Technology Collaboration Programme
by IEA

ISBN: 978-91-89821-53-8
DOI.org/10.23697/bp31-dm12
www.hpc2023.com

14th IEA Heat Pump Conference

May 15-18 2023, Chicago, US

"Heat Pumps – Resilient and Efficient"

Conference Proceedings

- Full Papers

ORGANIZED BY

Collaboration Program on Heat Pumping Technologies (TCP HPT) by International Energy Agency Technology (IEA)

CO-ORGANIZED BY

Air-Conditioning, Heating & Refrigeration Institute

American Society of Heating, Refrigerating and Air Conditioning Engineers

Preface
This conference was carried out within the Technology Collaboration Programme on Heat Pumping Technologies (HPT TCP), which is a Technology Collaboration Programme within the International Energy Agency, IEA.

The IEA
The IEA was established in 1974 within the framework of the Organization for Economic Cooperation and Development (OECD) to implement an International Energy Programme. A basic aim of the IEA is to foster cooperation among the IEA participating countries to increase energy security through energy conservation, development of alternative energy sources, new energy technology and research and development (R&D). This is achieved, in part, through a programme of energy technology and R&D collaboration, currently within the framework of nearly 40 Technology Collaboration Programmes.

The Technology Collaboration Programme on Heat Pumping Technologies (HPT TCP)
The Technology Collaboration Programme on Heat Pumping Technologies (HPT TCP) forms the legal basis for the implementing agreement for a programme of research, development, demonstration and promotion of heat pumping technologies. Signatories of the TCP are either governments or organizations designated by their respective governments to conduct programmes in the field of energy conservation. The Programme is governed by an Executive Committee, which monitors existing projects and identifies new areas where collaborative effort may be beneficial.

Disclaimer
The HPT TCP is part of a network of autonomous collaborative partnerships focused on a wide range of energy technologies known as Technology Collaboration Programmes or TCPs. The TCPs are organised under the auspices of the International Energy Agency (IEA), but the TCPs are functionally and legally autonomous. Views, findings and publications of the HPT TCP do not necessarily represent the views or policies of the IEA Secretariat or its individual member countries.

14th IEA Heat Pump Conference
15-18 May 2023, Chicago, Illinois

Abandoned mines as a source of heat and cold

Lukas Oppelt [a*], Thomas Grab [a], Thomas Storch [a], Timm Wunderlich [a], Tom Ebel [a], Tobias Fieback [a]

[a]TU Bergakademie Freiberg, Chair for technical thermodynamics, Gustav-Zeuner-Straße 7, 09599 Freiberg, Germany

Abstract

Mining has influenced and shaped the development of humankind for many thousands of years. After closure, these mines are often flooded and then offer a very high potential as a regenerative energy source for heating and cooling. Due to the almost constant temperature between about 10 to 30 °C throughout the year, an independent source of energy is permanently available, which can be brought to the necessary temperature level with heat pumps. In total 116 existing, planned and decommissioned systems were found worldwide. The observation of monitoring results of an example mine ("Reiche Zeche" in Freiberg/Germany) and a comparison to three other locations shows that the parallel use of mine water for heating and cooling can achieve coefficients of performance of the overall system of up to 10. Even with high electricity prices, operation costs for geothermal mine water energy of between 5 and 10 ct/kWh$_{heat}$ are possible. Compared to fossil fuels, at least 50 % CO_2 emissions are saved.
© HPC2023.
Selection and/or peer-review under the responsibility of the organizers of the 14th IEA Heat Pump Conference 2023.

Keywords: mine water, geothermal energy, heat pump monitoring, district heating cooling

1. Introduction

Mining is changing worldwide, e.g. in Germany the last hard coal mine was closed in 2018, brown coal is to be mined until 2035 at the latest [1]. In the Czech Republic, coal mining is planned to be finished in 2033 [2], similar to the situation of Canada, where coal mining is to end in 2030 [3]. The closure of the mines will inevitably lead to structural changes in the affected regions. Jobs in the mining sector will disappear and former mine sites will be renaturalized.

But these abandoned mines also offer potential: they can be used as a regenerative, geothermal energy source to provide heating and cooling. In most cases, abandoned mines are flooded and thus function as huge heat reservoirs. Depending on the location, the water temperatures are usually between 10 and 30°C. By using heat pumps, the temperature level necessary for the consumers can be provided. In the following, the basic structure of a typical geothermal mine water plant is presented and the current worldwide status quo is reviewed. Subsequently, the monitoring results of one plant in Germany are examined in more detail and compared to other plants located in Germany, the USA and Great Britain. Finally, the ecology and economy as well as identified problems are discussed.

2. Technological basics

The principle structure and possible extraction and return points of geothermal mine water systems are shown in figure 1. Firstly, the mine water is pumped to a heat exchanger (a) where heat is extracted (heating case) or supplied (cooling case) to a second fluid cycle. Afterwards, the heat will be transported in that intermediate circuit (b) to the heat pump (c), whereby the necessary temperature level is provided. If the temperature level is suitable for direct use as a heat sink for cooling, no heat pump is necessary. After heat is

* Corresponding author. Tel.: +49 (0) 3731 39-3277; fax: +49 (0) 3731 39-3963
E-mail address: Lukas.Oppelt@ttd.tu-freiberg.de.

extracted (heating case) from the mine water or supplied to it (cooling case), it is returned to the mine building. Depending on the location, other plant designs are also possible. [4, 5]:

- At pumping stations where mine water has to be pumped continuously, e.g. to protect groundwater level, and is discharged into surface waters, the pumped water can be used directly above ground, which is then transferred to surface waters. The same principle can be applied to active opencast mines where sump water is discharged.
- In the past, drainage galleries were built to transport the mine water out of the mines. Energetic utilisation is then also possible at the mouth holes, which avoids additional expenditures, e.g. for drilling.
- If there is enough space, it is also possible to install a closed loop system in the mine water, e.g. pipe bundles which are submerged in the mine water

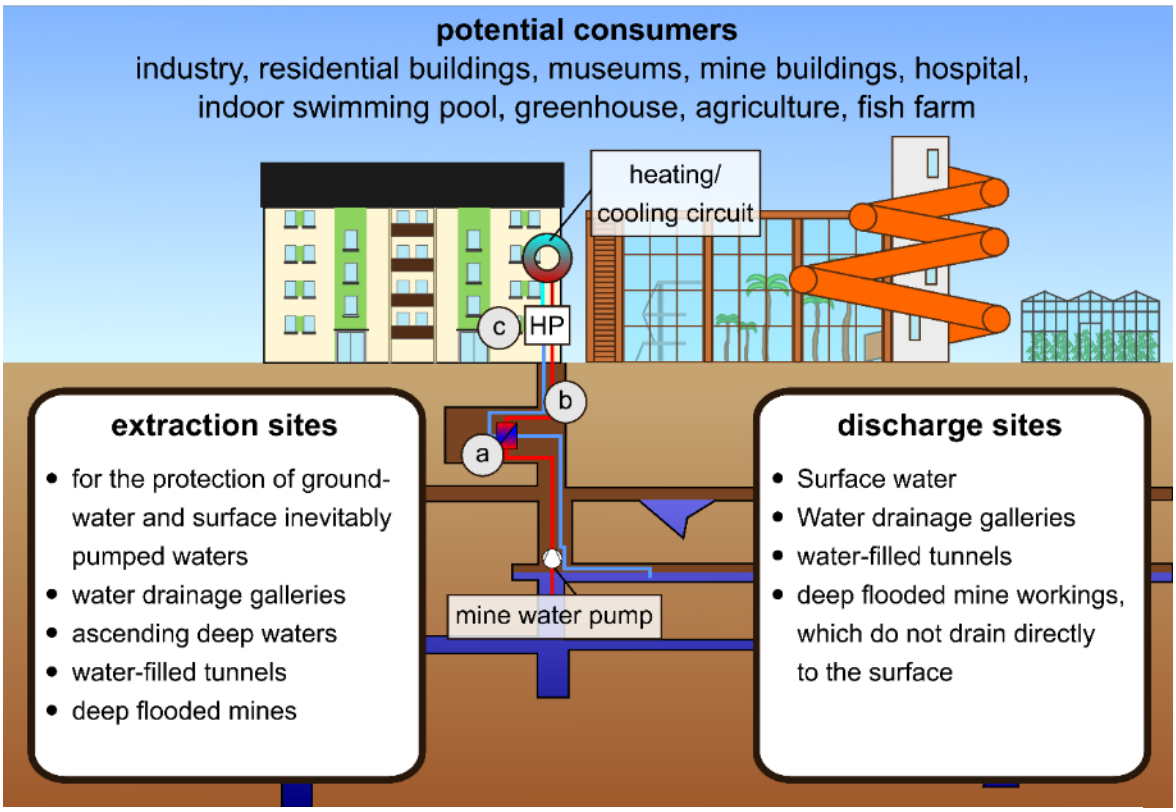


Fig. 1 Schematic structure of the geothermal mine water system as well as possible extraction and discharge sites and possible consumers (according to [4,6])

3. Current overview of geothermal mine water systems worldwide

In order to get an overview of the worldwide status quo of mine water geothermal systems, systems were searched in English and German literature, and a total of 42 active plants were founded worldwide. There are studies and construction plans for many more plants; a total of 116 plants could be found worldwide. Figure 2 gives an overview of the plants in Europe (up) and North America (down). It is clear that most plants are located in old mining areas in Germany, Great Britain, the USA and Canada. Outside these regions, only plants in China could still be found. However, there is also potential in other locations in South America and South Africa. Possible reasons for the lack of studies and planning for example could be a lack of investors or other, better available or cheaper renewable energy resources.

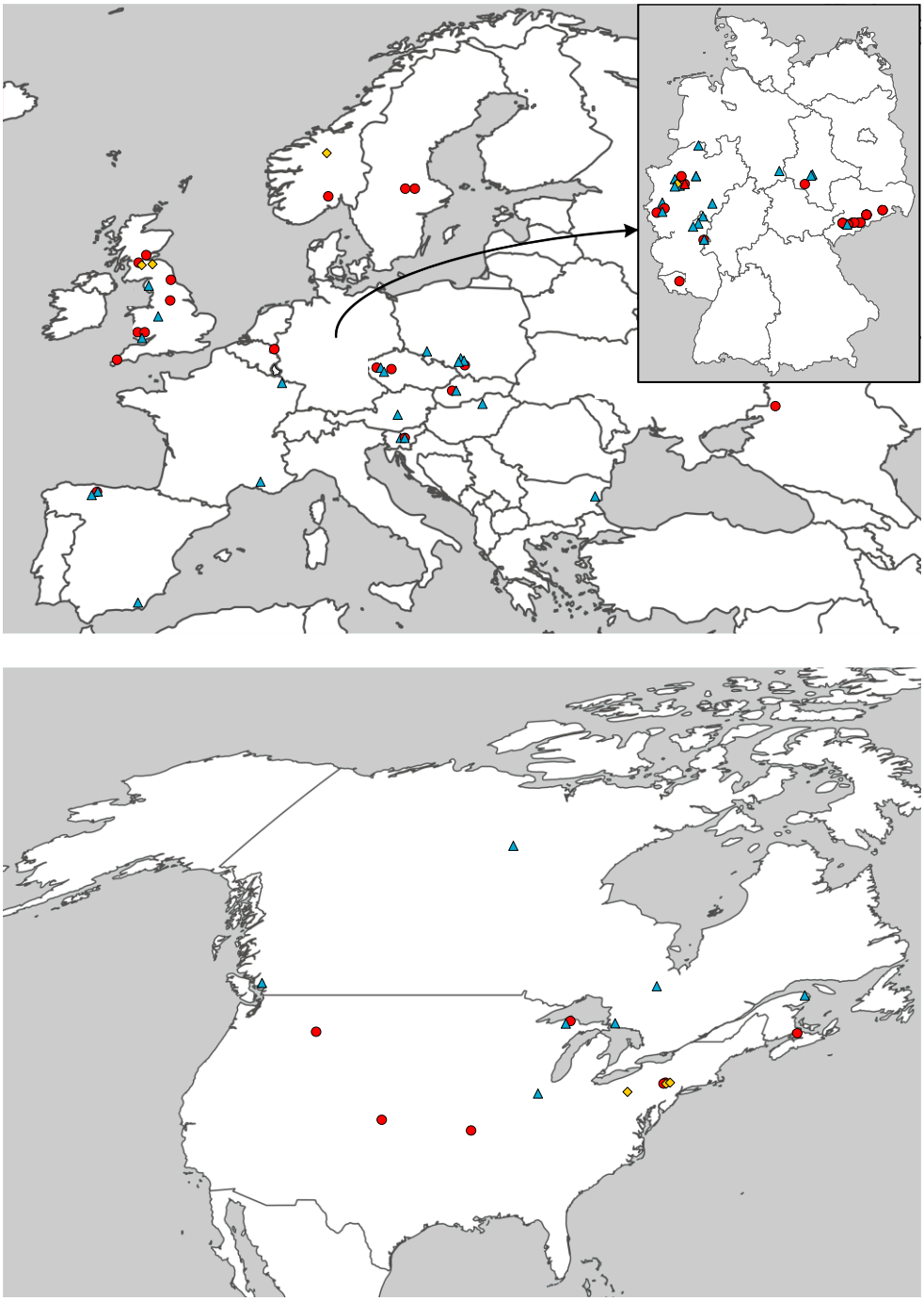


Fig. 2 Overview of current geothermal mine water plants in Germany/Europe (left) and North America (right) (o in operation, Δ planned/under construction/study, ◊ decommissioned, according to [5])

In order to give an overview of the amount of energy that is available through the geothermal energy of mine water, figure 3 shows the number of geothermal mine water plants built, planned and closed, summarized into freely chosen power classes. It can be seen from this that many existing plants worldwide are in smaller output ranges (below 200 kW), but new plants are more likely to be planned for larger output classes (over 500-1000 kW), or studies are being prepared for this. This is also evident in the projects currently planned and implemented in Europe:

- In Mieres in Spain, a large geothermal mine water plant is already in operation. There, mine water with a temperature of 23°C is used to supply various buildings, e.g. an university, with heat. The mine water is cooled down about 5 K, thus a heating power of about 4 MW is currently available after the heat pumps. In a further expansion stage, it is planned to increase it up to 6 MW. [7]
- Another big mine water project is also being planned in Germany: at the "Haus Aden" water extraction site (mine water must be pumped out permanently to protect the groundwater level) in Bergkamen in the Ruhr region, a new urban district is to be built on the former mine site and supplied proportionally with geothermal mine water energy. A mine water volume flow of about 1000 m³/h at about 20 °C is continuously available. This means that there is a theoretical potential of 30.6 MW, which will be exploited to set an example of how to safely supply renewable heat energy by mine water to urban districts. [8 bis 10]

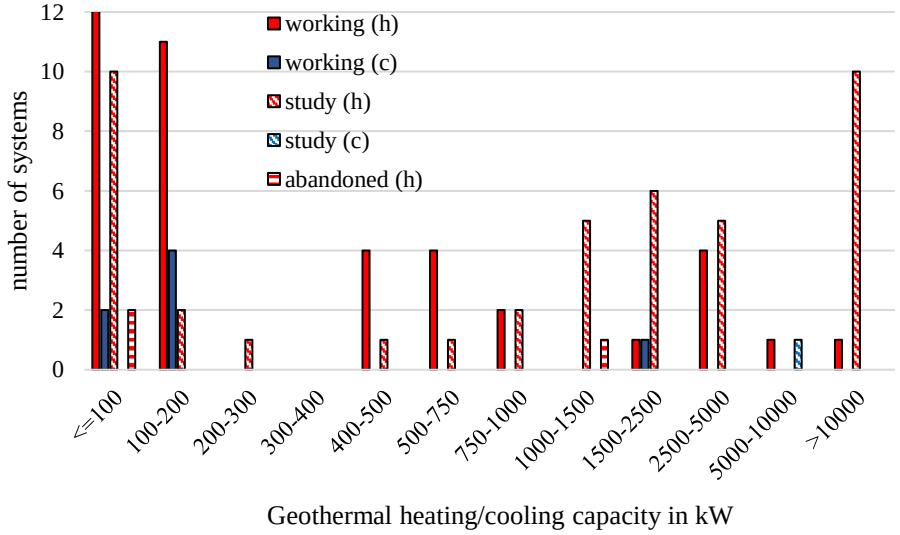


Fig. 3 Overview of the number of geothermal mine water plants in the different performance classes

4. Monitoring results

In 2013, a geothermal mine water system was put into operation at the former silver mine "Reiche Zeche" in Freiberg, Germany. In the current expansion stage, with a heating capacity of 175 kW and a cooling capacity of 100 kW it can supply several buildings at the university (offices, class rooms, laboratories, server rooms). The basic system design is shown in figure 4. The special feature here is that there are the three options for providing heating and/or cooling:

- Variant A (“Rothschönberger Stolln”): The mine water here is taken from the main drainage gallery of the Freiberg mining district, the “Rothschönberger Stolln”. This has a water temperature of about 14 °C.
  → Variant A is used when there is a predominant demand for cooling.
- Variant B (Shaft “Reiche Zeche”): Alternatively, the mine water can also be taken from the “Reiche Zeche” shaft, where the mine water has a temperature of about 19 °C due to rising deep water.
  → Variant B is used when there is a predominant demand for heating.
- Variant C (intermediate circuit): Only the fluid in the intermediate circuit between the heat exchanger at a depth of 228 m and the heat pumps on the surface is circulated. In the case of low heating or cooling requirements, the heat from the rock (Gneiss) that surrounds the intermediate circuit can be sufficient for heating and cooling.
  → Variant C is used when there is a low heating or cooling demand.

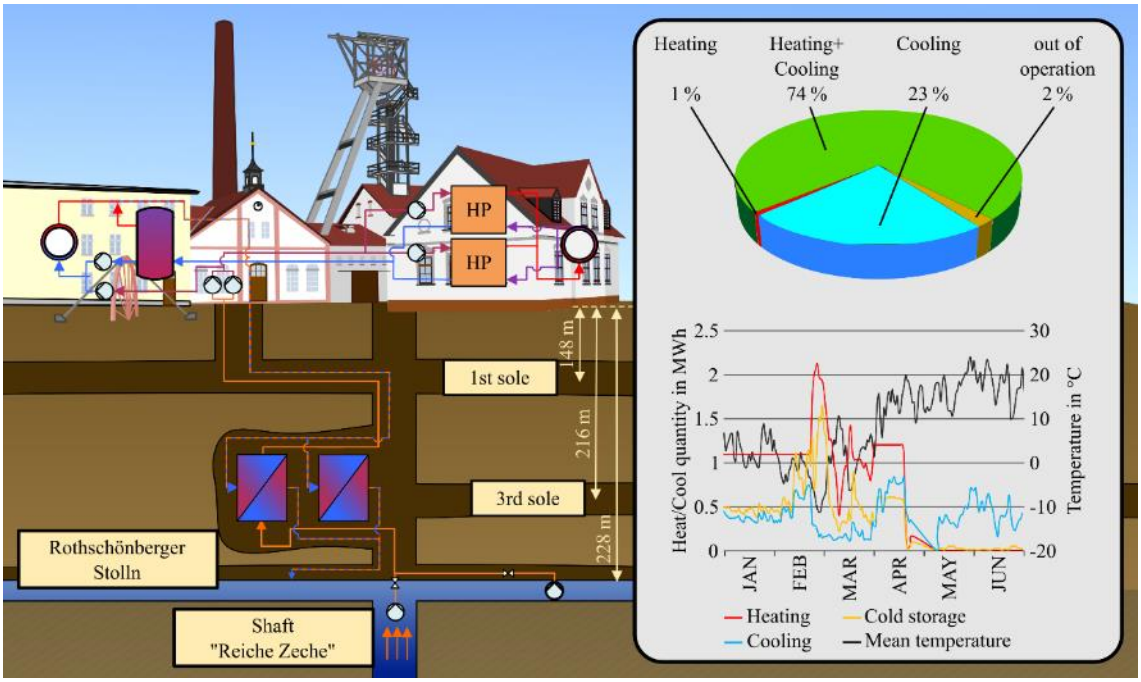


Fig. 4 Schematic structure of the "Reiche Zeche" mine water system and proportions of the operating modes over three years (top right) and heating and cooling quantities over half a year (bottom right)

This results in a total of 10 possible operating modes: for each of the three extraction options heating only, cooling only or combined heating and cooling can be selected. The 10th operating mode is "out of operation", e.g. because the system is being serviced. The diagram in figure 4 on the right top shows the proportions of the operating modes over an observation period of 3 years. Heating and cooling are used simultaneously for the most part; heating alone was only recorded in 1 % of the observation period. The reason for this is the basic cooling load that is necessary at the site for cooling the server and laboratory rooms. In most cases, there is also a need for cooling in the winter. Only on a few very cold winter days there is no cooling necessary for individual hours. Otherwise, cooling-only mode was only required in about a quarter of the period under review, and this was mainly the case during the warm summer months. This is also shown in the diagram of the amount of heat and cold shown in figure 4, bottom right. Until middle of April, the heat quantity is significantly higher than the amount for cooling. Afterwards the amount of cooling gets into the predominant position. In addition to direct heating and cooling operation, a cold storage tank is integrated in the system whereby the return flows from the heating circuit can be used for cooling. The cold flow from the cold storage tank is also mainly used until mid-April, as the storage tank is then no longer “loaded” due to the low heating requirements.

The almost continuous cooling demand has a significant influence on the efficiency of the overall system see figure 5. A representative summer and winter week is shown. As expected, the heating demand is predominant in winter, with overall system performance factor per hour (HPF_{HC4}) of about 3.5 to 4.5 (notation according to [11]). This also takes into account the expenditure for electricity of mine water pumps, pipeline pumps and the measurement equipment of the monitoring system. In comparison, significantly higher HPF_{HC4}s are achieved in summer. As can be seen in Figure 5, where the minimum HPF_{HC4} ranges between 5 and 6 but can also amount up to 10 in a representative summer week.

The reason for these HPF_{HC4}s is the predominant cooling demand. The mine water can be used directly as a heat sink and the electricity demand for the heat pump is omitted most of the time, unless there is a heat demand for hot water. The consideration of these two example weeks shows clearly that cooling can significantly increase the efficiency of geothermal mine water plants and thus make economic operation possible in the long term and in a stable manner. This issue is discussed in more detail in section 5.

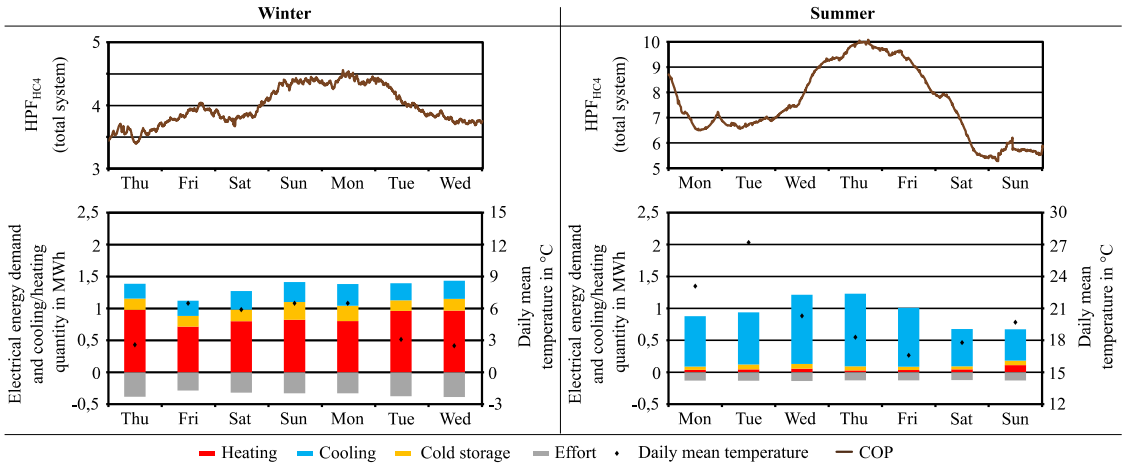


Fig. 5 Monitoring results of the geothermal mine water system "Reiche Zeche" in Germany of a representative winter week (left) and summer week (right)

In addition to the geothermal mine water system at the “Reiche Zeche”, other systems will be considered in the following:

- Since 2012, mine water from the former coal mine in Markham (Great Britain) has been used to heat company buildings. This system is an open system with mine water pumping to the surface. The mine water with an approximate temperature of 14 to 15 °C passes through the tubular heat exchanger within the mine water circuit, which heats the fluid in the intermediate circuit for a 20 kW heat pump. Due to the increased mine water level, the water extraction point was changed in 2015 so that water with a temperature between 13 and 14°C is now used. [12 bis 14]
- In Butte (Montana, USA), buildings at Montana Tech University are supplied with heating and cooling from mine water. The system uses water from the Orphan Boy shaft with a water level of 33.5 to 36.6 m below ground. The closed system includes a 175 kW heat pump that is connected to the building's heating or cooling loop, depending on the outdoor temperature. [15, 16]
- In Ehrenfriedersdorf in (Saxony, Germany) the buildings of the visitor mine are heated since 1992. The system has a total output of about 120 kW. The heat exchanger mine water–closed intermediate circuit is located at a depth of 110 m. Therefrom the heated fluid is pumped inside the intermediate cycle to the heat pump in the buildings [17]

Table 1 provides an overview of the seasonal performance factors (SPFs) of the presented individual systems and their operating modes. It is clear that for all systems, a SPF_{H1} of the heat pump of over 3 is achieved. In addition, the comparison of the SPF_{HC4} of the total system also shows except from location Markham for all other systems high SPF_{HC4}. Furthermore it’s obvious how worthwhile the combination of heating and cooling is (see “Reiche Zeche”), so that HPF_{HC4}s of over 5 can be achieved for the entire system over longer periods of time also in winter.

The coefficient of performance of the entire system in Markham is below 2. The main reason for this is probably the energy-intensive pumping of the mine water above ground in an open system. At the other sites, the mine water is pumped over lower altitudes and the heat is then transported in a closed system.

Table 1. Comparison of the performance factor of the selected geothermal plants (data: [12, 14, 15])

	Reiche Zeche Freiberg (GER)	Ehrenfriedersdorf (GER)	Markham (GRB)	Butte (USA)
Operating modes	Winter (more heating) /Summer (more cooling)	Heating	Heating	Heating
SPF_{H1} (heat pump)	3,6/-	3,8	3,6	4
SPF_{HC4} (total system)	4,2/7	3,6	1,6	3,5

5. Economic and ecological consideration

In addition to the investment costs, the operating costs during the operating period are a decisive factor in assessing the economic viability of geothermal mine water plants. Decisive influencing factors here are:

- Electricity price for the energy required for the heat pump, pumps, etc.
- SPF of the total system
- Costs for maintenance, servicing, etc.

Figure 6 shows the operating costs of a geothermal mine water system as a function of the electricity price in EURct/kWh and the SPF of the system. The operating costs can be read off from the sloping lines on the upper and right axes (in blue).

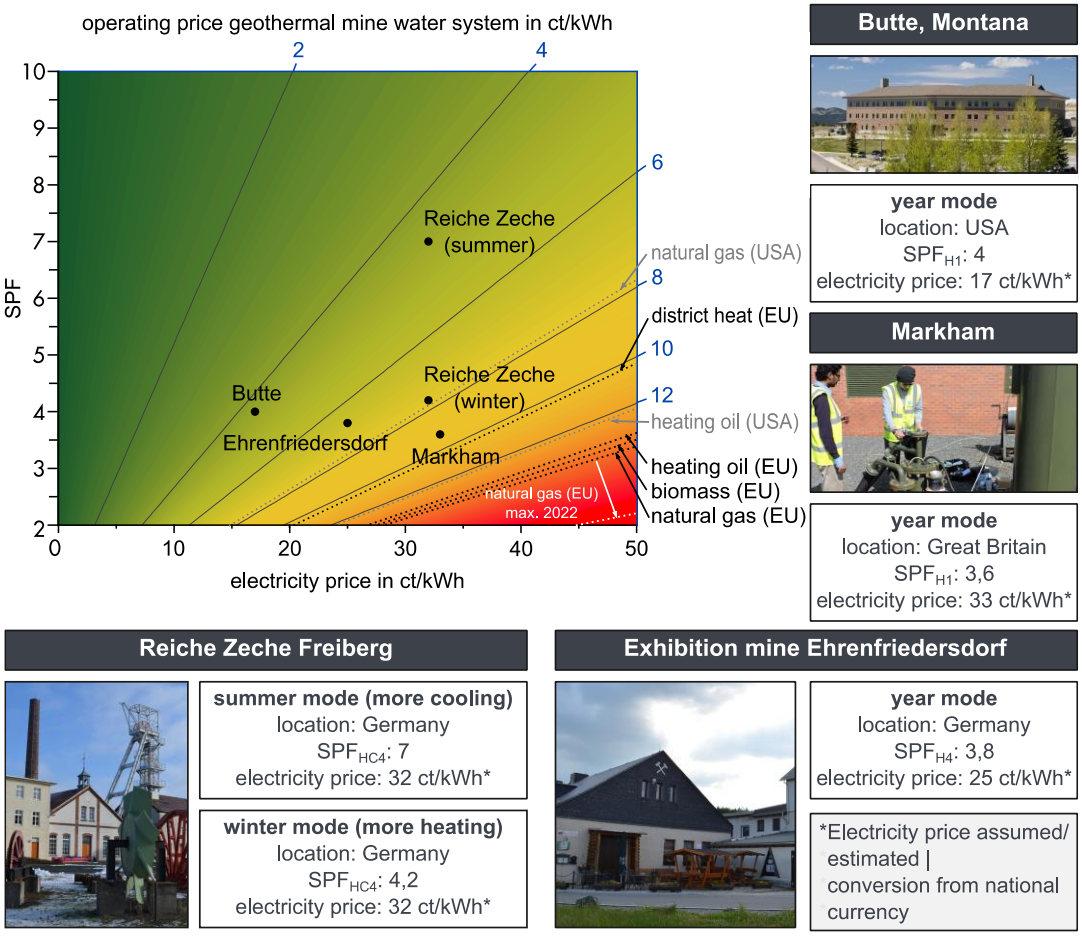


Fig. 6 Operating costs of a geothermal mine water system as a function of SPF_{HC4} and electricity price for various example plants compared to costs of other energy sources in the USA (grey dotted lines) and Europe (black dotted lines) data, pictures: [12, 14, 15]

The other costs, e.g. for maintenance, are included in the calculation as a percentage. The monitoring results presented in section 4 are integrated in figure 6, with country-specific electricity prices always converted to euros. It can be seen, that geothermal mine water energy is more economical than comparable fossil energy sources at all locations under the current framework conditions (as of November 2022). It can be seen that with high SPFs through combined heating and cooling, even with electricity prices above 30 EURct/kWh, working costs of the geothermal mine water system of about 5 EURct/kWh can be achieved. Favorable electricity prices, e.g. through special heat pump tariffs, as in the case of the plant in the Ehrenfriedersdorf visitor mine (Germany), then enable economic operation even with lower SPF_{H4}. The cost level of fossil fuels is always a decisive factor. The strong increase in the price of gas in Europe in 2022 is also shown in the diagram. With maximum gas prices of over 30 EURct/kWh, the energetic use of mine water is always more economical and might even present advantages in the short-term. In summary, at a current electricity price in Germany of 32 EURct/kWh, a working coefficient of the overall system of about 3 must be achieved in order to be cheaper than all comparable fossil energy sources. With an electricity price in the USA of the equivalent of 17 EURct/kWh, the systems are already more economical than fossil systems, also for e.g. gas prices in the USA. In a nutshell, the American plant in Butte must achieve a SPF_{H1} of at least 2.5 in order to be cheaper than fossil

fuels on the American market. In addition, electricity costs can be further reduced through local combination with the yields of e.g. photovoltaic or wind power plants. It should be noted, however, that the above consideration refers only to the operating costs; the investment costs of the systems are not integrated in this consideration. Depending on kind of construction activities are necessary (e.g. drilling), these can amount to several million euros.

In addition to the economic advantages, the use of geothermal mine water energy can also offer an ecological advantage by reducing CO_2 emissions. Figure 8 shows a comparison of the CO_2 equivalent of geothermal mine water systems compared to other energy sources. It is obvious that compared to the use of fossil fuels like brown coal or natural gas, CO_2 emissions can be reduced by 75% and by at least 56%, respectively. This factor will play an even greater role for the climate and economically in the future if CO_2 taxes are introduced or increased. The emissions that occur during the construction and operation of a geothermal mine water plant were considered in more detail in [18]. In summary, it is clear that emissions from geothermal mine water plants are mainly due to the electricity purchased and the refrigerant used in the heat pump, which in the future both will fall in their emission impact due to the rise of renewable electricity generation and natural refrigerants. [18]

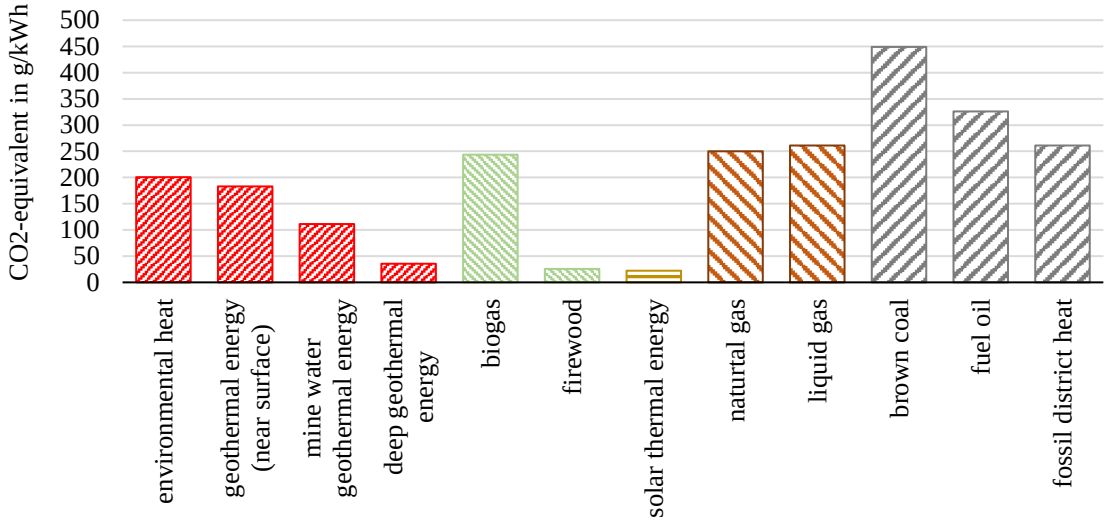


Fig. 7 Comparison of the CO_2 equivalent of geothermal mine water systems to other energy sources (data: [19], study for Germany)

6. Identified problems

One problem to be solved when using geothermal mine water energy is the formation of fouling/depositing in the heat exchanger or piplines. Depending on the site location, the mine water carries various loads, e.g. bacteria, dissolved and undissolved substances and other suspended matter. These substances can be deposited in the heat exchanger and thus significantly influence the plant efficiency. Even a biofilm of 250 µm can reduce the amount of heat transferred by 50 % [20]. In addition, the pressure loss across the heat exchanger increases, and the costs for maintenance also rise because cleaning is necessary. Furthermore, other sources of energy have to be used to compensate the resulting lack of heat. This also has a major impact on the SPF_{HC4}s of the plants, which can also be reduced by up to 50 % due to fouling. The TU Bergakademie Freiberg is currently researching optimized heat exchanger design to reduce fouling/depositing and increase the time between cleanings. [21]

In addition, there were problems in monitoring because the system at the “Reichen Zeche” was partially shut down due to technical defects and construction work in the mine, so that longer measurement periods could not be recorded.

Furthermore, depending on the system design, winter operation may be subject to low efficiencies. A possible solution for this could be the integration of a seasonal heat storage. Currently, only a cold storage facility is used in the “Reiche Zeche” system, but this already makes the potential visible. Seasonal storage in mine water, e.g. of heat dissipated for cooling purposes in summer which can be utilized in winter, would be

desirable. Two current projects, WINZER (Funding reference number: 03G0912C) and MineATES (Funding reference number: 03G0910A) are investigating the seasonal storage of heat and cold in mine water.

7. Conclusion and outlook

An evaluation of 116 geothermal mine water sites worldwide with plants and studies on the energetic use of mine water shows that these are mainly concentrated on locations in North America and Europe. 42 currently active plants are findable (German/English). Most of them are in the power range below 200 kW; new plants are planned mainly in a higher power range above 1 MW. The results of monitoring data at the "Reiche Zeche" plant in Freiberg, Germany, show that the geothermal use of mine water by means of heat pumps is ecological and economical favorable. The combined use of mine water for heating and cooling regularly achieves high annual averaged coefficients of performance of over 7. A comparison with three other systems worldwide shows annual averaged SPF_{HC4} of at least 3.5 can also be achieved in pure heating mode. Under the current purchase prices for alternative energy sources, geothermal mine water energy is already cheaper for a SPF_{HC4} of 2 to 2.5, and with more favorable electricity prices, as in the USA, even more economical, also mode modeefor fossil fuel prices in the USA. However, the partly high investment costs for development of mine water resources are not included in the direct operating costs and must be considered during the pre-planning phase before investment decisions. From the ecological point of view, the energetic use of mine water can save CO_2 emissions between 56 % up to 75 % compared to natural gas heating. In future a task to be solved is the location-dependent formation of fouling in the heat exchangers and components in contact with water due to the chemical composition of the mine water and its (un-)dissolved substances. This reduces the usable heat output and thus decreases the efficiency of plants. Research into optimized heat exchangers and plant design must be intensified in the future and adapted to the respective locations. In addition, intelligent monitoring is recommended for the plants currently planned and under construction in order to be able to monitor the actual efficiency and to compare it to other running mine water systems.

Acknowledgements

We would like to thank the German Federal Ministry of Education and Research and the project management organisation Jülich for their financial support of the WINZER (Funding reference number: 03G0912C) project. In addition, thanks go to all the technicians and students involved, especially: J. Balski, U. Fleischmann and R. Klink.

References

[1] Geinitz, C.: Kohleausstieg : Hart an einer Blamage vorbei. Frankfurter Allgemeine Zeitung (2020)
[2] Lazarová, D.: Coal mining in Czech Republic to be phased out by 2033. Radio Prague International (2022)
[3] Mihm, A.: Großbritannien und Kanada verkünden Kohleausstieg. Frankfurter Allgemeine Zeitung (2017)
[4] Oppelt, L., Grab, T., Pose, S., Storch, T. u. Fieback, T.: Mine water geothermal energy as a regenerative energy source - status quo and results from five years of monitoring. Oil Gas EUROPEAN MAGAZINE 47 (2021) 01/2021, S. 15–19
[5] Grab, T., Storch, T. u. Groß, U.: Energetische Nutzung von Grubenwasser aus gefluteten Bergwerken. In: Bauer, M., Freeden, W., Jacobi, H. u. Neu, T. (Hrsg.): Handbuch Oberflächennahe Geothermie. Berlin, Heidelberg: Springer Berlin Heidelberg (2018), S. 523–586
[6] Oppelt, L., Pose, S., Grab, T. u. Fieback, T.: Geothermische Nutzung von Grubenwasser zur regenerativen Energieversorgung. Geothermische Energie (2020) 95, S. 25–27
[7] "BARREDO COLLIERY" DISTRICT HEATING, HULLERAS DEL NORTE S.A., S.M.E., 2019
[8] Altieri, L., Wagner, H.-J., Gross, M. u. Reiners, T.: Kalte Nahwärmenetze mit Geothermischer Energie aus Grubenwasser. Der Geothermiekongress. Essen (2018)
[9] Kretschmann, J.: Sustainable Change of Coal-Mining Regions. Mining, Metallurgy & Exploration 37 (2020) 1, S. 167–178
[10] Potenzialstudie Warmes Grubenwasser. LANUV-Fachbericht 90, Landesamt für Natur, Umwelt und Verbraucherschutz Nordrhein-Westfalen, Recklinghausen (2018)
[11] IEA HPT Annex 53 - Long-term performance monitoring of GSHP systems for commercial, institutional, and multi-family buidlings. Subtask 3 report, Gehlin, S., Spitler, J., Witte, H., Andersson,

O., Berglöf, K., Davis, M., Javed, S., Bockelmann, F., Turner, J. u. Clauss, J., (2022)
[12] Banks, D., Athresh, A., Al-Habaibeh, A. u. Burnside, N.: Water from abandoned mines as a heat source: practical experiences of open- and closed-loop strategies, United Kingdom. Sustainable Water Resources Management 5 (2019) 1, S. 29–50
[13] Athresh, A. P., Al-Habaibeh, A. u. Parker, K.: The design and evaluation of an open loop ground source heat pump operating in an ochre-rich coal mine water environment. International Journal of Coal Geology 164 (2016), S. 69–76
[14] Burnside, N. M., Banks, D. u. Boyce, A. J.: Sustainability of thermal energy production at the flooded mine workings of the former Caphouse Colliery, Yorkshire, United Kingdom. International Journal of Coal Geology 164 (2016), S. 85–91
[15] Case Study of the ARRA-Funded GSHP Demonstration at the Natural Sources Building, Montana Tech, Malhotra, M., Liu, X. u. Walburger, A., (2014)
[16] Gammons, C. H., Metesh, J. J. u. Snyder, D. M.: A Survey of the Geochemistry of Flooded Mine Shaft Water in Butte, Montana. Mine Water and the Environment 25 (2006), S. 100–107
[17] Rottluff, F.: Neue Wärmepumpenanlage im Besucherbergwerk Zinngrube Ehrenfriedersdorf. Geothermische Energie - Mitteilungsblatt der Geothermischen Vereinigung e. V. 6 (1998) 21
[18] Oppelt, L., Grab, T., Wunderlich, T., Storch, T. u. Fieback, T.: Mine water geothermal energy - abandoned mines as a green energy source. CLIMA 2022 conference, 2022: CLIMA 2022 The 14th REHVA HVAC World Congress (2022)
[19] Emissionsbilanz erneuerbarer Energieträger, Memmler, M., Lauf, T. u. Sven, S., Dessau-Roßlau 2008
[20] Goodman, P. D.: Effect of chlorination on materials for sea water cooling systems: a review of chemical reactions. British Corrosion Journal 22 (1987) 1, S. 56–62
[21] Oppelt, L., Grab, T., Wunderlich, T., Pose, S., Storch, T. u. Fieback, T.: Innovative heat exchanger design to avoid fouling. European Geothermal Congress 2022 - Proceedings (2022)

14th IEA Heat Pump Conference
15-18 May 2023, Chicago, Illinois

Decarbonizing Steam Generation with High Temperature Heat Pumps: Refrigerant Selection and Flowsheet Evaluation

Christoph Höges[a, *], Valerius Venzik[a], Christian Vering[a], Dirk Müller[a]

[a] Institute for Energy Efficient Buildings and Indoor Climate, Mathieustr. 10, 52074 Aachen, Germany

Abstract

High temperature heat pumps have a high potential to reduce carbon emissions in industrial processes by replacing conventional heating systems for low-pressure steam generation. However, heat pump performance is sensitive to the selected refrigerant, flow sheet, and operating conditions complicating the design process. Thus, we conduct a refrigerant selection and evaluate five flow sheets for a low-pressure steam application, which heats liquid water from 80°C at 1.5 bar to 120°C steam. First, refrigerants are screened to identify suitable low-GWP (<150) refrigerants. We find 15 alternative refrigerants. Second, the performance of the selected refrigerants is evaluated in five flow sheets, including two vapor injection and a parallel-compression configurations. R717 outperforms all other solutions concerning cycle efficiency and heating capacity for all investigated cycles. However, R717 leads to high compressor discharge temperatures limiting the applicability with compressor lubricant. Here, lubricant-free technologies such as turbo compressors are promising. Besides R717, the investigation shows further solutions with high efficiencies. Most promising refrigerants, however, have a double bond in their molecule structure, reducing their chemical stability. Furthermore, the cycle configuration using vapor injection in combination with an internal heat exchanger yields the highest cycle efficiencies. Compared to the simple flow sheet, more than 20% of improvements are possible.

© HPC2023.
Selection and/or peer-review under the responsibility of the organizers of the 14th IEA Heat Pump Conference 2023.

Keywords: hydrocarbons ; loss-based compressor model ; low-pressure steam ; R717

1. Introduction

To achieve the goals of the Paris Climate Agreement, carbon emissions have to be reduced. One main source of carbon emissions is the combustion of fossil fuels in heat generation with conventional systems, e.g., a gas boiler [1]. Heat pumps are a possible solution to replace conventional systems in heat generation. Heat pumps use ambient or waste heat combined with electric power to provide the necessary heat demand. Thereby, the emissions of the heat pump depend on the specific emissions of the necessary power demand and the emissions related to refrigerant leakages on-site.

In industrial processes, heat over a wide range of temperatures is needed to satisfy all demands [2]. A large share of the necessary heat is utilized at temperatures below 200 °C, which current heat pumps can provide. Thus, a considerable reduction of carbon emissions is possible that be utilized with heat pumps [3].

For many industrial processes (e.g., drying, refining, and food processing), steam is used to distribute the heat due to its high heat capacity and good transfer properties. In addition, due to its high latent heat, a large amount of heat can be provided while keeping the temperature constant. However, the literature on steam generation using a heat pump is limited. Furthermore, steam generation is especially challenging due to the high isothermal heat demand, which leads to a more complex secondary temperature curve in the condenser.

In contrast to conventional heating systems, heat pump efficiency strongly depends on the operating point. Additionally, the selected refrigerant and cycle configuration influence operational performance, leading to lower efficiency or a reduced operating range. For refrigerants, current regulations regarding a low global

* Corresponding author. Tel.: +49 241 80 49598; fax: +49 241 80 49769.
E-mail address: christoph.hoeges@eonerc.rwth-aachen.de.

warming potential (GWP) and a zero ozone depletion potential (ODP) should be met [4]. Additionally, the refrigerant is subject to thermodynamic requirements regarding the critical temperature, the isobaric heat capacity, and the latent heat to achieve high efficiencies. Furthermore, the molecule has to offer long-term chemical stability to ensure a safe and efficient operation. Thus, the number of potential refrigerants is limited on the one hand, and the identification is more complex compared to the residential heat pumps on the other hand.

Besides the refrigerant [5, 6], the cycle configuration, i.e., the selected components [7, 8] and flowsheet [9, 10], has a significant influence on the overall cycle performance and the operating envelope. In contrast to residential heat pumps that are well known, industry heat pumps have a much higher heating capacity, which can exceed several Megawatts. Furthermore, due to the high energy flows, the overall share of the operation period is significantly higher than conventional, small-scale heat pumps. Thus, improving the efficiency as much as possible is one key aspect when designing large-scale heat pumps, resulting in a broader number of possible cycle configurations.

In this work, we investigate the potential of heat pumps to generate steam at 1.5 bar pressure and analyze the influence of the refrigerant and the selected flowsheet on the overall cycle performance. First, a refrigerant selection based on thermodynamic and ecologic properties is conducted for the defined application. The selection leads to 14 refrigerants that are not toxic and have GWP below 150. Additionally, ammonia (R717) and R245fa are included due to their wide usage. Furthermore, we include a zeotropic mixture based on R600a and R601a to analyze the potential of zeotropic mixtures for the defined application. Second, a case study is conducted that heats liquid water from 80 °C to steam at 120 °C. The investigation uses five cycle configurations to analyze their influence on the optimal refrigerant. Third, the present study's findings are discussed, and future research aspects are mentioned that should be directed in the future.

2. Methodology

The following sections present the used cycle models and the use case parameter. First, the general evaluation procedure is presented. Afterward, the component modeling followed by the investigated cycles is shown. Finally, section 2.4 presents the parameters of the case study and the selected refrigeration of the investigation.

2.1. Modeling approach

We use consistent thermodynamic models to predict the heat pump cycle behavior. The expansion valve is isenthalpic. Piping and all further components have no pressure and heat losses. For modeling the heat exchangers, a pinch model is used, enabling to determine the evaporation and condensation pressures related to the heat source and sink. Fig. 1 shows the temperature curves of the heat source (blue) and heat sink (red). The heat source uses sensible heat with a constant heat capacity resulting in a linear curve. The heat sink is split into a sensible part (preheating liquid water), a latent part (evaporation of water), and a sensible part (superheating of water).

Further degrees of freedom of the process are the superheating ΔT_{SH} at the compressor inlet and the subcooling ΔT_{SC} at the condenser outlet.

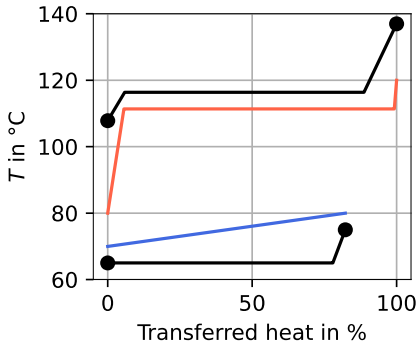


Fig. 1: Temperature curves of sink water (red) with cyclobutene (black) as the refrigerant and a heat source (blue).

As the main deviation from the standard heat pump model, the compressor efficiencies are calculated through a loss-based model of a reciprocating compressor [11]. The model calculates the isentropic and volumetric compressor efficiencies as a function of the operating point and the refrigerant. Equation (1) shows the general definition of the isentropic compressor efficiency η.

$$\eta = \frac{\dot{m}_{\text{refrigerant}} \cdot \Delta h_{\text{com}}^{\text{rev}}}{P_{\text{el}}} \tag{1}$$

The model includes multiple loss mechanisms within a compressor and combines them with analytical definitions of compressor efficiencies. Thereby, friction (parameter *a*), flow losses (parameter *b*), and electrical (parameter *c*) losses are considered. The model leads to the following expression for the isentropic compressor efficiency:

$$\eta = \frac{V_{\text{cyl}} \cdot n_{\text{cyl}} \cdot f_{\text{mech}} \cdot \rho_{\text{in}} \cdot \eta_{\text{vol}} \cdot \left(h_{\text{out}}^{\text{is}} - h_{\text{in}}\right)}{V_{\text{cyl}} \cdot n_{\text{cyl}} \cdot f_{\text{mech}} \cdot \rho_{\text{in}} \cdot \eta_{\text{vol}} \cdot \left(h_{\text{out}}^{\text{is}} - h_{\text{in}}\right) + a + b \cdot \rho_{\text{in}} \cdot (V_{\text{cyl}} \cdot n_{\text{cyl}} \cdot f_{\text{mech}} \cdot \eta_{\text{vol}})^3} (1 - c) \tag{2}$$

The volumetric compressor efficiency η_{vol} is approximated as a function of the pressure and refrigerant properties

$$\eta_{\text{vol}} = 1 - \frac{k_1}{H_{\text{ref}}} \cdot \left(\frac{p_{\text{out}} + k_2 \cdot \rho_{\text{in}}}{p_{\text{in}}}\right)^{\frac{c_{\text{v}}}{c_{\text{p}}}} \tag{3}$$

with k_1 and k_2 being fitting variables. Additionally, Roskosch et al. [11] proposed an approach that scales the loss parameters of friction (*a*) and flow losses (*b*) by the compressor geometry (piston diameter *D* and stroke *H*). We will use this scaling approach in our study to design the compressor geometry specifically for each refrigerant concerning the desired heating power of the heat pump.

For the cycle calculation, we use an optimization approach. As a result, each investigated flowsheet's coefficient of performance (COP) is maximized. Equation (4) states the optimization problem based on boundary conditions $\vec{\theta}$.

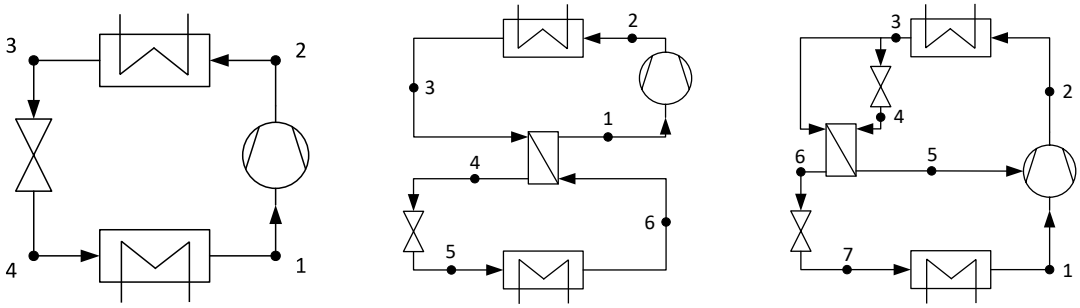
$$\begin{aligned} &\max_{\vec{x}} COP\left(\vec{x}, \vec{\theta}\right) \\ s.t. \quad &g\left(\vec{x}, \vec{\theta}\right) \geq 0 \\ &\vec{x}_{\min} \leq \vec{x} \leq \vec{x}_{\max} \end{aligned} \tag{4}$$

The optimizer permutes the optimization variables of vector $\vec{x}$, which depend on the flow sheet (see section 2.2). To speed up the calculation, reasonable lower and upper limits $\vec{x}_{\min}$ and $\vec{x}_{\max}$ are defined, respectively. Additionally, the cycle calculation is subject to multiple inequality constraints $g\left(\vec{x}, \vec{\theta}\right)$ that ensure a physical operation.

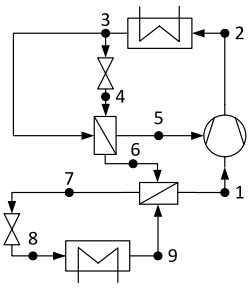
The inequality constraints *g* ensure a physically and technically feasible operation and include three main constraints. The first constraint prevents supercritical operation [12]. The second constraint verifies that no wet compression occurs, i.e., liquid droplets during compression [13]. The compression is discretized in thirty steps, and the respective specific enthalpy is compared to the dew line enthalpy. The third constraint is part of the pinch model and ensures that a minimum approach temperature within all heat exchangers (condenser, evaporator, internal heat exchanger) is kept.

2.2. Investigated flowsheets

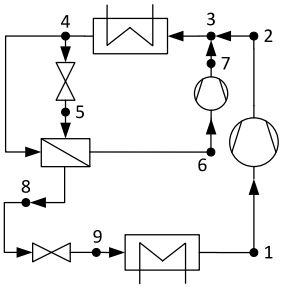
The present work investigates five flowsheets. Fig. 2 shows their schematics. In the following subsections, their general modeling assumptions are presented A detailed description can be found in [14]. To calculate the individual fluid properties, the *REFPROP* fluid database [15] is used.



(a) simple (b) ihx (c) vi



(d) vi-ihx



(e) pc

Fig. 2: Investigated flowsheets for steam generation heat pumps.

2.2.1. Simple cycle (Fig. 2a)

The cycle simulation of the simple cycle uses four degrees of freedom, which are defined by equation (5).

$$\vec{x}_{\text{simple}} = [p_{\text{eva}};\ p_{\text{con}};\ \Delta T_{\text{SH}};\ \Delta T_{\text{SC}}]^T \tag{5}$$

Here, the evaporation pressure p_{eva}, the condensation pressure p_{con}, the superheating ΔT_{SH} at the compressor inlet, and the subcooling ΔT_{SC} at the condenser outlet need to be defined. As the main assessment criterion, the *COP* is the ratio of transferred heat within the condenser and the electric power demand in the compressor. Equation (6) shows the formulation for the simple cycle assessment.

$$COP_{\text{simple}} = \frac{\dot{Q}_{\text{con}}}{P_{\text{el}}} = \frac{h_2 - h_3}{h_2 - h_1} \tag{6}$$

2.2.2. Internal heat exchanger cycle (Fig. 2b)

For the internal heat exchanger, we assume that a heat transfer from the condenser outlet realizes the entire superheating at the compressor inlet. Therefore, the refrigerant leaves the evaporator as saturated vapor and the condenser already as a subcooled liquid while it is superheated and further subcooled in the internal heat exchanger. Overall, the degrees of freedom, as well as the target function *COP*, are the same compared to the simple cycle (c.f. equation (5) and (6)). Here, we assume that the internal heat exchanger is designed ideally for the application. Thus, we optimize the transferred heat and do not use an efficiency based modeling approach.

2.2.3. Vapor injection cycle (Fig. 2c)

For the vapor injection (vi), a two-stage compression is used. After the first stage, the condenser outlet is split, and a partial mass flow rate $\dot{m}_{\text{inj}}$ (state 5) is injected into the compressor. Due to the vapor injection, the cycle includes additional degrees of freedom. Thus, the intermediate pressure p_{int} of states 4 and 5 is optimized. The injection ratio *y*, which is the ratio of injected vapor $\dot{m}_{\text{inj}}$ and total mass flow rate in the condenser $\dot{m}_{\text{con}}$, is included.

$$y = \frac{\dot{m}_{\text{inj}}}{\dot{m}_{\text{con}}} \tag{7}$$

$$\vec{x}_{\text{vi}} = [p_{\text{eva}};\ p_{\text{con}};\ \Delta T_{\text{SH}};\ \Delta T_{\text{SC}};\ p_{\text{int}};\ y]^T \tag{8}$$

The injected mass flow rate is at state 5 always saturated vapor. Due to the two-step compression and vapor injection into the compression chamber, the cycle efficiency calculation is more complex than the simple heat pump cycle. Equation (9) shows the definition of the *COP* for the vi cycle.

$$COP_{\text{vi}} = \frac{h_2 - h_3}{(1-y)\cdot \Delta h_{\text{com,step},1} + \Delta h_{\text{com,step},2}} \tag{9}$$

Thereby, $\Delta h_{\text{com,step } i}$ is the specific enthalpy difference due to the compression in step *i*. Since the mass flow within the evaporator and thus, the first compression step only includes a partial mass flow rate.

2.2.4. Vapor injection in combination with the internal heat exchanger cycle (Fig. 2d)

The fourth cycle combines the advantages of the internal heat exchanger cycle (cf. section 2.2.2) and the vapor injection cycle (cf. section 2.2.3). Degrees of freedom, and the COP calculation, are similar to the vapor injection cycle (cf. equation (8) and (9)).

2.2.5. Parallel compression cycle (Fig. 2e)

The parallel compression cycle (pc) functionality is similar to the vapor injection cycle. However, instead of a two-stage compression process with injection in a single compressor, the flowsheet includes two individual compressors. In parallel compression, the split and preheated mass flow rate (state 6) is not injected into the main compressor but compressed by a second compressor (state 7). Here, state 6 needs the minimum amount of superheating to ensure the compressor's safe operation. Afterward, compressor outlets are mixed (state 3) and enter the condenser. Overall, the degrees of freedom is similar to the vapor injection cycle (cf. section 2.2.3). However, the calculation of the *COP* deviates:

$$COP_{\mathrm{pc}} = \frac{h_2 - h_3}{y \cdot \Delta h_{\mathrm{com},67} + \Delta h_{\mathrm{com},12}} \tag{10}$$

2.3. Case study

The present investigation aims to cover the following research questions:

1. Which refrigerants show high efficiency and are suitable for a steam generation?
2. Which flowsheet shows the overall best performance?
3. How do the results regarding the optimal flowsheet deviate for different refrigerants?
4. How does the source temperature influence the overall results?

To do so, the investigation focuses on steam generation where liquid water enters the condenser at 80 °C and 1.5 bar and leaves the condenser as superheated vapor at 120 °C and 1.5 bar. Five different inlet temperatures are investigated for the heat source, ranging from 40 to 80 °C. For each temperature, the temperature difference of the source is set to 10 K. Fig. 1 shows the temperature curves in both heat exchangers for the sink, source, and refrigerant.

For the defined application, a fluid selection is conducted. The fluid selection accounts for global warming potential (GWP) limits and the minimum operating pressure at an evaporation temperature of 30 °C. Additionally, the filter only includes non-toxic fluids and limits the operation to subcritical. Thus, refrigerants with a critical temperature below 130 °C are dropped. As a result, 14 refrigerants satisfy the defined constraints. For some selected refrigerants, though, the actual GWP value is low. Since all of them are isomeres of known hydrocarbons, their expected GWP value should be below 150. Therefore, in addition to the selected refrigerants, ammonia and R245fa are added: Ammonia due to its high performance in the literature and R245fa as a reference refrigerant. Lastly, a zeotropic mixture based on R600a and R601a with a molar composition of 75/25 is included to analyze the potential of zeotropic mixtures for steam generation. Table 1 shows the selected refrigerants and their properties.

Table 1: Fluid properties of preselected pure refrigerants. Some fluid properties are not given in the literature, and their value is set to not available (n.a.).

Refrigerant	Molar mass [g/mol]	T_{crit} [°C]	NBP [°C]	ODP	GWP	Safety class	Molecule: Double or triple bind?
R601a (isopentane)	72.2	187.2	27.5	0	5	A3	no
R600a (isobutane)	58.1	134.6	-11.7	0	3	A3	no
R600 (butane)	58.1	152.0	-0.5	0	4	A3	no
R717 (ammonia)	17.0	132.4	-33.6	0	0	B2L	no
R1224yd(Z)	148.5	155.3	14.3	0.00012	< 1	A1	yes
R1233zd(E)	130.5	166.5	17.9	0.00034	1	A1	yes
R1234ze(Z)	114.0	150.1	9.4	0	1	A1	yes
R1336mzz(Z)	164.1	171.4	33.1	0	2	A1	yes
R1336mzz(E)	164.1	130.4	7.6	0	18	A1	yes
Butene	56.1	146.1	-6.6	0	n.a.	A3	yes
Isobutene	56.1	144.9	-7.3	0	n.a.	A3	yes
Cyclobutene	54.1	174.9	2.2	0	n.a.	A3	yes
1-Butyne	54.1	158.9	7.7	0	n.a.	A3	yes (3)
(Z)-But-2-ene	56.1	162.6	3.4	0	n.a.	A3	yes
(E)-But-2-ene	56.1	155.5	0.5	0	n.a.	A3	yes
R245fa	134.1	153.9	14.7	0	858	B1	no

Besides the parameters of the overall case study, the models presented in section 2.2 need lower and upper bounds for the defined degrees of freedom. The lower and upper bound should be set as close as possible to reduce the overall optimization time while not influencing the overall investigation results. Table 2 shows the selected bounds of the case study.

Table 2: The flowsheet evaluation's lower and upper bounds of optimization parameters.

Optimization parameters	Lower bound	Upper bound
Evaporation pressure p_{eva}	p_{dew}@283.15 K	$p_{\mathrm{dew}}@T_{\mathrm{eva,sec,in}}$
Condensation pressure p_{con}	$p_{\mathrm{dew}}@T_{\mathrm{con,sec,in}}$	$p_{\mathrm{dew}}@(T_{\mathrm{con,sec,out}} + 20$ K)
Amount of superheating ΔT_{SH} in K	10	30
Amount of subcooling ΔT_{SC} in K	0	40
Intermediate pressure ratio *r*	0	1
Injection ratio *y*	0	0.5

3. Results

The following section presents the results of the conducted investigation. The study includes all refrigerants mentioned in Table 1. However, the figures in this work show only a selected number of refrigerants that represent the overall findings. Table 3 in the attachment shows the complete results for all mentioned cycle configurations and refrigerants for the operating point W80/W120.

Fig. 3 shows the results for the *COP* for a sink and source inlet temperature of 80 °C. Starting with the simple cycle (red bars), ammonia (R717) shows the highest efficiency at 5.75, and R1336mzz(E) shows the lowest efficiency at 3.41. Besides ammonia, cyclobutane shows similar high efficiencies. However, all other refrigerants lead to significantly lower efficiencies.

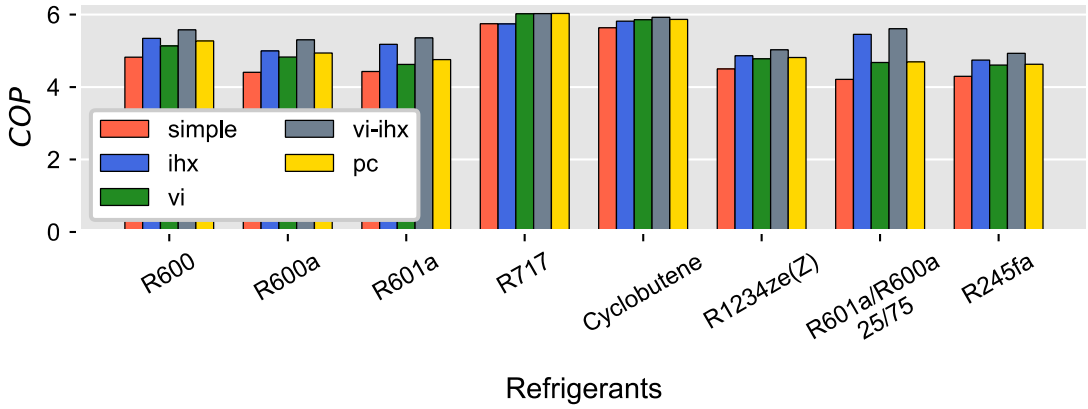


Fig. 3: *COP* of selected refrigerants with a sink and source inlet temperature of 80 °C.

Using the advanced flowsheets, ammonia and cyclobutane still lead to the highest efficiencies. The highest efficiency of 6.03 (R717) is reached when the vapor injection cycle, in combination with an internal heat exchanger, is used, leading to improvements of approximately 5 %. For both refrigerants, the improvements are relatively small compared to the other refrigerants. In contrast to both high-performance refrigerants, the efficiency of the zeotropic mixture based on R601a and R600a depends much more on the selected flowsheet. Here, the efficiency improves by up to 33 % with the advanced flowsheet vi-ihx. Thus, one observation is the strong interdependency of the refrigerant and the selected flowsheet.

The vi-ihx flowsheet leads to the highest overall efficiencies for all studied refrigerants, combining the ihx and the vi flowsheet. Additionally, the ihx flowsheet shows the second-highest efficiencies except for ammonia and cyclobutene. In the ihx flowsheet, the amount of superheating is shifted from the evaporator into the internal heat exchanger. Consequently, two effects occur for a perfect counterflow evaporator, which is assumed in the present work. First, the pinch-point shifts from the refrigerant outlet to the refrigerant inlet for a pure refrigerant. As a result, the lower pressure level increases, resulting in lower pressure ratios and, thus, higher efficiencies. Second, the heat that can be utilized in the evaporator increases due to the heat recovery

rate and the resulting lower vapor quality at the evaporator inlet. The heat recovery rate results from the higher superheating of the ihx cycle. Hence, the share of the provided heat received by the heat source increases, leading to higher efficiencies. However, one negative aspect is the increased maximum process temperatures (compressor discharge temperatures) due to the higher inlet temperatures in the compressor.

Fig. 4 shows the maximum process temperatures. Regarding the differences between the selected flowsheets, the ihx cycle shows the highest outlet temperatures for all refrigerants, followed by the vi-ihx cycle (except for ammonia). Due to the higher temperatures, the operating envelope of the compressor can be reduced. Thus, the overall operating range must be checked when selecting the compressor in combination with the flowsheet. On the other hand, the vi cycle leads to the lowest maximum temperatures. For the refrigerants, ammonia shows the highest process temperatures for all cycles, exceeding values above 160 °C.

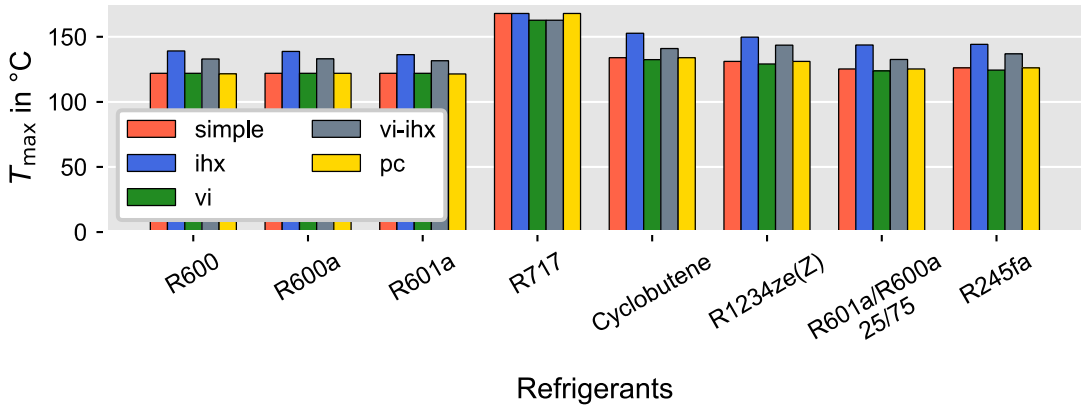


Fig. 4: Maximum process temperature for selected refrigerants in all cycle configurations for a source inlet temperature of 80 °C.

Besides the mentioned effects in the ihx cycle, the vi-ihx cycle adds the advantages of vapor injection to the ihx cycle, resulting in even higher efficiencies. When using vapor injection, the compressor outlet temperature decreases due to the injection of steam at a lower temperature. The lower compressor outlet and, thus, condenser inlet temperature leads to a lower mean temperature difference between the refrigerant and the secondary fluid (in this case, water) in the condenser, reducing the entropy production during the heat transfer and, thus, leading to higher efficiencies. Additionally, the throttling losses are reduced since only a partial mass flow rate is expanded to the evaporation pressure, whereas the other part only expands to the intermediate pressure. Thus, the overall losses can be reduced.

However, the amount of loss reduction when changing the flowsheet depends on the refrigerant. Thus, not all refrigerants show the same results. In this case, the most significant improvement when changing the flowsheet occurs for the zeotropic mixture. Here, up to 33 % improvements are presented when changing the flowsheets from the simple to the vi-ihx cycle. The main reason is the even higher effect of the internal heat exchanger for zeotropic mixtures. For pure fluids, the pinch point in the evaporator is located at the evaporator inlet in case no superheating is provided in the evaporator. For zeotropic mixtures with a temperature glide that perfectly matches the source temperature difference, however, the pinch-point can still be located at the evaporator outlet. Thus, the evaporation pressure can rise even further when using an internal heat exchanger, leading to higher efficiency improvements.

Nevertheless, the zeotropic mixtures still show far lower efficiencies than high-performing refrigerants like ammonia. The main reason here is the mainly latent temperature curve of the sink water in the condenser. In the condenser, the temperature glide can not be utilized due to the mainly isothermal heat transfer to the sink water. Therefore, the mean temperature difference between refrigerant and water increases if the refrigerant has a temperature glide. Once the mean temperature difference increases, the losses due to heat transfer also increase, resulting in lower overall efficiencies. Thus, zeotropic mixtures are not suitable for the generation of steam. However, azeotropic mixtures with similar behavior to pure fluids could increase efficiency since their overall fluid properties can be tailor-made by adjusting the mixture composition. Thus, azeotropic mixtures should be investigated further for applying steam generation heat pumps.

When comparing the pure refrigerants given in Fig. 3, most refrigerants show similar behavior when adjusting the flowsheet. Ammonia, however, deviates from the general performance adjustments. To analyze the effects further, Fig. 5 compares the results for all flowsheets for five source temperatures for the refrigerants ammonia (R717 – left) and butane (R600 – right). For both refrigerants, all flowsheets show the highest

efficiencies for the highest source temperature, which is the fundamental phenomenon related to the Carnot principle. The performance of the individual flowsheets, however, changes significantly. The pc, vi, and vi-ihx cycles for ammonia show similar efficiencies for all operating points.

Additionally, the ihx and simple cycle show similar performances but lower than the other three flowsheets. For butane, the vi-ihx cycle leads to the highest efficiency for all source temperatures, followed by the ihx, vi, and pc. However, the performance ranking of the ihx, vi, and pc flowsheets depends on the operating point. For high source temperatures (lower temperature lifts), the ihx flowsheet is superior to the other two. With decreasing source temperature and, thus, increasing temperature lift, the vi and pc flowsheet's potential increases, outperforming the ihx cycle's potential. Once again, the simple cycle shows the lowest efficiencies.

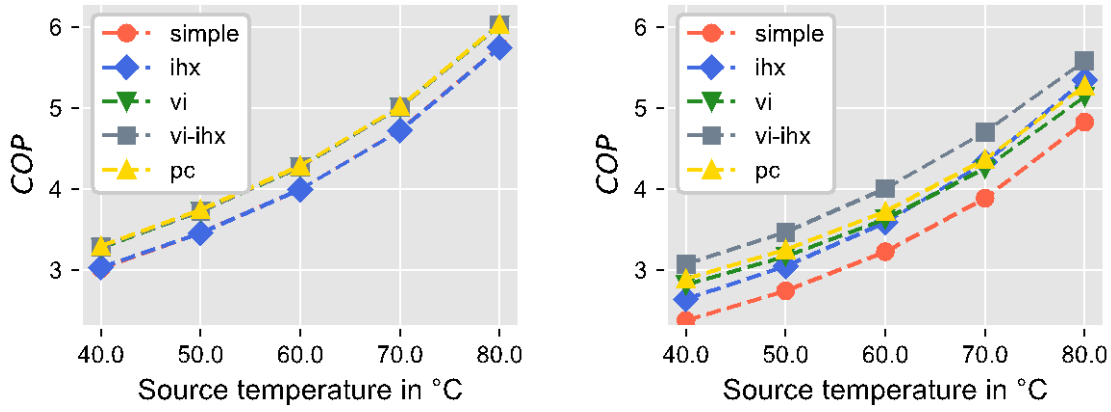


Fig. 5: *COP* results for ammonia (R717 – left) and butane (R600 – right).

The main differences between ammonia and butane result from two aspects: First, ammonia has far higher compressor discharge temperatures (cf. Fig. 4). Second, butane – similar to the other hydrocarbons – has a dewline with a comparably low slope. Thus, the amount of superheating at the compressor outlet and the condenser inlet is relatively low for most operating points and flowsheets. Both effects can improve or reduce the effects mentioned by the individual flowsheets and will be evaluated in the following.

In the ihx flowsheet, the main improvements result from the higher superheating at the compressor inlet and, thus, the higher degree of subcooling at the inlet into the expansion valve. Therefore, the potential can be fully utilized for butane with a low compressor discharge temperature. Furthermore, the improvements in additional heat in the condenser are greater than the additional compressor work due to the higher temperature at the compressor inlet, leading to efficiency improvements. For ammonia with a very high discharge temperature, however, the improvement in additional heat in the condenser is lower compared to the increase in compressor work. Thus, the optimizer does not increase the superheating at the compressor inlet compared to the simple cycle. Hence, the efficiencies are similar.

In the vi flowsheet, the compressor's discharge temperature can be reduced due to the injection of refrigerant vapor at a lower temperature. For ammonia, the throttling losses and the losses due to heat transfer in the condenser can be reduced. Similar effects occur for butane. However, since butane has a low amount of superheating at the compressor outlet (in the simple cycle 6 K for a source temperature of 80 °C), the overall possible improvement is limited. Additionally, the pinch-point temperature is influenced negatively, leading to higher condensation pressures (19.6 bar in the simple cycle compared to 20.5 bar in the vi cycle). In the vi cycle, the pinch-point is located in the superheated region of the sink water. In the simple cycle, the pinch-point is located at the evaporation region of the sink water. Hence, the sink temperature at the pinch-point is higher, leading to higher necessary refrigerant temperatures to satisfy the second law of thermodynamics. This effect negatively influences the overall performance of vi. Hence, vi shows greater improvements for refrigerants with moderate compressor discharge superheating. For lower source temperatures, the amount of discharge superheating at the compressor increases for butane. Therefore, the performance of the vi flowsheets increases also.

The pc flowsheet shows similar effects to the vi cycle. The main difference is the location where both enthalpy flows are mixed. In the vi cycle, the mixing occurs in the compressor leading to a mixing entropy production in the compressor. Simultaneously, the compressor is cooled, leading to lower maximum process temperatures. In the pc flowsheet, the mixing occurs after both compressors. Hence, two effects occur. First,

the maximum process temperature is not influenced compared to the simple cycle since a partial mass flow rate still overcomes the total pressure ratio (cf. Fig. 4). Second, the entropy production due to mixing does not influence the compression process since it occurs after both compressors. Due to the second effect, the efficiencies of pc flowsheet are overall slightly higher compared to the vi flowsheet.

For the vi-ihx flowsheet, the mentioned effects for vi and ihx are combined. However, in the case of ammonia, the ihx does not offer any improvement. Hence, the results of the vi and vi-ihx flowsheets are similar.

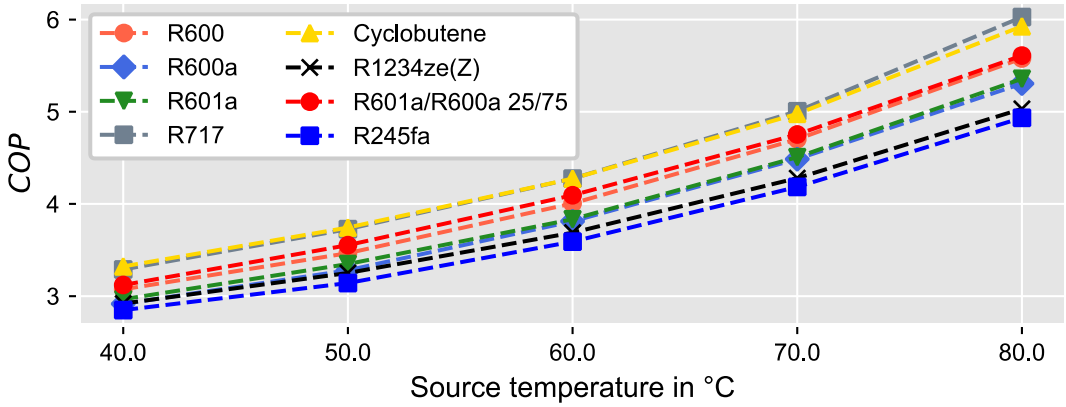


Fig. 6: *COP* for vi-ihx cycle for selected refrigerants.

Finally, Fig. 6 shows the best-performing flowsheet (vi-ihx) results for all refrigerants in dependency on the source inlet temperature. The *COP* increases when the sink inlet temperature increases for all refrigerants. However, the overall refrigerant ranking is not affected by the adjustment of the source temperature. Thus, ammonia and cyclobutene show the highest performances still. Nevertheless, the investigation could only cover some potential refrigerants for applying a steam generation heat pump. Thus, ammonia or cyclobutene are not necessarily the best possible refrigerants. Further research should investigate the possibility and the potential of tailor-made azeotropic mixtures that offers fluid properties for a defined application.

In the following section, the results of the present investigation are discussed.

4. Discussion

The previous section shows the results of the analysis of several refrigerants in five possible cycle configurations for the application in high temperature heat pumps to generate low-pressure steam. Regarding cycle efficiency, ammonia and cyclobutene show the highest values. Additionally, combining an internal heat exchanger and vapor injection in one flowsheet leads to the highest efficiencies for all refrigerants.

Besides the cycle efficiency, however, several further aspects must be addressed when selecting a refrigerant and a flowsheet for an application. One aspect is the long-term chemical stability of refrigerants. In high temperature applications, the refrigerant has to withstand the continuously high temperature compared to conventional heat pump systems (e.g., for space heating). However, long-term stability tests have yet to be conducted for many refrigerants. Thus, the long-term stability is unknown. However, one possible indicator is the molecule structure of a refrigerant. In this regard, double and triple bonds tend to be less chemically stable than regular bonds. Table 1 shows, there a refrigerant molecule includes at least one double or triple bond. Besides the natural refrigerant R717 (ammonia) and the hydrocarbons R600, R600a, and R601a, all investigated refrigerants have at least one double or triple bond. Hence, their chemical stability cannot be guaranteed, and further studies are necessary. Thus, ammonia is preferable to cyclobutane since its long-term stability has been tested widely already.

Ammonia is a toxic and moderately flammable (B2L) refrigerant. Therefore, additional safety measures are necessary, leading to higher costs and a more prolonged designing phase since many regulations must be satisfied. Furthermore, stainless steel is necessary for ammonia, resulting in higher investments. Additionally, processing stainless steel is more challenging and expensive compared to conventional materials for heat pumps, e.g., copper, making the construction part more challenging.

Besides the general fluid properties, ammonia has a critical temperature of 132.4 °C. Since the application of this paper is the generation of low-pressure steam with a water vapor outlet temperature of 120 °C, ammonia operates relatively close to the critical points. In case of higher dynamics or oscillations during the operation,

the critical point might be reached, leading to an unstable operation. Thus, ammonia might not be applicable for the given use case. Ammonia is applicable for lower sink temperatures with a sufficient difference from the critical temperature. Nevertheless, ammonia leads to very high operating pressures due to its high critical pressure of 112.8 bar. For operation closer to the critical temperature, there are limited components available to utilize ammonia's potential. Especially the compressor with its sealings leads to challenges regarding the design of new components.

Additionally, ammonia leads to very high discharge temperatures compared to other refrigerants (cf. Fig. 4), which can negatively affect the lubricant in the compressor. Therefore, oil-free compressor solutions, e.g., turbo compressors, can be possible when handling high temperatures. However, turbo compressors need several compression stages due to the high occurring pressure ratios and the simultaneously only limited pressure ratio a compression stage can overcome. Hence, additional investments are necessary for the system.

Nevertheless, ammonia has been applied in heat pumps for several decades. Thus, the mentioned challenges are well known, and possible solutions have been prepared and proven sufficient for a safe and efficient operation. Also, ammonia has the advantage of high volumetric heat capacities due to its high operating pressure. Due to the high volumetric heat capacities, the components of the heat pumps can be designed smaller, leading to more compact systems. Especially for large-scale heat pumps with heating demands in the range of several megawatts, compact systems are necessary due to the high demand for space. Thus, ammonia shows a high-performance solution for compact heat pump systems with solvable challenges regarding its safe operation.

Regardless of the high performance of ammonia, further research should still be conducted regarding possible alternatives. For example, for steam generation, zeotropic mixtures are not suitable due to the negative effect of the temperature glide. Tailor-made azeotropic mixtures optimized for the individual application, however, might improve the overall cycle performance (efficiency, volumetric heat capacity, maximum process temperature) further, leading to a further reduction in power demand and, thus, carbon emissions.

5. Conclusions

The present investigation analyzes the applicability of heat pumps for the generation of low-pressure steam. For the application, the water enters the heat pump condenser at 80 °C, evaporates at 1.5 bar (approx. 111 °C), and leaves the condenser at 120 °C as superheated vapor. First, a refrigerant selection is conducted to analyze the applicability of heat pumps. We identify 14 refrigerants that are not toxic and have a GWP below 150. Additionally, ammonia is included due to its high performance in existing heat pumps, and R245fa is added as a reference refrigerant. Second, we evaluate the performance of the refrigerants in five flowsheets and analyze the influence of shifting the source temperature from 40 °C to 80 °C.

The results show that ammonia and cyclobutene lead to the highest efficiencies with *COPs* of up to 6. Cyclobutene, however, has a double in its molecule structure and might be less chemically stable than ammonia. Hence, ammonia is to be preferred. Regarding the cycle configuration, a combination of vapor injection and an internal heat exchanger shows the highest efficiencies for all investigated refrigerants. For ammonia, however, the potential is similar to a basic vapor injection cycle since the potential of the internal heat exchanger cannot be utilized due to the high compressor discharge temperatures of ammonia.

Finally, the results are discussed. Due to its toxicity and flammability, additional safety measures are necessary when using ammonia as a refrigerant. Nevertheless, ammonia has been used in heat pumps for decades, showing its potential and solution when dealing with additional safety regulations. Additionally, ammonia leads to compact systems due to its high volumetric efficiency. Hence, ammonia is a performance solution, especially when combined with advanced flowsheets like a two-stage compression. So overall, ammonia is a high-efficiency replacement for conventional refrigerants such as R245fa. However, further research regarding the potential of tailor-made azeotropic mixtures should be conducted since the individual fluid properties can be optimized for generating low-pressure steam, improving the cycle efficiency even further.

Acknowledgements

We gratefully acknowledge the financial support by the German Federal Ministry for Economic Affairs and Climate Action (BMWK), promotional reference 03EN4011.

References

[1] V. Masson-Delmotte *et al., Climate Change 2021: The Physical Science Basis. Contribution of Working Group I to the Sixth Assessment Report of the Intergovernmental Panel on Climate Change*: Cambridge University Press, 2021. [Online]. Available: https://www.ipcc.ch/report/ar6/wg1/

[2] C. Arpagaus, F. Bless, M. Uhlmann, J. Schiffmann, and S. S. Bertsch, "High temperature heat pumps: Market overview, state of the art, research status, refrigerants, and application potentials," *Energy*, vol. 152, pp. 985–1010, 2018, doi: 10.1016/j.energy.2018.03.166.

[3] M. Papapetrou, G. Kosmadakis, A. Cipollina, U. La Commare, and G. Micale, "Industrial waste heat: Estimation of the technically available resource in the EU per industrial sector, temperature level and country," *Applied Thermal Engineering*, vol. 138, pp. 207–216, 2018, doi: 10.1016/j.applthermaleng.2018.04.043.

[4] M. O. McLinden, C. J. Seeton, and A. Pearson, "New refrigerants and system configurations for vapor-compression refrigeration," *Science (New York, N.Y.)*, vol. 370, no. 6518, pp. 791–796, 2020, doi: 10.1126/science.abe3692.

[5] M. O. McLinden, J. S. Brown, R. Brignoli, A. F. Kazakov, and P. A. Domanski, "Limited options for low-global-warming-potential refrigerants," *Nat Commun*, vol. 8, no. 1, p. 14476, 2017, doi: 10.1038/ncomms14476.

[6] J. Navarro-Esbrí, A. Fernández-Moreno, and A. Mota-Babiloni, "Modelling and evaluation of a high-temperature heat pump two-stage cascade with refrigerant mixtures as a fossil fuel boiler alternative for industry decarbonization," *Energy*, vol. 254, p. 124308, 2022, doi: 10.1016/j.energy.2022.124308.

[7] D. Roskosch, V. Venzik, J. Schilling, A. Bardow, and B. Atakan, "Beyond Temperature Glide: The Compressor is Key to Realizing Benefits of Zeotropic Mixtures in Heat Pumps," *Energy Technology*, p. 2000955, 2021, doi: 10.1002/ente.202000955.

[8] M. Jesper, F. Schlosser, F. Pag, T. G. Walmsley, B. Schmitt, and K. Vajen, "Large-scale heat pumps: Uptake and performance modelling of market-available devices," *Renewable and Sustainable Energy Reviews*, vol. 137, p. 110646, 2021, doi: 10.1016/j.rser.2020.110646.

[9] C. Mateu-Royo, C. Arpagaus, A. Mota-Babiloni, J. Navarro-Esbrí, and S. S. Bertsch, "Advanced high temperature heat pump configurations using low GWP refrigerants for industrial waste heat recovery: A comprehensive study," *Energy Conversion and Management*, vol. 229, p. 113752, 2021, doi: 10.1016/j.enconman.2020.113752.

[10] T. Bai, G. Yan, and J. Yu, "Thermodynamic assessment of a condenser outlet split ejector-based high temperature heat pump cycle using various low GWP refrigerants," *Energy*, vol. 179, pp. 850–862, 2019, doi: 10.1016/j.energy.2019.04.191.

[11] D. Roskosch, C. Arpagaus, S. Bertsch, and A. Bardow, "Compressor design vs. refrigerants properties: What is the main influence on compressor efficiency?," *26th International Compressor Engineering Conference at Purdue, July 10-14*, 2022.

[12] Z. Sun *et al.*, "Experimental study on CO2/R32 blends in a water-to-water heat pump system," *Applied Thermal Engineering*, vol. 162, p. 114303, 2019, doi: 10.1016/j.applthermaleng.2019.114303.

[13] M. R. Ally, V. Sharma, and K. Nawaz, "Options for low-global-warming-potential and natural refrigerants part I: Constrains of the shape of the P–T and T–S saturation phase boundaries," *International Journal of Refrigeration*, vol. 106, pp. 144–152, 2019, doi: 10.1016/j.ijrefrig.2019.05.010.

[14] C. Höges, D. Roskosch, J. Brach, C. Vering, V. Venzik, and D. Müller, "Investigation of the Interactions between Refrigerant, Flowsheet, and Compressor in Residential Heat Pumps," *Energy Technol.*, p. 2201295, 2023, doi: 10.1002/ente.202201295.

[15] E. W. Lemmon, I. H. Bell, M. L. Huber, and M. O. McLinden, "NIST Standard Reference Database 23: Reference Fluid Thermodynamic and Transport Properties-REFPROP, Version 10.0, National Institute of Standards and Technology," 2018, doi: 10.18434/T4/1502528.

Appendix

Table 3: Cycle efficiencies (*COP*) of evaluated refrigerants for operating point W80/W120.

Refrigerant	simple cycle	ihx cycle	vi cycle	vi-ihx cycle	pc cycle
R601a (isopentane)	4.43	5.18	4.63	5.36	4.76
R600a (isobutane)	4.41	5.00	4.83	5.31	4.94
R600 (butane)	4.83	5.34	5.14	5.58	5.27
R717 (ammonia)	5.75	5.74	6.02	6.03	6.03
R1224yd(Z)	4.06	4.50	4.35	4.62	4.36
R1233zd(E)	4.40	4.72	4.62	4.88	4.65
R1234ze(Z)	4.50	4.86	4.78	5.03	4.82
R1336mzz(Z)	3.80	4.29	4.04	4.34	4.08
R1336mzz(E)	3.41	4.01	3.82	4.30	3.83
Butene	4.95	5.35	5.35	5.58	5.36
Isobutene	4.41	5.31	5.30	5.56	5.31
Cyclobutene	5.64	5.82	5.86	5.93	5.87
1-Butyne	5.39	5.65	5.72	5.85	5.72
(Z)-But-2-ene	5.27	5.56	5.57	5.73	5.60
(E)-But-2-ene	5.13	5.49	5.48	5.69	5.49
R245fa	4.30	4.75	4.61	4.93	4.63
R601a/R600a 25/75	4.21	5.46	4.68	5.61	4.70

14th IEA Heat Pump Conference
15-18 May 2023, Chicago, Illinois

Analysis of the factors affecting the equilibrium temperature of the optimal performance of air source heat pump heating

Wang Shijie[a,b], Yang Lingyan[a,b,*], Xu Wei[a,b], Zhang Ruixue[a,b*]

[a]China Academy of Building Research, Chaoyang District of Beijing City, Beijing 100013,China
[b]Jianke EET Co., Ltd. Chaoyang District of Beijing City, Beijing 100013, China

Abstract

Driven by China's dual-carbon goals and the national strategy of clean heating, the application of air source heat pump heating is growing rapidly. So the determination of the equilibrium point in the heating design of the air source heat pump has an important influence on the determination of unit capacity, system heating performance and investment and operation cost. This paper analyzes the influence of the equilibrium point temperature selection of low ambient temperature and conventional air-source heat pump heating products in different regions, different energy-saving grades and different building types on the system performance. The results show that there is an obvious difference in the equilibrium point temperature corresponding to the optimal performance of air source heat pump heating in different regions. The equilibrium point temperature of different building types in the same region is different. In the same application situation, the equilibrium point of the low ambient temperature heat pump is generally lower than or equal to the conventional heat pump, the coefficient of performance of the heating season is higher, and has better application performance.

© HPC2023.
Selection and/or peer-review under the responsibility of the organizers of the 14th IEA Heat Pump Conference 2023.

Keywords: Air source heat pump heating; Equilibrium point; Heating season performance factor;

1. Introduction

In order to improve the atmospheric environment in northern China, the government has put forward a clean heating strategy, combined with the dual-carbon goals of "carbon peaking and carbon neutrality", and adopted electrified terminals to transform the seriously polluted bulk coal heating mode. Air source heat pump has the advantages of easy availability of low heat source and flexible installation[1]. Driven by demand, it continues to improve the applicability of low temperature and has become the dominant way of "electricity instead of coal". The current market scale is close to 7 billion yuan.

For the air source heat pump, the heating capacity and performance are positively correlated with the ambient temperature, that is, the higher the ambient temperature, the greater the heating capacity of the air source heat pump, the better the performance; for the user side, the indoor heat load is negatively correlated with the ambient temperature. when the indoor design temperature is the same, the higher the ambient temperature is, the lower the indoor heat load is, and the lower the outdoor temperature is, the higher the indoor heat load is.

The heating capacity of air source heat pump and building heat load have the opposite trend with the ambient temperature. When they are equal, the corresponding ambient temperature is the equilibrium point temperature. When the outdoor temperature is higher than the equilibrium point temperature, the heat pump unit runs under partial load, resulting in a decrease in the coefficient of performance; when the outdoor temperature is lower than the equilibrium point temperature, it is necessary for the auxiliary heat source to bear part of the heat load, which can't give full play to the energy-saving role of the air source heat pump. Therefore, a reasonable

* Corresponding author. Tel.: +86-15901118986.
E-mail address: yly8111@163.com

equilibrium point temperature can improve the coefficient of performance of the unit and give full play to the advantages of air source heat pump.

There have been many researches on the equilibrium point temperature of air source heat pump at home and abroad. Jiang's team[2]-[6] took the lead in putting forward the concepts of the optimal energy efficiency equilibrium point and the optimal energy equilibrium point, and took specific cities as examples to carry out relevant calculations. The research direction abroad is mostly focused on the method of determining the capacity of auxiliary heat source, including the difference of equilibrium point temperature when using different heating methods such as electric heating or gas heating as auxiliary heat source, which is also based on the temperature theory of heat pump equilibrium point.

The above research uses more steady-state calculation methods in the calculation of indoor heat load. With the development of computer technology, much simulation software has been developed to simulate indoor heating and cooling load, such as TRNSYS, DeST and so on. TRNSYS has the advantages of convenient use and flexible calculation, so this study uses TRNSYS software to simulate the cooling and heating load of different energy-saving buildings in different regions, and then uses the simulated indoor hourly heat load to calculate the optimal equilibrium point temperature of low ambient temperature air source heat pump(LATASHP) and conventional air source heat pump(CASHP).

2. Methods

The determination of the equilibrium point temperature depends on the choice of the final optimization objective. At present, there are two kinds of optimization objectives: the economic goal and the system performance goal. Using the annual cost value or the whole life cycle cost as the objective function to find the best economic equilibrium point temperature, its purpose is to ensure that the sum of the initial investment and operation cost of the heating system is the lowest. Using the seasonal coefficient of performance of the system heating HSPF or the seasonal coefficient of performance of the air source heat pump unit SCOP as the objective function to find the best performance equilibrium point temperature, the goal is to optimize the overall heating performance. The primary energy utilization coefficient of the air source heat pump and the primary energy utilization coefficient of the boiler are also used as the objective function, that is, when the heating energy utilization coefficient of the heat pump is equal to that of the auxiliary boiler, the primary energy efficiency of the heating system is the highest[7]. This paper mainly studies the balance point whose ultimate optimization goal is the system performance goal.

2.1. Optimal performance equilibrium point temperature of heating system

$$\mathrm{HSPF}=\frac{\sum_{\mathrm{i:T_l}}^{\mathrm{i:T_{max}}}\mathrm{Q_{1i}}}{\sum_{\mathrm{i:T_{min}}}^{\mathrm{i:T_{max}}}\mathrm{W_i}+\sum_{\mathrm{i:T_l}}^{\mathrm{i:T_b}}\mathrm{P_fQ_{fi}}}=\frac{\sum_{\mathrm{i:T_l}}^{\mathrm{i:T_{max}}}\mathrm{Q_{1i}}}{\sum_{\mathrm{i:T_{min}}}^{\mathrm{i:T_b}}\frac{\mathrm{Q_{hi}}}{\mathrm{COP_h}}+\sum_{\mathrm{j:T_b}}^{\mathrm{j:T_{max}}}\frac{\mathrm{Q_{hj}}}{\mathrm{COP_h\cdot PLF}}+\sum_{\mathrm{i:T_l}}^{\mathrm{i:T_b}}\mathrm{P_fQ_{fi}}}\tag{1}$$

In the formula:

$\mathrm{Q_{1i}}$ is the indoor heat load when the outdoor air temperature is I, kW;

$\mathrm{W_i}$ is the power consumption of the heat pump when the temperature is I, kW;

$\mathrm{Q_{fi}}$ is the heat consumption of the auxiliary heat source when the temperature is I, kW;

$\mathrm{T_l}$ is outdoor calculation temperature for design conditions for use region, ℃;

$\mathrm{T_{min}}$ is the higher value of the minimum outdoor temperature that can be operated for the heat pump unit and the outdoor calculated temperature under the design condition, ℃;

$\mathrm{T_{max}}$ is the highest outdoor temperature for heating operation of a heat pump unit, ℃;

$\mathrm{T_b}$ is the preset equilibrium temperature of the heating system, ℃;

$\mathrm{Q_{hi}}$、Q_{hj} are the heat generated by the heat pump unit at a certain outdoor temperature during the heating period, kW;

COP_h is the coefficient of heating performance of heat pump unit;

PLF is the COP correction factor of partial load heat pump unit;

P_f is the energy consumption conversion coefficient of auxiliary electric heating equipment, and the electric heating equipment generally takes 1;

$$PLF=\frac{PLR}{1-C_d(1-PLR)}\tag{2}$$

In the formula:

PLR is the partial load rate, which is defined as the ratio of actual heating capacity to the rated capacity of

the equipment;
C_d is the attenuation coefficient of heating performance of heat pump under partial load, which is generally 0.9;

$$Q_{h0} = \frac{Q'_0}{K_1 K_2} \tag{3}$$

In the formula:
Q'_0 is the heat output of the heat pump unit at the preset equilibrium point temperature, kW;
K_1 is the correction coefficient of heat pump unit at preset equilibrium point temperature;
K_2 is the defrosting loss coefficient of heat pump unit at preset equilibrium point temperature;

$$Q_h = K_1(T)K_2(T)Q_{h0} \tag{4}$$

In the formula:
Q_h is the heat produced by the heat pump unit at a certain outdoor temperature during the heating period;
$K_1(T)$ is the ambient temperature correction coefficient of a heat pump unit during the heating period;
$K_2(T)$ is the defrosting loss coefficient of the heat pump unit at a certain ambient temperature during the heating period;

$$Q_{fi} = Q_{1i} - Q_{hi} \tag{5}$$

When the heat load of the building, the air source heat pump unit and the auxiliary heat source are determined, HSPF is only a function of the equilibrium point temperature, so by changing the preset equilibrium point temperature, the curve of HSPF change can be obtained, and the equilibrium point temperature corresponding to the maximum value of HSPF is the optimal performance equilibrium point temperature.

2.2. Load simulation

Building energy efficiency in China is based on the building energy consumption in 1980-1981. It is a stage to improve energy efficiency by 30% on the basis of the previous stage in each step, that is, to save energy by 30%, 50%, 65% and 75% respectively compared with the benchmark building. On the basis of 65% energy saving rate, buildings that can save 60% - 75% more energy are near zero energy consumption buildings. Using TRNSYS to simulate the load of different types and different energy-saving buildings, the relevant parameters are based on the building energy efficiency standard system, and the residential building area is 2000 square meters, the office building area is 4000 square meters, and the commercial building area is 10000 square meters. The thermal disturbance factors such as enclosure structure, fresh air demand and internal personnel lighting are stipulated in the "Energy efficiency Design Standard of Public buildings GB 50189-2015" and the energy efficiency design standards of residential buildings in various areas(JGJ 26-2018, JGJ 134-2010, JGJ 75-2012). The following is an example of residential buildings in Beijing to analyze their load characteristics. It can be seen from Fig.1 that there is a linear relationship between indoor heat load and ambient temperature. The higher the energy saving level is, the lower the indoor heat load is at the same ambient temperature. Because of the interference of different factors, the relationship between indoor heat load and ambient temperature is not completely linear, and the fitted linear formula can be used to replace it in practical application. However, hourly heat load is used to calculate the energy consumption of air source heat pump in this study. For near-zero energy consumption buildings, the indoor heat load is basically less than 10W/m^2, and the performance of the building envelope is excellent, so the ambient temperature is only one of the factors affecting the indoor heat load, and the internal heat source also has a great influence on the indoor heat load, so the linear characteristic between the indoor heat load and the outdoor air temperature is not obvious. For near-zero energy consumption buildings, the heating load has almost no linear correlation with the outdoor temperature, and the building use mode and operation strategy have a decisive influence on the equilibrium point temperature, so it

is necessary to discuss everything in the application of near-zero energy consumption projects. According to the specific building demand, the equilibrium point is determined by calculation.

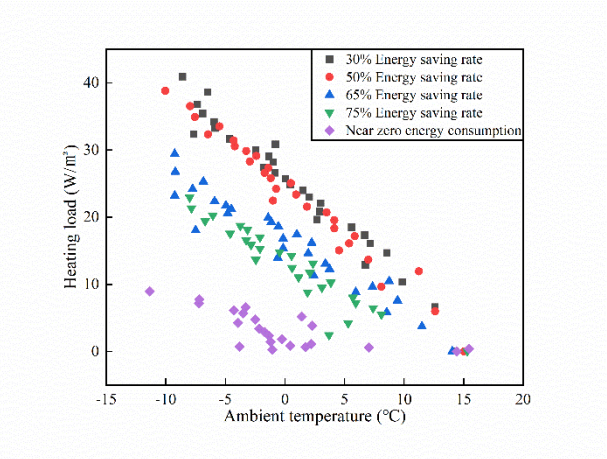


Fig. 1. Indoor heating load of residential buildings in Beijing.

2.3. Performance of air source heat pump

Through market investigation, the heating products of air source heat pump in the market are classified, and the representative ordinary air source heat pump products and jet enthalpy quasi-two-stage compressed LATASHP products are selected for performance analysis. The heating system is fixed as air source heat pump + fan coil end, and the water supply temperature is 41℃. The heating capacity and performance of the product are fitted by regression. As shown in Table 1, according to the heating capacity of the two products and the regression fitting formula of COP, we can know the change of the heat production of the air source heat pump with the outdoor temperature.

Table 1. Fitting Formula of Heat production and COP of Air Source Heat pump

LATASHP	Fitting formula	R^2
Heating capacity	$y=4.9952x^2+402.92x+15053$	$R^2=0.9729$
	$y=4.0734x^2+314.3x+11772$	$R^2=0.9829$
COP	$y=0.0005x^2+0.0632x+2.8982$	$R^2=0.9792$

Table 2. Fitting Formula of Heat production and COP of Air Source Heat pump

CASHP	Fitting formula	R^2
Heating capacity	$y=3.7364x^2+496.4x+14468$	$R^2=0.9839$
	$y=2.9226x^2+388.27x+11317$	$R^2=0.9899$
	$y=1.855x^2+246.44x+7182.9$	$R^2=0.9913$
COP	$y=0.0002x^2+0.0738x+2.7038$	$R^2=0.9892$

3. Results and discussion

The calculation results are analyzed from four directions: different climatic regions, different building types, different energy saving grades and different types of heat pumps.

3.1. Optimal performance equilibrium point in different climatic regions

Select typical cities in different climate zones: Harbin, Beijing, Wuhan. Harbin is located in a severe cold region, Beijing is located in a cold region, and Wuhan is located in a hot summer and cold winter region. The

buildings of the three are residential buildings, and the heat pump type is LATASHP. The current building energy efficiency in Harbin and Beijing is 75%. The current building energy efficiency rating is 50%.

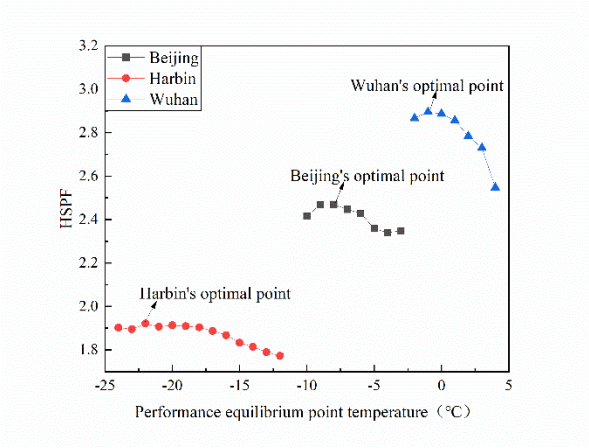


Fig. 2. Performance equilibrium point of typical cities in different regions

It can be seen from the Fig.2 that there is an obvious inflection point in the performance equilibrium point. The optimal performance equilibrium point in Harbin is -22°C, the optimal performance equilibrium point in Beijing is -8°C, and the optimal performance equilibrium point in Wuhan is -1°C. The reason why HSPF first increases and then decreases is that if the performance equilibrium point is too low, when the ambient temperature is high, the heat pump is in a partial load state, and the performance cannot be better utilized. If the performance equilibrium point is too high, when the ambient temperature is low, it can only rely on electric heating for heating, and cannot give full play to the advantages of the heat pump.

In addition, we can also see that the HSPF of the heat pump is greatly affected by the ambient temperature, and the HSPF of the typical cities in the three climate zones has obvious stratification. Region with hot summer and cold winter has great advantages in using heat pumps. The HSPF at the optimal performance equilibrium point in severe cold region is only 1.92, while that in region with hot summer and cold winters can reach 2.9. Therefore, improving the performance of heat pump at low temperature is one of the key research directions in the future.

3.2. Optimal performance equilibrium point for different types of buildings

Select different types of buildings in Beijing: residential buildings, office buildings, commercial buildings. The type of heat pump is LATASHP. The building energy saving rate is 65%. Different types of buildings mainly affect the indoor heating load. There are few indoor heat sources in residential buildings, and their winter heating load is mainly affected by outdoor temperature, while office buildings and commercial buildings have more indoor heat sources, and their winter heating load is affected in many ways. Fig.3 shows the heating load of different types of buildings.

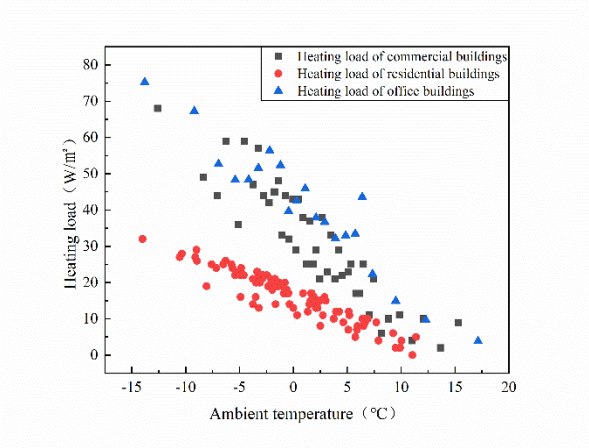


Fig. 3. Heating load of different types of buildings

Due to the work and rest of the staff, residential buildings are heated almost all day, while office buildings and commercial buildings need heating only half the time. Therefore, it can be seen from the picture that the heat load point of residential buildings is more than that of the other two buildings. However, the air exchange times of residential buildings are small and the thermal insulation performance is good, so the heating load per square meter of residential buildings is lower than that of office buildings and commercial buildings. Fig.4 shows how the HSPF of different building types varies with the performance balance point. The best performance balance point of office building and commercial building is -6℃, and that of residential building is -8℃. Because the load of office building and commercial building changes slowly in the low temperature section, and the influence of partial load is limited, so the optimal equilibrium point of office building and commercial building is higher than that of residential building. Similarly, the change of heating load of different types of buildings can be seen from the changes of HSPF. When the equilibrium point changes from -9℃ to -6℃, the HSPF change of office buildings and commercial buildings is not obvious, while that of residential buildings has obvious inflection point, indicating that the linear relationship between heat load and temperature of residential buildings is stronger.

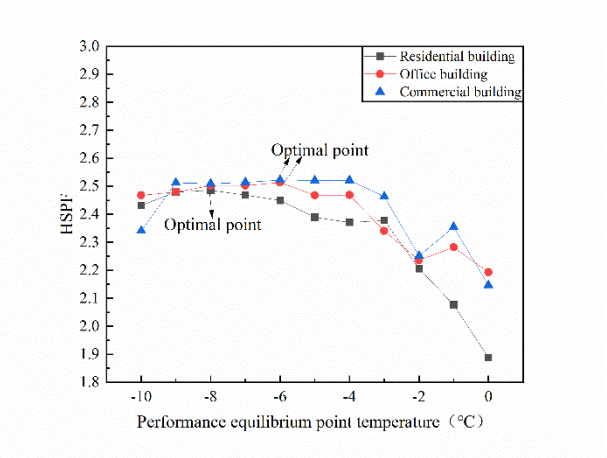


Fig. 4. The change of HSPF of different building types with the performance equilibrium point

3.3. Optimal performance equilibrium point for different levels of energy saving

Select residential buildings with different levels of energy conservation in Beijing: 30%, 50%, 65%, 75% and near zero energy consumption; the type of heat pump is LATASHP. For heating season, buildings with different energy saving levels mean that their indoor heat load is affected by ambient temperature.

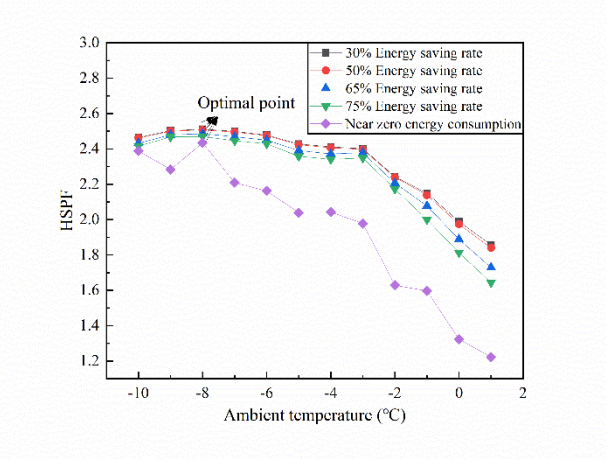


Fig. 5. The change of HSPF of different levels of energy saving with the performance equilibrium point

The higher energy saving grade has better performance of enclosure structure, less affected by ambient temperature, and less linear. However, after the actual calculation, it is found that the temperature of the

optimal performance equilibrium point is the same, which is -8℃. Based on the analysis of the load characteristics and other parameters in the calculation formula, it is found that this is because the linear degree is not reduced obviously, and the indoor heating load decreases proportionally with different energy saving levels, so it has little effect on the selection of the optimal equilibrium point temperature.

3.4. The optimal performance equilibrium point for different types of heat pumps

With the development of heat pump technology, the coefficient of performance of heat pump applied at low temperature is gradually increasing, and the applicable minimum temperature is also expanding. As the main difference between LATASHP and CASHP lies in the outdoor environment, this section analyzes the severe cold region city of Harbin and the cold region city of Beijing, and selects residential buildings with 75% energy-saving rate. Fig.6 shows the heating load of residential buildings in two cities.

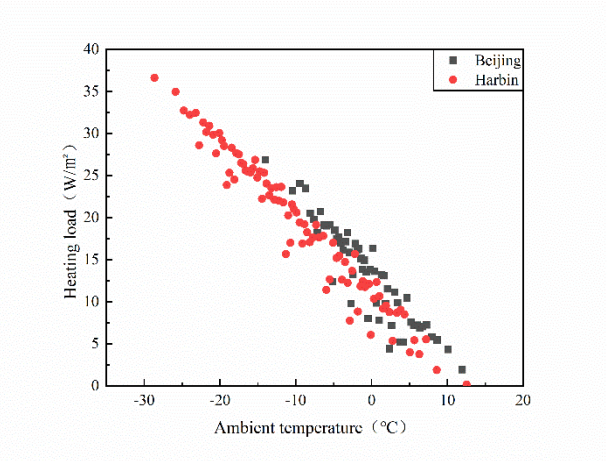


Fig. 6. Heating load of residential buildings in two cities

The lowest operating temperature of the CASHP used in this paper is -12℃, and that of the LATASHP is -27℃. The ambient temperature in Harbin is lower than -10℃ most of the time in winter, and the heating load of the building is significantly higher than that in Beijing. Therefore, in terms of ambient and heating load, for Beijing, the difference between LATASHP and CASHP should be small, and for Harbin, LATASHP should be significantly better than CASHP. Fig.7 shows the curve of HSPF of different types of heat pumps in two cities with the temperature of the performance equilibrium point. The HSPF of heat pump in Beijing is significantly higher than that in Harbin, and the outdoor temperature is an important factor restricting the performance of air source heat pump. For Beijing, the HSPF of CASHP and LATASHP has the same trend with equilibrium temperature, which is consistent with our above analysis. For Harbin, the change curve is completely different, because the lowest operating temperature of CASHP is -12℃, when the performance equilibrium point is lower than -12℃, the selection of air source heat pump is too large and can't be used at low temperature. On the contrary, it further increases the time of partial load of the unit, so the optimal performance equilibrium point of CASHP must be above -12℃, and it's -11℃. The working range of the LATASHP is relatively large, because its COP is always above 1, so as long as the air source heat pump is used, it must have an advantage over electric heating. Considering that the unit still has a long time of partial load operation, the optimal performance equilibrium point is -22℃. In addition, the HSPF of LATASHP is about 50% higher than that of CASHP.

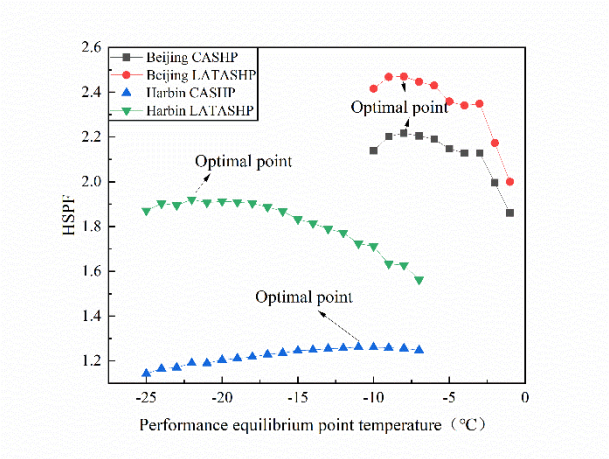


Fig. 7. HSPF curves of different types of heat pumps with performance equilibrium point

4. Conclusions

Through the optimization of the performance equilibrium point of the air source heat pump, the optimal equilibrium point temperature of typical cities in different climatic regions is determined. After analyzing the calculation results, the following conclusions are drawn:

(1) The HSPF of heat pump is greatly affected by ambient temperature, the HSPF of typical cities in different climatic regions have obvious stratification, the temperature of the optimal performance equilibrium point in hot summer and cold winter region is higher than that in cold region, and the optimal performance equilibrium point temperature in cold region is higher than that in severe cold region.

(2) Due to the slow change of load, the optimal performance equilibrium point of public buildings is higher than that of residential buildings in the same region.

(3) The optimal equilibrium points of different energy saving levels are close, but the corresponding seasonal coefficient of performance is different. The higher the energy saving grade, the better the performance.

(4) The optimal equilibrium point of the LATASHP is lower than that of the CASHP in the cold region, and the cold region is the focus of the next step of clean heating, so it is necessary to continue to develop a higher performance LATASHP.

(5) There are many parameters in the temperature optimization formula of the optimal performance equilibrium point, and the sensitivity analysis should be carried out later.

Acknowledgements

This research is supported by “National Key Research and Development Program of China (No.2019YFE0103000).

References

[1] CARROLL, P., CHESSER, M. & LYONS, P. (2020), "Air Source Heat Pumps field studies: A systematic literature review", Renewable & sustainable energy reviews, Vol. 134110275.
[2] YIQIANG, J. (1999) Study on heating optimal balance point of the water heater/chiller units of air source heat pump. Harbin University of C.E. & Architecture.
[3] JIANG YI-QIANG, Y. Y. M. Z. (2001), "Study on heating optimal energy balance point of the water heater/chiller units of air source heat pump", Journal of Harbin University of C.E. & Architecture, No.03, pp. 83-87.
[4] JIANG YIQIANG, Y. Y. M. Z. (2001), "Optimal economic balance point of air source heat pump heating systems", Heating Ventilating & Air Conditioning, No. 03, pp. 39-41.
[5] JIANG YIQIANG, Y. Y. D. S. (2003), "Selection of air source heat pump water chillers/heaters", Heating Ventilating & Air Conditioning, No. 06, pp. 30-33.
[6] JIANG YIQIANG, Y. Y. M. Z. (2000), "Study on Heating Optimal Energy Efficiency Balance Point Temperature of the Water Heater/Chiller Units of Air Source Heat Pump", Building Energy & Environment, No. 02, pp. 5-6.

[7] JIANG YIQIANG, Y. Y. M. Z. (2000), "Calculation of the loss coefficient for frosting-defrosting of air source heat pumps", Heating Ventilating & Air Conditioning, No. 05, pp. 24-26.

14th IEA Heat Pump Conference
15-18 May 2023, Chicago, Illinois

Development of a new GAX-based absorption heat pump for Domestic Hot Water production

Hai Trieu Phan*, Fabio Aste and Hélène Demasles

Université Grenoble Alpes, CEA, Liten, Campus INES, 73375 Le Bourget du Lac, France

Abstract

This paper presents the numerical and experimental results of an ammonia-water absorption heat pump based on a novel Generator Absorber heat eXchanger (GAX) architecture. A prototype at lab scale of 25 kW is developed in a perspective of performance, compactness and use of market-available components in order to address wide industrial applications. This machine is driven by a hot source at temperature above 100°C to produce hot water (> 60°C) from a lower temperature heat of about 30°C. The overall performance of the prototype under different operating conditions is characterized by measurements with high-quality temperature, pressure and mass flow rate sensors. The impacts of the external conditions are investigated while varying the evaporator temperature in the range of 25-50°C and the generator temperature in the range of 110-170°C. The experimental results show attractive performances with a maximum thermal Coefficient Of Performance (COP) of 1.72 and a maximum electrical COP of about 140. Preliminary techno-economic assessment has shown the interest of this technology.

© HPC2023.
Selection and/or peer-review under the responsibility of the organizers of the 14th IEA Heat Pump Conference 2023.

Keywords : absorption cycle, heat pump, GAX;

1. Introduction

In France, the residential and industrial sectors account for 23Mtoe of electric consumption, while the natural gas consumption attests on 24Mtoe (IEA database). In general, these two sectors are responsible of the 43.2% of the French total final consumption, and a great part of this share is converted into heat. In the residential sector, the 78% of the consumption is dedicated to space heating and cooling through systems that are fed for 58% with fossil fuels (https://www.ceren.fr/). Industry is as well dependent on fossil fuels (61% of the total consumption) for heat generation, with even a small share of the electricity consumption (18%, i.e. 21 TWh in 2013) used for thermal production. During the processes, about the 25-60% of the heat is lost to the environment, for a total amount of 8.56 Mtoe of waste heat (https://www.ademe.fr/). However, this rejected heat is available at different temperature levels: almost a third is available at >100°C and can be re-used on site or for feeding heating networks; the second third, between 40°C and 100°C, can be enhanced in temperature by heat pumps; the remaining third is rejected at a temperature < 40°C and is hardly exploitable. The challenge is saving the medium-and-low-temperature heat from being wasted, increasing the overall process performance and reducing the Greenhouse Gas (GHG) emissions. In this context, one of the most adapted solutions is represented by the absorption heat pumps, which use natural fluids and allow upgrading low-temperature sources to a higher temperature level using heat as fueling. In addition, such systems can also be configured in reverse mode to produce cooling, addressing both industrial and residential needs.

To operate, absorption machines need a heat driving source that can be indifferently gas, renewable heat (solar, geothermal, biomass) or waste heat, with an increased economical and environmental interest in the two last cases. Concerning heating, absorption heat pumps can effectively contribute to lower the global energy

* Corresponding author. Tel.: +33 4 79 79 23 72
E-mail address: haitrieu.phan@cea.fr.

consumption for both residential and industrial sectors, thus reducing the GHG emissions in accordance with the European Energy-Climate Framework 2030 and the international goals for limiting the global warming.

As absorption cycles require two fluids for operating, refrigerant and solvent, many possibilities of coupling exist in the literature according to Sun J. et al. (2012) [1]. The most diffused are ammonia-water and water-lithium bromide due to their interesting thermo-physical properties. This last couple has historically been chosen for air conditioning, and in the last decades, it found application even in some heat pumps [2-4]. Despite its good efficiency, especially in multi-stage systems, water-lithium bromide has two important drawbacks: a limited operating field, by both crystallization risk and water freezing temperature, and an important cost of lithium bromide. Ammonia-water couple avoids these problems, being suitable to operate in large temperature fields and having a lower cost, as ammonia is a common product. For the pursuit of the work, ammonia-water will be the chosen fluid couple.

Amongst the different ammonia-water absorption cycles, the Generator-Absorber heat eXchanger (GAX) cycle is the most interesting due to its flexibility and increased performance compared to the single stage cycle. This cycle can effectively be operated as a chiller, down to -40°C, or as a heat pump, even above 70°C with high efficiency. Despite that, few GAX heat pumps exist on the market and most of them based on expensive and bulky heat exchangers in the form of distillation columns. According to the literature, Aprile M. et al. (2016) [2] tested an industrial gas-driven, GAX heat pump that produces 20 kW of hot water at 60°C or 45°C (evaporator temperature TE,in=10°C) with Coefficient of Performances (COP) of 1.6 and 1.73 respectively. Dai E. et al. (2018) [3] tested an industrial 55 kW absorption heat pump that can produce 55°C hot water with an optimal COP of 1.63 at TE,in=20°C and generator temperature TG,in=200°C. The other heat pump present in the literature is a prototype made by Wang J. et al. (2019) [4], where the main heat exchangers consist in tailored-made shell-and-tube exchangers, thus not compact. The best performance obtained is COP = 1.51 with TE,in=15°C and TG,in=193°C. According to these works, the development of GAX heat pumps is particularly interesting for high-temperature waste heat recovery and, due to the COPs above 1.5, even the case of fuelling with fossil sources (gas, biomass, etc.) becomes environmentally and economically attractive.

In this paper, a novel GAX architecture is presented, together with the related numerical model. The prototype is designed, fabricated and tested according to this architecture using only commercially available components, such as plate-type heat exchangers in order to improve the compactness, the amount of charge (ammonia) as well as the minimize the constraint related to high pressure. During the experimental investigations in the laboratory test rig, a particular attention has been given to the operating conditions, which have been varied to test the response of the system in different situations. The experimental results are then discussed to analyse the impact of the main parameters, such as the generator temperature, the evaporator temperature and the solution flow rate. Preliminary techno-economic analysis is carried out to evaluate the interest of this technology.

2. Cycle description

As introduced before, ammonia/water is chosen for the study due to its favourable properties. In addition, this fluid couple is particularly interesting from an industrial point of view, being ammonia a well-known element used in plenty of domains, thus largely available and cheap. In this sense, the components of the GAX heat pump that is further proposed are chosen amongst commercial parts, as plate heat exchangers and pressurized tanks, to demonstrate the viability of such absorption systems.

Detailing the architecture, the GAX heat pump cycle shown in Fig. 1 features a novel architecture where the vapour generation process is discretized via different components, three heat exchangers (GAX2, generator and rectifier) and three pressurized tanks (N21, N22 and N3). This approach is quite the opposite of the concept of distillation column which has a more complex design in order to integrate in one component the vapour generation and separation from the two-phase flow.

2.1. Working principle

As the cycle works in heat pump mode, the absorber and the condenser are connected in series to maximize the hot water output temperature. Preliminary simulations show that the performance is better if the absorber is entered first. The useful effect consists in the heat delivered for production of hot water (yellow line), while the high-temperature heat entering the generator acts as the driving power (red line). The heat flux entering the evaporator can be from ambient or a waste free heat source at low temperature (20°C-35°C)

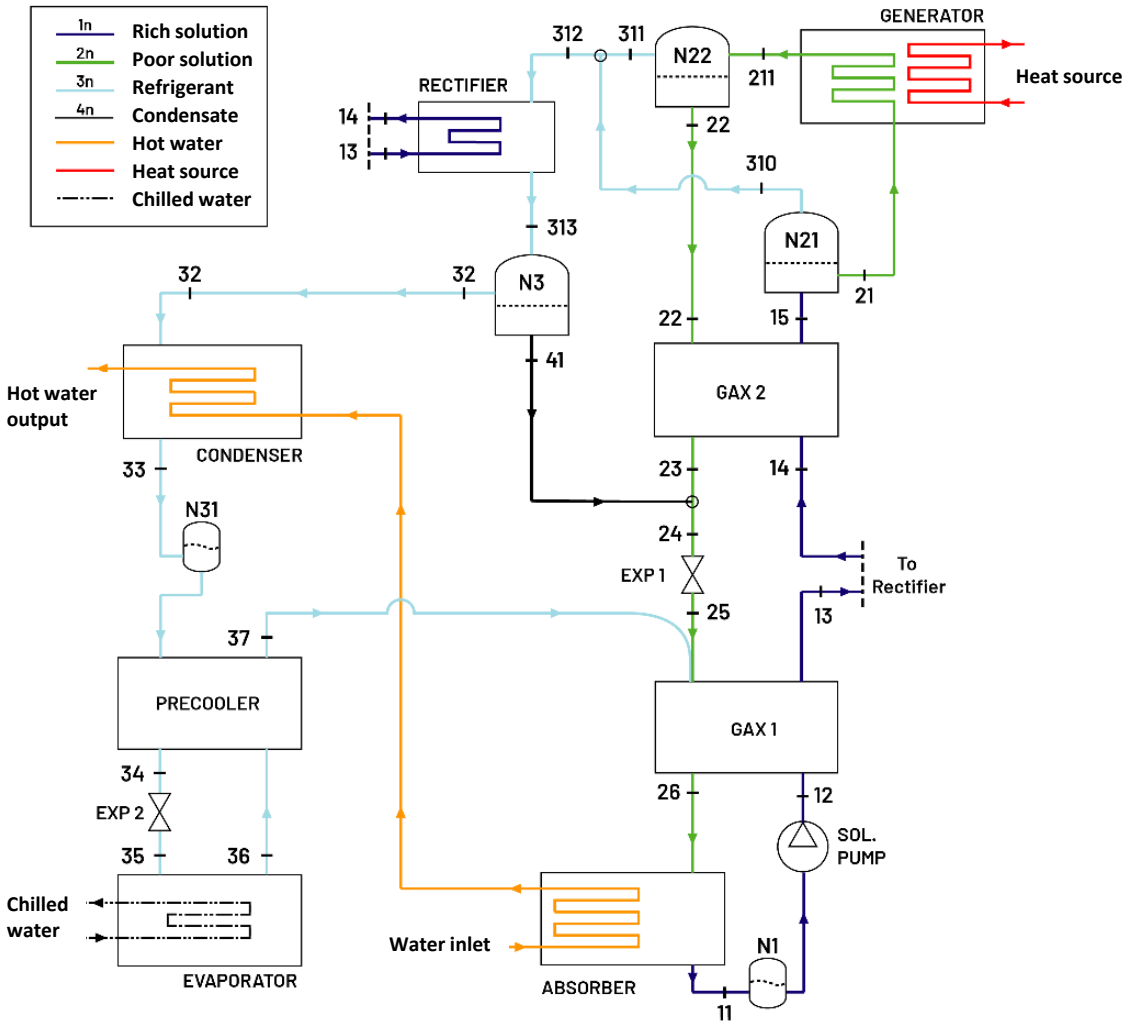


Fig. 1: Scheme of GAX prototype architecture.

For a convenient description, the heat pump cycle is divided into three sub-cycles according to the different flows of refrigerant, rich and poor solutions.

2.1.1. Refrigerant sub-cycle

Rich solution two-phase flows coming from the GAX2 and the generator enter the two separation tanks N21 and N22 respectively: there, the vapour separates by gravity from the liquid solution. Due to the difference in the saturation pressures, the liquid is richer in water and the vapour is richer in ammonia, but it is generally not pure. Therefore, the vapour is sent to the rectifier to be enriched in ammonia. The purification occurs through the refrigerant cooling, which causes a partial condensation of the fluid: the water-rich condensate is recirculated to the poor solution line. In parallel, the purified refrigerant is firstly condensed, then subcooled in the precooler before throttling, and finally vaporized in the evaporator. After that, the vapour refrigerant flows through the low-pressure side of the precooler and reaches the GAX1, where the absorption reaction with the poor solution begins.

2.1.2. Rich solution sub-cycle

The rich solution is obtained as the product of the absorption reaction, which begins in the GAX1 and ends in the absorber. There, the ammonia-water mixture presents the highest richness in ammonia and its thermodynamic state is subcooled liquid, which allows protecting the pump. This last component increases the pressure of the rich solution that is subsequently delivered to the GAX1 (12) to be heated. In this first heating phase, desorption might already occur. The desorption process continues in the rectifier and in the GAX2, as the rich solution recovers the available internal heat of the other fluid lines. Being diphasic after the GAX2, a

first phase separation is performed in the N21 tank to avoid sending vapour at the generator inlet. Here, the remaining rich solution is heated to the highest temperature to continue desorption process. The two-phase fluid undergoes a second and final phase separation in the N22 tank, resulting in the poor solution and some additional refrigerant vapour at the outlets.

2.1.3. Poor solution sub-cycle

After phase separation in the N22 tank, the poor solution features the lowest richness in ammonia in the cycle as well as its highest temperature. A first heat recovery occurs towards the rich solution in the GAX2. Then, the poor solution is mixed with the condensate, increasing ammonia richness and decreasing the temperature. The resulting solution is throttled before entering the GAX 1 (25). There, the ammonia vapour coming from the refrigerant sub-cycle (37) is absorbed by the poor solution and, as the absorption reaction is exothermic, heat generation occurs. The internal recovery is realized by the rich solution (13). The complete absorption in GAX1 is limited by the temperature level of the rich solution used for the cooling. Thus, the reaction is continued in the absorber where further absorption is done by cooling with a colder external source.

2.1.4. GAX effect

The GAX cycle is particularly interesting when a large temperature overlap between the generator and absorber occurs: in this case, absorption excess heat is partially available at a temperature that allows the rich solution desorption in GAX1. In GAX2 and rectifier, the desorption continues thanks to the internal heat recovery from the poor solution. Taking advantage of this temperature overlap decreases the input heat in the absorber and the generator, improving the global performance and reducing the absorber and generator components size.

2.2. Comparison with literature architectures

Only little experimental work has been done on GAX systems configured as heat pumps. Aprile M. et al. (2016) [2] tested an absorption heat pump manufactured by the Robur Company in Germany, Dai E. et al. (2018) [3] tested one manufactured by the Vicot Company in China, and only Wang J. et al. (2019) [4] tested a self-made prototype.

The main difference between the proposed architecture and the existing ones consists in the vapour generation system and the absorption system. An easy remark can be made about the rich solution circuit, which shows a different path: instead flowing first through the rectifier and then through the GAX, in the proposed version it encounters first the GAX1, then the rectifier, and finally the GAX2. This variation results from the pinch analysis of the system fluid lines and optimizes the internal heat recovery.

A more technical aspect concerns the heat exchangers technology. In the literature, the technologies used for the components where absorption takes place (GAX1 and absorber) vary according to the authors : two separated falling film heat exchangers tubes in tubes type [2] and [4] or shell-and-tubes exchangers, which allows piling the two units to form a single component [3]. However, all authors choose the same technology for the desorption block : Generator, GAX2 and rectifier are shell-and-tubes exchangers, which allows piling the three units where the ammonia vapour flows in counter-current respect to the solution, being cooled and rectified all along as in a distillation tower. Therefore, the refrigerant vapour is already purified when exiting the generation column and the condensate resulting from rectification is directly recirculated in the underlying sections. Since the vapour generation and separation occur simultaneously, the generation block is sized taking into account the two process. The novel architecture proposed in this work avoids dealing with this point: as the heat and mass transfers and the phase separation occur separately, each component is optimally sized to its function.

Another aspect to be considered is the system manufacturing. Generally, these distillation-column-like elements consist in a cylindrical vessel where the different sections are heated or cooled by coil exchangers. Such assembly requires a complex manufacturing and, due to the low heat transfer coefficient of coil exchangers, it presents a considerable volume that cannot be split without losing all the advantages of a coupled vapour generation and separation. Differently, the proposed architecture involves many smaller units that can be distributed in the space, thus allowing a more rational positioning inside the system and an easy maintenance.

3. Modelling for prototype sizing

To determine the most efficient solution for the novel GAX ammonia-water cycle, many architectures have been modelled and then implemented in the software EES (Engineer Equation Solver, http://www.fchart.com/) to be numerically studied. EES internally provides NH3/H2O mixture thermodynamic properties, which are calculated through the correlations proposed by Ibrahim O.M. and Klein S.A. (1993). By specifying the heat and mass efficiencies of the components and integrating the hypothesis listed in Table 1, the model returns the thermodynamic conditions of the state points of the cycle and the global performances.

Table 1: Hypothesis of the model for the prototype design

The system is at steady state;	Adiabatic components and pipes;
ΔEK and ΔEZ are negligible	Ideal heat sources and sinks;
Pressure drops are negligible;	Pump has ηel = 0.9 and ηm = 0.8;
Saturated fluid at separation tanks outlet;	The heat transfer efficiency is 0.8;
The approach temperature in heat exchangers is 5°C;	Absorption efficiency is 0.8 and desorption efficiency is 1 according to Boudehenn F. et al. (2014);
Evaporator temperature glide is 5°C;	

The model is established considering each component as a control volume, thus is 0D: the internal dynamics are excluded from the study, as the behaviour of the component is considered as a whole and included in the relative efficiency. Even if simple, this approach is reliable for the scope, as it has been largely demonstrated in previous works [5].

For each control volume, mass and energy conservation equations have been defined:

$$Total\ mass\ conservation \rightarrow \sum \dot{m}_{in} - \sum \dot{m}_{out} = 0 \tag{1}$$

$$Refrigerant\ mass\ conservation \rightarrow \sum \dot{m}_{in}\, x_{in} - \sum \dot{m}_{out}\, x_{out} = 0 \tag{2}$$

$$Energy\ conservation \rightarrow \sum \dot{m}_{in}\, h_{in} - \sum \dot{m}_{out}\, h_{out} + \sum \dot{Q} - \sum \dot{W} = 0 \tag{3}$$

In the last equation, Q and W are the heat and work fluxes exiting the system boundary. Signs respect the traditional convention.

The evaporator temperature glide is defined as $T_{36} - T_{35}$.

Finally, the Coefficient Of Performance (COP) of a generic heat pump is defined as the ratio between the heat rejected to the external cooling fluid at the condenser and the energy input in the compressor. In the case of absorption cycles, a heat rejection occurs also in the absorber, as the absorption reaction is exothermic. This heat being recuperated by the external cooling fluid, it becomes a part of the useful effect. The energy input changes too: in fact, besides the electric energy consumption, an additional and more consistent high-temperature heat consumption is necessary to power the system. Generally, it is good practice to distinguish the type of COP between electrical (ECOP) and thermal (COP) for the continuation, as heat consumption largely prevails on the electric). In particular, doing techno-economic analysis one of the two parameters is often negligible while the other drives the decision.

$$ECOP = \frac{\text{useful heat power}}{\text{electric power}} = \frac{\mathrm{Q_A} + Q_C}{\mathrm{W_{el,pump}}} \tag{4}$$

$$COP = \frac{\text{useful heat power}}{\text{heat power input}} = \frac{\mathrm{Q_A} + Q_C}{Q_G} \tag{5}$$

According to simulations, the best performance considering both COP and ECOP is obtained for the architecture given in Fig. 1. This model has also been used to size all the components of the prototype.

4. Experimental setup

4.1. Prototype

The sizing conditions are reported in Table 2. The generator inlet temperature is set at 170°C, corresponding to the optimal numerical COP. The target of the machine is to produce 25 kW of hot water (> 60°C) from a lower-temperature heat source (~ 30°C).

Table 2: Prototype sizing point

Parameters	Value	Measure Unit
Generator inlet temperature	170	°C
Absorber inlet temperature	30	°C
Evaporator inlet temperature	35	°C
Target hot fluid outlet temperature	> 60	°C
Target heating capacity	25	kW

Using these values as model inputs, the characteristic parameters of the components have been defined. Then, each element has been identified on the market, purchased and assembled. To respect the technological readiness asset, only industrial brazed/welded plates heat exchangers are implemented, as those last components are standardized and produced in series. Instead, the piping and separation tanks, even if they are well known industrial elements, must be designed and singularly manufactured to fit the operating conditions. In addition, as the ammonia/water mixture is very corrosive, a special care is taken by selecting only resistant components, mostly made in stainless steel. Considering the material costs of the assembly without instrumentation, the pressurized tanks (36%) and the piping (25%) represent a great share, while the plate heat exchangers affect for a littler amount (13%). A picture of the prototype is shown in Fig. 2.

Three stainless steel tanks are used to separate refrigerant vapour and liquid solution at the outputs of generator, GAX2 and rectifier. Two other tanks are provided as fluid storages: one to store the poor solution before pumping, in order to avoid pump cavitation during the start-up phase; the other one to store the refrigerant after the condenser. These two last tanks allow the heat pump to be operated over a wide temperature range. However, the system is filled with relatively low quantities of water and ammonia, 1.4 kg of water and 2.4 kg of ammonia. Finally, the GAX1 heat exchanger features an original, double distributor system for the poor solution and refrigerant inlet, allowing liquid and gas flows to be uniformly distributed into each channel.

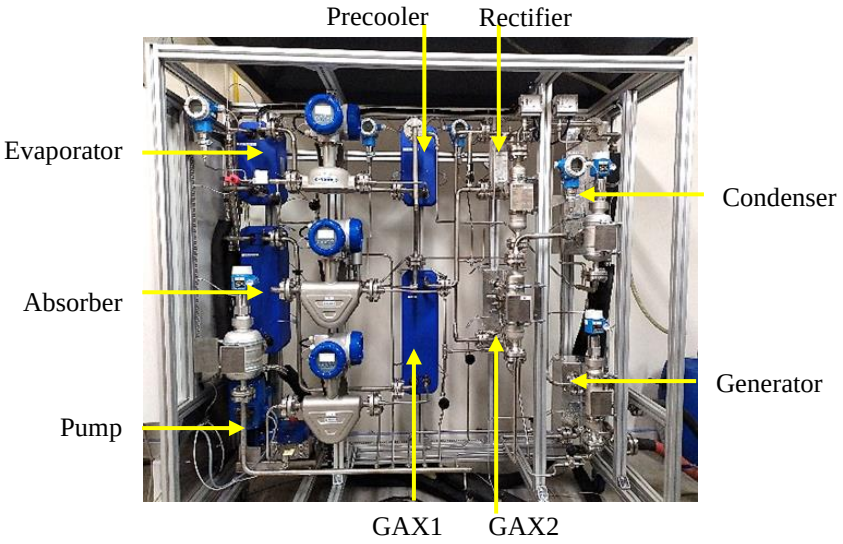


Fig. 2: Front view of the GAX prototype.

4.2. Characterization

Experimental tests were performed at the INES (French National Institute for Solar Energy) facility in a test rig that allowed providing adjustable temperatures and powers for the external fluids. The fluid chosen for all external circuits is pressurized water. The heat pump operating field during the tests is reported in Table 3.

Table 3: GAX heat pump operating range during experimental test. Data refers to external-side fluid for Evaporator, Absorber, Condenser and Generator and to the internal-side fluid (rich solution) for the Pump. In the case of the Pump, both upstream and downstream pressures are indicated.

		Evaporator	Absorber	Condenser	Generator	Pump
Inlet temperature [°C]	Nominal	34.6	29.5		170	41
	Minimal	25	29.5		110	35
	Maximal	50	29.5		170	47
Pressure [bar]	Nominal	9	10.5	23.4	23.6	10.5/23.6
	Minimal	7.5	7.5	19	19	7.5/19
	Maximal	13	13	24	24	13/24
Power [kW]	Maximal	13.4	16	14.6	18.9	0.2
Mass flow rate [kg/h]	Minimal	1700	320	320	950	
	Maximal		865	865		

4.3. Measurement apparatus

The prototype is instrumented with high-precision sensors in order to measure the parameters needed for a thorough comprehension of its functioning. Temperature sensors are positioned on the heat exchangers inlet/outlet. Pressure sensors are positioned on the high- and low-pressure solution and refrigerant circuits. Coriolis flowmeters are employed to measure mass flow, density and temperature of the internal fluids. Liquid level sensors are placed inside the pressurized tanks to measure the amount of the stocked liquid, thus describing the fluid distribution in the prototype. In addition, the level sensor in the storage tank upstream the pump has a protection function, as it shuts off the pump when the stocked liquid level is too low.

Type and uncertainty of the instrumentation are described in Table 4.

Table 4: Instrumentation characteristics

Parameters	Sensors type	Quantity	Uncertainty (+/-)
Heat transfer fluid temperature	Pt100	8	0.1 K
Refrigerant/Solution temperatures	Thermocouples	25	0.3 K
Refrigerant/Solution pressure	0-10 bar and 0-40 bar	4	0.2% full scale
Refrigerant/Solution flow	Mass flowmeter	3	0.20%
External fluid flow	Mass flowmeter	4	0.30%
Density	Mass flowmeter	3	2 kg/m3
Liquid level	Capacitance level sensor	3	0.50%

4.4. Data processing

Despite the number of sensors deployed across the system, many parameters cannot be directly measured and need to be calculated afterwards. In particular, it is the case of the flow rates in the poor solution and condensate lines, and the heat fluxes in the heat exchangers. The firsts are determined through total mass and refrigerant mass balances; the lasts require energy balances in addition. The heat flux can be properly calculated only on absorber, generator, condenser and evaporator where the measures are accurately done on external fluid. As an example, the absorber heat flux is defined:

$$Q_A = \dot{m}_A c_{P,w} \left(T_{A,out} - T_{A,in}\right) \tag{6}$$

Where $C_{P,w}$ is the specific heat of water and $\dot{M}$ is the heat carrier fluid flow. However, on internal heat exchangers where there are absorption or desorption reactions, the heat flux cannot be calculated as it is impossible to know the enthalpy of the fluid precisely.

4.5. NH3 concentration

Determining the ammonia concentration of the solution is an essential point to qualify the functioning of the system. Therefore, ammonia fractions are calculated from measured density, temperature and pressure through reverse correlations based on Ibrahim O.M. and Klein S.A. (1993) [6-7]. The maximum error is about ±2.5%.

5. Experimental results

5.1. Startup

For starting the prototype, we first ran the external circuits (cf. Fig. 1) at the target flow rates and inlet temperatures. Then we initiated the starts of the solution pump together with the openings of the expansion valves (EXP1 and EXP2) in order to regulate the flow rates and the pressure levels. As shown in Fig. 3, the machine took about 400s before reaching the stabilized conditions. This time mainly depends on the thermal inertia as well as the generation rate of the refrigerant vapor in order to reach the required high pressure level.

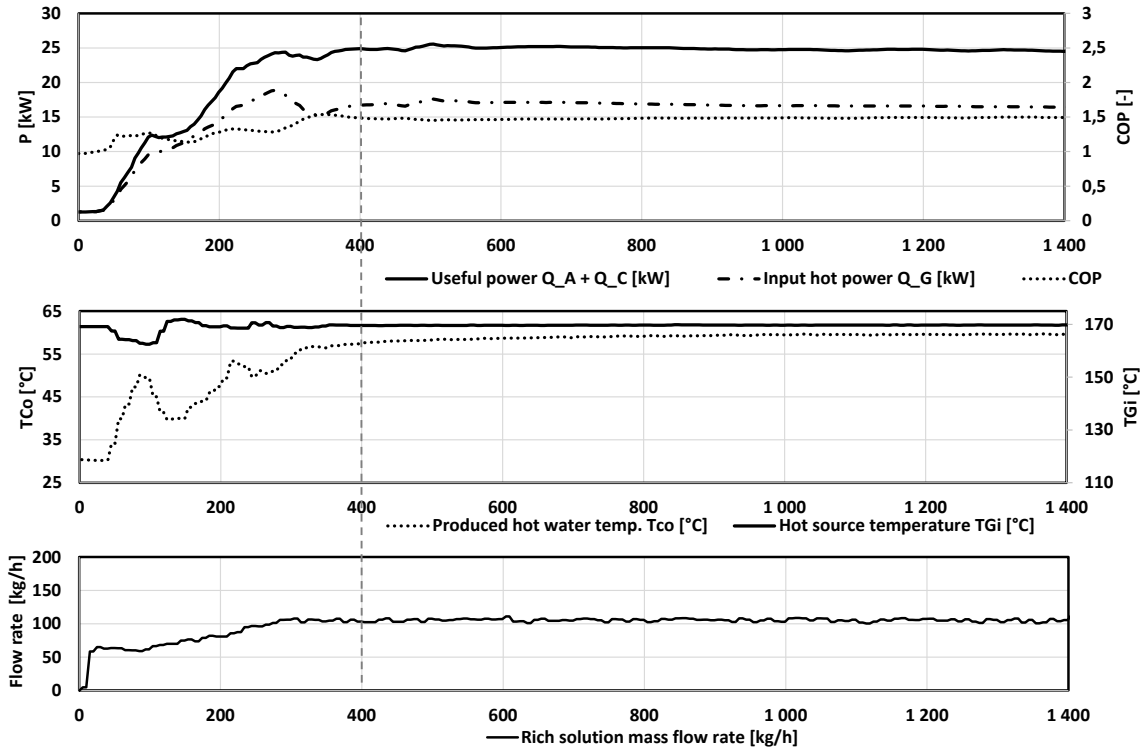


Fig. 3: Evolutions of different parameters during the startup of the prototype.

5.2. Stabilized performance

As the experimental campaign was carried through the conditions reported in Table 3, the impact of different parameters on the system performance has been evaluated. In particular, the study concerns the influences of the solution flowrate, the generator temperature and the evaporator temperature. Some preliminary observations can be presented with reference to Fig. 4. The target temperature for the hot water production ($T_{C,out}$=60°C) is reached for most points, despite the wide field of working conditions. Moreover, the hot water outlet temperature seems being stable at different system heat duty (from -50% to +30% nominal power), meaning that off-design operation is feasible.

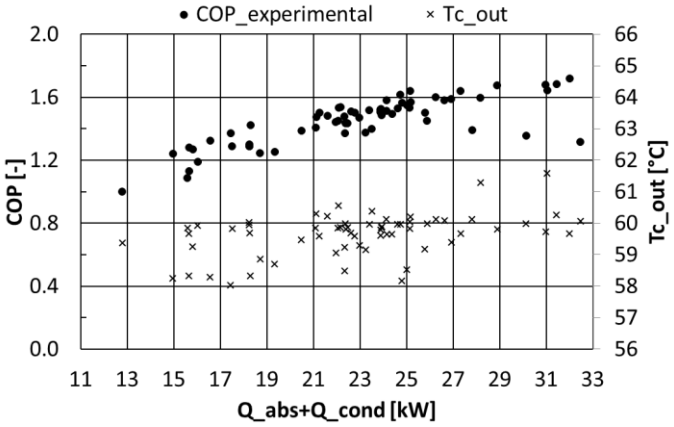


Fig. 4 : COP and the outlet hot water temperature as functions of the heating capacity.

Nevertheless, the COP strongly depends on the operating conditions, which reflect onto the absorber and condenser heat duties, with a sharp decrease below the nominal value (25 kW). Besides, in Fig. 5 the ECOP has an almost linear tendency with reference to the increase of the useful heat production. The highest heating power, 33kW, the best COP of 1.72 and the best ECOP of 170, are reached at 150°C, 30°C and 49.4°C respectively as generator, absorber and evaporator inlet temperatures.

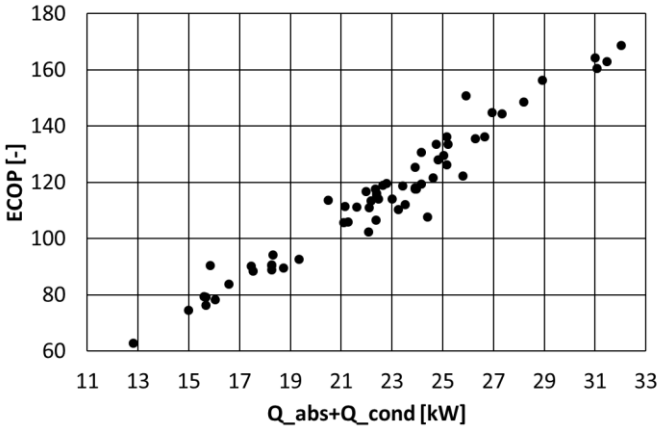
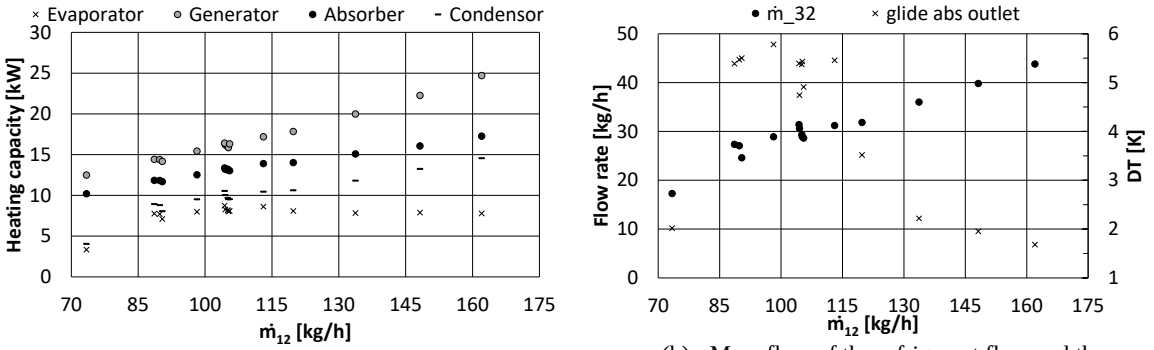


Fig. 5 : Electrical COP (ECOP) as a function of the heating capacity.

5.2.1. Rich solution flow variation

The impact of rich solution flow rate ($\dot{m}_{12}$) is studied at the nominal temperatures of $T_{a,in}$=29.4°C, $T_{g,in}$=169.8°C and $T_{e,in}$= 34.5°C. Fig. 6(a) shows that an increase in the rich solution flow rate leads to an increase in powers output of all heat exchangers, except for the evaporator. Despite the augmentation in the refrigerant vapour flow $\dot{m}_{32}$, its exchanged heat does not follow the same trend. The evaporator appears to be limited by its size, since a decrease of the temperature glide is observed, as shown in Fig. 6(b), even when a control target is set at 5K. In addition, we observed that the increase of the exchanged power in the absorber is smoother than in the generator (Fig. 6(a)). A possible explanation is that the mass transfer by absorption process in GAX1 and in the absorber deteriorates with an increase of liquid fraction at the outlet of the evaporator due to lower temperature glide. Indeed, a numerical calculation shows that at measured ammonia concentration of 96%, 80% of the refrigerant exits as vapour with a 5K glide at the evaporator outlet, while only 45% exits with a 1K glide.

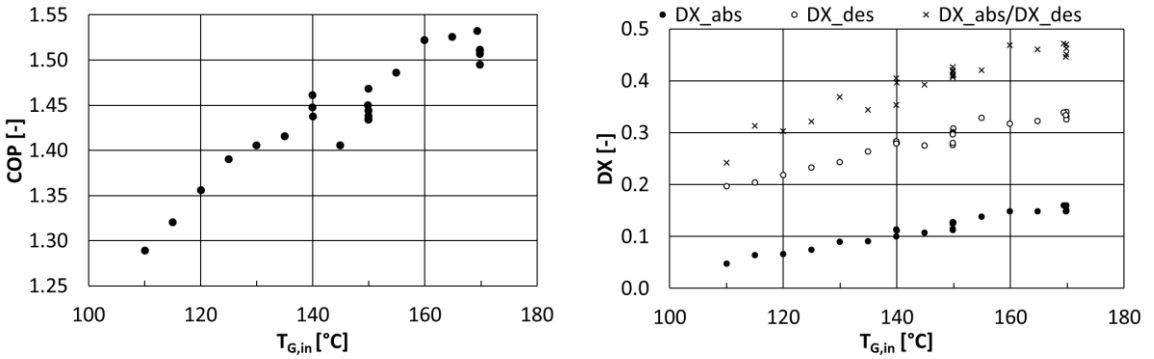


(a) Heating capacity (b) Mass flow of the refrigerant flow and the temperature glide

Fig. 6: Rich solution flow variation impact on different parameters with Tg,in=169.8°C, Ta,in=29.4°C, Te,in= 34.5°C.

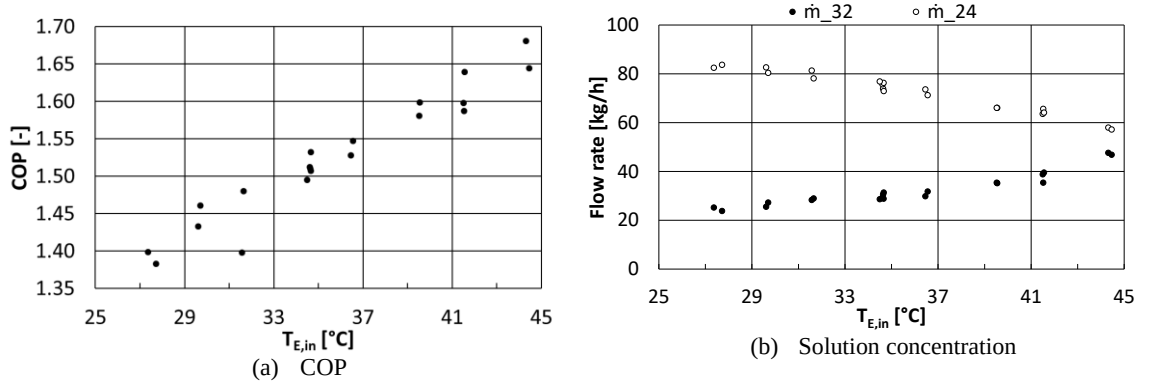
5.2.2. Generator temperature variation

The inlet temperature of the hot fluid at the generator is a relevant parameter because a flexibility in this sense would allow an easier management of the energy source and an increased working period. For a given solution flowrate, absorber temperature and evaporator temperature, Fig. 7(a) shows a COP increase with the generator temperature. This is in line with the observations about ammonia concentration in the solution. Indeed, increasing the temperature lead to increases in the capacities of absorption and desorption represented by $DX_{abs}=X_{12}-X_{24}$ and $DX_{des}=X_{12}-X_{22}$. In the order of magnitude, the heat production in the absorber and condenser is linked to DX_{abs} while the heat consumption in the generator is linked to DX_{des}. Therefore, the ratio between DX_{abs} and DX_{des} would represent the performance. As shown in Fig. 7(b), its tendency with the generator temperature is in agreement with that of the COP.



(a) COP (b) DX

Fig. 7: Generator temperature variation impact on different parameters with Ta,in=29.4°C, Te,in=34.6°C, MSR=106 kg/h.



(a) COP (b) Solution concentration

Fig. 8: Evaporator temperature variation impact on different parameters with $T_{a,in}$=29.4°C, $T_{g,in}$=169.8°C, M_{SR}=106kg/h.

5.2.3. Evaporator temperature variation

The inlet evaporator temperature is representative of the low-temperature source that feeds the cycle. However, it is not necessary the ambient that would provide the input heat: for example, low-temperature waste heat could be used for this task, with positive effects on the cycle performances.

According to the expectations, increasing $T_{e,in}$ leads to a better COP, as illustrated in Fig. 8(a). In particular, if the refrigerant evaporation can occur at higher temperatures, then higher pressures are allowed in the low-pressure side of the system. Operating at higher pressure is advantageous for the absorption reaction, as the equilibrium ammonia fraction of the rich solution increases with the pressure. As a result, the vapour generation flow rate ($\dot{m}_{32}$) increases with the evaporator temperature (while the poor solution mass flow rate $\dot{m}_{24}$ decreases due to a fixed pump flow rate), as shown in Fig. 8(b), leading to higher COP.

6. Conclusions

This paper presents a new architecture GAX NH3-H2O absorption heat pump designed with plate heat exchangers in order to offer a compact machine easy-to-manufacture. An innovative architecture has been proposed with the particularity of using an internal heat exchanger (GAX1) at two level of pressure: in one side, absorption occurs at low pressure and the heat produced is transferred to other side where the desorption at high pressure can be initiated. The desorption process is internally carried out by heat recovery in the rectifier and the solution heat exchanger (GAX2). A model has been developed for design and preliminary performance simulations. Based on the numerical results, a prototype has been built with a production target of 25 kW of hot water (> 60°C) from a lower-temperature heat source of around 30°C. Once the values of the regulation parameters are identified, the startup of the machine can be easily operated with a necessary time of about 400s for reaching stabilization. At nominal conditions, the machine produces a thermal coefficient of performance (COP) of 1.52 and an electrical coefficient of performance (ECOP) of 130. In favourable conditions, the maximum COP and power output are 1.72 and 32 kW, respectively. The tests show the capacity of the machine to operate in a wide range, especially in term of the inlet temperature of the heat driving source from 110°C to 170°C, which is interesting to address different applications with a flexibility in term of heat source temperature.

Nomenclature

			Subscripts	
C_P	Specific heat	[J/kg.K]	A	Absorber
DX	Concentration difference between rich and poor solution	[-]	abs	absorption
DT	Temperature glide	[K]	C	Condenser
h	Enthalpy	[J/kg]	des	desorption
ṁ	Mass flow	[kg/s]	el	electric
P	Pressure	[bar]	E	Evaporator
Q	Heat exchange rate	[W]	G	Generator
T	Temperature	[K]	in	input
x	Ammonia concentration	[-]	out	output
W	Work	[W]	sat	saturation
			sp	poor solution
			sr	rich solution
			v	vapour
Acronyms				
COP	Coefficient Of Performance	[-]		
ECOP	Electrical coefficient of performance	[-]		

Acknowledgements

The authors would like to express their gratitude to the French Alternative Energies and Atomic Energy Commission and the Auvergne-Rhône-Alpes region for the financial support.

References

[1] Sun J., Fu L. & Zhang S. A review of working fluis of absorption cycles. Renewable and sustainable energy review, Vol. 16, pp. 1899-1906, 2012.
[2] Aprile M., Scoccia R., Toppi T., Guerra M. & Motta M. Modelling and experimental analysis of a GAX NH3-H2O gas-driven absorption heat pump. International journal of refrigeration, Vol. 66, pp. 155-155, 2016.
[3] Dai E., Lin M., Xia J. & Dai Y. Experimental investigation on a GAX based absorption heat pump driven by hybrid liquefied petroleum gas and solar energy. Solar Energy, Vol. 169, pp. 167-178, 2018.
[4] Wang J., Wu W., Shi W., Li X. & Wang B. Experimental investigation on NH3-H2O generator-absorber heat exchange (GAX) absorption heat pump. Energy, Vol. 185, pp. 337-349, 2019.
[5] Herold K. E., Radermacher R. & Klein S. A. Absorption Chillers and Heat Pumps. CRC Press, 1996.
[6] Ibrahim O.M. and Klein S.A. Thermodynamic Properties of Ammonia-Water Mixtures. ASHRAE Trans.: Symposia, Vol. 21 (2), pp. 1495-1502, 1993.
[7] Wirtz M., Stutz B., Phan H.T. & Boudehenn F., Numerical modeling of falling-film plate generator and rectifier designed for NH3-H2O absorption machines. Heat and Mass Transfer, Vol. 58, pp. 431-446, 2021.

14th IEA Heat Pump Conference
15-18 May 2023, Chicago, Illinois

Industrial heat pumps: electrifying process heat supply in the United States through technology demonstration and market transformation actions

Paul Scheihing[a*], Andrew Hoffmeister[b] Ed Rightor[c], and Riyaz Papar[d]

[a]50001 Strategies LLC, Otis, Maine, USA, paul.scheihing@50001strategies.com
[b]ACEEE, Washington, D.C., USA, ahoffmeister@aceee.org
[c]Information Technology and Innovation Institute, Washington, DC, USA, erightor@itif.org
[d] C2A Sustainable Solutions, The Woodlands, TX, USA, rapapar@c2asustainable.com

Abstract

Industry accounts for almost a quarter of the energy use world-wide and energy-related carbon dioxide (CO_2) emissions. Industry has several pathways to step-change GHG reductions including electrification of process heat, which is responsible for 50% of on-site energy use. Industrial heat pumps (IHPs) can beneficially electrify much of the process heat needed for low to moderate temperature applications, helping to make dramatic cuts in industrial GHG emissions. Our research shows that moderate IHP deployment in industrial groups with high process heating demands (e.g., pulp and paper, chemicals, and food manufacturing) can save up to 30% of the source energy or 221.6 petajoules/year (equivalent energy use/year of 1.5 million U.S. homes). In parallel, IHPs can reduce CO_2 emissions up to 18.2 million metric tons /year (equivalent emissions from 4 million passenger cars or 1.3% of U.S. industrial CO_2 emissions). Expanded adoption of IHPs across all industrial sectors would save even more energy and CO_2 emissions.

© HPC2023.
Selection and/or peer-review under the responsibility of the organizers of the 14th IEA Heat Pump Conference 2023.

Keywords: Energy; Industrial heat pumps; Sustainability; GHG reductions; Beneficial electrification, pinch analysis.

1. Introduction

The industrial sector, which accounts for almost a quarter of the world's greenhouse gases (GHGs) and energy use (including feedstocks) must be decarbonized in order to transition the economy towards a low-carbon future. One crosscutting industrial decarbonization pathway that has been under-explored is the electrification of process heat, the generation and use of which in U.S. industry accounts for 51% of on-site energy use at 7992.7 petajoules (PJ) (or 7,576 trillion Btu/year) (EIA 2014). The potential for electrification to transform the GHG footprint of process heat is significant, as electricity currently accounts for only 5% of this heat, while carbon intensive fossil fuels combine for the rest (Whitlock et al., 2020).

Industrial heat pumps (IHPs) are a key technology for industrial decarbonization through electrification (Whitlock et al., 2020). Using electricity generated from low-carbon sources, they can provide adequate supply temperatures of process heat to replace reliance on fossil fuels in industrial processes. IHPs were being commercialized in the late 90s (IEA 1995), but the availability of inexpensive natural gas in the U.S. cut into economic favorability, and adoption stalled. The urgency of the climate crisis and advancements in IHP technology (some IHP types can now reach 160° C (320° F), more than double the supply temperature of earlier models), make them a logical decarbonization pathway. In addition to electrifying process heat, IHPs can also reduce industry's carbon footprint by improving efficiency (by avoiding complex, unbalanced and inefficient steam operating systems) and reusing or recovering wasted low temperature heat.

Although there are multiple studies examining IHP potential, there is a significant gap in the analysis of actual process heating and cooling streams at the unit operations level. Our research aims to bridge this gap by

* Corresponding author. E-mail address: paul.scheihing@50001strategies.com

examining the IHP market and demonstrations in varied industrial settings and geographical regions; matching capability fit with industrial needs via thermal energy analysis; determining the potential to reduce energy and GHGs; and finding enablers (including federal policy) needed to accelerate overall adoption.

2. Industry Processes and Heat Pumps

2.1. Process heat and thermal ranges of interest for IHPs

Figure 1 shows the temperature ranges of process heat demand in various industrial subsectors. Process heat is used in numerous applications that are common across these industry groups including fluid heating, distillation, evaporation, drying and melting. The temperature range of current IHP capabilities is between 60 and 160˚C.

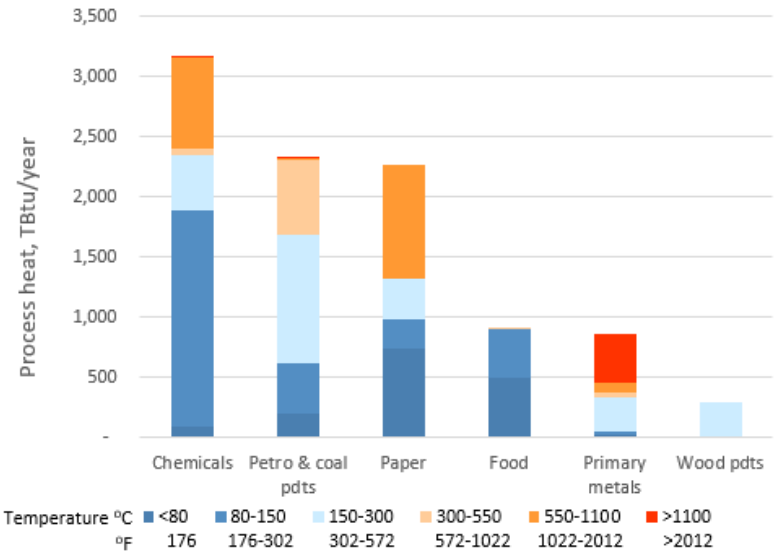


Fig. 1. Process heat demand at various temperature (°C) levels in select industries. Adapted from Adapted from "Manufacturing Thermal Energy Use in 2014," by C. McMillan, 2019, *National Renewable Energy Laboratory*

2.2. Industrial heat pumps

IHPs move heat up from a lower temperature heat source to a higher temperature heat sink. IHPs are similar in concept to residential/commercial heat pumps, however, they are more complicated, larger in capacity, engineered to integrate with industrial processes and expected to run continuously all-year round (high reliability). Figure 2 is a generic diagram of an IHP lifting waste heat at T_{source} and delivering heat to the process heat load at T_{sink}.

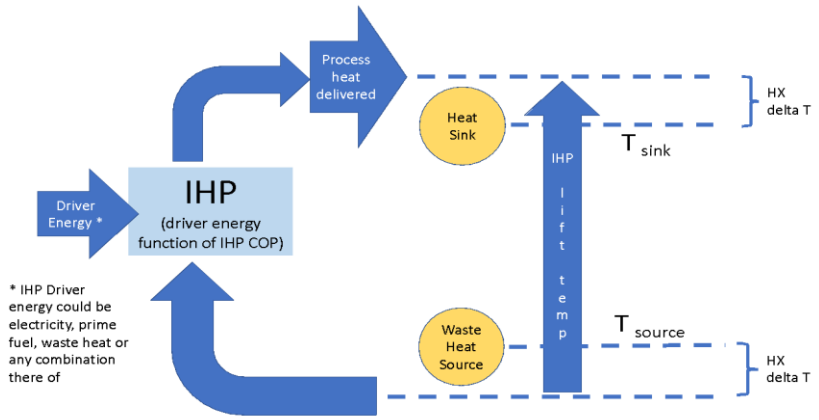


Fig. 2. Generic IHP diagram illustrating IHP lift temperature, T_{source} and T_{sink}. Source: this work

Our research examined six types of IHPs (more detail on their applications, data sources, and data treatment is provided below) (Rightor et al., 2022a). IHPs can be open cycle (where the heat pump working fluid is the process stream itself, such as, waste steam being compressed and returned to process) and closed cycle (where the heat pump has a heat exchanger on the heat source and sink sides to separate the heat pump working fluid from the processes). A classification of IHPs is provided in Figure 3.

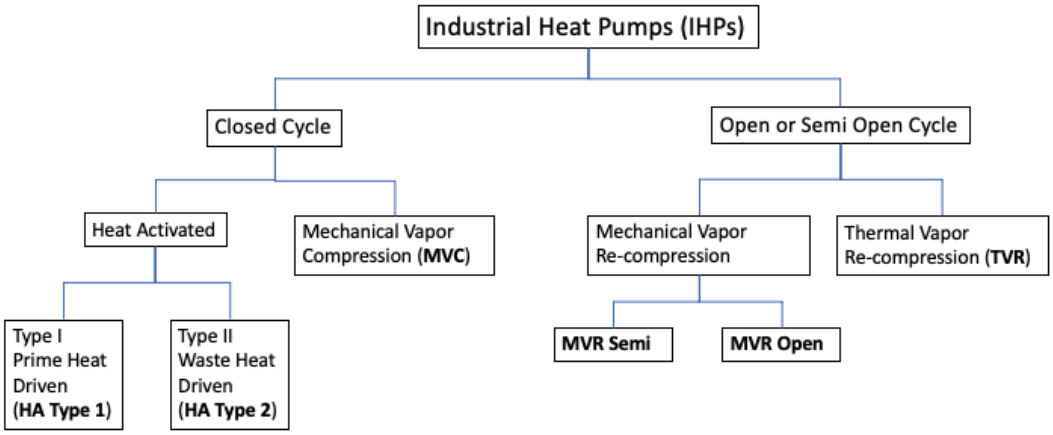


Fig. 3. Six different IHP types considered in this study (EPRI & RCG Hagler Bailly Inc., 1994). Adapted from "Industrial Heat Pump Report," by EPRI & RCG Hagler Bailly Inc, 1994.

The most common type of IHP is a mechanical vapor compression (MVC) heat pump which is a closed cycle system with an evaporator and condenser heat exchanger. Mechanical vapor re-compression (MVR) heat pumps are also applied in industry. MVRs directly compress the process fluid or steam without heat exchange on the heat sink or source side (semi-open cycle) or have no heat exchange (open cycle) on either side of the heat pump's compressor. Note: see appendix A of reference (Rightor et al., 2022a) for explanation of IHP types that were analyzed.

Prior studies show that moderate deployment of IHPs in manufacturing could avoid emissions of 12-25 million tons/year of CO_2 and save 2-5% of the total U.S. industrial process heat demand 180-370 PJ (or 170-350 trillion Btus/year) within 15 years (EPRI & RCG Hagler Bailly Inc., 1994). Advances in refrigerants (McLinden et al., 2014) and other working fluids to operate at higher delivery temperatures have broadened the range of IHP applications, such as in drying and recovery of waste heat, which can account for 12- 25% of industrial energy use (Lauermann et al., 2019). The market for IHPs is well-developed in Europe and Japan (Arpagaus et al., 2018), where there are strong policy incentives and economics. A recent study of the IHP potential in Europe indicates that 80% of the IHPs in industry would be less than 5 MW in thermal load capacity (Marina et al., 2021). Recent IHP demonstrations include those at 1 – 2 MW (Borealis, 2021).

2.3. Pinch analyses

Pinch analyses were used to find the optimum location for IHPs in the thermal flows of industrial processes (Rightor et al., 2022a). Pinch analysis is a method for minimizing energy consumption by optimizing energy supply and process heat recovery systems (Natural Resources Canada, 2003). It identifies the best hot streams which are being cooled (heat source) and cold streams which need to be heated (heat sink) for the heat pump to operate between heat source and sink. The Pinch analysis optimizes the heat transfer process between the hot and cold streams to minimize the amount of external process heating and cooling needed. This leads to defining a "pinch point" on the temperature scale in the whole process where heat transfer cannot occur anymore between the hot and cold streams since the temperature driving force required is not available. The ideally placed and integrated IHP takes heat from a heat source below the pinch point and upgrades or "lifts" the heat to a desired heat sink above the pinch point. An energy balance must be maintained between the heat source, heat sink, and the work done by the IHP. Optimal matching of the heat source temperature and the amount of heat required is the key to successful IHP implementation. If done efficiently, heat exchangers can be minimized, particularly above the pinch point.

Figure 4 shows an example of two pinch analysis simulations for a typical potato drying process. The x-axis shows the heat load (kW), and the y-axis shows the corresponding temperature levels for those heat loads. The blue lines represent the cold stream that needs to be heated and the red lines represent the hot stream that is being cooled. The overlap between the red and blue lines is the area of possible heat exchange. The difference between the cold stream heat load and the hot stream heat load, noted by the arrow in the upper right, represents the process heat demand which must be supplied by external sources (steam, direct firing) and is designated as Q_{hot}. The main goal of applying an IHP is to cost-effectively reduce Q_{hot} to the minimum possible amount. Figure 4 (left) shows the baseline case. Note the process heat demand of 3,725 kW and the pinch temperature at about 52°C. Figure 4 (right) shows the same process but with the application of an IHP used in an optimized configuration. Note that the process heat demand has been reduced to 2,314 kW and the pinch temperature has also moved up to about 70°C.

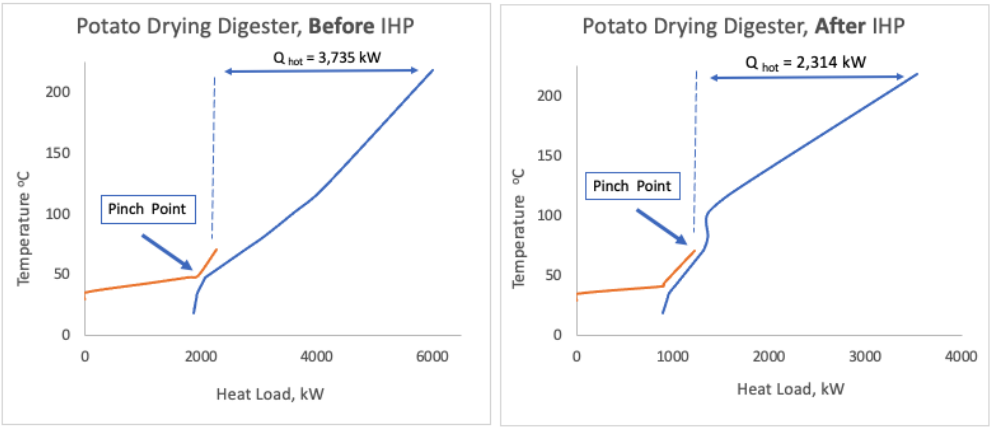


Fig. 4: Comparison of pinch analysis between the hot & cold composite curves for potato drying, with left being **Before** and right **After** the IHP installation. Source; this work.

3. IHP analysis

3.1. Industrial groups and unit operations analyzed.

The industrial groups and unit operations analyzed in this work are shown in Table 1 (Rightor et al., 2022a).

Table 1. Industrial groups and unit operation analyzed.

Industrial group	Unit operation
Paper	Pulp mill (PM)– digestor
	Pulp mill (PM)– multi-effect evaporator
	Non-integrated paper mill – pulper
Food	Wet corn milling (WCM) – steepwater
	Wet corn milling (WCM) – high fructose corn syrup starch conversion
	Potato processing – hot air dryer
Chemicals	Ethylene (above ambient) – process water stripper reboiler and debutanizer
	Ethanol fuel, dry mill

3.2. Industrial heat pump analysis approach.

All industrial process models used actual industrial heating and cooling stream data (ie., mass flow rate, specific heat and temperature increase or decrease for each stream) that was provided by Chalmers University from previous research (Franck et al., 2020). To assess the energy savings potential, we estimated both the "Economic" and "Technical" IHP potential. The Economic potential simply used one hot and one cold stream for the heat pump's heat source and sink. The IHP lift was limited to less than 40° C, which is within the capability of a single-staged compression IHP. The Technical potential case is more aggressive by using multiple heat sources and sinks at varying temperatures. Multiple staging of heat pumping (2 stages) were possible for the Technical case and the hot and cold streams were not limited to constant temperatures (Rightor et al., 2022a). Figure 5 illustrates the differences between the Economic and Technical IHP potential.

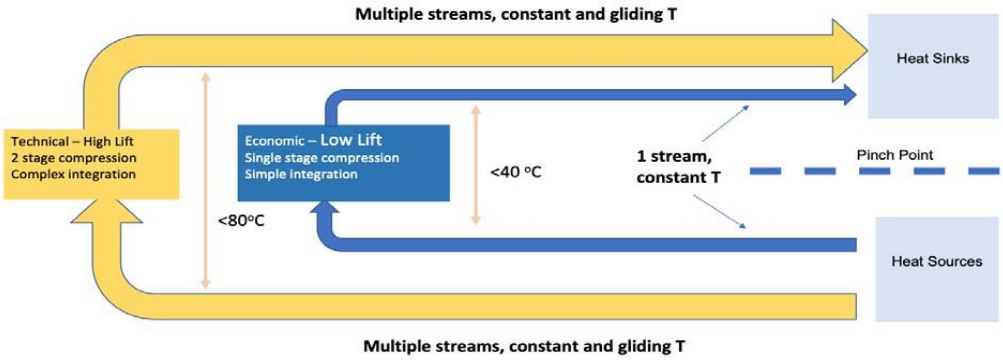


Figure 5. Economic and technical IHP potential energy savings

Energy savings across any sector were calculated based on the assumption that all U.S. production was impacted by heat pumping. Table 2 shows the overall approach to analyzing the energy savings and carbon reduction for the sectors shown in Table 1. The analysis progresses left to right: sector process analysis to pinch and heat pump analysis to sector energy savings and carbon emission analysis.

Table 2 – Heat pump analysis methodology to determine sector energy savings and carbon reduction.

Sector Process Analysis	Pinch and Heat Pump Analysis	Sector Energy Savings and Carbon Emissions
Overall U.S. sector production (tons product/year)	Process specific heating and cooling stream data – enthalpy and temperature for multiple streams	Apply heat pump unit operation savings for six IHP types across all sector facilities
Sector - # U.S. facilities with similar production	Pinch analysis of heating and cooling streams to identify streams (source/sink) for heat pumping	Calculate site and source energy savings based on natural gas saved and heat pump driver energy requirement for all 6 IHP types
Sector total process heat demand (GJ/year)	Calculate heat pump energy savings for 6 different IHP types	Calculate overall sector carbon emission reductions based on natural gas saved and heat pump driver energy type requirement for all 6 IHP types
Sector total carbon emissions (MMTCe/year)	Determine heat pump driver energy requirement for 6 IHP types – GJ and energy type (electricity, heat)	
Process heat unit operation hot utility targetable by IHP (GJ/ton)	Calculate heat pump energy savings on unit operation (site and source)	

The Pinch analysis model determined the amount of thermal energy recoverable by heat pumping relative to the overall process heat supplied. This represented the amount of thermal energy savings that was possible with the application of the heat pump. The actual percentage energy savings varied by heat pump type (Table 3 below shows results for MVC heat pump only) because different heat pump types could capture different amounts of waste heat (source) relative to the heat delivered (sink). Table 3 shows this as natural gas savings (%). Additionally, the different heat pumps have different COPs for the given lift temperature, and this results in different amounts of heat pump driver energy required. Table 3 below shows this as electricity increase (%). Therefore, unit operation natural gas savings for each heat pump type was found by multiplying tons of production for sector by production energy per ton and then by natural gas savings (%) per ton. Similarly, unit operation electricity increase for each heat pump type was found by multiplying tons of production for sector by production energy per ton and then by electricity increase (%) per ton.

Energy savings across any sector were calculated based on the assumption that all U.S. facilities making the product were impacted by heat pumping. This can be considered an upper estimate at 100% market penetration. While this may be a high estimate it should be noted that dual heating and cooling IHP opportunities were not yet included and the benefits of downsizing the process heat load from current steam systems (e.g., oversized boilers, steam losses) were not accounted for.

3.3. IHP summary across all industrial groups and unit operations studies

Results for IHP application across all industrial groups and unit operations studied are summarized in Table 3 (Rightor et al., 2022b) for the MVC IHP case. The simple payback was based on natural gas prices of

$6.86/ billion joules (or $6.5/MMBtu) and electricity price of 6 cents/kWh.

Table 3. Summary of results across all unit operations for the MVC IHP. Source: this work.

		Natural gas savings		Electricity increase		CO_2 decrease		Simple payback
Industry group	Unit operation	PJ/ year	%	MM kWh/ year	%	MMTCe/ year	%	years
Food	Potato drying	6.0	40.4	962	11.2	0.4	24.3	4.5
	WCM steepwater	2.1	20.4	128	5.5	0.1	1.2	3.7
	WCM, high fructose corn syrup	3.3	75.8	173	17.9	0.1	1.9	4.4
Paper	PM Digester	40.4	34.6	2,384	9.2	1.0	21.7	4.2
	PM multi effect evaporator	90.4	45.1	4,169	9.4	2.6	34.5	3.8
	Non-Integrated mill pulper	3.3	9.3	197	2.5	0.1	5.7	2.5
Chemicals	Ethylene debutanizer	5.3	18.4	6	3.4	0.2	15.1	1.9
	Ethylene water strip reboiler	1.3	9.8	66	2.2	0.0	7.0	2.2
	Ethanol fuel, dry mill	260.4	90.0	10,313	16.0	8.2	52.0	1.9
	Total	**422.1**		**18,398**		**12.6**		

Across all industrial groups and unit operations the total source energy savings are shown in Fig. 6. This plot shows that the total source energy savings is significantly higher for the Technical potential cases as expected given the more extensive application of IHPs assumed. Although lower energy savings are shown for the heat activated (HA) IHP types, it's expected that greater use of waste heat in the future will be enabled by heat-activated heat pumps since they can lift heat over higher temperatures without the penalty of high electricity operational costs. The MVR-Semi Open and MVR-Open IHPs each show higher energy savings improvement over the MVC heat pump, reflecting the fact that not requiring one (Semi-Open) or two (Open) heat exchangers to capture waste heat vapors yields higher heat pump COPs (e.g., high pump lift temperatures are lower than for the MVC type). The elimination of heat exchange translates into overall source energy savings.

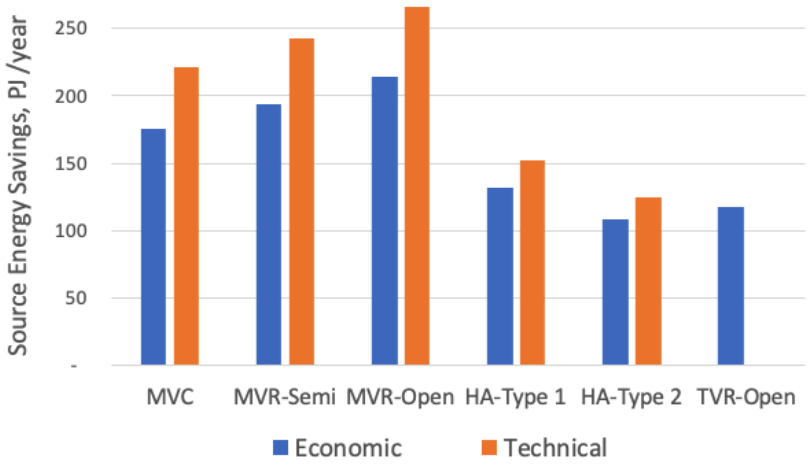


Fig. 6. Summary of source energy savings for all nine unit operations combined. Source this work.

While the IHPs save natural gas, electricity is required to run the compressors for the MVC, MVR Semi Open and MVR Open heat pumps. The heat-activated heat pumps (HA-Type 1 and HA-Type 2) do require less electricity than the MVC, MVR Semi Open and MVR Open heat pumps, but their COPs are lower and thus the thermal energy (natural gas) savings are lower.

3.4. Magnitude of energy and GHG reductions

Figure 7 shows the magnitude of the energy changes for natural gas and electricity usage for all nine unit operations analyzed. The increased electric load is shown to the right of the y-axis, and the natural gas reduction is shown to the left. Looking at the MVC, MVR-Semi, and MVR-Open types, the natural gas savings are similar, but the electricity demand decreases in this order. For the MVC (closed cycle), electricity is used

to compress refrigerant vapors, and there are heat exchangers at both the source and sink so the heat pump lift will be higher requiring additional electrical energy. The MVR Semi Open eliminates one heat exchanger and the MVR Open two heat exchangers, so the lift is lower resulting in lower electricity needs. The HA types require much lower amounts of electricity since they pump liquids and do not compress vapors but their lower heating COP vs. vapor compression heat pumps yield lower net energy savings.

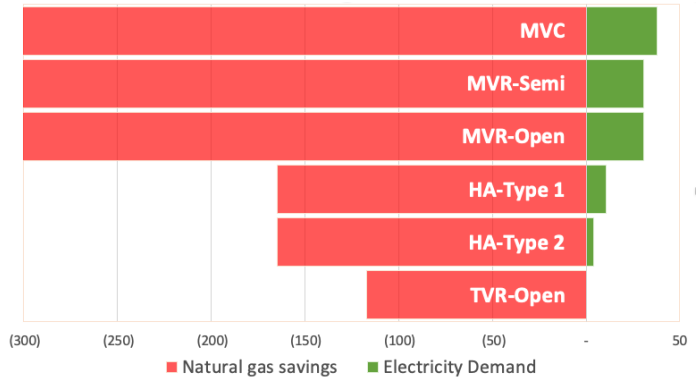


Fig. 7. Energy changes across all nine unit operations, Economic case, PJ/year. Source: this work.

Figure 8 shows the changes from a carbon perspective, where it's evident that the increase in carbon emissions from electricity (right, green) is significantly less than carbon emissions reduction from the decrease in natural gas use (red, left), indicating an overall net decrease in CO_2e emissions. As the electric grid incorporates more low-carbon energy and the emissions factors decrease, the carbon emissions footprint for electricity will also decrease, and the difference between the electricity and natural gas bars will become larger for the MVC types (as the electricity to run the compressors will have a lower carbon intensity).

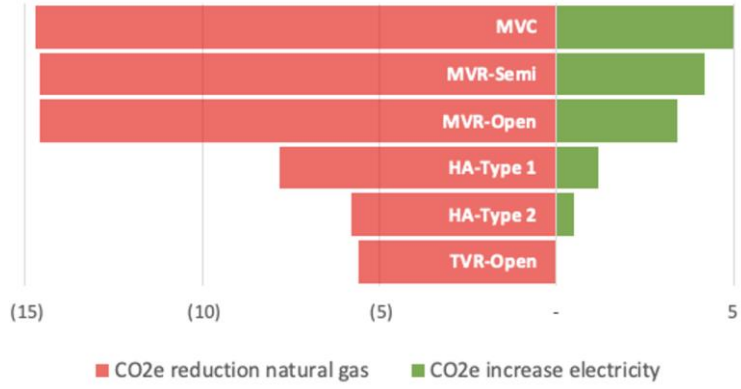


Fig. 8. Changes in CO_2e across all nine unit operations, Economic case, in millions of metric tons CO_2e/year. Source: this work.

3.5. Scale of impact

There can be multiple unit operations for each process considered in this work, so it can be challenging to understand the scale of impact. For example, the ethylene debutanizer and the process water stripper reboiler were examined for IHP potential, but these operations are a small portion of those in ethylene production and only the unit operations above ambient were considered in this work (e.g., no analysis was performed in the cold section). An estimate was made then for the application of IHPs not only in the nine unit operations analyzed but also an extrapolation across a broader application base in the three industrial groups examined. Table 4 summarizes the results for the nine unit operations analyzed in the 3 industrial groups, as well as the Industrial group-wide adoption extrapolation for natural gas, source energy savings, electricity demand increase and carbon reduction —near and long-term (when more low-carbon generation capacity decreases emissions factors for the electric grid).

Table 4. Energy savings and carbon reduction for IHP applications. Source: (Rightor et al., 2022a)

Unit Operations analyses only*	Food, min.	Food, max.	Paper, min.	Paper, max.	Chemicals	Total, min.	Total, max.
Natural gas savings, PJ/year	6.0	21.1	36.3	134.1	267.0	309.3	422.0
Source energy savings, PJ/year	2.9	7.5	20.1	61.2	152.6	175.6	221.6
Electricity consumption, MM kWh/year	288.0	1263.2	1500.0	6750.3	10595.4	12383.3	18609.0
Electricity demand increase, MW	32.9	144.2	171.2	770.6	1209.5	1413.6	2124.0
Heat pump output, MW	152.6	535.3	921.9	3402.8	6773.1	7847.6	10711.0
CO_2 savings, near term MTCe/year	0.20	0.50	1.10	3.70	8.40	9.7	12.6
CO_2 savings, long term MTCe/year	0.30	0.90	1.60	5.70	11.60	13.4	18.2
Sector-wide projection							
Natural gas savings, PJ/year	21.1	76.0	50.6	188.8	721.6	793.4	986.4
Source energy savings, PJ/year	10.2	26.8	28.1	86.2	412.3	450.4	517.9
Electricity consumption, MM kWh/year	1010.5	4547.8	2090.3	9504.1	28639.2	31761.0	43498.5
Electricity demand increase, MW	115.3	519.2	238.6	1084.9	3269.3	3625.7	4964.9
Heat pump output, MW	535.3	1927.1	1284.7	4791.0	18307.7	20127.7	25037.0
CO_2 savings, near term MTCe/year	0.7	1.8	1.5	5.2	22.7	24.9	29.5
CO_2 savings, long term MTCe/year	1.1	3.2	2.2	8.0	31.4	34.4	42.5

* PJ = petajoules, MM = millions, Ce = carbon equivalents for CO_2, M =1000, kW = kilowatts

4. IHP Deployment and Market Transformation

4.1. IHP Demonstrations

The next phase of our research includes IHP demonstrations where we are partnering with several utilities and a state research energy agency. Demonstrations aim to remove the technical risk, demonstrate IHP energy performance and economics in a variety of sectors and common industry processes. Evaluation factors in choosing at least 3-5 IHP demonstrations that will enable accelerate U.S. IHP deployment, include the following:

- Significant energy saving and GHG emission reduction potential in the currently available temperature range and IHP lift temperature required (e.g., <120° C heat sink range and <40° C lift) and thus favorable economics (e.g., < three-year payback)
- Widespread replicability potential within a sector or sectors due to common unit operation or process across the sector which minimizes technical risk.
- High replicability with a standard IHP designs that minimize significant site-specific engineering (e.g., fuel ethanol, alcoholic beverage, wet corn milling, lumber drying)
- High value product where non-energy benefits (better temperature control, lower maintenance costs, improved yield) are significant in addition to the energy saving benefits (e.g., applications in pharmaceutical, food & beverage.)

We are working with our regional utility and state energy agency partners and their customers to identify other good IHP candidates. Industrial sectors to pinpoint as good candidates for IHP application include the nine unit operations from our research (Rightor et al. 2022a), 13 industrial sectors and subsectors identified from another recent IHP study (Zuberi et al., 2022), and those highlighted by our regional partners with input from their industrial customers. Those high potential sectors include beer brewing, wet corn milling, high fructose corn syrup, lumber drying, paper drying, ethanol, ethylene, automotive processes, and metal manufacturing processes, among many others.

4.2. Regionality

The payback estimates above (Table 2) demonstrate that for the MVC and MVR IHPs with natural gas at $6.86/ billion joules (BJ) (or $6.5/MMBtu) and electricity at 6 cents/ kWh, the paybacks range from 2 to 4 years, which is considered economical for U.S. industry. This is a ratio of approximately 2.7 with electricity/natural gas price. Figure 9 shows the many U.S. states where the ratio of electricity/ natural gas is near that number (note data used was 2021 industrial rates). There could be early IHP adoption opportunities in those states.

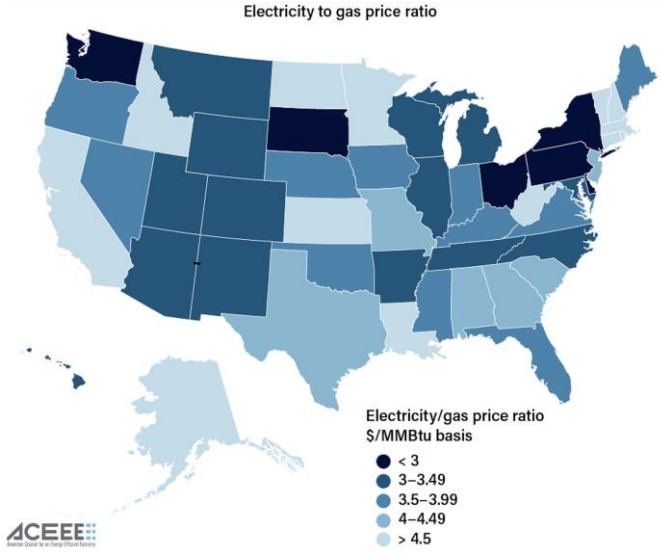


Fig. 9. Illustration of electricity/ gas price ratio by state. Source: this work. .

4.3. IHP market barriers

The barriers to IHP adoption must be identified and considered to form an effective market transformation strategy for IHP deployment that is scaleable throughout U.S. industry. IHPs are currently a niche product today in the U.S. market due to a variety of market constraints. The major constraints that a market transformation initiative will need to address are:

- *Limited product availability in North America:* A recent survey of IHP suppliers found that 24 of them were headquartered and manufactured in Europe and another 3 based in Japan (Arpagaus, 2022; IEA, 2022). Although, there are a few U.S.-produced products that center on industrial applications (mainly wood products and process heat as a service). IHPs are large products that can be expensive to ship so in order for a large IHP market to grow in the U.S., more products will need to be produced in North America. Additionally, European, Japanese and non-U.S. domestic IHP suppliers will need to modify their designs to account for U.S. code differences (heat exchangers, electrical service rating, etc.). IHP equipment manufacturers need to see sufficient market demand to justify both marketing of their products and/or investment to scale up North American production.
- *Limited knowledge by industrial decision-makers and engineers:* Most industrial decision makers are not familiar with IHPs and even many engineering firms have limited knowledge. Experienced engineers can optimize systems in ways that reduce system size and costs while providing important operating benefits, but most engineers presently lack this awareness, expertise, and experience. Many industrial applications cannot simply implement a one-size-fits-all solution so may require tailored system designs.
- *Economic challenges:* The economics of IHPs not only depend on the relative cost of electricity and natural gas, but also on the electric rate structures (e.g., demand and interconnection charges). Site specific timing and considerations are important. Strategies are needed to focus on the applications with the best economics, provide the tools to help manage project costs, and realize the greatest non-energy benefits for the process changes.
- *Service and maintenance:* Personnel to service and help maintain equipment are in limited supply and are often not local to the plants, risking extended production outages. More staff need to be trained and service infrastructure scaled up in parallel with expanding installations to support these projects in the field.

- *Electrical service capacity increase limitations:* U.S. industry is experiencing limitations on how much and/or how fast they can expand the amount of electric supply they can accommodate in their facilities due to long lead times by electrical equipment suppliers to increase electrical capacity. IHPs will require a substantial change in electricity capacity in facilities and could be limited by electrical service available.
- *Equipment certification:* IHPs made abroad haven't been through Underwriters Laboratory (UL) listing. Also, building code challenges exist for using some low-global warming potential, or regulations on using refrigerants that are potentially flammable.

4.4. Strategies to initiate market transformation.

The following strategic near-term actions could help to propel the manufacture and implementation of IHPs in the U.S.:

- *Support manufacturers to scale-up domestic availability of equipment:* Activities to expand domestic product offerings and bring manufacturing to the U.S., such as, government financial incentives to grow manufacturing for IHP technologies and components.
- *Coordinate with utilities, regulators, large customers, and federal agencies to foster a market for substantial growth in IHP sales:* Collaboration amongst the key IHP stakeholders to support technology demonstrations and education of large customers is critical. For example, U.S. Department of Energy announced the Industrial Heat Shot initiative in September 2022 (DOE Industrial Heat Shot, 2022) to drastically reduce emissions from the energy-intensive process heating applications. Industrial heat pumps can play an important role, as was identified in the recent DOE Industrial Decarbonization Roadmap (DOE, 2022).
- *IHP demonstrations, information and tools:* Support the identification, design, installation and validation of performance on IHPs in varied industrial applications with case studies documenting the cost-benefits of each demonstration.
- *Create awareness, knowledge, and workforce:* A communication campaign needs to be developed and deployed to raise the awareness of IHP technologies and benefits among utilities, engineering firms, service personnel and large customers. Training of engineering firms and service personnel needs to be delivered to build IHP related skills.
- *Work with utilities and regulators to develop rate structures in support of IHP:* Rate structures that incentivize IHP installation and yet fairly recovers the utility's fixed costs.
- *Tax incentives and low interest loans:* Federal tax credits for industrial end users to purchase IHPs and low interest loans for IHP equipment manufacturers to establish and/or expand IHP manufacturing capacity would further help to grow the U.S. IHP market.

5. Summary

IHPs can significantly improve the energy efficiency of process heating and cooling applications and reduce CO_2 emissions across the industrial sector. The sectors with applications that are most applicable for IHP implementations are pulp and paper, food and beverages manufacturing, and the chemicals industry, where there are significant proportions of process heating needs at low-moderate temperatures (60 to 200° C). Barriers must be overcome including economics, technical risk, integration, and development of local service capabilities. Enabling policies and programs by government and utilities would accelerate IHP adoption. IHPs can be a key technology in aiding beneficial electrification, with CO_2 reduction benefits increasing as the electric grid becomes less carbon intensive. Key learnings from our research include:

- IHPs were typically able to save 10 to 30% of the energy used for process heat generation.
- The vapor compression type IHPs natural gas savings were typically 2.7 to 3.7X the increases in electricity use . Similarly, the CO_2 reductions from natural gas savings were 3.5-4.7 X the CO_2 associated with electricity use. Simple paybacks for the compression type IHPs were near or under 3 years at a natural gas price of $6.86 /BJ when electricity/natural gas price ratio was 3 or less.
- Although the energy savings potential for heat activated type IHPs was lower than vapor compression heat pumps for the applications studied, as the technology advances these type of IHPs can potentially have greater impact due to their flexibility and ability to lift heat higher without the penalty of higher electricity consumption and cost as with vapor compression systems.
- Across all unit operations, the IHP analyses showed the potential to reduce process heat energy 309 - 422 PJs/year (42-57% of the process heat energy in the industrial groups). The potential for CO_{2e}

reductions was 25 - 29 million metric tons CO_{2e} /year. With lower emissions factors for grid produced electricity by 2050, the reductions potential would be 34 - 43 MMT CO_{2e} /year.

A variety of market transformation initiatives could be deployed to build the U.S. market for IHPs, including:

- Support manufacturers to scale-up domestic availability of equipment
- Coordinating with utilities, regulators, large customers, and federal agencies to foster a market for substantial growth in IHP sales.
- Supporting IHP demonstrations with validation and verification of the cost/benefits as well as developing more up-to-date process data and IHP analysis tools
- Creating awareness, knowledge, and workforce with comprehensive training at all levels.
- Working with utilities and regulators to develop rate structures in support of IHP.
- Creating tax incentives and low interest loans

Acknowledgements

The authors would like to thank Southern Company, New York State Energy Research and Development Authority, Tennessee Valley Authority, and Bonneville Power Administration, for their support of this research. We appreciate the advice given by Neal Elliott of ACEEE in shaping this paper. We would also like to thank Per Ake Franck (Chalmers University) for sharing process information on industrial processes and Ian Kemp (consultant, U.K) for guidance on use of the IChemE pinch analysis software. We are grateful to Cordin Arpagaus (Eastern Switzerland University of Applied Sciences) for sharing information on IHP technology, economics, and emerging capabilities, Jarrod Leak (Australian Alliance for Energy Productivity) for sharing a database of IHP case studies, and Benjamin Zühlsdorf (Danish Technological Institute) for sharing advances from the Annex 58 partnership on high temperature IHP capabilities.

Nomenclature

Acronym	**Definition**
Btu	British thermal unit
BJ	Billion Joules
CO_2e	Carbon dioxide equivalent
COP	Coefficient of performance
GHG	Greenhouse gases
HA	Heat activated (heat pump)
IHP	Industrial heat pump
KWh	Kilowatt hour
Lift	Lift is the magnitude of temperature, by which the IHP raises the temperature from T_{source} to T_{sink}
MMBtu	Millions of British thermal units
MT	Metric tonne
MMT	Millions of metric tons
MVC	Mechanical vapor compression
MVR	Mechanical vapor recompression
MW	Megawatt
PJ	Petajoules
Q_{hot}	Process heat demand which has to be supplied by external sources
RD&D	Research development and deployment
TBtus	Trillions of British thermal units
T_{source}	Temperature of the waste heat or heat source of the industrial heat pump to be lifted to the heat sink
T_{sink}	Temperature of the heat sink to be heated by the industrial heat pump
TVR	Thermal vapor recompression
WCM	Wet corn milling

References

Arpagaus, C. (2022). High-Temperature Heat Pumps for Industrial Applications – New Developments and Products for Supply Temperatures above 100 °C, *China Heat Pump Conference*.

Arpagaus, C., Bless, F., Uhlmann, M., Schiffmann, J., & Betsch, S. (2018). High Temperature Heat Pumps: Market Overview, State of the Art, Research Status, Refrigerant's, and Application Potentials, *Energy, 152* 985-1010.

Borealis Announces Start-up of Heat Recovery Unit Based on Revolutionary Qpinch Technology. (2021). https://www.borealisgroup.com/news/borealis-announces-start-up-of-heat-recovery-unit-based-on-revolutionary-qpinch-technology

Franck, Per-Ake. (2020). Pinch Analysis of Hot and Cold Stream Data for 140 Industrial Processes. *E-Sectionens Teletekniska Avdelnining (ETA).*

IEA Annex 58. https://heatpumpingtechnologies.org/annex58/task1

Industrial Decarbonization Roadmap. (2022). *U.S. Department of Energy [USDOE].* https://www.energy.gov/eere/doe-industrial-decarbonization-roadmap

Industrial Heat Pumps: Experience, Potential and Global Environmental Benefits. (1995). International Energy Agency [IEA], Heat Pump Centre.

Industrial Heat Pump Report. (1994). Electric Power Research Institute [EPRI] & RCG Hagler Bailly, Inc.

Industrial Heat Shot. (2022). *U.S. Department of Energy [USDOE].* https://www.energy.gov/eere/industrial-heat-shot

Lauermann, M., Wilk, V., Bantle, M., Sannan, S., & Schneeberger, A. (2019). DryFiciency: Waste Heat Recovery in Industrial Drying Processes, Interim Report on grant agreement 723576, *European Commission*.

Manufacturing Energy Consumption Survey. (2014). *Manufacturing Energy Footprint, U.S. Energy Information Administration [EIA]*. *https://www.eia.gov/consumption/manufacturing/*

Marina, A., Spoelstra, S., Zondag, H., & Wemmers, A. (2021). An Estimation of the European Industrial Heat Pump Potential, *Renewable and Sustainable Energy Reviews*, *139*. Task 1: Technologies – State of the art and ongoing developments for systems and components. (2020). https://doi.org/10.1016/j.rser.2020.110545

McLinden, M., Kazakov, A., Brown J., & Domanski, P. (2014). Thermodynamic Analysis of Refrigerants: Possibilities and Tradeoffs for Low-GWP Refrigerants, *Int. Jnl. Refrigerants, 38,* 80-92. https://doi.org/10.1016/j.ijrefrig.2013.09.032

McMillan, C. (1995). Manufacturing Thermal Energy Use in 2014, *National Renewable Energy Laboratory*. https://doi.org10.7799/1570008

Pinch Analysis: For the Efficient Use of: Energy, Water and Hydrogen. (2003). *Natural Resources Canada*. https://natural-resources.canada.ca/sites/www.nrcan.gc.ca/files/canmetenergy/pdf/fichier.php/codectec/En/2009-052/2009-052_PM-FAC_404-DEPLOI_e.pdf

Rightor, E., Scheihing, P., & Hoffmeister, A. (2022a). Industrial Heat Pumps: Electrifying Industry's Process Heat Supply report, *American Council for an Energy-Efficient Economy*. https://www.aceee.org/research-report/ie2201

Rightor, E., Scheihing, P., Hoffmeister, A., & Papar, R. (2022b). Industrial heat pumps: electrifying & optimizing industry's process heat supply, *International Conference on Efficiency, Costs, Optimization, Simulation and Environmental Impact of Energy Systems*.

Whitlock, A., Rightor, E., & Elliott, N. (2020). Transforming Industry: Paths to Industrial Decarbonization in

the United States, *ACEEE*. https://www.aceee.org/research-report/IE2001

Zuberi, J., Hasanbeigi, A., Morrow, W., & October. (2022). Electrification of U.S Manufacturing with Industrial Heat Pumps, Lawrence Berkely National Laboratory. https://eta.lbl.gov/publications/electrification-us-manufacturing

14th IEA Heat Pump Conference
15-18 May 2023, Chicago, Illinois

Industrial High Temperature Heat Pumps – Ongoing Research in the USA

Ammi Amarnath[a*], Baskar Vairamohan[a]

[a]Electric Power Research Institute, 3420 Hillview Avenue, Palo Alto, CA 94304. USA

Abstract

According to the U.S. Department of Energy, it is estimated that approximately 35% of industrial energy input for process heating is lost as waste heat in the form of exhaust gases, cooling water, and heat loss from product heating. The waste heat inventory in the industrial sector in the United States is estimated to be on the order of 1500–3000 trillion Btu per year [1.58 – 3.17 EJ]. The development and testing of a novel heat pump funded by the California Energy Commission in the United States is presented in this paper. This work effort is aimed at developing an industrial heat pump that can capture low-grade industrial waste heat (around 70 – 80°C) and transform it into high-temperature useful heat, specifically in the form of steam. The paper also discusses the use of a low Global Warming Potential (GWP) refrigerant (R1233zd (E)) that can provide a temperature lift of at least 40°C, thereby producing steam, with coefficient of performance (COP) greater than 3.4. Industries such as food processing, chemicals, paper and textile industries can make use of this steam.

© HPC2023.
Selection and/or peer-review under the responsibility of the organizers of the 14th IEA Heat Pump Conference 2023.

Keywords: Industrial heat pump; chemical industry; food industry; paper industry; steam production; waste heat recovery; industrial decarbonization.

1. Introduction to Industrial Decarbonization

Addressing climate crisis is in the limelight globally and almost every country in the world is on a path to decarbonize the buildings, transportation and industry. It is imperative that economy-wide decarbonization is the way to achieve carbon goals and meet the targets set forth in the 2015 Paris agreement and the electric power industry is leading the charge. Since 2005, the US reduced its carbon footprint by one gigaton, primarily by switching to cleaner fuels, expanding renewables and driving efficiencies. To get to the next gigaton, we need solutions to integrate and manage more low carbon energy generation: from distributed to utility scale solutions covering wind, solar, hydro and nuclear; to systems that help us optimize their output. According to a recent EPRI analysis, the annual U.S. emissions can be reduced by at least an additional 3 gigaton (Gt) from 2030–2050 (refer to Figure 1), consistent with an 80% drop since 2005, through strategic R&D focused on post- 2030 deployment of innovations for using clean electricity to capture a growing share of final energy markets. As efficient electrification accelerates, technologies for indirectly electrifying challenging end uses will emerge for deep decarbonization of all major energy sectors.

At the same time, electrification of the end use is a primary option for reducing direct emissions outside the electric sector, particularly in transportation but also in buildings and industry. Combining clean electric power and electrification can help bring about cost-effective decarbonization throughout the economy, although reaching economy-wide net-zero targets will likely require additional breakthrough technologies.

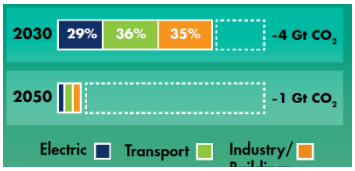


Figure 1 Emissions by US Energy Sector (Source: EPRI)

* Corresponding author. E-mail address: aamarnath@epri.com

Industrial-scale energy systems integration technologies, such as waste heat recovery and distributed energy generation, can reduce the manufacturing sector's reliance on the electric grid and increase industrial efficiency. Low-temperature waste heat streams account for the majority of the industrial waste heat inventory. The waste heat inventory in the industrial sector in the United States was analyzed and is estimated to be on the order of 1500–3000 trillion Btu [1.58-3.16 EJ] annually. According to US Department of Energy, process heating account for nearly 70% of the total process energy, accounting for approximately 7500 TBtu [7.91 EJ]. Of this total process heating energy (see Figure 2), only about 5% is direct electricity use and the remaining 95% is contributed by fossil-fuel and steam. Thus, industrial process heating has a very high potential for decarbonization as steam production and fossil-fuel fired processes contribute heavily to the global carbon emissions.

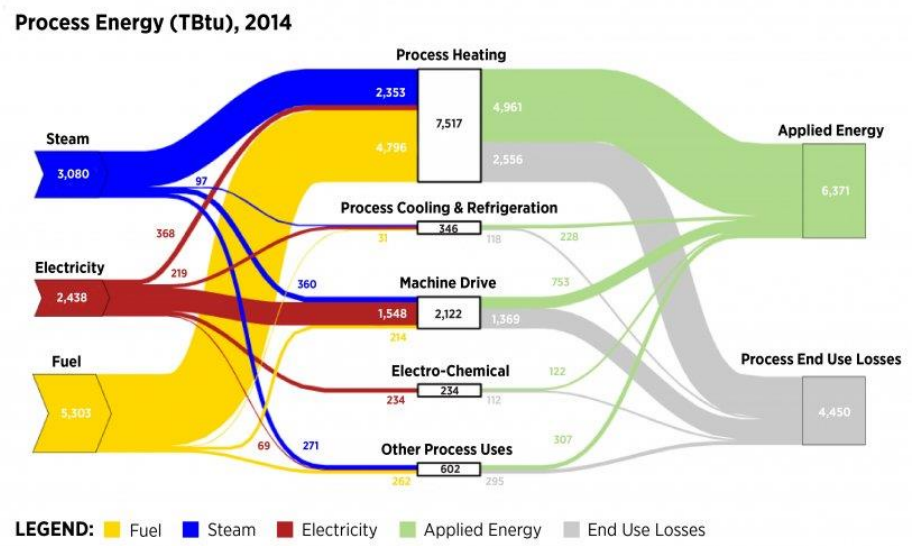


Figure 2 US manufacturing sector energy use and losses by fuel types (Source: US Department of Energy)

Recovering waste heat, though difficult to achieve, could offer a decarbonization solution to the industrial sector. By utilizing wasted heat energy and putting it back to the process reduces the fuel intake which in turn reduces the emissions. Additionally, using heat pump technology – an electric solution – for waste heat recovery reduces the steam and fossil-fuel dependence which effectively lowers the industrial emissions as well.

Waste heat recovery is often utilized in two different ways, (i) generated waste heat from an industrial facility can be captured and re-used by redirecting waste streams for use in other thermal processes, or (ii) the waste heat stream can be converted to electricity.

In this paper, an innovative heat pump technology that is currently in development which can capture the low-grade industrial waste heat (around 70 - 80ºC) and transform it into high-temperature useful heat, specifically in the form of steam will be discussed. Unfortunately, heat pumps that are currently available commercially cannot take advantage of high-temperature industrial processes, as currently available heat pumps have an upper-temperature range limit around 94°C.

Currently, the heat pumps that can produce steam are mostly in developmental stages across the world. Low-temperature waste heat streams available abundantly in industries. Typical waste heat sources are at temperatures in the 70-80ºC range. The sources of the waste heat in industry typically are chillers, cooling processes, return steam condensate. Most of the industry need for steam is in the range of 115 to 125ºC and industries such as food processing, dairy, paper and chemical can make use of this steam. This will provide an immediate high impact heat pump solution to the industries in not only California but also around the world once successfully developed, tested, and verified in the laboratory.

2. Market Characteristics

The most dominant existing technology for steam production is gas-fired boilers. Such boilers have significant carbon footprint – the GHG emission factor for gas boilers is about 235.6 g CO_2 equivalent per thermal kWh of heat produced[i]. Some boilers have electric resistance heaters (costly electricity, with COP~1)

that add to carbon emission based on the electric power generation mix. The cost of the electric resistance boilers is in the range of $30-$50/kW of heating capacity produced.

The challenge is to bring down the cost of heat pump to be closer to boiler costs. The current projected costs (in literature) are about an order of magnitude higher. This project is exploring the use of existing components with innovative design, in order to be cost effective, as compared to boilers. Details on the bill of materials for low-cost heat pumps are being developed in the project described in Section 5 of this Paper.

Another aspect of this project is to widely transfer knowledge gained. EPRI, through its utility membership consortia, is well qualified to do that. Targeted technology transfer activities are planned to be conducted during the latter part of 2023.

3. Other Emerging Heat Pump Technologies and Pilots Around the World

There are several organizations around the world involved in developing high temperature heat pumps some attempts to develop HTHPs. Several heat pumps in the category discussed in this paper from Japan, Norway, France etc. are still in R&D stage and are nearing commercialization status. Some information about the status of technology is given in Table 1 below through the literature survey. This is just a snapshot of example organizations that are developing high temperature heat pumps. Heat pump research is a hot research area and several other organizations in various countries developing breakthrough heat pump technologies as well as refrigerants.

In Japan, Fuji Electric has developed an early commercial heat pump prototype capable of producing steam from waste heat just recently. This heat pump is a smaller capacity (30 kW) exhaust heat recovery type steam generating heat pump system that can produce 120ºC saturated steam by means of efficiently recovering hot wastewater of less than 100ºC. Details as to the knowledge of refrigerants and other specifications are not available [ii].

Table 1 Sample of High Temperature Heat Pump research in various countries

Project	Country	Refrigerant	Heat Source (°C)	Heat Sink (°C)	Heating Capacity (kW)
Austrian Institute of Technology, Vienna, Chemours, Bitzer	Austria	R1336mzz(Z)	30 to 100	70 to 160	12
PACO, University of Lyon, EDF	France	R718	70 to 90	120 to 140	300
EDF, Johnson Controls, Alter ECO	France	R245fa	20 to 60	90 to 140	20 to 1,200
Tokyo Electric Power Company, Japan	Japan	R601	40 to 90	95 to 135	150 to 400
Austria: TU GAZ	Austria	R600	50 to 80	80 to 125	20 to 160
The Netherlands: ECN, SmurfitKappa, IBK, Bronswerk.	Netherlands				

4. Activities Under IEA Annex 58, Annex 59 and Annex 60

EPRI is a member of United States team that participates in three important international Heat Pump working groups, the IEA Annex 58, Annex 59 and Annex 60. More details about the three working groups are summarized below.

4.1. IEA Annex 58: High Temperature Heat Pump Technologies

This Annex gives an overview of available and close-to-market technologies regarding high-temperature heat pumps. The need for further RD&D developments will be outlined. In order to maximize the impact of high-temperature heat pumps, this Annex also looks at process integration by development of concepts for heat pump-based process heat supply and the implementation of these concepts [iii].

4.2. IEA Annex 59: Heat Pumps for Drying

The Annex aims to structure and describe the numerous possibilities and advantages of heat pump integration in dryers. Drying processes are widely used in industry and commerce (food industry, paper industry, chemical industry, ceramics industry, laundries etc.) as well as in household applications (white goods, tumble dryers, dishwashers) in various forms and contribute significantly to energy consumption. (10-25% of industrial energy consumption is used for drying processes)[iv].

4.3. IEA Annex 60: Retrofitting Heat Pump Systems in Large Non-domestic Buildings

The Annex focus on providing straightforward, high-level guidance for building owners and other decision-makers. Retrofitting heat pumps for larger non-domestic buildings is challenging as it contain a variety of complex heating, ventilation and cooling (HVAC) systems. These present different challenges and opportunities. In practice the retrofitting of heat pumps will often be part of more general refurbishment of a building. The scale and extent of anticipated refurbishment will be an important factor in determining which options for heat pump systems are technically or economically feasible. This annex aims to provide evidence of the practical feasibility and satisfactory operation of a range of installed retrofit systems in large non-domestic buildings in a number of countries, together with insights into the thinking that led to the choice of system[v].

5. EPRI Project on High Temperature Heat Pump for Industrial Decarbonization

This section outlines the general operational characteristics of heat pumps, current heat pump research project funded by the California Energy Commission (CEC), and the details of a prototype high temperature industrial waste heat recovery heat pump that is currently being developed under this funding.

5.1. Heat Pump Operation

This section provides a brief overview of the heat pump operating principles as applicable to heat recovery and using it within a process in a manufacturing facility. A heat pump consists of a closed loop containing a refrigerant that is either in the liquid or gaseous phase or both. The refrigerant or the working fluid passes through four main components (see Figure 3), i.e.:

- An evaporator where the refrigerant absorbs heat from the waste heat by evaporating.
- A compressor which increases the enthalpy and pressure of the refrigerant (and therefore its condensation temperature),
- A condenser in which the refrigerant transfers its latent heat to the industrial source by condensing,
- A pressure release valve that adjusts the evaporator supply and transfers the refrigerant from high to low pressure.

Energy is recovered by the successive changes in the states of the refrigerant.

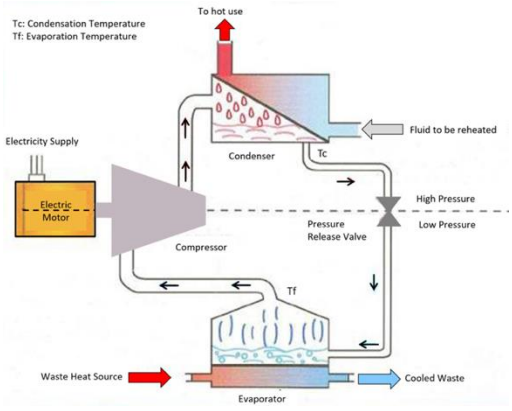


Figure 3 Schematics of a heat pump cycle

5.2. EPRI's CEC Project on Development of Industrial Heat Pump

EPRI has been funded by the CEC to lead this effort to develop an industry wide acceptable decarbonization solution. This high temperature heat pump (HTHP) technology once developed has the potential to meet the industrial steam need of industries such as food processing, chemical, paper and textile industries. Lack of commercial availability of high temperature heat pump technology to convert industrial waste heat to useful heat in the form of low-pressure steam was the motivation behind this project. In this project funded by the CEC[vi], EPRI is working with a research company called the Creative Thermal Solutions, Inc. (CTS) in the US to develop a high temperature industrial waste heat recovery heat pump that can produce steam. The project

uses an innovative design of building this prototype from commercially available components such as compressors, variable frequency drives, heat exchangers etc. The project requirements are that the developed technology should have a COP of 3.4 or better and provide a temperature lift of at least 40ºC. The table, Table 2, below shows the project success criteria that need to be met at the end of the project. This is an ongoing project that was started in 2020 with a planned completion of 2023.

The project innovation lies in two main areas: first, the near-zero GWP and ODP refrigerant that has the characteristics to operate in a sub-critical mode with an ability to exist in two-phases can help to extract low grade waste heat to transform to high temperature useful steam; second, the control system as well as the heat pump design that could deliver the temperature lift of 40°C or more at a coefficient of performance (COP) of at least 3.4. The advantages of this heat pump design are two-fold – first, it will provide an immediate high impact heat pump based decarbonization solution to the industries in California and second, the heat pump will reclaim the waste heat from the industry and utilize it by returning it back to the industrial processes and reduces fossil-fuel consumption and therefore reduces overall emissions associated with the combustion.

Table 2 Performance metric for the industrial high temperature heat pump (HTHP)

Performance Metric	**Baseline Performance**	**Target Performance**	**Evaluation Method**	**End-of-Project Performance**
Waste Heat Temperature Limits	70 - 80ºC	>120 ºC	Laboratory Testing	125 ºC
Coefficient of Performance (COP)	0.8	3.4	Laboratory Testing	3.6
Estimated Equipment Capital and Installation Costs	$2540/unit or $85/kW	$60,000/unit or $2000/kW	Market Available Cost	$45,000/unit or $1500/kW
Estimated Operation and Maintenance Costs (annual)	$916	$215 (based on 3.4 COP)	Market Available Cost	$203 (based on 3.6 COP)
Other	Size = 3 boiler horsepower (bhp) [equivalent to 29.43kW]	Size = 30kW	Power Measurements in Lab	30kW

5.2.1. Refrigerants

One of the requirements of this project is to create a vapor compression system that will be able to operate between temperatures 70 ºC and 135ºC. A low GWP refrigerant such as R245fa, R1233zd(E) or R1336mzz(Z) will be utilized as the working fluid. These three refrigerants were selected based on literature studies conducted during the project design and specification stages [1][2][3] & [4]. In addition to creating a higher efficiency and lower emission technology the project team is also committed to choosing a refrigerant that has close to zero GWP and ozone depletion potential (ODP) with additional characteristics of lower toxicity (A1) and no flame propagation (A1) as shown in Figure 4[vii]. The system will operate with one of low GWP refrigerants (working fluids) such as R1233zd(E) or R1336mzz(Z). To take it one notch further, the project team is using R1233zd(E) as a working fluid in the prototype because a) it is a non-flammable fluid, b) it has a GWP of 1 and Ozone Depletion Potential (ODP) of 0, and c) it is a non-toxic fluid. The tests conducted with the breadboard system with the three refrigerants have also shown that the R1233zd(E) has better performance compared to the other two refrigerants.

The following charts (see Figure 5) shows various refrigerants used in various high temperature heat pump research around the world [4] [5] & [6]. Table 3 shows the characteristics of three emerging refrigerants that have been considered for this project – R245fa (as baseline), R1336mzz(Z) and R1233zd(E). The latter two refrigerants are considered promising for industrial applications.

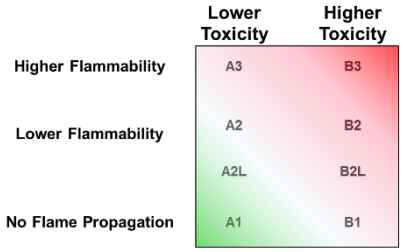


Figure 4 Characteristics of Refrigerants: ASHRAE Safety Designations

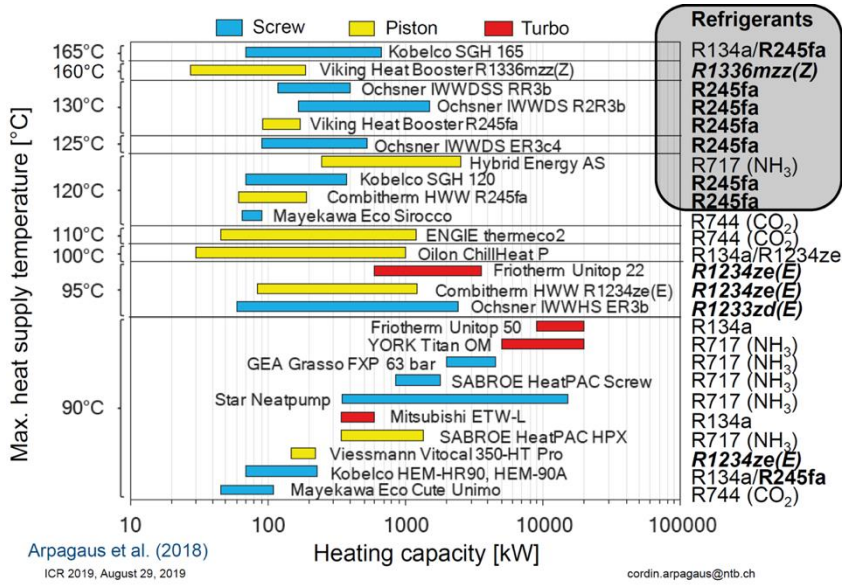


Figure 5 Typical refrigerants used in industrial high temperature heat pumps globally

Table 3 Characteristics of Emerging Refrigerants

Refrigerant	**Type**	**Chemical Description**	**Heat Sink Temperatures (°C)**	**Heating Capacity (kW)**
R245fa	HFC- Hydrofluorocarbons	Unsaturated organic comprising of hydrogen, fluorine, and carbon	120	60 to 370
		Chemical: Fluorine and Propane		
R1336mzz(Z)	HFO- Hydrofluoroolefins	Unsaturated organic comprising of hydrogen, fluorine, and carbon	150	28 to 188
		Chemical: Fluorine and Butene		
R1233zd(E)	HCFO – Hydrochlorofluoroolefins	Unsaturated organic comprising of hydrogen, chlorine, fluorine, and carbon	80 to 150	20 to 200
		Chemical: Chlorine, Fluorine, Propene		

The preliminary simulation results from the refrigerant testing shows that the required COP could be met.. In summary, when generating 120°C steam from 80°C heat source, both R1233zd(E) and R1336mzz(Z) show a higher COP than R245fa. R1233zd(E) benefits from its larger specific heat of vaporization at 125°C, while R1336mzz(Z) benefits from its smaller specific compression work and they both have significantly lower GWP than R245fa which was used as a baseline. The characteristics of the three refrigerants are shown in Table 4.

Table 4 Thermophysical properties of the refrigerants selected for the HTHP

Refrigerants	**MW [g/mol]**	**T_{crit} [°C]**	**P_{crit} [Mpa]**	**Vaporization Heat [kJ/kg] @ 125 °C**	**Sat Vapor Density [kg/m^3] @ 75 °C**	**ODP**	**GWP**	**ASHRAE Std 34 Safety Class**
R245fa	134.0	153.9	3.65	105.1	38.3	0	858	B1
R1233zd(E)	130.5	166.5	3.62	117.6	30.7	0.00034	1	A1
R1336mzz(Z)	164.1	171.4	2.90	107.1	24.4	0	2	A1

5.2.2. Heat Pump Design

This section presents the simplified, single-stage heat pump design approach taken for this project that meets the performance specifications set forth in the project. The simplified schematic design is presented in Figure 6. below. In the following drawing the refrigerant lines are shown in black while water lines are shown in blue.

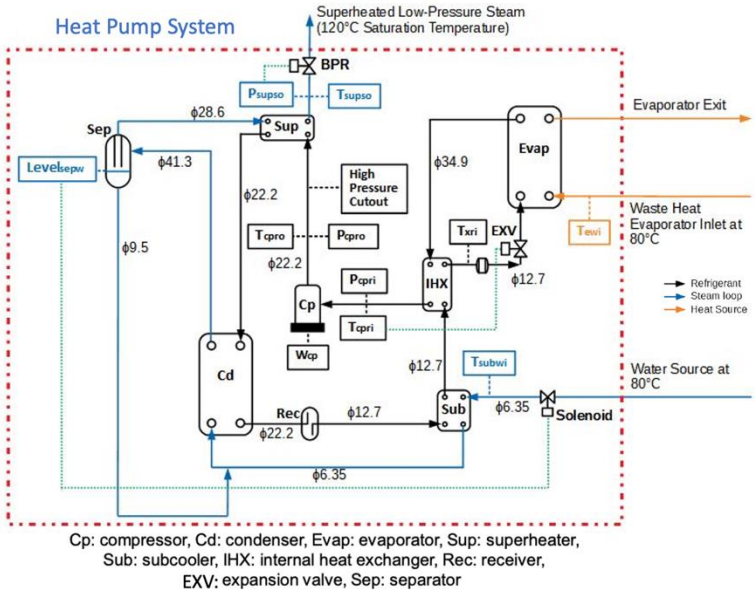


Figure 6 Simplified Schematic Diagram of the Heat Pump System

Compressor ***Cp*** discharges refrigerant to a superheater ***Sup***. The superheater serves to superheat the steam generated in the condenser ***Cd***. After the superheater, the refrigerant flows to the condenser ***Cd*** to be condensed. In that process, water on the other side is evaporated. The mixture of steam and water droplets goes to the separator ***Sep*** that sends saturated vapor to the superheater to be additionally heated and effectively prepare for transportation to the user. The condensed refrigerant flows to the high-pressure receiver ***Rec***. Liquid after the receiver will be subcooled in the subcooler ***Sub***, heating in that process water that will be later evaporated in the condenser. Recuperative "internal heat exchanger" ***IHX*** improves the performance of the system, taking care of the dry-out in the evaporator, and increases the reliability of the compressor by reducing the chance of sending liquid to the compressor. Expansion valve ***EXV*** controls the flow of the refrigerant through the evaporator ***Evap***, which will generate refrigerant vapor to be sent to the suction of the compressor. In this way, we have closed the refrigerant flow loop and explained the flow of water to be evaporated and turned into the superheated steam. The schematics also shows the pipe dimensions in the diagram.

After considering various heat exchanger options, the brazed plate type was chosen because it was by far the most compact and cost-effective option available. Acknowledged potential issues of scaling are to be handled with softened water where possible and periodic chemical cleaning that is conventional and commercially available. Table 5 shows the actual components and the make and model numbers of the parts used in the heat pump design.

Table 5 Components Used in the Heat Pump System

Component Description	**Model #**
Compressors	Copeland ZB45KCE-TFD (460V-3ph-60Hz)
Superheater	BAODE-BL26C-30D
Condenser	SWEP B45-060
Subcooler	BAODE-BL26C-30D
IHX	GEA-FP5X12L-80
Evaporator	SWEP V45-060
Steam separator	Custom built
Pump for m_{sepwo}	Micropump GJSN27.PVT.G
XV Valve	Sporlan (Parker) SERI-F
Back pressure regulator	Danfoss KVP28 evaporator pressure regulator
Refrigerant receiver	Refrigeration Research 3 liters
Variable Frequency Drive (VFD)	Drivecon N2
Watt Transducer (Compressor Power Measurement)	OSI PC5-015C, 3ph, 380-550V, 0-10A

The heat pump has controls to start and stop the compressor and one water pump. The heat pump is connected to a three-phase 480 V nominal power source at 60 Hz. A variable frequency drive (VFD) has been installed to vary the compressor speed. A 0-20 mA analog control signal must be connected to the drive to control the compressor speed. The speed of the compressor is controlled by adjusting the frequency of the VFD. Full rated compressor speed is achieved when the VFD frequency is set to 60Hz (line frequency of the AC power supply). The frequency of the drive directly correlates to the compressor speed, for example, 60Hz of VFD frequency is 100% of rated compressor speed, while 30Hz of VFD frequency is equal to 50% of the rated compressor speed. Subsequently over speeding of the compressor can be achieved by increasing the frequency to beyond 60 Hz, for example, 90Hz corresponds to 150% of the compressor rated speed.

5.2.3. Heat Pump Control System

The key features of the heat pump control system over the existing state-of-the-art technologies that are commercially available today are as follows:

- A new control strategy specifically for new refrigerants in the HTHP applications. Normal control of the expansion valve is based on the superheat exiting the evaporator. Isentropic line (that compressor follows in an idealized way) would enter into the two-phase zone, causing the liquid in the compression volume. To avoid that, the project team is using a novel control based on superheat at the compressor discharge stage.
- Modified compressor. New refrigerants bring several other new challenges. Their specific volume of vapor is significantly higher than in conventional refrigerants so a compressor with a much higher ratio of displacement vs. motor power will be used. Compressor with economized suction or compound type are preferential to maintain simplicity. That is another uniqueness of this approach. The compressor used in the design are commercially available.
- Modified heat exchangers (IHX). Another consequence of specific thermophysical properties (vapor volume) is a need for a special IHXs that will have different channels on the water and refrigerant side. The team would be using a Brazed Plate Heat Exchangers for heat transfer. A Brazed Plate Heat Exchanger (BPHE) offers the highest level of thermal efficiency and durability in a compact, low-cost unit.

5.2.4. Configuration of Laboratory Heat Pump System

The heat pump system and the components of the system are depicted in the figure (Figure 7) below.

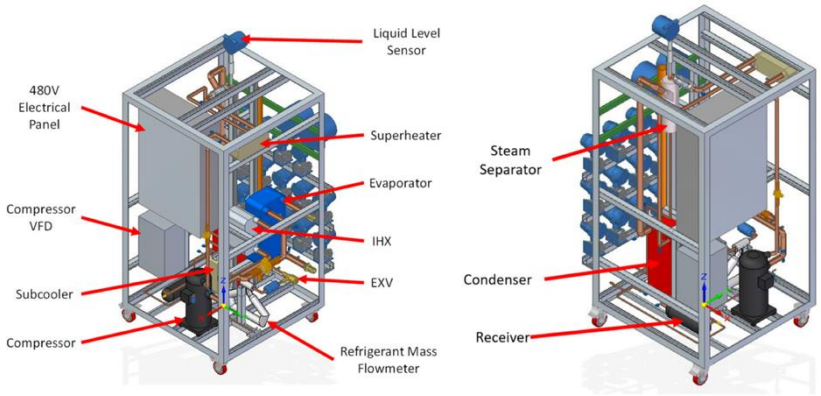


Figure 7 Schematic of a heat recovery heat pump currently being developed in California, USA funded by California Energy Commission (CEC)

Some of the key features of the heat pump design are summarized below:

- Simple single-stage vapor-compression cycle design
- Closed loop refrigerant and closed loop steam system design
- Hermetic sealed compressor to prevent refrigerant leakage
- Emerson (Copeland) scroll compressor is selected and is expected to be a robust and efficient option. The same compressor was used to test all the 3 refrigerants.
- Water conserving design that incorporates a closed loop steam system which returns the steam condensate back to the water reservoir.

The prototype system that is currently being tested at CTS's facility in Harmony, California is completely instrumented with multiple flow sensors, thermal sensors, steam flow sensors and electrical power meters to monitor and log the data for a thorough and detailed analysis. Multiple iterations have been conducted in the preliminary laboratory testing to ensure the sensitivity of the system load (capacity), input and output temperatures as well as other parameters. The photos in Figure 8 shows the actual prototype system built for this project.



Figure 8 Photos of the Actual HTHP Prototype System

The chart shown in Figure 9 below compares the compressor speed test results for R245fa (green), R1233zd(E) (blue), and R1336mzz(Z) (orange). The data shows that R1233zd(E) achieves the highest overall COP of 4.54 with a VFD set point of 40Hz (2/3rd rated compressor speed). The x-axis represents the heating capacity (Qh) of the heat pump and the y-axis represents the COP of the heat pump. The curves plotted for each refrigerant represents the COP of the system at various load conditions, which is represented by the frequency set point in the VFD (in Hz).

In the following chart, it can be seen that for the same heating capacity of Qh (= 18.3kW), the COP of R1233zd(E) is 4.8% higher than the COP of R1336mzz(Z). As Qh increases, the percent difference also increases, with the COP of R1233zd(E) being an estimated 13.8% higher at Qh (= 22.4kW). However, the most important comparison is between the three maximum COPs for each refrigerant, as the project's primary goal is to maximize COP. The maximum COP of R1233zd(E) is 2.2% higher than the maximum COP of R1336mzz(Z), and 10% higher than 245fa's maximum. Both R245fa and R1336mzz(Z) are within about 10% of the suggested 30kW capacity. Refrigerant R1233zd(E) shows better performance than R1336mzz(Z) in drop-in replacement mode. R1233zd(E) benefits from its larger specific vaporization heat, while R1336mzz(Z) benefits from its smaller specific compression work. R1233zd(E) leads to the highest COP of 4.5, which is 2.2% higher than R1336mzz(Z)'s maximum COP of 4.4, and about 10% higher than R245fa's maximum COP of 4.1.

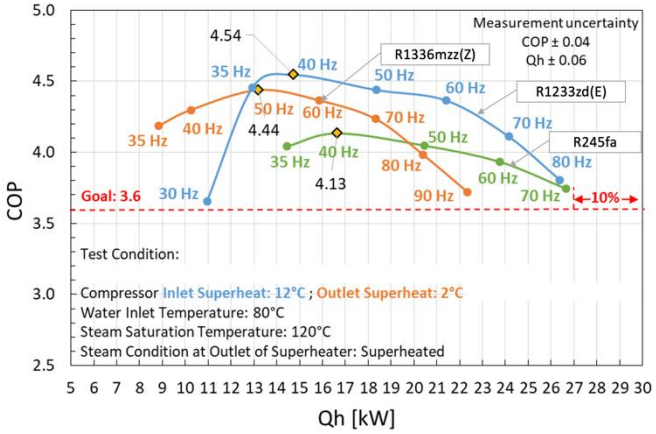


Figure 9 Comparison of COP for a given Qh between R245fa, R1233zd(E) and R1336mzz(Z)

The compressor efficiency of all refrigerants in the VFD set point of 40-70 Hz range are nearly identical, hovering in the 0.65 to 0.7 range. For a given VFD set point of 60 Hz (100% rated compressor speed), the total heating capacity of R1233zd(E) is about 0.89 times R245fa capacity and about 1.35 times of R1336mzz(Z)

capacity. Based on these results as well as other characteristics analyzed per earlier discussion, R1233zd(E) has been chosen as the refrigerant of choice, based on its high capacity, high COP, and lower risk for air to leak into the system.

The heating capacity Q_h is obtained from three heat exchangers (subcooler, condenser, and superheater) where the refrigerant heats the water source, evaporates it, and then superheats the steam flow. The heat energy supplied to the water is given by Eq.1:

$$Q_h = m_{subw} * [h_{supso}(T_{supso}, P_{supso}) - h_{subwi}(T_{subwi}, P_{subwi})] \quad Eq.1$$

Enthalpy h_{subwi} is found with the temperature T_{subwi} and P_{subwj}. Pressure measurement here is not needed because the water is subcooled, and the pressure will not change substantially due to temperature.

Efficiency or Coefficient of Performance (COP) is computed with the Eq.2 given below.

$$COP = Q_h / W_{cp} \quad Eq.2$$

where W_{cp} is the power drawn by the compressor which is measured by a Watt Transducer.

The testing of this system for more than six months has provided consistent, repeatable, and stable results that meet the project goals set forth at the beginning of this project. Table 6, Figures 10 and Figures 11 show the test results from 6 months of heat pump testing. Some of the salient findings from the laboratory tests are given below:

- The COP shows results above the target values of 3.4
- The heating capacity of 25 kW is achieved at compressor speeds around VFD set point of 80 Hz (=1.3 times rated compressor speed)
- Repeatability: The prototype system runs reliably and has shown that repeated test conditions produce similar results
- System has been optimized to achieve an average COP of 3.6 at an average heating capacity of 25kW (Q_h) and COP of 4.0 is easily achieved at an average heating capacity of 20kW (Q_h).

Table 6 Test results from 6 months of Heat Pump Testing at CTS Laboratory

Refrigerant	VFD Set Point (Hz)	Temp Lift (oC)	Average COP (-)	Average Qh (kW)
R1233zd(E)	60	40	4.0	20
	80	40	3.6	26

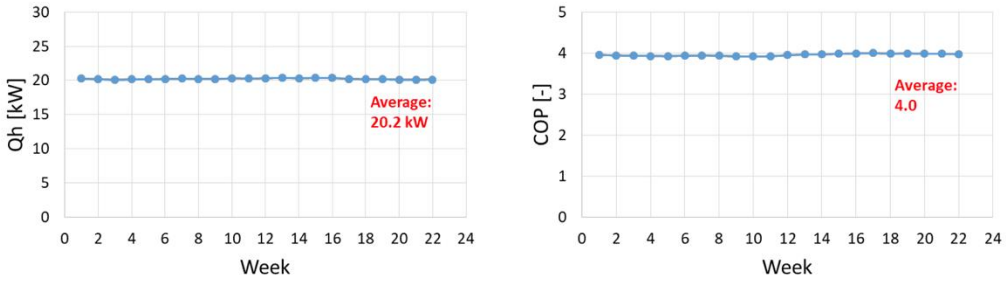


Figure 10 Heating capacity (left) and coefficient of performance (right) of the prototype heat pump system at rated compressor speed (VFD set point = 60 Hz)

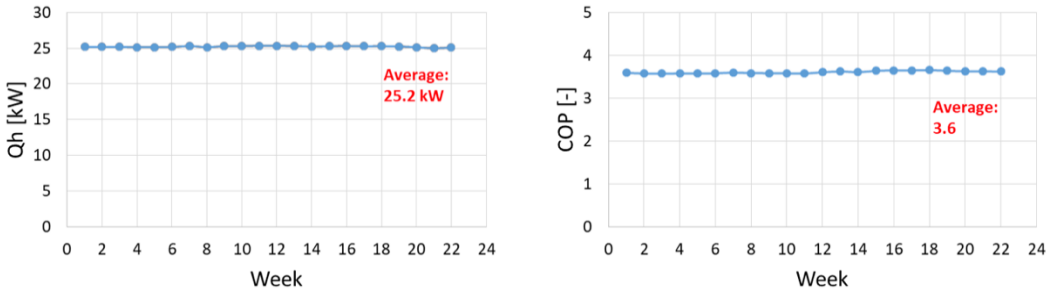


Figure 11 Heating capacity (left) and coefficient of performance (right) of the prototype heat pump system at 1.3 times the rated compressor speed (VFD set point = 80 Hz)

6. Summary

This paper provides an overview of an innovative, high temperature, industrial heat recovery heat pump that is currently developed by EPRI under the auspices of the California Energy Commission. This is an ongoing project that has a planned completion timeline of 2023. Results from the prototype laboratory testing show that with the newer and emerging refrigerants, efficient compressors, and innovative control designs, a higher COP heat pump that can effectively recover waste heat from the industrial processes is achievable. The industrial waste heat recovery heat pumps offer multiple benefits to the industrial customers, firstly it produces useful heat in the form of steam; secondly it lowers the fossil fuel energy use by reusing the otherwise wasted heat energy and thereby reduces emissions due to combustion; and finally, by using clean energy electricity it additionally lowers the emissions and helps in industrial decarbonization. The project will also look into market characteristics and develop pricing of the heat pumps, determine the incentives that electric utilities as well as other governmental agencies can provide to help increase the market adoption. In summary, even though there is no one “silver bullet” solution to decarbonize the world, heat pumps offer a great pathway for industries to achieve their carbon reduction targets. Governments around the world should fund more research to develop high performance refrigerants and innovations in heat pump technology designs that could potentially combat the climate crisis more effectively and efficiently.

Acknowledgements

The authors would like to first thank the CEC for funding the project described in this paper, and the CEC’s Contract Agreement Manager, Rajesh Kapoor, for providing guidance. The authors would also like to acknowledge the team at CTS who have contributed to the development of the prototype high temperature industrial waste heat recovery heat pump system as a sub-contractor to EPRI under the CEC contract.

References

[1] Arpagaus, Cordin; Bless, Frédéric; Uhlmann, Michael; Büchel, Elias; Frei, Stefan; Schiffmann, Jürg; and Bertsch, Stefan, "High temperature heat pump using HFO and HCFO refrigerants - System design, simulation, and first experimental results" (2018). International Refrigeration and Air Conditioning Conference. Paper 1875. https://docs.lib.purdue.edu/iracc/1875

[2] Jingye Yang, Ziyang Sun, Binbin Yu, Jiangping Chen, Experimental comparison and optimization guidance of R1233zd(E) as a drop-in replacement to R245fa for organic Rankine cycle application, Applied Thermal Engineering 141 (2018) 10–19

[3] Arpagaus, Cordin; Bless, Frédéric; Uhlmann, Michael; Büchel, Elias; Frei, Stefan; Schiffmann, Jürg; and Bertsch, Stefan, "High temperature heat pump using HFO and HCFO refrigerants - System design, and experimental results" (2019). Manuscript ID: 242, DOI: 10.18462/iir.icr.2019.0242

[4] Arpagaus, C., Bless, F., Schiffmann, J., Bertsch, S.S., 2017. Review on High Temperature Heat Pumps – Market Overview and Research Status. In: International Workshop on High Temperature Heat Pumps, September 9, 2017, Copenhagen, Denmark. pp. 1–25.

[5] Arpagaus, C., Bless, F., Uhlmann, M., Schiffmann, J., Bertsch, S.S., 2018b. High temperature heat pumps: Market overview, state of the art, research status, refrigerants, and application potentials (Lizenz-/Genehmigungsnummer: 4432121433391). Energy 152, 985–1010.

[6] Viking Heat Engines, 2018. HeatBooster HBS4: Industrial heat pump for clean energy production up to 160 °C.

[i] Source: https://www.researchgate.net/figure/GHG-emission-factors-for-different-boilers-Data-sources-are-GEMIS-495-37-except-for_tbl2_334164530

[ii] Source: https://www.fujielectric.com/company/research_development/theme/heatpump.html

[iii] Source: https://heatpumpingtechnologies.org/annex58/

[iv] Source: https://heatpumpingtechnologies.org/annex59/

[v] Source: https://heatpumpingtechnologies.org/annex60/

[vi] Source: https://www.energy.ca.gov/filebrowser/download/280

[vii] Source: http://www.epa.gov/ozone/snap/refrigerants/safety.html

14th IEA Heat Pump Conference
15-18 May 2023, Chicago, Illinois

Design of non-flammable mixed-refrigerants Joule-Thomson refrigerator below -100℃

Taejin Park[a], Junhyuk Bae[a*], Sangkwon Jeong[a *]

[a]Korea Advanced Institute of Science and Technology, 291, Daehak-ro, Yuseong-gu, Daejeon 34141, Republic of Korea

Abstract

Refrigeration below -100℃ (170 K) is often demanded in various industrial applications such as biomedicine, food stocks, and semi-conductor processing. It is difficult to pump heat from 170 K to room temperature by a single pure refrigerant in Joule-Thomson (JT) refrigerator due to the insufficient thermodynamic properties. Mixed-refrigerants (MR) possess some attractive merit as an alternative for that temperature range. We select the non-flammable refrigerants to avoid the operation safety issues such as flammability and explosiveness of hydrocarbon refrigerants. This paper validates a possibility for obtaining 170 K by using a non-flammable mixture refrigerant and determines its maximum COP. A two-stage cascade cycle is selected for design simulation in order to achieve a high efficiency. In the main cycle, R14, R23, and R218 are used after we consider the characteristics of the iso-thermal enthalpy difference. In addition, R410A, which is broadly used in commercial refrigerators, is utilized in the precooling cycle. The optimal design and the operating condition are evaluated with several parameters in the main and the precooling cycles, such as the suction and discharge pressures of the compressors, the mass flow rate, the precooling temperature, and the MR compositions. The simulation assumes the ideal conditions to analyze the performance of the cycle. Consequently, the maximum COP is calculated at 0.78 when the mole composition of the ternary refrigerants (R14:R23:R218) is 0.7:0.1:0.2.

© HPC2023.
Selection and/or peer-review under the responsibility of the organizers of the 14th IEA Heat Pump Conference 2023.

Keywords: mixed-refrigerant; non-flammable refrigerants; MR-JT refrigerator; SMR cycle; cascade cycle;

1. Introduction

With the 4th industrial revolution, the need for treating the amount and time of data is explosively increasing. As this tendency is accelerated, the demand of higher density semi-conductor is inevitable. In the previous semi-conductor manufacturing process such as an etching process, the required temperature of manufacturing chamber ranged from -20℃ to -30℃. Recently, as a new method for fabricating the advanced high-density semi-conductor, cryogenic-etching process where the lowest temperature is below -100℃ (170 K) is emerging as a novel technology for efficient production and precise manufacturing of the semi-conductor [1]. To obtain the low temperature below 170 K, the Joule-Thomson (JT) refrigeration could be utilized because of the several advantages such as high reliability due to no moving parts, low capital cost, simple structure, and adjustability of the cooling capacity. On the other hand, JT refrigerator has also several disadvantages such as clogging problem in the lowest temperature parts, large pressure ratio, which results in low efficiency. The substitution of a pure refrigerant with a mixed-refrigerant (MR) as the working fluid can be a solution to these problems in the JT refrigeration cycle. Recently, the global environmental issue is to cope with the global warming and the destruction of ozone layer. Many researches have focused on the investigation of the MR-JT refrigerator using flammable refrigerants, which could reduce the emission of the CO2 and increase the efficiency [2]. However, it has critical disadvantages such as the flammability and explosiveness when the system size grows. In the manufacturing process of semi-conductor, it is essential to facilitate a cleanroom which is designed to maintain extremely low levels of pollutant. When the flammable refrigerants are utilized as the working fluid of the

* Corresponding author. Tel.:82-042-350-3079; fax: 82-042-350-8207.
E-mail address: bjh0201@kaist.ac.kr

refrigerator, it has a critical fire hazard, which is the single greatest risk among the cleanroom accidents. The damage from a fire can generate tremendous loss of the cost and time-consumption within several minutes. Due to these peculiar issues in the manufacturing process of semi-conductor, the concern of the safety is an essential factor. Therefore, in specific industrial applications, which need highest safety concerns like semi-conductor process, it is justifiable to construct a refrigeration system by using non-flammable refrigerants even though they have relatively high GWPs.

Over the past years, numerous investigations of the MR-JT refrigerator are concentrated on the flammable refrigerants as the working fluids due to their advantages such as high efficiency and lower global warming potential. On the other hand, few researches have addressed the non-flammable refrigerants in the past years. The cycle efficiency is affected by not only the composition of the MR but also the configuration of the cycle. The investigation by using non-flammable refrigerants for below 170 K needs more attention for various inevitable applications. Zhili Sun et al. (2019) explore the alternatives of refrigerant substitution in three cascade refrigeration system (TCRS) [2]. In the Zhili paper, the maximum COP is about 0.59 when the lowest temperature is about 170 K by using flammable refrigerants. In 2017, Cheonkyu Lee et al. presented a high-performance mixed-refrigerants JT refrigerator cycle by using non-flammable refrigerants for obtaining about 100 K [3]. The applied refrigerants for main and precooling cycle consist of Ar (Argon), R14, R23, and R218 in the main cycle and R410A in precooling cycle, respectively. In this research, the optimum operating condition is discussed and presented. In the research by Jisung Lee et al. (2011), three-stage cascade cycle was proposed for cooling HTS cables at the refrigeration temperature of about 70 K [4]. For reaching the temperature about 70 K, the non-flammable mixture of neon-nitrogen was selected as the working fluid of the main cycle. However, the flammable mixture of nitrogen, methane, ethane, and propane have been used as the components of MR to improve the cycle's efficiency. Since then, Jisung Lee et al. (2017) conducted the experimental investigation for validating the results of the previous numerical simulation [5].

The objective of this paper is to design a high efficiency MR-JT refrigerator for 170 K by using non-flammable refrigerants. The concepts of phase-liquid diagram and iso-thermal enthalpy difference are exploited to select the appropriate working fluid. Also, the comparison between the single-stage mixed-refrigerant and the cascade mixed-refrigerant cycle is performed in order to examine what configuration of cycle has a higher efficiency [6, 7].

2. Methodology

2.1. Selection of proper refrigerants and optimal compositions of MR

Cryogenic refrigerators were to be operated over wide temperature ranges from below 1 K to higher than 100 K usually up to 120 K. The traditional target temperature is below 170 K, which specifically dictates heat pumping from 170 K to 300 K. To cope with this wide temperature range (nearly 130 K), the mixed-refrigerants are preferred. One of the methods for selecting proper mixed-refrigerants as the working fluid is to utilize the liquid-phase diagram, which indicates the available range of liquid-phase between triple point and critical point. Fig. 1. shows the liquid-phase range diagram for several refrigerants with various temperature. Whenever the refrigerator is operating below 170 K, it is imperative to avoid any freezing problem of the working fluid.

According to Fig.1, Tetra-fluoro-methane (R14,CF_4), Tri-fluoro-methane (R23,C_2F_6), and Octa-fluoro-propane (R218,C_3F_8) can be selected as the non-flammable refrigerants. The total number of the divided cases per 0.1 mole with respect to their molar compositions of the ternary mixed-refrigerant is about 36 cases. Before we conduct the simulations for all cases, it is useful to sift out several cases for the analysis by considering their iso-thermal enthalpy differences. The iso-thermal enthalpy differences of the selected refrigerants (R14, R23, and R218) are presented in Fig. 2 both for the pure and the mixture refrigerants. The precooling refrigerant in the case of cascade configuration, is chosen as R410A which is one of the frequently used refrigerants in commercial refrigerators. R410A is the well-known near-zeotropic mixture of difluoromethane (R32,$CH2F_2$) and pentafluoroethane (R125,CHF_2CF_3).

From Fig. 2, it is possible to determine proper compositions of the mixture and estimate its ideal cooling capacity. To lift heat from 170 K to the ambient temperature (300 K), each of the ternary refrigerants of R14, R23, and R218 plays its role at the lowest, middle, and highest temperature ranges, respectively. It is important to recognize that the minimum iso-thermal enthalpy difference for the whole temperature range actually determines the cooling capacity of the cycle and its COP. This fact justifies the use of precooling cycle in a cascade configuration to narrow down the required temperature range, for example from 170 K to 240 K

instead of 170 K to 300 K. Since the iso-thermal enthalpy difference of R14 is relatively smaller than the others, the composition ratio of R14 should be larger than that of the other refrigerants for approaching below 170 K. The candidates of the mixture for the analysis is summarized in Table. 1.

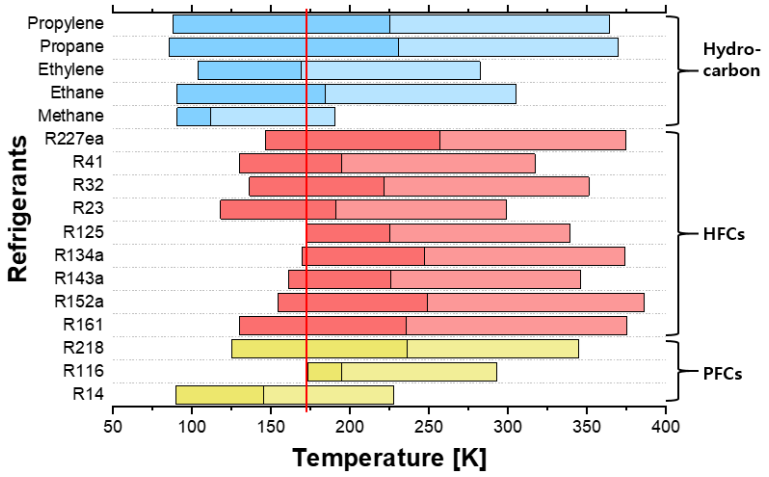
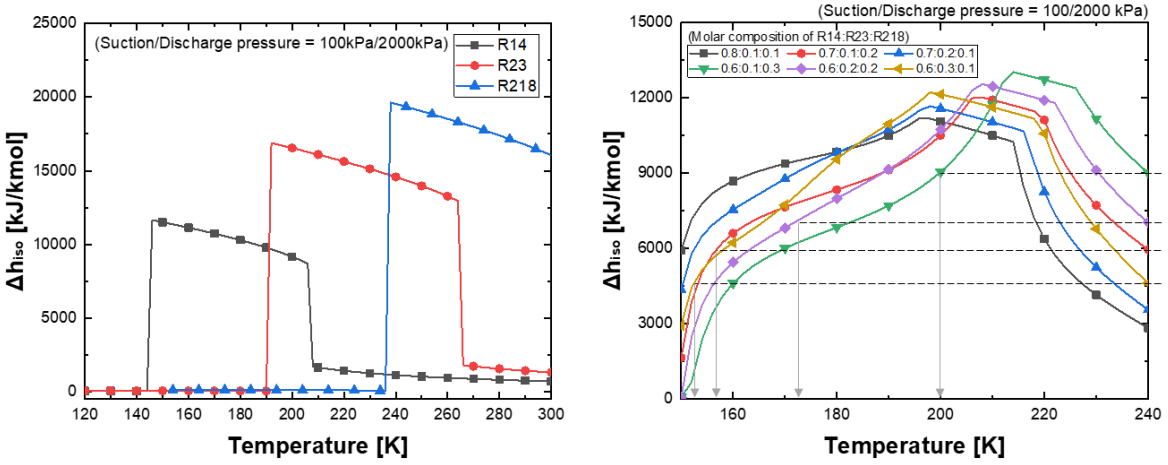


Fig. 1 Liquid-phase range diagram for various refrigerants



(a) Iso-thermal enthalpy difference for pure refrigerants

(b) Iso-thermal enthalpy difference for various mixture

Fig. 2 Iso-thermal enthalpy difference for non-flammable refrigerants (R14, R23, R218)

Table 1. Details of molar compositions for the non-flammable mixed-refrigerant

Case	Composition		
	R14	R23	R218
(1)	0.8	0.1	0.1
(2)	0.7	0.1	0.2
(3)	0.7	0.2	0.1
(4)	0.6	0.1	0.3
(5)	0.6	0.2	0.2
(6)	0.6	0.3	0.1

2.2. Cycle description

2.2.1. Single-stage mixed-refrigerant cycle (SMR)

SMR cycle, which is referred to as Linde-Hampson cycle and illustrated in Fig.3., comprises a compression unit, which includes compressor and after-cooler, a heat exchanger, an expansion valve, and an evaporator. By using two-stage compression system, the compression work and the compression ratio can be reduced effectively. Also, the operational soundness of the compressor is improved.

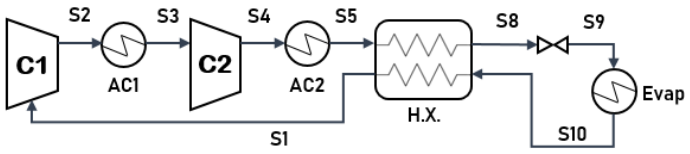


Fig. 3. Schematic of single-stage mixed-refrigerant cycle (SMR)

2.2.2. Cascade mixed-refrigerant cycle

Cascade cycle mainly consists of two cycles; the main (red-line) and precooling cycle (blue-line) in Fig.4. The configuration of the main cycle is derived from the basic Linde-Hampson cycle by adding the precooling cycle for the reduction of irreversibility inside H.X.2. In the previous research of C. Lee et al. and J. Lee et al., the two-stage cascade cycle used was proposed to enhance the cooling capacity [3, 4]. For the simplicity and ideal analysis, the minimum temperature approach in all heat exchangers is set to 3 K except for the low temperature side of H.X.1 between the temperature of Main6 and Main11. Generally, after the heat exchanger (H.X.1), the magnitude of the temperature difference inside the H.X.1 increases along the high-pressure stream. The increasing temperature difference inside the heat exchanger causes the area of heat exchange to be extended or the irreversibility in the heat exchanger to be increased. By deploying the precooling cycle inside the main cycle, these problems can be mitigated.

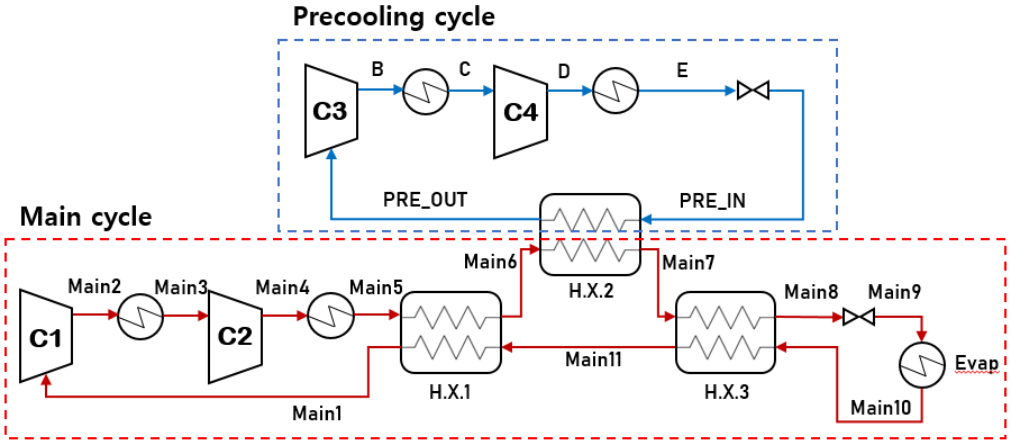


Fig. 4. Schematic of cascade mixed-refrigerant cycle (Cascade-MR cycle)

2.3. Simulation conditions and constraints

SMR and Cascade-MR are analyzed and compared to investigate the effect of precooling-cycle on the efficiency of the MR-JT refrigerator. For analyzing both refrigeration cycles, a commercial simulator, ASPEN HYSY V8.0 is utilized. In this paper, EOS is chosen Peng-Robinson equation in order to calculate the mixed refrigerant properties and the cycle efficiency. This EOS, which is presented below, has been commonly used for evaluating mixture properties in many previous researches [3-5]. P, R, T, v, a and b are pressure, universal gas constant, temperature, specific volume, fluid specific constants. P_c, T_c and w are critical pressure, critical temperature and acentric factor.

$$P = \frac{RT}{v-b} - \frac{a}{v^2+2bv-b^2} \quad (1)$$

$$a = \left(0.45724\frac{R^2T_c^2}{P_C}\right)\left[1 + (0.37464 + 1.54226\omega - 0.26992\omega^2)\left(1 - \sqrt{\frac{T}{T_c}}\right)\right]^2 \quad (2)$$

$$b = 0.07780\frac{RT_c}{P_c} \quad (3)$$

For simplifying the cycle analysis, we apply the following conditions and assumptions into the refrigeration cycle.

2.3.1. Compression part
- Two stage compression in the main and precooling cycle is implemented to reduce the compression work.
- It is assumed that the compression occurs with the isentropic efficiency of 80%.
- Each compressor in the main and precooling cycle has the same compression ratio.

2.3.2. Heat exchanger parts including after-coolers
- It is assumed that the pressure drops in both hot and cold streams are negligible except for the Joule-Thomson valve.
- Minimum temperature approach is 3 K inside heat exchangers.
- The type of heat exchangers is counter-flow.

2.3.3. Expansion part
- The expansion process is an isenthalpic process.

2.3.4. Simulation constraints
In general, the maximum pressure (discharge pressure) of MR-JT refrigerator is set to 3500 kPa for efficient operation. The minimum limitation of the suction pressure is nearly 100 kPa (1atm) due to the operational safety issue. The summary of the simulation constraints is presented in Table. 2.

Table 2. Summary of the simulation constraints

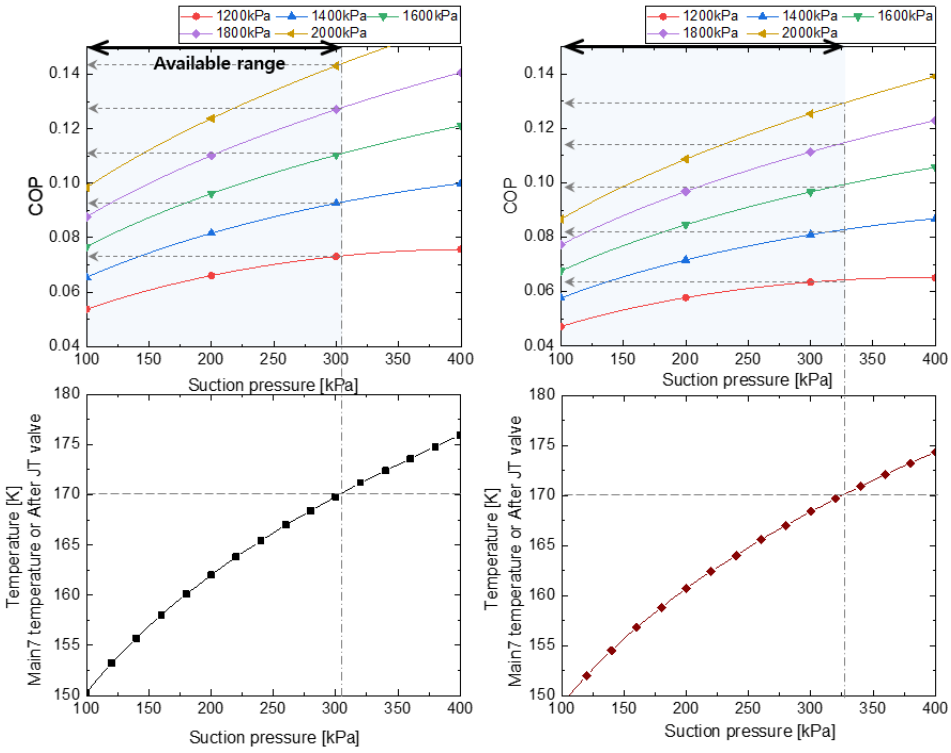
	Specification	Min	Max	Variation
Main cycle	Lower(suction) pressure [kPa]	100	500	40
	Higher(discharge) pressure [kPa]	1800	3400	200
	Mass flow rate [kg/s]	1	1	-
Precooling cycle	Higher(discharge) pressure [kPa]	1750	1750	-
	Temperature [K]	230	250	5

The mass flow rate of the main cycle is set as 1kg/s for the simplicity of the analysis. On the other hand, that of the precooling cycle is determined automatically in order to satisfy the minimum temperature approach 3 K in H.X.2. The discharge pressure of the precooling cycle is 1750 kPa, which means the subcooled or compressed state of R410A at ambient temperature (300 K).

3. Results

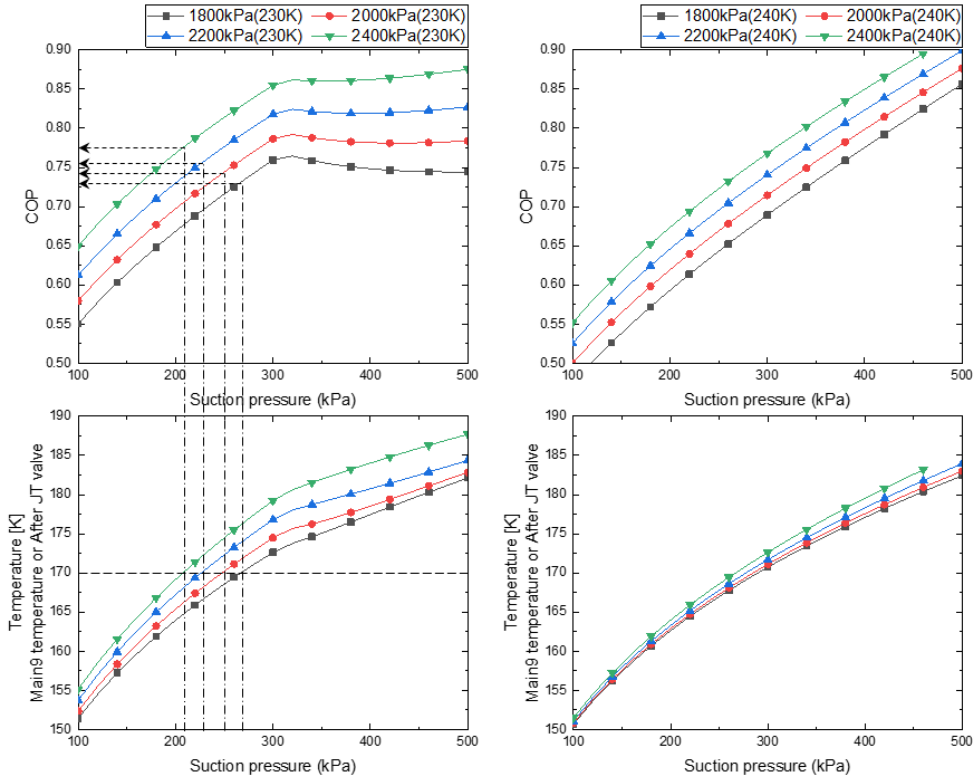
3.1. SMR cycle

Fig. 5. describes the variation of COP and the temperature of after-JT valve with the suction pressure of the SMR cycle for two cases of ternary MR compositions of R14, R23, and R218 (0.7:0.1:0.2 and 0.75:0.1:0.15). The longitudinal scales of the upper and the lower graphs are fitted equally for the convenience. Both (a) and (b) in Fig. 5. have the similar tendency. As the suction pressure increases from the 100 kPa, the cycle efficiency and the temperature of after-JT valve also increase gradually. The available suction pressure to achieve the target temperature of 170 K are up to 300 kPa and 330 kPa as indicated in Fig.5. (a) and (b), respectively. The COP of the case (a) is larger than that of the case (b) with more molar composition of R218.



(a) R14:R23:R218 = 0.7:0.1:0.2 (b) R14:R23:R218 = 0.75:0.1:0.15

Fig. 5. COP and after-JT temperature with respect to the molar compositions in SMR cycle



(a) Precooling temperature 230 K (b) Precooling temperature 240 K

Fig. 6. COP and after-JT temperature with respect to precooling temperature in cascade cycle

3.2. Cascade cycle

Fig. 6. (a) and (b) illustrate the variation of the achievable COP and the lowest temperature with the suction pressure and the discharge pressure in accordance with the precooling temperature in the cascade cycle. The overall tendency for the COP and the temperature of after-JT valve is similar with the SMR cycle's results as mentioned in the previous section. In the cascade cycle, the efficiency is primarily influenced by three main parameters, that are the suction, the discharge pressure, and the precooling temperature of Main7 which is the precooled temperature through H.X.2. From Fig. 6, it is evident that the lower precooling temperature leads to the higher efficiency of the cycle. Although the precooling temperature is controlled by the suction pressure in the precooling cycle, the temperature is limited by the suction pressure in the precooling cycle which isn't allowed below 100 kPa for the stable operation.

For more precise analyses in cascade cycles with different molar compositions, we considered several cases of 0.05 mole variations as presented in Table. 3. Also, in order to find the optimal operating conditions, the constraint range of discharge pressure in the main cycle extends from 2400 kPa to 3200 kPa with the variation of 200 kPa.

Table 3. Subdivided cases for several molar compositions

Case	Composition		
	R14	R23	R218
(1-1)	0.7	0.1	0.2
(2-1)	0.75	0.1	0.15
(3-1)	0.75	0.05	0.2
(4-1)	0.75	0.15	0.1

The sub-divided four cases are simulated and the results are plotted in Fig. 7. As a result, the maximum COP is obtained as 0.785 in the case of (1-1) with the compositions of R14, R23, and R218 (0.7:0.1:0.2). In that case, the suction and the discharge pressures are about 200 kPa and 2600 kPa for 170 K, respectively. The mass flow rate of the precooling cycle is estimated at 0.476 kg/s. Another case also has similar tendencies and the estimated maximum COP for 170 K is about 0.78. Table. 4 summarizes the simulation results in terms of the suction and the discharge pressures with the parameters of the precooling cycle.

Furthermore, the second law efficiencies of the sub-divided four cases in Table 3 are calculated to compare their realistic efficiencies with other cycles. The Carnot COP and the second law efficiencies can be calculated by eq.(4) and eq.(5), respectively. with the Carnot COP of 1.31. T_e and COP_{Carnot} stand for the evaporator temperature and the Carnot COP, respectively.

$$COP = \frac{T_e}{300 - T_e} \tag{4}$$

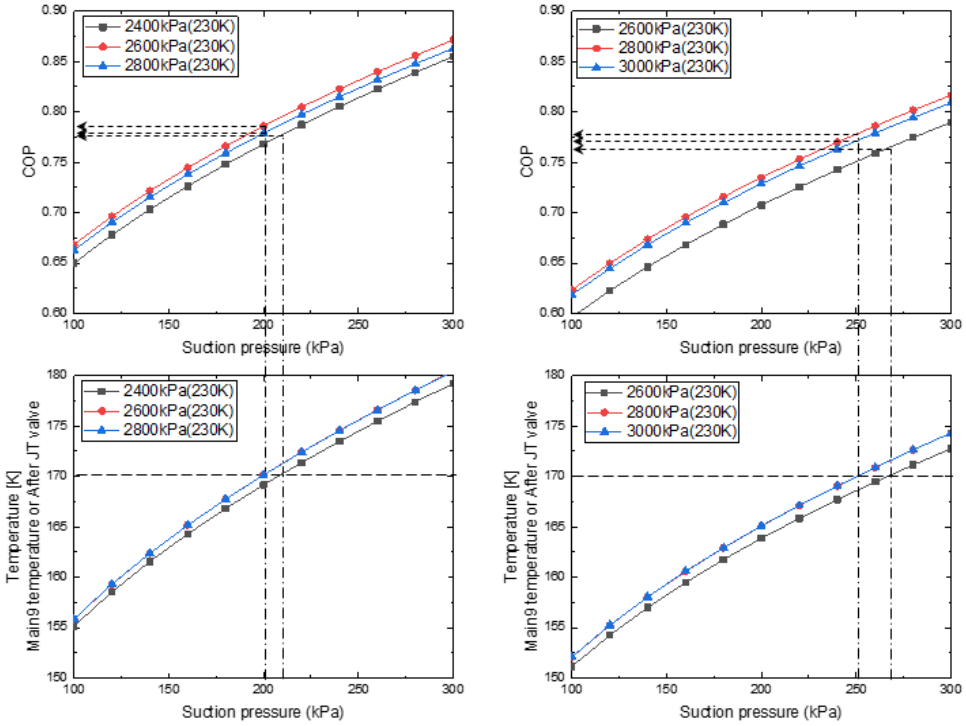
$$\eta_{II} = \frac{COP}{COP_{Carnot}} \tag{5}$$

The calculated results are depicted in Fig.8.

From the previous section, we deduce that the higher efficiency can be achieved when the precooling temperature decreases. In this numerical analysis, the suction pressure in the precooling cycle with R410A is primarily determined by the precooling temperature, 230 K.

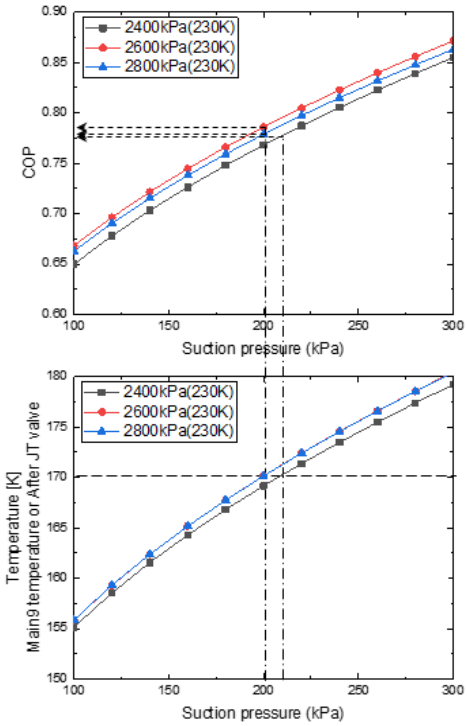
Table 4. Summary of simulated results in cascade cycle

CASE	Main cycle		Precooling cycle			COP
	Suction pressure [kPa]	Discharge pressure [kPa]	Mass flow rate [kg/s]	Suction pressure [kPa]	Temperature [K]	
(1-1)	198.67	2600	0.476	134.4	230	0.7847
(2-1)	249.57	2800	0.479	134.4	230	0.7784
(3-1)	220.00	2600	0.458	134.4	230	0.7787
(4-1)	284.28	2800	0.501	134.4	230	0.7767

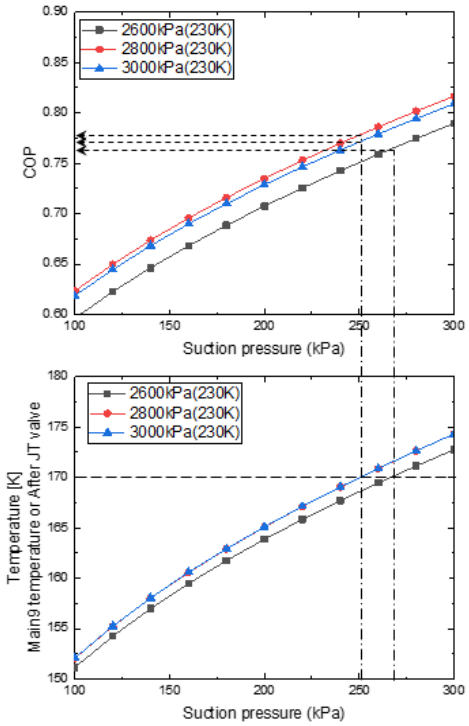


(a) R14:R23:R218 = 0.7:0.1:0.2 (CASE 1-1)

(b) R14:R23:R218 = 0.75:0.1:0.15 (CASE 2-1)



(c) R14:R23:R218 = 0.75:0.05:0.2 (CASE 3-1)



(d) R14:R23:R218 = 0.75:0.15:0.1 CASE(4-1)

Fig. 7. COP and after-JT temperature for four molar compositions

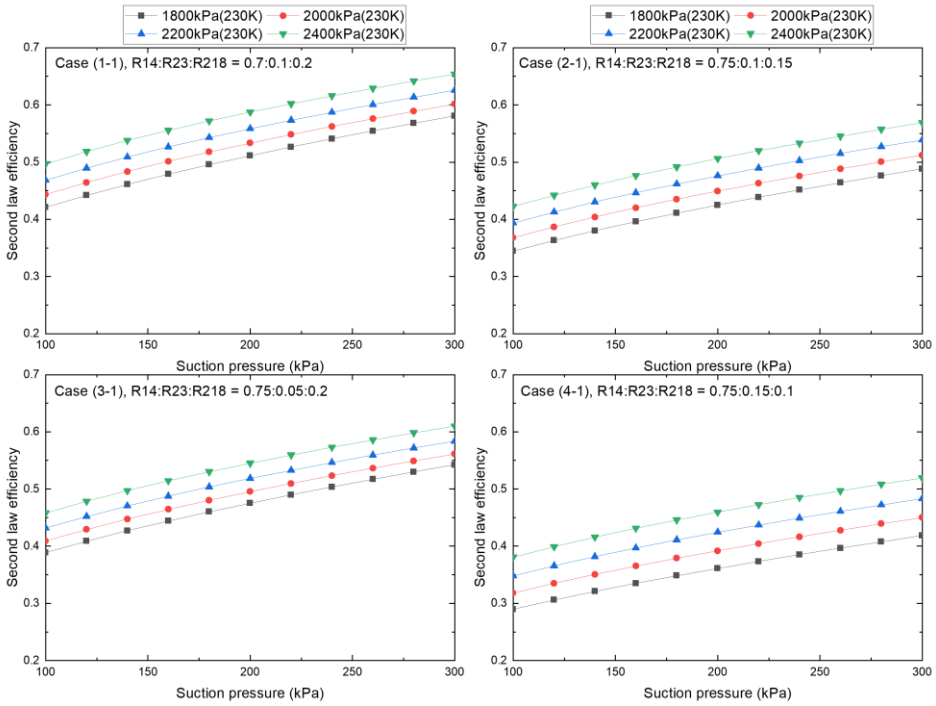


Fig. 8. The calculated second law efficiencies for four molar compositions

4. Discussion

Both SMR and cascade cycles with non-flammable refrigerants are analyzed by using commercial software ASPEN HYSYS V8.0. Both results of SMR and cascade cycles represent a similar tendency that the COP and the temperature of after-JT increase in accordance with the increase of the suction pressure. The reason for these characteristics is related to the pressure ratio between the suction (lower) and the discharge (higher) pressures. In condition with the same discharge pressure and the precooling temperature, as the suction pressure increases, the pressure ratio is reduced. As a result, the compression work is reduced by the decreased pressure ratio. By the definition of COP, a ratio of compression work and cooling capacity, the COP increases gradually to some extent. For example, the consumption of work and the cooling capacity in the case of (1-1) is illustrated in Fig. 9.

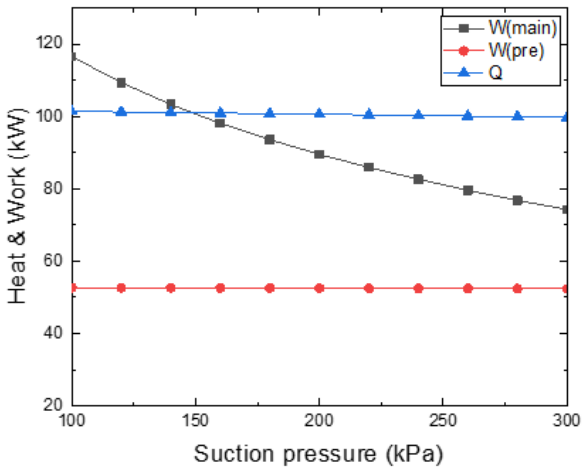


Fig. 9. Comparison between compression work and cooling capacity in the case of (1-1)

As the suction pressure increases, the temperature of after-JT also increases. It can be explained by the Joule-Thomson effect, where the difference between the lower and the higher pressures is a major factor in determining the temperature drop. In addition, as shown in the Fig.10, the precooling stage in the cascade cycle can decrease the temperature difference of hot and cold streams at the low temperature side of the heat exchanger. Therefore, the cascade cycle can result in higher efficiency with less entropy generation associated with the finite-temperature heat exchange in the counterflow heat exchangers.

This study has taken several ideal assumptions such as zero-pressure drop except for the expansion valve, higher compressor efficiency of 80%, and the minimum temperature difference of 3 K. For the realistic results, the effect of minimum temperature in the heat exchangers and the pressure drop in the cycle on COP should be considered as a future work. Furthermore, the predicted results should be validated by experiments.

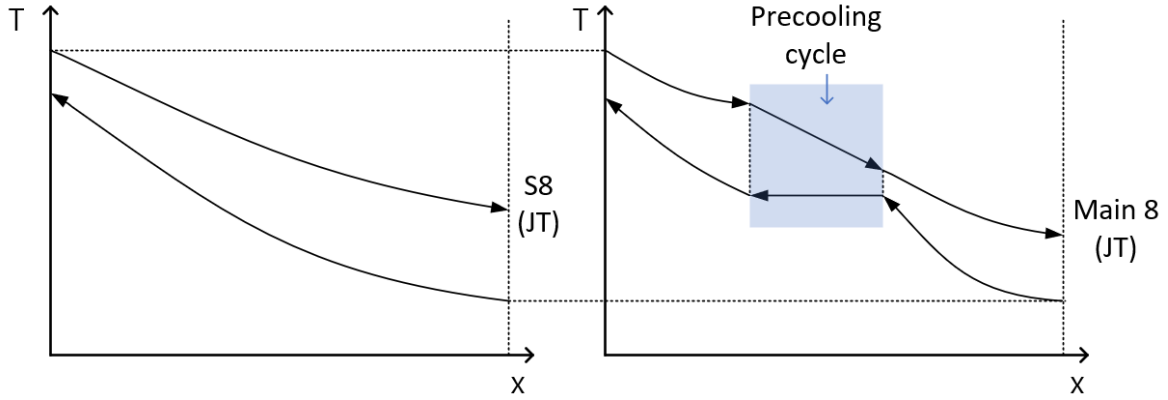


Fig. 10 Temperature distribution in the heat exchanger for SMR cycle (left) and cascade cycle (right)

5. Conclusion

The purpose of this paper is to show the possibility of efficient MR-JT refrigerator for 170 K by using non-flammable refrigerants only. At first, R14, R23, and R218 are sifted out and selected as the working fluids for the simulation. To achieve the target temperature, 170 K, the molar ratio of R14 should be larger than those of the other refrigerants. In this paper, the mixture composition is R14:R23:R218 = 0.7:0.1:0.2 for maximum COP. The analyzed configuration of the cycles is two-types; SMR and cascade-MR cycle. The comparison between the SMR and the cascade cycle clearly reveals that the efficiency of the low-temperature MR cycle is greatly enhanced by the implementation of precooling cycle. Deploying the precooling cycle in the appropriate location in the main cycle effectively reduces the generation of irreversibility in the recuperative heat exchanger of the refrigeration cycle.

Acknowledgements

This research was founded by the National R&D project (RS-2022-00143652).

References

[1] Dussart R, Tillocher T, Lefaucheux P, Boufnichel M. Plasma cryogenic etching of silicon: from the early days to today's advanced technologies. Journal of Physics D: Applied Physics. 2014;47(12):123001.
[2] Sun Z, Wang Q, Dai B, Wang M, Xie Z. Options of low global warming potential refrigerant group for a three-stage cascade refrigeration system. International Journal of Refrigeration. 2019;100471-83.
[3] Lee C, Jin L, Park C, Jeong S. Design of non-flammable mixed refrigerant Joule-Thomson refrigerator for precooling stage of high temperature superconducting power cable. Cryogenics. 2017;8114-23.
[4] Lee J, Hwang G, Jeong S, Park BJ, Han YH. Design of high efficiency mixed refrigerant Joule–Thomson refrigerator for cooling HTS cable. Cryogenics. 2011;51(7):408-14.
[5] Lee J, Lee C, Baek S, Jeong S. Investigation of ejector-equipped Joule–Thomson refrigerator operating below 77 K. International Journal of Refrigeration. 2017;7893-107.

[6] Reddy KR, Murthy SS, Venkatarathnam G. Relationship between the cooldown characteristics of J–T refrigerators and mixture composition. Cryogenics. 2010;50(6-7):421-5.
[7] Tzabar N. Binary mixed-refrigerants for steady cooling temperatures between 80 K and 150 K with Joule–Thomson cryocoolers. Cryogenics. 2014;6470-6.

14th IEA Heat Pump Conference
15-18 May 2023, Chicago, Illinois

Industrial high temperature heat pump for steam and hot water production

Tim Hamacher[a,*]

[a]SPH Sustainable Process Heat GmbH, Zur Kaule 1, 51491 Overath, Germany

Abstract

In industrial processes, heat is often required in the form of saturated steam. Due to their thermodynamic process, compression heat pumps are ideal for converting waste heat back into high quality saturated steam. The advantage over steam compressors is the ability to perform the phase change efficiently. An industrial high temperature heat pump capable of generating saturated steam up to approx. 6 bar absolute (approx. 160°C) or hot water at approx. 165°C is presented in this paper. For this purpose, a self-developed high-performance piston compressor is used, which was specially designed for high temperature applications with HFO refrigerants, such as R1336mzz-Z or R1233zd.The article presents two industrial applications in which large amounts of CO_2 are saved or avoided by using innovative high temperature heat pumps. One is 2 bar absolute steam production from cooling water heat of combined heat and power systems, used in the gelatine production. The other is the production of 130°C hot water for a drying process in the recycling industry. The paper shows that steam production in the industry with high temperature heat pumps is possible.

Selection and/or peer-review under the responsibility of the organizers of the 14th IEA Heat Pump Conference 2023.

Keywords: high temperature heat pump, steam, HFO, R1233zd;

1. Introduction

Global warming, climate change and the dependence on fossil fuels are defining challenges in the coming years and decades. In order to achieve the goals set by the EU for 2030 [1], a variety of measures are necessary. In addition to the expansion of renewable energies, it is essential to increase energy efficiency and thus reduce primary energy consumption.

About 21% of the total CO_2 emissions in Europe are due to industry [2]. Today, process heat in the range above 100°C is mainly generated with the help of fossil fuels, such as natural gas or fuel oil. A large part of the process heat in the range up to 200°C is used in the form of saturated steam. Saturated steam has the advantage of a large energy content when using the phase change and at the same time low transport costs from the point of generation to the consumer.

In recent years, the use of heat pumps as an alternative to fossil fuel heat generators has become increasingly popular for heating residential buildings. Here, mainly electrically driven compression heat pumps are used, which use environmental heat (outside air, geothermal heat) as a heat source to generate the required useful heat. When used with renewable electricity, quasi CO_2-free heat generation is thus possible.

This article shows the possibility of providing process steam or hot water from unused industrial waste heat with the help of compression heat pumps. The ThermBooster system can generate temperatures up to 165°C, or saturated steam pressures up to 6 bar absolute. The system is based on a piston compressor specially developed for use in industrial high temperature heat pumps. HFOs such as R1233zd are used as refrigerants.

Two industrial applications are shown. On shows the use of the system to produce 2 bar absolute saturated steam for use in the gelatine production. The other shows an innovative heat concept in the production of an innovative thermoplastic compound material, where the high temperature heat pump delivers 130°C hot water for a drying process.

*Tim Hamacher, Tel.: +49-2206-9050661
E-mail address: tim.hamacher@spheat.de

2. ThermBooster pilot system and process

2.1. Compressor

The core of the high temperature heat pump is a specially developed 4-cylinder piston compressor with a displacement of approx. 540 m³/h at 1500 RPM. The compressor is designed for up to 35 bar on the high-pressure side and 18 bar on the low-pressure side. Hot gas temperatures of 250°C and suction gas temperatures of 200°C are possible without any problems. The compressor is optimized by a patented valve system for HFO refrigerants of the latest generation (e.g. R1233zd, R1336mzz-Z) and achieves high isentropic and volumetric efficiencies. The valve system is characterized by an optimized arrangement and the use of the available area, thus reducing the pressure drop in the valve system to a minimum while maintaining a low clearance volume. First measurements on the testbed have shown isentropic efficiencies η_{is}, with R1233zd(E) as working fluid, in the range of 85%-95% for pressure ratios between 2,5 and 3,5. These values are calculated by measuring the pressure and temperature at compressor inlet and outlet and comparing the enthalpy difference according to formular 1. The volumetric efficiencies showed to be between 92% and 95%.

$$\eta_{is} = \frac{h_{Out,ideal} - h_{in}}{h_{Out,measured} - h_{in}} \quad (1)$$

To achieve long lifetimes and service intervals with these high temperatures, the heat pump is equipped with an oil conditioning system which always keeps the oil in a temperature range which is as low as possible, but still high enough to prevent too much refrigerant solving into the oil. The cylinder surface of the compressor together with its piston and piston rings is optimized for very low oil transport into the refrigerant circuit. It is also equipped with an oil separator in the crankcase ventilation system to reduce oil transport into the refrigeration circuit to nearly zero. Up to now, no detailed measurement was done but currently no oil transport could be observed. Depending on the refrigerant used, different type of oils will be used. For R1233zd(E) POE (Polyolester) or CE (Complexester) oils are used.

2.2. System layout

The system is designed as a compression heat pump with internal heat exchanger. Figure 1 shows the schematic structure of the system while Figure 2 shows the realised design as a CAD model.

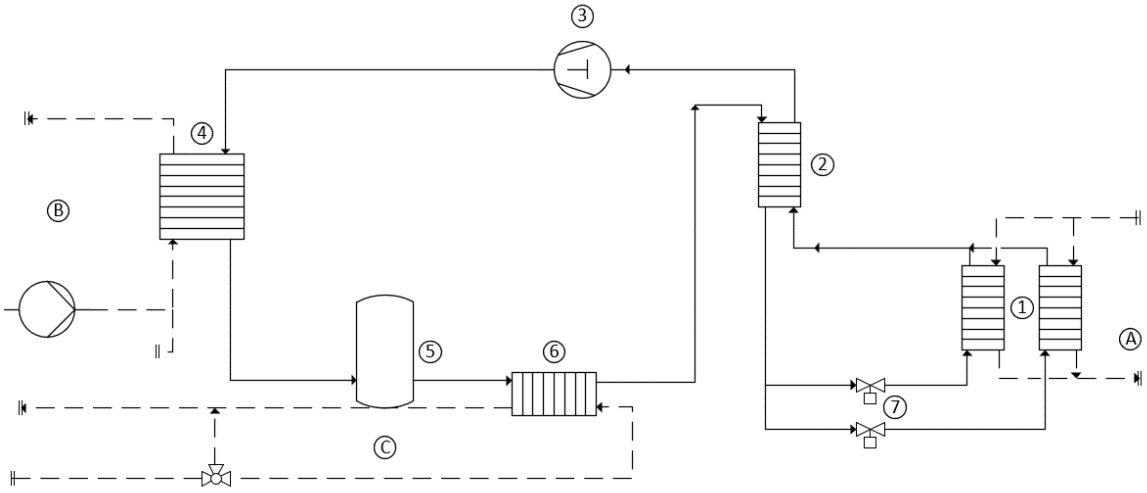


Fig. 1: principle P&ID of the heat pump

Table 1: legend for figure 1-3

Part	Description
1	Evaporator
2	Internal Heat Exchanger
3	Piston Compressor
4	Condenser / Steam Boiler
5	Receiver
6	Subcooler
7	Expansion Valve
A	Heat Source Circuit
B	Heat Sink Circuit for steam production including feed water pump
C	Subcooler Circuit for hot water

Highly efficient plate heat exchangers are used as evaporators and as internal heat exchangers. The condenser in the refrigeration circuit, which is also the steam generator in the heat sink circuit, is implemented as a Plate & Shell heat exchanger.
Plate & Shell heat exchangers offer for this application a good combination of efficiency of heat transfer from refrigerant to water and the required robustness for use in industrial steam systems. Evaporation is controlled by electronic expansion valves. To further increase efficiency, an additional subcooler has been integrated. With this subcooler, thermal energy as hot water can be extracted in parallel to the steam generation by subcooling the working fluid to lower temperatures to use it, for example, for feed water preheating or to feed it into another heating circuit.

For optimal oil conditioning, the oil sump of the compressor is equipped with a water jacket, which serves to preheat the oil and expel the dissolved refrigerant from the oil, as well as for oil cooling in high temperature operation. The required water is heated or cooled to the required temperatures by a conditioning unit integrated on the frame of the heat pump.

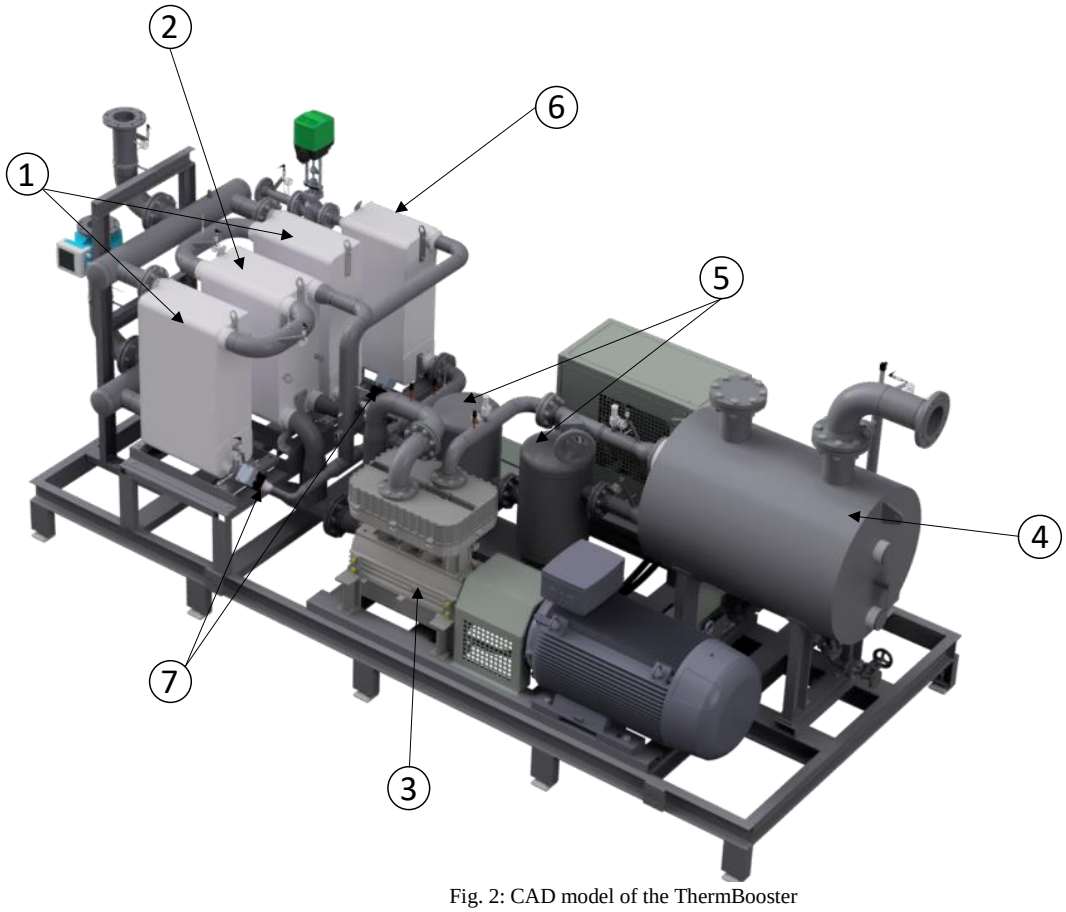


Fig. 2: CAD model of the ThermBooster

2.3. Thermodynamical cycle

The system operates as a compression heat pump with internal heat exchanger. Figure 3 shows the cycle in the log pH diagram for R1233zd(E).

Here, the process is as follows:
1) Evaporation with low superheat.
2) Superheating in the internal heat exchanger
3) Compression in piston compressor
4) Desuperheating and condensation
6) Subcooling in water-cooled subcooler
2) Subcooling in internal heat exchanger
7) Expansion in expansion valve and evaporator

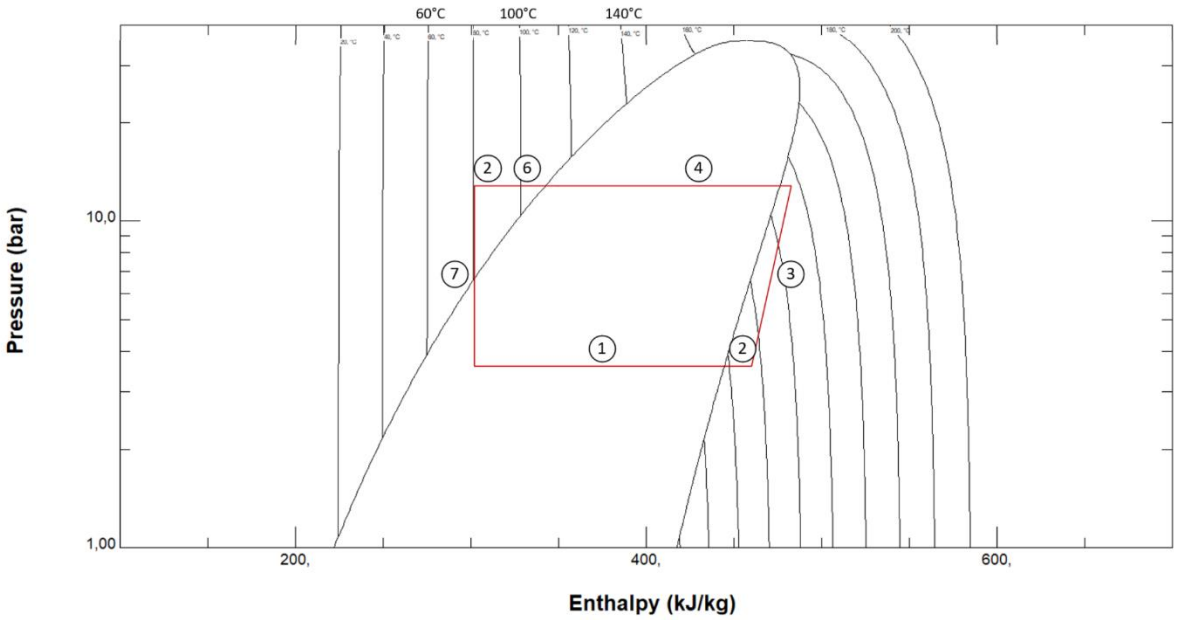


Fig. 3: log PH diagram of the thermodynamical cycle

3. Applications in industry

In the following, several project examples in industry are presented. The examples come from the food and recycling sector and show the wide range of possible applications of such systems for the generation of process heat with heat pumps. In addition to the integration, the effects on CO2 emissions are shown with the help of model calculations.

3.1. Gelatine production

Gelatine is mainly obtained from animal components, such as hides and bones of cattle and pigs. For this purpose, after thorough cleaning, the animal products must be pre-treated with the aid of acids so that the gelatine can then be extracted. The extraction is then carried out in several stages using hot water, with the water temperature being increased at each stage. The gelatine solution obtained, which now contains 2-5% gelatine, is then purified of solids before being concentrated to about 20-40%. This is usually done by vacuum evaporator. After leaving the concentration, the gelatine is thermally sterilized. Depending on the desired product (powder or sheet gelatine), various thermal drying processes are now used.

It can be clearly seen that thermal energy is required for most of the different process steps. Most of the thermal energy is required for the drying processes, where also the highest temperatures are needed.

3.1.1. Boundaries/ pre installation status

Currently, heat is generated by a gas-fired steam generator and several cogeneration units, which are used to supply electricity to the plant. There are two heat rails at the plant. A hot water rail at about 85°C and a steam rail at 2 bar absolute, corresponding to 120°C. The hot water rail is mainly fed by the cooling water heat from the CHP units and is used to provide process heat and heat for heating the buildings. The steam line is used exclusively to provide process heat. Since the demand for floor heating varies greatly from season to season and the demand for hot water is also relatively low, there is unused heat at this temperature level, most of which is now discharged to the environment via dry coolers. Figure 4 schematically shows the current situation in heat generation.

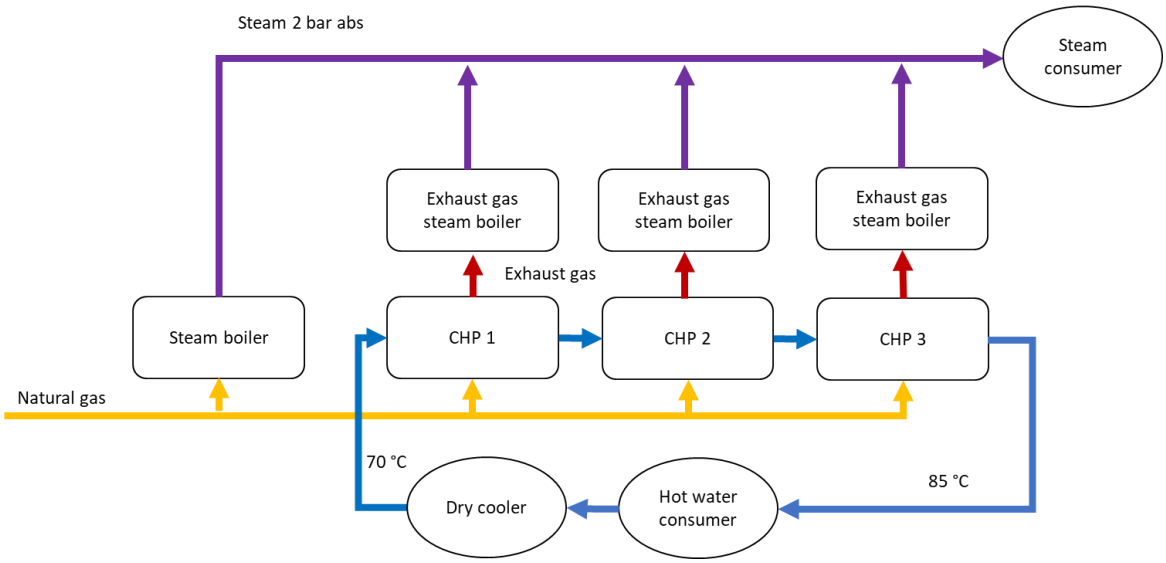


Fig. 4: current heat generation concept

3.1.2. Integration

In the future, the heat pump will replace the dry coolers and ensure that 100% of the heat generated is used on the 80°C hot water rail for production and space heating and not-longer wasted into the environment. For this purpose, the heat pump is integrated into the circuit parallel to the existing consumers and thus uses the 80°C heat rail as a heat source.

The heat pump used corresponds to the system presented in chapter 2, only without using the subcooler. Figure 5 shows the planned integration. The heat pump has to cool down the heat source to 70°C in order to use all available energy of the cooling water, because this 70°C is needed to be able to cool the CHP units.

Table 2 shows the integration conditions and the resulting performance data of the heat pump. All results are currently mostly based on simulations in combination with first results from the testbed. The heat pump will be installed beginning of 2023. The heat pump evaporates at about 67°C and condenses at about 125°C, giving an internal temperature lift of 58K. The theoretical Carnot efficiency related to evaporation and condensation temperature results from formula 2 to 6.9, this means that we reach here with the achieved COP of 4,4 a Carnot quality of 64% related to evaporation and condensation temperature. This is one used definition of the Carnot quality, another possibility is to calculate it related to the hottest and coldest process temperatures which are here the steam temperature of 120,2 °C and the heat source outlet temperature of 70°C. Using these temperatures, the Carnot quality reduces to 56%.

$$COP_{Carnot} = \frac{T_{Cond}}{T_{Cond} - T_{Evap}} \quad (2)$$

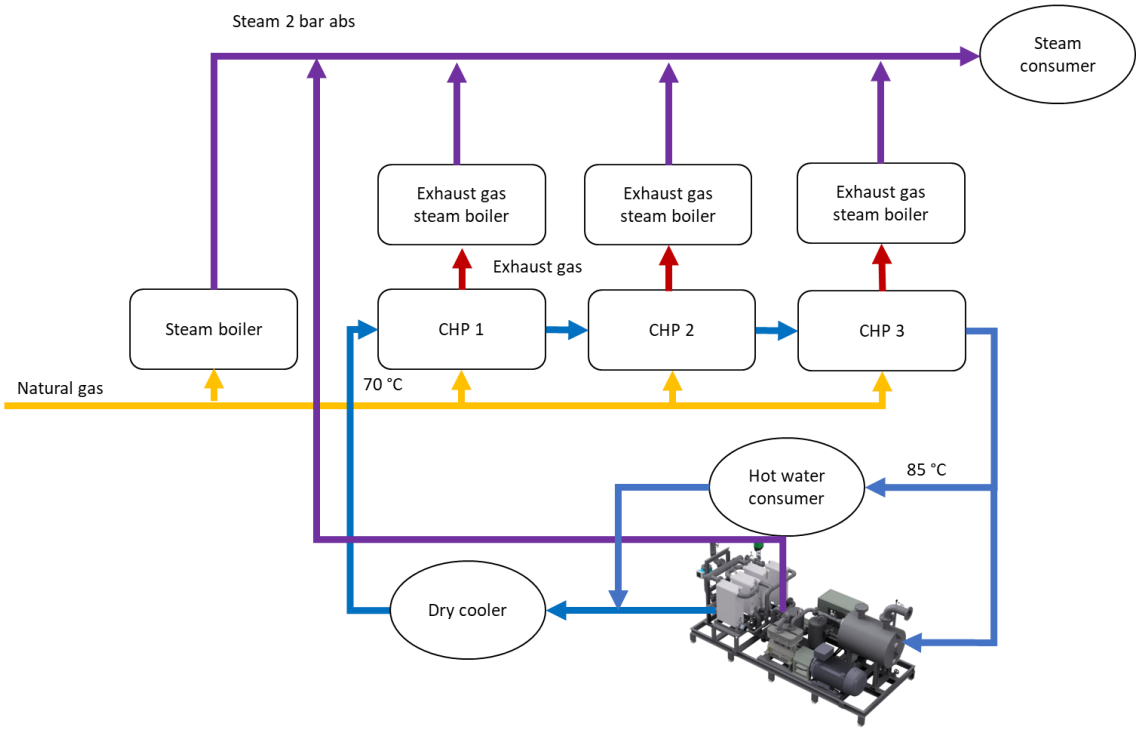


Fig. 5: planned integration of the heat pump

Table 2: boundary conditions and simulated performance data for heat pump integration

Parameter	Value
Heat Source Inlet	85°C
Heat Source Outlet	70°C
Feedwater In	85°C
Saturated Steam Pressure	2 bar absolute
Thermal Output	514 kW (812 kg/h)
Cooling Power	407 kW
Electrical Consumption	118 kW
COP	4,4
Refrigerant	R1233zd(E)

3.1.3. Environmental impact

Since the plant uses the heat supply about 8000h per year, about 6500 t of steam will be produced by the heat pump in the future with an electrical consumption of about 944 MWh yearly. This corresponds approximately to 4,1 GWh of thermal energy as steam. Assuming an efficiency of 85% in relation to the fuel input for a standard gas-fired steam boiler, approx. 4.8 GWh of natural gas will be saved. If a CO_2 emission factor of 0,201 t/MWh_gas [2] is taken as the basis for calculation, approx. 960 t CO_2 are avoided here. The exact CO_2 emission factor of the electricity used is not known. Different approaches can be used here.

1. CO_2 emission factor of CHP electricity (42% electrical efficiency) = 0,479 t/MWh_el.
2. CO_2 emission factor when changing the energy source to electricity = 0,366 t/MWh_el [3].
3. use of own electricity from the existing and planned PV systems + purchase of electricity from renewable sources = 0 t/MWh_el.

Thus, depending on the approach, the CO2 savings result in values between 508t and 960t savings per year.

Table 3: yearly CO2 savings

Electrical Energy Source	**CO_2 emission factor**	**Yearly CO_2 emission from electricity**	**Yearly CO_2 savings**
1 CHP produced	0,479 t/MWh_el	452 t	508 t
2 Change to electricity	0,366 t/MWh_el	345,5 t	614,5 t
3 Own + renewable electricity	0 t/MWh_el	0 t	960 t

3.2. Recycling industry

Recycling of used materials and raw materials is becoming increasingly important. More and more new processes for recycling waste are being developed and implemented on an industrial scale. In the following process, conventional household waste is converted into a high-quality thermoplastic composite material. For this purpose, household waste, previously considered non-recyclable, is taken and split into its basic components of lignin, cellulose, fibers and sugar in a complex process and then reassembled into a new matrix, the thermoplastic composite material. This is to be used in various applications in the future, e.g., for vehicle interiors.

One process step in the production is the drying of the material. Temperatures of around 130°C are required for this.

3.2.1. Boundaries

This project involves the construction of the first industrial application for the production of the new thermoplastic composite material. It was decided that the use of fossil fuel was not an alternative, so a comprehensive heat utilization concept was developed from the outset to bundle various waste heat streams and use them as a source for a high temperature heat pump. The concept includes various cooling and heating circuits at different temperature levels, all of which are interconnected.

3.2.2. Integration

The high temperature heat pump is the last link in a series of heat pumps providing thermal energy at different temperature levels. The schematic in Figure 6 shows only a very rough concept focusing on the different heat pumps. In addition to these heat pumps, there are several other thermal exchangers such as process heat exchangers or dry coolers for winter relief (delivering cooling water from cold outside temperatures instead of using the chiller) or even buffer storage. The circuit with the lowest temperature operates at 8°C and is used to cool various process steps. This temperature is generated by a chiller, which condensing heat is used in a water circuit at about 35°C. This level is used for cooling or heat recovery from warm material and exhaust air streams as well as for preheating material streams. It then serves as a source for a medium temperature heat pump that raises the temperature level to about 75°C-80°C. This level in turn serves as a source for various process steps, as well as a source for the high temperature heat pump. This then provides 130°C hot water for the drying processes. Approximately 1.5 MW of heating power is required for drying. Two heat pump systems, each with two independent refrigeration circuits, are used here, each with a thermal output of approx. 1 MW, so that only three of the installed refrigeration circuits are in operation at any one time and one circuit serves as redundancy or can cover power peaks in certain situations.

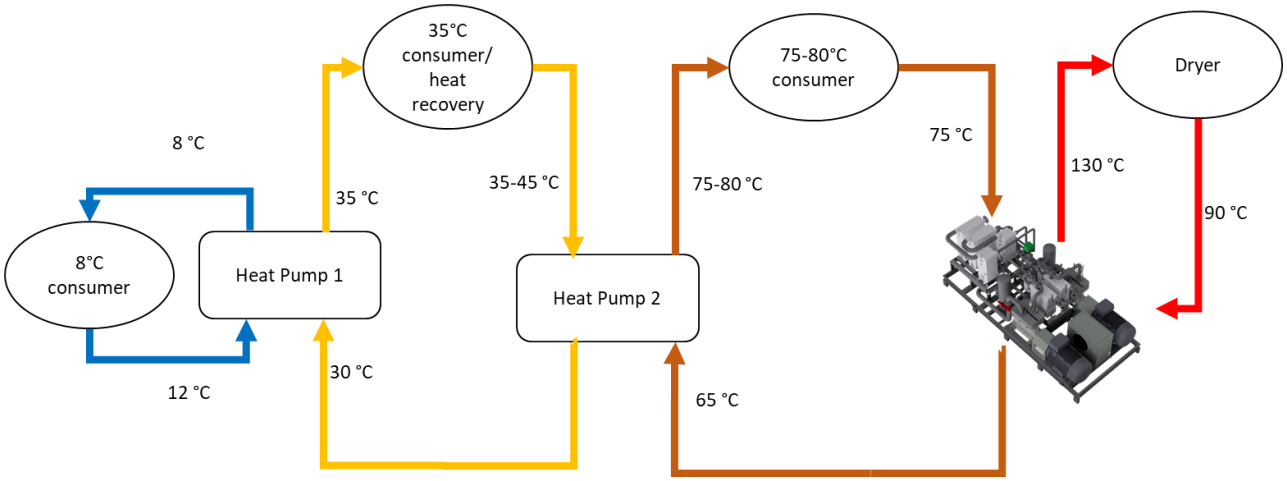


Fig. 6: thermal concept of the combination of cooling and heating circuits

3.2.3. High temperature heat pump system

Since this application does not use steam as a heat transfer medium, but hot water, the setup differs from the pilot system shown in chapter 2. Figure 7 shows the circuit diagram for the systems used.

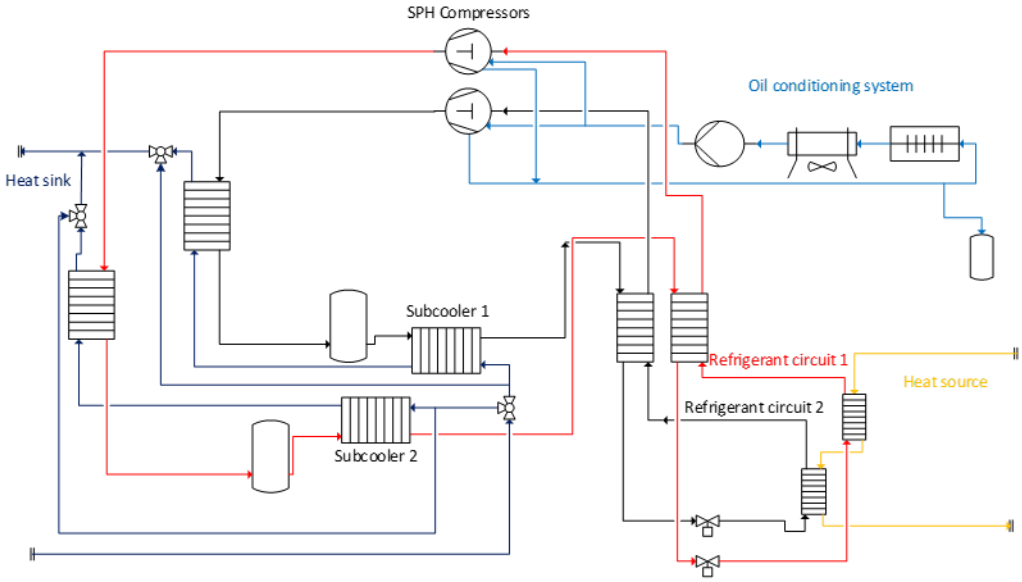


Fig. 7: P&ID 2 circuit hot water system

In the CAD model in Figure 8, you can see the compact design with the two compressors on the outside, condensers and subcoolers placed in between. At the other end are the evaporators connected in series and the internal heat exchangers. The design data applicable to this application can be found in Table 4. Because of the series-connected evaporators, the two refrigeration circuits operate at different evaporating pressure levels. In the first circuit, the evaporating temperature is about 67°C and in the second about 62°C. The condensing temperature, in turn, is very similar in both circuits at about 129°C. To make optimum use of the large spread in the heat sink, a subcooler was placed downstream of the condenser in each case to be able to subcool the refrigerant further and extract thermal energy. Due to the different evaporation temperatures od the two circuits, they don't have an identical power output. To be able to reach 130°C in each circuit a distribution valve is integrated between in the heat source water circuits. An additional distribution valve in each subpart of the water circuit helps to speed up the warm-up process if the complete water circuit is cold. In this case

only a small part of the flow goes through the subcooler and condenser to reach higher refrigerant temperatures in the condenser. This helps in the warm up process due to higher temperatures in liquid part of the internal heat exchangers which then lead to higher superheat before the compressor and the possibility to go to higher evaporation temperatures earlier. In the case of water as a heat sink, the Lorenz COP (2) is often used instead of the Carnot COP to assess the efficiency of the system. Here, no individual temperatures of the process are used as reference, but the entropic mean temperatures are used.

$$COP_{Lorenz} = \frac{\hat{T}_H}{\hat{T}_H - \hat{T}_L} \tag{2}$$

The entropic mean temperatures are defined as follows.

$$\hat{T}_H = \frac{\Delta T_H}{\ln\left(\frac{T_{H,o}}{T_{H,i}}\right)} \qquad \hat{T}_C = \frac{\Delta T_C}{\ln\left(\frac{T_{C,i}}{T_{C,o}}\right)} \tag{3}$$

With T_H the temperatures on the heat sink side and T_C the temperatures on the heat source side.

In this application, the Lorenz COP is 9.6. With a designed and simulated COP of 4,4 for the high temperature lift from 75°C to 130°C, this means a Lorenz quality of approx. 46%. The system will be installed in the first half of 2023.

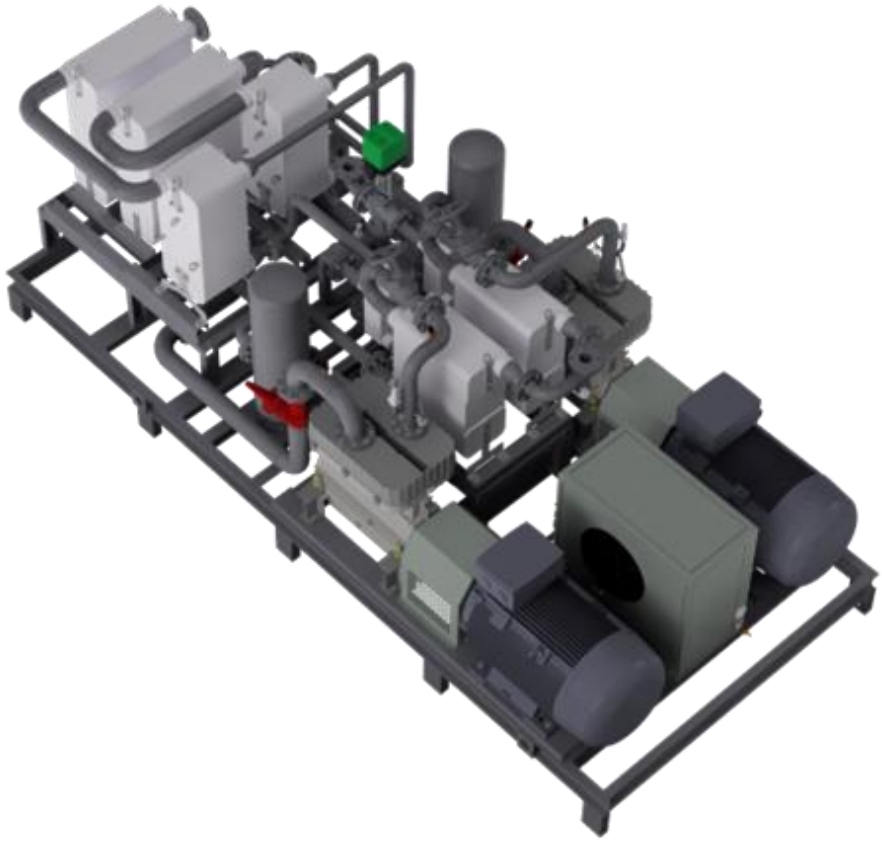


Fig. 8: CAD model of hot water system

Table 4: boundary conditions and simulated performance data for hot water heat pump

Parameter	Value
Heat Source Inlet	75°C
Heat Source Outlet	65°C
Heat Sink Inlet	90°C
Heat Sink Outlet	130°C
Thermal Output	1017 kW
Cooling Power	809 kW
Electrical Consumption	229 kW
COP	4,4
Refrigerant	R1233zd(E)

3.2.4. Environmental impact

With a planned annual service life of approx. 8000h, about 10.8 GWh of thermal process energy will be produced in the future. This corresponds to approx. 1.25 Mm^3 of natural gas, which will not be required through the use of the heat pump. As the user consequently follows the principle of sustainability, only CO_2 neutral produced electricity is used in this project, so that approx. 2400 t CO_2 per year are avoided compared to a natural gas fired process heat production.

4. Summary

This paper shows the commercial availability of a high temperature heat pump system to produce steam and hot pressurized water in industrial applications. With current HFO fluids temperatures up to 165°C are possible. The system is based on a newly developed piston compressor, optimized for the use in high temperature heat pumps. The system is built as a standard compression cycle heat pump with internal heat exchanger.

The first application which will be delivered into the galantine production and produces steam at 2 bar abs (120°C) with using cooling water from CHP units at a level of 85°C/70°C. For this application a COP of 4,4 has been simulated. The second application is production of 130°C hot water for a drying process in the recycling industry. Here the heat source is given by the waste heat from chiller systems which are combined between 8°C up to 130°C. Here the last step of this cascade, the high temperature heat pump, reaches a COP of 4,4.

References

[1] European Commission, *2030 climate & energy framework*,Website of the European Commission, https://climate.ec.europa.eu/eu-action/climate-strategies-targets/2030-climate-energy-framework_de, 9.2.2023

[2] Eurostat, *EU economy greenhouse gas emissions in Q2 2022*, WebsiteEurostat, https://ec.europa.eu/eurostat/de/, online data code: env_ac_aigg_q

[3] Bundesamt für Wirtschaft und Ausfuhrkontrolle der Bundesrepublik Deutschland, *Informationsblatt CO2-Faktoren*, Version 1.2, Stand 1.10.22

14th IEA Heat Pump Conference
15-18 May 2023, Chicago, Illinois

Application of multipurpose heat pumps in museums: a case study

Eva Schito*, Paolo Conti, Daniele Testi

Department of Energy, Systems, Territory and Construction Engineering (DESTEC), University of Pisa, Largo Lucio Lazzarino 1, 56122 Pisa, Italy

Abstract

The present work deals with the achievable benefits of using multipurpose heat pumps in museums, where heating and cooling are simultaneously required to ensure proper indoor conditions for artworks preservation. Air-handling units are usually installed to control temperature and relative humidity through both hot and cold coils that are usually fed by dedicated heat generators (e.g., heat pumps, boilers, and chillers). Using a multipurpose heat pump can reduce electrical input, as the same device can concurrently provide both heating and cooling power with a single energy input and recovering energy between the cold and the hot coils. In this perspective, the present work presents a representative real case study for Mediterranean climate. The building thermal load and the HVAC performances have been simulated in TRNSYS 17 and MATLAB with an hourly time step. The multipurpose heat pump provides an energy saving equal to 25% in cooling season compared to the use of a separate heat pump and a chiller. Indeed, the heating load is almost entirely met through the recovery of the condenser heat without significant additional energy input.

© HPC2023.
Selection and/or peer-review under the responsibility of the organizers of the 14th IEA Heat Pump Conference 2023.

Keywords: Multi-purpose heat pump; energy savings; building dynamic simulation; heat recovery.

1. Introduction

1.1. Context

Energy reduction in the building sector is crucial to achieve the objectives set by the United Nations and European Union for the reduction of greenhouse gas emissions [1-2]. Currently, buildings in the European Union are responsible for about 40% of the total energy consumption for the services of heating and cooling [3].

In the last decades, the use of heat pumps (HP) for heating purposes has increased, thanks to their performance especially in the case of low supply temperatures and mild climates. Modern HPs also provide cooling service if a reversing valve is present resulting in an advantageous device that can be used in both winter and summer.

The market share of HP has been notably increasing in recent years: in 2020 the sold heat pumps in EU Countries were more than 1.5 million, about 50% more than the sold units in 2016 [4]. Air-to-water units account for ~13% of the total air-source market with 1.5 M units sold in the 2015–2019 period and a total installed capacity of ~24 GW at the end of 2019. HPs are also strategic devices for increasing the renewable share in nearly Zero Energy Buildings (nZEB), integrated hybrid systems, smart microgrids, and energy communities thanks to the energy shifts between heat to electricity: better exploitation and storage of renewable production (e.g., photovoltaic modules) is thus possible, also through advanced and optimally controlled demand response and power-to-heat strategies. Therefore, HP installation in new or existing buildings is often supported by national governments through several forms of incentives.

* Corresponding author. Tel.: +39 050 2217 111, *E-mail address:* eva.schito@for.unipi.it

An additional possible application of HP technology for energy efficiency purposes is the use of the so-called *multipurpose heat pumps (MP-HP)*, which are chillers where a total recovery of the heat at the condenser is possible. This type of generator, also called *total recovery chiller*, can be particularly useful in buildings where heating and cooling are simultaneously required. MP-HPs can be seen as both co-generators able to provide two different energy services by using a single energy input, or as a recovery solution as the removed "cold energy" is not dissipated into the environment, but it is re-injected at a higher temperature.

1.2. Literature review

The analysis of the state of the art on MP-HPs has shown a limited application of this technology on scientific research, even if the found results has hinted that this generator allows significant energy savings compared to traditional systems. The literature analysis results fragmented, also because this technology is presented with a variety of different names (such as multipurpose heat pump, multi-heat pump, total recovery chiller, multifunctional heat pump), making the literature research difficult.

Most of the papers on this topic presents experimental tests on MP-HP. Agrawal et al. [5] present the results of experimental test on a CO2 transcritical MP-HP for simultaneously production of heating and cooling services. Kang et al [6] carry out measurements on a MP-HP directly exchanging with indoor air, evaluating COP when varying compressor speed ratio. Liu et al [7] present the performance of a prototype MP-HP for both heating and domestic hot water services. At evaporator, this prototype can use external air, gray water, or both these sources with an either parallel or series configuration. The results show that the optimal performance is reached with the parallel configuration at evaporator, using both sources. Other works are aimed at enhancing the MP-HP performances with different methods. As an example, Boahen et al [8] tested a cascade MP-HP for the simultaneous delivering of heating, cooling and domestic hot water at different level of temperatures. In their series of papers, Byrne et al. [9-11] present the results of an in-house designed heat pump for multiple services. First, the performance was measured in steady-state conditions, using R407C as refrigerant [9]. In their second paper [10], the dynamic behavior of the heat pump was analyzed, focusing on the performance during transition among operational modes (e.g., from only cooling delivering to both cooling and heating delivering) and on the possibility of partially recovering heating to be used for defrosting. Finally [11], two refrigerants are compared (i.e., R407C and R290) to evaluate best energetic and exergetic performances. Cho et al [12] designed and tested a MP-HP, seeking the optimal refrigerant charge to enhance the total efficiency of the system, in different load and operation conditions. Chiu et al [13] show the results of a monitoring campaign on an air conditioning system where the heat recovery at the condenser is used for domestic hot water purposes.

A small amount of research papers focuses instead on the simulation of MP-HP performances when applied to case studies. Diaby et al. [14] compare two possible applications of a CO2 transcritical MP-HPs in a hotel: in the first case, the heat pump is used for heating, cooling and domestic hot water services; in the second one, the heat pump is used for simultaneous cooling and desalinization purposes. The latter application shows better performances due to the more suitable process temperatures. In [15], the authors expose the outputs of the application of MP-HPs in three climates and three different buildings: a low-energy residential building, a retail store and a small office building. The results hint that applying MP-HP in low-energy residential building allows higher energy savings, as this type of building has often simultaneous heating and cooling load, depending on the solar gains. Shen et al. [16] simulated the performance of MP-HPs in ten different US cities, using a restaurant as case study, for simultaneous production of either heating and domestic hot water, or cooling and domestic hot water. The comparison of electrical energy needs with this technology and a classical solution with heat pump/chiller and electric heater shows savings ranging between 47% and 64%.

1.3. Aim and presentation of the research

The present research aims at evaluating the achievable energy savings when a MP-HP is used as the thermal generator in an environment where heating and cooling services are simultaneously required. The MP-HP performance is compared to a classical configuration where two different generators are used, namely an electric heat pump and an electric chiller. After a presentation of the energy models of the generators (Section 2), we show a case study consisting of a museum room in Italy where temperature and relative humidity should be carefully controlled to avoid artwork degradation (Section 3). To maintain the indoor setpoint values, an air handling unit (AHU) is used, thus requiring both heating and cooling services, especially in the cooling period where the dehumidification demand is high. Two different configurations are compared: the so-called "separate configuration" with two separate hot and cold generators: e.g., the heat pump and the chiller, and an

MP-HP configuration where a unique multipurpose heat pump is used (see Fig. 1 and 2, respectively). The Results Section (Section 4) presents the comparison of the total electrical energy consumption of the two configurations, demonstrating the effectiveness of the multipurpose heat pump.

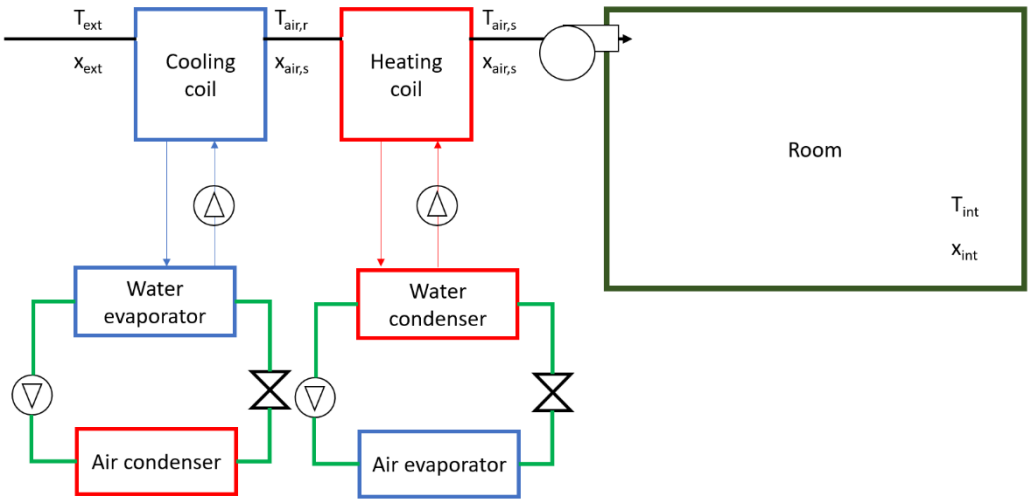


Fig. 1. The separate configuration, with a chiller and a heat pump, working separately for the AHU cooling and heating coil.

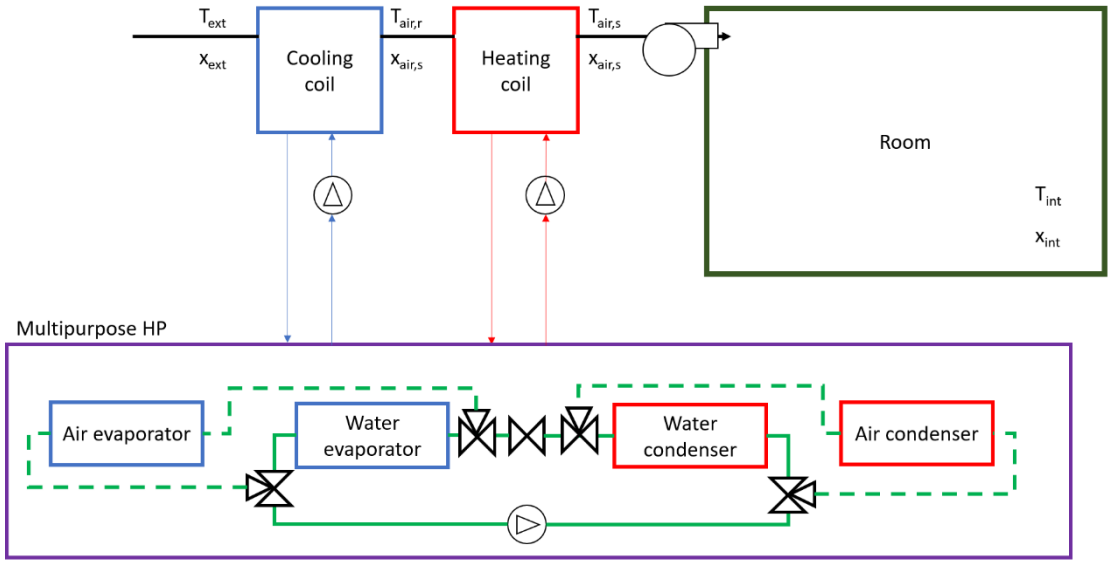


Fig. 2. MP-HP configuration where the generator provides both hot and cold water for the AHU cooling and heating coil..

2. The model

2.1. Multipurpose heat pump (MP-HP)

The considered MP-HP unit is a market-available device and the energy model is based on the manufacturer datasheets [17]. Depending on the dynamic load profile, external air temperature, and humidity, the AHU can only require heating power at the reheat coil ($\dot{Q}_{H,r}$), cooling power at the cooling coil ($\dot{Q}_{C,r}$), or both services

at the same time ($\dot{Q}_{H,r}$ and $\dot{Q}_{C,r}$). According to the manufacturer's data [17], the considered multipurpose heat pump can work in three different operational modes (see also Fig. 3):

1. as a classical chiller, only providing cold water to the AHU cooling coil and using an outdoor-air heat exchanger as a condenser (Mode 1). In this case, the absorbed electrical energy at the compressor is evaluated as a function of the supply temperatures to the cooling coil ($T_{C,s}$) and partial load conditions (CR):

$$\frac{\dot{Q}_{C,r}}{\dot{E}_{el}} = EER_{C,MP-HP}(T_{C,s}, CR) \tag{1}$$

2. as a classical heat pump, only providing hot water to the AHU reheat coil and using an outdoor-air heat exchanger as an evaporator (Mode 2) In this case, the absorbed electrical energy at the compressor is evaluated as a function of the supply temperatures to the reheat coil ($T_{H,s}$) and partial load conditions (CR):

$$\frac{\dot{Q}_{H,r}}{\dot{E}_{el}} = COP_{H,MP-HP}(T_{H,s}, CR) \tag{2}$$

3. as a multipurpose heat pump; providing both cold and hot water to the AHU. In other words, the MP-HP operates as a chiller with a total recovery of the heat at the condenser (Mode 3). Air heat exchangers do not operate and possible discrepancies between hot/cold generations and thermal loads are managed using ad buffer water storages, according to the following control strategy [17]:
   - The MP-HP tries meeting the cooling load, evaluating the absorbed electrical energy at the compressor as a function of the supply temperatures to the hot and cold coils ($T_{H,s}$ and $T_{C,s}$, respectively) and partial load conditions (CR):

$$\dot{E}_{el} = \frac{\dot{Q}_{C,r}}{EER_{H\&C,MP-HP}(T_{H,s}, T_{C,s}, CR)} \tag{3a}$$

$$\dot{Q}_{H,MP-HP} = \dot{Q}_{C,r} + \dot{E}_{el} \tag{3b}$$

   - If $\dot{Q}_{H,MP-HP} \geq Q_{H,r}$, the multi-purpose heat pump follows the cooling load ($\dot{Q}_{C,MP-HP,eff} = Q_{C,r}$, $\dot{Q}_{H,MP-HP,eff} = \dot{Q}_{H,MP-HP}$), storing the possible heating surplus ($\dot{Q}_{H,MP-HP} - \dot{Q}_{H,r}$) in the hot thermal buffer. In this case, Eqs. 3a and 3b apply.
   - If $\dot{Q}_{H,MP-HP} < Q_{H,r}$, the multi-purpose heat pump follows the heating load by increasing its thermal output at the condensing section ($\dot{Q}_{H,MP-HP,eff} = Q_{H,r}$). The corresponding effective cooling production ($\dot{Q}_{C,MP-HP,eff}$) at the evaporator increases to a value higher than the cooling load ($\dot{Q}_{C,r}$), thus the cooling surplus ($\dot{Q}_{C,MP-HP,eff} - \dot{Q}_{C,r}$) is stored in the cold thermal buffer. In this case, Eqs. 3a and 3b are slightly modified as:

$$\dot{E}_{el} = \frac{\dot{Q}_{C,MP-HP,eff}}{EER_{H\&C,MP-HP}(T_{H,s}, T_{C,s}, CR)} = \frac{\dot{Q}_{H,r}}{\left(1 + EER_{H\&C,MP-HP}(T_{H,s}, T_{C,s}, CR)\right)} \tag{4a}$$

$$\dot{Q}_{H,MP-HP,eff} = \dot{Q}_{H,r} = \dot{Q}_{C,MP-HP,eff} + \dot{E}_{el} \tag{4b}$$

We arbitrarily chose the EER as the reference thermodynamic coefficient of performance of the MP – HP. Analogous formulae can be deployed by using condenser output and COP definition to model the MP-HP performances. Moreover, for the sake of simplification, the cold and hot thermal buffers are considered as ideal, without thermal losses or energy exchange constraints.

The values of $EER_{C,MP-HP}(T_{C,s}, CR)$, $COP_{H,MP-HP}(T_{H,s}, CR)$, and $EER_{H\&C,MP-HP}$ are obtained through the polynomial fitting of the nameplate data provided by the manufacturer [17] (see, for instance, Eqs. 5).

$$TR = \left(\frac{T_{H,s} + 273.15}{T_{C,s} + 273.15}\right) \tag{5a}$$

$$CR = \left(\frac{\dot{Q}_{C,r}}{\dot{Q}_{C,NOM,MP-HP}}\right) \tag{5b}$$

$$EER_{H\&C,MP-HP}(T_{H,s}, T_{C,s}, CR) = [\alpha_0 + \alpha_1 \times TR + \alpha_2 \times CR + \alpha_3 \times TR^2 + \alpha_4 \times TR \times CR] \times \left(\frac{T_{C,s} + 273.15}{T_{H,s} - T_{C,s}}\right) \quad (5c)$$

In Eqs. 5, the values of temperatures are in °C.

The nameplate data of the multipurpose heat pump working in Mode 1, Mode 2, and Mode 3 are reported in Table 1, Table 2, and Table 3, respectively.

Table 1. Values of cooling load, input electrical energy, and performance of a multipurpose heat pump operating in Mode 1 (data from [17]).

		$T_{ext} = 35\ °C$			$T_{ext} = 30\ °C$			$T_{ext} = 20\ °C$		
		$\dot{Q}_{C,MP-HP}$	$\dot{E}_{el}$	$EER_{C,MP-HP}$	$\dot{Q}_{C,MP-HP}$	$\dot{E}_{el}$	$EER_{C,MP-HP}$	$\dot{Q}_{C,MP-HP}$	$\dot{E}_{el}$	$EER_{C,MP-HP}$
		[kW]	[kW]	[-]	[kW]	[kW]	[-]	[kW]	[kW]	[-]
CR=1	$T_{C,s} = 7\ °C$	43.0	14.0	3.07	46.4	12.9	3.61	52.5	10.9	4.80
	$T_{C,s} = 12\ °C$	49.8	14.7	3.39	53.8	13.7	3.92	59.8	11.5	5.21
	$T_{C,s} = 15\ °C$	54.2	15.1	3.58	57.2	14.0	4.09	63.6	11.9	5.35
CR=0.55	$T_{C,s} = 7\ °C$	23.7	6.3	3.75	25.5	5.8	4.41	28.9	4.9	5.87
	$T_{C,s} = 12\ °C$	27.4	6.6	4.15	29.6	6.2	4.79	32.9	5.2	6.36
	$T_{C,s} = 15\ °C$	29.8	6.8	4.38	31.5	6.3	4.99	35.0	5.4	6.54

Table 2. Values of heating load, input electrical energy, and performance of a multipurpose heat pump operating in Mode 2 (data from [17]).

		$T_{H,s} = 35\ °C$			$T_{H,s} = 45\ °C$			$T_{H,s} = 55\ °C$		
		$\dot{Q}_{H,MP-HP}$	$\dot{E}_{el}$	$COP_{H,MP-HP}$	$\dot{Q}_{H,MP-HP}$	$\dot{E}_{el}$	$COP_{H,MP-HP}$	$\dot{Q}_{H,MP-HP}$	$\dot{E}_{el}$	$COP_{H,MP-HP}$
		[kW]	[kW]	[-]	[kW]	[kW]	[-]	[kW]	[kW]	[-]
CR=1	$T_{ext} = 0\ °C$	48.8	10.6	3.05	30.8	12.8	2.41	28.5	15.8	1.83
	$T_{ext} = 7\ °C$	55.7	11.0	4.45	46.0	13.2	3.48	42.3	16.0	2.65
	$T_{ext} = 15\ °C$	32.2	11.1	5.02	53.4	13.3	4.00	46.7	16.1	3.08
CR=0.55	$T_{ext} = 0\ °C$	15.4	4.8	3.39	23.0	5.8	2.67	14.3	7.0	2.03
	$T_{ext} = 7\ °C$	24.4	4.9	4.95	26.7	5.9	3.87	21.2	7.2	2.94
	$T_{ext} = 15\ °C$	27.8	5.0	5.58	15.4	6.0	4.45	24.8	7.2	3.43

Table 3. Values of cooling load, input electrical energy, and performance of a multipurpose heat pump operating in Mode 3 (data from [17]).

		$T_{H,s} = 35\ °C$			$T_{H,s} = 40\ °C$			$T_{H,s} = 55\ °C$		
		$\dot{Q}_{C,MP-HP}$	$\dot{E}_{el}$	$EER_{H\&C,MP-HP}$	$\dot{Q}_{C,MP-HP}$	$\dot{E}_{el}$	$EER_{H\&C,MP-HP}$	$\dot{Q}_{C,MP-HP}$	$\dot{E}_{el}$	$EER_{H\&C,MP-HP}$
		[kW]	[kW]	[-]	[kW]	[kW]	[-]	[kW]	[kW]	[-]
CR=1	$T_{C,s} = 6\ °C$	49.6	11.3	4.37	45.2	13.4	3.38	36.3	15.9	2.28
	$T_{C,s} = 10\ °C$	54.8	11.9	4.61	46.3	17.6	2.64	41.5	16.5	2.52
	$T_{C,s} = 15\ °C$	61.1	12.6	4.87	56.8	14.6	3.89	48.4	17.1	2.82
CR=0.55	$T_{C,s} = 6\ °C$	28.3	5.10	5.34	24.9	6.01	4.14	19.9	7.17	2.78
	$T_{C,s} = 10\ °C$	30.2	5.35	5.64	25.4	7.90	3.22	22.8	7.41	3.08
	$T_{C,s} = 15\ °C$	33.6	5.65	5.95	31.2	6.56	4.76	26.6	7.71	3.45

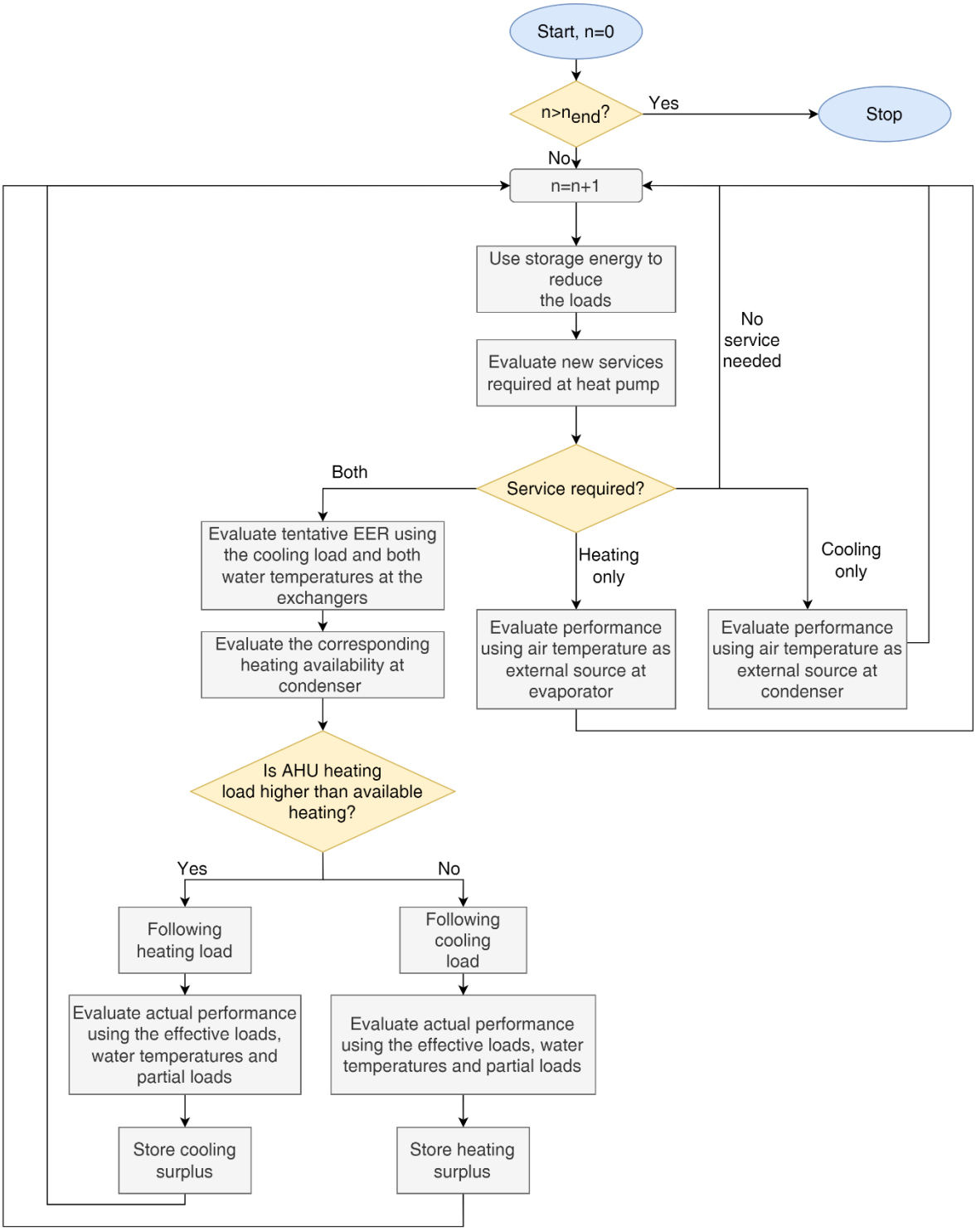


Fig. 3. MP-HP control strategy adopted in this study.

2.2. Separate heat pump and chiller configuration

For the separate configuration, the same regression coefficients obtained by fitting the data in Tables 1 and 2 are used. Using these values, the performances of the two generators in the separate configuration are evaluated as in Mode 1 (“Only cooling”) and Mode 2 (“Only heating”). The performance coefficients are named $COP_{H,SC}$ and $EER_{C,SC}$.Application of the model to a museum showroom

To compare the efficiency of a multipurpose heat pump with the two separate generators, we selected a case study consisting of a room of a museum hosting temporary exhibitions in Pisa, Italy. The simulation period starts on July 1st up to August 31st, with a one-hour timestep. The reference outdoor climate (external temperature, relative humidity, horizontal solar radiation) refers to the TMY provided by the Italian Thermotechnical Committee [18].

The considered room has a floor area of 100 m^2 and a volume of 500 m^3; walls are made of bricks and masonry (U-value of external walls: 1.1 W/(m^2K)) and no glazed elements. For the maintenance of indoor conditions, an AHU is used, consisting of a cooling/dehumidifier coil, a reheat coil, a steam vaporizer, and a fan.

The room is kept at precise internal conditions to avoid artwork deterioration:

- The indoor temperature setpoint is equal to 25 °C, with a control dead band of $\pm$1K;
- The indoor relative humidity is equal to 50%, with a control dead band of $\pm$2%.

An hourly profile of visitors has been used as the source of both sensible and latent internal gains; the maximum peak is 100 visitors. The visitors can visit the museum every day from 9:00 a.m. to 7:00 p.m. However, to ensure the maintenance of the indoor air setpoints, the AHU can be activated 24/7.

Other details on the case study and visitors' presence profile can be found in [19-20]. For the simulation of the AHU, a dynamic model has been used [21]: this model simulates the behavior of the various components (two heating coils, a vaporizer, and a cooling coil) using ϵ-NTU equations, mass and heat balance. The model evaluates the temperature and humidity ratio exiting the single coils ($T_{air,r}$ and $x_{air,r}$, at the end of the cooling coil, and $T_{air,s}$ and $x_{air,s}$ at the end of heating coil), knowing the external parameters (T_{ext} and x_{ext}), ensuring the room energy requirements. The energy balance at the coils allows the evaluation of the supply temperatures $T_{H,s}$.and $T_{C,s}$, More information on this model can be found in [21].

The building-HVAC system has been simulated in TRNSYS 17 [22] and MATLAB [23] obtaining the hourly values of the performance coefficients and electrical energy input as presented in Section 2. The two configurations in previous Figs. 1 and 2 are then compared in terms of seasonal energy input.

3. Energy performance results

Through the dynamic simulation of the building-AHU system, hourly values of supply temperatures $T_{H,s}$.and $T_{C,s}$ at the cooling and heating coils are calculated. Those temperatures are the required temperatures at the evaporator and condenser of the devices, the same in both "separate" and "combined" configurations as they depend on the same thermal loads and heat transfer performances of the two coils. Through the thermal loads, the supply temperatures and (in case of a single energy load) the external temperature, the performance of the heat pump is evaluated.

On average, the required supply temperature at the heating coil is 39.5 °C, and the one at the cooling coil is 7.7 °C. The average external temperature is 22.5 °C. Table 4 shows the results of the comparison of the two generator configurations of the case study, using the previously presented indicators. Also the value of Total Efficiency Ratio (TER), defined as the ratio between the total provided energy and the total electrical energy input, is shown.

The results show that the simultaneous operation of the MP-HP for both services frequently occurs: more than 90% of the heating load is delivered through this operation mode (Mode 3). In this case, considering the greater relevance of the cooling load, the hot thermal storage is charged. Mode 2 ("Only heating") is rarely used: it only applies in those timesteps when only the heating load occurs. On the contrary, the MP-HP frequently works in Mode 1 ("Only cooling") using the hot water buffer to meet the heating load and recover the heat stored in the previous Mode-3 operation.

Fig.4 shows the operation of the MP-HP for a typical day in July. During the night, the cooling load is low, so the MP-HP follows the heating profile. As an example, at "Hour 1" the MP-HP provides the AHU heating requirements, but the cooling output results in an overproduction compared to the actual load and the surplus energy is stored in the cold water storage. At "Hour 2", the stored energy in the cold water storage is sufficient to cover the AHU cooling load, so the MP-HP works in Mode 2 ("Only heating" mode). During the opening hours of the museum, the high cooling load drives the AHU operations that switch between Mode 1 and Mode 3, depending on the charging/discharging status of the hot water storage. As an example, at "Hour 16", the heating output at MP-HP is over 14 kW, even if the actual requirement is around 6 kW. The surplus is stored in the hot water buffer and used to meet the heating load at "Hour 17", where the generator works in Mode 1 ("Only cooling").

Table 4. Comparison of indicators in combined vs. separate configuration.

	MP-HP case	Separate case
Total cooling load required at AHU [MWh]	13.9	13.9
Total heating load required at AHU [MWh]	8.8	8.8
Total electrical energy input [MWh]	3.2	4.3
Cooling load provided by the generator in Mode 1 ("Only cooling") [MWh]	7.3	13.9
Share of cooling load provided in Mode 1 ("Only cooling") [%]	53	100
Seasonal coefficient of performance in Mode 1 ("Only cooling"), $SEER_{C,MP-HP}$ or $SEER_{C,SC}$	4.63	5.00
Heating load provided by the generator in Mode 2 ("Only heating") [MWh]	0.7	8.8
Share of heating load provided in Mode 2 ("Only heating") [%]	8	100
Seasonal coefficient of performance in Mode 2 ("Only heating") (Mode 2), $SCOP_{H,MP-HP}$ or $SCOP_{H,SC}$	5.20	5.70
Cooling load provided by the generator in Mode 3 ("Both heating and cooling") [MWh]	6.6	0
Share of cooling load provided in Mode 3 ("Both heating and cooling") [%]	47	0
Heating load provided by the generator in Mode 3 ("Both heating and cooling") [MWh]	8.1	0
Share of heating load provided in Mode 3 ("Both heating and cooling") [%]	92	0
Seasonal coefficient of performance in Mode 3 ("Both heating and cooling"), $SEER_{H\&C,MP-HP}$	4.11	-
Seasonal total efficiency ratio, TER_{MP-HP}or TER_{SC}	7.09	5.27

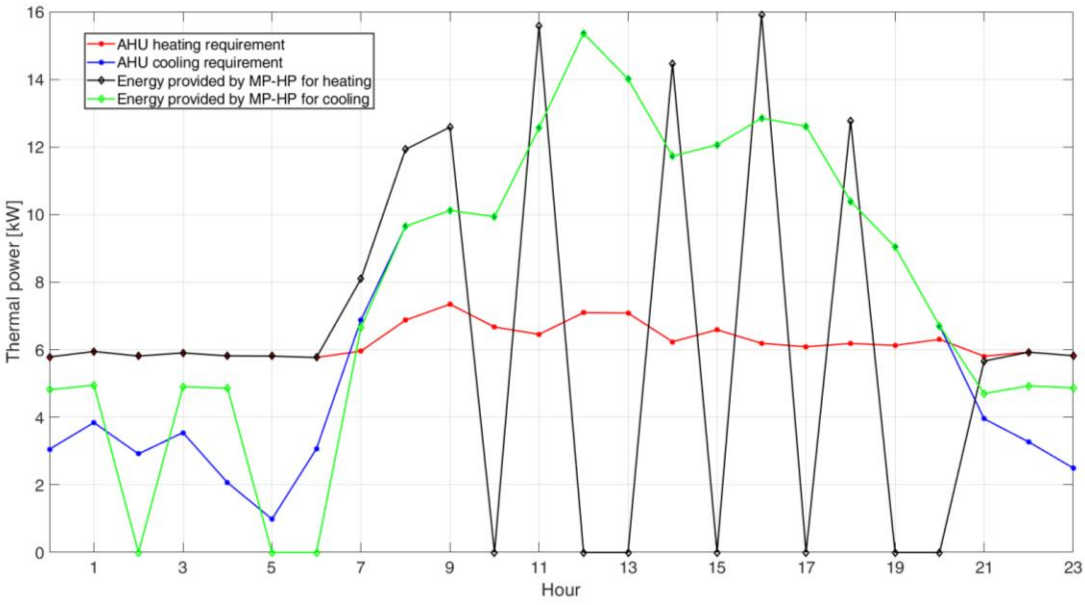


Fig. 4. Modes of operation of MP-HP in a day of July: energy delivered by the heat pump compared to the energy requirements at AHU. The position of the line representing delivered energy and required energy indicates the surplus of heating/cooling stored in dedicated buffers and later used.

Table 4 shows that the average MP-HP coefficient of performance is lower than in the case of separate configuration, namely, $SEER_{H\&C,MP-HP} < SEER_{C,MP-HP}$. Indeed, the average temperature difference between the supply water temperature (7.7 °C) and the outdoor air temperature (22.5 °C) is lower than the temperature difference between the two supply temperatures in Mode 3 (7.7 °C and 39.5 °C). However, the latter comparison is affected by our choice of using EER as the coefficient of performance for the MP-HP and it does not consider the simultaneous delivery of both heating and cooling loads. The TER indexes in Table 4 provide a better comparison of the two configurations, accounting for both hot and cold services. As previously mentioned, this indicator is defined as:

$$TER_{MP-HP} = \frac{\left(\sum \dot{Q}_{H,MP-HP,eff} + \sum \dot{Q}_{C,MP-HP,eff}\right)}{\sum \dot{E}_{el}} \quad (6a)$$

$$TER_{SC} = \frac{\left(\sum \dot{Q}_{H,r} + \sum \dot{Q}_{C,r}\right)}{\sum \dot{E}_{el}} \quad (6b)$$

Thus, the comparison of this index in combined and separate configuration hints the better exploitation of electrical energy in the MP-HP use. In this case study, using an MP-HP allows a decrease of electrical energy input equal to 25%. In Fig. 5, the daily electrical energy inputs for the "separate" and "combined" configurations are compared over a typical week (from 1st August to 7th August). For each day, the electrical energy consumptions in the three operational modes are independently visible. The figure shows that the heating load is almost always delivered as a total recovery of heat at the condenser when providing also cooling service. The daily reduction of electrical energy ranges between 20% and 30%.

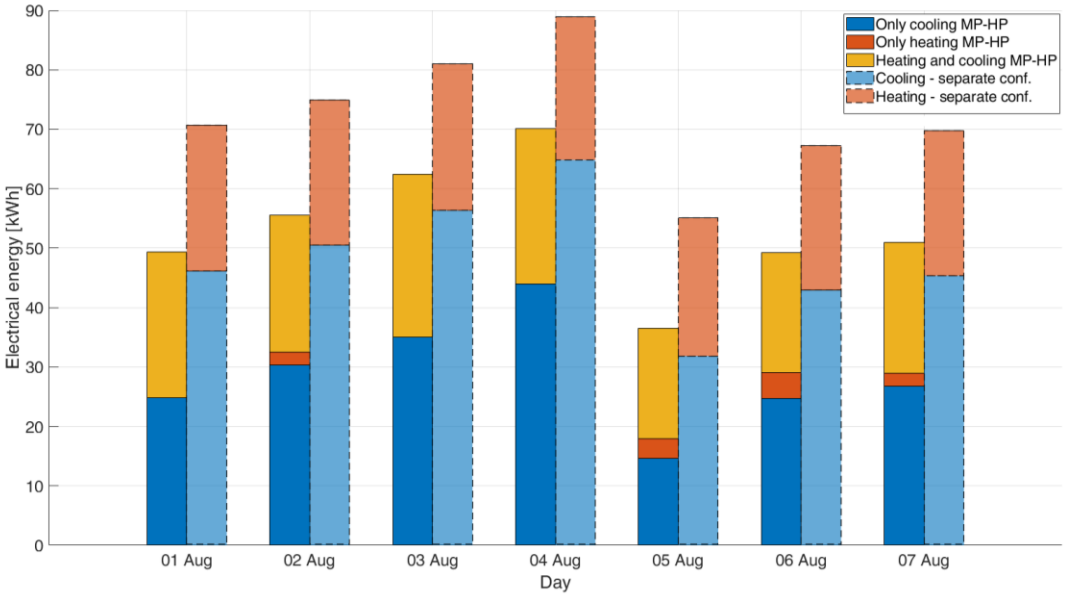


Fig. 5. Comparison of daily electrical energy input for combinate and separate configurations for a typical week.

4. Conclusions

In this paper, we have shown the potential of using a multi-purpose heat pump in a building where heating and cooling loads are simultaneously required. The analysis has compared the energy requirements of a "separate" configuration, using an independent air-source chiller and a heat pump, with a "combined" configuration using a MP-HP to feed the same AHU.

For the analysis, a case study has been identified: a room of a museum in the Mediterranean area where indoor temperature and relative humidity are kept constant using the AHU. Through an hourly dynamic simulation, the electrical energy consumptions required to operate the cooling and reheat coils have been calculated for both "separate" and "combined" configurations. The results show a reduction of electrical energy input of about 25% in the case of a "combined" configuration and MP-HP use. Due to the greater relevance of the cooling load in the presented case study, the MP-HP mainly operates in "Both heating and cooling" mode (Mode 3) and "Cooling only" mode (Mode 1). The system uses the surplus of the heating production in Mode 3 to charge the hot storage and then uses this energy in Mode 1 avoiding the need for another heating generator.

As a matter of fact, together with possible energy savings, the paper has also investigated the importance of the two "energy buffers" in MP-HP systems: indeed, depending on hot and cold load profiles, energy recovery would not be feasible where the two instantaneous load profiles were not properly synchronized. Thus, further development of the research will include the modeling of other MP-HPs devices (also using more efficient refrigerants as R744), a more accurate model of the thermal buffers in the MP-HP contexts, including the effects of their optimal sizing and control required to assess the actual potentiality of those systems. In addition, the efficiency of this technology in a whole-year simulation, also in different climates, and various types of buildings and services will also be investigated.

Nomenclature and acronyms

Acronyms	
AHU	Air handling unit
HP	Heat pump
MP-HP	Multi-purpose heat pump
nZEB	Nearly zero energy building
Nomenclature	
$COP_{H,MP-HP}$	Coefficient of performance of the multi-purpose heat pump in "Only heating" mode
$COP_{H,SC}$	Coefficient of performance of classical heat pump in separate configuration
CR	Capacity ratio
$\dot{E}_{el}$	Electrical energy needs at compressor
$EER_{H\&C,MP-HP}$	Coefficient of performance of multi-purpose heat pump in "Both heating and cooling" mode
$EER_{C,MP-HP}$	Coefficient of performance of the multi-purpose heat pump in "Only cooling" mode
$EER_{C,SC}$	Coefficient of performance of the classical chiller in separate configuration
$\dot{Q}_{C,MP-HP}$	Thermal output available at evaporator of multi-purpose heat pump
$\dot{Q}_{C,MP-HP,eff}$	Effective thermal output delivered at evaporator of multi-purpose heat pump
$\dot{Q}_{C,NOM,MP-HP}$	Nominal cooling heat of the multi-purpose heat pump
$\dot{Q}_{C,r}$	Cooling load required at the cooling coil of the air handling unit
$\dot{Q}_{H,MP-HP}$	Thermal output available at condenser of multi-purpose heat pump
$\dot{Q}_{H,MP-HP,eff}$	Effective thermal output delivered at condenser of multi-purpose heat pump
$\dot{Q}_{H,r}$	Heating load required at the heating coil of the air handling unit
$SCOP_{H,MP-HP}$	Average coefficient of performance of multi-purpose heat pump in "Only heating" mode
$SCOP_{H,SC}$	Average coefficient of performance of classical heat pump in separate configuration
$SEER_{C,MP-HP}$	Average coefficient of performance of multi-purpose heat pump in "Only cooling" mode
$SEER_{C,SC}$	Average coefficient of performance of classical chiller in separate configuration
$T_{air,r}$	Temperature of the air after the cooling and dehumidification process in the AHU
$T_{air,s}$	Temperature of the supply air entering the room
$T_{C,s}$	Supply temperature at cooling coil
T_{ext}	External temperature
$T_{H,s}$	Supply temperature at heating coil
T_{int}	Temperature of the thermal zone (Museum's rooms)
TER_{MP-HP}	Total efficiency ratio of multi-purpose heat pump
TER_{SC}	Total efficiency ratio of separate configuration
TR	Supply temperatures ratio
$x_{air,r}$	Humidity ratio of the air after the cooling and dehumidification process in the AHU
$x_{air,s}$	Humidity ratio of the supply air entering the room
x_{ext}	Humidity ratio of the external air
x_{int}	Humidity ratio of the internal air
$\alpha_1 - \alpha_5$	Coefficients of the polynomial fitting of nameplate data of performances of multi-purpose heat pump

Acknowledgments

We gratefully acknowledge AERMEC S.p.A. and, in particular, Mr. Davide Cucurnia, for sending us the performance data of their multi-purpose heat pump. The financial supports of the Italian Ministry of Education, University and Research (MIUR), in the framework of the Research Project of Relevant National Interest (PRIN) "The energy FLEXibility of enhanced HEAT pumps for the next generation of sustainable buildings (FLEXHEAT)" (PRIN 2017, Sector PE8, Line A, Grant n. 33) are acknowledged.

References

[1] United Nations. Sustainable Development Goals. Goal 13: Take urgent action to combat climate change and its impacts. 2015. https://www.un.org/sustainabledevelopment/climate-change/
[2] Communication from the Commission to the European Parliament, the European Council, the Council, the European Economic and Social Committee and the Committee of the Regions: The European Green Deal. 2019. https://eur-lex.europa.eu/resource.html?uri=cellar:b828d165-1c22-11ea-8c1f-01aa75ed71a1.0002.02/DOC_1&format=PDF
[3] The European Commission, 2021. Proposal for a Directive of the European Parliament and of the Council on the energy performance of buildings. https://eur-lex.europa.eu/resource.html?uri=cellar:c51fe6d1-5da2-11ec-9c6c-01aa75ed71a1.0001.02/DOC_1&format=PDF
[4] European Heat Pump Association (EHPA), 2022, Market data. https://www.ehpa.org/market-data/#:~:text=Heat%20pump%20sales%20grew%20by,560%2C000%20more%20than%20in%202020.
[5] Agrawal N., Bhattacharyya S. Experimental investigations on adiabatic capillary tube in a transcritical CO2 heat pump system for simultaneous water cooling and heating. *Int. J. Refr.* 2011, **34**: 476-483.
[6] Kang H., Joo Y., Chung H., Kim Y., Choi J. Experimental study on the performance of a simultaneous heating and cooling multi-heat pump with the variation of operation mode. *Int. J. Refr*. 2009, **32**: 1452-1459.
[7] Liu X., Lau S, Li H. Optimization and analysis of a multi-functional heat pump system with air source and gray water source in heating mode. *En. Build*. 2014, **69**: 1-13.
[8] Boahen S. Anka S.A., Lee K.H., Choi J.M. Performance characteristics of a cascade multi-functional heat pump in the winter season. *En. Build.* 2021, **253**:111511.
[9] Byrne P., Miriel J., Lenat Y. Design and simulation of a heat pump for simultaneous heating and cooling using HFC or CO2 as a working fluid. *Int. J. Refr*. 2009, **32**:1711-1723.
[10] Byrne P., Miriel J,, Lenat Y. Experimental study of an air-source heat pump for simultaneous heating and cooling – Part 1: Basic concepts and performance verification. *Appl. En*. 2011, **88**:1841-1847.
[11] Byrne P., Miriel J,, Lenat Y. Experimental study of an air-source heat pump for simultaneous heating and cooling – Part 2: Dynamic behaviour and two-phase thermosiphon defrosting technique. *Appl. En*. 2011, **88**:3072-3078.
[12] Cho C., Choi J.M. Experimental investigation of a multi-function heat pump under various operating modes. *Ren. En.* 2013, **54**: 253-258.
[13] Chiu Y., Chiu W., Kuan Y. Heat recovery system for reducing smart building carbon footprint. *Sens. Mat.* 2020, **32**(3): 885-893.
[14] Diaby A. T., Byrne P., Maré T. Simulation of heat pumps for simultaneous heating and cooling using CO2. *Int. J. Refr.* 2019, **106**:616-627.
[15] Ghoubali R., Byrne P., Miriel J., Bazantay F. Simulation study of a heat pump for simultaneous heating and cooling coupled to buildings. *En. Build.* 2014, **72**:141-149.
[16] Shen B., New J., Baxter V. Air source integrated heat pump simulation model for EnergyPlus. *En. Build.* 2017, **156**:197-206.
[17] AERMEC. Technical Datasheet of multi-functional heat pump. https://global.aermec.com/it/products/scheda-prodotto/?t=Unit%C3%A0%20multifunzione&c=CAT_50HZ_UE&f=chiller_polivalent&Code=NRP_PO
[18] CTI (Italian Thermotechnical Committee). 2012. Italian typical meteorological years. https://www.cti2000.it/index.php?controller=news&action=show&%20newsid=34985
[19] Schito E., Testi D. A visitors' presence model for a museum environment: description and validation. *Build. Simul.* 2017, **10**:977-987.
[20] Schito E., Conti P., Urbanucci L., Testi D. Multi-objective optimization of HVAC control in museum environment for artwork preservation, visitors' thermal comfort and energy efficiency. *Build. Env.* 2020, **180**:107018.
[21] Schito E. Dynamic simulation of an air handling unit and validation through monitoring data. *En. Proc.* 2018, **148**:1206-1213.
[22] Klein SA, 2010. TRNSYS 17: A Transient System Simulation Program, Solar Energy Laboratory, University of Wisconsin, Madison, USA.
[23] MATLAB R2022b, The Mathworks, Inc. Natick, MA, USA.

14th IEA Heat Pump Conference
15-18 May 2023, Chicago, Illinois

Techno-economic optimization of high-temperature heat pumps using pure fluids and binary mixtures

Elias Vieren[a,*], Toon Demeester[a] , Wim Beyne[a], Martin Pihl Andersen[b], Brian Elmegaard[b], Michel De Paepe[a,c], Steven Lecompte[a,c]

[a]Department of Electromechanical, Systems and Metal Engineering, Ghent University, Sint-Pietersnieuwstraat 41, 9000 Ghent, Belgium
[b]Department of Civil and Mechanical Engineering, Technical University of Denmark, Kgs. Lyngby, 2800
[c]FlandersMake@UGent–Core lab EEDT-MP, Gaston Geenslaan 8, 3001 Leuven, Belgium

Abstract

Electrically driven high-temperature heat pumps (HTHPs) are becoming a promising and cost-effective technology to replace fossil-fuel driven boilers through residual heat recovery and revalorization. HTHPs are however often designed and optimized in terms of thermodynamic performance, neglecting financial aspects such as the levelized cost of heat (LCOH). In this study, the heat pump design and operating conditions are optimized by minimizing the LCOH. This is done for a wide set of working fluids and boundary conditions. Both subcritical, transcritical and supercritical cycles, as well as (zeotropic) binary mixtures, are considered. Depending on the boundary conditions, both pure fluids as well as (zeotropic) binary mixtures, mostly operating in the subcritical region, are financially attractive. The potential benefits of zeotropic mixtures are twofold: (1) more favorable operating conditions and (2) higher COPs. Transcritical cycles only showed to be attractive for large temperature glides at the heat sink side. The results also shows that the financial and thermodynamic optima differ in many cases. One reason for this is that working fluids with a high COP often induce high compressor inlet volume flow rates, resulting in high compressor costs.

© HPC2023.
Selection and/or peer-review under the responsibility of the organizers of the 14th IEA Heat Pump Conference 2023.

Keywords: High-temperature heat pumps; binary mixtures; pure working fluids; techno-economic

1. Introduction

High-temperature heat pumps (HTHPs) are an emerging technology, allowing for efficient electrification in the industrial heating sector. It is expected that HTHPs will soon be able to supply process heat up to 200 °C [1]. By reaching supply temperatures of 200 °C heat pumps could deliver 37 % of the process heat demand in the European industry [2]. Consequently, there is an increasing amount of research on working fluids and cycle configurations for these HTHPs. This research mainly focusses on achieving a maximum COP and therefore minimal electricity use.

However, some working fluids with a high COP may require large compressors, or multiple compression stages, while configurations with a high COP may be more complex and therefore expensive. The discrepancy in thermodynamic and financial optima for some boundary conditions has been shown for organic Rankine cycles [3]. For HTHPs however, less research is performed on financially optimal heat pump cycles and working fluids. Moreover, if a financial analysis is performed it is typically done for just one application. In addition, the amount of working fluids screened and configurations considered is often not complete.

This research focusses on the selection of optimal working fluids for HTHPs, by optimizing and analyzing the levelized cost of heat (LCOH) for each working fluid. Both pure working fluids as well as binary (zeotropic) mixtures are considered as candidates. For this purpose, a financial framework is developed and applied to a large set of generic data, rather than to one, or a limited amount of, case studies(s).

* *Corresponding author.*
E-mail address: Elias.Vieren@ugent.be

2. Methods

In this section, the financial framework is first explained. Afterwards, an overview of the refrigerant candidates is given. Subsequently, the large set of generic boundary conditions, to which the financial framework will be applied, is presented. Finally, the post-processing of the results is explained. In this procedure, working fluids may be eliminated because they violate technical constraints.

2.1. Financial framework

The financial framework is an extension of the thermodynamic simulation and optimization framework developed by Vieren et al. [4,5]. This framework allows for optimizing the COP for pure fluids and binary (zeotropic) mixtures, both in the subcritical, transcritical and supercritical regime. A single-stage heat pump cycle was chosen as reference cycle, with the option for an internal heat exchanger (IHX). Based on the obtained optimal, or sub-optimal working fluids, more advanced cycles can be modelled. The optimization framework maximizes the COP of the heat pump cycle by varying the superheat (ΔT_{sh}), subcooling (ΔT_{sc}), pressure during heat delivery (p_{high}) and pressure during heat extraction (p_{low}). For operation above the critical point, ΔT_{sh} and ΔT_{sc} are defined with respect to the critical point. For the binary mixtures, the molar fraction of the components is also optimized.

Because the LCOH is a function of the COP, the developed thermodynamic framework acts as a well-suited basis. Next to changing the objective function from COP to LCOH, the main adaptions to the existing model are:

- Removal of the constraints on the pinch point temperature difference (PPTD). From a thermodynamic point of view the COP would be maximal for a PPTD of 0 K. This would however require infinitely large heat exchangers. Therefore, a PPTD of 5 K in the heat exchangers was imposed in the thermodynamic model. In this financial analysis however, a low PPTD will be automatically penalized by a strong increase in heat exchanger costs, while the COP increases only marginally.
- Introduction of multiple compression stages. In the financial model, multiple compression stages will be considered if the compression ratio is high. This was not done in the thermodynamic model, because the use of multiple compression stages will not drastically influence the COP. For the financial model however the impact can be much higher. A maximum compression ratio per stage of 6 is selected.

2.1.1. Levelized cost of heat

The LCOH is the average net present cost of the heat production (€/kWh$_{th}$) over the lifetime of the heat generating system. The LCOH is calculated by use of Eq. 1.

$$LCOH = \frac{C_{CAPEX} + \sum_{t=1}^{n} \frac{C_{OPEX,t}}{(1+i)^t}}{\sum_{t=1}^{n} \frac{Q_t}{(1+i)^t}} \quad (1)$$

With C_{CAPEX} the capital expenditure (€), $C_{OPEX,t}$ the operational expenditure at year t (€/year), n the heat pump lifetime (year), i the interest rate (%) and Q_t the amount of heat produced at year t (kWh$_{th}$/year).

2.1.1.1. Capital expenditure

The capital investment cost of the heat pump (C_{CAPEX}) is determined according to the preliminary and study cost estimation method of Turton et al. [6], providing estimates in the accuracy range of -25 % to +40 %. In addition to the equipment purchase costs, the method also accounts direct and indirect project expenses, contingency and fees and auxiliary facilities.

First the purchasing cost of each component (C^0) was determined. An overview of each component cost function can be found in Table 1.

Table 1: Overview of the bare module cost (C^0) of each component.

Component	Cost equation	Variable	Reference
Plate heat exchanger	$C^0_{hex} = 0.88 \cdot (1600 + 210A^{0.95})$	A: Heat transfer surface (m²)	[7]
Reciprocating compressor	$C^0_{comp} = 19\,850 \cdot \left(\frac{\dot{v}_{comp,i}}{279.8}\right)^{0.73}$	$\dot{v}_{comp,i}$: Volume flow rate at the compressor inlet (m³/h)	[8]
Compressor drive	$C^0_{drive} = 10\,710 \cdot \left(\frac{\dot{W}_{drive}}{250\,000}\right)^{0.65}$	$\dot{W}_{drive}$: Power use of the electrical drive (W)	[8]
Expansion valve	$C^0_{valve} = 114.5 \cdot \dot{m}_{ref}$	$\dot{m}_{ref}$: Mass flow rate of the refrigerant (kg/s)	[9]

The heat exchanger cost is based on the heat transfer area, which is based on heat transfer coefficients (HTCs). These HTCs depend on the working fluid, Reynolds number and Prandtl number. Since a large set of pure working fluids and binary mixtures will be screened, it is not feasible to implement heat transfer correlations. Moreover, high uncertainties are expected for the binary mixtures. Therefore, fixed HTCs, depending on the phase of the working fluid or secondary medium, are chosen in this high-level analysis. An overview of the selected HTCs can be found in Table 2. The HTC for the liquid phase, two-phase and gas phase where determined based on extrapolation of overall HTCs reported in the VDI Heat Atlas [10]. For the supercritical phase the same HTC is chosen as for the liquid phase.

Table 2: Overview of the considered heat transfer coefficients for each phase.

Phase	Heat transfer coefficient α [W/(m²K)]
Liquid	2000
Two-phase	3000
Gas	100
Supercritical	2000

In order to account for inflation the cost functions reported in Table 1, which are derived in the past, are adjusted to the year 2021 by use of the chemical engineering plant cost index (CEPCI) [8]. The indexed purchased equipment cost is used to calculate the bare module cost (C_{BM}) of each component. This cost also accounts additional direct costs (e.g. labour) and indirect costs (e.g. engineering expenses) for each component. The bare module cost is found by multiplying the purchased equipment cost (C^0) with a bare module cost factor (F_{BM}):

$$C_{BM} = C^0 \cdot F_{BM} \tag{2}$$

An overview of the bare module cost factor of each component can be found in Table 3.

Table 3: Bare module factor (F_{BM}) for each component, according to Turton et al. [6].

Component	F_{BM}
Plate heat exchanger	1.16
Positive displacement compressor	2.4
Compressor drive	1.5
Expansion valve	2

The total module cost (C_{TM}), which equals the capital expenditure, is the summation of each bare module costs with an additional 15 % and 3 % added for contingency costs and fees respectively:

$$C_{TM} = 1.18 \cdot \sum_{i=1}^{n} C_{BM,i} = C_{CAPEX} \tag{3}$$

2.1.1.2. Operational expenditure

The yearly operational expenditure is determined by the total yearly electricity use and the yearly maintenance cost:

$$C_{OPEX} = c_{el} \cdot \left(\frac{\dot{Q}process}{COP}\right) \cdot h_a + f_{maint} \cdot C_{CAPEX} \quad (4)$$

The total yearly electricity use is determined by the specific electricity costs c_{el} (€/kWh$_{el}$), the electricity use rate (kW$_{el}$) and the annual operation hours h_a (h). The electricity use rate is determined by dividing the heat demand rate of the industrial process ($\dot{Q}_{process}$) by the COP. The yearly maintenance cost is calculated as a fraction (f_{maint}) of the capital expenditure.

2.1.2. Financial boundary conditions

For the computation of the LCOH, several external parameters are required that depend, amongst others, on the type of industry and country where the HTHP is to be integrated. In this work financial boundary conditions are chosen that represent a typical energy-intensive industry in Belgium, as shown in Table 4.

Table 4: Overview of the considered financial boundary conditions.

Parameter	Value	Reference
Heat pump lifetime (n)	15 year	[8,11,12]
Interest rate (i)	5 %	-
Maintenance cost fraction (f_{maint})	0.06	[12]
Annual operating hours (h_a)	7000 h	[12,13]
Specific electricity cost (c_{el})	0.0806 €/kWh$_{el}$	[14]

For the specific electricity cost, the bi-annual electricity costs reported by Eurostat for Belgium between 2016-2020 [14] is averaged. This was done for the prices reported in the yearly electricity consumption range of 500 MWh$_e$ to 2000 MWh$_e$. According to Eurostat, most of the EU non-household consumers fall in this use range.

2.2. Refrigerant selection

Regarding the pure working fluids, a selection is made based on the REFPROP10.0 database [15]. The following selection criteria are applied:

- Ozone depletion potential (ODP) of approximately zero.
- Global warming potential (GWP) below 150.
- National Fire Protection Association (NFPA) 704 instability grade of 0.
- Thermally stable up to 200 °C or higher.

Based on the selection of the pure working fluids a pool of binary mixtures is made. From this pool, mixtures where both components have a critical temperature below 160 °C are eliminated, because the goal is to study these mixtures in the subcritical region. All these working fluids are examined for the configuration with and without IHX.

2.3. Operational boundary conditions

First the financial model is applied to two boundary conditions reported in earlier work of Vieren et al. [4], where the COP was optimized by this simulation framework. The temperature levels of the two selected boundary conditions can be found in Table 5.

Table 5: Temperature data of the two selected case studies.

Case study (source-sink)	Heat source inlet temperature	Heat source outlet temperature	Heat sink inlet temperature	Heat sink outlet temperature
Sensible-sensible	120 °C	100 °C	160 °C	180 °C
Latent-sensible	100 °C	100 °C	120 °C	180 °C

After these cases are discussed, an estimate of the financial performance for the selected refrigerants is formulated for a wide range of generic boundary conditions. The generic data is classified in four groups

depending on the nature of the heat source or sink. An overview of the classifications, and the amount of datapoints (i.e. boundary conditions) selected, can be found in Table 6.

Table 6: Overview of the four classifications depending on the nature of the heat source or sink.

Heat source	Heat sink	Datapoints
Latent	Latent	4
Latent	Sensible	12
Sensible	Latent	12
Sensible	Sensible	36

Each datapoint has a heat sink outlet temperature between 160-200 °C, whereas the heat source inlet temperature varies between 80-120 °C. Because the degrees of freedom increase when the secondary stream is of sensible nature (addition of a temperature glide next to the absolute temperature level), more datapoints are selected in these scenarios. However, less datapoints are selected compared to the COP optimization [4] due to the increased complexity and therefore computational power.

Important to note is that whilst the COP computation of the developed framework is independent of the capacity of the heat pump system, the LCOH is not because non-linear cost functions are used. In this work a heat pump with a heating capacity of 500 kW_{th} is considered.

2.4. Post-processing

After the pool of refrigerants is simulated, the results are post-processed. During post-processing working fluids which require a compressor discharge pressure above 60 bar are discarded. The reason is that few compressors exist for pressures above 60 bar, except for CO2. Moreover, for the binary mixtures a minimum deviation in molar fraction and LCOH from the respective pure fluids is imposed. A minimum deviation of respectively 2 mol % and 2 % is selected so that there is a clear distinction between pure working fluid and binary mixture.

3. Results

3.1. Sensible-sensible boundary condition

An overview of the financially best performing working fluids for the ‘sensible-sensible boundary condition’ can be found in Table 7. This table reports the working fluid, molar fraction of the first component, number of stages, use of an IHX, COP, LCOH and the specific investment cost (c_{inv}) of the 5 best performing fluids. The specific investment cost is obtained by dividing the capital expenditure (Eq. 3) by the heating capacity (500 kW_{th}).

Table 7: Overview of the financially best performing refrigerants for the ‘sensible-sensible boundary condition’.

Working fluid	Molar fraction first component	Stages	IHX	COP	LCOH [€/kWh_{th}]	$c_{,inv}$ [€/kW_{th}]
Methanol/ammonia	0.685	1	No	3.84	0.0290	372
Cis-2-Butene/methanol	0.585	1	Yes	3.56	0.0305	363
Benzene/methanol	0.648	1	Yes	4.10	0.0307	512
Cyclobutene/toluene	0.955	1	Yes	3.45	0.0309	351
Cyclobutene/heptane	0.963	1	Yes	3.46	0.0310	357

Based on the reported results it can be observed that the financially most attractive refrigerants are (zeotropic) binary mixtures. These binary refrigerants are made up entirely of natural refrigerants, or more specifically, of hydrocarbons and ammonia. To reveal the potential of these mixtures, the results of the respective pure working fluids with the largest molar fraction are reported in Table 8.

Table 8: Overview of the financially best performing pure refrigerants for the 'sensible-sensible boundary condition'.

Working fluid	Stages	IHX	COP	LCOH [€/kWh$_{th}$]	c_{inv} [€/kW$_{th}$]
Cyclobutene	1	Yes	3.37	0.0317	357
Methanol	2	No	3.71	0.0331	528
Cis-2-Butene	1	Yes	3.18	0.0339	396
Benzene	2	Yes	3.82	0.0400	871

Comparing these tables shows that mixtures are able to increase the COP and decrease the specific investment costs compared to the pure fluids. One of the reasons for the increase in COP can be explained by the non-isothermal phase change of these mixtures. This may result in a better temperature match between refrigerant and secondary medium, decreasing the exergy destruction. As an example, the T,Q-diagram of both methanol/ammonia and pure methanol is given in Figure 1, where it can be observed that methanol/ammonia results in a better temperature match. Moreover, the pressure levels shown in the figure indicate that the addition of ammonia to methanol increases the pressure levels. As the increase in evaporator pressure is relatively more outspoken compared to the condenser pressure, the compression ratio decreases from about 8 to 5.7, resulting in the possibility of using one compression stage. Moreover, mixing the pure fluids may result in a lower volume flow rate at the compressor inlet compared to one of the pure constituents and therefore a lower compressor cost. For the methanol/ammonia mixture for example the volume flow rate at the compressor inlet is 0.083 m³/s whereas for pure methanol a flow rate of 0.130 m³/s at the inlet of the compressor is needed.

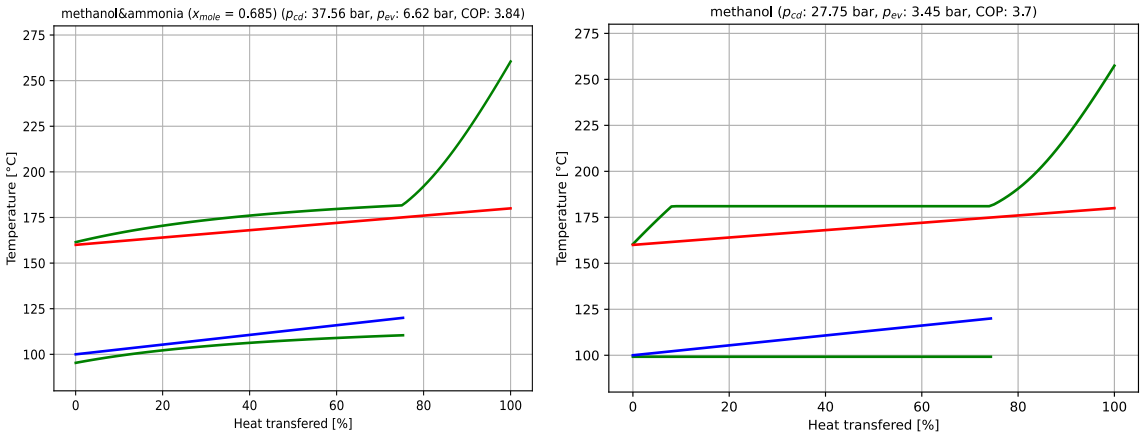


Figure 1: T,Q-diagram of methanol/ammonia and methanol for the 'sensible-sensible boundary condition'.

Table 7 and Table 8 also demonstrates that the financially most attractive heat pump does not necessarily have the highest COP. Benzene for example has a COP of 3.82 which is about 13 % higher than for cyclobutene (3.37). However, the LCOH of a heat pump with benzene is 26 % higher compared to a heat pump with cyclobutene. This is because a heat pump with benzene would have a specific investment cost of 871 €/kW$_{th}$, compared to 357 €/kW$_{th}$ for cyclobutene. The investment cost of the benzene heat pump is high because of the high pressure ratio resulting in the need for two compression stages, and the high volume flow rate resulting in large compressors. Both the high-pressure ratio and high volume flow rate are caused by the low evaporation pressure, associated to the high normal boiling point (NBP) of benzene (80.1 °C).

3.2. Latent-sensible boundary condition

An overview of the financially best performing working fluids for the 'latent-sensible boundary condition' can be found in Table 9, which has the same structure as Table 7.

Table 9: Overview of the financially best performing refrigerants for the 'latent-sensible boundary condition'.

Working fluid	Stages	IHX	COP	LCOH [€/kWh$_{th}$]	c_{inv} [€/kW$_{th}$]
Cyclobutene	1	No	4.16	0.0249	278
Cis-2-Butene	1	No	4.27	0.0255	306
R1233zd(E)	1	No	4.33	0.0258	332
R1234ze(Z)	1	No	4.27	0.0259	325
R1224yd(Z)	1	No	4.24	0.0265	345

Table 9 shows that all best performing working fluids are pure fluids. These fluids operate as transcritical cycles. For applications with a large temperature glide at the heat sink side and a small or zero temperature glide at the heat source side, these cycles are able to provide a good temperature match. In fact binary mixtures were able to increase the COP and LCOH, but only in such a minor degree that they were eliminated by the post-processing. Both natural refrigerants (i.e. hydrocarbons) and synthetic refrigerants hydrofuoloro-olefins (HFOs) and hydrochlorofluro-olefins (HCFOs) are found to be well performing. Again, the working fluid with the highest COP is not necessarily the working fluid showing the best financial aspects. This is shown in Figure 2, where the LCOH of the 100 best performing refrigerants is plotted as a function of the COP, showing no correlation between the two parameters. This is an important result: even though a higher COP inherently lowers the LCOH by reducing electricity consumption, other factors determine the financial optimum. The figure also shows that for the best performing fluids, the optimized LCOH does not show large variations. This is partly due to the large number of working fluids simulated. It should also be noted that due to the uncertainty in LOCH, the working fluid with the lowest simulated LCOH may not have the lowest LCOH in practice. Therefore, the generalized selection matrix will show the best performing refrigerant types (e.g. hydrocarbons or mixtures of HFOs) rather than a single working fluid.

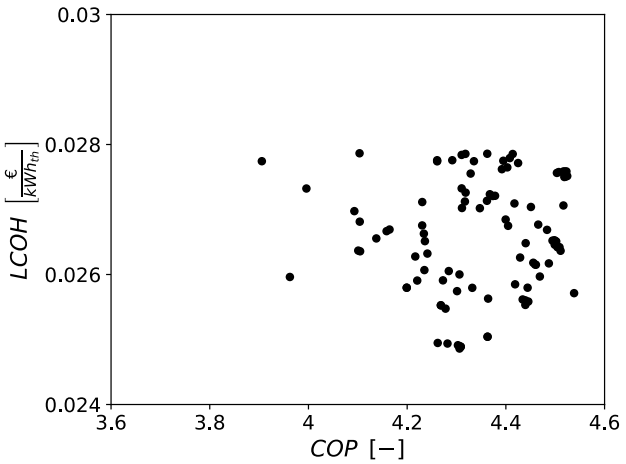


Figure 2: LCOH as a function of the COP for the 100 best performing working fluids of the 'latent-sensible boundary condition'.

3.3. Selection matrix

Based on a large amount of simulated boundary conditions, explained in Table 6, the results are generalized in the form of a 'selection matrix', as shown in Table 10. This selection matrix reports the best performing working fluid(s) for each type of heat source and sink. Since flammability concerns may prevent the installation of the heat pump, and the cost of ATEX related regulations is not considered, a distinction is made between flammable refrigerants and non/mildly-flammable refrigerants. As the feasibility also depends on the absolute temperature levels, it is also indicated for which temperature level (low, medium and high, within the studied temperature ranges) of heat source and/or heat sink the working fluid is recommended. Water for example is only recommended for high source temperatures, because for low source temperatures the evaporation pressure is low, resulting in high suction volume flow rates. Cyclobutene, cis-2-butene or HFOs and HCFOs on the other hand are only recommended for lower heat sink temperatures, as for high heat sink temperatures the compressor discharge pressure becomes too high (> 60 bar), resulting in elimination by the post-processing.

Table 10: Generalization of the financially best performing refrigerant for the different classifications of heat sources and heat sinks.

		Heat source	
		Latent	*Sensible*
Heat sink	*Latent*	**<u>Near-azeotropic mixtures</u>** **Flammable:** ➢ Mixtures of hydrocarbons (always) ➢ Mixtures of water and hydrocarbons (medium T_{source}) **Non/mildly flammable:** ➢ None **<u>Pure fluids</u>** **Flammable:** ➢ Acetone, methanol, ethanol (always) ➢ Cyclobutene (low T_{source} and T_{sink}) **Non-flammable:** ➢ Water (high T_{source}) ➢ HFOs and HCFOs (low T_{source} and T_{sink})	**<u>Zeotropic mixtures</u>** **Flammable**: ➢ Mixtures of hydrocarbons and mixtures of hydrocarbons and ammonia (always) ➢ Mixtures of water and hydrocarbons (medium T_{source}) **Non/mildly-flammable**: ➢ Water/ammonia (high T_{source}) **<u>Pure fluids</u>** **Flammable**: ➢ Cyclobutene, Cyclopentane, Cis-2-Butene (low T_{sink}) ➢ Acetone, Methanol, Ethanol (high T_{sink}) **Non/mildly-flammable**: ➢ Water (high T_{sink} and T_{source}) ➢ HFOs and HCFOs (low T_{sink} and T_{source})
	Sensible	**<u>Zeotropic mixtures</u>** **Flammable:** ➢ Mixtures of hydrocarbons (high T_{sink}) ➢ Mixtures of hydrocarbons and water or ammonia (high T_{source} and high T_{sink}) **Non/mildly-flammable:** ➢ None **<u>Pure fluids</u>** **Flammable:** ➢ Cyclobutene and Cis-2-Butene (low T_{sink}) **Non/mildly-flammable**: ➢ HFOs and HCFOs (low T_{sink}) ➢ Water (high T_{source} and T_{sink})	**<u>Zeotropic mixtures</u>** **Flammable:** ➢ Mixtures of hydrocarbons and mixtures of hydrocarbons and ammonia (always) ➢ Mixtures of water and hydrocarbons (medium T_{source}) **Non/mildly-flammable:** ➢ Water/ammonia (medium T_{source})

Interestingly, binary mixtures almost always show to be (near-) optimal, also for boundary conditions where the temperature glide of the heat source and sink differ, or there are no temperature glides at all. As an example, the T,Q-diagram of acetone/water is shown for a sensible (120-90 °C) latent (160 °C) boundary condition (Figure 3.a) and a latent (120 °C) latent (200 °C) boundary condition (Figure 3.b). From Figure 3.a it can be observed that for the optimized pressures and molar fraction the temperature glide of the acetone/water mixture during condensation is rather small (~10 °C) compared to the temperature glide during vaporization (~20 °C), resulting in a decent temperature match. For other molar fractions and pressures, the temperature glide of the mixture during evaporation and condensation may approach zero (i.e. near-azeotropic mixture) as shown in Figure 3.b. In these scenarios binary mixtures do not necessarily increase the COP (although in this case they did), but they may result in better operational parameters and therefore financial aspects. The only scenario where the potential of zeotropic mixtures is limited, is for boundary conditions with large temperature glides as the heat sink ($\geq$ 60 °C) and small to zero temperature glide at the heat source, as has been shown in section 3.2.

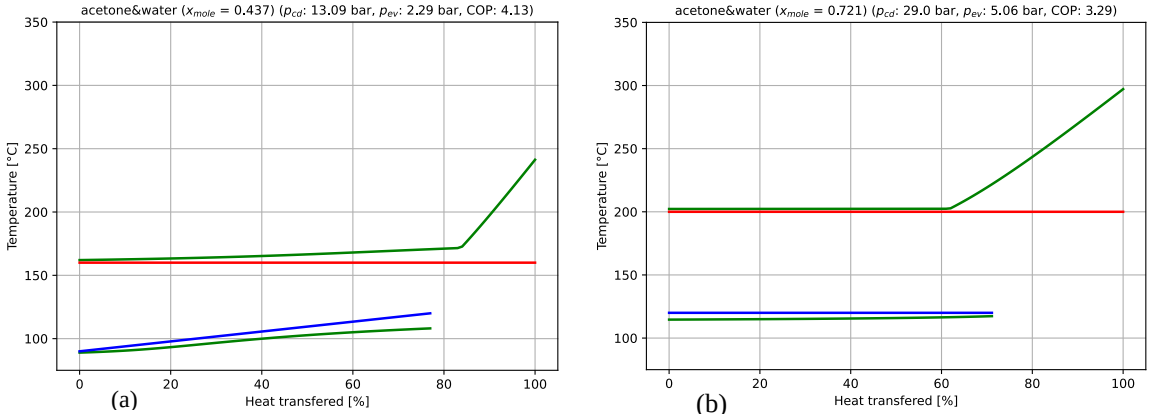


Figure 3: Optimized T,Q-diagram for acetone/water for a sensible (120-90 °C) latent (160 °C) boundary condition and latent (120 °C) latent (200 °C) boundary condition.

The reported (near-) optimal working fluids are, or consist of at least one, highly flammable hydrocarbon. If these highly flammable working fluids are not taken into consideration the options are limited. Generally, HFOs and HCFOs show the best feasibility if the source and sink temperature are low. For higher temperatures (where the pressure of the HFOs and HCFOs becomes too high) water is recommended. In some scenarios, addition of ammonia to the water can have beneficial effects in financial performance.

4. Discussion

A framework is developed that is capable of simulating single- and double-stage heat pump cycles, with and without internal heat exchanger. It is also able to simulate all the refrigerants in REFPROP 10.0 and the binary mixtures of these refrigerants. By assigning costs to the components of the heat pump, the financial performance over the lifetime of each heat pump cycle was estimated and ranked.

A preliminary financial screening is carried out for a wide range of generalized boundary conditions, rather than for a limited number of specific case studies. Generally, there is a common misconception in the literature that the payback period is used instead of LCOH. In such cases, the configurations with the optimum payback tend to be those with the lower investment costs, while they may not have the lowest LCOH, as has been shown in the work of Zühlsdorf et al. [19]. The LCOH is used in this work because it takes into account the period after the investment has been paid back. Moreover, the LCOH is independent of external boundary conditions such as gas prices. It is expected in this work that the calculated LCOH provides a good first estimate of the financial appraisal. The results showed that binary mixtures often have beneficial effects compared to their pure components, either by increasing the COP through improved temperature matching in the heat exchangers, or by improving the operating conditions due to the flexibility in thermophysical properties. Moreover, due to the presence of azeotropic behavior in the vapor-liquid equilibrium, these binary mixtures are also interesting for applications with no temperature glides. For applications where the temperature glides of the binary mixture cannot be matched with the secondary fluids, some authors even propose heat pump cycles with a variable mixture composition regulation, so that a satisfactory temperature match can be achieved in both condenser as evaporator [16], [17]. Nevertheless, the increase in COP for such cycles may not outweigh the additional cost. The only region where binary mixtures operating in the subcritical region are less interesting, is for applications with large temperature glides at the heat sink side. In such scenarios, pure fluids operating in the transcritical regime are the most favorable. In addition, in event of large temperature glides, zeotropic mixtures may experience fractionation and composition shift [18]. Furthermore, the results shows that there is a mismatch between thermodynamic and financial optima. The financially optimal working fluids do not have the highest COP. Furthermore, the best performing working fluid does also not have the lowest investment cost.

For the best performing working fluids reported in this work, the financial performance could be analyzed in more depth by (re)considering the following aspects:

1. The assumption of a fixed heat transfer coefficient. This assumption is particularly favorable for zeotropic mixtures, as these may experience a degradation of heat transfer [18]. Nevertheless, the breakdown of the LCOH showed that the contribution of the heat exchangers with respect to the total LCOH is often small.
2. The cost of the refrigerant, especially synthetic refrigerants shows to be more expensive [20].
3. The influence of material compatibility or pressure on the equipment costs.

4. The off-design behaviour.
5. An isentropic compression efficiency, which depends on the properties of the working fluid [21].
6. Influence of costs related to ATEX compliance.

In addition, there is a clear dependency of the results towards the considered financial boundary conditions reported in Table 4. Arpagaus et al. [22] showed that the electricity costs and operating hours in particular have a large impact on the LCOH, and thus could influence the most optimal heat pump cycle from a financial point of view. A sensitivity of the selection matrix towards these parameters could be included in future work.

5. Conclusion

A financial framework, able to optimize the LCOH of a heat pump is developed. This framework is used to give a preliminary indication of the financial appraisal for a broad range of pure fluids and binary mixtures. The model is applied to a large set of generic data.

The results show that there is a discrepancy between optimum COP and optimum LCOH. Consequently, selection of a refrigerant just based on maximal COP, may lead to a sub-optimal financial solution. Moreover, the selection matrix shows the optimal working fluid strongly depends on the boundary conditions. However, binary mixtures of natural refrigerants (hydrocarbons, ammonia and water) showed to be (near) optimal for a large range of boundary conditions. The potential of these mixtures is twofold: the COP can be improved by temperature matching in event of zeotropic mixtures and mixing working fluids allows for more advantageous operating conditions (e.g., lower compression ratio or lower volume flow rate).

Acknowledgements

We gratefully acknowledge the financial support of the Flemish Government and Flanders Innovation & Entrepreneurship (VLAIO) through the Moonshot project Upheat-INES (HBC.2020.2616).

The computational resources (Stevin Supercomputer Infrastructure) and services used in this work were provided by the VSC (Flemish Supercomputer Center), funded by Ghent University, FWO and the Flemish Government – department EWI.

Martin Pihl Andersen received funding from The Energy Technology Development and Demonstration Programme (EUDP), under the project title: “SuPrHeat - Sustainable process heating with high-temperature heat pumps using NatRefs” number 64020-1074.

References

[1] A. Marina, S. Spoelstra, H. A. Zondag, and A. K. Wemmers, “An estimation of the European industrial heat pump market potential,” *Renewable and Sustainable Energy Reviews*, vol. 139, p. 110545, Apr. 2021, doi: 10.1016/j.rser.2020.110545.

[2] “Strengthening Industrial Heat Pump Innovation Decarbonizing Industrial Heat”.

[3] S. Quoilin, S. Declaye, B. F. Tchanche, and V. Lemort, “Thermo-economic optimization of waste heat recovery Organic Rankine Cycles,” *Appl Therm Eng*, vol. 31, no. 14–15, pp. 2885–2893, Oct. 2011, doi: 10.1016/J.APPLTHERMALENG.2011.05.014.

[4] E. Vieren *et al.*, “Optimal temperature matching in high-temperature heat pumps,” *3rd High-Temperature Heat Pump Symposium 2022 : book of presentations*, pp. 225–229, 2022, Accessed: Nov. 07, 2022. [Online]. Available: http://hdl.handle.net/1854/LU-8757241

[5] E. Vieren *et al.*, “Natural refrigerants versus synthetic refrigerants for steam-generating heat pumps,” *GL2022, the 15th IIR-Gustav Lorentzen Conference on Natural Refrigerants, Proceedings*, 2022, doi: 10.18462/IIR.GL2022.0020.

[6] “Richard Turton et al. - Analysis Synthesis and Design of Chemical Processes-Pearson Education (2018).pdf.”

[7] Gavin Towler Ray Sinnott, *Capital Cost Estimating*, vol. 76, no. 6. 2013. doi: 10.1021/ie50502a032.

[8] T. Ommen, J. K. Jensen, W. B. Markussen, L. Reinholdt, and B. Elmegaard, “Technical and economic working domains of industrial heat pumps: Part 1 - Single stage vapour compression heat pumps,” *International Journal of Refrigeration*, vol. 55, pp. 168–182, 2015, doi: 10.1016/j.ijrefrig.2015.02.012.

[9] S. Sanaye and A. Shirazi, “Four e analysis and multi-objective optimization of an ice thermal energy storage for air-conditioning applications,” *International Journal of Refrigeration*, vol. 36, no. 3, pp. 828–841, May 2013, doi: 10.1016/J.IJREFRIG.2012.10.014.

[10] "VDI Heat Atlas," *VDI Heat Atlas*, 2010, doi: 10.1007/978-3-540-77877-6.
[11] F. Bless, C. Arpagaus, and S. Bertsch, "Theoretical investigation of high-temperature heat pump cycles for steam generation," *13th IEA Heat Pump Conference, May 11-14, 2020, Jeju, Korea, postponed to 26-29 April 2021*, pp. 1–9, 2020.
[12] G. B. Wang and X. R. Zhang, "Thermoeconomic analysis of optimization potential for CO2 vapor compression cycle: From transcritical to supercritical operation for waste heat recovery from the steam condenser," *Int J Energy Res*, vol. 43, no. 1, pp. 297–312, 2019, doi: 10.1002/er.4263.
[13] B. Zühlsdorf, F. Bühler, M. Bantle, and B. Elmegaard, "Analysis of technologies and potentials for heat pump-based process heat supply above 150 °C," *Energy Conversion and Management: X*, vol. 2, p. 100011, Apr. 2019, doi: 10.1016/J.ECMX.2019.100011.
[14] "Database - Energy - Eurostat." https://ec.europa.eu/eurostat/web/energy/data/database (accessed Apr. 26, 2022).
[15] E. W. Lemmon, I. H. Bell, M. L. Huber, and M. O. McLinden, "NIST Standard Reference Database 23: Reference Fluid Thermodynamic and Transport Properties-REFPROP, Version 10.0, National Institute of Standards and Technology." 2018. doi: https://doi.org/10.18434/T4/1502528.
[16] W. Xu, S. Deng, W. Su, Y. Zhang, L. Zhao, and Z. Yu, "How to approach Carnot cycle via zeotropic working fluid: Research methodology and case study," *Energy*, vol. 144, pp. 576–586, 2018, doi: 10.1016/j.energy.2017.12.041.
[17] C. Liu and T. Gao, "Off-design performance analysis of basic ORC, ORC using zeotropic mixtures and composition-adjustable ORC under optimal control strategy," *Energy*, vol. 171, pp. 95–108, Mar. 2019, doi: 10.1016/J.ENERGY.2018.12.195.
[18] G. Bamorovat Abadi and K. C. Kim, "Investigation of organic Rankine cycles with zeotropic mixtures as a working fluid: Advantages and issues," *Renewable and Sustainable Energy Reviews*, vol. 73, no. January, pp. 1000–1013, 2017, doi: 10.1016/j.rser.2017.02.020.
[19] B. Zühlsdorf, J. K. Jensen, and B. Elmegaard, "Heat pump working fluid selection—economic and thermodynamic comparison of criteria and boundary conditions," *International Journal of Refrigeration*, vol. 98, pp. 500–513, Feb. 2019, doi: 10.1016/J.IJREFRIG.2018.11.034.
[20] C. Arpagaus, F. Bless, M. Uhlmann, J. Schiffmann, and S. S. Bertsch, "High temperature heat pumps: Market overview, state of the art, research status, refrigerants, and application potentials," *Energy*, vol. 152, pp. 985–1010, 2018, doi: 10.1016/j.energy.2018.03.166.
[21] D. Roskosch, V. Venzik, J. Schilling, A. Bardow, and B. Atakan, "Beyond Temperature Glide: The Compressor is Key to Realizing Benefits of Zeotropic Mixtures in Heat Pumps," *Energy Technology*, vol. 9, no. 4, pp. 1–10, 2021, doi: 10.1002/ente.202000955.
[22] C. Arpagaus, F. Bless and S. S. Bertsch, "Techno-economic analysis f steam-generating heat pumps in distillation processes" *3rd High-Temperature Heat Pump Symposium 2022 : book of presentations*, pp. 371–386, 2022, Accessed: Nov. 07, 2022. [Online]. Available: http://hdl.handle.net/1854/LU-8757241

14th IEA Heat Pump Conference
15-18 May 2023, Chicago, Illinois

High Efficiency Heat Pump Industrial Drying with Water Vapor-Selective Membranes

Andrew J. Fix, James E. Braun, David M. Warsinger*

Purdue University, School of Mechanical Engineering & Herrick Laboratories, 585 Purdue Mall, West Lafayette, IN 47907

Abstract

Convective drying processes consume a significant amount of energy within the industrial sector. Heat pump-based drying processes are gaining attention as a potential technology for enabling efficient, electricity-driven drying for various applications. In this work, we propose a new heat pump drying system concept that employs water vapor-selective membranes for active control of the air humidity in drying processes, termed the MemDry system. We developed system-level models for the MemDry and representative baseline systems based on the first and second laws of thermodynamics to explore energy trends and limitations of the concept. It was found that energy savings on the order of 30-40% are possible when high temperature, low humidity conditions are required for the drying process. Furthermore, membrane dehumidification could theoretically reduce required drying temperatures by 10-20℃ while still saving energy. The unique design of the MemDry system and its use of exhaust air condensation may improve heat pump COPs by as much as 2x. This theoretical work shows that the MemDry concept has significant potential to provide efficient, feasible, and controllable conditions for industrial heat pump drying applications.

© HPC2023.
Selection and/or peer-review under the responsibility of the organizers of the 14th IEA Heat Pump Conference 2023.

Keywords: selective membranes; dehumidification; drying; Carnot; high temperature; thermodynamics; heat pump

1. Introduction and Background

1.1. Convective Drying Technologies

It has been estimated that thermal dehydration technologies account for anywhere between 10-20% of industrial energy consumption in developed countries [1]. Convective drying is one of the most common types of drying technologies, employed in drying food, pharmaceuticals, fabrics, chemicals, and more. Another common application for convective drying is residential clothes dryers, which constitute 3% of residential energy consumption [2]. Currently, industrial drying processes rely heavily on the combustion of fossil fuels [3]. More recently, there has been increased interest in moving away from combustion-based drying technologies, in favor of heat pump drying technologies [4].

Many different configurations and combinations of heat pump drying technologies have been proposed, including air-source [5], ground-source [6], solar assisted [7], chemical heat pumps [8], various forms of energy recovery, and more [4]. However, in their simplest form, the two categories of heat pump dryers are closed and open systems. Open dryers pull in ambient air, heat it up, send it to the drying process, and then simply exhaust the warm and humid air that leaves the drying process. In a closed heat pump dryer, instead of exhausting the warm and humid air leaving the drying process, it is instead passed through the vapor compression cycle's evaporator to condense water out of the air and is then reheated and recirculated [9].

Open heat pump systems can achieve high efficiency performance if the ambient conditions are very low humidity, but otherwise may be limited by the ambient conditions [3]. On the other hand, closed systems are not as dependent on the ambient conditions but must spend a considerable amount of energy condensing water

* Corresponding author. Tel.: +1-240-205-0440. *E-mail address:* dwarsing@purdue.edu.

out of the air. Conventional air conditioning technologies experience similar energy penalties when dealing with humidity [10]. Generally, closed heat pump dryers are more common in the literature, but even open systems could benefit from pre-dehumidification technologies. Thus, there is a need to identify innovative solutions to address the energy demands associated with air dehumidification in heat pump drying processes.

1.2. Water Vapor-Selective Membranes for Air Dehumidification

Recently, water vapor-selective membranes have gained interest in air conditioning research [11]. Conventional air conditioning technologies rely on cooling the air below its dew point to induce condensation dehumidification, and condensing water vapor requires a significant amount of energy [12]. Instead of relying on energy-intense phase-change dehumidification, selective membranes can mechanically separate water vapor out of air, which can save energy input depending on the system design [12], [13].

Most membranes used for air dehumidification are referred to as "dense" membranes [14]. For dehumidification membranes, a dense (non-porous) hygroscopic material, usually a polymer, is coated onto a support material. Because this hygroscopic layer is non-porous, air cannot easily penetrate, though the hygroscopic nature of the layer enables water vapor to transport across via the solution-diffusion process [15]. Some high-performance membrane materials for dehumidification include Pebax 1657 combined with graphene oxide [16], polyvinyl alcohol combined with triethylene glycol [17], and cellulose [19].

The two important performance metrics for the membrane materials are the permeance to water vapor and the air selectivity. The water vapor permeance simply describes the membrane's ability to pass water vapor. The air selectivity describes how well the membrane blocks air transport and is generally taken as the ratio of the water vapor permeance to the air permeance. Optimal membranes achieve both high selectivity and water vapor permeance. Top performing membranes generally achieve water vapor permeance on the order of 1,000-5,000 GPU, and selectivity up to 10,000 [16], [17]. However, the analysis in this work will provide high-level thermodynamic insight into the application of membrane dehumidification in industrial drying applications in a manner that does not rely on knowing or assuming values for these membrane material properties.

1.3. Scope and Novelty

While thermodynamic modeling for vacuum membrane dehumidification has been carried out extensively for air conditioning applications [13], [20]–[22], little-to-no work has been done in the field of industrial heat pump drying. This work, to the best of our knowledge, is the first to propose a hybrid membrane dehumidification and heat pump system configuration for efficient industrial drying applications. This analysis provides an introduction to the concept and explores the potential energy benefits through high-level, thermodynamic models that employ both theoretical and practical assumptions. The results provided in this paper will serve as a basis for further detailed modeling and prototyping efforts and can help establish a new sub-field within the heat pump and membrane research communities.

2. System Descriptions

2.1. Membrane Dehumidifier and Heat Pump Dryer System Description

In this work, we will refer to the system that combines membrane dehumidification and heat pump drying as the "MemDry" system. The left half of Figure 1 depicts the flow schematic of the MemDry system. Starting at State 1, relatively warm, saturated (100% relative humidity) air leaves the drying process and enters the dehumidification membrane module. A water vapor compressor maintains a low water vapor partial pressure on the top (permeate) side of the membrane at State 7 [23]. This difference in water vapor partial pressure draws humidity out of the drying process exhaust air while requiring no heat transfer. Then, the dry air at State 2 is reheated before being sent back to the drying process. The humidity that was removed between State 1 and State 2, is then slightly pressurized by the water vapor compressor to the second membrane module at State 8 and rejected across a membrane to the ambient air at State 4 [24].

The humid air at State 5 then passes through the evaporator of the vapor compression cycle, where heat is absorbed for reheating the process air (States 2 to 3). Condensing water vapor in this exhaust air is beneficial, as a significant portion of the heat transfer will come from the latent heat of vaporization. This means that, under certain conditions, warmer evaporator temperatures can be used, resulting in higher heat pump COPs. Plus, heat pump capacity requirements are lower, meaning smaller heat pump systems can be implemented.

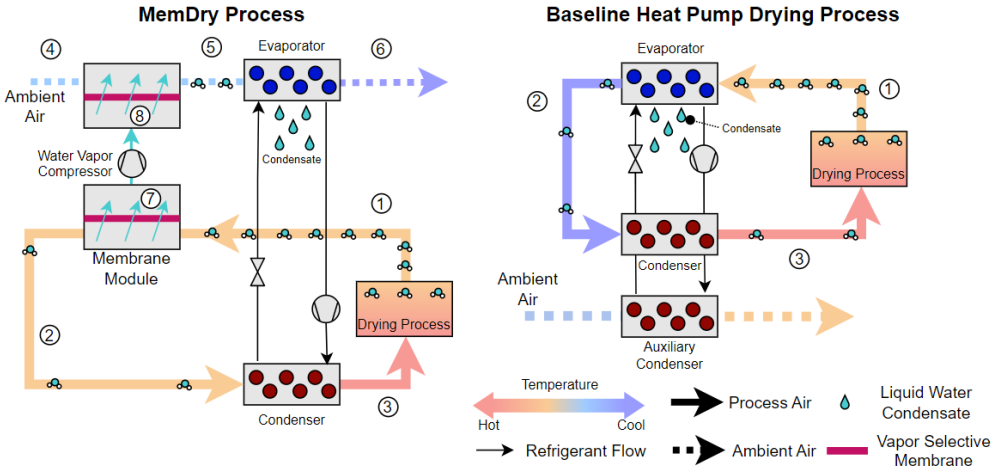


Figure 1. System schematics. (left) Membrane dehumidifier and heat pump dryer system schematic, referred to herein as the MemDry system. (right) Baseline, closed heat pump drying process.

2.2. Baseline Heat Pump Dryer System Description

In the baseline closed heat pump dryer system, shown in Figure 1 (right), State 1 and State 3 are identical to those states in the MemDry system. However, the relatively warm and humid air at State 1 is cooled to a lower temperature to induce condensation dehumidification. In this work, we model both systems such that the absolute humidity at State 2 is equivalent between both systems. But, because the air was cooled to induce condensation dehumidification, a significant amount of reheating must be provided by the condenser. While the condensation will provide a significant source of heat transfer in the baseline system as well, it is not strictly beneficial (as it is in the MemDry system) since it induces significant reheating requirements and lower evaporator temperatures are needed to maintain the desired humidity levels. Additionally, the condenser rate of heat transfer will be higher than the evaporator, so in order to maintain an energy balance within the drying process flow, an auxiliary condenser would be included to reject excess heat to an ambient air stream [2]. Figure 2 provides a sample psychrometric plot of the thermodynamic states in the two drying systems.

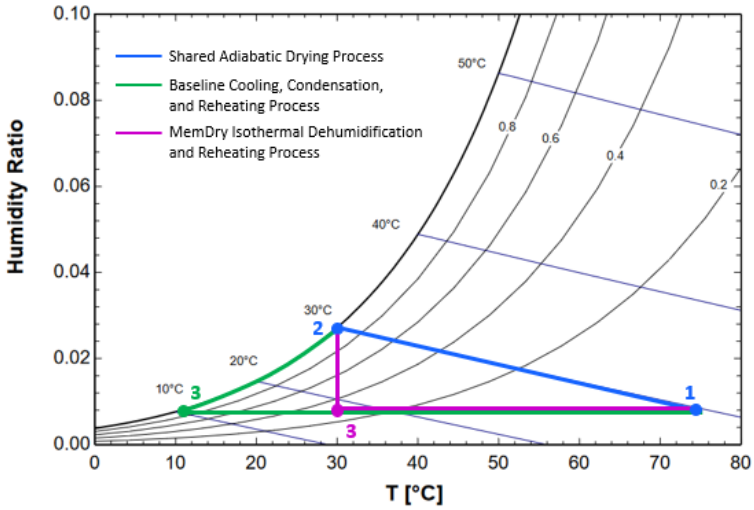


Figure 2. Sample psychrometric process plot showing the thermodynamic states within the drying cycle specific to the baseline system (green), MemDry system (pink), and shared isenthalpic drying process (blue). The supply temperature is shown as 75°C as an example.

3. Modeling Methodology

3.1. Modeling Overview

The models developed in this work are system-level, steady-state thermodynamic models based on a first-law analysis. Specific components are not modeled in detail (e.g., membrane area, heat exchanger area, membrane properties are not included in the model). This will become clear as the model is derived in the following sections. The models were developed in Engineering Equation Solver (EES), which is an iterative

solving software with built-in thermodynamic property functions for many fluids, including humid air [25]. Furthermore, some portions of the model were first replicated from prior published drying technology models before extending the framework to the MemDry system to ensure reasonable assumptions for the model. Overall, the intent of these theoretical models is to capture performance trends for the systems with both highly idealized assumptions and more practical assumptions and to assess key benefits and limitations.

3.2. Convective Drying Process Model and Validity

The convective drying process is modeled the same way for both systems in this work and is assumed to be a relatively ideal drying process. The supply temperature, T_3, and supply dew point temperature, $T_{\mathrm{DP},3}$, are set as inputs for most of the analyses. The supply dew point temperature is used as the metric for setting the dryer inlet humidity condition for convenience, as this will be directly tied to the evaporator temperature in the baseline system shown later. Thus, the inlet conditions, including the inlet humid air enthalpy, h_3, are known. To determine the dryer outlet conditions, we assume an ideal dryer where the drying occurs adiabatically (constant enthalpy) and the air leaving the drying process reaches 100% relative humidity [2]. These two critical assumptions are given by Equations 1 and 2.

$$h_1 = h_3 \tag{1}$$

$$RH_1 = 100\% \tag{2}$$

Thus, the inlet and outlet humid air conditions are known. In this work, a specific drying process is not explicitly modeled (conveyer drying, batch drying, etc.) Furthermore, we do not consider any dynamic behavior associated with the type of material being dried, thermal mass, or the change in drying rate as the water content changes in the product material. Similar simplifications have been made in other works and are justified here since the focus is on providing a comparative analysis between two heat pump technologies meeting the same theoretical drying load. Models from prior published work [2] were obtained for comparing inlet and outlet temperature conditions for different scenarios. It was found that the maximum error between our model and the prior model's temperature calculations was less than 1%, giving confidence that our drying process model was consistent with other works.

3.3. Vapor Compression Cycle Model

Both the MemDry and baseline systems incorporate a heat pump for process air heating. Due to the high temperature lift in this application (up to 130℃ in some cases), a more complex cycle architecture would be needed to achieve competitive COPs. However, this work focuses more on the comparison of the MemDry system to the baseline system, emphasizing the benefits of membrane dehumidification. So, to simplify the modeling of the vapor compression cycle energy requirements, two sets of results are presented. One set of results looks at the most ideal scenario and applies Carnot COPs to evaluate energy input requirements for the heat pumps. The Carnot cooling COP and heating COP, based on the thermodynamic states in the baseline system, are given by Equations 3 and 4, respectively.

$$COP_{Carnot,C} = \frac{T_2}{T_3 - T_2} \tag{3}$$

$$COP_{Carnot,H} = \frac{T_3}{T_3 - T_2} \tag{4}$$

Similar equations can be applied to the MemDry system but replacing T_2 with T_6. The second set of results that are presented apply a second law efficiency (η_{II}) to estimate real vapor compression cycle COPs for high temperature lift applications. Based on a review of detailed modeling efforts for high-temperature heat pumps employing two stage compression with some form of economization, it was found that the second law efficiency was around 0.40 across a broad range of conditions [26], [27]. The "practical" results in this work apply this second law efficiency to the Carnot COP to estimate "real" COPs, shown in Equation 5.

$$COP = COP_{Carnot} * \eta_{II} \tag{5}$$

Thus, the vapor compression cycle performance can be reasonably captured using the straightforward framework to compare the two systems and assess the benefits of adding membrane dehumidification.

3.4. Baseline Heat Pump Dryer System Model

Since the drying process is modeled identically in both systems, the remaining model derivations will focus on the portions of the two systems that remove humidity from the process air and reheat the process air.

3.4.1. Evaporator Energy Balance

The primary purpose of the evaporator in the baseline system is to provide dehumidification to the process air before it is reheated and sent back into the drying process. The temperature of the air at State 2 is used as an input or is varied in some of the following analyses. Since the air at State 1 is 100% relative humidity, State 2 will also be 100% relative humidity. The air-side energy balance on the evaporator in the baseline system is then given by Equation 6.

$$\dot{Q}_{evap,b} = \dot{m}_a(h_1 - h_2 - (\omega_1 - \omega_2)h_w) \tag{6}$$

Here, $\dot{m}_\mathrm{a}$ is the mass flowrate of air (on a dry basis) in the drying cycle, h represents the enthalpy of humid air, ω is the air humidity ratio, and h_w is the enthalpy of liquid water. In a steady state vapor compression cycle, the evaporator heat transfer rate is always less than the condenser heat transfer rate. So, we know that if the latent load is met by the evaporator, we will have sufficient (actually excess) heat available to reheat the process air in the condenser. Thus, the power consumption for the baseline heat pump system is based on the evaporator load, given by Equation 7 [28].

$$\dot{W}_b = \frac{\dot{Q}_{evap,b}}{COP_c} \tag{7}$$

Here, COP_c is the cooling coefficient of performance and can either be the Carnot COP ($\eta_\mathrm{II} = 1$) or practical COP ($\eta_\mathrm{II} = 0.4$), depending on the result being presented.

3.4.2. Condenser Energy Balance

Based on an energy balance for a vapor compression cycle, we can calculate the heat transfer rate in the condenser ($\dot{Q}_\mathrm{cond,b}$) according to Equation 8.

$$\dot{Q}_{cond,b} = \dot{W}_b + \dot{Q}_{evap,b} \tag{8}$$

The actual heat transfer rate required for reheating the process air ($\dot{Q}_\mathrm{heat,b}$) from State 2 to State 3 is given by Equation 9.

$$\dot{Q}_{heat,b} = \dot{m}_a(h_3 - h_2) \tag{9}$$

The enthalpy at State 2 (h_2) is known based on the set temperature and knowing the relative humidity is 100%, and the enthalpy at State 3 (h_3) is known based on the set drying temperature (T_3) and knowing that $\omega_3 = \omega_2$. As discussed before, excess heat is available on the condenser side of the vapor compression cycle due to the energy balance, therefore, the heat transfer rate in the auxiliary condenser is given by Equation 10.

$$\dot{Q}_{aux} = \dot{Q}_{cond,b} - \dot{Q}_{heat,b} \tag{10}$$

3.5. MemDry System Model

For the MemDry system, the vapor compression cycle is implemented slightly differently, requiring different energy balances, and the membrane dehumidification portion of the system model must be presented.

3.5.1. Membrane Dehumidification Governing Equations

Air leaving the drying process at State 1 enters the membrane module. In order to fairly compare both systems in this analysis, the dew point temperature at State 2 ($T_\mathrm{DP,2}$) is equivalent in both systems for all analyses. This dew point temperature has an associated humidity ratio (ω_2) and water vapor partial pressure

($P_{v,2}$). Thus, $P_{v,2}$ is known/set in the model. The low vacuum vapor pressure ($P_{v,7}$) required to meet this dehumidification load is set based on a given pinch point vapor pressure difference ($\Delta P_{v,pinch}$). Thus, $P_{v,7}$ can be calculated according to Equation 11.

$$P_{v,7} = P_{v,2} - \Delta P_{v,pinch} \tag{11}$$

Estimating vacuum vapor pressure in this manner is analogous to estimating vapor compression cycle evaporator or condenser temperatures based on assumed pinch point temperature differences. In this work, we use a pinch vapor pressure difference of 0.5 kPa for the practical scenarios, falling in the range analyzed by [21], and 0 kPa for the ideal scenarios, representing a mass exchanger with 100% effectiveness. State 7 and State 8 are both assumed to be pure water vapor, which implies that the membranes are perfectly selective. This assumption has been applied in many modeling works for assessing theoretical thermodynamic energy requirements of the technology [20], [21]. The mass flowrate of water vapor removed in the dehumidification process is given by Equation 12.

$$\dot{m}_v = \dot{m}_a(\omega_1 - \omega_2) \tag{12}$$

Next, we assume that when the water vapor is rejected to the exhaust air, the relative humidity is brought to 90% at State 5. With this assumption, a mass balance can determine the exhaust air flowrate ($\dot{m}_{a,ex}$) needed to achieve this condition.

$$RH_5 = 90\% \tag{13}$$

$$\dot{m}_v = \dot{m}_{a,ex}(\omega_5 - \omega_4) \tag{14}$$

Now, knowing the water vapor partial pressure at State 5, the rejection side water vapor partial pressure, $P_{v,8}$, can be calculated using the same pinch point vapor pressure difference as before.

$$P_{v,8} = P_{v,5} + \Delta P_{v,pinch} \tag{15}$$

The power consumption of the water vapor compressor is calculated by assuming an isentropic efficiency, as shown in Equation 16 [22], [28].

$$\dot{W}_{WVC} = \dot{m}_v \frac{h_{v,8s} - h_{v,7}}{\eta_{WVC}} \tag{16}$$

Here, $h_{v,7}$ is the enthalpy of water vapor at a pressure of $P_{v,7}$ and a temperature of T_1. $h_{v,8s}$ is the enthalpy of the water vapor at a pressure of $P_{v,8}$ under isentropic compression from State 7. η_{WVC} is the compressor isentropic efficiency, taken as 1 for the ideal scenarios and 0.7 for the practical scenarios [22].

3.5.2. Condenser Governing Equations

The membrane dehumidification process is assumed to be isothermal ($T_2 = T_1$). Therefore, the condenser energy balance is simply given by Equation 17.

$$\dot{Q}_{cond,M} = \dot{m}_a(h_3 - h_2) \tag{17}$$

It should be noted that, in the baseline system, the evaporator was the minimum load that must be met in the system, and we know that as long as the evaporator load is met, there will be sufficient heat for reheating in the condenser. However, in the MemDry system, the reheating load in the condenser is the minimum load that must be met, and the evaporator load does not affect the drying process (other than the evaporator temperature affecting the heat pump COP). Thus, the energy input for reheating the process air is given by Equation 18 and is based on the condenser load.

$$\dot{W}_{cond,M} = \frac{\dot{Q}_{cond,M}}{COP_H} \tag{18}$$

Here, COP_H is the heating coefficient of performance and can either be the Carnot COP or practical COP (depending on the result being presented).

3.5.3. Ambient Air Evaporator Governing Equations

As was stated previously, the ambient air evaporator makes use of the condensation to enable higher evaporating temperatures and therefore higher vapor compression cycle COPs. By assuming that $RH_6 = 100\%$ (since RH_5 is set at 90%), T_6 is calculated iteratively by three coupled equations (Equations 3, 19, and 20). Essentially, the condenser load ($\dot{Q}_{\mathrm{heat,M}}$) is set, the evaporator load depends on the heat pump COP, which depends on T_6 (which is dependent on the energy balance in Equation 20). Thus, three unknowns ($\dot{Q}_{\mathrm{evap,M}}$, T_6, and COP_c) are solved iteratively by the EES software.

$$\dot{Q}_{evap,M} = \dot{m}_{a,ex}(h_5 - h_6 - (\omega_5 - \omega_6)h_w) \tag{19}$$

$$\dot{Q}_{evap,M} = \dot{Q}_{cond,M} - \dot{W}_{cond,M} \tag{20}$$

Having determined T_6, the latent heat ratio on the evaporator can be expressed according to Equation 21.

$$LHR = \frac{\dot{m}_{a,ex}(\omega_5 - \omega_6)h_{fg}}{\dot{Q}_{evap,M}} \tag{21}$$

Additionally, the framework can be modified to assess the value of T_6 if no latent heat was available, which can then be used to estimate the heat pump COP when no latent heat is available, as will be shown later.

3.6. Key Performance Metrics

Several performance metrics will be evaluated in this work. The first is the energy savings. The energy savings metric simply compares baseline system power consumption to the MemDry power consumption. The baseline power consumption is simply equal to the vapor compression cycle power consumption. The MemDry total power consumption is given by Equation 22.

$$\dot{W}_M = \dot{W}_{WVC} + \dot{W}_{cond,M} \tag{22}$$

In both systems, fan power consumption is not included in the current models. This would be specific to the system design and is therefore outside the scope of this high-level analysis. Instead, we are more concerned in evaluating the fundamental thermodynamic requirements of heating and dehumidification in the two systems. Next, the drying efficiency relates the latent heat removal rate of the drying process divided by the total system power input, represented generally by Equation 23 [2], [29].

$$\eta_d = \frac{\dot{m}_a(\omega_3 - \omega_1)h_{fg}}{\dot{W}_{sys}} \tag{23}$$

Here, $\dot{W}_{\mathrm{sys}}$ generically represents the total system power consumption for either system (either $\dot{W}_{\mathrm{b}}$ or $\dot{W}_{\mathrm{M}}$). The drying time (t_{dry}) represents the time to remove all of the water from a product. The mass of water in the product to be dried ($m_{\mathrm{w,p}}$) can be set arbitrarily, and then for a given dry time and drying conditions, the air flowrate ($\dot{m}_{\mathrm{a}}$) can be calculated iteratively by the model.

$$t_{dry} = \frac{m_{w,p}}{\dot{m}_a(\omega_1 - \omega_3)} \tag{24}$$

In the analyses of this work, $\dot{m}_{\mathrm{a}}$ is set at 0.0646 kg/s and $m_{\mathrm{w,p}}$ is set at 2.05 kg based on typical clothes drying applications [2]. Of course, the eventual application for this technology is focused on industrial drying, through these clothes drying conditions provide a test case to study the thermodynamics.

4. Results and Discussion

The following results explore the thermodynamic performance of the MemDry concept and compare it to the baseline heat pump system. As has been alluded to in the prior sections, two sets of results are presented in this section: one for the "ideal" scenario and one for a "practical" scenario. Table 1 summarizes the model inputs for these two scenarios.

Table 1. Summary of the model inputs for the ideal and practical scenarios

Variable/Input	Ideal Scenario	Practical Scenario	Practical Scenario Reference
Pinch vapor pressure difference, $\Delta P_{v,pinch}$	0 [kPa]	0.5 [kPa]	[21]
Compressor isentropic efficiency, η_{WVC}	1 [-]	0.70 [-]	[22]
Heat pump second law efficiency, η_{II}	1 [-]	0.40 [-]	[26], [27]

4.1. Energy Savings Over Baseline System

First, the energy savings of the MemDry system compared to the baseline heat pump drying system are evaluated. Figure 3 displays the energy savings for the ideal scenario, and Figure 4 displays the energy savings for the practical scenario.

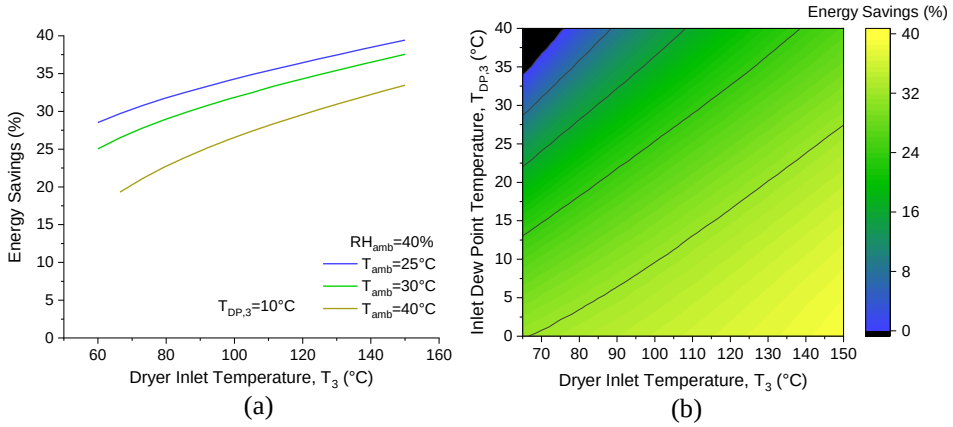


Figure 3. Ideal scenario energy savings. (a) Energy savings of the MemDry system as a function of the drying temperature (T_3) for different ambient temperatures. (b) Energy savings of the MemDry system as a function of the drying temperature (T_3) and dryer inlet dew point temperature ($T_{DP,2}$) for an ambient condition of 30℃ and 40% relative humidity.

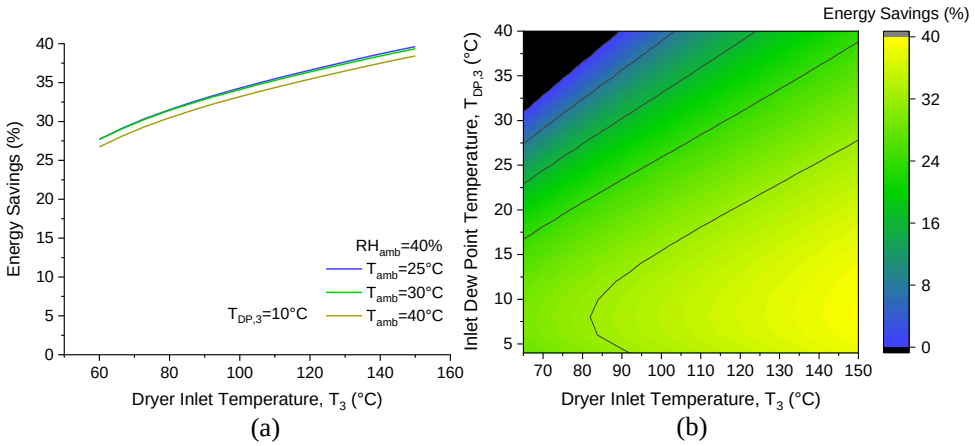


Figure 4. Practical scenario energy savings. (a) Energy savings of the MemDry system as a function of the drying temperature (T_3) for different ambient temperatures. (b) Energy savings of the MemDry system as a function of the drying temperature (T_3) and dryer inlet dew point temperature ($T_{DP,2}$) for an ambient condition of 30℃ and 40% relative humidity.

A few interesting trends can be noticed from these plots. First is that energy savings are generally higher for drying applications with high drying temperatures. As drying temperature increases, the dehumidification load increases exponentially, and reheating energy requirements increase linearly. Since membrane dehumidification specifically targets improving the energy input associated with the humidity loads, it is expected that greater energy savings would be achieved when these humidity loads become more significant. Also, as the ambient humidity ratio increases (increasing temperature at constant relative humidity) the energy savings decrease because the water vapor compressor must pressurize the water vapor to a higher pressure in order to reject it, thus requiring more power input.

In Figure 3a and Figure 4a, it appears as though the "ideal" MemDry system (Figure 3) achieves less energy savings than the "practical" MemDry system (Figure 4) in some conditions, however this is only

because the ideal MemDry system is compared against an ideal baseline system in Figure 3a (both with 100% Carnot efficiency). When practical operating conditions are imposed in Figure 4, the MemDry system does achieve higher savings relative to the baseline system than it did under the ideal operating scenario in Figure 3a because the membrane dehumidification helps alleviate the practical inefficiencies associated with condensation dehumidification in the baseline system that are less pronounced under ideal conditions.

Additionally, for a given drying temperature, an optimal dryer inlet dew point temperature (for the practical scenario) will exist, shown by Figure 4b. At sufficiently low inlet dew point temperatures, very low vacuum pressures are required to achieve this inlet dew point, and therefore the MemDry system achieves lower energy savings. Furthermore, at high inlet dew point temperatures, vapor compression cycles will have a high COP, and therefore the energy savings of membrane dehumidification become less pronounced.

Lastly, the MemDry is not suitable for low-temperature applications with high dryer inlet dew point temperatures (shown by the negative energy savings in the top left of Figure 3b and Figure 4b). In these scenarios, humidity loads would be relatively small and heat pump COPs would be very high, negating the need for energy efficient membrane dehumidification. However, these conditions are not conducive for convective drying and are therefore not likely to be used in many applications.

4.2. MemDry Evaporator Enhancement from Condensation

Next, the enhancement from air-side condensation in the MemDry evaporator is quantified. To clarify this concept, a certain amount of heat must be absorbed by the evaporator to sufficiently reheat the air in the condenser. Without condensation from State 5 to State 6, the evaporator would need to impose a large temperature change to the exhaust air stream. This in turn would mean that lower evaporator temperatures would be required, lowering the heat pump COP. But, with a substantial amount of the evaporator heat being pulled from the condensation process, less temperature change (sensible cooling) is provided to the exhaust air. Therefore, higher evaporator temperatures and higher COPs can be achieved when latent heat is available. The COP assuming no latent heat is available is denoted as COP_{dry}, whereas the COP with available latent heat is denoted COP_{wet} in this section.

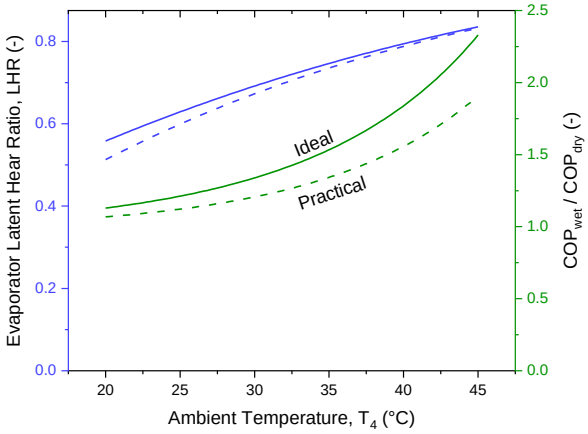


Figure 5. Evaporator latent heat fraction (left axis) and heat pump COP improvement ratio (right axis) as a function of the ambient air temperature for both ideal and practical scenarios. $T_3 = 100℃$ and $T_{DP,3} = 10℃$. Ambient humidity was constant at 40% RH.

For the conditions analyzed in Figure 5, we showed that the latent heat fraction ranged between 0.5 to 0.8. As the LHR increased and the evaporator temperature increased, the heat pump COP could be nearly doubled. Compounding this improved heat pump COP with the lower heating loads and efficient membrane dehumidification, the MemDry concept has great potential to provide significant savings.

4.3. MemDry System Drying Efficiency

Next, we evaluate the drying efficiency, defined by Equation 23, in Figure 6. The drying efficiency is evaluated as function of the drying temperature and inlet dew point temperature for a set ambient condition. As can be seen in Figure 6, the ideal drying efficiency ranges between 3-10 whereas in the practical scenario, the drying efficiency ranges between 0.8-3. A drying efficiency greater than 1 implies that the specific energy input for drying was less than the enthalpy of vaporization for water. A drying efficiency of 1 should be considered the minimum acceptable efficiency. The range of drying efficiencies below 1 in Figure 6a occur

where the heat pump supply temperature is very high (high heat pump energy input and low heat pump COP) and the inlet dew point temperature is low (requiring significant energy consumption from the water vapor compressor). This represents a rather extreme application/condition, though it is important to recall that, even though the drying efficiency dips below 1, the energy savings would still be positive relative the baseline system. Some combination of heat pump heating and resistive heating could potentially bring this drying efficiency closer to 1. Additionally, for a constant dryer temperature, higher inlet dew point temperatures yield a higher drying efficiency, but the drying time will also increase since the air cannot remove as much humidity due to the higher inlet air humidity. Drying time is considered in the next section.

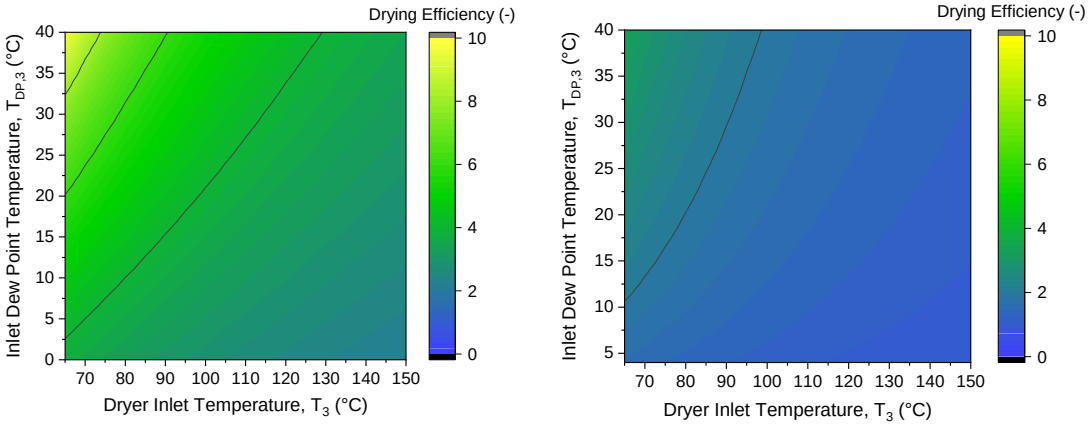


Figure 6. MemDry drying efficiency at the ambient conditions of 30℃ and 40% relative humidity. (a) Drying efficiency in the ideal scenario (b) Drying efficiency in the practical scenario.

4.4. Drying Temperature Reduction

Lastly, we evaluate the impact that the dryer inlet dew point temperature has on the required inlet dryer temperature. The inlet dryer temperature (T_3) is plotted as a function of the dryer inlet dew point temperature for a constant drying time in Figure 7. Essentially, as the inlet to the dryer becomes more humid (higher dew point temperature), a higher drying temperature (T_3) is required to compensate and maintain a constant drying time.

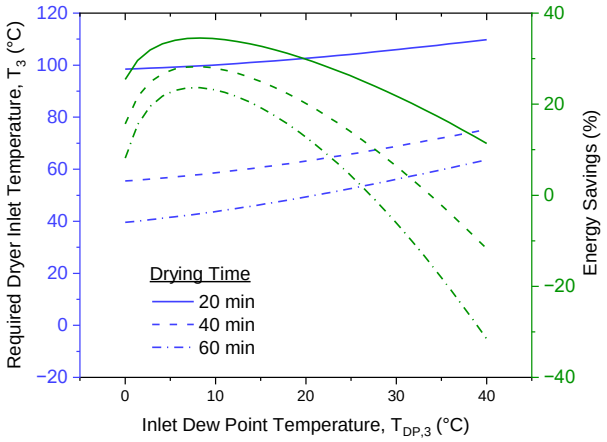


Figure 7. Required drying temperature as a function of the dryer inlet dew point temperature ($T_{DP,3}$) for different constant drying times for the ambient conditions of 30℃ and 40% relative humidity. The energy savings are plotted on the right axis.

As can be seen, reducing the dryer inlet dew point temperature could lead to drying temperature reductions on the order of 10-20℃. This is important for the technology because, achieving exceptionally high temperatures for drying with heat pumps can be challenging. However, if the goal is to electrify many drying processes, reducing inlet humidity conditions with membrane dehumidification can enable lower dryer temperatures (attainable with heat pumps) without sacrificing drying time. Plus, compared to the baseline heat pump system providing the same supply and dew point conditions, the MemDry system may provide energy savings on the order of 20-25% for lower inlet dew point temperature conditions.

5. Conclusions

In conclusion, this work has presented a novel system concept, termed the MemDry system, that combines selective membrane dehumidification with a heat pump for industrial drying applications. The theoretical models were used to explore energy savings and efficiency trends, relative to a baseline heat pump drying system modeled under an identical set of assumptions for fair comparison. It was found that, for the conditions analyzed, up to 40% energy savings could be possible, and negative energy savings are also possible under some extreme conditions. The vapor compression cycle COP can be improved by almost 2x due to the available latent heat in the evaporator for the MemDry, marking a unique advantage to the clever thermal system design. The drying efficiency was found to range between 3-10 under ideal conditions and 0.8-3 under more practical conditions. Furthermore, drying temperatures could be reduced by 10-20℃ while maintaining equivalent drying times and saving up to 25% of the energy input for drying. Overall, the concept shows great potential to offer significant energy savings and process control for industrial drying applications. Future work will focus on prototype development, detailed model development, and detailed model validation.

Nomenclature

Variables and Acronyms

Variable/Acronym Name	Symbol/Abbreviation	Units
Coefficient of Performance	COP	-
Compressor Isentropic Efficiency	η_{WVC}	-
Drying Time	t_{dry}	s
Drying Efficiency	η_{d}	-
Engineering Equation Solver	EES	
Enthalpy	h	kJ/kg
Gas Permeance Units	GPU	-
Humidity Ratio	ω	-
Heat Transfer Rate	$\dot{Q}$	kW
Latent Heat Ratio	LHR	-
Mass Flowrate	$\dot{m}$	kg/s
Mass of Water in Product	$m_{\mathrm{w,p}}$	kg
Power Consumption	$\dot{W}$	kW
Pressure	P	kPa
Pressure Difference	ΔP	kPa
Relative Humidity	RH	%
Second Law Efficiency	η_{II}	-
Temperature	T	℃

Subscripts

Subscript Meaning	Symbol
Air flow	a
Auxiliary Condenser	aux
Ambient Conditions (state 4)	amb
Ambient Exhaust Airflow	ex
Baseline system	b
Condenser	cond
Carnot Heat Pump	Carnot
Cooling	C
Evaporator	evap
Heat of Vaporization	fg
Heating	H
Liquid Water Property	w
MemDry System	M
Pinch Point Difference	pinch
Reheating Requirement	heat
Total System Energy	sys
Water Vapor Property	v
Water Vapor Compressor	WVC

Acknowledgements

We would like to thank Professor Davide Ziviani, Jinwoo Oh and Anand Balaraman for their review and suggestions for the paper. We thank Dr. Kyle Gluesenkamp for sharing his published models [2] for validating our own models. Furthermore, this work has been partially supported by the Center for High Performance Buildings (grant number CHPB-50) at Purdue University. This material is based upon work supported by the U.S. Department of Energy's Office of Energy Efficiency and Renewable Energy (EERE) under the Advanced Manufacturing Office, award number DE-EE0010199. Upon submitting this work, Andrew Fix is supported by an appointment to the Building Technologies Office (BTO) IBUILD Graduate Research Fellowship administered by the Oak Ridge Institute for Science and Education (ORISE) and managed by Oak Ridge National Laboratory (ORNL) for the U.S. Department of Energy (DOE). ORISE is managed by Oak Ridge Associated Universities (ORAU). All opinions expressed in this paper are the authors' and do not necessarily reflect the policies and views of DOE, EERE, BTO, ORISE, ORAU or ORNL.

References

[1] A. S. Mujumdar and Z. H. Wu, "Thermal Drying Technologies: New Developments and Future R&D Potential," *International Conference on Heat Transfer, Fluid Mechanics, and Thermodynamics*, 2007, doi: 10.1142/9789812771957_0001.

[2] K. R. Gluesenkamp and V. K. Patel, "Carnot Analysis of Heat Pump Drying: Ideal Efficiency and Dry Time," in *Purdue Conferences*, 2022.

[3] DOE, "Manufacturing Energy and Carbon Footprints," *Office of Energy Efficiency & Renewable Energy*, 2018. https://www.energy.gov/eere/amo/manufacturing-energy-and-carbon-footprints-2018-mecs (accessed Apr. 11, 2022).

[4] L. J. Goh, M. Y. Othman, S. Mat, H. Ruslan, and K. Sopian, "Review of heat pump systems for drying application," *Renewable and Sustainable Energy Reviews*, vol. 15, no. 9, pp. 4788–4796, 2011, doi: 10.1016/j.rser.2011.07.072.

[5] N. Colak and A. Hepbasli, "A review of heat-pump drying (HPD): Part 2 - Applications and performance assessments," *Energy Convers Manag*, vol. 50, no. 9, pp. 2187–2199, Sep. 2009, doi: 10.1016/j.enconman.2009.04.037.

[6] Z. Erbay and A. Hepbasli, "Application of conventional and advanced exergy analyses to evaluate the performance of a ground-source heat pump (GSHP) dryer used in food drying," *Energy Convers Manag*, vol. 78, pp. 499–507, Feb. 2014, doi: 10.1016/j.enconman.2013.11.009.

[7] Y. Qiu, M. Li, R. H. E. Hassanien, Y. Wang, X. Luo, and Q. Yu, "Performance and operation mode analysis of a heat recovery and thermal storage solar-assisted heat pump drying system," *Solar Energy*, vol. 137, pp. 225–235, Nov. 2016, doi: 10.1016/j.solener.2016.08.016.

[8] M. I. Fadhel, K. Sopian, W. R. W. Daud, and M. A. Alghoul, "Review on advanced of solar assisted chemical heat pump dryer for agriculture produce," *Renewable and Sustainable Energy Reviews*, vol. 15, no. 2. pp. 1152–1168, Feb. 2011. doi: 10.1016/j.rser.2010.10.007.

[9] J. H. Cheng, W. Yu, X. Cao, L. L. Shao, and C. L. Zhang, "Evaluation of heat pump dryers from the perspective of energy efficiency and operational robustness," *Appl Therm Eng*, vol. 215, Oct. 2022, doi: 10.1016/j.applthermaleng.2022.118995.

[10] J. Woods, "Membrane processes for heating, ventilation, and air conditioning," *Renewable and Sustainable Energy Reviews*, vol. 33, pp. 290–304, 2014, doi: 10.1016/j.rser.2014.01.092.

[11] B. Yang, W. Yuan, F. Gao, and B. Guo, "A review of membrane-based air dehumidification," *Indoor and Built Environment*, vol. 24, pp. 11–26, 2015, doi: 10.1177/1420326X13500294.

[12] A. J. Fix, J. E. Braun, and D. M. Warsinger, "Vapor-selective active membrane energy exchanger with mechanical ventilation and indoor air recirculation," *Appl Energy*, vol. 312, p. 118768, 2022, doi: 10.1016/j.apenergy.2022.118768.

[13] D. E. Claridge *et al.*, "A new approach for drying moist air: The ideal Claridge-Culp-Liu dehumidification process with membrane separation, vacuum compression and sub-atmospheric condensation," *International Journal of Refrigeration*, vol. 101, pp. 211–217, 2019, doi: 10.1016/j.ijrefrig.2019.03.025.

[14] M. Qu, O. Abdelaziz, Z. Gao, and H. Yin, "Isothermal membrane-based air dehumidification: A comprehensive review," *Renewable and Sustainable Energy Reviews*, vol. 82, pp. 4060–4069, 2018, doi: 10.1016/j.rser.2017.10.067.

[15] J. G. Wijmans and R. W. Baker, "The solution-diffusion model: a review," *J Memb Sci*, vol. 107, pp. 1–21, 1995, doi: 10.1016/0376-7388(95)00102-I.

[16] F. H. Akhtar, M. Kumar, and K. V. Peinemann, "Pebax®1657/Graphene oxide composite membranes for improved water vapor separation," *J Memb Sci*, vol. 525, pp. 187–194, 2017, doi: 10.1016/j.memsci.2016.10.045.

[17] T. D. Bui *et al.*, "Effect of hygroscopic materials on water vapor permeation and dehumidification performance of poly(vinyl alcohol) membranes," *J Appl Polym Sci*, vol. 134, p. 44765, 2017, doi: 10.1002/app.44765.

[18] Y. Shin *et al.*, "Graphene oxide membranes with high permeability and selectivity for dehumidification of air," *Carbon N Y*, vol. 106, pp. 164–170, 2016, doi: 10.1016/j.carbon.2016.05.023.

[19] T. Puspasari, F. H. Akhtar, W. Ogieglo, O. Alharbi, and K. V. Peinemann, "High dehumidification performance of amorphous cellulose composite membranes prepared from trimethylsilyl cellulose," *J Mater Chem A Mater*, vol. 6, pp. 9271–9279, 2018, doi: 10.1039/c8ta00350e.

[20] O. Labban, T. Chen, A. F. Ghoniem, J. H. Lienhard, and L. K. Norford, "Next-generation HVAC: Prospects for and limitations of desiccant and membrane-based dehumidification and cooling," *Appl Energy*, vol. 200, pp. 330–346, 2017, doi: 10.1016/j.apenergy.2017.05.051.

[21] H. Lim, S. Choi, Y. Cho, S. Kim, and M. Kim, "Comparative thermodynamic analysis of membrane-based vacuum air dehumidification systems," *Appl Therm Eng*, vol. 179, p. 115676, 2020, doi: 10.1016/j.applthermaleng.2020.115676.

[22] A. J. Fix, J. E. Braun, and D. M. Warsinger, "Vapor-selective active membrane energy exchanger for high efficiency outdoor air treatment," *Appl Energy*, vol. 295, p. 116950, 2021, doi: 10.1016/j.apenergy.2021.116950.

[23] A. J. Fix, J. E. Braun, and D. M. Warsinger, "Vapor-Selective Nanostructured Membrane Heat Exchangers for Cooling and Dehumidification," PCT/US2021/019314, 2021

[24] D. E. Claridge and C. Culp, "Systems and methods for air dehumidification and cooling with membrane vapor rejection," US 8,500,848 B2, 2013

[25] S. Klein, "Engineering Equation Solver," vol. v. 10.643, 2019.

[26] C. Mateu-Royo, C. Arpagaus, A. Mota-Babiloni, J. Navarro-Esbrí, and S. S. Bertsch, "Advanced high temperature heat pump configurations using low GWP refrigerants for industrial waste heat recovery: A comprehensive study," *Energy Convers Manag*, vol. 229, 2021, doi: 10.1016/j.enconman.2020.113752.

[27] G. Kosmadakis, C. Arpagaus, P. Neofytou, and S. Bertsch, "Techno-economic analysis of high-temperature heat pumps with low-global warming potential refrigerants for upgrading waste heat up to 150 °C," *Energy Convers Manag*, vol. 226, p. 113488, 2020, doi: 10.1016/j.enconman.2020.113488.

[28] Y. Cengel and M. Boles, *Thermodynamics: An Engineering Approach*, 5th ed. New York: McGraw Hill, 2006.

[29] K. R. Gluesenkamp, V. K. Patel, and A. M. Momen, "Efficiency limits of evaporative fabric drying methods," *Drying Technology*, vol. 39, no. 1, pp. 104–124, 2021, doi: 10.1080/07373937.2020.1839486.

14th IEA Heat Pump Conference
15-18 May 2023, Chicago, Illinois

Case Study of the Largest Air Source Heat Pumps Central Heating Project in China

Zhao Mishen[a], Wang Huping[a], Zhao Hengyi[b], Xie Sherry[c*], Ni Long[d]

[a] Guangdong New Energy Technology Development Co.,Ltd., Guangzhou, 511340, China
[b] China Heat Pump Alliance (CHPA), Beijing 100029, China
[c] Emerson Climate Technologies (Suzhou) Co., Ltd., Shanghai 200233, China
[d] School of Architecture, Harbin Institute of Technology; Key Laboratory of Cold Region Urban and Rural Human Settlement Environment Science and Technology, Ministry of Industry and Information Technology, Harbin, 150090, China

Abstract

This paper summarizes the best practices for Air Source Heat Pump (ASHP) central heating systems in large-scale residential buildings. Central heating of residential buildings in northern China typically depends on coal-burning power plants, which are the main sources of reducing such pollution as well as carbon emissions. The project described in this paper is one biggest ongoing ASHP heating projects in the world. More than 1,200 units of ASHPs were deployed as heating sources in northern China, heating approximately 4 million square meters of living spaces in large residential buildings. Various parameters were monitored and collected over about 120 days during the heating season from 2019 to 2020. Operating costs and carbon dioxide emissions were measured and compared to the corresponding figures for equivalent heating by other systems. It is demonstrated that ASHP systems are well suited for meeting the heating requirements of this region while reducing operating costs and greenhouse gas emissions.

© HPC2023.
Selection and/or peer-review under the responsibility of the organizers of the 14th IEA Heat Pump Conference 2023.

Keywords: air sources heat pump, large scale central heating project, carbon reduction.

1. Introduction

The heating project in Zhao County is located in Hebei province, north China, it is a typical cold winter area, and space heating in winter is managed by the government. The heat source that came from two coal-burning power plant caused serious air pollution significantly. In 2019, the local government decided to replace the coal-burning power plants with ASHP to reduce running cost and air pollution. Therefore, 1,200 ASHP units (input power is 60HP for each) are used for a 4.07 million square meters heating area; the terminals in the buildings are radiator and floor heating. The operation data of the 2018-2019 heating season provide favorable support for the heating system renovation. To fit the existing heating pipe network the whole heating project is designed to build 42 distributed air source heat pump stations with the 1200 units ASHP for heat supply. The old heating pipe network consists of two coal-fired power plants (A and B) as shown in Fig. 1(a), and the ASHP heating stations as shown in Fig. 1(b). Fig. 2 illustrates the Beling temple station and the Lichun station with ASHP units.

For large-scale ASHP projects, multiple sets of units placed together will impact the performance of the unit is a big problem. In the Zhao County project, many sites faced this challenge. There are also many other factors that affect the sites of the air source heat pump heat source selection, distributed heat source arrangement for the urban heating project is recommended to minimize the heat loss of the pipe network.

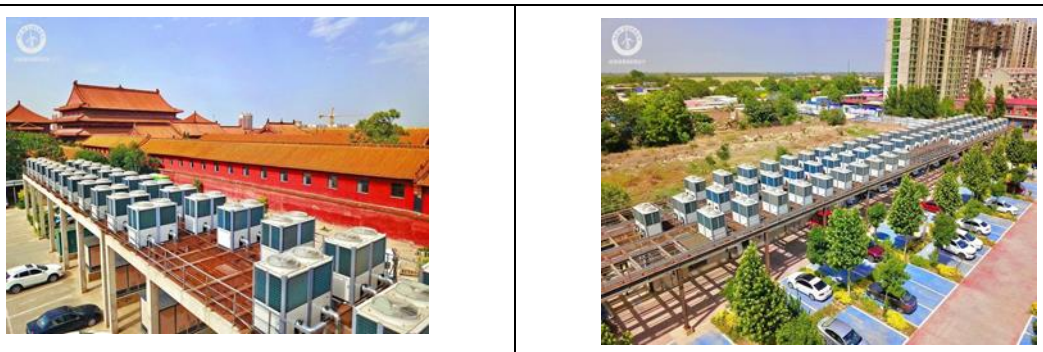
* Corresponding author. Wang Huping, Guangdong New Energy Technology Development Co., Ltd., Guangzhou, 511340, China
Tel: +86 189 2897 6897; *E-mail address:* 419961197@qq.com.



(a) The old heating pipe network (red ones) by two coal burning power plants (A and B)

(b) The ASHP heating stations (green ones) distribution with1200 units

Fig.1. The old heating pipe network and the new ASHP heating stations in Zhao County.



(a) Beling temple station with ASHP units

(b) Lichun station with ASHP units

Fig.2. The layout of ASHP units in the two stations.

2. Project overview

2.1. The system configuration scheme

The heat load of this project was calculated using the real-time calculation method (secondary stations with monitoring conditions) and the area index method (secondary stations without monitoring conditions). The average heat load during the heating period was calculated to be 137.9 MW. Combining with the heating load and development of the urban area of Zhao County and the fuel characteristics, 1200 ASHP units (120 KW of heat production per unit under heating condition) were selected for this project, and the development end was reserved in the heat source to meet the demand of future heating heat load growth. Low temperature water was adopted as the heating medium, with the supply and return water temperature of 55 ℃/45 ℃ at the end of radiator and 45 ℃/35 ℃ at the end of floor heating. The system configuration scheme of a station is shown in Fig. 3. Considering factors such as system drainage, the make-up water rate of this project was taken as 1%-2%, and the make-up water pump was used for variable frequency continuous pressure fixing.

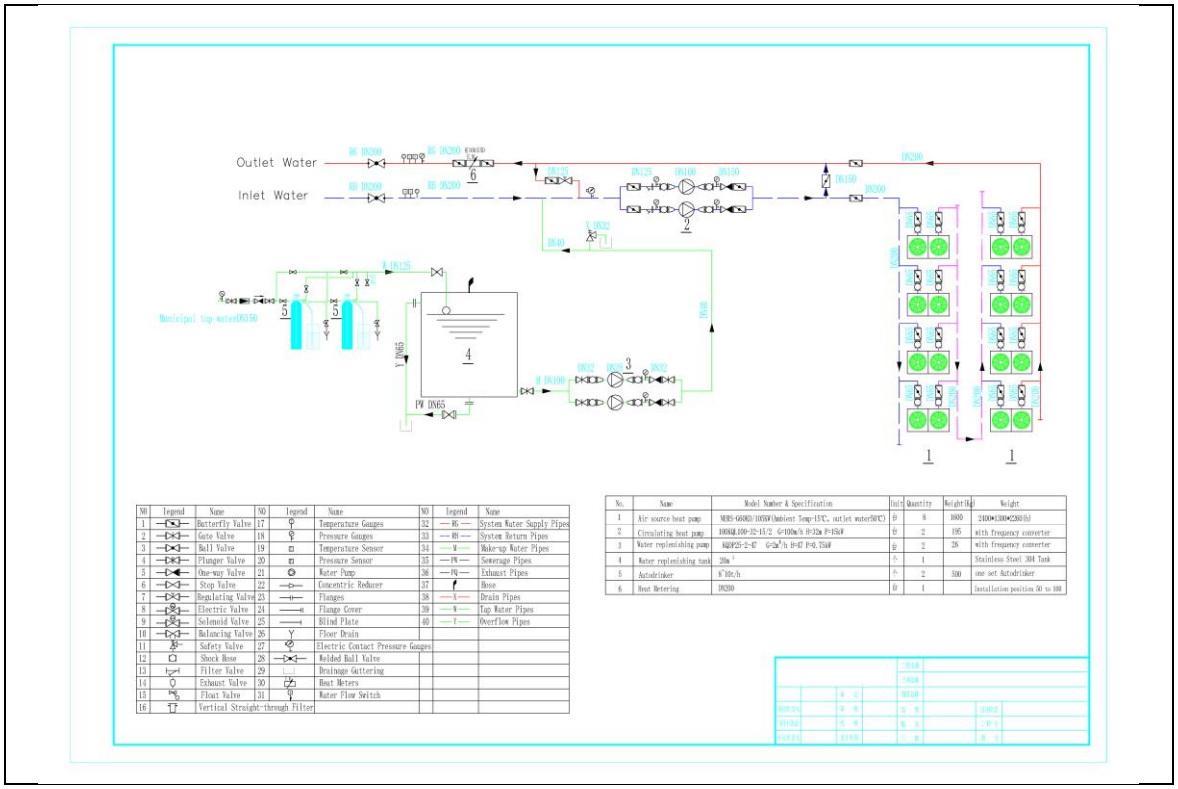


Fig.3. The system configuration scheme of a station in the large ASHP heating project.

2.2. The system operation scheme

The system adopts group control automatic management, which can realize to present the site water temperature and operation status of heat pump unit on the computer and cell phone, and also adjust the site parameters and remote switch operation. As shown in Fig. 4, the low-temperature hot water produced by the air source heat pump is transported to the heat users through the pipeline, and the whole heating process is monitored in its entirety.

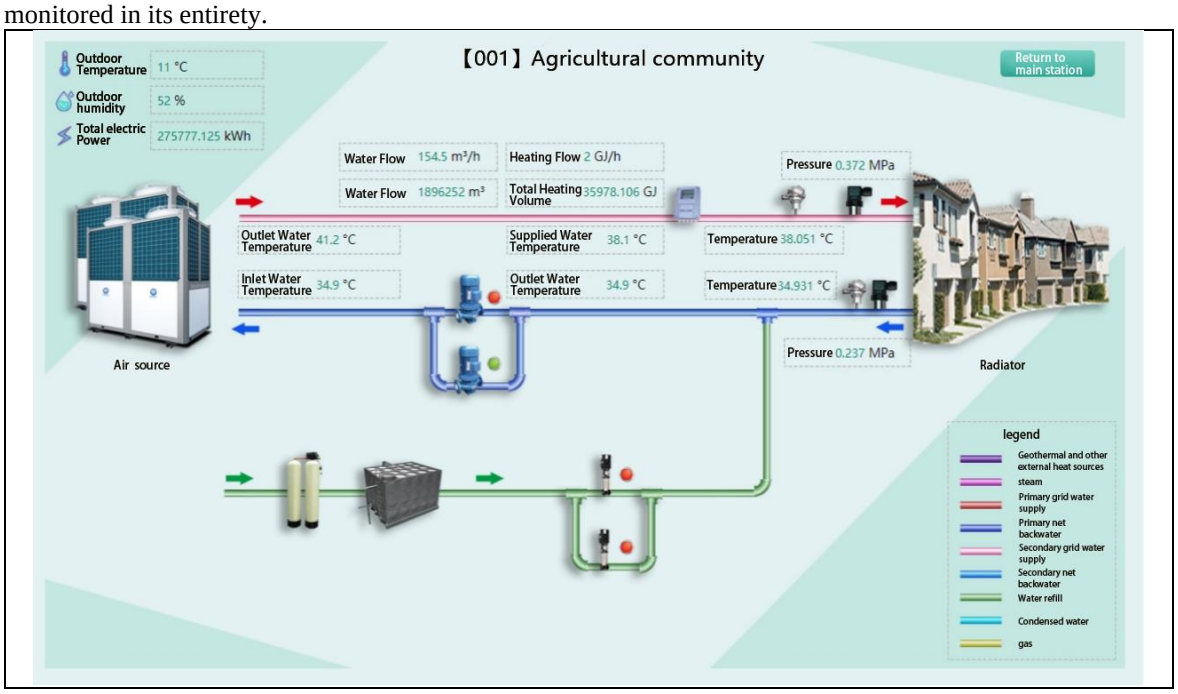


Fig.4. operation scheme and monitoring data for key parameters of an ASHP station.

3. Operating data and unit performance analysis

3.1. The system performance test data

The ASHP unit in the project has 4 compressors systems with the same configuration for each one as shown in Fig. 5.

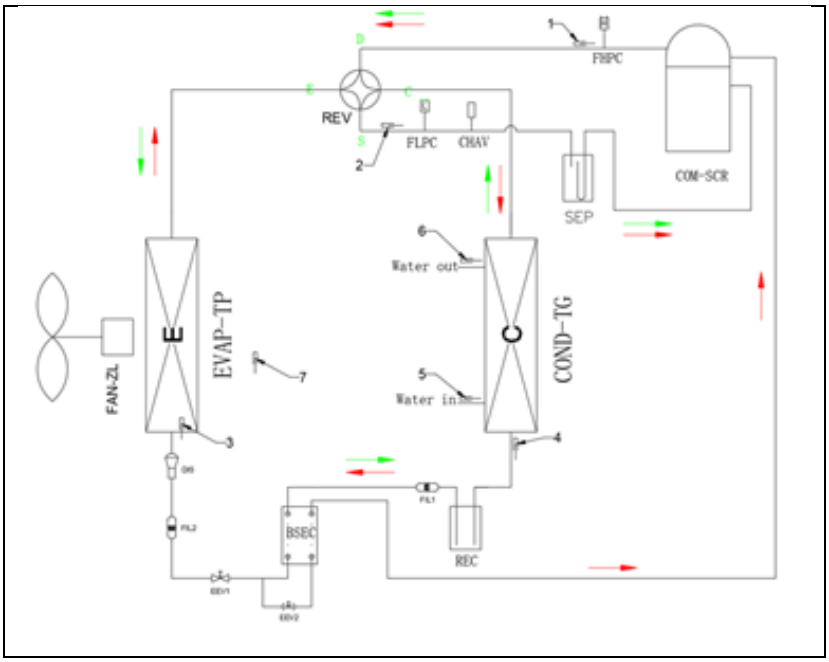


Fig.5. The system configuration scheme of the unit.

The system performance test data under the different ambient temperatures and different outlet temperatures of the ASHP unit has been listed in Table 1.

Table 1 The performance test data of the ASHP unit in the test lab.

NO.	Outlet water temperature (℃)	Ambient Temperature -5 ℃		Ambient Temperature -12 ℃		Ambient Temperature -20 ℃	
		Heating capacity (kW)	COP	Heating capacity (kW)	COP	Heating capacity (kW)	COP
1	41	130.5	3.03	112	2.62	94	2.32
2	45	131.05	2.85	112.87	2.46	95.77	2.11
3	50	133.5	2.55	114	2.18	98	1.91
4	55	135.2	2.45	116	2.12	100	1.8

3.2. The unit performance analysis

Based on the Fig.4 scheme, the monitoring data of the key parameters for corresponding systems such as outside ambient temperature, humidity, total electric energy consumption, transient flow rate of the heating water, and total flow rate of the heating water, the temperature of inlet and outlet water, the pressure of inlet and outlet water, the water pump running status and so on.

The heating capacity of the unit is calculated according to Eq. (1).

$$Q = \frac{c\rho V\left(t_g - t_h\right)}{3600} \tag{1}$$

Where, Q is the heating capacity of the unit, ρ is the density of the water, V is the water flow rate, t_g and t_h are the supply and return water temperature, respectively.

The heat dissipation of the cable comes from the heat loss of the current-carrying conductor. The single cable power loss can be calculated according to Eq. (2).

$$Q' = \frac{I^2 R}{A} \tag{2}$$

Where, *Q*' is the power loss, *I* is the cable current flow, *A* is the cable cross-sectional area, and *R* is the resistance value per meter of cable.

The coefficient of performance (COP) of the unit is calculated by Eq. (3).

$$COP = \frac{Q}{W} \tag{3}$$

Where, COP is the coefficient of performance of the heat pump unit, *W* is the power consumption of the heat pump unit.

The key operating parameters of the system and the performance of the unit are shown in Table 2.

Table 2 The key parameters and the COP for a unit in the 5 stations.

Contents	System 1	System 2	System 3	System 4	System 5
ASHP station name	Lichun school	Shihao	Shuiliju	Dianli 3	Sichangxiqu
Ambient temperature (℃)	-3.7	0	2.2	4.2	7.3
Inlet temperature (℃)	44	42.1	46.4	42.8	43.1
Outlet temperature (℃)	48.5	47.3	52.9	51.4	49.8
Water flow rate (m^3 /h)	28.336	24.194	21.99	15.868	20.44
Heating power（kW）	148.27	146.29	166.2	158.68	159.31
Total electric power input（kW）	52.13	51	55.52	53.6	54.67
Heating COP（kW/kW)	2.84	2.87	2.99	2.96	2.91

According to the monitoring data, the ambient temperatures in the heating season 2019-2020 are listed in the table 3, in which the energy consumed by water pumps and the heat losses from the pipes are not included. The percentage of each ambient temperature zone has been shown in the Fig. 6.

Table 3 The ambient temperature and corresponding data in the heating season 2019-2020.

Ambient Temp. (℃)	Hours (h)	Peak time (h)	Off peak time (h)	COP
-15~-10	12	6	6	2.26
-10~-5	90	52.5	37.5	2.47
-5~0	891	519.75	371.25	2.66
0~5	1068	623	445	2.88
5~10	597	348.25	248.75	3.16
10~15	234	136.5	97.5	3.55
15~20	30	17.5	12.5	3.96
20~25	6	3.5	2.5	4.37

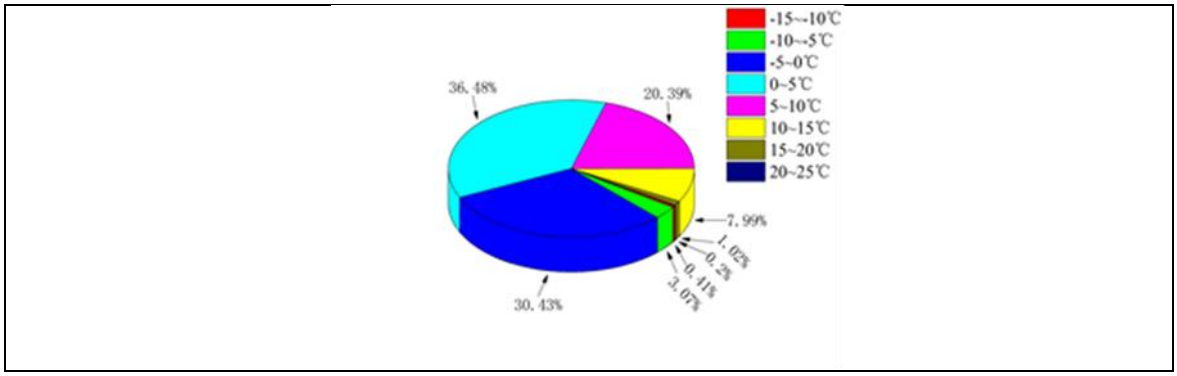


Fig.6. The percentages of each ambient temperature zone.

3.3. Air source heat pump for low ambient zone space heating

Air source heat pumps for heating in cold areas will face many challenges for efficiency and reliability, vapor injection technology for compressors of ASHP unit is a solution to resolve these issues. According to the winter climate record data of Zhao County, the lowest ambient temperature goes to -15 ℃.

Vapor inject technology brings great benefits for ASHP heating in cold ambient conditions. According to the lab test result by Emerson Climate technology, it shows 21% - 40% heating capacity improvement and 7% - 22% efficiency improvement. (Table 4)

Table 4 Vapor injection technology benefits.

Ambient temperature (℃)	Heating capacities improve (%)	Efficiency improves (%)
7	21%	7%
2	23%	6%
-7	37%	16%
-12	40%	22%

Vapor injection technology also can improve the reliability of the heat pump unit, it allows the system to be used in a -30℃ ambient area and deliver high enough temperature water even for radiators. The envelop of the compressor in Figure 7 shows the improvement.

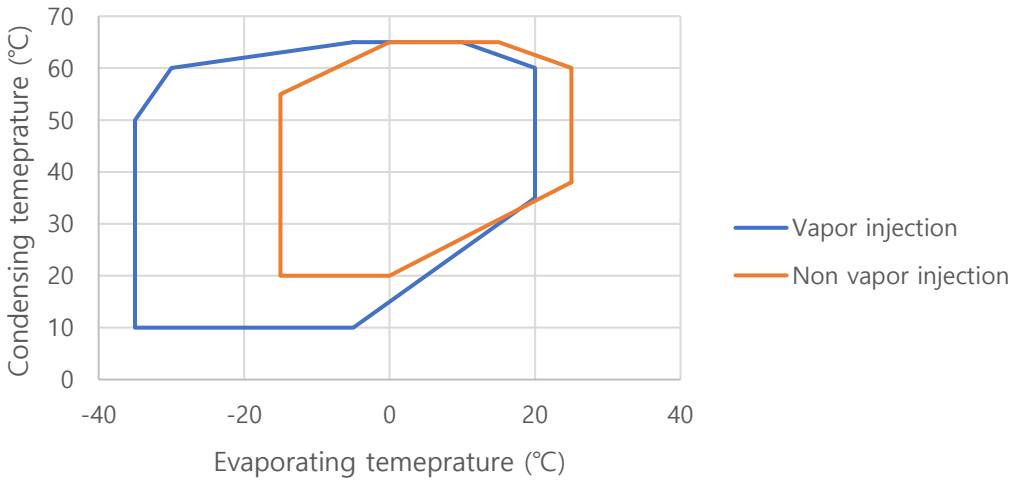


Fig.7. Compressor envelope with and without vapor injection.

4. Heating project optimization

The project is large in scale, short in the cycle, complex at the end, and diverse in construction conditions. How to accurately divide district heating in a complex on-site environment, how to solve the cold island effect and ensure that the selected air source heat pump can exert its maximum performance, how to solve the noise problem, how to achieve the pre-designed control effect, etc. are very critical to ensure that the overall project can meet the requirements of high efficiency, stability, and energy saving. According to the actual specific situation, from design to product, the manufacturer New Energy has repeatedly improved, tested, adjusted, and optimized the unit and the installation.

4.1. Equipment performance matching and tuning optimization

a. Environmental climate is a key factor affecting the use of air-source heat pumps, which determines the initial investment and operating costs of the project, as well as the performance advantages of ASHP. At the beginning of the project design, the historical climate and environmental characteristics of Zhao County were investigated, and make the analysis of the data as shown in Fig. 6.

b. “Cold Island” effect in the large ASHP heating project is a common issue if the air circulation around the ASHP units is not optimized. In order to ensure the good circulation of the air around the units, all the stations have been designed as frame structures with a height of above about 8 meters from the ground, so that the cold air from the units will flow to bottom and other open spaces. Besides, the layout of the units in each station is in line and has a max. 2 or 3 units in the row direction. In this way, the cold island effect in the project is avoided. Refers to Fig. 2.

4.2. Noise reduction

Large scale ASHP heating project could have higher noise for the environment. It is important of sound reduction for this heating project. Sound insulation wall (Fig. 8) is installed on field to reduce the noise impact.



Fig. 8. Noise insulation wall.

4.3. Radiator and floor heating combination

To get same heating performance from the terminals, the water temperature in the radiator will be higher than in floor heating. The hot water temperature leaves the radiator still is high enough for floor heating. But the water quantity for floor heating is bigger than the radiator. Some additional equipment and pipe are needed to balance the water system. Fig. 9 shows the scheme of the combination of the radiator and floor heating.

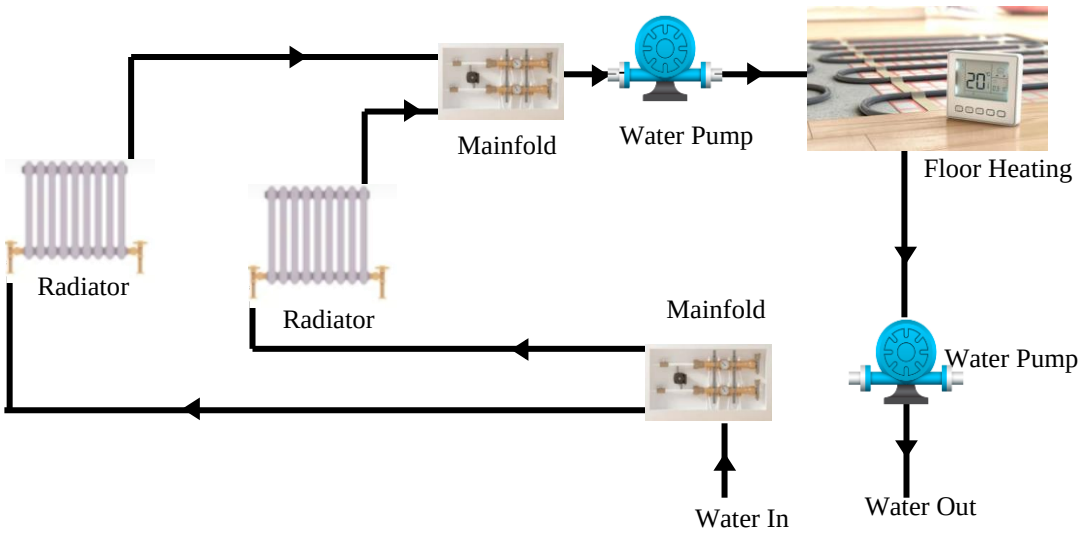


Fig.9. Scheme of radiator and floor heating combination.

4.4. System control

Heating load is determined by ambient temperature and residential behavior, it means the heating capacity requirement constantly changes. The management of 1,200 units ASHP with a higher system performance is important for energy saving. With IoT technology, depending on the temperature of outlet water and return water, automatically adjust the ASHPs for a better system efficiency. Fig. 10 shows the scheme of system control and interface.

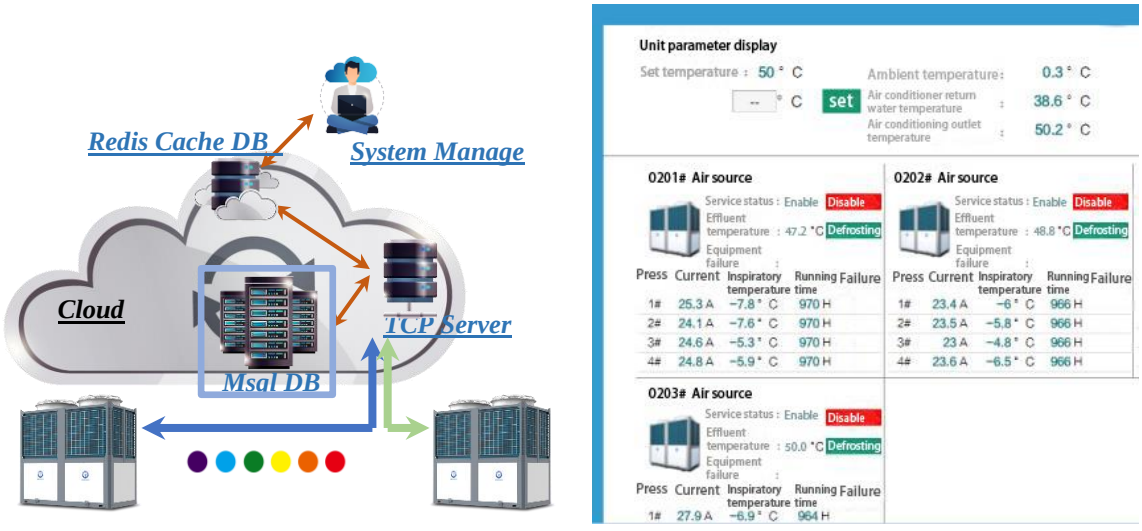


Fig. 10. System control and interface.

5. The economic and environmental analysis

5.1. Economic calculation

According to the statistical data from the monitoring system of the whole project, the total electric energy consumption in the heating season of 2019-2020 is 100.37 million kWh in the project. The average electrical energy consumption is 30.88 kWh per square meter. The detail data for economy calculation is as in Table 5.

Table 5 economy calculation for a heating season of 2019-2020.

Actual heating area	km^2	3250
Total electrical energy cons.	Mil. kWh	100.37
Total water consumption	ton	155678
Total cost paid	k CNY	43000
Ave. electric energy consumption	kWh/ m^2	30.88
The average price of the power	CNY/kWh	0.43
Average Operation cost	CNY/ m^2	12.23

In the same project, about 220k square meter area lack of electrical power is heated with gas boilers. The average heating cost of the area is 27.27 CNY/ m^2 for the heating season 2019-2020, more than twice of ASHP heating cost.

5.2. Cost saving

Total actual heating area in 2019-2020 heating season is 3.25 million square meters, according to the data recorded in cloud, comparing with another heating project with gas boiler that located in Zhao County as well, the running cost has more than 50% saving. Table 6 shows the comparison:

Table 6 Running cost comparison.

	ASHP	Gas boiler
Energy cost (million CNY)	43	6
Heating area (m^2)	3.25	0.22
CNY/ m^2	13.23	27.27

5.3. CO2 emission reduction

Air source heat pump is recognized as a green technology which can collect heat energy in the air to heat indoor space. It can reduce the CO_2 emission by replacing coal boiler. Comparing with gas boiler, the running cost is lower.

Ambient temperature has great impact on the ASHP efficiency, according to the climate bin data of Zhao County and the COP of ASHP under different ambient temperature, the average COP is 2.93 for whole heating season. Fig. 11 shows the detail data of ambient condition of Zhao County and COP of ASHP.

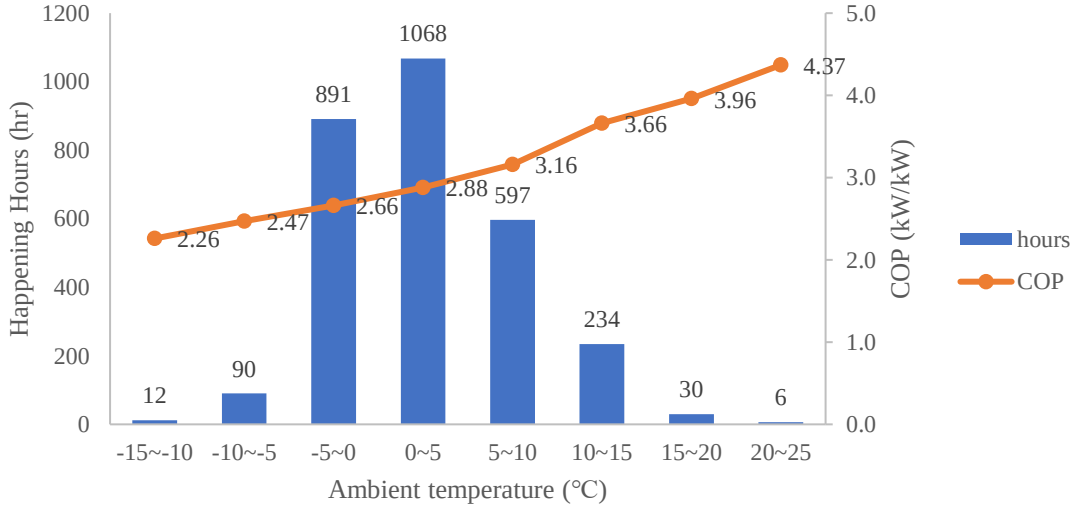


Fig.11. Climate bin data of Zhao County and COP of ASHP.

CO_2 emission comparing with coal boiler is show in Table 7, based on standard coal, ASHP can reduce around 38% CO_2 emission.

Table 7 CO_2 emission comparison.

	ASHP	Coal boiler
efficiency	293%	60%
CO_2 emission unit	0.997 kg/kWh	2.7 kg/kg
heating energy per unit	10548 kJ/kWh	17584 kJ/kg
CO_2 emission per kJ	0.095 g/kJ	0.154 g/kJ

The total electrical energy consumption in the heating season of 2019-2020 is 100.37 million kWh. The energy consumed by the water pumps is about 8% of the total one. Therefore, the ASHP unit's actual consumption of energy is 92.34million kWh, and the total heating energy produced by the ASHP units is 974002.32 million kJ. The reduction of the CO_2 is 57466.1 tons, and the standard coal reduction is 21522.9 tons.

5.4. Feedback on ASHP heating project

By on site interview, average indoor temperature can reach 20-22 ℃, no air polluted in Zhao County, residential people are satisfied with the heating project. Heat company also saves the cost by replacing coal boiler with ASHPs.

6. Conclusion

This paper presents a large air source heat pump project in Zhao County, which has the advantages of fast fault response, low maintenance cost, and significant energy savings. The main conclusions are as follows.

- The COP of the air source heat pump stations selected was above 2.8. When the outdoor temperature was -15 ~ -10 ℃, the heat pump cop could still reach 2.26.
- The cost of gas boiler heating is more than twice that of air source heat pump heating.
- Based on standard coal, air source heat pump can reduce carbon dioxide emissions by about 38% compared with coal-fired boilers.

Acknowledgements

We gratefully acknowledge the valuable cooperation of heat company of Zhao County, and their history data plays an important role in the system design.

14th IEA Heat Pump Conference
15-18 May 2023, Chicago, Illinois

Investigation of a Novel Hybrid Heat Pump Concept

Tobias Reum*, David Schmitt, Thorsten Summ, Tobias Schrag

Institute for new Energy Systems (InES), Technische Hochschule Ingolstadt, Germany

Abstract

Hybrid heat pumps can utilize two low-grade ambient heat sources to provide heating energy. However, efficient operation of two heat sources and its effect on heat source dimensioning has not been thoroughly examined. In this research, a hybrid heat pump is developed which can switch between an air heat exchanger and a ground source heat exchanger as the heat source. The hybrid heat pump interconnection also allows parallel operation of both heat sources. Based on an experimental investigation, a black box model is created including a suitable control strategy. An annual simulation for space heating of a domestic building is conducted. The hybrid heat pump provides about 18.9 MWh of heat while extracting only 47.1 % of this heat from the ground source heat exchanger. Parallel operation allows a heating capacity reduction of the ground source heat exchanger to about 80 % compared to a conventional ground source heat pump. The hybrid heat pump therefore allows a smaller design size.

© HPC2023.
Selection and/or peer-review under the responsibility of the organizers of the 14th IEA Heat Pump Conference 2023.

Keywords: hybrid heat pump; dual source heat pump; parallel operation; black box model; annual simulation

1. Introduction

1.1. Background and motivation

Heat pumps are one of the main heat generators for future heating systems. The heat pump market is growing rapidly. In 2021, the heat pump sales in Germany grew by about 28 % [1], even before the current energy crisis in Europe. Heat pumps are expected to become a main heat generator in the domestic sector [2].

Heat pumps provide heat using highly efficient refrigerant cycles, operating as reverse Carnot engines [3]. A small amount of (usually electrical) work is needed to provide a large amount of heat. Heat pumps therefore enable a transition of the heat generation into a fully electrical system. Electricity can be provided by renewable energy sources, e.g. wind power and photovoltaics. The remaining heat is drawn from ambient low-grade reservoirs. This means they are also significantly more efficient than direct electric heaters for domestic purposes. The fraction between the delivered heat capacity $\dot{Q}_{heat}$ and the necessary electrical power P_{el} is called the coefficient of performance (COP):

$$\mathrm{COP} = \frac{\dot{Q}_{heat}}{P_{el}} \tag{1}$$

In practice, the COP usually varies between 2 and 6 depending on the temperature above levels of the ambient reservoir and the temperature needed for the heating system [4, 5]. This requires proper

* Corresponding author. Tel.: +49-841-9348-6841; fax: +49-0841-9348-996841.
E-mail address: tobias.reum@thi.de.

implementation into the buildings for high efficiencies, for example by adding thermal insulation or large area heating systems like floor heating. Common ambient heat reservoirs serving as the heat source are air, the soil and ground water. While air source heat pumps are relatively cheap and easy to install, the efficiency especially during peak heating load hours in winter is lacking due to low ambient (outside air) temperatures. Using the soil or ground water as the heat source promises higher efficiencies due to higher reservoir temperatures during winter months, but the installation costs for either heat source are usually higher and there are higher geological requirements. Ground water needs careful examination of the underground water flow. Using the soil with vertical boreholes demands geological investigations and often longer time scales due to bureaucratic allowances, while horizontal heat exchangers occupy large areas, which are an issue especially in urban spaces. Each heat source for heat pumps therefore has their own advantages and disadvantages.

1.2. Hybrid heat pumps

Hybrid heat pumps (HHPs) – in literature often also referred to as dual source heat pumps to not confuse these systems with systems combining a heat pump with a gas boiler – combine several ambient heat sources to utilize the aforementioned advantages while minimizing the disadvantages. Commonly, HHPs optimize the usage of the heat sources to increase either the efficiency of the system, to reduce the energy extracted from the secondary (commonly the ground) heat source to limit ground source heat exchanger (GSHX) size or to profit from both benefits.

Allaerts et al. [6] combined two borehole GSHX with an air-based regenerator. The system was designed for an office building, where the cooling load was the dominating requirement. The HHP operated with one of the GSHXs while the other could be regenerated passively (i.e., not using the refrigerant cycle) over the ambient air. Serially, the HHP operated either in heating mode or cooling mode with one of the GSHXs. They researchers still found that a decrease of about 47 % in borehole sizing was possible due to regeneration with this air-based regenerator as compared to a single ground-source heat pump system.

Another project by Cannistraro et al. [7] extended an existing air-to-air heat pump into a HHP for an air-conditioning system. The heat pump could utilize either an air source or a flat-plate GSHX to provide heating and cooling. During cold ambient air conditions, the HHP used the GSHX to provide heating. A mixed operation was possible without stating further details. They found an improved efficiency compared to the original air-to-air heat pump at specific operating conditions No annual comparison was given.

In a simulation-based study, Dongellini et al. [8] attempted to reduce the sizing for the borehole GSHX of an HHP. This HHP could also switch between the air and the GSHX as the heat source. Based on previous experimental results, a model of the HHP was developed. This model was then used with different borehole GSHX sizes and compared to a pure air source and a conventional ground source heat pump. They found that a significant reduction of the borehole dimensioning to 50 % showed only minor reductions in annual efficiency compared to a conventional ground source heat pump (-11 %), while improving the efficiency compared to the air source heat pump system (+26 %).

1.3. Research gap and scope

HHPs currently focus on utilizing one heat source at a time. However, utilizing both heat sources in parallel operation can provide significant flexibility to the heating system: while it is relatively simple to reduce the energetic load on a GSHX by reducing the heating load during comparatively high ambient temperatures by switching to air source operation (ASO), the peak load still requires a large heat exchanger area. This research aims at investigating the potential on efficiency and GSHX sizing by including parallel operation of both heat sources into a HHP by utilizing two compressors compared to conventional ground source heat pumps (GSHP).

This study focuses on building a model of a HHP which can not only switch between utilization of either heat source, but also allows parallel operation of both heat sources. An air as well as a ground source is used. The HHP was developed and tested experimentally in [9]. This paper aims at (a) developing a model based on this investigation including an operation mode controller for the single heat source operations as well as the parallel operation of both heat sources, and (b) an annual simulation to determine the effect on the annual efficiency, the total energy extracted from the GSHX and the heating capacity the GSHX needs to provide. By this, the energetic advantages of parallel operation are evaluated.

2. Methodology

The overall method of this paper includes the development of a black box model for the HHP including both the single source operations with the air source (ASO) and the ground source (ground source operation; GSO) as well as the parallel operation (PO). The experimental investigation in [9] provides the necessary data. This model is then implemented into an annual simulation with weather data, soil temperatures and a building heating load.

To evaluate the annual efficiency, the seasonal performance factor (SPF) is used with the cumulative energies for the heat Q_{heat} and the electricity E_{el} over the whole year:

$$\mathrm{SPF} = \frac{Q_{heat}}{E_{el}} = \frac{\sum \dot{Q}_{heat} * dt}{\sum P_{el} * dt} \tag{2}$$

The HHP model needs to yield the heating load $\dot{Q}_{heat}$ as well as the necessary electrical power P_{el} for each simulation time step dt. These values are also required for the evaluation of the energetic and power load on the GSHX. The extracted energy over a whole year E_{GSHX} can be calculated by evaluating the GSO and the corresponding difference between the heating capacity $\dot{Q}_{heat,\mathrm{GSO}}$ and the electrical power $P_{el,\mathrm{GSO}}$, also summed up over the simulation time steps dt. The energy extracted during PO is included here, since PO is assumed to be a combination of full power GSO and additional ASO.

$$E_{\mathrm{GSHX}} = \sum (\dot{Q}_{heat,\mathrm{GSO}} - P_{el,\mathrm{GSO}})\, dt \tag{3}$$

The maximum power load on the GSHX $\dot{Q}_{\mathrm{GSHX,max}}$ can be evaluated by finding the maximum of the aforementioned difference between the vectorial values of the heating capacity $\dot{Q}_{heat,\mathrm{GSO}}$ and the electrical power $P_{el,\mathrm{GSO}}$ during GSO:

$$\dot{Q}_{\mathrm{GSHX,max}} = max(\dot{Q}_{heat,\mathrm{GSO}} - P_{el,\mathrm{GSO}}) \tag{4}$$

2.1. Development of the black box model

The model type of the heat pump was chosen to be a black box model to limit the computing time. For each operation mode one performance map was developed based on the measurements in [9]. These measurements described the heating and electrical powers ($\dot{Q}_{heat,\mathrm{GSO}}$ and $P_{el,\mathrm{GSO}}$ respectively) depending on boundary conditions like ambient temperature T_a, source inlet temperature $T_{\mathrm{so,GSO}}$ and sink outlet temperature T_{si} based on [10]. The detailed control of the HHP model described below was then realized within the simulation model.

The heating controller switched between the operation modes depending on the ambient temperature. The inverter frequency f_{inverter} resulted in a non-linear behavior of the heating and electrical power. This was included into the model. The range allowed for the inverter was $0 - 100$ %.

Two bivalence points were defined: bivalence point 1 T_{biv1} is the temperature, when the HHP switches from ASO to GSO and vice versa. Bivalence point 2 T_{biv2} is the temperature, when the HHP switches from GSO to PO and vice versa. A heating threshold temperature T_{thr} was implemented, at which the general operation of the HHP switched on and off depending on the moving mean ambient temperature $T_{a,\mathrm{mean}}$ over the last seven days. Figure 1 shows the general structure of the decision tree to determine the operation mode.

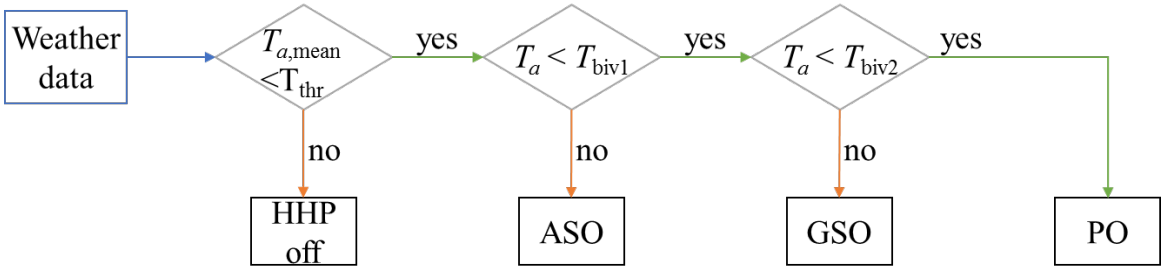


Fig. 1: Decision tree of the HHP model to derive the operation mode. Each check includes a hysteresis.

The GSO model had the inputs of source temperature from the GSHX, the outlet temperature of the heating system and the inverter frequency. The performance map along with the inverter correction factor then determined the output heating capacity and the electrical power.

The ASO model worked similar, except that the input for the source was the ambient temperature.

The PO was the combination of both operation modes. In this work, below the bivalence point 2 T_{biv2}, the GSO continued at maximum inverter frequency. Additionally, the ASO was added to the GSO at maximum inverter frequency: the inverter frequency fed into the PO model then only changed the frequency of the ASO. Both source temperatures for the ground source and the ambient temperature were needed for PO, since both compressors are running in this operation mode.

2.2. Description of the annual simulation

This HHP model was then implemented into an annual simulation. The general scheme of the annual simulation is shown in Figure 2. The input data consisted of a weather data set for Ingolstadt, Germany, in the format of a test reference year [11]. For the GSO, the source temperature was derived from an undisturbed ground temperature model. This ground temperature model was based on approaches for seasonal temperature variations in the ground [12, 13]. A horizontal GSHX was used, buried in a depth of 1.5 m. Additionally, for the heat transfer to the brine cycle, a temperature difference of 3 K was assumed below this undisturbed ground temperature for the source temperature.

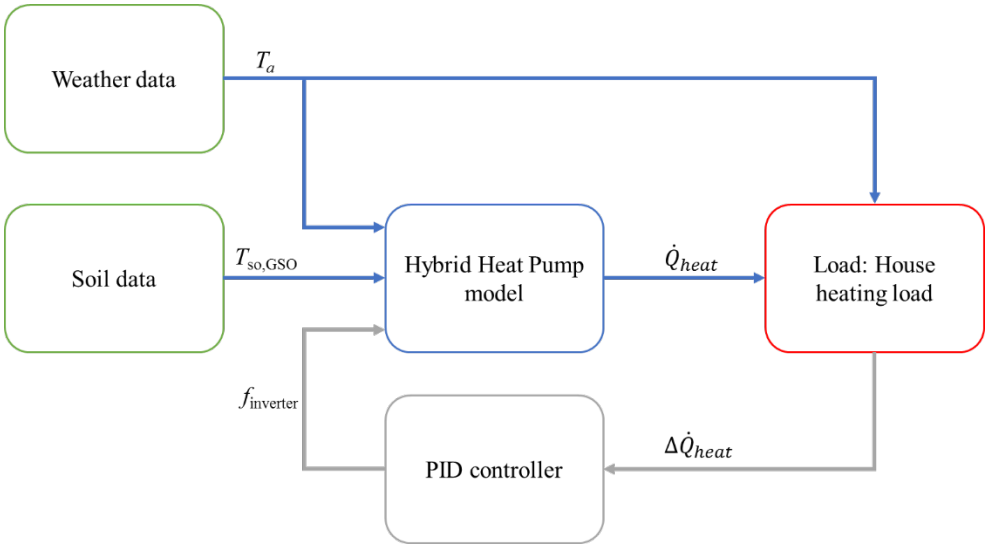


Fig. 2: Scheme of the annual simulation for the HHP. Sources (green) and load (red) are integrated as the periphery for the HHP model, a PID controller (grey) is used for determination of the necessary inverter frequency.

The load was described by a simple linear house heating load $\dot{Q}_{heat,\mathrm{set}}$ dependent on the ambient temperature. The conditions were:

- $\dot{Q}_{heat,\mathrm{set}}(T_a = 20\ °\mathrm{C}) = 0$ kW, assuming a target room temperature of 20 °C and no internal gains.
- $\dot{Q}_{heat,\mathrm{set}}(T_a = -20\ °\mathrm{C}) = 10$ kW, assuming maximum load at −20 °C.

This led to the following calculation for the necessary heating load of the house dependent on the ambient temperature:

$$\dot{Q}_{heat,\mathrm{set}} = -0.25\ \frac{\mathrm{kW}}{\mathrm{K}} * T_a + 5\ \mathrm{kW} \tag{5}$$

Then PID controller compared the necessary heating load with the delivered heating load delivered by the HHP $\dot{Q}_{heat}$. It then changed the frequency accordingly to minimize the error $\Delta\dot{Q}_{heat}$. It is important to note, that only one single inverter frequency is varied at a time: for the active compressor during ASO and GSO and during PO, the GSO compressor worked at maximum frequency and only the ASO compressor was controlled by the PID controller signal. The PID controller operated only with a proportional gain P = 0.5 and an integral

gain I = 0.1. The derivative gain was found to be not necessary. Also, the PID controller reset with every operation change of the HHP model due to non-linear behavior.

Since the heating system was designed around a buffer storage tank, the sink temperature of the HHP was assumed to be constant $T_{\mathrm{si}} = 35$ °C. Only space heating on floor heating temperature levels was considered. Bivalence point 1 was chosen to be $T_{\mathrm{biv1}} = 4$ °C with a hysteresis of ±1 K. Each change of operation mode leads to one compressor start (either the GSO compressor switches off and the ASO compressor switches on or vice versa), which should be limited to avoid damaging the compressor. Bivalence point 2 was set to be $T_{\mathrm{biv2}} = -3$ °C. A lower hysteresis of +1 K was chosen, because only the change from GSO to PO leads to one compressor start (from PO to GSO only deactivates the ASO compressor). This indicates that repeated switching between GSO and PO is half as harmful to the number of compressor starts compared to a switching between ASO and GSO. The heating threshold temperature was $T_{\mathrm{thr}} = 12$ °C with a hysteresis of +1 K.

The output data consisted of the current operation mode (ASO, GSO or PO) including the inverter frequency, the weather and soil data and the HHP output data for the heating and electrical power.

3. Annual simulation results

3.1. Analysis of the HHP black box model within the simulation

The main inputs of the simulation are shown in Figure 3(a). While the ambient temperature fluctuated significantly on a short time frame, the moving average ambient temperature showed a much smoother behavior. This led to a clearer distinction of whether heating is necessary or not, which finally resulted in less on-off cycles. This clear separation of no operation in summer time due to dependency of the mean ambient temperature can be observed in Figure 3(b). The inverter frequency was normalized to a relative value of its maximum. During summer time, the relative inverter frequency remained at zero, which here means the heat pump is switched off. Also shown in Figure 3(a) is the source temperature of the GSHX. The large thermal

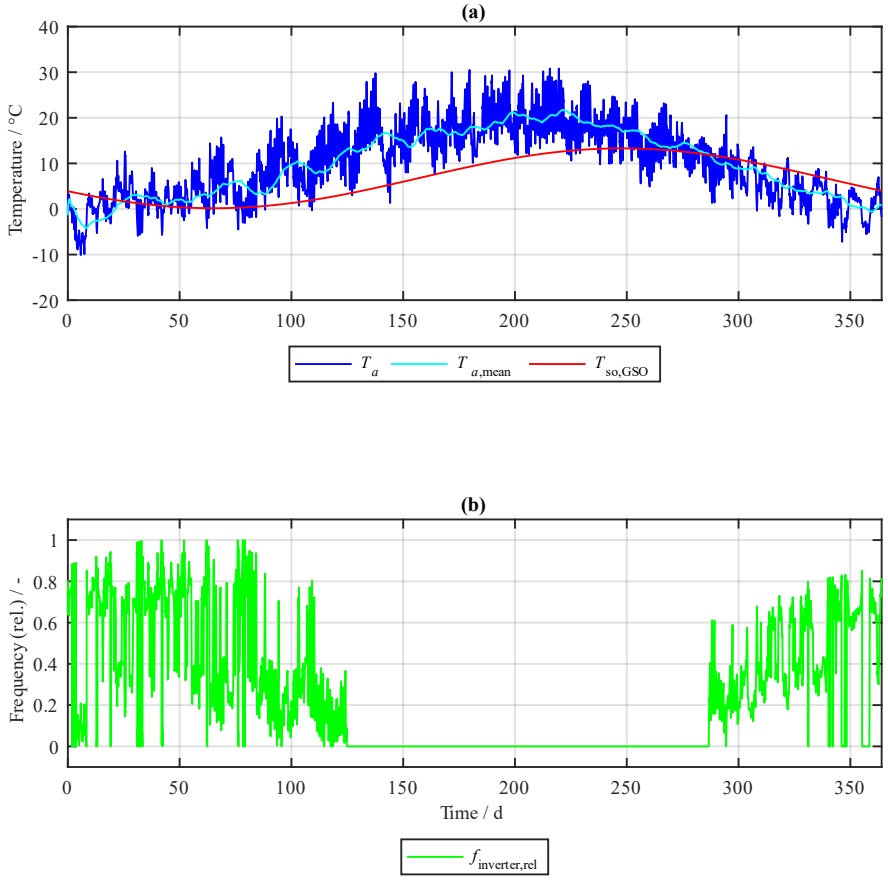


Fig. 3: Overview of the annual operation of the HHP. (a) shows the input parameters of the ambient temperature T_a, the moving mean ambient temperature over 7 days $T_{a,\mathrm{mean}}$ and the source temperature of the GSHX $T_{\mathrm{so,GSO}}$. (b) shows the relative inverter frequency $f_{\mathrm{inverter,rel}}$.

inertia of the ground leads to smaller amplitudes and a phase shift. It can be seen that especially in the last weeks of the year, the ground source temperature was notably higher than the ambient temperature, leading to a higher source temperature for the refrigeration cycle and therefore more efficient GSO compared to ASO. At the same time, however, in spring it seemed to be more beneficial to let the HHP run in ASO mode due to a cooled GSHX. A flexible bivalence point 1 depending on the ground source temperature should be analyzed, even though the increasing ambient temperatures indicate lower heating loads and therefore less impact on the annual efficiency. More detailed GSHX models are needed to verify this behavior of the slowly changing ground source temperatures which could impact the dependencies used for the bivalence points.

Next, the switching around the bivalence points 1 and 2 was analyzed exemplarily. In Figure 4, the ambient temperature during the last two weeks of the year can be observed. Additionally, the state of the GSO is shown: at 1, the state is ON, so GSO is active. At 0, GSO is off/inactive. Around day 356, the ambient temperature dropped below $T_{\mathrm{biv2}} = -3\ °\mathrm{C}$ and GSO was replaced with PO. For this, the GSO operates at maximum inverter frequency and ASO is added to cover the necessary heating load. This remained the case until the ambient temperature rose above the bivalence point including the hysteresis $T_{\mathrm{biv2}} + 1\ \mathrm{K} = -2\ °\mathrm{C}$ about two days later. Then, GSO reactivated instead of PO. GSO remained active until the ambient temperature increased above bivalence point 1 including hysteresis $T_{\mathrm{biv1}} + 1\ \mathrm{K} = 5\ °\mathrm{C}$ on day 362. GSO deactivated and ASO started instead until the ambient temperature decreased below the bivalence point 1 including hysteresis one day later $T_{\mathrm{biv1}} - 1\ \mathrm{K} = 3\ °\mathrm{C}$. The switching was operative and worked according to the rules.

The inverter frequency was controlled as expected. However, during PO the low inverter frequency indicates that PO was not really needed yet and the bivalence point 2 was set too high for these weeks. During GSO – when the state of the GSO is on –, the relative inverter frequency varied to match the heating capacity of the HHP to the necessary heating capacity defined by equation (6). The same was the case during ASO from day 362 to 363. One notable difference was the lower relative inverter frequency during ASO compared to GSO. The reason for this was a higher heating capacity by the ASO compressor than the GSO compressor's capacity. This led to a lower necessary inverter frequency to cover the load, which in turn led to the non-linear jump in the inverter frequency. The PID controller was reset during the operation mode change and therefore reacted quickly to minimize the heating capacity difference to the necessary heating load.

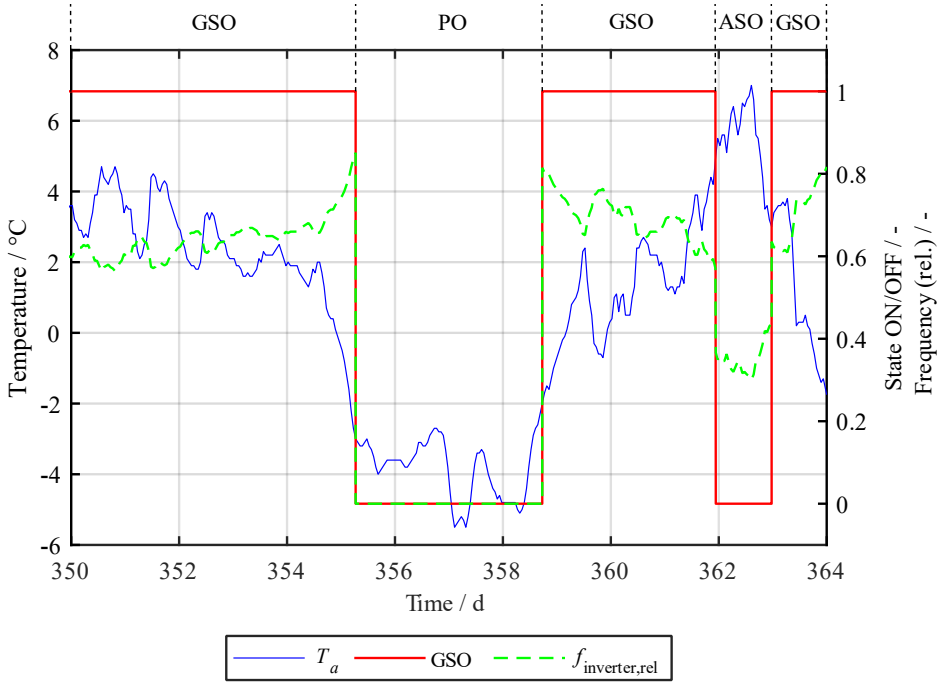


Fig. 4: Example of the switching procedure for both bivalence points 1 and 2 during the last two weeks of the year. For visibility, only the GSO is shown switching on and off.

Non-intuitive was the relative inverter frequency during PO from day 356 to 359. The value during this time was zero, indicating a switched-off air source compressor, since the ground source compressor was supposed to run at full inverter frequency during this operation mode. The explanation is, that the GSO was still able to cover the necessary heating load below maximum inverter frequency. This is an indicator, that the parallel operation was activated at too high temperatures when it was not yet necessary. However, at earlier

stages during the year, this was not the case: since the heating capacity of the GSO depends on the ground source temperature as well, the heating capacity of the GSO is reduced during late winter/early spring as shown in the GSHX source temperature in Figure 3. During times of still high source temperatures during GSO in late autumn/early winter, GSO could therefore provide enough heating capacity on its own and PO was activated with a deactivated air source compressor.

Figure 5 shows the operation modes (here: GSO and PO) during the first week of the year. Here, during PO starting at day 4 the frequency actually varied up to around 20 %, indicating that the GSO cannot cover the full heating load anymore due to a lower source temperature level of the GSHX. In this week PO was therefore necessary. This indicated that a flexible bivalence point 2 is required for proper coverage of the necessary heating load.

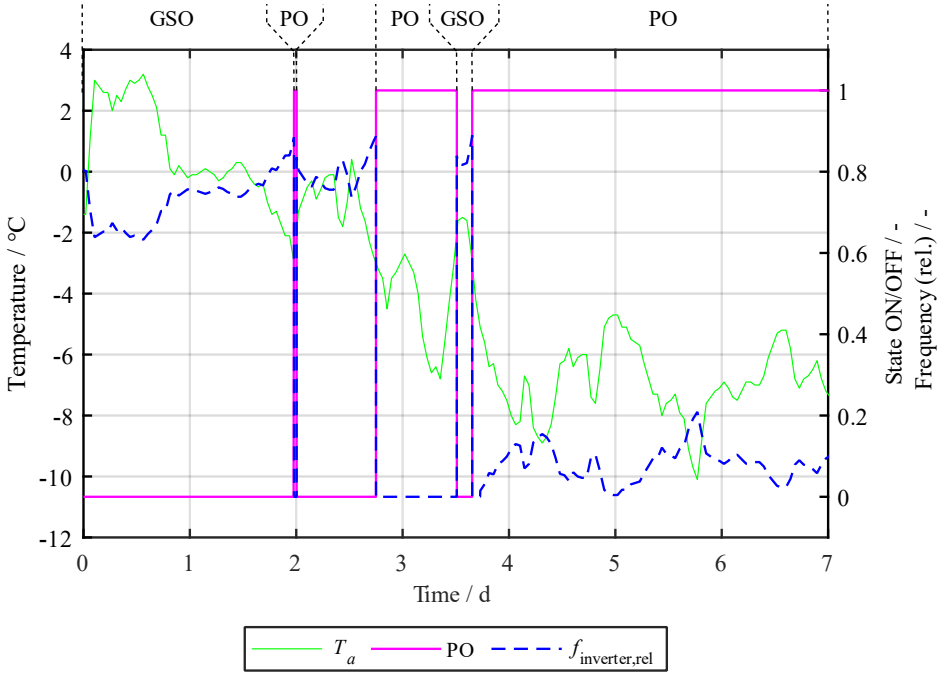


Fig. 5: Example of the relative inverter frequency at certain operation modes (ASO, GSO, PO) during the last two weeks of the year.

3.2. Effects of PO on annual efficiency and the GSHX

Still, the HHP showed an annual efficiency calculated using equation (2) of SPF = 4.37 for floor heating operation. The total delivered heating energy was $E_{heat} = 18.9$ MWh and the electrical energy $E_{el} = 4.3$ MWh. The energy extracted from the soil is the sum of the energy extracted during GSO and the GSHX energy extracted during PO. Equation (3) yielded $E_{\text{GSHX}} = 8.9$ MWh, which is a fraction equal to about 47.1 % of the delivered heating energy. The remaining energy was taken from the ambient air:

$$E_{\text{air}} = E_{heat} - E_{\text{GSHX}} - E_{el} = 5.7\ MWh \tag{7}$$

Using the same periphery (source and load), a conventional GSHP yielded an annual efficiency of $\text{SPF}_{\text{GSHP}} = 4.27$ and extracted heat energy from the GSHX of $E_{\text{GSHX,GSHP}} = 14.4$ MWh. The HHP showed improvements on both values: The SPF increased by about 2 %, the energy extracted from the soil to about 62 %. The bivalence points need to be examined further to not only allow flexibility as mentioned before, but also to analyze further reduction in GSHX size.

The heating capacity necessary by the GSHX was evaluated as well. The maximum difference per time step between the heating capacity $\dot{Q}_{heat}$ and the electrical power P_{el} resulted in $\dot{Q}_{\text{GSHX,max}} = 4.5$ kW. The comparison with a GSHP led to $\dot{Q}_{\text{GSHX,max,GSHP}} = 5.6$ kW. This was a relatively small difference of about 1 kW (or down to almost 80 %), indicating a limited power reduction due to PO of the HHP. This power reduction should be evaluated further: with an increased necessary heating load during PO, this effect should

be more distinct, because further air source power needs to be added to cover the heating load, while the power on the GSHX remains the same.

Lastly, the PID controller was operating properly. The mean error of heating load and necessary heating load over the whole year was $\Delta\dot{Q}_{heat,\mathrm{mean}} = -2.9\ \mathrm{W}$. So even though the PO mode often led to significant heating capacity differences when it was activated at too high ambient temperatures, the mean error heating capacity difference over the whole year was reasonably small.

3.3. Discussion of the results

The decision tree for the operation mode determination worked as intended: depending on the ambient temperature, one operation mode was active to cover the necessary heating load. Appropriate hysteresis's prevented repeated switching between the operation modes, which in turn would lead to an increase in compressor starts. The $\mathrm{SPF} = 4.37$ was comparable to market available GSHPs and the heat extracted from the soil $E_{\mathrm{GSHX}} = 8.9\ \mathrm{MWh}$ was reduced to about 62 % compared to conventional ground source heat pumps.

This can allow a reduction in size of the GSHX. However, the potential needs to be further evaluated with varying bivalence points as described in chapter 3.1 and also varying sink temperature levels with radiant heaters and/or without buffer storage.

Also, the inverter frequency control was working properly, covering the necessary heating load over the whole year at a small error. Especially during ASO and GSO, the PID controller worked well, while it struggled matching the heating load during PO. However, this was an issue of the bivalence point 2, not the PID controller. Also, in practice most inverters do not allow lower frequencies below about 25 %, which needs to be included in future simulations.

There are several steps which need to be improved in the simulation to enable further more detailed evaluations: first, the model of the PO is a simple combination of the single source operations. Since both operation modes share one condenser heat exchanger (see the interconnection in [9]), this is a simplification. The PO needs to be examined more closely in the laboratory to determine a proper PO model. Also, allowing a variation of the GSO inverter frequency during PO can add another level of flexibility: even at higher ambient temperatures, when GSO is more efficient than ASO but PO is not strictly necessary yet, running both inverters in part-load can reduce the energy extracted from the GSHX without a large influence on the efficiency.

The bivalence points are the second necessity: during the annual simulation, the ASO was often not used to its full extend. It is even possible that the annual efficiency increases by decreasing bivalence point 1. Also, bivalence point 2 needs dependencies to allow a more beneficial PO. Dependencies on the ground source temperature, building or buffer storage temperature or on the year's month are options for further examinations.

The periphery for the annual simulation is currently still simplified. The load is a linear heating load, which requires not the highest heating capacities possible by the HHP. Domestic hot water is not included yet, which also makes the heating controller more complex. The sources need to be modelled more in detail to show more complex behavior. Especially the GSHX was simplified in this work. Dynamic behavior of heat extraction and regeneration could therefore not yet be simulated.

Further operation modes possible to the interconnection [9] need to be implemented. Some of these requirements, especially active regeneration, need more detailed GSHX models to show their potential.

4. Conclusion

The interconnection of the HHP allows for an increased efficiency compared to conventional GSHPs. The increase in SPF from 4.27 for the GSHP to 4.37 for the HHP is an increase by only about 2 %, which is marginal. The HHP also reduced the extracted energy from the GSHX to about 62 %. PO specifically reduced the maximum heating load to about 80 %. These findings indicate a significant reduction possibility in dimensioning of the GSHX, while the increase in efficiency is marginal.

Further improvements of the simulation need to be applied. Most important are detailed heat source and heat sink models. The HHP model needs to include non-linear inverter frequency influence and limits as well as comprehensive PO modelling. On the controller side, especially the bivalence points – when to switch between ASO, GSO and PO – need to be examined and optimized.

Acknowledgements

The Project “Hybrid Heat Pump+” is supported by the Federal Ministry for Economic Affairs and Climate Action (BMWK) on the basis of a decision by the German Bundestag.

References

[1] Bundesverband Wärmepumpe e.V., "www.waermepumpe.de," BWP Marketing & Service GmbH, 20 January 2022. [Online]. Available: https://www.waermepumpe.de/presse/pressemitteilungen/details/starkes-wachstum-im-waermepumpenmarkt/. [Accessed 20 October 2022].

[2] Agora Energiewende, "Wärmewende 2030 - Schlüsseltechnologien zur Erreichung der mittel- und langfristigen Klimaschutzziele im Gebäudesektor," Berlin, 2017.

[3] I. Dincer, "Energy and Exergy Efficiencies," in *Comprehensive Energy Systems*, Oshawa, ON, Canada, Elsevier, 2018, pp. 265-339.

[4] John Cantor Heat Pumps, "https://heatpumps.co.uk," n.d.. [Online]. Available: https://heatpumps.co.uk/heat-pump-information-without-the-hype/what-is-the-cop/. [Accessed 01 September 2022].

[5] C. Naldi, E. Zanchini and G. L. Morini, "A method for the choice of the optimal balance-point temperature of air-to water heat pumps for heating," *Sustainable Cities and Society,* vol. 12, pp. 85-91, 01 July 2014.

[6] K. Allaerts, M. Coomans and R. Salenbien, "Hybrid ground-source heat pump system with active air source regeneration," *Energy Conversion and Management,* vol. 90, pp. 230-237, 04 November 2014.

[7] M. Cannistraro, E. Mainardi and M. Bottarelli, "Testing a dual-source heat pump," *Mathematical Modelling of Engineering Problems,* vol. 5, pp. 205-210, 2018.

[8] M. Dongellini, C. Naldi, C. Natale and G. L. Morini, "Modelling of a dual-source heat pump with Matlab/Simulink and Almabuild/Carnot," in *Simulation assisted design and optimisation of heat pumps and heat pump applications - from refrigerant cycle simulation to building and district heating integration*, Innsbruck, 2022.

[9] T. Reum, T. Summ, M. Ehrenwirth and T. Schrag, "Experimental Investigation of a Novel Hybrid Heat Pump," *Submitted to EuroSun 2022: ISES and IEA SHC Conference on Solar Energy for Buildings and Industry,* 2022.

[10] DIN e.V., DIN EN 14511:2019-07, Air conditioners, liquid chilling packages and heat pumps for space heating and cooling and process chillers, with electrically driven compressors, Berlin: Beuth Verlag GmbH, 2019.

[11] Deutscher Wetterdienst, "Testreferenzjahre (TRY)," 2017. [Online]. Available: https://www.dwd.de/DE/leistungen/testreferenzjahre/testreferenzjahre.html. [Accessed 25 October 2022].

[12] H. D. Baehr and K. Stephan, Wärme- und Stoffübertragung, Heidelberg: Springer-Verlag, 2006.

[13] V. Wesselak and T. Schabbach, Regenerative Energietechnik, Heidelberg: Springer-Verlag, 2009.

14th IEA Heat Pump Conference
15-18 May 2023, Chicago, Illinois

Green Solutions To Facilitate Heat Pump Technology Adoption For Tobacco Baking Application In China

Yanchun Han[a], Hengyi Zhao[b*], Ying Xie[a]

[a]Emerson Research and Solutions Center, Suzhou 215021, Jiangsu, China
[b]China Heat Pump Alliance, CHPA, Beijing 100013, China

Abstract

In the motivation of energy conservation and emission reduction, several provinces in China are promoting and subsidizing heat pump (HP) technology adoption for tobacco baking rooms to replace conventional baking room with heat resources by coal burning and others. HP technology used in tobacco baking room illustrates significant benefits for better baked tobacco leaves quality, more automation by occupying less manpower and more environment friendly with less emissions. Total solution for this application is developed with dedicated designated ZW/ZWD compressor and customized system controller, in order to facilitate OEMs and contractors to better serve end users and quickly grasp the opportunity to enter the market. One field project explains processes of tobacco baking in baking room and how Emerson solutions secure good quality of finished tobacco.

© HPC2023.
Selection and/or peer-review under the responsibility of the organizers of the 14th IEA Heat Pump Conference 2023.

Keywords: Tobacco baking; Heat pump; Total solution for baking; CO2 emission reduction

1. Introduction

China is the largest country in the world for its planting area of flue-cured tobacco, and also the largest tobacco consumer [1]. The annual planting area of flue-cured tobacco is about 2.5 million acres, and the annual output of flue-cured tobacco leaves is about 2 million tons, accounting for more than half of the world's total volume of cured tobacco [2]. Also, flue cured tobacco is an important agricultural product among China's crops, the main raw material for cigarette production, and one of the major agricultural products exported by China, making positive contributions to the national and local financial income increase and economic development [3].

At present, the tobacco curing technology in China is still relatively backward, and coal burning intensive curing houses are widely used to bake tobacco [4]. As the main way for baking, the total coal consumption of coal-fired baking is about 3.5 million tons per year. The coal consumption is large, and the cost of baking fuel is high. The flue gas emitted after the combustion of bulk coal carries a large amount of CO2, CO, SO2, NO, H2S and PM2.5 particles, and it is unable to conduct centralized desulfurization, and dust removal, causing serious environmental pollution, which has become a serious environmental problem in the tobacco baking regions [5]. According to statistics, the annual CO2 emissions of flue-cured tobacco leaves in China are close to 8 million tons, about 600 thousand tons of smoke and dust, and 30 to 50 thousand tons of toxic gases. The anthropogenic emission of air pollution particles and carbon dioxide has become a serious environmental problem [6-8]. With the increasing shortage of fossil energy and the continuous promotion of green ecological civilization construction, new and clean energy will become the new direction used in tobacco baking in China.

Since the year of the Fifth Plenary Session of the 18th Central Committee of the Communist Party of China, China announced to take "green development" as one of the five development concepts, and clearly proposed that: to adhere to green development, we must adhere to the basic national policy of saving resources and protecting the environment, adhere to sustainable development, and form a harmonious development between

* Hengyi Zhao. Tel.: +86 18916181988
*E-mail address:*zhaohy@cecaweb.org.cn

human and nature. In recent years, President Xi has repeatedly emphasized that "green water and green mountains are golden and silver mountains", and he pointed out that "we should accelerate the formation of a green development mode, promote win-win economic development and environmental protection, and build a global society where economy and the environment advance together."

At the same time, on September 22, 2020, at the general debate of the 75th United Nations General Assembly, President Xi announced that China's carbon dioxide emissions would strive to reach the peak by 2030, and would get to be carbon neutral by 2060, including greenhouse gas emissions in the whole economy, from carbon dioxide to all greenhouse gases. This has brought huge challenges and market opportunities to China's refrigeration, air-conditioning and heat pump industry, including agricultural drying and baking.

It is said that by the end of 2017, China has built 1.2 million intensive curing rooms, including 1.19 million coal-fired curing ones, 3000 heat pump curing rooms and 6690 other energy types [5]. With the increasing awareness of environmental protection throughout China, the voice against the traditional flue-cured tobacco production mode is becoming stronger and stronger [9]. Coal fired flue-cured tobacco is no longer in line with the development in terms of heating mode and resource utilization efficiency [10]. It is an urgent problem to develop a clean and green tobacco curing room, which also brings huge business opportunities. The upgrading, reconstruction of the old intensive curing rooms and new constructions will add a market of 70 billion yuan. The following is a further description of the relevant policies in China and technical routes of new environment-friendly tobacco curing room combined with air source heat pump technology.

2. Application and promotion of modern baking room technology

This section describes the process and development related to the baking room and tobacco baking. In the past 100 years, the baking room equipment has changed from low to high level and simple to complex. Before the 1950s, China has been using the simple clay baking room, directly making a fire to heat in it. In the 1960s, the baking technology was improved with the popularization and application of dry and wet thermometer in tobacco baking, but the baking process was mainly empirical. Into the 1970s, the baking process adopted the “high temperature and fast baking” operation technology to pursue the goal of yellow, freshness and clean. From the mid-late 1980s to the early 1990s, the 5-stage, 7-stage and 6-stage of low temperature and humidity baking processes were proposed around the country successively based on the study of baking process, but it still stayed at the low level of inspecting tobacco by human experience and burning by personal feeling. In the 1990s, the baking technology and baking room equipment in China had obvious technical progress and innovation. And the 3-stage baking process was proposed, which achieved the similar level of the international general advanced baking [11].

Now, here introduces the 3-stage process in tobacco baking, which is divided as yellow discoloration, color fixing and stem drying stage, and each stage is divided into multiple temperature rising and holding stages, as shown in Figure 1.

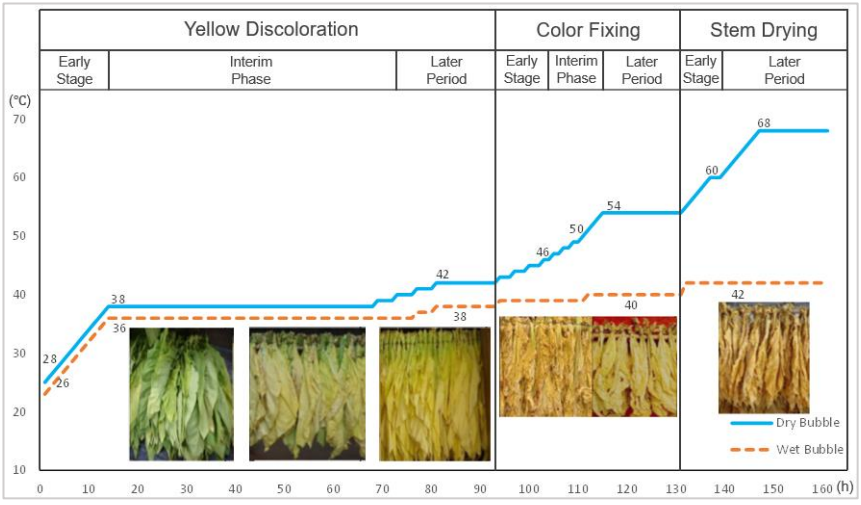


Fig.1. Tobacco Drying Process Curve

Yellow discoloration stage: The temperature and humidity in baking room should be gradually increased. And the temperature, humidity and baking time should be adjusted according to the actual situation of tobacco leaf change. The fresh tobacco leaves are tied reasonably and conveyed to the baking room, then start the heat pump unit. Gradually increase the temperature in the baking room to 38℃ and keep stable, with a difference of 2~3℃ between dry and wet bulb temperatures. When the tobacco leaves reach about 80% yellow, the

temperature in the baking room gradually rises to 42℃ and keeps stable. The difference between dry and wet bulb temperatures changes from 2℃ to 4℃. When the leaves become soft to fall on the shelf and yellow with little cyan, the yellow discoloration stage is completed.

Color fixing stage: The temperature in the baking room gradually rises to 54℃ with low to high heating rate. Before the temperature in the baking room reaches 50℃, the wet bulb temperature should be stabilized at 38~39℃. After the temperature in the baking room reaches 50℃, the wet bulb temperature should be stabilized at 39~40℃. The color fixing should be timely in this stage to improve the appearance grade quality and internal quality of tobacco leaves.

Stem drying stage: Temperature in the baking room gradually rises to 68℃, and the wet bulb temperature is rapidly adjusted to 41~42℃, to ensure that the whole tobacco leaves are dry and baked through, without wet stems and pieces, and swelled stems phenomenon.

With many years practice, air source heat pump system is proven that it's well controlled to stabilize the moisture content of tobacco and meet the temperature and humidity requirement of yellow discoloration, color fixing and Stem drying stage. Associated with modern control technology, heat pump system controller has multiple baking curves, which can modify the dry ball temperature, wet ball temperature and baking duration of each stage according to the local tobacco and climate status.

After seeing many and many successful projects from several provinces in China by introducing heat pump baking room technology, in order to further standardize the bidding and procurement behavior of baking room equipment, unify the construction standards and specifications of dense baking rooms, and promote the construction of new type baking rooms, the Office of the State Tobacco Monopoly Administration issued the "Management Measures for Bidding and Procurement of Baking Room Equipment" and "Revised Technical Specifications for Dense Baking Rooms (Trial)" in 2009. According to this policy, the baking room equipment to be bid must be designed and processed in strict accordance with the relevant requirements of the "Revised Technical Specifications for Dense Baking Rooms (Trial)", and suppliers are encouraged to actively carry out technological innovation and development of new equipment.

Meanwhile, Henan Tobacco Company released "Air Source Heat Pump Dense Baking Rooms" on December 15, 2020, which has been implemented on January 1, 2021. The standard specifies the basic structure, main equipment, and technical parameters of the air source heat pump dense baking rooms, and is also applicable to the new construction, reconstruction, and installation of heat pump baking room. The main components of the heat pump baking room are heating room, tobacco filling room, heat pump unit and controller. Figure 2 shows the standard requirements for the basic structure of the heat pump baking room (heating room, tobacco filling room), and Figure 3 shows the standard requirements for the display content of the main interface of the heat pump baking room controller.

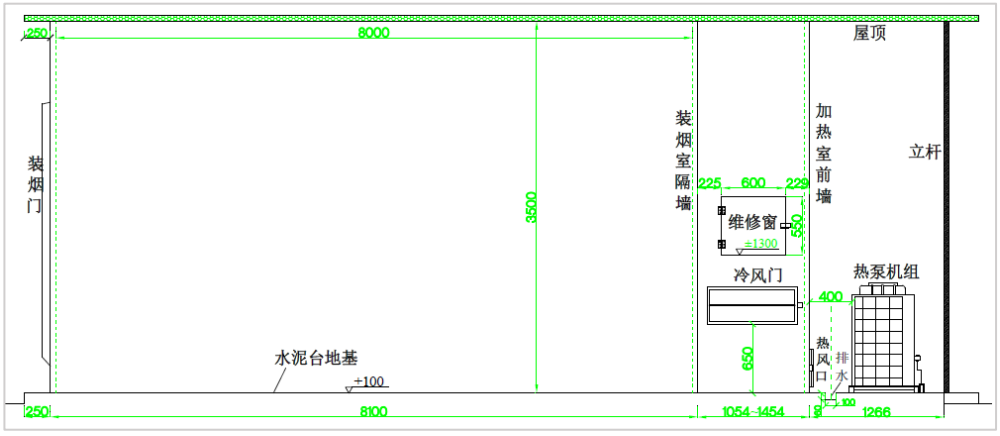


Fig.2. Defined Baking Room Size and Structure (For Reference)

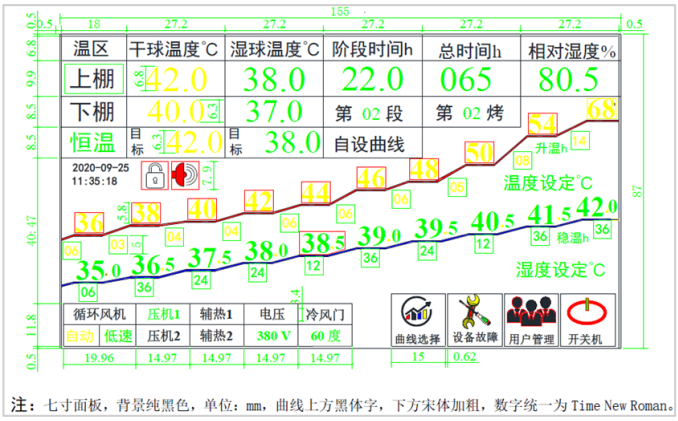


Fig.3. Defined Contents in HMI (For Reference)

3. Heat pump system design

The current application of heat pump system for tobacco baking can be roughly categorized as open loop system and closed loop system. Figure 4 shows the open loop system.

The low-temperature and low-pressure liquid refrigerant enters the evaporator to absorb the heat of the ambient air, and the refrigerant evaporates into medium-temperature and low-pressure vapor. The compressor consumes electric energy to make the pressure and temperature of gaseous refrigerant rise. Then the high-temperature and high-pressure gaseous refrigerant enters the condenser to release heat. The process of refrigerant heat release heats the return air on the other side of the condenser, so that the return air rises to a certain temperature. The refrigerant condensed into liquid is throttled by the throttle valve, and then becomes a low-temperature and low-pressure liquid, and then enters the evaporator to absorb heat. In this way, the thermal cycle process from the evaporator side to the condenser side is realized.

The performance of open loop system is greatly affected by ambient temperature. The starting and ending time of tobacco baking in different regions are not the same. When the weather is continuously rainy or the night temperature is lower than 10℃, the energy efficiency of the open loop heat pump is significantly reduced, COP is even less than 2.0, and the heat output may not meet the requirements of baking [12]. And in the late baking period, the moisture content of tobacco leaves is already low. The humidity of outdoor air can no longer meet the requirements of tobacco drying in the baking room, the only way is to reduce the relative humidity by rising the temperature of circulating air, but this will increase the load of the heat pump system. Meanwhile, the baking process requires that the temperature of the baking room should be maintained at 65~68℃ during the stem drying stage, which means the room for reducing the relative humidity by rising temperature is limited, so there are certain disadvantages and limitations for open loop system.

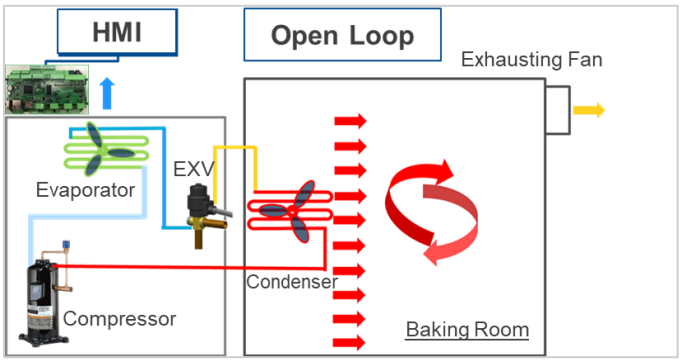


Fig.4. Open Loop Heat Pump System

Figure 5 shows a closed loop system, and the enthalpy-humidity chart of hot air cycle in the baking room is shown in Figure 6: Point R is the state of the hot air from the baking room, and it is divided into two parts. One first enters the sensible heat exchanger and is cooled from point R to point C without specific humidity change. Then enters the evaporator and is cooled and dehumidified from point C to point L. After coming out of the evaporator, it enters the sensible heat exchanger to pre-cool the high temperature air, and itself is heated from point L to point H without specific humidity change. Then it is mixed with another part of air along H-R

to point M, and the mixed air enters the condenser and is heated to point S, and the air at point S is sent into the baking room along the heat-humidity ratio line to complete the hot air cycle.

Different from the open loop system, the cycle medium air of the closed loop system absorbs the moisture in the tobacco leaves in the baking room, and then dries tobacco leaves again after being dehumidified by the evaporator. The whole system basically does not introduce outdoor fresh air. Therefore, in the middle and late period of tobacco baking, the system can effectively reduce the humidity of cycle air to meet the requirements of drying process and reduce the heat load, but the dehumidification efficiency of evaporator will affect the drying efficiency of the whole tobacco baking process [12].

The closed loop system circulates the hot air in the baking room to form a closed loop heating for the baking room. So, the heat provided by it is the compressor power consumption. In the late period of tobacco baking, the heat load of the baking room decreases, but to ensure the dehumidification efficiency of the evaporator, compressor need to run continuously, causing the temperature in the baking room to continuously rise. At this time, part of the fresh air needs to be introduced to meet the requirement of baking process temperature in the baking room. The closed loop system is not affected by the ambient temperature and maximizes the retention of various fragrance substances in tobacco leaves. The heat load in the middle and late period of tobacco baking is lower than that of the open loop system because the closed loop system recycles the latent heat absorbed by the moisture in tobacco leaves when evaporating.

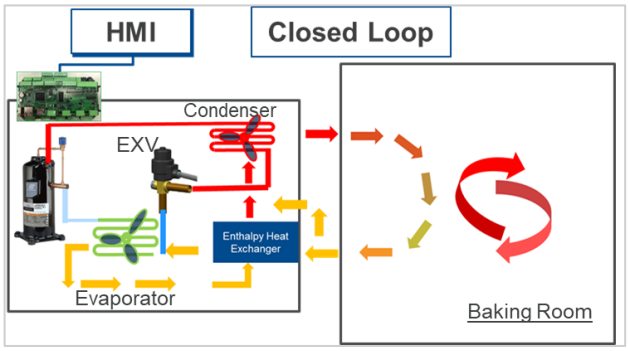


Fig.5. Closed Loop Heat Pump System

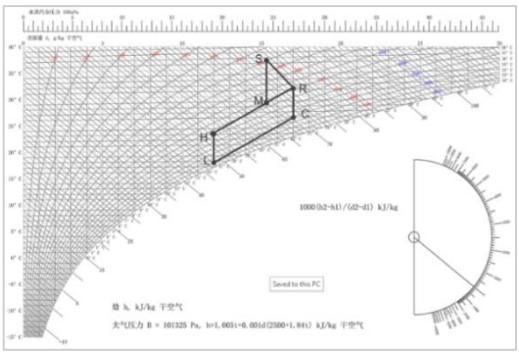


Fig.6. Enthalpy-humidity Chart Of Hot Air Cycle

After comparing the difference between open and closed loop heat pump system, these two types are commonly used in field, which reallly depend on HP OEM technical readiness and ambinent temperature. In order to promote heat pump drying technology more efficiently, Emerson Asia provides an integrated and total soution for heat pump drying system from, which provide great convinent for customers to adopt with one-stop shopping. As shown in Figure 7, which offers all key compoents and then greatly simplifies the application of heat pump in drying system. This total solution includes digital and fixed compressors, programmable controller as system control, X-web monitoring, HMI (human and machine interface), temperature and pressure sensor, and electronic expansion valve for high temperature application.



Fig.7. Emerson Total Solution for Tobacco Baking

Digital and fixed compressors are designed for high evaporating and condensing temperature dyring and baking application and have superior reliability, proven in the field. Digital compressor, called ZWD, have capacity modulation with range adjustment from 10% to 100%, which could deliver precise temperature control to have better baking quality of specimen including tobacco leaves. Together with ZWD compressor, modulation controller, called XC35, is also provide to control capacity output for customer to easily adopt digital compressor with minor change to their existing HP system main controller. An optimized system control scheme is built into the system controller, called iPro Lite, to enhence system performance and reliability. It is also embedded the program for tobacco drying processes with lots of flexibilities. The electronic expansion valve (EXV), dedicated design for high temperature, is one body structure design for best sealing and qualified with high reliability. HMI is slim design and has a 7 inches LCD display with high resolution. X-web monitoring can be connected with system controller through RS485 to inspect the operating conditions and real status in baking room, and provides data for remote moniotring system.

ZWD digital scroll compressor features stepless energy regulation in the range of 10-100% to ensure accurate temperature control and reduce dry consumption of goods. To compare the temperature control curves of fixed speed compressor and digital compressor, we carried out the experiments of mushroom drying in fixed drying system and digital drying system respectively. Figure 8 shows the temperature and humidity curves in drying system's baking room with fixed speed compressor, and Figure. 9 shows that in drying system's baking room with digital scroll. It can be seen from the figures that the temperature and humidity curve in the digital drying system has a higher coincidence with the control target. In addition, compared with inverter technology, the structure of digital scroll compressor is less complex. A large number of practical applications also prove that digital scroll technology can provide higher reliability and energy efficiency thanks to mechanical modulation technology.

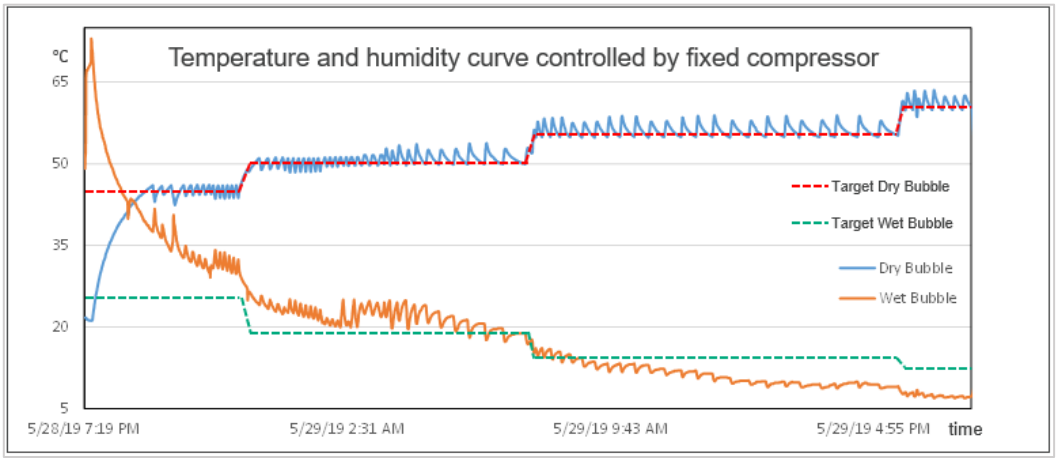


Fig.8. Temperature and Humidity Curve in Fixed Speed Drying System Baking Room

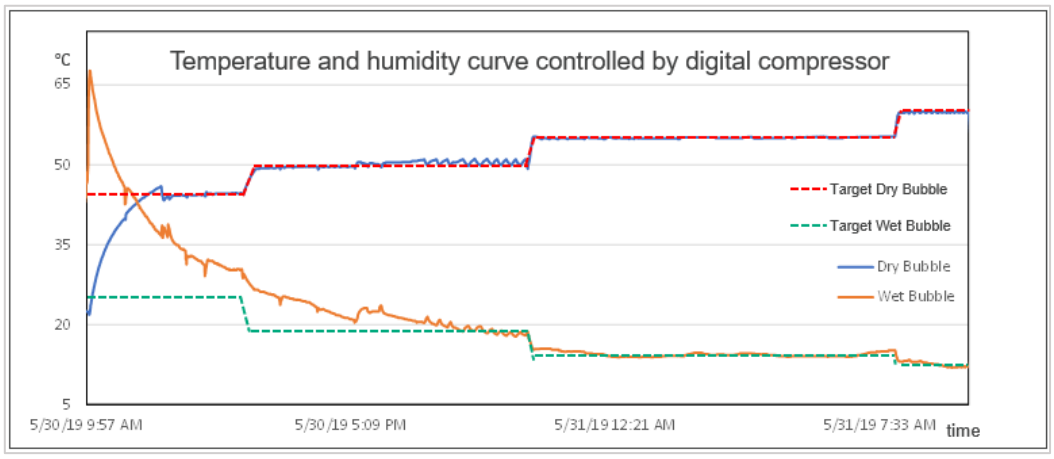


Fig.9. Temperature and Humidity Curve in Digital Drying System Baking Room

4. Field project summary

As mentioned above, when the traditional coal-burning drying is used, it is necessary to hire an experienced tobacco baking master to operate. In view of the pain points above, Emerson Asia has been doing in-depth researches and developing tobacco baking process, using iPro Lite programmable controller as the main control for air source heat pump system.

Taking the tobacco baking field test in Yuxi, Yunnan Province as an example, the system is an open loop heat pump system. The structure of the baking room is 8000mm×2900mm×4800mm, as shown in Figure 10, the wall material is double-sided color steel polyurethane plate. Its thermal conductivity is 0.023W/(m·K), indoor surface convection heat transfer coefficient is 8.7W/(m2·K), and outdoor surface convection heat transfer coefficient is 23.3W/(m2·K). Indoor temperature and humidity are given by tobacco baking process curve, as shown in Figure 1. The outdoor temperature is selected as the ambient temperature of 18~32℃ during the local baking period. Taking the tobacco leaves Yunyan 97 as an example, the weight of fresh tobacco leaves before baking was 3150kg, and the baking duration was determined to be 154h according to relevant literature and tobacco baking practice [13]. According to the existing references and relevant data, the law of water loss in tobacco baking can be obtained. The approximate water loss of tobacco leaves in the baking process is as follows: 27%-35% water loss in yellow discoloration stage, 50%-55% water loss in color fixing stage and 10%-23% water loss in stem drying stage[14]. The wet base moisture content of Yunyan 97 fresh tobacco is 88%, and about 6.5% at the end of baking[15], so the total water loss is 3150×(88%-6.5%)/(1-6.5%) = 2746kg. The water loss rate of each stage obtained from literature[15-16] is shown in Table 1.

Table.1. Water Loss Rate in Each Baking Stage

Baking Stage	Yellow Discoloration			Color Fixing		Stem Drying	
	30-36℃	36-38℃	38-42℃	42-48℃	48-54℃	54-60℃	60-68℃
Water Loss Rate %/℃	0.826	5.347	3.837	4.585	4.165	0.726	1.518



Fig.10. Baking Room Appearance

The sensible heat load of the baking room was the highest at the initial temperature rise, followed by the temperature rise of each stage, and the lowest at the temperature holding of each stage. In the early baking period, the moisture content of tobacco leaves is high, the water evaporation is more, the wet load is larger, but the duration is short. In the yellow discoloration temperature holding stage, the baking room needs to maintain a high humidity environment, the humidity load decreased. To the color fixing stage, the temperature of the baking room rises to 54℃, and the baking room needs to maintain a low humidity environment, and the humidity load increases to the maximum. The moisture content of tobacco leaves in stem drying stage decreased significantly, and the moisture evaporation was less, and the humidity load decreased to the lowest. The calculation result shows that the maximum heat load in the color fixing stage is 31.15kW. According to the calculated load of the baking room and the evaporating and condensing temperature of the heat pump operation, two ZW79KBC compressors are equipped for the baking room heat pump unit. Figure 11 shows the heat pump unit, control board and HMI.

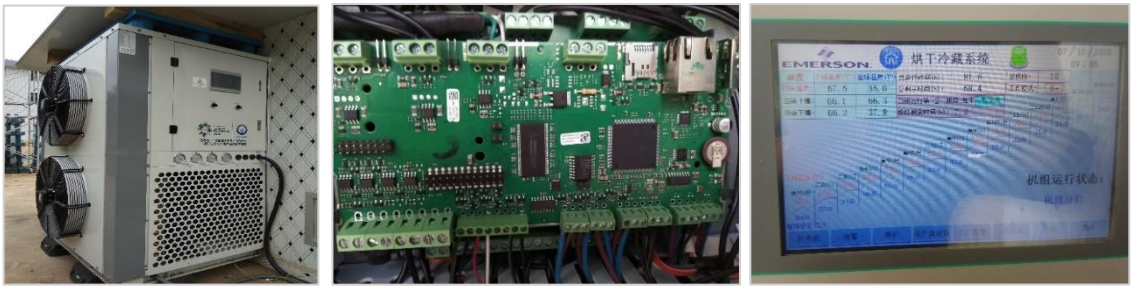


Fig.11. Heat Pump Unit, Control Board and HMI

Two exhaust fans are added to the baking room for strongly discharging humidity to enlarge the dedumudification capacity. Test data collection is shown in Figure 12 and comparison of tobacco leaves before and after baking is shown in Figure 13. The first stage is the low temperature yellow discoloration , compressor running rate is low as heat load is small. The second stage is color fixing, compressor runing rate is high, up to more than 90% as the heat and humidity load is large. The third stage is mesophyll drying, heat load is the main demand and humidity load need is affiliated. And compressor running rate is about 60%. Stage 4 is stem dryiny, basically heat load. And compressor running rate is consistent with stage 3. This tobacco baking test took 164 hours, and consumed 929.2kWh. The longer baking time is mainly due to the lengthening of yellow discoloration and stem drying. From the perspective of the whole drying process, the trend of the measured temperature and humidity curves in the baking room is highly consistent with the requirement of tobacco baking process shown in Figure 1. The air source heat pump drying technology has incomparable advantages in the accurate control of temperature and humidity.

In order to ensure the quality of tobacco baking, the baking room dry and wet bulb temperature control strategies are different at each stage. In the first stage, yellow discoloration of tobacco needs high humidity condition, so only dry bulb temperature needs to be controlled by adjusting the output of compressor. The exhaust fans are off and exhaust valaves are closed since there is no requirement for discharging humidity. In the second stage, baking room dry bulb temperature needs to rise gradually by increasing compressor output. At this time, the exhaust fans are on and the wet bulb temperature can be controlled by adjusting the opening of exhaust valves. For example, if baking room wet bulb temperature > setting value + offset, increase the exhaust valve opening. If baking room wet bulb temperature < setting value, decrease the exhaust valve opening. When baking room wet bulb temperature is between setting value and setting value + offset, keep the exhaust valve opening. When coming to the third stage, baking room dry and wet bulb temperature needs to be kept near the target value by controlling compressor output and exhaust valve opening. For the last stage, it is necessary to hit higher dry bulb temperature and keep wet bulb temperature close to the target in baking room by controlling compressor output and exhaust valve opening.

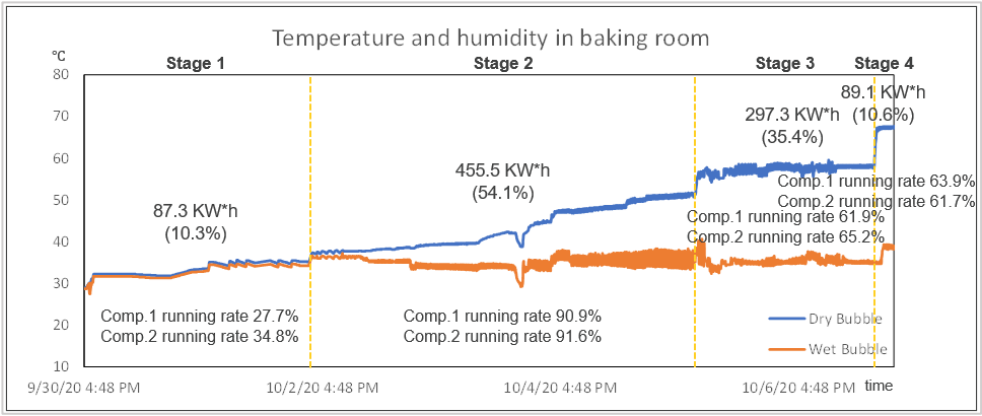


Fig.12. Tobacco Baking Test Data Curve for Heat Pump



Fig.13. Tobacco Leaves Before and After Baking

Compared to the coal-burning baking, the results are shown in Table 2. The power consumption of the heat pump baking room is 929.2kWh, and the labor cost of baking 1kg dry tobacco is 0.11 yuan. In coal-burning side, the electricity consumption of the coal-fired baking room is 181.8 kWh, the coal consumption is 808kg, and the labor cost of baking 1kg dry tobacco is 0.38 yuan. The electricity price is calculated as 0.53 yuan/kWh (the electricity price for agricultural production in the provincial power grid electricity price standard) and the coal price is calculated as 775 yuan/t. The total operating cost of 1kg dry tobacco in the heat pump baking room is 1.33 yuan, and that in the coal-fired baking room is 2.17 yuan. The baking cost of heat pump baking room is about 61% of that of coal-fired baking room, which saves 39% of the cost of tobacco baking. Moreover, the carbon emission of heat pump baking room is only 32% of that of coal-fired baking room, so the effect of cost saving and emission reduction is significant.

Table.2. Economic Comparison between Heat Pump and Coal-burning for Tobacco Baking

Item	Heat Pump Baking	Coal-burning Baking
Total weight of fresh tobacco leaves /kg	3150	3150
Total weight of dry tobacco after baking /kg	404	404
Power consumption /kWh	929.2	181.8
Coal consumption /kg	0	808
Electricity price per kWh /yuan	0.53	0.53
Coal price per t /yuan	775	775
Labor cost for 1kg dry tobacco /yuan	0.11	0.38
Baking cost for 1kg dry tobacco /yuan	1.33	2.17
Carbon emission /kg	473	1491

5. Summary and prospect

Traditional coal-fired tobacco baking not only has higher cost, but also has some uncertainty in baking quality, even brings serious environmental problems to tobacco regions. Under the influence of environmental policy, clean energy, especially air source heat pump technology has made great progress. Combing with the requirement of tobacco baking process, this paper expounds the important role of heat pump drying technology in energy conservation and environmental protection and improvement of tobacco baking quality and efficiency. Following summaries can be drawed:

(1) Even the initial equipment investment of heat pump drying technology is large, but its energy consumption and manual operation cost are quite low, and the long-term comprehensive benefit is attractive.
(2) Heat pump drying technology is highly electrified, and the temperature and humidity in the baking room can be accurately controlled, which greatly improves the proportion of top-grade tobacco.
(3) Heat pump drying technology can partically recover the waste heat from the baking room and realize a high degree of automation, significantly reduce the tobacco baking cost and improve the economic income of tobacco farmers.

In the future, with the continuous development of heat pump drying technology, the heat pump drying system and its control will be further optimized to make the temperature and humidity control of the whole baking process be more accurate, and the temperature fluctuation tends to be minimized. With more studies and practise on closed loop heat pump drying system, energy utilization efficiency could be further improved. In China, heat pump based tobacco baking room will has prospective future and it will contribute a lot to China national carbon emission targerts.

References

[1] Liang Liu. Study on the application of solar energy + heat pump technology to dense tobacco baking rooms in southern Anhui Province: [Master's degree paper]. Anhui: Anhui Jianzhu University Library, 2019

[2] Jianan Wang. Study on the effect of intelligent heating with clean energy on the tobacco baking: [Master's degree paper]. Shanxi: Northwest A&F University

[3] "Market Demand Forecast and Investment Strategy Planning Analysis Report of Chinese Tobacco Product Industry"

[4] Tobacco Research Institute of Chinese Academy of Agricultural Sciences. Chinese Tobacco Culture Science. First edition. Shanghai: Shanghai Science and Technology Press, 2005. 1-26.

[5] "Current Situation of Chinese Tobacco Baking and Prospect of Heat Pump Tobacco Baking"

[6] Givan W, Moore J M, Chi L P, et al. Effect of fuel cost on tobacco baking production [J]. Chinese Journal of Tobacco, 2008(3):55.

[7] Campbell J S. Tobacco and the environment: the continuous reduction of worldwide energy source use for green leaf curing[J]. Nephron Clinical Practice, 2015, 16(3): 107-117.

[8] Chaopeng Song, Fuxin Li, Shaobin Chen, et al. Current situation and development trend of tobacco baking technology [J]. Crops Journal, 2010(1):6-8.

[9] Shen D Y, Xia M Y, Zhang Q Y, et al. The impact of public appeals on the performance of environmental governance in China: A perspective of provincial panel data[J]. Journal of Cleaner Production,2019(231):290-296.

[10] He, Mei Wang, Tao Wang, et al. Spatial distribution of sulfur dioxide around dense tobacco baking rooms [J]. Journal of Applied Ecology,2014,25(3):857-862

[11] Xueying Jia, Kunfeng Liang, Lin Wang, et al. Thermal Analysis of Self-overlapping Heat pump System with Energy Tower [J]. Refrigeration Technology, 2015, 43(8) : 77-82.

[12] Faliang Zhu, Xi Yu, Leining Shi, et al. Study on Performance of Tobacco Baking Heat Pump Combined Cycle [J] Agriculture and Technology, 2022, 42 (04): 49-52.

[13] Zhicheng Ye, Xiong Liu. Performance optimization and analysis of a new closed loop heat pump tobacco baking system [J]. Building Thermal Energy Ventilation and Air Conditioning, 2020, 39 (05): 79-83.

[14] Changrong Rong, Xiaojian Wang, Jingmin Ma, et al. Study on the relationship between moisture dynamics and physiological changes of tobacco leaves during baking[J]. Journal of Henan Agricultural University, 2000, 34 (3): 229-231.

[15] Wei Huang. Study on the law of moisture change of tobacco leaves of different varieties and parts during baking[D]. Changsha: Hunan Agricultural University, 2009.

[16] Yafeng Bao, Yong Wang. Thermal and Moisture Analysis for Tobacco Leaf Flue-curing with Heat Pump Technology[J]. Procedia Engineering, 2016, 146: 481-493.

14th IEA Heat Pump Conference
15-18 May 2023, Chicago, Illinois

Evaluation of lower GWP alternatives to R410A in AC and HP applications

Michael Petersen[a*], Steve Kujak[b], Gurudath Nayak[c]

[a] Trane Technologies, Bloomington, Minnesota 55420, USA
[b] Trane Technologies, La Crosse, Wisconsin, 54601, USA
[c] Trane Technologies, Bengaluru, 560029, India

Abstract

R410A is a refrigerant commonly used in air conditioning and heat pump applications that has become the target to be replaced by lower global warming potential (GWP) alternatives. R-454B with a GWP of 466 has been proposed as a lower GWP replacement for R-410A with similar performance and operating characteristics. Long-term refrigerant solutions are required to provide similar to improved efficiency with comparable capacity while having a GWP of less than 300. This threshold has been identified as an industry-wide average in line with global climate commitments.
This paper investigates alternative refrigerant options to replace R-410A including R-454B, as well as DR-4 and R-479A with a GWP of less than 300 and less than 150 respectively. Thermodynamic simulations followed by an investigation using a component system model of a 3-ton unitary heat pump are performed. Varying ambient temperatures in cooling operation as well as standard rating conditions for both heating and cooling operation for each candidate are considered, to compare refrigerant performance and to determine their viability as a replacement option. Drop-in performance and adjusted compressor speeds are used to compensate for the capacity penalty the lower GWP options experience to achieve relative COP and capacity within 5% of R-410A for investigated heating and cooling conditions.
© HPC2023.
Selection and/or peer-review under the responsibility of the organizers of the 14th IEA Heat Pump Conference 2023.

Keywords: R-410A; Low GWP; Air conditioning; Heat pump, R-479A, DR-4

1. Introduction

Global climate change has brought the scientific community together through the research performed within the Intergovernmental Panel for Climate Change (IPCC, [1]). The reports that document the findings of experts confirm mankind's impact on ever increasing carbon dioxide emissions that drive temperature rise. Refrigerants with high global warming potential (GWP) are estimated to potentially contribute an average global temperature rise of 0.5˚C if no action was to be taken with reducing the GWP of fluorinated hydrocarbons in use today in HVACR equipment. Air conditioning and heat pump applications are hereby an important factor for which R410A is one of the leading refrigerants with a GWP of 2088 [2].

Multiple studies have been performed to investigate refrigerant options with a lower GWP to replace R-410A. The reduction of refrigerant GWP requires in many cases a blend design which contains lower GWP hydrofluoroolefin (HFO) refrigerant components that are often, ASHRAE Standard 34 flammability Class 2L [3]. For example, R-410A is a blend of R-32 which has a flammability classification of 2L and R-125 (Class 1) is added only to render the blend non-flammable. An industry wide test program that evaluated lower GWP R-410A replacements included R-744 as a nonflammable option along with nine lower flammability options with classification of 2L based on R-1234yf and R-1234ze(E) in combination with R-32 in most cases [4]. The GWP of the investigated 2L candidates offered hereby significant reduction compared to R-410A in a range from a GWP of about 200 to 1500 as described in [5]. Another lower flammability candidate with a GWP of 466 is the binary blend R-454B formulated with 68.9% R32 and 31.1% R-1234yf as presented by Hughes et

*Corresponding author
E-mail address: michael.petersen@tranetechnologies.com

al. [6]. This blend provides similar capacity with slight improvements in efficiency while having higher compressor discharge temperatures compared to R-410A. Considering a weighted average approach of GWP of refrigerants being used today throughout the industry, the GWP will need to be less than 300 to meet the phase-down targets of the Kigali Amendment to the Montreal Protocol as described by Schultz et al. [7]. Schultz describes the potential blend development opportunity by using newly introduced low GWP molecules CF3I, R-1123, R-1132a. Candidate blends were identified to have suitable properties to be considered as R410A replacement candidates. However, the expectable capacity would be 10 to 15% lower compared to R410A. Additional challenges remain in chemical and material compatibility considerations of these new molecules that need to be investigated for a successful implementation in air conditioning and heat pump applications. Recently another low GWP (GWP<1) molecule has been introduced with R-1132(E) as described by Rydkin et al. [8]. This molecule which has a safety classification of B2 by ASHRAE Standard 34 [3] has been formulated in the blend R-479A with 21.5% R32 and 50.5% R1234yf.

For the investigation performed in this study R410A is compared to R-454B and the binary blend option DR-4 as evaluated by Schultz et al. in [9] with a GWP of less than 300 and R-479A with a GWP of less than 150 as summarized in Table 1. All the investigated replacement blend candidates are of lower flammability and provide significant GWP reduction potential. The normal boiling point temperatures as well as the critical properties of the replacement candidates are similar while their temperature glide increases with decreasing GWP.

Table 1. Properties of investigated refrigerants

Refrigerant	**R-410A**	**R-454B**	**DR-4**	**R-479A**
Composition	R-32/R-125, (50/50)	R-32/R-1234yf, (68.9/31.1)	R-32/R-1234yf, (43.5/56.5)	R-1132(E)/R-32/R-1234yf, (28/21.5/50.5)
ASHRAE	A1	A2L	A2L	A2L
GWP_{100} AR4	2088	466	299	148
NBP [°C]	-51.7	-50.8	-49.0	-50.7
NDP [°C]	-51.6	-49.8	-44.9	-44.9
Glide [K]	0.1	1.0	4.1	5.8
Pcrit [MPa]	4.9	5.3	4.8	4.8
Tcrit [°C]	71.3	78.1	80.1	79.7

Figure 1 shows the property diagrams for all four compared blends visualizing their similarity in terms of heat of vaporization for R-410A, DR-4 and R-479A (pressure-enthalpy) as well as compressor discharge temperature (temperature -entropy). R-454B has a wider two-phase dome due to its larger R-32 blend fraction causing higher compressor discharge temperatures at the same time. The larger glide of DR-4 and R-479A compared to R-410A and R-454B becomes noticeable in the condenser and evaporator.

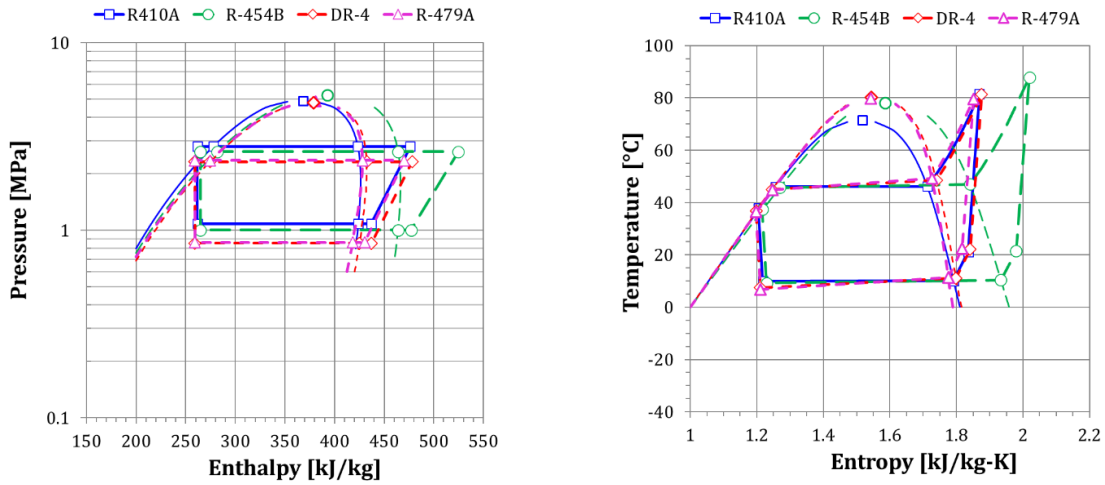


Figure 1. Pressure- Enthalpy and Temperature- Entropy property comparison of evaluated refrigerants

A thermodynamic model was set up using REFPROP 10 [10] refrigerant properties to evaluate the R-410A lower GWP alternatives in terms of expected performance and operating characteristics as outlined in Petersen et al. [11]. Pressure drops are hereby not accounted for in the heat exchangers and connecting lines. AHRI 210/240 A test point [12] conditions were used for the study with an evaporation temperature of 10°C considering 8.3K superheat and an approach of 8.4K based on an indoor air side temperature of 26.7°C. Similarly, the condensing temperature was set at 46.1°C with 8.3K subcooling and an approach temperature difference of 2.8K based on 35°C air temperature entering the outdoor unit. A heat exchanger weighting of 0.7 is applied for the evaporator and the condenser as a weighted average of the dew point and bubble point temperatures. Figure 2 summarizes the relative COP (COP*), relative capacity (CAP*) and relative compressor discharge temperature difference (ΔCDT) compared to R-410A.

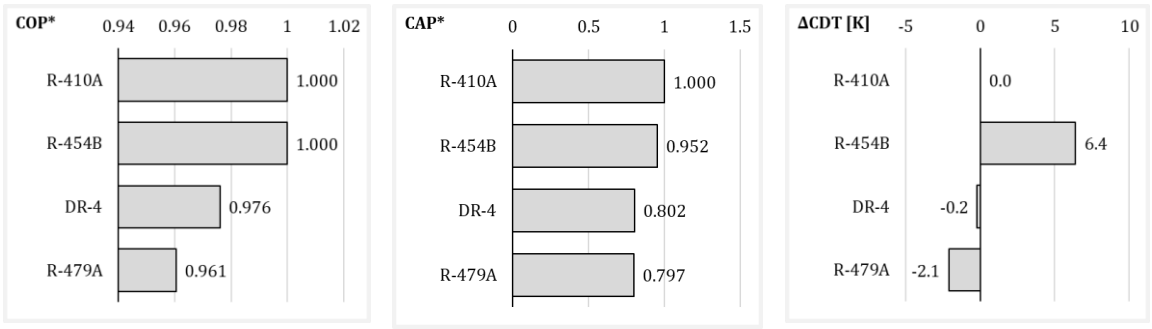


Figure 2. Relative COP (COP*), capacity (CAP*) and compressor discharge temperature difference (ΔCDT)

The relative COP of the alternative candidates are all within 5% of R-410A making them viable options, whereas the only R-454B provides this margin for relative capacity. The lower GWP alternatives DR-4 and R-479A both have a roughly 20% lower capacity compared to R-410A as well as similar to lower compressor discharge temperatures. Both lower GWP options provide similar performance characteristics whereas R-479A has a GWP below 150 or half of DR-4 with a GWP of less than 300. To better understand the relative performance and operating characteristics of the refrigerants exhibiting pressure drop and utilize their transport properties in the heat exchanger a system model was developed and investigated.

2. System and model description

A unitary packaged rooftop heat pump unit was chosen for the refrigerant system modeling. The unit is rated with a cooling capacity of 3 RT or 10.6kW while operating at 60 Hz. The nameplate R-410A refrigerant charge is 7.7 lbm or 3.5 kg. The unit is driven by a scroll compressor and uses indoor and outdoor heat exchangers with aluminum-fin/copper-tube construction with fixed speed fans. The Modelica platform with TiL suite library [13] has been used to create the heat pump unit system model. The system comprises of a physics based refrigerant independent compressor model which is developed using the R-410A test data. The compressor model parameters can then be used to predict the performance with other refrigerants over the entire operating map. Both the indoor and outdoor coils used have fin and tube heat exchanger configurations. The heat transfer (Shah [14],[15], [16] for two-phase and Dittus-Boelter [17] for Single-phase) and pressure drop (Konakov [18]) correlations from the literature are used both on the refrigerant side and air side (Haaf, [19]), while a discretized calculation method is applied for the heat exchangers. Correction factors are then applied to these correlations to accurately represent the test data in both cooling and heating modes for the baseline R-410A resulting in a match of the experimental data within 3%. Pressure-drop and heat transfer is also calculated for the refrigerant lines which are used to connect the above components and a 4-way reversing valve which enables switching between cooling and heating modes. NIST REFPROP 10.0 [10] has been used to generate the refrigerant properties lookup table for each of the refrigerant mixtures simulated here. Moist air properties are sourced from TiL Media [13]. The refrigerant R-410A is used as a baseline for relative performance as well as R-454B as a baseline for matching capacity in AHRI 210/240 [12] A condition for adjusting the compressor speed for the low GWP alternative refrigerant options DR-4 and R-479A. The baseline compressor speed hereby set at 50Hz with higher adjusted speed for DR-4 and R-479A to accommodate the lower relative capacity of around 20% as determined in the thermodynamic model in the previous paragraph. The system model design in Dymola/ Modelica is shown in Figure 3.

The investigated conditions for cooling and heating operations include both standard test conditions as defined in AHRI 210/240 for cooling (A, B) and heating (H1, H3) as well as ambient temperature sweeps in cooling operation to investigate the performance at varying ambient temperatures. The investigated conditions are summarized in Table 2.

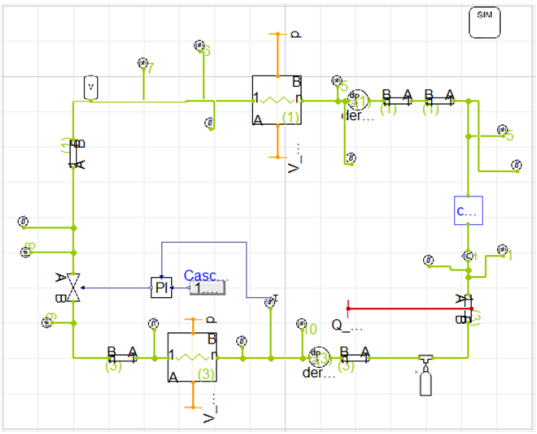


Figure 3. Schematic diagram of the system model developed

Table 2. Cooling and heating modeling conditions

Mode	**Description**	**Indoor**		**Outdoor**	
		Dry bulb temperature [˚C]	Wet bulb temperature [˚C]	Dry bulb temperature [˚C]	Wet bulb temperature [˚C]
Cooling	A	26.7	19.4	35.0	n/a
	B			26.7	
	Sweep			18.3	
				23.9	
				27.8	
				29.4	
				35.0	
				40.6	
				46.1	
				51.7	
Heating	H1	21.1	<15.6	8.3	6.1
	H3			-8.3	-9.4

3. Modeling results

In cooling condition “A” the baseline capacity was established with R-454B at a compressor frequency of 50Hz. The determined cooling capacity was then matched with the low GWP alternatives DR-4 and R-479A and the compressor speed at this adjusted condition was maintained for the temperature sweep and heating conditions to obtain both performance results at drop in compressor speeds of 50Hz and adjusted compressor speeds. The results for relative COP compared to R-410A are shown in Figure 4.

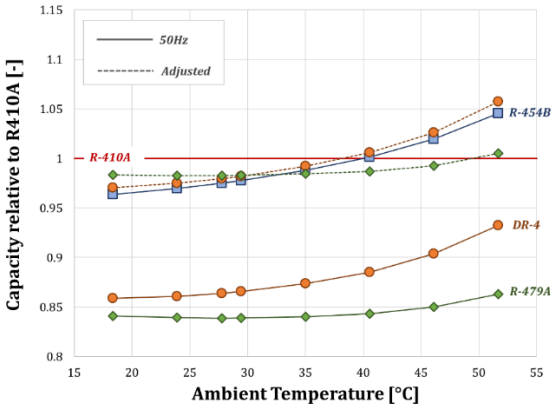


Figure 4. Capacity relative to R-410A for baseline and adjusted compressor speed

R-454B has similar capacity compared to R-410A at a rating ambient temperature of 29.4˚C. The low GWP alternative refrigerants DR-4 and R-479A have approximately 15% lower capacity compared to R-410A and have therefore been investigated at adjusted compressor speeds to match the higher capacity of R-454B. These adjusted compressor speeds were then used in the following conditions. DR-4 at baseline compressor speed of 50Hz provides a relative capacity of roughly 0.86 to 0.94 compared to R-410A with R-479A achieving 0.84 to 0.86. With adjusted compressor speeds both low GWP alternatives remain within ±5% of relative capacity compared to R-410A with slightly more improvement for DR-4 at elevated temperatures of 51.7˚C exceeding 5% relative capacity. The adjustment of compressor speed therefore confirms a viable option to match relative capacity requirements. However, the increase in refrigerant flow rate while maintaining the rest of the system design unchanged has an impact on the system COP as shown in Figure 5.

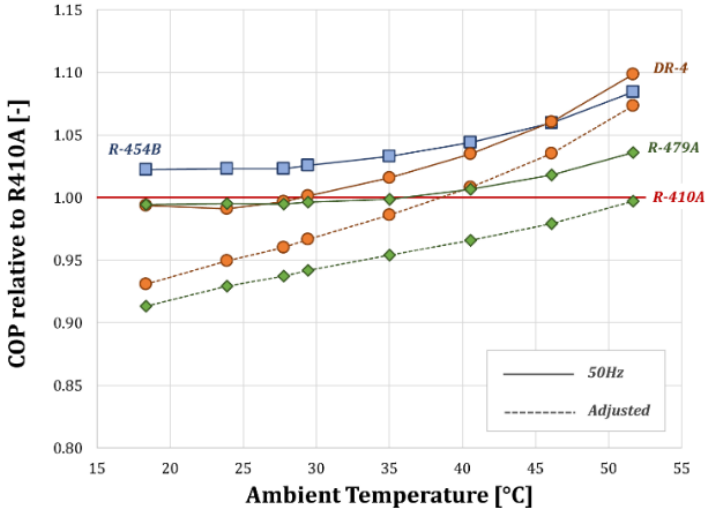


Figure 5. COP relative to R-410A for baseline and adjusted compressor speed

The baseline system efficiency for R-454B shows improvement over R-410A throughout the investigated ambient temperature range within 2% to 8%. DR-4 has similar COP at lower ambient temperatures up to 30˚C with benefits at higher ambient temperatures up to 10% at 51.7˚C. R-479A has a similar response with comparable COP up to 40˚C and improved values up to 4% at high ambient temperatures for the drop-in compressor speed of 50Hz. Adjusting the compressor speed to match relative capacity penalizes the achievable COP leading to a maximum penalty of approximately 8% at low ambient temperatures which decreases with increasing ambient temperatures up to parity with R-410A at 51.7˚C. Another important system operating parameter is the compressor discharge temperature which needs to be evaluated closely to ensure compressor operation throughout the operating map is not affected. The compressor discharge temperature difference compared to R-410A is shown in Figure 6.

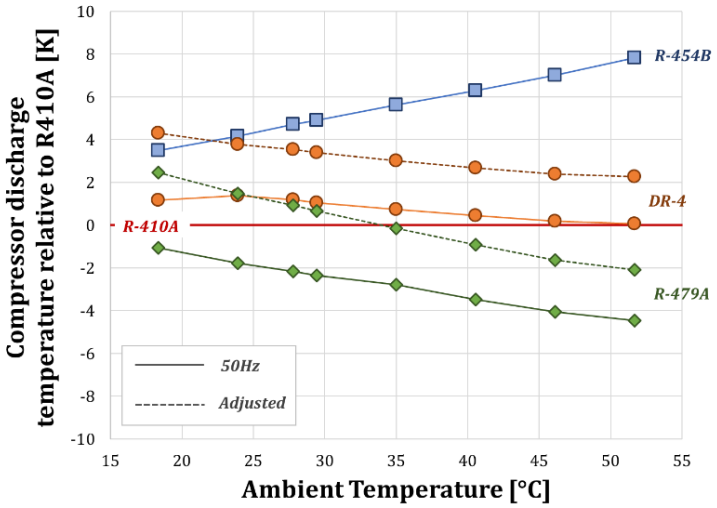


Figure 6. Relative compressor discharge temperature for baseline and adjusted compressor speed

R-454B shows higher compressor discharge temperatures compared to R-410A between roughly 4K at low ambient temperatures increasing to around 8K for high ambient temperatures. For drop in compressor speeds of 50Hz DR-4 shows similar CDT with slightly elevated values within 2K. R-479A provides lower compressor discharge temperatures ranging from 1K at low ambient temperatures to 4.5K at high ambient temperatures. With adjusted compressor speeds to match R-454B capacities at "A" condition the relative compressor discharge temperature difference increases for both low GWP options by approximately 2K to 3K. R-479A still provides lower relative temperatures compared to DR-4 and maintains lower temperatures compared to R-410A at ambient temperatures above 35˚C.

In heating operation, the investigation was done in a similar way with a drop-in situation using a compressor speed of 50Hz as well as the adjusted speed as determined in cooling "A" condition. The results for relative COP at condition H1 are summarized in Figure 7.

Both low GWP refrigerant blend options show relative COP compared to R-410A within 5% with similar results for both 50Hz and adjusted compressor speeds. R-454B due to its larger R-32 blend fraction has a match in heating efficiency compared to R-410A. The relative capacity results in Figure 8 show the impact of increased compressor speed to make up the inherent lower capacity of the low GWP blends due to their properties.

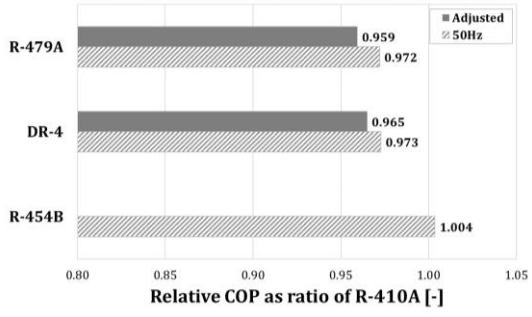


Figure 7. Relative heating COP of R454B and low GWP options compared to R-410A at H1 condition

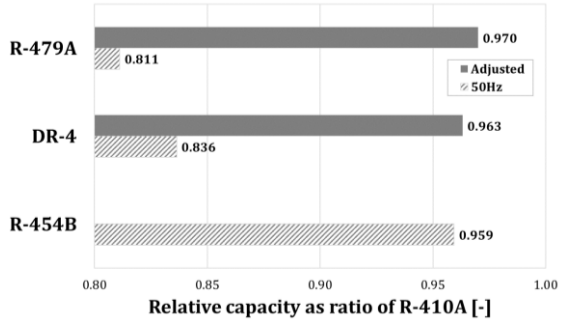


Figure 8. Relative heating capacity of R454B and low GWP options compared to R-410A at H1 condition

R-454B shows slightly lower capacity compared to R-410A at H1 condition with an ambient temperature of 8.3˚C. DR-4 and R-479A have about 18% lower heating capacity at drop in compressor speed of 50Hz. This can be recovered with the adjusted compressor speed and brings it within 5% of R-410A and slightly above R-454B. The effect on compressor discharge temperature can be seen in Figure 9. Similar to cooling operation R-454B shows higher compressor discharge temperature with 4.5K over R-410A. Both DR-4 and R-479A provide lower CDT with 2K and 6.7K respectively. Adjusting the compressor speed reduces this benefit of

lower compressor discharge temperature by about 4K for both candidates which results in about 2K lower CDT for R-479A and 2.2K higher CDT compared to R-410A for DR-4.

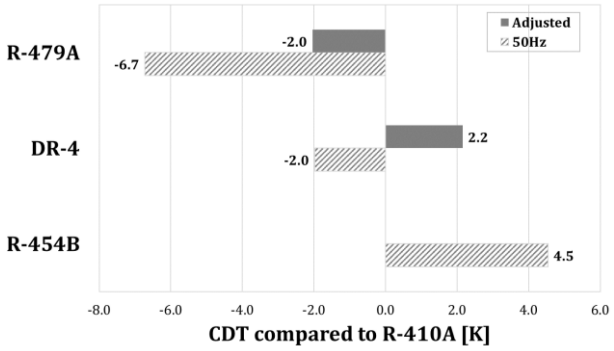


Figure 9. Compressor discharge temperature of R454B and low GWP options compared to R-410A at H1 condition

At even lower ambient temperatures of -8.3˚C at H3 condition the relative performance of all investigated refrigerants decreases compared to R-410A as shown in Figure 10.

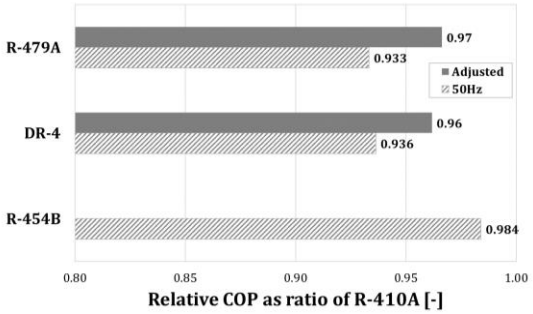


Figure 10. Relative heating COP of R454B and low GWP options compared to R-410A at H3 condition

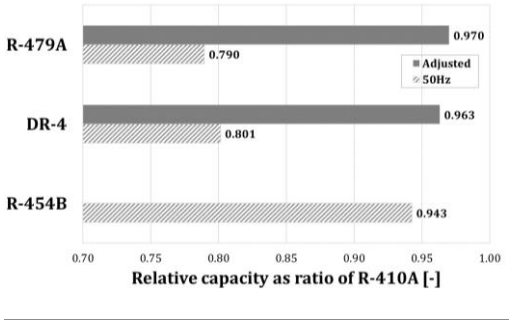


Figure 11. Relative heating capacity of R454B and low GWP options compared to R-410A at H3 condition

For adjusted compressor speeds DR-4 and R-479A achieve similar capacity to R-454B within 5% of R-410A. The relative capacity as shown in Figure 11 confirms the trends seen for cooling operation with drop-in capacity of about 80% compared to R-410A. By adjusting the compressor speed the relative capacity is recovered to within 5% with slight improvement for R-479A over DR-4. R-454B shows slightly lower relative capacity compared to R-410A while operated at the same compressor speed of 50Hz. The impact of compressor discharge temperature is shown in Figure 12 confirming the offsetting impact of necessary compressor speed increase to accommodate for the lower capacity of low GWP blends DR-4 and R-479A.

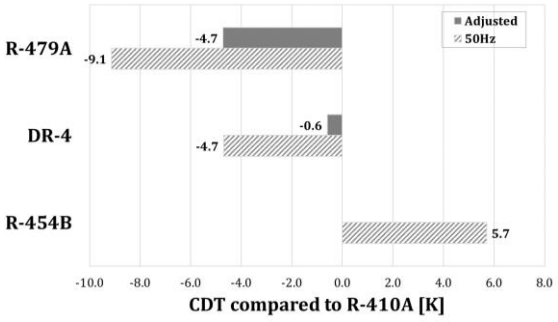


Figure 12. Compressor discharge temperature of R454B and low GWP options compared to R-410A at H3 condition

For the drop-in compressor speed lower compressor discharge temperatures of 9.1K to 4.7K are achieved for R-479A and DR-4 respectively compared to R-410A. When adjusting the compressor speed to make up the lower capacity of the blends the CDT increases to 4.7K and 0.6K lower values compared to R-410A.

4. Conclusions

This paper described the investigation of low GWP alternatives to R-410A for new system designs due to their flammable characteristics. The three investigated alternatives represent different GWP levels ranging from around 450 with R-454B as well as 300 (DR-4) and 150 for R-479A. R-479A is hereby utilizing the recently classified molecule R-1132(E) that provides a GWP<1. The thermodynamic model showed good agreement with the modeling results of a detailed system model of a unitary heat pump under standard rating conditions. The drop in case with same compressor speed confirmed the lower relative capacity for the low GWP options DR-4 and R-479A with approximately 17% lower capacity as seen in the initial thermodynamic model. Increasing the compressor speed allowed for recovery of relative capacity within 5% for all investigated conditions for both heating and cooling. The lower compressor discharge temperature that can be achieved with DR-4 and R-479A is offset when increasing the compressor speed but remains lower compared to R-410A and R-454B which can be beneficial to avoid limitations of the compressor operating map due to compressor discharge temperature limitations. The evaluation of a detailed system model that considers a physical compressor model as well as heat transfer and pressure drop provides good insight and indication of expectable performance. However, experimental evaluations are needed to validate these findings. In conclusion R-479A has been found to provide comparable to superior performance and operating characteristics to DR-4 while having approximately half the GWP. Further improvement of the system design is expected to improve the overall efficiency from the drop-in situation that was evaluated in this study.

Acknowledgements

The authors would like to thank Ken Schultz of Trane Technologies for his guidance and valuable comments.

References

[1] IPCC, 2021: Summary for Policymakers. In: Climate Change 2021: The Physical Science Basis. Contribution of Working Group I to the Sixth Assessment Report of the Intergovernmental Panel on Climate Change
[2] Forster, P., V. Ramaswamy, P. Artaxo, T. Berntsen, R. Betts, D.W. Fahey, J. Haywood, J. Lean, D.C. Lowe, G. Myhre, J. Nganga, R. Prinn, G. Raga, M. Schulz and R. Van Dorland, 2007: Changes in Atmospheric Constituents and in Radiative Forcing. In: Climate Change 2007: The Physical Science Basis. Contribution of Working Group I to the Fourth Assessment Report of the Intergovernmental Panel on Climate Change
[3] ANSI/ASHRAE Standard 34-2019, Designation and Safety Classification of Refrigerants, American Society of Heating, Refrigerating and Air-Conditioning Engineers, Inc., Atlanta, GA 30329.
[4] AHRI, 2015, Participants' Handbook: AHRI Low-GWP Alternative Refrigerants evaluation program (Low-GWP-AREP), Air-Conditioning, Heating and Refrigeration Institute, Arlington, VA 22201
[5] Schultz KJ, Perez-Blanco M, Kujak SA. System Soft-optimization Tests of Refrigerant R-32, DR-5A, and DR-55 in a R-410A 4-ton Unitary Rooftop Heat Pump-Cooling Mode Performance. *AHRI Low-GWP AREP* 2015; R056P.
[6] Hughes, Joshua and Shah, Sonali, "Testing of Low GWP Replacements for R-410A in Stationary Air Conditioning" (2016). International Refrigeration and Air Conditioning Conference. Paper 1805.
[7] Schultz, K, Replacements for R410A with GWPs less than 300, Proceedings of the 25th IIR International Congress of Refrigeration: Montréal , Canada, August 24-30, 2019
[8] Rydkin, I., Gobou, K., Karube, D., Ajioka, S., Nakaue, T., Leon, A., Overview of novel GWP 1 HFO Refrigerant 1132E and the Mixture of 1132E and R-1234yf, International Refrigeration and Air Conditioning Conference. Paper 2491. 2022, https://docs.lib.purdue.edu/iracc/2491
[9] Schultz, K., Kujak, S., Performance comparison of optimized R-410A replacements, Proceedings of the 24th IIR International Congress of Refrigeration: Yokohama, Japan, August 16-22, 2015.
[10] Lemmon, E.W., Bell, I.H., Huber, M.L., McLinden, M.O., 2018, NIST Standard Reference Database 23: Reference Fluid Thermodynamic and Transport Properties-REFPROP, Version 10.0, National Institute of Standards and Technology, Standard Reference Data Program, Gaithersburg
[11] Petersen, M. and Kujak, S., "Review of Lower GWP Refrigerants For Retrofitting R-410A Applications" (2022). International Refrigeration and Air Conditioning Conference. Paper 2280.

https://docs.lib.purdue.edu/iracc/2280
[12] AHRI Standard 210/240, 2020, Air conditioning, Heating and Refrigeration Institute, Arlington VA
[13] TIL Suite, Version 3.8.0, TLK-Thermo GmbH, Braunschweig, Germany, 2020
[14] Shah, MM.: "A general correlation for Heat Transfer during film condensation inside pipes", Int. J. Heat Mass Transfer, 1979, Vol. 22, p 547-556
[15] Shah, MM, “Chart Correlation for Saturated Boiling Heat transfer Equations and Further Study” ASHRAE Transactions, 1982, Vol.88, Part 2, 66-86
[16] Shah, MM., Two-Phase Heat Transfer, Wiley, ISBN: 978-1-119-61861-4 February 2021
[17] Dittus, F. and L. Boelter, University of California publications on engineering. University of California publications in Engineering, 1930. 2: p. 371.
[18] Konakov, P.K.: "A New Correlation for the Friction Coefficient in Smooth Tubes", Report of the Academy of Science USSR, Vol. 51: 503-506
[19] Haaf, S., Wärmeübertragung in Luftkühlern, Handbuch der Kältechnik, Bd. 6, Teil B: Wärmeaustauscher, Berlin u.a. : Springer Verlag, pp. 435-491,1988

14th IEA Heat Pump Conference
15-18 May 2023, Chicago, Illinois

Testing of alternative refrigerants for unitary air-conditioning and heat pump applications

Sarah Kim[a,*], Robert Elliott Low[b], Christopher Seeton[a], Ke Tang[c], Francesco Botticella[c]

[a]Koura, 950 Winter Street, Waltham, MA 02451, USA
[b]Koura, Runcorn, Cheshire WA7 4QX, UK
[c]Creative Thermal Solutions Inc, 2209 N. Willow Road, Urbana, IL 61802, USA

Abstract

The unitary air-conditioning and heat pump application sector is one of the largest single consumers of refrigerant today mostly with R-410A having Global Warming Potential (GWP) of 2088 or R-32 (GWP 675). Legislative phase-down of fluorinated refrigerants is driving a search for alternatives for this application with target to lower average GWP – ideally below 300. While some alternatives such as R-454B (GWP 466) or R-290 have already been identified as technically feasible, the flammability and charge size of systems may present an additional barrier to use these fluids. Use of R-744 has been considered in the past but the energy efficiency and cost of prototype systems has rendered it unattractive. A non-flammable refrigerant blend of R-744, R-1132a and R-32, working name LFR3 (submitted to standards bodies for classification), GWP 142, has been developed, which in testing has demonstrated significant energy efficiency advantage over R-744. A project is now underway to assess the feasibility of using this fluid for heat pumps. The goal is to develop baseline performance on a production system designed for R-410A then to retrofit the system with new heat exchangers and compressor suitable for use with R-744 and to assess whether comparable efficiency (EER) to the R-410A may be achieved. Performance testing with R-410A, with a near drop-in low-GWP alternative (R-468C, GWP 284)) and of the prototype high pressure system will also be presented.

© HPC2023.
Selection and/or peer-review under the responsibility of the organizers of the 14th IEA Heat Pump Conference 2023.

Keywords: refrigerants; low gwp, HFO, heat pumps

1. Introduction

The direct impact of refrigerant emissions and their global warming effect, measured by Global Warming Potential (GWP), have been a long focus by regulators. With another HFC allowance step down scheduled in 2024 as set forth by the F-gas regulation and the Kigali Amendment to the Montreal Protocol, the HVAC&R industry worked diligently in developing lower GWP refrigerants while updating standards and procedures to safely use the increasingly common mildly flammable refrigerants in systems and buildings. In addition, the HVAC sector, heat pumps to be specific, has been identified as key in accomplishing net zero energy goals established by corporations as well as governments. The US Department of Energy (DOE) published an industry decarbonization roadmap [1] in September of 2022 that laid out pathways in reaching the net-zero GHG emissions by 2050 in the US. Amongst the four pillars that were identified by the DOE, it is clear that heat pumps will be an integral technology for the energy efficiency and industrial electrification pillars. With ever increasing demand for more efficient HVAC systems, it is critical to take a wholistic approach when selecting a new refrigerant beyond the GWP value.

Refrigerant development activities were centered around designing fluids as closely as possible to incumbent refrigerants that would allow for easy adoption for both new and retrofit applications. To that end, the first part of this paper will present a drop-in assessment of a lower GWP R-410A replacement refrigerant,

* Corresponding author. E-mail address: sarah.kim@kouraglobal.com

R-468C. The second part of the paper will focus on a very high pressure low GWP refrigerant LFR3, blend of R-1132a, R-744, and R-32 (10/69/21 in mass %), which was developed to improve the efficiency of R-744 and expand the fluid usage to warmer climate zones. It is also nonflammable as formulated, which can be a promising solution for applications with larger refrigerant charges. A R-744 based prototype unit was built within the R-410A system frame, which was then assessed for cooling and heating performance of R-744 and LFR3.

2. Description

2.1. Refrigerant properties

As described in the previous section, four refrigerants have been experimentally evaluated in this work. They can be further categorized into two groups based on the pressure ranges: high pressure and very high pressure. Thermodynamic properties of the fluids are summarized in Table 1.

Table 1. Thermodynamic properties of test refrigerants

Property	Units	R-410A	R-468C	R-744 (CO_2)	LFR3
GWP (AR4)		2088	286	1	143
Molecular mass	g/mol	72.6	73.7	44.0	47.0
Critical temperature	°C	71.4	77.0	31.0	41.2
Critical pressure	kPa	4900	4880	7377	7170
Liquid density (0°C)	kg/m^3	1170	1084	927	935
Bubble pressure (0°C)	kPa	801	838	3485	2875

2.2. Test description

A commercially available R-410A packaged heat pump with a capacity of 17.6 kW (5 Ton) was used for R-410A and R-468C drop-in testing. The thermostatic expansion valve (TXV) was set to maintain a superheat of 3 K for cooling at A condition and was not readjusted for other conditions. Capacity was measured for both air and refrigerant side, which showed good agreement throughout the testing.

Upon completion of the high pressure refrigerant testing, a prototype unit was built within the frame of the R-410A unit with a goal to maintain the same cooling capacity of 17.6 kW, Figure 1. The same baseline indoor blower (air flow rate) and outdoor fan were used while a reciprocating compressor, indoor and outdoor heat exchanger, internal heat exchanger (IHX), accumulator, and EEV designed for R-744 were implemented. The purpose of this study was to evaluate the feasibility of using very high pressure low GWP refrigerants (R-744 and LFR3) in heat pumps while maintaining the same footprint as existing equipment with lower pressure.

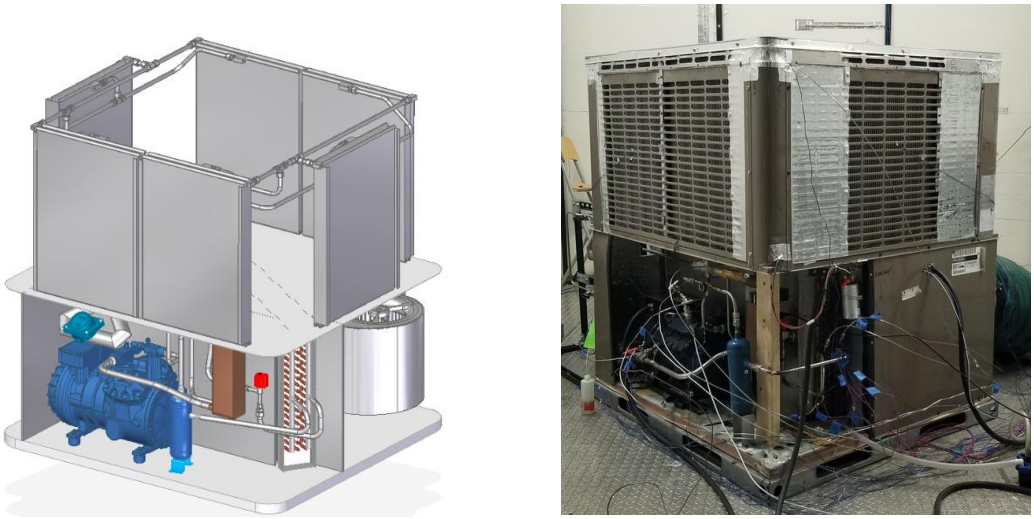


Fig. 1. R-744 system components fitted into the R-410A unit frame

3. Results and Discussion

3.1. Drop in test results for high pressure refrigerants

Refrigerants were evaluated at two cooling (A and B) and two heating conditions (H1 and H3) as described in the AHRI 210/240 standard [2]. The optimum charge of R-468C was determined to be 5.8 kg, 9% higher than the R-410A baseline, where sufficient subcooling was observed while maximizing the cooling capacity and COP. Uncertainty values were determined as ±0.7% for COP and ±0.2% for capacity.

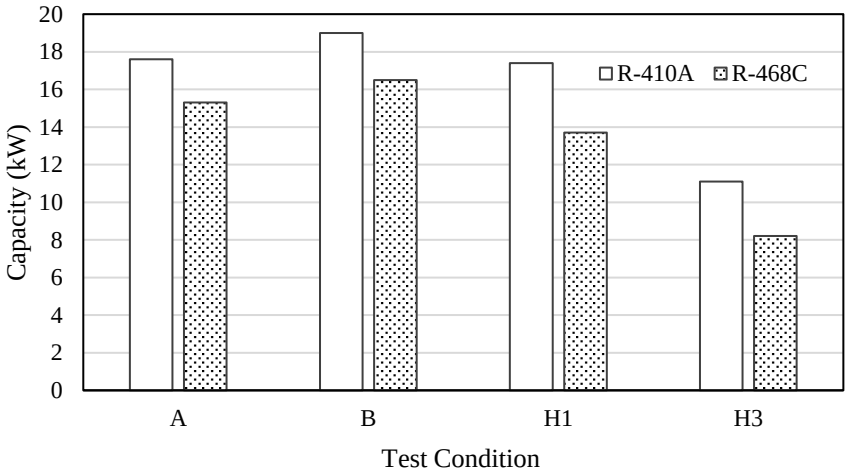


Fig. 2. Capacity of R-410A and R-468C at cooling and heating modes

R-468C showed slightly lower capacity values than R-410A especially during heating mode, Fig. 2. COP also showed a similar trend where R-468C exhibited comparable results to R-410A at cooling mode and lower efficiencies at heating mode, Fig. 3. These results are similar, but somewhat lower compared to previous drop in test results conducted in a R-410A split system where R-468C was reported as LFR1C [3]. Low reported similar or higher COP of R-468C than R-410A especially in heating mode. One potential reason for this discrepancy could be due to the testing in this work being carried out and optimized around cooling mode, which may have inadvertently hurt the heating performance. Also, it was noted that the performance was sensitive to the TXV opening and thus the superheat values, however, the TXV setting was not adjusted once it was set for A condition. A use of an electronic expansion valve (EEV) may help better modulate between the two modes. R-468C also has a higher glide of 4 to 5 K compared to R-410A's glide of 0.1 K, therefore the direction of flow in the heat exchangers can favor one mode over the other and provides an opportunity to optimize the system based on primary operations.

3.2. Test results for very high pressure refrigerants in the prototype unit

Three parameters can be changed to adjust the capacity and high side pressure of the R-744 based system:

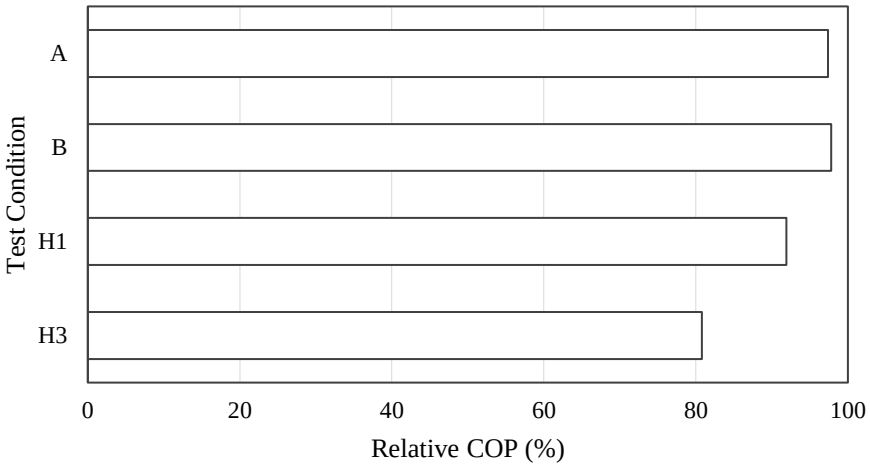


Fig. 3. COP of R-468C relative to R-410A at cooling and heating modes

1. Refrigerant charge,
2. Compressor speed, and
3. EEV opening.

3.2.1. Cooling mode

At each refrigerant charge, the EEV opening and thus the gas cooler inlet pressure was adjusted to maximize the COP. Then the corresponding compressor speed was set accordingly in order to match the cooling capacity of 17.6 kW. Summary of the test results at optimum refrigerant charge are shown in Table 2. Uncertainty was determined as ±1.0% for COP and ±0.3% for capacity. LFR3 operated at a higher compressor speed compared to R-744, but showed higher COP and compressor volumetric efficiency (η_{vol}) while exhibiting 20% lower optimal gas cooler pressure.

Table 2. Test summary of R-744 and LFR3 at A condition

Fluid	COP	Optimal gas cooler pressure (MPa)	Refrigerant charge (kg)	Compressor frequency (Hz)	η_{vol}
R-744	2.51	9	4.1	40.9	0.69
LFR3	2.64	7.3	4	47.1	0.75

Compressor speed and refrigerant charge found in A condition were kept constant for B condition tests. The result trends for B condition were consistent to those observed in A condition, Table 3. The consistently higher cooling efficiency of LFR3 over R-744 was also reported when tested in a heat pump system for bus applications [4].

Table 3. Test summary of R-744 and LFR3 at B condition

Fluid	COP	Optimal gas cooler pressure (MPa)	Refrigerant charge (kg)	Compressor frequency (Hz)	η_{vol}
R-744	3.3	7.0	4.1	40.9	0.72
LFR3	3.49	6.4	4	47.1	0.77

3.2.2. Heat pump mode

As the prototype unit was not assembled as a reversable system, the unit needed to be modified and re-piped prior to heat pump testing. It was also noted that the IHX was probably oversized and the combination of IHX and the accumulator contributed to additional pressure drop. Therefore, the accumulator was removed during the conversion. For cooling mode, the evaporator was mounted in parallel flow in order to have the same heat exchanger performing in counter flow in heat pump mode. As LFR3 is a zeotropic refrigerant, it was expected that the performance would further improve from the flow direction. The EEV opening was adjusted to maximize the COP while refrigerant charge and compressor frequency were kept at the previously determined values. The uncertainty was found to be ±0.6% for COP and ±0.3% for capacity.

Table 4. Test summary of R-744 and LFR3 at H1 condition

Fluid	COP	Capacity (kW)	Optimal gas cooler pressure (MPa)	η_{vol}
R-744	3.27	21.9	8.2	0.72
LFR3	3.26	21.5	7.0	0.70

LFR3 and R-744 showed similar efficiencies, which is contrary to previous testing of LFR3 in an air-source heat pump water heater designed for R-744 where 15% higher heating capacity and 35% higher COP of LFR3 relative to R-744 were reported [5]. These very high pressure refrigerants, however, showed approximately 25% improvement in heating capacities at the H1 condition compared to R-410A. The noticeable frost formation during the LFR3 runs may have led to lower than expected COP value, which is due to the combination of glide as well as parallel flow in the evaporator that brought down the evaporator inlet temperature to below 0°C.

Further testing on H3 condition is on-going and will be presented at the conference.

4. Conclusion

R-468C and LFR3 were evaluated as low GWP solutions in a packaged heat pump system. R-468C showed comparable performance as a R-410A alternative while providing more than 85% reduction in GWP. It should be noted that R-468C is an A2L safety class per ASHRAE 34 and should only be used in systems designed for mildly flammable refrigerants.

It was also demonstrated that it is feasible to use very high pressure refrigerant LFR3 while providing matching capacity and footprint as existing commercially available equipment. The heating results were particularly promising considering that a reciprocating compressor was used in lieu of a higher efficiency scroll compressor. While LFR3's COP was measured to be approximately 20% lower than R-410A in average, the

results are encouraging given that they were obtained from a first-generation prototype unit. Proper sizing and selection of components with optimized heat exchanger designs will allow for further performance improvement.

Disclaimer

Although all statements and information contained herein by Koura Global are believed to be of sound scientific judgement, they are presented without guarantee or warranty of any kind, expressed or implied. Information provided herein does not relieve the user from the responsibility of carrying out its own tests and experiments, and the user assumes all risks and liability for use of the information and results obtained. Statements or suggestions concerning the use of materials and processes are made without representation or warranty that any such use is free of patent infringement and are not recommendations to infringe on any patents.

Nomenclature

η_{vol}	Compressor volumetric efficiency

References

[1] United States Department of Energy. Industrial Decarbonization Roadmap. *DOE/EE*-2635; 2022.
[2] AHRI Standard 210/240-2023(2020), Performance Rating of Unitary Air-conditioning & Air-source Heat Pump Equipment, 2023, Air-Conditioning, Heating, and Refrigeration Institute, 2311 Wilson Boulevard, Suite 400, Arlington, VA 22201, U.S.A.
[3] Low R., 2021. "High-Performance Air-Conditioning Refrigerants With Low GWP," 2nd IIR Conference on HFOs and Low GWP blends. Japan.
[4] Petersen, M., Kujak, S., Galanský, M., Houdek, P., Kolda, M., Nayak, G., 2022. "Comparison of R744 and R744-based HFC/HFO blend in mass transit mobile AC and HP applications," 15th IIR-Gustav Lorentzen conference on Natural Refrigerants. Trondheim, Norway.
[5] Low R., 2020. "Pushing The Envelope: Extending The Range And Performance Of R-744," IIR International Rankine 2020 Conference – Heating, Cooling and Power Generation. Glasgow, UK.

14th IEA Heat Pump Conference
15-18 May 2023, Chicago, Illinois

Investigation of the performance of a ground-coupled CO_2 heat pump for space and water heating

Thor Alexis Sazon[a*], Homam Nikpey[a]

[a]University of Stavanger, Kjell Arholms gate 41, Stavanger 4021, Norway

Abstract

A parametric investigation on a ground-coupled CO_2 heat pump for space and water heating was performed using a model developed with Modelica. The CO_2 heat pump, with a tripartite gas cooler configuration, was modeled using the Thermal Systems library and then calibrated with experimental data, while the Borehole Heat Exchangers (BHEs) were modeled using the MoBTES library and sized following the ASHRAE methodology. Different design and operating parameters were varied to see their effects on the system's coefficient of performance (COP). Simulations showed that there is an optimal high-side pressure that maximizes the COP. The evaporator's water-side mass flow, the BHE's length, the grout's thermal conductivity, and the compressor speed all have an inverse relationship with the COP, while the low-side pressure of the heat pump and the valve's throttle area are directly related to it. However, changing these parameters to increase the COP has limits because doing so decreases the amount of heat that the system can deliver. This study serves as a starting point for the design and optimization of a bigger system that utilizes other low-temperature resources with the CO_2 heat pump.

© HPC2023.
Selection and/or peer-review under the responsibility of the organizers of the 14th IEA Heat Pump Conference 2023.

Keywords: trans-critical CO_2 heat pump; borehole heat exchanger; Modelica; Space and water heating

1. Introduction

Heating/cooling accounts for around 50% of the total energy consumption in Europe, the majority of which (~45%) comes from the residential sector [1]. Burning fuels just to provide for the thermodynamically-lower grade demands of space and water heating, which only requires ~40 - 80 °C, is highly inefficient. It wastes the thermodynamic potential of combustible fuels, resulting in large exergy losses, and leads to emissions that could have been avoidable [2]. Heat pumps are devices that can harness heat from low-temperature resources and increase it to useful temperature levels. Given the substantial consumption associated with residential heating, displacing the inefficient use of combustible fuels through heat pumps, which also promotes the use of diversified and local energy resources, can contribute to increasing energy security and to decreasing CO_2 emissions.

Most heat pumps nowadays operate through a sub-critical vapor-compression cycle that uses Hydrofluorocarbons (HFCs) as working fluid. HFCs replaced the once widely-used ozone-depleting Chlorofluorocarbons (CFCs) because they exhibited similarly good performance, efficiency, low toxicity, and non-flammability. However, they were later discovered to be very potent greenhouse gases. Recent initiatives seem to point out the inevitable phase-out of HFCs. The EU's F-gases regulation (EC517/2014) aims to gradually decrease the usage of important fluorinated gases in the EU, such as R404A, R410A, R407C, and R134a to one-fifth of 2014 in 2030 [3]. In addition, in January 2019, the Kigali amendment to the Montreal Protocol, wherein several countries committed to cutting the production and consumption of HFCs by more than 80% over the next 30 years, entered into force [4].

* Corresponding author. Tel.: +47-51-832534
E-mail address: thor.a.sazon@uis.no

The growing environmental concerns about the use of conventional synthetic heat pump refrigerants have revived the interest in natural working fluids. Carbon dioxide is one of the few non-toxic and non-flammable natural refrigerants that have zero effect on ozone layer destruction and a substantially lower global warming potential (GWP) relative to commercially available alternatives [5]. Lorentzen first proposed the modern use of CO_2 in a trans-critical heat pump cycle [6]. One of the notable configurations of the CO_2 heat pump includes the tri-partite gas cooler, first proposed by Stene [7], [8], as a way to allow simultaneous and separate production of space heating and domestic hot water in an integrated design that simplifies the heat pump layout and piping requirements.

Due to substantial irreversibility during compression and gas cooling, the performance of a CO_2 heat pump is generally lower than that of a system using a subcritical cycle [9]. In addition, the reliability of the system is not as good because of the large performance variations with operating conditions. One of the ways to improve the performance of the CO_2 heat pump is by integrating it with borehole heat exchangers (BHEs). Generally, ground temperature down to depths of 5 - 10 m is influenced by solar radiation and ambient air temperature. Below 15 m, the ground temperature remains undisturbed by seasonal temperature variations [2], [10]. The undisturbed ground temperature then increases with depth due to the heat from within the Earth's core [11]. Stable temperatures on the ground provide a more reliable heat pump performance as compared to using air as the heat source, given that air temperature varies greatly with the weather. Vertical BHEs are usually around 50-150 m in depth and may have a single U-type, double U-type, or coaxial configuration [12].

Wang et al. [13] compared the performance of a CO_2 trans-critical heat pump system that uses a U-tube BHE with the performance of conventional R22 and R134a systems. Their results suggest that if the system is applied for space conditioning and tap water heating, where high water temperature is desired, then it could reach efficiencies similar to that of a conventional R134a cycle. Kim and Chang [14] focused on the development of a model that could perform a steady-state thermodynamic performance analysis of a CO_2 geothermal heat pump system that implements a suction gas heat exchanger (SGHX). The model was implemented in Digital Visual Fortran with the graphical user interface (GUI) implemented in Visual Basic. Their simulations indicated that, in cooling mode, the COPs of the cycle with SGHX were 2-6% better than the typical trans-critical CO_2 heat pump cycle COPs. However, in heating mode, the configuration that uses an SGHX got slightly smaller COPs than those of the basic cycle. Kim et al. [9] performed a simulation study of a hybrid solar-geothermal CO_2 heat pump system for residential space heating in the winter. They considered a system configuration where heat from both the solar collector and heat pump is collected in a thermal energy storage tank whose temperature is controlled at a designated level. Engineering Equation Solver (EES) was used to model the system components and calculate the thermodynamic properties of the refrigerant. This study is also limited to steady-state performance calculations.

Replacing HFCs with alternative refrigerants requires systems with comparable efficiencies. If the new system has significantly lower efficiency and if the electricity that runs the compressor is mainly generated with the use of fossil fuels, the replacement of the existing system will just contribute more to global warming [15]. To push for wider technology uptake, careful investigation of the effects of various design and operating conditions on the performance and operating characteristics of the system is needed. Bellos and Tzivanidis [16] performed a parametric investigation on a ground-coupled CO_2 heat pump using steady-state calculations with EES. Their analysis shows the effects of ten parameters on the system's coefficient of performance, five from the heat pump and five from the BHE.

Similarly, this work performs a parametric investigation on a ground-coupled CO_2 heat pump for simultaneous space and water heating using a system model developed with the Modelica language [17]. Modelica is an equation-based, object-oriented modeling language that allows dynamic simulations. While most studies performed steady-state calculations, the model developed here can consider time-varying system characteristics, particularly the reduction of ground temperature as it is used for space and water heating. Different design and operating parameters from both the heat pump side and the BHE side were varied to see their individual effects on the system's COP. The result of this study serves as a starting point for the design and optimization of a bigger system that utilizes other low-temperature energy resources integrated with the CO_2 heat pump, and the model developed can be utilized for further simulation studies that entail time-varying inputs and responses.

2. Methods

In this work, the model was developed using Modelica with the Dymola [18] user interface. The CO_2 heat pump was modeled using the Thermal Systems library [19] in Dymola and then calibrated with experimental

data; while the BHEs were modeled using the MoBTES library [20] and then sized based on the ASHRAE methodology [21].

2.1. CO_2 heat pump modeling

The CO_2 heat pump model developed in this work was based on a 6.5 kW prototype unit constructed and tested by Stene [7, 8]. It consists of the counter-flow tripartite gas coolers, an evaporator, a compressor, a throttle valve, an SGHX, a sub-cooler, and a low-pressure receiver. Although the prototype can function in three modes (space heating only, domestic hot water (DHW) heating only, and simultaneous space and DHW heating), the model in this work was only calibrated for simultaneous space and DHW heating. Preheating of the incoming water from the supply line occurs at the first gas cooler while further increasing its temperature to a useful level is achieved at the third gas cooler. The second gas cooler separately provides the thermal energy needed for space heating.

This reference system was then converted into a Modelica model using the Thermal Systems library in the Dymola GUI. The Thermal Systems library, also synonymous with the TIL suite, is a commercial Modelica library for modeling thermo-fluid systems. It can be used to model various components, such as heat pump cycles, hydraulic networks, ventilation, and so on. It uses the TSMedia library to calculate the thermophysical properties of fluid and fluid mixtures [19].

The CO_2 heat pump model developed is shown in Fig. 1. The control strategy implemented includes: (a) controlling the DHW temperature by adjusting the water pump speed, (b) controlling the supply temperature for SH by adjusting the water pump speed, (c) controlling the high-side pressure of the heat pump by adjusting the throttle area of the valve, and (d) controlling the low-side pressure by adjusting the compressor speed. All of these were implemented in the model using proportional-integral (PI) controllers (Fig. 1).

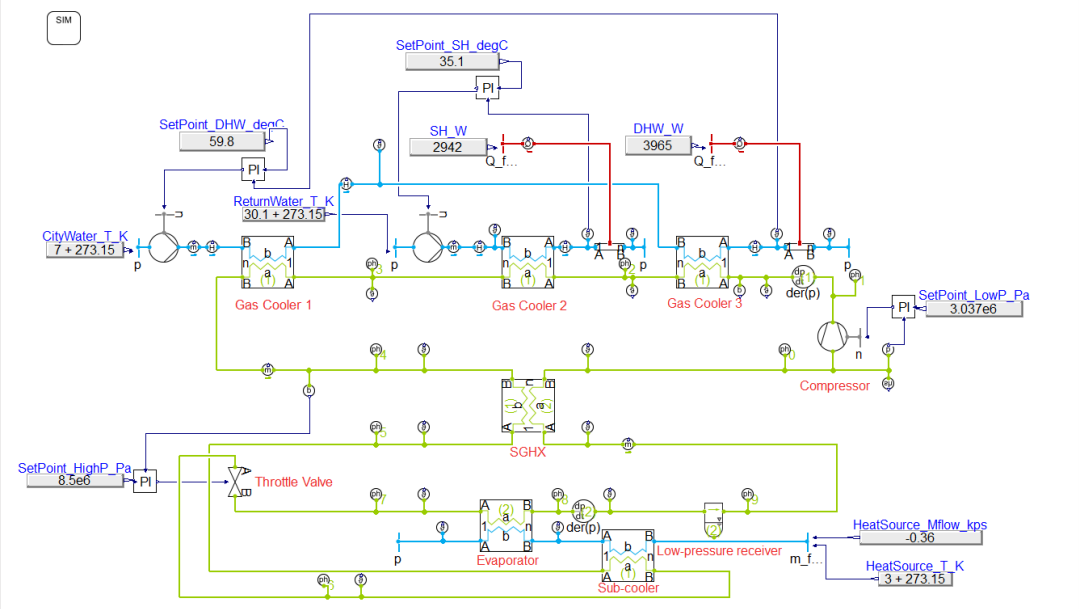


Fig. 1. CO_2 heat pump model developed in Modelica (Dymola) using the Thermal Systems library

Table 1 shows the design conditions of the prototype CO_2 heat pump unit when utilized for simultaneous space and water heating. At design conditions, the heat pump unit gives off ~3 kW of heat to a floor heating system at a supply/return temperature of 35/30 °C and ~3.5 kW to heat to the DHW from ~5 °C to ~60 °C. The compressor discharge pressure is around 85 to 90 bars, and the evaporation temperature is -5 °C. The specifications for the compressor used in the prototype are given in Table 2.

Table 1. Design conditions for the prototype CO_2 heat pump unit for simultaneous space and water heating (taken from [7])

Component	Parameter	Value
Compressor	Suction pressure (-5°C)	3.046 MPa
	Suction temperature	0°C
	Discharge pressure	8.5 to 9.0 MPa
	CO_2 mass flow rate	~1.40 kg/min
Evaporator	Evaporation temperature	-5°C
	LMTD	~5 K
Tripartite gas cooler	Space Heating (SH) -Water temperatures	35/30 °C
	SH - Heating Capacity	~3 kW
	SH - Temperature approach	<0.2 K
	DHW - Water temperatures	5/60 °C
	DHW - Heating capacity	~3.5 kW
	DHW - Temperature approach	<3 K

Table 2. Specifications for the rolling piston compressor (prototype) (taken from [7])

Type	Hermetic two-stage rolling piston unit operated as a single-stage unit (LP + HP)
Operating range	1800 to 7200 rpm (39 to 120 Hz)
Displacement volume	3.33 cm^3/rev (LP) and 1.88 cm^3/rev (HP)
Swept volume	1.439 m^3/h at 7200 rpm
Max operating pressure	14 MPa
Max discharge temperature	125 °C
Motor type	Digitally controlled brushless motor – 4 poles
Maximum power input	2500 W

During the calibration of the CO_2 heat pump, the mass flow and temperature of the BHE fluid (propylene glycol) entering the evaporator were fixed at 0.36 kg/s and 3°C, respectively. These were assumed using some rule of thumb given in the ASHRAE handbook [21] since this information was not available in the reference material used.

The measured data for the design condition at 85 bars were used to calibrate the model. The information available in Stene's work [7] was used to set the values of some parameters in the different component models, including the tube diameters of all the tube-in-tube heat exchangers, as well as their weights, material of construction, and length; the size of the low-pressure receiver; and the compressor displacement and operating range. The parameters adjusted during calibration include (a) the coefficient of heat transfer in each heat exchanger and (b) the isentropic and overall efficiencies of the compressor. A compressor model with fixed efficiencies was utilized for simplicity.

2.2. BHE modeling and sizing

Fig. 2 shows the BHE model developed in Dymola using the MoBTES library [20]. The MoBTES library is a free and open Modelica library that comprises components for the simulation of BHEs and Borehole Thermal Energy Storage (BTES) systems. It is built with objects from the Modelica Standard Library (MSL) for fluid heat flow and heat transfer. MoBTES was developed in accordance with MSL version 3.4, but in this work, it was revised to work with MSL version 4.0.

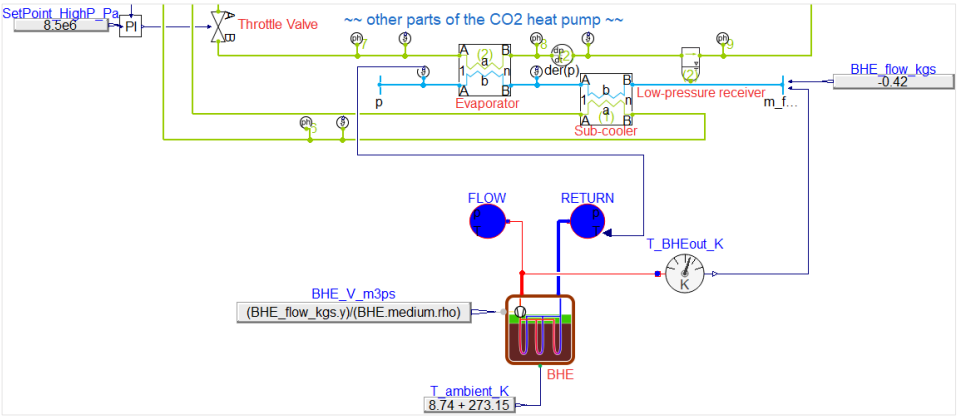


Fig. 2. The BHE model in Dymola (with a portion of the CO_2 heat pump model to show how they are connected)

The BHE was connected to the CO_2 heat pump model by considering the BHE fluid mass flow rate and temperatures. The temperature of the fluid entering the heat pump (evaporator's water side) was assumed equal to the temperature of the fluid exiting the BHE, while the temperature of the fluid exiting the evaporator's water-side was assumed equal to the temperature of the fluid entering the BHE. The mass flow rate of the fluid circulating through the BHE and the water side of the evaporator was calculated by following the ASHRAE methodology. For simplicity, the ambient temperature was fixed to a constant value equivalent to the annual average temperature in Western, Norway.

The sizing of the BHE was implemented using the ASHRAE methodology [21]. In this method, the length of the borehole required for heating purposes L_h is calculated using the Equation below.

$$L_h = \frac{Q_a R_{sa} + Q_h (R_b + PLF_m R_{sm} + F_{sc} R_{sd})}{T_0 - \frac{T_{in,hp} + T_{out,hp}}{2} - T_p} \cdot \frac{COP_h - 1}{COP_h} \quad (1)$$

Where Q_a is the net annual average heat transfer to the ground; PLF_m is the part-load factor for the design month; R_{sa}, R_{sm}, and R_{sd} are the effective thermal resistances of the ground to the annual pulse, monthly pulse, and daily pulse, respectively; F_{sc} is the short-circuit heat loss factor; R_b is the overall borehole thermal resistance; and T_p is the temperature penalty for the interference of adjacent bores.

The overall thermal resistance R_b is the sum of the heat exchanger thermal resistance R_p, which is the average of the thermal resistance of the tube R_{tube} and the film thermal resistance of the fluid R_{film}, and the thermal resistance of the grout R_{grt}.

$$R_b = R_p + R_{grt} \quad (2)$$

$$R_p = \frac{R_{tube} + R_{film}}{2} \quad (3)$$

$$R_{film} = \frac{1}{\pi d_{in} h_f} \quad (4)$$

$$R_{tube} = \frac{ln \frac{d_{out}}{d_{in}}}{2\pi k_{tube}} \quad (5)$$

$$R_{grt} = \left(k_{grt} b_0 \left[\frac{d_p}{d_{out}} \right]^{b_1} \right)^{-1} \quad (6)$$

Where d_{in}, d_{out}, and d_p are the inner, and outer diameters of the tube, and the borehole diameter, respectively; h_f is the convective heat transfer of the fluid; k_{tube} and k_{grout} are the conductive heat transfer coefficients of the tube and the grout, respectively; and b_0 and b_1 are coefficients found in the ASHRAE handbook specific to the position of the tube in the borehole.

The heat transfer coefficient of the fluid h_f is calculated using the Colburn equation [22]. In this work, the Reynold's number Re has values in the turbulent regime, so it follows that:

$$Nu = 0.023 Re^{0.08} Pr_f^{1/3} \quad (7)$$

$$Nu = h_f d_{in}/k_f \quad (8)$$

$$Re = 4m_{f,0}/\pi d_{in}\mu_f \quad (9)$$

$$Pr_f = \mu_f c_{p,f}/k_f \quad (10)$$

Where Nu is the Nusselt number; Pr is the Prandtl number; k_f is the thermal conductivity of the fluid; $m_{f,0}$ is the mass flow of the geothermal fluid in one borehole; μ_f is the fluid viscosity; and $c_{p,f}$ is the geothermal fluid heat capacity.

2.3. Parametric simulation runs

The parametric investigation was implemented by varying the values of chosen parameters one at a time. Table 3 shows the heat pump and BHE parameters varied, with their default values and the ranges of the variations implemented. Five of these parameters pertain to the heat pump and the other three pertain to the BHE. During these simulation runs, the space and water heating demand were fixed to the value used during the calibration simulation. The mass flow of the BHE fluid was also fixed to the value calculated from the ASHRAE methodology (0.42 kg/s). Each simulation case was run for 980 hours [21]. Note that this only covers the full load hours in a year. Since the COP of the system changes with time, given that the input temperature of the heat source changes with utilization, only the COP values at the end of the simulation time were compared.

Table 3. Parameters varied during the parametric analysis

Parameter Varied	**Default Value**	**Range of variation**
Heat pump high-side pressure, bar	85	77 - 100
Heat pump low-side pressure, bar	30.37	29.69 - 31
Throttle valve area, $x10^{-7}$ m^2*	2.5	2.1 - 2.7
Compressor speed, Hz*	115	108 - 120
Evaporator water-side flow rate, kg/s	0.42	0.3 - 0.5
BHE length, m	95	85 - 110
BHE spacing, m	6	3 - 10
Grout thermal conductivity, W/m-K	1.5	1 - 5

**Varying these parameters requires the removal of the high- and low-side pressure controllers*

3. Results and discussions

In this work, the model was developed using Modelica with the Dymola [18] user interface. The CO_2 heat pump was modeled using the Thermal Systems library [19] in Dymola and then calibrated with experimental data; while the BHEs were modeled using the MoBTES library [20] and then sized based on the ASHRAE methodology [21].

3.1. Calibration of the CO_2 heat pump model

The heat pump model was calibrated using the measured data at the high-side pressure of 85 bars; this represents the design conditions of the heat pump. Some component specifications were obtained from the reference material while some were determined through the calibration process. Table 4 shows the values of the heat exchanger parameters whileTable 5 shows the parameters for the other heat pump components, such as the low-pressure receiver and the compressor. During calibration, the values of the heat transfer coefficients were assumed equal for the two sides of each heat exchanger and then adjusted so that the heat flows and the available inlet/outlet temperatures (Table 1 (water) and Table 6 (CO_2)) and temperature approach data (Table 1) are matched. Some of them required to have different water-side and CO_2-side heat transfer coefficients to match the data. The efficiencies of the compressor were adjusted to simulate measured heat flows, power consumption and CO_2 inlet temperature. The effective isentropic efficiency (Table 4) also takes into account the supplied mechanical power.

Table 4. CO_2 heat pump heat exchanger specifications

	Gas Cooler 1	**Gas Cooler 2**	**Gas Cooler 3**	**Evaporator**	**Sub-cooler**	**SGHX**
CO_2-side tube length, m	14	15	3.5	12	6	2.3
CO_2-side tube inner diameter, m	0.006	0.006	0.006	0.008	0.008	0.08/0.12
CO_2-side heat transfer coefficient, W/m^2-K*	9000	7000	3500	6500	150	550
Water-side tube length, m	14	15	3.5	12	1	NA
Water-side tube inner diameter, m	0.012	0.018	0.012	0.02	0.025	NA
Water-side heat transfer coefficient, W/m^2-K*	9000	7000	5500	4500	150	NA
Wall thermal resistance, K/W (Stainless Steel)	0.00025	0.00025	0.00025	0.00025	0.0001538	0.00025
Mass, kg	13	18	6	17	17	2.5

**Values determined from the calibration process*

Table 5. Other CO_2 heat pump component specifications

Compressor		
Displacement, m^3	3.33x10^{-06}	
Volumetric Efficiency*	0.85	
Isentropic Efficiency	0.8	
Effective Isentropic Efficiency*	0.62	
Pumps	DHW	SH
Volume of liquid in pump, m^3	1.60x10^{-05}	1.00x10^{-04}
Volumetric flow rate at nominal speed, m^3/s	6.00x10^{-05}	6.00x10^{-05}
Pressure increase at 0 flow, bar	2	2
Speed, Hz	5 - 150	5 - 150
Nominal efficiency	0.4	0.4
Low-pressure receiver		
Volume, m^3	0.004	
Initial filling level	0.5	

**Values determined from the calibration process*

Table 6 gives the results of the CO_2 heat pump calibration runs. The model was calibrated against the data for P_{GC} = 85 bars, while the other measured data were used to test the calibrated model. Calibration and test errors were obtained by comparing the measured and simulated COPs. As shown, the error generated by the calibrated model increases when it is used to simulate an off-design condition (design conditions: 85 to 90 bars, as given in Table 1). This can be partly attributed to the choice of using a simplified compressor model that assumes constant efficiencies.

Table 6. Results of the calibration CO_2 heat pump unit at ~60°C DHW temperature, ~35/30°C supply /return temperature for SH (data taken from [7]; $Q_{DHW} = Q_{GC1} + Q_{GC3,} Q_{GC2}$ is the heat for SH, T_E is the evaporator temperature in the CO_2 loop)

Data type	**P_{GC}, bars**	**T_E, °C**	**Q_{GC}, W**	**Q_{DHW}, W**	**Q_{GC1}, W**	**Q_{GC2}, W**	**Q_{GC3}, W**	**Power$_C$, W**	**Tin/out$_{CO2_GC}$, °C**	**$M_{CO2,}$ kg/s**	**COP**	**Error**
Measured*	85	-5.1	6907	3965	1608	2942	2357	1775	86.40/9.80	1.441	3.89	-0.26%
Calibrated	85	-5.1	6710	3776	1534	2934	2242	1730	86.56/9.80	1.449	3.88	
Measured*	89.8	-5	6947	4351	1550	2596	2801	1878	90.60/8.50	1.442	3.70	1.89%
Simulated	89.8	-5	6711	4074	1480	2637	2594	1779	90.76/8.17	1.417	3.77	
Measured	80.3	-5.1	6230	3502	1674	2728	1828	1699	81.60/18.00	1.440	3.67	4.90%
Simulated	80.3	-5.1	6595	3615	1707	2981	1907	1715	83.82/15.41	1.500	3.85	

**Design conditions*

3.2. Modeling and sizing of the BHE

The parameters assumed to calculate the size of the BHE using the ASHRAE methodology are given in Table 7. As shown, it was assumed that 4 BHEs are needed to provide the ~6.5 - 7 KW heat required by the system. A yearly equivalent heating full-load hours of 980 h then was assumed based on the data given in the ASHRAE handbook for Portland, Maine [21], assuming that the weather there is comparable to that of western Norway. The ground was assumed to have the characteristics of Slate, one of the common rock types in some parts of Norway [23] while the thermal gradient was assumed to be 0.0125 K/m, similar to that of some wells drilled in Bergen, Norway [24].

Following the procedure in the ASHRAE method, a borehole length of 82 m/well was calculated. Consequently, the calculated BHE length, as well as the assumed BHE parameters, were inputted to the BHE model, and a simulation was run to see if it can maintain the output of the heat pump system to around 6.7 kW (value used in the calibration) for the equivalent full-load hours of 980 h.

The result of the simulation shows that a BHE length of 82 m was not enough to maintain the output of the heat pump system to at least 6.7 kW for 980 h of continuous operation. Of course, in reality, the heat pump is not expected to be operated continuously for 980 h at full load, so this BHE length might already be enough for the expected usage. However, it is normal to oversize the BHE to take into account the changes in the performance that can be expected from the changes in ground temperature upon utilization [25]. Therefore, the BHE length was increased until simulation shows that it can support at least 6.7 kW by the end of 980 h of continuous full-load run. From this, a borehole length of 95 m was determined and used as the base value for the parametric simulation runs.

Table 7. BHE parameters

BHE parameter	Value
Average ambient temperature, °C	7
Geothermal gradient, K/m	0.0125
Ground density, kg/m^3	2760
Ground specific heat, J/kg-K	920
Ground thermal conductivity, W/m-K	2.1
Layout	Rectangle
BHE type	Single U
Number of BHEs	4
Borehole diameter, m	0.15
Tube inner diameter, m	0.034
Tube thickness, m	0.003
Tube thermal conductivity, W/m-K	0.4
Shank spacing, m	0.08
Number of BHE in series	1
Grout density, kg/m^3	1900
Grout thermal capacity, J/kg-K	1300
Grout thermal conductivity, W/m-K	1.5
Calculated BHE length, m/well*	82
Adjusted BHE length, m/well**	95

**Calculated using the ASHRAE method **Determined through simulation*

3.3. Parametric Simulation Runs

Simulation runs were performed to see the effects of varying some of the heat pump and BHE design and operating parameters on the COP (Table 3). Before the parametric runs, the performance of the base model, which uses the default values of the parameters, was determined. Fig. 3 shows the COP, the heat extracted from the BHE, the total heat from the gas coolers, and the power input to the compressor with the time of the base model. It can be seen that the heat derived from the BTES and consequently from the gas coolers decreased with time. This is expected as thermal energy from the ground, as well as its temperature (Fig. 4), would decrease if it were continuously used to provide the heating demand without recharge. Nonetheless, the

COP throughout the full-load period of 980 h remained between 3.8 and 4.

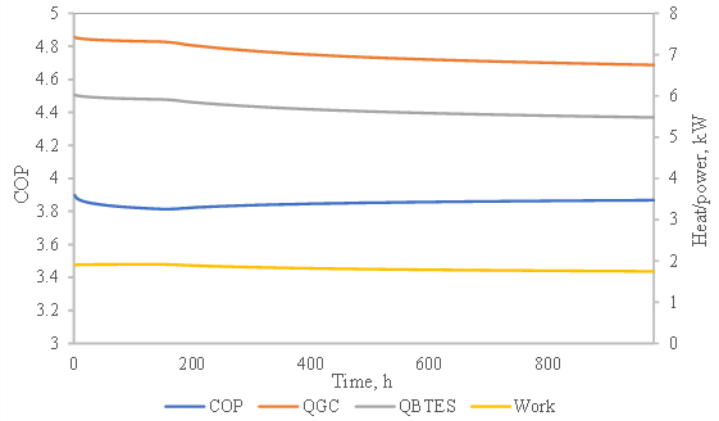


Fig. 3. Performance of the base model with time

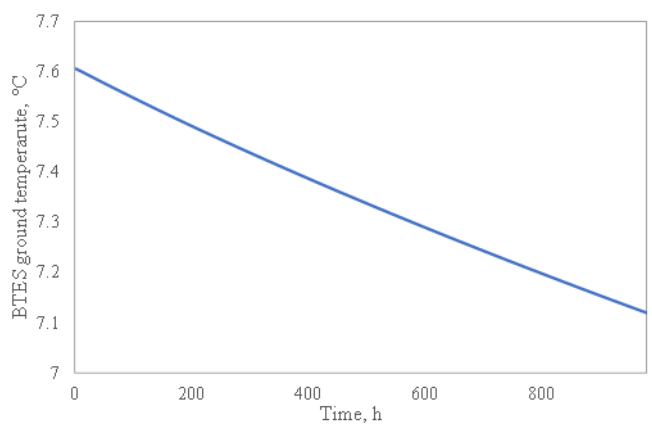


Fig. 4. Ground temperature with time

Fig. 5 gives the results of the parametric simulation runs. To make the comparison easier, only the performance values at the end of the 980 h simulation runs were used. It should be noted that the variation in the compressor speed and throttle valve area were both implemented by removing the PI controllers that maintain the high-side and low-side pressure at fixed levels. This means that for these two sets of simulation runs, the high- and low-side pressure varies with the parameter variation, unlike in the other parametric simulation runs performed here. Stene [7] pointed out that the high-side pressure of the CO_2 heat pump is controlled by using the low-pressure receiver and by adjusting the opening of the expansion valve, which temporarily changes the balance between the mass flow rate in the compressor and the valve. Reducing the valve opening accumulates more CO_2 in the gas cooler piping, thereby increasing the high-side pressure until a new balance point for the mass flow rate in the compressor and the valve is reached. The extra CO_2 charge needed to increase the pressure is boiled off from the liquid reservoir in the receiver. On the other hand, opening the expansion valve reduces the high-side pressure and the surplus CO_2 is stored as a liquid in the receiver.

It can be seen from Fig. 5a that an optimum high-side pressure that maximizes the COP of the system is present. In this case, it occurs at the design operating pressure of 85 bars. The compressor speed, the evaporator's water-side mass flow, the BHE's length, BHE spacing, and the grout's thermal conductivity all have an inverse relationship with the COP. However, as any of these parameters were lowered to increase the COP, the amount of heat that the system can deliver also decreased. This points out that they can only be decreased to certain limits when they could still sufficiently provide the value of the heat demand. On the other hand, as the low-side pressure of the heat pump and the throttle valve area were increased, the COP also increased. Similarly, there are also limits on these since increasing their respective values decreases the heat that could be delivered by the system.

Given the assumed variation range of the parameters, it can also be observed that the performance of the heat pump is most reactive to the high-side (discharge) heat pump pressure and the throttle vale area, followed

by the low-side (suction) heat pump pressure and the compressor speed. Conversely, it is least reactive to the variation in the BHE spacing and the grout thermal conductivity.

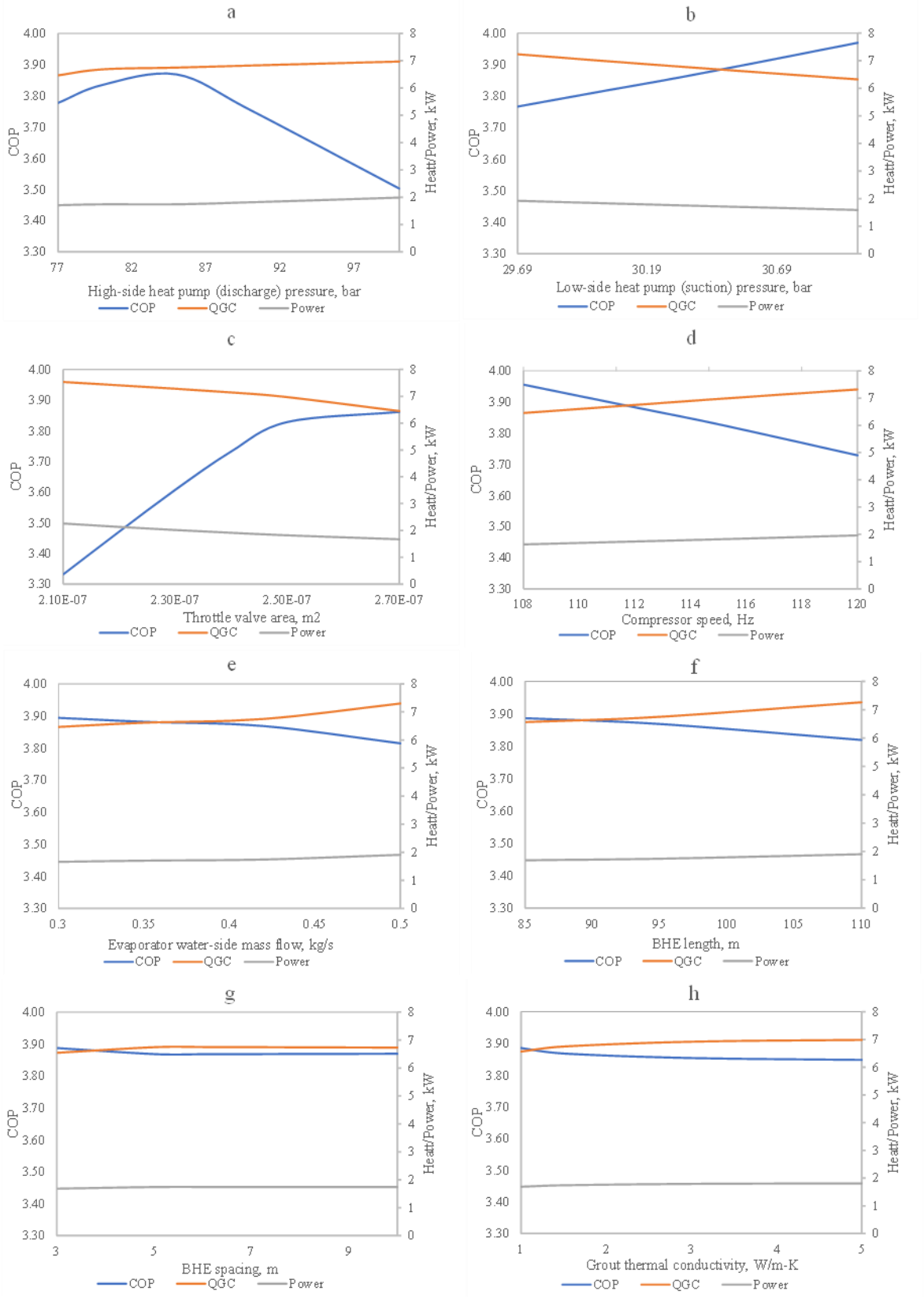


Fig. 5. Variation of COP with different heat pump and BHE parameters: (a) high-side pressure, (b) low-side pressure, (c) throttle valve area, (d) compressor speed, (e) evaporator water-side mass flow rate, (f) BHE length, (g) BHE spacing, and (h) grout thermal conductivity

4. Conclusion

A parametric analysis was performed on a ground-coupled CO_2 heat pump system that is designed to simultaneously provide for both space and water heating demands. The CO_2 heat pump model was first developed and calibrated using data from an experimental setup. Afterward, the BHE was modelled and then sized using the ASHRAE methodology.

The calibration shows that the model performs closely to the experimental rig when it operates within design conditions. The results of the parametric studies show that an optimum high-side pressure maximizes the COP of the system. The compressor speed, the evaporator's water-side mass flow, the BHE's length, and the grout's thermal conductivity all have an inverse relationship with the COP, while the low-side pressure of the heat pump and the throttle area of the expansion valve are directly related to it. However, changing all these parameters to increase the COP has limits since they all impose a decrease in the amount of heat that can be delivered by the system. It was also observed that the performance of the heat pump is most reactive to the high-side (discharge) heat pump pressure and the throttle vale area, followed by the low-side (suction) heat pump pressure and the compressor speed. Conversely, it is least reactive to the variation in the BHE spacing and the grout thermal conductivity.

This work is planned to be further extended to investigate other performance indicators, such as the total annual cost, seasonal performance factor, and ground temperature change. It is also planned to expand the system to include a solar thermal collector component, a tank thermal energy storage, and energy demand specifications that follow realistic patterns for a given year.

Acknowledgments

This paper is part of the Ph.D. work funded internally by the University of Stavanger.

References

[1] European Commission, An EU Strategy on Heating and Cooling. 2016. Accessed: May 23, 2022. [Online]. Available: https://eur-lex.europa.eu/legal-content/EN/TXT/?qid=1575551754568&uri=CELEX:52016DC0051

[2] T. Sliwa and M. A. Rosen, "Natural and Artificial Methods for Regeneration of Heat Resources for Borehole Heat Exchangers to Enhance the Sustainability of Underground Thermal Storages: A Review," Sustainability, vol. 7, no. 10, Art. no. 10, Oct. 2015, doi: 10.3390/su71013104.

[3] "EU legislation to control F-gases." https://ec.europa.eu/clima/eu-action/fluorinated-greenhouse-gases/eu-legislation-control-f-gases_en (accessed Apr. 01, 2022).

[4] United Nations, "The Kigali Amendment (2016): The amendment to the Montreal Protocol agreed by the Twenty-Eighth Meeting of the Parties (Kigali, 10-15 October 2016) | Ozone Secretariat," 2016. https://ozone.unep.org/treaties/montreal-protocol/amendments/kigali-amendment-2016-amendment-montreal-protocol-agreed (accessed Mar. 18, 2021).

[5] R. U. Rony, H. Yang, S. Krishnan, and J. Song, "Recent Advances in Transcritical CO2 (R744) Heat Pump System: A Review," Energies, vol. 12, no. 3, Art. no. 3, Jan. 2019, doi: 10.3390/en12030457.

[6] G. Lorentzen, "Trans-critical vapour compression cycle device," WO1990007683A1, Jul. 12, 1990 Accessed: Feb. 17, 2021. [Online]. Available: https://patents.google.com/patent/WO1990007683A1/en

[7] J. Stene, Residential CO2 Heat Pump System for Combined Space Heating and Hot Water Heating. Fakultet for ingeniørvitenskap og teknologi, 2004. Accessed: May 23, 2022. [Online]. Available: https://ntnuopen.ntnu.no/ntnu-xmlui/handle/11250/233381

[8] J. Stene, "Residential CO2 heat pump system for combined space heating and hot water heating," International Journal of Refrigeration, vol. 28, no. 8, pp. 1259–1265, Dec. 2005, doi: 10.1016/j.ijrefrig.2005.07.006.

[9] W. Kim, J. Choi, and H. Cho, "Performance analysis of hybrid solar-geothermal CO2 heat pump system for residential heating," Renewable Energy, vol. 50, pp. 596–604, Feb. 2013, doi: 10.1016/j.renene.2012.07.020.

[10] S. Gehlin, "Thermal response test: method development and evaluation," Doctoral Thesis, Luleå University of Technology, Luleå, Sweden, 2002. [Online]. Available: http://www.diva-portal.org/smash/get/diva2:991442/FULLTEXT01.pdf

[11] D. Banks, An Introduction to Thermogeology: Ground Source Heating and Cooling. John Wiley & Sons, 2009.

[12] G. Florides and S. Kalogirou, “Ground heat exchangers—A review of systems, models and applications,” Renewable Energy, vol. 32, no. 15, pp. 2461–2478, Dec. 2007, doi: 10.1016/j.renene.2006.12.014.
[13] J. Wang, L. Kang, and J. Liu, “CO2 Transcritical Cycle for Ground Source Heat Pump,” in 2009 WRI World Congress on Computer Science and Information Engineering, Mar. 2009, vol. 2, pp. 213–217. doi: 10.1109/CSIE.2009.235.
[14] Y.-J. Kim and K.-S. Chang, “Development of a thermodynamic performance-analysis program for CO2 geothermal heat pump system,” Journal of Industrial and Engineering Chemistry, vol. 19, no. 6, pp. 1827–1837, Nov. 2013, doi: 10.1016/j.jiec.2013.02.028.
[15] S. Riffat, D. Aydin, R. Powell, and Y. Yuan, “Overview of working fluids and sustainable heating, cooling and power generation technologies,” International Journal of Low-Carbon Technologies, vol. 12, no. 4, pp. 369–382, Dec. 2017, doi: 10.1093/ijlct/ctx008.
[16] E. Bellos and C. Tzivanidis, “Parametric Investigation of a Ground Source CO2 Heat Pump for Space Heating,” Energies, vol. 14, no. 12, Art. no. 12, Jan. 2021, doi: 10.3390/en14123563.
[17] Modelica Association, “Modelica Language,” 2021. https://modelica.org/modelicalanguage.html (accessed Sep. 02, 2021).
[18] Dassault Systèmes, “Dymola,” 2022. https://www.3ds.com/products-services/catia/products/dymola/ (accessed May 23, 2022).
[19] Claytex Technia Company, “Thermal Systems Library & TIL Suite,” Claytex, 2022. https://www.claytex.com/products/dymola/model-libraries/thermal-systems-library/ (accessed May 23, 2022).
[20] J. Formhals, H. Hemmatabady, B. Welsch, D. O. Schulte, and I. Sass, “A Modelica Toolbox for the Simulation of Borehole Thermal Energy Storage Systems,” Energies, vol. 13, no. 9, Art. no. 9, Jan. 2020, doi: 10.3390/en13092327.
[21] S. P. Kavanaugh and K. D. Rafferty, Geothermal Heating and Cooling: Design of Ground-source Heat Pump Systems. ASHRAE, 2014.
[22] A. P. Colburn, “A method of correlating forced convection heat-transfer data and a comparison with fluid friction,” International Journal of Heat and Mass Transfer, vol. 7, no. 12, pp. 1359–1384, Dec. 1964, doi: 10.1016/0017-9310(64)90125-5.
[23] J. Stene, “Ground-source heat pump systems in Norway IEA HPP Annex 29 (2004-2006),” Norway, NEI-NO--0706407, 2007. [Online]. Available: https://inis.iaea.org/search/search.aspx?orig_q=RN:38097084
[24] K. Midttømme, “Geothermal Energy in Norway and Hordaland,” Bergen Energy Lab, 06 2017. [Online]. Available: https://www.uib.no/en/energy/108628/kirsti-midtt%C3%B8mme-geothermal-energy-norway-and-hordaland
[25] T. Persson, O. Stavset, R. K. Ramstad, M. J. Alonso, and K. Lorenz, “Software for modelling and simulation of ground source heating and cooling systems,” SINTEF Energy Research, Trondheim, Norway, TR A7570, 2016. Accessed: Feb. 17, 2021. [Online]. Available: https://www.sintef.no/globalassets/sintef-energi/interact/tr-a7570-software-for-modelling-and-simulation-of-ground-source-heating-and-cooling-systems-2016.pdf

14th IEA Heat Pump Conference
15-18 May 2023, Chicago, Illinois

Efficiency Improvement Of A High Capacity Transcritical CO_2 Heat Pump For Human Comfort In Large Buildings

Hakim Nesreddine[a], Dominique Monney[b*], Wayne Wehber[c]

[a]Hydro Quebec, 600 avenue de la Montagne, Shawinigan, QC G9N 7N5, Canada
[b] Emerson Commercial & Residential Solutions | 145 Sherwood Drive, Brantford, ON N3T 1N8, Canada
[c]Vilter Manufacturing LLC, 5555 S Packard Ave, Cudahy WI 53110-8904, USA

Abstract

Transcritical CO_2 heat pumps have the potential to be environmentally friendly to decarbonize buildings. This technology is very efficient for water heating applications. However, they generally exhibit poor efficiencies for space heating due to high return temperatures. This paper presents new experimental test data obtained by operating a single screw industrial heat pump for space heating and cooling in large buildings. This transcritical CO_2 pilot-scale prototype has a maximum heating and cooling thermal capacity of 1.35 and 1.05 MW, respectively. The results show that decoupling the thermal load from the CO_2 heat pump by the use of thermal storage tanks increases substantially the coefficient of performance (COP) of the system compared to the reference case (without heat storage and temperature conditioning).

© HPC2023.
Selection and/or peer-review under the responsibility of the organizers of the 14th IEA Heat Pump Conference 2023.

Keywords: Building; Heat pump; Transcritical CO_2; Pilot-scale prototype

1. Introduction

Heat pumps are increasingly recognized as an efficient and low-carbon energy technology for heating, cooling and sometimes for providing hot water to buildings. The global heat pump market has expanded rapidly over the last few years, with around 190 million units in operation in buildings worldwide in 2021, the three main markets being in China (33%), North America (23%) and Europe (12%) [1,2]. Though being considered as a key and cost-effective component towards the reduction of carbon emissions in the residential and commercial sectors, heat pumps currently provide only 10% of the global heating need in buildings. In the 2050 carbon neutrality scenario, the world heat pump stock should reach 600 million by 2030, representing 20% of the global heating needs and having a more preponderant position to face the increased cooling needs. Countries currently develop different strategies (constraining building codes and standards, performance-based labels, grants to support system's acquisition or privileged electricity tariff) to accelerate the deployment of heat pumps in residential and commercial buildings. Some markets also credit the heat supplied by heat pumps as renewable such that they get eligible to specific grants [1]. However, their market penetration remains relatively slow. Gaur et al. [3] discussed the main barriers to their integration: high upfront costs, uncertainty in policy, lack of standards, public acceptance and limitation of the electrical networks.

Heat pump technology allows to uplift low-grade temperature heat sources to a useful temperature level (sink) using electricity. Thus, they can operate using low-grade renewable energy sources (air, water, ground or solar), but also using waste heat. They can provide both heating and cooling (reversible heat pumps), separately or simultaneously, with no heat dissipation. They are then highly efficient with coefficients of performance (COP) typically ranging from 3 to 5 [4]. When the electricity used to drive the compressor comes from a renewable source (like hydroelectricity as it is the case in the Québec province for example), all the

*Corresponding author. Tel.: +1 514 946 1882
E-mail address: Dominique.Monney@Emerson.com

useful heat provided by the heat pump gets zero-carbon. Besides the prime objective of efficient decarbonation, heat pumps may also play a role to enhance the energy security of countries.

As shown by Gaur et al. [3], the literature on heat pumps is quite abundant and the number of publications continues to rise exponentially. The interested reader can refer to the recent review of Ni et al. [5] for more details about heat pump systems for heating and cooling of buildings. The authors focused on air and ground heat pumps integrating a thermal energy storage under the form of water, phase change materials or ground. Wang et al. [4] discussed the main parameters affecting the performance of heat pumps: hybridization of the different heat sources and sinks depending on the temperature levels, compressor efficiency and potential integration of a thermal energy storage.

There is no consensus on the appropriate definition of a large-scale heat pump. For the European Heat Pump Association (EHPA), heat pump is considered large if its capacity exceeds 100 kW. Their potential integration for district heating systems and their impact are constantly investigated through case studies mainly in North Europe : Baltic countries [6], Germany [7] or Denmark [8] among other examples. These different works enable to compare the benefit of heat pumps compared to other sources (biomass [6], coal-fired combined heat and power system [7], mixed sources [8]) but also demonstrate that results are strongly case-dependent. David et al. [9] analyzed the existing electricity-driven heat pumps with a thermal capacity output equal or greater to 1 MW installed in Europe. They highlighted the huge potential for using sewage water and ambient water as the main heat sources followed by geothermal energy. Ground source heat pumps are indeed preferred over air source ones in Nordic climates as they are more constant and at higher temperature levels. Schlosser et al. [10] reviewed the applications, performance, economic feasibility and industrial integration of large-scale heat pumps. Their analysis, which gathers 155 large-scale heat pumps, covered all types of refrigerants, compressors, heat sources, etc.

As already mentioned, compressor efficiency plays a crucial role on the system performance. Jesper et al. [11] analyzed a database of 33 large-scale heat pumps from 11 different manufacturers. The distribution between reciprocating piston, screw and scroll compressors was well balanced. Screw compressor-based heat pumps exhibited the highest lift temperature difference and the largest nominal thermal output range. Wang et al. [12] proposed a matching strategy for a screw compressor integrated in a heat pump. It consists in the matching of the built-in volume of the compressor and the annual heating and cooling demands. They also introduced a new performance index denoted ACOPA (Annual integrated Coefficient of Performance under Actual operating conditions). For a ground-source heat pump, they showed numerically that such a strategy may improve the ACOPA by 6%.

R134a and R245fa are certainly the most used refrigerants in large-scale heat pumps [10, 11]. Due to their progressive phase-out, new low Global Warming Potential (GWP) refrigerants have to be considered. Hydrocarbons like R600 (n-butane) or R601 (pentane) have a low GWP but are highly flammable such that their filling capacity is limited to 2.5 kg in heat pumps in Europe, excluding them from potential large-scale applications. The use of alternative natural refrigerants in large-scale heat pumps with a low GWP and a favourable safety classification like R718 (water) or R744 (carbon dioxide), though being highly attractive, is still not state-of-the-art technology according to Jesper et al. [11]. As shown recently by Song et al. [13], transcritical CO_2 heat pumps are widely considered for water heating in buildings or for industrial processes and attention is now turned more on their performance optimization by ejector or vortex tube. Their application for space heating is scarcer. Schlosser et al. [10] proposed a correlation for the COP of transcritical CO_2 heat pumps based on four series from the same manufacturer, all using a reciprocating piston compressor. It represents 936 operating points in total. COP does not depend on the logarithmic mean temperature on the heat sink but depends only on the lift temperature difference.

To fully benefit from the heat pump potential, thermal energy storage is deemed necessary to continuously operate the system, shift the heat production to off-peak hours and decrease the thermal capacity to less than the maximum heating requirement among other benefits. It results in reduced installation and operating costs. Osterman and Stritih [14] proposed a recent review on compression heat pump systems including thermal energy storage (TES) for heating and cooling in buildings. Energy can be stored under three different forms, namely sensible storage, latent storage and thermo-chemical heat storage. Sensible TES through water storage tanks are the more simple and common solution. The authors found that in most cases, air is used as a balancing source and the capacities of heat pumps and the size of storage tanks remains relatively small. No study concerned the experimental investigation of a ground source transcritical CO_2 large-scale heat pump coupled to a TES for space heating and cooling, as in the present work. Liu et al. [15] considered a water source CO_2 heat pump with TES but at a small scale: 3 kW of nominal thermal capacity and small water storage tanks (around 170 L each for the hot and cold tanks). Alkhwildi et al. [16] developed a numerical model based on TRNSYS of ground source heat pump with hybrid TES (water and salt-hydrate) used to reduce the peak electricity demand of a 180 m² house in Toronto, Canada. A 2.5 m³ water tank was found sufficient to fully shift load. The results are theoretical and difficult to reproduce as no details on the type of heat pump and refrigerant used are provided.

Scientific and technical innovation is still required to improve the performance and durability of heat pumps, enhance their flexibility for the heating and cooling of large buildings and accelerate their market penetration. To the best of the authors' knowledge, the present work is the first to demonstrate the potential of a single screw industrial transcritical CO_2 heat pump for space heating and cooling in large buildings at the pilot scale. The addition of a water storage tank having a thin thermocline separating its hot and cold sections drastically improves the performance of the system by enabling to decouple the thermal load from the heat pump. It also allows to feed the heat pump's evaporator when the heat source is insufficient, which has never been demonstrated at this scale for this particular heat pump.

The paper is organized as follows: the experimental set-up and the associated instrumentation are described in detail in Section 2. The results are presented in Section 3. The discussion focuses on the benefit of decoupling the thermal load from the heat pump cycle by adding a large capacity thermal storage tank. Conclusions and future views are finally provided in Section 4.

2. Prototype Description

The test rig of the water source transcritical CO_2 heat-pump consists of three major components: water-loop system, heat-pump system, and data collection system. The schematic diagram of this experimental system is shown in Figure 1. It is composed of a gas cooler, an evaporator, a compressor, a flash tank, an internal heat exchanger, and an electronic expansion valve (EEV). The water loop system includes thermal storage tanks that decouple the thermal load from the CO_2 heat pump and allow performance enhancements. Detailed information about the main components is summarized in Table 1.

Table 1. Main components.

Component	**Type**	**Characteristics**
Compressor	Open Single Screw	Displacement: 452 m³/h Maximum rotating speed: 4200 rpm Maximum operating pressure: 103.4 bar Maximum Motor capacity: 643 kW
Gas cooler	Shell & Tubes Heat Exchanger	Shell: ϕ323.85mm (CO_2) Tube (Nb: 138): ϕ 12.7 mm (Water)
Evaporator	Flooded Shell & Tubes Heat Exchanger	Shell: ϕ*609.6*mm (CO_2) Tubes (Nb: 360): ϕ *19.05* mm (Water)
Flash tank	Custom built	-
Expansion valves	Electronic	Opening: 0-100%
Internal heat exchanger	Copper brazed plates	-
Thermal storage tanks	Custom built	Total volume of 40,000 l[2]

T-type thermocouples were adopted to measure the temperatures in the experimental system. The measurement accuracy is ±0.2 °C in the range of −10 °C to 150 °C. CO_2 mass flowrate was measured by a Coriolis mass flowmeter with the accuracy at ±0.1% in the range of 26 to 9,072 kg/h. Pressure transmitters with the accuracy at ±0.25% (0–6 MPa and 0–16 MPa, respectively) were used to measure the CO_2 pressures. Turbine volumetric flowmeters with the accuracy at ±0.5% were used to measure water flowrates.

[2] The volume and geometry characteristics have been determined using CFD simulation.

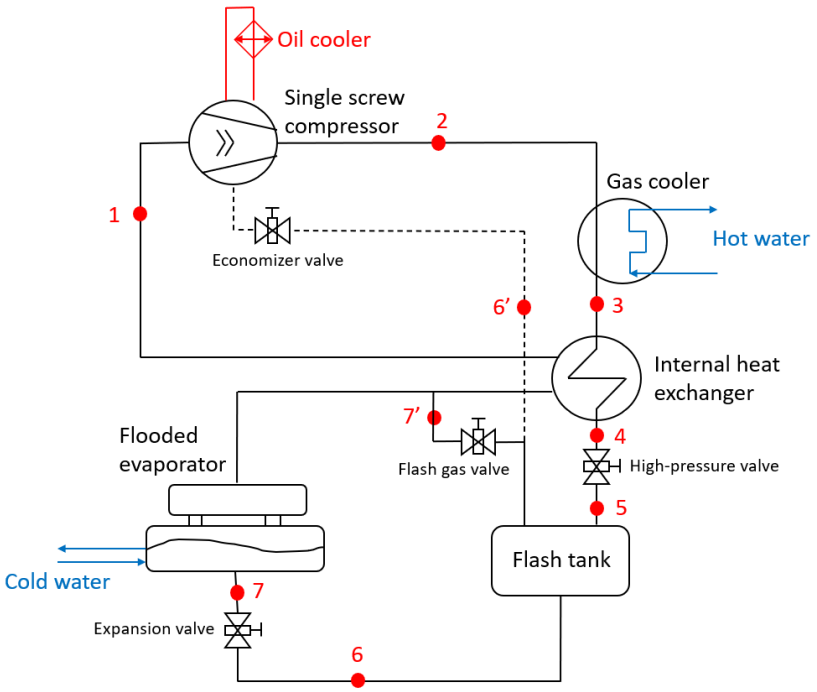


Fig. 1. Simplified configuration of transcritical CO_2 heat pump

Figure 2 shows the p-h diagram of the heat pump system under study. The main system cycle is 1-2-3-4-5-6-7-1. The refrigerant is compressed from point 1 (superheated vapour) to point 2 (supercritical fluid) by the compressor. The water is heated in the gas cooler by the heat released from point 2 to point 3. The water is cooled from point 7 to the gas saturation line by the CO_2 evaporation and CO2 is overheating from the saturation vapour line to point 1 by the heat absorbed in the internal heat exchanger. (Point 3 to 4)

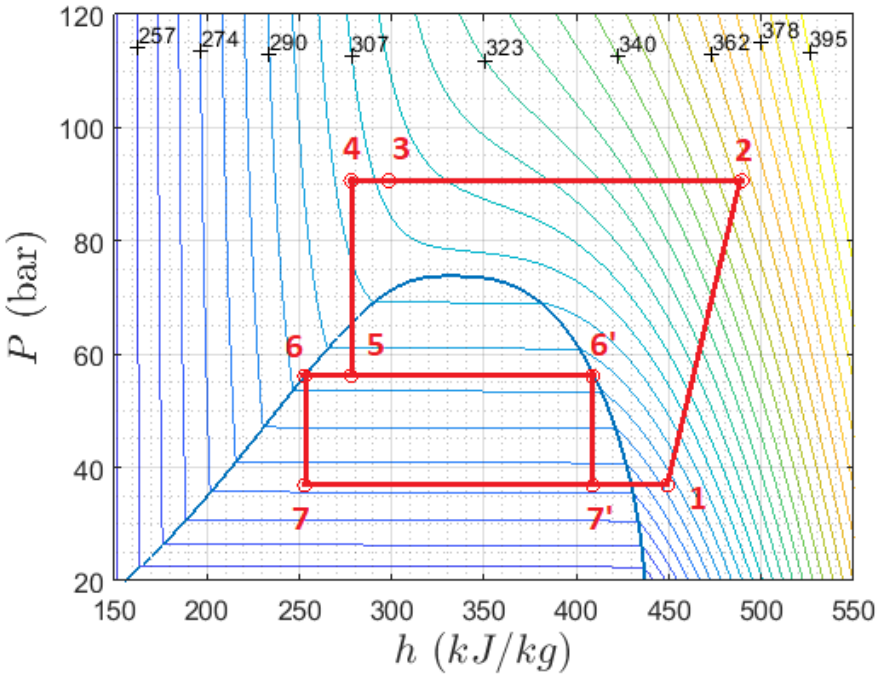


Fig. 2. P-h diagram of transcritical CO_2 heat pump

The CO_2 heat pump COP is calculated by the following relation:

$$COP = \frac{Q_h}{W_c} \tag{1}$$

where Q_h and W_c represent the heating capacity and the compressor power, respectively.

Q_h is calculated as follows:

$$Q_h = \dot{m}_g C_g (T_{go} - T_{gi}) \tag{2}$$

where $\dot{m}_g$and C_g denote mass flowrate and heat capacity, respectively, of the thermal fluid circulating in the gas cooler. T_{go} and T_{gi} are the outlet and inlet temperatures of the thermal fluid.

Similarly the combined COP for heating and cooling is determined by adding the cooling capacity Q_c to the numerator of equation 1.

Q_c is calculated as follows:

$$Q_c = \dot{m}_e C_e (T_{ei} - T_{eo}) \tag{3}$$

where $\dot{m}_e$and C_e denote mass flowrate and heat capacity, respectively, of the thermal fluid circulating in the evaporator. T_{eo} and T_{ei} are the outlet and inlet temperatures of the thermal fluid.

The root-sum-square method was applied for calculating uncertainties of measured variables as follows

$$\varepsilon_v = \sqrt{\sum_{i=1}^{k} \left(\frac{\partial v}{\partial \alpha_i} \varepsilon_{\alpha_i}\right)^2} \tag{4}$$

where v denotes the analyzed variable. α_i denotes the variable affecting v. ε_v and ε_{α_i} denote the uncertainties of v and α_i, respectively. This method is utilized for calculating uncertainties of measured variables in Equations 1 and 2. Uncertainty of COP (ε_{COP}) is calculated by:

$$\varepsilon_{COP} = \sqrt{\left(\frac{\partial COP}{\partial Q_h} \varepsilon_{Q_h}\right)^2 + \left(\frac{\partial COP}{\partial W_c} \varepsilon_{W_c}\right)^2} \tag{5}$$

where ε_{Q_h} and ε_{W_c} represent the uncertainties of Q_h and W_c, respectively. ε_{COP} is calculated by:

$$\varepsilon_{COP} = \sqrt{\left(\frac{\partial Q_h}{\partial \dot{m}_g} \varepsilon_{\dot{m}_g}\right)^2 + \left(\frac{\partial Q_h}{\partial T_{gi}} \varepsilon_{T_{gi}}\right)^2 + \left(\frac{\partial Q_h}{\partial T_{go}} \varepsilon_{T_{go}}\right)^2} \tag{6}$$

where $\varepsilon_{\dot{m}_g}$, $\varepsilon_{T_{gi}}$, and $\varepsilon_{T_{go}}$, denote the uncertainties of $\dot{m}_g$, T_{gi} , and T_{go}, respectively. Using measured data, ε_{COP} could be determined by Equations 1 to 6. Calculations shows that the maximum ε_{COP} is 3.92%.

3. Experimental Results and Discussion

The prototype previously described has been operated in order to assess its performances and study the effect of some governing parameters such as: discharge pressure, compressor speed, heat source and sink temperatures. Experimental results are presented hereafter.

3.1. Discharge pressure effect

The effects of the discharge pressure upon the key parameters characterizing the transcritical CO_2 heat-pump system are illustrated in Figures 3–5. The other influencing parameters are kept constant.

As shown in Figure 3, upon increasing the discharge pressure, the CO_2 mass flowrate gradually decreases. This results from the regulation of the discharge pressure by adjusting the EEV opening. If the EEV opening is reduced, the mass flowrate of CO_2 flowing through EEV decreases, leading to an excessive accumulation of CO_2 in the gas cooler. As a result, the discharge pressure and temperature increase and consequently, the heat generated at the gas cooler increases as displayed in Figure 4. Since the water temperature at the outlet of the gas cooler is regulated by the water flowrate to keep it close to a setpoint, the water flowrate is adjusted automatically as the discharge pressure increases by a PID that controls the pump's speed.

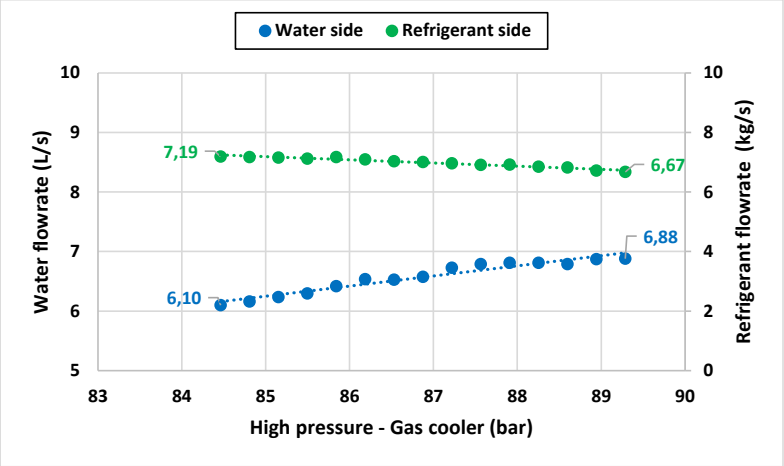


Fig. 3. Effect of discharge pressure on flowrates

Figure 4 displays the heating-cooling output and the compressor power demand as a function of the discharge pressure. It observed that an increase of discharge pressure results in a higher heating and cooling capacities. As the EEV closes, the discharge pressure increases, and the suction pressure decreases. Consequently, the discharge temperature is higher, and the evaporating temperature is lower. Thus, water flowrates increase in both the gas cooler and the evaporator to keep the pre-set temperatures at the exists constant. This explains the augmentation of the heating and cooling capacities. Upon increasing the discharge pressure, the specific work of the compressor increases significantly due to the increase of the compression ratio. However, the CO_2 mass flowrate decreases with the increase of the discharge pressure. It is important to mention that the influence of the specific work is much larger than that of the CO_2 mass flowrate, hence, the cross effect of the two factors lead to the increase of the power demand of the compressor.

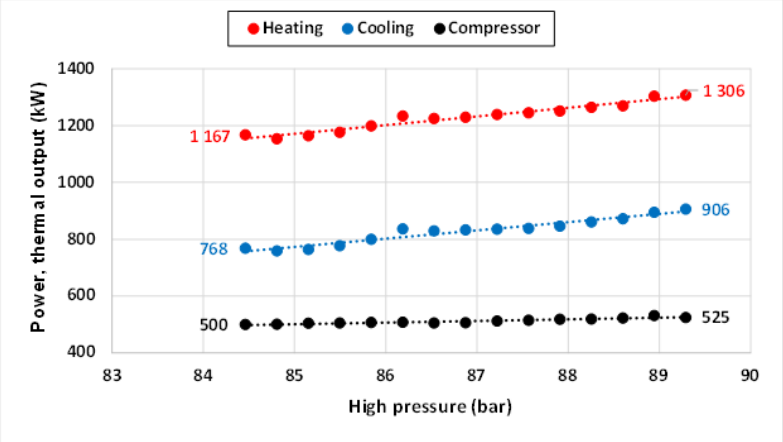


Fig. 4. Effect of discharge pressure on HP thermal outputs and power demand (HP: high pressure)

Figure 5 shows that with the increase of the discharge pressure, the COP rises steadily. Since the discharge pressures tested do not exceed 90 bar, it is unlikely to reach the optimum discharge pressure for which the COP is at its maximum. Based on the previous analysis, the power consumption increases monotonously with the increase of the discharge pressure.

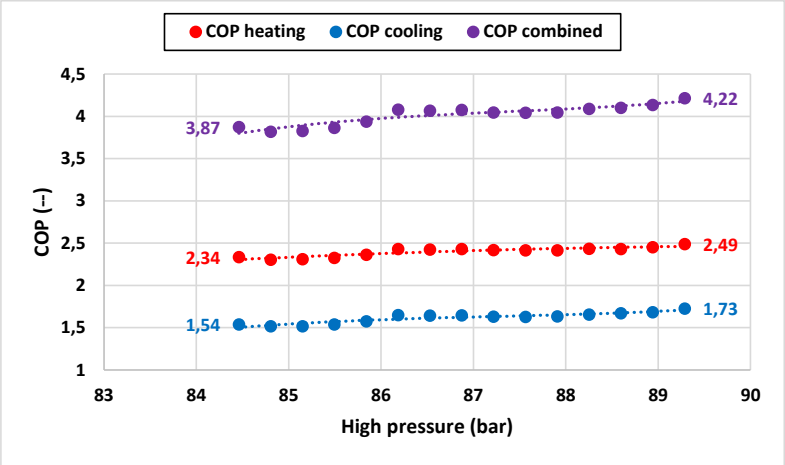


Fig. 5. Effect of discharge pressure on HP performance

3.2. Effect of compressor speed

Figure 6 presents the compressor power demand for different rotational speed: 2000 to 4200 rpm. As the compressor speed increases, the EEV opens to maintain the discharge pressure constant. Thus, the refrigerant flowrate increases as well as the flowrate of water since more thermal energy must be evacuated.

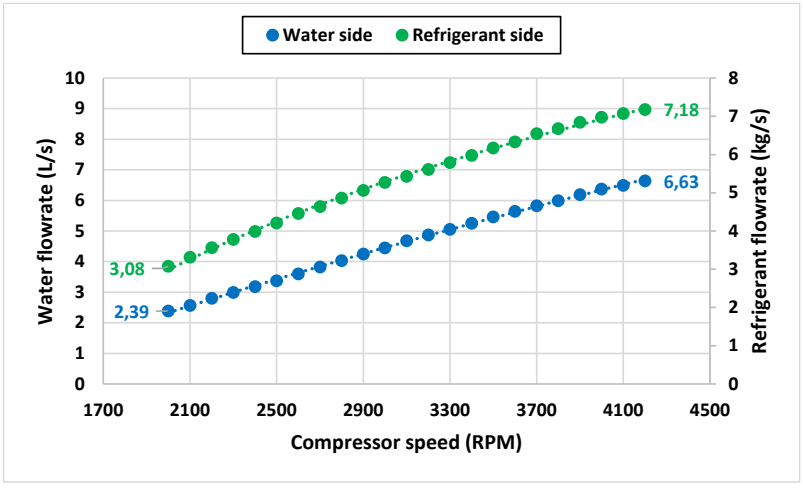


Fig. 6. Effect of compressor speed on flowrates

Indeed, Figure 7 shows that the heating output through the gas cooler increases as the compressor's speed evolves. It is worth mentioning that the decrease of the compressor speed reduces substantially the compressor power demand. For example, when the compressor speed drops from 4200 to 2000 rpm, the power demand is reduced by 57%.

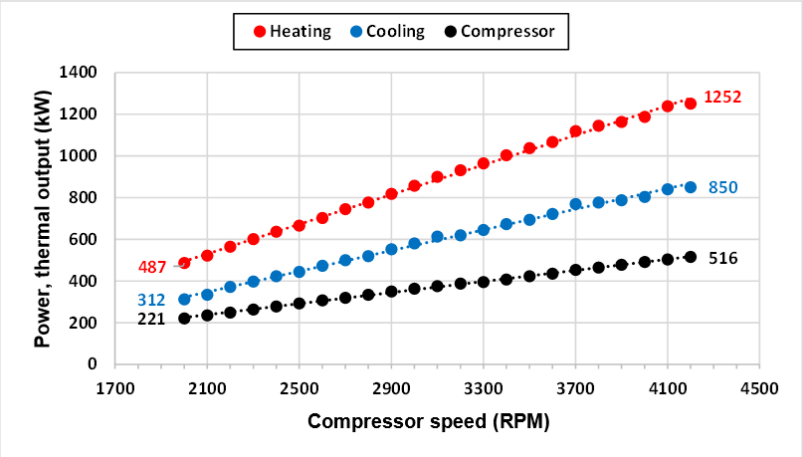


Fig. 7. Effect of compressor speed on HP thermal outputs and power demand

It is important to point that the influence of the compressor speed on the COP is not pronounced namely for speeds exceeding 3300 rpm as displayed in Figure 8. Indeed, the performance decreases by only 12% when the compressor speed drops from 4200 to 2000 rpm. This finding is important as it has an important impact for demand response applications for which the compressor speed variation is an advantage.

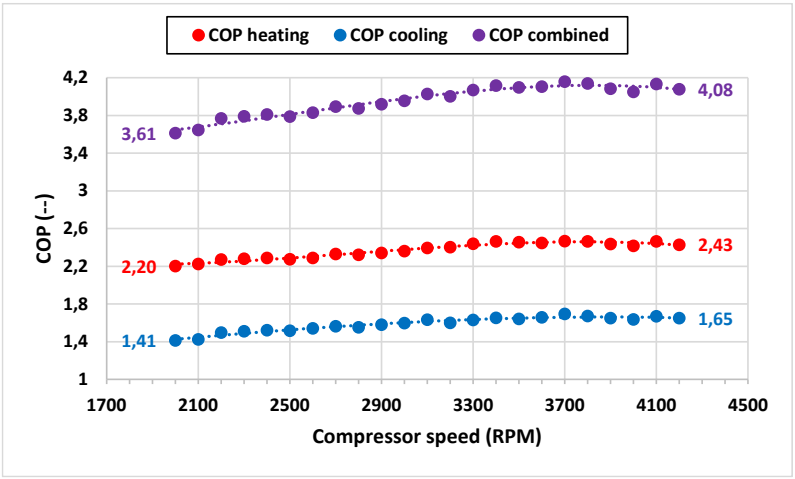


Fig. 8. Effect of compressor speed on HP performance

3.3. Heat source temperature effect

Heat source temperature is represented by the inlet water temperature at the evaporator. This parameter has been varied from 12°C to 20°C while the temperatures at the inlet and outlet of the gas cooler have been maintained constant at 20°C and 60°C respectively. The compressor speed was set at 4200 rpm and the high pressure was fixed at 86.2 bar.

Figure 9 displays that an increase in the heat source temperature results in an increase of the flowrates on both sides of the gas cooler. The increase of the refrigerant flowrate is due to an enhancement of the evaporating kinetic as more heat is supplied to the evaporator even though the compressor speed is kept constant. Since more heat is absorbed by the evaporator, it is expected that more heat will be released at the gas cooler (Fig. 9). In this case, the water flowrate will increase to maintain the water outlet temperature at the set-point of 60°C.

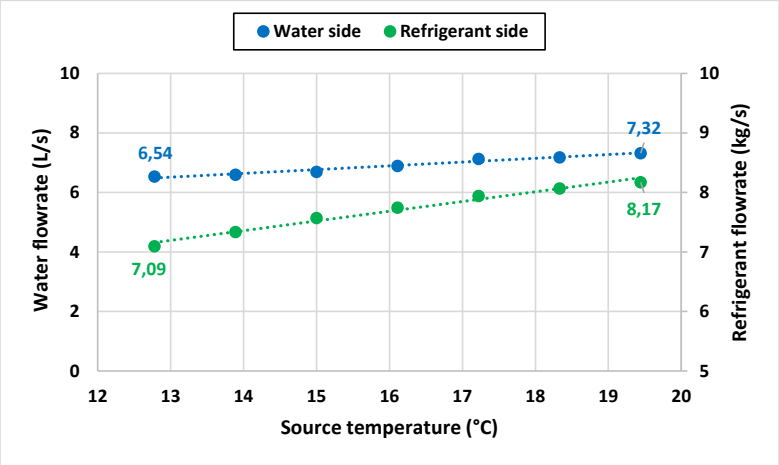


Fig. 9. Effect of heat source temperature on flowrates

Figure 10 displays the impact of heat source temperature on thermal outputs and compressor power demand. The increase of the heat source temperature at the evaporator increases the heat adsorbed and rejected by the heat pump as mentioned before. The power demand of the compressor rises as well because of an increase of the refrigerant flowrate occurs due to an enhancement of the vaporizing process in the evaporator. As a consequence, the performance of the heat pump is improved as shown in Figure 11.

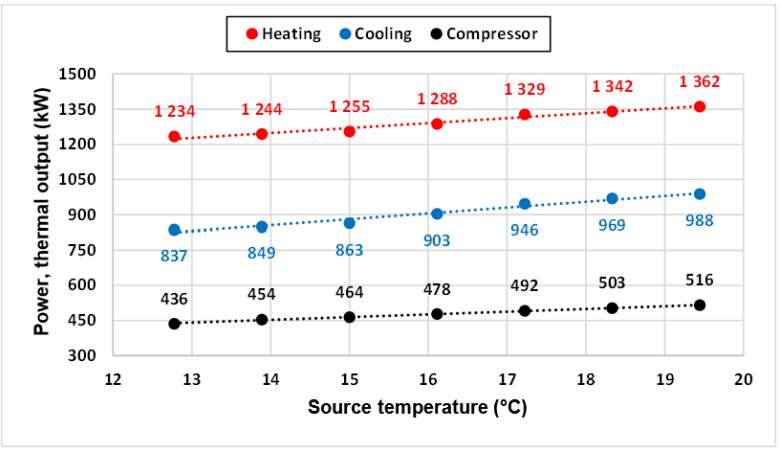


Fig. 10. Effect of heat source temperature on HP thermal outputs and power demand

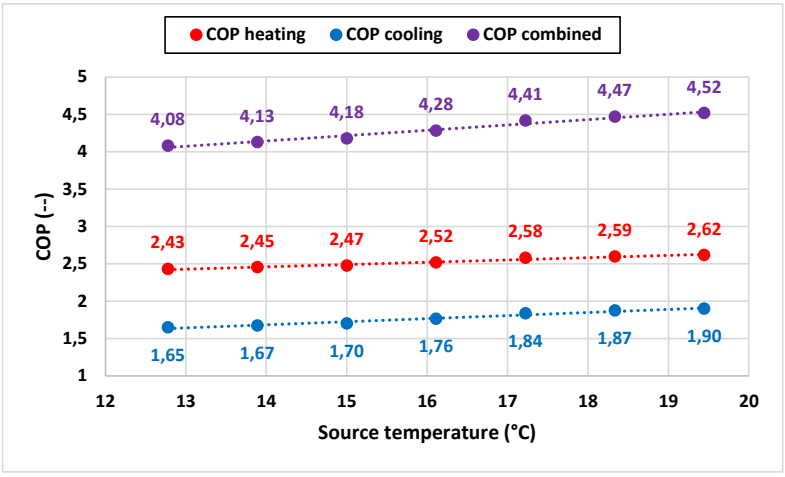


Fig. 11. Effect of heat source temperature on HP performance

3.4. Heat sink temperature effect

Figure 12 displays the variation of the COP for both heating and cooling as a function of the water temperatures at the inlet and outlet of the gas cooler for different discharge pressures. The compressor speed and the heat source temperature are kept constant at 3500 rpm and 12 °C, respectively.

Results show that for a constant outlet temperature at the gas cooler when the inlet temperature increases, the performance deteriorates. Since an increase in the inlet temperature results in an increase of the CO_2 temperature at the outlet of the gas cooler, the heat absorbed at the evaporator is less and consequently, the thermal output decreases.

On the other hand, when the inlet temperature is kept constant, any reduction in the outlet temperature will lead to an increase of the COP. In fact, the water flowrate through the gas cooler is higher when the outlet temperature is reduced.

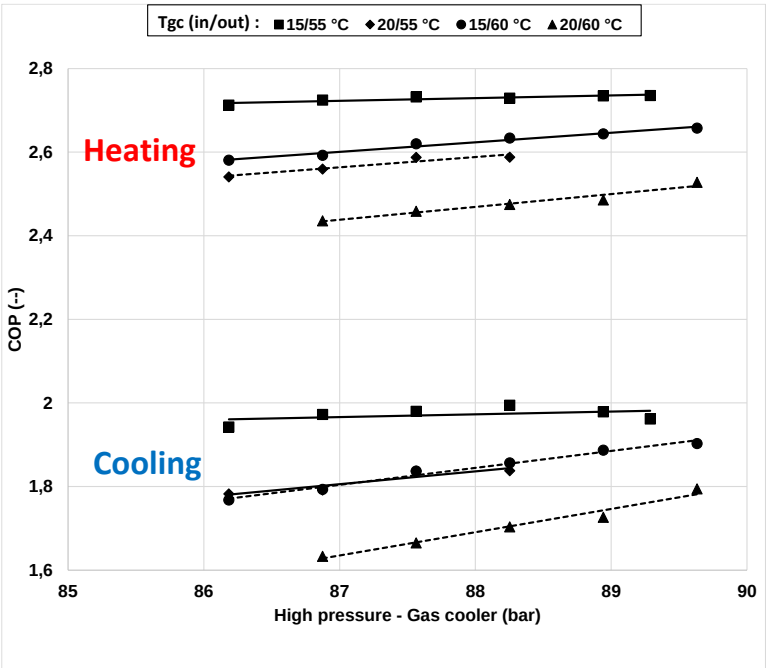


Fig. 12. Effect of gas cooler inlet outlet temperatures on HP performance (3500 rpm and T_{source} = 12°C)

4. Conclusion

A transcritical CO_2 heat pump has been built at the pilot-scale to demonstrate the potential of such a technology to provide heating and cooling to large buildings. The heat pump is composed of an open single screw compressor, shell and tube heat exchangers (flooded at the evaporator), expansion valves, a flash tank and a copper brazed plates internal heat exchanger. The water loop system includes thermal storage tanks that decouple the thermal load from the CO2 heat pump and enable performance enhancement. Detailed information about the main components is summarized in Table 1.

The influences of the discharge pressure, compressor speed, and heat source and sink temperatures on the main performances of the system have been quantified in detail and discussed. The main results may be summarized as follows:

- Both heating and cooling COPs are increasing as a function of the discharge pressure, compressor speed, and heat source / sink temperatures.
- The maximum heating and cooling power capacities are 1.362 and 0.988 MW, respectively.
- The maximum COP values are 2.75 and 2 for heating and cooling, respectively, leading to a maximum combined COP of 4.75. (Real COP measured based on heat outputs on the water sides).

This technology appears as a valuable way for the decarbonization and efficient electrification of large commercial or residential building, Future works include the detailed investigation of the water storage tank and more particularly its optimal design to manage the thermocline.

Acknowledgements

The authors would like to thank the engineering team of Vilter and Ceptek for their technical support and the technical staff of Hydro Quebec for the build-up and operation of the industrial prototype.

References

[1] Delmastro C, Heat pumps – more efforts needed, Tracking report of International Energy Agency, 2022.
[2] Rosenow J, Gibb D, Nowak T, Lowes R. Heating up the global heat pump market. *Nature Energy* 2022.
[3] Gaur AS, Fitiwi DZ, Curtis J. Heat pumps and our low-carbon future: A comprehensive review. *Energy Res Soc Sci* 2021; **71**:101764.
[4] Wang Y, Wang J, He W. Development of efficient, flexible and affordable heat pumps for supporting heat and power decarbonisation in the UK and beyond: Review and perspectives. *Renew Sust Energy Rev* 2022; **154**: 111747.
[5] Ni L, Dong J, Yao Y, Shen C, Qv D, Zhang X. A review of heat pump systems for heating and cooling of buildings in China in the last decade. *Renew Energy* 2015;**84**:30-45.
[6] Volkova A, Koduvere H, Pieper H. Large-scale heat pumps for district heating systems in the Baltics: Potential and impact. *Renew Sust Energy Rev* 2022; **167**: 112749.
[7] Popovski E , Aydemir A, Fleiter T, Bellstadt D, Büchele R, Steinbach J. The role and costs of large-scale heat pumps in decarbonising existing district heating networks - A case study for the city of Herten in Germany. *Energy* 2019; **180**: 918-933.
[8] Bach B, Werling J, Ommen T, Munster M, Morales JM, Elmegaard B. Integration of large-scale heat pumps in the district heating systems of Greater Copenhagen. *Energy* 2016; **107** : 321-334.
[9] David A, Vad Mathiesen B, Averfalk H, Werner S, Lund H. Heat Roadmap Europe: Large-Scale Electric Heat Pumps in District Heating Systems. *Energies* 2017; **10** : 578.
[10] Schlosser F, Jesper M, Vogelsang J, Walmsley TG, Arpagaus C, Hessekbach J. Large-scale heat pumps: Applications, performance, economic feasibility and industrial integration. *Renew Sust Energy Rev* 2020; **133**: 110219.
[11] Jesper M, Schlosser F, Pag F, Walmsley TG, Schmitt B, Vajen K. Large-scale heat pumps: Uptake and performance modelling of market-available devices. *Renew Sust Energy Rev* 2021; **137**: 110646.
[12] Wang Y, Wang Z, Li M, Chen T, Wang Z. An optimal matching strategy for screw compressor for heat pump applications. *Appl Therm Eng* 2018; **132**: 333-340.
[13] Song Y, Cui C, Yin X, Cao F. Advanced development and application of transcritical CO_2 refrigeration and heat pump technology—A review. *Energy Reports* 2022; **8**: 7840-7869.
[14] Osterman E, Stritih U. Review on compression heat pump systems with thermal energy storage for heating and cooling of buildings. *J Energy Storage* 2021; **39**:102569.
[15] Liu F, Zhu W, Cai Y. Experimental study of a dual-mode CO_2 heat pump system with thermal storage. *Energy Proc* 2017; **105** : 4078–4083.
[16] Alkhwildi A, Elhashmi R, Chiasson A. Parametric modeling and simulation of Low temperature energy storage for cold-climate multi-family residences using a geothermal heat pump system with integrated phase change material storage tank. *Geothermics* 2020; **86** : 101864.

14th IEA Heat Pump Conference
15-18 May 2023, Chicago, Illinois

Progress and challenges in rolling bearing technology for compressors in industrial heat pumps

Guillermo E. Morales-Espejel[a,b], Rudolf Hauleitner[c*], Paul Dietl[d]

[a] SKF Research and Technology Development, Houten, The Netherlands
[b] Université de Lyon, INSA-Lyon, CNRS, LaMCoS UMR5259, F69621, France
[c] SKF Product Development and Engineering Americas, Plymouth, MI, USA
[d] SKF Fluid Machinery, Steyr, Austria

Abstract

The introduction of new process media like refrigerants with low GWP (Global Warming Potential) and the specific operating conditions of heat pumps can create challenges for traditional bearing technology: dilution of the lubricating oil by process media is increasing, lubrication films are getting thinner, and risk of corrosion and chemical compatibility need to be investigated upfront. Furthermore, the use of variable frequency drives (VFD) extends the speed range to both lower and higher values for which the bearings must operate reliably. In certain cases this even requires a change of bearing technology like from hydrodynamic to rolling element bearings. But also rolling bearings can suffer from above mentioned conditions. Therefore this article summarises the extensive research and development to provide state-of-the-art rolling bearing solutions and related engineering advice. This involves tribological testing and lubrication characterization of refrigerants and oil-refrigerant mixtures. The article also touches on the use of hybrid ceramic bearings, stainless materials, coatings, and advanced cage materials. The effect of oil dilution and poor lubrication and its impact on surface distress and rolling bearing life, as well as the effect of contaminating particles have been captured in models to allow engineers to give improved predictions of bearing performance and durability. Finally, different rolling bearing solutions to deal with the challenges related to lubrication and bearing life in heat pump compressors are described, all the way from oil-refrigerant mixture lubrication with moderate high dilution rates, up to a major innovation related to oil-free lubrication, so-called Pure Refrigerant Lubrication (PRL).

© HPC2023.
Selection and/or peer-review under the responsibility of the organizers of the 14th IEA Heat Pump Conference 2023.

Keywords: bearings; ceramic, tribology; lubrication; refrigerants, heat pump; compressor

1. Introduction

In the UN COP26 conference on climate change in 2021 one of the priorities was securing agreements for reducing emissions, with the goal of limiting the increase of global temperatures to 1.5 °C. Investment in renewable energy sources is encouraged while phasing out fossil fuels is identified as crucial to delivering this target [1]. Heat pump technology is seen as a key technology to replace fossil fuel usage and reduce carbon emissions. One major advantage of heat pump technology is that heat can be collected from a variety of renewable or other sources, such as air and water as well as geothermal and waste heat, producing no direct local emissions (as long as heat pump drive energy is also renewable).

Industrial heat pumps and heat pumps for district heating often use waste heat from processes in industries like food & beverage, pulp & paper, cement and building materials industry, chemical and petrochemical industries as well as refineries, and even large computer or data centres that need significant cooling for their operations. Heat pumps can help to cut operating costs and enable the electrification of the heating process.

Different from chillers, compressors in heat pumps must enable higher temperature (and pressure) lifts, often with discharge temperatures larger than 100°C to be applicable e. g. for drying operations and steam

* Corresponding author. Tel.: +1 734 892 9263
E-mail address: rudolf.hauleitner@skf.com.

production. The higher temperatures and pressures, together with the use of (new) refrigerants, lead to bearing lubrication regimes with a mixture of lubricant oil and refrigerant, in some cases with very high rations of low-viscous refrigerant in the oil. At higher temperatures the lubricating films become thinner than in conventional chillers, affecting the life of the bearings. The use of new low-GWP refrigerants, which are typically less chemically stable or more chemically active, or the use of ammonia as a refrigerant might in certain cases (like in the presence of humidity or water) harm the bearing materials by chemical attack, corrosion, ageing or close contact with hydrogen derivatives. The use of variable frequency drives (VFD) broadens the speed range in which the bearing solution must operate reliably. These challenges make rolling bearings one of the most critical machine elements in the evolution of heat pump technology, and reliable solutions need to be developed.

There is good amount of research work dedicated to rolling bearings lubricated with oil-refrigerant mixtures (ORM) and pure refrigerant lubrication (PRL). However, for the purpose of this publication, focus is put on the research that aims to describe and understand the effects of these types of lubrication on bearing performance and bearing life. For refrigeration compressors, the reader is kindly referred to the review paper published earlier by some of the current authors [2].

Early work in the 1990's related to the ORM lubrication of bearings and life effects is described in [3-4]. The effect of refrigerant dilution in lubricated contacts and film thickness is studied experimentally and numerically in [5-9]. Detailed numerical work of the elasto-hydrodynamically lubricated (EHL) contacts with ORM, including thermodynamic effects in dilution is presented in [10]. Recent work related to the modelling of the lubrication quality in rolling bearings with ORM is described in [11-12]. Work related to describing damage and life effects in rolling bearings running under ORM conditions is found in [13]. In relation to study the film thickness and rheological properties of refrigerants in EHL conditions, several experimental and numerical works can be cited [14-18]. Rolling bearings lubricated PRL conditions are studied in [19-22].

The current publication describes the tribological challenges faced by rolling bearings in typical industrial heat pumps, including such that work beyond discharge temperatures of 100°C. It presents information on modelling and experimental aspects which provide explanations for successful technological solutions. It will be impossible to have a complete review of the topic, since there is a very large and diverse literature database, and more research is ongoing while this publication is written. However, the objective of this article is two-fold: (i) to briefly summarize application aspects of rolling bearings above mentioned conditions, including different bearing designs and technologies, and (ii) to more extensively present scientific aspects on lubricant properties of (pure) refrigerants and oil-refrigerant mixtures, including modelling of surface life in rolling bearings. This double objective is difficult to find in existing publications.

Description of Compressor Designs used in Heat Pumps

In heat pumps utilising the vapour compression cycle, the compressor is the main mechanical component. There are two important compressor types used in heat pumps of industrial size with typical drive motor power above 50 kW [23] where rolling bearings play a key role for compressor reliability and efficiency: screw and centrifugal compressors (Figure 1). For detailed description of these compressor designs and typical bearing arrangements, the reader is referred to [2] and [24].

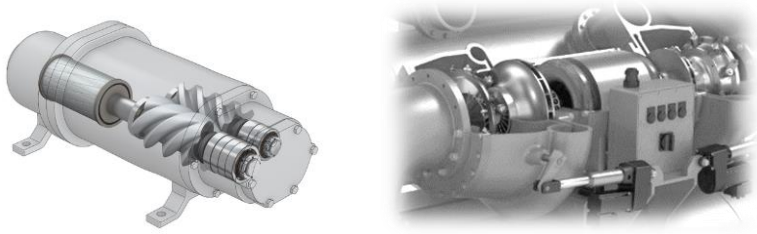


Fig. 1. Left: screw compressor. Right: centrifugal refrigerant compressor.

The bearing arrangements are usually the same or very similar for refrigerant compressors used in air-conditioning (i.e. for chillers) or in heating applications. Nevertheless, the operating conditions are heavily influenced by the needed temperatures and used refrigerants. Every refrigerant has its own characteristics which is commonly visualised in the pressure-enthalpy diagram (Figure 2). Within the "vapour dome" (the two-phase region) pressure and temperature are linked with each other. Therefore, if the source and the sink temperature (evaporator and condenser temperatures) of a specific application are known, the characteristics of the used refrigerant will link it to the pressure levels – which set the suction and discharge pressure of the

compressor. A heat pump operating at higher temperature will create higher gas pressures leading to higher bearing forces. At the same time the change in pressure and temperature affects the dilution of the lubricant and its viscosity.

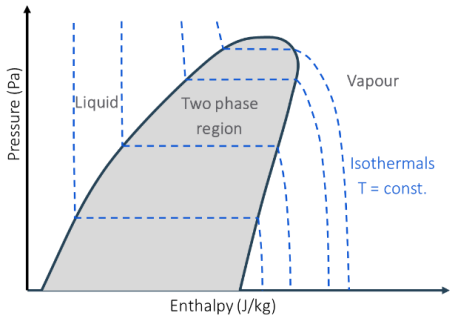


Fig. 2. Characteristics of a refrigerant in the pressure-enthalpy diagram.

1.1. Description of Oils and Refrigerants

In the past, commonly used refrigerants for compressors were the low-pressure chlorofluorocarbon CFC-11, and medium-pressure refrigerants like CFC-12 and hydrochlorofluorocarbon HCFC-22. In 1989, a global ban of ozone depleting refrigerants – indicated by their Ozone Depletion Potential (ODP) - was agreed upon in the Montreal Protocol. New HCFC and hydrofluorocarbon (HFC) refrigerants were developed having low or no ODP. Low pressure refrigerant HCFC-123 replaced CFC-11 and medium pressure refrigerant HFC-134a became a substitute for CFC-12 and HCFC-22.

When global warming started to become a bigger concern in the 1990s, another unintended characteristic of refrigerants got more attention, namely their high Global Warming Potential (GWP). For example, HFC-134a has a GWP of 1300 times that of CO2. In 1997 the so called Kyoto Protocol agreement on reduction of global greenhouse gases was proposed - but not ratified by major countries and never fully implemented. In 2016 it was decided to use the more successful format of the Montreal Protocol to control phase down of HFCs, referred to as the Kigali Amendment of the Montreal Protocol.

The newer refrigerants were not necessarily simple substitutes for CFCs. HFC-134a refrigerant, for example, is incompatible (due to different molecular polarity) with common mineral oils normally used with CFCs. An important property of any refrigerant and oil combination is the ability to dissolve with one another. It is therefore necessary to use synthetic lubricants like Polyol-Ester (POE) or polyalkylene glycol (PAG). Refrigerant HFC-134a is used in screw and centrifugal compressors at higher speeds and its phase out is governed by the Kigali Amendment. Refrigerant HCFC-123 is still used mainly in centrifugal compressors and is being phased out in accordance with the Montreal Protocol.

1.2. Later Generation Refrigerants and Natural Refrigerants

1.2.1. Hydrofluoroolefins (HFO) and Hydrochlorofluoroolefins (HCFO)

New refrigerants with low GWP and zero ODP are now being developed and phased in by the global refrigeration and air conditioning industries. Two promising new refrigerants are low pressure refrigerant HCFO-1233zd(E) and medium pressure refrigerant HFO-1234ze(E) and various blends containing these refrigerants. The GWP of the new refrigerants is less than five and the ODP is zero. These refrigerants have a very short atmospheric lifetime, thus they are chemically more active, which can lead to corrosion or material incompatibility, especially in the presence of moisture, adding an extra element in the equation. Besides all this, the thermodynamics of the new refrigerants make the oil-refrigerant mixtures more prone to having high concentrations of refrigerants (30 % or higher) during important times of the operation cycle.

1.2.2. Natural refrigerants

Natural refrigerants such as ammonia (NH3, R717) and carbon dioxide (CO2, R744) are also used increasingly, although ammonia has limitations due to some toxicity and flammability, and carbon dioxide is used at high pressures, which explains why mainly reciprocating compressors are applied for CO2 cycles.

Ammonia (NH3, R717) is toxic for humans, but its strong smell makes leaks easily detectable. There are different grades of ammonia based on application with different requirements on the water content. Industrial-grade anhydrous ammonia, commonly called metallurgical or refrigeration grade, has very little water

contamination. Refrigeration-grade ammonia has a maximum of about 150 ppm water content. Ammonia is flammable and has a lower explosive limit (LEL) of 15 percent and an upper explosive limit (UEL) of 28 percent. When the ammonia vapor is mixed with a miscible oil, the LEL can be as low as 8 percent.

Considering only its thermodynamic properties CO2 (R744) is not the ideal refrigerant candidate. However, this is compensated by its very good heat transfer coefficient, very low viscosity and its relatively insensitiveness to pressure losses. From the environmental point of view, CO2 is very attractive, with OPD equal to zero and GWP equal to 1, and CO2 is non-corrosive and basically non-toxic. Recently, mixtures of CO2 and ammonia are considered to increase efficiency. NH3/CO2 mixture is extremely efficient for low and very low temperature applications (below -40 °C). And CO2 is also used in supercritical conditions (sCO2) for higher temperature regimes.

2. Lubrication with Refrigerants

In most refrigerant compressors (except e.g. such using magnetic bearings) the refrigerant plays a role in the lubrication of the bearings, either as a component in the oil-refrigerant mixture or as the sole bearing lubricant in pure refrigerant lubrication (PRL) applications. In any case, the knowledge of the lubricating properties of the refrigerants is needed. And of course, lubrication and tribological aspects are important parameters in the estimation of bearing life and other aspects like frictional losses.

2.1. Model for Oil-Refrigerant Mixtures

Studies have been carried out in the past to model lubrication properties of oil-refrigerant mixtures. In reference [7] the Eyring theory is used to derive equations for the piezo-viscosity coefficient and viscosity:

$$\boldsymbol{\alpha_{mix}} = \frac{\boldsymbol{ms_{ref}(\alpha_{ref}-\alpha_{lub})}}{\boldsymbol{s_{ref}(m-1)+1}} + \boldsymbol{\alpha_{lub}} \tag{1}$$

$$\boldsymbol{ln(\eta_{mix})} = \boldsymbol{\left(ln\,\eta_{ref} - ln\,\eta_{lub}\right)\left(\frac{ms_{ref}}{(m-1)s_{ref}+1}\right) + ln\,\eta_{lub}} \tag{2}$$

where $\boldsymbol{m = M_{lub}/M}$, being $\boldsymbol{M}$ the molecular mass of the component.

Bair [16] offers an alternative mixing law to equation (2). Reference [11] offers an adaptation to these equations in consideration of any refrigerant and lubricant, see equations (3) and (4). Equations (1) and (2) are modified with constants (k_{al}, k_{et}) multiplying the molecular mass ratio, as follows:

$$\boldsymbol{\alpha_{mix}} = \frac{\boldsymbol{k_{al}ms_{ref}(\alpha_{ref}-\alpha_{lub})}}{\boldsymbol{s_{ref}(k_{al}m-1)+1}} + \boldsymbol{\alpha_{lub}} \tag{3}$$

$$\boldsymbol{ln(\eta_{mix})} = \boldsymbol{\left(ln\,\eta_{ref} - ln\,\eta_{lub}\right)\left(\frac{k_{et}ms_{ref}}{(k_{et}m-1)s_{ref}+1}\right) + ln\,\eta_{lub}} \tag{4}$$

These constants are calibrated from measurements of viscosity of different oil-refrigerant mixtures, so calibration functions that depend on oil viscosity and working temperature can replace the originally constant parameters ($\boldsymbol{k_{al}, k_{et}}$), thus,

$$\boldsymbol{k_{al} = f(\eta_{0.lub}, T)} \quad \text{and} \quad \boldsymbol{k_{et} = f(\eta_{0.lub}, T)} \tag{5a, 5b}$$

These equations have been proven to be more accurate than the original ones for several mixtures of refrigerants and oils when compared with measured values [19].

Now, in rolling bearing life calculation the lubrication quality parameter kappa (κ) is used as a measure of the lubrication condition in the bearing. This parameter is defined as the ratio between the actual viscosity used in the bearing at the working temperature and the required viscosity recommended by the manufacturer and it is properly defined and explained in ISO 281:2007 [34]. The required viscosity is a parameter provided by the bearing manufacturer. Thus, the only parameter that remains to be estimated for calculation of κ in oil-refrigerant mixture conditions is the actual lubricant viscosity and equation (2) can be used for this purpose.

For bearing life calculations, reference [4] recommends increasing the required kinematic viscosity of the bearing (ν_1) calculated as oil by multiplying it with a factor $f = 3$, for HFC-134a and POE oil. This is to

account for the reduction in piezo-viscosity plus other unaccounted effects (e.g.: lubricity reduction and chemical aggressiveness) in the actual viscosity estimated with equation (2). For very compressible refrigerants an extra increase factor should be derived for correction in the final calculated κ, but here this will be disregarded. Bearing life can be calculated from this final adjusted value of κ called $\kappa_{oil/ref}$. Therefore, according to [11] it is:

$$\boldsymbol{\nu_{adj} = \nu f_{adj}} \tag{6}$$

where ν is the actual kinematic viscosity calculated as oil but with the value obtained from the mixture. Thus,

$$\boldsymbol{\kappa_{oil/ref} = \kappa_{oil}(f_{adj})} \tag{7}$$

with, κ_{oil} being the lubrication quality factor calculated as oil but with the viscosity of the mixture. And, by neglecting the difference in compressibility between oil and refrigerant,

$$\boldsymbol{f_{adj} = \left[\left(\frac{\alpha_{mix}}{\alpha_{oil}}\right)^{0.7} \frac{1}{f_s}\right]} \tag{8}$$

Where

$$\boldsymbol{f_s = 1 + (f - 1)tanh\left(\frac{4s_{ref}}{s_{ref.c}}\right)} \tag{9}$$

and $\boldsymbol{f}$ being the safety factor as described by Meyers [4], but because it was initially introduced by Jacobson it will be called the "Jacobson" safety factor here, defined at a reference refrigerant dilution fraction $\boldsymbol{s_{ref.c}}$. Notice that f_s will become 1 when the dilution of refrigerant s_{ref} becomes zero i.e. when there is no refrigerant mixed into the oil.

The above model has been substantially validated with several HFO, HCFO and HFC refrigerants, but it is likely that some adaptation will be required for Ammonia and CO2. Unfortunately, not much experimental data are available in the literature to either verify this model or to adapt it for those important natural refrigerants. For example, when it comes to ammonia only limited literature is available [25], mainly on the development of Daniel plots for mixtures of ammonia and various oils with dilution rates up to 6% ammonia in saturation conditions. And on the piezo-viscosity behaviour of ammonia no information has been found, (except for relatively low pressures [26], though it is likely that this simple molecule - similar to CO2 - will be an iso-viscous liquids, similar to water. So this could be a "safe" approach for design purposes until more data becomes available. Equation (1) is still valid for $\alpha_{ref} = 0$.

3. Rolling Bearing Life and Other Bearing Failure Modes

The typical life-critical issues in refrigerant compressor bearings, where usual maximum Hertzian pressures are below 2 GPa, are surface-related problems, caused by e. g. poor lubrication and contamination, which leads to wear and/or surface distress, also known as micropitting. Other surface failure modes are also possible e.g. smearing (or adhesive wear), however, those are less often observed in these applications since in general no large rotational accelerations are experienced. Thus, most of the effort invested to increase the life of the bearings goes to preventing or delaying surface distress from poor lubrication conditions. This is why the authors in an earlier publication [2] have included a special section to this topic. Details about performed reliability studies can be found in the following publications: on the accuracy of high reliability values in bearing life calculation [43] and on the accuracy of comparing life models with endurance testing [44].

In [2], the authors also included a modelling example for indications of surface distress occurrence and ways of mitigation. Surface distress is thus strongly influenced by high oil dilution rates, low viscosities of the oil-refrigerant mixture, low piezo-viscosity and higher compressibility of the refrigerants, plus sometimes some corrosive attack due to the chemical activity of the refrigerants, especially in combination with moisture. Note that in [27] a new bearing life model is described that separates the surface distress from subsurface fatigue. This model – which is briefly described in the next section - should be better suitable to handle life calculations in this type of diluted applications, not only because of its better link to physics but also due to its flexibility to accommodate different surface related failure modes.

3.1. The Generalized Bearing Life Model (GBLM)

Following [27] the bearing life equation associated to a reliability (S) can be written as:

$$\boldsymbol{L = \frac{\left[ln\left(\frac{1}{S}\right)\right]^{1/e}}{u}\left[\overline{A}\int_{V_v}\frac{\langle\sigma_v-\sigma_u\rangle^c}{z^h}dV_v + \overline{B}\int_A\langle\sigma_s-\sigma_u\rangle^c dA\right]^{-1/e}} \quad (10)$$

For nomenclature see the mentioned references. In rolling bearings the chosen reliability is usually 0.9, thus the life L will be known as the L_{10} life of the bearing. The first integral in equation (10) is the usual subsurface term [28], while the second integral is a new integral accounting for the fatigue damage at the surface, which can be assessed with a numerical model for e.g. surface distress [29] or indentations [30], etc.

In order to understand the different tribological processes happening at the surface of a rolling bearing, one can take the example of hybrid ceramic bearings, i.e. bearings that use rolling elements made out of ceramic materials instead of steel. It is well known that hybrid bearings are more resilient against poor lubrication conditions and indentations than steel-steel bearings [31, 32]. Therefore, the assessment of the surface integral in equation (10) for this type of bearings is customized [27, 33]. If the new GBLM model is applied [33] much longer lives for hybrid than steel-steel bearings are predicted under difficult conditions, i.e. poor lubrication and contamination. Of course, in case of good and clean lubrication conditions but heavy loads, subsurface fatigue will dominate and hybrid bearing life will be penalised by GBLM due to the higher elastic modulus of ceramics creating somewhat higher contact stresses – which is consistent with test results.

3.2. Bearing Damage due to Particles and Indentations

Particle entrapment in all-steel and hybrid bearings is discussed in [35] and [36]. In [35], the indentation process is described in addition to particle entrapment, presenting some modelling tools for this. The entrapment results where summarised with the use of an arbitrary indentation severity parameter defined as:

$$\boldsymbol{IS = \frac{h_p s_p}{\phi a}} \quad (11)$$

Equation (11) refers to the schematics of an indentation profile along the rolling direction as depicted in Figure 3 left. Where *a* refers to the Hertzian semi-width along the rolling direction of the contact.

The reference discusses a simple entrapment model based on the friction coefficient between the particle and the bearing surfaces μ_p and also based on the rolling element diameter D_w and negligible lubricating central film thickness h_c. Giving the maximum size of a spherical particle to be entrapped as:

$$\boldsymbol{d_{p.max} = \frac{D_w}{cos(tan^{-1}\mu_p)} - D_w} \quad (12)$$

The fact that a particle is entrapped in a contact does not necessarily mean that it will indent the rolling surface and generate damage. It all depends on size, material and hardness of this particle in relation to the counter face. Very small particles will move through the lubricant film without causing any damage to the mating surfaces. Larger and very hard brittle particles may shatter in the contact producing many smaller particles. Figure 3 (right) depicts some predicted maximum entrapment particle diameters for varying rolling element diameter and particle-surface friction coefficient. The minimum particle diameter according to equation [37] that might still indent the bearing surfaces is also depicted in the plot (as a reference) using the horizontal black dotted line, notice that the minimum steel particle diameter causing an indentation would be of the order of the central film thickness h_c - for a typical heat pump bearing $h_c \approx 0.1\,\mu m$. Notice that experiment estimated values for μ_p steel-steel are reported in [35] of about $\mu_p = 0.15$, but it will be lower for the case of ceramic rolling elements.

Of course, most contamination particles are not spherical, however the model is valid for particle diameters estimated from the shortest particle length, e.g. for a cylindrically shaped particle the parameter d_p would refer to the cylinder diameter and not to the length. The damage produced by indentations in the context of GBLM and EHL contacts is described in detail in [30].

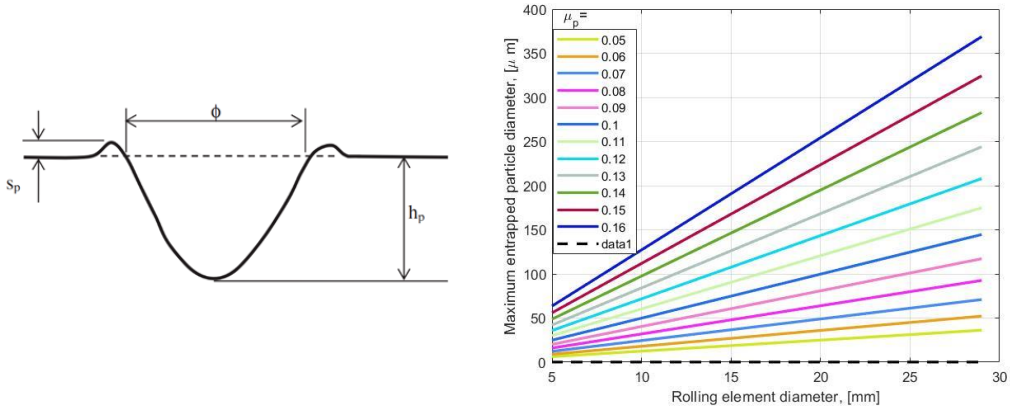


Fig. 3. Left: Schematics of an indentation profile along the rolling direction of the contact.
Right: Maximum entrapment diameter particle as calculated from equation (12). The horizontal black dotted line gives an indication of the minimum steel particle diameter that could produce an indentation on the bearing surfaces according to equation [37].

3.3. Surface Distress Phenomenon

Micropitting is a term widely used in the gearbox industry to describe micro surface spalls and cracks, which sometimes appear on the surface of rolling–sliding contacts. ISO 15243 [38] refers to this failure mode as surface distress or surface initiated fatigue, i.e. the failure of the rolling contact metal surface asperities under poor lubrication conditions and with certain amount of sliding motion causing the formation of (1) burnished areas (glazed; grey stained), (2) asperity microcracks, and (3) asperity micro-spalls, see Figure 4 (left). This failure mode will be described here using the term of surface distress. It is well known that surface distress is the result of the competition between surface fatigue and mild wear [29]. Mild wear (wear at asperity level) modifies the initial topography reducing the asperity heights and also removes fatigued surface layers - refreshing the exposed material and thus delaying surface fatigue. The modelling of this phenomenon is possible, and one of the current authors has developed a numerical model for surface distress [29] that can be applied for the present case of oil-refrigerant mixtures [2]. The model requires 3D digitised roughness data from several positions of the two contacting surfaces (inner - or outer - ring raceway and roller - or ball). A calculation example simulating the fatigue weakening by corrosion from refrigerants is given in [2].

3.4. Integrating Surface Failure Modes in GBLM

The model described in [29] can be used to generate tendency curves by simulating surface distress from using roughness samples of many bearings (all types and sizes) under different loads and lubrication conditions (In the bearing industry the parameter κ is used [34] rather than the film thickness/roughness ratio Λ used in other engineering fields to describe the quality of lubrication). In [29] a curve-fitted equation to model the surface integral representing surface distress is obtained from the simulations. An example of the graphical representation of this equation is depicted in Figure 4 (right), where the normalized value of the surface integral ($\tilde{I}_s$) is plotted for different normalised equivalent loads (P/P_u) under different lubrication qualities (κ).

The surface integral is defined as

$$\tilde{\boldsymbol{I}}_{\boldsymbol{s}} = \boldsymbol{I}_{\boldsymbol{s}}\boldsymbol{u}^{\boldsymbol{e}}\left(\frac{\boldsymbol{C}}{\boldsymbol{P}}\right)^{\boldsymbol{p}} / \left(\boldsymbol{K}\,\boldsymbol{ln}\left(\frac{\boldsymbol{1}}{\boldsymbol{0.9}}\right)\right) \tag{13}$$

with K being a scaling factor and,

$$\boldsymbol{I}_{\boldsymbol{s}} = \overline{\boldsymbol{B}}\int_{\boldsymbol{A}} \langle \boldsymbol{\sigma}_{\boldsymbol{s}} - \boldsymbol{\sigma}_{\boldsymbol{u}} \rangle^{\boldsymbol{c}} \boldsymbol{dA} \tag{14}$$

As can be seen in Figure 4 (right) when lubrication conditions deteriorate (low values of κ) the surface integral increases in value, this is an indication of higher probability of surface distress. When the load increases in general the integral increases, except in the cases of very poor lubrication where the integral is slightly reduced due to the increase of mild wear. The scaling and behaviour of these curves can be adapted

for the case of material weakness, e. g. due to corrosion from refrigerants and moisture. Other adaptations are possible depending on the balance wear and fatigue, or with the use of hybrid bearings [27], etc.

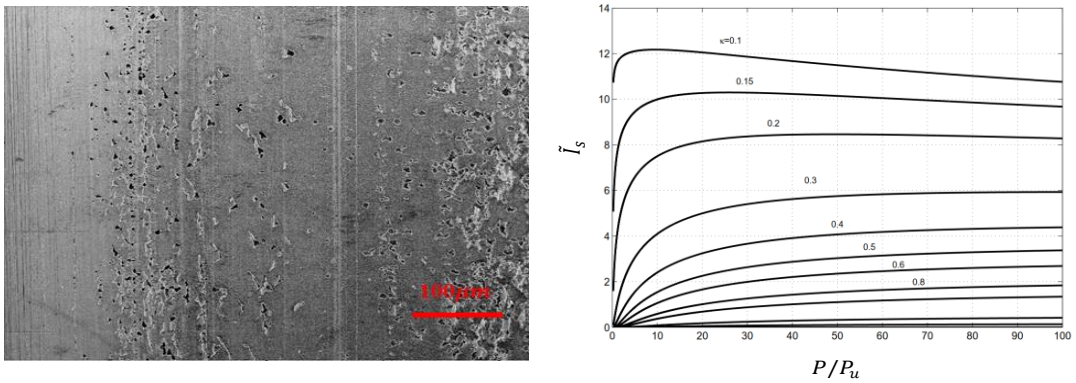


Fig. 4. Left: Surface distress in a raceway bearing surface; Right: Example of normalised surface integral for the GBLM model as a function of normalised equivalent load and lubrication quality in the bearing, as given in [29].

3.5. Relative Surface Fatigue Index in GBLM

One of the advantages of separating the subsurface and surface damage integrals is that they can be compared and in this way an indication of the most fatigued area can be determined. Consider the parameter called "relative surface fatigue index" denoted by the symbol S_R:

$$\boldsymbol{S_R = \frac{I_s}{I_s + I_{ss}}} \tag{15}$$

where I_s is given by equation (14) and I_{ss} by

$$\boldsymbol{I_{ss} = \overline{A} \int_{V_v} \frac{\langle \sigma_v - \sigma_u \rangle^c}{z^h} dV_v} \tag{16}$$

Notice that when $S_R \to 1$ the surface integral is dominant which means that the higher damage is expected at the surface. When $S_R \to 0$ fatigue is taken mainly by the subsurface. This parameter is important because when operating conditions are changed, changes in this parameter will indicate how the surface or the subsurface is being affected. The parameter S_R can also be calculated locally, for example along the raceway profile in a roller bearing, reflecting the effect of the local stresses. Reference [30] shows good examples of the use of S_R for the case of indentations and the interaction with the lubrication quality parameter.

4. Technical Bearing Solutions for Heat Pump Compressors

In the following, some technical solutions to address the challenges in heat pump compressors bearings as indicated above are presented.

4.1. Surface Treatments in Conventional Rolling Bearings

For oil-refrigerant mixtures under poor lubrication and/or high contamination, surface (heat) treatments that have a large potential for rolling bearings are nitriding and carbonitriding. The latter one is an added surface heat treatment with the addition of ammonia to the standard gas carburisation process. This introduces N and C atoms diffusing into the surface steel, improving the fatigue strength and reducing wear. Carbonitrided (HN code) bearings have been tested and compared with normal heat treated bearings in harsh contaminated conditions in [39]. Wear rate was reduced to about 45 % of the normal bearings and bearing life was roughly doubled for those particular test conditions. In addition, the surface distress model described before was used to simulate the behaviour and provide understanding.

4.2. Semi-Hybrid Rolling Bearings

It has been verified by testing [40] that steel rolling bearings which contain at least one rolling element made of ceramic (Si3N4) material can substantially improve performance under poor lubrication and high contamination conditions. Therefore, the next "line of defence" after nitriding or carbonitriding for lubrication with oil-refrigerant mixtures should be this type of rolling bearings, sometimes also called "semi-hybrid" or "self-healing" bearings. The working mechanism is similar to hybrid bearings as explained in [35, 37].

4.3. Raceway Coatings

If a bearing raceway coating has to be chosen in harsh oil-refrigerant lubrication conditions, it is recommended to select a sacrificial coating that will mainly help to run-in the surfaces improving the tribology and smearing itself for the steel surfaces. In this way, it will also protect the surfaces from mild chemical attacks (mild corrosion). This is the case for special bearing-grade black oxide coating [41], which could be a rolling bearing performance improver in mild severity conditions of poor lubrication with oil-refrigerant mixture. An alternative coating solution against corrosion is zinc-coated bearings.

For lower refrigerant dilution rates other coatings may be used that can provide the bearings with some protection. This is the case for special DLC (NoWear^{TM}) with and without porosity seal, made to endure in poor lubrication conditions and to fight adhesive wear.

4.4. Hybrid ceramic bearings

For extreme conditions such as dilution rates much higher than say 20%, for very low operating viscosity, and/or very high or low speeds, hybrid bearings comprising ceramic rolling elements (usually made out of Si3N4/silicon nitride) and steel rings are a favourable solution. The reasons for the superior performance of hybrid bearings under such conditions was already explained in section 3.1. In case the chemical conditions in the compressor also bear the risk of corrosive attack, or if the bearings should be lubricated only by the refrigerant in oil-free compressors, the rings need to be made out of a bearing-grade corrosion resistant material with high toughness, see next section (Figure 5).

4.5. High-nitrogen stainless steel hybrid bearings

When the bearing rings cannot be protected by oil or grease against corrosive media in the machine, rings made out of stainless steel are often the most reliable solution. Various stainless material options exist, which have to be selected based on their corrosion resistance as well as their mechanical strength in rolling bearing application. Inner and outer rings made of through-hardened martensitic stainless steel with high nitrogen content show high corrosion-protection capability and fatigue toughness. It is of high importance to tune the steel making and heat treatment process parameters to obtain a fine microstructure that leads to high toughness and so making the steel an excellent material for the demanding conditions in highly loaded rolling contacts.

With thinner lubrication films or in media lubricated applications (like for PRL) also the raceway surface finishing quality tends to play a more important role for the bearing performance. This is why more stringent raceway honing specifications are applied related to surface roughness and imperfections, as well as to manufacturing process cleanliness applied for media lubricated applications.

For extreme conditions, a specific high-nitrogen steel with a dedicated heat treatment for high corrosion resistance, fatigue toughness and also higher temperature stability was developed. It was proven to be a reliable solution for applications like sour gas compressors, cryogenic pumps, and pure refrigerant lubricated compressors. Some examples for media- and mixed-media lubricated applications are presented in [42].



Figure 5: Special hybrid ceramic bearings with super-tough high-nitrogen stainless steel rings

4.6. Cage Material Selection

There is a large variety of cage designs and materials for any bearing type. In demanding application, the cage design choice is often either a massive metal cage or a lightweight polymer cage. Common materials for metal cages are brass, steel, or sometimes also aluminium alloys. Massive metal cages offer high mechanical strength and for very critical applications special pocket designs or surface coatings can be applied. Massive (stress-free) brass cages have also a proven track recorded in ammonia compressors.

Besides standard polymer cages, different high-performance polymers have been developed for bearing applications. Fibre reinforced PEEK (polyether-ether-ketone) is a very robust solution in demanding applications, especially where an extended temperature range, chemical stability, and a lightweight design are required. The combination of ceramic rolling elements and a polymer cage allows for a very low weight of the rotating components in the bearing which are not directly mounted on the shaft or in the housing, reducing their inertia which is especially beneficial in high acceleration or very low load conditions. PEEK cages have also been proven to work in ammonia compressors up to 120°C operating temperature

5. Discussion

The present publication summarises the current status of rolling bearing technology for refrigerant compressor applications, with emphasis on the special conditions found in heat pumps, where the lubrication with oil-refrigerant mixtures is common practice and the bearing operating conditions are harsher than for most other compressor applications. It is suggested that standard bearing technologies for conventional refrigerants and requirements with oil-dilution rates usually lower than 20% will be increasingly challenged by new and more chemically active low-GWP refrigerants (according to Kyoto protocol requirements). Dilution rates up to 60% or even higher in some sections of the thermodynamic duty cycle, and also much higher process temperatures and pressures leads to challenging conditions for the rolling contacts in the bearings.

As a graphical summary of the application of the different rolling bearing technologies, the authors propose the schematics of Figure 6 to describe the possible usage ranges and technology sophistication level of the different rolling bearing technologies discussed in the current paper, as a function of the tribological and chemistry complexity and risks.

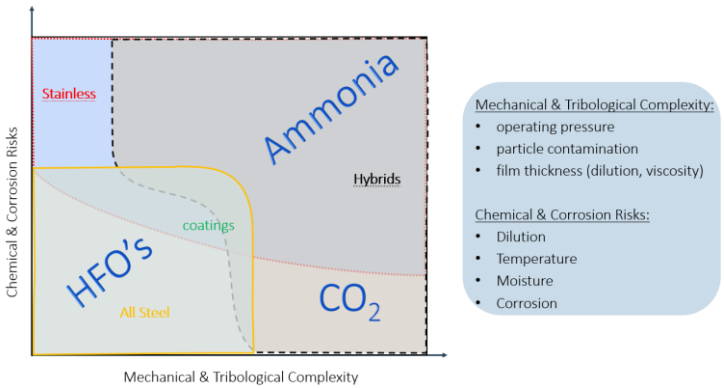


Fig. 6. Schematics of potential solutions for rolling bearings depending on the application and tribological and corrosion risks.

Notice that the ordinate in Figure 6 (mechanical & tribological complexity) represents a qualitative scale where no values are given, but it should illustrate the experience of the authors. The abscissa of the figure represents the risks related to chemical aspects. Note that tribological risks (i.e. due to very low viscosity or speeds) can be mitigated with the use of hybrid bearings. High chemical risks (high corrosion potential) can be mitigated with the use of special bearing-grade stainless steels. In the transition area between all-steel bearings to hybrid bearing and stainless steel rings, the use of special heat treatments, coatings, or semi-hybrid bearings can be an appropriate fit-for purpose solution – in economic and as well as technical terms.

6. Conclusions

The following conclusions can be drawn based on the above presented research and also practical experience:

1. Standard all-steel rolling bearing technology is currently challenged by the arrival of new, more environmentally friendly refrigerants in the industrial compressor sector, which bring higher refrigerant dilution rates, more chemically active compounds and – for heat pumps or also data centre chillers - much higher temperatures.
2. As a response to this challenge, different rolling bearing technologies are proposed, like the use of special heat treatments as well as hybrid ceramic rolling bearings.
3. A better understanding still needs to be obtained for specific lubrication mechanisms and failure initiation mechanisms in heat pumps with low-GWP refrigerants. This implies work to be done on tribological refrigerant characterisation, tribology contact modelling, tribo-testing, and bearing testing under representative compressor conditions.

Acknowledgements

The authors wish to thank SKF for the permission to publish this article.

References

[1] SKF Evolution online magazine, Industry: Heat pumps favour global drive for zero emissions. January 20th 2022. https://evolution.skf.com/heat-pumps-favour-global-drive-for-zero-emissions/
[2] Morales-Espejel, G.E., Wallin, H. H., Hauleitner, R., Arvidsson, M., Progress in Rolling Bearing Technology for Refrigerant Compressors, IMechE, Part C, J. of Mech Engineering Science, vol. 232(16), pp. 2948-2961, 2017.
[3] Wardle, F.P., Jacobson, B., Dolfsma, H., Hoglund, E. Jonsson, U. The Effect of Refrigerants on the Lubrication of Rolling Element Bearings used in Screw Compressors, Proc. Int. Comp. Conf. Purdue 1992; pp. 523-534. http://docs.lib.purdue.edu/cgi/viewcontent.cgi?article=1842&context=icec (1992, accessed 21 June 2017).
[4] Meyers, K. Creating the Right Environment for Compressors Bearings, SKF Evolution Magazine 1997; No. 4, November. http://evolution.skf.com/creating-the-right-environment-for-compressor-bearings/
[5] Gunsel, S., "Elastohydrodynamic Lubrication with Polyolester Lubricants and HFC Refrigerants", Final Report, vol 1, prepared for The Air Conditioning and Refrigeration Technology Institute under ARTI MCLR Project Number 670-54400, 1999. DOE/CE/23810-102.
[6] Gunsel, S., Pozebanchuk, M., "Elastohydrodynamic Lubrication with Polyolester Lubricants and HFC Refrigerants", Final Report, vol 2, prepared for The Air Conditioning and Refrigeration Technology Institute under ARTI MCLR Project Number 670-54400, 1999. DOE/CE/23810-102.
[7] Akei, M., Mizuhara, K. The Elastohydrodynamic Properties of Lubricants in Refrigerant Environments, Trib. Trans. 1997, vol. 40, 1, pp. 1-10.
[8] Jonsson, U. J., Lilje, K.C. Elastohydrodynamic Lubrication Properties of Polyol Ester Lubricants-R134a Mixtures, International Compressor Engineering Conference 1998, Purdue University, paper 1227, pp 123-128. http://docs.lib.purdue.edu/cgi/viewcontent.cgi?article=2226&context=icec
[9] Bair, S., Habchi, W., Baker, M., Pallister, D.M., "Quantitative Elastohydrodynamic Film-Forming for an Oil/Refrigerant System", Trans. ASME, J. of Trib., 139, 2017, 061501-1-7.
[10] Zhang, F., Fillot, N., Hauleitner, R., Morales-Espejel, G.E., "Thermal-Elastohydrodynamic Contacts Lubricated With Oil/ Refrigerant Solutions: A New Cavitation Modeling Approach Based on Refrigerant Solubility", Trans. ASME, J. of Trib., 144, 2022, 081602-1-13.
[11] Morales-Espejel, G.E., Hauleitner, R., "Lubrication Quality of Compressor Rolling Bearings with Oil-Refrigerant Mixtures", Tribology Online, vol. 15(1), pp. 45-52, 2020.
[12] Hauleitner, R., Morales-Espejel, G.E., "Lubrication Quality of Compressor Rolling Bearings with Oil-Refrigerant Mixtures", in Proceedings of the International Compressor Engineering Conference, Purdue University 2020, paper 1258, pp. 1-5.
[13] Tuomas, R., "Properties of Oil Refrigerant Mixtures – Lubrication of Ball Bearings in Refrigerant Compressors", PhD Thesis, Lulea University of Technology 2006:70, Sweden. http://www.diva-portal.org/smash/get/diva2:990000/FULLTEXT01.pdf (2006, accessed 21 June 2017).
[14] Laesecke, A., Bair, S., "High-pressure viscosity measurements of 1,1,1,2-tetrafluoroethane", Int. J. Thermophysics 2011, 32, pp. 925–941.
[15] Vergne, P., Fillot, N., Bouscharain, N., Devaux, N., Morales-Espejel, G.E., "An Experimental and Modelling Assessment of the HCFC-R123 Refrigerant Capabilities for Lubricating Rolling EHD Circular Contacts", Proc IMechE, Part J, J. of Eng. Tribology 2015, vol. 229(8), pp. 950-961.
[16] Jacobson, B.O., Morales-Espejel, G.E., High Pressure Investigation of Refrigerants HFC245fa, R134a and R123, in Proceedings of the International Compressor Engineering Conference, Purdue University 2006, paper 1789, pp. 1-8.
[17] Morales-Espejel, G.E., Meeuwenoord, R., Félix-Quiñonez, A., Hauleitner, R., "Film thickness and traction measurements of refrigerant R1233zd used as lubricant in elastohydrodynamic conditions", IMechE, Part C, J. of Mech Engineering Science, vol. 229(2), pp. 244-253, 2014.

[18]Habchi, W., Vergne, P., Eyheramendy, D., Morales-Espejel, G.E., Numerical investigation of the use of machinery low-viscosity working fluids as lubricants in elastohydrodynamic lubricated point contacts. Proc IMechE, Part J: J Engineering Tribology 2011; 225: 465–477.
[19]Wallin, H.H., Morales-Espejel, G.E., Hybrid Bearings in Oil-Free Air Conditioning and Refrigeration Compressors, SKF Evolution Magazine 2002, No. 2. http://evolution.skf.com/hybrid-bearings-in-oil-free-air-conditioning-and-refrigeration-compressors/ (2002, accessed 21 June 2017).
[20]Morales-Espejel, G.E., Hauleitner, R. , Wallin, H., Pure Refrigerant Lubrication Technology in Oil-Free Centrifugal Compressors, SKF Evolution Magazine 2017, No. 1. http://evolution.skf.com/us/pure-refrigerant-lubrication-technology-in-oil-free-centrifugal-compressors/
[21]Hauleitner, R.; Morales-Espejel, G. E.; Meeuwenoord, R.; and Arvidsson, M., "Rolling Bearings Lubricated With Refrigerant" (2018). International Compressor Engineering Conference. Paper 2556. https://docs.lib.purdue.edu/icec/2556
[22]Jacobson, B.O., Morales-Espejel, G.E., High Pressure Investigation of Refrigerants HFC245fa, R134a and R123, in Proceedings of the International Compressor Engineering Conference, Purdue University 2006, paper 1789, pp. 1-8. http://docs.lib.purdue.edu/cgi/viewcontent.cgi?article=2788&context=icec
[23]Gużda, A., Szmolke, N.: Compressors in Heat Pumps. Machine Dynamics Research 2015, Vol. 39, No 2, 71–83, Opole University of Technology
[24]SKF: Bearings in twin screw compressors, Applic. handbook, PUB BU/P7 14510 EN, Jan. 2018
[25]Feja, S., Hanzelmann, C., Zuber, S., PVT-Measurements for High-Temp Ammonia Heat Pump Lubricants, 7th IIR Conference: Ammonia and CO2 Refrigeration Technologies, Ohrid, 2017, pp. 1-8 (doi: 10.18462/iir.nh3-co2.2017.0013).
[26]Fenghour, A., Wakeham, W. A., Vesovic, V., Watson, J. T. R., Millat, J., Vogel, E. The Viscosity of Ammonia, Journal of Physical and Chemical Reference Data 24, 1649 (1995); https://doi.org/10.1063/1.555961
[27]Gabelli, A. Morales-Espejel, G.E., A Model for Hybrid Bearing Life with Surface and Subsurface Survival, Wear 422-423, pp. 223-234, 2019.
[28]Ioannides, E., Harris, T.H., A New Life Model for Rolling Bearings, Journal of Tribology, 107, 367-378, 1985.
[29]Morales-Espejel, G.E., Brizmer, V., Micropitting Modelling in Rolling–Sliding Contacts: Application to Rolling Bearings, Trib. Trans. 2011, vol. 54, 4, pp. 625-643.
[30]Morales-Espejel, G.E., Gabelli, A. A Model for Rolling Bearing Life with Surface and Subsurface Survival: Sporadic Surface Damage from Deterministic Indentations, Trib. Int.. 2016, vol. 96, pp. 279ff.
[31]Gabelli, A., Kahlman, L., Bearings that Heal Themselves, SKF Evolution Magazine 1999, No. 3, September. http://evolution.skf.com/bearings-that-heal-themselves-2/ (1999, accessed 21 June 2017).
[32]Brizmer, V., Gabelli, A., Vieillard, C., Morales-Espejel, G.E., An Experimental and Theoretical Study of Hybrid Bearing Micropitting Performance under Reduced Lubrication, Trib. Trans. 2015, vol. 58, pp. 829-835.
[33]Morales-Espejel, G.E., Gabelli, A., Application of a rolling bearing life model with surface and subsurface survival to hybrid bearing cases, Proc IMechE, Part C, J. of Mech. Eng. Science 2019, vol. 233(15), pp. 5491-5498.
[34]ISO 281, International Standard. Rolling bearings - dynamic load ratings and rating life. 2007.
[35]Morales-Espejel, G.E., Gabelli, A., Particle entrapment and indentation process in rolling bearings, Proc IMechE, Part J, J. of Eng. Tribology 2016, vol. 230(12), pp. 1572-1587.
[36]Strubel, V., Fillot, N., Ville, F., Cavoret, J., Vergne, P., Mondelin A., Maheo, Y., Particle Entrapment in Hybrid Lubricated Point Contacts, Trib. Trans., 2016, vol 59(4), 768–779.
[37]Ai, X., Effect of debris contamination on the fatigue life of roller bearings. Proc IMechE, Part J: J Engineering Tribology 2001; 215: 563–575.
[38]ISO Standard 15243. Rolling bearings—Damage and failures—Terms, characteristics and causes. Geneva, Switzerland: ISO, 2017.
[39]Gabelli, A., Kerrigan, A., De Blic, E., HN Rolling Bearings for Extended Service Life, Progress in Heat Treatment and Surface Engineering, Proceedings of the Fifth ASM Heat Treatment Conference, Mittemeijer, E.J. and Grosch, J., Ed. June 2000, Gothenburg, Sweden.
[40]Gabelli, A., Kahlman, L., Bearings that Heal Themselves, SKF Evolution Magazine 1999, No. 3, September. http://evolution.skf.com/bearings-that-heal-themselves-2/ (1999, accessed 21 June 2017).
[41]Brizmer, V., Stadler, K., van Drogen, M., Han, B., Matta, C., Piras, E.: The Tribological Performance of Black Oxide Coating in Rolling/Sliding Contacts, Tribology Transactions, published online 2016. DOI: 10.1080/10402004.2016.1186258
[42]Hauleitner, R., Dietl, P., Arvidsson, M.: Rolling bearing solutions for mixed-media and media lubrication in compressors or pumps, 4th International Rotating Equipment Conference 2019, paper no. 2019-036, Wiesbaden. https://evolution.skf.com/wp-content/uploads/sites/5/2020/08/pump-and-compressor-performance-under-thin-film-and-oil-free-conditions-1.pdf
[43]Blachère, S., Morales-Espejel, G.E.: Extrapolating Rolling Bearing Life Data to Very High Reliabilities: Friend or Foe, Bearing World Journal, vol 6, pp. 23-39, 2021.
[44]Blachère, S., Gabelli, A., Morales-Espejel, G.E.: Experimental Conformity Level for comparison between endurance tests and life calculation models, Bearing World Journal, vol 6, pp. 15-22, 2021.

14th IEA Heat Pump Conference
15-18 May 2023, Chicago, Illinois

Resorption heat pump development

G. H. Atkinson[a*], R. E. Critoph[a], S. J. Metcalf[a], G. S. F. Shire[a]

[a] University of Warwick, Coventry CV4 7AL, UK

Abstract

The development of a resorption heat pump for domestic use is described. The cycle uses the alternate adsorption and desorption of ammonia between two salts – sodium bromide and manganese chloride. The equilibrium and dynamic behaviour of both salts with ammonia has been measured using the Large Temperature Jump (LTJ) technique and a good match found between experimental and modelled data. This has been used to design a nominal 2.5 kW heat pump as a demonstrator to confirm the results. The bench scale machine can be driven by a high temperature source of pressurised water at up to 170 °C, the low temperature input is from water between 5 and 15 °C and the output is between 40 and 60 °C. It uses a simple cycle consisting of one low-pressure phase followed by a high-pressure phase, without any heat recovery, moving ammonia from the Low Temperature Salt (LTS) sodium bromide reactor to the High Temperature Salt (HTS) manganese chloride reactor and vice versa. A practical machine would have two such sets of reactors and recover heat between them, but this level of complexity is avoided in the demonstrator. Despite this, initial results are extremely encouraging having achieved repeatable ammonia cycling between the reactors.

© HPC2023.
Selection and/or peer-review under the responsibility of the organizers of the 14th IEA Heat Pump Conference 2023.

Keywords: Ammonia; Heat pump; Resorption.

1. Introduction

The chemisorption of ammonia into halide salts has been studied over many years: it was first observed by Faraday [1] who recognised its potential for generating a heating or cooling effect; more recently it gained attention in the ‘80s and ‘90s, primarily by Spinner [2], and many others: Goetz et al., [3], Lebrun and Spinner, [4]; Mazet and Spinner [5].

Cycles using chemisorption can be applied to refrigeration, heat pumping, and thermal transformation and may either use a single salt in a reactor together with a system for evaporating and condensing the refrigerant, or a resorption cycle in which the refrigerant is adsorbed or desorbed between two salts. More complex three salt cycles with varying degrees of complexity and heat recovery are also possible. A simple heat-pumping cycle is illustrated in Figure 1.

A Low Temperature Salt (LTS) and a High Temperature Salt (HTS) are contained in separate reactors that are connected, the whole being in the presence of ammonia that is either present as a gas, or a chemically adsorbed phase with the salts. The equilibrium lines for the reaction with each salt are illustrated on the Clapeyron diagram, Figure 1. In reality, there can be hysteresis between adsorption and desorption, but this is omitted for clarity. Starting at low pressure, the LTS is heated from ambient, perhaps at 0°C, which desorbs ammonia. In the case of NaBr as illustrated 5.25 mols are desorbed. The ammonia is adsorbed in the HTS (4 mols for $MnCl_2$) generating useful output at 60°C. When the reactions are complete in the low-pressure phase, the HTS is heated by a high temperature heat source at around 150°C. Both salts’ state moves up the equilibrium line until they are at 60° and 150°. During the pressure rise there is little adsorption or desorption because no heat is removed from the LTS, but on reaching the high-pressure phase, heat can be removed from the LTS at 60 °C whilst more heat enters the HTS at 150 °C. The reactions proceed at a nominal constant temperature until complete and the LTS again contains its maximum quantity of ammonia. To return to the

* Corresponding author. Tel.: +44 2476 1 50465;
E-mail address: George.H.Atkinson@warwick.ac.uk.

starting condition in the low-pressure phase, the LTS is cooled back to ambient whilst the HTS is adiabatic. A real machine would most likely feature two sets of reactors operating out of phase so that heat from the cooling LTS could be used to pre-heat the other HTS. Advantages of a resorption cycle are the absence of an evaporator, condenser, or any refrigerant control valves, plus a wide range of salts to choose from that may be matched to required temperatures.

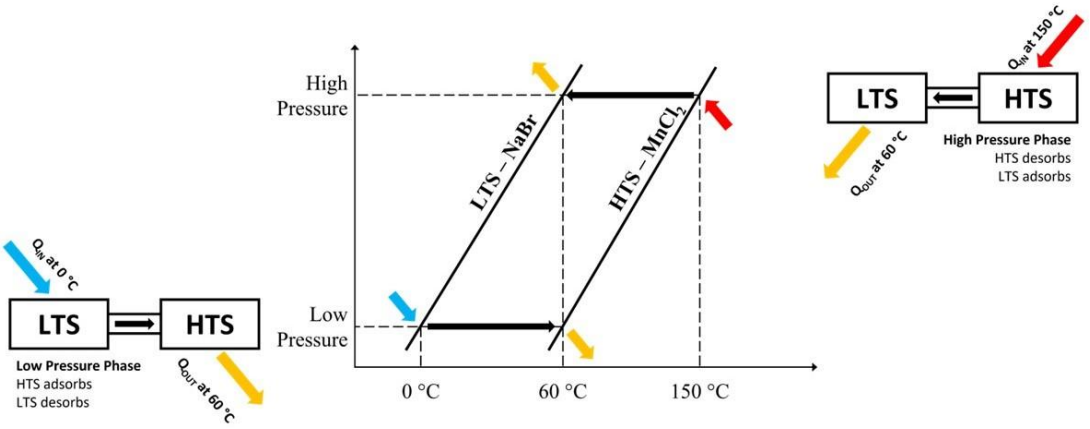


Fig. 1. Simple resorption heat pump cycle. Red, orange and blue arrows indicate heat flows, black arrows are used for ammonia flow.

However, practical difficulties have prevented successful exploitation of the cycle in the past. These are mainly due to slow reaction dynamics (hour-long cycles) and agglomeration of the salts (when used in bulk form) leading to a loss in reactivity. Both drawbacks can be overcome by dispersion of the salt within a porous matrix. Keeping the crystals small and separate prevents agglomeration. Additionally, if the matrix is highly conductive, such as Expanded Natural Graphite (ENG), the overall heat transfer is improved and reaction times reduced, as reported by van der Pal [6]. In this study the salts are impregnated into ENG sheet (SIGRATHERM® Graphite Lightweight Board, ECOPHIT® L10/1500). The measured sheet density is 196 kg m^{-3} and the thermal conductivity in the plane of the sheet is 26 $Wm^{-1}K^{-1}$ as obtained from the manufacturer's data sheets.

2. Material Thermodynamic and Rate Equations

The methodology used to determine properties and governing rate equations is described by Hinmers et al. [7]. The Large Temperature Jump (LTJ) technique is used on small (approx. 10 mm diameter impregnated ENG discs) samples that are rapidly heated or cooled. The reactor vessel is connected to an empty buffer vessel which maintains a nearly constant pressure, similar to that in a full system in desorption (or adsorption), whilst careful measurement of the small increase in pressure yields the time history of ammonia evolution (or devolution). Matching the experimental results with a simulation model reveals the controlling parameters that can be used to design a full system. The reaction is dominated by heat transfer, but chemical reaction rate parameters are also revealed, together with the proportion of the impregnated salt that is able to take part in the reaction. The reaction rate equation used is:

Desorption:

$$\frac{dX}{dt} = A_{DES}\left(1 - \frac{p_{EQ}}{p}\right)(1 - X)^{n_{DES}} \quad (1)$$

Adsorption:

$$\frac{dX}{dt} = A_{ADS}\left(1 - \frac{p_{EQ}}{p}\right)(X)^{n_{ADS}} \quad (2)$$

where: X = reaction advancement ($1 > X > 0$)
t = time (s)
p = pressure
p_{EQ} = equilibrium pressure
$A_{DES}, A_{ADS}, n_{DES}, n_{ADS}$ are constants

When there is hysteresis the lines on the Clapeyron diagram indicating adsorption and desorption are not equilibrium lines and so the slope does not correspond to the enthalpy of reaction which is determined as in [7], by heating the sample slowly and isosterically in a vessel with minimal void volume.

An interesting outcome of identifying the different parameters is that the overall power density and rate of ammonia sorption/desorption is found to be dominated by heat transfer rather than chemical kinetics. We suppose that in previous studies insufficient attention was paid to heat transfer. In particular, the overall cycle time (for a complete reaction) is highly sensitive to the thermal contact resistance between the ENG and the metal surface used to conduct heat in and out of it.

3. Design of 2.5 kW Demonstrator

The LTJ tests were carried out on 10 mm diameter ENG-salt composite discs contained within the tube of a heated, or cooled, stainless steel double-pipe heat exchanger. However, this would not be a suitable design for a demonstrator since the sensible heat load of the stainless steel would result in low COPs. Instead, the design was based on hexagonal ENG plates with a central hole, Figure 2 (a). Many such 'nut-shaped' discs may be mounted on a stainless-steel tube which heats or cools them from their centre. The model parameters and heat transfer properties were used in a simulation model to explore the design trade-off between COP and power density with different central hole diameters and across-flat dimensions. There is no precise optimum, but one criterion was to achieve a mean power density of at least 1 kW per litre of reactor volume.

The dimensions decided on were a central hole diameter of 12.7 mm and 32 mm across the flats, Figure 2 (a), with a predicted power density of 1.4 kW per litre [8]. Since several metres of tube would be needed the concept was to have seven tubes in a hexagonal bundle within a stainless-steel shell that contains the ammonia, as in Figure 2 (b) and (c).

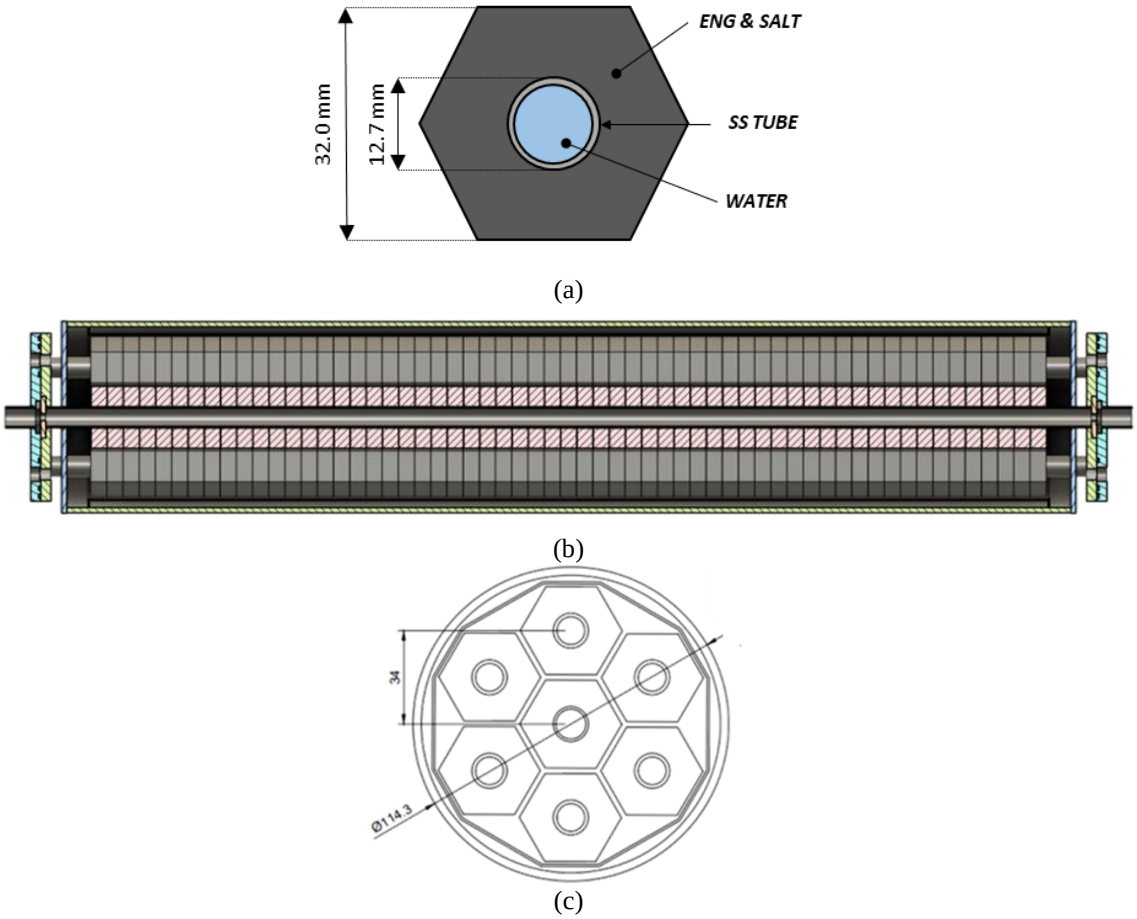


Fig. 2. (a) ENG-salt composite dimensions, (b) longitudinal cross-section through the reactor design concept with a bundle of seven tubes and (c) frontal cross-section through the reactor design concept.

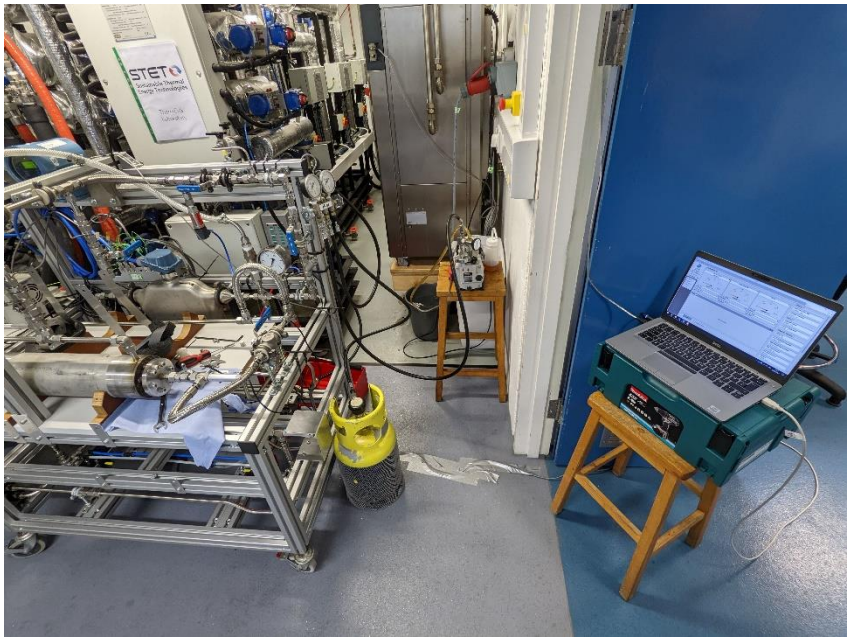


Fig. 3. Demonstrator and ThermExS rig during charging.

The complete demonstrator is connected to the laboratory 'ThermExS' test stand which can supply pressurised water from three different thermostatically controlled baths. Pneumatically controlled valves are used to switch hot water to the HTS reactor during the high-pressure phase, cold water to the LTS during the low-pressure phase and to remove heat (simulating the heat pump load) from both reactors as required, as in Figure 1. Inlet and outlet stream temperatures are measured using PRTs and the flow rate is measured by Coriolis meters. In addition, the mass flow of ammonia gas moving from one reactor to another is measured using a Coriolis meter. The demonstrator is controlled and monitored by an NI cDAQ linked to a PC and using LabView™. Figure 3 shows the nearly completed demonstrator being charged with ammonia, whilst monitoring the pressure and temperature.

4. Preliminary Results

At the time of writing a limited number of test conditions have been conducted and not fully analysed; however, initial results show that the resorption machine operates well.

In the following figures the test conditions were:

4 cycles at 165/40/15 °C with a cycle time of 2600 seconds (43 minutes 20 seconds).

5 cycles at 170/40/15 °C with a cycle time of 2500 seconds (41 minutes 40 seconds).

The cycle times were designed to allow full ammoniation and de-ammoniation of each salt reactor in both pressure phases, therefore allowing the resorption reaction to run to completion. Figure 4 shows the mass flow rate of ammonia being transferred from one salt reactor to the other, taken directly from the Coriolis meter. Positive values are during the low-pressure phase, peaking at around 1.6 to 1.7 g/s of ammonia, and negative values are during the high-pressure phase, peaking at -0.5 to -0.6 g/s.

Figure 5 shows the pressure variation over the cycles between the low- and high- pressure phases. Note there are three pressure transducers in the ammonia line (LTS-side, Mid and HTS-side), which match well across the pressure range. In the 165/40/15 °C tests, the demonstrator cycles between 0.35 bar and 9.00 bar. In the 170/40/15 °C tests, the pressure cycles between 0.35 bar and 9.45 bar.

Although the preliminary data is encouraging in showing the consistency of the resorption cycle, when analysing the initial data during the first cycles, the power output is less than the designed target of 2.5 kW. However, the cycle times used are much longer than optimal to ensure the resorption reaction completes. Future work will test the demonstrator at a variety of temperature and cycle time conditions to ascertain overall system performance; in particular, by optimising and reducing the cycle time the power should increase.

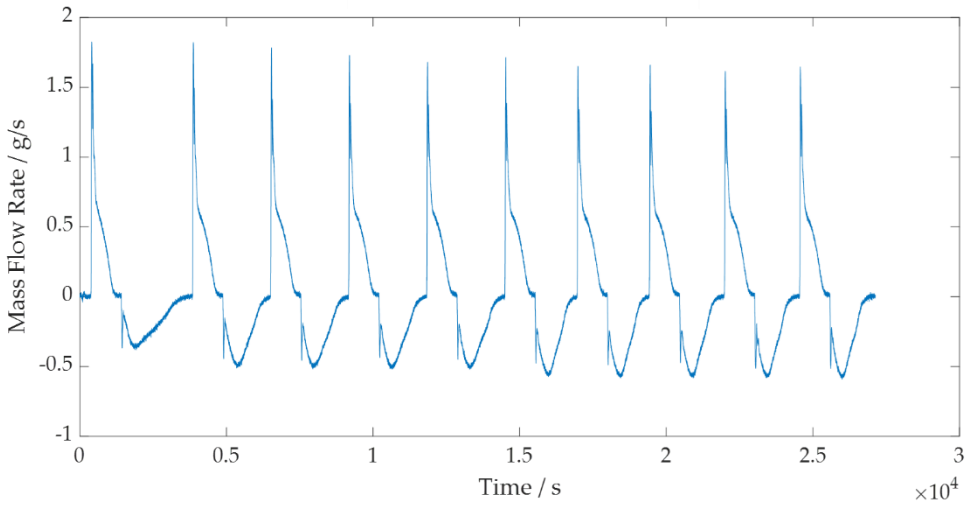


Fig. 4. Mass flow rate of ammonia in each salt during repeated resorption cycles.

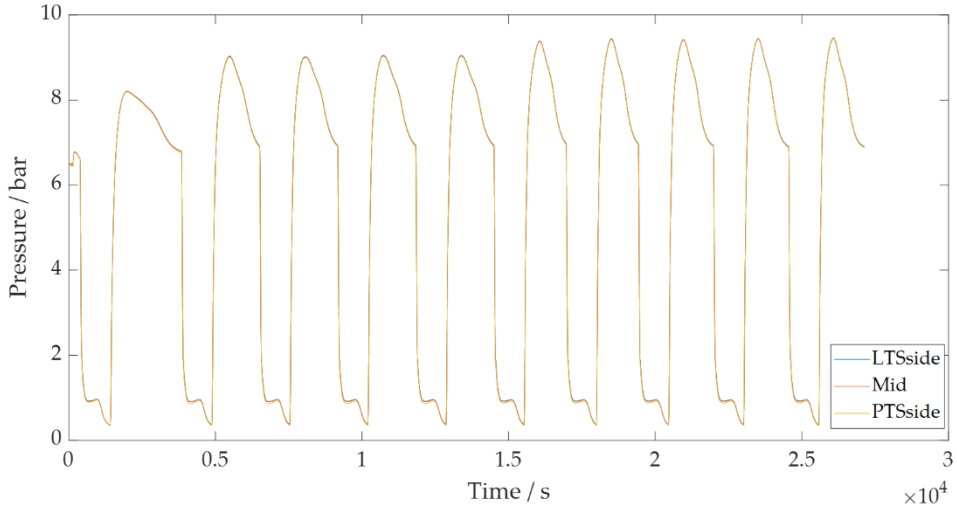


Fig. 5. Pressure variation between the low- and high- pressure phases during repeated resorption cycles.

5. Conclusions

A resorption heat pump cycle using ammonia as the refrigerant, sodium bromide as the low temperature salt and manganese chloride as the high temperature salt is proposed. The salts are dispersed in ENG to improve conductivity and remove any danger of salt agglomeration. LTJ testing on small samples was used to determine equilibrium properties, hysteresis effects, heat transfer and reaction rate limitations. This data was used to design a nominal 2.5 kW demonstrator. The reactors utilise seven parallel heating/cooling tubes in a shell and tube arrangement, with pressurised water on the tube side and the ENG-salt composite on the ammoniated shell side. Each tube fits tightly within many ENG hexagons impregnated with a salt.

Initial testing is very encouraging, showing repeatability and good transfer of ammonia between salts during resorption. Further testing will optimise the cycle time and enable a performance envelope to be calculated and checked against theory. A practical machine would use two pairs of reactors with a heat recovery phase between reactors to enhance the performance.

Acknowledgements

Project funding is from the UK Mission Innovation programme, via EPSRC grant EP/R045496/1 and an EPSRC PhD studentship, EP/R513374/1 (2199243).

Thanks to Michel van der Pal for his guidance and for sharing his expertise on ammonia-salt reactions. Thanks also to Charles Joyce for his technical and manufacturing guidance.

References

[1] Faraday, M., 1823. On the Condensation of Several Gases into Liquids. Philosophical Transactions of the Royal Society of London 113, 189-198.
[2] Spinner, B., 1988. Pompes à chaleur basées sur la réaction renversable entre un gaz et un solide on un liquide ou une solution saturée. Récents Progrés en Génie des Procédés, 2, 222.
[3] Goetz, V., Elie, F., Spinner, B., 1993. The structure and performance of single effect solid-gas chemical heat pumps. Heat Recovery Systems and CHP 13, 79-96.
[4] Lebrun, M., Spinner, B., 1990b. Simulation for the development of solid—gas chemical heat pump pilot plants Part I. simulation and dimensioning. Chemical Engineering and Processing: Process Intensification 28, 55-66.
[5] Mazet, N., Spinner, B., 1994. Analyses of irreversibilities and research and development on solid-gas reaction thermochemical transformers. International Journal of Refrigeration 17, 329-337.
[6] van der Pal, M., Critoph, R.E., 2017. Performance of CaCl2-reactor for application in ammonia-salt based thermal transformers. Applied Thermal Engineering 126, 518-524.
[7] S. Hinmers , G.H. Atkinson , R.E. Critoph , M. van der Pal , Modelling and Analysis of Ammonia Sorption Reactions in Halide Salts, International Journal of Refrigeration (2022), doi: 10.1016/j.ijrefrig.2022.01.032
[8] S. Hinmers, G. H. Atkinson, R. E. Critoph, and M. van der Pal, "Resorption Thermal Transformer Generator Design," Energies, vol. 15, no. 6, 2022, doi: 10.3390/en15062058

14th IEA Heat Pump Conference
15-18 May 2023, Chicago, Illinois

Load-based performance characterization of air conditioners using an emulator-type assessment technique

D. Dondini[a*], R. Mori[a], N. Giannetti[b], Y. Miyaoka[c], K. Saito[a]

[a] Department of Applied Mechanics and Aerospace Engineering, Waseda University, 3-4-1 Okubo, Shinjuku, Tokyo, 169-8555, Japan
[b] Waseda Institute for Advanced Study, Waseda University, 1-6-1 Nishiwaseda, Shinjuku, Tokyo, 169-8050, Japan
[c] Research Organization for Open Innovation Strategy, Waseda University, Tokyo 169-8555, Japan

Abstract

The operation of air conditioning installations may respond to different thermal load scenarios with variable or intermittent modulations of the compressor speed and expansion valve opening, according to the native control system. Therefore, the representativeness of the standard performance rating procedures obtained at a fixed compressor speed is limited and may be misleading for the efficient development of this technology.
The emulator-type performance assessment technique was developed by combining the equipment of air-enthalpy testing facilities for real-time measurement of the cooling capacity supplied by the air conditioner and a room emulator to reproducibly generate arbitrary indoor load conditions. This study demonstrates the ability of the developed assessment approach to characterize the performance of air conditioners in response to variations in the indoor air state according to the native control system. Specifically, an R32 ceiling-type commercial unit was tested under the conditions necessary for the calculation of the annual performance factor over a load range between 25 and 100% of the nominal system capacity for a 147 m^3 virtual room with a total thermal capacity of 1470 kJ/K. The steady, fluctuating, and intermittent controllability of the system was captured. Finally, the efficiency of the system operating according to its native control system was compared with the results obtained according to the current standard procedure defined by the Japanese Industrial Standard at a fixed compressor speed.

Keywords: Dynamic performance evaluation; Testing facility; Emulator; Cyclic operation; Load-based test;

1. Introduction

The need to decarbonize the energy sector through efficient energy management has steadily become more relevant in recent years as policymakers and stakeholders, as well as manufacturers, are reacting to the rising climate threat. Air conditioners and heat pumps are among the most frequently deployed devices worldwide, with billions of operative installations. Although vapor compression air conditioning is generally recognized as a well-developed technology, the actual performance of these systems remains largely unknown. Specifically, standard testing and rating methods were conducted with a fixed compressor speed while deactivating system control. Therefore, the rated performances are not representative of the actual operation of air conditioners (AC). In addition, the sensors required by conventional measurement techniques are too costly and complex to capture the actual performance of a statistically meaningful number of AC installations. For example, air flow meters are too bulky, and the installation of refrigerant pressure sensors and flow meters requires cutting refrigerant pipelines. Consequently, owing to this gap in knowledge regarding the actual performance of ACs, optimal control strategies that are able to efficiently respond to different building structures, occupant lifestyles, and climates of different air conditioning installations are yet to be understood and developed. Sholahudin et al. 2021 [1] demonstrated the ability of machine learning techniques to deal with the latter issue through broadly applicable and cost-effective performance-monitoring techniques. Nonetheless, this monitoring approach requires training data to be collected with dedicated testing methodologies. However, standardized testing methodologies are conducted with a fixed compressor speed while deactivating the system

* Corresponding author. E-mail address: damiano@moegi.waseda.jp

control, thus deviating from the actual performance of operating installations. To overcome this challenge, an emulator-type testing facility was designed and built for load-based tests. Contextually, the time evolution of indoor conditions, such as temperature and humidity, is recreated by a condition generator to represent the dynamic thermal response of the conditioned room in accordance with the system capacity and building loads. The system reacts to deviations from the setpoint of the thermostat according to its native control with variable compressor speed and fan speed, allowing this testing method to capture actual field operation performance. Although standardization of such a methodology is yet to be conclusively defined, load-based testing methodologies have been recognized as an effective approach for capturing system controllability and representative performance [2-4]. Accordingly, load-based testing methodologies are being endorsed to form the basis for new rating standards (CSA [5]) and are being investigated to ensure test reproducibility [6-9]. In this study, the current Japanese standard testing methodology (JIS B 8615-1/2:2015) [10] was compared with the proposed emulator-type load-based testing methodology to clarify the difference between the two approaches and discuss the advantages of capturing the interdependencies between the controllability and system performance. The testing conditions were defined according to the requirements for calculating the seasonal performance index adopted in Japan (Annual Performance Factor, APF). Finally, the APF was evaluated with reference to the test results obtained from the testing facility and from the manufacturer.

2. JIS test methodology

JIS tests are conducted with reference to the JIS B 8615-1/2:2015 [10] regulations. The system is operated at a maximum volumetric air flow rate, constant outdoor conditions, and return conditions to the indoor unit while overriding the native control of the system to constantly maintain the prescribed compressor speed and valve opening. These tests adopt the air-enthalpy method for cooling and heating capacity measurement.

3. Testing Facility and Methodology

Load-based tests require a real-time evaluation of the supplied cooling capacity for the considered system operating under constant load conditions and the set value of the indoor temperature. During operation, the native control of the system is kept active, regulating both the valve opening and compressor speed. To perform load-based tests, it is necessary to calculate and reproduce the time variation of the indoor condition in its interaction with the variable-speed control of the air conditioner (Figure 1).
The experimental setup was composed of two psychrometric rooms. Both rooms were equipped with a condition generator to reproduce the operational environment, and a measurement chamber instrumented for the measurement of the sensible and latent cooling capacities with dedicated temperature and humidity sensors. Other round-robin tests are in progress with other companies that possess calorimetric testing facilities to statistically confirm the conclusions of this study and spread the effectiveness of this methodology in capturing the controllability and dynamic performance of air conditioners.

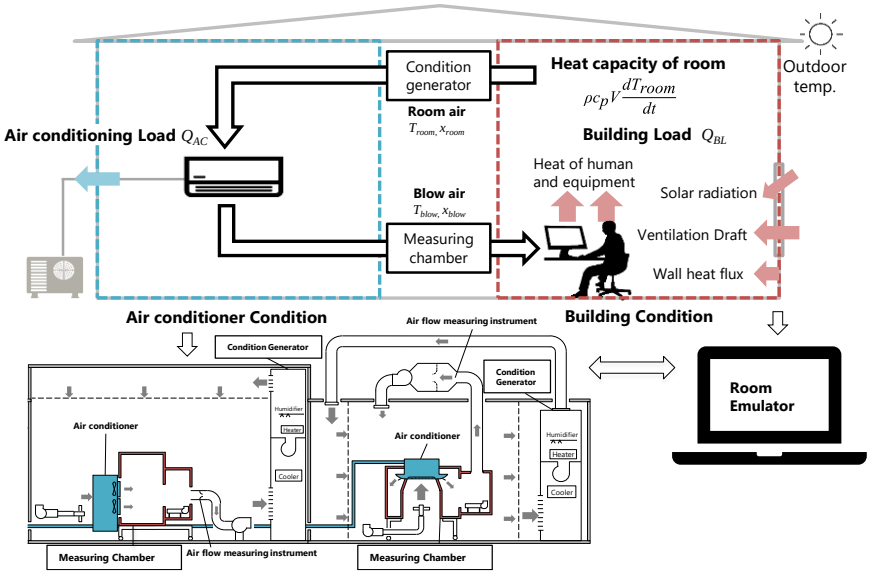


Fig. 1. Testing Facility schematic.

4. Emulator

The virtual room emulator is a central element for the reproducibility and representativeness of the time-dependent response resulting from the interaction of the system control with specific heat load conditions.

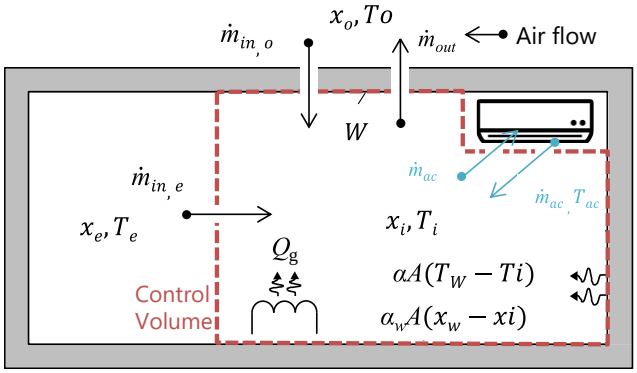


Fig. 2. Testing Facility Indoor room schematic.

The numerical model of the room (schematically represented in Figure 2) accounts for heat infiltration from the external environment, ventilation, and heat transfer from solar radiation through windows. Furthermore, the model considers the internal generation of sensible and latent heat from the occupants, lighting, and indoor equipment, in addition to heat and moisture accumulation owing to the heat and mass capacities of the volume of indoor air, fixtures, walls, and floors.

$$\dot{m}_{out} = \dot{m}_{in,o} + \dot{m}_{in,e} \tag{1}$$

$$C_{S,i}\frac{dT_i}{dt} = Q_{ac,S} + Q_{bld,S} \tag{2}$$

$$M_{L,i}\frac{dx_i}{dt} = \dot{m}_{ac}(x_{ch} - x_i) + L_g \tag{3}$$

$$Q_{ac,S} = \dot{m}_{ac}\, c_p(T_i - T_{ch}) + \alpha_{ch}A_{ch}(T_i - T_{ch}) \tag{4}$$

In the present study, the mathematical model was based on the continuity of indoor air (Eq. 1), energy balance (Eq. 2), moisture balance (Eq. 3), and the auxiliary relations for heat and mass transfer of walls and fixtures considering the thermal and moisture capacity of a 147 m^3 room (details of the present formulation can be found in [9]). In the following tests, the terms $Q_{bld,S}$ and L_g summarize the combination of effects defining the sensible and latent load scenarios, respectively, and are kept constant during the load-based tests. The cooling capacity $Q_{ac,S}$ accounts for the sensible part of the overall system capacity and, in these preliminary tests, it is calculated as in Eq. (4). Accordingly, it accounts for the sensible heat transfer between the return air conditions and the supply air condition measured at the measurement chamber, plus the correction factor that represents heat infiltration through the chamber walls. Here the factor $\alpha_{ch}A_{ch}$ indicates the thermal conductance of the chamber, which is measured at standard conditions as in [10]. More detailed investigations on the influence of such measurement methodology for the supply air condition is referred to [7].

5. System

The system tested in this study is an R32 ceiling-type air conditioner that features a nominal cooling/heating capacity of 10 kW/11.2 kW with the main specifications summarized in Table 1.

Table 1. System characteristics

Type	Cooling [W]	Heating [W]	Refrigerant	Mass Charge [kg]	Maximum air flow rate [m^3/min]
Ceiling	10000	11200	R32	3.3	32

6. Annual Performance Factor

The Annual Performance Factor (APF) is an index used in Japan to assess the seasonal efficiency of thermal systems such as air conditioners and heat pumps, accounting for both geographical and seasonal conditions. The tests conducted under the conditions listed in Table 2 were referenced for defining a COP value for each outdoor temperature and calculating the APF index as an overall value weighted on the annual hourly distribution of each temperature bin. During the JIS tests, the load condition was defined with reference to the maximum compressor speed, whereas for load-based tests, it refers to the nominal cooling/heating capacity of the system. In accordance with JIS B8615 [10] and JIS B8616 [11], the APF can only be obtained in the cooling mode, heat pump operation, or both. The temperature distribution used in the Tokyo area is shown in Fig. 3.

Table 2. Measurements required for APF calculations

Cooling/Heating load (% of compressor speed at rated capacity)	Outdoor Temperature Dry/Wet bulb °C	Indoor Temperature setpoint Dry/Wet bulb °C	Operation Mode
Full Load (100)	35/24	27/19	Cooling
Half Load (50)	35 /24	27/19	Cooling
Half Load (50)	29 /19	27/19	Cooling
Low Load (25)	29/19	27/19	Cooling
Full Load (100)	7 /6	20/15	Heating
Half Load (50)	7 /6	20/15	Heating
Low Load (25)	7 /6	20/15	Heating
Full Load (100)	2 /1	20/15	Heating

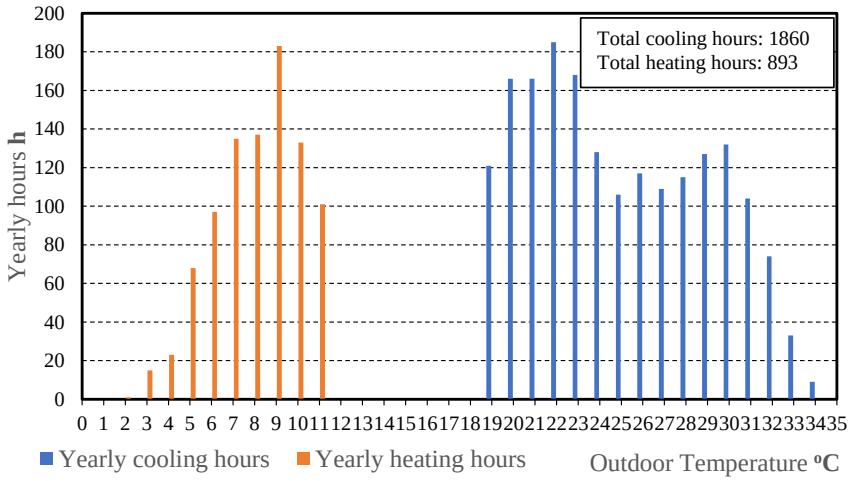


Fig. 3. Representative yearly heating and cooling hours distribution in the Tokyo prefecture

7. Data analysis

7.1. JIS tests

The COP obtained under the aforementioned operating conditions for the JIS standard testing methodology is reported in Table 3, along with the load-based test results. Peak efficiency was demonstrated at low-load conditions for the cooling operation, whereas for the heating mode, the highest COP was achieved at half-load operation. JIS standard testing results reported in the study are obtained from the manufacturer catalogue of the specific system used in load-based tests. Because of the regulation on such performance tests [10-11], the test condition is set by fixing the compressor speed and setting the valve opening to achieve a safe degree of superheating at the compressor suction. Operating conditions set in this manner are not necessarily resulting in a cooling/heating capacity equivalent to the percentage of the rated value reported in Table 2.

7.2. Load-based tests

The following charts represent the four conditions used to measure the cooling performance of the system, as listed in Table 2. COP, power consumption, and cooling capacity were calculated with reference to the interval between the vertical dotted lines, representing an integer number of regular cycles.

Figure 4 Illustrates the results of a load-based test conducted for a load equivalent to 25% of the nominal cooling capacity at 29 ºC outdoor temperature. In this operating condition, the control system is driving the air conditioner with on-off cycling operation. This type of regulation is required when the inverter is unable to stably maintain a low compressor speed, such as the one imposed during JIS tests. Such cycling operation, along with a lower air flow rate led to a 35% gap in COP when compared with steady operation JIS test.

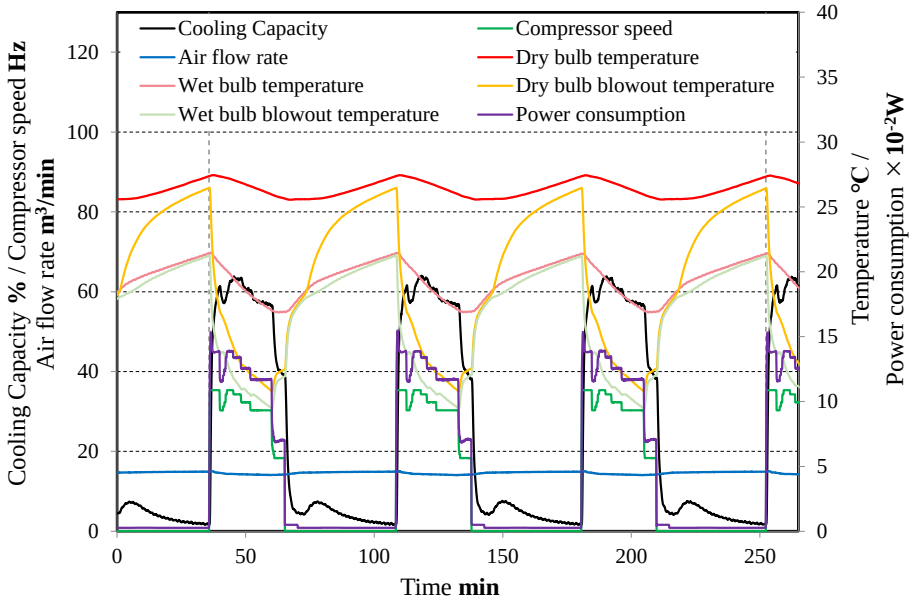


Fig. 4. 29 ºC Outdoor Temperature, Low Load

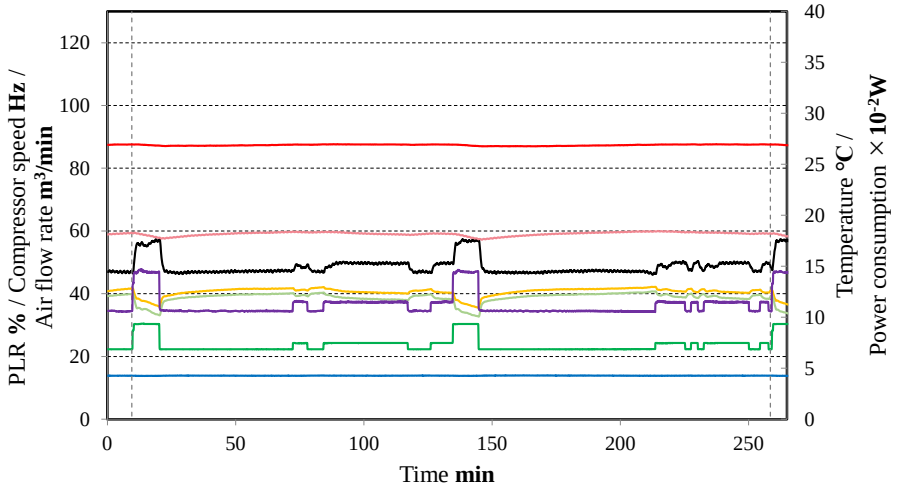


Fig. 5. 29 ºC Outdoor Temperature, Half Load

The load-based test results reported in Figure 5 and 6 demonstrate the ability of the variable speed control to achieve a close-to-stationary operation (except for minor compressor speed adjustments owing to oil management processes), but a lower air flow rate than the corresponding JIS test results led to a lower COP value for load-based tests. Under this load condition, the control system operated the air conditioner with a supply airflow rate that was approximately half of the maximum value used during the JIS measurements. Accordingly, the compressor speed required to compensate for the less efficient heat exchange was

approximately 20% higher, resulting in a higher power consumption to balance the same heat load and maintain the target indoor temperature.

The test results obtained at full capacity at 35 ºC outdoor temperature are shown in Figure 7. Under this limiting condition, it was necessary to override the air flow rate of the native control system during load-based tests to achieve the target room air temperature. Figure 7 demonstrates that the system control manages this load with a variable speed and results in a lower COP than that obtained during the JIS tests at a constant compressor speed.

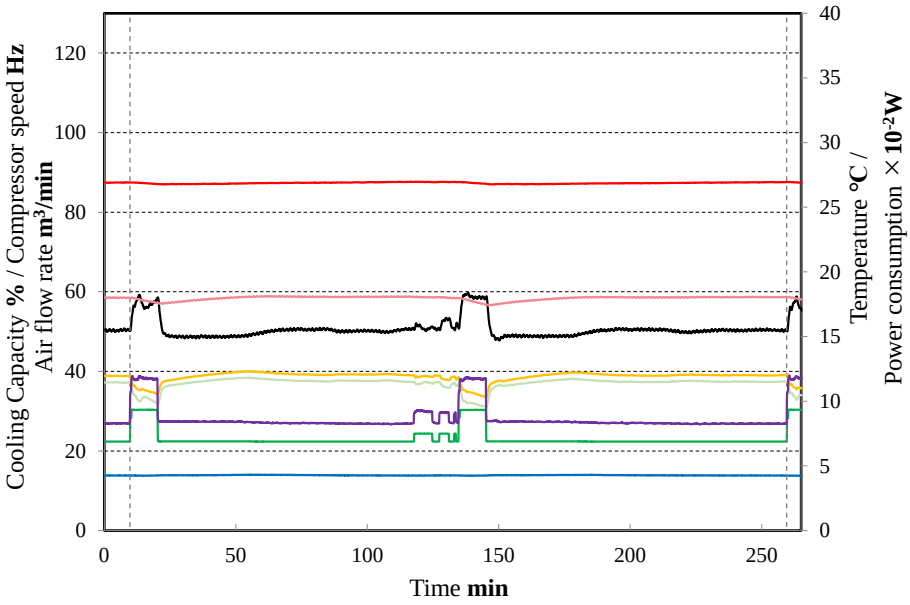


Fig. 6. 35ºC Outdoor Temperature, Half Load

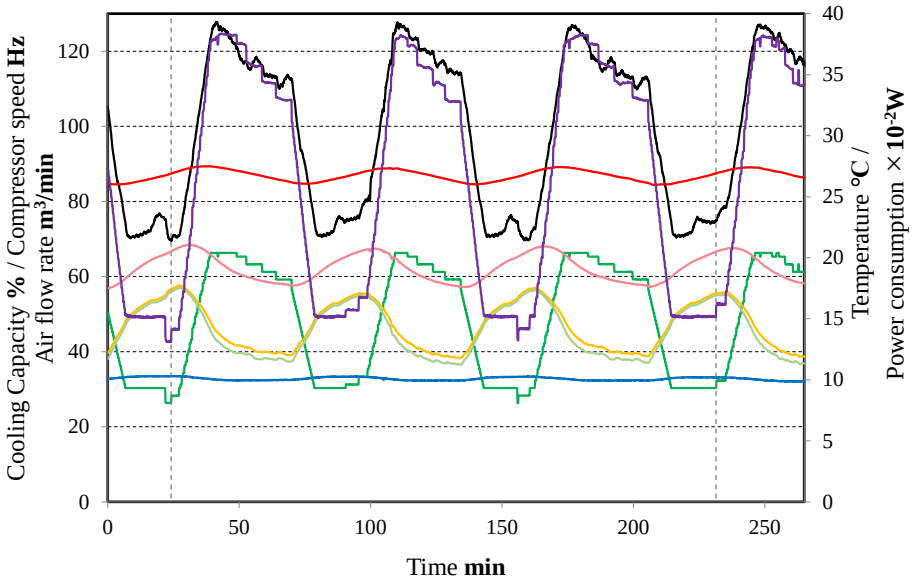


Fig. 7. 35ºC Outdoor Temperature, High Load

Consequently, the heating performance of the system was evaluated with reference to the four representative conditions listed in Table 2. Correspondingly, COP, power consumption, and cooling capacity, were evaluated in the time interval between the vertical dotted lines, representing an integer number of regular cycles. In accordance with the cooling case, in the heating mode, the on-off operation is performed at low loads (Figure 8), and to ensure a comfortable temperature for blowout air flow, a further adjustment of the compressor speed is performed between cycles.

As shown in Figure 9, the same observations for the half-load cooling conditions could be made. Despite relatively steady functioning, the lower air flow rate led to a less efficient heat exchange and compression ratio; thus, the COP values obtained were 36% lower.

In Figure 10, it is possible to notice an unsteady operation performed by the native control system aimed at maintaining a comfortable blowout air flow rate and temperature, lowering the airflow when the blowout temperature is low, and increasing the compressor speed between peaks to avoid relatively colder air blows that may result in discomfort for users.

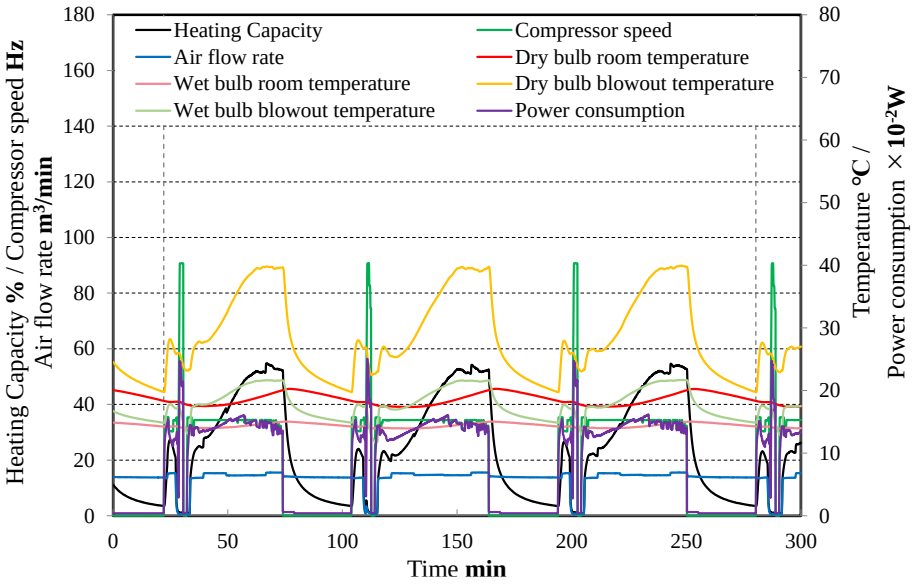


Fig. 8. 7 ºC Outdoor Temperature, Low Load

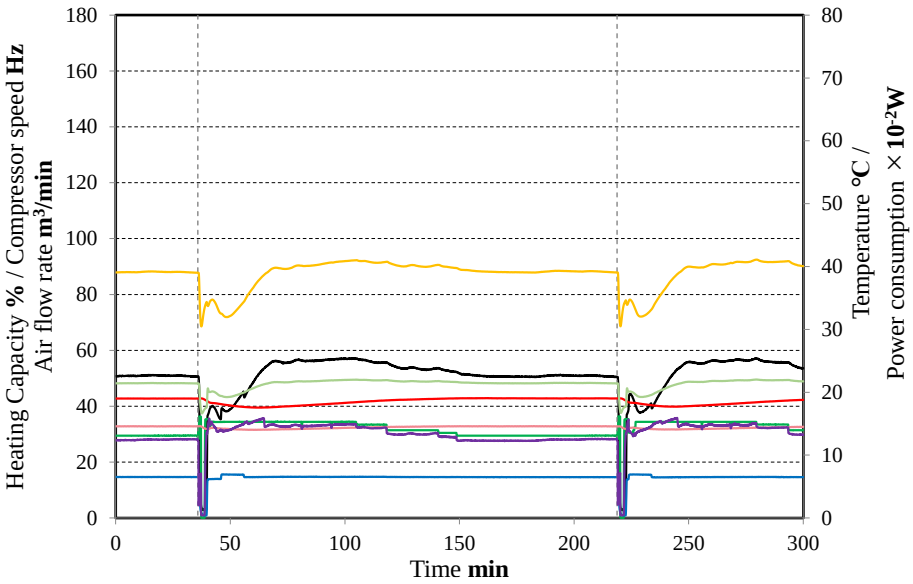


Fig. 9. 7 ºC Outdoor Temperature, Half Load

In Figure 11, the full-load and low outdoor temperatures represent the most demanding operating conditions for the system. They present the overall lowest COP in both the load-based and fixed compressor speed rating methods. Moreover, this is the only condition where the load-based COP value is higher than the steady-state counterpart, and the ability of the control system to maintain the room temperature around the set point value of 20 ºC with cyclic operation and a high air flow rate, along with a relatively broad dead band of the thermostat around the set value, results in a higher system COP when compared to the full load JIS test where the compressor speed is maintained at its maximum value.

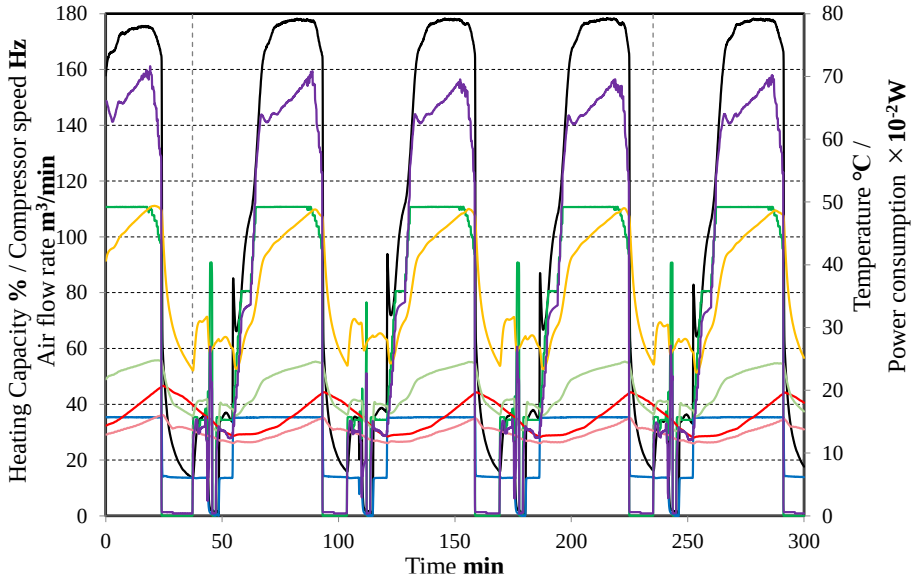


Fig. 10. 7 ºC Outdoor Temperature, High Load

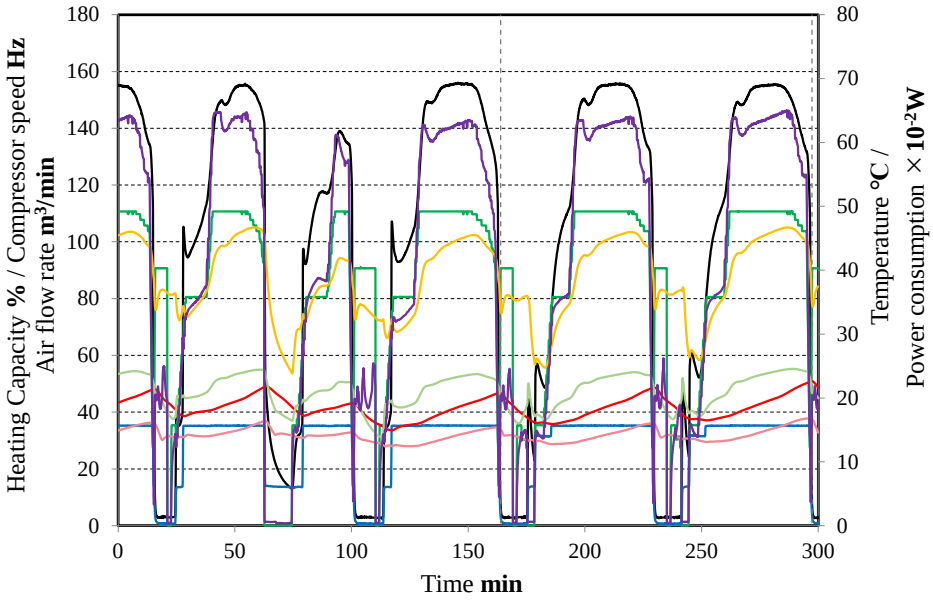


Fig.11. 2 ºC Outdoor Temperature, Full Load

Table 3. Measurement results required for APF calculation

Cooling/Heating Condition	Load-based test* Capacity/Power Consumption **kW**	Load-based test COP	JIS test Capacity/Power Consumption **kW**	JIS test COP	COP % Difference
Full 35ºC	9.88 / 2.66	3.70**	10.00 / 2.41	4.15	10.8
Half 35 ºC	4.86 / 1.12	4.34	4.50 / 0.79	5.66	23.3
Half 29 ºC	5.06 / 0.86	5.85	4.70 / 0.61	7.70	24.0
Low 29 ºC	2.53 / 0.49	5.15	3.30 / 0.41	7.97	35.4
Full 7 ºC	11.15 / 3.56	3.13	11.20 / 2.35	4.77	34.4
Half 7 ºC	5.70 / 1.33	4.28	5.10 / 0.76	6.67	35.8
Low 7 ºC	2.85 / 0.91	3.13	2.80 / 0.50	5.60	44.1
Full 2 ºC	11.22 / 4.12	2.72	13.50 / 5.30	2.55	-6.7

*Average values, ** Air flow rate manually managed

As shown in Table 3., the results of the measurement process in the testing facilities lead to 10–44% lower COP values compared with the data reported in the manufacturer catalogue, obtained through fixed compressor speed testing following the JIS guidelines.

The corresponding APF values are listed in Table 4 for a standard office in the Tokyo area. This result provides evidence for a difference of approximately 27% between standard and load-based tests, which is sensitively related to the number of hours of functioning encounter cycling on-off or modulating variable speed mode when driven by the native control system. Further, this may sensitively depend on the interactions with the specific building characteristics and load scenarios of different installations.

Table 4. APF calculation

APF Load-based tests	APF JIS tests
4.76	6.40

8. Conclusions

In this study, an emulator-type load-based testing methodology was proposed to overcome the limitations of the current JIS testing procedures conducted at constant compressor and fan speeds by disabling the native control system of the air conditioner. The proposed method allows the system to respond to the dynamic variation in the return air condition according to its native control system, as it responds during field operation. This was made possible by combining an emulator simulating the time variation of the room condition during its interaction with arbitrary load scenarios and air-enthalpy testing equipment for the real-time measurement of the output capacity.

The ability of this testing methodology to capture the controllability and dynamic response of air conditioners to constant load and set indoor temperature conditions is presented and discussed herein. The heating and cooling operation performance of an R32 ceiling-type air-conditioning unit was investigated under the prescribed conditions required for the characterization of the annual performance factor. A qualitative and quantitative comparison between the results of the JIS constant-speed tests and emulator-type load-based tests was conducted to clarify the differences and connotations of the two approaches.

During the cooling mode operation at high loads, the COP difference between the JIS and load-based tests was approximately 10% and it increased with decreasing cooling load, showing no substantial difference for the two different conditions at half load (23 and 24% COP difference) despite the different outdoor temperatures, reaching the maximum gap for the low-load condition (35% COP difference). For heat pump operation, the efficiency comparison follows the same trend, but with higher discrepancies of up to 44% for lower loads. These results, even though affected by the aforementioned discrepancies of cooling/heating capacities between JIS and load-based, show a substantial performance difference between the fixed compressor speed and native control-driven functioning, especially at lower loads, where the divergences between the on and off cyclic operation and steady operation are significant and closely related to the specific control method integrated in the system.

Accordingly, the results suggest the importance of accounting for the system controllability, load scenario, and room characteristics to improve current standard rating procedures and demonstrate the ability of the proposed emulator-type load-based testing methodology to capture these operating characteristics. The use of such an emulator-type load-based testing approach is critical for effectively developing high-efficiency control methods for air conditioners and heat pumps.

Nomenclature

Symbol:

A	Area [m^2]
C	Heat [J/K]
c_p	Constant pressure specific heat [J/(kg･K)]
d	Thickness [m]
H	Internal heating of the walls [W/m^2]
h	Specific enthalpy [kJ/kg]
L	Vapor generation rate [kg/s]
$\dot{m}$	Mass flow rate [kg/s]
Q	Heat transfer rate (load/capacity) [W]
T	temperature [K]

t	Time [s]
V	Volume [m^3]
W	Wall
x	Specific humidity [kg/kg_a]

Greek symbols:

α	Heat transfer coefficient [$W/(m^2 \cdot K)$]
α_L	Moisture transfer coefficient [$(kg/s)/(kg/kg_a \cdot m^2)$]
λ	Thermal conductivity [$W/(m \cdot K)$]
ρ	Density [kg/m^3]

Subscript:

ac	Supply
bld	Overall building coefficient
ch	Measuring chamber
e	Exterior
g	Internal generation
i	Indoor
in	Inflow
L	Latent heat
o	Outdoor
out	Outflow
S	Sensible heat
w	Water
W	Wall

Acknowledgement

This paper is based on results obtained from a project commissioned by the New Energy and Industrial Technology Development Organization (NEDO).

References

[1] Sholahudin, Giannetti, N., Yamaguchi, S., Saito, K., Miyaoka, Y., Tanaka, K. & Ogami, H., Experimental implementation of artificial neural network for cost effective and non-intrusive performance estimation of air conditioning systems. *Applied Thermal Engineering* 181 (2020), 115985.
[2] T. Ban, D. Nakano, K. Ohno, S. Yamaguchi, K. Saito, H. Yamaguchi. (2017). Testing facility for unsteady performance of air conditioning System. *Proceedings of 12th IEA Heat Pump Conference* 2017, Rotterdam.
[3] J. Liu, D.-H. Chung, M. Chung, Y.-H. Im. Development of load models and operation simulator for a building complex with mixtures of multi-type engines and renewable devices. *Energy and Buildings* 158 (2018), 831-847.
[4] L. Cheng, P. Dhillon, W. T. Horton, J. E. Braun. Automated laboratory load-based testing and performance rating of residential cooling equipment. *International Journal of Refigeration* 123 (2021), 124-137.
[5] CSA. (2019). CSA EXP07:19 Load-based and climate-specific testing and rating procedures for heat pumps and air conditioners.
[6] P. Dhillon, D. Welch, B. Butler, W.T. Horton, J.E. Braun. Validation of a Load-Based Testing Methodology for Residential Heat Pump Performance Characterization in Heating Mode. *Purdue ePubs International Refrigeration and Air Conditioning Conference* 2022, 2524.
[7] N. Giannetti, J. Jeong, H. Ariyadi, Y. Miyaoka, K. Saito. Development of an Emulator-Based Assessment Method for Representative Evaluation of the Dynamic Performance of Air Conditioners. *Purdue ePubs International Refrigeration and Air Conditioning Conference* 2022, 2458.
[8] L. Cheng, W. T. Horton, J. E. Braun. Load-based testing using a thermostat environment emulator. *International Journal of Refigeration* 126 (2021), 109-122.
[9] N. Giannetti, S. Matsui, R. Mori, J. Jeong, H. Ariyadi, Y. Miyaoka, E. Togashi, K. Saito. Emulator-type load-based tests for dynamic performance characterization of air conditioners. *Energy and Buildings* 273 (2022), 112411.
[10] Japanese Standards Association Committee: Package air conditioner JIS B 8615-1/2:2015, (2015). (In Japanese).
[11] Japanese Standards Association Committee: Package air conditioner JIS B 8616:2015, (2015). (In Japanese).

14th IEA Heat Pump Conference
15-18 May 2023, Chicago, Illinois

Steam generating heat pumps – Measuring results and market potential

Bernd Windholz[a,*1], Johannes Riedl[a], Sophie Knöttner[a], Paula Schmidberger[a], Franz Helminger[a], Annemarie Schneeberger[a], Clément Gachot[b], Florence de Carlan[b], Yannick Beucher[b]

[a]AIT Austrian Institute of Technology GmbH, Giefinggasse 2, 1210 Vienna, Austria
[b]EDF LAB Les Renardières, Département Technologies et Recherche pour l'Efficacité Energétique, Avenue des Renardières – Ecuelles, 77250 Moret Loing et Orvanne, France

Abstract

Heat recovery becomes increasingly important for the decarbonization of industry. In addition to direct heat recovery, industrial heat pumps are increasingly used to valorize low-temperature waste heat for industrial processes. Increased utilization temperatures of heat pumps in recent years allow for generation of steam, serves as an efficient medium for heat transfer and as a process reactant in industry. For that, different types of heat pumps are available, but nearly no reference plants. In the H2020 project BAMBOO, different heat pump systems were investigated and a demonstrator consisting of a water-to-water heat pump and a flash tank system was built and tested to analyze steam production and efficiency in different operating conditions.
Furthermore, a market potential assessment for steam-generating heat pumps in European countries was done, considering production volumes, steam demand for selected products, and energy prices for different consumption bands (generally speaking different company sizes), showing the influence of different boundary conditions on the economic potential of integrating heat pumps in specific sectors.
This paper describes the measurement results of the demonstrator and the results of the market study.

© HPC2023.
Selection and/or peer-review under the responsibility of the organizers of the 14th IEA Heat Pump Conference 2023.

Keywords: Steam generating heat pump; measurement results; market potential; heat recovery; industrial processes; decarbonization;

1. Introduction

The growing interest in industrial heat pumps already shows their great potential for decarbonizing process heat. On the one hand, by increasing energy efficiency through the use and recovery of waste heat, and on the other hand, by using electricity from renewable resources to power heat pumps, it is possible to completely decarbonize process heat. [1] For low and medium temperature levels in industrial processes, heat pump applications are projected to cover 30% of total heat demand by 2050. Thus, to achieve the International Energy Agency's "Net-Zero Emissions by 2050" scenario, heat pump capacities of about 500 MW need to be installed each month over the next 30 years. [2]

As far as European industry is concerned, low-temperature process heat forms a significant proportion of energy consumption. About 30% of the process heat is in a temperature range below 200°C. In many cases, steam is used as efficient heat transfer medium for production processes (e.g. drying, sterilization and cooking) and as a reactant. The use of steam is not only well proven in practice but steam itself can also be classified as environmentally safe. [3]

Due to the attractive market potential, there are already some developments in the European market for industrial high-temperature heat pumps that offer the provision of saturated steam up to 5 bar_a for industrial processes. [4], [5], [6] Nevertheless, there is still a lack of reference and demonstration plants to prove and

[1] Corresponding author. Tel.: +43-50550-6385 ; fax: +43-50550-6679 .
E-mail address: bernd.windholz@ait.ac.at .

visualize the functionality of these novel steam supply systems - especially under real operating conditions. Apart from the European market, steam-generating heat pump systems at high TRL with several 100 kW_{th} to a few MW_{th} heating capacity for saturated steam generation up to 9 bar_a can only be found in Japan. [7], [8] In this context, the system studied by Kaida et al [7] is comparable to the one analyzed in this publication, but has a higher heating capacity and a lower level of utilization temperature. In the publications of Bless et al [9] and Wilk et al [10], different cycle and technical approaches to heat pump-based steam generation have already been theoretically investigated. Marina et al. presented experimental results of a steam generating heat pump system for up to 4.8 bar_a saturated steam. [11]

Within this publication, results and findings of initial experimental investigations of a heat pump-based steam generation system using flash tanks are shown, which are based on the previous work of Helminger et al [12], Wilk et al [10], and mainly on Riedl et al. [13], among others. Extending these works within this publication the heat pump of the steam generating system is focused on.

Results from market potential analyses already carried out [14] [15] indicate potentials for high-temperature heat pumps in selected production areas (food, paper industry, wood-based materials industry, etc.). The market potential assessment for steam-generating heat pumps (< 150 °C) presented in this paper, which takes into account country-specific production volumes from statistics databases [16] and process-specific steam demand volumes for the production of selected products, and current energy prices of European countries, extends the works of Windholz et al. [17] by analyses with prices for different consumption bands (generally speaking different company sizes).

The paper is organized as follows: After this introduction, the steam-generating heat pump system is described, followed by measurement results and findings. After the market potential study is presented, the paper concludes with a summary.

2. Description of the steam-generating heat pump system, [13]

As stated in [13], Figure 1 shows the complete steam-generating heat pump system (SGHP) in the laboratory of EDF LAB Les Renardières. It is composed of the high-temperature heat pump (HTHP) HeatBooster HBS4 of the no longer existing manufacturer Viking Heat Engines (VHE), and a flash tank unit (FT) for steam generation from hot pressurized water.

The water-to-water HTHP is equipped with four oil-cooled reciprocating compressors and is capable of providing a maximum useful temperature of 160 °C by using HFO-R1336mzz(Z) refrigerant. It has a nominal heating capacity of 200 kW_{th}.

The FT was designed and manufactured specifically for the HTHP (i.e., 200 kW_{th}) and for test operation in the laboratory and subsequent demonstration operation in a semi-industrial environment. With this FT it is possible to generate saturated steam up to about 5 bar_a (~152 °C).

According to the schematic representation of the SGHP in Figure 2 the idealized steam generation of the SGHP works as follows [13]:

The refrigerant circulating in the heat pump (HP) extracts heat from the heat source by its evaporation, and after compression is in compressed form with higher temperature. By liquefying the refrigerant in the condenser, it adds heat to the circulating pressurized water on the secondary side, increasing the water temperature (ideally isobaric) to a still subcooled state.

- The speed of the water circulation pump and the use of its bypass together with the opening degree of the flash valve mainly define the circulation flow and the pressure drop of the pressurized water along the flash valve. The (ideally isenthalpic) expansion (exergy loss) of the subcooled water flow causes partial evaporation of the water, resulting in a certain steam quality after the flash valve. The higher the pressure drop, the higher are steam quality but also the exergy loss.
- In the flash tank, saturated steam is subsequently separated from the saturated liquid and discharged in a usable manner (ideally isobaric).
- The mass predominant saturated water collects in the flash tank and is pumped back to the condenser by the circulation pump (ideally isentropic), increasing its pressure.
- To keep the water level in the flash tank constant or to refill the flash tank, the evaporated water is replenished via the feedwater pump.

Since the studied object is a heat pump-based energy system, in addition to the COP of the heat pump COP_{HP}, the COP of the SGHP COP_{system} was also calculated, also considering the performance of the circulation pump.

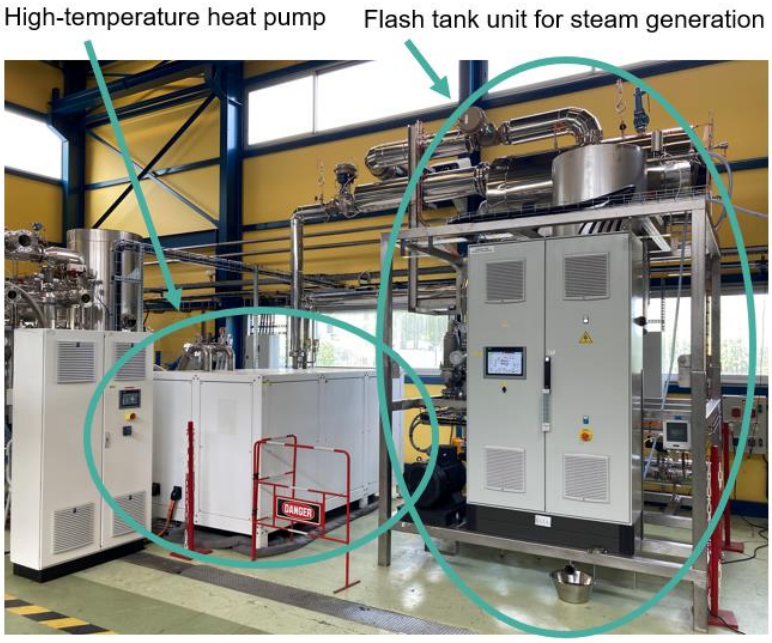


Figure 1: HTHP in the lab of EDF, adapted from [13]

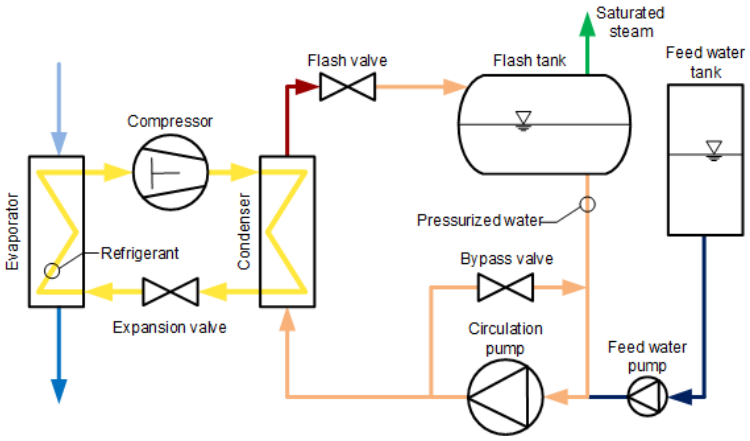


Figure 2: Scheme of the SGHP, adapted from [13]

3. Measurement results and findings

To the knowledge of the authors, the data of the measurement campaign are the first ones of a steam generating heat pump system like this, i.e., a saturated steam pressure of up to 5.5 bar_a with a high-temperature heat pump using a low GWP refrigerant and a flash tank.

As partly stated in [13], a maximum steam pressure of 5.5 bar_a (~155 °C) was reached, and a maximum saturated steam mass flow rate of 218 kg/h was achieved. Relevant system conditions at these two maximum operating points are listed in Table 1.

In [13], results of stationary operating points were presented by COP_{system} and corresponding steam mass flow, see Figure 3. The COP_{system} was broken down by saturated steam pressure (2/3.5/5 bar_a), source-side inlet temperature of the heat pump source (65/80 °C), and whether the circulation pump bypass valve was open or closed (cmp. scheme in Figure 2).

Table 1. System conditions at maximum values of steam pressure and steam mass flow reached during the test campaign

Steam pressure / temperature (bar_a / °C)	**Steam mass flow (kg/h)**	COP_{system} (-)	Sink-side water inlet/outlet temperatures of the heat pump (°C)	Source-side water inlet/outlet temperatures of the heat pump (°C)
5.5 / ~155	56	~1.7	154/157	80/77
2.0 / ~120	**218**	~4.2	121/129	80/74

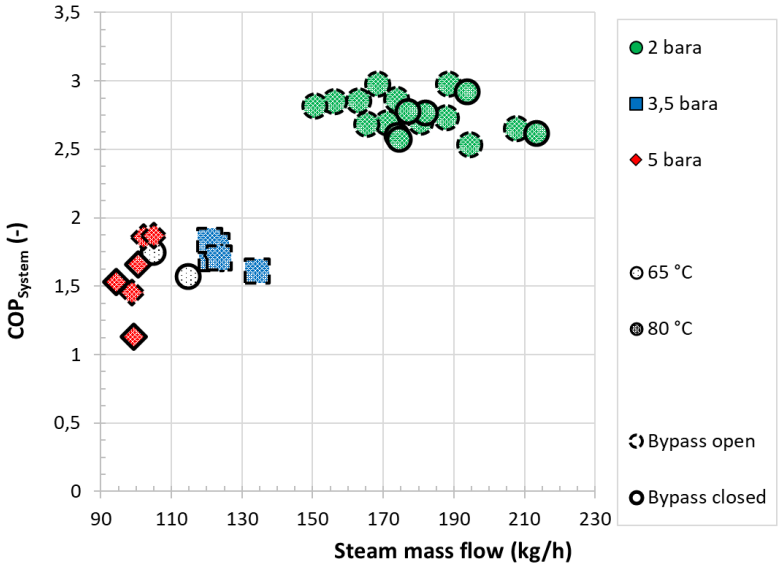


Figure 3: COP_{system} and different steam mass flows, broken down by saturated steam pressure (2/3.5/5 bar_a), source-side heat pump inlet temperature (65/80 °C), and whether the circulation pump bypass valve was open or closed. Adapted from [13]

Extending the earlier work of the authors, a deeper analysis of the heat pump's COP_{HP} (without flash tank system) is carried out within this paper to gain knowledge about the demonstrator and improve the design of future SGHPs. During the measurement campaign, the boundary conditions and setpoints of the SGHP were changed systematically, e.g., inlet/outlet temperatures and mass flows. Due to different issues (i.e., operation at operating limits, controls of the components and the test rig) not all combinations of boundary conditions and setpoints delivered stationary operation of the SGHP. The boundary conditions of the resulting 31 stationary operating points are shown in Figure 4. The diagram shows the volume flows on the sink and the source side of the heat pump, as well as the resulting temperature lift between sink outlet and source outlet at 100% rotational speed of the compressor. While the flow rate on the sink side had a range of 8.5 to 38.0 m³/h (ratio 1:4.5), the volume flow rate on the source side had only 2 concrete values 9.9 and 12.0 m³/h (ratio 1:1.2). The allowed volume flow range is 5 to 50 m³/h on both sides of the heat pump. The resulting temperature lift ranged from 49.2 to 79.2 K (ratio 1:1.6), distinguished within the diagram by 5 K groups (color and marker).

Given these boundary conditions, Figure 5 shows the resulting COP_{HP} of the heat pump at different temperature lifts between sink outlet and source outlet, broken down by the temperature difference (spread) of the pressurized water (sink). The authors focused on lift and spread since the lift is known to have a strong influence on the COP_{HP} of a compression heat pump (rising lift generally decreases COP_{HP}), and the spread on the sink side is also expected to play a role (at constant lift, rising spread reduces condensation pressure thereby increasing the COP). Analyzing the available measurement data, the expected trends are not fully confirmed, lift and spread are apparently not the only relevant parameters for the COP_{HP}, as can be seen especially at the operating points having a lift of about 78 K but different COP_{HP} values from 1.6 to 2.1 for different spreads, and on the other hand having nearly the same COP_{HP} values of around 3.5 (lift around 50 K) at spreads from 2 to 7 K. Unambiguous influences of other parameters could not be obtained with the available data.

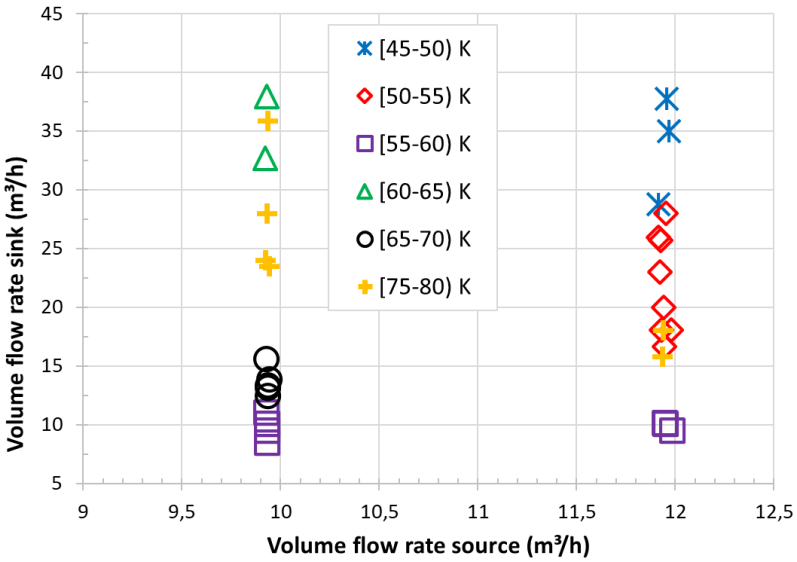


Figure 4: Boundary conditions at available operation points of the measurement campaign: Volume flow rates at heat source and heat sink (axes) and resulting temperature lift between sink outlet and source outlet

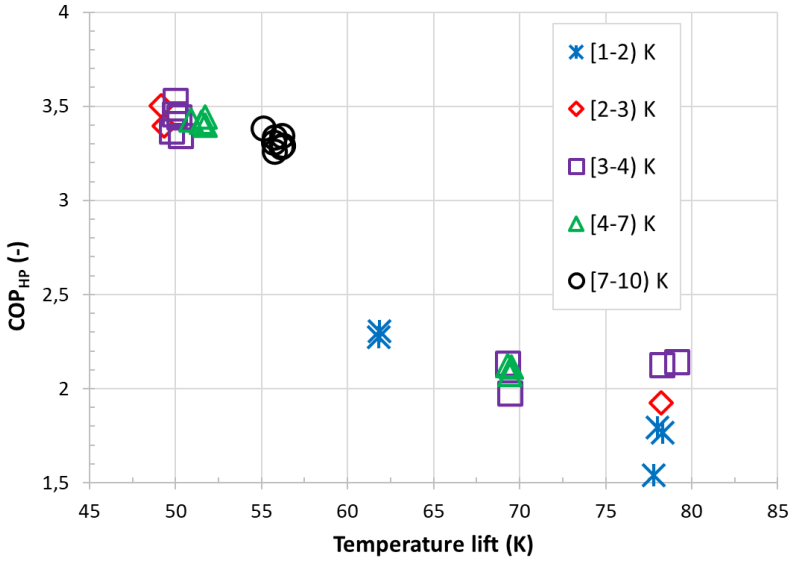


Figure 5: COP_{HP} at different temperature lifts between sink outlet and source outlet, broken down by the temperature difference (spread) of the pressurized water (sink)

The second law efficiency presented in the following compares the actual COP_{HP} with the maximum possible COP of a Lorenz cycle. For the correct calculation of this efficiency value, the difference of the logarithmic mean sink and source temperatures takes the place of the above used simple temperature lift between sink outlet and source outlet. But again, temperature difference between sink and source (though calculated differently) and spread was focused on since they are expected to have influence on the second law efficiency. The results for the available operating points are shown in Figure 6 with the corresponding volume flows on the heat source and the heat sink shown in Figure 7 over the resulting temperature difference between sink and source, broken down by the temperature difference (spread) of the pressurized water (sink). The diagrams indicate a lower second law efficiency at a higher difference between sink and source temperature (esp. spread group [1-2) K, having occasional comparable volume flows). Considering the spread on the heat sink (different colors and marker symbols) at comparable temperature differences between sink and source temperature (esp. 75 K), the second law efficiency tends to rise with rising spread.

Another observation at a temperature difference between sink and source of around 75 K and a constant source volume flow (spread groups [1-2) K and [3-4) K) is a decrease of second law efficiency with rising sink volume flow. This effect is not that strong at lower temperature differences between sink and source.

The current findings within this paper are that the second law efficiency (Lorenz cycle) of the heat pump is far from being constant, it increases when the temperature difference between sink and source is decreased, and with a rising temperature difference between sink and source the second law efficiency increases with rising spread of the pressurized water (respectively a lower sink volume flow). Even though unambiguous influences of all the parameters could not be obtained with the available data, the so far derived trends can help to operate the SGHP more efficient.

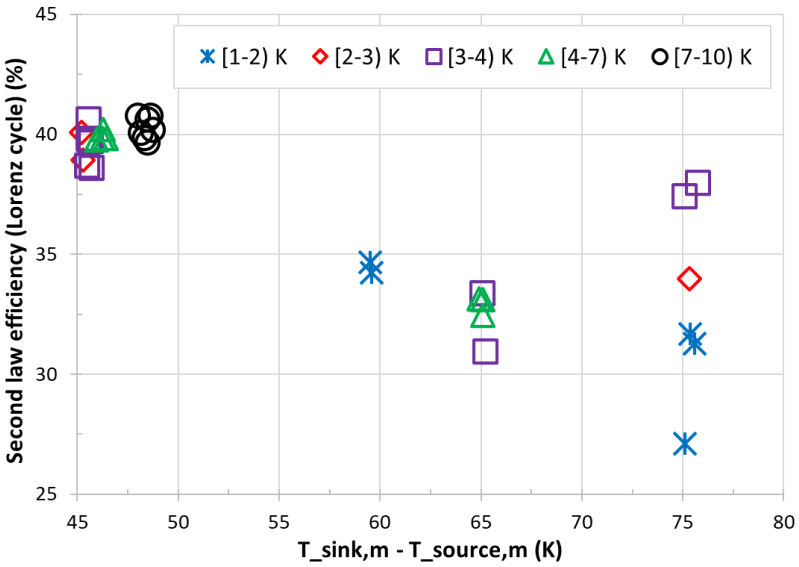


Figure 6: Second law efficiency (Lorenz cycle) over the difference between logarithmic mean sink and source temperature, broken down by the temperature difference (spread) of the pressurized water (sink)

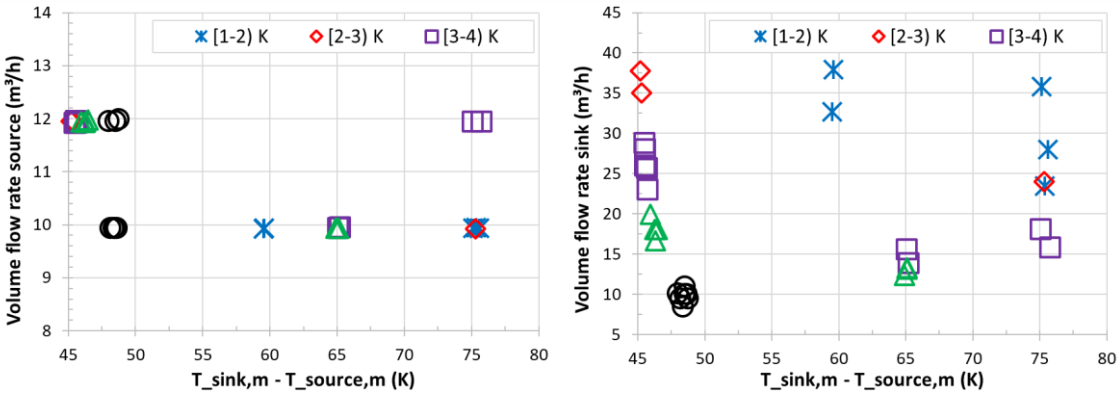


Figure 7: Boundary conditions at available operation points of the measurement campaign: Volume flow rates at heat source (left) and heat sink (right) over the resulting temperature difference between sink and source, broken down by the temperature difference (spread) of the pressurized water (sink)

4. Market potential

Within this paper, the market potential assessment of steam-generating high-temperature heat pumps up to 150 °C by Windholz et al. [17] is extended by analyses with prices for different consumption bands. Prices for different annual consumption bands of electricity and gas were extracted from the eurostat database [16] for the year 2021, see Table 2. Figure 8 shows the calculated effective ratios of electricity to gas prices in various European countries.

As stated in [17] for consumption bands IF/I4 (centre): Countries with relatively cheap electricity - above all Finland and Sweden - are particularly suitable for the substitution of gas by electricity, for example with heat pumps. In contrast, the implementation of heat pump projects in countries with relatively expensive

electricity - especially Slovakia, Ireland and Germany - is only economically viable over longer periods of time, if at all.

In comparison with the maps in the left (consumption bands IA/I1) and the right diagram (consumption bands IG/I5), price ratios – against first expectations – do not decrease with higher consumption bands in each country. In Bulgaria, Netherlands, Portugal, and Sweden, price ratios increase strictly monotonically from IA/I1 over IF/I4 to IG/I5. In Ireland, Hungary, Austria, Romania and Finland, price ratios only increase from IF/I4 to IG/I5.

Table 2. Energy consumption bands of non-household consumers for electricity and gas according to eurostat database [16]

Name of consumption band	Energy carrier	Band of annual consumption
IA	Electricity	Less than 20 MWh
IF	Electricity	70,000 MWh – 149,999 MWh
IG	Electricity	150,000 MWh or over
I1	Gas	Less than 1,000 GJ
I4	Gas	100,000 GJ – 999,999 GJ
I5	Gas	1,000,000 GJ – 3,999,999 GJ

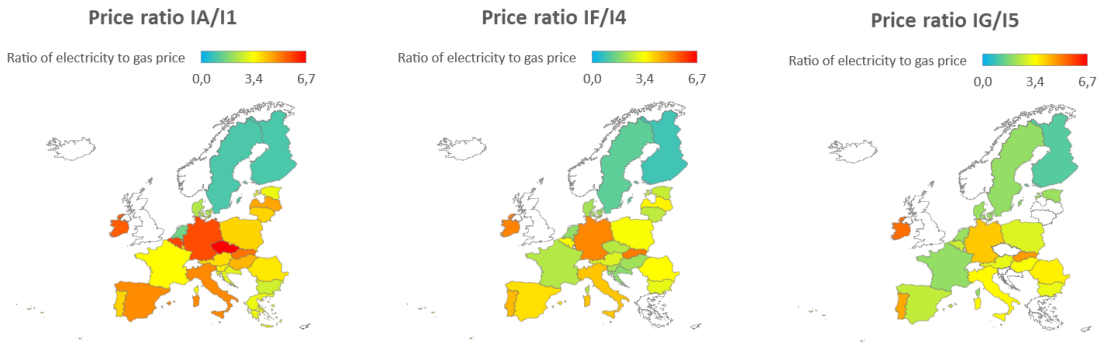


Figure 8: Ratio of electricity to gas prices in various European countries in 2021 according to *[16]*.
Left: Electricity consumption band IA, gas consumption band I1. Center: Electr. cons. band IG, gas cons. band I4 - adapted from *[17]*.
Right: Electr. cons. band IF, gas cons. band I5.
Supported by Bing, © GeoNames, Microsoft, OpenStreetMap, TomTom

4.1. Pulp and paper sector

Windholz et al. [17] found a total installed heating capacity in the paper industry in the European countries considered of around 12.6 GW_{th}. Germany achieves the highest individual value in this respect with 3.0 GW_{th}, followed by Finland and Sweden with 1.3 GW_{th} each. The technical potential for the use of steam-generating high-temperature heat pumps (< 150 °C) in the paper industry in various European countries was found to be around 6.1 GW_{th} or, at 48%, almost half of the installed heating capacity that could be provided by heat pumps - a heat recovery measure that saves primary energy.

The economic viability of heat pump systems is strongly dependent on the energy price ratio (electricity to natural gas) and the pricing of greenhouse gas emissions. Under the assumption that the use of heat pump systems must be financially worthwhile for the operator in addition to the primary energy savings, at a certificate price of 60 €/t and the three different price ratios of consumption bands a heating capacity of 1.3, 1.7 or 1.9 GW_{th} of HT heat pumps can be installed, i.e., only around 22, 28 or 31% of the technical potential in the paper industry.

As can be seen in the upper three images in Figure 9, Finland and Sweden as well as the Netherlands, Hungary and Croatia can leverage 100% of their technical potential with financial gain already with price ratio IA/I1. In Estonia and France this goal can only be reached with price ratio IG/I5. Note: Relevant information for the evaluation is missing for the countries shown in white.

An increase of the emission pricing (certificates) to e.g., 200 €/t increases the economic efficiency of heat pump systems, so that with the three different price ratios a total of about 1.4, 3.4, or 3.6 GW_{th}, or a share of 24, 55, or 58% of the technical potential can be raised in an economically profitable way, see in the lower three

images in Figure 9. While with price ratio IA/I1 6 countries could possibly leverage 100% of their technical potential, this number increases to 15 or 14 with price ratios IF/I4 or IG/I5, respectively (As before: Relevant information for the evaluation is missing for the countries shown in white).

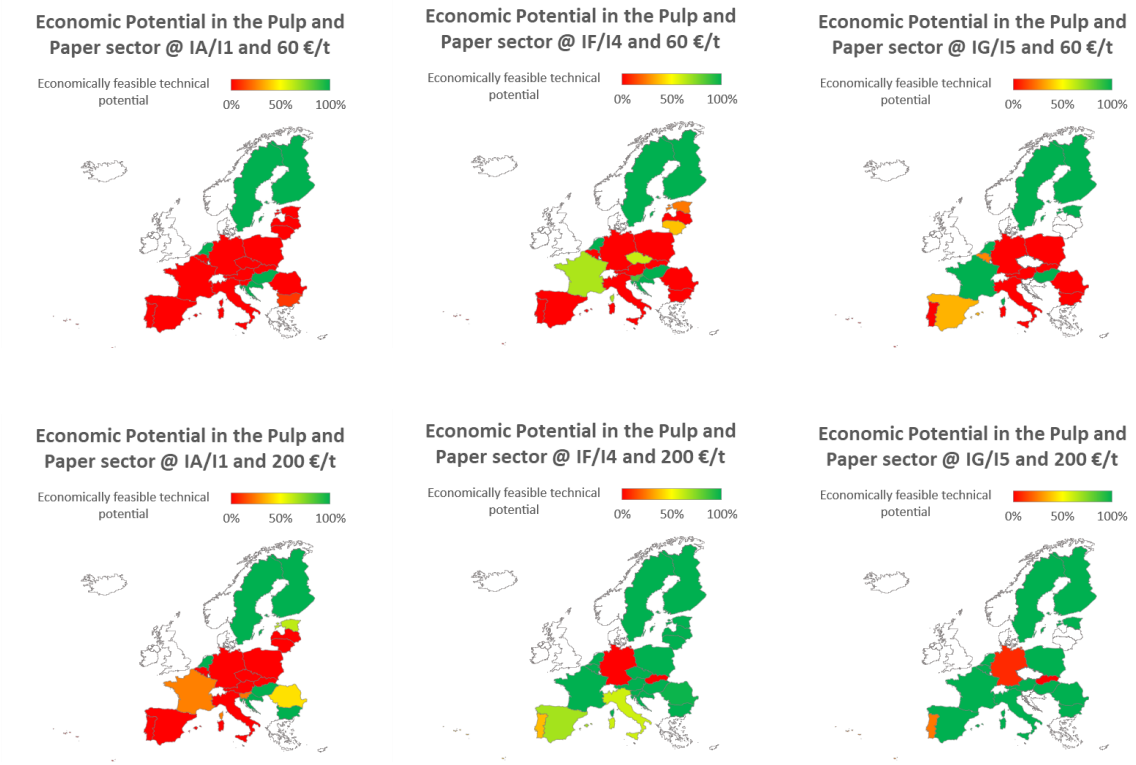


Figure 9: Economically feasible technical potential for steam-generating heat pumps (< 150 °C) in the paper industry in various European countries with a certificate price of 60 €/t.
Left: Price ratio IA/I1. Center: IG/I4. Right: IF/I5
Top: 60 €/t. Bottom: 200 €/t.
Supported by Bing, © GeoNames, Microsoft, OpenStreetMap, TomTom

4.2. Dairies, breweries, and meat processing

Windholz et al. [17] found a total installed heating capacity in subsectors (Dairies, breweries, and meat processing) of the food & beverage sector in the European countries considered of around 5.1 GW_{th}. Ireland achieves the highest individual value in this respect with 1.1 GW_{th}, followed by France with 875 MW_{th} and United Kingdom with 558 MW_{th}. The technical potential for the use of steam-generating high-temperature heat pumps (< 150 °C) in these subsectors of the food & beverage sector in various European countries was found to be around 2.2 GW_{th} or, at 44%, almost half of the installed heating capacity that could be provided by heat pumps - a heat recovery measure that saves primary energy.

The economic viability of heat pump systems is strongly dependent on the energy price ratio (electricity to natural gas) and the pricing of greenhouse gas emissions. Under the assumption that the use of heat pump systems must be financially worthwhile for the operator in addition to the primary energy savings, at a certificate price of 0 €/t and the three different price ratios of consumption bands a heating capacity of 136, 106 or 134 MW_{th} of HT heat pumps can be installed, i.e., only around 6, 5 or 6% of the technical potential in the considered subsectors of the food & beverage sector, see upper three images in Figure 10. These not really rising but partly even decreasing numbers are a direct consequence of the increasing price ratios with increasing consumption bands in some countries as explained above. While with price ratio IA/I1 three countries (Finland, Sweden, Netherlands) could possibly leverage 100% of their technical potential, this number decreases to two or one with price ratios IF/I4 or IG/I5, respectively.

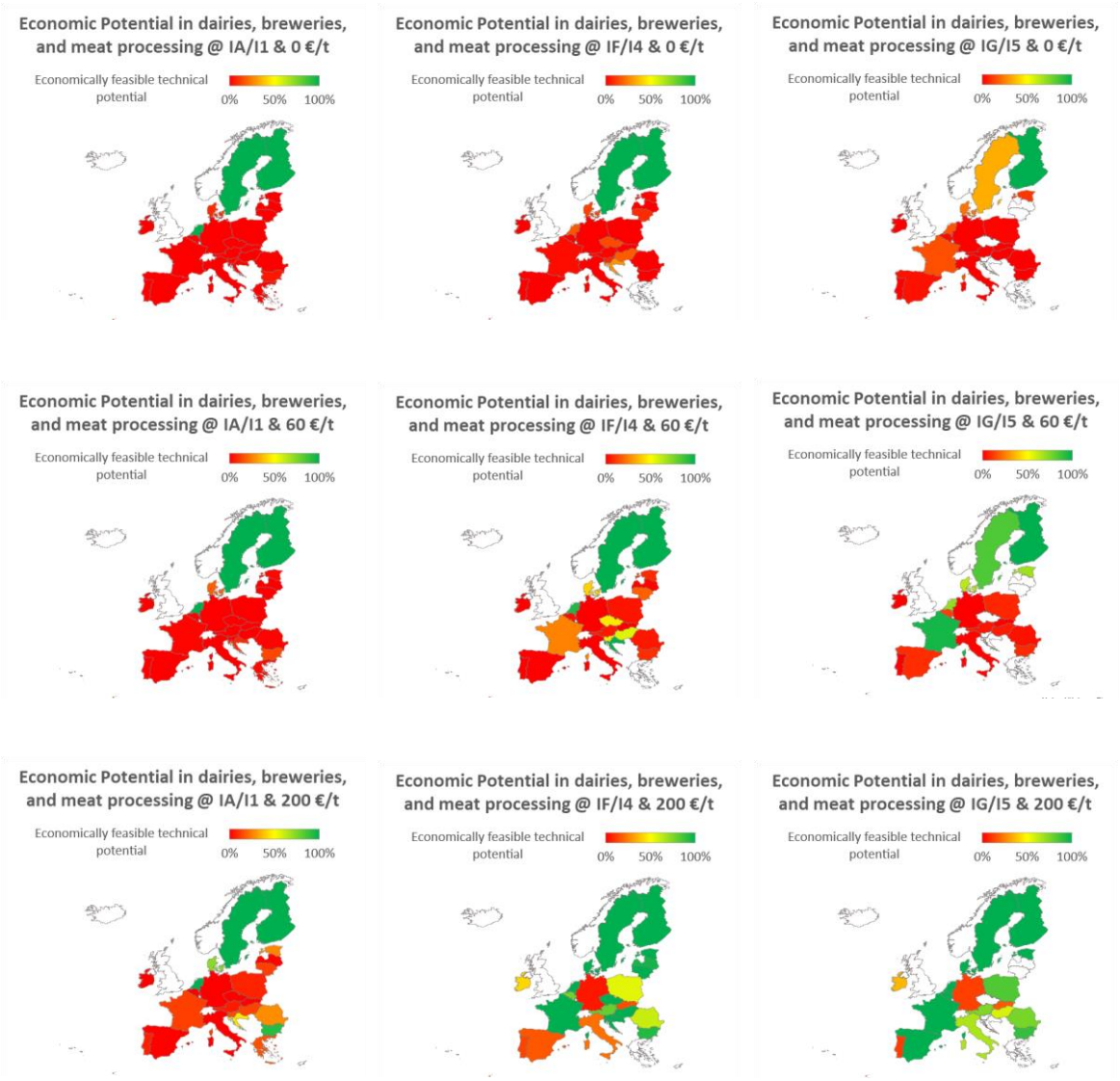


Figure 10: Economically feasible technical potential for steam-generating heat pumps (< 150 °C) in dairies, breweries, and meat processing in various European countries with a certificate price of 0 €/t. Left: Price ratio IA/I1. Center: IG/I4. Right: IF/I5 Top: 0 €/t. Middle: 60 €/t. Bottom: 200 €/t. Supported by Bing, © GeoNames, Microsoft, OpenStreetMap, TomTom

An increase of the emission pricing (certificates) to e.g., 60 €/t increases the economic efficiency of heat pump systems, so that with the three different price ratios a total of about 151, 300, or 545 MW_{th}, or a share of 7, 13, or 24% of the technical potential can be raised in an economically profitable way, see middle three images in Figure 10. While with price ratio IA/I1 three countries could possibly leverage 100% of their technical potential, this number stays three or decreases to one with price ratios IF/I4 or IG/I5, respectively. On the other hands, in countries with decreasing price ratios (with rising consumption bands), e.g. France and Denmark, the economic potential rises from IA/I1 to IG/I5.

An increase of the emission pricing (certificates) to e.g., 200 €/t increases the economic efficiency of heat pump systems, so that with the three different price ratios a total of about 284, 1084, or 1318 MW_{th}, or a share of 13, 48, or 59% of the technical potential can be raised in an economically profitable way, see lower three images in Figure 10. While with price ratio IA/I1 three countries could possibly leverage 100% of their technical potential, this number increases to eleven or eight with price ratios IF/I4 or IG/I5, respectively. On the other hands, in countries with decreasing price ratios (with rising consumption bands), e.g. Poland and Spain, the economic potential rises from IA/I1 to IG/I5.

The current findings add a new aspect to the results of Windholz et al. [17], namely that in some countries the price ratio of electricity to gas is not strictly monotonically decreasing with rising consumption bands, but

even increasing. This means, that in the countries concerned, smaller companies in the considered subsectors of the food & beverage sector, due to their better price ratio, have more economic potential to integrate heat pumps than larger companies (generally speaking having price ratios of higher consumption bands). However, despite the same price ratios, this effect was not found in the results of the pulp and paper sector, mainly due to different annual operating hours (8000 h/a in pulp & paper, 6000 h/a in the food & beverage sector) as boundary conditions.

Nevertheless, the influence of certificate prices on the economic potential of heat pump integration is clear, higher prices increase the economic potential.

5. Summary

Within this publication, results and findings of initial experimental investigations of a heat pump-based steam generation system using flash tanks were shown, which are based on the previous work of Helminger et al [12], Wilk et al [10], and mainly on Riedl et al. [13], among others. Extending these works within this publication the heat pump of the steam generating system was focused on. The current findings within this paper are that the second law efficiency (Lorenz cycle) of the heat pump is far from being constant, it increases when the temperature difference between sink and source is decreased, and with a rising temperature difference between sink and source the second law efficiency increases with rising spread of the pressurized water (respectively a lower sink volume flow). Even though unambiguous influences of all the parameters could not be obtained with the available data, the so far derived trends can help to operate the SGHP more efficient.

Results from market potential analyses already carried out [14] [15] indicate potentials for high-temperature heat pumps in selected production areas (food, paper industry, wood-based materials industry, etc.). The market potential assessment for steam-generating heat pumps (< 150 °C) presented in this paper, which takes into account country-specific production volumes from statistics databases [16] and process-specific steam demand volumes for the production of selected products, and current energy prices of European countries, extends the works of Windholz et al. [17] by analyses with prices for different consumption bands (generally speaking different company sizes). The current findings add a new aspect to the results of Windholz et al. [17], especially for the considered subsectors of the food & beverage sector, namely that in some countries the price ratio of electricity to gas is not strictly monotonically decreasing with rising consumption bands, but even increasing. This means, that in the countries concerned, smaller companies in the considered subsectors of the food & beverage sector, due to their better price ratio, have more economic potential to integrate heat pumps than larger companies (generally speaking having price ratios of higher consumption bands). However, despite the same price ratios, this effect was not found in the results of the pulp and paper sector, mainly due to different annual operating hours (8000 h/a in pulp & paper, 6000 h/a in the food & beverage sector) as boundary conditions, increasing the economic potential.

Nevertheless, the influence of certificate prices on the economic potential of heat pump integration is clear, higher prices increase the economic potential.

Nomenclature

Abbreviation/symbol		Subscript	
COP	Coefficient of performance	a	absolute
FT	Flash tank	HP	Heat pump
HFO	Hydrofluoroolefin	m	mean
HP	Heat pump	th	thermal
HT	High-temperature		
HTHP	High-temperature heat pump		
SGHP	Steam-generating heat pump system		
TRL	Technology readiness level		

Acknowledgements



The project has received funding from the European Union's Horizon 2020 programme for energy efficiency and innovation action under grant agreement Nr. 820771.

References

[1] R. de Boer, A. Marina, B. Zühlsdorf, C. Arpagaus, M. Bantle, V. Wilk, B. Elmegaard, J. Corberán and J. Benson, "Strengthening Industrial Heat Pump Innovation: Decarbonizing Industrial Heat," 2020.

[2] IEA, "Net Zero by 2050 - A Roadmap for the Global Energy Sector," 2021.

[3] IEA, "HEATING AND COOLING facts and figures: The transformation towards a low-carbon Heating & Cooling sector," 2017.

[4] SPH Sustainable Process Heat, "Die Wärmepumpe: Produktbeschreibung.," [Online]. Available: https://www.spheat.de/. [Accessed 11 2022].

[5] Heaten AS, "HeatBooster," [Online]. Available: https://www.heaten.com/product/. [Accessed 11 2022].

[6] Turboden, "Large Heat Pump," [Online]. Available: https://www.turboden.com/solutions/2602/large-heat-pump. [Accessed 11 2022].

[7] T. Kaida, I. Sakuraba, K. Hashimoto and H. Hasegawa, "Experimental performance evaluation of heat pump-based steam supply system," *IOP Conference Series: Materials Science and Engineering,* vol. 90, p. 12076, 2015.

[8] Fuji Electric, "Steam Generating Heat Pump," [Online]. Available: https://www.fujielectric.com/company/research_development/theme/heatpump.html. [Accessed 11 2022].

[9] F. Bless, C. Arpagaus and S. Bertsch, "Theoretical investigation of high-temperature heat pump cycles for steam generation," *13th IEA Heat Pump Conference,* p. 357–369, 2021.

[10] V. Wilk, F. Helminger, S. Dusek, M. Lauermann and T. Fleckl, "Steam generation from waste heat with heat pumps".*Proceedings of DKV Tagung 2019.*

[11] A. Marina, S. Smeding, A. Wemmers, S. Spoelstra and P. Kremers, "Design and Experimental Results of a Two-Stage Steam Producing Industrial Heat Pump," *13th IEA Heat Pump Conference,* p. 908–919.

[12] F. Helminger, "Steam generating heat pumps – Upcoming technology for heat recovery," [Online]. Available: https://www.hp-summit.de/de/events/vortrag/steam-generating-heat-pumps--upcoming-technology-for-heat-recovery-24/768038. [Accessed 11 2022].

[13] J. Riedl, F. Hubmann, B. Windholz, C. Gachot, F. de Carlan and Y. Beucher, "Messergebnisse einer dampferzeugenden Wärmepumpe mit Flash tank".*Proceedings of DKV-Tagung 2022.*

[14] G. Kosmadakis, "Estimating the potential of industrial (high-temperature) heat pumps for exploiting waste heat in EU industries," *Applied Thermal Engineering,* vol. 156, pp. 287-298, 2019.

[15] A. Marina, S. Spoelstra, H. Zondag and A. Wemmers, "An estimation of the European industrial heat pump market potential," *Renewable and Sustainable Energy Reviews,* vol. 139, p. 110545, 2021.

[16] "Database - Production - Eurostat," 2021. [Online]. Available: https://ec.europa.eu/eurostat/web/energy/data/database.

[17] B. Windholz, S. Knöttner, P. Schmidberger, F. Helminger and A. Schneeberger, "Marktpotentialabschätzung dampferzeugender Hochtemperatur-Wärmepumpen bis 150°C".*Proceedings of DKV-Tagung 2022.*

14th IEA Heat Pump Conference
15-18 May 2023, Chicago, Illinois

Numerical performance assessment of heat pumps in Rankine-based Carnot battery systems for grid balancing services

Robin Tassenoy[a,*] Jari De Craecker[a], , Katarina Simić [a], Toon Demeester[a], Michel De Paepe[a,b], Steven Lecompte[a,b]

[a]Ghent University, Sint-Pietersnieuwstraat 41, Ghent 9000, Belgium
[b]FlandersMake@UGent – Core lab EEDT-MP, Gaston Geenslaan 8, Heverlee 3001, Belgium

Abstract

Due to the increasing share of renewable sources in the energy mix, large-scale energy storage systems are becoming essential to ensure secure and stable energy supply. Carnot batteries, a combination of a power-to-heat, a thermal storage and a heat-to-power system, could provide a possible solution. Heat pump systems have been considered as the power-to-heat technology for Carnot batteries. However, it is not clear which grid services these heat pumps could deliver. To answer this question, a 1 MW vapour compression heat pump, suitable for integration in a Carnot battery, was modelled in Modelica. Quasi-steady state operation of compressor and expansion valve was considered, while dynamic finite volume models were used for the heat exchangers. Behavior of the sensible storage tanks was assumed ideal and quasi-steady boundary conditions were imposed. Furthermore, a control strategy driven by the requirements of the electrical grid was proposed. The dynamic model simulates and evaluates the heat pump's response to the qualification test profiles for grid balancing services. It was found that the heat pump can deliver a symmetric capacity of 125 kW for primary reserve while maintaining a correct delivery temperature to the thermal storage system. In addition, the system qualifies for delivering a capacity of 250 kW for secondary and tertiary reserve. These results indicate that the delivery of grid balancing services could be another revenue stream to increase the financial feasibility of Carnot battery systems and it is thus worthwhile to investigate its potential financial benefits.

© HPC2023.
Selection and/or peer-review under the responsibility of the organizers of the 14th IEA Heat Pump Conference 2023.

Keywords: Carnot battery; Rankine-based heat pump; grid balancing services; FCR; aFRR; mFRR

1. Introduction

1.1. Carnot batteries

The share of renewables in the worldwide energy generation is continuously increasing, peaking at 23.2% in 2019. This increase was even steeper in member states of the European Union, where renewable electricity production accounted for 33.2% [1]. This large deployment of variable renewable energy sources (RES) challenges the stability of the electrical grid due to their intermittent nature. Energy storage can address these problems by power and voltage smoothing, energy management, frequency regulation, peak shaving, load leveling, seasonal storage and standby generation during a fault [2]. Therefore, energy storage is considered one of the main drivers to provide the flexibility needed to completely decarbonize the electricity grid [3].

Carnot batteries are an emerging large-scale electrical energy storage (EES) concept that may provide additional flexibility to the grid. The concept involves three steps. First, electrical energy is converted into heat using a heat pump or joule heater after which the heat is stored in the second step.

* Corresponding author. Tel.: +32 9 264 33 59 .
E-mail address: Robin.Tassenoy@UGent.be .

Finally, heat engine technology is used to convert the heat back to electricity when needed. One of the Carnot battery's subsets is pumped thermal energy storage (PTES), in which an electrically driven heat pump is used to deliver heat to a hot store and/or extract heat from a cold store [4]. The majority of studies currently available have focused on the steady-state analysis and optimization of the storage concept and the obtainable round-trip efficiencies [5]. More recently, the techno-economic optimization of PTES have gained interest as well [6, 7]. Vecchi et al. [7] collected and compared the techno-economic performance data of different Carnot battery systems in literature. Moreover, they discussed the applications of Carnot batteries at energy system scale and the most recent commercial developments in Carnot battery technologies. Their literature review reveals that Carnot batteries have been considered mainly for load-shifting and arbitraging services. The authors concluded that these services alone may not be sufficient to recover the investment cost of the technology. The importance of a portfolio of grid services to provide different revenue streams is thus highlighted.

1.2. Grid balancing services

Within the portfolio of grid services, providing grid flexibility is highly promising as the need intensifies due to the large deployment of variable RES [8]. Grid flexibility is usually defined as the possibility of modifying generation and/or consumption patterns in reaction to an external signal (e.g. price) to contribute to the power system stability in a cost-effective manner. At the transmission grid level, flexibility is linked to grid balancing services offered to transmission system operators (TSOs) [9]. These services match the instantaneous electricity production and demand, which is essential to ensure stable grid operation. According to their time scale, three balancing products can be distinguished: primary or frequency containment reserve (FCR), secondary or automatically activated frequency restoration reserve (aFRR) and tertiary or manually activated frequency restoration reserve (mFRR). The FCR stabilizes the frequency deviation on the European grid at a stationary value, after which the aFRR and mFRR restore the frequency to its original value [10]. An overview of the main service characteristics is presented in Table 1.

Table 1. Characteristics of balancing services in the European electricity grid.

Balancing service	Direction	Full activation time	Min. delivery time	Min. bid size	Ref.
FCR	symmetric	30 s	15 min	1 MW	[11]
aFRR	up / down	7.5 min (to 5 min)	15 min	1 MW	[12]
mFRR	up / down	15 min	15 min	1 MW	[13]

1.3. Dynamic modelling of PTES and large-scale heat pumps with respect to grid balancing services

From the discussion above, it is clear that PTES-dynamics are essential for the delivery of grid balancing services. However, there is a lack of research on these dynamic characteristics which makes it difficult to predict, regulate and optimize the performance of PTES in actual operation processes [14].

This knowledge gap has partially been addressed for Brayton-based PTES recently [14, 15]. Lu et al. [14] constructed a dynamic simulation model of a PTES based on the closed Brayton-cycle with a nominal charging- and discharging power of 2.27 and 1.49 MW, respectively. The model was used to optimize the control strategy and dynamic performance of the system during the start-up process. It was found that the rotational speed increase rate had a negligible effect on the system startup time for the charging process but affected the start-up time of the discharging process significantly. Moreover, high rotational speed increase rates caused fluctuation and overshoot in the rotational speed. Depending on the control parameters, start-up to full load took 50 min in charging mode and 15 min in discharging mode. While the start-up was discussed, the system's reaction to disturbances of electrical power input in nominal operation was not studied. This topic was addressed by Yang et al. [15] for a 5 MW Brayton-heat pump in a PTES-system. Next to a study of the step response to the system control parameters, a closed loop inventory control strategy was proposed to ensure correct storage temperatures and high efficiency even at part-load. Although control of the system to maintain a desired power uptake, as needed for delivery of grid balancing services, was not discussed, the authors showed the system's capability to maintain correct charging conditions for the storage system despite reduced electrical power input.

To the best of the authors' knowledge, no study on the dynamics and control of a full Rankine-based PTES-system or of a heat pump cycle to be implemented in a PTES-system is currently available. Stand-alone large-scale Rankine-based heat pumps are currently mainly used in district heating applications and are thus not

optimized to react quickly to the needs of the electrical grid. Consequently, providing grid flexibility using large-scale Rankine-based heat pumps is not well understood [16]. Meesenburg et al. [17] were probably first to address this issue. A detailed numerical system model of a two-stage ammonia heat pump used in district heating applications was developed and calibrated based on experimental data. Rooted on this model, they assessed how fast large-scale heat pumps can adapt their load according to grid requirements, the dynamic effects during fast-regulation and the limitations of currently implemented units with regard to fast-regulation. It was found that after optimization of the control structure, the heat pump power could be regulated from 250 kW to 175 kW in 54 s and from 250 kW to 100 kW in 99 s without the risk of condensation in the suction line.

1.4. Scope of this study

As illustrated by the discussion above, the dynamic response and control of PTES driven by requirements of the electrical grid is a clear gap in literature. For Brayton-based PTES, the dynamic response to power disturbances has been addressed. Nevertheless, control of the system to follow a desired electrical consumption or production profile as required for grid balancing has not yet been studied. For Rankine-based PTES, no study discussing the dynamic response of the complete system has been found. In fact, only one study addressing this subject for a stand-alone large-scale heat pump has been identified. However, this study focused on an existing heat pump for district heating, which means the topology, working temperatures and temperature requirements of the heat transfer fluid to the thermal storage were less strict compared to PTES-applications. As such, it remains unclear whether PTES is capable of delivering grid balancing services. This study aims to make a first step towards answering this question by focusing on the heat pump component of Rankine-based PTES. A dynamic model of a 1 MW Rankine-based heat pump cycle suitable for implementation in a PTES was constructed. Then, a suitable control strategy to follow the desired power uptake was developed, while maintaining correct storage temperatures. Finally, the controlled system was validated against pre-qualification tests of the European grid to assess its technical potential to deliver grid balancing services.

The system description, nominal operating conditions, sizing and dynamic modelling of the components and test conditions, are described in Section 2. The modelling results are shown and discussed in Section 3. First, the Modelica model is validated by a steady-state comparison to the Python cycle calculation. Then, the maximum capacity is determined and the qualification tests for mFRR, aFRR and FCR are successively discussed before a conclusion is formulated in Section 4.

2. Methodology

2.1. Carnot-battery lay-out and heat pump boundary conditions

This work focusses on the dynamic modelling of a vapour compression heat pump to be implemented in a Carnot battery. These PTES-systems usually consists of a heat pump, a thermal storage system and a thermal engine, as shown in Figure 1.

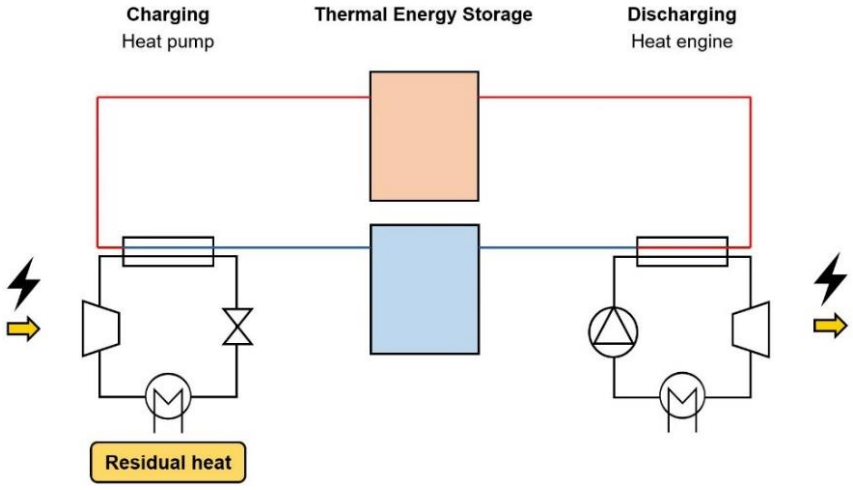


Fig. 1. Schematic representation of a Rankine-based, thermally integrated Carnot battery.

Rankine-based PTES typically takes advantage of a low-grade heat source to boost the electric round-trip efficiency of the system [18]. Apart from low grade geothermal heat and solar thermal energy, heat sources of suitable thermal capacity and temperature level can be found mostly in the industrial sector. Marina et al. [19] inventoried these industrial residual heat sources suitable for heat pump integration. The amount of residual heat available reduces with increasing heat temperature. Balancing the heat availability and efficiency improvement of the PTES, a residual heat source of 65°C was adopted in this study.

Sensible liquid heat storage is often applied as it is reliable, mature and cost-efficient. A two-tank configuration guarantees almost constant charge and discharge profiles and was therefore selected instead of a single tank solution, despite the cost of doubling the storage volume [18, 20]. Pressurized water tanks were opted for as they are cheap, have low environmental impact and are suitable for the temperature range of interest [5, 21]. As typical temperature lifts of heat pumps reported in literature range from 40 to 80 °C [22, 23], the tank temperatures were chosen to fit within this lift range. The temperature of the hot tank was chosen as 125 °C, while a cold tank temperature of 95 °C was assumed.

A basic heat pump cycle was chosen in this work. It has four main components: an evaporator, a compressor, a condenser and an expansion valve (see Fig. 1). In literature, more advanced cycles have been proposed [20, 22, 24]. Although these systems have higher coefficients of performance, the additional components increase the thermal inertia of the system and are thus expected to slow down the system's dynamic response. Therefore, the most basic system was assessed first. If this topology proves to be suitable to deliver grid balancing services, more complex topologies can be addressed in future work.

2.2. Nominal operating conditions and refrigerant selection

Once the temperature range of the heat pump had been fixed, the working fluid was selected. Based on different studies, R-1233zd(E) was selected because of its good thermodynamic performance in the intended operating range and low global warming and ozone depletion potential compared to refrigerants commonly applied [25, 26].

The steady-state operating conditions were calculated using a Python toolbox to model basic and advanced heat pump concepts [27]. Fluid property data were imported from REFPROP 10.0 [28]. Based on these estimates, more detailed component selection and modelling were performed, as discussed in Section 2.3. An overview of the modelling assumptions and resulting nominal conditions is given in Table 2.

Table 2. Nominal operating conditions: modelling assumptions and results.

Assumed parameter	Value	Unit	Output parameter	Value	Unit
$T_{water,source,in}$	65	°C	$P_{evaporator}$	2.93	bar
$T_{water,sink,in}$	95	°C	$P_{condenser}$	19.08	bar
$T_{refrigerant,sat,evaporator}$	50	°C	PR	6.5	-
$T_{refrigerant,sat,condenser}$	130	°C	$\dot{m}_{water,source}$	43.4	kg/s
$\Delta T_{superheat}$	9	°C	$\dot{m}_{water,sink}$	20.7	kg/s
$\Delta T_{subcooling}$	4	°C	$\dot{m}_{refrigerant}$	22.4	kg/s
$\dot{Q}_{condenser}$	2.8	MW	$\dot{Q}_{evaporator}$	1.81	MW
$PP_{evaporator}$	5	°C	$\dot{Q}_{condenser}$	2.80	MW
$PP_{condenser}$	5	°C	$P_{el,compressor}$	0.99	MW
$\eta_{is,compressor}$	0.8	-			
Refrigerant	R-1233zd(E)	-			

2.3. Component selection and modelling

A dynamic heat pump model was built in the object-oriented modelling language Modelica [29], using the simulation software Dymola 2022 [30] and the TIL-library [31]. The component models of this library were used, and extended when necessary. The piping pressure losses on the low and high pressure side were merged in one common pressure loss model at each pressure side to ensure right inlet and outlet pressure for the compressor. Fluid properties were calculated using the REFPROP-database [28]. In the following subsections, the component selection and assumptions made for their modelling are briefly discussed.

2.3.1. Heat exchangers

Plate heat exchangers (PHE) were selected for both the evaporator and condenser because they are relatively cheap, compact and have a modular design [20, 32]. Funke [33] produces gasketed PHE with capacities up to 30 MW and volume flow rates up to 4500 m³/h. SWEP [34] manufactures smaller capacity heat exchangers, but provides an intuitive sizing tool for high-level sizing of the heat exchangers. Based on this tool, five VH500TM PHEs and two B500TM PHEs were selected as evaporator and condenser respectively. The PHEs were modelled using the finite volume (FV) model available in the TIL-library [31], assuming countercurrent flow. Instead of modelling five separate evaporators, only one PHE model was used with the total amount of plates. The dimensions of one plate were based on the actual heat exchanger. A similar approach was implemented for the condenser. The suitability of FV-models for dynamic simulation of evaporators and condensers has extensively been demonstrated [32]. Moreover, the PHE model from the TIL-library used in this study has been successfully used to simulate a two-stage ammonia heat pump with a thermal capacity of 800 kW [17]. The authors validated the model to experimental measurements of an actual heat pump with shell-and-plate heat exchangers under identical operating conditions. Despite the different heat exchanger type, the alternative heat exchanger model accurately represented the general trends of the heat pump behavior during load change and could thus be used to assess to study the system control. In the current study, not all model parameters were made available by the PHE manufacturer. Therefore, the values reported by Meesenburg et al. [17] were used initially and adapted so that the heat exchanger mass, volume and heat exchanger area matched the values proposed by the SWEP-software [35]. Consequently, the inertia of the modelled heat exchangers is representative for the selected components. On the refrigerant side, following heat transfer correlations were applied: Shah Chen [36] for evaporation, Chen [36] for condensation and Gnielinski Dittus Boelter for single-phase flow [37]. Heat transfer at the water side was modelled by the VDI Plate alpha correlation [38]. Finally, all pressure drops in the heat exchangers were assumed proportional to quadratic mass flow [17].

2.3.2. Compressor model

A screw compressor or centrifugal compressor would be most suitable for the nominal flow rate and pressure ratio [39]. However, performance data at variable rotational speeds was not found for both. Therefore, performance maps for an axial compressor, suitable for higher flow rates, were retrieved from the GasTurb performance map collection [40] and scaled to the intended nominal conditions. An important remark to make is that the performance map used is representative for gas compressors, while in the current study a refrigerant was used. Nevertheless, the performance map of the gas compressor allowed to construct a performance map-based compressor model. The reported isentropic efficiencies range from 65 to 87 % depending on the operating conditions, which corresponds with common assumptions in performance studies for Carnot batteries. Therefore, this assumption was considered acceptable for the current purpose and the results can be updated when more suitable performance data becomes available. Immediate response of the compressor was assumed [17, 41, 42].

2.3.3. Valve model

The valve model was retrieved from the TIL-library [31]. The operating point was adapted by regulating the effective flow area of the valve.

2.3.4. Other components

The sensible storage was not modelled in detail. Instead, it was assumed that the tank was perfectly stratified and the water temperature at the inlet of the condenser stayed constant. A boundary model was used to impose a constant pressure and temperature, while the mass flow could be regulated.

2.4. Controller design

The control system should make sure the heat pump responds quickly to a desired power uptake, while maintaining correct storage temperatures and maximizing operational efficiency. Therefore, three inputs were controlled using PI-controllers: the compressor rotational speed, the valve through-flow area and the water mass flow rate in the condenser. Variable speed control of the compressor is an effective way to modulate the power uptake. A PI-controller compared the desired power consumption with the effective one and changed the rotational speed accordingly. As the operating point is determined by the intersection of the compressor- and valve characteristic, the effective through-flow area of the valve was varied to acquire the mass flow corresponding with the maximal efficiency of the compressor for a given pressure ratio. The value of the

refrigerant mass flow was calculated based on a fourth degree polynomial derived from the efficiency map of the compressor optimizing the relation between pressure ratio and mass flow rate. Finally, the water mass flow rate in the evaporator was adapted by a PI-controller to maintain a hot storage temperature of 125°C. All PI-constants were determined by analyzing the corresponding system step response using a dedicated online toolbox [43]. The resulting PI-constants are summarized in Table 3.

Table 3. PI-control parameters.

Controller	k [-]	T_i [s]
Compressor	2.412325169e-7	0.739237526841722
Valve	4.034429164e-6	0.162573741351303
Water mass flow	5	7

2.5. Test conditions for ancillary services

The Belgian TSO Elia provides prequalification tests for all balancing services discussed in Table 1. All tests follow the same approach. A power profile that represents the most extreme testing situation is provided. The service is then evaluated in terms of the full activation time (FAT), the maximum power delivery, the duration of the service and the deviation of the power. The delivery of FCR is always symmetric and the capacity should react linearly to the frequency deviation of the grid. aFRR and mFRR on the other hand can deliver up- or down regulation separately, or do both. It should be noted that Elia sets a minimum capacity bid for aFRR and mFRR at 1MW, but it is allowed to split this capacity over multiple assets. The main criterium is that the requested power uptake or production (within predefined accuracy) is reached within the prescribed maximum activation time. In this study, the combination of up-and down regulation was not tested as it follows from the separate tests. The pre-regulation tests also aim at verifying that the service can be delivered for a sufficiently long time. For Carnot batteries, this duration is closely related with the capacity and state-of-charge of the thermal storage system. Here, focus was given to the reaction time and it was assumed the TES was sized adequately, fulfilling the duration requirement.

3. Results and discussion

3.1. Steady-state model validation

A direct validation of the separate component models to experimental data is not possible, as this data is not available. Instead, the component sizing and modelling are partially validated by comparison of the steady-state results to the steady-state Python calculation. The dynamic model (and implemented control) are tested by simulating the steady-state system response to constant controller setpoints. An overview of the assumed boundary conditions, controller setpoints and corresponding simulation results is given in Table 4. The simulation results show good correspondence with the steady-state cycle calculations in Table 2. The deviation can be explained by the model strategy. While the thermodynamic states are fixed directly in the Python model, they follow from the physical component characteristics and choice of controlled parameters in the Modelica model. A one-on-one match is thus not to be expected. Nevertheless, the good correspondence between results indicates proper sizing and modelling of the different components. Moreover, the controllers reach the desired setpoint illustrating the effectiveness of the implemented control method.

Table 4: Steady-state model validation - boundary conditions and simulation results.

Assumed parameter	Value	Unit	Output variable	Value	Unit
$T_{water,source,in}$	65	°C	$T_{water,sink,out}$	125	°C
$T_{water,sink,in}$	95	°C	$P_{el,compressor}$	1.00	MW
$T_{water,sink,out,set}$	125	°C	$P_{evaporator}$	2.98	bar
$\dot{m}_{water,source}$	43.4	kg/s	$P_{condenser}$	19.52	bar
$P_{el,compressor,set}$	1	MW	PR	6.54	-
Refrigerant	R-1233zd(E)	-	$\dot{m}_{water,sink}$	19.41	kg/s
			$\dot{m}_{refrigerant}$	23.05	kg/s

$\dot{Q}_{evaporator}$	1.48	MW
$\dot{Q}_{condenser}$	2.46	MW
$\Delta T_{superheat}$	12.68	°C
$\Delta T_{subcooling}$	0	°C
$PP_{evaporator}$	3.1	°C
$PP_{condenser}$	8.096	°C
$\eta_{is,compressor}$	0.86	-

3.2. Maximum power regulation

To assess the possibility of delivering grid balancing services, the maximum capacity available should be determined first. The minimum part-load capacity the system can run at is determined by:

- The minimum rotational speed of the compressor, which is 50% of the nominal speed according to the performance map.
- Condensation of the refrigerant at the inlet or outlet of the compressor due to insufficient superheating.
- The condenser temperature, as the heat pump may not be able to sustain a water outlet temperature of 125°C to the storage tank.

In order to test which condition limits the part-load capacity of the system, the compressor power setpoint was gradually reduced. This was done sufficiently slow so that all operating points could be considered steady-state and the operating range was not determined by transient responses. The superheating at the outlet of the compressor became insufficient first, at a compressor power uptake of 750 kW. The compressor power can thus be modulated between 750 and 1000 kW. The potential capacity for aFRR and mFRR is hence 250 kW. As FCR should always be delivered symmetrically, the potential power band for FCR is limited to 125 kW around a nominal operating point of 875 kW.

3.3. Tertiary reserve

The Carnot battery should fulfill two requirements in order to qualify for mFRR: the system should have a sufficiently low response time and should be able to maintain the correct charging temperatures to the TES.

The mFRR has a maximum FAT of 15 min, implying that the full offered capacity should be activated within 15 min. In Figure 2, the step response of the heat pump system to a step change in compressor power setpoint in the downward- and upward direction is shown. As summarized in Table 5, the FAT of the heat pump is well below the limit of 15 minutes. The response time found is significantly shorter than the minimal regulation time of 54 s obtained by Meesenburg et al. [17], who made similar modelling assumptions. This difference can be attributed to the more complex system lay-out. The one-stage heat pump reacts significantly quicker than a two-stage variant because of its lower system inertia and omitted control of the intermediate pressure level. Yang et al. [15] studied the dynamic response of a 5 MW Brayton-based heat pump integrated in a Carnot battery and found a response time of 14.28 s for a 250 kW downward ramp. The response times found for the 1MW Rankine-heat pump are thus lower, but have a similar order of magnitude for the same mFRR capacity delivered.

Table 5. FAT of a 1 MW heat pump system in downward and upward direction.

Full activation time [s]	Downward step	Upward step
Within 1% deviation	4.1	3.7
Within 0.1 %	6.4	7.3

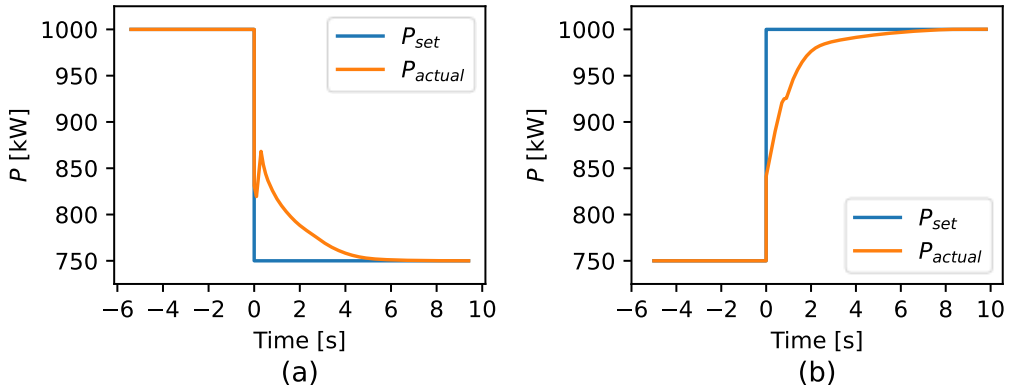


Fig. 2. Response of a 1 MW heat pump to a 250 kW downward (a) and upward (b) step in compressor power.

Next to this suitable response time, it is crucial that the delivery temperature to the TES-system remains correct during the power modulation. In Figure 3, the variation of the water temperature at the outlet of the condenser is shown for the downward and upward step. The maximum absolute deviation is 0.59 °C and 0.66 °C for the downward and upward step, respectively. Besides, the duration of the deviation is lower than 50 s. Despite this short duration, it is still noticeable that the temperature response is significantly slower than the power response.

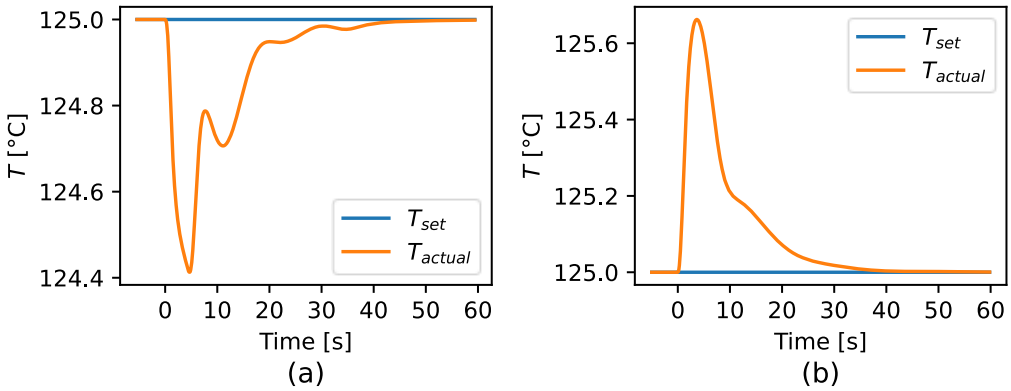


Fig. 3. Water temperature at the outlet of the condenser for a 250 kW downward (a) and upward (b) step in compressor power.

To better understand this delayed thermal response, the system's reaction to a 250 kW downward step in compressor power setpoint (P_{set}) is investigated. The response to the upward step is analogous. In Figure 4, it can be seen that the PI-controller of the compressor reacts immediately on the reduced power setpoint by lowering the compressor speed (n). Consequently, the refrigerant mass flow ($\dot{m}_r$) reduces. Moreover, the evaporator pressure drops and the condenser pressure increases, which results in a reducing pressure ratio (PR) over the compressor. As both changes happen quickly, the compressor power settles rapidly at the desired setpoint. The delayed temperature response of the sink water can be explained by the thermal inertia of the heat exchanger. As visualized in Figure 5, the thermal inertia causes the condenser heat rate ($\dot{Q}_{cond,out}$) to drop slower compared to the refrigerant mass flow and enthalpy of the refrigerant at the compressor outlet. Therefore, the water temperature at the sink outlet drops more slowly as well. As the heat sink PI-controller reacts based on the difference between this temperature and the desired temperature setpoint, its reaction is delayed compared to the compressor PI-controller that reacts directly on the desired electrical power consumption. The sink PI-controller's response is thus cushioned by the inertia of the heat exchanger. Nevertheless, the PI-controller of the sink reacts sufficiently quickly to maintain a suitable water temperature at the condenser outlet.

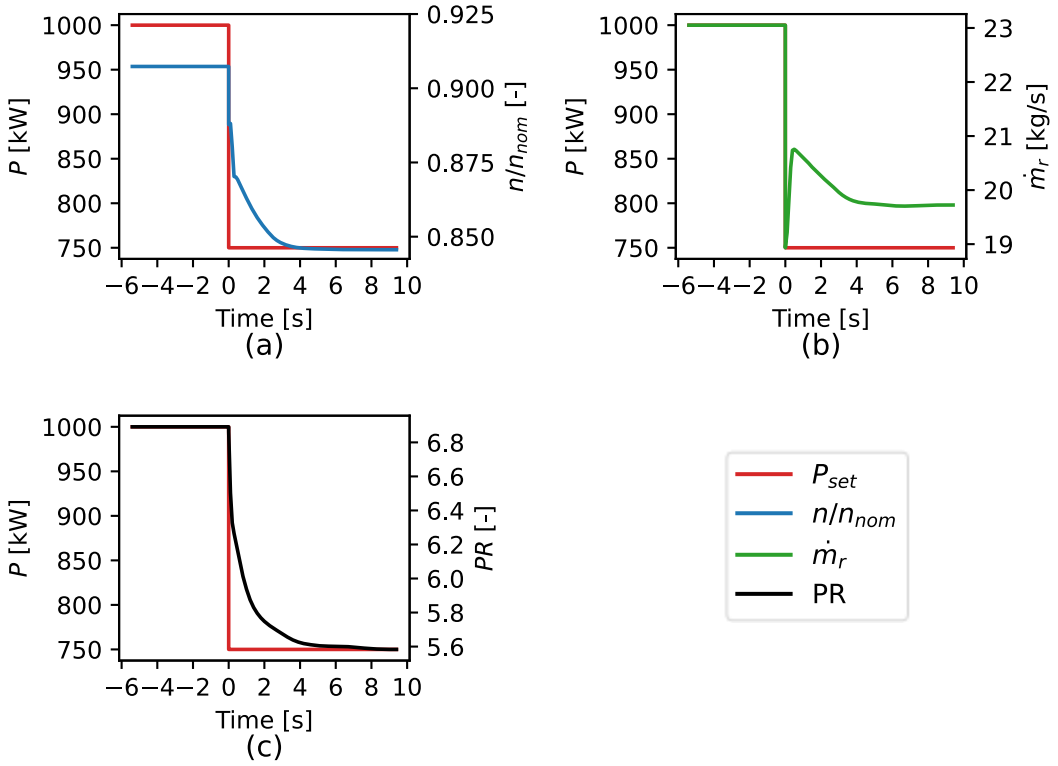


Fig. 4. System response for a 250 kW downward step in compressor power: (a) relative compressor speed, (b) refrigerant mass flow rate, (c) pressure ratio.

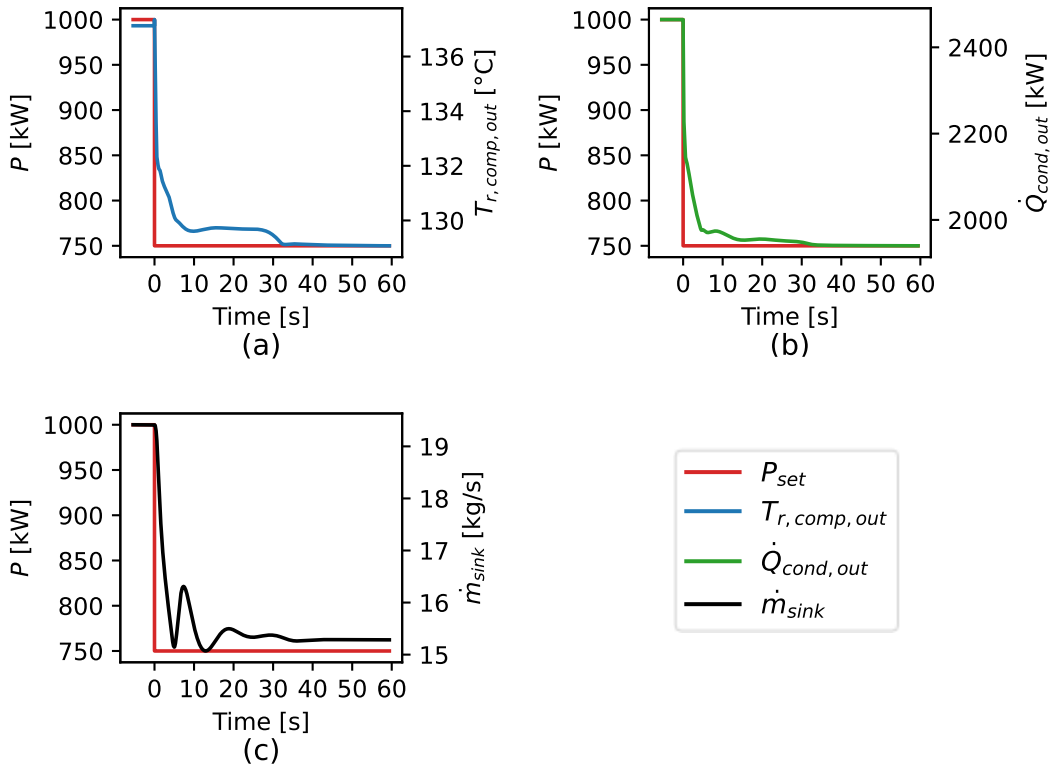


Fig. 5. System response for a 250 kW downward step in compressor power: (a) refrigerant temperature at compressor outlet, (b) condenser heat rate, (c) water mass flow heat sink.

As the FAT is well below the required limit while maintaining adequate supply temperatures to the TES, it can be concluded that the heat pump system is capable of delivering a capacity of 250 kW mFRR in both the upward and downward direction. However, it is important to note that the power control acts directly on the compressor setpoint and that this compressor is modelled assuming quasi-steady state. Given the low FAT found, taking the compressor dynamics into account may thus be important for grid supporting applications in contrast to traditional heat pump applications where the heat pump is controlled based on heat demand. The sensitivity of the system's response to the compressor inertia will be evaluated in future work.

3.4. Secondary reserve

Compared to tertiary reserve, aFRR requires a faster response with a FAT lower than 7.5 min. This limit will be reduced to 5 minutes by 17/12/2024 [12]. As discussed in Section 3.3, the heat pump meets this requirement while maintaining suitable TES-temperatures. Next to the FAT requirement, the heat pump should be able to follow a synthetic load pattern within a margin of 7.5 %. Figure 6 shows this load-pattern for upward and downward aFRR, which corresponds to lowering and increasing the compressor power consumption respectively. A maximum power deviation of 0.85 % and 0.79 % is observed for the upward and downward aFRR product, which is within the allowable limit. The corresponding maximum absolute deviations of the water temperature at the outlet of the condenser are 0.30 °C in both directions. The heat pump thus qualifies for an aFRR capacity of 250 kW in the upward and downward direction.

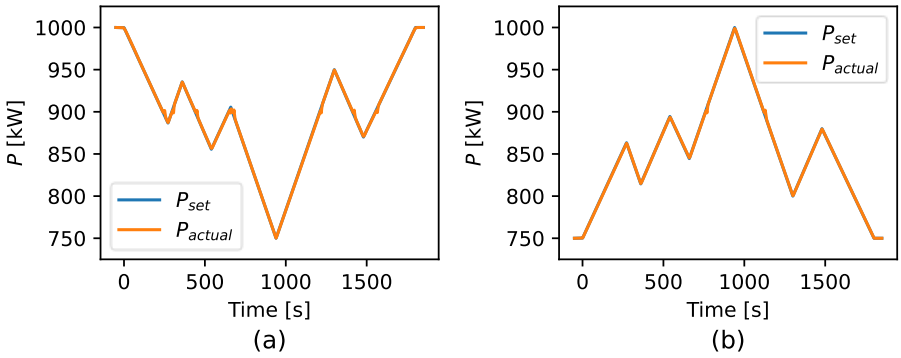


Fig. 6. Load-following test for the (a) upward and (b) downward aFRR product.

3.5. Primary reserve

The qualification test for FCR consists of two parts. First, the FAT of the full contracted reserve should be delivered within 30 s in both directions, a requirement which is met as shown in Table 5. Besides, the system should react adequately to step changes of one fourth of the contracted capacity. The maximum allowable deviation after 12.5 s is 10% of the step (3.125 kW). As explained in Section 3.1, the heat pump is tested for a symmetric capacity of 125 kW. Figure 7 shows the system response on the stepwise decrease and increase of the requested compressor power. The deviation values per step are summarized in Table 6. The maximum absolute deviation of the water temperature at the outlet of the condenser over the whole ramping interval is 0.27 and 0.13 °C for the stepwise decrease and increase in requested compressor power, respectively. The system thus qualifies for a symmetric FCR capacity of 125 kW.

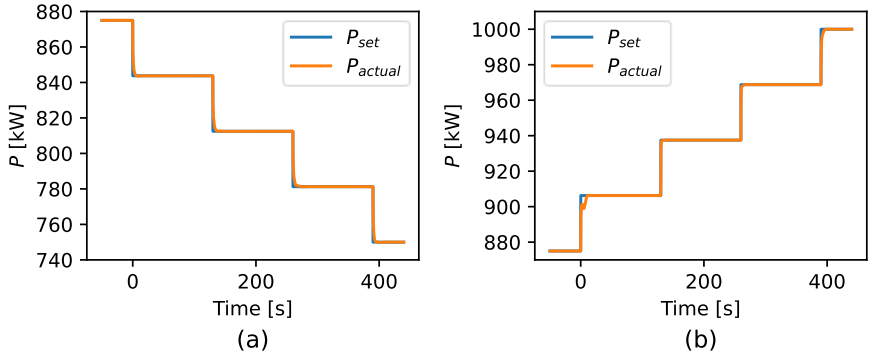


Fig. 7. System's response to stepwise (a) decrease and (b) increase of requested compressor power.

Table 6. Overview of power deviations in FCR qualification test.

	Decrease compressor power		Increase compressor power	
Step	P_{set} [kW]	Largest deviation [kW]	P_{set} [kW]	Largest deviation [kW]
1	843.750	0.0435	906.250	0.0339
2	812.500	0.0397	937.500	0.0100
3	781.250	0.157	968.750	0.009
4	750.00	0.213	1000.00	0.006

4. Conclusion

The possibility to deliver grid balancing services with large-scale heat pumps in Rankine-based Carnot battery systems was investigated. Therefore, a basic Rankine-based 1 MW heat pump cycle, suitable for implementation in a Carnot battery using two-tank liquid storage, was modelled dynamically in Modelica. Afterwards, a suitable system control strategy was developed and the system was evaluated according to the pre-qualification tests for grid balancing services in the European grid. Under the assumption of quasi-steady state compressor modelling and ideal behavior of the sensible storage tanks, the heat pump can deliver a symmetric capacity of 125 kW for FCR while maintaining correct delivery temperatures to the TES. Alternatively, the system can offer a capacity of 250 kW for aFRR and mFRR in both the upward and downward direction. These results indicate that the delivery of grid balancing services could be another revenue stream to increase the financial feasibility of Carnot battery systems and it is thus worthwhile to investigate the potential financial benefits. In future work, the sensitivity of the results to the compressor's inertia will be validated and the dynamic model will be extended to a full dynamic Carnot battery model including detailed modelling of the TES and organic Rankine cycle, hence further investigating optimal system scheduling within the energy system.

References

[1] International Energy Agency, Energy transition indicators, 2020. https://www.iea.org/data-and-statistics/data-browser?country=WORLD&fuel=Energy%20transition%20indicators&indicator=ETISharesInPowerGen (Accessed 30.06.2021.
[2] M.C. Argyrou, P. Christodoulides, S.A. Kalogirou, Energy storage for electricity generation and related processes: Technologies appraisal and grid scale applications, Renewable and Sustainable Energy Reviews 94 (2018) 804-821.
[3] C. Andrey, P. Barberi, L. Lacombe, L. van Nuffel, F. Gérard, J.G. Dedecca, K. Rademaekers, Y. El Idrissi, M. Crenes, Study on energy storage – Contribution to the security of the electricity supply in Europe, European Commission, Luxembourg, 2020.
[4] J.D. McTigue, P. Farres-Antunez, K.S. J, C.N. Markides, A.J. White, Techno-economic analysis of recuperated Joule-Brayton pumped thermal energy storage, Energy Conversion and Management 252 (2022).
[5] O. Dumont, G.F. Frate, A. Pillai, S. Lecompte, M. De paepe, V. Lemort, Carnot battery technology: A state-of-the-art review, Journal of Energy Storage 32 (2020).
[6] R. Tassenoy, K. Couvreur, W. Beyne, M. De Paepe, S. Lecompte, Techno-economic assessment of Carnot batteries for load-shifting of solar PV production of an office building, Renewable Energy 199 (2022) 1133-1144.
[7] A. Vecchi, K. Knobloch, T. Liang, H. Kildahl, A. Sciacovelli, K. Engelbrecht, Y. Li, Y. Ding, Carnot Battery development: A review on system performance, applications and commercial state-of-the-art, Journal of Energy Storage 55 (2022).
[8] T. Heggarty, J.-Y. Bourmaud, R. Girard, G. Kariniotakis, Multi-temporal assessment of power system flexibility requirement, Applied Energy 238 (2019) 1327-1336.
[9] J. Villar, R. Bessa, M. Matos, Flexibility products and markets: Literature review, Electric Power Systems Research 154 (2018) 329-340.
[10] elia, Keeping the Balance, 2022. https://www.elia.be/en/electricity-market-and-system/system-services/keeping-the-balance. (Accessed 06/11/2022.
[11] elia, FCR service design note, 2019.
[12] elia, Automatic Frequency Restoration Process (aFRR/R2), 2022. https://www.elia.be/en/electricity-market-and-system/system-services/keeping-the-balance/afrr. (Accessed 06/11/2022.

[13] elia, Balancing services: mFRR - design note, 2022.
[14] C. Lu, X. Shi, Q. He, Y. Liu, X. An, S. Cui, D. Du, Dynamic modeling and numerical investigation of novel pumped thermal electricity storage system during startup process, Journal of Energy Storage 55 (2022).
[15] H. Yang, J. Li, Z. Ge, L. Yang, X. Du, Dynamic characteristics and control strategy of pumped thermal electricity storage with reversible Brayton cycle, Renewable Energy 198 (2022) 1341-1353.
[16] A. David, B.V. Mathiesen, H. Averfalk, S. Werner, H. Lund, Heat Roadmap Europe: Large-Scale Electric Heat Pumps in District Heating Systems, Energies 10(4) (2017).
[17] W. Meesenburg, W.B. Markussen, T. Ommen, B. Elmegaard, Optimizing control of two-stage ammonia heat pump for fast regulation of power uptake, Applied Energy 271 (2020).
[18] G.F. Frate, M. Antonelli, U. Desideri, A novel Pumped Thermal Electricity Storage (PTES) system with thermal integration, Applied Thermal Engineering 121 (2017) 1051-1058.
[19] A. Marina, S. Spoelstra, H.A. Zondag, A.K. Wemmers, An estimation of the European industrial heat pump market potential, Renewable and Sustainable Energy Reviews 139 (2021).
[20] G.F. Frate, L. Ferrari, U. Desideri, Multi-Criteria Economic Analysis of a Pumped Thermal Electricity Storage (PTES) With Thermal Integration, Frontiers in Energy Research 8 (2020).
[21] A. Rahman, A.D. Smith, N. Fumo, Performance modeling and parametric study of a stratified water thermal storage tank, Applied Thermal Engineering 100 (2016) 668-679.
[22] C. Arpagaus, F. Bless, M. Uhlmann, J. Schiffmann, S.S. Bertsch, High temperature heat pumps: Market overview, state of the art, research status, refrigerants, and application potentials, Energy 152 (2018) 985-1010.
[23] A.H.H. Jose M Corberan, Jorge Paya, Thermodynamic analysis and selection of refrigerants for high temperature heat pumps, in: I.E.S. Vasile Minea (Ed.) 25th IIR International Congress of Refrigeration, International Institute of Refrigeration IIR, Montréal, Canada, 2019.
[24] G. Kosmadakis, C. Arpagaus, P. Neofytou, S. Bertsch, Techno-economic analysis of high-temperature heat pumps with low-global warming potential refrigerants for upgrading waste heat up to 150 °C, Energy Conversion and Management 226 (2020).
[25] G.F. Frate, L. Ferrari, U. Desideri, Analysis of suitability ranges of high temperature heat pump working fluids, Applied Thermal Engineering 150 (2019) 628-640.
[26] B. Eppinger, L. Zigan, J. Karl, S. Will, Pumped thermal energy storage with heat pump-ORC-systems: Comparison of latent and sensible thermal storages for various fluids, Applied Energy 280 (2020).
[27] S. Quoilin, Next Generation Heat Pumps, 2020.
[28] I.H.B. Eric W. Lemmon, Marcia L. Huber, Mark O. McLinden, REFPROP Documentation, Release 10.0, 2018.
[29] T.M. Association, 2022. https://modelica.org/. (Accessed 06/11/2022.
[30] D.S. AB, Dymola - Dynamic Modelling Laboratory - Full User Manual, 2021.
[31] TLK Thermo GmbH & IfT TIL 3.7 – Model library for thermal components and systems, 2020.
[32] M. Imran, R. Pili, M. Usman, F. Haglind, Dynamic modeling and control strategies of organic Rankine cycle systems: Methods and challenges, Applied Energy 276 (2020).
[33] Funke, PLATE HEAT EXCHANGERS - Variety and top product quality, 2022. 26/04/2022).
[34] Swep, Plate Heat Exchangers - products, 2022. https://www.swep.net/products/.
[35] J.D. Craecker, Performance analysis of heat pumps in Carnot battery systems for grid balancing services, in: G. University (Ed.) 2022, p. 90.
[36] J.G. Collier, Thome, J.R., Convective Boiling and Condensation, 3rd ed.1996.
[37] H.D. Baehr, Stephan, K., Wärme- und Stoffübertragung, 2 ed.1996.
[38] M. Holger, Pressure Drop and Heat Transfer in Plate Heat Exchangers, 2010.
[39] K. Hoopes, T.C. Allison, R. Kurz, Oil and Gas Compressor Basics, Compression Machinery for Oil and Gas2019, pp. 3-11.
[40] GasTurb, GasTurb 14 - free trail, 2022.
[41] R. Pili, A. Romagnoli, M. Jiménez-Arreola, H. Spliethoff, C. Wieland, Simulation of Organic Rankine Cycle – Quasi-steady state vs dynamic approach for optimal economic performance, Energy 167 (2019) 619-640.
[42] W.K. Meesenburg, René; Ommen, Torben; Markussen, Wiebke Brix; Elmegaard, Brian, Design considerations for dynamically operated large-scale ammonia heat pumps, 25th IIR International Congress of Refrigeration, International Institute of Refrigeration, Montréal, Canada, 2019.
[43] pidtuner, pidtuner - tune your PID, 2022. https://pidtuner.com/#/.

14th IEA Heat Pump Conference
15-18 May 2023, Chicago, Illinois

Simplified ground-source heat pump models for predicting heat extraction

Sara Bordignon[a,b,*], Jeffrey D. Spitler[a], Angelo Zarrella[b]

[a]School of Mechanical and Aerospace Engineering, Oklahoma State University, Stillwater, OK 74074, United States
[b]Department of Industrial Engineering, University of Padova, Via Venezia 1, Padova 35121, Italy

Abstract

Simplified heat pump models are needed for design of ground heat exchangers used with ground-source heat pump systems. Design engineers commonly have only manufacturer's data with which to construct a heat pump model that can predict heat extraction given building heating load. Earlier work has used simple polynomials to predict the ratio of heat extraction to heating. Unfortunately, manufacturers' catalog data do not always provide sufficient support to calculate the polynomial coefficients. Therefore, in the absence of experimental data, there is a need for simplified and acceptably accurate models exploiting a limited number of operating points. This paper presents a study of available manufacturers' data in North American and European markets. The available data vary from country-to-country, depending on the standards in use in each country. Then, a range of models are investigated, characterizing the results by the required inputs and the root mean square error. Results show acceptable accuracy of the models when compared to catalog data and allow providing recommendations on models to be used or avoided, depending on the available data.

© HPC2023.
Selection and/or peer-review under the responsibility of the organizers of the 14th IEA Heat Pump Conference 2023.

Keywords: Ground-source heat pump; simplified models;

1. Introduction

Ground source heat pumps (GSHPs) represent a good solution to abate energy usage and reduce greenhouse gas emissions. However, the design of ground heat exchanger (GHE) fields is crucial to minimize installation costs and guarantee high efficiencies of the system for long-term operation.

The heat pump selection is important to the design of ground heat exchangers because it affects heat extraction from the ground during heating operation. Conversely, the ground heat exchanger performance (specifically, fluid temperatures provided to the heat pumps) affects the heat pump performance. In the common situation where systems are designed to meet building-specific hourly heating loads, simulations are used to predict the combined performance of the GSHPs and the ground heat exchanger field to achieve a solution that provides the needed heating capacity while minimizing energy consumption and installation cost.

Besides affecting the electrical consumption of the system and related operating costs, the choice of heat pumps directly affects the size of the ground heat exchanger field. Therefore, GSHP models are needed to design the ground heat exchanger field.

Detailed models of heat pumps, e.g. those that are based on vapor compression cycle simulations, are widely described in the literature. However, for most designers, only limited heat pump data from manufacturers' catalogs are available. The availability of data and temperature ranges for which data are provided vary from country-to-country, often depending on local standards. For example, North American manufacturers usually provide a wide range of operating points; fewer data points are presented in European catalogs and, in some cases, limited to a few specific rating conditions recommended by the standards.

* Corresponding author. Tel.: +39-049-827-6895;
E-mail address: sara.bordignon@unipd.it.

Therefore, simpler heat pump models are needed to calculate the ground heat extraction. In contrast to detailed models, these models should depend on easy-to-obtain catalog data rather than specific measurement campaigns.

International and national standards play a key role in defining the minimum energy efficiency requirements for new heat pumps and providing manufacturers with guidelines regarding the testing conditions and the documentation to be made available to users. Standards suggest performance calculation methods and define standard rating conditions for each country or area. In many cases, the standard rating conditions suggest a minimum data set to be presented in manufacturers' catalogs. Commonly, the performance of a heat pump is defined using the Coefficient of Performance (COP), which corresponds to the heating provided, divided by the heat pump's electrical consumption.

ISO 13612-2 Appendix A [1] describes a method to calculate a heat pump performance matrix with a single test result. The model is based on the Carnot method for calculating the COP of the heat pump, knowing the performance at the rating conditions. The Carnot COP corresponds to the COP for an ideal inverse thermodynamic cycle at specific operating temperatures. If the value of the actual COP is known for the real heat pump working at the same operating temperatures, it is possible to define how much worse the real inverse thermodynamic cycle is compared to the ideal one, using the Carnot effectiveness $\eta_{Carnot,0}$, (also known as 2nd law efficiency). As stated in [1], the accuracy of this model drops when the operating conditions are far from the rating point. A higher level of accuracy can be obtained using a larger number of operating points.

Some standard energy simulation programs incorporate simplified heat pump models with various levels of detail. In Energy Plus [2], two types of models for water-to-air and water-to-water heat pumps are used: equation fit models [3], [4], based on simple non-dimensional curves and parameter estimation models [5], incorporating a vapor compression cycle simulation, with parameters for internal components that require estimation.

In TRNSYS [6], the TESS [7] library contains a water-to-water heat pump model that linearly interpolates between the performance data provided in manufacturer's catalogs, given the values of the air flow rate, fluid flow rate, and entering fluid temperature. Users who want to provide their own performance data must adhere closely to the syntax of the sample file [8].

In a previous work [9], a novel TRNSYS type was developed modeling a heat pump with a vapor compression cycle simulation that incorporated the compressor's performance polynomials. The type is also available with a link to Refprop [10] for deriving the properties of the refrigerant. Although it is very flexible, the need for compressor polynomials might be a problem when they are unavailable from heat pump manufacturers or when the compressor brand and model are not specified in catalogs.

The Modelica Buildings Library [11] contains several heat pump models. The simplest model is based on the Carnot efficiency method. Moreover, models based on the equation fit model [4] and the parameter estimation model [5] from EnergyPlus are implemented.

For GLHEPRO [12], [13], manufacturer's data are used to fit 2nd order polynomials for the ratio of heat extraction to heat pump heating capacity and heat rejection to heat pump cooling capacity as functions of heat pump entering fluid temperature.

Similar equations used to quantify the performance of water-source heat pumps have been described in the literature. Proposed simplified models are generally based on industrial surveys and field test trials [14]-[16] used to derive the COP of ground source heat pumps.

This paper provides an overview of catalog data availability for the North American and European markets and reviews the literature on simplified and acceptably accurate models for predicting the ratios of heat extraction to heating. A range of models are tested for different data availability scenarios, and finally recommendations are made for models that can be used within ground heat exchanger design tools. The basis for most of the work is manufacturers' catalog data.

2. Methodology

Generally, water-source heat pump catalogs provide data on heat pump performance and heating capacity, depending on the source and load side temperature levels. Once the performance of a heat pump is known, it is possible to compute the heat extraction, given building heating load, using Eq. 1.

$$HE = HC \cdot \left(1 - \frac{1}{COP}\right) \quad (1)$$

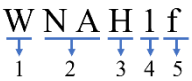
Therefore, once the building heating load is determined using building simulation software and is assumed to be met by the heat pump, simplified models for calculating the COP make the calculation of extraction extremely straightforward. This formulation neglects compressor shell losses, which are usually small (less than 5% of the heating provided [17]).

After presenting the main characteristics of water-source heat pump datasheets, some selected catalogs are used in this paper to evaluate several models for extraction calculation for GSHP design purposes. This section presents the characteristics of the utilized data and the proposed models, along with conventions for labeling the data.

2.1. Availability of manufacturers' data

The availability of manufacturers' data strongly affects the accuracy of models that do not rely on user-measured experimental data. As already mentioned, standards influence the documentation that manufacturers publish. However, many manufacturers provide data that goes beyond the minimal requirements, e.g., several values measured at different inlet temperatures when only a single point is required. The available data often differ from country to country, even for the same heat pump, depending on the selected market. In North America, data about the heat pump performance outside the rating conditions are often available and complete. The range of inlet water temperatures at the ground-coupled side of the heat pump is usually broad and covers temperatures that can go outside standard operating conditions. When available, manufacturers' data of operating points outside rating conditions are more limited in Europe than in North America. Characteristics and features of ground source heat pumps can also vary in different areas: for example, in North America, water-to-air heat pumps are the most widespread, while in Europe, ground-source heat pumps are generally water-to-water.

In order to characterize the data availability for the selected water-to-water heat pumps operating in heating mode, the data sets are labeled using the following code composed of five letters and one number:



Where:

1. The first letter defines the type of heat carrier fluid at the heat pump load side, W-water;
2. The second and third letters represents the market's area, NA-North America, NE-Northern Europe, SE-Southern Europe;
3. The fourth letter defines the heat pump mode, H-Heating;
4. A sequential number is used to identify the different investigated units;
5. The last letter clarifies if the data refer to p-partial or f-full load operation.

The symbol reported under each variable in Table 1 indicates if it can be found in the catalog, varying for the different operating conditions ("Yes"), if it is omitted ("No"), or if it is derivable ("Der") using other information provided in the datasheet. The last row of Table 1 reports the rating heating capacity of the specific heat pump.

In Table 1, data sets of water-to-water heat pumps in heating mode can be subdivided into three main categories. The first group ("Group 1") includes data from North American manufacturers, characterized by the wide availability of operating points and variables, given for a range of entering temperatures and flow rates. In the second group ("Group 2"), catalogs do not provide data about the source and load fluid flow rates and leaving fluid temperature (typical of Central/Northern Europe). The third group ("Group 3") collects catalogs typical of Southern European manufacturers. In this case, generally, data are provided for a range of source and load side temperatures, considering a fixed temperature difference between the inlet and the outlet of the heat exchangers. Catalog WSEH4f, of a machine produced in South Europe, is part of Group 3. However, in this case the number of available operating points is limited to four rating points, provided for heating model only.

Table 1. Data availability for selected water-to-water heat pumps in heating mode.

	Group 1							Group 2		Group 3			
Variable	WNAH1f	WNAH2f	WNAH3f	WNAH4f	WNAH5f	WNAH6p	WNAH6f	WNEH1f	WNEH2f	WSEH1f	WSEH2f	WSEH3f	WSEH4f
SEFT	Yes	Yes	Yes	Yes	Yes	Yes	Yes	Yes	Yes	Der	Der	Der	Yes
SFfr	Yes	Yes	Yes	Yes	Yes	Yes	Yes	No	No	Yes	Der	No	Der
LEFT	Yes	Yes	Yes	Yes	Yes	Yes	Yes	No	No	Der	Der	Der	Yes
LExFT	Yes	Yes	Yes	Yes	Yes	Yes	Yes	Yes	Yes	Yes	Yes	Yes	Yes
LFfr	Yes	Yes	Yes	Yes	Yes	Yes	Yes	No	No	Yes	Der	No	Der
HC	Yes	Yes	Yes	Yes	Yes	Yes	Yes	Yes	Yes	Yes	Yes	Yes	Yes
Pel	Yes	Yes	Yes	Yes	Yes	Yes	Yes	No	No	Yes	Yes	Yes	Yes
HE	Yes	Yes	Yes	Yes	Yes	Yes	Yes	Der	Der	Yes	Yes	Yes	Der
COP	Yes	Yes	Yes	Yes	Yes	Yes	Yes	Yes	Yes	Yes	Der	Der	Yes
HC rating [kW]	50.6	14.7	14.2	16.4	24.5	10.8	13.3	7.57	3.51	8.3	13.1	8.2	18

2.2. Proposed Models

Depending on the data availability discussed in the previous section, several models to calculate the performance of ground source heat pumps have been assessed based on the methods from the literature. First, these models have been applied to catalog data of the selected heat pump models. Afterward, based on the data availability, some models have been modified to reduce the RMSE in the COP calculation. Each model can or cannot be applied to a specific group of catalog data, depending on the data availability, as discussed in the previous section 2.1.

Once the COP is computed, the heat extraction can also be calculated using heating capacity reported in the datasheets using Eq. 1.

Table 2 summarizes the models applied to the catalogs of water-to-water heat pumps operating in heating mode. Some points can be made regarding the models:

- Models applicable to catalog data of the heat pumps produced in Northern Europe are different than the models suggested for North American and Southern Europe catalogs. The differences are because information about the source fluid flow rate and load fluid entering temperature are generally unavailable in the Northern European cases.
- Wh01 is the most complex model, as it is a function of the SFfr, the SEFT, and the temperature difference between the load-side outlet and the source-side inlet and its square. The equation's coefficients can be generated using the generalized least square (GLS) method from the catalog's data. The generalized least squares method is used to generate the equations' coefficients starting from the catalog data at determined reference conditions, giving the least differences between the model outputs and the catalog data. This model can be used when data for more than four operating conditions are available, due to the high number of required coefficients.
- Model wh03 uses generic coefficients given in [14]. Model wh02 uses the same equation form as wh03 but fits the coefficients using the GLS method.
- Model wh04 is the same proposed in [16], and coefficients can be computed using the GRG (Generalized Reduced Gradient) non-linear solver implemented in Microsoft Excel [18]. (The GLS method fits coefficients for linear combinations of functions, but cannot handle, for example, the multiple terms used to form an exponent in wh04).
- Equation wh05 is supposed to improve method wh04 using SEFT and LExFT as inputs, instead of SExFT and LEFT, as these data are generally available in all catalogs.
- Model wh06 is based on the work presented in [15], with a difference: the method consists in computing the COP starting from catalog data, while in [15], it was derived only after calculating the electrical power and heating capacity. This variation reduces the computational effort and allows the calculation in case data about the electrical consumption are unavailable.
- Model wh07 improves the wh06 by considering the whole temperature lift between the heat pump source and load sides, using the LExFT instead of the LEFT.

- Model wh08 is based on the Carnot method, but the COP is calculated differently from the standards. For the sake of simplicity and for minimizing the assumptions, it directly depends on the entering source and load side temperatures (the same is done for the Carnot COP at rating conditions), as in Eq. 2, instead of depending on the condensing and evaporating temperatures.
  The set temperature difference can be adjusted so that the COP does not reach remarkably high values (for example, higher than 8) for low temperature differences. In this work, the computation of the COP is calibrated using the available data sets. If only one rating condition is available, the ΔT_{set} can be set equal to 15°C and, the user can reduce or increase this value if the considered operating conditions lead to high values of COP.

$$COP_{Carnot} = \frac{LEFT+273}{\Delta T_{set}} \quad (2)$$

- For the Northern European catalogs, the LExFT replaces the LEFT in the equation, and the control on the Carnot COP is done on the SEFT: if the SEFT is higher than 13°C, it is considered equal to 13°C.
- Model wh09 is an alternative to model wh01 when data on the SEFT and the SFfr are unavailable, like in Northern European datasheets.
  When at least three operating points at rating conditions are available, they can be used to compute the coefficients for a model dependent on the temperature differences between the LEFT and the SEFT in North America (wh11) and the LExFT and the SEFT in Northern Europe (wh10).

Table 2. Data availability for selected water-to-water heat pumps in heating mode.

		Group 1							Group 2		Group 3			
	Model	WNAH1f	WNAH2f	WNAH3f	WNAH4f	WNAH5f	WNAH6p	WNAH6f	WNEH1f	WNEH2f	WSEH1f	WSEH2f	WSEH3f	WSEH4f
wh01	$COP = c_0 + c_1 \cdot SEFT + c_2 \cdot SFfr + c_3 \cdot (LExFT - SFET) + c_4 \cdot (LExFT - SEFT)^2$	x	x	x	x	x	x	x	x	x	x	x	x	x
wh02	$COP = c_0 + c_1 \cdot (LExFT - SEFT) + c_2 \cdot (LExFT - SEFT)^2$	x	x	x	x	x	x	x	x	x	x	x	x	x
wh03	$COP = 8.77 - 0.15 \cdot (LExFT - SEFT) + 0.000734 \cdot (LExFT - SEFT)^2$	x	x	x	x	x	x	x	x	x	x	x	x	x
wh04	$COP = c_0 \cdot \exp(c_1 \cdot SFExT + c_2 \cdot LEFT) + c_3 \cdot \frac{SFExT}{LFET} + c_4$	x	x	x	x	x	x	x	x	x	x	x	x	x
wh05	$COP = c_0 \cdot \exp(c_1 \cdot SEFT + c_2 \cdot LExFT) + c_3 \cdot \frac{SEFT}{LExFT} + c_4$	x	x	x	x	x	x	x	x	x	x	x	x	x
wh06	$COP = c_0 + c_1 \cdot SEFT + c_2 \cdot LEFT + c_3(SEFT \cdot LEFT)$	x	x	x	x	x	x	x	x	x	x	x	x	x
wh07	$COP = c_0 + c_1 \cdot SEFT + c_2 \cdot LExFT + c_3(SEFT \cdot LExFT)$	x	x	x	x	x	x	x	x	x	x	x	x	x
wh08	$COP = COP_{Carnot} \cdot \eta_{carnot,0}$	x	x	x	x	x	x	x	x	x	x	x	x	x
wh09	$COP = c_0 + c_1 \cdot LExFT + c_2 \cdot (LExFT - SEFT) + c_3 \cdot (LExFT - SEFT)^2$	x	x	x	x	x	x	x	x	x	x	x	x	x
wh10	$COP = c_0 + c_1 \cdot (LExFT - SEFT) + c_2 \cdot (LExFT - SEFT)^2$ Stand.	x	x	x	x	x	x	x	x	x	x	x	x	x
wh11	$COP = c_0 + c_1 \cdot (LEFT - SEFT) + c_2 \cdot (LEFT - SEFT)^2$ Stand.	x	x	x	x	x	x	x	x	x	x	x	x	x

The models presented in this section are evaluated using the RMSE (Eq. 3) calculated for the COP and heat extraction from the ground in heating operation. In Eq. 3, y_c is the catalog value, y_m is the modeled value, and N is the number data.

$$RMSE = 100\sqrt{\frac{1}{N}\sum_{i=1}^{N}\left(\frac{y_{c,i}-y_{m,i}}{y_{c,i}}\right)^2} \quad (3)$$

3. Results

The present section analyzes the performance of the models characterized by RMSE. Figures 1 and 2 show the RMSE values calculated as in Eq. 3 for each set of catalog data of water-to-water heat pumps. The RMSE is relative to the COP (Figure 1), computed by applying the models discussed in section 2.2, and to the heat extracted from the ground (Figure 2). This last value is calculated using Eq. 1, starting from the thermal load demanded by the building, and met by the heat pump at different operating conditions, according to the catalog data. If the error is higher than 15%, in the graphs, a control bar is shown in the pink area (RMSE>15%) in place of the actual value for the specific model's RMSE. In the case of non-applicable models, the RMSE value is not shown.

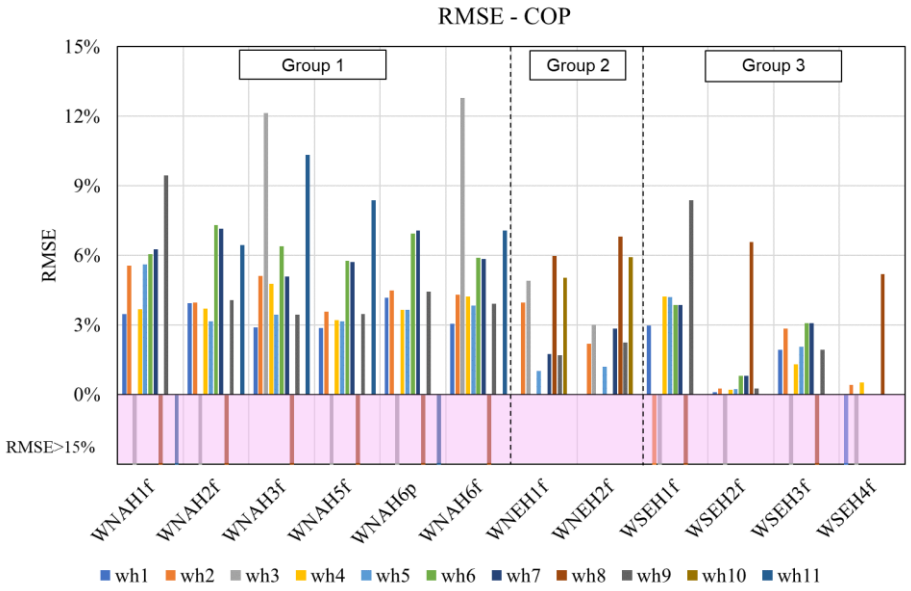


Fig. 1. RMSE for COP for the different catalogs and models.

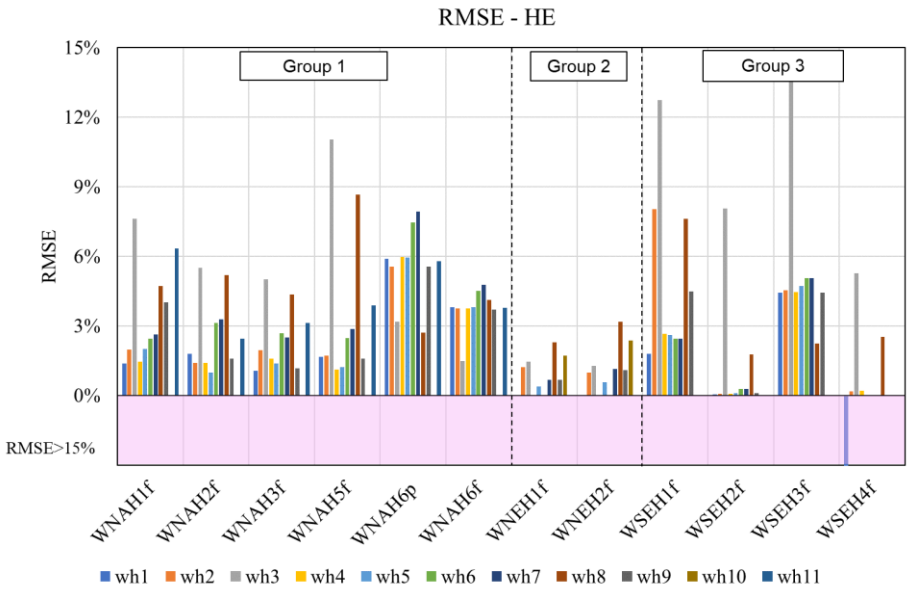


Fig. 2. RMSE for HE for the different catalogs and models.

In general, the deviation between catalog and simulated data is higher for COP values than for the heat extraction values. For example, the application of models wh03 and wh08 to all selected data sets leads to an average $RMSE_{COP}$ of 21% and 17%, respectively, but only to an $RMSE_{HE}$ of 6% and 4%. Moreover, models wh03 and wh08 are likely to overestimate the COP and the HE, compared to catalog data. The application of model wh01 leads to very good results when a wide range of data is available. However, model wh01 leads to high $RMSE_{COP}$ and $RMSE_{HE}$ when the number of operation conditions provided in the manufacturer's catalog is limited, like for the case of theWSEH4f data set.

The application of model wh11 leads to an $RMSE_{COP}$ up to 20% (WNAH1f) but results in an $RMSE_{HE}$ of only 6%. The application of the other models to the catalog data leads to an average maximum $RMSE_{COP}$ of 5% and an average maximum $RMSE_{HE}$ equal to 3%.

4. Recommendations

This section provides recommendations for applying the proposed models based on the available quantity of manufacturers' catalog data. In Section 2.1, the type of data available was used to divide the heat pumps into three groups. Table 3 show the average $RMSE_{COP}$ and $RMSE_{HE}$ for each group of water-to-water heat pumps operating in heating mode. In the table, when a model is applicable to the catalogs, the average RMSE is highlighted with a color: (a) green if the RMSE is lower than 5% (the results of the model are good), (b) light orange if its value is between 5% and 10% (the results of the model are acceptable), (c) orange when the RMSE is higher than 10% (the model is not recommended for that set of data). When the model is not applicable to a specific group of catalogs, it is indicated with "N/A".

Therefore, a decision-making process for choosing the most suitable model can be outlined as follows, depending on what types of catalog data are provided for the heat pump:

a. If only one data point is available, the only applicable models are the ones derived from the Carnot efficiency calculation (wh08) or from an experimentally derived curve (wh03). These models, in general, lead to higher $RMSE_{COP}$ but more than acceptable $RMSE_{HE}$.

b. If only rating conditions (three or four operating points) are available, models wh10, wh11 can be used. However, model wh08 can also be a good option.

c. If more than four operating points are available in the catalog data, the corresponding group from Table 1 can be identified by comparing the data available for the type of heat pump and operation mode to the data available for each group in Tables 1. With the group identified, Table 3 can be used to identify the best choices – that is the model or models with the lowest $RMSE_{HE}$. A secondary consideration may be the model performance in predicting COP, also summarized in Table 3. Taking first the model performance in predicting HE, and secondarily, the model performance in predicting COP, a final recommendation is made for each group in Tables 3. A "x" is used to identify the recommended model or models.

Table 3. Average RMSE by group of data and model and final recommendations.

	Groups	wh01	wh02	wh03	wh04	wh05	wh06	wh07	wh08	wh09	wh10	wh11
$RMSE_{COP}$	Group 1	**3%**	4%	19%	4%	4%	6%	6%	24%	5%	N/A	12%
	Group 2	N/A	3%	4%	N/A	**1%**	N/A	**2%**	6%	**2%**	5%	N/A
	Group 3	**2%***	5%	32%	**2%**	**2%**	**2%**	**2%**	12%	3%	N/A	N/A
$RMSE_{HE}$	Group 1	**3%**	**3%**	6%	**3%**	**3%**	4%	4%	5%	**3%**	N/A	4%
	Group 2	N/A	**1%**	**1%**	N/A	**0%**	N/A	**1%**	3%	**1%**	2%	N/A
	Group 3	**2%**	**3%**	10%	**2%**	**2%**	**2%**	**2%**	4%	**2%**	N/A	N/A
Recommendations	Group 1	x										
	Group 2					x		x		x		
	Group 3	x			x	x	x	x				

** model wh01 is considered not-applicable to catalog WSEH4f, where only four operating points are provided.*

The results of the models are strongly affected by the accuracy and the level of detail of the manufacturer's catalog data: if the accuracy is high, the agreement between the models' results and field measurements will also be high. Moreover, the accuracy of the models improves if the catalog contains detailed information about the operation of the heat pump, for example, correction factors for different temperature differences at the load

and source sides, or for the use of a mixture of water and glycol, or, in general, if it includes a relevant number of operating points.

Although the primary objective of these models is to derive the heat extraction from the ground, they might also be used to compute the COP of the heat pump. As already pointed out, the COP results are more accurate when the catalog data are numerous and precise.

5. Conclusions

This paper addresses a problem encountered when designing ground heat exchangers that are used with ground-source heat pump systems. Engineers designing the system typically only have catalog data for the heat pumps and the data provided vary with manufacturer and location. This paper focuses on simple models that can be used to determine the GSHP heat extraction required to meet building loads.

A review of available manufacturers' catalog data for water-to-water heat pumps in North American and European markets is presented, and catalog data are categorized by data availability. A range of models are investigated; their accuracy is evaluated by their ability to reproduce the catalog data and recommendations on which model to use are provided. The recommended models give acceptable accuracy in the calculation of the heat extraction, with no more than 3% RMSE when compared to catalog data. Nevertheless, the model accuracy depends on the range and quantity of catalog data.

The recommended models presented in this paper are suitable for single-speed water-to-water heat pumps in heating mode and quasi-steady operation. Further work is in progress to address water-to-air heat pumps and cooling mode. Additional research is needed to treat multi-stage and variable-speed heat pumps.

The investigation presented here is limited by its use of catalog data, which is based on steady-state operation and, in many cases, by proprietary models developed by the manufacturer. Comparisons against field measurements are in progress. However, additional comparisons to field measurements would be welcome.

Nomenclature

c_i		Equation coefficients
COP	kW/kW	Coefficient of Performance
COP_{Carnot}	°C/°C	Carnot COP
Der		Derivable data
GLS		Generalized least square
GRG		Generalized reduced gradient
GSHP		Ground source heat pump
HC	kW	Heating capacity
HE	kW	Heat extraction
LEFT	°C	Load entering fluid temperature
LExFT	°C	Load exiting fluid temperature
LFfr	l/s	Load fluid flow rate
N		Number of data
Pel	kW	Electrical power
RMSE		Root mean square relative error
SEFT	°C	Source entering fluid temperature
SFfr	l/s	Source fluid flow rate
Stand		Data from rating conditions defined in the standards
ΔT_{set}	°C	Temperature lift between source and load side
$\eta_{Carnot,0}$	[-]	Carnot effectiveness
y_c		Variable's value in the catalog
Y_m		Variable's value in the model

Acknowledgements

The second author's work was supported by the OG&E Energy Technology Chair.

References

[1] ISO 13612-2:2014, Heating and cooling systems in buildings — Method for calculation of the system performance and system design for heat pump systems Part 2 : Energy calculation," 2014.
[2] U.S. Department of Energy (DOE). 2019. EnergyPlus version 9.2, Washington, DC: U.S. Department of Energy.
[3] Shenoy, A. 2004. Simulation, Modeling and Analysis of Water to Air Heat Pump. Ph.D. Thesis, Oklahoma State University.
[4] Tang, C. C. 2004. Modeling Packaged Heat Pumps in a Quasi-Steady State Energy Simulation Program. Ph.D. Thesis, Oklahoma State University.
[5] Jin, H. 2002. Parameter Estimation Based Models of Water Source Heat Pumps. Ph.D. Thesis, Oklahoma State University.
[6] Klein, S.A. et al, 2017, TRNSYS 18: A Transient System Simulation Program, Solar Energy Laboratory, University of Wisconsin, Madison, USA, http://sel.me.wisc.edu/trnsys.
[7] J. W. Thornton, D.E. Bradley, T.P. McDowell, N.J. Blair, M.J. Duffy, N.D. LaHam, A.V. Naik,, "TESSLibs 17 - Volume 6 HVAC Library Mathematical Reference," Madison, Wisconsin, 2012, pp. 214–218.
[8] The Solar Energy Laboratory, 2019, Trnsys 18 a transient system simulation program. Volume 4: Mathematical Reference. Solar Energy Laboratory, University of Wisconsin, Madison, USA. vol. 4, 2019.
[9] S. Bordignon, G. Emmi, A. Zarrella, and M. De Carli, "Energy analysis of different configurations for a reversible ground source heat pump using a new flexible TRNSYS Type," Applied Thermal Engineering, vol. 197, no. July, p. 117413, 2021.
[10] Lemmon, E.W., Bell, I.H., Huber, M.L., McLinden, M.O. NIST Standard Reference Database 23: Reference Fluid Thermodynamic and Transport Properties-REFPROP, Version 10.0, National Institute of Standards and Technology, Standard Reference Data Program, Gaithersburg, 2018.
[11] Michael Wetter, Wangda Zuo, Thierry S. Nouidui and Xiufeng Pang. 2014. Modelica Buildings library. Journal of Building Performance Simulation, 7(4), 253–270.
[12] Spitler, J.D. 2000. GLHEPRO -- A Design Tool For Commercial Building Ground Loop Heat Exchangers. Proceedings of the Fourth International Heat Pumps in Cold Climates Conference, Aylmer, Québec. August 17-18, 2000.
[13] School of Mechanical and Aerospace Engineering, Oklahoma State University. GLHEPro 5.0 for Windows Users' Guide; International Ground Source Heat Pump Association: Stillwater, OK, USA, 2016.
[14] I. Staffell, D. Brett, N. Brandon, and A. Hawkes, "A review of domestic heat pumps," Energy Environ. Sci., vol. 5, no. 11, pp. 9291–9306, 2012.
[15] B. Perers, E. Anderssen, R. Nordman, and P. Kovacs, "A simplified heat pump model for use in solar plus heat pump system simulation studies," Energy Procedia, vol. 30, pp. 664–667, 2012.
[16] Y. Liu, J. X. Liu, and G. Ding, "Mathematical model of water-source heat pump uni ts under variant working conditions," HVAC 37, pp. 21–24, 2007.
[17] M. Goossens, C. Teuillieres, P. Riviere, O. Cauret, and D. Marchio, "An Instrumented Method for the Evaluation of Compressor Heat Losses in Heat Pumps On-Field," 12th IEA Heat Pump Conference, no. May, p. 9, 2017.
[18] Microsoft Corporation. (2018). Microsoft Excel. Retrieved from https://office.microsoft.com/excel

14th IEA Heat Pump Conference
15-18 May 2023, Chicago, Illinois

A novel heat pump-based energy recycling system of an industrial building utilizing waste heat flows and geothermal energy

Niklas Söderholm [a, b,**], Tuomo Niemelä [a]

a Granlund Oy, Malminkaari 21, FI-00701 Helsinki, Finland
b Aalto University, School of Engineering, Otakaari 4, PO Box 14100, FI-00076 Aalto, Finland

Abstract

The energy efficiency improvement potential in industrial buildings is often significant, considering all unutilized waste heat flows. Cost efficient and innovative renovation concepts are needed for a good balance between cost savings and investment costs including energy grants for new energy systems. The paper presents a case study, motivated by financial savings and CO_2 emission reductions for an industrial building in Finland based on realized costs and measured energy consumption. The building belongs to a company with multiple industrial facilities in Finland and around the world and the company fulfils its energy program Mission to Zero, significantly reducing the carbon footprint of its buildings. The energy renovation concept studied in this study relies on a novel heat pump-based energy recycling system utilizing boreholes for thermal storage and free cooling. Sources for energy recycling are the cooling and pressurized air systems serving the production line. The long-term renovation plan is included to improve the overall cost efficiency. The energy concept is compared to the initial situation and a conventional ground source heat pump system utilizing free cooling from the boreholes. The measurements indicate that the performance, (SCOP 3.3) and heating energy covered by the heat pump system (about 97%), has been better than expected based on the energy calculations.

© HPC2023.
Selection and/or peer-review under the responsibility of the organizers of the 14th IEA Heat Pump Conference 2023.

Keywords:ground source heat pump; energy recycling; hybrid heat pump system;

1. Introduction

The demand for energy efficiency measures in energy intensive industrial buildings is rising to cope with the rising energy prices and to meet the ambitious goals of leading companies to cut down the CO_2 emissions. A key issue is to find the most efficient measures to reach the goals with a decent price tag. However, some measures might even be free of charge such as set-point adjustments, which are important to trace before any major energy renovations are planned. Utilization of waste heat flows is on the contrary not free of charge but extensive utilization of waste heat flows in a heat pump-based energy recycling system will most likely pay itself back in 5 to 8 years depending on the system design. For the customer paying the investment, it is also important that the energy system will receive the maximum amount of government grants to produce a decent payback time. For example, in Finland 20 % lower investment costs can be achieved if energy system design fully complies with the grant requirements.

The ABB Group is an example of a leading industrial company that strives to significantly reduce its carbon footprint through its own energy efficiency program Mission to Zero. The investigated industrial building in this study, ABB assembly parts, is located near the Gulf of Finland in the city of Porvoo approximately 50 km from the Helsinki capital. It is characterized by both high heating and cooling demand, making it ideal for a heat pump-based energy recycling system. Firstly, to live up with the expectations, the objective was to design a cost-efficient hybrid heat pump system utilizing all feasible heat sources. Secondly, a high heating energy coverage rate (at least 95%) by the heat pump system should be reached.

* Corresponding author. E-mail address: niklas.soderholm@granlund.fi

The investigated heat pump system in this paper, designed by the Granlund company, has been operational and monitored since November 2021. The objective of the presented study was to compare the installed hybrid heat pump system to a conventional ground source heat pump system utilizing free cooling as concerns the energy performance of the system and financial viability.

Energy recycling systems coupled with boreholes have been studied in the Nordic climate and a key dimensioning parameter is the relation between extracted heat from the ground and heat loaded into the ground and how it affects the average COP (Coefficient of Performance) in the long run [1]. For a pure ground source heat pump system, a conventional COP value to be used in energy calculations is 3.0 for a building in the cold climate (Nordic countries) and 3.6 in an average climate [2].

2. Methods

2.1. The investigated industrial building

The present study was made for an industrial building located in southern Finland as a part of an energy efficiency project carried out by Granlund Oy. The industrial building in question has high cooling demand all year round due to cooling intensive manufacturing process. The manufacturing line is operating from Monday to Friday implying that energy recycling from the cooling process is not available during the weekend. Another source for energy recycling in the building is heat from the pressurized air compressor also used from Monday to Friday. The original compressor (nominal motor power 75 kW) was air cooled but as a part of the energy efficiency project it was replaced with a liquid cooled version (nominal motor power 90 kW) suitable for the energy recycling system.

Heating consumption in the investigated building is mostly space and ventilation heating divided between the office and manufacturing parts of the building. The warehouse itself is energy intensive in terms of heating as the ventilation system and the circulation air heaters consume the most part of heating in the manufacturing area. Volume flow rates and heat recovery used in the ventilation system are 3 m^3/s in the office region (plate heat exchanger for heat recovery) and approximately 12 m^3/s in the manufacturing area (glycol-based heat recovery). The building is connected to the local district heating system and initial heating consumption before the heat pump project was approximately 960 MWh in 2019. Cooling is managed through two chiller units utilizing free cooling, one for the office area and the second for the manufacturing area. The cooling demand for the manufacturing part was estimated to be 840 MWh.

2.2. Description of the installed energy recycling system with boreholes

The installed heat pump system is a hybrid heat pump system consisting of energy recycling and boreholes. Boreholes are primarily used to support the energy recycling system especially during weekends when no recycling potential is available and to store unused heat from the energy recycling system into the ground. The borehole field is primarily charged during the summer months providing free cooling to the process cooling network. Free cooling is limited by the ground temperature and the cooling system temperature levels 8 / 13 °C, thus leading to a maximum brine temperature of 9 - 10 °C. However, the brine temperature supplied to the ground may increase even higher during the summer when the boreholes are charged with heat from the pressurized air compressors. A schematic drawing of the hybrid heat pump system is presented in Fig. 1.

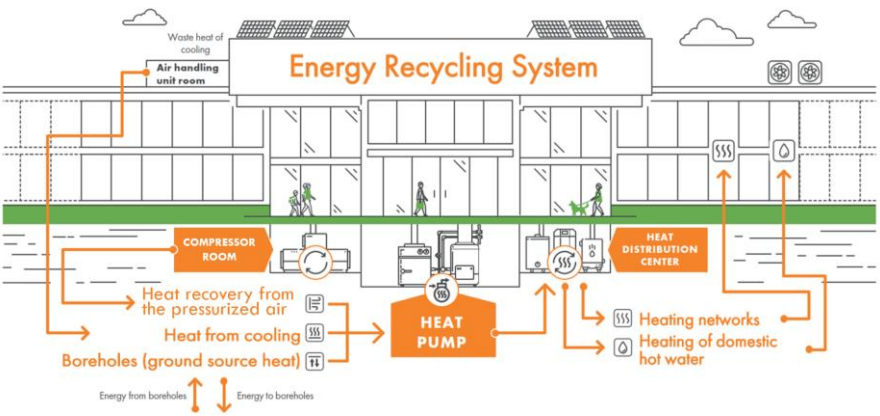


Fig. 1. Schematic drawing of the hybrid heat pump system.

Altogether three on-off controlled heat pump units are used in the heat pump system with a total heating capacity of about 330 kW. Buffer tanks were included in the heat pump system on the condenser side, 2 m^3 for space and ventilation heating and 2 m^3 for domestic hot water heating. On the evaporator side, the buffer tank was left out because the energy recycling potential was known to be almost constant during the workdays. Dimensioning parameters of the heat pump system are shown in Table 1.

Table 1. Dimensioning parameters of the heat pump system.

Parameter	Dimensioning data
Heat pump models	3x Gebwell Taurus EVI 110, 3x 104 kW at 5 / 45 °C (T_{e_Out} / T_{c_Out})
Heat pumps for domestic hot water heating	One heat pump out of three working in alternating mode (domestic hot water / space heating)
Heat pump COP at rating points	4.0 at 5 / 45 °C and 2.6 at 5 / 65 °C (T_{e_Out} / T_{c_Out})
Heat exchanger capacity for energy recycling from the cooling network	Dimensioning heating capacity 100 kW at temperature levels 10 / 5 °C on the brine side
Heat exchanger capacity for energy recycling from the pressurized air compressors	Dimensioning heating capacity 60 kW at temperature levels 20 / 5 °C on the brine side
Borehole field	18 pcs of boreholes in two rows, depth 250 m and distance between the holes 20 m
Heating system setpoint curve for the supply water temperature (targeted design values)	Supply water temperature at -29 °C: 66 °C, supply water temperature at 0 °C: 46 °C *[1])

*[1]) The actual heating curve in the building automation system was higher at 0 °C, approximately 52 °C.

The chosen heat pumps are on-off controlled with two compressors per heat pump, altogether 6 compressors in the whole system. All heat pumps take advantage of superheating of the refrigerant R410A to produce small fractions of domestic hot water at a high COP value. Domestic hot water is produced separately with one of the heat pumps particularly during the summer months. The borehole field, 18 x 250 meters, was sized based on the heating capacity requirements especially during the weekends when no energy recycling is available. Despite of heating capacity-based dimensioning of the borehole field, temperature is still very stable from year to year due to balanced extraction and loading of the boreholes.

Compared to a conventional heat pump system utilizing geothermal energy, the most significant difference is energy recycling from the pressurized air compressors and loading of unused heat in the ground to stabilize the temperature profile in the borehole field. Energy recycling from the cooling networks and free cooling from the ground can be seen as the conventional approach in the Nordic countries. The existing chiller is used as backup whenever the heat pumps are not able to recycle heat from the cooling network to the heating networks or when the free cooling capacity from the ground is insufficient.

2.3. Simulation model for the hybrid heat pump system

The energy system simulations were performed with the energy simulation tool IDA ICE 4.8.2 (Indoor Climate and Energy) in combination with its ESBO plant interface (Early Stage Building Optimization) for simulation of energy systems. IDA ICE is especially used in the Nordic countries for building energy simulation purposes and it is extensively validated in previous studies [3-7]. In this work the original ESBO plant model for energy system simulations has been reworked to match more closely the real heat pump system. Moreover, the original heat pump model has been replaced by a parametric heat pump model working accurately based on performance data given for a specific heat pump model at all possible operation points as also parametrized in [1]. Measurement data from the heat pump manufacturer Gebwell (heating capacity and COP at different operation points) was used in the simulation model describing the Taurus EVI 110 heat pump. Despite of the real on-off controlled compressors in the heat pump, the part load behaviour of the heat pump

was modelled in line with the standard EN 14825 degradation coefficient Cc [8], with a given value of Cc = 0.97. The same modelling approach is also used in the original heat pump model included in IDA ICE.

It has been shown that the original heat pump model in IDA ICE can be used quite accurately within an error of ±1 % in energy system simulations if the heat pump is calibrated using 7 calibration parameters against measured data [9].

An overview of the customized energy system interface in IDA ICE is shown in Fig. 2 and the most important components of the model are numbered and explained below. Calculation of supplied and extracted heat to and from the energy model is done in dedicated macros, but in this context the details of the model are not discussed.

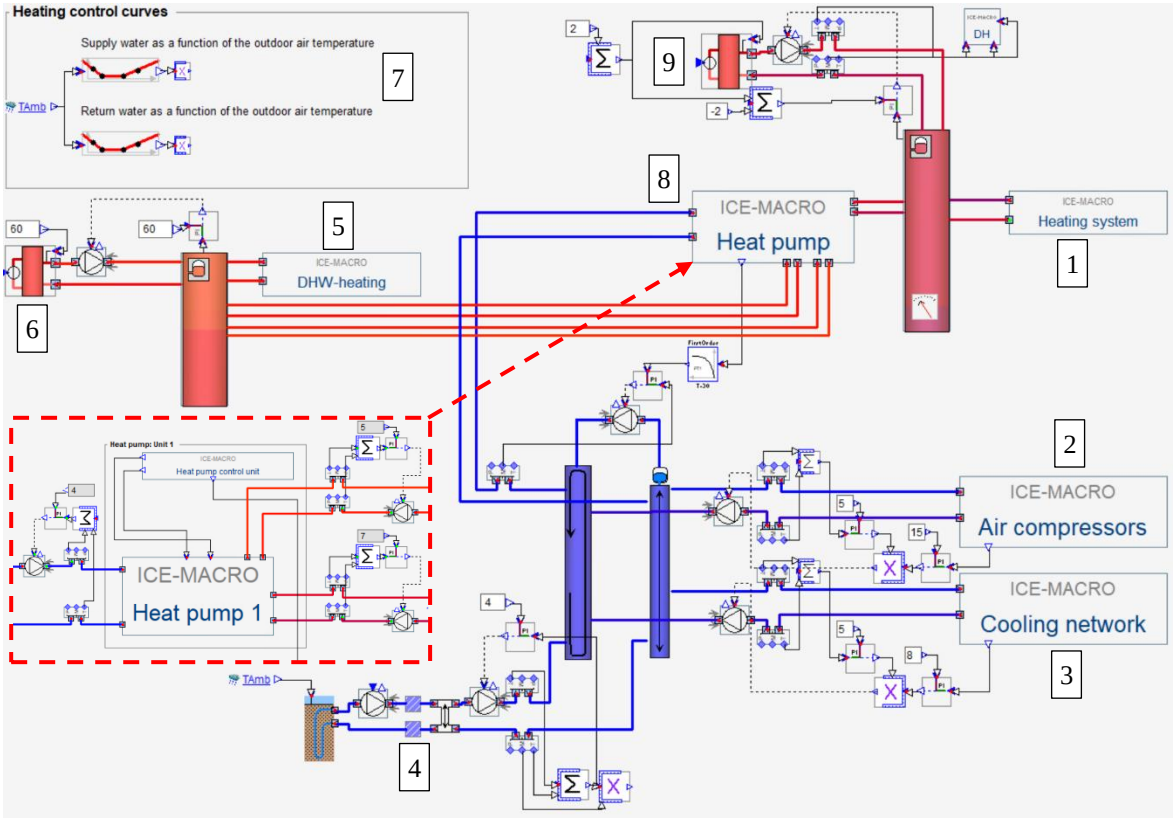


Fig. 2. The customized energy system interface in IDA ICE for energy system simulations.

Numbering and explanations referring to Fig. 2:

1. Space and ventilation heating systems in the building. Set points for the supply and return water temperature are given according to the heating control curves (7) and the measured heating power is used as input data.
2. Heat recovery from the pressurized air compressors including temperature control on the primary and secondary sides of the heat exchanger (brine / water). The measured heating power data of the compressors is used as input data.
3. Cooling network connected to the brine side with a heat exchanger including temperature controls. The measured and partly estimated cooling heating power data is used as input data.
4. Borehole field and its temperature control.
5. Consumption of domestic hot water. The estimated domestic hot water profile is used as input data.
6. Additional heating (district heating) supplied to the domestic hot water network if necessary.
7. Supply and return water set point curves as a function of the outdoor air temperature. The maximum supply water temperature is 66 °C at the outdoor air temperature of -28 °C.
8. Parametric heat pump model and a snapshot of it showing its pipe connections. On the condenser side there are pipe connections for space heating and for super-heating supplied to the DHW tank. One of the three heat pumps is working in alternating mode (space heating / DHW heating) and therefore four hot pipes are connected to the DHW tank in the simulation model.
9. Additional heating (district heating) supplied to the space heating network if necessary.

Exemplified profiles for estimating the energy recycling potential are shown in Fig. 3 for cooling as well as for the pressurized air networks. The profiles were determined from the building automation system before the beginning of the heat pump project. Both energy recycling profiles are almost constant during workdays Monday to Friday. Heat recovery potential from the pressurized air compressors is 50 – 70 kW and heat to be recovered from the cooling network 100 – 140 kW. The energy simulations were performed based on measurement data from the original air-cooled compressors (motor power 75 kW), although it was known that the recoverable power from the new water-cooled versions (Atlas Copco GA90, motor power 90 kW) would be somewhat higher than before. The manufacturing line is closed from Friday evening to Monday morning, implying that the system works as a pure ground source heat pump system during weekends.

Duration curves of the heating demand and energy recycling potential throughout the year are shown in Fig. 4. The duration curves for the heating demand are presented both without the ventilation adjustments (initial situation in the project planning phase) and with the adjustments to show the final situation.

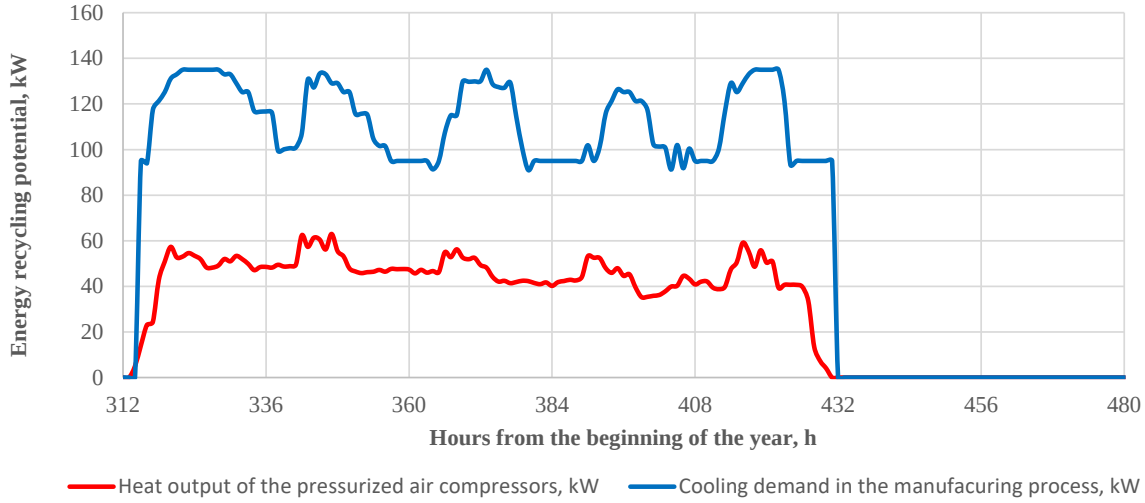


Fig. 3. Energy recycling profiles for one week during the heating season.

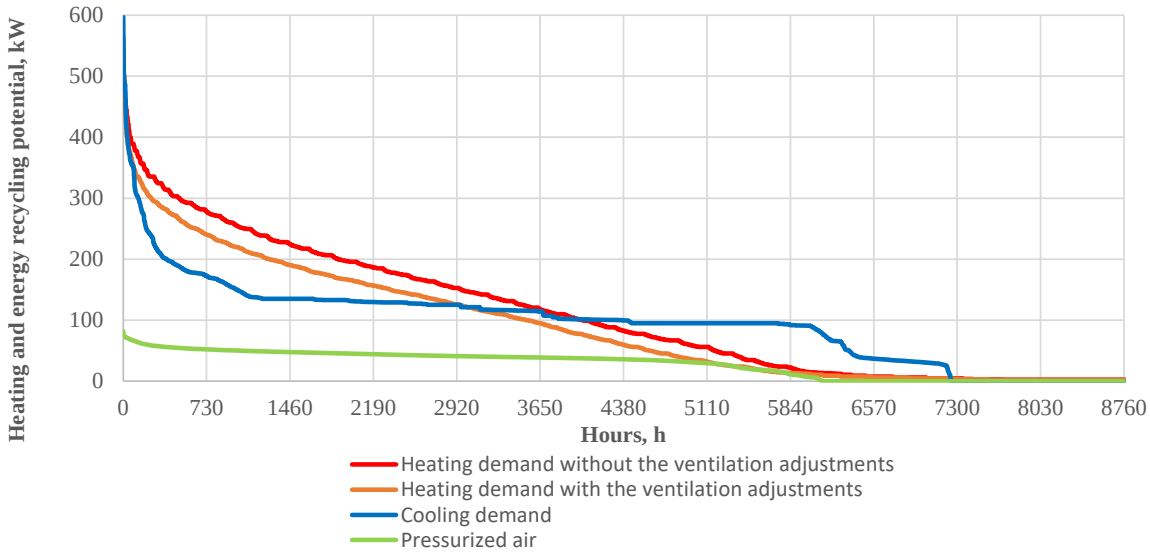


Fig. 4. Duration curves of the heating demand and energy recycling potential throughout the year.

The temperature profile in the borehole field was investigated in the GLHEPRO simulation software using the simulated heat extraction and loading profiles from the single year IDA ICE simulation. GLHEPRO is developed at the Oklahoma State University, and it has been validated against measured data from working ground heat exchangers [10] and compared with the ASHRAE Handbook method [11]. The GLHEPRO

simulations performed on a monthly level and for a period of 40 years will show if the dimensioning of the borehole field is sufficient.

3. Case study

3.1. Simulation of the installed heat the pump system and comparison to a conventional ground source heat pump system

The installed hybrid heat pump system was investigated using the energy system interface in IDA ICE described earlier. Attention was especially paid to the heat extraction and loading pattern of the borehole field and that all available heat is either recycled or stored in the ground. The target was to achieve a high heating energy coverage rate using the heat pump system, at least 95% in accordance with the ABB's energy program "Mission to Zero". Hourly simulation results shown in this paper are calculated based on the measured district heating consumption from 2019 without any ventilation adjustments to represent the initial situation at the project planning phase. The heat extraction and loading rates (kW) of the borehole field are presented in Fig. 5 for the installed system and for the conventional ground source heat pump system with free cooling.

Simulation results for the installed hybrid heat pump system show, that heat is mostly extracted from the borehole field during the weekends and heat is stored in the ground almost during the whole year with emphasis on the summer months. The peak heat extraction from the boreholes is about 38 W/m and loading 9 – 13 W/m depending on the ground temperature. The amount of heat stored in the ground is primarily limited by the temperature level of the liquid in the cooling network, but slightly more heat can still be stored in the ground from the pressurized air compressors if the free cooling mode is not available due to a high brine temperature. The rest of the cooling demand in the manufacturing area, which cannot be produced through energy recycling or by utilizing free cooling from the ground is covered by the existing chiller either as free or mechanical cooling.

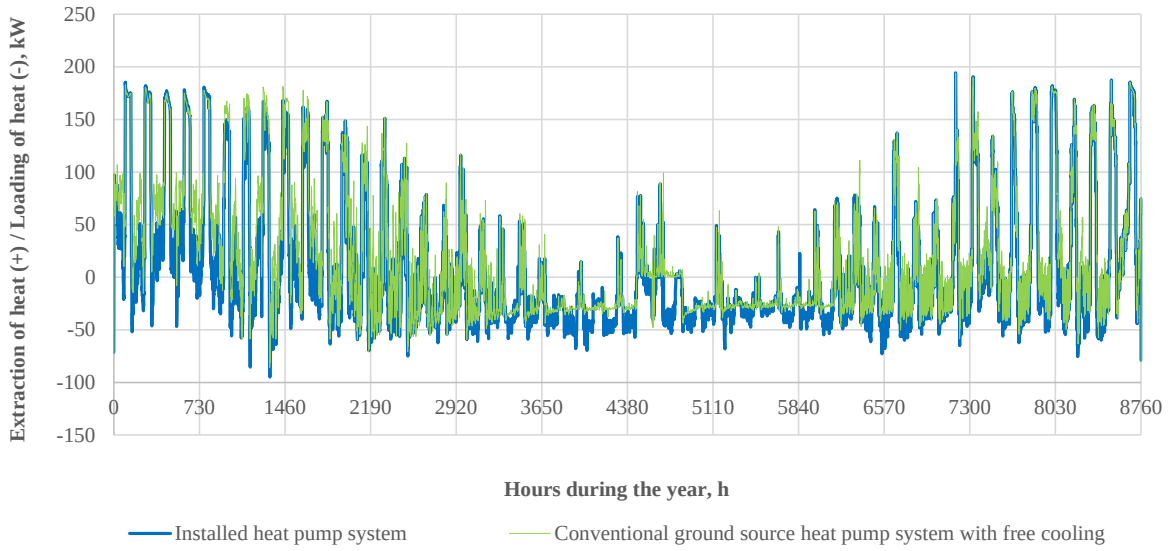


Fig 5. Net heat extraction rates (positive value) and loading rates (negative value) are shown on the left axis. The results shown with a thick blue line belong to the installed system and the results shown with a thin green line represent the conventional ground source heat pump system with free cooling.

An overview of the utilization of the installed hybrid heat pump system compared to the conventional ground source heat pump system with free cooling is presented in Table 2. The results are focusing on the energy balance of the borehole field and on the amount of free cooling available.

The energy simulations indicate that extensive loading of the ground comes at a price when it comes to the utilization of free cooling from the ground. Hence, 139 MWh less cooling energy (17% of the cooling demand) is utilized either through energy recycling or through free cooling from the ground. Considering possible free cooling with the existing chiller, the amount of compressor cooling is increased by 86 MWh (10% of the cooling demand). Altogether 103 MWh of more heat is still utilized in the installed energy system either through energy recycling or by loading the borehole field. From the numbers it can be observed that the

borehole field is almost fully charged bearing in mind the liquid temperatures in the cooling network (8 / 13 °C) and that all available heat from the pressurized air compressors is used in the energy system.

Table 2. Utilization of the hybrid heat pump system based on the energy simulations.

Investigated variable	Installed heat pump system (MWh)	Conventional heat pump system with free cooling (MWh)
Heat extraction from the boreholes	218 MWh	275 MWh
Heat loaded into the boreholes	170 MWh	124 MWh
Cooling energy utilized by the heat pump system	332 MWh	471 MWh
Heat from the pressurized air compressors utilized in the hybrid heat pump system	242 MWh	0 MWh

Monthly averaged liquid temperatures in the borehole field are compared in Fig. 6. for an anticipated life span of 40 years (480 months). The results shown with a thick blue line belong to the installed system and the results shown with a thin green line represent the conventional ground source heat pump system with free cooling. The number of boreholes is identical 18 x 250 m in both energy systems because dimensioning of the borehole field was made based on the required heat extraction rate (kW) and secondly to enable an adequate brine flow rate (dm^3/s) on the evaporator side of the heat pumps. Dimensioning parameters of the borehole field are as follows: Heat conductivity of the ground 3.1 W/mK, undisturbed ground temperature 7.5 °C, collector pipe diameter DN45, borehole thermal resistance 0.12 K/(W/m) and distance between the boreholes 20 meters. Thermal response tests for the ground were not made during the project, implying that the parameters used in the calculation are commonly used in ground source heat pump applications.

According to the simulation results, the monthly averaged temperatures in the borehole field fluctuate between 4 – 9 °C during the whole investigation period of 40 years. The temperature level in the conventional system is on the other hand constantly decreasing with same borehole dimensioning but it is still on the safe side regarding freezing. Without heat recovery from the air compressors, a constantly fluctuating temperature profile can be reached with free cooling only, but according to the simulations the energy system would need 8 – 10 additional boreholes (depth 250 m) to reach that level.

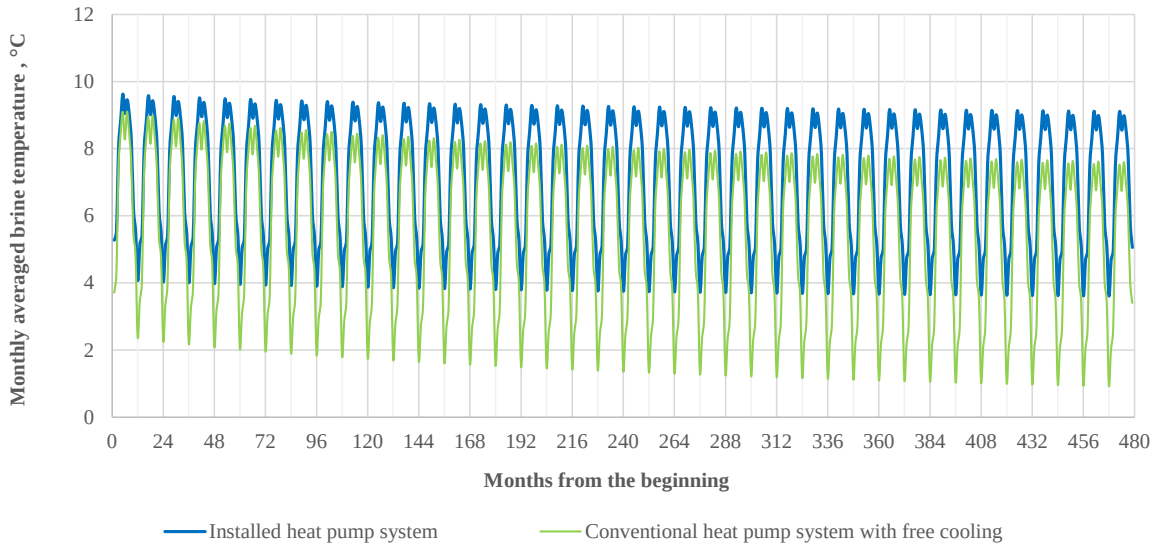


Fig 6. Monthly average liquid temperatures in the borehole field of the two compared energy systems.

The simulated seasonal coefficient of performance (SCOP) for the installed heat pump system is 3.19 and as seen from the monthly average liquid temperatures shown in Fig. 6, the SCOP will not decrease during the

lifecycle of the heat pump system. During the heating season the COP value fluctuates between about 3.5 during workdays and close to 3 during weekends when no energy recycling is available. The corresponding simulated SCOP for the conventional heat pump system with free cooling is 3.08 during the first year of operation and 3.04 on average.

3.2. Energy monitoring of the installed heat pump system

The installed heat pump system has been operational since November 2021 and its performance is monitored through a new building automation system interface provided by Schneider Electric. Key temperatures, status information of control valves as well as capacity data in the heat pump system are monitored at a time interval of 10 minutes. Measurements indicate that the building has consumed only 28 MWh of district heating since November 2021 and all additional heating took place in December 2021 and January 2022, approximately 80% in December and 20% in January. Compared to preliminary simulations performed in 2020, district heating consumption should have been approximately 34 MWh during the whole year when calculated with the measured district heating consumption data from 2019. During the year 2019 the amount of degree days (S17 degree day method) was 3419 in the Helsinki region and in 2021 correspondingly 3831. That is to say, the heating demand should be approximately 12% higher with the 2019 weather data compared to the year 2021. The before mentioned heating degree days are maintained by the Finnish Meteorological Institute [12].

An explanation to lower district heating consumption is that a schedule-based ventilation strategy has been deployed in the manufacturing spaces since mid-December 2021. A ventilation schedule with 100% air flow rate is used at workdays from 7 – 20 and a lower air flow rate of 67% of the nominal flow rate has been introduced to lower heating consumption at periods of absence. The operational hours of the ventilation unit serving the office region were also readjusted to further lower heating consumption. The adjustments to the ventilation system were proposed as a part of the energy efficiency project, leading to a 17% smaller heating energy consumption compared to measured consumption data from 2019. The total district heating consumption should have been higher if the ventilation system had operated as initially simulated, considering the ventilation adjustments at the end of 2021 and that 80% of the district heating was consumed during 2021. Measured consumption data from 2021 and the corresponding calculated data using district heating consumption from 2019 are compared in Table 3. DH in Table 3 stands for district heating.

Table 3. Measured heating consumption data compared to preliminary calculation data from 2019.

Consumption	Calculated value	Measured value
DH consumption without the heat pump system: 2019 measured data		956 MWh
Seasonal COP (SCOP) of the heat pump system: 2019 consumption data without ventilation adjustments	3.2	
DH consumption without the heat pump system: estimated consumption with ventilation adjustments (calculated based on the measured data from 2019)	796 MWh	
DH consumption with the heat pump system: 2019 consumption data without ventilation adjustments	34 MWh	
DH consumption with the heat pump system: 2019 consumption data with ventilation adjustments	12 MWh	
DH consumption with the heat pump system: 2021 actual consumption data		28 MWh
Heating energy produced by the heat pump system: 2021 actual consumption data		810 MWh
Seasonal COP (SCOP) of the heat pump system: 2021 actual consumption data		3.3

Energy simulations comparing the installed and the conventional heat pump system with free cooling indicate that there is only a minor difference of about 9 MWh in the district heating consumption in favour of the installed heat pump system (34 MWh compared to 43 MWh).

3.3. Analysis of life cycle costs and reductions of CO_2 emissions

The life cycle costs, and payback time of the hybrid heat pump system were investigated with a typical life span of 20 years including yearly maintenance costs and compressor renewals after 15 years of operation. All presented life cycle costs are proportioned to the initial state of the building: all heating energy is purchased from the district heating network and chillers with free cooling produce the cooling energy. Energy tariffs used in the calculation were gathered in November 2022, tariffs for district heating (energy tariff €/MWh and capacity fee €/kW) and the transfer fees for electricity (consumption related tariff €/MWh and power related fee €/kW). Especially the year 2022 has shown, that the electricity price has heavily fluctuated in Europe and the future is therefore difficult to predict. Due to the before mentioned uncertainties, the life cycle cost calculations were made based on two assumptions: 1. Energy tariff for electricity is 55 €/MWh without tax (assumption that the price will be stabilized to the same level as before the energy crisis in Europe) 2. Energy tariff for electricity is 80 €/MWh without tax (assumption that the price will not return to the same level during the upcoming decades). Hence, the total tariff in the first scenario is 84.7 €/MWh including the transfer fee, tax, and the energy tariff and 109.7 €/MWh respectively in the second scenario. An additional power fee of 2.4 €/kW/month is charged for the electrical power peek consumed every month. The district heating tariff is 68.2 €/MWh and the capacity fee is determined by 2604.26 + Q x 13.31 €/kW, where Q stands for the peak capacity during one year. The CO_2 reduction potential of the installed heat pump system was determined using averaged emission factors for a district heating network and electricity generation in Finland. Emission factors used in the calculation are 177 kg CO_2/MWh for district heating and 89 kg CO_2/MWh for electricity production [13].

Life cycle cost savings, investment costs, payback time and reduction of CO_2 emissions compared to the initial state are presented in Table 4 using the electricity tariff 55 €/MWh. The calculation results are shown both for the installed heat pump system and the alternative conventional heat pump system with free cooling.

Table 4. Financial analysis of the heat pump system compared to the initial state of the building.

Variable	Installed heat pump system	Conventional heat pump system with free cooling
Investment cost	447 k€	442 k€
Savings in heating energy	34 MWh	43 MWh
Electricity consumption increased due to the heat pump system	166 MWh *[1]	149 MWh *[2]
Life cycle cost savings during a life span of 20 years with energy grants (-20% of the investment cost)	661 k€	663 k€
Payback time without energy grants	9.1 years	8.8 years
Payback time with energy grants (-20% of the investment cost)	7.3 years	7.1 years
Reduction of CO_2 emissions	148.5 ton CO_2/year	148.5 ton CO_2/year

*[1]) The electricity consumption of the installed heat pump system is 280 MWh/year and electricity consumed by the chillers 155 MWh.
*[2]) The electricity consumption of the installed heat pump system is 292MWh/year and electricity consumed by the chillers 126 MWh. The initial level electricity consumption of the chillers is 269 MWh without any heat pump system.

A higher electricity tariff of 109.7 €/MWh (scenario 2) compared to 55 €/MWh would increase the payback time by 0.6 years and reduce the life cycle cost savings by 75 k€ with energy grants (-20% of the investment cost).

4. Discussion

The investigated hybrid heat pump system in the industrial building owned by the ABB Group in Finland has been operational since November 2021 and monitoring of the system indicates that the performance has exceeded the expectations. The most obvious explanation for better performance compared to the energy

calculations shown in this paper is the ventilation adjustments in the manufacturing area lowering net heating energy consumption during off hours. The adjustments to the ventilation system were proposed as a part of the energy efficiency project but the heat pump system itself was dimensioned based on the original consumption profile of the building. A dimensioning approach on the safe side was chosen because it was unclear if the proposed changes would be implemented due to high quality requirements of contaminant removal from the air. Secondly, the safe side dimensioning approach was motivated by the fact that the operation line at the industrial building will most likely be active also during the weekends in the future. The extended operation time would noticeably increase the net heating consumption of the building, but then again also the energy recycling potential would increase leading to a better overall system performance. In the present situation the COP of the heat pump system is approximately 3.5 during workdays and close to 3 during weekends during the coldest winter months. With the extended operational hours in the future, the seasonal COP value (SCOP) would consequently be over 3.5 when the current value is 3.3.

Compared to a conventional heat pump system with free cooling from the boreholes, the current situation reveals that the installed system is slightly over dimensioned proportioned to the net heating demand of the building. That is, the life cycle savings are even slightly higher in the conventional approach and same borehole dimensioning is applicable in both cases. From the design viewpoint, the pressurized air compressors would anyway have been replaced soon in the alternative approach by adding a separate liquid cooler on the roof of the building transferring waste heat into the outdoor air. Waste heat transfer into the outdoor air was, on the other hand, not in line with the ABB Group energy program Mission to Zero and secondly it was not a future proof solution bearing in mind the extended operational hours of the manufacturing line in the future. Hence, the conventional heat pump system (alternative approach) would have required more boreholes with a future proof dimensioning to cope with the increased heating demand, which then again would have influenced the profitability of the energy system negatively. The installed heat pump system can be seen as an encouraging example for other hybrid heat pump systems to be used within the ABB Group. In other industrial buildings a pure energy recycling system without boreholes might for instance be the only option due to strict ground water requirements in the area and in these cases an energy recycling system with a solid performance is the most valuable solution. For the investigated building ABB assembly parts in Finland, the use of a pure energy recycling system would have led to a decent heating energy coverage ratio of 63%.

The energy system simulation model in IDA ICE turned out to produce reasonable results compared to the measurements. The greatest uncertainties in the modelling relate to the borehole field, the properties of the ground and the amount of heat loaded into the borehole field by the new liquid cooled air compressors. Thermal response tests for the ground were not carried out during the project because the dimensioning on the energy system was known to be well on the safe side. The energy simulation of the borehole field was, on the contrary, made with conservative input parameters and the heat load of the air compressor was estimated based on measured data from the smaller old compressor (old compressor 75 kW and new compressor 90 kW). From this point of view, it was known that energy modelling would not overestimate the energy performance. The most significant uncertainties in heat pump modelling itself were found in the part load behaviour of the on-off controlled heat pumps at small loads and the effect on the average COP value.

5. Conclusions

The hybrid heat pump system investigated in this study was a part of the energy efficiency project carried out by the Granlund company to significantly improve the energy performance of an industrial building owned by the ABB Group in Finland. An incentive to the chosen design approach came from the ABB Group, aiming to significantly reduce the carbon footprint of its buildings in line with the energy program Mission to Zero. Monitoring of the installed heat pump system has revealed that the industrial building has been almost self-sufficient after the proposed adjustments to the ventilation system were made to lower the net heating consumption of the building. In fact, the hybrid heat pump system is for the present use of the building slightly over dimensioned and economically not the most feasible alternative compared to a conventional ground source heat pump system with free cooling. The system was on the contrary dimensioned for the future usage of the building when the manufacturing line is used every day instead of the present usage pattern from Monday to Friday. Hence, extensive energy recycling will pay itself well back in the future compared to a conventional heat pump system requiring more boreholes to cope with the increased heating demand.

The current design approach emphasises a good collaboration with the end user, understanding the current situation and future evolution. A key premise to success is to consider the long-term investment plan and include additional useful investments into the project, improving the overall cost efficiency of the project and making use of the energy grants for investments promoting the use of new energy technology. In this case the

existing air compressor was at the end of its life cycle, meaning that it should have been replaced anyway soon. The integration of the compressor to the energy system for energy recycling and loading the borehole field was a key measure in this project improving long-term energy efficiency of the heat pump system. A lesson learned was the importance of reducing unnecessary heating in the building, in this case unnecessary ventilation during off hours and dimensioning the heat pump system based on new heating consumption. The investigated heat pump system was dimensioned on the safe side based on the higher heating demand and by considering the future needs. Hence, the energy system could have been optimized slightly further and made somewhat cheaper but as a conclusion, it matches or even exceeds the expectations of the Abb's own energy program Mission to Zero. The energy recycling approach investigated in this study is applicable to all kinds of buildings, either as a pure energy recycling system or coupled with boreholes for additional heat extraction and buffering of waste heat into the ground. The system is also scalable in terms of heat pump capacity and the energy recycling sources and dimensioning of the system is tailored to match the consumptions profiles of a specific building. The payback time of the investigated system is without energy grants approximately 9 years and with the energy grants in Finland (-20% of the investment cost) approximately 7 years. The energy performance of the energy recycling system could be optimized further based on the readings from the building automation system. With the present setpoints the supply water heating curve has been too high at warmer air temperatures, especially at 0 – 5 °C, over 50 °C. The temperature setpoint should according to the design parameters be more than 5 °C lower, implying that the seasonal COP (SCOP) could be close to 3.5 instead of the measured 3.3.

From the energy modelling point of view, the most important need for future research is to validate the energy system model used in the calculations especially at part loads but also on system level considering the operation of buffer tanks and mixing valves. The existing heat pump calculation models are generalized, and they are not related to a particular heat pump type, in this case to the on-off behaviour of the compressors.

Acknowledgements

The study presented in this conference paper was carried out as an individual research project as an extension to the project work performed at Granlund Oy. The authors would like to thank especially ABB in Finland for the research opportunity and for providing measurement and investment cost data for the project.

References

[1] Shakerin, M., Eikeskog, V., Li, Y., Harsem, T., Nord, N., Li, H., 2022. Investigation of Combined Heating and Cooling Systems with Short- and Long-Term Storages. Sustainability 2022, 14, 5709. https://doi.org/10.3390/su14095709.

[2] Laitinen, A., Tuominen, P., Holopainen, R., Tuomaala, P., Jokisalo, J., Eskola, L., Sirén, K., 2014. Renewable energy production of Finnish heat pumps. Final report of the SPF-project: VTT Technology publication 164.

[3] Sahlin, P., 1996. Modelling and Simulation Methods for Modular Continuous Systems in Buildings. Doctoral Dissertation, Department of Building Sciences, Division of Building Services Engineering, Royal Institute of Technology 1996, Stockholm, Sweden. ISSN 0284-141X.

[4] Björsell, N., Bring, A., Eriksson, L., Grozman, P., Lindgren, M., Sahlin, P., Shapovalov, A., Vuolle, M., 1999. IDA indoor climate and energy, Proceedings of the IBPSA Building Simulation '99 conference, Kyoto, Japan.

[5] Achermann, M. and Zweifel, G., 2003. RADTEST – Radiant heating and cooling test cases, Subtask C, A Report of IEA Task 22, Building Energy Analysis Tools, 2003.

[6] Loutzenhiser, P., Manz, H., Maxwell, G., 2007. Empirical Validations of Shading / Daylighting / load Interactions in building energy simulation tools, A Report for the International energy Agency SHC Task 34, ECBCS Annex 43 Project C, 2007.

[7] Travesi, J., Maxwell, G., Klaassen, C., Holtz, M., 2001. Empirical validation of Iowa.

[8] SFS-EN 14825. Air conditioners, liquid chilling packages and heat pumps, with electrically driven compressors, for space heating and cooling. Testing and rating at part load conditions and calculation of seasonal performance.

[9] Niemelä, T., Kosonen, R., Jokisalo, J., 2017. Comparison of energy performance of simulated and measured heat pump systems in existing multi-family residential buildings. 12th IEA Heat Pump Conference 2017.

[10] ASHRAE. 2011. ASHRAE Handbook-Application. Atlanta: American Society of Heating Refrigeration and Air Conditioning Engineers, Inc.

[11] Cullin, J.R., J.D. Spitler, C. Montagud, F. Ruiz-Calvo, S.J. Rees, S.S. Naicker, P. Konečný, and L.E. Southard. 2015. Validation of Vertical Ground Heat Exchanger Design Methodologies. Science and Technology for the Built Environment. 21(2):137-149.
[12] The Finnish Meteorological Institute, 2022. The annual S17 degree day numbers of Finnish cities. Available online at: https://www.ilmatieteenlaitos.fi/lammitystarveluvut (in Finnish).
[13] Motiva Oy, 2022. CO_2 emission factors for the average district heating network and electricity production in Finland. Moving average values during 2018 – 2020. Available online at: https://www.motiva.fi/ratkaisut/energiankaytto_suomessa/co2-paastokertoimet (in Finnish).

14th IEA Heat Pump Conference
15-18 May 2023, Chicago, Illinois

Enabling Electrification of Domestic Hot Water and Space Conditioning with Multi-function Heat Pumps

Subhrajit Chakraborty[a*], Stephen Chally[b], Timothy Levering[a]

[a]Western Cooling Efficiency Center, 215 Sage St., Davis CA 95616, U.S.A

[b]Frontier Energy, 123 C St., Davis CA 95616, U.S.A.

Abstract

Heat Pumps, although imperative to eliminate building onsite emissions, are required to be both energy efficient and capable of retrofitting in existing homes. In this study, we focus on Multi-function Heat Pump (MFHP) system, that uses one outdoor unit to provide both domestic hot water (DHW) along with space cooling and heating. An air-to-air MFHP, demonstrated in this study, reduces barriers to home electrification by avoiding electric resistance and lowering peak demand. The MFHP system is retrofitted in a 2000 sq-ft residential home to evaluate ease of installation, reliability, energy efficiency, and thermal comfort in terms of the space and water temperatures. Performance metrics of the MFHP are monitored over the summer in various modes and reported in this study. Coefficient of Performance (COP) of the AC mode was observed to be about 2.8 for an outdoor dry bulb of 35°C and COP of the water heating mode was observed to be about 2.3 for an outdoor dry bulb of 19.7°C. MFHP system provides a unique opportunity to move the heat from space into the DHW tank while operating in a simultaneous space cooling and hot water heating mode. The simultaneous mode performed 36% better than individual two modes if operated separately. The study demonstrates energy savings potential with MFHP while adequately meeting multiple loads in residential buildings without electric resistance heating. Refrigerant charge optimization and advanced controls to increase the run-time of the simultaneous AC and DHW mode are the next steps to improve the air-to-air MFHP system.

© HPC2023.
Keywords: Heat Pump; Domestic Hot Water, Electrification, Residential Building

1. Introduction

Residential buildings generate about 20% of the Unites States (US) energy-related greenhouse gas (GHG) emissions mainly from heating, cooling and hot water heating [1]. The main source of residential onsite emissions is from burning fossil fuels (mainly natural gas) for space and water heating which contributes about 323 million metric tons of GHG yearly[2]. Thus, residential heat pumps (HP) for domestic hot water (DHW) and space conditioning along with a clean electricity grid is the future of the decarbonized world. It is observed that even for the current predictions of the electricity grid, installation of heat pumps to replace natural gas furnaces for residential space heating leads to an average of 45% GHG emission reduction across the US over the lifetime of the equipment [3]. Electrifying existing space and water heating with heat pumps is a critical step in building decarbonization and poses a big challenge with electrical service upgrades. Requirements for home electrical service upgrades add cost and installation delays for retrofit customers who are considering HP for space conditioning and or hot water heating [4]. Around half of all homes are expected to need electrical service panel upgrades that cause system installation delays to fully electrify [5]. Furthermore, heat pump water heaters (HPWH) come with space constraints for closet installations and require air supply for the evaporator coil.

* Corresponding author. E-mail address: sjchakra@ucdavis.edu

Multi-Function Heat Pumps (MFHP) use one efficient compressor and outdoor heat exchanger coil to provide space cooling, space heating, and domestic hot water heating. Air-to-air MFHP systems (shown in Figure 1) use refrigerant to provide end-use heating and cooling services and have the potential to be easily retrofitted in ducted central air-conditioned (AC) homes and eliminate the need for electric resistance backup heaters. Eliminating electric resistance backup heaters can greatly reduce the maximum power requirements and eliminate the need for electrical service upgrades, which is one of the major barriers to electrification. The DHW tank of the MFHP obviates the need for exhaust connections, inlet air flow, or electrical power and has a smaller footprint. Uniquely, air-to-air MFHP systems can also operate in a simultaneous space cooling and DHW heating mode, which utilizes the heat from space cooling to heat DHW. The simultaneous AC-DHW mode usually has higher efficiency and can meet both space cooling and water heating loads flexibly [6].

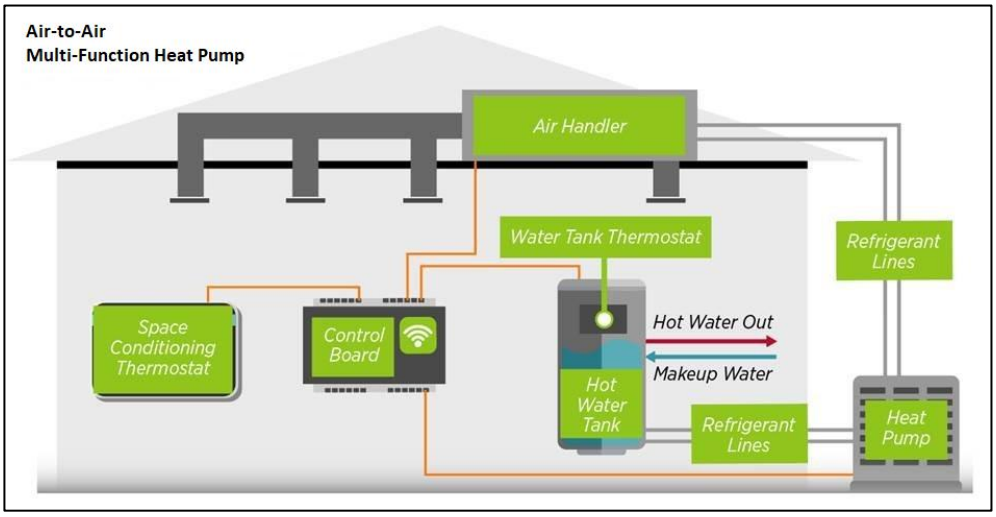


Figure 1 Air-to-air MSHP using refrigerant to provide end-use heating and cooling

Previous studies have focused on heat pumps utilizing carbon-dioxide (CO_2) as a refrigerant that can provide high temperature water for both space and water heating [7], [8]. However, these systems did not provide cooling to the household during hot summer months which is a requirement in most climate zones [9]. Heat pumps are best known for their ability to switch between cooling and heating, which is an opportunity to reduce equipment redundancies. Integrated heat pump systems have been available in Europe and a relevant testing standard was made available by International Energy Agency (IEA) through Annex 28 [10]. Although the testing procedure developed by IEA encompassed a multi-function heat pump, the scope was limited to space heating, DHW and ventilation. There has been a lack of understanding of MSHPs in space cooling (AC) with DHW mode and its overall potential to save costs and energy for the typical single-family house in the US. This study attempts to fill that gap by evaluating an air-to-air MSHP in a 2000 sq-ft household in Davis, California. Results from the study about the ease of retrofit installation, performance of the MSHP during summer, and ability of the MSHP to meet space comfort and DHW requirements are presented in this paper. Insights gained from this study will pave the path for further research in MSHP systems for easy electrification while saving energy and costs for existing residential buildings in the US.

2. Site and Installation

MSHP system uses an off-the-shelf standard split system heat pump outdoor unit with refrigerant line set serving an indoor direct expansion (DX) air handler and adds a second refrigerant line set serving a DHW tank (Figure 1). The custom made DHW tank consists of both refrigerant-to-water and water-to-water heat exchangers. City water supply flows separately through the water-to-water heat exchanger and exchanges heat with the thermal storage water from the tank. With this innovative design the DHW tank stays at ambient pressure and does not need to be certified as a pressure vessel with a relief valve. This MFHP product has been certified for capacity and efficiency for water heating by third party tests at Intertek.

As seen in Figure 2, the site before retrofit consisted of a 12.3kW (3.5 ref ton) AC, a 29.3kW (100 MBH/hr) natural gas furnace with a blower, and a 189-liter (50 gallon) tank with natural gas boiler of 11.7 kW (40

MBH/hr) capacity. The house electrical panel was limited to maximum 100 amp with the line to the utility transformer limited to maximum 125 amp. An electrification of the space and water heating would be replacing the AC with HP but would require strip heaters in the 220V air-handler requiring additional 30 amp. Additionally, a unitary hybrid HPWH installation in the closet would require 30 amp more in the electrical panel. This was avoided by electrifying the space conditioning and water heating with an air-to-air MFHP.

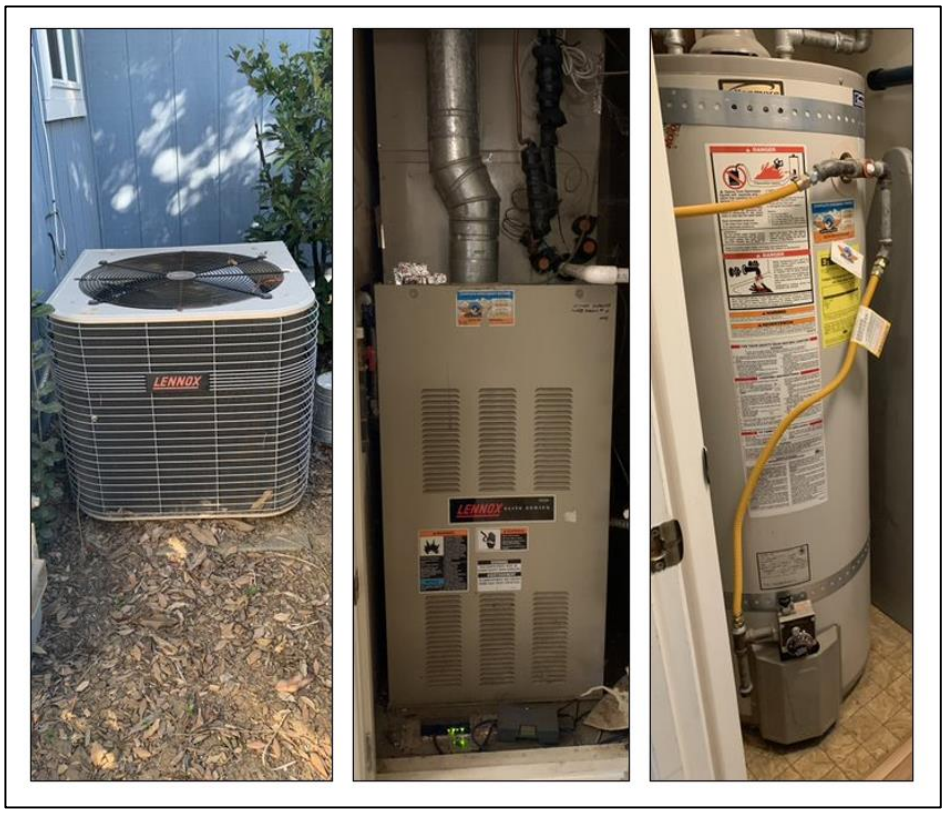


Figure 2: Pre-retrofit space conditioning and water heating equipment

The retrofitted air-to-air MFHP consisted of a 14 kW (4 ref ton) cooling capacity outdoor unit (16 SEER) connected to an air-handler in the attic, which circulates 2480 m3/hr (1460 CFM) of air through the house. The innovative refrigerant to water tank was placed in the same closet as the pre-retrofit natural gas DHW tank and did not need any additional air flow paths. Refrigerant (R410A) line sets were connected from the outdoor unit to the AHU and the DHW tank with proper temperature and sound insulation. The main control board of the MFHP is connected to the water tank thermostat and space conditioning thermostat. The main control board decides the mode of the MFHP based on the heating and cooling calls from each thermostat. For the summer monitoring period, the MFHP operated in three modes Space cooling (AC), DHW heating mode, and concurrent AC and DHW heating mode.



Figure 3: Post-retrofit MSHP components installed

3. Methodology

3.1. Instrumentation

To determine the overall performance of the MFHP system, the system was monitored using Frontier Energy's proprietary data logger. The following were instrumented and logged at 5-second intervals using the data logger:

- Detailed DHW monitoring: An Onicon ultrasonic BTU meter collected temperature, flow, and delivered energy between the hot water storage tank and the heat pump outdoor unit. Three Omega PR-10L RTDs were used to measure water temperature stratification within the DHW tank.
- Detailed HVAC system monitoring: Three ICP M-7059D modules were installed between the inputs and outputs of the MSHP controller to monitor every time the controller activates a new setting, i.e. dehumidification, cooling, heating, heat recycling, etc. Nine thermocouples were installed inside the primary supply duct leaving the supply plenum to create a 3x3 sensor averaging temperature grid to measure supply temperature. A Vaisala HMD62 was installed in the return plenum, and another in the supply plenum to measure temperature and relative humidity. A Wattnode WND-WR-MB1 True-RMS energy meter was installed on both the air handler and the outdoor unit to measure power. Five Omega PR-10L RTDs were mounted around the outdoor unit to monitor the airflow temperature entering and leaving the outdoor unit refrigerant coil.
- Weather monitoring: A Vaisala HMS110 humidity and temperature sensor was mounted outside to collect the local weather data.

In addition to the detailed DHW, HVAC, and weather monitoring, the indoor conditions of the home were monitored using an ecobee thermostat with five remote temperature sensors which provided the following data points in 5-minute intervals:

- Thermostat setpoint
- System mode
- Component operation time
- Current temperature
- Relative humidity at the ecobee
- Occupancy

The specifications for all sensors used are presented in Table 1 and Table 2.

Table 1: Data Logger Sensor Specifications.

Type	Locations	Mfr/Model	Signal	Span	Accuracy
Temperature/RH	Supply and Return Plenum	Vaisala HMD62	Modbus	-40-176°F	0.18°F
				0-100 %RH	1.5 %RH
Temperature/RH	Outside	Vaisala HMS100	Modbus	-40-140°F	0.36°F
				0-100 %RH	2 %RH
Temperature	Supply duct and return plenum	Type T	Analog	-200 to 200°C	±0.5°C
Temperature	Outdoor unit and Hot Water Tank	Omega PR-10L RTD	Analog	-50-250°C	Class A ± (0.15 + 0.002T)°C
AC Voltage Digital Input/Output State	AquaThermAire Controller	ICP DAS M-7059D	Modbus	10 – 70 V AC	N/A
RTD Analog Input Module	Outdoor unit and Hot Water Tank	ICP DAS M-7015P	Modbus	-13 – 167°F	0.05%
Power meter	Heat Pump Outdoor unit and Air Handler	Wattnode WND-WR-MB	Modbus	CT dependent	0.5%
BTU meter	Hot Water Tank	Onicon System 40	Modbus	0.15-15 gpm	±2%
					±0.18°C

Table 2. Ecobee sensor Specifications.

Type	Mfr/Model	Signal	Span	Accuracy
Temperature	ecobee and remote sensors	N/A	5 to 37 °C	±0.5 °C
Relative Humidity	ecobee and remote sensors	N/A	20 to 90% RH	±5% RH

The installation locations of the sensors and monitoring equipment are shown in Figure 4. The data logger was installed with the cell modem, in a lockable NEMA enclosure. Other equipment, such as remote sending units, were installed behind hatches or other removable coverings. The Ecobee thermostat is part of the HVAC system and property of the homeowner.

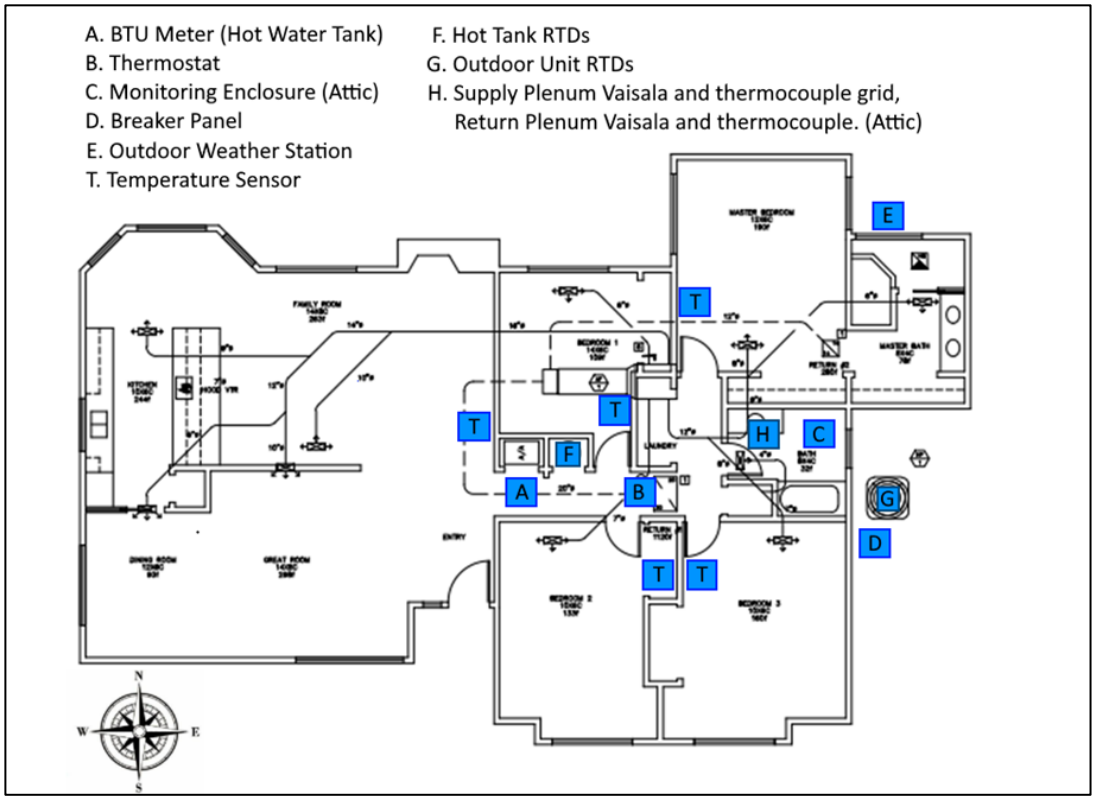


Figure 4. Monitoring System Install Locations in house floor plan

3.2. Data Analysis

3.2.1. DHW Performance

Detailed domestic hot water (DHW) system data was analyzed to calculate operating efficiencies. The BTU meters performed the necessary calculations for the amount of energy of the water delivered from the hot water tank. The standard heat balance equation follows:

$$Q_{Water} = c_{p_{water}} \rho_{water} \dot{V}_{water} \Delta T \quad (1)$$

The capacity measured from the BTU meter only accounted for the DHW energy leaving the tank as water was used throughout the home. To determine the capacity delivered to the tank during a water heating cycle, the following equation was used:

$$Q_{TES} = m_{TES} c_{p_{water}} \frac{\Delta T_{avg,Tank}}{\Delta t} \quad (2)$$

To determine the total capacity during a water heating cycle, the sum of the heat delivered to and leaving the tank was taken shown in the following equation:

$$Q_{DHW} = Q_{TES} + Q_{Water} \quad (3)$$

3.2.2. Heat Pump Performance

The output cooling capacity was calculated in real time using the enthalpies calculated using the Vaisala HMD62 sensors and Type T thermocouples in the supply and return plenums, with the one-time airflow measurement taken when commissioning the system.

$$Q_{cooling} = \rho_{air} \cdot \dot{V}_{air} \cdot \left(H_{return} - H_{supply}\right) \quad (4)$$

To determine the overall performance of the space cooling mode, the Coefficient of Performance (COP) was calculated:

$$COP = \frac{Q_{cooling}}{P_{total}} \quad (5)$$

3.2.3. Overall Performance

Due to the design of the tank (an atmospheric storage tank with two coincident coils, one carrying refrigerant and one carrying potable water), it is very difficult to measure the performance of the combined modes. For this reason, overall system efficiency was generalized using the ratio of the total daily delivered cooling and DHW energy to the total electrical energy consumed.

$$COP_{combined} = \frac{Q_{DHW}+Q_{cooling}}{P_{total}} \quad (6)$$

3.2.4. Equation Nomenclature

c_p is the specific heat.
CFM is the total return airflow in cooling.
COP is Coefficient of Performance at AHRI standard conditions.
P_{total} is the total HVAC electrical power including AHU
η is the overall system efficiency.
H is supply and return enthalpies.
m_{TES} is the mass of water within the thermal storage tank.
$Q_{cooling}$ is the cooling delivery rate.
Q_{DHW} is the total rate of heat delivered to the tank during a water heating cycle.
Q_{TES} is the rate of heat added to the thermal storage tank.
Q_{Water} is the rate of heat delivered from the thermal storage tank to the point of use.
ρ is the density.
Δt is the time period of the cycle.
ΔT is the temperature difference between the hot and cold side.
$\Delta T_{avg,Tank}$ is the change in average tank temperature during a tank heating cycle.
$\dot{V}$ is the volumetric flow rate.

4. Results and Discussion

The significant findings from the summer monitoring period for the MFHP are shown below as results. An hourly average of the indoor, outdoor, and DHW tank temperatures are shown in Figure 4 (top). The modes of the MFHP observed during the summer along with their respective runtimes during that three-day period are shown as bars on the secondary y-axis. It is evident from the indoor temperature that the MFHP is able to hold the indoor temperature steady across fluctuating outdoor conditions. The first 12 hours of the day had cold outdoor conditions and did not have AC runtime, however DHW heating runtimes were triggered by significant water draws. The concurrent AC-DHW mode was also seen to run during times when there is call for both space cooling and water heating. The frequency and run-times of the concurrent mode were low, which provides a scope of improvement for the MFHP with advanced controls. Figure 4(bottom) shows the performance of the MFHP over the three-day period in terms of cooling capacity, total power consumption, and volumetric flow of hot water. The volumetric flow is represented in liters of hot water provided per minute on the secondar y-axis. The average DHW tank temperature would drop due to water draws but would go up due the MFHP operation in water heating or the concurrent AC and DHW mode. As expected, the cooling capacity was seen to be larger than the total power draw, suggesting a COP higher than unity.

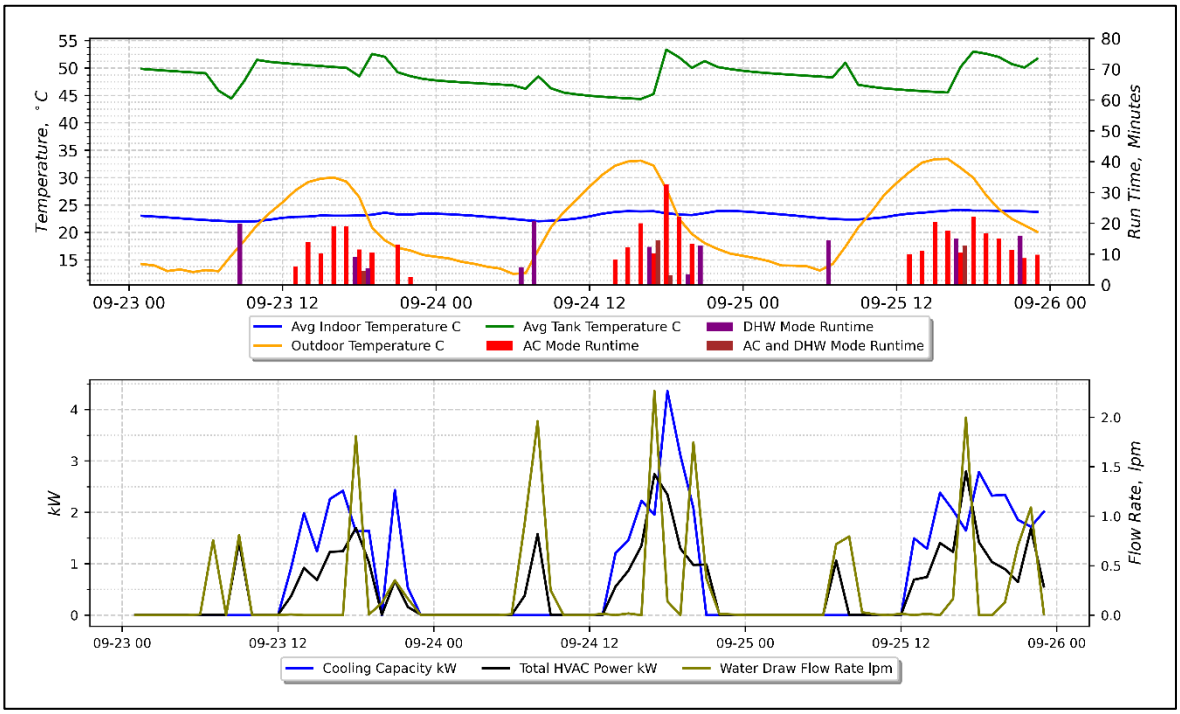


Figure 4: Hourly runtimes, average temperature, and performance of the MSHP system over a 3 day period in summer

A compressor cycle level analysis was performed to understand the efficiency of each mode of the MFHP. Coefficient of Performance (COP) for compressor cycles above four minutes in the duration between May 21 and October 21 with the outdoor dry-bulb temperature are shown in Figure 5. The cycle level COPs are sorted into three modes: AC mode (top left), DHW mode (top right), and concurrent AC and DHW mode (bottom).

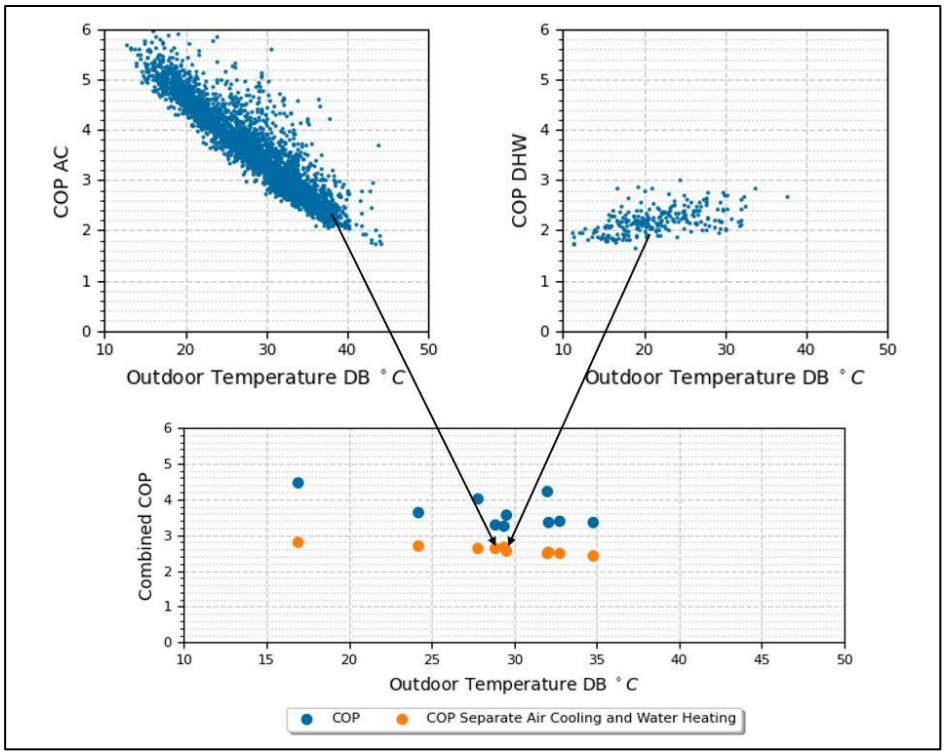


Figure 5: Compressor cycle level COP of each mode of the MFHP during the summer

Each blue dot in Figure 5 represents a compressor cycle in the respective mode. As shown, the MFHP ran very frequently in AC mode, followed by the DHW heating mode, and very infrequently in concurrent AC and DHW mode. This is because most of the concurrent mode occurrences throughout the monitoring period usually had lower than 4-minute runtimes, which was taken as the minimum amount of time for a cycle to reach steady state. The AC mode was observed to be drawing a power at 4.1 kW for a COP of 2.8 at 35°C outdoor dry bulb which was lower than the manufacturer published COP data (3.5) for a heat pump without the MFHP modifications. The reason for this difference in COP could be many. Firstly, there is higher refrigerant pressure drop expected from the addition of the three-way valves for changing modes and longer refrigerant line sets compared to the AHRI rated line set length of 25 feet. Secondly, return air conditions and supply air pressure drop in the current installation of the house are probably different than AHRI rating conditions. And lastly, the MFHP refrigerant charge is still being optimized by the manufacturer to accommodate wide range of conditions in the various modes. The DHW mode demonstrated a COP of 2.3 delivering 9.8 kW of thermal power into the water at 19.7°C outdoor dry bulb temperature, several times higher than the regular heat pump water heaters.

The bottom chart shows the measured combined COP of the concurrent mode (blue) and the combined calculated COP of the separate modes (orange), that is, if the MFHP were to run in AC and DHW mode separately to meet the same loads at the same outdoor condition. The calculated combined COP of the separate modes was based on data driven efficiency models of the AC and DHW modes separately. The measured COP of the concurrent AC and DHW mode was 36% better on average than two separate modes and thus, there is potential for energy savings by maximizing the runtime of the concurrent mode.

Figure 6 shows the transient response curve of the temperature in home to a setpoint change. The thick blue line represents the thermostat cooling setpoint which was initially set to 26.7°C as the occupants were away and was dropped to 23.3°C at 16:00 hours. The thick orange line is the temperature as measured by the thermostat and started to drop as the MFHP ran the AC mode. The thin lines with the shading in between are the individual room temperatures and shows the spread in room temperatures across the house. The dotted red line is the outdoor temperature, plotted on the secondary y-axis, stayed relatively constant over the time period. The thermostat temperature was seen to drop by 1.5°C in the first 30 minutes for the 2000 sq-ft house and was able to meet the comfort needs of the occupants. The span temperatures in all the rooms of the house denoted by the shaded region increases as the system operates due to heat gains on the house envelope and unequal distribution of air in rooms.

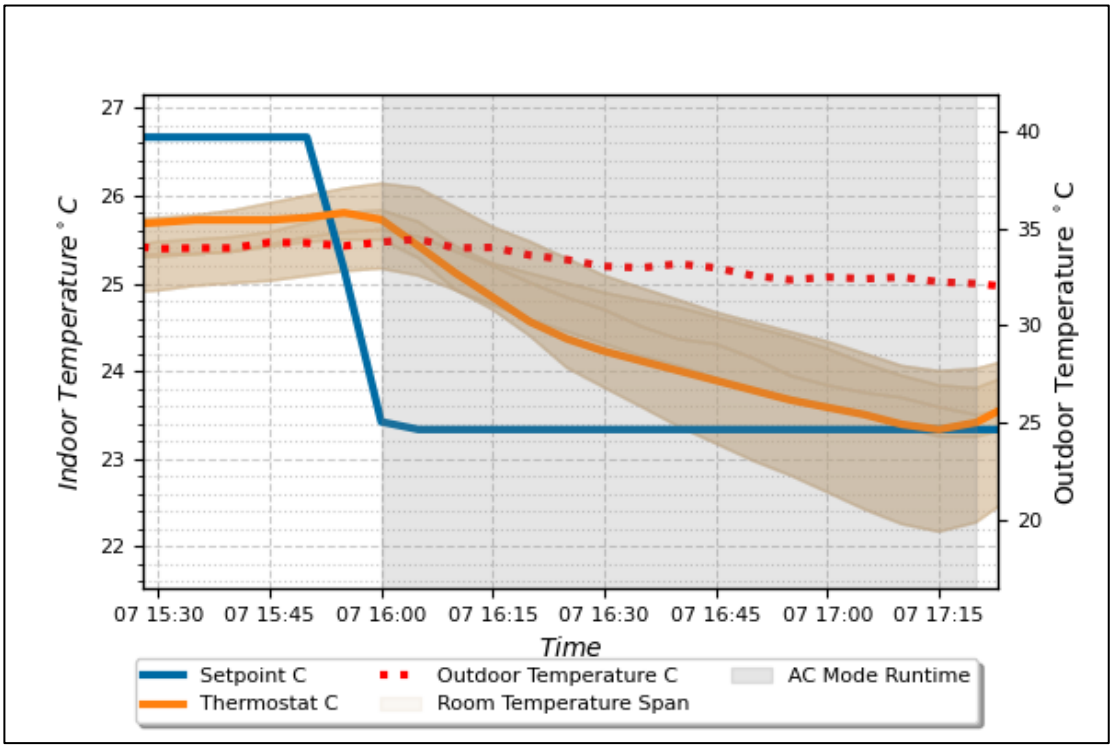


Figure 6: Indoor temperature transient response to a cooling call in AC mode

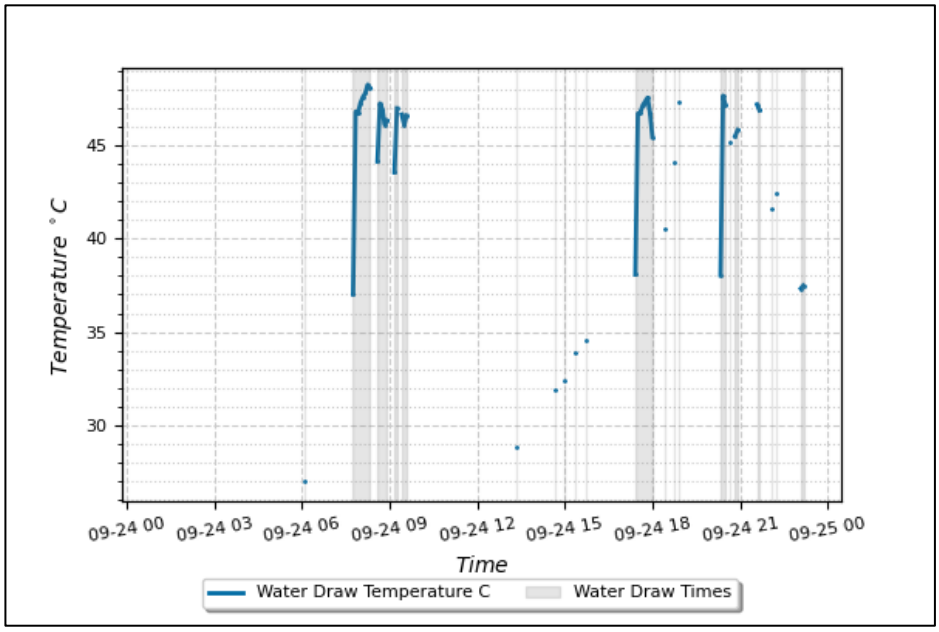


Figure 7: DHW tank delivered temperature during hot water draws

Figure 7 shows the water draw temperature over a day measured at the exit of the DHW tank during times of hot water draws, denoted by grey shading. The water temperature data was filtered on this basis to better illustrate the water delivered to point of use since the water at the tank exit cools down and does not heat up until there is flow. At start of every long draw the water temperature was seen to have a lower temperature and quickly increasing in temperature to about 45°C. This is due to the thermal mass in and around the outlet temperature sensor, which takes time to heat up to give a more accurate reading of the water flow temperature. The blue dots denote temperatures at water draws with a duration lasting less than 5 minutes. These points generally have lower temperatures similar reason to the starting measurements of the longer draws. The temperature profiles of the longer draws shows drop in temperature after a peak temperature value is achieved indicating depletion of thermal storage in the DHW tank.

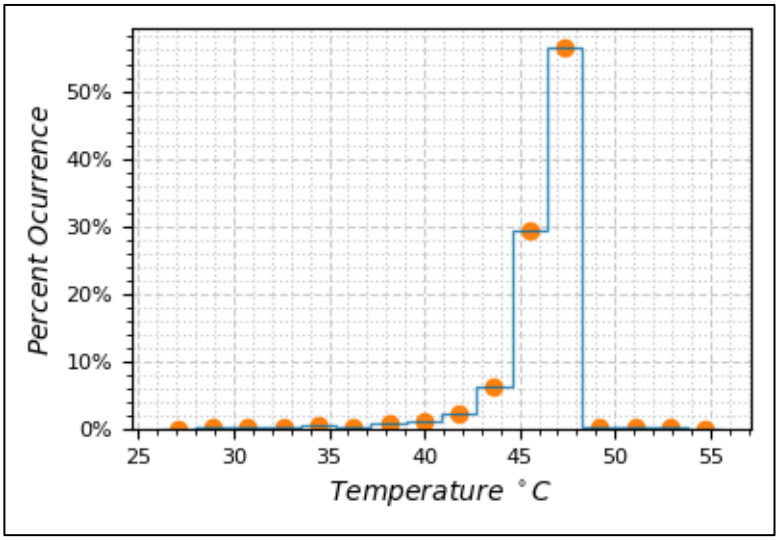


Figure 8: Hot Water temperature distribution of draws lasting above 5 minutes

The water temperature distribution shown in

Figure 8 was filtered for data when there was a water draw in the 5 minutes prior to the current water draw. This was done to filter out temperature data at the beginning of a draw before the sensor has time to heat up

which was not deemed representative of hot water delivered by MFHP to meet comfort. About 15% of the total water draw occurrences, or 3.2% of the total hot water volume flow, had a hot water delivery temperature of below 45°C, which is the considered the lowest acceptable value for a shower. This shows that the MFHP system reasonably meets the hot water needs of the household during the summer while meeting the space cooling loads.

5. Conclusion

Electrification of space conditioning and hot water heating in homes require installation of separate air source heat pump equipment with each having electrical resistance heaters, which leads to increase in demand and ampacity of the electrical panel. Additional cost and complexity of electrical panel upgrades is one of the main challenges of electrification of older homes in the US. An air-to-air R410A MFHP system, capable of providing DHW and space conditioning, is investigated as a retrofit in a single-family home in Davis, California without electric resistance heaters. The system is monitored over the summer (May 21 to October 21) to analyze efficiencies of the MFHP in each mode and to evaluate its capability in meeting the space cooling and hot water loads. The household was instrumented with several sensors to calculate the metrics necessary for assessing the performance of the MFHP system and the thermal comfort of the occupants. The average COP of the MFHP AC mode was observed to be 2.8 (at 35°C Outdoor dry bulb), lower than heat pump without MFHP modifications. The reasons could be sub-optimal refrigerant charge and higher pressure drop due to longer lineset and refrigerant valving. The measured COP of the concurrent cooling and DHW mode was better than the COP estimated for meeting those loads in separate cycles by an average of 36%. Altering the controls to favor the concurrent mode rather than tackling the space cooling and DHW loads separately, this system can provide major energy and cost savings to the homeowner. Continued monitoring of the operation of MFHP and evaluating the heating performance of the system in the winter is ongoing. The MFHP space heating mode is demonstrated an average COP of 3.25 (at 8.3°C Outdoor dry bulb). Future work will assess the year-round performance and capability of MFHP in providing required household space conditioning and domestic hot water.

References

[1] EIA, “U.S. CO2 emissions from energy consumption by source and sector,” *Total Energy Monthly Data - U.S. Energy Information Administration (EIA)*, Apr. 2021. https://www.eia.gov/totalenergy/data/monthly/ (accessed Mar. 16, 2022).

[2] U.S. EIA, “U.S. Energy-Related Carbon Dioxide Emissions, 2020,” 2021. Accessed: Jul. 17, 2022. [Online]. Available: https://www.eia.gov/environment/emissions/carbon/

[3] T. Pistochini, M. Dichter, S. Chakraborty, N. Dichter, and A. Aboud, “Greenhouse gas emission forecasts for electrification of space heating in residential homes in the US,” *Energy Policy*, vol. 163, p. 112813, Apr. 2022, doi: 10.1016/J.ENPOL.2022.112813.

[4] S. Outcault, A. Depew, Y. Akoda, and A. Meier, “Residential Electrification in Sacramento and Its Impact on Residential Appliance Sales,” 2021. Accessed: Nov. 08, 2022. [Online]. Available: https://ucdavis.app.box.com/s/hcrzfp7a6md77g6q21db2k6agkt88406

[5] Pecan Street Inc., “Addressing an Electrification Roadblock: Residential Electric Panel Capacity Analysis and Policy Recommendations on Electric Panel Sizing,” 2021. [Online]. Available: https://www.pecanstreet.org/electrification-tool]

[6] S. Chakraborty, R. Mcmurry, and C. Harrington, “Concurrent Space Cooling and Hot water Heating through Compact Heat Pumps for All-electric Residential Buildings,” Aug. 2022. Accessed: Feb. 25, 2023. [Online]. Available: https://escholarship.org/uc/item/9565g85j

[7] J. Stene, “Residential CO2 heat pump system for combined space heating and hot water heating,” *International Journal of Refrigeration*, vol. 28, no. 8, pp. 1259–1265, Dec. 2005, doi: 10.1016/j.ijrefrig.2005.07.006.

[8] K. Eklund and A. Banks, “Combined Space and Water CO 2 Heat Pump System Performance Research,” 2016.

[9] K. Janowitz, C. Dymond, C. Roos, and M. Jerome, “Is the CO 2 Heat Pump Ideal for Combination Space and Water Heating ? Field Data from Seven CO 2 Heat Pump-Based Combined Space and Water Heating Systems,” 2020, pp. 126–141.

[10] C. Wemhoener, T. Afjei, and R. Dott, “IEA HPP Annex 28 – standardised testing and seasonal performance calculation for multifunctional heat pump systems,” *Appl Therm Eng*, vol. 28, no. 16, pp. 2062–2069, Nov. 2008, doi: 10.1016/J.APPLTHERMALENG.2007.12.003.

14th IEA Heat Pump Conference
15-18 May 2023, Chicago, Illinois

Industrial Heat Pumps in Japan: Current Status and Future Prospects

Takenobu Kaida[a,b,*], Toshihiro Mukai[c], Tsuyoshi Hamayashiki[d,**]

[a] Grid Innovation Research Laboratory, Central Research Institute of Electric Power Industry (CRIEPI), Yokosuka 240-0196, Japan
[b] Department of Mechanical Engineering, Kyushu University, Fukuoka 819-0395, Japan
[c] Socio-Economic Research Center, Central Research Institute of Electric Power Industry (CRIEPI), Tokyo 100-8126, Japan
[d] Japan Electro-Heat Center (JEHC), Tokyo 103-0011, Japan

Abstract

The importance of industrial heat pumps for decarbonization has gained widespread recognition. Japan has demonstrated preeminence in the realm of industrial heat pump innovation and implementation. This paper overviews the current technology and market status of industrial heat pumps in Japan, demonstrating the maturity of heat-pumping technology to some extent. However, it shows a need to accelerate the introduction. Through a comprehensive questionnaire survey and barrier analysis, this study clarifies the challenges faced in the widespread adoption of industrial heat pumps and proposes measures to address these barriers in the future.

© HPC2023.
Selection and/or peer review under the responsibility of the organizers of the 14th IEA Heat Pump Conference 2023.

Keywords: Industrial heat pump; Technology status, Market status, Barrier analysis, Questionnaire survey

1. Introduction

Industrial heat pumps are recognized as a technology for decarbonizing industries due to their high efficiency and ability to be electrified with low-carbon electricity. According to the net-zero scenario of the International Energy Agency (IEA) by 2050 [1], industrial heat pumps will play an important role for low- (<100°C) and some medium- (100°C–400°C) temperature heat demand in light industries, accounting for approximately 30% of the total heat demand by 2050. To achieve this scenario, it is estimated that approximately 500 MW of industrial heat pumps must be installed each month over the next 30 years.

In Japan, the "Clean Energy Strategy," published in May 2022, prioritizes industrial heat pumps as a key decarbonization technology for heat demands below 200°C [2]. This strategy maps out the shift from our current energy system to one with a targeted 46% reduction in emissions by 2030 and an ultimate aim of reaching net-zero emissions by 2050. Industrial heat pumps are considered a practical solution due to their high efficiency and high technology readiness level compared to other alternatives.

The industrial heat pump technologies in Japan are regarded as unparalleled globally, and previous studies have reported on their technologies and application examples [3-5]. However, prior research has focused on specific and individual technologies. Conversely, this study takes a broader perspective, providing a comprehensive overview of the current status of industrial heat pumps in Japan. Moreover, it clarifies the barriers to its widespread adoption through a questionnaire survey and barrier analysis and proposes measures for future development.

* Corresponding author.
E-mail address: kaida@criepi.denken.or.jp.
** Present affiliation: TEPCO Energy Partner, Tokyo 104-0061, Japan.

2. Current Status

This chapter provides an overview of the technology and market status of industrial heat pumps in Japan.

2.1. Technology status

Various types of industrial heat pumps have been commercialized in Japan, including closed and open systems such as mechanical vapor recompression (MVR). The closed-system is further divided into two categories: the air-source type (Fig. 1) and the water-source type (Fig. 2).

The air-source heat pump typically utilizes ambient air as the heat source. Given the latitudinal expanse of Japan, from north to south, the ambient temperature varies across regions and seasons, with an average temperature of approximately 15°C. In the light of the cost-competitive coefficient of performance (COP), the maximum heat supply temperature is limited to approximately 90°C. Some products have a maximum heating capacity of 150 kW–200 kW, whereas many others have a heating capacity of less than 50 kW. It is assumed to be distributed throughout each heating process. This distribution arrangement presents two potential benefits. Firstly, it has the potential to reduce the heat dissipation loss from the long steam pipes of a steam boiler system. Typically, steam boilers have a thermal efficiency of ~ 90%. However, considering the heat dissipation loss from steam pipes, the end-use efficiency was only ~ 50% [6]. Secondly, this distribution arrangement also offers the possibility of utilizing heat dissipation from industrial processes. Many heating processes raise the internal temperature of a factory by dissipating heat, leading to decreased worker comfort or increased air conditioning demand. By placing an air-source heat pump near the heating process within the factory, it is possible to reduce air conditioning demand and improve the heat pump COP by increasing its heat source temperature.

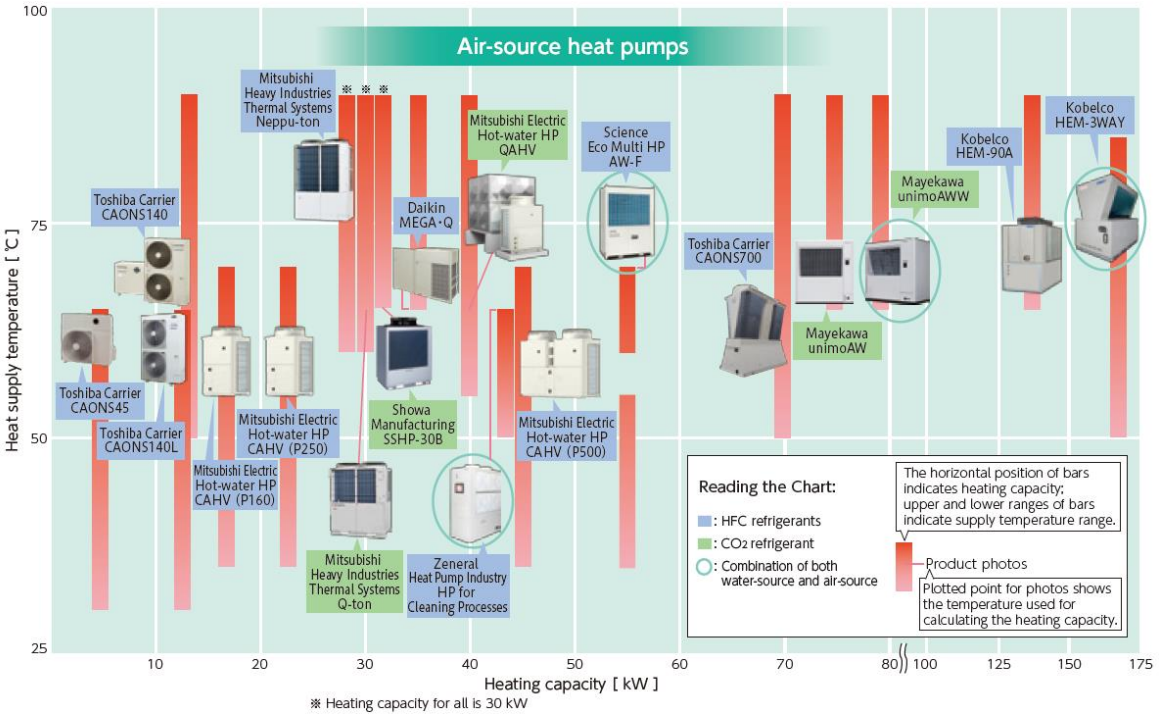


Fig. 1. Air-source industrial heat pumps available in the Japanese market [6].

Compared to the aforementioned air-source type heat pumps, water-source type heat pumps exhibit a wider range of heat supply temperature and heating capacity. They have a maximum supply temperature of 175°C, with a maximum heating capacity of ~ 600 kW. This type is primarily employed for waste heat recovery or simultaneous heating and cooling applications. To achieve economic viability for heat supply temperatures exceeding 100°C, relatively high-temperature waste heat is typically utilized as the heat source. At present in Japan, a COP of four is considered optimal for heat pump applications where heating is the sole objective. For combined heating and cooling applications, a total COP of five (with a heating COP of three) is recommended. The integration of a thermal storage tank is often required for simultaneous heating and cooling operations, as

heating and cooling demands may not occur concurrently. However, the addition of this tank can present barriers to the implementation of heat pumps, particularly in terms of capital cost and spatial constraint. Products circled in Fig. 1 are equipped with two evaporators and can switch between water and air heat sources. During periods where both heating and cooling are required, the water heat source is utilized. During periods where cooling is not necessary, the air heat source is employed.

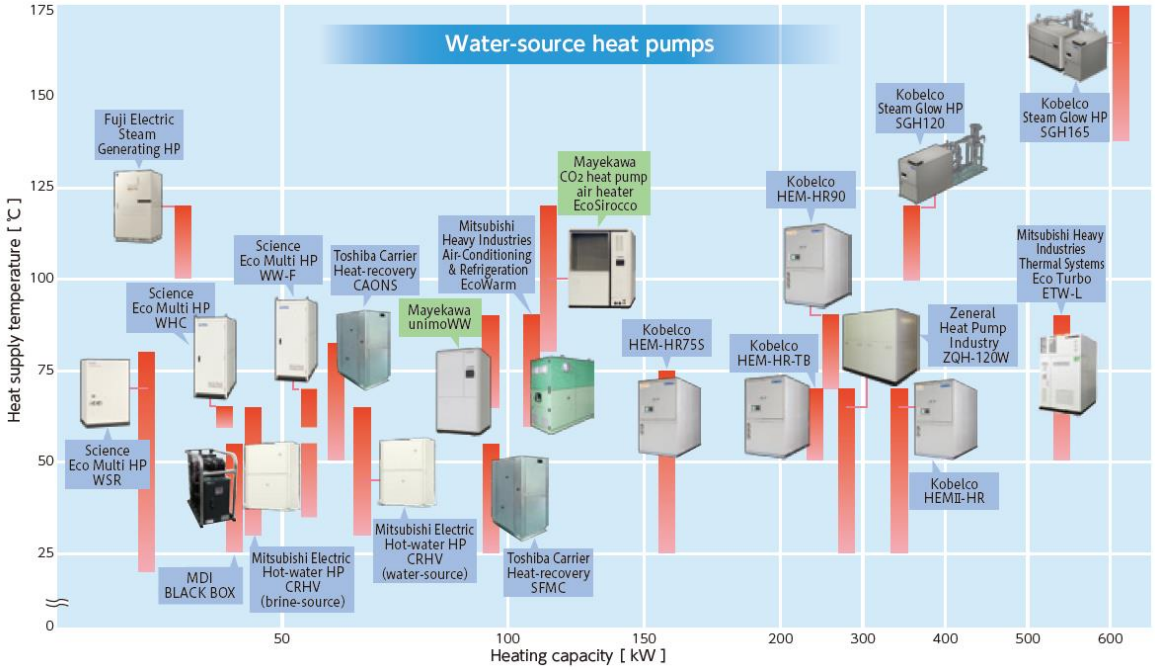


Fig. 2. Water-source industrial heat pumps available in the Japanese market [6].

While most of the heat pumps shown in Figures 1 and 2 have been commercially available for over a decade, they are still reliant on hydrofluorocarbon (HFC) refrigerants. Future technical challenges include lowering the global warming potential (GWP) of refrigerants and expanding the product lineup for high-temperature ranges. In national R&D projects led by New Energy and Industrial Technology Development Organization (NEDO), some manufacturers such as Fuji Electric, Mayekawa, and Mitsubishi Heavy Industries Thermal Systems are actively working on developing heat pumps with the capacity to supply heat at temperatures of 150°C or greater. Table 1 provides a comprehensive overview of this technology. The expansion of the product lineup for high-temperature range is expected in the near future.

Table 1. Under development high-temperature heat pumps in Japan

Manufacturer	Fuji Electric	Mayekawa	Mayekawa	Mitsubishi Heavy Industries Thermal Systems	Mitsubishi Heavy Industries Thermal Systems
Supply temperature	120–150°C (steam)	150°C (steam)	80°Cin / 180°Cout	70°Cin / 160°Cout	100°Cin / 200°Cout
Heat source temperature	60–90°C	80°C	80°C	80°C	95°C
Heating capacity	30 kW	260 kW	500 kW	600 kW	600 kW
Refrigerant	R1336mzz(Z)	R601	R600 or HFO	R1336mzz(Z)	HFE356mmZ
Compressor	Scroll	Screw	Centrifugal	Centrifugal	Centrifugal

2.2. Market status

The market status of industrial heat pumps in Japan is reflected in two statistics, as shown in Table 2. The first statistic is an annual publication by the Ministry of Environment (MOE) that tracks progress on the Plan for Global Warming Countermeasures [7], which was established by the Japanese Cabinet in May 2016. This report describes the cumulative heating capacity of installed industrial heat pumps and is based on surveys

conducted by the Ministry of Economy, Trade, and Industry (METI) and the Japan Refrigeration and Air Conditioning Industry Association (JRAIA). Although the data are limited to products from seven suppliers and do not represent the whole market, they are used as a policy indicator, and it is pertinent to monitor their progress.

The second statistic, published annually by the Japan Electro-Heat Center (JEHC) [8], is used as a basic material for the promotion of industrial heat pumps. This report covers a wider range of suppliers and their products, including MVR systems. In addition to the total heating capacity, the report also provides information on the capacity and number of units in the heat pump category, as well as information on the industries and processes in which heat pumps have been installed.

Table 2. Two statistics on the market status of industrial heat pumps in Japan [7, 8]

Publication	MOE (Ministry of Environment)	JEHC (Japan Electro-Heat Center)
Surveyed organization	METI (Ministry of Economy, Trade, and Industry) and JRAIA (Japan Refrigeration and Air Conditioning Industry Association)	JEHC and Fuji Keizai
Purpose	Policy indicator	Basic material for promotion
Coverage	7 suppliers	24 suppliers
Items	• Total capacity	• The capacity and number of units for each heat pump category • Installed industries and processes

Figure 3 shows the cumulative heating capacity of industrial heat pumps, as reported by the MOE. The Japanese government expects that the total capacity will reach 1,673 MW in FY2030. However, the actual installation in FY2020 was 168.4 MW, indicating a need to accelerate the installation.

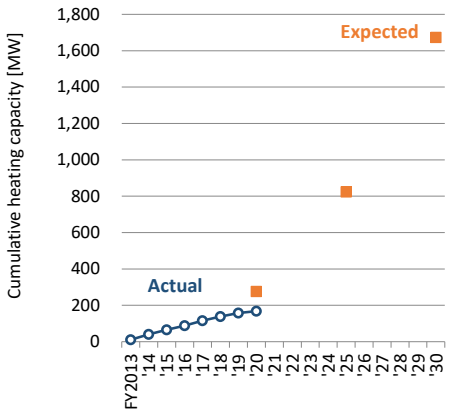


Fig. 3. The policy indicator and actual cumulative heating capacity of industrial heat pumps in Japan [7].

Figure 4 shows the entire installation of industrial heat pumps, as documented by the JEHC. As of FY2020, the cumulative capacity of closed-system heat pumps stands at 877 MW, while that of open-type heat pumps (MVRs) is 440 MW, totaling 1,317 MW. The actual installation is approximately 7.8 times greater than the data used in the government's policy indicator. The cumulative number of installed MVRs was 248, with a total heating capacity of 440 MW and an average unit capacity of 1.8 MW. Conversely, for air-source hot water heating heat pumps, although 981 units are installed, the average unit capacity is 24 kW. The demand for industrial heat pumps with a broad range of capacities remains evident.

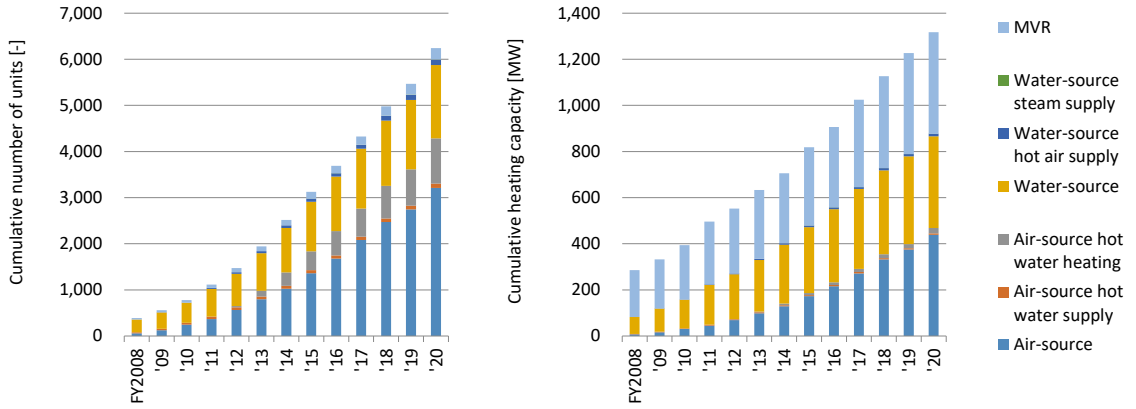


Fig. 4. The entire installations of industrial heat pumps in Japan [8].

For closed-system heat pumps, the breakdown of the installed industries is shown in Fig. 5. The machinery industry, including the automobile and electronics industries, demonstrates the highest installation density. This distribution pattern reflects the prevalent orientation of the Japanese industrial landscape towards machinery development.

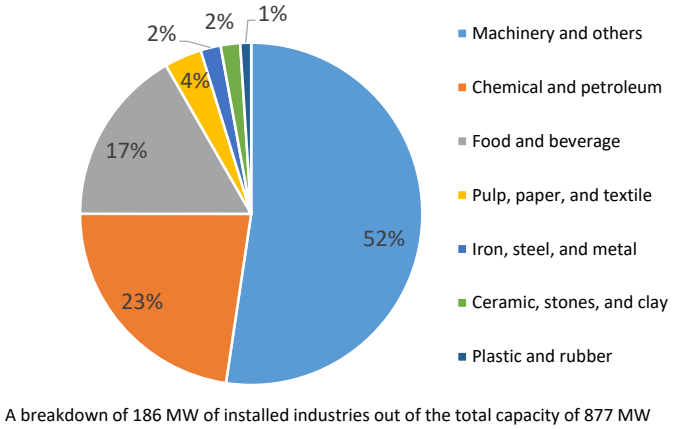


Fig. 5. Installed industries for closed-system industrial heat pumps in Japan [8].

2.3. Summary of the current status

In Japan, various types of industrial heat pumps with a wide range of specifications have been commercialized, largely due to the support provided by the government and electric utilities towards heat pump manufacturers in their developmental endeavors. Industrial heat pumps are considered to have achieved a high level of technological maturity. However, the rate of adoption has not progressed as anticipated. To foster widespread adoption, it is imperative to mitigate not only technological impediments, but also economic and site-specific obstacles.

3. Barrier Analysis

This chapter presents the results of a questionnaire survey of industries, clarifies why the installation of industrial heat pumps has not progressed, and discusses future measures.

3.1. Questionnaire survey

The authors conducted a questionnaire survey regarding the current status of decarbonization efforts in the manufacturing industry and the adoption of industrial electrification technologies, including heat pumps,

resistance heating, induction heating, dielectric heating, infrared heating and arc furnace. In this paper, we introduce extracts related to industrial heat pumps.

This survey was conducted by mail. The response period was from October 15 to November 5, 2021. This survey covered factories in which energy management was specified in the Energy Efficiency Act. Out of the 6,016 mailed questionnaires, there were 690 valid responses, yielding a response rate of 11.5%. This study provides answers to the following questions:

- Q1. Are you currently planning or making progress towards decarbonization in your factory?
- Q2. Are you currently planning or making progress towards electrification?
- Q3. What specific decarbonization efforts are you taking?
- Q4. Have you installed heat pumps in your factory yet?
- Q5. Are you satisfied with your heat pumps?
- Q6. Are you satisfied with your heating equipment?
- Q7. Do you plan to install heat pumps in your factory in the near future?
- Q8. What reasons are making you reluctant to install heat pumps?

Questions one to three are about the status of the efforts towards decarbonization. The survey responses from 671 companies, as depicted in Fig. 6, reveal that 29% of the companies have already initiated efforts towards decarbonization and 47% are in the planning stage. However, 25% of the companies have yet to begin planning for decarbonization. Companies with fewer employees were noted to be less active. The same trend was observed for electrification. Of the companies that have either initiated or are planning for decarbonization, 90% reported that improving energy efficiency was a specific action, as depicted in Fig. 7. Energy efficiency improvement is directly linked to energy cost reduction, which explains its high priority. On the other hand, only 17% of the companies have adopted electrification as a specific action, as it does not guarantee energy cost reduction at present.

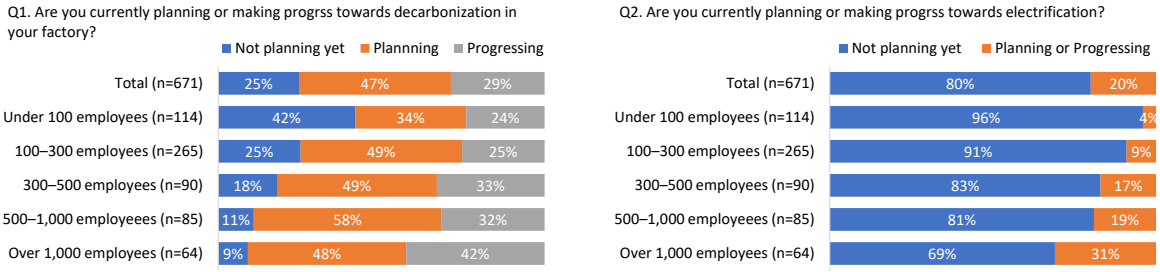


Fig. 6. Questionnaire for decarbonization and electrification.

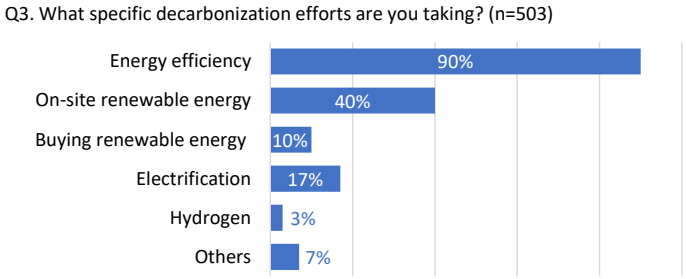


Fig. 7. Questionnaire for specific efforts toward decarbonization.

A heat pump is a technology that can simultaneously improve energy efficiency and electrification. Figure 8 shows the status of industrial heat pump installations, which encompasses both relatively low-temperature heat pumps, such as air conditioning in clean rooms, as well as high-temperature heat pumps. Of the 476 companies that responded, 38% have already installed heat pumps, while 48% acknowledge their importance but have yet to install them. Moreover, 13% of the companies do not recognize the value of heat pumps.

Of the 155 companies that have already installed heat pumps, 89% reported satisfaction with their performance. Figure 9 shows a comparison of satisfaction with heat pumps and combustion equipment, demonstrating that heat pumps are on par with combustion steam boilers and water heaters in terms of user

satisfaction. Despite any initial concerns that companies may have had prior to the installation of heat pumps, the survey results indicate a high degree of satisfaction post-installation.

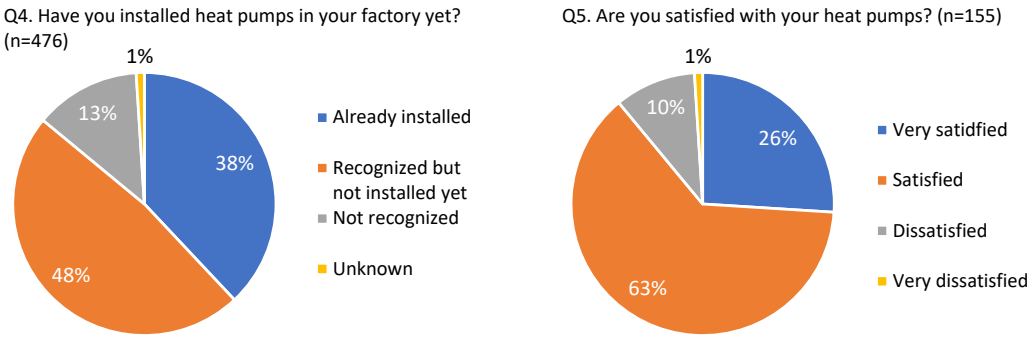


Fig. 8. Questionnaire for installation of and satisfaction with heat pumps.

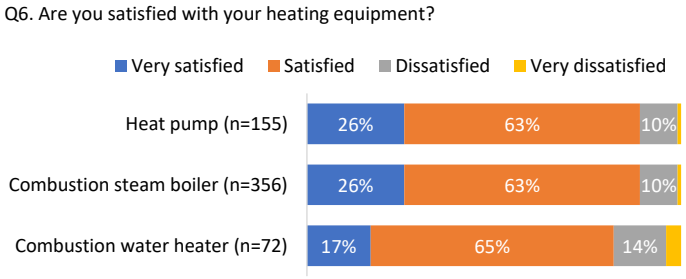


Fig. 9. Questionnaire for satisfaction with heat pumps compared to boilers.

Figure 10 shows the responses to the question regarding the future plans for the introduction of heat pumps. Of the 126 companies that have already partially installed heat pumps, 30% are planning new installations, and 32% are contemplating such installations. Conversely, only 4% of the companies that have not yet installed heat pumps are planning to do so. Therefore, it appears that prior experience with heat pump installations may facilitate further adoption.

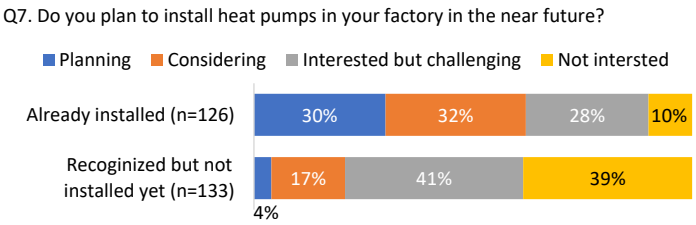


Fig. 10. Questionnaire for those having the intention to install heat pumps in the near future.

As shown in Fig. 10, many companies, 28% of those that have already partially installed and 41% of those that have recognized the importance of heat pumps but have not yet installed them, answered that they were interested in heat pumps but found the installation process challenging. Figure 11 sheds light on the reasons behind their reluctance to install heat pumps, with most of these companies not being concerned with the technological maturity, energy efficiency, or CO_2 reduction capabilities of heat pumps. Nonetheless, there are technological considerations other than heat pump equipment that may be impediments to the widespread introduction of heat pumps.

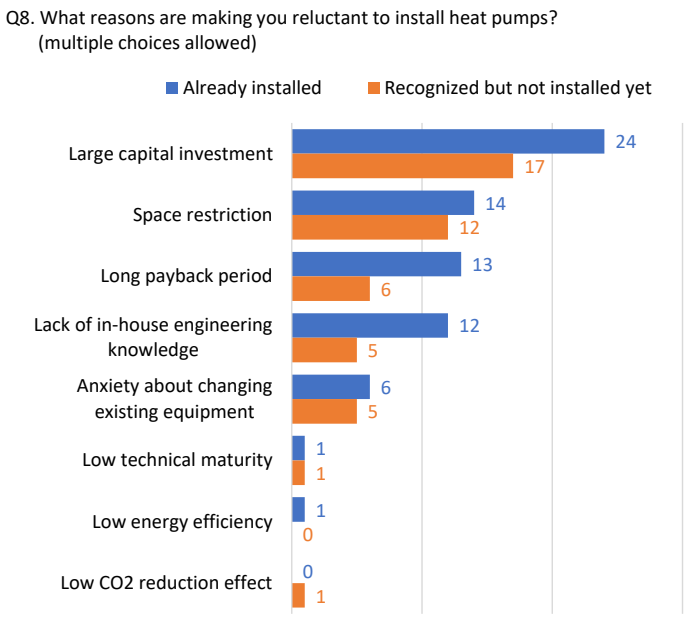


Fig. 11. Questionnaire showing the reasons for the reluctance to install heat pumps.

The major impediments to the widespread adoption of heat pump technology are primarily of an economic and financial nature. Companies are concerned about large capital investments and extended payback periods. Interestingly, some companies are only concerned about large capital investments; others have complaints about the payback period. These findings suggest that the introduction of more favorable financing arrangements could help to overcome these barriers.

Moreover, site-specific factors, such as the lack of installation space or in-house engineering expertise, were also identified as key challenges by some companies. Some existing factories may not have enough space to install heat pumps, especially when considering the recovery of waste heat from heating processes. In addition, some companies lack in-house engineering capabilities, thereby making it challenging for them to assess the benefits and feasibility of heat pump adoption.

3.2. Barriers and solutions

So far, the support for industrial heat pumps by the Japanese government has mainly focused on technological developments, such as the development of high-temperature heat pumps. These supports have successfully improved the technical potential and maturity of the industrial heat pumps. Nevertheless, it is imperative to continue to support the development of low-GWP refrigerants as well as related lubricants, oils, and compressors. However, for the widespread adoption of industrial heat pumps, it is crucial to extend support beyond heat pump equipment technology in the future.

Table 3 summarizes the main barriers and possible solutions for industrial heat pump applications. As for the solutions, while there may be a number of measures that private entities can undertake voluntarily, this table only considers the solutions that the government can implement.

The installation of a heat pump system requires a thorough analysis of the sources of heat and the areas in which it needs to be supplied. Therefore, it is necessary to establish a process integration methodology and to conduct research on technology deployment as well as technology development.

To provide support in terms of capital expenditure (CapEx), it would be effective to focus on small and medium-sized enterprises (SMEs) and new factories. Additionally, in terms of operating expenses (OpEx), rebalancing the renewable energy levy can be a fair and effective measure.

Table 3. Main barriers and possible solutions for widespread adoptions of industrial heat pumps in Japan

Barrier	Current status	Possible Solution (by the government)
High capital investment	• Companies with fewer employees are challenged to initiate efforts toward decarbonization.	• It is necessary to support capital investment, mainly targeting small and medium-sized enterprises (SMEs).
Long payback period	• Electricity price is relatively expensive compared to fuel prices. One of the factors is that renewable energy levy is imposed only on electricity.	• Rebalancing the renewable energy levy can be a fair and effective measure.
Space restriction	• It is difficult to address the lack of installation space in existing factories.	• It would be useful to take measures to encourage the introduction of industrial heat pumps in new factories.
Lack of in-house engineering knowledge	• Many companies lack the necessary knowledge and skills to integrate heat pumps into their processes or utilities.	• It is necessary to strengthen the demonstration and deployment projects for the purpose of establishing process integration methodology and to cultivate process integrators.

4. Conclusions

The integration of industrial heat pumps is deemed crucial for decarbonization. Despite the advancements and commercialization of various types of industrial heat pumps in Japan, their widespread adoption has not materialized as anticipated.

To gain a deeper understanding of the barriers hindering the implementation of industrial heat pumps, a questionnaire survey was conducted. The results highlight four main barriers: high capital investment, a long payback period, spatial restrictions, and a lack of in-house engineering expertise. In addition, we listed the possible solutions that can be provided by the government for each barrier.

These barriers are believed to be common worldwide, and it is our aim to contribute to overcoming these obstacles by sharing our findings and insights with other countries and promoting the utilization of industrial heat pumps globally.

References

[1] IEA (Interntional Energy Agency), Net Zero by 2050: A roadmap for the global energy sector, May, 2021.
[2] METI (Ministry of Economy, Trade and Insutry), Clean Energy Strategy, Interim report, May, 2022.
[3] Watanabe C., Uchiyama Y., Hirano S., Hikawa T., Pioneering industrial heat pump technology in Japan, 11th IEA Heat Pump Conference, Montreal, Canada, May, 2014.
[4] Watanabe C., Uchiyama Y., Hirano S., Okumura H.,Industrial heat pumps and their application examples in Japan, 12th IEA Heat Pump Conference, Rotterdam, the Netherlands, May, 2017.
[5] Kaida T., Industrial heat pump applications in Japan, Chillventa Congress, Nuremberg, Germany, October, 2018.
[6] JEHC (Japan Electro-Heat Center), Industrial Heat Pump Utilization Guide, March, 2021.
[7] MOE (Ministry of Environment), Progress report of the plan for global warming countermeasures, June, 2021. [in Japanese] https://www.env.go.jp/content/000040099.pdf
[8] JEHC (Japan Electro-Heat Center), Investigation report of installed industrial heat pumps, October, 2021. [in Japanese] https://sangyo-hp.jeh-center.org/asset/00032/library/IHP_hokoku_2021.10.pdf

14th IEA Heat Pump Conference
15-18 May 2023, Chicago, Illinois

An energetical, exergetical and experimental analysis of an absorption-heat exchanger used as transfer sub-station in an already existing district heating grid

Gerald Zotter[a*], Damian Eberhöfer[a], Carina Seidnitzer-Gallien[a]

[a]AEE INTEC; Feldgasse 19, Gleisdorf 82002, Austria
[b]Second affiliation, Address, City and Postcode, Country

Abstract

The application of an absorption-heat exchangers as transfer sub-station in a district heating grid can use the temperature difference between the primary (up to145 °C) and secondary supply temperature (ca. 70 °C) of the circuits for subcooling the primary return temperature below the secondary one. This leads to the advantages of increased heat capacity within an existing grid up to 30% at unchanged flow and temperature inlet conditions on the one hand-side, and on the other hand-side, more renewables can be more easily integrated. To proof the required temperature gap between the two supply temperatures to ensure a subcooling of the primary return flow temperature below the secondary one has been experimentally investigated by a small pilot-scaled absorption-heat exchangers (about 10 kW max) at the laboratory of AEE INTEC at different inlet conditions. This analysis has shown that a subcooling up to 20.7 K is achievable between the return temperatures with an AHX at highly primary supply and low secondary return temperatures as long the mass flow of the secondary grid gets increased accordingly to the heat capacity increase.

© HPC2023.
Selection and/or peer-review under the responsibility of the organizers of the 14th IEA Heat Pump Conference 2023.

Keywords: heat exchanger effectivness, transfer sub-station, exergy analysis, pinch point, renewables

1. Introduction

In Austria, more than about a quarter of the entire population and numerous companies are currently supplied of thermal energy by means of district heating (DH) [1], with a forecasted growing rate of 0.8%/anno in average for the next 5 years. This increasing demand is currently being covered by investments in network infrastructure and supply units. At the same time, however, a complete phase out of Gas (about 28% [1]) is limited by the fact that a considerable proportion of renewables and waste heat cannot be integrated in Austrians existing DH-grids based on not fitting temperature levels, which means that the temperature levels, particular in the so-called primary circuit is still too high. A further advantage of a reduction of the used supply temperature in the DH-Grid is the reduction of the distribution heat losses.

But for already existing heating networks - based on already installed pipelines, which means that the diameters of the pipes are also fixed - the maximum possible mass flow ($\dot{m}$) is limited and thus also the maximum possible heat capacity ($\dot{Q}$) of the network is limited, according to Eq. (1). The limitation of $\dot{m}$ in existing pipes is based on cavitation avoidance reasons, where the flow velocity cannot be increased so that the local static pressure in the pipe does not fall below that of the saturation pressure. So, an increase of the heat capacity could be only achieved, if bigger pipes would be installed. But this creates high investment cost and long periods to refurbish the entire grid. To overcome this situation, the (primary) return temperature ($t_{R,Pr}$) has to be lowered by a higher value than the (primary) supply temperature ($t_{S,Pr}$), in order to achieve a bigger temperature-spread and thus ensure an increase of the heat capacity of the existing DH-grid, according to. With a sufficiently high reduction of the return temperature, the supply temperature could also be reduced

* Gerald Zotter. Tel.: +43 650 891 819 5
E-mail address: g.zotter@aee.at.

at a high value, which leads to a reduction of losses and significantly increases the possibility for the integration of renewables, such as deep geothermal or industrial waste heat (compare Figure 1 to Figure 2).

$$\dot{Q} = \dot{m} * c_p * (t_{S,Pr} - t_{R,Pr}) \quad (1)$$

Technologies such as electrically driven heat pumps and thermally absorption heat pumps (AHPs) are widely used to improve the overall efficiency of different energy supply systems in different applications [3-7]. The possibilities to use thermally-driven AHP in district heating and/or cooling grids are wide and cover a broad spectrum for increasing the energy efficiency. According to Hu et. al (2020) [8] the absorption heat exchanger (AHX) is one of the most commonly used technologies to improve performance of district heating grids. In comparison to a conventional heat exchanger (HX) an AHX can use the exergetic potential (second law of thermodynamics) based on the temperature difference between the supply temperatures ($\Delta t_{S,Pr/Se}$) (see Eq. 2) to sub-cool $t_{R,Pr}$ below the return temperature of the secondary circuit ($t_{R,SE}$), which is the inlet temperature of the on the secondary side of the TSS. This subcooling ($\Delta T_{Sub-R,Pr/Se}$, according to Eq.3) allows the improvement of the DH-grid, as already mentioned above, and the reason to use an AHX. A detailed explanation of the working principal of an AHX and a comparison to a HX are given in chapter **Error! Reference source not found.**.

$$\Delta T_{S,Pr/Se} = (t_{S,Pr} - t_{S,Se}) \quad (2)$$

$$\Delta T_{Sub-R,Pr/Se} = (t_{R,Se} - t_{R,PR}) \quad (3)$$

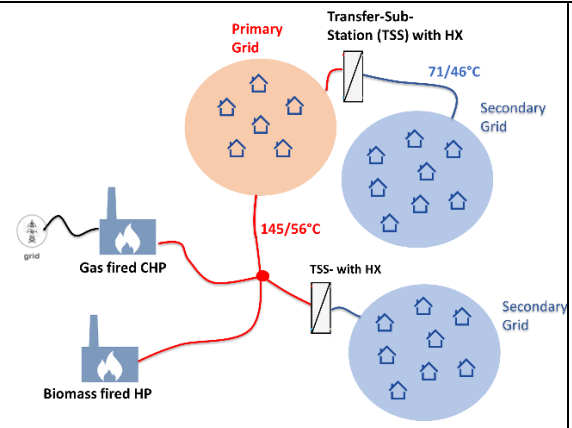


Figure 1: Schematic drawing of an old district heating grid supplied by Gas fired combined heat and power plants (CHP) and biomass fired with a transfer-substation (TSS) with conventional heat exchangers (HX) between primary and secondary grid with different temperature levels (145/56°C at primary circuit and 71/46°C at secondary grid)

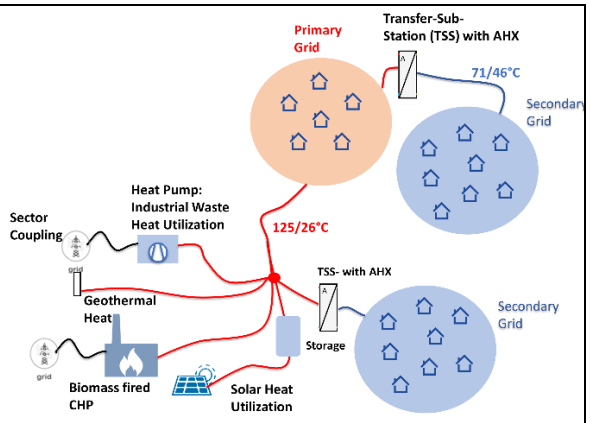


Figure 2: Schematic drawing of the optimized future district heating grid supplied only by renewables (geothermal, industrial waste & solar thermal heat, etc.), where the primary circuit is operated at lower temperature levels of compared to the schematic in Figure 1 by using absorption heat exchanger (AHX) instead of an HX as transfer-substation (TSS) (125/56°C at primary circuit and 71/46°C at secondary grid)

So, using an AHX for transfer-subs-stations (TSS) instead of conventional heat exchangers (HX) are key for lowering the temperature levels of already existing DH-grids. Although, AHXs have a high potential for return flow temperature reduction of heating grids [9-10], those applications are still very rare in Austria. To overcome that situation, within this work a small pilot-scaled AHX (of about 10 kW, see Figure 10) has been experimentally investigated in detail at different boundary conditions at the laboratory of AEE INTEC.

2. Optimized transfer-sub-station

When a DH-grid is separated in circuits with different temperature levels (primary and secondary), the circuits are connected via TSS using conventional HX (see Figure 3). Generally, the temperature levels in the DH-grid depend on the ambient temperature. This is based on the fact that grid is operated by a weather-compensating control for the supply temperature, where minima supply temperatures have to be ensured

depending on a floating set value considering the weather conditions. For colder ambient conditions the supply temperature has to be higher than for warmer days. For the design point of about -10°C ambient temperature the supply/return temperature in the primary grid is about 145°C/58°C, where else on the secondary grid it is about 70°C/45°C.

2.1. Using heat exchanger as TSS

As mentioned in chapter 1, from an energetical point of view the primary return temperature should be as low as possible. The primary return temperature depends at that case on the arrangement of the HX (parallel- or counter-flow) and the so-called pinch-point temperature difference (Δt_{PP}). Δt_{PP} is influenced by the heat transmission coefficient (U) and the heat transfer area of the HX (A). This means for example that an increase of A of about 40% (see Figure 3and Figure 5) could lower Δt_{PP} to the half and this raises $\dot{Q}$ of about 7% at constant inlet conditions, as shown by a comparison of the- two t vs $\dot{Q}$ - diagram in Figure 4 and Figure 6.

Even if, the heat exchanger efficiency (η, see Eg. 5) is mostly 100% as long as the heat losses ($\dot{Q}_{loss}$) are neglectable, but a change of Δt_{PP} has an influence on the heat exchanger effectiveness (ϵ, see Eq. 4) as well as different inlet conditions concerning $\dot{m}$, c_p and temperature. Based on the conditions shown in Figure 4 the HX has an ϵ of 0.9, where else the HX with the increased A has an effectiveness of 0.95.

$$\epsilon = \frac{actual\ heat\ transfer}{maximal\ possible\ heat\ transfer} = \frac{\dot{m}_{Pr} * c_{p,PR} * (t_{S,Pr} - t_{R,Pr})}{|\dot{m} * c_p|_{min} * (t_{S,Pr} - t_{R,se})} \quad (4)$$

$$\eta = \frac{\dot{Q}_{Pr}\,(-\dot{Q}_{loss})}{\dot{Q}_{Se}} \quad (5)$$

2.2. Using absorption heat exchanger as TSS

A (single-stage) AHP is driven by heat and consists of an evaporator, where heat gets absorbed from a cold heat source (cold water). The vaporized refrigerant flow to the absorber, where the solution fluid absorbs the refrigerant by rejecting heat to a mid-temperate heat sink (cooling water). The (refrigerant) rich solution gets pumped over the solution HX (where sensible heat between the hotter poor solution and colder rich solution is transferred) into the generator. The generator gets driven by heat from the hot heat source (hot water) to desorb the refrigerant from the solution. The poor solution flows via a throttle and the solution HX back to the absorber, where else the refrigerant flows to the condenser. The condenser rejects latent heat to the mid-temperate heat source to fully condensate the refrigerant. The condensate gets expanded via another throttle to the evaporator. Evaporator and absorber operate (if pressure losses could be neglected) at the same low-pressure level. Condenser and generator operate (if pressure losses could be neglected) at the same high-pressure level.

The AHX is a combination of an absorption chiller with an HX, as shown Figure 7, which is not used as a chiller or heat pump, but as an exergetically optimized HX. As though, the hot water- (external heat transfer fluid-circuit) is short-circuited with the cold water-circuit (external heat transfer fluid-circuit) of the absorption chiller via the heat exchanger; this side represents the primary circuit of the AHX. For the secondary side, the cooling water (external heat transfer fluid-circuit) gets partitioned between the HX and the absorber chiller via the distribution valve (D-valve).

2.3. Analysis of TSS based on the second law of thermodynamics

The AHX is using the exergetical potential (ex_{pot}) of the otherwise unused big temperature gab between the two supply temperatures ($\Delta t_{S,Pr/Se}$) to drive an AHP for subcooling $t_{R,Pr}$ below $t_{R,Se}$ in the evaporator of the AHP. At the given boundary conditions, according to Figure 6, the HX offers a theoretical ex_{pot} of ca. 15% (T_a = 293.15 K) which could be used to operate an AHX (according to Eq. 6), but would be irreversible wasted in a conventional HX. That potential is shrinking to zero when $\Delta t_{S,Pr/Se}$ is decreasing to zero: However, this is a theoretical potential not covering the temperature glides. pressure losses, irreversibility in each single heat exchanger etc. is not covered. However, as shown in Figure 8, which is based on an 0D simulation model in EES [13] a subcooling ($\Delta t_{Sub-R,Pr/Se}$) of 21 K can be achieved by a first principal model, with Δt_{PP} > 3 K in every single heat exchanger of the AHX. According to that, see Figure 8, the heat capacity

could be increased of about 30%, in which the secondary mass flow has to be increased also of the same 30% that the surplus of $\dot{Q}$ could be transferred without raising $t_{S,Se}$. This is required to avoid that the $\mathrm{ex_{pot}}$ would not be lowered, which is required to drive the AHX.

Furthermore, a detailed exergy analysis - based on the Gouy-Stodola-Equation, considering the different entropy changes (see Eq. 7) on primary ($\dot{m}_{Pr} * \Delta s_{Ps}$) and secondary ($\dot{m}_{Se} * \Delta s_{Se}$) side - shows irreversible exergy losses within the HX and AHX. This analysis shows that up to 30% of the irreversibility can be reduced using an AHX compared to an HX (neglecting the pumps and each single pinch point temperature difference from generator to evaporator). Within this exergetical improvement the AHX could achieve an ϵ of 1.15. This is only possible due to counter-clockwise rotated cycle is used within the AHX and the driving source comes from the otherwise unused exergetical potential, as already mentioned. However, the exergetical efficiency of the AHX is of course still below 1 and amounts to 0.93 for the boundary conditions listed in table 1.

$$ex_{pot} = \frac{\dot{Ex}}{\dot{Q}} = T_a \frac{(T_{S,Pr} - T_{S,Se})}{(T_{S,Pr} * T_{S,Se})} \tag{6}$$

$$-\frac{dEx_{Irr}}{d\tau} = T_a * [\sum \dot{m}_{Se} * s_{Se} - \sum \dot{m}_{Pr} * s_{Pr}] \tag{7}$$

$$\eta_{ex} = \frac{\dot{Ex}_{in} - \dot{Ex}_{irr}}{\dot{Q}\dot{Ex}_{in}} \tag{8}$$

Table 1. A comparison of the boundaries and efficiencies/effectiveness for HX and AHX

Transfer-sub-station using	$t_{S,Pr}$ (°C)	$t_{R,Pr}$ (°C)	$\dot{m}_{Pr}$ (kg/s)	$t_{S,SE}$ (°C)	$t_{R,Se}$ (°C)	$\dot{m}_{Se}$ (kg/s)	$\dot{Q}$ (MW)	ϵ -	η_{ex} -
HX	145	52	16.1	71	46	62.5	6.3	0.95	0.91
AHX	145	25	16.1	71	46	77.4	8.1	1.15	0.93

According to Figure 8, the exergetical benefit of an AHX is that the high temperature level of the supply-side of the primary circuit is used to drive the generator, where that high temperature level is required. All pinch point temperature in the AHX is positive. The directly sub-cooling ($\Delta T_{Sub-R,Pr/Se}$) happens in the evaporator of the AHX. To count the energetical potential of an AHX not only $\Delta T_{Sub-R,Pr/Se}$ should be considered, but also the pinch point temperature difference which is required for a conventional HX. This means that the entire temperature difference between the primary return temperature of a HX and an AHX is in that particular case 27 K (compare Figure 5to Figure 7).

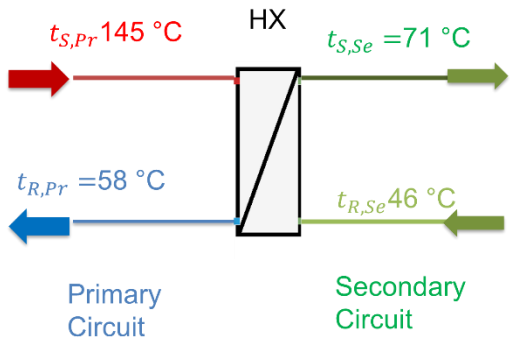


Figure 3: Principal picture of a conventional heat exchanger (HX) used as transfer sub-station (TSS) in a district heating grid (DH) including temperature levels of external heat transfer fluids of primary and secondary site

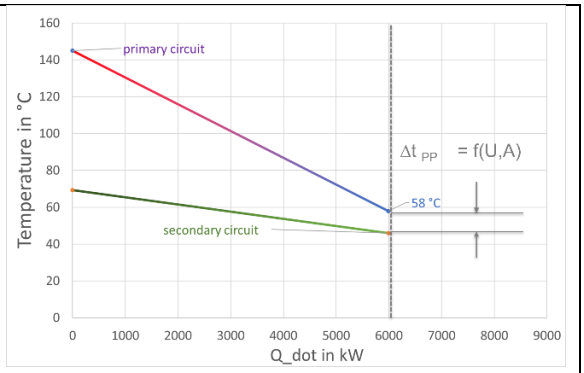


Figure 4: Pinch point temperature difference (Δt_{PP}) in the temperature vs. heat capacity – diagram (t vs. $\dot{Q}$ – diagram) of a transfer sub-station

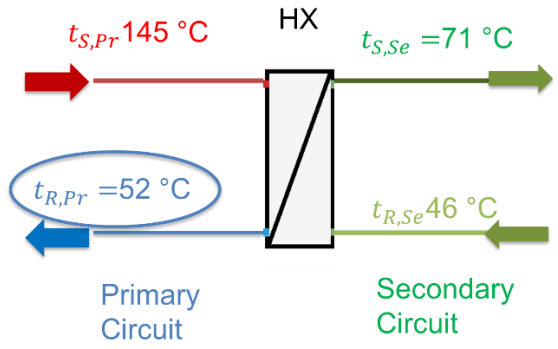


Figure 5: Principal picture of a conventional HX used as TSS in a DH-grid including temperature levels of external heat transfer fluids of primary and secondary site with 40% bigger heat transfer area (A) compared to Figure 3

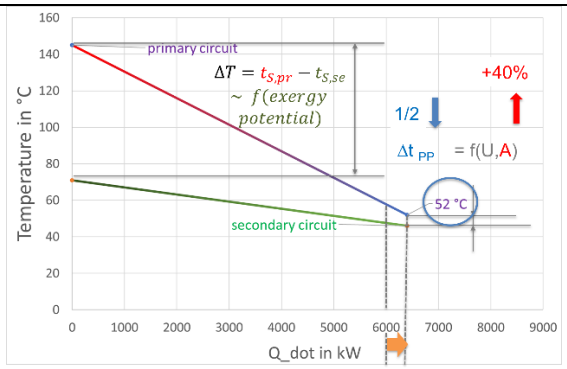


Figure 6: t vs. $\dot{Q}$ – diagram of a 40% bigger HX compared to Figure 5 lowering Δt_{PP} to the half and increasing $\dot{Q}$ of about 7%; furthermore, also the big temperature difference between the supply temperature of the primary circuit

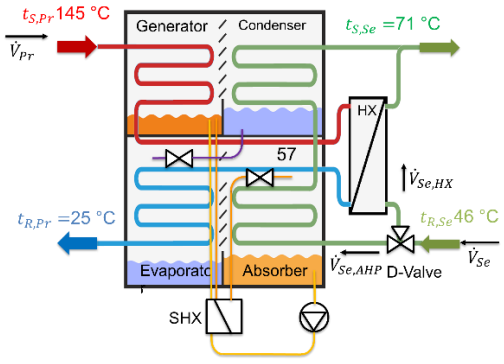


Figure 7: Principal picture of an absorption heat exchanger (AHX) consisting of an AHP and a HX and a distribution valve (D-valve)

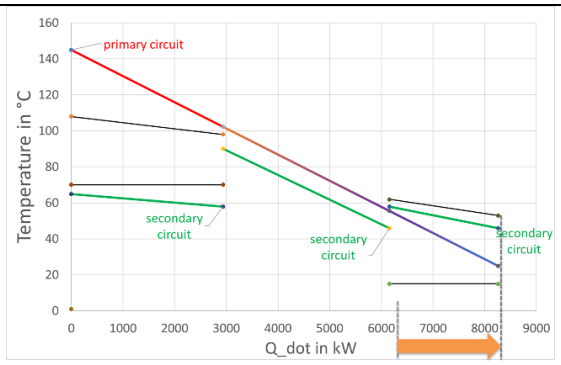


Figure 8: t vs. $\dot{Q}$ – diagram of all heat exchangers of an AHX and an increased $\dot{Q}$ of about 30%; furthermore,

From a thermodynamical point of view, an AHX can be seen as a combination of a Rankine cycle and compression chiller, as shown in Figure 9. The supply side of the primary circuit is used as heat sink of the Rankine cycle and the supply side of the secondary circuit is used as its heat sink. The electrical power produced by a Rankine cycle is used to drive a Perkins/Evans cycle, where the return-side of the secondary circuit is used as heat sink and the return-side of the primary circuit is used as heat source. So, an AHX is a combination of a HX and a clockwise- and counterclockwise rotating thermodynamical cycles, where exergy fluxes are used regarding its temperature levels.

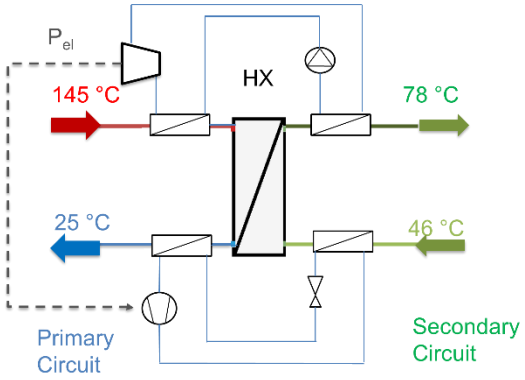


Figure 9: Principal drawing of a combination of a Rankine Cycle and a Perkin/Evans Cycle to sub-cool the return temperature below the one of the

3. Test bench of the pilot-scaled AHX

Within this work a pilot-scaled AHX was designed and set up as a combination of an AHP (absorption chiller: single-stage chiller with solution HX, available on the market with a nominal cooling capacity of 15 kW, see Figure 9 in orange) and a plate-HX (see Figure 9 in green, with A of 2.46 m²), in a counterflow arrangement. The working pair used in the AHP was water/Lithium-Bromide (H_2O-LiBr). As shown in Figure 10, the AHX been equipped with the required measurement equipment and integrated into the infrastructure of the laboratory of the AEE INTEC (blue-marked) consists of a heat-sink/-source system, and analyzed at different operating conditions. For that, the primary inlet ("supply") and the secondary inlet ("return") temperature and as well as volume flow ratio between primary and secondary site has been varied, as well as the secondary distribution ratio (see table 2). All energy fluxes have been measured at internal AHX cycle as well as on the external primary and secondary circuits. After calibration of the measurement equipment the uncertainties of the temperature sensors amount only ± 0.2 K, of the volume flow meter only about ± 0.5% of the measured value.

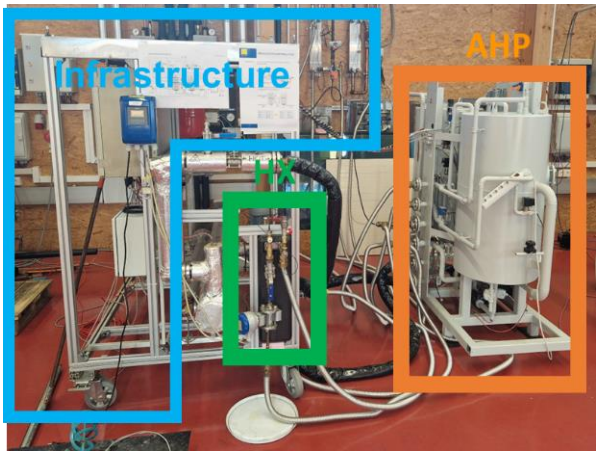


Figure 10: Picture of the AHX test bench at AEE INTEC, consist of an AHP (in orange) and a HX (in green) integrated in the infrastructure of the laboratory

At that point it has to be mentioned, that regarding safety reasons thermo-oil was used as heat transfer fluid for the primary side instead of pressurized hot water (up to 20 bar, avoiding cavitation for 145 °C). This had in influence on lowering the possible heat capacity of the tested AHX down to max. 10 kW. Particularly, the differences between heat transfer coefficients (HTC) and specific heat capacities (c_{ps}) of the two fluids must be taken into account. In addition, the energy balance was drawn for stationary points and the corresponding heat losses were analyzed, see. The convective and radiative heat losses were evident (of about 10%) due to the lack of thermal insulation, but could be balanced out for the analysis.

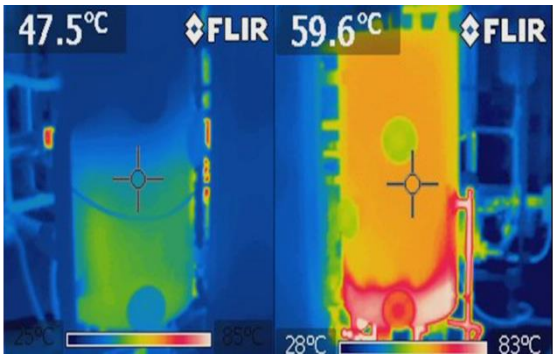


Figure 11: Infrared photograph of the evaporator-absorber reactor (left) and the condenser-generator reactor (right); to determine the heat losses [14]

However, to simplify the data collection parameter for the ratios of volume flows, as mentioned above, has been determined. So, the ration of volume flows between primary and

secondary circuit is called general volume flow ratio (GVR, see Eq. 9)- and the ratio between the secondary volume flow through the HX and the AHP is called secondary volume flow ratio (SVR, see Eq.9)

$$GVR = \frac{\dot{V}_{Se}}{\dot{V}_{Pr}} \tag{9}$$

$$SVR = \frac{\dot{V}_{Se,HX}}{\dot{V}_{Se,AHX}} \tag{9}$$

Table 2. Parameter (and values) for measurement matrix of AHX

Name of parameter	Values	Measurement uncertainties
$t_{S,Pr}$ in °C	145, 125, 105	± 0.2 K
$t_{R,Se}$ in °C	38, 44, 50, 56	± 0.2 K
$\dot{V}_{Pr}$ in m³/h	250	± 0.5% of the measured value
GVR in -	3, 4.5, 6	$\pm\sqrt{\left(\left({}_{\pm 0.5\%MVSE}/_{\pm 0.5\%MVPR}\right)^2+\left({}_{\pm 0.5\%MVPR^4}/_{\pm 0.5\%MVPR^4}\right)\right)}$
SVR in -	2, 0.5, 0.2	$\pm\sqrt{\left(\left({}_{\pm 0.5\%MVHX}/_{\pm 0.5\%MVAHP}\right)^2+\left({}_{\pm 0.5\%MVAHP^2}/_{\pm 0.5\%MVHX^2}\right)\right)}$

4. The measurement results

Within this experimental analysis the maximal possible subcooling $(t_{R,Se} - t_{R,PR})$ within the pilot-scaled AHX has been investigated in detail, according given boundaries in table 2. Covering all the different variants by changing that parameter as shown in table 2, the measurement matrix consists of 36 different measurement points. Each individual measurement point was recorded dynamically and when the external temperatures and volume flows as well as the internal (high and low) pressure levels settled to a stable asymptote, the steady state was evaluated. In those experimental investigations, the transient behavior of the AHX was also determined, but this is not the subject of this paper.

Figure 12 shows the subcooling of the primary return temperature below the secondary one $(t_{R,Se} - t_{R,PR})$ depending on primary supply temperature at different $t_{R,Se}$ and constant $\dot{V}_{Pr}$ of 250 m³/h; GVR of 4.5 and a SVR of 0.2. The highest $(t_{R,Se} - t_{R,PR})$ can achieved at high supply temperatures on the primary circuit and low return temperatures of the secondary circuit. However, high $(t_{R,Se} - t_{R,PR})$ has been measured also at higher $t_{R,Se}$ up to 56 °C, as long as $t_{S,Pr}$ is high. Furthermore, even at a low $t_{S,Pr}$ of 105 °C a sub-cooling of about 12 K could be measured as long as $t_{R,Se}$ is not warmer than 44 °C. No sub-cooling could be achieved at low $t_{S,Pr}$ and high $t_{R,Se}$.

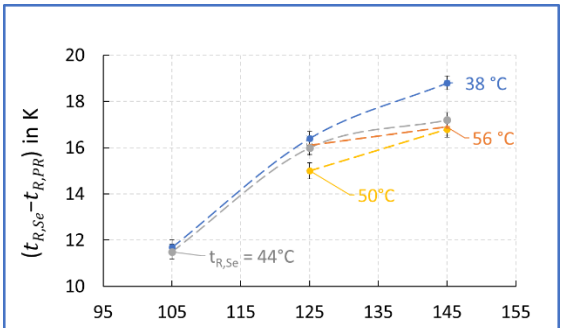


Figure 12: Subcooling of the primary return temperature below the secondary one $(t_{R,Se} - t_{R,PR})$ depending on primary supply temperature at different $t_{R,Se}$ and constant $\dot{V}_{Pr} = 250$ m³/sh; GVR =4.5, SVR = 0.2

Figure 14 shows the subcooling of the primary return temperature below the secondary one $(t_{R,Se} - t_{R,PR})$ depending on GVR at different SVR and constant $\dot{V}_{Pr}$ of 250 m³/h; $t_{R,Se}$ of 44°C. For higher sub-cooling the ratio between volume flow rate of the secondary circuit to the one of the primary circuits has to be high. The same is valid for the SVR, as shown in the Figure 13. Figure 13 shows the sub-cooling of the primary return temperature below the secondary one $(t_{R,Se} - t_{R,PR})$depending on SVR at different $t_{R,Se}$ and constant $\dot{V}_{Pr}$ of 250 m³/h and GVR of 6. As more volume flow rate passes the AHP as higher is the sub-cooling. There is a limitation based on the required pump power and on the heat which has to be transferred of the HX to cool down the primary circuit coming from the generator and before entering the evaporator. Furthermore, within this investigation room for improvements has been detected regarding thermal insulation of the AHP, the internal control of the solution pump and the throttles, as well as on changes by the cycle of the AHP itself, like connecting the absorber and the condenser not in a serial but in a parallel arrangement.

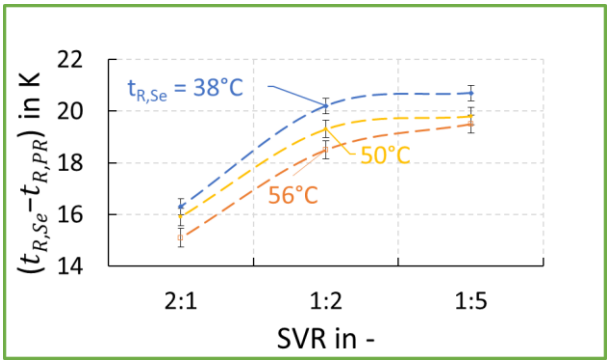


Figure 13: Subcooling of the primary return temperature below the secondary one $(t_{R,Se} - t_{R,PR})$depending on SVR at different $t_{R,Se}$ and constant $\dot{V}_{Pr} = 250$ m³/h and GVR of 6

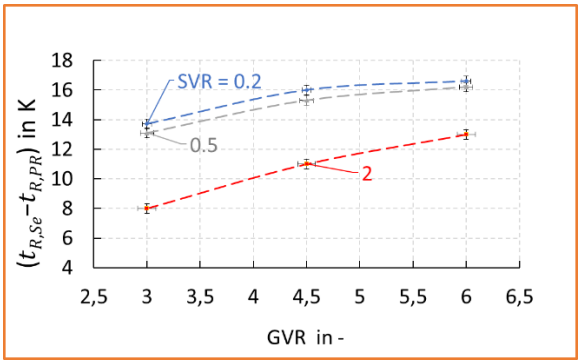


Figure 14: Subcooling of the primary return temperature below the secondary one $(t_{R,Se} - t_{R,PR})$ depending on GVR at different SVRs and constant $\dot{V}_{Pr} = 250$ m³/h; $t_{R,Se}$ = 44°C

5. Conclusions

The application of an AHX as a TSS in a DH-grid can use the temperature difference between the primary (up to145 °C) and secondary supply temperature (ca. 70 °C) of the circuits for subcooling the primary return temperature below the secondary one. This leads to the advantages of increased heat capacity within an existing grid up to 30% at unchanged flow and temperature inlet conditions on the one hand-side, and on the other hand-side, more renewables can be more easily integrated. As shown in this work, this is based on the fact that the exergy losses could be reduced by about 30% compared to a conventional HX and the heat capacity could be extended of about 30%. Furthermore, an AHX offers that the heat exchanger effectiveness could be increased to 115%, but the exergetical efficiency is of course still below 1 (0.94 at the same boundary conditions). However, this exergetical potential for optimization depends on the difference between the supply temperatures of the primary and secondary circuit. If the supply temperature of the primary circuit is close to the one of the secondary side no driving potential for subcooling the return temperature is available.

Considering that, within this work an experimental investigation of an AHX was covered and described in order to analyze its performance as a TSS being considered in DH-grids. The main focus was on the subcooling performance of the return temperature of primary circuit influenced by the difference between the supply temperatures of the primary and secondary circuits. For this research, an AHX at pilot-scale was designed, consist on a H_2O-LiBr - absorption chiller, available on the market (nominal cooling capacity of 15 kW) and the plate heat exchanger with a heat transfer Aera of (2.46 m²) and integrated in the test facility of the laboratory of AEE INTEC. The test rig was driven by various temperature and mass flow inlet parameter variations in order to analyze the optimal operating points, the limitation for subcooling based on the minimal required difference between the supply temperature on steady-state points as well as to investigate the transient behavior of the AHX and explore a fit ting control strategy regarding the mass flow distribution. Energy balancing was also carried out to determine the heat losses or inputs from the ambience.

The results of the experimental measurement series show that a high primary supply temperature, a low secondary return temperature and a high secondary-to-primary mass flow rate are required for a high subcooling performance. The partitioning of the secondary mass flow between the absorption chiller and the heat exchanger also had an effective effect, with a high mass flow through the chiller increasing subcooling. At $t_{S,Pr}$ of 145 °C and $t_{R,Se}$ of 38 °C, a SVR of 0.2 and GVR of 6 the highest subcooling with 20.7K could be achieved within the pilot scaled AHX. But even under suboptimal conditions, like low primary supply temperatures of 105 °C the AHX subcooled the primary return temperature below the secondary of 12.4K, but for that a low return temperature on the secondary side below 44 °C is required. For $t_{R,Se}$ higher than 50 °C a minimal $t_{S,Pr}$ of 125 °C is required.

Furthermore, the measurements have underlined the theoretical considerations about the exergetical driving potential that can be used by the AHX. Namely a big difference between the supply temperatures between primary and secondary circuit is required to sub-cool the return temperature at its most. This means that, for a constant mass flow of the primary circuit, the temperature spread has to increase by raising heat capacity of the AHX. Therefore, the mass flow on the secondary side must also be increased so that the heat capacity can be increased without increasing the supply temperature on the secondary circuit, that the exergetical driving potential stays constant. So at higher GVR a higher sub-cooling ($\Delta T_{Sub\text{-}R,Pr/Se}$) could be achieved within the

AHX. In addition, a distribution valve is needed on the secondary side so split the secondary volume flow between a part which flows through the AHP and through the HX (SVR). This experimental investigation shows that if more volume flow rate flows through the AHP part of the AHX the sub-cooling ($\Delta T_{Sub\text{-}R,Pr/Se}$) raises.

In conclusion, an AHX have high potential avoiding exergetical losses in a transfer-sub-station of a DH-grid and therefore the heat capacity in existing DH-grids could be increased, particular if renewables like deep geothermal heat or solar heat is used for suppling it.

6. Outlook

The experimental investigation of an AHX shows a high potential for reducing the primary return temperature of district heating networks and thus also a high replication potential for other substations, which can thus contribute to the increased use of exclusively renewable energy sources in DH-grids in Austria and Europe. This potential is based on the reduction of the return temperature, as this can also reduce the flow temperature, and thus renewable such as 'deep geothermal energy, solar thermal energy' and regenerative such as waste heat can be integrated much more efficiently into the grid. However, a necessary reduction of the flow and return temperatures on the secondary side must also be provided.

However, a necessary reduction of the flow and return temperatures on the secondary side must also be provided. Ergo, suitable measures must also be provided for the end user, such as for example surface heating, building mass activations, sufficiently large house transfer stations, etc.

But before that, from a technical point of view, it is important to convert results that are partly related to thermal-oil, which was used as heat transfer fluid for the primary side should be transferred to pressurized hot water. The measured values have to be transformed considering the higher cp and HTC of water compared to thermo-oil on the primary side. Before the AHX is used in full-scale as a transfer substation, an optimized flow-layout, such as parallel connection of condenser and absorber, use of a multi-chamber machine and a corresponding control strategy for the distribution between secondary mass flow by the absorption machine part and the heat exchanger part has to be investigated in detail.

From an economical point of view, a further dynamic year-round simulation is essential for the economic evaluation in order to determine by how much the primary return can be supercooled. However, the economic consideration also requires a precise analysis of the supply side used. Especially renewables such as geothermal energy are extremely interesting; because by lowering the return temperature at the same flow rate, more heat can be drawn from this regenerative source free of charge. But, also the bigger packing and the issue with the required space of an AHX has to be considered. A planned demonstration of this integration concept of an AHX into a DH-grid shows high replication potential for other TSS, which can therefore contribute to the increased market penetration of these systems in Austria and Europe.

Acknowledgements

This work has been carried out within the project “AbSolut” (FFG-Nr.: 879433), which was financially supported by the “Klima und Energiefonds” within the national research program “Vorzeigeregion Energie” by the Austrian research funding association “FFG”. The authors also wish to thank the project partners, “WIEN ENERGIE GmbH”, “StepsAhead Energiesysteme GmbH”, “LINZ STROM GASWÄRME GmbH”, “EQUANS Energie GmbH” for their support and contributions.

Nomenclature

A	heat transfer area of the heat exchanger	$t_{S,Pr}$	primary supply temperature
AHP	absorption heat pump	$t_{S,Se}$	secondary supply temperature
AHP	absorption heat exchanger	U	heat transmission coefficient
COP	coefficient of performance	$\dot{V}$	volume flow rate
c_p	(isobaric) specific heat capacity	$\dot{V}_{Pr}$	volume flow rate on the primary circuit
DH	district heating	$\dot{V}_{Se}$	volume flow rate on the secondary circuit
D-valve	distribution valve	$\dot{V}_{Se,HX}$	volume flow rate through HX on the secondary circuit
EER	energy efficiency ratio	$\dot{V}_{Se,AHP}$	volume flow rate through AHP on the secondary circuit
Ex	exergy flux	TSS	transfer-subs-stations
ex_{pot}	exergetica potential		
$\dot{Ex}$	exergy flux		

$\dot{E}x_{irr}$	exergy losses	s	entropy
GVR	general volume flow ratio	SVR	secondary voume flow ratios
HTC	heat transfer coefficient	ΔT_{PP}	pinch-point temperature difference
$\dot{m}$	mass flow rate	$\Delta T_{S,Pr/Se}$	difference of supply temperatures
$\dot{Q}$	heat capacity, heat flux	$\Delta T_{Sub-R,Pr/Se}$	subcooling: difference between secondary and primary return temperature
$\dot{Q}_{Pr}$	heat flux emitted from the primary circuit	Δs_{Pr}	entropy change on the primary side
$\dot{Q}_{Se}$	heat flux absorbed to the secondary circuit	Δs_{Se}	entropy change on the secondary side
T, t	temperature (K, °C)	ϵ	heat exchanger effectiveness
T_a	ambient temperature	η	heat exchanger efficiency
$t_{R,Pr}$	primary return temperature	η_{ex}	exergetical efficiency
$t_{R,Se}$	secondary return temperature		

References

[1] Federal Ministry for Climate Protection, Environment, Energy, Mobility, Innovation and Technology (BMK), 2020: Energy in Austria Figures, data, facts, Vienna,in German: Bundesministerium für Klimaschutz, Umwelt, Energie, Mobilität, Innovation und Technologie (BMK), 2020: Energie in Österreich Zahlen, Daten, Fakten, Wien, https://www.bmk.gv.at/themen/energie/publikationen/zahlen.html

[2] Zotter, G, Seidnitzer-Gallien, C., Eberhöfer, D. (2022) Analysis of an absorption-heat exchangers used as transfer sub-station in a district heating grid based on the first and second law of thermodynamicsPoster Contribution at EuroSun 2022: ISES and IEA SHC Conference on Solar Energy for Buildings and Industry, 25 - 29 September 2022, Kassel

[3] Altenkirch E., 1954: „*Absorptionskältemaschinen*“, VEB Verlag Technik, Berlin

[4] Bosnjakovic F. 1960. „*Technische Thermodynamik, II.* Teil“, 3. Auflage, in Wärmelehre und Wärmewirtschaft in Einzeldarstellungen (Band 12), Verlag von Theodor Steinkopff Dresden und Leipzig, p. 222 – 244

[5] Radermacher R., Ling J., Gluesenkamp K. 2013. „Design of a Combined Cooling, Heating and Power Unit driven by IC Engine“, in Proc. *Deutsche Kälte-Klimatagung 2013*, Hannover, Deutscher Kälte-Klimatechnischer Verein (DKV), Band 4, ISBN 978-3-932715-49-5

[6] Ziegler F. 2002: “State of the art in sorption heat pumping and cooling technologies” *International Journal of Refrigeration*, Vol. 25/4, 06.2002, pp. 450-459

[7] Zotter, G., Rieberer, R., 2014: Increasing energy efficiency in Austrian industry through internal waste heat utilization by means of heat pump systems using two examples (in German) – Proc. Paper @ 13. *Symposium Energieinnovation*, 12.-14.2.2014, Graz/Austria

[8] Hu, J,, Xie , X., Jiang, Yi, 2020: Design and experimental study of a second type absorption heat exchanger: *International Journal of Refrigeration* 118 (2020) 50–60

[9] Fu, L., Li, Y., Zhang, S., & Jiang, Y. (2010). A district heating system based on absorption heat exchange with CHP systems. Frontiers of Energy and Power Engineering in China, 4(1), 77–83. https://doi.org/10.1007/s11708-010-0022-0

[10] Li, Y., Fu, L., Zhang. Sh., Jiang, Y., Xiling, Z., 2011: A new type of district heating method with co-generation based on absorption heat exchange (co-ah cycle) - *Energy Conversion and Management* 52 (2011) 1200–1207

[11] Li Zhu, C., Xie, X., Jiang, Y., 2016: A multi-section vertical absorption heat exchanger for district heating systems - *International Journal of Refrigeration* 71 (2 0 1 6) 69–84

[12] Zotter, G., Rieberer, R., 2014: Increasing energy efficiency in Austrian industry through internal waste heat utilization by means of heat pump systems using two examples (in German) – Proc. Paper @ 13. *Symposium Energieinnovation*, 12.-14.2.2014, Graz/Austria

[13] EES 2010. “Engineering Equation Solver”, © 1992-2010 S.A. Klein, Academic Professional V8.659-3D (09/1/10), F-Chart Software, Madison, Wisconsin

14th IEA Heat Pump Conference
15-18 May 2023, Chicago, Illinois

Fields of application of large-scale heat pumps and challenges in planning

Franziska Bockelmann*, Joris Zimmermann

SIZ energieplus, Hamburger Strasse 277, 38114 Braunschweig, Germany

Abstract

Large-scale heat pumps are increasingly used in the heat supply. The challenge in creating a heating concept for the use of large-scale heat pumps is the balance between cost efficiency and CO_2-emissions. certain criteria such as the innovation of supply concept and technologies, the reduction of CO_2-emission and the acceptance as well as the cost-effectiveness must be taken into account in advance. Heat pump systems and concepts on this scale require appropriate design and pre-planning.
Large-scale heat pumps have the potential to be used in many different ways. In this paper, five examples of heat pump integration will be presented, from neighborhoods, building blocks and the use of waste heat for district supply. These projects show that a significant contribution can be made to increase the share of renewable energy in the heat supply. It can be shown that it is theoretically possible to cover the heat demand up to 100% via the application of heat pumps. Furthermore, enormous ecological potentials can be demonstrated. Compared to gas boilers, CO_2 reductions of 50 - 90% can be achieved.

© HPC2023.
Selection and/or peer-review under the responsibility of the organizers of the 14th IEA Heat Pump Conference 2023.

Keywords: large-scale heat pumps; energy concepts; planing and design; examples

1. Introduction

On average, each person in Germany emits around 7.75 t of CO_2 per year (energy-related – electricity and heat, 2019) [1]. An emission per person of less than 1 t CO_2 per year would be climate compatible [2]. This shows that sustainable consumption requires great efforts and a reduction of around 90 % compared to the current level. A major contribution to achieve climate neutrality can be achieved by reducing emissions in the residential sector. Here, heating offers large potential. Energy consumption must be reduced in the long term, e.g. through thermal insulation of the building envelope. The same time there must be a coupling of the heat and electricity sector, as electricity can more easily be replaced by renewable energy. This coupling can be achieved by using heat pumps.

These positive effects of heat pumps can be scaled up if they are integrated into district heating grids. This can result in modern supply concepts, where smart controllable large-scale heat pumps are integrated for energy-efficient operation. However, these systems face many challenges. Suitable environmental heat sources for the residential energy supply must be dimensioned and developed to the required extent. For resilient and cost-efficient operation, heat pumps may need to be used bivalently in combination with other heat sources of the heating grid. The difference in temperature levels required for new and existing buildings connected to the network needs to be considered.

Such supply concepts should be developed holistically together with the electricity sector. The integration of heat pumps results in a high level of electrification, which should be covered by renewable electricity. Furthermore, the energy concept must enable the energy supply in the neighborhood with the highest possible share of renewable energy at economically justifiable investments and operating costs. In order to consider the costs of the project holistically, land acquisition, grid connection costs and general development costs must be

* Corresponding author. Tel.: +49-531-793893-17; fax: +49-531-793893-98.
E-mail address: franziska.bockelmann@siz-energieplus.de.

taken into account. The transferability of the energy concept to other projects depends strongly on the existing infrastructure and the specific requirements of the residential area, which often results in individual solutions.

To sum up, for designing and choosing an energy supply system for districts, certain criteria have to be met:

- Innovation (using innovative technologies and supply concepts)
- Renewability (including reduction of carbon dioxide emissions)
- Resilience (against internal and external disturbances)
- Potential for servicing the electricity grid
- Transferability (of the system design to other districts / cities)
- Acceptance (among the local population)
- Economic efficiency

The framework conditions and prerequisites for the integration of large-scale heat pumps into supply concepts are given. In addition to the actual concept, the technical components are also available. In addition to the already existing use in the metal processing industry and the food industry, the application area "district heat supply" is seen as a great potential for large-scale heat pumps. For a CO2-neutral heat supply, the transition to large-scale heat pumps is indispensable. The reason why large-scale heat pumps have only been installed sporadically so far is that the price ratio of electricity to gas has been high until now. Therefore, people resorted to a heat supply via gas.

Despite the small number of units installed, the Technology Readiness Level (TLR) of large-scale heat pumps is 6 - 8, and even 9 for large industrial heat pumps.

Large-scale heat pumps are still largely manufactured as individual solutions and are therefore not as inexpensive to purchase as series products. Individual manufacturers offer their systems in a kind of modular system and can thus cover a heat output range of 350 – 3,100 kW. Large-scale heat pumps can cover temperature levels up to 130°C and achieve COPs of 4 to 7. [3]

2. Planning of energy concepts with large-scale heat pumps

The conceptual design is about the intelligent networking of electricity, heat and mobility in everyday life and the sensible integration of renewable energies into existing supply networks. One aspect of this is the use of existing heat sources on site, for example using waste heat from industry to provide heat to neighborhoods.

While smaller heat pumps with lower supply temperatures and low heating capacities have been established for many years in both residential and non-residential buildings, a supply concept with large-scale heat pump makes higher demands. Heat pumps suitable for these operating conditions are not yet standard products but are designed for the specific application. Frequently used air-to-water heat pumps, for example, must be able to raise the temperature of the ambient air to at least 80°C for a neighborhood supply (temperature level for the network if existing buildings are to be supplied and decentralized reheating or decentralized heat generators should not to be used) and may need to provide a thermal output of several megawatts, depending on the size of the heat network and the intended supply share of the heat pump. Many manufacturers of large-scale heat pumps have specialized in high performance and temperatures up to 90°C in the meantime and can offer models with good COPs.

2.1. Evaluation criteria

The conceptualization and elaboration of the supply system include the following points:

1. Demand assessment and load profiles

   For dimensioning the temperature of the supply network to e.g. neighborhoods, where the building-ages varies and usually several decades old, it is necessary to increase the flow temperature due to the associated heat losses.

   In order to consider the dimensioning of the components holistically, several potential expansion and connection stages of the supply network as well as the users must be taken into account. Therefore, variants must be considered with network expansion in the unrefurbished state of the houses and with reduced heating capacity in the refurbished state.

2. Simplicity and multifunctionality

   The biggest challenge in suppling existing neighborhoods is to provide heat at a temperature level where residents can decide today whether to replace their old oil or gas boiler with a local heating solution without having to immediately invest in insulation measures for their buildings. The concept

should work both today and in several years, but in the long term the focus should be on reducing demand.

In terms of reducing complexity, the supply concept should be as simple as possible, while also maintaining a necessary degree of diversity and redundancy.

In order to implement the concepts, the individual systems, from heating systems to central storage facilities, must work together in a way that serves the system. For this purpose, the grids for heat, electricity and e.g. gas as a bivalent heat generator are intelligently connected to the individual systems in order to optimally use the mutual flexibility potentials.

3. Space requirements and suitability for an energy center

When determining a suitable location for the energy center - building or room in which all components for heat and power generation are placed, a basic requirement is that the location of the energy center be close to the key connection users and be accessible by transportation. In order to keep installation costs and distribution losses low, the distances between the heat storage facility, energy center and heating network should also be kept as short as possible.

In the conceptual design, attention must be paid to where large open spaces, which also offer space for redensification, are available in the area under consideration.

Furthermore, the location of the energy center must be compatible with the urban development plans. Conflicts of use must be avoided. A minimum distance from residential buildings must be maintained. The necessary redesignations in the land use plan to enable the construction of the heating center must be verified and clarified in advance.

The resulting space requirement of the energy center is determined by the size of the systems to be built, the dimensions (installation areas), the space requirement of the inspection areas and the maintenance of the distance to trees (treetops), neighboring buildings, neighboring properties, etc. In outdoor area, additional space must be provided for the transport infrastructure or the installation of the air-to-water heat pumps (incl. distance compliance). The area of the energy center is often largely determined by the air-to-water heat pumps.

When determining the space requirements, it should also be taken into account that the heating center can be expanded for future expansion scenarios of the network and the heat demand. Therefore, there should be potential for the energy center to be supplemented with additional components.

4. Time frame

An important criterion nowadays is the quick realizability of projects.

If the area is owned by the city/municipality or can alternatively be secured quickly, this is advantageous for the progress of the project. A critical path in the project is the preparation and amendment of development plans; in Germany, this should be planned for approximately 12 months. If an area is already earmarked for energy production in the development plan, this significantly increases the likelihood of implementation within the specified timeframe.

A longer time period of several years or even decades must be seen and planned, if the energetic refurbishment of the buildings have to be considered.

5. Noise protection

The heat generator, all supply components and especially air heat pumps can generate noise levels that may exceed the limits of residential areas. Therefore, noise barriers must be integrated into the installation concept. An evaluation of the noise emissions (sound calculator) is required in order to plan the necessary measures such as shielding wall / noise barrier or additional protection (cover damped 1.5 m depth).

A heat supply system or the implementation of a large-scale heat pump in a supply structure requires not only a suitable concept, but also good communication between different parties to achieve practical implementation. In addition to the points in above (section 2.1), the corresponding tasks should also include:

- approaching the main potential customers,
- educating local residents about the project.

Acceptance has a great influence on the achievement of the project's goals but it is difficult to assess regarding to the location of the energy center. An acceptance phenomenon is often described as "not in my backyard", i.e. general endorsement of a project as opposed to direct and personal influence. If the project is

in an existing neighborhood, it is also complicated by the fact that almost every building has a different owner who has to be convinced of the project and can exert influence.

3. Project examples with large-scale heat pumps

Large-scale heat pumps have the potential to be used in many different ways. Due to their variability, they can cover large capacities as well as high temperatures (up to 130°C). In the following, projects will be presented, in which a large-scale heat pump is to be or has been integrated.

All projects presented are still in the planning stage, which is why only the initial planning results and calculations can be presented.

3.1. Project 1 – District in Heide

The first example shows the integration of heat pumps into a medium-sized district heating system currently planned for the city of Heide in northern Germany. The planned air/water heat pump should produce a supply temperature of at least 80°C and provide a thermal output of 1 to 2 MW_{th}. The project aims to design and implement a multimodal and sustainable energy supply system for the existing and future buildings in the district. (Fig. 1)

The selected district with an area of 20 ha is inhabited by approximately 500 people and features a diverse building structure. There are 108 single-family- and 47 multi-family-houses, as well as 27 non-residential buildings that are mostly businesses. Most of the buildings are heated with natural gas, some with oil and electricity. The annual energy demands of the existing buildings in the neighbourhood are approximately 1,683 MWh electricity, 4,932 MWh natural gas and 2,216 MWh oil, equivalent to a total of 3,410 t/a CO_2-emissions.

In the most ambitious planned stage for the district heating network, 125 buildings are connected. This includes 40 new buildings that are planned for the near future, resulting in a connection rate of 56%. Including the additional heat demand of the new buildings, the total heat demand provided by the heating grid adds up to 6,560 MWh/a.

In order to supply this heat and meet all the design criteria of the project, the energy supply system (Fig. 2) consists of various components:

- Photovoltaic installation spread over the roofs of the buildings in the district
- Dedicated electrical grid for collecting the PV electricity in the energy control central (required for regulatory reasons)
- Battery
- High temperature air/water heat pump (up to 90°C)
- Electrolysis (small, for research purposes)
- Combined heat and power plant (CHP), able to use natural gas and hydrogen
- Gas boiler used as back-up heater
- Thermal storage (water tank)
- District heating grid

An air/water heat pump is the primary heat generator, which is powered either by the photovoltaic, the output of a combined heat and power unit (CHP) or the public electricity grid. The latter is an important option for further CO_2-reductions, when electricity from the grid becomes less carbon intensive over time. Electricity can also be used to produce hydrogen in an electrolyser, which is installed for research and demonstration purposes. The use of hydrogen can be tested in the CHP in combination with natural gas, potentially used for hydrogen mobility or fed into the public gas grid. The electrolyser's waste heat can be used for heating, but only if the temperature is further increased. For this purpose, the waste heat can become a source for the heat pump. However, the available thermal power from the electrolyser is very small compared to the demand of the heat pump. Therefore, the ambient air remains the main source for the heat pump and the system is not dependent on the electrolysis, which makes the concept more easily transferable. The CHP is the secondary heat generator and, finally, a gas boiler is used as a back-up heater. The heat produced can be stored in a large water heat storage of about 500 m^3 which can store heat for several days of use. A heating grid is used to transport the heat to the buildings.

Technically, the heat pump is the most challenging component. While smaller heat pumps with lower flow temperatures used in modern buildings have been established for many years, the presented concept has more demanding requirements. The buildings supplied are from different time periods and mostly several decades old. Supplying the heat via a heating grid with its inherent heat losses further raises the required flow

temperature. Heat storage adds an additional requirement. The available thermal energy is defined by the usable temperature difference. To store the highest possible amount of heat in a given volume of water, a relatively high temperature with up to 90°C must be achieved. For those times when the storage alone is expected to meet the full demand of the grid, it can only do so while its outlet temperature surpasses the set temperature of the grid. The lower coefficients of performance resulting from the high supply temperature can be accepted if the heat pump is powered by local photovoltaic.

As a result, air/water heat pumps of this concept must raise the temperature of the heat source (environmental air) to 80 - 90°C, while providing thermal output power of 1 to 2 MW_{th}, depending on the final size of the heating grid and the targeted share of the heat pump (in relation to the CHP). Heat pumps suitable for these operating conditions are not yet of-the-shelf products, but instead designed for each use case. Due to the large temperature difference between source and load, manufacturers use a two stage process of either screw or piston compressors. The most common refrigerants are R717 (ammoniac) and R1234yf.

The air heat exchangers required to provide sufficient thermal source power need a large installation surface and create a noise level above the limits for residential areas of 60 dB(A) during day and 45 dB(A) at night. Therefore, noise protection barriers must be integrated into the installation concept.

Ground-source heat pumps using geothermal energy have been considered as an alternative, promising higher coefficients of performance and lower noise emissions. However, exploration drilling showed that the area available nearby for boreholes could provide only a fraction of the required annual energy demand, while increasing the investment costs drastically.

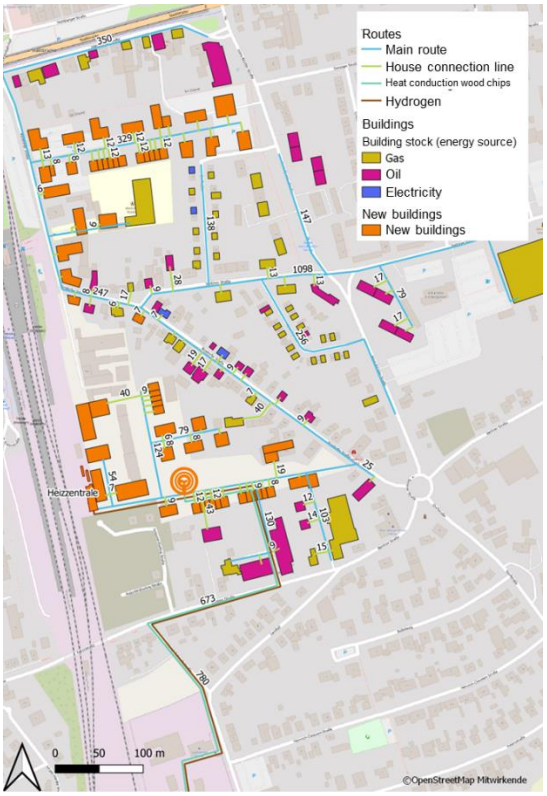


Fig. 1. Location plan project 1.

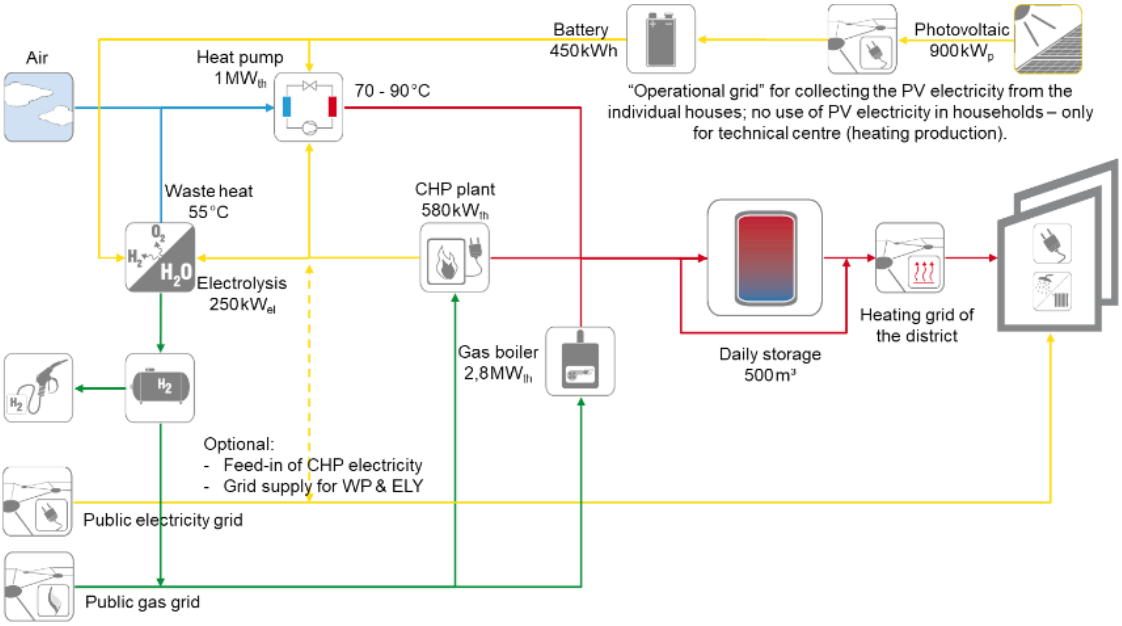


Fig. 2. Energy supply concept (below).

3.2. Project 2 – Building block in Kassel

Project 2 shows the implementation of a large-scale heat pump within a building block with around 150 residential units. The planned air/water heat pump must produce a supply temperature of at least 70 to 80°C and provide a thermal output of 640 kW. The aim of the project and the guiding principle of the building owner is the motto "away from gas"; all buildings in the building owner's portfolio are to be operated with renewable energy in the future. The project is still in the design phase; all boundary conditions are currently being defined and the energy consumption to date is being determined.



Fig. 3. Location plan project 2. [google maps]

3.3. Project 3 – District supply via four heating centers

Project 3 shows the implementation in four single small heating grids. The planned air/water heat pumps are to produce a supply temperature of at least 80 to 90°C and provide a thermal output of 7 MW in total (depending on the final size of the bivalent producer). The aim of the project is to convert four existing heating centers as a first step towards making all of the client's buildings and facilities fit for the future. The desire is to achieve climate neutrality for the properties.

In order to make all of the owner's sites sustainable in terms of construction and renovation activities as well as heat and power supply, the properties shown (Fig. 4) and the development potentials towards climate neutrality have to be assessed first. For the location examined, 90 buildings with about 550 residential units and a heated floor space of about 50,000 m² are assumed. The buildings accommodate different uses such as housing/assisted living or care facilities, workshop/warehouse, administration and social facilities.

Project 3 involves the conversion of four existing heating centers in the owner's entire property, which are currently operated via gas boilers and CHP units. The supply concepts to be developed should have a high share of renewable energy. The goal is to implement a share of 65 - 95% of the heat supply per heating center via air-water heat pumps (Fig. 5).

At present, the tasks are to examine the expandability of the respective heating system and the combination with thermal storage and photovoltaics for the use of self-produced electricity. The different building age classes and varying energy conditions of the buildings as well as the inhomogeneous structure at the site represent a challenge in the concept development and dimensioning. In addition, development scenarios for the site have to be worked out and defined with regard to future expansions and space requirements, as well as requirements for space- and use-specific needs.

The individual heating centers must cover a heat output of 485 kW to 5,145 kW and operate at a temperature level of 80/60°C or 90/70°C.

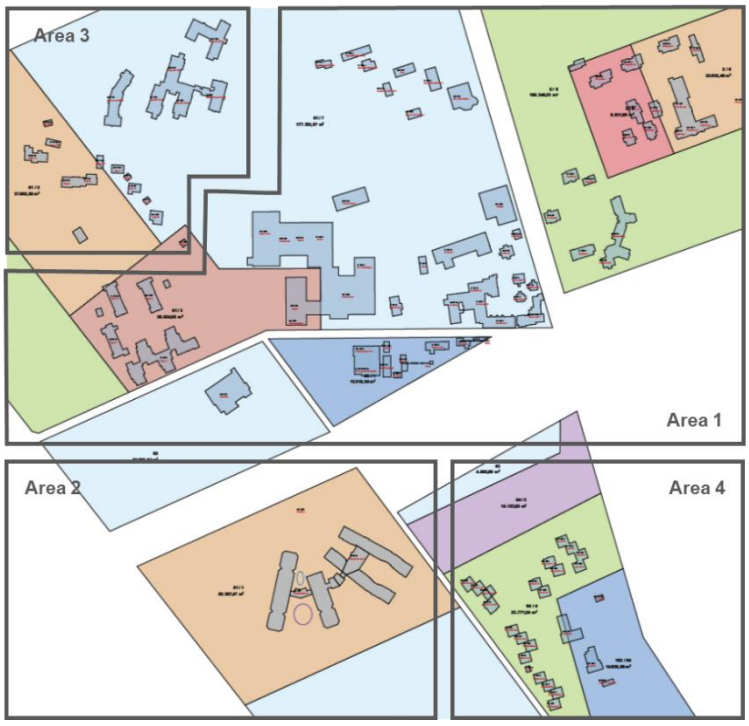


Fig. 4. Location plan project 3. [energydesign braunschweig GmbH]

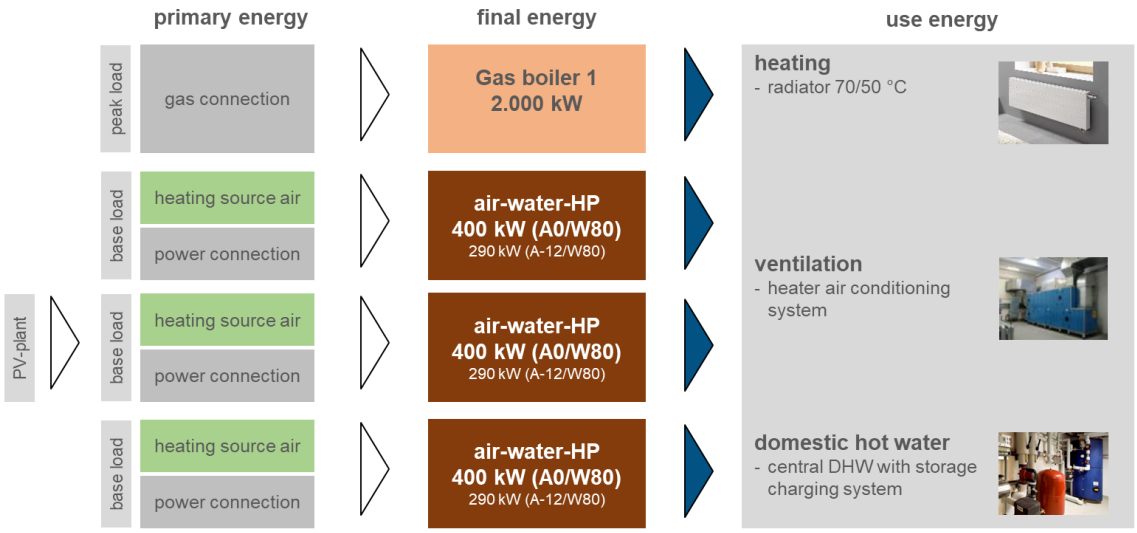


Fig. 5. Concept proposal for one heating center. [energydesign braunschweig GmbH]

The ecological assessment refers to the emissions that are emitted during the generation of heat via the current supply concept with gas boiler compared to the heat pump solution. The balance also includes the yields of the added PV systems and the electricity consumption. (see (1))

$$CO_2 emission = CO_2 emission\ factor\ x\ final\ energy\ (energy\ source) - CO_2 emission\ factor\ x\ electricity\ production\ PV\ plant \quad (1)$$

Based on the examples of the new energy concepts with heat pumps for the heating centers in Area 1 and Area 3, there is an annual CO_2 saving potential of 53 and 78 % respectively compared to the current supply concept with gas boilers. This would mean a CO_2 reduction of around 515 to 1,210 tCO_2 annually.

- V1: heating center Area 1 – gas boiler
- V2: heating center Area 1 – Air to water heat pump
- V3: heating center Area 3 – gas boiler
- V4: heating center Area 3 – Air to water heat pump

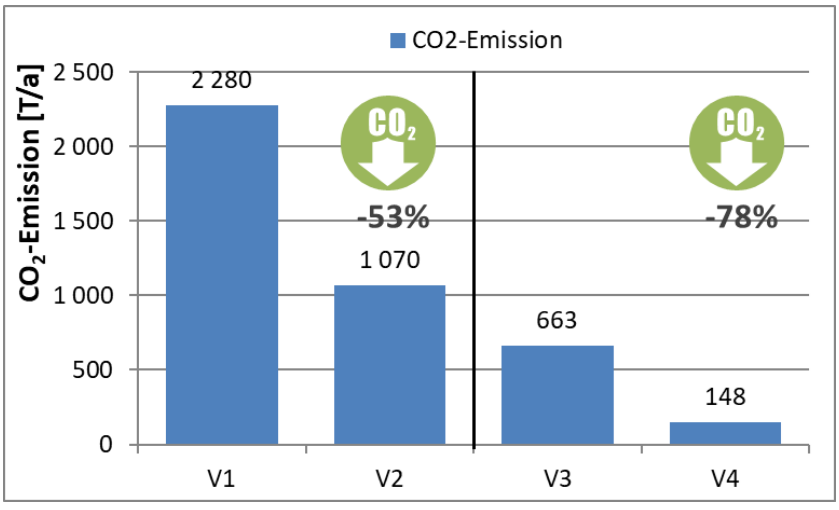


Fig. 6. CO_2-emission of the different variants of the heating center Area 1 + Area 3 (CO_2 emission factors: natural gas 270 g/kWh, electricity 400 g/kWh, displacement electricity -700 g/kWh) [energydesign braunschweig GmbH]

3.4. Projekt 4 – Data center concept study

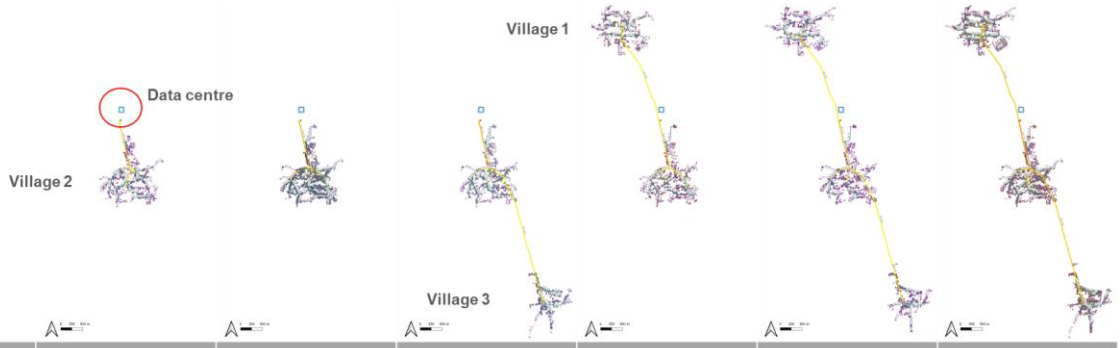
Project 4 shows the implementation of a large-scale heat pump with waste heat from a data center in a heating network. The planned water/water heat pump must produce a supply temperature of 80 to 90°C and provide a thermal output of 10 MW. The aim of the project is to use the waste heat from the data center under consideration, which has so far been released into the environment by conventional means via cooling fans, as a source for a new district heating network.

The data center is located between two rural villages with approx. 2,000 to 2,500 inhabitants each, which are currently mainly supplied with individual heating systems and fossil fuels. It is possible to implement waste heat recovery to supply the buildings via local heating networks. Other locations that could also be considered as heat consumers can be included. (Fig. 7)

In connection with the use of waste heat, a climate-neutral supply can be established for the surrounding villages in the building stock. The waste heat from the data center is available throughout the year at a temperature level of 20 - 36°C. (Fig. 8) Currently, a waste heat output of the data center (source) of 7 - 8 MW can be assumed (full expansion of the data center). With an annual performance factor for the heat pumps of 3.3, a theoretical 87,600 MWh/a of heat can be provided to the grid. This would even exceed the total heat demand of the expansion stages to supply the villages (Fig. 7).

Even if the data center could theoretically cover the total energy for the neighborhoods, it is assumed that the heat must be stored - need for a large heat storage tank - and that additional heat generators must be integrated. The following variants are still considered in the study as additional heat generators and heat grid feeders:

- Variant A: Heat pump + electrode boiler (as back-up heating)
- Variant B: Heat pump + electrode boiler + CHP (electricity energy system)
- Variant C: Heat pump + electrode boiler + CHP (electricity energy system) + heat pump for storage (to extract heat from the storage above a certain temperature level)
- Variant D: Heat pump + high voltage electrode boiler [4] + CHP (electricity-fired power plant) + heat pump for storage + wind turbines
- Variant E: Heat pump + electrode boiler (as back-up heating) + wind turbines
- Variant F: Heat pump + electrode boiler + CHP (straw-fired energy plant) + wind turbines



	Level 1	Level 2	Level 3	Level 4	Level 5	Level 6
	Village 2	Village 2	Village 2 + 3	Village 1 + 2	Village 1 - 3	Village 1 - 3
Connection to the grid	60%	100%	60%	60%	60%	100%
Inhabitants	1,455	2,432	2,076	2,569	3,183	5,300
Buildings	482	804	735	847	1,099	1,833
Total heating demand	16.2 GWh	28.5 GWh	25.7 GWh	28.8 GWh	37.0 GWh	62.5 GWh
Total heating capacity	5.8 MW	10.0 MW	9.1 MW	10.3 MW	12.4 MW	20.1 MW
Route length	14.0 km	16.0 km	22.8 km	27.1 km	35.5 km	39.2 km

Fig. 7. Location plan and Expansion scenarios for the heating supply grid.

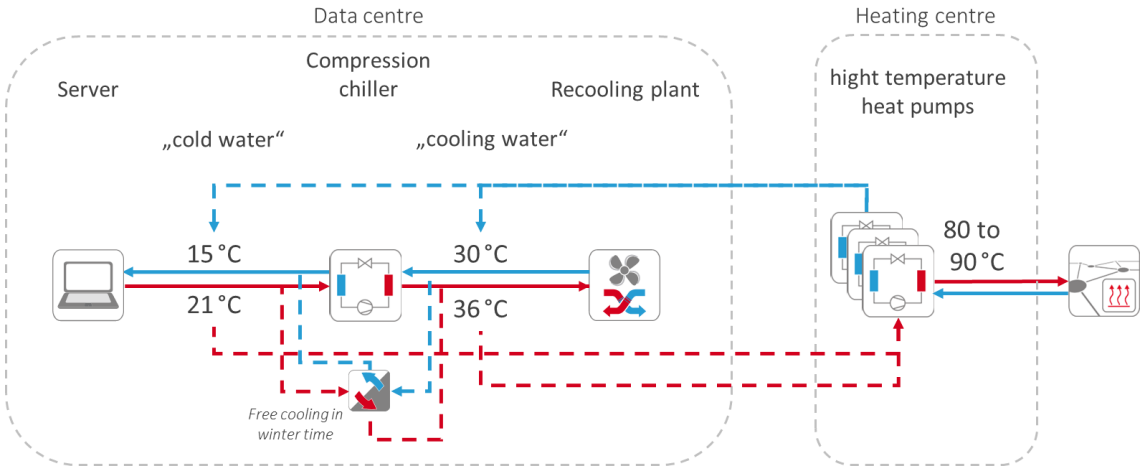


Fig. 8. Supply concept of the heating grid with integration of the data center as a heating source

The ecological assessment refers to the emissions (see (1)) that are emitted during the generation of heat via the current supply concept using decentralized gas boilers (in Fig 9 the reference) compared to the neighborhood supply with heat pumps (in Fig. 9 Variant A, B, E and F). The balance also includes the yields of the wind turbines.

The concept variants were worked out using level 3 as an example. The results show an enormous ecological savings potential. An annual CO_2 saving potential of about 45 - 97 % (depending on the wind power implementation) compared to the current supply concept is available. This would mean a CO_2 reduction of around 3,185 to 7,122 tCO_2 annually.

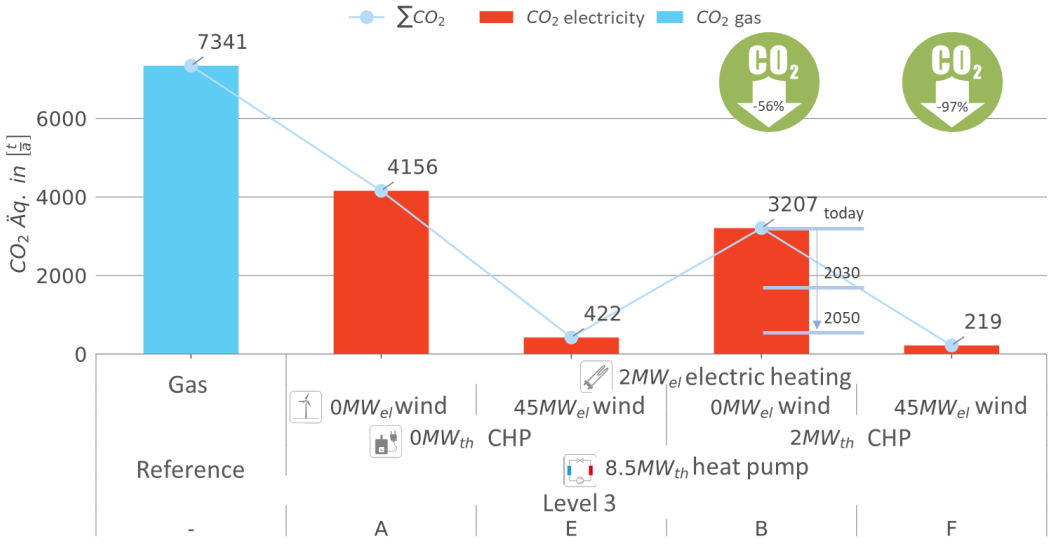


Fig. 9. CO_2 emissions of the different variants for heat generation (CO_2 emission factors: natural gas 250 g/kWh, grid electricity 401 g/kWh)

3.5. Projekt 5 – research center for hydrogen technology

Another example is the integration of a large-scale heat pump in a hydrogen technology research facility. The project aims to improve the overall efficiency of the electrolysis by decoupling the waste heat and using it for heating applications. For this purpose, different heat exchangers are to be implemented in combination with a heat pump.

4. Conclusion

Germany is to become greenhouse gas neutral by 2045, to reach this the 65% renewable energy target for heat generation has been introduced. However, this target can only be achieved if the heat supply is restructured in terms of energy and can do without fossil fuels. Large-scale heat pumps will therefore play an important role in the medium and long-term transformation of the heat supply.

In newly built residential buildings (single-family and multi-family buildings) and non-residential buildings (office buildings), the heat pump has already become the standard heating appliance. However, the situation is different in the commercial sector, in existing buildings and at the neighborhood level. Here, the heat pump is still too rarely seen as the ideal technology. The examples given show that this should no longer be a problem in the future at the neighborhood and commercial level, and that municipalities, project developers, public utilities and other energy suppliers in particular see the opportunity to massively advance climate protection when building or modernizing neighborhoods and building blocks - and, quite incidentally, to establish sustainable business models with long-term customer relationships. An individual solution can now be found for every large property/project thanks to the very diverse use of large-scale heat pumps.

However, in order to be able to exploit the potential of this energy supply variant in the best possible way, the design and dimensioning as well as the integration into the overall supply concept are relevant. At present, unfortunately, the large-scale heat pump is still a special design that has to be planned according to the specific application.

The planning and dimensioning of supply concepts with large-scale heat pumps includes in advance an inventory to present the basics and objectives of the concept. In the first step, the demand and load profiles must be determined. If the project involves existing systems / existing buildings, future renovations and changes to the buildings must be taken into account. But also necessary changes to the existing concept, like the adjustment of the supply temperatures, have to be considered. Existing systems require increased attention during replanning so that all individual systems, from the heating system to the central storage tank, are coordinated and work together in the future.

Other factors, albeit secondary locations, should not be neglected. For example, the new location of the energy center, if required, or in general the space requirements of the new supply system must be examined and defined. Existing technical rooms could become too small if additional components such as storage tanks or the heat pump itself have to be installed.

In the entire planning process, attention must be paid to early coordination and clarification of goals and target values, as well as communication with all stakeholders and their involvement in the processing and concept development.

The projects shown relate primarily to the replacement and exchange of gas boilers and the implementation of large-scale heat pumps in the existing supply. The supply concepts are increasingly changing from a decentralized to a centralized supply. All concepts have the goal of saving as much CO_2 as possible in order to meet climate protection targets. It can be clearly seen that just by exchanging the old heat generators (fossil fuels, gas) to a heat pump (regenerative energy source) the CO_2 emissions can be reduced more than 50%. Furthermore, a high share of the heat supply should be covered by the heat pump and thus renewable. Depending on the concept, “>50% “up to 100% (total exchange) can be achieved as coverage share.

Acknowledgements

We would like to thank the clients and energydesign braunschweig GmbH for their help and support and for making the projects available. We would like to thank them for the orders and the confidence in the processing.

References

[1] Statista Research Department. Energiebedingte CO_2-Emissionen pro Kopf weltweit nach ausgewählten Ländern im Jahr 2019. 2022; https://de.statista.com/statistik/daten/studie/167877/umfrage/co-emissionen-nach-laendern-je-einwohner/.

[2] Umweltbundesmat. Wie hoch sind die Treibhausgasemissionen pro Person in Deutschland durchschnittlich?. 2021; https://www.umweltbundesamt.de/service/uba-fragen/wie-hoch-sind-die-treibhausgasemissionen-pro-person.

[3] Fraunhofer-Institut für Solare Energiesysteme ISE (10/2021). Innovative Energietechnologien – Analyse ausgewählter innovativer Technologien zur Energieerzeugung, -umwandlung und -speicherung. Kurzgutachten zur dena-Leitstudie Aufbruch Klimaneutralität. Deutschen Energie-Agentur GmbH (dena).

[4] www.parat.no/en/products/industry/parat-ieh-high-voltage-electrode-boiler

14th IEA Heat Pump Conference
15-18 May 2023, Chicago, Illinois

Evaluation of proper HFO refrigerant/ionic liquid mixture for absorption refrigeration system

Younggyun Lee[a], Gilbong Lee[b], Junhyun Cho[b], Bongsu Choi[b], Nyeon Gu Han[a], Dong Kyu Kim[a,c*]

[a]Department of mechanical Engineering, Chung-Ang University, Seoul 06974, Korea
[b]Thermal Energy Conversion systems laboratory, Korea Institute of Energy Research, Daejeon 34127, Korea
[c]Schoold of Computer Science and Engineering, Chung-Ang University, Seoul 06974, Korea

Abstract

This study is to evaluate ionic liquid as absorbents for absorption refrigeration system using Hydrofluoro-olefin (HFO) refrigerant. By examining properties of absorbent/refrigerant mixture, we found the most efficient absorbent/refrigerant pair for the absorption refrigeration system. First, we analyzed characteristics of ionic liquid as absorbent in absorption refrigeration system. Imidazolium ionic liquids have relatively low viscosity of about 10 mPa.s at 70 ºC and high stability to water and air, so that we decided to apply imidazolium ionic liquid as absorbent. Then, we examined proper HFO refrigerant for the system. Among the refrigerants, R1336mzz(Z) and R1234ze(Z) are applicable for the absorption refrigeration system because both have low inflammability, and high critical points over 150 ºC. Next, we analyzed characteristics of absorbent/refrigerant pair. When [OMIM][BF4] is used as absorbent, R1336mzz(Z) and R1234ze(Z) have the highest solubility of 0.05848 and 0.66149 at absorber, respectively. Lastly, we analyzed performance of the refrigeration system. Since difference of solubility of [OMIM][BF4]/R1234ze(Z) is large between absorber and generator, it shows the highest COP than other pairs.

© HPC2023.
Selection and/or peer-review under the responsibility of the organizers of the 14th IEA Heat Pump Conference 2023.

Keywords: Absorption refrigeration system; Absrobent/refrigerant pair; Ionic liquid; Hydrofluoro-olefin; Non-Random two liquid model

1. Introduction

To maintain indoor thermal comfort in summer days, the use of refrigerator is rapidly increasing. Among various refrigeration system, absorption refrigeration system is promising due to its low operating cost and low heat source temperature. The absorption refrigeration system usually used H_2O/LiBr or NH_3/H_2O as refrigerant/absorbent pair. Those refrigerant/absorbent pairs, however, have fatal problems, such as crystallization of absorbent and corrosion [1-2]. Therefore, it is necessary to find proper refrigerant/absorbent pairs that can be used in absorption refrigeration system.

Ionic liquid has gained attraction as absorbent in absorption refrigeration system, because asymmetric structure between cation and anion of ionic liquid can help dissolve polar refrigerant, and it has good stability in air and water. Therefore, many studies are trying to apply ionic liquid in absorption refrigeration system. Firstly, research on finding substitute of LiBr in H_2O/LiBr absorption refrigeration system is conducted. Some researchers examined performance of absorption refrigeration system using H_2O/[EMIM][DMP] pair. The COP of refrigeration system using ionic liquid as absorbent is about 7% lower than that of H_2O/LiBr system, but it still showed relatively high COP over 0.7 [3]. Other researchers tried to increase COP of absorption refrigeration system using H_2O/[DMIM][DMP] pair [4]. They insisted that COP of the refrigeration system using H_2O/[DMIM][DMP] pair can provide higher COP of 0.78 compared to the system using H_2O/LiBr pair by proper system optimization. Others analyzed pair of water and various imidazolium-type ionic liquids for

* Corresponding author. Tel.: +82-2-820-5192.
E-mail address: dkyukim@cau.ac.kr.

absorption refrigeration system, and showed that H2O/[EMIM][$(CH_3)_2PO_4$] showed the highest COP of 0.69 [5]. Others tried to apply EMISE to absorb water in absorption refrigeration system [6]. Although COP of absorption refrigeration system with H_2O/EMISE pair showed relatively high value of 0.66, the COP is lower than the refrigeration system with H_2O/LiBr pair. Although many previous studies analyzed application of ILs as absorbent to use water as refrigerant, water is frozen below zero temperature, so that operating range of the refrigeration system using water as refrigerant is limited. Therefore, research on various refrigerant for absorption refrigeration system is needed.

Due to environmental issue, research of low global warming point (GWP) refrigerant has been actively conducted, so that researchers tried to apply ionic liquid as absorbent with low GWP refrigerant. Some researchers analyzed application of [HMIM][PF_6] and [HMIM][Tf_2N] as absorbent for R134a refrigerant [7]. When [HMIM][Tf_2N] is used as absorbent, about 0.1 higher COP is obtained compared to the absorption refrigeration system using [HMIM][PF_6] as absorbent. Other researchers analyzed performance of absorption refrigeration system with HFO/ionic liquid pairs [8]. Since high solubility of R32 to [C_2MIM][Tf_2N], the COP of the system with R32/[C_2MIM][Tf_2N] pair showed the highest value of 0.734 among various working pairs. Others examined six imidazolium-type ionic liquids as absorbent for using R1234yf as refrigerant [9]. Among the ionic liquids, [HMIM][Tf_2N] showed the highest COP of 0.35 among IL absorbents. The R1234yf /[HMIM][Tf_2N] pair, however, showed lower COP than conventional working fluids due to low specific volume of R1234yf. Although various studies have been conducted to find proper ionic liquid for absorption refrigeration system, studies on finding proper ionic liquid for absorbing hydrofluoroolefin refrigerant is insufficient.

2. Methods

The purpose of this study is to find proper working fluid/absorbent mixture for double effect absorption refrigeration system. Therefore, we have to develop the refrigeration system model and express behavior of the mixture. The double effect absorption refrigeration system model is developed using MATLAB. Properties of HFO refrigerants are obtained by REFPROP 10.0, and that of the mixture is calculated using COSMO-RS.

The absorption cooling system is largely composed of a generator, a condenser, an evaporator, and an absorber. The double-effect absorption system is a device that aims to improve performance by adding a regenerator and a condenser, respectively, to the existing system. The working pressure of the double-effect absorption cooling system is divided into three levels, and the concentration is also divided into three levels. The schematic diagram is shown in fig 1. For the study of this system, it is necessary to assume the understanding of the phenomena of each component. The whole system is calculated assuming a steady state. At the outlet point of the low-pressure condenser, the refrigerant from the low-temperature condenser is assumed to condense to saturation, where the pressure determines the operating pressure at the mid-level. The refrigerant vaporized in the evaporator is also assumed to be saturated, where the pressure determines the low level operating pressures in the evaporator and absorber. In the absorber, the gaseous refrigerant is absorbed by the working fluid with a low concentration to become a saturated working fluid with a high concentration that satisfies the phase equilibrium state under the operating conditions. In the high-pressure regenerator and the low-pressure regenerator, the refrigerant is separated due to the difference in boiling point between the two liquids constituting the working fluid. Since only the refrigerant is separated in the regenerator, the concentration of the outlet is calculated using the same amount of absorbent. Concentration calculation and thermal equilibrium are calculated through the following equations.

$$\sum \dot{m}_i = \sum \dot{m}_o \tag{1}$$

$$\sum \dot{m}_i h_i = \sum \dot{m}_o h_o \tag{2}$$

$$\dot{m}_i x_i = \dot{m}_o x_o \tag{3}$$

When calculating the coefficient of performance of the cycle, the energy consumed by the pump is very small and is therefore neglected.

$$COP = \frac{Q_{Evaporator}}{Q_{High\ Pressure\ Generator} + W_{Pump}} \cong \frac{Q_{Evaporator}}{Q_{High\ Pressure\ Generator}} \tag{4}$$

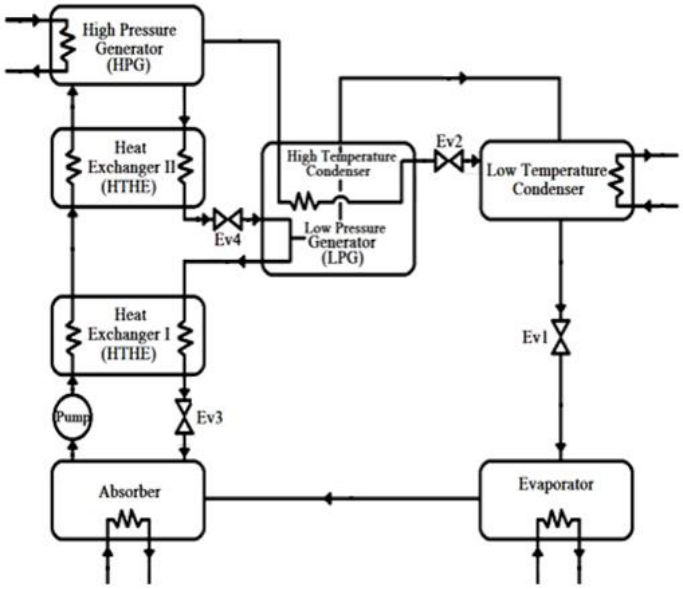


Fig. 1. Schematic of double effect absorption refrigerator.

The pressure at vapor-liquid phase equilibrium in the absorber and the two regenerators of the double-effect absorption chiller is calculated using Raoult's law, which introduces the activity coefficient.

$$y_i P = x_i \gamma_i P_i^{sat} \tag{5}$$

x_i denotes the mole fraction in the liquid phase, and y_i denotes the mole fraction in the vapor state. The activity coefficient is introduced in consideration of the fact that the gas has not great non-ideality with respect to the actual gas, but the liquid phase has large non-ideality. The enthalpy of various working fluids used in a double-effect absorption chiller is calculated as follows.

$$h = h_{Ref} x_{Ref} + h_{IL} x_{IL} + h_{mix} \tag{6}$$

$$h_{IL} = h_o + \int_{T_o}^{T} C_{p,IL} dT \tag{7}$$

$$h_{mix} = -RT^2 \left[\frac{\partial \left(\frac{G^E}{RT} \right)}{\partial T} \right]_P \tag{8}$$

3. Results and discussion

3.1. HFO refrigerants and ionic liquid absorbents

In this study, we examined HFO refrigerants that are usually used in refrigeration system. Most of GWPs of HFO refrigerants and flammability are also low, so most HFO refrigerants are applicable to the refrigeration system. Moreover, these refrigerants have lower freezing point than water, so we can generate more cold heat source with refrigeration system using HFO refrigerants than that using water. Next, we examined possibility of application of HFO refrigerants to double effect absorption refrigeration system. The desirable operating ranges of HFO refrigerants are listed in Fig. 2. Here, we assumed that the desirable operating range is between triple point and critical point. Heat source temperature of double effect absorption refrigeration system is usually over 120 °C. Therefore, when refrigerants which has low critical point than heat source temperature, the thermodynamic cycle will be operated in super critical state. Unfortunately, the studies on super critical state of HFO refrigerant are insufficient. Therefore, the refrigerant which has higher critical point than heat source temperature is recommended, such as, R1336mzz(Z) and R1234ze(Z).

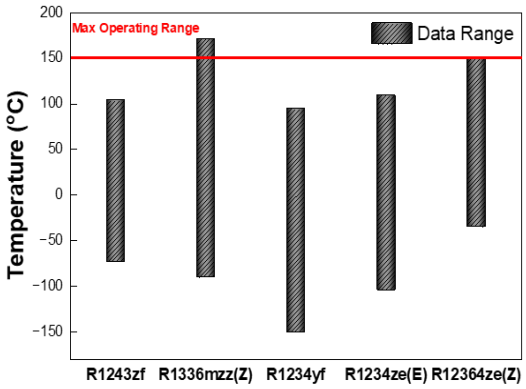


Fig. 2. Comparison of operating ranges of HFO refrigerants.

Next, proper ionic liquids are examined. Ionic liquids consist of large cation and small anion. This asymmetry leads to weak attractive force, so that ionic liquids have low melting point. Characteristics of ionic liquids are determined by combination of cation and anion. Especially, flow characteristics of ionic liquids are mainly determined by structure of cation. The characteristics of various cation are listed in table 1.

Table 1. Characteristics of $N(SO_2CH_3)_2$ anion-based ionic liquids

Name	Chemical Formula	Molecular weight (g/mol)	Volume (cm^3/mol)
1-Ethyl-3-methylimidazolium	$C_6H_{11}N_2^+$	111.17	259.5
1-Methyl-1-propyrrolidinium	$C_8H_{18}N^+$	128.24	287.0
Trimethylpropylammonium	$C_6H_{16}N^+$	102.20	268.7
1-Ethyl-2,3,5-trimethylpyrazolium	$C_8H_{15}N_2^+$	139.22	288.4
1-Methyl-1-propylpiperidinium	$C_9H_{20}N^+$	142.26	300.8

Among the flow characteristics, viscosity is one of important factors that affects performance of the refrigeration system. Therefore, we examined viscosities of ionic liquids based on cations shown in Fig. 3. In this study, we examined viscosity of ionic liquids with 1-ethyl-3-methylimidazolium (EMIM), N-methyl-N-propylpyrrolidinium (P13), trimethyl propylammonium (TMPA), and 1-ethly-2,3,5-trimethylpyrazolium (ETMP) comparing with H2O/LiBr solution of 59.9 wt%. Most ionic liquids have higher viscosity than that of H_2O/LiBr solution. Among the ionic liquids, however, imidazolium type ionic liquid has relatively low viscosity. Over 50 °C, viscosity of EMIM is lower than 20 mPa.s. Therefore, we concluded that EMIM ionic liquids are promising for absorption refrigeration system.

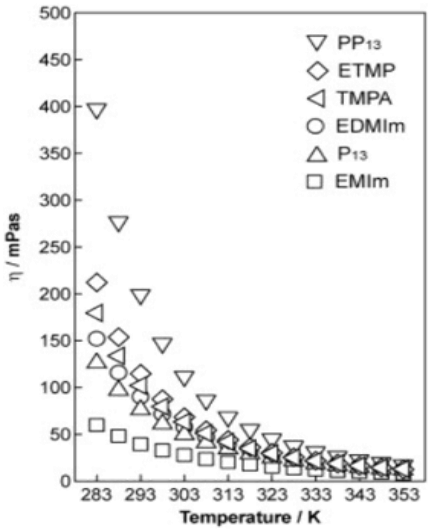
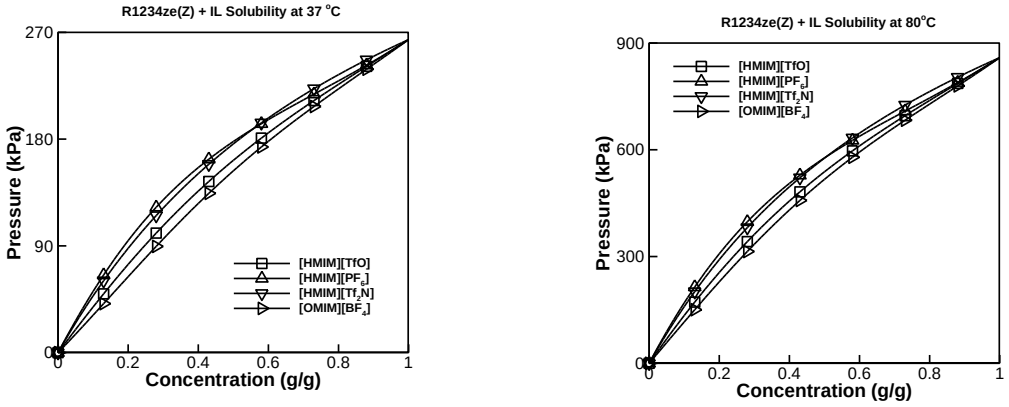


Fig. 3. Changes in viscosity of ionic liquids depending on various cation with Tf_2N anion [10].

3.2. Examination of HFO refrigerants/ionic liquid absorbents solution

In this section, we analyzed application of HFO refrigerant/ionic liquid mixture for double absorption refrigeration system. Here, heat source temperature of the refrigeration system is 140 °C, and temperatures of pressure generator and absorber are 37 °C and 80 °C, respectively. Candidate of HFO refrigerants are R1336mzz(Z) and R1234ze(Z) and that of ionic liquids are imidazolium type ionic liquids. Results of the mixture is compared to water/ionic liquid pair.

Solubility of R1234ze(Z) with various ionic liquids are shown in Fig. 4. Here, solubility of refrigerant is expressed using concentration that is defined by mass fraction of refrigerant weight and solution weight. Since the highest concentration is observed absorber and the lowest concentration is observed in low-pressure generator. Therefore, we compared concentration in low-pressure generator and absorber. The Concentration of R1234ze(Z) is increased according to saturation pressure. For example, concentration of R1234ze(Z) /[OMIM][BF_4] mixture increased from 0.15 to 0.32 when saturation pressure increased from 30 kPa to 90 kPa. The concentration of the mixtures, however, inversely proportional to temperature. For example, the solubility of R1234ze(Z)/[OMIM][BF_4] mixture at 100 kPa decreased from 0.37 to 0.14 when the temperature increased from 37 °C to 80 °C.



(a) Change in solubility at absorber (b) Change in solubility at low pressure generator

Fig. 4. Comparison of solubility of R1234ze(Z) with various ionic liquids in double effect absorption refrigeration system.

Among the refrigerant/absorbent mixtures, R1234ze(Z)/[OMIM][BF_4] pair is the only promising pair for the double absorption refrigeration system. Because the concentration at absorber is lower than that in low-pressure generator when other refrigerant/absorbent mixtures except R1234ze(Z)/[OMIM][BF_4] pair. When we use [OMIM][BF_4] as absorbent, the concentration of refrigerant at absorber is 0.01 higher than that at low-

pressure generator shown in Fig. 5. Therefore, R1234ze(Z)/[OMIM][BF_4] is good for double effect absorption refrigeration system.

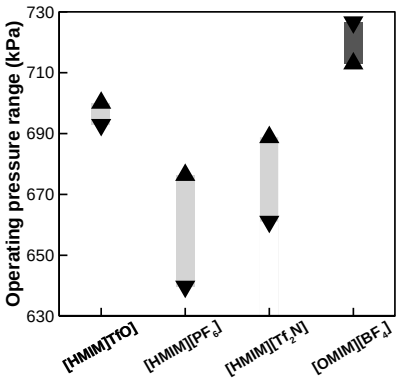
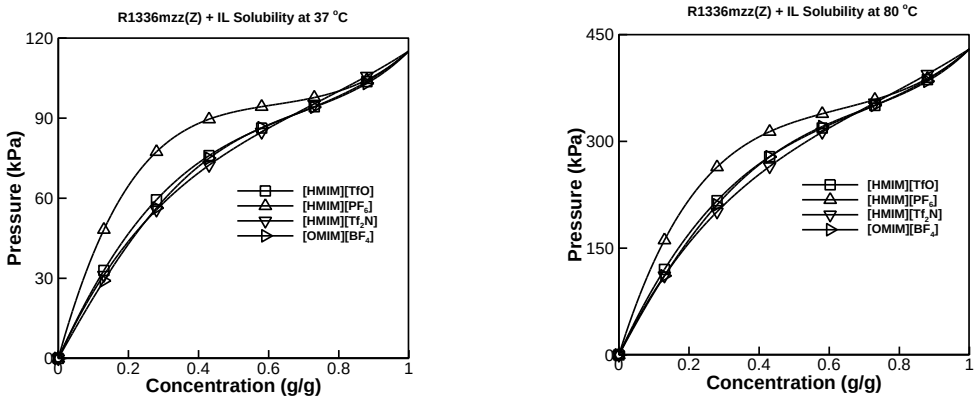


Fig. 5. Concertation of R1234ze(Z) at absorber and low-pressure generator with various ionic liquids.

Next, solubility of R1336mzz(Z) examined with various ionic liquids shown in Fig. 6. Similar to R1234ze(Z), solubility of R1336mzz(Z) is proportional to pressure, and inversely proportional to temperature. In case of R1336mzz(Z) with [HMIM][TfO], concentration is increase from 0.22 to 0.58 when saturation pressure increased from 150 kPa to 300 kPa. Concentration decreased from 0.8 to 0.15 when the temperature increased from 37 °C to 80 °C at saturation pressure of 100 kPa. Among the mixtures, R1336mzz(Z)/[HMIM][Tf2N] pair showed the highest solubility. At 600 kPa, concentration of R1336mzz(Z) with [HMIM][Tf_2N] is about 0.42.

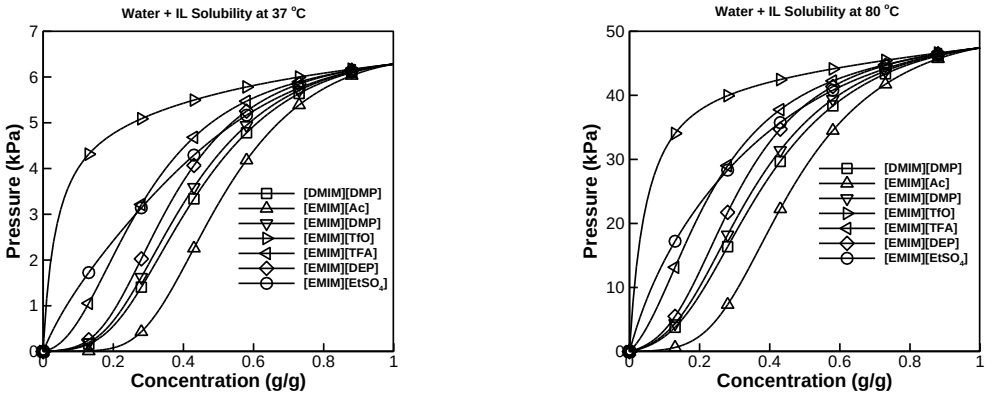


(a) Change in solubility at absorber (b) Change in solubility at low pressure generator

Fig. 6. Comparison of solubility of R1336mzz(Z) with various ionic liquids in double effect absorption refrigeration system.

In case of R1336mzz(Z), however, the concentration of refrigerant at absorber is lower than that at generators. To operate absorption refrigeration system, the concentration of refrigerant at absorber should be higher than that at generator. Because refrigerants are absorbed to absorbent at absorber. Therefore, R1336mzz(Z) is inappropriate refrigerant for absorption refrigeration system in given condition.

Solubility of water with various ionic liquids also analyzed shown in Fig.7. Changes in solubility of water with ionic liquids are similar to other refrigerants. The higher the saturation pressure, the higher the solubility, and the higher the temperature, the lower the solubility. Among the mixture, H_2O/[EMIM][Ac] pair shows the largest solubility. In low-pressure generator, the concentration is about 0.65 at 5 kPa.



(a) Changes in solubility at absorber (b) Changes in solubility at low pressure generator

Fig. 7 Comparison of solubility of water with various ionic liquids in double effect absorption refrigeration system.

However, concentration difference between at absorber and low pressure generator is the largest for H_2O/[DMIM][DMP] mixture shown in Fig. 8. Therefore, H_2O/[DMIM][DMP] is suitable for the absorption refrigeration system.

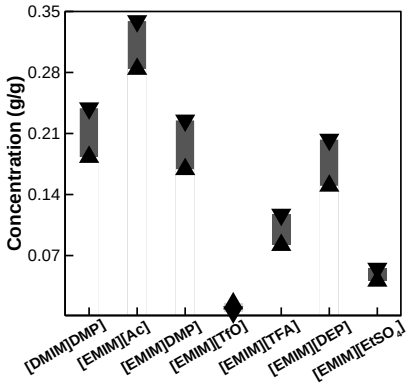


Fig. 8. Operating range of high pressure generator for the absorption refrigeration system using water with various ionic liquids.

4. Conclusion

In this study, proper HFO refrigerant/ionic liquid pairs for double effect refrigeration system are examined. We analyzed properties of various mixtures for the double effect absorption refrigeration system depending on working fluid/ionic liquid.

(1) Among HFO refrigerants, R1234ze(Z) and R1336mzz(Z) are promising refrigerants for double effect absorption refrigeration system. Because heat source temperature of double effect absorption refrigeration system is higher than the critical point of rest of HFO refrigerants. Therefore, only R1234ze(Z) and R1336mzz(Z) can be exited in stable condition under operating condition of double effect refrigeration system. In case of ionic liquid, imidazolium type ionic liquids are suitable for the refrigeration system. Because viscosity of imidazolium ionic liquid has relatively low value compared to other ionic liquids.

(2) The solubility of HFO refrigerant/ionic liquids are examined to find promising mixture for the absorption refrigeration system. For R1234ze(Z), [OMIM][BF4] is promising due to high solubility of 0.28 in low pressure generator at 300 kPa. It also has high concentration difference between absorber and generator, so that large amount of refrigerant can be supplied to evaporator. In case of R1336mzz(Z), however, concentration of refrigerant at absorber is lower than that at generators, it is not suitable refrigerant for the absorption refrigeration system. We also analyzed solubility of water to ionic liquid absorbent. Although the highest solubility can be found for H2O/[EMIM][Ac] mixture, concentration difference between absorber and generator is relatively small. Therefore, we recommended that H2O/[DMIM][DMP] is promising absorbent for water.

Acknowledgements

This research was supported by the National Fir Agency and the Korea Institute of Energy Technology Evaluation and Planning (KETEP) (No. 20008021), the Korea government (MOTIE) (No. 20212050100010), framework of research and development program of the Korea Institute of Energy Research (KIER) (C2-2417), and National Research Foundation of Korea (NRF) grant by the Korea Government (MSIT) (NRF-2022R1C1C1010338)

References

[1] A. Mota-Babiloni, J. Navarro-Esbrí, Á. Barragán-Cervera, F. Molés, B.o Peris, G. Verdú, Commercial refrigeration – An overview of current status, International Journal of Refrigeration,
Vol. 57 (2015): Pages 186-196.
[2] M. Bentrcia, M. Alshitawi, H. Omar, Developments of alternative systems for automotive air conditioning – A review, Journal of Mechanical Science and Technology, Vol 32 (2018): page 1857-1867.
[3] Xiaodong Zhang, Dapeng Hu,, Performance simulation of the absorption chiller using water and ionic liquid 1-ethyl-3-methylimidazolium dimethylphosphate as the working pair, Applied Thermal Engineering, Volume 31, Issue 16, 2011, Pages 3316-3321.
[4] Chong Zhai, Zengguang Sui, Wei Wu, Geometry optimization of plate heat exchangers as absorbers in compact absorption refrigeration systems using H2O/ionic liquids, Applied Thermal Engineering, Volume 186, 2021, 116554.
[5] Yokozeki A, Shiflett MB. Water solubility in ionic liquids and application to absorption cycles. Ind Eng Chem Res 2010;49:9496–503.
[6] Gorakshnath D. Takalkar, Rahul R. Bhosale, Nilesh A. Mali, Sunil S. Bhagwat, Thermodynamic analysis of EMISE–Water as a working pair for absorption refrigeration system, Applied Thermal Engineering, Volume 148, 2019, Pages 787-795.
[7] S. Kim, P.A. Kohl, Analysis of [hmim][PF6] and [hmim][Tf2N] ionic liquids as absorbents for an absorption refrigeration system, Int. J. Refrig 48 (2014) 105–113.
[8] José M. Asensio-Delgado, Salvador Asensio-Delgado, Gabriel Zarca, Ane Urtiaga, Analysis of hybrid compression absorption refrigeration using low-GWP HFC or HFO/ionic liquid working pairs, International Journal of Refrigeration, Volume 134, 2022, Pages 232-241.
[9] Y. Sun, G. Di, J. Wang, X. Wang, W. Wu, Performance analysis of R1234yf/ionic liquid working fluids for single-effect and compression-assisted absorption refrigeration systems, Int. J. Refrig. 109 (2020) 25–36.
[10] S. Seki, T. Kobayashi, Y. Kobayashi, K. Takei, H. Miyashiro, K. Hayamizu, S. Tsuzuki, T. Mitsugi, Y. Umebayashi, Effects of cation and anion on physical properties of room-temperature ionic liquids, Journal of Molecular Liquids, 152 (2010) 9-13.

14th IEA Heat Pump Conference
15-18 May 2023, Chicago, Illinois

Development of a Near-isothermal Compressor for Transcritical Carbon Dioxide Cycle

Cheng-Yi Lee, Timothy Kim, Jan Muehlbauer, Yunho Hwang*,

Reinhard Radermacher

Center for Environmental Energy Engineering
Department of Mechanical Engineering, University of Maryland,
4164 Glenn Martin Hall Bldg., College Park, MD 20742, United States

Abstract

This study demonstrates the feasibility of a near-isothermal compressor for the transcritical CO_2 compression cycle. A copper tube-based compression chamber was designed, built, and installed in the open-loop liquid piston compression system. The oil compressed the CO_2 in the chamber from 40°C, 4,000 kPa to 10,000 kPa by an external gear pump. A 59% isothermal compression efficiency was measured at 900 RPM motor speed. To increase the efficiency, we tried the following two options: (1) lower the operation speed and (2) enhance the heat transfer rate. Evaporative cooling was applied by installing a mist generator in front of the chamber to improve the outer heat transfer performance. According to the experimental results, simply slowing down the operation to 270 RPM increases the efficiency to 80%, and combining evaporative cooling and slower operation delivers 93.8% of isothermal efficiency. Under this enhancement, the compression power can be 30% less than the isentropic compression. Several suggestions have been proposed to improve the current prototype's performance.

Keywords: Isothermal compression; Trans-critical CO2; Efficiency; Heat pump; Refrigeration

1. Introduction

The transcritical CO_2 application has been getting much attention recently, considering it has numerous advantages over traditional HFC refrigerants. First, CO_2 refrigerant is much cheaper than the HFC or HFO system. Second, CO_2 is a natural refrigerant with a global warming potential of 1, which will not be regulated. Hence, many researchers in academia and industry have considered CO_2 as a long-term solution for approaching carbon neutrality. Many applications are being studied and investigated, including vehicle heat pumps, residential heat pumps, heat pump water heaters, heat pump dryers, and commercial refrigeration [1].

Many methods can improve the efficiency of the transcritical CO_2 system, such as optimizing the gas cooler design, improving the control logic through artificial intelligence, or recovering the expansion work by using an expander, ejector, vortex tube, and so on. One of the intriguing approaches is reducing the compression work through isothermal compression. It can be commonly seen in Compressed Air Energy Storage (CAES) for isothermal compression technology to reduce the work required for compression, increasing the charge-discharge efficiency for CAES [2]. Unlike these conventional approaches, we proposed an integrated gas cooler compression system combining the gas cooler and compression chamber. In the typical transcritical CO_2 system, refrigerants are compressed isentropically, carrying the compression work to the gas cooler. Then the compression work and inherent internal energy are discharged into the environment. So the refrigerant enthalpy can reach the designed conditions. This study integrates these two processes into a single isothermal compression process, compressing the refrigerant and discharging the heat simultaneously and isothermally to

* Corresponding author. Tel.: +1-301-405-5247
E-mail address: yhhwang@umd.edu.

improve the system's efficiency. This work demonstrates the suggested idea's feasibility and proposes future design improvement suggestions.

2. Isothermal and Isentropic Compression in Transcritical CO_2

The transcritical CO_2 near-isothermal compression demonstrated excellent potential for compression work reduction and is compared with the isentropic compression process using the property chart in EES (Engineering Equation Solver). In Figure 1, the red square symboled curve illustrates the CO_2 refrigerant being isentropically compressed from 40°C and 4,000 kPa inlet to 10,000 kPa outlet. It should be noted that this suction condition is after considering the suction line heat exchanger to be employed. For isentropic compression, the compression work is the enthalpy difference between the initial and final state, which follows the isentropic line in the P-h diagram. On the contrary, the compression work of isothermal compression includes heat discharged out of the compression chamber to keep the constant compression temperature. Hence, the isothermal compression work could not be shown in the P-h diagram but can be evaluated in another way as follows. First, the isothermal compression process is divided into many finite segments. As an example, 100 segments are shown in Figure 1. Each segment comprises an isentropic compression and an isobaric cooling along the isothermal line. Then the isothermal compression work was derived by integrating the tiny consecutive compression and cooling operation for 100 segments. The other way is to integrate the pressure and volume variation during the compression process, as shown in Eq. (1).

$$W = \int_{V_i}^{V_f} P dV = \int_{V_i}^{V_f} \frac{ZnRT}{V} dV = ZnRTln\frac{V_f}{V_i} \quad (1)$$

where Z is the compressibility factor.

By comparing the finite segments approach with the ideal gas law approach, the calculated work difference is only 0.2%. Since pressure and temperature sensors are installed in the system, the refrigerant status can be calculated immediately and reflected in the P-h diagram. Therefore, the finite segments method would be applied to the following calculation to facilitate the compression work estimation.

Table 1. Compression Work Comparison

Initial Compression Conditions	Final Compression Condition	Isothermal Compression Work	Isentropic Compression Work	Work Reduction
40°C, 4,000 kPa	10,000 kPa	32.9 kJ/kg	48.5 kJ/kg	32.1 %

Table 1 illustrates the work input requirement to compress the CO_2 refrigerant from 40°C, 4,000 kPa to 10,000 kPa isothermally or isentropically. The isothermal compression work is 32.9 kJ/kg, and the isentropic compression work is 48.5 kJ/kg. Therefore, if the isothermal compression process replaces the isentropic compression in transcritical CO_2, the overall potential work reduction can achieve 32.1%, which benefits the refrigeration industry by cutting off the carbon footprint. The following chapter explains how this study experimentally approaches the near-isothermal process and demonstrates the possible work reduction using this technology.

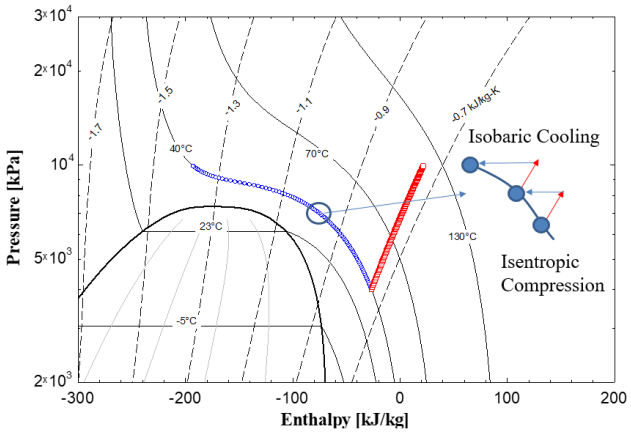


Fig. 1. CO_2 Compression Processes in P-h Diagram

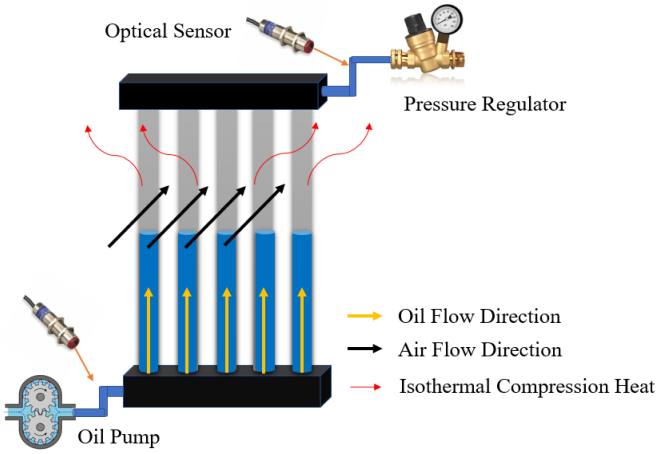


Fig. 2. Isothermal Compression Mechanism Schematic Diagram

3. Experimental Facility

3.1. Isothermal Compression Process Mechanism

A simple figure illustrating the fluids' movement was created to give the readers a better understanding of how we approach near-isothermal compression. In Figure 2, the CO_2 refrigerant stored in the compression chamber was compressed by pressurized oil, and the CO_2 pressure increased when the oil level elevated. Meanwhile, forced air cooling discharged the CO2 compression work and its internal energy from the compression chamber, maintaining the isothermal process. Once the CO_2 pressure reached the designed pressure, the pressure regulator opened, and the compressed CO2 was delivered downstream. The compression process finished when the upper optical sensor detected the oil level.

3.2. Experimental Facility

The first open-loop liquid piston isothermal compressor prototype has been designed for CO_2 and built to demonstrate the near-isothermal compression process, as shown in Figure 3 and the actual picture in Figure 4. The dimensions of the experimental facility, including integrated gas cooler compression chamber, tube diameters, and gear pump capacities, were developed based on delivering 1.75 kW of cooling capacity. Therefore, the self-built compression chamber utilized 17 of 6.2 mm inner diameter copper tubes with an outer diameter of 9.5 mm. The 1.65 mm wall thickness was designed to have a working pressure of 16,500 kPa and a burst pressure of 25,000 kPa with a safety factor of 1.5. The overall dimensions of the chamber are 0.61 m wide and 0.55 m height. And the overall heat transfer area is 0.279 m^2. The detailed chamber design parameters are listed in Table 2.

Table 2. Chamber Design Parameters

Parameter	Unit	Value
Compressor Suction Temperature	°C	40
Evaporating Temperature	°C	5
Mass Flow Rate	g/s	13.3
Cooling Capacity	kW	1.75
Operating Pressure	kPa	4,000 - 10,000
Cycle Frequency	Hz	0.1
Chamber Volume	m^3	0.00117
Chamber Heat Transfer Area	m^2	0.279

In Figure 3, the experimental facility is categorized into three major sections: (1) The left-hand side liquid oil circulation section. (2) The integrated gas cooler compression chamber. (3) The right-hand side compressed CO_2 storage and release section. At the beginning of the compression process, the mineral oil was fed into the 9.5 c.c gear pump at a given driven speed from the open oil tank. The atmosphere pressure oil was compressed

to 11,000 kPa limited by a back pressure regulator to ensure the liquid piston pressure was large enough to compress CO_2 to 10,000 kPa. In parallel, there is a relief valve set to 12,000 kPa for its bypass back to the oil tank in case of any unexpected situation. Since the gear pump operated continuously, even not in the compression process, the friction loss would increase the oil temperature. Before entering the compression chamber, an oil heat exchanger was placed to prevent heat accumulation and maintain the constant oil temperature. Two solenoid valves break down the liquid piston cycle into compression and suction process. If the compression solenoid valve opens and the suction solenoid closes, the oil flows into the compression chamber and starts compressing, and if the compression solenoid closes and the suction solenoid opens, the oil flows back to the oil tank. The compression speed depends on the driving speed of the motor. On the other hand, the suction speed depends on the opening of the needle valves. The longer the suction time, the more accurate the replenishment mass flow rate would be, but it reduced the cycle frequency or cooling capacity.

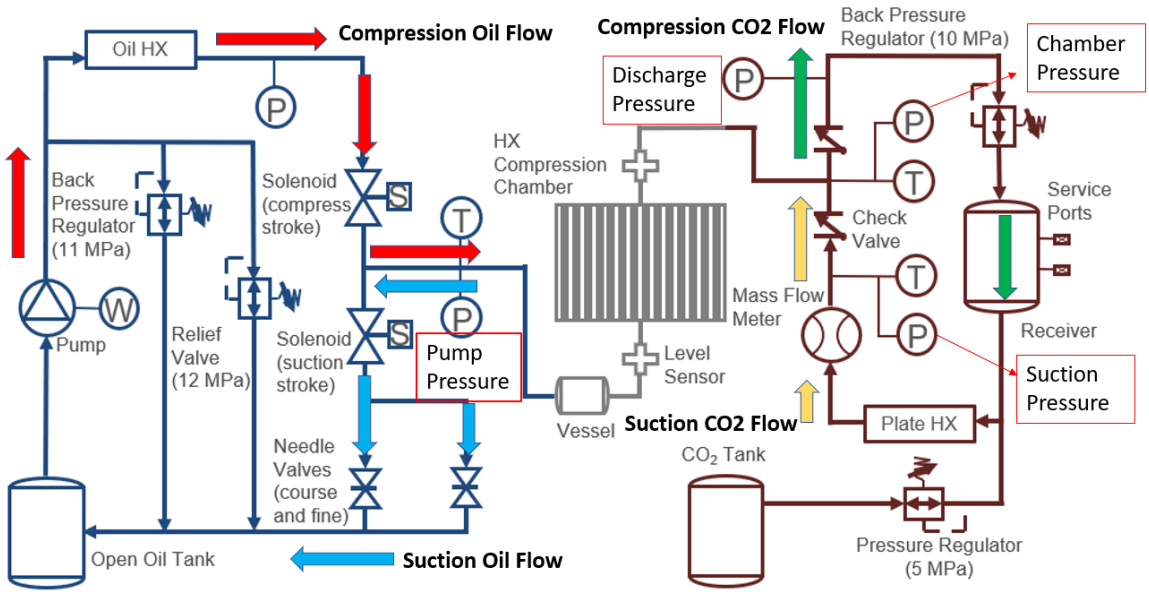


Fig. 3. Experimental Facility Schematic Diagram

The aforementioned integrated gas cooler compression chamber is located in the middle of the facility. The system's criteria for deciding when to compress and release depends on two optical leveling sensors. When the dyed mineral oil passes through the bottom-level sensors during the suction process, the detected sensor signal change makes the compression solenoid open, the suction solenoid close, and the compression process starts. When the oil reaches the top of the level sensor, the system responds vice versa.

Upon reaching 10,000 kPa for the CO_2 refrigerant compression, the compressed CO_2 passes the upper back pressure regulator and enters the receiver. During the suction process, a certain amount of CO2 was degassed from the mineral oil because of the solubility difference between 10,000 kPa and atmosphere pressure. Hence, the CO_2 from the supply tank would compensate for this loss and be mixed with CO_2 from the receiver. Altogether, the mixed CO_2 was conditioned to 40°C and recorded by the mass flow meter before flowing back into the compression chamber.

3.3. Instruments and Uncertainties

Table 3 lists the experimental facility's instruments and their systematic error. All the instruments were calibrated before being installed in the facility. The data were acquired when the system operated for at least half an hour and reached a steady state.

Table 3. Instruments and Uncertainties

Instrument	Model	Range	Systematic Error
Pressure Transducer	Setra, 280E	0 – 20,684 kPa	± 0.11% FS
RTD	Omega, 1/10 DIN	-100 °C – 400 °C	± 1/10 x (0.3 + 0.005 x t) °C
Mass Flow Meter	Micromotion CMFS010M	0 – 30 g/s	± 0.25% of reading
Watt Meter	Ohio Semitronics, PC5-062D	0 – 10 kW	± 0.5% F.S.
Gear Pump	Honor Externa,l 2GG1U09R	9.5 c.c. per rev.	N.A.
Motor	Baldor, EJMM.401T	10 hp, 1770 RPM max.	N.A
Axial Fan	N.A	1000 CFM	N.A

3.4 Test Matrix

The experimental facility was built inside the environmental chamber, which was set at 35°C and 20% in humidity. The initial chamber's temperature and pressure were set to 40 °C and 4000 kPa, respectively. And the final chamber pressure is 10,000 kPa. Two pump speeds, 270 RPM and 900 RPM have been chosen. In addition to the fan cooling, the room-temperature water mist was sprayed on the compression chamber surface as a heat transfer enhancement method in test #3, and an additional fan was installed to facilitate the water evaporation.

Table 4. Test Matrix

Test Number	Initial Chamber Temperature °C	Initial Chamber Pressure kPa	Final Chamber Pressure kPa	Pump Speed RPM	Evaporative Cooling Mist Temperature °C	Axial Fan Number
#1	40	4,000	10,000	900	NA	1
#2	40	4,000	10,000	270	NA	1
#3	40	4,000	10,000	270	35	2

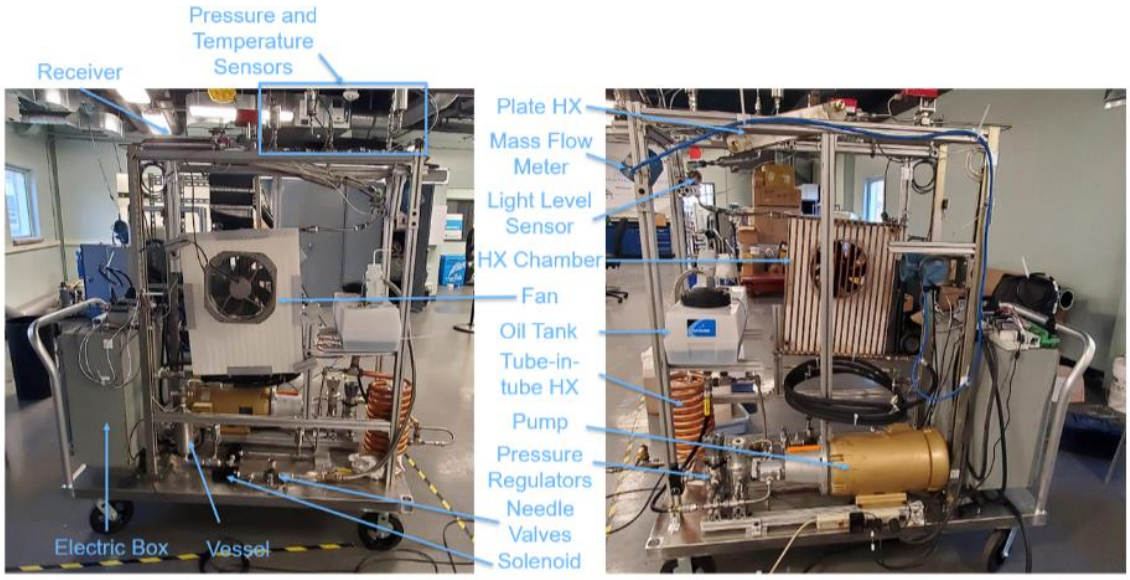


Fig. 4. Picture of Compression Chamber (left) and Experimental Facility (right)

4. Results and Discussion

4.1. 900 RPM Operation with Axial Fan Cooling: Test #1

The motor operation speed of 900 RPM has been chosen to observe the compression chamber's temperature and pressure variation under the isothermal compression process. In Figure 4, the upper graph displays the pressure variation in each measuring section. When the compression process starts, the pump elevates the liquid piston and compresses the refrigerant in the chamber, increasing the pump and chamber pressure simultaneously. Once the chamber pressure reaches 10,000 kPa, the upper back pressure regulator opens, and the compressed CO_2 flows into the receiver, which causes the suction pressure to increase. After the oil level reaches the upper-level sensors, the solenoid valves are switched, and the suction process is started. Consequently, the pump pressure built up because the compression solenoid valve closed, and the chamber started to decompress to the initial conditions (40°C, 4,000 kPa) and then started the compression process over again.

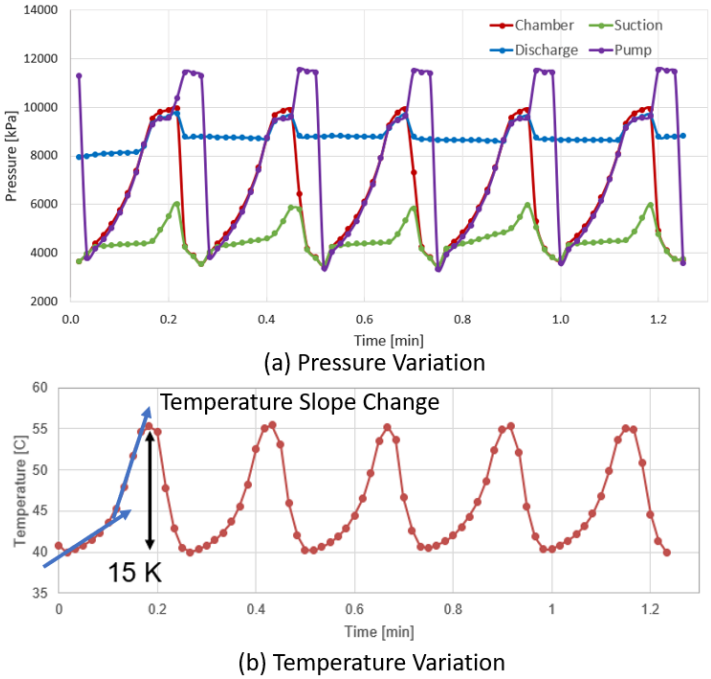


Fig. 4. Pressure and Temperature versus Time Plot at 900 RPM

Compared with the isentropic compression, which would result in a 117°C chamber temperature under the same given conditions, the current temperature increased to 55°C with a 15 K lift, demonstrating a 62 K temperature suppression. The chamber temperature in Figure 4 describes this temperature suppression for the test #1 condition. One thing worth noting is that the temperature curve has a noticeable slope change at around 7,000 kPa. It can be attributed to heat transfer area reduction and the reaching of the local CO_2 pseudocritical point. First, the heat transfer area between the compressed CO_2 and the environment becomes less as the liquid oil level upraises during compression. Second, Figure 5 shows that CO_2 density and specific heat increased dramatically from 4,000 kPa to 10,000 kPa, which means the internal energy is significantly different. The same thing can be observed in the P-h diagram, shown in Figure 1. A significant enthalpy drop can be found along the 40°C isothermal line. These factors make the chamber temperature inevitably deviate from the isothermal process.

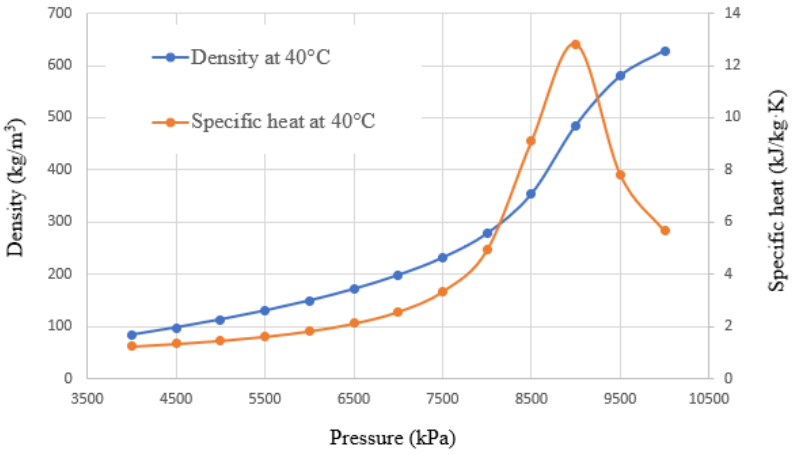


Fig. 5. Density and Specific Heat of CO_2 at 40°C and Various Pressures

The compression power curve and the mass flow rate of replenished CO_2 are depicted in Figure 6. Due to the open-loop design, the gear pump has to consume energy to hold the pump pressure to 4,000 kPa from atmospheric pressure, corresponding to the power consumption below the black line, which is about 1 kW. The motor power can be derived by integrating along the power line above the black line. According to the given product specification, the gear pump and motor have a combined efficiency of 0.72, and the actual work input for compressing the CO_2 must consider this factor. At the bottom of Figure 6, refrigerant replenishment can be derived by integrating the mass flow rate curve, and the integrated value stands for the initial CO_2 mass stored in the chamber for the next compression cycle.

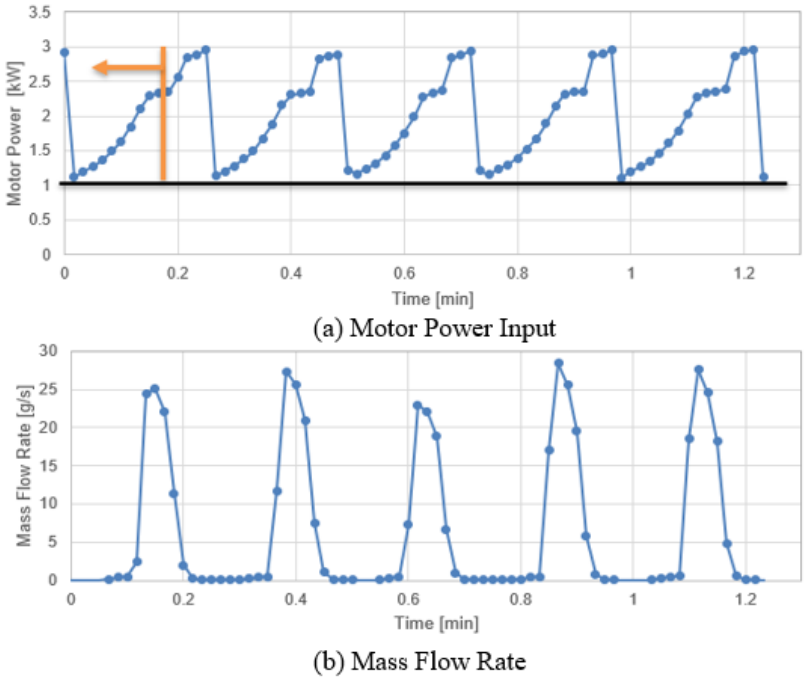


Fig. 6. Motor Power Input and CO_2 Mass Flow Rate

4.2. 270 RPM Operation and Evaporative Cooling Heat Transfer Enhancement: Tests #2 and 3

Based on the experimental results from the 900 RPM operation, which has 59.7% of isothermal efficiency, the current chamber design was too small to approach the near-isothermal operation for 1.75 kW cooling capacity. Nevertheless, the near-isothermal operation is still achievable by manipulating the control operation and heat transfer enhancement.

First, the motor compression speed is decreased to 270 RPM, the minimum allowable operating speed for the installed gear pump (Test #2). By slowing down the compression process, the extended heat transfer time helps discharge the accumulated heat inside the compression chamber. In contrast to Figures 5 and 6, Figure 7 only focuses on the single compression stroke. As shown in the upper left of Figure 7, the temperature lift is reduced to 10.6 K compared to 15 K in 900 RPM operation. For evaluating how the entire process is close to the isothermal compression, isothermal efficiency is defined as the ideal isothermal compression work divided by the actual compression work, which can be found in Eq. (2). And the motor plus pump efficiency was defined as actual compression work divided by the integrated work from the measurement, as shown in Eq. (3).

$$\eta_{iso} = \frac{W_{isothermal}}{W_{actual}} = \frac{Mass_{chamber} \cdot w_{isothermal}}{W_{integrated} \cdot \eta_{motor+pump}} \tag{2}$$

$$\eta_{motor+pump} = \frac{W_{actual\ work}}{W_{integrated\ work}} \tag{3}$$

In Eq. (2), the $W_{isothermal}$ represents the ideal compression work for the amount of CO_2 in the compression chamber, which was the product of CO_2 mass and the specific ideal isothermal work. The CO_2 mass can be derived from the initial CO_2 density and chamber volume. And $w_{isothermal}$ is the specific ideal isothermal work calculated from the second section, 32.9 kJ/kg. The actual work is calculated from the integrated work multiplied by the efficiency of the motor and pump. A 59.7 % isothermal efficiency can be found for operating the system at 900 RPM. As a comparison, a significant improvement to 80% isothermal efficiency can be achieved by slowing down the pump speed to 270 RPM.

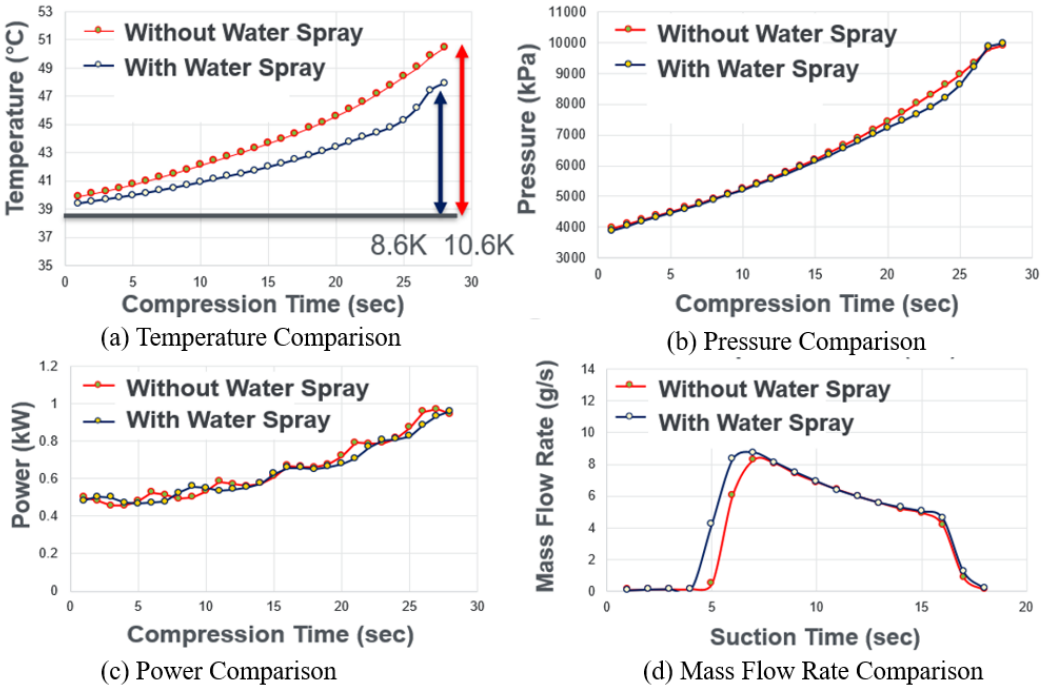


Fig. 7. Compression Behaviour Comparison at 270 RPM

Except for slowing down the rotation speed, additional heat transfer enhancement can be applied to the integrated gas cooler compression chamber (Test #3). While the current chamber's configuration limited the improvement method, evaporative cooling was chosen to help further enhance the heat transfer. According to Heyns and Kroger (2010), the water film heat transfer coefficient ranges from 1,500 to 3,000 $W/m^2 \cdot K$, which is the function of the deluge water mass flow rate, air mass flow rate, and deluge water temperature. The enhancement can significantly reduce the thermal resistance at the outer surface. Hence, a water mist generator was placed in front of the compression chamber. We made sure all the tubes were sufficiently wet during the compression chamber. In addition, one more axial fan was installed to improve the air volumetric flow rate, helping the water evaporate from the tube surface. By doing so, the temperature curve in Figure 7 shows further temperature suppression and maintains a relatively low-temperature increase compared to test #2. In the upper right of Figure 7, the pressure shows an evident suppression from 7,000 to 9,000 kPa, which has the most heat needed to be removed in the entire process.

However, a rapid increase in temperature and pressure occurred around 9,000 to 10,000 kPa because the heat transfer area was still too small to discharge heat. Evaporative cooling effectively improves the heat transfer rate and isothermal efficiency, which results in a 93.8% achievement. A detailed comparison can be found in Table 5. However, the lower motor RPM results in a decrease in cooling capacity. Assuming a gas cooler and a suction line heat exchanger were installed in the system, the cooling capacity in each test would be 1719, 674, and 743 W, respectively.

Table 5. Compression Performance Comparison

Objective	Unit	900 RPM	270 RPM	270 RPM with Evaporative Cooling
Energy per Cycle	kJ	6.12	3.91	3.67
Initial CO_2 Density	kg/m^3	84	83	81
CO_2 in Chamber	g	107	106	103.5
$W_{isothermal}/W_{actual}$	%	59.7	80.0	93.8
Average CO_2 Mass Flow Rate	g/s	7.4	2.9	3.2
Cooling Capacity	W	1719	674	743

Although the demonstrated prototype achieved high isothermal efficiency, many future design opportunities can improve furthermore. First, water has become scarce as climate change exacerbates yearly, and using it as heat transfer enhancement is not the ideal option. Instead, different geometries or fins would be applied to the outer compression chamber to increase the heat transfer area and coefficient. Second, the preliminary thermal resistance analysis shows that the CO_2 side was the dominant contributor to the overall thermal resistance compared with the conduction resistance and external resistance. Therefore, the heat transfer enhancement technique should also be applied to the internal chamber to lower the thermal resistance. Third, due to the lower operation speed, the average CO_2 mass flow rate was much lower than the design capacity. The number of tubes for the compression chamber should be increased accordingly to increase the heat transfer area and cooling capacity

5. Conclusions

The prototype of a near-isothermal compressor for transcritical CO_2 has been built and demonstrated the capability of achieving high isothermal efficiency. In this study, a 0.61 m by 0.55 m integrated gas cooler compression chamber was self-built, utilizing 17 tubes in 9.5 mm diameter. The compression process was set to compress 40°C, 4,000 kPa CO_2 to 10,000 kPa. Three different operation conditions were performed and compared: (1) 900 RPM compression with fan cooling, (2) 270 RPM compression with fan cooling, and (3) 270 RPM compression with evaporative cooling. The demonstrated isothermal efficiency was 59.7%, 80%, and 93.8%, respectively. Based on the current experimental results, three main improvement options were suggested: (1) enhance the outer heat transfer area and geometry of the compression chamber, (2) improve the inner heat transfer rate by applying turbulators or internal fins, and (3) increase the number of such tubes to enable a faster compression speed for higher system capacity. This study demonstrated that the near-isothermal compression process could be achieved. The 93.8% isothermal efficiency contributes 30% of the compression power input savings compared to traditional isentropic compression, which may facilitate the world and industry to achieve net-zero emissions.

Acknowledgments

This work was supported by the United States Department of Energy Award Number DE-EE0009685, the Consortium for Energy Efficiency and Heat Pumps, and the Center for Environmental Energy Engineering (CEEE) at the University of Maryland.

References

[1] Song, Y., Cui, C., Yin, X., & Cao, F. (2022). Advanced development and application of transcritical CO2 refrigeration and heat pump technology—A review. Energy Reports, 8, 7840-7869.
[2] Kim, T., Lee, C. Y., Hwang, Y., & Radermacher, R. (2022). A review on nearly isothermal compression technology. International Journal of Refrigeration.
[3] Heyns, J. A., & Kröger, D. G. (2010). Experimental investigation into the thermal-flow performance characteristics of an evaporative cooler. Applied Thermal Engineering, 30(5), 492-498.

14th IEA Heat Pump Conference
15-18 May 2023, Chicago, Illinois

Heat pumps in the United States: Market potentials, challenges and opportunities, technology advances

Mini Malhotra[a*], Zhenning Li[a], Xiaobing Liu[a], Melissa Lapsa[a], Tony Bouza[b], Edward Vineyard[c]

[a]Oak Ridge National Laboratory, P.O. Box 2008, Oak Ridge, TN, 37831, USA
[b]U.S. Department of Energy, 1000 Independence Ave, S.W., Washington, DC, 20585, USA
[c]Strata-G, 2027 Castaic Ln, Knoxville, TN, 37932, USA

Abstract

The US heat pump market has been affected by the socioeconomic impacts of the COVID-19 pandemic. However, the Biden administration's goal of net-zero greenhouse gas emissions by 2050 through electrification and clean energy technologies is accelerating the research, development, and deployment of heat pumps in the United States for improved energy performance, reduced greenhouse gas emissions, and wider adoption. The US heat pump market has experienced steady growth since 2010. In 2020, heat pumps surpassed gas furnace shipments for the first time, and the trend maintains through 2022. The current priority is to improve the affordability of energy and equitable access to heat pump technologies through cost reductions and further accelerate this trend. In addition, current R&D includes emphases on alternative refrigeration technology and lower–global warming potential refrigerants to reduce direct emissions. Heat pump market share is expected to grow as regulatory policies and financial incentives steer the building sector toward decarbonization. This paper reviews policies and market trends, discusses the challenges and opportunities in the current policy landscape, and reviews current research in the United States.

© HPC2023.
Selection and/or peer-review under the responsibility of the organizers of the 14th IEA Heat Pump Conference 2023.

Keywords: Heat pumps; US policy; shipments; heat pump market; research, development and deployment; electrification

1. Introduction

The halt in manufacturing and construction activities due to partial or complete lockdown during the COVID-19 pandemic severely impacted the global economy, including the heat pump market, in 2020 [1]. In 2021, global economy recovery began. However, the growth has been fragile because of the continued pandemic and geopolitical and economic uncertainties [2]. According to the United Nations [3], the economic impacts of the war in Ukraine has had both positive and negative effects on climate action. In particular, countries have an opportunity to address high prices and resource availability concerns by accelerating the adoption of clean energy, which also strengthens the fight against climate change [3]. Specifically, heat pump technologies are receiving unprecedented priority to reduce the use of fossil fuels and vulnerability to supply disruptions in response to the global energy crisis [4].

* Corresponding author. Tel.: +1-865-574-4317. *E-mail address:* malhotram@ornl.gov.
This manuscript has been authored by UT-Battelle, LLC, under contract DE-AC05-00OR22725 with the US Department of Energy (DOE). The US government retains and the publisher, by accepting the article for publication, acknowledges that the US government retains a nonexclusive, paid-up, irrevocable, worldwide license to publish or reproduce the published form of this manuscript, or allow others to do so, for US government purposes. DOE will provide public access to these results of federally sponsored research in accordance with the DOE Public Access Plan (http://energy.gov/downloads/doe-public-access-plan).

2. US Policies and Programs

The Biden administration's affirmatory response to international climate change agreements, including Paris Climate Accord to limit and resist climate change [5], and the Kigali Amendment to Montreal Protocol to phase down the consumption and production of hydrofluorocarbons [6], confirms a commitment toward global clean energy economy. The United States has set forth the goals to reduce greenhouse gas (GHG) emissions by 50%–52% from 2005 levels in 2030, decarbonize the US power sector by 2035, and achieve a net-zero emissions economy by 2050 [7]. Minimizing the emissions from buildings has been a priority to accomplish these goals [8]. Federal investments have been allocated to modernizing and upgrading buildings to be affordable, resilient, accessible, energy-efficient, and electrified [9]. A number of policies have been implemented, and targeted actions are taken to support heat pump technology research, expand deployment, and address supply chain vulnerabilities. Figure 1 shows a timeline of policies since 2020 that have supported the development and adoption of heat pump–related technologies.

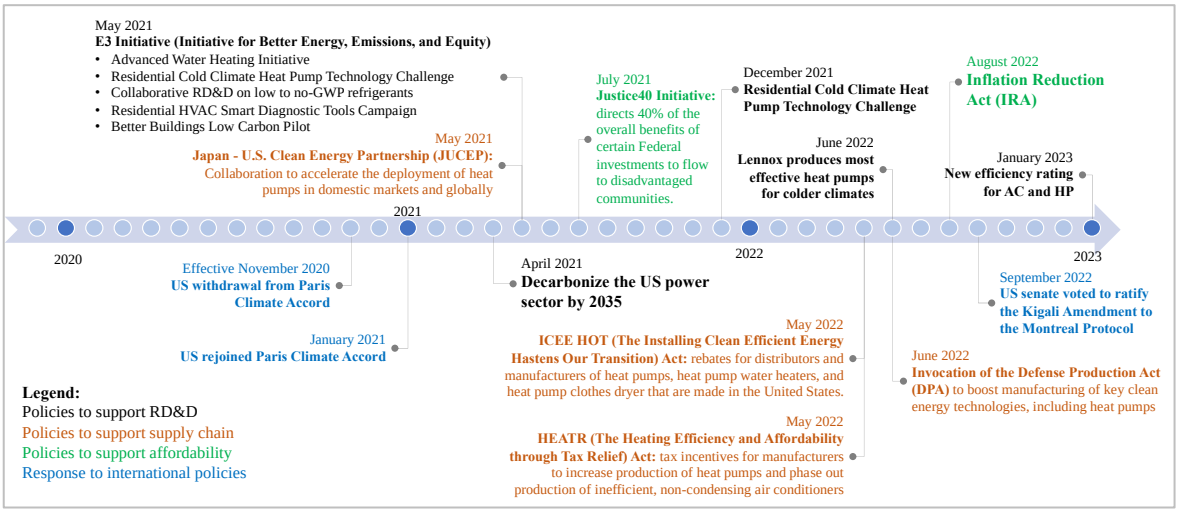


Fig. 1. Heat pump–related policies since 2020.

2.1. Policies and programs to support heat pump research, development, and deployment

In May 2021, the US Department of Energy (DOE) launched the E3 Initiative for improved energy, emissions, and equity to advance the research and adoption of clean energy technologies, including heat pumps. Initial actions under the E3 initiative included a nationwide Advanced Water Heating Initiative to increase market adoption of high-efficiency, grid-connected heat pump water heaters in residential and commercial buildings; the Residential Cold Climate Heat Pump Technology Challenge to accelerate the performance of cold climate heat pump technologies; and new collaborative research, development, and deployment efforts partnering national laboratories and manufacturers to accelerate the development of low– to no–global warming potential (GWP) refrigerants [10]. The focus of the E3 Initiative expanded to workforce solutions that ensure proper installation and maintenance through the Residential HVAC Smart Diagnostic Tools Campaign; and understanding implementation challenges through the Better Buildings Low Carbon Pilot [11].

2.2. Policies and programs to support heat pump supply chain

The United States has implemented international and domestic policies to respond to supply chain vulnerabilities and build up domestic manufacturing capacity. In May 2021, Japan and the United States collaborated under the Japan–US Clean Energy Partnership to accelerate the deployment of heat pumps in their respective domestic and global markets through support for manufacturing, training, and promotion [12]. On May 22, 2021, two bills—the ICEE HOT Act and HEATR Act—were introduced, which provide incentives for manufacturers and distributors of heat pumps [13]. In June 2022, the Defense Production Act was invoked to rapidly expand US manufacturing of five critical clean energy technologies, including heat pumps [14].

2.3. Policies and programs to increase affordability for heat pump technologies

To improve the affordability of energy and equitable access to heat pump technologies, the United States launched the Justice40 Initiative in January 2021, with the aim to direct 40% of the overall benefits of certain federal investments, including clean energy and energy efficiency, toward disadvantaged communities [15],[16]. These include R&D investments in the development of low-cost heat pump technology solutions and financial incentives for consumers. In August 2022, the Inflation Reduction Act was introduced, which offers tax credits and rebates for families to buy heat pumps and other energy-efficient home appliances, and rebates to low- to moderate-income households to electrify their homes [17].

3. Heat Pump Market

A review of the US heat pump market is presented in terms of prevalent heat pump technologies, market growth compared with competing heating and cooling technologies, and share in existing and new residential and commercial building sectors. Potential factors such as climate, energy price, efficiency standards, and financial incentives that impact the heat pump market are discussed.

3.1. Shipment

As shown in Figure 2, US heat pump market shipments predominantly comprises air source heat pumps. Heat pump water heaters, water loop heat pumps, and ground source heat pumps comprised a little over 7% of heat pump sales in 2022 [18]. More than 96% of air source heat pumps have a capacity of 19 kW or less [19].

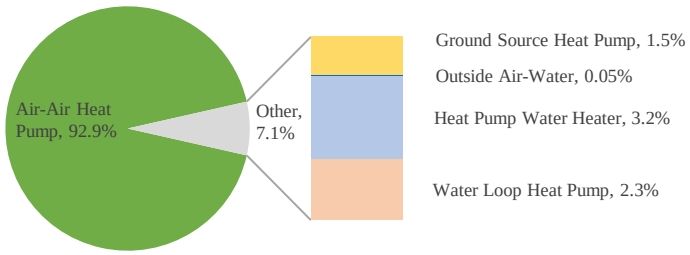


Fig. 2. 2022 market distribution of heat pump technologies.

Figure 3 shows the annual shipments of air source heat pumps (green) compared with gas and oil furnaces (orange and yellow, respectively) and central air conditioners (blue) since 2001. Despite the sharp drop in the shipments of all heating and cooling equipment during the 2006–2007 housing market collapse, the share of heat pumps (black dotted) has shown a relatively consistent increasing trend. In 2020, heat pumps surpassed gas furnace shipments for the first time and the trend maintains through 2022, reaching 52.6%. Meanwhile, the heat pump share in cooling equipment market reached 41.7% in 2022 [19].

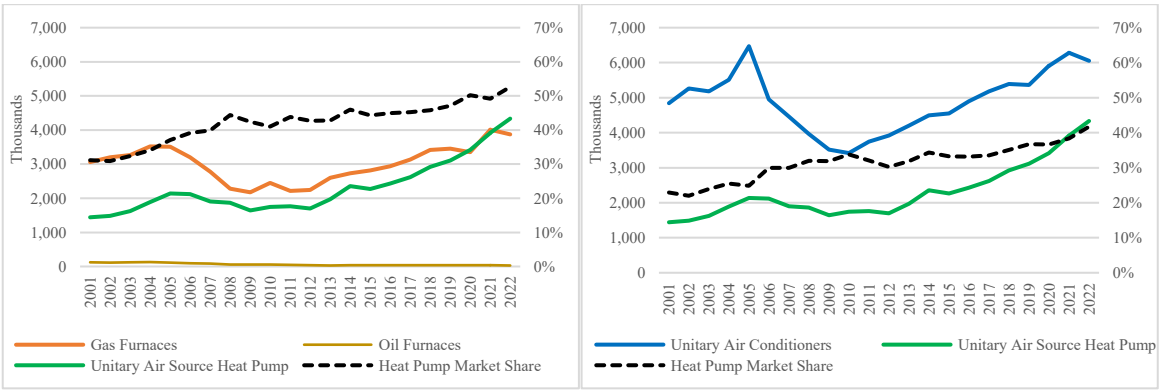


Fig. 3. Air source heat pump shipments compared with furnaces (left) and central air conditioners (right).

Figure 4 shows the sales of water loop heat pumps and heat pump water heaters since 2006 [18]. Water loop heat pumps are typically installed in multifamily buildings, hotels, dormitories, and so on, which may require simultaneous heating and cooling. Water loop heat pump shipments also saw a drop since 2007 due to the housing market collapse, and again, since 2019 as construction activities slowed down due to COVID-19 pandemic [18]. Heat pump water heaters have experienced a dramatic increase in sales due to the National Appliance Energy Conservation Act 2015 that requires higher energy factor ratings on all residential and some light-duty commercial products, and requires all electric water heaters of over 55 gal to use heat pump water heating technology [18].



Fig. 4. Water loop heat pump and heat pump water heater sales.

Figure 5 shows the annual shipments of ground source heat pumps (GSHP) in the last 20 years [18]. It shows a steady increase from 2003 to 2011, first, due to increasing natural gas price, and since 2009, when the federal government started offering tax rebates for GSHP installation. GSHP shipments were apparently affected when tax credits expired in 2016, but jumped back in 2019 when tax credits were reinstated. The GSHP shipment dropped again in 2020 due to the COVID-19 pandemic and the resulting halt in construction activities and supply chain issues [18]. The low natural gas price during the pandemic may also have contributed to the staggering growth of GSHP applications in the United States.

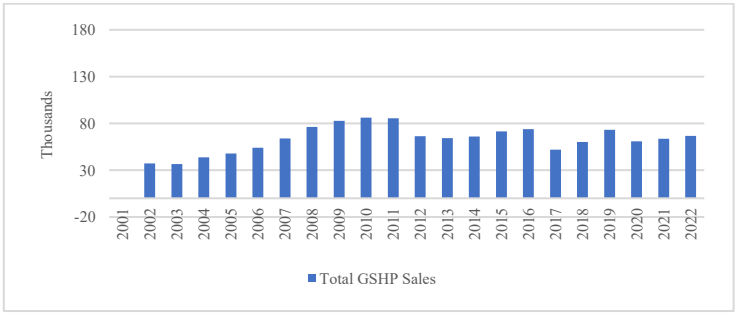


Fig. 5. GSHP sales.

3.2. Market share

The US Energy Information Administration's (EIA's) 2020 Residential Energy Consumption Survey estimates that approximately 15% of existing US homes use electric heat pumps as their primary heating source. The heat pump market share is higher in the South, where heat pumps serve one-third of existing homes [20]. The heat pump market share is smaller in the commercial building sector. According to EIA's 2018 Commercial Building Energy Consumption Survey, only 4.5% of existing US commercial building floorspace is served by electric heat pumps [21].

Based on the US Census Bureau's housing data [22], the market share of heat pumps in new single-family construction has stayed relatively constant since 2012. More than 39% of single-family homes completed in the United States in 2021 used a heat pump as their primary heating source (Figure 6, left). An estimated 59% of single-family homes completed in the South in 2021 used a heat pump for heating. The share has remained at 60% or more since 2011 (Figure 6, right). In the West, the installation of heat pumps has been ramping up, reaching 17% in 2021—the highest share since 1986. The housing construction, as well as the heat pump share, has declined in the Midwest. The heat pump market share has fluctuated in the Northeast, but stayed at a share of less than 10% [18].

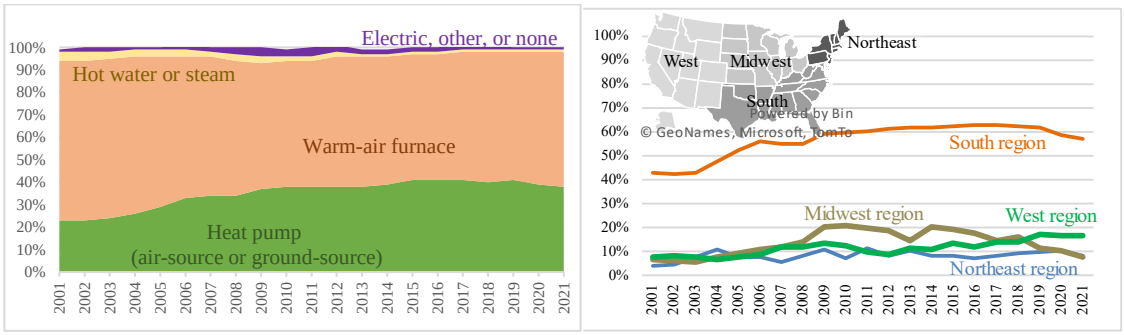


Fig. 6. Share of heat pumps in new single-family houses: (left) Comparison with other heating system types across the United States, and (right) heat pump share by US census region.

3.3. Energy price

Figure 7 shows the historical and projected prices of electricity and natural gas for residential sector in the United States [23],[24]. Both nominal and real prices[1] are shown to allow for a more accurate comparison between the past and predicted values. Over the 2007–2018 period, natural gas prices have decreased, and electricity prices gradually risen (or remained relatively level in terms of real price). Under nominal conditions[2], the prices are predicted to change with a 2022–2050 growth rate of 2.2% for electricity (-0.2%, considering real price) and 1.8% for natural gas (-0.5%, considering real price) [24].

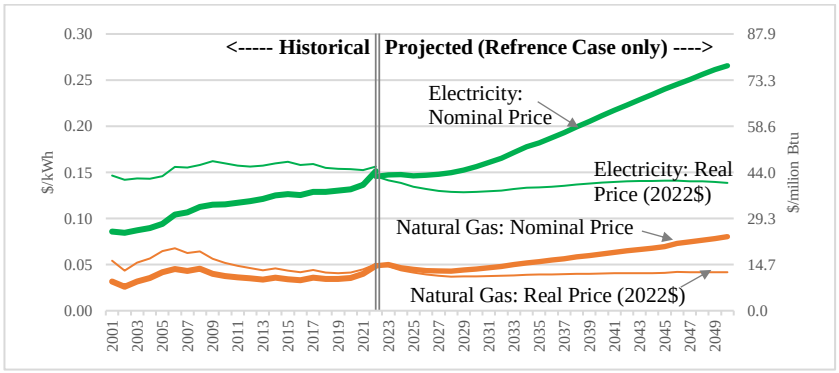


Fig. 7. US average historical and projected residential electricity and natural gas prices.

Figure 8 shows the 2021 natural gas and electricity prices by state [25],[26]. The regional differences in the heat pump market share, as noted in Figure 6 (right), can be attributed to the mild winter combined with lower electricity and higher natural gas prices in the southern states.

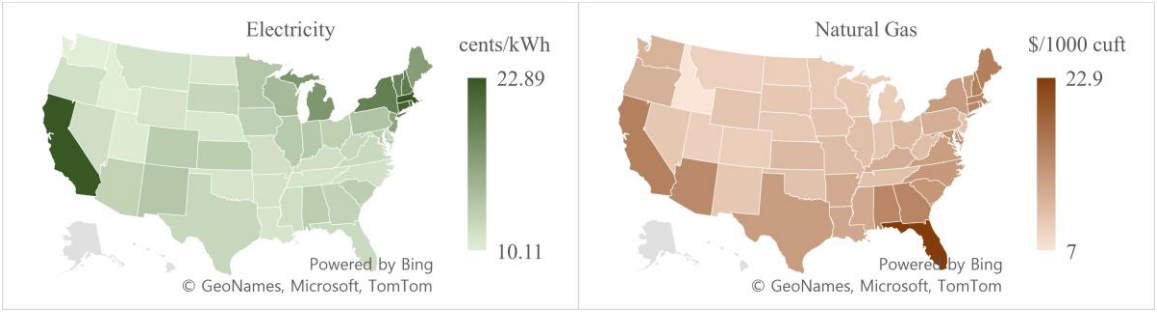


Fig. 8. 2021 residential energy prices by US state: (left) electricity and (right) natural gas.

[1] Nominal price is the price paid for a product or service at the time of the transaction. Real price is a price that has been adjusted to remove the effect of changes in the purchasing power of the dollar, expressed in constant dollars relative to a base year.
[2] The EIA's Annual Energy Outlook modeled projections include cases with different assumptions about macroeconomic growth, world oil prices, and technological progress. The Reference Case represents projections under nominal conditions, which presumes no new policy or laws over the modeled time horizon.

3.4. Financial incentives

Heat pump installations in the United States have been in part driven by an array of tax credits. As part of the Inflation Reduction Act of 2022, federal tax credits have been extended through 2032 [27]. Equipment tax credits of $300 is available for installing air source heat pumps and heat pump water heaters in existing homes that meet specified efficiency criteria. Renewable energy tax credits are available for geothermal heat pump installation in existing homes and new construction, with a gradual step down in the credit value (i.e., 22%–30% of system cost) based on the year the system is placed in service. In addition, most states offer rebate programs for air source and geothermal heat pump installation [28]. Other common financial incentive mechanisms are available as loan programs, grant programs, and Property-Assessed Clean Energy financing [28]. The recent high natural gas prices and the uncertainties in natural gas supplies make the investment in GSHP systems more economically viable than during the pandemic. For example, New York and Massachusetts have invested in several pilot projects for district-scale GSHP systems [29].

Furthermore, under the High-Efficiency Electric Home Rebate Act, a part of the Inflation Reduction Act of 2022, point-of-sale consumer rebates are available for low- and moderate-income households to electrify their homes. The rebate covers 50%–100% of purchase and installation costs up to $14,000 on electrification measures, including heat pumps, heat pump water heaters, panel/service upgrades, electric stoves, clothes dryers, and insulation/air sealing measures [30].

These financial incentives help reduce the cost burden on consumers of heat pump technologies and support electrification.

3.5. Efficiency Standards

In the United States, the cooling and heating efficiency of central heat pumps is measured by seasonal energy efficiency ratio (SEER)[3] and heating seasonal performance factor (HSPF)[4]. The minimum efficiency standards for heat pumps were established in 1992 and were updated in 2006 and 2015 [31]. In 2017, DOE announced changes to the testing procedure and rating descriptor for central air conditioners and air source heat pumps. Effective January 2023, they will be rated by SEER2 and HSPF2 (as opposed to the current SEER and HSPF rating descriptors) following a more stringent testing procedure. The new testing procedure increases the systems' external static pressure by a factor of five to better reflect field conditions of installed equipment in a typical ducted system and results in a lower numerical rating value for the same product [32]. Thus, beginning in 2023, all new residential air source heat pump systems sold in the United States are required to meet or exceed 14.3 SEER2 and 7.5 HSPF2 (equivalent to 15 SEER and 8.8 HSPF) compared with 14 SEER and 8.2 HSPF required by the current standard that went into effect in 2015 [33]. The efficiency standards for other heat pump technologies are unchanged and are summarized in Joe *et al.* [34].

4. Challenges and Opportunities

The US government's decarbonization goal and the supporting policies and programs have presented an unprecedented opportunity for advancing the research, development, and deployment of heat pump technologies. Electrification of buildings and large-scale deployment of heat pumps are key to accomplishing this goal. A review of the heat pump market indicated areas and sectors that need dedicated solutions to encourage heat pump adoption. Solutions for increasing the supply chain capacity; workforce expansion, training, and education; affordability and accessibility for heat pump technologies; and a supporting grid infrastructure are needed. Key technological challenges include lack of regional solutions for cold climates, high upfront cost, complicated design and control of the components and system for hybrid heat pumps with multiple heat sources, compromised energy benefits due to installation challenges, and space constraints that potentially limit the installation of heat pumps.

Specific research topics to address these challenges include the following:

1. Improve efficiency and capacity of heat pumps for cold climates, and efficiency of systems for warm climates
2. Reduce installed cost and improve reliability of high-efficiency systems

[3] The total heat removed from the conditioned space during the annual cooling season, expressed in Btu's, divided by the total electrical energy consumed by the central air conditioner or heat pump during the same season, expressed in watt-hours.

[4] The total space heating required during the heating season, expressed in Btu, divided by the total electrical energy consumed by the heat pump system during the same season, expressed in watt-hours.

3. Develop solutions for problematic heat pump installations, such as space and electrical panels, particularly for retrofit and renovation applications
4. Develop alternative refrigeration technologies and lower-GWP refrigerants to reduce direct emissions

Tackling these challenges requires technological, economic, social, and political innovations from all stakeholders by developing efficient systems with efficient components, smart monitoring, optimal control, innovative system integration, aggregation, and servicing.

5. Current R&D Focus

This section reviews recent research and developments in heat pump systems in the United States. The goals of R&D efforts are to increase the energy efficiency, reduce system cost, expand single-function equipment to be multi-function systems, and reduce environmental impacts. The focuses of these developments are depicted in Figure 9.

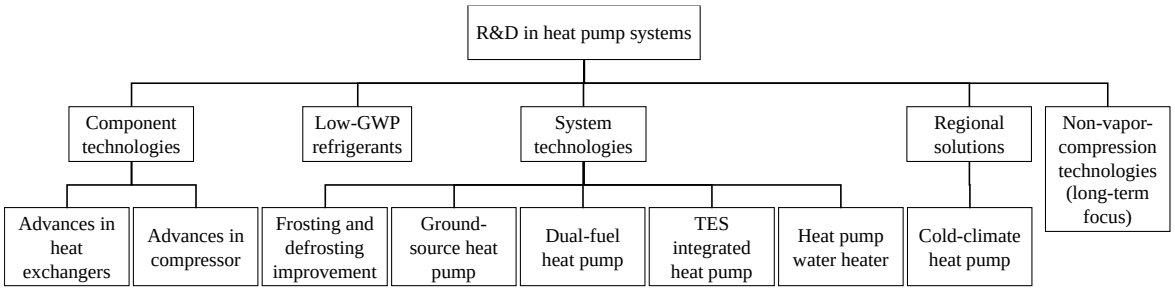


Fig. 9. Research and development focus for heat pump systems.

Advances in heat exchangers: The evolving simulation and manufacturing capabilities have given engineers new opportunities to pursue high-performance, cost-efficient heat exchanger designs. Figure 10 shows a topology optimized heat exchanger fabricated by additive manufacturing [35]. There has always been a great emphasis on understanding the underlying physics and improving the performance of these heat exchangers. Recently, researchers have been investigating the use of small hydraulic diameter flow channels and novel heat transfer surfaces based on topology optimization. The designs include shape-optimized tubes, as well as tube bundles with varying tube and fin geometries and refrigerant flow paths. The research interests for heat exchangers include mitigating the impact of airflow and refrigerant maldistribution, developing methods to reduce material/cost, developing advanced manufacturing techniques, and using technologies such as desiccant-coated, water-sorbing heat exchangers to reduce energy for dehumidification [36].

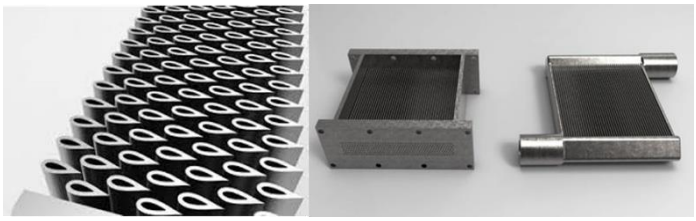


Fig. 10. Topology optimized heat exchanger fabricated by additive manufacturing [35].

Advances in compressors: The goal for new compressors is to reduce the power consumption, and one effective way is to keep compression temperature low. Most recently, several teams in US universities and national labs invest efforts to develop isothermal compressors that transfer heat out of the chamber during the compression process [37].

Low-GWP refrigerants: Natural refrigerants, HFO (hydrofluoroolefins), and HFO mixtures have significantly lower GWPs than traditional HFC (hydrofluorocarbons) refrigerants. Researchers have selected HFO refrigerants via drop-in testing and optimized heat pump components to achieve optimal solutions considering the trade-offs among low GWP, low flammability, and high system performance. Air-Conditioning, Heating, and Refrigeration Institute (AHRI) has established this industry-wide cooperative research program to identify and evaluate promising alternative refrigerants for major product categories. The

AHRI Low-GWP Alternative Refrigerants Evaluation Program (AREP) includes compressor calorimeter testing, system drop-in testing, soft-optimized system testing, and heat transfer testing [38]. For component soft optimization with goal of improving system performance with low-GWP refrigerants, the major efforts are on heat exchanger and compressor designs [39]. The IEA Annex 53 on advanced cooling/refrigeration technology development is exploring two directions on low-GWP refrigerants application: advanced vapor compression with low- or ultralow-GWP refrigerants, and nontraditional technologies such as zero-GWP refrigerants. McLinden *et al.* [40] identified 138 low-GWP refrigerants by screening more than 60 million chemical formulas. They filtered out the refrigerants according to several criteria. For instance, only molecules that consist of eight chemical elements were chosen, and the maximum number of atoms in a molecule was limited to 18. In addition, the critical temperature was limited to between 320K and 420 K. After filtering out highly toxic and unstable fluids, the screening identified 23 fluids with GWP values below 1000.

Frosting and defrosting improvements: Problems of frosting and defrosting are one of the biggest obstacles restricting the promotion of air source heat pumps. Research includes understanding the frosting and defrosting mechanism; comparing different defrosting technologies, including hot gas bypass, reverse cycle defrosting, electric heater, and dual hot gas bypass; thermal energy storage–based new reverse cycle defrosting to mitigate the indoor thermal discomfort during defrosting cycle; using frost-free air source heat pumps by different latent heat removal technologies to dehumidify the outdoor coil; and optimizing heat exchanger circuitry for uniform frost formation [41].

GSHPs: To enable wider adoption of GSHP systems, several recent projects have tried to reduce the cost of ground heat exchanger by developing shallow bore ground heat exchanger [42],[43] and advanced design tool for borehole field to minimize needed drilling [44],[45]. In addition, a web based GSHP screening tool has also be developed and released to public [46],[47]. This tool allows potential consumers of GSHP system to quickly evaluate the costs and benefits of retrofitting almost any existing commercial and residential buildings in the United States. To enable quick retrofit/replacement of existing conventional HVAC equipment, a dual-source heat pump (DSHP) has been prototyped and tested in an experimental house. DSHP can use the ambient air or the ground as heat sink or heat sources. It can switch between the two sources based on the available temperature of each. Therefore, it has potential to solve the performance degradation problem of ASHP in cold climate and cost less than conventional GSHP system by using a smaller ground heat exchanger. The DSHP system can also be integrated with thermal energy storage to shift electric demand from peak hours to off-peak hours or provide active demand side response according to control signals of electric grid operators [48]. DOE's Geothermal Technologies Office released its roadmap for developing geothermal energy, including geothermal heat pump, in its GeoVision study [49]. One of the goals of Multi-Year Program Plan of the Geothermal Technologies Office is to implement geothermal heat pumps in 28 million homes by 2050.

Dual-fuel heat pumps (DFHPs): DFHPs, consisting of an electric heat pump and a natural gas furnace, are a promising compromise between economic and environmental impacts in the transition period toward zero emissions and eliminating the use of fossil fuels. Dual fuel heat pumps allow customers to adapt to changing temperatures and fuel prices, since they can easily alternate power or fuel sources. Plus, like other advanced electric technologies, many dual fuel heat pumps can be programmed to optimize economic or environmental impacts according to utility goals. Current research focuses on smart control of DFHPs to optimize their switching/mode of operation between furnace and heat pump modes in response to the outdoor temperature, gas and electricity prices, desired indoor temperature, and renewable energy generation to improve energy efficiency, minimize energy cost, and minimize carbon footprint [50].

Thermal energy storage (TES)-integrated heat pumps: Integrating heat pumps with a TES component to shift most of the electricity used for space cooling and heating from peak to off-peak periods is a popular research topic [51]. Commonly used phase change materials (PCMs) include paraffin wax, ice, and salt hydrates. Taking advantage of the thermal energy storage ability, several feasible PCM application schemes have been proposed. One of the recent research focuses is to develop a model-predictive control strategy to regulate the PCM tank charging and discharging mode switching based on weather, utility, and grid emission signals. Simulation based research have demonstrated the efficacy of TES-integrated heat pumps for electrification of space cooling and heating devices without overtaxing the grid [52]. Most recently, under the auspices of IEA Annex 55, the project "Comfort and Climate Box" develops nearly market-ready TES-integrated heat pump systems for cooling-dominated climate regions for 11 countries including the United States [53].

Heat pump water heaters: Potential research areas to improve heat pump water heater performance include incorporating defrost strategies to boost performance under low or extreme ambient conditions; considering suitable refrigerants for heat pump water heater applications; applying advanced materials and

components to increase storage capacity; developing smart control strategies to optimize energy use, reduce operation cost, and reduce CO_2 emission; developing products with multi-function applications; and developing plug-in 120 V heat pump water heater units [54].

Cold-climate heat pumps (CCHPs): Driven by the building sector electrification policy in the United States, CCHPs are a popular research focus. For CCHPs, research challenges include the following: First, the maximum COP of the advanced system under low ambient temperature condition is relatively small in terms of primary energy ratio. Second, the heating capacity needs to be further enhanced to satisfy the building load, especially under extreme conditions. In addition, low-temperature start-up technology and year-round control strategy have potential to improve the reliability of CCHP systems. CCHPs can be classified into three categories: single-stage, dual-stage, and multi-stage compression systems [55]. For single-stage compression systems, employing an ejector and new refrigerant can improve the heating performance but cannot reduce the discharge temperature of the compressor. For dual-stage compression systems, various intermediate configurations, such as flash tank, sub-cooler, and ejector, are employed to enhance the heating performance to the maximum extent. For multi-stage compression systems, the theoretical COP increases with the number of compression stages. In general, CCHP technologies includes innovations on compressor technology, new system configuration, new cycle types such as vapor injection, defrosting technology and expansion loss recovery [56]. Long-term research, development, and deployment efforts have made heat pumps a viable option even in cold climates. DOE recently launched the Residential Cold Climate Heat Pump Technology Challenge to accelerate the deployment of technologies in very cold climates. Optimized heat pump solutions differentiated by climate needs could lower equipment costs.

Non-vapor compression technologies, as listed in Figure 11 [57], have also been developed to eliminate high GWP refrigerants, improve source energy efficiency, or expand operating conditions. Long-term R&D is still needed to improve performance, reliability, and cost effectiveness.

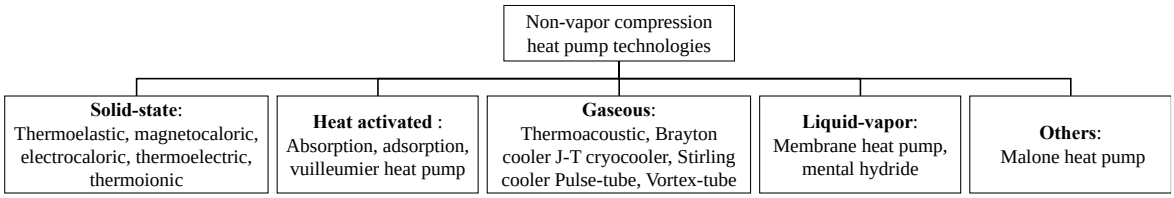


Fig. 11. Summary of non-vapor compression heat pump technologies

DOE's Building Technologies Office (BTO) characterized the non-vapor compression technologies based on their technical energy savings potential and development status as shown in Figure 12 [58]. The top favored technologies are thermoelastic, membrane heat pumps, evaporative liquid desiccant, magnetocaloric, and vuilleumier heat pump.

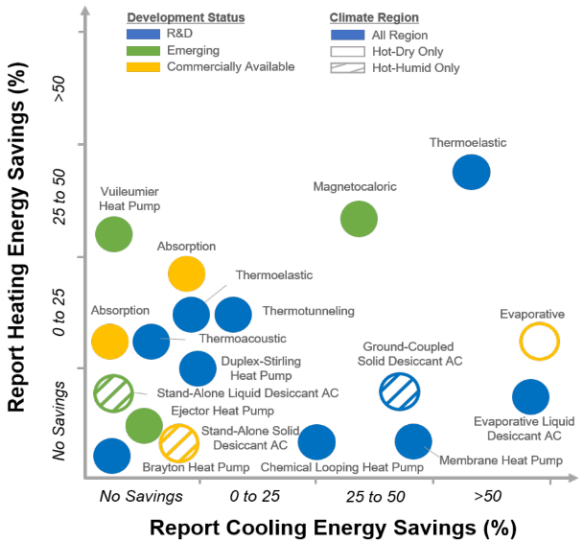


Fig. 12. Energy saving potential for different non-vapor compression technologies reorganized based on [58].

6. Summary and Outlook

This paper presents a review of the US policies, heat pump market potentials, identifies challenges and barriers facing large-scale deployment of heat pumps, and provides a brief review of recent developments in heat pump technologies.

The US government's decarbonization goal and the supporting policies and programs have presented an unprecedented opportunity for advancing the research, development, and deployment of heat pump technologies [59]. A large increase in heat pump policies and incentives, notably in the US Inflation Reduction Act, is set to accelerate their deployment [4]. Governmental actions, along with public and private sector incentive programs for heat pump and building electrification, promote deploying more efficient heat pump systems.

The US heat pump market has shown steady growth since 2010—faster relative to competing space heating technologies. However, the market growth is uneven geographically, with a very small market share in cold climates. The heat pump market share is also very small in the commercial sector. GSHP market trends show a direct and immediate influence of tax credits.

There are several hurdles to expanding heat pump deployment, including the relatively high cost of installation; high operational costs in cold climates; various supply chain constraints such as limited manufacturing capacity and shortages of skilled workers; and existing building stock with fossil fuel systems and constraints for fuel-switching.

DOE is investing heavily in heat pump technology. Research efforts have significantly improved the energy efficiency of heat pumps, as evidenced by the evolving efficiency standards. The development of component technologies effectively reduces the energy consumption, and the expansion of multi-functional equipment has enabled heat pumps to perform efficiently with wider applications. To further expand the usage of heat pumps, continuous efforts are needed to improve performance and reliability while discovering novel applications.

As the share of renewables in the energy mix increases, heat pumps can play an important role in electrifying the building sector. Heat pump technology is mature, and production and installation can, in principle, be scaled up quickly. Long-term solutions, including policy consistency, targeted action to strengthen supply chains, building the grid capacity, and expanding renewables, thermal storage, and smart technology (such as smart thermostats, zoning control, and auxiliary heat control) at lower costs, are needed to encourage further investment [4]. The future of heat pump technologies will be highly influenced by the evolving minimum standards, R&D, tax credits, and incentive programs.

Acknowledgments

This research used resources at the Building Technologies Research and Integration Center, a DOE Office of Science User Facility operated by the Oak Ridge National Laboratory. The authors would like to acknowledge Brian Fricke, Bo Shen, and Kyle Gluesenkamp from Oak Ridge National Laboratory and the DOE Building Technologies Office for their support.

References

[1] Grand View Research. Heat Pump Market Size, Share & Trends Analysis Report by Technology (Water Source, Air Source, Ground Source), by Application (Commercial, Residential, Industrial), by Region, and Segment Forecasts, 2022–2030. GVR-3-68038-589-2. March 15, 2022.

[2] United Nations Department of Economic and Social Affairs. Fragile economic recovery from COVID-19 pandemic upended by war in Ukraine. https://www.un.org/en/desa/fragile-economic-recovery-covid-19-pandemic-upended-war-ukraine, accessed March 15, 2023.

[3] United Nations Department of Economic and Social Affairs. World Economic Situation and Prospects as of mid-2022. May 18, 2022. https://www.un.org/development/desa/dpad/publication/world-economic-situation-and-prospects-as-of-mid-2022/

[4] International Energy Agency. The Future of Heat Pumps. World Energy Outlook Special Report, Revised December 2022.

[5] Whitehouse.gov. Paris Climate Agreement. January 20, 2021.

[6] Whitehouse.gov. Statement by President Joe Biden on Senate Ratification of the Kigali Amendment to the Montreal Protocol. September 21, 2022.

[7] Whitehouse.gov. FACT SHEET: President Biden Sets 2030 Greenhouse Gas Pollution Reduction Target Aimed at Creating Good-Paying Union Jobs and Securing U.S. Leadership on Clean Energy Technologies. April 22, 2021.

[8] US Department of Energy. Net Zero Buildings Week: Commercial Buildings. March 31, 2021.

[9] Whitehouse.gov. FACT SHEET: Biden Administration Accelerates Efforts to Create Jobs Making American Buildings More Affordable, Cleaner, and Resilient. May 17, 2021.

[10] US Department of Energy. FACT SHEET: The E3 Initiative. DOE/EE-235, May 2021, Revised June 2022.

[11] US Department of Energy. Energy, Emissions and Equity (E3) Initiative. https://www.energy.gov/eere/buildings/energy-emissions-and-equity-e3-initiative, accessed March 15, 2023.

[12] Whitehouse.gov. FACT SHEET: U.S.- Japan Climate Partnership. May 23, 2022.

[13] Garry, M. U.S. Senate Introduces Two Bills Supporting Transition to Heat Pumps. June 3, 2022. https://r744.com/u-s-senate-introduces-two-bills-supporting-transition-to-heat-pumps/

[14] US Department of Energy. President Biden Invokes Defense Production Act to Accelerate Domestic Manufacturing of Clean Energy. June 6, 2022.

[15] Whitehouse.gov. Justice40 – A Whole-of-government Initiative. https://www.whitehouse.gov/environmentaljustice/justice40/, accessed March 15, 2023.

[16] US Department of Energy. Justice40 Initiative, Office of Economic Impact and Diversity. https://www.energy.gov/diversity/justice40-initiative, accessed March 15, 2023.

[17] Whitehouse.gov. BY THE NUMBERS: The Inflation Reduction Act. August 15, 2022.

[18] BRG, 2022. The North American Heating & Cooling Product Markets, 2022 Edition. BRG Building Solutions.

[19] The Air-Conditioning, Heating, and Refrigeration Institute (AHRI). Historical Data. https://www.ahrinet.org/analytics/statistics/historical-data, accessed March 15, 2023.

[20] US Energy Information Administration. 2020 Residential Energy Consumption Survey. March 2023. https://www.eia.gov/consumption/residential/data/2020/

[21] US Energy Information Administration. 2018 Commercial Building Energy Consumption Survey. Revised December 2022. https://www.eia.gov/consumption/commercial/data/2018/

[22] US Census Bureau, 2022. Type of Heating System Used in New Single-Family Houses Completed. https://www.census.gov/construction/chars/xls/heatsystem_cust.xls

[23] US Energy Information Administration, 2022. Real Prices Viewer, EIA Short-Term Energy Outlook, March 2023. https://www.eia.gov/outlooks/steo/realprices/

[24] US Energy Information Administration. Annual Energy Outlook 2023. March 16, 2023. https://www.eia.gov/outlooks/aeo/

[25] US Energy Information Administration. Natural Gas Prices. https://www.eia.gov/naturalgas/data.php#prices, accessed March 15, 2023.

[26] US Energy Information Administration. Electricity Sales (consumption), revenue, prices & customers. https://www.eia.gov/electricity/data.php#sales, accessed March 15, 2023.

[27] Energy Star. Federal Income Tax Credits and Other Incentives for Energy Efficiency. Information updated 12/30/2022. https://www.energystar.gov/about/federal_tax_credits

[28] Database of State Incentives for Renewables & Efficiency (DSIRE). http://www.dsireusa.org/, accessed November 2, 2022.

[29] Gilman, S. New York, Massachusetts Utilities Investigate Potential New Business Model: Community-Scale Geothermal. January 26, 2021. https://energycentral.com/o/EPRI/new-york-massachusetts-utilities-investigate-potential-new-business-model

[30] US Department of Energy. Biden-Harris Administration Announces State And Tribe Allocations For Home Energy Rebate Program. November 2, 2022.

[31] Vineyard, E., Baxter, V. US Heat Pump Market – 2021 Update. International Energy Agency, Technology Collaboration Programme. September 7, 2021. https://heatpumpingtechnologies.org/wp-content/uploads/2021/09/mcr-iea-hpt-presentation-us-20210907.pdf

[32] Code of Federal Regulations, Title 10, Part 430, Subpart B, Appendix M1 – Uniform Test Method for Measuring the Energy Consumption of Central Air Conditioners and Heat Pumps. January 1, 2022.

[33] Code of Federal Regulations, Title 10, Section §430.32 Energy and water conservation standards and their compliance dates. January 1, 2022.

[34] Joe, J., Malhotra, M., Lapsa, M., Baxter, V. US Heat Pump Market Overview – 2020. *Proceedings of the 13th IEA Heat Pump Conference*, Jeju, South Korea, April 26–29, 2021.

[35] Bacellar, D., Aute, V., Huang, Z., Radermacher, R. Design optimization and validation of high-performance heat exchangers using approximation assisted optimization and additive manufacturing. *Science and Technology for the Built Environment* (2017) 23:896–911. DOI:10.1080/23744731.2017.1333877

[36] Li, Z. Advanced Modeling and Refrigerant Flow Path Optimization for Air-to-refrigerant Heat Exchangers with Generalized Geometries. Ph.D. dissertation, University of Maryland, College Park, MD, 2019.

[37] Kowalski, S., Rendall, J., Abuheiba, A., Cheekatamarls, P., Gehl, A., Momen, A., Nawaz, K. Initial Design and Experimental Results of a Novel Near-Isothermal Compressor for Heat Pump Applications. Paper 2776. *Proceedings of the 26th International Compressor Engineering Conference at Purdue*, West Lafayette, IN, July 10–14, 2022.

[38] The Air-Conditioning, Heating, and Refrigeration Institute (AHRI). AHRI Low-GWP Alternative Refrigerants Evaluation Program. https://www.ahrinet.org/analytics/research/ahri-low-gwp-alternative-refrigerants-evaluation-program, accessed March 15, 2023.

[39] Li, Z., Shen, B. Gluesenkamp, K.R. Multi-objective optimization of low-GWP mixture composition and heat exchanger circuitry configuration for improved system performance and reduced refrigerant flammability. *International Journal of Refrigeration* 126 (2021):133–142. DOI:10.1016/j.ijrefrig.2021.01.003

[40] McLinden, M.O., Brown, J.S., Brignoli, R., Kazakov, A.F., Domanski, P.A. Limited options for low-global-warming-potential refrigerants. *Nature Communications* 8:14476 (2017). DOI:10.1038/ncomms14476

[41] Li, Z., Qiao, H., Aute, V. Tube-fin Heat Exchanger Circuitry Optimization For Improved Performance Under Frosting Conditions. *Proceedings of the 13th International Modelica Conference*, Regensburg, Germany, March 4–6, 2019. DOI:10.3384/ecp19157259

[42] Warner, J., Liu, X., Shi, L., Qu, M., Zhang, M. A novel shallow bore ground heat exchanger for ground source heat pump applications—Model development and validation. *Applied Thermal Engineering* 164(2020):114460. DOI:10.1016/j.applthermaleng.2019.114460

[43] Shi, L., Qu, M., Liu, X., Wang, L., Zhang, M. Numerical modeling and parametric study of a dual purpose underground thermal battery. *Energy & Buildings* 275(2022):112472. DOI:10.1016/j.enbuild.2022.112472

[44] Spitler, J.D., West, T., Liu, X., 2022. Ground Heat Exchanger Design Tool with RowWise Placement of Boreholes. IGSHPA Research Track. Las Vegas, December 6–8, 2022. DOI:10.22488/okstate.22.000016

[45] Liu, X., Spitler, J.D., Qu, M., Shi, L., 2021. Recent developments in the design of vertical borehole ground heat exchangers for cost reduction and thermal energy storage. *Journal of Energy Resources Technology* 143(10):100803. DOI:10.1115/1.4050418

[46] Liu, X., DeGraw, J., Malhotra, M., Forman, W., Adams, M., Accawi, G., Bass, B., Kunwar, N., New, J., Guo, J. Development of a Web-based Screening Tool for Ground Source Heat Pump Applications. IGSHPA Research Track. Las Vegas, December 6–8, 2022. DOI:10.22488/okstate.22.000042

[47] Liu, X., Li, Y., Malhotra, M., Lian, J., Wang, X., Ho, J., Impact Analysis of Heating Electrification in US Buildings with Geothermal Heat Pumps. IGSHPA Research Track. Las Vegas, December 6–8, 2022. DOI:10.22488/okstate.22.000011

[48] Wang, L., Liu, X., Shen, B., Liu, X., Gehl, A., Shi, L., Qu. M. Experimental Performance Analysis of a Dual-Source Heat Pump Integrated with Thermal Energy Storage. IGSHPA Research Track. Las Vegas, December 6–8, 2022. DOI:10.22488/okstate.22.000036

[49] Liu, X., Hughes, P., McCabe, K., Spitler, J., Southard, L. GeoVision analysis supporting task force report: thermal applications—Geothermal heat pumps. ORNL/TM-2019/502. Oak Ridge National Laboratory, Oak Ridge, TN, April 2019. DOI:10.2172/1507876

[50] Li, Z., Gluesenkamp, K., Shen, B., Munk, J., Zandi, H., Cheekatamarla, P., Kowalski, S., 2022. Seamlessly Fuel Flexible Heat Pump with Optimal Model-based Control Strategies to Reduce Peak Demand, Utility Cost and CO_2 Emission. *Proceedings of the 2022 ACEEE Summer Study on Energy Efficiency in Buildings*, Monterey, CA, August 21–26, 2022.

[51] Shi, L., Liu, X., Qu, M., Liu, G., Li, Z., 2021. Potential of Utilizing Thermal Energy Storage Integrated Ground Source Heat Pump System to Reshape Electricity Demand in the United States. *Journal of Engineering for Sustainable Buildings and Cities* 2(3):031003. DOI:10.1115/1.4051992

[52] Li, Z., Catano, J., Gluesenkamp, K., Shen, B., LaClair, T., Comparin, R., Welch, D. Simulation of a PCM Integrated Heat Pump Using Time-of-Use Utility Structure based Control Strategy for Demand Response. Paper 2469. *19th International Refrigeration and Air Conditioning Conference at Purdue*, West Lafayette, IN, July 10–14, 2022.

[53] Hewitt, N. IEA HPT Annex 55: Comfort & Climate Box – towards better integration of heat pumps and storage, Final Report – Part 5, Report no. HPT-AN55-5, September 2022.

[54] Willem, H., Lin, Y., Lekov, A. Review of energy efficiency and system performance of residential heat pump water heaters. *Energy & Buildings* 143(2017):191–201. DOI:10.1016/j.enbuild.2017.02.023

[55] Zhang, L., Jiang, Y., Dong, J., Yao, Y. Advances in vapor compression air source heat pump system in cold regions: A review. *Renewable and Sustainable Energy Reviews* 81(2018):353–365. DOI:10.1016/j.rser.2017.08.009

[56] Konrad, M.E. Improving cold climate performance of heat pumps using market-available systems. Master Thesis. Ontario Tech University, Oshawa, Ontario, Canada. October 2022.

[57] Qian, S., Nasuta, D., Rhoads, A., Wang, Y., Geng, Y., Hwang, Y., Radermacher, R., Takeuchi, I. Not-in-kind cooling technologies: A quantitative comparison of refrigerants and system performance. *International Journal of Refrigeration* 62(2016):177–192.

[58] Goetzler, W., Shandross, R., Young, J., Petritchenko, O., Ringo, D., McClive, S. Energy savings potential and RD&D opportunities for commercial building HVAC systems, DOE/EE-1703, December 2017.

[59] Moore-Bloom, R. Policies Could Jumpstart Heat Pump Adoption. June 20, 2022. https://www.cleanenergytransition.org/post/policies-could-jumpstart-heat-pump-adoption

14th IEA Heat Pump Conference
15-18 May 2023, Chicago, Illinois

Frost Detection with Neural Networks: Determining Necessary Sensors to Predict Optimal Defrost Initiation Time for Air Source Heat Pumps

Jonas Klingebiel[a,*], Paul Salomon [a], Christian Vering [a] and Dirk Müller [a]

[a]Institute for Energy Efficient Buildings and Indoor Climate, Aachen, Germany

Abstract

Air Source Heat Pumps (ASHPs) are the most common heat pump type in Europe's residential buildings. To increase the energy efficiency of ASHPs, a main research field focuses on defrosting management. Currently, researchers showed that optimal defrosting initiation time (ODT) exists, which exhibits great potential to improve operational efficiency. However, ODT depends on multiple factors such as ASHP operation (e.g., compressor RPM) and ambient conditions (e.g., relative humidity). While mapping all correlations between ODT and all relevant factors can be accomplished with artificial neural networks (ANN), gaining sufficient test-bench data is time-consuming. When combining ANNs with reinforcement learning (RL) the data can be automatically generated on-site. A key aspect for the successful realization of RL is the determination of necessary sensors to detect frost under dynamic ASHP operation and varying ambient conditions. This work studies the applicability of different sensor sets to predict frost. Therefore, we use a heat pump model with valid frosting and defrosting behavior. The model is calibrated with test bench data. The results indicate that commonly available sensors in heat pumps are suitable for robust frost detection. Using only the ambient and evaporation temperature, the RL agent can separate frosting behavior from heat pump control and improves energy efficiency by up to 9.4 % compared to conventional time-controlled defrosting.

© HPC2023.
Selection and/or peer-review under the responsibility of the organizers of the 14th IEA Heat Pump Conference 2023.

Keywords: defrost initiation; self-optimizing control; artificial neural network; reinforcement learning; simulation

1. Introduction

The federal government of Germany has set itself ambitious and legally binding climate protection goals: Greenhouse gas emissions must be reduced by 65% until 2030 and by 88% until 2040, relative to 1990 levels. [1]. Since heat pumps are an resource-efficient option to convert electricity from renewable energy sources to heat, the Federal Environmental Agency attributes a key role to heat pumps in achieving the goals [2]. Currently, Air-Source Heat Pumps (ASHPs) make up 82% of heat pumps installed in Germany's building sector (2021), and their market share rises continuously [3] as they are easier to install and retrofit. Thereby ASHP are more cost-effective while performing only marginally worse than Ground Source Heat Pumps (GSHPs) [4].

During the heating operation of ASHPs, frost may form on the evaporator's fins due to the temperature difference between the heat-transferring surface and the ambient air, depending on the ambient conditions. The frost deteriorates the evaporator capacity and, thus, the heat pump efficiency. To maintain safe and efficient operation, defrosting operations are performed. Wang et al. experimentally show that optimal defrosting initiation time (ODT) exists [5]. Further, they conclude that ODT varies significantly depending on ambient conditions and ASHP operation. However, simple defrosting strategies such as time-based defrosting (TBD) are widely used in commercial applications [6] because of their ease of implementation. In TBD, a defrosting

* Corresponding author.
E-mail address: jonas.klingebiel@eonerc.rwth-aachen.de

operation is performed at a fixed time interval, ranging typically between 60 to 90 minutes [7]. TBD inevitably leads to sub-optimal defrost initiations, so-called "mal-defrost phenomena" [8], which comprise either too early or too late defrost initiations.

To limit the inherent mal-defrost losses of TBD, several attempts have been made to develop demand-based defrosting (DBD) strategies. DBD strategies aim to enhance the defrost initiation by determining correlations between measurable operational parameters and the current state of frosting on the ASHP. Recent works study the application of artificial neural networks (ANNs) [9], [10]. ANNs seem promising for the complex control task due to their capability of capturing complex system relations [11]. Wang et al. [9] propose a supervised learning approach using convolutional neural networks (CNNs). The researcher use samples from a time-based defrosting approach as labeled data for the supervised learning task. The data was manually filtered for mal-defrost operations leading to a data set without apparent mal-defrost phenomena. The trained CNN reached a root mean squared error (RMSE) of 7.2 % and avoided mal-defrosting for most of the investigated test cases. However, the authors constituted that the quality of the labeled data limits the quality of the CNN defrosting strategy. Generating labeled data in sufficient quantities is often a core limitation in ANN applications.

To support this research, we considered the application of Reinforcement Learning (RL) algorithms for DBD in a previous simulation study [12]. In difference from pure ANN approaches, RL allows for learning independent of labeled data since it autonomously discovers the inherent patterns in a dataset. Thus, an RL agent does not impose the limitation of high-quality data but gradually evolves by learning from previous experiences. The investigated Deep-Q-Network (DQN) Agent achieved an average improvement of 5.6% over TBD for a 24h dynamic interval and avoided mal-defrosting operation. However, we used the air-side pressure drop as a frost indicator, among other sensor data, which might not be available in real-world application. In this context, this parameter represents a comparatively direct correlation to frost mass but is difficult to determine experimentally.

Therefore, this paper studies the applicability of different sensor sets to predict frost formation. The paper is organized as follows: In the 2. section we present the basics of RL, and the algorithms used to analyze the results. In the 3. section we describe the case study system, our implementation approaches, and the experiment design. In the 4. section we present the results, which are discussed in the 5. section in more detail. In the 6. section we give a concluding summary as well as inspirations for future work.

2. Methodology

2.1. Reinforcement Learning

RL is a model-free, self-optimizing control algorithm in which an agent interacts with an environment without providing it with instructions on how to act correctly. However, the agent receives feedback on the quality of its actions in the form of a reward r. The goal of the agent is to maximize its immediate and future rewards. Therefore, actions leading to higher rewards are reinforced during the learning process. Based on experience, the agent derives a policy π which maps an action a to each environment state s. The state s is a set of features/sensors representing the environment and includes all information upon which the agent chooses the action. With increasing training, the agent's policy converges toward the optimal policy. Figure 1 illustrates the agents' interactions with the environment.

In Q-Learning, a standard reinforcement learning algorithm, the values of state-action pairs (s, a) with respect to the reward signal are established. In basic Q-Learning the relation between (s, a) and value is stored in a table. While this works well for simple systems with limited states and actions [13], complex problems make use of function approximators. Deep Q-Networks (DQN), a state-of-the-art RL algorithm, use artificial neural networks (ANN) as function approximators [14].

Many design principles have been published over the years, enabling stable ANN training in dynamic environments and improving training data efficiency. As part of our last study, we used two principles: a target network and a replay buffer. The target network is a second ANN, which is used to calculate the Q-values. Its trainable parameters are frozen for a fixed number of interactions. Unlike the main Q-network, the target network's parameters are not trained but periodically synchronized with them. Using a target network prevents instabilities (or even divergence) during training that may arise from rapidly changing policies. The second principle is the use of a replay buffer for experience replay. This overcomes two issues when combining RL with ANNs. First, the data set of RL is non-stationary since the RL algorithm constantly learns new behaviors, but ANNs need stationary data sets. Second, classical ANNs see training samples independent from each other but the training data of RL is sampled from a sequence of correlated states. The replay buffer serves as a growing but stationary data set, breaking the correlation between data samples during training. When RL is

applied to slow-responding thermal systems, including past observations is important because an important design principle (the Markov property) requires that future states depend only on the current state [20].

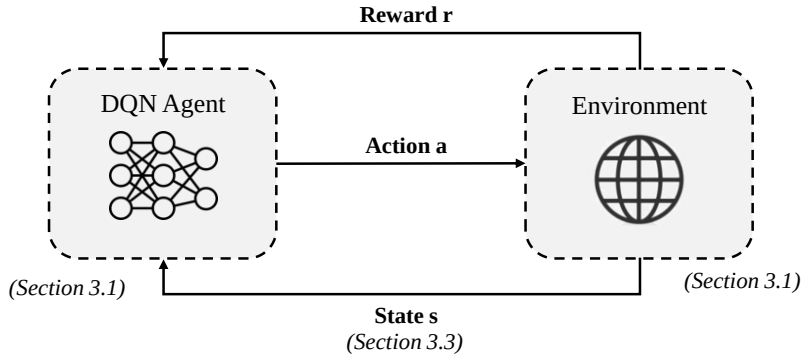


Fig. 1. Schematic illustration of reinforcement learning.

2.2. Feature Importance

Machine learning models can be interpreted by assessing feature importance. To quantify a feature's importance, the model's prediction error is calculated after it has been permuted. As a result of this procedure, the relationship between the feature and the target is broken, thus causing the model score to drop, indicating the model's dependence on it. The feature is considered "important" if randomizing its values increases model error since the model relies on the feature to make predictions. A feature is "unimportant" if shuffling its values leaves the model error unchanged. [15], [16]

3. Experimental design

In this section, we describe the case study system, our implementations in Python and Modelica, and the different configurations of our experiment.

3.1. The Case Study

In the conducted case study, a DQN agent is implemented as a defrost controller and applied to a dynamic heat pump simulation model. The simulation model and the RL agent are described below.

3.1.1. Simulation Model

The dynamic simulation model of the ASHP is implemented in Modelica [17] using Dymola [18] and TIL Library [19], [20]. A detailed description of the calibrated simulation model can be derived from [12]. In the following, the essential principles of the model are outlined.

At the core of the ASHP model is a finite-volume model of the evaporator. The control volume is discretized into several small volumes (cells), and the conservation equations for energy, mass, and impulse are solved for each cell. To model the effect of frost on the heating capacity, the two dominant loss mechanisms are incorporated into the evaporator model:

- **Thermal Resistance**: Frost acts as a thermal insulation layer between the air and the fin. The thermal resistance is a function of frost density and frost layer thickness.
- **Hydraulic Resistance**: Frost reduces the air-side cross-sectional area. For a constant fan power, the air volume flow decreases with increasing frost layer thickness.

To determine the described mechanisms, the frost density and the frost thickness must be modelled sufficiently accurately. For this purpose, the convective water mass flow from the moist air to the frost is divided into frost densification and frost thickening by applying literature correlations. The evaporator model is embedded in a model of the refrigerant cycle with lower complexity to preserve high simulation speeds. The complete refrigerant cycle model is calibrated using measurement data from an ASHP test bench. To enable the dynamic operation of the heat pump model a compressor control is implemented, which adjusts compressor

power to match a set value for supply temperature. Further, a superheating controller regulates a constant superheat at the evaporator outlet.

The resulting heat pump model takes the ambient temperature, the relative humidity, the condenser capacity, and the supply temperature of the heat sink as model inputs as illustrated in Figure 2. Dynamic profiles are generated with AixLib library [21] to simulate real-world scenarios with varying ambient conditions and heat demands. This study uses a building model of a 120 m² single dwelling in Berlin as a case study.

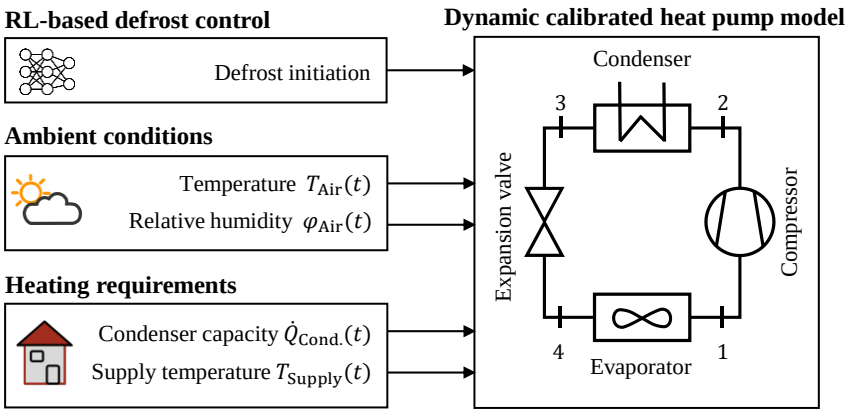


Fig. 2. Inputs of dynamic heat pump simulation model.

3.1.2. Reinforcement Learning Agent

In the following, the design of the control problem is formulated. We use a DQN Agent with the extensions outlined in section 2. The agent interacts with the ASHP model every 100 seconds (simulation time). Every interaction step consists of taking an action, observing the environment, and receiving a reward. The agent decides whether defrosting should be initiated (**action** a). Thereby the agent's action space is discrete:

$$a = \begin{cases} 1\text{: initate defrost operation} \\ 0\text{: stay in heating operation} \end{cases} \tag{1}$$

While defrost initiation is controlled by the RL agent, defrost termination is not part of the agent's control domain. The defrosting operation is terminated by a threshold value with regard to the frost mass.
The agents' state s, which is composed of several features, is varied in this study. The selection of suitable state spaces is described in section 3.3. The *COP* of the system can serve as a **reward** function, but its value is strongly dependent on ambient conditions. Therefore, selecting COP as reward would penalize the agent for thermodynamic demanding ambient conditions. To eliminate this deficiency, we use the Carnot efficiency as a reward function:

$$r = \frac{COP}{COP_{\mathrm{Carnot}}} \tag{2}$$

The Carnot efficiency normalizes the *COP* to the physical optimum. As a result, ambient conditions do not directly affect the reward signal. The described interaction approach exhibits temporarily delayed rewards: The agent has to learn that occasional defrosting operations positively impact the future reward trajectory even though it receives a penalty in the short term.

3.2. Implementation

Figure 3 shows the overall framework in which the agent and the environment (heat pump simulation model) interact. The simulation model written in Modelica is exported as Functional Mock-up Unit (FMU).

FMI is an open-source standard for the simulation of dynamic models generated in Dymola or Simulink in other frameworks such as Python. The FMU is embedded in Python with the Python library FmPY [22]. In order to develop reinforcement learning agents, the FMU is embedded into an OpenAI Gym environment [23]. These provide standardized interfaces in the field of RL research to test and compare algorithms efficiently. The algorithms used are provided by the Pytorch-based stable-baselines library [24]. The library provides tested state-of-the-art RL algorithms, a comparatively user-friendly API, and many recurringly needed evaluation and backup methods.

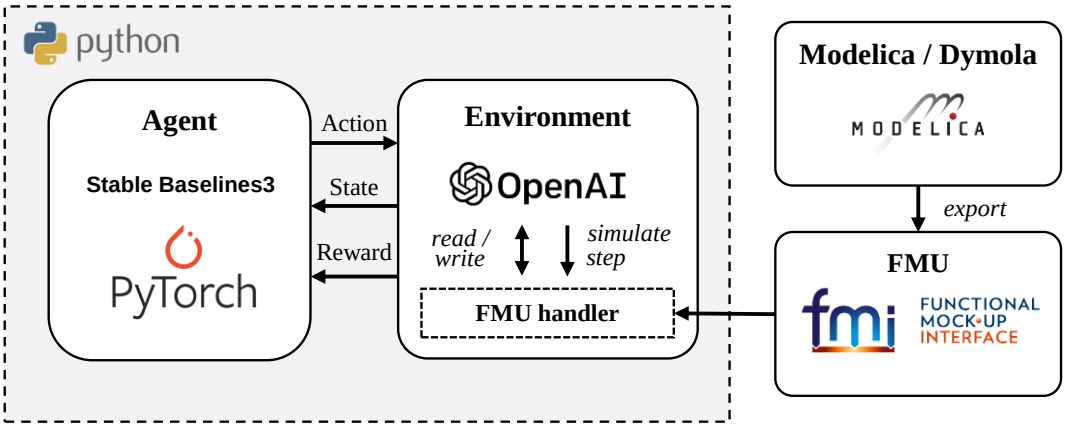


Fig. 3. The software modules used in this study and their functional relationships.

3.3. State space variations

In this study, we investigate the influence of different state spaces on the performance of an RL-based defrosting controller. In many cases, the environment is not fully observable, preventing the agent from developing an accurate picture of its environment. The features must contain sufficient information about frost accumulation and its impact on the operation. To develop a reasonable strategy, the agent must separate between phenomena caused by frost formation and other unrelated influences. For this purpose, sensors which directly measure the existence of frost while having few external influences are advantageous. However, these sensors are usually not installed in conventional heat pumps and may be expensive and unreliable.

For example, frost mass or air-side static pressure difference over evaporator are good frost indicators, but they represent an additional asset in terms of cost and reliability. On the contrary, the evaporating temperature is robust and inexpensive to measure but contains only an indirect link to frost mass. Other parameters, such as fan or compressor speed, influence the evaporation temperature, complicating the control problem. In general, a small state with high-quality information leads to faster convergence. Considering the abovementioned limitations, we selected the following features:

- Ambient temperature T_{Air}
- Prior action a_{t-1}
- Evaporating temperature $\mathrm{T_{Evaporator}}$
- Evaporator outlet temperature $\mathrm{T_{Evaporator,out}}$
- Condensing temperature $\mathrm{T_{Condenser}}$
- Air-side static pressure difference over evaporator Δp_{Air}
- Electrical power consumption of the compressor $\mathrm{P_{el,compressor}}$

Section 4.1 describes the influence of frost and external disturbances on each parameter. The features were grouped into state spaces based on expert knowledge. Tab. 1 displays five state spaces that were investigated in this study. The state spaces are increasingly difficult (from #1 to #5) since number and information quality are reduced successively. While the first state space (#1) contains variables that exhibit a direct link to frost mass (air-side pressure difference Δp_{Air}), the last one (#5) only includes the ambient temperature and the prior action, which significantly complicates the control problem. All state spaces contain the air temperature T_{Air} and the last performed action a_{t-1} since they are easy to determine and have proven to be relevant parameters for the agent's decision. Additionally, except for #5, each state space contains the evaporating temperature.

Since the air-side pressure difference Δp_{Air} has to be determined by additional sensors, it is only utilized for state space #1. From #3 on, the compressor power $\mathrm{P_{el,compressor}}$ is also discarded since measuring this parameter is costly. As a result, only standard sensory is used from #3 - #5.

Table 1. Investigated state spaces

#1	#2	#3	#4	#5
T_{Air}	T_{Air}	T_{Air}	T_{Air}	T_{Air}
$a_{\mathrm{t-1}}$	$a_{\mathrm{t-1}}$	$a_{\mathrm{t-1}}$	$a_{\mathrm{t-1}}$	$a_{\mathrm{t-1}}$
$T_{\mathrm{Evaporator}}$	$T_{\mathrm{Evaporator}}$	$T_{\mathrm{Evaporator}}$	$T_{\mathrm{Evaporator}}$	
$P_{\mathrm{el,compressor}}$	$T_{\mathrm{Evaporator,out}}$	$T_{\mathrm{Evaporator,out}}$		
Δp_{Air}	$P_{\mathrm{el,compressor}}$	$\mathrm{T_{Condenser}}$		
	$\mathrm{T_{Condenser}}$			

Besides the sensor values listed above, historical sensor values are also included in the state space. In addition to the current sensor value at time t, the last 39 historical sensor values are provided as input to the agent.

3.4. Training

The training is divided into two phases. The goals of the training stages are explained in the following:

- **Pre-training**: Pre-training aims to train the agent to cope with constant ambient conditions. After pre-training, the agent should recognize patterns between ambient conditions and frost growth rate. Therefore, the agent should be capable of adjusting the time point of defrost initiation concerning the ambient conditions in a static case. The agent is required to generalize as the ambient conditions are random and nonrepetitive. Pre-Training is terminated when a certain reward threshold is reached.
- **Main training**: Main training aims to train the agent in a dynamic environment. After the main training, the agent exhibits a reasonable defrosting strategy for dynamic ambient conditions and heat loads. The agent is also required to identify conditions in which no frost formation occurs and not to initiate defrosting when these conditions are present. The agent is trained for 150.000 steps, corresponding to 170 days of simulation time.

4. Results

In this section, we present the results obtained with our experiment design.

4.1. System dynamics

In the following, the state spaces' features and their influence on frost are analyzed. Figure 4 displays selected features for a frosting-defrosting cycle. Two scenarios were simulated for constant ambient conditions and heat demands to highlight the influence of frost growth velocity on the corresponding features. The first represents severe frosting conditions, and the second mild frosting conditions. Table 2 summarizes the simulation set values for both scenarios. The frost growth rate is high in the severe frosting scenario due to high absolute humidity. In contrast, the frost growth rate is lower in the "mild frosting" scenario.

The frost growth is reflected in the accumulated frost mass. The gradient is higher for severe frosting than for mild frosting. This relationship can be extracted directly from the signal for the air-side pressure drop: The pressure drop increases faster in the severe frosting scenario. Faster growth of frost causes the air-side cross-sectional area to decrease rapidly so that the pressure drop increases and the volume flow decreases. In the severe frosting scenario, the air-side pressure drop at t = 2000 converges to a limit at 100 Pa. Here, the air-side cross-sectional area is completely blocked. The increase in frost mass is only due to frost densification.

Table 2. Boundary conditions for simulation (see figure 4)

Scenario	Air temperature T_{Air} in °C	Relative humidity φ_{Air} in %	Condenser capacity $\dot{Q}_{\mathrm{cond.}}$ in kW	Supply temperature T_{Supply} in °C
Severe frosting	4	80	7000	35
Mild frosting	-6	80	7000	35

The compressor's electrical power shows similar characteristics: As the frost mass increases, the transferred heat at the evaporator decreases. To maintain a constant condenser capacity, compressor power is increased by the heat pump controller to compensate for the reduction in evaporator capacity. If heat demand, ambient temperature, and supply temperature are constant during the heating phase (frosting), the electrical power is a valid frosting indicator. Under frost-free conditions, the air-side pressure drop is identical for both scenarios and is thus independent of external influences (see figure 4, t=0). In contrast, the compressor's electrical power depends on the heat demand and the supply temperature and thus differs under frost-free conditions.

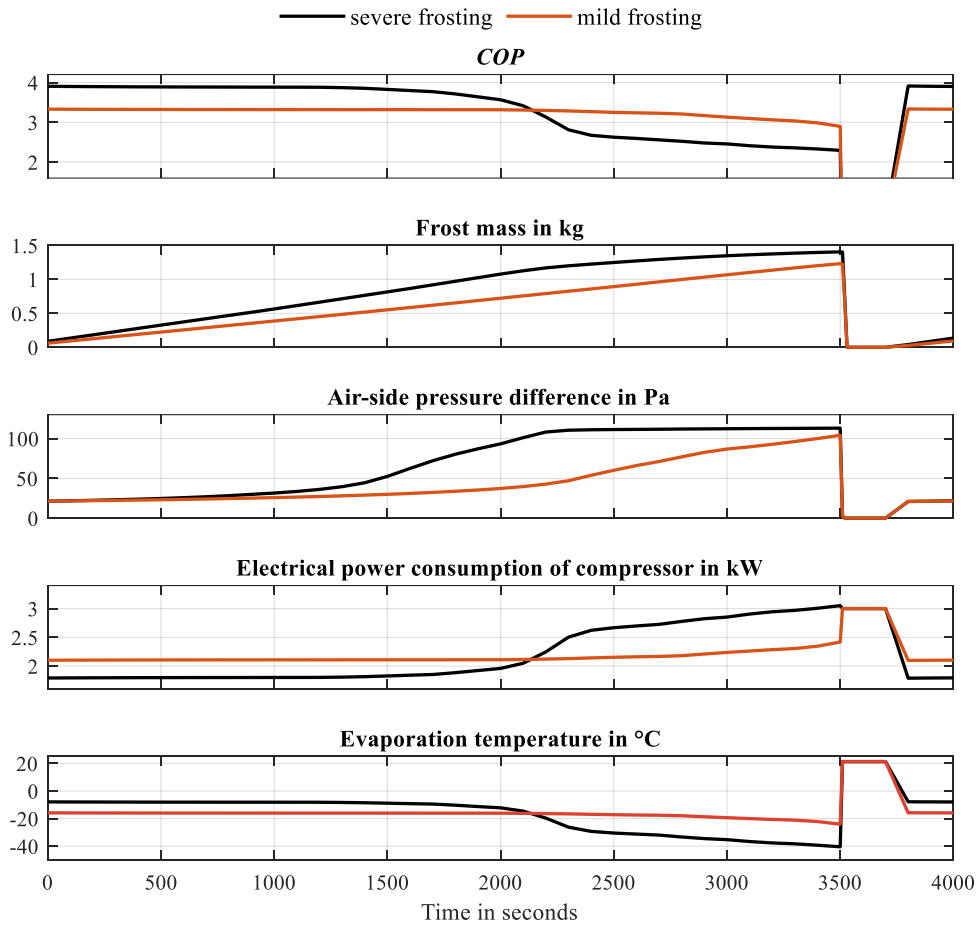


Fig.4. Influence of frost on heat pump system.

Figure 4 also displays the evaporating temperature. The evaporating temperature decreases with increasing frost mass due to the expansion valve control, which regulates a constant superheat. The evaporating temperature shows a qualitatively similar curve to the compressor's electrical power consumption. While the evaporating temperature decreases significantly in the severe frosting scenario, only a slight decrease can be seen in the "mild frosting" scenario. The evaporating temperature differs under frost-free conditions due to the varying ambient temperatures.

In addition to the quantities shown in figure 4, additional features were selected for frost detection. The temperature at the output of the evaporator differs from the evaporation temperature by a constant value (superheat). The condensation temperature correlates with the ambient temperature according to the heating curve and thus has an indirect influence on frost growth.

4.2. State space variations

The agents with the state spaces defined in Table 1 were trained according to the description in section 3.4. After training, the performance of the agents was evaluated for ten randomly selected test periods with varying environmental conditions and heat demands with a length of 72 h. The average reward per step for each test period was calculated to compare the agent's performance. The reward corresponds to the Carnot efficiency (see equation 2). The value was then averaged over the ten episodes.

Additionally, a time-based defrost controller that initiates a defrosting operation every 60 minutes was evaluated. The 60 minutes correspond to a typical value from the literature [7]. Figure 5 displays the average reward per step over the ten test periods for RL and TBD. Additionally, minimum and maximum deviation is displayed.

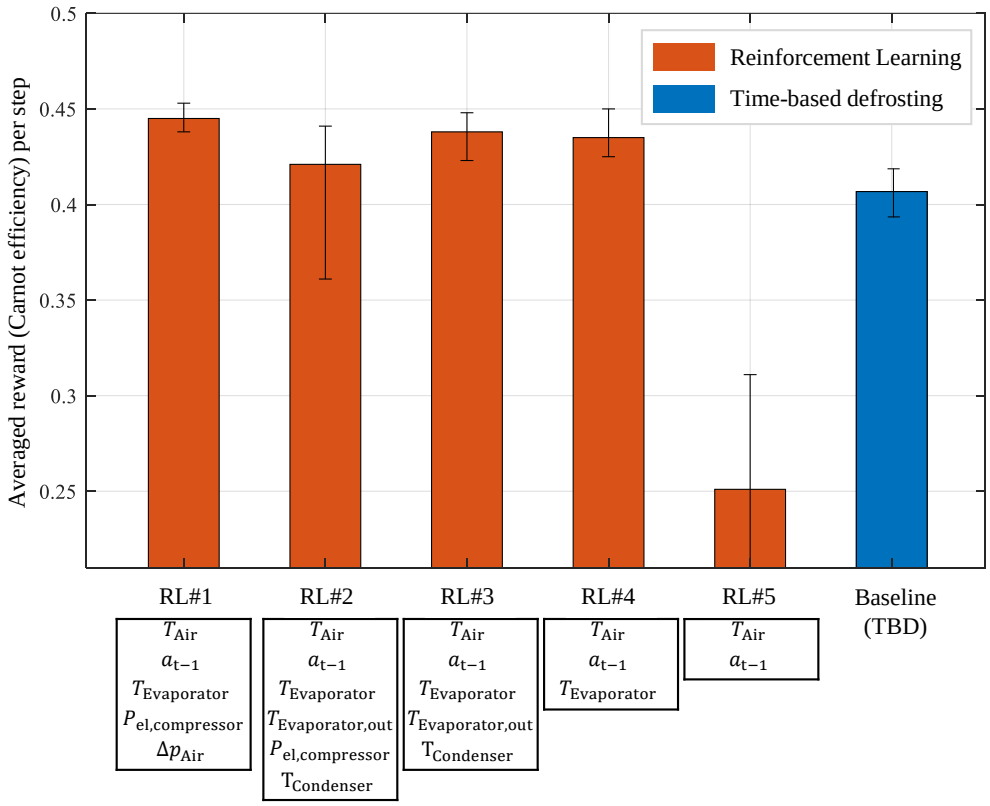


Fig.5. Results of state space variation.

RL with state space #1 (RL#1) achieves the highest reward per step. However, RL#3 and RL#4 achieve comparable scores. While the performance of RL#4 is marginally worse compared to RL#3, this may be due to the randomness of the selected test conditions. The similar performance between RL#3 and RL#4 implies that the evaporator output temperature and condensing temperature do not add beneficial information. Based on the results, we conclude that demand-based defrosting can be accomplished with just the air temperature, the evaporation temperature, and the last action.

RL#2 performs significantly worse compared to RL#3. At first, this seems counterintuitive since RL#2 contains all features of RL#3. The difference between RL#2 and RL#3 is in the electrical compressor power signal, which was classified as a reasonable frost indicator in the previous section. The weaker performance can be attributed to the higher number of features. The additional information provided by the sensor is not valuable enough for the agent to achieve higher performance. Conversely, the additional feature increases the

complexity of frost detection. As a result, the RL#2 agent requires more training time to achieve similar results as RL#3.

RL#5 shows significantly worse performance compared to all other RL agents. The included features do not exhibit sufficient information to perform demand-based defrosting operations. The agent has to develop a defrosting control based on the ambient temperature. However, since frost growth is, among others, dependent on relative humidity and condenser power, the agent cannot establish a reasonable defrosting strategy.

Compared to TBD, the RL agents #1 - #4 achieved significant efficiency improvements. The increase in efficiency between TBD and RL#1 is 9.4 %. The efficiency improvement between TBD and RL#4 is 8.9 %.

4.3. Feature importance

We performed permutation tests in order to measure feature importance. Therefore, each feature was randomly permuted, while the remaining features were kept untouched. After a permutation was performed, the loss of the model prediction was calculated. This was repeated 100 times (for each feature), and the average prediction loss was evaluated.

Figure 6 displays the model loss due to feature permutation for different state spaces. Across the three state spaces presented, there is no dominant feature. While the absolute value of the model error has a low information value, the relative differences within a state space can be interpreted.

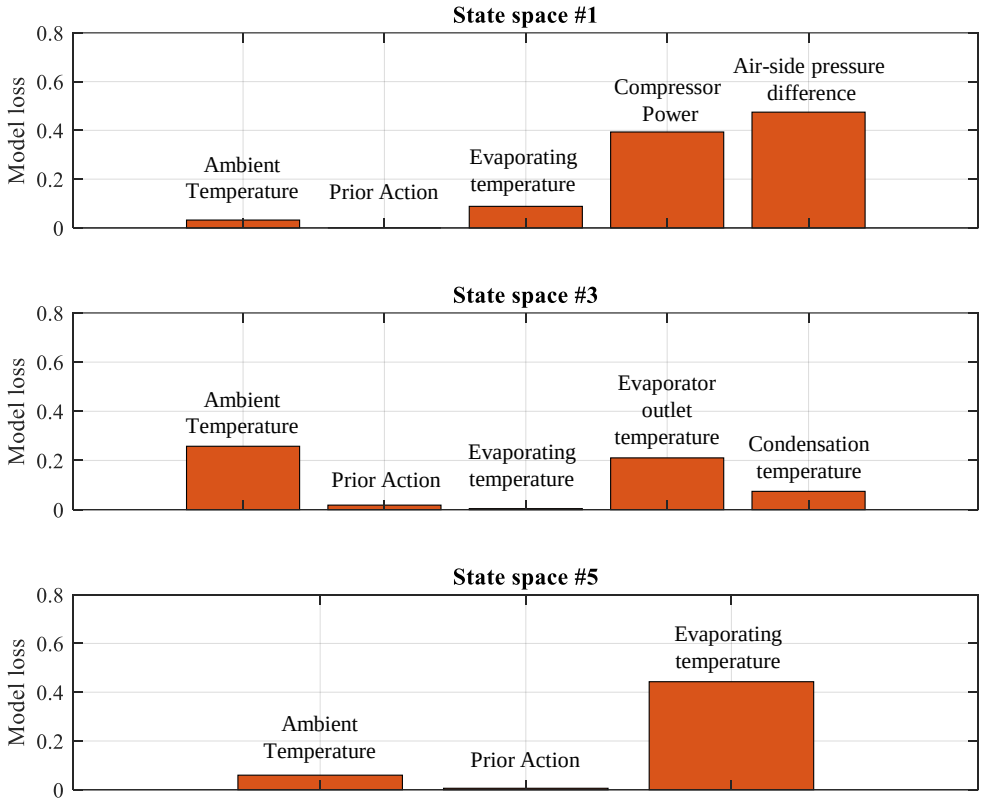


Fig.6. Feature importance of different state spaces.

In state space #1 the air-side pressure difference and the compressor power show the most significant influence on the agent's actions. The remaining features have a minor impact on the agent's decisions. Consequently, the agent has discovered that the two dominant features provide sufficient information to learn a reasonable defrosting strategy.

Ambient temperature and evaporator outlet temperature have the most decisive influence on the agent in state space #3. The feature importance of the evaporating temperature is negligible. The agent has detected that the difference between both features consists of a constant offset (superheating). Thus, the features share identical information as long as the superheat is kept constant by expansion valve control. In state space #5 the

evaporation temperature is the dominant feature since evaporator outlet temperature is not part of the state space. The decisive influence of the ambient temperature is significantly smaller.

5. Discussion

The results show that RL can serve as a demand-controlled defrost algorithm using only standard temperature sensors of the refrigerant cycle as frost indicators. The state space variation and the feature importance evaluation demonstrate that the agent successfully recognizes the sensor values with the highest information quality and assigns the greatest influence to these values in the decision process. Furthermore, we observed that a larger state space leads to a lower performance for the same training time. For this reason, the number of features should be kept reasonably small.

In the calibrated simulation model, the evaporation temperature shows a characteristic drop due to frost. The absolute value of the evaporation temperature is dependent on the ambient temperature. Thus, the agent needs both features to predict defrosting necessity. An improvement could be achieved by applying feature engineering. Here, multiple features are combined into a single value to decrease state space dimension and accelerate convergence speed. With regard to the results of section 4.2, it seems promising to pass the temperature difference between ambient and evaporation temperature to the agent as a single value.

Although the results of this simulation study are promising, the simulation did not take into account several effects that arise in heat pumps in the field and might complicate the control problem significantly. In this study, the fan speed was assumed constant. Since fan speed affects the evaporating temperature, its set value should be implemented as a feature when applying RL to real heat pumps. Furthermore, we did not investigate the effect of controller-related oscillations on the agents' performance. In real-world applications, the frosting influences the controlled system of the expansion valve because system dynamics differ from no-frost conditions. Altered system dynamics can result in an oscillation of the superheat and, thus, of the evaporating temperature. Smoothing the features with respect to time may resolve the issue.

Furthermore, we defined the reward using Carnot efficiency. While this is an excellent quantity to optimize, the computation of the value is subject to variances due to measurement uncertainties. In addition, many frost-unrelated factors influence the Carnot efficiency, e.g., isentropic compressor efficiency. Contrary to the assumption implied in this study, the isentropic efficiency is not constant. Consequently, the reward function will fluctuate in absolute value over the operating range, which is a disturbance factor for the agent. Hence, alternative reward functions that directly relate to frost growth should be investigated.

6. Conclusion and future work

In this paper, we apply a State-of-the-Art RL algorithm to perform demand-controlled defrosting for a calibrated dynamic ASHP simulation model. The results indicate that RL can serve as a demand-controlled defrost algorithm while using only standard sensors of the refrigerant cycle as frost indicators. The agent extracts all necessary information and outperforms conventional time-controlled defrosting by 9.2% by only using two temperature sensors in the state space (ambient temperature and evaporation temperature). We conclude that the selected state space significantly impacts the agent's convergence speed and final energy efficiency. Further, we apply a feature importance analysis to quantify the impact of individual features on the agent's decision.

However, some aspects must be addressed to exploit the full potential for real-word applications. Future work should focus on accelerating convergence speed (e.g., feature engineering) and implementing more on-site effects (e.g., measurement uncertainty) into the simulation model. Additionally, research that investigates the reusability of already trained algorithms to heat pumps with different evaporator geometries could accelerate the deployment of RL algorithms to commercial heat pumps.

Acknowledgements

We gratefully acknowledge the financial support by the German Federal Ministry for Economic Affairs and Climate Action (BMWK) through the AiF (German Federation of Industrial Research Associations eV) based on a decision taken by the German Bundestag (IGF no. 20701 N / 2).

References

[1] W. Frenz, “Bundes-Klimaschutzgesetz (KSG),” in *Klimaschutzrecht: EU-Klimagesetz, KSG Bund und NRW, BEHG, Steuerrecht, Querschnittsthemen*, W. Frenz, Ed. Berlin: Erich Schmidt Verlag GmbH & Co. KG, 2022, pp. 525–841. doi: 10.37307/b.978-3-503-20687-2.04.

[2] D. V. Bürger *et al.*, “Klimaneutraler Gebäudebestand 2050 - Energieeffizienzpotenziale und die Auswirkungen des Klimawandels auf den Gebäudebestand,” p. 289.

[3] Bundesverband Wärmepumpe e.V., “Absatzzahlen für Heizungswärmepumpen in Deutschland 2013-2019,” *Bundesverband Wärmepumpe e.V. Zahlen & Daten*, Aug. 18, 2020. https://www.waermepumpe.de/typo3temp/yag/11/58/Diagramm_AbsatzzahlenHWP_2013-2019_115809_5e42bdc64.jpg (accessed Aug. 18, 2020).

[4] P. Christodoulides, L. Aresti, and G. Florides, "Air-conditioning of a typical house in moderate climates with Ground Source Heat Pumps and cost comparison with Air Source Heat Pumps," *Applied Thermal Engineering*, vol. 158, p. 113772, Jul. 2019, doi: 10.1016/j.applthermaleng.2019.113772.

[5] W. Wang, S. Zhang, Z. Li, Y. Sun, S. Deng, and X. Wu, "Determination of the optimal defrosting initiating time point for an ASHP unit based on the minimum loss coefficient in the nominal output heating energy," *Energy*, vol. 191, p. 116505, Jan. 2020, doi: 10.1016/j.energy.2019.116505.

[6] M. Song, S. Deng, C. Dang, N. Mao, and Z. Wang, "Review on improvement for air source heat pump units during frosting and defrosting," *Applied Energy*, vol. 211, pp. 1150–1170, Feb. 2018, doi: 10.1016/j.apenergy.2017.12.022.

[7] M. Song, G. Gong, N. Mao, S. Deng, and Z. Wang, "Experimental investigation on an air source heat pump unit with a three-circuit outdoor coil for its reverse cycle defrosting termination temperature," *Applied Energy*, vol. 204, pp. 1388–1398, Oct. 2017, doi: 10.1016/j.apenergy.2017.01.068.

[8] W. Wang, J. Xiao, Q. C. Guo, W. P. Lu, and Y. C. Feng, "Field test investigation of the characteristics for the air source heat pump under two typical mal-defrost phenomena," *Applied Energy*, vol. 88, no. 12, Art. no. 12, Dec. 2011, doi: 10.1016/j.apenergy.2011.05.047.

[9] W. Wang, Q. Zhou, G. Tian, Y. Wang, Z. Zhao, and F. Cao, "A novel defrosting initiation strategy based on convolutional neural network for air-source heat pump," *International Journal of Refrigeration*, vol. 128, pp. 95–103, Aug. 2021, doi: 10.1016/j.ijrefrig.2021.04.001.

[10] Y. H. Eom, Y. Chung, M. Park, S. B. Hong, and M. S. Kim, "Deep learning-based prediction method on performance change of air source heat pump system under frosting conditions," *Energy*, vol. 228, p. 120542, Aug. 2021, doi: 10.1016/j.energy.2021.120542.

[11] S. Kollias, Ed., *Artificial neural networks -- ICANN 2006: 16th international conference, Athens, Greece, September 10-14, 2006, proceedings, part I*, 1st ed. Berlin: Springer, 2006.

[12] J. Klingebiel, S. Göbel, V. Venzik, and D. Müller, "Evaluation of machine learning methods for optimizing the defrosting process of air-to-water heat pumps," *15th IIR-Gustav Lorentzen Conference on Natural Refrigerants*, 2022, doi: 10.18462/iir.gl2022.117.

[13] E. Even-Dar and Y. Mansour, "Learning Rates for Q-Learning," in *Computational Learning Theory*, vol. 2111, D. Helmbold and B. Williamson, Eds. Berlin, Heidelberg: Springer Berlin Heidelberg, 2001, pp. 589–604. doi: 10.1007/3-540-44581-1_39.

[14] V. Mnih *et al.*, "Playing Atari with Deep Reinforcement Learning," Dec. 2013, doi: 10.48550/arXiv.1312.5602.

[15] L. Breiman, "Random Forests," *Machine Learning*, vol. 45, no. 1, pp. 5–32, Oct. 2001, doi: 10.1023/A:1010933404324.

[16] A. Fisher, C. Rudin, and F. Dominici, "All Models are Wrong, but Many are Useful: Learning a Variable's Importance by Studying an Entire Class of Prediction Models Simultaneously," p. 81.

[17] Modelica Association, *Modelica\circledR - A Unified Object-Oriented Language for Physical Systems Modeling: Version 3.2 Revision 2*. 2013.

[18] Dymola, *Dassault Systems. Dymola - multi-engineering modelling and simulation. Dymola 2017 (64-bit)*. 2016. [Online]. Available: http://www.3ds.com/products/catia/portfolio/dymola

[19] C. Richter, “Proposal of New Object-Oriented Equation-Based Model Libraries for Thermodynamic Systems,” Universitätsbibliothek Braunschweig, 2008. doi: 10.24355/DBBS.084-200806100200-3.

[20] M. Gräber, K. Kosowski, C. Richter, and W. Tegethoff, "Modelling of heat pumps with an object-oriented model library for thermodynamic systems," *Mathematical and Computer Modelling of Dynamical Systems*, vol. 16, no. 3, pp. 195–209, Oct. 2010, doi: 10/bvtz37.

[21] EBC, *AixLib: A Modelica model library for building performance simulations*. 2018. [Online]. Available: https://github.com/RWTH-EBC/AixLib

[22] GitHub, *FMPy*. 2020. [Online]. Available: https://github.com/CATIA-Systems/FMPy

[23] OpenAI, "Gym: A toolkit for developing and comparing reinforcement learning algorithms." https://gym.openai.com (accessed Aug. 10, 2021).

[24] A. Raffin, A. Hill, A. Gleave, A. Kanervisto, M. Ernestus, and N. Dormann, "Stable-Baselines3: Reliable Reinforcement Learning Implementations," p. 8.

14th IEA Heat Pump Conference
15-18 May 2023, Chicago, Illinois

Interconnected heat pumps in Austria: A technology implementation survey

Veronika Wilk[a*], Reinhard Jentsch[a], Tilman Barz[a]

[a] AIT Austrian Institute of Technology GmbH, Giefinggasse 2, 1210 Vienna, Austria

Abstract

Heat pumps become increasingly connected devices enabled to participate in the Internet of Things (IoT). Such heat pumps, both in domestic and industrial applications, allow for operation optimization to reduce energy consumption, to reduce the carbon footprint, to realize economic benefits or to increase comfort. They also enable grid services, which is of increasing importance due to the rising share of renewable energy. This contribution presents results of a survey among companies of the Austrian heat pump industry which was conducted to gather and evaluate the general sentiment on the relevance of interconnected heat pumps, state-of-the-art use cases, market availability and selected technology trends. The collected feedback clearly indicates significant progress in technology implementation. All participating companies offer both, IoT products (e.g. heat pumps with connectivity or intelligent components such as compressors or sensors), and related services (e.g. marketing of flexibility, remote service, monitoring, etc.). While two thirds of these products are already available either in the product portfolio of the companies, or in a large number in use, another third is currently under evaluation, under development or in a pilot phase. IoT technology is expected to bring significant changes in product development, business models and maintenance. For IoT enabled heat pumps this means that instead of being an autonomous smart component, they will be increasingly integrated and will be part of connected energy systems in the future.

© HPC2023.
Selection and/or peer-review under the responsibility of the organizers of the 14th IEA Heat Pump Conference 2023.

Keywords: products; services; data transmission protocols; communication interfaces; trends

1. Introduction

Ambitious climate, energy and environmental goals require the transformation of the energy system into an efficient and renewable system with low CO_2 emissions. Digitalization is one of the important factors for this transformation. According to the IEA, digitalization is the increasing interaction and convergence between the digital and physical worlds. The digital world comprises data (digital information), analytics (the use of data to produce useful information and insights) and connectivity (exchange of data between humans, devices and machines) through digital communication networks. Digitalization is driven by increasing volume of data due to the declining costs of sensors and data storage, rapid progress in advanced analytics and computing capabilities, and greater connectivity with faster and cheaper data transmission. [1] Intelligent, digital solutions are increasingly in demand to efficiently use various flexibility options such as power-based heat generation, the use of storage facilities or e-mobility as well as to safely control the electricity grid. The EU has high expectations for digital technologies in the energy transition, as they should unlock the full potential of flexible energy generation and consumption. Digital technologies enable system optimization, operational savings and savings in network infrastructure, as they should provide the necessary data to match supply and demand both locally and system wide. Therefore, the EU Commission has adopted an action plan in October 2022 that aims to contribute to the EU energy policy objectives by the development of a sustainable, cyber-secure and competitive market for digital energy services and digital energy infrastructure. Main pillars are the

* Corresponding author. Tel.: 0043 664 6207794; fax: 0043 50550 6679.
E-mail address: veronika.wilk@ait.ac.at

establishment of a common European energy data space for sharing and using energy data, a code of conduct for interoperability, enhanced participation in demand-response schemes for energy-smart appliances and strengthening cyber security and resilience of the energy system. [2]

Heat pumps are a versatile technology for the provision of domestic hot water and process heat, and for cooling of buildings and processes. According to the IEA's Net Zero by 2050 report, a total of 1800 million heat pumps have to be installed in buildings world-wide to provide more than half of the heating needs. It is a tenfold increase compared to the level of 2020 [3]. The EU aims at doubling the current deployment rate of individual heat pumps, resulting in a cumulative 10 million units over the next 5 years to be installed. [4]

As digitalization progresses, heat pumps increasingly become connected devices that participate in the Internet of Things (IoT). They can be designed to intelligently meet demand, enabling real-time energy efficiency, flexible use of electricity, optimized load profiles and an optimized compromise in terms of comfort and operating costs. IEA's Net Zero by 2050 report also elaborates on the impact of digitalization on emission reduction. Advances in technology, e.g. smart thermostats or other smart appliances lower carbon emissions, as they reduce the necessity for people to play an active role in energy savings. It is expected that emissions from the building sector will be reduced by 350 Mt CO_2 by 2050 due to digitalization and smart controls. [3]

Recently, the impact of digitalization was assessed for Austria and Germany. The Austrian study analyzed the potential for reducing energy consumption and GHG emissions through applications of digitalization by 2040. It was found that, taking into account the increased energy consumption of the necessary ICT infrastructure, effective savings of 4 – 9% of energy consumption can be reached by 2040. This is equivalent to a 2-10% reduction of greenhouse gas emissions and reductions of up to 2.3 million t CO_{2eq}. The highest net effect on energy consumption can be realized by process automation in industry, smart homes, simulation and digital twins in industry and building automation in the service sector. [5] Similar high potential was identified for Germany, where digitalization could contribute up to 34% of the CO_2 emission reduction that is required according to the climate targets for 2030 (up to 126 Mt CO_{2eq}). The highest reductions can be achieved in industrial production, mobility, energy, and buildings. Important technologies in buildings are intelligent energy management and intelligent HVAC components. [6]

In the Technology Collaboration Programme on Heat Pumping Technologies of the IEA, the IoT Annex project was launched in 2020. In this collaborative project, researchers from Germany, France, Sweden, Norway, Denmark, Switzerland and Austria explore the opportunities and challenges of connected heat pumps. Both, typically mass-produced heat pumps for household applications, and heat pumps with large capacities for industrial and district heating are included. The Annex project has a broad scope looking at different aspects of digitalization and aims to create a knowledge base on connected heat pumps to provide information for heat pump manufacturers, component manufacturers, system integrators and other actors involved in IoT. This contribution presents the results of a survey among companies of the Austrian heat pump industry to assess the relevance of interconnected heat pumps, state-of-the-art use cases, market availability and selected technology trends.

2. Manufacturer Survey in Austria

2.1. Methodology

The purpose of the survey was to collect feedback from companies in the heat pump market segment to gather and evaluate the general sentiment on the importance of IoT. The survey had more than 50 questions, which were single and multiple choice, rating and ranking as well as free text questions. The average time for completing the survey was about 20 min. The survey was divided in two different parts. The first part was equal for all participants. The second part was different for participants active either on the residential, commercial and office buildings market, or on the industrial heat pump market, with specific questions relevant for each group.

The questionnaire was designed after conduction of interviews and focus groups with domain experts in residential and industrial heat pump technology, buildings automation, data security and electricity market from the IEA HPC Annex 56 expert group. Companies were contacted by the Austrian Heat Pump Association "Wärmepumpe Austria" (WPA) and asked for their participation in the survey. WPA covers the entire value chain of the heat pump industry in Austria and includes heat pump manufacturers, as well as all electricity supply companies, component suppliers and drilling companies as well as planners, installers and engineering companies. Answers were collected from May to June 2022.

2.2. Survey participants

A total of 16 companies participated in the survey. 13 participants answered all questions in the survey, 3 participants only answered a part of them (76%, 84% and 91% completion). All company sizes, from small SME to large companies are covered by the survey: 6 companies have less than 50 employees, 5 companies 50 – 250 employees, and 5 companies have more than 250 employees.

Most companies identified themselves as heat pump manufacturers and heat pump vendors (8), three are heat pump installers (thereof 2 also vendors) and 3 component manufacturers (thereof 1 also heat pump manufacturer and vendor), see Fig. 1. Among the current members of WPA, there are 44 companies that manufacture or import heat pumps, thereof 17 that manufacture a part or all of their products in Austria and 12 component manufacturers. From the numbers of participating companies, it can be concluded that 53% of the heat pump manufacturers, 37% of the vendors and 17% of the component manufacturers were reached.

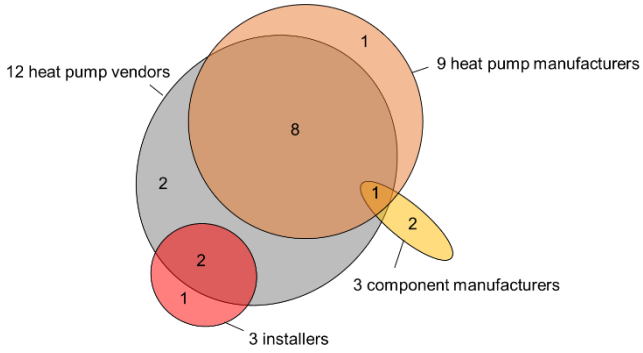


Fig. 1: Participants in the Austrian IoT survey

Activities in market segments: All 16 companies are active on the residential heat pump market including commercial and office buildings. From these 16 companies only 6 have indicated that they are also active in the industrial and district heating market segment (Fig. 2). However, because this second market segment is smaller, and because it is likely that not all companies address this second market segment, no direct conclusions can be drawn about different relevance of IoT in the two different market segments.

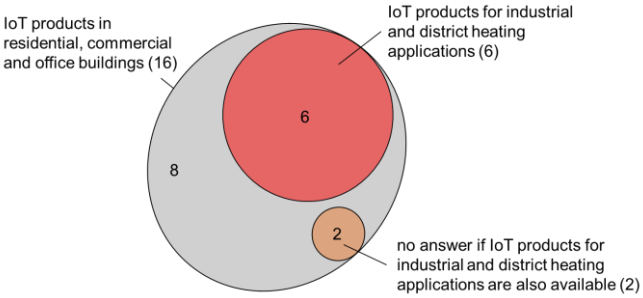


Fig. 2: Market segment covered by the participating companies

2.3. Availability of products and services

The feedback clearly indicates that participating companies have IoT products and services. 66 % are available, which means either in their product portfolio (in implementation), or in a large number in use (extensive implementation). 33% are currently under evaluation, under development or in a pilot phase. All companies offer both IoT products (e.g. heat pumps with connectivity or intelligent components such as compressors or sensors) and services based on IoT products (e.g. marketing of flexibility, remote service, monitoring, etc.). In 56% of the companies, the product and service portfolio have the same maturity level, in 31% the services are further developed than the products and in 13% the products are more advanced and the services still under development.

2.4. Relevance and implementation of IoT related products and services

A self-assessment and comparison to international competitors revealed that 2 companies identify themselves as a pioneer in offering IoT products. The remaining answers from manufacturers are more conservative, 8 regard their products as state of the art, 6 companies see development needs. With regard to the use of IoT services, the feedback is very similar, 1 company regards itself as a pioneer, 7 regard services as state of the art, 8 see development needs.

The feedback on the question who deals with IoT in the company is expectedly diverse, considering the different company sizes among the participants. It ranges from external developers and individual employees, as found in small companies to dedicated IoT departments and company-wide digitalization strategies in medium and large companies. Most commonly, project teams or a part of the development department deals with IoT.

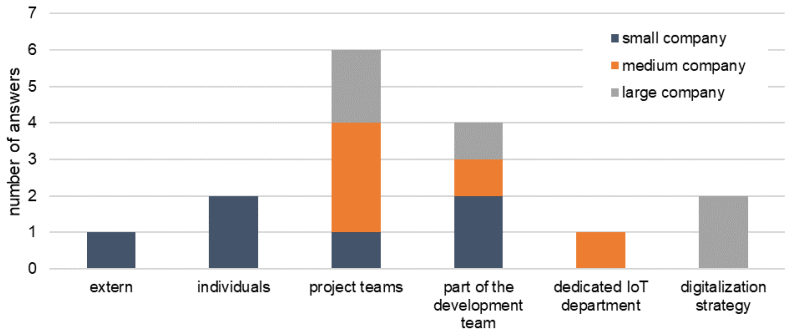


Fig. 3: IoT development by company size

Asked about the motivation for adopting IoT products, the top three selected answers were customer loyalty, service improvement and new business models, see Fig. 4. Cost reduction has been ranked higher than environment awareness. For most companies, IoT products are not seen as a unique selling proposition.

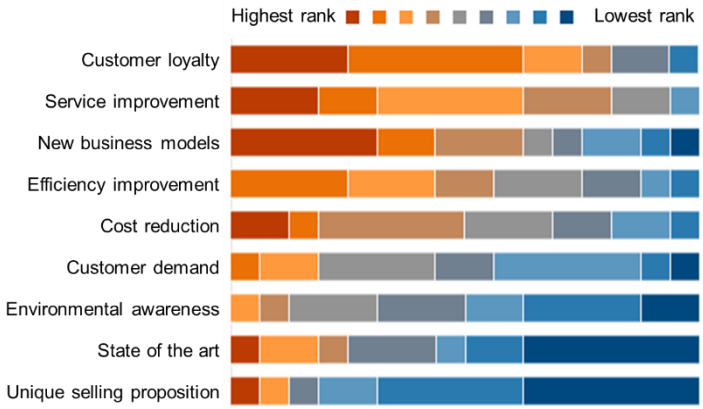


Fig. 4: Motivation to introduce IoT products

2.4.1. IoT in residential, commercial and office buildings

Operation data is collected locally at the heat pump or in a cloud service. For residential, commercial and office buildings, 50% of the companies use both, local storage and the cloud, 31% use the cloud and 13% only local storage. All these companies offer data-based features for the customers, such as operation monitoring and control, visualization of operation data and historic data and integration in a home automation system. To access these features, 93% of the companies provide an app for the customers, 73% have a control panel on the heat pump, 73% provide access to a website and 67% allow for integration in a home automation system. 47% of the companies offer all four ways of access.

The most common interface to collect operation and field data is LAN (81% of the companies), followed by WLAN (63%). 31% offer all interfaces that were mentioned: LAN, WLAN, local wireless, local wired, GSM, interfaces for smart grid ready. The most common transmission protocol is Modbus (75%), followed by

KNX (50%). Data security, transmission security and availability are most frequent reasons to choose the transmission protocol.

On the one side, certain IoT features are explicitly requested by customers. The participants confirmed that the following features are important for their customers: monitoring; interfaces for home automation; interfaces for smart tariffs and marketing of flexibility; coordinated operation with local PV and storage; and optimized maintenance intervals. On the other side, the companies confirm that the following IoT features are of great and almost equal importance for themselves: efficiency improvement; anomaly detection and operational monitoring; installation error detection; improved service offering (e.g. PV or price optimization); and product improvement and development. Interestingly, those IoT features which are seen as important by the companies are also those features which are already in use. A total of 88% of the companies apply data analytics for the following applications: installation error detection; efficiency improvement; anomaly detection and operational monitoring; product improvement and development.

2.4.2. IoT in industrial and district heating applications

For industrial and district heating applications, heat pump data is collected in the cloud and locally, most of the companies have both types. All of them offer integration of the data in the process control system and provide access to features in the cloud. The features comprise visualization of operation and historic data, monitoring and control and integration in the process control system. This is in good agreement with the IoT features requested by the customers. Unlike residential applications, smart tariffs are of less importance in industry.

The most common interface to collect operation and field data is LAN, which is used by all companies, (100%), followed by WLAN (67%). The most common transmission protocol is Modbus (83%), followed by OPC-UA and BACNET (each used by 50% of the companies). The reason to choose the transmission protocol are similar to the residential applications (data security, transmission security and availability).

2.5. Trends and future developments

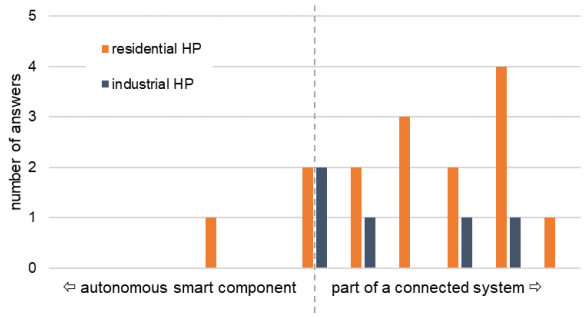


Fig. 5: IoT enabled heat pumps in the energy system

Generally, most participants agree that IoT technology brings significant changes. These changes are especially expected in product development, business models, maintenance and partially in sales. Less or insignificant impact is anticipated in the customer segment, production, installation, and supply. Most companies (except one) explicitly foresee the option to add or change IoT features through software updates after heat pump installation. This can be accomplished mainly via internet or manually by service personal. Three participants state that customers can also manually do software updates.

Clearly, IoT enabled heat pumps are expected to be rather a part of a connected system in the future than an autonomous smart component. As shown in Fig. 5, this was found for both residential and industrial heat pumps. The most important barriers for IoT technologies are the availability of qualified personnel, data protection and legal requirements as well as lack of standards. There is less concern about communication protocols and interfaces and the availability of suitable hardware.

It should be noted that IoT technology is seen as one of several digital transformation technologies to which a high importance is attached for the future. According to Fig. 6, equal or similar importance is attached to machine learning, predictive maintenance and building information modelling. Privacy requirements are ranked neutrally. In contrast, asset administration shell, semantic modeling and digital twin are considered as less important.

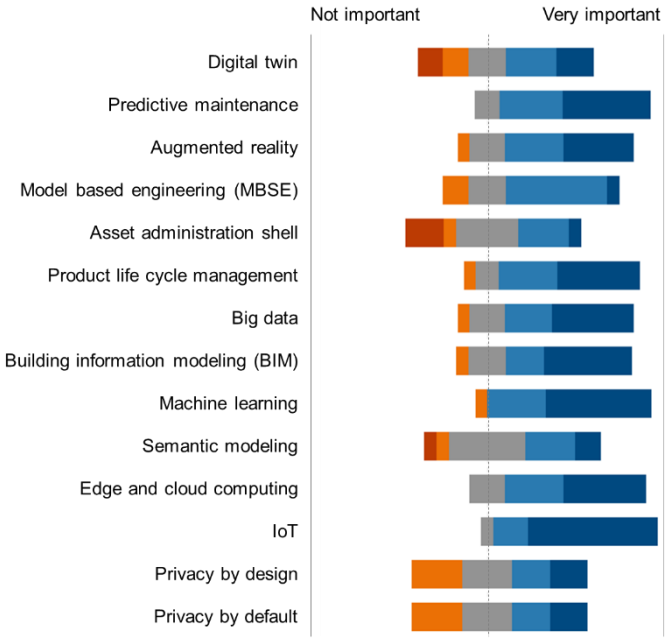


Fig. 6: Importance of digital transformation technologies for the future

3. Conclusions and outlook

A survey on the importance of IoT was carried out among companies of the Austrian heat pump industry. The participants represent 53% of the Austrian heat pump manufacturers and 27% of the heat pump vendors allowing for meaningful results. All companies offer both, IoT products (e.g. heat pumps with connectivity or intelligent components such as compressors or sensors), and services based on IoT products (e.g. marketing of flexibility, remote service, monitoring, etc.). Two thirds of the evaluated products are available, which means either in their product portfolio (in implementation), or already in a large number in use (extensive implementation). Another third is currently under evaluation, under development or in a pilot phase.

Most commonly, IoT products and services are developed by project teams or by a part of the development department. The main drivers for these products and services are customer loyalty, service improvement and new business models. The most important barriers for IoT technologies are the availability of qualified personnel, data protection and legal requirements, as well as lack of standards. There is less concern about communication protocols and interfaces and the availability of suitable hardware. The general expectation shared by all participants is that IoT technology will bring significant changes in product development, business models and maintenance. Moreover, IoT enabled heat pumps are expected to be a part of connected systems, and IoT technology is seen as one of several important digital transformation technologies for the future.

Digitalization is an important factor in the transformation of the energy system. It is expected to facilitate matching of supply and demand with increasing volatile energy production and to significantly contribute to end energy savings and CO_2 emission reductions. Connected heat pumps will play a vital role in the future energy system. Important fields of action are the establishment of common standards and interoperability of the appliances in the energy system. This is now also addressed in the latest EU action plan aiming at a common European energy data space for sharing and using energy data, a code of conduct for interoperability, enhanced participation in demand-response schemes for energy-smart appliances and strengthening cyber security and resilience of the energy system.

Acknowledgements

The Austrian IoT Annex project is being carried out within the framework of the IEA research cooperation on behalf of the Federal Ministry for Climate Action, Environment, Energy, Mobility, Innovation and Technology. The financial support is gratefully acknowledged.

References

[1] IEA. Digitalization & Energy. Paris: International Energy Agency, 2017
[2] EU Communication from the Commission to the European Parliament, the Council, the European Economic and Social Committee and the Committee of the Regions. Digitalising the energy system - EU action plan. COM(2022) 552 final, October 2022, https://eur-lex.europa.eu/legal-content/EN/TXT/PDF/?uri=CELEX:52022DC0552&from=EN
[3] IEA, Net Zero by 2050, IEA, Paris, 2021. https://www.iea.org/reports/net-zero-by-2050
[4] EU Communication from the Commission to the European Parliament, the Council, the European Economic and Social Committee and the Committee of the Regions. REPower EU Plan. COM(2022) 230 final, May 2022, https://eur-lex.europa.eu/legal-content/EN/TXT/?uri=COM%3A2022%3A230%3AFIN&qid=1653033742483
[5] Baumann M, Eggler L, Pauritsch G, Rohrer M. Auswirkungen der Digitalisierung auf Energieverbrauch und Klima in Österreich, D4.1 Quantifizierung der Szenarien. 2022, https://www.energyagency.at/fileadmin/1_energyagency/projekte/digitalisierung/digat/digat2040_d4.1_modelergebnisse_final.pdf
[6] Accenture. Klimaeffekte der Digitalisierung. Studie zur Abschätzung des Beitrags digitaler Technologien zum Klimaschutz. Bitkom, 2021. https://www.bitkom.org/sites/default/files/2021-10/20211010_bitkom_studie_klimaeffekte_der_digitalisierung.pdf

14th IEA Heat Pump Conference
15-18 May 2023, Chicago, Illinois

Numerical study of the part load operation for a reverse Brayton high-temperature heat pump

Enrico Jende[a*], Nancy Kabat[a], Panagiotis Stathopoulos[a]

[a] Institute of Low-Carbon Industrial Processes, German Aerospace Center, 03046 Cottbus, Germany

Abstract

Electrification of industrial process heat from renewable sources can contribute to the reduction of energy-related CO2 emissions. High-temperature heat pumps are one of the most important technologies to realize this electrification while reducing the electrical energy required for it. The Institute of Low-Carbon Industrial Processes of the German Aerospace Center (DLR) is developing high-temperature heat pumps (HTHP) based on reverse Brayton and Rankine cycles for heat transfer temperatures above 150 °C. The development and integration process of HTHPs for industrial processes often starts with their sizing at nominal operating conditions. Once the operational boundary conditions are defined, the individual components are sized. A large proportion of industrial heat pumps operate at a fixed point and are not optimized or designed for frequent part-load operation. This is expected to change, especially when heat pumps are required for industrial processes with part load operation. The current work presents an analysis of the part load operation of a reverse Brayton HTHP built in the laboratory of DLR and investigates its operational limits.

© HPC2023.
Selection and/or peer-review under the responsibility of the organizers of the 14th IEA Heat Pump Conference 2023.

Keywords: high temperature heat pumps; reverse Brayton cycle; process heat; stationary process simulation

1. Introduction

1.1. Motivation

Reducing greenhouse gas (GHG) emissions by 2050 is one of the most important steps to achieve the European Union's (EU) climate goals [1]. An interim target for 2030 is to reduce GHG emissions by at least 55% compared to 1990 levels [2]. Industrial heating and cooling demand in the EU accounts for over 25 % of these emissions [3]. More than 30 % of the cumulative energy demand for heating and cooling is used for industrial processes. This heating and cooling demand is mainly met by fossil fuels and a transformation to a GHG-free energy system is required to achieve the EU climate goals [4]. Several studies have been carried out in the past to estimate the heat demand for different process temperatures and industrial sectors in the EU. Naegler et al. [5] and Rehfeldt et al. [6] analysed several industrial processes and concluded that there is a large demand for heat at temperature levels from 100 °C to 500 °C mainly in industrial sectors such as chemical, paper and food industry. It is shown that the total final energy demand for heat in the EU-28 Member States in 2012 was 8518 PJ. The resulting total energy demand for heat at process heat temperature levels of 100 - 400 °C is 2214 PJ and above 400 °C 3859 PJ [5]. Marina et al. [7] identified the potential of heat pumps with heat sink temperatures up to 200 °C and analyzed their application in the food, paper, chemical and refinery sectors. They highlighted that a total of 641 PJ/year of process waste heat could be covered by industrial heat pumps. Wolf [8] investigated the application potential for heat use in German industry. He found a technical potential of 611 PJ using heat pumps with a maximum heat sink temperature of 140 °C. Kosmadakis [9] analyzed the possibilities of waste heat recovery using industrial heat pumps. He concluded that industrial heat pumps in the EU have a total potential of 28.37 TWh/year (102.132 PJ).

* Corresponding author. Tel.: +49 355 355645 32; *E-mail address:* enrico.jende@dlr.de.

All authors also emphasized that high-temperature heat pumps (HTHP) driven by renewable energy can make a significant contribution to the decarbonization of industrial heat supply in Europe and also significantly reduce the necessary primary energy demand for industrial heating [10], [11].

Nomenclature

Abbreviations		*Variables*	
3WV	Three-way-valve	COP	Coefficient of performance
CoBra	Cottbus Brayton cycle heat pump	COP_{Lorenz}	Lorenz COP
DLR	German Aerospace Center	P_c	Mechanical power of compressor, kW
EU	European Union	P_T	Mechanical power of turbine, kW
GHG	greenhouse gas	$\dot{Q}_{in}$	Heat sink heat flow of LTHX, kW
HP	heat pump	$\dot{Q}_{int}$	Internal heat flow of IHX, kW
HTHP	high-temperature heat pump	$\dot{Q}_{out}$	Heat source heat flow of HTHX, kW
HTHX	high-temperature heat exchanger	T	Temperature, K
IHX	Recuperator (internal heat exchanger)	T_m	Logarithmic mean temperatures, K
LTHX	low-temperature heat exchanger	η_{Lorenz}	Lorenz efficiency
TRL	Technology Readiness Level		

1.2. Short overview of the state of the art on HTHPs

The literature provides a first overview of the state of the art. For example, Wolf et al. [12] compared available types and technologies of heat pumps (HP), focusing on compression, absorption and hybrid HPs with a temperature delivery limit of 120 °C. Schlosser [13] investigated the decarbonization of industrial heat supply through the integration of heat pumps and presents methods for techno-economic detailed planning. Arpagaus et al. [14] give an overview of HPs already available on the market and the state of the art.

The IEA HPT Annex 58 project is currently underway to provide an overview of the state of the art and ongoing developments for HTHP systems and components [15]. This overview of the development of supplier technologies for HTHP shows that maximum supply heat sink temperatures between 115 °C and 280 °C with heating capacities up to 70 MW are available at the highest Technology Readiness Level (TRL) of 9 [15]. In addition, the demonstration cases of different technologies for HTHP have heat sink temperatures up to 211 °C, heating capacities up to 12 MW, and a coefficient of performance (COP) of 5.3 maximum [15].

In addition, published work with a simulative background has focused on the on-design operation of HTHPs and their techno-economic evaluation. For example Zühlsdorf et al. [11] presented possible solutions for a HTHP with sink temperatures around 250 °C and recommended a closed-loop reverse Brayton or Rankine cycle. Oehler et al. [16] investigated the part load capability of a HTHP based on a closed loop reverse Brayton cycle. They presented a combined method to operate such heat pumps at part load either by changing the speed of their compressor or by actively controlling the working fluid mass in the closed loop of the heat pump. As part of investigations on the load strategy of a gas turbine using the Brayton cycle, the benefits of fluid inventory control were also investigated by Pradeep Kumar et al. [17]. Both studies have shown that a Brayton cycle based HP can achieve high efficiencies and provide good flexibility by using an appropriate part load strategy [16], [17].

1.3. Motivation and contributions of this study

Potential applications for Brayton heat pumps are drying processes, e.g. in the food industry with temperature requirements up to 280 °C [11], [18]. Another application is preheating processes, for example in the metal industry [11] In some cases, variations in production conditions (temporary production line shutdowns, etc.) often lead to variations in the mass flow rate of the heating medium, even though the same product is being processed. To accomplish this task, it is necessary to understand the operating behavior, especially at partial load.

The DLR Institute of Low-Carbon Industrial Processes is developing a HTHP pilot plant based on the Reverse Brayton Cycle to analyze the feasibility of heat sink temperatures up to 300 °C. The aim of the present work is to analyze the steady-state part-load performance of this Reverse Brayton Cycle pilot plant under different boundary conditions. The ability and limitations of part load operation play an important role in the integration of HTHP into existing industrial processes with different operating conditions. The conclusions of this work are expected to pave the way for further investigations on the part load operation of HTHP.

2. Research object

This work focuses on the part load operation for reverse Brayton high-temperature heat pumps in the context of industrial process integration. The following subsections outline the research object of this considerations. First, the reverse Brayton process and the main evaluation parameters are described. The technical basis for the simulations and a detailed description of a prototype are then presented.

2.1. Brayton process and coefficient of performance

The reverse Brayton process considered in this study is shown in Figure 1. By absorbing mechanical power from the compressor shaft (P_c), the compressor (C) raises pressure and temperature of the working fluid (1 → 2). After that, the high-temperature heat exchanger (HTHX) transfers sensible heat ($\dot{Q}_{out}$) to the heat sink and cools down the working fluid (2 → 3'). If the cycle uses recuperation, heat is transferred ($\dot{Q}_{int}$) over an internal heat exchanger (IHX) to further reduce the temperature of the working fluid (3' → 3) before it expands through a turbine. The output mechanical power of the latter (P_T) is used directly to partially drive the compressor. In the DLR design, the turbine and the compressor are mechanically decoupled and the exchange of energy takes place through a power electronics system. After expansion the working fluid pressure drops to the initial level while its temperature decreases significantly (3 → 4). Finally, the working fluid absorbs heat ($\dot{Q}_{in}$, 4 → 1') first from the environment in the low-temperature heat exchanger (LTHX) and subsequently from the fluid exiting the HTHX in the internal heat transfer of the IHX (3' → 1) to close the cycle.

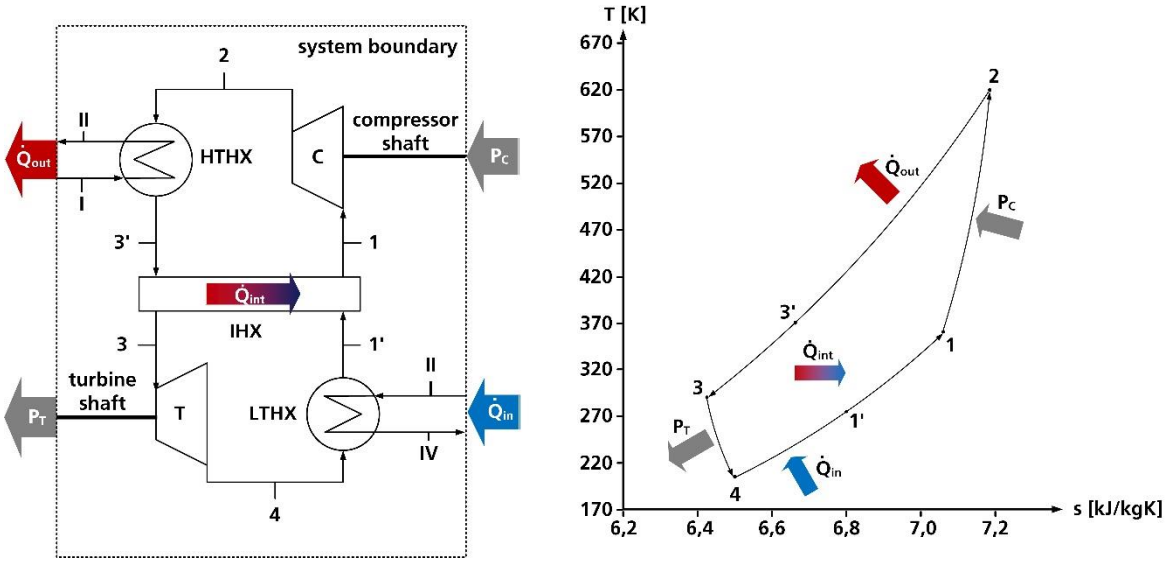


Figure 1. Scheme of the recuperated Brayton process (left) and sketched T-s-diagram of the simulation model of the CoBra

With regard to the following investigations, process parameters of heat sink, heat source, heat flow, temperature, and drive power outside the system boundaries of the Brayton process - see Figure 1- are mainly evaluated. In addition, the investigations on the heat pump system also need a main indicator to evaluate the results of the different part load operations. Arpagaus et al. [19] described the key efficiency indicator of a heat pump as the coefficient of performance (COP). The COP is defined as the ratio between the output heat power and the applied drive power. Considering the application of the Brayton process shown in Figure 1, the COP (Equation 1) is defined in these considerations as the ratio between the transferred heat flow $\dot{Q}_{out}$ and the difference between the drive power at the compressor shaft P_C and output power of the turbine P_T.

$$COP = \frac{\dot{Q}_{out}}{P_C - P_T} \tag{1}$$

Arpagaus et al. [19] and Marina et al. [7] described, that operating between process and waste heat streams with constant heat capacities and varying temperatures (temperature glides), the maximum theoretical COP is known as the Lorenz COP. Considering the application of the Brayton process shown in Figure 1, the Lorenz-COP (Equation 2) is defined as the ratio between the logarithmic mean temperatures T_m at the HTHX (Equation 3) and the LTHX (Equation 4). The Lorenz efficiency will not be reached in practice due to all kind of losses. To determine the real COP, a system efficiency must be considered [19]. An efficiency term, which relates the actual COP to the maximum Lorenz COP is given in Equation 5.

$$COP_{Lorenz} = \frac{T_{m,HTHX}}{(T_{m,HTHX} - T_{m,LTHX})} \tag{2}$$

$$T_{m,HTHX} = \frac{T_I - T_{II}}{\ln(T_I/T_{II})} \tag{3}$$

$$T_{m,LTHX} = \frac{T_{III} - T_{IV}}{\ln(T_{III}/T_{IV})} \tag{4}$$

$$\eta_{Lorenz} = \frac{COP}{COP_{Lorenz}} \tag{5}$$

2.2. DLR-HTHP Prototype CoBra

At the DLR Institute of Low-Carbon Industrial Processes, a prototype of a high-temperature heat pump based on the reverse, closed-loop and recuperated Brayton cycle was developed and built. The prototype is called CoBra (**Co**ttbus **Bra**yton). The main components are the two turbo machines and three shell-and-tube heat exchangers. To accommodate a large number of possible experimental investigations, the following design features are included:

- Designed for two working fluids - air and argon
- Compressor and turbine with own shafts and coupled to their electric machines through gearboxes
- Three-way-valve (3WV) to vary the mass flow of the hot fluid entering the recuperator
- Electrical heater upstream of the compressor to simulate an additional waste heat application
- Fluid inventory control by actively controlling the working fluid mass in the cycle
- Simultaneous supply of process heating and cooling
- Flexible secondary heat sink circuit to experimentally simulate various industrial processes / customers
- Flexible secondary heat source circuit with controllable fan and electrical heater as heat source to simulate an industrial cooling process with waste heat recovery

In addition to the design features of the prototype CoBra, the plant has been equipped with a comprehensive range of instrumentation to monitor the operation of all components in detail. Each circuit - the Brayton primary and the two secondary circuits - has a mass flow meter (MFM) and the necessary temperature and pressure measurements to evaluate the performance of the system under all operating conditions.

3. Methodology

A simulation model of the Brayton HTHP based on the CoBra has been developed in order to study the part-load operation in the context of industrial process integration and as a function of different process conditions. Furthermore, it is necessary to consider the possible industrial process integration of the Brayton HTHP. The following subsections outline the simulation model used for the numerical study and set up different Scenarios for the integration of the Brayton HTHP.

3.1. Simulation model of the Brayton HTHP

The first part of the development process of an industrial heat pump requires a design of the system based on defined boundary conditions. A simplified thermodynamic model of a reverse, recuperated Brayton cycle has been implemented in the software tool EBSILON® Professional [20]. This model considers the detailed operating maps of each component and is capable of simulating part-load operation of the entire cycle for steady-state operating conditions. The additional features of the off-design model can be summarized as follows:

- The compressor operation has been modelled with its operational maps
- The reduced mass flow rate in the turbine is considered constant. In other words, it is assumed that the turbine is always operating in the chocked region of its operational map.
- Heat exchanger with exchange surfaces and a standard map for off-design in EBSILON®
- Pipes with geometric based pressure losses and heat losses
- 3WV, electrical heater and MFM (based on CoBra) with constant pressure losses

The simulation model derived by the Brayton HTHP is based on parameters and maps of the main components and design features of the CoBra (see subsection 2.2). Environment conditions used for the first approach of the design was dry air as working fluid, the inlet temperatures of the HTHX and LTHX is set equal to 15 °C and the heat sink outlet temperature equal or higher than 250 °C. Based on this boundary conditions, Figure 2 shows the process design parameter of the fully recuperated CoBra at the maximum compressor speed of 105 000 min^{-1}. In general, the allowable range of tests is based on the operating limits of the plant. (see Table 1). The resulting model is conditionally switchable, allowing investigations of the Brayton heat pump in the context of industrial process integration and as a function of different process conditions.

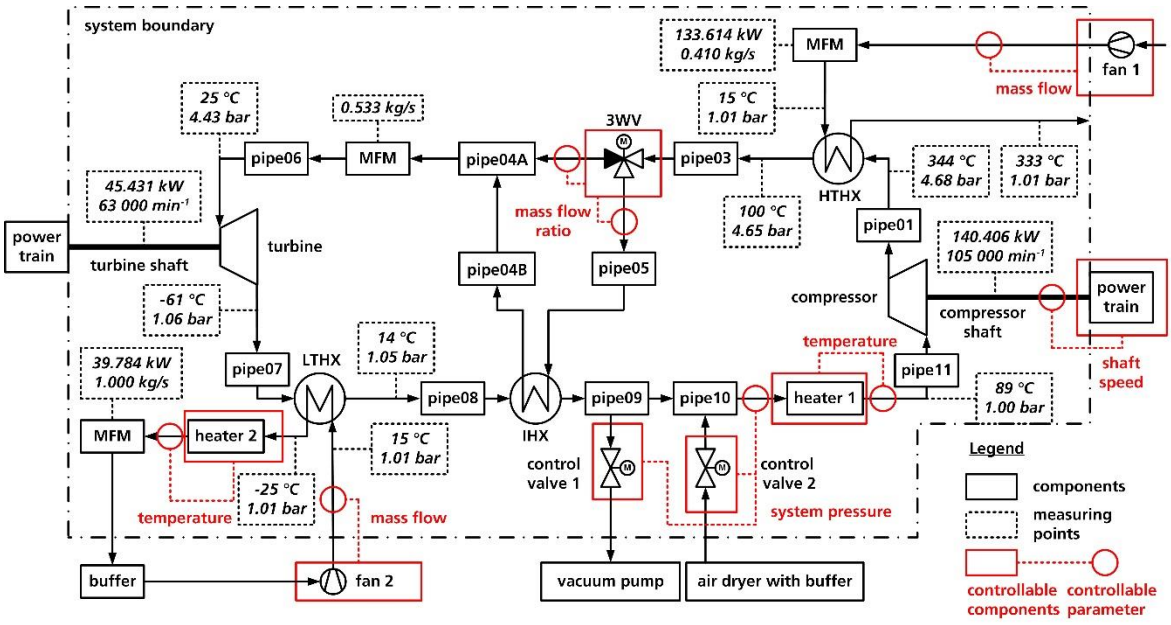


Figure 2. Scheme of the recuperated simulation model with design parameter (black dotted line) and controllable components (red line)

Table 1. Operating limits and ranges of the controllable components of the CoBra

Components	Control parameter	Operating limits	Operating range
Compressor	Compressor shaft speed	Surge and choke limit of the compressor	Map specific
		Maximum shaft speed	max. 105 000 min^{-1}
3WV	Mass flow rate of hot fluid into recuperator	Limits of 3WV	0 … 100 %
Fan 1	Mass flow rate at heat sink secondary	Maximum delivery rate	max. 0.67 kg/s
Fan 2	Mass flow rate of heat source secondary	Maximum delivery rate	max. 1.2 kg/s
Heater 1	Compressor inlet temperature	Maximum compressor inlet temperature	max. 100 °C
Heater 2	Heat source inlet temperature	Maximum fan 2 inlet temperature	max. 40 °C (+ 10 °C temperature lift of fan 2)
Control valve 1	Compressor inlet pressure based on mass in the primary HTHP loop	Minimal pressure of vacuum pump	min. 0.25 bar(g)
Control valve 2		Maximum pressure after the compressor	max. 7 bar(g)

3.2. Industrial process integration of the Brayton HTHP

In order to investigate the integration of the Brayton HTHP into an industrial process, it is necessary to define an appropriate integration Scenario. In the current work, a generic industrial process is assumed that requires a flow of hot air with a fixed temperature of 250°C and a mass flow of 0.5 kg/s (heat flow of 120 kW_{th}). In addition, it is assumed that this industrial process returns an exhaust air heat flow with a temperature of 50 °C at a mass flow of 1 kg/s (based on the heat mass flow rate of the CoBra). In general, the output temperature of the heat source is considered as a free parameter. Depending on its temperature, this flow can be made available for a cooling process or can be discharged to the environment. Finally, Figure 3 shows the two integration Scenarios. The first considers a Brayton HTHP with CoBra boundary conditions. The second introduces a recirculation of the exhaust air heat flow for the heat source of the Brayton HTHP.

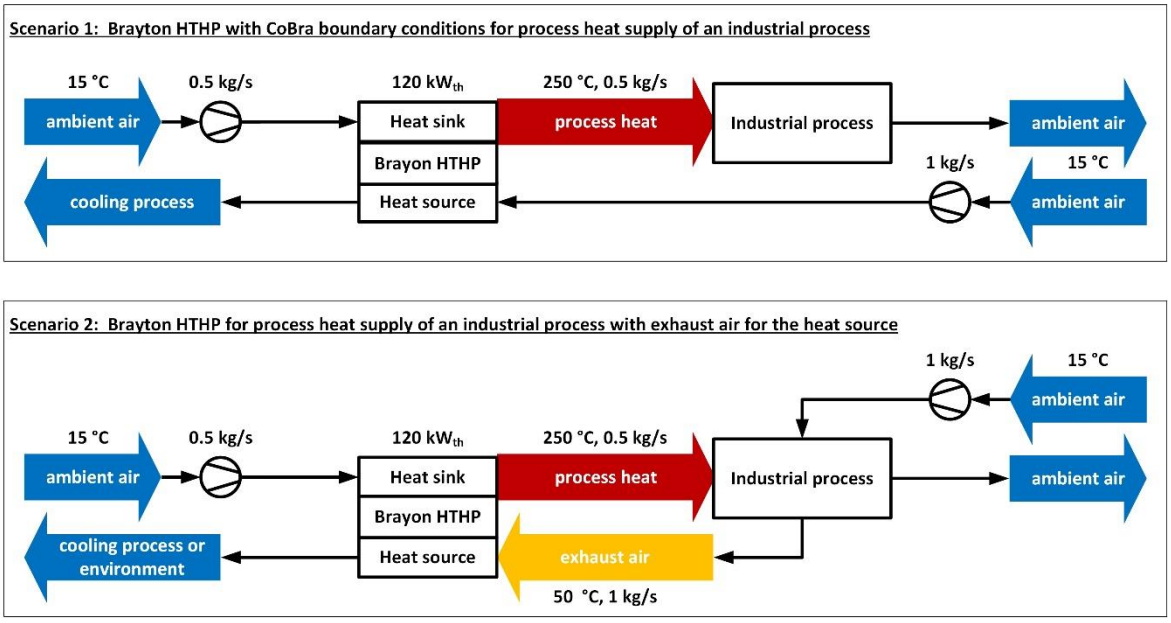


Figure 3. Schemes of process integrations Scenarios of a Brayton HTHP into an industrial process

4. Results and discussion

Table 2 shows the operating range that used to study the off-design operation of the HTHP. It should be noted that, based on the compressor map, the minimum possible load is equal to approximately 60 % due to the compressor surge limit. In general, the heat sink outlet temperature is specified fixed at 250 °C. The heat source outlet temperature is considered as a free parameter that can potentially be made available for a cooling process.

Table 2. Range of industrial process conditions for the part load operations

Investigation Scenario	unit	Scenario 1		Scenario 2	
Load	%	100	60	100	60
Heating capacity	kW_{th}	120	72	120	72
Heat sink inlet temperature	°C	15	15	15	15
Heat sink mass flow rate	kg/s	0.5	0.3	0.5	0.3
Heat source heat capacity	kW_{th}	-	-	40	20
Heat source inlet temperature	°C	15	15	50	50
Heat source mass flow rate	kg/s	1	1	1	1

For the described integration Scenarios (see Figure 3), the results are presented in the following subsection. The HTHP load has been varied between 60 – 100 % (fan 1 as control parameter, mass flows see in Table 2) and the operating modes with and without recuperation have been studied. The degree of recuperation (3WV as control parameter, 0 % is non-recuperated, 100 % is recuperated) and the speed of the compressor (free parameter between 80 000 and 105 000 rpm) are the only variable control parameters. The other control parameters are fixed (fan 2 is 1 kg/s, heaters 1 and 2 with no heat input, control valves 1 and 2 are deactivated for no fluid inventory control).

4.1. Results of the Scenario 1

Figure 4 shows the compressor efficiency for the part load operations of Scenario 1. The comparison shows that the recuperated HTHP generally has a higher COP and Lorenz efficiency in all part load modes. The reason for the higher HTHP efficiency can be explained by the compressor and turbine mechanical powers conditions, inlet temperatures and compressor pressure ratio (Figure 5).

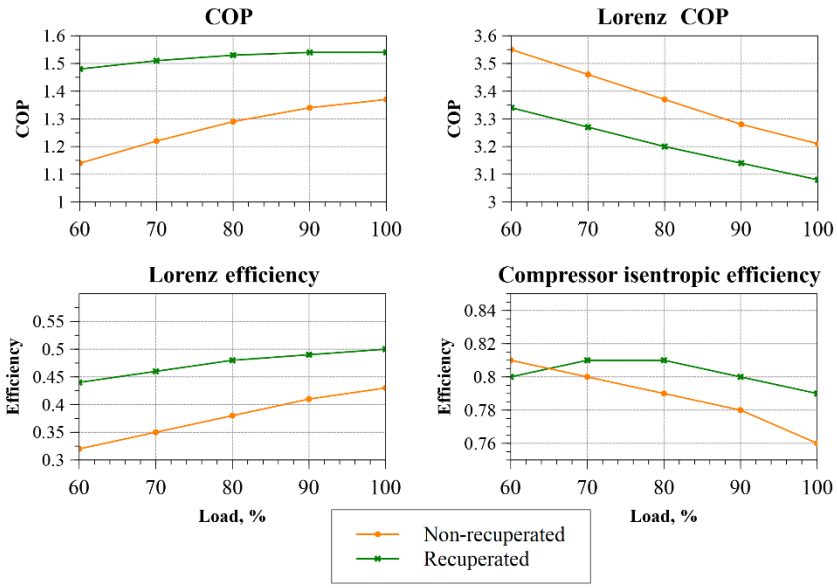


Figure 4. Process parameter of the Brayton HTHP (Part 1) - Scenario 1

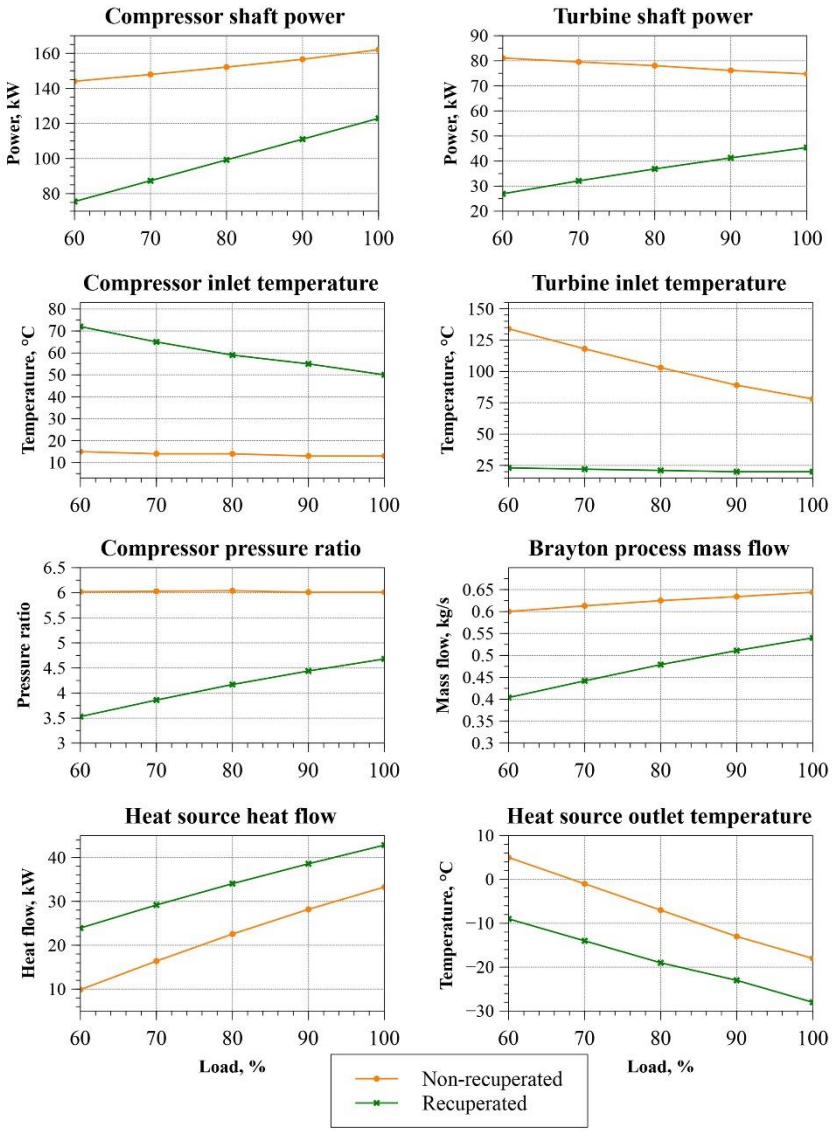


Figure 5. Process parameter of the Brayton HTHP (Part 2) - Scenario 1

Figure 5 shows that the recuperated operation mode has a significantly lower compressor power at all part load conditions, which is not compensated by the lower turbine power. Relative to the constant heat flow through the heat sink, this effect results in a higher COP (see equation 1 in subsection 2.1). The lower compressor and turbine power is due to the internal heat transfer through the IHX, which generally results in higher compressor inlet temperatures and lower turbine inlet temperatures. This is due to the fact that the only controllable parameter to run at part load is the compressor speed, which is controlled for an appropriate pressure ratio, which in turn provides the 250°C. When the compressor shaft speed is reduced, the Brayton mass flow and the compressor pressure ratio in the primary circuit are also reduced. This effect shifts the compressor operating condition to points on its map with higher isentropic efficiencies compared to non-recuperated operation (Figure 4).

In addition, Figure 5 shows that the consistently low turbine inlet temperatures and the generally lower Brayton mass flow in the recuperated mode in turn ensure consistently very low heat sink outlet temperatures and a higher heat source heat flow. With increasing part load, the outlet temperatures increase in both operating modes, which in turn leads to higher theoretical maximum efficiencies in the form of the Lorenz COP (Figure 4).

4.2. Results of the Scenario 2

Figure 6 shows the complete process parameters of Scenario 2 and the difference between the Brayton HTHP for the part load operation of Scenario 2 compared to Scenario 1. In general, it can be seen that the higher inlet temperature at the heat source results in a higher COP and, at full load, nullifies the effects and benefits of recuperation described above. This can also be seen where the turbomachinery capacities are almost the same at full load. This effect is cancelled as the partial load increases, as the internal heat transfer increases and the conditions become more similar to those in Scenario 1. In general, the inlet temperatures at the turbomachinery are higher, which leads to better conditions (e.g. compressor pressure ratio and Brayton mass flow) and ultimately to better but more similar efficiencies - compared between operating modes - as well as higher heat source flows and outlet temperatures in Figure 6.

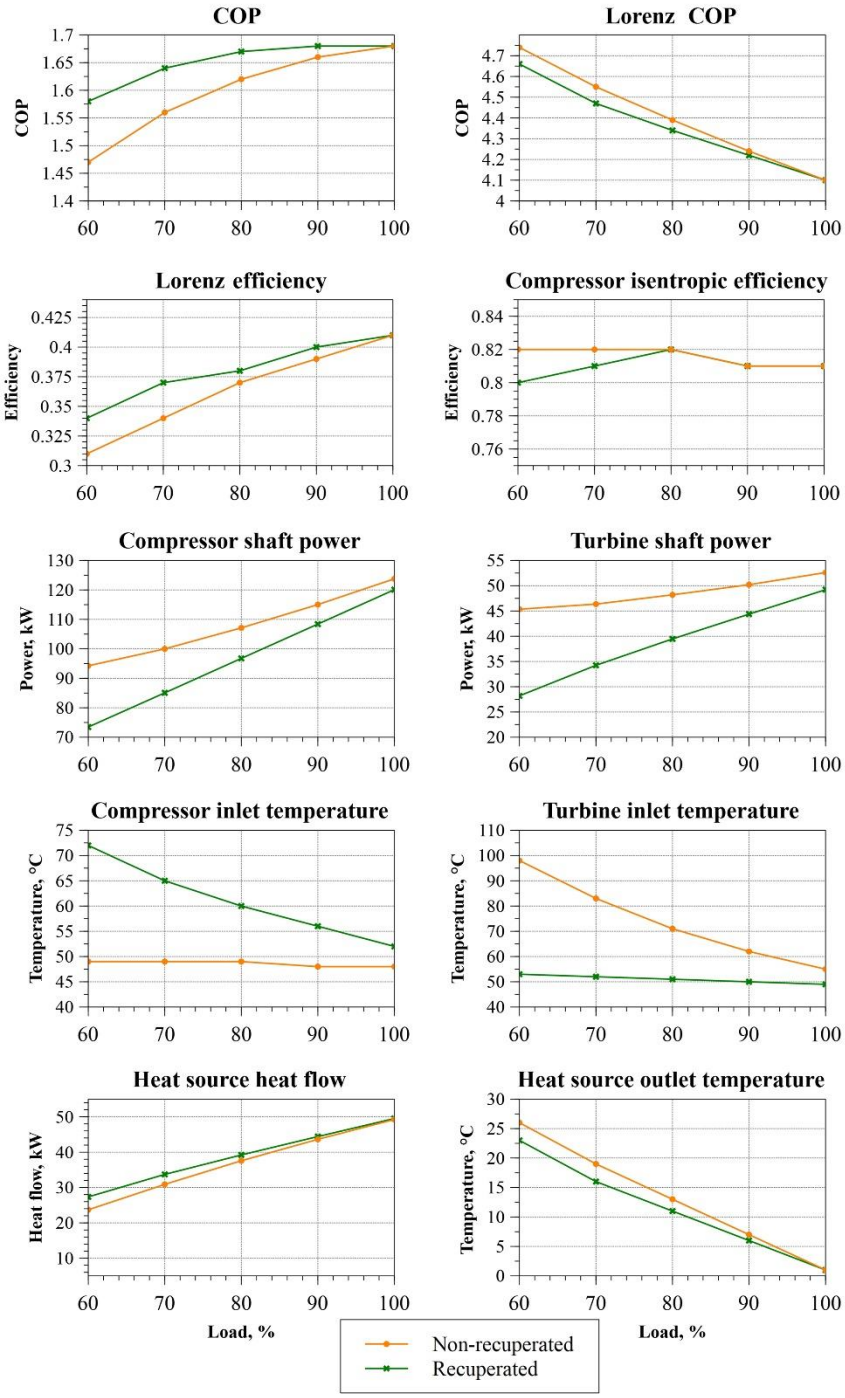


Figure 6. Process parameter of the Brayton HTHP - Scenario 2

4.3. Comparison of the two Scenarios of industrial process integration of the Brayton HTHP

Firstly, the graphs of the key efficiency indicator COP show the typical increase in COP for heat pumps as the heat source inlet temperature rises. Scenario 2 has a significantly higher efficiency than Scenario 1 at all load conditions.

In relation to the influence of recuperation, both Scenarios show that the recuperated mode has a higher COP than the non-recuperated mode in part load operation. However, Scenario 2 shows that recuperation has no effect on the heat sink and heat source conditions and the COP of the Brayton HTHP as the heat source inlet temperatures increase. From this effect it can be concluded that as the available temperature increases, the decision of whether a recuperated process is required becomes obsolete.

A consideration of the heat sink conditions indicates that the type of process integration is critical to the intended application. This is because the outlet temperatures drop significantly at lower temperatures (see Scenario 1) and the use of the Brayton HTHP only makes sense if the cold temperatures are used in a cooling process.

Finally, a look at the controllable parameter of the compressor shaft speed of the two Scenarios in Figure 7 reflects the behavior of the heat pump in both Scenarios, where at low heat source inlet temperatures (Scenario 1) a higher demand is placed on the compressor than at increasing heat source inlet temperatures (Scenario 2), up to the approximate balance at full load due to cancellation of the positive recuperation effect.

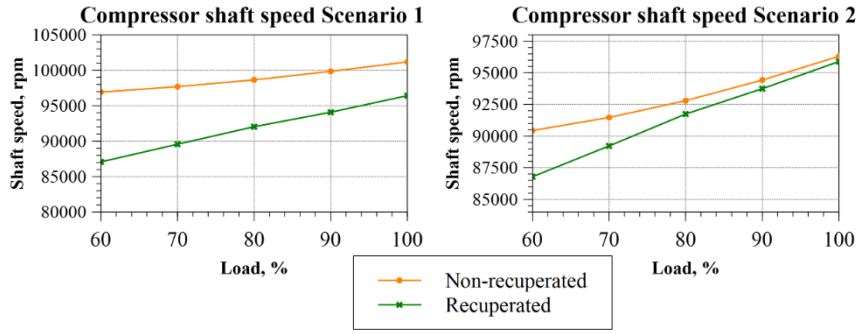


Figure 7. Compressor shaft speed of Scenario 1 (left) and compressor shaft speed of Scenario 2

5. Conclusion and outlook

High temperature heat pumps based on the reverse Brayton process can contribute to the decarbonisation of industrial drying processes. For process integration into existing industrial processes with variable conditions, the ability and limitations to operate at part load play an important role. A simulation model based on a DLR-HTHP prototype was developed in these investigations and integrated into the simulation environment of EBSILON® Professional for off-design simulation considerations. An industrial process was then assumed and described which provided two investigation Scenarios for the Brayton HTHP integration and the part load study. These investigations were initially carried out with the two controllable components, the compressor to vary the compressor shaft speed and the 3-way valve to vary the recuperation rate.

The part load studies show that the conditions of the heat source and ultimately the nature of the industrial process are critical. If efficiencies increase as expected at low inlet temperatures and increasing recuperation, the advantage of recuperation is cancelled out as inlet temperatures increase.

Based on the controllable components presented in the methodology of this research, further studies on partial load operation can be carried out with DLR-HTHP prototype CoBra. Examples include fluid inventory control, or investigating further process architectures with the electric heater upstream of the compressor to simulate an additional waste heat application.

Furthermore, in the context of process integration, it should be noted that an experimentally designed HTHP has been studied in the context of these considerations. Although this will allow future experimental verification of the results with the DLR-HTHP prototype CoBra test facility, a potential Brayton HTHP integrated into an industrial process must be optimized for the industrial process with variable part-load conditions already in the design phase. The above considerations can serve as a basis for this.

Acknowledgements

The authors thanks Eberhard Nicke, Leander Schleuß and all members of the department of high-temperature heat pumps for their support.

References

[1] Brian Vad Mathiesen, Nis Bertelsen, Noémi Cécile Adèle Schneider, Luis Sánchez García, Susana Paardekooper, Jakob Zinck Thellufsen et al. *Towards a decarbonised heating and cooling sector in Europe: Unlocking the potential of energy efficiency and district energy* 2019.

[2] Webseite der Bundesregierung | Startseite. *Klimaschutzpaket der EU-Kommission | Bundesregierung*. [September 22, 2022]; Available from: https://www.bundesregierung.de/breg-de/themen/europa/fit-for-55-eu-1942402.

[3] Umweltbundesamt. *Energieverbrauch nach Energieträgern und Sektoren*. [November 11, 2022]; Available from: https://www.umweltbundesamt.de/daten/energie/energieverbrauch-nach-energietraegern-sektoren#allgemeine-entwicklung-und-einflussfaktoren.

[4] Tobias Fleiter, Rainer Elsland, Matthias Rehfeldt, Jan Steinbach, Ulrich Reiter, Giacomo Catenazzi, Martin Jakob, Cathelijne Rutten, Robert Harmsen, Florian Dittmann, Philippe Rivière, Pascal Stabat. *Heat Roadmap Europe: EU Profile of heating and cooling demand in 2015;* 2017.

[5] Naegler T, Simon S, Klein M, Gils HC. *Quantification of the European industrial heat demand by branch and temperature level*. *Int. J. Energy Res.* 2015;**39**(15):2019–30, DOI: 10.1002/er.3436.

[6] Rehfeldt M, Fleiter T, Toro F. *A bottom-up estimation of the heating and cooling demand in European industry*. *Energy Efficiency* 2018;**11**(5):1057–82, DOI: 10.1007/s12053-017-9571-y.

[7] Marina A, Spoelstra S, Zondag HA, Wemmers AK. *An estimation of the European industrial heat pump market potential*. *Renewable and Sustainable Energy Reviews* 2021;**139**:110545, DOI: 10.1016/j.rser.2020.110545.

[8] Wolf S. *Analyse des Potenzials von Industriewärmepumpen in Deutschland Forschungsbericht Endbericht*. Stuttgart; 2014.

[9] Kosmadakis G. *Estimating the potential of industrial (high-temperature) heat pumps for exploiting waste heat in EU industries*. *Applied Thermal Engineering* 2019;**156**:287–98, DOI: 10.1016/j.applthermaleng.2019.04.082.

[10] Prognos, Öko-Institut, Wuppertal-Institut. *Towards a Climate-Neutral Germany. Executive Summary conducted for Agora Energiewende, Agora Verkehrswende and Stiftung Klimaneutralität;* 2020.

[11] Zühlsdorf B, Bühler F, Bantle M, Elmegaard B. *Analysis of technologies and potentials for heat pump-based process heat supply above 150 °C*. *Energy Conversion and Management: X* 2019;**2**:100011, DOI: 10.1016/j.ecmx.2019.100011.

[12] Wolf S, Blesl M. *Model-based quantification of the contribution of industrial heat pumps to the European climate change mitigation strategy*. *ECEEE Ind Summer Study Proc* 2016:477-87.

[13] Schlosser F. *Integration von Wärmepumpen zur Dekarbonisierung der industriellen Wärmeversorgung*: Universität Kassel; 2021.

[14] Arpagaus C, Bless F, Uhlmann M, Schiffmann J, Bertsch SS. *High temperature heat pumps: Market overview, state of the art, research status, refrigerants, and application potentials*. *Energy* 2018;**152**:985–1010, DOI: 10.1016/j.energy.2018.03.166.

[15] Annex 58. *Task 1 - Technologies - Annex 58*. [February 20, 2023]; Available from: https://heatpumpingtechnologies.org/annex58/task1/.

[16] Johannes Oehler, Jens Gollasch, A. Phong Tran, Eberhard Nicke. Part Load Capability of a High Temperature Heat Pump with Reversed Brayton Cycle. In: *13th IEA Heat Pump Conference 2021 (HPC2020) Conference Proceedings. 13th IEA Heat Pump Conference, 26.-29. April, Jeju, Korea.*

[17] Pradeep Kumar KN, Tourlidakis A, Pilidis P. *Performance review: PBMR closed cycle gas turbine power plant*. International Atomic Energy Agency (IAEA); 2001.

[18] Dipl.-Ing.Jörg Schulz. *Leitfaden"Energieeffizienz in Bäckereien - Energieeinsparungen in Backstube und Filialen"*; Available from: https://www.selbstaendig-im-handwerk.de/downloads/News/EnEffBaeckerei-Leitfaden-Juli2014.pdf.

[19] Arpagaus C. *Hochtemperatur-Wärmepumpen*: *Marktübersicht, Stand der Technik und Anwendungspotenziale*. Berlin, Offenbach: VDE Verlag GmbH; 2019.

[20] STEAG Ebsilon. *STEAG EBSILON*. [November 09, 2022]; Available from: https://www.ebsilon.com/de/.

14th IEA Heat Pump Conference
15-18 May 2023, Chicago, Illinois

Performance study of a dual-loop booster heat pump in the deep recovery of boiler flue gas waste heat

Yuepeng Jiang[a], Guoyuan Ma[a,*], Yuexuan Gong[a], Shuxue Xu[a]

[a]Department of Refrigeration and Cryogenic Engineering, Beijing University of Technology, Beijing 100124, China

Abstract

Traditional district heating systems face disadvantages such as low utilization of renewable energy and high system heat loss, while ultra-low temperature district heating (ULTDH) systems can make full use of low-temperature waste heat or renewable heat sources while reducing the heat loss of the pipe network. To deeply recover the low-temperature waste heat from the flue gas of a gas boiler in a heating project in Beijing, this paper designs a dual-loop booster heat pump system and uses it in the ULTDH system. The coefficient of performance (COP) and annual power consumption of the designed booster heat pump operating in the ULTDH system is simulated and analyzed using DeST software and actual compressor specifications. The results show that the average COP of the dual-loop booster heat pump is 0.92 higher than that of the conventional heat pump, which can save about 0.034 million kW·h of electrical energy during the heating period, and has a large energy-saving potential and broad market prospect.

© HPC2023.
Selection and/or peer-review under the responsibility of the organizers of the 14th IEA Heat Pump Conference 2023.

Keywords: Booster heat pump; ultra-low temperature district heating; deep flue gas heat recovery.

1. Background

Current energy systems worldwide consume vast amounts of energy, even triggering global climate change. To achieve sustainable development strategies, there is a need to reduce primary energy consumption and gradually transition to sustainable energy. Among all energy consumption, building energy consumption account for a huge proportion of energy consumption, so improving building energy consumption is an effective way to achieve efficient energy use[1-3]. Currently, the district heating of buildings in China is still dominated by coal-fired and gas-fired boilers, which pollutes the atmospheric environment and brings the problem of excessive energy utilization. Therefore, the effective recovery of low-grade waste heat or using renewable energy for building heating and hot water is an effective way to reduce energy consumption and achieve sustainable development[4-6].

In recent years, researchers have proposed an ultra-low temperature district heating system (ULTDH) that can fully use low-temperature heat sources or renewable energy, also known as the fifth generation district heating system. ULTDH improves the problems of significant heat loss, high energy consumption and less available heat sources in traditional district heating networks. The water temperature flowing from the heating network of the ULTDH is lower than 50 °C, even as low as 25 °C[7,8]. Since the hot water temperature of the ultra-low temperature district heating system is relatively low, the hot water should be heated by the heat pump (booster heat pump) before passing through the terminal equipment to meet the requirements of the user or terminal equipment. In this case, the heat loss can be minimized to the extent that no pipe insulation is required because the hot water is close to the ambient temperature as it flows through the pipe network[9-14].

The high-temperature flue gas emitted from conventional district heating boilers can be recovered and utilized by heat exchangers or absorption heat pumps. But in the low-temperature flue gas still contains a large amount of waste heat that can be used. The compression heat pump can deeply recover the low-temperature

* Corresponding author. Tel.: 010-67391363;
E-mail address: magy@bjut.edu.cn.

flue gas waste heat between 30~60℃[15-18]. Mu et al.[19] applied heat pumps to flue gas recovery and conducted an experimental analysis of the performance of heat pumps. Compared with the energy consumption of gas boilers, exhaust-source heat pumps can save 55% of standard coal. The comprehensive energy efficiency ratio of heat pumps can reach more than 4.0. However, because two sets of units are needed to supply heat and domestic hot water separately, there are problems with occupying large space and large installation and operation and maintenance costs. Wu et al.[20] analyzed the engineering application of exhaust-source heat pumps. The results show that although the traditional heat pump has greater advantages in waste heat utilization, the large-scale implementation of the application is more difficult due to the large number of equipment and complex system operation. Huang et al.[21] address the problem of low utilization of waste heat from flue gas boilers, combined with air source heat pump technology for low-level flue gas waste heat for gradient depth recovery and utilization. Results show that by recycling flue gas waste heat, with low valley electricity prices, the heating cost of domestic hot water can be reduced more significantly, with energy saving, emission reduction, water saving and other economic benefits. However, the initial investment cost of the system is large. In the face of large temperature differences, there are still problems of relatively low energy efficiency and poor system heat transfer efficiency.

Due to the problems of high initial investment cost, large floor space and low heat transfer efficiency of the system under large temperature difference conditions, this paper designs a dual-loop heat pump system for boiler flue gas deep recovery. Integrating two independent heat pump loops into one device improves the uniformity of the heat transfer process and the coefficient of performance (COP) of the heat pump. The dual-loop booster heat pump is applied to the deep recovery of boiler flue gas waste heat in a district heating project in Beijing. Based on the performance of the actual compressor, the operating performance of this dual-loop booster heat pump was simulated and analyzed using DeST software.

2. System design and application scheme

2.1. Dual-loop booster heat pump system

The flue gas waste heat recovery device integrated with the heat pump is shown in Fig. 1. Firstly, the boiler flue gas and part of the heating return water for heat exchange, then the flue gas is discharged to the flue gas heat exchanger, in the flue gas heat exchanger for intermediate water heating, flue gas reduced to a certain temperature and then discharged to the heat exchanger, the heated intermediate water as a low-temperature heat source into the heat pump, the heat pump will be the remaining heat network return water heated to the heating temperature.

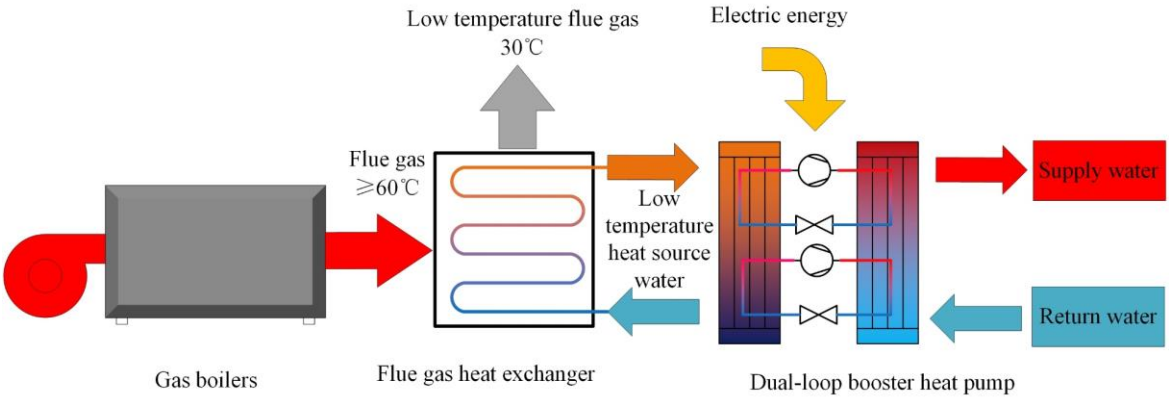


Fig. 1. Combined utilization of flue gas waste heat recovery device and booster heat pump.

Fig. 2(a) shows the designed new dual-loop heat pump system. After absorbing the flue gas waste heat, the hot intermediate water enters the evaporator of the heat pump to exchange heat with the refrigerant, the booster heat pump absorbs heat from the intermediate water and raises the refrigerant to a higher temperature with the input of electrical energy to heat the heating return water in the condenser. The designed dual-loop system contains two compressors, two expansion valves, an evaporator and a condenser. The return water enters from the inlet of the condenser and carries out counter-current heat exchange with the refrigerant in the low-temperature loop and the high-temperature loop successively, and then discharges from the outlet of the condenser after reaching the required temperature of the user and flows to the user side for heating; the heat

source water enters from the inlet of the evaporator and carries out counter-current heat exchange with the refrigerant in the high-temperature loop and the low-temperature loop successively. The pressure-enthalpy diagram of the dual-loop heat pump system is shown in Fig. 2(b), where cycle 1-2-3-4-1 represents the low-temperature loop and cycle 5-6-7-8-5 for the high-temperature loop.

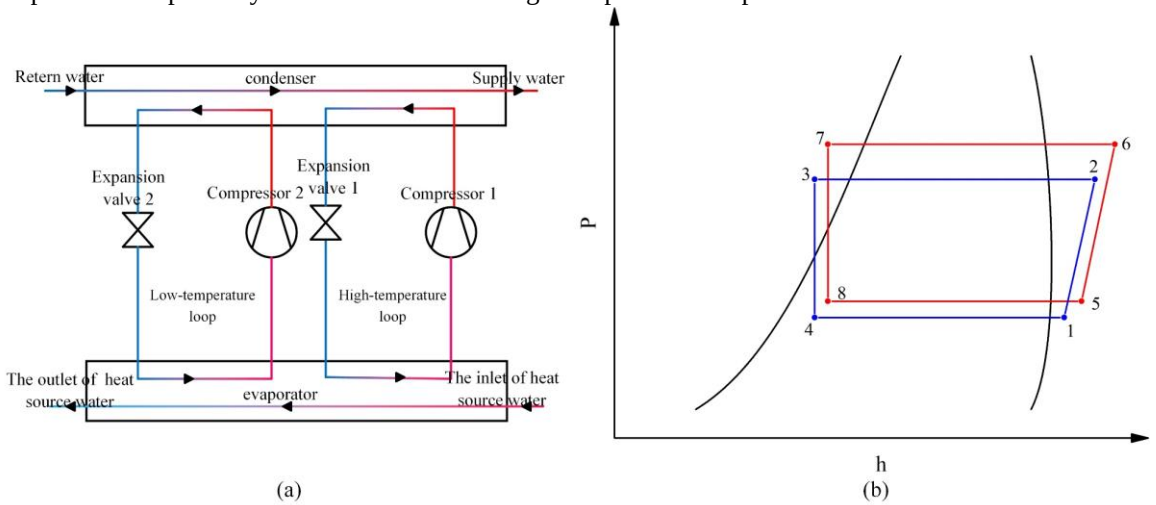


Fig. 2. (a) Schematic of the dual-loop system; (b) P-h diagram of dual-loop heat pump system.

2.2. Application scheme

This paper designs a traditional single-loop and a new dual-loop booster heat pump for flue gas waste heat recovery in a heating boiler room in Beijing, and the heat recovered by the booster heat pump heat some commercial buildings in the area, and this boiler room is divided into two rooms in the North and South, covering 188,848 m² and 353,603 m², respectively, the design indexes are shown in Table 1.

Table 1. Waste heat recovery indexes

Building location	Heating load for commercial (*kW*)	Heating load for residential (*kW*)	Total heating load (*kW*)	Index of waste heat recovery (*kW*)
South area	8498.19	893.82	9392.02	470
North area	15912.15	957.83	16869.99	843.5

The main heating form of the project is gas boiler heating, and the flue gas is the main waste heat source of the project itself. The waste heat recovery index is 5% of the total heat load, the total installed capacity of the South area is 9392kW, and the total installed capacity of the North area is 16870kW. The waste heat recovery index of the heat pump in the South area is 470kW, and the waste heat recovery index of the heat pump in the North area is 843.5kW. The heat recovered from the heat pump will be used to meet the heat demand of some buildings in the area, the main load of this part of the building is commercial heat load, mainly concentrated during the daytime, with insulation running at night.

For the traditional single-loop booster heat pump systems, each unit is set to have a rated heat capacity of 150kW. For the new dual-loop booster heat pump systems, each unit is set to have a rated heat capacity of 240kW, and the heat production is made to meet the heat load requirements by connecting multip le units in parallel. For the South area, the index of waste heat recovery is 470kW, so the single-loop heat pump in the South area is set to 4 units in parallel, and the dual-loop heat pump is set to 2 units in parallel. In the North area, the waste heat recovery index is 843.5kW, so the single-loop system in the North area is set to 6 units in parallel, and the dual-loop heat pump is set to 4 units in parallel.

Due to the large amount of low-temperature flue gas discharged from the district heating boiler, it is necessary to select a large-capacity compressor that can operate at low-temperature conditions. According to the compressor's applicable temperature range and heat capacity, the working fluid's safety and economy. Danfoss DSH381-4 scroll compressor and R410A are selected, and the curve of COP with temperature is shown in Fig. 3.

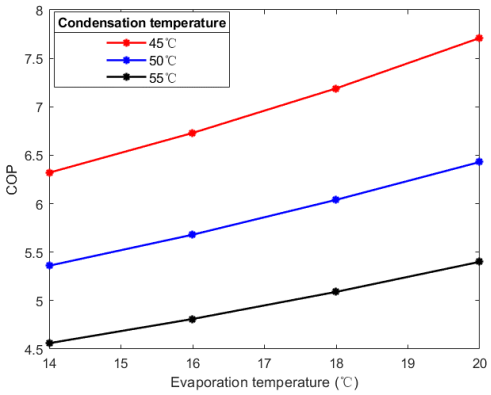


Fig. 3. Danfoss DSH381-4 Compressor Performance Curve.

2.3. The curve of the heating load

In this case, the heat recovered from waste heat is used for heating some buildings in this area. To meet the real-time heat demand of users, this paper has used DeST software to conduct modeling and simulation and obtains the hourly heating load curve of the whole heating period of some buildings in this area. As shown in Fig. 4(a), the heating period is from November 15 to March 15 of the following year, totaling 2904 hours. In Fig. 4, the horizontal coordinate represents the time and the vertical coordinate represents the heating load, the blue curve is the heating load of some buildings in the North area and the red curve is the heating load of some buildings in the South area. The average hourly heating load of the buildings in the North area is 261.76kW, and the maximum heating load can be 710.75kW, while the average hourly heating load of the buildings in the South area is 145.75kW, and the maximum heating load is 395.74kW, the waste heat recovery index can fully meet the heating load demand of this part of the buildings. From the perspective of the whole heating period, the overall trend of hourly heating load in both the South and North areas is first increased and then decreased, which is consistent with the actual local climate change. It is shown in Fig.4 (a) that the heating load fluctuates greatly in a short time interval, this is because the buildings are mainly commercial buildings, and there are many people in the daytime, so they need high thermal comfort and high heating load. However, there are few people in commercial buildings at night, and the thermal comfort is low. Therefore, the heating load of the buildings at night is low.

Instantaneous heating load on the customer side is variable, so heating regulation is required during operation. In this paper, temperature regulation is utilized as a centralized regulation method for the hot water heating system, that is, the mass flow rate of heating water is unchanged, and only the temperature of the supply water is changed. Fig. 4(b) shows the variation in the temperature of the supply and return water in the heating system regarding the number of days. At the beginning of the heating period, the required heating load on the customer side is low, the temperature of the supply water is slightly lower, the temperature of the return water is high, and the temperature difference between the supply and return water is small; at this stage, the average temperature of the supply water is 45.29 ℃, the average temperature of the return water is 34.43 ℃, and the average temperature difference between supply and return water is 10.86 ℃. As time passes, the ambient temperature gradually decreases, the heating demand on the customer side becomes higher, the temperature of the supply water rises continuously up to 48.45 ℃, the temperature of the return water gradually decreases, down to 32.92 ℃, and the maximum temperature difference between supply and return water is up to 15.53 ℃. At the later stage of the heating period, the ambient temperature gradually rises, the heating load of the customers is lower, the temperature of the supply water gradually decreases, the temperature of the return water gradually increases, and the temperature difference between the supply and return water becomes smaller, at this stage the average temperature of the supply water is 45.63 ℃, the average temperature of the return water is 35.86 ℃, and the average temperature difference between supply and return water is 9.77 ℃.

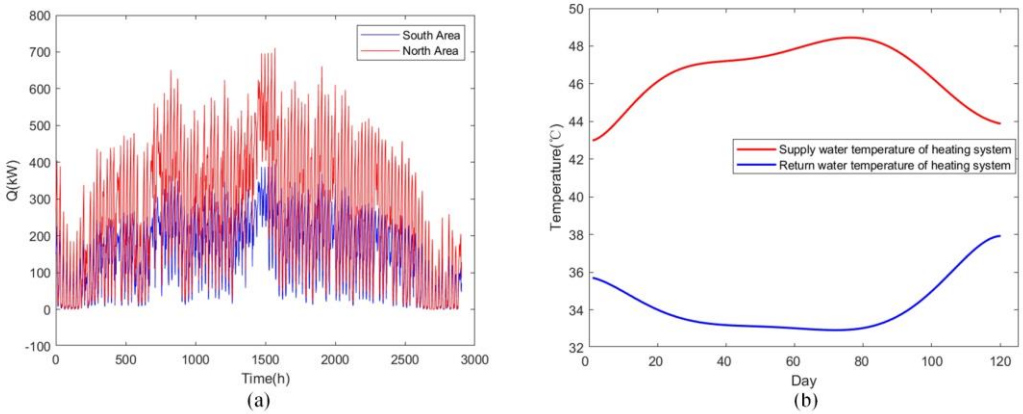


Fig. 4. (a) Hourly heating load of buildings in the heating period in this area; (b) Temperature of the supply and return water during the heating period.

2.4. Control strategy of heat pump

Based on the hourly heating load curve and the temperature variation curve of the supply and return water obtained from the above simulation throughout the heating period, this paper carries out the analysis of the year-round control strategy of the booster heat pump system, which controls the heat production by controlling the compressor on and off, and the higher the heating load, the more the number of compressors on. When the heating load is lower than the rated heat capacity of one unit, only one heat pump unit is turned on. It is important to note that two compressors need to be started for the dual-loop heat pumps for each unit.

On the day with the highest heating load during the whole heating period, the number of started compressors hour by hour for the North and South areas are shown in Fig. 5(a) and 5(b), respectively. It can be seen that the number of started compressors is higher in the North area than in the South area due to the difference in heating load. Since the dual-loop systems contain two compressors in one unit, the number of started compressors is greater than or equal to that of the single-loop systems. At night, there are few people in the commercial buildings, the heating load is low, and the number of started compressors is small; during the daytime, the number of people in the commercial buildings increases, the heating load rises, and the number of started compressors increases and reaches the highest from 7:00 a.m to 9:00 a.m. After 9:00 a.m, solar heat radiation gradually becomes more robust, the heating load decreases, and the number of started compressors decreases. From 11:00 a.m to 3:00 p.m, the heating load is lowest and the compressor is turned on the least.

During the heating period, solar radiation, ambient temperature, as well as the number of people in the building, vary almost cyclically, which means that the trend of the number of compressors starting and stopping each day is the same, and there will only be quantitative differences, so the day with the highest heating load is chosen for the control strategy analysis to be more representative.

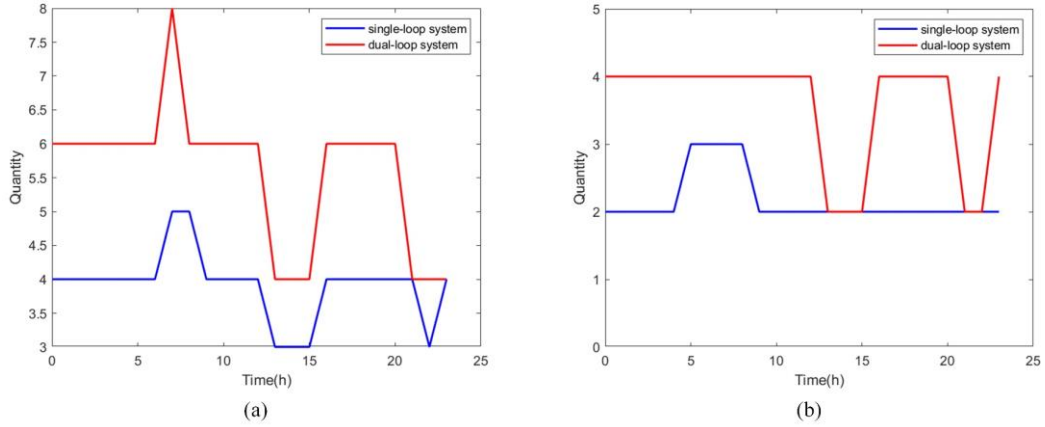


Fig. 5. (a) Number of compressors started by the hour in North area; (b) Number of compressors started by the hour in South area.

3. Calculation and result analysis of booster heat pump system

3.1. Thermal cycle calculation process of the heat pump unit

The temperature of the supply and return water and heating load obtained in section 2.3 are used as input to calculate the parameters of the thermal process for the conventional single-loop system and the new dual-loop system based on the control strategy of compressors, and the calculated parameters include the condensation and evaporation temperature temperatures, condensation and evaporation pressures, water-side mass flow rate, refrigerant mass flow rate, the heating capacity, heat taking and power consumption.

For the whole dual-loop system, the heating capacity, power consumption and COP of the system can be calculated by equations (1), (2) and (3). The heating capacity and power consumption of the whole system are the sum of the two loops. Equations (4) and (5) are the power consumption calculation process of the low-temperature loop, and the calculation process of the high-temperature loop is similar to that of the low-temperature loop.

$$Q_e = cm_1(t_{w,1,i} - t_{w,1,o}) \tag{1}$$

$$Q_c = cm_2(t_{w,2,o} - t_{w,2,i}) \tag{2}$$

$$COP = Q_c/W \tag{3}$$

$$m_{r1} = Q_{c1}/(h_2 - h_3) \tag{4}$$

$$W_1 = m_{r1}(h_2 - h_1) \tag{5}$$

Where, Q_c is the heating capacity of the whole system, kW; Q_e is the quantity of heat taken from the low-temperature heat source side, kW; c is the specific heat capacity of water, J/(kg·℃); m_1 is the mass flow rate of the heat source water, m³/h; m_2 is the mass flow rate of the supply water, m³/h; m_r is the mass flow rate of refrigerant, kg/s; W is the power consumption of the compressors, kW; COP is the coefficient of performance; $t_{w,1,i}$ is the inlet temperature of low-temperature heat source water, ℃; $t_{w,2,i}$ is the temperature of the return water, ℃; $t_{w,1,o}$ is the outlet temperature of low-temperature heat source water, ℃; $t_{w,2,o}$ is the temperature of the supply water, ℃.

3.2. Flowchart for calculating dual-loop booster heat pump

Since a dual-loop heat pump system has two loops and the two loops interact, the calculation process differs from that of a single-loop heat pump. Using the heat balance equation of the water side and the refrigerant side, input the known temperatures of the supply water and the return water, the inlet and outlet temperatures of the heat source water side, the average temperature of the inlet and outlet temperatures of the hot water side and the average temperature of the inlet and outlet temperatures of the heat source water side can be selected as the assumed temperature of the middle point respectively, and after repeated iterations to reach equilibrium, simulations are performed to calculate the low-temperature loop, high-temperature loop and the overall unit performance parameters. The flowchart of the calculation of the dual-loop heat pump is shown in Fig. 6 below.

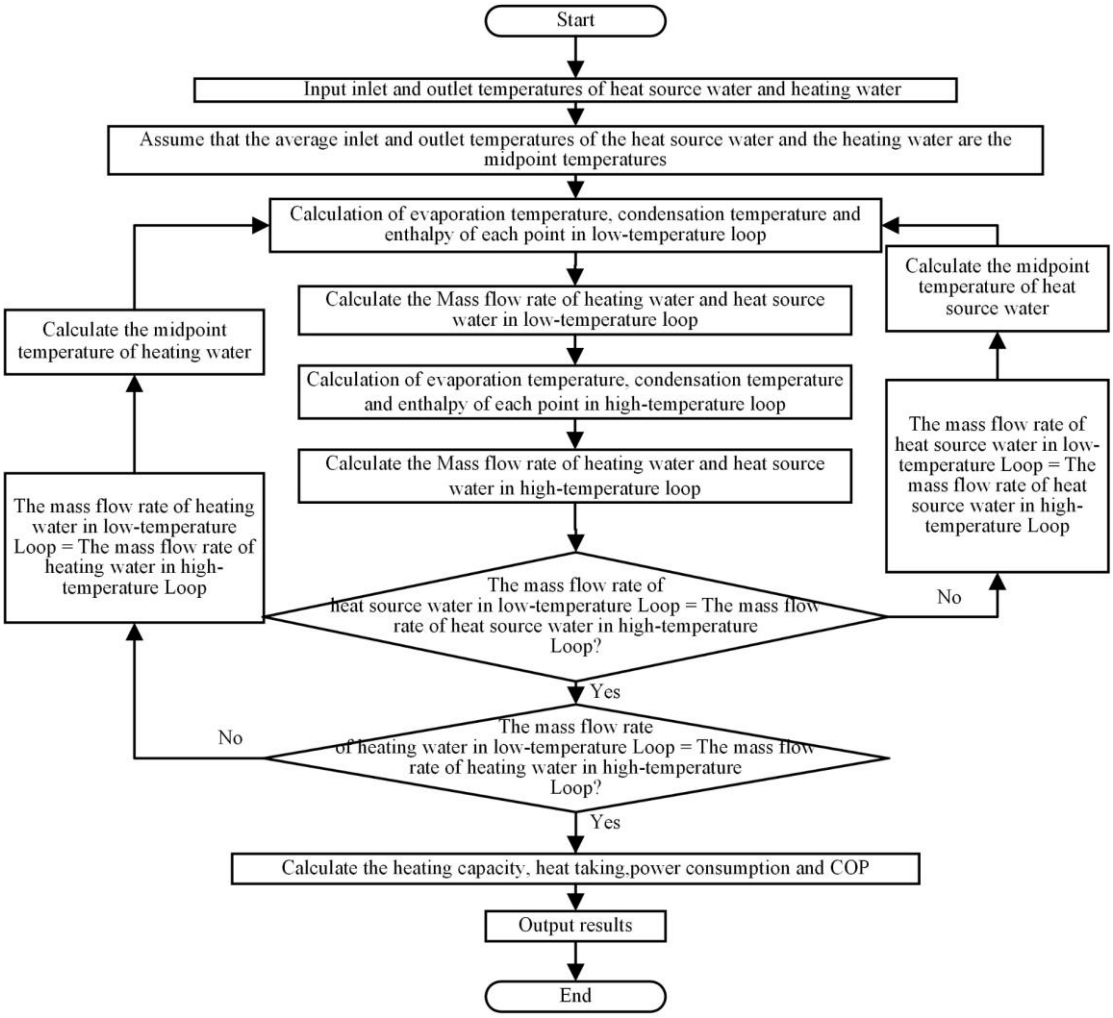


Fig. 6. Flowchart for calculating the dual-loop booster heat pump.

3.3. Verification of calculation results

In order to verify the accuracy of the calculation results in this paper, the working condition of supply/return water temperature of 60/50 ℃ and heat source water inlet/outlet temperature of 30/25 ℃ are calculated and compared with the results in Ref. [22]. The results are shown in Table 2. From Table 2, the deviation of COP is 4.36%, the deviation of power consumption is 4.82% and the deviation of heat capacity is 9.06% compared with the data in the literature, which are less than 10%, which can indicate the reliability and accuracy of the calculation results.

Table 2. Calculated results compared with experimental results in Ref. [22]

Items	Literature	This paper	Deviation (%)
COP	6.70	6.42	4.36
Power consumption (*kW*)	1418.0	1352.8	4.82
Heating capacity (*kW*)	9550.0	9492.5	9.06

3.4. Calculation results

Calculations are performed according to the calculation procedure shown in Fig. 7, keeping the inlet temperature of heat source water at 28 ℃ and outlet temperature at 18 ℃, heat transfer temperature difference of the heat exchanger at 3 ℃. The inlet and outlet temperatures of heating water vary according to the curves shown in Fig. 4(b).

Fig. 7 shows the dynamic variation of the COP of the conventional single-loop booster heat pump and the new dual-loop booster heat pump in terms of days. Under the same conditions, the COP of the dual-loop heat pump is significantly higher than that of the conventional single-loop heat pump. The COP of the single-loop heat pump and the dual-loop system has roughly the same trend over time, both decrease first and then increase, mainly because the temperatures of the supply and return water are different at different times, as shown in section 2.3, the temperature of the supply water increases first and then decreases over time during the heating period. When the temperature of the supply water increases, the system needs to reach a higher condensation temperature. The compressor's compression ratio increases, the refrigerant mass flow rate decreases, and the system performance decreases. The average COP of the single-loop heat pump was 5.42 and the average COP of the dual-loop system was 6.34, with a difference of 0.92. The highest COP of the single-loop heat pump was 6.28 and the lowest was 5.03, with a variation of 1.25, and the highest COP of the dual-loop heat pump was 7.12 and the lowest was 6.01, with a variation of 1.11.

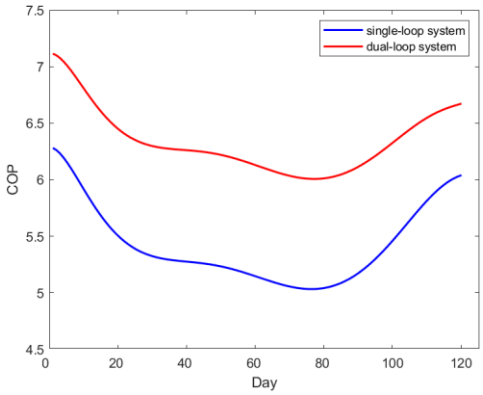


Fig. 7. COP of booster heat pump systems.

3.5. Energy saving effect

Fig. 8 shows the daily power consumption of the traditional single-loop booster heat pump and the dual-loop booster heat pump in the North area. The horizontal coordinate is time and the vertical coordinate is the power consumption of the heat pump. The red curve represents the dual-loop heat pumps and the blue curve represents the single-loop heat pumps. It can be seen that in the middle of the heating period, the power consumption is higher than that at the beginning and end of the heating period, which is the same as the trend of the heating load. The power consumption of the dual-loop heat pumps is generally lower than that of the single-loop heat pumps, which is more obvious when the heating load is high.

After calculation, this ultra-low temperature district heating system can produce 4260 GJ of heat per year during the heating period, of which the single-loop heat pumps need to consume 0.217 million kW·h of electric energy and the dual-loop heat pumps need to consume 0.183 million kW·h of electric energy. In the whole heating period, compared with the single-loop heat pump system, the dual-loop heat pump system saves 0.034 million kW·h of electric energy, and the electricity saving rate is up to 15.6%.

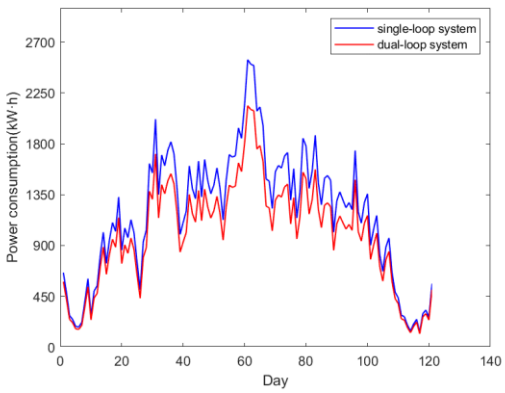


Fig. 8. Power consumption of the booster heat pump.

4. Conclusions

In this paper, a new dual-loop booster heat pump for ultra-low temperature district heating is designed and applied to a gas boiler flue gas deep recovery project in Beijing. Simulations were performed using DeST software to obtain the hourly heating load for the entire heating period, and then the annual energy consumption and COP of the dual-loop booster heat pump system were calculated and analyzed, with the following conclusions:

The heating load of the building is affected by the ambient temperature more obviously, from the beginning to the end of the heating period, the heating load of the buildings rises first and then decreases, in the middle of the heating period when the weather is cold, the heating load is larger, at the beginning and the end of the heating period the heating load of the buildings is smaller, among which the maximum heating load of the buildings in the North area can reach up to 710.75 kW, and the highest heating load of the buildings in the South area is 395.74 kW. The waste heat recovery capacity of the booster heat pump designed in this paper can fully meet the heating demand of this part of the building.

Compared with the traditional single-loop heat pump, the dual-loop heat pump has a significant energy-saving effect, with an average COP increase of 0.92. The traditional single-loop heat pumps need to consume 0.217 million kW·h of electric energy in the whole heating period. In comparison, the dual-loop heat pumps consume 0.183 million kW·h, saving 0.034 million kW·h of electric energy, with an electricity saving rate of up to 15.6%.

Acknowledgements

The study has been supported by the National Key R&D Program of China (2022YFC3802501-5)

References

[1] PENG Xiang, LIU Di, XU Yimin. Research on The Path of Ultra-Low Energy Consumption Building Helping to Achieve the Goal of "Double Carbon". Construction Economy 2022;43(S1):550-556. (in Chinese).
[2] China Association of Building Energy Efficiency. 2019 China Building Energy Consumption Research Report. Construction and Architecture 2020;(07):30-39. (in Chinese).
[3] JIANG Yi. Study on Building Energy Conservation Strategy in China. Strategic Study of CAE 2011;13(06):30-38. (in Chinese).
[4] FANG Xiumu, ZHOU Zhigang. Development and prospect of heating technology. Heating Ventilating & Air Conditioning 2016;46(03):14-19+8. (in Chinese).
[5] Breembroek Gerdi, Dieleman Maus. Domestic heating and cooling distribution and ventilation systems and their use with residential heat pumps. IEA Heat Pump Center Analysis Report HPC-AR8 2001;ISBN 90-72741-40-8.
[6] Dokka. T. H, Hermstad. K. Energy efficient houses for the future-A Handbook for Planning of Passive Houses and Low-Energy Houses. Norwegian final report from ECBCS Annex 38, Sustainable Solar Housing. SINTEF Building and Infrastructure 2006.
[7] Zühlsdorf B, Meesenburg W, Ommen TS, Thorsen JE, Markussen WB, Elmegaard B. Improving the performance of booster heat pumps using zeotropic mixtures. Energy 2018;154:390–402.
[8] Yang X, Li H, Svendsen S. Evaluations of different domestic hot water preparing methods with ultra-low-temperature district heating. Energy 2016;109:248-259.
[9] Ziemele J, Talcis N, Osis U, Dace E. A methodology for selecting a sustainable development strategy for connecting low heat density consumers to a district heating system by cascading of heat carriers. Energy 2021;230:120776.
[10] Reiners T, Gross M, Altieri L, Wagner H-J, Bertsch V. Heat Pump Efficiency in fifth Generation Ultra-Low Temperature District Heating Networks using a Wastewater Heat Source. Energy 2021;121318.
[11] Pellegrini, Marco, Bianchini, et al. The Innovative Concept of Cold District Heating Networks: A Literature Review. Energies 2018.
[12] Ivar Baldvinsson, Toshihiko Nakata. A feasibility and performance assessment of a low temperature district heating system – A North Japanese case study. Energy 2016;95:155-174.
[13] Lund, R., Østergaard, D. S., Yang, X., Mathiesen B. V. Comparison of Low-temperature District Heating Concepts in a Long-Term Energy System Perspective. International Journal of Sustainable Energy Planning and Management 2017;12:5–18.
[14] Thorsen J E, Svendsen S, Smith K M, et al. Feasibility of a booster for DHW circulation in apartment buildings. 17th International Symposium on District Heating and Cooling (DHC), Energy Reports 2021;7:311-318.
[15] Dermentzis G, Ochs F, Thuer A, Streicher W. Supporting decision-making for heating and distribution

systems in a new residential district - An Austrian case study. Energy 2021;224:120-141.
[16] Rt A, Vca B, Mcb A. Impact of Legionella regulation on a 4th generation district heating substation energy use and cost: the case of a Swiss single-family household. Energy 2021.
[17] LI Qingwei. Discussion on the Selection of District Heating Source Allocation Mode. Total Corrosion Control 2021;35(09):58-59. (in Chinese).
[18] Gang Xianxiu. Research on deep recovery technology of low temperature flue gas waste heat of district heating industrial boiler. Harbin Institute of Technology 2016. (in Chinese).
[19] MU Lianbo. Application and analysis of heat pump system applied to the flue gas heat recovery for gas boiler. Heating Ventilating & Air Conditioning 2014;44(12):49-54. (in Chinese).
[20] WU Jianguo. Application of Waste Heat Recovery Heat Pump System for Gas Boiler Flue Gas. Chemical Engineering Design Communications 2018;44(06):181. (in Chinese).
[21] HUANG Dengjie. Application and analysis of gas boiler flue gas waste heat recovery air source heat pump. China Gas Operation and Safety Symposium (10th) & 2019 Annual Symposium of Gas Branch of China Civil Engineering Society (2nd volume) 2019;59-62. (in Chinese).
[22] Hu B, Xu S, Wang R Z, et al. Investigation on advanced heat pump systems with improved energy efficiency. Energy Conversion and Management 2019;192:161-170.

14th IEA Heat Pump Conference
15-18 May 2023, Chicago, Illinois

Performance Analysis of Heat Pump Water Heater System Operating on a New Storage Heat Pump Cycle to Achieve Higher Operating Range

Purav Patel[a], Stefan Elbel[a,b*]

[(a)]University of Illinois at Urbana-Champaign, Department of Mechanical Science and Engineering, Air Conditioning and Refrigeration Center, 1206 West Green Street, Urbana, IL 61801, USA
[(b)]Creative Thermal Solutions, Inc., 2209 North Willow Road, Urbana, IL 61802, USA
[(*)] Corresponding author: elbel@illinois.edu

Abstract

Heat pump systems are often restricted to operate within a certain temperature range due to the limits on pressure ratio and discharge temperature. A new storage heat pump concept aimed at improving the operating temperature range of a heat pump system is proposed. Performance of an R134a heat pump water heater (HPWH) system with wrap-around condenser coil operating based on the new concept is studied by means of a system model. The storage heat pump cycle involves system operation in two modes to achieve the high temperature lift. In Mode I, ambient air acts as heat source for the evaporator and full length of wrap-around coil is used as condenser, whereas in Mode II, a throttling valve splits the wrap-around coil into a condenser and evaporator. Here, the intermediate temperature water in the lower tank region acts as heat source for the evaporator. This lifts up the evaporating pressure which enables the heat pump to operate at a lower pressure ratio and reach a higher water end temperature. Modeling results obtained for the storage heat pump system are also compared with a conventional HPWH system that uses back-up electric elements to reach the required water temperature when the heat pump is unable to operate.

© HPC2023.
Selection and/or peer-review under the responsibility of the organizers of the 14th IEA Heat Pump Conference 2023.

Keywords: heat pump water heater; operating range; energy storage; modeling

1. Introduction

Heat pump systems operate on the principle of vapor compression cycle and thus offer a much higher energy utilization efficiency as compared to conventional methods like electric resistance heating. The maximum possible temperature difference between the heat source and heat sink for the system is referred as the operating temperature range of the system and it is limited by the compressor operating envelope in conjunction with the refrigerant used. Exceeding the operating temperature range can cause issues such as degradation of lubricant as well as lower heating capacity due to the high pressure ratio and discharge temperature. The heat pump water heater (HPWH) system faces this situation when it is required to provide hot water in cold ambient conditions. A new storage heat pump concept aimed at improving the operating temperature range of a heat pump system is introduced in this paper. The system under consideration is an R134a HPWH with wrap-around condenser coil.

Implementation of the new concept requires a split-condenser design, an energy storage element and the system operation in two different modes. Mode I is same as conventional system operation whereas as the wrap-around coil is split into condenser and evaporator in Mode II. The water contained in the lower portion of tank itself acts as energy storage element for the system, wherein energy stored by the system in Mode I is utilized in Mode II to enable the system to operate at a lower pressure ratio and discharge temperature compared to a conventional heat pump system. Objective of this study is to predict the performance of a storage heat pump system by the means of a system model. Model is used to obtain the system performance under different scenarios and determine the suitable wrap-around coil split ratio along with compressor speed and

* Corresponding author. E-mail address: elbel@illinois.edu

time duration for system operation in Mode II. System model consists of a quasi-steady vapor compression cycle model linked with a transient water tank CFD model. Performance of the storage heat pump system is also compared with a conventional HPWH that uses back-up electric heating elements to reach the target water temperature when heat pump is unable to operate.

Several authors have studied methods such as refrigerant injection in HPWH system (Liu *et al.*, 2008) and usage of cascade heat pump systems (Wu *et al.*, 2012) with an aim to overcome issues of high discharge temperature and low heating capacity when operating the heat pump in cold climate. Refrigerant injection can cause issues such as compressor slugging while the cascade system can lead to increased complexity and cost for the heat pump. The storage heat pump concept introduced in this paper is based on energy storage at an intermediate temperature and can be implemented through a single stage heat pump design.

1.1. New Storage Heat Pump Concept

A schematic of the storage heat pump system operating in two modes is shown in Figure 1. The system operation in Mode I shown in Figure 1a is same as the conventional system operation. For a conventional heat pump system, the ambient air is used as heat source for the fin-tube evaporator and water contained in tank is heated by heat rejection from the condenser. The schematic also shows the water tank temperature stratification which occurs due to the effect of natural convection. As the water contained in the tank heats up, the temperature difference between the ambient (heat source) and water (heat sink) increases. This results in an increase in the pressure ratio and discharge temperature for vapor compression cycle. If the pressure ratio becomes too high, then the compressor has to be cycled off and the system is unable to reach the target water temperature while using the heat pump. Conventional HPWH system often uses back-up electric heating elements to reach the higher water temperature when the heat pump is unable to operate.

The storage heat pump system involves switching between the two modes to achieve the high temperature lift. In Mode I, the water contained in the tank is heated from a low to intermediate temperature while using the full length of wrap-around coil as condenser. Then the system operation switches to Mode II, in which the wrap-around coil is split by means of a throttle valve to use top portion of coil as condenser and the bottom portion as evaporator. The fan attached to the fin-tube heat exchanger is kept off so that the heat exchanger is unused in this mode. In Mode II, the intermediate temperature water present in lower region of tank would act as heat source for the evaporator. This increases the evaporating pressure and reduces the pressure ratio which allows the system to continue to operate and reach a higher water temperature in the upper region of the tank.

Thus, instead of using the back-up electric elements to reach a higher water temperature the storage heat pump system in Mode II would use the heat pump compressor to pump the energy contained in the water in lower tank region to that in the upper region. While evaporator received energy from the ambient in Mode I, the energy received by evaporator in Mode II comes from within the system and the temperature of water in lower tank region reduces. It should be noted that the tank will not heat up faster than in the conventional HPWH because the heating capacity of vapor compression cycle is lower than the heating capacity of back up electric elements used in conventional HPWH system. Instead, the storage heat pump concept allows the system to reach a higher water end temperature that could otherwise not be reached with a conventional system while only using the heat pump.

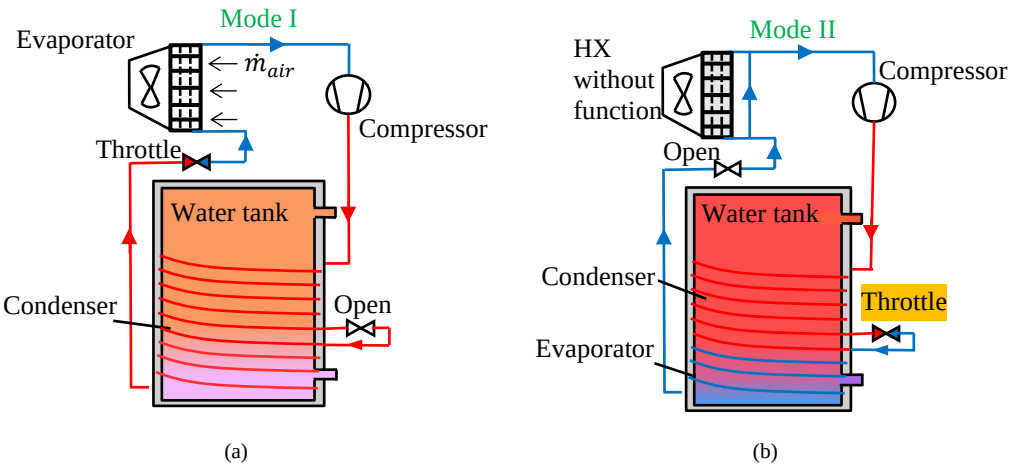


Figure 1. Heat pump water heat system operating in the two modes: a) Mode I and b) Mode II

2. Model Description

HPWH systems are commonly modeled by combining a quasi-steady vapor compression cycle model with a transient water tank model. Ibrahim *et al.* (2014) developed a dynamic simulation model for an air source HPWH with immersed coil condenser to obtain system performance under different climatic conditions. Vapor compression system was modeled under quasi-steady assumption and the water tank was modeled through a lumped parameter approach. Shen *et al.* (2018) developed a quasi-steady HPWH model with wrap-around condenser coil. Water tank was modeled by dividing the tank into several nodes in 1D to model the temperature stratification in the tank. Deutz *et al.* (2018) used the zonal tank model approach in their HPWH model. The zonal water tank model takes into account the thermal and inertial boundary layer forming along the tank wall when heated by the condenser. Li and Hrnjak (2018) presented an experimentally validated HWPH model in which the vapor compression system model was linked with a transient water tank CFD model. The CFD model of the water tank could give accurate estimation of the water side temperature and flow field inside the water tank.

The linked modeling approach from Li and Hrnjak is used to model the storage heat pump system in this work. System model consists of a quasi-steady vapor compression system model linked with a transient water tank CFD model. The linked modeling algorithm is shown in Figure 2b. System is simulated with water in *warm-up* condition, where the water in the tank is heated from an initial to set point temperature without any water draw from the system. The vapor compression system model consists of a compressor model, condenser and evaporator models and an expansion valve modeled by isenthalpic process. This model is solved by using an iteration algorithm (shown in Figure 2a) based on the Newton Raphson method adopted from Inampudi *et al.* (2021). Pressure and specific enthalpy are taken as connecting variables between the various components and the system model is solved iteratively until the refrigerant states at connecting points do not need further modification.

2.1. Compressor Model

For the given refrigerant inlet pressure, inlet specific enthalpy and outlet pressure, the compressor model uses three variables: volumetric efficiency, compression efficiency and isentropic efficiency to compute the refrigerant mass flow rate, discharge specific enthalpy and the electric power consumed by the compressor.

$$\eta_{vol} = \frac{\dot{m}}{\rho_{suc} * V_{disp} * f} \tag{1}$$

$$\eta_{comp} = \frac{(h_{cpro,isen} - h_{cpri})}{(h_{cpro} - h_{cpri})} \tag{2}$$

$$\eta_{isen} = \frac{\dot{m} * (h_{cpro,isen} - h_{cpri})}{\dot{W}_{electric}} \tag{3}$$

Curve fitting equations that relate efficiencies to pressure ratio were obtained from experimental data. A linear curve fitting between efficiencies and pressure ratio was found to give a reasonable result. Mass flow rate, discharge specific enthalpy and electric power consumption is obtained by solving equations (1), (2) and (3) respectively.

2.2. Heat Exchanger Models

Heat exchangers in the system are modeled by using the finite volume approach. The heat exchanger is divided into discrete elements along the refrigerant flow circuit and the heat transfer and pressure drop in each element is obtained by applying equations for conservation of energy and momentum. Refrigerant inlet pressure and specific enthalpy, mass flow rate and external fluid (air for fin-tube evaporator and water for wrap-around coil heat exchanger) conditions are taken as inputs for the heat exchanger model. Discrete elements are solved sequentially to obtain the refrigerant specific enthalpy and pressure at exit of each element. The model finally gives the refrigerant specific enthalpy and pressure at the outlet of the heat exchanger. The $\varepsilon - NTU$ method is used for calculating the heat transfer in each element considering a cross flow configuration between external fluid and refrigerant. Table 1 shows the correlations used in calculating pressure drop and heat transfer coefficient for the evaporator and condenser. Water side heat transfer coefficient for the wrap-around coil heat exchanger is obtained from the water tank CFD model.

Table 1. Correlations used to obtain heat transfer coefficient and pressure drop in each element for heat exchanger models

	Condenser		**Evaporator**	
	HTC	ΔP	HTC	ΔP
Single phase refrigerant	Gnielinski (1976)	Churchill (1977)	Gnielinski (1976)	Churchill (1977)
Two-phase refrigerant	Dobson and Chato (1998)	Souza *et al.* (1992)	Wattelet *et al.* (1994)	Souza *et al.* (1992)
Air	-	-	Wang *et al.* (2009)	

2.3. Water Tank CFD Model

A transient water tank CFD model is developed in ANSYS Fluent. The three-dimensional cylindrical water tank is simplified to a two-dimensional axis-symmetric model by assuming the heat flux from each coil turn to be uniform in the circumferential direction. Each turn of the wrap-around coil is represented by a line segment (of the length equal to the pitch of coil turn) at the tank wall. The heat flux from each coil turn is implemented as a time varying boundary condition by using User Defined Functions in Fluent. The natural convection of water is modeled by computing the density based on Boussinesq approximation. Laminar flow model is selected for the simulation and the SIMPLE scheme is selected for the pressure velocity coupling.

2.4. HPWH System Model Solving Procedure

The system model consists of a quasi-steady vapor compression cycle model linked with a transient water tank CFD model using the linked modeling approach of Li and Hrnjak (2018). Starting from a guess value of heat flux profile q''(n,t) (here n is the coil turn number and t is time) at the tank wall, the CFD model is solved for the full water heating period. The resulting water side temperature and heat transfer coefficient are used as inputs for the vapor compression system model which is then run at various time instances to obtain the new temporal heat flux profile. The water tank model is run again with the new heat flux profile as input and the iterations continue until convergence in heat flux profile through tank wall is obtained. The vapor compression system model takes the air side mass flow rate and temperature (for the fin-tube evaporator), water side temperature and heat transfer coefficient (for the wrap-around coil heat exchanger), compressor speed, superheat (set by EXV) and subcooling (set by system charge) as inputs.

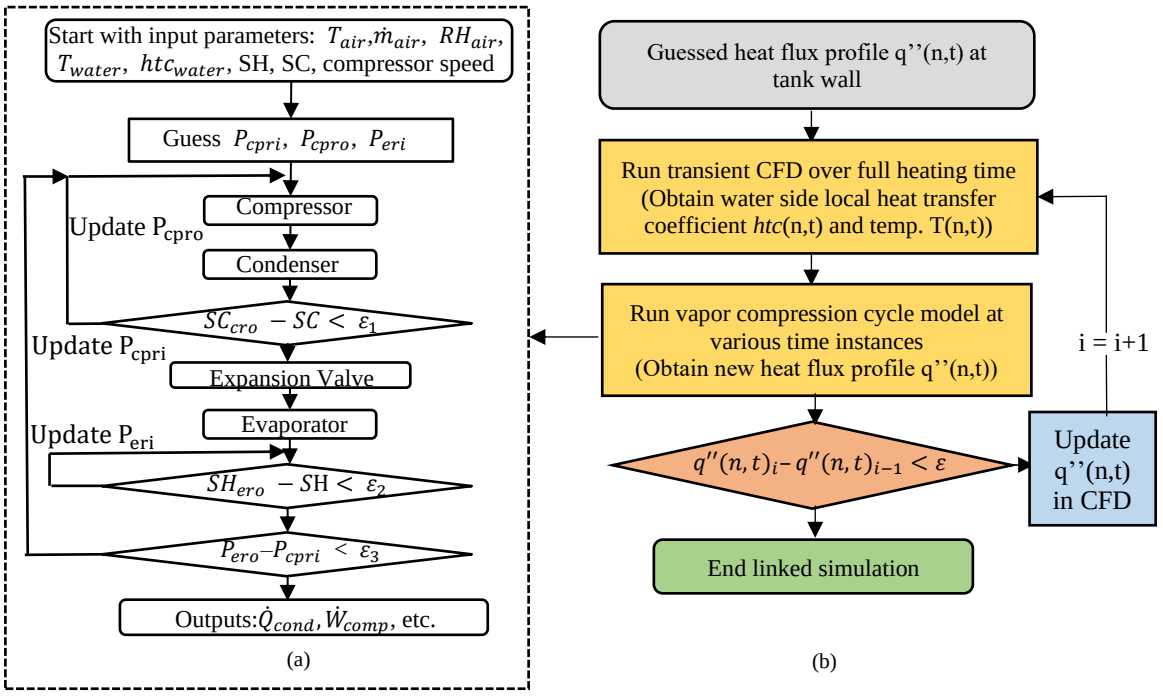


Figure 2. a) Vapor compression cycle model solving algorithm, b) Linked modeling algorithm

3. Modeling Results

3.1. Storage Heat Pump System

A previous experimental study (Patel and Elbel, 2022) carried out on a conventional HPWH showed that for an initial water temperature of 25℃ the system could heat water only to a bulk average temperature of 48℃ by using the heat pump. The heat pump compressor is cut-off when the water temperature reaches 48℃ and the conventional HPWH would use a back-up electric coil to reach a higher water temperature. The time taken for the system to heat the water from 25℃ to 48℃ in warm-up condition (no water draw from tank) was about 180 minutes.

The storage heat pump cycle involves system operation in two modes to reach a higher water temperature than a conventional HPWH could reach while using the heat pump. Performance of the storage heat pump system is obtained for the operating conditions shown in Table 2. System operates in Mode I until the water contained in the tank is heated to bulk average temperature of 48℃. Then the system operation switches to Mode II in order to get the reduction in pressure ratio and discharge temperature.

Table 2. Operating conditions for the storage heat pump system model

$T_{ambient}$=25℃, $T_{water,initial}$=25℃, Subcooling = 5℃, Superheat = 5℃	
Compressor Speed in Mode I = 3600min^{-1}, Mode II = 1800min^{-1}	
Split ratio for wrap-around coil in Mode II (no. of coil turns used as evaporator/ no. of coil turns used as condenser = Ne/Nc) = 3/7	
Time	Mode
t=0 to 180 minutes (until T_{water} = 48℃)	I
t=180 to 240 minutes	II
t=240 to 265 minutes	I
t=265 to 300 minutes	II

As show in Table 2, the compressor speed in Mode I is 3600min^{-1}, while in Mode II it is taken as 1800min^{-1}. The compressor speed for storage heat pump system operating in Mode II is lowered by 50% compared to speed in Mode I. The compressor speed is reduced in order to match the compressor capacity with the smaller size of heat exchangers in Mode II. The system uses fin-tube evaporator and full length of wrap-around coil as condenser in Mode I, while splitting the wrap-around coil into condenser and evaporator in Mode II. Due to this, there is a change in the size of the heat exchangers in the system upon switching to the Mode II. The ΔT $\left(\Delta T_{hx} = T_{ri,sat} - T_{ext,fluid}\right)$ for a heat exchanger is defined as the difference between the refrigerant saturation temperature and the external fluid temperature. The ΔT values of condenser and evaporator for the system operating in Mode I are listed in Table 3. The ΔT values predicted for the system upon switching to Mode II and operating with two different compressor speeds are also shown in the Table 3.

It can be observed that if the compressor speed in Mode II is kept the same as the speed in Mode I then the ΔT values for the heat exchangers in Mode II are much higher than the corresponding values in Mode I. This indicates that the compressor is oversized for the size of heat exchanger in Mode II and the high ΔT values will be detrimental to reducing the pressure ratio in Mode II. Thus, to keep the ΔT for heat exchanger in Mode II closer to the value in Mode I, the compressor speed is reduced by 50% in Mode II. The reduction in compressor speed will result in a lower heating capacity for the vapor compression cycle in Mode II compared to Mode I.

Table 3. The ΔT values for condenser and evaporator in Mode I and Mode II

	Mode I (at t=180min)	**Mode II (at t=182min)**	
Compressor speed	3600min^{-1}	3600min^{-1}	1800min^{-1}
ΔT_{cond} [℃]	8.4	15.7	10.5
ΔT_{evap} [℃]	11.9	20.5	14.6

The P-h plot obtained for the storage heat pump system for various time instances from t=0 to 240 minutes is shown in Figure 3. The system achieves a lift in evaporating pressure upon switching to Mode II at t=180 minutes. This is because the evaporator in Mode II will use the water contained in the bottom region of the tank as the heat source. The water contained in the tank (heat source in Mode II) would be at a higher temperature than the ambient air (heat source in Mode I) as the water temperature was elevated during system

operation in Mode I. The condensing pressure for the system also increases upon switching to Mode II. This is due to a slightly higher ΔT_{cond} (resulting from a smaller condenser size in Mode II compared to Mode I) for system in Mode II. However, the lift in evaporating pressure achieved upon switching to Mode II enables the system to maintain a lower pressure ratio and discharge temperature while the water in the upper tank region continues to heat up.

Figure 4a shows the variation in water temperature with time (at 10 different vertical locations spaced uniformly) as system switches operation between the two modes. The water tank CFD model showed that the water temperature in the tank remains almost uniform in the radial direction other than within a small boundary layer region near the tank wall. The water tank temperature contour at t=240 minutes is shown in Figure 4b. It can be observed from Figure 4a that the water temperature in the upper tank region (4/5th of total tank height for wrap-around coil split-ratio Ne/Nc = 3/7) continues to increase while the water temperature in the lower region increases in Mode I and reduces when operating in Mode II. Water contained in the lower tank region is used an energy storage element, wherein the energy stored in Mode I is utilized by the system in Mode II.

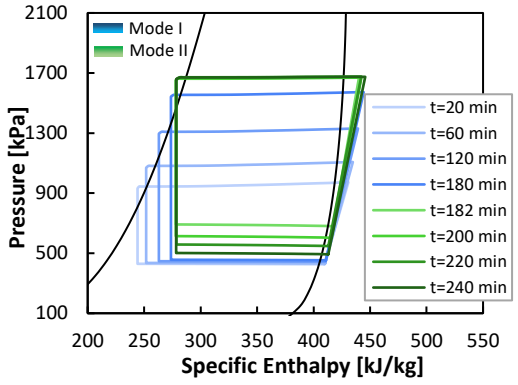


Figure 3. Pressure vs Specific enthalpy plot for system at different time instances

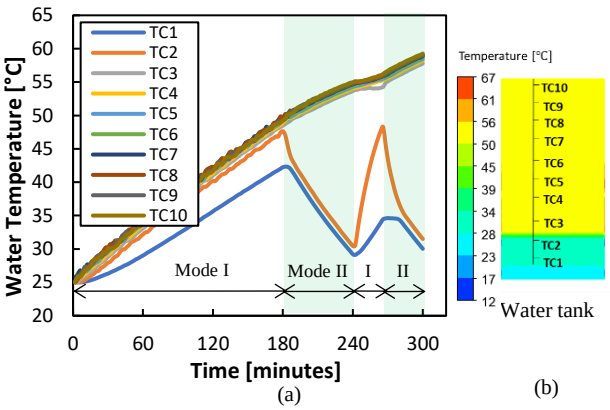


Figure 4. a) Water temperature measured at different vertical locations in the tank b) Water temperature contour at t=240 minutes

While operating in Mode II (from t=180 to 240 minutes), the water temperature in the bottom tank region reduces due to the heat extraction by the evaporator. The lift in evaporating pressure achieved upon switching to Mode II also diminishes with time. This limits the time duration for which it is advantageous (in terms of reduced pressure ratio and discharge temperature) for the system to operate in Mode II. However, the system can again switch back to Mode I (at t=240 minutes) as the intermediate operation in Mode II would have resulted in lowering the temperature of water in the bottom tank region. This enables the system to maintain a lower pressure ratio and discharge temperature compared to a system with continuous operation in Mode I. Now when the system operates in Mode I (from t=240 to 265 minutes), most of the heat transfer from the condenser coil would happen from the coil turns located around bottom region of tank. The temperature of water in bottom tank region increases at a much faster rate and once the water in bottom tank region is heated up to an intermediate temperature level, the system can again switch back to Mode II (at t=265 minutes) to use this water as heat source for the evaporator.

The variation in discharge temperature and pressure ratio with time for the storage heat pump system are shown in Figure 5. When operating in Mode I (between t=0 to 180 minutes) the pressure ratio increases as the water heats up and results in an increase in condensing pressure while the evaporating pressure remains almost same due to the ambient temperature being constant. The pressure ratio reduces as the system switches to Mode II (at t=180 minutes). This is due to the lift in evaporating pressure achieved upon switching to Mode II. The reduction in pressure ratio would contribute to lowering the discharge temperature for the system while the higher condensing pressure in Mode II will contribute to increasing the discharge temperature. The combined effect causes the discharge temperature to reduce slightly upon switching to Mode II

When operating in Mode II (between t=180 and 240 minutes) the pressure ratio increases as the water in upper tank region (heat sink) heats up while the water in the lower tank region (heat source) cools down. The discharge pressure also increases when operating in Mode II. As the system again switches to Mode I (at t=240 minutes) and uses full length of wrap-around coil as condenser, the discharge temperature and pressure ratio drop due to the lower condensing pressure for the system caused by the low temperature of water in the bottom tank region. When operating in Mode I (between t=240 and 265 minutes) the pressure ratio and discharge temperature increase as water in the tank is heated up. Now, when the system switches again to mode II (at

t=265 minutes) the pressure ratio drops while the combined effect of lower pressure ratio and higher condensing pressure causes the discharge temperature to increase slightly. Compared to a conventional heat pump system (which is equivalent to a continuous operation in Mode I) the storage heat pump system can maintain the lower discharge temperature and pressure ratio. The heating capacity and compressor power consumption are shown in Figure 6. The heating capacity is lower in Mode II due to the reduction in size of heat exchangers and compressor speed in Mode II as compared to Mode I.

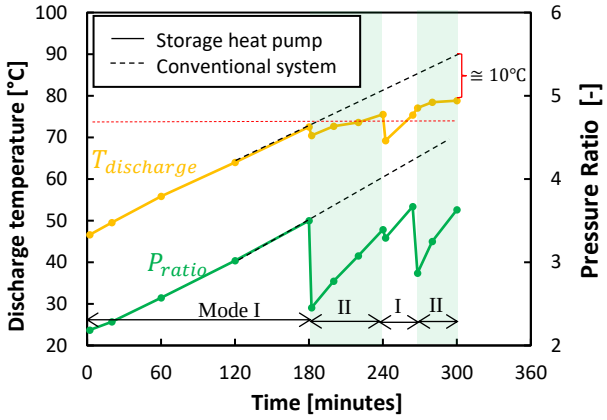


Figure 5. Discharge temperature and pressure ratio vs time for the storage heat pump system

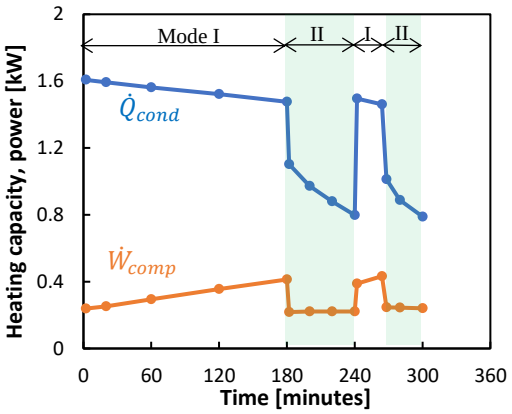


Figure 6. Heating capacity and compressor power consumption vs time for the storage heat pump system

3.2. Effect of Wrap-Around Coil Split Ratio on System Performance

The storage heat pump system uses full length of wrap-around coil as condenser in Mode I while splitting the wrap-around coil to use top portion of coil as condenser and bottom portion as evaporator in Mode II. The split ratio for wrap-around coil in Mode II is defined as (Ne/Nc) = number of coil turns used as evaporator/ number of coil turns used as condenser in Mode II. The split ratio determines the relative sizes of condenser and evaporator in Mode II and thus impacts the system performance. The model is used to study the system performance in Mode II for four different split ratios. Other than varying the split ratio all the other conditions for the four cases were kept same as listed in Table 4.

Table 4. Operating conditions for the system model to study effect of wrap-around coil split ratio on system performance in Mode II

$T_{ambient}$=25°C, $T_{water,initial}$=25°C, Subcooling = 5°C, Superheat = 5°C
System operates in Mode I from t=0 to 180 minutes and in Mode II from t=180 to 240 minutes
Compressor Speed in Mode I = 3600min^{-1}, Mode II = 1800min^{-1}
Four different cases considered are: Split ratio for wrap-around coil in Mode II (Ne/Nc) = 2/8, 3/7, 4/6 and 5/5

Figure 7 shows the comparison between P-h plot of the different cases upon switching Mode II. It can be observed that a system with a higher split ratio achieves a higher lift in the evaporating pressure upon switching to Mode II. This is because the system with a higher split ratio will have a larger size of evaporator compared to the lower split ratio case and this results in a lower ΔT_{evap} $(T_{w,lower} - T_{ref,evap})$ for the system with higher split ratio. The system with a higher split ratio also shows a higher condensing pressure in Mode II because of the relatively smaller condenser size that results in a higher ΔT_{cond} $(T_{ref,cond} - T_{w,upper})$ for the system. The discharge temperature and pressure ratio for the different cases is shown in Figure 8. The pressure ratio is almost the same for all the cases while the system with higher split ratio shows a higher discharge temperature due to the higher condensing pressure in Mode II.

The average heating capacity for the system in Mode II (average $\dot{Q}_{cond}$ from t=180 to 240 minutes) for the different cases is listed in Table 5. The compressor speed in Mode II is kept same for all the cases due to which there is not much difference between the heating capacity among the different cases. With the pressure ratio being almost same for all the cases, the system with a higher split ratio has a higher evaporating pressure which results in higher refrigerant mass flow rate. This leads to a higher heating capacity for system with higher split ratio in Mode II. The average value of the ratio of heating capacity and compressor power consumption in Mode II is also listed in the Table 5. This system with intermediate split ratio such as

Ne/Nc=3/7 and Ne/Nc=4/6 have a higher heating capacity per unit power consumption as compared to other cases which is due to better matching between the compressor capacity and size of condenser and evaporator in these systems. It should be noted that the heating capacity of system is the rate of energy transfer to the water in upper region of the tank while water in lower tank region acts as heat source for the evaporator. Thus, energy received by the evaporator comes from within the system and temperature of water in lower tank region (within bottom of tank to the height at which wrap-around coil is split) reduces when operating in Mode II.

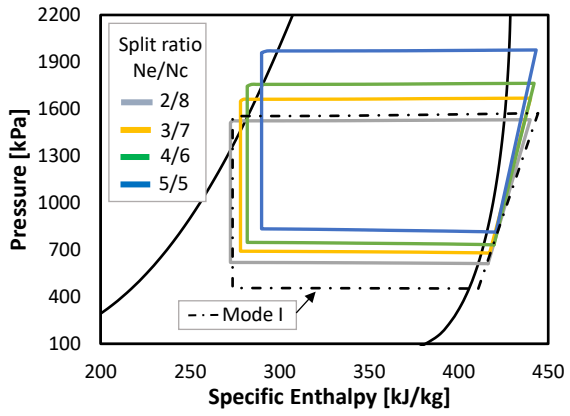


Figure 7. P-h plot upon switching to Mode II (at t=182 minutes) for different split ratio cases

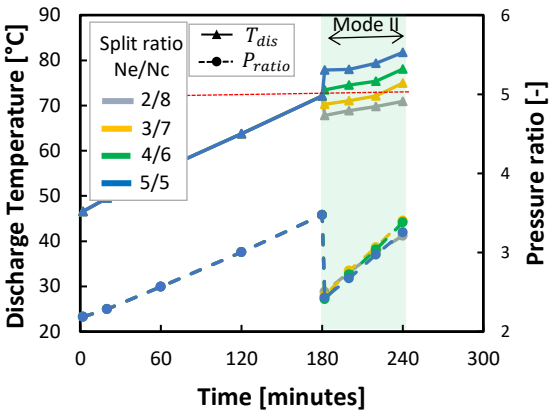


Figure 8. Discharge temperature and pressure ratio vs time for different split ratio cases

Table 5. Average heating capacity and heating capacity per unit compressor power consumption in Mode II (from t=180 to 240 minutes) for the different cases

Split ratio Ne/Nc	Average $\dot{Q}_{cond}$ [kW] in Mode II	Average $\dot{Q}_{cond}/\dot{W}_{comp}$[-] in Mode II
2/8	0.93	4.41
3/7	0.98	4.49
4/6	1.04	4.50
5/5	1.13	4.40

While the higher split ratio of Ne/Nc=5/5 gives a higher heating capacity, the absolute value of discharge temperature for this case becomes even higher than its value before in Mode I (at t=180 minutes). The lower split ratio case of Ne/Nc=2/8 will have a lower value of condensing pressure and discharge temperature but the heating capacity for this case is lowest and it would take a longer time to reach the required hot water temperature. Thus, an intermediate split-ratio such as Ne/Nc=3/7 can be selected for the wrap-around coil in the storage heat pump system. This split ratio will result in the system having a medium heating capacity (when compared with other split-ratio cases) while also maintaining the value of discharge temperature lower than the value in Mode I.

3.3. Effect of Compressor Speed in Mode II on System Performance

The storage heat pump system operates with a reduced compressor speed in Mode II in order to match the compressor capacity with the smaller size of heat exchangers in Mode I. The compressor speed in Mode I is $3600 min^{-1}$(corresponding to full compressor capacity) while it is reduced in Mode II. For a certain split ratio, the upper limit on the compressor speed in Mode II is based on the consideration that the compressor should not be oversized compared to condenser and evaporator in the system.

In the previous section, the system performance was obtained for system with four different values of split ratio and with a compressor speed of $1800 min^{-1}$ in Mode II. The system with higher wrap-around coil split ratio (Ne/Nc=5/5) in Mode II showed a higher heating capacity due to its higher evaporating pressure compared to system with lower split ratio. However, the higher split ratio could not be selected for the system because the condenser is undersized compared to the compressor capacity in Mode II which leads to system having a much higher condensing pressure and discharge temperature. In order to bring down the condensing pressure and discharge temperature for the high split ratio case the compressor speed would have to be reduced.

Table 6 shows the discharge temperature (at t= 182 minutes) for the system with split ratio Ne/Nc=5/5 and two different compressor speeds in Mode II. By lowering the compressor speed from 1800 min^{-1} to 1200min^{-1} in Mode II, the reduction in condensing pressure and discharge temperature is obtained but the heating capacity of the system also reduces. The system with split ratio Ne/Nc=5/5 and compressor 1200min^{-1} perhaps shows a lower heating capacity than system with split ratio Ne/Nc=3/7 and with compressor speed 1800min^{-1} in Mode II. This shows that the split ratio affects size of heat exchangers and the absolute value of evaporating and condensing pressure for the system in Mode II, but the heating capacity of the system in Mode II is much more sensitive to the compressor speed than the split ratio. Thus, it is more advantageous in terms of heating capacity to keep a higher compressor speed in Mode II with the upper limit on speed being that the reduction in discharge temperature and pressure ratio is achieved upon switching from Mode I to II.

Table 6. Discharge temperature and heating capacity for the system upon switching to Mode II

	Storage heat pump system in Mode II (at t=182 minutes)		
Wrap-around coil split ratio	Ne/Nc=5/5		Ne/Nc=3/7
Compressor speed	1800min^{-1}	1200min^{-1}	1800min^{-1}
$T_{discharge}$ ($T_{discharge}$ = 72.1℃ in Mode I at t=180minutes)	77.8℃	71.7℃	70.3℃
Heating Capacity ($\dot{Q}_{cond}$ =1.48 kW in Mode I at t=180minutes)	1.24 kW	0.93 kW	1.10 kW

3.4. Comparing System Performance with Conventional System

Conventional heat pump water heater (HPWH) systems often use back-up electric elements to heat the water to the target temperature when the heat pump is unable to operate. Performance of the storage heat pump system obtained for the operating conditions shown in Table 2 is compared to a conventional HPWH that uses heat pump to heat water from 25℃ to 48℃ (t=0 to 180 minutes) and then uses back-up electric elements to achieve the water heating from 48℃ to 58℃ (t>180 minutes). The water contained in the tank is heated without any water draw from the system.

The conventional HPWH system usually contains one upper and one lower heating element mounted on the tank wall. Both the elements have the same power rating and only one of the elements is operated at a time to avoid exceeding the limits on the allowable current draw. When using the electric element, the heating capacity for the system will be equal to the power of the electric element. Most conventional HPWH operate on 240V with current draw limited to about 20A and having 4500W heating element. Assuming that the system is powered by a limited electric supply of 120V the power of the electric element reduces to 1125W. Systems having 1125W electric element are not common and the example is used only for comparing storage heat pump system performance with two conventional systems having different power rating of electric elements. The Figure 9 shows the water temperature vs time predicted for conventional HPWH operating on two different electric supplies - a) operating on 120V with limited current draw (1125W electric elements) and b) operating on 240V (4500W electric elements).

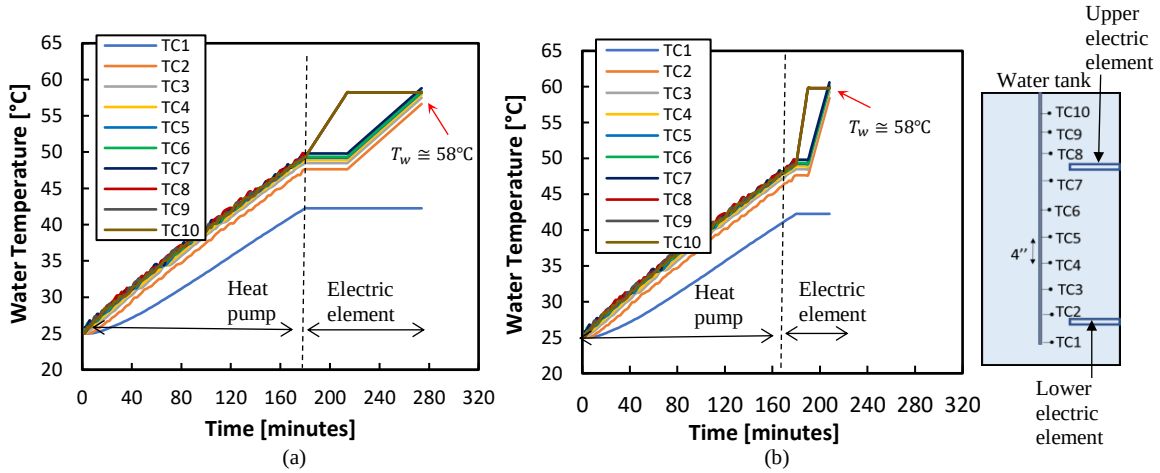


Figure 9. Water temperature vs time for conventional HPWH: a) 1125W electric elements b) 4500 W electric elements

The conventional heat pump water heater system uses the heat pump to heat water until 48℃ and then uses the upper and lower electric heating elements until the water temperature reaches 58℃. The system uses the upper electric element first and then uses the lower electric element. When the upper electric element operates, the water contained in the region between upper element and top wall of tank will heat up due the effect of natural convention. Thus, locations T8, T9 and T10 in Figure 9 show an increase in temperature. The upper electric element is turned off once the water in this region reaches the target temperature. The rate of heat conduction between the water layers in vertical direction is negligible and hence the water contained in the tank below the height of upper element stays at almost the same temperature. Then the lower electric element is turned on to finish heating up the remaining water. When the lower electric element operates, water contained in the tank above the height of lower electric element shows an increase in temperature. Thus, locations T2 to T7 in Figure 9 show an increase in temperature. The natural convection in the tank causes the hot water to remain above the relatively cold water and thus a small volume of water located between lower element and bottom of tank does not show a rise in temperature when the lower element operates. The water temperature vs time for the storage heat pump system was shown in Figure 4. Table 7 shows the comparison between storage heat pump system and conventional heat pump water heater system.

Table 7. Comparison between storage heat pump system and conventional heat pump water heater system

		Conventional HPWH		**Storage HP**
		1125W electric elements	4500W electric elements	-
Overall energy consumed	T_{water} from 25℃ to 48℃ (t = 0 to 180 minutes)	0.9 kWh (Using heat pump)	0.9 kWh (Using heat pump)	0.9 kWh (Mode I)
	T_{water} from 48℃ to 58℃ (t > 180 minutes)	1.8 kWh (Using electric coil)	1.8 kWh (Using electric coil)	0.53 kWh (Mode II, I)
Time taken for T_{water} to reach from 48℃ to 58℃		96 minutes	24 minutes	120 minutes
Hot water available at end of warm-up (Total tank capacity = 50 gallons)		44.6 gallons	44.6 gallons	40 gallons

The performance of storage heat pump system is same as conventional system for water heating from 25℃ to 48℃ (i.e. from t=0 to 180 minutes). The storage heat pump system operates in Mode I until water is heated to 48℃ and then switches to Mode II for the first time to get reduction in pressure ratio and discharge temperature. The conventional system uses heat pump to heat water from 25℃ to 48℃ and then uses the back-up electric elements to heat the water from 48℃ to 58℃.

The storage heat pump system takes additional time of 120 minutes to heat the water from 48℃ to 58℃. The time taken is 25% more compared to conventional system operating on 120V (1125W electric elements) and 5 times more compared to conventional system operating on 240V (4500W electric elements). This is because of the lower heating capacity of vapor compression cycle in the storage heat pump system compared to the heating capacity (power) of the electric elements used by the conventional system. The overall energy consumed by the storage heat pump system is about 70% less than that consumed by the conventional system. For a total tank capacity of 50 gallons, the total hot water available at end of the warm-up is lower than the total tank capacity for all the systems. For the conventional system, the water contained in tank located below the height of lower heating element does not get heated. For the storage heat pump system, the water contained in the tank at a height below which the wrap-around is split into evaporator and condenser is not heated up. The storage heat pump system uses this water as the heat source for evaporator in Mode II.

4. Conclusions

System model for the heat pump water heater system operating based on a new storage heat pump cycle is developed. Storage heat pump cycle involves system operation in two modes to reach the required water temperature while using the heat pump compressor instead of the back-up electric elements. Water contained in lower region of tank is used as energy storage element by implementing a split-condenser design. Mode I is same as conventional system operation, while the wrap-around coil is split to use the top portion as condenser and the bottom portion as evaporator in Mode II. The intermediate temperature water in the lower tank region acts as heat source for the evaporator which lifts up the evaporating pressure and reduces pressure ratio upon switching to Mode II.

Model is used to study the effect of wrap-around coil split ratio and compressor speed on system performance in Mode II. The wrap-around coil split ratio determines the size of condenser and evaporator in Mode II which affects the absolute values of condensing and evaporating pressure for the system in Mode II. System performance for four different split ratios is obtained and it is shown that an intermediate split ratio such as Ne/Nc=3/7 which gives medium heating capacity while giving a reduction in the discharge temperature and pressure ratio can be selected for the split condenser design. The split ratio also limits the compressor speed in Mode II as the speed has to be reduced to match compressor capacity with the smaller size of condenser and evaporator in Mode II compared to Mode I.

Modeling results for storage heat pump system with wrap-around coil split ratio Ne/Nc=3/7 and compressor reduced by 50% in Mode II show that the system can reach a higher water end temperature while maintaining relatively lower pressure ratio and discharge temperature than a conventional system. System performance is also compared with conventional heat pump water heater system that uses back-up electric elements to reach the higher water temperature when the heat pump is unable to operate. The additional time taken by the storage heat pump system to heat the water to a higher temperature is 25% more compared to conventional system operating on 120V (1125W electric elements) and 5 times more compared to conventional system operating on 240V (4500W electric elements). However, the energy consumed by the storage heat pump system is about 70% lower than the energy consumed by the electric elements in the conventional system. The power consumption for storage heat pump system is lower as it uses the vapor compression cycle to heat water to higher temperature instead of using electric elements. The storage heat pump concept is to be evaluated experimentally by modifying a conventional heat pump water heater system to implement the system operation in two modes.

Nomenclature

Symbols

f	Operating frequency of compressor [revolutions per second]
h	specific enthalpy [kJ/kg]
htc	heat transfer coefficient [W/m^{2}K]
$\dot{m}$	mass flow rate [kg/s]
Nc	number of wrap-around coil turns used as condenser in Mode II
Ne	number of wrap-around coil turns used as evaporator in Mode II
P	pressure [kPa]
$\dot{Q}$	heat transfer rate/heat exchanger capacity [kW]
q''	heat flux [W/m^2]
SC	subcooling [°C]
SH	superheat [°C]
T	temperature [°C]
$T_{w,lower}$	bulk average water temperature in lower tank region [°C] (the region between bottom tank wall to height at which coil is split in Mode II)
$T_{w,upper}$	bulk average water temperature in upper tank region [°C] (the region between top tank wall to height at which coil is split in Mode II)
ΔT_{hx}	difference between ref. saturation and external fluid temperature [°C]
$\dot{W}$	power consumption [kW]

Subscripts

comp	compressor
cond	condenser
cpri	comp. inlet
cpro	comp. outlet
cro	cond. outlet
disp	displacement
dis	discharge
eri	evap. inlet
ero	evap. outlet
evap	evaporator
hx	heat exchanger
isen	isentropic
ref	refrigerant
ri	ref. inlet
sat	saturation
suc	suction
vol	volumetric
w	water

Greek

ε	epsilon [-]
η	efficiency [-]
ρ	density [kg/m^3]
Δ	difference [-]

References

[1] Churchill, S.W. (1977). Friction-factor equation spans all fluid flow regimes. *Chem. Eng.*, 7, 91-92.

[2] Deutz, K.R., Charles, G.L., Cauret, O., & Rulli*è*re, R. (2018). Detailed and dynamic variable speed air source heat pump water heater model: Combining a zonal tank model approach with a grey box heat pump model. *Int. J. Refrig.*, 92, 55-69.

[3] Dobson, M.K., Chato, J.C. (1998) Condensation in smooth horizontal tubes. *J. Heat Transfer,* 120(1), 193-213

[4] Gnielinski, V. (1976). New equations for heat and mass transfer in turbulent pipe and channel flow. *Int. Chem. Eng.*, 16(2), 359-368.

[5] Ibrahim, O., Fardoun, F., Younes, R., & Louahlia-Gualous, H. (2014). Air source heat pump water water heater: dynamic modeling, optimal energy management and mini-tube condensers. *Energy*, 64, 1102-1116.

[6] Inampudi, S., Boticella, F., & Elbel, S. (2021). Modeling and comparison of different capacity modulation strategies with focus on seasonal performance, *Int. Conf. on Compressor and their Systems*, Paper 185, London.

[7] Li, W., Hrnjak, P. (2018). Experimentally validated model of heat pump water heater with a water tank in heating-up transients. *Int. J. Refrig.*, 88, 420–431.

[8] Liu, F., Huang, H., Ma, Y., & Zhuang, R. (2008). Experimental study on the heat pump water heater system with refrigerant injection. *Int. Refrig. and Air Cond. Conference*, Paper 955. Purdue University. USA.

[9] Patel, P., Elbel, S. (2022). Study of a conventional heat pump water heater system for implementation of a new storage heat pump concept. *Int. Refrig. and Air Cond. Conf. at Purdue,* Paper 2257. Purdue University. USA.

[10] Shen, B., Nawaz, K., Baxter, V., & Elater, A. (2018). Development and validation of quasi-steady-state heat pump water heater model having stratified water tank and wrapped-tank condenser. *Int. J. Refrig.*, 87,78-90.

[11] Souza, A.L., Chato, J.C., Jabardo, J.M.S. *et al.* (1992). Pressure drop during two-phase flow of refrigerants in horizontal smooth tubes, *Technical Report ACRC TR-25*, University of Illinois at Urbana-Champaign.

[12] Wang, C., Chi, K., Chang, C. (2009). Heat transfer and friction characteristics of plain fin-and-tube heat exchangers part II: correlation. *Int. J. Heat Mass Transf.*, 43, 2693-2700.

[13] Wattelet, J.P., Chato, J.C., Christoffersen, B.R. *et al.* (1994), Heat transfer flow regimes of refrigerants in a horizontal-tube evaporator, *Technical Report ACRC TR-055*, University of Illinois at Urbana-Champaign.

[14] Wu, J., Yang, Z., Wu, Q., & Zhu, Y. (2012). Transient thermal behavior and dynamic performance of cascade heat pump water heater with thermal storage system. *Applied Energy*, 91(1), 187-196.

14th IEA Heat Pump Conference
15-18 May 2023, Chicago, Illinois

The Dynamic behaviors on Drying Performance of Heat Pump Dryer using a Reduced Order Model

Yoonjei Hwang*, Jinwook Lee, Wansoo Kim, Kangwook Lee, Yeonha Seong, Mansu Park and Saikee Oh

H&A R&D Center, LG Electronics Inc., 08592 Seoul, Korea

Abstract

Dynamic behaviors be observed on a heat pump dryer to maximize drying performance under various condition through the change of compressor frequency. In order to optimize the drying performance, it is necessary to predict the dynamic behavior of air side and refrigerant side together. However, as the refrigeration cycle is optimized by a constant state condition of air at the design stage, it has less chance to implement design parameters to air flow path. In the study, simulation has been done to refrigerant and air side simultaneously under a concept of model based environment. There was no issues for integrated model because the geometrical model(3D) for air side converted to a reduced order model to make shorten the simulation time. The model for heat exchangers took a finite volume method that calculates the governing equations for several segments. The compressor model came from the analytical models for gas compression in control volumes. For the model for drum, it was predicted through the artificial neural network(ANN) learned by the test data set from experimental set up. In order to verify the system model that integrates the refrigeration and air cycle including drum model in the Dymola® environment, the dynamic characteristics data of the dryer for 2 ~ 8 kg drying load conditions were acquired. The result of numerical study shows reasonably low errors when compared with the experimental data. The pressure of refrigeration cycle and drying time at the drying section showed an error of 10% or less.

© HPC2023.
Selection and/or peer-review under the responsibility of the organizers of the 14th IEA Heat Pump Conference 2023.

Keywords: Heat pump dryer, Model-based design, Reduced order model, ANN(Artificial Neural Network);

1. Introduction

A dryer for clothes be divided into a direct heating using an electric heater and a heating by heat pump using a refrigerant cycle according to a heating method. The heat pump-based clothes dryer is more energy efficient than the electric heater-based because it reuses waste heat to remove moisture from the clothes inside the drum.[1] The heat pump clothes dryer is a closed-loop system where the air passed through drum be cooled to low temperature at the evaporator and re-heated it to high-temperature air through the condenser. The design of the closed loop dryer is more difficult than the direct exhaust dryer, in which the air absorbed a moisture from the clothes in the drum is directly discharged out of the dryer. A Chailoet et al. investigated the effects of key parameters through experiments on the energy efficiency of the clothes dryer[2] and Xiang Cao et al developed a quasi-steady-state simulation of the heat pump clothes dryer to optimize the design parameter.[3]

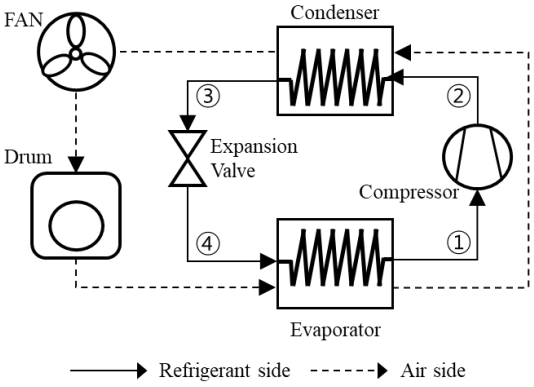
The transient behavior, in which the state of air and refrigerant is changed continuously from the start of product operation to the end, be observed at the heat pump-based clothes dryer. Therefore, considering the change of air state according to the evaporation amount of moisture in the clothes inside the drum is important to predict the drying performance. A bunch of tests are repeated to optimize parameters of performance during the design stage of the dryer because the range of operation modes is wide depending on the purpose of

* Corresponding author. Tel.: +82-10-2343-3830
E-mail address:yj.hwang@lge.com.

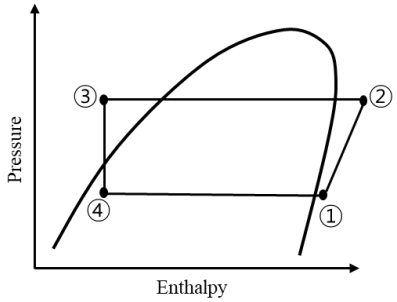
customer needs. As a result, it causes low product competitiveness and high cost of product development. The analytical model for simulation is need to solve these issues and predict the physical phenomenon at the transient state in the drying process. During the design process of the product, the main components of refrigerant cycle are designed to achieve maximum drying performance after deciding the geometrical parameters of the circulated air flow path to minimize flow resistance through three-dimensional CFD model. In general, the simultaneous simulation in a same environment is limited since each simulation is highly dependent on their own simulation environment. Therefore, optimization must be required at the system level, and a model-based simulation environment makes it happen. The overall system divides into sub-component models based on functional classification and it provides convenient environment where the entire system can be evaluated through only modification and validation for sub-components even if there has a needs to design modification. The mass flow rate of the circulated air at the flow path in the dryer is calculated using a reduced-order model in the model-based environment for simultaneous analysis. The reduced-order model could be a surrogate model, in which the complexity of numerical simulation is simplified even there has a loss of fidelity, it provides shorten analyzing time to the airflow path resistance according to various geometrical parameters. In the study, a dynamic simulation for clothes dryer of a closed-loop using R134a refrigerant as a working fluid was developed to evaluate drying performance and optimize design parameters. The Modelica language in the Dymola be used for system modeling of the heat pump-based dryer. The developed system model was verified through comparison with experiments by loads of clothes and operating conditions.

2. System Overview

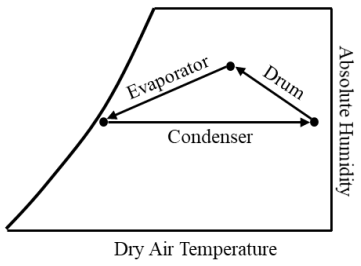
The schematic of the heat pump dryer cycle and the change of thermodynamic properties according to the air and refrigerant side conditions are shown in Fig.1. The refrigerant of low-temperature and low-pressure is flowed into a compressor and compressed to the high-temperature and the high-pressure as a vapor state, and phase changes to liquid state through heat exchange with airside. Refrigerant after the expansion valve flows into the evaporator in a low-temperature and low-pressure state, the phase changes to the vapor state through heat exchange with high-humidity air, and the air flows into the drum again through the condenser.



(a) Schematic diagram of the heat pump dryer



(b) P-h diagram of refrigeration side



(c) Psychrometric chart of air side

Fig. 1. Schematic diagram of the heat pump-based dryer

The dynamic model for dryer have to respond to the changes by control logic for individual optimization as well as respond to wide variety of operating modes depending on the user's requirements. A model considering various physics was implemented to simulate the dynamic characteristics of each component caused by the real-time change of the operating frequency of the compressor, the rotation speed of the fan and drum, and the opening of the electronic expansion valve.

3. Modeling Approach

3.1. Modeling for Refrigerant cycle

The dynamic model developed in the study was created using the Modelica language in the Dymola environment utilizing TIL suite (2022) by TLK Energy. The version of TIL used in the study is 3.10.0. The rotary compressor model was defined as the mass flow rate and power consumption according to condensing and evaporating temperature calculated from both the displacement and frequency as shown in equation from (1) to (3). Each of efficiency was defined using the performance data of the compressor by LGE. The mass flow rate of the refrigerant is calculated from the volumetric efficiency, and the compressor outlet enthalpy can be predicted from the isentropic efficiency. Therefore the power consumption of the compressor can be predicted as well.

$$\eta_{vol} = \frac{\dot{m}_{ref}}{\rho_{ref,s} \cdot rps \cdot \mathrm{V}_{dis}} \tag{1}$$

$$\eta_{isen} = \frac{h_{dis,isen} - h_{suc}}{h_{dis} - h_{suc}} \tag{2}$$

$$\eta_{eff,isen} = \frac{\dot{m}_{ref}(h_{discharge,isen} - h_{suction})}{P_{shaft}} \tag{3}$$

In the case of model for the electronic expansion valve, an empirical correlation was proposed using not only the diameter, but also length of the orifice as the geometrical parameter because the characteristics of mass flow rate to an electronic expansion valve are depended on the pressure drop of the refrigerant in orifice.[4] As the coefficient of flow rate is the shape coefficient of the orifice, the variable coefficient was developed based on the experimental data reflecting the component characteristics, because the characteristics are normally different depends on manufacturers even if the diameter is the same.

$$\dot{m}_{eev} = C_D A \sqrt{2\rho_{in}(P_{in} - P_{out})} \tag{4}$$

Both the condenser and evaporators are fin-and-tube type heat exchangers. Heat and mass transfer in the heat exchanger occurs relatively slow compared to the compressor or the expansion device, however the boundary conditions keep on changed continuously. The change of state properties were calculated through a differential equation including a time derivative by a finite volume method, it calculates a tube through which refrigerant flows by dividing it into multiple control volumes. The heat exchanger model provided by TIL can be divided into a moist air cell and a tube wall cell for airside analysis, as well as VLE Fluid cell for refrigerant side analysis. All cells reflected a geometric information for fin and tube such as number of row, columns, fin pitch, and thickness. Each cell also contains the equations of mass, energy, and momentum balance for the analysis of unsteady states.

3.2. Modeling for Airflow loop cycle

The model for circulated rate of air flow in dryer was developed through the law of similarity based on the data measured from the fan test. After taking P-Q curve for fan by fan test, the pressure losses for each component must be predicted to take a system resistance curve. Eventually, the mass flow rate of air is

calculated at the point where curves the system resistance and the pressure loss intersect. Simulation by three-dimensional CFD model for a complex shape of airflow path must be carried out so that detailed dimensions of components be considered, moreover simultaneous simulation with the refrigerant cycle system should be performed. There have limitations when trying to perform simultaneous analysis, it is limited due to the simulation speed difference between the refrigerant cycle and the three-dimensional CFD for airflow path. The reduced-order model for air flow rate can be a solution to synchronizing time difference. The response surface models for components were prepared based on simulation data for the airflow path to make the reduced-order model. The main advantage of doing that, it doesn't need to re-simulate performance for the entire area when a new event occurred like partial change of configuration, but only calculate performance using the configured reduced model maintaining fidelity.

The schematic of the cycle of the airflow path is shown in Figure 2. The airflow rate by fan is flowed into the drum inlet after pass through a porous plate and the rear duct sequentially. The air passed through the drum circulates continuously, to the front duct and through two mid ducts between the evaporator and the condenser. The model for air circulation flow was divided into four parts, which are front duct, mid duct (a), mid duct (b) and rear duct respectively, also the factors affecting flow path resistance were defined as input parameters when designing each component. For four sorts of duct, DOE based parameter optimization was conducted by 14 factors, which consist of the shape parameters selected and operating conditions. And then data from flow path analysis were collected through the simulation of the three-dimensional CFD. After, a total of 560 data were generated by this way, the reduced-order models for each duct were developed based on this data.

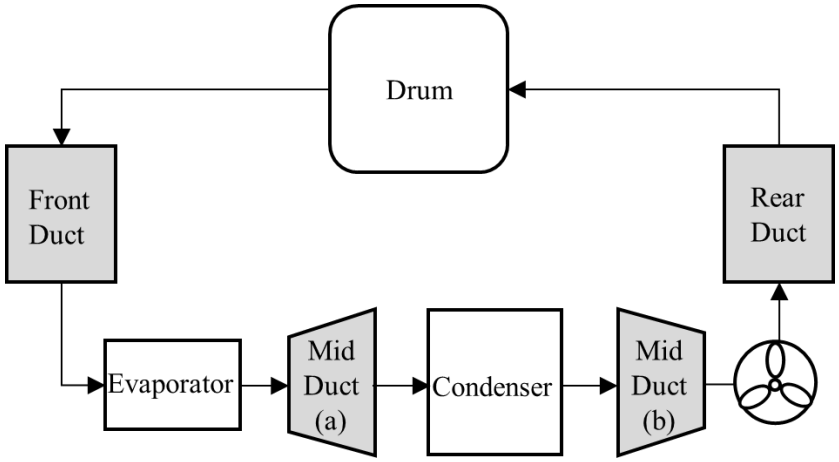


Fig. 2. Schematic of the circulated airflow path in a closed loop system

The heat exchanger model is defined by seven factors, which can be a tube diameter and relative humidity as an example, and by flow velocity that affect pressure loss. Coil Designer, a heat exchanger design tool, was used to find the data for pressure difference according to the pre-defined factors. During the process, the equation of correlation for pressure difference that be selected as an input to the coil designer, takes the equation developed by LGE. The result of process provides 80,000 simulation data.[5][6] The model for pressure loss in heat exchanger comes the result of learning process from ANN(Artificial Neural Network) based on the collected pressure loss data. For the model of Drum, 32-course data based on the drying loads from 1 to 20 kg, and pre-set drying mode like a Speed, Eco and Auto were collected. To make an ANN model, define first to main influencing factors such as drying load, drying status, moisture content, air temperature and humidity as an input parameter. When comparing the predicted value with the data which is not used for model learning, it was confirmed that there was no overestimation issues because it observed within 5% of the average error of cross-validation. The airflow rate of the system can be predicted by comparing the pressure at various operating conditions of the blowing fan with each of pressure drop model for components. It will be combined with the refrigerant cycle model in Dymola platform for simultaneous simulation. The concept of airside model has shown in Figure 3. When predict a value by implemented model, which is combined air flow and refrigeration cycle, compared with test data, it was confirmed that the accuracy was 97% as shown in Figure 4.

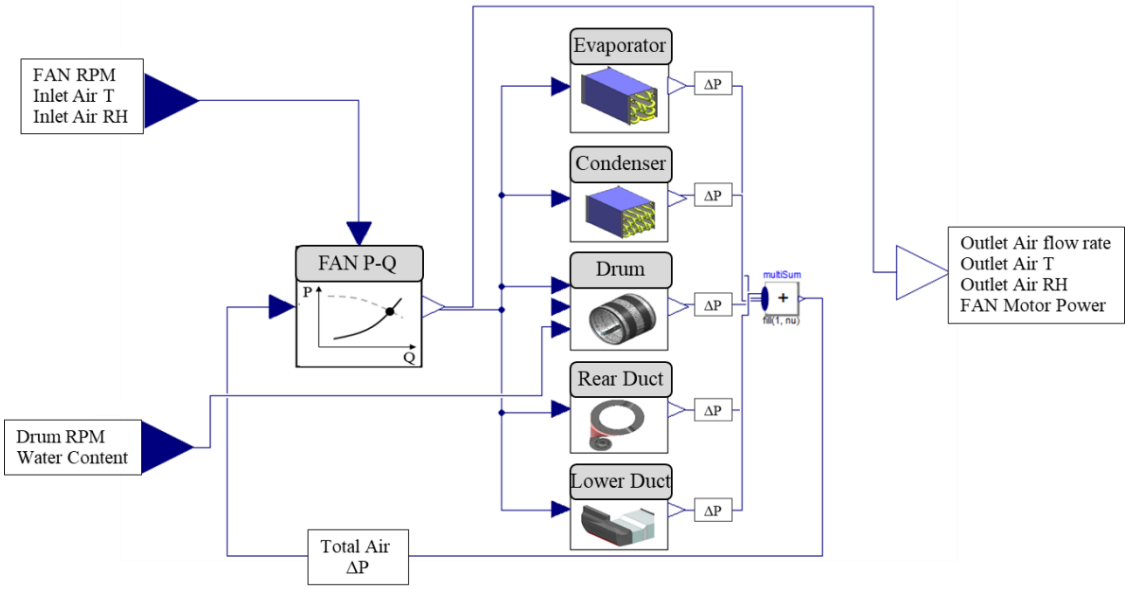


Fig. 3. The concept of the model for air flow rate in Dymola®

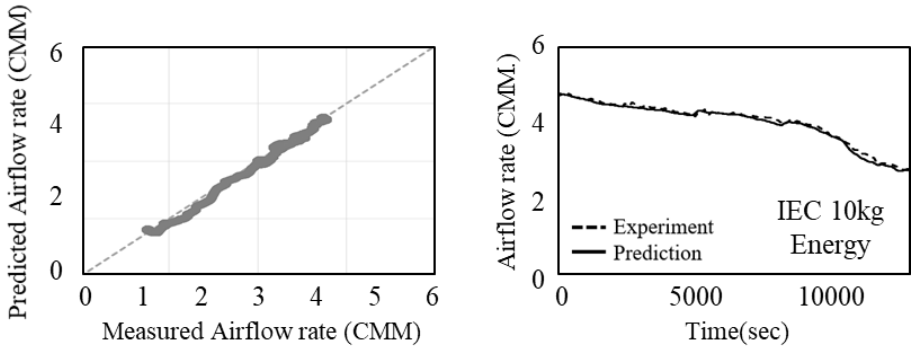


Fig.4 Comparison between measured and predicted air flow rate

3.3. Modeling for Drum

The rate of moisture extraction from clothes, where occurred inside of drum during the process of drying, be affected by the surface area of clothes when it contact with air flow. Therefore, the behavior of the clothes that changes as the drum rotates must be predicted by simulation model. However, there have many difficulties in numerically analyze physical phenomena because there happens heat transfer between air and cloth each other, together with heat exchange occurs between drum and the outside air at the same time. In the study, the data through experiments for the moisture extraction in drums is collected, and the model was developed by techniques for machine learning from based on the data. As shown in Figure 5, the experimental apparatus excluded the influence of the refrigerant cycle to measure only the change of air properties in the drum, and there have a device to make a constant temperature and humidity at inlet through a separate ducting system. The experiment was conducted for various operation modes until the initial moisture content of the clothes reached 0% from start at 60% based on the load commercially used, as shown in Table 1. The type of clothes follows the IEC 61121(International Electrotechnical Commission) standard and consists of Sheet, Pillowcase, Towel combinations. The measuring of a moisture content takes the signal from an electrode sensor of the dryer. ANN technique be introduced for modeling of the drum, the structure of input layer for ANN consists of three factors related to air characteristics (dry bulb temperature, absolute humidity, mass flow rate) and two factors related to clothes (amount of moisture, mass of clothes). Moreover, it has 3 hidden layers consist of 12 nodes per layer to calculate the sensible heat and the rate of moisture extraction between clothes in the drum as a output layer.[6]

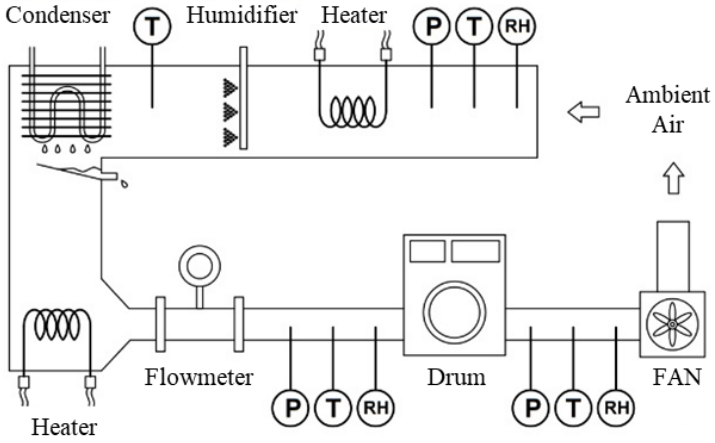


Fig. 5. Experimental equipment for acquiring learning data for drum

Pre-processing on the learning data has done to improve the performance of the drum model. During the experiment on drying, there has a tendency to sampled more data under high load conditions compared to low load conditions, and it caused a poor prediction performance to low load conditions. To solve it, not only additional sampling process has done to make a data samples as an even to the load conditions but also data samples, based on moving average line at 200-second, removed to avoid a noise caused by the measuring error from both to humidity sensor and the airflow meter. Figure 6 shows the results of comparing the model with the experimental data at the condition of 10kg and 20kg load. The prediction value for both to the sensible heat and the moisture extraction showed an 8% error if it compared with the experiment data based on movement average besides shown 13% error if it compared with the experiment data including noise.

Table 1. Test condition for drum

Parameter	Range
Clothes Load (kg)	10, 20
Circulated Airflow Rate (CMM)	3.0, 5.0
Drum Inlet Temperature (℃)	20, 40, 60, 80
Absolute Humidity (kg/kgDA)	0.01, 0.03, 0.05, 0.08

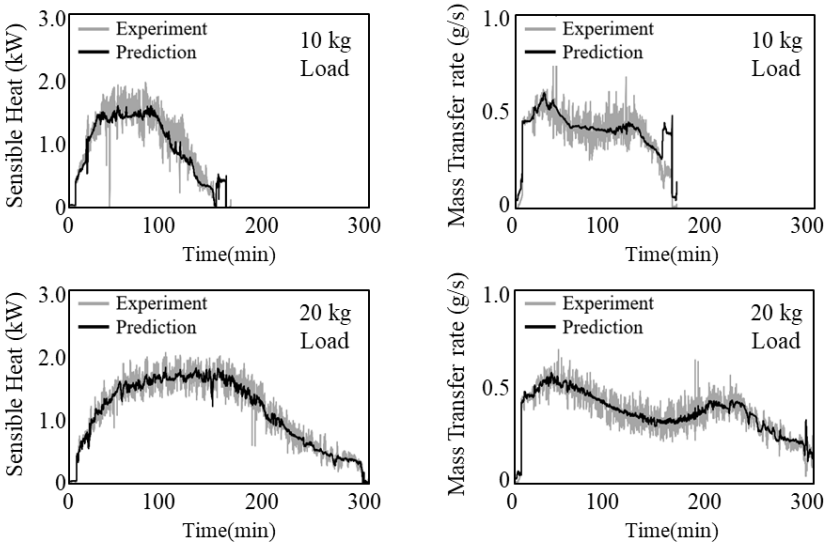
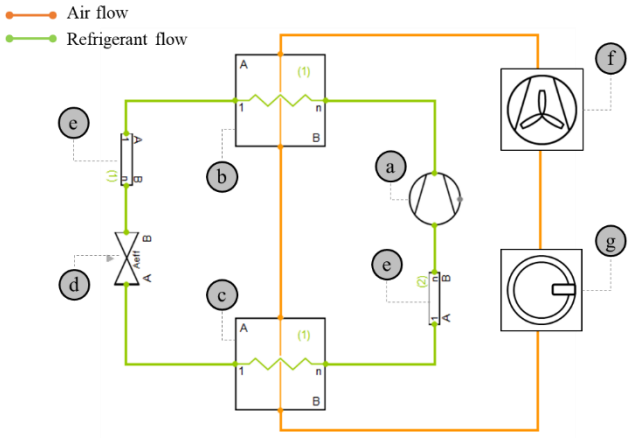


Fig. 6 Verification of drum ANN model

3.4. The system modeling for co-simulation

The study implemented the dynamic model that enables simulation together with refrigerant-side and air-side as combined systems that affect drying performance. For air flow path, the three-dimensional model be made first, and then it combined with refrigerant cycle model for co-simulation after three-dimensional model converted to 1D model through reduced order technique. The reason why it simulated as a three-dimensional CFD first is that the dimension of structure becomes dominant factor to determine accurate airflow rate, which should be affect to the drying performance in the dryer system, moreover, it could be a reliability issue if the structure model not be handled leakage properly. The 1D model for air-side validated before combining with refrigerant-side model to see how stably data transferred during order change from 3D to 1D. As a next step, the combined 1D system model synchronized again with real time control logic at every time intervals after combining two cycles. System simulation in a model-based environment was run through Dymola as a platform software. Figure 7 is a schematic diagram of the simultaneous simulation of refrigerant cycle and airflow cycle in the heat pump dryer system. The input and output values of the model to the main components of refrigerant cycle be defined as temperature, pressure, and flow rate of the refrigerant. The model for airflow rate calculates the airflow rate during circulation of air from the performance curve of the FAN and the total resistance by the system. Total resistance from the reduced order model of the ducting system that considered the shape of airflow path structures, included the heat exchangers and drum. The air properties during circulation is defined through the models both to heat exchangers and drum.



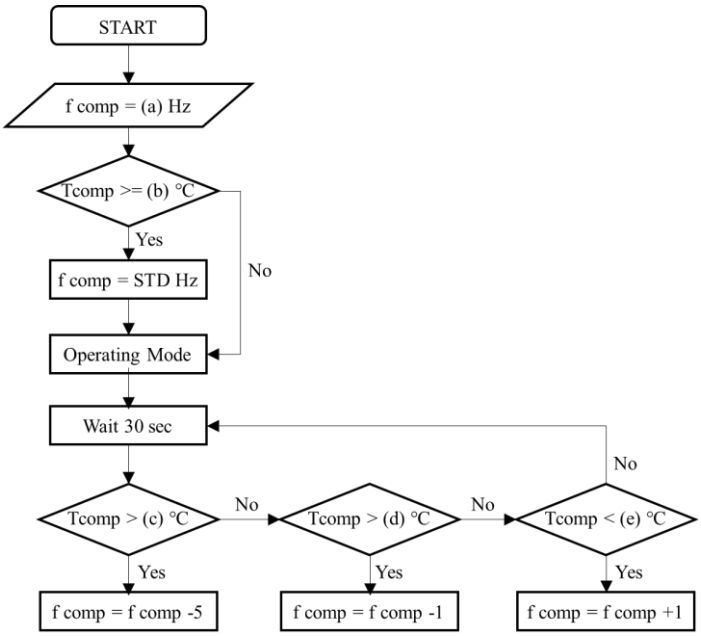
	Model	Input Parameter	Output Parameter
a	Compressor	Ref. P, h Operating Hz	Ref. P, h, $\dot{m}$
b	Condenser	Ref. P, h, $\dot{m}$ Air P, T, RH, $\dot{m}$	Ref. P, h, $\dot{m}$ Air P, T, RH, $\dot{m}$
c	Evaporator	Ref. P, h, $\dot{m}$ Air P, T, RH, $\dot{m}$	Ref. P, h, $\dot{m}$ Air P, T, RH, $\dot{m}$
d	Expansion Valve	Ref. P, h Operating Pulse	Ref. P, h, $\dot{m}$
e	Pipe	Ref. P, h, $\dot{m}$	Ref. P, h, $\dot{m}$
f	FAN	Air P, T, RH Operating RPM	Air P, T, RH, $\dot{m}$
g	Drum	Air P, T, RH, $\dot{m}$ Operating RPM	Air P, T, RH, $\dot{m}$

Fig. 7 Heat pump dryer system dynamic model in Dymola.

3.5. System Controls

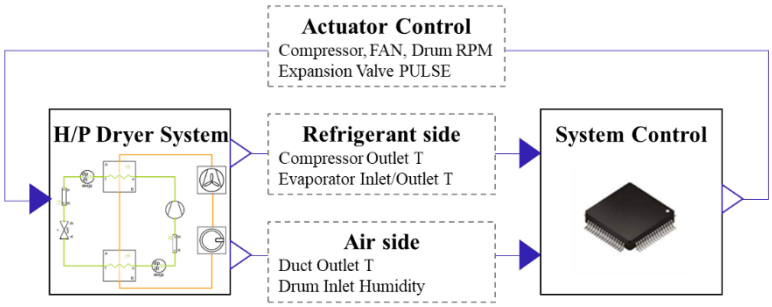
In the heat pump-based dryer, the control strategy at starting point is determined depending on the amount of moisture in the clothes initially detected. The compressor frequency is controlled to adjust the drying level, and also the opening of the electronic expansion valve is controlled based on the level of super-heating at compressor suction port. In addition, the fan rpm be set to control the circulating flow rate on the air side, and the rotation speed of the drum is controlled for drying the clothes. Pre-defined algorithm determines the end time by checking the moisture amount of the clothes. Generally, the compressor operating frequency is the most influential factor on the cycle behavior. When the dryer started up, compressor frequency maintains at a high to maximize drying performance for a while. Resulting that the temperature of the circulated air raised as much as the increased pressure difference between evaporation and condensation. However, high frequency mode couldn't be kept long because the cloth may be damaged by overheating or might be happen to reliability issue of compressor. There has a protection algorithm to control compressor frequency not to cross the specific value based on the outlet temperature of compressor and a target frequency depends on it as well. The reference temperatures for frequency control is pre-defined according to the cloth and operation mode. The control logic for compressor frequency is shown in Figure 8 (a). In the study, input/output variables of control logic for cycles implemented from a dryer product were defined, and all sensors implemented in the product were modeled for connection with the heat pump system model. As shown in Figure 8(b), the control model for cycles receives a feedback from the heat pump model based on the information of the air and refrigerant state, and then the model for cycle control provides a command signal to the heat pump model through the interface,

it should be a compressor frequency, EEV opening, and RPM target values of fan and drum at real-time. Finally co-simulation between the heat pump system model and the control model was performed as an entire system model.



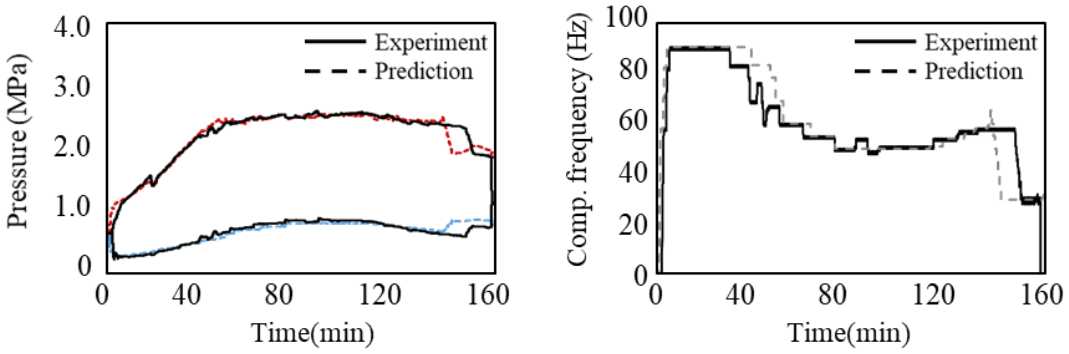
(a) Control strategy for compressor frequency

.



(b) Co-Simulation of integrated system model in Dymola

Fig. 8 The concept of co-simulation between control logic for cycles and heat pump system.



(a) Refrigerant pressure (b) Compressor frequency

Fig. 9 The comparison between experiments and predictions for 10kg load.

4. Simulation results and discussion

The validation of the heat pump-based dryer system model is confirmed by whether it predicts well by the change of air and refrigerant cycles according to the change in compressor frequency. The drying process can be defined into three stages. The first stage is a heating section where the drying speed increases as the temperature of the clothes rise to the wet bulb temperature, followed by a constant drying section as a second stage where the surface temperature of the clothes is maintained at the wet bulb temperature, and finally a reduction drying section where the surface temperature of the clothes rises to the dry bulb temperature of the dry air. The result of the simulation to the pressure of the refrigerant cycle under the load condition of 10 kg, it showed an error of 5% during the first and second stages, and it showed about 8% during the reduction section as a last stage. There observed a gap between prediction and experiment as time goes on as shown in Figure 9. The output values from the control model for cycles will be varies depending on the feedback values from the heat pump model in real time. If there happened an underestimation of the discharge temperature of the compressor from the model, it caused an error to predict proper frequency because the compressor frequency be determined by the discharge temperature of compressor during the stage of heating and constant drying as well. Moreover, the cycle control criterion for determining the completion of drying during the reduction drying stage set to the amount of moisture in the fabric. If the amount of fabric moisture is under predicted, there occurred a time difference to reach the minimum operating frequency. The amount of fabric moisture is determined by predicted values of air and refrigerant properties from heat pump system model at the initial stage of drying, in case there has an error and it accumulated continuously as time goes on, it affects the cycle control in the second half of drying. Therefore, the overall error of drying performance is the result of accumulated errors of the physical models for each component. Accuracy of the model for the drying performance depends on the prediction accuracy both of drying time and power consumption with various loads for the clothes. Three sorts of loads for the clothes from 5kg to 20kg were compared, where the drying time was calculated based on the time it took to reach the final moisture content from the initial moisture content of 60%. As the load of the clothes increased, the drying time and accumulated amount of electric power tended to increase as well. When it compared to the experiment, the drying time showed an error of 10%, and the accumulated power consumption showed an error of up to 7%.

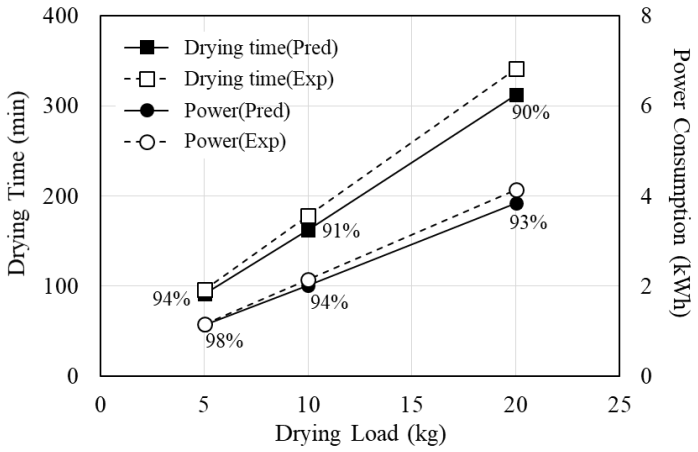


Fig. 10 Validation of the drying time and accumulated power consumption according to drying load

To make a further improvement of prediction to drying performance of the model, there have to consider a couple of things as follows. Because the rate of moisture content is the critical value for decision to system control during the drying process, accurate prediction of it serves as the most important factor in predicting the drying time and power consumption. Therefore, in order to improve the accuracy of the simulation, it is necessary to enhance the precision of the electrode sensor that measures the moisture content equipped in a product. In addition, the structure of the airflow path consist of a series of ducts, so it is necessary to more considering to leakage loss between components. And add a heat loss model to the current model can be a good way for improving accuracy because there has a heat transfer between product and environmental condition where it installed.

5. Conclusion

In the study, a dynamic model where combined a functional model and geometric model, was developed to predict the dynamic performance of the heat pump-based dryer system as a design tool. The model has verified that it simulates the drying performance well and control logic works accurately to the changes in various operating conditions. The decision of the end of drying be set at the high load condition because the prediction result of the rate of moisture content shows a relatively not a good accuracy at the condition. From based on this, it was confirmed that the error of the drying time and power consumption was up to 10% and 7%, respectively.
The main contributions brought by the modeling and simulation is that 1) The dynamic model for dryer system can be useful as a platform for design that can shorten the development time by optimizing the design parameters for the target performance in the earlier stage of product design. 2) The dynamic model for dryer system is a combined model where control algorithm and heat pump cycle, it can contribute to find the optimal algorithm scenario without or minimal testing by trying the maximum number of algorithm scenario cases at all design stages. 3) The dynamic model for dryer system consist of a functional model as well as a geometric model, there is flexibility to check the performance in advance by exploring various types of structures without relying on tests when structural or physical changes occur in the air flow ducting system. Finally, due to high energy efficiency, the demand for heat pump type dryers keeps on increasing, and the need for this model is even greater because there are many demands for responding quickly to the complexity and diversity of products in market. The result of the study can be applied very similarly to the washing machine system whose have a washing drum.

References

[1] Aceves-Saborio S, 1993, “Analysis energy consumption in heat pump and conventional driers”, Heat Recovery Systems &CHP, Vol.13, 419-428.
[2] A. Chailoet, T. Kliniam, R. Muangpisan, P. Kiatkungwankai, T. Leephakpreeda, 2010, “Analytical and Experimental Studies of Rapid Cloth Drying for Technological Innovation”, 2nd International Conference on Mechanical, System and Control Engineering, Moscow (Russia), June 21-23.
[3] Xiang C, Jing Z, Zhen Y, Liang S, Chun Z, 2021, “Process simulation and analysis of a closed loop heat pump clothes dryer”, Appl. Therm. Eng. 199 (2021) 117545
[4] C. Park, H. Cho, Y. Lee, Y. Kim, 2007, “Mass flow characteristics and empirical modeling of R22 and R410A flowing through electronic expansion valves”, Int. J. Refrigeration 30, 1401-1407.
[5] N.-H. Kim, J.-H. Yun and R. L. Webb, 1997, Heat Transfer and Friction Correlations for Wavy Plate Fin-and-Tube Heat Exchangers, *Journal of Heat Transfer*, Vol. 119, pp. 560~567
[6] Y. T. Lin, Y. M. Hwang, and C. C. Wang, 2002, Performance of the herringbone wavy fin under dehumidifying conditions, *International J. of Heat and Mass Transfer*, Vol. 45, pp. 5035-5044
[7] D. Lee, M. Lee, M. Park, Y. Kim, 2022,”Experimental evaluation and prediction model development on the heat and mass transfer characteristics of tumble drum in clothes dryers”, Appl. Therm. Eng. 202 (2022) 117900.
[8] Y. Do, M. Kim, T. Kim, S. Jeong, S. Park, S. Woo, Y. Kwon, Y. Jung, J. Lee, Y. Ahn, 2013, “An experimental study on the performance of a condensing tumbler dryer with an air-to-air heat exchanger”, Korean J. Chem. Eng. 30, 195-1200.
[9] K. Lee, J. Lee, Y. Hwang, M. Park, S. Oh, 2022, “Development of heat pump dryer system model through integrating thermodynamic model and data learning model”, SAREK Annual Conference 2022
[10] W. Kim, J. Lee, K. Lee, Y. Hwang, M. Park, S. Oh, 2022, “Data driven model of circulation air flow rate for heat pump dryer”, KSME Annual Meeting 2022

14th IEA Heat Pump Conference
15-18 May 2023, Chicago, Illinois

Novel HFO Refrigerant Blend R-474A for GWP <1 Automotive Heatpump Application

Ivan Rydkin*[a] Tsubasa Nakaue [b] Alvaro Leon [b]

[a] Daikin America Inc., 20 Olympic Drive, Orangeburg, NY USA
[b] Daikin Industries, Ltd., Chemicals Division, Settsu-shi, Osaka, 566-8585, Japan

Abstract

The introduction of novel Hydrofluorooelefin (HFO) component R-1132E allows for significant improvements in Global Warming Potential (GWP) and thermophysical performance of ultralow GWP refrigerant blends. This paper will provide laboratory test results with R-474A, a binary blend of R-1132E, R-1234yf and provide an comparison and LCCP. It was found that R-474A as a drop-in replacement demonstrated up to a 50% heating and cooling capacity increase compared to R-1234yf and a up to a 30% Coefficient of Performance (COP) increase over R-744 (CO_2)

© HPC2023.
Selection and/or peer-review under the responsibility of the organizers of the 14th IEA Heat Pump Conference 2023.

Keywords: Type your keywords here, separated by semicolons ;

1. Introduction

The 1987 adoption of the Montreal Protocol for the protection of the ozone layer led to the ban of Chlorofluorocarbons (CFC's) and eventual phaseout of Hydrochlorofluorocarbons (HCFC's). However, the Hydrofluorocarbon (HFC) gases selected to replace the previous generation have been found to have high levels of global warming potential and are considered to be a contributor to climate change. The parties to the Montreal Protocol agreed to phase down the use of HFC's, as measured in equivalents of CO_2, under the Kigali Amendment ratified in 2016. The United States took action with the passing of the US AIM Act [1] in 2021, seeking an 85% reduction by 2036, measured in CO_2 equivalents, in the use of HFC's.

To lower the overall use of HFC's, new innovations in developing molecules with shorter atmospheric lifetimes and therefore lower GWP's are necessary. A class of unsaturated fluorocarbons or HFO's has been identified as meeting those requirements. Unfortunately, the same factors that create lower atmospheric lifetimes that reduce GWP, also have the potential to reduce thermal and chemical stability that was the foundational strength of HFC's. As an example, while having similar thermodynamic properties R-1234yf is less stable and more flammable than the low pressure HFC-134a which it replaced in automotive air conditioning applications.

End uses such as automotive, where previously ample waste heat was provided from internal combustion engines, are accelerating the move towards electrification, and thus to the proliferation of heat pumps. As these heat pumps are introduced there is a growing need to identify higher capacity and higher performance refrigerants to meet these additional performance demands. However, automotive was the first sector to move en-masse to GPW <5 solutions such as R-1234yf, thus any replacement alternative would need to not only improve on performance but also meet this extreme GWP threshold expectation.

In this study we will present laboratory test results of R-474A a refrigerant based on novel HFO molecule R-1132E ((E) 1,2, Difluoroethylene) as it compares to R-1234yf, R-134a and R-744. The physical properties of the R-1132 were first defined in studies by Higashi et. al [2] and Pererra et. al [3] and the critical parameters

* Corresponding author. Tel.: 1-585-315-5148.
E-mail address: irydkin@daikin-america.com.

and equation of state for R-474A, a binary refrigerant blend of 23% by mass R-1132E and 77% by mas R-12347f, was determined by Akasaka et. al [4]. Table 1 summarizes relevant refrigerant properties.

Previous studies [5] have already covered theoretical modeling, material compatibility and stability of R-1132E Blend R-474A.

Table 1. List of Refrigerant Properties

Refrigerant	R-1132E	R1234yf	R-474A
GWP (AR4)	<1*	4	<3
Boiling Point (101.3kPa)	-52.5°C	-29.4°C	-44.6°C
Critical Temperature	75.6°C	94.7°C	87.1°C
Critical Pressure (MPa)	5.16	0.59	4.04
Pressure at 20°C (MPa)	1.46	0.59	0.94
ODP	0	0	0
Safety Class**	B2	A2L	A2L
LFL (Vol %)	4.3	6.2	5.5
BV WCF (cm/s)	32.9	1.5	2.9

*Evaluated under AR5 conditions **ASHRAE 34 Safety Group Classification

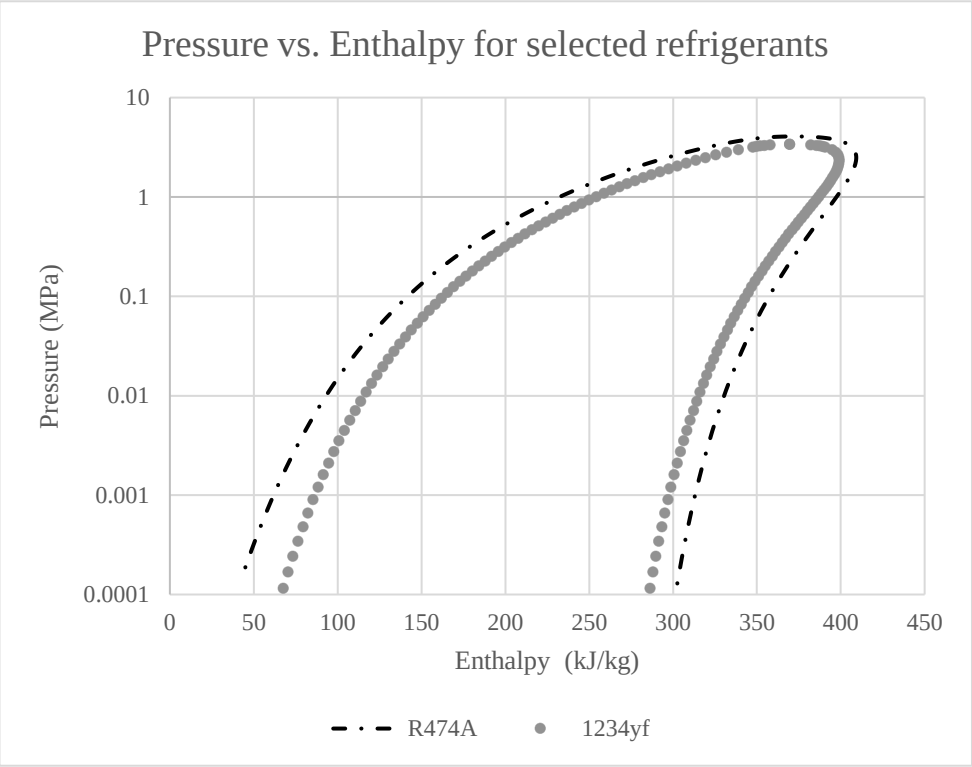


Figure 1: Pressure Enthalpy Diagram for R-1234yf and R-474A

2. Laboratory Tests

Two tests were performed in order to evaluate Refrigerant R-474A. First was an evaluation compared to R-1234yf using a standard compressor bench system at Ipetronik laboratories. The compressor calorimeter is shown in figure 2 system utilized a commercial off the shelf 34cc Brose compressor with PAG oil. The compressor tests included both heating and cooling conditions to estimate the compressor COP and capacity impacts of a refrigerant change.

Second, bench testing was performed utilizing two VW ID3 systems one a traditional R-1234yf AC only system with electric heat, and one utilizing an R-744 heat pump system. In the R-1234yf system the TXV was

replaced with an electronic expansion valve. In both systems pressure, temperature and mass flow rate was measured as described in figure 3 and figure 4. Comparative testing was only performed in cooling mode.



Figure 2. Compressor Calorimeter

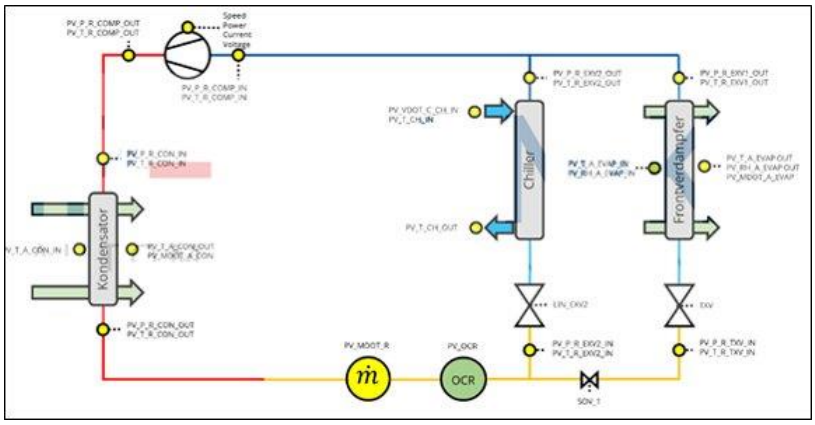


Figure 3. R-474A and R-1234yf Bench System Layout

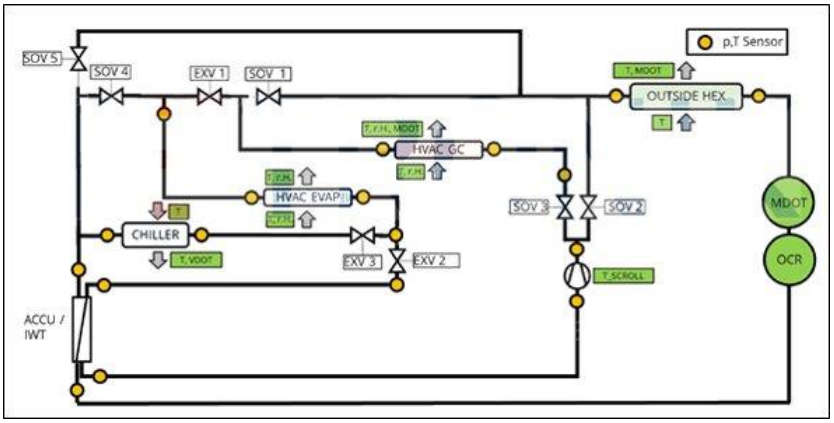


Figure 4. R-744 Bench System Layout

For the compressor calorimetry test, the conditions evaluated are identified in table 2.

Table 2: Compressor Calorimeter Test Parameters

Test	Condenser (°C)	Evaporator (°C)	Superheat (K)	Subcooling (K)
Cooling 1	40	-1.5	25	5
Cooling 2	69	-1.5	25	5
Heating 1	0	50	10	5
Heating 2	-10	60	10	5

For system bench evaluation, measurement points were selected from the list of tests available per SAE Standard J2765 [6]; The first set of tests, I60 through H35a were run as an evaluation of max performance / and at max allowable RPM; The second set of tests, I40a through I15 were run at a fixed cooling load to evaluate best case COP. Uncertainty and instrumentation tolerances are listed in section 4 of SAE J2765 for the test equipment and section 5 for the test room. In general, per J2765 section 1.5.2, the test apparatus is designed to give agreement within ±4% between two independent balances.

Lastly before evaluation for the bench system could be performed, a charge determination step was done by measuring superheat, subcooling pressure and temperature, and trying to identify the subcooling plateau. The test was performed with the condenser, coolant temperature and evaporator at 40°C; The compressor at max speed of 8500RPM. The charge determination graph is shown in figure 5 and indicates a 10% charge reduction with R-474A vs R-1234yf

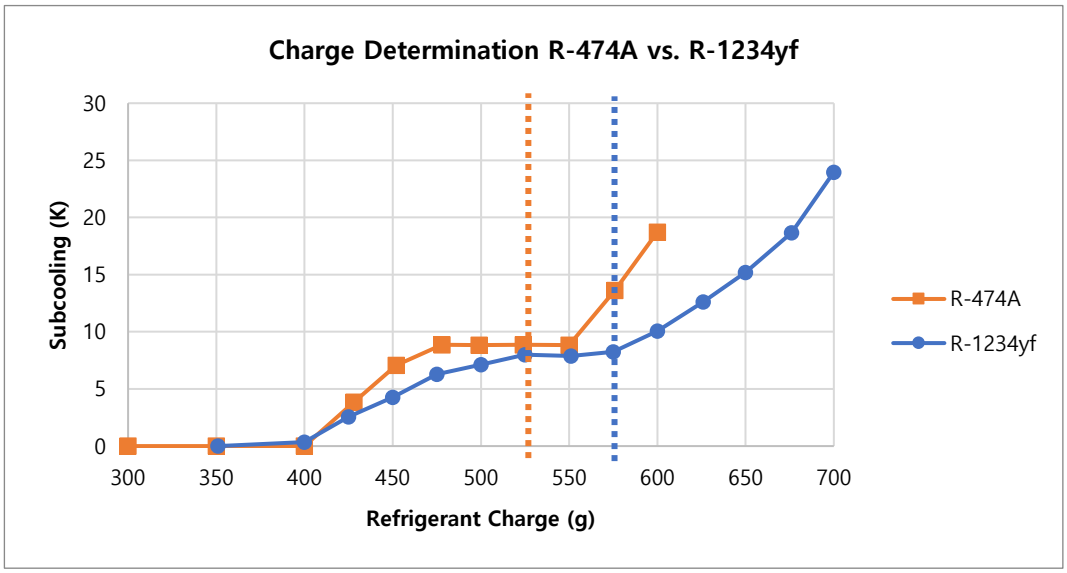


Figure 5. Bench System Charge determination

Table 3: Bench System Evaluation Points

Test	Condenser Air Temp (°C)	Condenser Air Flow (m/s)	Evaporator Air Temp (°C)	Evaporator Humidity (%)	Evaporator Air Mass Flow (kg/h)	Chiller Inlet Temperature (°C)	Coolant Flow Rate (l/min)	Air Temperature Target (°C)	Coolant ΔT (K)
I60	60	1.5	35	25	300	40	10	3	10
I45	45	1.5	35	25	300	40	10	3	10
M45	45	3	35	25	300	40	10	3	10
H45a	45	4	35	25	300	40	10	3	10
I50a	50	1.5	35	40	300	30	6.7	3	10
I35a	35	1.5	35	40	300	30	6.7	3	10
L35a	35	2	35	40	300	30	6.7	3	10
H35a	35	4	35	40	300	30	6.7	3	10
I40a	40	1.5	25	80	210	25	2.0	3	5
I25a	25	1.5	25	80	210	25	2.0	3	5
H25a	25	4	25	80	210	25	2.0	3	5
I40c	40	1.5	25	50	210	25	2.0	3	5
I25c	25	1.5	25	50	210	25	2	3	5
I30	30	1.5	15	80	210	Off	Off	3	Off
I15	15	1.5	15	80	210	Off	Off	3	Off

3. Results

Results for the compressor calorimeter test are summarized in table 4 where capacity is given in kW. In general R-474A showed a significant increase in capacity, almost 40-60% greater capacity than R-1234yf in heating mode. R-474A also demonstrated a significant improvement in COP over R-744 and R-1234yf in cooling mode while maintaining a 40% capacity improvement.

Table 4: Compressor Calorimeter Test Results

Cooling Point 1

	Compressor RPM				
	1500	3000	5000	7000	8500
1234yf COP	1.75	2.12	2.14	2.05	1.91
R474A COP	1.82	2.2	2.24	2.15	2.024
R134a COP	1.9	2.2	2.3	2.2	2.1
R744 COP		1.57	1.78	1.74	1.7
1234yf Capacity	1.19	2.54	4.45	6.23	7.41
R474A Capacity	1.71	3.63	6.24	8.72	10.41
R134a Capacity	1.39	2.96	5.10	7.15	8.53
R744 Capacity	0.00	2.57	4.76	6.88	8.49

Cooling Point 2

	Compressor RPM				
	1500	3000	5000	7000	8500
1234yf COP		0.92	1.01	1.02	0.98
R474A COP	0.76	0.97	1.08	1.09	1.05
R134a COP		2.2	3.7	5.2	6.2
R744 COP			0.91	0.91	0.91
1234yf Capacity		1.62	2.87	4.02	4.8
R474A Capacity	1.35	2.39	4.17	5.86	7.03
R134a Capacity		2.15	3.73	5.21	6.22
R744 Capacity			3.01	4.41	5.52

Heating Point 1

	Compressor RPM				
	1500	3000	5000	7000	8500
1234yf COP			1.02	0.97	0.92
R474A COP			1.14	1.1	1.05
R744 COP			1.2	1.2	1.2
1234yf Capacity			1.85	2.57	3.03
R474A Capacity			2.57	3.58	4.28
R744 Capacity			3.42	4.91	6.13

Heating Point 2

	Compressor RPM				
	1500	3000	5000	7000	8500
1234yf COP			0.57	0.55	0.52
R474A COP			0.67	0.66	0.637
R744 COP			1	0.98	0.97
1234yf Capacity			1.07	1.55	1.83
R474A Capacity			1.72	2.42	2.88
R744 Capacity			2.64	3.82	4.76

Results for the bench test when comparing max cooling are shown in figure 6. R-474A demonstrates a 1200 to 2200 watt improvement in cooling output across the test conditions as compared to both R744 and R1234yf and a small decrease in COP compared to R-1234yf and a significant increase in COP when compared to R-744

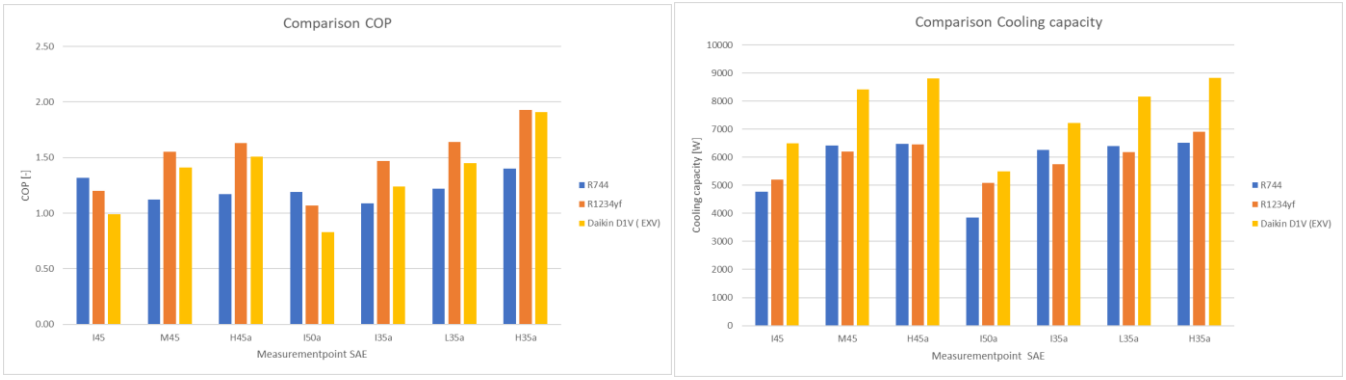


Figure 6. Bench System Max Load results

Results when matching cooling capacity are shown in figure 7. We note that R-474A shows an improvement in COP across the entire range of test conditions. We also observe a decrease in the COP of R744.

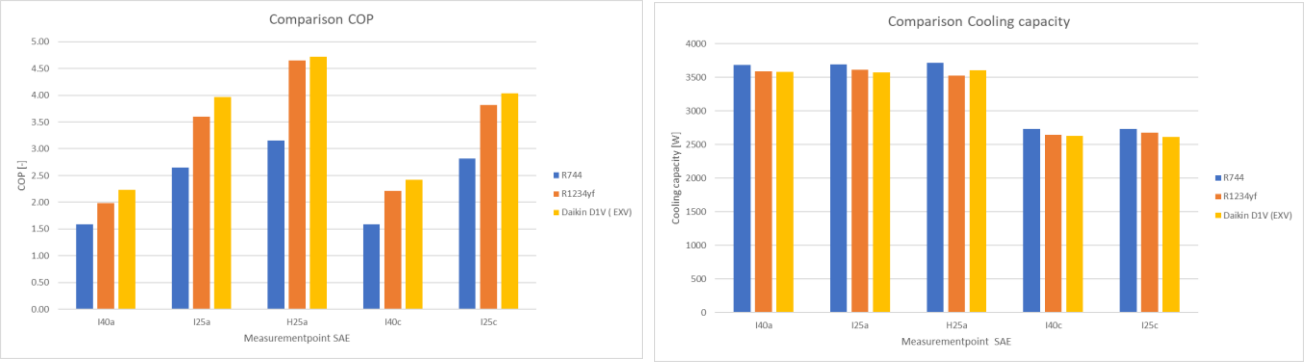


Figure 7. Bench System Max Load results

4. Conclusion

Based on the bench test results observed, R-474A is capable of extending the heating range of a traditional R-1234yf heatpump system beyond 0°C to -10°C and with this trend extending likely a significant amount of heat being available at -20°C. This indicates that a reduction in the quantity and use of PTC heaters Is possible as a potential weight and cost savings.

Additionally at mild cooling conditions when matching capacity, there is a significant improvement in COP, indicating that for a typical automotive drive cycle, there is opportunity to reduce total HVAC energy consumption and thus improve cruising range.

Furthermore, charge determination experiment indicates that the total refrigerant charge for an R-474A system when dropped into an existing commercial system can be as much as 10%.

Lastly, the significant observed improvement in capacity is shown at many of the test points. This can be utilized to either improve HVAC system noise vibration and harshness (NVH) characteristics by reducing RPM, which is significantly more important in generally quieter electric vehicles, or to down size the compressor.

Acknowledgements

This paper is based on results obtained in part from a project, JPNP18005, subsidized by the New Energy and Industrial Technology Development Organization (NEDO). This paper is based on testing results obtained by IPETRONIK GmbH & Co. KG.

References

[1]. US AIM Act. Title 42 US Code 7675 American innovation and manufacturing
[2]. Higashi Y., Sakoda N., Kondou C. (2020), Determination of Saturated Densities, Critical Temperature and Critical Density for New Refrigerant HFO1132(E), Proc. 2020 JSRAE Annual Conference, JSRAE, D142
[3]. Perera U., Thu K., Miyazaki T., Sakoda N., Higashi Y. (2020). Determination of Saturation Pressure and Critical Pressure for New Refrigerant HFO1132(E), Proc. 2020 JSRAE Annual Conference, JSRAE, D143
[4]. Akasaka R., Lemmon E. (2021). A New ISO 17584 Standard Equation of State for 2,3,3,3-Tetrafluoroprop-1-ene (R1234yf) and its Modification for trans-1,2-Difluoroethene [R1132(E)], 2nd IIR Conference on HFO Refrigerants and Low GWP Blends (2021)
[5]. Rydkin, Ivan; Gobou, Kenji; Karube, Daisuke; Ajioka, Shohei; Nakaue, Tsubasa; and Leon, Alvaro, "Overview of novel GWP 1 HFO Refrigerant 1132E and the Mixture of 1132E and R-1234yf" (2022). International Refrigeration and Air Conditioning Conference. Paper 2491
[6]. SAE J2765 Procedure for Measuring System COP [Coefficient of Performance] of a Mobile Air Conditioning System on a Test Bench (2017). SAE International 400 Commonwealth Drive Warrendale, PA 15096

14th IEA Heat Pump Conference
15-18 May 2023, Chicago, Illinois

Investigation of industrial high-temperature heat pumps for simultaneous heating and cooling: A brewery case study

Martin Pihl Andersen[a], Roger Padullés I Solé[a], Benjamin Zühlsdorf[b], Wiebke Brix Markussen[b], Jonas Kjær Jensen[a], Brian Elmegaard[a]

[a]Department of Civil and Mechanical Engineering, Technical University of Denmark, Kgs. Lyngby, 2800, Denmark
[b]Danish Technological Institute, Taastrup, 2630, Denmark
*Corresponding author, mapian@dtu.dk

Abstract

Process industries are responsible for a large share of the global energy demand. While refrigeration systems are used in the industry for the supply of cooling, the introduction of high-temperature heat pumps (HTHPs) and electric boilers to supply heat is necessary for the electrification of this industry. Combining the refrigeration system and the HTHP may offer an opportunity to improve the overall efficiency and facilitate the integration of HTHP. However, fluctuating, and non-continuous demands make the integration of a combined heat pump for simultaneous heating and cooling (HPS) more challenging as the heating and cooling capacity for such a system is coupled.
This study compared a cascade HPS with an R-717 bottom cycle and R-718 top cycle to a reference system consisting of a R-717 refrigeration system releasing excess heat to the ambient and a HTHP with R-717 and R-718 using the ambient as a heat source. The HPS configuration included heat exchangers with ambient air, and ambient heat sources to meet all combinations of heating and cooling demands. The comparison was carried out for an industrial brewery case and was based on numerical modelling.
For each combination of heating and cooling load the usage of ambient air as heat source and sink was adapted and simultaneously the pressure levels in the HPS were optimized for minimum electricity consumption. The influence of the ambient temperature was also analysed.
At design conditions the electricity consumption of the HPS was 9.8 % lower than the electricity consumption of reference system, but only 2.1 % lower on a yearly basis, due to the fluctuating demand profiles. This indicates that the HPS did not offer a substantial improvement in in terms of thermal efficiency compared to the reference system.

© HPC2023.
Selection and/or peer-review under the responsibility of the organizers of the 14th IEA Heat Pump Conference 2023.

Keywords: industry; high temperature; heat pump; cooling; HPS

1. Introduction

Process industries are responsible for a large share of the global energy demand and comparably large CO_2 emissions. According to [1], 69 % of the European industry's energy consumption is used for process heating and cooling, with 40 % being delivered at temperatures below 200 °C. These processes show great potential for electrification, and through this reducing overall greenhouse gas emissions [2].

Refrigeration systems based on vapour compression cycles have been used in the industry for the supply of cooling since the mid-19th century [3] but the introduction of high-temperature heat pumps (HTHPs) and electric boilers to supply heat is not as prevalent in today's market in comparison. Nevertheless, HTHPs are an efficient and feasible solution for the total electrification of this industry [4]. However, increasing the temperature lift of the HTHPs to reach higher supply temperatures yields a lower coefficient of performance (COP) resulting in higher operating expenses (OPEX) challenging the economic potential.

Combining the refrigeration system and the HTHP into a single heat pump for simultaneous heating and cooling (HPS) offers an opportunity to improve the overall efficiency of delivering heating and cooling requiring one system instead of two [5]. However, the part-load performance of such systems has not been

analysed. At the same time, the existing cooling utility could be fully or partly replaced facilitating the electrification of the industry.

When operating a HPS, two thermal energy streams, one for cooling and one for heating, are produced simultaneously. Therefore, it is interesting for the user that the HPS operates in simultaneous mode as much as possible. However, the energy demand of industrial processes varies throughout the day.

The combination of batch processes and continuous demands dictates load variations on an hourly and daily basis [6], but weekly and seasonal variations also exist. As the heating and cooling capacity of the HPS are coupled, either heating or cooling will be in excess in most operating conditions when fulfilling the needed heating and cooling demands of the processes. The HPS will therefore either expel the excess to the ambient or fill a thermal storage. However, for large demand variations like seasonal trends, a thermal storage requires substantial amounts of space [7]. The HPS needs to adapt its operation to fulfil its function. Hence, the variability of the non-continuous energy demands makes the integration of a HPS more challenging where both operation during design conditions and during part-load are essential.

This study conducted a case study of supplying simultaneous heating and cooling with a HPS for a Danish brewery. The analysis was based on daily average consumption data assuming that daily variations were covered by existing heat storages. The HPS was designed to cover all demands of cold- and hot water with no further required utilities. The daily and yearly operations were evaluated in terms of electricity consumption and Lorenz efficiency, while being compared to a reference system which consisted of two separate utilities, a HTHP and a refrigeration cycle, respectively.

2. Method

This section presents the method and concepts used for the modelling, analysis, and evaluation of the HPS. First, the investigated case study is presented followed by the thermodynamic modelling of the HPS system and the reference system. Finally, relevant performance indicators are introduced which were used to assess this strategy for electrifying industrial processes.

2.1. Brewery case study

The industrial facilities chosen for this study was a Danish brewery producing a large variety of products. The consumption data and the ambient temperature for the year 2021 was used in the case study. The heating demand of the actual production facilities was traditionally covered by a natural gas boiler supplying hot water. The cold water was supplied by a refrigeration plant covering the cooling of products both during production and storage. The demand profiles used are presented in Figure 1 together with the ambient temperature. The orange curve shows the heat load, the blue curve shows the cooling load, and the grey curve shows the ambient temperature.

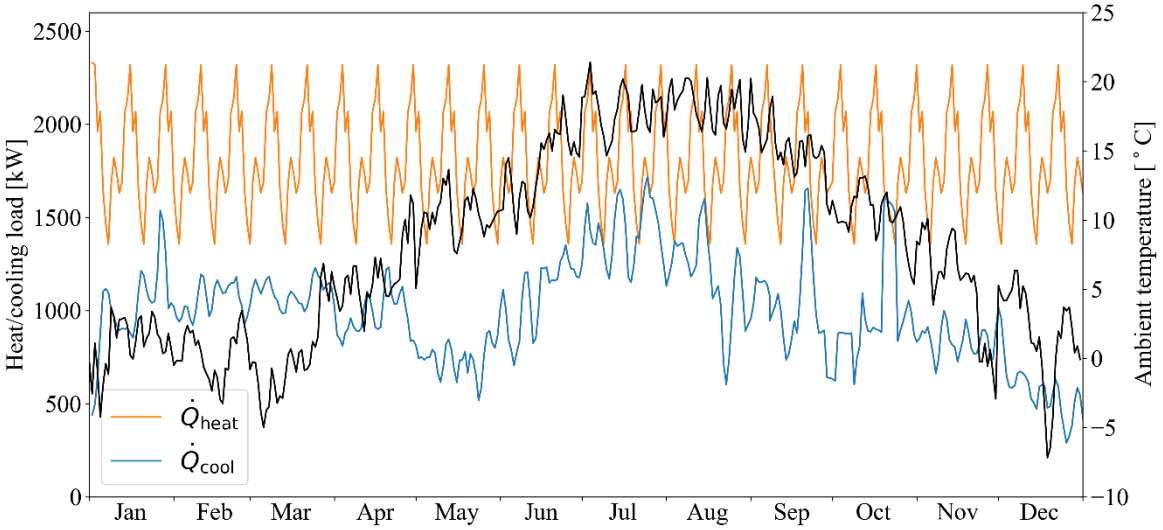


Figure 1: Daily average heating and cooling load supplied by hot water and cold water, respectively. The daily average temperature is presented on the secondary axis.

The heating demand follows a bi-weekly schedule with very little influence from the season. The demand fluctuates between 1350 kW and 2330 kW depending on the day. The demand for cold water follows a seasonal trend with lower loads during colder months. The cooling load is also low in May due to the product being transported directly to the customers to a higher degree. The demand varies between 290 kW and 1720 kW. This means that the ratio between the heating and the cooling demand is largest during the winter and smallest during the summer. The ambient changes with a seasonal trend between -7 °C and 21 °C.

The hot water is produced at a temperature of 145 °C by reheating the return water at 110 °C. The cold-water supply temperature is 2 °C while it returns at a temperature of 8 °C as presented in Table 1. The design cooling load of the HPS was chosen as 80 % of the maximum cooling demand, i.e., 1380 kW. The design heat load was corresponding to running the described cooling load without expelling any excess heat, resulting in a design heat load of 2230 kW. It is assumed that there is already a storage big enough to mitigate the daily variations in demand.

Table 1: Design conditions for the HPS at 80 % load given by the case study.

Design parameter		Value
Hot water supply temperature	$T_{\text{sink,out}}$	145 °C
Hot water return temperature	$T_{\text{sink,in}}$	110 °C
Cold water supply temperature	$T_{\text{source,out}}$	2 °C
Cold water return temperature	$T_{\text{source,in}}$	8 °C
Design heat load	$\dot{Q}_{\text{heat}}$	2230 kW
Design cooling load	$\dot{Q}_{\text{cool}}$	1380 kW
Lorenz COP	$\text{COP}_{\text{Lor,comb}}$	5.37

2.2. Heat pump modelling

The HPS considered for this case study was an electrically driven vapour compression cycle in a cascade configuration.

The model consisted of an evaporator at the heat source and a desuperheater, condenser and subcooler at the heat sink as visualised in Figure 2 to the left producing hot water at 145 °C and cold water at 2 °C at the sink and source, respectively.

In between the source and the sink, a cascade of two two-stage vapour compression cycles was applied. Both cycles were modelled in a configuration with a bubble-through intercooler minimizing the superheat at the inlet of the high stage compressors. The bottom cycle was modelled with ammonia (R-717) as the refrigerant while the top cycle was modelled with water (R-718) as the refrigerant. The two cycles were connected through a set of cascade heat exchangers (HEX). The first one responsible for desuperheating the ammonia (4→5) while the second HEX was assumed to condense the ammonia (5→6). On the secondary side, the mass flow of R-718 was controlled such that a superheat (ΔT_{SH}) of 0.5 K was ensured at state point 21 shown in Figure 2.

The four compressors (1→2, 3→4, 21→22, and 23→24 in Figure 2) represent a compression process. An isentropic efficiency of 70 % was applied for all compressors, since this value is common for theoretical calculations [8]. The expansion valves (7→8, 10→11, 27→28, and 30→31) were modelled as isenthalpic expansion processes leading the refrigerant into the evaporation process or the liquid separator. The liquid separators (state points 9 and 29) were assumed ideally mixed with pure liquid exiting out the bottom (state points 10 and 30) and vapour leaving with a ΔT_{SH}=0.5 K out the top (state points 3 and 23).

The heat exchangers with ambient air (5a→6a and 11a→11b) were used to expel excess heating or cooling capacity of the HPS. A fraction of the mass flows at point 4 and point 11 went to the ambient air heat exchanger to match demand from the process (see Figure 1). The two ambient air heat exchangers were assumed to always be able to transfer enough heat so the conditions of 6a was equal to 6 and 11b was equal to the conditions of 13.

All heat transfer processes were assumed isobaric. A minimum temperature difference of 5 K was chosen for all the heat exchangers at design conditions as in [9]. The subcooling process in the top cycle (26→27)

and the bottom cycle (6b→7) was maximised so the outlet conditions were set to 5 K above the sink inlet temperature and the ambient, respectively.

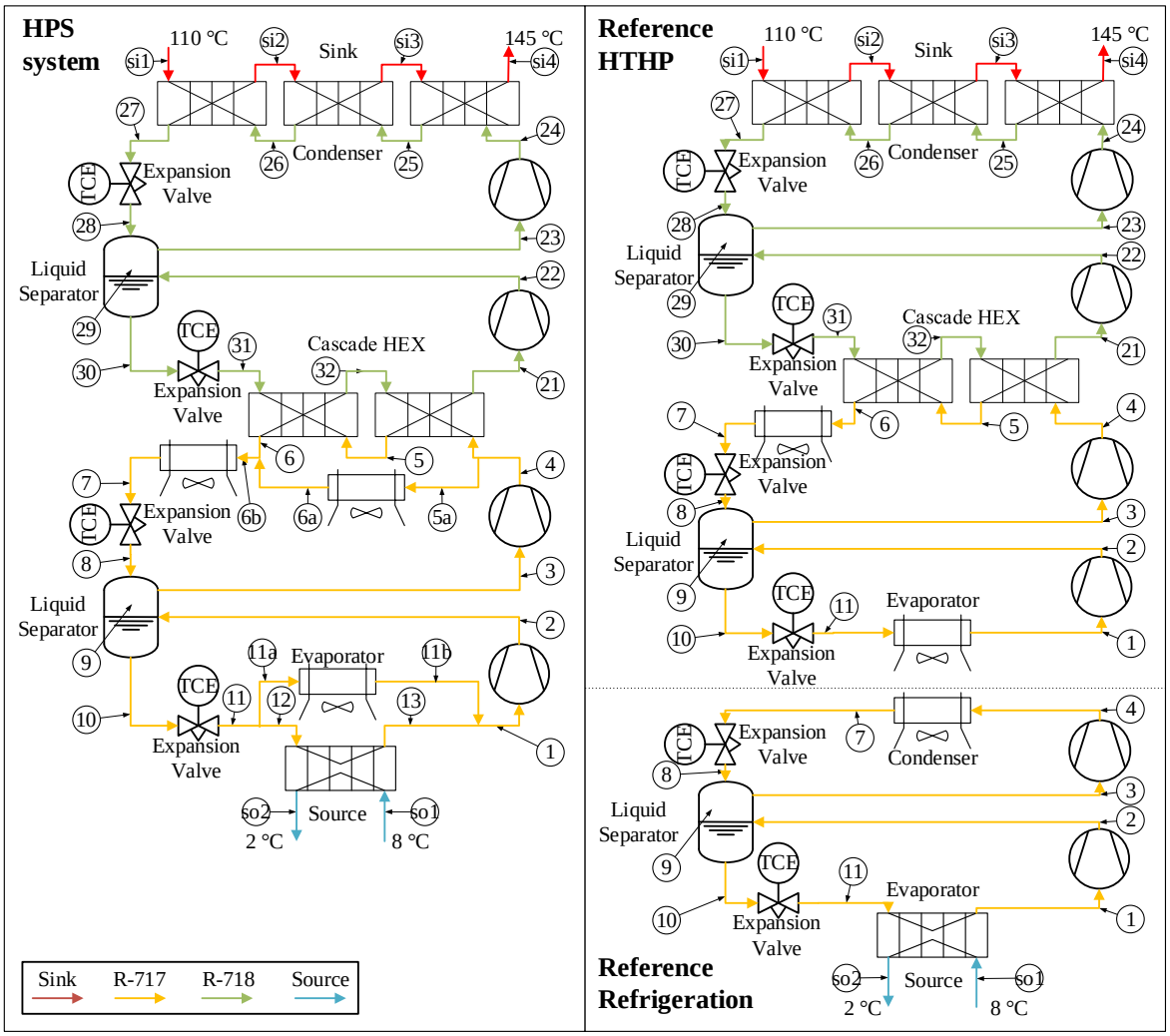


Figure 2:PI-diagram of the combined heating and cooling system, HPS to the left, and the reference systems to the right.

As described, the heat exchangers with ambient air (5a→6a and 11a→11b) were used to expel excess heating or cooling capacity of the HPS to match the process demand. The corresponding control narrative is presented in Table 3 when heat is either in excess or lacking compared to operation according to the design point.

Table 3: Control narrative of the HPS system during different load conditions.

Load conditions	Operational condition
Heat and cooling load is balanced according to design point	The HPS delivers heat to the sink and cooling to the source.
Heat load exceeds excess heat from the cooling system	Absorb heat by operating the air HEX parallel w. the evaporator
Cooling load offering more excess heat then the HP system requires	Expel excess heat by operating the air HEX parallel w. the cascade HEX

A minimum of 0.5 K superheating was considered before the low-pressure compressor of each cycle (point 1 and 21). The condensing temperature of the bottom cycle was optimized for the highest Lorenz efficiency (Equation 2), while fan power pressure losses were neglected. The assumptions at design conditions as in Table 1 are summarised in Table 2.

Table 2: Assumptions for thermodynamic model of the heat pump used in simulations at design conditions as in Table 1.

Component	Assumptions	Value
Evaporator	Pinch point temperature difference	$\Delta T_{\text{pinch}} = 5$ K
	Minimum superheating	$\Delta T_{\text{SH}} = 0.5$ K
Condenser	Pinch point temperature difference in the desuperheater, condenser, and subcooler.	$\Delta T_{\text{pinch}} = 5$ K
	Design heat load	$\dot{Q}_{\text{heat}} = 2230$ kW
Shared cascade heat exchanger	Pinch point temperature difference	$\Delta T_{\text{pinch}} = 5$ K
	Condensing temperature of bottom cycle optimized for highest η_{Lor}	
Heat exchangers with ambient air (5a→6a and 11a→11b)	Same conditions out of HEX as the parallel HEX	$h_{6a} = h_6$ and $h_{11b} = h_{13}$
Air subcooler (6b→7)	Refrigerant maximally subcooled by the ambient temperature.	$\Delta T_{\text{pinch}} = 5$ K
Liquid separator	Intermediate pressures optimized for highest overall η_{Lor}	ΔT_{SH}=0.5 K
	Saturated liquid and slightly superheated vapour towards lower pressure and intermediate pressure side, respectively.	
Compressor	Fixed isentropic efficiency	$\eta_{\text{is}} = 70$ %
Throttling valve	Isenthalpic expansion	
Overall system	Fan power neglected	
	No pressure losses considered	
	R-717 and R-718 used as refrigerants for the bottom and top cycle respectively.	

At the design conditions, the required UA-value of each heat exchanger of the HPS was determined using Equation 1.

$$\dot{Q}_k = (U \cdot A)_k \cdot \text{LMTD}_k \tag{1}$$

Where $\dot{Q}_k$ is the given heat load, $(U \cdot A)_k$ is product of the heat exchanger area and the heat transfer coefficient at design conditions, and LMTD_k is the logarithmic mean temperature difference [10], all for HEX *k*.

During operation at conditions away from the design point, the LMTD changed depending on the heat load experienced by the specific HEX as the UA-values were assumed to be constant.

For the comparison a reference system was modelled as presented to the right in Figure 2. The refence HTHP was modelled using the same configuration as the HPS system with a heat load at design conditions of 2230 kW but utilizing ambient air as an isothermal heat source. Similarly, a refrigeration cycle was modelled for the cold utility. This system was represented by an ammonia cycle like the one shown in the bottom right Figure 2 with the ambient air as an isothermal heat sink. The condensing temperature of the refrigeration cycle was given a lower bound of 10 °C.

The parameter variations are done by varying the total compressor power between 360 kW and 1320 kW and the utilisation of the heat exchangers with ambient air between 0 % and 100 % while optimising the η_{Lor}.

2.3. Performance parameters

For evaluating the performance of the HPS two performance indicators were used. The first one is the power consumption of the compressors while the second was the second law efficiency, η_{Lor}. This was defined as the ratio between the combined COP, COP_{comb}, of the HPS and the maximally achievable COP, as in Equation 2.

$$\eta_{\text{Lor}} = \frac{\text{COP}_{\text{comb}}}{\text{COP}_{\text{Lor,comb}}} \tag{2}$$

Where the $\text{COP}_{\text{Lor,comb}}$ denotes the COP of a Lorenz cycle where both heating and cooling is considered a product at the given boundary conditions defined in Equation 3 [5].

$$\mathrm{COP}_{\mathrm{Lor,comb}} = \frac{T_{\mathrm{sink,av}} + T_{\mathrm{source,av}}}{T_{\mathrm{sink,av}} - T_{\mathrm{source,av}}} \tag{3}$$

With $T_{\mathrm{sink,av}}$ and $T_{\mathrm{source,av}}$ being the thermodynamic average temperatures of the sink and source streams. They are defined as the logarithmic means as in Equation 4.

$$T_{\mathrm{sink,av}} = \frac{T_{\mathrm{sink,out}} - T_{\mathrm{sink,in}}}{\ln\left(\frac{T_{\mathrm{sink,out}}}{T_{\mathrm{sink,in}}}\right)} \qquad T_{\mathrm{source,av}} = \frac{T_{\mathrm{source,in}} - T_{\mathrm{source,out}}}{\ln\left(\frac{T_{\mathrm{source,in}}}{T_{\mathrm{source,out}}}\right)} \tag{4}$$

Here sink out is the hot water supply, sink in is the hot water return, source in is the cold water return temperature, and source out denotes the cold-water supply temperature.

The $\mathrm{COP}_{\mathrm{comb}}$ is defined in Equation 5 as the sum of the supplied heating, $\dot{Q}_{\mathrm{heat}}$, and the supplied cooling, $\dot{Q}_{\mathrm{cool}}$, divided by the sum of each of the compressor's power, $\dot{W}_k$.

$$\mathrm{COP}_{\mathrm{comb}} = \frac{\dot{Q}_{\mathrm{heat}} + \dot{Q}_{\mathrm{cool}}}{\sum \dot{W}_k} \tag{5}$$

The difference in total compressor power of the two solutions, $\dot{W}_{\mathrm{diff}}$, was used as a measure to compare the OPEX of the two solutions. This was defined as the difference in compressor power of the HPS, $\dot{W}_{\mathrm{HPS}}$, and compressor power of the reference system, $\dot{W}_{\mathrm{ref}}$. This is defined as the sum of the compressor power of the high temperature heat pump, $\dot{W}_{\mathrm{HTHP}}$, and reference system refrigeration cycle, $\dot{W}_{\mathrm{refri}}$ as in Equation 6.

$$\dot{W}_{\mathrm{diff}} = \dot{W}_{\mathrm{HPS}} - (\dot{W}_{\mathrm{HTHP}} + \dot{W}_{\mathrm{refri}}) = \dot{W}_{\mathrm{HPS}} - \dot{W}_{\mathrm{ref}} \tag{6}$$

Lastly, the normalized difference in power, $\dot{W}_{\mathrm{diff,norm}}$, is defined using the power of the HPS system at the design conditions, $\dot{W}_{\mathrm{HPS,des}}$ as in Equation 7.

$$\dot{W}_{\mathrm{diff,norm}} = \frac{\dot{W}_{\mathrm{diff}}}{\dot{W}_{\mathrm{HPS,des}}} \tag{7}$$

The performance of the cycles was examined by numerical modelling based on energy and mass balances as described in this section using Python [11] and CoolProp [12] for its thermophysical properties. The minimize function in [13] was used for the optimisation of the COP by changing the condensing temperature of the bottom cycle and the intermediate pressures of both the top- and the bottom cycle. All data was collected, analysed, and visualised using the Pandas library [14].

3. Results

The HPS and the reference system models were used to assess the performance at design conditions for varying ambient temperatures. Additionally, the compressor power at varying heat- and cooling loads were mapped to assess the off-design performance of the HPS compared to the reference system. Finally, the systems were compared in terms of yearly energy consumption using a quasi-steady state approach.

The calculated compressor power of the HPS is presented in Figure 3 as a function of the required heating and cooling load. The utilisation of each heat exchanger with ambient air was varied from 0 % to 100 % in steps of 5 % for all combinations. The total compressor power is varied from 360 kW to 1320 kW in increments of 120 kW. Each grey diamond represents the results of a simulation with a specific utilisation of the heat exchangers with ambient air. The grey curves indicate the pareto fronts in terms of supplied heating and cooling for a specific sum of compressor power. The design point, as defined in Table 1 is marked with a red dot. The simulations were done at an ambient temperature of 20 °C.

The grey curves in Figure 3 are the most efficient operating points for the HPS for a specific combination of demands. The inclination of the grey curves changes with a varying cooling load. At 0 kW cooling load the evaporator is completely bypassed getting all heat for the bottom cycle from the air source. Following the grey curve for 1200 kW compressor power, for higher cooling the potential heat load decreases. This is due to the higher evaporator utilisation increasing the heat load of the component, increasing the LMTD as in

Equation 1. This trend continues until reaching the design point in the steps of about 5 % in correlation with the utilisation of the bottom heat exchanger with the ambient air.

From here, the heat load decreases rapidly for an increased cooling load. This is the second heat exchanger with ambient air bypassing the cascade HEX being used increasingly until the top cycle is fully bypassed. Thereby, the compressor power from the top cycle can be utilised in the bottom cycle instead, hence increasing the potential cooling load. However, the maximal cooling load will reach a maximum, when the bottom cycle compressors reach their maximal operating conditions which are not considered in this study. The remaining combinations of heat exchangers with ambient air utilisation and compressor power yield non-optimal working conditions with lower efficiency.

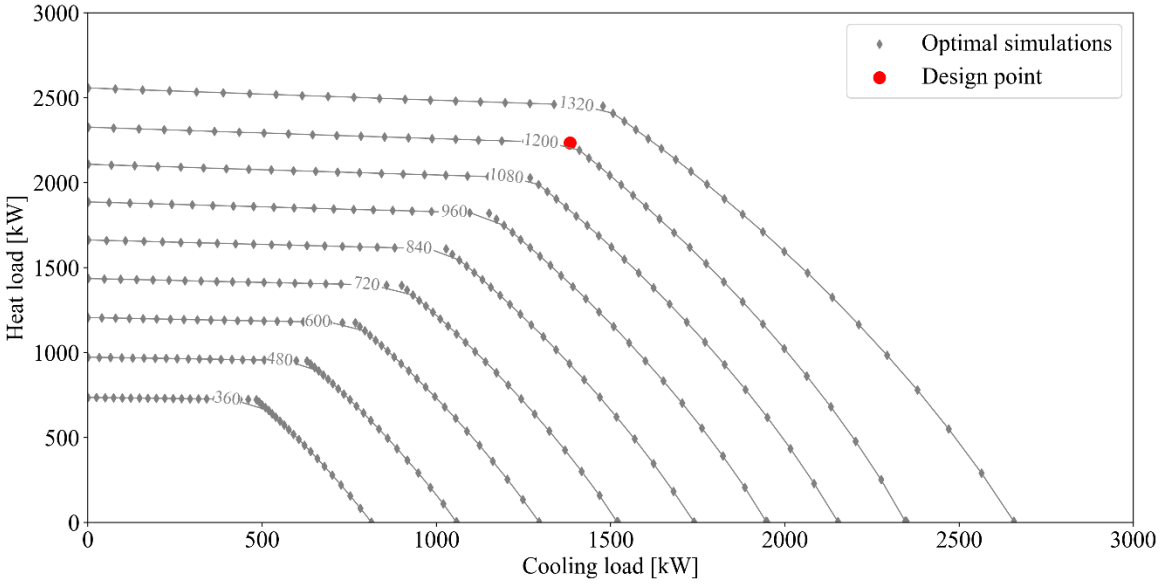


Figure 3: Compressor power at varying heating and cooling loads of the HPS at an ambient temperature of 20 °C.

Similar simulations were performed for the HTHP and the refrigeration cycle as in Figure 3. The normalized difference in compressor power of the HPS and the reference system at the same heating and cooling load is presented in Figure 4. The heat load ranges from 0 kW to 2500 kW and the cooling load from 0 kW to 1750 kW. An ambient temperature of 20 °C was assumed. The result is normalised with the compressor power of the HPS at the design point. Negative $\dot{W}_{\mathrm{diff,norm}}$ indicates a lower compressor power for the HPS. The opposite is true for positive $\dot{W}_{\mathrm{diff,norm}}$, where the HPS will perform worse than the refence HTHP and refrigeration cycle.

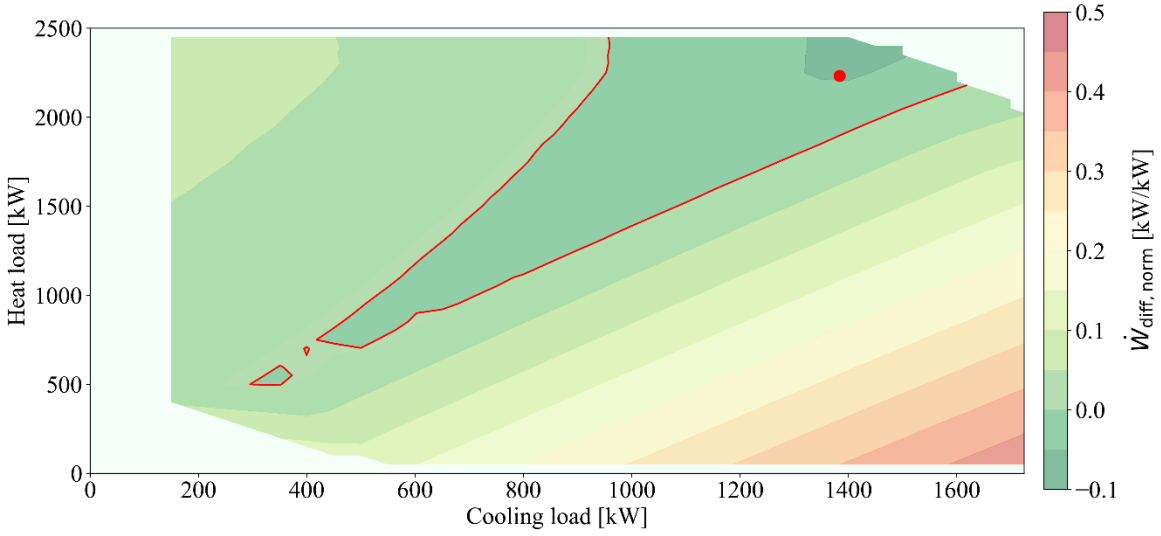


Figure 4: Difference in compressor power of the HPS compared to the separate systems at 20 °C ambient temperature.

From the contour plot in Figure 4 we observe values of $\dot{W}_{\text{diff,norm}}$ between -9.8 % and +47.1 %. The result may be divided into three cases:

- **Heat and cooling load is balanced according to design point:** The efficiency of HPS is higher as shown by the dark green area. $\dot{W}_{\text{diff}}$ is from 0 % to 9.8 % lower for the HPS than for the reference system in this area, with the highest values close to the design point. The area is a wedge shape (outlined with red) spanning from the design point towards the origin. This is as expected since the HPS will operate at similar ratios between the heating and cooling load in this region with minimal usage of the heat exchangers with ambient air.
- **Heat load exceeds excess heat from the cooling system:** The HPS is less efficient than the reference system by up to 10 %. This is due to the expelling of excess cooling which does not significantly affect the power consumption of the HPS as seen in Figure 3.
- **Cooling load offering more excess heat then the HP system requires:** The HPS is less efficient than the reference system by up to 47.1 %. The HPS is penalised comparatively more from an increased cooling load, especially for low heat loads. This is due to the high lift of the bottom cycle compared to the to the reference system.

This indicates, that the HPS will benefit from a high, and stable heat load, where the dark green area is the largest. At the same time, oversizing the HPS will lead to a smaller benefit as the area with negative $\dot{W}_{\text{diff}}$ gets relatively slimmer. A lower cooling load than expected will not hurt the performance as much.

Figure 3-4 show results for constant ambient temperature. This is not the case during yearly operation. Therefore, the effect of varying the air temperatures on the HPS and the reference system was analysed. The performance was evaluated in terms of Lorenz efficiencies at the design point (a heat load of 2230 kW and a cooling load of 1380 kW). The results are shown in Figure 5 both as a function of the ambient temperature and the time of year.

The air temperature affects the two systems differently. The Lorenz efficiency of the HPS (blue) is close to constant for varying air temperatures. This is expected since only the possible subcooling of the bottom cycle is affected by the ambient temperature. η_{Lor} increases for lower temperatures, since a higher subcooling can be obtained. The HTHP and refrigeration cycle (orange) experience a larger effect from the air temperature. η_{Lor} increase with higher temperatures. Higher temperatures result in a larger temperature lift of the refrigeration cycle while the HTHP will overcome a smaller temperature lift. The same is seen through the year (Figure 5 to the right), where the HTHP and refrigeration cycle have a higher η_{Lor} in the summer months, while the efficiency of the HPS is close to constant.

The overall result is the same independent of the ambient temperature. The HPS has a higher η_{Lor} at the design point for every ambient temperature. The difference decreases from 6.24 %p for an ambient temperature of 0 °C to 3.99 %p at 21 °C. This is due to the ambient temperature getting closer to the temperature in the cascade HEX. The HPS has the advantage of being able to optimize the temperature between the two cycles which increases the η_{Lor}. This means that the difference in performance will be more pronounced during the colder months.

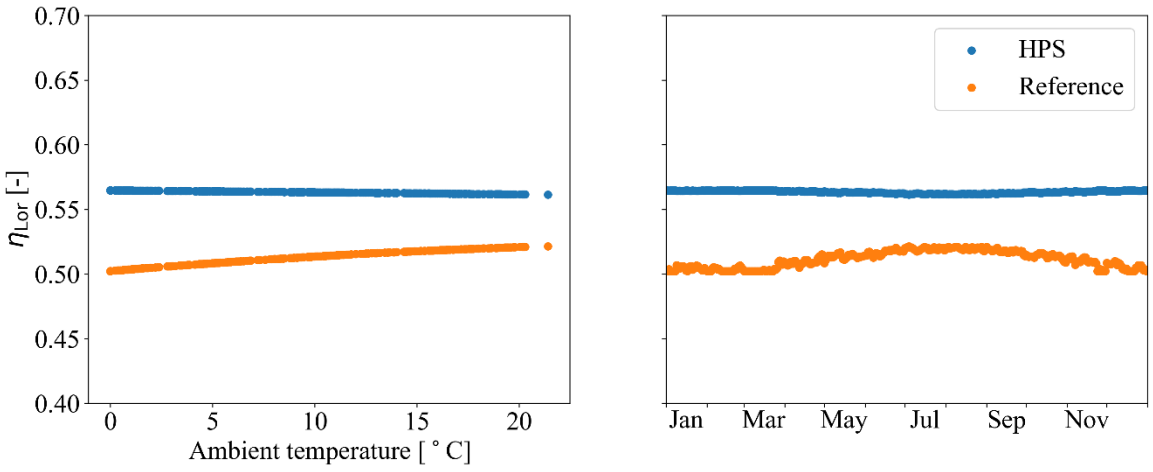


Figure 5: The Lorenz efficiency of the systems at the design loads for varying ambient temperatures (left) and for each of the days of the year of 2021 (right).

In Figure 6 the compressor power of the HPS (blue) is compared to the HTHP and refrigeration cycle (orange) throughout the year 2021. The top figure of Figure 6 shows the compressor power for every day for both solutions. The compressor power varies between 676 kW and 1348 kW for the separate systems and between 684 kW and 1282 kW for the HPS. The biggest differences are during July and August when the HPS has both the highest and the lowest compressor power.

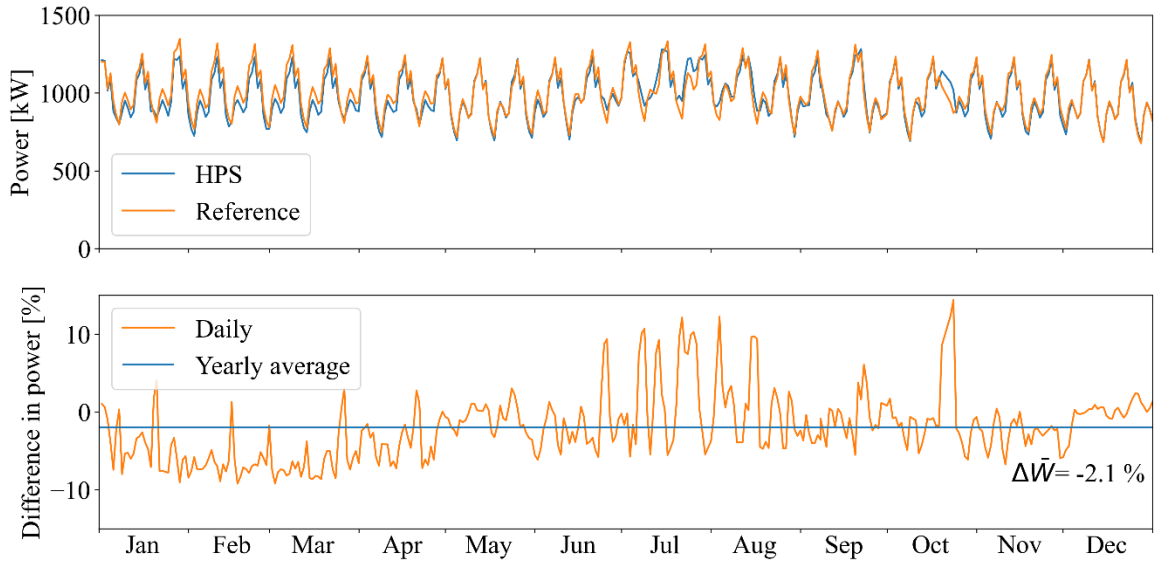


Figure 6: Compressor power of the HPS compared to the HTHP and refrigeration cycle throughout the year 2021. The top figure is the compressor power at every day, while the bottom figure shows the difference in the average power used by the compressors up til that date.

The bottom figure of Figure 6 shows the difference in the compressor power throughout the year. The difference is normalised with the compressor power of the HPS. The blue line indicates the average difference through the year which is 2.1 % in favour of the HPS. The difference in power varies between -9.2 % and 14.2 % being highest in August and the end of October while being lowest in February and March. This is expected as the ratio between the heating and the cooling demand is largest during the winter and smallest during the summer as seen in Figure 1. This yields operating points that are further away from the design point, which is in favour of the separate systems, as shown in Figure 4. Furthermore, the warmer temperatures during the summer months yield a higher η_{Lor} for the separate systems as seen in Figure 5.

4. Discussion

4.1. Alternative configurations of the HPS

The presented HPS is one potential configuration of a vapour compression cycle. Several other refrigerants and configurations could potentially supply the heating and cooling required by the processes. The work in [15]–[17] shows promising performance for heat pumps with hydrocarbons, water, or zeotropic mixtures as the refrigerant with improvements of up to 36 % compared to conventional solutions.

An alternative cycle that could be analysed was presented in [18] utilising two bottom cycles to produce hot and cold water and the top cycle to produce steam. The cycles were connected by a flooded cascade HEX, which additionally acted as a buffer tank. This buffering effect could potentially mitigate some of the penalties of operating away from the design point. The two bottom cycles will, however, introduce further energy demands to consider for a similar study as in this work. Another alternative is the inclusion of a back-up refrigeration cycle with air-cooled condensers or a condenser after the first pressure stage in the bottom of the HPS. This would grant additional cooling capacity with a temperature lift of the ammonia to the ambient temperature instead of the cascade HEX temperature. This will increase the COP following Equation 3 as $T_{\mathrm{sink,av}}$ will decrease.

4.2. Choice of design point

The choice of design point is not trivial and requires full knowledge of the future energy demands. Even when knowing this, it is not possible to choose a design point matching both the heating demand and the cooling demand. By choosing one, the other one is given by the energy balance and the cycle COP. This is in strong contrast to other HPS cycles like in [19] where a CO_2 refrigeration cycle produces space heating as a by-product and cooling as the main product. Thereby, the cooling demand will not define the operating conditions. If the average heating and cooling demand do not correspond to the balanced energy flows of the installed system, off-design conditions will inevitably lead to lower efficiencies for the specific case. In these cases, a HPS will not be suited to deliver the needed heating and cooling without auxiliary equipment. Therefore, more work is needed to determine the optimal design point of the HPS.

4.3. Practical challenges related to the modelled HPS and reference system

The modelled systems were based on a set of decisions that might affect the result. The superheating before all compressors is assumed to be 0.5 K which is normal for flooded evaporators but not for HEX's controlled using thermostatic expansion valves as depicted in in Figure 2. It is not obvious if changing the assumed superheat, will benefit the HPS or the reference system the most. However, the low superheat potentially favours the reference system as it has three evaporators being affected opposed to two for the HPS.

Additionally, the minimum condensing temperature of 10 °C for the ammonia refrigeration cycle potentially implies a two small temperature lift for a 2-stage system. A single-stage cycle could be needed lowering the COP of the cycle, which would favour the HPS. Furthermore, alternative isentropic efficiencies or pinch temperature differences could impact the result.

4.4. Fluctuating heating and cooling demand profiles and potential for the inclusion of storages

As indicated by Figure 4 and 6, the varying demands for heating and cooling substantially lowered the efficiency of the HPS. This was also mentioned by [5], who experienced difficulty delivering the correct amount of heating and cooling simultaneously. The same problem is not addressed by [7], as the HPS only provided 80 % of the heat demand with several backup systems and built-in hot water tanks mitigating the problem, but not leading to full electrification.

An assumption for this study was that all daily fluctuations in the heating and cooling demand profiles could be covered by an already installed storage or buffer capacity. Expanding this assumption with larger storage capacities could mitigate the bi-weekly variations in the heating demand of this case. However, this will require further investigation. Nevertheless, even an infinitely large storage cannot solve this problem if the average heating and cooling demand on a seasonal timescale does fit with the energy balance of the installed system.

4.5. Economic potential

This study showed a 2.1 % decrease in power consumption over a year of operation. This margin indicated that the lower OPEX should not be the only reason for choosing a HPS as the only heating and cooling utility for all industrial cases. It should be noted that fan power has been neglected which will be biggest for the reference system. The operation of large air HEXs could also lead to increased maintenance cost and down-time from required defrosting. Nevertheless, as the HPS had fewer total components than the separate systems, the capital cost could be lower, leading to a better pay-back time on the initial investment. However, the capital cost of the system was shown to be neglectable in [21 - 22] in comparison to the OPEX for high operating hours such as industrial breweries. Therefore, the best solution would allow the HPS to operate at design conditions most of the time while having flexible, auxiliary utilities to cover the variations in demand maximizing the overall efficiency even at higher initial investments.

5. Conclusion

Industrial processes require substantial amounts of energy to cover their heating- and cooling demands. Increased use of electricity in the industry will be necessary for a reduction in the emitted greenhouse gases emitted by the current equipment.

This study evaluated the potential of using a HPS for simultaneously producing hot water at 145 °C and cold water at 2 °C with higher efficiency than a separate HTHP and a refrigeration cycle. The HPS was evaluated by using a case of a Danish brewery with continuous energy demands.

The results showed that the electricity consumption of the HPS decreased by 9.8 % at design conditions compared to a separate heat pump and a refrigeration system. However, the separate systems perform better when the ratio between heating and cooling demand differs substantially from the design point. This trend is more pronounced for low heat loads and high cooling loads. The ambient temperature shows a neglectable effect on the combined system while separate utilities vary by 6 % in Lorenz efficiency.

A yearly quasi-steady simulation showed a 2.1 % lower electricity consumption for the HPS indicating neglectable benefits in terms of operational costs. However, the HPS may present a lower initial investment compared to the supply of heating and cooling individually.

Acknowledgements

This research project was funded by The Energy Technology Development and Demonstration Programme (EUDP), under the project title: “SuPrHeat - Sustainable process heating with high-temperature heat pumps using NatRefs”. The authors are grateful of the financial support from the EUDP and the project partners of SuPrHeat.

Nomenclature

Description (unit)	Symbol	Subscripts and superscripts	Symbol
Heat exchanger area (m^2)	A	Average	av
Coefficient of Performance (-)	COP	Combined heating and cooling	comb
Enthalpy (J/kg·K)	h	Cooling	cool
Logarithmic mean temperature difference (K)	LMTD	Design conditions	des
Efficiency (-)	η	Difference	diff
Heat flow (W)	$\dot{Q}$	Heating	heat
Temperature (K)	T	Into heat exchanger	in
Temperature difference (K)	ΔT	Isentropic	is
Overall heat transfer coefficient ($W/m^2 \cdot K$)	U	Indices	k
Compressor power (W)	$\dot{W}$	Lorenz	Lor
		Normalized	norm
		Out of heat exchanger	out
		Superheating	SH
		Heat sink	sink
		Heat source	source
		Heat pump for simultaneous heating and cooling	HPS
		High temperature heat pump	HTHP
		Pinch point	Pinch
		Reference cycle	ref
		Refrigeration cycle	refri

References

[1] R. de Boer *et al.*, “Strengthening Industrial Heat Pump Innovation: Decarbonizing Industrial Heat,” *Whitepaper*, p. 32, 2020, [Online]. Available: https://www.sintef.no/globalassets/sintef-energi/industrial-heat-pump-whitepaper/2020-07-10-whitepaper-ihp-a4.pdf.

[2] IEA Heat Pump Centre, “Annex 35: Application of Industrial Heat Pumps - Final Report (No. Report HPP-AN35-1&2),” Borås, Sweden, 2014.

[3] R. M. Jakobs and C. Stadtländer, *Final Report Annex 48: Industrial Heat Pumps, Second Phase*, no.

October. 2020.
[4] B. Zühlsdorf, “Annex 58: High-Temperature Heat Pumps,” 2021. https://heatpumpingtechnologies.org/annex58/# (accessed Apr. 18, 2022).
[5] X. D. ZHENG and X. C. LIN, “The Economics of Industrial Heat Pump Systems for Simultaneously Cooling and Heating,” *Heat Pumps*, pp. 327–335, Jan. 1990, doi: 10.1016/B978-0-08-040193-5.50043-2.
[6] P. Byrne and R. Ghoubali, “Exergy analysis of heat pumps for simultaneous heating and cooling,” *Appl. Therm. Eng.*, vol. 149, pp. 414–424, Feb. 2019, doi: 10.1016/j.applthermaleng.2018.12.069.
[7] C. Schlemminger, M. Bantle, and S. Jenssen, “Industrial high temperature heat pump for simultaneous production of ice-water and process-heat,” 2022, doi: 10.18462/iir.gl2022.166.
[8] C. Arpagaus, F. Bless, M. Uhlmann, J. Schiffmann, and S. S. Bertsch, “High temperature heat pumps: Market overview, state of the art, research status, refrigerants, and application potentials,” *Energy*, vol. 152, pp. 985–1010, 2018, doi: 10.1016/j.energy.2018.03.166.
[9] F. Bühler, B. Zühlsdorf, T. Van Nguyen, and B. Elmegaard, “A comparative assessment of electrification strategies for industrial sites: Case of milk powder production,” *Appl. Energy*, vol. 250, no. May, pp. 1383–1401, 2019, doi: 10.1016/j.apenergy.2019.05.071.
[10] F. P. Incropera, *Fundamentals of Heat and Mass Transfer*, 8th ed. John Wiley & Sons, Inc., 2017.
[11] G. Van Rossum and F. L. Drake, “Python 3 Reference Manual.” Scotts Valley, California, 2009.
[12] I. Bell, J. Wronski, S. Quoilin, and V. Lemort, “Pure and Pseudo-pure Fluid Thermophysical Property Evaluation and the Open-Source Thermophysical Property Library CoolProp,” *Ind. Eng. Chem. Res.*, no. 53, pp. 2498–2508, 2014, doi: https://doi.org/10.1021/ie4033999.
[13] P. Virtanen, R. Gommers, and T. E. Oliphant, “SciPy 1.0: fundamental algorithms for scientific computing in Python,” *Nat. Methods*, vol. 17, no. 3, pp. 261–272, Mar. 2020, doi: 10.1038/s41592-019-0686-2.
[14] W. McKinney, “Data structures for statistical computing in python,” in *Proceedings of the 9th Python in Science Conference*, 2010, pp. 51–56, doi: 10.25080/Majora-92bf1922-00a.
[15] M. P. Andersen, B. Zühlsdorf, W. B. Markussen, J. K. Jensen, J. L. Poulsen, and B. Elmegaard, “Thermodynamic analysis of vapour compression heat pump cycles for high-temperature applications,” 2022, doi: 10.18462/iir.gl2022.099.
[16] B. Zühlsdorf, J. K. Jensen, and B. Elmegaard, “Heat pump working fluid selection—economic and thermodynamic comparison of criteria and boundary conditions,” *Int. J. Refrig.*, vol. 98, pp. 500–513, 2019, doi: 10.1016/j.ijrefrig.2018.11.034.
[17] J. K. Jensen, T. Ommen, L. Reinholdt, W. B. Markussen, and B. Elmegaard, “Heat pump COP, part 2: Generalized COP estimation of heat pump processes,” *Refrig. Sci. Technol.*, vol. 2018-June, pp. 1255–1264, 2018, doi: 10.18462/iir.gl.2018.1386.
[18] B. Zühlsdorf, F. Bühler, M. Bantle, and B. Elmegaard, “Analysis of technologies and potentials for heat pump-based process heat supply above 150 °C,” *Energy Convers. Manag. X*, vol. 2, no. January, p. 100011, 2019, doi: 10.1016/j.ecmx.2019.100011.
[19] G. Maouris, E. J. Sarabia Escriva, S. Acha, N. Shah, and C. N. Markides, “CO2 refrigeration system heat recovery and thermal storage modelling for space heating provision in supermarkets: An integrated approach,” *Appl. Energy*, vol. 264, p. 114722, Apr. 2020, doi: 10.1016/j.apenergy.2020.114722.
[20] M. P. Andersen *et al.*, “Economic potential of lowering supply temperatures when using industrial heat pumps,” 2022. In *Proceedings of ECOS 2022 - The 35th International Conference on Efficiency, Cost, Optimization, Simulation and Environmental Impact of Energy Systems 2022*. Copenhagen, Denmark, paper #322.
[21] G. Kosmadakis, C. Arpagaus, P. Neofytou, and S. Bertsch, “Techno-economic analysis of high-temperature heat pumps with low-global warming potential refrigerants for upgrading waste heat up to 150 °C,” *Energy Convers. Manag.*, vol. 226, no. July, p. 113488, 2020, doi: 10.1016/j.enconman.2020.113488.

14th IEA Heat Pump Conference
15-18 May 2023, Chicago, Illinois

New Perspectives for the Application of large-scale Heat Pumps

Christian Huettl[a*], Norbert Wenn[a], Juergen Voss[b], Florian Reissner[c], Jochen Schaefer[a]

[a] *Siemens Energy, Schuckertstrasse 3, 91058 Erlangen, Germany*
[b] *Siemens Energy, Rheinstrasse 100, 45478 Muelheim, Germany*
[c] *Siemens Technology, Schuckertstrasse 2, 91058 Erlangen, Germany*

Abstract

Large-scale heat pumps are an efficient and cost-effective solution for the generation of industrial heat and district heating. They take up thermal energy from a low-temperature heat source (e.g. waste heat from industries or ambient heat from sea, lakes, rivers, or geothermal sources) and supply thermal energy at higher temperature to a heat sink.

During the next years, heat supply will be electrified and decarbonized step by step, due to the gradual replacement of fossil-fired heat supply by natural gas, coal, and oil. As the electricity generation will be decarbonized further in the upcoming years, more and more renewable electric energy will be available to achieve a climate neutral heat supply.

Siemens Energy has long-term experiences with large-scale heat pump solutions up to 95°C and 30 MW of thermal output per heat pump unit. Several industrial segments need heat pumps with even higher temperatures and higher thermal output. Thus, new heat pump solutions and an enhanced heat pump portfolio to higher temperatures (up to 150°C) and larger thermal output (up to 70 MW in one unit) are being developed. Low pressure steam requirements can be met by these high temperature heat pumps. By adding an additional steam compressor to the high temperature heat pump, even higher steam temperatures and pressures can be achieved (up to 270°C and 55 bara).

Heat pump solutions and possible applications for industrial hot water, steam supply and district heating are presented in this paper. Furthermore, ongoing and future projects of large-scale heat pump installations are shown.

© HPC2023.

Keywords: High temperature heat pump; Industrial heat pump; Industrial heat supply; Steam generation

1. Introduction

According to the International Energy Agency (IEA), heat is the world's largest energy end use, accounting for almost half of global final energy consumption in 2021. Industrial processes are responsible for 51% of the energy consumed for heat, while another 46% is consumed in buildings for space and water heating. Along with this heat consumption comes a significant amount of CO_2 emissions. Heat consumption and its related supply structure contributed to more than 40% of global energy-related CO_2 emissions in 2020 [1].

Worldwide industrial heat consumption remains heavily fossil fuel dependent. The share of renewable heat for industrial heat stagnated over the last decade, see figure 1. The growth rate of the renewable share in the heating sector (building and industry) is anticipated to grow from 11% in 2020 to 13% in 2026. To achieve IEA's "Net Zero Emissions Scenario" (NZE), the renewable share would need to grow 2.5 times faster than currently anticipated [1].

* Corresponding author. *E-mail address:* christian.huettl@siemens-energy.com

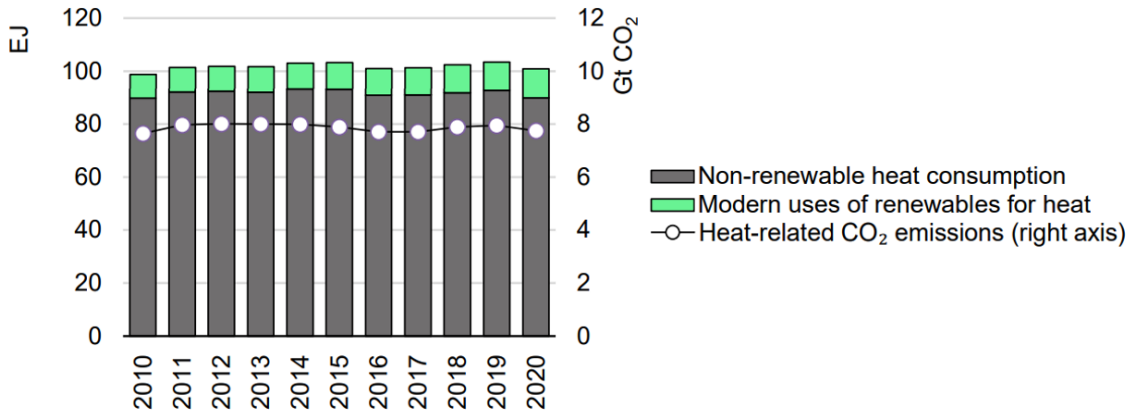


Fig. 1. Renewable and non-renewable heat consumption and heat-related CO_2 emissions in industry (world). Renewable heat covers bioenergy, solar thermal and geothermal energy, renewable electricity for heat, etc. reference [1]

There are several technologies that can supply renewable heat such as solar thermal, geothermal, synthetic climate-neutral fuels (e.g. hydrogen), biomass, and electricity-based systems like electric heaters and heat pumps. The applicability and economic viability of these different technologies depend on the application and its corresponding required temperature levels. For example, it is very efficient and economically viable to apply heat pumps for space and water heating in buildings due to the relative low temperature and easy access to heat sources for heat pumps such as ambient air. The IEA projects for the NZE that more than 50% of all buildings worldwide will be heated by heat pumps (approximately 1.8 billion units) in 2050 [2], see figure 2.

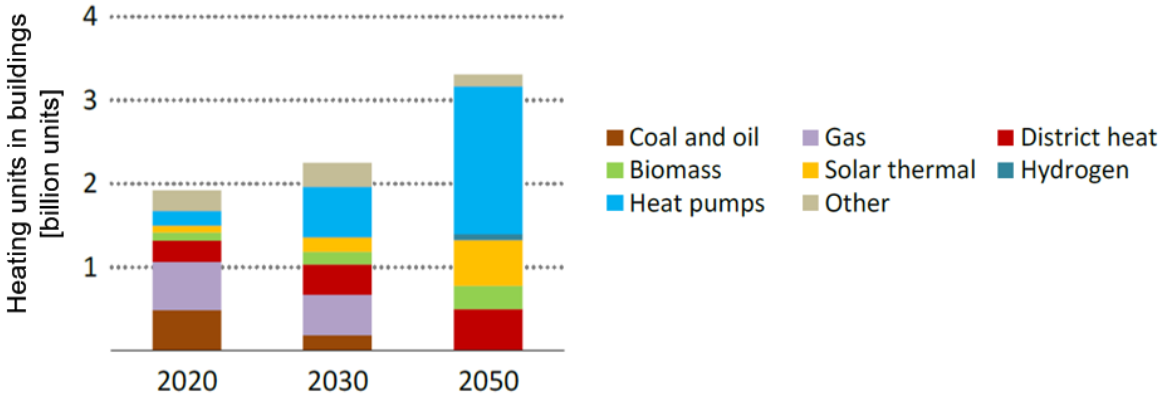


Fig. 2. Global building heating equipment stock by type in 2020 and projection in the NZE for 2030 and 2050 [2]

The industrial heating sector shows other requirements regarding the temperature level and energy density. Consequently, the projection of the IEA for the NZE shows a more diverse technology distribution for the heat demand up to 400 °C, see figure 3 [2]. Electricity-based technologies such as heat pumps and electric heaters have the highest share followed by biomass and hydrogen [2].

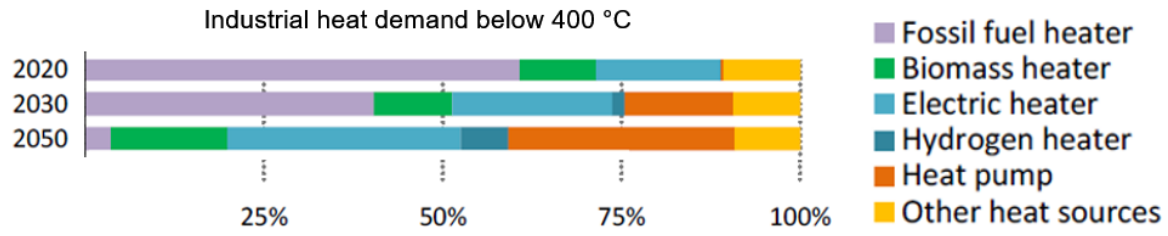


Fig. 3. Global share of heating technology for industries in 2020 and projection in the NZE for 2030 and 2050 [2]

Today, the share of heat pumps for industrial heating is insignificant and needs to grow very fast to meet the projections in 2030 and 2050. For that the IEA states that "around 500 MW of industrial heat pumps need to be installed every month over the next 30 years" [2]. It is a huge effort for all stakeholders like heat pump manufacturers, heat suppliers, and numerous industry branches to achieve such a growth worldwide.

There are already a few countries in which the number of applications of industrial heat pumps grew substantially in recent years. Figure 4 shows Denmark and Austria as an example [3, 4].

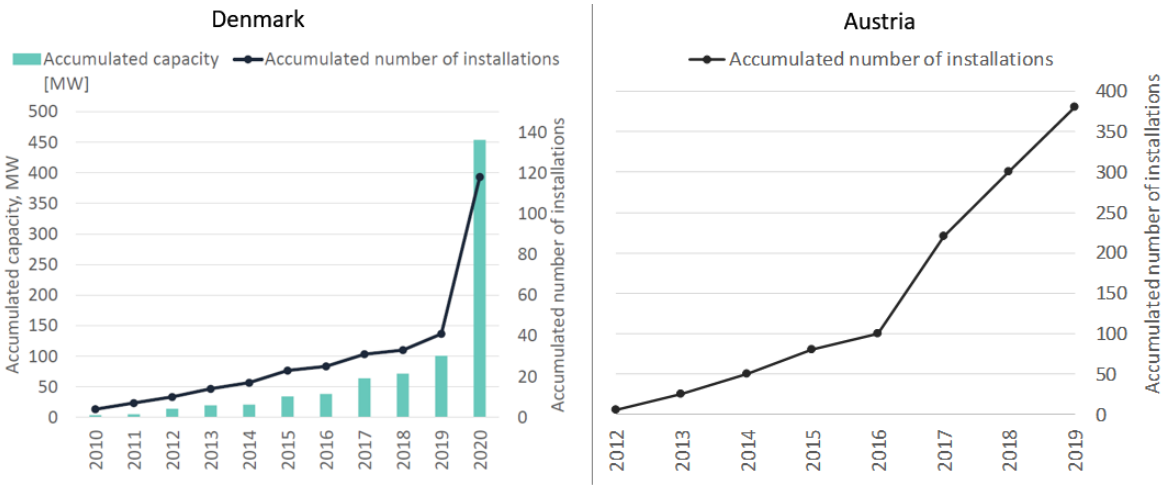


Fig. 4. Installed industrial heat pumps, left: Denmark accumulated capacity and accumulated number of installations; Right: Austria accumulated number of installations [3, 4]

2. Heat pump technologies for large scale heat supply at medium, high and very high temperatures

Industrial heat demand shows a large variety of required temperature levels depending on industry segment and its heat demanding processes [5]. It is important to distinguish heat pumps upon their achievable temperature level as the state of technology is very different depending on the temperature level. Within this paper the following nomenclature is used to categorize heat pumps upon their achievable temperature level:

- Medium temperature: below 100 °C
- High temperature: between 100 °C and 150 °C
- Very high temperature above 150 °C

2.1. Medium temperature heat pumps (MTHP)

Medium temperature heat pumps (MTHP) are a well-proven and widely implemented technology. There are numerous heat pump installations at large scale (single- and double-digit Megawatt range of thermal

output). These large-scale MTHP are mostly applied for district heating, with the first ones installed in the 1980s. There are several heat pump installations that operate since then for over four decades already. For example, Averfalk et al. [6] and David [7] list about 150 heat pump installations for district heating in 13 countries with an overall installed thermal output of approximately 1.5 GW.

Among them are 50 MTHP units of Siemens Energy that were installed in the 1980s and 1990s. 40 units of them are still in operation today. These units have a thermal output of 5 to 30 MW and an overall combined thermal output of 850 MW [8]. New large-scale MTHP are being installed e.g., for district heating in the city of Mannheim in Germany with up to 20 MW thermal output. This heat pump installation will be commissioned end of 2023 and is described in detail in section 3.

2.2. High temperature heat pumps (HTHP)

Over the last decade, the development of HTHP technology gained momentum. There are several technological developments of research institutes and companies, which increased the applicable temperature range of heat pumps to 150 °C [9-12].

Some of these developments led to new heat pump products and solutions. First large-scale pilot plants for full-scale operation are being commissioned. A HTHP in the city of Berlin in Germany with 8 MW thermal output and temperatures up to 120 °C is installed. This heat pump installation and its application is described in detail in section 3.

2.3. Very high temperature heat pumps (VHTHP)

There are several heat pump concepts with applicable temperature levels above 150 °C. It is important to distinguish these concepts.

There is the well-established technology of mechanical vapor recompression. It is a very efficient method of waste heat recovery under the requirement that the heat source is steam and can directly be recompressed. It is not possible to use this technology by an indirect heat transfer of other media, which closed loop heat pumps do. Some manufacturers call their mechanical vapor recompression product “heat pump” anyway [12]. Due to the previous mentioned requirement and thus widely limited application potential, mechanical vapor recompression as single technology alone is not further considered in this paper.

Some VHTHP concepts use Brayton or Joule cycles in which the working fluid shows no phase change and thus has a sensible heat transfer to the heat source and sink. There are some technological developments with such cycles [12]. However, the largest application potential at temperature levels above 150 °C in the industry is for steam generation. Steam generation requires isothermal heat transfer as liquid water evaporates at a constant temperature to become steam. Thus, a sensible heat transfer is not efficient to generate steam. Consequently, Brayton or Joule cycles are not considered further in this paper.

VHTHP concepts that allow a predominantly isothermal heat transfer to the heat sink and thus are suitable for e.g. steam generation are reverse Rankine cycles. Recently published concepts for large-scale that are currently in technological development consist of one closed loop heat pump cycle combined with a steam compressor. Siemens Energy has developed several of such concepts for applications in the refinery, paper and chemical industry. One of these concepts is described in detail in section 3. A first pilot plant in full scale operation for steam generation in the industry is anticipated to be commissioned in the coming years.

3. Large-scale heat pump applications at medium, high and very high temperatures

Most existing urban district heating networks still operate on a maximum required temperature typically between 90 and 130 °C [13]. Consequently, most district heating applications with heat pumps can be realized by using MTHP or HTHP under the conditions that a suitable heat source is present. Existing MTHP, for example, use sea water, lake water, river water, sewage water or industrial waste heat as heat source [7].

Industrial heat demand shows a much broader temperature range than district heating. Figure 5 shows the industrial final energy demand end-use of the 28 European Union countries in the year 2015 by temperature [14].

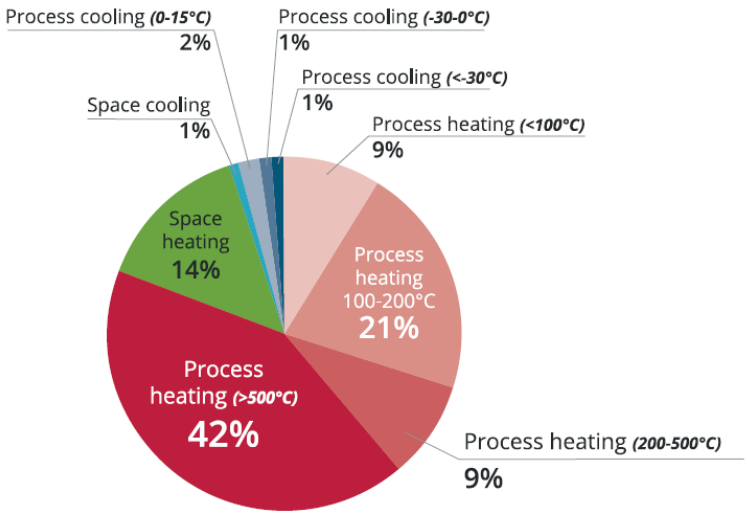


Fig. 5. Industrial final energy demand end-use of the 28 European Union countries in the year 2015 by temperature [14]

Currently developed VHTHP and further anticipated mid-term developments of heat pump technology do not allow to cover the whole temperature range of industrial heat demand. Space heating and process heating below 100 °C can be supplied by MTHP technology. Process heating between 100 and 200 °C can be supplied by HTHP and VHTHP technology. Process heating above 200°C can be partially supplied by VHTHP. This makes up a share that can be supplied by heat pumps of approximately half of the industrial heat demand when considering only the supply temperature. It is important to note that these heat pumps always require a suitable heat source. The higher the heat supply temperature the more challenging it is to identify a suitable heat source that allows an economically viable heat pump operation.

In the following, applications of MTHP, HTHP and VHTHP will be shown. Some of them are existing installations that are commissioned in 2022 or will be commissioned in 2023 (section 3.1). Others are concepts of applications that are very promising to be realized in pilot plants in the coming years (section 3.2).

3.1. Large-scale MTHP and HTHP for district heating

3.1.1. Large-scale MTHP for district heating, existing installation, Mannheim, Germany

Siemens Energy has started building a new large-scale heat pump installation in April 2022 in Germany in the city of Mannheim (under construction as of 16th February 2023). It is built for the utility MVV (Mannheimer Versorgungs- und Verkehrsgesellschaft) next to the power plant “Grosskraftwerk Mannheim”. This heat pump is part of the “Living Lab” for Energy Transition with the title “Large-scale heat pumps in district heating networks”. It is a funded program of the German Federal Ministry for Economic Affairs and Climate Action.

This heat pump bases on a reverse Rankine closed loop cycle with refrigerant R1234ze(E). Figure 6 shows the basic cycle configuration of this heat pump. This heat pumps uses the water of the river Rhine as heat source. The Rhine water has a temperature of about 5 to 25 °C depending on the season. The heat source is used to evaporate and superheat the refrigerant in the evaporator. A two-stage centrifugal compressor driven by an electric motor sucks the refrigerant and discharges it at higher pressure and temperature to the condenser. In the condenser and subcooler, heat is transferred from the refrigerant to the district heating water. The heat pump supplies up to 20 MW of thermal output to the district heating network at temperatures up to 99 °C. The expected average COP for the overall system including all kinds of losses (thermal, electrical, mechanical, pressure and so on) is 2.7. After the subcooler, the cycle has two expansion stages. There is a flash tank in between the stages. The part of the refrigerant flow, which is in vapor phase in the flash tank, is fed directly to the second compressor stage. This increases the overall cycle efficiency. Figure 7 shows a model of the heat pump type used for this heat pump installation.

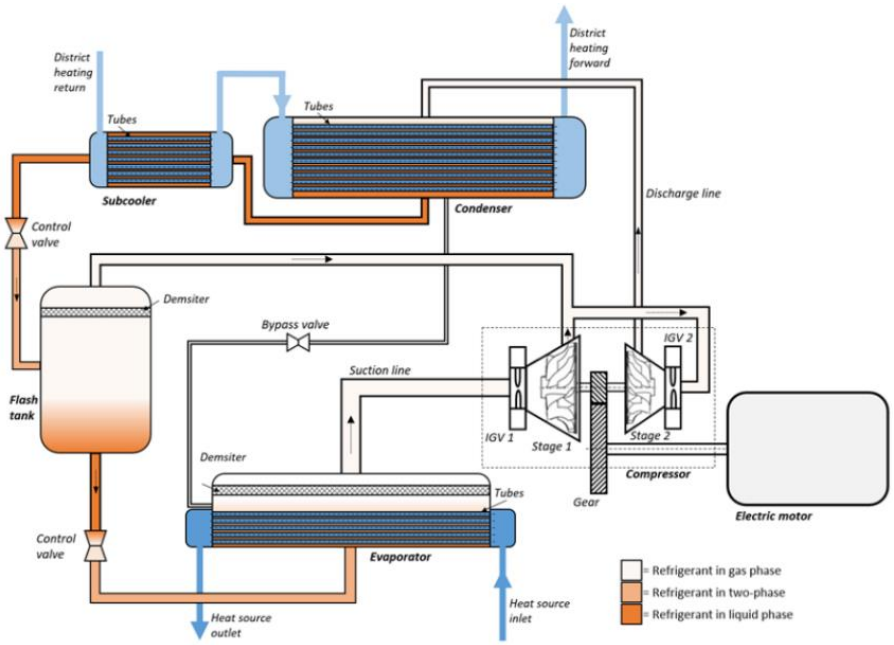


Fig. 6. Basic cycle configuration of MTHP for utility MVV in Mannheim, Germany



Fig. 7. Model of MTHP type used for utility MVV in Mannheim, Germany

It is expected that this heat pump supplies heat to approximately 3,500 households and will save around 10,000 metric tons of CO_2 emissions per year.

3.1.2. Large-scale HTHP for district heating, existing installation, Berlin, Germany

Siemens Energy started building a new large-scale heat pump installation at the end of 2021 in Germany in the city of Berlin (construction finished, under commissioning as of 16th February 2023). It is built for the utility Vattenfall within their existing site chiller plant ("Kaeltezentrale"), which supplies cold water to a district cooling grid in the center of Berlin. This heat pump project is funded by the German Federal Ministry for Economic Affairs and Climate Action within the program "EnEff:Waerme".

At Vattenfall's site, there are several compression chillers that produce waste heat. This waste heat is currently re-cooled by wet cooling towers at the building's roof. The heat pump is integrated in a way, that the waste heat can be recovered and utilized for district heating. Figure 8 shows the integration of the heat pump.

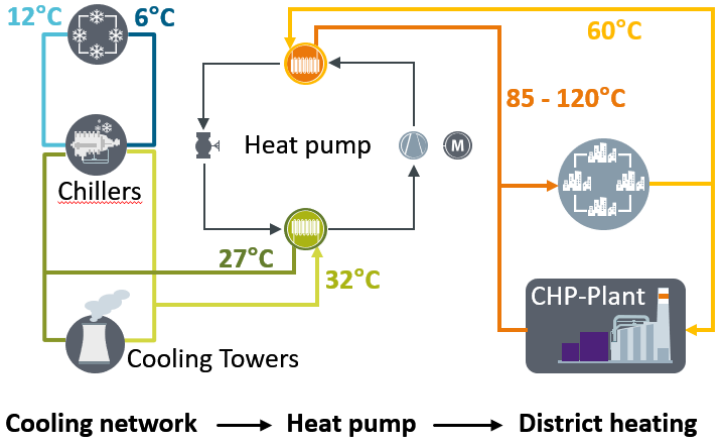


Fig. 8. Integration of HTHP at utility Vattenfall in Berlin, Germany, CHP stands for combined heat and power

The evaporator of the heat pump cools the waste heat of the chillers from 32 to 27 °C and thus recovers this waste heat. The refrigerant R1233zd(E) evaporates and superheats by the heat transfer from the waste heat in the evaporator. A single-shaft centrifugal compressor, see figure 9, sucks the refrigerant and discharges it at higher pressure to the condenser. In the condenser, heat is transferred from the refrigerant to the district heating water. The district heating water enters with about 60 °C and is heated up to between 85 and 120 °C depending on district heating network requirements.



Fig. 9. Picture of the centrifugal compressor of the heat pump for utility Vattenfall in Berlin, Germany after delivery to site

The heat pump has a thermal output of 8 MW and delivers about 55 GWh of district heat per year at an expected average COP of 3 for the overall system including all kinds of losses (thermal, electrical, mechanical, pressure and so on). It is expected that approximately 6,500 metric tons of CO_2 emissions will be saved per year. Another advantage is that less cooling water for the cooling towers will be needed, i.e. around 120,000 m^3 of cooling water will be saved per year.

3.2. Large-scale VHTHP for steam production in industry

Steam is a universal heat carrier for industrial plants with heat demand e.g. in chemical, refinery and paper industries. Most plants with heat demand in these industries use steam as heat carrier. Usually there is a steam distribution system that supplies the heat to the various production plants. The steam distribution system has a certain pressure level or consists of different pressure levels enabling the heat supply at different temperature levels.

The pressure levels, amount of steam demand per level and time-dependent demand per level varies greatly among different industrial steam distribution systems. It is crucial for the heat pump technology that steam can be supplied to those different systems in a very flexible way.

Siemens Energy has developed a flexible heat pump system where a closed loop heat pump cycle generates steam with pressures up to 3.5 bara. If a high superheat is required at this pressure, the heat pump can be combined with an electric superheater. For even higher steam pressures, the heat pump can be combined with a steam compressor.

The combination of heat pump with an electric superheater is described exemplary by an application developed with a company from the paper industry (see section 3.2.1). The combination of heat pump with a steam compressor is described by an application developed with a company from the chemical industry (see section 3.2.2).

3.2.1. Large-scale VHTHP for steam generation in fiber industry

The following application example has been developed together with a company from the paper industry. The company operates an industrial site with several waste heat flows that are not recovered currently. At the same time, steam at a pressure of 3.3 bara and at a temperature of 157 °C is required, which is currently supplied by natural gas boilers. Figure 10 shows the heat pump integration concept into the industrial site's heat sources and heat sink.

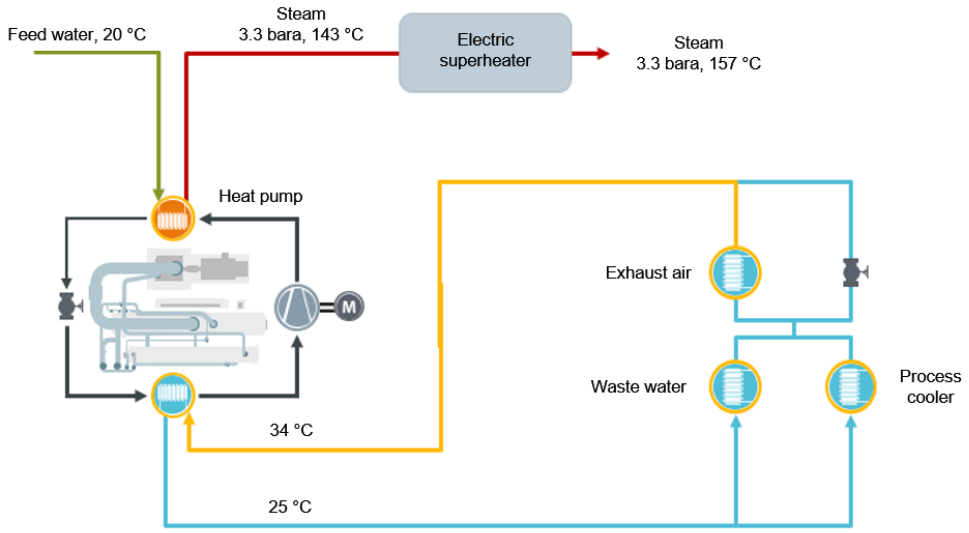


Fig. 10. VHTHP integration concept, combination of heat pump and electric superheater, application in paper industry

Three different heat sources (process cooler, waste water and exhaust air) are combined and recovered. The heat from the heat sources is transferred to the refrigerant in the evaporator. A centrifugal compressor, driven by an electric motor, sucks and compresses the refrigerant to a higher pressure. The refrigerant enters the condenser and transfers heat to the feed water (heat sink). The feed water enters the condenser with 20 °C and is heated up and evaporated to steam at 3.3 bara and 143 °C. The electric superheater increases the temperature of the steam to the required temperature at 157 °C. The expected average COP for the overall system including all kinds of losses (thermal, electrical, mechanical, pressure and so on) is 1.9.

This heat pump integration is one example of many different possibilities with this combination of closed loop heat pump cycle and electric superheater. As long as there is a sufficient heat source, the heat pump can supply steam at pressure from 1 bara to 3.5 bara and the electric superheater can be flexibly adapted to the required steam temperature.

3.2.2. Large-scale VHTHP for steam generation in chemical industry

The following application example has been developed together with a company from the chemical industry. The company operates an industrial site at which process water is available as heat source, which is currently not recovered. At the same time, steam at a pressure of 7 bara and at a temperature of 195 °C is required, which is currently supplied by natural gas boilers. Figure 11 shows the heat pump integration concept into the industrial site's heat sources and heat sink.

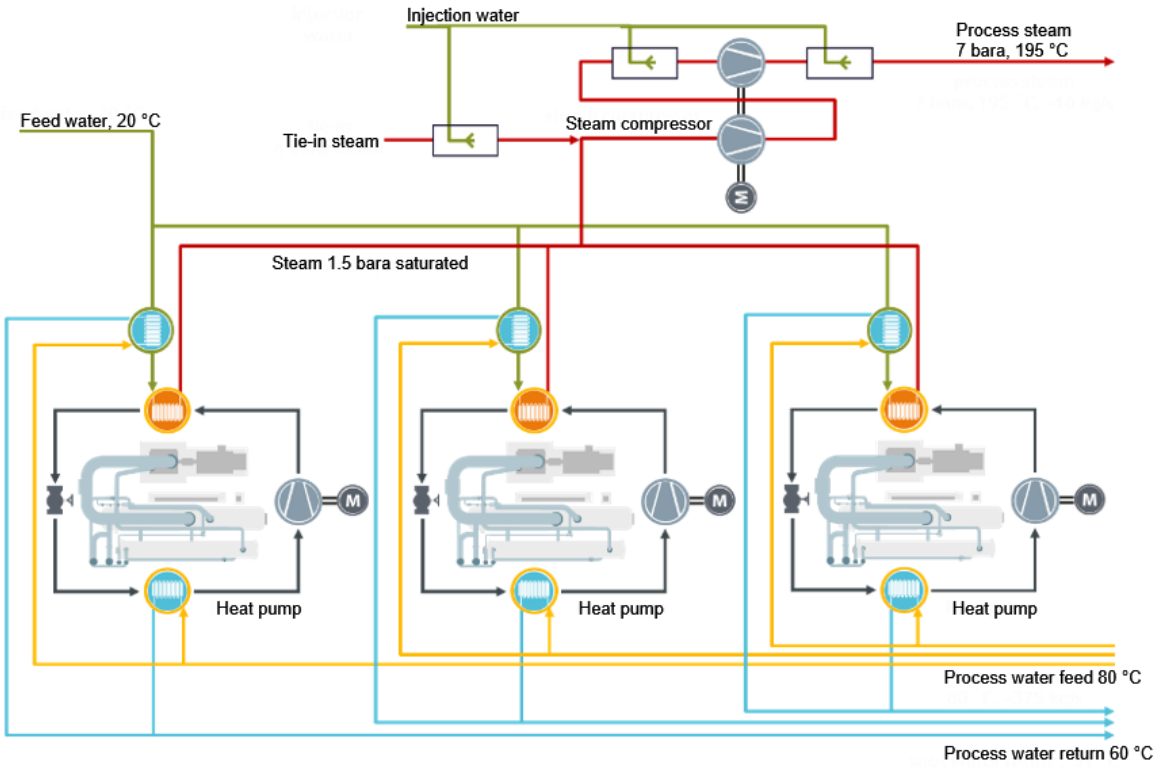


Fig. 11. VHTHP integration concept, combination of heat pump and steam compressor, application in chemical industry

The concept consists of three heat pumps in parallel that are identical in construction. There are several reasons for the parallelization like redundancy and part-load capability.

The heat source (process water) is recovered by cooling it from 80 °C to 60 °C in the evaporators of the heat pumps and partly in the pre-heaters of the heat sink. The heat from the heat source in the evaporators is transferred to the refrigerant to evaporate and superheat it. Centrifugal compressors, driven by electric motors, suck and compress the refrigerant to a higher pressure. The refrigerant enters the condensers and transfers heat to the feed water (heat sink). At first, the feed water is preheated by the heat sources and then enters the condensers. In the condensers, the feed water is heated up and evaporated to saturated steam at 1.5 bara. A two-stage steam compressor sucks the steam and increases the pressure to 7 bara in two stages. There are water injections before, between and after the stages to decrease the superheat. After the last stage, the required pressure of 7 bara and temperature of 195 °C is reached. The expected average COP for the overall system including all kinds of losses (thermal, electrical, mechanical, pressure and so on) is 2.8.

This heat pump integration is one example of many different possibilities with this combination of closed loop heat pump cycle and steam compressor. As long as there is a sufficient heat source, the heat pump can supply steam at a pressure of 1.5 bara and the steam compressor and water injection system can be flexibly adapted to the required steam pressure and temperature.

3.3. Large-scale HTHP and VHTHP integrated with other energy supply systems

The transition of the heat sector from fossil fuel-based heat supply to a climate neutral heat supply requires the installation of new and adapted heat supply units in industry and for district heating. There will be a large variety of different technologies for the heat sector. In the following two heat supply systems are described that can be integrated with heat pumps to increase the overall efficiency and are anticipated to show a high market share in the future.

3.3.1. Hydrogen production by thermally integrated Electrolyzer

Hydrogen will play a major role in future climate neutral energy supply systems. Hydrogen can be produced by electrolysis in electrolyzers. The IEA “Net Zero Emission” scenario projects that in 2030 there will be 850 GW (electric power input) and in 2045 there will be 3 TW (electric power input) of electrolyzers be installed [2].

The production of hydrogen in Electrolyzers also generates waste heat. This waste heat can be recovered and upgraded in its temperature level by heat pumps. Figure 12 shows the integration of a heat pump for steam generation.

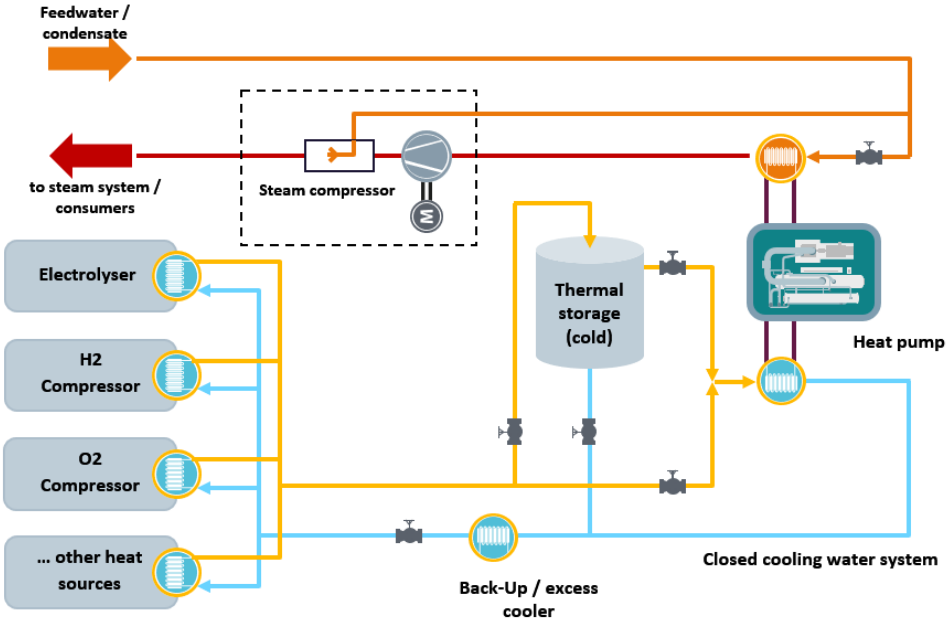


Fig. 12. Heat pump integration concept into Electrolyzer system

The heat pump can recover waste heat from various heat sources like electrolyzer, hydrogen compressor, oxygen compressor and other heat sources. A cold thermal storage that buffers the heat from the heat sources can be integrated if the electrolyzer operation is fluctuating strongly.

The waste heat is typically in the range of 35 to 50 °C. The heat pump lifts the temperature level to supply heat to a heat sink. The heat sink can be hot water or, as in figure 12 shown, steam. For steam at 8 bara and 190 °C, the expected average COP for the overall system including all kinds of losses (thermal, electrical, mechanical, pressure and so on) is 2.1.

Combinations of heat pumps and electrolyzers are being developed together with companies from different industrial branches.

3.3.2. Heat supply by exhaust gas condensation for natural gas / hydrogen fired boilers and gas turbines

Natural gas-fired boilers and gas turbines are well-established and widely used technologies. Exhaust gas condensation is often not applied at large-scale and especially when the temperature of the return flow of the heat sink is too high. The integration of a heat pump enables to further cool the exhaust gas and condense the water content in the exhaust gas. In doing so, a large amount of additional heat can be recovered from exhaust gas streams. Figure 13 shows a concept of combining a gas turbine with a heat pump.

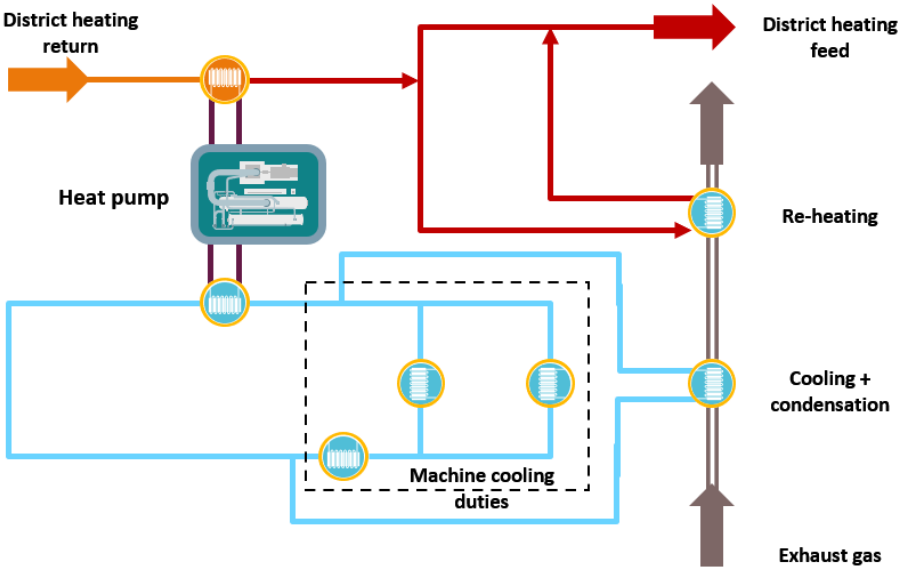


Fig. 13. Heat pump integration concept into gas turbine system

There is an intermediate loop (blue lines) that takes up the heat from the heat sources. The heat sources are various machine cooling duties like the generator of the gas turbine and the exhaust gas. The exhaust gas stream is cooled below the dew point of its containing moisture. The heat pump takes up the heat from the intermediate loop in the evaporator and supplies heat at a higher temperature for example for district heating. In some cases, a re-heating of the exhaust gas is required to ensure a stable flow through the chimney.

A typical case is the supply of district heating at 115 °C. The expected average COP for the overall system including all kinds of losses (thermal, electrical, mechanical, pressure and so on) is 2.2.

Combinations of heat pumps and gas turbines are being developed together with companies from different industrial branches and district heating network operators.

In the future it is anticipated that natural gas-fired boilers and turbines will be adapted to use hydrogen or a mixture of hydrogen and natural gas as fuel. The exhaust gas cooling and condensation also works with hydrogen or a mixture of hydrogen and natural gas as fuel.

4. Summary and conclusion

The transition of the heat sector towards climate neutral heat supply is a very challenging undertaking. District heating and industrial heat are still predominantly based on fossil fuel and thus contribute to a large portion of worldwide CO_2 emissions.

There are several technologies that will support the decarbonization of the heat sector. Large-scale heat pumps with supply temperatures below 100 °C for district heating are a well-established technology since decades. The share of these heat pumps for the overall heat supply needs to grow substantially. Siemens Energy has built 50 large-scale heat pumps in the past already and new heat pump installations are being built.

District heating also requires temperatures above 100 °C. There are numerous developing activities for products and solutions for large-scale high temperature (> 100 °C) heat pumps. Siemens Energy builds and commissions a first large-scale high temperature heat pump for district heating for the utility Vattenfall in Berlin with 8 MW of thermal output and supply temperatures of up to 120 °C. This pilot plant is an outstanding step in the advancement of heat pump technology.

Industrial heat supply requires even higher temperatures. Often, steam is used as heat carrier at industrial sites. There are numerous developing activities for products and solutions for large-scale very high temperature (> 150 °C) heat pumps. Several concepts have been developed for the steam generation with very high temperature heat pumps. These concepts can easily be adapted to meet various steam pressure and temperature requirements.

There are technologies that are anticipated to be largely present in future climate neutral energy supply systems, such as electrolyzers and hydrogen-fired gas turbines. Concepts have been elaborated to integrate heat pumps that recover the waste heat of these technologies.

It can be concluded that heat pumps will play a major role in future carbon neutral heat supply systems for district heating and industrial heat supply. More and more pilot plants of high temperature and very high temperature heat pumps will start its operation in full-scale in the coming years until these heat pump technologies are well-established and are widely accepted as standard technology by the involved stakeholders.

References

[1] International Energy Agency, Renewables, Analysis and forecast, Chapter 3 Renewable heat, December 2021.
[2] International Energy Agency, Net Zero by 2050, A Roadmap for the Global Energy Sector, Ocotober 2021.
[3] Danish Technological Institute, B. Zuehlsdorf, DKV/IZW webinar, March 2021
[4] Austrian Institute of Technology, V. Wilk, DKV/IZW webinar, March 2021
[5] Interstaatliche Hochschule für Technik Buchs, C. Arpagaus, Hochtemperatur-Wärmepumpen für industrielle Anwendung, 4. Internationaler Großwärmepumpen Kongress, Zurich, May 2019.
[6] H. Averfalk, P. Ingvarsson, U. Persson, M. Gong, S. Werner, Large heat pumps in Swedish district heating systems, Renewable and Sustainable Energy Reviews 79 (2017) 1275-1284.
[7] A. David, Large heat pumps in European district heating systems, 22nd International Trade Fair and Congress, Frankfurt, April 2016.
[8] Siemens Energy, C. Huettl, F. Reissner, N. Wenn, J. Voss, New perspectives for industrial heat pumps, Chillventa Congress, Nuremberg, October 2022
[9] Austrian Institute of Technology, V. Wilk, B. Windholz, F. Helminger, M. Lauermann, J. Riedl, A. Sporr, A. Schneeberger, T. Fleckl, DryFiciency Cloesd Loop HP Operation and Experience and Outlook, 3rd High Temperature Heat Pump Symposium, Copenhagen, March 2022
[10] F. Reissner, J. Schaefer, B. Gromoll, J. Karl, Basic development of a novel high temperature heat pump system using very low-GWP fluids, International Energy Agency Heat Pump Conference, Montreal, May 2014
[11] C. Arpagaus, F. Bless, S. Bertsch, Techno-Economic Analysis of Steam-Generating Heat Pumps in Distillation Processes, 3rd High Temperature Heat Pump Symposium, Copenhagen, March 2022
[12] B. Zuehlsdorf, J. Poulsen, F. Schlosser, IEA HPT Annex 58 about High Temperature Heat Pumps State of the Art Review, Demonstration Cases and Development Perspectives, 3rd High Temperature Heat Pump Symposium, Copenhagen, March 2022
[13] S. Puschnigg, G. Jauschnik, S. Moser, A. Volkova, M. Linhart, A review of low-temperature sub-networks in existing district heating networks: examples, conditions, replicability, 17th International Symposium on District Heating and Cooling, IEA DHC CHP, Nottingham, United Kingdom, September 2021.
[14] Heat Roadmap Europe, Heating and Cooling facts and figures the transformation towards a low-carbon Heating & Cooling sector, June 2017

14th IEA Heat Pump Conference
15-18 May 2023, Chicago, Illinois

Modelling and Simulation of a Thermoelectric Heat Pump with Micro-Channel Heat Transfer

Hanlong Wan*, Bo Shen, Kyle R. Gluesenkamp, Zhenning Li

Oak Ridge National Laboratory, Oak Ridge, TN 37831, USA

Abstract

Thermoelectric heat pumps (TEHPs) have advantages of modularity and simple design for heating and cooling in some applications. Models of thermoelectric (TE) heat pumps are widely studied. Nevertheless, most existing modeling work focuses on the TE material or air-sourced TE modules. TEHP modeling, especially the relationship between modules and heat exchangers, has not been comprehensively conducted. This work presents a water-to-water TEHP modeling framework that combines Goldsmid's approach for TE material performance, Gnielinski's correlation for convective heat transfer, and thermal balance theory for heat exchange networks. This combined framework provides an accurate theoretical analysis of the water-to-water TEHP system. Subsequently, the framework was used to empirically determine TE material properties (electric resistivity, thermal conductivity, and Seebeck coefficient) that minimize modeling errors versus experimentally observed values from the literature. Finally, an additional set of experimental TEHP data was used to validate the model, all with relative absolute deviations of approximately 10% when predicting heating capacity and 10%–20% when forecasting cooling capacity at a 30 K temperature lift. For future work, people can further develop models of TEHPs with an air-based heat sink on one side and water channels on the other side.

© HPC2023.
Selection and/or peer-review under the responsibility of the organizers of the 14th IEA Heat Pump Conference 2023.

Keywords: thermoelectric, heat pump, Seebeck coefficient, coefficient of performance;

1. Introduction

In the 1950s, thermoelectric (TE) techniques were originally studied [1]; later, their applications for heat pumps were taken into consideration [2]. TE modules provide benefits such as cheap cost, modularity, easy design, and environmental friendliness [1] while being less efficient than conventional vapor-compression heat pumps [3]. As a result, there has been an increase in interest in using TE modules for applications like building heating and cooling [4–7], refrigeration [8], personal thermal comfort [9], electronics cooling [10], and clothes dryers [11,12].

Some researchers treated the TE modules' lumped property parameters (Seebeck coefficient S, thermal conductivity K, and electrical resistance *R*) as temperature-dependent. For instance, Nemati et al. estimated the property parameters using a second-order polynomial correlation with the mean temperatures of the hot and cold sides of the TEHP [13]. However, they neglected to take into account the variation in samples and measurements and instead utilized the coefficients from a study that was published in 2020 [14], which were generated using a different TE module. The identical techniques and coefficients were used by Kaushik et al.

* Corresponding author. *E-mail address:* wanh@ornl.gov.
This manuscript has been authored by UT-Battelle, LLC, under contract DE-AC05-00OR22725 with the US Department of Energy (DOE). The US government retains and the publisher, by accepting the article for publication, acknowledges that the US government retains a nonexclusive, paid-up, irrevocable, worldwide license to publish or reproduce the published form of this manuscript, or allow others to do so, for US government purposes. DOE will provide public access to these results of federally sponsored research in accordance with the DOE Public Access Plan (http://energy.gov/downloads/doe-public-access-plan).

and Feng et al.[15,16]. The attributes were handled as a function of the hot-side temperature by Chen and Snyder et al. [17,18]. Their coefficients, which came directly from the producers, were more trustworthy.

Other researchers treated all or some of the parameters as temperature-independent. Cai et al. treated the properties as constants from the manufacturers' datasheets [19]. Patel et al. treated S and K as constants but the electric resistance *R* as a linear function of the temperature difference between the hot and the cold sides [11].

This paper used Cheon's model [18] to evaluate TE property parameters. In addition, by plugging in the property parameters and applying Goldsmid's method [21] and Gnielinski's correlation [22], this paper developed a detailed liquid-to-liquid TEHP model. Furthermore, the proposed model was validated through quasi-steady-state data from a laboratory test.

2. Methodology

Water-to-water TEHPs, which are simply built and often used in several investigations, is the subject of this study [11,20]; an example is shown in Fig.1. Two mini-channel heat exchangers containing fluid (for example, water) were put on the two sides of one or more TE modules for the TEHP in this investigation. A short distance was maintained between the hot and cold mini-channel heat exchangers using an aluminum space block. UA_{hw} and UA_{cw} are the overall heat transfer coefficients and area of the hot side and cold side, respectively. The model is broadly applicable to scenarios involving liquid-to-liquid, liquid-to-air, and air-to-air interactions thanks to the use of various UA values. This work developed and validated a thermodynamic model using a water-to-water TEHP as a case study. The temperature and UA variables used are marked in Fig.1., as well.

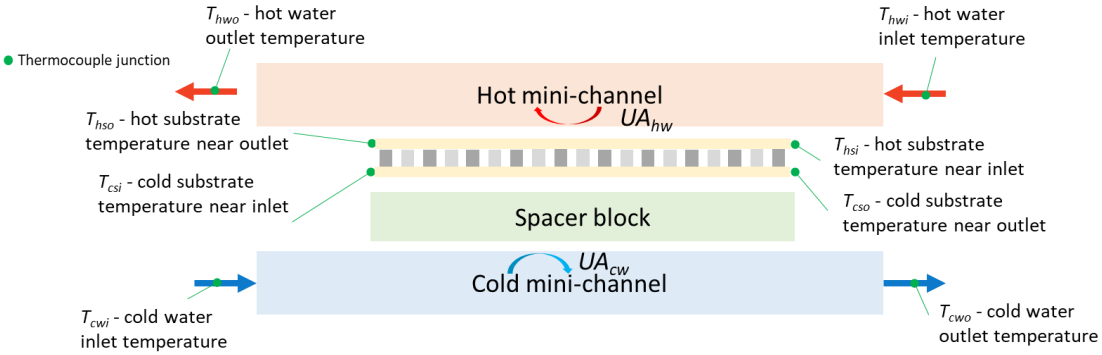


Fig. 1. A general liquid-to-liquid TEHP schematic.

The inlet and outlet water temperatures in the TEHP system under consideration were relatively similar (within 1 K). Thus, the system was made simpler by using lumped approaches. T_h and T_c are the lumped hot- and cold-side temperatures of the TE modules, respectively. The TE surface temperatures can be estimated by measuring the substrate temperatures near the inlet and outlet.

$$T_h \approx \frac{T_{hsi} + T_{hso}}{2} \tag{1}$$

$$T_c \approx \frac{T_{csi} + T_{cso}}{2} \tag{2}$$

Similarly, the lumped hot and cold side water temperatures can be estimated using the inlet and outlet water temperatures.

$$T_{cw} \approx \frac{T_{cwi} + T_{cwo}}{2} \tag{3}$$

$$T_{hw} \approx \frac{T_{hwi} + T_{hwo}}{2} \tag{4}$$

2.1. TE module model

Goldsmid's method is commonly agreed upon and used to describe TE module performance [21]. The heat transfer across the cold side and hot side of one TE module can be given by

$$Q_c = Q_{c_GS} = SIT_c - \mathrm{K}(T_h - T_c) - I^2 R/2 \quad (5)$$

$$Q_h = Q_{h_GS} = SIT_h - \mathrm{K}(T_h - T_c) + I^2 R/2 \quad (6)$$

where Q_{c_GS} and Q_{h_GS} are the predicted heat capacities across the cool and hot sides, respectively, and I is the current. When multiple modules are used in one TEHP, the capacity needs to be multiplied by the number of the modules used, or the number of models should be connected and iterated in series.

From Goldsmid's method [21], the lumped parameters (S, R, and K) can be expressed by the parameters of the couples in one module:

$$Af = N \cdot (A_n + A_p) \quad (7)$$

$$S = N \cdot \alpha_i = N \cdot 2\alpha \quad (8)$$

$$R = N \cdot R_i = N \cdot \left(\frac{l_n \rho_n}{A_n} + \frac{l_p \rho_p}{A_p} + R_l\right) = \frac{N^2 l}{Af} 4\rho \quad (9)$$

$$\mathrm{K} = N \cdot \mathrm{K}_i = N \cdot \left(\frac{A_n \kappa_n}{l_n} + \frac{A_p \kappa_p}{l_p}\right) = \frac{Af}{l}\kappa \quad (10)$$

where *N* is the couple number; Af is the packing area of the TE module; ρ, κ, and α are the property parameters of the nodes; and l and A are the geometry parameters of the nodes. We can assume the following:

$$l_p = l_n = l \quad (11)$$

$$A_n = A_p = d_1 d_2 \quad (12)$$

Cheon's model was applied in the proposed model [18]. From the manufacturer's specifications, ΔT_{max}, I_{max}, and $\dot{Q}_{max}$ (performance parameters of TE modules, which are commonly given in the specifications) are 70 K, 8.4 A, and 90 W, respectively, when T_h equals 27°C, and they are 83 K, 8.4 A, and 98 W, respectively, when T_h equals 50°C. The literature indicates that ΔT_{max} was related to T_h by Eq. (13) (Z is the effective device figure of merit) [18]. The linear interpolation method was used to predict $\dot{Q}_{max}$ at other hot-side temperature points.

$$\Delta T_{\max} = \left(T_h + \frac{1}{Z}\right) - \sqrt{\left(T_h + \frac{1}{Z}\right)^2 - {T_h}^2} \quad (13)$$

The node properties can be achieved using the following equations:

$$\alpha = \frac{\dot{Q}_{max}(T_h - \Delta T_{max})}{N T_h^2 I_{max}} \quad (14)$$

$$\rho = \frac{Af(T_h - \Delta T_{max})^2}{2T_h^2 l} \frac{\dot{Q}_{max}}{N^2 I_{max}^2} \quad (15)$$

$$\kappa = \frac{l(T_h - \Delta T_{max})^2}{Af T_h^2} \frac{\dot{Q}_{max}}{\Delta T_{max}} \quad (16)$$

By plugging in the properties, the lumped parameters can be obtained. In the process, the Af is eliminated, and thus, the lumped parameters are not related to Af directly. When the modules' hot side surface temperature varies from 27 °C to 50 °C, the S, R, and K will be in the range of 0.054–0.054 V·K−1, 1.42–1.57 Ω, and 0.633–0.706 W·m−1·K−1, respectively. S changes very small (less than 1%) in the temperature difference range.

2.2. Heat convection model

In this case study, to estimate UA, the heat transfer coefficient between the fluid and the inner surface of the channel was predicted using Gnielinski's correlation [22]. For different fluid regimes and channel geometries, other appropriate correlations [23] can be used to predict the heat transfer coefficient.

$$Nu = \frac{UA \cdot L}{k_w A} = \frac{(f/8)(Re - 1000)\mathrm{Pr}}{1 + 12.7(f/8)^{1/2}(\mathrm{Pr}^{2/3} - 1)} \quad (17)$$

$$f = (0.79\ln(Re) - 1.64)^{-2} \quad (18)$$

$$Pr = \frac{c_p \mu_w}{k_w} \quad (19)$$

$$Re = \frac{\rho_w u L}{\mu_w} \tag{20}$$

μ_w is the dynamic viscosity of water and is a function of water temperature. u is the water flow speed and can be calculated from m_h and m_c. c_p is the specific heat of water, k_w is the thermal conductivity of water, L is the characteristic linear dimension (the inner height of the mini-channel in this study), Re is the Reynolds number, Pr is the Prandtl number; and Nu is the Nusselt number.

2.3. TEHP model

The proposed TEHP model used any two temperatures in $T_{cwi}, T_{cwo}, T_{hwi}, T_{hwo}$ as the inputs and could predict the other two temperatures and the system performance. Fig.2. shows the thermal resistance network of the system and the modeling flow.

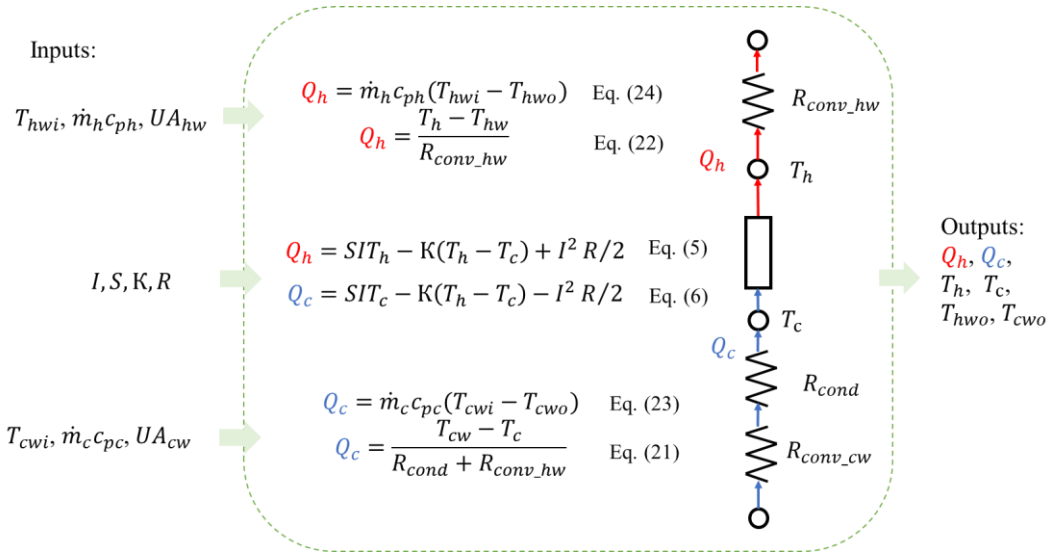


Fig. 2. Resistance network and model flow diagram.

The thermal resistance of the aluminum space block was very small (UA_{hot} is about 8 W/K, while UA_{block} equals 188 W/K) and could be ignored in the analysis. The cooling capacity and heating capacity can be derived as follows:

$$Q_c = \frac{LMTD_c}{\frac{l_s}{k_{alu}A_s} + \frac{1}{UA_{cw}}} \approx UA_{cw}(T_{cw} - T_c) = \frac{T_{cw} - T_c}{R_{cond} + R_{conv_hw}} \tag{21}$$

$$Q_h \approx UA_{hw}(T_h - T_{hw}) = \frac{T_h - T_{hw}}{R_{conv_hw}} \tag{22}$$

LMTD is the log mean temperature difference. Considering the water temperature change,

$$Q_c = \dot{m}_c(h_{cwo} - h_{cwi}) \cong \dot{m}_c c_p(T_{cwo} - T_{cwi}) \tag{23}$$

$$Q_h \cong \dot{m}_h c_p(T_{hwi} - T_{hwo}) \tag{24}$$

$\dot{m}$ is the mass flow rate of the water, and h is the enthalpy of the water, and c_p is the specific heat of water. Since the channel surface temperature and the fluid temperature are close and no phase change exists, the capacity can be simplified using Eqs. (11) and (12). Water was used in this study, and its specific heat was treated as a constant. Using Eqs. (1)–(6) and Eqs. (11)–(14) and knowing property parameters and UA values, all the temperature variables can be solved.

2.4. Data source

A dishwasher using TEHPs was developed by the authors' group [24]. Two TEHPs were used in the dishwasher, and transient laboratory test data from one of the TEHPs were used to validate the proposed model. Compared with the quasi-steady-state TEHP testing previously described, in this testing, two space blocks

were used for each TE module. However, the conductivity of the space blocks is very high, so the resistance can be ignored, and the same model can be applied. In addition, the TEHPs used in this project contained five TE modules.

3. Results and discussion

The results of the transient testing are plotted in Fig.3.

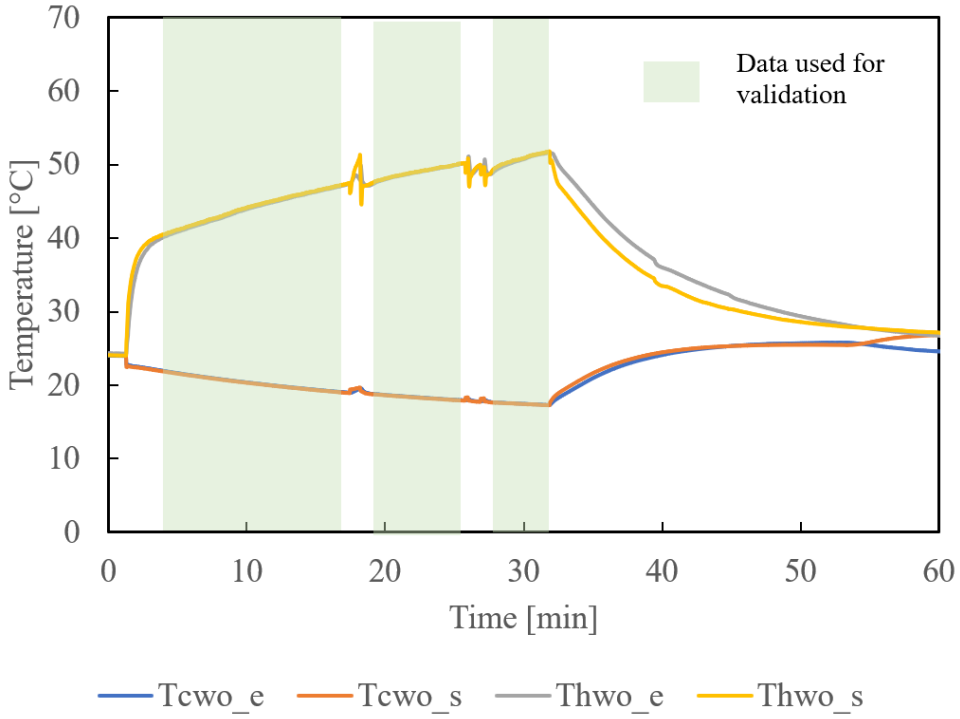


Fig. 3. Experimental and model-predicted outlet water temperature.

When the TE module is on (i.e., the current passing through the module is greater than 0) and the system is stable, the model has good agreement with the measured values. However, when the module is off, the model cannot predict the outlet conditions perfectly because the thermal mass of the system is not considered in the model. Thus, when the module is off, the predicted temperature of the TE module changes immediately and causes water temperature to change at the same time. However, because of the system's thermal mass, the experimental water temperature change is delayed.

Unlike in the steady-state test, some noise exists in the temperature signals. The data with positive current were screened out, and the outliers were excluded (as shown in the shaded area in Fig.3.). The performance of the models using the data set is listed in Table 1. The results are close for all three approaches, which implies that the slight change in the parameters (S, R, and K) will not significantly affect the model. The hot- and cold-side temperatures of the TE module were not predicted perfectly because the temperature sensors installed may not reflect the lumped surface temperature of the modules.

Table 1. TEHP model performance

RME_{DT} (%)	RME_{DT_w} (%)	RME_{Q_c} (%)	RME_{Q_h} (%)	COP_c(-)
35.10	0.61	7.09	8.84	0.6

Table 2 provides the systematic uncertainty of measured and derived values. Using the information from the quasi-steady-state TEHP test and Lecompte's approach [24], Propagated uncertainties of the resulting values were computed. The uncertainty of capacity computed from the water side is high due to the low accuracy of thermocouples and the tiny difference between the input and output water temperatures.

Comparatively, the projected cooling capacity was just 50 W. Therefore, utilizing the water-side capacity to calculate the system coefficient of performance (COP) and assess the performance of the models would not yield useful information. On the other hand, the calculation of capacity from the TE module side has little uncertainty when all of the TE material parameters are accurate. The TE hot- and cold-side temperature measurements have the biggest impact on the TE module performance uncertainty. As a result, a suitable metric for assessing the performance of the models is the difference between the measured and simulated TE module surface temperature. A more accurate system COP may also be obtained by computing COP using the TE module-side capacity. Experiments will be conducted in future with RTDs for better water side capacity accuracy.

Table 2. Uncertainties of measured and derived quantities

	Quantity	Instrument	Uncertainty
Measurement	Geometry	Vernier Caliper	±0.02 mm
	Temperature	Omega TMQSS-062G-6 Type T thermocouple read by NI 9214 module	±0.5 K
	Mass flow rate (water)	Bronkhorst M-15 Coriolis flowmeter	±0.5%
	Applied voltage to TE banks	Sorensen XG150-5.6 DC Programmable Power Supply	±2 V
	Current through TE banks	Sorensen XG150-5.6 DC Programmable Power Supply	±0.05 A
Derived quantity	Capacity (water side)	N/A	±40 W
	Capacity (TE module side)	N/A	±0.5 W
	TE power	N/A	±10 W

4. Conclusions

A thorough modeling framework was given in this study based on a numerical method that incorporates three sub-models: Goldsmid's method for TE material performance, Gnielinski's correlation for convective heat transfer, and thermal balance theory for a heat exchange network. Using this modeling framework, a water-to-water TEHP system was precisely assessed. The TE material performance was estimated through Cheon's model. Finally, quasi-steady-state experimental data were used to validate the overall modeling framework. The findings are as follows:

- The proposed water-to-water TEHP model can achieve a *RME* of approximately 10% when predicting heating capacity and 10%–20% when forecasting cooling capacity at a 30 K temperature lift. For larger lifts, the cooling capacity becomes small, and the relative uncertainty in cooling capacity gets larger.
- TE surface temperatures have a major impact on the TEHP capacity and efficiency. In contrast, the impact of temperature-based variations in TE material properties was minor, over the evaluated range of 20 to 50 °C.
- It is common in TEHP applications to have small changes in water temperature across the TE, leading to difficulty in accurately measuring water-side capacity. This work allows engineers to predict capacities and system COP from knowledge of TE properties and heat transfer, without high accuracy measurements of differential temperatures.

For future work, a more accurate liquid temperature measurement method is needed. Furthermore, customer-designed TE modules are also necessary. Models of TEHPs with an air-based heat sink on one side and water channels on the other side should also be developed.

Nomenclature

A	area (m^2)
c_p	specific heat ($J \cdot kg^{-1} \cdot K^{-1}$)

D	width (m)
d	length of side (m)
DT	temperature difference (K)
f	correction factor
h	enthalpy ($J \cdot kg^{-1}$)
H	height (m)
I	current (A)
k	liquid thermal conductivity ($W \cdot m^{-1} \cdot K^{-1}$)
L	length (m)
l	thickness (m)
m	mass flow rate ($kg \cdot s^{-1}$)
N	number
Nu	Nusselt number
Pr	Prandtl number
Q	capacity (J)
R	lumped electric resistance (Ω)
Re	Reynolds number
RME	relative mean error
S	lumped Seebeck coefficient ($V \cdot K^{-1}$)
T	surface or liquid temperature (K or °C)
TE	thermoelectric
TEHP	thermoelectric heat pump
u	liquid flow speed ($m \cdot s^{-1}$)
UA	heat transfer coefficient and area ($W \cdot K^{-1}$)
Z	effective device figure of merit (K^{-1})

Greek symbols

α	Seebeck coefficient ($V \cdot K^{-1}$)
κ	thermal conductivity ($W \cdot m^{-1} \cdot K^{-1}$)
μ	dynamic viscosity ($kg \cdot m^{-1} \cdot s^{-1}$)
ρ	electric resistivity ($\Omega \cdot m^{-1}$), density ($kg \cdot m^{-3}$)
σ	electrical conductivity ($m \cdot \Omega^{-1}$)
Κ	lumped conductivity ($W \cdot m^{-1} \cdot K^{-1}$)

Subscripts

c	cold side, cooling
exp	experimental
GS	Goldsmid's method
h	hot side, heating
i	inlet
max	maximum
n	n-type node
o	outlet
p	p-type node
s	side
sim	simulation
test	empirical method
w	water

Acknowledgements

This work was sponsored by the US Department of Energy's (DOE's) Building Technologies Office under Contract No. DE-AC05-00OR22725 with UT-Battelle LLC. This research used resources at the Building Technologies Research and Integration Center, a DOE Office of Science User Facility operated by the Oak Ridge National Laboratory. The authors would also like to acknowledge Tony Bouza, Technology Manager – HVAC&R, Water Heating, and Appliance, DOE Building Technologies Office.

References

[1] Riffat SB, Ma X, Wilson R. Performance simulation and experimental testing of a novel thermoelectric heat pump system. Applied Thermal Engineering 2006;26:494–501. https://doi.org/10.1016/j.applthermaleng.2005.07.016.
[2] Rowe DM. Thermoelectrics Handbook: Macro to Nano. Boca Raton, FL: CRC press - Taylor & Francis Group; 2005.
[3] Zhao D, Tan G. A review of thermoelectric cooling: Materials, modeling and applications. Applied Thermal Engineering 2014;66:15–24. https://doi.org/10.1016/j.applthermaleng.2014.01.074.
[4] He W, Zhou J, Chen C, Ji J. Experimental study and performance analysis of a thermoelectric cooling and heating system driven by a photovoltaic/thermal system in summer and winter operation modes. Energy Conversion and Management 2014;84:41–9. https://doi.org/10.1016/j.enconman.2014.04.019.
[5] Ibañez-Puy M, Bermejo-Busto J, Martín-Gómez C, Vidaurre-Arbizu M, Sacristán-Fernández JA. Thermoelectric cooling heating unit performance under real conditions. Applied Energy 2017;200:303–14. https://doi.org/10.1016/j.apenergy.2017.05.020.
[6] Irshad K, Habib K, Basrawi F, Saha BB. Study of a thermoelectric air duct system assisted by photovoltaic wall for space cooling in tropical climate. Energy 2017;119:504–22. https://doi.org/10.1016/j.energy.2016.10.110.
[7] Zhao D, Yin X, Xu J, Tan G, Yang R. Radiative sky cooling-assisted thermoelectric cooling system for building applications. Energy 2019:116322. https://doi.org/10.1016/j.energy.2019.116322.
[8] Liu X, Fu RS, Wang ZQ, Lin L, Sun ZX, Li XL. Thermodynamic analysis of transcritical CO2 refrigeration cycle integrated with thermoelectric subcooler and ejector. Energy Conversion and Management 2019;188:354–65. https://doi.org/10.1016/j.enconman.2019.02.088.
[9] Duan L, Han J, Cao L, Huo C. Experimental study on heat transfer characteristics of CNTs/Al2O3nanofluids in personal cooling system based on thermoelectric refrigeration. Procedia Engineering 2017;205:588–95. https://doi.org/10.1016/j.proeng.2017.10.421.
[10] Liang K, Li Z, Chen M, Jiang H. Comparisons between heat pipe, thermoelectric system, and vapour compression refrigeration system for electronics cooling. Applied Thermal Engineering 2019;146:260–7. https://doi.org/10.1016/j.applthermaleng.2018.09.120.
[11] Patel VK, Gluesenkamp KR, Goodman D, Gehl A. Experimental evaluation and thermodynamic system modeling of thermoelectric heat pump clothes dryer. Applied Energy 2018;217:221–32. https://doi.org/10.1016/j.apenergy.2018.02.055.
[12] Patel V, Gluesenkamp KR. Thermoelectric Heat Pump Clothes Dryer using Secondary Loop Heat Exchangers: Experimental Evaluation and System Modeling, 2018.
[13] Nemati A, Nami H, Yari M, Ranjbar F, Rashid Kolvir H. Development of an exergoeconomic model for analysis and multi-objective optimization of a thermoelectric heat pump. Energy Conversion and Management 2016;130:1–13. https://doi.org/10.1016/j.enconman.2016.10.045.
[14] Xuan XC, Ng KC, Yap C, Chua HT. The maximum temperature difference and polar characteristic of two-stage thermoelectric coolers. Cryogenics 2002;42:273–8. https://doi.org/10.1016/S0011-2275(02)00035-8.
[15] Kaushik SC, Manikandan S, Hans R. Energy and exergy analysis of thermoelectric heat pump system. International Journal of Heat and Mass Transfer 2015;86:843–52. https://doi.org/10.1016/j.ijheatmasstransfer.2015.03.069.
[16] Feng Y, Chen L, Meng F, Sun F. Influences of the Thomson Effect on the Performance of a Thermoelectric Generator-Driven Thermoelectric Heat Pump Combined Device. Entropy 2018;20:29. https://doi.org/10.3390/e20010029.
[17] Chen M, Snyder GJ. Analytical and numerical parameter extraction for compact modeling of thermoelectric coolers. International Journal of Heat and Mass Transfer 2013;60:689–99. https://doi.org/10.1016/j.ijheatmasstransfer.2013.01.020.
[18] Cheon S-Y, Lim H, Jeong J-W. Applicability of thermoelectric heat pump in a dedicated outdoor air

system. Energy 2019;173:244–62. https://doi.org/10.1016/j.energy.2019.02.012.
[19] Cai Y, Zhang D-D, Liu D, Zhao F-Y, Wang H-Q. Air source thermoelectric heat pump for simultaneous cold air delivery and hot water supply: Full modeling and performance evaluation. Renewable Energy 2019;130:968–81. https://doi.org/10.1016/j.renene.2018.07.007.
[20] Kumar N, Gluesenkamp KR, Turnaoglu T, Patel V, Gehl AC, Abuheiba A, et al. Novel Dishwasher with Thermal Storage and Thermoelectric Heat Recovery. Oak Ridge National Laboratory, Oak Ridge, TN (United States); 2021.
[21] Goldsmid H. Thermoelectric Refrigeration. Springer; 2013.
[22] Gnielinski V. Heat Transfer Coefficients for Turbulent Flow in Concentric Annular Ducts. Heat Transfer Engineering 2009;30:431–6. https://doi.org/10.1080/01457630802528661.
[23] Bergman TL, Lavine AS, Incropera FP, DeWitt DP. Introduction to heat transfer. John Wiley & Sons; 2011.
[24] Lecompte S, Gusev S, Vanslambrouck B, De Paepe M. Experimental results of a small-scale organic Rankine cycle: Steady state identification and application to off-design model validation. Applied Energy 2018;226:82–106. https://doi.org/10.1016/j.apenergy.2018.05.103.

14th IEA Heat Pump Conference
15-18 May 2023, Chicago, Illinois

Carbon Mitigation Potential of Heat Pump Integrated with Thermal Storage for Grid-Interactive Residential Buildings

Sara Sultan[a*], Jason Hirschey[b], Zhenning Li[c], Bo Shen[c], Samuel Graham[c], Kyle R. Gluesenkamp[c*]

[a]University of Tennessee, Bredesen Center of Interdisciplinary Education, Knoxville, TN, USA
[b]Georgia Institute of Technology, Atlanta, GA, USA
[c]Oak Ridge National Laboratory, Oak Ridge, TN, USA

Abstract

Residential buildings' heating and cooling loads are associated with significant carbon emissions and peak electricity demand. Phase change material (PCM) based thermal energy storage (TES) can be used for space heating and cooling by embedding into the heat pump equipment. Past work on TES integrated with heat pumps (HP) has demonstrated significant load shifting and economic benefits. However, the potential for TES to reduce carbon emissions has not been widely explored. This study evaluates carbon mitigation potential of an ice-based TES coupled to HP (HP-TES) based on a simple rule-based control strategy accounting for electric grid emissions data. A vapor compression HP model using Engineering Equation Solver (EES). The modeled HP-TES system for single-family residential building demonstrates decreased carbon emissions with reduced peak utility cost.

© HPC2023.
Selection and/or peer-review under the responsibility of the organizers of the 14th IEA Heat Pump Conference 2023.

Keywords: Thermal Energy Storage; Marginal Grid Emissions; Carbon Mitigation; Heat pump; Space cooling; Residential Buildings;

1. Introduction

Heating, cooling, and ventilation loads in residential buildings account for about 10% of energy consumption and CO_2 emissions worldwide and comprises 50% of the building electricity consumption [1]–[3]. More than 74% of electric use in United States is attributed to buildings where heat pumps (HP) exacerbate the demand issues, as, during the summer peak times, 50% of the electric load comes from residential buildings, which is largely HVAC (Heating, Ventilation, and Air Conditioning) load [4]. The potential of onsite thermal energy storage (TES) has mostly been underestimated even though its significance for decarbonization and demand reduction has been established by researchers [2].

TES systems locally decouple heating or cooling demand from its production. The thermal storage properties can be leveraged from phase change materials (PCM) to not only design a demand response strategy for peak load shifting, but also for decarbonization. PCM which can be incorporated as passive or active storage, have a capability to store the off-peak energy that can be released during on-peak time.

Studies can be found in literature that investigate the demand response potential of TES. Peak thermal loads have been shifted to off peak time using utility pricing and demand-based controls [2], [5]–[7]. However, only a handful of research works reported in literature have investigated TES for carbon emissions reduction accounting for HP loads. The table below summarizes the literature investigating TES potential for demand management and carbon mitigation. Noticeably, gas consumption for furnace as a base case is compared against electric HP in most papers.

* Corresponding author. Tel.: +1-865-241-2952;
E-mail address: gluesenkampk@ornl.gov; ssultan1@vols.utk.edu.

Table 1: Load shifting, and carbon mitigation reported in literature using PCM-TES

Author	Location	System Description	Demand Impact	Carbon Mitigation
[8]	Turkey, Spain	PCM in buildings using passive TES and Active Aquifer TES	Loads reduced by 7% for cooling and 10% for heating	~26%* CO_2 emission reduction
[9]	Ithaca, NY	Borehole TES coupled to heat pump	Not reported	64% CO_2 emission reduction
[10]	Spain	Passive PCM in buildings	HVAC loads reduced by 20%	5.5% CO_2 emission reduction
[11]	Italy	TES with Photo Voltaic system and heat pump	41% energy cost reduced by peak load shifting	50% CO_2 emission reduction
[12]	Iran	Bio PCM integrated in wall and construction material of building	4% annual cooling and heating load reduction	2-5% CO_2 emission reduction
[13]	Saudi Arabia	3 different PCMs (18, 23, 25°C) in building envelope	Not reported	6.8-56.9% CO_2 emission reduction
[14]	UK	PCM in floor, coupled to air source HP	50% annual load reduction	36% CO_2 emission reduction
[15]	Saudi Arabia	PCMs (18, 21, 24, 25, 28°C) in wall, coupled to HVAC	Not reported	9.4-61% CO_2 emission reduction
[16]	Mexico	PCM (25°C) in building envelope	11-58% annual load reduction	~25%* CO_2 emission reduction
[17]	Turkey	PCM in wall, configuration and temperature optimized	17.2% annual energy savings	18.4% CO_2 emission reduction

*Calculated from the data given in the paper

As shown in Table 1, the papers reported in literature are either passive or hybrid TES systems. Most researchers either employed passive cooling or heating by using PCM in building envelope or in case of active system, integrated TES with an additional energy production sources like PV systems. There is a large disparity in savings reported. Majority of the works evaluate the electric heat pump CO_2 emission reduction in comparison to gas furnaces as a reference, which yields more than 40% reduction [9], [11], [14]. Other studies compared PCMs with various insulations and passive configurations [13], [16]. In optimization studies, different PCMs and their melting points have been investigated to optimize the savings [15], [17].

Figure 1 below shows the reduced carbon emissions in literature for different regions. Passive TES have varying benefits but for all regions, heat pump coupled systems consistently report more than 35% reduction.

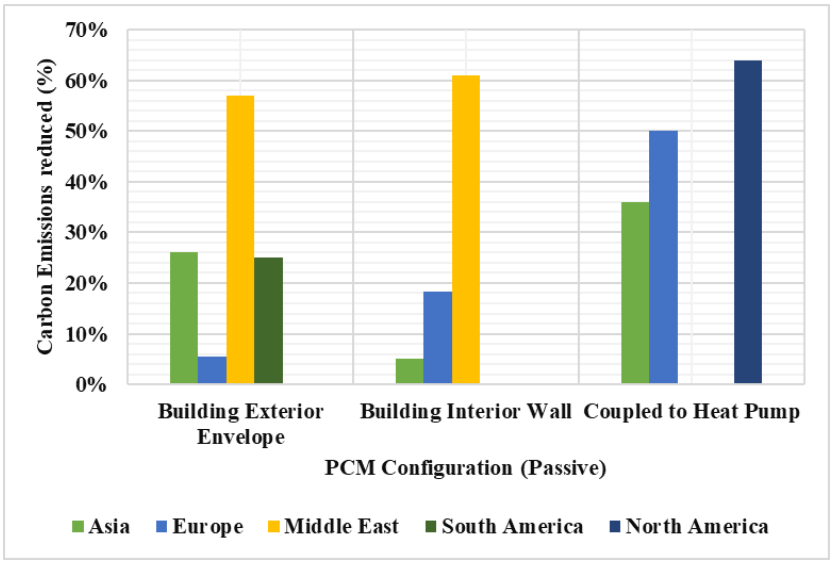


Figure 1: One representative reference reporting emission reduction by using PCM in various locations and configurations

The focus of this paper is to evaluate the carbon mitigation potential of TES assisted heat pumps against the normal heat pump operation, to compare the emissions with and without TES using a rule-based control strategy. Heat pump integrated TES has especially garnered attention for its demand response potential, flexible configurations, and less space requirements. Active HP-TES systems were reviewed to establish that peak loads and cost associated with HVAC loads can be successfully reduced [18]. Many researchers have used demand response control strategies to shift the peak load, but very few papers have investigated the decarbonization potential of TES. Peak load was shifted using various controls and configurations for residential HP-TES, and corresponding emissions were reported [19]. The emissions have been calculated by deriving relations to the energy consumption and power usage. Abu Hamdeh *et al.* (2022) multiplied the power usage by the amount of greenhouse gases emission per kWh [13]. Arce *et al.* (2011) used European Commission emission factors, load reduction and energy savings to calculate the carbon emissions reduced [10]. Cabeza *et al.* (2015) defined CO_2 factor as a corelation between CO_2 emissions (g) and energy consumption (kWh). The CO_2 footprint (g/kWh) is 0.08 times energy consumption [8]. No studies were found that utilize emissions data into the control strategy of HP-TES systems.

Table 2: Table showing gap in literature and scope of this work

Reference	Active HP-TES mediated by heat pump	Carbon Emission controls for HP-TES	CO_2 emissions reported	Electric heat pump baseline vs PCM	Utility based controls for peak load shifting
[8]	×	×	■	×	×
[9]	×	×	■	×	■
[10]	×	×	■	×	×
[11]	×	×	■	×	■
[19]	×	×	■	×	■
[12]	×	×	■	■	×
[13]	×	×	■	■	×
[14]	×	×	■	×	■
[3]	■	×	×	■	■
This work	■	■	■	■	■

The electricity sector has seen a shift from traditional centralized system to a smart grid device. This phenomenon has been ushered in by the increased integration of renewable energies. The rapid proliferation of the 'Internet of Things' (IoT) [20], allow major loads, such as HP, to be controlled with the goal of reducing peak power consumption on the electrical grid. In a smart grid, HP can be considered part of the demand side that can be actively managed to stabilize voltage fluctuations caused by high demand or high penetration of renewable energy [21]. With smart control of HP-TES, the system can switch between charging and discharging mode depending on the outdoor temperature, electricity price, desired indoor temperature, renewable energy generation, and COP of HP [20]. It is important to describe how to incorporate a grid's GHG (greenhouse gases) condition into a site-specific MPC. The grid system-wide emission rate in a specific grid region depends on the total power production rate from grid power generators, and other factors that affect system operating conditions, such as weather. The marginal operating emissions rate (MOER) is the partial derivative of the systemwide emission rate with respect to the total production rate [22]. It means the change of the emission rate in the grid region with respect to the last megawatt produced by dispatchable generators having the unit of metric Ton CO_2-equivalent per MWh [mTonCO_2/MWh]. Intuitively, this indicates how much carbon emission rate increases/decreases in a grid region when one consumes one megawatt more/less. Therefore, MOER allows for associating the power usage at a specific site with the carbon emission rate in the grid region by simply multiplying the on-site power consumption with the MOER signal. In this paper, we used the MOER signal, based on a proprietary model [22], but adapted for real-time use [23].

In our previous work, we used time-based pricing to determine the economic value of residential TES system [6]. The PCM was incorporated into the conventional HVAC and time-of-use (TOU) utility rate schedule was analysed to evaluate the demand impact and energy savings. The objective of this present work is to evaluate the simple control strategy to reduce grid emissions while shifting the peak load, accounting for both grid and utility data. Marginal grid emissions data is used to determine if the emissions are relatively higher than the average of the previous day. The controls are then applied for the heat pump and TES operation,

and emissions are reported.

A simple building thermal energy model and HP model is evaluated with an active configuration implying direct use of TES for the building cooling during the discharge. The TES is based on water/ice PCM with 0°C storage temperature. TES is not directly conditioning the building but interacts with HP to mediate the heat transfer. The potential reduction in grid emissions is assessed using marginal grid emissions data and peak load is shifted using residential TOU utility tariff. Both correspond to the ASHRAE climate zone 3B, in California. For modelling, Engineering Equation Solver (EES) and Microsoft Excel are used. System overview and decision controls are explained in the Methodology (Section 2).

2. Methodology

The model comprises of various components connected to the building and HP using R410-a refrigerant. A TES heat exchanger with embedded PCM is integrated into HP to modify the vapor compression system and is transferring energy to and from the ambient. Thermostat controls monitor the building indoor temperature. The ambient weather data, TOU utility data, and marginal grid emissions data obtained for the same climate location, ASHRAE climate zone 3B. Marginal grid emissions data and electric utility schedule controls the heat pump to cool the building, and charge and discharge the ice-based TES. The analysis is performed for cooling only during the hottest week of June. The building energy consumption, HP work, and emissions are calculated in Microsoft Excel according to the rule-based control strategy in the minutely time steps.

2.1. System Overview and Configuration

The conventional vapor compression cycle of HP is modified by coupling TES to the system. TES is integrated with HP via active configuration and assists the HP cooling. TES does not cool the building directly, but heat transfer occurs through HP, as shown in Figure 2. PCM-TES can function either as a condenser or an evaporator, dependent upon the mode of operation. It is assumed that TES has an infinite coefficient of heat transfer and is always at constant temperature of 0°C.

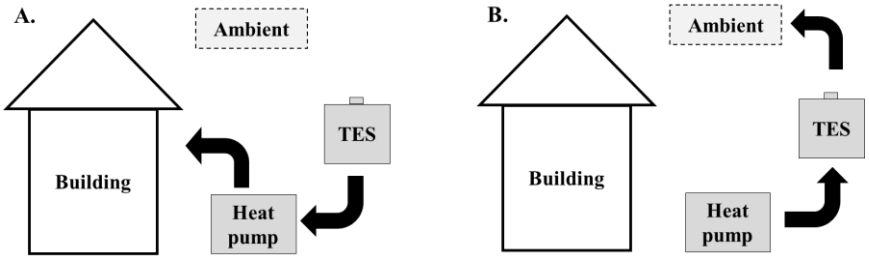


Figure 2: HP-TES configuration in cooling mode (A. TES Discharging B. TES Charging)

HP has four modes of operation. HP is turned off in the standby mode and only thermal energy from outdoors is being transferred to the building. HP is turned on to cool the building through refrigeration cycle in normal mode, and no TES is involved. During charging mode, TES stores the energy from HP as Q_{PCM} to be used at later time. During discharging mode, TES releases the already stored energy into the building via HP. This mode has increased COP than the normal mode due to favourable temperature gradient. TES, which is at a colder temperature, is coupled to HP condenser and creates a negative temperature lift to move the condenser heat from building to TES.

2.1.1. Cooling Mode

Operating modes for cooling and respective energy flows are shown in Figure 3. Ambient is at a higher temperature than the building. During cooling normal operation, the condenser heat, Q_{cond}, is discarded to the ambient while the heat of the evaporator, Q_{evap}, is removed from the building and directed to the heat pump.

TES behaves as condenser or evaporator depending on the mode of operation. Evaporator is assumed to be the TES during charging. So, the TES is being cooled directly. The heat, Q_{evap}, is removed from the TES though latent heat of freezing. TES solidifies as the heat stored from the TES is discarded to the ambient via heat pump. In the discharging mode, the TES is defined as the condenser and the evaporator was tied to the building. The Q_{cond} is now being stored to the TES instead of ambient and the PCM within the TES is being liquified.

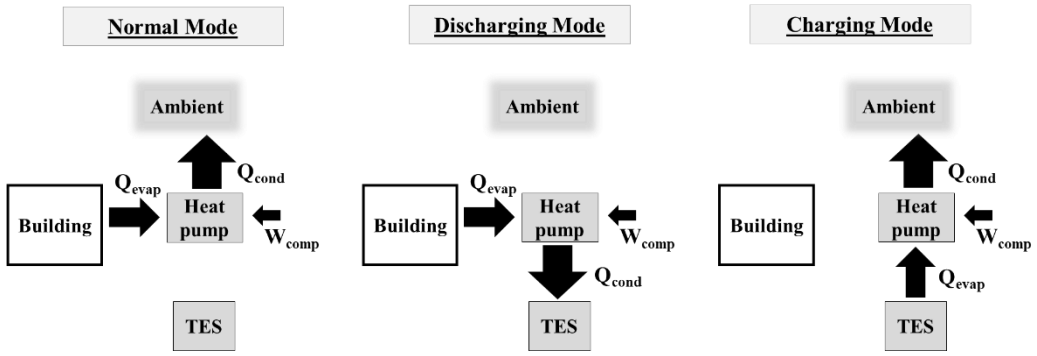


Figure 3: Operating modes in cooling

2.2. System Controls

The operating mode of HP-TES is determined by the thermostat decision whether the building needs to be cooled or not, utility off-peak and on-peak time, state of charge of PCM (SOC), and grid emissions. The control strategy of HP-TES model is regulated based on four decision variables: 'Thermostat call', 'Utility Peak', 'Emissions Peak' and 'State of Charge'.

The thermostat model (section 3.5) regulates the indoor temperature and determines if cooling is needed at a given time to call for cooling. A cooling temperature setpoint is fixed at 21°C, and the need is determined when the indoor temperature is higher than the cooling setpoint. The utility model, explained in section 3.1, determines the utility peak time. The emissions are obtained from the grid emissions model in section 3.6, while the TES model (section 3.5) determines the PCM state of charge.

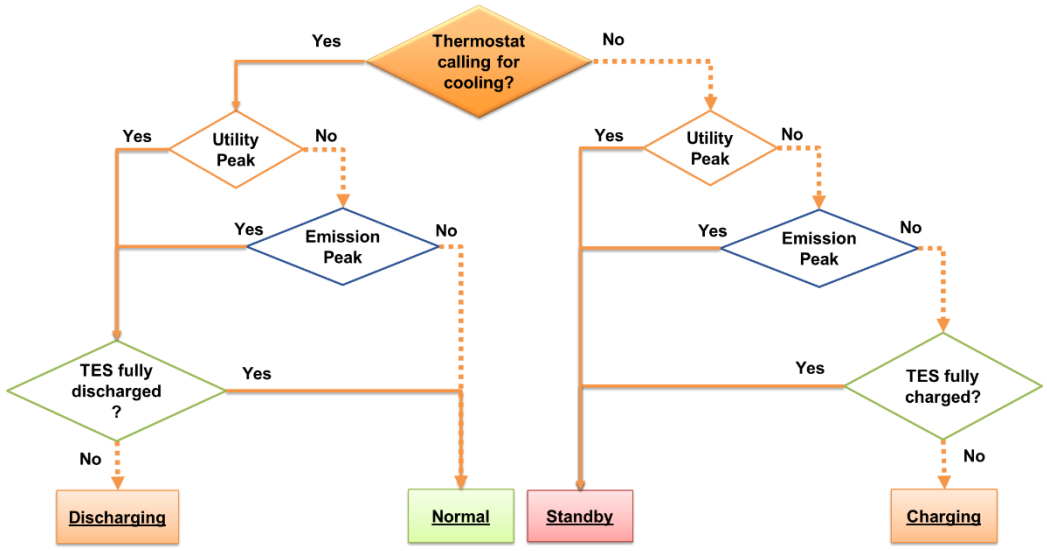


Figure 4: Controls decision tree used in this work

The operating modes are shown in the decision tree diagram (Figure 4). Assuming the initial PCM SOC as 50%, if the thermostat is calling for cooling during the utility peak time defined by TOU tariff, PCM discharging mode will turn on. But during utility off peak, the emissions peak will determine if the discharging mode should be on. Charging mode is only activated during off-peak times to take advantage of the lower electrical cost and emissions, while thermostat is not calling for cooling, and PCM is not already charged. If during utility off-peak time, thermostat is calling for cooling, the HP goes into normal operation depending on emissions peak. Emissions peak is determined by average of grid emissions in the past 24 hours, if emissions are greater than the average of last 24 hours at a given point, it's emissions peak. In previous work [6], emissions were not included, and controls were based only on utility data.

2.3. Information Flow

The overall system flow is depicted in Figure 5, which depends on the component models to analyze the

weather, utility and emissions data. All the components are mainly coordinated by the decision tree as a main control to maximize the system efficiency. Some values are updated to use as intermediate inputs in the model, represented by feedback arrows. The building model, HP model, and TES model are used from the previous work [6].

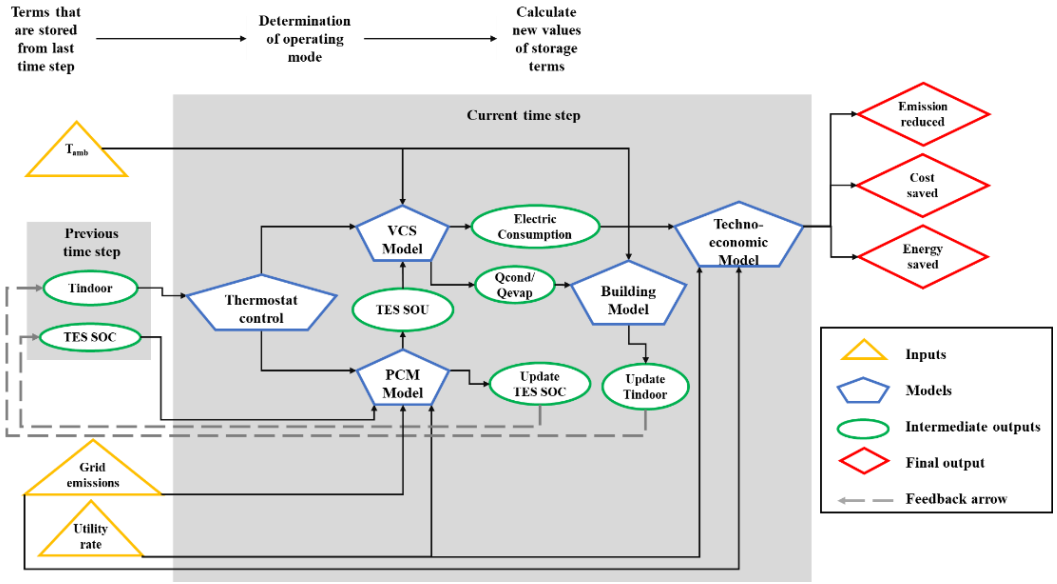


Figure 5: Information Flow Diagram

3. Component Models

3.1. Weather and Utility Data

The TMY 3 weather data used is of Fresno, CA which corresponds to ASHRAE climate zone 3B. The location correlates to marginal grid emissions and utility tariff. The Time of Use (TOU) utility data is a fixed utility rate schedule from Pacific Gas and Electric (PG&E) Electric Schedule E-TOU-B. The analysis for cooling is performed considering both peak and off-peak hours for a hot week of June 24-30, 1994. The peak hours vary by season. For cooling season defined from June till September, on-peak hours are observed from 4pm to 9pm on weekdays, and the utility rate is $0. 39689/kWh. At other times, including the weekends, the off-peak rate is $0. 29383/kWh. The difference between on-peak and off-peak utility rate is $0.103/kWh.

Figure 6 shows ambient temperature versus utility rate for cooling season. The cost for cooling increases when the demand increases as a function of outdoor dry bulb temperature. The design objective is to take advantage of the low rates and assist heat pump operation using TES when the cost is high during peak hours.

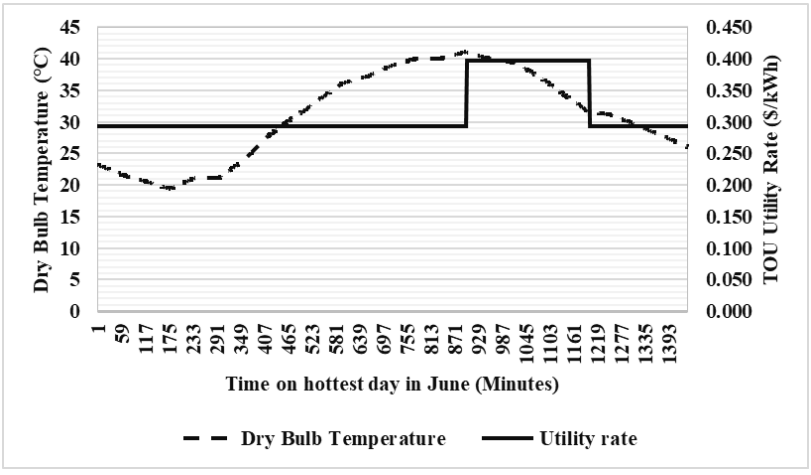


Figure 6: Ambient Temperature and Utility data for cooling day

3.2. Building Model

Building's thermal response is simulated by a simple building model that calculates indoor temperature. The model takes into account the heat pump load, building's thermal capacitance, and ambient load. A balance point temperature of 18℃ is assumed to model the ambient load, as shown in Equation 2. An overall heat transfer coefficient of 0.25 kW/K is estimated based on cooling design day.

$$Q_{amb} = U * (T_{amb} - T_{bal}) \quad (1)$$

Indoor temperature is determined by the energy balance where Q_{VCS} is the cooling or heating load output from the heat pump model in either normal or discharging modes, in one minute time step. A single-family house with 223 m^2 (2400 ft^2) area was selected and the building capacitance was estimated to be 16459 J/K [6]. It was chosen to result in a reasonable rate of change of building.

$$T_{indoor,i+1} = \frac{-(Q_{VCS} - Q_{amb}) * dt}{C} + T_{indoor,i} \quad (2)$$

3.3. Thermostat Model

The thermostat model tracks the indoor temperature and calculates the variable 'thermostat call'. It uses a constant setpoint temperature to turn on cooling mode. Due to thermal loading from the ambient temperature, when the building indoor temperature exceeds the setpoint cooling temperature of 21°C (with a dead band of +/- 0.5°C), the thermostat calls for cooling. Depending on other conditions (time of day, emissions, and outdoor temperature), the HP will enter into either discharging mode where TES will be used, or normal mode where HP cools the building without TES.

3.4. Heat Pump Model

A heat pump model was simulated in EES and the operating modes with TES were modelled separately. The vapor compression model calculates the COP for cooling from the evaporator output and electric consumption by compressor [6]. The compressor has a constant volumetric flow rate of $2.5e^{-6}$ m^3. Equation 4 defines the cooling COP.

$$COP_c = \frac{Q_{evap}}{W_{comp}} \quad (3)$$

The outputs of heat pump model, Q_{evap} from the evaporator and Q_{cond} from the condenser are called into Excel, where they are coupled to the PCM-TES or ambient depending on the operating mode. The condenser is tied to the ambient in normal mode, thus the dry bulb temperature was used as an input. The condenser is paired to the TES in the discharging mode. Where TES is kept at a constant 0°C. The discharging mode does not depend on ambient temperature and thus its operating parameters are constant. Because the temperature gradient is more favourable, total work during discharging is 0.748 kW, much lower than the normal mode which varies between 2.65 and 7 kW depending on the ambient temperature.

The condenser is coupled to the ambient in charging mode, and now the evaporator interacts with the TES. The decision tree (Figure 4) and thermostat model was used to control the HP and PCM state of use.

3.5. TES Model

The HP vapor compression system is coupled to PCM via heat exchanger in such a way that TES does not interact directly with the building and is not affected by the ambient temperature. An ice/water based PCM with phase change temperature of 0°C is embedded in the TES. TES heat exchanger is assumed to have an indefinite heat transfer rate at a constant temperature maintained at 0°C. TES is modelled as an 80-gallon tank, which can provide up to 27.8 kWh of cooling capacity. The operating modes are controlled by the PCM state of charge which is a function of peak time, and indoor temperature.

The fraction of maximum energy that can be stored by TES is defined as state of charge of PCM (PCM SOC). The PCM SOC is increased during charging to store the energy and reduced during discharging mode when it is consumed. For charging mode, the state of use of PCM (SOU) is -1, for discharging it is +1, and PCM SOU is 0 when it is not being used.

3.6. Grid Emissions Model

Marginal grid emissions schedule is obtained for Fresno, CA from a data driven tool that uses an empirical model. The tool generates emissions schedule based on continuous emissions and electricity generation data from major fossil fuel plants in the U.S. Figure 7 shows the hourly emissions data for the year of 2022 obtained on November 15. The data from January until November 15 is real time, and rest is projected based on historical data. Controls are designed based on average of the last 24 hours and variable called 'Emission Peak' is defined. If at any given point, the emissions exceed the average of last 24 hours, it will be considered emission peak. Discharging mode will be turned on if cooling is needed at that time. This strategy avoids using HP during both utility and emission peak times, to assess the maximum grid emission savings.

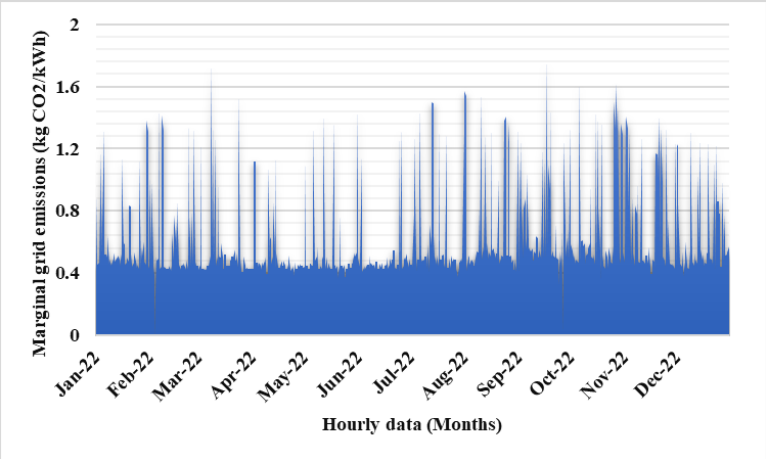


Figure 7: Fresno annual grid emissions during 2022

4. Results and Discussions

The analysis is performed for one week of cooling season to report utility cost, electric consumption, and carbon emission reduction. The indoor temperature was maintained at 20℃ for cooling. For the simulated 7-day period, the grid emissions corresponding to the HP electric consumption are compared for the cases with and without PCM TES. The baseline system is defined as the case without TES.

4.1. Carbon Emissions

Figure 8 shows the grid emissions for both baseline and TES systems. The no-TES baseline case resulted in 181.78 kg of CO_2 over the simulated week, while using the TES system, emissions were 160.1 kgCO_2, reducing 11.92% grid emissions for the simulated week. These savings were achieved by using TES to discharge during emission peak and utility peak.

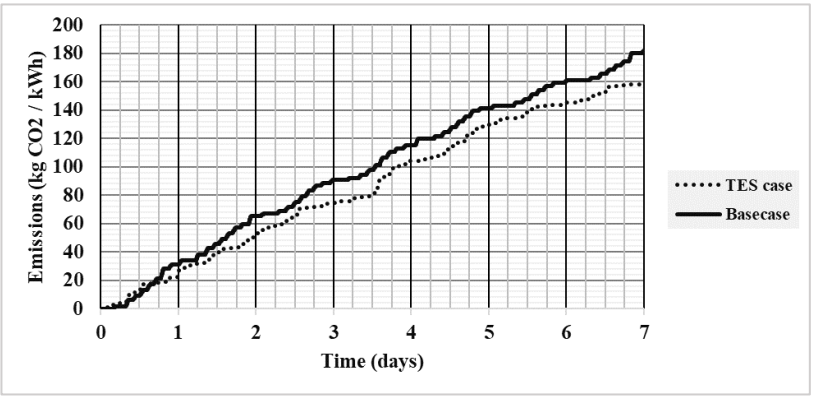


Figure 8: Emissions reduced using TES

4.2. Electric Consumption

Figure 9 shows the HVAC electric consumption and the peak electric consumption for both baseline and TES systems. TOU tariff for Fresno, CA is used for this study and the on-peak pricing applies from Monday through Friday only, excluding weekends. For the baseline system, where no TES was used, total electric consumption was 353.2 kWh, and on-peak consumption was 98.1 kWh. For the system with TES, the total electric consumption was reduced by 10.19% to 317.2 kWh. TES on-peak usage was 48.8 kWh, which means 50.2% of peak load was shifted. In our previous study [6], 87% of peak load was shifted to off-peak hours using TES under TOU tariff. The present study also implements grid emissions-based controls and TES is more frequently used in discharging mode than in previous study.

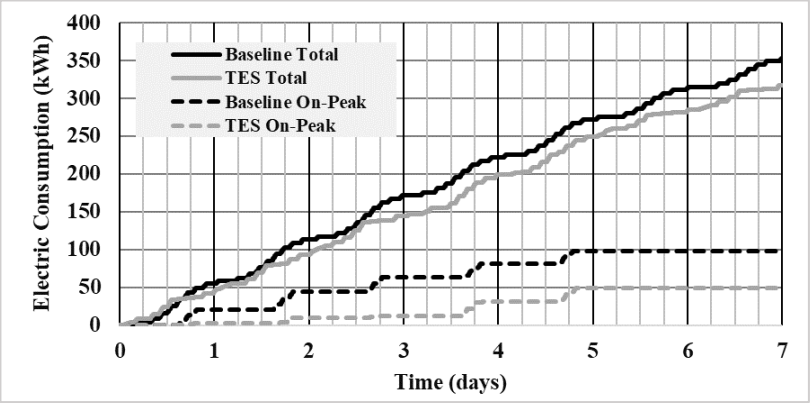


Figure 9: Electric Consumption with and without TES

4.3. Operating Cost

The utility cost to cool the building is shown in Figure 10. Compared to baseline, 12.68% of system operating cost was saved using TES. The baseline system without TES accumulated $112.52 for cooling during the simulated week, while TES accounted for $98.25. In the previous study [6], 20% utility cost was saved using TES. The cost for the present system has increased when additional emission-based controls were introduced. In the control strategy, the emissions peak has precedent over the utility peak. Therefore, cost savings are not as significant as was seen in the previous study when only cost peak was considered.

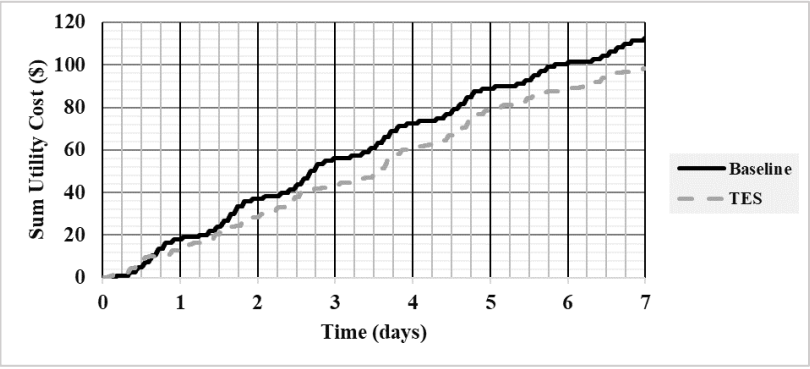


Figure 10: Utility Cost reduced using TES

5. Conclusion

The objective of this work is to assess the carbon emissions reduction potential of HP-TES using a rule-based strategy accounting for marginal grid emissions data and time-of-use utility tariff. An HP-TES configuration was evaluated with an ice/water based PCM coupled to the HP. A vapor compression model was developed using EES, and Excel was used to compute results for the integrated HP-TES system. The analysis was performed for one week of cooling season. The utility cost for cooling was reduced by 12.68% using TES

while also maintaining occupant comfort. The total electric consumption was also reduced by 10.19% and 50.2% of peak electric load was shifted to off-peak time. 11.92% of grid emissions were reduced by using TES during emissions and utility peak times defined in the control strategy. The study concluded that while this configuration can still create some economic advantage with a simple control strategy, controls should be further optimized to reduce peak energy consumption. The analysis was performed for 7 days only, and the results should not be extrapolated for annual savings. This work highlights the potential for reducing grid emissions using a rule-based strategy.

Nomenclature

PCM	Phase Change Material	
TES	Thermal Energy Storage	
EES	Engineering Equation Solver	
HP-TES	Heat Pump integrated Thermal Energy Storage	
MGE	Marginal Grid Emissions	
TOU	Time of Use	
VCS	Vapor Compression System	
SOC	State of Charge	
COP	Coefficient of Performance	
Q	Energy	(kW)
W	Electric Consumption	(kWh)
C	Building Thermal Capacitance	($J\text{-}°C^{-1}$)

Acknowledgements

This manuscript has been authored by UT-Battelle, LLC under Contract No. DE-AC05-00OR22725 with the U.S. Department of Energy. The United States Government retains and the publisher, by accepting the article for publication, acknowledges that the United States Government retains a non-exclusive, paid-up, irrevocable, world-wide license to publish or reproduce the published form of this manuscript, or allow others to do so, for United States Government purposes. The Department of Energy will provide public access to these results of federally sponsored research in accordance with the DOE Public Access Plan (http://energy.gov/downloads/doe-public-access-plan).

References

[1] U.S. EIA, “Annual Energy Outlook 2020,” 2020. Accessed: Apr. 19, 2020. [Online]. Available: https://www.eia.gov/outlooks/aeo/

[2] A. Odukomaiya *et al.*, “Addressing energy storage needs at lower cost via on-site thermal energy storage in buildings,” *Energy Environ Sci*, vol. 14, no. 10, pp. 5315–5329, Oct. 2021, doi: 10.1039/D1EE01992A.

[3] J. Dong, B. Shen, J. Munk, K. R. Gluesenkamp, T. Laclair, and T. Kuruganti, “Novel PCM Integration with Electrical Heat Pump for Demand Response,” in *IEEE Power and Energy Society General Meeting*, 2019. doi: 10.1109/PESGM40551.2019.8973936.

[4] B. Cui, J. Munk, R. Jackson, D. Fugate, and M. Starke, “Building thermal model development of typical house in U.S. for virtual storage control of aggregated building loads based on limited available information,” in *30th International Conference on Efficiency, Cost, Optimization, Simulation and Environmental Impact of Energy Systems, ECOS 2017*, 2017.

[5] F. Li, B. Sun, C. Zhang, and C. Liu, “A hybrid optimization-based scheduling strategy for combined cooling, heating, and power system with thermal energy storage,” *Energy*, vol. 188, p. 115948, Dec. 2019, doi: 10.1016/J.ENERGY.2019.115948.

[6] S. Sultan, J. Hirschey, K. Gluesenkamp, and S. Graham, “Analysis of Residential Time-of-Use Utility Rate Structures and Economic Implications for Thermal Energy Storage,” 2021, pp. 1–10. Accessed: Aug. 31, 2021. [Online]. Available: https://docs.lib.purdue.edu/cgi/viewcontent.cgi?article=1369&context=ihpbc

[7] N. Zhu, S. Wang, Z. Ma, and Y. Sun, “Energy performance and optimal control of air-conditioned buildings with envelopes enhanced by phase change materials,” *Energy Convers Manag*, vol. 52, no.

10, pp. 3197–3205, Sep. 2011, doi: 10.1016/j.enconman.2011.05.011.
[8] L. F. Cabeza *et al.*, "CO2 mitigation accounting for Thermal Energy Storage (TES) case studies," *Appl Energy*, vol. 155, pp. 365–377, Oct. 2015, doi: 10.1016/J.APENERGY.2015.05.121.
[9] S. Durga, K. F. Beckers, M. Taam, F. Horowitz, L. M. Cathles, and J. W. Tester, "Techno-economic analysis of decarbonizing building heating in Upstate New York using seasonal borehole thermal energy storage," *Energy Build*, vol. 241, p. 110890, Jun. 2021, doi: 10.1016/J.ENBUILD.2021.110890.
[10] P. Arce, M. Medrano, A. Gil, E. Oró, and L. F. Cabeza, "Overview of thermal energy storage (TES) potential energy savings and climate change mitigation in Spain and Europe," *Appl Energy*, vol. 88, no. 8, pp. 2764–2774, Aug. 2011, doi: 10.1016/J.APENERGY.2011.01.067.
[11] A. L. Facci, V. K. Krastev, G. Falcucci, and S. Ubertini, "Smart integration of photovoltaic production, heat pump and thermal energy storage in residential applications," *Solar Energy*, vol. 192, pp. 133–143, Nov. 2019, doi: 10.1016/J.SOLENER.2018.06.017.
[12] E. Markarian and F. Fazelpour, "Multi-objective optimization of energy performance of a building considering different configurations and types of PCM," *Solar Energy*, vol. 191, pp. 481–496, Oct. 2019, doi: 10.1016/J.SOLENER.2019.09.003.
[13] N. H. Abu-Hamdeh, R. A. R. Bantan, and R. I. Hatamleh, "Carbon dioxide reduction using passive technique of incorporating phase change materials into envelopes: A case study of climate data from Saudi Arabia," *J Energy Storage*, vol. 49, p. 104153, May 2022, doi: 10.1016/J.EST.2022.104153.
[14] L. Cabrol and P. Rowley, "Towards low carbon homes – A simulation analysis of building-integrated air-source heat pump systems," *Energy Build*, vol. 48, pp. 127–136, May 2012, doi: 10.1016/J.ENBUILD.2012.01.019.
[15] N. Farouk, M. A. El-Rahman, M. Sharifpur, and W. Guo, "Assessment of CO2 emissions associated with HVAC system in buildings equipped with phase change materials," *Journal of Building Engineering*, vol. 51, p. 104236, Jul. 2022, doi: 10.1016/J.JOBE.2022.104236.
[16] S. Mousavi, M. Gijón-Rivera, C. I. Rivera-Solorio, and C. Godoy Rangel, "Energy, comfort, and environmental assessment of passive techniques integrated into low-energy residential buildings in semi-arid climate," *Energy Build*, vol. 263, p. 112053, May 2022, doi: 10.1016/J.ENBUILD.2022.112053.
[17] M. Arıcı, F. Bilgin, M. Krajčík, S. Nižetić, and H. Karabay, "Energy saving and CO2 reduction potential of external building walls containing two layers of phase change material," *Energy*, p. 124010, Apr. 2022, doi: 10.1016/J.ENERGY.2022.124010.
[18] S. Sultan, K. R. Gluesenkamp, and U. States, "The State of Art of Heat-Pump integrated Thermal Energy Storage for Demand Response," *IEA Heat Pump Technologies Magazine*, vol. 40, no. 2, pp. 27–30, 2021. doi: https://doi.org/10.23697/62tr-nt79.
[19] R. Renaldi, A. Kiprakis, and D. Friedrich, "An optimisation framework for thermal energy storage integration in a residential heat pump heating system," *Appl Energy*, vol. 186, pp. 520–529, Jan. 2017, doi: 10.1016/J.APENERGY.2016.02.067.
[20] P. Siano, "Demand response and smart grids—A survey," *Renewable and Sustainable Energy Reviews*, vol. 30, pp. 461–478, Feb. 2014, doi: 10.1016/J.RSER.2013.10.022.
[21] D. Fischer, H. M.-R. and S. E. Reviews, and undefined 2017, "On heat pumps in smart grids: A review," *Elsevier*, Accessed: Nov. 21, 2022. [Online]. Available: https://www.sciencedirect.com/science/article/pii/S1364032116309418?casa_token=Qh18EGJLZLwAAAAA:vpcm3J1pwdEV8U5QYm_IU7cE3i4I6Wuv_Zp3WoY2Sf95l1BAIPqXKo95rW9jIkSZs6zNmasuGQ
[22] K. Siler-Evans, I. L. Azevedo, M. G. Morgan, and J. Apt, "Regional variations in the health, environmental, and climate benefits of wind and solar generation," *Proc Natl Acad Sci U S A*, vol. 110, no. 29, pp. 11768–11773, Jul. 2013, doi: 10.1073/PNAS.1221978110.
[23] D. S. Callaway, M. Fowlie, and G. McCormick, "Location, location, location: The variable value of renewable energy and demand-side efficiency resources," *J Assoc Environ Resour Econ*, vol. 5, no. 1, pp. 39–75, Jan. 2018, doi: 10.1086/694179.

14th IEA Heat Pump Conference
15-18 May 2023, Chicago, Illinois

Numerical comparison of the yearly performance of an indirect vapour compression heat pump working with R290 with R410A systems

Nicholas Croci[a], Matteo Fusaro[a], Luca Molinaroli[a,*]

[a]Dipartimento di Energia, Politecnico di Milano, Via Raffaele Lambruschini 4/A, 20156, Milano, Italy

Abstract

In the last years, the environmental awareness is pushing the air-conditioning and refrigeration industry towards a massive use of low GWP refrigerants. Generally, despite being environmentally friendly, these new working fluids are mildly flammable, or even flammable, and therefore safety concerns arise. One possible way to cope with the flammability hazard is the reduction of the charge of the refrigerant inside the system. In this scenario, indirect systems, i.e. brine-to-water system with a remote air-to-brine heat exchanger, seem to be a viable solution since they may be built with low internal volume which, in turn, leads to a low refrigerant charge. However, the use of heat transfer fluid between the air and the refrigerant results in an increase in the energy consumption of the system, making this solution less attractive.
In the present paper, a numerical assessment of the use of R290 in an indirect expansion vapour compression system is presented. The analysed system consists of a reversible brine-to-water heat pump able to supply space heating or space cooling depending on the season. The results are compared with those of a baseline R410A system, both in direct and indirect configurations. Although the refrigerant charge is well below the maximum value currently allowed, the indirect systems show a reduction in the energy performance by around 20% with respect to the direct one.

© HPC2023.
Selection and/or peer-review under the responsibility of the organizers of the 14th IEA Heat Pump Conference 2023.

Keywords: Heat pump; Indirect expansion; R290.

1. Introduction

In the last years, the constraints introduced by the environmental regulations such as the EU 517/2014 regulation [1] and the Kigali amendment to the Montreal Protocol [2] are pushing the air conditioning and refrigeration industry is facing the transition towards the use of low-GWP refrigerants.

Among the possible options, natural refrigerants such as R290 and R744 [3] have received a lot of attention, especially in heat pump applications and/or refrigeration application and their application is becoming more and more widespread. Focusing on propane only, it has very good thermodynamic properties that may lead to high performance systems but has the drawback of flammability that may limit its diffusion. Indeed, in the open literature it is possible to find a lot of studies that deal with the reduction of the charge in propane-based systems [4-7].

In this scenario, for air-to-water heat pumps one interesting option lies in indirect expansion systems, i.e. systems in which the air is not used directly as cold heat source directly in an air-to-refrigerant evaporator, but is used in an air-to-brine heat exchanger to heat a brine flow which, in turn, acts as cold heat source in a brine-to-refrigerant evaporator. This layout leads to significant reduction in the inner volume of the refrigerant circuit, and of the refrigerant charge, which is beneficial for the system safety and risk reduction. However, some inherent energy penalization may arise since the evaporating temperature in indirect systems is generally lower than that found in direct ones because of the use on an intermediate heat transfer fluid.

* Corresponding author. Tel.: +39-02-23993872.
E-mail address: luca.molinaroli@polimi.it.

This paper wants to contribute to this general discussion presenting the results of a numerical study aimed to analyse the performance of an indirect expansion heat pump working with R290. The results are compared with those achieved by a traditional air-to-water heat pump working with R410A, which is the baseline for the comparison, and by an indirect heat pump, again operated with high-GWP refrigerant R410A.

2. Modelling

As stated, in the present study the performance of an indirect expansion heat pump is analysed and compared with that of classical air-to-water systems. Figure 1 shows the layouts of the two heat pumps considered. The main difference between the direct expansion system and the indirect one is the addition of a heat exchanger beyond the condenser-evaporator pair. Indeed, while in an air-to-water system the evaporator is a fin-and-tube coil that exchanges heat directly with the air, i.e. the cold heat source of the heat pump, in an indirect system the evaporator is a plate heat exchanger that transfers heat between the refrigerant and a secondary fluid in liquid state. This fluid, which is the "direct" cold heat source of the heat pump, is then heated in a finned coil in which a heat transfer process with air occurs. Air is then the "indirect" cold heat source of the heat pump. When the operation of the heat pump is reversed from heating to cooling, i.e. the heat pump behaves like a chiller, the secondary fluid receives heat in the plate heat exchanger, that acts as a condenser, and, in turn, rejects heat to the environmental air through the fin-and-tube heat exchanger.

The simulation model of each system is built with a bottom-up approach, i.e. connecting the sub-models of each component of the heat pump.

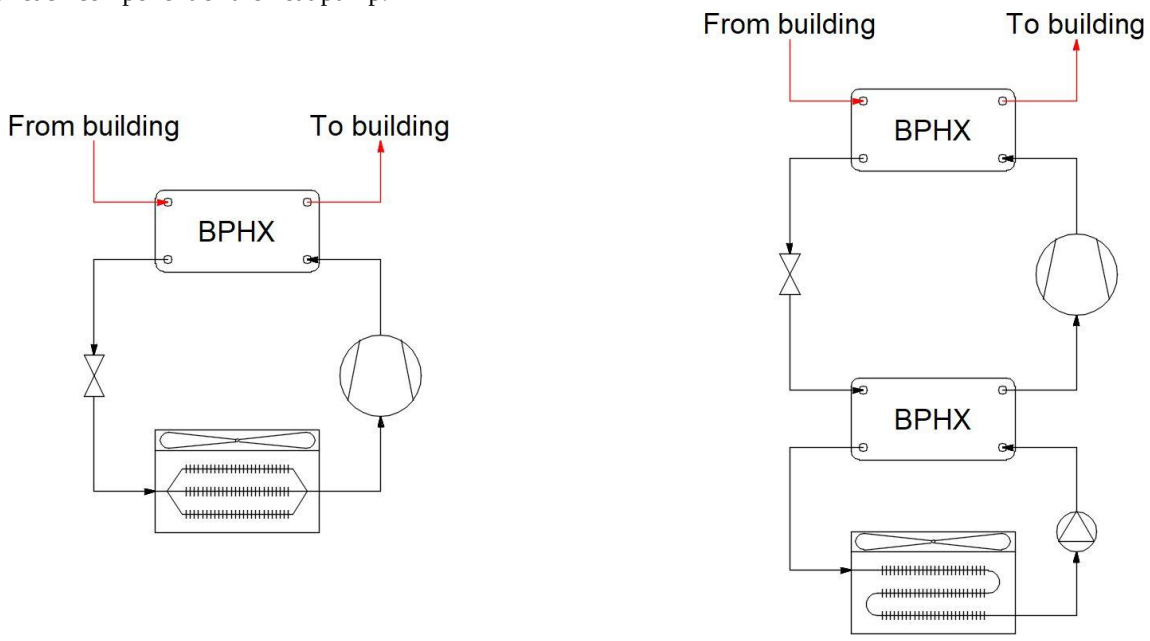


Fig. 1. Layout of the direct system (left) and indirect system (right) considered in the present study.

2.1. Compressor modelling

The compressors considered in the present study are hermetical, variable speed scroll compressors that are modelled through the ten coefficients polynomial curves that express the refrigerant mass flow rate processed by the compressor and its power consumption as per EN 12900 [8]:

$$\dot{m} = a_0 + a_1 T_{EVAP} + a_2 T_{COND} + a_3 T_{EVAP}^2 + a_4 T_{EVAP} T_{COND} + a_5 T_{COND}^2 + a_6 T_{EVAP}^3 + a_7 T_{EVAP}^2 T_{COND} + a_8 T_{EVAP} T_{COND}^2 + a_9 T_{COND}^3 \quad (1)$$

$$P = b_0 + b_1 T_{EVAP} + b_2 T_{COND} + b_3 T_{EVAP}^2 + b_4 T_{EVAP} T_{COND} + b_5 T_{COND}^2 + b_6 T_{EVAP}^3 + b_7 T_{EVAP}^2 T_{COND} + b_8 T_{EVAP} T_{COND}^2 + b_9 T_{COND}^3 \quad (2)$$

The coefficients that appear in Eqs. (1-2) are valid for a well-defined rotational speed, so different sets of coefficients are needed to compute the compressor performance when its rotational speed is changed. Finally, due to the heat pump application, the compressor is assumed to be adiabatic and, therefore, the refrigerant enthalpy at the compressor discharge is calculated through the following equation:

$$h_{DIS} = h_{SUC} + P/\dot{m} \quad (3)$$

2.2. Plate heat exchanger modelling

Plate heat exchangers models are developed using the finite volume method. Each heat exchanger is divided in small slices and the amount of heat transferred between the hot and cold fluid in the small volume is calculated using the ε-NTU method according to the following equations:

$$\varepsilon = \frac{\dot{Q}}{\dot{Q}_{MAX}} = \begin{cases} \dfrac{1 - e^{-NTU(1-R^*)}}{1 - R^* e^{-NTU(1-R^*)}} & counterflow \\ \dfrac{1 - e^{-NTU(1+R^*)}}{1 + R^*} & parallel\ flow \end{cases} \quad (4)$$

$$\dot{Q} = \dot{m}_H c_{P,H} \left(T_{H,IN} - T_{H,OUT}\right) = \dot{m}_C c_{P,C} \left(T_{C,OUT} - T_{C,IN}\right) \quad (5)$$

$$\dot{Q}_{MAX} = min\ (\dot{m}_H c_{P,H}, \dot{m}_C c_{P,C}) \left(T_{H,IN} - T_{C,IN}\right) \quad (6)$$

$$R^* = \frac{min\ (\dot{m}_H c_{P,H}, \dot{m}_C c_{P,C}) \left(T_{H,IN} - T_{C,IN}\right)}{max\ (\dot{m}_H c_{P,H}, \dot{m}_C c_{P,C}) \left(T_{H,IN} - T_{C,IN}\right)} \quad (7)$$

$$NTU = \frac{UA}{min\ (\dot{m}_H c_{P,H}, \dot{m}_C c_{P,C}) \left(T_{H,IN} - T_{C,IN}\right)} \quad (8)$$

$$(UA)^{-1} = R_H + R_{FOU,H} + R_{WALL} + R_{FOU,C} + R_C \quad (9)$$

The overall heat transfer rate is, then, the sum of the infinitesimal heat transfer rate at volume scale.

The correlation used for the calculation of the heat transfer coefficient are the correlations proposed by Longo et al. [9-10] for the evaporation, for the condensation and for the single phase fluid (water in the condenser/evaporator, secondary fluid in the evaporator/condenser, refrigerant in the vapour zone and liquid zone in the condenser and refrigerant in the vapour zone in evaporator).

The heat exchangers are designed with counterflow arrangement in the heating mode and with a parallel flow during the cooling mode.

2.3. Expansion valve modelling

The expansion valve is modelled considering an isenthalpic process and assuming that it is able to keep the superheat at the evaporator outlet at the set value of 5 K in any operating conditions.

2.4. Fin-and-tube heat exchanger modelling

The model of the fin-and-tube heat exchanger is developed using a finite volume approach [11]. Furthermore, since the flow rate of fluid is evenly divided in the exchanger circuits, it is decided to model only one circuit to reduce computational effort. Similarly to the plate heat exchangers, the heat transfer within the single element is solved by applying the ε-NTU method. Indeed, the same set of equations (5(9) is used with an update of the equation for the effectiveness calculation to account for the flow arrangement:

$$\varepsilon = \frac{\dot{Q}}{\dot{Q}_{MAX}} = \begin{cases} \frac{1}{R^*}\left(1 - e^{-R^*\left(1-e^{-NTU}\right)}\right) \; if \; (\dot{m}c_P)_{AIR} < (\dot{m}c_P)_{INN} \\ 1 - e^{-\left(1-e^{-NTU\cdot R^*}\right)/R^*} \; if \; (\dot{m}c_P)_{AIR} > (\dot{m}c_P)_{INN} \end{cases} \tag{10}$$

The correlations used for the convective heat transfer coefficient calculation are the Gnielinski correlation [12] for single phase flow inside tubes, the Diani et al. [13], for evaporation and the Kedzierski and Goncalves [14] for condensation. The air side heat transfer coefficient is calculated using the Wang et al. correlation [15] in dry mode and the Wang et al. [16] in wet mode.

Depending on the season and on the characteristics of the air, there can be different types of heat transfer (dry, wet and frost) as detailed in the next sections.

2.4.1 Dry mode: sensible heat exchange

The simplest case is related to the sensible heat transfer. In the dry mode, the surface temperature of the heat exchanger is higher than the dew point temperature of the air. The air changes its enthalpy by changing only the temperature whereas the water content, i.e. the humidity ratio, is constant. In the ε-NTU method, the dry bulb temperature is used to characterize air conditions and the Schmidt's model [17] is used to compute the fin efficiency. In the counterflow arrangement, the process to solve all the elements is iterative, since the fluids enter from two opposite sides and only the inlet temperatures are available. It is necessary to assume the outlet temperature and iterate to check the convergence. Instead, in the parallel flow, the resolution is straightforward.

2.4.2 Wet mode: latent heat exchange by air dehumidification

In the wet mode, the surface temperature of the heat exchanger is lower than the dew point temperature of the air but higher than 0 °C. In this situation, air dehumidification occurs. This phenomenon consists of the condensation of the water vapour which is in the air and it involves both the sensible heat transfer and the mass transfer (latent heat transfer).

The resolving method is the same as reported for the dry mode. However, it is necessary to modify some parameters in order to consider the mass transfer. First, the latent heat of condensation of water has to be considered in the calculation of the overall heat transfer rate as per eq. (11) in which the condensed water flow rate is computed using the mass transfer coefficient which, in turn, is estimated through the Lewis' analogy [18].

$$\dot{Q}_{LAT} = \dot{m}_{COND}\Delta h_{LV} = h_{MT}(x_{AIR} - x_{WALL})A\Delta h_{LV} \tag{11}$$

Additionally, considering that the heat transfer takes place between air and a wet surface, both the convective heat transfer coefficient and the fin efficiency change. The former is computed through an appropriate model [18] whereas the latter is modified to account for the mass transfer resistance as done in the model proposed by McQuinston et al. [18]. Finally, in order to use the ε-NTU method, the wet bulb temperature of the air must be used instead of the dry bulb temperature, which is directly connected to the air enthalpy.

2.4.3 Frost mode

In the frost mode, the surface temperature of the heat exchanger is lower than the dew point temperature of the air and, at the same time, lower than 0 °C. In this situation, frost formation and accumulation on the finned surface occurs.

In this case, the water vapour directly sublimates on the surface of the heat exchanger, passing from the gaseous state to the solid state. The heat transfer is determined by the temperature gradients between the air flow and the frost surface, while the mass transfer is determined by the vapour concentration gradients. Part of the total transferred water vapour diffuses into the existing porous frost layer, and undergoes phase transformation to ice, contributing to increase the frost density. The remainder freezes on the frost surface, contributing to increase the frost thickness [19].

Following Qiao et al. [19], the mass balance of the total water vapour transferred from the air stream to the frost layer can be expressed as:

$$\dot{m}_V = \dot{m}_\rho + \dot{m}_\delta \tag{12}$$

The sensible heat flux exchanged between the air stream and the frost surface is:

$$\dot{Q}_{SENS} = \dot{m}_{AIR} c_{P,AIR} \left(T_{AIR,IN} - T_{WALL}\right)\left(1 - e^{-UA/\dot{m}_{AIR} c_{P,AIR}}\right) \tag{13}$$

Similarly, the flow rate of vapour transferred to the surface of the exchanger is calculated as:

$$\dot{m}_V = \dot{m}_{AIR}\left(x_{AIR,IN} - x_{WALL}\right)\left(1 - e^{-h_{MT} A/\dot{m}_{AIR}}\right) \tag{14}$$

The latent heat flow due to the solidification of the vapour that freezes on the frost surface is calculated by the following equation:

$$\dot{Q}_{LAT,\delta} = \dot{m}_\delta \Delta h_{SL} \tag{15}$$

The total flux transferred during the frost formation process is given by the sum of sensible and latent contributions.

The frost formation, besides influencing the heat transfer process, also determines a variation of the fan consumption. Indeed, the frost thickness reduces the air cross-sectional area which, in turn, increases the pressure drop and changes the operating point of the fan. The new operating point, that changes over time as frost accumulates, has typically a lower flow rate and a higher power consumption.

In order to remove the frost, bringing the finned surface back to the initial, frost-free condition, defrosting cycles are designed. Two main issues are considered: the defrosting time and defrosting cycle frequency. The defrosting time is the period required to ensure the correct melting of the frost accumulated on the surface. The value is proportional to the mass of ice, which can be calculated as:

$$M_F = \rho_F A \delta_F \tag{16}$$

While the energy needed to melt the frost mass is:

$$E_F = M_F \Delta h_{SL} \tag{17}$$

For the sake of simplicity, a constant defrosting time equal to 300 s is assumed.

On the other hand, the choice of the defrost frequency is essential to ensure proper heat pump operation. Indeed, too infrequent defrosting cycles lead to the formation of large thicknesses of ice on the surface, while too frequent defrosting involves waste of energy. To accurately define the correct defrost start time, the defined thickness should be evaluated instantaneously. However, the frost thickness is difficult to measure, so, the defrost frequency is set on the excess of the fan pressure increase that arises from the increase of air pressure drop. Indeed, once the maximum value of the pressure increase is reached, the operation of the fan is stopped and the 300 s defrosting cycle starts.

3. Case study description

3.1. Building

The building considered in the present study is taken from the scientific literature [20]. It is a new single-family house that consists of two levels with a floor area of 70 m^2 each. Radiant floor is considered as the indoor emitting system. The main feature of the building are reported in Table 1.

Table 1. Main feature of the building

U_{WALL}	0.15 W/(m^2K)
U_{ROOF}	0.13 W/(m^2K)
U_{FLOOR}	0.15 W/(m^2K)
$U_{WINDOWS}$	1.10 W/(m^2K)
U_{DOOR}	1.30 W/(m^2K)
$\Delta U_{THERMAL\ BRIDGE}$	0.05 W/(m^2K)
Infiltration	0.10 h^{-1}
Ventilation System	Yes

The thermal loads are calculated in TRNSYS environment and considering the two levels as a single thermal zone. From the annual simulation, the maximum heating load is equal to 6340 W (T_{AIR} = -12 °C) while the maximum cooling load is equal to 6317 W (T_{AIR} = 32 °C). For the sizing of the heating/cooling system, these values are "rounded" to reproduce a slight oversizing that would be found in a real application. The building is characterized by a heating period longer than the cooling period. For this reason, the system works mainly as a heat pump. The guideline used to choose the components is to prefer and guarantee the maximum efficiency in winter conditions. As a result, the nominal conditions on which the systems are designed are: T_{AIR} = -12 °C, $\dot{Q}_{BUILDING}$ = 7000 W, duration of heating season equal to 2822 h.

3.2. Heat pump

In the present study, three different heat pumps are considered:

- The first heat pump is an air-to-water heat pump working with R410A. This heat pump allows for the direct installation and, therefore, is considered as the current, largely diffused baseline technology.
- The second heat pump is a water-to-water heat pump working with R410A. This heat pump allows for indirect installation. It is considered as the term of comparison for indirect systems.
- The third heat pump is a water-to-water heat pump working with R290. This heat pump works with propane and is used in indirect installation with the aim of reducing refrigerant charge. It is the innovative system in indirect systems.

Air-to-water heat pump working with R290 is not considered in the present study since it requires a large refrigerant charge.

The R410A air-to-water heat pump is sized considering the constraint shown in **Error! Reference source not found.**. On the other side, considering the water-to-water heat pumps, to allow them to work even when the outside air temperature drops below 0 °C, a mixture of water and ethylene glycol is chosen as secondary fluid to avoid mixture freezing. The glycol concentration is set to 40% so that the freezing temperature is -24.8 °C whereas the inlet and outlet design temperatures are -20 °C and -17 °C respectively since the minimum air temperature is -12 °C.

All the three heat pumps are sized considering real, commercially available components. The characteristics of the main components of the three heat pumps considered are collected in Table 2.

Table 2. Main characteristics of the components of the three heat pumps

Component	Air-to-water R410A	Water-to-water R410A	Water-to-water R290
Compressor	Scroll compressor	Scroll compressor	Scroll compressor

	Variable speed	Variable speed	Variable speed
	Swept volume: 25 cm^3/rev	Swept volume: 25 cm^3/rev	Swept volume: 45 cm^3/rev
	Rotational frequency: 35 Hz – 110 Hz	Rotational frequency: 35 Hz – 110 Hz	Rotational frequency: 35 Hz – 110 Hz
	Oil charge: 0.74 dm^3	Oil charge: 0.74 dm^3	Oil charge: 1.45 dm^3
Condenser	Plate height: 526 mm	Plate height: 526 mm	Plate height: 526 mm
(plate heat exchanger)	Plate width: 119 mm	Plate width: 119 mm	Plate width: 119 mm
	Plate pitch: 1.56 mm	Plate pitch: 1.56 mm	Plate pitch: 1.56 mm
	φ = 1.24	φ = 1.24	φ = 1.24
	Plate number: 18	Plate number: 18	Plate number: 18
Evaporator	Tube inner diameter: 9.52 mm	-	-
(fin-and-tube heat exchanger)	Tube outer diameter: 10.12 mm		
	Tube length: 1000 mm		
	Transversal pitch: 25 mm		
	Longitudinal pitch: 21.65 mm		
	Fin pitch: 4.2 mm		
	Fin thickness: 0.15 mm		
	Number of tubes: 40		
	Number of rows: 4		
	Number of circuits: 4		
Evaporator	-	Plate height: 526 mm	Plate height: 526 mm
(plate heat exchanger)		Plate width: 119 mm	Plate width: 119 mm
		Plate pitch: 1.56 mm	Plate pitch: 1.56 mm
		φ = 1.24	φ = 1.24
		Plate number: 24	Plate number: 22
Finned coil		Tube inner diameter: 9.52 mm	Tube inner diameter: 9.52 mm
(indirect evaporator)		Tube outer diameter: 10.12 mm	Tube outer diameter: 10.12 mm
		Tube length: 810 mm	Tube length: 810 mm
		Transversal pitch: 25 mm	Transversal pitch: 25 mm
		Longitudinal pitch: 21.65 mm	Longitudinal pitch: 21.65 mm
		Fin pitch: 4.2 mm	Fin pitch: 4.2 mm
		Fin thickness: 0.15 mm	Fin thickness: 0.15 mm
		Number of tubes: 32	Number of tubes: 32
		Number of rows: 4	Number of rows: 4
		Number of circuits: 8	Number of circuits: 8

It is worth mentioning that the compressor for R290 is not a native variable speed compressor. However, for the sake of homogenous comparison, in the present study it is assumed that it is possible to drive it through an inverter. In order to compute the compressor performance at rotational speed different from 50 Hz, corrective look-up tables are prepared starting from the data available with the R410A, variable speed compressor. Tables that report the refrigerant mass flow rate and compressor power consumption as a function of the shaft rotational frequency and in broad ranges of evaporating and condensing temperatures are first generated and, then, normalised considering the nominal rotational frequency equal to 50 Hz. This results in correction coefficients that represent the reduction (increase) in the refrigerant mass flow rate or compressor power as a result of the reduction (increase) in the shaft rotational frequency. These values are applied to the R290 compressor to simulate its behaviour under variable speed regime.

The heat pumps sizing is then completed with the estimation of the refrigerant charge. The amount of refrigerant which is contained in each component is computed dividing the inner volume by the refrigerant specific volume. More in detail, for the components in which the refrigerant is in single phase, i.e. compressor, pipes, desuperheating zone and subcooling zone of the condenser and superheating zone of the evaporator, the specific volume is calculated considering the average inlet-outlet pressure and temperature. On the other hand, for the components in which the refrigerant undergoes a phase change, i.e. the condensing

zone of the condenser and the evaporating zone of the evaporator, the average specific volume is computed starting from those of the saturated liquid and saturated vapour and using the void fraction models proposed by Steiner [21] in the fin-and-tube heat exchanger and by Smith [22], as suggested by Mancini [23], in the plate heat exchangers. Finally, refrigerant mass trapped in the oil is accounted for considering the solubility diagram of the refrigerant-oil pair that is provided by the compressor manufacturer. Overall, the refrigerant charge in the R410A air-to-water heat pump is estimated to be 3561 g. This value is 20% lower than that of a real air-to-water heat pump of similar capacity which, as per the manufacturer's catalogue, is filled with 4320 g of R410A [24]. However, it must be mentioned that the calculation of the charge does not consider any liquid receiver which, in turn, is installed in the real heat pump. As a result, it is possible to state that the charge calculation is quite accurate. For the water-to-water heat pumps, the refrigerant charge is estimated in 899 g with R410A and in 467 g with R290. The water-to-water heat pump has a lower internal volume with respect to the air-to-water one since the fin-and-tube evaporator is replaced by a plate heat exchanger. As a result, the refrigerant charge of R410A reduces by 75%. The charge of the R290 heat pump is even lower since the density of R290 is significantly lower than that of R410A in the full set of operating conditions.

Finally, pumps and fans used to supply the secondary fluid flow rate are chosen. The main characteristics of these devices are reported in Table 3.

Table 3. Main characteristics of the pumps and fans

Component	Air-to-water R410A	Water-to-water R410A	Water-to-water R290
Pump (end-user side)	Not considered since it is the same in each system	Not considered since it is the same in each system	Not considered since it is the same in each system
Fan (fin-and-tube evaporator)	Air flow rate: 6386 m^3/h Power consumption: 293 W	-	-
Pump (plate evaporator	-	Water flow rate: 1.8 m^3/h Power consumption: 115 W	Water flow rate: 1.8 m^3/h Power consumption: 119 W
Fan (indirect evaporator)	-	Air flow rate: 7712 m^3/h Power consumption: 628 W	Air flow rate: 7712 m^3/h Power consumption: 628 W

3.3. Seasonal simulation and performance index

The analysis of the performance of the three heat pumps is carried out considering one year of operation. The yearly simulation is carried out considering a time step equal to 3600 s and assuming that the heat pump operates in steady state regime in it. If frost formation occurs, the time step is reduced to 300 s but, again, the heat pump is assumed to work in steady state in the time step while it changes its operating point from one time step to the other.

At each time step the building load is available from the building simulation whereas the heat pump heating capacity is computed from the simulation tool. Since each heat pump is built with a variable speed compressor, the matching between the end-user need and the capacity delivered by the heat pump may occur by varying the rotational frequency of the compressor shaft, or by on-off cycling. In the former situation, the compressor speed is changed so that the heat pump delivers exactly the building load; in this scenario, the heat pump is assumed operate continuously for the full time step. On the other hand, in the latter situation, which typically occurs at high ambient temperatures, despite the compressor speed is set to the minimum value, the heat pump capacity is higher than the building load and, so, it undergoes on-off cycling with the aim of providing a time step average capacity equal to the building energy need. This working condition is not optimal since additional power consumption related to electronic board arises even when the compressor is switched off. To account for it, a correction of the COP as proposed by EN 14825 [25] is used:

$$COP_{ON-OFF} = \frac{CR}{1 - C_D + C_D \cdot CR} COP_{CONTINUOS} \quad (18)$$

In eq. (18) CR is the capacity ratio, i.e. the ratio between the building load and the heat pump capacity, whereas C_D is the degradation coefficient for on-off cycling, equal to 0.9, and $COP_{CONTINUOS}$ is the coefficient of performance of the heat pump that operates without on-off cycling. It is worth specifying that the control of the heat pump capacity is achieved acting simply on the rotational frequency of the compressor shaft. All the other components that may vary their rotational speed, i.e. the fan of the evaporator for the

direct system and the fan of the air-to-glycol heat exchanger and the glycol pump for the indirect ones, are instead kept at the maximum speed.

Overall, the performance indexes that are used to compare the three different heat pumps are the seasonal coefficient of performance and the Total Equivalent Warming Impact ($TEWI$) that are calculated as follows:

$$SCOP = \frac{\sum_{i=1}^{n} \dot{Q}_{BUILDING,i} \Delta t}{\sum_{i=1}^{n} \left(P_{COMP,i} + P_{PUMP,i} + P_{FAN,i} + P_{DEFROST,i}\right) \Delta t} \tag{19}$$

$$TEWI = \alpha_{LEAK} M_{REF} nGWP + (1 - \varepsilon_{REC}) M_{REF} GWP + E_{EL} n M_{CO_2} \tag{20}$$

4. Results

Starting from, the energy performance index, Fig. 2 shows the $SCOP$ and the $SCOP_{HP}$ of the three different heat pumps considered in the present study. $SCOP$ is defined as per Eq. (19) and accounts for the power consumption of the compressor, the auxiliaries and the defrost, whereas the $SCOP_{HP}$ is the Seasonal Coefficient Of Performance of the heat pump only, i.e. it accounts for the compressor consumption only. The rationale behind these indexes is pointing out the differences that arise not only from the system layout, i.e. direct and indirect, but also to highlight the performance of the use of different refrigerants.

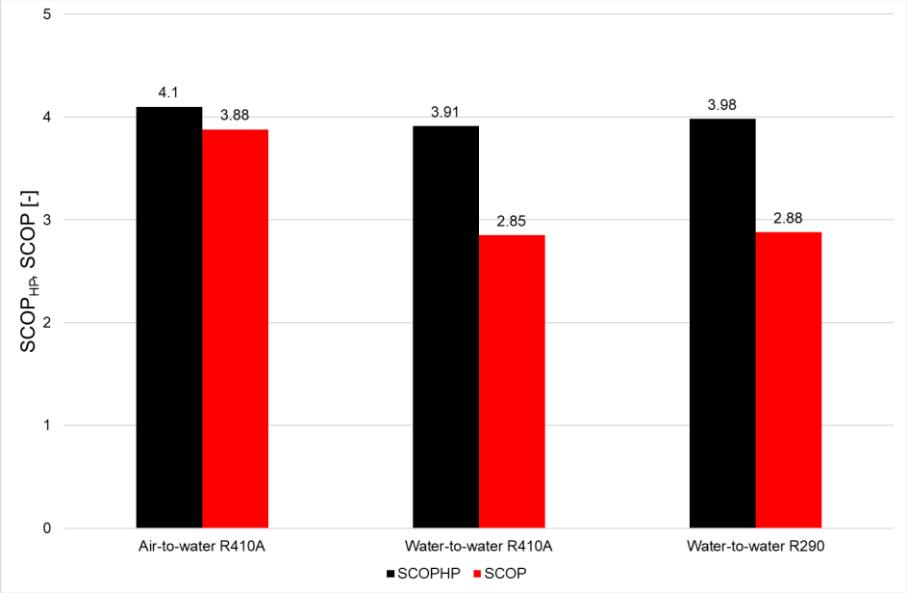


Fig. 2. $SCOP_{HP}$ and SCOP of the three systems.

From the analysis of the figure, it is possible to conclude that the performance of the heat pump only is very similar since a reduction in the $SCOP_{HP}$ of around 3% is found passing from direct R410A system to indirect ones. Additionally, in indirect systems a slight tendency of R290 to perform better than R410A may be found because the $SCOP_{HP}$ of the heat pump that uses the natural refrigerant is around 2% higher than that of R410A-based heat pump. However, a significant difference arises when the consumptions related to the auxiliaries and the defrosting cycles are taken into consideration. Indeed, the $SCOP$ of the overall system is around 26% lower for the indirect heat pumps with respect to the direct one. This is related to the strong increase in the fan and pump consumptions that arises in the indirect systems. Indeed, as shown in **Error! Not a valid bookmark self-reference.**, in these systems the fan consumption is around 5 times higher than the fan consumption in direct system and also the consumption of the water-ethylene glycol mixture is not negligible since it is even higher than the consumption of the fan of direct systems. The first result is not surprising: in indirect system, the evaporating temperature is significantly lower than the air temperature since heat is extracted from the water-ethylene glycol mixture which, in turn, is colder than air. As a result, in indirect systems there is an increase in the range of air temperature and humidity conditions in which the frost formation and accumulation phenomenon occurs. This result in an increase in the air side pressure drop

which, in turn, leads to an increase in the fan consumption. Similarly, although the pump power consumption is small, the large number of operating hours, i.e. the full heating season, leads to a not negligible energy consumption.

Table 4. Details on energy consumption of the three heat pumps

	Fan	Pump
Air-to-water R410A	122.5 kWh	-
Water-to-water R410A	670.9 kWh	202.4 kWh
Water-to-water R290	674.4 kWh	204.6 kWh

Finally, the $TEWI$ of the three systems is in Fig. 3. For the calculation of this environmental index, the GWP values are taken from the last IPCC report [26] resulting in GWP_{100} = 0.02 and GWP_{100} = 2256 for R290 and R410A respectively. The refrigerant leakage is assumed to be 2% and, additionally, it is assumed that it does not influence the heat pump performance. This may be a source of error, especially for indirect systems that might not be built with liquid receiver, but it is done for the sake of simplicity since the model developed for this study is not able to simulate the operation of a heat pump in undercharged conditions. The other parameters are: lifetime of the system equal to 10 years, end-of-life recovery efficiency 90% and emission of CO_2 per unit of electrical energy 247 g/kWh [27]. Comparing the results, it is possible to state that, despite its lower energy performance, the system using R290 largely benefits from the low-GWP of this refrigerant since its $TEWI$ is around 5% lower than that of the baseline solution despite its higher energy consumption. On the other hand, comparing the two systems working with R410A, the indirect one has a lower direct impact, as a consequence of the lower charge, but higher indirect emission since it shows higher energy consumption. Overall, the two effects approximately compensate each other resulting in a $TEWI$ only around 4% higher than that of the baseline system.

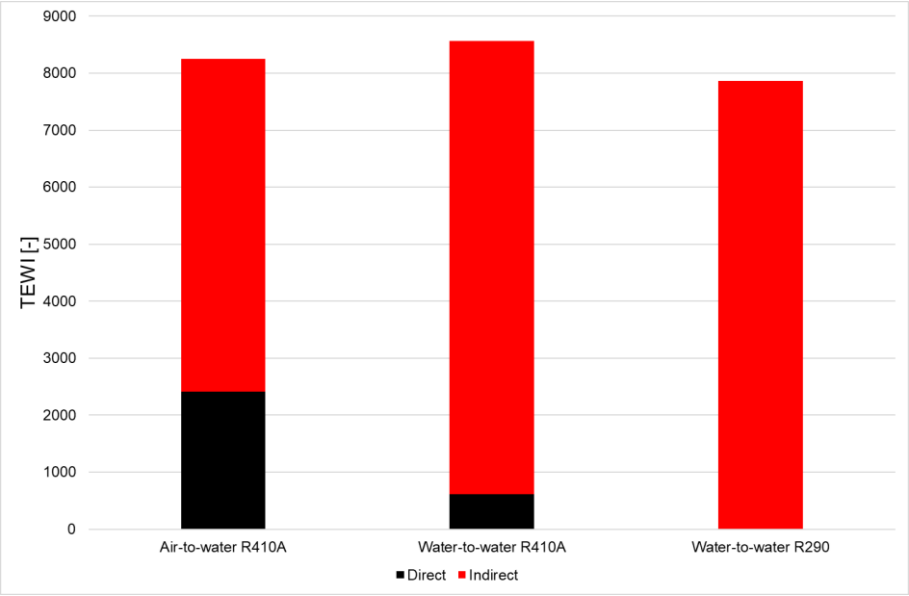


Fig. 3. TEWI of the three systems.

5. Conclusions

In the present paper, the performance of an indirect expansion heat pump working with R290 is analysed and compared with that of R410A heat pumping systems. For this refrigerant, both well-established air-to-water heat pump, i.e. direct system, and water-to-water heat pump, i.e. indirect system, are considered.

The analysis is carried out on a yearly basis using a simulation tool designed and built for this purpose. Seasonal coefficient of performance ($SCOP$) is used as energy performance index whereas total equivalent warming impact ($TEWI$) is used to measure the equivalent carbon dioxide emissions of the three systems.

Overall, the direct system performs better than the indirect ones both from the energy efficiency point of view and the environmental point of view. Indeed, the $SCOP$ of the indirect systems are around 25% lower than that of the direct system whereas the $TEWI$ is around 9%-15% higher. However, the refrigerant charge in indirect system is significantly lower than that required in a direct system, resulting in an improvement in the system safety.

Nomenclature

$a_0 \dots a_9$	Coefficients in eq. (1)
A	Area [m^2]
$b_0 \dots b_9$	Coefficients in eq. (2)
c_P	Isobaric heating capacity [J/(kg·K)]
C_D	Degradation coefficient [-]
COP	Coefficient of performance [-]
CR	Capacity ratio [-]
E	Energy [J]
GWP	Global warming potential [-]
h	Enthalpy [J/kg]
h_{MT}	Mass transfer coefficient [kg/(m^2·s)]
M	Mass [kg]
M_{CO_2}	Emission of carbon dioxide per unit of energy [kg/kWh]
$\dot{m}$	Mass flow rate [kg/s]
$\dot{m}_\rho$	Mass flow rate of vapour that increases the frost density [kg/s]
$\dot{m}_\delta$	Mass flow rate of vapour that increases the frost thickness [kg/s]
n	Number of years [-]
NTU	Number of Transfer Unit [-]
P	Power [W]
$\dot{Q}$	Heat transfer rate [W]
R	Thermal resistance [K/W]
R^*	Heat capacity ratio [-]
$SCOP$	Seasonal coefficient of performance [-]
T	Temperature [K]
$TEWI$	Total equivalent warming impact [kg]
U	Overall heat transfer coefficient [W/K]
x	Humidity ratio [kg/kg$_{DA}$]
Greek symbols	
α_{LEAK}	Leakage rate [-]
δ	Thickness [m]
Δh_{LV}	Liquid-to-vapour phase change enthalpy [J/kg]
Δh_{SL}	Solid-to-liquid phase change enthalpy [J/kg]
Δt	Time step [s]
ε	Effectiveness [-]
ε_{REC}	Recovery efficiency [-]
ρ	Density [kg/m^3]

Subscript			
AIR	Air	*FOU*	Fouling
BUILDING	Building	*H*	Hot
C	Cold	*IN*	Inlet
COMP	Compressor	*INN*	Inner
COND	Condensing	*LAT*	Latent
DEFROST	Defrost	*PUMP*	Pump
DIS	Discharge	*REF*	Refrigerant
EL	Electrical	*SENS*	Sensible
EVAP	Evaporating	*SUC*	Suction
F	Frost	*V*	Vapour that frosts
FAN	Fan	*WALL*	Wall

References

[1] European Union , 2014. Regulation (EU) no 517/2014 of the european parliament and the EU Council of 16 april 2014 on fluorinated greenhouse gases and repealing Regulation (EC) no 842/2006. Off. J. Eur. Union 150, 195–230.
[2] United Nations, 2016. The amendment to the Montreal Protocol agreed by the Twenty-Eighth Meeting of the Parties (Kigali, 10–15 October 2016).
[3] Tammaro, M., Montagud, C., Corberán, J.M., Mauro, A.W., Mastrullo, R., 2017. Seasonal performance assessment of sanitary hot water production systems using propane and CO2 heat pumps. International Journal of Refrigeration 74, pp. 224-239.
[4] Fernando, P., Palm, B., Lundqvist, P., Granryd, E. Propane heat pump with low refrigerant charge: design and laboratory tests. International Journal of Refrigeration 27, pp. 761-773.
[5] Corberán, J.M., Martínez, I.M., Gonzálvez, J. Charge optimisation study of a reversible water-to-water propane heat pump. International Journal of Refrigeration 31, pp. 716-726.
[6] Cavallini, A., Da Riva, E., Del Col, D., Performance of a large capacity propane heat pump with low charge heat exchangers. International Journal of Refrigeration 33, pp. 242-250.
[7] Ghoubali, R., Byrne, P., Bazantay, F., 2017. Refrigerant charge optimisation for propane heat pump water heaters. International Journal of Refrigeration 76, pp. 230-244.
[8] European Committee for Standardization, 2013. EN 12900 - Refrigerant compressors - Rating conditions, tolerances and presentation of manufacturer's performance data.
[9] Longo, G.A., Mancin, S., Richetti, G., Zilio, C., 2015. A new model for refrigerant boiling inside Brazed Plate Heat Exchangers (BPHEs). International Journal of Heat and Mass Transfer 91, pp. 144–149.
[10] Longo, G.A., Richetti, G., Zilio, C., 2015. A new computational procedure for refrigerant condensation inside herringbone-type Brazed Plate Heat Exchangers. International Journal of Heat and Mass Transfer 82, pp. 530–536.
[11] Joppolo, C.M., Molinaroli, L., Pasini, A., 2015. Numerical analysis of the influence of circuit arrangement on a fin-and-tube condenser performance. Case Studies in Thermal Engineering 6, pp.136-146.
[12] Gnielinski, V., 2013. On heat transfer in tubes. International Journal of Heat and Mass Transfer, 63, pp. 134-140.
[13] Diani, A., Mancin, S., Rossetto, L., 2014. R1234ze(E) flow boiling inside a 3.4 mm id microfin tube. International Journal of Refrigeration 47, pp. 105-119.
[14] Kedzierski, M.A., Goncalves, J.M., 1999. Horizontal convective condensation of alternative refrigerants within a micro-fin tubes. Enhanced Heat Transfer 6, pp. 161-178.
[15] Wang, C.-C., Lee, C.-J., Chang, C.-T., Lin, S.-P., 1999. Heat transfer and friction correlation for compact louvered fin-and-tube heat exchangers. International Journal of Heat and Mass Transfer 42, pp. 1945-1956.
[16] Wang, C.-C., Lin, Y.-T., Lee, C.-J., 2000. Heat and momentum transfer for compact louvered fin-and-tube heat exchangers in wet conditions. International Journal of Heat and Mass Transfer 43, pp. 3443-3452.
[17] Schmidt, T.E., 1949. Heat transfer calculations for extended surfaces. Refrigerating engineering, pp. 351-357.
[18] Mc Quiston, F.C., Parker, J.D., Spitler, J.D. Heating, ventilating, and air conditioning: analysis and design. John Wiley & Sons, 2004.
[19] Qiao, H., Aute, V., Radermacher, R., 2017. Dynamic modeling and characteristic analysis of a two-stage vapor injection heat pump system under frosting conditions. International Journal of Refrigeration 84, pp. 181-197.
[20] Scoccia, R., Toppi, T., Aprile, M., Motta, M., 2018. Absorption and compression heat pump systems for space heating and dhw in european buildings: Energy, environmental and economic analysis. Journal of Building Engineering 16, pp. 94-105.
[21] Steiner, D., 1993. Heat transfer to boiling saturated liquids. VDI Heat Atlas
[22] Smith, S.L., 1969. Void fraction in two-phase flow: a correlation based upon an equal velocity head model. Proceedings of the Institution of Mechanical Engineers 184, 647-664
[23] Mancini, R., 2019. Design and performance analysis of plate heat exchangers for heat pumps using pure and mixed refrigerants. PhD thesis, Danish Technical University.
[24] Aermec, ANK 020-085 Installation manual.
[25] European Committee for Standardisation, 2018.EN 14825 - Air conditioners, liquid chilling packages and heat pumps, with electrically driven compressors, for space heating and cooling - Testing and rating at part load conditions and calculation of seasonal performance
[26] IPCC, 2022: Climate Change 2022: Impacts, Adaptation and Vulnerability. Contribution of Working Group II to the Sixth Assessment Report of the Intergovernmental Panel on Climate Change. Cambridge University Press. Cambridge University Press, Cambridge, UK and New York, NY, USA, 3056 pp.
[27] European Environment Agency, 2022. https://www.eea.europa.eu/data-and-maps/daviz/co2-emission-intensity-12/#tab-chart_2.

14th IEA Heat Pump Conference
15-18 May 2023, Chicago, Illinois

Decarbonization of Affordable Multifamily Housing – Application of high-efficiency monoblock heat pumps

Maggie Sheng[a], Zack Allen[b], Siva Sankaranarayanan[a*]

[a]*EPRI, 3420 Hillview Ave, Palo Alto, CA 94340, USA,* [b]*Silicon Valley Mechanical, Palo Alto, CA.*

Abstract

Affordable multifamily housing presents one of the hardest residential sectors to decarbonize. Many of these housing units have the bare minimum in terms of HVAC (e.g., swamp coolers + gas wall furnaces, etc.) and are compromised on occupant comfort. A recent innovation in the heat pump retrofit market is the development of monoblock heat pumps which do not have separate indoor-outdoor units and are relatively simple to install. These are also high-efficiency inverter-driven systems that operate on a 120V single phase. The authors were part of a project team that worked with a multifamily affordable housing complex in Fresno, CA to install 140 monoblock heat pumps in 60 living units. The project investigated various aspects of the retrofit process and collected energy use data from all the units to derive insights into the efficacy of these heat pumps for providing comfort while reducing GHG emissions. The results indicate that residents used their heat pumps similar to swamp coolers in the main living areas, and with additional heat pumps in the bedrooms, were able to achieve better cooling while staying within the building's overall current capacity. In winter, the use of heat pumps significantly reduced energy use consequently reducing the overall GHG emissions from this community. A set of recommendations on applying these heat pumps in utility customer programs to help to decarbonize affordable multifamily housing is developed.

© HPC2023.
Selection and/or peer-review under the responsibility of the organizers of the 14th IEA Heat Pump Conference 2023.

Keywords: affordable housing; decarbonization; retrofits; monoblock heat pumps; 120V heat pumps;

1. Introduction

Historically, higher-income communities have been the early adopters of emerging energy technologies—such as rooftop solar photovoltaics (PV), high-efficiency appliances, light-emitting diode (LED) lights, heat pumps, heat pump water heaters (HPWHs), and electric vehicles. The idea behind this market-driven approach is that as deployment becomes more widespread, the technologies will eventually become more affordable to low-income communities, further expanding the market.

Today, as governments and utilities establish aggressive climate goals, the need to electrify and decarbonize residential and commercial buildings—which account for about 12% of U.S. greenhouse gas emissions—becomes more urgent. However, advanced electric building technologies such as electric heat pumps and HPWHs are generally expensive and out-of-reach for low-income households.

The cost of adoption of heat pump technologies goes beyond the equipment and labor costs for affordable multifamily housing (which houses low-to-moderate income residents) as these buildings are heavily constrained by existing electrical capacity. In a recent study conducted by the authors in a garden-style multifamily affordable housing complex in Fresno, CA, each building with up to 8 apartments each had a total capacity of 200A with each apartment having 100A panels. Full scale electrification of this community using traditional mini-split heat pumps and heat-pump water heaters would have significantly exceeded the capacity constraints in many of the buildings. The solution to this challenge required scouting, analyzing, certifying,

* Corresponding author. Tel.: +1-510-821-1756
E-mail address: ssankaranarayanan@epri.com.

and installing 120V monoblock air-source heat pumps for space conditioning. The use of 120V monoblock[1] heat pumps helped to eliminate costs for panel upgrades, additional wiring (for 240V), and potentially higher costs associated with increasing a building's current capacity all of which collectively would have doubled the per unit cost of the overall retrofit. In the following sections, we describe why the use of these monoblock heat pumps and other decarbonization measures that can form a "package" solution for decarbonizing affordable multifamily housing.

Recognized as a critical technology for efficient space conditioning and building decarbonization, electric heat pumps have become an increasingly popular option in residential buildings across the country and the globe. Using electricity instead of fossil fuel as energy source, heat pumps enable the large majority of current space heating demand to be met with lower carbon emissions. By leveraging a vapor compression refrigeration cycle to harness ambient thermal energy, heat pumps can efficiently provide heat with one-third to one-fifth of the electricity consumed by conventional electric heating equipment [1].

In the US, electric heat pumps are most adopted in single-family houses, but there is an increasing trend of electric heat pump adoption in multi-family apartment buildings as well. As of 2005, apartment buildings accounted for about 10.2% of total installed residential electric heat pump. This number has increased to 13.2% in 2015 [2]. 2021 has been a record-high year for heat pump sales. In the US, heat pump sales grew by around 15% year-on-year. Air-source heat pumps (ASHP) account for most sales, with a market share of more than 60% [1] . With continued advances in heat pump technology, heat pumps can perform well across nearly all climate zones in the country [1]. ASHPs operate most efficiently in mild and coastal climates [3]. Therefore, California climate is ideal for ASHP implementation. According to the survey of California Heat Pump Residential Market Characterization and Baseline Study, most of the construction professionals in the survey expected the heat pump market to grow in the next five years in California. Half of these professionals reported they already install heat pumps regularly and see heat pumps becoming increasingly critical to meet California's energy goals. Even in cold places like Lake Tahoe, manufacturers make heat pumps that work effectively at very cold temperatures [4].

However, there are still some barriers to widespread adoption. In addition to the negative perception carried by historical poor performance at low outdoor temperature, heat pumps require more complex and proper maintenance than furnaces to keep optimal performance. The expected average lifetime for a heat pump is 10 years or more, while 15-20 years for a gas furnace [5]. Moreover, customers and technicians are more familiar with gas furnaces and air conditioners. The lack of appropriate skills and knowledge and high upfront costs are the two other major barriers to widespread heat pump adoption, especially in the placement of the equipment of the compressor unit [4].

In the Net Zero Emission by 2050 scenario, the global heat pump stock should cover at least 20% of global heating needs in buildings, while heat pumps still only meet about 10% of the need for now [1]. Policy support for heat pumps is rapidly increasing to meet decarbonization ambitions [1]. Several manufacturers are expanding heat pump production with emerging business models. Further policy support and technical innovation are still needed to reduce upfront purchase and installations costs, remove market barriers, improve energy performance, and exploit potential to enable power system integration and flexibility [1].

2. Decarbonizing Affordable Multifamily Housing

2.1. What is the motivation?

Affordable multifamily housing is one of the most challenging segments of buildings to decarbonize and this is especially true for retrofits. There are several extenuating circumstances that makes this challenging, some of these are listed below:

- **Energy Burden**: Any upgrades and technology investments made cannot result in increasing the energy burden in affordable housing communities. With decarbonization pathways that utilize electrification, there is a need to be cognizant of the potential for electrified end-uses being higher operating costs for community residents and measures to help mitigate these cost increases are necessary.
- **Split Incentives**: Given that community residents don't own the infrastructure in affordable multifamily housing communities, there is a need to make sure that the investment made by the building owner/operator has a return for the building owner/operator.

[1] Throughout the paper, the term monoblock heat pumps refer to specific class of heat pumps that have a single unit form-factor (indoor unit only) as opposed to the traditional indoor/outdoor (dual-unit) form factor.

- **Retrofit Costs**: In addition to the cost of equipment and labor, retrofits need to explicitly account for retrofit costs which could include costs for additional panel capacity, wiring for 240-V end-use devices, cost of removal of existing (old) infrastructure, asbestos abatement for older vintage buildings, etc. These costs could significantly add to the overall cost of decarbonizing affordable housing communities.
- **Infrastructure upgrade costs**: This impacts electrification based decarbonization measures which are currently being served for space and water heating via natural gas. The additional electrical load that may arise can trigger the need for upgrading distribution infrastructure such as service transformers and requires the local utility to invest in these upgrades.

Given these set of challenges, it is safe to say that if there is a way to engineer a decarbonization solution for affordable multifamily housing, there is a very high likelihood of these decarbonization solutions to find wider applicability. In that sense, this challenge has high innovation potential both in terms of technology as well as business model. The above list is not exhaustive as each community is different and may have their own set of issues that makes decarbonization challenging. However, the market availability of 120V monoblock heat pump products present a viable answer to many of these challenges.

2.2. How does 120V Monoblock heat pumps help?

To help address the challenges with decarbonizing affordable multifamily housing, the use of 120V monoblock heat pumps in conjunction with other electrification and decarbonization technologies can be considered to develop packages of energy conservation measures that can provide for decarbonization while reducing the first cost of upgrades and operating cost of energy.

- **High Efficiency**: The 120V monoblock heat pumps that are currently available in the market are high efficiency inverter driven variable speed heat pumps which have operating Coefficient of Performance (COP) of 3.0 or higher. This effectively provides for a 3x increase in efficiency compared to even the most efficient natural gas heating solutions. This increased efficiency helps to offset the cost of natural gas with higher electricity use that is more efficient for the same amount of heat.
- **120V as opposed to 240V**: The use of 120V as the operating voltage and less than 15A as the operating maximum current draw allows these heat pumps to used in capacity constrained multifamily buildings. This is especially true if these heat pumps are replacing existing low-efficiency evaporative coolers or window air-conditioning units. This also significantly reduces the risk of higher costs related to retrofit constraints. The unit's operation at lower power draws also allows for not requiring distribution infrastructure upgrades if the unit is replacing an existing low-efficiency system at the living unit level.
- **Monoblock requires less construction**: The use of monoblock heat pump technology also requires less construction impacts as the heat pump unit does not have any ducting, wires, tubes that runs from the outdoor unit to the indoor unit. Additionally, the models used in our case study use two 6" holes for air intake and exhaust allowing for tighter air sealing.
- **Additional decarbonization**: Additional measures such as envelope improvements, community-scale solar PV, etc. with the ability to avail of federal, state, and utility level incentives such as the U.S. Department of Energy's Weatherization Assistance Program (WAP), California's Solar on Multifamily Housing (SOMAH) all help to address issues with split incentives, reducing energy burden, etc. and when done in conjunction with the installation of 120-V monoblock heat pumps helps to further address the challenges with decarbonizing affordable multifamily housing.

3. Case Study

3.1. Project Description

Constructed 50 years ago, Pleasant View is a 60-unit affordable housing community in Fresno, California. It is a family community comprised of 1-, 2-, 3-, and 4-bedroom units spread across ten buildings, each of which contain between four and ten apartments. The units were previously cooled by evaporative coolers and heated by natural gas wall furnaces. A closet in each apartment stored a 40-gallon natural gas water heater. The community is master metered for both electricity and natural gas, with the property owner LINC Housing paying all utility costs to PG&E, the serving utility. Each apartment is served by a 100-A electric panel, while

each building is served by 200-A mains panel (regardless of number of apartments). Limits on the local distribution system precluded full-scale electrification of the property.

The project team installed the monoblock heat pump and limited (limited to 3 of the 10 buildings) centralized HPWH retrofits in the first half of 2020. Retrofits involved installing 120-V, 12-hp Innova D.C. inverter heat pump units with an energy efficiency ratio (EER) of 3.3 (min outside ambient temp of 14F in heating mode) in each apartment. Two advantages of the Innova heat pumps, also referred to as packaged terminal air conditioning (PTAC) stood out: 1) Historically most residential heat pumps installed in the U.S. are 240-V units, which would have required new electric panels and rewiring at Pleasant Hill. The 120-V Innova units minimized any need for upgrades and represented one of the first large scale retrofit installation of 120-V heat pumps in affordable multifamily housing; 2) Historically, heat pumps have been split systems, requiring heat pump components to be installed on opposite sides of the inner and outer wall. Innova's monoblock unit involves installing only a single heat pump component on the inner wall. The monoblock configuration lowers installation costs and possibly long-term maintenance costs. Innova units were installed in the living room of all living units in the building. In two-bedroom units, Innova units were installed in the living room and master bedroom. In three- and four-bedroom units, Innova units were installed in the living room, master bedroom, and secondary bedroom. No further electrical infrastructure changes were made to the living units.

The project team performed the following additional energy efficiency upgrades listed in Table 1. The utility energy savings assistance programs covered some of the common area measures, but the air conditioning upgrades were out of pocket for the property owner.

Table 1. Summary of energy efficiency measures

Energy System	Pre-Retrofit	Post-Retrofit
Wall Insulation	None	R-19
Roof Insulation	R-13	R-25 with blown insulation
Patio Doors	Single Pane	Double pane with low-e and frame sealing
Space Cooling	Direct Evaporative Cooler	120-V Innova Heat Pump
Space Heating	Natural Gas Wall furnace	120-V Innova Heat Pump
Water Heating	40-gallon gas storage water heater	Sanden CO2 shared HPWH (in 3/10 buildings)
Indoor lighting	CFL	LED
Outdoor lighting	Metal halide parking lot lights	LED integrated lamps, fixtures, and posts for parking lot lights
		LED replacement in wall scones
Appliances	Electric coil cooktop	Glass-top electric cooktop
Renewables	None	137-kW community solar PV system

3.2. Data Collection and Methodology

Data collection from the community was performed primarily at the circuit level wherein each living unit was fitted with a current-transformer based circuit level load monitors that helps to provide highly granular (1-min level frequency) disaggregated load data. The need for this level of disaggregated load monitoring was motivated by the fact that the community is master metered for both electricity and natural gas thereby not having granular energy consumption at the individual unit level. Data was collected over a 3-year period ranging from 2019 (pre-retrofit) into 2020 (mid-retrofit) and 2021 (post-retrofit). While the heat pump retrofit was done in 2020, many of the other measures such as envelope and solar PV installation happened much before (2018-2019 timeframe). Load calculations were all based on disaggregated circuit level loads with a dedicated CT monitoring the living room Innova unit and master and second bedroom Innova units monitored via 15A shared circuit CTs. The monitors provide cumulative energy data based on per-minute current and voltage measurements which was aggregated to obtain appropriate hourly energy use values. Additionally master metered electric and gas data was used to calculate community level energy use and associated GHG using CAISO provided emissions factors.

3.3. Results

3.3.1. Summary

Total energy increased a small amount in the summer (shown as the small negative orange bars in Figure 1) but decreased significantly in the winter (shown as the orange bars at right). In other words, gas consumption decreased, while electricity consumption increased. Gross energy use decreased by 22%, mostly from winter gas savings.

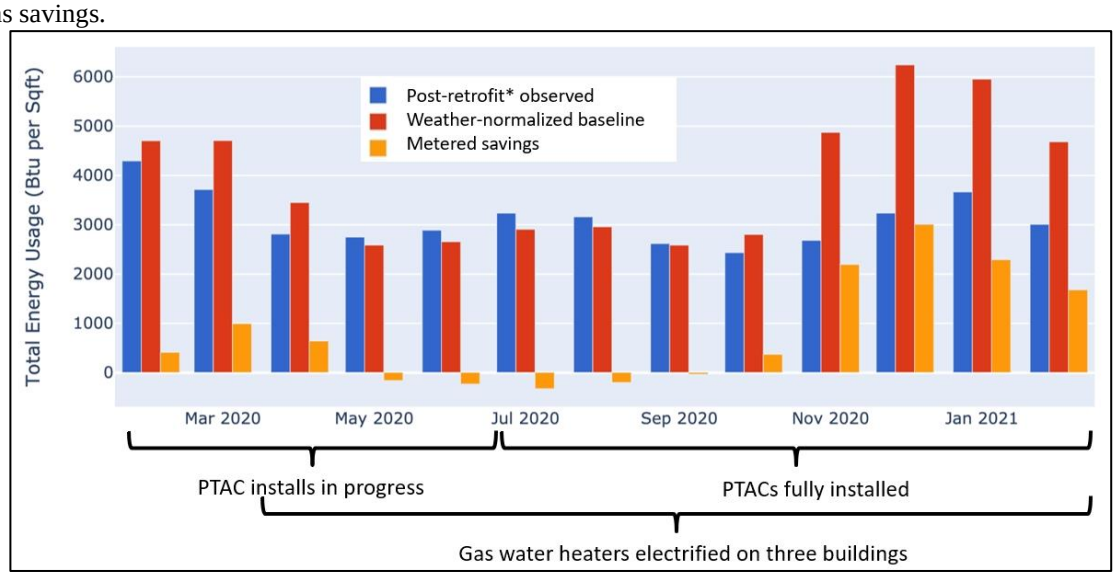


Figure 1 Total Energy (Gas and Electric) Usage[2]

Replacing evaporative cooling with compressor-based cooling, combined with the stay-at-home Covid-19 effect, increased summer GHG emissions. Electrification of water heating all year round overcame these increases, leading to a net GHG emission reduction. Figure 2 indicates the energy use converted to lb CO2e using California Independent System Operator (CAISO) published hourly emissions intensity. Overall emissions (site emissions + source emissions from grid electricity) decreased by 13%, largely due to winter gas savings.

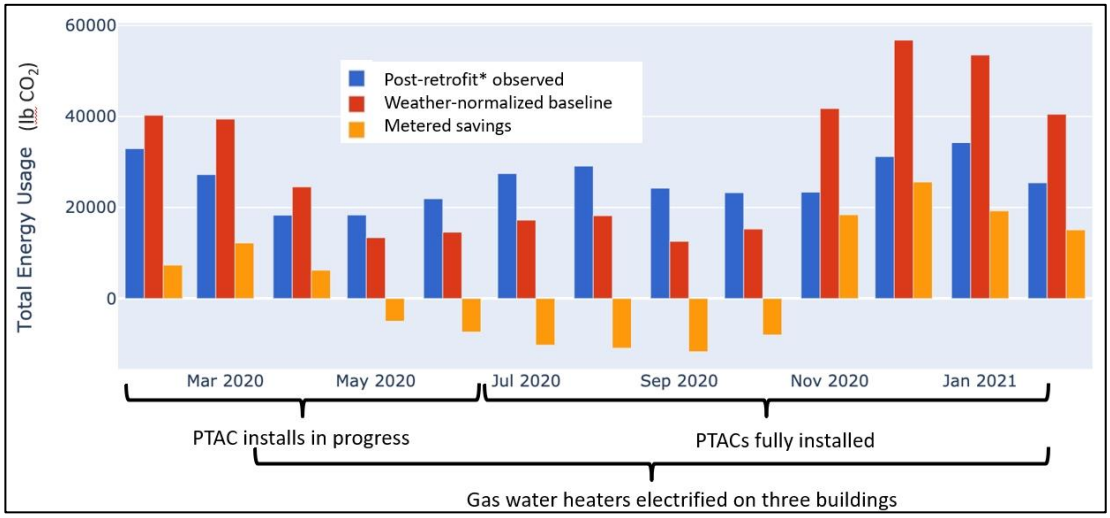


Figure 2 Monthly GHG emissions

While these results indicate the overall effect of PTAC and heat pump water heaters for the time periods under consideration (as indicated in Figure 1 and Figure 2), a detailed analysis of the 120V monoblock heat pumps was conducted to characterize the field performance of this new & emerging heat pump technology.

[2] This is total community level energy use based on master metered gas and electric meter data could not be further disaggregated for the periods shown without combining data from utility meters and circuit level monitors which don't have the same levels of accuracy.

3.3.2. Field performance of monoblock heat pumps

The field performance of monoblock heat pumps (PTAC units) were analyzed from the point of view of four research questions:

- How are residents of the community using these PTAC units? Is there a significant behavioral difference between living units?
- How does the load shape of the PTAC unit relate to the load shape of status-quo cooling solution? Can the load shape differences be attributed to efficiency or more to customer behavior?
- What happens when multiple PTAC units are used concurrently in buildings? Does simultaneous use of multiple PTAC units cause significant current draws that can potentially trip circuit breakers?
- What is the result of the use of PTAC units compared to status quo in terms of overall energy use (and potentially energy bills) in summer and winter?

3.3.2.1. Average user behavior

The July performance of the Innova heat pumps in the 1-bedroom units are shown in Figure 4. Most one-bedroom units show continuous, low-power draw, without significant periods of non-use. There is high-efficiency due to variable-speed performance. The load increases moderately with higher outdoor air temperatures. The data shows afternoon peaking performance and significant differences between living units with some living units running the PTAC units continuously in summer. With the status quo being inefficient evaporative coolers, which were under-utilized because of non-performance, many residents were happy to use a functioning high efficiency air conditioning unit. A qualitative survey of customer satisfaction was corroborated by data collected from the living units.

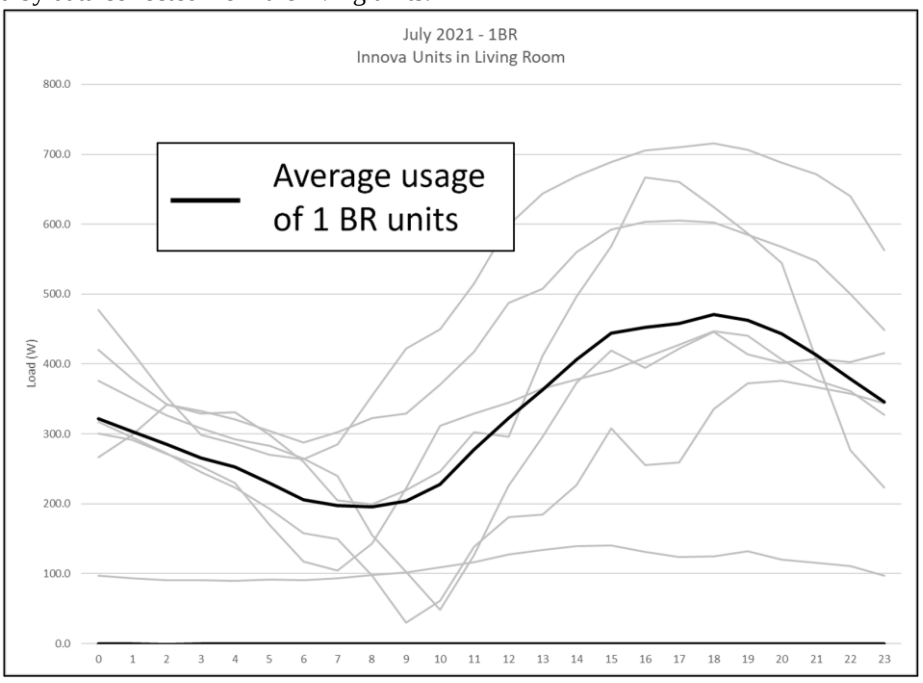


Figure 3 Innova Heat Pump Use Characterization (July 2021 – 1BR)

The January performance of the Innova heat pumps in the 1-bedroom units are shown in Figure 4. The data shows very low energy draw during the winter for heating. Significant variation between units is observed. When actively being used, the data shows dual peaking behavior corresponding to early morning and late evening hours, which is to be expected.

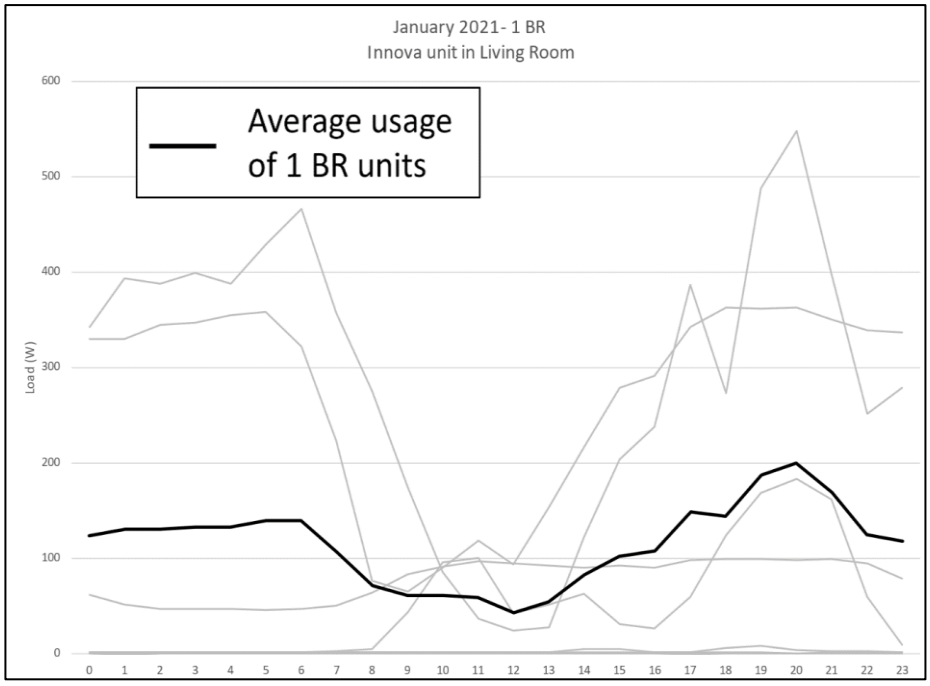


Figure 4 Innova Heat Pump Use Characterization (January 2021 – 1BR)

3.3.2.2. Comparison of monoblock heat pump load shape to status quo

The average summer load shapes for 1-bedroom units, displayed in Figure 5, show that 1-bedroom units use the heat pump to gain more comfort and that the living room Innova performance is similar to the swamp cooler. The higher efficiency mode allows less power despite continuous use. Note that winter load shapes couldn't be compared because the status quo is a natural gas wall furnace.

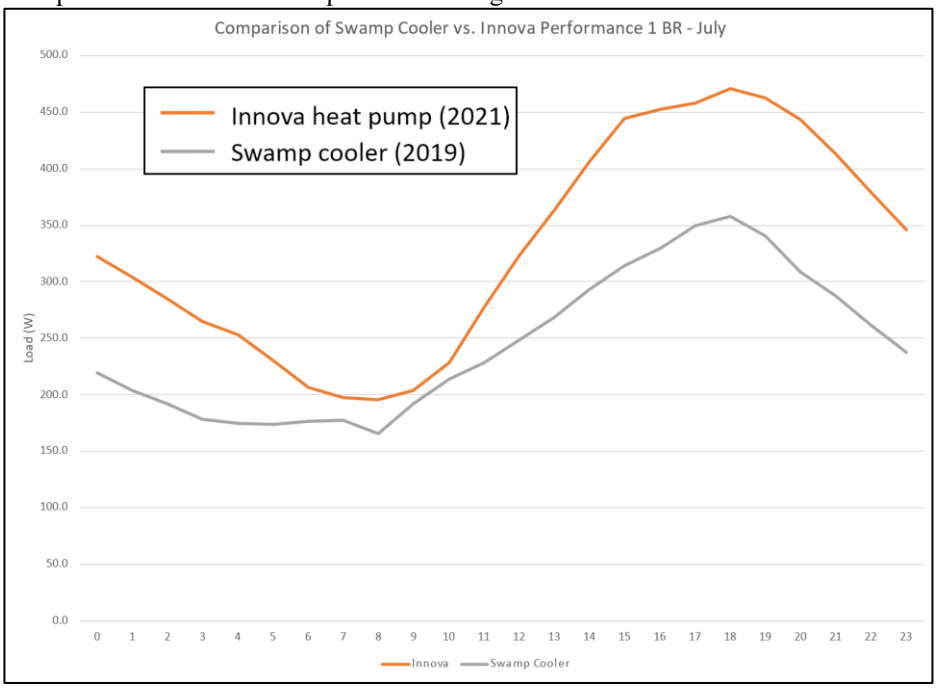


Figure 5 Comparison of swamp cooler vs. Innova heat pump performance (July – 1BR)

3.3.2.3. Impact of simultaneous multiple PTAC use on building's current draw

Figure 6 shows the hourly building level current draw in July 2021. The maximum current draw with multiple Innova heat pumps is an average of about 15-A per living unit. At a maximum of about 7.5-Aper Innova, use of a second Innova is not likely to cause the circuit breaker to trip unless other current loads are on the same circuit.

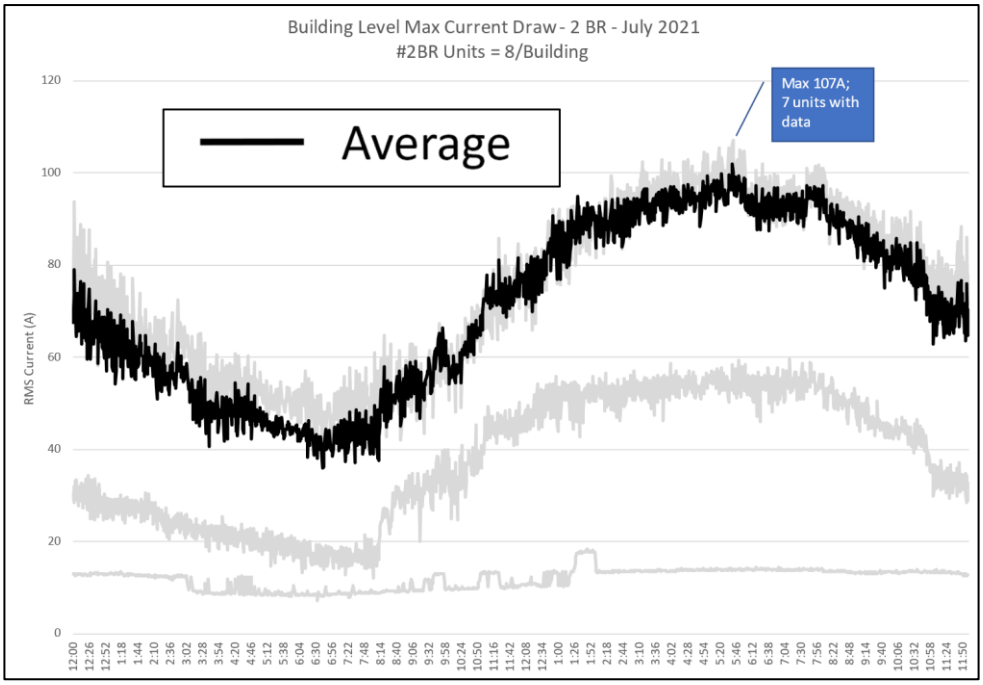


Figure 6 Innova Heat Pump Current Draw at Building Level in July 2021 (2 BR)

Figure 7 show the maximum current draw with multiple Innova heat pumps is an average of about 6-A per heat pump (or 42-Atotal for the 7 units). At a maximum of about 6-Aper Innova, use of a second Innova is not likely to cause the circuit breaker to trip unless other current loads are on the same circuit

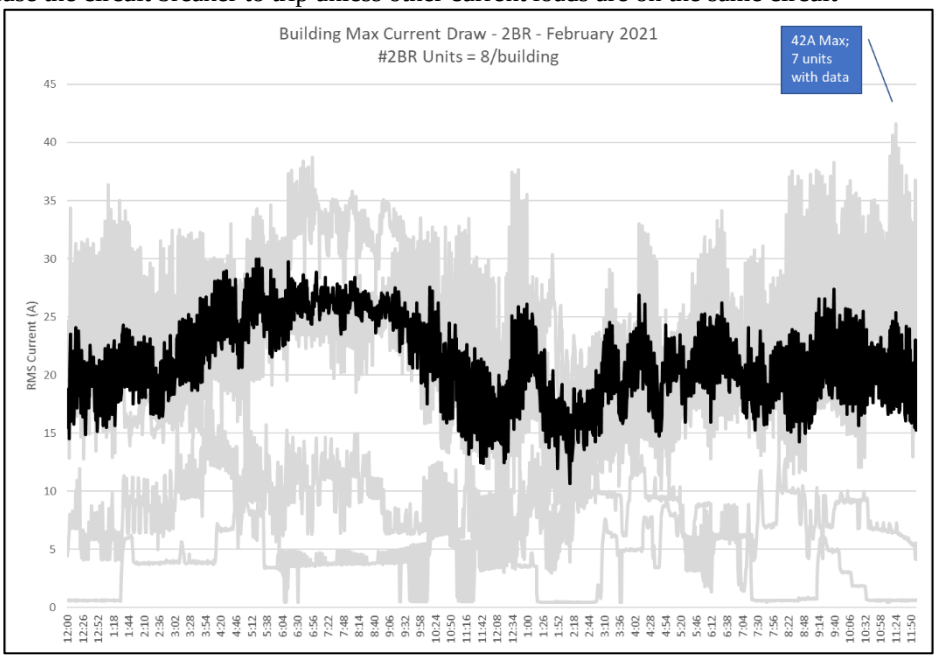


Figure 7 Innova heat pump current draw at building level in February 2021 (2 BR)

3.3.2.4. Summer and Winter energy performance of PTAC and status quo

Figure 8 shows that the monthly energy consumption is slightly higher for the Innova heat pumps than for the swamp coolers due to Innova continuous use. Higher energy use of Innova is also due to increased cooling needs in 2021 compared to 2019. However, Figure 9 show that energy consumption is significantly lower for the Innova heat pumps than for the gas wall furnace in the winter (electricity consumption in kWh was converted to US Therms for comparison). Significant performance improvement may also be attributed to envelope improvements that were added.

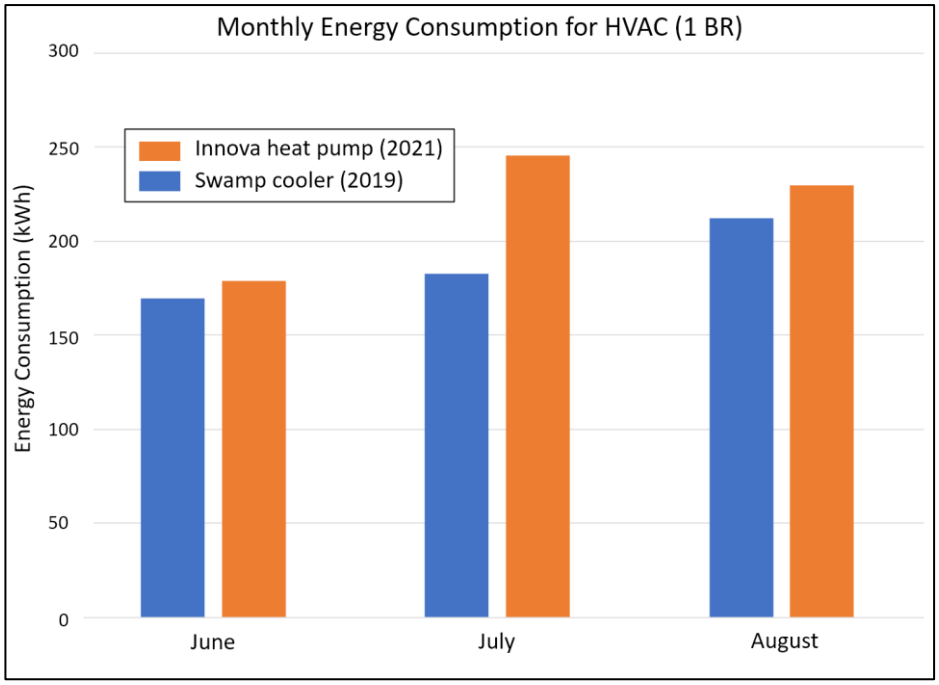


Figure 8 Energy Performance: Innova heat pump comparison to swamp cooler (1 BR)

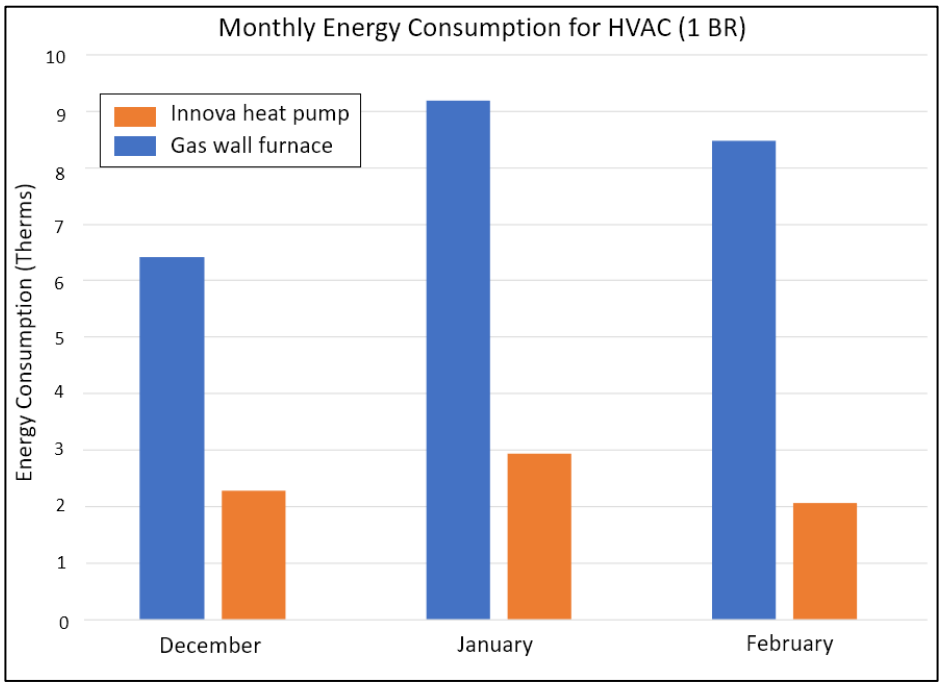


Figure 9 Energy Performance: Innova Heat Pump Comparison to gas wall furnace (1 BR)

4. Conclusions & Recommendations

The Pleasant View project was a showcase illustration of the unique application of emerging technologies to surmount barriers to electrification.

The results indicate that the Innova units are ideal for smaller living units, given the increased usage (and possibility for increased energy bills) in summer compared to reduction in gas use in winter. In a few cases, high overall usage (indicated by continuous use and low thermostat set points) caused maintenance issues. The product supports a “hoteling” mode that can help prevent extreme set points from causing maintenance issues, especially in master-metered facilities. Further, with a peak around 700-W and an average load of about 400-

W, each of these monoblock heat pumps represent about 300-W in flexibility potential, assuming adoption of a suitable controls platform that can implement demand-side flexibility.

While the technology itself shows promise in terms of performance, projects need to address split-incentives, and consider that total energy costs may increase with electrification depending on the energy use patterns and local utility rates. Improved energy efficiency and on-site PV are important steps to reduce tenant and owner energy costs.

The project team recommends the following actions to develop better pathways for the scaling of electrification retrofits of affordable multifamily and other residential markets to maximize decarbonization impacts.

- **Improve planning and implementation models**: The process for understanding and integrating the many support programs for the affordable multifamily market is daunting. For example, coordinating solar PV, roof upgrades, and energy conservation measures is essential for optimizing the electrical upgrades needed for the entire decarbonization retrofit.
- **Improve economic models for split incentives:** Scaled community decarbonization retrofits are emerging as evidenced by this project. To accelerate market adoption, improved models for overcoming split incentives and distribute savings from the community solar and other decarbonization retrofits are needed.
- **Upgrade policy or codes for electrification/decarbonization:** The shift to carbon-based metrics and incentives is underway in many utility service territories and are important to the successful scaling of decarbonization retrofits for affordable multifamily communities. Using carbon savings metrics can increase the incentives and cover a significant portion of the first cost of decarbonization retrofits as shown by California's Low-Income Weatherization Program incentives. Solutions for mitigating the electric infrastructure costs are essential for stimulating the electrification/decarbonization retrofits. New federal, state, and utility programs need to be developed and tested to cover these costs.
- **Work with manufacturers and stakeholders:** A significant barrier to the electrification retrofits of affordable multifamily communities is the lack of heat pump products for the retrofit market. New heat pump products designed for the retrofit market are needed. Recent advances such as the Innova monoblock heat pumps and Gradient window cold-climate heat pumps are good examples. A sustained program working with domestic and international manufacturers, utilities, designers, installers, and government organizations is recommended.
- **Demonstrate evaluation of integrated solutions:** Demonstration programs and test beds for utilities and stakeholders is needed for rapid evaluation of new integrated decarbonization retrofit solutions to accelerate market adoption of these new solutions.

Acknowledgements

The authors would like to thank the California Energy Commission which funded the research conducted in this paper under grant CEC-EPC-15-053. The authors would also like to thank their colleagues Corey Shono, Evan Giarta, and Herb Yaptinchay for all the help with data collection and project management.

References

[1] IEA, 2022. "Heat Pumps", IEA, Paris, https://www.iea.org/reports/heat-pumps, License: CC BY 4.0
[2] Hill, M., Veilleux, N., Strauss, Z., 2022. "Trends in Residential Heat Pump Adoption in the United States," *Buildings Hub*. https://atlasbuildingshub.com/2022/04/22/trends-in-residential-heat-pump-adoption-in-the-united-states/
[3] Deetjen, T., Walsh, L., Vaishnav, P., 2021. "US residential heat pumps: the private economic potential and its emissions, health, and grid impacts," *Environmental Research Letters* 16(8): 084024. https://dx.doi.org/10.1088/1748-9326/ac10dc
[4] Opinion Dynamics, 2022. "California Heat Pump Residential Market Characterization and Baseline Study," California Measurement Advisory Council
[5] EPRI, 2018, "*Heat Pump and Heat Pump Water heater Economic Assessment: Applicability for Residential and Small Commercial Markets.* EPRI, Palo Alto, CA: 2020. 3002013328

14th IEA Heat Pump Conference
15-18 May 2023, Chicago, Illinois

Tracking the carbon impact of space heating appliances from cradle to grave

Laure Meljac[a,*], Martin Forsen[a]

[a] NIBE, Hannabadsvägen 5, 285 32 Markaryd, Sweden

Abstract

To keep the global warming below 1.5°C, the European Union (EU) committed to carbon neutrality by 2050. The EU acknowledge that achieving this goal will require to track the greenhouse gases (GHG) emissions of organisations, products and buildings, from cradle to grave. Carbon, and more generally environmental, impact of products and buildings is evaluated while performing life cycle assessments (LCAs). LCAs are not widespread so far in the EU. However, several signs show that LCAs will become the norm sooner or later.
LCAs are governed by precise and strict rules that are described in standards which describe the LCA's process as well as how the environmental product declaration shall be performed and handled.
In the French law, before any building construction, it is compulsory to perform a LCAs. Construction projects shall demonstrate that GHG emissions from cradle to grave do not exceed defined thresholds.
LCAs provide a much wider picture of the environmental impact of products or buildings and can serve for building up the best strategy for reducing the GHG emissions.

Keywords: space heating appliances, carbon footprint, climate change, carbon neutrality

1. Greenhouse gases emissions tracking

1.1. Worldwide commitment

In order to fight against the climate change, the United Nations Framework Convention on Climate Change (UNFCCC) was adopted in 1992 and has since been ratified by 195 Parties. The Kyoto Protocol was adopted in 1997 to implement the UNFCCC and entered into force in 2005.

In short, the Kyoto Protocol operationalizes the United Nations Framework Convention on Climate Change by committing industrialized countries and economies in transition to limit and reduce greenhouse gases (GHG) emissions in accordance with agreed individual targets.

Under the Protocol, countries' actual emissions have to be monitored and precise records have to be kept. Reporting is done by Parties by submitting annual emission inventories and national reports under the Protocol at regular intervals.

A compliance system ensures that Parties are meeting their commitments and support them to meet their commitments if they have problems doing so.

At the conference of the parties organized in 2015 in Paris (COP 21) 196 Parties signed a legally binding international treaty on climate change.

Its goal is to limit global warming to well below 2, preferably to 1.5 degrees Celsius, compared to pre-industrial levels.

To achieve this long-term temperature goal, countries aim to reach global peaking of GHG emissions as soon as possible to achieve a climate neutral world by mid-century.

The Paris Agreement is a landmark in the multilateral climate change process because, for the first time, a binding agreement brings all nations into a common cause to undertake ambitious efforts to combat climate change and adapt to its effects.

* * Corresponding author. Tel.: +33 6 07 98 45 28
E-mail address: laure.melac@nibe.se

The Paris Agreement works on a 5-years cycle of increasingly ambitious climate action carried out by countries. By 2020, countries submit their plans for climate action known as nationally determined contributions (NDCs).

In their NDCs, countries communicate actions they will take to reduce their GHG emissions in order to reach the goals of the Paris Agreement. Countries also communicate in the NDCs actions they will take to build resilience to adapt to the impacts of rising temperatures [1].

In 2020, the European Union (EU) published its NDC where the EU set a binding target of a net domestic reduction of at least 55% GHG emissions by 2030 compared to 1990 [2]. The EU is pushing even further and targeting carbon emissions neutrality by 2050.

1.2. European Union actions

After the Kyoto protocol was signed, the EU put in place the first measures aiming at tracking and limiting the GHG emitted by the energy related activities, and several other very high GHG emitting sectors. However, the carbon neutrality cannot be achieved unless, the emissions in almost all the human activity sectors are tracked and limited. Therefore, the EU launched the Emission Trading System (ETS) that tracks the GHG emitted by the energy utilities and industries and other pieces of legislation addressing energy related products; buildings, transportation and many more.. The EU also set GHG reporting obligation (DIRECTIVE 2014/95/EU) for the largest organisations, both public and private and set the ambition of tracking both direct and indirect GHG emission.

This paper is focusing on the measures impacting products, and more specifically energy related products, such as heat pumps.

- Large organisations' GHG emissions

Every company employing more than 500 persons must report on their direct and indirect GHG emissions as well as on information on the management's approach to reduce them. The reporting periodicity is defined at the member state level. It is recommended to report according to the scope 1 and scope 2 as defined by the GHG protocol standards.

The GHG protocol is a partnership of businesses, non-governmental organisations (NGOS), governments, and other organisations convened by the World Resources Institute (WRI) and the World Business Council for Sustainable Development (WBCSD). It first established in 2001 the most widely used international accounting tool for quantifying and measuring GHG emissions.

The GHG Protocol breaks GHG emissions down into three categories: scope 1 emissions are defined as those caused directly by an organization's activities while scope 2 emissions count indirect emissions resulting from an organisation's energy consumption. Scope 3 encompasses all other indirect emissions, caused along an organisation's value chain, included the products that are purchased and placed on the market [3]. The three scopes concepts are illustrated on figure 1.

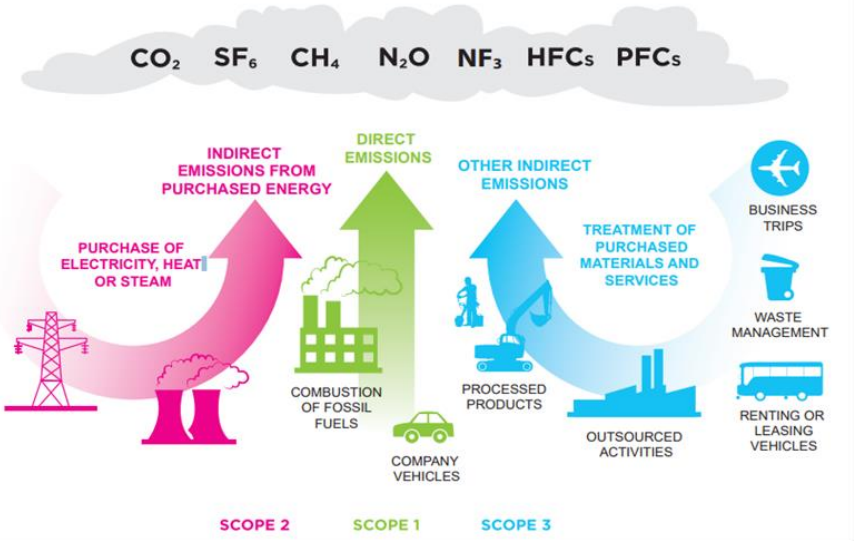


Fig. 1. Overview of the GHG Protocol scopes and emissions across the value chain [4]

As of today, reporting on emissions under scope 1 and 2 is mandatory while reporting under scope 3 is optional. However, in some member states, like France, reporting under scope 3, which requires accounting for the carbon footprint of products and goods, is recommended.

- Energy using products

The EU started to tackle the energy related products already back in 1994 when the energy label was introduced for several household appliances before being subsequently expanded in 2004.

The EU energy label has been a key driver for helping consumers choose products which are more energy efficient. At the same time, it also encourages manufacturers to drive innovation by using more energy efficient technologies.

The energy labelling directive was then followed, in 2009 by an eco-design directive. This directive is an effective tool for improving the environmental performance of products by setting minimum energy performance standards. This eliminates the least performing products from the market, significantly contributing to the EU's energy and climate targets.

The Ecodesign directive and Energy labelling regulation are both addressing energy efficiency, meaning the energy used by products during their life stage. Even though the GHG emissions from the usage phase of the energy using product often stand for a significant share of the overall GHG emissions, the GHG emissions from energy using products start when the raw material is extracted from the mines and stop when the products are either recycled, burned or land filled. To reach the 2050 zero emission target, the EU has to reduce the GHG emissions of products while taking in account their entire life cycle. An assessment limited to the usage phase is not enough.

A proposal for "Ecodesign for sustainable products regulation" is under development [5]. This regulation will replace the present Eco-design directive and is aiming at adding criteria addressing resource efficiency. In particular, the regulation proposes a mandatory carbon and environmental footprint declaration for the energy using products.

In parallel, the EU aims at switching its economy from a linear to a circular one. The actions taken in the framework of the circular economy action plan [6] will further speed up the GHG emissions' reductions and favor EU independency towards raw material.

- Buildings

In the EU, buildings represent 40% of the total energy consumption and 36 % of all GHG-emissions [7]. The GHG emission reduction target cannot be met without substantial reduction of the GHG emitted by buildings. The European Energy Performance of Building directive is the legislative instrument aiming at reducing the energy consumed by new buildings. As addressing new built buildings is not enough, the EU initiated, in 2020, the renovation wave which is targeting the existing buildings and is aiming at increasing the speed of renovation of the building stock. The renovation wave action plan includes a 2050 whole life-cycle performance roadmap to reduce GHG emissions form buildings [8].

Improving the energy efficiency of building is a good start as it helps reducing the GHG emissions over the life stage of the buildings. However, measuring the GHG emissions exclusively over the use phase of the building is misleading. As for the energy using products, reducing the energy use during the life stage would not be enough to reduce the GHG emissions so that carbon neutrality can be achieved by 2050. Indeed, a study on the Austrian building stock showed that the GHG "embodied" in building-related processes (e.g., material production, transport, refurbishment, or end-of-life) is four times higher than the GHG emitted during the use phase of the buildings [9].

In the recast of the Energy Performance of Building directive, a new requirement is added on a mandatory calculation of the life-cycle Global Warming Potential (GWP) of new buildings [7]. This new directive is to be published in 2023.

- General rules for life cycle assessment

Reporting on the GHG emitted over the use phase of products and buildings and directly or indirectly emitted by organisations is not enough to cut down GHG emissions so that the 2050 goal can be achieved. For that reason, carbon or environment footprint criteria are appearing in pieces of legislation related to reporting obligations for organisations, products and buildings.

The European Commission acknowledged that Life Cycle Assessments (LCA) provide the best framework for assessing the potential environmental impacts of products currently available. The need for consistent data and consensus LCA methodologies was underlined. Mid-2005. A joint project between DG Environment and the Commission's Directorate-General Joint Research Centre was initiated and the European Platform on Life Cycle Assessment was created.

2. Life Cycle Assessment

2.1. Definitions

The term "carbon footprint' has been widely established, including the public domain. However, this term is not clearly defined and moreover, several definitions can be found in the literature [8].

In the proposal for a regulation on Ecodesign for sustainable products [5], the carbon footprint is defined as "the sum of greenhouse gas (GHG) emissions and GHG removals in a product system, expressed as CO_2 equivalents and based on a life cycle assessment using the single impact category of climate change".

The "environmental footprint" is defined as "a quantification of a product's environmental impacts, whether in relation to a single environmental impact category or an aggregated set of impact categories based on the Product Environmental Footprint method".

Looking at the above-mentioned definitions, it seems that the "carbon footprint" is limited to the GHG emissions, whereas "the environmental footprint" has a wider scope and includes other types of impact than GHG emissions. In any case, both the carbon and environmental footprints are quantified by performing a life cycle assessment (LCA).

2.2. LCA methodologies

Two LCA methodologies are described in the literature: the bottom-up, based on process analysis and the top-down, based on environmental input-output (EIO) analysis [10]. The top-down method is an economic quantitative method to study the interdependence between various parts of the economic system, which runs in the whole industry cycle. The method aims at estimating all purchases and activities in a supply chain leading up to final manufacture in an industry. The carbon or environmental footprints are then calculated based on these transactions within the supply chain.

Process analysis is a bottom-up method, which has been developed to understand the environmental impacts of individual products from cradle to grave. The bottom-up approach describes the environmental footprint calculation of individual materials, products or processes. Setting the boundary conditions is key while performing a LCA using the process analysis method. Omrany et al [11] made an extensive review of existing LCA in buildings and showed that there is no common way of defining boundary conditions. However, comparing carbon or environmental footprint of similar materials, products or services is only possible if the boundary conditions are identical. For that reason, it is essential to describe common ways and method for performing LCA.

2.3. LCA international standards, process-based method

The development of the international standards for life cycle assessments by the International Standardisation Committee (ISO), ISO 14040 series was an important step to consolidate procedures and methods of LCA. Their contribution to the general acceptance of LCA by all stakeholders and by the international community was crucial.

ISO 14040 describes the four phases of an LCA: goal and scope definition, life cycle inventory analysis (LCI), life cycle impact assessment (LCIA) and life cycle interpretation. The scope definition includes, among others, the boundary conditions. ISO 14041, ISO 14042, ISO 14043 ISO 14044 provide details and guidelines on the four phases.

ISO 14040 series contains overarching standards that are addressing a very wide audience. In order to establish the carbon or environmental footprint of materials, products, services… the ISO 14040 series is complemented by more specific standards addressing specifically material, buildings, products…

2.3.1. Environmental product declaration (EPD)

EPDs are Type III environmental declarations, according to ISO 14025 (2006) and are often a good source of environmental data for a life cycle analysis.

ISO 14025 standard establishes the principles and specifies the procedures for developing Type III environmental declaration programs and Type III environmental declarations. It specifically establishes the use of the ISO 14040 series of standards in the development of Type III environmental declaration programs and Type III environmental declarations.

Type III environmental declarations present quantified environmental information on the life cycle of a product to enable comparisons between products fulfilling the same function. Such declarations

– are provided by one or more organisations,
– are based on independently verified life cycle assessment (LCA) data, life cycle inventory analysis (LCI) data or information modules in accordance with the ISO 14040 series of standards and, where relevant, additional environmental information,
– are developed using predetermined parameters, and
– are subject to the administration of a program operator, such as a company or a group of companies, industrial sector or trade association, public authorities or agencies, or an independent scientific body or other organisation.

Type III declaration process is illustrated in figure 2.

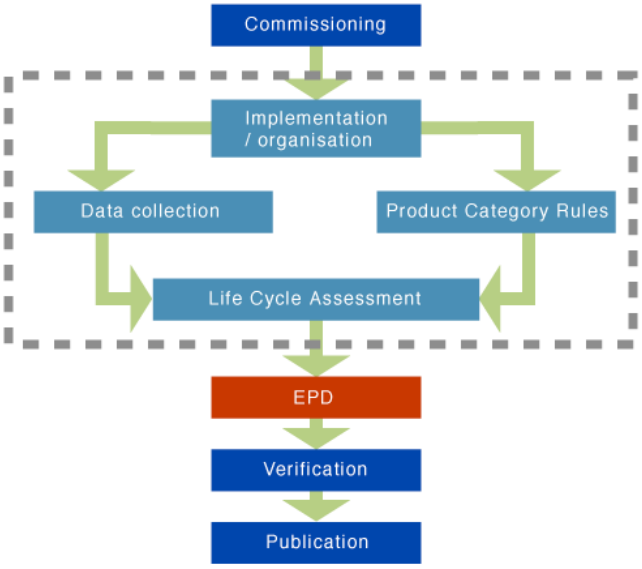


Fig. 2. Type III declaration process (Source: https://www.greenspec.co.uk)

In the development of Type III environmental declarations, all relevant environmental aspects of the product throughout its life cycle shall be taken into consideration and become part of the declaration. If the aspects considered to be relevant do not cover all stages of the life cycle then this shall be stated and justified. The data shall be generated using the principles, framework, methodologies and practices established by the ISO 14040 series of standards (i.e. ISO 14040 and ISO 14044).

The organisations acting as program operator are elaborating product category rules (PCR) which are defined as a set of specific rules, requirements and guidelines for developing Type III environmental declarations. PCRs set the rules, among other, for the environmental aspect and the life cycle stages to be considered, for the data quality requirements and the boundary conditions.

An EPD is a particular type of LCA, conducted using a defined set of Product Category Rules (PCR). Many PCR can be used for construction products (CPA, 2012) but only EPD following the same PCR can be compared.

EPDS are stored in dedicated database such as the INIES database or “the international EPD system” database.

2.3.2. Product standards

The European Committee for Standardisation (CEN) was mandated in 2004 for the development of horisontal standardised methods for the assessment of the integrated environmental performance of buildings. CEN TC350 works on the two standards dedicated to the evaluation of the environmental impacts of buildings: the EN 15978 (2011) and the EN 15804 (2012), for the building and material/product levels, respectively.

- Building level (EN 15978)

EN 15978 provides calculation rules for the assessment of the environmental performance of new and existing buildings based on a life cycle approach. It is intended to support the decision-making process and documentation of the assessment of the environmental performance of a building.

- Product level (EN 15804)

At the product level, EN 15804 standard defines the product category rules to develop Environmental Product Declarations (EPD) of construction products. The product category referred to in this standard includes all construction products and construction services for buildings and other construction works.

2.4. EU recommendations for LCA

The European Platform on Life Cycle Assessment (LCA) was created in 2008. This platform is aiming at proposing common methods to quantify the environmental impacts of products (goods or services) and organisations.

The European Commission proposed the Product Environmental Footprint (PEF) and Organisation Environmental Footprint (OEF) methods as a common way of measuring environmental performance.

The overarching purpose of PEF and OEF information is to enable to reduce the environmental impacts of goods, services and organisations taking into account supply chain activities (from extraction of raw materials, through production and use to final waste management). This purpose is achieved through the provision of detailed requirements for modelling the environmental impacts of the flows of material/energy and the emissions and waste streams associated with a product or an organisation throughout the life cycle.

The EU in COMMISSION RECOMMENDATION (EU) 2021/2279 sets the rules for establishing product environmental footprint. The document describes general procedure to conduct a LCA and the rules for establishing the Product Environmental Footprint Category Rules (PEFCR). The general procedure follows the same steps as these describes in ISO 14040 while the rules to establish the PEFCR are based on the minimum recommendation of ISO 14025. The recommendation also provides guidance to elaborate Product Specific Rules (PSR) which are vertical rules addressing specific products. While PEFCR describe horisontal rules to be followed by products belonging to the same category, the PSR are addressing sub-categories.

The term PEFCR is used instead of PCR in order to avoid confusion between ISO 14025 and EU recommendations.

The recommendation 2021/2279 goes into the very details of each phase of the LCA and PEFCR.

3. LCA in the French building code

3.1. French building code RE2020

The first building code was introduced in France in 1974. The building code aims at ensuring a minimum energy performance of new buildings. Since the first edition of the EU Energy Performance of Buildings Directive in 2002, the French building code serves as the national implementing regulation of the EU directive.

The building code is associated to a calculation tool that calculates the yearly energy consumption of a building based on its structural characteristics (shape, insulation, walls, windows…), equipment (heating, ventilation systems…) and location. Prior to each new building construction, the building project shall demonstrate compliancy with the building code requirements.

Until 2022, the building code requirements were mainly addressing the energy consumption, the building envelop performance and the amount of renewable energy used.

On 1st of January 2022, the new French building code, RE2020 entered into force. The RE2020 includes the calculation of the LCA of the buildings, including equipment. from cradle to grave.

3.2. Buildings' LCA

3.2.1. General methodology

The whole process for the LCA follows the approach as recommended by the EU in COMMISSION RECOMMENDATION (EU) 2021/2279.

The buildings' LCA is conducted according to ISO 14040 and ISO 14044 and follows the four steps of the LCA as defined in ISO 14040: definition of scope and goal, life cycle inventory, life cycle impact assessment, interpretation and declaration. The buildings' LCA is performed according to NF EN 15978 and comes as the sum of the LCA of the construction material, including heating, ventilation and air conditioning (HVAC) equipment, the impact from the energy used during the life phase and the impact of the construction services.

The LCA of construction materials and HVAC equipment are conducted according to ISO 14025, NF EN 15804 and NF EN 15804/CN (national complement to the standard for construction products) and are delivered as EPD.

The energy used during the use phase includes the energy needed for lighting, ventilation, space heating and domestic hot water production. In tertiary buildings and multifamily houses, energy needed for the lift and for lighting the car parks are also accounted for.

The impact of the building on the climate change is defined as the global warming potential (GWP) expressed in kg CO_2 eq/m².

The life-time of the building is assumed to be 50 years. A life-time is also defined for each piece of equipment. As an example, the life-time of heat pumps is 17 years. The GWP is calculated over the 50 years and the calculation takes into account the replacement of equipment. Primary energy factor for electricity is equal to 2.3 and it is considered constant for the entire life time of the building. The CO_2 content of the energy carriers are also considered constant over the 50 years.

3.2.2. Boundary conditions for the EPD

LCAs are performed from cradle to grave (according to NF EN 15804). The EPD shall be established while considering the following stages of the building life:

- Production: (modules A1-A3 according to NF EN 15804) extraction of raw material, transportation to the manufacturing site, manufacturing. Management of residues including packaging not leaving the factory gates are including in this stage
- Construction: (modules A4-A5 according to NF EN 15804) transportation from the production gate to the manufacturing site, construction or installation of the material or product, management of waste and packaging
- Usage: (modules B1-B7 according to NF EN 15804) use stage including maintenance, repair and replacement, energy and water used
- End of life: (modules C1-C4 according to NF EN 15804) deconstruction, transportation of the discarded products, waste processing
- Benefits and loads beyond the product system boundaries: (modules D according to NF EN 15804) environmental benefits or loads resulting from reusable products, recyclable materials and/or useful energy carriers leaving a product system.

The details of all the modules are describes in NF EN 15804.

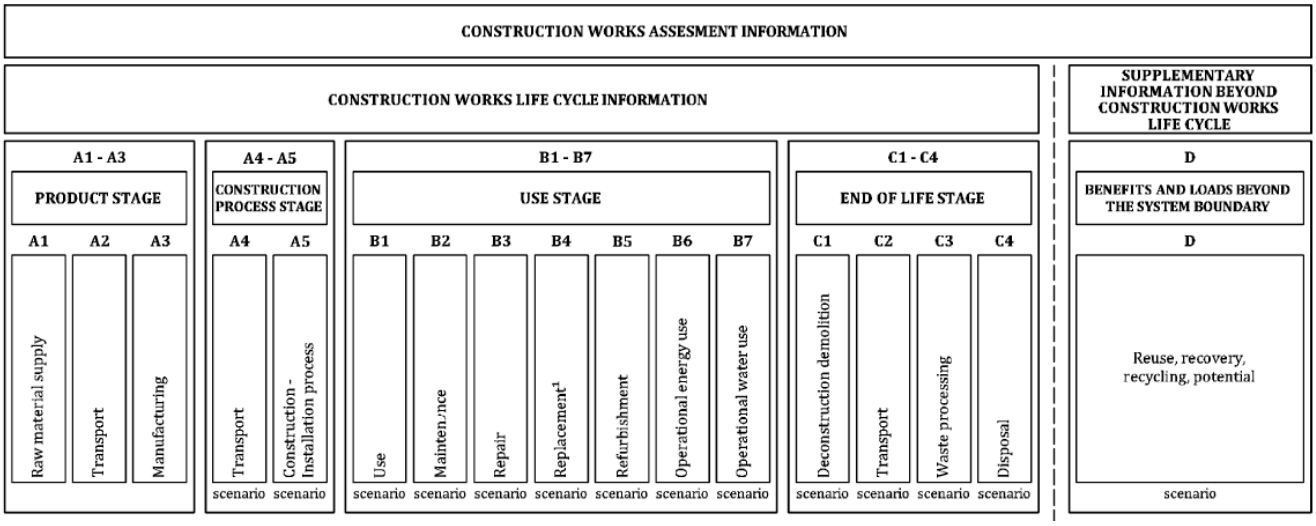


Fig. 3. Stages that shall be observed for a cradle to grave LCA (Source: NF EN 15804)

The EPD might be established for equipment providing one or several functions or for material and services.

The EPD shall be established for clearly defined and measurable functional (equipment) or declared (material and services) units to allow for the comparison of equipment, material and services.

3.2.3. Environmental impacts covered in the EPD

The EPD shall provide, at least:

- The global warming potential indicator

This indicator accounts for the GHG emitted over the entire life cycle of the product. It is expressed in CO_2 equivalent.

6 energy indicators: basically the renewable and non-renewable energy used during the use phase of an equipment.

- 12 indicators related to circular economy.
- 11 indicators related to biodiversity which include air, water and sea pollution.

3.2.4. EPD types

- General rules

  The environmental product data shall be made available through EPD. However, in cases where no EPD is available, default values might be used.

  The EPD are managed by the organization called INIES and made available on INIES database publicly and freely accessible on the internet.
- Default values

  Default values are established for construction material and equipment by the French authorities (ministry . They are penalizing compared to specific data from EPD.

  Default values are also established for services that are not covered by any program and thus cannot beneficiate from any EPD. These services are: waste treatment, transportation…, energies (electricity, wood, district heating…), refrigerants…
- FDES

  FDES (Fiche de Données Environnementales et Sanitaires) are the EPD for construction material. INIES is the operator for the FDES and defines the program rules.

  There are two main categories of FDES: collective and individual FDES. The collective FDES are established by several companies and concern a given material type (eg: clay roof tiles) while individual FDES is established for a given material reference of a given manufacturer.

  The FDESs are valid for 5 years.
- Product Environmental Profile (PEP)

The operator for the equipment's EPD is an organization called PEP Ecopassport which is dedicated to electric, electronic and HVAC-R products. The EPD managed by PEP Ecopassport are called PEP (product environmental profile).

PEP Ecopassport is managing the electric, electronic and HVAC-R product category rules as well as specific product rules.

Just as FDES, there are two main categories of PEP: collective and individual PEP. The collective PEP are established by several companies and concern a given material type (eg: combination air to water heat pumps using R410A) while individual PEP is established for a given material reference of a given manufacturer.

The PEPs are valid for 5 years.

3.3. Minimum RE2020 criteria

RE2020 set minimum requirements related to the global warming potential (GWP). Two thresholds are defined, one addressing the construction phase: construction work, material and equipment, one addressing the energy used during the usage phase.

In order to be compliant, the calculated GWP of the construction phase and the calculated GWP of the energy used during the usage phase shall be lower than the thresholds.

- GWP of the material and equipment

The GWP is calculated as the sum of the GWP calculated in modules A, C and D for all the construction service and material, equipment that constitute the building

- GWP of the energy used during the usage phase

The GWP is calculated as the sum of the GWP calculated in modules B for all the material, equipment and services that constitute the building

3.4. Example of results of LCA performed on a single-family house

The LCA is performed on a 100m² single family house located in the West part of France. Table 1 shows the GWP values for both construction and use phase achieved if both the space heating and domestic hot water demand are covered by either an air to water heat pump or a wall-hung condensing gas boiler providing both space heating and domestic hot water. The heat pump considered in the example has a seasonal energy performance equal to 3 while the gas boiler has an efficiency of 94%.

Table 1. GWP calculated and GWP thresholds in kg CO_2 eq/m² when an air to water heat pump is installed

Phase	Construction phase	Use phase
	Air to water combination heat pump / wall hung gas boiler	Air to water combination heat pump / wall hung gas boiler
LCA GWP values kg CO_2 eq /m²	630 / 528	52 / 419
RE2020 thresholds kg CO_2 eq /m²	640	140

One can observed that the GWP impact of the construction phase is higher for the air to water heat pump than for the wall-hung gas boiler. However, the gas boiler is not compliant as the GWP on the use phase is higher than the authorized threshold.

4. Opportunities of the LCA calculations

So far, the EPBD mainly focus on the yearly energy use in buildings. However, setting up a building construction strategy on the basis of the energy consumption might be completely different from the one that might be adopted while considering the GHG emissions during the life-time of the building or the total GHG emissions from cradle to grave.

Let's consider the example above (100m² single family home in the West part of France). Let's consider an existing similar house, located in the West part of France as well, built in the 60s and equipped with a 20-years-old non condensing gas boiler which achieve 75% efficiency. The primary energy used for space heating and domestic hot water for the new built house and the existing one over 50 years (for the existing building, the web tool [13] has been used) are shown in figure 4. Figure 5 shows the GHG emissions, calculated for 50 years corresponding to the energy used for space heating and domestic hot water production while considering the data listed in table 2.

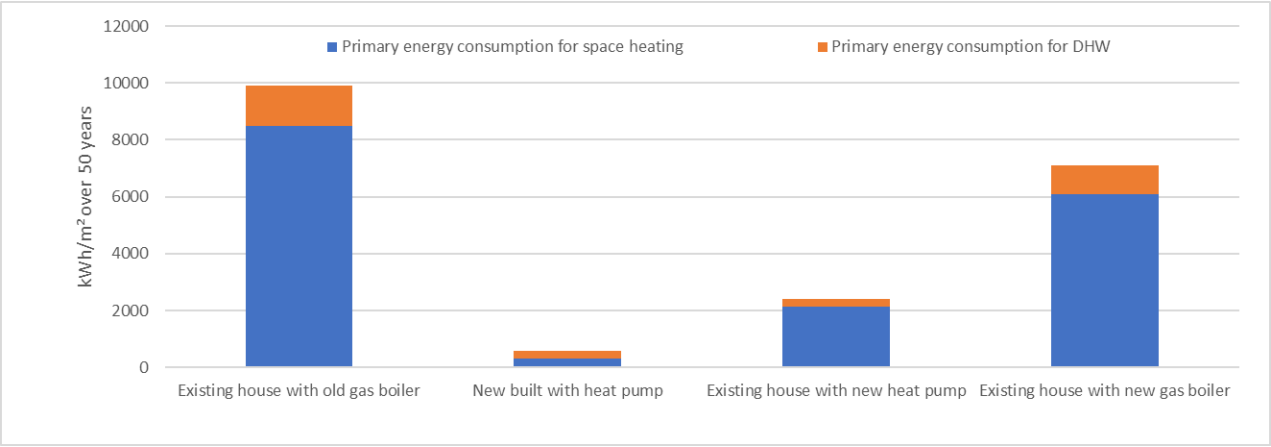


Fig. 4. Primary energy used for space heating and domestic hot water production over 50 years in kWh/m²

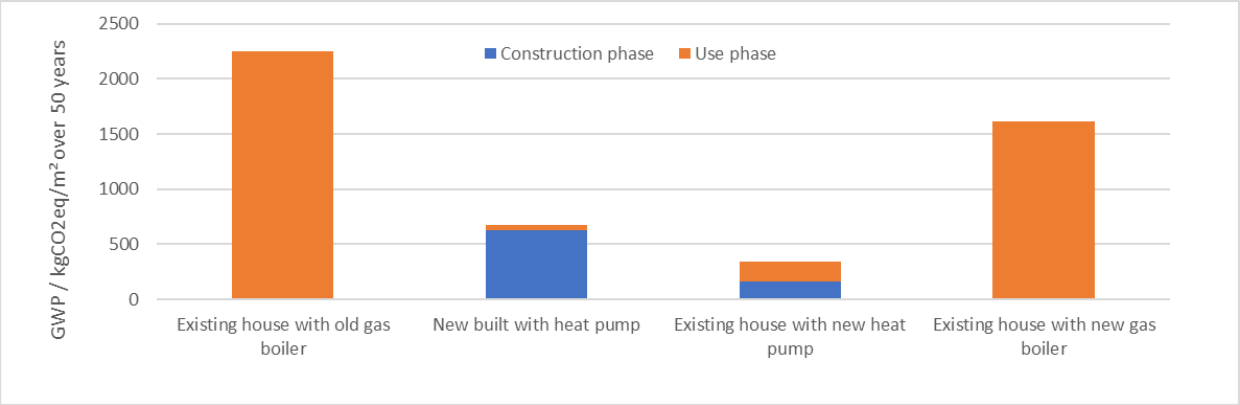


Fig. 5. GWP for construction and use phases for new built and existing house

In figure 5, the GHG impact of the heat pump and new gas boiler installation and two replacements are considered, while it is assumed that the existing boiler will last for 50 years.

Table 2. Assumptions [12]

	GWP kg CO_2 eq / kWh	Primary energy factor
Electricity for heating	0,079	2.3
Electricity for domestic hot water	0.065	2.3
Natural gas	0,227	1
	GHG emission kg CO_2 eq	
GWP for the construction of a 12kW air to water combination heat pump (PEP UNICLIMA [14])	5358	
GWP for the construction of a 23kW wall-hung condensing boiler (PEP UNICLIMA [15])	228	
Seasonal Performance factor of heat pump	3	
Energy efficiency of the new gas boiler	94%	
Energy efficiency of the old gas boiler	75%	

Figure 6 shows the emissions savings achieved while considering the following scenario:

- Scenario a: only the GHG emitted during the use phase of the house are considered
- Scenario b: GHG emitted by both the use and construction phase of the house are considered

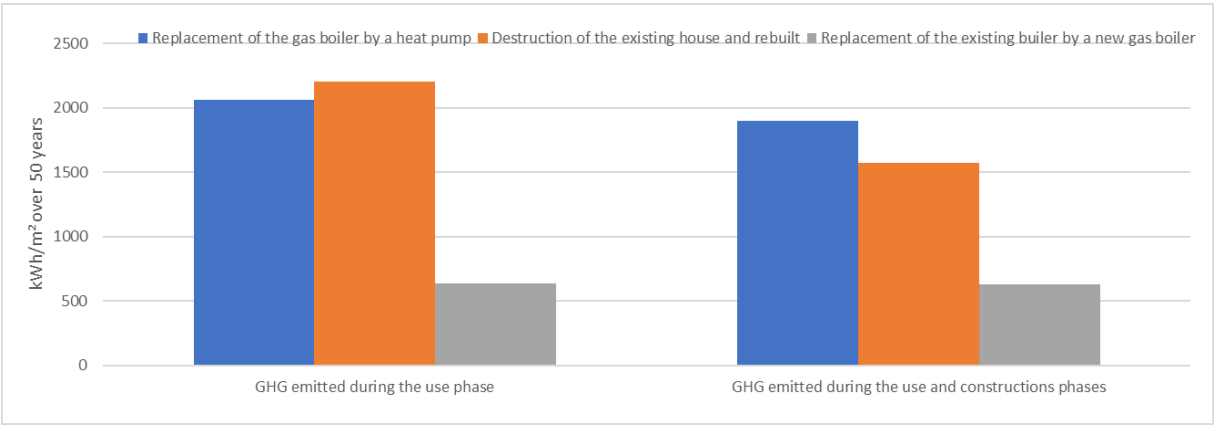


Fig. 6. Energy savings achieved while considering scenario a and b

Would only the use phase be considered, the conclusion would be that in order to achieve the highest GHG saving the old house should be teared down and replaced by a new one.

However, would both the use and the construction phases be considered, the best option would be to replace the existing gas boiler by a heat pump.

The conclusion here is only valid for France. Indeed, the conclusion could be very much different in countries where the CO_2 content of electricity is higher than the one in France. Figure 7 illustrates where the breaking point is.

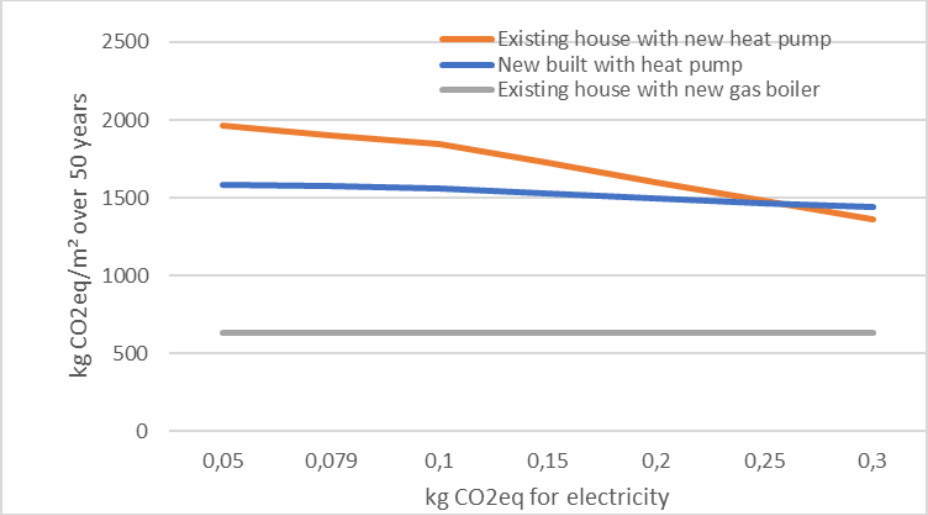


Fig. 7. CO_2 savings achieved depending on the CO_2 content of electricity

In countries where carbon intensity of electricity is lower or equal to the emission factor of gas, 0.25kg CO_2eq/kWh, it is worthwhile tearing down the existing building and rebuild a new one. Indeed, the GWP of the use phase become much more impacting than this of the construction phase.

This calculation illustrates the potential behind the life cycle assessment. Moreover, the calculation done here is only considering the GHG emissions impact. While accounting for more than one environmental impact, it would be possible to be sharper on the best strategy to adapt in order to protect our environment and preserve the natural resources.

5. Conclusion

In order to meet the COP 21 target and to achieve carbon neutrality by 2050, it is not enough to track the GHG directly and indirectly emitted by organizations and the GHG emitted during the use phase of the energy related product and buildings. Tracking the GHG emitted over the entire life cycle of products and buildings, from cradle to grave, has become a necessity. The tracking is done through the LCA that leads to environmental impact declarations for product, material and services. EPDs allow for a fair comparison of equivalent products and help choosing the less harming products in order to reduce the impact on the climate change.

In the EU, signs show that EPDs will become the norm soon or later for material and products, and in particular for heat pumps.

In France, since January 2022, EPDs are needed for construction material and HVAC equipment where installed in new buildings. In their national building code, RE2020, the French authorities go even beyond the GHG emissions as a full LCA is to be performed prior to every building construction. The LCAs include many impacts and not only the GWP impact. Even so, for the time being, minimum requirements are only addressing the GWP.

LCAs provides much more information than the GHG impact of a product, material or service. Other environmental impacts are assessed that give a much broader overview of how armful a product, material or service can be for the environment. Indeed, Life cycle assessment allows for establishing construction strategy based on more extensive environmental criteria. In France, because the CO_2 content of electricity is low, it is better to replace existing boilers by heat pumps than to tear down the building and build up new ones.

References

[1] https://unfccc.int
[2] EU report, Update of the NDC of the European Union and its Member States; Berlin 2020
[3] https://ghgprotocol.org/calculation-tools
[4] https://www.epa.gov/
[5] EU draft regulation: Ecodesign for sustainable products regulation; Brussels, 30/03/2022
[6] EU communication: A new Circular Economy Action Plan for a cleaner and more competitive Europe, Brussels, 11/03/2020
[7] EU draft proposal: DIRECTIVE OF THE EUROPEAN PARLIAMENT AND OF THE COUNCIL on the energy performance of buildings; Brussels, 15/12/2021
[8] Communication from the commission to the European parliament of the council, the European economic and social committee and the committee of the region: a Renovation Wave for Europe, Brussels, 14/10/2020
[9] B Truger1 *, S Nabernegg2 , T Lackner2 , M Röck1,3, N Alaux1 , E Hoxha1,4, M Ruschi Mendes Saade1 , A Passer1 *: Life cycle GHG emissions of the Austrian building stock: A combined bottom-up and top-down approach; article for conference serie "Earth and Environmental Science", Berlin, 2022
[10] Thomas Wiedmann and Jan Minx: "A Definition of 'Carbon Footprint'"; ISA^{UK} Research report 07/01
[11] Hossein Omrany * , Veronica Soebarto , Jian Zuo and Ruidong Chang: "A Comprehensive Framework for Standardising System Boundary Definition in Life Cycle Energy Assessments", article, Buildings 2021, 11, 230
[12] Arrêté du 4 août 2021 relatif aux exigences de performance énergétique et environnementale des constructions de bâtiments en France métropolitaine et portant approbation de la méthode de calcul prévue à l'article R. 172-6 du code de la construction et de l'habitation
[13] Selectra group, https://selectra.info/
[14] UNICLIMA PEP reference: 25841
[15] UNICLIMA PEP reference: 14080

14th IEA Heat Pump Conference
15-18 May 2023, Chicago, Illinois

Comparative Analysis on Ejector and Converging Tee-driven Refrigeration Systems

Gwang Soo Ko[a], Waseem Raza[a], Youn Cheol Park[a,*]

[a] Department of Mechanical Engineering, Jeju National University, 102, Jejudaehak-ro, Jeju, 63243, South Korea

Abstract

The growing need for thermal comfort has resulted in an increase in refrigeration systems and, as a result, increased electricity demand for these systems. Waste heat-driven devices for refrigeration systems appear to be a potential alternative to traditional compression-based refrigeration technologies for reducing energy consumption. These devices in the refrigeration cycle can be driven by waste heat (free or inexpensive low-temperature energy source) as the primary energy source instead of electricity. This study investigates the ejector-driven and converging Tee-driven refrigeration systems (EDRS & CTDRS) using waste heat, aiming to provide an alternative to traditional VCC. An experimental setup is developed with a 3.6 mm nozzle size of an ejector and a converging tee diameter of 12.7 mm. A comparative experiment was conducted to assess the coefficient of performance (COP). In terms of performance, the EDRS COP outperformed the converging-tee-driven refrigeration cycle. The results showed that the proposed concept is promising to develop an alternative to the traditional refrigeration cycle and heat recovery.

Keywords:Refrigeration; Vapor Compression Cycle; Waste Heat; Ejector; converging Tee;

1. Introduction

Air conditioning is a need for humans in everyday life. Air-conditioning using a large amount of electric power results in a considerable proportion of fossil fuel combustion. Air conditioning and refrigeration systems consume a big part of the electricity used worldwide. There has been a huge growth in air conditioning usage, particularly in southern nations, causing major supply challenges during peak load hours. Furthermore, predictions show a tremendous increase in energy use. Another effect is the rising energy cost. Thus, many alternatives need to be considered to overcome the electricity demand. An ejector is a widely used device for energy conversion [1], [2]. A refrigeration system powered by an ejector has the ability to minimize energy usage and consequently increase performance.

The EDRS is a vapor compression cycle (VCC) modification. Low-grade thermal energy use is considered as an essential kind of energy conversion that is both ecologically friendly and energy-saving. Low-grade thermal energy is an energy resource, and its recovery will improve energy efficiency. The ejector-driven refrigeration system, being a heat-driven device, provides a practical technique for converting low-grade heat into useful cooling. Low-grade heat sources, such as solar collectors [3], industrial processes, and automobiles [4] power the ejector. An ejector compresses refrigerant vapor from the evaporator and discharges it to the condenser rather of pressuring it with a mechanical compressor. The vapor generator, which is heated by a low-temperature heat source generated the motive vapor. An appropriate ejector substantially increases the system's performance.

Many studies have demonstrated that a suitable ejector increases the system's performance. For instance, the authors [5] developed an ejector-driven refrigeration system to overcome the throttling losses. The system performed optimally, with a 5 to 13% greater COP than a typical refrigeration system with a nozzle diameter

* Corresponding author. Tel.: +82-64-754-3626.
E-mail address: ycpark@jejunu.ac.kr.

of 2.3 mm and a corresponding ratio of 15.3. The researchers of [6] investigated the variable area ratio on a multi-evaporator refrigeration system. The results indicate that the energy saving increased by 112% by the variable area ratio compared to the traditional refrigeration system. An experimental investigation of the R134a EDRS was conducted by [7]. The outcomes indicate that with the rise in boiler temperature (motive), capacity, COP, and entrainment ratio improved and then reduced. Hence, the motive temperature must be optimized for the set condenser and evaporator temperatures to achieve maximum COP. Our previous study [8] compared the ejector nozzle sizes for an EDRS. The findings revealed that an ejector with a nozzle size of 3.6 mm performed well compared to 1.8 and 5.4mm nozzle sizes. Moreover, compared to the VCC, the refrigeration cycle performed well at below 0ºC. A similar study by Chaiwongsa et al. [9] investigated a motive nozzle's various nozzle outlet diameters for system performance. The ejector-nozzle with an outlet diameter of 2 mm yielded the highest COP.

This study aims to utilize the ejector and converging tee to reduce power consumption and improve the COP of conventional refrigeration systems. An ejector and converging tee with nozzle sizes of 3.6 mm and 12.7 mm are considered, respectively. A comparative analysis is discussed in this study. The present study is subdivided into four sections. The first section provides an introduction, while the second is about methodology. Section 3 contains the results and discussion, and section 4 has the conclusions.

2. Materials and Methods

A heat-driven ejector and converging tee may be used to power a refrigeration system instead of or in addition to a compressor. The ejector and the converging tee have no moving parts, are cost-effective, have high reliability, have simple construction, and have minimal installation and operating expenses. Furthermore, both the ejector and converging tee have two intake ports, a motive, and a suction port, as well as one discharge port, allowing the primary high-pressure stream to hold the secondary low-pressure stream. Two streams are mixed in an ejector, discharged at a predetermined intermediate pressure, and actuated by fluid energy rather than electricity.

Both devices (ejector and converging tee) operate on low-grade thermal energy generated by waste heat. Second, the second level of compression is known to exist in order to lower the energy required by the input of a mechanical compressor. Furthermore, these devices serve as a pump to transport refrigerant via the refrigerant circulation channel. The efficiency of the ejector and converging tee directly influences the effectiveness of the refrigeration system. According to the working conditions, the ejector and converging tee have the maximum entertainment ratio, continuously allowing the system to operate optimally.

Table 1. Test conditions of ejector and converging tee

Cycle	Diameter (mm)	Motive Ref. State	Eva. Inlet Temp (ºC)	Cooling water temp. (ºC)
Converging tee system	12.7	Liquid	5	35
			10	
Ejector refrigerant system	5.4		15	
			20	

The proposed refrigeration system uses an ejector and a converging nozzle to investigate the system's energy consumption and COP. The refrigeration systems' key parts are the expansion valve, receiver, condenser, ejector or converging tee, generator, evaporator, accumulator, and compressor. A system's performance relies on the working fluid's thermal characteristics. Thus, R134a refrigerant is employed as a working fluid, while waste heat is used as a primary fluid for the ejector and converging tee motive. In order to circulate the condensing water and waste heat (in the form of hot water) to the generator, two circulation pumps are employed. Table 1 displays the test conditions for the ejector and converging tee-driven refrigeration systems.

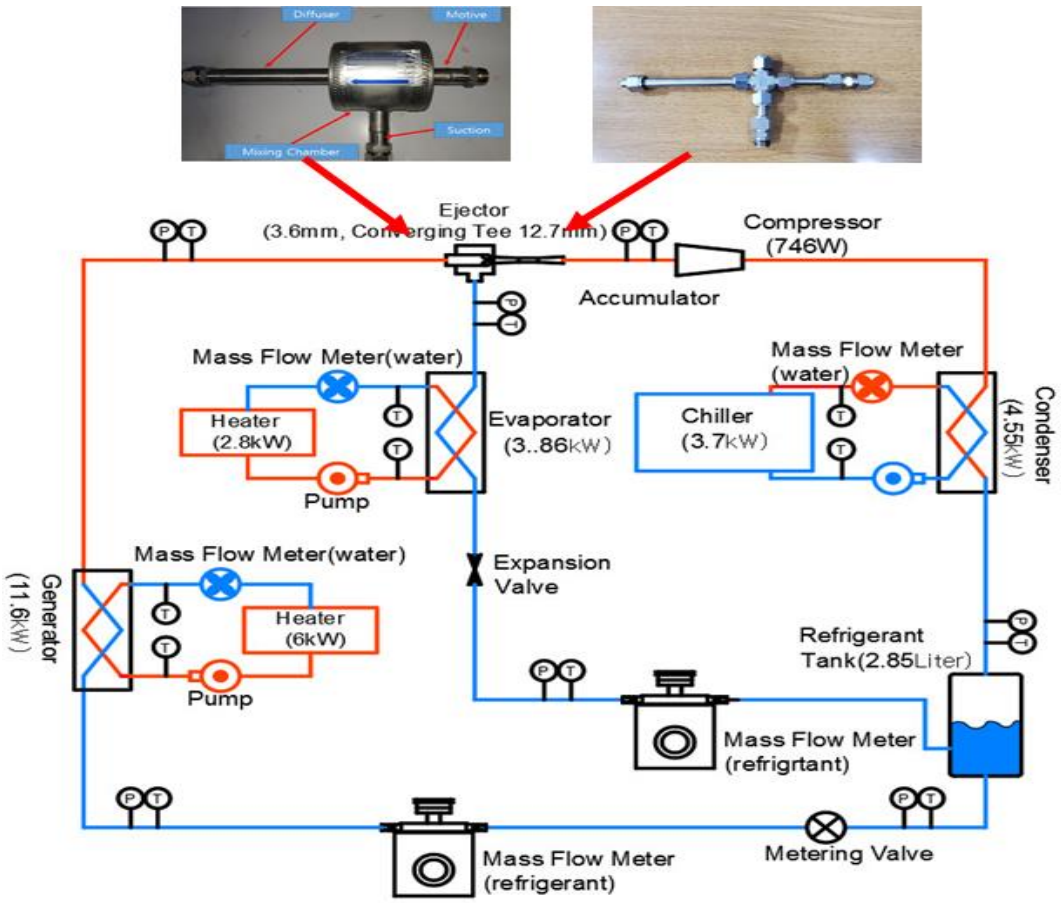


Fig. 1. Schematic diagram of comparison system of ejector and converging tee

Moreover, pressure sensors, T-type thermometers, and refrigerant and water flow meters are used to measure the system's characteristics. A refrigerant receiver is installed at the condenser outlet to ensure that refrigerant flows continuously toward the expansion valve and generator. The primary flow reaches the ejector's motive or converging tee to entertain and compress the secondary refrigerant flow from the evaporator at high temperature and pressure. A heater with an output of 2.8 kW (Rainbow) is employed as the evaporator load. Brazed-plate heat exchangers are both a condenser and an evaporator. As a generator, a brazed-plate heat exchanger is used. Table 2 contains all additional technical characteristics. The refrigeration system schematic diagram for understanding the performance characteristics is depicted in Figure 1.

Table 2. Specification of refrigeration system

Condenser	12.25 kW
Compressor	746 W
Refrigerant tank	2.5 Liter
Expansion valve	Manual
Evaporator	1.93 kW
Generator	11.6 kW
Ejector nozzle size	3.6 mm
Converging Tee pipe size	12.7 mm
Waste heat	80ºC
Refrigerant	R134a

3. Results and Discussion

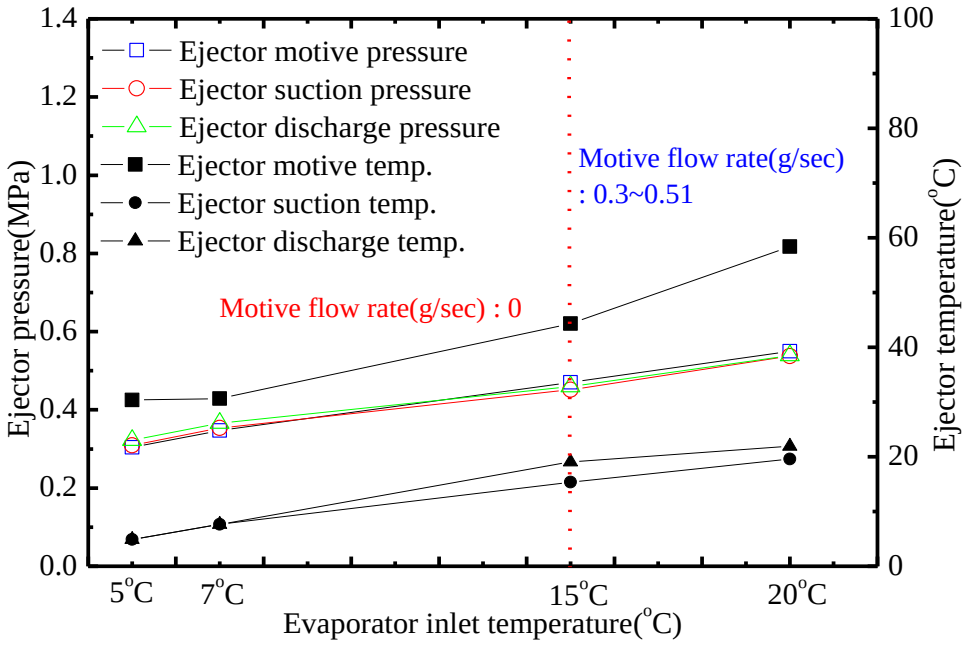


Fig. 2. Variation of ejector discharge pressure and temperature according to evaporator inlet temperature

An ejector refrigeration system operating characteristics, such as pressure and temperature at the motive against the evaporator inlet temperature, are depicted in Figure 2. In this refrigeration system, an ejector is installed with a nozzle size of 3.6 mm. The pressure and temperature of the ejector motive change with the change of evaporator inlet temperatures such as 5, 7, 10, and 20ºC. As the evaporator's inlet temperature decreased, the ejector motive's pressure and temperature also decreased. As a result, there is no refrigerant flow, as shown in Figure 2. The motive flow rate is 0 g/sec. This phenomenon is because as the refrigerant temperature at the ejector motive and evaporator inlet decreases, the opening degree of the expansion valve and metering valve decreases, resulting in much resistance to the refrigerant flow.

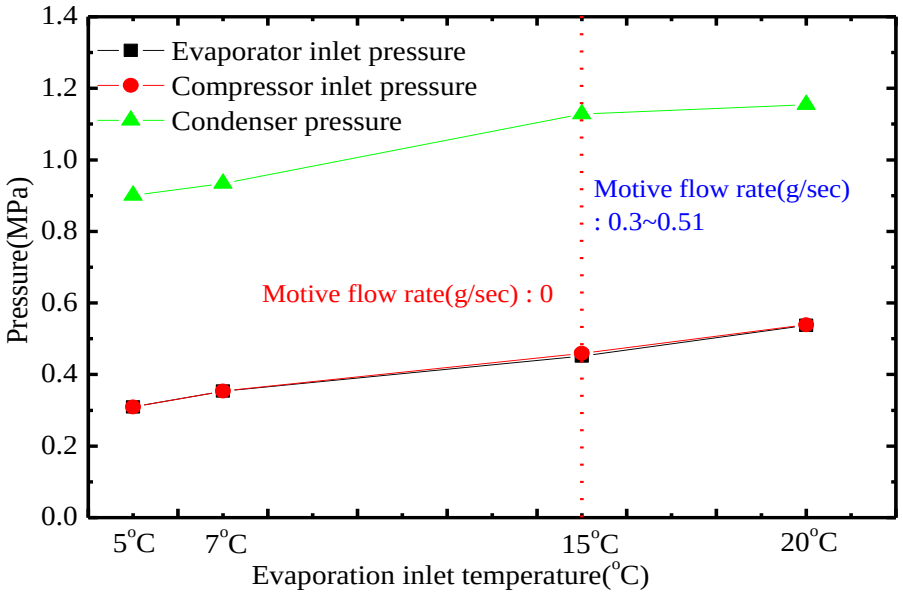


Fig. 3. Variation of the evaporator, compressor, motive, and condenser pressure according to evaporator inlet temperature

At 15 and 20ºC, the refrigerant flow rate is 0.3 to 0.51 g/sec when the refrigerant passes through the generator, and heat exchanges between the hot water and refrigerant. So, the pressure discharged from the generator goes higher before entering the ejector. On the other hand, the pressure discharged from the ejector did not change significantly. This phenomenon is believed to be because of the refrigerant temperature at the ejector inlet increases. The pressure of the refrigerant discharged from the ejector is further affected by the refrigerant flow rate in the ejector. The change in ejector motive temperature due to the generator was not affected at 5ºC and 7ºC temperatures of the evaporator inlet. So, the ejector temperature discharged was 4.9 ºC and 7.6 ºC. However, at 15 ºC and 20 ºC evaporator temperatures, where the mass flow rate of the refrigerant at the ejector motive is 0.3 to 0.51 g/sec, the refrigerant temperature of the ejector motive was 44 ºC and 58 ºC by exchanging the heat through a generator. So, the ejector discharged temperature was 19 ºC and 21 ºC at the evaporator inlet temperature of 15ºC and 20ºC.

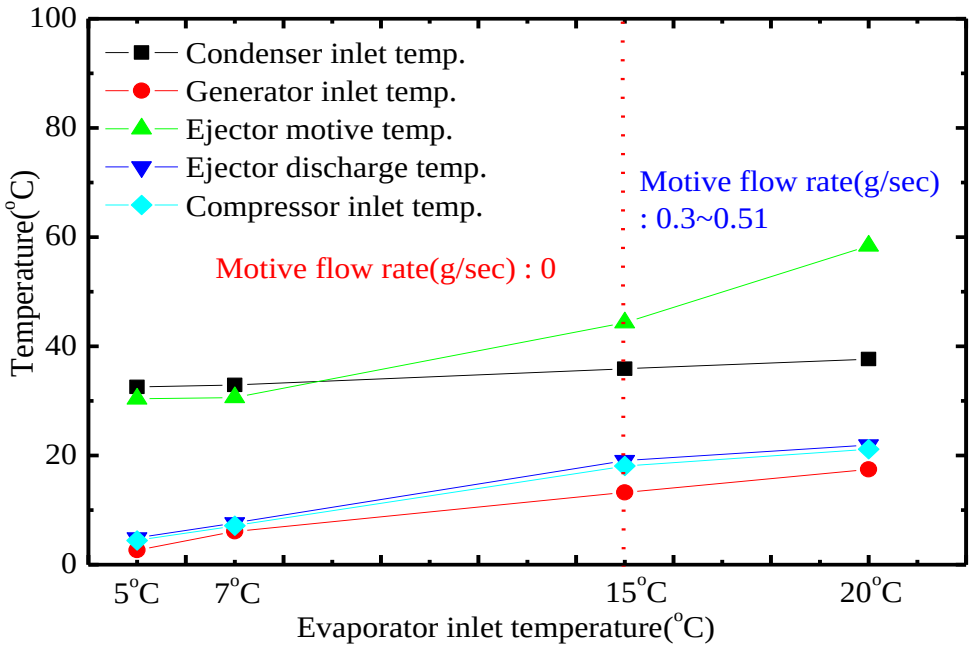


Fig. 4. Variation of the refrigerant temperature of an ejector refrigeration system according to evaporator inlet temperature

Figure 3 shows the inlet pressures of a compressor, condenser, and evaporator versus the evaporator inlet temperature. The results revealed that the refrigerant pressure at the inlet of the compressor and evaporator is almost the same at 5 ºC and 7 ºC, where there is no flow at the ejector motive. However, the compressor inlet pressure is slightly higher at 15 ºC and 20 ºC. This is because of the refrigerant flow rate at the ejector motive. The inlet pressure of the condenser is higher than the inlet pressure of the compressor. It is also depicted that condenser pressure increases with evaporation inlet temperature. Nevertheless, the operation remained stable as the condenser capacity was designed to be larger than the compressor capacity. Figure 4 represents the compressor, condenser, generator, and ejector motive and discharge temperatures against the evaporator inlet temperature. There is a slight difference in ejector discharge and compressor inlet temperatures. The generator inlet temperature is the lowest among others because a metering device is used to maintain the required experimental conditions. Regarding the ejector motive, the temperature remained the same at 5 ºC and 7 ºC because of no refrigerant flow from the motive. Besides, the refrigerant temperature increased at 15 ºC and 20 ºC because of refrigerant flow at the ejector motive.

The refrigerant flow rate (g/sec), power consumption, and cooling capacity versus the evaporator inlet temperature are presented in Figure 5. As shown, there is a slight change in the capacity and power consumption at 5 ºC and 7 ºC, whereas cooling capacity and power consumption increased at 15 ºC and 20 ºC. Although, the increase in cooling capacity trend was higher than the power consumption trend. On the other hand, the ejector motive flow rate remained constant at 5 ºC and 7 ºC, while slightly increasing from 15 ºC to 20 ºC. The generator capacity and COP of an ejector refrigeration system are depicted against the evaporator

inlet temperature in Figure 6. There is no change in the generator capacity at 5 ºC and 7 ºC; there is no flow at the ejector motive as well. Nevertheless, the generator capacity is 45.61 and 65.86W at 15 ºC and 20 ºC, respectively. On the other hand, in the COP of the ejector-driven refrigeration system, there is a slight increase from 5 ºC to 7 ºC, after slightly increasing to 15 ºC after that, COP rose dramatically but remained below one on all evaporating inlet temperatures. Although, the COP of the system remained low in the experimental results. The COP can be improved by optimizing capacity and ejector nozzle size. This is one of the solutions to improve the COP.

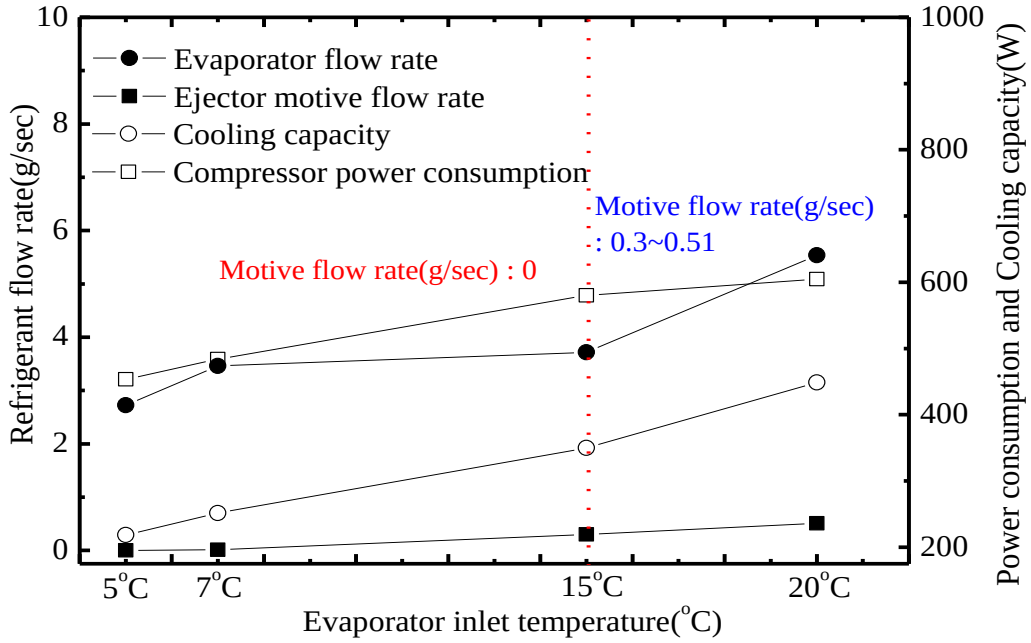


Fig. 5. Variation cooling capacity and compressor power consumption according to evaporator inlet temperature and ejector motive flow rate

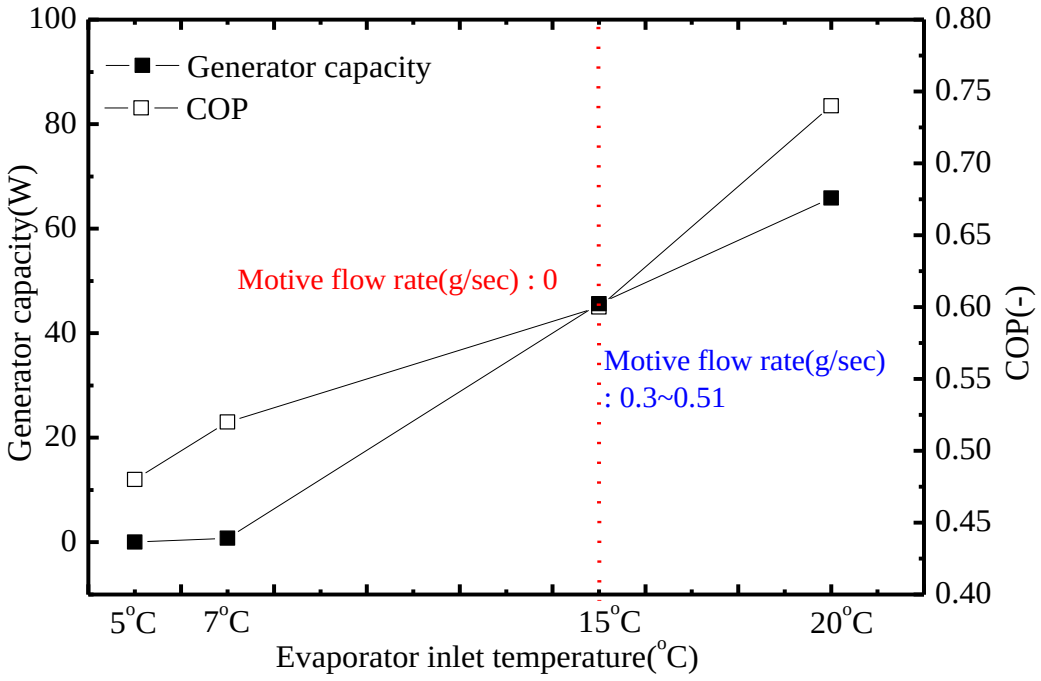


Fig. 6. Variation of generator capacity and COP according to evaporator inlet temperature

A comparative experiment was conducted on the operation and performance characteristics of the refrigeration system installed with the ejector and converging tee to confirm the ejector's effectiveness. A comparison of the ejector and converging tee discharge temperature and pressure is presented in Figure 7. As shown, the ejector discharge pressure is dominant on all temperatures 5 ºC, 10 ºC, 15 ºC, and 20 ºC. On the other hand, in terms of ejector and converging tee discharge temperatures, the ejector discharge temperature is higher on all temperatures, such as 5 ºC, 10 ºC, 15 ºC, and 20 ºC, indicating the domination of ejector-driven refrigeration systems over converging-tee-driven refrigeration system. The cause of this phenomenon is that in the converging tee, only the refrigerant is mixed inside, and in the case of the ejector, refrigerant is sucked from the evaporator outlet and mixed inside. The refrigerant temperature rises and leaves the ejector diffuser with intermediate pressure.

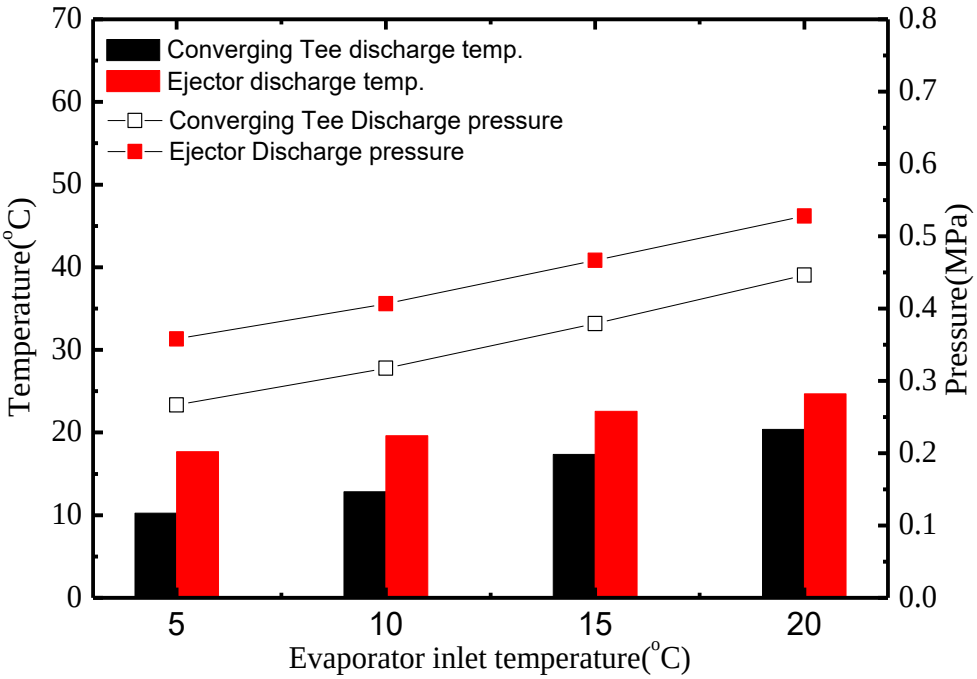


Fig. 7. Variation of discharge temperature and discharge pressure in an ejector and converging tee

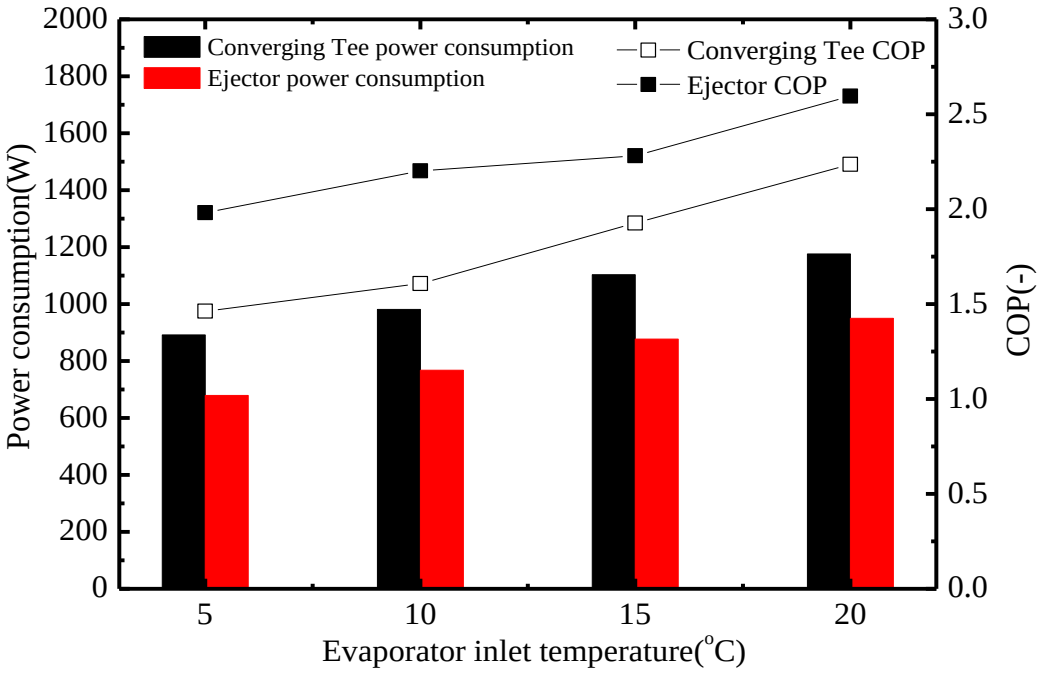


Fig. 8. Variation of power consumption and COP in an ejector refrigeration system and converging tee

Figure 8 shows the power consumption and COP of the ejector-driven and converging tee-driven refrigeration systems according to the evaporator inlet temperature. As a result of the comparative analysis, it is found that the power consumption of the CTDRS was higher than the ejector-driven refrigeration system in all cases of temperature. This is because of the high pressure and temperature in the ejector-driven refrigeration system, causing the compressor to do less work. Regarding COP, the ejector-driven refrigeration system COP is higher than the converging tee-driven refrigeration system. For instance, at 20 ºC, the converging tee-driven refrigeration system COP is 2.25, and the EDRS COP is 2.65 showing the higher COP of the ejector-driven refrigeration system. It is evident that when the ejector-driven refrigeration system power consumption is low, the COP will be higher.

4. Conclusions

A vapor compression cycle-driven refrigeration cycle integrated with an ejector and converging tee is investigated in this study. This study has two goals: to minimize power use in order to achieve energy savings which will result in cost savings and to use waste heat as a renewable energy source. Thus, a comparative analysis has been conducted to identify the results of both cycles. The ejector nozzle & converging tee diameter sizes were 3.6 mm and 12.7 mm. In terms of power consumption, the ejector refrigeration system showed less power consumption against the evaporator inlet temperature in comparison to the converging tee refrigeration system. In terms of COP, the results revealed that the ejector-driven refrigeration system COP is better than the converging tee refrigeration system COP.

Acknowledgments

This research was funded by the National Research Foundation of Korea (No. 2020R1A2C1011871).

References

[1] J. H. Keenan and E. P. Neumann, "A Simple Air Ejector," *J. Appl. Mech.*, vol. 9, no. 2, pp. A75–A81, Mar. 2021, doi: 10.1115/1.4009187.
[2] J. H. Keenan, E. P. Neumann, and F. Lustwerk, "An Investigation of Ejector Design by Analysis and Experiment," *J. Appl. Mech.*, vol. 17, no. 3, pp. 299–309, Apr. 2021, doi: 10.1115/1.4010131.
[3] D.-W. Sun, "Solar powered combined ejector-vapour compression cycle for air conditioning and refrigeration," *Energy Convers. Manag.*, vol. 38, no. 5, pp. 479–491, Mar. 1997, doi: 10.1016/S0196-8904(96)00063-5.
[4] L. Wang, W. Cai, H. Zhao, C. Lin, and J. Yan, "Experimentation and cycle performance prediction of hybrid A/C system using automobile exhaust waste heat," *Appl. Therm. Eng.*, vol. 94, pp. 314–323, Feb. 2016, doi: 10.1016/j.applthermaleng.2015.10.051.
[5] S. Sag *et al.*, "Early atherosclerosis in normotensive patients with autosomal dominant polycystic kidney disease: the relation between epicardial adipose tissue thickness and carotid intima-media thickness," *SpringerPlus*, vol. 5, no. 1, pp. 1–7, 2016, doi: 10.1186/s40064-016-1871-8.
[6] X. Ma, W. Zhang, S. A. Omer, and S. B. Riffat, "Experimental investigation of a novel steam ejector refrigerator suitable for solar energy applications," *Appl. Therm. Eng.*, vol. 30, no. 11, pp. 1320–1325, Aug. 2010, doi: 10.1016/j.applthermaleng.2010.02.011.
[7] A. Selvaraju and A. Mani, "Experimental investigation on R134a vapour ejector refrigeration system," *Int. J. Refrig.*, vol. 29, no. 7, pp. 1160–1166, Nov. 2006, doi: 10.1016/j.ijrefrig.2006.01.004.
[8] W. Raza, G. S. Ko, and Y. C. Park, "A Study on the Combined Driven Refrigeration Cycle Using Ejector," *Int. J. Air-Cond. Refrig.*, vol. 29, no. 01, p. 2150004, Mar. 2021, doi: 10.1142/S2010132521500048.
[9] P. Chaiwongsa and S. Wongwises, "[논문]Experimental study on R-134a refrigeration system using a two-phase ejector as an expansion device," *Appl. Therm. Eng.*, vol. 28, no. 5, pp. 467–477, 2008, doi: 10.1016/j.applthermaleng.2007.05.005.

14th IEA Heat Pump Conference
15-18 May 2023, Chicago, Illinois

Heat pump system performance measurement in Annex 52

Signhild Gehlin[a*] Jeffrey D Spitler[b]

[a]The Swedish Geoenergy Center, Box 1127, 22104 Lund, Sweden
[b]School of Mechanical and Aerospace Engineering, Oklahoma State University, Stillwater, Oklahoma, USA

Abstract

This paper presents an overview of the IEA HPT Annex 52, "Long term performance measurement of ground-source heat pump (GSHP) systems serving commercial, institutional and multi-family buildings." Energy use intensities are a common system metric, but comingle the performance of the building envelope, occupancy effects and the system performance. The annex utilizes performance factors and a new boundary schema which facilitates characterizing the performance of different parts of the system. The annex delivered a library of quality long-term system performance measurements in the form of case studies, improved methodologies to better characterize system performance in larger buildings, and guidelines for instrumentation, uncertainty analysis, key performance indicators, data management and quality assurance. This paper focuses on performance measurements of the heat pumps, covering both internal and external approaches, instrumentation and uncertainty guidelines. Though aimed at water-source heat pumps, the annex schema and guidelines are applicable to air-source heat pumps (ASHP) and air-conditioning systems also.

© HPC2023.
Selection and/or peer-review under the responsibility of the organizers of the 14th IEA Heat Pump Conference 2023.

Keywords: Ground source heat pumps;GSHP;performance measurement;SPF;HPT Annex 52;

1. Introduction

Field measurements of building heating and cooling system performance are rarely made but are essential to ensure that performance expectations are actually met. For GSHP systems, owners have made significant investments with expectations of high performance. Hence, it is particularly important that high performance is achieved. Though some field measurements have been reported in the literature, there is little or no consistency on how to measure the performance or how to report the results. Cost-effective measurement programs are hindered by this lack of consistency and a lack of guidance regarding measurement system design.

The four-year international collaboration project IEA HPT Annex 52 - Long-term performance monitoring of GSHP systems for commercial, institutional and multi-family buildings - was carried out by seven countries: Sweden, the USA, the UK, the Netherlands, Germany, Norway and Finland. The Annex was initiated to improve the state-of-the-art in GSHP system performance measurement, going beyond energy use intensity (EUI) measurements that comingle the performance of the building envelope, occupancy effects and the system performance. Instead, performance factors are used to characterize the system performance. As introduced by a 1948 Edison Electric Institute report [1], a performance factor (PF) is similar to a coefficient of performance (COP) except the COP is an instantaneous value and the PF covers a specified time period. Performance factors are field measured; COPs may be field measured, but most commonly COP measurements are made in a laboratory. Performance factors are commonly defined for different system boundaries (e.g. the heat pump, the heat pump & source-side circulating pump) and different time periods (e.g. daily, weekly, monthly,

* Corresponding author. Tel.: +46 75 700 88 23
E-mail address: signhild.gehlin@geoenergicentrum.se

seasonal). Performance factors depend on system design and operational parameters such as setpoints, part-load conditions, source- and sink temperatures. The high degree of granularity with five system boundaries aids in analysis of the system performance. The specific objectives of Annex 52 were to:

- Create a library of quality long-term measurements of GSHP system performance for commercial, institutional, and multi-family buildings served by any type of ground source (e.g. vertical boreholes in rock, pile heat exchangers in soil, open-loop groundwater wells.)
- Refine and extend current methodology to better characterize large-scale GSHP system performance and to provide a set of benchmarks for comparisons of such systems. The improved methodology will be beneficial for the IEA and will facilitate collection of more accurate and uniform statistics, and thus help in estimating, with less uncertainty, how much energy we can produce and how much CO2 emissions we can reduce with GSHP systems.
- Provide guidance for instrumentation, uncertainty calculation, key performance indicators and system boundaries that cover as many GSHP system features as possible.

Outcomes from the Annex include new boundary schema and guidelines for instrumentation, uncertainty, key performance indicators, data management, and quality assurance. In addition to the final report [2], four subtask reports [3-6] and 27 case study reports [7,8] containing 29 monitoring projects have been published, comprising more than 1000 pages in total. These reports are published on the Annex 52 webpage https://heatpumpingtechnologies.org/annex52/documents/. In addition, the Annex has so far resulted in three sets of open-source measurement data from two GSHP systems, seven published peer reviewed scientific journal papers and 14 peer reviewed conference papers.

Prior to the Annex, there have been relatively few long-term performance measurements of ground-source heat pump systems serving larger commercial buildings. Gleeson and Lowe [9] reported a meta-analysis of field measurements for residential buildings in Europe in which 216 ground-source heat pumps were included, but the analysis was complicated by inconsistent boundary schemas. Spitler and Gehlin [10] reported on 55 GSHP systems serving commercial and multifamily residential buildings. Both references [9,10] noted a significant range in SPF values that cannot be explained solely by different equipment or different climatic conditions.

This paper gives an overview of the boundary schema, then focuses on methods and results for the heat pump boundary (Level 1). Measured SPF for the heat pump only are summarized for 20 systems with a total of 78 years of measurements.

2. Boundary Schema

The overall performance of a GSHP system is affected by the performance of the source side ground circuit, as well as the heat pump (HP) unit performance and the load side circuit performance, including supplementary heating and cooling. Hence, performance factors are necessarily defined for a specific set of boundaries. However, in the literature, there is little consistency in the use of system boundaries, and, in many cases, the system boundaries are not clearly defined. This makes it difficult to compare published performance factors for GSHP systems. The SEPEMO system boundary schema [11] was initially used for calculation of performance factors within Annex 52. However, the SEPEMO system boundary schema has limitations when accounting for the complexity of larger GSHP systems used in commercial, institutional, and multi-family residential buildings.

Annex 52 has sought to harmonize system boundary definitions and identify and recommend performance indicators that will allow evaluation at multiple clearly stated system boundaries. A new system boundary schema consisting of six defined boundaries and an indicator for use of supplemental heating or cooling was defined within Annex 52 [2]. It is based on the SEPEMO schema but is revised and extended, such that every SEPEMO boundary matches one of the Annex 52 boundaries (see Figure 1 and Table 1). This improves the applicability to larger and more complex GSHP systems of various types. The Annex 52 system boundary schema has been applied on all case studies within Annex 52.

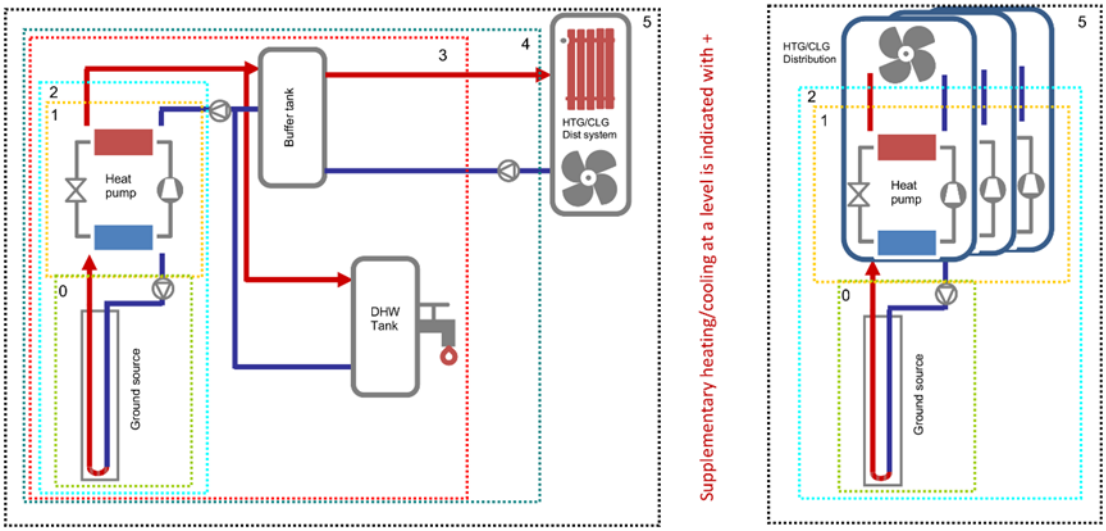


Fig. 1 Annex 52 system boundary schema for centralized systems (left) and distributed systems (right).

Table 1: Annex 52 system boundary schema and its relation to the SEPEMO boundary schema. [2]

	Boundary Levels											
Boundary description	0	0^+	1	1^+	2	2^+	3	3^+	4	4^+	5	5^+
Ground Source (circ. pump + ground heat exchanger)	x	x			x	x	x	x	x	x	x	x
Heat pump unit incl. internal energy use, excluding internal circ. pump.			x	x	x	x	x	x	x	x	x	x
Buffer tank (incl. circ. pump between heat pump and buffer tank)							x	x	x	x	x	x
Circ. pump on load side (between buffer tank & building heating/cooling distribution system)									x	x	x	x
Building heating/cooling distribution system											x	x
Auxiliary heating or cooling		x		x		x		x		x		x
Corresponding SEPEMO boundary level			H1/C1		H2/C2	H3			C3		H4	C4

3. Heat Pump Boundary (Level 1) Methods

There are two approaches for determining heat pump performance factors – the so-called external and internal approaches [12]. Further diagrams illustrating these two approaches are found in the Annex 52 instrumentation guideline [4].

3.1. External Approach

The external approach makes use of measurements that are made external to the vapor compression cycle of the ground-source heat pump:

- Power measurements of the compressor, and other devices if needed to establish performance factors at different boundaries.
- Entering and exiting temperature measurements of the secondary refrigerant or air on the load side of the heat pump.
- Mass flow measurements made of the secondary refrigerant (heat transfer fluid) or air on the load side of the heat pump.
- For measurement of cooling performance factors with water-to-air heat pumps, humidity measurements of the air entering and exiting the evaporator are also needed.
- Thermodynamic properties or thermodynamic property routines for the secondary refrigerant or air.

The cooling or heating capacity is determined calorimetrically – by multiplying the measured mass flow rate by the difference in enthalpy. For flows without phase change, the enthalpy difference would usually be estimated as the product of the specific heat and the temperature difference. Uncertainty calculations are illustrated for this method in [5].

3.2. Internal Approach

The internal approach [13] makes use of:

- Pressure and temperature measurements of the refrigerant at the compressor suction and discharge.
- Temperature measurement of the refrigerant at the condenser discharge.
- Power measurements of the compressor, and other devices if needed to establish performance factors at different boundaries.
- An estimate of the compressor heat loss.
- Thermodynamic property routines for the refrigerant.
- Temperature measurements of the entering and exiting temperatures of the condenser and evaporator on the secondary refrigerant or air side.

The pressure and temperature measurements at the compressor suction and discharge and the temperature measurement at the condenser discharge are used, with the aid of the refrigerant property routines, to determine the enthalpies at all state points in the cycle. Coupled with the compressor power measurement and the estimate of the compressor heat loss, the refrigerant mass flow rate can be determined. With this information, instantaneous values of COP, cooling capacity, heating capacity, and isentropic efficiency can be determined. By making enough time series measurements, the performance factor for the heat pump can be determined by integrating the instantaneous values of the cooling or heating provided and the electrical power input. The temperature measurements of the secondary refrigerant and/or air are used to determine 2nd law efficiencies of the individual components. This capability allows better diagnosis of internal heat pump problems, compared to the external approach. Further refinements and uncertainty analysis are discussed in references [5,12,13].

3.3. Discussion

Both approaches may be used to determine performance factors and both approaches require careful attention to propagation of uncertainties. Each approach has its own advantages and disadvantages, which may be summarized as follows:

- The internal approach uses more sensors but can provide additional information about the performance of the individual components in the heat pump. This information is very useful for diagnosing problems.
- In some systems, the secondary refrigerant may be "over-pumped", that is, the pump has been conservatively selected and delivers high flow rates and low temperature differences. If insufficient care has been taken in specifying the sensors, the low temperature differences may lead to low accuracy with the external approach.
- The external approach does not require making connections (pressure measurements) to the refrigerant, and, so, is less invasive. On the other hand, heat pumps increasingly have more and more internal measurement points, decreasing the required additional instrumentation and connections.

As internal heat pump controls and monitoring become more sophisticated with additional sensors, it seems likely that the internal approach or a variation on it could be implemented by the manufacturer, if desired. This would further lower the cost of monitoring and fault detection and diagnosis.

4. Heat Pump Boundary (Level 1) Results

In this section, we present seasonal performance factor results based on measurements made in the Annex 52 case studies. 20 systems that provided building heating and cooling (in some cases) were monitored that could provide SPF at boundary level 1; a total of 78 years of SPFs were measured. The measured values are summarized in Table 2. With three exceptions (IKEA Uppsala, Backadalen and Rosenborg), the external method has been used for these case studies. Unfortunately, there were no case studies within Annex 52 comparing the internal and external approaches.

For heat pumps operating in heating mode, the average SPF_{H1} is 3.9, whether taken as the simple average of 12 systems, or the average of 78 years of operation. For cooling operation, the average SPF_{C1} is 3.9 taken as the average of 8 systems or 3.7 as the average for all years. For heat pumps that provide both heating and cooling, the combined SPF_{HC1} is 3.7 as the average for 6 systems, or 3.5 taken as the average for all years. For comparison purposes, Spitler and Gehlin [9] found an average SPF_{H1} of 4.0 for 39 systems and an SPFC1 of 5.5 for 12 systems reported in the literature.

Table 2. Annex 52 case studies presenting SPF1 results

Building name	Country	Years	HC1 Min	***HC1 Avg.***	HC1 Max	H1 Min	***H1 Avg.***	H1 Max	C1 Min	***C1 Avg.***	C1 Max	UGT [°C]
Aalto University [14]	Finland	*1*		***3.7***								8.6
Hugh Aston Building [15]	UK	*2*	3.3	***3.5***	3.7	2.9	***3.2***	3.6	3.9	***3.9***	4.0	12.3
The Crystal [16]	UK	*8*	1.5	***2.5***	3.3	2.3	***3.0***	3.7	1.1	***2.2***	2.9	13.1
Kalnes [17]	Norway	*5*	4.3	***4.6***	4.8							8.1
KIWI Dalgård [18]	Norway	*1*					***2.9***					5.0*
Sweco building [18]	Norway	*1*					***3.4***			***3.5***		8.0*
Moholt 50/50 [18]	Norway	*1*					***3.2***					5.0*
Frescati [19]	Sweden	*3*				5.6	***6.2***	6.5	4.7	***5.2***	5.6	9.0
Forskningen [20]	Sweden	*1*					***3.6***					9.8
Rosenborg [21]	Sweden	*1*		***4.9***			***5.0***			***4.4***		10.0
Frölunda Club house [22]	Sweden	*3*				3.6	***3.8***	3.9				8.0*
Studenthuset [23]	Sweden	*5*				3.8	***3.9***	4.1				9.2
Traktorn [24]	Sweden	*2*				3.9	***4.0***	4.0				11.1
Briljanten [25]	Sweden	*4*				3.1	***3.2***	3.4				11.1
IKEA Uppsala [26]	Sweden	*3*	3.6	***3.7***	3.9	3.6	***3.8***	4.0	3.6	***3.7***	3.9	6.8
Backadalen [27]	Sweden	*1*					***3.9***					7.8
AOV [28]	Germany	*9*	3.0	***3.4***	4.3	2.9	***3.4***	4.5	1.8	***4.0***	5.1	11.3
GEW [29]	Germany	*11*	2.0	***3.6***	4.6	1.7	***2.5***	2.8	1.6	***4.1***	6.8	12.0
EFB [30]	Germany	*14*				5.1	***5.7***	7.2				10.6
WGG [31]	Germany	*2*				4.8	***5.1***	5.3				11.7

*Estimated undisturbed ground temperatures (UGT) based on local annual mean air temperature.

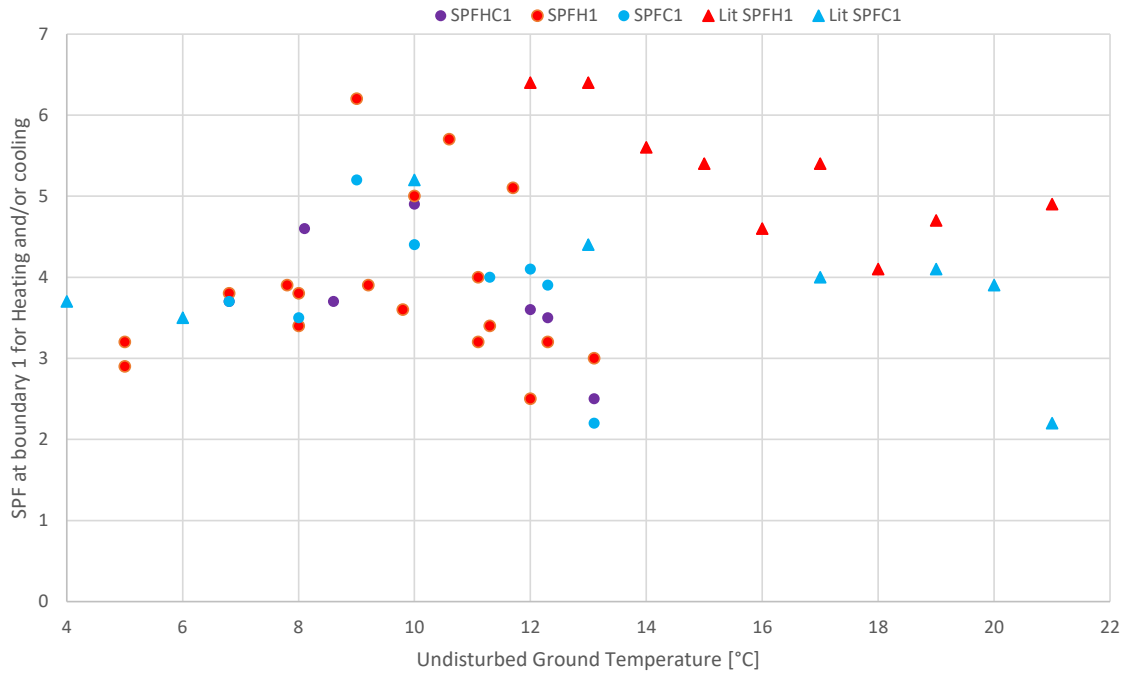


Fig. 2 SPF for level 1 vs Undisturbed Ground Temperature (UGT) -Values from Annex 52 Case Studies and Literature Review [10]

One finding of multiple studies, e.g. [9,10] is, that there is no clear relationship between ground temperature, system type, or other variables and the reported SPF. Figure 2 illustrates this, showing average SPF_{H1}, SPF_{C1} and SPF_{HC1} for (1) the 20 Annex 52 case studies and (2) 55 systems reviewed in [10] versus undisturbed ground temperature (UGT) at the locations. Not all systems reported all measures; SPFH1 is reported by 8 of the Annex 52 studies and 39 of the literature review studies; SPFC1 is reported by 8 of the Annex 52 studies and 12 of the literature review studies. SPFHC1 is reported by 8 of the Annex 52 studies and none of the literature review studies. All but four of the Annex 52 locations have measured UGT and the remaining values were estimated by the case study authors based on the annual mean air temperature at the locations. UGT values for the literature review cases have been estimated with a model [32-34] based on weather data.

Some of the systems in Table 2 show marked variation in year-to-year values of SPF. For some systems, these changes in SPF are connected to changes in load or equipment. The Crystal Building in London undergoes some abrupt changes in SPF_{C1} due to apparent control and operation issues. In the system serving the AOV building [28] a modest decline in the ground temperatures occurs over nine years of operation, as evidenced by the heat pump entering and exiting fluid temperatures shown in Figure 3. The SPF_{H1} values in Figure 4 show a corresponding decline in performance associated with the heat pump entering fluid temperatures. However, with the limited sample size, it seems year-to-year variations are more likely to be caused by other factors than changes in the ground temperatures.

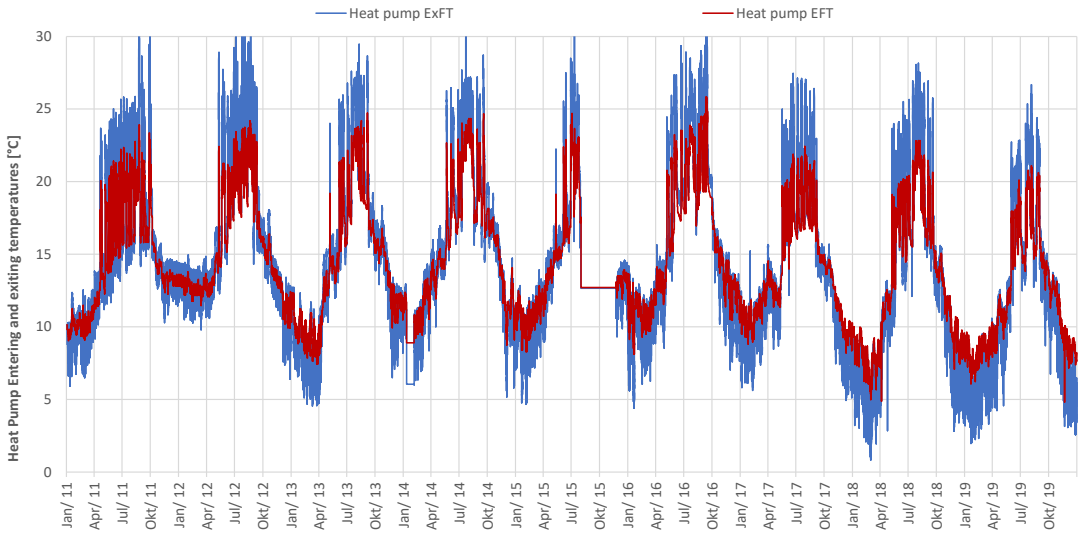


Fig. 3 Heat pump entering and exiting fluid temperatures for AOV building [28] Adapted from original figure; used by permission.

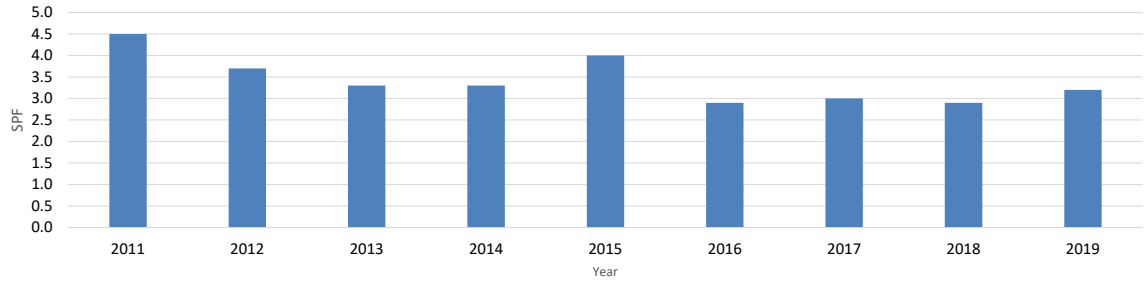


Fig. 4 SPF_{H1} for AOV building [28]

The Frescati building [19] has exceptionally high SPF_{H1} and SPF_{HC1}. The borehole system is connected to a local thermal network and operates with three parallel heat pumps of which the two larger heat pumps are frequency regulated and deliver heat at 30°C while the third heat pump is a smaller on-off regulated heat pump delivering heat at 40°C. The small heat pump has lower performance but is used less frequently than the other two heat pumps, so has little influence on the combined SPF_{H1} for all three heat pumps. The system uses district heating to meet peak loads. This allows the lower supply temperature and higher performance.

The EFB building [30] is another building with very high performance at system level 1. The heat pumps are connected to a large number of energy piles below the building and provide heating via concrete core activation, with a very low distribution temperature (22°C). Significant supplementary heating is provided from a district heating system via radiators and ventilation. The heat pumps are operated in this way to cool the ground surrounding the pile heat exchangers so that free cooling can be provided in the summer. This combined with the very low distribution temperatures leads to high values of SPF_{H1}. The system has been monitored over 14 years and although SPF_{H1} has been above 5 all the measured years, the performance has increased significantly to values around 7 in the later three years (2017-2019) after refining the operating strategy.

Apart from the 20 buildings listed in Table 2, the Emmaboda case study [35] also reported SPF for system level 1. The Emmaboda system is, however, an industrial system, originally a high-temperature borehole thermal energy storage (HT-BTES) without heat pumps, used to store waste heat from the foundry. After several years in operation, the system design and operation were altered by installing heat pumps and decreasing the average storage temperature from ~45°C to ~30°C. The system now serves as a high-temperature process cooling with very high performance at system level 1. The measured SPF_{C1} over the three measured years after the heat pumps were installed reach 13.1 on average but can't really be compared with the performance of ordinary building heat pump systems.

5. Discussion, Conclusions and Recommendations

Some of the main findings of Annex 52 include the following:

- Annex 52 has contributed to systematization of field measurements by introducing a new boundary schema that accounts for a wide range of system features that go beyond typical residential systems.
- Annex 52 has developed guidelines for key performance indicators, instrumentation, measurement, and uncertainty analysis. These guidelines will allow better planning of field measurements at lower costs and facilitate fault detection/diagnosis and optimization of system design and operation.
- While field measurements of ground-source heat pump system performance factors are still relatively rare and uncertainty analysis of performance measurements is even rarer, the Annex has contributed a significant increase in the number of published field measurements of larger GSHP systems. The Annex sought to collect data for benchmarking, but this is only provided to a limited degree. Most of the systems are located in northern Europe. Further studies covering a larger geographic area would be welcome.
- This paper has only presented SPF for the heat pumps, but the Annex is much broader, covering SPF for a range of boundaries. A general trend is that SPF decreases as the boundary is extended to include the source-side distribution system and some or all of the load-side distribution system. In fact, even systems with "free cooling" via use of ground loop fluid to provide cooling may have SPF_{C5} that is not markedly different from GSHP systems that use the heat pump to provide cooling. It should also be noted that, though often ignored, the energy used by distribution systems is not unique to GSHP systems or ASHP systems. Field measurements of energy at all boundaries used by other competing heating and cooling systems would be a welcome contribution to the field, as this would shed light on the need for increased efficiency in heating and cooling distribution systems.
- System SPFs at all boundary levels are highly variable from system to system, with, for the most part, no clear relationship between SPF and other factors. This was illustrated in this paper for the heat pumps, but similar disparities were found at other boundary levels.
- A number of the case studies found that short-term performance factors (e.g. hourly and daily) were generally higher during periods of higher load, even though source temperatures were less favorable.

With regards to seasonal performance of the heat pumps:

- The measured system average heat pump SPFs (Level 1) presented in this paper range between 2.2-4.9 for SPF_{HC1}, 2.5-6.2 for SPF_{H1}, and 2.2-5.2 for SPF_{C1}, with overall average values for all systems being 3.9 for SPF_{HC1}, 3.9 for SPF_{H1}, and 3.7 for SPF_{C1}. These are in line with results from systems previously reported in the literature.
- Two systems with very high SPF_{H1} had significant supplementary heating and were designed so that the heat pumps used a very low distribution temperature allowing excellent heat pump performance.

The Internet of Things (IoT) is rapidly developing. Many of the measurements needed to calculate seasonal and other performance factors are already internally measured within currently available heat pumps, though this information is often not available to end users. It seems likely to us that making this information available and lowering the cost of field measurement combined with a higher degree of automated evaluation would lead to wider use of field measurements and much better understanding of real-world performance. This in turn will lead to improved system performance and a higher degree of renewable energy in our heating and cooling systems. Finally, we note that though the focus of the annex and this paper is ground-source heat pump systems, much of the work on field measurements can be and should be directly applied to air-source heat pump systems and air-conditioning systems also.

Acknowledgements

The support from the authors' employers and the Swedish Energy Agency (TERMO research program Grant 45979-1) is gratefully acknowledged. The second author's work was supported by the OG&E Energy

Technology Chair. This work is part of the IEA HPT Annex 52, *Long-term performance measurement of GSHP systems serving commercial, institutional and multi-family buildings*.

References

[1] Edison Electric Institute. 1948. Suggested Field Test Procedure for Determination of Coefficient of Performance and Performance Factor of an Electric Heat Pump While Operating on the Heating Cycle, New York City, Edison Electric Institute. Report No. Q-11.
[2] Gehlin, S. and J.D. Spitler. 2022. Final report. IEA HPT Annex 52 – Long-term performance monitoring of GSHP systems serving commercial, institutional and multi-family buildings. https://doi.org/10.23697/xsbr-xn83
[3] Gehlin, S., Spitler, J.D. 2022. Subtask 1 Report – Annotated Bibliography – Final Document. IEA HPT Annex 52 – Long-term performance monitoring of GSHP systems serving commercial, institutional and multi-family buildings. https://doi.org/10.23697/dzpy-yp81
[4] Davis, M.J., Martinkauppi, I., Witte, H., Berglöf, K., Vallin, S. 2021. Guideline for Instrumentation and Data – Final Document. IEA HPT Annex 52 – Long-term performance monitoring of GSHP systems serving commercial, institutional and multi-family buildings. https://doi.org/10.23697/tgr4-qn89
[5] Spitler, J.D., Berglöf, K., Mazzotti-Pallard, W., Witte, H. 2021. Guideline for Calculation of Uncertainties – Final Document. IEA HPT Annex 52 – Long-term performance monitoring of GSHP systems serving commercial, institutional, and multi-family buildings. https://doi.org/10.23697/m2em-xq83
[6] Gehlin, S., Spitler, J.D. Witte, H., Andersson, O., Berglöf, K., Davis,M., Javed, S., Bockelmann, F., Turner, J., Clauss, J. 2022. Subtask 3 Report – Guide for analysis and reporting of GSHP system performance – system boundaries and key performance indicators (KPI) – Final Document. IEA HPT Annex 52 – Long-term performance monitoring of GSHP systems serving commercial, institutional and multi-family buildings. https://doi.org/10.23697/xa7z-vd92
[7] Gehlin, S., Spitler, J.D. 2022. Case Study Summary Report. IEA HPT Annex 52 – Long-term performance monitoring of GSHP systems serving commercial, institutional and multi-family buildings. https://doi.org/10.23697/qfnt-rb80
[8] https://heatpumpingtechnologies.org/annex52/documents/
[9] Gleeson, C. P. and R. Lowe. 2013. Meta-analysis of European heat pump field trial efficiencies. Energy and Buildings 66(0): 637-647. https://doi.org/10.1016/j.enbuild.2013.07.064
[10] Spitler, J. D. and S. Gehlin. 2019. Measured Performance of a Mixed-Use Commercial-Building Ground Source Heat Pump System in Sweden. Energies 12(10): 2020. https://doi.org/10.3390/en12102020
[11] Nordman, R., O. Kleefkens, P. Riviere, T. Nowak, A. Zottl, C. Arzano-Daurelle, A. Lehmann, O. Polyzou, K. Karytsas, P. Riederer, M. Miara, M. Lindahl, K. Andersson and M. Olsson. 2012. SEPEMO - Seasonal performance factor and monitoring for heat pump systems in the building sector., SP Technical Research Institute of Sweden.
[12] Fahlén, P. 2005. Performance audits of heat pumps - procedures and uncertainties. 8th International Energy Agency Heat Pump Conference. Las Vegas, International Energy Agency.
[13] Berglöf, K. 2005. Methods and potential for on-sire performance validation of air conditioning, refrigeration, and hat pump systems. 8th International Energy Agency Heat Pump Conference. Las Vegas.
[14] Todorov, O., Vallin, S., Virtanen, M., Leppäharju, N. (2021). Case study report for monitoring project – Aalto University New Campus Complex, Otaniemi (Espoo). Finland. IEA HPT Annex 52 – Long-term performance monitoring of GSHP systems serving commercial, institutional and multi-family buildings. https://doi.org/10.23697/cm70-g204
[15] Rees, S.J. 2021. Case study report for a large university building, UK. The Hugh Aston Building at De Montfort University. IEA HPT Annex 52 – Long-term performance monitoring of GSHP systems serving commercial, institutional and multi-family buildings. https://doi.org/10.23697/qwab-0818
[16] Turner, J., Loveridge, F. Rees, S.J. 2021. Case study report for the Crystal Building, United Kingdom. IEA HPT Annex 52 – Long-term performance monitoring of GSHP systems serving commercial, institutional and multi-family buildings. https://doi.org/10.23697/kmxr-hw82
[17] Clauß, J., Taveres-Cachat, E., Erstad, E. 2021. Case study report for Kalnes energy central, Sarpsborg, Norway. IEA HPT Annex 52 – Long-term performance monitoring of GSHP systems serving commercial, institutional and multi-family buildings. https://doi.org/10.23697/jh1q-4k55
[18] Stene, J. 2021. Case Study report for 1) KIWI Dalgård, 2) The SWECO Building and 3) Moholt 50|50 – Norway. IEA HPT Annex 52 – Long-term performance monitoring of GSHP systems serving commercial, institutional and multi-family buildings. https://doi.org/10.23697/wa60-2121
[19] Lazzarotto, A. 2021. Case study report for Frescati NPQ, Sweden. IEA HPT Annex 52 – Long-term performance monitoring of GSHP systems serving commercial, institutional and multi-family buildings. https://doi.org/10.23697/emqr-m785
[20] Mazzotti-Pallard, W. 2021. Case study report for Forskningen, Stockholm, Sweden. Three plus energy buildings (by design) with GSHPs, variable-length boreholes, ventilation recovery and pre-heating, wastewater recovery & PV panels. IEA HPT Annex 52 – Long-term performance monitoring of

GSHP systems serving commercial, institutional and multi-family buildings. https://doi.org/10.23697/dfs2-v474

[21] Abuasbeh, M. 2021. Case study report for Rosenborg, Sweden. GSHP installation coupled with aquifer thermal energy storage ATES supplying heating and cooling for two commercial buildings. IEA HPT Annex 52 – Long-term performance monitoring of GSHP systems serving commercial, institutional and multi-family buildings. https://doi.org/10.23697/6h7v-bt33

[22] Javed, S., Zhang, H., Liu, H. 2021. Case study report for a small Clubhouse building in Gothenburg, Sweden. IEA HPT Annex 52 – Long-term performance monitoring of GSHP systems serving commercial, institutional and multi-family buildings. https://doi.org/10.23697/8n0p-3n24

[23] Gehlin, S., Spitler, J.D. 2021. Case study report for Studenthuset, Stockholm, Sweden. Long-term performance analysis of the GSHP system for a student union building. IEA HPT Annex 52 – Long-term performance monitoring of GSHP systems serving commercial, institutional and multi-family buildings. https://doi.org/10.23697/pmr0-0778

[24] Ekestubbe, J. 2021. Case study report for Kv Traktorn, Lund, Sweden. Long-term performance analysis of the GSHP system for an office building. IEA HPT Annex 52 – Long-term performance monitoring of GSHP systems serving commercial, institutional and multi-family buildings. https://doi.org/10.23697/92qm-rr10

[25] Ekestubbe, J. 2021. Case study report for Brf Briljanten, Lund, Sweden. Long-term performance analysis of the GSHP system for a multi-family building. IEA HPT Annex 52 – Long-term performance monitoring of GSHP systems serving commercial, institutional and multi-family buildings. https://doi.org/10.23697/te3s-cb70

[26] Walfridson, T. 2021. Case study report for IKEA Uppsala, Sweden. IEA HPT Annex 52 – Long-term performance monitoring of GSHP systems serving commercial, institutional and multi-family buildings. https://doi.org/10.23697/vda5-8s77

[27] Walfridson, T. 2021. Case study report for Backadalen, Göteborg, Sweden. IEA HPT Annex 52 – Long-term performance monitoring of GSHP systems serving commercial, institutional and multi-family buildings. https://doi.org/10.23697/r7zd-s388

[28] Bockelmann, F. 2021. Case study report for AOV, Germany. Office building with borehole heat exchanger. IEA HPT Annex 52 – Long-term performance monitoring of GSHP systems serving commercial, institutional and multi-family buildings. https://doi.org/10.23697/s338-wf13

[29] Bockelmann, F. 2021. Case study report for EFB, Germany. Office building with energy piles. IEA HPT Annex 52 – Long-term performance monitoring of GSHP systems serving commercial, institutional and multi-family buildings. https://doi.org/10.23697/2hb1-h641

[30] Bockelmann, F. 2021. Case study report for GEW, Germany. Office building with borehole heat exchanger. IEA HPT Annex 52 – Long-term performance monitoring of GSHP systems serving commercial, institutional and multi-family buildings. https://doi.org/10.23697/0cfw-xw78

[31] Bockelmann, F. 2021. Case study report for WGG, Germany. School with gym and energy piles as well as agrothermal field. IEA HPT Annex 52 – Long-term performance monitoring of GSHP systems serving commercial, institutional and multi-family buildings. https://doi.org/10.23697/ek2v-c43

[32] Xing, L. and J. D. Spitler. 2017. Prediction of undisturbed ground temperature using analytical and numerical modeling. Part I: Model development and experimental validation. Science and Technology for the Built Environment 23(5): 787-808. https://doi.org/10.1080/23744731.2016.1258371

[33] Xing, L. and J. D. Spitler. 2017. Prediction of undisturbed ground temperature using analytical and numerical modeling. Part II: Methodology for developing a world-wide dataset. Science and Technology for the Built Environment 23(5): 809-825. https://doi.org/10.1080/23744731.2016.1262705

[34] Xing, L., J. D. Spitler and A. Bandyopadhyay. 2017. Prediction of undisturbed ground temperature using analytical and numerical modeling. Part III: Experimental validation of a world-wide dataset. Science and Technology for the Built Environment 23(5): 826-842. https://doi.org/10.1080/23744731.2016.1253978

[35] Andersson, O., Rydell, L., Håkansson, N. 2021. Case study report for the Xylem HT-BTES plant in Emmaboda, Sweden. Efficiency by using heat pumps for extraction of stored heat. IEA HPT Annex 52 – Long-term performance monitoring of GSHP systems serving commercial, institutional and multi-family buildings. https://doi.org/10.23697/j2hk-4×61

14th IEA Heat Pump Conference
15-18 May 2023, Chicago, Illinois

Towards integral assessment of heat pumps and refrigerants using LCA: A case study for the German building stock

Christian Vering[a,*], Christian Zibunas[b], Felix Tessarek[a,b], Nils Moschner[a], Katharina Breuer[a], Christoph Höges[a], Hannah Romberg[a], Niklas von der Aßen[b], Dirk Müller[a]

[a]Institute for Energy Efficient Buildings and Indoor Climate, RWTH Aachen University, Mathieustraße 10, 52074 Aachen, Germany
[b] Chair of Thermodynamics, RWTH Aachen University, Schinkelstraße 8, 52064 Aachen, Germany

Abstract

Heat pumps are the key technology to defossilize the heat supply of buildings, which for now is predominantly based on burning fossil fuels. In Germany, 19 Million residential buildings consume about 865 TWh of fossil fuels and emit about 120 Million tons of CO2 each year, mainly for heating purposes. Reducing GHG emissions is critical to achieving climate goals, and replacing combustion-based heating technologies is crucial to GHG mitigation. To recommend appropriate alternative technologies and accelerate the corresponding deployment, there are standardized indicators for heat pumps in each sustainability dimension: For instance, economic and environmental aspects can be represented by energy labels, while social aspects (e.g., acoustics) are currently not in focus. In particular, from an environmental point of view, the focus is on labeling emissions due to the refrigerants' Global Warming Potential (GWP) and operating-related emissions. However, the focus on GHG emissions bears the risk of unnoticed burden shifting to other environmental impacts, such as ecotoxicity or land use. To avoid burden shifting, a holistic assessment of heat pumps and refrigerants using life cycle assessment (LCA) is necessary.

This work investigates the environmental assessment metrics beyond climate change and applies them to heat pumps and refrigerants in existing buildings in Germany. To evaluate essential assessment metrics simultaneously, a fundamental data basis is prepared through an extensive literature and database review. While there is scientific consensus on the fundamental understanding of heat pumps and refrigerants, some assumptions still need to be made to obtain meaningful results. Therefore, a key finding of this work is that further research is mandatory. In addition, we identify the main contributors to improving the environmental impacts of heat pumps and refrigerants using LCA: For low GWP refrigerants in heat pumps, the refrigerant choice is less important in terms of environmental aspects, here resource availability (flour range) and proper handling (avoidance of leakage) are essential. Currently, emissions from electricity generation dominate the environmental impacts of heating with heat pumps. Using renewable electricity instead will lead to some burden shifting but reduce most environmental impacts so that the production of heat pumps and refrigerants gains importance for further impact reduction. For future research, consider potential improvements in the supply chains of materials and refrigerants using dynamic LCA.

© HPC2023.
Selection and/or peer-review under the responsibility of the organizers of the 14th IEA Heat Pump Conference 2023.
Keywords: Environmental impact, low-emission heating, burden-shifting

1. Introduction

To adjust to comfortable indoor conditions, heating and cooling are crucial in the building sector. Particularly during the heating season, the building sector throughout Europe requires enormous energy to meet its heating demands. Currently, most residential heating systems are based on conventional combustion

* Corresponding author. *E-mail address:* cvering@eonerc.rwth-aachen.de

technologies, which cause greenhouse gas (GHG) emissions during operation, mainly in the form of CO_2. However, GHG emissions must be drastically reduced by 2050 to achieve climate targets. In this context, the transition to low-carbon heating systems is taking place with increasing acceleration replacing conventional with heat pump-based systems. Heat pumps use refrigerants to upgrade environmental heat and provide suitable heat for buildings. The upgrading requires an additional energy supply to raise the temperature level of environmental heat. In building applications, the energy supply powers an electricity-driven compressor with refrigerant-dependent efficiency. Therefore, the overall heat pump performance and emission reduction potential depend mainly on the refrigerant and the refrigerant-dependent compressor efficiency. In the past, heat pumps used refrigerants (Hydrochlorofluorocarbons, HCFC) that were very efficient and simultaneously neither flammable nor toxic. These favorable properties were achieved using fluorine (F) and chlorine (C) atoms in the hydrocarbon chains of the refrigerant. However, in the event of a leak, chlorine was released into the atmosphere, contributing to ozone depletion. Therefore, refrigerants with ozone depletion potential (ODP) were largely banned. [1]

The ban has led to the developing of new refrigerants that are also efficient and safe but do not require a chlorine atom to make a stable molecule. This group of refrigerants is called hydrofluorocarbons (HFCs), which consist of hydrocarbons and fluorine. However, many HFCs have high global warming potential (GWP) due to the fluorine atoms. Therefore, in the event of leakage, HFCs would contribute to global warming and climate change. Therefore, HFCs should also be used less or even completely banned in heat pumps to comply with long-term climate targets to reduce this risk. According to current research, the most superior alternatives for the future are natural refrigerants such as hydrocarbons (HCs) or other organic refrigerants such as ammonia or CO_2 and hydrofluorolefines (HFOs). These refrigerant groups have no ODP and a low GWP (<150), thus potentially not compromising climate goals. However, future refrigerants must also be very efficient to achieve a high performance of heat pumps and, accordingly, low GHG emissions. [2]

To extend the environmental assessment of refrigerants to heat pumps, the (extended) Total Equivalent Warming Impact (eTEWI) [3], [4] or Lifecycle Climate Performance (LCCP) [5] evaluation methods are often used in the current literature. Both methods focus on evaluating the climate change impact of refrigerants and heat pumps' operation, i.e., the electricity consumption of the compressor. However, in the future, regenerative energy sources can reduce the climate impact of the operation, potentially shifting the impact to other life cycle stages, e.g., emissions from the production of heat pumps, or increase other environmental impacts, which is called burden shifting. To avoid burden shifting, more advanced environmental assessment methods must be applied, which consider further impact categories. For example, in addition to operation, the heat pump's production, disposal, and recycling will gain importance. However, the influence of these phases is insufficiently considered in current methods. Therefore, Life Cycle Assessment (LCA) [6] is needed to consider all phases and impacts adequately. Moreover, in the early design stages, LCA will already help identify potential environmentally friendly refrigerants that have less impact on the environment than conventional refrigerant groups.

Compared to conventional eTEWI and LCCP, this work investigates the environmental assessment metrics beyond climate change by using LCA and applies them consistently to heat pumps and refrigerants in existing buildings in Germany. An LCA model is formulated to evaluate essential assessment metrics simultaneously (Section 2), and an extensive literature and database review provide relevant information and assumptions. As a case study (Section 3), we use seven refrigerants in a simple heat pump cycle and assess 16 environmental impact categories. For discussion (Section 4), we apply different electricity mixes and compare our results to a conventional gas boiler system. Finally, we summarize our findings and give a perspective for future work (Section 5).

2. LCA Modelling

This section addresses the Goal and Scope definition (Section 2.1) of this study, the Life Cycle Inventory (LCI, Section 2.2), and the data sources (Section 2.3).

2.1. Goal and Scope Definition

The LCA serves for the environmental evaluation of heat pumps and refrigerants in residential buildings in Germany. The LCA aims to investigate the influence of the refrigerant on the GHG emissions caused within the life cycle of a heat pump. In addition, trade-offs with other environmental categories will be considered, and levers to reduce the overall environmental impact will be identified.

This work investigates the life cycle of a simple air-to-water heat pump according to Figure 1. While the production of refrigerants and heat pumps and the operation of the heat pumps are in the foreground of the investigations (red), additional aspects (black) must also be modeled to develop reasonable conclusions. The function of the air-to-water heat pump is to provide space heating over an observation period of 20 years, matching the heat pump's lifetime [7]. This paper does not consider other parts of the building energy system, such as the distribution system, the buffer tanks, or the building envelope, as this work is intended to provide a basis. However, these other parts of the building energy system should be integrated into future work. The functional unit in the LCA is the provision of space heating for a German residential building over the heat pump's life cycle (20 years). The system boundaries include the production of refrigerant and heat pump, the operation of the heat pump, any leakage of refrigerant, and upstream processes, e.g., materials and energy. In contrast to the LCCP method, the recycling of heat pump and refrigerant is not included in the system boundaries, as there are no sufficient data sets for the environmental impacts of the recycling processes.

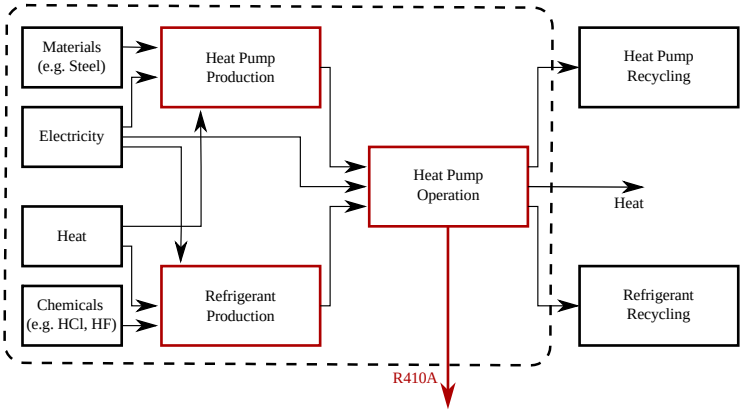


Figure 1: Life cycle of an air-water heat pump and assumed system boundaries.

This study follows the ILCD (International Life Cycle Data system) recommendations to characterize elementary flows to environmental impacts, comprising 16 environmental impact categories, e.g., climate change, acidification, and ozone depletion [8], [9]. All 16 categories are assessed, while the focus lies on climate change.

2.2. Life Cycle Inventory

To conduct the LCA, we need a sound basis comprising the assumptions within the calculation procedure. Table 1 sums up all assumptions depending on the refrigerant. To exchange the conventional refrigerant R410A, we investigate six potential refrigerants with lower GWP than 1000 and no ODP from four substance groups: R1234yf (HFO), R32 (HFC), R290, R1270, and R600a (HC), and R717 (Anorganic). Except for R717 (safety class B), all refrigerants are assigned to safety class A. However, all potential refrigerants are at least low flammable (2L and higher). Thus, if one of these six refrigerants prevails in the long term, increased safety requirements will be imposed on heat pumps. To assess the environmental impacts concerning the entire life cycle, we need additional information about the production (refrigerant and heat pump), the heat pump operation, and refrigerant leakage during the heat pump operation and end-of-life (EOL).

Table 1: Main assumptions to model the life cycle of an air-water-heat pump. Most of the assumptions are independent of the refrigerant choice, while some are influenced by the refrigerant.

Refrigerant	R410A	R32	R1234yf	R290	R1270	R600a	R717
Group	HFC	HFC	HFO	HC	HC	HC	Anorganic
Safety Class	A1	A2L	A2L	A3	A3	A3	B2L
GWP_{100}	2,256	771	4	3	1.8	4	0
Heat pump operation							
SCOP / -	3.71	3.99	3.82	4.20	4.19	3.81	4.27

Annual Heat Demand	20,400 kWh	20,400 kWh	20,400 kWh	20,400 kWh	20,400 kWh	20,400 kWh	20,400 kWh
Maximum Heat Demand	7.5 kW	7.5 kW	7.5 kW	7.5 kW	7.5 kW	7.5 kW	7.5 kW
Refrigerant	R410A	R32	R1234yf	R290	R1270	R600a	R717
Heat pump production							
Specific HP size	18 kg/kW	18 kg/kW	18 kg/kW	18 kg/kW	18 kg/kW	18 kg/kW	18 kg/kW
Mass Composition HP	Heck et al.	Heck et al.	Heck et al.	Heck et al.	Heck et al.	Heck et al.	Heck et al. w/o Copper
Refrigerant production							
Specific Refrigerant charge	0.3 kg/kW	0.25 kg/kW	0.35 kg/kW	0.15 kg/kW	0.15 kg/kW	0.15 kg/kW	0.1 kg/kW
Production Impacts	Frischknecht	Frischknecht	Baral et al.	ecoinvent	ecoinvent	ecoinvent	ecoinvent
Leakage rate / production	1% total	1% total	1% total	-	-	-	-
Refrigerant Leakage							
Leakage rate / operation	5 %/a	5 %/a	5 %/a	5 %/a	5 %/a	5 %/a	5 %/a
Leakage rate / EOL	30 %	30 %	30 %	30 %	30 %	30 %	30 %

2.2.1. Refrigerant Production

While potential environmental impacts are known and available in ecoinvent [10] for producing natural refrigerants R290, R1270, R600a, and R717, few primary sources exist for the refrigerants R410A, R32, and R1234yf, which generally consider only GHG emissions. Therefore, for R410A and R32 production, data sets from Frischknecht et al. are used [11], [12]. Frischknecht models the production of refrigerants using chemical reaction equations with additional assumptions about the energy required, recovery, chemical leakage, and the production route. Data sets from Baral et al. are used for R1234yf production [13]. Baral et al. study the GHG emissions from the production of R1234yf using the CHEMCAD simulation tool. The reported production process starts with the reactants chlorotrifluoroethylene and chloromethane. Moreover, leakages of chemicals, reactants, or intermediates can occur during refrigerant production. In particular, the leaking of substances with high GWP or ODP can account for a large portion of the total environmental impact of production and thus have to be modeled for a holistic assessment. As a first estimate, an emission rate of one mass percent is assumed, made up of the reactants and intermediates.

The required charge in the heat pump depends on the refrigerant considered and determines the amount of refrigerant that needs to be produced. Commercial heat pumps for residential buildings exist for the three refrigerants R410A, R32, and R290 so that data sheets can be accessed. The data sheets approximate the specific charge for R410A, R32, and R290. The specific charge of the remaining refrigerants is estimated using the UNEP report published in 2014 [14]. In addition to the amount of refrigerant required for operation, we consider the heat pump production and refrigerant leakage that may occur during operation. The leakage reduces the heat pump's charge, so refilling the system becomes necessary to ensure its efficiency.

2.2.2. Heat Pump Production

The mass composition of the heat pump under study is based on a 10 kW brine-to-water heat pump from Hoval, operated with R134a. In Heck et al. [15], the masses and compositions of the individual components are reported. The mass composition of a heat pump will vary depending on the production company and the choice of components used. Since no known mass compositions of heat pumps operating with the refrigerants studied, the mass composition is used for all refrigerants studied except R717 (Figure 2).

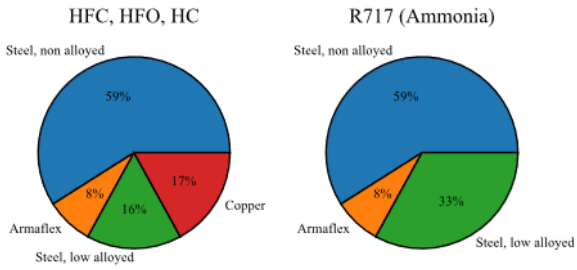


Figure 2: Mass composition of the studied air-water heat pumps.

R717 attacks copper and copper alloys, so copper for piping and heat exchangers is not currently approved. Since no sources on mass composition and weight of R717 small heat pumps are known, any other system technology is neglected below, and the mass fraction of copper is replaced by low-alloy steel. These material compositions can be scaled to the heating power of the heating system under study using specific gravity, i.e., the total weight per heating power.

The specific gravity of the heat pump depends on the design of the heat pump and the refrigerant used. The volumetric heating capacity (VHC) influences the required installation space as well as the size of the heat pump. In addition, the required wall thicknesses of the tubes depend on the maximum operating pressures of the heat pumps, which are determined by the refrigerant used. Examining data sheets of commercial heat pumps results in a specific weight of 15 kg/kW for heat pumps operating with R32 and R410A and a specific weight of 20 kg/kW for heat pumps operating with R290. Differences could not be attributed to the refrigerant and thus might result from design choices by the manufacturers. To the author's knowledge, no publication exists that examines the refrigerant's influence on the heat pump's weight in isolation from other influencing factors. Therefore, the same specific weight of 18 kg/kW is assumed for all refrigerants, as it is the average of the reported specific weight based on manufacturer data. In addition to the environmental impacts from material production, we consider the heat pump's assembly and the subcomponents' manufacture using the generic ecoinvent data set for metalworking.

2.2.3. Refrigerant Leakage

Leakage to the atmosphere results in different environmental effects depending on the refrigerant. As described in Section 1, the use of CFCs was regulated by the Montreal Protocol in 1989 because leakage of CFCs depletes the ozone layer. While the refrigerants studied in this work do not have ODP as a measured characteristic, i.e., do not cause ozone layer depletion when released, refrigerant leakage may contribute to the heat pump's total impact in other environmental categories. This work assumes a leakage rate L_{Use} of 5% per year in operation and a leakage rate L_{EOL} of 30 % at the end of life (EOL) [16], [17]. Although leakage of refrigerants has no direct impact on ozone layer depletion, during the production of some of the refrigerants, leakage of intermediates (see 2.2.1.) can cause ozone layer depletion, which we attribute to refrigerant manufacturing.

2.2.4. Heat Pump Operation

Since a large share of the emissions is related to indirect emissions from electricity consumption, it is critical to consistently model the energy demand of the buildings and the corresponding heat pump operation. The heat pump operation is driven by the building's heat demand, which is determined via TEASER [18]. TEASER is a framework for data enrichment of building performance simulation models to simplify simulating the heat demand of buildings, neighborhoods, and city districts. Based on the location, building type, building area, year of construction, and modernization standard, TEASER approximates the building's envelope area and insulation standard. In this paper, a two-story single-family house in Aachen is considered. The building has a living area of 150 m^2 and an insulation standard according to the 2nd Thermal Insulation Ordinance of 1984.

As the building model’s boundary condition serves a weather data set (Test Reference Year (TRY), 2015) representing an hourly resolved annual temperature profile. The TRY data set used represents Aachen to match the building location and was published by the German Weather Service. In general, TRY data sets exist for each square kilometer in Germany. Thus, spatially-resolved temperature profiles can be used in further studies to exploit the change of environmental impacts depending on the location.

TEASER enriches a parameterized building performance simulation model with data sets and a weather data set to create a simulation model. Then, the energetic performance is calculated based on the heat demand, which is required to balance heat losses to the environment while maintaining an indoor air set temperature,

which is 21 °C in our case study (cf. Figure 3). In total, the annual heat demand of the considered building is about 20,400 kWh with a maximum heat load $\dot{Q}_{max}$ of 7.5 kW.

To meet the building's heating demand based on the outdoor air temperature, a heating system is required. We use an air-to-water heat pump model to provide heat that meets the hourly resolved demand. Outdoor air temperature and heating demand serve as the boundary condition for the calculation procedure. The nominal flow temperature is calculated using a conventional heating curve. The heat pump model includes a fluid dependency and calculates the fluid behavior in a basic refrigeration cycle, according to Figure 4. The model is used from Hoeges et al. and covers fluid dependence with a validated loss-based compressor model.

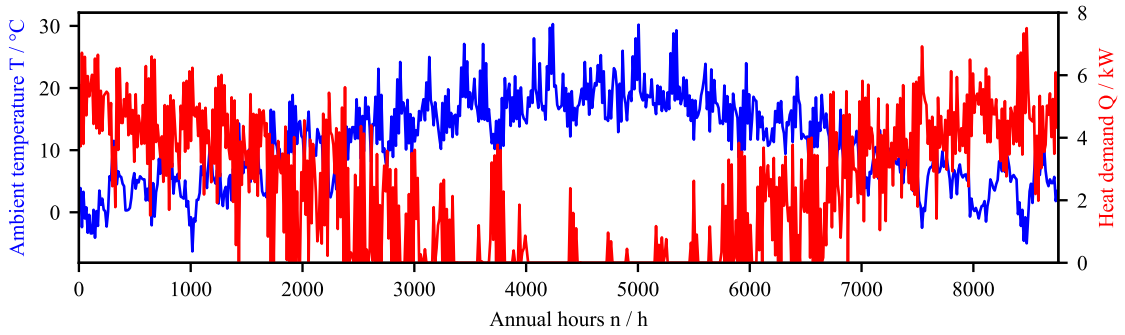


Figure 3: Hourly resolved temperature profile and corresponding heating demand of the investigated building.

Based on the boundary conditions, the heat pump model optimizes the pressure levels in the evaporator and the condenser. In addition, the degree of subcooling at the condenser outlet and the degree of superheating at the compressor inlet is maximized for each operating point subject to maximum Coefficient of Performance (COP). For more details on the heat pump model we refer to Hoeges et al. [2]. Using the heat pump model, the heat demand profile, and the outdoor air temperature profile, the required electrical power for space heating is determined for each refrigerant.

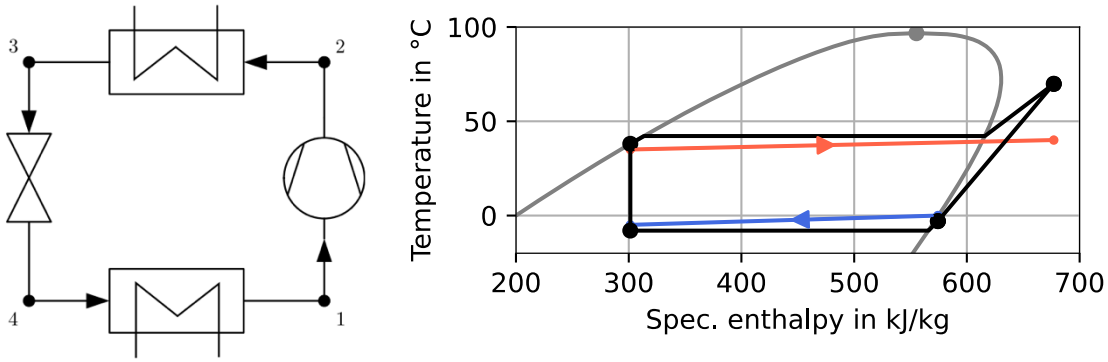


Figure 4: Process scheme (left) and exemplary T-h diagram (right) of a simple heat pump circuit.

2.3. Data Sources and Calculation of Environmental Impacts

This work uses the LCA database ecoinvent [10] to obtain the environmental impacts of material and energy used for the production of refrigerants, the construction and operation of heat pumps. (cf. Table 1).
The ecoinvent datasets already contain the characterization models and, thus, the environmental impacts of each material or energy flow needed in this study. When using the ecoinvent datasets, the environmental impacts must be scaled by the amount of material or energy flow necessary to supply the functional unit. The characterization factors for elementary flows representing refrigerants are used to estimate the impact of refrigerant leakage. The characterization factors indicate the extent to which the refrigerant leakage contributes to an impact category.

3. Life Cycle Impact Assessment

In this section, we provide the general Life Cycle Impact Assessment and conduct a sensitivity study with respect to the grid mix.

3.1. General Assessment

The electricity demand from heat pump operation accounts for the largest share of the total environmental impacts in most categories (orange, Figure 5). The only exception is ozone depletion of fluorine-containing refrigerants due to leakage of intermediates during the refrigerant production. In all other categories, refrigerant production is negligible, and heat pump production is the second largest contributor to environmental impacts. In particular, heat pump production results in significant environmental impacts in ecotoxicity, human toxicity, and resource consumption for all refrigerants except the R717 due to not involving copper (see Section 2.2.2).

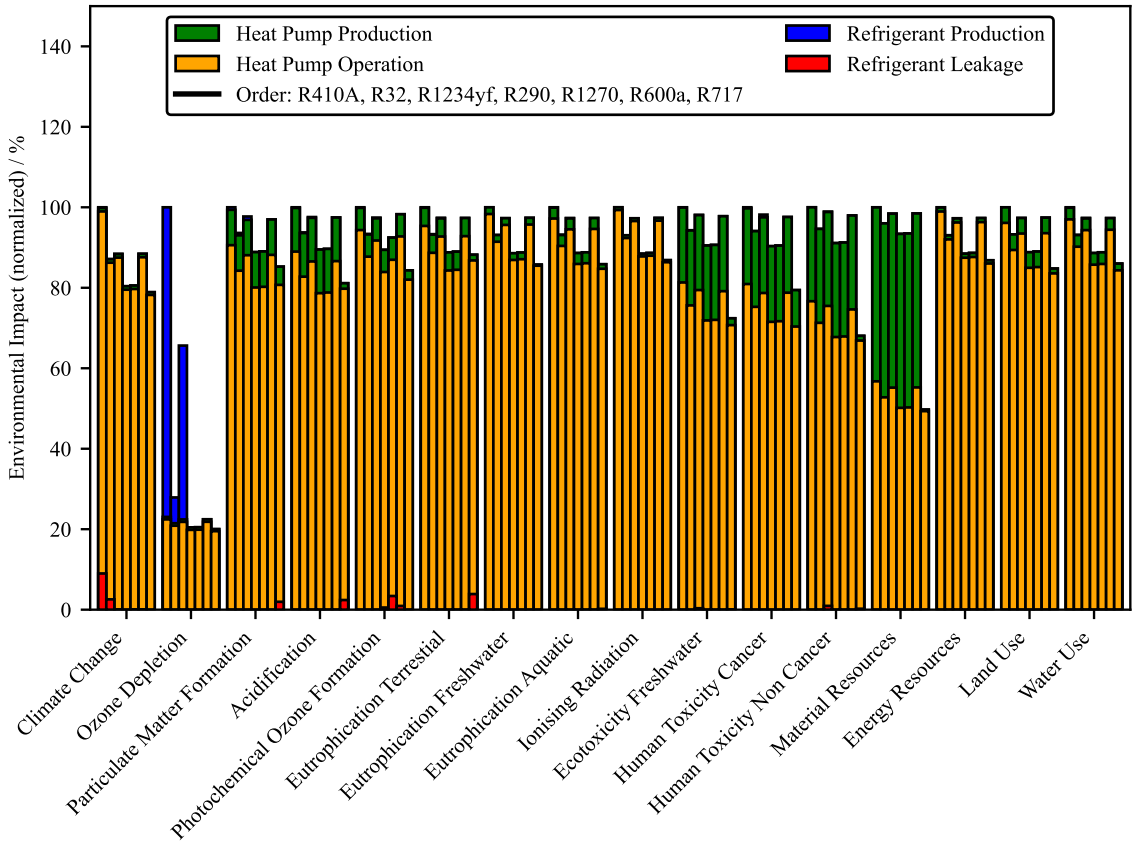


Figure 5: Environmental impacts of a heat pump for each environmental category and each refrigerant (normalized to R410A). Considered is heat supply over 20 years using the German electricity mix (2018) (521 gCO_2/kWh). The shares of the individual phases are color-coded.

Refrigerant leakage during the operation (red) is the smallest contributor and depends on the refrigerant and the environmental category: The high-GWP refrigerants R410A and R32 lead to an increase in GHG emissions and leakage of the toxic refrigerant R717 leads to minor environmental impacts, in particulate matter formation, acidification, and terrestrial eutrophication.

Across all refrigerants, R717 causes the lowest environmental impacts in all categories due to the high efficiencies. Due to the high SCOP that can be achieved with R717, the electricity required to operate the heat pump is lower, resulting in lower environmental impacts. In addition, the production of the R717 heat pump causes lower environmental impacts. Since the environmental impacts are lowest for a heat pump with R717, the refrigerant R717 is recommended in the context of a purely environmental evaluation. After R717, the environmental impacts are lowest for the hydrocarbons R290 and R1270. The use of R290 and R1270 allows high efficiencies and thus lower environmental impacts due to electricity demand than the HFOs and R600a. The next efficient refrigerant is R32. A disadvantage is the high GWP, so the leakage of R32 significantly

increases GHG emissions. Using R600a and R1234yf causes high environmental impacts due to the lower efficiencies. The highest environmental impacts in all environmental categories are caused by using R410A with the lowest efficiency. Moreover, R410A leakage significantly increases GHG emissions. The production of R410A also causes the highest environmental impacts in the ozone depletion category. Since the electricity demand and the grid mix have the highest influence on all environmental impacts, we analyze its sensitivity.

3.2. Influence of Grid Mix

The environmental impacts of the heat pump (Figure 5) were calculated assuming the German electricity mix from 2018 (GE) for the heat pump's entire lifetime. However, the share of renewable energies in electricity production is forecast to increase while the share of fossil fuels is forecast to decrease. Thus, in the following, we assume a dynamic electricity mix (GE-to-SDS) that changes over the heat pump's lifetime to account for the influence of possible decarbonization. We assume a linear progression between the German electricity mix from 2018 and the European electricity mix from the Sustainable Development Scenario (SDS) of the International Energy Agency (IEA) for 2040 [19]. The Sustainable Development Scenario models the measures needed to achieve the goals of the Paris Climate Agreement. The resulting environmental impacts of the heat pump considering the GE-to-SDS electricity mix (Figure 6).

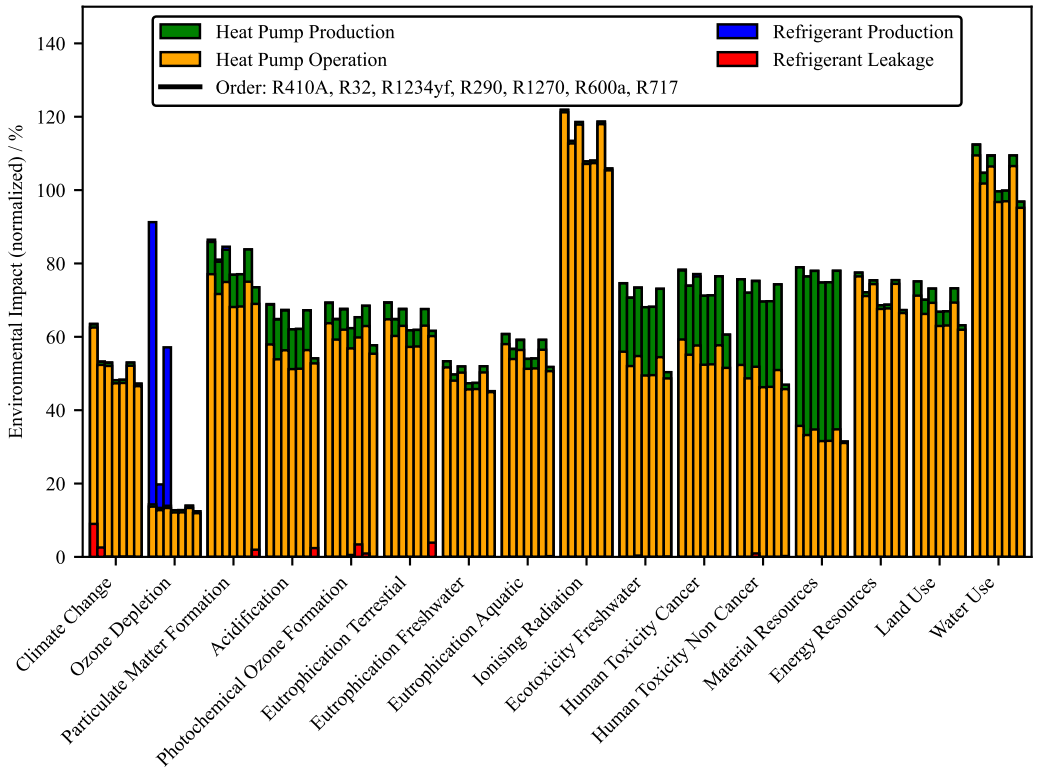


Figure 6: Sensitivity analysis of electricity mix (normalized to refrigerant R410A with German electricity mix). Instead of the static, German electricity mix, a more and more sustainable electricity mix is assumed (GE-to-SDS), where specific CO_2 emissions decrease linearly over the lifetime of the heatpump, from 521 gCO_2/kWh (GE) to 114 gCO_2/kWh (SDS). The environmental impacts of the heat pump are normalized to the refrigerant R410A with the static German electricity mix from 2018.

The environmental impacts of the heat pump decrease in most environmental categories due to a higher share of renewable energy sources and nuclear energy compared to the German electricity mix. Only ionizing radiation and water demand increase due to the higher proportion of nuclear and hydro energy in the SDS electricity mix. Not only do the environmental impacts in most environmental categories decrease due to the change in the electricity mix, but the ranking of refrigerants is also affected. For example, for the static German electricity mix, the R32 heat pump produces lower GHG emissions than the heat pumps of the low-GWP refrigerants R1234yf and R600a due to good efficiency despite leakage (see Figure 6). For the GE-to-SDS electricity mix, this statement is no longer valid, as GHG emissions are higher for the use of R32.

Furthermore, changing the electricity mix does not affect the environmental impacts from production of heat pump and refrigerant, even though these phases require electricity. This is because the production is based

on aggregated datasets from ecoinvent, which does not directly allow to exchange the electricity mix, e.g., for the upstream copper production. The refrigerant leakage is also unaffected since no electricity is involved.

4. Discussion

To evaluate whether changing from a gas condensing heating system to an air-to-water heat pump increases or decreases the enviromental impact we show a list of all impact categories and different grid mixes in Table 2. A heat pump with R410A refrigerant is used for the comparison to conservatively assess potential GHG mitigation. For this comparison, the SCOP of the heat pump is based on measured values of air-to-water heat pumps in the field. The SCOP of 3.1 used comes from the research project WPsmart in the inventory of Fraunhofer ISE. The gas condensing heating system is modeled using an ecoinvent dataset. Table 2 shows that the heat pump's potential to reduce environmental impacts depends on the electricity mix and the impact category. If the heat pump would use the current German electricity mix (GE) throughout its entire life cycle, GHG emissions decrease by 30% compared to the gas condensing system.

Further reductions are expected in ozone depletion, photochemical ozone formation and energy resources. All other environmental categories increase significantly. The GE-to-SDS electricity mix approximates the electricity mix of a heat pump installed in 2020 that has a 20-year lifetime. In the GE-to-SDS electricity mix, the environmental categories increase or decrease in the same environmental categories. In the climate change categories, the changing electricity mix achieves a higher reduction in GHG emissions (-54%). Further significant savings are also possible in the ozone depletion, and energy resources. In the remaining environmental categories, except for ionizing radiation and water consumption, the environmental impacts increase less for the GE-to-SDS electricity mix than for the GE electricity mix.

While the environmental impacts of switching to a heat pump with the GE-to-SDS electricity mix can only be reduced in 4 out of 16 environmental categories, the number increases to 9 out of 16 for the static SDS electricity mix. Using the SDS electricity mix, a heat pump reduces GHG emissions by 79% down to one-fifth of the GHG emissions that would be caused by providing space heating through gas heating.

By switching to the SDS electricity mix, the environmental impacts of a heat pump can be significantly reduced compared to the GE electricity mix in all environmental categories except ionizing radiation and water consumption. Furthermore, the less environmental impact caused by the generation of the purchased electricity, the better the air-to-water heat pump performs in an environmental comparison with a gas condensing boiler. In addition to the three electricity mixes, the comparison between gas heating and heat pumps is listed for electricity supply by wind power and photovoltaic (PV) technologies. The data sets for both technologies come from ecoinvent [10]. The use of wind power can reduce GHG emissions by 89%, and environmental impacts are reduced in 11 of 16 environmental categories. With the use of PV, a reduction of 81% is possible, or in 8 of 16 environmental categories.

To summarize, in the categories of climate change, ozone depletion, photochemical ozone formation, and energy resource consumption, environmental impacts can be reduced for all five electricity mixes. However, in the categories of eutrophication, freshwater, and human toxicity, the environmental impacts of carcinogenic, resource consumption, and water consumption increase when switching to a heat pump for all five electricity mixes. The environmental impacts cannot be reduced in all environmental categories, even if renewable energy sources, wind power, and photovoltaics provide electricity.

When switching from a gas condensing heating system to a heat pump, burden-shifting always occurs. Burden shifting describes the increase of environmental impacts in one or more impact categories when reducing environmental impacts in another category. For example, when switching from a gas condensing heating system to an air-to-water heat pump, GHG emissions can be saved, while environmental impacts increase in other environmental categories.

The extent to which burden-shifting is acceptable depends on the environmental categories affected. Reducing GHG emissions is currently a high priority, so burden-shifting could be acceptable. The Planetary Boundary framework provides an initial guide for assessing whether burden-shifting compromises the overall sustainability. Planetary Boundaries are boundaries in nine categories, the crossing of which threatens the stability of the Earth's ecosystem. Climate change is one of the nine categories. Other categories address the biogeochemical cycles of nitrogen and phosphorus, freshwater use, and land use. However, an exact mapping between the EF environmental categories used in this study and the Planetary Boundaries is only partially possible. Five of the nine boundaries have already been transgressed so that burden-shifting to these categories should be avoided. These categories among others include climate change, land-system change (similar to land

use), and the biogeochemical cycles of nitrogen and phosphorus (similar to eutrophication), which are also addressed in the EF environmental categories.

Table 2: Changes of the environmental impact when switching from a gas condensing heating system to an air-to-water heat pump depending on the electricity mix. The gas heating system is used as a reference. (R410A, n = 20 a, SCOP = 3.1)

	GE (521 gCO_2/kWh)	GE-to-SDS (317 gCO_2/kWh)	SDS (114 gCO_2/kWh)	Wind Energy (32 gCO_2/kWh)	Photovoltaic (99 gCO_2/kWh)
Climate Change	-30%	-54%	-79%	-89%	-81%
Ozone Depletion	-37%	-43%	-50%	-51%	-40%
Particulate Matter Formation	60%	38%	16%	-1%	92%
Acidification	65%	12%	-40%	-41%	-11%
Photochemical Ozone Formation	-4%	-34%	-63%	-74%	-45%
Eutrophication, terrestrial	86%	29%	-29%	-61%	-17%
Eutrophication, freshwater	3458%	1793%	128%	87%	175%
Eutrophication, aquatic	166%	61%	-44%	-63%	-13%
Ionizing Radiation	894%	1112%	1330%	-74%	-9%
Ecotoxicity, freshwater	59%	18%	-24%	-7%	10%
Human toxicity, cancer	80%	40%	-1%	61%	55%
Human toxicity, non cancer	306%	204%	101%	187%	201%
Material Resources	650%	481%	311%	882%	753%
Energy Resources	-41%	-54%	-67%	-97%	-90%
Land Use	282%	187%	91%	-2%	3426%
Water Use	652%	746%	840%	15%	849%

Burden-shifting occurs in land use and eutrophication when switching from a gas condensing heating system to a heat pump. However, further assessment is needed to determine the magnitude of the burden-shift compared to the boundary value. If the shift is low enough, other sectors might be able to efficiently reduce impacts in these two categories and compensate for the burden-shift from switching to heat pumps, for the cause of overall GHG mitigation without pressuring already transgressed planetary boundaries. Ultimately, all sectors in sum need to comply with the planetary boundaries to be sustainable and the strength of heat pumps lies in comparably energy-efficient GHG mitigation [20].

Another criterion besides the immediate environmental impacts that influence the refrigerant selection is the F-Gas regulation [21]. The F-Gas regulation restricts the distribution of high-GWP refrigerants containing fluorine. This restriction can negatively affect the supply and price of refrigerants such as R410A and R32,. Another aspect that has to be considered is the degradation of refrigerants in the atmosphere. The refrigerant R1234yf degrades to TFA within a few weeks [22]. TFA belongs to the group of PFAS chemicals that have been reported to be carcinogenic. Therefore, there are efforts to ban the distribution of PFAS chemicals [23] in the next years which in turn could restrict the option of using R1234yf.

These two criteria are among many that further restrict the possible choice of refrigerants for heat pump applications. In summary, achieving overall sustainable domestic heating will comprise environmental, social, and economic aspects, such as health and refrigerant price.

5. Conclusion

This work performs a life cycle analysis (LCA) for air-to-water heat pumps for use in German residential buildings. Particular focus is put on the influence of refrigerants, which can potentially be used in heat pumps. The refrigerants investigated are the hydrofluorocarbons R410A and R32, the hydrofluoroolefin R1234yf, the

hydrocarbons R290, R1270, and R600a, and the inorganic refrigerant R717. The LCA results can be used to estimate which of these refrigerants leads to the lowest environmental impact over the entire life cycle and should be used in heat pumps for residential buildings.

The LCA is divided into four steps according to DIN EN ISO 14040. First, the objective and the scope of the LCA are defined. Then, the life cycle of the heat pump is modeled, consisting of the production and operation of the heat pump and the production and leakage of the refrigerant. Based on these four life cycle phases, a heat pump's environmental impacts are estimated in 16 environmental categories recommended by the ILCD. The LCA results show that the largest share of environmental impacts in the life cycle is due to electricity demand. Therefore, the lowest environmental impacts are achieved by using refrigerants that enable high heat pump efficiency and reduce the required electricity demand. These include R717, R290, and R1270. In contrast, using R410A, R1234yf, and R600a result in the highest environmental impacts, as only low efficiencies are achieved through these refrigerants. Other phases of the life cycle have only a secondary impact. Sensitivity analyses confirm the high significance of the electricity demand for the total environmental impact also until mid-century. Simultaneously, impacts from production become more important with increasingly renewable electricity generation.

One possibility to reduce the environmental impacts due to electricity demand is to increase the efficiency of the heat pump which reduces the electricity demand. A second possibility is reducing the specific environmental impacts of electricity generation by using more renewable energy sources. The expected increase of renewable energy sources in the German electricity mix would decrease the environmental impacts of a heat pump significantly. Therefore, the current electricity mix should not be used for the environmental assessment of a newly installed heat pump. Instead, a possible change in the electricity mix during the heat pump's lifetime should be considered.

Based on the results of the LCA and other selection criteria, such as the F-Gas regulation, a recommendation for action is made, and the use of R290 in residential heat pumps is recommended. The use of R290 leads to low environmental impacts due to its high achievable efficiency. In addition, R290 is non-toxic, has a low GWP, and is already used in heat pumps for residential buildings. The disadvantage of R290 is its high flammability and classification in safety class A3. In addition, DIN EN 378 [3] restricts possible installation sites for R290 heat pumps. If R290 is not possible, alternative refrigerants must be used.

With the environmental impacts of a heat pump determined, an ecological comparison is then made between a heat pump and a gas condensing boiler. As mentioned before, the efficiency of the heat pump and the origin of the purchased electricity significantly influence the environmental impact of a heat pump and, thus, also the ecological comparison. For example, with a SCOP = 3.1 and a predicted increase in the share of renewable energies in the German electricity mix, a heat pump decreases greenhouse gas emissions over the entire life cycle by 54% compared to a gas condensing boiler. However, the environmental impacts can only be reduced in 4 of the 16 environmental categories investigated; in the remaining 12 environmental categories, a heat pump causes higher environmental impacts than gas condensing heating. Therefore, reducing greenhouse gas emissions is achieved by shifting the environmental impact to other categories, i.e., burden shifting. By increasing the heat pump's efficiency, the environmental impacts can be further reduced, but burden-shifting can still not be avoided. Thus, further research has to assess the relevance of the identified burden-shifting, while either way heat pumps offer an opportunity for significant greenhouse gas mitigation.

Acknowledgements

We gratefully acknowledge funding by the German Federal Ministry for Economic Affairs and Climate Action (BMWK) with the promotional references: 03EN4011 and 03EN1022B as well as the Ministry of Economic Affairs, Innovation, Digitalization, and Energy of the State of North-Rhine Westphalia for the SCI4climate.NRW founded project (EFO 0001 G). We additionally acknowledge funding by the European Regional Development Fund (ERFD-0500029).

References

[1] J. M. Calm, “The next generation of refrigerants - Historical review, considerations, and outlook,” *International Journal of Refrigeration*, vol. 31, no. 7, pp. 1123–1133, 2008, doi: 10.1016/j.ijrefrig.2008.01.013.

[2] C. Höges, V. Venzik, C. Vering, and D. Müller, “Bewertung alternativer Arbeitsmittel für Wärmepumpen im Gebäudesektor,” 2022, doi: 10.1007/s10010-022-00584-0.

[3] D. I. N. e.V., “DIN EN 378-1 - Kälteanlagen und Wärmepumpen – Sicherheitstechnische

und umweltrelevante Anforderungen.” 2021.
[4] F. Ceglia, E. Marrasso, C. Roselli, and M. Sasso, “An innovative environmental parameter: Expanded Total Equivalent Warming Impact,” *International Journal of Refrigeration*, vol. 131, pp. 980–989, 2021, doi: 10.1016/j.ijrefrig.2021.08.019.
[5] Life Cycle Climate Performance Working Group, “Guideline for Life Cycle Climate Performance January 2016,” *Int. Institute of Refrigeration*, no. January, pp. 1–26, 2016.
[6] D. I. N. e.V., “DIN EN ISO 14040:2021-2 Umweltmanagement – Ökobilanz – Grundsätze und Rahmenbedingungen.” 2021.
[7] C. Vering, D. Schwarz, P. Stefaniak, V. Venzik, and D. Müller, “Kältemittel in Wärmepumpen für die Gebäudeheizung: Ökologische Auswirkungen im gesamten Lebenszyklus,” *Chem Ing Tech*, vol. 94, no. 4, pp. 542–554, 2022, doi: 10.1002/cite.202100016.
[8] D. R. Tobergte and S. Curtis, *ILCD Handbook - Recommendations for Life Cycle Impact Assessment in the European context*, vol. 53, no. 9. 2013. doi: 10.278/33030.
[9] L. Zampori and R. Pant, *Suggestions for updating the Product Environmental Footprint (PEF) method*. 2019. doi: 10.2760/424613.
[10] G. Wernet, C. Bauer, B. Steubing, J. Reinhard, E. Moreno-Ruiz, and B. Weidema, “The ecoinvent database version 3 (part I): overview and methodology,” *Int. Journal of Life Cycle Assessment*, vol. 21, no. 9, pp. 1218–1230, 2016, doi: 10.1007/s11367-016-1087-8.
[11] R. Frischknecht, “Umweltrelevanz natürlicher Kältemittel - Ökobilanzen von Wärmepumpen und Kälteanlagen,” Bern, 1999. [Online]. Available: http://www.esu-services.ch/download/frischknecht-1999-LCA_SB.pdf
[12] R. Frischknecht, “Umweltrelevanz natürlicher Kältemittel - Ökobilanzen von Wärmepumpen und Kälteanlagen, Anhang zum Schlussbericht,” Bern, 1999.
[13] A. Baral, R. Minjares, U. Robert, “Upstream climate impacts from production of R-134a and r-1234yf refrigerants Used in mobile air conditioning systems,” *White Paper*, August, 2013.
[14] UNEP, *UNEP 2014 Report of the Refrigeration, Air Conditioning and Heat Pumps Technical Options Committee*. 2014.
[15] T. Heck, “Wärmepumpen,” in *Sachbilanzen von Energiesystemen: Grundlagen für den ökologischen Vergleich von Energiesystemen und den Einbezug von Energiesystemen in Ökobilanzen für die Schweiz*, vol. 0, no. 6, 2007, pp. 1–327. [Online]. Available: http://db.ecoinvent.org/ecoquery/files.php?area=463ee7e58cbf8&action=list%5Cnpapers2://publication/uuid/5C1B29FC-20E9-4F65-8B4E-1475A6FBAFBF
[16] IPCC, “Industrial Processes - IPCC good practice guidance,” in *IPCC Good Practice Guidance and Uncertainty Management in National Greenhouse Gas Inventory*, 2000, pp. 3.1-3.131. [Online]. Available: http://www.ipcc-nggip.iges.or.jp/public/gp/english/3_Industry.pdf
[17] Umweltbundesamt, “Berichterstattung unter der Klimarahmenkonvention der Vereinten Nationen und dem Kyoto-Protokoll 2012 - Nationaler Inventarbericht zum Deutschen Treibhausgasinventar 1990 - 2010,” *Nationaler Inventarbericht Deutschland - 2012*, p. 841, 2012, [Online]. Available: https://www.umweltbundesamt.de/sites/default/files/medien/461/publikationen/4292.pdf
[18] P. Remmen, M. Lauster, M. Mans, M. Fuchs, T. Osterhage, and D. Müller, “TEASER: an open tool for urban energy modelling of building stocks,” *J Build Perform Simul*, vol. 11, no. 1, pp. 84–98, 2018, doi: 10.1080/19401493.2017.1283539.
[19] International Energy Agency, “IEA: World Energy Outlook 2018,” *Iea*, 2018.
[20] A. Sternberg and A. Bardow, “Power-to-What?-Environmental assessment of energy storage systems,” *Energy Environ Sci*, vol. 8, no. 2, pp. 389–400, 2015, doi: 10.1039/c4ee03051f.
[21] E. Union, *Regulation (EU) on fluorinated greenhouse gases and repealing Regulation (EC) No 842/2006*, vol. 2014, no. 517. 2014, p. L150/195-230. [Online]. Available: http://eur-lex.europa.eu/eli/reg/2014/517/oj
[22] K. R. Solomon *et al.*, “Sources, fates, toxicity, and risks of trifluoroacetic acid and its salts: Relevance to substances regulated under the Montreal and Kyoto Protocols,” *J Toxicol Environ Health B Crit Rev*, vol. 19, no. 7, pp. 289–304, 2016, doi: 10.1080/10937404.2016.1175981.
[23] European Chemicals Agency (ECHA), “Five European states call for evidence on broad PFAS restriction,” 2023. https://echa.europa.eu/-/five-european-states-call-for-evidence-on-broad-pfas-restriction (accessed Feb. 09, 2023).

14th IEA Heat Pump Conference
15-18 May 2023, Chicago, Illinois

Experimental Investigation of a Phase Change Material Charged Serpentine Heat Exchanger with Louvered Fins

Jangho YANG[a], Jan MUEHLBAUER[a], Daniel BACELLAR[a], Vikrant AUTE[a], Yunho HWANG[a*]

[1]Center for Environmental Energy Engineering
Department of Mechanical Engineering, University of Maryland
College Park, MD 20742, United States

Abstract

Phase change material heat exchangers (PCM-HX) can be used as a latent heat thermal energy storage (LHTES) component in heat pump applications to further enhance the efficiency of a heat pump as well as to yield financial savings by peak-load shifting. In this paper, a low-cost commercially available aluminum serpentine heat exchanger with louvered fins was experimentally investigated to check its thermal performance as a PCM-HX. A transparent rectangular box fabricated from acrylic plates served as a PCM container. Two cameras were used to capture the phase change process of the PCM on the front and top sides of the container during the experiment. A total of 88 installed temperature sensors throughout the test setup and a mass flow meter enabled a quantitative analysis of the PCM-HX as well. The energy balance deviation between the estimated theoretical and experimentally calculated PCM storage was ±14% considering the often-neglected heat loss and thermal mass of the PCM-HX. PCM temperature profiles, charge and discharge rates, and energy densities under different test conditions were also investigated.

© HPC2023.
Selection and/or peer-review under the responsibility of the organizers of the 14th IEA Heat Pump Conference 2023.

Keywords: Phase change material; Serpentine; Thermal energy storage; RT35HC; Experimental investigation; Louvered fins;

1. Introduction

The demands for energy-efficient heat pump technology have been steadily increasing worldwide with the goal of decreasing carbon footprints. A latent heat thermal energy storage (LHTES) integration into heat pump systems can potentially help shave the peak load demand of the residential and commercial energy sectors while using off-peak electricity, ultimately realizing both financial and energy savings. Phase change material heat exchangers (PCM-HXs) can be excellent candidates for LHTES as they can utilize the latent heat during the charging and discharging processes. When integrating LHTES into heat pump systems, heat exchanger should be designed to overcome the challenge of low thermal conductivities of PCMs. Hence, it is essential to explore different heat exchanger configuration options and expand the list of high-potential candidates that are economical and easy to implement [1]. In this paper, a commercially available serpentine tube heat exchanger with louvered fins was experimentally investigated as the first-order analysis revealed that this type of heat exchanger has a very competitive compactness and a material utilization value as compared to the other commercially available configurations such as crimped fin, wire fin, and spine fin heat exchangers. A comprehensive thermal performance analysis including PCM temperature profiles, charge/discharge rates, energy densities, and energy balance of the PCM-HX under different operating conditions are presented in this study. Often-neglected visual observation and heat loss and thermal mass calculations were experimentally

* Corresponding author. *E-mail address:* yhhwang@umd.edu

considered in the study for more of an in-depth analysis as well as to capture the practical side of the experiments. There are a number of existing literature for experimental investigations of compact PCM-HXs [1]–[4]. However, the experimental study regarding the selected heat exchanger configuration in this paper is scarce. Therefore, this study will provide one of the initial experimental data for this heat exchanger configuration when used as a PCM-HX.

2. Experimental Setup

2.1. PCM properties

RT35HC from Rubitherm [5] was chosen as a PCM for the experiments as it is known to be stable in terms of cyclic durability and has a relatively high heat storage capacity (HSC) for an organic-based PCM. Its nominal phase change temperature, thermal conductivity, specific heat, and volume expansion ratio are around 35 °C, 0.2 W/m-K, 2 kJ/kg, and 12.5%, respectively. Choosing a specific PCM with an actual hot storage applicable phase change temperature was not the main concern for this study as the main focus was to assess the thermal performance of the heat exchanger configuration itself. This statement can be further supported by the PCM heat sink topology optimization results from Ho et al. [6] where the optimization runs with PCMs with different melting temperatures yielded nearly identical optimized designs for conduction-dominated cases. Hence, the use of RT35HC in this study can be justified because if the heat exchanger showed a good performance with certain PCM, it would also show a good performance with other PCMs with different melting/solidification points for conduction-dominated cases. The original equipment manufacturer (OEM) claims that the nominal HSC within the selected temperature range is 240 kJ/kg with ±7.5% accuracy. It is important to mention that a separate differential scanning calorimetry (DSC) test was conducted to have additional reference to the enthalpy information of the PCM. The HSC values from the DSC results with a 5 °C/min heat rate yielded 180.6 kJ/kg and 203.7 kJ/kg for melting and solidification, respectively. Lastly, the total amount of PCM mass that was charged into the PCM-HX container was 3.979 kg.

2.2. PCM-to-HTF (Heat Transfer Fluid) Test Facility

An in-house test facility was used to conduct PCM-to-HTF experiments. As shown in Fig. 1, the test facility was placed inside the temperature- and humidity-controlled environmental chamber for reliable test conditions. The facility consists of main components such as Coriolis mass flow meter, gear pump, resistance heater, air-to-HTF heat exchanger with a fan, and the PCM-HX test section. T-type thermocouples and resistance temperature detectors (RTD) were installed for PCM and HTF-side temperature measurements. For HTF, deionized water was chosen for this study. The National Instruments (NI)'s data acquisition (DAQ) system together with the LabVIEW software was used for controls and data collection. It is worth mentioning the test facility could function bi-directionally using the 3-way valve and ball valves depending on the orientation of the PCM-HX. However, only one HTF direction was investigated in this study since the PCM-HX was oriented horizontally. For melting experiments, heater proportional-integral-derivative (PID) control was used to stabilize the inlet temperature of the HTF, while the air-to-HTF heat exchanger with a fan was used to control the HTF inlet temperature during the solidification experiments. The mass flow rate (MFR) was controlled by the PID control using the Coriolis mass flow meter and the pump driver during both experiments.

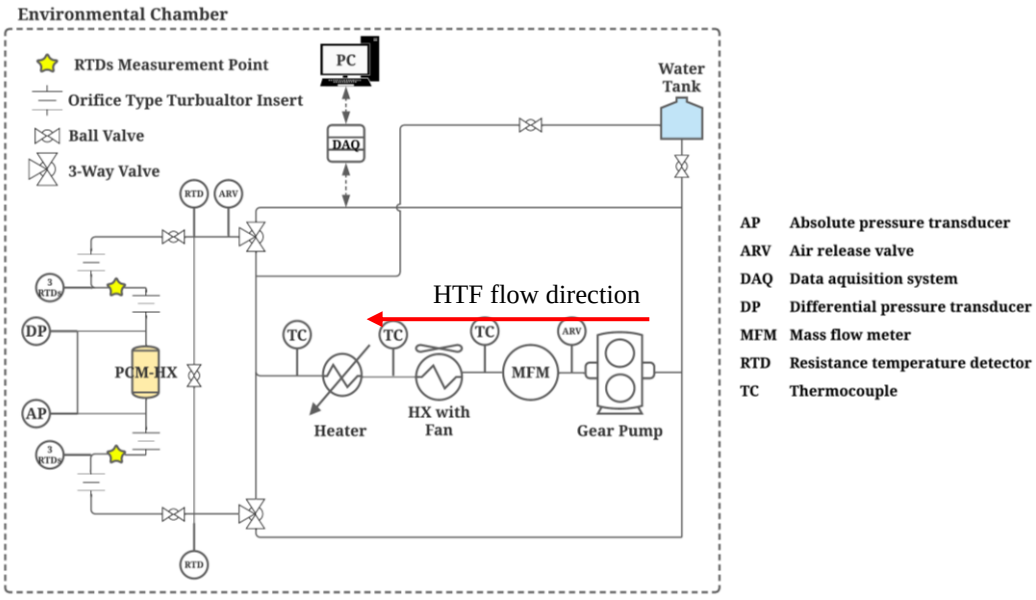
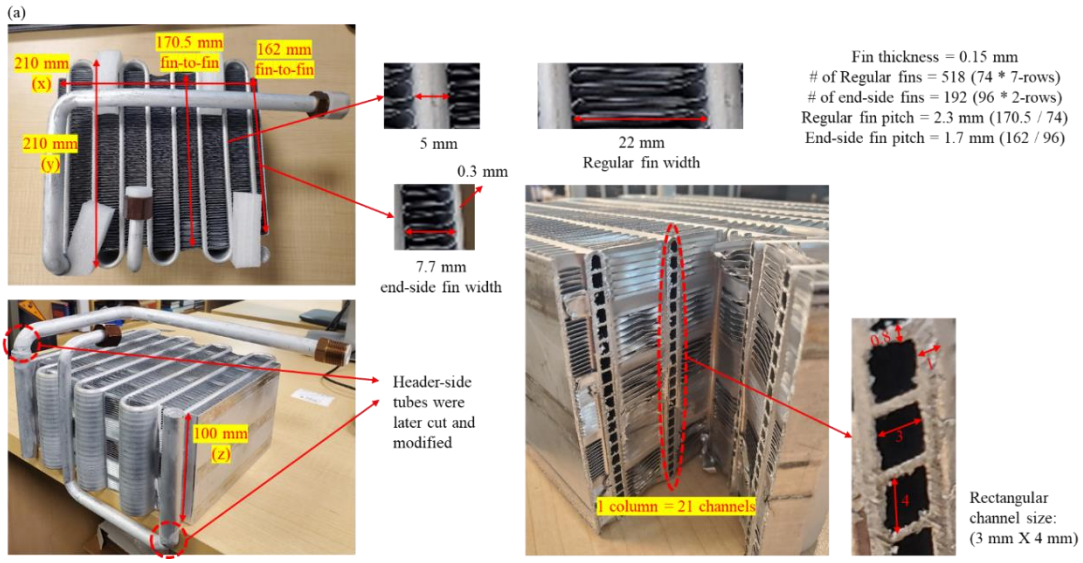


Fig. 1. PCM-to-HTF test facility schematic diagram

Sub-components such as the orifice-type turbulator inserts, 3D printed RTD guides with multi-cord grips, and 90° elbows were installed near the PCM-HX's inlet and outlet side for accurate HTF-side temperature measurement. The elbows and turbulator inserts allow the HTF to be well-mixed before the measurement points whereas the RTD guides prevent the RTD end tips from touching the tube wall and keep them concentric. Hence, the systematic uncertainties of the HTF side measurement could be minimized even with flows in a laminar regime.

2.3. Serpentine Heat Exchanger and Thermocouple Positions

A commercially available serpentine tube heat exchanger was selected as a PCM-HX candidate. A single-path serpentine tube heat exchanger consisted of 21 individual rectangular channels. The detailed dimensions and its configuration are shown in Fig. 2 – (a).



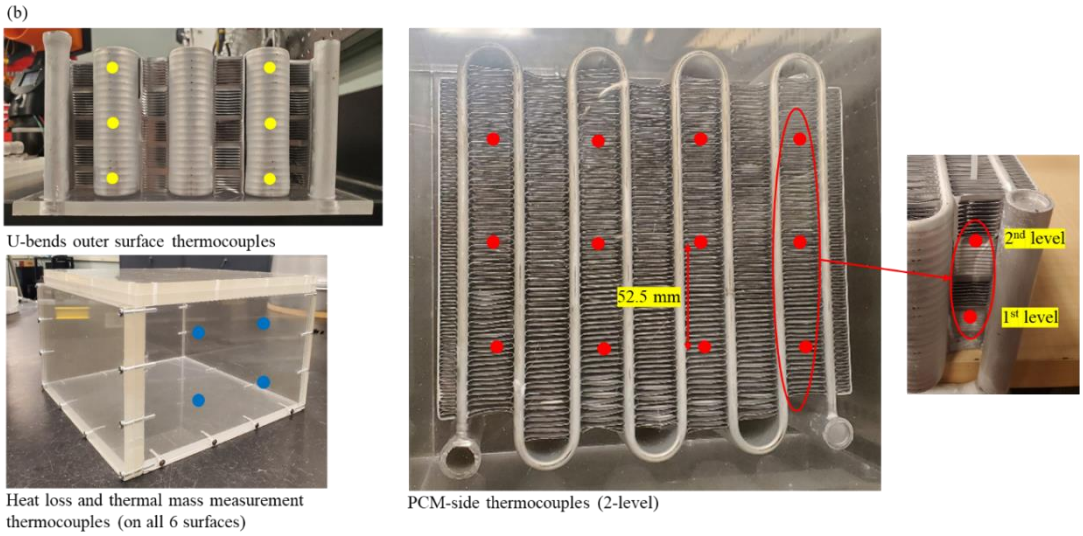


Fig. 2. (a) Serpentine tube PCM-HX dimensions and details and (b) Thermocouple distributions

In total, 78 T-type calibrated thermocouples with ±0.5 K absolute uncertainty were installed in and around the test section. After calibration, the measured maximum temperature deviation across all thermocouples was about 0.15 K when a few test points were measured. First, as shown in the top left corner of Fig. 2 - (b), six thermocouples were attached to the surfaces of the 1st and 3rd U-bends on the front side of the heat exchanger. From the bottom, the thermocouples were attached to the outer surfaces of the 3rd, 11th, and 20th rectangular channels for both U-bends. Next, as shown in the bottom left corner of the same figure, four thermocouple pairs were evenly distributed in each quadrant of the acrylic plate's inner and outer surfaces. These heat loss and thermal mass measurement thermocouples were installed on all six container surfaces. Lastly, two levels of twelve thermocouples were installed in between the fins to measure the PCM temperatures, as shown in Fig. 2 - (b). The thermocouples were installed every 52.5 mm from the front to back surfaces. The 1st and 2nd levels are 43 mm and 77 mm from the bottom surface of the container.

2.4. Container Configuration

Clear high-strength acrylic plates were used as container walls. The acrylic plates were cut to the designed dimensions using the laser cutting machine. Modified acrylic plates were later assembled with screws and acrylic epoxy for the container construction. The detailed dimensions of the container's inner volume are shown in **Error! Reference source not found.**. A 10 mm gap between the heat exchanger surfaces and the inner wall of the container was given around all heat exchanger surfaces except for the top surface. For the bottom gap, small 3D-printed blocks were attached to the bottom surface of the heat exchanger. The height of the container's inner volume was designed to have at least a 15 mm air gap at the top to prevent any unexpected PCM leakage through the top plate. The front and top surfaces used for visual observation angles were double-plated to increase the thermal resistance while maintaining transparency. The rest of the single acrylic plates were later covered with 1" thick insulation sheets.

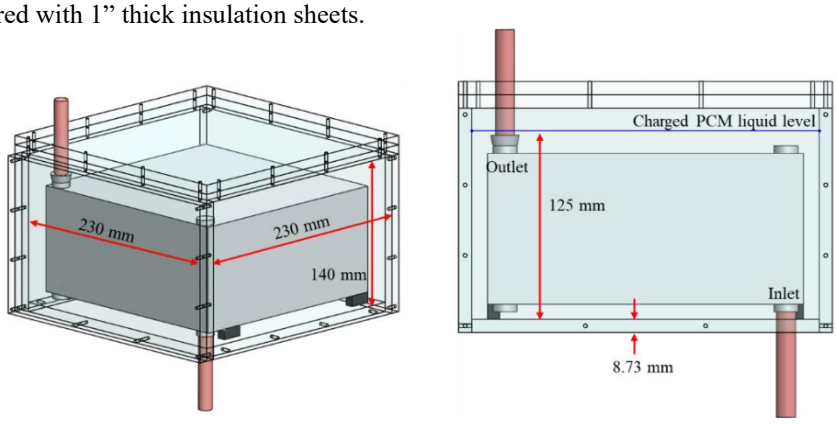


Fig. 3. A 3D model of a container and heat exchanger assembly dimensions

3. Data Reduction

The theoretical storages of the PCM-HX with the given initial and final PCM temperatures along with PCM properties were estimated using the average value of the PCM-side thermocouples temperature readings. The sensible and latent portions of the theoretical storages during both phase change processes were calculated using the temperature range that was specified by the OEM. Also, the thermal mass of the aluminum heat exchanger was considered as a part of the theoretical storage as shown in Equations (1) and (2).

$$Q_{m,theor.} = \sum M\left[C_{p,s}(27 - T_{ini.}) + L_{PCM} + C_{p,l}(T_{fin.} - 42)\right] + \sum TM_{HX} \quad (1)$$

$$Q_{s,theor.} = \sum M\left[C_{p,l}(T_{ini.} - 42) + L_{PCM} + C_{p,s}(27 - T_{fin.})\right] + \sum TM_{HX} \quad (2)$$

The accumulated HTF energies during melting and solidification were calculated using Equation (3). The time step of 10 sec was chosen as a data collecting interval.

$$Q_{(m/s),HTF} = \int_{\tau_{ini.}}^{\tau_{fin.}} \dot{m} C_{p,HTF}\left(T_{RTD_{(in/out)}} - T_{RTD_{(out/in)}}\right) d\tau \quad (3)$$

For estimating the actual charged and discharged energies, the heat loss and thermal mass considerations of the test section were necessary. Hence, Equations (4) and (5) were used. Importantly, the heat loss sum and thermal mass sum terms each contain different equations inside for charging and discharging scenarios. This was to avoid heat loss or thermal mass double counting depending on the directions of the heat transfer during each process and the defined control volumes. As this test setup only consisted of flat rectangular surfaces, a simple 1-D flat heat flow approach was assumed as shown in Equation (6).

$$Q_{charged} = Q_{m,HTF} - \sum Heat\ Loss\ - \sum Thermal\ Mass \quad (4)$$

$$Q_{discharged} = Q_{s,HTF} + \sum Heat\ Loss \pm \sum Thermal\ Mass \quad (5)$$

$$Heat\ Flow_{flat} = \int_{\tau_{ini.}}^{\tau_{fin.}} U \cdot A \cdot \Delta T\ d\tau \quad (6)$$

Moreover, Equations (7) and (8) were used to calculate the systematic uncertainties of the measured HTF side energies. The systematic uncertainties were minimized by using two sets of three 1/8-inch diameter RTDs with ±0.03 K absolute uncertainty and a Coriolis mass flow meter with ±0.2% relative uncertainty.

$$U_{Q_{water}} = \sqrt{\sum \left(\frac{\partial Q_{water}}{\partial x_i}\right)^2 U_x^2} \qquad U_{Q_{water},total} = \sum \left(U_{Q_{water}}\right)_\tau \quad (7) \text{ and } (8)$$

Two dimensionless numbers, the Reynolds number, a ratio of fluid inertial to viscous forces, and the Stefan number [7] and [8], a ratio of sensible to latent heats were calculated using Equations (9) and (10).

$$Re = \frac{\rho u D_H}{\mu} \qquad Ste = \frac{C_{p,PCM}\left|T_{in} - T_{phase\ change}\right|}{L} \quad (9) \text{ and } (10)$$

4. Results and Discussion

4.1. Test Conditions

The summary of the test matrix is described in Table 1. The [M] and [S] in the table represent the melting and solidification cases. The test matrix was designed to test a combination of two melting inlet temperatures and three mass flow rates. The ambient temperature for all test conditions was within the range of 25.0~25.1 °C. The Reynolds numbers for a single rectangular channel for all chosen test conditions were under a laminar flow regime due to a slow flow velocity in each channel as the main flow diverges into 21 channels. Compared with the melting cases, the solidification cases had lower Reynolds numbers as the dynamic viscosity of water increased as the water temperature decreased. The Stefan number for each test condition was also calculated

to have a dimensionless parameter as a reference. The melting process was considered finished when all the heat loss and thermal mass measurement thermocouples that were installed on the inner surfaces of the acrylic plates reached 40 °C. Similarly, the solidification process was thought to be completed when the same group of thermocouples all reached 27 °C. For melting, the thermocouples located at the inner surface of the bottom acrylic reached 40 °C at last. For solidification, the thermocouples installed at the inner surface of the back-side acrylic took the longest to reach 27 °C. Importantly, the test condition 2 was repeated three times to check the test facility's repeatability before completing the test matrix, and excellent repeatability results were obtained.

The test durations and average charge and discharge rates of the PCM-HX for each test condition are shown in Table 1 as well. The higher mass flow rates yielded both faster melting and solidification and higher average charge and discharge rates. The higher average HTF inlet temperature for melting yielded faster melting, as expected. Test conditions 1 through 3 have slightly longer solidification durations than the lower average inlet T group with same MFRs as the only difference was the initial PCM temperature for the solidification process that was affected by the higher HTF inlet temperature for melting. Finally, the energy densities had negligible differences among the test conditions within the same melting HTF inlet temperature group.

Table 1. Summary of test conditions

Test	MFR [g/s]	Re for single channel	Avg. Inlet T [°C]	Ste	Test Durations [min]	Avg. Charge/Discharge rates [W]	Energy density [kWh/m^3]
1	5	143.4 [M], 78.4 [S]	58.9 [M], 26.1 [S]	0.215 [M], 0.0802 [S]	73.8 [M], 258.2 [S]	256.7 / 65.8	42.2 [M], 43.1 [S]
2	10	287.3 [M], 155.7 [S]	59.0 [M], 25.8 [S]	0.216 [M], 0.0829 [S]	62.7 [M], 224.7 [S]	299.1 / 74.8	41.8 [M], 42.0 [S]
3	15	431.0 [M], 231.9 [S]	59.0 [M], 25.5 [S]	0.216 [M], 0.0856 [S]	59.0 [M], 213.7 [S]	316.9 / 80.3	41.8 [M], 42.5 [S]
4	5	132.8 [M], 78.2 [S]	54.0 [M], 26.0 [S]	0.171 [M], 0.0811 [S]	90.5 [M], 254.3 [S]	201.6 / 61.5	40.4 [M], 39.7 [S]
5	10	265.7 [M], 156.4 [S]	54.0 [M], 26.0 [S]	0.171 [M], 0.0811 [S]	76.5 [M], 223.5 [S]	231.8 / 72.2	39.3 [M], 40.3 [S]
6	15	398.5 [M], 231.4 [S]	54.0 [M], 25.4 [S]	0.171 [M], 0.0865 [S]	73.2 [M], 212.8 [S]	242.1 / 76.2	39.3 [M], 40.3 [S]

4.2. HTF inlet Temperature, PCM Average Temperature, and ΔT

Test condition 2 from Table 1's HTF inlet temperature, PCM average temperature, and heat exchanger temperature difference between inlet and outlet are shown in Fig. 4. The HTF inlet temperature was controlled within ±1 °C during the melting process. The heater was switched off when the melting process was considered completed, then the HTF inlet temperature was brought down to the room temperature for the solidification process. The PCM average temperature was plotted using the average value of all PCM-side thermocouples. Lastly, as shown in the plot, the ΔT was measured the highest during the beginning of both melting and solidification processes, then both decreased towards to zero as the PCM absorbed and discharged most of the HTF's energy and its absorbed energy, respectively.

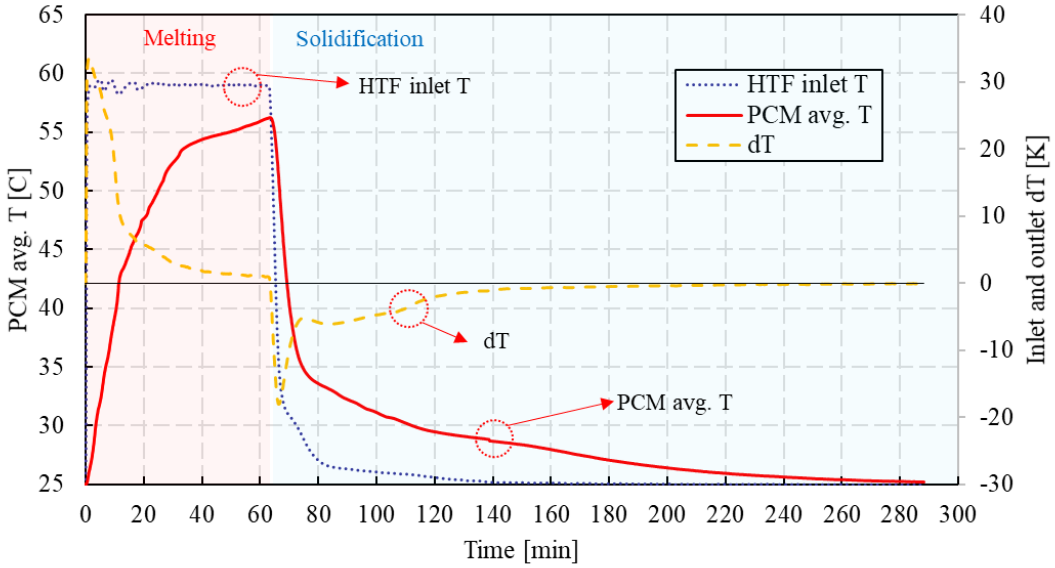
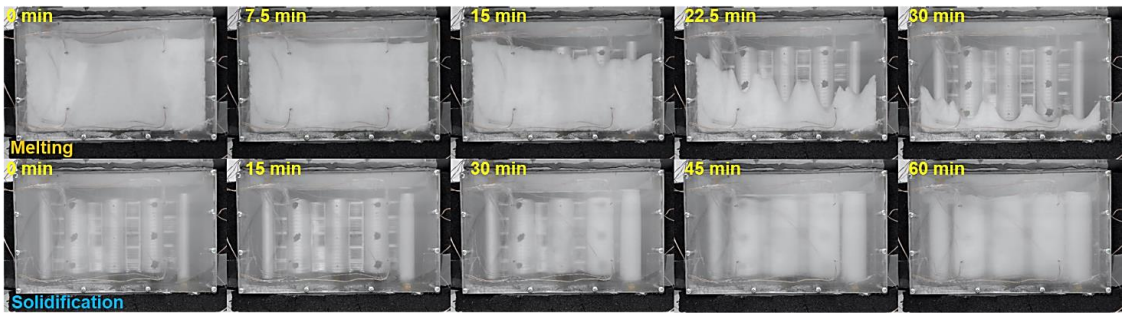


Fig. 4. Test condition 2's HTF inlet temperature, PCM average temperature, and ΔT

4.3. Visual Observation

As mentioned in section 2.4, the front and top angles were selected to visually observe the experiments. In Fig. 5, the front and top angles images of test condition 2 from Table 1 are displayed for both the melting and solidification processes. For melting, it was shown that the melting progression was from right to left and top to bottom from the front angle. It is essential to mention that the front angle view shows only the outer boundary of the PCM that touches the inner surface of the container wall. Therefore, for a more complete observation, top angle images could be investigated for comparison. The top-angle images show that the PCM in close contact with the heat exchanger surfaces quickly melted as compared with the PCM close to the container's inner walls. This could be verified by checking the ΔT plot of the heat exchanger inlet and outlet from Fig. 4 where the slope became less stiff around the 15 min mark. The charging rate slowed as only the outer PCM was left to melt. Hence, it was observed that the major portion of the PCM near the heat exchanger melted almost uniformly regardless of the height with the help of louvered fins, then the outer PCM that was closer to the container's inner walls took longer to melt due to the higher thermal resistance in the PCM layer without fins. Thus, the outer PCM melting front was from top to bottom as the melted PCM's natural convection effect was the dominant driver of heat transfer. For solidification, since conduction became the main mode of heat transfer, the solidification fronts showed more of a uniform trend that followed the serpentine path, as shown in the bottom images of Fig. 5 - (TOP) and (BOTTOM). Additionally, the PCM volume change was observed near the top section of the container as PCM solidified and increased its density, as shown in the front angle images.



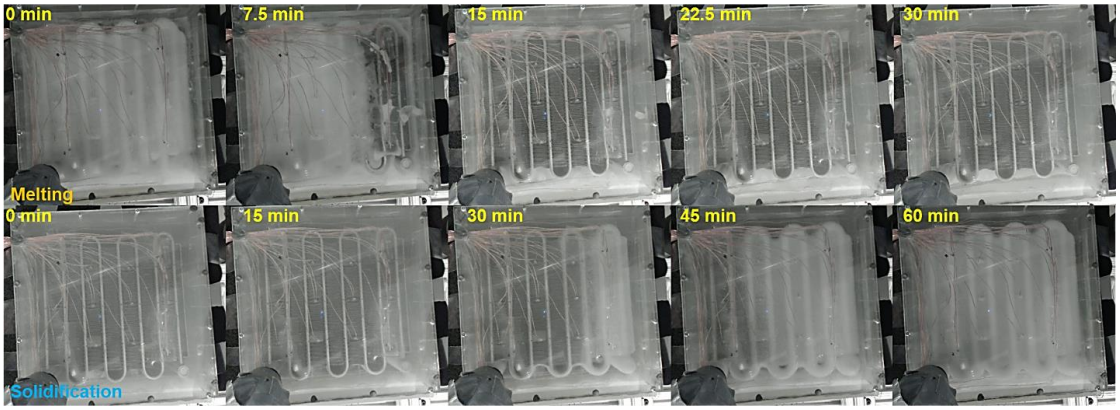


Fig. 5. Test condition 2's (TOP) front angle and (BOTTOM) top angle visual observation of first 30 mins of melting and first 60 mins of solidification

4.4. PCM Temperature Profiles

Fig. 6 – (TOP) shows test condition 2's temperature profiles for the selected PCM locations during the melting process. As shown in the image and the naming convention, the front four pairs (locations 1, 4, 7, and 10) of thermocouples were chosen for a temperature profile comparison. As mentioned in the previous section, the thermal conductivity of the PCM was largely enhanced by the louvered fins. Hence, the temperature delays between the bottom- and top-level PCM locations were relatively smaller than the vertically oriented finless PCM-HX test results from the literature [9]–[11]. The top-level PCM thermocouples started to increase the temperature gaps from the bottom-level thermocouples as the PCM around them were fully melted and the natural convection effect kicked in. Then as most of the PCM melted and their temperatures nearly reached the HTF temperature, the gaps were reduced. For all top-level PCM thermocouples, there were minor temperature dips right before they started to get flattened out, reaching the HTF temperature. This was due to the solid PCM at the top surface melting and traveling down the cracks between the fins as they became small enough to fall through. This was verified by comparing the timing of the recorded images from the top-angle camera. Also, the temperature delays across the horizontal PCM thermocouple locations were clearly shown from right to left as they followed the serpentine path.

Test condition 2's temperature profiles for the same PCM locations during the solidification process are presented in Fig. 6 – (BOTTOM). As mentioned previously, conduction became the dominant mode of heat transfer during solidification. Therefore, the temperature gaps between the bottom and top thermocouples were relatively smaller than the temperature gaps of the melting test results throughout the test. Furthermore, the temperature delays across the horizontal PCM thermocouple locations following the serpentine path were shown again during the solidification process. Lastly, a minor supercooling phenomenon was observed near 31 °C for all PCM locations.

The temperature profile data of the U-bends in different locations were also collected as well. However, for the sake of brevity, such information was not included in this study.

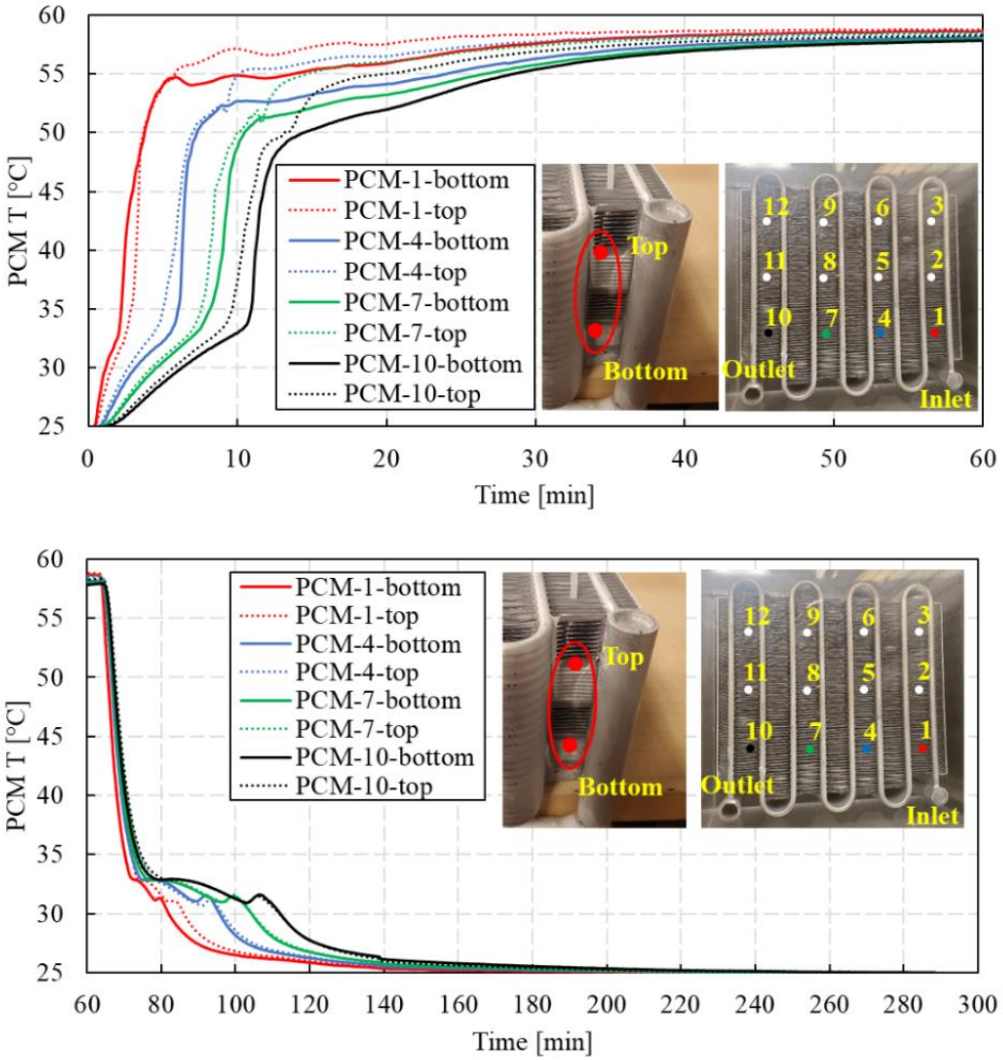


Fig. 6. Test condition 2's temperature profiles for the selected PCM locations during (TOP) melting and (BOTTOM) solidification

4.5. Energy Balance

The summary of the energy balance results for each test condition's melting [M] and solidification [S] process is presented in Table 2. The energy balance deviations were calculated using the data reduction approach in section 3. The energy balance deviation was calculated by comparing the theoretical storage and the estimated charged/discharged energy values. The average of the systematic uncertainties of the HTF (water) side energy for all test conditions was calculated to be 0.5% for melting and 1.4% for solidification, while the maximum uncertainties were 0.7% for melting and 2.1% for solidification.

Initially, although not shown here for brevity, when the nominal HSC value (240 kJ/kg) given from the OEM was used, the Q_{water} values for test conditions 2, 3, 5, and 6 during melting were smaller than their theoretical storage values which is unintuitive. The Q_{water} values contain the information of heat loss and thermal mass of the test setup on top of the PCM-HX charging process. Hence, the Q_{water} values for melting should always be larger than the theoretical storage values. Furthermore, existing literature [12]–[14] show that their in-house DSC analysis yielded 11.9%, 6.3%, and 13.8% fewer HSC values compared with the nominal value from the manufacturer's datasheet. Therefore, the HSC values from the DSC results and the lower bound of the HSC value from the OEM's datasheet were used for energy balance estimation.

As shown in the grey energy balance column, all test conditions' energy balances were within ±14% deviation when using the HSC values obtained by the DSC results. On the other hand, as presented in the green energy balance column, the melting energy balance deviations were improved significantly while the solidification energy balance worsened when the theoretical storages were calculated using the lower bound of the HSC range. For more accurate energy balance estimation in the future, the DSC test should be conducted

with multiple heat rates to get the best result as they are highly dependent on different heat rates as well as the sample size and test temperature range.

Table 2. Summary of energy balance estimation

Test	Q_{water} [kJ]	Theoretical Storage [kJ] w/ DSC HSC values	Theoretical Storage [kJ] w/ -7.5% HSC values	Estimated Charged / Discharged Energy [kJ]	Energy Balance Deviation [%] w/ DSC HSC values	Energy Balance Deviation [%] w/ -7.5% HSC values
1	1140 [M], 1020 [S]	887 [M], 979 [S]	1052 [M], 1052 [S]	1006 [M], 1025 [S]	-13.3 [M], -4.7 [S]	4.4 [M], 2.6 [S]
2	1128 [M], 1009 [S]	896 [M], 986 [S]	1061 [M], 1059 [S]	996 [M], 1000 [S]	-11.1 [M], -1.4 [S]	6.1 [M], 5.5 [S]
3	1126 [M], 1031 [S]	898 [M], 990 [S]	1063 [M], 1063 [S]	996 [M], 1012 [S]	-10.8 [M], -2.2 [S]	6.4 [M], 4.8 [S]
4	1097 [M], 938 [S]	850 [M], 940 [S]	1015 [M], 1013 [S]	961 [M], 945 [S]	-13.0 [M], -0.6 [S]	5.3 [M], 6.7 [S]
5	1067 [M], 969 [S]	854 [M], 946 [S]	1019 [M], 1019 [S]	936 [M], 960 [S]	-9.6 [M], -1.5 [S]	8.1 [M], 5.7 [S]
6	1066 [M], 974 [S]	856 [M], 947 [S]	1022 [M], 1020 [S]	937 [M], 960 [S]	-9.3 [M], -1.3 [S]	8.3 [M], 5.9 [S]

4.6. Practical Considerations

One should not only pay attention to the theoretical considerations but also carefully look into the practical considerations when implementing or designing the PCM-HX-based thermal energy storage. From this study, several practical issues were identified. One of the most common challenges with PCM-based storage is a pressure build-up in the container as the PCM undergoes a phase change process. This is caused by the volume expansion of the PCM as its density decreases as it undergoes the melting process. In this test setup, a portion of liquid PCM squirted onto the ceiling plate could be observed around the 7.5 min-mark of the melting process shown in Fig. 5 – (BOTTOM) due to the pressure build-up. Additionally, the PCM container even experienced a minor leakage issue after a number of cycles due to the repeating rounds of volume expansion and contraction cracked the acrylic epoxy adhesion. Hence, in a case where one can control the HTF direction, the HTF direction should be carefully chosen with the effort of minimizing the pressure build-up in the container. For example, one can flow the HTF downwards when the straight tube PCM-HX is oriented vertically, promoting the downwards melting trend so that the melted PCM would have a free space to expand to right away.

Another consideration that stems from the PCM volume change that one should beware of is the changing boundary condition. In a scenario where the container is narrow and long, the PCM level change during the phase changes will be relatively large. Hence, one should make sure to have the PCM-HX surfaces always submerged in the PCM during both charging and discharging modes to take full advantage of the heat transfer area.

Moreover, when initially charging the PCM liquid into the container, extra effort should be made not to create or trap any air bubbles in the container, especially in between the fins. These air bubbles can negatively affect the heat transfer between the PCM and the heat exchanger surfaces.

5. Conclusions

Overall, a PCM-HX assembly from a commercially available serpentine heat exchanger with louvered fins was embedded in RT35HC and experimentally investigated to check its thermal performance. A test matrix consisted of six test conditions with varying inlet HTF temperature and MFR. According to the obtained test results, particular conclusions were derived and can be summarized as follows:

- Increase in both Re and Ste had considerable effects on reducing the test durations while increasing the average charge and discharge rates in a laminar regime.
- For test conditions 1 to 3, the melting test durations were decreased by 15% and 20%, respectively when increasing the MFR from 5 g/s to 10 g/s and 15 g/s, whereas the solidification test duration decreased by 13% and 17%, respectively.

- For test conditions 4 to 6, the melting test durations were decreased by 15% and 19%, respectively when increasing the MFR from 5 g/s to 10 g/s and 15 g/s, whereas the solidification test duration decreased by 12% and 16%, respectively.
- For test conditions 4 to 6, the melting test durations were decreased by 18%, 18%, and 19%, respectively when the melting HTF inlet T was increased by 5 K.
- For test conditions 1 to 3, the average charge rates were increased by 16% and 23%, respectively when increasing the MFR from 5 g/s to 10 g/s and 15 g/s, whereas the average discharge rates were increased by 14% and 22%, respectively.
- For test conditions 4 to 6, the average charge rates were increased by 15% and 20%, respectively when increasing the MFR from 5 g/s to 10 g/s and 15 g/s, whereas the average discharge rates were increased by 17% and 24%, respectively.
- For test conditions 4 to 6, the average charge rates were increased by 27%, 29%, and 31%, respectively when the melting HTF inlet T was increased by 5 K.
- The energy balance deviations were within ±14% and ±9%, respectively when the HSC values from DSC results and the lower bound of the OEM datasheet were used.

In the future, for constructing a various types of PCM-HXs' performance database, the operating conditions and applications should be clearly defined so that meaningful comparisons could be made when using useful comparison approaches like rate capability and Ragone plots [15] and ε-NTU method [3], [4], [7], [16].

Nomenclature

Variables			*Subscripts*	
ρ	density	(kg/m^3)	*f*	fin
μ	dynamic viscosity	(kg/m-s)	*fin.*	final
Q	heat energy	(kJ)	*HTF*	heat transfer fluid
D_H	hydraulic diameter	(m)	*HX*	heat exchanger
L	latent heat	(m) (kJ/kg)	*ini.*	initial
M	mass	(kg)	*in*	inlet, inner
$\dot{m}$	mass flow rate	(kg/sec)	*l*	liquid state
Re	Reynolds number		*m*	melting
C_p	specific heat	(kJ/kg-K)	*out*	outlet, outer
A	surface area	(m^2)	*s*	solidification, solid state
Ste	Stefan number		*theor.*	theoretical
T	temperature	(°C)	*x*	variable
TM	thermal mass	(kJ)	*i*	variable number
τ	time step	(sec)		
U	uncertainty, U-value	(W/m^2-K)		
u	velocity	(m/s)		

Acknowledgements

The authors would like to acknowledge the funding support from the U.S. Department of Energy Award Number DE-EE0009158 and the Energy Efficiency and Heat Pump Consortium (EEHP) at the Center for Environmental Energy Engineering (CEEE), University of Maryland, College Park.

References

[1] M. Medrano, M. O. Yilmaz, M. Nogués, I. Martorell, J. Roca, and L. F. Cabeza, "Experimental evaluation of commercial heat exchangers for use as PCM thermal storage systems," *Appl. Energy*, vol. 86, no. 10, pp. 2047–2055, 2009, doi: 10.1016/j.apenergy.2009.01.014.

[2] J. P. da Cunha and P. Eames, "Compact latent heat storage decarbonisation potential for domestic hot water and space heating applications in the UK," *Appl. Therm. Eng.*, vol. 134, no. May 2017, pp. 396–406, 2018, doi: 10.1016/j.applthermaleng.2018.01.120.

[3] M. Fadl, D. Mahon, and P. C. Eames, "Thermal performance analysis of compact thermal energy storage unit-An experimental study," *Int. J. Heat Mass Transf.*, vol. 173, p. 121262, 2021, doi:

10.1016/j.ijheatmasstransfer.2021.121262.

[4] M. E. H. Amagour, A. Rachek, M. Bennajah, and M. Ebn Touhami, "Experimental investigation and comparative performance analysis of a compact finned-tube heat exchanger uniformly filled with a phase change material for thermal energy storage," *Energy Convers. Manag.*, vol. 165, no. December 2017, pp. 137–151, 2018, doi: 10.1016/j.enconman.2018.03.041.

[5] "RT35HC Data Sheet," Rubitherm Technologies, 2020. https://www.rubitherm.eu/media/products/datasheets/Techdata_-RT35HC_EN_09102020.PDF.

[6] J. Y. Ho, Y. S. See, K. C. Leong, and T. N. Wong, "An experimental investigation of a PCM-based heat sink enhanced with a topology-optimized tree-like structure," *Energy Convers. Manag.*, vol. 245, 2021, doi: 10.1016/j.enconman.2021.114608.

[7] Z. Khan and Z. A. Khan, "Thermodynamic performance of a novel shell-and-tube heat exchanger incorporating paraffin as thermal storage solution for domestic and commercial applications," *Appl. Therm. Eng.*, vol. 160, no. January, 2019, doi: 10.1016/j.applthermaleng.2019.114007.

[8] R. E. Murray and D. Groulx, "Experimental study of the phase change and energy characteristics inside a cylindrical latent heat energy storage system: Part 1 consecutive charging and discharging," *Renew. Energy*, vol. 62, pp. 571–581, 2014, doi: 10.1016/j.renene.2013.08.007.

[9] J. Yang, J. Muehlbauer, D. Bacellar, V. Aute, and Y. Hwang, "Experimental Investigation of Melting and Solidification Processes of Phase Change Material Heat Exchanger," 2021, doi: 10.18462/iir.PCM.2021.2034.

[10] D. S. Mehta, K. Solanki, M. K. Rathod, and J. Banerjee, "Thermal performance of shell and tube latent heat storage unit: Comparative assessment of horizontal and vertical orientation," *J. Energy Storage*, vol. 23, no. March, pp. 344–362, 2019, doi: 10.1016/j.est.2019.03.007.

[11] M. Longeon, A. Soupart, J. F. Fourmigué, A. Bruch, and P. Marty, "Experimental and numerical study of annular PCM storage in the presence of natural convection," *Appl. Energy*, vol. 112, pp. 175–184, 2013, doi: 10.1016/j.apenergy.2013.06.007.

[12] M. Kraiem, M. Karkri, S. Ben Nasrallah, P. Sobolciak, and M. Fois, "Thermophysical characterization and numerical investigation of three paraffin waxes as Latent Heat Storage Materials .," *Energy fuel Technol.*, no. March, 2019, doi: 10.20944/preprints201903.0034.v1.

[13] T. Barz, J. Krämer, and J. Emhofer, "Identification of phase fraction⇓temperature curves from heat capacity data for numerical modeling of heat transfer in commercial paraffin waxes," *Energies*, vol. 13, no. 19, 2020, doi: 10.3390/en13195149.

[14] H. İ. Yamaç and A. Koca, "Experimental investigation of water flow window system and numerical modeling of solar thermal energy storage with phase change materials on the way of nearly zero energy buildings," *J. Energy Storage*, vol. 43, no. September, 2021, doi: 10.1016/j.est.2021.103118.

[15] J. Woods, A. Mahvi, A. Goyal, E. Kozubal, A. Odukomaiya, and R. Jackson, "Rate capability and Ragone plots for phase change thermal energy storage," *Nat. Energy*, vol. 6, no. 3, pp. 295–302, 2021, doi: 10.1038/s41560-021-00778-w.

[16] N. H. S. Tay, M. Belusko, and F. Bruno, "An effectiveness-NTU technique for characterising tube-in-tank phase change thermal energy storage systems," *Appl. Energy*, vol. 91, no. 1, pp. 309–319, 2012, doi: 10.1016/j.apenergy.2011.09.039.

14th IEA Heat Pump Conference
15-18 May 2023, Chicago, Illinois

TECH Clean California: Paving the Way to Heat Pump Market Transformation

Evan Kamei[a*], Teddy Kisch[a]

[a]Energy Solutions, 449 15th Street, Oakland, California, 94612, United States of America

Abstract

In the United States, over 90 percent of direct residential carbon emissions come from fossil fuel-fired space and water heating [1]. A critical strategy to decarbonize this sector is scaling adoption of high-efficiency, electric heat pumps for space and water heating. However, the market share for heat pumps for both is less than 10 percent in most states in the U.S. and will need to scale exponentially over the next decade to meet greenhouse gas (GHG) reduction goals. TECH Clean California is a $120 million, multi-year market transformation initiative focused on accelerating adoption of heat pump technology by driving down costs, finding new value streams, and scaling successful approaches through market and policy changes. The initiative includes three concurrent efforts: 1) motivating the supply chain through midstream incentives, providing accessible workforce training, and driving consumer demand; 2) demonstrating scalable solutions to key market barriers; and 3) using data from TECH installations to create a public database that can inform policy. This paper provides an overview of the initiative's theory of change and illustrates the relevancy of its results to resiliency, efficiency, and the heat pump industry at large.

© HPC2023.
Selection and/or peer-review under the responsibility of the organizers of the 14th IEA Heat Pump Conference 2023.

Keywords: Decarbonization; heat pumps; water heating; space heating; market transformation; California

1. Overview

TECH Clean California (TECH) is a market transformation initiative aimed at driving market adoption of zero-emissions space and water heating technologies for existing single family and multifamily residential homes to help achieve California's goal of six million installed heat pumps by 2030 and carbon neutrality by 2045 [2]. In 2022, the California Air Resources Board (CARB) finalized their State Implementation Plan proposed a zero-emission standard for space and water heaters effective 2030 [3]. The initiative was created through the passage of California Senate Bill 1477 and is funded by revenues collected through California's Cap-and-Trade program.

TECH is designed to be a centralized flagship implementation program for all existing and potential heat pump HVAC (HP HVAC) and heat pump water heater (HPWH) programs and to create best practices to inform statewide consistency. To achieve lasting scale, the initiative will pave a path for favorable decarbonization policy and make heat pumps cost-competitive with incumbent technologies.

There are three main pillars to the initiative. First, to meet California's aggressive decarbonization goals, there must be a significant increase in market scale and a rapid shift towards clean heating technologies. To achieve this, TECH provides a combination of market incentives, supply chain engagement, workforce development, and consumer education. The second pillar of TECH leverages regional pilots and Quick Start Grants to address specific barriers to scale within specific markets, such as low income or multifamily, as well as and explore ways to push through existing barriers such as with identifying customers, project finance, streamlining permitting, and load control. Lastly, the third pillar of TECH informs long-term, building decarbonization policy frameworks by collecting, analyzing, and publicly publishing energy and GHG impacts

* Corresponding author. *E-mail address:* ekamei@energy-solution.com

and detailed program case studies, results and processes that can be used to inform long-term decarbonization planning**.**

2. Initiative Description

2.1. The initiative framework

2.1.1. Pillar One: Spur the clean heating market for electrification through statewide strategies

Focus on contractors to prime the market: TECH Clean California employs several strategies to prime the market throughout the supply chain. TECH actively coordinates with manufacturers, distributors, contractors, and consumers to holistically support market transformation. TECH Clean California concluded that contractors would have the greatest impact on market transformation since they directly influence the sales process for most heat pump installations, including customer decisions on fuel substitution. To impact heat pump sales in the near-term, engaging these supply chain actors is critical. However, contractors are often hesitant to break away from their existing profitable sales model and invest time and effort to sell and install nascent technologies with yet-to-be proven demand [4]. Given these findings, this initiative is designed to train contractors on the technology, value proposition, and business model aspects of electrification; and to motivate contractors to sell heat pump technologies by providing contractor incentives, sales rewards, and bonuses.

Provide incentives for both single-family and multifamily residences: Providing incentives for both residence types helps ensure demand is supported across the market, including customer segments that can be hard to reach. TECH provides both HPWH and HP HVAC installation incentives for single-family residences, while encouraging best installation practices associated with each project. TECH also provides incentives installed in multifamily properties, thus reaching renters who may not be in charge of infrastructure upgrade decisions. Incentives are available for various equipment types that serve residential apartments as well as communal spaces used by residents and multifamily building staff.

Leverage existing marketing infrastructure to drive consumer demand: The Building Decarbonization Coalition (BDC) has played a prominent leadership role in consumer education, outreach, and engagement thus far. To drive demand, TECH integrates with and enhances their consumer inspiration campaign, the *Switch Is On*, which has been a key means of engaging in mass market communications for the initiative and has also been supported by heat pump manufacturers. This resource provides information for every step of the customer journey, such as guides to electrification, as well as resources that enable them to take direct action such as finding qualified contractors and available incentives.

2.1.2. Pillar Two: Create scalable models for market transformation through regional pilots and focused outreach

Test strategies through regional pilots and Quick Start Grants: Six regional pilots are designed to address key barriers to heat pump adoption, in a small-scale targeted fashion. The focus for two of the six pilots is to address adoption barriers within particular market segments — low-income households and multifamily housing — important for supporting an equitable transition. The remaining four pilots address key barriers along the customer journey: identifying the customers most likely to save money by switching to heat pumps, enabling high-volume project finance structures, streamlining equipment installation, and managing the new electrical load once the appliance is installed. TECH Clean California launched these pilots and also funded seventeen Quick Start Grants. Pilot details are discussed further in section 2.5 below.

Target low-income, hard-to-reach, disadvantaged communities (DACs): Investments in impacted communities help fuel economic recovery and respond to the needs of those hit hardest by historical environmental and social inequities as well as the ongoing COVID-19 pandemic. TECH Clean California has deployed targeted strategies and localized investments to enable equitable, impactful decarbonization. The initiative has a goal to invest 40 percent of program incentives in low-income households and DACs. To promote program collaboration, with advisement of the California Public Utilities Commission (CPUC) Low-income Oversight Board (LIOB), TECH Clean California assembled a Low-Income Ambassador Panel, consisting of low-income regional representatives from across the state. The objective of these activities is to gather the requisite data and market experience to inform policies and program designs that will transition low-income weatherization programs towards electrification, ensuring that low-income households have access to the health and safety benefits associated with decarbonization.

2.1.3. Pillar Three: Inform long-term building decarbonization framework

Public reporting drives policy: As a market transformation program TECH Clean California's role is to support structural shifts through policy and market mechanisms, and create sustained, long-term impacts. The initiative provides a single source of heat pump market data for California through its public reporting website, www.techcleanca.com, offering market transparency with program information on installation details, project prices, deployment progress, and meter-based impacts.

Quantify the value of decarbonization: A key barrier to decarbonization is the existing deficiency of the market to monetize grid and climate value. Many of the primary benefits of decarbonization are grid- and climate-related (bill savings are generally secondary), and thus a key near-term opportunity is using installation data from the initiative to quantify these values and support the development of more formal markets. Achieving zero carbon homes by 2045 will require significant public and private capital investment and robust project finance that supports this investment. By rigorously quantifying GHG impacts and all other decarbonization value streams for heat pumps by means of interval meter data, TECH Clean California hopes to achieve an actuarial level of impacts quantification required for large-scale project finance, similar to the wind and solar industry.

2.2. *Demonstrating scalability*

Like many other states, decarbonization efforts in California need to balance multiple priorities: 1) maximizing GHG reductions, 2) maintaining grid reliability, 3) ensuring equity and minimizing consumer bill impacts, and 4) achieving project cost declines and mature business models so that a large-scale transition is economically feasible. Programs like TECH Clean California can support scale to help pave the way for market transformation by demonstrating market demand and supporting a scalable process that can accommodate the high project volume needed to achieve California's heat pump goals. Within California, energy reliability remains an ongoing concern with respect to peak electricity demand in the summer. The California Independent System Operator (CAISO) conducted analyses and concluded that additional resources are needed to ultimately achieve long term reliability margins and need to consider growing risks of more extreme events stemming from climate change and supply chain disruptions. This stresses the need for approaches that support reliability and resiliency, such as HPWHs with load-shifting capability or customer targeting that maximizes peak load reductions [5].

In the United States, the Inflation Reduction Act is set to infuse approximately $300 billion into energy and climate reform measures, including $9 billion for rebates on efficient equipment — including HP HVAC and HPWH — and corresponding contractor training and education. The information gained from TECH Clean California will be invaluable in guiding other programs within California and nationwide as others create their own programs in response to the Act. The statewide initiative coordinates directly with the CPUC to deliver results across the four investor-owned gas utilities: Pacific Gas & Electric (PG&E), San Diego Gas & Electric (SDG&E), Southern California Gas (SoCalGas), and Southwest Gas (SWGas). TECH Clean California has also layered $5.4 million in incentives funded by partner utility programs, adding to the $31.7 million paid through the Cap-and-Trade funding that directly supports the initiative. These partner utility programs include those offered by community choice aggregators such as Central Coast Community Energy, municipal utilities such as Sacramento Municipal Utility District (SMUD), and regional energy networks such as BayREN. This incentive layering strategy is especially important as the Inflation Reduction Act will soon launch new programs such as the High-Efficiency Electric Home Rebates Program (HEEHRA) and the Whole-Home Energy Efficiency Program (HOMES) throughout the United States. These programs will need to coordinate and layer with local, existing energy efficiency programs. The lessons learned from TECH Clean California and the data available through our public reporting site offer unparalleled value to state energy offices and implementers and will guide and support the future of the industry.

2.3. Incentive design

TECH Clean California is designed to provide a simplified and consistent statewide incentive structure that integrates with existing local heat pump programs. A large-scale, statewide initiative brings significant benefits by simplifying two key areas: contractor participation and general program communication. To support this, TECH developed the Incentive Clearinghouse to layer incentives across integrated programs. This approach enables multiple organizations to provide funding for a single product type. TECH Clean California has now integrated its application process with five additional heat pump programs.

TECH Clean California's single-family incentive structure was designed with two goals in mind: 1) stretch the incentive budget by encouraging layering with local programs, and 2) provide a baseline set of incentives everywhere to ensure an equitable rollout. TECH concluded that the best approach would be to provide a statewide level of baseline incentives focused on overcoming the financial barriers associated with fuel switching, while coordinating with local energy efficiency programs to enhance incentives.

Facilitating a truly seamless experience for the contractor requires that all programs adopt consistent eligibility rules and application processes. In the first phase of incentive layering integration, each program still had its own rules, which caused contractor confusion and uncertainty. TECH Clean California and the other programs continue to work to streamline requirements and processes.

In addition to single-family incentives, TECH Clean California provides incentives for HPWH and HP HVAC equipment installed in multifamily properties for both retrofit and new construction applications. Incentives are available for various equipment types that serve residential apartments and communal spaces. For multifamily dwellings or properties with five or more dwelling units, TECH opted for a single incentive structure available throughout the investor-owned utility (IOU) gas territories to make the program simple and consistent for building owners and property managers.

2.4. Progress-to-date

2.4.1. Single-family incentives

TECH Clean California launched statewide, single-family incentives on December 7, 2021, and enrolled contractors ramped up participation quickly and enthusiastically. This is evidenced by the month-over-month growth in submissions shown in Fig. 1 below. Within six months, TECH enrolled over 900 contractors (3.5% of total California HVAC and water heating contractors) and received over 20,000 completed projects or reservations.[6]

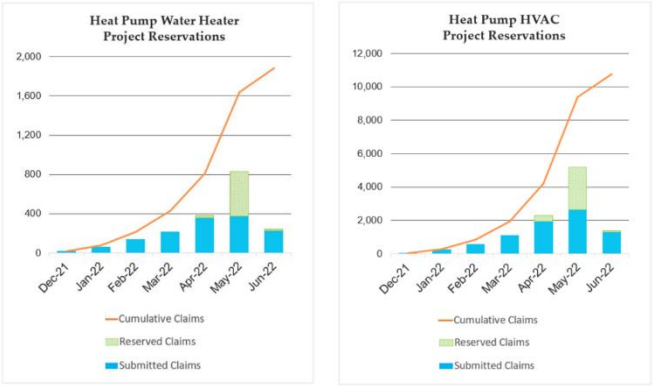


Fig. 1. Single-family incentives over time

Incentive spending in certain gas IOU territories gained momentum much more quickly than others, resulting in program suspensions due to budgetary limits required by the California Air and Resources Board funding allocations. These suspensions started with SDG&E on April 26, 2022, and extended to PG&E and SoCal Gas (HVAC only) on May 13, 2022.

To address the potential for exceeding the amount of available incentives, TECH Clean California introduced an incentive reservation system in May 2022 which allowed contractors to reserve incentives prior to project completion to ensure that funding would still be available when they were ready to submit applications for reimbursement. The team worked with participating contractors and energy raters to develop the reservation process and obtain feedback. The team sent out several communications to stakeholders to ensure that contractors were aware of the new system and in the span of a single week TECH received over 5,000 incentive claims, which quickly exhausted the remaining incentive budget and forced the program to suspend further incentive reservations.

Overall, both HPWHs and HP HVAC show significant growth, but initial sales were dominated by HVAC projects in single family homes: market-rate single-family TECH incentives applications had a 7.1:1 ratio of HP HVAC heat pump installations to those for HPWHs. This dramatic success of HP HVAC is likely due to selling on increased comfort and a combined heating and cooling solution, and the additional infrastructure

and complexity involved with HPWHs. For HPWHs, most installs took place in the Bay Area and Sacramento regions, which had existing programs and a more mature installer network. This suggests that HPWH programs in new areas should include robust investment in supply chain engagement and training, requiring time to build up a set of qualified and motivated contractors.

2.4.2. Multifamily incentives

TECH Clean California launched multifamily incentives with an incentive reservation system to accommodate the long pre-construction and construction timelines, the need to track incentive budgets, and the need for a contractor to provide property owners and managers with firm pricing proposals prior to decision-maker approval.

The TECH Clean California incentives enabled owners to move forward with heat pump projects that they could not otherwise fund themselves. To date, reservations have been made for over $12 million in multifamily incentives representing over 7,400 housing units, with the majority set aside for disadvantaged communities and affordable housing. In addition to the reserved incentives, about $7 million worth of incentives are on the multifamily waitlist, representing projects in the pipeline that can be completed if funding becomes available from new sources, such as IOU energy efficiency programs and state funding, or from projects that do not materialize. These incentive reservations were mostly for projects in SoCalGas and PG&E territory with a smaller portion in SDG&E territory (see Fig. 2 for breakout).

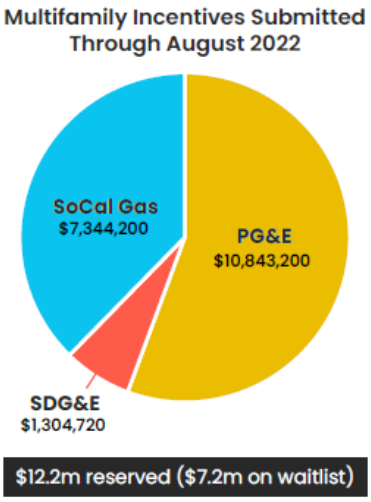


Fig. 2. Multifamily incentives reservations through August 2022

For multifamily installations, HPWHs comprised roughly 60 percent of projects. Of HPWH installations, 85 percent were in-unit installations, with 15 percent of units being served by central HPWHs. These heat pump investment decisions were often driven by project economics, or property owners looking to electrify to manage long-term fuel costs, decrease GHG impacts, and integrate with solar.

2.5. Overcoming barriers

The six TECH Clean California regional pilots, summarized in Table 1, are designed to test potential solutions to discrete market barriers, including impediments to widespread technology deployment and meeting California's GHG reduction goals. The solutions that prove effective will be incorporated into the TECH Clean California framework and scaled into statewide approaches where feasible.

Two of the six pilots address adoption barriers for market segments that are particularly important for supporting equitable transition: low-income households and multifamily housing. The remaining four pilots address key barriers along the customer journey: identifying the customers most likely to save money by switching to heat pumps, financing the project, streamlining equipment installation, and managing the new electrical load once the appliance is installed.

Table 1. Summary of TECH Clean California Pilots

Pilot	Objective
Inclusive Utility Investment Program	Launch Tariffed On-Bill (TOB) program with partner utility to expand access to financing
Low Income Integration	Collaborate with existing low-income programs to more fully incorporate heat pumps
Multifamily Housing	Provide deep technical support for designing building systems that reduces the perceived risk of electrifying
HPWH Load Shifting	Target contractors as key market actors to maximize use of HPWH for load shifting
Streamlining Permitting	Design code-compliant, one-day HPWH permit process
Customer Targeting	Identify and engage customers who can benefit most from heat pumps

2.5.1. Inclusive Utility Investment Program

The Inclusive Utility Investment Pilot aims to demonstrate and expand the Tariffed On-Bill (TOB) or Inclusive Utility Investment (IUI) model through a partnership with a Load Serving Entity (LSE). TOB/IUI programs allow utilities to pay for cost-effective energy improvements, such as home heating and cooling units, at a specific residence. TOB/IUI also recover costs for improvements over time through a dedicated charge on the utility bill less than the estimated savings from the improvements. TOU and IUI are not forms of debt or lending, and cost recovery survives across successor occupants, making it more inclusive and allowing longer cost recovery terms. TOB/IUI is a new concept and exact impacts of a larger program are unknown. Results from this pilot can be used to inform the statewide framework to support future programs.

2.5.2. Low-Income Integration Pilot

The Low-Income Integration Pilot aims to expand access to building decarbonization technologies among low-income households by partnering with existing energy efficiency or income-based retrofit programs to ensure heat pumps are available in more programs and to more customers.

In 2019 the CPUC initiated the San Joaquin Valley Disadvantaged Communities (SJV DAC) Pilots, seeking to increase access to affordable energy sources and reduce use of fossil fuels for generators. A key focus is on creating pathways to electrification for low-income households. The TECH Clean California Low Income Integration Pilot team collaborated with this program to address issues in low-income homes that must be remediated before electrification can proceed. The SJV DAC program had a limited budget for pre-existing homes that was proving inadequate to cover unforeseen repair needs. The goal of the TECH Clean California collaboration pilot is to address 70 single-family homes that were not originally able to participate in the SJV DAC program, by providing each home with additional funding for remediation. As of June 2022, TECH Clean California has funded remediation on 13 homes in the San Joaquin Valley, with more in the pipeline. A central learning of the pilot is that the initial costs for retrofitting and repairs that are essential before installing heat pumps are often underestimated and the bill impacts of heat pumps are uncertain due to variables unique to each installation site. The lessons learned from this pilot will inform other equity-based programs throughout the state.

2.5.3. Multifamily Housing Pilot

The Multifamily Housing Pilot seeks to address barriers associated with electrification and energy efficiency upgrades in multifamily properties specifically by reducing the perceived risk of heat pump systems, by providing deep technical support in building system design. The strategy is to increase market familiarity with technologies and build capacity within design teams at multiple levels: from owners and architects to mechanical, electrical, and plumbing engineers. By accelerating the learning curve, the pilot will reduce the time and cost for developers to transition to all-electric buildings. The pilot has three tracks of activity:

- Project Specific and Portfolio Level Electrification Advising
- Central Heat Pump Water Heater Technical Support
- Property Electrification Readiness Plan

By addressing these multifamily housing barriers, this pilot can help provide a framework to support future efforts to transition properties to all-electric service.

2.5.4. HPWH Load-Shifting Pilot

This pilot aims to establish market readiness and ensure that the full load-shifting benefits of HPWHs can be realized. It addresses this by motivating contractors to set up a HPWH to load-shift upon installation and encouraging them to sign customers up for demand response (DR) programs.

The initial focus of the pilot through 2021 and early 2022 was to educate contractors about the value of load shifting. The pilot team created an HPWH load-shifting training curriculum, and as of May 2022, more than 700 contractors had begun to enroll. Of these contractors, more than 150 had viewed the training video, and 75 percent of those who responded to the post-training survey reported that they had a positive view of the training, with only six percent being less than satisfied.

Initially, the pilot team also offered a $200 incentive to contractors who installed a thermostatic mixing valve (TMV), a component that greatly expands the load-shifting potential of an HPWH. The pilot received and paid 209 TMV incentive claims, and early results from the launch of general TECH Clean California incentives revealed that about 70 percent of installs were already including TMVs as a matter of course. In the fall of 2021, the Self Generation Incentive Program (SGIP) announced HPWH incentives with requirements that included the inclusion of TMVs for all installations. To align the TECH Clean California requirements with SGIP, and after consultation with contractors to ensure the market was ready to include TMVs as a standard part of installations, TMVs were made a requirement for receiving standard TECH Clean California incentives, and TMV bonus incentives were discontinued on June 20, 2022.

With the discontinuation of TMV incentives, the pilot team expanded the portion of this pilot that encourages contractors to enroll customers in DR programs by providing an additional $50 incentive for each customer enrolled. Originally, the HPWH Load Shifting Pilot focused on collaboration with PG&E's WatterSaver DR program; however, standard TECH Clean California incentives were exhausted in PG&E territory in May 2022. The team expanded its focus and now offers the $50 incentive for enrollment in DR programs statewide and is currently collaborating with WatterSaver, SMUD's PowerMinder program, and OhmConnect, and open to other collaborations in the future. The pilot team will continue to educate contractors – and through them, customers – on the benefits of DR enrollment for both the grid and customer savings and will collect data on the barriers and challenges that dissuade contractors and their customers from enrolling in these programs.

2.5.5. Streamlining Permitting Pilot

This pilot aims to close the gap in permitting times between natural gas water heaters and HPWHs, by adopting a single-day HPWH permitting process within single-family homes where code compliance could be demonstrated easily and effectively. The permitting process for HPWHs can currently span multiple days, deterring both homeowners and installers from making the switch from gas water heating to electric HPWHs. In emergency replacement scenarios, longer installation periods due to permitting delays are an even more significant barrier.

Throughout the second half of 2021 and into 2022, the pilot team convened numerous meetings with stakeholders to identify permitting challenges and solutions and help shape the potential goals of the pilot. Incorporating feedback from these sessions, the group reviewed a permit guidance package intended to aid building permit offices and contractors in creating a more expedited HPWH permitting process.

2.5.6. Customer Targeting Pilot

This pilot seeks to identify and test outreach strategies to drive demand among customers for whom the value of electrification is most compelling. It addresses two key market barriers hindering adoption of heat pumps in California:

- A lack of large-scale data demonstrating which customers are most likely to benefit from upgrading to a heat pump, and how to motivate those customers to buy a heat pump instead of an alternative.
- Poor outcomes from recruitment of customers with low potential to save, which can have an outsize effect on adoption in early-stage technology markets. This highlights the need to recruit customers whose energy profiles indicate high potential to save.

This work transitioned from planning to implementation in early 2022 after receiving the necessary customer data from the utility. Working with SCE, the team devised an email campaign to be sent to SCE customers with a high likelihood of energy bill savings from installing HP HVAC systems. The pilot will compare the effectiveness of a general message about the efficiency and benefits of heat pumps to a specific

message stating that a customer's energy use indicates their household is a particularly suitable candidate. The lessons learned from this comparison will demonstrate the value of targeting customers based on energy use, which may be leveraged by future programs.

2.5.7. Quick Start Grants

Along with other TECH pilots, the Quick Start Grant (QSG) program aims to identify and fund targeted, innovative pilots that test approaches to overcome market barriers to heat pump deployment. The QSG program has funding for two solicitations annually. With these, the QSG program aims to promote the development and refinement of interventions that meet our solicitation criteria:

- Test solution to a barrier to residential building decarbonization.
- Have the potential to scale up to become statewide solutions.
- Ensure feasibility within the budget proposed and can be implemented within one year.

The first solicitation sought QSG pilots in the fall of 2021, received 35 grant applications and selected 11 projects for funding. Of the winning projects, 73 percent of overall funding went to projects expected to serve low-income households or historically underserved populations. The projects launched in early 2022. Since then, each of the grants has made progress in hitting individual milestones.

Fig. 3 provides a summary of the Quick Start Grants from the first solicitation.

The second solicitation was completed in the fourth quarter of 2022 and selected six projects for funding. Several changes were made to the second solicitation to reflect input from stakeholders as well as the implementation team's experience. These include expanding stakeholder outreach, extending the open time of the solicitation, adding an interview stage for grant finalists, and increasing the focus on projects addressing barriers in historically underserved communities.



Enabling Faster Installations

Barnett Plumbing, Loaner Water Heaters for Emergency Fuel-Switching

Small Planet Supply, Parkside Apartments HPWH

New Buildings Institute, 120V HPWH Field Test

IHACI, Virtual Technician Software Platform

Making Programs More Inclusive

Redwood Coast Energy Authority, Air Source Heat Pump Incentives for Unregulated Fuel Customers

Franklin Energy and MCE, Augmentation of Income-Qualified Electrification Program

Reducing Energy Costs

The Energy Coalition, Basset Avocado Heights Advanced Energy Community HPWH

AESC, Interactive Impacts of HPWH in Manufactured and Mobile Homes

Innovation for Multifamily Housing

BlocPower and City of San Luis Obispo, Better Buildings SLO Pilot

Revalue, Green and Healthy Homes

USGBC-LA, Electrification in Green and Affordable Homes Program

Fig. 3. Quick Start Grant summary

TECH will analyze the collected data, review the gained experience, and make the findings known to key decision makers through the public reporting website.

2.6. Public reporting

The vision for TECH Clean California public reporting is to bring a variety of data sources together and layer them into a robust and scalable data pipeline that offers novel visibility into the California heat pump market as shown in Fig. below. In the first year of implementation, TECH focused on building a core infrastructure to collect useful, actionable data. First-year accomplishments include building a robust incentive application data collection pipeline, unlocking access to historical meter data via CPUC to measure key participant outcomes, and launching the public reporting website to collect data and key findings, including anonymized project-level data and evaluation data as of July 2022.

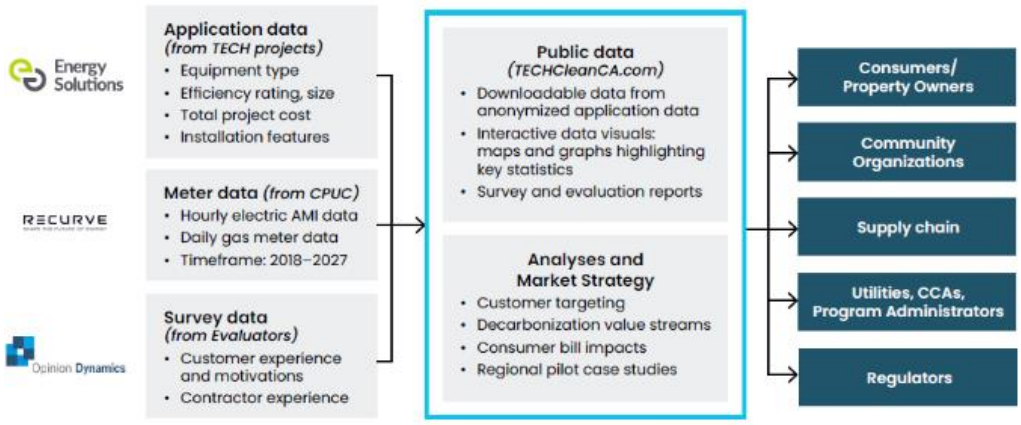


Fig. 4. TECH Clean California data mapping

The primary data pipeline starts with the Incentive Clearinghouse, where contractors submit incentive applications and data about project installation. An early focus area has been to outfit the Incentive Clearinghouse with all the features needed to fulfill TECH Clean California's ambitious goals — programs for two distinct technologies, each with high data quality requirements, and each capable of layering with other partner programs — while making the combined incentive consistent enough for contractors to understand and predict. Once this functionality was in place, incentives for thousands of projects could be quickly deployed in just a few months, layered with four partner programs, each with a distinct layering structure. The Incentive Clearinghouse can continue to serve as a processing and layering center for new incentive programs anywhere in the state.

Concurrently, TECH worked with CPUC and California Energy Commission to gain access to statewide residential historical electricity and gas meter data (approximately 11 million meters) to understand the impacts of heat pump installations on the utility bills and GHG emissions of TECH Clean California participants. After collaborating with CPUC to resolve unforeseen legal barriers preventing access to the necessary meter data, TECH was able to start auditing the database that stores statewide residential electricity and gas meter data. TECH has started building a baseline understanding of residential gas and electricity consumption throughout the state and using this data to inform customer targeting and regional pilots. Meter-based results for TECH Clean California participants will become available starting one year after heat pump installation – the third quarter of 2023 for most TECH Clean California participants.

Finally, TECH has established regular data exchange with our evaluators, Opinion Dynamics, to further our understanding of customers' and contractors' experience with TECH Clean California and heat pumps in general. For example, Opinion Dynamics' participant surveys [n=596] found that the TECH incentive was at least somewhat important to their purchase decision for 93% of customers, and that over 90% of respondents were satisfied with their contractor experience. This rapid feedback significantly helped inform ongoing program decisions. TECH is also working on data sharing arrangements with key market actors to obtain sales and product price data for the overall California heat pump market. Given the importance of this data to these companies' business models, traction on this is still in progress and obtaining the data requires persistent and attentive negotiation.

With a data pipeline built atop the Incentive Clearinghouse, and integrated meter-based impacts and TECH Clean California participant surveys, TECH will publish data-driven insights to catalyze market transformation. These will be hosted on our public reporting website, which launched in July 2022. Hosting downloadable data and interactive data visuals, the public reporting site makes data engaging and impactful for both casual visitors as well as researchers. The site currently hosts application data from the several thousand market rate single-family projects that received TECH Clean California incentives since December 2021, and this data is updated monthly as more incentives are paid.

3. Key Lessons Learned

3.1. Balancing the need for scale with consistent funding streams

A key challenge for TECH was balancing its market transformation mandate to drive adoption and send clear market signals, with its incentive funding limitations. The enthusiastic overall response led to incentive

funding being suspended in much of the state by May 2022, well ahead of schedule but still at a pace far below the annual installation numbers and growth rates required to achieve the state target of six million heat pumps by 2030. While TECH funding provided incentives to over 20,000 projects and exhausted funds relatively quickly, over 500,000 water heaters and 500,000 furnaces or air conditioners are installed each year in California. The inherent trade off was that high incentives were needed to initially attract contractor attention and create the market shifts necessary to rapid uptake, yet, given the scale of the California market TECH did not have sufficient funding to move the market alone. To achieve the level of scale needed, incentives per project need to decrease over time and long-term sources of private and public investment are needed to sustain significant transformation. The 20,000 projects deployed through TECH data should provide a robust data set to inform development of a longer-term funding approach that aligns with California's 2030 heat pump goals. As TECH integrates additional funding, the initiative will refine its offering by lowering incentives to match growing customer demand in support of market transformation.

As the number of incentivized technologies grows, and TECH gathers empirical data on their energy use, an analysis of what is driving — or impeding — heat pump adoption will become available. The first year of the program has produced key process-based lessons on the essential components of program design necessary to meet heat pump goals at the scale set by California.

3.2. Robust heat pump incentives drive the market

A market shift toward heat pumps will require large-scale shifts in equipment production towards lower emissions products. To ensure there is sufficient equipment supply and manufacturers are incorporating these decarbonization goals into their product roadmaps, it is critical that the state outline investment strategies commensurate with these goals to send a clear signal to supply chain actors. California has recently begun to step up its public investment in decarbonization: through equipment incentive programs like TECH and SGIP which will provide $80 million in incentives for HPWH; through incentives for all-electric new construction like the Building Initiative for Low-Emissions Development; and through the proposed $1 billion investment from the legislature to support equitable building decarbonization. However, the state should establish a clearer, long-term funding roadmap.

3.3. Consumer education and outreach is an important complement to incentives

TECH's consumer education website and outreach efforts, through www.SwitchIsOn.org and its Ambassador Program, played a crucial role in supporting consumers at each point of the customer journey. The website achieved over 326,000 unique visitors and facilitated over 4,500 contractor quotes. Website visits scaled with project installations, with the most popular pages being the Rebate Finder tool and the Find a Contractor tool. Anecdotal evidence from contractors suggests that the website provided critical support for contractors to help educate prospective customers. In addition, the Ambassador Program, which focuses on individuals sharing their heat pump and home electrification journey with others, received over 100 initial ambassador volunteers throughout the state to promote and offer their experience as a resource to other prospective customers. These resources are particularly important when considering broader community engagement campaigns.

3.4. Providing statewide support and creating consistency among the many heat pump programs

There are many heat pump programs within California, and a project may be eligible for multiple programs based on its location. A large-scale, statewide initiative brings significant benefits by simplifying two key areas: contractor participation and general program communication. To simplify the contractor experience and eliminate the need for applying separately for multiple programs, TECH integrated its application process with other five additional heat pump programs. This layering approach enables multiple organizations to provide funding for a single product. This approach is particularly important for decarbonization measures, since the NOx, GHG, energy efficiency, and peak demand benefits may have different funders or organizations interested in those respective values. For example, an air quality management agency may be interested in NOx reductions, while a utility is focused on efficiency and peak load reduction. Additionally, incentive layering equips programs with funding that can tackle key barriers seen through the TECH pilots, such as remediation costs, bill impacts, or cost effectiveness for low-income programs or split incentive challenge for multifamily programs.

While streamlining multiple incentives provided benefits to create standardized incentive amounts across the state, there were significant implementation challenges due to differences in eligibility criteria. These differences made it difficult for contractors to understand which programs they qualified for. The difficulty in communicating consistent eligibility requirements across programs was a sufficient barrier that the TECH program decoupled incentives from multiple programs. That made it easier to communicate flat amounts provided by each program. Ultimately, TECH believes the best approach is having a robust statewide baseline incentive, sufficient to move the market, with as-needed supplemental incentives in areas to drive specific adoption. Numerous contractors noted that the statewide simplicity across utility borders was a major benefit and made participation more straightforward. Scaling heat pump adoption is a statewide priority and thus it makes sense to have a statewide initiative rather than a patchwork of smaller efforts. It also requires significant non-incentive market development efforts, such as workforce education and training, consumer education and data reporting, all of which benefit from economies of scale at the statewide level.

4. Conclusion

TECH Clean California has launched a combination of market incentives, supply chain engagement, workforce development, consumer education, regional pilots, and Quick Start Grants. TECH Clean California has resulted in the rapid deployment of heat pumps and has established data infrastructure to inform statewide consistency. Through these efforts, TECH Clean California has identified key lessons learned, including the effectiveness of incentives, importance of consumer and contractor engagement, and value of consistency among heat pump programs.

During the next year of TECH Clean California implementation, the focus of data reporting efforts will shift from building new infrastructure to scaling and improving the initiative. As the depth and breadth of the data increases over time, TECH will continue to refine its ongoing strategies to maximize impacts as well as conducting analyses that inform statewide decarbonization policies and investments. The initiative's goal is to make application data and meter-based results for every TECH-funded project easily accessible and comparable, in one place, to showcase important differences between the various TECH Clean California programs, such as single-family versus multifamily projects. In addition to public data, TECH has also initiated a process of customized quarterly reporting for key heat pump manufacturers, giving them critical insight into TECH Clean California participation. Manufacturers are just one key consumer of TECH Clean California data, though, and it will be critical for TECH to strategize where and how the initiative focuses its analysis and outreach to meet the most important needs for decarbonization policymakers and investors.

Funded with an additional $50M through the California State budget, TECH Clean California will continue to enable the installation of zero-emissions space and water heating technologies and will collect and publish energy and GHG impacts with market data to inform California's long-term decarbonization framework and beyond.

References

[1] Kenney, M., Wahlgren, J., Duloglo, K., Mateo, T., Drozdowicz, D., Bailey, S. 2022. "Final 2021 Integrated Energy Policy Report, Volume I: Building Decarbonization." California Energy Commission. Publication Number: CEC-100-2021-001- V1.

[2] Office of Governor Gavin Newsom. 2022. "Governor Newsom Calls for Gold Actions to Move Faster Toward Climate Goals." https://www.gov.ca.gov/2022/07/22/governor-newsom-calls-for-bold-actions-to-move-faster-toward-climate-goals/

[3] California Air Resources Board. 2022. 2022 State Strategy for the State Implementation Plan. https://ww2.arb.ca.gov/sites/default/files/2022-08/2022_State_SIP_Strategy.pdf

[4] Opinion Dynamics. 2022. California Heat Pump Residential Market Characterization and Baseline Study. https://pda.energydataweb.com/api/view/2610/OD-CPUC-Heat-Pump-Market-Study-Report-final-4-2022.pdf

[5] Emmert, B. 2022. "Briefing on 2022 Summer Loads and Resources Assessment results." http://www.caiso.com/Documents/Briefingon2022SummerLoadsandResourcesAssessmentResults-Presentation-May2022.pdf

[6] Energy Solutions. 2023. 6th Quarterly Stakeholder Meeting: February 7, 2023. https://www.techcleanca.com/

14th IEA Heat Pump Conference
15-18 May 2023, Chicago, Illinois

A Review of Recent Residential Heat Pump Systems and Applications in Cold Climates

Hanlong Wan[a,b], Yunho Hwang[a *]

[a]4164 Glenn Martin Hall Bldg., Center for Environmental Energy Engineering
Department of Mechanical Engineering, University of Maryland, College Park, MD, 20742, United States
[b]Oak Ridge National Laboratory, Oak Ridge, TN, USA

Abstract

The heat pump (HP) system is one of the environmentally friendly solutions to reduce the carbon footprint of buildings due to its high efficiency and low added initial cost from the cooling-only systems. This paper presents a literature review of the recent advances in HP systems applied in cold climate regions categorizing the systems into two major types depending on energy source types. The first type is the systems with an air source without additional energy sources, i.e., Air Source HP (ASHP) systems, which use various working fluids and configurations. However, several issues impede their widespread applications. When the systems are used for space or water heating in cold climates, ASHP systems suffer a high discharge temperature and pressure ratio at low ambient temperature, which leads to low efficiency and heating capacity. Furthermore, some researchers reported that the defrost penalty reduced the energy efficiency by up to 30%, leading to a degradation of heating capacity by 43%. The second type is the systems with additional energy sources, like solar-assisted HP systems, which can partly improve energy performance but have difficulties in coupling different sub-systems to achieve increased operational time and are limited to locations with enough solar radiation. This study identifies the future research directions as (1) developing multi-source heat pumps with efficient control; (2) utilizing waste heat for defrosting; and (3) optimizing HP configurations and minimizing refrigerant charge while achieving higher efficiency.

© HPC2023.
Selection and/or peer-review under the responsibility of the organizers of the 14th IEA Heat Pump Conference 2023.

Keywords: heat pump; cold climate; air source; multi-source; defrost

1. Introduction

A number of researchers have reported that the high energy consumption of the building sector is among the significant global challenges for sustainable human development [1]. Space and water heating take up more than half of residential energy consumption [2]. This ratio increases significantly in cold climate regions [3]. Over the last two decades, residential buildings have widely adopted Heat Pump (HP) systems due to their simple structure and low added initial cost [2]. Several different HP technologies exist. Air Source Heat Pump (ASHP) systems take low-grade heat from the air and produce high-temperature heat for domestic heating or other purposes [4]. Solar Assisted Heat Pump (SAHP) systems, which combine solar thermal panels with heat pumps, have been widely used to provide residential hot water owing to their simple structure, low cost, stable operation, and effective solar energy collection [5]. Ground Source Heat Pump (GSHP) and Water Source Heat Pump (WSHP) systems use heat energy naturally stored in either the ground or water, taking advantage of the

* Corresponding author. Tel.: +1-301-405-5247
E-mail address: yhhwang@umd.edu.

Notice: This manuscript has been authored by UT-Battelle, LLC under Contract No. DE-AC05-00OR22725 with the U.S. Department of Energy. The United States Government retains and the publisher, by accepting the article for publication, acknowledges that the United States Government retains a non-exclusive, paid-up, irrevocable, world-wide license to publish or reproduce the published form of this manuscript, or allow others to do so, for United States Government purposes. The Department of Energy will provide public access to these results of federally sponsored research in accordance with the DOE Public Access Plan (http://energy.gov/downloads/doe-public-access-plan).

relatively constant temperatures of the earth or waterbody throughout the seasons [6]. However, there are many challenges when people are using HP systems in cold climate regions. This paper groups the so-called cold climate heat pump (CCHP) systems into two major types depending on energy sources for clear discussion. The first type is the systems with an air source only without any additional energy sources, i.e., ASHP systems. The second type is the systems coupled with additional energy sources, like GSHP or SAHP systems. This study summarizes the challenge of different HP types to penetrate the cold climate region application.

2. Challenges of Heat Pump Application in Cold Climates

Challenges exist for almost all current CCHP systems. First, typical ASHP systems work under a high discharge temperature and pressure ratio at low ambient temperature, which leads to low efficiency and heating capacity [7]. For instance, with a decline in ambient temperature, a decreased heating capacity of the ASHP system may be insufficient for the building's heating load requirement, and the high compression ratio may lead to an extremely high discharge temperature and system shutdown. Furthermore, frost on the outdoor heat exchanger coil surface degrades thermal performance by reducing airflow area due to the blockage caused by the layer of frost [8]. Also, an insulating area is built up over the evaporator coils, thereby reducing their ability to absorb heat from the outdoor environment [8]. Defrost is a non-eligible problem in cold climate region. The heating COP would decrease by 30% if the heat exchanger was fully frost [9].

SAHP systems face challenges as well. The constant operation of the heat pump in the systems usually leads to a large carbon footprint, significant electrical energy use, and an energy inefficient operation [10]. However, owing to the fluctuation of solar radiation during the day time, the SAHP system may have a low efficiency without a proper control strategy or energy storage device [10]. As for the GSHP and WSHP systems, the installation region is restricted.

3. Air Source Heat Pump

Zhang et al. (2018) [2] reviewed the literature on vapor compression ASHP systems from 2005 to 2017 and classified the systems into single-stage, dual-stage, and multi-stage compression systems. They concluded that the quasi-two-stage compression system showed enormous potential for heating performance and initial cost. No similar study exists after Zhang's work summarizing new CCHP techniques based on the authors' knowledge. This section mainly focuses on reviewing the experimental studies conducted in the recent five years while comparing the new works with three old studies [11–13].

Table 1 summarizes the authors and some features of the target studies. In the "cycle type" column, "cascade" refers to two-stage systems using two separate compressors [14,15], while "VI" refers to the systems using the Vapor Injection (VI) technique. "-" in this column refers to single-stage systems. In the "discharge temperature" column, "-" means the information is not given in the related studies. Among the studies, Zhang et al. (2017) and Fan et al. (2022) [16,17] highlighted the need to reduce defrosting process power consumption in cold climates. Zhang et al. (2019) developed and investigated a novel thermal storage refrigerant-heated radiator coupled with an ASHP heating system. Zhang et al. (2017), Wei et al. (2020), and Wu et al. (2022) [16,19,20] examined the long-term performance of the ASHP system in the field test.

Fig. 1 plots these studies using the ambient temperature as the x-axis and COP as the y-axis. All points were tested under the same indoor condition (21 °C). The linear regression line of the data points shows that most of the ASHP systems can reach 1.5 COP under extreme conditions. One outstanding piece of research was carried out by Bertsch and Groll (2008) [11,12]. They applied a special low-pressure stage compressor with an oil tap in the VI system and mentioned that this compressor with a suction volume of approximately 90 cm^3/rev was not commercially available, which might explain the impressive performance.

First, the data suggest that VI using R410A is the primary trend technique applied for cold climate ASHP system. However, the discharge temperature of the upper stage cycle typically exceeds 90 °C. Except for some limited studies, the COP limitation exists under the extreme ambient conditions of -20 °C to -30 °C. Second, frost-caused performance degradation is non-negligible [9]. Supplying an auxiliary heat source, e.g., an electric heater, seems necessary for cold-climate ASHP systems.

In summary, from the existing studies, the maximum COP of the advanced system under low ambient temperature conditions based on the published literature is still low from the viewpoint of the primary energy ratio. Secondly, its heating capacity deserves to be further enhanced to satisfy building heating loads, especially under extreme conditions. Finally, more research on the technology about system start-up at low ambient temperature and year-round control strategy is required to ensure the reliability of the advanced system.

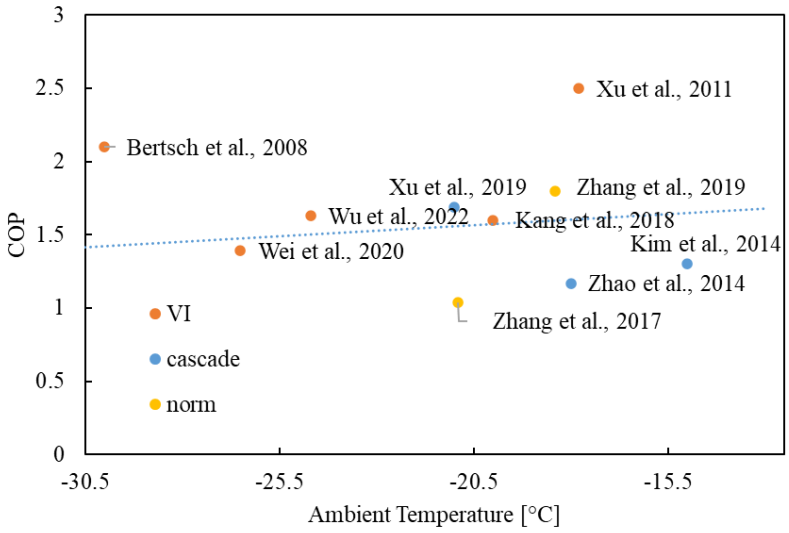


Fig. 1. Comparison of existing studies under extremely cold conditions

Table 1. Existing ASHP performance under extreme conditions

Authors, year	COP	Ambient Temp. [°C]	Cycle Type	Refrigerant	Discharge Temp. [°C]
Bertsch and Groll, 2008 [11]	2.1	-30.0	VI	R410A	93.0~102.0
Xu et al., 2011 [12]	2.5	-17.8	VI	R410A	-
Kim and Kim, 2014 [13]	1.3	-15.0	cascade	R410A/R134a	80.0~90.0
Zhang et al., 2017 [16]	1.1	-20.9	-	R22	-
Kang et al., 2018 [21]	1.6	-20.0	VI	R410A	97.3~101.2
Xu et al., 2019 [22]	1.7	-21.0	cascade	R404A/R134a	93.9~91.4
Zhang et al., 2019 [18]	1.8	-18.4	-	R410A	-
Wei et al., 2020 [19]	1.4	-26.5	VI	R410A	90.6
Wu et al., 2022 [20]	1.6	-24.7	VI	R410A	-

4. Systems with additional energy sources

4.1. Solar Assisted Heat Pump

Some researchers identified the merits of SAHP systems as flexibility, efficiency, and stability in cold regions [23]. Others argued that cold regions in winter usually lack solar energy [7]. Many studies exist to improve the thermal performance of SAHP systems. Ji et al. (2008) and Fu et al. (2012) [24,25] optimized the structure of the solar thermal panels and evaporator; Zhang et al. (2014) [26] studied the optimal geometrical sizes and capacity; Gorozabel Chata et al. (2005) and Kong et al. (2017) [27,28] concentrated on the refrigerant type; Chaturvedi et al. (1998) and Kong et al. (2018) [29,30] focused on the control strategy for compressor and electronic expansion valve, and Chaturvedi et al. (2009) [31] combined the cascade structure with Thermal-SAHP water heater to reach higher supply temperature. Nevertheless, none of the research mentioned how their proposed system could match the requirements under low ambient temperature or radiation conditions. Qiu et al. (2018) [32] investigated a low-temperature heat-collecting system and got a simulation COP result of only 1.6 at -25 °C ambient temperature and 200 W/m^2 solar radiation intensity. Only limited scholars studied combined photovoltaic-thermal (PV/T) SAHP (air-source). Li et al. (2015) [33] developed a mathematical model of a PV/T-SAHP system and optimized the flow distribution and velocity to reach the COP as high as 4.6 at 10 °C ambient conditions. However, this result was given with 400 W/m^2 radiation, and the authors also mentioned that the performance could reduce to 21% when the outdoor air temperature was -5 °C. Cao et al. (2016) [34] simulated a PV/T-SAHP performance using Computational Fluid Dynamics (CFD). The COP could reach 3.5 when the ambient temperature was around 0 °C. However, they did not study the performance under further lower temperature conditions.

A comparative study of different seasonal Thermal Energy Storage (TES) systems using HPs with solar collectors identified the heat pump's COP and the solar fraction as the main factors that influenced the efficiency of the system, with both factors being a function of the collector area and storage volume [35]. Pensini et al. (2014) [36] undertook an economic analysis of using excess renewable energy for heating purposes, and reported that HPs with centralized thermal storage met heat demand at lower costs than conventional systems even if there was a charge for producing excess renewable energy. Kapsalis and Karamanis (2016) [37] considered solar TES and heat pumps with Phase Change Materials (PCMs) and concluded that further investigation and experimental work were necessary to determine the combined effect PCMs in building components and HP operation within different climates.

This section discussed the merits and limitations of SAHP systems in cold regions. Several studies have been conducted to improve the thermal performance of SAHP systems. SAHP could improve the COP in cold regions with high solar radiation, but the benefit is limited in low solar radiation regions.

4.2. Ground Source Heat Pump

It was reported that Ground Source Heat Pump (GSHP) systems have relatively stable performance throughout a year but can only be installed at specific locations [38]. One study shows that such systems are 40% more energy efficient than ASHPs [39]. Huang et al. (2019) [40] reported that the GSHP system had higher installation costs but higher energy efficiency and 10% lower costs across 10 years. Direct expansion GSHPs, a variant of the common GSHP that uses a buried copper piping network through which refrigerant is circulated, can deliver superior performance relative to GSHPs and ASHPs in Canadian and Chinese locations [41,42]. Mattinen et al. (2015) [43] compared carbon emissions across direct electric heating, ASHP, and GSHP systems and found that GSHPs perform better in colder climates due to higher COP at lower outdoor temperatures. Carbon emissions in ASHP systems were 40% lower than direct electric heating and 70% lower in the GSHP system. From an emissions perspective, this makes GSHP systems the best option; however, reducing emissions is only possible if the heat pumps are integrated with low-carbon power systems. Otherwise, deploying large quantities of heat pumps in a power system where there is a low level of decarbonization of electricity generation merely results in shifting emissions from one sector to another. Wu compared ASHPs with GSHPs and concluded that GSHPs have the advantages of higher efficiency; lower life cycle cost; lower impact on environment; and better reliability [44]. Safa et al. got a result that for cooling mode, the COP of ASHP ranged from 4.7 to 5.7 at an outdoor temperature of 33 °C and 16 °C respectively, while the COP of GSHP ranged from 4.9 (at an ELT of 8.5 °C and EST of 19.2 °C) to 5.6 (at an ELT of 12.4 °C and EST of 17.8 °C) [45]. Garber et al.'s results of the analysis show that potential savings from a full-size GSHP system largely depend on projected HVAC system efficiencies and gas and electricity prices [46].

This section summarizes that GSHP systems can be more efficient than ASHP systems. However, their emissions benefits are only realized if they are integrated with low-carbon power systems.

4.3. Water Source Heat pump

Water source heat pumps (WSHPs) use lakes, ponds, rivers, groundwater, and other water sources, as a source of heat. They convert low-grade heat from the water source to a higher grade. The temperature of the waterbody fluctuates less than that of air; thus, the performance of WSHP is relatively stable. Bach et al. (2016) [47] from Denmark found the seasonal variation of COP had little or no impact on the transmission and distribution networks of the district heating system, as COPs of WSHPs did not vary much throughout the year. Thus, such systems can work well in cold weather. However, WSHP applications are limited due to the requirement of large water bodies or storage tanks near dwellings. Moreover, the need to adhere to specific environmental regulations may further result in a low uptake rate of WSHPs.

5. Discussion

5.1. Existing studies

First, based on existing literature for ASHP systems, the two-stage compression system shows tremendous potential for performance and cost [2]. Furthermore, Table 1 suggests that VI systems using R410A are the main trend technique. However, the discharge temperature of the upper stage cycle was usually high. In addition, the COP of all the systems is still a bit small from the viewpoint of the primary energy ratio. The

defrost power consumption, low-temperature start-up technology, and year-round control strategy are significant but are seldom mentioned in current published literature.

Some studies concluded that SAHP and GSHP systems are better options than ASHP systems in colder regions [4]. However, the type of heat pump to be installed is location and application specific. This is due to the concern that ASHPs may not be able to meet the thermal comfort and energy efficiency requirements when ambient temperatures are immensely low. The requirement of solar radiation, ground thermal sources, and other environmental concerns limit SAHP, WSHP, and GSHP systems' overall uptake rate.

5.2. Current Barriers

Several issues that impede the widespread of above applications still exist: 1) the lack of clear decarbonization pathways, technology acceptance, and funding are the primary sources of barriers to cold climate heat pump uptake [48]; 2) public acceptance and awareness issues, i.e., emanate from unwarranted fear, misperception, misinformation, and previous experiences on the reliability, also pose significant challenges in adopting the new technology [49]; 3) existing market structures combined with public perception can also hinder the penetration of cold climate heat pumps [50]; 4) barriers related to lack of standards and mandatory policies can also considerably constrain some special HP systems deployments, like GSHP and WSHP [51]; 5) an essential barrier to widespread adoption of heat pumps in cold climate is the limitation of the electrical network, which may be further increased at peak periods and in turn may require additional electricity grid infrastructure investment to satisfy the demand [52]; and 6) proper sizing and installation of a heat pump is essential in order to achieve the desired design objectives and overcome the barriers to widespread adoption.

5.3. Future work

The future research directions were identified: (1) multi-source heat pumps, for example, the systems using both solar energy and ground source energy, could be proposed; for these systems, an efficient control to coordinate each part is necessary; (2) waste heat or low-grade heat shall be used for heat pump defrosting in cold climate regions; identification of more heat source other than the ground source or water source could be investigated; (3) people may also study advanced heat storage technology and heat exchanger design strategies; and (4) researcher may continue to optimize the configuration and refrigerant usage to achieve low discharge temperature in cold climate heat pumps.

6. Conclusions

Due to the great efficiency and minimal added initial cost compared to cooling-only systems, HP systems are one of the ecologically sustainable ways to lower the carbon footprint of buildings. In this research, the HP systems are divided into two main categories depending on supplementary energy sources, and current HP system developments for cold climate regions are thoroughly assessed. Following is a list of the conclusions:

The two-stage compression system shows tremendous potential for performance and cost, and VI systems using R410A are the primary trend technique for ASHP systems. However, the discharge temperature of the upper stage cycle was usually high. In addition, the COPs of all the systems are still a bit low from the primary energy ratio viewpoint.

Some researchers reported that the defrost penalty reduced energy efficiency by up to 30%, leading to further degradation of heating capacity by 43%. Thus, defrost is a non-negligible factor for CCHP application.

Low-temperature start-up technology and year-round control strategy are significant but are seldom mentioned in published literature.

Some studies concluded that SAHP and GSHP systems are better options than ASHP systems in colder regions. However, the type of heat pump installed is location and application specific. This is due to the concern that ASHPs may not be able to meet the thermal comfort and energy efficiency requirements when the ambient temperature is immensely low. The requirement of solar radiation, ground thermal sources, and other environmental concerns limit SAHP, WSHP, and GSHP systems' overall uptake rate.

Current barriers to CCHP systems include policy limitation, public acceptance, economic reasons, a lack of standards and funding, and insufficient studies on an electronic network.

Future research should focus on the following topics: (1) multi-source heat pump with effective control; (2) heat pump defrosting capability utilizing waste heat; (3) advanced Heat Storage and Heat Exchange Unit technology; and (4) optimized structure and refrigerant usage to obtain low discharge temperature.

Acknowledgements

We gratefully acknowledge the support of the Center for Environmental Energy Engineering (CEEE) at the University of Maryland.

References

[1] D. Ürge-Vorsatz, L.F. Cabeza, S. Serrano, C. Barreneche, K. Petrichenko, Heating and cooling energy trends and drivers in buildings, Renewable and Sustainable Energy Reviews. 41 (2015) 85–98. https://doi.org/10.1016/j.rser.2014.08.039.

[2] L. Zhang, Y. Jiang, J. Dong, Y. Yao, Advances in vapor compression air source heat pump system in cold regions: A review, Renewable and Sustainable Energy Reviews. 81 (2018) 353–365. https://doi.org/10.1016/j.rser.2017.08.009.

[3] A. Hakkaki-Fard, Z. Aidoun, M. Ouzzane, Improving cold climate air-source heat pump performance with refrigerant mixtures, Applied Thermal Engineering. 78 (2015) 695–703. https://doi.org/10.1016/j.applthermaleng.2014.11.036.

[4] A.S. Gaur, D.Z. Fitiwi, J. Curtis, Heat pumps and our low-carbon future: A comprehensive review, Energy Research & Social Science. 71 (2021) 101764. https://doi.org/10.1016/j.erss.2020.101764.

[5] Y. Fan, X. Zhao, Z. Han, J. Li, A. Badiei, Y.G. Akhlaghi, Z. Liu, Scientific and technological progress and future perspectives of the solar assisted heat pump (SAHP) system, Energy. 229 (2021) 120719. https://doi.org/10.1016/j.energy.2021.120719.

[6] I. Sarbu, C. Sebarchievici, General review of ground-source heat pump systems for heating and cooling of buildings, Energy and Buildings. 70 (2014) 441–454. https://doi.org/10.1016/j.enbuild.2013.11.068.

[7] B. Shen, M.R. Ally, Energy and Exergy Analysis of Low-Global Warming Potential Refrigerants as Replacement for R410A in Two-Speed Heat Pumps for Cold Climates, Energies. 13 (2020) 5666. https://doi.org/10.3390/en13215666.

[8] H.-J. Choi, B.-S. Kim, D. Kang, K.C. Kim, Defrosting method adopting dual hot gas bypass for an air-to-air heat pump, Applied Energy. 88 (2011) 4544–4555. https://doi.org/10.1016/j.apenergy.2011.05.039.

[9] W. Wang, J. Xiao, Y. Feng, Q. Guo, L. Wang, Characteristics of an air source heat pump with novel photoelectric sensors during periodic frost–defrost cycles, Applied Thermal Engineering. 50 (2013) 177–186. https://doi.org/10.1016/j.applthermaleng.2012.06.019.

[10] A. Moreno-Rodriguez, N. Garcia-Hernando, A. González-Gil, M. Izquierdo, Experimental validation of a theoretical model for a direct-expansion solar-assisted heat pump applied to heating, Energy. 60 (2013) 242–253. https://doi.org/10.1016/j.energy.2013.08.021.

[11] S.S. Bertsch, E.A. Groll, Two-stage air-source heat pump for residential heating and cooling applications in northern U.S. climates, International Journal of Refrigeration. 31 (2008) 1282–1292. https://doi.org/10.1016/j.ijrefrig.2008.01.006.

[12] X. Xu, Y. Hwang, R. Radermacher, Transient and steady-state experimental investigation of flash tank vapor injection heat pump cycle control strategy, International Journal of Refrigeration. 34 (2011) 1922–1933. https://doi.org/10.1016/j.ijrefrig.2011.08.003.

[13] D.H. Kim, M.S. Kim, The effect of water temperature lift on the performance of cascade heat pump system, Applied Thermal Engineering. 67 (2014) 273–282. https://doi.org/10.1016/j.applthermaleng.2014.03.036.

[14] H. Lee, Y. Hwang, R. Radermacher, H.-H. Chun, Performance investigation of multi-stage saturation cycle with natural working fluids and low GWP working fluids, International Journal of Refrigeration. 51 (2015) 103–111.

[15] H. Lee, Y. Hwang, R. Radermacher, H.-H. Chun, Potential benefits of saturation cycle with two-phase refrigerant injection, Applied Thermal Engineering. 56 (2013) 27–37.

[16] Y. Zhang, Q. Ma, B. Li, X. Fan, Z. Fu, Application of an air source heat pump (ASHP) for heating in Harbin, the coldest provincial capital of China, Energy and Buildings. 138 (2017) 96–103. https://doi.org/10.1016/j.enbuild.2016.12.044.

[17] Y. Fan, J. Li, X. Zhao, S. Myers, Y. Cheng, M. Yu, Y. Golizadeh Akhlaghi, X. Ma, S. Yu, A proof-of-concept study of a novel ventilation heat recovery vapour injection air source heat pump, Energy Conversion and Management. 256 (2022) 115404. https://doi.org/10.1016/j.enconman.2022.115404.
[18] H. Zhang, L. Jiang, W. Zheng, S. You, T. Jiang, S. Shao, X. Zhu, Experimental study on a novel thermal storage refrigerant-heated radiator coupled with air source heat pump heating system, Building and Environment. 164 (2019) 106341. https://doi.org/10.1016/j.buildenv.2019.106341.
[19] W. Wei, L. Ni, L. Xu, Y. Yang, Y. Yao, Application characteristics of variable refrigerant flow heat pump system with vapor injection in severe cold region, Energy and Buildings. 211 (2020) 109798. https://doi.org/10.1016/j.enbuild.2020.109798.
[20] C. Wu, F. Liu, X. Li, Z. Wang, Z. Xu, W. Zhao, Y. Yang, P. Wu, C. Xu, Y. Wang, Low-temperature air source heat pump system for heating in severely cold area: Long-term applicability evaluation, Building and Environment. 208 (2022) 108594. https://doi.org/10.1016/j.buildenv.2021.108594.
[21] D. Kang, J.H. Jeong, B. Ryu, Heating performance of a VRF heat pump system incorporating double vapor injection in scroll compressor, International Journal of Refrigeration. 96 (2018) 50–62. https://doi.org/10.1016/j.ijrefrig.2018.09.027.
[22] Y. Xu, Y. Huang, N. Jiang, M. Song, X. Xie, X. Xu, Experimental and theoretical study on an air-source heat pump water heater for northern China in cold winter: Effects of environment temperature and switch of operating modes, Energy and Buildings. 191 (2019) 164–173. https://doi.org/10.1016/j.enbuild.2019.03.028.
[23] X. Wang, L. Xia, C. Bales, X. Zhang, B. Copertaro, S. Pan, J. Wu, A systematic review of recent air source heat pump (ASHP) systems assisted by solar thermal, photovoltaic and photovoltaic/thermal sources, Renewable Energy. 146 (2020) 2472–2487. https://doi.org/10.1016/j.renene.2019.08.096.
[24] J. Ji, G. Pei, T. Chow, K. Liu, H. He, J. Lu, C. Han, Experimental study of photovoltaic solar assisted heat pump system, Solar Energy. 82 (2008) 43–52. https://doi.org/10.1016/j.solener.2007.04.006.
[25] H.D. Fu, G. Pei, J. Ji, H. Long, T. Zhang, T.T. Chow, Experimental study of a photovoltaic solar-assisted heat-pump/heat-pipe system, Applied Thermal Engineering. 40 (2012) 343–350. https://doi.org/10.1016/j.applthermaleng.2012.02.036.
[26] D. Zhang, Q.B. Wu, J.P. Li, X.Q. Kong, Effects of refrigerant charge and structural parameters on the performance of a direct-expansion solar-assisted heat pump system, Applied Thermal Engineering. 73 (2014) 522–528. https://doi.org/10.1016/j.applthermaleng.2014.07.077.
[27] F.B. Gorozabel Chata, S.K. Chaturvedi, A. Almogbel, Analysis of a direct expansion solar assisted heat pump using different refrigerants, Energy Conversion and Management. 46 (2005) 2614–2624. https://doi.org/10.1016/j.enconman.2004.12.001.
[28] X.Q. Kong, Y. Li, L. Lin, Y.G. Yang, Modeling evaluation of a direct-expansion solar-assisted heat pump water heater using R410A, International Journal of Refrigeration. 76 (2017) 136–146. https://doi.org/10.1016/j.ijrefrig.2017.01.020.
[29] S.K. Chaturvedi, D.T. Chen, A. Kheireddine, Thermal performance of a variable capacity direct expansion solar-assisted heat pump, Energy Conversion and Management. 39 (1998) 181–191. https://doi.org/10.1016/S0196-8904(96)00228-2.
[30] X. Kong, K. Jiang, S. Dong, Y. Li, J. Li, Control strategy and experimental analysis of a direct-expansion solar-assisted heat pump water heater with R134a, Energy. 145 (2018) 17–24. https://doi.org/10.1016/j.energy.2017.12.114.
[31] S.K. Chaturvedi, T.M. Abdel-Salam, S.S. Sreedharan, F.B. Gorozabel, Two-stage direct expansion solar-assisted heat pump for high temperature applications, Applied Thermal Engineering. 29 (2009) 2093–2099. https://doi.org/10.1016/j.applthermaleng.2008.10.010.
[32] G. Qiu, X. Wei, Z. Xu, W. Cai, A novel integrated heating system of solar energy and air source heat pumps and its optimal working condition range in cold regions, Energy Conversion and Management. 174 (2018) 922–931. https://doi.org/10.1016/j.enconman.2018.08.072.
[33] H. Li, C. Cao, G. Feng, R. Zhang, K. Huang, A BIPV/T System Design Based on Simulation and its Application in Integrated Heating System, Procedia Engineering. 121 (2015) 1590–1596. https://doi.org/10.1016/j.proeng.2015.09.184.
[34] C. Cao, H. Li, G. Feng, R. Zhang, K. Huang, Research on PV/T – Air Source Heat Pump Integrated Heating System in Severe Cold Region, Procedia Engineering. 146 (2016) 410–414. https://doi.org/10.1016/j.proeng.2016.06.422.
[35] A.G. Devecioğlu, Seasonal performance assessment of refrigerants with low GWP as substitutes for R410A in heat pump air conditioning devices, Applied Thermal Engineering. 125 (2017) 401–411. https://doi.org/10.1016/j.applthermaleng.2017.07.034.
[36] A. Pensini, C.N. Rasmussen, W. Kempton, Economic analysis of using excess renewable electricity to displace heating fuels, Applied Energy. 131 (2014) 530–543. https://doi.org/10.1016/j.apenergy.2014.04.111.

[37] V. Kapsalis, D. Karamanis, Solar thermal energy storage and heat pumps with phase change materials, Applied Thermal Engineering. 99 (2016) 1212–1224. https://doi.org/10.1016/j.applthermaleng.2016.01.071.
[38] A.A. Safa, A.S. Fung, R. Kumar, Comparative thermal performances of a ground source heat pump and a variable capacity air source heat pump systems for sustainable houses, Applied Thermal Engineering. 81 (2015) 279–287. https://doi.org/10.1016/j.applthermaleng.2015.02.039.
[39] B. Huang, V. Mauerhofer, Life cycle sustainability assessment of ground source heat pump in Shanghai, China, Journal of Cleaner Production. 119 (2016) 207–214. https://doi.org/10.1016/j.jclepro.2015.08.048.
[40] S. Huang, W. Zuo, H. Lu, C. Liang, X. Zhang, Performance comparison of a heating tower heat pump and an air-source heat pump: A comprehensive modeling and simulation study, Energy Conversion and Management. 180 (2019) 1039–1054. https://doi.org/10.1016/j.enconman.2018.11.050.
[41] A. Hakkaki-Fard, P. Eslami-Nejad, Z. Aidoun, M. Ouzzane, A techno-economic comparison of a direct expansion ground-source and an air-source heat pump system in Canadian cold climates, Energy. 87 (2015) 49–59. https://doi.org/10.1016/j.energy.2015.04.093.
[42] W. Yang, Experimental performance analysis of a direct-expansion ground source heat pump in Xiangtan, China, Energy. 59 (2013) 334–339. https://doi.org/10.1016/j.energy.2013.07.036.
[43] M.K. Mattinen, A. Nissinen, S. Hyysalo, J.K. Juntunen, Energy Use and Greenhouse Gas Emissions of Air-Source Heat Pump and Innovative Ground-Source Air Heat Pump in a Cold Climate, Journal of Industrial Ecology. 19 (2015) 61–70. https://doi.org/10.1111/jiec.12166.
[44] R. Wu, Energy efficiency technologies–air source heat pump vs. ground source heat pump, Journal of Sustainable Development. 2 (2009) 14–23.
[45] A.A. Safa, A.S. Fung, R. Kumar, Comparative thermal performances of a ground source heat pump and a variable capacity air source heat pump systems for sustainable houses, Applied Thermal Engineering. 81 (2015) 279–287.
[46] D. Garber, R. Choudhary, K. Soga, Risk based lifetime costs assessment of a ground source heat pump (GSHP) system design: Methodology and case study, Building and Environment. 60 (2013) 66–80.
[47] B. Bach, J. Werling, T. Ommen, M. Münster, J.M. Morales, B. Elmegaard, Integration of large-scale heat pumps in the district heating systems of Greater Copenhagen, Energy. 107 (2016) 321–334. https://doi.org/10.1016/j.energy.2016.04.029.
[48] S. Nyborg, I. Røpke, Heat pumps in Denmark—From ugly duckling to white swan, Energy Research & Social Science. 9 (2015) 166–177. https://doi.org/10.1016/j.erss.2015.08.021.
[49] S. Karytsas, I. Kostakis, Barriers and diffusion actions of residential ground source heat pump systems in Greece: An ordered regression model analysis, 2014.
[50] Z. Wang, Heat pumps with district heating for the UK's domestic heating: individual versus district level, Energy Procedia. 149 (2018) 354–362. https://doi.org/10.1016/j.egypro.2018.08.199.
[51] J. Globisch, M. Kühnbach, E. Dütschke, A. Bekk, The stranger in the German energy system? How energy system requirements misalign with household preferences for flexible heat pumps, Energy Research & Social Science. 67 (2020) 101604. https://doi.org/10.1016/j.erss.2020.101604.
[52] T. Fawcett, N. Eyre, R. Layberry, Heat pumps and global residential heating, 2015.

14th IEA Heat Pump Conference
15-18 May 2023, Chicago, Illinois

An Assessment of Gas Absorption Heat Pump Integration Strategies with Combination and Commercial Space Conditioning Systems

Abinesh Ravi[a*], Michael Mensinger Jr.[b], Paul Glanville[c], Jason LaFleur[d], Steven Arnold[e]

[a]Principal Engineer, GTI Energy, 1700 Mt Prospect Rd, Des Plaines 60018, USA
[b]Engineer, GTI Energy, 1700 Mt Prospect Rd, Des Plaines 60018, USA
[c]Director of R&D Heat and Power, GTI Energy, 1700 Mt Prospect Rd, Des Plaines 60018, USA
[d]Senior Manager, GTI Energy, 1700 Mt Prospect Rd, Des Plaines 60018, USA
[e]Director of Operations, Building Energy Solutions Ltd., 550 West Broadway, Vancouver V5Z 0A9, Canada

Abstract

Gas absorption heat pumps (GHP) are an emerging class of high efficiency heating equipment that upgrade low-quality ambient heat via an ammonia-water absorption process. This technology can reduce fuel consumption of space heating systems served by furnaces or boilers by 35%-55%, with rated seasonal heating efficiencies of 140% AFUE or greater, based on the application and climate region. GHPs are commercially available, but the commercial space conditioning market adoption is low due to the upfront investments and a lack of installation and maintenance experience. Drawing from multiple case studies, the authors explored the implementation of heat pumps in cold climates for water heating and / or hydronic space conditioning applications. This paper summarizes important design considerations, installation best practices, controls, commissioning and lessons learned from successfully integrating GHPs into hot water plants, often with existing equipment to boost overall plant efficiencies.

Keywords: Gas Absorption Heat Pumps; Reversible Cycle; Space Heating; Space Cooling; Chilled Water; Service Hot Water; Ammonia Absorption Cycle; Combination Heating Systems;

1. Introduction

Commercial space conditioning (heating, cooling and ventilation) accounted for about 7.0 quads per year, or about 40% of total commercial energy use, in terms of primary energy consumption, in the United States [1]. Per a 2018 survey of commercial buildings [2], total number of buildings increased 6% from 2012 to 2018 or about 11% increase in floorspace. By 2050, commercial building floor space is estimated to reach 124 billion square feet, or a 33% increase from 2020 [3]. Natural gas or electricity was the primary fuel source for commercial space heating, while electricity was primarily used for cooling. Packaged heating units and furnaces were used to condition 50% of commercial floor space, boilers accounted for 30% and heat pumps accounted for 15%. For commercial space cooling, packaged A/C units conditioned 58% commercial floor space, central chillers accounted for 19% and heat pumps accounted for 12%.

EIA forecasts short term commercial electricity pricing to increase from 11.27 cents / kWh in 2021 to 12.23 cents in 2023. Natural gas spot pricing is expected to remain high into early 2023, due to lower than average natural gas inventories. Rapid electrification of buildings to achieve decarbonization and sustainability goals may increase grid reliance from 20% to 50% [4]. As systems decarbonize and shift towards pumped hydroelectric, wind, solar, battery storage, etc., there will be a renewed reliance on natural gas to provide peak load balancing to allow for this transition to be seamless. The above factors may contribute to higher prices for commercial space conditioning.

* Corresponding author. *E-mail address:* aravi@gti.energy

Conventional fuel fired heating systems such as gas fired furnaces and boilers have approached their thermodynamic limit over the past few decades. Electric heat pumps are highly efficient and have been growing in popularity (where electrification for existing buildings is economically feasible), but their heating performance in cold climate retrofits is low [5]. Additional barriers include high capital and maintenance costs of equipment [7] and associated electric infrastructure upgrades, and challenges in maintaining SHW supply temperatures at peak winter conditions.

Gas absorption heat pumps (GHPs) are an emerging class of high efficiency Thermally Driven Heat Pump (TDHP) equipment that upgrade low-quality ambient heat via an ammonia-water absorption cycle process. This technology can reduce fuel consumption of space heating systems served by furnaces or boilers by 35%-55%, with rated seasonal heating efficiencies of 140% AFUE or greater, based on the application and climate region [8]. GHPs also employ internal heat recovery for coil defrost such that the Coefficient of Performance (COP) and output capacity reduction at low ambient temperatures is less significant when compared to other heat pump technologies. In a study of ammonia absorption cycle heat pump installs across multiple types of commercial buildings in the US Midwest and Canada, TDHPs have shown a consistent Coefficient of Performance for Gas Consumed (COPg) of >1 in cold climate installs. Despite the benefits outlined above, and the commercial availability of GHPs, integration and adoption of GHPs in the commercial space conditioning market is low.

2. A Summary of GHP Integration Strategies with Water Heating, Space Heating, Combination, and Space Cooling Systems

This section aims to assess and summarize key aspects of a hybrid GHP-Boiler integration into water heating and / or space conditioning systems. The term 'Hybrid' here refers to a combination of 2 heating sources. Information such as the site selection process, capacity sizing and storage design considerations, construction and commissioning, controls integration, and operational lessons learnt are also discussed.

2.1. Hybrid GHP-Boiler Integration in Combination SHW Systems

The Toronto Atmospheric Fund's case study [9] in association with a local utility selected a social housing complex in Toronto, ON, Canada to demonstrate GHP integration into a gas-fired SHW and space heating system to maximize emissions reductions.

Existing Conditions: The existing oversized boilers provided both space and SHW heating at an average of 54% TE (thermal efficiency) baselined through a 12,133-liter SHW storage tank.

System Design and Sizing: Two (2) heating only GHPs with a heating capacity of 36.2 kW were selected through a SHW system modelling approach to provide 58% of the overall SHW capacity, while also being able to handle 100% of the baseload non-peak demand at a 54 ºC SHW setpoint. A brazed plate and frame double-walled heat exchanger (PFHX) separated the glycol and potable water systems, and supplemental SHW and space heating demand was met by a pair of high-efficiency condensing boilers. Since GHPs are installed in unconditioned or exterior spaces exposed to weather elements, a water-glycol mixture was used as a heat transfer medium to prevent freezing of pipes. The equipment manufacturer provided performance correction factors which were utilized during the design and selection process. Although, these correction factors were developed only under an ambient temperature of 35ºC and a supply water temperature of 6.6ºC. It would be helpful to explore capacity correction factors under a range of glycol operating temperatures in the future.

Modelled seasonal efficiency of the condensing boiler and GHP system providing SHW and space heating was expected to reach 110%. The study restricted the GHP sizing to two (2) units only due to space constraints in the mechanical room, and to reduce construction costs required to install equipment on the roof. In addition, utilization of the 'N'th unit would be limited to peak SHW load conditions only. The installed system configuration and associated monitoring devices is shown in Figure 1**Error! Reference source not found.**.

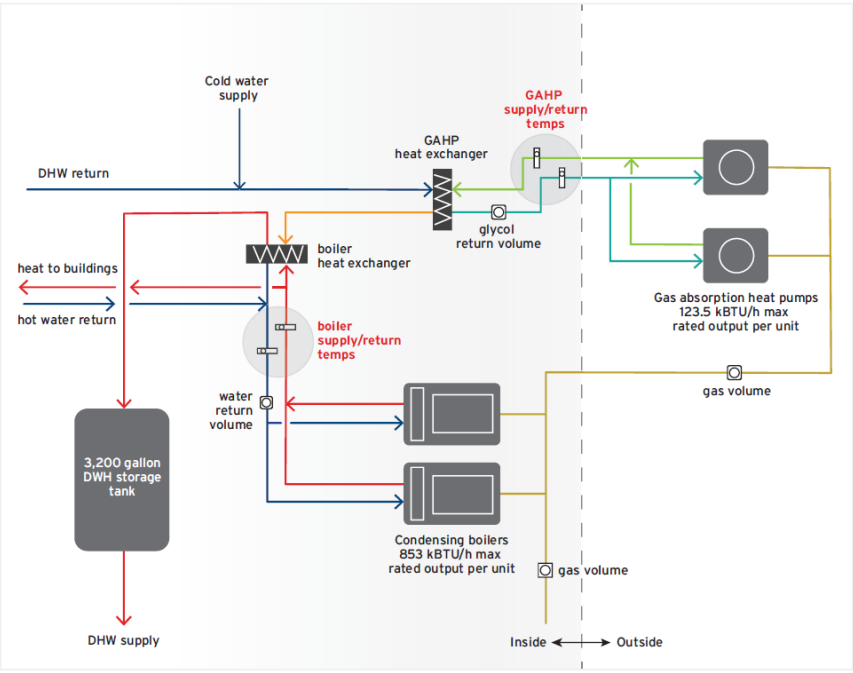


Figure 1. GHP Integration with a Combination Space and Water Heating System [9]

System Performance: GHP performance was represented using the COP measure as shown below.

$$COP = \frac{usable\ heat\ supplied\ by\ GAHP}{natural\ gas\ consumed + electricity\ consumed\ by\ GAHP} \quad (1)$$

The study achieved a mean (averaged during cooler weather operation) COP of 1.14 and at an average GHP Supply Water Temperature (SWT) of 46.6 ºC. When the Outside Air Temperature (OAT) fell below -12 ºC, COP fell below 1.0. It is important here to understand the GHP's cold climate performance to contextualize its COP. This heating only GHP (36 kW, 6ºC ambient, 50ºC outlet temperature) is a commercially available product developed by Manufacturer A and works on a Generator-Absorber Heat Exchange (GAX) cycle and does not modulate in capacity. Figure 2 shows the performance impact of manufacturer A's product due to OAT under laboratory test conditions. The mean COP achieved in this case study was realistic due to variabilities in the field such as glycol percentage, system flowrates, cyclic operation, etc, which may impact performance. Also shown is the laboratory tested performance of a product from Manufacturer B. This was a prototype operating on a single effect direct fired ammonia absorption cycle with capacity modulation, but was not commercially available at this time.

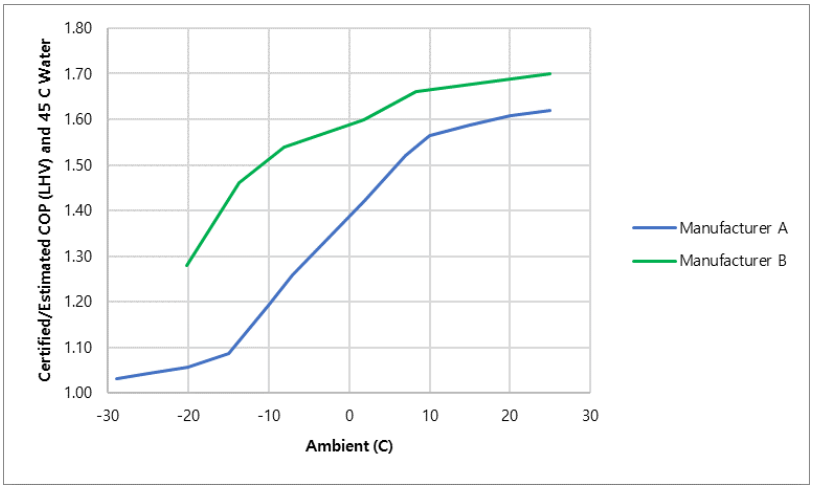


Figure 2. Comparison of Laboratory Performance of two GHPs at different Ambient Temperatures [10]

Operational Challenges and Lessons Learned:

1. Boilers were manually operated for two weeks which resulted in high Return Water Temperatures (RWT) that were close to or exceeded the GHP RWT limit of 50 ºC. This error in sequencing impaired the operation and performance of the GHPs.
2. During periods of no SHW demand, or when the RWT exceeded 50 ºC, the GHPs and their associated glycol circulation pumps were sequenced to shut down. Unfortunately, the GHP flow switches would trip due to premature stopping of the circulation pumps thereby transferring SHW heating load to the backup boilers. This issue was resolved by sequencing the pumps to shut down only after the GHPs stopped consuming electricity.
3. SHW use at the site resulted in fluctuating utilization of the GHP capacity with peak SHW use occurring between 8-10am, and a second peak occurring between 4-6pm. Hourly average capacity utilization was 40% and peaked to 61% at 9am. Capacity utilization of the GHP was lower than pre-installed modelling where it was expected to meet 100% of the daily-off peak loads. To address this underutilization, the GHP will be prioritized when there is an SHW demand instead of calling for heat from the GHPs and boilers simultaneously. This is expected to increase GHP utilization in summer, but not during the shoulder and winter seasons since the boilers will be operational at colder ambient temperatures.
4. When specifying equipment, it is important to determine the % glycol in the glycol-water mixture and apply performance correction factors. An optical refractometer is recommended for this purpose.

2.2. Hybrid GHP-Boiler Integration with a Re-designed Buffer Tank in Combination SHW Systems

GTI Energy's (GTI) study in association with NEEA [11] selected a multifamily residential site in Evanston, IL to demonstrate GHP integration into a gas fired SHW and space heating (or combination) system. The GHP was a prototype developed by manufacturer B (see Figure 2 above) and tested under laboratory conditions [8].

Existing Conditions: One (1) existing oversized non-condensing 80% TE boiler (123 kW) provided both space and SHW heating to six (6) housing units. Daily SHW load is approximately 757-946 liters/day.

System Design and Sizing: Analysis of past utility bills estimated the baseline boiler to have only 6-8 equivalent full load hours (EFLH) during peak winter conditions. During summer with SHW loads only, peak load was estimated as 879.3 kW/day. One (1) heating only GHP with a heating capacity of 23.4 kW, 4:1 modulation, a peak delivered temperature of 73.8 ºC and active defrost was selected. If the GHP was expected to meet 40% of SHW load assuming a COPg of 1.10 during peak winter conditions, it yielded 20 EFLH which indicates the GHP may be well sized for this application. A brazed plate double walled PFHX separated the glycol and potable water systems. A buffer tank was designed and installed as a 'volume' where the GHP loop and the main return loop mixed to preheat cold service makeup water through a coil, to avoid cyclic GHP operation. The existing oversized boiler was replaced with two (2) 84% AFUE and 58.6 kW boilers. One boiler was installed in series with an indirect storage tank to handle SHW loads, and both boilers can provide full redundancy to the GHP. A dedicated Plant Controller was installed and configured to stage the GHP and Boiler operation based on RWT, Space or SHW demand, and OAT reset. Details of the control strategy were published [8] and the installed system configuration is shown in Figure 3**Error! Reference source not found.**.

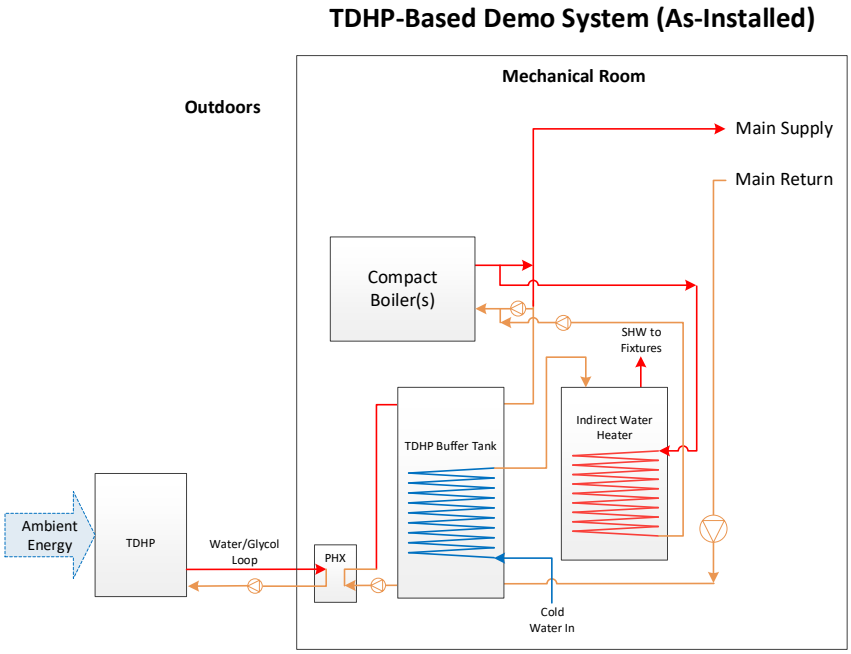


Figure 3. Final Integrated GHP-Boiler Combination Piping Layout (as-installed)

System Performance: At steady state operation under laboratory conditions (50% fire, ambient 0ºC, 49.4ºC RWT), COPg was measured at 1.20. This demonstration saw a COPg of 1.24 under steady state field conditions. During a 13-day continuous operating period between February and March 2020 of the GHP, where RWT is above 51.6 ºC and close to maximum operating capacity, the GHP's efficiency was close to the laboratory measured COPs of 1.12 at -10 ºC and 1.32 at 8 ºC [8]. The system efficiency formula is below:

$$System\ Efficiency = \frac{\Sigma(Q\ Hydronic,THP + Q\ Hydronic,Boiler1 + Q\ Hydronic,Boiler2)}{\Sigma(Q\ NG,Boilers + Q\ NG,THP + Q\ Elec,Pumps + Q\ Elec,Boilers + Q\ Elec,THP)} \quad (2)$$

$$COPgas = \frac{\Sigma(Q\ Hydronic,THP)}{\Sigma(Q\ NG,THP)} \quad (3)$$

Despite this room for optimization, the projected annual therm savings and GHG emissions reductions were estimated to be 43% for SHW mode and 41% for combined space heating and SHW mode for the GHP/boiler system over the original equipment, or 24% for the compact boiler only architecture. Using the rated 80% TE as the baseline, this corresponds to a hybrid GHP/boiler system delivered efficiency of 136%. On financial payback for the 2835 therms saved/year, at $0.76/therm this system as installed with two compact boilers would have a 4-year payback, or 1.3 years for an optimized system with a single boiler.

Operational Challenges and Lessons Learned:

1. This was a 1st of its kind demonstration of GHP-Boiler integration to multifamily hybrid combination systems with a new product developed by the manufacturer and GTI and tested through this field demonstration. The GHP underwent repairs and a full replacement due to unique failure modes caused by excess wear and tear of the prototype GHP leading to service interruptions. Subsequent design improvements were undertaken on key components (such as the solution pump). The project team recommissioned the system as of spring 2022 and will monitor performance for one (1) year.
2. A parallel study by GTI to utilize GHPs for SHW in full-service restaurants identified a sweet spot for sizing the GHP to carry 30%-60% of peak water heating demand.
3. Capacity and efficiency loss are often a strong function of higher RWTs. High RWTs also lead to high-limit shutdowns, thereby reducing utilization of the GHP. Use of variable speed circulation pumps and a reduced boiler reset temperature setting can help with lowering RWTs.
4. Design and sizing of buffer tanks is critical to manage the high thermal inertias associated with GHPs, variable SHW loads and to smooth out cyclic GHP operation. Depending on GHP size, technology and setpoints, GHPs can require between 5 – 15 minutes to reach steady state capacity and efficiency.

5. The original piping scenario was designed so that the backup boilers would be installed to serve the main space heating loop and the indirect water heating tanks. The GHP would still be installed outdoors and the glycol and service hot water loops would be separated by a PFHX. The first zone is the higher priority water heating tank, and the return is mixed with the main return line. The second zone is the buffer tank, which allows the GHP to preheat return water to the boilers. An alternate layout includes all the above but includes a second PFHX that allows the GHP to heat the SHW directly and is shown in Figure 4. The team identified pitfalls with both layouts:
    a. Combination operation could lead to warming up the RWT as the indirect SHW tank warms up, which would lead to premature shutdowns.
    b. In space heating only mode, as the circulation pumps cycle, adverse mixing on the hot and cold sides of the PFHX would hurt the GHP performance due to temperature swings in the buffer tank.
    c. For SHW only, since the feed water to the indirect water heater tank is a mix of cold water and building recirculation, RWTs to the GHP PFHX would be warm / hot

    These issues led the team towards the piping design described under "System Design and Sizing".

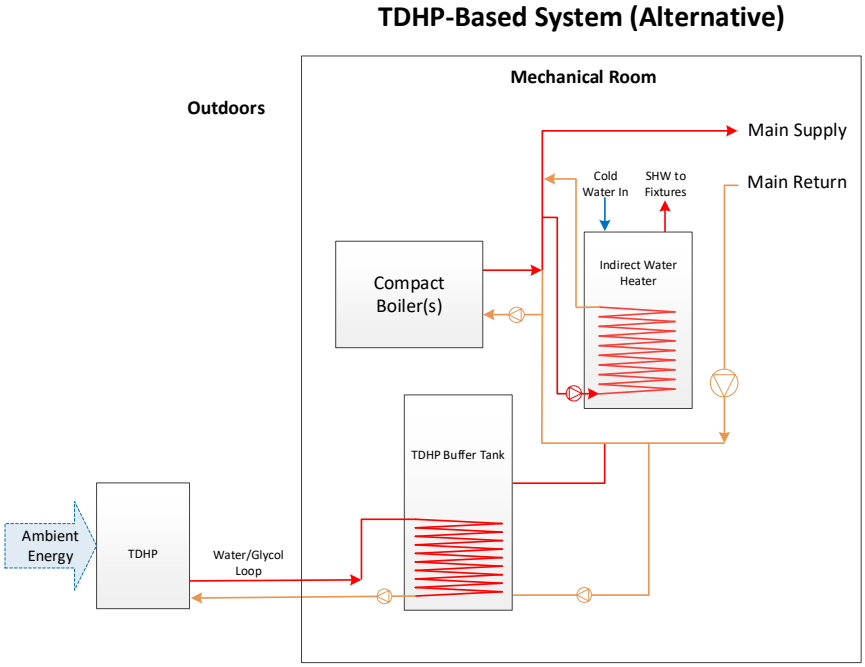


Figure 4. Preliminary Integrated GHP-Boiler Combination Piping Layouts

2.3. Hybrid GHP-Boiler Integration in SHW Systems, with future Space Heating Considerations

Building Energy Solutions Ltd. (BES) and Fortis BC collaborated on a measurement and verification study to investigate the performance of GHPs integrated into SHW systems at five (5) multi-unit residential buildings in Canada. This paper reviews the work performed at site #4 (site numbers designated by the study). The results of the study will be published by the authors at a later date.

Existing Conditions: The SHW system consists of one (1) existing standard efficiency (80%) boiler with a 296 kW capacity, a separate standard efficiency (80%) SHW boiler with a 116.9 kW capacity, and a 435-liter SHW storage tank. The project team estimated that the actual boiler operating efficiency of both boilers was between 65% - 79% based on a number of factors including submetering of boiler input and output parameters, independent flue gas analysis, age and condition of the boilers, and losses in efficiency due to cyclic operation.

System Design and Sizing: Historical gas utility data was weather normalized over a 10-year period (2008-2018) to determine baseline SHW consumption. Since natural gas is used for space and SHW heating, a baseline average of historical gas consumption during summer months was calculated for sizing considerations. The design team developed and built a prefabricated skid that housed the double wall heat exchanger, pumps and control valves, and the skid was installed within the mechanical room. Two (2) heating only GHPs from manufacturer A with a combined capacity of 76.2 kW were installed on the roof with reinforcement. One of the existing SHW storage tanks was replaced with a similarly sized preheat buffer tank

with an internal heat exchanger. Per local building codes, SHW must be heated to 60 ºC prior to consumption to eliminate harmful bacteria. A 3-way control valve was installed to bypass the existing hot water boiler when the GHPs were operational to prevent internal corrosion of the standard efficiency boiler's tubes. The project team installed advanced controls to automatically sequence, schedule and change setpoints of the integrated systems to boost energy savings and efficiencies. The installed system configuration is shown in Figure 5**Error! Reference source not found.**.

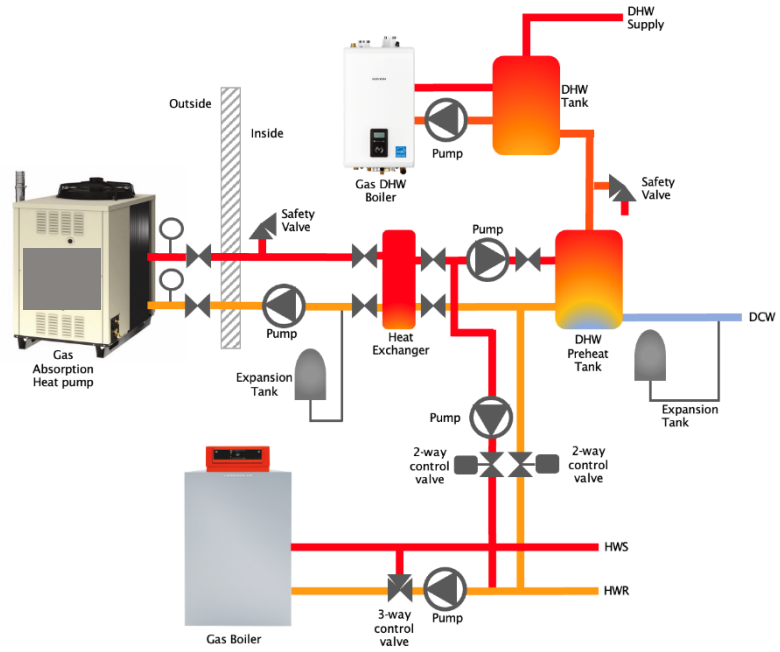


Figure 5. GHP Integration into an existing combination system

System Performance: The GHP was able to operate efficiently in heating mode between 15 ºC - 17 ºC ambient air temperatures due to the high heating load requirement of the building below these temperatures. i.e., the output of the GHPs was approximately 25% of the output of the existing SHW boiler. A 15.7% reduction in the site's SHW natural gas consumption and a 8.9% reduction in space heating natural gas consumption from baseline was achieved when test results were extrapolated over a full year. The project team attempted to right-size the GHP capacity by using one of the two installed GHPs to handle SHW demands. A 19.0% SHW gas consumption savings was achieved through this effort. In addition, with a differential temperature of greater than 2ºC across the GHP, the average COP was measured at 1.14. At differential temperatures greater than 8ºC, the GHP can achieve a COP of 1.2 to 1.4.

Operational Challenges and Lessons Learned:

1. The project team installed two (2) gas meters to measure consumption for the site versus the GHPs respectively. There were inconsistent readings between the site versus GHP gas flowrate measurements which pointed to data collection and instrumentation errors. In a similar vein, a few sites within the demonstration's portfolio of test sites had 0.1-meter diameter SHW flow meters installed, which was unable to record flowrates below 227 liters/min. Unfortunately, these factors limited calculation of the system efficiency. For critical parameters, it is important to use high accuracy sensors with the right measurement ranges and calibration certificates.
2. Standard efficiency boilers are on average 80% efficient per their nameplates. Based on the age and condition of the boilers, the baseline efficiency of the boilers at full fire was determined to be between 70% - 78%.
3. Efficiency of the GHP is strongly tied to the SHW load profile, which is typically intermittent. Maintaining a large and sustained temperature differential across the GHP (greater than 2 ºC) helps boost efficiencies. Right sizing of the GHP is also very important to improve response times and the temperature differentials.
4. The project estimated a 3.7% thermal efficiency loss occurs across the heat exchanger between the glycol loop and SHW loop. Other sources of efficiency loss included the use of glycol in the loop and

the inadvertent effect of short cycling of the existing boiler under reduced load (~>10%) due to introduction of the GHP for SHW heating. Short cycling significantly reduces efficiencies especially for boilers with limited turndown ratios.

5. The project determined that replacing the existing standard boiler with a minimum 5:1 modulating condensing boilers and improving system sequencing controls as detailed on point #6 could achieve an overall system COP of above 1.0. Introducing condensing boilers can eliminate corrosion concerns thereby modifying the system to a hybrid configuration where the GHP can meet stage 1 demands. In addition, integrating GHP operation with smaller and more consistent heating loads such as Make-Up air handling unit coils or swimming pool heating could allow the GHP to operate for longer periods, thereby improving the COP. This would require additional system design / controls considerations which BES and Fortis BC are exploring in the next phase of their pilot study.
6. Important control parameters for the GHP system are the heating temperature setpoint and the deadband. 'Deadband' is the difference between the supply water temperature when the system cycles off, and the return water temperature when the system cycles on and can vary between products and for a given product-based controls. The heating outlet temperature limit of a GHP is generally between 55 ºC – 58 ºC. The GHP would shutoff due to internal limits before it approaches 60 ºC supply water temperature.

2.4. Hybrid GHP-Water Heater Integration with a Space Cooling Application

GTI in association with the California Energy Commission [6] demonstrated a low-cost gas-fired heat pump integrated with existing commercial water heating and air-conditioning at two (2) restaurants in Los Angeles. The commercial restaurant sector consumes more natural gas per square foot than other commercial building types, with water heating being the largest thermal load. With condensing efficiencies being the ceiling for water heating technologies, the project looked towards deploying gas-fired GHPs. GHPs had the ability to operate at 140% or greater efficiencies and reduce gas consumption by 43% [12]. In addition, GHPs could displace up to 20% electricity demand for air conditioning providing greater operational savings. The project team assumed that an added 0.5 – 2.2 tons of cooling capacity could be useful in all instances with the range dependent on the GHP modulation. Los Angeles has only 1,200 heating degree days per year on average and the internal loads in the kitchen are expected to demand cooling year-round.

Existing Conditions: Depending on SHW loads and redundancy requirements, typical restaurants have one or two hot water heaters with integrated or external storage tank(s) and a recirculation loop to provide 60 ºC SHW for kitchen operation. HVAC equipment should be sized to handle high ventilation loads and internal heat gain totalling to 5-7 times greater energy consumption than other commercial building types. This paper reviews the work performed at site #1 (site numbers designated by the study). Site #1 has two identical storage type 82% TE gas-fired water heaters (79.1 kW input) with 378 liters of storage each. Site #1 consumed 10,290 liters on average of SHW per day, with a peak of 14,142 liters, and a peak flowrate of 45 lpm. The annualized gas input was 875.5 GJ at an average delivered efficiency of 70%. Space conditioning is provided by five heat pumps of 17.5 kW capacity each and one RTU of 44 kW capacity. Weather normalized power demand for the RTU was estimated to be 79 MWh.

System Design and Sizing: A 23.4 kW output GHP, a 427.7-liter indirect storage tank, associated piping and controls were assembled on a 1.2 m x 2.4 m skid to allow for ease of install and maintenance. The GHP skid was installed to act as a preheater for the existing gas fired water heaters. This system was sized and controlled to be SHW demand led, with the GHP carrying most of the SHW load and the gas fired water heaters handling peak loads. For space conditioning, an indoor fan coil unit was sized to deliver 9.3 kW/h and installed in the kitchen which typically experiences year-round cooling requirements. The installed system configuration is shown in Figure 6**Error! Reference source not found.**.

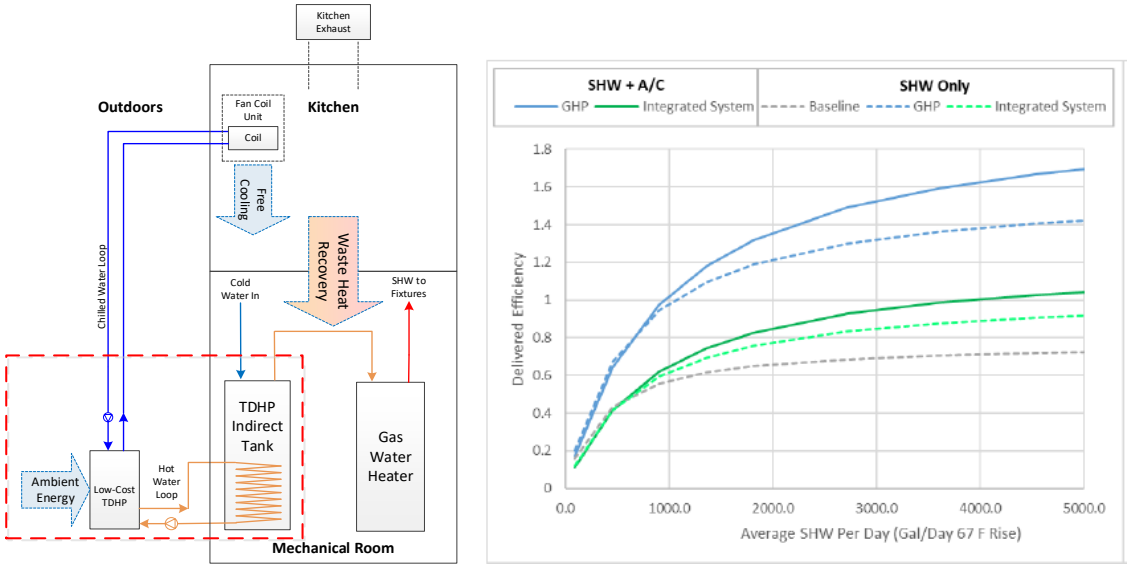


Figure 6. GHP Integration with SHW and Space Conditioning Equipment (Left); Delivered Efficiencies Projection (Right)

System Performance: The GHP system operated for 4,790 hours and 1,150 cycles through a 1-year monitoring period. The project recorded a heating only COPg range of 1.10 - 1.30, and a heating / cooling COPg range of 1.30 - 1.70. Figure 6**Error! Reference source not found.** shows the projected delivered efficiencies of the GHP system and the integrated system (GHP + Existing Gas Water Heaters). Ambient temperatures for the site varied between 1.6 ºC - 43.8 ºC. Use of the retrofit space conditioning system yielded a 14% electric savings (10,820 kWh/year). The GHP carried most of the SHW load through the day, which was approximately 30-60% of the total SHW load.

Operational Challenges and Lessons Learned:

1. Skid assembly and pre-shipment preparations included development of contractor training materials and instructions to ensure a smooth install and on-site commissioning.
2. The GHP skid was to be installed beside an exterior parking space or on the rooftop due to the lack of extra space within the mechanical room or the roof. To minimize hot water piping to the indirect storage tank and chilled water lines to the FCU, an alternate location closer to the water heaters was chosen. Although, the manufacturer required clearance / setback to install a portion of the evaporator coil was not achieved which limited the airflow thereby reducing performance of the GHP.
3. The GHP and FCU were integrated with glycol and chilled water lines respectively. The host site expressed concerns with the glycol mixture's proximity to the cooking areas due to potential leaks. Unfortunately, the final placement of the FCU was less useful in improving thermal comfort of restaurant employees as they were not directed at portions of the cookline and food preparation areas. Although, as discussed in the "system performance" section, there was a 14% reduction in AC kWh usage for a year-round cooling requirement. In addition, the chef and cooks provided positive feedback on the retrofit AC's functionality.
4. The length of and restrictions within the FCU Chilled Water loop prevented the installed system from reaching its designed chilled water flowrates as recommended by the manufacturer. Supplemental A/C effectiveness was further reduced due to a lack of effective air removal from the hydronic loops during routine service. Site #1 achieved only 55% of the target CHW flowrate.
5. Nuisance "blocked vent" errors caused early interruptions of GHPWH operation. Issue was resolved when vents were properly sloped for condensate disposal.
6. Due to prototype status of this product from manufacturer B, hardware / software issues were identified during operation and resolved. The first issue was with a faulty startup capacitor which stopped condenser fan motor operation. The fan motor was replaced, and the issue did not recur. Second, the solution pump showed signs of wear on the bearing which required a pump replacement. Third, over the course of the 12-month study, the evaporator coil had accumulated excessive dust /

lint due to site conditions. Exterior fouling was addressed by simply hosing down the coil. Each issue was identified and rectified with the manufacturer, and design improvements were recommended.

3. Conclusion

With the push towards electrification and decarbonization in a steadily growing commercial building market, it is important to integrate high efficiency heating technologies such as GHPs into water heating or space conditioning systems. Utilities are already using natural gas fired plants to meet increased electricity demand due to electrification of water and space heating systems. Extreme cold and hot weather events can also trigger unexpected spikes, grid instability, and power outages. Depending on the geographic fuel mix for electricity generation, the consumer may pay more for electricity consumption and demand. GHPs can help flatten peak electricity demand especially during the heating season and maintain efficiencies above conventional heating systems. GHPs can also serve as a drop-in replacement for conventional boilers / water heaters and require minimum updates to existing infrastructure. However, attention must be paid to critical design considerations and integration strategies for a successful deployment of GHPs.

This paper summarizes key design considerations and operational lessons learned from four (4) field demonstrations across North America, with a few aspects highlighted below:

- Existing SHW or Combination systems typically have an oversized 80% TE non-condensing boiler with redundant capacity. SHW systems also have large storage tanks and variable demand through the day which lead to the boilers cycling and hence reduce overall system efficiency.
- A retrofit GHP system can be sized to meet baseload non-peak demand with supplemental heating provided by existing boilers. Design and right-sizing can also consider analyses of past utility bills, sub metered / monitored data for a range of OATs and building loads, results from system modeling, capacity correction factors when using a glycol-water mixture and utilization of a heat exchanger internal or external to a buffer tank (review manufacturer published recommendations for buffer capacity). OAT reset controls for space conditioning systems must consider the GHP's SWT limit of 60ºC and RWT limit of 50ºC. GHPs must be installed exterior to the building with adequate access and clearances provided.
- A majority of lessons learned are from implementation of control parameters / limits used to stage the hybrid heating plant. GHPs must be prioritized to handle baseload and to maximize runtime (reduce cycling). Controls for ancillary equipment such as 3-way control valves and circulation pumps must be commissioned on a system level to prevent premature shutdown of GHPs. Other mechanical and plumbing considerations are to maintain appropriate slope for condensate vents, clean condenser coils prone to fouling due to dust, and install air removal vents at high points of hydronic systems.

The authors hope to provide a roadmap to design, install and operate hybrid heating systems with heat pumps, which would ultimately increase adoption of this emerging technology.

4. Nomenclature

A/C	Air Conditioning
AFUE	Annual Fuel Utilization Efficiency
COP	Coefficient of Performance
EIA	Energy Information Administration
EFLH	Equivalent Full Load Hours
GAX	Generator-Absorber Heat Exchange Cycle
GHP	Gas Absorption Heat Pumps
NEEA	Northwest Energy Efficiency Alliance
OAT	Outside Air Temperature
PFHX	Plate and Frame HX
RWT	Return Water Temperature
SHW	Service Hot Water
SWT	Supply Water Temperature
$Q_{Hydronic, THP}$	GHP's hot water output
$Q_{Hydronic, Boiler}$	Boiler's hot water output
$Q_{NG, THP}$	Gas consumed by the GHP
$Q_{NG, Boiler}$	Gas consumed by the boiler
$Q_{Elec, Pumps}$	Electricity consumed by pumps
$Q_{Elec, Boilers}$	Electricity consumed by the boilers

$Q_{Elec, THP}$	Electricity consumed by the GHP during operation
TDHP	Thermally Driven Heat Pump
%TE	% Thermal Efficiency
BES	Building Energy Solutions Ltd
RTU	Rooftop Unit
FCU	Fan Coil Unit

References

[1] Better buildings Solution Center, Energy.gov
[2] U.S. Energy Information Administration, *2018 Commercial Buildings Energy Consumption Survey*, 2021
[3] U.S. Energy Information Administration, *Annual Energy Outlook 2022*, 2022
[4] Electric Power Research Institute, *Enhancing Energy System Reliability And Resiliency In A Net-Zero Economy*, 2022.
[5] Fridlyand, A., Glanville, P., & Garrabrant, M. (2021). *Pathways to Decarbonization of Residential Heating.*
[6] Glanville, P., Mahderekal, I., Mensinger, M., Bingham, L., Keinath, C. 2021. *Demonstrating an Integrated Thermal Heat Pump System for Hot Water and Air-Conditioning at Full-Service Restaurants*, ASHRAE Transactions; Vol. 127 363-370.
[7] The National Energy Modeling System, Commercial Demand Module, DOE/EIA-0581(2009), Table 4
[8] Glanville, P., Suchorabski, D., Keinath, C., and Garrabrant, M. 2018. *Laboratory and Field Evaluation of a Gas Heat Pump-Driven Residential Combination Space and Water Heating System,* proceedings of the 2018 ASHRAE Winter Conference, Chicago, IL.
[9] The Atmospheric Fund, *Gas Absorption Heat Pumps, Technology assessment and Field Test Findings*, 2018
[10] GTI & Brio, Gas Heat Pump Technology and Market Roadmap (2019)
[11] Glanville, P., Mensinger Jr, M., Stein, J., Suchorabski, D., M. 2022. *Multifamily Thermal Heat Pump / Boiler Hybrid Demonstration*.
[12] Glanville, P, Fridlyand, A., Keinath, C., and Garrabrant, M. *Demonstration and Simulation of Gas Heat Pump-Driven Residential Combination Space and Water Heating System Performance*. ASHRAE Transactions; Atlanta Vol. 125, (2019): 264-272.

14th IEA Heat Pump Conference
15-18 May 2023, Chicago, Illinois

Performance of a State-of-Art Packaged Heat Pump for Residential Space Conditioning and Hot Water

Navin Kumar[a*], Alejandro Guada[a],William Asher[a], Alex Fridlyand[a], Paul Glanville[a], Matt Blaylock[b], Thao Strong[b]

[a]GTI Energy, 1700 S Mt Prospect Rd, Des Plaines 60018, USA
[b]Stone Mountain Technologies Inc, 609 Wesinpar, Johnson City 37604, USA

Abstract

Residential space conditioning and hot water loads in the US are typically decoupled and served by separate equipment. A residential home in four and above IECC climate zones can have two to three systems, typically a gas furnace for space heating, a gas-fired storage water heater, and an electric air conditioning (A/C) unit for space cooling. The decoupled nature of these individual systems prevents the units from working in a tandem nature, limiting the benefit of shared system costs and internal heat recovery. In addition, gas-fired furnaces and water heaters operate at less than 100% thermal efficiencies, insufficient for most CO2e emission reduction schemes. This manuscript summarizes data and key findings from the laboratory evaluation of a hybrid heat pump, a packaged Thermal Heat Pump (THP), and an Electrical Air Conditioning (EAC) unit for the combined operation of space conditioning and water heating. The packaged heat pump prototype achieved an AFUE of 121.6% and SEER of 8.

© HPC2023.
Selection and/or peer-review under the responsibility of the organizers of the 14th IEA Heat Pump Conference 2023.

Keywords: Gas Absorption Heat Pump; Electric Air Conditioning, Space Conditioning, Water Heating, Packaged Heat Pump

1. Introduction

The annual heating needs are more significant than the yearly cooling needs for residential buildings in most climate regions in the US [1]. Gas-fired appliances predominantly provide US residential space and water heating. As of the 2018 EIA report [2], more than 26 million homes in the cold climate regions of the US are heated by gas-fired furnaces, water heaters, and boilers. These gas-fired appliances have approached their thermodynamics limits in terms of efficiency (<100%), and any further improvements will have diminishing returns. The most recent residential energy consumption survey data highlighted that the total natural gas consumption for residential space and water heating is 38 billion therms, 68% of all residential heating in the US [2]. Natural gas is primarily consumed in cold and very-cold climate regions, with more than 5,400 heating degree days (HDD) and more than 9,000 HDD, respectively.

Electric Heat Pumps (EHP) have recently grown in demand and popularity due to policy changes and push for electrification and low-carbon initiatives. EHPs, primarily as air-source heat pumps (ASHP), are in demand in milder climates for new retrofit homes, where local electricity rates are competitive (namely in the south and the pacific northwest). The significant advantages of ASHPs are (a) the ability to reduce heating costs and (b) the integration of cooling and heating with a reversible heat pump. Improvements in ASHP technology and new constructions have driven the adoption of ASHP further. As of 2015, more ASHPs are being shipped than gas furnaces and electric resistance heating [3].

In cold climates, where gas heating is well established, ASHP adoption has been slow because: (a) highly efficient condensing gas-fired appliances are well established and can be cost-effective, (b) drop-off in

* Corresponding author. Tel.: +1 386-898-2292
E-mail address: nkumar@gtienergy.com

Coefficient of Performance (COP) and capacity at cold ambient temperatures, and the requirement for supplementary resistance heating, and (c) the initial cost of owning a cold-climate ASHPs (ccASHPs).

Therefore, the current market and changes in regulatory requirements have created the pathway and need for gas heating equipment with COPs higher than 100%, namely Gas Heat Pumps (GHP). The air-source Gas-Fired Absorption Heat Pump (GAHP) uses natural gas as energy input to extract heat from the outdoors to a conditioned indoor environment. GAHP products and prototypes in the market use the vapor absorption cycles where the sorbent is in the liquid phase and work on the principle that by combining refrigerant/working fluid with a sorbent, significantly less input energy is required to raise refrigerant pressure. During these cycles, thermal energy input is necessary to "desorb" the refrigerant/working fluid from the sorbent to yield a high-pressure vapor. At the core of the GAHP is a group of heat exchangers, vessels, and a pump that comprise the 'thermal compressor." LiBr/H2O (chilling) and NH3/H2O (heating) are common absorptions working fluid pairs. GAHP for heating is a developing technology with a notable advantage in heating performance in cold climates that exceeds ASHPs performance. In a single-effect vapor absorption cycle, approximately 40% of the heat delivered to the building is from the ambient ("heat pumping effect" and the remaining is from internal heat recovery [4]. For this reason, GAHP's in heating mode is much less sensitive to cold conditions and commonly do not require supplementary heating.

In the majority of residential applications in the US, space conditioning and hot water loads are typically decoupled and served by different types of equipment. A residential home in four and above IECC climate zones can have two to three types of equipment, typically a gas furnace for space heating, a gas-fired storage tank for water heating, and an electric air conditioning (A/C) unit for space cooling. The decoupled nature of these individual systems prevents the units from working in a tandem nature, limiting the benefit of shared system costs and internal heat recovery. Previous studies have described developing and demonstrating gas-fired "combi" systems for space and water heating, achieving a projected 140% AFUE while reducing water heating energy consumption and emissions by up to 50% [5–7]. One approach to address these challenges is an optimized and cost-effective packaged heat pump unit for combined space conditioning and water heating. The packaged unit offers advantages by coupling the space conditioning and water heating with a single unit to reduce the overall equipment and installation cost and operate at efficiencies of more than one.

This manuscript summarizes data and key findings from the lab evaluation of a hybrid heat pump, a packaged Thermal Heat Pump (THP), and an Electrical Air Conditioning (EAC) unit for the combined operation of space conditioning and water heating.

2. Concept

This effort is to take a pre-commercial GAHP product that only provides whole-house heating and domestic hot water (DHW) and add a cost-effective cooling function to provide space conditioning and water heating in a single packaged unit. Figure 1 illustrates the 4-pipe configuration of the hybrid GAHP–EAC (system for space conditioning and water heating. The GAHP–EAC systems consist of (1) an air handling unit (AHU), (2) a DHW storage tank, and (3) an outdoor unit. The outdoor unit is a four-pipe hydronic system that provides heating and cooling with two independent systems, a 3:1 modulating GAHP and a standard two-stage EAC system through a refrigerant/water heat exchanger. The outdoor unit heating and cooling streams are connected to an indoor hydronic coil AHU with internal pumps and three-way valves to independently manage space conditioning and water heating processes. The AHU system provides heating or cooling based on two-stage 24 VAC thermostat calls and water heating via a separate recirculating loop connected to the indirect storage water heater controlled by an aquastat.

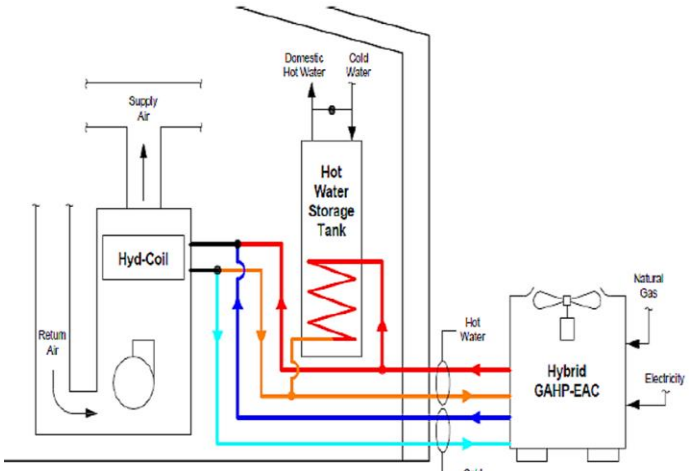


Figure 1: The hybrid GAHP-EAC concept for combined space conditioning and water heating

The GAHP is based on an economical single-effect, ammonia/water absorption cycle. With previously estimated Annual Fuel Utilization Efficiency (AFUE) of >140% [7,8]. Acknowledging that a reversible GAHP product is neither novel nor efficient compared to modern electrically-driven Air-Conditioning (A/C) technologies, this effort sought to add a vapor compression module using R410a as the refrigerant to provide cooling. Table 1 highlights the hybrid GAHP-EAC system specifications. The prototype system is illustrated in Figure 2.

Table 1: The hybrid GAHP-EAC specifications.

Outdoor Unit			
Thermal	**Heating**	Maximum capacity at 47°F	40 kBtu/hr (3.3 RT)
		Modulation	3:1
		Nominal water flow rate	4 GPM (15.1 lpm)
		Estimated AFUE	140%
	Cooling	High-stage capacity at 85°F	19 kBtu/hr (1.6 RT)
		Low-stage capacity at 85°F	15 kBtu/hr (1.25 RT)
		Nominal water flow rate	4.5 GPM (17 lpm)
		Compressor EER	10.10 (Btu/Wh)
	Water heating	Storage	80 gal
		Tank Temperature	120°F
Air Handling Unit			
Airflow		Maximum	700 scfm
		Minimum	200 scfm

The hybrid GAHP-EAC system relies upon the logic built into the system that responds to a 2-stage 24VAC thermostat and aquastat demand calls. This logic monitors the outdoor ambient temperature (OAT) and indirect storage water heater temperature, amongst other variables, to appropriately respond to space conditioning and water heating demands.

The hybrid GAHP-EAC system provides space and water heating with the GAHP. A configurable outdoor reset curve for space heating is based on the OAT and supply water temperature to modulate the GAHP between the maximum and minimum heating capacity as a function of OAT. During a heating call, hot glycol/water Heat Transfer Fluid (HTF) from the GAHP is delivered to the AHU at a constant water flow rate, with the AHU increasing the airflow as a function of the time of actuation at thermostat stages. The GAHP operation is centered around maximizing run-on-time and efficiency. In DHW mode, after receiving a call from the aquastat, the GAHP will turn on and supply water at 120-125°F until the aquastat is satisfied. The control will prioritize water heating if both space and water heating are being called.

The hybrid GAHP-EAC can simultaneously provide space cooling from the EAC and water heating from the GAHP. Since the EAC is a two-stage compressor air conditioner, it provides space cooling based on 1st

and 2nd cooling stage calls from the thermostat. The second stage cooling call will be triggered if the thermostat is 3.0°F above the set point. The AHU will start at medium speed and increase the airflow as a function of time.



Figure 2: The "Hybrid" GAHP-EAC unit. (Left) The outdoor unit in the environmental chamber; (Middle) The AHU unit system; (Right) The 80-gallon storage water heater.

3. Experimental Procedures

The hybrid GAHP-EAC system's performance for residential space conditioning and water heating applications was evaluated in a laboratory environment. The seasonal performance and capacities for space heating and cooling were characterized using standardized steady-state testing based on the North American rating method (ANSI Z21.40.4) and (AHRI 210/240), respectively. In addition to standardized testing, extended 24-hour Simulated Use Tests (SUT) on GTI Energy's Virtual Test Home (VTH) were conducted for real-world operation.

Both standardized steady-state test methods comprised a series of steady-state rating points under static conditions at full and partial loadings, including considering defrost modes and cycling degradation. Data from test rating points were used to calculate the seasonal performance metrics for the GAHP and EAC. The test conditions for the steady-steady testing can be referenced in the following standard's manual for ANSI Z21.40.4 [9] and AHRI 210/240 [10].

The hybrid GAHP-EAC system for space conditioning and water heating performance was evaluated in a simulated environment over 24 hours. In SUT testing, one space heating and cooling profile was implemented to present the heating and cooling season. One daily water heating profile was superimposed onto the space heating or cooling profile to simulate DHW usage for these two operating seasons. The SUTs space conditioning and water heating load profiles were based on yearly EnergyPlus modeling of a 3,016 sq-ft Vintage IECC 2012 home in Chicago, IL, as illustrated in Figure 3.

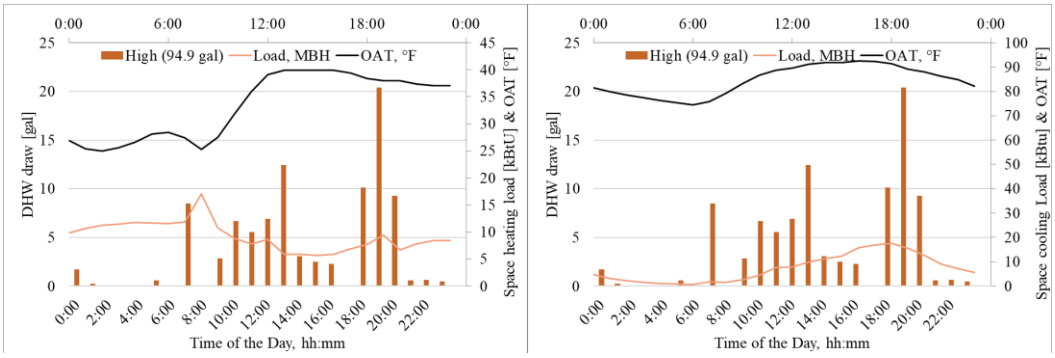


Figure 3: The load profiles for space conditioning and water heating. (Left) Heating season, (Right) Cooling season.

The SUTs implemented thermostat DHW simulators to evaluate the hybrid GAHP-EAC system performance and logic features to as-installed operating conditions. The thermostat simulator for simulated-use space conditioning evaluation is an algorithm based on a whole-home lumped heat capacity approach to simulate space conditioning part-load operation with HVAC equipment. This approach has been well documented in literatures [11,12].

A purpose-built test stand with instrumentation and the environmental chamber was used to evaluate the hybrid GAHP-EAC system, as illustrated in Figure 4. A National Instrument was used to record all data continuously throughout the data collection period with a maximum data sample interval of 5 seconds. The instrumentation list with make model and accuracy are summarized in Table 2.

Table 2: Instrumentation list and accuracy.

Measurement/ Component	Instrument Used	Instrument Accuracy
Natural Gas Pressure	Dwyer ISDP-008	±0.5% of reading
Natural Gas/Flue Temperatures	Omega T-type thermocouples	±1.1°C of reading
Natural Gas Flow	AM-250 and 500 pulses/cF	500 pulses/cubic foot
Flue Gas Composition	Bacharach PCA3 Analyzer	O_2: ±0.3% CO: Greater of ±5% of reading or ±10ppm NO/NO_2: Greater of ±5% of reading or ±5ppm
Air Temperature	Omega T-type thermocouples	± 0.75%
Air Relative Humidity (AHU)	Dwyer RHP-2D11	±2.0%RH (10– 90 % R.H.)
Air Relative Humidity (Outdoor)	Vaisala HMT120-130	±1.5%RH (0-90 % RH) @>0°C ±3.0%RH (0-90 % RH) @<0°C
Air Flow Rate	FE-1500-1-A-0-16x08-R-0-FX-1	± 2% of reading ± 0.12% of Full-scale
Air Flow Differential Pressure	Setra 2641-R25WD-11-C	± 0.25% of full scale (0" to 0.25" wc)
Pressure Rise	Setra 2641-2R5WD-11-C	± 0.25% of full scale (0" to 2.5" wc)
Ambient Pressure	Traceable Excursion-Trac Barometer	± 406 Pa
Glycol/Water Temperature	Omega RTDs PR-10L-3-100-1/8-9	Class B
Glycol/Water Flowrate	Dwyer MFS2-3	± 1% of reading
AHU Power (120Vac)	CCS WattNode Pulse RWNB-3Y-208-P and ACTL-0750-020	± 1% (5 to 100% rated current)
Outdoor Unit Power (240Vac)	CCS WattNode Pulse RWNB-3Y-208-P and ACTL-0750-020	± 1% (5 to 100% rated current)

The electrical input at the System Boundary is the total power measurement of the indoor and outdoor units as:

$$E_{Sys} = E_{AHU} + E_{OU} \quad (1)$$

Where:

E_{Sys} = accumulated electrical power at the System Boundary (kWh)
E_{AHU} = accumulated electrical power at the AHU (kWh)
E_{OU} = accumulated electrical power at the outdoor unit (kWh)

The following basic equation is used to calculate the gas consumption by the system:

$$Q_f = \sum HHV \cdot \dot{V}_f \cdot \Delta t \cdot \rho_{fs}/\rho_{fa} \quad (2)$$

Where:

Q_f = accumulated HHV fuel energy input (Btu)
HHV = fuel higher heating value (Btu/ft³)
$\dot{V}_f$ = flow rate of fuel (lbm/h)
Δt = testing period (h)
ρ_{fs} = fuel standard density (lbm/ft³)
ρ_{fa} = fuel actual density (lbm/ft³)

Thermal output at AHU is determined by measuring the airflow rate, supply and return temperature, and relative humidity. The enthalpy difference was computed using the measured temperatures and relative humidity in Engineering Equation Solver. The heating and cooling output was calculated with the following equation for heating:

$$Q_{SH} = \dot{V}_a \cdot \rho_{as} \cdot -\Delta h \cdot t \cdot \sqrt{\rho_{as}/\rho_{aa}} \quad (3)$$

Where:

Q = accumulated heating/cooling output of the AHU, (Btu)
$\dot{V}_a$ = AHU airflow, (acfm)
Δh = enthalpy difference between leaving and entering air temperatures at the AHU, (°F)
ρ_{as} = dry-air density based on the fluid temperature at the flow meter (lbm/cF)
ρ_{ss} = dry-air density at standard at 14.69psia and 70°F, (lbm/cF)
t = data collection time step, (min)

The DHW output was measured and calculated with the direct measurement of the water flow rate, city water, and DHW supply water temperatures at the indirect storage tank as:

$$Q_{DHW} = \dot{V}_w \cdot \rho_w \cdot c_{p_w} \cdot \Delta T_{DHW} \cdot t \quad (4)$$

Where:

Q_{DHW} = accumulated DHW output, (Btu)
$\dot{V}_w$ = city water flow rate, (gpm)
ΔT_{DHW} = temperature difference between city water and DHW temperatures at the indirect storage water heater, (°F)
ρ_w = water density based on the fluid temperature at the flow meter (lbm/gal)
c_{p_w} = specific heat based on average entering and leaving water temperatures across the indirect storage water heater (BTU/lbm -°F)
t = data collection time step, (min)

The coefficient of performance (COP) at the GAHP is calculated by the accumulated heat produced by the GAHP over the gas consumption as:

$$COP_{gas} = \frac{\sum_{t_o}^{t}(\dot{Q_{SH}} \cdot \Delta t) + \sum_{t_o}^{t}(\dot{Q_{DHW}} \cdot \Delta t) +}{\sum_{t_o}^{t}(\dot{Q_g} \cdot \Delta t)} \quad (5)$$

Where:

COP_{gas} = coefficient of performance at the GAHP, gas only
Δt = data collection time-step
t_o = start of steady-state measurement
t = data collection time step, (min)

The COP for the system is calculated by the accumulated heat produced by the GAHP over the gas and electric consumption as:

$$COP = \frac{\sum_{t_o}^{t}(\dot{Q_{SH}} \cdot \Delta t) + \sum_{t_o}^{t}(\dot{Q_{DHW}} \cdot \Delta t) +}{\sum_{t_o}^{t}(\dot{Q_g} \cdot \Delta t) + E_{Sys}} \quad (6)$$

Where:

COP = coefficient of performance at the GAHP

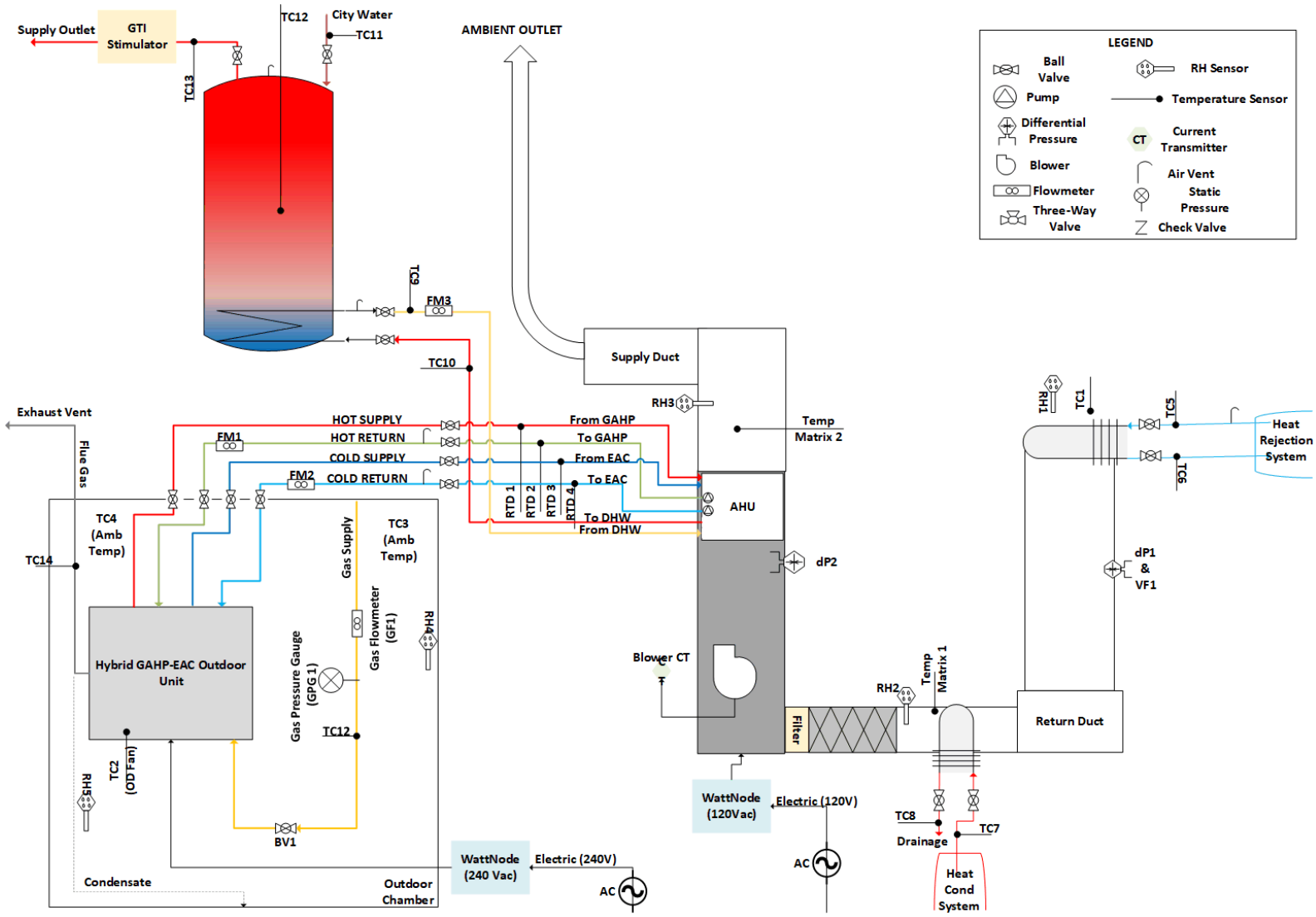


Figure 4: The purpose-built test stand and instrumentation.

4. Results and Discussion

The results of the steady-state heating and cooling test are summarized in Figure 5 and Figure 6, respectively. Using the data from Figure 5, the seasonal AFUE for US average climate bin conditions per ANSI Z21.40.4 was 121.6% for the US average climate bins based on a cycling degradation coefficient (Cd) of 0.25 as per the standard of ANSI Z21.40.4 based on air-water evaluation at a water return temperature of 95°F.

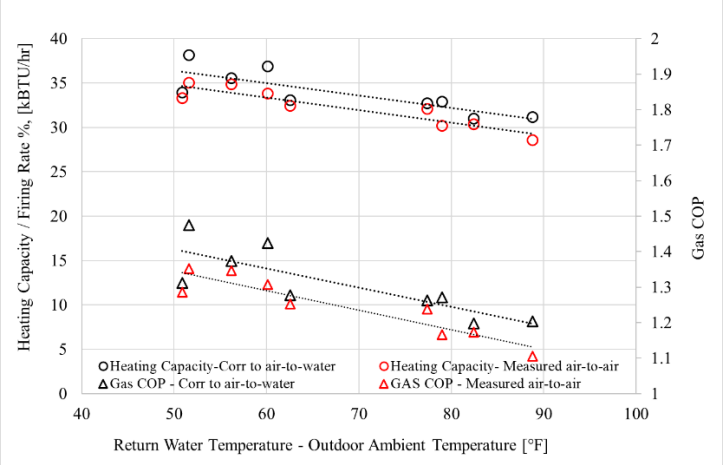


Figure 5: The ANSIZ21.40.4 steady-state testing results normalized at different modulation rates for air-to-water and air-to-air testing.

At lower and intermediate firing rates, the air-air GAHP was maintained close to 95°F return hydronic temperature (RHT), similar to an air-water GAHP. Whereas, at level 2 firing rate, the performance and capacity of the air-air GAHP are 9 to 12% lower than an air-water GAHP. At a higher firing rate, the air-air GAHP RHT was 13 °F higher than the air-water GAHP.

Using the data from Figure 6, the Seasonal Energy Efficiency Rating (SEER) was 10.1 (EAC only) and 8.24 (EAC + AHU) with a cycling degradation coefficient (Cd) of 0.59. As per standard Cd of 0.2 as per AHRI 210/240, the SEER was 12.4 (EAC only) and 10.1 (EAC +AHU). The EAC's cycling degradation coefficient and electric consumption were considered high in this prototype due to (1) an additional refrigeration/water heat exchanger and (2) an additional pump needed for the water loop.

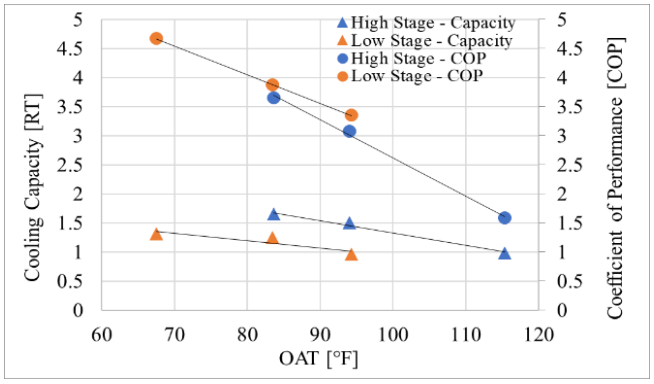


Figure 6: The AHRI 210/240 steady-state cooling test results.

Figure 7 summarizes and compares the supply air temperature of hybrid GAHP and EAC to other manufacturers' state-of-the-art technology. The GAHP supplied air at a higher temperature than ccASHPs in the market. At level 2 firing rate, the GAHP supplied air above 100°F. The EAC with hydronic loop provided supply air at ±2°F of manufacturer A's 16 SEER system.

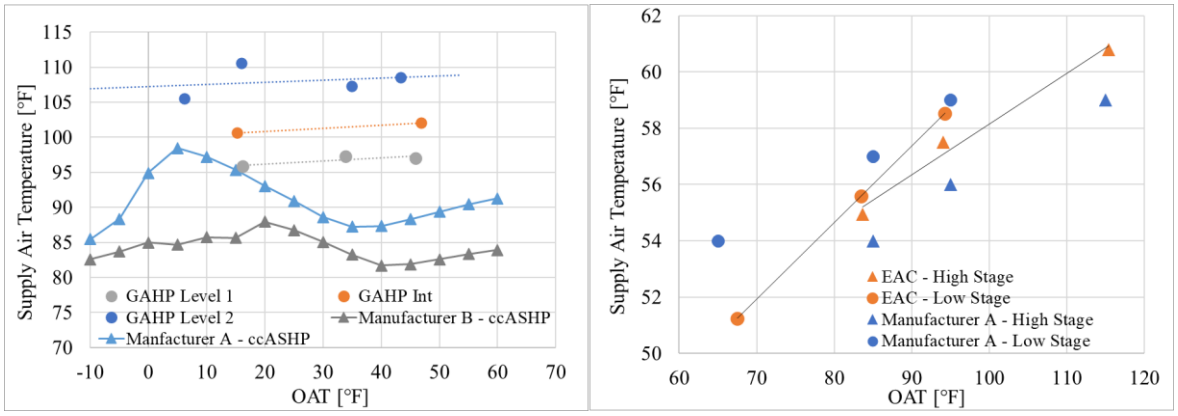


Figure 7: The supply temperature of the prototype in comparison to state-of-art system. (Left) Heating supply air temperature, (Right) Cooling supply air temperature.

The GHAP's flue gas composition and emissions were measured during steady-state tests. Table 3 summarizes the average measurements of flue gas composition on a dry basis. Compared to the 40 kBtu/hr gas furnaces, the hybrid's GAHP-EAC carbon monoxide (CO) in free air is 3 - 4 times lower. The NOx emission of 7.8 ng/J is roughly 45% lower than the requirement per Rule 1146 and SCAQMD requirements for residential and commercial space heating of 14 ng/J. Therefore, the hybrid GAHP-EAC can be classified as a low-NOx system.

Table 3: The steady-state emission measurement of the GAHP at different modulation levels

Modulation Level	O_2 %	CO_2 %	CO Air Free (ppm)	NO Air Free (ppm)	NO_2 Air Free (ppm)	NO_x (ng/J)
Level 1	4.6±0.3	9.2±0.3	11.5 ±12.7	10±6.3	6±6.3	7.8
Intermediate	5.2±0.3	8.9±0.3	32±12.8	8±6.4	7±6.4	7.3
Level 2	5.3±0.3	8.8±0.3	101±12.6	9.1±6.2	7±6.2	7.8

Figure 8 summarizes the hourly heating load, COP gas, OAT, and the indoor temperature during the simulated use testing over 24 hours. As outlined in Figure 8 (Left), the hybrid GAHP – EAC mainly operated in the intermediate firing rate region at a heating rate of 15 to 20 kBtu/hr. During the cyclic operation, the GAHP took about 25-30 minutes to reach steady-state operation, of which 6-10 minutes of initial load were used to heat the system's mass. Therefore, during the 24-hour duration, the GAHP only operated on the first stage of the heating call. The heating call's second stage was programmed to be triggered only when the indoor temperature is 3°F above the thermostat set point. The GAHP took an average of 60 minutes to 145 minutes to raise the home's temperature by 2°F from 69°F to 71°F, as shown in Figure 8 (Right).

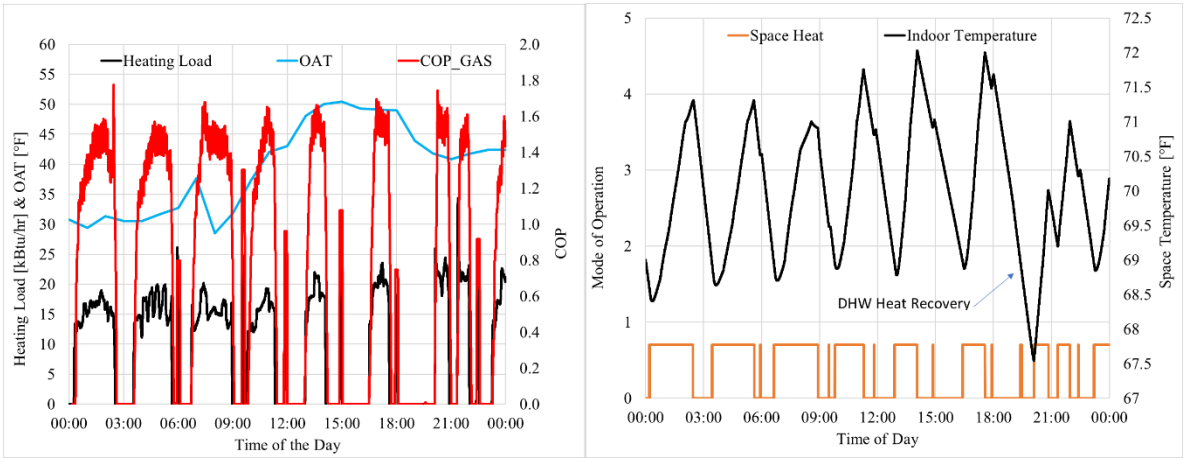


Figure 8: The 24-hour simulated use test results. (Left) The space heating load, COP gas, and OAT. (Right) The indoor temperature during space heating.

Table 4 summarizes the average space, water, and combi performance of GAHP when operated at an average OAT of 39.3 °F over 24 hours. The electric load made up 9% of the total energy used in a combi operation, and heat loss from the tank was 0.57 kBtu/hr (0.86 °F/hr), with a 24-hour standby electrical usage of 0.623 kWh. The combined system COP was 1.08. The significant electrical load due to the additional pumps and blower affects the system COP, as these are roughly 50% of the total electric load.

Table 4: The daily average of the SUT data for space heating and water heating

	Space Heating	**Water Heating**	**Combined**
Gas [kBtu]	177	44.84	223.1
Heating Supplied - @GAHP [kBtu]	231	53.19	284.19
Heating Supplied – @AHU [kBtu]	215	50.02	265.02
GAHP Electric Load [kWh]	2.24	0.586	2.98
AHU/Pump Electric Load [kWh]	2.79	0.371	3.63
COP_{gas}	1.21	1.11	1.19
COP_{total}	1.10	1.02	1.08
Standby-by Electric usage [kWh]			0.623
Water Drawn [Gal]	-	91.42 [37.2 kBtu]	-
Heat Loss [kBtu/hr]	-	0.57 [0.86°F/hr]	-
Tank Initial Temp [°F]	-	120.1	-
Tank Final Temp [°F]	-	118.7	-
Average City Water Temp [°F]	-	70.43	-
Average OAT [°F]	39.3		

An approximately 13% performance degradation between the GAHP performance rating and an optimized GAHP system can be found. This degradation percentage is anticipated with other technologies such as furnaces and ASHPs. Figure 9 shows the resulting performance of a 96% AFUE furnace at the same testing conditions implemented for the SMTI 40k hybrid GAHP system at 36 °F ambient temperature day. This testing condition was used for comparison since it represents the majority of load hours of heating equipment in the US national average climate. The 96% AFUE furnace sized per Air Conditioning Contractors of America (ACCA) Manual S scored 89% daily gas efficiency. The difference between AFUE and installed performance was about 7%, similar to the difference observed between air-to-air configuration ANSI Z21.40.4 testing and SUT evaluation in the 40k hybrid GAHP system.

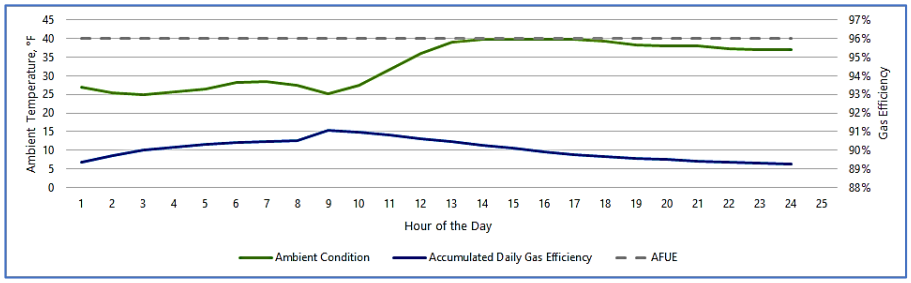


Figure 9: Daily efficiency of a 96 AFUE furnace at VTH 36 °F ambient test used for the SMTI 40k hybrid GAHP system.

Similarly, Table 5 summarizes the average space cooling with EAC and water heating with GAHP performance over 24 hours. The average COP of EAC for space cooling was 2.56 at average OAT of 92.2 ˚F. Similarly, the average system COP of water heating with GAHP was 1.3, and the heat loss from the tank was similar to the heating test at 0.62 kBtu/hr. Compared to the heating test, the 24-hour standby electrical load was 0.36 kWh; the lower standby electrical load in the cooling test was due to the EAC's extended long-time over the 24 hours.

Table 5: Summary of the SUT testing for space cooling with EAC and DHW with GAHP

	Space Cooling	**Water Heating**
Gas [kBtu]	-	32
Cooling Supplied - @EAC [kBtu]	205.1	-
Cooling Supplied – @AHU [kBtu]	191.3	-
Heating Supplied - @ DHW	-	48.1
GAHP/EAC Electric Load [kWh]	16.3	0.7
AHU/Pump Electric Load [kWh]	5.5	0.8
COP_{gas}		1.5
COP_{total}	2.56	1.3
Standby-by Electric usage [kWh]	0.36	
Water Drawn [Gal]	-	86.3
Heat Loss [kBtu/hr]	-	0.62 (0.94˚F/hr)
Tank Initial Temp [°F]	-	118.7
Tank Final Temp [°F]	-	117.9
Average City Water Temp [°F]	-	70.8
Average OAT [°F]	92.2	

5. Conclusion and Future Work

A series of laboratory evaluations were conducted to map the performance of the Hybrid GAHP-EAC system for residential HVAC and water heating applications. The seasonal heating and cooling performance of the Hybrid GAHP-EAC system were: (1) AFUE: 121.6%; (2) SEER: 8. In the SUT testing for space and water heating, the system performance degraded by 6- 11% in comparison to the steady-state testing. The average system COP, including the gas and the electrical load, was 1.10 (space heating), 1.02 (water heating), and 1.08 (combined) at an average OAT of 39.3 ˚F. The electric consumption was 9% of the energy consumption.

In the SUT testing for space cooling and water heating, the system performance degraded by less than 7% due to the long runtime of the EAC. The EAC operated at extended periods in stage 1, as the trigger from stage 1 to stage 2 was ±3 ˚F above the thermostat set point. The average COP was 2.56 for space cooling and 1.3 for water heating at an OAT of 92.2 ˚F.

Future work for space heating are:

- Improvement in controls for the time taken for space heating to maintain comfort. The 3 ˚F trigger for the next stage seems high to keep the required comfort in the home.

- The electric load should be considered in the design phase. The electric load makes up 9% of the energy usage. As observed in the SUT testing, the combined COP of the system was 1.08 at 39.3 ˚F.

Future work for space cooling are:

- Like space heating, a 3 ˚F trigger for the next stage seems high to maintain the required comfort in the home and reduce the EAC's performance. Therefore, the motivation for the next step should be a combination of time-based and OAT reset.

Acknowledgments

The authors would like to thank the Utilization Technology Development (UTD) and Natural Gas Innovation Fund of the Canadian Gas Association for their support of this work under project #1.18. H

References

[1] Montgomery D. 8 Charts on How Amercians Use Air Conditioning. Bloomberg 2019.
[2] Berry C. Space heating and water heating account for nearly two thirds of US home energy use. 2018.
[3] The Air-Conditioning, Heating and RI. Monthly Shipments 2022. https://www.ahrinet.org/analytics/statistics/monthly-shipments.
[4] Garrabrant M, Stout R, Glanville P, Fitzgerald J. Residential Gas Absorption Heat Pump Water Heater Prototype Performance Test Results. Int. Sorption Heat Pump Conf., 2014.
[5] Glanville P, Suchorabski D, Keinath C, Garrabrant M. Laboratory and Field Evaluation of a Gas Heat Pump-Driven Residential Combination Space and Water Heating System. ASHRAE Winter Conf., 2018.
[6] Garrabrant M, Stout R, Glanville P, Keinath C, Garimella S. Development of Ammonia-Water Absorption Heat Pump Water Heater for Residential and Commercial Applications. ASME 2013 7th Int. Conf. Energy Sustain., ASME; 2013, p. V001T04A002. https://doi.org/10.1115/ES2013-18121.
[7] Garrabrant M, Stout R, Keinath C, Glanville P. Experimental Evaluation of Low-Cost Gas Heat Pump Prototypes for Building Space Heating. Int. Refrig. Air Cond. Conf. Purdue, 2016.
[8] Fridlyand A, Glanville P, Kumar N. A Review and an Evaluation of the Updated Method of Test for Rating Fuel-fired Heat Pumps in HVAC. ASHRAE Winter Conf., Las Vegas, NV: 2022.
[9] CSA America I. ANSI Z21.40.4-1996 (R2017)/CGA 2.94-M96 (R2017) - Performance Testing And Rating Of Gas-Fired, Air Conditioning And Heat Pump Appliances. 2017.
[10] The Air-Conditioning, Heating and RI. Performance Rating of Unitary Air-Conditioning & Air-Source Heat Pump Equipment. n.d.
[11] Patil, Akash; Hjortland, Andrew L.; Cheng, Li; Dhillon, Parveen; Braun, James E; Horton WT. Load-based testing to characterize the performance of variable-speed equipment. Int. Refrig. Air Cond. Conf., 2018.
[12] Antonopoulos KA, Koronaki E. Apparent and effective thermal capacitance of buildings. Energy 1998;23:183–92. https://doi.org/10.1016/S0360-5442(97)00088-1.

14th IEA Heat Pump Conference
15-18 May 2023, Chicago, Illinois

Ionic liquid absorption system for dehumidification and IAQ enhancement in built environment

Rohit Bhagwat[a], Michael Schmid[b], Abbas Ahsan[c], Navin Kumar[c], Paul Glanville[c], and Saeed Moghaddam[a*]

[a]University of Florida, 939 Sweetwater Dr, MAE-A Bldg, RM 310, Gainesville, FL, 32611, USA
[b]Micro Nano Technologies, 747 SW 2nd Ave, Gainesville, FL, 32601, USA
[c]GTI Energy, 1700 S Mt Prospect Rd, Des Plaines, IL, 60018, USA

Abstract

Cooling systems are a necessity of modern civilization that have greatly enhanced our standard of living and enabled the development of large population centers in harsh climates. However, a key shortcoming of the existing prominent cooling system i.e., vapor compression system is the need for overcooling of air to condense its moisture content. This limitation often leads to implementation of reheat to bring the air to a desired supply temperature to maintain comfort and indoor air quality (IAQ). Liquid desiccant absorption systems have been considered to handle the latent load such that need for reheat is eliminated. However, a low energy efficiency, high cost, and operational and maintenance complexities have prevented such systems from becoming a mainstream product. Here, we report progress on development of ionic liquid desiccant dehumidification systems with a membrane-based absorber that promise to overcome shortcomings of the existing desiccant dehumidification systems. We compare performance of the system operating with adiabatic and internally cooled membrane-based absorbers. The studies are conducted at Integrated Seasonal Moisture Removal Efficiency (ISMRE) inlet air conditions. Effect of dew point temperature on system capacity and coefficient of performance (COP) is studied. A maximum COP of 0.82 is reached, showing promise in terms of energy efficiency. The studies also suggest that further enhancement in dehumidification level is required to meet the needs of HVAC systems.

© HPC2023.
Selection and/or peer-review under the responsibility of the organizers of the 14th IEA Heat Pump Conference 2023.

Keywords: Absorption; Dehumidification; Liquid desiccant; Ionic liquid

1. Introduction

Cooling systems are responsible for nearly 10% of the global electricity consumption [1]. This energy use is steadily rising due to the increase in the number of installed cooling systems and climate temperature. Currently, only 8% of the 2.8 billion people living in the hottest parts of the world possess an air conditioner [1]. As the living standard in these areas rises, the number of air conditioners is expected to increase [2]. It is projected that the global energy consumption associated with cooling could reach 6,200 TWh by year 2050 [1]. The use of dedicated outdoor air systems (DOAS) for applications with large ventilation loads have shown reduction in the overall building energy use and improvements in the indoor air quality (IAQ). A DOAS is designed to handle the outdoor ventilation air latent load. However, to remove moisture from air, vapor compression systems must overcool air to saturation conditions. The use of a more thermodynamically efficient process to remove moisture from air has the potential to improve energy efficiency in HVAC systems.

In this study, an experimental analysis of a membrane-based ionic liquid (IL) desiccant dehumidification system is presented. This work builds upon our invention of specific aspects of this absorption cycle [4,5] and demonstration of its performance using ILs [5–7] as well as characterization of a membrane-based absorber for dehumidification [8,9]. In the following sections, the system configuration, and its components, including

* Corresponding author. *E-mail address:* saeedmog@ufl.edu

the absorber, desorber, and the implemented IL are introduced. The experimental system is presented, and measurement uncertainties are discussed. The system dehumidification performance is measured at the Integrated Seasonal Moisture Removal Efficiency (ISMRE) inlet air conditions used to establish dedicated outdoor air systems (DOAS) performance characteristics.

2. Experimental System

2.1. Process and instrumentation diagram

A single-effect liquid desiccant absorption dehumidification system was fabricated and integrated into a test suite (Figure 1). This system operates in a cycle in which water vapor is absorbed from the airflow in the absorber and is subsequently liberated in the desorber (via heating). Within the absorber, the concentrated desiccant solution flows down the absorber plate while interfacing with the airflow through the membrane. The water vapor is absorbed by the solution. The dilute (i.e., water-rich) solution then exits the absorber and is pumped to the desorber where it is regenerated. A heat exchanger (i.e., solution heat exchanger, SHX) recovers heat of the desorber outbound solution to elevate temperature of the desorber inbound solution. This internal energy recovery stage plays a key role in energy efficiency of the system as well as absorber performance, as it lowers the absorber inlet solution temperature. The water vapor liberated from the solution is condensed, metered, and drained.

This experimental test setup consists of two primary flow loops including the solution and airflow loops as well as three secondary flow loops; the heating oil loop, the condenser/absorber cooling water loop, and the air-cooling loop (cf. Figures 1 and 2). The IL solution exiting the absorber is pumped to the desorber by a small variable speed gear pump. The absorber is located within the closed air loop (cf. Figure 2). To control the humidity level within the air loop, a steam generator in conjunction with a custom-made steam distribution manifold are utilized. To control the air temperature, a secondary water loop is connected to a heating/cooling coil installed within the air duct. A variable speed axial fan is used to circulate air through the air loop. The heating oil loop, which powers the desorber, utilizes a heating oil bath and synthetic oil SIL 180. An additional water chiller is used to cool the absorber (in inter-cooled operation) and the condenser. Temperature, relative humidity, and flow sensors (Figure 1) are installed throughout the system to enable components and system level characterizations.

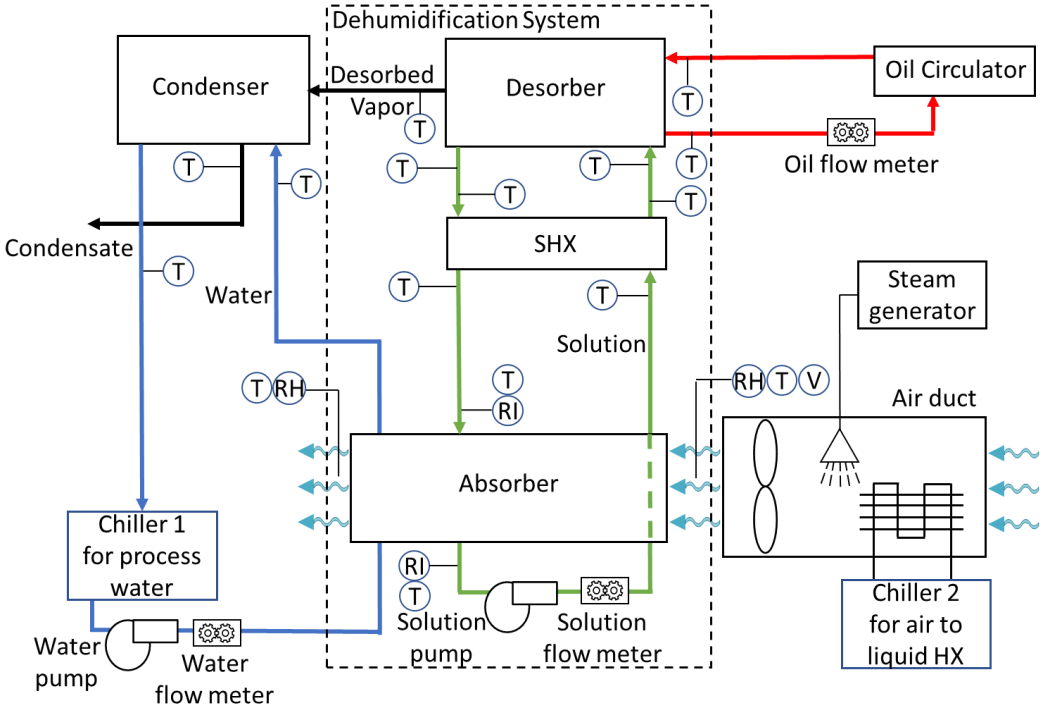


Figure. 1. Process and instrumentation diagram of the experimental test system.

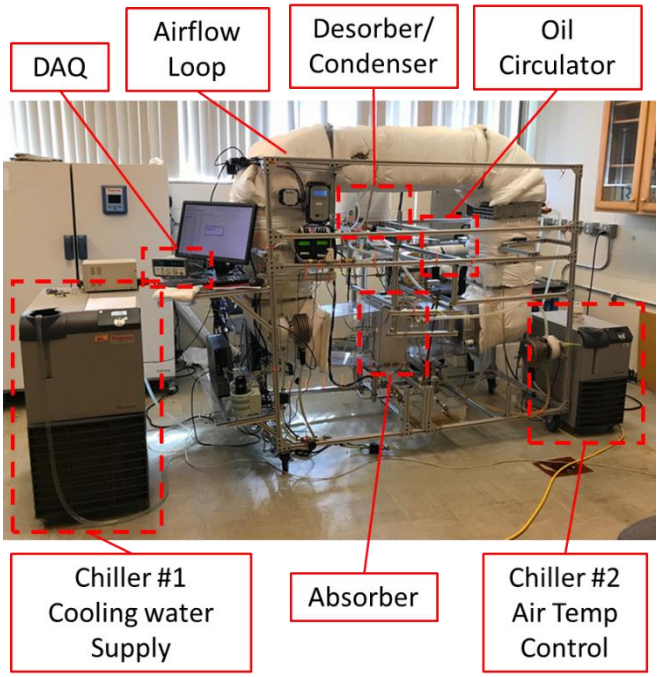


Figure. 2. Photograph of the experimental system with the key components identified.

2.2. Absorber

A schematic of an absorber panel showing the desiccant solution, cooling water, and airflow is shown in Figure 3. The absorber is fabricated from Acrylonitrile Butadiene Styrene (ABS) sheets. Each absorber plate has an internal cooling water core containing water channels and distribution manifolds. The desiccant solution flows on the two outer surfaces of each plate. The plate surfaces are machined to include features designed to slow and spread the solution flow to "wet" the entire surface (front and back) of each sheet [10,11]. A membrane is then bonded over the surface features to constrain the solution. Lastly, manifolds are bonded on the top and bottom of each side of the ABS sheet-membrane assembly (i.e., a panel) to direct the IL flow through the gap formed in between the ABS surface and membrane, and the water to the internal water cavity. Air flows across the panels (cf. Figure 3) through 3 mm gaps formed in between them within the absorber assembly. Geometrical characteristics of the absorber is listed in Table 1.

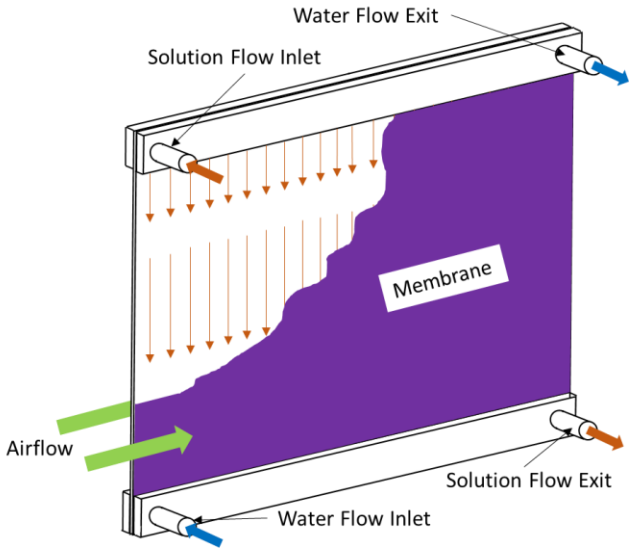


Figure 3. A schematic of a single absorber plate showing airflow across the membrane while exchanging moisture with the desiccant solution constrained behind the membrane.

Table 1. Absorber geometrical characteristics

Parameter	Value
Number of panels	14
Active Surface area (m^2)	3.30
Active plate Volume (m^3)	0.0091
Active surface area/volume ratio (m^{-1})	363.6

2.3. Desorber and Condenser

Figure 4 depicts the desorber, showing the dilute solution supplied by a distribution manifold over the desorber surface. To ensure uniform supply of solution over the surface (Figure 4A) and enhancement of the desorption rate, surface structures described in our earlier studies are utilized here [12]. The desorber surface is heated using silicone oil in a counter flow heat exchange configuration (Figure 4A). To capture and condense the vapor, a condensing surface is built adjacent to the desorber surface, separated by a porous polytetrafluoroethylene (PTFE) membrane (Figure 4B). A critical function of this membrane is to eliminate IL carryover from the desorber while permitting water vapor migration to the condensing surface. The condensing surface is cooled using a water loop.

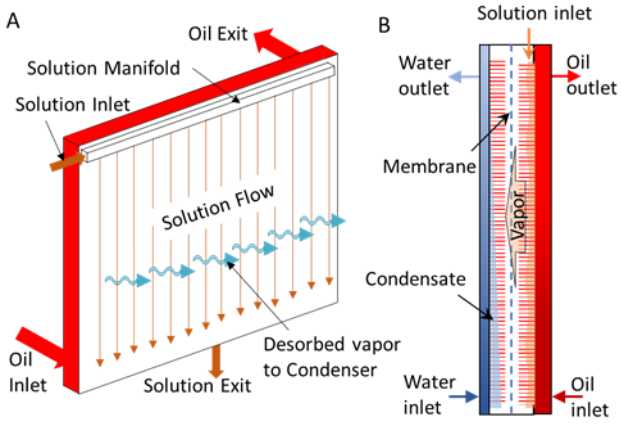


Figure 4. A schematic of the desorber and condenser assembly showing solution falling film flow configuration (A) and the desorption of water vapor, its flow through a PTFE membrane, and subsequent condensation in the condenser (B).

2.4. Measurement System

The solution flow rate is measured using a positive displacement flow meter. Due to the elevated temperature of the oil flow loop, a high-temperature positive displacement flow meter is used to measure the oil flow rate. The water flow rate is measured using a turbine flow meter. All flow meters were calibrated in house using a bucket-stopwatch method. The airflow rate is measured using a pitot tube sensing element mounted within the air loop duct. Multiple sensing ports along the length of the sensing element are used, and internally averaged to ensure accurate airflow rate measurement. All liquid temperatures were measured using T-type thermocouples. The process air temperature and relative humidity are measured using thin-film capacitive sensors. The absorber solution inlet and outlet concentrations are measured using two inline refractive index (RI) sensors. RI instead of Coriolis effect is used because the variation in density for ILs is insignificant over a wide concentration range, making accurate measurement of the concentration infeasible. Curve fits have been developed to establish RI values as a function of IL concentration and temperature. The primary system temperature, flow rate, RI, and air velocity are recorded using a data acquisition system. A second data acquisition system is used to record the air temperature and relative humidity. Time stamps are used to combine the data collected by each data acquisition system to enable a system level data analysis.

2.5. Data reduction and uncertainty analysis

The system performance presented in the results and discussion section is calculated based on the measured data described above. The system latent capacity is calculated using Eq. (1).

$$Q_{latent} = \dot{V}_{air}\, \rho_{air}\, h_{fg}\, (\omega_{air_in} - \omega_{air_out}) \quad (1)$$

where $\dot{V}_{air}$ is the absorber airflow rate; ω_{air_in} and ω_{air_out} are the absorber air inlet and exit absolute humidity, respectively; ρ_{air} is the air density as calculated from standard tables using the measured air inlet conditions; and h_{fg} is the water latent heat of evaporation. The desorber heat input is calculated using Eq. (2).

$$Q_{oil} = \dot{V}_{oil}\, \rho_{oil}\, c_{p_oil} (T_{des_oil_in} - T_{des_oil_out}) \quad (2)$$

where $\dot{V}_{oil}$ is the desorber oil flow rate; $T_{des_oil_in}$ and $T_{des_oil_out}$ are the desorber oil inlet and outlet temperatures, respectively; ρ_{oil} is the oil density; and c_{p_oil} is the oil thermal capacity calculated using curve fits derived from data provided by Clearco for their SIL 180 silicone oil. The system latent heat capacity along with the desorber heat input are used in Eq. (3) to calculate the system COP.

$$COP = \frac{Q_{latent}}{Q_{oil}} \quad (3)$$

The absorber moisture removal rate (MRR) is calculated using Eq. (4).

$$MRR = \dot{V}_{air}\, \rho_{air}\, (\omega_{air_in} - \omega_{air_out}) \quad (4)$$

The uncertainty was calculated using an engineering equation solver (EES) uncertainty propagation subroutine. The subroutine is based on NIST guidelines[13] and assuming that the individual measurements are uncorrelated and random, the uncertainty in the calculated quantity can be estimated using Eq. (5).

$$U_Y = \sqrt{\sum_i \left[\frac{\partial Y}{\partial X}\right]^2 U_{X_i}^2} \quad (5)$$

Table 2 below lists all the relevant measurement errors and uncertainties in this experimental study.

Table 2. Measurement error and uncertainty propagation.

Variable	Uncertainty
Fluid temperatures -All T-type TC	±0.8°C
Solution volumetric flow rate	±0.25% reading
Solution RI	±0.5% scale range (0.0003nD)
Water volumetric flow rate	±1% full scale (0.5 LPM)
Air volumetric flow rate	±2% reading
Oil volumetric flow rate	±0.5% reading
Air temperature	±0.3% reading
Air relative humidity	±1.8% RH
Oil heat	±3.7%
Water heat	±2.0%
Concentration (X%)	±0.15%
COP	±4.2%

2.6. Test Conditions

The test conditions listed in Table 3 represent the ISMRE [14] inlet air conditions used to establish DOAS performance characteristics. The inlet air, IL solution, and oil flow rates as well as the oil inlet temperature have been held constant at 155 cfm, 300 mlpm, 2.85 lpm, and 148 °C, respectively.

Table 3. Inlet air test conditions.

Test Condition	Inlet Air Conditions			Notes
	Dry Bulb Temp [°C]	Dew Point Temp [°C]	Rel. Hum. [%]	
1	35.0	22.1	47.29	ISMRE A
2	26.7	21.2	72.03	ISMRE B
3	21.1	17.8	81.36	ISMRE C
4	17.2	13.6	79.41	ISMRE D

3. Results

Figure 5 shows results of a typical run conducted at the ISMRE A test condition operating with an intercooled absorber at an air inlet temperature of ~35 °C and ~52% relative humidity. It is noted that due to the low thermal mass of the system, the system quickly reaches steady state conditions. In these steady state conditions, the difference in the inlet and exit air absolute humidity remains constant (Figure 5A), resulting in an essentially constant moisture removal rate (Figure 5B).

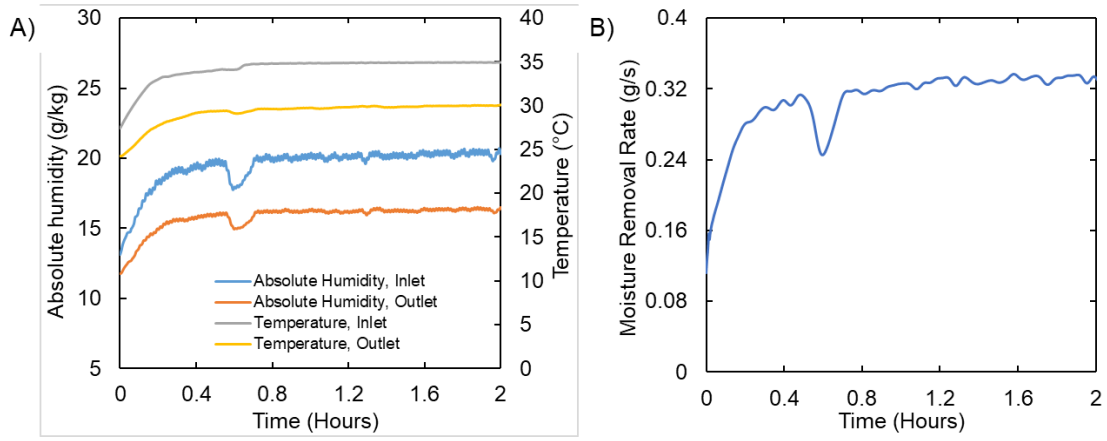


Figure 5. System inlet and exit air conditions (a) and water removal (b) with an intercooled absorber at ISRME A conditions. The inlet air, IL solution, and oil flow rates as well as the oil and water inlet temperatures have been held constant at 155 cfm, 300 mlpm, 2.85 lpm, 148 °C, and 10 °C, respectively.

3.1. Dehumidification performance

The dehumidification performance of the system was experimentally evaluated at each of the four ISRME test conditions, with the absorber operating in both adiabatic and intercooled configurations. In these flow configurations, the water flow rate was varied between 0 lpm (no flow) and 0.82 lpm for the adiabatic and intercooled configurations, respectively. The absorber inlet water temperature for the intercooled condition was held constant at 10 °C. The dehumidification performance of the system is plotted on the psychometric chart shown in Figure 6. In the adiabatic configuration, the heat associated with condensation of the water vapor into the solution is returned to the air stream. As a result, the air is dehumidified and heated in a nearly isenthalpic process. In the intercooled configuration, the absorber heat energy is removed by the cooling water enabling latent and sensible cooling of the process air.

Typically, in DOAS applications, outdoor ventilation air is dehumidified and conditioned to a room or neutral state (Figure 6). As can be seen, dehumidification of the process air to neutral conditions was not achieved during these tests. For ISMRE conditions C and D, it is believed that slight changes in the water and airflow rates will enable the existing system to deliver neutral air. For ISMRE conditions A and B, in addition to changes to air and water flow rates, a larger absorber is required. This experiment demonstrated that this absorber configuration, with proper air/water flow control can provide a wide range of air conditioning (above isenthalpic to constant relative humidity cooling). This range of air conditioning is enabled by the dehumidification capacity of the solution and the heat transfer between the absorber fluids. This is exemplified by performing above isenthalpic dehumidification because of the additional sensible heat transfer from the solution to the air emanating from high temperature of the solution entering the absorber.

The absorber implemented for this test, was approximately 35 cm tall, 35 cm long, and 8 cm wide with an active surface area of 3.3 m2 (Table 1). The dehumidification capacity, in latent cooling (W) and the moisture removal rate (kg/hr) of the absorber in the two configurations is shown in Figure 7. As shown in Figure 7, the dehumidification performance of the intercooled configuration is significantly better than that of the adiabatic configuration. The water absorption process is driven by the difference in vapor pressure between the process air and the desiccant solution. As the desiccant solution is heated its vapor pressure increases, reducing the absorption rate. As the cooling water in the intercooled configuration cools the solution, it is intuitive that under the same physical conditions (size, surface area, flow rates, etc.) the intercooled configuration will have a greater dehumidification capacity than the adiabatic configuration. As the architecture of both the absorber and desorber are modular, the addition of plates serves to increase system capacity.

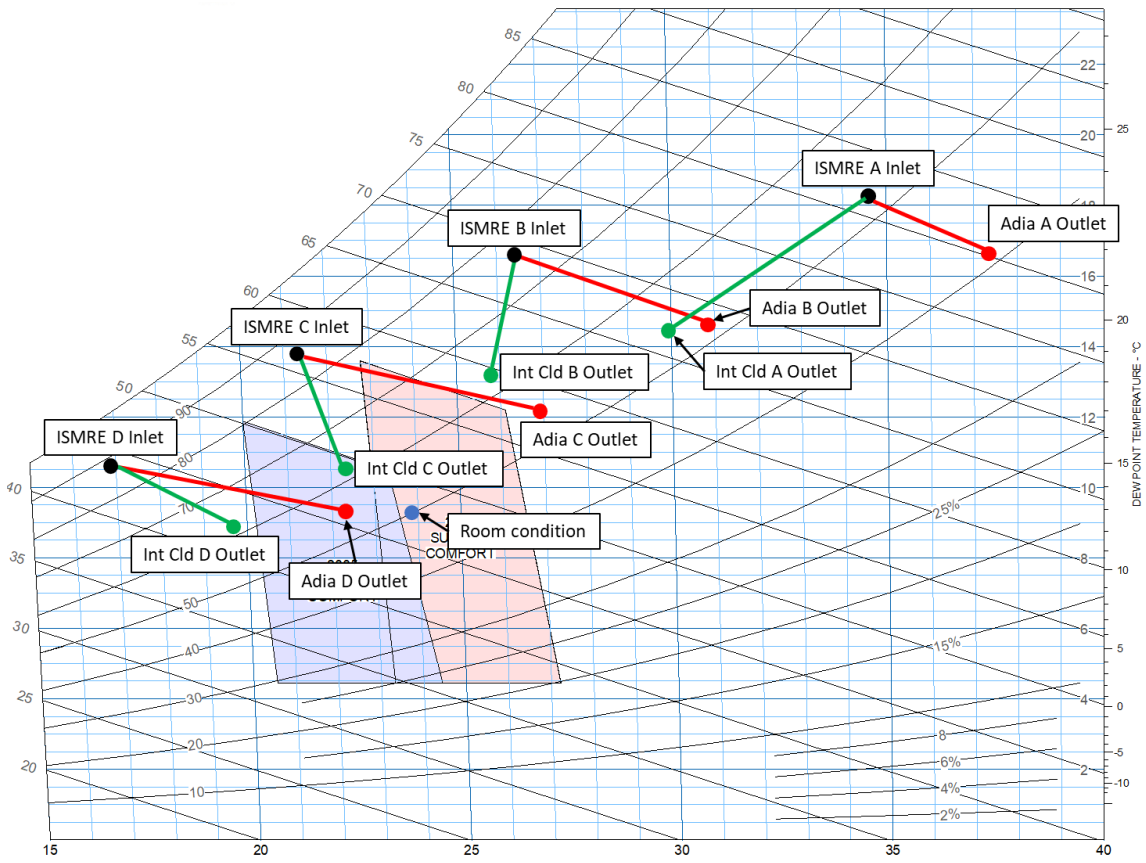


Figure 6. System inlet and exit air conditions for the system operating in the adiabatic and intercooled configurations at the four ISMRE conditions. The inlet air, IL solution, and oil flow rates as well as the oil and water inlets temperature have been held constant at 155 cfm, 300 mlpm, 2.85 lpm, 148 °C, and 10 °C, respectively.

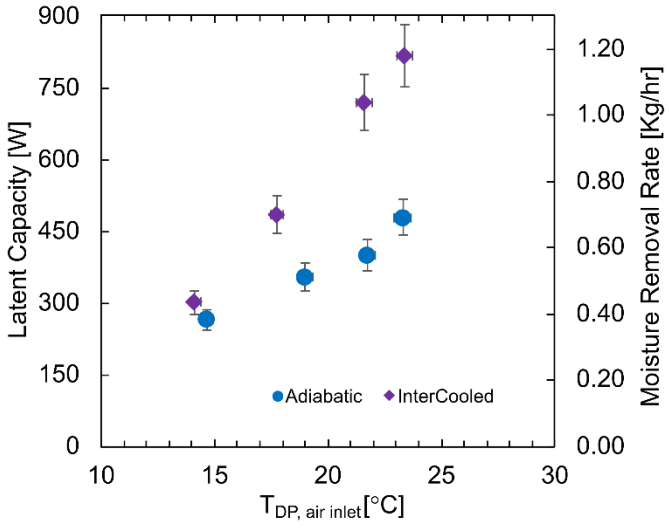


Figure 7. System latent capacity and moisture removal rate as a function of inlet air dewpoint temperatures which approximate the ISMRE conditions for the adiabatic and intercooled absorber configurations. The inlet air, IL solution, and oil flow rates as well as the oil and water inlet temperatures have been held constant at 155 cfm, 300 mlpm, 2.85 lpm, 148 °C and 10°C, respectively.

3.2. Coefficient of performance (COP)

As the primary function of the system is dehumidification, its COP (calculated using Eq. 3) represents the system's dehumidification (latent cooling) efficiency. This COP is plotted in Figure 8 as a function of the inlet

air dew point temperatures representative of the four ISMRE conditions. As shown in Figure 8, the COP of the system with the intercooled absorber (chilled water inlet temperature of 10 °C) is greater than that of the adiabatic configuration at higher dewpoint temperatures. The highest COP is associated with the maximum latent load, as dew point temperature is an indicator of the air moisture content. Although the system performance is presented in Figure 8 as a function of the inlet air dew point temperature, the inlet water and air drybulb temperatures also impact system performance. For the intercooled absorber, the inlet chilled water temperature has been maintained as 10 °C, which cools the solution within the absorber, ultimately resulting in the absorber inlet temperature being held essentially constant across the four test conditions. In contrast, the solution inlet temperature of the adiabatic absorber increases with increasing air inlet dewpoint/drybulb temperatures, such that for ISMRE A (22.1 °C $T_{DP, air\ inlet}$) it is 15 °C higher than its intercooled counterpart. While the cooling water dominates the heat transfer characteristics of the absorber, cooling both the solution and the air, the air inlet dry bulb temperature increased the solution temperature within the adiabatic absorber. The resulting increase in solution temperature decreased the latent capacity of the adiabatic absorber relative to the intercooled absorber at the higher inlet air dewpoint/drybulb conditions.

As shown in Figure 8, the system COP declines, regardless of absorber configuration, as the inlet air dewpoint temperature decreases. The system performance at these low dewpoint conditions was negatively impacted by maintaining a constant solution flow rate. The COP is expected to improve by lowering the solution flow rate such that change in the solution concentration between the absorber inlet and outlet is maximized. In other words, the solution flow rate should match the air dehumidification requirement.

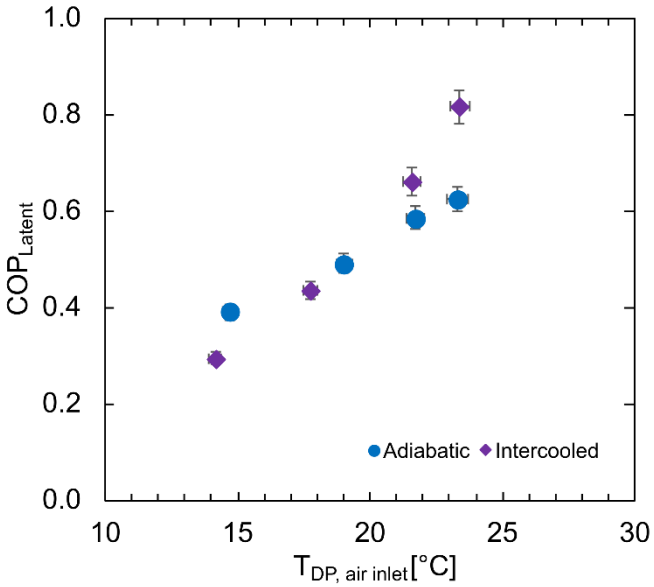


Figure 8. System COP as a function of air inlet dew point temperatures that approximate the ISMRE condition for the adiabatic and intercooled absorber configuration. The inlet air, IL solution, and oil flow rates as well as the oil and water inlet temperatures have been held constant at 155 cfm, 300 mlpm, 2.85 lpm, 148 °C, and 10°C, respectively.

4. Conclusions

A lab scale IL dehumidification system was experimentally tested in two configurations, adiabatic and intercooled, at the inlet air conditions representative of the four ISMRE test conditions, while the system internal operating conditions were maintained constant. The use of IL demonstrated the robustness of the system in providing dehumidification across a wide operational range, without control equipment for mitigating crystallization. An all polymer plate-and-frame membrane-based absorber effectively demonstrated dehumidification of the airflow in a small volume format. The measured system latent performance and system COP ranged from ~265 W to ~820 W, and 0.30 to 0.82 respectively across the test conditions. These tests demonstrated that this absorber configuration, with proper air/water flow control can provide a wide range (beyond isenthalpic to constant relative humidity cooling) of air conditioning, which when properly sized can deliver ventilation air at neutral air conditions.

Nomenclature

ABS	acrylonitrile butadiene styrene
Adia	adiabatic
CFM	cubic feet per minute
COP	coefficient of performance
D	depth
H	height
HX	heat exchanger
IL	ionic liquid
ISMRE	integrated seasonal moisture removal efficiency
Int Cld	intercooled
L	length
LPM	liters per minute
mLPM	milliliters per minute
PTFE	Polytetrafluoroethylene
RI	refractive index
RH	relative humidity
SHX	solution heat exchanger
$\dot{m}$	mass flow rate (kg/sec)
T	temperature (°C)
$T_{DP,in}$	Inlet air dew point temperature (°C)
TWh	terawatt hour
V	volumetric flow rate

Acknowledgements

This work was sponsored by the U. S. Department of Energy, Office of Energy Efficiency and Renewable Energy (EERE), under Award Number DE-EE0009162 with the University of Florida. The authors would also like to acknowledge Mr. Antonio Bouza, Ms. Coriana Fitz, and Dr. Isaac Mahderekal from the U.S. DOE Building Technologies Office (BTO) for their support of this research.

References

[1] OECD/IEA. The Future of Cooling Opportunities for energy-efficient air conditioning Together Secure Sustainable 2018:92.

[2] Davis L, Gertler P, Jarvis S, Wolfram C. Air conditioning and global inequality. Global Environmental Change 2021;69:102299. https://doi.org/10.1016/j.gloenvcha.2021.102299.

[3] Woods J, James N, Kozubal E, Bonnema E, Brief K, Voeller L, et al. Humidity's impact on greenhouse gas emissions from air conditioning. Joule 2022:1–16. https://doi.org/10.1016/j.joule.2022.02.013.

[4] Moghaddam S, Chugh D, Nasrisfahani R, Bigham S, Fazeli SA, Yu D, et al. Open absorption cycle for combined dehumidification, water heating, and evaporative cooling, 2018.

[5] Gluesenkamp KR, Chugh D, Abdelaziz O, Moghaddam S. Efficiency analysis of semi-open sorption heat pump systems. Renew Energy 2016:1–10. https://doi.org/10.1016/j.renene.2016.07.075.

[6] Chugh D, Gluesenkamp K, Abdelaziz O, Moghaddam S. Ionic liquid-based hybrid absorption cycle for water heating, dehumidification, and cooling. Appl Energy 2017;202. https://doi.org/10.1016/j.apenergy.2017.05.161.

[7] Chugh D, Gluesenkamp KR, Abu-Heiba A, Alipanah M, Fazeli A, Rode R, et al. Experimental evaluation of a semi-open membrane-based absorption heat pump system utilizing ionic liquids. Appl Energy 2019;239:919–27. https://doi.org/10.1016/j.apenergy.2019.01.251.

[8] Bhagwat R, Schmid M, Moghaddam S. Experimental and numerical analysis of a three-fluid membrane-based ionic liquid desiccant absorber. Int J Heat Mass Transf 2022;183:122122. https://doi.org/10.1016/j.ijheatmasstransfer.2021.122122.

[9] Bhagwat R, Sanadhya S, Gulotty E, Tucker Z, Ashfeld B, Moghaddam S. High-precision vapor pressure measurement apparatus with facile and inexpensive construction. Meas Sci Technol

2022;33:067002. https://doi.org/10.1088/1361-6501/ac5135.
[10] Mortazavi M, Isfahani Nasr R, Bigham S, Moghaddam S. Absorption characteristics of falling film LiBr (lithium bromide) solution over a finned structure. Energy 2015;87:270–8.
[11] Nasr Isfahani R, Bigham S, Mortazavi M, Wei X, Moghaddam S. Impact of micromixing on performance of a membrane-based absorber. Energy 2015. https://doi.org/10.1016/j.energy.2015.08.006.
[12] Mortazavi M, Schmid M, Moghaddam S. Compact and efficient generator for low grade solar and waste heat driven absorption systems. Appl Energy 2017;198:173–9. https://doi.org/10.1016/j.apenergy.2017.04.054.
[13] Taylor BN, Kuyatt CE. Guidelines for Evaluating and Expressing the Uncertainty of NIST Measurement Results. Technology (Singap World Sci) 1994:2.
[14] AHRI Standard 921-2020. Performance Rating of Direct Expansion-Dedicated Outdoor Air System Units 2021;920.

14th IEA Heat Pump Conference
15-18 May 2023, Chicago, Illinois

Thermally driven industrial ionic liquid absorption heat pump dryer

Michael Schmid[a], Rohit Bhagwat[b], and Saeed Moghaddam[b*]

[a]Micro Nano Technologies, 747 SW 2nd Ave, Gainesville, FL, 32601, USA
[b]University of Florida, 939 Sweetwater Dr, MAE-A Bldg, RM 310, Gainesville, FL, 32611, USA
*Email: saeedmog@ufl.edu

Abstract

Drying, an energy-intensive process that is indispensable to many industries, accounts for 10–20% of the total industrial energy use in most developed countries. Thus, there are great incentives to reduce energy use in drying to lower its carbon footprint and improve process economics. However, challenging thermodynamic barriers have limited the opportunities to reduce energy consumption in the drying industry. The vapor compression system heat pump (VCSHP) has been established as a promising technology to improve the drying process efficiency. Fuel-flexible heat pump systems (operated by waste heat, solar-thermal, biomass, and green hydrogen) provide an off-grid alternative to VCSHP with attractive efficiency and economics. Here, two configurations of a thermally-driven ionic liquid semi-open absorption heat pump drying system are studied. Both systems utilize an adiabatic absorber to remove latent heat (moisture) from the process air and return its latent energy content as sensible heat to the process air (i.e., latent to sensible energy exchange takes place in the absorber). The systems' condenser heat is then recovered to further increase the process air temperature prior to its entry into the drying kiln. Test results show that our semi-open ionic liquid absorption heat pump approaches a moisture removal efficiency (MRE) of ~1.2 kg $H_2O/kWh_{primary}$ comparable with the VCSHP drying systems (available products have an average MRE 1.4 kg $H_2O/kWh_{primary}$). This level of performance, coupled with its fuel-flexibility, demonstrates the viability of the ionic liquid absorption heat pump technology in industrial drying.

© HPC2023.
Selection and/or peer-review under the responsibility of the organizers of the 14th IEA Heat Pump Conference 2023

Keywords: Absorption; Heat Pump; Drying;

1. Introduction

Drying is an indispensable technique for large-scale food preservation and lumber production. Dried foods offer numerous benefits including storage stability, ease of packaging, and reduction in transportation cost. Lumber is dried to enhance its stability and strength. However, drying is one of the most energy-intensive processes, accounting for 10–20% of the total industrial energy use in most developed countries [1]. The main reason for this is the high latent heat of evaporation of water and the relatively low energy efficiency of industrial dryers [2]. Thus, there are clear incentives to reduce energy use in drying to lower its carbon footprint and improve process economics. However, challenging thermodynamic barriers have limited the opportunities to reduce energy consumption.

Current vapor compression system heat pump (VCSHP) drying has been demonstrated as a state of the art, low energy drying technology applicable to the food and lumber industries [3]. VSCHP drying is a technology in which an air-to-air heat pump is used to dehumidify and heat air as the convective medium for drying of food and lumber materials [4]. Since the system is entirely re-circulatory, food and lumber products are dried in environmentally friendly conditions in an operation that is independent of outside ambient weather

* Corresponding author. *E-mail address:* saeedmog@ufl.edu

conditions. Energy consumption is significantly reduced with respect to other commonly used industrial drying technologies [5].

Recent work has demonstrated the dehumidification capability of a thermally driven semi-open absorption heat pump [6–9]. The semi-open absorption cycle operates at near ambient pressure, eliminating complexities and costs associated with conventional absorption cycles. An ionic liquid (IL) has been successfully implemented enabling the system operation at cycle conditions not possible with conventional salts and operation with inexpensive and passive controls. Herein, two configurations of the system are studied to establish their moisture removal efficiency (MRE). The performance of these two configurations is compared with VCSHP technology.

2. System

Single- (Figure 1a) and double-effect (Figure 1b) semi-open heat pump absorption cycles with heat recovery are studied at conditions representative of lumber drying kilns. These systems operate in a cycle in which water vapor is absorbed from the warm and humid air of the drying kiln. The water vapor is absorbed in the absorber and is subsequently liberated in the desorber(s) via heating. Within the absorber, the concentrated desiccant solution flows down the absorber plates while interfacing with the air flow through a porous membrane. The water vapor is absorbed by the solution. The dilute (i.e., water-rich) solution then exits the absorber and is pumped to the desorbers where it is regenerated. Depending on the configuration, one or two heat exchangers (SHXs) are used to recover heat of the solution exiting the desorber to elevate the temperature of the solution entering the desorber. In this application, the heat of the desorbed vapor/condensate is used to heat the process air. This enables the cycle to dehumidify and reheat the process air, prior to its reentry into the drying kiln.

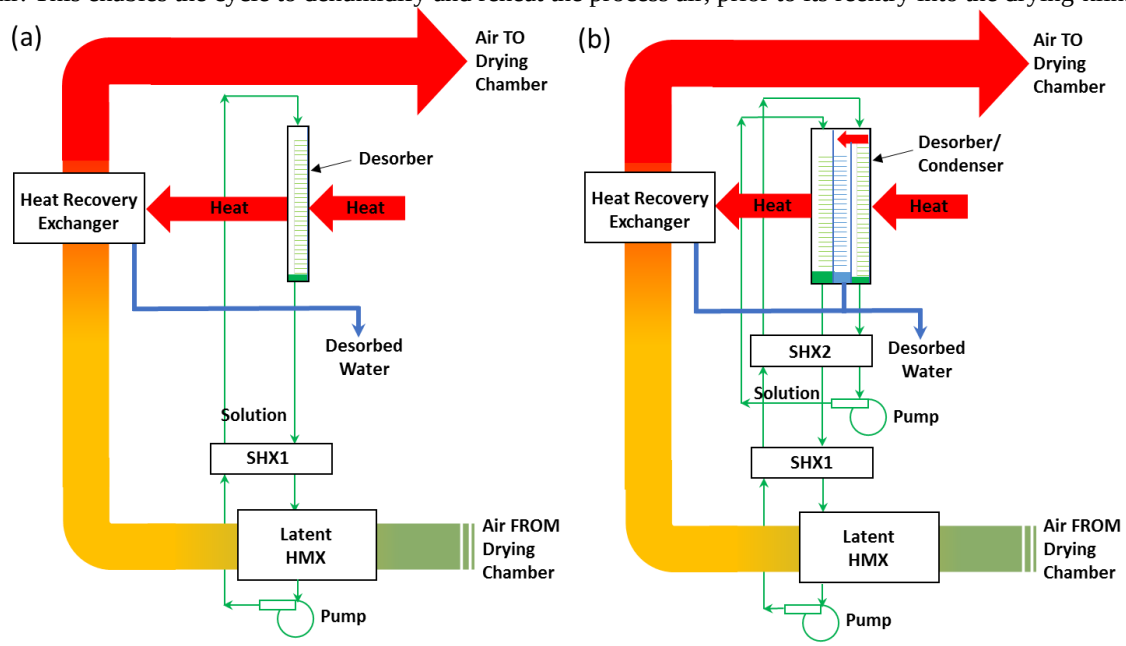


Figure. 1. The semi-open absorption single-effect (a) and double-effect (b) heat pump drying system configuration schematics.

2.1. Instrumentation Diagram

To validate performance of the single- and double-effect semi-open absorption cycles, and their associated moisture removal efficiencies, two systems were studied. Each experimental test setup consisted of two primary flow loops including the solution and air flow loops as well as three secondary flow loops; the heating oil loop, the condenser/absorber cooling water loop, and the air-cooling loop (Figure 2). The IL solution exiting the absorber is pumped to the desorber by a small variable speed gear pump. The absorber is located within the closed air loop (cf. Figure 2). In the single-effect configuration (Figure 2a), the solution exiting the desorber returns to the absorber to complete the solution flow loop. In the double-effect configuration, the solution exiting the upper desorber is pumped to the lower desorber by a second variable speed gear pump. The solution exiting the lower desorber returns to the absorber to complete the solution flow loop. To control the humidity level within the air loop, a steam generator in conjunction with a custom-made steam distribution manifold are utilized. To control the air temperature, a secondary water loop is connected to a heating/cooling coil installed

within the air duct. A variable speed axial fan is used to circulate air through the air loop. The heating oil loop, which powers the upper desorber, utilizes a heating oil bath and synthetic oil SIL 180. As the test setups only validated the cycle performance, they did not contain a heat recovery exchanger (Figure 1) to sensibly heat the air prior to its exit back into the drying kiln. As such, a water chiller is used to maintain the lower condenser at the desired temperature.

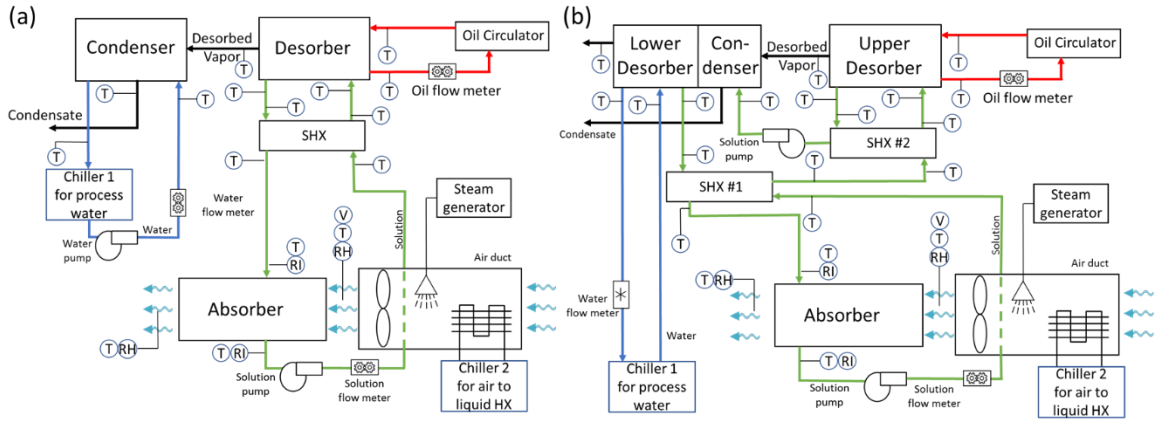


Figure. 2. Instrumentation diagram of the single-effect (a) and double-effect (b) experimental test systems.

The solution and water flow rates are measured using positive displacement and turbine flow meters, respectively. Due to the elevated temperature of the oil flow loop, a high-temperature positive displacement flow meter is used to measure the oil flow rate. The air flow rate is measured using a pitot tube sensing element mounted within the air loop duct. Multiple sensing ports along the length of the sensing element are used, and internally averaged to ensure accurate air flow rate measurement. All liquid temperatures were measured using T-type thermocouples. The process air temperature and relative humidity are measured using thin-film capacitive sensors. The absorber solution inlet and outlet concentrations are measured using two inline refractive index (RI) sensors. RI instead of Coriolis effect is used because the variation in density for ILs is insignificant over a wide concentration range, making accurate measurement of the concentration infeasible. Curve fits have been developed to establish RI values as a function of IL concentration and temperature. The primary system temperature, flow rate, RI, and air velocity are recorded using a data acquisition system. A second data acquisition system is used to record the air temperature and relative humidity. Time stamps are used to combine the data collected by each data acquisition system to enable a cycle level data analysis.

2.2. Absorber

In the HP drying application, humid warm air is removed, dehumidified, heated, and returned to the drying kiln. To support this process, an adiabatic absorber fabricated from Acrylonitrile Butadiene Styrene (ABS) sheets is used. The desiccant solution flows on the two surfaces of each absorber plate. The plate surfaces are machined to include features designed to slow and spread the solution flow to “wet” the entire surface (front and back) of each sheet [10,11]. A membrane is then bonded over the surface features to constrain the solution. Lastly, manifolds are bonded on the top and bottom of each side of the ABS sheet-membrane assembly (i.e., a panel) to direct the IL flow through the gap formed in between the ABS surface and membrane. Air flows across the panels (cf. Figure 3) through 3 mm gaps formed in between them within the absorber assembly. To support our modelling efforts, an absorber was fabricated and tested. Geometrical characteristics of the absorber are provided in Table 1. The test data was used to validate the absorber model [12].

Table 1: Absorber design properties and parameters.

Parameter	Value
Number of panels	14
Active Surface area (m^2)	3.30
Active plate Volume (m^3)	0.0091
Active surface area/volume ratio (m^{-1})	363.6

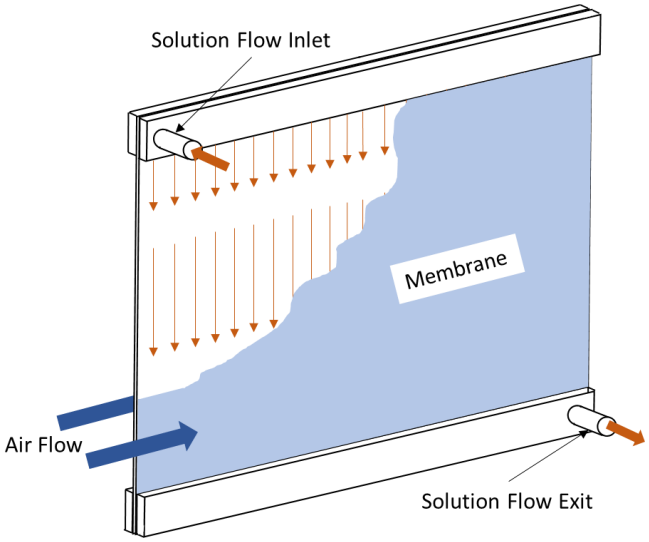


Figure 3. A schematic of a single absorber plate showing that air flows across the membrane while exchanging moisture with the desiccant solution constrained behind the membrane.

2.3. Desorbers and Condensers

In the double-effect configuration, the desorber/condenser module contains upper and lower desorbers and condensers (Figure 4a). In this configuration, heat is added to the dilute solution in the upper desorber using silicone oil in a counter flow heat exchange configuration. The desorbed vapor is then condensed in the upper condenser. The heat released from the vapor is used to heat the solution in the lower desorber. The solution leaving the upper desorber is cycled back to the low desorber after it passes through a heat recovery heat exchanger (Figure 1). The vapor desorbed in the lower desorber is condensed in the lower condenser. In the single-effect configuration (Figure 2a), heat is only used once in the desorption process. Thus, only a single desorber and condenser are contained in the module. The heat from the lower condenser (double-effect) and the condenser (single-effect) are used in a steam/air heat exchanger to heat the process air. A single- and a double-effect desorbers/condensers module (Figure 4b) were fabricated and have been used to test the performance of the single and double-effect test systems.

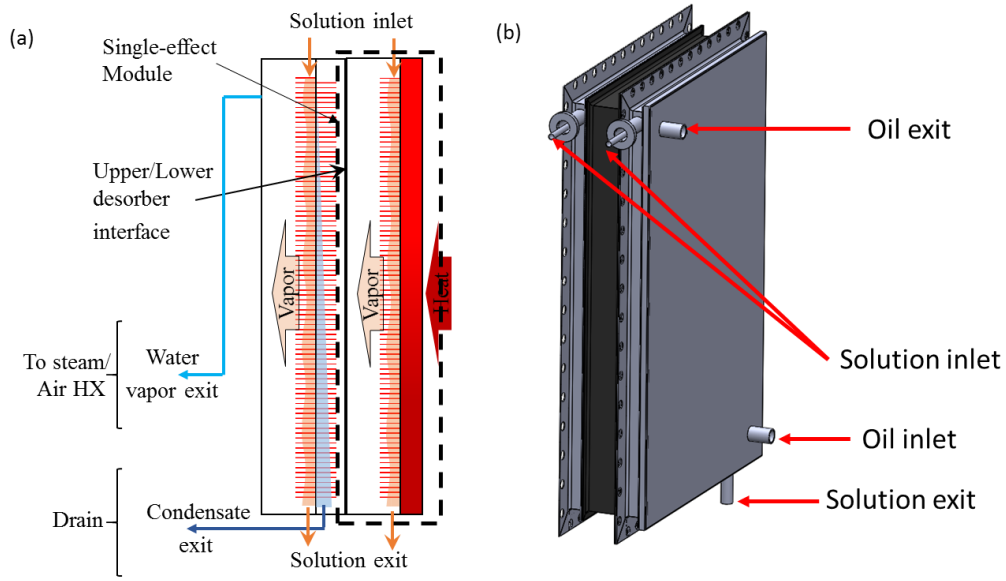


Figure 4. The absorption cycle desorber/condenser assembly schematic (a) and assembly 3-D model (b).

2.4. Ionic Liquids

ILs are broadly defined as low temperature molten salts composed of large asymmetric organic cations and inorganic or organic anions that are moisture and air stable at room temperature [13], [14]. ILs exhibit properties required for absorption dehumidification systems including thermal stability, negligible vapor pressure, high solubility in water, and low corrosion towards metals, making their use promising in absorption systems [15]. In liquid desiccant absorption systems, the dehumidification capability of the desiccant is considered its most critical thermo-physical property. This characteristic of the desiccant is best represented by its water vapor pressure at a given concentration and temperature.

Another key factor that dictates the dehumidification system design and whether an IL-based system can be successfully built is the IL viscosity. Our studies [9], [7], [16], have shown that the IL viscosity impacts the design of middle and low temperature components of the system the most, consisting of the absorber and solution heat exchanger. The high operating temperature of our desorber greatly reduces the IL solution viscosity such it is not the prominent factor in design considerations. Viscosity is a key constrain in design of the solution heat exchanger when the IL flow from the desorber to absorber is driven by gravity. Furthermore, design of the IL flow distribution within the absorber is impacted by the IL viscosity. Hence, assessing utility of one IL versus another involves comparing their viscosity..Table 2 compares viscosity of the IL used in this study and LiBr, LiCl, and [EMIM]OAc. While viscosity of both ILs is similar, it is 2-3 times higher than that of the LiBr and LiCl.

Table 2. Dynamic viscosity comparison for different liquid desiccants.

Desiccant	Viscosity (Pa-s)	Stability Limit (°C)
LiCl (20 °C, 40%)	0.0096	NA
LiBr (20°C, 53%)	0.0051	NA
[EMIM]OAc (20°C, 73%)	0.0233	~100

2.5. Data reduction and uncertainty analysis

The system performance presented in the results and discussion section is calculated based on the measured data described above. The system latent capacity is calculated using Eq. (1).

$$Q_{latent} = \dot{V}_{air}\, \rho_{air}\, h_{fg}\, (\omega_{air_in} - \omega_{air_out}) \tag{1}$$

where $\dot{V}_{air}$ is the absorber air flow rate; ω_{air_in} and ω_{air_out} are the absorber air inlet and exit absolute humidity, respectively; ρ_{air} is the air density as calculated from standard tables using the measured air inlet conditions; and h_{fg} is the water latent heat of evaporation. The desorber heat input is calculated using Eq. (2).

$$Q_{oil} = \dot{V}_{oil}\, \rho_{oil}\, c_{p_oil} (T_{des_oil_in} - T_{des_oil_out}) \tag{2}$$

where $\dot{V}_{oil}$ is the desorber oil flow rate; $T_{des_oil_in}$ and $T_{des_oil_out}$ are the desorber oil inlet and outlet temperatures, respectively; ρ_{oil} is the oil density; and c_{p_oil} is the oil thermal capacity calculated using curve fits derived from data provided by Clearco for their SIL 180 silicone oil. The system latent heat capacity along with the desorber heat input are used in Eq. (3) to calculate the system dehumidification COP.

$$COP_{dehumidification} = \frac{Q_{latent}}{Q_{oil}} \tag{3}$$

The moisture removal efficiency (MRE) was estimated using Eq. (4).

$$MRE = \frac{\dot{V}_{air}\, \rho_{air}\, (\omega_{air_in} - \omega_{air_out})}{Q_{oil}} \tag{4}$$

The uncertainty was calculated using an engineering equation solver (EES) uncertainty propagation subroutine. The subroutine is based on NIST guidelines[17] and assuming that the individual measurements are uncorrelated and random, the uncertainty in the calculated quantity can be estimated using Eq. (5).

$$U_Y = \sqrt{\sum_i \left[\frac{\partial Y}{\partial X}\right]^2 U_{X_i}^2} \tag{5}$$

Table 2 below lists all the relevant measurement errors and uncertainties in this experimental study.

Table 2. Measurement error and uncertainty propagation.

Variable	Uncertainty
Fluid temperatures -All T-type TC	±0.8°C
Solution volumetric flow rate	±0.25% reading
Solution RI	±0.5% scale range (0.0003nD)
Water volumetric flow rate	±1% full scale (0.5 LPM)
Air volumetric flow rate	±2% reading
Oil volumetric flow rate	±0.5% reading
Air temperature	±0.3°C
Air relative humidity	±1.8% RH
Oil heat	±3.7%
Water heat	±2.0%
Concentration (X%)	±0.15%
COP	±4.2%

3. Results and discussions

The experimental test loop was run to validate the dehumidification performance of the two different configurations of the semi-open absorption cycle as a heat pump dryer. The absorber implemented for this test was approximately 35×35×8 cm (H×W×D) in size with 3.3m^2 of active surface area (Table 1). It is noted that the absorber and desorber architectures are modular, enabling the increase in capacity through the addition of plates, without loss in efficiency. In typical drying applications, it is desirable to dehumidify the process air and elevate its temperature within the absorber. As shown in Figure 5, the system latent capacity is a function of the inlet air dewpoint temperature because the air moisture increases with increasing the dewpoint temperature. Within the absorber, the primary difference between the single- and double-effect system configurations is the inlet solution concentration and temperature. In this study, across the spectrum of single-effect experimental data, the absorber solution inlet concentration was kept constant at ~88%. The absorber inlet solution concentration in the double-effect experimental is maintained constant at ~92%. As the water absorption process is driven by the difference in vapor pressure between the process air and the desiccant solution (solution vapor pressure decreases with increasing concentration), the latent capacity of the double-effect system at these same conditions (Figure 5) is expected to be greater.

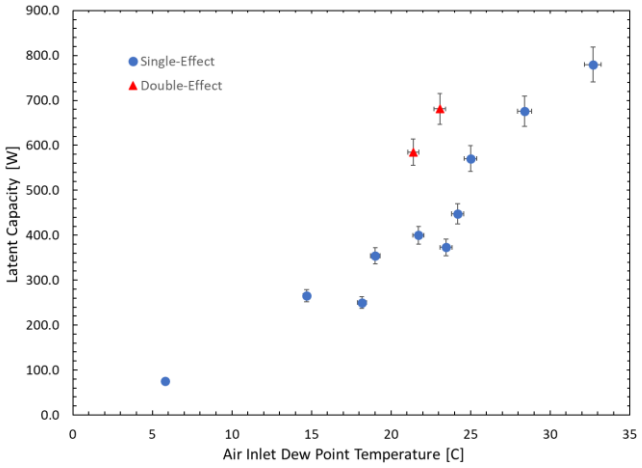


Figure. 5. Single- and double- effect system latent capacity as a function of inlet air dewpoint temperatures. The inlet air, IL solution, and oil flow rates as well as the oil inlet temperatures have been held constant at 155 cfm, 300 mlpm, 2.85 lpm, and 148 °C, respectively. The solution flow rate for the two double-effect data points is 125 mlpm.

In the drying application it is also beneficial to raise the temperature of the process air at the absorber exit. This limits the amount of condenser heat recovery required to achieve the desired exit air temperature conditions. The amount of sensible heat transferred to the process air is a function of the absorber inlet air dry bulb temperature and the inlet solution temperature. As shown in Figure 6, as the difference between the solution and air inlet temperatures increases (the solution is hotter than the inlet air) the process air dry bulb temperature rises. At large solution/air inlet temperature differences, the process air is heated up to ~6 °C. It is

noted that although the same solution and air inlet temperature difference can be observed at different operating conditions, leading to a range of absorber air temperature increases, there is a general trend of increasing absorber with increasing solution/air inlet temperature difference. The low air temperature rise in the double-effect system is attributable to the low solution flow rate (125 mlpm). At this low flow rate, the heat transfer resistance between the solution and the air flows increases due to an increased air gap between the membrane and the solution.

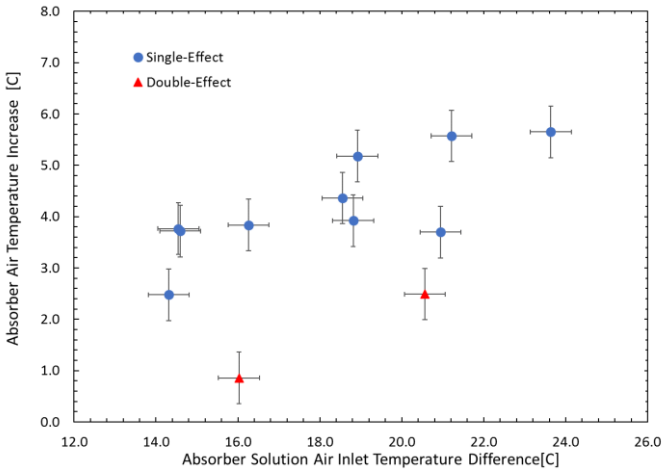


Figure 6. 1. Process air dry bulb temperature increase, as a function of the single- and double-effect absorber inlet solution/air temperature difference. The inlet air, IL solution, and oil flow rates as well as the oil inlet temperature have been held constant at 155 cfm, 300 mlpm, 2.85 lpm, and 148 °C, respectively. The solution flow rate for the two double-effect data points is 125 mlpm.

The MRE of the single- and double-effect systems as calculated on a primary energy basis is shown in Figure 7. To convert the MRE as calculated by Eq. 4, a burner efficiency of 0.85 and a site-to-source ratio of 1.05 (natural gas) has been used to adjust the amount of energy (Q_{oil}) required to drive the system. As this system can use solar thermal, biomass, waste heat, etc., it is believed that this burner efficiency/natural gas site-to-source ratio provides a representative estimate of the system's primary energy consumption. As can be seen in Figure 7, the single-effect primary MRE approaches 1.25 kg/kWh$_{primary}$ with increasing inlet air dewpoint. At the same conditions, the estimated theoretical performance of the double-effect system (Figure 7) approaches an MRE of 2.35 kg/kWh$_{primary.}$ As the testing has just begun, the MRE performance of the double-effect system at a low solution flow rate of 125 mplm is presented in Figure 7. As the double-effect testing continues over the coming month, a complete set of data at a solution flow rate of 300 mlpm will be incorporated in this figure.

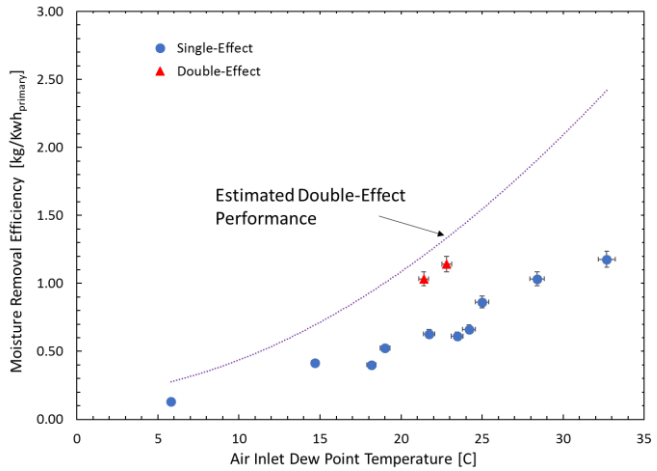


Figure 7. Single- and double-effect system primary moisture removal efficiency as a function of the air inlet dew point temperature. The inlet air, IL solution, and oil flow rates as well as the oil and inlet temperature have been held constant at 155 cfm, 300 mlpm, 2.85 lpm, and 148 °C respectively for the single effect system. The solution flow rate for the two double-effect data points is 125 mlpm.

This preliminary MRE data compares well to the performance of current VCSHP systems (0.65-1.53 $Kg/kWh_{primary}$) [18–20] (Figure 8) when the data is converted from site to primary energy using a primary energy factor of 2.8. Improvements in the system's MRE performance are expected with the optimization of the solution and air flow rates as well as system components.

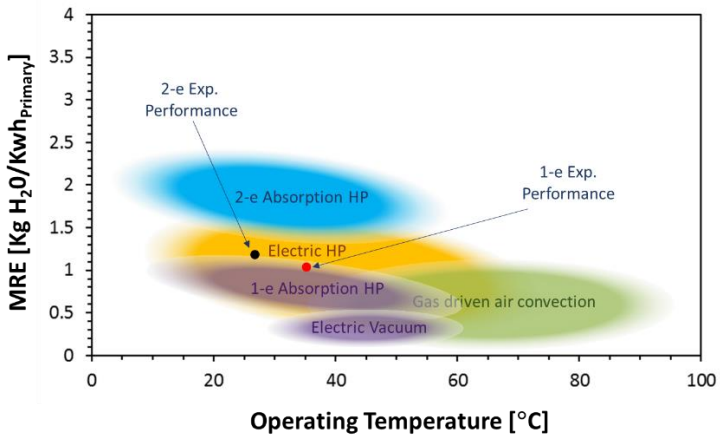


Figure 8. A comparison of drying technologies primary energy MRE as a function of system operating temperature.

4. Conclusions

Laboratory-scale IL single- and double-effect absorption heat pump drying systems were experimentally tested across a range of inlet air conditions representative of those found in low temperature drying applications. The single-effect system demonstrated a MRE of 1.2 $kg/kWh_{primary}$. The MRE performance of the double-effect system is projected to reach 2.35 $kg/kWh_{primary}$. This preliminary performance compares well with the current state-of-the-art VCSHP performance based on the primary energy consumption. The use of IL demonstrated the robustness of the system without control equipment for mitigating crystallization. Further optimization of the system operating conditions and components are ongoing. This thermally-driven technology could facilitate implementation of waste heat, solar thermal, biomass, and green hydrogen powered industrial drying systems.

Nomenclature

ABS	acrylonitrile butadiene styrene
CFM	cubic feet per minute
COP	coefficient of performance
$COP_{dehumidification}$	dehumidification capacity (latent cooling)/thermal energy consumed
HP	heat pump
HX	heat exchanger
IL	ionic liquid
LPM	liters per minute
mLPM	milliliters per minute
PTFE	polytetrafluoroethylene
RI	refractive index
RH	relative humidity
SHX	solution heat exchanger
$\dot{m}$	mass flow rate (kg/sec)
MRE	moisture removal efficiency
T	temperature (°C)
VCSHP	vapor compression system heat pump

Acknowledgements

This work was sponsored by the U. S. Department of Energy, Advanced Research Projects Agency (Arpa-e), under Award Number DE-AR0001488 with Micro Nano Technologies. The authors would also like to acknowledge Mr. Pieter De Bock from Arpa-e for his support of this research.

References

[1] Kemp IC. Fundamentals of Energy Analysis of Dryers. Modern Drying Technology, John Wiley & Sons, Ltd; 2014, p. 1–45. https://doi.org/https://doi.org/10.1002/9783527631728.ch21.

[2] Brunetti L, Giametta F, Catalano P, Villani F, Fioralba J, Fucci F, et al. Energy consumption and analysis of industrial drying plants for fresh pasta process. Journal of Agricultural Engineering 2015;46:167–71. https://doi.org/10.4081/jae.2015.478.

[3] Menon A, Stojceska V, Tassou SA. A systematic review on the recent advances of the energy efficiency improvements in non-conventional food drying technologies. Trends Food Sci Technol 2020;100:67–76. https://doi.org/10.1016/j.tifs.2020.03.014.

[4] Perera CO, Rahman MS. Heat pump dehumidifier drying of food. Trends Food Sci Technol 1997;8:75–9. https://doi.org/10.1016/S0924-2244(97)01013-3.

[5] Fayose F, Huan Z. Heat pump drying of fruits and vegetables: Principles and potentials for Sub-Saharan Africa. Int J Food Sci 2016;2016. https://doi.org/10.1155/2016/9673029.

[6] Chugh D, Gluesenkamp K, Abdelaziz O, Moghaddam S. Ionic liquid-based hybrid absorption cycle for water heating, dehumidification, and cooling. Appl Energy 2017;202:746–54. https://doi.org/10.1016/j.apenergy.2017.05.161.

[7] Chugh D, Gluesenkamp KR, Abu-Heiba A, Alipanah M, Fazeli A, Rode R, et al. Experimental evaluation of a semi-open membrane-based absorption heat pump system utilizing ionic liquids. Appl Energy 2019;239:919–27. https://doi.org/10.1016/j.apenergy.2019.01.251.

[8] Gluesenkamp KR, Kumar N, Abu-heiba A, Patel V. Semi-open absorption water heater : experimental results 2020:1–11.

[9] Gluesenkamp KR, Chugh D, Abdelaziz O, Moghaddam S. Efficiency analysis of semi-open sorption heat pump systems. Renew Energy 2016:1–10. https://doi.org/10.1016/j.renene.2016.07.075.

[10] Mortazavi M, Isfahani Nasr R, Bigham S, Moghaddam S. Absorption characteristics of falling film LiBr (lithium bromide) solution over a finned structure. Energy 2015;87:270–8.

[11] Nasr Isfahani R, Bigham S, Mortazavi M, Wei X, Moghaddam S. Impact of micromixing on performance of a membrane-based absorber. Energy 2015. https://doi.org/10.1016/j.energy.2015.08.006.

[12] Bhagwat R, Schmid M, Moghaddam S. Experimental and numerical analysis of a three-fluid membrane-based ionic liquid desiccant absorber. Int J Heat Mass Transf 2022;183:122122. https://doi.org/10.1016/j.ijheatmasstransfer.2021.122122.

[13] Shah FU, An R, Muhammad N. Editorial: Properties and Applications of Ionic Liquids in Energy and Environmental Science. Front Chem 2020;8:1–3. https://doi.org/10.3389/fchem.2020.627213.

[14] Kim YJ, Kim S, Joshi YK, Fedorov AG, Kohl PA. Thermodynamic analysis of an absorption refrigeration system with ionic-liquid/refrigerant mixture as a working fluid. Energy 2012;44:1005–16. https://doi.org/10.1016/j.energy.2012.04.048.

[15] Qu M, Abdelaziz O, Sun XG, Yin H. Aqueous solution of [EMIM][OAc]: Property formulations for use in air conditioning equipment design. Appl Therm Eng 2017;124:271–8. https://doi.org/10.1016/j.applthermaleng.2017.05.167.

[16] Chugh D, Gluesenkamp K, Abdelaziz O, Moghaddam S. Ionic liquid-based hybrid absorption cycle for water heating, dehumidification, and cooling. Appl Energy 2017;202. https://doi.org/10.1016/j.apenergy.2017.05.161.

[17] Taylor BN, Kuyatt CE. Guidelines for Evaluating and Expressing the Uncertainty of NIST Measurement Results. Technology (Singap World Sci) 1994:2.

[18] Closas AA, Villanueva EP. Determination of Specific Moisture Evaporation Rate, Energy Consumption and Specific Energy Consumption at Varying Sample Load Capacity per Batch Drying in a Heat Pump Dryer. International Journal of Engineering and Techniques 2017;3.

[19] Yang KS, Hamid K, Wu SK, Sajjad U, Wang CC. Experimental analysis of a heat pump dryer with an external desiccant wheel dryer. Processes 2021;9. https://doi.org/10.3390/pr9071216.

[20] Stawreberg L, Nilsson L. Modelling of Specific Moisture Extraction Rate and Leakage Ratio in a Condensing Tumble Dryer. Appl Therm Eng 2010;30:2173–9. https://doi.org/10.1016/j.applthermaleng.2010.05.030.

14th IEA Heat Pump Conference
15-18 May 2023, Chicago, Illinois

Hybrid thermally driven ionic liquid heat pump water heater and dehumidifer for commercial applications

Rohit Bhagwat[a], Michael Schmid[b], Paul Glanville[c], and Saeed Moghaddam[a*]

[a]University of Florida, 939 Sweetwater Dr, MAE-A Bldg, RM 310, Gainesville, FL, 32611, USA
[b]*Micro Nano Technologies, 747 SW 2nd Ave, Gainesville, FL, 32601, USA*
[c]GTI Energy, 1700 S Mt Prospect Rd, Des Plaines, IL, 60018, USA

Abstract

Water heating and indoor latent cooling loads are great sources of primary energy consumption in many applications. Recently, a semi-open ionic liquid absorption heat pump water heater (AHPWH) has been proposed in which the latent energy in humid air (ventilation, process air, etc.) is used to heat water. This APHWH operates at near ambient pressure, using a novel ionic liquid, enabling stable operation across a wide range of conditions using inexpensive and passive controls eliminating the complexities and costs associated with typical absorption cycles. In this work, we experimentally compare the performance of three configurations of the semi-open heat pump water heater internal heat recovery, at several conditions, including those representative of the standard rating tests as applied to commercial storage-type water heating equipment, to determine their impact on system capacity, coefficient of performance (COP), and water delivery temperature. The results suggest that the impacts varies with the inlet air dewpoint temperature and are substantial at low dewpoints. In hot and humid inlet air conditions, the combined COP reached to 2.55 with a 52 °C water delivery temperature. In these same hot and humid inlet air conditions, the combined COP decreased to 1.93 as the delivery water temperature was increased to 82 °C. These measurements demonstrated the viability of this technology in hot water-intensive applications such as commercial kitchens and food and beverage processing facilities.

© HPC2023.
Selection and/or peer-review under the responsibility of the organizers of the 14th IEA Heat Pump Conference 2023.

Keywords: Absorption; Ionic Liquid; Heat Pump; Water Heater; Dehumidification; Decarbonization

1. Introduction

With rising energy demand and the dependence on fossil fuels, the world is facing the unprecedented challenges of climate change and energy security [1]. Energy efficiency improvements offer the greatest opportunities for near term decarbonization solutions [2]. Water heating and dehumidification represent two energy intensive processes that have wide-spread application across the industrial and building sector. Several applications such as commercial kitchens and food and beverage processing facilities utilize both processes simultaneously. Recent work has demonstrated the ability of a semi-open absorption heat pump water heater (AHPWH) [3] to harvest the latent energy of air moisture for water heating [4–7]. This AHPWH operates at near ambient pressure, eliminating complexities and costs associated with conventional absorption cycles. A novel ionic liquid (IL) has been successfully implemented enabling the system operation at cycle conditions not possible with conventional salts due to crystallization, and stable operation with inexpensive and passive controls. The system also benefits from compact, light, low-cost plate-and-frame membrane-based heat and mass exchangers [8,9].

Herein, three configurations of the AHPWH system involving different ways of recovering the solution heat leaving the desorber are studied to determine the impacts on system coefficient of performance (COP) and water exit temperature. In the following sections, first, the three system configurations are introduced. Then,

* Corresponding author. *E-mail address:* saeedmog@ufl.edu

details of an experimental setup developed for testing these configurations is discussed. Finally, test results on performance of these systems are compared and the ability of the technology to deliver hot water in commercial applications is analyzed.

2. Experimental system

2.1. System configurations

Previous semi-open AHPWH research has been conducted using the system architecture presented in Figure 1a. In this architecture, heat is added to the process water in the absorber, solution-water heat exchanger (SWHX), and condenser. The use of the SWHX serves to increase the process water temperature, while lowering the desiccant solution temperature prior to its entry into the absorber. A heating oil loop (not shown) is used in all three configurations (Figure 1) to add heat to the desorber. The solution-oil heat exchanger (SOHX) represents the use of flue gas heat to preheat the desiccant solution prior to its entry into the desorber. Figure 1b presents a semi-open AHPWH architecture wherein heat is added to the process water in the absorber and condenser. In this architecture a solution heat exchanger (SHX) is used to recover heat in the solution flow loop, preheating the desiccant solution prior to its entry into the desorber, while cooling the desiccant solution prior to its entry into the absorber. Figure 1c represents a hybrid version of the previous two configurations. In this configuration, heat is added to the process water in the absorber, SWHX, and condenser similar to the configuration shown in Figure 1a. Heat recovery in the desiccant solution flow loop is performed by the SHX in a similar fashion as the configuration shown in Figure 1b. The addition of the SWHX in this configuration is intended to lower solution desiccant temperature entering the absorber to increase the system's latent capacity. In this paper, the experimental performance of these configurations is compared.

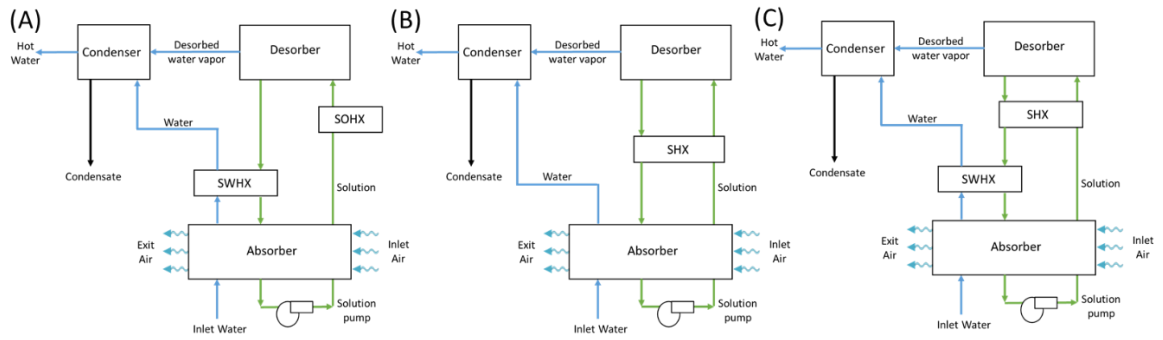


Figure 1. The semi-open absorption heat pump water heater system configuration schematics using solution-water and solution-oil heat exchangers (A), solution heat exchanger (B), and solution-water and solution heat exchangers (C).

2.2. Instrumentation Diagram

A single-effect liquid desiccant AHPWH was fabricated and integrated into a test suite (Figure 2). Two configurations of this AHPWH system (Figure 1b and 1c) were tested in this study. This experimental data was compared with legacy data for the AHPWH operating in the configuration shown in Figure 1a [4,6,7]. In each configuration, the system operates in a cycle in which water vapor is absorbed from the air flow in the absorber and is subsequently liberated in the desorber (via heating) with the heat of absorption, condensation, and recovery being used to heat the process water. Within the absorber, the concentrated desiccant solution flows down the absorber plate while interfacing with the air flow through the membrane. The water vapor is absorbed by the solution. The dilute (i.e., water-rich) solution then exits the absorber and is pumped to the desorber where it is regenerated. Depending on the system configuration, one or more heat exchangers are used to recover energy of the solution exiting the desorber to either heat the desorber inlet solution and/or the process water.

The experimental test setup consists of three primary flow loops including the solution, water, and air flow loops as well as two secondary flow loops: the heating oil loop and the air flow loop (cf. Figure 2). The IL solution exiting the absorber is pumped to the desorber by a small variable speed gear pump. The absorber is located within the closed air loop (cf. Figure 2). A chiller is used in the process water loop to control the inlet temperature and water flow rate to the system absorber, condenser, and heat exchangers (as applicable). To control the humidity level within the air loop, a steam generator in conjunction with a custom-made steam distribution manifold are utilized. To control the air temperature, a secondary water loop is connected to a

heating/cooling coil installed within the air duct. A variable speed axial fan is used to circulate air through the air loop. The heating oil loop, which powers the desorber, utilizes a heating oil bath and synthetic oil SIL 180.

The solution and water flow rates are measured using positive displacement and turbine flow meters, respectively. Due to the elevated temperature of the oil flow loop, a high-temperature positive displacement flow meter is used to measure the oil flow rate. The air flow rate is measured using a pitot tube sensing element mounted within the air loop duct. Multiple sensing ports along the length of the sensing element are used, and internally averaged to ensure accurate air flow rate measurement. All liquid temperatures were measured using T-type thermocouples. The process air temperature and relative humidity are measured using thin-film capacitive sensors. The absorber solution inlet and outlet concentrations are measured using two inline refractive index (RI) sensors. RI instead of Coriolis effect is used because the variation in density for ILs is insignificant over a wide concentration range, making accurate measurement of the concentration infeasible. Curve fits have been developed to establish RI values as a function of IL concentration and temperature. The primary system temperature, flow rate, RI, and air velocity are recorded using a data acquisition system. A second data acquisition system is used to record the air temperature and relative humidity. Time stamps are used to combine the data collected by each data acquisition system to enable a system level data analysis.

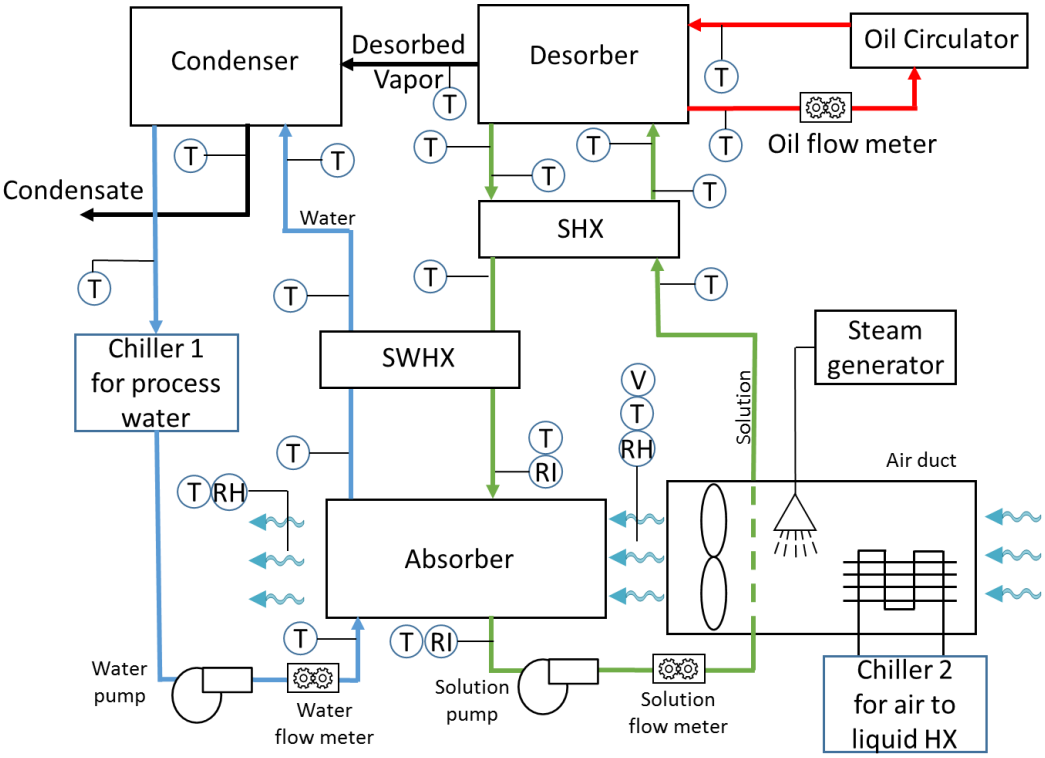


Figure 2. Instrumentation diagram of the experimental test system, when testing the system configuration shown in Figure 1c.

2.3. Absorber

A new generation absorber is utilized in this study. Comparison of this absorber with the configurations of absorbers used in our previous studies are presented in Table 1. The overall absorber configuration has remained the same between different generations. A schematic of an absorber panel showing the desiccant solution, cooling water, and air flows is shown in Figure 3. The absorber used in this study is fabricated from acrylonitrile butadiene styrene (ABS) sheets. Each absorber plate has an internal cooling water core containing water channels and distribution manifolds. The desiccant solution flows on the two outer surfaces of each plate. The plate surfaces are machined to include features designed to slow and spread the solution flow to "wet" the entire surface (front and back) of each panel [8,9]. A membrane is then bonded over the surface features to constrain the solution. Lastly, manifolds are bonded on the top and bottom of each side of the ABS sheet-membrane assembly (i.e., a panel) to direct the IL flow through the gap formed in between the ABS surface and membrane, and the water to the internal water cavity. Air flows across the panels (cf. Figure 3) through 3 mm gaps formed in between them within the absorber assembly.

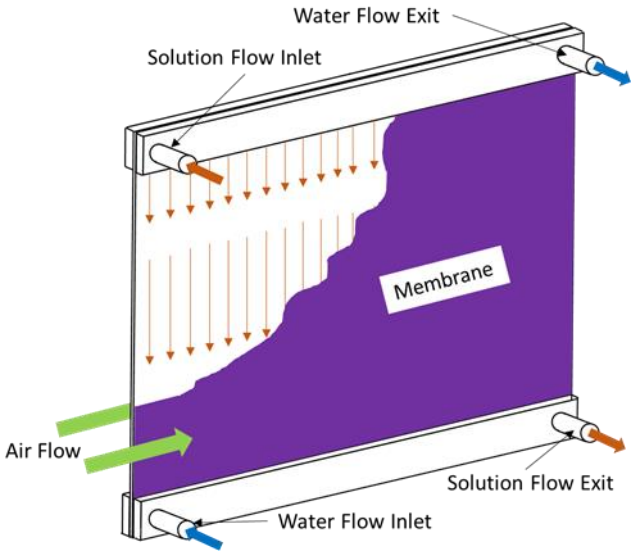


Figure 3. A schematic of a single absorber plate showing that air flows across the membrane while exchanging moisture with the desiccant solution constrained behind the membrane.

Table 1: Absorber design properties and parameters.

Absorber	Gen 1[4]	Gen2[5]	Gen 3[6]	This study
Number of panels	4	7	13	14
Active surface area (m^2)	0.42	0.92	1.89	3.30
Active plate volume (m^3)	0.0084	0.008	0.01191	0.0091
Active surface area/volume ratio (m^{-1})	50	115	158.59	363.6
Plate material	Metal & 3D printed polymer	Polycarbonate	Polycarbonate	ABS
Plate construction	CNC Machined, Adhesive bonded	CNC Machined; Thermal & Adhesive bonded	CNC Machined; Thermal & Adhesive bonded	CNC Machined; Thermal & Adhesive bonded
Solution side fin height	1.5 mm	1mm	0.6 mm	0.6 mm
Membrane constraint	Not bonded on the fins	Thermally bonded on fins	Thermally bonded on fins	Thermally bonded on fins
Membrane pore size	1 µm	1 µm	1 µm	1 µm

2.4. Desorber and Condenser

In contrast to the absorber, the desorber design has remained the same in all our studies. In the desorber, the dilute solution is supplied to the desorber surface by a distribution manifold located at the top of the desorber surface (Figure 4). To ensure a uniform distribution of the solution over the desorber surface (Figure 4A) and to enhance the desorption rate, surface structures described in our earlier studies are utilized here [10]. The desorber surface is heated using silicone oil in a counter flow heat exchange configuration (Figure 4A). To utilize the heat of the desorbed vapor, a condensing surface is built adjacent to the desorber surface, separated by a porous polytetrafluoroethylene (PTFE) membrane (Figure 4B). A critical function of this membrane is to eliminate IL carryover from the desorber while permitting water vapor migration to the condensing surface. The condensing surface is used as the final heating stage of the process water within the AHPWH.

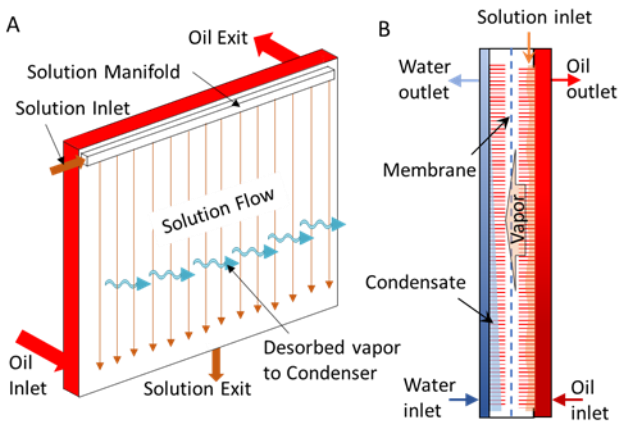


Figure 4. A schematic of the desorber and condenser assembly showing solution falling film flow configuration (A) and the desorption of water vapor, its flow through a PTFE membrane, and subsequent condensation and heating of the process water in the condenser (B).

2.5. Data reduction and uncertainty analysis

The system performance presented in the results and discussion section is calculated based on the measured data described above. The system latent capacity is calculated using Eq. (1).

$$Q_{latent} = \dot{V}_{air}\, \rho_{air}\, h_{fg}\, (\omega_{air_in} - \omega_{air_out}) \tag{1}$$

where $\dot{V}_{air}$ is the absorber air flow rate; ω_{air_in} and ω_{air_out} are the absorber air inlet and exit absolute humidity, respectively; ρ_{air} is the air density as calculated from standard tables using the measured air inlet conditions; and h_{fg} is the water latent heat of evaporation. The desorber heat input is calculated using Eq. (2).

$$Q_{oil} = \dot{V}_{oil}\, \rho_{oil}\, c_{p_oil} (T_{des_oil_in} - T_{des_oil_out}) \tag{2}$$

where $\dot{V}_{oil}$ is the desorber oil flow rate; $T_{des_oil_in}$ and $T_{des_oil_out}$ are the desorber oil inlet and outlet temperatures, respectively; ρ_{oil} is the oil density; and c_{p_oil} is the oil thermal capacity calculated using curve fits derived from data provided by Clearco for their SIL 180 silicone oil. The system water heating capacity is calculated using Eq (3).

$$Q_{water} = \dot{V}_{water}\, \rho_{water}\, c_{p_water} (T_{water,cond_out} - T_{water,abs_in}) \tag{3}$$

where $\dot{V}_{water}$ is the process water flow rate; $T_{water,\ cond_out}$ and $T_{water,\ abs_out}$ are the condenser water outlet and absorber water inlet temperatures, respectively; ρ_{water} is the water density; and c_{p_water} is the water thermal capacity. The system latent heat capacity along with the desorber heat input are used in Eq. (4) to calculate the system dehumidification COP.

$$COP_{dehumidification} = \frac{Q_{latent}}{Q_{oil}} \tag{4}$$

The system water heating capacity along with the desorber heat input are used in Eq. (5) to calculate the system heating COP.

$$COP_{heating} = \frac{Q_{water}}{Q_{oil}} \tag{5}$$

The combined system COP is the addition of the system water heating and system dehumidification COPs as shown in Eq. (6).

$$COP_{combined} = COP_{heating} + COP_{dehumidification} \tag{6}$$

The uncertainty was calculated using an engineering equation solver (EES) uncertainty propagation subroutine. The subroutine is based on NIST guidelines[11] and assuming that the individual measurements are uncorrelated and random, the uncertainty in the calculated quantity can be estimated using Eq. (7).

$$U_Y = \sqrt{\sum_i \left[\frac{\partial Y}{\partial X}\right]^2 U_{X_i}^2} \tag{7}$$

Table 2 below lists all the relevant measurement errors and uncertainties in this experimental study.

Table 2. Measurement error and uncertainty propagation.

Variable	Uncertainty
Fluid temperatures -All T-type TC	±0.8°C
Solution volumetric flow rate	±0.25% reading
Solution RI	±0.5% scale range (0.0003nD)
Water volumetric flow rate	±1% full scale (0.5 LPM)
Air volumetric flow rate	±2% reading
Oil volumetric flow rate	±0.5% reading
Air temperature	±0.3% reading
Air relative humidity	±1.8% RH
Oil heat	±3.7%
Water heat	±2.0%
Concentration (X%)	±0.15%
COP	±4.2%

2.6. Test Conditions

Each configuration was tested at the inlet air and water conditions listed in Table 3. The first test condition represents the inlet water and air temperatures outlined in the Electronic Code of Federal Regulations (e-CFR) to establish water heating Uniform Energy Factor (UEF) performance[12]. The inlet air, IL solution, and oil flow rates as well as the oil inlet temperature have been held constant at 155 cfm, 300 mlpm, 2.85 lpm, and 148 °C, respectively.

Table 3. System inlet air and water test conditions.

Test Condition	Inlet Air Conditions			Water Inlet Conditions	Notes
	Dry Bulb Temp [°C]	Dew Point Temp [°C]	Rel Hum [%]	Temp [°C]	
1	19.7	8.99	50.00	14.4	UEF Conditions
2	19.7	8.99	50.00	30.0	
3	26.8	24.1	85.00	15.0	
4	26.8	24.1	85.00	30.0	
5	30.0	23.9	70.00	15.0	
6	30.0	23.9	70.00	30.0	
7	21.3	13.2	60.00	15.0	
8	21.3	13.2	60.00	30.0	
9	35.0	33.1	90.00	15.0	
10	35.0	33.1	90.00	30.0	

3. Results

Legacy data is presented herein to compare the performance of system configuration A (cf. Figure 1) to configurations B and C [4–7]. The system performance data presented for configurations b and c has been collected as part of this experimental study.

3.1. Configuration B

As shown in Figure 5 for configuration B (cf. Figure 1b), the system water heating capacity depends on both the air and water inlet conditions. As expected, the system water heating capacity increases as the inlet air dewpoint increases. This is due to the increase in the air temperature and moisture content with increasing dewpoint temperature, meaning that more energy is available in the air (more humidity). Also, the water heating capacity decreases as the inlet water temperature increases, because increasing the water temperature elevates the solution temperature resulting in reduction in the heat added to the water.

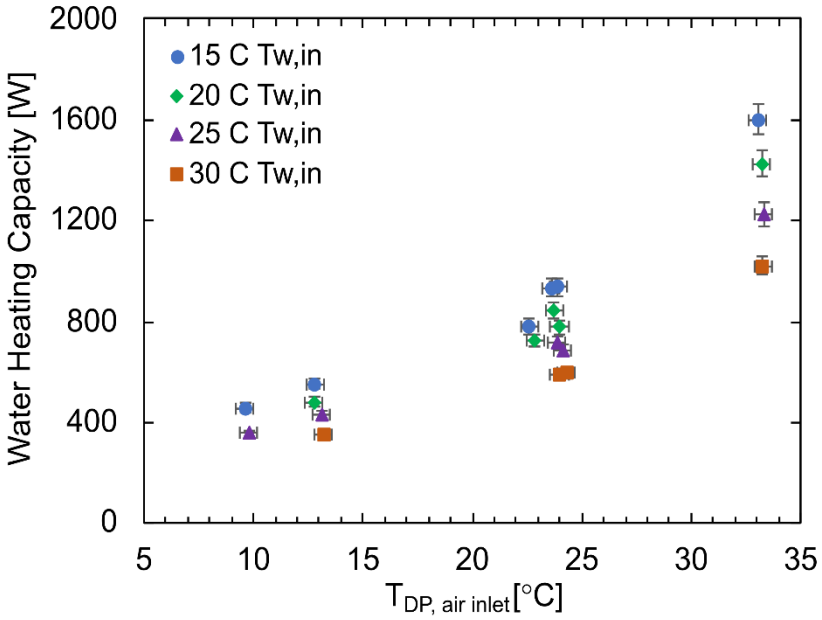


Figure 5. System water heating capacity as function of air inlet dew point temperature and water inlet temperature (Tw, in) when operating in configuration B. The inlet air, IL solution, and oil flow rates as well as the oil inlet temperature have been held constant at 155 cfm, 300 mlpm, 2.85 lpm, and 148 °C, respectively.

Similarly, as the system water heating capacity increases as a function of the increasing inlet air dewpoint temperature and decreasing water temperature, the system heating COP (Figure 6a) and dehumidification COP (Figure 6b) also show similar trends. The very low dehumidification COP at low inlet air dewpoint temperatures is a result of the relatively high absorber solution inlet temperatures (~ 40 °C). While these temperatures served to heat the water in the absorber, they limit the amount of latent heat removed from the air, lowering the system dehumidification COP.

3.2. Configuration C

Similar to configuration A (cf. Figure 1a), configuration C (cf. Figure 1c) uses heat recovery from the solution flow loop for process water heating. However, in configuration C, the solution inlet temperature to SWHX used for heat recovery is substantially lower than that in configuration A, as the solution flow has already been used for heat recovery in the SHX. The water heating capacity, and heating and dehumidification COPs trends for configuration C (cf. Figure 1c) are consistent with those exhibited in configuration B (Figure 7). At a given inlet water temperature, the water heating capacity and heating and dehumidification COPs all increase with increase inlet air dewpoint temperature. As discussed in the section above, this is due to the increase in the energy available in the inlet air as its dewpoint temperature is increased. Although not shown in Figure 7, similar to the trend in configuration B the system capacity and performance decreases with increasing absorber water inlet temperature.

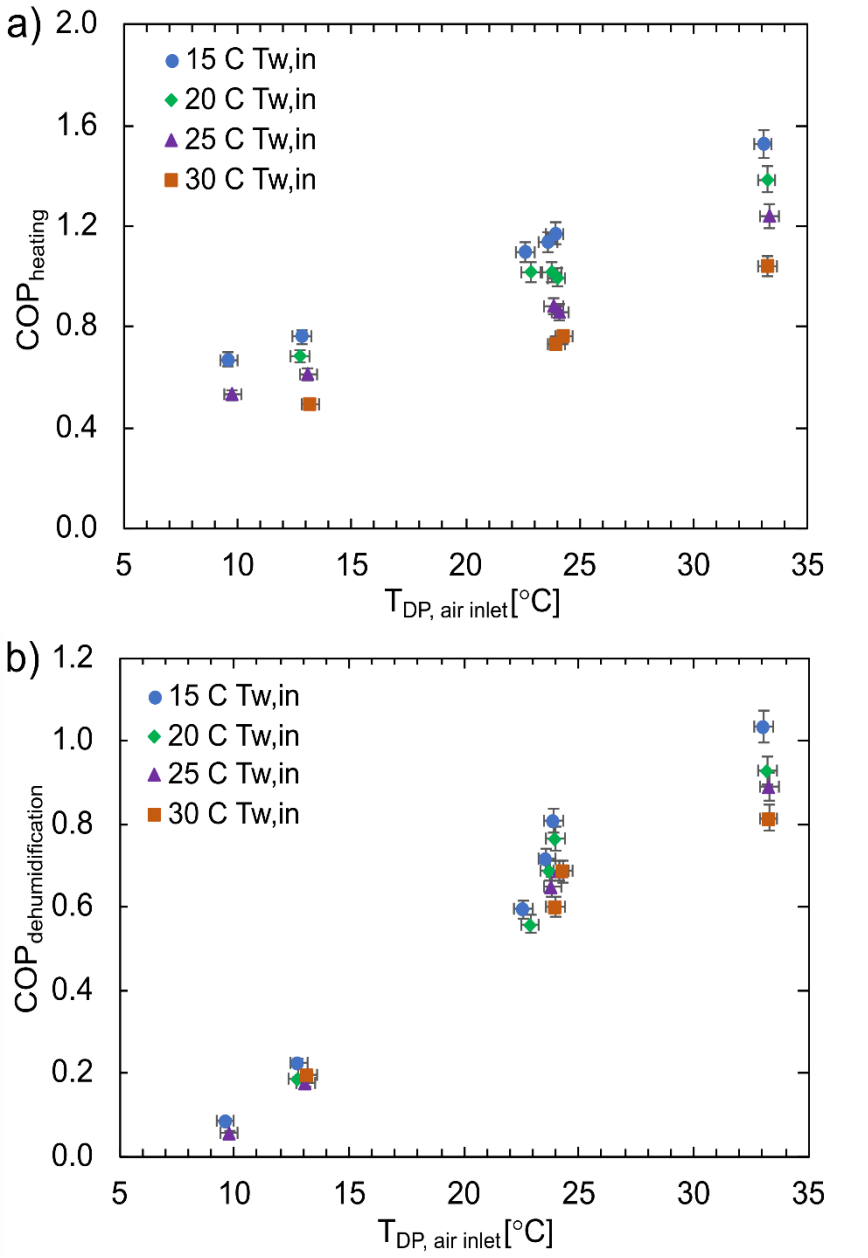


Figure 6. System heating (a) and dehumidification (b) COP as a function of air inlet dew point temperature and water inlet temperature (Tw,in) when operating in configuration B. The inlet air, IL solution, and oil flow rates as well as the oil inlet temperature have been held constant at 155 cfm, 300 mlpm, 2.85 lpm, and 148 °C, respectively.

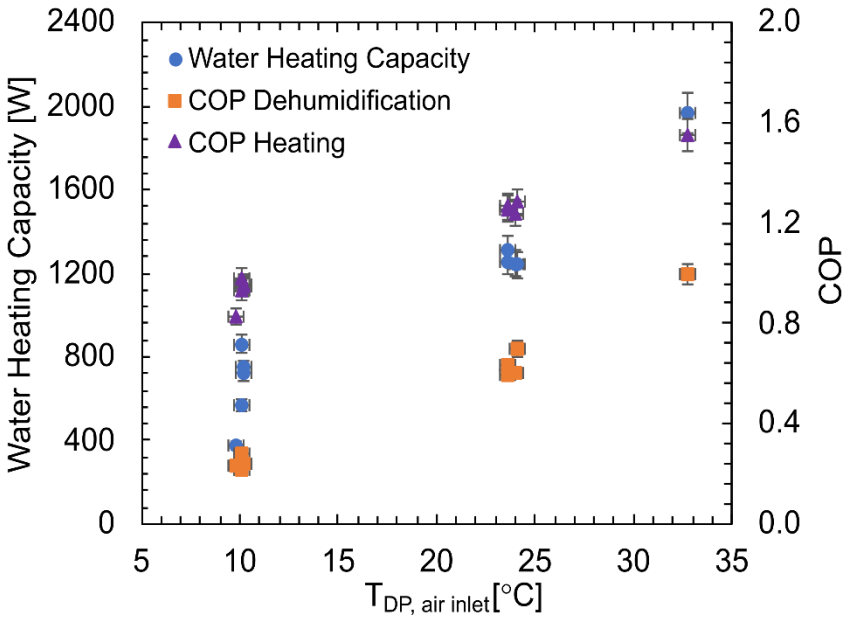


Figure 7. System water heating capacity as function of air inlet dew point temperature when operating in Configuration C. The inlet air, IL solution, and oil flow rates as well as the oil and water inlet temperature have been held constant at 155 cfm, 300 mlpm, 2.85 lpm, 148 °C, and 15 °C respectively.

3.3. Comparison between Different System Configurations

As shown in Figure 8, the differences in the solution heat recovery process as defined by Configurations A, B, and C impact the system water heating capacity. As is shown in Figure 8, the addition of the SWHX in the solution loop (Configuration C) provides a fairly constant increase in system water heating capacity relative to Configuration B over a wide range of inlet air dewpoint temperature. The legacy water heating capacity data for Configuration A, does not demonstrate the same increasing capacity with increasing inlet air dewpoint temperatures [5].

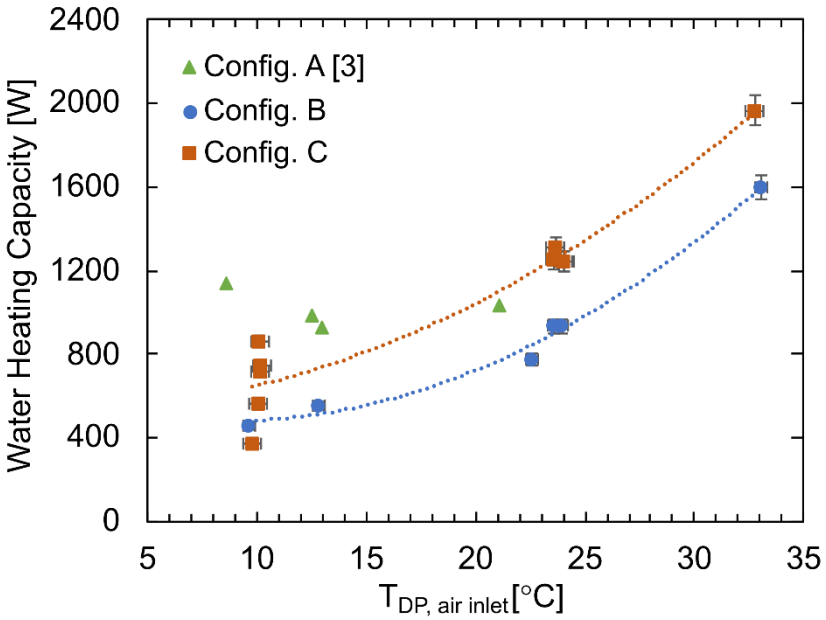


Figure 8. System water heating capacity as a function of air inlet dew point temperature for all three configurations. The inlet air, IL solution, and oil flow rates as well as the oil and water inlet temperatures have been held constant at 155 cfm, 300 mlpm, 2.85 lpm, 148 °C, and 15 °C, respectively.

As shown in Figure 9, the addition of the SWHX has increased both the heating and dehumidification COPs in at low inlet air dewpoints when compared to the COPs of configuration B (Figure 6). However, as

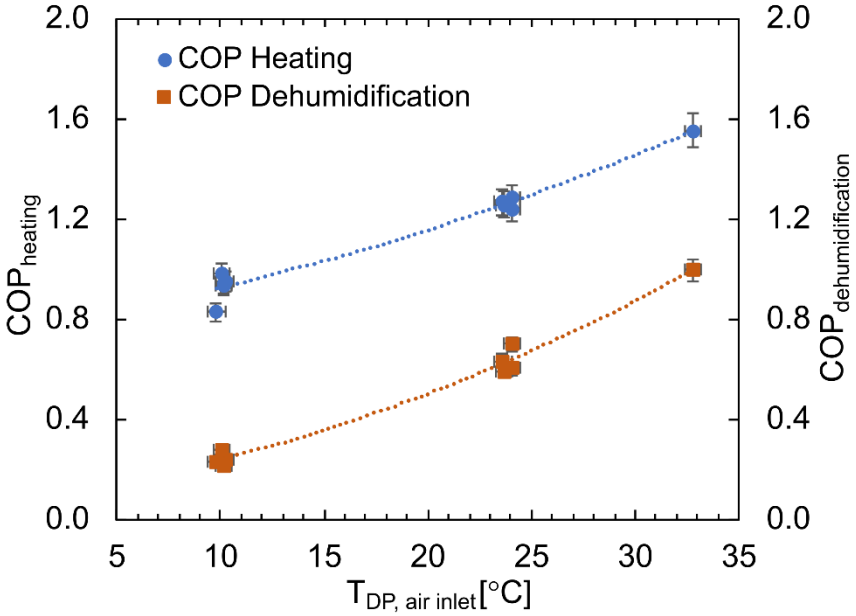


Figure 9. System heating and dehumidification COP as a function of air inlet dew point temperature for configuration C. The inlet air, IL solution, and oil flow rates as well as the oil and water inlet temperatures have been held constant at 155 cfm, 300 mlpm, 2.85 lpm, 148 °C, and 15 °C, respectively.

can be seen in Figure 10 this improved COP of configuration C as compared to configuration B at low inlet air dewpoint temperatures, becomes smaller as the inlet air dewpoint increases. In comparison the combined COP of configuration A, is the best at low inlet air dewpoint temperatures, with its performance being relatively flat as the inlet air dewpoint is increased. This demonstrates the configuration C, provides the best performance

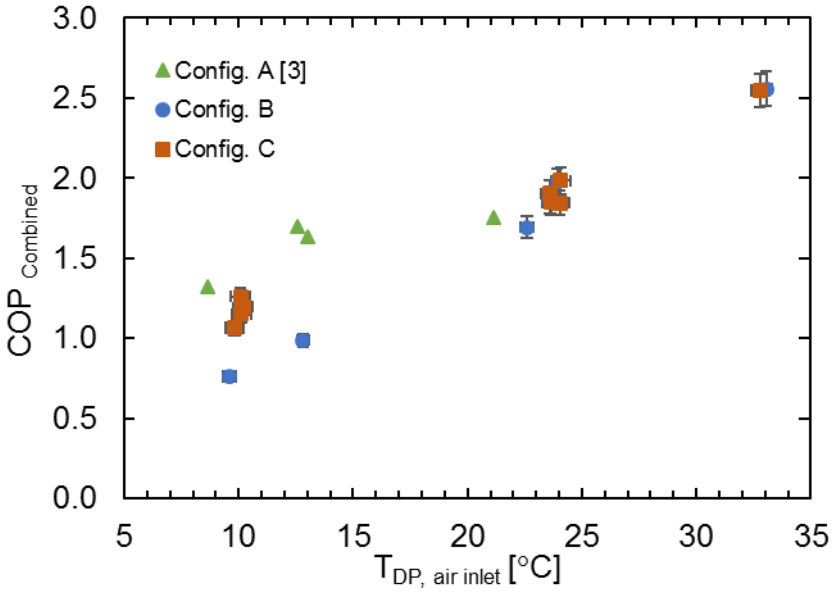


Figure 10. Combined system COP as a function of air inlet dew point temperature for all three configurations. The inlet air, IL solution, and oil flow rates as well as the oil and water inlet temperatures have been held constant at 155 cfm, 300 mlpm, 2.85 lpm, 148 °C, and 15 °C, respectively.

across a wide range of inlet air conditions. At low inlet air dewpoint conditions, the performance of configuration A and C are comparable, but better than that of configuration B. At high inlet dewpoint conditions, the performance of configuration B and C are comparable, but better than that of configuration A.

3.4. Delivery water temperature

For residential water heating applications, the UEF test conditions dictate a water delivery temperature of 51.7 °C. In legacy research, the water delivery rate was held constant, and the water delivery temperature was allowed to fluctuate based on the inlet air and water conditions[5]. In this study, for configurations B and C, the delivery water temperature was maintained at ~ 52 °C, and the water delivery rate was varied based on the inlet air and water conditions. As the performance of this AHPWH improves with increasing air inlet temperature and humidity, a potential application is commercial water heating for kitchens using the kitchen latent load.

The commercial water delivery temperature is 82.2 °C. As such, the ability of the system to deliver water at this temperature, at hot and humid air inlet temperatures, and the impact on system performance was investigated. At an inlet air dewpoint temperature of 32.7 °C and an inlet water temperature of 15 °C, the heating COP of the system decreases from 1.55 to 1.07 as the water delivery temperature is increased from 52 °C to 82 °C for the system operating in Configuration C. Under this same conditions and configuration, the dehumidification COP decreases slightly from 0.99 to 0.86. The decrease in heating COP is expected as the condenser operating temperature has been increased, while the desorber oil inlet temperature has been held constant. Future studies are warranted to increase the system COP by changing its regeneration temperature as well as IL properties.

4. Conclusions

A lab scale IL absorption heat pump water heater system was experimentally tested in two configurations, across a range of inlet air and water conditions, including those delineated for UEF testing. The system performance of these two configurations were compared to each other, as well as, a third configuration used in previous research efforts. These configurations demonstrated the ability to deliver 52 °C water at UEF conditions at a heating COP of 1.26 [6] (configuration A), 0.67 (configuration b), and 0.98 (configuration C). This performance increased to a heating COP of 1.52 (configuration B) and 1.55 (configuration C) at an inlet air dewpoint of ~ 32 °C. These COPs compare well to the primary COP of 1.42 [13] of the most efficient electric HPWH (UEF = 4.07) on the market today.[14] Additionally, the ability to deliver 82 °C water at hot and humid inlet air conditions demonstrated the viability of this technology in commercial water heating applications. The use of IL demonstrated the robustness of the system in providing water heating across a wide operational range, without control equipment for mitigating crystallization. Further optimization of the system flow rates offers the ability to improve.

Nomenclature

ABS	acrylonitrile butadiene styrene
AHPWH	absorption heat pump water heater
CFM	cubic feet per minute
COP	coefficient of performance
$COP_{combined}$	sum of $COP_{heating}$ and $COP_{dehumidification}$
$COP_{dehumidification}$	dehumidification capacity (latent cooling)/thermal energy consumed
$COP_{heating}$	water heating capacity/thermal energy consumed
e-CFR	electronic code of federal regulations
HX	heat exchanger
IL	ionic liquid
LPM	liters per minute
GHG	greenhouse gas
mLPM	milliliters per minute
PTFE	polytetrafluoroethylene
RI	refractive index
RH	relative humidity
SHX	solution heat exchanger
SOHX	solution-oil heat exchanger
SWHX	solution-water heat exchanger
$\dot{m}$	mass flow rate (kg/sec)

T	temperature (°C)
Tw,in	water inlet temperature (°C)
$T_{DP,in}$	inlet air dew point temperature (°C)
UEF	uniform energy factor

Acknowledgements

This work was sponsored by the U. S. Department of Energy, Office of Energy Efficiency and Renewable Energy (EERE), under Award Number DE-EE0009162 with the University of Florida. The authors would also like to acknowledge Mr. Antonio Bouza, Ms. Coriana Fitz, and Dr. Isaac Mahderekal from the U.S. DOE Building Technologies Office (BTO) for their support of this research.

References

[1] Jarraud M, Steiner A. Summary for policymakers. vol. 9781107025. 2012. https://doi.org/10.1017/CBO9781139177245.003.
[2] Cresko J. Industrial Decarbonization Roadmap 2022.
[3] Moghaddam S, Chugh D, Nasrisfahani R, Bigham S, Fazeli SA, Yu D, et al. Open absorption cycle for combined dehumidification, water heating, and evaporative cooling, 2018.
[4] Chugh D, Gluesenkamp K, Abdelaziz O, Moghaddam S. Ionic liquid-based hybrid absorption cycle for water heating, dehumidification, and cooling. Appl Energy 2017;202:746–54. https://doi.org/10.1016/j.apenergy.2017.05.161.
[5] Chugh D, Gluesenkamp KR, Abu-Heiba A, Alipanah M, Fazeli A, Rode R, et al. Experimental evaluation of a semi-open membrane-based absorption heat pump system utilizing ionic liquids. Appl Energy 2019;239:919–27. https://doi.org/10.1016/j.apenergy.2019.01.251.
[6] Gluesenkamp KR, Kumar N, Abu-heiba A, Patel V. Semi-open absorption water heater : experimental results 2020:1–11.
[7] Gluesenkamp KR, Chugh D, Abdelaziz O, Moghaddam S. Efficiency analysis of semi-open sorption heat pump systems. Renew Energy 2016:1–10. https://doi.org/10.1016/j.renene.2016.07.075.
[8] Mortazavi M, Isfahani Nasr R, Bigham S, Moghaddam S. Absorption characteristics of falling film LiBr (lithium bromide) solution over a finned structure. Energy 2015;87:270–8.
[9] Nasr Isfahani R, Bigham S, Mortazavi M, Wei X, Moghaddam S. Impact of micromixing on performance of a membrane-based absorber. Energy 2015. https://doi.org/10.1016/j.energy.2015.08.006.
[10] Mortazavi M, Schmid M, Moghaddam S. Compact and efficient generator for low grade solar and waste heat driven absorption systems. Appl Energy 2017;198:173–9. https://doi.org/10.1016/j.apenergy.2017.04.054.
[11] Taylor BN, Kuyatt CE. Guidelines for Evaluating and Expressing the Uncertainty of NIST Measurement Results. Technology (Singap World Sci) 1994:2.
[12] Subpt B, App E. Pt. 430, Subpt. B, App. E 2016.
[13] April U. DNV GL - ENERGY DEER Water Heater Calculator Documentation 2022.
[14] ENERGY STAR Certified New Homes : ENERGY STAR n.d.

14th IEA Heat Pump Conference
15-18 May 2023, Chicago, Illinois

Thermodynamic analysis of the cascade economization cycle for high temperature heat pump applications

Elias N. Pergantis[a,*], Abd Alrhman M. Bani Issa[a], John K. Brehm, Andreas J. Hoess[a], Eckhard A. Groll[a], Davide Ziviani[a]

[a]Ray W. Herrick Laboratories, School of Mechanical Engineering, Purdue University West Lafayette, 47907-2099, USA

Abstract

High-temperature heat pumps (HTHP), supply temperatures > 100°C, have received significant traction in recent years due to the high total energy usage by processing industries and the phasing down of hydrocarbons. However, despite their potential to significantly reduce greenhouse gas emissions, electrically driven HTHPs suffer considerable performance losses at temperature lifts greater than 60 °C. However, multiple industrial sectors require supply temperature > 120°C while at the same time high temperature high-capacity waste heat sources are often not readily available. Currently, the most widely used cycle for HTHPs with a large temperature lift is the cascade arrangement with different refrigerants on the high side and low side. In this work, we propose staging either the high-side or the low-side compressor, and as such, we investigated different types of economization through a thermodynamic simulation in EES. The refrigerants selected were R-32 and R-1233zd(E). It was found that by using open economization on the high side and by optimizing the cascade temperature, performance enhancements in the order of 25% are achievable over the baseline cascade cycle.

© HPC2023.
Selection and/or peer-review under the responsibility of the organizers of the 14th IEA Heat Pump Conference 2023.

Keywords: High Temperature Heat Pumps; Cascade; GWP; Decarbonization

1. Introduction

Decarbonization policies, government initiatives (e.g., carbon taxes), and many other measures have resulted in rapid replacement of fossil fuels in applications where heating can be effectively electrified by means of heat pumps. Although the debate is mostly focused on buildings, industrial processes require vast amounts of heat, primarily supplemented by fossil fuel sources. In the work of Fox et al. (2021), it was estimated that 3416 PJ of heat are required in the U.S. for process heat, with roughly 50% used for supply temperatures between 120 to 160 °C, 30% for 160 to 200 °C and the rest for supply temperatures less than 120 °C [1,2]. Although trends from Germany and France indicate lower usage of process heat above 140 °C, it is immediately apparent that a vast potential of decarbonization potential exists in switching these processes from gas/oil burners to heat pumps. These heat pumps, labeled as High Temperature Heat Pumps (HTHPs), are usually characterized by heat sink temperatures greater than 100 °C and can be further categorized as a very high temperature heat pumps (VHTHP). However, since the specific limits are not clearly defined, this differentiation will not be used in this work. Additionally, this work will focus on closed systems, compression heat pumps, although open systems (mechanical vapor recompression, thermal vapor recompression) and closed (sorption) have been investigated elsewhere [3,4,5].

HTHPs in the recent scientific literature have received significant academic traction, with multiple review papers [2,6,7], work on refrigerant selection [8,9], advanced thermodynamic cycles [10,11], experimental pilot studies [12,13] and technoeconomic analyses [14]. This interest has not only been restricted to academia, but

* Corresponding author. Tel.: +1-734-263-4421.
E-mail address: epergant@purdue.edu

multiple companies have also come up with industrial models, some of which are shown in Table 1, a more comprehensive list is provided in [2].

Table 1. Some industrial HTHP models available in the market.

	Model 1	Model 2	Model 3	Model 4
Name	SGH 120/165	HEM-HR90	Ochsner IWDSS R2R3B	Viking HeatBooster S4
Company	Kobelco	Kobelco	Ochsner	Viking Heat Engines
Capacity [kW]	380/660	160	400	28/188
Operating Evaporator [°C]	25 - 65	-10 - 40	8 - 45	60 - 100
Operating Condenser [°C]	120 - 165	65 - 90	70 – 130	110 - 150
Type of Cycle	Single Stage	Single Stage	Cascade	Single Stage
Refrigerants	R245fa	R-134a/R245fa	R245fa(H)/R-134a(L)[†]	R-1336mzz(Z)
GWP Category	High	High	High	Low
Compressor Type	Twin Screw	Twin Screw	Screw	Piston
Heat Source Type	Water	Air	Air/Water	Water
Purpose	Steam Delivery	Process Heat	Process Heat	Process Heat

The widespread adoption of this technology is, however, restricted by several challenges, including the following:

- **Compressor design and oil management:** The large capacities of industrial applications, the high superheat temperature and material stresses are significant challenges to compressor designs and their longevity. Additionally, synthetic lubricants that can withstand such high temperatures and operate with the selected refrigerants need to be identified.
- **Refrigerant selection:** For most of the available high temperature heat pump applications, refrigerant R245fa is used. This essentially has to do with the familiarity of the manufacturers with this refrigerant due to its extensive use in waste heat recovery Rankine cycles. However, this refrigerant has a high GWP, and due to the large refrigerant charge of these systems, its usage can be detrimental to the environment. Therefore, much research is focused on finding low GWP refrigerants, with non-flammability also being a vital attribute [15].
- **Coefficient of Performance (COP):** The process heat industry requires massive sums of heat to be supplied. The transition to electricity would result in significant loads to the distribution grid. Additionally, the lower price of gas over kWh in most of the world gives a considerable incentive for the industry to continue using fossil fuels. Therefore, thermodynamic cycles with high COP are required to meet this challenge and incentivize HTHP adoption.
- **Cost:** Currently, HTHP presents a more costly solution over gas burners, although this difference can decrease with market maturity, economies of volume, higher gas pricing, and tax incentives.

The aim of this work is to address some of the challenges with respect to the COP decrease as the lift temperature (ΔT_{lift}), defined as the difference between the sink and the source temperature, increases. In the recent works of Kosmadakis et al. (2020) and Mateu-Royo et al (2021), it was identified that for low temperature lifts (50 K or below), single-stage with economization and internal heat exchanger (IHX) performed best, while at higher lifts (60 K or above), two-stage cascade with different refrigerants on the high side and the low side selected appropriately performs better [10,14]. However, in many cases, a far greater ΔT_{lift} is necessary, in the order of 80 to 100 K, with some applications requiring an even greater temperature lift. An example of this could be a pulp factory in the U.S., receiving waste heat at 40 °C and needing to provide heat for its processes in the 120 to 140 °C range. Although higher source temperatures would be preferred, that is not readily available in many cases. Another example is that of air source systems, such as the HEM-HR90 (see Table 1), which are subject to atmospheric variations even at lower sink temperatures. Through a literature review, it was identified that limited research has been on this topic [16,17], and in particular, that of triple stage (treble) compression, an option widely used in the LNG and cold process industry where a large ΔT_{lift} is also necessary. A benefit of triple stage compression is that the pressure across each compressor is limited, increasing its performance while decreasing the superheat losses. As such, we propose comparing a number of possible triple stage compression architectures with some of the currently available two stage, in particular,

two-refrigerant cascade cycle, with or without internal heat exchangers, to quantify the potential expected improvements.

The novelty of the work lies in investigating multiple potential architectures as well as using a variable compressor map, unlike the previous authors [16], as well as proposing in so far as the authors are aware, a novel treble compression cycle that of cascade economization, presented in Section 2.1. This cycle can achieve three compression processes with only two compressors by staging one of these compressors. The paper is structured in the following manner:

- **Thermodynamic Modeling & Cycles:** Cycles analyzed, thermodynamic equations and assumptions.
- **Refrigerant Selection:** Selecting refrigerant the best refrigerant candidates for the cycles.
- **Parametric Analysis:** Comparative performance of different cycles and impact of operating conditions. Optimal system parameters ($T_{cascade}$). Impact of modeling assumptions and system parameters (pinch analysis, compressor map).
- **Discussion:** Outcomes from parametric analysis, identified trends, and proposed future work.

2. Thermodynamic Modeling & Cycles

2.1. Cycle Architectures

Economization cycles are able to improve thermodynamic performance of cycles by splitting one larger less efficient compression process to two smaller more efficient ones which results in performance gains. Since

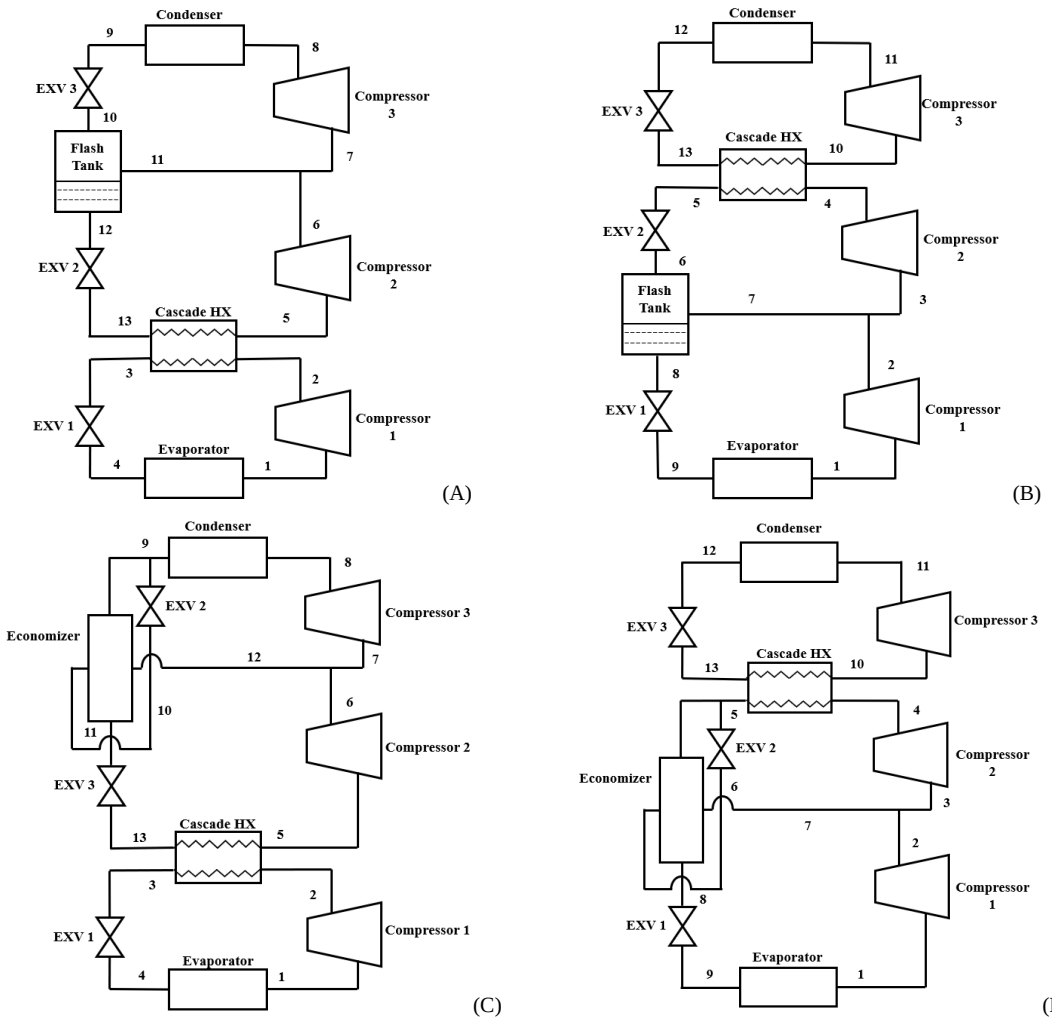


Fig 1. Cascade economization cycles investigated: (A) Open economization HT, (B) Open economization LT, (C) Closed economization HT, (D) Closed economization LT.

this work aims to analyze the potential of staging compressors in HTHPs, closed and open economization were investigated. In particular, given the high lift temperatures sought, the cycles are proposed in a cascade format, where staging occurs either on the low or high side. These cascade sides use different refrigerants to optimize cycle performance and are henceforth referred to in this paper as LT for the low temperature loop and HT for the high temperature loops. These cycles are illustrated in Figure 1.

The cycles were compared to the industry standard for high lift temperatures, namely the cascade cycle (see Ochsner IWDSS R2R3B). Additionally, an improved cascade cycle given in [24] was investigated using two internal heat exchangers. Lastly, a triple cascade cycle with three separate compressors, rather than staged as in Figure 1(A), was also analyzed. These cycles are provided in Figure 2.

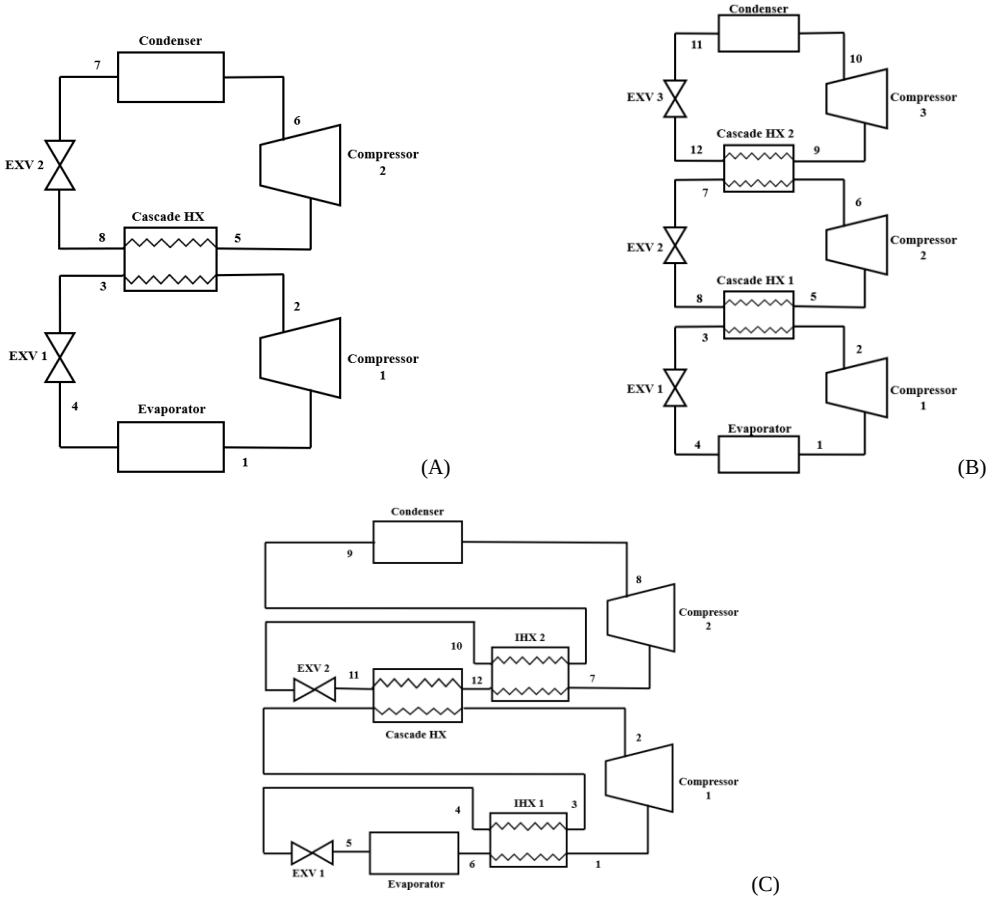


Fig 2. Variations of the simple cascade investigated: (A) Baseline cascade, (B) Triple cascade, (C) Cascade with internal HXs.

2.2. Thermodynamic Model

A thermodynamic model was developed to investigate the system performance. Calculations were performed in EES [18]. The following modeling assumptions were made to develop the models:

- Steady-state, steady-flow analysis.
- Kinetic Energy and Potential Energy are neglected.
- Negligible pressure drops and heat losses to the surrounding in heat exchangers and piping.
- Adiabatic expansion valves with isenthalpic expansion.

The compressor power can be expressed in terms of isentropic efficiency:

$$\dot{W}_c = \frac{\dot{m}(h_{out,is} - h_{in,is})}{\eta_{is}} \quad (1)$$

To define isentropic efficiency, one must select a compressor technology, which is mainly subject to the refrigerant used and capacity of the system. For HTHP applications, the vast majority of research and industrial development is focused on piston, screw, twin-screw, and turbo compressors, of which the most prominent type is that of screw. As such, we will primarily focus on screw compressors, with Equations 2 and 3

representing the compressor's isentropic and volumetric efficiency as a function of the pressure ratio. The impact of compressor isentropic efficiency will be further investigated in Section 4.3.

$$\eta_{is} = b + cln\left(\frac{\dot{v}_{in}}{3600}\right) + d(r_{vc,i}) \quad (2)$$

$$\eta_{vol} = 0.95 - 0.0125 r_{pc,i} \quad (3)$$

These correlations were obtained from [14,22] and the fit variables are given in [22]. The volumetric heat capacity (VHC) was used to select the best refrigerant in the cascade cycle. It was modeled accounting for the low and high sides as per [10]:

$$VHC = \rho_{c,in}\eta_{vol}\Delta H_{cond} \quad (4)$$

Heat exchangers were modeled using pinch analysis, the values shown in Table 2. For the internal heat exchanger effectiveness, Equation 5 was used.

$$\varepsilon_{IHX} = \frac{h_{vap,out} - h_{vap,in}}{h_{vap,out} - h_{liq,in}} \quad (5)$$

$$\dot{Q}_{HX} = \dot{m}(h_{out} - h_{in}) \quad (6)$$

For the cascade HX, the approach of [19] was used. In terms of the economization, the optimum pressure from the two-stage economization cycle was used (no cascade) [20].

$$P_{int} = \sqrt{P_{high}P_{low}} \quad (7)$$

Finally, the system COP and 2nd Law efficiency can be defined as:

$$COP = \frac{\dot{Q}_{sink}}{\sum_i \dot{W}_{c,i}} \quad (8)$$

$$COP_{Carnot} = \frac{T_{sink}}{T_{sink} - T_{source}} \quad (9)$$

$$\eta_{II} = \frac{COP}{COP_{Carnot}} \quad (10)$$

Table 2. Assumptions and conditions used in modeling simulations.

Parameter	Assumed Value
Sink Temperature [°C]	100 – 150
Source Temperature [°C]	-10 – 40
ΔT_{lift} (T_{source}- T_{sink}) [°C]	60 – 110
Compressor Type	Screw
Pinch [°C]	10
Subcooling [°C]	5
Superheat [°C]	5
ΔT_{casc} [°C]	5
IHX effectiveness (ε)	0.7
T_{cas}	Obtained by using Golden Section Algorithm in EES for COP maximization
Nominal state for refrigerant selection†	T_{source} = 40 °C T_{sink} = 120 °C

†The nominal state was used in the simulation (Section 3) on the refrigerant selection section to compute the VHC and COP.

3. Refrigerant Selection

To compare the performance of the cycles in Section 2.1, it was necessary to select some appropriate refrigerants. However, choosing refrigerants in a cascade cycle for a high temperature heat pump system is not straightforward. An optimal refrigerant should address thermodynamic aspects (e.g., thermal stability at high temperatures, volumetric capacity, etc.), environmental and safety concerns (e.g., GWP, ODP, flammability and toxicity), and techno-economic considerations. The following analysis shows all relevant parameters for a proper selection. Due to the cascade nature of the cycles investigated, two refrigerants have to be selected, one to operate on the high side and one on the low side. The normal boiling point (NBP) should be low enough to allow vaporization during regular operation , while the critical temperature of the refrigerant defines the upper temperature border for a system that is not supposed to run in supercritical operation. So especially for the high temperature loop, selecting a refrigerant whose critical point is above the anticipated condensation temperature is essential. From an environmental standpoint, the refrigerant should have an ODP of 0 and a GWP that is as low as possible. Furthermore, the safety classes helped to distinguish between lower toxicity (class A) and higher toxicity (class B) as well as to estimate the flammability (increasing in the order of 1, 2L, 2, and 3) [21]. Low toxicity and flammability are generally preferred, but the thermodynamic properties sometimes require a tradeoff. Finally, the techno-economic parameters are important. Values like the volumetric heat capacity (VHC) can tell how big the components will be, so this value should be high to reduce component sizing. At the same time a high COP is preferred to allow an efficient operation. To initiate the calculations, R-290 was used as a reference fluid in the low-temperature cycle, while R-600 was the reference fluid for the low temperature loop refrigerant.

The comparison for the low-temperature cycle refrigerants (Table 3) shows that the highest COP can be achieved with R-717 (ammonia). The pros of this refrigerant are its high VHC, which is the third highest in the comparison. Also, it is a natural refrigerant with an ODP and a GWP of 0. However, it is toxic and mildly flammable. In addition, the economic factor comes into place. Ammonia systems require stainless steel components and cannot be manufactured with copper parts. Therefore, when accounting for VHC, COP, GWP, and classification, **R-32** is the appropriate candidate. In this work, A3 refrigerants were eliminated due to adoption issues in practical applications, although the reader is directed to the following [9,12]. R-600 and R-601 are attractive options for the HT side, albeit flammable. As such, research has been focused on the following HFOs: R-1336mzz(Z), R-1234ze(Z), R-1233zd(E), and R-1224yd(Z) [8]. Of these, **R-1233zd(E)** was selected primarily due to its high performance and critical temperature. In the case of the triple cascade cycle, R-32 was used for the LT loop, while R-1233zd(E) for MT and HT. A different choice for the MT loop was not made since the analysis was limited to T_{sink} = 150 °C. Had a higher sink temperature been required, a 3rd choice, such as R-601, would have been made.

Table 3. Low Temperature Loop Refrigerants

Refrigerant	**NBP**	**Critical Temperature**	**ODP**	**GWP**	**Safety Classification**	**T_{CAS}**	**VHC**	**COP**
	(°C)	(°C)	(-)	(kg CO_2)	ASHRAE [25]	(°C)	(kJ/m3)	(-)
R-290	-42.1	96.7	0	~10	A3	72.9	5724	2.41
R-744 (CO2)	-78.5	31.0	0	1	A1	-	-	-
R-717 (NH3)	**-33.3**	**132.4**	**0**	**0**	**B2L**	**87.7**	**9717**	**2.62**
R-718 (H2O)	-33.3	132.4	0	<1	A1	103.3	63	2.55
R-1216	-30.3	85.7	0	<1	B3	66.1	4577	2.30
R-1234yf	-29.5	94.7	0	4	A2	70.1	4395	2.36
R-125	-48.1	66.0	0	3500	A1	58.0	7760	2.18
R-134a	-26.1	101.1	0	1430	A1	74.2	4896	2.44
R-143a	-47.2	72.7	0	4470	A2	64.6	7188	2.26
R-161	-37.5	102.1	0	12	A3	77.8	6493	2.48
R-32	**-51.6**	**78.1**	**0**	**675**	**A2L**	**69.9**	**11496**	**2.34**
R-404A	-46.2	72.1	0	3900	A1	63.6	7105	2.24
R-507A	-46.7	70.6	0	3985	A1	61.0	7459	2.23
R-600	**- 0.5**	**152.0**	**0**	**4**	**A3**	**81.4**	**1992**	**2.59**

Table 4. High Temperature Loop Refrigerants

Refrigerant	**NBP**	**Critical Temperature**	**ODP**	**GWP**	**Safety Classification**	**T_{CAS}**	**VHC**	**COP**
	(℃)	(℃)	(-)	(kg CO_2)	ASHRAE [25]	(℃)	(kJ/m3)	(-)
R-600	**-0.5**	**152.0**	**0**	**4**	**A3**	**72.9**	**3990**	**2.41**
R-601	36.1	196.6	0	5	A3	69.4	1697	2.57
R-1336mzz(Z)	**33.4**	**171.3**	**0.0003**	**2**	**A1**	**71.2**	**1966**	**2.47**
R-1234ze(Z)	**9.8**	**150.1**	**0.0001**	**<1**	**A2L**	**70.8**	**3714**	**2.47**
R-1233zd(E)	**18.0**	**166.5**	**0**	**1**	**A1**	**69.5**	**2936**	**2.53**
R-1224yd(Z)	**14.0**	**155.5**	**0**	**<1**	**A1**	**72.5**	**3223**	**2.44**
Novec 649	49.0	168.7	0	<1	N/A	83.4	1304	2.19
R-717 (NH_3)	-33.3	132.4	0	0	B2L	64.2	17512	2.46
R-718 (H_2O)	**100.0**	**373.9**	**0**	**0**	**A1**	**56.6**	**242**	**2.78**
R-744 (CO_2)	-78.5	31.0	0	1	A1	-	-	-
R-245fa	58.8	154.0	0	1030	B1	73.2	3594	2.43
R-365mfc	40.2	186.85	0	782	N/A	69.6	1629	2.51

4. Results

4.1. Impact of operating conditions and Second Law Efficiency

The cycles presented in Section 2.1 were numerically investigated in EES. The purpose of this analysis was to quantify the performance degradations resulting from compression across a range of ΔTlift and the potential benefit of staging one of the compression processes. Firstly, the source temperature was fixed at 40 ℃, and the sink temperature was increased. This would indicate a process with a stable waste heat source, and the sink is required at a high temperature, similar to the pulp process industry. The results are shown in Figure 3.

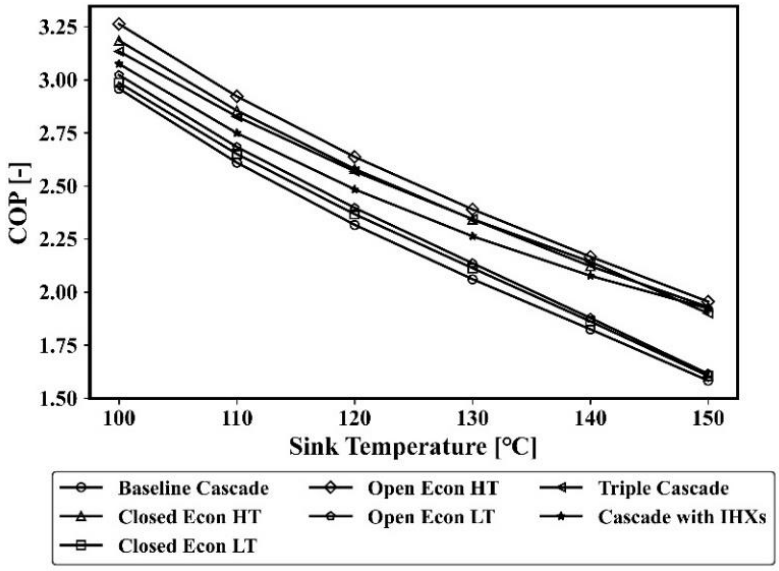


Fig 3. Performance (COP) of different cycles for increasing sink temperature.

The results indicate that cycles that perform the two-stage compression on the HS outperform those that do not. Of these, open economization beats closed economization. Open economization on the high side offers an increasing COP enhancement with ΔT_{lift} over the simple cascade, starting at 10% (ΔT_{lift} = 60 ℃) and increasing up to 25% for (ΔT_{lift} = 110 ℃). Cascade with IHXs and triple cascade are the 3rd and 4th performing cycles, respectively, even when not accounting for the pressure drops in the IHXs. These trends are also shown in Figure 4 with respect to the second law efficiencies of these systems.

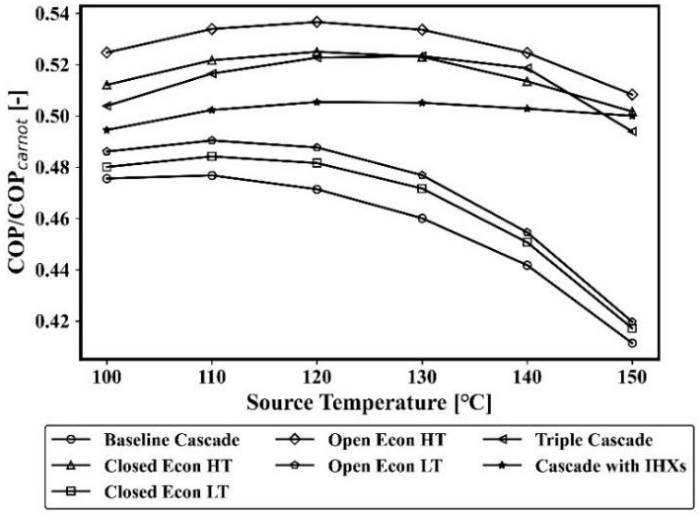


Fig 4. Second law efficiency of different cycles for increasing sink temperature.

With the goal of HTHPs to replace typical gas furnaces, it is also vital to investigate scenarios where waste heat is not readily available and rather air source systems is used. An industrial example of such a heat pump is Ochsner IWDSS R2R3B. The sink temperature is fixed at 120 °C. This is shown in Figure 5.

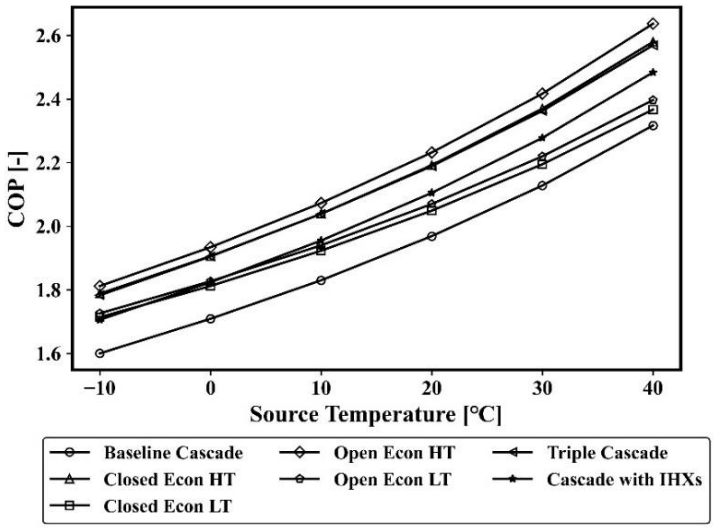


Fig 5. Performance (COP) of different cycles for decreasing source temperature

The results presented so far indicate that the performance of the cascade cycle rapidly deteriorates since the lift at each compression process is significant. To understand this further, by redefining the lift temperature as $\Delta T_{lift,LT} = T_{cas} - T_{source}$ and $\Delta T_{lift,HT} = T_{sink} - T_{cas}$, and assuming that the optimal cascade temperature is approximately $(T_{sink} + T_{source})/2$, at T_{sink} = 140 °C and T_{source} = 40 °C we can compute $\Delta T_{lift,LT} = \Delta T_{lift,HT}$ = 50 °C. This represents an adverse temperature lift, resulting in high-pressure ratios and that a staging process similar to the ones presented in this paper are required. The impact of T_{cas} is further investigated in Section 4.2

4.2. Optimizing Cycle Parameters for COP

It was identified that two system parameters could be treated as open for optimization. Those are the intermediate pressure used in the staging of the compressor and the cascade temperature. In this work, the empirical expression shown in equation 7 has been used to simplify the analysis. Instead, optimization in EES was performed by noting that COP(T_{cas}) and using the golden-section algorithm to find the best combination of COP and T_{cas}. In the case of the triple cascade, COP($T_{cas,LT}$, $T_{cas,HT}$) was used to perform combined optimization. Future work should also be directed at identifying COP(T_{cas}, P_{inter}) since the square root rule

(widely adopted empirical relation in Eq. 7) might not hold. The results presented in Section 4.1 are based on the optimized cascade temperatures.

Figure 6 indicates that based on which side the staging occurs, T_{cas} is calculated so that the temperature across this side increases given that the isentropic efficiency is better for the dual-stage compressor on that side. This means that for the cascade cycle, the cascade temperature remains close to $(T_{sink} + T_{source})/2$ since staging does not occur [10]. A similar trend is seen for the triple cascade cycle, where the temperatures are attempting to split ΔT_{lift} in three equal fractions. The slight for the triple cascade in Fig 6 occurs to the refrigerant properties.

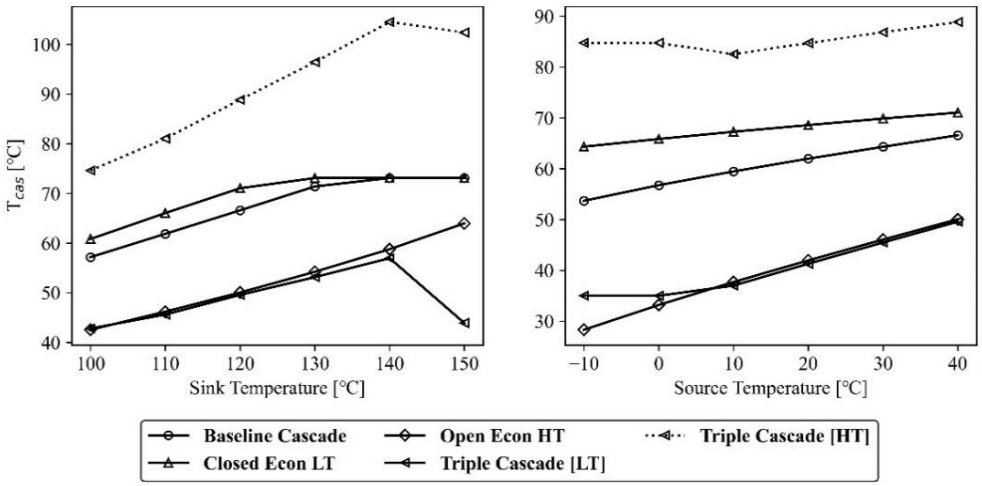


Fig 6. Optimum cascade temperature for different arrangements and different sink and source temperatures.

4.3. Impact of System Assumptions

Finally in this section we investigate the impact of the system assumptions on the heat exchanger modeling as well as the compressor map used.

4.3.1. Heat Exchanger Modeling

Simple thermodynamic models were selected for the heat exchangers given the comparative nature of the analysis. For the refrigerant-to-refrigerant (non IHX, cascade) HXs and the air/water to refrigerant HXs, a pinch analysis approach was used since temperature on the refrigerant side remains relatively constant due to phase change. From the thermodynamic results. it was identified that while the superheat has negligible impact to the performance of the cycle, while increasing subcooling enhances capacity and therefore the COP. Figure 7 indicates the importance of using high performance heat exchangers and that an open economization cycle on the HT side can achieve a COP of almost 2.5 at a ΔT_{lift} = 100 °C (20 – 120 °C), at a pinch of 5 K which is achievable with current heat exchanger technology.

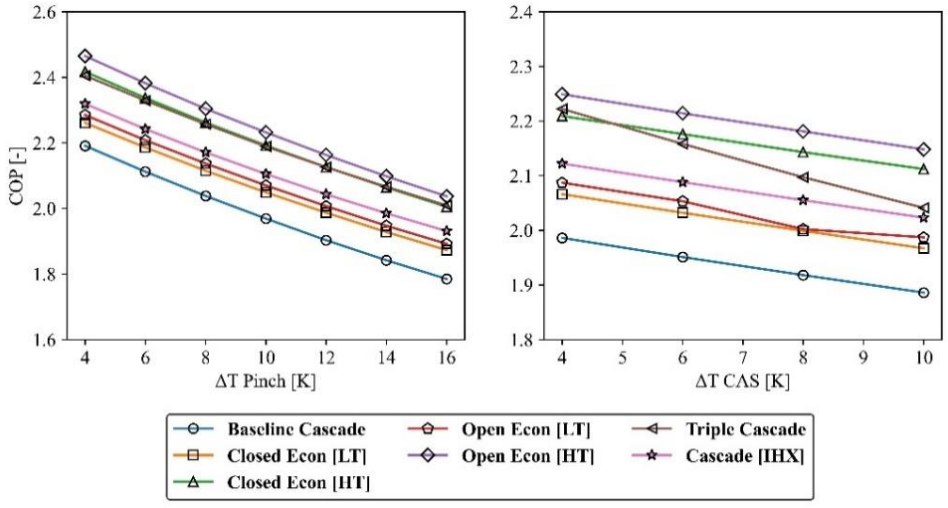


Fig 7. Impact of HX modeling, pinch, superheat, subcooling and cascade pinch on cycle performance.

While the pinch analysis could be used in the case of the phase change processes, it cannot be used in the modeling of the IHX given that the refrigerant (same refrigerant on both sides) is in the subcooled and superheated regions. As such, the effectiveness approach was adopted. Figure 8 serves a two-fold purpose. Firstly, the impact of the IHX effectiveness was analyzed. By changing the value from 0.5 to 0.9, it was found that the IHX on the high side (see Figure 2C) had significantly greater impact on the performance of the cycle. As such, the impact of the effectiveness (ε) was investigated on a cycle with one IHX, two IHXs and compared to the cascade open economization cycle. It was found that using only a single higher performing IHX on the HT loop outperforms having two IHXs. However, even when using highly efficient IHXs are used on either both sides or the high side, and not accounting for pressure drops, this cycle was not able to outperform the open economization cycle.

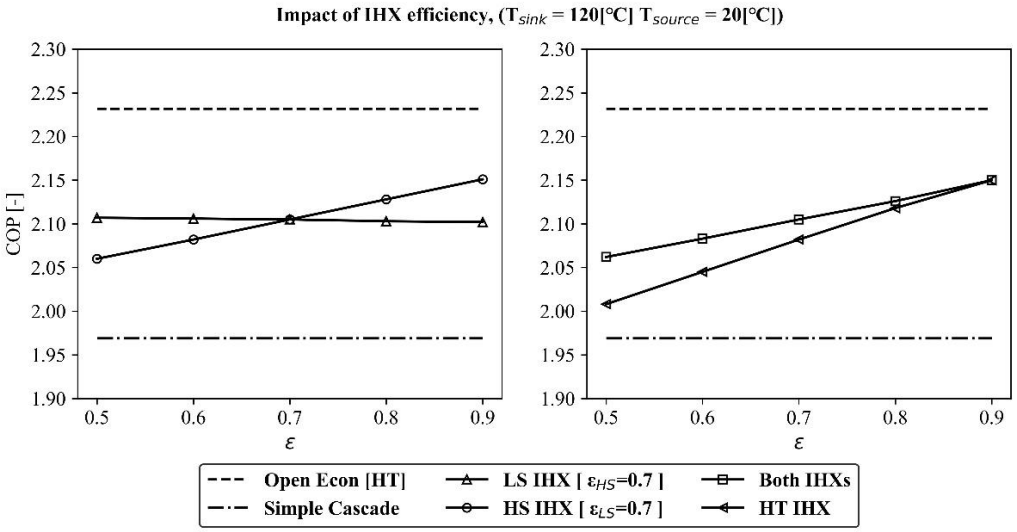


Fig 8. COP as a function of ε for T_{sink} = 120 °C and T_{source} = 20 °C.

4.3.2. Compressor Mapping

Using the compressor map in [14, 22] for a single screw compressor, it was identified that the compressor isentropic efficiency was approximately 0.7 for the cascade cycle. In contrast, the cycles with two-stage compressions were in the order of 0.75 ~ 0.8 due to the improved distribution of temperature lifts and compression ratios across the system. However, it should be noted that limited information and experimental studies exist on compressors for HTHPs, given that this is a nascent field.

5. Discussion

The results of the previous analysis show that a cascade cycle with economization has clear advantages compared to a simple cascade cycle. Economized cycles use a flash tank between the condenser and evaporator under a predefined intermediate pressure controlled by the expansion valve. The gaseous fraction of the refrigerant is used to cool down the compression process. Therefore, the gas at intermediate pressure gets expanded and injected into the compressor. This technology cools down the gas temperature during the compression process and therefore improves the isentropic efficiency of the compressor. Even if that cycle is more cost-intensive due to additional components and an adapted compressor design, the performance enhancements of 25% are significant. An example of a two-stage screw compressor was prosed in [23]. It should be noted that this compressor is different from a twin-screw compressor in that the two screws do not mesh, but rather, compression occurs in two different single screws driven in a single planar arrangement.

The analysis used a compressor map that changes the isentropic efficiency based on the volume ratio the compressor has to achieve (typical to use volume ratio for screw compressor). For the comparison, the map of a screw compressor was used [14, 22]. The benefits of staging can be adopted by either compressor types (reciprocating, centrifugal), such as scroll for smaller capacities with the impact varying based on the impact of pressure ratio its isentropic efficiency.

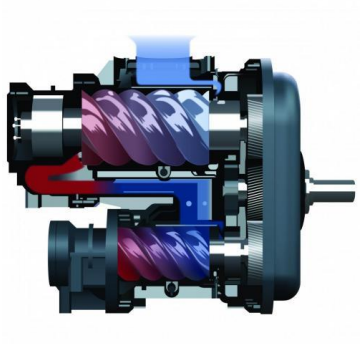


Fig 9. An example of a two-stage screw compressor for air applications, the two screws have a common stator housing and drive [23].

Even cascades with two internal heat exchangers, as used in other publications, show lower efficiencies than the economized cycle [24]. Therefore, based on the technoeconomic results of Kosmadakis [14], it seems that the additional cost of an improved compressor with a flash tank coupled with significant performance enhancements in high lift cycles outweighs using a standard cascade cycle. Further, with respect to introducing IHXs to as an efficiency measure to the cascade cycle, limited benefit is gained by using two while using only one on the HS seems to offer some performance enhancements, albeit lower than staging. It should be noted that plate internal heat exchangers pose additional detriments, such as oil separation, pressure drops, and have a significant cost. From our preliminary analysis, the staging proposed seems to outperform this efficiency measure.

However, additional work is needed with detailed component models, particularly for the compressor, given that limited experimental data are available for HTHP compressors, to reach a conclusive outcome. This work aims to initiate this conversation, particularly in the case of high temperature lift applications, which represent a significant proportion of the process heat industry where heat pumps are or could be used.

6. Conclusions

High temperature heat pump is a technology that can offer significant greenhouse gas reduction in the area of industrial processing. However, they suffer from substantial performance losses and irreversibilities largely due to the extreme temperature lifts they need to achieve. In this work, the potential of staging one of the compression processes was investigated. A number of proposed thermodynamic cycles were investigated by varying the type of economization (open or closed) as well as the location (high or low side). These arrangements were compared against the industry standard cycle for high lift applications, the cascade cycle, with two different refrigerants, one selected for the high side and one for the low side. Additionally, a modified high performance cascade cycle was investigated with two IHXs before the compression processes. The refrigerants selected for the investigation were R-32 and R-1233zd(E) for the low-side and high-side, respectively, based on their thermodynamic properties, low GWP, and ASHRAE classifications. It was found that staging the compression process can lead to performance enhancements (COP) in the order of 25% for high temperature lift applications over the baseline cascade cycles. The highest performing cycle with a staged compression process used two-stage economization on the high side with an open economizer (flash tank). This work highlights the need for integrated cycle and compressor design to achieve widespread HTHP integration at realistic supply temperatures.

Acknowledgements

This work was partially supported by the Center for High Performance Buildings (CHPB) at Purdue University and the Onassis Foundation Fellowship awarded to Elias Pergantis, one of the foundation's Scholars.

References

[1] Fox DB, Sutter D, Tester JW. The thermal spectrum of low-temperature energy use in the United States. Energy Environ Sci 4, p. 3731.
[2] Arpagaus C, Bless F, Uhlmann M, Schiffmann J, Bertsch SS. High temperature heat pumps: Market overview, state of the art, research status, refrigerants, and application potentials. Energy 152, p. 985-1010.

[3] Kim J, Park, SR, B YJ, Chang KC, Ra HS, Kim M, Kim Y,. Experimental study of operating characteristics of compression/absorption high-temperature hybrid heat pump using waste heat. Renewable Energy 54, p. 13-19.
[4] Furukawa T. Industrial high-temperature heat pump for waste heat recovery. New Energy Conservation Technologies and Their Commercialization, Proceedings of an International Conference, Berlin, Germany, Springer-Verlag Berlin Heidelberg, New York (April 6-10 1981), pp. 1483-1493
[5] Jensen JK, Markussen WB, Reinholdt L, Elmegaard B. On the development of high temperature ammonia-water hybrid absorption- compression heat pumps Int J Refrig, 58 (2015), p. 79-89
[6] Jiang J, Hu B, Wang RZ, Deng N, Cao F, Wang CC. A review and perspective on industry high-temperature heat pumps. Renewable and Sustainable Energy Reviews 161, 2022, 112106.
[7] Adamnson KM, Walmsley TG, Carson JK, Chen Q, Schlosser F, Kong L, Cleland DJ. High-temperature and transcritical heat pump cycles and advancements: A review. Renewable and Sustainable Energy Reviews 167, 2022.
[8] Fukuda S, Kondou C, Takata N, Koyama S. Low GWP refrigerants R1234ze(E) and R1234ze(Z) for high temperature heat pumps. Int J Refrig, 40 (2014), p. 161-173
[9] Bamigbetan O, Eikevik TM, Neska P, Bantle M, Schlemminger C. Theoretical analysis of suitable fluids for high temperature heat pumps up to 125 °C heat delivery. Int. J. Refrig. 92, 2018, p. 185-195.
[10] Mateu-Royo C, Arpagaus C, Mota-Babiloni A, Navarro-Esbri J, Bertsch SS. Advanced high temperature heat pump configurations using low GWP refrigerants for industrial waste heat recovery: A comprehensive study. Energy Conversion and Management 229 (2021) 113752.
[11] Mota-Babiloni A, Mateu-Royo C, Navarro-Esbri J, Moles F, Amat-Albuixech M, Barragan-Cervera A. Optimisation of high-temperature heat pump cascades with internal heat exchangers using refrigerants with low global warming potential. Energy 165 (2018), p. 1248 - 1258.
[12] Bamigbetan O, Eikevik TM, Nekså P, Bantle M. Development of propane-butane cascade high temperature heat pump: early test rig results International Workshop on High Temperature Heat Pumps, Copenhagen, Denmark (September 9, 2017), pp. 1-12
[13] Mateu-Royo C, Navarro-Esbri J, Mota-Babiloni A, Moles F, Amat-Albuixech M. Experimental exergy and energy analysis of a novel high-temperature heat pump with scroll compressor for waste heat recovery. Applied Energy 253, 2019.
[14] Kosmadakis G, Arpagaus C, Neofytou P, Bertsch SS. Techno-economic analysis of high-temperature heat pumps with low-global warming potential refrigerants for upgrading waste heat up to 150 C, Energy Conversion and Management 226 (2020) 113488.
[15] Fernandez-Moreno A, Mota-Babiloni A, Gimenez-Prades P, Navarro-Esbri J. Optimal refrigerant mixture in single-stage high-temperature heat pumps based on a multiparameter evaluation. Sustainable Energy Technologies and Assessments 52, Part A, 2022.
[16] Kondou C, Koyama S. Thermodynamic assessment of high-temperature heat pumps using Low-GWP HFO refrigerants for heat recovery. Int. J. Refrig. 53, 2015, p. 126-141.
[17] Hu B, Wu D, Wang LW, Wang RZ. Exergy analysis of R1234ze(Z) as high temperature heat pump working fluid with multi-stage compression. Front. Energy 2017, 11(4): 493–502.
[18] Klein S, Alvarado F. Engineering equation solver. F-Chart Software (2002), Madison, WI.
[19] Arpagaus C, Bless F, Schiffmann J, Bertsch SS. Multi-temperature heat pumps: A literature review. Int J Refrig, 69 (2016), p. 437-465.
COPStoecker, W. F. (1998). Industrial Refrigeration Handbook. McGraw-Hill Education.
[21] ASHRAE Safety Standard for Refrigeration Systems, ANSI/ASHRAE 34-2019, *Designation and Safety Classification of Refrigerants*.
[22] Astolfi M. Techno-economic optimization of low temperature CSP systems based on ORC with Screw expanders. Energy Procedia 2015;69:1100–12
[23] FS Curtis, NxHE Series Two-Stage 90-260kW, URL: https://us.fscurtis.com/product/nxhe-series-90-260kw-two-stage-rotary-screw/, Accessed: 10/10.
[24] Mota-Babiloni A, Mateu-Royo C, Navarro-Esbrí J, Molés F, Amat-Albuixech M, Barrágan-Cervera A. Optimisation of high-temperature heat pump cascades with internal heat exchangers using refrigerants with low global warming potential, Energy 165 (2018), p. 1248-1258.
[25] ANSI/ASHRAE 34-2019, Designation and Safety Classification of Refrigerants.

Nomenclature

$\dot{W}c,i$	Power of ith compressor [kW]	$r_{vc,i}$	Volume ratio across ith comp. [-]
$\dot{Q}$	Heat Supply [kW]	ρ	Density [kg/m$_3$]
$\dot{m}$	Mass flow rate [kg/s]	vap	vapor
h	Specific enthalpy [kJ/kg]	cond	condenser
η_{is}	Isentropic efficiency [-]	EXV	Electronic expansion valve
η_{vol}	Volumetric efficiency [-]	Econ	Economizer
η_{II}	Second law efficiency [-]	CAS	Cascade
P	Pressure [kPa]	Δ	Difference
$\dot{v}$	Volumetric flow rate [m^3/s]	Σ	Sum
$r_{pc,i}$	Pressure ratio across ith comp. [-]	ε	Effectiveness [-]

14th IEA Heat Pump Conference
15-18 May 2023, Chicago, Illinois

Methodologies for high-density domestic heat pump deployment in the UK

Nicola Lazenby[a1], Alex Hobley[b],

[a]Government Department for Energy Security & Net Zero (DESNZ), 1 Victoria St, London, SW1H 0ET, UK
[b]Government Department for Energy Security & Net Zero (DESNZ), 1 Victoria St, London, SW1H 0ET, UK

Abstract

The UK Government's Department for Business, Energy & Industrial Strategy (BEIS) has embarked on a 3-year innovation programme, 'Heat Pump Ready', part of its Net Zero Innovation Portfolio. This paper considers one of the programme's objectives to drive forward methodologies which support the high-density deployment of domestic heat pumps across urban and rural areas. Projects delivering against this objective have conducted feasibility studies which address both technical and consumer barriers to high-density heat pump deployment, bringing together key stakeholders in the journey to ensure a 'joined up' approach from the energy networks right through to installers and consumers. Emphasis is being placed on providing a cost-effective installation and on-going support package to consumers. The key findings from these feasibility studies, carried out by project teams across Great Britain, are presented in this paper alongside proposals for the trial of these methodologies in order to achieve high-density heat pump deployment within the project's specific locations.

© HPC2023.
Selection and/or peer-review under the responsibility of the organizers of the 14th IEA Heat Pump Conference 2023.

Keywords: heat pumps; high density; deployment; coordinated deployment; net zero;

1. Introduction

By 2028, the UK aims to be installing 600,000 hydronic heat pumps per year [1], this is a considerable increase from the reported rate of 55,000 heat pumps installed in 2021 [2]. To achieve this deployment aim, as set out in the 'Heat and Buildings Strategy' [1], many factors must be considered including elements such as: achieving significant growth in the heat pump supply chain; affordability of heat pumps; the ability of the electricity network to accommodate an increase in electricity demand; and enabling the timely connection of heat pumps to the network.

The UK government have set out a package of measures to support the increase in heat pump deployment [3] which includes:

- Reducing the cost of heat pumps to consumers through zero-rate value added tax for the next 5 years on the installation of low carbon heating technologies
- Launching £450m Boiler Upgrade Scheme to provide consumers with up to £6,000 off the cost of a heat pump
- Expanding the UK's manufacturing capacity through a £30m Heat Pump Investment Accelerator
- Investing in heat pump innovation through a £60m Heat Pump Ready Programme, part of the Net Zero Innovation Portfolio [4], which aims to develop innovative methodologies for high density heat pump deployment, in addition to supporting the development of innovative tools and technologies to overcome barriers to heat pump deployment.

This paper sets out the development and delivery of the Heat Pump Ready Programme (HPR), considering the learnings from the programme to date.

[1] Corresponding author: Email address: Nicola.lazenby2@beis.gov.uk

2. Requirement for heat pump innovation

In the development stage of HPR, it was important to establish the bench-mark of current market and industry practice for heat pumps, in order to establish the areas for innovation. To determine this benchmark, an evidence review alongside stakeholder engagement was conducted. The programme design also drew upon the learning from the department's previous heat pump innovation programme, the Electrification of Heat Demonstration project.

2.1 Evidence review

A rapid evidence assessment (REA) of existing literature was carried out in order to establish the current benchmark for innovation [5]. This evidence review was carried out across 4 key areas:

1. Financial Innovations: What are the necessary financial innovations required to deliver a large-scale roll-out of heat pumps in the United Kingdom (UK)?
2. Low Voltage Grid Issues: What are the Low Voltage (LV) grid issues associated with a concentrated deployment of heat pumps and how can we mitigate these? What is the necessary size of a heat pump cluster to achieve appropriate grid impact learnings?
3. Roll-out Facilitation: What are the necessary innovations or learnings required to facilitate the large-scale roll-out of heat pumps? What tools or established processes of stakeholder coordination exist that could support the effective roll-out of heat pumps and are there examples of coordinated deployment?
4. Performance and Deployment: What are the technological improvements to the heat pump system and tools that could be developed to support any of the above aims - i.e. the large-scale deployment of heat pumps in the UK?

The REA found that significant benefit could be gained through innovation in the following areas:

- Design improvements - considering heat pumps as modular systems and how innovation could support the ease of design, installation, and optimization of low temperature systems. Design improvements could also support the ease of connection between heat pumps and other technologies such as heat storage.
- New ways of manufacturing - the use of computer modelling simulation tools to provide flexible, user-friendly interfaces to overcome inefficient designs, in addition to new methods of mass production such as 3D printing. These come with the opportunity to increase resilience in the UK supply chain.
- Installation – the use of 'plug and play' software and hardware.
- Monitoring, maintenance, and operation – the opportunity for improvements to the user interface and inclusion of internet of things data-gathering to support optimization, remote diagnostics, and predictive maintenance of heat pump systems. This presents the opportunity for an enhanced consumer experience, in addition to cost savings.

These areas were supported by recommendations for future innovation programs and research to consider:

- Trials which build on the scale of previous heat pump trials, utilizing up-to-date installation, commissioning, and operational practices.
- The performance gap between system design, installation and operational use of a heat pump and the role which different approaches to on-going monitoring and optimization can play in improving performance.
- Innovation 'horizon scanning' to seek out early-stage technology and tools which may be at lower technology readiness levels.
- Broader areas for innovation relating to the uptake and performance of heat pumps in areas such as noise and disruption.

2.2 Learnings from Electrification of Heat Demonstration Project

The Electrification of Heat Demonstration Project (EoH) [6] began in 2020, with the aim of demonstrating the feasibility of a large-scale roll-out of heat pumps in Great Britain. This project deployed 742 heat pumps in 3 different locations within the UK. Results from the EoH have produced the following 2 key findings:

1. All UK housing types are suitable for a heat pump [7] with no property or architecture, ranging from Victorian mid-terraces and pre-world war two semi-detached homes to 1960s blocks of flats, found to be unsuitable for a heat pump.
2. Heat pumps installed in the UK have been shown to be 3 times as efficient as gas boilers [8]. Measured real-world performance of heat pumps has shown a significant increase in performance through this

trial when compared to previous UK field trials. The study found that the heat pumps performed well even on the coldest observed days with only a relatively small reduction in performance.

EoH has demonstrated that heat pumps work in domestic properties from a technical perspective and data shows their efficiency. The Heat Pump Ready programme therefore looked to explore the tangential barriers associated with the increased uptake in heat pump deployment.

2.3 Stakeholder engagement event

To understand remaining innovation requirements for heat pumps, BEIS held a virtual stakeholder engagement session [9]. This event was attended by 342 representatives from across the sector. A total of 1,241 comments were received from participants with the key suggestions including:

- The use of smart controls to monitor heat pumps, improve consumer experience, and enable response to grid demands.
- The use of thermal storage to improve heat pump efficiency, consumer experience and enable demand reduction of electricity from heat pump users.
- Options for leasing heat pumps or heat charged as a service to a consumer.
- Green mortgage options which include heat pump and energy efficiency funding.
- The coordination of heat pumps by local authorities
- Heating engineers and installers are the most trusted to advise consumers on heat pumps
- The use of national media outlets, e.g. TV and radio, to raise the profile of heat pumps
- The use of clear and simple heat pump communication

3. Heat Pump Ready Programme

The funding opportunities available under HPR were launched in 2021 [10] with the aims of the programme being to:

- Reduce lifetime costs of domestic heat pumps
- Improve lifetime consumer experience of heat pumps
- Stimulate innovative research and solutions to address the impact of domestic heat pumps on the electricity system
- Develop and strengthen partnerships between the many players involved in the domestic heat pump sector
- Develop effective approaches and products to engage effectively on heat pump issues with homeowners and with other key players in the sector
- Establish an evidence base to enable effective design and development of future heat pump policy and regulation

The programme is split in line with its aims across 3 key objectives:

1. Innovative methodologies for high-density deployment: Recognizing the need for a shift from a very dispersed, consumer led approach in deployment to a coordinated, ‘street-by-street’ high-density deployment of heat pumps (Stream 1)
2. Support innovative tools and technologies to overcome barriers to high-density heat pump deployment (Stream 2) across key areas including [11]:
    a. increasing the performance whilst reducing the cost of domestic heat pumps
    b. minimizing home disruption whilst providing high quality installations
    c. providing financial solutions for heat pumps
    d. improving the consumer journey through their transition to heat pumps
    e. creating a smart home energy system
3. Providing the opportunity for knowledge transfer and the dissemination of learnings across HPR projects and the broader heat pump sector (Stream 3).

This paper provides an overview of the Heat Pump Ready Programme (HPR) with a particular focus on objective 1 – the development of innovative methodologies developed which support high-density heat pump deployment within specific locations in Great Britain.

4. Scope for Innovative methodologies for high density deployment

In the development of the scope for the funding competition for project teams to carry out feasibility studies on innovative methodologies for coordinated, high-density deployment of heat pumps it was important to ensure the projects would add to the existing evidence based within this area. One of the greatest challenges

for heat pumps is increase their attractiveness to the able-to-pay, owner occupier and private landlord market – those who are responsible for the capital and on-going cost and maintenance of heat pumps installed within their homes. Coupled with this is understanding the impact on the electricity network of mass transition to heat pumps. This funding competition was divided into 2 Phases: Phase 1 developing feasibility studies for innovative methodologies for high-density heat pump deployment (6 months); and Phase 2 trialing these feasibility studies developed (24 months).

To ensure project developed methodologies which targets this demographic and scenario the following key elements of eligibility criteria [6] were applied to all applications:

1. Project costs must not exceed £200,000, as funding was being deployed through the mechanism of Small Business Research Initiative (SBRI) [12] with this funding being required to cover 100% of the total eligible costs of the project.
2. Projects must be up to 6 months in duration, ending 30th November 2022 to enable projects to apply their learnings to their Phase 2 application to trial the methodology they developed
3. Projects must be looking to achieve deployment of heat pumps in at least 25% of homes either on a low voltage network feeder, supplied from a secondary substation or supplied from a primary substation, during Phase 2, in order to be considered as achieving high-density deployment.
4. Funding for the cost of the heat pump, installation and on-going maintenance of the heat pump, in Phase 2, is capped in line with the Boiler Upgrade Scheme at £5,000 per air source heat pump and £6,000 per ground source heat pump.
5. Heat pumps are to be deployed, during Phase 2, in predominately on-gas grid, domestic, private existing homes, with a cap of 30% of trial buildings being eligible to be social housing, new build or non-domestic properties. Applicants could opt to include up to 15% of their trial homes as off-gas homes.
6. The technology eligible for deployment as limited to hydronic air source or ground source heat pumps, with only a maximum of 20% of the trial homes being eligible for hybrid or air-to-air heat pumps or other sources of direct electric heating. Shared ambient temperature ground loops were eligible, however high temperature ground loops and heat networks were not eligible for deployment.
7. All innovative methodologies for deployment were required to be replicable in other areas of the UK.
8. All technologies, tools and finance models deployed into consumers' homes must have already been trialed and be a commercial offering to the consumer.

5. Overview of Phase 1 projects

Following the assessment of applications, 11 projects were awarded Phase 1 funding to carry out a feasibility study into their innovative methodology for coordinated, high-density heat pump deployment [7]. The locations of project are shown below on Figure 1 with:

- Urban projects (shown in purple) based in Newcastle-upon-Tyne, Sunderland, Leeds, Oxford, Greenwich and Bristol.
- Urban with significant rural projects (shown in red) based in Perth & Kinross, Cherwell and Bridgend.
- Rural projects (shown in blue) based in Fenland and Teinbridge.



Figure 1: Map of Heat Pump Ready Stream 1, Phase 1 projects.

Across the project teams' feasibility studies there was a mix of projects focusing on the deployment of either air source heat pumps or shared ground loops. The number of heat pumps which project teams were looking to deploy in their locations ranged from 30 to 1000 heat pumps, with a mixture of financial offerings being considered such as upfront capital funding from the consumer, heat pump leasing and financial loans.

6. Findings of feasibility projects

Through the delivery of Phase 1 feasibility studies [13], project teams identified a range of challenges and opportunities to support coordinated, high-density heat pump deployment. This section will consider each of these in turn.

6.1. Coordination of stakeholders

To achieve high-density deployment within a given location, there is a strong requirement for the various actors supporting deployment in that location to come together. The actors which projects have identified as having a core role in deployment include:

- Management entity: across the projects, this role was carried out by a range of organisations. For the majority of projects, this role was carried out by engineering/project management consultancies [14-19] with energy suppliers [20-21] also taking on this role. For a small proportion of projects, a technology provider/coordinator took on this role [22-23] with one local authority [14]. For the local authority, they were supported by an engineering consultancy as part of their consortium to deliver the project management elements of their feasibility study. This role was responsible for bringing together the organizations necessary to deliver a coordinated methodology, developing the project communication plan alongside their approach to data sharing and governance.
- Place based entity: where a local authority was not fulfilling the management entity, the majority of projects included within their project team a local authority to provide support within depth knowledge of the local area.
- Engagement coordinator: most of the project teams had an organization specifically responsible for coordinating the consumer engagement within their location. This role typically delivered elements such as consumer surveys, developed marketing campaigns and conducted focus groups. For some projects, this role was carried out by an organization specializing in consumer engagement whilst others utilized local community groups to support this engagement.
- Housing data modeler: Some of the projects [15, 18-19, 21] included a specific role within their feasibility study project team for an organization responsible for utilizing available data on elements

such as housing architypes, social-economic data on occupants and energy data. How this data was utilized by the projects is discussed in Section 6.2.

- Financing partner: Developing an understanding of the consumer finance offer was a key element of the project's feasibility, which ultimately decided whether a project was confident to apply for Phase 2 of the programme to trial their methodology developed. The inclusion of a financing partner, as part of the feasibility studies was not necessarily required, however it was found to be very beneficial to have a member of the project team focused on developing the project's consumer financing offers [17-20, 24].
- Technology provider: Across the projects, there was a split between whether they chose a technology provider in advance of completing their feasibility study. 4 projects [15, 17, 21, 24] opted to include a member of the Kensa Group within their project team with the aim of deploying a shared ground loop (SGL) solution, in addition to the Oxford project, which was led by Samsung, aiming to deploy specifically Samsung air source heat pumps (ASHP). Choosing a technology provider upfront enabled the projects to focus their feasibility study on delivering that specific technology. Contrast to other projects who retained the ability to adapt their specific technology offers to the needs of the consumers depending largely on their house type and financial circumstances, demonstrating high levels of replicability for their innovative, coordinated methodology developed.
- Distribution Network Operator (DNO): Within the phase 1 project teams, there was limited representation of DNO's, with only a couple of projects formally including their DNO in the project team [17, 22]. It was found however through the feasibility studies that the role of the DNO was vital to deliver an innovative coordinated methodology for heat pump deployment. The key knowledge which was required from the DNO was an understanding of the network configuration and capacity within the areas the project teams were targeting, to understand whether network reinforcement would be required and to explore the opportunity for flexibility across the network to reduce peak demand. Early engagement with the local DNO provided the opportunity to develop a more in-depth feasibility study.

A key element throughout each of the feasibility studies was the understanding that a customer relationship management (CRM) platform which operated between the organizations within the project team was essential. The governance for the operation varied with approaches included a combined CRM platform across all project partners [18-19, 23], utilizing existing CRM platforms [20, 21] and the development of a cross organization 'data hub' architecture to support data sharing [15].

6.2. Technical appraisal of location and homes

Coordinating the deployment of heat pumps within a specific location unlocks the opportunity to optimize the process of technical appraisal of homes for their suitability of heat pumps. Many of the projects used a 'data led approach' to narrow down their location for high density deployment. Two projects which considered this in detail were Samsung's project in Oxford [16] and Buro Happold's project in Bristol [15]. This process included bringing together the following data (in compliance with data protection protocols):

- Network data: working within a specific location enables network capacity to be considered for all residents within that specific location, creating efficiencies in the network assessment process and coordinated sequencing of any grid reinforcement required. To access this data, projects established relationships with the relevant Distribution Network Operator within their location. For the Samsung project they combined this data with Oxford Brookes University's LEMAP tool to understand the load profile on the electricity network. Buro Happold utilized the DNO substation polygon areas and distribution substation capacity data available from National Grid to support their understanding.
- Housing stock model: Samsung drew upon the Energy Performance Certificate (EPC) dataset to feed into the analysis of the housing stock within the location they were targeting, with Buro Happold using data provided by Parity Projects, which also included energy data. Another project, E.On [17] working in Newcastle, took this analysis further by testing the feasibility of carrying out drone surveys across the location they were targeting, to develop a thorough understanding of the archetypes and features of the homes which would impact the heat pump system design.
- Energy data: For Samsung's project, work was led by the University of Oxford and Oxford Brookes University to develop analytical approaches which reveal the attributes, capabilities and priorities of the target communities. This project drew upon the Energy Demand Research Project

(EDRP) dataset and The Smart Energy Research Lab (SERL) dataset to enable demand profiling to be conducted for the homes within their focused location.

- Occupant data: For Samsung's project, the ACORN classification and MOSAIC datasets were used to determine the defined socio-economic types for each of the homes within the location. This classification was used to identify common factors which explain the energy demand profile associated with the home and enable the project team to explore the demographic, socio-economic status and lifestyle of the consumer. Buro Happold utilized social housing data from Bristol City Council regarding council owned properties in addition to other social housing providers data.

This flow of data is presented in Figure 2 below, which shows how the collection of data feeds into decision making regarding the location for heat pump deployment. For most of the project teams, the decision was made to trial their methodology in a location which met the following criteria:

1. The properties have high levels of energy efficiency, requiring little to no additional fabric upgrades.
2. The majority of consumers being classified as able-to-pay, middle income residents, enabling access to a wide range of financial products such as loans or heat pump rental.
3. There is sufficient headroom on the electricity network within that location, or a Distribution Network Operator (DNO) on board with the project, supporting the required upgrades within that location.

Most projects focused on location whereby they had an existing relationship with an organization within the location; this was typically with a local authority or a community energy group.

Once this data was collected, project teams planned how it would flow through the consumer journey, to support the trial of their methodology. This data was identified to support the design and survey of the heat pump by:

- Enabling remote survey and triaging of the properties: Enabling an understanding of what would be required from a heat pump install to be developed prior to visiting the consumer. This data allows the project teams to make an informed choice as to where to target the high-density deployment of heat pumps.
- Streamlining in home surveys: Having an established data set of property details will enable the project team to reduce the number of visits to a property, but also allow for data about the property to be pre-populated into surveys so that data is checked and verified during the surveys rather than collected for the first time, leading to a reduction in errors and re-visits required.
- Supporting occupant surveys: Ensuring that consumers are not required to repeatedly provide their personal information, in addition to providing pre-populated information within their surveys for consumers to verify rather than specific, for example asking consumers to confirm they have cavity wall insulation, based on data drawn from their EPC, rather than having to select what type of insulation their home has.

Bringing together this data centrally was identified as being key for the project teams to support the development of their specific offer to the consumer, in Phase 2, with regards the size of heat pump they required, any energy efficiency or home upgrades required and consumer financing.

Through the understanding of the role of data throughout the consumer journey and how this data supports stakeholders throughout the journey, the project teams are able to develop a standardized process for data storage and transfer which could be replicated in other locations.

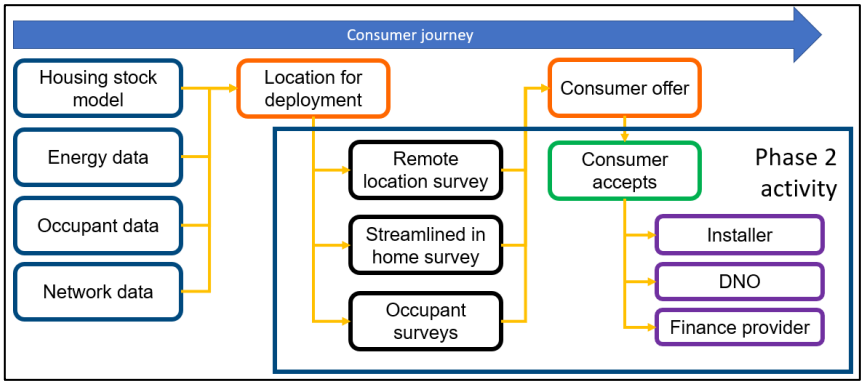


Figure 2: Diagram showing the flow of data identified in Phase 1 feasibility studies

Consumer journey and engagement

For each of the projects, a key emphasis of their feasibility study was placed on how to support the consumer throughout their heat pump journey. For each of the projects, a 'consumer platform' was proposed which brought together various elements of the innovative coordinated methodology. For projects with an existing consumer base, such as the energy suppliers [16, 20-21], the project teams looked to utilize their existing consumer platforms, adding to them the functionality to support their heat pump journey, including registering interest for a heat pump installation, find heat pump installers and providing post-installation guidance.

Each of the project teams conducted early consumer engagement within the location they were working. The early consumer engagement largely consisted of either focus groups, online surveys/expression of interests and/or face to face surveys either at the consumer's home or at a community event. Where surveys were conducted, the project teams findings predominately aligned with findings from existing literature, with limited local variation regarding consumers' perspectives or motivations . Surveys however, especially when conducted face to face, did provide the first 'touch point' with the consumer to open the conversation regarding the project and establish early trust in the project team and build momentum for the project.

Through location specific deployment, project teams were able to consider more bespoke engagement with their communities. Project teams identified the importance of local engagement to generate interest across the community, in addition to building momentum across residents. The findings of the consumer engagement are provided in each project's feasibility reports [13].

7. Projects progressing to Phase 2

During Phase 1, projects were eligible to apply for funding under Phase 2 of the programme in order to proceed to trial the methodology developed as part of their Phase 1 feasibility study. Upon successful completion of Phase 1, 4 projects were awarded Phase 2 funding [18]:

1. Urban projects, one led by Samsung (project value £3,206,448) focusing on heat pump deployment in Rose hill, Oxford and another by Bristol City Council (project value £2,925,450.72) focusing on heat pump deployment in Westbury on Trym, Bristol.
2. Rural project being led by City Science (project value £1,815,391) focusing on heat pump deployment in Fenland, Cambridgeshire.
3. Urban with significant rural project led by City Science (project value £1,799,245) focusing on heat pump deployment in Cherwell, Oxfordshire.

Across three of the four Phase 2 applications, there was a significant decrease in ambition in comparison to their Phase 1 applications, this was primarily due to the 'cost of living' crisis which is ongoing in the UK. These project teams looked to minimize their delivery risk by reducing the scale of their deployment from the range of 500-700 heat pumps to 100-150 heat pumps, whilst still meeting the high-density eligibility criteria. They achieve this by reducing down from doing multiple areas of the electricity network to just limited elements. Bristol City Council were the only project to maintain their deployment ambition of approximately 200 from Phase 1 into Phase 2. From a project perspective, this reduced ambition will still provide the opportunity to trial the project innovative methodologies for coordination and gather the learnings required from the programme.

Through the trial of the projects' innovative, coordinated methodologies for high-density heat pump deployment, some of the key overarching barriers and challenges being addressed include:

- Capital vs lifetime cost of heat pumps: projects are looking to demonstrate and present a detailed overview and understanding of lifetime costs of a heat pump to consumer. Through lifetime cost modelling project teams are including capital cost pay by the consumer and financing options, in addition to their projected operational cost of the heat pump and any income from electricity demand flexibility. Through trialing their methodologies, project teams will be able to establish exactly the cost associated with coordinated deployment of heat pump installations and the potential capital cost reduction available to consumers through this approach.
- Perceived disruption of homes: for the locations which the projects have selected, minimal home retrofits will be required, however some of the homes are likely to require radiator upgrades, for example. To demonstrate the level of distribution required, project teams are looking to set-up 'open homes' and 'show homes' to enable consumers to see and feel a heat pump installation in real-life.
- Limited installer capacity: project teams are taking a variety of approaches with regards to ensuring the installer capacity is in place for their deployment. The 3 approaches being trialed are: tendering for installers; including an installer provider on the project team; and including an installer training provider on the project team to develop a local installer hub and training programme.

- Requirement for network reinforcements: City Science's Fenland project is aiming to deploy heat pumps in a constrained part of the electricity network. Here the project team are working closely with the DNO in the area to understand how to coordinate heat pump deployment alongside network reinforcements and the role of flexible demand profiles from the heat pumps. The other City Science project in Oxfordshire, and the Samsung project, whilst not working in a constrained part of the network, are using this project to demonstrate how to coordinate heat pump deployment (with DNO monitoring) in the area, to understand the network impact of deploying heat pumps at high density.
- Coherent consumer journey: All Phase 2 projects have a strong emphasis on providing a coherent consumer journey from a consumer's initial expression of interest in a heat pump through to the operation, maintenance and getting the best performance from their heat pump once installed. All projects are establishing a 'consumer portal' through which consumers manage their heat pump journey, rather than having to navigate various websites and platforms of the various actors who play a role in their transition to heat pump adoption.

8. Conclusion

From the initial 6 month's feasibility studies developed by the Heat Pump Ready, Stream 1 – Phase 1 projects, key learnings have already been provided:

- The support required for the future of heat pump deployment in terms of the actions which stakeholders can take to increase the uptake of heat pumps within their local areas.
- The role of data has been shown to be vital in unlocking the coordination of high-density heat pump deployment and supporting the consumer through their heat pump journey.
- The potential role of future policy regarding the role of DNO's, flexibility in the energy network, developing installer capacity and engaging consumers.

The Heat Pump Ready, Stream 1 – Phase 2 projects will continue to provide vital learnings as they progress through their mobilisation stage into heat pump deployment.

Acknowledgements

This research and development has been funded under the Heat Pump Ready programme, part of BEIS' £1bn Net Zero Innovation Portfolio. Acknowledgement is made to project teams responsible for delivery of the projects.

References

[1] Department for Business, Energy & Industrial Strategy, "Heat & Buildings Strategy," 2021. [Online]. Available: https://www.gov.uk/government/publications/heat-and-buildings-strategy.

[2] BSRIA, "Heat pumps market analysis," 2020. [Online]. Available: https://www.bsria.com/uk/.

[3] Department for Business, Energy & Industrial Strategy, "British Energy Security Strategy," 2022. [Online]. Available: https://www.gov.uk/government/publications/british-energy-security-strategy/british-energy-security-strategy.

[4] Department for Business, Energy & Industrial Strategy, "Net Zero Innovation Portfolio," 2022. [Online]. Available: https://www.gov.uk/government/collections/net-zero-innovation-portfolio.

[5] Department for Business, Energy & Industrial Strategy, "Background on innovation needs," 2021. [Online]. Available: https://assets.publishing.service.gov.uk/government/uploads/system/uploads/attachment_data/file/1043227/heat-pump-ready-innovation-needs.pdf.

[6] Department for Business, Energy & Industrial Strategy, "Electrification of Heat Demonstration Project: winning bids, case studies and project data," 2020. [Online]. Available: https://www.gov.uk/government/publications/electrification-of-heat-demonstration-project-successful-bids.

[7] Energy Systems Catapult, "All housing types are suitable for heat pumps, finds Electrification of Heat project," [Online]. Available: https://es.catapult.org.uk/news/electrification-of-heat-trial-finds-heat-pumps-suitable-for-all-housing-types/.

[8] Energy Systems Catapult, “Heat pumps shown to be three times more efficient than gas boilers,” 2023. [Online]. Available: https://es.catapult.org.uk/news/heat-pumps-shown-to-be-three-times-more-efficient-than-gas-boilers/.

[9] Department for Business, Energy & Industrial Strategy, “Heat Pump Ready: Supporting Information. Stakeholder Engagement Feedback,” 2021. [Online]. Available: https://assets.publishing.service.gov.uk/government/uploads/system/uploads/attachment_data/file/1043235/heat-pump-ready-engagement-summary.pdf.

[10] Department for Business, Energy & Industrial Strategy, “Heat Pump Ready Programme,” 2021. [Online]. Available: https://www.gov.uk/government/publications/heat-pump-ready-programme.

[11] Department for Business, Energy & Industrial Strategy, “Heat Pump Ready Programme: Stream 2 projects,” [Online]. Available: https://www.gov.uk/government/publications/heat-pump-ready-programme-successful-projects/heat-pump-ready-programme-stream-2-projects.

[12] UK Government, “SBRI: the Small Business Research Initiative,” [Online]. Available: https://www.gov.uk/government/collections/sbri-the-small-business-research-initiative.

[13] Carbon Trust, “Feasibility Reports,” [Online]. Available: https://heatpumpready.org.uk/feasibility-reports/.

[14] Leeds City Council, “Leeds RHINOS,” February 2023. [Online]. Available: https://heatpumpready.org.uk/wp-content/uploads/2023/02/renewable-heat-infrastructure-network-operating-system-RHINOS-feasibility-report.pdf/.

[15] Buro Happold, “Bristol Heat Pump Ready,” February 2023. [Online]. Available: https://heatpumpready.org.uk/wp-content/uploads/2023/02/bristol-heat-pump-ready-feasibility-report.pdf/.

[16] Samsung, “Clean Heat Streets,” February 2023. [Online]. Available: https://heatpumpready.org.uk/wp-content/uploads/2023/02/clean-heat-streets-feasibility-report.pdf/.

[17] E.On, “The Newcastle Heat Pump Ready Feasibility Report,” February 2023. [Online]. Available: https://heatpumpready.org.uk/wp-content/uploads/2023/02/heat-pump-ready-newcastle-feasibility-report.pdf/.

[18] Department for Business, Energy & Industrial Strategy, “Heat Pump Ready Programme: Stream 1 Phase 2 projects,” [Online]. Available: https://www.gov.uk/government/publications/heat-pump-ready-programme-successful-projects/heat-pump-ready-programme-stream-1-phase-2-projects.

[19] City Science, “Cambridgeshire Final Report,” February 2023. [Online].

[20] Department for Business, Energy & Industrial Strategy, “Heat Pump Ready: Stream 1 – Solutions for high-density heat pump deployment. Phase 1 competition guidance.,” 2021. [Online]. Available: https://www.contractsfinder.service.gov.uk/Notice/Attachment/003dd4f0-cfb1-4d61-b85d-5b1633376c6c.

[21] Energy Systems Catapult, “All housing types are suitable for heat pumps, finds Electrification of Heat project,” 2022. [Online]. Available: https://es.catapult.org.uk/news/electrification-of-heat-trial-finds-heat-pumps-suitable-for-all-housing-types/.

[22] Department for Business, Energy & Industrial Strategy, “Heat pump Ready Programme: Stream 1 Phase 1 Projects,” 2022. [Online]. Available: https://www.gov.uk/government/publications/heat-pump-ready-programme-successful-projects/heat-pump-ready-programme-stream-1-phase-1-projects.

[23] Department for Business, Energy & Industrial Strategy, “Heat Pump Ready Programme,” 10 2021. [Online]. Available: https://www.gov.uk/government/publications/heat-pump-ready-programme.

[24] Element Energy, “Greenwich TIME,” February 2023. [Online]. Available: https://heatpumpready.org.uk/wp-content/uploads/2023/02/greenwich-thermal-infrastructure-motivating-electrification-Greenwich-TIME-feasibility-report.pdf/.

[25] Buro Happold, “HPR Bridgend,” February 2023. [Online]. Available: https://heatpumpready.org.uk/wp-content/uploads/2023/02/heat-pump-ready-bridgend-feasibility-report.pdf/.

[26] EDF, “Project Gaia,” February 2023. [Online]. Available: https://heatpumpready.org.uk/wp-content/uploads/2023/02/project-gaia-feasibility-report.pdf/.

[27] City Science, “Oxfordshire Final Report,” February 2023. [Online]. Available: https://heatpumpready.org.uk/wp-content/uploads/2023/02/prosumer-model-for-heat-pump-

deployment-in-cherwell-feasibility-report.pdf/.

[28] Power Circle Projects, “SAPPHIRE Solo,” February 2023. [Online]. Available: https://heatpumpready.org.uk/wp-content/uploads/2023/02/SAPPHIRE-solo-feasibility-report.pdf/.

[29] Utilita, “Heat Pump Ready Programme Stream 1, Phase 1,” February 2023. [Online]. Available: https://heatpumpready.org.uk/wp-content/uploads/2023/02/utilita-energy-heat-pump-ready-programme-feasibility-report.pdf/.

14th IEA Heat Pump Conference
15-18 May 2023, Chicago, Illinois

Innovative technologies and tools to increase deployment of domestic heat pumps in the UK

Alex Hobley[a], Nicola Lazenby[b*]

[a]Government Department for Energy Security & Net Zero, 1 Victoria St, London, SW1H 0ET, UK
[b]Government Department for Energy Security & Net Zero, 1 Victoria St, London, SW1H 0ET, UK

Abstract

The UK Government's Department for Energy Security & Net Zero has undertaken a 3-year innovation programme titled 'Heat Pump Ready' (HPR) as part of its £1bn Net Zero Innovation Portfolio. Heat Pump Ready is split into three complementary work streams. This paper focuses on stream 2 of the up to £60m programme which aims to support the development of innovative tools and technologies addressing barriers to domestic heat pump deployment across five thematic areas of: increasing the performance of domestic heat pumps whilst reducing their cost; minimising home disruption whilst providing high quality installations; providing financial solutions for heat pumps; improving the consumer journey through the transition to heat pumps; and creating a smart home energy system for heat pumps. This paper will provide an insight into the high-potential, innovative technologies and tools being developed under the programme across the thematic areas and their potential impact in supporting the deployment of heat pumps across the UK and in countries with similar climates and housing archetypes. [162 words]

© HPC2023.
Selection and/or peer-review under the responsibility of the organizers of the 14th IEA Heat Pump Conference 2023.

Keywords:heat pumps; innovation; supporting deployment;

1. Introduction & background

The heating of buildings is responsible for approximately 22% of the UK's carbon emissions [1]. Therefore, to meet the UK's legally binding net zero target, nearly all heat in buildings in the UK needs to be decarbonised. Without government investment in innovation and other measures to create an enabling environment for the large-scale adoption of heat pumps, gas boilers will remain the default for consumers heating their homes and there is a significant risk that net zero and interim emissions targets will not be met.

There are several potential solutions to meeting the challenge of decarbonising heat in homes and other buildings. The main potential decarbonisation pathways are: approaches involving electrification of heating, using heat pumps; those which rely on low-carbon gas, in the form of biogas or hydrogen; or a mixture of the two. In the short-term, electrification of heat is the only commercially available option for decarbonising heat. In order for the UK to meet its legally binding interim carbon budgets, it will need to rapidly scale-up deployment of heat pumps during the 2020s, both off and on the gas grid, from current levels, of about 55,000 in 2021 [2], up to the government's aim of 600,000 installs per year by 2028 [3].

Specifically, the HPR programme supports the ambition of 600,000 UK heat pump installs per year by 2028, which was set out in the Government's 2020 Ten Point Plan [3]. The barriers to overcome to enable a scale up of domestic heat pump deployment include: consumer acceptability, installer expertise and capacity, technology performance and cost, home suitability, electricity network suitability; installation quality and availability of financing options [4]. There are some solutions available to overcome these barriers, however, they are not at a commercial scale, or deployed most effectively, as part of a coordinated heat pump landscape. In responding to this challenge the UK Government's Heat Pump Ready (HPR) programme seeks to accelerate the development and deployment of innovative solutions in all these areas.

* Corresponding author. *E-mail address:* nicola.lazenby2@beis.gov.uk

The overarching objective of the HPR Programme (which is split into 3 complementary streams [5]) is to create an enabling environment for heat pump deployment at a significantly increased density and scale than current deployment levels. This enabling environment - to stimulate and support the high-density2 deployment of domestic heat pumps in the UK – is to be achieved under the HPR programme stream 2 – the focus of this paper - through the development and trial of innovative tools and technology and to address barriers faced across the landscape. The parallel stream 1 of HPR programme focuses on the development and trial of innovative methodologies and solutions for local coordination of high-density heat pump deployment, consumer engagement and network upgrades.

2. Heat pump ready programme development

2.1. Evidence review

During the process of designing the HPR programme, a Rapid Evidence Assessment (REA) [6] was undertaken on behalf of the department to review available evidence on heat pump innovation in the UK and internationally including identifying any gaps in research. The REA used four questions to help focus and guide the research:

1. Financial Innovations: What are the necessary financial innovations required to deliver a large-scale roll-out of heat pumps in the United Kingdom (UK)?
2. Low Voltage Grid Issues: What are the Low Voltage (LV) grid issues associated with a concentrated deployment of heat pumps and how can we mitigate these? What is the necessary size of a heat pump cluster to achieve appropriate grid impact learnings?
3. Roll-out Facilitation: What are the necessary innovations or learnings required to facilitate the large-scale roll-out of heat pumps? What tools or established processes of stakeholder coordination exist that could support the effective roll-out of heat pumps and are there examples of coordinated deployment?
4. Performance and Deployment: What are the technological improvements to the heat pump system and tools that could be developed to support any of the above aims - i.e. the large-scale deployment of heat pumps in the UK?

Analysis of existing literature focusing on these four questions included the following four findings:

1. Considerable research has been undertaken on the business models needed to stimulate the uptake of domestic heat pumps, particularly when coupled with other energy efficiency measures. However, while there is plenty of discussion of the different models few have been trialled in-situ and at scale. Further trials and development of heat as a service (HaaS) is required to increase consumer understanding, identify what motivates consumers, and address concerns around the disruption and long-term commitment element associated with HaaS.
2. The level of impact that the electrification of heat, through the use of heat pumps, will have on the LV network will depend on a number of factors that include rate of uptake and load profile. The body of evidence suggests that LV network issues (e.g. voltage problems or overloading) can be expected from a level of heat pump penetration on the LV network. The availability of field data is limited especially at a larger scale. In order for a deployment programme to achieve the appropriate grid impact learnings, the deployment size should target achieving heat pump penetration across at least 20% of dwellings on an individual LV network.
3. A clear theme running through the body of evidence, is the benefit of effective coordination between relevant stakeholder groups. A consumer-focused framework which considers area characteristics that define the stakeholder engagement strategy may lead to increased take-up. An increased understanding of how more effective and accurate modelling of local and household energy demand approaches can assist in both scheme design and management, and operational ease-of-use and performance. It is worth noting that the evidence base for question 3 suggests using the social aspects of this kind of rollout, e.g. consumer engagement and satisfaction as a metric to compare the effectiveness of various modelling scenarios.

[2] In the context of the Heat Pump Ready programme, high-density is defined as deployment of heat pumps to at least 25% of properties on a single low-voltage feeder, secondary substation or primary substation.

4. To bring the actual performance of heat pump systems closer to the projected performance, innovations which allow existing heat pump technology to perform in a more repeatable way could be of significant benefit. Several studies observed that there are installations where the performance gap is very small and there are installations where there is a significant gap. Potential areas where research and innovation are listed as being of significant benefit include design improvements, manufacturing, installation and monitoring, maintenance, and operation.

2.2. Heat Pump Ready Programme objectives

An assessment of the evidence as part of the rapid evidence assessment identified the following widespread key barriers to large-scale heat pump deployment:

- affordability: the high cost of heat pumps
- lack of availability: lack of a strong market presence
- lack of awareness: of systems and benefits by households and the industry
- acceptance: heat pumps are perceived to be harder to install and use than gas boilers
- consumer willingness: resistance against potential disruption during installations
- consumer behaviour: demanding and using heat as if it were being produced by a fossil fuel boiler
- long-term demand: lack of certainty required for investors and businesses

In responding to these identified barriers the key objectives of the £60 million HPR programme are:

- reduce the lifetime costs of domestic heat pumps (including capital equipment costs, installation costs and operating costs);
- improve the lifetime consumer experience of heat pumps (including the experiences of: learning about and choosing a heat pump and how to pay for it; having a heat pump installed in the home and living with a heat pump);
- stimulate innovative research and solutions to address the impact of domestic heat pumps on the electricity system;
- improve the interoperability of domestic heat pumps with other smart technology in the home;
- develop and strengthen partnerships between the many players involved in the domestic heat pump sector;
- develop effective approaches and products to engage stakeholders effectively on heat pump issues with homeowners and with the key players who can help to deliver high-density heat pump deployment across the UK;
- establish an evidence base to enable effective design and development of future heat pump policy and regulation

The HPR programme covers three streams. Stream 1 supports the design and trial of innovative, optimised solutions delivering a more cost-effective and higher-density domestic heat pump roll out. High-density deployment will be piloted in a number of areas across the UK. Stream 2 focuses on supporting the development of innovative tools and technologies addressing barriers to domestic heat pump deployment. Stream 3 is focused on capturing and sharing progress, evidence, knowledge, and lessons learned between all the different projects across the programme as well as developing tailored knowledge to disseminate amongst key stakeholders including industry.

2.3. Stream 2 objectives

Under stream 2 – which is the focus of this paper - the UK government has provided more than £15million in funding to support innovation to make heat pumps cheaper and easier to install, helping accelerate the UK's move away from fossil fuel heating [7]. The solutions supported are at Technology Readiness Levels (TRL) 5 to 7 at the start of the projects. A total of 24 projects [8] in England and Scotland were awarded funding under stream 2. Stream 2 objectives specifically relate to supporting the development of innovative tools and technologies addressing barriers to domestic heat pump deployment under five main category objectives:

- increasing the performance whilst reducing the cost of domestic heat pumps
- minimising home disruption whilst providing high quality installations
- providing financial solutions for heat pumps
- improving the consumer journey through the transition to heat pumps
- and creating a smart home energy system

2.4. Stream 2 tools & technology outputs

Each project runs for a period of either 18 or 30 months with the programme concluding by early 2025. The tools and technologies being developed can be categorised by the expected output in the following way:

- Apps being created, for example:
  - for installers to use to ensure correct heat pump install & commission
  - for surveyors to generate heat loss calculations, radiator sizing and heat pump sizing
  - for consumers/installers going through heat pump related decisions including selection and install process
- Control systems:
  - for utilising smart meter data to embed heat pumps in a Home Energy Management System to optimise behaviour of house/renewable technology
  - for remote adjustment of heat pumps
- Data utilization, for example:
  - smart meter data enabling thermal modeling of the home considering heat pump suitability and sizing
  - data-driven solutions for installer decision-making/upskilling. Data and learning from every installation undertaken captured in structured Case Studies (including post-installation assessment)
- Financial products:
  - low interest loan products for consumers spreading the cost over the life of a heat pump
- Heat pump design:
  - design solutions for non-traditional housing archetypes
  - remote survey tool for surveyors
- Manufacturing:
  - to include; redesign of heat pump assembly processes, reducing heat pump part-count, modular heat pump design
  - heat pump and energy storage system combining energy recovery from the wastewater streams leaving a house
- Software:
  - to predict & monitor fuel usage savings from heat pump & fabric savings
  - installer selection tool allowing consumers to request installation quotes from Microgeneration Certificate Scheme (MCS)[3] certified installers, filtering by name, type and location
  - to ensure improved assurance of heat pump design and installation to manage financial risk

This paper will explore these innovative outputs and their potential impact in more detail.

3. Overview of stream 2 projects by category objective

The stream 2 projects are categorized from an innovation activity perspective as either Industrial Research or Experimental Development.

Industrial Research can involve planned research or critical investigation aimed at the acquisition of new knowledge and skills for developing new products, processes or services or for bringing about a significant improvement in existing products, processes or services. It comprises the creation of components parts of complex systems and may include the construction of prototypes in a laboratory environment or in an environment with simulated interfaces to existing systems as well as of pilot lines, when necessary for the industrial research and notably for generic technology validation.

Experimental Development can involve acquiring, combining, shaping and using existing scientific, technological, business and other relevant knowledge and skills with the aim of developing new or improved products, processes or services. This may include, for example, activities aiming at the conceptual definition, planning and documentation of new products, processes or services. Experimental development may comprise prototyping, demonstrating, piloting, testing and validation of new or improved products, processes or services in environments representative of real-life operating conditions where the primary objective is to make further technical improvements on products, processes or services that are not substantially set. This may include the

[3] MCS works with industry to define, maintain and improve quality by certifying low-carbon energy technology contractors including heat pumps.

development of a commercially usable prototype or pilot which is necessarily the final commercial product, and which is too expensive to produce for it to be used only for demonstration and validation purposes.

3.1. Category objective 1: to increase the performance whilst reducing the cost of domestic heat pumps;

The five projects within this category objective are outlined below.

3.1.1.

In the UK, housing associations and local authorities often find themselves as large landlords managing sites of multiple homes. In working to understand the context of the existing heating system prior to the installation of a heat pump and through continuous monitoring and analysing of ongoing heat pump performance, this Guru Systems Ltd project's objective is to provide operators the ability to remotely adjust the heating system settings as required. The intended outcomes for this project are to enable reduced initial capital expenditure spend, improved heat pump performance in operation, resulting in fewer maintenance callouts, lower carbon emissions, and, more comfortable residents with reduced heating costs. Tools and monitoring equipment are being developed to allow landlords to actively manage their heating systems as part of the project.

3.1.2.

To improve heat pump manufacturing processes this ICAX Ltd project aims to tackle the cost barriers of heat pump deployment by designing and building a trial manufacturing assembly line for residential heat pumps, using analytical and physical tools. This is in order to offer a systemic approach to optimised manufacturing based on current intelligent manufacturing design and operation capabilities. By re-designing the heat pump assembly process, the objective is to reduce unit costs and increase product quality.

3.1.3.

By combining electrically-driven heat pumps with heat storing batteries the aim of this project is to shift heat production from times of peak electrical demand on the National Grid, enabling consumers to charge heating systems to store lower cost and lower carbon heat in anticipation of their peak heating demand. This Kensa Heat Pump Ltd project aims to achieve this by decoupling the times of heating demand in the property from the time of electrical heat production. By shifting energy demands, the project also aims to negate some of the challenges faced by the grid from electrifying and decarbonising heat.

3.1.4.

This Mixergy Ltd project aims to reduce the lifetime costs of domestic heat pump installation whilst delivering higher system efficiency throughout the year. In turn it is expected this will reduce capital and operational costs, ensuring a more seamless installation process and holistic approach to design. The project team are focusing on ground-breaking technologies which reduce installation complexity and elevate the seasonally adjusted Coefficient of Performance of real-world heat pump installations.

3.1.5.

Modular heat pump design may be able to provide significant cost and CO2 savings across the installation, operation and production phases. Ventive's heat pumps are demand responsive, fully integrated with indoor environment control systems providing integrated ventilation, heating, and hot water with free summer cooling. The Heat Pump will arrive pre-plumbed and pre-configured with monitoring and renewable energy storage to enable quick and simple installation. Since each home is different (size, heat loss, thermal mass, occupancy, user behaviour), the project will use an array of integrated sensors to assess the indoor environment and adapt the performance of each system, learning and optimising its operation to drive improvements in energy efficiency, energy storage and load shifting capacity.

3.2. Category objective 2: to minimise home disruption whilst providing high quality installations;

The six projects within this category objective are outlined below.

3.2.1.

This project aims to create a new method to optimise heat pump specification, design and management by using on-site measurement of building performance parameters as design inputs. Through using smart meters, low-cost sensors and newly established techniques to directly measure key performance parameters on a property basis, this Build Test Solution project aims to determine:

- how calculations and measurements can co-exist, the latter providing improved confidence as well as optimisation and calibration of heat pump system specification and design
- a publicly available protocol that defines the measurement options, the standards that must be followed, what the outputs must comprise and how these should be presented
- optimal delivery models with respect to the use of quick tests, low disruption short term monitoring and/ or use of existing smart infrastructure and Internet of Things (IoT) devices already installed.
- the role of ongoing measurement and condition monitoring services to validate system performance in-use

3.2.2.

This project focuses on creating a mobile app and web platform which supports the correct installation, commissioning and maintenance of heat pumps. The Guru Systems Ltd platform verifies outcomes and stores heat pump settings in order to benchmark for future maintenance and efficiency improvements, and acts as a training resource for new heat pump engineers. The modular nature of the product will allow for a dynamic service to provide apps and platforms for surveys, commissioning and subsequent maintenance which can be easily adjusted for different heat pumps and adapt to changing verification regimes depending on how the market evolves.

3.2.3.

Hoare Lea's 'Right Sizing Heat Pumps' project aims to reduce capital costs, operational costs, and grid infrastructure upgrade costs through developing a tool to properly size, efficiently monitor and optimise heat pump performance. This will be achieved by improving cost and viability through standardising the approach to sizing heat pumps.

3.2.4.

A free heat pump home survey and design tool to help consumers make informed decisions regarding heat pump installation providing a knowledge base to facilitate the national rollout of heat pumps. As there are different types of Heat Pumps available with vastly different applicability, thermal output, installation complexity and cost, Q-BOT Ltd's tool will help consumers confidently match the heat pump to the thermal demand of the house and other specific needs on a case-by-case basis.

3.2.5.

1 million non-traditional homes in the UK have poor energy performance, putting their occupiers at increased risk of fuel poverty, and presenting a key challenge to standardised energy efficiency measures that typically precede a heat pump installation. RJ Barwick's project will utilise the Energiesprong approach to develop optimum standardised whole house retrofit solutions for four of the most challenging and/or common non-traditional home archetypes. The housing stock of West Kent Housing Association & Gravesham Borough Council will be used for these pilots, with selected archetypes that have inherent design complexities, assisting the development of optimum solutions in the future. Each house has its own complexities and sharing of practical archetypal retrofit knowledge on 'hard to treat' non-traditional homes underpins this project.

3.2.6.

An all-encompassing integrated software package and app for installers to streamline the survey, installation and commissioning processes required when installing a heat pump. Thormer Solutions Ltd's project will provide a digital survey platform and a fully automated design facility. It aims to allows the system to be optimised from the beginning and uses augmented reality to provide the consumer with an upfront feel for how the system and components will look and sound when installed. The platform will also ensure that all documentation is stored and logged against the installation. There will be full traceability for consumers and installers to access in the future when it comes to heat pump maintenance and service. Overall the project will aim to streamline the installation process, significantly reducing the time and effort it takes to complete any installation.

3.3. Category objective 3: to provide financial solutions for heat pumps;

The four projects within this category objective are outlined below.

3.3.1.

This project aims to transform current understanding of heat in the domestic setting and provide a scalable approach to heat pump financing and deployment throughout the UK. This will be achieved via the prototyping, deployment, and testing of a Heat as a Service (HaaS) modeling solution, which will provide decarbonisation pathways and financing models. The City Science Corporation solution features a modular design, interacting to provide a full HaaS offering. Sub-sets of these modules will also provide highly valuable use-cases, for example by enabling key insights into which buildings heat pumps can provide a viable and attractive heating solution. Through the facilitation of a complete and accurate financing package, this project hopes to enable increased financing for combined heat pump and retrofit solutions, thus accelerating heat pump deployment at the lowest cost to the consumer.

3.3.2.

Heat pumps can deliver energy cost savings of over 50% when deployed as part of a high performance and high-quality retrofit. This creates an opportunity for a 'Comfort Plan' to be offered, which provides guaranteed heating outcomes for occupants in return for a fee (which is no more than the total savings). This could help to fund the heat pump retrofit enabling greater deployment and support access to heat pumps through reducing the requirement for upfront capital investment. This Energiesprong project will finalise the process and technology requirements to offer a seamless end to end Comfort Plan management service, and then develop and test the technical solutions required to enable delivery of this. Developments in this scheme will be shared in an initial contracted pipeline of 1,550 homes, aiming for solutions to be demonstrated within live projects.

3.3.3.

The aim of this Home Infrastructure Technology project is to develop a Green Homeowner Loan to pave the way for mass adoption of green home improvements, by developing a fintech platform specifically designed to fund heat pumps and other green measures. Aiming to be financially attainable, this has the aim to help gain consumer buy-in and increase the sale of heat pumps.

3.3.4.

This project from Parity Projects Ltd aims to directly address the cost and quality assurance barriers of decarbonising heat in homes, by creating a low-cost cost-effective options analysis and verification protocol to enable the offer of a financially insurable performance guarantee to homeowners and landlords. The project outcome will be software that integrates existing retrofit supply chain components to ensure improved assurance of design and installation of a suitable package of measures, with a particular focus on managing financial risk.

3.4. Category objective 4: to improve the consumer journey through the transition to heat pumps;

The six projects within this category objective are outlined below.

3.4.1.

The project aims to simplify and improve the efficiency of the heat pump installation process by creating a consumer-centric digital platform to support customers through the whole heat pump installation journey. This EDF digital solution aims to improve the customer journey by streamlining the required pre-installation steps into one remote survey, adopting a self-serve approach and reducing the amount of information required upfront. The outcome will be an end-to-end digital solution which will support customers in identifying innovative heat pump solutions, tailored to their profile. The solution will split into three main digital modules:

- pre-survey assessment using basic customer-provided data and housing stock data, determining heat pump eligibility or providing advice on other steps required (e.g. insulation) to become eligible
- remote survey and analysis, carrying out detailed design, quotation and installation plan
- post-installation monitoring and customer 'after care' package to build long term relationships with customers

3.4.2.

The project is proposing an artificial intelligence (AI) Smart Heat Pathway to enable rapid, high-quality and scalable heat pump deployment. This will be achieved through leveraging AI on Smart Meter and Smart Thermostat data to determine a personal net-zero pathway for each home, and size the subsequent appropriate heat pump, from actual measured data. Green Energy Option's project aims to help reduce the upfront costs of property survey and design and provide a viable customer success pathway towards net-zero heat for hard-to-treat homes. The project will be piloted across 150 homes, with the aim of scaling the AI Smart Heat Pathway nationwide subsequently.

3.4.3.

Hildebrand Technology Ltd's project is focused on improving the heat pump adoption customer journey, installer expertise, and outcomes by leveraging data from installations and enabling peer-to-peer learning and transparency. The project will provide a data-driven solution to reduce complexity and uncertainty for consumers and provide data, tools and resources for installer decision-making and upskilling. Data and learning from every installation will be captured in structured Case Studies (including post-installation assessment) to share insights in a structured, useful and engaging way. The goal is to create a feedback loop of peer-to-peer learning, among consumers and installers, that continuously improves advice and stakeholder confidence, based on practical real-world experience.

3.4.4.

This Switchee Ltd project aims to provide tools and research to overcome the current scaling barriers relating to heat pump acceptance, lack of awareness and consumer behaviour. The project is producing smart heat pump tools specifically aimed at improving the consumer journey for residents in Social Housing. This will be delivered by:

- allowing remote reading of error warning messages from the heat pump to alert the housing association
- using heat pump specific metrics including live and historic data. Heat pump specific algorithms will be developed to alert detected heat pump performance issues i.e. excessive energy consumption
- offering tailored heat pump advice focused on resident experience
- empowering the housing association to trigger when a new resident has moved into the property so that heat pump advice and educational material can be made available to them

3.4.5.

Developing a new consumer journey for heat pumps, guiding consumers from their first engagement through to receiving quotes for installation. The journey will build a technology selection tool based on the existing, tried and tested solution provided through Home Energy Scotland to assess a property's suitability for a heat pump. This will be linked to an enhanced version of the Microgeneration Certification Scheme's (MCS) 'find a contractor' tool to allow consumers to request installation quotes from installers. The project will seek an assessment partner, to increase the accuracy and dependability of the home information data. The intention being to provide multiple installers with sufficient information to quote to 90% accuracy, without the need for several pre-quote site surveys, whilst still complying with MCS standards.

3.4.6.

This is a software project aimed at improving the customer journey. Significant barriers need to be overcome at a household level to accelerate adoption of Heat Pumps technology and to meet the target of 600,000 system installations per year by 2028. These include costs, understanding of the technology, and appreciation of the long-term benefits (financial and environmental). VIA Analytics' project aims to help meet the 600,000 per year target by developing an online property level analytics platform enabling end to end management of the customer journey, particularly through:

- identification of suitable opportunities for domestic heat pump installations (and benefits) through digital customer engagement
- providing a platform that brings the customers and supply chain together in an efficient, optimised, digitally driven way

- developing a framework to provide accurate data management of engagement, installation, and post completion – with the objective of increasing investor confidence, to promote accelerated investment into heat pumps technology

3.5. Category objective 5: to create a smart home energy system.

The three projects within this category objective are outlined below.

3.5.1.

Creating a heat pump specialist Home Energy Management System (HEMS) supported by a full-package solution to help customers understand and maximise the benefits to their home. The Gen Game project aims to reduce costs and carbon by:

- using smart meter data to identify customers who would benefit from heat pumps and inform them of savings
- sizing heat pumps based on a variety of data sources
- optimising home energy management systems across heat pumps, PV, electric vehicle charging, battery storage and other energy assets to reduce costs and carbon
- providing access to flexibility markets to enhance the benefits and business case
- remaining energy supplier and product manufacturer agnostic, giving customers choice

3.5.2.

This Thermoelectric Conversion Systems Ltd project aims to overcome several major infrastructural challenges of heat pump adoption, by harnessing demand-side management to cope with peak loads and time-shifting energy use. By utilising otherwise wasted energy, this solution aims to give economic and reliable products for retrofit in existing homes and new-build properties to dramatically improve energy efficiency of buildings and cut running costs. The aim is to achieve this by:

- drawing energy from the household wastewater stream by re-using energy lost, e.g. from the shower or bath, by fitting the heat pump in the drainage system to recover energy stored in a hot water cylinder
- using a small air source heat pump to 'top up' the hot water tank temperature to provide the domestic hot water supply
- operating both heat pumps from a mains plug
- using a smart controller to manage both heat pumps and integrate with demand-side management systems to ensure sufficient hot water and heat are available

3.5.3.

The final project is working to overcome the key technical barriers to integration and energy performance optimisation, reducing running costs of heat pumps, and more broadly support improved end-user experiences and acceptance of these systems. The Wondrwall project aims to achieve this by optimising energy management to provide a platform that underpins advanced time-shifting strategies alongside proprietary artificial software intelligence software, using machine learning for dynamic predictive modelling of energy requirements based on their patented sensing technologies.

4. Potential impact of developing the innovative tools & technology

This next section of the paper considers what impact collectively the development of the tools and technologies under HPR Stream 2 may have on supporting meeting the category objectives listed in section 2.3 of the paper.

In order to increase the performance whilst reducing the cost of domestic heat pumps there is a real focus on the manufacturing of heat pumps and how innovation can positively impact current practices. This encompasses tackling the high number of parts utilized in heat pump manufacturing and reducing this where possible to bring about cost savings. In a similar vein modular heat pump manufacturing is being closely looked at as this may also have cost saving benefits. Taking a detailed look and reassessment of how heat pumps are assembled may also enable cost savings which could be passed on to consumers in time. Efforts focused on reducing installation complexity may also support the objective of reducing costs. Finally, it will be worthwhile to quantify potential cost savings that can be made in the remote controlling of a portfolio of operating heat

pumps through, for example, a housing association. Allowing heat pump operators to adjust settings based on continuous monitoring should allow identified savings to be realized across capital expenditure, lower maintenance costs and improved performance.

In minimising home disruption whilst ensuring high quality installations there is a real focus from the funded projects on producing mobile phone apps for a range of people involved in the process of getting a heat pump.

Taking the consumer (e.g. home owner), as an example, a whole range of information needs to be considered by them in order to make decisions relating to changing their heating system. With many different heat pump types and manufacturers available on the market with vastly different applicability, thermal output, installation complexity and cost, this app will help consumers confidently match the heat pump to thermal demand of the house and other specific needs on a case-by-case basis. The market at present often means that a consumer might be advised to get a heat pump from the manufacturer that the installer is more familiar with rather than what makes most sense for the home in question.

The surveyor app being proposed aims to properly size, efficiently monitor and optimise heat pump performance. At the moment there are a range of tools open to surveyors to undertake heat loss calculations for a home and this app is an attempt to move closer towards an easier, more standardized approach to calculating this. Finally, regarding apps they are also being produced for heat pump installers. The app would allow the installer to complete a digital survey and a fully automated design allowing for system optimisation from the beginning of the process. The platform would also ensure that all documentation is stored and logged against the installation, there will be full traceability for consumers and installers to access in the future when it comes to heat pump maintenance and service. Documents received by a consumer at handover of a heat pump can be extensive so having this in one place through an app could be very beneficial. The impact of this could facilitate a more streamlined installation process, significantly reducing the time and effort it takes to complete any installation. As well additional benefits could be derived from an installer app as it could store heat pump settings in order to benchmark for future maintenance and efficiency improvements whilst also acting as a training resource for new heat pump engineers. Better heat pump system design is being investigated through utilizing properties' smart meter data and low-cost sensors to directly measure key performance parameters on a property basis. The output from this is a publicly available protocol that defines the measurement options, standards that must be followed, what the outputs must comprise and how these should be presented. Finally standardised heat pump system design as part of a wider retrofit for non-traditional hard to treat homes is being considered.

In providing financial solutions to support wider heat pump deployment three key initiatives are underway. The purchase of a car through finance is a widely utilized financial product. Creating a financial product for the purposes of making the purchase of a heat pump more feasible by spreading out the upfront cost is being done as part of HPR stream 2. The Green Homeowner Loan aims to be financially attainable to help increase the sale of heat pumps and allow them to be a mainstream home purchase. Heat as a service is seen as another means to provide a financial solution to accelerating heat pump deployment at the lowest cost to the consumer. Consumers that buy heat as a service choose how much to spend on the experience they want – feeling warm and comfortable when and where they want in their homes – instead of paying for kilowatt-hours of energy [9]. Finally, the offer of a financially insurable performance guarantee to homeowners and landlords aims to use software integrated with existing retrofit supply chain components to quality assure quality design and installation of a heat pump system. This may be able to assist with ensuring installations are of good quality.

To address improving the consumer journey through the transition to heat pumps a number of data utilization initiatives amongst others are being delivered. The power of data clearly has a role within this area across surveying homes, heat pump installation, optimization and maintenance. Across these points of the consumer's heat pump journey projects are looking into smart meter data enabling better thermal modeling of the home to support accurate heat pump sizing and type suitability for a home. Installers can then obtain data of a heat pump system they've installed post-install to support their own learning. Housing associations responsible for heat pumps across a portfolio of homes might be interested in the ability to undertake remote reading of error warning messages from a heat pump to alert and enable a response to a heat pump performance issues. Heat pump system design is being considered through a digital solution to improve the customer journey by streamlining the required pre-installation steps into one remote survey reducing the amount of information required upfront ahead of an installation. The end-to-end digital solution could support customers in identifying innovative heat pump solutions, tailored to their profile. Other project offerings under this category objective include the ability to select MCS certified installers, filtering by name, type and location to obtain quotes. This would save the consumer considerable time in identifying an installer in what has been a difficult task due to a lack of installers in certain geographical locations.

In supporting the creation of a smart home energy system an output from the projects is to utilise smart meter data to embed heat pumps within a Home Energy Management System to optimize energy-related behavior within the home including renewable energy technology usage. This might involve for example accessing flexibility markets. Optimised energy management is also being considered through a platform that underpins advanced time-shifting strategies alongside proprietary artificial software intelligence software. This would take place through the use of machine learning for dynamic predictive modelling of energy requirements based on their patented sensing technologies. Finally, the potential for demand side management is being looked at through a heat pump and energy storage system combining energy recovery from the wastewater streams leaving a house. This will be done by drawing energy from the household wastewater stream by re-using energy lost, e.g. from the shower or bath, by fitting the heat pump in the drainage system to recover energy stored in a hot water cylinder.

5. Conclusions

This paper has showcased the high-potential innovative tools and technologies being developed under stream 2 of the HPR programme addressing barriers to domestic heat pump deployment across the five thematic areas. The paper has also considered the potential impact in supporting the deployment of heat pumps across the UK and in countries with similar climates and housing archetypes. The rapid evidence assessment undertaken during programme design highlighted the need for further trials and development of heat as a service to increase consumer understanding. HPR is directly addressing this through a heat as a service project and will obtain learnings on this. Similarly understanding the impact on the electricity grid of high-density heat pump deployment will be facilitated through stream 1 deployment as well as potentially better understood on how to mitigate this through the Kensa project. Effective coordination between heat pump stakeholder groups is being well tackled through the various apps being produced under stream 2 of which all are outlined in this paper. Finally the potential areas where research and innovation are listed under the rapid evidence assessment as being of significant benefit includes design improvements of heat pumps, manufacturing, installation, monitoring, maintenance and operational. The rationale for interventions in these areas are to address the performance gap between theoretical and actual heat pump performance. The ICAX, Ventive and Thermoelectric Conversion Systems projects should all provide interesting insights into improving heat pump manufacturing.

Acknowledgments

The research and development funded under the Heat Pump Ready programme is part of the Department for Energy Security & Net Zero's £1bn Net Zero Innovation Portfolio. Acknowledgment is made to all the project lead organisations that comprise the programme [5].

References

[1] BEIS. (2021, February 2). Final UK greenhouse gas emissions national statistics: 1990 to 2019. Retrieved from Gov.uk: https://www.gov.uk/government/statistics/final-uk-greenhouse-gas-emissions-national-statistics-1990-to-2019

[2] BSIRA. (2021). Heat pumps market analysis 2020: United Kingdom. BSIRA.

[3] HM Government. (2020). The Ten Point Plan for a Green Industrial Revolution,: Retrieved from Gov.Uk: https://assets.publishing.service.gov.uk/government/uploads/system/uploads/attachment_data/file/936567/10_POINT_PLAN_BOOKLET.pdf

[4] Heat Pumps and Their Role in Decarbonising Heating Sector: A Comprehensive Review, Ankita Singh Gaur, Desta Z. Fitiwia,b and John Curtisa, ESRI Working Paper, June 2019

[5] BEIS. (2022, January 22). Heat Pump Ready Programme. Retrieved from Gov.Uk: https://www.gov.uk/government/publications/heat-pump-ready-programme

[6] BEIS. (2021, December 30). Heat Pump Ready: Supporting Information Background on innovation Needs. Retrieved from Gov.Uk:

https://assets.publishing.service.gov.uk/government/uploads/system/uploads/attachment_data/file/1043227/heat-pump-ready-innovation-needs.pdf

[7] BEIS. (2022, September 30). Boost for innovative heat pump projects to drive cleaner heating. Retrieved from Gov.uk: https://www.gov.uk/government/news/boost-for-innovative-heat-pump-projects-to-drive-cleaner-heating

[8] BEIS. (2022, September 27). Heat Pump Ready Programme: Stream 2 Projects. Retrieved from Gov.uk: https://www.gov.uk/government/publications/heat-pump-ready-programme-successful-projects/heat-pump-ready-programme-stream-2-projects

[9] Energy Systems Catapult. (2022, October 7). SSH2: Introduction to Heat as a Service. Retrieved from Energy Systesms Catapult: https://es.catapult.org.uk/report/ssh2-introduction-to-heat-as-a-service/#:~:text=Heat%20as%20a%20Service%20is,for%20kilowatt%2Dhours%20of%20energy

14th IEA Heat Pump Conference
15-18 May 2023, Chicago, Illinois

Experimental testing of solar photovoltaic/thermal collector as a heat pump source under outdoor laboratory conditions

Francisco Beltrán*, Nelson Sommerfeldt, Hatef Madani

KTH Royal Institute of Technology, Stockholm 100 44, Sweden

Abstract

The integration of photovoltaic-thermal (PVT) and heat pumps appears as a promising technology for the decarbonization of European buildings. Some of the benefits include the simultaneous production of renewable electricity and heat, as well as an improved system efficiency. However, there has been little research dedicated to collectors designed specifically for heat pump integration. This study aims at characterizing the performance of an unglazed and uninsulated PVT collector with fins, acting as a source for heat pump systems. Tests are performed at an outdoor testing facility in Stockholm Sweden, over two weeks in October 2022. Specific thermal output in W/m^2 is presented against temperature difference between ambient and mean fluid temperature for a wide range of boundary conditions. The results show that the PVT collector field can generate a peak thermal power of 9 kW during sunny days, and 5 kW during nighttime operation. In order to meet the peak heating capacity in a Swedish villa, however, the collector field should be at least 40 m^2.

© HPC2023.
Selection and/or peer-review under the responsibility of the organizers of the 14th IEA Heat Pump Conference 2023.

Keywords:Solar sourced heat pumps, PVT, testing facility, heat exchanger;solar hybrid

1. Introduction

Solar photovoltaic-thermal (PVT) modules can produce electricity and heat simultaneously, thus reducing the amount of required roof area if compared to stand-alone solar PV and thermal systems. At the same time, heat pumps are the most efficient technology to produce space heating and domestic hot water in a highly electrified scenario. There are currently 190 million heat pumps installed worldwide and, according to the Net Zero by 2050 scenario developed by IEA, this number should increase to 600 million by 2030 if climate targets are to be met (IEA, 2022). Therefore, the integration of PVT with heat pumps appears as a promising technology for the decarbonization of European buildings.

When combined with heat pumps, solar thermal systems can provide a higher seasonal performance factor due to the reduction in heat pump electricity use, whereas solar PV allows for the use of less electricity from the grid (Poppi et al., 2018). There are many ways of combining these two technologies, but one that has gained attention in recent years are PVT sourced heat pumps (Sommerfeldt and Madani, 2017). In this configuration, uncovered PVT collectors are connected in series with a heat pump system to act as an additional or sole heat source, in order to lift the evaporator temperature and improve system efficiency (Giovannetti et al., 2019; Hadorn, 2015). The low temperatures in the PVT circuit allow heat to be captured not only from the sun but also from ambient air, thus increasing thermal efficiency to a level on par with a high performance solar thermal system (Sommerfeldt and Madani, 2018; Weiss and Spörk-Dür, 2019). The low operating temperatures also enable the use of cheaper and lighter materials such as plastic, and an improved electrical efficiency due to the cooling effect on the PV cells. The increased electrical power generation can be enough to cover the additional pumping power, making the captured heat from the PVT a free resource (Sommerfeldt and Madani, 2018).

Schmidt et al. (2018) investigated the performance of rear insulated and unglazed PVT collectors acting as the sole source of a heat pump. The results showed that this system configuration was able to cover the space

*Corresponding author.
E-mail address: fbeltran@kth.se

heating and domestic hot water demand for winter days down to -10°C, and suggested that better results could be achieved if using uninsulated PVT collectors.

Although solar PVT and heat pump systems have been studied extensively in the past, there has been little research dedicated to collectors designed or optimized specifically for heat pump integration. For example, the heat capture could be enhanced by adding fins on the rear side of the absorber/exchanger, improving heat production even at low solar irradiance levels. A few studies have looked at the performance of PVT+HP systems with unglazed and uninsulated PVT collectors with fins. Chhugani et al. (2020) looked at the performance of an unglazed and uninsulated PVT collector with fins serving as a sole source of a heat pump in a single-family house in Germany. The system was tested under a Hardware in the Loop test environment, and the results showed that the seasonal performance factor (SPF) during the winter months reached daily averages of 3.3. It was suggested that the PVT collectors could replace the noisy heat exchanger in an air source heat pump, while keeping a good system efficiency. Giovannetti et al. (2020) calculated the U-values of a 20m^2 PVT collector array with fins under no solar irradiance conditions according to ISO 9806:2017, and found that they were in the range of 22.9 and 27.0 Wm^{-2}K^{-1} at specific heat flows between 75 and 175 W/m^2.

2. Objective and Methodology

This study aims at empirically characterizing the performance of an unglazed and uninsulated PVT collector with fins designed specifically for heat pump integration. The tests are performed at an outdoor testing facility between the 4th and 20th of October 2022, for different inlet temperatures and flow rates, which provides a wide range of solar irradiance levels (G) and ambient temperatures (T_{amb}). Three different volumetric flow rate ranges are considered: 30 to 35 lh^{-1}m^{-2}, 40 to 45 lh^{-1}m^{-2} and 50 to 55 lh^{-1}m^{-2}. Thermal power output is monitored for the collector array and plotted against the temperature difference between ambient and mean fluid temperature of the collector field ($T_{f,m}$). Linear regression is used to determine the thermal performance curves, and the key parameters such as the slope of the curve, the performance at $\Delta T=0$ and the coefficient of determination (R^2) are presented and discussed. The U-value obtained from the collector field is then compared against the results for the same stand-alone collector and other finned collector designs. Finally, time series data for the days between 15th and 18th of October is presented, looking at daily heat and electricity generation.

2.1. Testing facility

The testing facility is located on the rooftop of the Energy Technology Laboratory at KTH Royal Institute of Technology in Stockholm, Sweden, and consists of a 14 PVT collector array with an area of 20 m^2, connected in series to a 12 kW variable speed heat pump. The array is oriented to the south and has a tilt angle of 45°. It is made up of two subarrays connected in series, where each subarray has seven collectors connected in parallel. The testing facility also includes a hot water tank and air to water heat exchanger for heat dissipation. Figure 1 shows the PVT collector array and mechanical room of the testing facility at KTH.



Figure 1. PVT+HP testing facility at KTH with collector array (left) and mechanical room (right)

The facility allows for two operation modes:

- brine circulates directly into the solar PVT loop
- brine and solar loops operate independently, with a cold storage tank connecting both circuits

For the purpose of this study, only the operation mode in which the tank is bypassed is utilized.

2.2. PVT module

The PVT collector is manufactured by the company Solhybrid i Småland and consists of an extruded aluminum manifold mechanically pressed to the rear side of a glass-glass PV module. The manifold has a trough that fits a 12 mm copper pipe, also mechanically pressed. To increase heat transfer between the different absorber materials, thermal grease is added between manifold and rear glass, as well as between the aluminum trough and the copper pipe. A picture of the PVT absorber can be seen in Figure 2.



Figure 2. Unglazed and uninsulated sheet and tube PVT collector from Solhybrid i Småland

The PV module is an off-the-shelf 60 monocrystalline-cell panel manufactured by Perlight Solar. The electrical ratings and specifications are presented in Table 1. Each PV module is connected to a micro inverter for DC/AC conversion.

Table 1. PV module specifications

Pmax *(Wp)*	Efficiency *(ηel)*	Open-circuit voltage *(Voc)*	Short-circuit current *(Isc)*	Voltage @ Pmax *(Vmp)*	Current @ Pmax *(Imp)*	Temp. coeff. Pmax *(β)*
285 W	17.52%	38.80 V	9.32 A	32.43 V	8.79 A	-0.40 %/°C

The monitoring system consists of a weather station for ambient temperature measurement, dew point and wind speed; a solar irradiance meter for measurement of the incident solar irradiation on the collector plane; a heat power meter for the measurement of flow rate, inlet temperature, outlet temperature and thermal power; the already mentioned micro inverters for electrical power measurement. All the measured data is obtained in 1-minute time steps, except for the electricity generation that is measured every five minutes. A schematic diagram of the testing facility with the monitoring equipment is presented in Figure 3.

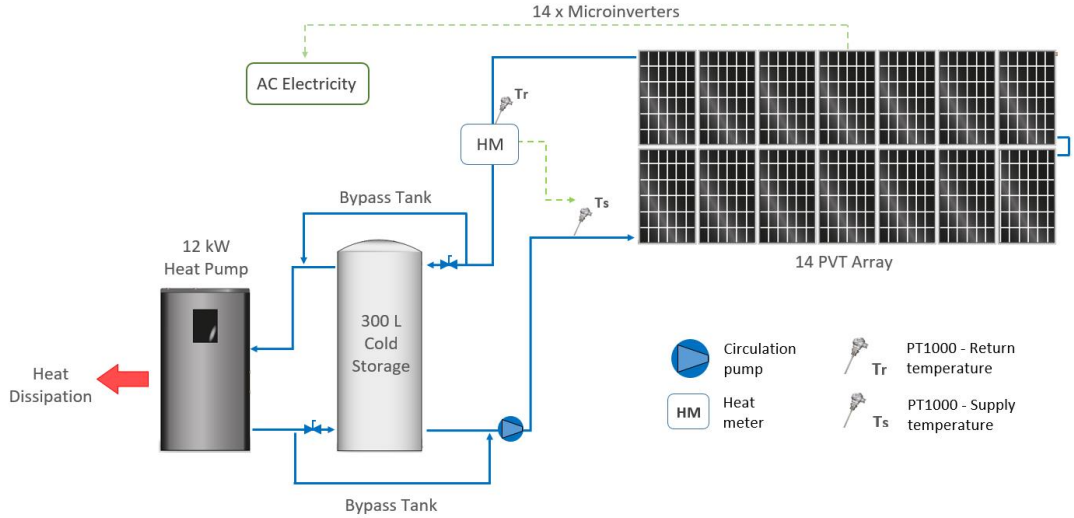


Figure 3. Test rig diagram

3. Results and discussion

Firstly, the weather data for the period of study is presented in Figure 4. The range of ambient and dew point temperatures is 2 to 16°C and 0 to 13°C, respectively, throughout the experiments. Regarding in-plane solar irradiance levels, there is a wide range of conditions, from zero to around 1000 W/m^2. Looking at the daily solar irradiation on the collector plane, the sunniest day is October 9th with 5.1 kWh/m^2, and the lowest is October 5th with 0.4 kWh/m^2.

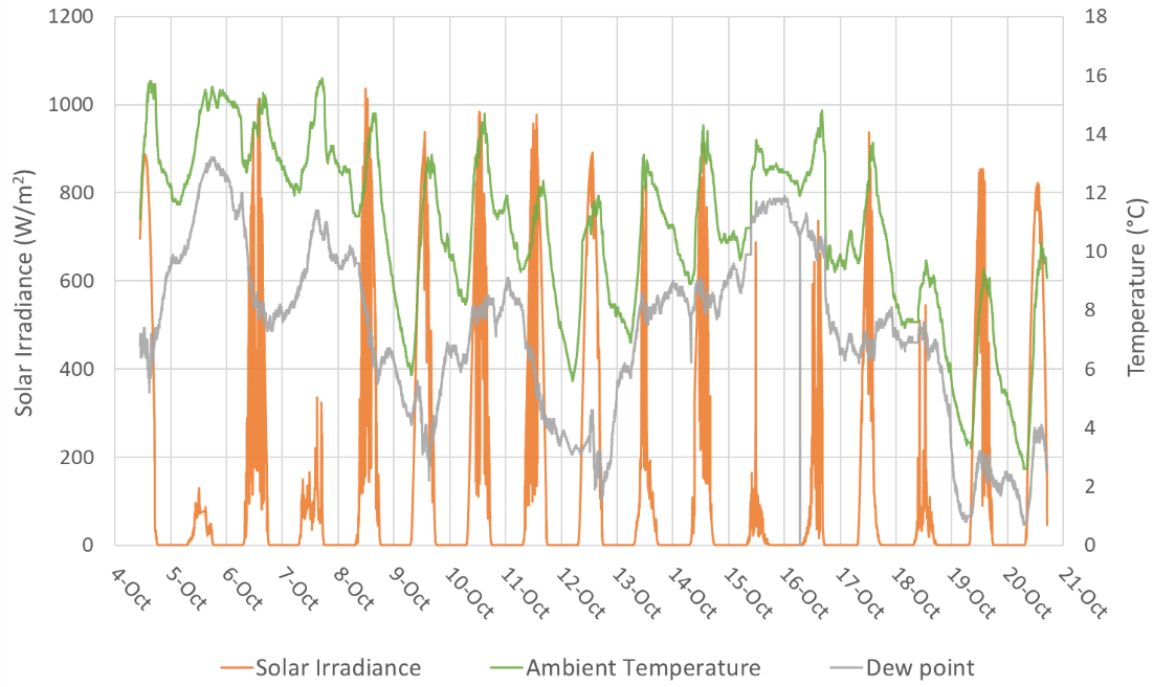


Figure 4. Weather data between 4th and 20th of October

The results for specific thermal production of the PVT collector in W/m^2 are presented against the temperature difference between ambient and mean fluid temperature of the collector field, separated by solar irradiance levels and volumetric flow rates.

3.1. Volumetric flow rate of 30 to 35 lh^{-1}m^{-2}

Figure 5 shows the results when the volumetric flow rate is set in the range of 30 to 35 lh^{-1}m^{-2}. In this case, the thermal output can reach a value of 425 W/m^2 for solar irradiances in the range of 700 to 900 W/m^2 and a ΔT of around 13 K. It can also be seen that, even at low solar irradiance levels (200 - 400 W/m^2), the thermal output of the collector field can be over 300 W/m^2 for ΔT=14K, which shows the importance of the heat exchange with ambient air. However, such high ΔTs can be a limitation for the heat pump as ambient air temperatures approach the evaporator's limit. Looking at lower temperature differences of 6K or 7K, we can see that the thermal output goes from just over 100 W/m^2 for low solar irradiances, up to 300 W/m^2 for the upper range. For the 14 PVT collector array, this equals a total thermal power production between 2 and 6 kW fed directly into the heat pump evaporator.

Linear regression is used to represent the thermal performance curve of the collectors as a function of temperature difference between ambient and mean fluid temperature of the collector field for different solar irradiance levels. The key parameters of such curves, such as the slope of the curve in W/K, the thermal output at a ΔT=0 and the coefficient of determination (R^2), are shown in Table 2.

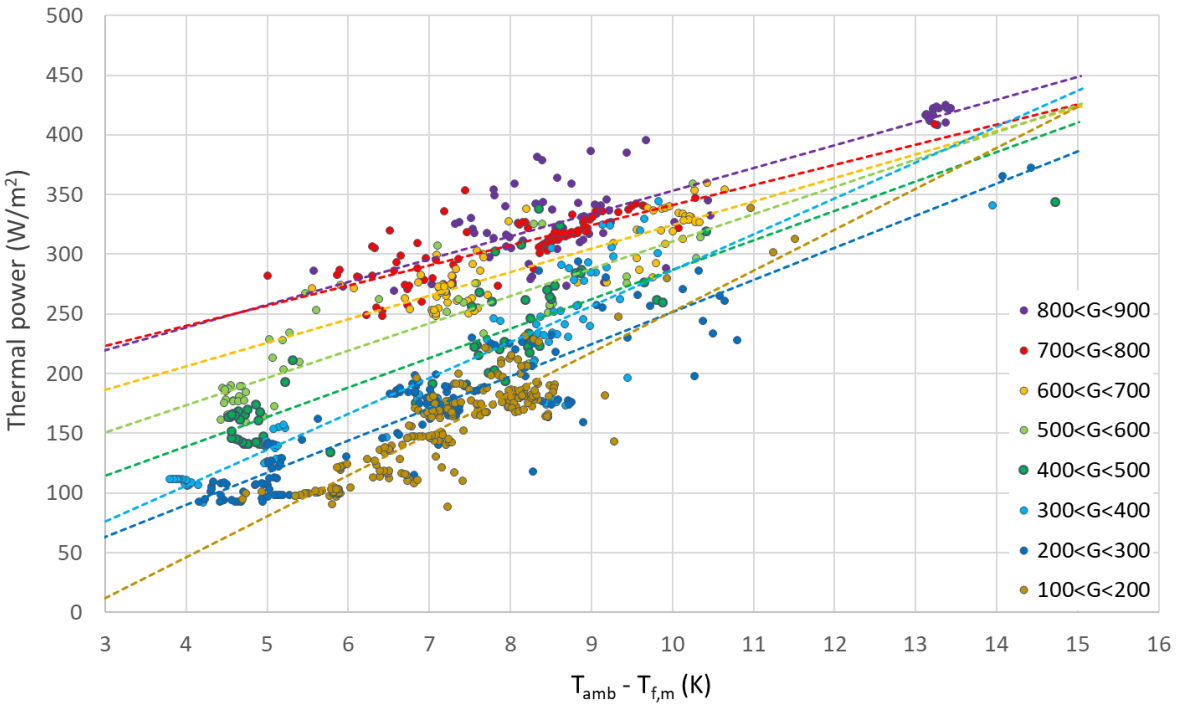


Figure 5. Specific thermal output of collector array as a function of $T_{amb} - T_{f,m}$ for different solar irradiance levels and flow rate of 30 to 35 $lh^{-1}m^{-2}$

As the solar irradiance increases, the U-value of the collector field decreases (i.e. slope of the curve) and the thermal output at ΔT=0 increases (y-intercept). Another aspect to highlight is the fact that the coefficient of determination decreases as the solar irradiance increases. This can be explained by the fact that the PVT collector has a limit on how much heat it can capture based on the flow rate and absorber geometry, so the curve tends to start flattening as we increase the difference between T_{amb} and $T_{f,m}$. The coefficient of determination is between 65% and 82% for all cases, which shows that the presented linear relationships are relatively weak. This is primarily due to missing aspects of wind velocity, sky temperature or thermal capacity in the regression model, as described by (Fischer et al., 2004; Perers, 1997) for quasi-dynamic conditions.

Table 2. Main parameters of thermal performance curve for a flow rate of 30 to 35 $lh^{-1}m^{-2}$

Solar Irradiance W/m^2	HEX U-value $Wm^{-2}K^{-1}$	Y-intercept Wm^{-2}@ΔT=0	R^2
100<G<200	34.3	-90.9	0.78
200<G<300	26.9	-17.8	0.82
300<G<400	30.1	-14.3	0.84
400<G<500	24.6	40.8	0.75
500<G<600	22.8	82.6	0.73
600<G<700	19.7	127.3	0.71
700<G<800	16.9	172.8	0.65
800<G<900	19.1	162.6	0.73

3.2. Volumetric flow rate of 40 to 45 $lh^{-1}m^{-2}$

Figure 6 shows the results when the flow rate is increased by 10 $lh^{-1}m^{-2}$. The specific thermal output can reach a value of approximately 450 W/m^2 for solar irradiances over 500 W/m^2 and a ΔT of around 13-14 K, representing a 5% increase in thermal output if compared to the previous case. For the 14 PVT collector array, this equals an increase in thermal power of 0.5 kW. Looking at a ΔT of 6-7 K we can see that thermal output

is in the range of 150 to 325 W/m^2. For the 14 PVT collector array, this equals a total thermal power production of between 3 and 6.5 kW that could be fed directly into the heat pump evaporator.

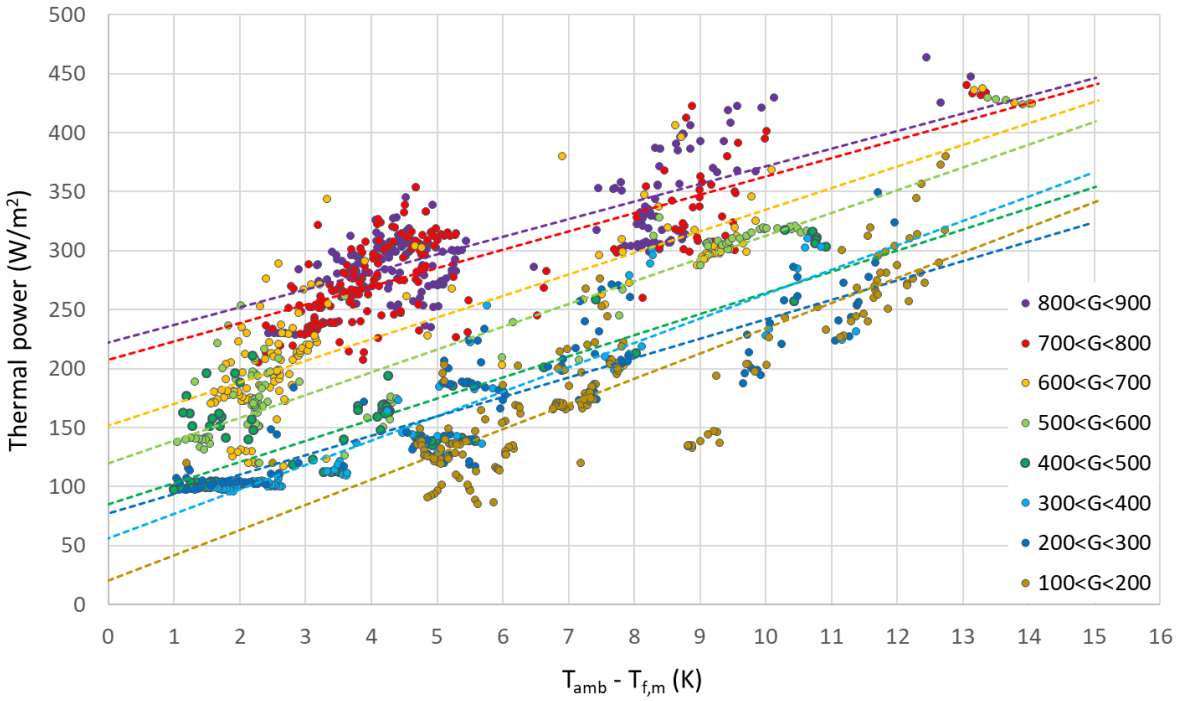


Figure 6. Specific thermal output of collector array as a function of $T_{amb} - T_{f,m}$ for different solar irradiance levels and flow rate of 40 to 45 lh^{-1}m^{-2}

The main parameters of the thermal performance curve are presented in Table 3. As solar irradiance increases, the U-value of the collector field decreases and the y-intercept increases, as was observed for the 30 to 35 lh^{-1}m^{-2} case. Another aspect to highlight is that even when there is no temperature difference between ambient and mean fluid temperature, the PVT collector can still generate heat regardless of the solar irradiance level. The coefficient of determination is between 61% and 85% for all cases, which shows that the presented linear relationships are relatively weak, as explained in the previous section. When comparing the values in the Table to the previous case, the U-values of the collector field are lower at higher flow rates, but the specific heat production at ΔT=0 becomes higher as the flow rate increases.

Table 3. Main parameters of thermal performance curve for a flow rate of 40 to 45 lh^{-1}m^{-2}

Solar Irradiance W/m^2	HEX U-value Wm^{-2}K^{-1}	Y-intercept Wm^{-2}@ΔT=0	R^2
100<G<200	21.4	20.3	0.73
200<G<300	16.5	77.1	0.74
300<G<400	20.7	56.4	0.85
400<G<500	17.9	85.4	0.71
500<G<600	19.3	119.9	0.83
600<G<700	18.3	151.8	0.74
700<G<800	15.6	207.4	0.62
800<G<900	14.9	222.5	0.61

3.3. Volumetric flow rate of 50 to 55 lh^{-1}m^{-2}

Figure 7 shows the thermal performance of the PVT collector when the flow rate is further increased to the range between 50 and 55 lh^{-1}m^{-2}. In this case, the thermal output can reach values of around 450 W/m^2 for ΔTs as low as 8 K and high solar irradiance levels. Once again, if we look at a more likely 6 to 7 K temperature

difference, we can see that the thermal power production is in the 150 – 350 W/m^2 range, or 3 to 7 kW for the full collector field.

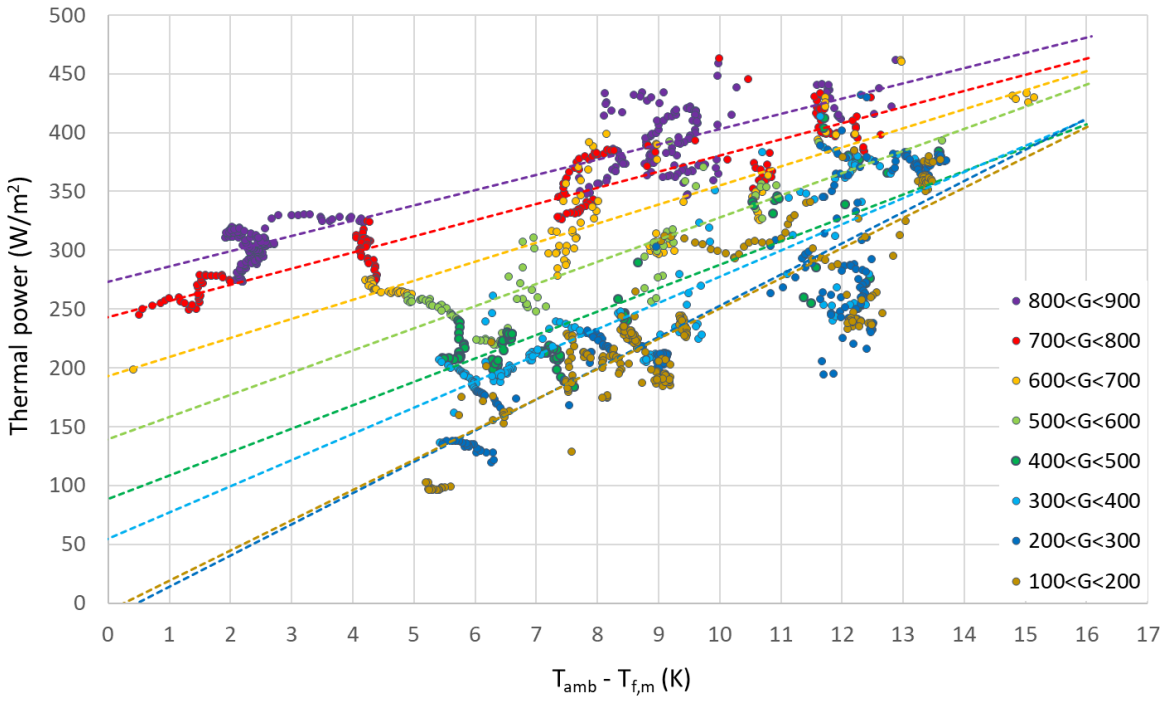


Figure 7. Specific thermal output of collector array as a function of $T_{amb} - T_{f,m}$ for different solar irradiance levels and flow rate of 50 to 55 lh^{-1}m^{-2}

An interesting observation when looking at the thermal performance curves is that they start to spread out for lower irradiance levels, but tend to converge as ΔT increases. This can be explained by the fact that the PVT collector has a limit on how much heat it can capture based on the flow rate and absorber geometry, so the curve tends to start flattening as we increase the temperature difference between ambient and mean fluid temperature. Another aspect to consider is that as the temperature difference increases, the relative importance of solar irradiance decreases within the overall heat transfer, meaning that convection will play a larger role. An important takeaway of this is that it seems to be convenient to work at higher flow rates at lower ΔTs, and lower flow rates at higher ΔTs.

The main parameters of the linear regression curves are presented in Table 4. As happened with the previous two cases, it can be seen that as the solar irradiance increases, the U-value decreases and the thermal output value for ΔT=0 increases. If compared with the 40 to 45 lh^{-1}m^{-2} case, the slope of the curves are higher for lower solar irradiance levels and lower for higher solar irradiance levels. The same occurs with the specific thermal output at ΔT=0. Opposite to what happened with lower flow rates, the value of R^2 increase as solar irradiance increases and is higher than 70% for all cases.

Table 4. Main parameters of thermal performance curve for a flow rate of 50 to 55 lh^{-1}m^{-2}

	W/K	W@ΔT=0	R^2
100<G<200	25.7	-6.8	0.75
200<G<300	26.5	-12.5	0.73
300<G<400	22.3	55.0	0.72
400<G<500	19.9	89.0	0.72
500<G<600	18.8	139.4	0.75
600<G<700	16.1	193.5	0.77
700<G<800	13.7	243.5	0.89
800<G<900	13.0	273.1	0.87

3.4. No solar irradiance

Figure 8 shows the performance of the PVT collector for a solar irradiance level of 0 W/m^2, for different ΔTs and volumetric flow rates. It can be seen in the chart that when working exclusively as an air to water heat exchanger, the PVT collector can generate up to 250 W/m^2 for a ΔT of 10 K, and as high as 150 W/m^2 when ΔT is in the 6-7 K range. The latter means a total thermal energy production for the collector field of more than 3 kW.

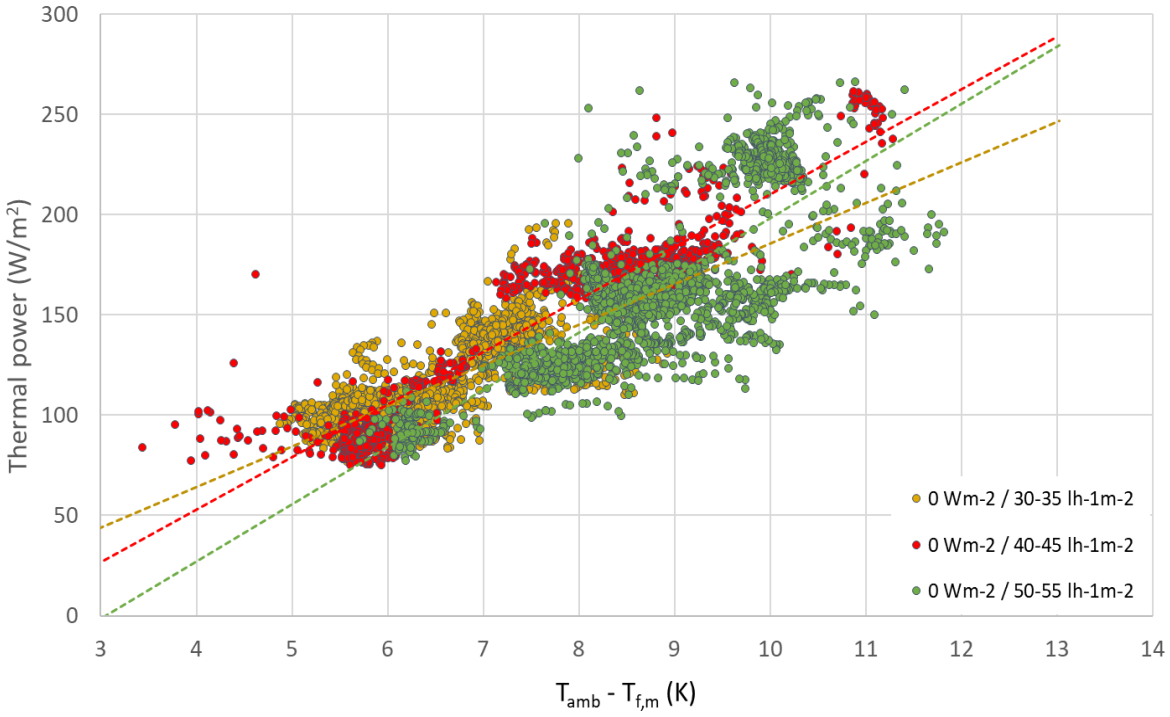


Figure 8. Specific thermal output of collector array as a function of $T_{amb} - T_{f,m}$ for solar irradiance levels of 0, 400 and 800 W/m^2 and varying flow rates

The main parameters of the thermal performance curves are presented in Table 5. It can be observed that the slope of the curve increases together with the flow rate. When looking at the thermal output at ΔT=0, it decreases with increasing flow rate. Finally, the coefficient of determination is higher than 60% for all cases, meaning that the linear regression curves are a good fit for the empirical data.

Table 5. Main parameters of thermal performance curve for solar irradiance 0 W/m^2 and varying flow rates

lh^{-1}m^{-2}	No solar irradiance		
	W/K	W@ΔT=0	R^2
30-35	20.3	-16.8	0.60
40-45	23.8	-32.2	0.80
50-55	28.5	-86.8	0.61

3.5. Time-series performance between 15th and 18th of October

Figure 9 shows the time-series specific thermal and electrical output of the 14 PVT collector array for 4 days between the 15th and 18th of October. The temperature difference between ambient and mean fluid temperature is also plotted. It can be seen that the thermal and electrical output are the highest for the 17th of October, which coincides with day with highest solar irradiation and temperature difference between T_{amb} and $T_{f,m}$.

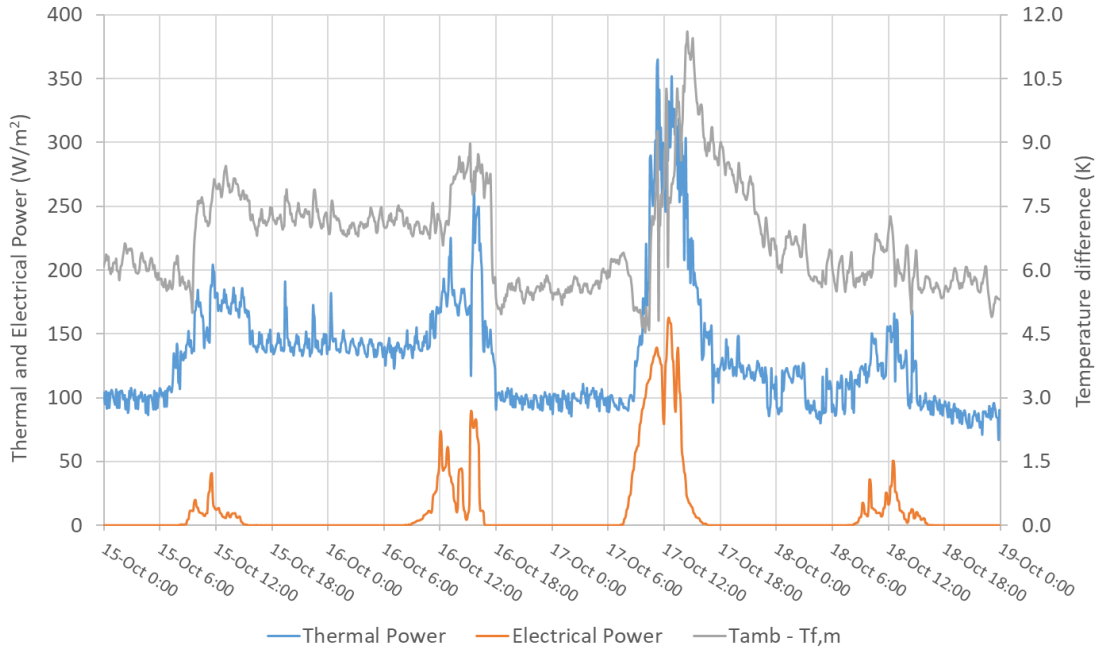


Figure 9. Time-series thermal and electrical performance of PVT collector field between 15th and 18th of October

Table 6 shows a summary with the total heat and electricity production for each day per m^2 of collector, together with the daily solar irradiation, average ambient temperature and average temperature difference between ambient and fluid. One of the main observations here is that the performance of an unglazed-uninsulated PVT collector with fins is more dependent on temperature difference with ambient than solar irradiation. For example, the total solar irradiation for the 16th of October is three times more than that of the 15th of October; however, the total heat production from the PVT collectors only experiences a 3.7% increase. This is because the average ΔT is practically the same, with a value close to 9°C. On the other hand, electrical power production is highly dependent on solar irradiance levels and very little on ambient and/or fluid temperature. For the day with the highest solar irradiation levels, the electricity production of the full array is 12.9 kWh, with a peak power of 3.2 kW. For the considered study period, the 20-m^2 PVT collector array generated a daily average of 64 kWh of heat and 5.2 kWh of electricity. This translates into a daily average solar efficiency of 370% for heat and 17.1% for electricity, which is near the rated efficiency for the PV module.

Table 6. Daily performance of PVT collector field and weather data

Day	Heat *(kWh/m²-day)*	Electricity *(kWh/m²-day)*	Solar Irradiation *(kWh/m²-day)*	Solar efficiency Heat	Solar efficiency Electricity	Ambient Temperature *(°C)*	Average T_{amb}-$T_{f,m}$ *(°C)*
15-Oct	3.25	0.07	0.46	707%	15.2%	11.94	8.88
16-Oct	3.37	0.23	1.30	259%	17.7%	12.06	8.98
17-Oct	3.58	0.64	3.31	108%	19.3%	10.68	9.36
18-Oct	2.51	0.10	0.62	405%	16.1%	7.92	7.29

4. Discussion

For this study, the U-value calculated as the slope of the thermal performance curve, is in the range of 13 to 19 $Wm^{-2}K^{-1}$ for high solar irradiance levels, which is on the upper range of what a typical unglazed and uninsulated PVT collector would have (Brötje et al., 2018). However, it is 40 to 60% lower than other PVT collectors specifically designed for heat pump integration that were found in the literature.

Most residential heat pumps in villas are in the range of 10-15 kW, and likely to have a COP of 2 when operating at peak capacity. Assuming those operating conditions, the PVT field should be able to supply between 5 and 7.5 kW at the evaporator, meaning a minimum of 250 W/m^2 with the 20-m^2 array presented. The results in this study show that during sunny days, this could be achieved by the 20-m^2 collector array when temperature difference between ambient and mean fluid temperature is higher than 3 or 4 K. However, when looking at nighttime performance, it would be required to have a ΔT higher than 10 K, which is unlikely to happen during low ambient temperatures when the heat pump needs to operate at maximum capacity due to temperature limits at the evaporator. Under those circumstances, a PVT array of at least double the size would be required to meet the heating needs.

With regards to the seasonal performance factor (SPF) of a solar PVT sourced heat pump system, previous simulation research by the authors showed that an SPF of 1.6 can be achieved for a typical multi-family house in Stockholm with a PVT collector area of 4.5 m^2 per kW_{th} of nominal heat pump power (Sommerfeldt et al., 2020). Although this is on the lower end of what would be expected for an air source heat pump system, several design improvements to enhance heat capture with the air were also demonstrated that could bring the SPF up to 2.6, making it competitive with an air source heat pump in Stockholm. This performance is corroborated by studies carried out in Germany, where Chhugani et al., (2020) found that an SPF of 3.3 can be achieved during the winter period in Hamelin, using a sheet and tube collector with fins with an area of 2.5 m^2/kW_{th}. Lämmle and Munz, (2022) showed that an SPF of up to 3.6 can be achieved when using double-finned micro-channel PVT collector, with a collector area as little as 3 $m^2/kW_{th.}$

Although the effect of wind velocity or direction was not considered in this study, it has been proven significantly lower for a collector array than for a stand-alone collector. Chhugani et al. (2021) found that the overall heat transfer coefficient of a 20-m^2 PVT array is around 20% lower than that of a single PVT collector, and the wind dependence of the heat loss coefficient is reduced by half.

The effects of condensation and frost formation were not considered either, which could enhance the thermal performance of the collectors. However, once an ice layer is formed, it decreases the thermal output of the collector. Chhugani et al. (2021), found a 15% reduction in measured against simulated thermal output when frost formation occurs, showing that ice formation hinders the heat exchange with ambient air considerably.

Even though the coefficient of determination for the different thermal performance curves was within an acceptable range for certain data sets, there was a large variance of the data around the linear regression curve. This can be explained by the previous two limitations in the study: the effect of wind velocity (even if not as high as for a stand-alone collector) and the effect of condensation and frost. Usually tests on PVT collectors are performed at indoor testing facilities with fixed solar irradiance, wind velocity, ambient temperature and humidity. In this case it was tested outdoors, so there was no control on the weather conditions. Another limitation is that instead of using fixed values of solar irradiance or flow rates, ranges are used, which can bring differences in the measured values. Besides, as can be seen from the weather data, most of the days were partially cloudy which adds another layer of uncertainty.

The coefficient of determination for all curves was between 60 and 90%, which is relatively weak for a regression model. However, it was not the aim of this study to present a regression model for PVT collectors, rather use it to help in the description of the data that was gathered. A widely accepted empirical model of unglazed and uninsulated PVT collectors already exists, where factors such as wind speed, radiation to sky and thermal capacity of the collector are considered and will be part of future work.

5. Conclusion

The performance of a 20-m^2 PVT collector array specifically designed for heat pump integration was tested under outdoor weather conditions for 16 days in October 2022, in Stockholm, Sweden. The results show that the specific thermal output of such collectors varies primarily with the difference between ambient temperature and mean fluid temperature. With a specific thermal output in the range of 100 and 250 W/m^2 when there is no solar irradiance, a standard villa-sized PVT array can act as an air to water heat exchanger producing

between 2 kW and 5 kW of heat to use as a source for a heat pump. Looking at peak heat capture capacity, the 20 m^2 PVT field is expected to provide 9 kW peak on a sunny day, and 5 kW peak during nighttime.

The U-values found for this collector at high solar irradiances are in the range of 13 to 19 $Wm^{-2}K^{-1}$, which compared to other collectors found in the literature, shows that there is room for improvement in the design. The addition of more and thinner fins can improve these values to a level with state-of-the-art heat pump PVT collectors. However, this could lead to an increase in collector weight and manufacturing costs, which need to be considered in a detailed techno-economic analysis.

The presented 20 m^2 PVT field is likely to meet the demand at the evaporator of the heat pump working at full capacity during cold and sunny winter days, but at least double the size would be required to meet the demand at night. Alternatively, more fins would increase the U-value, but even still it is likely that a larger area would be necessary. This study does not analyze how PVT and HP work together to meet building loads, but it gives some perspective on the required area and temperature difference that is needed.

The period of study produced a wide range of boundary conditions, which capture a wide range of possible operating conditions. It is observed that as solar irradiance, flow rate and temperature difference increase, so does the specific thermal output of the collector. A maximum value of 450 W/m^2 is registered throughout the experiments, suggesting that the thermal output may be limited at around that number for this particular design.

Finally, the time-series performance of the PVT collector array was studied, where it was found that the daily electricity production for four days in October was 7.5% of the daily heat production. However, the percentage of electricity production during the summer and spring should increase thanks to more hours of available sunshine. Looking at the solar efficiency of the collector, the daily average for heat is around 370%, meaning that around 75% of the energy captured by the PVT collector throughout a day in October comes from the ambient air. The daily average for electrical efficiency is 17.1%, which is around the rated electrical efficiency of the PV module.

6. Future work

This study looks exclusively at the thermal and electrical performance of an uninsulated/unglazed PVT collector with extruded fins. Future work should expand the system boundaries by examining the empirical performance of the heat pump when using PVT as the source, as a way to understand how PVT collectors can improve COP and SPF of the heat pump for real operating conditions under Nordic climate conditions. Moreover, different collector designs should be evaluated for benchmarking and better understanding of the characteristics that make a collector suitable for heat pump integration. Condensation and frost formation were not considered in this study, but these phenomena are going to be the focus of future work, particularly strategies for defrosting. Finally, it would be interesting to look at the benefits of having a cold water storage tank between heat pump and PVT array. The heat production fluctuations that are experienced by the PVT with changes in solar irradiance levels, can put a lot of stress on the compressor, which can affect its lifetime. The addition of a cold storage tank would act as a buffer tank with a certain thermal inertia, which would keep the heat flux to the evaporator at a constant rate.

Acknowledgements

This research study is part of the SmartSol^2 project (Smart Solar Hybrid Solutions for Sustainable European Buildings) funded by Mistra Innovation as part of the MI23 program.

References

Brötje, S., Kirchner, M., Giovannetti, F., 2018. Performance and heat transfer analysis of uncoveredphotovoltaic-thermal collectors with detachable compound. Sol. Energy 170, 406–418. https://doi.org/10.1016/j.solener.2018.05.030

Chhugani, B., Kirchner, M., Littwin, M., Giovannetti, F., 2020. Investigation of photovoltaic-thermal (PVT) collector for direct coupling with heat pumps: Hardware in the Loop (HiL) and Trnsys simulations, in: BauSIM 2020. Online.

Chhugani, B., Pärisch, P., Kirchner, M., Littwin, M., Lampe, C., Giovannetti, F., 2021. Model Validation and Performance Assessment of Unglazed Photovoltaic-Thermal Collectors with Heat Pump Systems 1–12. https://doi.org/10.18086/eurosun.2020.05.13

Fischer, S., Heidemann, W., Müller-Steinhagen, H., Perers, B., Bergquist, P., Hellström, B., 2004. Collector test method under quasi-dynamic conditions according to the European Standard EN 12975-2. Sol. Energy 76, 117–123. https://doi.org/10.1016/j.solener.2003.07.021

Giovannetti, F., Lampe, C., Kirchner, M., Littwin, M., Asenbeck, S., Fischer, S., 2019. Experimental investigations on photovoltaic-thermal arrays designed for the use as heat pump source. Proc. ISES Sol. World Congr. 2019 IEA SHC Int. Conf. Sol. Heat. Cool. Build. Ind. 2019 177–188. https://doi.org/10.18086/swc.2019.05.03

Hadorn, J.-C. (Editor), 2015. Solar and Heat Pump Systems for Residential Buildings, First. ed. Ernst & Sohn GmbH & Co., Berlin.

IEA, 2022. Heat Pumps. Paris.

Lämmle, M., Munz, G., 2022. Performance of Heat Pump Systems with PVT Collectors with optimized Finned Heat Exchangers integrated as single Heat Source, in: EuroSun 2022. pp. 0–4.

Perers, B., 1997. An improved dynamic solar collector test method for determination of non-linear optical and thermal characteristics with multiple regression. Sol. Energy 59, 163–178. https://doi.org/10.1016/S0038-092X(97)00147-3

Poppi, S., Sommerfeldt, N., Bales, C., Madani, H., Lundqvist, P., 2018. Techno-economic review of solar heat pump systems for residential heating applications. Renew. Sustain. Energy Rev. https://doi.org/10.1016/j.rser.2017.07.041

Schmidt, C., Schäfer, A., Kramer, K., 2018. Single source “solar thermal” heat pump for residential heat supply: Performance with an array of unglazed PVT collectors, in: 12th ISES Eurosun Conference. Rapperswil, Switzerland.

Sommerfeldt, N., Beltran, F., Madani, H., 2020. High Market Potential Applications for PVT with Heat Pumps. https://doi.org/10.18086/eurosun.2020.05.11

Sommerfeldt, N., Madani, H., 2018. Ground Source Heat Pumps for Swedish Multi-Family Houses: Innovative co-generation and thermal storage strategies.

Sommerfeldt, N., Madani, H., 2017. Review of Solar PV/Thermal Plus Ground Source Heat Pump Systems for European Multi-Family Houses 1–12. https://doi.org/10.18086/eurosun.2016.08.15

Weiss, W., Spörk-Dür, M., 2019. Solar Heat Worldwide. Global Market Development and Trends in 2018. Sol. Heat Worldw. Rep. 1, 86.

14th IEA Heat Pump Conference
15-18 May 2023, Chicago, Illinois

Flow Boiling Heat Transfer Performance of R448A inside Multiports Mini-Channel tubes with different geometry

Hoang Ngoc Hieu[a], Nurlaily Agustiarini[a], Jong-Taek Oh[b*], Jong Kyu Kim[c]

[(a)] Department of Refrigeration and Air-Conditioning Engineering, Graduate School, Chonnam National University Yeosu, 59626, South Korea
[(b)] Department of Refrigeration and Air-Conditioning Engineering, Chonnam National University, Yeosu, 59626, South Korea
[(c)] Department of Naval Architecture & Ocean Engineering, Chonnam National University, Yeosu, 59626, South Korea

Abstract

R448A, a zeotropic blend with GWP of 1390, is being proposed as an alternative refrigerant working in air-conditioning and heat pump systems. Despite being suitable as drop-in refrigerants, some redesigning of R448A systems was recommended for achieving maximum efficiency. In the work, the heat transfer coefficient of R448A inside multiple multiport mini-channel tube with different geometries were experimentally investigated. The experimental range of mass flux is from 100 to 500 kg/m^{2}s, heat flux from 3 to 15 kW/m^2 at a fixed saturated temperature of 6^{o}C, in 3 multiport tubes with varying hydraulic diameter, number of ports and aspect ratio. The influence of mass flux, heat flux, and vapor quality are examined, as well as the effect of channel geometry on the heat transfer performance. Finally, a correlation including the channel geometrical effect is proposed for the prediction of R448A heat transfer coefficient.

© HPC2023.
Selection and/or peer-review under the responsibility of the organizers of the 14th IEA Heat Pump Conference 2023.

Keywords: multiport mini-channels;flow boiling; heat transfer coefficient;correlatio;, R448A

1. Introduction

The HVAC industry have been rushing in research and development toward the 4th generation of refrigerant. Ultra-low GWP HFOs blend are currently considered best candidate as they can reduce GWP while retaining a good system performance. R448A is among those candidates, which is a zeotropic blend of 5 different components, consisting of R32, R125, R134a and the HFO's R1234ze and R1234yf. With non-flammability, non-toxicity (safety class A1), and a GWP of 1387, which is over 60% lower in GWP than R404A, it intended replacement, R448A has met many requirements of a high priority candidate.

Theoretical evaluation by Mota-Babiloni et al. [1] of alternative refrigerant with R404A as a baseline considered R448A (N-40) to be the best option in term of energy efficiency among 6 candidates in application which non-flammability is required. Past retrofit testing of R448A in different systems has also been available with the experimental work by Mota-Babiloni et al. [2], which tested R448A and compared against R404A in vapor compression systems. They found R448A charged systems to have lower mass flow rate, cooling capacity, power consumption and higher COP than R404A. The authors considered R448A to be a good alternative for R404A for medium temperature (food conservation) application, and warm climate countries would benefit from R448A due to it higher discharge temperature.

Investigation of R448A flow boiling heat transfer has been available within literatures. Lilio et al [3] experimentally measured R448A heat transfer coefficient and pressure drop in a 6mm steel tube. Heat transfer degradation observed at the mass flux of 150 kg/m^{2}s, which was attributed due to flow stratification. The higher mass flux shows convective behavior, with the heat transfer coefficient increases with quality. Heat flux does

* Corresponding author. Tel.: +82-61-659-7273, fax: +82-61-659-7279.
E-mail address: ohjt@chonnam.ac.kr

not only increase the heat transfer coefficient but also change the data trend with quality and dry-out characteristic. Kim & Kim [4] investigated the heat transfer coefficient and pressure drop of 4 different alternative refrigerants of R404A inside a smooth tube, the interims (R448A, R449A) and long-terms (R455A and R454C) in a smooth tube. At lower mass flux (100 kg/m^{2}s) and low vapor quality at the high mass flux of 300 kg/m^{2}s, R404A heat transfer coefficient is larger than the alternative refrigerant, due to the heat transfer penalization from the alternatives larger temperature glide. However, at the high mass flux of 300 kg/m^{2}s and high vapor quality, R404A heat transfer coefficient is exceeded by the alternative refrigerants, due to their more favorable thermos-physical properties. By the same author, Kim & Kim [5] studied those same blends heat transfer coefficient and pressure drop but in multiport mini-channel tube. Here the heat transfer coefficient of R404A is higher than all of the alternatives. At lower mass flux of 200 kg/m^{2}s, heat transfer coefficient of the alternatives is higher than the interim, while the reverse is true at 400 kg/m^{2}s. Like in Kim & Kim [6], the finding was attributed to the relationship between temperature glide and thermos-physical properties.

A literature survey shows that although R448A is a relatively well research blend recently, their database for multiport mini-channel tube should be supplemented with further data, for better consideration when applying to refrigeration or heat pump systems. Up to date, only Kim & Kim [4] had investigated heat transfer coefficient and pressure drop of R448A inside multiport mini-channel, albeit with only one channel. The current work extends the data for various different channels with varying geometry. The experimental range of mass flux is from 100 to 500 kg/m^{2}s, heat flux from 3 to 15 kW/m^2 at a fixed saturated temperature of 6^{o}C, in 3 multiport tubes with varying geometry. The effect of mass flux, heat flux as well as channel geometry are discussed. Finally, correlations are examined and new one proposed for practical prediction.

2. Experimental Apparatus and Methodology

2.1. Experimental Apparatus

The investigation is carried out through a testing apparatus shown in the following schematic diagram 1.

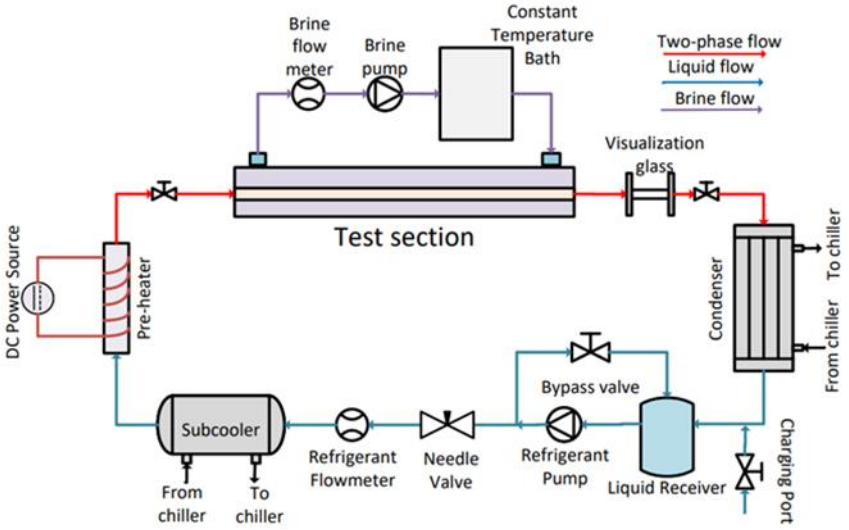


Fig. 1. Experimental systems.

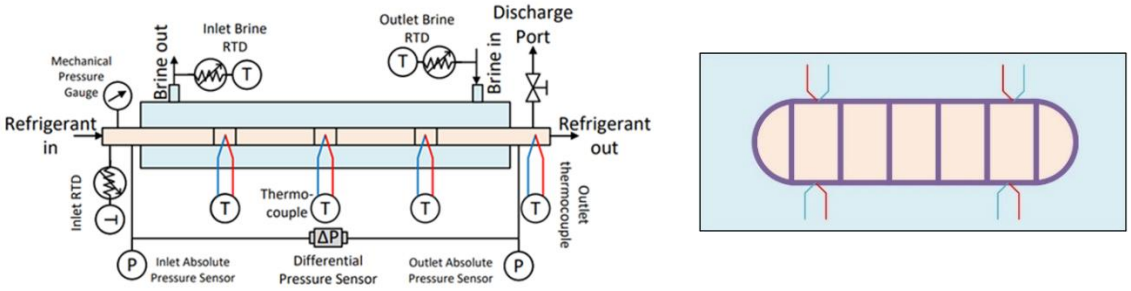


Fig. 2. Test section in detail and layout of thermocouple attachment

The refrigerant micro-gear pump is the driving force of flow circulation. The mass flow rate can be varied using an inverter controlled, while measurement is done by a flow meter installed after the pump. Heating was provided via preheater section, which is a 4m length tube wired to a DC power source. The DC power source power output can be controlled up to 1500W, so as to heat refrigerant up to desired quality before entering the test section, where the measurement of heat transfer coefficient and pressure drop took place. Outlet of the test section is the condenser, where the refrigerant return to liquid phase for next circulation. Refrigeration load for both condenser and sub-cooler come from a chilled brine bath, which is chilled by a separated chiller system. All sensor from the systems is connected to a data-logger then onto a PC for monitoring and recording of data.

Heating for the test section is provided from a warm brine bath. The test section is a counter current heat exchanger, with two acrylic slab sealed a multiport mini-channel tube in the middle. The brine pump was also connected to an inverter controlled to varying the mass flow rate, and a flow meter of same type is used for the measurement of it. Inlet and outlet temperature of the test section are both measured by RTDs, and is used along with mass flow meter for the calculation of applied heat flux. The pair of inlet temperature RTD and inlet absolute pressure transducer is used together to determine the inlet condition (vapor quality and enthalpy). The pressure drop is monitored with a differential pressure sensor, connected from 2 ports from the inlet and outlet of the test section. In order to calculate the heat transfer coefficient, the wall temperature was measured using thin thermos-couples wire. In total 12 was embedded at the surface, in 3 different positions from the inlet, 2 on top and 2 down the bottom in each position, as it is shown in figure 3.

The geometry of testing tube in table 1.

Table 1. Geometrical configuration of test tubes

Tube	H	W	d_h	AR	n
B	2	0.77	1.14	0.345	11
D	1.4	0.87	1.07	0.56	16
E	1.42	0.7	0.969	0.493	9

2.2. Data reduction

With inlet temperature and inlet pressure, it is possible to deduce the vapor quality and enthalpy at the inlet.

$$x_{in} = f(T_{in}, P_{in}), i_{in} = f(T_{in}, P_{in}) \tag{1}$$

The heat flux can be calculated using the brine inlet, outlet temperature and the brine mass flow rate

$$q = \frac{m_{water} C_{p,water} \left(T_{water,in} - T_{water,out}\right)}{A_{ext}} \tag{2}$$

Assuming an even distribution of heat flux across the tube, the enthalpy of i^{th} measurement point can be calculated as follow:

$$i_i = i_{in} + \frac{qP_{tube}}{m_{ref}} z_i \tag{3}$$

Likewise, assuming linear pressure drop, the pressure at the i^{th} measurement point can be calculated as

$$P_i = P_{in} - \Delta P \frac{z_i}{L} \tag{4}$$

With both pressure and enthalpy, it is possible to infer the saturated temperature at that location:

$$T_{sat,i} = f(P_i, i_i) \tag{5}$$

The internal wall temperature can be readily calculated with one dimensional thermal conduction equation through wall. Generally, the difference between internal and external wall temperature is insignificantly small due to the thin wall. The wall temperature is the average temperature of the 4 thermocouples

$$T_{w,in_i} = T_{w,out_i} + \frac{qD}{k} \tag{6}$$

Finally, the heat transfer coefficient can be calculated with the internal wall temperature and the corresponding saturated temperature.

$$h_i = \frac{A_{ext}}{A_{int}} \frac{q}{T_{w,in_i} - T_{sat,i}} \tag{7}$$

The average uncertainty for heat transfer coefficient is roughly 15.4%, while for vapor quality it is kept small at about 0.02.

3. Result and Discussion

3.1. Heat transfer coefficient result

Figure 3 displays the effect of mass flux on the heat transfer coefficient.

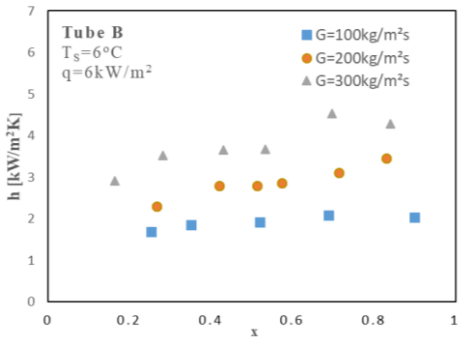


Fig. 3. The effect of mass flux on heat transfer coefficient.

As shown increase the mass flux increases the heat transfer coefficient. The current trend is universal within literature. The contribution of convective boiling in flow boiling heat transfer coefficient is mainly driven by mass flux. With increase mass flux, the annular regime is expanded due to strong inertia of vapor phase. Under annular flow, thin film evaporation occurring at the interface is driven significantly by the effect of interfacial shear stress, which increases along with mass flux. Additionally, an increase in mass flux will decrease the thermal resistance between the liquid film and the vapor core by enhancing the effective turbulent thermal conductivity. Improved turbulent effect at high velocity also help to offset the effect of mass transfer resistance on heat transfer of mixture by improving compositional mixing, as mentioned in Li [6] or Berto [7].

Figure 4 displays the effect of heat flux on the heat transfer coefficient.

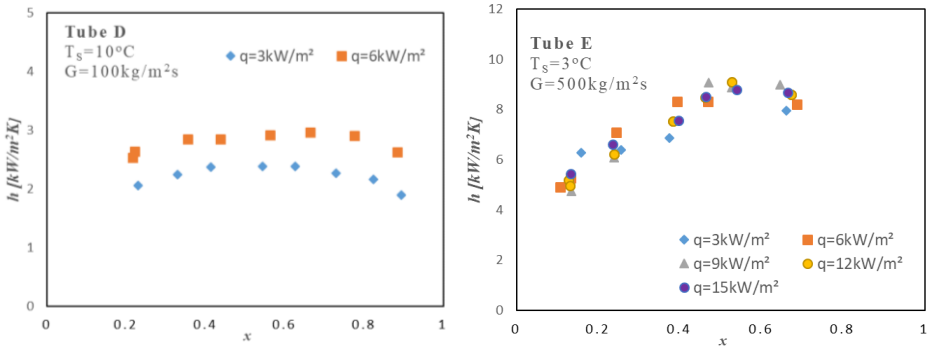


Fig. 4. The effect of heat flux on heat transfer coefficient.

Heat flux affects heat transfer coefficient differently, as it is more dependable on the specific mass flux condition. As explained in conventional nucleate boiling theory as well as being well reported in literature,

increasing heat flux activate more nucleate site and hasten the bubble nucleation and growth cycle, overall enhancing convective boiling. However, with an increasing of mass flux, convective boiling become a dominate flow boiling mechanism, owning to strong effect of interfacial shear and turbulent. Consequently, the effect of heat flux become less noticeable at high mass flux.

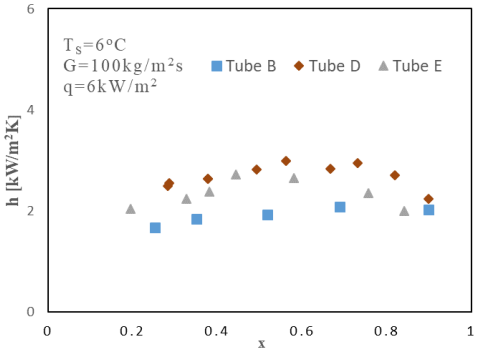


Fig. 5. Heat transfer coefficient comparison between different channels.

Evidently, at lower mass flux condition, where nucleate boiling have more noticeable effect on heat transfer, the heat transfer coefficient follows the descending order of B, D and E. From table 2, the heat transfer was found to generally increase with the decreasing of hydraulic diameter, although tube D is higher than tube E heat transfer coefficient, despite having larger hydraulic diameter, suggesting hydraulic diameter alone is not the only geometrical feature that is important toward heat transfer. Literature survey of heat transfer investigation using multiport mini-channel evaporator types was performed to compare against the current trend with past trend. Yun et al. [8] commented that decreasing the hydraulic diameter was found to increase the overall heat transfer coefficient. However, Yun [10], claimed the enhancement of heat transfer was found with the increasing of internal perimeter. Additionally, Al-Zaidi et al [11] comments that for rectangular mini-channel, increase the aspect ratio also increase heat transfer coefficient. This explain why despite having larger hydraulic diameter, tube D heat transfer coefficient than tube E.

3.2. Evaluation of existing correlation

The current experimental database was compared against various correlations in literature. In 2015, Shah [12] presented a simple method of correcting the heat transfer coefficient of zeotropic mixture when applying correlation of pure fluid. The database is compared against the heat transfer coefficient correlation in its original form and its modified form.

The comparison result is shown in table 3

Table 2. Performance of existing correlation

Correlation	MAD (%)		MSE (%)	
	Original	Modified	Original	Modified
Bertsch et al. [13]	82.5	24.5	68.9	-19.4
Grungor&Winterton [14]	40.2	26.7	40	25.7
Kim & Mudawar [15]	28.7	19.2	22.4	7.8
Saitoh et al. [16]	25.5	18.3	6.4	18.6

As it is shown, the heat transfer coefficient database is relatively well predicted by the current database, and improvement upon original was observed, with the most spectacular improvement from the model of the Bertsch [13]. Although they are well predicted, it is preferable to introduce an optimized correlation for the best prediction of the present database for the more precision design of heat exchanger. In addition, since the Shah [12] method was found to made improvement to original prediction, this method is also employed during the development of correlation.

3.3. Correlation proposal

Enhancement and suppression factor can be proposed by optimizing the coefficient from the experimental data as follow:

$$E = 1 + 12000Bo^{1.5} + 0.9X_{tt}^{-0.85} \quad (14)$$

$$S = \frac{1}{1+1.1Re_l^{0.5}F^{1.15}10^{-6}} \quad (15)$$

With the nucleate boiling and single phase liquid heat transfer coefficient both used the common equations of Cooper and Dittius-Boelter respectively

$$h_{nb} = 55M^{-0.5}q^{-0.67}P_{red}^{0.12}(-log_{10}P_{red})^{-0.55} \quad (16)$$

$$h_l = 0.023Re_l^{0.8}Pr_l^{0.4}\frac{k_l}{d_h} \quad (17)$$

The evaluation was done with MAD and MAE as previously and shown the new correlation performed the best against the current experimental database.

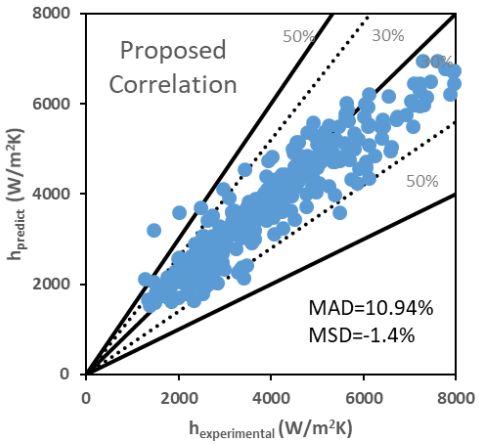


Fig. 4. Heat transfer coefficient comparison with new correlation and experimental data.

4. Conclusion

The current work investigates the heat transfer coefficient of R448A inside 3 different multiport mini-channel tube. The key findings can be summarized as follow:

1. The heat transfer coefficient is a strong function of mass flux. Heat transfer coefficient increase with increase heat flux under low mass flux conditions but display insignificant effect at higher mass flux conditions.
2. Channel geometry have important effect at lower mass flux conditions. It is found that decreasing hydraulic diameter, increasing aspect ratio (W/H), and increasing number of multiport to have favourable effect on heat transfer coefficient.
3. Past correlation can provide a reasonable prediction against the current database, with modification to account for temperature glide effect can reduce the error further. A new correlation is proposed which achieved a good accuracy with present data.

Acknowledgements

This work is supported by a National Research Foundation of Korea (NRF) grant funded by the Korea government (MSIT) (No. NRF-2020R1A2C1010902).

Nomenclature

A	: Area [m^2]	Y	: Bell-Ghaly term
B	: Scaling factor (in Thome-Shakir model)	z	: Distance from the inlet [m]
C_{pv}	: Vapor phase specific heat [kJ/kgK]	Greek letter	
C_{pl}	: Liquid phase specific heat [kJ/kgK]	β	: Liquid mass transfer coefficient (=0.0003) [m/s]
d_h	: Hydraulic diameter [m]	Δ	: Difference
E	: Convective boiling enhancement factor	μ	: Viscosity
F_{TS}	: Thome-Shakir factor	ρ	: Density
G	: Mass flux [kg/ m^{2}s]	Suscript:	
h	: Heat transfer coefficient [kW/ m^{2}K]	cb	: Convective boiling
i	: Specific enthalpy [kJ/kg]	io	: Liquid/vapor only (i=l/v)
i_{lv}	: Latent heat of vaporization [kJ/kg]	$pred$	: Predicted
k	: Thermal conductivity [W/mK]	exp	: Experimental
m	: Mass flow rate [kg/s]	ext	: External
M	: Molar mass [kg/kmol]	$glide$	: Glide (temperature)
MAD	: Mean Absolute Deviation [%]	in	: Inlet
MSE	: Mean Signed Deviation [%]	int	: Internal
P	: Pressure [kPa]	l	: Liquid phase
P_{crit}	: Critical pressure [kPa]	nb	: Nucleate Boiling
Pr	: Prandtl number	out	: Outlet
p_{tube}	: Tube perimeter [m]	$pool$	: Pool boiling
q	: Heat Flux [kW/m^2]	ref	: Refrigerant
Re	: Reynolds number	sat	: Saturated
S	: Suppression factor of Nucleate boiling	v	: Vapor phase
T	: Temperature [K], [^{o}C]	$water$	: Water
u	: Uncertainty		
x	: Vapor quality		

References

[1] A. Mota-Babiloni, J. Navarro-Esbrí, B. Peris, F. Molés, and G. Verdú, "Experimental evaluation of R448A as R404A lower-GWP alternative in refrigeration systems," *Energy Convers. Manag.*, vol. 105, pp. 756–762, Nov. 2015, doi: 10.1016/j.enconman.2015.08.034.

[2] A. Mota-Babiloni, J. Navarro-Esbrí, Á. Barragán, F. Molés, and B. Peris, "Theoretical comparison of low GWP alternatives for different refrigeration configurations taking R404A as baseline," *Int. J. Refrig.*, vol. 44, pp. 81–90, Aug. 2014, doi: 10.1016/j.ijrefrig.2014.04.015.

[3] G. Lillo, R. Mastrullo, A. W. Mauro, F. Pelella, and L. Viscito, "Experimental thermal and hydraulic characterization of R448A and comparison with R404A during flow boiling," *Appl. Therm. Eng.*, vol. 161, p. 114146, Oct. 2019, doi: 10.1016/j.applthermaleng.2019.114146.

[4] C.-H. Kim and N.-H. Kim, "Evaporation heat transfer and pressure drop of the interim (R-448A, R-449A) and long term (R-455A, R-454C) low GWP R-404A alternative refrigerants in a smooth tube," *Int. J. Heat Mass Transf.*, vol. 181, p. 121903, Dec. 2021, doi: 10.1016/j.ijheatmasstransfer.2021.121903.

[5] C.-H. Kim and N.-H. Kim, "Evaporation heat transfer and pressure drop of low GWP R-404A alternative refrigerants in a multiport tube," *Int. J. Heat Mass Transf.*, vol. 184, p. 122386, Mar. 2022, doi: 10.1016/j.ijheatmasstransfer.2021.122386.

[6] M. Li, C. Dang, and E. Hihara, "Flow boiling heat transfer of HFO1234yf and R32 refrigerant mixtures in a smooth horizontal tube: Part I. Experimental investigation," *Int. J. Heat Mass Transf.*, vol. 55, no. 13, pp. 3437–3446, Jun. 2012, doi: 10.1016/j.ijheatmasstransfer.2012.03.002.

[7] A. Berto, M. Azzolin, S. Bortolin, C. Guzzardi, and D. Del Col, "Measurements and modelling of R455A and R452B flow boiling heat transfer inside channels," *Int. J. Refrig.*, vol. 120, pp. 271–284, Dec. 2020, doi: 10.1016/j.ijrefrig.2020.08.007.

[8] R. Yun, Y. Kim, and M. S. Kim, "Convective boiling heat transfer characteristics of CO2 in microchannels," *Int. J. Heat Mass Transf.*, vol. 48, no. 2, pp. 235–242, Jan. 2005, doi: 10.1016/j.ijheatmasstransfer.2004.08.019.

[9] J. Kaew-On, K. Sakamatapan, and S. Wongwises, "Flow boiling heat transfer of R134a in the multiport

minichannel heat exchangers," *Exp. Therm. Fluid Sci.*, vol. 35, no. 2, pp. 364–374, Feb. 2011, doi: 10.1016/j.expthermflusci.2010.10.007.
[10] R. Yun, J. Hyeok Heo, and Y. Kim, "Evaporative heat transfer and pressure drop of R410A in microchannels," *Int. J. Refrig.*, vol. 29, no. 1, pp. 92–100, Jan. 2006, doi: 10.1016/j.ijrefrig.2005.08.005.
[11] A. H. Al-Zaidi, M. M. Mahmoud, and T. G. Karayiannis, "Effect of aspect ratio on flow boiling characteristics in microchannels," *Int. J. Heat Mass Transf.*, vol. 164, p. 120587, Jan. 2021, doi: 10.1016/j.ijheatmasstransfer.2020.120587.
[12] M. M. Shah, "A method for predicting heat transfer during boiling of mixtures in plain tubes," *Appl. Therm. Eng.*, vol. 89, pp. 812–821, Oct. 2015, doi: 10.1016/j.applthermaleng.2015.06.047.
[13] S. S. Bertsch, E. A. Groll, and S. V. Garimella, "A composite heat transfer correlation for saturated flow boiling in small channels," *Int. J. Heat Mass Transf.*, vol. 52, no. 7, pp. 2110–2118, Mar. 2009, doi: 10.1016/j.ijheatmasstransfer.2008.10.022.
[14] K. E. Gungor and R. H. S. Winterton, "A general correlation for flow boiling in tubes and annuli," *Int. J. Heat Mass Transf.*, vol. 29, no. 3, pp. 351–358, Mar. 1986, doi: 10.1016/0017-9310(86)90205-X.
[15] S.-M. Kim and I. Mudawar, "Universal approach to predicting saturated flow boiling heat transfer in mini/micro-channels – Part II. Two-phase heat transfer coefficient," *Int. J. Heat Mass Transf.*, vol. 64, pp. 1239–1256, Sep. 2013, doi: 10.1016/j.ijheatmasstransfer.2013.04.014.
[16] S. Saitoh, H. Daiguji, and E. Hihara, "Correlation for boiling heat transfer of R-134a in horizontal tubes including effect of tube diameter," *Int. J. Heat Mass Transf.*, vol. 50, no. 25, pp. 5215–5225, Dec. 2007, doi: 10.1016/j.ijheatmasstransfer.2007.06.019.

14th IEA Heat Pump Conference
15-18 May 2023, Chicago, Illinois

Techno-environmental evaluation of a river-source heat pump system using a hot gas bypass valve

Hyun Ku Cho[a], Hyun Ho Shin[b], Se Hyeon Ham[b], Sun An Jeong[c], Kyoung-Tae Park[c], Yongchan Kim[b] *

[a]Department of Smart Convergence, Korea University, 145 Anam-ro, Sungbuk-gu, Seoul 02841, Republic of Korea
[b]Department of Mechanical Engineering, Korea University, 145 Anam-ro, Sungbuk-gu, Seoul 02841, Republic of Korea
[c]Myoung Shin Co., 34 Jayuro Gunsansi, Jeollabukdo, 54006, Republic of Korea

Abstract

River water-source heat pumps show higher energy efficiency than conventional air-source heat pumps because water has better thermal characteristics than air. However, as the river water temperature decreases in winter, there is a risk of freezing in heat exchangers during the heating season. In this study, the performance of a hybrid heat pump system using a hot gas bypass valve (HBHPS) was compared analytically to that of a conventional hybrid heat pump system (CHHPS). In the HBHPS, the refrigerant flow rate can be controlled by the hot gas bypass valve to decrease the heating capacity, hence reducing the temperature difference of the secondary fluid on the evaporator side. Accordingly, it can increase the heat pump operation time in winter. Mechanical components of the HBHPS were modeled analytically. The performances of the two energy conversion systems were compared through transient simulations based on a water temperature measurement in Han River, South Korea. As a result, the HBHPS showed higher life cycle climate performance than the CHHPS owing to the increase in the heat pump operation time.

© HPC2023.
Selection and/or peer-review under the responsibility of the organizers of the 14th IEA Heat Pump Conference 2023.

Keywords: River source heat pump, Heat pump simulation, Hot gat bypass, TRNSYS, Hybrid heat pump system;

1. Introduction

Many efforts are being carried out to reduce greenhouse gas emissions around the world. Among these efforts, research related to renewable energy conversion systems is actively being conducted. A heat pump system that uses surface water as a heat source is one of them. The water source heat pump system obtains energy required for heating and cooling loads by using the energy of water sources including river water, lake water, and seawater. The temperature of the water source is higher in winter and lower in summer than that of the air source, which has the advantage of a lower seasonal temperature difference. Therefore, water source heat pumps have the advantage of being able to operate at high efficiency year-round compared to conventional air source heat pumps [1]. However, there is a disadvantage that the use is limited due to the problem of freezing in the heat pump evaporator or source-side heat exchanger when the water temperature is low in winter. For this reason it is difficult for water source heat pumps to be operated alone even though they show high efficiency in summer. To overcome this problem, the conventional water source heat pump system mainly adopted a hybrid configuration in which a gas boiler is installed to satisfy the heating load when the heat pump is not operable. The use of boilers reduces the efficiency of the entire system but allows the system to operate reliable annually. However, the gas boiler is less energy efficient and emits a larger amount of carbon dioxide than the heat pump. Therefore, to reduce the operation time of the gas boiler and increase the operation time of the heat pump, it is essential to control the capacity of the heat pump to broaden the operable water temperature range.

* Corresponding author. Tel.: +82-2-921-5946.
E-mail address: yongckim@korea.ac.kr.

There are several ways to control the capacity of heat pumps. The first way is to use a variable-speed compressor. It uses energy efficiently by changing the compressor frequency in response to the load and heat source. Nasution and Wan Hassan [2] showed that controlling the compressor through the inverter can save energy consumption more than the compressor on-off control. Jeong et al. [3] compared the hot gas bypass method and the variable-speed compressor method and showed that the COP was higher in the variable-speed compressor control using the inverter during a partial load operation. Generally, most of heat pumps use variable-speed compressors to control the capacity. To continuously operate the heat pump using the low water temperature in winter, it is necessary to reduce the temperature difference of the primary fluid by controlling the capacity of the heat pump. However, in the case of a large heat pump system, limitation exists to control capacity through the compressor owing to the surging problem or degradation of the volumetric efficiency. Therefore, the operation of heat pumps is not available during the winter season when the water temperature is low.

The second way to control the capacity of heat pumps is to apply a hot gas bypass valve. It controls the evaporator inlet enthalpy by bypassing a part of the high-temperature and high-pressure refrigerant gas at the compressor discharge to the evaporator inlet or controlling the mass flow rate of refrigerant by bypassing a part of the high-temperature and high-pressure refrigerant gas at the compressor discharge to the compressor inlet. Yaqub et al. [4] suggested three methods of capacity control in refrigeration and air conditioning systems through the hot gas bypass method and analyzed the performance characteristics of each method through experiments and analysis. Baek et al. [5–6] analyzed the performance characteristics of the three methods proposed by Yaqub et al. according to changes in load and operating conditions. Ahn et al. [7] experimentally compared the hot gas bypass method in which a part of the refrigerant gas at the compressor outlet bypassing to the compressor inlet and the method in which a part of the liquid refrigerant at the discharge of the condenser bypassing to the suction of the compressor. It was shown that the hot gas bypass method was advantageous during the heating period, the pressure of the condenser was lowered, and the COP was also lowered as the bypass ratio increased.

In this study, the heating performance of a hybrid heat pump system using hot gas bypass (HBHPS) was analyzed analytically. The river water was used as a heat source. The heat pump system using hot gas bypass was simulated by using Python. In the simulation, the characteristics of controlling the capacity of the heat pump by the hot gas bypass valve in the low water temperature condition were simulated. Through the heat pump simulation, performance map data were obtained according to the conditions of the heat source and the load side. The transient simulation program, TRNSYS, was used for the simulation, and the performance change was analyzed compared to the conventional boiler hybrid heat pump system (CHHPS).

2. Simulation method

2.1. Heat pump simulation method

The heat pump simulation was performed with the algorithm shown in Figure 1, based on the ORNL method [8] proposed by Fischer and Rice. The algorithm started by assuming an initial condensing pressure and an evaporation pressure. Then, the state of each component was calculated. The calculation proceeded until the energy balance converged, and when the convergence was reached. The efficiency model was used for the compressor modeling. The heat transfer occurring in the evaporator and the condenser was calculated using the ε-NTU method. To simplify the simulation, the effectiveness (ε) was fixed at 0.7. In addition, the heat transfer was calculated by dividing the section according to the phase of the refrigerant. Accordingly, energy balance convergence conditions in the evaporator and condenser were set considering the degree of subcooling and superheating. The hot gas bypass method was applied in which some refrigerant was bypassed from the compressor outlet to the inlet. The opening ratio of the hot gas bypass valve (x) was set as an input value. However, the mass flow rate that can be bypassed is limited because the high bypassed mass flow rate can cause the compressor to overheat severely. The maximum ratio of bypassed flow rate can be expressed as y, which is the point where heating capacity can be controlled down to 73% of design capacity [7]. The bypass opening ratio (x) became 1 when the ratio of actual bypassed mass flow rate (y') is that of the maximum bypassed mass flow rate (y). R-134a was used as the refrigerant, and the physical properties at each point were obtained through CoolProp [9], which is a Python module. The schematic of the hot gas bypass heat pump is shown in Figure 2. The process of from points 2 to 6 is assumed to be the isenthalpic process because the hot gas bypass valve is an expansion valve for reducing the pressure. The operating characteristics of the hot gas bypass method were obtained by Equations (1)–(4).

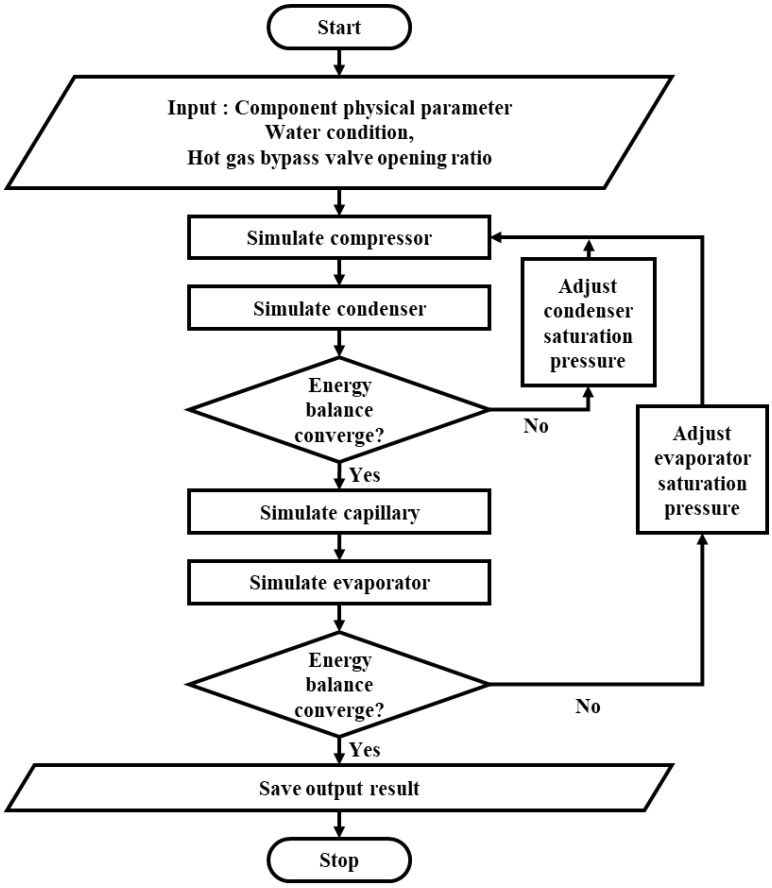


Fig. 1. Flow chart of heat pump simulation.

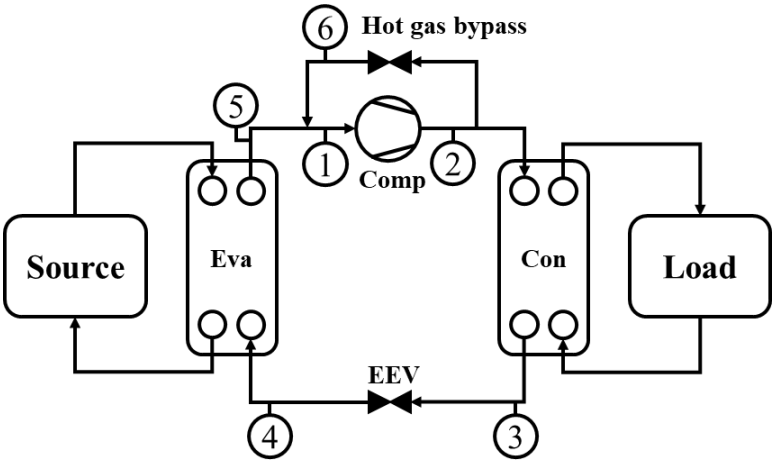


Fig. 2. Schematic of hot gas bypass water source heat pump.

$$x = y'/y \ (\ 0 \le y' \le y\ ) \tag{1}$$

$$y' = \dot{m}_6/\dot{m}_1 \tag{2}$$

$$y' = (h_1 - h_5)/(h_2 - h_5) \tag{3}$$

$$COP = [(1 - y')(h_5 - h_4)]/(h_2 - h_1) \tag{4}$$

2.2. TRNSYS simulation method

Based on the heat pump simulation, the performance map data was obtained according to the temperature and flow rate of the heat source and load, and the ratio of bypass valve opening. The schematic of the TRNSYS model is shown in Figure 3, and the simulation conditions are shown in Table 1. The load for simulation was based on the actual measured data of a commercial building in Gwacheon in 2020. The actual measured temperature of the Paldang Dam basin in 2018 was used for the river water temperature. The average water temperature in winter was 5.3 °C and the range of temperature was 1.3–13.5 °C. Simulations were performed during the heating period in Korea, January–March, and November–December. A 500 RT heat pump system was used based on the maximum heating and cooling load, and water was used for both the heat and load side secondary fluid. When water is used as the secondary fluid, freezing can occur at the outlet of the heat pump evaporator when the river water temperature is low in winter, which makes the entire heat pump system inoperable. Therefore, when the heat pump is not operable, a gas boiler was mainly used for heating. To prevent freezing in the evaporator, the flow rate of source-side water can be increased or the capacity of the heat pump decreased to reduce the water-side temperature change in the evaporator.

As shown in Figure 4, the performance comparison was analyzed by TRNSYS modeling of two cases according to the control method of the heat pump system. The first case was a conventional hybrid heat pump system (CHHPS) which conventional water source heat pump applied. When the low water temperature condition was reached, the temperature change between the inlet and outlet of the primary and secondary fluids can be reduced by increasing the pump flow rate of the heat source. It is possible to increase the flow rate up to 2.0 times for P0 and 1.2 times for P1. Accordingly, the operation time of the heat pump can be extended. However, the power consumption can increase.

In the second case, the hot gas bypass heat pump was used in the hybrid heat pump system (HBHPS). The temperature change between the inlet and outlet of the evaporator of the heat pump can be further reduced by lowering the heat pump capacity through the hot gas bypass method in the low water temperature condition that even CHHPS cannot operate. However, the capacity in the condenser is also reduced, so to maintain the temperature difference on the load side, the flow rate of P2 must be reduced by 0.7 times. The coefficient of performance decreases as the opening of the hot gas bypass valve increases.

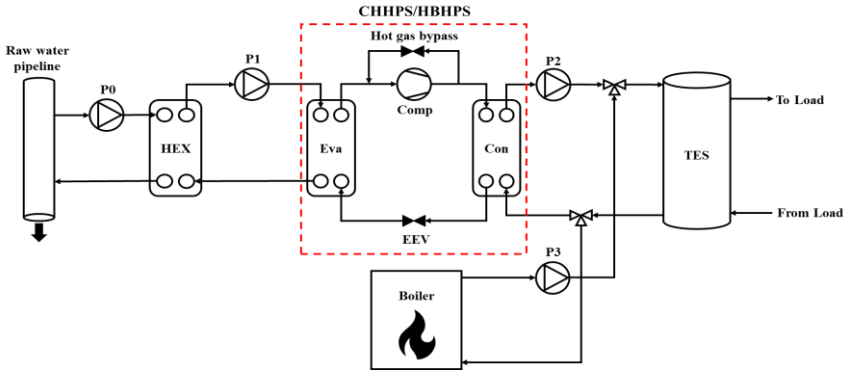


Fig. 3. Configuration of the hybrid heat pump system applying CHHPS and HBHPS.

Table 1. Main simulation condition for the TRNSYS model

Description	Units	Value
Water source temperature	℃	Measured
Load	kWh	Measured
Heat pump capacity	RT	500
Evaporator design capacity	RT	391
Evaporator minimum leaving temperature	℃	1
Pump design flow rate (P0, P1)	LPM	6533
Pump design flow rate (P2, P3)	LPM	5040
TES load side minimum leaving temperature	℃	45
Gas boiler combustion efficiency	%	80
Electricity bill	$/kWh	[10]
Gas bill	$/kWh	[11]

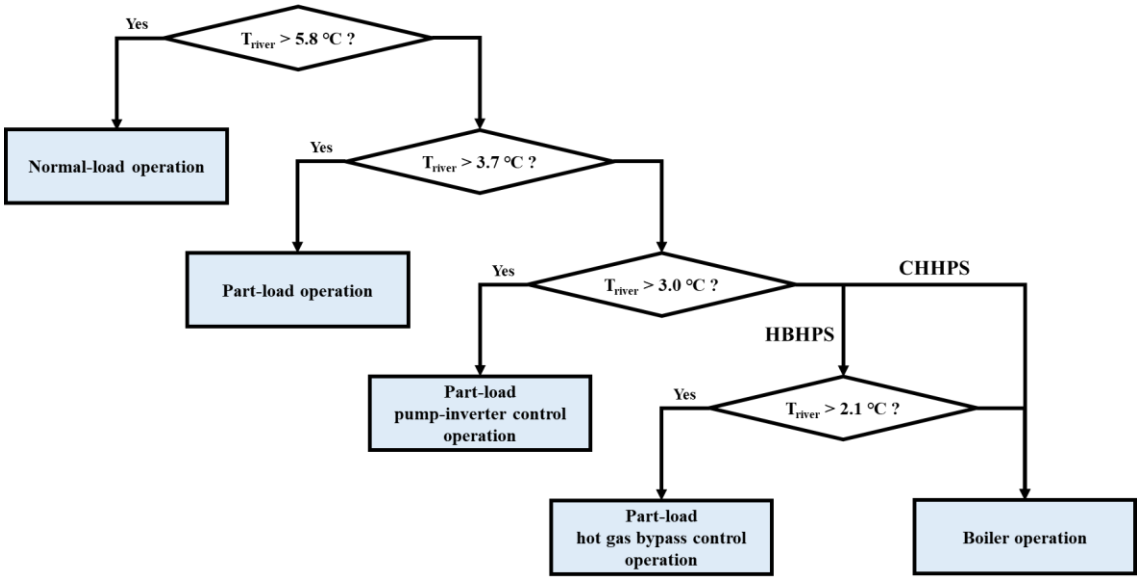


Fig. 4. Control strategy for HBHPS and CHHPS.

2.3. Performance indices

For the above two cases, the performance change was analyzed with various evaluation indices. Performance change was compared with seasonal performance factor (SPF), operation time, greenhouse gas emissions (GHGE), and operation costs. The formulas of each evaluation index are as follows. The SPF is the factor of efficiency for the whole heat pump operation period. The SPF is expressed as the heat supplied by the heat pump system ($E_{th,HP}$) divided by whole energy consumption ($E_{p,tot,P} + E_{p,tot,HP}$) for the operation period. The greenhouse gas emission factors for electric power and gas were 0.4594 (EF_e) and 0.2016 (EF_g), respectively, which are based on the Korean standard. Each emission factor was multiplied by the annual energy consumption of electricity and gas (AEC). In addition, for the annular operation costs of electricity and gas (AOC), rate tables based on Korean standards [10–12] were used. The exchange rate of the dollar was as of November 1, 2022. Greenhouse gas emissions and operating costs were compared under the assumption that the heat pump was operated for 16 years, which is the life cycle of the heat pump (L), under the same water temperature and load conditions. Inflation rate (i) and discount rate (d) were both set as 0.1.

$$SPF = \frac{E_{th,HP}}{E_{p,tot,P} + E_{p,tot,HP}} \tag{5}$$

$$GHGE = L * (AEC_e * EF_e + AEC_g * EF_g) \tag{6}$$

$$Operation\ cost = \sum_n \{\frac{1+i}{1+d}\}^{n-1} (AOC_e + AOC_g) \tag{7}$$

3. Simulation results

3.1. Heat pump simulation results

Figure 5 shows the change in the P-h diagram when the condenser water inlet temperature was 40 ˚C, the evaporator water inlet temperature was 12 ˚C, and the x was 0.5. As a part of the refrigerant gas at the compressor outlet passed through the hot gas bypass valve and flowed into the compressor inlet, the condensing pressure was lowered. However, the evaporating pressure was slightly increased because a part of the high-temperature and high-pressure refrigerant gas flows into the outlet of the evaporator. Additionally, the compression ratio and compressor work were reduced, but the heat pump capacity reduction was larger. Accordingly, the COP was lowered.

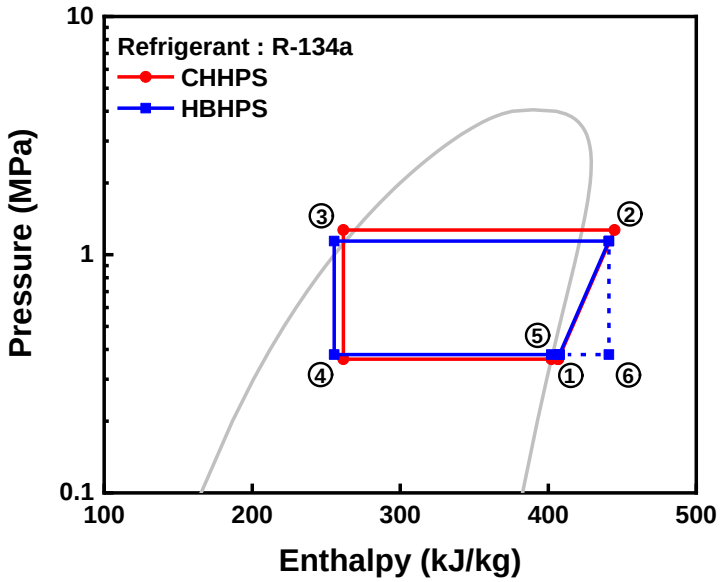


Fig. 5. P-h diagram of the heat pump applied in CHHPS and HBHPS of bypass opening ratio 0.5.

3.2. TRNSYS simulation result

Figure 6 shows the load supply period by the heat pump of CHHPS and HBHPS. The operating time of the HBHPS was 97 hours longer than that of the CHHPS. This corresponded to 2.68% of the total heating period. This was because the capacity of the heat pump was lowered by the hot gas bypass valve and can operate until the water source temperature was 2.38 ˚C compared to CHHPS which can operate until 3.03 ˚C. Both cases cannot cover the heat load by heat pump operation alone during the coldest season in winter because the river water temperature was below than 2.38 ˚C.

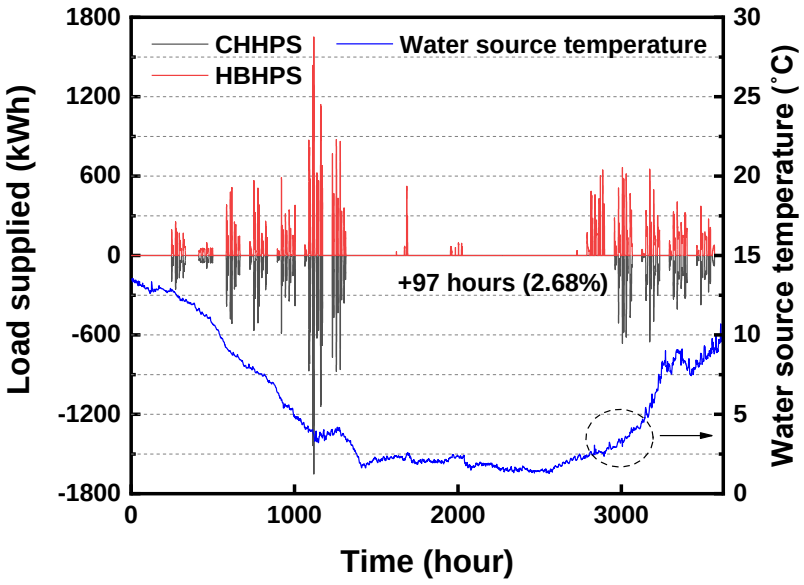


Fig. 6. Operation time of CHHPS and HBHPS and winter season river water source temperature.

Figure 7 shows the energy consumption, heat supply, and SPF for the heat pump operation period by the heat pump systems of CHHPS and HBHPS. Since HBHPS had a longer operating time compared to CHHPS,

the energy consumption was 28.30% higher and heat supply was 16.43% higher. The increase in energy consumption was larger than the amount of heat supplied, resulting in a lower SPF of 9.26%.

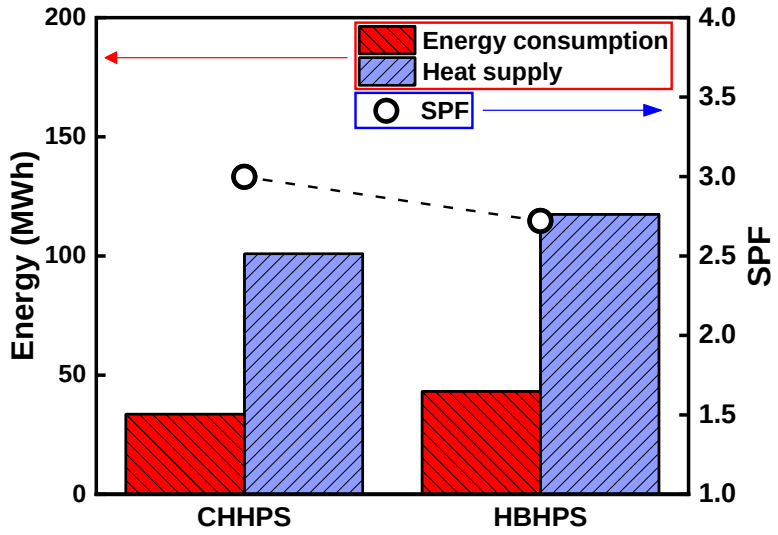


Fig. 7. Energy consumption, heat supply and SPF for CHHPS and HBHPS.

Figure 8 shows the greenhouse gas emissions of CHHPS and HBHPS, and Figure 9 shows the operating costs of CHHPS and HBHPS. As the heat pump operation time in HBHPS increased, the boiler operation time decreased. The decrease in gas usage was larger than the increase in electric energy usage. Accordingly, GHGE was reduced by 2.23%, and winter season operating cost was reduced by 5.88% in HBHPS compared to CHHPS.

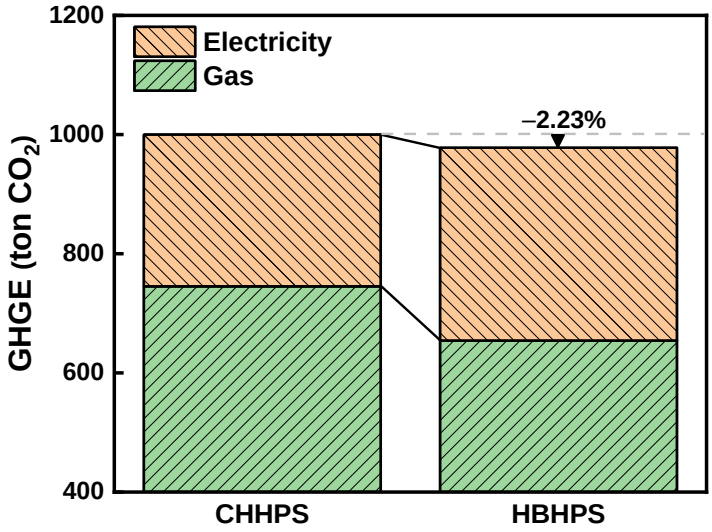


Fig. 8. GHGE of CHHPS and HBHPS for life cycle.

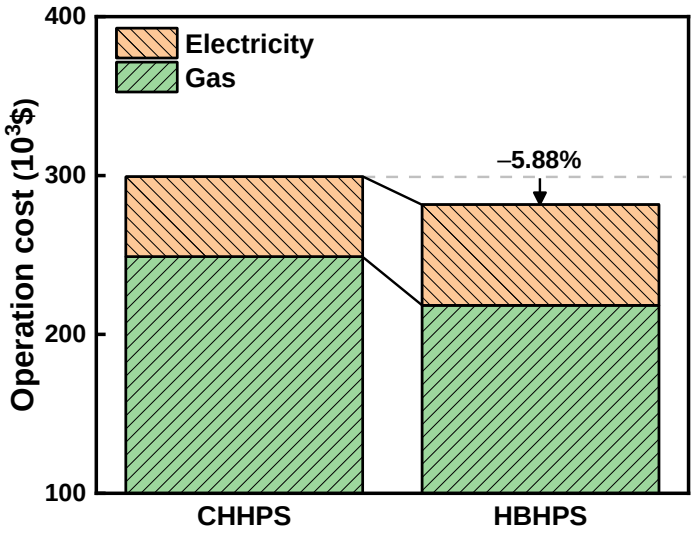


Fig. 9. Operation costs of CHHPS and HBHPS for the life cycle.

4. Conclusion

In this study, the performance change according to the hot gas bypass heat pump application of the hybrid heat pump system for heating load in winter was analyzed. As a result, when the hot gas bypass heat pump was used, the SPF of the heat pump system was reduced by 9.26%. However, the operating time increased by 2.68%, GHGE was reduced by 2.23%, and operating cost by 5.88%. This study was based on the water temperature in the Paldang Dam basin in 2018, where the average water temperature condition in winter was very low. The hot gas bypass heat pump system is expected to show better performances in areas where the water temperature is relatively higher.

Acknowledgments

This work was supported by the Technology Innovation Program (No. 20011094) funded By the Ministry of Trade, Industry & Energy (MOTIE, Korea).

References

[1] Park, C. S., Jung, T. H., Park, H. H., Kim, Y. C., 2009. Performance characteristics and economic assessment of a river water: source heat pump system. Korean Journal of Air-Conditioning and Refrigeration Engineering, 21(11), 621-628.
[2] Nasution, H., Wan Hassan, M. N., 2006. Potential electricity savings by variable speed control of compressor for air conditioning systems. Clean Technologies and Environmental Policy, 8(2), 105-111.
[3] Jeong, S. K., Lee, D. B., Yoon, J. I., 2012. Comparison of system performances of hot-gas bypass and compressor variable speed control of water coolers for machine tools. Korean Journal of Air-Conditioning and Refrigeration Engineering, 24(1), 1-8.
[4] Yaqub, M., Zubair, S. M., 2000. Performance evaluation of hot-gas by-pass capacity control schemes for refrigeration and air-conditioning systems. Energy, 25(6), 543-561.
[5] Baek, S. M., Yoon, J. I., Son, C. H., Heo, J. H., 2014. Performance Comparison of Hot-gas Bypass Types with the Variation of Refrigeration Load. Journal of Power System Engineering, 18(5), 48-54.
[6] Baek, S. M., Son, C. H., Heo, J. H., Choi, I. S., Yoon, J. I., 2014. Performance characteristics of hot-gas bypass refrigerator with the variation of operation conditions. Journal of Advanced Marine Engineering and Technology, 38(9), 1021-1026.
[7] Ahn, J. H., Joo, Y., Yoon, W. J., Kang, H., Kim, Y., 2013. An experimental study on the performance characteristics of hot-gas and liquid bypass heat pump systems for capacity modulation. Korean Journal of Air-Conditioning and Refrigeration Engineering, 25(3), 137-142.
[8] Fischer, S. K., Rice, C. K., 1983. Oak Ridge heat-pump models. I. A steady-state computer design model for air-to-air heat pumps (No. ORNL/CON-80/R1). Oak Ridge National Lab., TN (USA).

[9] Bell, I. H., Wronski, J., Quoilin, S., Lemort, V., 2014. Pure and pseudo-pure fluid thermophysical property evaluation and the open-source thermophysical property library CoolProp. Industrial & engineering chemistry research, 53(6), 2498-2508.
[10] Korea Electric Power Corporation., Electric Rates Table. https://home.kepco.co.kr/kepco/EN/F/htmlView/ENFBHP00101.do?menuCd=EN060201; [accessed 1 November 2022].
[11] Samchully Corpration., City gas rates table. https://www.samchully.co.kr/customer/gas/info/fee/system.do; [accessed 1 November 2022].
[12] Korea Ministry of Environment., 2022. Guidelines for Reporting and Certification of Emissions of Greenhouse Gas Emissions Trading System.

14th IEA Heat Pump Conference
15-18 May 2023, Chicago, Illinois

Optimum Capacity-Matching Performance of a Heat-Pump-driven Liquid-Desiccant Air-conditioning System

Jae-Hee Lee [a], Yong-Kwon Kang[a], Seheon Kim [a], Gyu-Bae Lee [a], Jae-Weon Jeong [a,*]

[a]Department of Architectural Engineering, College of Engineering, Hanyang University,
222 Wangsimni-Ro, Seongdong-Gu, Seoul, 04763, Republic of Korea

Abstract

In heat-pump-driven liquid-desiccant (HPLD) air-conditioning systems, the release of condensing heat from the heat pump to the regenerator solution and exhaust air (i.e., capacity matching) is very important to maintain the dehumidification performance as well as the operational feasibility and stability of the system. Therefore, in this study, the capacity matching especially focusing on the release of extra condensing heat of the HPLD air-conditioning system is optimized in conjunction with the energy performance. With four design variables under the various outdoor air conditions, a multi-objective optimization is conducted to simultaneously maximize a system coefficient of performance and minimize a newly defined capacity matching index of extra condenser. Pareto front which is a set of optimum points is obtained using multi-objective genetic algorithm, and final optimum solutions are then determined and discussed based on a decision-making scenario. In conclusion, the system coefficient of performance is maximally increased by 24 % and the capacity matching index of extra condenser is maximally decreased by 55 %, compared with each initial value.

© HPC2023.
Selection and/or peer-review under the responsibility of the organizers of the 14th IEA Heat Pump Conference 2023.

Keywords: Liquid desiccant; Heat pump; Capacity-matching performance; Energy performance; Multi-objective optimization

1. Introduction

Recently, as the significance of indoor humidity control has increased [1], a liquid-desiccant (LD) system which has an energy saving potential due to its decoupled control of the indoor temperature and humidity has emerged as a promising alternative to the traditional dehumidification systems [2]. Both the dehumidification and regeneration performances in the LD system improve via increase of the vapor pressure difference between the desiccant-solution and air. Thus, the desiccant-solution should be cooled before the absorber and heated before the regenerator [3]. Therefore, the integration of a heat pump to the LD system, referred to as a heat-pump-driven liquid-desiccant (HPLD) system, would be a practical approach because the heat pump can provide the solution cooling and heating simultaneously [4].

Many previous studies have mainly focused on improving the energy performance of the HPLD air-conditioning system and demonstrating its energy saving potential [5,6]. By contrast, some previous studies have been performed to match the solution heating load and the actual heat released from the solution-side condenser, and to control the extra condensing load which generates as the heat released from the solution-side condenser is higher than the solution heating load, referred to as capacity matching. Niu et al. [7] defined a novel performance index to evaluate the capacity matching and concluded that the HPLD system should possess double-condenser to handle the extra condensing load. Abdel-Salam and Simonson performed the parametric study on both the capacity matching and energy performance with varying the operating parameters and finally revealed the most influential parameter based on a sensitivity analysis [8]. In addition, they established an operating logic under the various capacity matching situations [9].

* Corresponding author. Tel.: +82-2-2220-2370; fax: +82-2-2220-1945.
E-mail address: jjwarc@hanyang.ac.kr

The abovementioned previous studies focused only on the capacity matching of the solution-side condenser; however, to ensure the operational feasibility and stability of the system, the release of the extra condensing heat in the extra condenser based on thermodynamics should also be concretely handled in the capacity matching research. Furthermore, although the capacity matching, including releasing the extra condensing heat, must finally be optimized considering the energy performance together, no related optimization study has been previously conducted. Therefore, in this study, a multi-objective optimization of the HPLD air-conditioning system which can provide both the latent and sensible cooling is presented. With four design variables under the various outdoor air conditions, the two objectives are optimized as follows: extra condenser's capacity matching index (CMI) which is much focused on releasing the extra condensing heat and coefficient of performance (COP) of the entire system for the energy performance index. A parametric study is first conducted to help to select the design variables and also understand the results of multi-objective optimization. Subsequently, a set of optimum points (i.e., Pareto front) is obtained using multi-objective genetic algorithm (MOGA). This would significantly contribute to providing engineers with a guideline for optimally designing and operating the HPLD air-conditioning system in various situations.

2. System Overview

2.1. System description

Figure 1 shows the proposed HPLD air-conditioning system. The process air as the room-return air mixed with outdoor air is initially dehumidified in the absorber via contact with the desiccant-solution which is cooled to the target temperature by the solution-side evaporator of heat pump. The dried process air is then sensible cooled to the target supply air temperature (i.e., $T_{sa} = 15$ °C) in the air-side evaporator of heat pump. In the regenerator, the desiccant-solution which is heated to the target temperature by the solution-side condenser of heat pump discharges moisture to the outdoor air (i.e., scavenging air) to increase its concentration (i.e., regeneration process). When the amount of heat released from the solution-side condenser is greater than the solution heating load, the extra condenser which is a kind of the air-cooled condenser is activated to release the extra condensing heat into the regenerator outlet air.

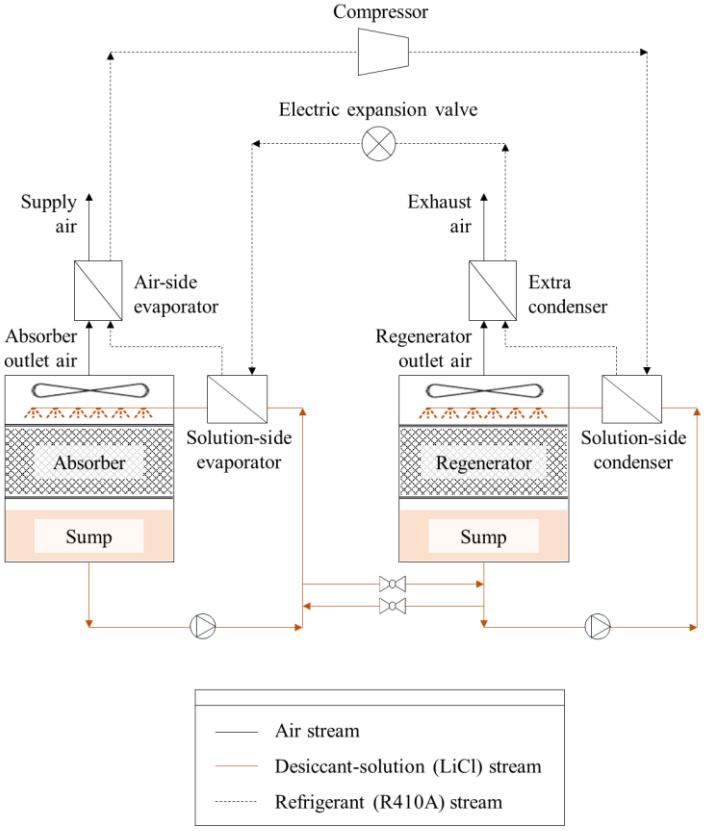


Fig. 1. Proposed HPLD air-conditioning system.

2.2. Performance indices

Before defining the CMI, the amount of heat absorbed by both the solution-side evaporator and air-side evaporator is assumed to be equal to the amount of heat required to cool the absorber solution and process air, respectively. In other words, the actual cooling capacity of evaporator is always the same as the cooling load of evaporator by adjusting the refrigerant flow rate in accordance with the inverter control. Therefore, two evaporators' CMIs (i.e., the ratio of the actual cooling capacity of evaporator to the cooling load of evaporator) are 1.0 all the time, which is not the focus and will not be more discussed in this study. The CMIs of both the solution-side condenser and particularly the extra condenser are the major performance indices to assess the condensing heat release and quantify the capacity matching. The solution-side condenser's CMI ($CMI_{sol,cond}$) is defined as the ratio of the total condensing heat to be released, referred to as total condensing load ($\dot{Q}_{tot,cond,load}$), to the heat required to heating the regenerator solution to the target solution temperature ($\dot{Q}_{reg,load}$) (Eq. (1)).

$$CMI_{sol,cond} = \frac{\dot{Q}_{tot,cond,load}}{\dot{Q}_{reg,load}} = \frac{\dot{m}_{ref}\cdot(h_{cond,i}-h_{cond,o})}{(\dot{m}\cdot c_p)_{reg,i,s}\cdot(T_{reg,i,s}-T_{reg,sump})} \quad (1)$$

Therefore, the increase in $CMI_{sol,cond}$ indicates the increase in the total condensing load, and when $CMI_{sol,cond}$ is greater than 1.0, the extra condensing load ($\dot{Q}_{extra,cond,load}$) then occurs. The extra condenser is a kind of the air-cooled heat exchanger; therefore, the maximum thermodynamically possible heat transfer rate of the extra condenser ($\dot{Q}_{extra,cond,max}$) should be estimated via multiplication of the minimum capacitance rate by the maximum possible temperature difference [10]. Accordingly, the extra condenser's CMI ($CMI_{extra,cond}$) is defined as the ratio of $\dot{Q}_{extra,cond,load}$ to $\dot{Q}_{extra,cond,max}$ (Eq. (2)) to assess the operating stability and feasibility of the extra condenser based on thermodynamics. The decrease in $CMI_{extra,cond}$ indicates the decrease in the extra condensing load, which is ideal in terms of reducing the waste heat and extra condenser size. In addition, when $CMI_{extra,cond}$ is lower than 1.0, the extra condensing heat is well released at the extra condenser. On the other hand, when $CMI_{extra,cond}$ is higher than 1.0, the extra condensing heat is not completely released and remains inside the heat pump, which results in a fatal entire system failure.

$$CMI_{extra,cond} = \frac{\dot{Q}_{extra,cond,load}}{\dot{Q}_{extra,cond,max}} = \frac{\dot{Q}_{tot,cond,load}-\dot{Q}_{reg,load}}{(\dot{m}\cdot c_p)_{reg,o,a}\cdot(T_{cond}-T_{reg,o,a})} \quad (2)$$

The system COP (COP_{sys}) is selected as the energy performance index and defined as the ratio of total cooling capacity ($\dot{Q}_{cooling}$) to total input power ($\dot{W}_{tot}$), as shown in Eq. (3).

$$COP_{sys} = \frac{\dot{Q}_{cooling}}{\dot{W}_{tot}} = \frac{\dot{m}_{abs,i,a}\cdot(h_{abs,i,a}-h_{sa})}{\dot{W}_{comp}+\dot{W}_{fan}+\dot{W}_{pump}} \quad (3)$$

3. Optimization Overview

3.1. Design problem formulation

In the design and operation of the proposed HPLD air-conditioning system, the design problem of multi-objective optimization is formulated to derive the optimum combination of design variables both to achieve the capacity matching including the release of extra condensing heat and to improve the energy performance. The overall design problem formulation is outlined in Table 1.

3.1.1. Design variables

The influential design variables commonly used in the previous studies on the LD systems are as follows: inlet air temperature, inlet air humidity, packing geometry, air flow rate of absorber and regenerator, solution flow rate of absorber and regenerator, solution temperatures of absorber and regenerator, solution concentrations of absorber and regenerator. However, in this study, some of the conventional influential design variables which meet the following criteria are fixed, excluded, or neglected:

- First, the relatively less influential variables
- Second, the uncontrollable or nonmanipulable variables
- Third, the variables related to the latent cooling for a target conditioned zone

Based on the criterion assessment, the multi-objective optimization is conducted for three cases of summer outdoor air temperatures (i.e., low temperature, standard temperature and high temperature), and finally four design variables are selected as follows: the ratio of the air flow rate of regenerator to absorber (R_{air}), the ratio of the solution flow rate of regenerator to absorber (R_{sol}), the solution temperature of absorber ($T_{abs,i,s}$) and the solution temperature of regenerator ($T_{reg,i,s}$). The range of design variables is set in consideration of the range commonly used in the previous studies of the HPLD systems [11] and also the system practicality. Then, the medium of each variable's min-max range was considered as the representative value for each variable and put as its initial value.

3.1.2. Objective function and constraint

Among the performance indices, COP_{sys} and $CMI_{extra,cond}$ are selected as the objective functions to be maximized and minimized, respectively. They also correspond to the constraints because they should be improved compared with their initial values. Particularly, $CMI_{extra,cond}$ must be lower than 1.0 to completely release the extra condensing heat within $\dot{Q}_{extra,cond,max}$, as specified in Section 2.2. In addition, $CMI_{sol,cond}$ corresponds to the constraint too and should be greater than 1.0 because $\dot{Q}_{reg,load}$ should be satisfied to heat the regenerator solution to the target temperature. The humidity ratio of the absorber outlet air ($\omega_{abs,o,a}$) is the final constraint which should be lower than 0.010 kg/kg to handle the room latent load of the target zone [12].

Table 1. Design problem formulation

Category		Parameter	Value
Classification of cases by outdoor air temperature (T_{oa})		Case 1: Low T_{oa} [°C]	$T_{oa} = 27$
		Case 2: Standard T_{oa} [°C]	$T_{oa} = 31$
		Case 3: High T_{oa} [°C]	$T_{oa} = 35$
Design variable	*Find*	R_{air} [-]	$0.5 \leq R_{air} \leq 1.5$ (Initial value: $R_{air} = 1.0$)
		R_{sol} [-]	$0.5 \leq R_{sol} \leq 1.5$ (Initial value: $R_{sol} = 1.0$)
		$T_{abs,i,s}$ [°C]	$15 \leq T_{abs,i,s} \leq 25$ (Initial value: $T_{abs,i,s} = 20$)
		$T_{reg,i,s}$ [°C]	$40 \leq T_{reg,i,s} \leq 50$ (Initial value: $T_{reg,i,s} = 45$)
Objective function	*To maximize*	COP_{sys} [-]	
	To minimize	$CMI_{extra,cond}$ [-]	
Constraint	*Subject to*	COP_{sys} [-]	$COP_{sys} \geq$ Initial value
		$CMI_{extra,cond}$ [-]	$CMI_{extra,cond} \leq$ Initial value, $CMI_{extra,cond} \leq 1.0$
		$CMI_{sol,cond}$ [-]	$CMI_{sol,cond} \geq 1.0$
		$\omega_{abs,o,a}$ [kg/kg]	$\omega_{abs,o,a} \leq 0.010$

3.2. Optimization algorithm

The optimization algorithm should be appropriately selected according to the type of optimization problems. All four design variables are the continuous variables, and because one of the objective functions and constraints has nonlinearity based on the parametric study which will be described later in Section 4.1, nonlinear programming should be handled. In addition, the multi-objective optimization problem with two conflicting objective functions should be solved, and global optimization results, not local optimization results, should be derived. Therefore, MOGA which is based on the genetic algorithm for the multi-objective optimization problem is selected as the optimization algorithm. MOGA is noted as one of the most popular multi-objective optimization algorithms and can generate a better spread of Pareto front for the multi-objective functions. Particularly, two specialized multi-objective operators, corresponding to crowding distance sorting and non-dominated sorting, are applied to MOGA, which is referred to as a non-dominated sorting genetic algorithm-II (NSGA-II) [13]. The population size is 100, and the crossover rate is 0.9. The mutation rate is 0.25 considering the number of design variables, and the random speed is 100. The maximum number of generations is 250, and the violated constraint limit is 0.003. The multi-objective optimization is conducted using a commercial process integration, automation and optimization (PIAnO) software.

4. Results and Discussion

4.1. Parametric study

To help to understand the selection of design variables and the optimization results, the parametric study is first conducted on the two objective functions (i.e., COP_{sys} and $CMI_{extra,cond}$) by varying all possible operating parameters as follows: outdoor air temperature (T_{oa}), outdoor air humidity ratio (ω_{oa}), the ratio of the air flow rate of regenerator to absorber (R_{air}), the ratio of the solution flow rate of regenerator to absorber (R_{sol}), the solution temperature of absorber ($T_{abs,i,s}$) and the solution temperature of regenerator ($T_{reg,i,s}$).

Figure 2 shows the results of parametric study for each operating parameter. As T_{oa} increases, both COP_{sys} and $CMI_{extra,cond}$ are increased (Fig. 2(a)). The increase in COP_{sys} at the high T_{oa} is attributed to the significant increase in the total cooling capacity ($\dot{Q}_{cooling}$). The increase in the heat absorption rate of evaporators and input power of compressor result in the increase in total condensing load ($\dot{Q}_{tot,cond,load}$) and then extra condensing load ($\dot{Q}_{extra,cond,load}$). However, $\dot{Q}_{extra,cond,max}$ is decreased because the difference in the temperature between the regenerator outlet air and condenser is decreased, which increases $CMI_{extra,cond}$.

On the other hand, in Fig. 2(b), COP_{sys} is slightly decreased as ω_{oa} increases because the increase in $\dot{Q}_{cooling}$ is insignificant. In addition, $CMI_{extra,cond}$ is almost constant regardless of the change in ω_{oa} because ω_{oa} is not directly involved in the parameters that make up $CMI_{extra,cond}$.

In Fig. 2(c), COP_{sys} is slightly increased when R_{air} increases because as regenerator air flow rate increases, it could increase the regeneration performance and solution concentration, which increases the dehumidification performance and $\dot{Q}_{cooling}$. However, because the fan power is increased and also the solution cooling load is increased due to the increase in the exothermic reaction during the dehumidification process, COP_{sys} cannot be increased significantly. Meanwhile, $CMI_{extra,cond}$ is found to be much significantly decreased as R_{air} increases due to the increase in the air flow rate of regenerator and the increase in $\dot{Q}_{extra,cond,max}$ accordingly.

In Fig. 2(d), as R_{sol} increases, COP_{sys} is shown to be decreased mainly due to the increase in the pump input power. However, $CMI_{extra,cond}$ is slightly increased as R_{sol} increases. The higher solution flow rate of regenerator is less influenced by the decrease in solution temperature caused by the endothermic reaction during the regeneration process. Therefore, the solution temperature of regenerator sump is increased, and then the condensing temperature is decreased. Consequently, the difference in the temperature between the condenser and the regenerator outlet air is decreased at the high R_{sol}, which results in the $CMI_{extra,cond}$ increase.

In Fig. 4(e), COP_{sys} is maximized between 15–20 °C of $T_{abs,i,s}$. This is because at the higher $T_{abs,i,s}$, the dehumidification rate is decreased due to the decrease in the vapor pressure difference, and at the lower $T_{abs,i,s}$, the dehumidification rate is also decreased according to the previous absorber model used in this study [14]. Therefore, the dehumidification rate is maximized at the intermediate $T_{abs,i,s}$, which results in COP_{sys} being maximized between 15–20 °C of $T_{abs,i,s}$. Meanwhile, as the dehumidification rate is maximized, the regeneration rate is also maximized between 15–20 °C of $T_{abs,i,s}$. Accordingly, the solution temperature of regenerator sump is minimized due to the decrease in solution temperature caused by the endothermic reaction during the regeneration process. Therefore, between 15–20 °C of $T_{abs,i,s}$, $\dot{Q}_{reg,load}$ is maximized and $\dot{Q}_{extra,cond,load}$ is then minimized, which causes the minimization of $CMI_{extra,cond}$.

In Fig. 4(f), as $T_{reg,i,s}$ increases, both COP_{sys} and $CMI_{extra,cond}$ are noted to be decreased. The decrease in COP_{sys} at the high $T_{reg,i,s}$ is resulted from the high input power of the compressor as the condensing temperature is increased to produce the high $T_{reg,i,s}$. On the other hand, the increase in the condensing temperature at the high $T_{reg,i,s}$ increases the temperature difference between the condenser and the regenerator outlet air, thereby decreasing $CMI_{extra,cond}$.

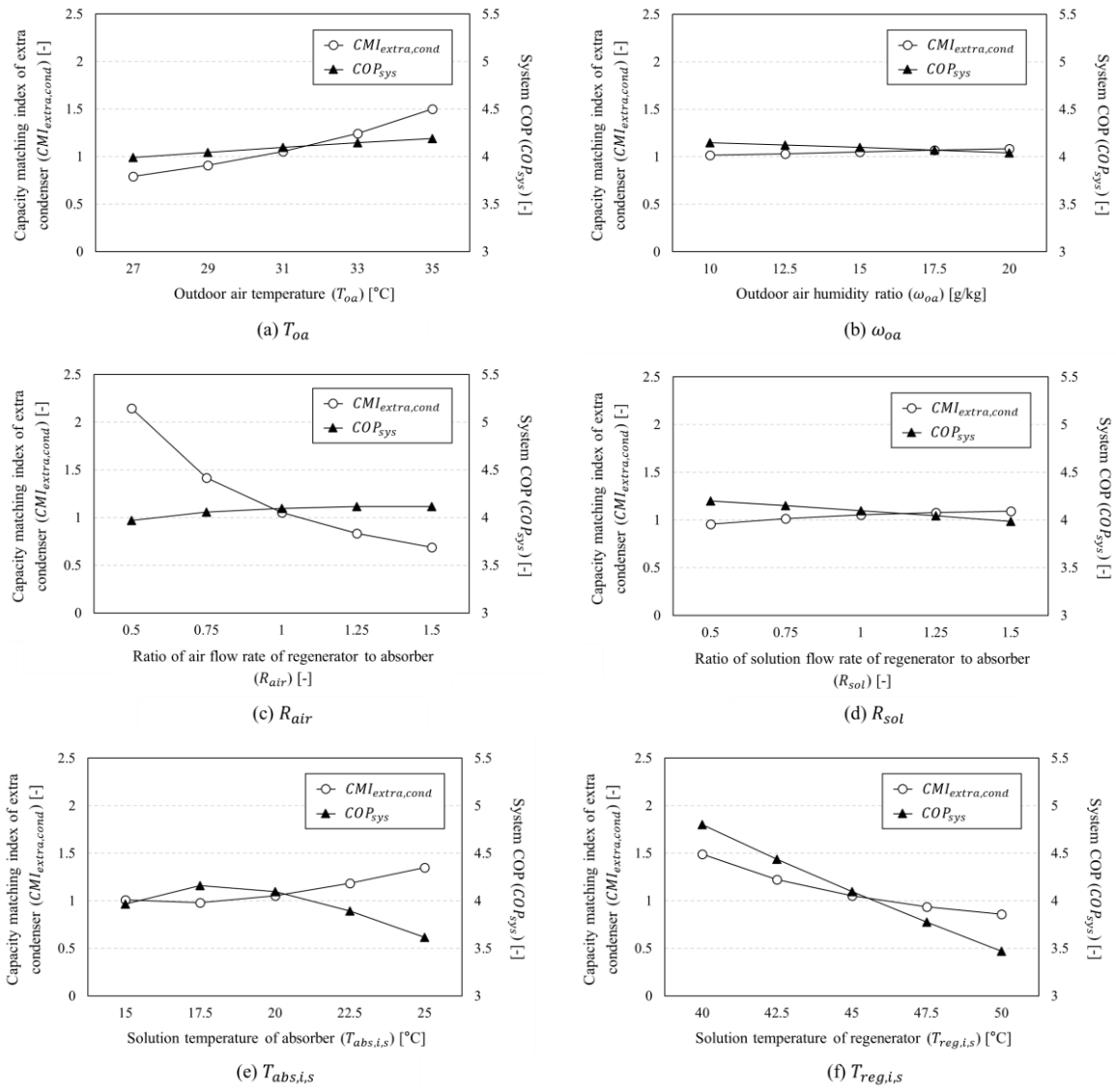


Fig. 2. Effect of operating parameters on two objective functions.

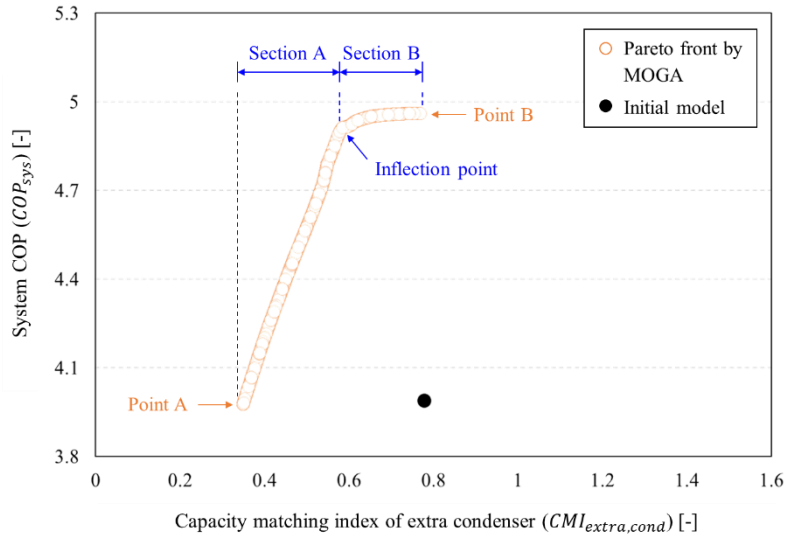
4.2. Optimization results

4.2.1. Pareto front

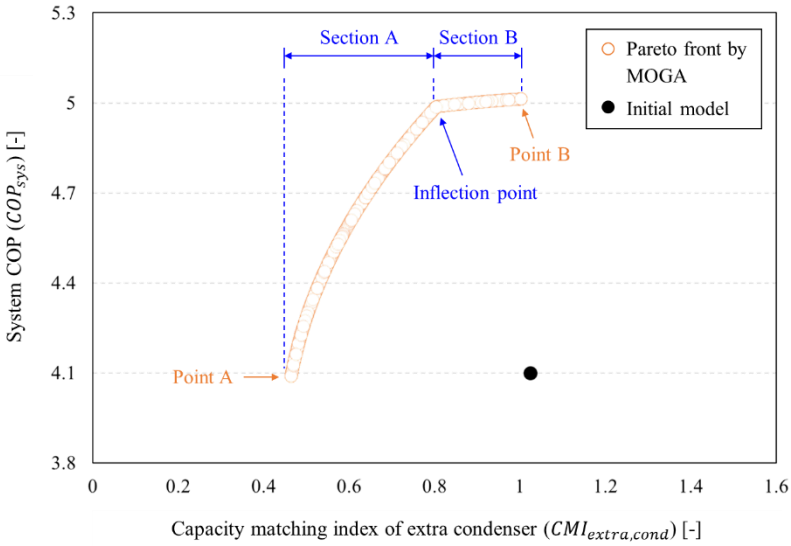
Pareto front which is a curve presenting a set of optimized non-dominated points obtained by MOGA should be generated to find the optimum solution. Figure 3 shows both the initial model and the generated Pareto fronts by MOGA for each case of T_{oa}. In all three Pareto fronts, all non-dominated optimized points are indicated to be adequately plotted in maximizing COP_{sys} and minimizing $CMI_{extra,cond}$. In addition, the constraints are noted to be satisfied in that all optimized non-dominated points have greater COP_{sys} and lower $CMI_{extra,cond}$ compared to the initial values, respectively, and particularly, all optimized non-dominated points have $CMI_{extra,cond}$ lower than 1.0.

According to the parametric study, when T_{oa} increases, the points of the Pareto front generally have a higher $CMI_{extra,cond}$ value because at the high T_{oa}, releasing the condensing heat is more difficult. Moreover, the maximization of COP_{sys} on the Pareto front in Case 3 is found to be insignificant compared with that in Case 1 and Case 2. This is because in Case 3, in most cases, $CMI_{extra,cond}$ is greater than 1.0 which violates the constraint. Therefore, although COP_{sys} could be further maximized, the points that violate the constraints were excluded from the Pareto front. Meanwhile, in Case 1 and Case 2, a section, names as Section B, is shown on the Pareto front wherein $CMI_{extra,cond}$ is further minimized while COP_{sys} is almost constant. Because R_{air} is the most influential parameter in $CMI_{extra,cond}$, R_{air} is primarily increased in

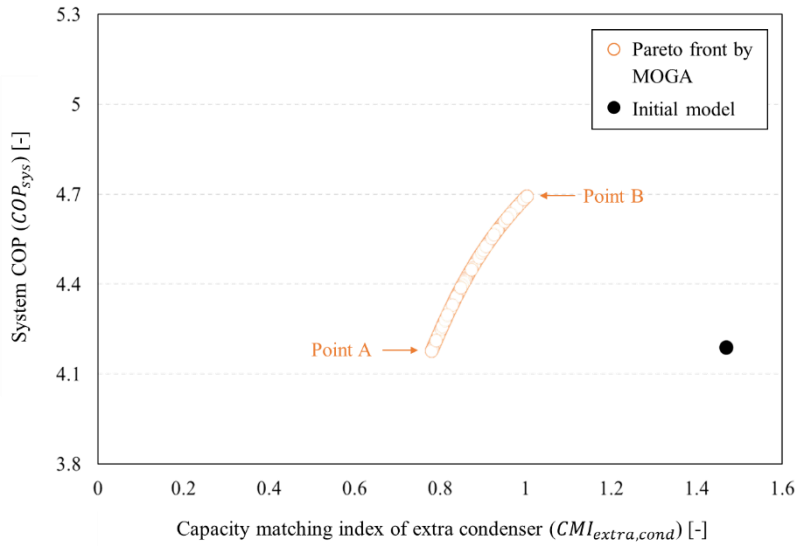
section B. However, R_{air} is the least influential parameter in COP_{sys}, therefore COP_{sys} is almost constant in Section B. In section A, R_{air} has maximum value and does not change, and then $T_{reg,i,s}$ which corresponds to the next most influential parameter in $CMI_{extra,cond}$ primarily minimizes $CMI_{extra,cond}$. However, $T_{reg,i,s}$ also corresponds to the influential parameter in COP_{sys}, thus the graph rapidly changes in Section A.



(a) Case 1 ($T_{oa} = 27$ °C).



(b) Case 2 ($T_{oa} = 31$ °C).



(c) Case 3 (T_{oa} = 35 °C).

Fig. 3. Pareto front generated by MOGA.

4.2.2. Final optimum solutions by decision-making scenario

All non-dominated points on the Pareto front are the acceptable optimum solutions to the multi-objective optimization problem. However, the final optimum solutions should be presented based on a decision-making process to provide the designers and engineers with a practical guideline for optimally designing and operating the HPLD air-conditioning system.

The established decision-making scenario consists of three different scenarios with respect to the different weights allotted to each objective function. First, in Scenario I, COP_{sys} maximization and $CMI_{extra,cond}$ minimization have weights of 0.0 and 1.0, respectively, which corresponds to point A in Fig. 3. Scenario I focuses only on improving the operational feasibility and stability of the system and reducing the extra condensing load while maintaining the energy performance just at its initial value. Second, in Scenario II, COP_{sys} maximization and $CMI_{extra,cond}$ minimization have weights of 0.5 and 0.5, respectively, which places the same importance on both the system energy performance and the heat release. Finally, in Scenario III, COP_{sys} maximization and $CMI_{extra,cond}$ minimization have weights of 1.0 and 0.0, respectively, which corresponds to point B in Fig. 3. Scenario III focuses only on improving the energy performance while maintaining the operational feasibility and stability of the system just at its initial value. Tables 2, 3 and 4 reveal the selected final optimum solutions in all scenarios for each case of T_{oa}.

Table 2. Final optimum solutions based on decision-making scenario for Case 1 (T_{oa} = 27 °C)

Parameter		Decision-making scenario		
		Scenario I	Scenario II	Scenario III
Design variables	R_{air} [-]	1.5	1.5	1.13
	R_{sol} [-]	0.5	0.5	0.5
	$T_{abs,i,s}$ [°C]	15	15	17.3
	$T_{reg,i,s}$ [°C]	46.3	46.3	40.0
Objective functions and Constraints	COP_{sys} [-]	3.99	3.99	4.96
	$CMI_{extra,cond}$ [-]	0.35	0.35	0.77
	$CMI_{sol,cond}$ [-]	1.81	1.81	2.02
	$\omega_{abs,o,a}$ [kg/kg]	0.00798	0.00798	0.00897

Table 3. Final optimum solutions based on decision-making scenario for Case 2 ($T_{oa} = 31$ °C)

Parameter		Decision-making scenario		
		Scenario I	Scenario II	Scenario III
Design variables	R_{air} [-]	1.5	1.5	1.32
	R_{sol} [-]	0.5	0.5	0.5
	$T_{abs,i,s}$ [°C]	18.4	18.2	18.3
	$T_{reg,i,s}$ [°C]	46.3	44.7	40.0
Objective functions and Constraints	COP_{sys} [-]	4.10	4.31	5.01
	$CMI_{extra,cond}$ [-]	0.46	0.51	1.00
	$CMI_{sol,cond}$ [-]	1.93	1.95	2.16
	$\omega_{abs,o,a}$ [kg/kg]	0.00773	0.00800	0.00890

Table 4. Final optimum solutions based on decision-making scenario for Case 3 ($T_{oa} = 35$ °C)

Parameter		Decision-making scenario		
		Scenario I	Scenario II	Scenario III
Design variables	R_{air} [-]	1.5	1.5	1.5
	R_{sol} [-]	0.5	0.5	0.5
	$T_{abs,i,s}$ [°C]	17.0	17.5	18.4
	$T_{reg,i,s}$ [°C]	45.6	44.6	42.4
Objective functions and Constraints	COP_{sys} [-]	4.19	4.35	4.69
	$CMI_{extra,cond}$ [-]	0.78	0.84	1.00
	$CMI_{sol,cond}$ [-]	2.04	2.06	2.15
	$\omega_{abs,o,a}$ [kg/kg]	0.00815	0.00823	0.00849

5. Conclusion

In this study, the multi-objective optimization of the HPLD air-conditioning system was conducted to simultaneously improve the energy performance and achieve the capacity matching especially focusing on the release of extra condensing heat. The capacity matching indices were defined for solution-side condenser and extra condenser, respectively to assess the release of condensing heat and quantify the capacity matching. With four design variables (i.e., R_{air}, R_{sol}, $T_{abs,i,s}$, $T_{reg,i,s}$), a set of optimum points, referred to as Pareto front, which aims maximizing COP_{sys} and minimizing $CMI_{extra,cond}$, was generated based on MOGA for each case of outdoor temperature (T_{oa}). Subsequently, the final optimum solutions were determined based on the decision-making scenario which is established by diversely assigning weights to the objective functions.

Finally, at the low T_{oa}, COP_{sys} and $CMI_{extra,cond}$ maximally increased and decreased by 24 % and 55 %, respectively, compared with initial value, and at the standard T_{oa}, by 22 % and 55 %, respectively, and at the high T_{oa}, by 12 % and 47 %, respectively. The results of this study would be a practical guideline for engineers to optimally design and operate the HPLD air-conditioning system while simultaneously improving the energy performance and capacity matching in various situations. In future, an experimental investigation will be conducted to validate the optimization results in this study, and an optimal prototype will also be constructed based on the optimization results in this study.

Acknowledgements

This work was supported by the National Research Foundation of Korea(NRF) grant funded by the Korea government(MSIT) (No. 2022R1A2B5B02001975 and No. 2022R1A4A1026503) and Korea Environment Industry & Technology Institute (KEITI) through Prospective green technology innovation project, funded by Korea Ministry of Environment (MOE) (RE202103243).

References

[1] Winkler, J., Munk, J., Woods, J. Effect of occupant behavior and air-conditioner controls on humidity in typical and high-efficiency homes. *Energy Build.* 2018;**165**:364–78.
[2] Liu, X., Jiang, Y., Zhang, T. *Temperature and humidity independent control (THIC) of air-conditioning system*. Springer; 2014.
[3] Qi, R., Lu, L., Huang, Y. Energy performance of solar-assisted liquid desiccant air-conditioning system for commercial building in main climate zones. *Energy Convers. Manag*. 2014;**88**:749–57.
[4] Mohammad, A.T., Bin Mat S., Sulaiman, M.Y., Sopian, K., Al-Abidi, A.A. Survey of liquid desiccant dehumidification system based on integrated vapor compression technology for building applications. *Energy Build*. 2013;**62**:1–14.
[5] Cai, D., Qiu, C., Zhang, J., Liu, Y., Liang, X., He, G. Performance analysis of a novel heat pump type air conditioner coupled with a liquid dehumidification/humidification cycle. *Energy Convers. Manag*. 2017;**148**:1291–305.
[6] Liu, X., Xie, Y., Zhang, T., Chen, L., Cong, L. Experimental investigation of a counter-flow heat pump driven liquid desiccant dehumidification system. *Energy Build.* 2018;**179**:223–38.
[7] Niu, X., Xiao, F., Ma, Z. Investigation on capacity matching in liquid desiccant and heat pump hybrid air-conditioning systems. *Int. J. Refrig*. 2012;**35**:160–70.
[8] Abdel-Salam, A.H., Simonson, C.J. Capacity matching in heat-pump membrane liquid desiccant air conditioning systems. *Int. J. Refrig*. 2014;**48**:166–77.
[9] Abdel-Salam, A.H., Simonson, C.J. Optimal design, sizing and operation of heat-pump liquid desiccant air conditioning systems. *Sci. Technol. Built Environ*. 2020;**26**:161–76.
[10] Mitchell, J.W., Braun, J.E. *Principles of heating, ventilation, and air conditioning in buildings*. John Wiley & Sons; 2012.
[11] Liu, X., Yi, X., Jiang, Y. Mass transfer performance comparison of two commonly used liquid desiccants: LiBr and LiCl aqueous solutions. *Energy Convers. Manag*. 2011;**52**:180–90.
[12] Lee, J.H., Jeong, J.W. Hybrid Heat-Pump-driven Liquid-Desiccant System: Experimental Performance Analysis for Residential Air-conditioning Applications. *Appl. Therm. Eng*. 2021;**195**:117236.
[13] Deb, K., Pratap, A., Agarwal, S., Meyarivan, T. fast and elitist multiobjective genetic algorithm: NSGA-II. *IEEE Trans. Evol. Comput*. 2002;**6**:182–197.
[14] Chung, T.W., Luo, C.M. Vapor pressures of the aqueous desiccants. *J. Chem. Eng. Data*. 1999;**44**:1024–27.

14th IEA Heat Pump Conference
15-18 May 2023, Chicago, Illinois

Flexibility potential of heat pumps in Swedish thermal grids: for district heating companies and end users

Meng Song[a], Anna-Lena Lane[b], Markus Lindahl[b*], Tommy Walfridson[c], Metkel Yebiyo[c]

[a]Electric Power Systems, RISE Research Institutes of Sweden, Stockholm, Sweden
[b]Energy and Resources, RISE Research Institutes of Sweden, Borås , Sweden
[c]Energy and Resources, RISE Research Institutes of Sweden, Stockholm, Sweden

Abstract

In a power system with a large share of intermittent sources, the need for flexibility to balance variations in electricity production will increase. Flexibility can also help to reduce problems with bottle necks in the electricity grids. An advantage of using a combination of heat pumping technology and thermal networks is the larger flexibility in heat production and storage options that it entails. This article discusses the potential of using the flexibility of heat pumps in Swedish thermal grids from the perspective of energy company and end users. In an interview study with district heating companies that have heat pumps in their thermal grids, possibilities and barriers to use heat pumps for flexibility was investigated. It was found that those who have heat pumps already use them for flexibility. Barriers for even more use was investment cost for new heat pumps. More frequent shifts are connected to organizational, behavioral, and technical barriers. The study also investigates the economic benefits for end users by utilizing the flexibility of heat pumps combined with district heating. Simulations are carried out for buildings located in different electricity price areas and climate zones in Sweden. It also considers different price scenarios for electricity, grid tariff, district heating and system services The result shows that the energy cost for end users could be effectively reduced by using the flexibility of the hybrid heating system. The cost saving potential varies among locations, price scenarios and the type of system services provided by the heat pump.

© HPC2023.
Selection and/or peer-review under the responsibility of the organizers of the 14th IEA Heat Pump Conference 2023.

Keywords: Heat Pump; Thermal grid; District heating; Flexibility; Demand response; Load control

1. Introduction

In a power system with a large share of intermittent sources, the need for flexibility to balance variations in electricity production will increase. Flexibility can also help to reduce problems with bottle necks and shortage of capacity in the electricity grids. An advantage of using a combination of heat pumping technology and thermal networks is the greater flexibility in heat production and storage options that it entails. Today, there is an ongoing work to find affordable solutions to increase the robustness and flexibility of the power system. Several international reports [1]-[3] have in recent years pointed out the combination of heat pumps and district heating as a technical solution that can help to manage an increasing share of electricity from intermittent sources. Here Sweden is an interesting county to evaluate since the country has well-developed district heating systems in almost all cities as well as a large number of heat pumps installed, giving good conditions to combine district heating and heat pumps for a more flexible energy system.

Within EU there is an ongoing trend with an increasing share of electricity from renewable sources. EUs Renewable Energy Directive towards 2030 [4] sets a binding target for the EU for 2030 that 32% of the final energy consumption should come from renewable sources, and there are ongoing discussions to increase the target to 40% as part of the European green deal [5]. Sweden has similar targets, with a political goal that 100% of the electricity should be fossil-free by 2040 [6][7]. There is also an ongoing electrification of the whole

* Corresponding author. Tel.: +46 10 516 5529
E-mail address: markus.lindahl@ri.se

Swedish society. "Fossilfritt Sverige", an initiative to reduce the climate impact from different industrial sectors in Sweden, has developed several roadmaps for different industrial sectors and many of them points out an increased electrification as the way forward to reduce the climate impact of their respective industries [9]. In order to support the transition, the Swedish government has published an electrification strategy [8]. The strategy highlights a flexible use of electricity as one important part and mention especially a higher degree of flexibility related to electrical heating. All this indicates that an increased load on the electricity grid is to be expected in the future and a large part will be covered by intermittent sources.

1.1. Background

Most Swedish buildings are today heated by district heating, followed by electricity, either by a heat pump or electrical heaters, on third place comes biofuel-boilers. While heat pumps and electric heaters are most common in single-family homes, district heating dominates in apartment buildings. Today there are almost 1,5 million installed heat pumps in Sweden, mainly in the approximately 2 million single family-houses in the country [11]. When it comes to heat pumps installed for production of district heating a survey from 2016 identified 149 units of large-scale heat pumps (>1 MW_{th}) from 11 different countries. According to the survey Sweden is by far the country with the largest installed capacity in Europe (approximately 1200 MW). Many of these Swedish heat pumps was installed during the 80´s and have now been in operation for many years [12].

Using heat pumps located at the end users for demand response, without altering the heat source between heat pump and district heating, makes use of the thermal inertia of the building to shift the heat production in time. The thermal inertia makes it possible to start or stop the heat production for a while without any large impact on the indoor comfort, for how long depends highly on the thermal inertia of the building. A study simulating single family buildings in Denmark [14] concluded that it is possible to shift the heat production by 2-5 h in poorly insulated buildings and still maintain a good comfort. For well isolated buildings (passive house standard) the allowed shifted period could be even longer, a complete shutdown of the heating system is possible for more than 24h while still fulfilling the defined comfort criteria. Weiβ et al. [13] showed by simulations in IDA ICE that for residential buildings in Austria, built according to Austrian standards after 1980, at least 50% of domestic heating peak loads can be shifted to off-peak periods during the day, using a comfort band between 19-22°. For heat pumps located in the district heating grids the thermal inertia is many times larger due to the possibilities to store heat in pipes and accumulator tanks. [28]

1.2. Scope

The scope of the study is to evaluate potentials and constrains to use heat pumps for increasing the flexibility of energy systems. It investigates two types of heat pump systems: 1) centrally placed heat pumps in thermal grids which are operated by district heating companies; and 2) decentralized heat pumps which are installed on customer side and combined with district heating as a hybrid heating solution.

1.2.1. Delimitations

The article focusses on Swedish conditions in terms of climate, demand for space heating and hot water consumption, prices for heating and electricity, market conditions for frequency regulation services, projection of future scenarios, etc.

1.3. Definition flexibility

Flexibility and demand response are broad terms without a clear definition. EU:s Electricity Directive [10] states that: "*demand response' means the change of electricity load by final customers from their normal or current consumption patterns in response to market signals, including in response to time-variable electricity prices or incentive payments, or in response to the acceptance of the final customer's bid to sell demand reduction or increase at a price in an organised market … whether alone or through aggregation*."

In this study, we focus on demand response of heat pumps that are owned either by district heating companies or by property owners with a hybrid heating solution. The demand response refers to the adjustment of heat pump operation for two purposes:

1. Respond to dynamic prices such as the variations in price for electricity, district heating or fuels.
2. Respond to dedicated markets for flexible resources such as local flexibility markets or TSO's market for ancillary services.

The flexibility is achieved by varying the running order between different heat sources, or utilizing the

heat storage in the thermal grid, accumulator tanks or thermal inertia of buildings.

2. Interview study with district heating companies using heat pumps

2.1. Method in interview study

An interview study has been done with district heating companies in Sweden that have heat pumps in their production mix. Statistics about heat production in district heating system for 2020 and 2017 [15][16] have been used to find companies for interviews. About 17 companies with heat pumps in the production in 2020 was found. To find informants on these companies the contact network within the project has been used along with contact details from the energy companies. Some contacts have been found on the energy companies web pages. Contacts has been taken by email with 16 persons representing 14 different companies. The contact details did not match for 4 and 3 did not answer and 1 turned out to not have a heat pump in the grid. Finally, 8 interviews, (named I1-I8 in the study), with 13 persons were booked and finalized, representing 10 district heating grids distributed across Sweden. The interviews were done with the digital meeting tool zoom and recorded. Notes were also taken during the interviews that lasted between 30-60 min. The informants had both strategical roles and works closely with the production.

Before the interviews was conducted a semi structured interview guide was developed including the following themes: background about the informants and the company, facts about their thermal grids and production, their heat pumps, their attitudes and actions for flexibility, and finally their attitudes on decentralized heat pump at end consumers. Recordings and notes from the interview have been analyzed to find how heat pumps in district heating grids are used and what possibilities and barriers there are for contribution to flexibility.

2.2. Results from the interview study

2.2.1. Heat pumps in the district heating grids

In the 1980's many heat pumps were installed in district heating grids in Sweden. Since these decisions were taken about 40-50 years ago, knowledge about the accurate basis for decisions may only be found in old documentation.

" They wanted to replace heavy oil... I found some old document from when decisions were made, and then it was expected that there were quite high electricity prices for that time, but they were stable and then you dared to make this investment." I5

The informant I5 talks about ambitions to reduce fossil fuels in combination with a lot of available electricity from nuclear plants and with stable electricity prices as motivation of the investment back in the 1980's. Some of those heat pumps are still in use in district heating grids, but in need of reparation and maintenance. Three different ways to handle this have been found in the study. The first way is to replace the heat pump by other heat production. One example is described by I7:

" It was old, since 1984, and expensive to renovate. More power was needed as the city grow, then they installed a new heating plant with bark and wood chips. . . and scrapped pellets and heat pump. They had calculated that it was much cheaper to run on bark and wood chips than the electricity price for the heat pump. I don't think the heat factor was very good. ... I know that when I ran it, it took water from about 8 m depth. It was about 2 degrees Celsius. It wasn't even 4 degrees." I7

The heat pump was scrapped because of age, high costs for renovation and a low coefficient of performance, COP, which contributed to calculated higher energy production cost than with bark and wood chips. One reason for low COP was that the inlet of seawater was not deep enough to deliver 4 degrees C which normally is the bottom temperature due to high density, during winter when the sea water is cold. For some of the old heat pumps in the study there are plans for replacing them with other kind of production further on. This is the most common way and probably the answer to why there is less heat pumps in 2020 than 2017. The second way is to maintain the heat pumps to pro long their lifetime. There is a variation from smaller reparations to replacement of vital parts. Lack of spare parts is a barrier for reparations that some companies overcome it with special manufacturing based on old drawings. The most deep-going renovation is described by I3 where the control system and vital parts are renovated to prolong the lifetime with 30 years. This was motivated by a good heat source on the cold side and that there was no other heat production that was suitable in the system near a city with limitations for combustion. The third way is to replace the old heat pump with a new. I8, describes how the old heat pumps were demolished as they were found unprofitable since they had built new production with biogas as fuel. A few years later the gas price was high, and it was considered profitable to install new heat pumps, which was done in 2017.

There are also some other heat pumps that are installed in recent years in district heating grids where there is an available heat source for the cold side of the heat pump. District cooling is an upcoming product for energy companies. Some of these plants are also used for production of heat during winter. Other more recent heat pump installations are "island installations" where the normal grid is not connected.

2.2.2. District heating production and heat pumps

The informants describe how their district heating production is planned based on a forecasted heat need in the coming day and week according to weather forecasts, historical data and fuel prices. Available production units and personal resources are also considered as input for the planning. The planning results in a dispatch order for the different production units connected to the grid.

2.2.3. Flexibility in district heating grids

One way to create more flexibility than the thermal inertia of the supply pipes is to add an accumulator tank in the grid. This has been adopted by almost every grid in the study. The companies who have heat pumps in their grid describe the accumulator tank as an asset for accessing flexibility when the electricity price varies. On the other hand, it is hard to motivate an investment in heat pump only for getting more flexibility because of the low profitability. The startup time for heat pumps is shorter than that for other heat production units e.g. boiler with wood chips. Technically it is possible to start or stop heat pumps almost immediately, but in practice the minimum running time for heat pumps lasts from at least 3-4 hours to 12 hours in most grids. Frequent start and stop increases the risk of higher maintenance costs, especially for older heat pumps. Many of the informants also talk about the easy capacity regulation as an advantage of heat pumps. But there is a limitation in delivered temperature that must be supplemented by other fuels, at least in wintertime.

Barriers for the use of existing heat pumps, even when electricity prices are low, have been found in the study. The first barrier is that other production must be up and running and then fulfills the heat demand. A Typical example is the waste combustion i.e. where there is a commitment to combust a specific volume of waste and it is not possible to save it for later needs. The second barrier is the monthly electrical power fee that occurs when a heat pump is used. The size of the fee is so high that it is unprofitable to start a heat pump if it is not going to be used at least for about 7 days in the actual calendar month. The third barrier found is the lack of capacity on the cold side of the heat pump, caused by for example low water temperatures in sea water, low volumes of wastewater or lack of waste heat caused by revision or lower production. The fourth barrier is a need of both available and motivated personnel to start or stop a heat pump when the electricity price change. The larger energy production units are seldom fully automated, so active control by personnel is needed to change between production units.

2.2.4. District heating companies' view of smaller heat pumps located at end-users in their grid

Informants from the district heating companies in the study describe existing or possible customers using heat pumps as a competitor situation and how they use pricing to overcome this.

"We price against customers who have heat pumps so that we outcompete it." I8

The reason why combination of heat pumps and district heating is rarely seen as a referable combination from the district heating companies is because it causes more costs and is hard to plan.

"Nope... But really, we think they're free riding on us. They remove the base load when we have the best production and then they want to buy peak load production from us that is expensive, difficult to provide and has poor environmental performance." I2

They also say that using district heating as peak load often results in the need to have and use fossil production, which causes bad environmental performance. In the company in I7 they have handled the situation with a special agreement for customers who only use district heating as peak load. The aim is to make it more profitable for the district heating company and provide fairer pricing for their other customers who use district heating for all their consumption. One argument against the smaller heat pumps is that the district heating company cannot control them. In the study there are few examples of the collaboration between energy companies and customers for and controlling the smaller heat pumps in the grid. The company in interview I8 gives one example: where the district company has bought a 0,8 MW-size heat pump installation, (which are seen as a small heat pump), from a customer and now use and control it. The informant I8 describe it as a win-win situation for both customer and district heating company. Heat pumps out in the grid compensate for heat losses and contribute with higher temperature and capacity out in the grid. Economic benefits for energy customers to use the flexibility of heat pumps.

3. Economic benefits for energy customers to use the flexibility of heat pumps

This section analyses the economic benefits of Swedish property owners for utilizing the flexibility of heat pumps. It focuses on the customers who use a hybrid heating system i.e. heat pump combined with district heating. It firstly identifies the cost and revenue streams for the common Swedish energy customers with hybrid heating solutions. Then it introduces a simulation model for analyzing the energy usage and operation cost of the heating system. The model is applied in a case study to simulate the operation of a hybrid heating system under different conditions. The simulation results are shown and discussed in the end.

3.1. Cost and revenue of property owners with both heat pump and district heating

A Swedish property owner with a hybrid heating system needs to pay both electricity cost and district heating cost. The electricity cost is related to the electricity consumed by the heat pump. It consists of two parts: one part is paid to the DSO (distribution system operator) for connection and usage of the power grid; another part is paid to the electricity retailer for buying the electricity. The district heating cost is paid to the heat supplier for extracting heat from the thermal grid. The property owner signs separate contracts with DSO, electricity retailer and district heating supplier. [18] Table 1 lists the cost components that are usually included in the three contracts. The electricity price paid to retailer is mainly affected by the price on the wholesale electricity market. The grid tariff and district heating tariff are defined by DSO and heat supplier and supervised by Swedish Energy Markets Inspectorate.

Table 1. Cost components in customer contracts with DSO, electricity retailer and heat supplier [17][18]

DSO contract (Grid tariff)	**Electricity retailer contract**	**Heat supplier contract (District heating tariff)**
Annual fee	Electricity price	Energy price
Subscription fee	Green certificate	Flow price
Distribution fee	Fixed fee	Effect price
(Power fee)		(Fixed annual cost)
Energy tax		

Note: the cots components in the parentheses are not always included in the contract.

With the thermal inertia of the building envelope, the property owner can also provide flexibility to the power system by adjusting the default set points of the heat pump. The flexibility can be used as different types of services. This study focuses on four frequency regulation services purchased by TSO (transmission system operator) on the corresponding reserve markets. Table 2 is an overview of the four reserve markets [19]. As a service provider, the property owner could get compensation for the reserved capacity and/or the actual delivered regulation volume.

Table 2. Overview of the four frequency regulation services analyzed in the study [19]

	FCR-N	**FCR-D up**	**aFRR**	**mFRR**
Full name	Frequency containment reserves for normal operation	Frequency containment reserves for disturbances	Automatic frequency restoration reserves	Manual frequency restoration reserves (“regulating market”)
Regulation direction of the product on markets	Symmetric	Up-regulation	Separate products for up- and down-regulation	Separate products for up- and down-regulation
Minimum bid size	0.1 MW	0.1 MW	5 MW	10 MW (5 MW in price area SE4)
Activation	Automatically activated when the frequency deviates within 49.90 – 50.10 Hz	Automatically activated when the frequency deviates within 49.9 – 49.50 Hz	Automatically activated through a central control signal if the frequency deviates from 50.00 Hz.	Manually activated at the request of Svenska Kraftnät
Activation time	63% within 60 sec. and 100 % within 3 min.	50% within 5 sec. and 100% within 30 sec.	100 % within 120 sec.	100% within 15 min.
Endurance	1 hour	at least 20 minutes	1 hour	1 hour
Capacity compensation	Pay-as-bid. Will change to marginal pricing in 2024.	Pay-as-bid. Will change to marginal pricing in 2024.	Pay-as-bid. Has changed to marginal pricing since 2022.	None
Energy compensation	According to up/down regulation prices.	None	According to up/down regulation prices.	According to up/down regulation prices.

3.2. Simulation model

A python-based model is developed to simulate the operation of the hybrid heating system in buildings. The model structure is illustrated in Figure 1. The input of the model includes parameters about the building, heating devices, climate, and the information from market and system. The model simulates both normal and flexible operation modes of the heating system. Both operation modes are formulated as optimization problem.

For the normal operation mode, the objective function is to minimize the indoor temperature deviation from the desired set point during the planning horizon. It subjects to the constraints for estimating the heat balance and indoor temperature at each time step, and the capacity limits of the heating devices. The solution of the optimization problem is the total heat demand at each time step. It is assumed that the heat pump is always prioritized in the normal operation mode. District heating is only used when the demand exceeds the heat pump capacity. Accordingly, the heat power provided by heat pump and district heating are estimated for each time step, respectively. Then the corresponding cost is calculated. For the flexible operation mode, the objective function is to minimize the energy cost during the planning horizon considering the potential revenue from providing frequency regulation services. It subjects to similar constraints as in the normal operation mode. Additional constraints are considered to fulfill the requirements of the specific reserve markets. The heat power

provided by heat pump and district heating are estimated by solving the optimization problem. The corresponding cost and revenue are calculated accordingly.

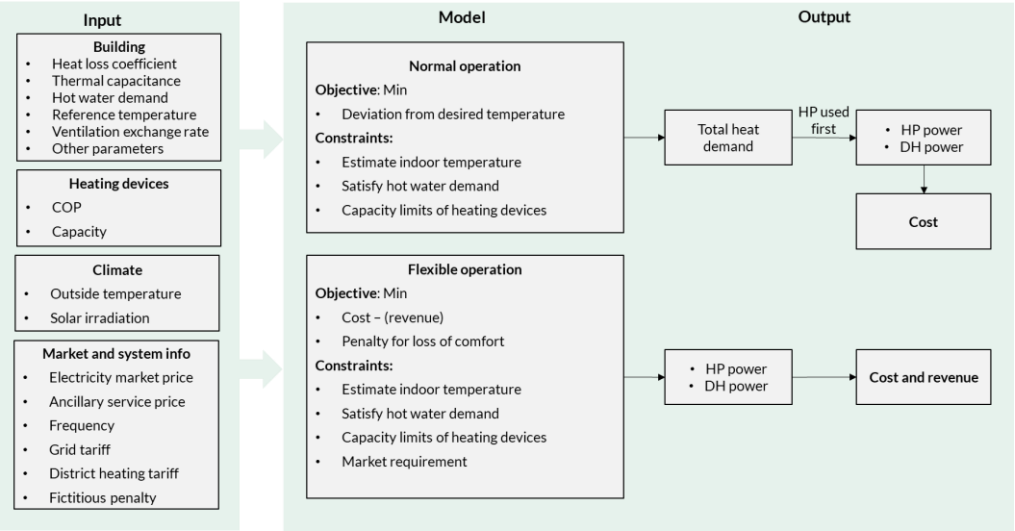


Figure 1. Simulation model for the hybrid heating system in a building

3.3. Case study

The case study analyzes the economic benefits of a property owner in different situations. It is based on a residential building with 93 apartments and 7161m^2 heating areas. The thermal inertia of the building is estimated based on parameters specified in **Error! Reference source not found.**. The building is installed with a ground source heat pump system and district heating. The COP of the heat pumps are affected by the outdoor temperature as shown in Table 3 and has a maximum heating capacity of approximately 350 kW (at +2°C), giving the building in the case study a bivalent temperature of -12°C. A validation of the model has been carried out by comparing the modelling results in the normal operation mode with a previous study [29]. The yearly energy consumption and cost estimated from the model are on the similar level as in the previous study.

Table 3. COP of the heat pump

Outdoor temperature (°C)	**COP Space heating**	**COP Hot water**
-21	3.50	3.00
-15	3.75	3.00
- 7	4.00	3.00
2	4.50	3.00
7	5.00	3.00
12	5.50	3.00

Four locations are investigated for the building: Kiruna, Östersund, Stockholm and Malmö. The four cities represent different climate zones in Sweden from north to south. In addition, they belong to the four electricity price areas which are divided because of the transmission bottlenecks. For the building at each location, six operation modes are simulated for the heating system:

- ref: normal operation, prioritize HP, no frequency regulation service is provided.
- DR_None: flexible operation, cost minimization, no frequency regulation service is provided.
- DR_FCRN: flexible operation, cost minimization, provide FCR-N service.
- DR_FCRD: flexible operation, cost minimization, provide FCR-D service.
- DR_aFRR: flexible operation, cost minimization, provide aFRR service.
- DR_mFRR: flexible operation, cost minimization, provide mFRR service.

For each operation mode, 16 scenarios are analyzed to represent the possible price for energy and frequency regulation services in the future. The spot price scenarios are based on the long-term market analysis by Svenska Kraftnät [20]. The scenarios are defined for the Nordic power system in 2035 and 2045, considering the growing electricity demand, higher penetration of renewable energy, coupling with hydrogen production and grid expansion. The grid tariff and district heating tariff in 2035 and 2045 are estimated according to the base tariffs in 2021 [22][23] and the historical price development trend [24][25]. The price on different reserve markets and system frequency are based on the historical data in 2018-2021, which are extracted from ENTSO Transparency Platform [26] and FinGrid Open Data [27].

Figure 2 shows the simulation results of the yearly heating cost of the building. Each box indicates the cost distribution among the 16 scenarios. In general, the cost increases from Malmö in the south of Sweden to Kiruna in the north. It is mainly due to the climate conditions i.e. more heating energy is needed in colder regions. For each location, the costs in the five DR cases are apparently lower than the cost in the reference case. It implies that the flexible operations with cost minimization can effectively reduce the overall cost for heating. The cost reduction is achieved by utilizing the thermal inertial of the building and actively selecting the heating source with a favorable price. Figure 3 shows the annual bought energy for the heating system in an example case, in which the building is assumed to be in Stockholm and the spot price scenario for 2035 is adopted. It indicates that the heating system consumes more district heating energy and less electricity in DR modes compared with the reference operation mode. Further analysis shows that the increased heat extraction from the thermal grid mainly happens in summer when the heating price is low.

The cost could be further reduced when the heat pumps provide frequency regulation services. However, the economic potential may vary among locations and scenarios. In most scenarios, the lowest cost can be found when the heat pumps provide FCR-N or aFRR service. Taking the building in Östersund as an example, the lowest cost is found when the heat pumps provide FCR-N service. The reason is that the property owner gets both capacity and energy compensation from TSO when participating in FCR-N and aFRR markets.

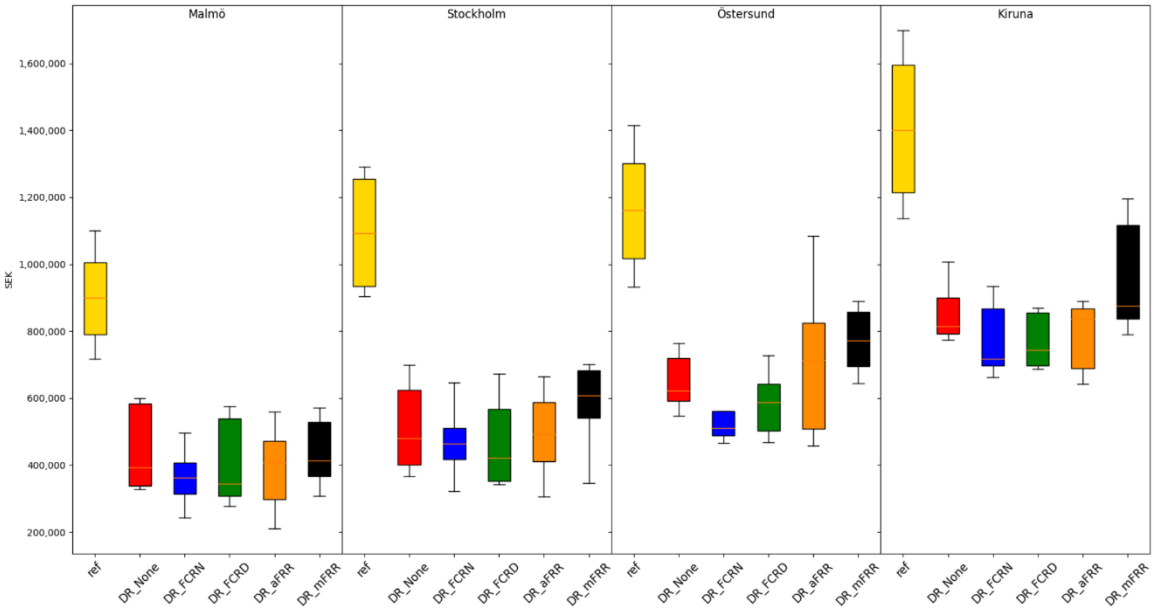


Figure 2. Annual heating cost for the building in different conditions

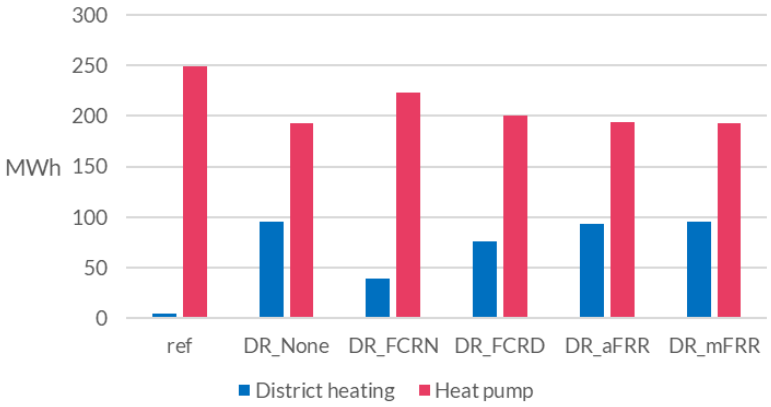


Figure 3. Annual bought energy (district heating and electricity to the heat pump system) for the example heating system: Stockholm, spot price scenario 2035

4. Discussion

In the interview study with district heating companies, it was found that it is an asset to have heat pumps in the district heating grid for flexibility. They also are perceived as easy to regulate and have shorter start and stop time than many other production units. The largest barrier to an increased use of heat pumps in the thermal grids is the investment. The investment cost is high, and it is mostly hard to motivate new installations and it compete with investments in combustion units that could cover all temperatures and heat need and may also produce electricity. Only in one of the interviews they had found it more profitable with a heat pump, but then their other production was based on gas, which have rising prices. To plan and produce heat to the lowest cost and to use inertia in grid and accumulator tank to cut peak loads is an everyday activity in district heating companies and how things have been done for long time. Heat pumps could be used more in the thermal grid if some barriers could be removed as for example monthly calendar basis for power fee. There is also a potential for more flexibility with motivated and available resources in personnel, so the fast variation in electricity price could be met. Traditional planning goes out from the nearest 24 hours and the coming week.

The case study of decentralized heat pumps shows that large economic potentials could be expected for the property owners when utilizing the flexibility of heat pumps. However, the potentials vary among scenarios, and it is based on the assumption of perfect market forecasts. Further studies are needed to investigate how the uncertainties in the market price and required regulation directions would affect the benefits for the property owners. Economic potential of delivering ancillary services to the TSO is a focus of the analysis. But in practice, before this is up and running there are still technical issues to solve on how to communicate with the heat pumps and how the heat pumps should react on signals to deliver the demand response to the grid. One barrier to solve is to make sure that the heat pumps can react and adjust the power consumption fast enough on signals for demand response, although the ramping rate of heat pump is not considered in the model. Among the frequency regulation services analyzed in this study, FCR-D up is the fastest reserve with an activation time of 50% within 5s and 100% within 30s. Discussions with the Swedish heat pump manufacturers indicate that it should be possible from a technical point of view to fulfill the demands for FCR-D, but updates of today's heat pumps might be needed. Another issue to solve is how to fulfill the requirements on the verification of delivered flexibility since todays' heat pumps have no electric meters installed.

The interview study shows that energy companies consider customers with the hybrid heating solution, i.e. heat pumps combined with district heating, as lost customers or free riders. The customers are blamed for only using district heating during peak load period and causing more combustion with expensive fossil fuels. Some district heating companies choose to use a special pricing scheme to overcome it. On the other hand, the case study of decentralized heat pump shows that the property owners may consume more district heating energy annually in DR modes compared with the reference level. If more customers in the thermal grid adopt the hybrid heating solution and apply similar flexible operation modes, the heat demand could be significantly changed from today and consequently affect the planning and operation of district heating production. However, this does not necessarily lead to an increase of peak load in the thermal grid. The analysis shows that in DR modes district heating would be mainly used during summer when the heat demand is conventionally low.

Therefore, more studies are needed to further clarify the effects of decentralized heat pumps on the thermal grid, especially when demand response is taken into account. Better data exchange between energy companies and end customers would be needed to enable energy companies to have a better overview of the grid. More active actions should be taken by the energy companies by e.g. improving the forecast of heat demand and flexibility potential of customers, and enhancing the efficient planning and operation of the heat plants with different energy mix. A holistic strategy is needed to coordinate the flexibility from both centralized and decentralized heat pumps and utilize them in a more efficient manner.

5. Conclusions

This article discusses the potential and constraints of using the flexibility of heat pumps in Swedish thermal grids from the perspective of energy company and end users, respectively. An interview study with district heating companies has been carried out to identify the possibilities and barriers to use heat pumps for flexibility services. The study shows that the companies with heat pumps in their grids today think it is an advantage to use them for flexibility when electricity prices variates. But to invest in a new heat pump to get additional flexibility is described as hard to motivate and to get profitable. Technically it is possible to start or stop heat pumps almost immediately, but in practice the minimum running time for the heat pump is from at least 3-4 hours or 12 hours in most grids. Other identified barriers for additional use of existing heat pumps are: 1) other heat production must be up and running, e.g. waste combustion; 2) a high monthly electrical power fee makes it unprofitable to start a heat pump if it is not going to be used at least for about 7 days in the calendar month; 3) lack of capacity on the cold side of the heat pump, caused by for example low temperatures in sea water, low volumes of wastewater or lack of waste heat; 4) need of both available and motivated personnel to start or stop a heat pump.

In addition, a quantitative analysis has been performed to investigate the economic benefits for end users by utilizing the flexibility of heat pumps combined with district heating. It is based on the simulations for buildings located in different electricity price areas and climate zones in Sweden, and considers the future price scenarios for electricity, grid tariff, district heating and system services. The analysis shows that the energy cost for end users could be effectively reduced by using flexibility of the hybrid heating system, whereas the cost saving potential may vary among locations, price scenarios and the type of system services provided by the heat pump. More studies are needed in the future to further clarify how demand response of customers may affect the operation of the district heating production, and how the flexibility from centralized and decentralized heat pumps can be coordinated and utilized in a more efficient manner.

Acknowledgements

This work was supported by the Swedish Energy Agency, project Flexibility by implementation of heat pumps in thermal networks – Swedish participation in the IEA HPT annex [grant number 51525-1].

References

[1] European Commission, *COMMUNICATION FROM THE COMMISSION TO THE EUROPEAN PARLIAMENT, THE COUNCIL, THE EUROPEAN ECONOMIC AND SOCIAL COMMITTEE AND THE COMMITTEE OF THE REGIONS An EU Strategy on Heating and Cooling*, COM 51 Final, Brussels, Belgium, 2016

[2] S. Paardekooper et.al., *Heat Roadmap Europe 4: Quantifying the Impact of Low-Carbon Heating and Cooling Roadmaps*. Aalborg Universitetsforlag, 2017

[3] R. Geyer, D. Hangartner, M. Lindahl, and S. V. Pedersen, *Heat Pumps in District Heating and Cooling Systems - Final report*, IEA Heat Pumping Technologies Annex 47, https://heatpumpingtechnologies.org/annex47/, 2019

[4] EU, *Directive (EU) 2018/2001 of the European parliament and of the council of 11 December 2018 on the promotion of the use of energy from renewable sources (recast)*, Official Journal of the European Union, L 328/82, 2018

[5] European Parliament, *Fact sheets on the European Union, Renewable energy*, https://www.europarl.europa.eu/factsheets/en/sheet/70/fornybar-energi, 2022-11-02

[6] Regeringskansliet, *Mål för energipolitiken*, https://www.regeringen.se/regeringens-politik/energi/mal-och-visioner-for-energi/, 2022-10-25 (In Swedish)

[7] Sverigedemokraterna, Moderaterna, Kristdemokraterna, Liberalerna, *Tidöavtalet: Överenskommelse för Sverige*, https://www.xn--tidavtalet-gcb.se/, 2022-10-25 (In Swedish)

[8] Regeringskansliet. *Nationell strategi för elektrifiering*, 2022 (In Swedish)

[9] Energiföretagen & Fossilfritt Sverige, *Färdplan för fossilfri konkurrenskraft -Elbranschen*, 2020 (In Swedish)

[10] European Union, *DIRECTIVE (EU) 2019/944 OF THE EUROPEAN PARLIAMENT AND OF THE COUNCIL of 5 June 2019 on common rules for the internal market for electricity and amending Directive 2012/27/EU*, Official Journal of the European Union, L158, https://eur-lex.europa.eu/legal-content/EN/TXT/PDF/?uri=CELEX:32019L0944, 2019

[11] Swedish Energy Agency, *Energistatistik för småhus, flerbostadshus och lokaler*, https://www.energimyndigheten.se/statistik/den-officiella-statistiken/statistikprodukter/energistatistik-for-smahus-flerbostadshus-och-lokaler/, 2022

[12] J. Neves, and B. Mathiesen, *Heat Roadmap Europe: Potentials for Large-Scale Heat Pumps in District Heating*, Alborg University, Denmark, 2018

[13] T. Weiβ, A. Fulterer, and A. Knotzer, *Energy flexibility of domestic thermal loads -a building typology approach of the residential building stock in Austria*, Advances in Building Energy Research, 13:1, 122-137, DOI: 10.1080/17512549.2017.1420606, 2019

[14] J. Le Dréau, and P. Heiselberg, *Energy flexibility of residential buildings using short term heat storage in the thermal mass*, Energy 111 p. 991-1002, 2016

[15] Energiföretagen, *Fjärrvärmens bränslen och produktion 2017och 2020*, Tillförd energi till fjärrvärme och kraftvärme - äldre statistik - Energiföretagen Sverige (energiforetagen.se) (2022-11-16)

[16] Swedish Energy Market Inspectorate, *Produktion per prisområde fjärrvärme tekniska uppgifter 2015-2020*, https://www.ei.se/om-oss/statistik-och-oppna-data/tekniska-uppgifter---fjarrvarme, (2022-11-16)

[17] H. Li, F. Wallin, and J. Song, *A Dynamic Pricing Mechanism for District Heating Based on Levelized Cost of Heat and Prediction of Total Heat Demand*, Energiforsk, 2017:408, 2017. [Online]. Available: www.energiforsk.se

[18] Energimarknadsbyrån, *Elräkningen*. https://www.energimarknadsbyran.se/ (accessed Nov. 09, 2022) (In Swedish)

[19] E. Abdollahi, P. Chaves-Ávila, T. Gerres, P. Mastropietro, P. Rodilla, and Y. Vardanyan, *Review of The Regulatory Environment for CHP - Identification of Relevant Markets*, Bio-FlexGen project, 2022. [Online]. Available: https://bioflexgen.eu/

[20] O. Gustafsson and J. Karlsson, *Resurseffektiv energieffektivisering av flerbostadshus*, master thesis, Linköpings Universitet, LIU-IEI-TEK-A-15/02179-SE, 2015 (in Swedish)

[21] K. Brunge, E. Hellström, M. Jakobsson, and E. Thornberg, *Långsiktig Marknadsanalys 2021 Scenarier för Elsystemets Utveckling fram till 2050*, 2021. [Online]. Available: www.svk.se (In Swedish)

[22] Tekniska verken, *Lågspänning, effekt från 50 kW och högspänning*. https://www.tekniskaverken.se/kundservice/priser-och-avtal/elnat/utgaende-priser/ (accessed Jun. 01, 2022) (In Swedish)

[23] Tekniska verken, *Linköping: företag, bostadsrättföreningar och samfälligheter, Tekniska verken*. https://www.tekniskaverken.se/kundservice/priser-och-avtal/fjarrvarmepriser-2021/foretag/ (accessed Jun. 01, 2022) (In Swedish)

[24] Nils Holgersson Rapporten, *Rapport 2021: El*. https://nilsholgersson.nu/rapporter/rapport-2021/el-2021/ (accessed Nov. 09, 2022) (In Swedish)

[25] Nils Holgersson Rapporten, *Fjärrvärme – Historik*. https://nilsholgersson.nu/rapporter/rapporthistorik/fjarrvarme-historik/ (accessed Nov. 09, 2022) (In Swedish)

[26] ENTSO, *ENTSO Transparency platform*. https://transparency.entsoe.eu/ (accessed Nov. 11, 2022)

[27] Fingrid Open data, *Frequency - historical data*. https://data.fingrid.fi/en/dataset/frequency-historical-data (accessed Nov. 11, 2022)

[28] J. Hennessy, H. Li, F. Wallin, and E. Thorin, *Flexibility in thermal grids: a review of short-term storage in district heating distribution networks*, Energy Procedia, Volume 158, 2019, Pages 2430-2434, ISSN 1876-6102, https://doi.org/10.1016/j.egypro.2019.01.302. (https://www.sciencedirect.com/science/article/pii/S1876610219303224)

[29] M. Lindahl, O. Gustafsson, C. Markusson, and C. Haglund Stignor, *Hybrid heat pumps in combination with district heating*, 12th IEA Heat Pump Conference 2017, 2017

14th IEA Heat Pump Conference
15-18 May 2023, Chicago, Illinois

Theoretical analysis of membrane based liquid desiccant air conditioning system

Seong-Yong Cheon [a], Beom-Jun Kim [a], Jae-Hee Lee [a], Minseong Kim [a], Hyo-Lim Park [a], Jae-Weon Jeong[a,*]

[a]Department of Architectural Engineering, College of Engineering, Hanyang University,
222 Wangsimni-Ro, Seongdong-Gu, Seoul, 04763, Republic of Korea

Abstract

Air conditioning systems using liquid desiccant have been gaining attention due to their great energy-saving potential, but cooling and heating load for dehumidification and regeneration process remained a vital role in energy consumption. In this research, we proposed a membrane-based liquid desiccant air conditioning system, which is a vapor transportation driven system with gas separation membrane technology, and evaluated its thermodynamic performance by equation-based simulation. The proposed system has five components: an absorber, a regenerator, a membrane for dehydration, a membrane for hydration, and a vacuum compressor. The membranes were used to control solution concertation without heating and cooling; the water vapor separated by the membrane is transported from the dehydration solution to the hydration solution. The vacuum compressor operated to separate the water vapor from the solution and then transport the separated vapor to the membranes. The results showed that the ideal COP (coefficient of performance) of the proposed system in the thermodynamic analysis is 1.55, which is 5.17 higher than that of the conventional liquid desiccant (heat driven dehumidification and regeneration system), which is 0.3 COP at the design air.

© HPC2023.
Selection and/or peer-review under the responsibility of the organizers of the 14th IEA Heat Pump Conference 2023.

Keywords: Seperation membrane, liquid deisccant air coniditiong, Dehydration, Hydration

1. Introduction

The importance of humidity control in air-conditioning systems has increased as the ratio of sensible load to total air-conditioning load of a building has decreased dramatically due to improved building envelope thermal performance [1]. Decoupling the sensible and latent cooling functions of air conditioning has been suggested as a possible alternative to the typical condensation dehumidification technique. Several unique energy-efficient systems that can individually accommodate sensible and latent loads have been disclosed in the open literature [2].

One of these systems is the liquid-desiccant-assisted air-conditioning system [3, 4], in which the process air is dehumidified by a liquid-desiccant solution and then sensible cooling to the supply air's setpoint temperature. To improve the dehumidification performance, the concentrated desiccant solution should be cooled, and the diluted desiccant solution should be regenerated in the regenerator by heating. The heating and cooling of the desiccant solution are the most energy-intensive processes [5].

Numerous research have investigated the performance of various types of liquid desiccant systems to enhance the dehumidification performance. In the previous studies, air to liquid flow direction (i.e., cross flow, counter flow), has been investigated. Recently, internally-cooling [6] and heating [7] system was introduced to increase the system performance. Nevertheless, heating and cooling of the desiccant solution, which has high regeneration temperatures between 50 and 80 °C results in considerable energy consumption if free heat sources are unavailable [8, 9].

* Corresponding author. Tel.: +82-2-2220-2370; fax: +82-2-2220-1945.
E-mail address: jjwarc@hanyang.ac.kr (J.-W. Jeong).

In previous research, heat (heating and cooling) based liquid desiccant air conditioning system have been mainly conducted for evaluating energy performance; however, it is rare to evaluate the thermodynamic and energy performance using vacuum pressure driven liquid desiccant system. In this study, we proposed a novel system that uses dehydration and hydration in the liquid desiccant with separation membrane. The sensitivity of the operating conditions to the dehumidification performance of the proposed system was analyzed by numerical simulation. The energy performance of the proposed system was also evaluated by comparing the existing liquid dehumidification system (heating and cooling-based system) with design conditions.

2. System overview

2.1. System overview

Figure 1 depicts the five components of the proposed system: an absorber, a regenerator, a membrane for dehydration, a membrane for hydration, and a vacuum compressor. The membranes were utilized to regulate solution concentration without the use of heating and cooling; the water vapor separated by the membrane is delivered from the dehydration solution to the hydration solution. The vacuum compressor was used to separate the water vapor from the solution and transfer it to the membranes.

The diluted liquid desiccant solution leaving the absorber is preheated by the sensible heat exchanger and then hydrated by the hydration membrane, which make increase of the partial vapor pressure as decreasing solution concentration. The desiccant solution is regenerated in the regenerator, and the strong solution is precooled by the heat exchanger (HX). Finally, the supply air is dehumidified by the strong solution that is made by the dehydration membrane.

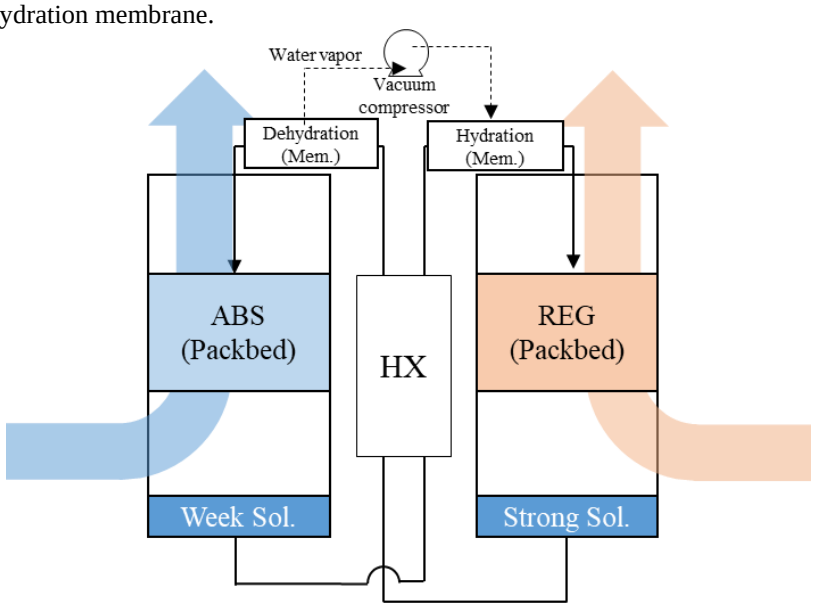


Fig. 1. Proposed system: Hydration/dehydration integrated liquid desiccant air conditioning system

Figure 2 showed the detailed configuration of the dehydration and hydration membrane (DHM) system used in the proposed system as a device for concentration control of the solution. The DHM consists of a dehydration membrane, a hydration membrane and a vacuum compressor. The dehydration and hydration membrane is separation membrane, which permeate the water vapor from solution because of the partial vapor difference between the feed-side (solution) and the permeate-side (vacuum) channels. When the week solution is introduced into the dehydration membrane, the water vapor in the dehydration membrane permeate to the vacuum compressor inlet. Then, the water vapor compressed by vacuum compressor permeate into strong solution in the hydration membrane.

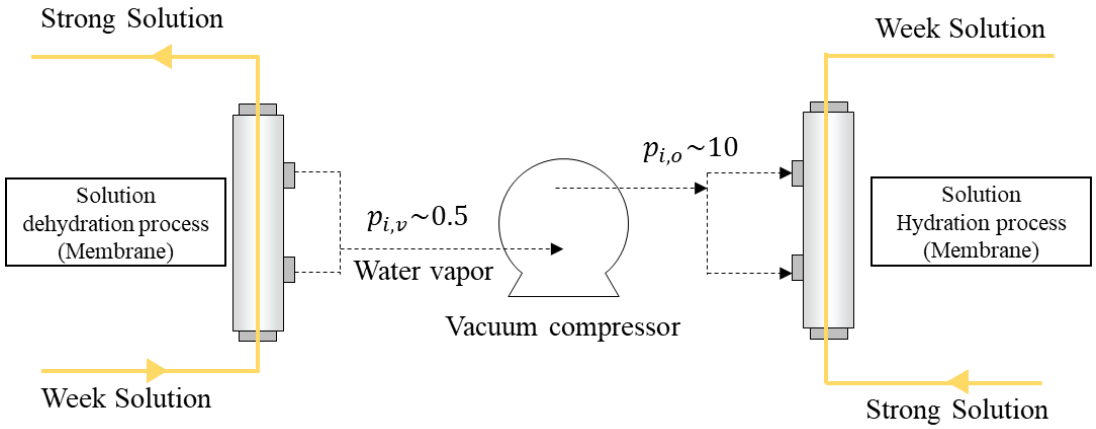


Fig. 2. Hydration and dehydration membrane

2.2. Reference system

As a reference system, a typical liquid desiccant-based air conditioning system consisting of an absorber, a regenerator, a cooling coil, a heating coil, and a liquid-to-liquid type sensible heat exchanger was chosen (Figure 3). In case of the reference system, the partial water vapor pressure of the diluted solution leaving the absorber and regenerated solution leaving the regenerator were controlled by varying the solution temperature. In an absorber, before hot, humid air and desiccant solution coincidently cross the packing media, the desiccant solution is cooled by the cooling coil until the water vapor pressure of the desiccant solution is lower than that of the target supply air. The diluted desiccant solution leaving the absorber is then heated by the heating coil so that the water vapor pressure of desiccant solution is higher than the air introduced to the regenerator. The sensible heat exchanger precools and preheats the regenerated and diluted solutions, which leads to reduction in solution heating and cooling loads.

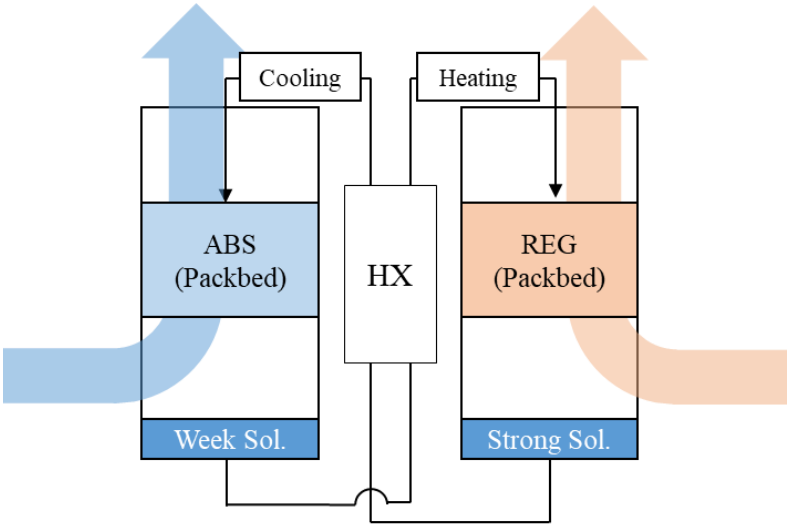


Fig. 3. Reference system: Cooling/heating coil based liquid desiccant air conditioning system

3. Simulation model

3.1. Numerical model of separation membrane: Dehydration and hydration

The process of dehydration and hydration in the membranes transfers the water vapor by the partial vapor pressure gradient between the feed and permeate sides as shown in Figure X. To estimate the mass transfer of the dehydration and hydration, the gas separation model with infinity selectivity for Water vapor was used as shown in Equation 1. The governing equation of the mass transfer driven by partial vapor gradient between membrane layers for each node. The change of the solution concentration along the membrane was estimated by mass balance equation (Equation 2), which address that the concentration change is driven by ratio of the permeated water vapor to the solution mass flow rate. As shown in Equation 3, the solution temperature change in the dehydration membrane is calculated by the evaporative cooling from desorption process of the membrane, whereas the solution temperature change in the hydration membrane is calculated by the condensation heating and air compressed heat from the vacuum compressor. To evaluate the partial vapor pressure of the solution, the desiccant solution model (Equation 4), which is driven by solution temperature and concentration was used.

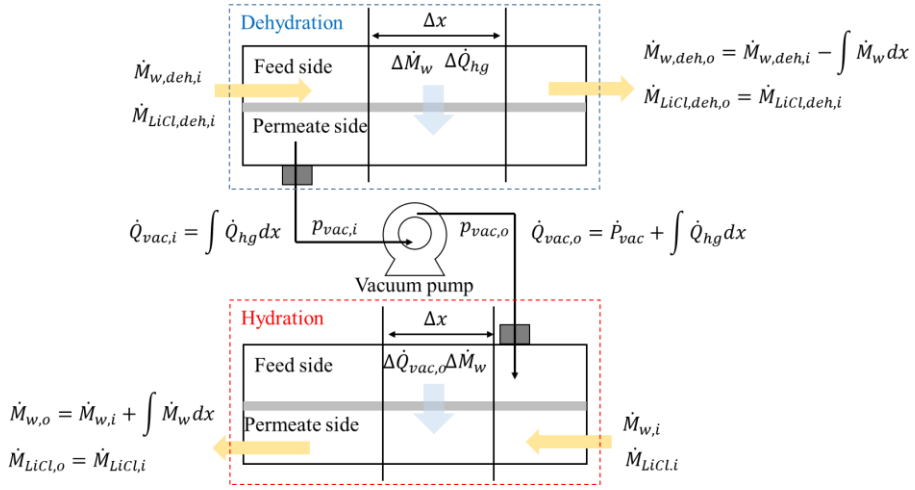


Fig. 4. Heat and mass balance of the dehydration and the hydration membrane

$$\Delta\dot{M}_{deh} = Permeance(p^{i}_{v,sol} - p_{vac})M_{mass}\Delta A \quad (1)$$

$$p^{i}_{v,sol} = f(T^{i}_{s,i}, X^{i}_{s,i}) \quad (2)$$

$$X^{i+1}_{s,i} = X^{i}_{s,i}/(1-(1+X^{i}_{s,i})) \times (\Delta\dot{M}_{deh}/\dot{m}_{sol}) \quad (3)$$

$$T^{i+1}_{s,i} = T^{i}_{s,i} - (h_{fg}\Delta\dot{M}_{deh})/(c_{p,sol}\dot{m}_{sol}) \quad (4)$$

3.2. Liquid desiccant

The temperature and concentration of the liquid desiccant at each point (i.e., inlet and outlet conditions at the absorber and regenerator) were calculated by using the empirical models predicting the dehumidification/regeneration effectivenesses the absorber and regenerator.

The first model for the dehumidification effectiveness of the absorber ($\varepsilon_{abs,m}$) was derived by Chung and Luo [10]. As shown in Equation 5, this model was derived for the packed-bed type liquid desiccant dehumidifier using the seven variables – the inlet temperature of air ($T_{abs,i,a}$), inlet partial water vapor pressure of air ($p_{v,abs,i,a}$), inlet temperature of desiccant solution ($T_{abs,i,s}$), inlet partial water vapor pressure of solution

($p_{v,abs,i,s}$), mass flow rate of air ($\dot{m}_{abs,a}$), and mass flow rate of solution ($\dot{m}_{abs,s}$), and packing specific surface area (aZ). Based on the existing literature, it was assumed that the heat exchange effectiveness of the absorber ($\varepsilon_{abs,T}$) between the air and solution was similar to the dehumidification effectiveness [11].

$$\varepsilon_{abs,m} = \left(1 - \frac{0.024\cdot\left(\frac{\dot{m}_{sa}}{\dot{m}_{abs,i,s}}\right)^{0.6}\cdot exp\left(1.057\cdot\frac{T_{abs,i,a}}{T_{abs,i,s}}\right)}{(aZ)^{-0.185}\cdot\left(\frac{p_{v,abs,i,a}-p_{v,abs,i,s}}{p_{v,abs,i,a}}\right)^{0.638}}\right)\Bigg/\left(1 - \frac{0.192\cdot exp\left(0.615\cdot\frac{T_{abs,i,a}}{T_{abs,i,s}}\right)}{\left(\frac{p_{v,abs,i,a}-p_{v,abs,i,s}}{p_{v,abs,i,a}}\right)^{-21.498}}\right) = \frac{\omega_{abs,i,a}-\omega_{abs,o,a}}{\omega_{abs,i,a}-\omega_{abs,eq,s}} \quad (5)$$

$$\varepsilon_{abs,T} = \frac{T_{abs,i,a}-T_{abs,o,a}}{T_{abs,i,a}-T_{abs,i,s}} \quad (6)$$

As for the empirical model of the regenerator, the model established by the Martin and Goswami [12] was used in this study (Equation 7). As shown in Equation 8, the regeneration effectiveness ($\varepsilon_{reg,\mathrm{m}}$) is predicted by using five parameters – enthalpy of inlet air ($\mathrm{h}_{reg,i,a}$), enthalpy of inlet desiccant solution, mass flow rate of air ($\dot{m}_{reg,a}$), and mass flow rate of solution ($\dot{m}_{reg,s}$), and packing specific surface area (aZ). Identical to the absorber, the thermal effectiveness of regenerator was assumed to be similar to the regeneration effectiveness.

$$\varepsilon_{reg,m} = 1 - 48.3\left(\frac{\dot{m}_{reg,a}}{\dot{m}_{reg,s}}\right)^{(0.396(\gamma_L/\gamma_c)-1.57)}\left(\frac{h_{reg,i,a}}{h_{reg,i,s}}\right)^{-0.751}(aZ)^{(0.0331(\gamma_L/\gamma_c)-0.906)} = \frac{\omega_{reg,o,a}-\omega_{reg,i,a}}{\omega_{reg,i,s}-\omega_{reg,i,a}} \quad (7)$$

$$\varepsilon_{reg,T} = \frac{T_{reg,o,a}-T_{reg,i,a}}{T_{reg,eq,a}-T_{reg,i,a}} \quad (8)$$

The equilibrium humidity ratio of desiccant solution, which determines the ideal maximum humidity ratio variance between the process air and the desiccant solution, was obtained by Equation (9).

$$\omega_{eq,s} = 0.622\cdot\frac{p_{v,s}}{101.325-p_{v,s}} \quad (9)$$

4. Results

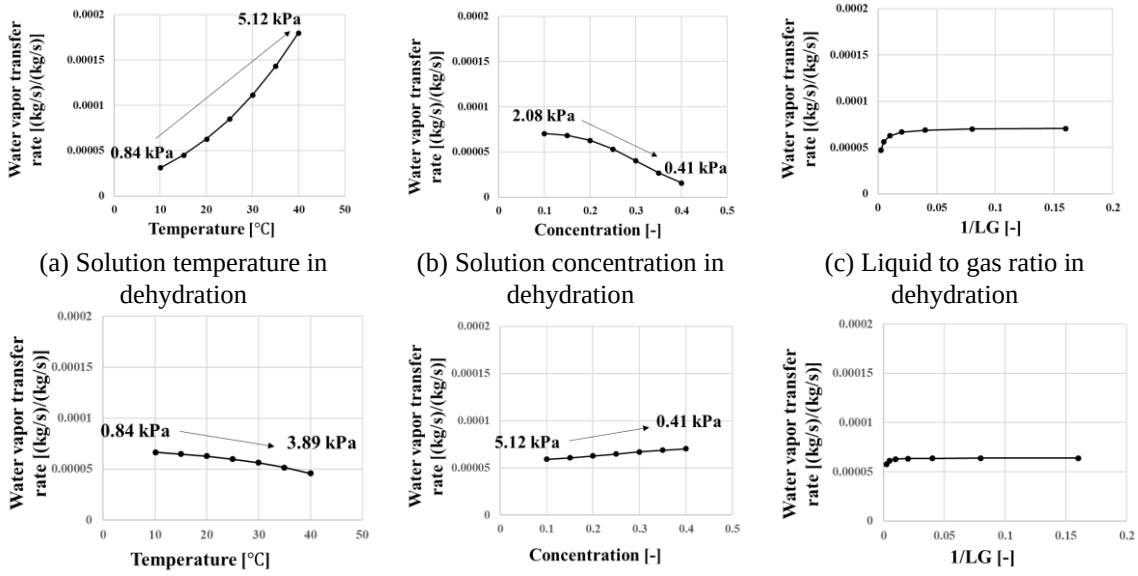
4.1. Parametric analysis of the separation membrane: mass transfer of the water vapor

In order to estimate the dehumidification performance of dehydration and hydration of the membrane, the effect of mass transfer was evaluated by varying the desiccant solution conditions. Parametric analysis was performed by solution temperature, solution concentration, and liquid to gas ratio in the dehydration and the hydration side. The base case of the solution in the dehydration and the hydration side set to 20 °C, 20%, and 0.01 of liquid to gas ratio. The compression ratio of the vacuum compressor was set to 10. Range of each parameter was set 10 °C to 40 °C (temperature), 10% to 40% (concentration), and 0.0025 to 0.16 (liquid to gas ratio).

In the Figure 5 (a) to (c), as the dehydration solution changes, the solution temperature and concentration have the greatest effect. As the temperature of the solution increases and the concentration of the solution decreases, the partial pressure of water vapor in the solution increases. As the temperature changes, the partial pressure of water vapor in the steam solution rises from 0.84 kPa to 5.12 kPa, and as the concentration changes, the partial pressure of water vapor decreases from 2.08 kPa to 0.41 kPa. Therefore, it can be confirmed that the mass transfer increases as the driving force between the membranes increases.

In the Figure 5 (d) to (f), the solution temperature and concentration have the greatest effect as solution changes in the hydration membrane. When the water vapor partial pressure of the solution increases, the water vapor partial pressure difference (driving force) between the membranes decreases, and thus the overall mass transfer of the proposed system decreases. As the temperature changes, the partial pressure of water vapor in the steam solution rises from 0.84 kPa to 3.89 kPa, and as the concentration changes, the partial pressure of water vapor decreases from 5.12 kPa to 0.41 kPa. The effect of solution of hydration was lower than that of

solution of dehydration, which shows that the effect of water permeation in hydration is greater than the effect of water permeation of dehydration.



(a) Solution temperature in dehydration

(b) Solution concentration in dehydration

(c) Liquid to gas ratio in dehydration

(d) Solution temperature in hydration

(e) Solution concentration in hydration

(f) Liquid to gas ratio in hydration

Fig. 5. Effect of water vapor transfer rate

4.2. Performance evaluation: COP

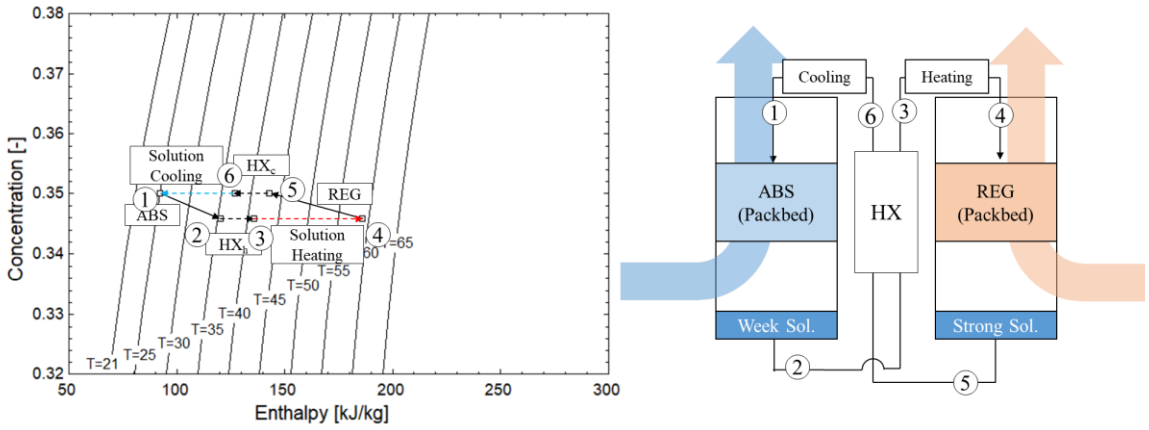
For the performance evaluation of the proposed system, the thermodynamic changes of the existing system, heat demand and solution were confirmed. (Figure 6) The design air condition of the absorber and regeneration was set to 32 °C and 60%, and LG was assumed to be 1. The solutions of the reference system were 25 °C and 35% (Absorber) and 58 °C and 34.5% (Regeneration) respectively, and the proposed system reference system solutions were 25 °C and 35% (Absorber) and 63 °C and 33.5% (Regeneration) respectively.

As shown in Equation 10, in the reference system, the enthalpy change of the absorber was 27.96 kJ/kg (120.2 kJ/kg to 92.24 kJ/kg), and the enthalpy change of heating and cooling was 54.7 kJ/kg and 36.66 kJ/kg, respectively. The COP of the reference system is 0.3.

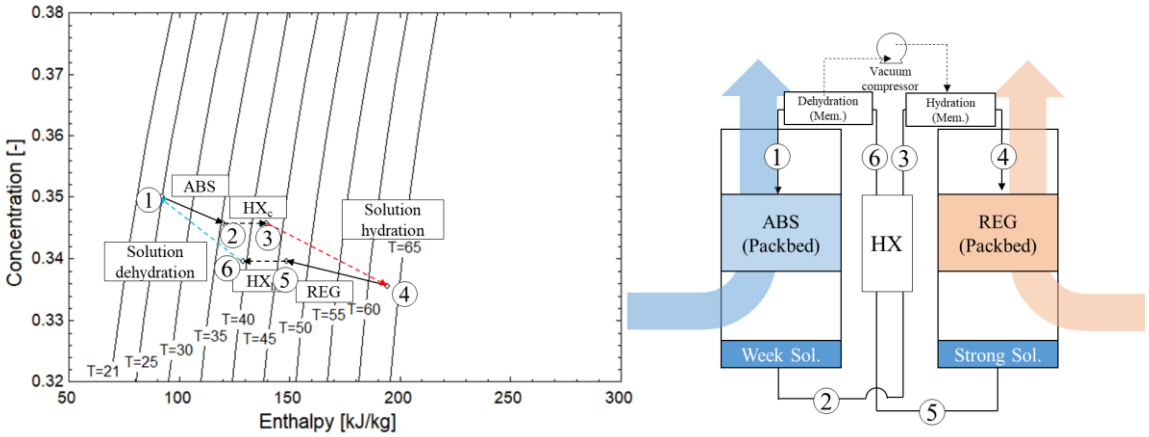
On the other hand, in the proposed system, the absorber's enthalpy change was 27.96 kJ/kg (120.2 kJ/kg to 92.24 kJ/kg) as in the reference system. As shown in Equation 11, The power of the vacuum pump can be expressed as the enthalpy change of hydration and the enthalpy change of dehydration, and was 54.7 kJ/kg (hydration) and 36.66 kJ/kg, respectively. Therefore, the power of the vacuum pump at unit mass flow rate (1 kg/s) is 18.04 kW/(kg/s). The COP of the proposed system is 1.55. The results showed that the ideal COP (coefficient of performance) of the proposed system in the thermodynamic analysis is 5.17 higher than that of the conventional system.

$$COP_{Ref} = \frac{Q_{a,c}}{Q_{h,s}+Q_{c,s}} \tag{10}$$

$$COP_{Ref} = \frac{Q_{a,c}}{P_{vac}} = \frac{Q_{a,c}}{Q_{Hyd}-Q_{dehyd}} \tag{11}$$



(a) Reference system



(a) Proposed system

Fig. 6. Thermodynamic characteristic of desiccant solution in the systems

5. Conclusion

In this research, a membrane-based liquid desiccant air conditioning system, which is a vapor transportation driven system with gas separation membrane technology, was proposed and its thermodynamic performance (dehumidification and energy performance) evaluated by equation-based simulation.

The parametric study of the proposed system for dehumidification performance (mass transfer) showed that the solution temperature and concentration is mainly affected as driving force. Especially, the mass transfer of the dehydration membrane side is more affected than that of the hydration membrane side on dehumidification performance. The vacuum compressor operated to separate the water vapor from the solution and then transport the separated vapor to the membranes. The results showed that the ideal COP (coefficient of performance) of the proposed system in the thermodynamic analysis is 1.55, which is 5.17 higher than that of the conventional liquid desiccant (heat driven dehumidification and regeneration system), which is 0.3 COP at the design air condition. This study demonstrates the thermodynamic analysis of the proposed system in simple principles. In further studies, we will construct a prototype unit of proposed system, and experimentally analyze the effect of thermodynamic and energy performance of the proposed system.

Acknowledgements

This work was supported by the National Research Foundation of Korea(NRF) grant funded by the Korea government(MSIT) (No. 2022R1A2B5B02001975 and No. 2022R1A4A1026503) and Korea Environment Industry & Technology Institute (KEITI) through Prospective green technology innovation project, funded by Korea Ministry of Environment (MOE) (RE202103243).

References

[1] Winkler J, Munk J, Woods J. Effect of occupant behavior and air-conditioner controls on humidity in typical and high-efficiency homes. Energy Build 2018;165:364–378.
[2] Wang RZ, Yu X, Ge TS, Li TX. The present and future of residential refrigeration, power generation and energy storage. Appl Therm Eng 2013;53:256–270.
[3] Daou K, Wang RZ, Xia ZZ. Desiccant cooling air conditioning: A review. Renew Sustain Energy Rev 2016;10:55–77.
[4] Rafique MM, Gandhidasan P, Bahaidarah HMS. Liquid desiccant materials and dehumidifiers - A review. Renew Sustain Energy Rev 2016; 56:179–195.
[5] Nóbrega CEL, Brum NCL. Desiccant-Assisted Cooling: Fundamentals and Applications, Springer; 2013.
[6] Park JY, Kim BJ, Yoon SY, Byon YS, Jeong JW. Experimental analysis of dehumidification performance of an evaporative cooling-assisted internally cooled liquid desiccant dehumidifier. Applied Energy 2019;235:177-185.
[7] Yin Y, Zhang X. Comparative study on internally heated and adiabatic regenerators in liquid desiccant air conditioning system. Build Environ 2010;45:1799–807.
[8] Caliskan H, Hong H, Jang JK. Thermodynamic assessments of the novel cascade air cooling system including solar heating and desiccant cooling units. Energy Conversion and Management 2019;199:112013.
[9] Angrisani G, Roselli C, Sasso M, Tariello F. Dynamic performance assessment of a solar-assisted desiccant-based air handling unit in two Italian cities. Energy Conversion and Management 2016;113:538–550
[10] Chung TW, Luo CM. Vapor pressures of the aqueous desiccants. J Chem Eng Data 1999;44:1024–1027.
[11] Katejanekarn T, Kumar S. Performance of a solar-regenerated liquid desiccant ventilation pre-conditioning system. Energy Build 2008;40:1252–1267.
[12] Martin V, Goswami DY. Effectiveness of heat and mass transfer processes ina packed bed liquid desiccant dehumidifier/regenerator. HVAC&R Research 2000;6(1):21–39.

14th IEA Heat Pump Conference
15-18 May 2023, Chicago, Illinois

Heat pumps in existing heating and hot water systems: an evaluation of primary energy savings and reduction of CO_2 produced

Alberta Carella[a,*], Luca Del Ferraro[b], Annunziata D'Orazio[a]

[a]Dipartimento di Ingegneria Astronautica, Elettrica ed Energetica, Sapienza Università di Roma, Via Eudossiana 18, Rome, 00184, Italy
[b]Daikin Applied Europe S.p.A., Via Piani di S.Maria 72, Ariccia, 00072, Italy

Abstract

In a previous work we recorded a significant contribution to urban air pollution attributable to heating systems powered by fuel. Thus, we propose the replacement of existing boilers for heating and domestic hot water (DHW) production systems with high temperature air-to-water heat pumps as an intervention to improve urban air quality and energy use. We analyze replacement scenarios within the entire residential building stock of two Italian cities, Milan and Salerno, belonging to different climate zones and with their own thermophysical characteristics.
For each of them, the consequences of the replacement intervention in terms of primary energy savings and lower CO_2 production are evaluated.
The results show a reduction of primary energy consumption by 34% in Milan and 43% in Salerno, and of CO_2 production by 30% in Milan and 39% in Salerno.

© HPC2023.
Selection and/or peer-review under the responsibility of the organizers of the 14th IEA Heat Pump Conference 2023.

Keywords: Urban air quality; Heat pumps; Primary energy; CO_2 emissions.

1. Introduction

In a previous work [1], a significant contribution to urban air pollution, related to fuel-fired heating systems, was recorded. Based on an analysis of the heating and domestic hot water (DHW) requirements of the residential building stock of two different Italian cities and the installed thermal systems, we propose to replace these systems with high temperature air-to-water heat pump systems of a suitable size that can supply the existing radiator systems.

The proposed measure is studied for two different Italian cities, Milan and Salerno, characterised by different outdoor air temperatures and with different thermophysical characteristics of the building stock.

In particular, replacement scenarios are analysed in the case of an outdoor temperature equal to the design temperature and for heat pump power generation equal to the current mix.

The evaluation of the intervention, while considering some approximations and working hypotheses, confirms to varying degrees for both cities a substantial reduction in both primary energy and CO_2 production needs, thanks to the highest generation efficiencies obtainable in the large thermoelectric power plants and the abatement systems present there.

Finally, it can be minimally invasive for citizens (since the existing radiator systems are not modified) to reduce air pollution in the long term, since it implies a significant decrease of emissions of pollutants in urban areas, with reduced energy (and, therefore, environmental) costs, towards environmentally sustainable cities.

* Corresponding author. Tel.: +39 3347684769
E-mail address: alberta.carella@uniroma1.it

2. Materials and methods

2.1. Climatic characterization

Two Italian cities were considered, belonging to two different climate zones according to national legislation. Milan, in Lombardy, located in the north-west of the Italian peninsula and characterised by an external design temperature [2] of -5 °C, and Salerno, a city in central-southern Italy facing the Tyrrhenian Sea and having an external design temperature of 2 °C.

2.2. Characterization of building stocks

According to ISTAT [3], Milan is outlined as a city made up of approximately 70% of buildings constructed between 1919 and 1970. Only 5% of the buildings were built after 1990. Most (66%) are four and more storeys above ground, while only 7% are one storey. This is confirmed by the fact that more than half of them (55%) have more than eight interiors.

Although less evident also in Salerno, the majority (55%) of residential buildings were built between 1919 and 1970. Only 7.5 % of the buildings were built after 1990. Most (46%) are 2 or 3 storeys above ground with 37% consisting of 1 or 2 interiors.

In order to characterise the building stock of the city of Milan from an energy point of view, the CENED +1.2 database [4] of the Lombardy Region was taken into consideration, which contains information useful for drawing up energy certificates.

From the database it was possible to obtain the average values of the thermal transmittances of the dwellings in the Municipality of Milan for each period of construction. Figure 1 shows the trend of the thermal transmittances of the windows and vertical opaque envelope, the basement and the roof.

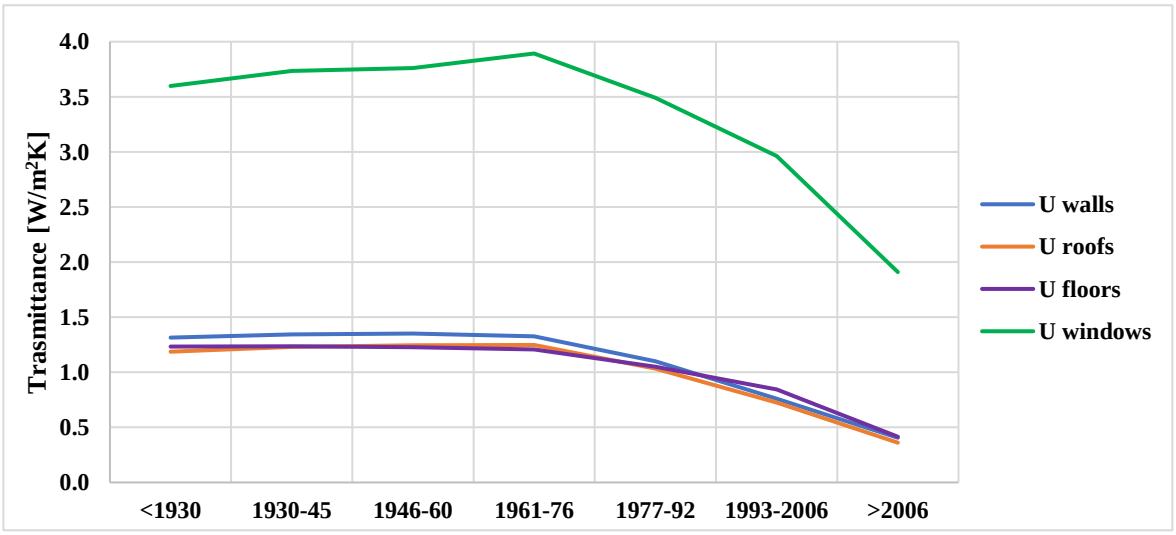


Fig. 1. Trend of the average thermal transmittances of the walls, floors, roofs and windows of the average flat in Milan by age of construction

It can be seen that up to 1976 the average thermal transmittance of all components remained fairly constant and then decreased, probably due to the approval of Law 373 of 1976 on energy efficiency and Law 10 of 1991.

The energy analysis for private buildings carried out in the Municipal Energy Plan of the Municipality of Salerno [5] shows the trend of average thermal transmittances of opaque components and windows shown in Figure 2.

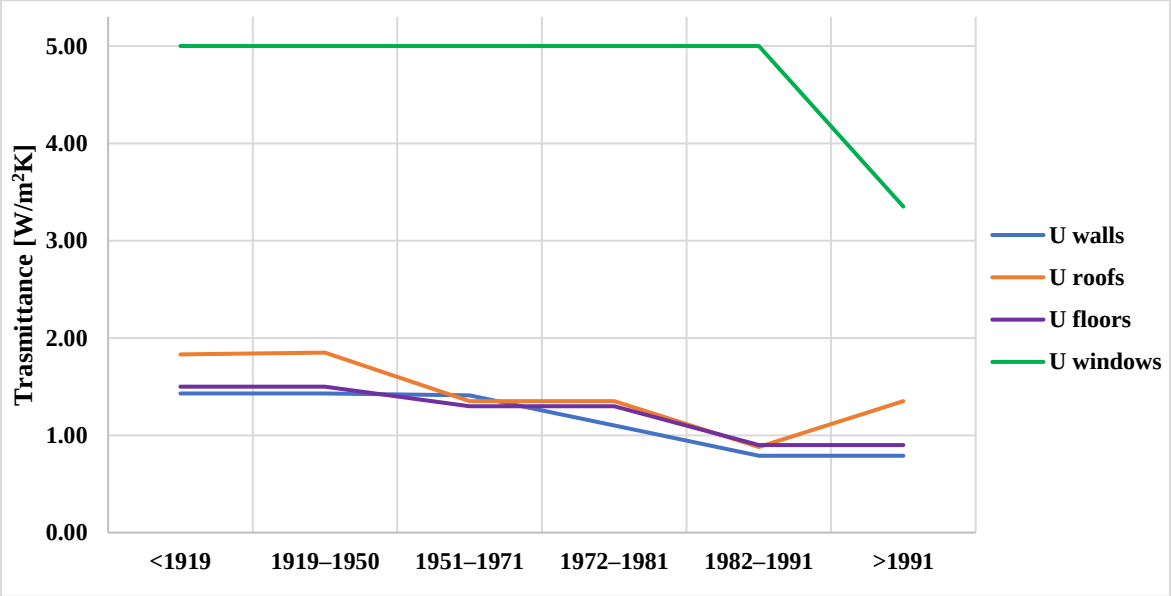


Fig. 2. Trend of the average thermal transmittances of the walls, floors, roofs and windows of the average flat in Salerno by age of construction (data from [5])

It can be seen that up to the 1970s, the average thermal transmittance of all components remained fairly constant, but then decreased, again due to the passing of Law 373 of 1976 on energy efficiency and Law 10 of 1991. In the case of roofs, on the other hand, an anomalous increase was noted for the data available in [5].

2.3. Thermal energy needs associated with building stocks

In order to evaluate the average thermal requirements for heating associated with the flats in the Municipality of Milan, from the entire CENED +1.2 database the certificates of dwellings with destination of use E.1(1) [D.P.R. 412/93] were taken into consideration, dwellings used as residences with a continuous character, relative to a single sub-terrain, so as to exclude those referring to entire blocks of flats.

For simplicity's sake, it was decided to consider only the inter-floor building units, identifiable in the database as those without a numerical transmittance value of the basement and roof, indicating the absence of these dispersing elements.

From the values of the transmittances and the dispersing surfaces, the heat requirement for heating was thus calculated, assumed as a first approximation to be equal to the heat dispersion by transmission through the vertical opaque envelope and windows.

The simplified calculation of the heating heat requirement was carried out in line with what was adopted by UNI TS 11300-1-2:2014 [6], by summing the monthly heating needs, relative to the period of the winter season, for twenty-four hours per day.

An internal temperature t_i of 20°C was assumed and an external temperature equal to the monthly average value of the daily average external temperature, obtained from UNI 10349:1994 [7].

The calculation was applied to all the certificates present in the Cened +1.2 database, from which the average characteristic values of relative to each period of construction shown in the Table 1 were then obtained.

The thermal energy requirements for domestic hot water Q_w were obtained according to UNI TS 11300-1-2:2014 [6], considering a 24-hour daily use period extended to the entire year (1).

$$Q_w = \rho_w \times c_w \times V_w \times (\theta_{er} - \theta_0) \times G \quad (1)$$

Where:

ρ_w is the density of the water, which is approximately 1000 [kg/m^3];
c_w is the specific heat of water equal to 1,162 [Wh/kgK];
V_w is the volume of water required during the calculation period [m^3];
θ_{er} is the hot water supply temperature [°C];
θ_0 is the cold water inlet temperature [°C];
G the number of days in the calculation period considered [d].

The domestic hot water supply temperature θ_{er} is assumed to be 40°C and the cold water inlet temperature θ_0 is assumed to be equal to the annual average of the monthly average outside air temperatures taken from UNI 10349. The required volumes of water V_w are obtained according to table 30, reported in [6] as a function of the useful surface area of the dwelling, which is present as data in the Cened +1.2 certificates.

The formula was applied to all the certificates present in the Cened +1.2 database, from which the average characteristic values for each period of construction were then derived. The results are shown in the Table 1.

In order to represent and compare the data of the two different cities, coming from two different databases with different periodization, it was decided to use the subdivision of construction periods adopted by ISTAT. The average values of thermal needs related to the time periods of the ISTAT database were obtained by taking into account the degrees of temporal overlapping between the two periodization systems and using them as weights for the computation of the weighted average.

Table 1. Thermal energy requirements for winter heating and DHW production per year of construction CY for the city of Milan; Portion of the buildings stock %BS.

CY	%BS	Thermal energy needs kWh$_t$ / year for the city of Milan		
		Heating	DHW	Heating and DHW
<1918	8,8%	7744	1140	8883
1919-45	16,3%	7733	1130	8863
1946-60	25,0%	7933	1151	9084
1961-70	28,1%	8709	1209	9919
1971-80	11,2%	8564	1233	9797
1981-90	4,2%	8346	1269	9615
>1991	6,3%	5791	1159	6950

The results show higher thermal needs associated with the average intermediate flats after the 1960s, probably associated with higher average transmittance by windows and walls together with higher dispersing surfaces.

In order to evaluate the average heating requirements associated with the flats in the Municipality of Salerno, the dispersing surfaces were first obtained.

In particular, reference was made to Annexes A and B of the Salerno Municipal Energy Plan, where the recurring architectural types in the building stock are represented.

These are shown in succession, according to the number of floors above ground and the number of interiors present. From the diagrams shown it was possible to deduce the net floor area and the lateral area of the buildings.

From Annex D, on the other hand, the values of the net heights, the surfaces of the walls and the windows, and the surfaces dispersing towards the stairwell were obtained. The latter ones were subtracted from the lateral surfaces to obtain the side opaque surfaces.

From each building typology reported, characterised by a certain number of floors and interiors, the individual flats of which each building typology is composed were approximated, focusing attention, as in Milan, on the inter-floor building units. Their characteristic dimensions correspond to a weighted average of the various inter-floor flat sizes available in the building stock.

Once the heating requirements for each of them had been calculated, a weighted average was made on the basis of ISTAT data on the number of buildings by number of interiors and above ground floors, in order to obtain a representative average value for each period of construction. Table 2 shows the results obtained in summary.

Similarly for Milan, thermal energy requirements for domestic hot water were then calculated according to UNI TS 11300-1-2:2014 [6] and reported in Table 2.

For Salerno, the division of construction epochs adopted by ISTAT was also used.

Table 2. Thermal energy requirements for winter heating and DHW production per year of construction CY for the city of Salerno; Portion of the buildings stock %BS

CY	%BS	Thermal energy needs kWh_t / year for the city of Salerno		
		Heating	DHW	Heating and DHW
<1918	8,1%	4778	1239	6017
1919-45	9,8%	4782	1239	6022
1946-60	24,1%	4205	1375	5580
1961-70	31,4%	3916	1443	5359
1971-80	12,9%	3304	1443	4746
1981-90	9,4%	2774	1443	4217
>1991	4,3%	2525	1443	3968

From the data obtained, a progressive decrease in thermal requirements could be observed as the years progressed.

2.4. Heating systems fleet

According to the ISTAT census of 2011 on the type of fuel or energy source that fuels the heating system of homes in the Municipality of Milan [8], methane gas is the most widely used source (81.92%), followed by diesel (12.12%) and electricity (3.10%).

The percentage of homes using solid fuel such as wood or coal (0.47%), LPG (0.57%), fuel oil (0.15%) or other types of fuel or energy is lower.

According to the "Catasto Unico Regionale degli Impianti Termici", the regional register of the thermal plants, (CURIT) [9], the number of heating systems in the Municipality of Milan is composed of approximately 153.000 autonomous systems with a capacity of less than 35 kW and 27.000 centralised systems with a capacity of more than 35 kW and typically serving more than one property unit.

According to the 2011 ISTAT census on the type of fuel or energy source that fuels the heating system of homes in the Province of Salerno [8], the most used source (53.88%) is methane, followed by solid fuel such as wood or coal (24.92%) and LPG (10.29%).

The percentage of dwellings using electricity (6.64%), diesel (2.14%), fuel oil (0.07%) or other types of fuel or energy is lower.

The census on the number of dwellings equipped with a heating system [10] shows that there are approximately 38.000 autonomous and 3.000 centralised heating systems in the municipality of Salerno.

With regard to the combustion efficiency for winter air conditioning of the systems present in the Municipality of Milan, CURIT deduces an average value of 0.9.

In order to calculate the average global efficiency, the tables contained in UNI TS 11300-2 of 2014 [6] are used to estimate the distribution, regulation and emission efficiency values, assumed to be 0.98, 0.95 and 0.94 respectively. The average global efficiency value obtained from the product of the four efficiencies is 0.8.

From the 2014 UNI TS 11300-2 prospectuses [6], the average global efficiency of the generator for the production of domestic hot water is also estimated at 0.7, obtained from the product of the efficiencies of generation equal to 0.8, supply equal to 1, and distribution equal to 0.9.

Since we do not have data on the efficiency of the thermal plants in the Municipality of Salerno, we assume the same efficiency value for winter air conditioning equal to 0.8 and for the production of domestic hot water equal to 0.7. As in the case of the Municipality of Milan, Salerno's thermal plants are mainly made up of autonomous plants (over 90%) that use methane gas as their main fuel.

2.5. Heat pumps identified in the proposal

Considering the scenario of replacing the entire thermal systems of the two cities with high-temperature air-water heat pumps, the nominal capacities are evaluated.

Considering a configuration based on the logic of prioritizing DHW production overheating, and since the two thermal needs are never satisfied simultaneously, the sizing is carried out on the basis of the thermal load for winter heating.

In particular, for both cities, from the values of the transmittances and the dispersing surfaces, the winter heat load NP at the external design temperature was calculated, assumed as a first approximation equal to the heat dispersion by transmission through the vertical opaque envelope and the windows, as follows:

$$NP = (H_o \times S_o + H_w \times S_w) \times (t_i - t_p) \quad (2)$$

Where H_o and S_o are respectively the transmittance and the dispersing surface of opaque walls, H_w and S_w the transmittance and the dispersing surface of windows, t_i the desired internal temperature equal to 20°C, t_p the design external temperature, equal to -5°C for Milan and +2 for Salerno. Tables 3 and 4 show the nominal powers NP of the heat pumps (HPs) at the design external temperature by year of construction.

In particular, air-water heat pumps are considered to be those that can work with radiators, the most common terminals in the existing building stock, and are therefore capable of producing flow water at a temperature of 70°C or higher.

The compressor of the HPs selected is a scroll type with inverter capacity control and economizers to increase the efficiency of the system. The refrigerant they use is R32, which offers a low global warming potential (GWP) compared to standard refrigerants and ensures higher energy efficiency and lower CO_2 emissions.

The size of the machine was chosen in line with the commercial state of the art from a manufacturer's catalogue considering an outside temperature not higher than the design outside temperature and closer to this.

In order to ensure operation at high temperature, an oversizing choice is made with respect to the required heat output. The analysis carried out was related to full load performance at design conditions. The real working conditions imply different values of outdoor temperature during the heating season, with favorable consequences for HP performance, as a result of a direct thermodynamic effect and reduced heat losses from machines (with inverter) operating under partial load conditions. The present study concerned, thus, the worst-case scenario.

The plate power (PP) values of the selected heat pumps, obtained from the manufacturers' catalogues as the heating capacity at the design outdoor temperature and outlet water temperature of 70°C, are shown in Tables 3 and 4 for each requirement.

The COP of the selected HP is provided by the manufacturer as the ratio between the heating capacity and the electrical power input; the heating capacity is defined as the integrated power between the power for heating and the power used between the start of one defrosting cycle and the start of the next, also provided by the manufacturer for a value of outside air temperature and a value of water supply temperature.

To derive the COP at design conditions, if not present in the values declared by the manufacturer (as in the case of Milan with an external design temperature of -5), proceed according to UNI EN 14825 [11].

Specifically, with the same outlet water flow temperature, if the design outdoor air temperature is within the range of values provided by the manufacturer, the COP is calculated by linear interpolation of the second principle efficiency values η_{II}, calculated on the basis of the known data. If the outdoor air temperature is outside the range of values provided by the manufacturer, but within a maximum deviation of 5 K, the efficiencies η_{II} calculated on the basis of the nearest possible known data can be extrapolated (i.e. η_{II} is considered to remain constant up to a temperature difference of 5 K). The second-principle efficiency η_{II} is defined for electric heat pumps as the ratio of equation (3) between the actual efficiency of the heat pump declared by the manufacturer (COP) and the theoretically achievable maximum efficiency (theoretical maximum COP_{max}).

$$\eta_{II} = \frac{COP}{COP_{max}} = COP \frac{t_h - t_c}{t_h + 273{,}15} \quad (3)$$

where t_h is the outlet water temperature (at the condenser) and t_c is the cold source temperature (at the evaporator). The COP value at conditions x is therefore obtained by the efficiency ηII interpolated to conditions x as in equation (4).

$$COP_x = \eta_{II,x} \frac{t_h+273,15}{t_h-t_{c,x}} \quad (4)$$

Since the COP values for the desired value of the design external temperature of Milan (−5 ◦C) were not available from the manufacturer, we proceeded by analogy with the interpolation of the second principle efficiencies of the known data.

Table 3 for Milan and 4 for Salerno show, for each selected HP and by year of construction of the buildings, the calculated COP values referring to the desired delivery water temperature (70°C), as it is reiterated that the current radiators are to be left as terminals, and to the external temperature of -5°C (Milan) and +2°C (Salerno).

Table 3. Nominal (NP) and plate powers (PP) and COP of the HP required for the design value of the external temperature of Milan (-5 ◦C) , per year of construction CY (outlet water temperature 70 ◦C); portion of the buildings stock %BS.

CY	%BS	NP kW	PP kW	COP (-5°C,70°C)
<1918	8,8%	3,35	8,73	1,78
1919-45	16,3%	3,34	8,73	1,78
1946-60	25,0%	3,43	8,73	1,78
1961-70	28,1%	3,76	8,73	1,78
1971-80	11,2%	3,70	8,73	1,78
1981-90	4,2%	3,61	8,73	1,78
>1991	6,3%	2,50	8,73	1,78

Table 4. Nominal (NP) and plate powers (PP) and COP of the HP required for the design value of the external temperature of Salerno (2 ◦C), per year of construction CY (outlet water temperature 70 ◦C); portion of the buildings stock %BS.

CY	%BS	NP kW	PP kW	COP (2°C,70°C)
<1918	8,1%	3,40	9,13	2,00
1919-45	9,8%	3,41	9,13	2,00
1946-60	24,1%	3,03	9,13	2,00
1961-70	31,4%	2,85	9,13	2,00
1971-80	12,9%	2,68	9,13	2,00
1981-90	9,4%	2,53	9,13	2,00
>1991	4,3%	2,46	9,13	2,00

2.6. Impact of replacement interventions

In order to assess the overall impact, in terms of primary energy consumed, tonnes of CO_2 produced and pollutants emitted, that replacing the boilers currently most used in homes in Milan and Salerno with HPs would entail, the 153.000 autonomous systems with a power output of less than 35 kW and the approximately 27.000 centralised systems are considered for the Municipality of Milan.

The latter, considering a condominium composed of an average of 12 flats, are considered equivalent to 324.000 autonomous systems. Therefore, 480.000 HPs are considered installed, with the characteristics described above, distributed in number as summarised in Table 7.

For the Municipality of Salerno, given the 38.000 autonomous systems and 3.000 centralised systems, considered as 36.000 autonomous systems, we have a total of 74.000 HPs installed, distributed as in Table 8.

In the following evaluations, the methane gas/primary energy conversion factor and the renewable electricity conversion ratio are considered unitary; the efficiency of the existing boilers is 0.8 for heating and 0.7 for DHW production, the distribution losses in the electricity grid are 10% [12][13]. Concerning electricity

generation, a 35% renewable fraction and a fuel fraction of 65% are considered, the latter mainly composed of natural gas (Terna source [12][13]). The fossil-to-electric conversion efficiency for 2021 is assumed equal to 48%. The COP considered is that relative to the external air temperature conditions of the project, -5 °C for Milan and +2 °C for Salerno.

The useful coefficient for the calculation of CO_2 emissions related to the consumption of methane used to fuel the boilers is found in the table of the UNFCCC national inventory of CO_2 emission coefficients [14] for which the result is 202.36 g CO_2 /kWh thermal. The coefficient useful for the calculation of CO_2 emissions related to the production of electricity used to fuel the boilers is found in the ISPRA report on emissions in the electricity sector [14] for which the result is 449.1 g CO_2 /kWh electricity for the current mix of fuels relative to the non-renewable fraction.

Tables 5 and 6 show, by building construction period, the thermal needs for heating and DHW production and the relative primary energy needs for the current boilers and for the selected HP for the current energy mix for the cities of Milan and Salerno.

Table 5. Total heat requirement and primary energy requirement for boilers (η_h**=0,8;** η_w**=0,7**) and for selected HPs, per year of construction CY of buildings of the city of Milan (generation fraction from renewable energies 35%, grid losses 10%, COP at design temperature of -5°C)

CY	Thermal Energy needs for heating and DHW production kWh_t/year	Primary energy requirement for single boiler kWh_t/year	Primary energy requirement for HP ($COP_{-5°C/70°C}$) from fossil fuels kWh_t/year
<1918	8883	11307	7434
1919-45	8863	11281	7417
1946-60	9084	11560	7602
1961-70	9919	12614	8300
1971-80	9797	12467	8199
1981-90	9615	12245	8046
>1991	6950	8894	5816

Table 6. Total heat requirement and primary energy requirement for boilers (η_h**=0,8;** η_w**=0,7**) and for selected HPs per year of construction CY of buildings of the city of Salerno (generation fraction from renewable energies 35%, grid losses 10%, COP at design temperature of 2°C)

CY	Thermal Energy needs for heating and DHW production kWh_t/year	Primary energy requirement for single boiler kWh_t/year	Primary energy requirement for HP ($COP_{2°C/70°C}$) from fossil fuels kWh_t/year
<1918	6017	7743	4482
1919-45	6022	7748	4485
1946-60	5580	7220	4156
1961-70	5359	6957	3991
1971-80	4746	6190	3535
1981-90	4217	5529	3141
>1991	3968	5218	2955

As expected, the heat requirements, and corresponding the primary energy requirements were significantly higher for the older buildings in Salerno.

In Milan, on the other hand, the thermal needs, and consequently in the primary energy needs, were higher if associated with the average intermediate flats built after the 1960s, probably due to the higher average transmittance values of windows and walls, together with higher dispersing surfaces.

Primary energy requirements when using HPs are always lower than those of boilers, both for Milan and Salerno and for all years of construction.

The overall primary energy consumption from fossil fuels, in the case of the current boilers and the proposed replacement HPs, are shown in Tables 7 and 8. Results are presented in terms of percentage ratio, between heat pumps and boilers, of global primary energy from fossil fuel and CO_2 production.

Table 7. Distribution by year of construction CY of the buildings of Milan of the 480.000 selected HPs, percentage ratio of global primary energy requirement from fossil fuel and CO_2 emissions of heat pumps to that of boilers (generation fraction from renewable energies 35%, grid losses 10%, COP at design temperature of −5 °C), portion of building stock %BS, nominal power NP.

CY	%BS	NP kW	Number of HPs	Global primary energy from fossil fuel HPs / global primary energy from fossil fuel boilers	CO_2 HPs / CO_2 boilers
<1918	8,8%	3,35	42328	66%	70%
1919-45	16,3%	3,34	78379	66%	70%
1946-60	25,0%	3,43	119867	66%	70%
1961-70	28,1%	3,76	134816	66%	70%
1971-80	11,2%	3,70	53821	66%	70%
1981-90	4,2%	3,61	20379	66%	70%
>1991	6,3%	2,50	30410	65%	70%
TOTAL			480000	66%	70%

Table 8. Distribution by year of construction CY of the buildings of Salerno of the 74.000 selected HPs, percentage ratio of global primary energy requirement from fossil fuel and CO_2 emissions of heat pumps to that of boilers; (generation fraction from renewable energies 35%, grid losses 10%, COP at design temperature of 2 °C), portion of building stock %BS, nominal power NP.

CY	%BS	NP kW	Number of HPs	Global primary energy from fossil fuel HPs / global primary energy from fossil fuel boilers	CO_2 HPs / CO_2 boilers
<1918	8,1%	3,40	6022	58%	62%
1919-45	9,8%	3,41	7255	58%	62%
1946-60	24,1%	3,03	17860	58%	61%
1961-70	31,4%	2,85	23226	57%	61%
1971-80	12,9%	2,68	9546	57%	61%
1981-90	9,4%	2,53	6934	57%	61%
>1991	4,3%	2,46	3158	57%	60%
TOTAL			74000	57%	61%

One can see that the percentage ratios, representative of the reduction in consumption and CO_2 production, were irrespective of the year of construction; this was due to the fact that the same machine, with a certain COP under design conditions, was selected to ensure operation at high temperatures (70 °C) with radiators.

The replacement of the entire boiler fleet, considering the external design conditions, implies a reduction in primary energy consumption of 34% for Milan and 43% for Salerno and a reduction in emissions of 30% for Milan and 39% for Salerno.

The greater reductions obtained in the case of the city of Salerno are probably associated with the more favourable external design temperature conditions for the use of HP, which assume higher COP values in those conditions.

3. Conclusions

Starting from the results obtained in a previous work [1] on the analysis of pollutant concentrations and from the identification of the weight of heating systems as an emissive source, the replacement of boilers in current heating and domestic hot water production systems with high temperature air/water heat pumps was proposed as an intervention to improve urban air quality.

The study was mainly dedicated to assessing whether the proposed replacement of the approximately 480.000 autonomous methane gas boilers for the city of Milan and 74.000 for the city of Salerno, all with the same efficiency of 80% for heating and 70% for the production of DHW, of which, to a first approximation, the entire thermal systems of the municipalities of Milan and Salerno can be considered to be made up,

implying a significant reduction in polluting emissions in the urban area, would on the other hand entail additional energy (and therefore environmental) costs. Replacing the current boilers would eliminate individual local emission sources, concentrating emissions at a thermal power plant, located in suburban areas, characterised by the highest generation efficiencies, equipped with pollutant abatement systems (sulphur oxides, nitrogen oxides, particulate matter, CO_2), with a discharge into the atmosphere at significant heights compared to those in urban areas.

The study demonstrated the validity of the proposal in terms of reducing primary energy needs and CO_2 emissions for the two different cities considered, in particular for an external temperature at design conditions and for electricity generation mixes that in the future will be modified in favour of increasing shares of renewable sources. The proposal analysed is also in line with the electrification targets set in recent years, essential to achieve the energy transition and aimed at a sustainable development model.

The results obtained are a useful indication for overall incentive measures, given the low invasiveness of the interventions for individual citizens, and cannot be considered a feasibility study of the individual intervention.

It should be remembered that the assumptions made (average efficiency of boilers) and selections performed (the machines) were a first approximation and, therefore, cannot be used for the evaluation of the individual intervention, which will also have to take into account the real overall dimensions (with on average little space available for old buildings, for which the use of centralised heat pump systems could be considered).

It is worth noted that full load operating condition at design temperature are not the most frequent. The real working conditions characterize by different external temperature and partial load performance imply greater advantage in terms of COP.

A more in-depth analysis will be carried out in a future work, to evaluate the behavior of the systems in real operating conditions. Future works will also investigate more favorable/unfavorable climatic conditions related to different Italian and European cities.

References

[1] Carella A.,D'Orazio A., The heat pumps for better air quality, Sustainable Cities and Society, 75 (2021) 103314
[2] UNI EN 12831, Design heat load calculation method, December 2006
[3] National Institute of Statistics. (2011). Residential buildings by age of construction- ISTAT Census 2011 (italian language) ISTAT, Edifici residenziali per epoca di costruzione.
http://dati-censimentopopolazione.istat.it.
[4] Cened Data, https://www.cened.it/opendata-cened-1.2
[5] Municipality of Salerno, University of Salerno, Municipal Energy Plan for the Municipality of Salerno (PEC), Energy Analysis for Private Buildings, Annexes A, B, C, D
http://www.dimec.unisa.it/PEC_Salerno/materiali.asp
[6] UNI TS 11300-2, Energy Performance of Buildings Part 2: Determination of the Primary Energy Needs and Yields for Winter Air Conditioning, For the Production of Sanitary Hot Water, For Ventilation and For Lighting in Non-Residential Buildings, October 2014
[7] UNI 10349:1994, Heating and cooling of buildings, climate data, (1994)
[8] National Institute of Statistics. (2011). Houses with heating system by type of fuel or energy supplying the heating system - ISTAT Census 2011 (italian language) ISTAT, Abitazioni con impianto di riscaldamento per tipo di combustibile o energia che alimenta l'impianto di riscaldamento.
http://dati-censimentopopolazione.istat.it.
[9] Curit, Catasto Unico Regionale degli Impianti Termici, https://www.curit.it/consulta-i-dati
[10] [National Institute of Statistics. (2011). Dwellings occupied by residents - Dwellings by availability of services- ISTAT Census 2011 (italian language) ISTAT, Abitazioni occupate da persone residenti - Abitazioni per disponibilità di servizi, http://dati-censimentopopolazione.istat.it.
[11] EN 14825:2018 Air conditioners, liquid chilling packages and heat pumps, with electrically driven compressors, for space heating and cooling - Testing and rating at part load conditions and calculation of seasonal performance - UNI EN 14825: 2019 Condizionatori d'aria, refrigeratori di liquido e pompe di calore, con compressore elettrico, per il riscaldamento e il raffrescamento degli ambienti - Metodi di prova e valutazione a carico parziale e calcolo del rendimento stagionale, Newark (2018).
[12] TERNA National Electricity Grid, production data (italian language), Rome (2021).
https://download.terna.it/terna/5%20-%20PRODUZIONE_8da7ab6394701ad.pdf
[13] TERNA National Electricity Grid, generation data (italian language), Rome (2021).

https://download.terna.it/terna/3%20-%20IMPIANTI%20DI%20GENERAZIONE_8da7ab6ef9ad0ea.pdf
[14] Caputo, A. Indicators of Efficiency and Decarbonisation of the National Energy System and the Electricity Sector, (Italian Language) Istituto Superiore per la Protezione e la Ricerca Ambientale ISPRA, Indicatori di Efficienza e Decarbonizzazione del Sistema Energetico Nazionale e del Settore Elettrico; Higher Institute for Environmental Protection and Research ISPRA: Rome, Italy, 2022; pp. 1–108.

14th IEA Heat Pump Conference
15-18 May 2023, Chicago, Illinois

High temperature test results and application cases of a Rotation Heat Pump

Andreas Längauer[a*], Bernhard Adler[a]

[a]ecop Technologies GmbH, Perfektastraße 73/Top A1, 1230 Vienna, Austria

Abstract

The environmentally friendly working fluid, based on noble gases like Helium, Argon and Krypton, is used in the counterclockwise Joule-cycle in a Rotation Heat Pump (RHP). Combined with centrifugal compression this leads to a very high Coefficient of Performance (COP) at high sink outlet temperatures compared to conventional compression heat pumps. Since the realized Joule-Cycle is based on an always gaseous working fluid, the heat transfer in the heat exchangers is sensible. Therefore, neither the issue of lubrication of the compressor nor the critical point of the working fluid limit the maximum sink output temperature. The data shown provides information about the electricity consumption, the flow temperatures and the heat output provided by the system. The results show that the prototype of the RHP K7 can achieve a COP >3.5 for sink outlet temperatures *higher* than *100 °C*. The correlations between the main rotor speed, temperature spread and thermal power are analyzed for the test run as well. Based on this, application cases in the industry and the field of energy services are presented and the advantages of the Rotation Heat Pump are described. Those are, for example, the high spread of sink and source when providing cooling and heating as well as the flexibility using one machine at different temperature levels. Further, an outlook for adaptions to realize sink outlet temperatures >150°C will be given.

© HPC2023.
Selection and/or peer-review under the responsibility of the organizers of the 14th IEA Heat Pump Conference 2023.

Keywords: Rotation Heat Pump, Test Results, High Temperature, Application Cases

Introduction

An enormous amount of energy is required in industry in the form of heat, De Boer et al [1]. In many cases, the temperature level is between 100 °C and 200 °C, Fleiter et al. [2], whereby the availability of heat pumps is limited, especially above 100 °C utilisation temperature. For this reason, many research projects and developments are being carried out with the aim of tapping this potential. Heat pumps are one of the key technologies in industrial applications and make a very large contribution to the reduction of CO2 emissions. By integrating them into different processes such as brick, food and feed drying, pasteurisation, distillation as well as chemical processes, the consumption of fossil fuels can be greatly reduced. The variety of applications, Schlosser et al [3], requires maximum flexibility of heat pumps as well as different technologies that can be used. The great potential of high temperature heat pumps in general and different implementation possibilities were described in Arpagaus et al [4], [5] and [6] as well as the currently still existing market barriers. Furthermore, the use of heat pumps in Austrian district heating networks is presented with examples in Arnitz [7] and the status quo and potentials of industrial heat pumps in Wilk et al [7]. Applications and potentials for industrial heat pumps in Switzerland are presented in Arpagaus et al [8]. Results of a propane-butane heat

* Corresponding author. Tel.: +43 -1-865-10-62-27
E-mail address: andreas.laengauer@ecop.at

pump for high temperature applications are shown in Bantle [9]. Further synthetic refrigerants with low global warming potential and heat pump cycles are analysed in [10].

Due to the design of conventional compression heat pumps (CHP) with the main components - compressor, condenser, evaporator and expansion valve - heat is in most cases transferred latently (i.e. by evaporation or condensation of a refrigerant). This means that comparatively high mass flows of the process media are necessary to scale up the performance if small temperature spreads between source inlet and outlet are to be achieved. Smaller spreads in conventional CHP are therefore to be aimed for, as this also keeps the temperature lift between condensation and evaporation low. The electrical power consumption of the compressor is reduced. The required compressor power has a direct effect on the COP (Coefficient of Performance).

The special characteristics and the design of the Rotation Heat Pump (RHP) make it possible to use heat pumps in new areas of application (hot air, steam, water) that have not been exploited so far.

Providing heat pumps for higher temperatures is very important and there has a lot of research been done in this area by different manufactures. Most of standard compressors in CHP are limited in terms of temperature by the working fluids and the lubrication. The RHP, using the Joule-cycle, is not limited by those factors for a temperature range >100°C. Based on previous publications, where the basic function, design, calculation methods and first test results of a Rotation Heat Pump have been published (Längauer et al., [11]), further tests are finished. Those are focused on higher temperatures at sink and source as well as showing how different parameters effect the Joule-Cycle in the RHP. Therefore, beside steady state conditions for sink and source also the start-up period and the shutdown process are explained. The test setup in terms of a scheme is described as well, which is essential to allow a comprehensible analyse of the test results. The aim is not to give a detailed calculation about COP including error estimations and tolerances but more to give an overview of the test procedure and how a certain measuring period looks like. Of course, detailed analyses are essential for accurate results when the COP is focused on. In this case tolerances of sensors are given but further calculations will not be implemented in this paper to keep the focus on temperature curves. The first part of the paper will give a short overview of the technology and references and further deal with this high temperature test of a RHP. After the results and discussion an outlook will be given for further tests. Also, the possibility to reach higher temperatures will be addressed and necessary changes will be given.

The Joule process implemented in the RHP realises a wide spread of both heat source and heat sink due to the sensitive heat transfer and is especially optimally suited for this purpose. In contrast to CHP, the temperature lift and the compressor capacity are decoupled from the spread. They can be controlled almost independently of each other. The COP therefore remains at a high level compared to the CHP, with a similar temperature range and a spread of up to 30 K. The strong cooling of the source offers the advantage of transferring very large heat outputs from the process water to the working fluid at lower mass flows. This means that not only the pipelines, but also other peripherals such as pumps, filters, etc. can be dimensioned much smaller. The high efficiency of RHP with large spreads brings great advantages in terms of costs and application in industrial processes with specified cooling or target temperatures (provision of cooling water).

The efficiency of heat pumps is usually compared using the COP at certain operating points. Together with other criteria, this is ultimately decisive for the final selection. As boundary conditions, often only the temperature at the inlet of the source and the temperature to be aimed for at the outlet of the sink are mentioned here. In combination with the thermal power and the mass flow, the other temperature levels are finally determined based on thermodynamics. If a fluid with a very high heat capacity flow is available as the source, it is of little or no relevance if the thermal power is primarily achieved via the mass flow. This could be the case, for example, when using river water, geothermal energy or similar heat sources. In many industrial processes, however, these mass flows are limited and thus thermal power must be seen as a product in which the temperature difference factor is much more important. This plays a major role in the dimensioning of heat pumps. It is therefore essential to consider the temperature spread of source and sink when designing and considering implementation options. Examples of this are various heating processes such as the provision of hot air, hot water or steam or air preheating for drying processes (e.g.: Wilk et al. [12]). A second part of this paper will discuss and show how the thermodynamic process is affected by having high spreads for sink and source in a CHP and RHP. For this purpose, a conventional HFO (Hydrofluoroolefine) refrigerant - R1336mzz(Z) with low GWP (Global Warming Potential) and the Joule process as implemented in the RHP with a noble gas mixture as working fluid are compared in an industrial process for distillation. Also, some more application cases will be shown and discussed where the temperature spread is essential and an advantage.

1. Main Principle

In the RHP, the counterclockwise Joule cycle is realised whereby the working medium used is always gaseous. The compression is realised by centrifugal forces, the pressure and the temperature increase outwards due to the rotation (approximately adiabatic compression). This principle was first presented in Adler [13] and further in Adler [14], [15]. Further descriptions, explanations and test results can be found in Adler and Mauthner [16], Längauer [11], [17]. Since the technology is worldwide patented and there is no other manufacturer providing it, only references by ecop can be given. Essential for the function is the centrifugal acceleration occurring due to the rotation, which causes the compression of the working gas. Thus, a very efficient compression can be realised, since the relative velocity of the working gas in the pipes is very small compared to the absolute velocities. Figure 1 schematically shows the Joule process in an RHP**.**

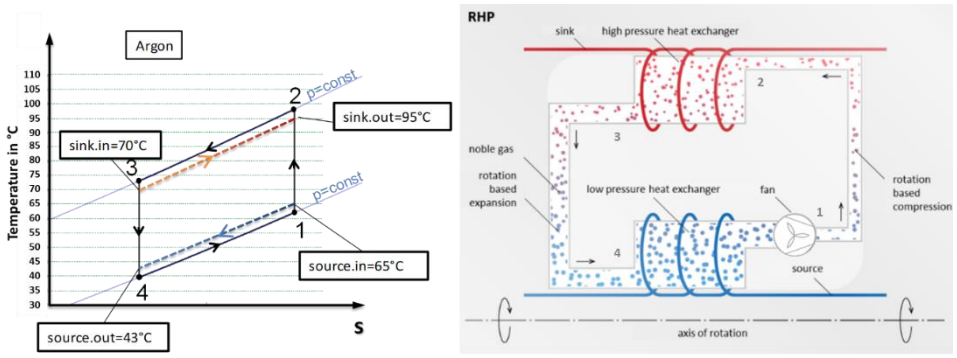


Figure 1: Schematic representation of the cycle process in an RHP [17]

2. High temperature test

2.1. Test setup

To test the performance of a RHP a test rig is used which is connected to the sink and source of the RHP. The two different circuits are each closed and mass flow is ensured by pumps. Temperatures are measured at the RHP as well as at the test rig where also the mass flow is captured. The electrical power consumption is measured via frequency converters which are used for controlling the rotational speed of the components as well. All sensors and components necessary are connected by a Bus-system with the programmable logic controller where the signals are postprocessed and the final value is stored in a file. Beside several sensors and pumps the test rig also includes heat exchangers which are used to recover heat during the test process. Much less energy than the thermal output at the sink has to be dissipated to the environment because of this arrangement. For steady state conditions the electrical power consumption of the fan and rotor, which are finally transformed to heat, have to be dissipated. Therefore, a separate circuit including two water-air heat exchangers with fans (Fan1, Fan2), is used. The following Figure 2 shows the RHP-K7 and the test rig during the test process.

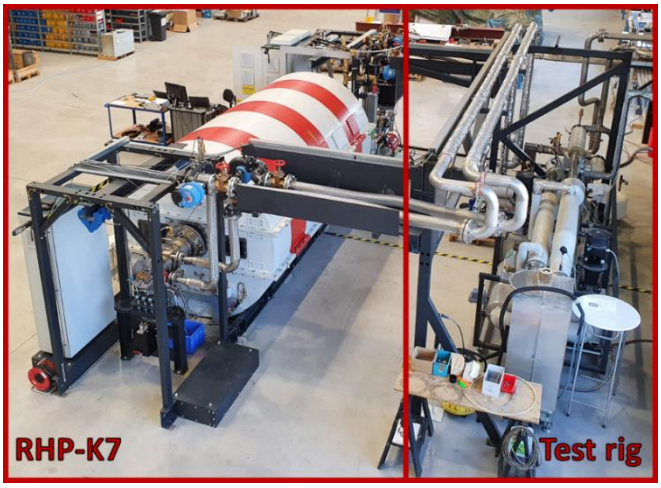


Figure 2: RHP-K7 and Test rig at production site

Essential components and sensors as wells as details about the measurement system and configuration are given in [11]. They will not be summed up here again. Also, the COP calculation is based on this publication, it should only be mentioned here, that for the COP the thermal power at the sink side and the electrical power consumption of the main rotor plus the fan engine are used.

2.2. Results and discussion

In the following section test results based on the test setup described above will be shown and discussed. Therefore, one day of testing is split in three sections which will each be illustrated in a quartet of diagrams. They will include measured values of temperatures (sink and source), electrical power consumption, mass flows, thermal power (sink and source) and COP. This is useful to explain the behaviour of the RHP for different conditions and the corresponding results. The first section will describe the ramp up of the Rotation Heat Pump, the second section will discuss the curves for almost steady state and the third section will be about the shutdown of the System. To give an overview, the following diagram (Figure 3) of the temperature curves shows the related sections. The shown test was started at 07:00h and lasted till 17:30h. After the results are presented, a short discussion will follow where different effects of changed boundary conditions are analysed.

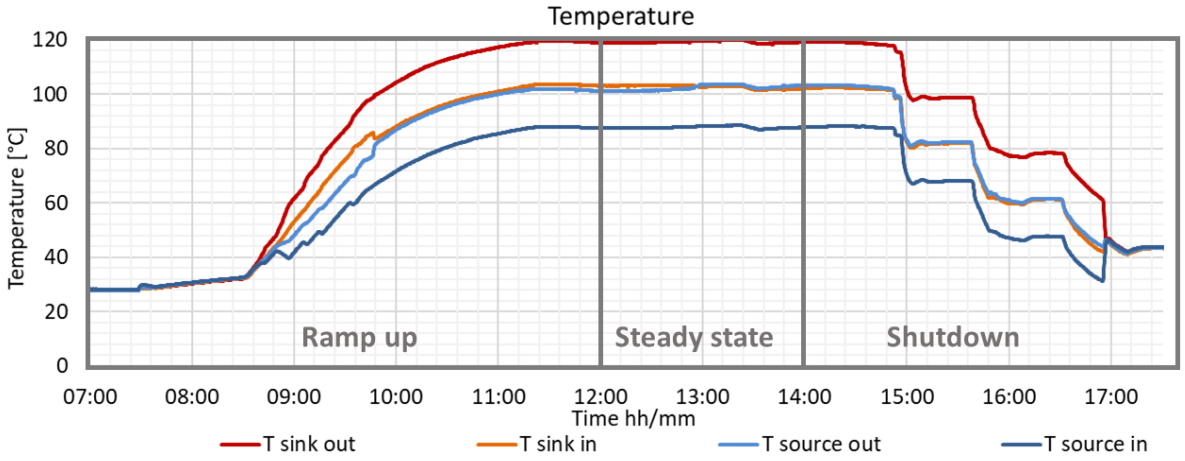


Figure 3: Temperature curves of sink and source of testing day including different time periods

The ramp up time represents the time where the system is started and heated up from initial conditions. Figure 4 shows the mentioned curves for these conditions. Initial conditions means that there is no rotation whether of the main rotor or the fan and there is no mass flow of working fluid or process fluid. The temperature level of sink and source are almost equal at the inlet as well as at the output. The test run starts by ensuring mass flow of sink and source just after 07:30h (Figure 4b) while at around 8:30h the fan, which provides the mass flow of the working fluid, is switched on. This can be seen by the electric power of the fan in Figure 4c. It is essential, that the mass flow of the working fluid is already built up before transferring thermal power at sink and source because otherwise the pressure increase necessary for the process can't be ensured by the fan. Last step is to start up the main rotation which generates the temperature lift between sink and source, Figure 4b. This can be seen just a few minutes after 08:30h, the mass flow of the working fluid is already ensured. The COP at this time is not representative because there is still a certain amount of heat necessary to heat up the whole machine. As can be seen in Figure 4a, the temperature of sink and source generally increases over time while the temperature difference between sink outlet and source inlet increases as well. General increase is caused by heating up the system by internal electrical components and an external heater mounted on the pipe system at the test rig. The temperature difference, means the temperature lift between sink and source, increases because of the increasing rotational speed of the rotor.

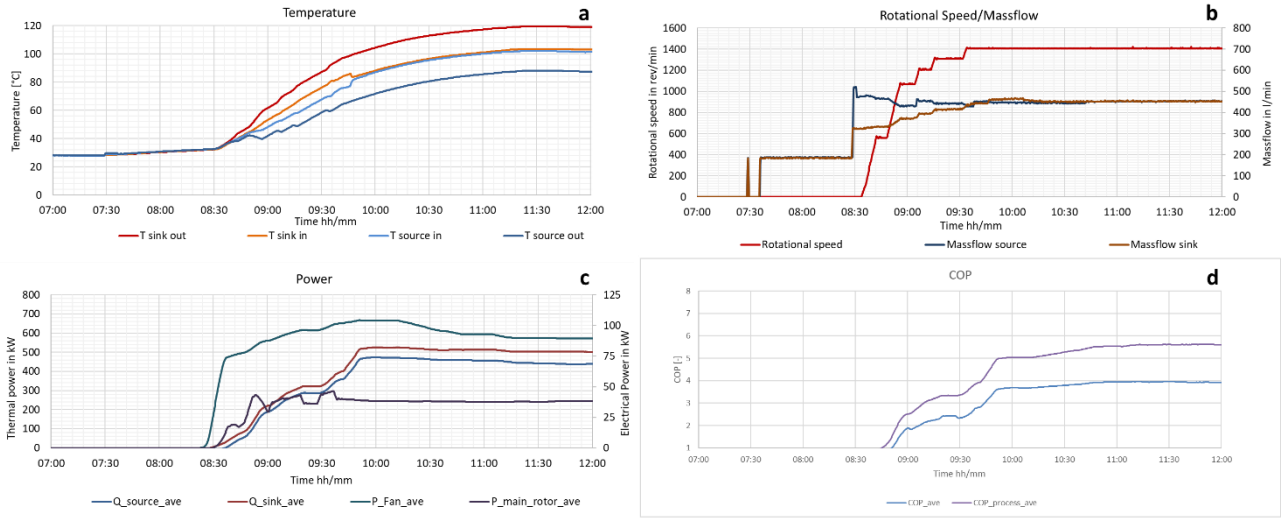


Figure 4: Ramp up – Temperature (a), rotational speed and mass flow (b), thermal and electrical power (c) and COP (d)

The second time section displays the performance of the RHP at almost constant boundary conditions, shown in Figure 5. After the ramp up the temperatures for sink and source at the inlet are kept constant. Also, mass flow and rotational speed of the main rotor are set to a certain level. For this test 1400rpm are defined for the main rotor and approximately 460l/min are the flow rate of sink and source. Since the test rig is a circuit of limited volume, the controller is not finally optimised yet and as much heat as possible is tried to be recovered, some small drifts of temperature and thermal power occur. Nevertheless, the temperature at sink outlet is kept at around 120°C, which demonstrates the possibility of providing high temperatures while the COP results in around 4 and COP_process is around 5,7-6. The thermal power at the outlet is 500-550kW. A small deviation of thermal power and COP can be seen a few minutes before 13:00h, where the rotational speed of the fan engine was increased slightly and the inlet temperatures have been adjusted.

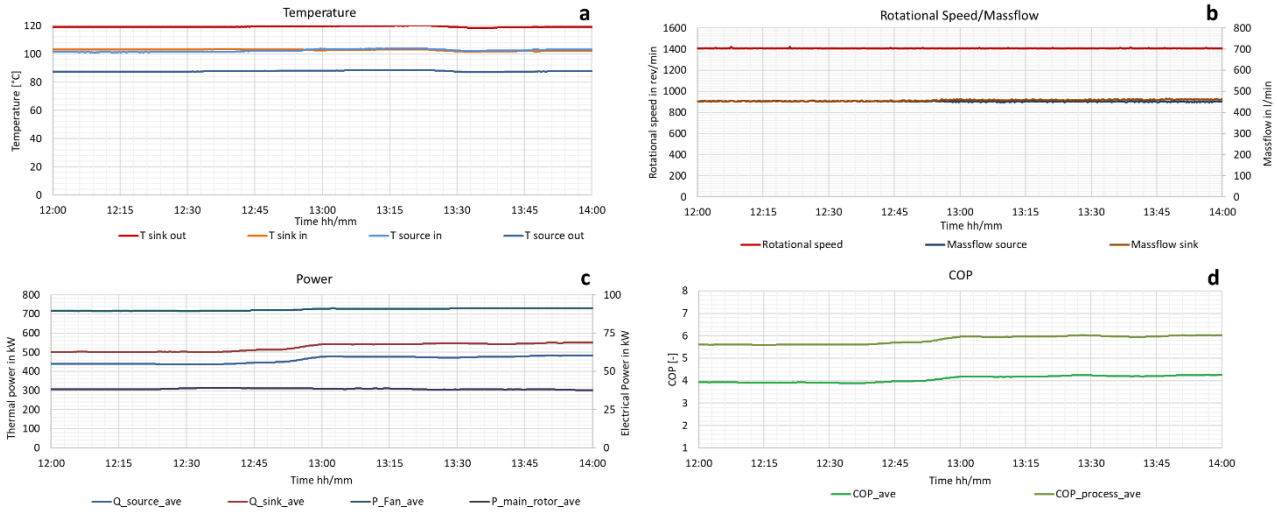


Figure 5: Steady state – Temperature (a), rotational speed and mass flow (b), thermal and electrical power (c) and COP (d)

The last section, Figure 6, describes variations and the shutdown of the system which means that it shows how the temperature is lowered and finally the rotational speed of the rotor decreases until it stops. Also, at the beginning variations of the rotational speed of the fan and how they affect the Joule-cycle and the system are shown. Starting at 14:00h, the temperatures correspond to the level of the steady state shown earlier. A few minutes after 14:00h the rotational speed of the fan is reduced which can be seen by the decreased power consumption of the fan-engine. Because of fluid mechanics, lowering the fan speed goes along with reducing mass flow and pressure increase. This results in lower flow velocities and less flow losses but also less heat transfer in the heat exchangers. Consequently, the transferred heat also decreases, as can be seen in Figure 6c. As a result, however, the COP increases because the ratio of thermal power and electrical power consumption increases. In particular, the COP_process increases since the fan works more efficient. After lowering the rotational speed of the fan, the first temperature step downwards takes place at around 15:00h. At this time more heat is dissipated via the external heat exchangers of Fan1 and Fan2. Sink outlet temperature decreases from 120°C to 100°C and also inlet and outlet temperatures of sink and source are dropping around 20K. Since this is a dynamic process the thermal power and the COP calculation are showing values for unsteady conditions. The heat capacity of the rotor and the whole system would have to be included at this point because the temperature level of all components is decreased. After this drop the system is in a steady state condition after a few minutes again. About half an hour later the next temperature drop takes place and the system temperature is lowered again 20K. Heat output and COP show the same characteristics as before and after a few minutes steady state operation is reached again. Looking at the COP in general, it almost does not depend on the temperature in steady state. In the next steps the temperature is further lowered and just a few minutes before 17:00h the fan is switches off and there is no more thermal power delivered, all temperatures equalise and finally the values for COP are not representative anymore. Before the last step, where the pumps for the process fluids are switched off, the engine for the main rotor is switched off and the rotational speed is reduced. The peak of the main rotor power consumption at 17:00h can be explained as follows. For a final shutdown when the rotor has to stop, valves in the housing are opened to allow ambient air to flow into. Basically, till all tests a vacuum is provided inside the housing to reduce ventilation losses of the rotor. In this case, just before the engine is switched off, the valves are opened, air flows into the housing and so the power consumption of the main rotor is for a short time higher than usual.

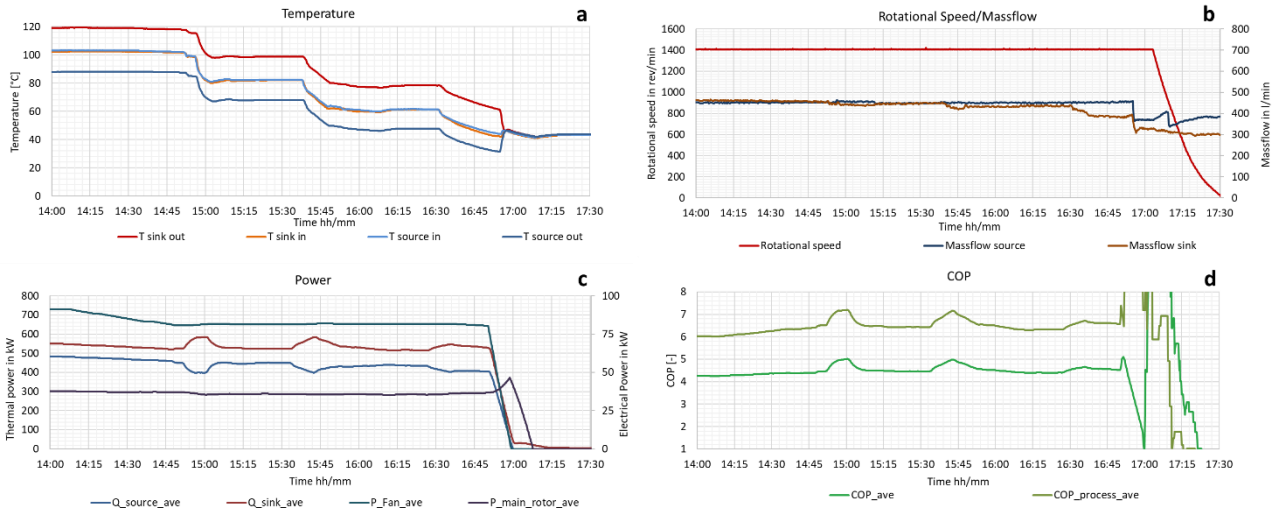


Figure 6: Shutdown – Temperature (a), rotational speed and mass flow (b), thermal and electrical power (c) and COP (d)

3. Application Cases

3.1. Distillation

For the calculation of the thermodynamic processes, the same values for the CHP and RHP were assumed regarding the temperatures of the source and sink, the mass flow and the thermal power. The results are based on [18], where more detailed analyses are given. The spread given in the calculations is assumed to be the same for both source and sink. Since the refrigerant R1336mzz(Z) has a strongly overhanging wet vapor region (see also Helminger [19]), superheating after the evaporator is also applied in the calculation. Furthermore, in the CHP process, no peripheral losses such as the power of the control system or auxiliary devices that influence the process or COP are included. Application - Distillation process

In addition to the results presented so far with specified boundary conditions, as can occur in industrial processes, the two heat pump processes are compared below for the specific application case of a distillation process in whisky production. In this application, the ethanol-water mixture is evaporated in the still (distillation column). This takes place at 85 °C to 95 °C and is usually realised with saturated low-pressure steam. In this application, an inlet temperature of 120 °C and an outlet temperature of 90 °C are required. In principle, the distillation process (latent heat) is also possible at constant temperature. This process can also be implemented with process water, but the spread must be correspondingly large (30 K). At the same time, the heat of condensation and cooling that must be dissipated in the downstream condenser can be used as a source. This application thus has the advantage that both the cooling of the source and the heating of the sink can be used. Figure 7 shows the integration schematically. The boundary conditions are the

- Temperature at the inlet of the source with 85 °C,
- Temperature at the outlet of the source with 55 °C,
- Temperature at the inlet of the sink with 90 °C,

Temperature at the outlet of the sink with 120 °C

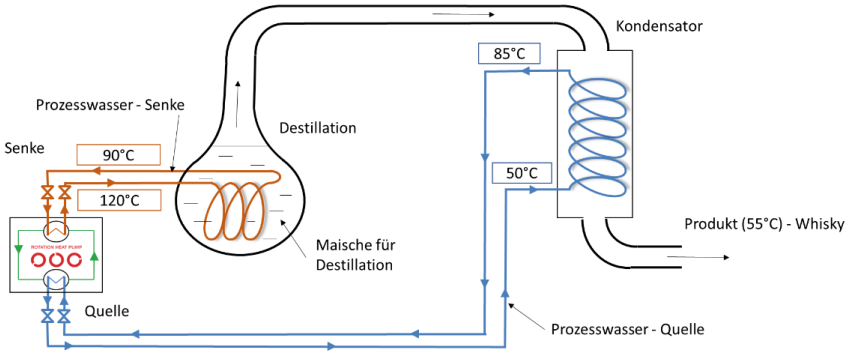


Figure 7: Continuous distillation process of ethanol in combination with an RHP

The spread is 30 K, whereby the lift for the evaluation according to source inlet to sink outlet temperature is 35 K and 65 K for source outlet to sink outlet temperature. The thermal power is also given in this case with 700 kW and is assumed to be the same in both designs. Figure 8 below show the thermodynamic cycle for the RHP and CHP for the given boundary conditions where a COP of 4,7 for the RHP and for the CHP a COP of 3,7 can be calculated.

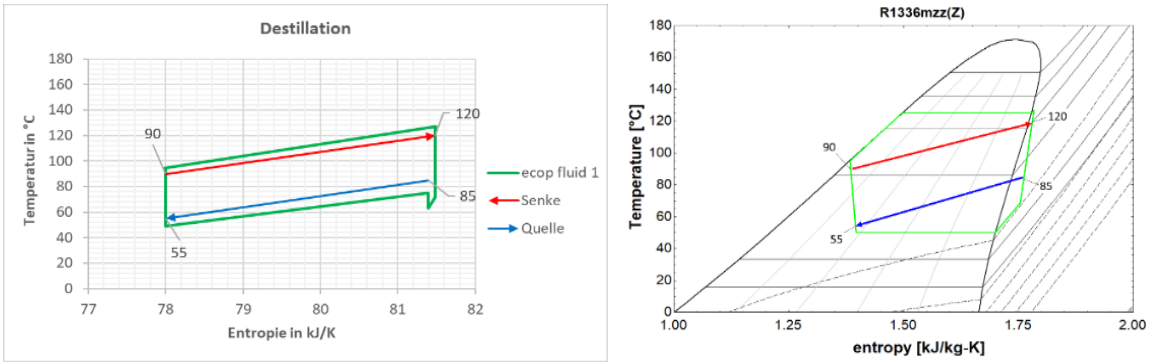


Figure 8: Calculated cycle for application in distillation (source inlet/outlet: 85 °C/55 °C, sink inlet/outlet 90 °C/120 °C), (left: Joule process of RHP, right: 2-phase process of CHP)

3.2. Cooling

Many industries need to dissipate enormous amounts of heat for the cooling of engines/generators/processes, this heat can often not be used directly due to a relatively low temperature level. With the Rotation Heat Pump, it is possible to both provide the cooling with high temperature spreads, this energy is used as a source, and to provide heat again at a high temperature level. E.g., for self-consumption for heating support or for feeding into a district heating network. Heat and cold can thus be provided with one system.

3.3. Pasteurization

In the pasteurization process, products must be heated in the first step and then cooled again. Until now, these processes have often been considered separately. However, it is much more energy-efficient to use the heat available during cooling and to use it for heating at the beginning by means of a temperature lift in a Rotation Heat Pump.

3.4. Hydrogen production

In hydrogen production, water is separated into Hydrogen (H_2) and Oxygen (O_2) by an electrolysis process. The water provided must be cooled and fed back into the process. To make hydrogen production as efficient as possible, it makes sense to use this heat for other processes. Depending on the operating temperature of the production process, many electrolyzers use temperature levels of around 40-70°C which is to less for direct using most of the time. Combined with a Rotation Heat Pump, a large spread at the source can be achieved to cool the water and then feed the heat into e.g., a district heating network or a production process at higher temperature levels.

3.5. Steam generation

Steam can be obtained directly from the hot water by pressure reduction in a steam drum. This eliminates the need for an additional heat exchanger and allows the full temperature level to be utilised, as steam is fed directly into the system via a steam lance. Pressure control units allow precise control of the steam pressure as well as the hot water to prevent evaporation in the heat pump. The amount of used steam is fed back into the system in form of feed water via a feed water tank.

4. Results and discussion

The presented results of a high temperature test run show that due to the flexibility of the Joule-cycle the temperature level is not essential to operate a RHP efficiently. During the ramp up time it is necessary that mass flow of the working fluid is already ensured before the main rotor speed is increased. Otherwise, it is not possible to overcome the pressure difference caused by the thermal power transferred at the heat exchangers. This pressure increase is mainly depending on the thermal power and the temperature lift. Temperature lift is mainly produced by the rotational speed of the main rotor. By adjusting the rotational speed of the rotor, the temperature lift can be controlled as well as the thermal power for given conditions can be adjusted. Of course, different control strategies can be obtained for this system by having those parameters to control. This is already in progress and will be tested as soon as possible in a first step on digital twins and finally at the test rig combined with the RHP. Having different control strategies also tests will be adapted and can be much more dynamical. Changes in temperature, mass flow, rotational speed and other parameters can then be made easily under exact control. This will allow a much more detailed analyse of the system under dynamic boundary conditions. Probably the sampling rate of the logging must be adjusted to get finer results since now it is set to 5 seconds. In addition, accuracy of sensors should be considered and analyzed in a next step.

Table 1 shows the COP for the given operating points before. They are based on theoretical calculations with 700 kW thermal power at the sink. Most of the values of conventional heat pumps used for the specification of the temperature spread usually refer to the inlet temperature of the source and the outlet temperature of the sink. This approach is referred to as case 1 in the results. Another possibility is to calculate the temperature spread from the outlet temperature of the source and the outlet temperature of the sink. Case 2 describes this value.

Table 1: Overview of the operating points and calculation results

	Temperature of source in °C		Temperature of sink in °C		Temperaturelift in K			
Spread in K	Inlet	Outlet	Inlet	Outlet	Case 1	Case 2	CHP-COP	RHP-COP
30	100	70	120	150	50	80	2,91	3,87
30	85	55	90	120	35	65	3,72	4,68

The results show that the COP has a strong dependence on the temperature lift or on the temperatures used for calculating the temperature lift (source inlet/source outlet).

At a spread of 30 K, the difference between the two technologies becomes clear, with the RHP achieving much higher COP values than the CHP. This is possible due to the sensitive heat transfer as it occurs in the Joule process in the RHP.

Table 1 shows that the RHP achieves comparatively higher COP values as the temperature level rises. The reason for this is the Joule process implemented in the RHP, which enables very efficient compression due to the always gaseous working fluid at different temperature levels. The 2-phase process in the CHP is limited in terms of the maximum temperature level by the refrigerant. The COP decreases in the subcritical cycle in the CHP close to the critical temperature [6]. This effect does not occur in the RHP, since the working fluid permanently runs through the cycle in a supercritical state. Specifically for distillation, the RHP has a COP of 4.68 and the CHP a COP of 3.72. This can be explained by the high spread in combination with the high temperature level (120 °C sink outlet, 90 °C sink inlet, 85 °C source inlet, 55 °C source outlet).

Beside the specific shown case for a distillation process different application cases are shown were the high temperature spread provides a significant advantage for the process. Those applications provide for example cooling of a specific system or a high temperature difference at the process fluids is beneficial. A very interesting topic for high temperature heat pumps is also steam production which can be realized by using a steam drum. As a next step the combination and testing of a Rotation Heat Pump with a steam production system will be the aim.

4.1. Outlook for very high temperatures

The demand on thermal power at temperatures higher than 150°C up to 250°C in the industry is enormous. While right now temperatures of 150°C are possible by using a Rotation Heat Pump, it is already the aim to provide also these temperature-levels. Therefore, a completely new design of the rotor is developed which uses new technologies of manufacturing. The new method is based on a diffusion bonded system which includes heat exchangers and also the pipe system for water and the working fluid (only one solid block). A massive simplification is possible because all sealings at the rotor can be removed and so this method allows simple mass production. While also the size is reduced by more than 50% the efficiency can be increased by around 30% (due to smaller delta T in heat exchanger and reduced pressure drop). Following Figure 9 shows the difference in size and grade of simplification for a rotor providing same thermal power and temperatures. This new design will allow temperatures of up to 250°C and will be included in a prototype till 2024.

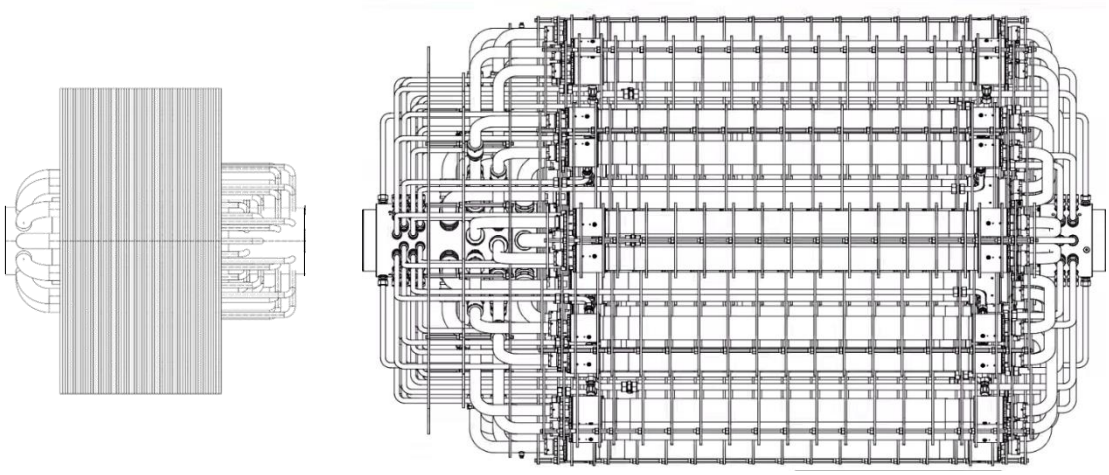


Figure 9: Comparison of rotor designs (same scale for both); Left: Integrated-Rotor design based on diffusion bonding, Right: assembled rotor-design

5. Conclusions

High temperature heat pumps play an important role to decrease CO_2 emissions since there are a lot of industrial applications using fossil fuels for heat supply now. The possibility to use the Joule cycle in a RHP allows using flexible temperatures and in addition the temperature level is not limited by the working fluid. To demonstrate the performance of a RHP at high temperatures, up to 120°C, a specific test run was set up and analyzed. Those test results were generated using a RHP-K7 in combination with a special test rig described in previous papers. The test data show an entire test day were also the startup period and shutdown time is included and analyzed. During the startup it is clearly shown how the temperature increases with time due to the heating up of the circuits. This takes some time but is not limited by the RHP but more by the electrical

heaters. The RHP could deal with faster changes in temperature which is demonstrated during the shutdown. Also, the effect of increasing the rotational speed of the rotor can be seen and how this influences the process. This is a dynamic process where no steady state conditions are present and the evaluated COP is not correct by using classic formulations. Because the machine and periphery are heated up and can be seen as a thermal storage, energy balances are not fulfilled during this time. After the components have reached steady temperature levels the second time period of testing starts. This mainly includes steady state analyses where the parameters should not be changed. During this period measured sensor values and COP are almost constant without discontinuities. After having this constant test period, the third part describes the shutdown of the machine when the temperature level is reduced in a few steps. This shows that the temperature level can be changed within some minutes. Also, the thermal power can be adjusted in a certain range by increasing or reducing the speed of the fan. If the fan is finally turned off, no more mass flow occurs, and the temperatures all drop to an equal level. This test at 120°C could also be achieved for 150°C at sink outlet, essential is the use of adequate seals for this case to prevent leakage. Since the working fluid is not limiting the Joule-process itself, higher temperatures are feasible but of course some components must be updated.

Acknowledgement

This project is supported by InnoEnergy and Co-funded by the European Union.

References

[1] R. De Boer, A. Marina, B. Zühlsdorf, C. Arpagaus, M. Bantle, V. Wilk, B. Elmeaard, J. Corberan and J. Benson, "Strenghening Industrial Heat Pump Innovation, Decarbonizing Industrial heat," White Paper, 2020.

[2] T. Fleiter, R. Elsland, M. Rehfeldt, J. Steinbach, U. Reiter, G. Catenazzi and e. al, "Heat roadmap Europe - Deliverable 3.1, Profile of heating and cooling demand in 2015," 2017.

[3] F. Schlosser, M. Jesper, J. Vogelsang, T. Walmsley, C. Arpagaus and J. Hesselbach, Large-Scale Heat Pumps: Applications, Performance, Economic Feasibility and Industrial integration, Renewable and Sustainable Energy Reviews, 2020.

[4] C. Arpagaus, Hochtemperatur-Wärmepumpen: Marktübersicht, Stand der Technik und, Berlin: VDE Verlag, 2018.

[5] C. Arpagaus, F. Bless, J. Schiffmann and S. S. Bertsch, "Hochtemperatur Wärmepumpen:," in *DKV-Tagung*, Bremen, 2017.

[6] C. Arpagaus, F. Bless, J. Schiffmann and S. S. Bertsch, "High temperature heat pumps: Market overview, state of the art, research status, refrigerants, and application potentials," in *17th International Refrigeration and Air Conditioning Conference*, Purdue, 2018.

[7] V. Wilk, T. Fleckl, A. Arnitz and R. Rieberer, "Industriewärmepumpen in Österreich: Status Quo und Potentiale, Internationale Energiewirtschaftstagung," White Paper, Wien, 2019.

[8] C. Arpagaus and S. Bertsch, "Industrial Heat Pumps in Switzerland – Application Potentials and Case Studies, Final Report, on behalf of the Swiss Federal Office of Energy," Bern, 2020.

[9] M. Bantle and C. Schlemminger, "Design und experimentelle Resultate einer Hochtemperatur Propan-Butan Wärmepumpe," DKV-Tagung, Aachen, 2018.

[10] C. Mateu-Royo, C. Arpagaus, A. Mota-Babiloni, J. Navarro-Esbrí and S. Bertsch, "Advanced High Temperature Heat Pump Configurations using low GWP Refrigerants for Industrial Waste Heat Recovery: A Comprehensive Study, Energy Conversion and Management," 2020.

[11] A. Längauer, B. Adler and C. Rakusch, "Testergebnisse einer Rotation Heat Pump," in *DKV-Tagung*, Ulm, 2019.

[12] V. Wilk, M. Lauermann and F. Helminger, "Decarbonization of industrial processes with heat pumps," in *25th IIR International Congress of Refrigeration*, Montreal, 2019.

[13] B. Adler et al, "Centrifugal compression turbo heat pump made by ECOP," in *10th IEA Heat Pump Conference*, Tokyo, 2011.

[14] B. Adler and S. Riepl, "Heat pump for process industry," in *11th IEA Heat Pump Conference*, Montreal, 2014.

[15] B. Adler et al., "Industrieller Einsatz einer Rotationswärmepumpe," in *DKV-Tagung*, Bremen, 2017.

[16] B. Adler and R. Mauthner, "Rotation Heat Pump (RHP)," in *12th IEA Heat Pump Conference*, Rotterdam, 2017.

[17] A. Längauer and B. Adler, "The Joule cycle realised in a Rotation Heat Pump," in *14th IIR Gustav Lorentzen Conference*, Kyoto online, 2020.

[18] A. Längauer, B. Adler, C. Arpagaus, F. Bless and S. Bertsch, "DKV-Tagung," in *AA IV 21*, Dresden, 2021.

[19] F. Helminger, M. Hartl, T. Fleckl, K. Kontomaris and J. Pfaffl, "Hochtemperatur Wärmepumpen Messergebnisse einer Laboranlage mit HFO-1336MZZ-Z bis 160 °C Kondensationstemperatur," in *14. Symposium Energieinnovation*, Graz, 2016.

14th IEA Heat Pump Conference
15-18 May 2023, Chicago, Illinois

Development of a liquid dessicant air conditioning system using ionic liquids

Hiroshi Nakayama[a], Masatoshi Harada[b], and Xinming Wang[c*]

[a]Chubu Electfric Power co., Inc., 20-1, Kitasekiyama, Midori-ku, Nagoya, Aichi, 459-8522, Japan
[b]Dyna Air co., Ltd., 3-4-2, Kandanishiki-cho, Chiyoda-ku, Tokyo,101-0054, Japan
[c]Evonik Japan co., Ltd., Shinjuku Monolith 12F, 2-3-1, Nishi-Shinjuku Shinjuku-ku, Tokyo 163-0938, Japan

Abstract

Liquid desiccant air-conditioners (LDAC) with heat pump can perform cooling dehumidification or heating humidification, and have high energy-saving and sterilization performance. Therefore, they are installed in hospitals, nursing homes, and food factories, where humidity control is required. However, lithium chloride (LiCl), a conventional humidity control liquid, is highly corrosive to metals, requiring the use of highly corrosion-resistant materials such for the pipes and the heat exchangers. This leads the problem that the manufacturing cost of the air conditioner increases.

Therefore, we developed an inexpensive and compact LDAC by adopting a novel ionic liquid (IL) that does not corrode the metals commonly used in air conditioners. In this study, we evaluated the metal solubility and sterilizing property of the ionic liquid. Based on the physical properties of the IL, the humidity control module was improved for the purpose of downsizing and cost reduction of the unit. Moreover, we conducted a performance evaluation of the LDAC in the environmental test room under the condition in which temperature and humidity change rapidly in short period of time to simulate the condition of sudden showers of rain in summer. Test results showed that processed air was supplied at very stable level.

© HPC2023.
Selection and/or peer-review under the responsibility of the organizers of the 14th IEA Heat Pump Conference 2023.

Keywords: Liquid Dessiccant Air Conditioning, Ionic Liquids, Heat pump, Dehumidification

1. Introduction

The development of an efficient air-conditioning system has become more and more important from the standpoint view of realizing a sustainable society. In hospitals and factories where temperature and humidity control throughout the year are required, gas as fuel have been used as heat sources of boilers and absorption chillers. However, there is a lot of heat loss in the boiler and the steam piping, and the energy consumption is high. LDAC is attracting attention as one of the most promising candidates to replace such inefficient air conditioning systems [1-3].

However, the present commercial LDAC uses an aqueous solution of LiCl as the humidity control liquid or desiccant. The LiCl is very caustic/corrosive to metals, in particular, iron or aluminium, both of which are popular resources of materials in the air-conditioner system; this requires expensive special corrosion-resistance pipes and heat exchangers, which causes a critical problem that the manufacturing cost of the air-conditioning system is rather high.

Ionic liquids (ILs) have gained strong interests due to their unique physical and chemical properties and their applied fields have been significantly expanding. ILs show a low volatility, unique solvation capability, and high stability and the liquids have thus been applied in various fields of electro-chemistry, organic and inorganic synthetic chemistry, catalysis, and gas absorption [4-5].

In these backgrounds, we have developed an inexpensive and compact LDAC by adopting a novel IL that does not corrode general-purpose metals such as iron and aluminium. In this study, we evaluated the metal

* Corresponding author. Tel.:+81-52-621-6101; fax:+81-52-624-9234.
E-mail address: Nakayama.Hiroshi2@chuden.co.jp

solubility and the sterilizing property of the IL. Based on the physical properties of the IL, we improved the heat exchanger and the humidity controller. Moreover, we conducted a performance evaluation of the LDAC in the environmental test room under the condition in the rated dehumidification condition and the transient condition.

2. Outline of LDAC

Figure 1 shows an outline of LDAC in the case of dehumidification. LDAC is a device that absorbs and releases water vapor in the air by bringing the outside air into direct contact with a gas-liquid contactor wetted with a liquid humidity control liquid to adjust the humidity and temperature of the air. It consists of a processor and a regenerator. The processor plays a role of supplying the treated air to the room, and can create air of any temperature and humidity by adjusting the temperature and concentration of the humidity control liquid. Also, the temperature and concentration of the humidity control liquid can be independently controlled, and the temperature and humidity of the air can be freely set. On the other hand, the regenerator has a role of concentrating the liquid by heating the humidity control liquid, which has been diluted by absorbing the moisture in the air, and bringing it into contact with the outside air. Humidification is performed by switching between cooling and heating of a heat source such as a heat pump. Various heat sources such as heat pumps, groundwater, exhaust heat, and solar heat are used to cool or heat the liquid. In particular, the use of heat pumps that can heat and cool at the same time will improve system efficiency.

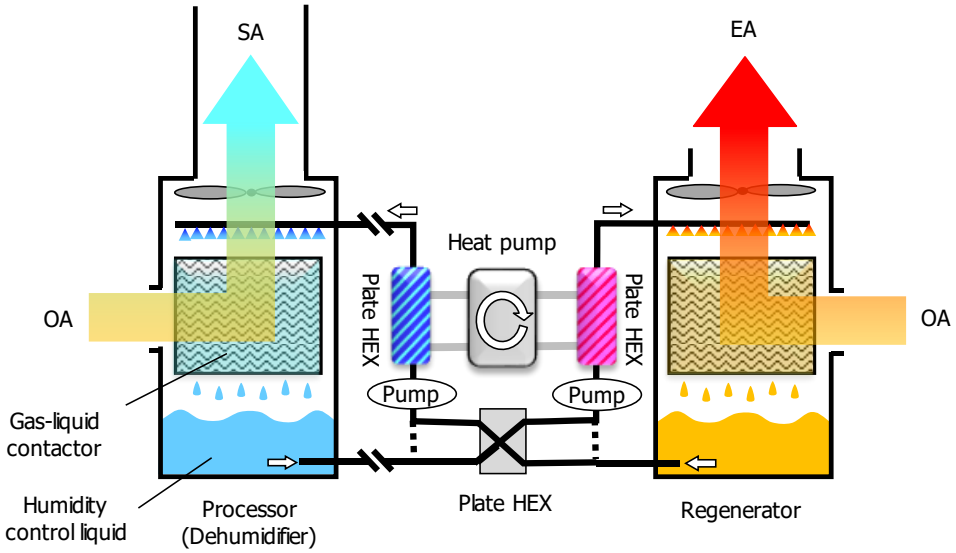


Fig.1 Outline of LDAC (Dehumidification case)

3. Physical properties of IL

In general, humidity control liquids are required to have high humidity control performance, inexpensive, satisfy, and high sterilization properties and so on. LiCl which is mainly used as a humidity control liquid for LDAC, satisfies such requirements, but has the problem of being highly corrosive to metals.

In this study, a novel IL developed by Evonik Industries was used as the humidity control liquid. This IL exhibits high dehumidification performance, thermal and chemical stability, low volatility, comparable heat mass transfer properties [6] and is suitable for LDAC. Table 1 shows comparison of thermophysical properties of humidity control liquid. At the same temperature and the equivalent liquid desiccant mass fraction at which the saturated vapor pressure is identical, the aqueous IL exhibits lower density and surface tension than aqueous LiCl. On the other hand, the viscosity of aqueous IL is higher than that of aqueous LiCl. In the following, the results of evaluating the level of metals dissolved into the IL and sterilization performance in comparison with LiCl are shown.

Table 1 Thermophysical properties of humidity control liquid (25°C)

	Mass fraction	Density	Viscosity	Surface tension	Thermal conductivity	Specific heat capacity
	%	kg/m^3	Pa ·s	N/m	W/mK	kJ/kgK
IL	0-80	1000-1150	0.001-0.03	0.072-0.039	0.607-0.271	4.2-2.2
LiCl	0-35	1000-1215	0.001-0.005	0.072-0.091	0.607-0.539	4.2-2.8

3.1. Level of Metal ions into the IL

Figure 2 and Fig.3 show the metal ions of stainless steel and aluminum dissolved into the IL. The test period is 3 weeks and the temperature of the solution is heated up to 70°C. The mass fraction of IL and LiCl are 80wt% and 35wt%, respectively. Saturated vapor pressure at these mass fractions is close to the value when dehumidifying the outside air in summer. The size of the metal sample is 40mm×10mm×3mm. The amount metal ions SUS and aluminum dissolved into the IL is much less than into the LiCl solution and is at a practically acceptable level. This result suggests that commonly used tubes and heat exchangers can be used, which is a great advantage in reducing the manufacturing cost of air conditioners.

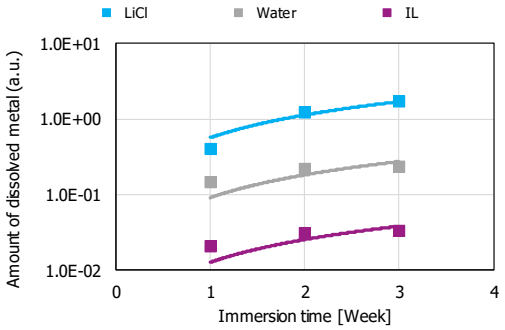


Fig.2 Amount of dissolved metal (Aluminum)

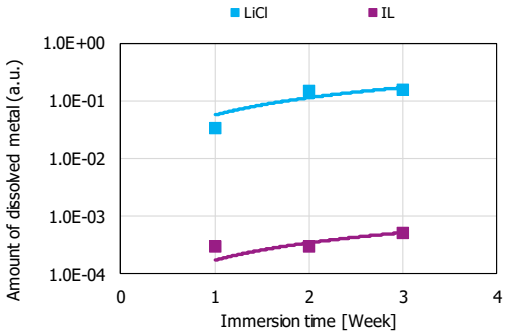


Fig.3 Amount of dissolved metal (SUS304)

3.2. Sterilization performance

In the COVID-19 pandemic, the air cleaning performance of air conditioners is also required as an additional factor. Therefore, we investigated the sterilization and virus inactivation performance of the IL. As an example, Fig. 4 and Fig. 5 show the results of the sterilization effect against *Legionella* and *Aspergillus niger* of the IL in comparison with LiCl solution. When each bacterium is brought into contact with the IL, it dies after 1 minute, and the sterilization performance is higher than that of LiCl.

Table 2 shows the inactivation effect of the IL on three types of viruses (*feline coronavirus*, *influenza virus*, and *feline calicivirus*). The IL was added to the liquid containing the virus cell line, and after a predetermined period of time, the amount of virus infection to the cell line was measured. In the case of the purified water for comparison, the amount of viral infection hardly changed after 60 minutes, but with the IL, the amount of viral infection decreased sharply down to the detection limit even after only 1 minute, demonstrating a remarkable viral inactivation effect.

Regarding the hazards of this IL, we conducted an acute toxicity test using mice in accordance with the OECD guidelines, and confirmed that the classification of hazards to health (GHS) is beyond the most mild class.

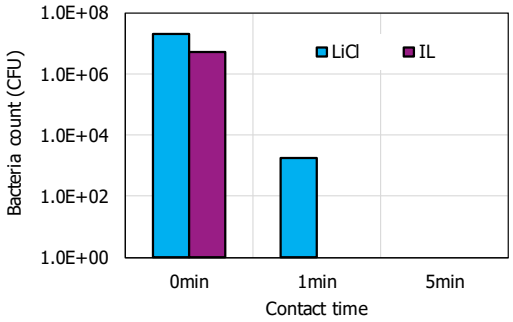


Fig. 4 Bacteria count (Legionera)

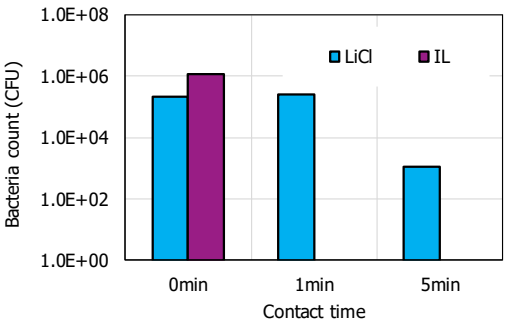


Fig.5 Bacteria count (Aspergillus niger)

Table 2 Virus inactivation performance result of ionic liquid

value of virus infectious dose (TCID50/mL)

	feline coronavirus		*influenza virus*		*feline calicivirus*	
	IL	Water	IL	Water	IL	Water
0min	1.7×10^5	1.7×10^5	1.0×10^5	1.0×10^6	2.4×10^5	2.4×10^5
1min	No count	–	No count	–	No count	–
5min	No count	–	No count	–	No count	–
60min	No count	1.1×10^5	No count	3.1×10^6	No count	2.4×10^5

4. Configuration of humidity control module

In LDAC, the supply air temperature is determined by controlling the temperature of the humidity control liquid, and the air humidity is determined by controlling the concentration of the humidity control liquid. In a typical LDAC, as shown in Fig. 6, the humidity control liquid is first cooled in a plate heat exchanger and then directly contacted with the outside air in an air-liquid contactor. The temperature and humidity of the outside air are regulated by direct contact with this liquid.

In the conventional LDAC systems using LiCl, as the humidity control liquid generates heat when it absorbs moisture, the temperature gradually rises in the downstream direction of the gas-liquid contactor. Since the dehumidifying ability of the humidity control liquid decreases as the temperature rises, it is necessary to flow a large amount of the liquid in order to prevent this, and the capacity of the solution pump and the solution tank have been increased. Therefore, from the viewpoint of the cost reduction and the compactness, it was necessary to reduce the liquid flow rate and the tank size as much as possible.

In this study, as shown in Fig. 7, a sandwich structure was adopted in which tube heat exchangers and gas-liquid contactors were alternately arranged, and dehumidification was performed while cooling the humidity control liquid. As a result, it becomes possible to reduce the liquid flow rate while reducing the temperature rise of the humidity control liquid in the downstream direction. We conducted tests using the tube layout and the type of gas-liquid contactor at various conditions of parameter, determined the optimal combination, and developed a compact integrated humidity control module that combines a heat exchanger and a humidity control mechanism. As a result, the circulation flow rate (liquid volume) was reduced by 90% compared to the conventional machine, and the tank size was also greatly reduced. As showed in Table 1, the IL has lower surface tension and higher viscosity than LiCl. Therefore, it should be noted that a stable and thin liquid film is likely to be formed even at a low flow rate [7].

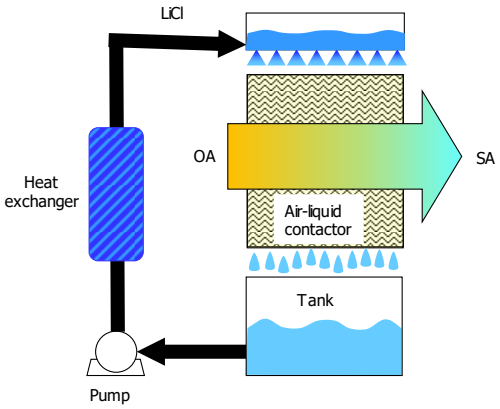


Fig.6 Conventional humidity control module

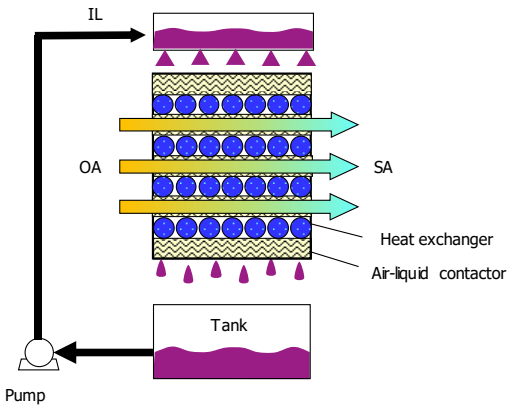


Fig.7 Developed humidity control module

5. Specifications

Figure 8 shows the appearance of the developed LDAC, and Table 3 shows the specifications. The processor and the regenerator have the same shape. As a heat source, not only hot and cold water from a heat pump chiller, but also hot water discharged from a factory, well water, etc. can be used. Compared to the conventional models of line-up, this unit has about 20% reduction in manufacturing cost, about 25% reduction in installation area, and about 90% reduction in the amount of humidity control liquid.

The LDAC shown in Fig. 8 has a rated air volume of 4,500 m^3/h, but customers in the industrial field require a variety of processing air volumes. Therefore, as shown in Fig.9, we made it possible to customize and incorporate it inside the air handling unit (AHU) used for general air conditioning. As a result, we have been able to respond to a wide range of processing air volumes according to customer needs.



Fig.8 Outside appearance of the LDAC (processor)

Table 3 Specifications of the LDAC

Dimensions (Width × Depth × Height)	1,600×1,830×2,000
Weight (kg)	1,620
Pump power supply (W)	200
Rated dehumidification capacity (kg/h)	67.5
Rated humidification capacity (kg/h)	68.6
Rated Air flow rate (m^3/h)	4,500

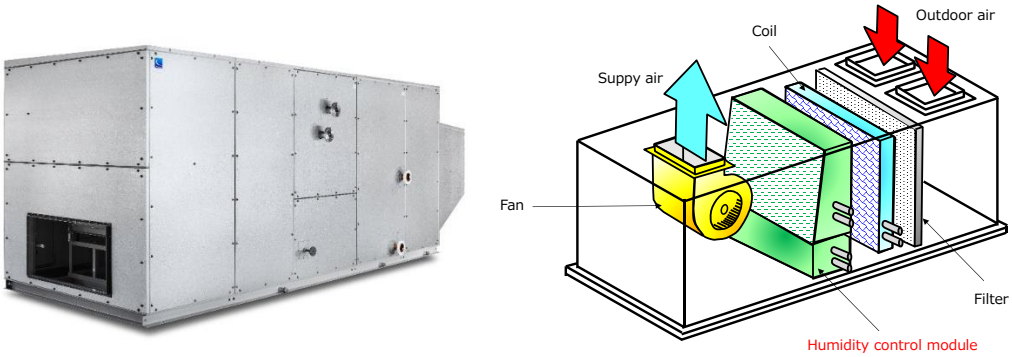


Fig.9 Outside appearance of the LDAC (AHU version)

6. Performance tests of the LDAC

The performance tests of the developed LDAC were conducted in the climatic environmental testing room in the research and development division of Chubu Electric Power Co., Inc. Rated humidification performance, dehumidification transient performance were measured. 100kW heat pump chiller was used as a heat source.

6.1. Rated dehumidification performance test

Table 4 shows the results of the rated performance test. This test was conducted under typical Japanese summer outdoor air conditions, assuming application to a commercial building. The measured value of the dehumidification capacity was close to the target value, confirming that stable performance were obtained.

Table 4 Results of rated performance test

		Target value	Measured value
Flow rate (m^3/h)		4,500	4,474
Temperature of cold water (°C)		10.0	9.6
Temperature of hot water (°C)		45.0	37.8
Outdoor air	Temperature (°C)	34.3	34.3
	Humidity (g/kgDA)	19.5	19.5
Supply air	Temperature (°C)	20.0	18.4
	Humidity (g/kgDA)	7.0	6.4
Cooling Capacity (kW)		70.3	73.2
Dehumidification capacity (kg/h)		67.5	70.3

6.2. Dehumidification transient performance test

This test was conducted for the purpose of verifying the humidity control during sudden weather changes. In manufacturing processes such as pharmaceutical and painting processes, it is important to maintain a stable state even under drastic change in ambient conditions.

Figure 10 shows changes in temperature and humidity processed by the developed LDAC in a situation simulating the condition in which temperature and humidity change rapidly in short period of time such as sudden showers of rain in summer. By control temperature and concentration of the IL suitably, test results showed that the processed air was supplied at very stable level. The averaged temperature, humidity, and humidity ratio during the test were 26°C, 44%, and 9.2g/kgDA, respectively. The temperature change of the supply air was ±0.6 °C and the humidity change was within ±1%.

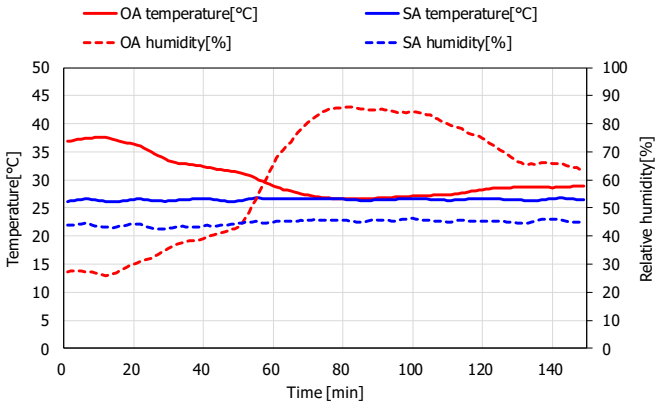


Fig.10 Supply air temperature and humidity characteristics when a shower is assumed

7. Primary energy consumption

Table 5 shows the result of estimating primary energy consumption and CO_2 emission of the conventional system and that of the developed LDAC system when the system is introduced to a hospital in Japan. The conventional system consists of a gas steam boiler and an air-cooled heat pump chiller. A substantial reduction in energy consumption of 72% and CO_2 emission of 49% from that of the conventional system can be expected when the new system is introduced. It is noted that although the LDAC system using LiCl considerably increases the power consumption of the pump compared to the developed system, the impact on the increase of primary energy consumption and CO_2 emission is not so large.

Table 5 Estimated primary energy consumption and CO_2 emission

	Conventional system	Developed system	Reduction rate
Primary energy consumption [GJ/year]	449	126	72% down
CO_2 emission [ton-CO_2/year]	111	56	49% down

-Estimate condition-
Building: Hospital (floor area: 2,000m^2)
Air conditioning operation: 24h/day, 365day, flow rate 10,000m^3/h
System Efficiency: Heat pump chiller (cooling COP:4.07, heating COP:4.06), Gas boiler 70%
Calorific value: Electric 9.70MJ/kWh, Gas 45MJ/m^3
CO_2 emission factor: Electric 0.449kg-CO_2/kWh, Gas 2.29kg-CO_2/m^3

8. Summary

We have developed an inexpensive and compact LDAC by using a novel IL that does not corrode general-purpose metals. The developed LDACs were already installed in hospitals, nursing homes, offices, food supermarkets, and beer factory as energy-saving and hygienic air conditioners. The results obtained during the research and development of this system are as follows:

- The amount of SUS and aluminum dissolved in the IL is much lower than that in LiCl solution. In addition, the IL has a higher sterilization effect against bacteria and viruses than LiCl solution.
- A sandwich structure in which tube heat exchangers and gas-liquid contactors are alternately arranged was developed for the direct contact of air to liquid. Consequently, the liquid flow rate can be reduced by 90% compared to the conventional unit.
- By appropriately controlling the temperature and IL concentration, extremely stable processing air can be supplied even under conditions where the outside air conditions change rapidly.
- It is expected that the energy consumed by conventional air conditioning system such as heat pump chiller and boiler, can be reduced 72% by introducing the new system.

References

[1] Lowenstein A., Review of liquid desiccant technology of HVAC applications, HVAC&R Research; 2008, **14**, p.819-839
[2] Yamaguchi S., Jeong J., Saito K., Miyauchi H., and Harada M., Hybrid liquid desiccant air-conditioning system: Experiments and simulations, *Appl Ther Eng*; 2011, **31**, p.3741-3747
[3] Kim M., Park J., and Jeong J., Energy saving potential of liquid desiccant in evaporative-cooling-assited 100% outdoor air, *Energy*; 2013, **59**, p.726-736
[4] Itoh T., Ionic liquids as tool to improve enzymatic organic synthesis, *Chm. Rev.*; 2017, **117**, p.10567-10607.
[5] Watanabe H., Komura T., Matsumoto R., Ito K., Nakayama H., Nokami T., Itoh T., Design of ionic liquid as liquid desiccant for an air conditioning system; Green Energy Env; 2019, **4**, p.139-145
[6] Cao B., Yin Y., Zhang F., Tong S., Che C., Chen W., Ji Q., Xu G, Li X, Experimental study on heat and mass transfer characteristics between a novel ionic liquid and air under low-humidity conditions, *Int J Heat Mass Trans*; 2022, **198**, 123373
[7] Varela R.J., Giannetti, N., Saito K., Wang X., and Nakayama H., Experimental performance of a three-fuid desiccant contactor using a novel ionic liquid, Appl Ther Eng; 2022, **210**, 118343

14th IEA Heat Pump Conference
15-18 May 2023, Chicago, Illinois

Boiling Heat Transfer of Ammonia in a Flooded Evaporator of Adsorption Heat Pumps

Jin Sub Kim[a,*], Dong Hwan Shin[a], Wookyoung Kim[a] and Seok Ho Yoon[a]

[a]Department of Thermal Energy Solutions, Korea Institute of Machinery and Materials, Daejeon, 34103, Republic of Korea

Abstract

Adsorption heat pumps can provide process heat to the industry by converting wasted heat from the plants to more useful heat of high temperature. Ammonia is suitable for a working fluid of the adsorption heat pump for decarbonization since it has zero global warming potential (GWP) and ozone depletion potential (ODP). Thermal performance of the ammonia adsorption heat pump is closely related to the boiling heat transfer in a flooded evaporator of the heat pump. Boiling heat transfer of ammonia on the plain stainless steel tube with an outer diameter of 15.87 mm was investigated at three different saturation pressures of 6.15, 8.57, and 11.7 bar (corresponding saturation temperatures of 10, 20, and 30 ℃). Considerable hysteresis between increasing heat flux and decreasing heat flux cases was observed. Measured boiling heat transfer coefficients were compared with previous correlations, and Stephan-Abdelsalam's correlation showed best agreement with the measurement. Boiling heat transfer on the enhanced tube with low fins was also examined, which exhibited large enhancement of the boiling heat transfer coefficient.

© HPC2023.
Selection and/or peer-review under the responsibility of the organizers of the 14th IEA Heat Pump Conference 2023.

Keywords: Adsorption heat pump; Ammonia; Pool boiling; Flooded evaporator; Hysteresis

1. Introduction

The decarbonization of thermal energy associated with building and industry sectors is essential for attaining the 2050 Net-zero goal. Thermally driven heat pumps such as absorption and adsorption heat pumps are regarded as one of the key technologies improving the energy efficiency in heating and cooling section, and eventually replacing conventional fossil fuels [1]. An adsorption heat pump can be operated with lower grade waste heat and is free from greenhouse gas emission because it utilizes natural refrigerants like water and ammonia [2]. Although ammonia is toxic and flammable, it has lots of advantages of high latent heat, chemical stability, and higher operating pressure above atmosphere [1].

Numerous previous studies have revealed basic heat transfer characteristics of ammonia in the heat exchange devices such as boiler and flooded evaporator. Spindler [3] thoroughly reviewed pool boiling heat transfer data of ammonia and compared them with general pool boiling correlations. Experimental data include pool boiling on a single tube [4], heat transfer enhancement techniques [5-6], boiling phenomena on tube bundles [7], and spray evaporation [8]. Zheng et al. [9] investigated the effect of lubricant oil on shell-side boiling heat transfer coefficient and concluded that the heat transfer coefficient first decreased with increasing oil concentration, then increased with a further increase in concentration. Abbas et al. [10] also reviewed various empirical correlations for outside boiling on single tube and bundles in ammonia. They concluded that existing correlations are to be cautiously applied because there is a wide disparity among them. Fernandez-Seara et al. [11] compared the heat transfer coefficient of spray evaporation with that of pool boiling on a horizontal plain tube in ammonia. They also showed boiling heat transfer improvement on an integral finned tube in a flooded evaporator [12]. They reported that a large hysteresis between increasing heat flux and decreasing heat flux was initially observed but diminished as the time passed (10 hours).

* Corresponding author. Tel.: +82-42-868-7807; fax: +82-42-868-7338.
E-mail address: jskim129@kimm.re.kr.

Despite abovementioned previous studies, there are still lots of unresolved phenomena about pool boiling of ammonia in a flooded evaporator. More elaborate investigation is required to understand the complicated phenomena of ammonia including boiling incipience, hysteresis, and effect of surface structures in the flooded evaporator. The present study is aimed to investigate the hysteresis in boiling curves of ammonia and to clarify the effect of low fin structure on boiling performance, and to compare the measured data with previous correlations.

2. Experimental Setup

2.1. Experimental apparatus

The test chamber was made of stainless steel with a wall thickness of 6.5 mm to withstand an internal pressure as high as 20 bar, which corresponds to the saturation pressure of ammonia at 49.4 ℃. The length of the test chamber is 796 mm, and the internal diameter is 254.4 mm. The chamber is filled with ammonia, and the liquid level of the ammonia pool reaches approximately to the center of the chamber. The test tube was located at the bottom-center of the liquid pool as shown in Fig. 1. The test tube was likewise made of stainless steel with an outer diameter of 15.87 mm, and the inner diameter was 13.39 mm. Smooth tube and enhanced tube were prepared to investigate the effect of surface geometry on boiling heat transfer performance. Important geometric parameters are designated in Fig. 2 and corresponding values for smooth and enhanced (low fin) tubes are tabulated in Table 1. A smooth tube has machine-roughened surface, whose arithmetic average roughness (R_a) was measured as 0.296 μm using the surface roughness tester. The enhanced tube has low fins with a height of 1.33 mm. The fin pitch was 0.977 mm (26 fins per inch), and wall thickness (t_w) was 0.63 mm. Since the tube was compressed by the fin rolling machine during the fabrication process, the outer and inner diameters of the enhanced tube were reduced to 13.07 mm and 11.81 mm, respectively. The outmost diameter including low fins was maintained to be 15.73 mm, which is nearly the same as the outer diameter of the smooth tube.

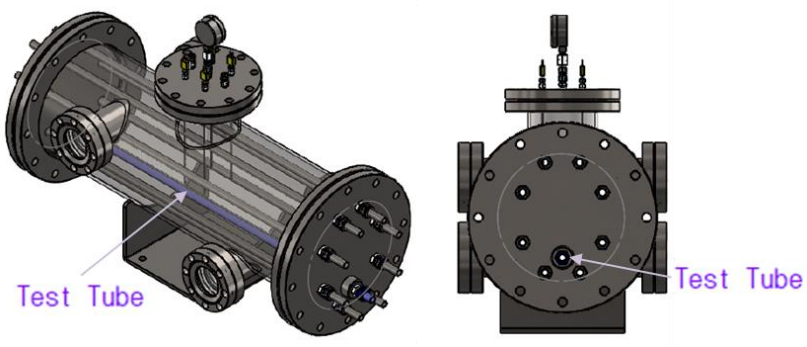


Fig. 1. Schematic drawing of test chamber and test tube.

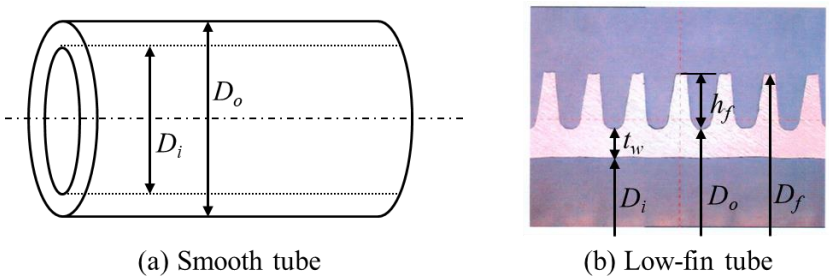


Fig. 2. Designation of geometric parameters for smooth and low-fin (enhanced) tubes.

Table 1. Geometric parameters of smooth and low-fin tubes

	D_i (mm)	D_o (mm)	t_w (mm)	D_f (mm)	h_f (mm)
Smooth tube	13.39	15.87	1.24	-	-
Low-fin tube	11.81	13.07	0.63	15.73	1.33

The chamber temperature was maintained using eight tubes embedded in the chamber, where water and ethylene glycol mixture flows. Four tubes are in the vapor region of the chamber and utilized to condense the ammonia vapor generated from the test tube. The remaining four tubes are located at the liquid region of the chamber and employed to maintain the saturation temperature of the liquid pool of ammonia. The liquid temperature of the ammonia pool was measured at two points using T-type thermocouples, and the internal pressure of the chamber was acquired from the pressure transducer. The temperature of the test tube was controlled by circulating hot distilled water through the tube. Inlet and outlet temperatures of the test tube were measured with precise RTD sensors with 1/10 DIN accuracy (±0.03 ℃ tolerance at 0 ℃). The hot distilled water was circulated by a gear pump and the flow rate was measured with Coriolis mass flowmeter. The flow rate through the test tube was maintained to be 3.8 kg/min over the entire tests. Two reinforced glass windows were equipped at the top and bottom regions of the chamber to observe the boiling and condensation phenomena at the liquid and vapor regions, respectively. A high-speed camera with a frame rate of 2,000 fps was utilized for capturing the bubble nucleation on the heated tube. The entire test chamber was thermally insulated with fiberglass insulation tapes having low thermal conductivity of 0.05 W/mK.

2.2. Experimental procedure and data reduction

Ammonia is filled into the test chamber in the following procedure. The internal pressure of the test chamber is lowered down to the absolute pressure of 3–5 mTorr using a rotary vacuum pump. Once the non-condensable gas is completely extracted from the chamber, the valve to the vacuum pump is closed. Then, the valve to the ammonia cylinder is open, and the liquid ammonia is injected into the chamber. When the liquid level of ammonia gets to the center of the chamber, the valve is closed to finish the filling process. The boiling experiment was conducted at three saturation pressures of 6.15, 8.57, and 11.7 bar, which correspond to the saturation temperatures of 10, 20, and 30 ℃, respectively. Once the internal temperature and pressure are maintained at the designated saturation temperature and pressure using eight temperature control tubes, the hot water begins to flow through the test tube. At the initial step, hot water temperature is merely 2.5 K higher than the saturation temperature of ammonia pool. Once the inlet and outlet temperatures of the test tube reach steady state, all data including temperature, pressure and flow rate are stored for 10 min, and the hot water temperature is increased to the next level stepwise.

Evaporation or boiling heat transfer rate, Q is obtained from the following energy balance equation.

$$Q = \dot{m} c_p \Delta T = \dot{m} c_p (T_i - T_o) \tag{1}$$

T_i and T_o refer to the inlet and outlet water temperature of the test tube, respectively. The heat transfer rate, Q is also expressed as multiplying overall heat conductance and log-mean temperature difference as shown in Eq. (2).

$$Q = UA\Delta T_{lm} \tag{2}$$

The LMTD (log-mean temperature difference) is defined as,

$$\Delta T_{lm} = \frac{\Delta T_i - \Delta T_o}{ln(\Delta T_i / \Delta T_o)} \tag{3}$$

$$\text{here,} \quad \Delta T_i = T_i - T_\infty, \ \Delta T_o = T_o - T_\infty$$

T_∞ refers to the liquid pool temperature surrounding the test tube. Boiling heat transfer coefficient, h_b can be acquired from the following thermal resistance relation.

$$\frac{1}{UA} = \frac{1}{h_i A_i} + \frac{ln(D_o/D_i)}{2\pi kL} + \frac{1}{h_b A_o} \tag{4}$$

Total thermal resistance comprises thermal resistance of internal convection, conduction thermal resistance through the tube wall, and thermal resistance of boiling heat transfer. Convective heat transfer coefficient of internal water flow through the test tube was obtained from the Gnielinski correlation [13].

$$Nu_D = \frac{(f/8)(Re_D - 1000)Pr}{1+12.7(f/8)^{1/2}\left(Pr^{2/3}-1\right)} \tag{5}$$

$$0.5 \le Pr \le 2000, \quad 3000 \le Re_D \le 5 \times 10^6$$

Since Reynolds numbers in the present study range from 5,282 to 14,531, the correlation is applicable to obtain the internal convective heat transfer coefficient. Then, boiling heat transfer coefficient (h_b), the remaining unknown in Eq. (4), can be acquired. The average wall temperature on the test tube is calculated in the following equation.

$$\overline{T_w} = (T_i + T_o)/2 + Q \times \left(\frac{1}{h_i A_i} + \frac{ln(D_o/D_i)}{2\pi kL}\right) \tag{6}$$

2.3. Uncertainty analysis

T-type thermocouple employed to measure the liquid pool temperature has an uncertainty of ±0.5 ℃. 1/10 DIN-class RTDs to measure inlet and outlet temperatures of the test tube are extremely accurate with an uncertainty of ±0.03 ℃ at 0 ℃. The uncertainty increases with temperature according to the following relation.

$$U(T) = (0.3 + 0.0005 \times T)/10 \tag{7}$$

where, T is measured temperature in ℃. The resultant uncertainty of LMTD (log mean temperature difference) are calculated to be from 1.9% to 14.4%. The mass flowmeter has an uncertainty of ±0.1%, and the pressure transducer has an accuracy of ±0.08%, both of which are provided by manufacturers. As a result, the uncertainty of obtained heat transfer rates ranges from 1.1% to 20.5%, and the uncertainty of boiling heat transfer coefficients is 16.1% in average.

3. Results and Discussion

3.1. Hysteresis in boiling curve

Figure 3(a) exhibits the boiling curve on the smooth tube in the ammonia pool at the saturation temperature of 30 ℃ corresponding to the saturation pressure of 11.7 bar. It is noticeable that there is discrepancy between boiling curves with increasing heat flux and decreasing heat flux. In case the heat flux is increased from low to high, bubble generation is observed only in some areas of the tube until the heat flux

reaches 11,000 W/m^2. It seems that boiling incipience is delayed until the superheat is large enough to sustain the bubble generation. The large superheat required to generate the bubble is attributed to the superior wettability of ammonia on the stainless steel surface owing to the small surface energy. Ammonia is highly wettable on most of metal surfaces, resulting in the low contact angle less than 10°. The low contact angle is responsible for the suppression of bubble nucleation because it decreases the initial radius of the vapor embryo. The small initial radius of the embryo results in the increase of the wall superheat for attaining bubble nucleation. In contrast, in case the heat flux decreases from high to low, nucleate boiling is preserved over the entire tube surface even at the low heat fluxes less than 10,000 W/m^2. The bubble generation is facilitated at the low heat flux because the remaining vapor after the departure is large enough to keep the bubble generation at the low wall superheat. Boiling heat transfer coefficients at two cases show maximum 46% difference near the heat flux of 7,800 W/m^2 as shown in Fig. 3(b). Since the large hysteresis leads to different heat transfer performance according to the heating and cooling paths, consistent operation of actual heat exchangers might be threatened. In real heat transfer applications, it is greatly important to minimize the hysteresis by using surface modification techniques such as wettability control or porous structures.

Figure 4 shows different boiling phenomena at the heat flux near 11,000 W/m^2 for both increasing and decreasing heat flux cases. At the increasing case, only a few bubbles can be seen at the low heat flux. In contrast, numerous bubbles are observed over the entire tube surface at the decreasing case. Certainly, the increased number of bubble nucleation is responsible for improvement of heat transfer performance at the decreasing case as shown in Fig. 3.

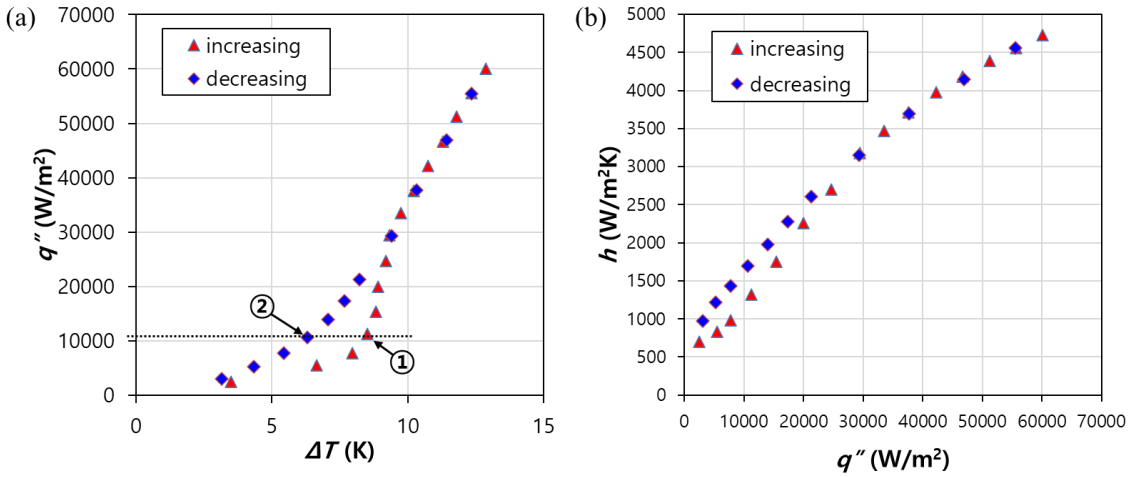


Fig. 3. Hysteresis in pool boiling of ammonia, (a) boiling curve and (b) heat transfer coefficient at P_{sat} = 11.7 bar.

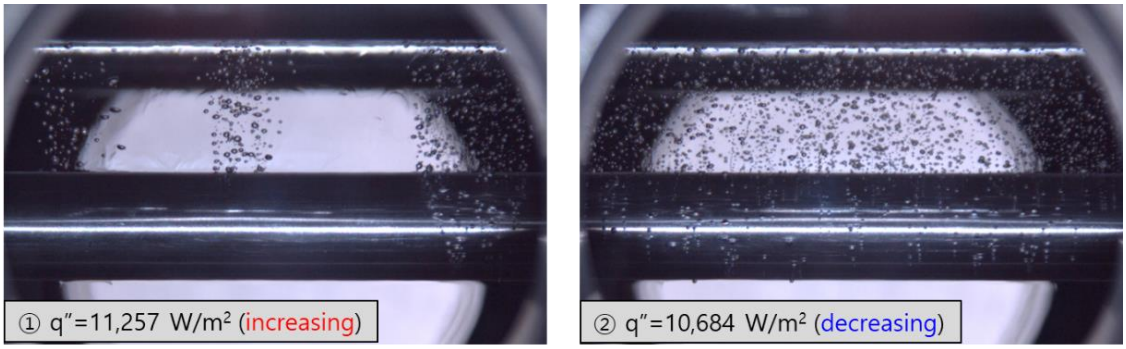


Fig. 4. Bubble nucleation comparison in increasing q'' and decreasing q'' cases at P_{sat} = 11.7 bar.

3.2. Effect of saturation pressure

With increasing the saturation pressure in the ammonia pool, thermodynamic properties such as liquid density, vapor density, surface tension, and heat of vaporization are changed. Since the variation of thermodynamic properties affect the boiling heat transfer performance, heat transfer coefficients at three different saturation pressure from 6.15 bar (T_{sat} = 10 ℃) to 11.7 bar (T_{sat} = 30 ℃) were compared as shown in Fig. 5. As the saturation pressure increases, boiling curves move to the left, implying that the boiling heat transfer is enhanced. It is known that bubble departure diameter decreases with increasing the saturation pressure owing to the variation of thermodynamic properties. Eq. (8) shows the correlation about the bubble departure diameter proposed by Cole [14].

$$Bo^{1/2} = 0.04Ja \tag{8}$$

$$\text{here,} \quad Bo = \frac{g(\rho_l - \rho_v){d_d}^2}{\sigma}, \quad Ja = \frac{\rho_l c_{pl}(T_w - T_{sat})}{\rho_v h_{lv}}$$

where, d_d refers to the bubble departure diameter. The bubble departure diameters of ammonia at the wall superheat of 7 ℃ are calculated to be 1.21, 1.08, and 0.97 mm at three different saturation pressures. Figure 6 clearly shows that the bubble departure diameter increases with increasing the saturation pressure. On the contrary, number of nucleation sites and departure frequency are increased with increasing the saturation pressure. More bubble nucleation sites at higher saturation pressure are also revealed in the captured images in Fig. 6.

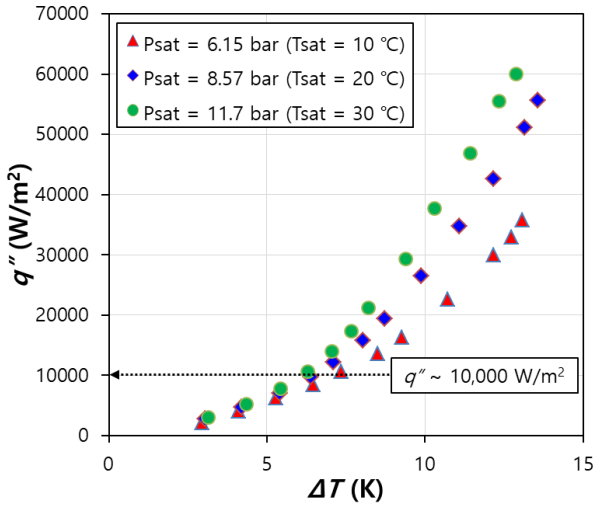


Fig. 5. Boiling curves according to the saturation pressure from 6.15 to 11.7 bar (decreasing q'').

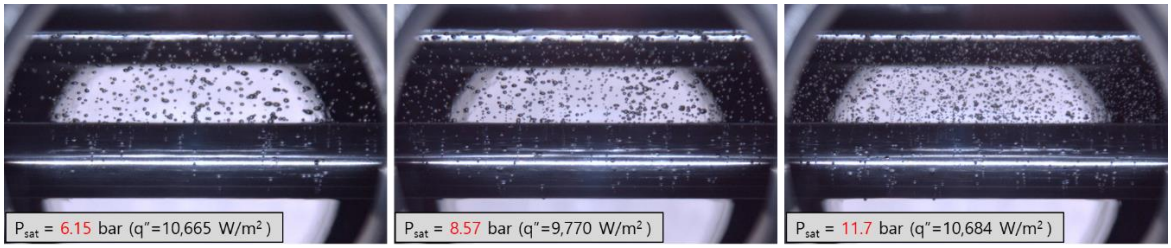


Fig. 6. Comparison of bubble nucleation according to the saturation pressure from 6.15 to 11.7 bar (decreasing q'').

3.3. Comparison with previous correlations

The present data are compared with previous correlations about pool boiling heat transfer coefficients on the smooth tube. Following four correlations (Mostinski [15], Gorenflo [16], Rohsenow [17], and Stephan-Abdelsalam [18]) were selected for comparison.

$$h_b = 0.1011(P_c)^{0.69} q^{0.7} \left[1.8\left(\frac{P}{P_c}\right)^{0.17} + 4\left(\frac{P}{P_c}\right)^{1.2} + 10\left(\frac{P}{P_c}\right)^{10}\right] \quad \text{(Mostinski)} \tag{9}$$

$$h_b = h_0 \left(\frac{q}{q_0}\right)^{n(P_r)} F(P_r) \left(\frac{R_a}{R_{a0}}\right)^{0.133} \quad \text{(Gorenflo)} \tag{10}$$

$$h_b = \frac{1}{C_{sf}} \frac{C_{pl}}{h_{fg}^{0.67}} \left[\frac{1}{\mu_l}\sqrt{\frac{\sigma}{g(\rho_l - \rho_v)}}\right]^{-0.33} (q)^{0.67} (Pr_l)^{-1.7} \quad \text{(Rohsenow)} \tag{11}$$

$$\frac{h_b D_b}{k_l} = 207 \left(\frac{q D_b}{k_l T_{sat}}\right)^{0.745} \left(\frac{\rho_v}{\rho_l}\right)^{0.581} (Pr_l)^{0.533} \quad \text{(Stephan-Abdelsalam)} \tag{12}$$

Gorenflo and Rohsenow's correlations exhibit relatively high heat transfer coefficients (upper bound), and Stephan-Abdelsalam correlation provides lower heat transfer coefficients (lower bound). The present data in case of increasing heat flux shows good agreement with the Stephan-Abdelsalam correlation, and the data in the decreasing case are somewhat higher than the Stephan-Abdelsalam correlation, and approach the Mostinski correlation, especially at the low heat flux region. The following empirical relations are deduced for the pool boiling heat transfer of ammonia at the saturation temperature of 30 ℃.

$$h = 0.9168(q'')^{0.7846} \quad \text{(increasing } q'') \tag{13}$$

$$h = 10.472(q'')^{0.5542} \quad \text{(decreasing } q'') \tag{14}$$

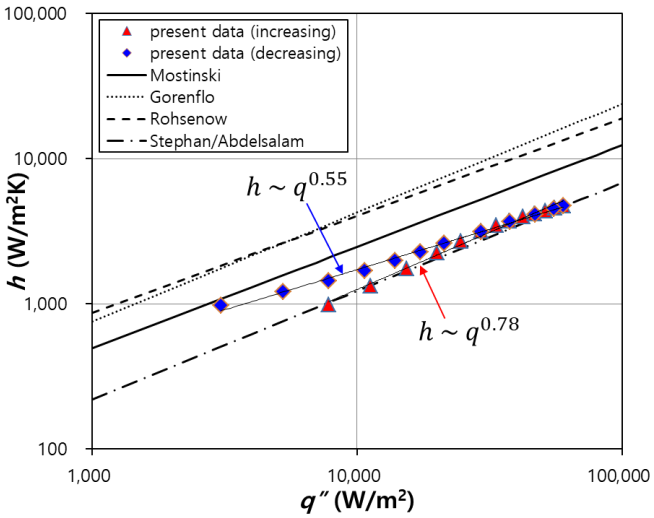


Fig. 7. Comparison with previous correlations at the saturation pressure of 11.7 bar.

3.4. Smooth tube vs. Low-fin tube

The low-fin tube has an outer diameter (D_o) of 13.07 mm as indicated in Fig. 2 and Table 1. The heat transfer coefficient, h_b, is calculated from the tube surface area based on the outer diameter. Total heat transfer rate (Q) is obtained from the following equation.

$$Q = h_b A_o \Delta T_w \tag{15}$$

Figure 8 shows boiling curve and boiling heat transfer coefficient on the low-fin tube compared with those on the smooth tube at the saturation pressure of 11.7 bar. It is noticeable that boiling hysteresis is enlarged on the low-fin tube compared with the smooth tube. The enlarged hysteresis resulted from the decrease in wall superheat on the finned surface compared with that on the smooth tube because there is temperature gradient along the fin height. Despite the hysteresis, the low-fin tube exhibits higher heat transfer coefficients in both increasing and decreasing heat flux cases. The heat transfer coefficient (h_b) increased by 61% in increasing q'' case and by 111% in decreasing q'' case.

Since the heat transfer area is varied, thermal performance of the low-fin tube can be compared with that of the smooth tube based on the thermal conductance which is defined as multiplying heat transfer coefficient and heat transfer area, h_bA_o. Figure 9 shows the thermal conductance of the low-fin tubes normalized with that of the smooth tube in increasing and decreasing heat flux cases. It is concluded that the boiling heat transfer on the low-fin tube is enhanced by 33% (increasing q'') and 74% (decreasing q'') over the smooth tube.

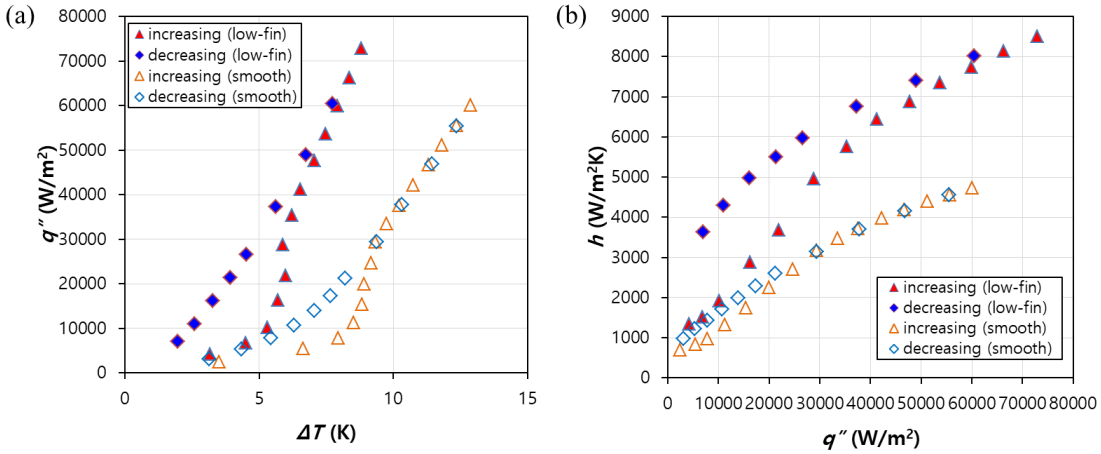


Fig. 8. Effect of enhanced structure (low fins) on boiling heat transfer of ammonia.

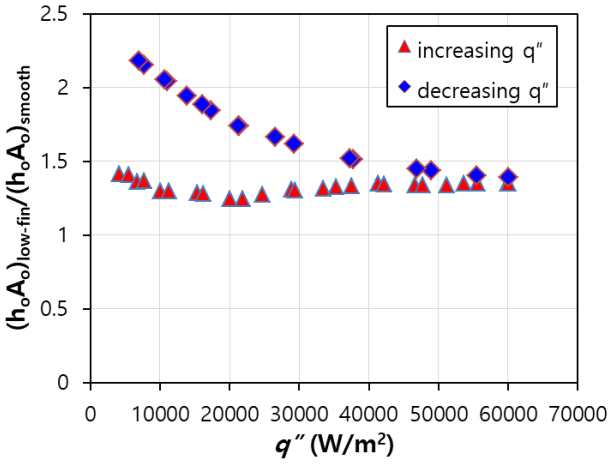


Fig. 9. Thermal conductance of the low-fin tube compared with the smooth tube.

4. Conclusion

Boiling heat transfer of ammonia was investigated in a flooded evaporator for an adsorption heat pump at the saturation pressures of 6.15, 8.57, and 11.7 bar. Large hysteresis between increasing heat flux case and decreasing heat flux case was observed in the boiling curves, which is ascribed to the low surface energy of ammonia. Higher heat transfer coefficients were obtained with increasing saturation pressure, and the measured heat transfer coefficients were best matched with the previous Stephan-Abdelsalam's correlation. Since the enhanced tube with low fins exhibited 33% (increasing q'') and 74% (decreasing q'') higher heat transfer performance compared with those on the smooth tube, employing the low-fin tubes in a flooded evaporator is expected to augment thermal performance of the adsorption heat pump system.

Acknowledgements

This work was supported by Korea Institute of Energy Technology Evaluation and Planning (KETEP) and the Ministry of Trade, Industry & Energy (MOTIE) of the Republic of Korea. (Grant No. 20212050100010).

References

[1] Yang Z, Qu M, Gluesenkamp KR. Ammonia-based chemisorption heat pumps for cold-climate heating applications: A comprehensive review. *Appl Therm Eng* 2020;**179**:115674.
[2] Dias JM, Costa VA. Adsorption heat pumps for heating applications: A review of current state, literature gaps and development challenges. *Renewable Sustainable Energy Rev* 2018;**98**:317-327.
[3] Spindler K. Overview and discussion on pool boiling heat transfer data and correlations of ammonia. *Int J Refrig* 2010;**33.7**:1292-1306.
[4] Arima H, Monde M, Mitsutake Y. Heat transfer in pool boiling of ammonia/water mixture. *Heat Mass Transf* 2003;**39.7**:535-543.
[5] Danilova GN, Dyundin VA, Borishanskaya AV, Soloviyov AG, Kozyrev AA. Effect of surface conditions on boiling heat transfer of refrigerants in shell-and-tube evaporators. *Heat Transf-Soviet Res* 1990;**22.1**:56-65.
[6] Djundin VA, Solov′ev AG, Borisanskaja AV, Vol′nych J. Influence of the type of surface on heat transfer in boiling. *Kholod Tekh* 1984;**5**:33-37..
[7] Ayub ZH, Chyu MC, Ayub AH. Different types of carbon steel enhanced tubes in ammonia flooded evaporator. *Heat transf eng* 2006;**27.5**:39-44..
[8] Zeng X, Chyu MC, Ayub ZH. Experimental investigation on ammonia spray evaporator with triangular-pitch plain-tube bundle, Part I: tube bundle effect. *Int J Heat Mass Transf* 2001;**44.12**:2299-2310..
[9] Zheng JX, Jin GP, Chyu MC, Ayub ZH. Flooded boiling of ammonia with miscible oil outside a horizontal plain tube. *HVAC&R Res* 2001;**7.2**:185-204..
[10] Abbas A, Ayub ZH, Khan TS, Ayub AH, Chattha JA. A Review of Correlations for Outside Boiling of Ammonia on Sinrgle Tube and Bundles. *Heat Transf Eng* 2018;**39.16**:1425-1436.
[11] Fernández-Seara J, Pardiñas ÁA, Diz R. Experimental heat transfer coefficients of pool boiling and spray evaporation of ammonia on a horizontal plain tube. *Int J Refrig* 2016;**67**:259-270.
[12] Fernández-Seara J, Pardiñas ÁÁ, Diz R. Heat transfer enhancement of ammonia pool boiling with an integral-fin tube. *Int J Refrig* 2016:**69**:175-185..
[13] Gnielinski V. New equations for heat and mass transfer in turbulent pipe and channel flow. *Int Chem Eng* 1976;**16.2**:359-368..
[14] Cole R. Bubble frequencies and departure volumes at subatmospheric pressures. *AIChE J* 1967;**13.4**:779-783..
[15] Mostinski IL. Application of the rule of corresponding states for calculation of heat transfer and critical heat flux. *Teploenergetika* 1963;**4.4**:66-71..
[16] Gorenflo D. *VDI Heat Atlas*. VDI-Verlag GmbH, Dusseldorf, Germany: Springer; 1993.
[17] Rohsenow WM. A method of correlating heat-transfer data for surface boiling of liquids. *Trans Am Soc Mech Eng* 1952;**74.6**:969-975..
[18] Stephan K, Abdelsalam M. Heat-transfer correlations for natural convection boiling. *Int J Heat Mass Transf* 1980;**23.1**:73-87..

14th IEA Heat Pump Conference
15-18 May 2023, Chicago, Illinois

Performance of a new ultra-high temperature industrial heat pump

Arne Høeg[a*], Kristian Løver[a], Trond-Atle Asphjell[a], Norbert Lümmen[b]

[a]Enerin AS, Torvveien 1, 1383 Asker, Norway
[b]Dept. of Mechanical and Marine Engineering, Western Norway University of Applied Sciences, Inndalsveien 28, 5063 Bergen, Norway

Abstract

This paper presents a new ultra-high temperature heat pump, working on the Stirling cycle, with helium as working medium. The heat pump can generate heat up to 200°C from sources as low as -10°C with high energy efficiency. A 400 kW prototype installation at a biogas facility is described, where the heat pump supplies steam and cooling to the CO_2 capture process. The performance of the heat pump is presented across a wide range of source and sink temperatures, in terms of heating capacity and share of Carnot COP. The experimental setup is described in detail, as well as the simulation model used for comparing simulated and experimental data. The performance figures are compared with published data for other heat pump cycles used for high temperature heat pumping. The results indicate that helium heat pumps may be more efficient than vapor compression heat pumps for temperature ratios above 1.3 K/K (sink temperature/source temperature).

© HPC2023.
Selection and/or peer-review under the responsibility of the organizers of the 14th IEA Heat Pump Conference 2023.

Keywords: ultra high-temperature lift heat pump; UHTHP; very high temperature heat pump; VHTHP; high temperature lift; steam generating heat pump; helium; CO2 capture

1. Introduction

A prototype of a new stirling-cycle heat pump is installed in a test rig at the biogas facility IVAR near Stavanger, Norway. The pilot installation is shown in Fig.1.

This paper presents the performance of a novel high temperature difference heat pump. The performance is measured at a non-commercial installation of the heat pump, operating with a heat source varying between

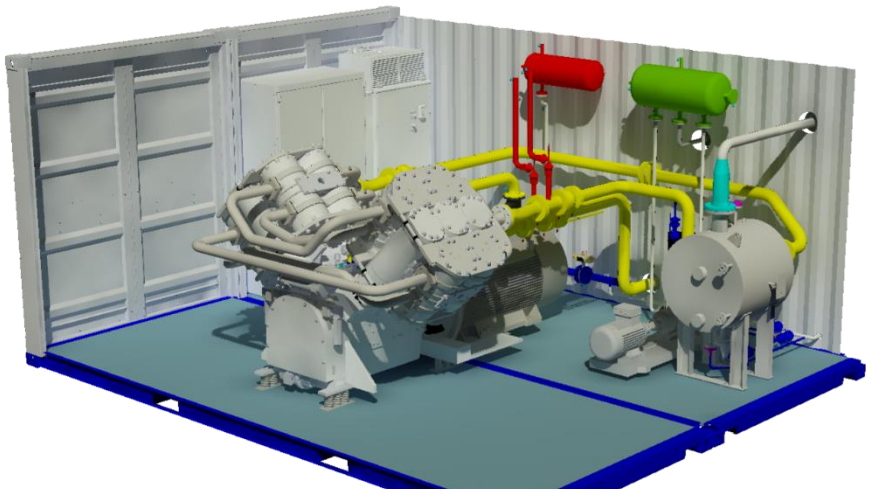


Fig. 1. Pilot installation with steam generator

* Corresponding author. *Email address:* arne@enerin.no

5°C and 45°C and with heat sink temperatures between 140°C and 190°C. The heat pump performance and COP are simulated across a wide range of temperatures and measured at the temperatures that were possible at the plant.

The first sections give a description of the heat pump, the thermodynamic process, the process layout and the instrumentation.

The next sections present the results from testing the heat pump at different loads and the comparison between the measured parameters and simulated values. The discussion and conclusions are given in the last section.

2. HoegTemp ultra high-temperature heat pump

The ultra-high temperature heat pump HoegTemp (Fig.2) from Enerin, is a Stirling-cycle heat pump with helium (refrigerant R-704) as working medium. As the Stirling cycle relies on compression and expansion of a gas, Stirling-cycle heat pumps are not characterized by boiling points and condensing temperatures of their refrigerant, but rather by the ratio of absolute temperatures for the source and sink.

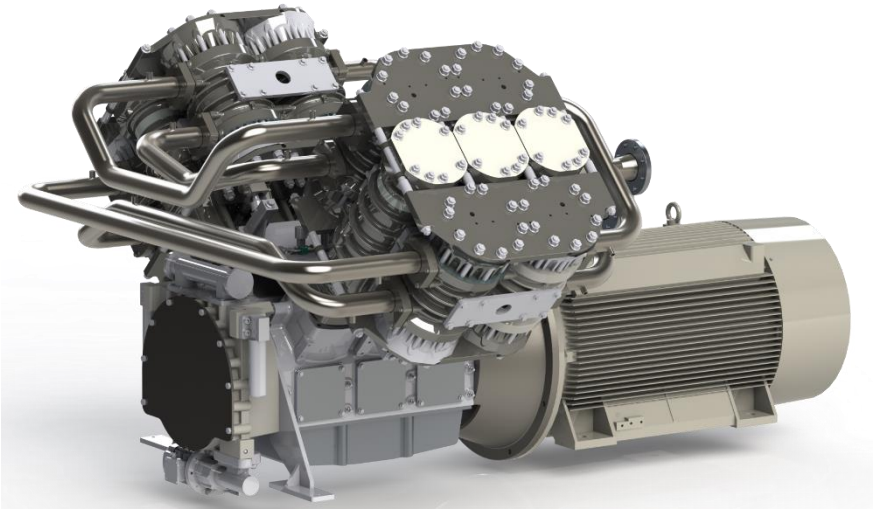


Fig. 2. HoegTemp heat pump

The HoegTemp is a 4-circuit piston compressor heat pump of the double-acting gamma configuration. Each

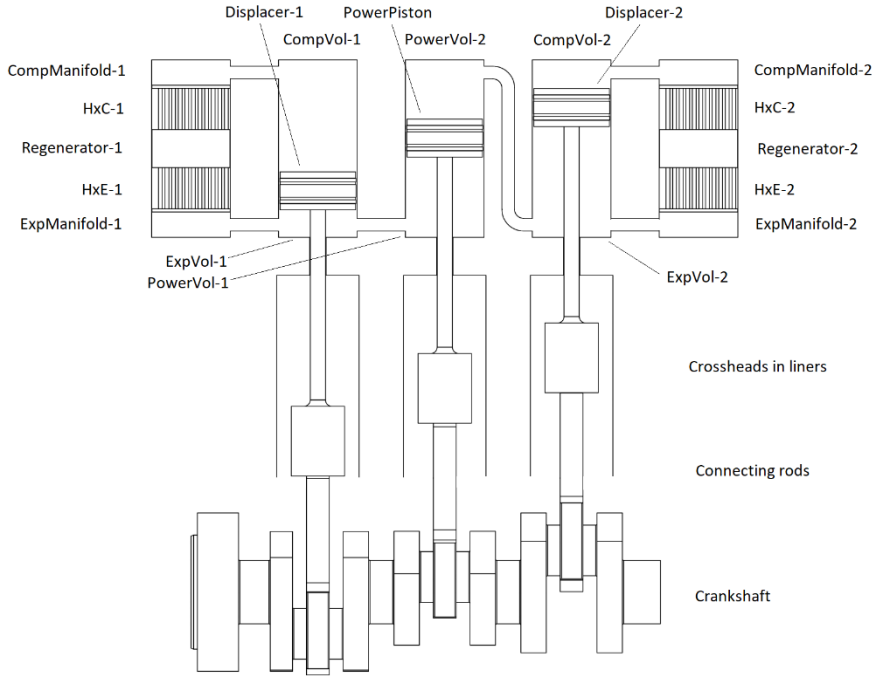


Fig. 3. A circuit pair

circuit consists of a pair of heat exchanger modules, a displacer cylinder, where a displacer piston pumps the working medium through the heat exchangers, and a power cylinder volume, where a power piston compresses and expands the working medium in the whole circuit. The power piston separates two circuits, hence the term double-acting. A pair of circuits is shown in Fig.3. The process components are also referred to in figures 8 and 9. The heat exchanger modules consist of a source heat exchanger and a sink heat exchanger, separated by a regenerative heat exchanger, where heat is stored in steel wire.

The heat pump operates on the Stirling cycle, and due to the cylinder configuration, the two circuits of a circuit pair undergo slightly different processes, as shown in fig. 4.

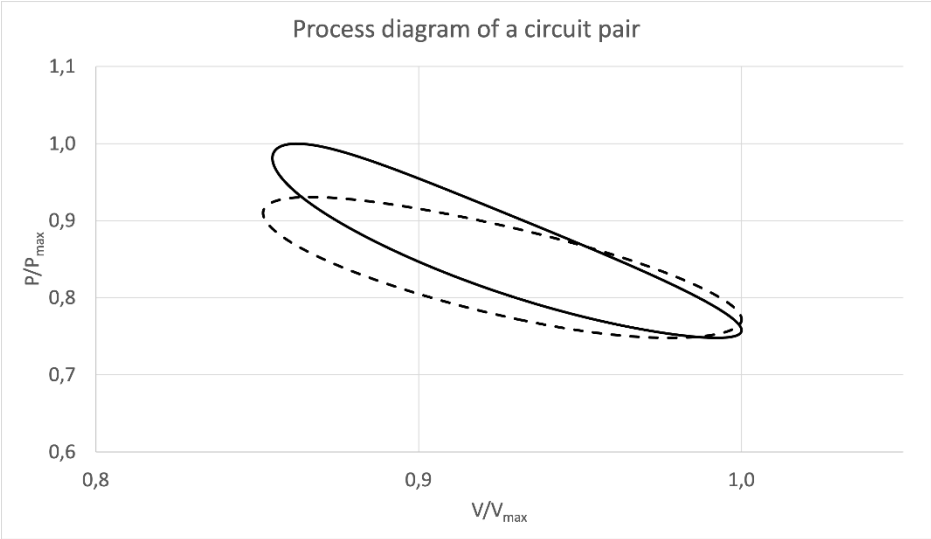


Fig. 4. Process diagram of a circuit pair

The maximum heating capacity of the current implementation of the HoegTemp heat pump is 400 kW. The heat can be generated at any temperature between 20°C and 200°C. The heat pump source can be at any temperature between -10°C and 120°C. If the source temperature is higher than the sink temperature, the heat

pump will work as a heat engine. In future implementations, the source temperature limit may be reduced to minus 250°C, and the sink temperature limit may be increased to +300°C.

Heat is transferred through closed water circuits, both for source and sink. Steam can be generated by a steam generator heated by the pressurized hot-water circuit. The heat pump has separate subsystems for oil lubrication and cooling, working medium handling and process control, diagnostics and data logging.

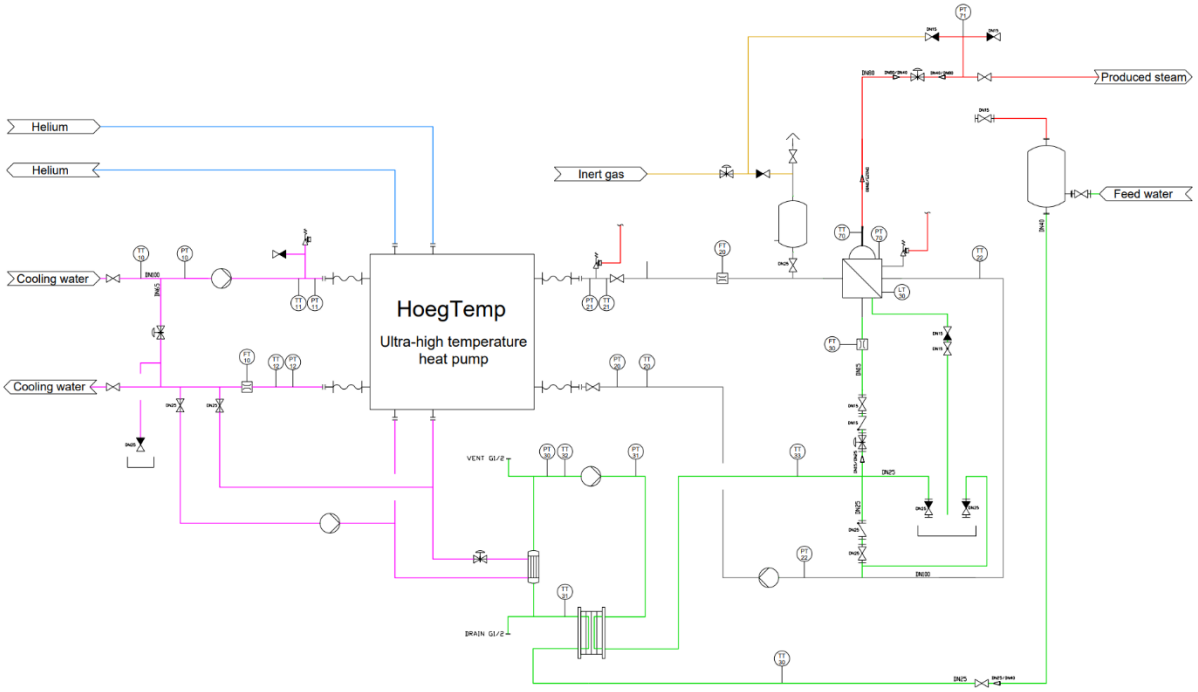


Fig. 5. P&ID of a steam generating installation

3. Pilot installation in biogas facility

Fig. 5 shows a P&ID of the steam generating installation. Heat is transferred to and from the heat pump through closed liquid circuits. Water is a very suitable heat transfer fluid at the temperatures of interest, but other fluids can also be used.

The cold or source side circuit (purple lines) uses pure water, and delivers heat from the external source by receiving and returning water at different temperatures. A shunt valve is used to recirculate a fraction of the water, thereby achieving two objectives:

- Control the heat pump inlet temperature
- Vary the mass flow x ΔT relationship independently from requirements set up by the external source

The hot side (sink side, grey lines) circuit uses water under pressure in a closed loop to transfer heat from the heat pump to a steam generator, without any direct contact with the external sink. The steam generator is a shell and plate design heat exchanger, where the hot side (hot side circuit) runs inside the plates, while the cold side (feed water, steam) runs between the outer shell and the plates. A pump is used to circulate the hot side circuit, pump work is predominantly caused by pressure loss in the heat exchangers of the heat pump.

Feed water (green lines) from an external source is pumped into the steam generator at the same rate that water is evaporated. Steam (red line) is finally delivered to the external heat sink at a pressure regulated by a control valve. Heat delivered from the hot side circuit is used for preheating of incoming feed water, evaporation of feed water and to a certain amount superheating of steam. It must be assumed that full crossflow conditions are not achieved in the steam generator.

3.1. Instrumentation and measurements

A complete overview of the system from the point of view of measurements is given in figure 6, with descriptions in table 1.

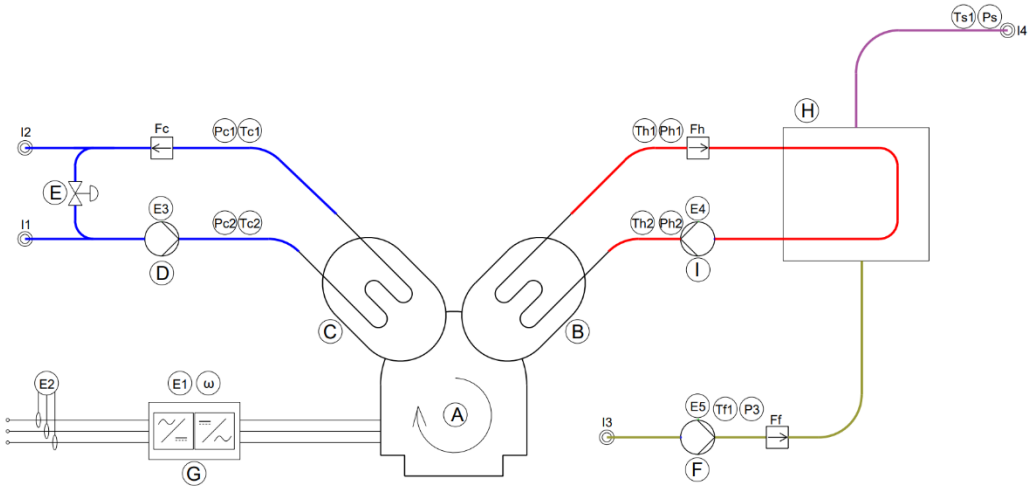


Fig. 6. Instrumentation

Table 1. Instrumentation

A	Heat pump	B	Heat pump hot side heat exchangers
C	Heat pump cold side heat exchangers	D	Cold side circulation pump
E	Shunt valve	F	Feed water pump
G	Variable frequency drive (VFD)	H	Steam generator
I	Hot side circulation pump		
I1	Tempered water from external source	Pc1	Pressure in cold side circuit after heat pump
I2	Tempered water return to external source	Pc2	Pressure in cold side circuit before heat pump
I3	Feed water from external sink	Ph1	Pressure in hot side circuit after heat pump
I4	Steam to external sink	Ph2	Pressure in hot side circuit before heat pump
Tc1	Cold side temperature after heat pump	P3	Pressure of feed water
Tc2	Cold side temperature before heat pump	Ps	Pressure of produced steam
Th1	Hot side temperature after heat pump	Fc	Flow in cold side circuit
Th2	Hot side temperature before heat pump	Fh	Flow in hot side circuit
Tf1	Feed water temperature after pump	Ff	Feed water and steam flow
Ts1	Produced steam temperature	ω	Heat pump speed
E1	VFD produced energy	E2	VFD consumed energy
E3	Hot side circulation pump consumed energy	E4	Cold side circulation pump consumed energy
E5	Feed water pump consumed energy		

3.2. Accuracy estimates

The main energy streams are measured as follows:

$$\dot{Q}_x = F_x\big(h(T_{x2}, p_{x2}) - h(T_{x1}, p_{x2})\big) \tag{1}$$

If the accuracy of an instrument is generically defined as $V = \bar{V}\big(1 \pm \dot{V}\big)$, where $\bar{V}$ is the apparent value, $\dot{V}$ is the relative deviation and V is the actual value, the total accuracy for the calculated energy flow is

$$\dot{Q}_c = \bar{F}\big(1 \pm \dot{F}\big)\Big(\bar{h}_2\big(1 + \dot{h}_2\big) - \bar{h}_1\big(1 + \dot{h}_1\big)\Big) \tag{2}$$

which becomes

$$Q_c = \bar{F}\bar{h}_2\left(1 \pm \dot{F}\right)\left(1 + \dot{h}_2\right) - \bar{F}\bar{h}_1\left(1 \pm \dot{F}\right)\left(1 + \dot{h}_1\right) \tag{3}$$

The latter can be transformed into

$$Q_c = \bar{F}\bar{h}_2\left(1 + \sqrt{\dot{F}^2 + \dot{h}_2^2}\right) - \bar{F}\bar{h}_1\left(1 + \sqrt{\dot{F}^2 + \dot{h}_1^2}\right) \tag{4}$$

The following equation can be used instead of eqn. (4).

$$Q_x = \bar{F}\left(\left(\bar{h}_2 - \bar{h}_1\right) + \sqrt{\left(\bar{h}_2\sqrt{\dot{F}^2 + \dot{h}_2^2}\right)^2 + \left(\bar{h}_1\sqrt{\dot{F}^2 + \dot{h}_1^2}\right)^2}\right) \tag{5}$$

It is assumed there is a linear relationship between temperature and enthalpy for small temperature spans (i.e. the uncertainty range of the temperature sensor)

For the cold side circuit

$$\dot{Q}_c = F_c\left(h(T_{c2}) - h(T_{c1})\right) \tag{6}$$

For the hot side circuit

$$\dot{Q}_h = F_h\left(h(T_{h2}) - h(T_{h1})\right) \tag{7}$$

The coefficient of performance of the heat pump is calculated as

$$COP = \frac{Q_h}{W_{E1}} \tag{8}$$

The relationship with Carnot efficiency is calculated by the mean temperature of the water-side of hot and cold side heat exchangers

$$COP_{ideal} = \frac{T_{h1}+T_{h2}}{T_{h1}+T_{h2}-T_{c1}-T_{c2}} \tag{9}$$

4. Simulated performance

4.1. Main energy flows

Figure 7 shows the main energy flows in the heat pump. The electric power W_{el}, the recycled heat Q_L, and the useful heat Q_H. The main losses are electric losses in the variable frequency drive, Q_{VFD}, the electric motor,

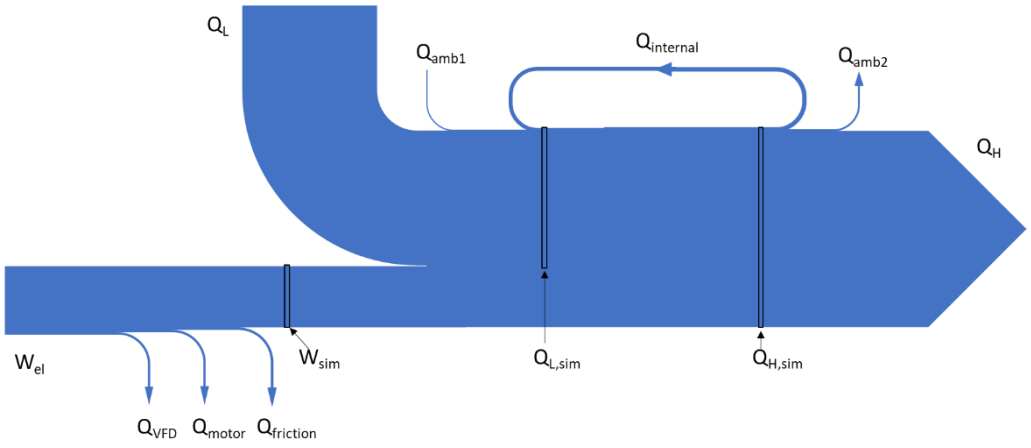


Fig. 7. Sankey diagram

Q_{motor}, friction in the bearings, crosshead, piston ring seals and piston rings, $Q_{friction}$, internal heat transfer from hot to cold volumes, $Q_{internal}$, and heat exchange with the ambient, Q_{amb1} and Q_{amb2}.

4.2. Simulation model

During the development of the process a simulation model of the engine was developed and refined as the design evolved. The simulation model was made in Sage, which is a software package specially designed to simulate Stirling engines. Sage is developed by David Gedeon [1]. The development and use of a simulation model for an earlier heat pump, is described in detail in a previous paper by Tveit et al [2]. Sage is a 1-dimensional finite element model, where each component is divided into a small number of elements (typically 3 to 9 elements each). Inputs to the model are the principal dimensions of each gas volume in terms of cylindrical equivalents, such as diameter, length, number of tubes, Bernoulli factor k, surface area and wall thickness, and the operating conditions such as shaft speed, average pressure and surface temperatures. The model calculates all heat flows and pv work. Internal heat transfer may be modelled, but the authors have chosen to model such losses outside of the simulation model.

The root model consists of three pistons, connected to a crankshaft, defined by geometry, the average charge pressure of each circuit, and the circuit model, shown in fig.8. As can also be seen in fig.3 Displacer-1 separates CompVol-1 and ExpVol-1, Displacer-2 separates CompVol-2 and ExpVol-2, and PowerPiston separates PowerVol-1 and PowerVol-2 in the circuit model 'GammaCircuits'.

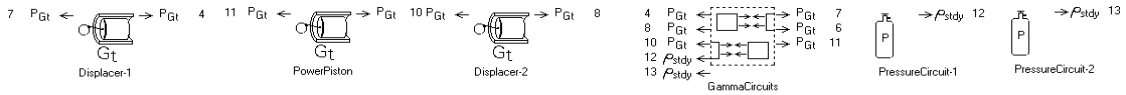


Fig. 8. Main elements of the simulation model implemented in Sage

The circuit model (fig.9) consists of two similar circuits, each with a compression volume and an expansion volume, connected by the heat exchangers and ducts, both circuits connected to each side of the power piston, via gas ducts. The gas flow is denoted with numbers: for Circuit 1, the connections are 6-7-20-21-9-10-29-30, and the components are shown principally in fig.3.

The simulation model takes into account certain losses, e.g., gas friction losses in the tube heat exchangers, hysteresis losses between gas and wall surfaces, but not the mechanical losses and heat losses by convection and radiation of the exposed surfaces. Internal heat transfer between parts are not included in the model either.

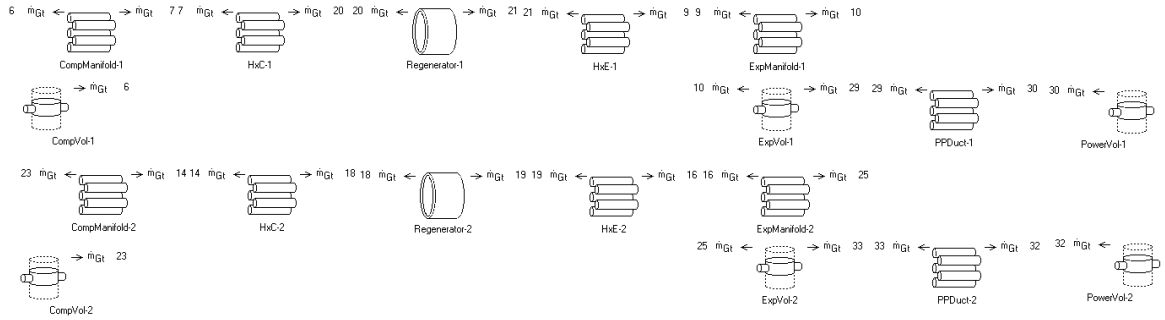


Fig. 9. Circuit model as implement in the software Sage

4.3. Decoupled losses

A model for decoupled losses, was developed, along the methods described by Lundqvist [3]. The main loss factors are defined as:

- Losses in the electric drive train: Q_{VFD}, Q_{motor}
- Mechanical losses outside the cylinders: $Q_{friction}$
- Mechanical losses inside the cylinders: $Q_{friction}$
- Direct heat transfer from hot to cold heat pump volumes: $Q_{internal}$
- Heat loss to the ambient: Q_{amb1}, Q_{amb2}

Internal heat transfer has been modelled as linear conduction, with temperature gradient and cross section. External heat transfer has been modelled as free convection and radiation.

Mechanical friction has been simulated by Daido Bearings, the bearing manufacturer for the rotating bearings. The crossheads and piston rod seals have been modelled like linear bearings, and the dry piston guide rings and piston rings, have been treated as linear dry bearings. The efficiency of the electric motor and VFD has been found from the specifications.

4.4. Simulated performance at expected operating conditions

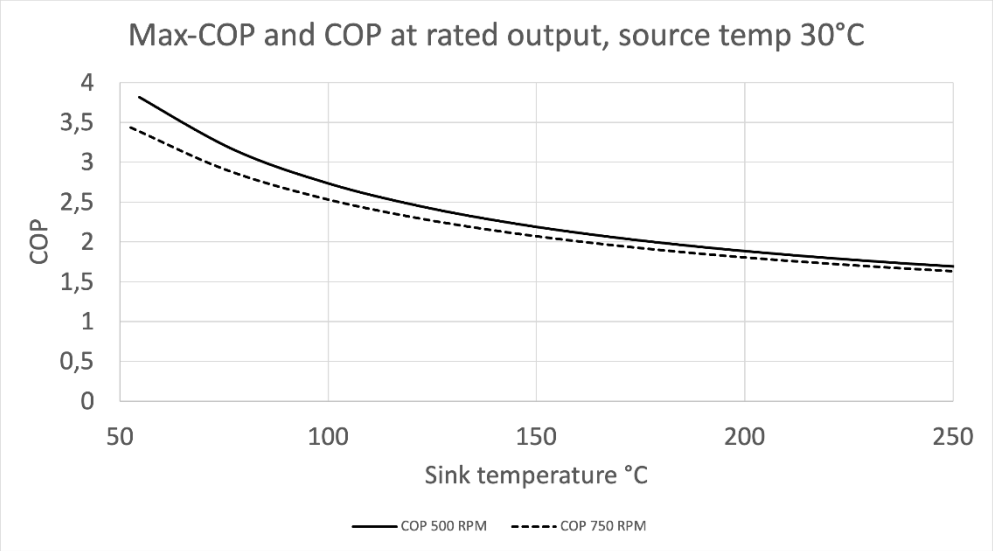


Fig. 10. Simulated COP for the HoegTemp heat pump

Fig. 10 shows the simulated performance of the process, simulated with source temperature 30°C (average between in and out flow temperatures of the water circuit, 35°/25° would be typical) and sink temperatures ranging from 60°C to 250°C (defined as average between in and out flow temperatures of the water circuit, ΔT 10-20° would be typical), at a shaft speed of 500 RPM, which is very close to the simulated maximum COP of the heat pump, and at a shaft speed of 750 RPM, which is the rated operating point, with a heat output, Q_H, of 400 kW across the sink temperature range.

5. Testing at the biogas facility

During operation, the available heat source temperature varies with the ambient temperature, and with the plant operation. The installation allows a reduced source temperature, as long as it is above 5°C to avoid freezing. The maximum expected source temperature is 50°C in the summer.

The plant needs saturated steam at minimum 2 barG, but the test cell is designed to allow heating of the steam generator with higher temperature hot water, or even a higher delivery pressure, that may be throttled to 2-3 barG. The piping and systems have been designed for 16 barG and 200°C. For testing purposes, it is possible to test the heat pump with sink temperatures below 133°C (2 barG), by cooling the steam generator with cold water.

During early testing, the available source temperatures will be 5-15°C, and heat generation will be tested at 130°C to 180°C. Steam will be generated at both 2-3 barG, and at up to 7 barG.

The installation is not ready at the time of writing, so measurements are not available yet.

6. Comparison of simulated results to other high-temperature heat pumps

The simulated performance of the Enerin HoegTemp heat pump is compared to other high-temperature heat pumps in figure 11. For reference, the performance of the stirling cycle heat pump from Single-Phase Power was documented by Høeg et al [4], the performance of heat pumps described in an overview by Bless et al [5], and the peak performance points of cooling machines with natural refrigerants, presented by NTNU [6], have been included. As the Carnot COP and also the COP of a stirling cycle heat pump, depends on the temperature ratio between sink and source temperatures, the chart is presented in terms of temperature ratio rather than the

more common temperature lift. A temperature lift from 5° to 105°C corresponds to 1.36 K/K, while a temperature lift from 70° to 170°C corresponds to 1.29 K/K, and the heat pumps would have different COPs, and different share of Carnot COP.

$$Temperature\ ratio = \frac{T_{sink,in}+T_{sink,out}}{T_{source,in}+T_{source,out}} \quad (10)$$

In order to compare the relative efficiency of the heat pump to other types of heat pumps and cooling machines, the cooling COP relative to the cooling COP of a carnot heat pump, is plotted against the ratio of sink temperature to source temperature, in fig.12. In the authors' opinion, this ratio more accurately assess the relative efficiency of different cycles, especially at high temperature lifts (large temperature fractions).

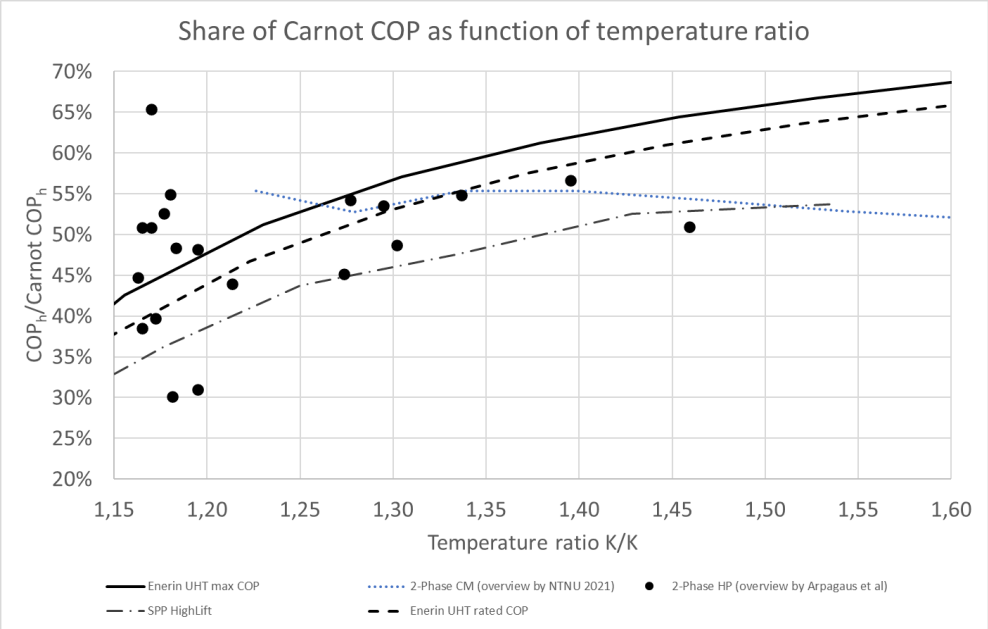


Fig. 12. Share of Carnot COP as function of temperature ratio

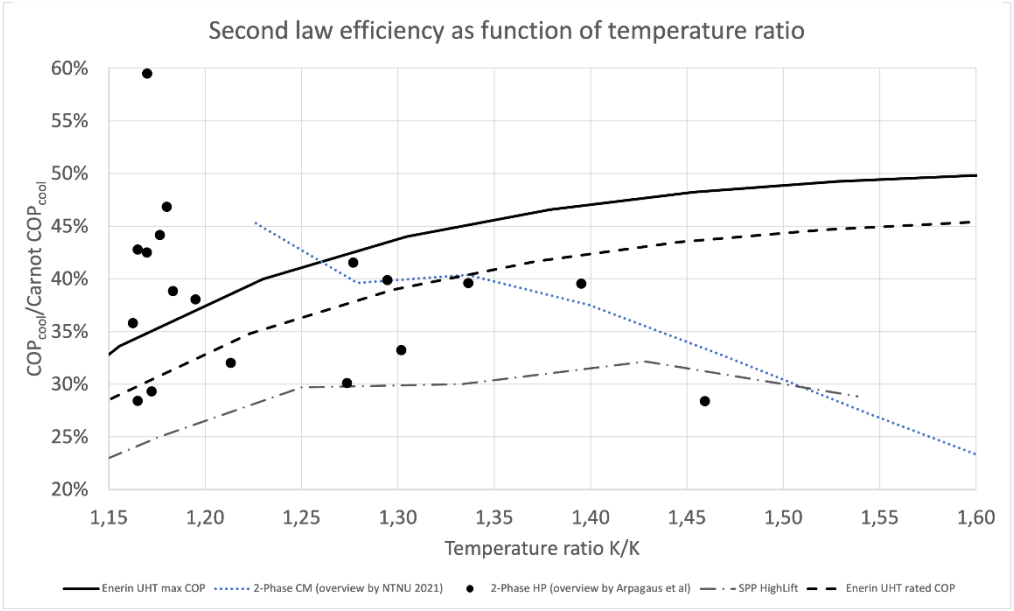


Fig. 11. Second law efficiency of the HoegTemp heat pump, compared to vapour compression heat pumps

7. Conclusions

The comparison shows that stirling-cycle heat pumps may be more efficient than vapour compression heat pumps when the ratio of sink to source temperature is above 1.3 K/K. That could be 114°C heating from a 25°C source, or a circuit at 162°/154°C to make 4 bar steam, with a source of 65°/50°C waste heat.

Acknowledgements

The R&D project has been part-funded by Innovation Norway, and the inter-municipal infrastructure company IVAR has provided the test installation at its biogas facility at Grødaland.

References

[1] Gedeon, D. Sage users guide, stirling pulse tube and low T model classes, Gedeon Associates 2009
[2] Tveit, TM, Høeg, A, Asphjell, TA. A simulation based interactive multi-criterion strategy for optimizing stirling engine designs, Proceedings of the 14th International Stirling Engine Conference, Groningen, The Netherlands, 2009
[3] Lundqvist, PG, Stirling cycle heat pumps and refrigerators. Doctoral dissertation, KTH, Stockholm, Sweden 1993
[4] Høeg, A, Tveit, TM. Low to very high temperature thermal energy recycling – 3 case studies, Proceedings of the 19th International Stirling Engine Conference, Rome, Italy, 2021
[5] Bless, F, Arpagaus, C, Bertsch, S. Theoretical investigation of high temperature heat pump cycles for steam generation, 13th IEA heat pump conference, Jeju, Korea, 2020
[6] Contiero, L, Saed MZ, Blust, S. Cooling between -40◦C and -80◦C, Norsk Kjøleteknisk Forenings Årsmøte 2021

14th IEA Heat Pump Conference
15-18 May 2023, Chicago, Illinois

Optimization of SPF or CO_2 emissions? Impact of control strategies on a bivalent waste water heat pump system for high energy standard buildings

Simon Callegari*, Fleury de Oliveira, Pauline Brischoux, Pierre Hollmuller

Groupe Systèmes Energétiques, Université de Genève, Bd Carl-Vogt 66, CH – 1211 Genève 4, Switzerland

Abstract

While heat pump (HP) systems could be a main solution to achieve the energy transition, their operation in actual condition of use still face specific issues, in particular when integrated in multi-energy systems with fossil complement. Based on detailed monitoring (hourly data, entire year), this paper concerns the monitoring and simulation of the heat production system of a new low energy multifamily buildings complex in Geneva - Switzerland, comprising a centralized HP on waste water (200 kW_{th}) and complementary gas boiler (600 kW_{th}). For SPF optimization reasons and in order to take advantage of the lower space heating temperatures, a seasonally differentiated operation mode was planned for the HP, with a lower temperature production setpoint in winter than in summer (when only domestic hot water is needed). However, this does in fact limit the operation of the HP to short periods, and leads to a lower HP share (45%) than expected. By way of numerical simulation, we show that alternative operation modes could induce a higher share of HP production, up to 70%. Despite a possible drop in SPF (from 3.2 in the current situation to 2.7 when maximizing the heat pump production), we highlight that this could actually lead to a better system performance in terms of CO_2 emissions, when taking into account the related reduction in gas consumption of the complementary gas boiler, as well as the actual hourly electricity mix for the HP.

© HPC2023.
Selection and/or peer-review under the responsibility of the organizers of the 14th IEA Heat Pump Conference 2023.

Keywords: waste water; heat recovery; HP performance; bivalent systems; in situ monitoring; simulation; system analysis; CO_2 emissions.

1. Introduction

1.1. Context and issues

In the canton of Geneva, CO_2 emissions from the energy system represent about 4.2 t/capita, of which 2.2 are emitted by the building heat supply sector, 1.1 by the transport sector (excluding the airport), and 0.8 by the electricity sector [1]. As a result, the greatest potential for reducing CO_2 emissions lies in the building heat supply sector, which also accounts for nearly half of the final energy consumption delivered to consumers. In 2018, the energy consumption of this sector (climate adjusted) amounted to 5'300 GWh or 10.6 MWh/capita, and was mainly based on fossil fuels.

One of the options to valorize local renewable resources is the use of heat pumps (HP). In 2018, this technology covered 1.7% of the heat demand of the Canton of Geneva [1]. However, a set of recent prospective scenarios [1, 2] shows that the development of HPs, in combination with other production methods such as medium-depth geothermal energy, the development of district heating networks, as well as the reduction of the demand for the building stock, would allow a reduction of CO_2 emissions related to this sector to about 1 t/capita by 2035, respectively 0.2 t/capita by 2050.

* Corresponding author.
E-mail address: simon.callegari@unige.ch.

In this respect, it is however crucial to know and control: i) the actual performances of HP systems, in condition of use; ii) the effective thermal demand of high and very high energy performance buildings (in terms of heat load and temperature). These points are particularly crucial with regard to multifamily buildings, which represent 79% of the heated surface of Geneva's residential building stock, against 21% for single family houses [3].

The issue of using HPs for multifamily buildings is addressed in [4], which analyzes the potentials and constraints of various cold sources (air, unglazed solar panels, geothermal boreholes, lake, river, groundwater) for different types of buildings (new and existing). In new constructions, with reduced space heating (SH) demand and distribution temperature, the important share of domestic hot water (DHW) turns out to have a significant impact on the HP performance.

In order to use the warmest possible heat sources, and with the idea that the majority of the heat demand is in winter, geothermal and hydrothermal energy are a priori well placed, since their temperature remains relatively constant during the year, unlike the outside air. However, in many cases, legislation prohibits geothermal boreholes or water collection in subsurface aquifers (protection of drinking water resources). In this respect, waste water of the proper buildings is an interesting resource, both because of its temperature level which is higher than for low enthalpy geothermal resources, and because of its local and temporal availability matching the heat demand of the buildings, especially for the heat supply of DHW.

1.2. Objectives and structure

This paper concerns the monitoring and simulation of the heat production system of a new low energy multifamily buildings complex in Geneva, comprising a centralized HP on waste water (200 kW_{th}) and complementary gas boiler (600 kW_{th}) with heat distribution by a local district heating.

After a brief description of the buildings and heat production system, we present the heat production balance over an entire year of operation, followed by a detailed analysis and characterization of the related subsystems (waste water pit, HP, gas boiler). CO_2 emissions are assessed by taking into account the hourly Swiss electricity mix. Finally, numerical simulation shows that alternative operation modes could induce a higher share of HP production, with a drop in SPF but a better system performance in terms of CO_2 emissions.

2. System description

2.1. Buildings

Constructed between 2014 and 2019, the residential complex under consideration consists of 7 buildings, 4 of which comply with the legal requirement of "high energy performance" (HEP) for new constructions, and 3 comply with a "very high energy performance" (VHEP) requirement, equivalent to the Minergie label [5]. In total, the complex includes 335 apartments totalizing a heated area of 29'192 m^2, as well as 1'245 m^2 for extracurricular activities. The buildings are built according to an identical structure and shape (ground floor + 8 floors). Their thermal envelope differs by triple glazing for the VHEP buildings instead of double glazing for the HEP buildings, as well as by a tested airtightness for the VHEP buildings.

2.2. Heat production

The schematic diagram of the heat production is shown in Fig. 1. The waste water from the 7 buildings is collected in a central pit (approx. 37 m^3), in which a filtration system retains and removes the solid waste. Heat extraction is realized by submerged heat exchanger, which is connected to the evaporator of the heat pump (HP) by way of a glycol water circuit. The cooled waste water is evacuated by a siphon from the bottom of the pit. The heat production of the HP (200 kW_{th}) is transferred to a buffer storage (2 x 10'000 l). A condensing gas boiler (600 kW_{th}), located downstream of the buffer, allows for complementary heat production. Except for the building that houses the boiler room and whose substation is directly connected to the primary circuit, the heat is transfered to the other six building substations by way of two heating networks (DH1 for the HEP buildings, DH2 for the VHEP buildings), which consist of classical 2-pipe distribution system. Within the substations (not depicted here), the hydraulic configuration allows for production or preheating of the domestic hot water tanks (DHW), with serial connection to the space heating (SH) distribution system.

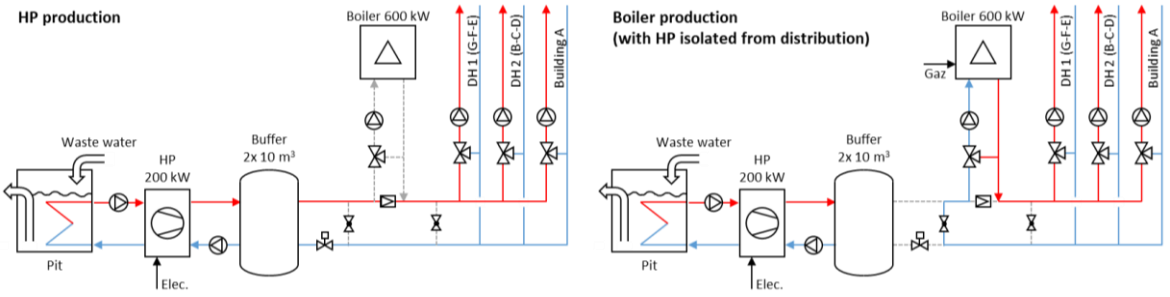


Fig. 1. Heat production scheme and modes.

The heat production system operates according to following alternative modes:

- HP production (Fig 1, left), which is engaged when the heat pump and its buffer can meet the demand (load and temperature).
- Boiler production (with the HP isolated from the distribution system - Fig 1, right), which is activated when the HP and its buffer can no longer meet the demand (in terms of load or temperature). In this case, in order to prevent the boiler from heating up the HP buffer via the return flow of the networks, the HP is isolated from the gas boiler and the DH networks, and operates in a closed loop for recharging of the buffer.

So as to improve the performance of the HP production and to limit the distribution losses, the system control includes temporary temperature rises (batches) several times a day for meeting the demand for domestic hot water (DHW), and differs between summer (DHW only) and winter (DHW + SH):

- In summer, the HP produces at its maximum temperature of 63°C, for covering of the DHW demand. The boiler only ensures the weekly rise in temperature for the treatment of legionella (heat production at 75°C during 2h), in which case the HP operates in closed loop with its buffer, which is maintained between 45 and 60°C (with an HP production at 63°C).
- In winter, the HP produces at 45°C, for covering of the SH demand along with preheating of the DHW tanks. As soon as there is a demand for DHW from any of the substation, the boiler ensures the production at 65°C for loading of all DHW tanks. During these periods, the HP operates in closed loop with its buffer, which is maintained between 40 and 55°C (with an HP production between 45 and 60°C).

2.3. Monitoring

The following data are collected from the centralized control system, in 20 minute time step, and aggregated into hourly and daily values: i) electricity for the HP, including associated circulating pumps (on evaporator and condenser side); ii) heat production by the HP and the gas boiler, as well as associated flow rates and temperatures (including HP buffer temperatures); iii) heat supply for SH and DHW production in each building, as well as associated flow rates and temperatures; iv) waste water temperatures (inlet and outlet of the waste water pit). In parallel, the inlet and outlet temperatures of the HP evaporator are collected by data-loggers placed by us.

3. Heat production balance

Within this study we focus on the year 2018, corresponding to the first full year of operation of the 4 HEP buildings (A, G, E, F - DH1), during which the VHEP buildings were still under construction. During that year, the heat demand (1'162 MWh, or 66.8 kWh/m^2) is split between 59% for DHW and 41% for SH. The production (Fig. 2) is covered at 45% by the HP with an annual COP of 3.04 (including auxiliaries on the evaporator and condenser side), the 55% complement being covered by the gas boiler (with an efficiency of 86% on the upper heating value). While the HP provides the entire DHW production during the summer (except for the weekly anti-legionella temperature rise), in winter it essentially provides SH as well as DHW preheating, the boiler providing the DHW production.

The last 3 buildings were completed and connected to the heating network in the following year (2019). During that year, the HP was temporarily taken out of service due to repeated blockages of the waste water pit by unwanted materials from the construction site [6], reason why we do not include 2019 in this article.

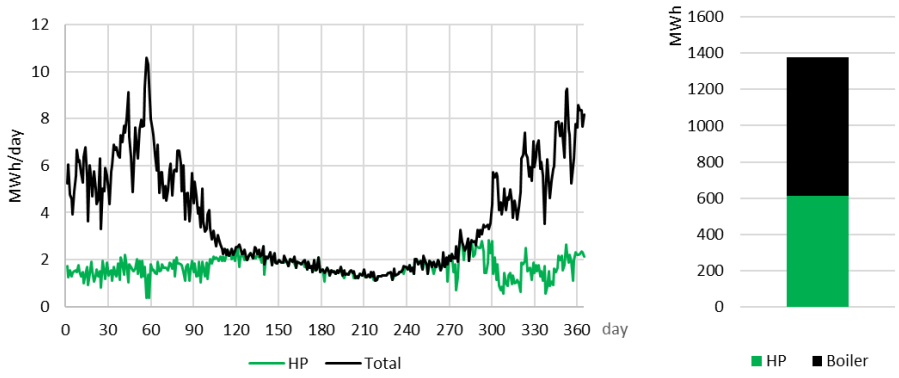


Fig. 2. Heat production dynamic and balance (daily and annual values).

4. Waste water pit

4.1. Temperatures

Operation of the waste water pit and its relationship to the HP is analyzed on the period ranging from February to December 2018, for which all the temperature data is available (in particular at HP evaporator as well as within the pit). In order to avoid intermittent operation, which make the analysis of the measurements more difficult, only the hours during which the HP operated continuously (60 min) are retained (corresponding to 85% of the HP production over the period). Finally, the filtered measurements are aggregated and analyzed in daily values (Fig. 3, left).

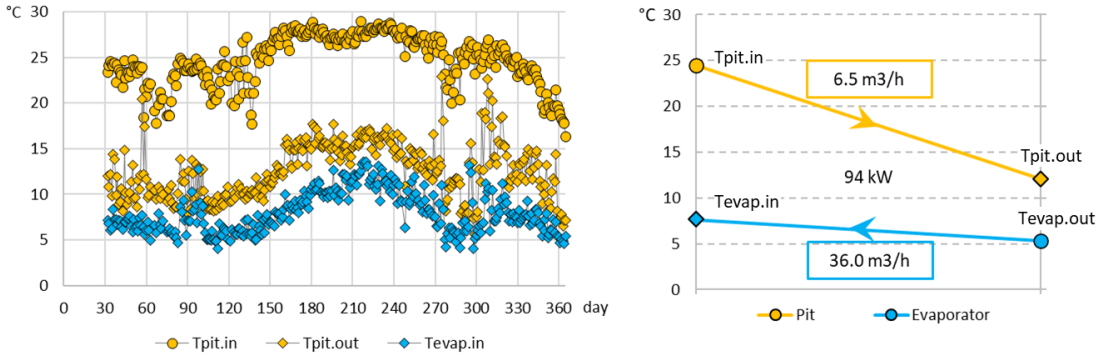


Fig. 3. Left: Temperature of pit (top and bottom) and evaporator inlet, daily values (Feb - Dec 2018); Right: Counterflow heat exchanger model (annual average).

Analysis of this figure leads to following observations:

- The temperature at the top of the pit (waste water inlet) varies between about 28°C in summer and 18°C in winter, with an annual average of 24.5°C. Based on a DHW share of 46% (as measured over a subsequent period, see further down), the latter value is about 7 K lower than the value resulting from the mixture of DHW (at 55°C) and cold water (at 12°C), which could be due to heat losses in the buildings and in the ground, especially in winter.
- In the pit, we observe a relatively important temperature drop (12.4 K in annual average) between the top of the pit (waste water inlet) and the bottom of the pit (waste water discharge, after exchange with the HP evaporator).
- Finally, the temperature at the evaporator inlet (corresponding to the heat exchanger outlet) has an average 7.6°C, i.e. 4.4 K below the bottom of the pit.

4.2. Flowrates

By transferring the daily power extracted from the evaporator (and therefore from the pit) to the temperature loss between the top and bottom of the pit, we can estimate the flow of waste water transiting through the pit

during HP operation. Except for a few peaks, this calculated flow is around 5 to 10 m^3/h, with an average of 6.5 m^3/h, i.e. 1.6 m^3/h per building. For the sake of comparison/validation, hourly monitoring of the DHW consumption yields values between 0.5 and 1 m^3/h per building (during day-time), and weekly readings of total water consumption yield an average share of 46% for DHW and 54% for cold water. Assuming that the cold-water consumption follows the same profile as the DHW, the total day-time water consumption would amount to about 1 - 2 m^3/h per building, compatible with the value of 1.6 m^3/h used here.

By comparison, the nominal flow rate in the evaporator is 36 m^3/h (5.5 times higher than the 6.5 m^3/h estimated for the waste water of the 4 buildings, in period of HP operation), corresponding to an evaporator inlet / outlet temperature differential of 2.2 K (i.e. 5.5 times lower than that observed between the top and bottom of the pit).

4.3. Characterization of the heat exchange

The average annual operation of the heat exchange between the pit and the HP evaporator can be characterized by way of a counterflow heat exchanger [7], which links the heat exchange efficiency ε to the flowrate ratio V_{ratio} and to the number of transfer units *NTU* (ratio between the heat exchange factor and the heat flowrate of the pit):

$$\varepsilon = \frac{1-exp\left(-NTU\left(1-V_{ratio}\right)\right)}{1-V_{ratio}\ exp\left(-NTU\left(1-V_{ratio}\right)\right)} \quad (1)$$

Where:

$$\varepsilon = \frac{T_{pit.in}-T_{pit.out}}{T_{evap.in}-T_{evap.out}} \quad (2)$$

$$V_{ratio} = \frac{V_{pit}}{V_{evap}} \quad (3)$$

$$NTU = \frac{H}{C_{water} \cdot V_{pit}} \quad (4)$$

With the average annual operation conditions described above (Fig. 3, right), the efficiency of the waste water heat exchanger amounts to 65%, which corresponds to a *NTU* of 1.1, i.e a heat exchange factor *H* of 8.5 kW/K.

4.4. Alternative scenarios

All other things remaining equal (load absorbed at the evaporator of 94 kW, pit inlet temperature of 24.5°C, heat exchange factor *H* of 8.5 kW/K), the model in question allows to evaluate the performance of the waste water / HP heat exchange, for various alternative configurations (Fig. 4):

- **4 Bld**: This configuration, which corresponds to the situation observed above, concerns the 4 buildings connected in 2018, with a waste water flow during HP operation of 6.5 m^3/h, for a flow in the evaporator of 36 m^3/h. It results in the observed evaporator inlet temperature $T_{evap.in}$ of 7.6°C, respectively an evaporator average temperature T_{evap} of 6.5°C (where $T_{evap} = (T_{evap.in} + T_{evap.out})/2$).
- **7 Bld**: This configuration corresponds to a waste water flow rate of 11.3 m^3/h (all 7 buildings), for an unchanged evaporator flow rate. It results in an evaporator inlet $T_{evap.in}$ of 10.9°C, i.e. an evaporator average T_{evap} of 9.8°C.
- **7 Bld + Veq**: This configuration is identical to the previous one for waste water, however with a reduced flowrate in the evaporator (11.3 m^3/h, equal to the one of the waste water). As a result, the evaporator inlet $T_{evap.in}$ rises to 13.5°C. However, the reduction of the evaporator flowrate results in an increased temperature drop in the evaporator (7.1 K, identical to that of the waste water), i.e. to an average evaporator temperature T_{evap} of 10.0°C, almost identical to the previous case.
- **7 Bld + 2 S**: This configuration corresponds to 7 buildings (without balancing of the evaporator flowrate), but with a doubled heat exchanger surface (i.e a doubled heat exchange factor *H*). It results in an evaporator inlet $T_{evap.in}$ of 16.2°C, respectively an evaporator average T_{evap} of 15.1°C.

- **7 Bld + Veq + 2 S**: This last configuration combines the balancing of the flow rates and the doubling of the exchange surface, resulting in evaporator inlet $T_{evap.in}$ of 19.0°C, respectively an evaporator average T_{evap} of 15.4°C, again almost identical to the previous case.

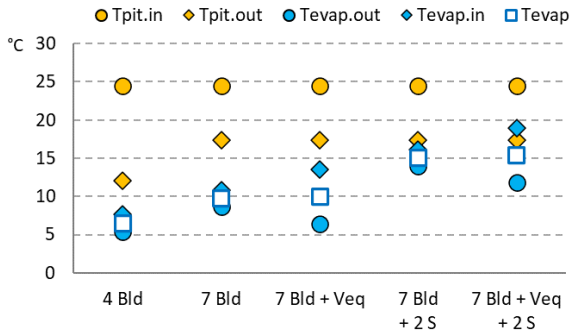


Fig. 4. Temperatures of waste water pit and HP evaporator, for various configurations.

With the connection of the last 3 buildings, the temperature in the evaporator should be around 3.3 K higher than the one observed in 2018. In principle, this performance could be further improved by 5.3 K with doubling of the submerged heat exchanger surface.

5. Heat production units

5.1. Heat pump

The dynamic of the ΔT (condenser outlet – evaporator inlet) and COP of the HP (including auxiliaries) is presented in Fig. 5. HP operation at a high ΔT mainly occurs in the summer, for DHW supply at 63°C. In the winter, the operation at a lower ΔT is mainly related to the production of SH at 45°C.

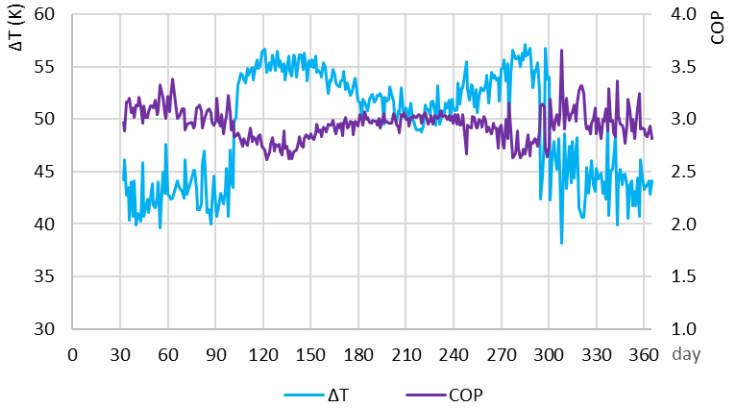


Fig. 5. HP performance (including auxiliaries) and temperature difference between condenser and evaporator (ΔT), daily values (COP filtered when the heat pump operates 60min/hour; ΔT weighted by the energy supplied by the heat pump).

The 2018 SPF is 3.04 including electricity for the auxiliaries (circulation pumps on evaporator and condenser side). This value is related to an energy-weighted temperature average of 7°C at the evaporator and 56°C at the condenser, representative of the average HP operation. The corresponding thermodynamic HP efficiency hence amounts to 45% (ratio between the actual SPF and the Carnot SPF, the latter corresponding to the maximum theoretical performance, for the same operating point).

For comparison, according to the HP data sheet, operation at 14°C / 60°C announces a COP of 3.67 (195 kW thermal supply, 53.2 kW electrical consumption), corresponding to a thermodynamic efficiency of 51%. However, note that latter values do not take into account the electricity of the circulation pumps on the evaporator and condenser side.

5.2. Gas boiler

Based on manual readings of the gas and heat production meters (taken between April 2019 and January 2020), the boiler efficiency is 86%, as calculated on the higher heating value of 11.39 kWh/m^3 of natural gas. This efficiency, which may seem low for a condensing boiler, is related to the relatively high operating temperatures of the boiler, mainly due to heat production for DHW, which limits the possibility of heat recovery by flue gas condensation. For the 2018-2019 period, the energy-weighted average temperatures for the boiler supply and return are 61°C and 50°C respectively. For comparison, the manufacturer announces an efficiency of 88% at a temperature regime of 70/50°C, respectively 92% at a regime of 60/40°C.

6. CO_2 balance

6.1. CO_2 content of gas and electricity

While the CO_2 content of gas is well established (228 gCO_2-eq/kWh on higher heating value [8]), the same is not true for electricity, whose origin is subject to debate. In this study, we use the Swiss consumption mix emission factor, calculated on an hourly basis [9]. This calculation takes into account domestic production and inflows into Switzerland from its neighboring countries. To do so, it uses hourly data of the production mix of the different European countries, by type of production, as well as hourly cross-border flows. On the basis of economic considerations with respect to merit order of the various types of production, it takes into account the impact of Swiss imports on the production mix of neighboring countries. Finally, the CO_2 content of the resulting electricity mix is calculated from the carbon intensity of each type of generation. During the winter of 2018, there were occasional peaks of more than 500 gCO_2-eq/kWh_{el}, mainly due to fossil electricity imports from Germany. These peaks are much smaller in daily values, rarely exceeding 300 gCO_2-eq/kWh_{el}. Finally, given a low-carbon electricity in summer, the annual average is 107 gCO_2-eq/kWh_{el}. Note that this value is very close to those observed over the previous two years (105 and 108 gCO_2-eq/kWh_{el}).

6.2. CO_2 content of the heat mix

The CO_2 content of the heat production is calculated in hourly values, based on the above data. It is represented in daily and annual values in Fig. 6. It can be seen that the dynamic of the emissions is strongly correlated to the heat demand, and is essentially linked to the use of the gas boiler, whose emissions largely dominate those of the HP. Thus, although the HP covers 45% of the annual heat production, it represents only 10% of the CO_2 emissions. In total (HP + boiler), the latter amounts to 224 tCO_2-eq (or 163 gCO_2-eq/kWh_{th}).

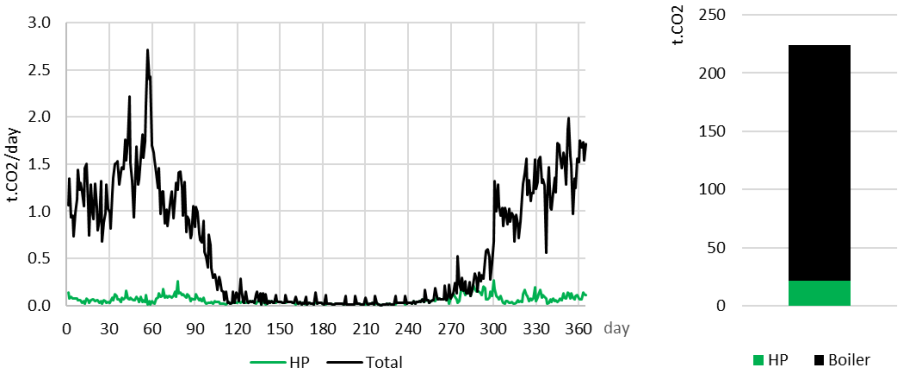


Fig. 6. CO_2 emissions, dynamic and balance (daily and annual values).

In other words, given an efficiency of 86%, the carbon content of the heat production by the boiler is 265 gCO_2-eq/kWh_{th}. Given a relatively constant COP of around 3, the carbon content of the heat production by the heat pump is 7 times lower, namely 35.4 gCO_2-eq/kWh_{th}. As a consequence, up to an electricity carbon content 7 times higher (820 gCO_2-eq/kWh_{el}), the HP heat production would still have a lower carbon content than that of the gas boiler.

7. Evolution and optimization potential

As we have just seen, the CO_2 content of the kWh produced by the heat pump is much lower than the one produced by the boiler, which argues a priori for the most intensive possible use of the HP. However, it turns out that with the current settings, the HP produces less in winter than in summer, despite a higher heat demand (see Fig. 2). In order to evaluate the system optimization potential in relation to the HP operation settings, we conduct an hourly numerical simulation, based on the values measured in 2018. The model also allows to evaluate the evolution of the heat production mix with the connection of the 3 additional buildings (not yet present in 2018).

7.1. Simulation model

The simulation model takes up, in a simplified way, the essential elements of the heat production system, namely: i) the HP and its buffer; ii) the gas boiler; iii) the primary distribution circuit (internal to the boiler room) and the outlet of the district heating / building substations. The algorithm, which is integrated in a spreadsheet, is executed in hourly time step.

The inputs to the model are as follows (in hourly values):

- At source level, the evaporator inlet temperature ($T_{evap.in}$), which is given by a sinusoidal between 5°C at the end of January and 12°C at the end of July, in accordance with what has been observed.
- The instantaneous heat demand, given in terms of load (Q_{dem}) by the demand measured at the substations, and in temperature (T_{dem}) by the temperature measured at the outlet of the boiler room / inlet to the district heating network (note: for simplification purposes, the thermal losses of the district heating network, as well as the phase shifts linked to the transit time to the substations, are not taken into account).

The main characteristics and parameters of the model correspond to the observed values, and are summarized as follows:

- The HP is characterized by a fixed electrical power of 50 kW, and a thermodynamic efficiency of 45%, which allow at each moment to calculate the COP and the heat production Q_{dem}, according to the temperatures at the condenser and evaporator (T_{HP} and $T_{evap.in}$).
- The buffer is represented by a non-stratified one-node model, characterized by a thermal capacity of 20 m^3 and a single temperature (T_{buffer}). Depending on the imbalance between production (Q_{HP}) and demand (Q_{dem}), the buffer is used for storing/retrieving of the excess/missing heat. Its operating range is limited by upper and lower temperature setpoints, which determine the on/off switching of the HP (see the control concept below).
- The gas boiler is characterized by an efficiency of 86% on the higher heating value.

The operating modes are as follows (in order of priority), and correspond to the observed operating modes:

- HP + buffer charge: this mode is activated when the HP production is sufficient to meet the demand (in terms of load and temperature), the excess heat being stored in the buffer.
- HP + buffer discharge: this mode is activated when both: i) the HP production allows to meet the demand temperature, but not the load; ii) the buffer temperature is sufficient to meet the demand.
- Buffer discharge alone: this mode is activated when the HP is stopped (buffer setpoint reached) and the buffer temperature is sufficient to meet the demand.
- Boiler on: this mode is activated when neither the HP nor the buffer can meet the demand (temperature and/or load). In this case, the HP and the buffer are isolated from the primary distribution circuit, and operate in a closed loop, for recharging of the buffer.

Finally, in accordance with what is observed at the level of monitoring, the control setpoints are adapted according to the season: i) in summer, the HP produces at its maximum temperature of 63°C, and the buffer is maintained between 45 and 60°C; ii) in winter, the HP produces at a temperature 5 K higher than that of the buffer, which is maintained between 40 and 55°C.

7.2. Validation

Initially the simulation is carried out on the basis of the demand observed in 2018, corresponding to the first 4 constructed buildings, connected to heating network DH1 (buildings A-F-G-E).

As shown in Fig. 7 the simulation reproduces very well the share of the heat production between HP and boiler. In the case of the boiler, the difference observed on the last 2 months of the year is due to the recent connection of an additional substation (building B), which is not accounted in the demand used for the

simulation. The consistency between simulation and measurement is also very satisfactory regarding the electrical consumption of the HP, with a simulated SPF of 3.10, against 3.04 for monitoring.

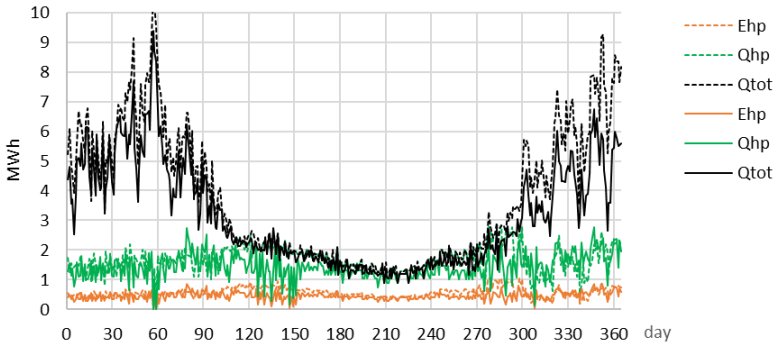


Fig. 7. Heat production (total and HP) and HP electricity, integrated daily values, monitoring (dashed lines) and simulation (solid line).

7.3. Sensitivity analysis

For the sake of comparison with the base case simulated above, we perform a sensitivity analysis for following HP operation scenarios:

- **Reference**: this is the basic scenario described above, in which: i) the HP and the boiler operate in alternating mode (the HP and its buffer being decoupled from the distribution network when they cannot meet the load and temperature of the demand); ii) the HP control setpoints are adapted according to the season (with lower production temperatures in winter than in summer).
- **Alternate**: in this scenario, the HP and the boiler also operate in alternate mode, but the HP control setpoints are maintained all year round at their high values (summer setpoints of the base case).
- **Series**: in this scenario, the heat pump and the boiler operate in series, the heat pump continuing to deliver heat to the network when its temperature is high enough, the additional load being provided by the boiler. In this scenario, the production setpoints of the HP are maintained throughout the year at their high values.
- **Series + 60°C**: this scenario corresponds to the previous scenario, but the network temperature never exceeds 60°C (except for the weekly rise for the anti-legionella treatment).

Fig. 8 represents the network demand and the heat production of the HP, for these various operation modes. Moreover, the various scenarios are simulated on the one hand for the demand of the first 4 buildings (as was the case in 2018), and on the other hand for a demand multiplied by a factor of 1.75, representing in a simplified way the demand of all 7 buildings. The following qualitative observations can be made:

- While in the **Reference** scenario the HP production drops during the winter, it remains at a slightly higher level in the **Alternate** scenario, when the summer setpoints are maintained throughout the year as.
- Winter HP productivity increases significantly in the **Series** scenario, with the HP operating in series with the boiler, and reaches its full potential when the network temperature is maintained below 60°C (**Series + 60°C**): the winter productivity ceiling of 3 MWh/day corresponds to 20 hours of operation at 150 kW, i.e., the available capacity for an evaporator temperature of 5°C and a production at an average of 50°C.
- When taking into account the demand of all 7 buildings, the HP productivity increases slightly (in MWh/day), but covers a proportionally smaller fraction of the demand. We observe in particular that the HP can no longer provide 100% of the summer DHW demand. Indeed, with 7 buildings, the demand linked to DHW batches typically reaches a daily peak of 400 kW, which can no longer be fully met by the HP.

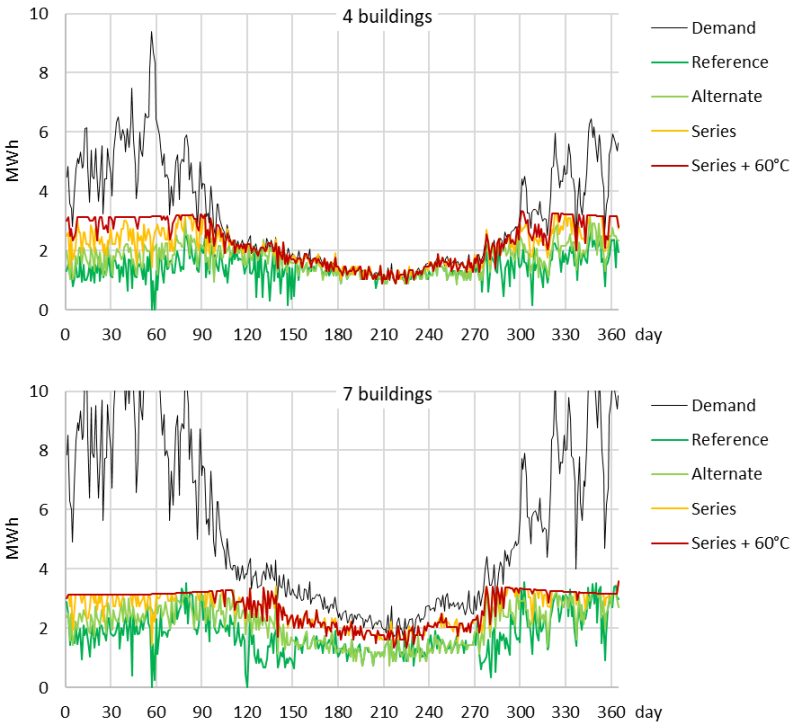


Fig. 8. Demand and HP production for various operating modes (daily values, 4 or 7 buildings).

Fig. 9 represents a set of annual performance indicators (boiler share in the heat mix, CO_2 content of total thermal kWh, SPF of the heat pump), for the various operating modes above, as well as for a 100% boiler scenario. The following conclusions are drawn:

- With 4 buildings to be supplied with heat, the **Reference** scenario allows to reach a coverage rate of 45% via the heat pump, but this rate might drop to about 30% with the connection of the 7 buildings. These rates could in principle increase significantly with the operation of the heat pump in series with the boiler, and a high production temperature maintained throughout the year: thus the **Series** and **Series + 60°C** scenarios both show coverage rates of about 70% (for 4 buildings), respectively 50% (for 7 buildings).
- Given the low CO_2 content of the heat produced by the heat pump, the carbon content of the heat mix falls in a totally correlated way with the fall in the boiler coverage rate, despite a slight fall in the COP of the heat pump (which goes from about 3.2 in the **Reference** scenario to about 2.7 in the other scenarios).
- The linear correlation between the carbon content of the heat mix and the boiler coverage rate is explicitly shown in Figure 9.

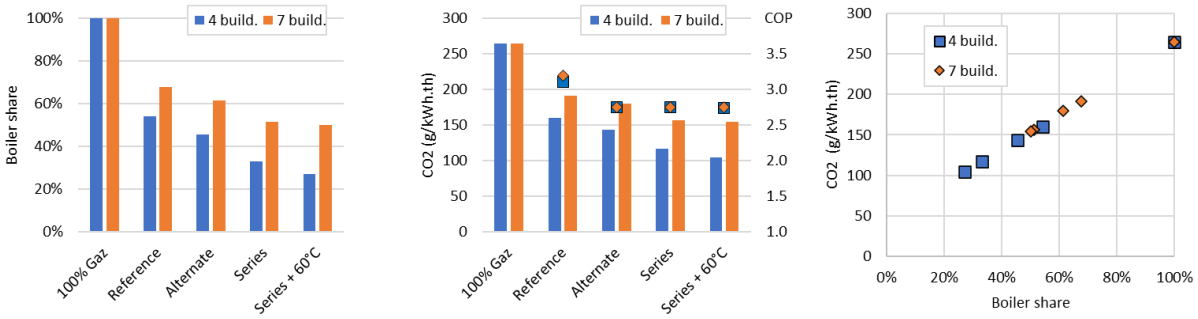


Fig. 9. Performance indicators (boiler share of the heat mix, CO_2 content of the thermal kWh and SPF of the heat pump) for various operating modes (annual values, for 4 or 7 buildings).

Note: in this model, the evaporator inlet temperature is in all cases defined in accordance with the monitored values of the reference case. As has been seen in section 4.4, such is strictly speaking not correct for 7 instead

of 4 connected buildings, in which case we would theoretically expect the evaporator temperature to be about 3.3 K higher. Latter would have a slight positive impact on the annual SPF and on the HP share of the heat production, but would not drastically change the insights gained by this analysis.

8. Conclusions

This paper concerns the monitoring and simulation of the heat production system of a new low energy multifamily buildings complex in Geneva, comprising a centralized HP on waste water (200 kW_{th}) and complementary gas boiler (600 kW_{th}) with heat distribution by a small-scale district heating network. For SPF optimization reasons and in order to take advantage of the lower space heating temperatures, a seasonally differentiated operation mode was planned for the HP, with a lower temperature production setpoint in winter than in summer (when only domestic hot water is needed). However, this does in fact limit the operation duration of the HP to short periods, and leads to a lower HP share than expected.

By way of numerical simulation, we show that alternative operation modes could induce a higher share of HP production, up to 70%. Despite a possible drop in SPF (from 3.2 in the current situation to 2.7 when maximizing the heat pump production), this could actually lead to a better system performance in terms of CO_2 emissions, when taking into account the related reduction in gas consumption, as well as the actual hourly Swiss electricity mix consumed by the HP. At this point, it is however important to emphasize that the current performance of the system is already much better than in the case of 100% fossil fuel production, especially as the heat demand remains low overall.

As a complement, future simulation work could include additional scenarios concerning issues like: i) enhanced flue gas heat recovery by coupling with the HP evaporator, which could also enhance latter's COP; ii) sensitivity analysis concerning HP sizing, in link with possible HP cascading,

Acknowledgements

The authors would like to thank following funding bodies: Fondation HBM Emma Kammacher, Office cantonal de l'énergie de Genève, Services industriels de Genève. We also emphasize the essential role played by the regular meetings of the monitoring panel, which allowed the various actors to discuss the results and issues raised by this study.

References

[1] de Oliveira Filho F. et al. (2020). Évaluation quantitative de scénarios de développement du marché de la chaleur à Genève à l'horizon 2050 : du fossile aux renouvelables, pistes pour décarboner le système thermique. http://archive-ouverte.unige.ch/unige:149640
[2] Quiquerez L. et al. (2016). The role of district heating in achieving sustainable cities: comparative analysis of different heat scenarios for Geneva. In: The 15th International Symposium on District Heating and Cooling. Seoul (South Korea). http://archive-ouverte.unige.ch/unige:86876
[3] Khoury J. (2014). Rénovation énergétique des bâtiments résidentiels collectifs: état des lieux, retours d'expérience et potentiels du parc genevois. Thèse, Université de Genève. Url: https://archive-ouverte.unige.ch/unige:48085
[4] De Sousa Fraga C. et al. (2018). Heat pump systems for multifamily buildings: Potential and constraints of several heat sources for diverse building demands. In: Applied Energy, 2018, vol. 225, p. 1033-1053. doi: 10.1016/j.apenergy.2018.05.004
[5] Minergie (2021) : Règlement des labels MINERGIE / MINERGIE-P / MINERGIE-A. Version 2022.1
[6] Callegari S. et al. (2021). La Fontenette – « Les Auréa » : Analyse technique et sociale d'un complexe d'immeubles HBM de haut standard énergétique, équipé d'une PAC centralisée sur eaux usées. Université de Genève : 2021. Url : http://archive-ouverte.unige.ch/unige:149374
[7] Bergnman T., Lavine A., Incropera F., Dewitt D. (2007). Fundamentals of Heat and Mass Transfer (7th edition). Ed.: John Wiley & Sons.
[8] KBOB (2016). Empfehlung Ökobilanzdaten im Baubereich 2009-1-2016. Koordinationskonferenz der Bau- und Liegenschaftsorgane der öffentlichen Bauherren. Bundesamt für Bauten und Logistik, Schweiz.
[9] Romano E. et al (2018). Romano E., Hollmuller P., Patel M. (2018). Émissions horaires de gaz à effet de serre liées à la consommation d'électricité – une approche incrémentale pour une économie ouverte : Le cas de la Suisse. Url : http://archive-ouverte.unige.ch/unige:131622

14th IEA Heat Pump Conference
15-18 May 2023, Chicago, Illinois

Field tests of variable speed heat pumps to compare load-based and fixed-speed test and rating methods

Bruce Harley[a*], James Butler[b], Christopher Dymond[c], Gary Hamer[d], Jennifer McWilliams[e], David P. Yuill[b]

[a]Bruce Harley Energy Consulting, 665 Boulger Road, Stamford VT 05352, USA
[b]University of Nebraska - Lincoln, Architectural Engineering, Omaha, NE, 68182, USA
[c]Northwest Energy Efficiency Alliance, 700 NE Multnomah Street, Suite 1300, Portland, Oregon 97232, USA
[d]BC Hydro, 333 Dunsmuir Street,Vancouver, BC V6B 5R3, Canada
[e]DNV Energy Insights USA Inc., 8 San Carlos Ave, Albany CA 94706, USA

Abstract

The improved performance of variable-speed heat pump systems has resulted in their widespread adoption globally. Heat pump rating methods such as AHRI 210/240-2023 (2020) were originally developed to characterize fixed-speed heat pump performance. Recently, load-based testing methods such as CSA EXP07:19 have been developed as a response to evidence that such fixed-speed tests don't represent realistic performance of variable-speed systems. EXP07 laboratory test results differ significantly from AHRI 210/240 ratings, yet neither approach has been validated as representative of field performance. This paper describes a field test in which six heat pumps are installed in three unoccupied test houses in Lincoln, Nebraska (a climate with a wide range of weather conditions, with heating and cooling design temperatures of -17°C and 34°C respectively. Each house has separate ducted and ductless systems, instrumented to collect performance data; the systems alternate operation weekly. After field testing, the same units will be tested in a certified laboratory using both AHRI 210/240 and an updated load-based method, SPE-07:23 facilitating comparison between the laboratory and in-situ performance. This will allow a fair assessment of the representativeness of each rating method.

© HPC2023.
Selection and/or peer-review under the responsibility of the organizers of the 14th IEA Heat Pump Conference 2023.

Keywords: Heat pump; rating; variable speed; load-based testing; field test; representativeness; EXP07; SPE07

1. Introduction

Interest in efficient, variable speed air conditioners and heat pumps has gained momentum around the world as efforts to decarbonize building systems increase and performance of variable-speed systems continues to improve. In many markets, however, air source heat pumps have a lingering negative reputation among contractors and consumers, particularly in cold climates where historically poor sizing and installation practices have led to low efficiency [1-2]. Inaccurate efficiency ratings increase the potential for poor product choices, disappointed customers, and unexpected high bills. When a contractor or consumer chooses a product based on an efficiency rating, they should reasonably expect that the ratings will realistically represent that product, especially when comparing efficiency ratings of similar products. The impact of unpredictable performance ratings can reinforce existing bias, reflect negatively on utility and other publicly supported market transformation programs, and offers little motivation for manufactures to improve product performance. A 2019 study conducted for the Northwest Energy Efficiency Alliance [3] suggests that when a test procedure is updated to better represent current equipment, new energy savings can be gained from "better characterizing the energy use of the product." The savings result from eliminating the less-reliable ratings that mischaracterize units as highly efficient, and the authors conclude that improving heat pump ratings (specifically the use of EXP07) is a high priority representing a high magnitude of new energy savings.

* Corresponding author. Tel.: +1-802-694-1719
E-mail address: bruce@bruceharleyenergy.com.

In 2015 the Canadian Standards Association (CSA) formed a development committee to develop testing and rating procedures that would better represent installed performance of variable capacity heat pumps (VCHPs). The relevance of Heating Seasonal Performance Factor (HSPF) and Seasonal Energy Efficiency Ratio (SEER) ratings [4] as realistic performance metrics to represent savings was increasingly called into question, and concerns included substantial variations in equipment performance when installed in climates that differ substantially from those used for the ratings. Further, in-field monitoring consistently suggested that current ratings do not predict installed performance well [5-6-7-8]. Many utilities and state/provincial agencies are increasing their market transformation efforts and funding to promote efficient HVAC installations, and are increasingly motivated to find rating metrics that reduce investment risk and improve evaluation results.

The development committee focused on variable-speed equipment, which depends on on-board firmware to operate, and for which field-measured performance has appeared to vary the most from published ratings. The result of this effort is a test procedure that includes the effects of on-board control algorithms and a wide range of outdoor conditions, driving a performance metric across a wide range of climates. CSA published EXP07:19 [9] as a technical review document; the updated version of the procedure based on technical review comment resolution has been published by CSA as SPE-07:23 [10]. Significant improvements have been incorporated with the primary intention of improving repeatability and reproducibility, yet it is expected that results of testing using SPE-07:23 will be generally similar to those using EXP-07:19.

Initial results of lab testing on numerous models using EXP07:19 have varied significantly from those units AHRI ratings of SEER and HSPF [11-12], with large variability in the load-based test results even among models with identical AHRI ratings, and very different relative rankings in relative efficiency levels for both heating and cooling performance. The load-based testing inherently includes the built-in control algorithms of variable-speed systems, whereas conventional tests require the use of "locked" or fixed-speed compressor and fan modes. The built-in controls appear to play a large role in the discrepancies in at least some cases. Although the load-based rating procedure has primarily been promoted for voluntary use (e.g. for qualified product lists and to differentiate high-performing products), stakeholders have suggested that better understanding of test-to-test repeatability, lab-to-lab reproducibility, and lab-to-field representativeness is needed to fully characterize the differences between load-based and fixed-speed testing.

Fixed-speed testing has an advantage in the rating process because steady-state operation makes measurements easier and reduces uncertainty. Load-based testing is conducted under "quasi-steady state" conditions, and depends on the behavior of built-in control algorithms, so uncertainty in the results will likely always be higher and repeatability lower. The high degree of lab familiarity with traditional fixed-speed tests (and by contrast, unfamiliarity with load-based methods) increases the potential for misunderstandings or diverse interpretations of testing procedures that can lead to discrepancies in results of load-based tests. An initial evaluation of repeatability and reproducibility [13] has shown that there is significant room for improvement. At the same time, many of the concerns raised by participants and stakeholders have been addressed during the comment resolution process leading to the updated SPE-07:23. Further study of repeatability and reproducibility using SPE-07:23 will be an important step in understanding these improvements and characterizing the differences between SPE-07 and more traditional test and rating methods. The focus of this paper is a further study, currently underway, that will focus on the representativeness of load-based and fixed-speed test methodologies to *in situ* field performance.

The authors of this paper are unaware of any systematic field validation of this nature that have previously been undertaken on any past versions of AHRI 210/240 and its precursors over several decades. Several studies have examined factors that introduce bias in the SEER and HSPF ratings [7-14-15]. Field studies and program evaluations generally cannot be taken as a direct comparison to standardized efficiency ratings. Many have found performance that varies from rated values, but such results can be influenced by numerous external factors including occupant behavior, indoor air conditions, duct leakage, load differences, and installation practices such as air flow and refrigerant charge. Recently, with the 2023 edition of AHRI 210/240 [16], an effort has been made to correct assumptions regarding the heating load lines used in different climates (related to both building thermal performance and equipment sizing assumptions) for both single and variable-speed equipment, and the assumed static pressure of duct systems has been increased from an unrealistically low 50 Pa (0.2 in.w.c) to 125 Pa (0.5 in.w.c) for most common ducted system types. These changes will result in new metrics of HSPF2 and SEER2, that will generally be numerically lower than those of HSPF and SEER. Both of these changes should reduce systematic bias in the new metrics, making them incrementally more representative of field conditions. However, the continued use of fixed-speed testing that ignores built-in equipment control algorithms is likely to miss some important performance variations.

Although the lab tests using CSA EXP07 revealed substantial differences between the fixed-speed ratings and load-based tests [12] and provided some evidence that these differences were largely driven by the

behavior of built-in equipment control algorithms in the load-based testing, to date there has been no clear proof that load based testing results in ratings that better approximate real-world performance. This paper describes an effort to address this gap.

2. Representativeness Study Overview

The study is divided into two phases, a field segment (Phase I, currently underway) and a laboratory segment (Phase II). Phase I studies the performance of six heat pumps installed the field in a simulated occupancy home environment. Phase II will test the same heat pumps in an accredited lab, using both SPE-07:23 and AHRI 210/240: 2023 [16]. Comparing the test and rating results will provide insight into which method (if either) more closely matches the performance of the actual systems in the field. Equally important, the detailed field monitoring and lab test results may provide insight into what aspects of performance drive the differences between the rating methods, as well as differences between both methods and the field performance. The intent is to examine the differences between the rating methods and provide insight into how either or both methods might be improved to represent real-world performance more closely. Ratings are always models based on limited testing and assumed applications, and as such are inherently simplifications; they are typically used for purposes such as comparing different products, roughly predicting product performance, and demonstrating regulatory and/or voluntary program compliance. But systematic biases and other significant errors in rating methodologies have the potential to dilute and confuse those purposes.

Phase I is being conducted in Lincoln, NE in a residential neighborhood using three identical, unoccupied mobile homes as test houses. Each test house is outfitted with two heat pumps, one ducted and the other ductless, that are being used in alternate weeks to heat or cool each house. The heat pumps were installed and set up to run in cooling mode, with data collection beginning in mid-August 2022, and were subsequently changed over to heating mode in late October. In March 2023 the tested systems will be uninstalled and shipped to the laboratory for Phase II. This time span will include a wide range of load conditions for both heating and cooling operation.

During Phase II, the laboratory will conduct the test procedure using a modified version of SPE-07:23. The modifications will be to approximate both the load line and thermal mass capacitance of the actual houses as measured during Phase I, so that the test method can be calibrated to the buildings used in the study. The laboratory will also conduct a set of heating and cooling tests from AHRI 210/240-2023, with manufacturer cooperation to access any required proprietary test modes. The lab testing may include additional testing such as the optional H_{4Full} test [16] at -15 °C (5 °F), the Min/Mild and/or the H4_Max/Cold tests as detailed in the DOE cold climate challenge specification [17].

3. Field Study Method

3.1. General approach

Each test house has two heat pumps installed; operation is alternated between the two systems approximately once each week, to capture a range of operating conditions for each. The test houses have been calibrated to approximately match the heat transfer and thermal mass characteristics of SPE-07. The test houses are operated with internal gains, and latent internal gains during cooling, to approximate occupied conditions. Detailed measurements of heat pump operating parameters are recorded, as well as conditions in the house, and outdoor conditions at the site, allowing measurements of equipment capacity and input power over the entire range of operating conditions at a 1-second time interval. All the recorded data is uploaded to a server for access and analysis.

3.2. Test house description and characterization

The test houses consist of three manufactured homes of identical design, built in 2021 at the same factory, sited in the same neighborhood and orientation to the compass. Each house has 113 m² floor area on one story (Figure 1), with low-slope vaulted ceilings and are insulated to current code requirements for manufactured homes. They are set on concrete blocks, raised off the ground level approximately 1 m. The existing heating system is an electric forced-air furnace of 15 kW nominal capacity, with a supply duct running the length of

the “belly” (enclosed joist/truss area) and a single branch duct running to each room; a single return register is located in the utility room.

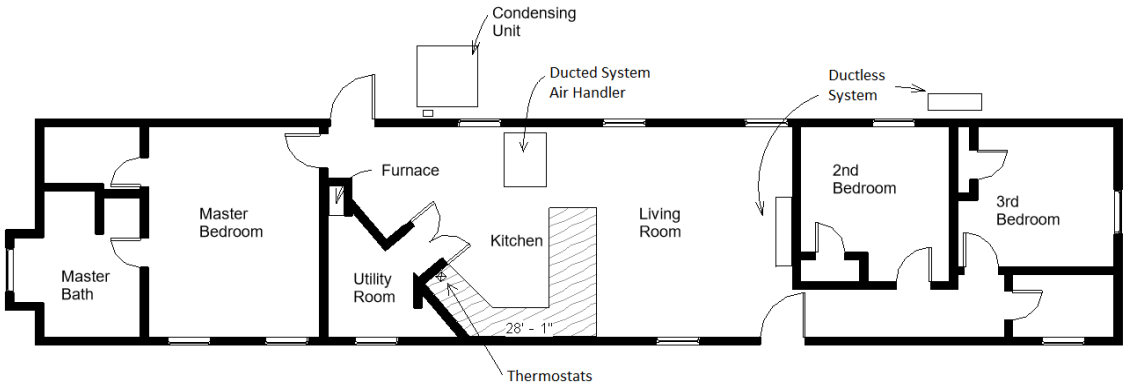


Fig 1: Plan View of Test House.

The houses were tested and calibrated prior to the test period, with enclosure thermal transfer (UA) and mass capacitance measured, as well as enclosure and duct leakage. Each home has one ducted and one ductless heat pump installed. The ductless heat pumps are high-wall mounted. The ducted heat pump air handlers are mounted off the floor, with return air at the bottom and a single supply duct that terminates inside the service closet near the return grille of the central system, as shown in Figure 2.

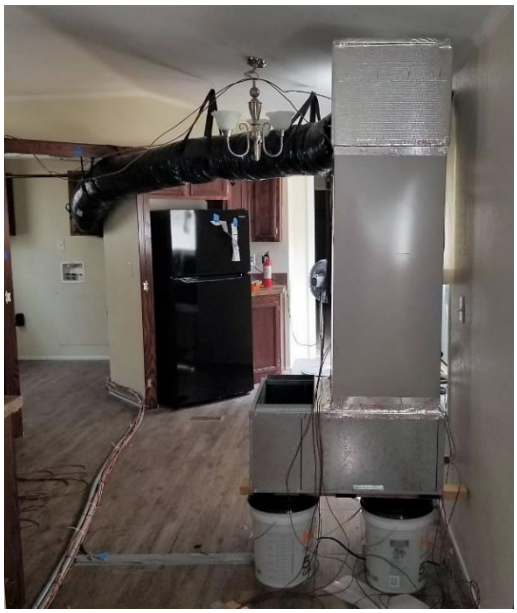


Fig. 2. Ducted Indoor Unit.

Each heat pump is controlled by a wall-mounted thermostat on an interior kitchen wall, near the entrance to the utility room. During the test period, the air handler fan of the pre-existing central furnace remains on, to promote air mixing. In addition, there are two ceiling fans, four box fans and two stand fans to mix the air throughout the house.

3.3. Test house calibration

The test method of SPE-07 relies on a model of the building load and shallow thermal mass typical of a residential building. The model is scaled to equipment capacity. The laboratory test mimics the thermal response of the modeled building as the equipment capacity varies during each load-based test condition. Measurements and modifications were made to bring the UA and mass capacitance of the test homes close to

the SPE-07 lab test values. The test method of AHRI 210/140 has no built-in assumptions about either parameter, so no conflict results from targeting those of SPE-07.

The UA can be defined as:

$$UA = \frac{Q_{heat\ loss} - c}{\Delta T} \quad (1)$$

Where:

UA is the U-value times the area of the building in W/K
$Q_{heat\ loss}$ is the heat loss of the house in W,
ΔT is the difference between indoor and outdoor temperature in K, and
c is the temperature-independent heat loss (internal gains)

To estimate the UA of the test houses, the houses were heated with electric resistance heaters at night to reduce transients and solar effects. By measuring the energy input and indoor/outdoor temperature differences, the UA can be estimated as the slope of a linear regression of those two variables. Figure 3 shows an example of a UA calculation for one house that is tested over a period of 26 nights.

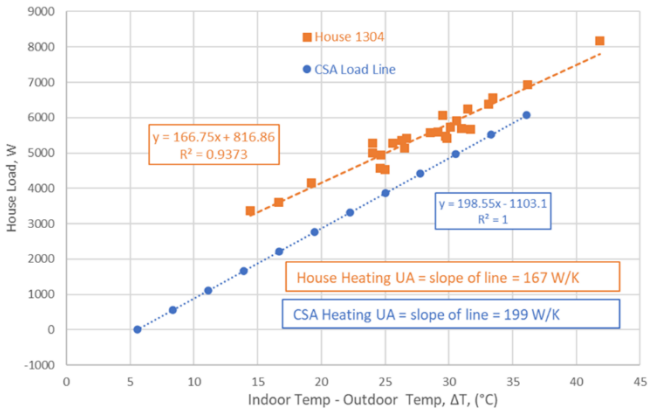


Fig. 3. Plot of Target CSA UA and Measured House UA.

The target UA for SPE-07 based on equipment nominal cooling capacity of 5.2 kW is 199 W/K. Measurements of the three houses ranged from 160 to 169 W/K, so modifications were made to increase the heat transfer. Some insulation and air barrier materials were removed from the belly (crawlspace) of the homes, and in each house four double-low-e glazing panels were replaced with sheet galvanized steel.

The target thermal capacitance for SPE-07 for a 5.2 kW capacity heat pump is 317 Wh/K. The capacitance of the houses was estimated by using the preexisting electric furnace and measuring the cycling rate of the furnace under a range of heating load conditions. The capacitance [18] is then calculated using:

$$C_s = \frac{Q_{h,s,D}}{4 \cdot N_{max} \cdot \Delta T_{db}} \quad (2)$$

Where:

C_s is the thermal capacitance in Wh/K,
$Q_{h,s,D}$ is the heater capacity in W,
N_{max} is the maximum cycling rate in hours^{-1}, and
ΔT_{db} is the thermostat deadband in K

N_{max} can be determined using the following relationship [18]:

$$N = 4 \cdot N_{max} \cdot X \cdot (1 - X) \quad (3)$$

Where *X* is the run time fraction, which is the heat on time divided by total cycle time.

By logging the behavior of the on/off heating cycles, as shown in Figure 4, across a range of load conditions (changing outdoor temperatures), the value of N_{max} can be determined empirically for each house as the slope of the linear regression formed by the cycling rates N vs the product of the run fraction and its complement $X \cdot (1 - X)$, for each cycle, divided by 4. The plots for each test house are shown in Figure 5. The coefficients of determination R^2 are 0.96, 0.96 and 0.98 respectively for House 1, 2 and 3, indicating a strong correlation.

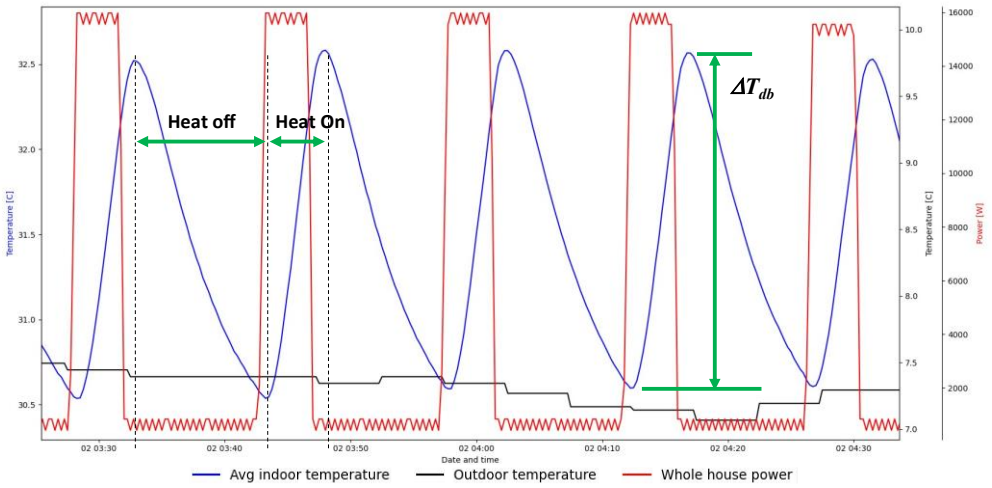


Fig. 4. Measurement of Cycle Times and Thermostat Deadband to Calculate Thermal Capacitance.

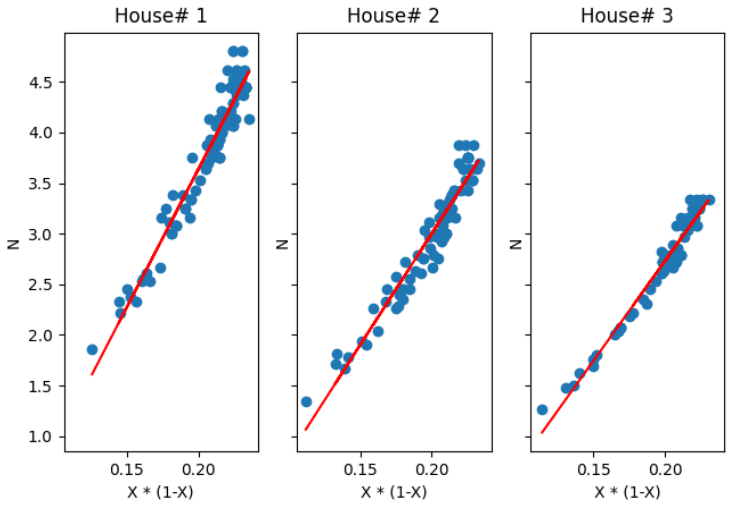


Fig. 5. Plots of Cycling Rate.

The value of C_s for the three houses were estimated to be 282, 296, and 298, slightly lower than the target of 317, and N_{max} was estimated between 4.9 and 6.8 for the three houses. In order to increase the shallow mass capacitance and increase the cycle time, 16 sheets of drywall were added to each house, divided into three rooms, and standing vertically and separated to increase surface exposure (Figure 6). The 16 sheets were estimated based on a comparison of interior surface area of a house contained within a residential home testing laboratory facility, which had been previously used to conduct validation testing and compare mass capacitance response using EXP07:19 [19].

The project schedule did not allow repeating the measurements with the final modifications in place, but data adequate to estimate the building heating and cooling loads and the equipment cycling behavior are being captured throughout the test period, so a more complete picture of the houses' dynamic response will be understood by the end of the test period. These parameters in the SPE-07 lab tests during Phase II will then be matched to the measured houses' performance.

The airtightness of each house was measured with a blower door, with results ranging from 3.1 to 3.9 air changes per hour at 50 Pa. The leakage impact on heating and cooling load is integrated into the overall UA value of each house and the houses are tight enough that wind effects should be small.



Fig. 6. Drywall Used to Increase Thermal Capacitance

3.4. Heat pump selection

The design heating load was estimated at 5.5 kW at the heating design temperature of -15 °C. This was done by analyzing billing data of identical homes, and with standard load calculations. The design cooling load was calculated to be 5.2 kW at a design temperature of 35°C. Heat pump models from manufacturers who are engaged in the project were selected, so that the manufacturers will be able provide testing support during Phase II to ensure that the proprietary test modes required for AHRI 210/240 testing can be accessed properly. Five of the selected systems are variable-speed, and one (a ducted system) has a 2-stage compressor. The variable-speed systems are all considered "cold-climate" systems according to the NEEP cold-climate air-source heat pump listing specification [20], whereas the 2-stage system (Unit B in Figure 7) has a steeper drop of heating capacity at colder ambient conditions, typical of more conventional heat pumps. It was important to choose systems that are not significantly oversized, so that they will typically run at full speed operation near design conditions and modulate well across a range of heating and cooling load conditions. Figure 7 shows the systems' heating and cooling capacities, compared with the estimated heating and cooling design loads. Because the UA measurements were done on the houses in advance, actual heating loads could be estimated with reasonable confidence, whereas cooling loads are driven by solar gain, which could not be measured in advance of test period.

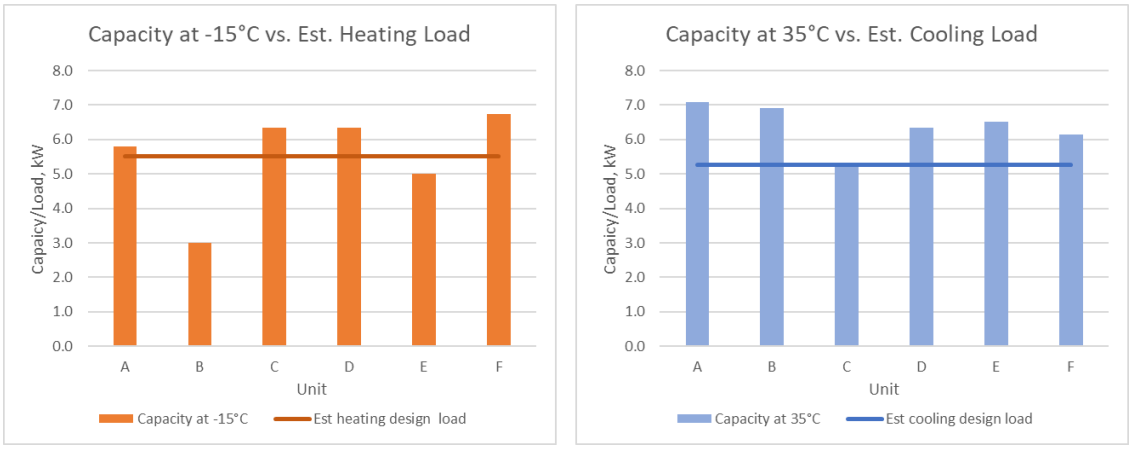


Fig. 7. Installed Heat Pump Heating and Cooling Capacities and Design Loads.

The heat pumps were installed carefully following manufacturers' specifications, with line lengths selected to require no adjustment to refrigerant charge amount. Line lengths were calculated to account for the interior volume of the mass flow sensors and bypass piping. Most systems' outdoor units came pre-charged, so that no refrigerant was added during installation. Two of the systems were charged at the site. Both had charge weighed in, and the charge amount was confirmed by comparing the liquid line subcooling measurement to the manufacturer specification.

Figure 8 shows a typical ductless outdoor unit installation, and one steel window panel, which was used as a location for mechanical penetrations.



Fig. 8. Typical Ductless Outdoor Unit Installation, Showing Steel Window Replacement.

3.5. Example test results

The systems were operated in cooling mode from 19 August and switched over to heating on 25 October, 2022, and are expected to run through early March 2023. The outdoor temperatures have ranged from 39.4 °C (103 °F) to -25 °C (-13 °F), providing a range of operating conditions that exceeds the normal design conditions. The units within each test house were alternated at intervals ranging from 3 days to a week. Figure 9 shows an example of two of the units operating from noon until 8:00 AM the following morning, during which a peak 39 °C ambient temperature occurred. The power to unit D (House 1) modulated over a wider range during the hottest hours, while unit F (House 3) appears to modulate more smoothly, and uses about 70% of the energy of unit D. Unit D appears to manage the supply air temperature within a narrow range when the cooling load is large. Analysis is still in progress, so calculated values (e.g., capacity) are not available at the time of writing.

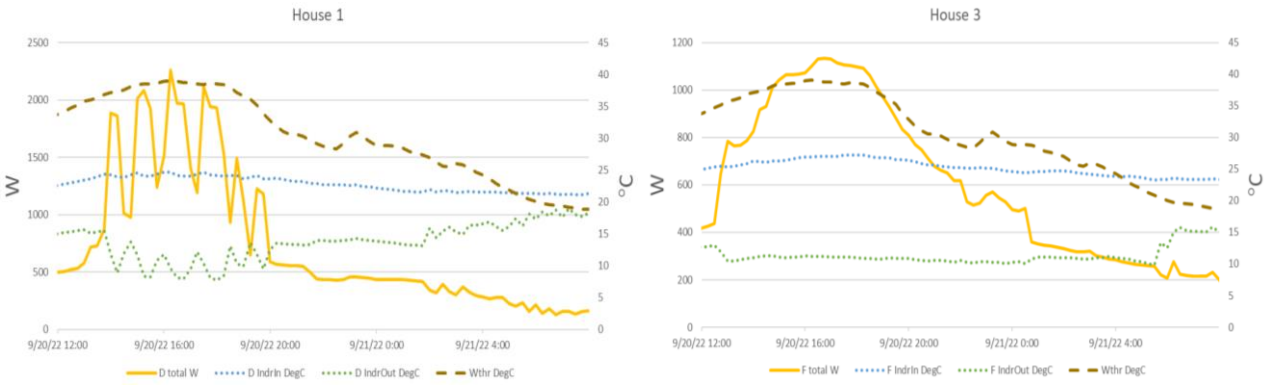


Fig. 9. Systems D and F in Cooling Mode During a 20-hour operating period with a 39 °C Peak Ambient Temperature.

3.6. Measurements and instrumentation

Each of the houses has almost 100 sensors connected to a data acquisition system (DAQ), which is cloud-connected, allowing real-time monitoring. The sensors provide a comprehensive set of measurements within the house, such as temperatures in important locations, and of the heat pumps. Electrical power is also monitored at end uses, including the heat pumps and air handlers, and for the house overall, so that internal heat gain is known. The set of monitored variables facilitates characterization of the houses' cooling and heating loads, as well as the capacity and efficiency of the heat pumps. Heat pump capacity is characterized both on the air-side (by measuring the air flow rate and the indoor coil entering and leaving temperature and humidity) and on the refrigerant side (by measuring refrigerant mass flow rate and characterizing enthalpy entering and leaving the indoor coil with temperature and pressure measurements). This provides redundant measurement of the key variable, heat pump capacity.

Coriolis mass flow sensors are used to measure refrigerant mass flow. Cutting into the liquid line was considered to be too invasive; for most systems it would involve substantial modification of the outdoor unit, and removal then replacement of the refrigerant. Instead, the mass flow sensors were installed in the line set, which carries vapor or mixed-phase refrigerant, depending on the mode of operation and the location of the expansion devices. Mass flow sensors can only measure single-phase refrigerant, so the sensors were located to provide vapor flow measurements.

Some systems do not have a pressure port that allows measurement of the high side pressure during cooling mode, which is needed to calculate liquid line enthalpy (that can be assumed to equal the enthalpy at the evaporator inlet). Because the outdoor unit could not be modified, additional pressure ports could not be added. In these systems, the pressure is inferred by measuring temperature at several locations in the condenser, finding the region of saturation, and using the saturation pressure at that temperature. Figure 10 shows two indoor units with the Coriolis mass flow sensors installed in the refrigerant lines near an indoor unit.



Fig. 10. Ducted (left) and Ductless (right) Indoor Units, Showing Refrigerant Mass-flow Sensors.

The houses each have temperature and humidity sensors measuring the air condition in several locations throughout the house. Each house also has temperature sensors on the: (1) interior surface of the drywall; (2) the outward-facing surface of the drywall; and (3) in the middle of the wall cavity. These trios of sensors are located on: (a) an interior wall; (b) a south facing wall; and (c) on a north-facing wall. A temperature sensor is also located at the location of the thermostats controlling the heat pumps. Outdoor conditions – temperature, humidity, wind and solar irradiance – are monitored with a weather station, and each outdoor unit is also outfitted with radiant-shielded temperature sensors in the air intake of the outdoor unit. Finally, condensate from the evaporator in cooling mode is measured with a tipping-bucket type sensor.

Table 1 gives a list of typical measurements in each house.

Table 1: List of measurements in each house

	Variable	Type	Description
1	W_dhp	Current transf.	Ducted heat pump power
2	W_dhp_i	Current transf.	Ducted indoor unit power
3	W_dlhp	Current transf.	Ductless heat pump power
4	W_dlhp_i	Current transf.	Ductless indoor unit power
5	W_house	Current transf.	Total house power
6	W_furnace	Current transf.	Furnace power
7	T_amb	RTD	Outdoor temp.
8	RH_amb	Capacitance	Outdoor humidity
9	WS_amb	Vane	Outdoor windspeed
10	WD_amb	Vane	Outdoor wind direction
11	p_amb	Piezoelectric	Atmospheric pressure
12	Q_solar	Si pyranometer	Solar irradiance
13	T_wall_ii	Thermocouple	Interior wall indoor surface temp.
14	T_wall_ib	Thermocouple	Interior wall back of drywall temp.
15	T_wall_ic	Thermocouple	Interior wall cavity temp.
16	T_wall_ni	Thermocouple	North wall indoor surface temp.
17	T_wall_nb	Thermocouple	North wall back of drywall temp.
18	T_wall_nc	Thermocouple	North wall cavity temp.
19	T_wall_si	Thermocouple	South wall indoor surface temp.
20	T_wall_sb	Thermocouple	South wall back of drywall temp.
21	T_wall_sc	Thermocouple	South wall cavity temp.
22	T_air_br1	RTD	BR1 space temp.
23	RH_air_br1	Capacitance	BR1 space humidity
24	T_air_br2	RTD	BR2 space temp.
25	RH_air_br2	Capacitance	BR2 space humidity
26	T_air_br3	RTD	BR3 space temp.
27	RH_air_br3	Capacitance	BR3 space humidity
28	T_stat	Thermocouple	Thermostat temp.
29	T_air_fur	Thermocouple	Furnace inlet air temp.
30	RH_air_fur	Capacitance	Furnace inlet air relative humidity
31	T_sa_dl1	RTD	Ductless supply air temp. 1
32	T_sa_dl2	RTD	Ductless supply air temp. 2
33	T_sa_dl3	RTD	Ductless supply air temp. 3
34	T_sa_dl4	RTD	Ductless supply air temp. 4
35	RH_sa_dl1	Capacitance	Ductless supply air humidity 1
36	RH_sa_dl2	Capacitance	Ductless supply air humidity 2
37	RH_sa_dl3	Capacitance	Ductless supply air humidity 3
38	RH_sa_dl4	Capacitance	Ductless supply air humidity 4
39	T_ra1	RTD	Ductless return air temp. 1
40	T_ra2	RTD	Ductless return air temp. 2
41	RH_ra_dl1	Capacitance	Ductless return air humidity 1
42	RH_ra_dl2	Capacitance	Ductless return air humidity 2
43	T_ref_mf	Thermocouple	Ductless MF sensor inlet temp.
44	T_ref_ei	Thermocouple	Ductless evaporator inlet temp.
45	T_ref_eo	Thermocouple	Ductless evaporator outlet temp.
46	T_ref_suc	Thermocouple	Ductless suction temp.
47	T_ref_tsuc	Thermocouple	Ductless suc. after rev. vlv temp.
48	T_ref_dis	Thermocouple	Ductless discharge temp.
49	T_ref_rvlv	Thermocouple	Ductless after rev. valve temp.
50	T_ref_c1	Thermocouple	Ductless condensing temp. 1
51	T_ref_c2	Thermocouple	Ductless condensing temp. 2
52	T_ref_c3	Thermocouple	Ductless condensing temp. 3
53	T_ref_c3	Thermocouple	Ductless condensing temp. 3
54	T_ref_ll	Thermocouple	Ductless liquid line temp.
55	m_ref1	Coriolis	Ductless Refrigerant mass flow
56	T_air_c1	RTD	Ductless cndnsr air in temp. 1
57	RH_air_c1	Capacitance	Ductless cndnsr air in rel humidity 1
58	T_air_c2	RTD	Ductless cndnsr air in temp. 2
59	RH_air_c2	Capacitance	Ductless cndnsr air in rel humidity 2
60	p_ref_suc	Piezoelectric	Ductless ref. suction pressure
61	p_ref_ll	Piezoelectric	Ductless ref. liquid line pressure
62	m_cond	Rain gauge	Evaporator condensate mass flow
63	V_ra	Orifice plate	Ducted indoor unit airflow
64	T_sa_d1	RTD	Ducted supply air temp. 1
65	T_sa_d2	RTD	Ducted supply air temp. 2
66	T_sa_d3	RTD	Ducted supply air temp. 3
67	T_sa_d4	RTD	Ducted supply air temp. 4
68	RH_sa_d1	Capacitance	Ducted supply air humidity 1
69	RH_sa_d2	Capacitance	Ducted supply air humidity 2
70	RH_sa_d3	Capacitance	Ducted supply air humidity 3
71	RH_sa_d4	Capacitance	Ducted supply air humidity 4
72	T_ra1	RTD	Ducted return air temp. 1
73	T_ra2	RTD	Ducted return air temp. 2
74	RH_ra_d1	Capacitance	Ducted return air humidity 1
75	RH_ra_d2	Capacitance	Ducted return air humidity 2
76	T_ref_mf	Thermocouple	Ducted MF sensor inlet temp.
77	T_ref_ei	Thermocouple	Ducted evaporator inlet temp.
78	T_ref_eo	Thermocouple	Ducted evaporator outlet temp.
79	T_ref_suc	Thermocouple	Ducted suction temp.
80	T_ref_tsuc	Thermocouple	Ducted suc. after rev. valve temp.
81	T_ref_dis	Thermocouple	Ducted discharge temp.
82	T_ref_rvlv	Thermocouple	Ducted after rev. valve temp.
83	T_ref_c1	Thermocouple	Ducted condensing temp. 1
84	T_ref_c2	Thermocouple	Ducted condensing temp. 2
85	T_ref_c3	Thermocouple	Ducted condensing temp. 3
86	T_ref_c3	Thermocouple	Ducted condensing temp. 3
87	T_ref_ll	Thermocouple	Ducted liquid line temp.
88	m_ref1	Coriolis	Ducted Refrigerant mass flow
89	T_air_c1	RTD	Ducted cndnsr air in temp. 1
90	RH_air_c1	Capacitance	Ducted cndnsr air in rel humidity 1
91	T_air_c2	RTD	Ducted cndnsr air in temp. 2
92	RH_air_c2	Capacitance	Ducted cndnsr air in rel humidity 2
93	p_ref_suc	Piezoelectric	Ducted ref. suction pressure
94	p_ref_ll	Piezoelectric	Ducted ref. liquid line pressure

4. Future Comparison of Lab and Field Performance

Properly comparing field performance and the two types of rating approaches requires that each system be run through the entire SPE-07 and AHRI testing process. From that process unofficial efficiency performance metrics can be calculated for each tested system, which may or may not correspond closely to the catalogued ratings. Further, because the load-based approach in SPE-07 inherently includes a virtual model of the building load and mass capacitance (scaled to the size of the tested system), this virtual model will be adjusted to match the actual test houses, to make the comparisons more meaningful. The initial characterization testing of the three houses showed that they were quite close to the SPE-07 virtual building model, providing an initial validation that the SPE-07 virtual building model is reasonable.

Finally, to compare the field- and lab-tested performance fairly, the field performance of each tested system will be characterized by a performance curve, primarily capacity and input power over a range of outdoor temperature conditions. That performance curve will then be fitted to the prototypical climates that have been defined for each test method, to create field equivalent performance metric results for each rating procedure, that can be compared with the unofficial efficiency performance metrics from the laboratory testing. The performance curve can also be fitted back to the actual weather from the field test sites, to determine how closely the simplified curve approximates the actual seasonal performance during the test period.

Besides simply making numerical comparisons of the unofficial rating results, the analysis will examine *where* in the testing processes there may be the largest discrepancies, and whether there are other factors that create systematic bias or other errors in one or both ratings methodologies.

5. Conclusions

This project is unique because it will provide field data that can be directly compared to multiple lab test methods. Having six heat pumps tested in nearly identical homes, under identical use patterns but without occupant behavior, enables researchers to evaluate how effective current and future test procedures are at generating representative ratings. Much of the lab testing to date [8-11-12] has shown that conducting tests under a heat pump's built-in algorithms sometimes reveals performance issues for variable speed and single speed heat pumps alike. As heat pumps increasingly become microprocessor controlled, it is imperative that we learn what conditions are most sensitive to the effects of built-in control algorithms. This research project will be able to inform improvements that can be made to both load-based and fixed-speed test methods, to provide ratings that better inform contractors and end users which product will perform better for their climate conditions. In addition, more representative test procedures can lead to better input parameters for simulations that are used for electrical utility forecasting and grid resilience, energy code compliance, engineering analysis and system designs.

Acknowledgements

Project partners for Phase I include the Air-Conditioning Heating and Refrigeration Institute (AHRI), BC Hydro, Carrier Corporation, ComEd, Daikin Comfort Technologies North America, Lincoln Electric System, Midea America, Mitsubishi Electric Trane HVAC, Natural Resources Canada (NRCan), New York State Energy Research and Development Agency (NYSERDA), Northwest Energy Efficiency Alliance (NEEA), Northeast Energy Efficiency Partnership (NEEP), Xcel Energy, American Public Power Association (APPA). The project is managed by NEEP, and DNV Energy Insights USA is the principal research implementer.

References

[1] Northeast Energy Efficiency Partnerships (NEEP). *Northeast/Mid-Atlantic Air-Source Heat Pump Market Strategies Report 2016 Update*, Lexington, MA: NEEP; 2017, p. 48–50. neep.org/sites/default/files/NEEP_ASHP_2016MTStrategy_Report_FINAL.pdf

[2] NEEP. *Assessment of Residential and Small Commercial Air-Source Heat pump (ASHP) Installation Practices in Cold Climates*, Lexington, MA: NEEP; 2017, p. 1 neep.org/sites/default/files/AssessmentofResandSmallCommASHPInstallationPracticesinCold-Climates.pdf

[3] Baker, N., Hessels, J., Widder, S. *Evaluation of Energy Savings from Test Procedures & Specifications*, Portland, OR: Northwest Energy Efficiency Alliance (NEEA), Development of Standards and Ratings for Commercial and Industrial Equipment (Contract No. 51033) – Task 5; 2019, p. 8–10, 13.

[4] Air-Conditioning, Heating, and Refrigeration Institute (AHRI). *AHRI Standard 210/240 with addendum 1: 2017 Standard for Performance Rating of Unitary Air-conditioning & Air-source Heat Pump Equipment*, Arlington, VA: AHRI; 2017. https://www.ahrinet.org/sites/default/files/2022-06/AHRI_Standard_210-240_2017_add1.pdf

[5] Proctor J, Wilcox B, Chitwood R. *Central Valley Research Homes Project Final Report*, Publication Number: CEC-500-2018-033. Sacramento, CA: California Energy Commission; 2018. ww2.energy.ca.gov/2018publications/CEC-500-2018-033/CEC-500-2018-033.pdf

[6] Wilcox B, Conant A, Chitwood R. *Central Valley Research Homes, Variable Compressor Speed Heat Pumps*, ET Project Number: ET14PGE8761. Sacramento, CA: Pacific Gas and Electric Company (PG&E); 2016. www.etcc-ca.com/reports/variable-compressor-speed-heat-pumps

[7] Larson B, Davis B, Uslan J, Gilman L. *Residential Variable Capacity Heat Pump Field Study*, BPA Energy Efficiency's Emerging Technologies Initiative. Portland, OR: Bonneville Power Authority; 2014,

p7, 26, 29. https://ecotope-publications-database.ecotope.com/2013_005_ResidentialVCHPFieldStudy.pdf
[8] Harley, B. *Heat Pump and Air Conditioner Efficiency Ratings: Why Metrics Matter*, NEEA Report #E22-329. Portland, OR: Northwest Energy Efficiency Alliance (NEEA); 2022, p. 2–3, 6–7. http://neea.org/resources/heat-pump-and-air-conditioner-efficiency-ratings-why-metrics-matter
[9] Canadian Standards Association (CSA). *EXP-07:19, Load-based and climate-specific testing and rating procedures for heat pumps and air conditioners.* Toronto, Ontario, Canada: CSA; 2019. https://community.csagroup.org/docs/DOC-115027
[10] Canadian Standards Association (CSA). *SPE-07:23, Load-based and climate-specific testing and rating procedures for heat pumps and air conditioners.* Toronto, Ontario, Canada: CSA; 2023. https://community.csagroup.org/docs/DOC-161850
[11] Harley B. *EXP07:19 Load-based and Climate-Specific Testing and Rating Procedures for Heat Pumps and Air Conditioners: Interim Lab Testing and Rating Results*, NEEA Report #E20-314. Portland, OR: NEEA; 2020. https://neea.org/resources/exp0719-load-based-and-climate-specific-testing-and-rating-procedures-for-heat-pumps-and-air-conditioners
[12] Harley B, Alatorre M, Dymond C, Hamer G. CSA EXP07: Ongoing Progress, Lessons Learned, and Future Work in Load-based Testing of Residential Heat Pumps Herrick Refrigeration and Air Conditioning 2022 Conference Proceedings. West Lafayette, IN: Purdue University; 2022. http://docs.lib.purdue.edu/iracc/2456/
[13] Dhillon P, Wang X, Horton WT, Braun J. Repeatability and Reproducibility Assessment of Residential Heat Pump Performance Evaluation Methodologies based on CSA EXP07 and AHRI 210/240. Herrick Refrigeration and Air Conditioning 2022 Conference Proceedings. West Lafayette, IN: Purdue University; 2022. http://docs.lib.purdue.edu/iracc/2477/
[14] Fairey P, Parker D, Wilcox B, Lombardi M. *Climate Impacts on Heating Seasonal Performance Factor (HSPF) and Seasonal Energy Efficiency Ratio (SEER) for Air Source Heat Pumps,* FSEC-PF-413-04. ASHRAE Transactions, June 2004. Atlanta, GA: American Society of Heating, Refrigerating and Air Conditioning Engineers, Inc. (ASHRAE); 2004. http://publications.energyresearch.ucf.edu/wp-content/uploads/2018/06/FSEC-PF-413-04.pdf
[15] Wilcox B, Conant A, Chitwood R. *Variable Capacity Heat Pumps – Evaluation of Sizing and Controls Settings 2017-2018,* ET Project Number PGE 2019. Sacramento, CA: PG&E; 2019. www.etcc-ca.com/reports/central-valley-researchhomes-evaluation-sizing-and-controls-settings-2017-2018
[16] AHRI. *AHRI Standard 210/240: 2023 (2020) Standard for Performance Rating of Unitary Air-conditioning & Air-source Heat Pump Equipment*, Arlington, VA: AHRI; 2020. https://www.ahrinet.org/sites/default/files/2022-06/AHRI%20Standard%20210.240-2023%20%282020%29.pdf
[17] U.S. Department Of Energy (DOE). *Residential Cold-Climate Heat Pump Technology Challenge Specification and Supporting Documents, Version 1.2*. Washington, DC: US DOE; 2021 p. 13, 16–17, 19–20. https://www.energy.gov/sites/default/files/2021-10/bto-cchp-tech-challenge-spec-102521.pdf
[18] Henderson H, Raustad R, Rengarajan K. *Measuring Thermostat And Air Conditioner Performance In Florida Homes*, Publication #FSEC-RR-24-91. Cocoa, FL: Florida Solar Energy Center (FSEC); 1991, p. A1–A4. https://stars.library.ucf.edu/cgi/viewcontent.cgi?article=1854&context=fsec
[19] Dhillon P, Welch D, Butler B, Horton, W.T, Braun, J. *Validation of a Load-Based Testing Method for Characterizing Residential Air-Conditioner Performance.* West Lafayette, IN: Purdue University; 2021. International Refrigeration and Air Conditioning Conference. Paper 2257. https://docs.lib.purdue.edu/iracc/2257
[20] NEEP. *Cold Climate Air Source Heat Pump (ccASHP) Product List and Specifications Version 4.0,* Lexington, MA: NEEP; 2022. https://neep.org/sites/default/files/media-files/cold_climate_air_source_heat_pump_specification_-_version_4.0_final_1.pdf

14th IEA Heat Pump Conference
15-18 May 2023, Chicago, Illinois

In-situ monitoring of a groundwater heat pump for a low-temperature district heating network: energy performance, issues and challenges

Pauline Brischoux[a,*], Stefan Schneider[a], Pierre Hollmuller[a]

[a]University of Geneva, 66 Bd Carl-Vogt, 1205 Geneva, Switzerland

Abstract

With the development of district heating networks and the need for decarbonization, heat pumps in district heating are expected to play a major role in the upcoming years. To facilitate the implementation of such systems by sharing lessons learned, this study presents monitoring results of a large-scale heat pump supplying a low-temperature district heating network (LTDH) in Switzerland. Detailed monitoring over a whole year of operation reveals an annual heat production of 8 GWh, of which 85% is covered by the heat pump with an annual SPF of 3.69 (pumping and auxiliaries excluded). However, about 25% of the heat for space heating is produced with very low energy performance. Analyzing the influence of temperatures and flow rates on the heat pump energy performance brings to light potential optimizations of the system and improvements for future LTDH. In particular, the results raise crucial questions related to heat pump sizing and domestic hot water production methods with LTDH, as well as reaffirm the importance of optimizing substations return temperatures when the main heat generator is a heat pump.

© HPC2023.
Selection and/or peer-review under the responsibility of the organizers of the 14th IEA Heat Pump Conference 2023.

Keywords: heat pump ; district heating and cooling ; in-situ monitoring ; faults in substations

1. Introduction

1.1. Context

In 2015, around 45% of the total European energy consumption was due to the heat supply of buildings for space heating and domestic hot water, and was based at 66% on fossil fuels [1]. This sector hence represents a huge potential for the reduction of greenhouse gas emissions.

District heating networks (DH) have long been recognized as a means to decarbonize the heat supply in dense urban areas, as it allows the use of waste heat, which would otherwise be rejected in the environment, and facilitates the integration of renewable energies.

However, renewable energy sources such as geothermal heat, solar heat, surface or underground water are often available at low temperature, unfit for direct use. Thus, their integration into buildings heat supply often requires a temperature lift with a heat pump (HP), either centralized or decentralized.

Therefore, with the development of DH and the need for decarbonization, HP are expected to play a major role in the upcoming years. Heat Roadmap Europe 2050 (HRE2050) prospective scenario [2] shows that DH could cost-effectively cover 50% of the total heat demand by 2050, compared to 12% currently, with 25% of the heat supplied by large-scale HP (520 TWh/year with a COP of 3 and a total capacity of 40 GW_{th}).

Large-scale HP are already in use across Europe for the supply of DH networks. A study made in 2017 [3] identifies 149 units (≥ 1 MW) across 11 European countries, installed between 1981 and 2016, for a total capacity of 1.6 GW_{th} (25 times lower than the HRE2050 scenario). This study also shows that many large-scale HP were commissioned in the last decade in several countries such as Finland, France, Denmark and Italy.

* Corresponding author.
E-mail address: pauline.brischoux@unige.ch.

Despite their use on many systems since the 1980s, there are still barriers to the implementation of HP in DH networks [4], such as the lack of knowledge compared to other technologies (like biomass or gas boilers) and investment cost. Therefore, documentation on existing projects could increase confidence of stakeholders, increase energy efficiency as well as reduce operation and maintenance costs of such systems. IEA HPT Annex 47 [5] produced a short description of 44 case studies of HP in DH networks to show examples of implementation. However, detailed information on the challenges/issues encountered are not always provided.

1.2. Objectives

The present study consists in analyzing the energy performance, in actual conditions of use, of a large-scale HP supplying a low temperature district heating network (LTDH). The aim is to determine whether the HP achieves the expected performance and to identify possible areas for improvement. This provides insight not only on this specific system, but also for the optimization of other existing or future HP in LTDH systems.

Based on detailed monitoring data over an entire year of operation, we first compute daily and annual energy balances of the HP to get an overview of its energy performance. Then, we proceed to an hourly analysis to examine the influence of various parameters on the HP performance, such as temperature levels and flow rates. Finally, based on the results of this study, we make recommendations regarding the use of large-scale HP in LTDH.

2. Case study

2.1. Description

The case study is an eco-district located in the canton of Geneva, Switzerland. It hosts around 1'350 dwellings and various activities, totalizing 170'000 m² of conditioned floor area. A local low temperature district heating network (LTDH) distributes heat to the buildings for space heating (SH) and domestic hot water (DHW). Because all connected buildings meet high energy performance standards, the LTDH supplies heat at a low temperature level (50°C). At fixed time, twice a day, the temperature of the network is raised from 50°C to 65°C to heat up DHW tanks within the buildings over a 2-hour period. Compared to a network operating at a constant supply temperature of 65°C, these DHW batches lower DH heat losses and increase the energy performance of the heat production.

As shown in Fig. 1, the LTDH is mainly supplied by a 5 MW_{th} heat pump (HP), whose heat source is shallow groundwater. Before reaching the HP, this cold water at approximately 12°C supplies a district cooling network, recovering waste heat from the nearby industries, thereby increasing the resource temperature for the HP and improving its efficiency. As a result, the HP source temperature ranges between 12°C (during the winter) and 16°C (during the summer). The HP delivers heat directly to the LTDH and the surplus is stored in two buffer tanks of 20 m³ each (i.e. a total volume of 40 m³) to add inertia to the system.

In addition to the HP, the LTDH is also connected to Geneva's high-temperature district heating network (HTDH), as complementary or back-up source. The objective is to cover at least 80% of the annual heat demand with the centralized HP, and reach a HP seasonal performance factor close to the nominal values presented below, pumping and auxiliaries excluded.

The HP has two variable-speed compressors, operating in parallel for SH mode or in series for DHW mode (to reach higher outlet temperatures). It admits condenser inlet temperature ranging from 20°C to 45°C, though it only stops when the temperature reaches 50°C to prevent damage. According to the manufacturer [6], the nominal coefficient of performance (COP) of the HP for each operation mode is as follows:

- DHW: COP of 3.62, for inlet/outlet condenser temperatures of 45°C/65°C
- SH : COP of 4.60, for inlet/outlet condenser temperatures of 35°C/50°C

It should be noted that these values are given for an evaporator inlet temperature of 12.5°C, i.e. the temperature of the water at the pumping site. The increase in temperature of this resource due to the heat supplied by the district cooling customers allows in principle to reach slightly higher COP.

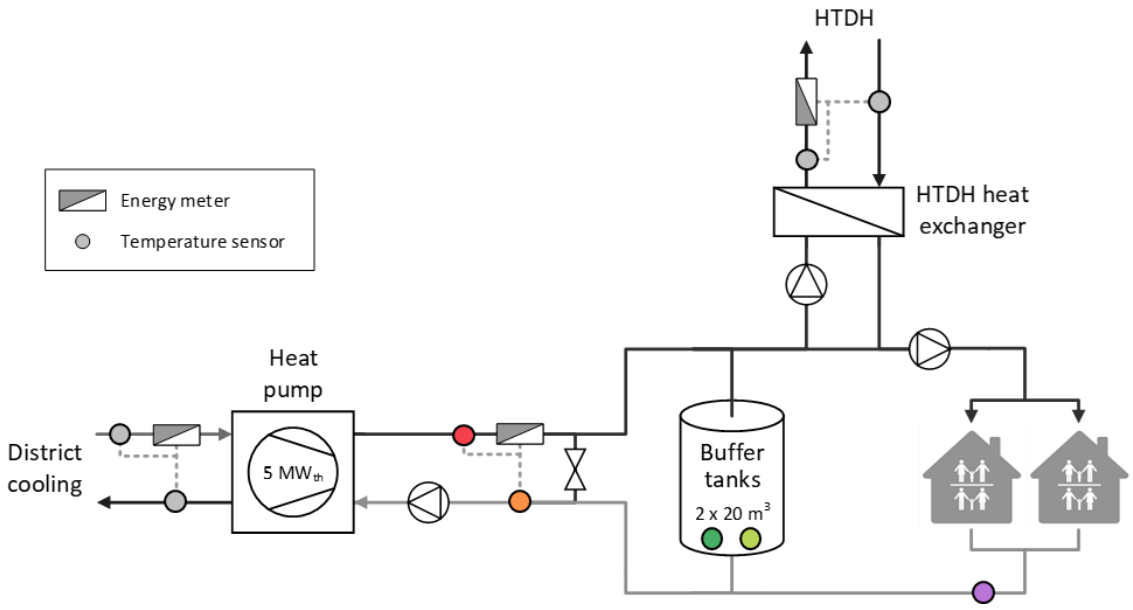


Fig. 1. Schematic of the district heating system. Colored circles indicate the location of the temperature sensors used in Fig. 5.

2.2. Monitoring

To evaluate the actual energy performance of the HP, we analyze monitoring data for a whole year, from June 2019 to June 2020. This time interval corresponds to the first year of operation of the HP and has the advantage of including all possible types of operation, namely:

- A summer period (from June to August 2019) where the HP operates only 4 hours per day (two 2-hour batches) for the preparation of DHW at 55°C-65°C.
- Mid-season periods (from September to October 2019 and from March to May 2020) during which the HP operates not only in DHW mode during the batches (at 55°C-65°C), but also in SH mode intermittently (at 50°C).
- A winter period (from November to March 2020) during which the HP operates almost continuously to maintain the LTDH at 50°C for SH of buildings, and at 55°C-65°C for DHW batches 4 hours per day.

Except for a few breakdowns in February and March 2020, partially due to high condenser inlet temperatures exceeding the HP limits of operation, the HP runs during most of the period. It stops voluntarily at the end of the heating season (mid-May) to test the behavior of the LTDH when the HTDH covers the entire heat demand during the summer.

Data is collected from the system with a 10-min time step and aggregated on an hourly, daily and annual basis. As indicated in Fig. 1, it includes, but is not limited to: i) energy meters, with their corresponding flow meters and temperature sensors, on the evaporator and condenser of the HP, as well as on the HTDH supply; ii) electricity meters on the HP compressors; iii) temperature sensors in the buffer tanks, in particular at the bottom of each tank, as well as on the DH return.

Since the high temperature DHW batches occur at fixed time each day, it is possible to dissociate the heat produced in DHW mode from SH mode (i.e. outside the batches) based on the timestamp. The DHW batches start at 5:00 and end at 7:10 each morning and evening.

The energy performance of the HP is evaluated on an hourly (COP) and annual basis (SPF) as the ratio of the heat produced at the condenser to the electricity consumption of the HP compressors (i.e. pumping and auxiliaries excluded).

To check the validity and consistency of the data, we calculate the hourly and daily energy balances between the load side (condenser) and the source side (evaporator and electricity) of the HP. Following the observation of the data, the limit is set at ± 10% error on the HP balance. Results exceeding the limit are excluded from the analysis. Similarly, outlier COP values are excluded (COP > 7 and COP < 1).

3. Results and discussion

3.1. Energy balance

Fig. 2a shows the daily and annual energy balance between energy source (HP evaporator, electricity and HTDH) and heat production per operation mode (SH / DHW).

The total heat production varies from 7 MWh/day in summer to nearly 50 MWh/day in winter. The heat production in DHW mode, i.e. during the high temperature batches (55°C-65°C), has a seasonal effect: it goes from 7 MWh/day in summer to about 12 MWh/day in winter. It is important to note that this corresponds to the heat production during this period of the day, and not the buildings DHW demand, because the HP stops at the end of each DHW batch and lets the DH temperature come back down to SH level before turning back on. Therefore, part of the heat produced during the DHW batches is used after the batch for SH. This control logic is visible on typical days presented later in Fig. 5.

The total heat production amounts to about 7.98 GWh, with a HP coverage of 85%, thus meeting the target of 80% despite the HP breakdowns (February-March). The HP produces 6.78 GWh of heat with an electricity consumption of 1.84 GWh, leading to an annual SPF of 3.69. Over an entire year of monitoring, the ratio of heat produced during the DHW batches, i.e. between 55°C and 65°C, to the total heat produced is close to 52%. Outside the heating season, from June to early October 2019, the SPF value of 3.25 is lower than the annual SPF (Fig. 2b). It corresponds to the operation of the HP in DHW mode only. During the heating season, from October 2019 to June 2020, the SPF is higher (3.77), indicating that the COP of the HP in SH mode is higher than in DHW mode, as specified by the HP manufacturer. In this regard, the highest daily SPF match the days with the highest share of SH.

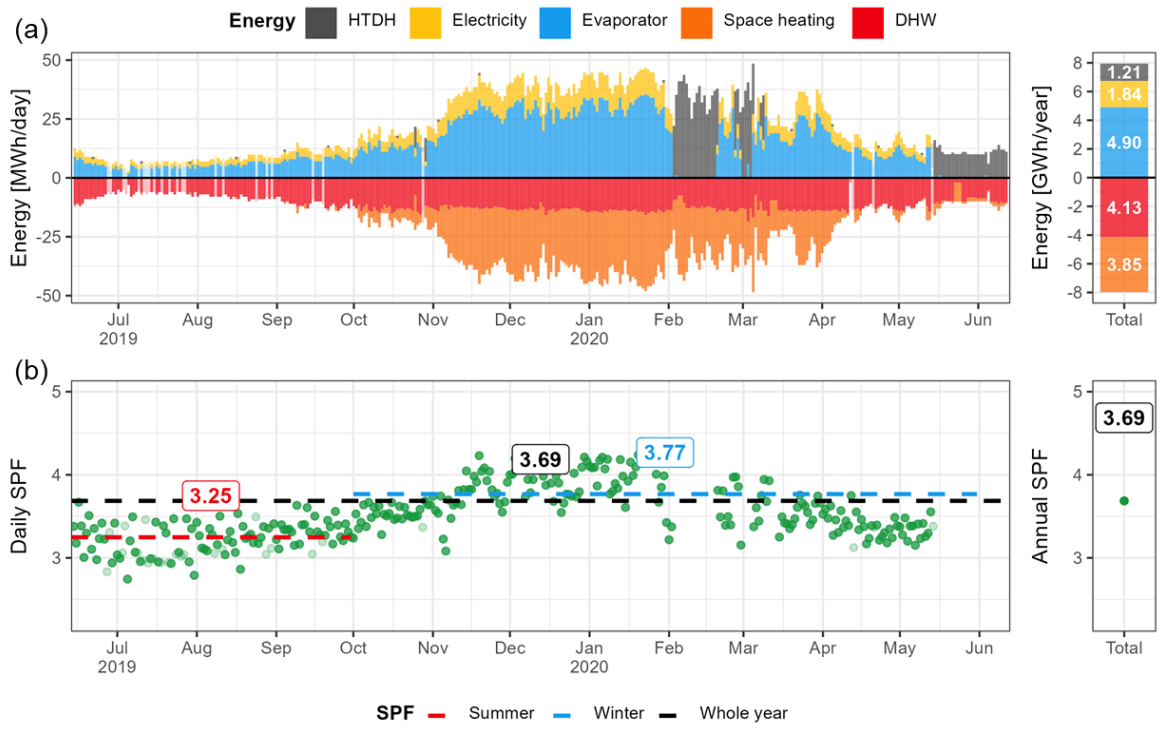


Fig. 2. Energy balance of the system and SPF of the heat pump on a daily and annual basis.

3.2. Measured and expected energy performance

Comparing hourly values of the measured COP with the expected COP provides a more accurate assessment of the HP performance, per operation mode (SH / DHW), than the daily or seasonal SPF presented before. In this regard, Fig. 3 shows, for each operation mode, the distribution of the measured hourly COP in bins of width 0.25, as well as the corresponding cumulative heat output, aggregated from the lowest to the highest COP. Vertical lines represent the measured SPF, as well as the expected COP provided by the manufacturer. These results confirm that the COP in DHW mode is generally lower than in SH mode.

In SH mode, the COP varies greatly, from 2.2 up to 5. A large share of the measured COP (41%) exceeds the expected COP of 4.60 provided by the manufacturer. The corresponding heat production represents nearly half of the heat production of the HP in SH mode. On the other hand, more than a third of the measured COP are below 4, representing about 25% of the heat production. For the whole period, the SPF (4.28) is only 7% below the nominal COP (4.60). Operation with high COP thus largely compensates for operation with very low COP. Hence, while the annual performance in this mode is close to expected, it could exceed expectations thanks to optimization measures.

In DHW mode, the COP is more stable as it varies from 2.8 to 3.5, but never reaches the COP announced by the manufacturer (3.62). While 45% of the measured hourly COP are below 3.25, most of the heat production (74%) is done with a COP between 3.25 and 3.5. Overall, the SPF is equal to 3.32, which is 8% less than the nominal COP (3.62).

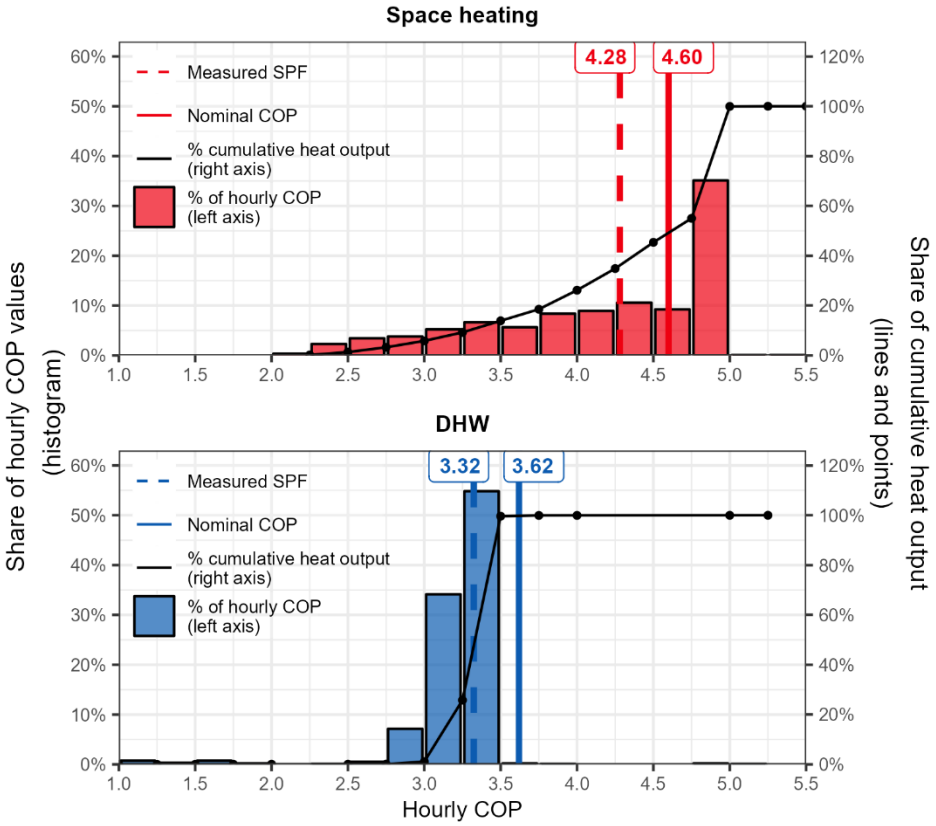


Fig. 3. Distribution of measured hourly COP per bins of width 0.25 (histogram), cumulative heat production aggregated from the lowest COP to the highest (black dots) and comparison with the manufacturer's data (vertical lines).

It should be noted that the results presented in Fig. 3 are based on available hourly data. As explained earlier, some data are either missing or inconsistent and have been excluded from the analysis. In the end, the valid hourly data presented correspond to a total heat production of 4.4 GWh, i.e. 64% of the HP heat production during this period.

With an annual electricity consumption of 1.84 GWh (Fig. 2), the HP is one of the main electricity consumer of the district since it represents about 30% of the total electricity demand (including heat pump and auxiliaries, as well as buildings' electricity consumption). Thus, even though the measured performance of the HP is close to the expected performance, there is a potential for optimization in both operation modes that could lead to significant electricity savings. To identify causes of low COP, the following sections focus mainly on SH mode. Reasons behind COP higher than the nominal COP in SH mode or lower than nominal COP in DHW mode could not be identified from the available information.

3.3. Factors of influence

To explain the performance gap between theoretical and measured COP and to identify optimization strategies, we first investigate the influence of the inlet and outlet temperatures at the evaporator and condenser.

The only temperature which can explain variations in COP within a given operation mode (SH / DHW) is the condenser inlet temperature, because: i) the evaporator inlet temperature is stable in SH mode, i.e. about 13°C, and varies only slightly in DHW mode (from 13°C to 16°C); ii) the condenser outlet temperature, i.e. the production temperature, is a setpoint for each operation mode (50°C in SH mode, 55°C at the beginning of the DHW batch and 65°C for the rest of the DHW batch). According to the system diagram in Fig. 1, the condenser inlet temperature results from two elements: i) the temperature at the bottom of the buffer tanks of the heating plant and ii) the DH return temperature.

Fig. 4a shows the measured hourly COP as a function of the temperature difference (ΔT) between the condenser inlet and the evaporator inlet, as well as the average temperature at the bottom of the storage tanks (color). As expected, the COP is higher in both operation modes when the ΔT is lower. The COP in SH mode is very sensitive to the ΔT: it varies from 2.2 for a ΔT of 28°C, to about 5 for a ΔT of 18°C. Furthermore, when the ΔT is lower than 23°C, there are significant variations in the COP, ranging from about 4 to 5 for the same ΔT. On the other hand, the COP in DHW mode is relatively unaffected by the ΔT since it varies from 2.8 to 3.5 over a wider range of ΔT, from 20°C to 38°C. In both modes, except for COP greater than 4 in SH mode, there is a clear correlation between the buffer tank temperature and the COP: the lower the temperature at the bottom of the tanks, the higher the COP. Besides, in DHW, the bottom of the tank reaches temperatures up to 50°C, which corresponds to the temperature at which the HP shuts down to prevent damage.

Not presented here, the same analysis with the DH return temperature instead of the buffer tanks temperature shows that, in SH mode, there is no systematic correlation between the DH return temperature and the COP. Whereas in DHW mode, results are similar to those of the buffer tanks temperature. Hence, the temperature at the bottom of the tanks is the main source of increase of the return temperature to the HP in SH mode. In DHW mode, the condenser inlet temperature is influenced both by the DH return temperature and by the temperature at the bottom of the tanks.

However, the variations of the condenser inlet temperature alone do not explain why, in SH mode, the hourly COP varies between 4 and 5 for the same ΔT of about 20°C (Fig. 4a). As shown in Fig. 4b, this is due to variations in condenser flow rate. The highest COP (4.8 to 5) occur for condenser flow rates of 90 m³/h or more, while the lowest (below 4.5) correspond to flow rates below 75 m³/h. Intermediate values are associated with the transition phase between these two flow rates.

Therefore, the COP of the HP is mainly influenced by: i) the condenser flow rate (Fig. 4b) and ii) the condenser inlet temperature, itself mainly influenced by the temperature at the bottom of the buffer tanks (Fig. 4a). The performance of the HP in SH is highest for flow rates above 90 m³/h and low condenser inlet temperatures (< 35°C).

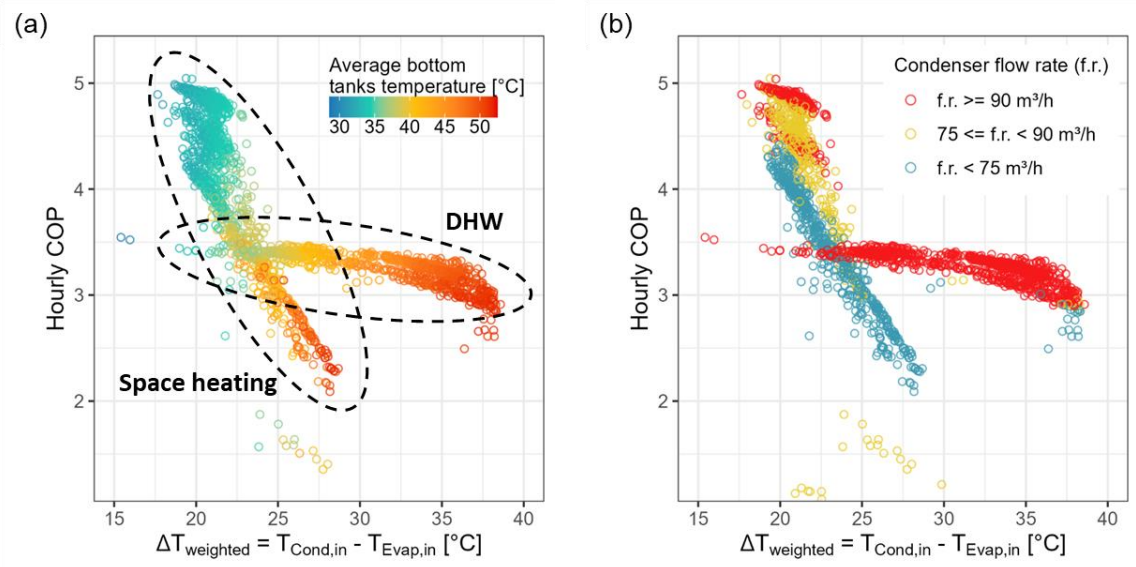


Fig. 4. Influence of the condenser flow rate and the temperature at the bottom of the buffer tanks on the hourly COP of the heat pump.

3.4. Typical Days

To understand more precisely the mechanisms involved in the degradation of the COP in SH, Fig. 5 presents typical days of operation of the HP during the winter. The location of the temperature sensors used to produce this figure is shown in the schematic of Fig. 1, where the colored circles correspond to the color of the lines. During those days (December 6th to December 8th), the HP operates at all times, except for approximately an hour and a half after each DHW batch, where it stops until the LTDH temperature lowers back to SH temperature levels (50°C).

The system dynamics indicates that low COP in SH generally occur before the DHW batches, while they are the highest after, following the temporary shutdown of the HP. During SH cycles *c2* and *c3*, there is a significant degradation of the COP, since it goes from 5 at the beginning of the cycle to about 3 at the end. First, the condenser flow rate decreases from 90 to 70 m³/h. Then, while the condenser flow rate is greater than the DH flow rate, the temperature at the bottom of the buffer tanks increases significantly (up to 50°C), thereby increasing the condenser inlet temperature. In SH cycle *c4*¸ the degradation of the COP is less important than for the two previous cycles (*c2* and *c3*) because the temperature at the bottom of the storage tanks remains low (around 34°C). There is only a reduction of the condenser flow rate in the middle of the cycle (between 1:00 a.m. and 3:00 a.m.). The only SH cycle illustrated here for which the COP of the HP is stable is cycle *c1*, during which the condenser flow rate remains high (equal to about 90 m³/h) and the temperature at the bottom of the tanks stays in the 30-35°C range. It is important to note that, in SH mode, the DH return temperature is stable. This indicates that, at this time of year, the degradation of the COP in SH is not due to high return temperatures from the DH substations. In DHW mode, the DH return temperature often reaches 50°C or more at the end of the batches, which can damage the HP and force it to shut down.

During the mid-season, the COP degradation phenomenon is amplified due to high imbalance between demand and HP production. Furthermore, the increase in condenser inlet temperature is not only due to an increase in buffer tank temperature, but also to high return temperatures of the DH substations.

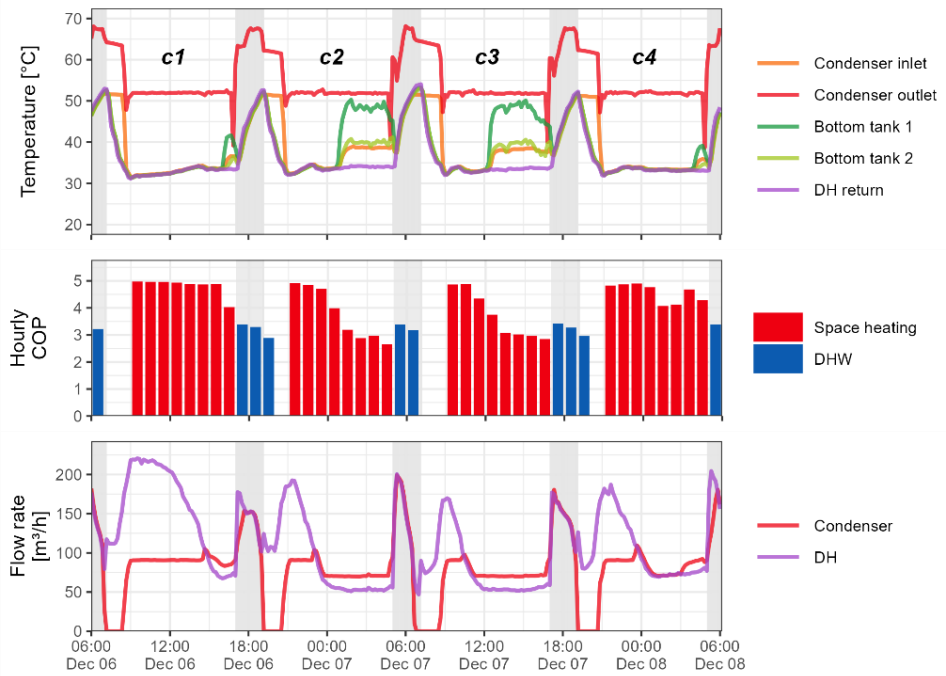


Fig. 5. Typical days of the system for December 6th to December 8th 2019. Gray background indicates the DHW batches. Refer to Fig. 1 for the location of temperature sensors.

In summary, the COP degradation phenomenon observed throughout the year can be caused by two elements:

- The high HP capacity compared to the demand which leads to: i) a reduction of the condenser flow rate to adapt to the demand, and ii) an increase of the buffer tanks temperature caused by storage of excess heat production.

- The substations and buildings control for SH which results in high DH return temperatures, in particular during the mid-season. Possible reasons are: i) a non-optimal control of the building SH circuits, which leads to high return temperature on the secondary side of the substations, thereby causing high return temperatures to the DH; ii) an excessive flow rate on the primary side of the substations, which leads to a low temperature difference between the inlet and outlet on that side, and thus to high return temperatures, regardless of the return temperature of the SH circuit on the secondary side.

3.5. Discussions and recommendations

The use of a HP with such a high capacity when the DH demand is low leads to an unsolvable problem. When the condenser flow rate is higher than the DH flow rate, the bottom of the tanks quickly heats up and increases the condenser inlet temperature. If the DH flow rate is increased, for the same heat demand, then the DH return also heats up. A solution would consist in lowering the production temperature of the HP: either punctually when the demand becomes too low during a SH cycle, or in a more systematic way by applying a heating curve to the DH supply temperature as a function of the outdoor temperature. This would allow to keep a relatively high flow rate at the condenser and to increase the DH flow rate while keeping DH return temperatures low.

It should be noted that the maximum capacity of the HP is 5 MW. However, the maximum heating power measured over this period is only about 2.5 MW in SH mode, while it reaches 4 MW in DHW mode. This difference between the two operation modes seems mainly related to the DHW batch system, gathering the whole daily DHW production in only 4 hours. Therefore, even if these batches avoid supplying the network constantly at 65°C, it raises an interesting point as for the sizing of the HP required for such a strategy, and thus of the necessary investment.

More generally, this analysis leads to the following recommendations, related to this case study in particular, but also to other HP in DH:

Control logic:

- **Adapt the DH supply temperature to the outdoor air temperature** to prevent operating with flow rates below the HP's operating limits, and thus degrading the HP performance. However, special attention should be paid to the network flow rates as such implementation leads to reduced temperature difference between DH supply and return, i.e. to higher DH flow rates. Therefore, to be beneficial, the increase in HP COP must compensate the additional electricity consumption for pumping.
- **Stop the HP sooner and operate on the DH inertia** to avoid reducing the flow rate and/or overheating the buffer tanks. The disadvantage of this solution is that heat pumps need time between each cycle to preserve their lifespan. It is thus challenging to decide when to switch it off, knowing it cannot turn back on immediately. Furthermore, if the HP stops shortly before a DHW batch, then the network temperature will decrease below 50°C. It will therefore take longer to reach the 65°C setpoint at the beginning of the DHW batch. As a result, it may prevent the DHW tanks within the buildings from being fully charged and thus cause comfort issues.
- **Optimize DH substations** to prevent high return temperatures, as pointed out in [7, 8], as high return temperatures reduce the HP energy performance and force it to shut down when it exceeds the operating limits. Such optimization might not only increase the HP performance, but also the overall efficiency of the district, if the faults identified also affect the energy performance of the buildings. For example, as shown in previous work [9], some buildings seem to have a high cut-off temperature of their SH system (> 15°C) despite their highly insulated thermal envelope. This suggests that some buildings are over-heated. Optimizing the control of the heat distribution system for these buildings would thus avoid having very low SH demand when the outdoor temperature is relatively high.

Sizing and system concept:

- **Use several smaller HP instead of one high capacity HP,** to better adapt to the DH demand and prevent overproduction compared to the demand, especially if the storage volume is low. This could however make the system control strategy more complex than with a single HP, because it is then necessary to manage several HPs.
- **Install bigger volumes for thermal storage compared to the minimum capacity of the HP,** to allow the HP to operate longer without overheating the storage and degrading the COP. Needless to say, there are economical and spatial constraints to such solution.

- **Use another strategy for DHW preparation**, as the DHW batch system leads to high return temperatures and causes HP breakdowns. It adds complexity to the system, both in terms of control strategy and equipment sizing compared to a substation that has the possibility to charge DHW tanks at any time of day. In addition, there has been complaints from building occupants regarding the lack of DHW, usually happening in the afternoon. Because supplying the DH network at 65°C at all time would mean achieving an annual SPF of 3-3.5 rather than 4-4.5, other, more energy efficient solutions should be explored. For example, installing booster heat pumps [10, 11] or flat substations [12, 13] with instantaneous water heating would allow to operate the network at lower temperatures than 65°C at all times, thanks to the limited risk of legionella bacteria proliferation. Both options would grant constant access to DHW preparation, thus an improved comfort for the occupants.

4. Conclusions

This study concerns the analysis, in actual conditions of use, of the energy performance of a large-scale heat pump supplying a low temperature district heating network. One of the specificities of this concept is that the district heating network is maintained at 50°C, and at fixed time, twice a day, its temperature is raised from 50°C to 65°C to heat up domestic hot water tanks within the buildings (batch).

Monitoring results show that the heat pump reaches an annual SPF of 3.69 (pumping excluded) and covers about 85% of the district heating demand. While the heat pump energy performance is close to the expected values (6-8% lower), the heat pump electricity consumption represents about 30% of the total electricity demand of the district, it is thus a consumption worthwhile to optimize.

The analysis of detailed monitoring data indicates that low energy performance is associated with low condenser flow rate and high return temperatures. This is mainly due to the high capacity of the heat pump compared to the demand and the storage volume, which leads to: i) a reduction of the condenser flow rate to adapt to the demand, and ii) an increase of the buffer tanks temperature of the heating plant, caused by storage of excess heat production. Furthermore, in mid-season, high return temperature from district heating substations in space heating also participate to the reduction of the heat pump performance, likely due to substations malfunctions. In domestic hot water mode, all substations of the district tend to have a high return temperature, partially due to the complexity of the domestic hot water batch strategy (control, equipment sizing, storage stratification etc.).

To prevent unexpectedly low energy performance of large-scale heat pumps in district heating, it is necessary to consider, but is not limited to, the following aspects: i) heat pump(s) and buffer tank sizing, which should allow to cover the highest demand, but also the lowest to avoid overheating the buffer tank; ii) control of the system, such as the use of a heating curve on the supply temperature of the network to operate the heat pump(s) at the lowest temperature possible, as well as to prevent high capacity heat pumps from operating at flow rates below operating limits; iii) substations monitoring and optimization, which allows to reduce the district heating return temperature to the heat pump(s), thereby increasing the energy efficiency and avoiding heat pump(s) shutdowns; iv) domestic hot water production strategies, as the batch system used in this case study has proven to be more challenging than anticipated, adding complexity to control and sizing of the system (heating plant and building substations) to guarantee the operation of the heat pump, the energy efficiency of the system and occupants comfort.

Because heat pump in district heating systems are expected to develop massively in the upcoming years, it would be interesting to explore alternative solutions to this concept, in actual conditions of use, such as the use of decentralized solutions for the domestic hot water production.

Acknowledgements

The authors are thankful to the following entities for funding the work presented in this paper: Services industriels de Genève (SIG), Office cantonal de l'énergie de Genève (OCEN) and Ville de Meyrin.

References

[1] Fleiter T, Elsland R, Rehfeldt M, Steinbach J, Reiter U, Catenazzi G, Jakob M. Profile of heating and cooling demand in 2015. Heat Roadmap Europe 2017.

[2] Paardekooper S, Lund RS, Mathiesen BV, Chang M, Petersen UR, Grundahl L, David A, Dahlbæk J, Kapetanakis IA, Lund H, Bertelsen N, Hansen K, Drysdale DW, Persson U. Heat Roadmap Europe 4: Quantifying the Impact of Low-Carbon Heating and Cooling Roadmaps. Aalborg Universitetsforlag 2018.
[3] David A, Mathiesen BV, Averfalk H, Werner S, Lund H. Heat Roadmap Europe: Large-Scale Electric Heat Pumps in District Heating Systems. *Energies* 2017;**10**:578.
[4] Geyer R, Hangartner D, Lindahl M, Pedersen SV. IEA HPT Annex 47 Heat Pumps in District Heating and Cooling Systems. Task 4: Implementation barriers, possibilities and solutions. 2019.
[5] Geyer R, Hangartner D, Lindahl M, Vinther Pedersen S, Betz M. IEA HPT Annex 47 Heat Pumps in District Heating and Cooling Systems. Task 2: Demonstration projects. 2019.
[6] R.G. Riedweg & Gendre SA. Ecoquartier 'Les Vergers' Meyrin : Centrale de production SIG - Energies annuelles consommées. Genève 2014.
[7] Gadd H, Werner S. Fault detection in district heating substations. *Applied Energy* 2015;**157**:51–9.
[8] Månsson S, Johansson Kallioniemi P-O, Thern M, Van Oevelen T, Sernhed K. Faults in district heating customer installations and ways to approach them: Experiences from Swedish utilities. *Energy* 2019;**180**:163–74.
[9] Brischoux P, Schneider S, Hollmuller P. Performance gap analysis of a new Minergie A/P district. *J Phys: Conf Ser* 2021;**2042**:012141.
[10] Østergaard PA, Andersen AN. Booster heat pumps and central heat pumps in district heating. *Applied Energy* 2016;**184**:1374–88.
[11] Yang X, Li H, Svendsen S. Evaluations of different domestic hot water preparing methods with ultra-low-temperature district heating. *Energy* 2016;**109**:248–59.
[12] Toffanin R, Curti V, Barbato MC. Impact of Legionella regulation on a 4th generation district heating substation energy use and cost: the case of a Swiss single-family household. *Energy* 2021;**228**:120473.
[13] Yang X, Li H, Svendsen S. Decentralized substations for low-temperature district heating with no Legionella risk, and low return temperatures. *Energy* 2016;**110**:65–74.

14th IEA Heat Pump Conference
15-18 May 2023, Chicago, Illinois

Characterization of the fluid flow phenomena in an ejector for a high temperature heat pump

Manuel Schieder[a,*], Constantin Zenz[a,b], Julian Unterluggauer[a], Michael Lauermann[a], Adam Buruzs[a], Veronika Wilk[a], Thomas Fleckl[a], Christoph Reichl[a]

[a]AIT Austrian Institude of Technology GmbH, Giefinggasse 4, 1210 Vienna, Austria
[b]TU Wien Institute for Production Engineering E311, Karlsplatz 13, 1040 Vienna, Austria

Abstract

Decarbonization of industrial processes is one important step towards a sustainable future. The usage of high-temperature heat pumps to provide heat for industrial processes is a promising way towards that goal. Heat pumps used for such high temperature applications have a large difference between condenser and evaporator pressure and therefore the losses due to irreversible dissipation within the expansion process are high. To make high-temperature heat pumps more efficient and therefore interesting for industrial applications, the ejector, which is an alternative expansion device to replace the conventional throttle valve, is investigated. The flow inside an ejector of a high temperature heat pump is simulated numerically to gain better understanding of the underlying fluid flow phenomena, its applicability to heat pump cycles and to give an outlook on possible cycle efficiency improvements. To reduce the computational demand of simulating the two-phase flow inside the ejector and to avoid the need for experimental-based fine-tuning as opposed to a full multiphase model, the Homogeneous Equilibrium Model (HEM), which assumes thermal and mechanical equilibrium between both phases, is applied. This model was implemented into the commercial Computational Fluid Dynamics (CFD) software Ansys Fluent. The main flow features are analyzed, and phenomena occurring at unfavorable operating points, obtained through an unsuitable geometry, are identified.

© HPC2023.
Selection and/or peer-review under the responsibility of the organizers of the 14th IEA Heat Pump Conference 2023.

Keywords: High-temperature heat pump, CFD, Ejector

1. Introduction

Performance enhancement of high temperature heat pump systems is an important topic to facilitate a change in industrial energy systems. One way is to do cycle modification with the intentions of decreasing the electrical energy input under the restrictions of as low costs as possible. Therefore, the introduction of a two-phase ejector has become a promising cycle modification recently. Contrary to an ordinary expansion valve, the ejector recovers some of the expansion energy which is normally wasted in throttling processes. It reduces the compressor work by raising the suction pressure to a higher level, which directly leads to an improvement of the COP. Nakagawa et al. [1] experimentally analyzed ejectors and achieved a COP increase of up to 26%. Moreover, the ejector technology also leads to an evaporator size reduction as it provides a flash gas bypass. The technology itself is not new, as in 1990 Kornhauser [1] analyzed the thermodynamic performance of the ejector expansion refrigeration cycle using R12 as a working fluid.
To improve the design of ejectors CFD has become a valuable tool to enhance the performance. For a given ejector geometry, there exists only a small bandwidth of operating conditions that is leading to optimum efficiency [3][4][5].

Smolka et al. [6] developed a Homogeneous Equilibrium Model (HEM) to perform CFD simulations of a two-phase transcritical CO_2 ejector with a commercial CFD code without having to employ a full multiphase

* Corresponding author. Tel.: +43 50550-6602; fax: +43 50550-6679
E-mail address: manuel.schieder@ait.ac.at

model, as through the assumption of a homogeneous equilibrium, the governing equations can be used in their single-phase formulation. Bodys et al. [7] expanded the model of Smolka et al. [6] to account for thermodynamic metastability effects, which was realized through solving an additional equation for the vapor quality which includes a relaxation factor to be experimentally tuned. This addition to the homogeneous model led to an improvement of the prediction of CO_2 ejectors with subcritical inlet conditions. Yazdani et al. [8] used a mixture model to simulate the two-phase flow of CO_2 in an ejector. The mass transfer between the phases was modeled including both boiling and cavitation phenomena. Additionally, a slip velocity between the phases was included in the model. The analysis did not show a better accuracy in predicting key performance parameters of an ejector than simpler models like that of [7]. Biferi et al. [9] used the HEM of [6] to simulate a supersonic ejector with R134 as working fluid. The simplification of constant material properties except for those of density and speed of sound was made without drawbacks in accuracy.

Zhu et al. [10] showed that their 2D axisymmetric CFD simulation can predict the entrainment ratio with good accuracy (<10% error) compared to their measurements using R141b as working fluid.

In this work the HEM approach is used to model the flow phenomena inside the given R600 (butane) ejector. The extracted data from 2D-axisymmetric CFD simulations is analyzed and compared to experimental results. The results of this paper are partly based on the work of Zenz [11].

2. Heat pump cycle

The ejector in a heat pump cycle fulfils two purposes, first mixing of the high-pressure with the low-pressure flow and secondly pressure recovery by expansion. It consists of a primary inlet where the fluid is in a liquid state, a secondary inlet also called suction inlet where the fluid is in a gaseous state and one outlet with mixed conditions. As there are different types of ejectors it must be noticed that the presented design can be characterized as a two-phase supersonic constant pressure mixing ejector. A high-pressure fluid enters through the primary inlet and accelerates in the motive nozzle which entrains a low-pressure fluid through the secondary inlet. After a mixing process and static pressure recovery in a diffuser, the fluid leaves the ejector at a pressure that lies between the two inlet pressures. In the motive nozzle the fluid reaches supersonic speed while at the beginning of the diffuser the Mach number is close to 1 so that no further acceleration occurs, and pressure recovery is obtained.

The idea of an ejector in a heat pump cycle is to replace the expansion valve which has the purpose of converting the potential energy of the high-pressure fluid into kinetic energy as it is accelerated. Therefore, the pressure level at the compressor inlet is increased which leads to lesser electric energy needed and as a result to an increase of the COP. In Figure 1 the heat pump cycle, using an ejector, is depicted. Based on the ejector technology applied, the vapor entering the compressor from the separator at state 1 lies at a higher-pressure level than that of the evaporator. The low-pressure vapor leaving the evaporator (10) enters the ejector through the secondary inlet (5) and is entrained by the high-pressure stream coming from the condenser and entering the ejector through the motive nozzle (4). After pressure recovery inside the diffuser, the mixed two-phase refrigerant leaves the ejector at a higher-pressure level (7) and is separated into vapor (1) and liquid (8) phases.

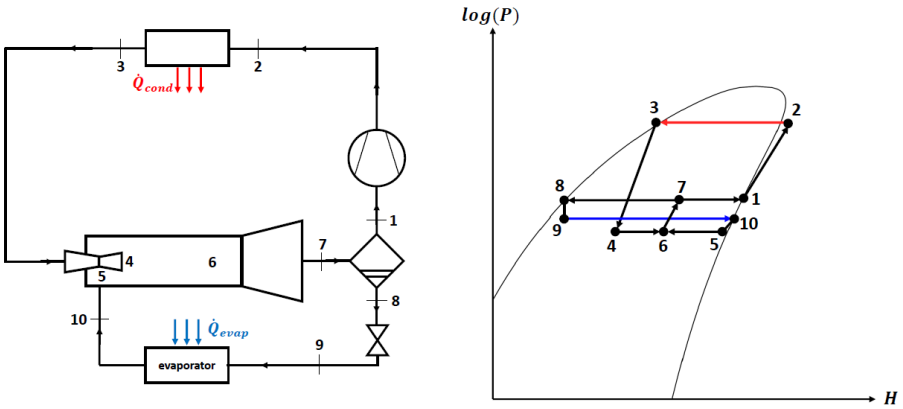


Fig. 1. Heat pump cycle and log(p)-H diagram. (see [11])

The ejector can be characterized by three key parameters. The first one is the entrainment ratio:

$$X = \frac{\dot{m}_{sec}}{\dot{m}_{prim}}, \tag{1}$$

with $\dot{m}_{sec}$ being the secondary inlet mass flow and $\dot{m}_{prim}$ the mass flow entering the motive nozzle at the primary inlet.
The second parameter is the suction pressure ratio:

$$\Pi_S = \frac{p_{out}}{p_{sec}}, \tag{2}$$

with p_{out} the absolute pressure at the outlet and p_{sec} the total pressure at the secondary inlet.
The last and third parameter is the ejector efficiency as it is defined by Elbel and Hrnjak [12]:

$$\eta_{ej} = X \frac{h(p_{out}, s_{sec}) - h(p_{sec}, s_{sec})}{h(p_{prim}, s_{prim}) - h(p_{out}, s_{prim})}, \tag{3}$$

Using the entrainment ratio X and enthalpy differences. In other words, the ejector efficiency can be described as the ratio of the amount of expansion work rate recovered to the maximum possible expansion work rate recovery potential of the ejector. Lawrence and Zhang et al. [13] found out that the ejector efficiency ranges from 20% to 30% for transcritical CO_2 heat pump cycles. They also mention that the best system performance may not occur when the ejector efficiency is at its peak for a given geometry.

3. Numerical Model

3.1. Geometry and Mesh

The geometry is designed by using an 1D simulation tool and is already published together with first measurement results by Schlemminger et al. [14].

Motive nozzle (A)	$D_{MN,1}$ [mm]	20
	$D_{MN,2}$ [mm]	4,4
	$D_{MN,3}$ [mm]	6,9
	$D_{MN,4}$ [mm]	26
	$\gamma_{MN,1}$ [°]	30
	$\gamma_{MN,2}$ [°]	10
	$\gamma_{MN,3}$ [°]	37
Mixing chamber (C)	L_{MCH} [mm]	11
	D_{TIP} [mm]	8,53
Suction nozzle (B) And Diffusor (D)	D_{SN} [mm]	38
	γ_{SN} [°]	37
	D_{MIX} [mm]	14
	L_{MIX} [mm]	112
	D_{DIF} [mm]	36
	γ_{DIF} [°]	5

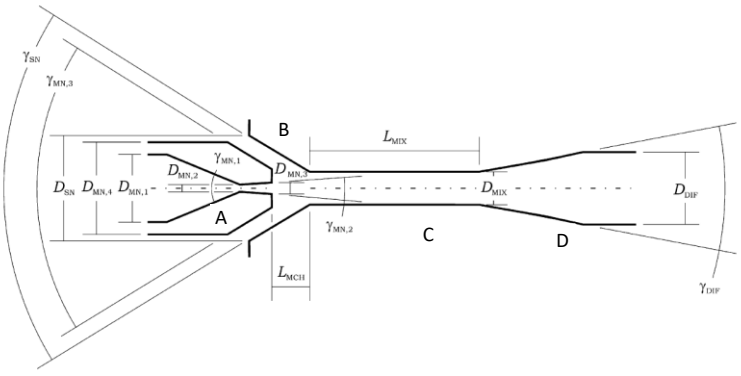


Fig. 2. Ejector design according to [14].

The domain is meshed using Ansys 19 Workbench to generate a full hexahedral grid with 167000 cells which is depicted in Figure 3.

The maximum skewness is well below 0.5 and refinements at the walls are included to keep the y^+ at a reasonable value (area-weighted average ≈ 2.5). The cells are stretched in axial direction which is increasing their aspect ratio in regions such as the mixing chamber and the diffuser, as there exists a clear direction of convective transport and therefore, the number of needed cells can be significantly reduced. Inside the primary nozzle and where the primary and secondary exit meet, the aspect ratio is kept near unity.

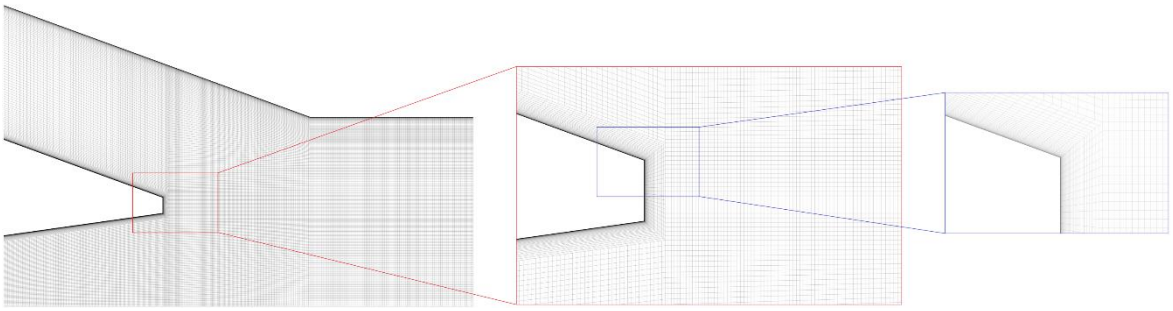


Fig. 3. Computational grid (167 000 cells).

3.2. Numerical setup and Boundary conditions

The boundary conditions are chosen accordingly to Schlemminger et al. [14] and are summarized in Table 1. The refrigerant entering the ejector through the motive nozzle is subcooled. However, in [14] it was assumed that a vapor quality of 2.7% was present at the primary inlet. Therefore, a two-phase state corresponding to a vapor quality of 2.7% was used as boundary condition for the value of enthalpy at the primary inlet. With the energy equation being enthalpy-based the temperature is not a variable used by the solver. The whole case is set up as a 2D-domain using Ansys 19 Fluent for steady-state simulations. To setup the Homogeneous Equilibrium Model, the energy equation needs to be solved in the enthalpy-based form. This is done with a User Defined Scalar (UDS), solving an additional transport equation for the enthalpy. Moreover, the material properties are updated by calling an User Defined Function (UDF) that contains the C-code to perform a bilinear interpolation in order to obtain material properties as functions of pressure and enthalpy based on the REFPROP 10.0 database [15]. To model turbulence the k-ω-SST taking compressibility effects into account is used. All equations are solved using first-order upwind schemes, except for pressure, where a second order pressure interpolation scheme is chosen. Second-order schemes are known to be more accurate and less diffusive, but also more numerical unstable. The drawback in accuracy of a first-order scheme over a second order scheme (given they are both of the same type, e.g. upwind schemes) can be compensated by using a denser computational grid. For the two-dimensional simulations performed in this work it was noticed that an increase in cell density comes at less computational cost than the needed measures to bring a simulation using second-order upwind schemes to convergence.

Table 1 Boundary conditions for R600 ejector

Boundary Condition	Value
Primary inlet total pressure (bar)	21.39
Primary inlet vapor quality (%)	2.7
Secondary inlet total pressure (bar)	4.3
Secondary inlet superheating ΔT (K)	8.06
Outlet static pressure (bar)	5.845

3.3. Homogeneous Equilibrium Model

To lower the computational demand, the Homogeneous Equilibrium Model was used as a two-phase model. In this model the liquid and the vapor phase are assumed to be in a thermal and mechanical equilibrium, meaning that pressure, temperature, velocity, turbulence kinetic energy and turbulence dissipation rate are the same in both phases [6].

All properties are a function of the specific enthalpy and the pressure. Since Ansys Fluent uses the temperature as an independent variable for the energy equation, an enthalpy-based energy equation was implemented, using the specific enthalpy as an independent variable. This was implemented as an UDS in the program.

The general form of a steady state transport equation of an arbitrary scalar ϕ (with Favre averaged quantities denoted with tilde and Reynolds averaged quantities denoted with a macron) in ANSYS Fluent has the form [6][16]:

$$\boldsymbol{\nabla} \cdot \left(\rho \tilde{\boldsymbol{u}} \tilde{\phi}\right) = \boldsymbol{\nabla} \cdot \left(\Gamma \boldsymbol{\nabla} \tilde{\phi}\right) + \dot{S}_{\phi}, \tag{4}$$

with $\dot{S}_{\phi}$ being an additional source term and Γ the diffusion coefficient of the scalar ϕ. The enthalpy-based energy equation for the implementation in Ansys Fluent has the following form, according to [6]:

$$\boldsymbol{\nabla} \cdot \left(\rho \tilde{\boldsymbol{u}} \tilde{h}\right) = \boldsymbol{\nabla} \cdot \left(\Gamma_h \boldsymbol{\nabla} \tilde{h}\right) + \dot{S}_{h1} + \dot{S}_{h2} + \dot{S}_{h3}, \tag{5}$$

with Γ_h being the diffusivity of h:

$$\Gamma_h = \frac{\lambda}{c_p} + \frac{\mu_t}{\sigma_t}. \tag{6}$$

where λ denotes the thermal conductivity, c_p the specific heat capacity at constant pressure, μ_t the turbulent viscosity and σ_t the turbulent Prandtl number.

The source terms represent the mechanical energy $\dot{S}_{h1}$, the irreversible dissipation of kinetic energy variations $\dot{S}_{h2}$ and the dissipation of turbulent kinetic energy $\dot{S}_{h3}$. These source terms have the following form [6]:

$$\dot{S}_{h1} = \tilde{\boldsymbol{u}} \cdot \boldsymbol{\nabla} \bar{p}, \tag{7a}$$

$$\dot{S}_{h2} = (\mu + \mu_t)\left\{2\left[\left(\frac{\partial \tilde{u}}{\partial x}\right)^2 + \left(\frac{\partial \tilde{v}}{\partial y}\right)^2 + \left(\frac{\partial \tilde{w}}{\partial z}\right)^2\right] + \left(\frac{\partial \tilde{u}}{\partial y} + \frac{\partial \tilde{v}}{\partial x}\right)^2 + \left(\frac{\partial \tilde{u}}{\partial z} + \frac{\partial \tilde{w}}{\partial x}\right)^2 + \left(\frac{\partial \tilde{v}}{\partial z} + \frac{\partial \tilde{w}}{\partial y}\right)^2 - \frac{2}{3}(\boldsymbol{\nabla} \cdot \tilde{\boldsymbol{u}})^2\right\} - \frac{2}{3}\bar{\rho} K \boldsymbol{\nabla} \cdot \tilde{\boldsymbol{u}}, \tag{7b}$$

$$\dot{S}_{h3} = -\bar{\rho} \tilde{\boldsymbol{u}} \cdot \boldsymbol{\nabla} K. \tag{7c}$$

For the implementation into Ansys Fluent, using the axisymmetric solver, all source terms need to be implemented in cylindrical coordinates, leading to:

$$\dot{S}_{h1} = \tilde{u}_r \frac{\partial \bar{p}}{\partial r} + \tilde{u}_\theta \frac{1}{r}\frac{\partial \bar{p}}{\partial \theta} + \tilde{u}_z \frac{\partial \bar{p}}{\partial z}, \tag{8a}$$

$$\dot{S}_{h2} = (\mu + \mu_t)\left\{2\left[\left(\frac{\partial \tilde{u}_r}{\partial r}\right)^2 + \left(\frac{1}{r}\frac{\partial \tilde{u}_\theta}{\partial \theta} + \frac{\tilde{u}_r}{r}\right)^2 + \left(\frac{\partial \tilde{u}_z}{\partial z}\right)^2\right] + \left[\frac{\partial}{\partial r}\left(\frac{\tilde{u}_\theta}{r}\right) + \frac{1}{r}\frac{\partial \tilde{u}_r}{\partial \theta}\right]^2 + \left(\frac{1}{r}\frac{\partial \tilde{u}_z}{\partial \theta} + \frac{\partial \tilde{u}_\theta}{\partial z}\right)^2 + \left(\frac{\partial \tilde{u}_r}{\partial z} + \frac{\partial \tilde{u}_z}{\partial r}\right)^2 - \frac{2}{3}(\boldsymbol{\nabla} \cdot \tilde{\boldsymbol{u}})^2\right\} - \frac{2}{3}\bar{\rho} K \boldsymbol{\nabla} \cdot \tilde{\boldsymbol{u}}, \tag{8b}$$

$$\dot{S}_{h3} = -\bar{\rho}\left(\tilde{u}_r \frac{\partial K}{\partial r} + \tilde{u}_\theta \frac{1}{r}\frac{\partial K}{\partial \theta} + \tilde{u}_z \frac{\partial K}{\partial z}\right). \tag{8c}$$

Since the velocities and derivatives in an axisymmetric simulation are zero, the source terms reduce to the following form:

$$\dot{S}_{h1} = \tilde{u}_r \frac{\partial \bar{p}}{\partial r} + \tilde{u}_z \frac{\partial \bar{p}}{\partial z}, \tag{9a}$$

$$\dot{S}_{h2} = (\mu + \mu_t)\left\{2\left[\left(\frac{\partial \tilde{u}_r}{\partial r}\right)^2 + \left(\frac{\tilde{u}_r}{r}\right)^2 + \left(\frac{\partial \tilde{u}_z}{\partial z}\right)^2\right] + \left(\frac{\partial \tilde{u}_r}{\partial z} + \frac{\partial \tilde{u}_z}{\partial r}\right)^2 - \frac{2}{3}(\boldsymbol{\nabla} \cdot \tilde{\boldsymbol{u}})^2\right\} - \frac{2}{3}\bar{\rho} K \boldsymbol{\nabla} \cdot \tilde{\boldsymbol{u}}, \tag{9b}$$

$$\dot{S}_{h3} = -\bar{\rho}\left(\tilde{u}_r \frac{\partial K}{\partial r} + \tilde{u}_z \frac{\partial K}{\partial z}\right), \tag{9c}$$

with the divergence of the velocity, assuming that velocity and derivatives in angular direction are zero:

$$\boldsymbol{\nabla} \cdot \tilde{\boldsymbol{u}} = \frac{\partial \tilde{u}_r}{\partial r} + \frac{\tilde{u}_r}{r} + \frac{\partial \tilde{u}_z}{\partial z}. \tag{10}$$

In the general form of cylindrical coordinates, the z-axis is considered as the symmetry axis. Ansys Fluent specifies the x-axis as the symmetry axis. Therefore, for the implementation in Ansys Fluent all terms in z-direction need to be implemented as x-direction terms.

4. Results

The mass flow rate and entrainment ratio were, in the experiment, measured as $\dot{m}_{\text{prim}} = 0.127$ kg/s and $X = 0.46$, respectively [13]. The simulation over-predicts the mass flow rate by 30% up to 45% and the entrainment ratio by 20% up to 50%, depending on the value of inlet vapor quality. The unsatisfactory prediction of mass flow rates by the HEM was also concluded by Bodys et al. [7] for subcritical inlet conditions (for CO_2 as working fluid). Therefore, they extended the underlying model to incorporate non-equilibrium effects. This led to an agreement between experimental and simulated mass flow rates of less than 10%. However, this model needs to be calibrated by a set of experiments which in not available for the presented R600 ejector.

The influence of vapor quality at the primary inlet on the primary mass flow rate and the entrainment ratio is shown in Figure 4. With an increase of the vapor quality the density decreases and therefore the mass flow changes quickly. However, the entrainment ratio X increases which suggests that the effect of the lower primary inlet mass flow is dominant over the effect on the physical process of entrainment.

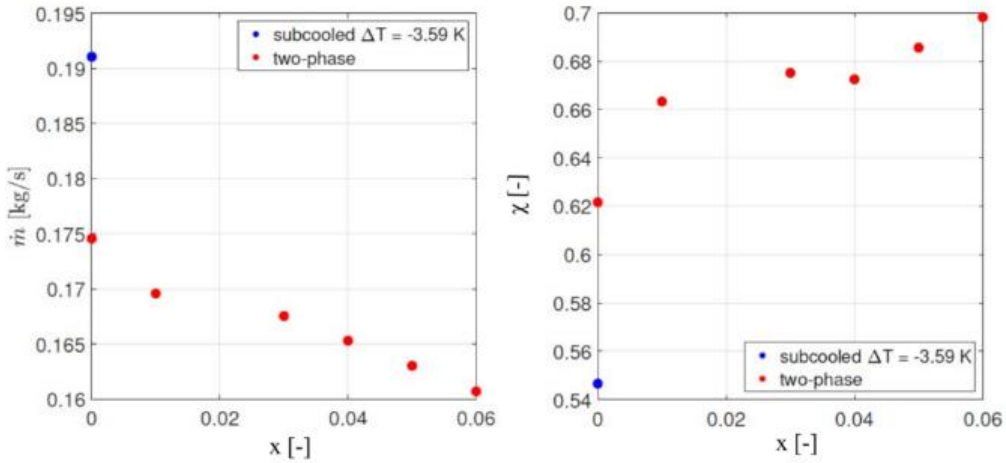


Fig. 4. Primary inlet mass flow rate $\dot{m}$ (left) and entrainment ratio $\boldsymbol{X}$ (right) for subcooled primary inlet condition and different levels of primary inlet vapor quality. (see [11])

Figure 5 shows the variation of static pressure along the ejector axis and wall compared to six measurement points obtained by the experiments published in [14]. In the mixing zone a deviation of the calculated pressure from experimental measurements is noticeable. This is also the location in which oblique shock waves occur. This might have affected the measurement results. However, specific potential errors in measurements due to condensation at the drilled hole for the pressure measurement, as well as thermal effects cannot be quantified.

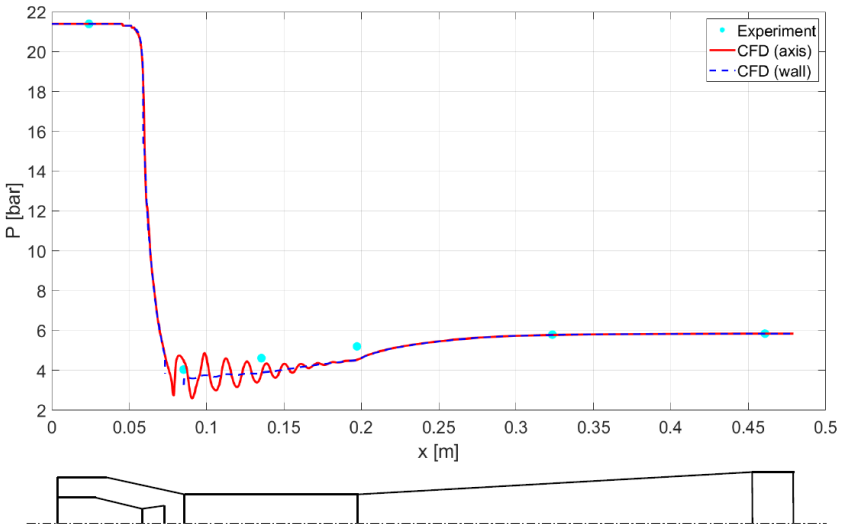


Fig. 5. Static pressure along the ejector axis and the wall, as well as experimental pressure measurements from [14]. (see [11])

Figure 6 shows the Mach number along the axis of the ejector. The oscillations in the mixing chamber correspond to supersonic shocks which can be noticed in the contour plot showed in Figure 7.

The velocity is decreasing, and no shocks are appearing at the beginning of the diffuser, which is a must have condition to guarantee the desired pressure recovery. This behavior can also be seen in the contour plot of the Mach number in Figure 7.

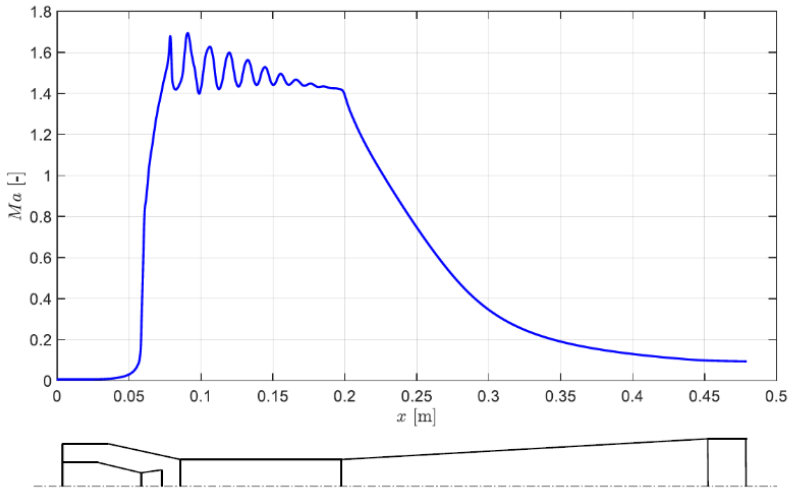


Fig. 6. Mach number along the ejector axis. (see [11])

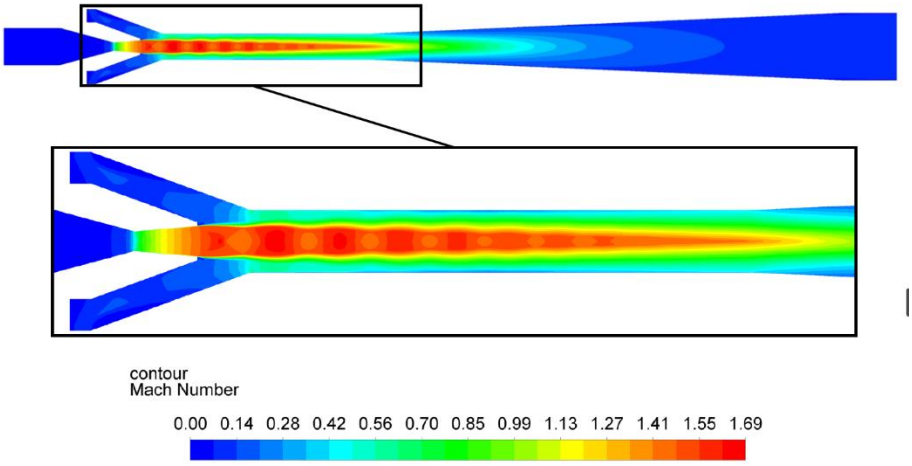


Fig. 7. Contour plot of the Mach number. (see [11])

How sensible the ejector design reacts to minor geometry variation in the motive nozzle can be seen in Figure 8. The primary nozzle throat and exit diameter are increased while keeping the converging and diverging angle constant, and the secondary nozzle cross-sectional area is decreased. In contrast to Figure 7 higher Mach numbers are reached and the flow stays supersonic until reaching the beginning of the diffuser, where a crucial shock occurs. As a result, boundary layer separation occurs and a recirculation region at the beginning of the diffuser forms. This leads to a performance drop with a decrease of the entrainment ratio to X = 0.082. Although, the simulation model is not able to capture non-equilibrium effects, qualitative conclusions on the suitability of an ejector geometry can be drawn. This model is especially interesting for drawing relative comparisons between different ejector geometries.

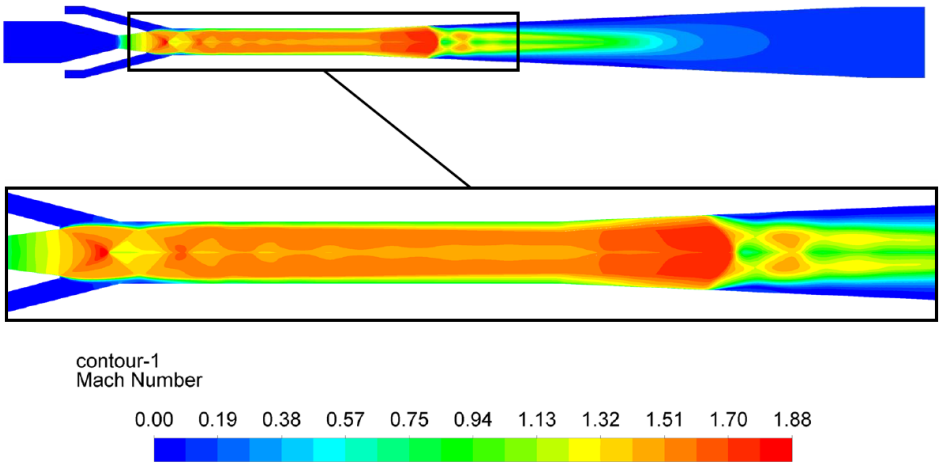


Fig. 8. Contour plot of the Mach number for a geometry variation of the motive nozzle. (see [11])

5. Conclusion

For the evaluation of the ejector performance in a high-temperature heat pump a CFD analysis was conducted.

A homogeneous equilibrium model was implemented in Ansys Fluent to allow for computationally affordable calculations of the two-phase flow. The benefit of the model is, that it does not need experimental fine-tuning, which is difficult, given that currently heat pumps featuring an ejector are still a topic of research and not commercially available. Even though the mathematical model is not capable of capturing metastability

effects, and therefore mass flow rate predictions are sometimes unsatisfactory, the model can still be used to make interesting qualitative observations. Furthermore, geometry shape optimizations can be extracted. Besides the limitations of the HEM approach, comparisons between different ejector geometries can be drawn. Concerning future work, a broader range of experimental data for ejectors operated under heat pump conditions is needed to calibrate more reliable numerical models. This is of importance as the main quantities of interest for heat pump cycle simulations, the mass flow rates and entrainment ratio, are found to be strongly affected by non-equilibrium thermodynamics. For further work, a subcooled state in the motive nozzle flow should be achieved in the experiments since the given ejector was originally designed for those conditions.

6. Copyright

By submittal of his or her full paper to the International Energy Agency for the 14th Heat Pump Conference, the author(s) assumes full responsibility for ensuring that his or her paper does not infringe on another party's intellectual property rights, which include copyright and agree that the paper has not previously been submitted for publication elsewhere. Furthermore, the author, by submittal of his or her conference paper to the conference, grants publishing rights of that paper to the Agency for the 14th Heat Pump Conference, which may:

1. Publish or arrange to publish the paper as part of the Conference proceedings,
2. Copy and distribute the paper in its entirety in print and electronic form, and
3. Copy and distribute excerpts from the paper.

Acknowledgements

This publication was conducted within the projects "ETHP" (FFG project number: 40165847) and "VWE" (FFG project number: 871723).
This project is funded by the Austrian national Research Funding Agency (FFG).

Nomenclature

Abbreviations

CFD	Computational Fluid Dynamics
COP	Coefficient of Performance
UDF	User Defined Function
UDS	User Defined Scalar

Greek Symbols

η_{ej}	Ejector efficiency
Γ	Diffusion coefficient
λ	Thermal conductivity
μ	Dynamic viscosity
μ_t	Turbulent viscosity
ϕ	Spare variable
Π_s	Suction pressure ratio
ρ	Density
σ_t	Turbulent Prandtl number

Latin Symbols

c_p	Specific heat capacity at constant pressure

h	Specific enthalpy
K	Turbulence kinetic energy
$\dot{m}$	Mass flow rate
p	Pressure
r	Radius
r, θ, z	Direction vector components in cylindrical coordinates
s	Specific entropy
$\dot{S}$	Source term in transport equation
$\boldsymbol{u}$	Velocity vector
u, v, w	Velocity components in cartesian coordinates
u_r, u_θ, u_z	Velocity components in cylindrical coordinates
x, y, z	Direction vector components in cartesian coordinates
X	Entrainment ratio

References

[1] Nakagawa, M., Marasigan, A., Matsukawa, T., and Kurashina, A. (2011). Experimental investigation on the effect of mixing length on the performance of two-phase ejector for CO2 refrigeration cycle with and without heat exchanger. International Journal of Refrigeration, 34(7):1604–1613. http://dx.doi.org/10.1016/j.ijrefrig.2010.07.021.

[2] Kornhauser AA. (1990). The use of an ejector as a refrigerant expander. Proceedings of USNC/IIR-Purdue refrigeration conference, USA.

[3] Grazzini G., Milazzo A., and Mazzelli F..(2018) Ejectors for Efficient Refrigeration. Design, Applications and Computational Fluid Dynamics. Springer. https://doi.org/10.1007/978-3-319-75244-0

[4] Varga S., Oliveira A. C., and Diaconu B.. (2009). Influence of geometrical factors on steam ejector performance - A numerical assessment. International Journal of Refrigeration 32, pp. 1694-1701. https://doi.org/10.1016/j.ijrefrig.2009.05.009

[5] Banasiak K. and Hafner a.. (2011). 1D Computational model of a two-phase R744 ejector for expansion work recovery. International Journal of Thermal Sciences 50, pp. 2235-2247. https://doi.org/10.1016/j.ijthermalsci.2011.06.007

[6] Smolka, J., Bulinski, Z., Fic, Z., Nowak, A. J., Banasiak, K., and Hafner, A. (2013). A computational model of a transcritical R744 ejector based on a homogeneous real fluid approach. Applied Mathematical Modelling, 37(3):1208–1224. http://dx.doi.org/10.1016/j.apm.2012.03.044.

[7] Bodys J. et al. (2020). Non-equilibrium approach for the simulation of CO2 expansion in two-phase ejector driven by subcritical motive pressure. International Journal of Refrigeration 114, pp. 32-46. http://dx.doi.org/10.1016/j.ijrefrig.2020.02.015.

[8] Yazdani M., Alahyari A.A., and Radcli T. D.. (2012). Numerical modeling of two-phase supersonic ejectors for work-recovery applications. In: International Journal of Heat and Mass Transfer 55, pp. 5744-5753. https://doi.org/10.1016/j.ijheatmasstransfer.2012.05.071

[9] Biferi G. et al. (2016). CFD modelling of the condensation inside a supersonic ejector working with R134a. Energy Procedia 101, pp. 1232-1239. https://doi.org/10.1016/j.egypro.2016.11.138

[10] Zhu Y., Cai W., Wen C., Li Y.. (2009). Numerical investigation of geometry parameters for design of high performance ejectors,Appl. Therm. Eng., 29 ,pp. 898-905. https://doi.org/10.1016/j.applthermaleng.2008.04.025

[11] Zenz, C. (2020). Numerical Analysis of Fluid Flow and Heat Transfer Characteristics of Ejectors and Vortex Tubes [Master's Thesis, TU Wien]. https://doi.org/10.34726/hss.2020.64243

[12] Elbel, S. and Hrnjak, P. (2008). Experimental validation of a prototype ejector designed to reduce throttling losses encountered in transcritical R744 system operation. International Journal of Refrigeration, 31(3):411–422. http://dx.doi.org/10.1016/j.ijrefrig.2007.07.013

[13] Zhang, Z., Feng, X., Tian, D., Yang, J., & Chang, L. (2020). Progress in ejector-expansion vapor compression refrigeration and heat pump systems. Energy Conversion and Management, 207, 112529. https://doi.org/10.1016/j.enconman.2020.112529

[14] Schlemminger, C., Kopp, C., Banasiak, K., Drexler-Schmid, G., Lauermann, M., Windholz, B., Zauner, C., & Baumhakel, A. (2019). Hochtemperatur Wärmepumpe mit Ejektor. *Deutsche Kälte- und Klimatagung 2019, Ulm.* DKV - Deutscher Kälte- und Klimatechnischer Verein.

[15] Lemmon, E. W., Bell, I. H., Huber, M. L., and McLinden, M. O. (2018). NIST Standard Reference Database 23: Reference Fluid Thermodynamic and Transport Properties-REFPROP, Version 10.0, National Institute of Standards and Technology

[16] ANSYS, Inc. (2022). Ansys® Fluent Theory Guide, Release 2022 R1. Canonsburg, USA, 2022.

14th IEA Heat Pump Conference
15-18 May 2023, Chicago, Illinois

Heat Pumps and Thermal Storage for Domestic Dwellings

Neil J Hewitt*, Babak Kamkari and Patrick Keatley

Ulster University, 2-24 York Street, Belfast, BT15 1AP, Northern Ireland, UK

Abstract

IEA HPT Annex 55 Comfort and Climate Box aligned with the UKRI funded Comfort and Climate Box to review the challenges and research necessary to deliver at scale heat pump and thermal storage solutions for single family homes across the partnering nations. Building on the deliverables to IEA HTP Annex 55, an updated review of the state of the art is presented here and how that was implemented in a small sample trial in social housing in Northern Ireland. Early results of this field trial indicate strong participant satisfaction with the air source heat pump and thermal store with reduced heating costs when allied to a modest upgrade to building thermal fabric i.e., improved glazing, insulation etc. and larger hydronic radiators to facilitate lower temperature heat delivery.

© HPC2023.
Selection and/or peer-review under the responsibility of the organizers of the 14th IEA Heat Pump Conference 2023.

Keywords: Heat Pump, Thermal Storage, Integration, Single-Family Homes

1. Introduction

IEA HTP Annex 55 Comfort and Climate Box and the subsequent UKRI//BEIS funded Comfort and Climate Box (EP/V011340/1, CCB, facilitating UK participation) targeted the implementation of typically air source vapour compression heat pumps and accompanying thermal storage in single family homes. It could be argued that such a focus was restrictive to global participation, but it was recognised that a focus had to be applied to deliver an in-depth analysis of the CCB concept to address concerns, that often are ultimately related to capital cost.

The Annex therefore identified several criteria that required inputs to deliver significant heat decarbonisation and integration with non-dispatchable and variable renewable electricity resources, such as:

- Affordability
- Suitability
- Compactness
- Efficiency
- Plug & Play, maintenance
- Integral design
- Smart Grid ready
- Controls & monitoring
- Appreciation

These factors were considered as the backbone of the research and implementation required to provide the necessary confidence for governments and other agencies to successfully promote the decarbonisation of space heating with electrically driven vapour compression heat pumps and thermal storage. Initially, observations were obtained from the participating countries of Austria, Belgium, Canada, China, Germany, Italy, the Netherlands, Sweden, Turkey, the UK, and the USA, but relevant results from other countries were also

* Corresponding author. Tel.: +44-28-95365239
E-mail address: nj.hewitt@ulster.ac.uk

incorporated. The purpose of this paper is then to update the reports that addressed aspects of these issues and to report on the implementation of this research that led to a demonstration of air-source heat pumps and thermal stores in social housing (alongside a modest retrofit) as a cost-effective decarbonisation approach to space and water heating in homes.

2. Vapour Compression Heat Pump – Examples of Technical and Financial Supports

At the core of this approach to the decarbonisation of space and water heating in single family homes is the vapour compression heat pump. New (and existing) working fluids that decrease/eliminate global warming potential, and indeed reduce capital costs, are noted. In terms of single-family home systems, the role of hybrid heat pumps may seem attractive. Natural gas is seen as a contributor to decarbonisation in the short-term and its replacement (by biomethane and/or hydrogen) in the longer term is being considered. The price of natural gas is a current challenge and the scale of switching to more decarbonised sources much be at such a scale that the decarbonised gas sources are not costed at international gas prices. An example of this is the US Henry Hub price for natural gas. The US (and Canada) was largely insulated from European price increases resulting from war in Europe due to availability of low-cost "fracking" (hydraulic fracturing) gas. Natural Gas prices are also of course two-sided. Lower natural gas prices may hinder heating decarbonisation with heat pumps but now, electrification of heating (aligning with large scale renewable energy resources such as wind and solar) has gained a significant driver beyond decarbonisation, and it is incumbent upon us to deliver this opportunity. Regarding hybrid heat pumps therefore, Beccali et al [1] noted existing gas boilers can be utilised in "parallel" or in "series" alongside various ground source and air source heat pumps, both with and without thermal storage. Series or parallel approaches lend themselves to demand side management in terms of reducing electrical load at peak electricity demand times, with obviously the parallel approach facilitating a significant electricity load reduction like that of thermal storage, but perhaps with a less time limiting factor i.e., the gas boiler can operate at peak electricity demand times and/or low (renewable) electricity supply times. Sun et al [2] noted that such "smart" hybrid heat pumps could avoid heat pump oversizing (reducing capital cost), avoid/minimise electricity distribution network capacity challenges (facilitating technology introduction), and overcoming social barriers to new technology adoption.

Vapour compression heat pumps need to be cost effective. Examples of how to achieve this is in the technology itself, selling heat as a service and demand response electricity market services. Regarding the technology, optimal sizing and impact on the electricity network is critical, as noted with gas boiler hybrid heat pumps. Unfortunately, not all countries with electrically driven vapour compression heat pump aspirations have sufficient capacity at local low voltage electrical distribution network level. Therefore, advanced high coefficient of performance (COP) heat pumps can be aided with the wider deployment of (5th Generation) heat networks (waste heat, renewable heat from excess renewable energy, geothermal heat etc.). So called "booster" heat pumps have upgraded heat for domestic applications with Thorsen et al [3] demonstrating an average seasonal COP of 5.25 and improved heat pump economics. Østergaard et al [4] noted that if district heating networks are operated in conjunction with lower heat distribution temperatures in the buildings, the overall efficiency of building/heat pump/heat network is significantly improved, with, again, cost savings as in some cases, little must be done to the building heating distribution system as the older hydronic radiators work sufficiently well at lower temperatures.

Regarding utilisation of the heat pump and thermal store as heat as a service and/or demand side response (electricity grid balancing), selling heat as a service to lower the barriers for heat pumps is noted by Kircher and Zhang [5]. A host purchases heat from a heat pump owned by an aggregator. The aggregator purchases power (at scale) and with the aid of thermal storage can address demand side response requirements of the local electricity market, whether renewable energy driven, electricity network constraint driven etc. It is claimed that the value of the heat pump investment is nearly doubled, i.e., a strong return on investment is possible. However, there is a concern over "data". While "the internet of things" facilitates significant data flows, the question must be "what is the minimum amount of data that can be securely interrogated to deliver demand side response?". The question arises as we become "smart", we also may become vulnerable to cyber-attack. The fear is not when something is turned off (which is very inconvenient and possibly personally challenging), but when a significant number of devices are turned on at the same time, thus potentially initiating long-term damage to an electricity network. The electrification of heating (and transport) will require an amount of control and an expectation that by a given time, heat (and power) will be provided. Thermal storage (and/or hybrid heat pumps) are an example of peak electricity demand avoidance. Other approaches (e.g., for electric vehicle charging) are more time manageable where we expect our car to be charged overnight for example. Smart domestic electricity load controllers will therefore "manage" electrical demands through an

understanding (whether a fixed concept of a maximum electrical demand or through a "floating" concept associated with available local electricity network capacity) or our needs and, for example, reduce/turn off demands for short periods when we (the end user) do not notice. Thus, our fear of a cyber-attack to turn everything on could destroy infrastructure.

However, on the positive side, the role of integrated renewable energy i.e., photovoltaics, solar thermal or indeed their combination in PVT, can be aligned to heat pumps and thermal storage. Typically (but not always the case), winter solar energy is limited (when we want it the most) and summer solar energy can be excessive. Affordable seasonal thermal storage that is also sufficiently dynamic for diurnal/demand side response operations would be an advantage. Returning to "solar-assisted" heat pumps, Gaonwe et al [6] describes the likely types, while Yang et al [7] addresses the traditional solar thermal approach, heating a storage vessel and the heat pump utilising this storage as a heat source utilising TRNSYS modelling. This model accounted for the UK geographical extremes in temperature encountered in the UK (represented by an additional 21 days in space heating requirements but still represented a 30% increase in COP when using solar assisted united compared to an air-source heat pump. Regarding financial supports, at an electricity market level, we see several markets addressing aggregated technologies to coordinate demand side response/management for the greater integration of variable, non-dispatchable renewable electricity. These include CAISO, ERCOT, Hawaii, Australia's NEM, GB's Smart Systems and Flexibility Plan, EU MCs, including Denmark's community renewables ownership model, etc). An example is the TenneT-Veissmann Viflex project where domestic heat pumps, thermal storage, and photovoltaics (PV) manage the electricity network in areas of high PV penetration. OpenADR is also being considered as a mechanism for standardised Demand Response control. In the UK, Gupta and Morey [8] assessed a domestic heat pump, PV and battery arrangement for single family homes noting 2-hour intervention times and their impact on electricity demand and export. Automation was deemed too be very important, as was transparency of financial transactions. Agile electricity tariffs were deemed advantageous.

3. Heat Pumps and Thermal Storage – What is emerging as best practice?

The Kigali Amendment to the Montreal Protocol requires developed countries to reduce their use of HFCs by 85% by 2036. This would challenge the use of the most popular air-source heat pump working fluid, namely R410A. Several alternatives are being explored namely R452B, R454B, R454C etc. e.g., Shen et al [9]. However, the question arises as to what is a low global warming potential (GWP) refrigerant? Very low GWP refrigerants refer to the natural fluids such as CO_2, Ammonia, Propane etc. with GWP's of less than 3. Low GWP refrigerants is accepted as those below 150 (on a 100-year basis), although there appears to be no absolute definition. Unfortunately, when taking the more extreme requirement of low GWP, there appears to be currently one no HFC, HFO replacement for the current incumbent R410a. Therefore, propane (R290) is of interest and Schnabel et al [10] demonstrated that for a charge of 200g of R290, a 10kW heat pump could achieve a COP of 3.5 across a 35ºC temperature lift. With R290 having a Lower Explosion Limit of 2.1% volume per volume, 200g of propane would be "safe" in a space as low as $0.11m^3$. Regarding alternative refrigerants to R410a for air-source heat pumps, the following refrigerants have been modelled (Table 1) for different heat pump configurations (Figure 1). These are not always drop-in replacements but are being considered for domestic heat pumps, given the challenges of finding a suitable (<150 GWP) direct replacement for R410a.

Table 1. Modelled Refrigerants

Refrigerant	Class	GWP	Flammability	Critical Temperature ºC	Critical Pressure Bar
R32	HFC	677	A2L	78.11	57.82
R410A	HFC	1924	A1	71.34	49.01
R1234ze(E)	HFO	<1	A2L	109.24	36.35
R1234yf	HFO	<1	A2L	94.7	33.82
R454B	HFC/HFO	466	A2L	78.1	52.67
R452B	HFC/HFO	676	A2L	77.1	52.2
R513A	HFC/HFO	631	A1	94.9	36.49
R515A	HFC/HFO	387	A1	108.71	35.65
R454C	HFC/HFO	148	A2L	85.7	43.2

The choice of system is interesting. Capital cost of domestic heat pumps has come under pressure and development of lower cost units is very worthy of effort. Energy Poverty and Fuel Poverty are themes at the time of writing that imply heat pumps and thermal storage for single family homes i.e., the pathway to space heating decarbonisation, may become the preserve of the wealthy. For mass adoption, capital costs must reduce and/or schemes for ownership spread that cost over the lifetime of the system. However, improving COP is also welcome.

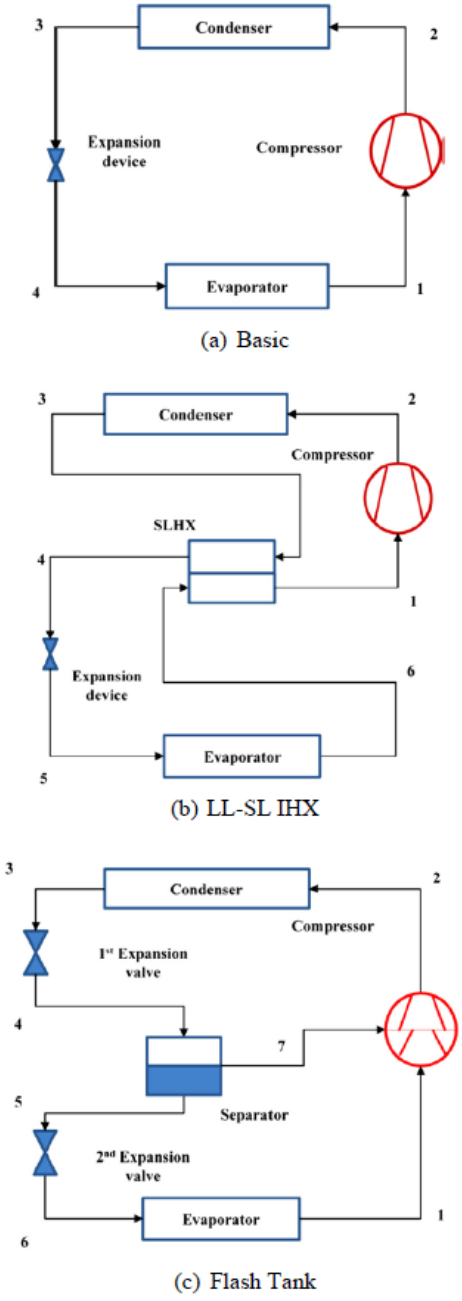


Fig. 1. Vapour Compression cycles considered in this analysis.

The performance of the alternative refrigerants is evaluated in three different heat pump cycles i.e., basic, liquid line-suction line internal heat exchanger (LL-SL IHX) and flash tank heat pump cycles. For all cycles, the condenser temperature is set at 60ºC, and the evaporator temperature changes ranging from 0ºC to 10ºC to calculate the COP, Volumetric Heat Capacity (VHC), discharge temperature, and pressure for systems working with different refrigerants. In the current analysis, the subcooling and superheating values are set at 0ºC and isentropic efficiency has been considered for the compressor operation based on the pressure lift.

Figure 2 shows the variation of COP with evaporator temperature in different heat pump cycles working with alternative refrigerants. As expected, the COP increases by increasing the evaporator temperature. For the basic cycle at an evaporator temperature of 0ºC, the R32 provides the best COP followed by R32, R454C, R452B, R1234ze(e), R515A, R454B, R513A, R1234yf, and R410A. The difference between the maximum (R32) and minimum (R410A) COPs is about 7%. The COP ranking differs with changing the evaporator temperature or cycle configuration. For example, at an evaporator temperature of 10ºC, R1234ze(e) performs marginally (1%) better than R32. Also, it is observed that the COPs may improve slightly by adding a LL-SL IHX to the cycle at the expense of higher discharge temperature. However, employing a flash tank can considerably enhance the COP compared to the basic cycle. Volumetric heat capacity reveals that R32 has the highest VHC followed by R452B, R454B, and R410A. Pure HFO refrigerants (R1234ze(e) and R1234yf) has considerably lower VHC values compared to R32 due to low vapor density.

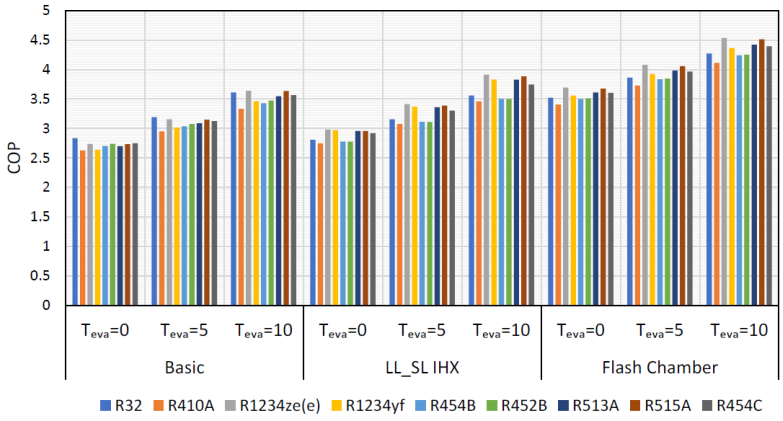


Fig. 2. Variation of COP.

By adding R32 to HFO refrigerants the VHC improves as is seen for R454B (69% R32 and 32% of R1234yf) with 153% improvement in VHC compared to that of R1234yf (Figure 3). Figure 4 illustrates the variation of discharge temperature of the compressor versus evaporator temperature in different heat pump cycles working

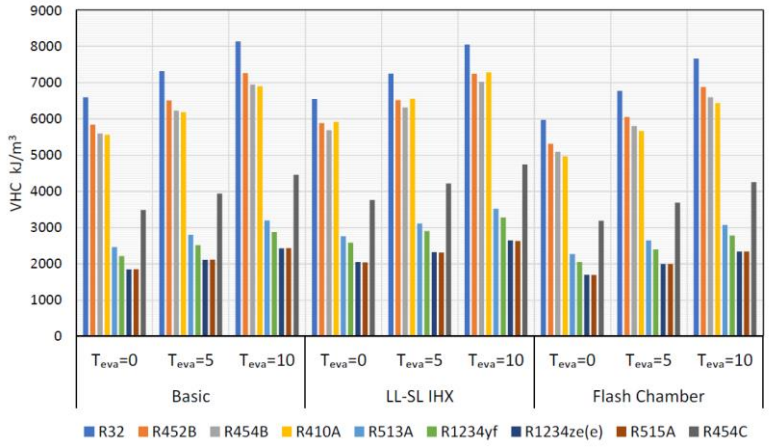


Fig. 3. Variation of volumetric heating capacity with evaporator temperature for different heat pump cycles

with alternative refrigerants. The maximum discharge temperature corresponds to the pure R32 and reduces by decreasing the share of R32 in the mixed refrigerant. The minimum discharge temperature belongs to R1234yf. It is seen that the discharge temperature increases with raising the evaporator temperature. The value of temperature rises in the case of LL-SL heat exchanger running with R32, R452B, and R454B are not realizable in practice, and they are shown just for comparison. The figure shows that depending on the refrigerant type, employing the flash tank decreases the discharge temperature by 9 to 17% compared to the basic cycle. Figure 4 also depicts the discharge temperature for different alternative refrigerants employed in basic, LLSL IHX, and flash tank heat pump cycles at evaporator temperatures of 0, 5, and 10ºC. As expected,

the pressure lift decreases by increasing the evaporator temperature. At 0ºC, the maximum pressure lift is about 5.9 which is related to R1234ze(e) and R515A, and the minimum pressure lift is 4.8 obtained by R410A. Thus,

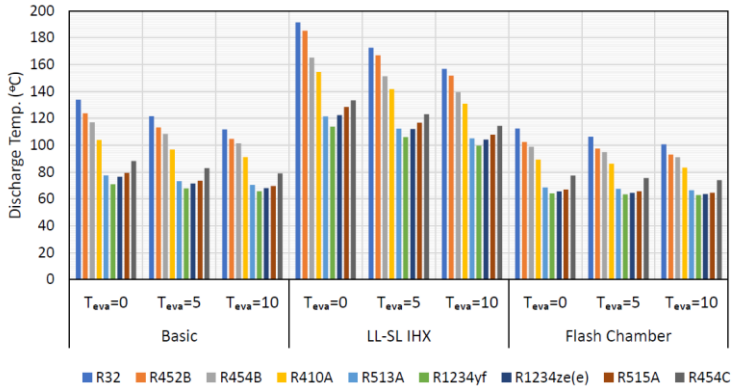


Fig. 4. Variation of discharge temperature with evaporator temperature for different heat pump cycles

we can conclude that from these choices, it is challenging to address a direct replacement for R410a that possesses a GWP <150. Therefore, new systems will emerge, or existing systems will re-emerge that can address low GWP (and safety) while, in the best traditions of the automotive mass manufacturing industry were saving in weight equate to manufacturing savings, retain of exceed the size of R410a units. About the control of alternative cycles, such as a flash tank, this requires additional expansion valves to manage superheat at the intermediate compression stage. There are the challenges of expansion valve sizing in that there is typically reduced pressure drops than those encountered with a traditional heat pump cycle. However, managing flow rate to maintain the usual minimum superheat is normal with a digital valve e.g., a stepper motor and pre-programmed refrigerant saturation temperature curves.

Finally, R290 and moving beyond F-Gas regulations to the future phase out of working fluids proposed by the European Chemicals Agency, we see proposal to cut perfluoroalkyls, leaving the domestic air-source heat pump sector with for example, R32 and R290 as their main choices. The US EPA has also banned certain working fluids. Utilising the data provided by OST (Switzerland), Air-Source Heat Pumps (ASHPs) are tested under conditions of both EN14511 (COP at certain temperatures, humidities etc.) and EN14825 (seasonal COP). The available data is summarised in Figure 5 for conventional air-source heat pump cycles.

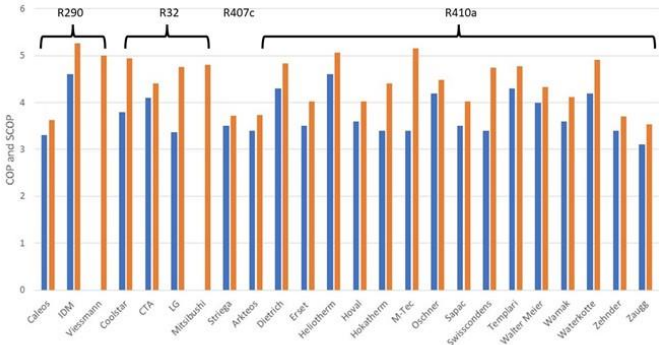


Fig. 5. COP Comparison of Existing Tested Air Source Heat Pumps

In terms of thermal storage, our understanding of electricity network constraints to be combined with our understanding of our heating and hot water needs to provide an optimal system. As previously reported, a 2-hour period was noted for demand response and the greater integration of non-dispatchable, variable renewable energy. For our domestic space heating and domestic hot water needs, water as a medium has flexibility in temperature (for weather compensated heating control), low cost and well understood systems and properties. However, the size of water-based systems (in both retrofit and expensive inner-city terms) along with heat losses, may deem water to have rival storage media. Nair et al [11] reviewed phase change materials (PCMs) for space heating and domestic hot water applications and noted that many organic PCMs are flammable (potentially limiting their application), salt hydrate types are highly corrosive and suffer from supercooling and phase separation, and long-term cycle stability is questioned by some. However, encouraging trials and examples are noted with for example, the then Department of Energy and Climate Change funded trial in 7 homes in the UK starting in 2013. Using an Air Source Heat Pump and a phase change material storage, an

average heating bill saving of 50% compared to fossil fuels was achieved [12]. There remain numerous studies on laboratory-based systems and thus the need to verify PCM based systems in the field.

4. Field Trials in Northern Ireland

Ulster University has been developing heat pumps for 50 years. Initial interest was in heat pump performance in a controlled environment during an energy crisis of the 1970's. This evolved into the challenge of compressor lubrication and oil transport, its effects on heat transfer and of course, compressor longevity based on refrigerant/lubricant solubility and miscibility. This work continued as we moved from CFC's to HCFC's and HFC's, with HFC's typically utilising Polyol Ester lubricants (POEs) and combined system performance comparisons, material compatibility and lubrication aspects. New heat exchangers such as all-welded compact plate types saw improvements in performance. Natural fluids also were noted and indeed their challenges as drop-in replacements for, for example, R407c heat pumps, where R290's lack of compatibility with POEs lead to compressor failures. Compressors for domestic heat pumps moved to scroll types (again with new lubrication concepts needed) and future developments such as the vapour injection for higher temperature lift applications where developed. R410a heat pumps where introduced and new working fluids such as R1233zd(E) are being evaluated for different applications, including industrial heat pumps. Therefore, it was correct to not only assess the heat pump system, but how it would be used in homes and how it would need thermal storage to address the electricity network, renewable energy integration and perhaps of increasing importance, the role of the end-user in the success of heating decarbonisation.

In understanding heat pumps and thermal storage in single family homes, Shah et al [13] utilised an air course heat pump and 600 litres of water to heat a "hard-to-treat" home, purposely built on a campus of Ulster University. This house, as part of "Terrace Street" was home to a family and was monitored for temperature, electricity consumption, gas consumption (when the boiler was required) with a heavily monitored heat pump and thermal store. The occupier and their family were free to heat the home as appropriate and the gas boiler was available for comparisons as well as a back-up during system modifications. In general, the occupants were happy with the level of heat provided but no formal test was carried out as the then objective was to observe what performance was required to maintain thermal comfort.

Overall COP of the high temperature heat pump could have been better and spurred our interest in an overall system methodology i.e., building improvements (a "Fabric First" approach) followed by a heat pump of appropriate size. About the size of thermal store, we had anticipated a time frame that approached 4 hours rather than a shorter time. The 3-to-4-hour time frame addressed the peak time for electricity usage (typically 4pm to 7pm) in the UK but was later proved to be not as important as the shorter term changes in for example, wind derived electricity from the network (as demonstrated by the 48 time periods incorporated into the current All-Ireland electricity market structures). A secondary (but important factor) was the heat losses associated with such a large (but still well insulated) water storage tank. Thus, smaller storage systems with less heat loss were required and therefore air source heat pumps and compact thermal stores applied to homes with improved building fabric (typically glazing and insulation).

Interreg VA Spire 2 and UKRI EPSRC CCB and Lot-NET projects provided the means to work with the Northern Ireland Housing Executive (one of the largest social housing providers in the UK) to deliver the solutions and the analysis of the installation of air source heat pumps and thermal storage into retrofitted homes in the west of Northern Ireland. This significance of the area chosen is to reassure those out of our major cities that cost-effective decarbonisation approaches can be delivered in rural communities, and secondly, the west of Northern Ireland is where our dominant wind energy resource is found, and therefore local demand response solution may have to be found soon. UKRI EPSRC CCB and IEA HPC Annex 55 gave confidence in delivering

a viable solution to decarbonisation of our homes. RULET – Rural-Led Energy Transition – is an initiative within the SPIRE 2 project (Figure 6) aimed at reducing or eliminating the risk of low-income households being left behind in the transition to clean, smart, integrated energy systems. Not only where air source heat pumps and thermal storage systems investigated, but also hybrid systems (with oil or gas boilers) to address



Fig. 6. Rulet Heat Pump and Thermal Storage Installations

the householder concerns regarding the "radical, new technology" of heat pumps.

Figure 7 shows typical operational data per home and Figure 8 illustrates the CO_2 seen from the different options across a three-month operating period. As expected, with Northern Ireland producing nearly half of its electricity from wind power, the heat pump has the lowest emissions. Furthermore, as part of the trial, a local electricity supplier agreed to provide an Economy 7 tariff i.e., a reduced cost from 12:00 to 07:00 daily as a prelude to flexible tariffs. Householders were generally pleased with their running costs.

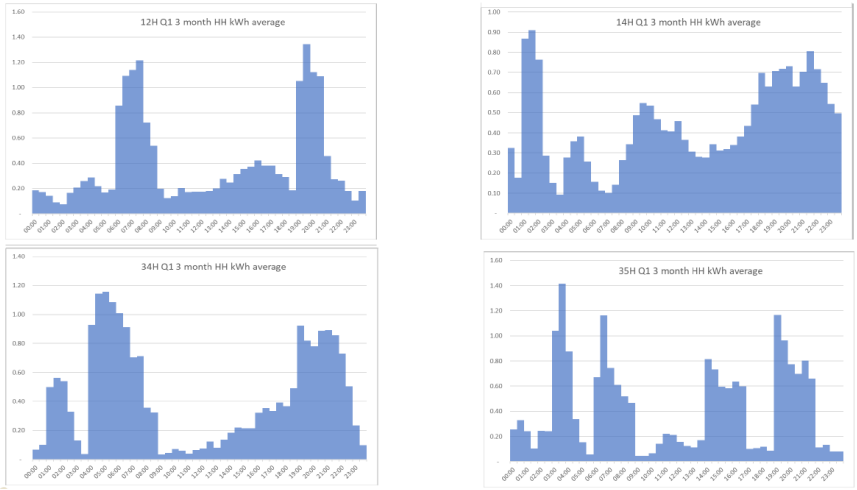


Fig. 7. Household electricity consumption profiles.

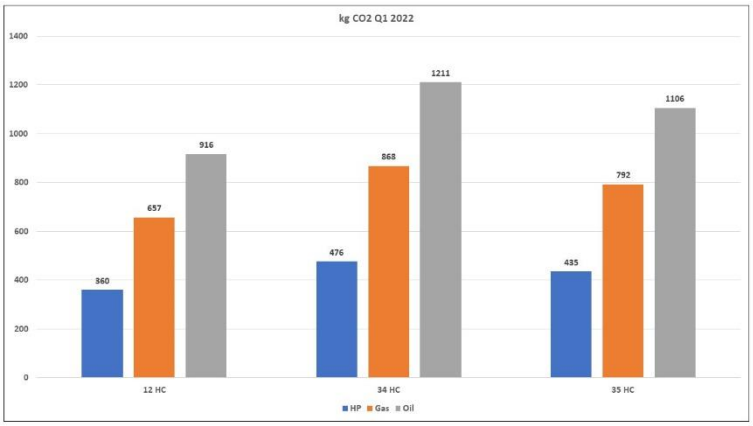


Fig. 8. CO2 Emissions for the Selected Options

However, the most important aspect during this energy crisis is that of running costs. Figures 9 and 10 illustrate the current running costs and the projected running costs for the Winter period 2022/2023.

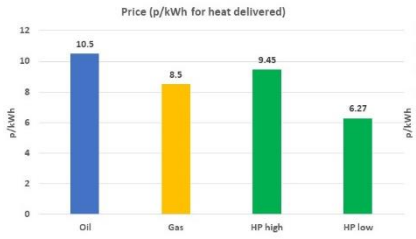
The small-scale trial has illustrated that an air source heat pump with thermal storage can mee the demands of householders, at least at a similar cost basis and, with the help of flexible tariffs, could reduce the running costs further. However, what of capital cost? For this field trial, approximately £18,000 was spend per home, with a building fabric upgrade of glazing and insulation being approximately £9,000 per home, the PCM thermal store of 6kW was £6000 and the 5kW (thermal) air source heat pump was £3,700. With 880,000 homes in Northern Ireland (not all requiring this level of retrofit prior to heat pump installation), Ogunrin et al [14] estimated approximately £2bn would be required for the building fabric upgrade alone. However, the kWh not used is the best kWh. Aggregation systems that use the heat pump and thermal storage as a renewable electricity integrator must become part of the value-added aspects of heat pump deployment.

Regarding reducing heat pump capital costs, in addition to mass production, smaller machines due to reduced heating demands and moving away from air to waste heat/geothermal heat networks, the use of lower cost components and natural working fluids that have lower pressures and no doubt other innovations not requiring copper and steel may make systems cheaper, while maintain reliability. Water for thermal storage with vacuum insulation tanks may be more cost effective.

Finally, the move towards R290 in the field of domestic air-source heat pumps is typically beneficial. A 5% increase in seasonal COP has been noted in Figure 5 and this would translate in an equivalent reduction in electricity demands.

5. Conclusions

Air source heat pumps and thermal storage are a solution to decarbonisation of space and domestic water heating. We have seen (albeit informally) that residents are happy with their decarbonisation solution, especially as in many cases is saves on running costs. The heat pumps and accompanying thermal stores need to be smart. The use of an Economy 7 tariff was successful, but a 10-hour tariff would be more beneficial. A flexible tariff following excess wind generation, thus reducing wind derived renewable electricity curtailment and constraint and operated by aggregators, should benefit electricity distribution companies (better utilisation of existing network capacity and lower rates of new builds), the aggregators themselves, and the end-users (the residents and as such, prosumers with lower tariffs). This help with affordability. Retrofit, even at a basic level improved building suitability. Compactness may be challenged by refrigerant changes. Efficiency will be improved with new components, a move to R290, and a move away from air-source. Finally, integral design of heat pumps, thermal store and building will see improved results.



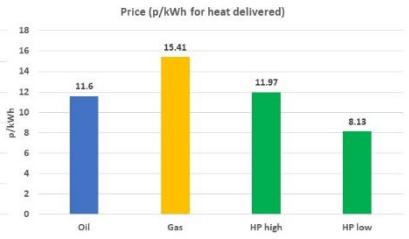


Fig. 9. Energy Price (left) and Fig. 10. Projected Running Costs with Likely Energy Cost Increases (right).

6. Copyright

By submittal of this full paper to the International Energy Agency for the 14th Heat Pump Conference, the authors assume full responsibility for ensuring that this paper does not infringe on another party's intellectual property rights, which include copyright and agree that the paper has not previously been submitted for publication elsewhere. Furthermore, the authors, by submittal of this conference paper to the conference, grants publishing rights of that paper to the Agency for the 14th Heat Pump Conference, which may:

1. Publish or arrange to publish the paper as part of the Conference proceedings,
2. Copy and distribute the paper in its entirety in print and electronic form, and
3. Copy and distribute excerpts from the paper.

Acknowledgements

The authors would like to acknowledge numerous projects, whose individual elements began to come together into heat pumps and thermal storage for single family homes including Interreg VA Spire 2, UKRI EPSRC CCB and Lot-NET.

References

[1] Beccali, M., Bonomolo M., Martorana, F., Catrini P., Buscemi, A. *Electrical hybrid heat pumps assisted by natural gas boilers: a review'* Applied Energy, 6 July 2022
[2] Sun M., Djapic, P., Aunedi, M., Pudjianto, D., Strbac, G., *Benefits of smart control of hybrid heat pumps: An analysis of field trial data*, Applied Energy 247 2019 525–536
[3] Thorsen, JE., Svendsen, S., Smith, K., Ommen T., Skov, M., *Feasibility of a booster for DHW circulation in apartment buildings*, Energy Reports 7, 2021, 311–318
[4] Østergaard PA, Werner P., Dyrelund A,, Lund H., Arabkoohsar A., Sorknæs P., Gudmundsson O., Thorsen JE., Mathiesen BV., *The four generations of district cooling - A categorization of the development in district cooling from origin to future prospect*, Energy, 253, 2022.
[5] Kircher KJ., Zhang KM., *Heat purchase agreements could lower barriers to heat pump adoption*, Applied Energy 286 (2021)
[6] Gaonwe TP., Kusakana K., Hohne PA., *A review of solar and air-source renewable water heating systems, under the energy management scheme*, Energy Reports 8 (2022) 1–10
[7] Yang LY., Li Y., Yang Y., Wang HS., *Low temperature heating operation performance of a domestic heating system based on indirect expansion solar assisted air source heat pump*, Solar Energy 244 (2022) 134–154
[8] Gupta R., Morey J., *Empirical evaluation of demand side response trials in UK dwellings with smart low carbon technologies*, Renewable Energy 199 (2022) 993–1004
[9] Shen B., Li Z., Gluesenkamp K., *Experimental study of R452B and R454B as drop-in replacement for R410A in split heat pumps having tube-fin and microchannel heat exchangers*, Applied Thermal Engineering 204 (2022)
[10] Schnabel l., Dankwerth C., Methler T., Schossig P. *Low Charge Heat Pump Module – development and evaluation of charge reduced designs using 150g of R-290*, Chillventa, 13-15 October 2020.
[11] Nair AM., Wilson C., Huang MJ., Griffiths P., Hewitt N., *Phase change materials in building integrated space heating and domestic hot water applications: A review*, Journal of Energy Storage, Volume 54, October 2022
[12] https://www.gov.uk/government/publications/advanced-heat-storage-competition
[13] Shah NN., Wilson C., Huang MJ., Hewitt NJ., *Analysis on field trial of high temperature heat pump integrated with thermal energy storage in domestic retrofit installation*, Applied Thermal Engineering Volume 143, October 2018
[14] Ogunrin OS., Vorushylo I., Okpako O., Hewitt N., *Domestic Energy Efficiency Scenarios for Northern Ireland*, Energies, April 2022.

14th IEA Heat Pump Conference
15-18 May 2023, Chicago, Illinois

Integration of High-Temperature Heat Pumps in Swiss Industrial Processes (HTHP-CH)

Cordin Arpagaus[a,*], Frédéric Bless[a], Stefan Bertsch[a], Pierre Krummenacher[b], Daniel A. Flórez-Orrego[c], Eduardo A. Pina[c], François Maréchal[c], Nicole Calame Darbellay[d], Fabrice Rognon[d], Stéphane Vesin[e], Pascal Achermann[f], Christian Jansen[g]

[a]Eastern Switzerland University of Applied Sciences, Institute for Energy Systems, CH-9471 Buchs,
[b]HEIG-VD Haute Ecole d'Ingénierie et de Gestion du Canton de Vaud, Institute of Thermal Engineering, CH-1401 Yverdon-les-Bains,
[c]EPFL Valais, Industrial Process and Energy Systems Engineering, CH-1951 Sion,
[d]CSD Ingénieurs SA, CH-1701 Fribourg,
[e]ESTAVAYER LAIT SA (ELSA), CH-1470 Estavayer-le-Lac,
[f]Cremo SA, CH-1752 Villars-sur-Glâne,
[g]Gustav Spiess AG, CH-9442 Berneck

Abstract

High-temperature heat pumps (HTHP) with supply temperatures above 100 °C are becoming increasingly important for the electrification and decarbonization of industry. However, their adoption is slow because there is still a lack of knowledge about their capabilities, design, control, and optimal integration, resulting in few practical implementation examples. This study investigates the technical and economic feasibility of HTHP integration based on case studies from the Swiss industry. ELSA (Estavayer Lait SA), Cremo SA, and Gustav Spiess AG support the research and provide access to industrial process data. ELSA, Switzerland's largest industrial dairy on a single site, is interested in a HTHP supplying steam for cleaning-in-place processes. Cremo SA manufactures dairy products and sees opportunities to integrate a HTHP in a milk permeate drying plant that consumes a large amount of 3 bar steam. Gustav Spiess AG produces meat products and sees potential for integrating a HTHP into sausage cooking processes for steam generation at about 115 °C. In addition, other Swiss industrial companies in the food, biotech, and chemical sectors also show interest in HTHPs for applications such as distillation, sterilization, drying, and steam generation. This study presents suitable HTHP integration concepts based on case studies with quantified efficiency gains, energy savings, CO_2 reduction, and cost-efficiency results. It also includes an up-to-date review of HTHP suppliers derived from participation in the IEA HPT Annex 58 that shares results and knowledge with international experts on HTHPs.

© HPC2023.
Selection and/or peer-review under the responsibility of the organizers of the 14th IEA Heat Pump Conference 2023.

Keywords: industrial processes; high-temperature heat pumps; techno-economic analysis; payback period; case studies; CO_2 emissions

1. Introduction

1.1. Application potential of industrial HTHPs in Switzerland

Switzerland has been pioneering in developing and commercializing heat pumps (HP). The first European HPs were realized in Switzerland (e.g., in 1877 at the salt works at Bex) [1]. In 2021, HP sales increased to an all-time high of 33'704 units (20% growth compared to 2020) [2]. Especially in the small-capacity range for single- and multi-family houses, HPs are an established technology for space heating and domestic hot water, with a market share of over 90% in new buildings. Above 100 kW heating capacity, 169 HPs were sold (around 0.5% of all units) since, in larger heating capacity ranges, oil and gas boilers still dominate process heat generation [3]–[5]. Therefore, replacing fossil heating systems with electrically-driven industrial HPs is

* Corresponding author. *Email address:* cordin.arpagaus@ost.ch

a possible scenario to reduce CO_2 emissions from industry. High-temperature heat pumps (HTHP) with supply temperatures above 100 °C are increasingly important to replace fossil fuels in industries [6]–[8]. The most relevant application areas for HTHPs are the food/beverage, chemicals, and pulp/paper industries for processes like drying, evaporation, sterilization, or similar thermal processes with available waste heat from about 30 °C to 70 °C and process heat demand from 80 °C to 150 °C [9]. Based on annual energy consumption of around 43 TWh in Switzerland [10], a 30% share of process heat and steam below 150 °C [11], and a moderate conversion rate of 40% to HPs and HTHPs [12], the addressable energy savings potential from the use of HTHPs in the Swiss industry can be roughly estimated at 2'893 GW/a which is approximately 6.7% of the total process heat demand [13] (Table 1).

Table 1. Potential energy savings through industrial HTHPs in Switzerland (top-down estimate) [13].

	Energy consumption	**Data source / Estimations**
Swiss industry	42'972 GWh	154,7 PJ as of 2018 [10]
Process heat demand	24'107 GWh	56,1% (>80 °C) [10]
Process heat and steam demand below 150 °C	7'232 GWh	30% (estimate based on Heat Roadmap Europe [11])
Energy savings potential through the use of HTHPs (= addressable process heat share)	2'893 GWh (6.7% of the process heat demand)	40% (moderate estimate of conversion rate to HPs and HTHPs based on technical analysis within SCCER EIP [12])

Compared to natural gas, which has an emission factor of 0.201 kg CO_2 per kWh_{th} of useful heat [14], the consumer electricity mix available in Switzerland is 0.128 kg CO_2/kWh_{el} [15]. On this basis and with an average COP of 3.0 to 4.0 for an industrial HTHP at about 40 K to 60 K temperature lift from heat source inlet to sink outlet (assuming 45% Carnot efficiency [6], [7], [16]), the generated CO_2 emissions per useful heat are about 0.032 to 0.043 kg CO_2/kWh, which is 5 to 7 times lower than for a gas boiler (assuming 90% boiler efficiency). Assuming that integrated HTHPs would run with 5'000 operating hours per year on average, this results in a total heating capacity of 579 MW and, with specific investment costs (incl. installation, without integration, valid for 500 kW_{th} HP size) of approx. 450 to 700 EUR per kW heating capacity [17], a potential market of 260 to 405 million EUR for Switzerland. Assuming an average heating capacity per HTHP unit of 1 MW_{th} is equivalent to installing around 579 HTHP units.

Thus, integrating industrial HTHPs will contribute to energy savings, CO_2 reduction, and a substantial new market. Furthermore, expanding renewable energy and increasing energy efficiency in industrial processes align with the federal government's Energy Strategy 2050 [18]. Consequently, HTHP technology supports the efforts of Switzerland's net carbon emissions to net zero by 2050 [19].

1.2. Existing challenges for the wider spread of HTHPs

However, HTHPs are just beginning to enter the market of industrial heat production. There is still a lack of knowledge about available HTHP technologies and products (>100 °C supply temperature), methods for optimal integration, proper sizing, control, dynamic behavior, and techno-economic feasibility, resulting in few realized references with operational experience. As highlighted in a white paper [20], demonstration projects with increased knowledge sharing at the international level are needed to drive further HTHP technology dissemination and achieve greater visibility, particularly in process electrification. In this context, the authors of this study participate as Swiss representatives in the IEA HPT Annex 58 on HTHPs to exchange results and knowledge with international experts. In recent studies, the techno-economic feasibility of integrating HTHPs for steam generation in distillation applications was investigated [21], [22], and an up-to-date overview of the latest HTHP developments and products for supply temperatures above 100 °C was presented at the China Heat Pump Conference 2022 [16]. The analysis of the integration of HTHPs into ammonia and pulp production was also presented at CPOTE 2022 [23] and ECOS 2022 [24].

1.3. Objectives of this study

This study investigates the technical and economic feasibility of HTHP integration based on case studies in Swiss industrial companies with heat source temperatures from 40 to 80 °C to provide process heat (e.g., steam) at 115 to 150 °C and about 0.5 to 3.5 MW heating capacity. First, a review of current HTHP products and the corresponding working domains (e.g., heating capacity, temperatures) is given. Next, a simple economic model is used at an early planning stage to assess whether a HTHP integration could be economically viable. Then, the investment and operating costs of HTHPs are analyzed for the case studies using a cost model with different

input parameters. Finally, the payback period, the avoided CO_2 emissions, and the energy savings are calculated, and the main influencing factors are discussed in a sensitivity analysis.

2. Market review of industrial HTHPs and operating ranges

The range of industrial HTHP products on the market has grown steadily in recent years (especially since 2018 [6]). Table 2 presents an overview of 33 HTHP products with heat supply temperatures above 100 °C based on information collected in the IEA HPT Annex 58 project [25]. The list includes closed-cycle and open-cycle HPs for mechanical vapor recompression (MVR). It is structured by maximum supply temperature, HTHP supplier, country, compressor type, the working fluid (refrigerant), maximum heating capacity, and technology readiness level (TRL) [16]. The specific investment costs are also given in EUR/kW_{th}. It should be noted that the HTHP suppliers provided the information without third-party validation. Therefore, the data is indicative and may vary in the final installations depending on the application-specific parameters.

Table 2. Overview of HTHP technologies and suppliers structured by maximum supply temperature above 100 °C [16] (Data based on IEA HPT Annex 58 [25]) (Note: The HTHP suppliers provided all information without third-party validation. Therefore, the information is indicative and may vary in final installations depending on application-specific parameters).

HTHP supplier (High-Temperature Heat Pump)	Country	Product	Compressor type	Working fluid (Refrigerant)	Max. heating capacity (MW)	Max. supply temp. (°C)	TRL (Technology Readiness Level)	Spec. invest. cost (EUR/kW_{th})
Spilling	DE	Steam Compressor	Piston (MVR)	R718 (water)	15	280	9	100 to 400
Enerin	NO	HoegTemp	Piston	R704 (helium)	10	250	6	600 to 800
Qpinch	BE	Heat Transformer	Chemical heat transformer	R718, H_3PO_4 and derivatives	2	230	9	1000 to 2000
Piller	DE	VapoFan	Turbo (MVR)	R718	70	212	8 to 9	850
Olvondo	NO	HighLift	Piston (double acting)	R704	5	200	9	1200
Turboden	IT	LHP	Turbo	Application specific	30	200	7 to 9	300 to 700
ToCircle	NO	TC-C920	Rotary vane	R717 (ammonia), R718	5	188	6 to 7	250 to 430
Kobelco MSRC160	JP	MSRC160	Twin -screw (MVR)	R718	0.8	175	9	n.a.
Kobelco SGH165	JP	SGH165	Twin-screw (MVR)	R245fa/R134a (mixture), R718	0.62	175	9	n.a.
Heaten	NO	HeatBooster	Reciprocating, custom design	HFOs (hydrofluorolefins)	6	165	7 to 9	250 to 350
SPH	DE	Thermbooster	Piston	HFOs (hydrofluorolefins)	5	165	6 to 8	150 to 1000
SRM	SE	Compressor for water vapor	Screw (MVR)	R718	2	165	5	n.a.
Siemens Energy	DE	Industrial Heat Pump	Turbo (geared or single-shaft)	R1233zd(E), R1234ze(E)	70	160	9 (to 90 °C)	250 to 800
Enertime	FR	HTHPs	1- or 2-stage centrifugal	R1336mzz(Z), R1224yd(Z), R1233zd(E)	10	160	4 to 8	300 to 400
Weel & Sandvig	DK	WS Turbo Steam	Turbo (MVR)	R718	5	160	4 to 9	150 to 250
Rank	ES	Rank® HP	Screw	R245fa, R1336mzz(Z), R1233zd(E)	2	160	7	200 to 400
MAN	DE	ETES CO_2 Heat Pump	Centrifugal turbo with expander	R744 (CO_2)	50	150	7 to 8	300 to 500
Epcon	NO	MVR-HP	Centrifugal fan / Blower	R718	30	150	9	200 to 400
Ohmia Industry	NO	SPHP	Piston, Centrifugal fan (MVR)	R717, R718	10	150	7 to 8	n.a.
ecop	AT	Rotation Heat Pump K7	Rotational heat pump	ecop fluid 1 (He, Kr, Ar)	0.7	150	6 to 7	700
Mayekawa FC Comp	BE	FC-compressor	Screw	R601 (n-pentane)	1	145	5	720
GEA Refrigeration	NL	CO_2 Heat Pump	Semi-hermetic piston	R744	1.2	130	8	200 to 300
Mitsubishi Heavy Ind.	JP	ETW-S	Two-stage centrifugal	R134a	0.6	130	9	n.a.
Hybrid Energy	NO	HyPAC-S	Piston/screw	R717/R718 mixture	5	120	9	200 to 600
Johnson Controls	DK	Cascade Heat Pump System	Reciprocating	R717, R600 (n-butane) (cascade)	5	120	7 to 8	n.a.
Fenagy	DK	H1800-AW/WW	Reciprocating	R744	1.8	120	5 to 6	250 to 425
Mayekawa HS Comp	BE	HS-compressor	Piston	R600 (n-butane)	0.75	120	7	450
Kobelco SGH120	JP	SGH120	2-stage twin-screw	R245fa	0.37	120	9	n.a.
Mayekawa EcoCircuit	JP	Eco Circuit 100	Reciprocating	R1234ze(Z)	0.1	120	9	n.a.
Fuji Electric	JP	Steam Generation Heat Pump	Reciprocating	R245fa	0.03	120	9	n.a.
Emerson	US	Cascade Solution	Scroll and EVI scroll	R245fa, R410a, R718	0.03	120	6	n.a.
Skala Fabrikk	NO	SkaleUP	Piston (semihermetic)	R290 (propane), R600 (cascade)	0.3	115	7	500 to 700
Mayekawa EcoSirocco	JP	Eco Sirocco	Reciprocating	R744 (CO2)	0.1	100	8 to 9	n.a.

Figure 1 shows the industrial HTHP products sorted by their maximum heat supply temperature and heating capacity. The heating capacities range from laboratory demonstrators of about 10 kW to larger 70 MW units. Illustrated in color are the compressor technologies, including screw, piston, turbo, and others like the rotary vane compressor from ToCircle, the heat transformer from QPinch, or the Rotational HP from Ecop using a noble gas in a Joule cycle. These last examples show various technologies emerging alongside more classical Carnot cycles.

In most cases, turbo compressors are used for large heating capacities. For HTHP applications and high temperature lifts, compressors must be able to handle high pressure ratios. Therefore, the compressor manufacturers offer optimized designs for special applications.

For HTHP application, the steam compressors must preferably offer high flow rates at low suction pressure, high pressure ratios to reduce the number of compression stages, temperature resistance (e.g., need for liquid injection), and long-term corrosion resistance. In particular, a development perspective is small steam compressors for integrating HTHPs in industrial processes with an open cycle or combined in a two-stage cycle with MVR [26].

For example, Spilling's piston steam compressors operate at suction pressures above 1.4 bar(a) (110 °C) and achieve temperature lifts of up to 100 K with a 3-stage compression design in one unit. Piller's VapoFans are used in multi-stage MVR applications with suction pressures down to about 100 mbar(a) (45 °C). Enerin and Olvondo provide HTHPs with helium (R704) as working fluid and double-acting piston compressors in a Stirling cycle, which allow flexible operation conditions, high lifts, and supply temperatures above 200 °C.

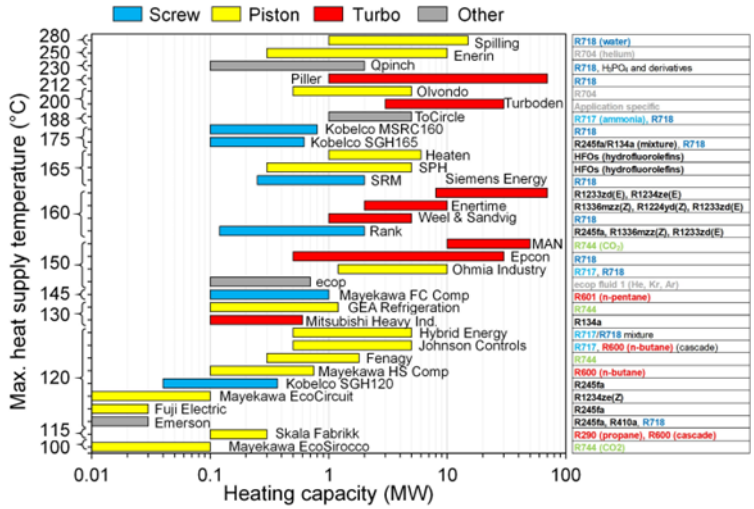


Fig. 1. Industrial HTHPs products sorted by maximum heat supply temperature (>100 °C) and heating capacity. The implemented compressor technology is color-coded (blue: screw, yellow: piston, red: turbo, grey: others). The table indicates the refrigerant [16].

Some HTHP suppliers provide closed-cycle HTHPs with up to 165 °C supply temperature using HFO refrigerants, e.g., the HeatBooster from Heaten or the ThermBooster from SPH. Other suppliers realize steam-generating HP using natural refrigerants, e.g., Ohmia Industry with ammonia (R717) in a bottom cycle and water (R718) in an open top cycle with MVR, Mayekawa with n-butane (R600), or Johnson Controls (Sabroe) with an R717/R600 cascade system using piston compressors.

Hybrid Energy uses ammonia/water (R717/R718) as the working medium in an absorption/compression cycle. As a result, temperatures up to 120 °C are achieved with high efficiency, and potentially high temperature glides on the heat source and sink. Recently, Fenagy commercialized CO_2 HPs for hot water heating from 30 to 120 °C with heating capacities up to about 1,800 kW.

Other manufacturers of HTHP products not listed in Table 2 and Figure 1 are Ago Calora (absorption-compression cycle, R717/R718, up to 150 °C), Ochsner (HFO refrigerants, up to 130 °C), Oilon (R1233zd(E), up to 120 °C), PureThermal (Pure PLUS, up to 120 °C), ThermoDraft (R1233zd(E), up to 120 °C), or Combitherm (HFO refrigerants, up to 120 °C). Finally, several large-scale HTHPs with > 10 MW heating capacity for industrial applications are supplied, for example, by Friotherm, MAN Energy Solutions, Turboden, Mitsubishi MHPS, or Siemens Energy.

Figure 2 shows the operating maps of some industrial HTHPs as a function of the heat source and sink temperature. In particular, there is a higher share around 50 °C heat source and 120 °C sink temperature. The operating limits are determined by the permissible condensation pressure, evaporation pressure, compression ratios, differential pressure across pistons, compressor speed, discharge gas temperatures, lubrication (e.g., oil temperature issues), and lowest allowable suction pressure.

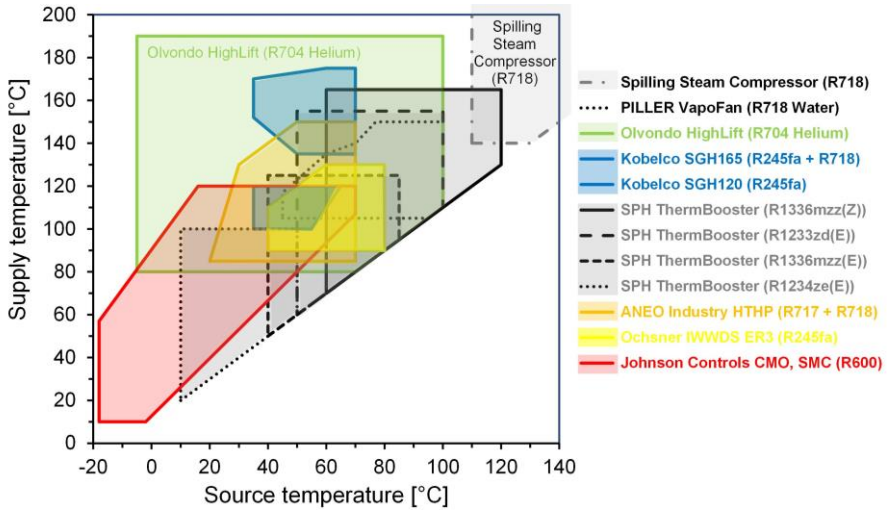


Fig. 2. Operating maps of some industrial HTHPs as a function of heat source and supply temperature.

Overall, Table 1 and Figures 2 and 3 demonstrate the availability of HTHP products and steam compressors and can be used as decision-support data for selecting appropriate HTHP suppliers. A preliminary technical feasibility check for HTHP integration consists of verifying the availability of a HTHP compatible with the temperature levels of the heat source and sink and heating capacity for a given project. In addition, industrial site constraints may further limit the HTHP integration options, such as the choice of refrigerant used (e.g., natural or synthetic), cycle concept (e.g., open, closed, or combinations), and space limitations.

Finally, a Pinch analysis can determine the optimal HTHP integration in an industrial context, which also identifies heat recovery options to increase efficiency and reduce energy consumption. Depending on the application, tailor-made HTHP designs are required (i.e., concepts for large temperature glides in the heat sink versus steam generation with no temperature glide).

3. Case studies and economic model

The following section describes case studies of potential HTHP integrations from the industrial companies ELSA, Cremo SA, and Gustav Spiess AG that support the Swiss project Annex 58 HTHP-CH by giving access to industrial process data. Furthermore, various other Swiss industrial companies (e.g., food, biotech, chemical) and HP suppliers are in contact with the project team showing interest in HTHP integration.

3.1. Case Study at ELSA (Estavayer Lait SA)

ELSA (Estavayer Lait SA) is Switzerland's largest dairy on a single site, processing around 260,000 t/a of milk into a wide range of fresh dairy products, such as UP/UHT milk, yogurt, quark, and cream. The main heat treatments are pasteurization and sterilization in the temperature range of 65 to 155 °C. In addition to the production processes, CIP processes (Cleaning in Place) require large amounts of water and are an important steam consumer (e.g., 4.5 bar(a), 148 °C) (Figure 3). Today, process steam is generated by a wood chip steam boiler and several natural gas boilers (71.6 GWh/a or 275 kWh/t milk processed).

The process requirement for CIP is keeping the circulating basic and acidic solutions at 75 °C and 60 °C respectively, while the"sterilization" step of processing equipment, taking place after cleaning and, if needed, before the next operation, requires circulating hot water at 90 °C. These requirements could, in principle, be fulfilled with a hot utility below 100 °C; however, retrofitting the CIP stations (comprising 65 heat exchangers in total) for a hot water utility at 95 to 100 °C instead of steam at 4.5 bar(a) would be both expensive and difficult to implement because of the lack of space.

Therefore, to save energy and water, ELSA is interested in integrating steam-generating HTHPs that use waste heat from the NH_3 chillers (about 23.7 GWh/a at 40 °C, currently discharged through cooling towers) or drain water (about 490,000 m^3/a at 50 °C) as a heat source to replace some of the steam required for the CIP processes (about 22.7 GWh/a steam in 7,200 h of operation corresponding to 3.15 MW). Although the heat sources and sinks have yet to be confirmed, Figure 3 shows potential HTHP integration points for the CIP plants. Measurements are ongoing to determine the mass and heat balance of CIP operations and to check whether a significant share of the consumed 4.5 bar(a) steam could, in practice, be supplied at a significantly lower temperature and affordable costs.

The electricity price for 2023 is around 0.18 CHF/kWh [27] in Estavayer for a large industrial company (Category C7), and the gas price (Type X) is about 0.13 CHF/kWh, including CO_2 tax of 0.02 CHF/kWh [28]. These conditions result in a favorable electricity-to-gas price ratio of around 1.4. Compared with natural gas, which has a CO_2 emission factor of 0.201 kg CO_2 per kWh_{th} [14], an average Swiss consumer electricity mix of 0.128 kg CO_2/kWh_{el} is considered [29]. The cost multiplication factor for planning and integration is assumed to be 3.0 because the installation environment is quite complex, and space is tight.

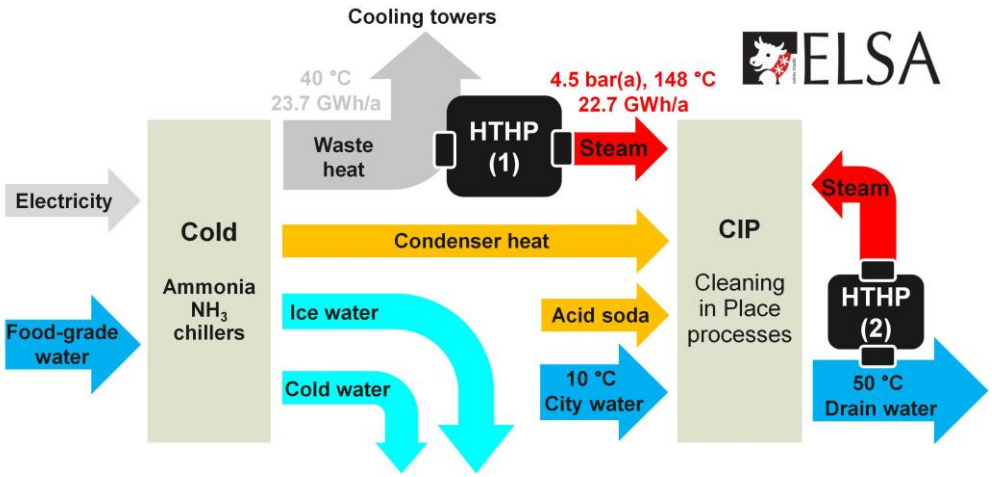


Fig. 3. Potential integration points for a steam-generating HTHP at ELSA using waste heat from the ammonia chillers at 40 °C as a heat source (1) or heat from drain water at 50 °C (2).

3.2. Case Study at Cremo SA

Cremo SA in Villars-sur-Glâne processes around 240,000 t/a of milk into various dairy products, including cheese (Gruyère, Vacherin fribourgeois, Raclette), butter, skim milk, milk proteins, and milk permeate powder. Today, the heat is supplied by two 5 MW gas-fired steam boilers (12 t/h steam, baseline consumption). In addition, a district heating network (105 °C/80 °C supply/return) from the nearby waste incineration plant provides heat to an internal hot water loop at 105 °C/60 °C that is connected to spray dryers (for preheating air), a TIXOTHERM™ drying process [30], evaporators, pasteurizers, CIP stations, building HVAC, and tap hot water. In case of a future reduction of the district heating temperature to 80 °C / 60 °C, the possibility of a large-scale HTHP is considered (around 5 to 10 MW_{th}) to adapt to the changing heat transfer rate (Figure 4).

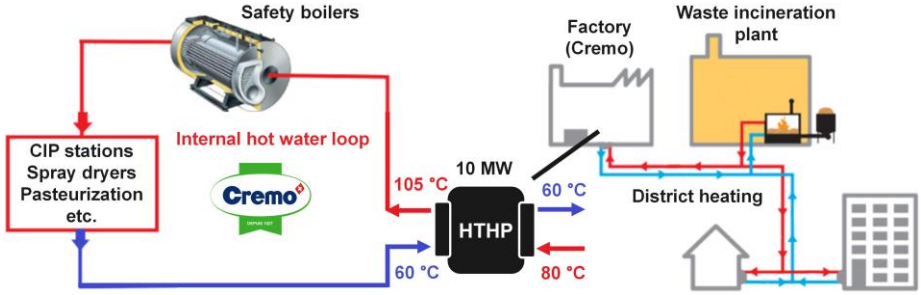


Fig. 4. Potential HTHP integration point at Cremo using district heat as a source and upgrading the heat to the internal hot water loop.

Another potential integration point for a HTHP has been identified in the TIXOTHERM™ drying plant (Figure 5), which produces milk permeate powder (containing milk sugars) and currently consumes about 10% to 15% of the total steam demand for heating a Rosinaire™ paddle dryer [30]. Presently, there is only limited heat recovery on the humid exhaust air. Therefore, this case study is *a priori* suitable for a HTHP integration to supply low-pressure steam at around 1.4 bar(a) (110 °C) to the paddle dryer using humid exhaust air as a heat source (65 °C) and substitute steam generation from the steam boilers.

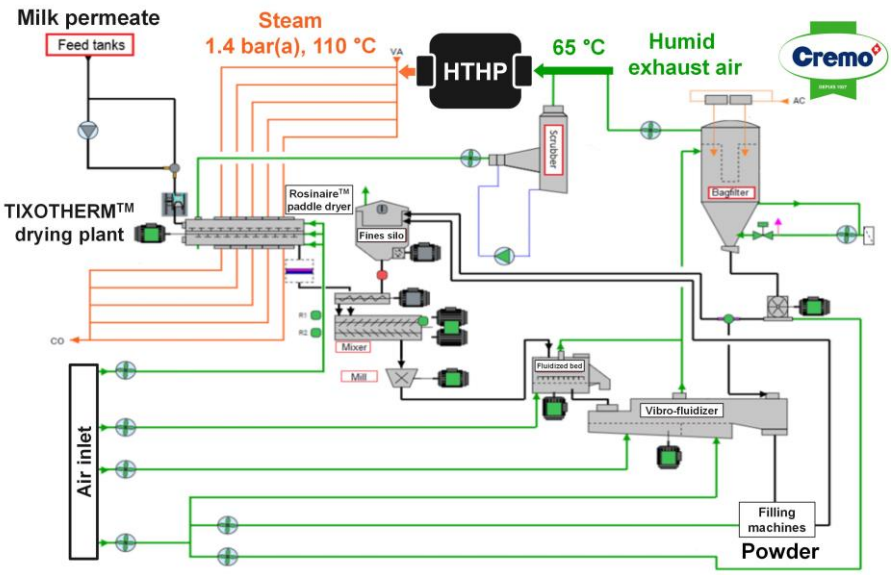


Fig. 5. Potential HTHP integration point at Cremo in the TIXOTHERMTM drying process with a RosinaireTM paddle dryer, where humid exhaust air could be used as a heat source to generate steam.

Figure 6 (left) shows the calculated Composite Curves (CCs) as the initial situation before the integration of a HTHP, indicating a Heat Recovery (HR) potential through direct heat transfer of about 600 kW between air flows and a Pinch temperature at around 70 °C. Furthermore, Figure 6 (middle) shows the corresponding Grand Composite Curve (GCC) with an integrated HTHP, providing a 940 kW condensation capacity at 120 °C and 570 kW evaporation capacity at 38 °C, from which a COP of 2.3 can be derived (see COP-fit formula in Figure 8). Finally, Figure 6 (right) shows the CCs after integrating the HTHP. The example demonstrates a potential reduction of the Hot Utility (HU) by 100% (from 940 to 0 kW) and the unused waste heat by 47% (from 1,204 to 634 kW), and an increase of the HR potential by 249% (from 605 to 2,113 kW).

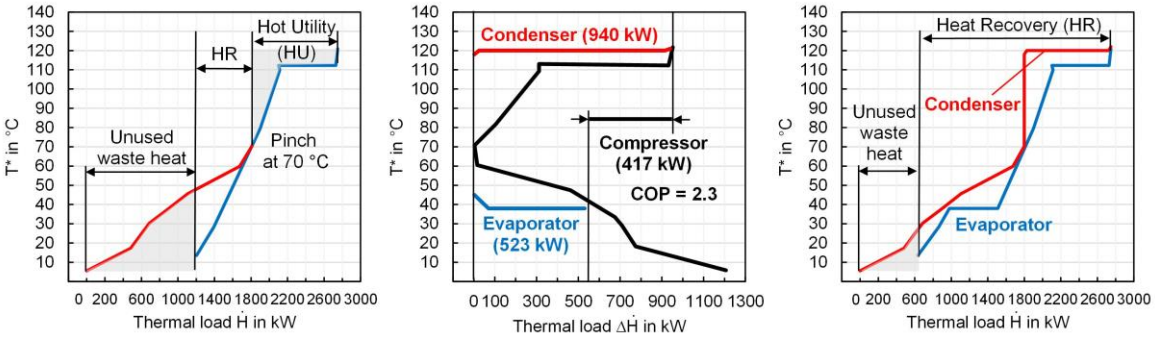


Fig. 6. Composite curves (CC, left) and grand composite curve (GCC, right) of the TIXOTHERM™ process with paddle dryer at Cremo showing the potential HTHP integration providing low-pressure steam at 110 °C and using humid exhaust air as a heat source (Pinch at 70 °C, evaporation temperature at 38 °C, condensation temperature at 120 °C, COP of 2.3).

A challenge is the low evaporation temperature (and thus the large temperature lift of 80 K) and the probably insufficient evaporation capacity if the waste heat is to be recovered exclusively from the drying process. Therefore, additional waste heat sources must be identified at about 35 to 40 °C. The estimated annual operating time of the potential HTHP is about 6,400 hours, which is within the range of various techno-economic studies presented in a literature review [21], [22]. The electricity price for a customer of the size of Cremo is 0.2 CHF/kWh$_{el}$, and the gas price is 0.11 CHF/kWh$_{th}$, corresponding to an electricity-to-gas price ratio of about 1.8. The CO_2 emission factor of electricity at Cremo is around the average Swiss consumer electricity mix of 0.128 kg CO_2/kWh$_{el}$ [29], as the mix contains renewables, just not purely renewables. Furthermore, a discount rate of 2% is used to estimate the discounted payback period of the HTHP investment. The cost multiplication factor for calculating planning and integration costs is assumed to be 2.0.

3.3. Case Study at Gustav Spiess AG

Gustav Spiess AG in Berneck (SG) produces meat products such as sausage, ham, and bacon. Today, a gas boiler provides steam (6 to 8 bar(a)) to heat the pasteurization and cooking/smoking cabinets (Figure 7). The steam pressure is reduced to 1.5 bar(a) (115 °C) to achieve cabinet temperatures of 85 to 90 °C and a sausage core temperature of about 72 °C. Here, integrating a 550 kW_{th} steam-generating HTHP is under consideration, using the waste heat from the NH_3 chillers as a possible heat source at 40 to 50 °C. Typical operation is 12 hours per day, 250 days per year, resulting in an annual operating time of about 3,000 hours. The expected payback period for new energy-related infrastructure investments is about 8 to 10 years. The electricity price for medium-sized customers in the given area is 0.25 CHF/kWh, and the gas price is 0.17 CHF/kWh resulting in an electricity-to-gas price ratio of 1.5, which appears favorable for electricity-powered heating and cooling technologies. The purchased electricity mix is nuclear energy with a low CO_2 emission factor of about 0.012 kg CO_2/kWh_{el}. The cost multiplication factor accounting for planning and integration is assumed to be 2.0.

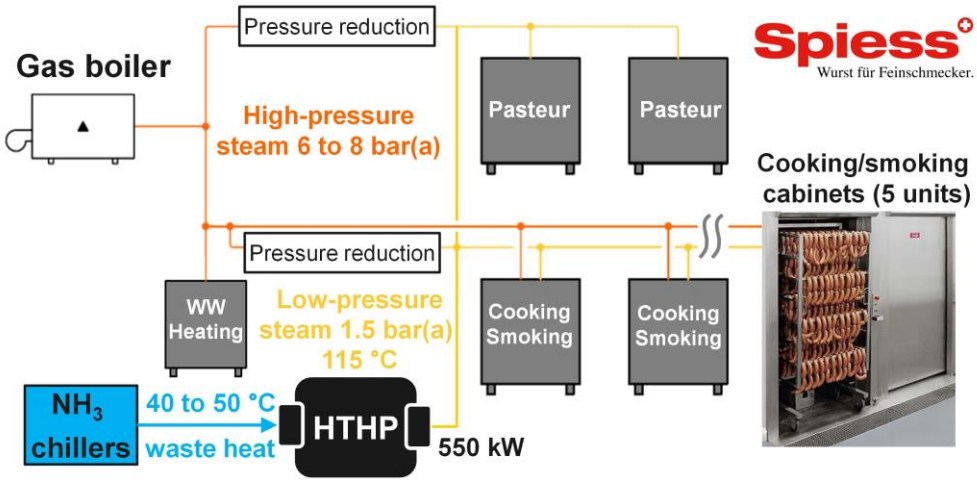


Fig. 7. Possible integration point of a steam-generating HTHP at Gustav Spiess AG for sausage cooking/smoking processes.

3.4. Economic evaluation and COP estimation

The economic evaluation of the case studies is based on a calculation tool developed in MS Excel, illustrated in Figure 8 [21], [22]. It assumes that the investment of the gas boilers is depreciated and that the gas boilers remain for production safety, redundancy, start-up operation, and peak load coverage. Input parameters to the evaluation tool are electricity price (c_{el}), gas price (c_{fuel}), operating hours (t), heating capacity ($\dot{Q}_h$), temperature lift between the heat source and sink (ΔT_{lift}), specific investment costs ($c_{inv,HP}$), maintenance cost factor ($f_{maintain}$), interest rate (i), the emissions factors of electricity and fuel (f_{CO2}), and CO_2 tax refund (subsidies). The output results are the COP, CO_2 emissions reduction ($\dot{m}_{CO2,reduction}$), annual cost savings ($C_{savings}$), and the payback periods (PP). The calculation tool helps to quickly evaluate the economic feasibility as a "go/no-go" decision.

1. First, the efficiency of the HTHP is estimated using the temperature lift (ΔT_{lift}) and a COP fit-curve ($COP = 52.94 \cdot {\Delta T_{lift}}^{-0.716}$) derived from quotes from various heat pump suppliers [21], [22].
2. Next, the investment costs ($C_{inv,HP}$) of the industrial HTHPs are evaluated based on the specific investment costs ($c_{inv,HP} = 3'157 \cdot {\dot{Q}_h}^{-0.322}$) according to price information from heat pump suppliers, the heating capacity ($\dot{Q}_h$), and a cost multiplication factor ($f_{inv,HP}$) accounting for planning and integration (typically between 1.5 to 4.0 depending on the complexity of integration, e.g., including heat storage, site's electrical installation, piping, hydraulics, etc.) [21], [22].
3. Then, the annual cost savings are calculated considering the following:
   - electricity cost (C_{el}) to operate the HTHP,
   - maintenance costs ($C_{maintain}$) of the HTHP using a multiplication factor ($f_{maintain}$) on capital cost (typically between 1.5% to 6%, in the case studies, 4% is used) [21], [22],
   - saved fuel costs (C_{fuel}) (assuming 90% boiler efficiency η_{fuel}), and
   - possible refunds of CO_2 reduction (C_{CO2}) (e.g., carbon taxes or subsidies).
4. After that, the payback period of the HTHP investment is evaluated as a trade-off between the investment costs versus the expected annual cost savings resulting from the heat pump investment.

5. Finally, the discount rates (i) are considered to calculate the discounted payback periods (DPP) [31], depending on the investor's risk tolerance (e.g., sector, company size, energy intensity, funding source, new technology, etc.) [32]. Typical discount rates for HP investments range from 5% to 15%, according to reviewed literature [21], [22]. The DPP (discounted payback period) is the period after which the cumulative discounted cash inflows cover the initial investment [31]. The DPP can therefore be interpreted as a period beyond which a project generates economic profit. In contrast, the static PP gives a period beyond which a project generates accounting profit.

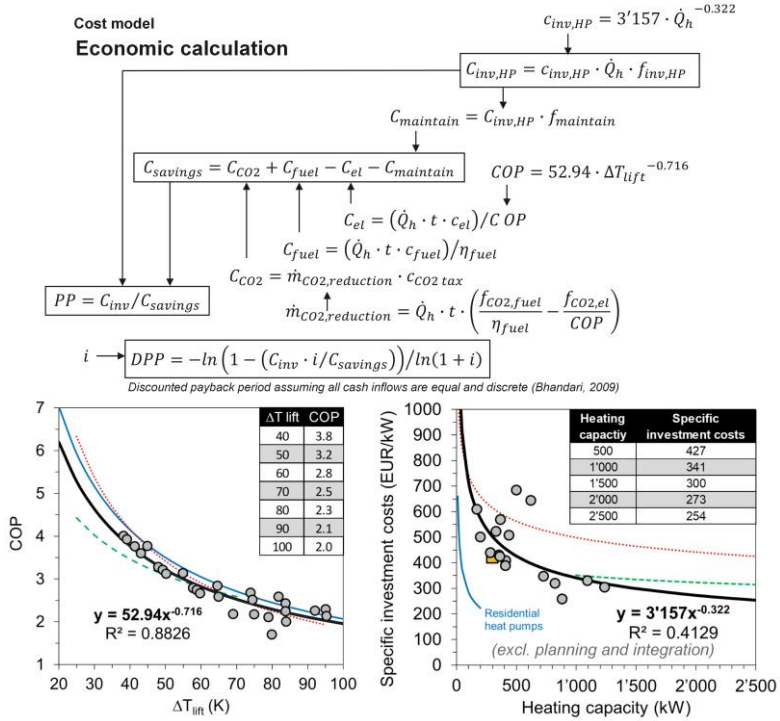


Fig. 8. Economic calculation, COP, and specific investment costs to derive the payback period for HTHP integration [21], [22].

4. Results and discussion

Table 3 summarizes the results of the three case studies. The calculations lead to payback periods of 2.0, 3.7, and 3.3 years, which means that HTHP integration would be cost-effective under current assumptions. Overall, the case study examples show significant annual energy savings of 55%, 60%, and 66%, and CO_2 emission reductions of 71%, 75%, and 98%, respectively. The COP varies between 2.0 and 2.7 according to the COP-fit function shown in Figure 8.

Table 3. Results of the case studies, with COP, energy savings, investment costs, reduction of CO_2 emissions, and payback periods.

Heat pump conditions	**Symbol**	**Unit**	**ELSA CIP process**	**Cremo Milk drying**	**Gustav Spiess Sausage cooking**	**Reference 2023 (Ref)**
Heat sink (outlet) temperature	$T_{h,out}$	°C	148	120	115	120
Heat source (inlet) temperature	$T_{c,in}$	°C	50	38	50	50
Temperature lift	ΔT_{lift}	K	98	82	65	70
Heating capacity	$\dot{Q}_h$	kW	3,150	940	550	1,000
Fuel (gas, oil) price	c_{fuel}	EUR/kWh	0.13	0.11	0.17	0.15
Electricity price	c_{el}	EUR/kWh	0.18	0.20	0.25	0.35
Electricity-to-fuel price ratio	$p_{el/fuel}$	-	1.38	1.82	1.47	2.33
CO_2 tax (or subsidies)	$c_{CO2\,tax}$	EUR/tCO_2	0	0	0	92.5
Electricity CO_2 emissions factor	$f_{CO2\,el}$	kgCO_2/kWh	0.128	0.128	0.012	0.128
Fuel CO_2 emissions factor	$f_{CO2\,fuel}$	kgCO_2/kWh	0.201	0.201	0.201	0.201
Annual operating time	t	h/a	7,200	6,400	3,000	6,400
The efficiency of fuel boiler	η_{fuel}	-	0.90	0.90	0.90	0.90

Maintenance factor (on capital costs)	$f_{maintain}$	-	0.04	0.04	0.04	0.04
Cost factor for planning & integration	$f_{inv,hp}$	-	3.0	2.0	2.0	3.0
COP ($COP = 52.94 \cdot \Delta T_{lift}{}^{-0.716}$)	COP	-	2.0	2.3	2.7	2.5
Specific investment costs ($c_{inv,HP} = 3'157 \cdot \dot{Q}_h{}^{-0.322}$)	$c_{inv,hp}$	EUR/kW	236	348	414	341
Annual CO_2 emissions reduction	$\dot{m}_{CO2,reduction}$	tCO_2/a	3,604	1,002	361	1,105
Annual CO_2 emissions reduction	-	-	71%	75%	98%	77%
Annual energy savings	$E_{savings}$	MWh/a	13,782	4,019	1,214	4,579
Annual energy savings	-	-	55%	60%	66%	64%
Investment costs	$C_{inv,hp}$	kEUR	2,230	655	455	1,024
Annual fuel cost savings	C_{fuel}	kEUR/a	3,276	735	312	1,067
Annual electricity costs	C_{el}	kEUR/a	2,055	533	155	886
Annual heat pump maintenance costs	$C_{maintain}$	kEUR/a	89	26	18	41
Annual CO_2 tax compensation	C_{CO2}	kEUR/a	0	0	0	102
Annual cost savings	$C_{savings}$	kEUR/a	1132	176	139	242
Discount rate	i	-	0.10	0.02	0.05	0.10
Payback period	PP	years	2.0	3.7	3.3	4.2
Discounted payback period	DPP	years	2.3	3.9	3.7	5.8

The case study ELSA has the highest temperature lift of 98 K and consequently the lowest COP as well as a cost multiplication factor for planning and integration of 3.0, but benefits from favorable electricity-to-gas price ratio and low specific investment costs due to the large HTHP (economies of scale).

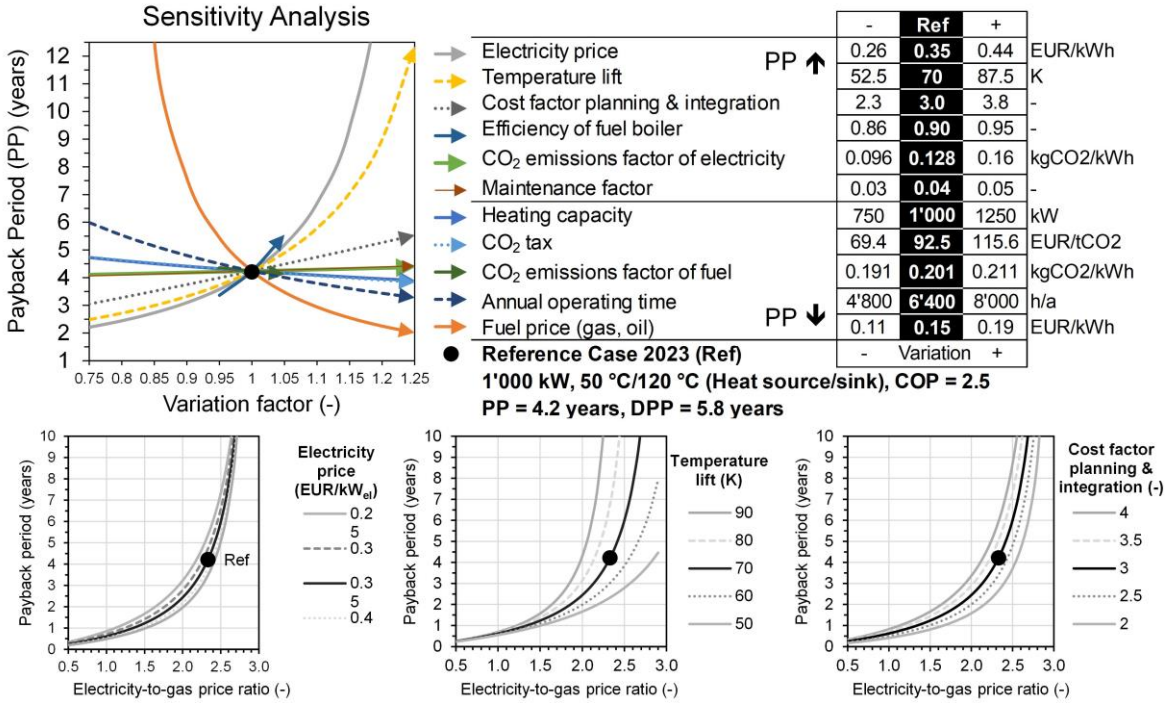
In the Cremo case study, the electricity-to-gas price ratio is higher, and the integration factor is 2.0, but the discount rate is low, leading to a DPP of 3.9 years. The pinch analysis is a powerful tool to determine the optimal placement of a HTHP, its size, and adequate evaporation and condensation temperatures.

The case study of Gustav Spiess AG shows a high CO_2 emission reduction of 98% because the company benefits from low CO_2 emissions by purchasing nuclear power. Using waste heat from the NH_3 chillers as a heat source shows great multiplication potential in other case studies in the Swiss food industry, where refrigeration machines for cooling foods are state of the art.

In addition to the three case studies, Table 3 also shows the results of the payback period for a possible Reference Case 2023 (Ref) with a heat source of 50 °C, a heat sink of 120 °C (COP of 2.5), and 1 MW heating capacity, and specific investment costs of 341 EUR/kW_{th}. This scenario uses a discount rate of 10%, an average Swiss consumer electricity mix with a CO_2 emission factor of 0.128 $kgCO_2/kWh_{el}$ [29], and a possible carbon tax refund of EUR 92.5/tCO_2 due to the reduction of CO_2 emissions. Electricity and gas prices are based on market data for 2023 [33] (0.15 EUR/kWh PEGAS NCG Year Future and 0.35 EUR/kWh Phelix Year Future, price ratio 2.33, as of December 11, 2022).

Figure 9 shows a sensitivity analysis of the payback period for the Reference Case 2023 (abbreviated as Ref). All input factors of the model were individually varied from -25% to +25% (factor 0.75 to 1.25), while the other parameters were kept constant. The sensitivity analysis reveals that the payback period is strongly sensitive to a change in electricity and fuel prices as well as the temperature lift of the heat pump.

Favorable conditions for HTHPs are higher values of fuel prices, operating time, fuel CO_2 emission factor, CO_2 tax, heating capacity, and lower electricity prices. In addition, an increasing CO_2 tax, along with subsidies and possible CO_2 compensation through the European emission trading system increase the financial incentives for HTHPs.



	-	Ref	+	
Electricity price (PP ↑)	0.26	**0.35**	0.44	EUR/kWh
Temperature lift (PP ↑)	52.5	**70**	87.5	K
Cost factor planning & integration (PP ↑)	2.3	**3.0**	3.8	-
Efficiency of fuel boiler	0.86	**0.90**	0.95	-
CO_2 emissions factor of electricity	0.096	**0.128**	0.16	kgCO2/kWh
Maintenance factor	0.03	**0.04**	0.05	-
Heating capacity	750	**1'000**	1250	kW
CO_2 tax	69.4	**92.5**	115.6	EUR/tCO2
CO_2 emissions factor of fuel	0.191	**0.201**	0.211	kgCO2/kWh
Annual operating time (PP ↓)	4'800	**6'400**	8'000	h/a
Fuel price (gas, oil) (PP ↓)	0.11	**0.15**	0.19	EUR/kWh

Fig. 9. Sensitivity analysis of the payback period for a Reference Case 2023 (Ref) at 50 °C/120 °C heat source/sink, 1'000 kW heating capacity, and an electricity-to-gas price ratio of 2.33. The graphs below show the impact of electricity price, temperature lift, and cost factor for planning & integration on the payback period as a function of the electricity-to-gas price ratio.

On the other hand, low gas and high electricity prices lead to unfavorable conditions and are significant barriers to the investment of industrial HTHPs. As seen in the lower diagrams of Figure 9, the payback period is strongly determined by the electricity-to-gas price ratio. Above a price ratio of 2.7, the payback period is more than 10 years. In addition, the payback period is strongly influenced by the temperature lift, which determines the COP and, thus, the operating cost of the HTHP and the avoided fuel consumption.

For given energy prices and temperature lift, the cost multiplication factor for planning & implementation leads to significant uncertainty in quantifying the payback period. The cost multiplication factor depends on the complexity of the HTHP integration and can only be properly determined after a thorough analysis of the project and indicative price quotations for the entire heating system implementation.

5. Conclusions

A simple cost model was developed to pre-assess the economic feasibility of integrating HTHPs into actual industrial processes based on investment costs and annual cost savings. The analyzed HTHP integrations at ELSA, Cremo, and Gustav Spiess show significant annual energy savings of 55%, 60%, and 66%, and CO_2 emission reductions of 71%, 75%, and 98%, respectively. The calculations lead to payback periods of 2.0, 3.7, and 3.3 years, which means that the integration of HTHP would be cost-effective under the current assumptions. However, it should be noted that the financial evaluation strongly depends on the individual case. A sensitivity analysis has shown that higher fuel prices mainly shorten the payback period. An electricity-to-gas price ratio below 2.7 leads to payback periods below 10 years. Temperature lifts below 70 K appear to be profitable. Economic challenges arise with high temperature lifts, low gas prices, and high discount rates. Overall, the availability of closed-cycle HTHP products and steam compressors shows that the case studies are technically feasible with the integration concepts presented. A wide range of HTHP products is available up to 120 to 160 °C supply temperature. Individual HTHP products achieve temperature lifts of up to 125 K. HTHPs are also available in the large heating capacity range >10 MW. More detailed discussions with HTHP manufacturers are required in the next step to clarify the end-user-specific integration conditions. In addition,

the cost model can be applied to other Swiss case studies for initial cost estimation. Future work could include integrating an advanced heat pump model that considers the effects of refrigerant, compressor efficiency, and cycle design.

Acknowledgments

The project team gratefully acknowledges the Swiss Federal Office of Energy (SFOE) for the financial support of the R&D project Annex 58 HTHP-CH (Contract number SI/502336-01) and the SWEET (SWiss Energy research for the Energy Transition) project DeCarbCH (DeCarbonisation of Cooling and Heating in Switzerland) (www.sweet-decarb.ch).

Nomenclature

$\dot{Q}_h$	Heating capacity	kW	$C_{inv,HP}$	Investment costs of HP	EUR
ΔT_{lift}	Temperature lift	K	$\dot{m}_{CO2,reduction}$	Annual CO_2 emissions reduction	tCO_2/a
$c_{inv,HP}$	Specific investment costs of HP	EUR/kW	$E_{savings}$	Annual energy savings	kWh/a
$f_{inv,HP}$	Cost factor for planning & HP integration	-	C_{fuel}	Annual fuel cost savings	EUR/a
t	Annual operating time	h/a	C_{el}	Annual electricity costs	EUR/a
$f_{maintain}$	Maintenance factor (on capital costs)	-	$C_{maintain}$	Annual HP maintenance costs	EUR/a
η_{fuel}	Efficiency of gas boiler	-	C_{CO2}	Annual CO_2 tax compensation	EUR/a
i	Discount rate	-	$C_{savings}$	Annual cost savings	EUR/a
c_{fuel}	Fuel price (gas, oil)	EUR/kWh	PP	Payback period	a
c_{el}	Electricity price	EUR/kWh	DPP	Discounted payback period	a
$c_{CO2\ tax}$	CO_2 tax	EUR/tCO_2			
$f_{CO2,el}$	CO_2 emissions factor electricity	$kgCO_2/kWh$			
$f_{CO2,fuel}$	CO_2 emissions factor fuel	$kgCO_2/kWh$			

References

[1] M. Zogg, “History of Heat pumps: Swiss Contributions and International Milestones,” 2008. https://www.zogg-engineering.ch/publi/HistoryHP.pdf.

[2] FWS, “Statistik 2021, Fachvereinigung Wärmepumpen Schweiz,” 2021. https://www.fws.ch/wp-content/uploads/2022/05/FWS-Statistiken-2021-V2.pdf.

[3] S. Renz, “Heat Pump Market Development in Switzerland, Market Report,” *Heat Pump. Technol. Mag.*, vol. 38, no. 1, pp. 19–22, 2020, [Online]. Available: https://heatpumpingtechnologies.org/publications/heat-pump-market-development-in-switzerland/.

[4] B. Vonlanthen, “Erfolgsgeschichte der Wärmepumpen in der Schweiz,” in *News aus der Wärmepumpen-Forschung, 25. Tagung des BFE-Forschungsprogramms “Wärmepumpen und Kälte”, 26. Juni 2019, BFH Burgdorf*, 2019, pp. 7–16.

[5] C. Arpagaus, F. Bless, S. S. Bertsch, and J. Schiffmann, “Wärmepumpen für die Industrie: Eine aktuelle Übersicht,” in *25. Tagung des BFE-Forschungsprogramms “Wärmepumpen und Kälte”, 26. Juni 2019, BFH Burgdorf, Schweiz*, 2019, pp. 1–15.

[6] C. Arpagaus, F. Bless, M. Uhlmann, J. Schiffmann, and S. S. Bertsch, “High temperature heat pumps: Market overview, state of the art, research status, refrigerants, and application potentials,” *Energy*, vol. 152, pp. 985–1010, Jun. 2018, doi: 10.1016/j.energy.2018.03.166.

[7] C. Arpagaus, *Hochtemperatur-Wärmepumpen: Marktübersicht, Stand der Technik und Anwendungspotenziale, 138 Seiten, ISBN 978-3-8007-4550-0 (Print), ISBN 978-3-8007-4551-7 (E-Book)*. Offenbach, Berlin: VDE Verlag GmbH, 2018.

[8] N. Calame, F. Rognon, and O. Sari, “High Temperature Heat Pumps for Industrial Processes - State of the Art and Research Needs,” in *23. Tagung des Forschungsprogramms Wärmepumpen und Kälte des Bundesamts für Energie BFE, 14. Juni 2017, Burgdorf*, 2017, pp. 1–17.

[9] C. Arpagaus, J. Payá, A. H. Hassan, and S. S. Bertsch, “Potential Impact of Industrial HTHPs on the European Market,” in *3rd HTHP Symposium, 29-30 March, 2022, Copenhagen, Denmark*, 2022, p. Poster, [Online]. Available: http://hthp-symposium.org/hthp-symposium-2022/.

[10] Bundesamt für Energie (BFE), “Analyse des schweizerischen Energieverbrauchs 2000 - 2018 nach Verwendungszwecken,” 2019. [Online]. Available: https://www.bfe.admin.ch/bfe/en/home/supply/statistics-and-

geodata/energy-statistics/analysis-of-energy-consumption-by-specific-use.html.

[11] T. Fleiter *et al.*, "Profile of heating and cooling demand in 2015, Deliverable D3.1 Report, Heat Roadmap Europe," *HeatRoadmapEU*, no. 695989, p. 70, 2017, [Online]. Available: https://heatroadmap.eu/wp-content/uploads/2018/11//HRE4_D3.1.pdf.

[12] M. J. S. Zuberi *et al.*, "Decarbonizing Swiss industrial sectors by process integration, electrification, and traditional energy efficiency measures," in *Eceee Industrial Summer Study Proceedings, Industrial Efficiency 2020 Decarbonise industry! 14–17 September 2020 Online event*, 2020, pp. 307–318, [Online]. Available: https://www.eceee.org/library/conference_proceedings/eceee_Industrial_Summer_Study/2020/4-technology-products-and-systems/decarbonizing-swiss-industrial-sectors-by-process-integration-electrification-and-traditional-energy-efficiency-measures.

[13] C. Arpagaus *et al.*, "HTHP-CH – Integration of High-Temperature Heat Pumps in Swiss Industrial Processes," in *28. Tagung des BFE-Forschungsprogramms «Wärmepumpen und Kältetechnik» 22. Juni 2022, BFH Burgdorf*, 2022, pp. 1–9, [Online]. Available: https://www.sweet-decarb.ch/fileadmin/downloads/Presentations_File/HTHP-CH_Tagungsband.pdf.

[14] BAFU, "CO2 -Emissionsfaktoren des Treibhausgasinventars der Schweiz, Faktenblatt, Januar 2022, Bundesamt für Umwelt BAFU," 2022. https://www.bafu.admin.ch/dam/bafu/en/dokumente/klima/fachinfo-daten/CO2_Emissionsfaktoren_THG_Inventar.pdf.download.pdf/Faktenblatt_CO2-Emissionsfaktoren_01-2022_DE.pdf.

[15] Bundesamt für Umwelt (BAFU), "8. How climate-friendly is the Swiss energy supply? Last modification 02.10.2018," 2018. www.bafu.admin.ch/bafu/de/home/themen/klima/klimawandel--fragen-und-antworten.html.

[16] C. Arpagaus, L. Brendel, S. Paranjape, F. Bless, M. Uhlmann, and S. Bertsch, "High-Temperature Heat Pumps for Industrial Applications - New Developments and Products for Supply Temperatures above 100 °C," 2022, [Online]. Available: https://www.youtube.com/watch?v=HvCEWrG4uR0.

[17] S. Wolf, R. Flatau, P. Radgen, and M. Blesl, "Systematische Anwendung von Großwärmepumpen in der Schweizer Industrie, Endbericht, 10. Mai 2017." pp. 1–47, 2017, [Online]. Available: https://www.bfe.admin.ch/bfe/de/home/news-und-medien/publikationen.exturl.html/aHR0cHM6Ly9wdWJkYi5iZmUuYWRtaW4uY2gvZGUvcHVibGljYX/Rpb24vZG93bmxvYWQvODY3Ng==.html.

[18] Bundesaft für Energie (BFE), "Energiestrategie 2050," 2021. https://www.bfe.admin.ch/bfe/de/home/politik/energiestrategie-2050.html.

[19] Bundesamt für Umwelt (BAFU), "Klimastrategie 2050," 2021. https://www.bafu.admin.ch/bafu/de/home/themen/klima/fachinformationen/emissionsverminderung/verminderungsziele/ziel-2050/klimastrategie-2050.html.

[20] R. De Boer *et al.*, "Strengthening Industrial Heat Pump Innovation, Decarbonizing Industrial Heat, White Paper," 2020.

[21] C. Arpagaus and F. Bless, "Techno-economic analysis of steam generating heat pumps for integration into distillation processes," 2022, doi: http://dx.doi.org/10.18462/iir.gl2022.0029.

[22] C. Arpagaus, F. Bless, and S. S. Bertsch, "Techno-Economic Analysis of Steam-Generating Heat Pumps in Distillation Processes," 2022, [Online]. Available: http://hthp-symposium.org/hthp-symposium-2022/.

[23] D. Flórez-Orrego, M. E. G. Domingos Ribeiro, and F. Maréchal, "A systematic framework for the multi-time integration of industrial complexes and urban systems," in *7th International Conference on Contemporary Problems of Thermal Engineering, CPOTE 2022, 20-23 September 2022, Warsaw, Poland*, 2022, pp. 1–23.

[24] D. Flórez-Orrego, E. A. Pina, M. Ribeiro Domingos, S. Sharma, and F. Maréchal, "High temperature heat pumps applications for industrial separation and drying processes," in *Proceedings of ECOS 2022 - The 35th International Conference on Efficiency, Cost, Optimization, Simulation and Environmental Impact of Energy Systems, July 4-7, 2022, Copenhagen, Denmark*, 2022, pp. 1001–1009.

[25] IEA HPT, "IEA HPT Annex 58 about HTHPs (Website), Task 1: Technologies - State of the art and ongoing developments for systems and components," 2022. https://heatpumpingtechnologies.org/annex58/task1/.

[26] F. Bless, C. Arpagaus, S. S. Bertsch, and J. Schiffmann, "Theoretical analysis of steam generation methods - Energy, CO 2 emission, and cost analysis," *Energy*, vol. 129, pp. 114–121, Jun. 2017, doi: 10.1016/j.energy.2017.04.088.

[27] ElCom, "Strompreise Schweiz, 17,97 Rp./kWh 2023, Groupe E SA, Estavayer," 2023. https://www.strompreis.elcom.admin.ch/municipality/2054?category=C7.

[28] WBF, "Preisüberwachung: Gaspreise in der Schweiz, Typ X," 2022. http://gaspreise.preisueberwacher.ch.

[29] FOEN, "Climate change: Questions and answers, 8. How climate-friendly is the Swiss energy supply? Federal Office for the Environment," 2022. https://www.bafu.admin.ch/bafu/en/home/topics/climate/questions-answers.html.

[30] J. Písecký, "Spray drying in the cheese industry," *Int. Dairy J.*, vol. 15, no. 6–9, pp. 531–536, Jun. 2005, doi:

10.1016/j.idairyj.2004.11.010.

[31] S. B. Bhandari, “Discounted Payback Period - Some Extensions,” in *Proceedings of ASBBS Annual Conference, Las Vegas, February 2009*, 2009, vol. 16, no. 1, pp. 1–10.

[32] European Commission, “EU Reference Scenario 2020 Energy, Transport and GHG Emissions - Trends to 2050,” 2021. https://op.europa.eu/s/shWr.

[33] Enerprice Partners AG, “Market prices 2023, as of December 11, 2022, Electricity - Phelix Year Future, Gas - PEGAS NCG Year Future,” 2022. https://www.enerprice.ch/charts.

14th IEA Heat Pump Conference
15-18 May 2023, Chicago, Illinois

Field Experience with Residential Heat Pumps in Switzerland: Potential for Improvement and Future Developments

Cordin Arpagaus *, Matthias Berthold, Michael Uhlmann, Ralph Kuster, Mick Eschmann, Stefan Bertsch

Eastern Switzerland University of Applied Sciences, Institute for Energy Systems (IES), Werdenbergstrasse 4, CH-9471 Buchs

Abstract

This study summarizes the main findings from field measurements with 14 air-to-water heat pumps (AWHP) and 12 brine-to-water heat pumps (BWHP) in Switzerland. The focus is on heat pump control optimization and possible future performance developments until 2050. The following statements can be derived so far:

- AWHPs with variable-speed compressors are particularly suitable for new buildings with low supply temperatures (e.g., floor heating).
- At a temperature lift of 25 K, AWHPs with inverter technology are 22 % more efficient on average than those with fixed speed. At 40 K, both compressor types operate equally efficiently.
- For retrofits and higher supply temperatures, BWHPs are preferable due to their higher efficiency and more stable source temperature. However, proper sizing, integration, and parameterization are key to the efficient and durable operation.
- AWHPs currently achieve a measured Seasonal Performance Factor (SPF) of 3.5 in new single-family houses (combined heating and hot water mode), while BWHPs achieve an SPF of 4.9.
- In an average-case scenario (new house, 30 °C to 35 °C floor heating, 60 % Carnot efficiency), SPFs of 6.3 and 7.9 are reachable by 2050.

© HPC2023.
Selection and/or peer-review under the responsibility of the organizers of the 14th IEA Heat Pump Conference 2023.

Keywords: field measurements; domestic heat pumps; air-to-water heat pumps; brine-to-water heat pumps; efficiency; optimization

1. Introduction

Heat pumps (HP) for heating and hot water production are on the rise in Swiss households. In 2021, 33,704 units were sold, corresponding to a growth rate of 20 % compared to 2020 (28,064 units) [1]. About 56 % of the HPs fall in the heating capacity range between 5 and 13 kW and over 86 % below 20 kW. Furthermore, 73 % are air-to-water heat pumps (AWHP), 25.6 % are brine-to-water heat pumps (BWHP), and 1.4 % are groundwater-to-water heat pumps (GWHP).

At the same time, estimating the field performance of such HP systems is becoming increasingly important, as the efficiency responds to their integration into the heating system and the settings of the HP control. Therefore, the Heat Pump Test Center (WPZ) and the Institute for Energy Systems (IES) at the Eastern Switzerland University of Applied Sciences in Buchs (SG) have been conducting field measurements of HPs on behalf of EnergieSchweiz since 2015.

The main objectives of the field measurements are to investigate the real performance of HP systems and identify the systems' optimization potential, which can then be implemented. Typically, five new HPs are included in the measurement series every year.

Until 2020, the field measurement campaign included mainly new HP systems installed in single-family houses (new buildings or renovations). However, from 2021 on, HP systems in multi-family homes with a heating capacity of approximately 20 to 30 kW have been included. Before on-site installation, the HPs are

* Corresponding author. Tel.: +41 58 257 34 94
E-mail address: cordin.arpagaus@ost.ch

evaluated in the laboratory at the Heat Pump Test Center (WPZ), and the measuring equipment (e.g., PT-100 sensors with four-wire technology and flow sensors) are calibrated [2], [3].

Compared to former field studies in the 1990s and early 2000s like FAWA (Field Analysis of Heat Pump Installations) [4], the measurement methodology and data acquisition technology have changed considerably. Thanks to digitalization, much more data is available and can be monitored. In addition, precise and automated measuring equipment and high sampling rates of 10 Hz enable meaningful measurement data. Between 30 and 40 sensors are installed in each HP system, and mean values are stored every 10 s. The goal is an overall uncertainty of the target values (e.g., COP, SPF, etc.) of <10 % [3], [5].

The most important results of the field measurements are published in the annual reports of EnergieSchweiz. In addition, many of the results are also presented in Swiss technical journals for planners and installers so that new findings can be implemented directly. The reports and publications are publicly available for download on the website [6] of the University of Applied Sciences Eastern Switzerland.

Moreover, the results from the field monitoring study from 2015 to 2019 have already been presented at the 13th IEA Heat Pump Conference 2020 [3] and the Purdue Conferences 2021 [5], [7], and 2022 [8]. The results clearly show the expected dependence of the seasonal performance factor (SPF) on the supply temperature (T_{supply}) and the selected heat source (e.g., air and brine) [8].

AWHPs in new buildings achieved an average SPF of 3.7 with floor heating (35 °C), while BWHPs had an average SPF of 5.7 [7]. At higher supply temperatures, such as about 50 °C in old buildings with radiator heating, average SPF values of about 2.9 for AWHPs and 4.4 for BWHPs were measured (see Table 1). Combined heating and hot water production systems showed 3 % to 9 % lower SPF due to increased supply temperatures. Typical optimization measures identified were adjusting the heating curve and the heating limit, legionella routines, increasing the charging time at midday for AWHPs and preheating the hot water with the compressor before starting the legionella program with an auxiliary heater. BWHPs were recommended for refurbished buildings.

As of August 2022, 26 HP systems are included in the field measurements campaign. This comprises 14 AWHPs, 9 of which are speed-controlled, and 12 BWHPs with 7 speed-controlled models. In 4 installations, hot water is heated with a separate domestic hot water heat pump (DHWHP). Cooling mode is activated at 6 objects. Meanwhile, up to 6 heating periods, i.e., 2016/17, 2017/18, 2018/19, 2019/20, 2020/21, and 2021/22, can be evaluated per system [9].

So far, the monitoring results have shown that most HP systems are efficient and run robustly. Severe deficiencies were found only rarely. However, the greatest optimization potential was identified in the HP control systems. Therefore, this paper summarizes important findings concerning the optimization of the controller settings.

2. System boundaries and key performance indicators

For the characterization of HP systems in the field monitoring study, EnergieSchweiz has defined different system boundaries and key performance indicators [2], [10]. Figure 1 shows an example of a BWHP with direct heating and domestic hot water storage.

The system boundaries are drawn not only in terms of sensor position but also in terms of time. In addition, a distinction is made between the operating modes “heating,” “hot water charging,” and “cooling.” The electrical standby power consumption (standby here means compressor standstill and no cooling operation) is assigned to the "space heating (SH)" or "domestic hot water charging (DHW)" operation, depending on the position of the three-way valve.

The seasonal performance factor (SPF^+) (Eq. 1) is the key indicator for the efficiency of the HP unit. Only the electrical energy of the compressor, fan (for AWHPs), source pump (for BWHPs), and control electronics of the HP are considered in this indicator. In contrast to the COP^+, the SPF^+ value also includes the energy demand of the source circulation pump ($E_{CP,source}$) for BWHPs.

The heat utilization ratio (HUR) (Eq. 2) also includes the electrical energies of the sink circulating pump ($E_{CP,sink}$) and all electrical auxiliary heaters ($E_{ext,HE}$). In this way, the efficiency of the entire heat generation, including the electricity consumption for the distribution system, is considered and thus made comparable to other heating systems.

Finally, the system utilization ratio of domestic hot water (SUR_{DHW}) (Eq. 3) defines the efficiency of the overall hot water generation concerning the used domestic hot water from the storage tank outlet. It includes all storage and distribution losses. A smaller DHW demand generally leads to lower energy demand and efficiency since the losses are more significant. In addition, the SUR_{DHW} can also be determined for DHWHPs, allowing comparison with DHW charging of combined HPs.

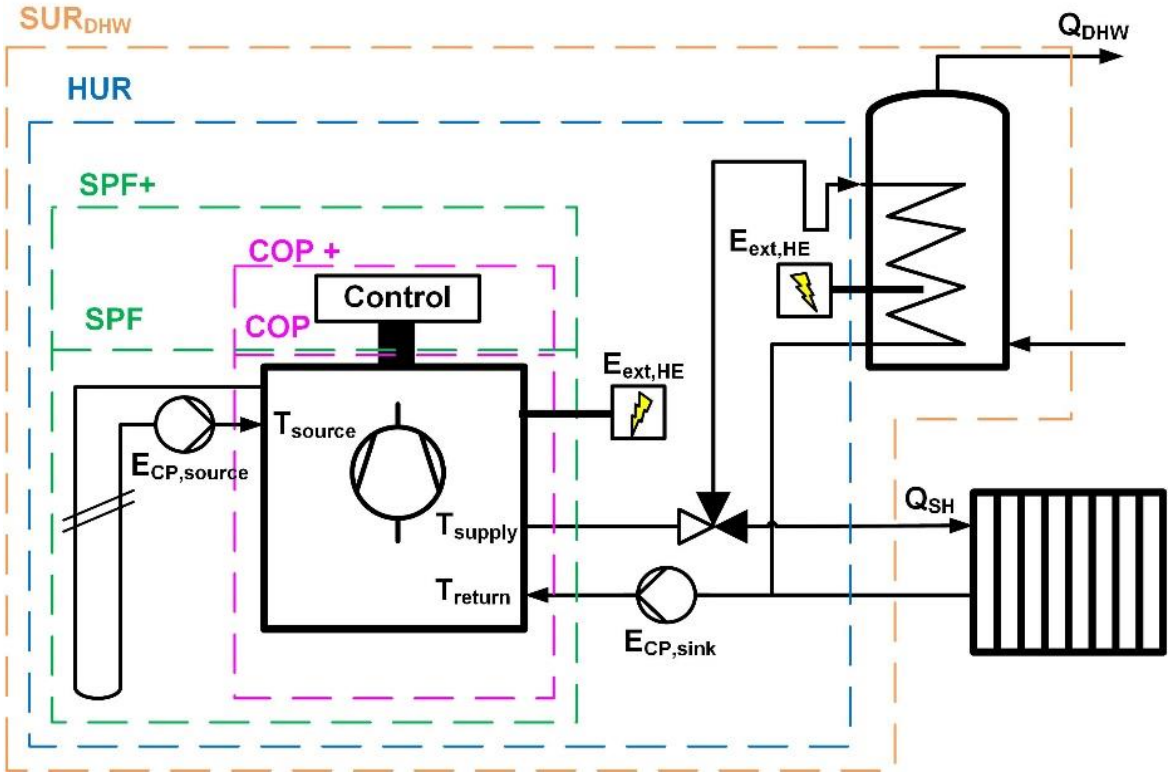


Fig 1. System boundaries and key performance indicators (SUR, HUR, SPF, COP) of a brine-to-water heat pump with a direct heating circuit and domestic hot water heating with a storage tank (Definitions based on EnergieSchweiz [2], [10]).

The total electrical energy requirements for the entire HP system, commonly referred to as electricity consumption, are summarized in the value E_{tot}. Notably, only the performance indicators SPF^{+}, SPF^{+}_{SH}, SPF^{+}_{DHW}, and SUR^{+}_{DHW} do not include standby losses since the electrical energies are only considered during active compressor operation. On average, the share of electrical standby losses is 2 % to 3 % of the total annual electrical energy demand [9].

The specific DHW heat requirement (HR_{DHW}) (Eq. 4) and the total heat requirement (THR) (Eq. 5) refer to the energy reference area of the building (ERA) for better comparability of different building sizes. For the evaluation of the specific heating and electrical energy demand (Q_{HD} and E_{HD}) (Eq. 6 and Eq. 7), the required charging energy (Q_{SH} and E_{SH}) is related to the ERA.

The heating degree days (HGT) reflect the weather influence of a period (month or heating season) and/or location. A heating limit temperature of 12 °C and an indoor target temperature of 20 °C are used for new buildings ($HGT_{20,12}$). For renovated buildings, the heating limit is usually set at 16 °C ($HGT_{20,16}$). Heating degree days are only counted if the average daily temperature is lower than the heating limit [9]. Finally, the HGT results from the difference between the average daily temperature and 20 °C.

To sum up, the following formulas and parameters are used for data evaluation of the field measurements:

$$SPF^{+} = \frac{Q_{SH}+Q_{DHW}}{E_{tot}-E_{CP,Sink}-E_{ext,HE}} \quad (1) \qquad HUR = \frac{Q_{SH}+Q_{DHW}}{E_{tot}} \quad (2) \qquad SUR_{DHW} = \frac{Q_{DHW}}{E_{DHW}+E_{ext,HE}} \quad (3)$$

$$HR_{DHW} = \frac{Q_{DHW}}{ERA} \quad (4) \qquad THR = \frac{Q_{SH}+Q_{DHW}}{ERA} \quad (5) \qquad Q_{HD} = \frac{Q_{SH}}{ERA} \quad (6)$$

$$E_{HD} = \frac{E_{SH}}{ERA} \quad (7) \qquad ER_{DHW} = \frac{E_{DHW}}{ERA} \quad (8)$$

with
SPF Seasonal performance factor [-]
HUR Heat utilization ratio [-]
SUR_{DHW} System utilization ratio of domestic hot water [-]
Q_{SH} Thermal energy requirement for space heating (SH) [kWh]

Q_{DHW}	Thermal energy requirement for DHW [kWh]
E_{tot}	Electrical energy input of the entire HP system [kWh]
$E_{CP,sink}$	Electrical energy of the circulating pump at the heat sink [kWh]
$E_{ext,HE}$	Electrical energy of the external heating elements [kWh]
E_{SH}	Electrical energy of the HP in SH operation [kWh]
E_{DHW}	Electrical energy of the HP in DHW operation [kWh]
E_{HD}	Specific electrical energy demand in heating operation[kWhel/m²]
Q_{HD}	Specific heating demand [kWh/m²]
HR_{DHW}	Specific DHW heat requirement [kWh/m²]
ER_{DHW}	Specific electrical energy requirement in DHW operation [kWh/m²]
THR	Total specific heat requirement (SH and DHW) [kWh/m²]
ERA	Energy reference area of the building [m²]
$HGT_{20,12}$ or $HGT_{20,16}$	Heating degree days [°C] with a heating limit of 12 °C (new house) or 16°C (renovation) and room temperature of 20 °C

3. Results

3.1. Effects of control optimization measures of a HP in a renovated building

This section presents some control optimization measures in a renovated single-family house from 1975 with inverter-regulated AWHP (Object No. 24 in the field study) [9]. Based on the evaluation of the heating season HS 2020/21 in the field monitoring study, some optimization measures could be implemented for the 2021/22 heating season. Data evaluation enables a direct performance comparison of the two heating seasons. The effects of control optimization on the HP system performance were as follows:

- **Speed reduction of the heat sink circulation pump:** The speed was reduced by approx. 10 % resulting in a decrease in the average pump power from 30.4 to 17.3 W. The running time decreased by 4 %, and the annual energy consumption of the pump reduced by 45 % (from 78.1 to 42.7 kWh/a).
- **Speed reduction of the compressor:** The compressor's minimum speed was reduced, lowering the minimum compressor power consumption from 4 to 2 kW. This increased the compressor's control range, and the compressor's annual operating hours increased by 2.5 % to 2,374 hours, although the total specific heat requirement (THR) decreased by 9 % to 66.3 MWh.
- **Reduction of the maximum heating capacity in the DHW mode:** The maximum thermal load in the DHW mode has been reduced from 8 to 6 kW to allow lower supply temperatures during storage tank charging and thus improve efficiency. Figure 2 (A) shows that the average supply temperature in DHW mode ($T_{supply,DHW}$) decreased from 51.4 °C in the heating season HS 2020/21 to 49.0 °C in HS 2021/22. At the same time, the specific DHW heat requirement (HR_{DHW}) decreased to 87 %, while the demand for electrical energy for DHW heating (ER_{DHW}) decreased to 61 % compared to the previous year (Figure 2, B).
- **Reduction of the heating curve and temperature rise in the buffer tank:** The temperature rise in the buffer tank was reduced in HS 2021/22, and thus the supply temperature in heating mode. Figure 2 (C) shows that the adjusted heating curve in HS 2021/22 is approx. 7 K lower than in HS 2020/21. The mean value of the supply temperature in heating mode ($T_{supply,SH}$) reduced from 45.0 °C to 37.8 °C (Figure 2, A). The heat source temperatures remained constant. There was no loss of comfort identified.

Figure 2 (B) compares the changes in the heating degree days and the thermal and electrical energy requirements. The heating degree days ($HGT_{20,16}$) decreased by 7 %, and the specific heating demand (Q_{HD}) by 8 %. However, the specific electrical energy demand in heating mode (E_{HD}) decreased by 31 %, which is attributed to higher efficiency (Figure 2, D) resulting from the mentioned improvements. The efficiencies increased in the heating and DHW operating modes. The SPF^{+}, *HUR*, and SPF_{SH}^{+} parameters increased by about 37 % (e.g., from 2.2 to 3.1), while the SPF_{DHW}^{+} and HUR_{DHW} increased by 42 %, and SUR_{DHW}^{+} even doubled (from 0.6 to 1.2). In DHW operation, the thermal energy demand (HR_{DHW}) decreased by 13 %, and electrical energy demand (ER_{DHW}) by 39 %.

Overall, the example of Object No. 24 shows that relatively simple control optimization measures can significantly impact the performance of an AWHP system.

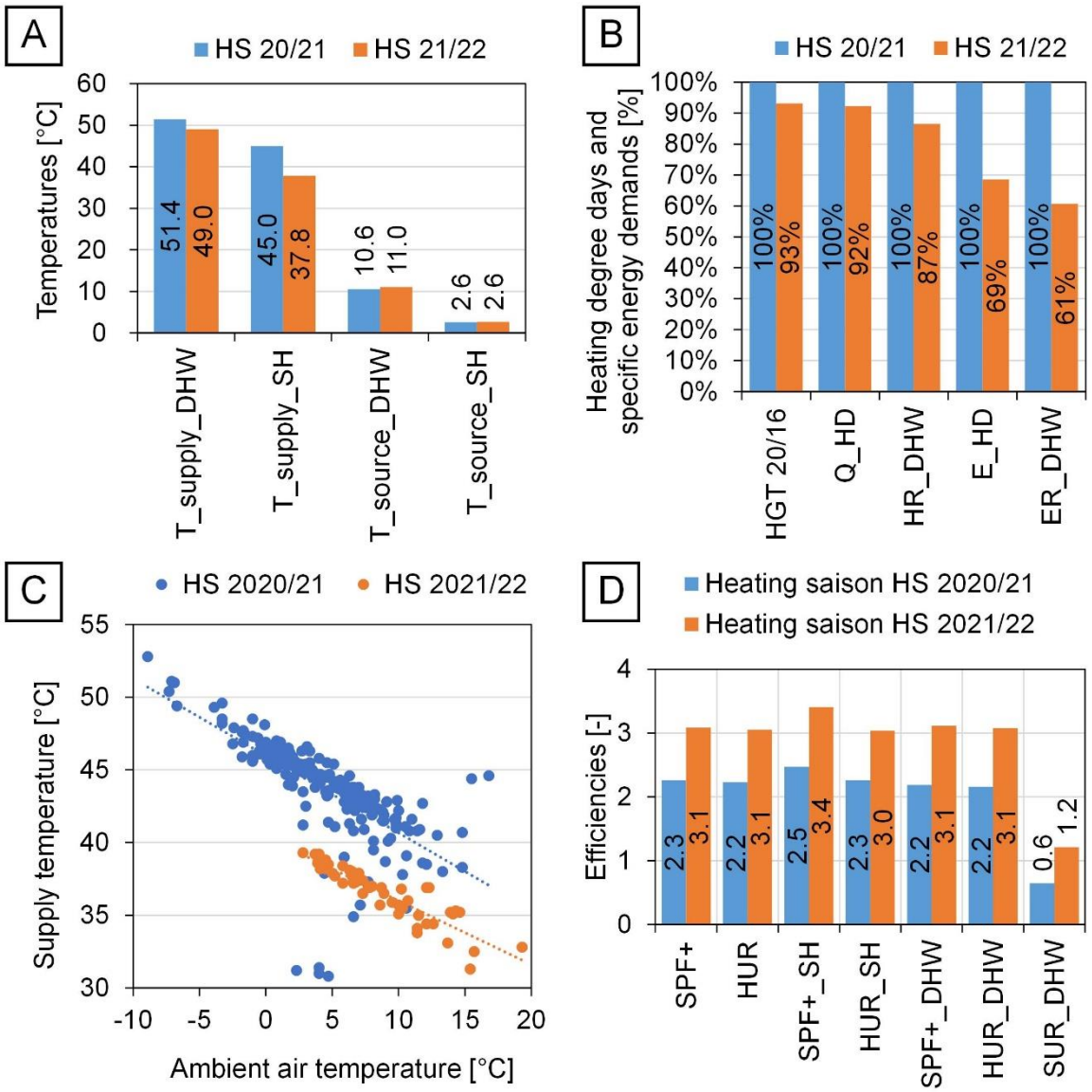


Fig. 2. Comparison of two heating seasons, HS 2020/21 and HS 2021/22, in a renovated single-family house from 1975 (Object No. 24 equipped with an inverter-regulated AWHP [9]) after control optimization on the HP. (A) Change of the supply and source temperatures in heating and DHW mode, (B) Comparison of the heating degree days and the specific thermal and electrical demands in heating and DHW mode (thermal demand decreased by 8 %, electrical demand decreased by 31 %), (C) Adjusted heating curve in HS 2021/22 (approx. 7 K lower supply temperature) compared to HS 2020/21 after a reduction of the temperature rise in the buffer tank, (D) Comparison of the efficiencies in heating, DHW, and combined operating modes for the heating seasons HS 2020/21 and HS 2021/22 (Data source: [9]).

3.2. Shifting the DHW charging operation to time windows with high outdoor air temperatures for AWHPs

As a next example, Figure 3 (A and B) compares the DHW charging characteristics of two renovated single-family houses (Objects No. 11 and No. 15) equipped with AWHPs. The graphs show hourly averaged data from 365 days (9/1/2021 to 9/1/2022) for several parameters over the daytime (00:00 to 24:00).

In Object No. 11 (Figure 3, A), the DHW operation often occurs in the morning between 7:00 to 8:00, accounting for about 48 % of the thermal energy. This time window corresponded to an annual average outdoor air temperature of 10.0 °C, thus the time with the lowest outdoor air temperature. Conversely, the highest outdoor air temperature was 16.6 °C and occurred between 15:00 and 16:00. Therefore, shifting the DHW mode operation to times with higher outdoor air temperatures would significantly increase the overall efficiency of the AWHP system if it does not result in a loss of comfort due to too low tapping temperatures.

As can be seen, in the time window from 11:00 to 12:00, the electrical consumption of the compressor was almost zero due to active power blocking by the local grid operator. Such blocking times are based on the load

profiles of grid utilization and prevent controllable devices like HPs from consuming electricity at peak loads. Thus, blocking time detection can help optimize PV self-consumption or source temperature maximization.

Figure 3 (B) shows an equal representation for Object No. 15 (renovated single-family house with inverter-driven AWHP). Here, the DHW charging operation by the AWHP was concentrated at midday. 88 % of the DHW was generated between 12:00 and 15:00. This means that most of the DHW charging occurred when the outdoor air temperature (or the heat source temperature of the AWHP) was close to its daily maximum. In the selected time frame from 12:00 to 15:00, the average outdoor temperature was 15.7 °C. Ideally, the DHW charging operation would have to occur even two hours later (i.e., from 14:00 to 17:00) to reach the highest possible heat source temperature of 17.2 °C. In this context, the summertime changeover must also be considered. A one-hour shift results from the change of the clock to summertime. Another time shift results from later daily maximum temperatures in summer.

To sum up, the analysis of the HP operation over the day of Objects No. 11 and No. 15 showed that the DHW heating demand is virtually identical (273 W thermal power on average). However, Object No. 11. required more than twice the electrical compressor power (693 W vs. 299 W on average) and heating power (1'997 W vs. 999 W) due to operation in the early morning at the lowest outdoor air temperatures. Therefore, the timing of DHW charging after noon, between 13:00 and 15:00, is crucial for the high efficiency of the AWHP system and can be set in the HP controller settings. As a rule of thumb, a 10 °C higher source temperature results in 25 % higher HP efficiency.

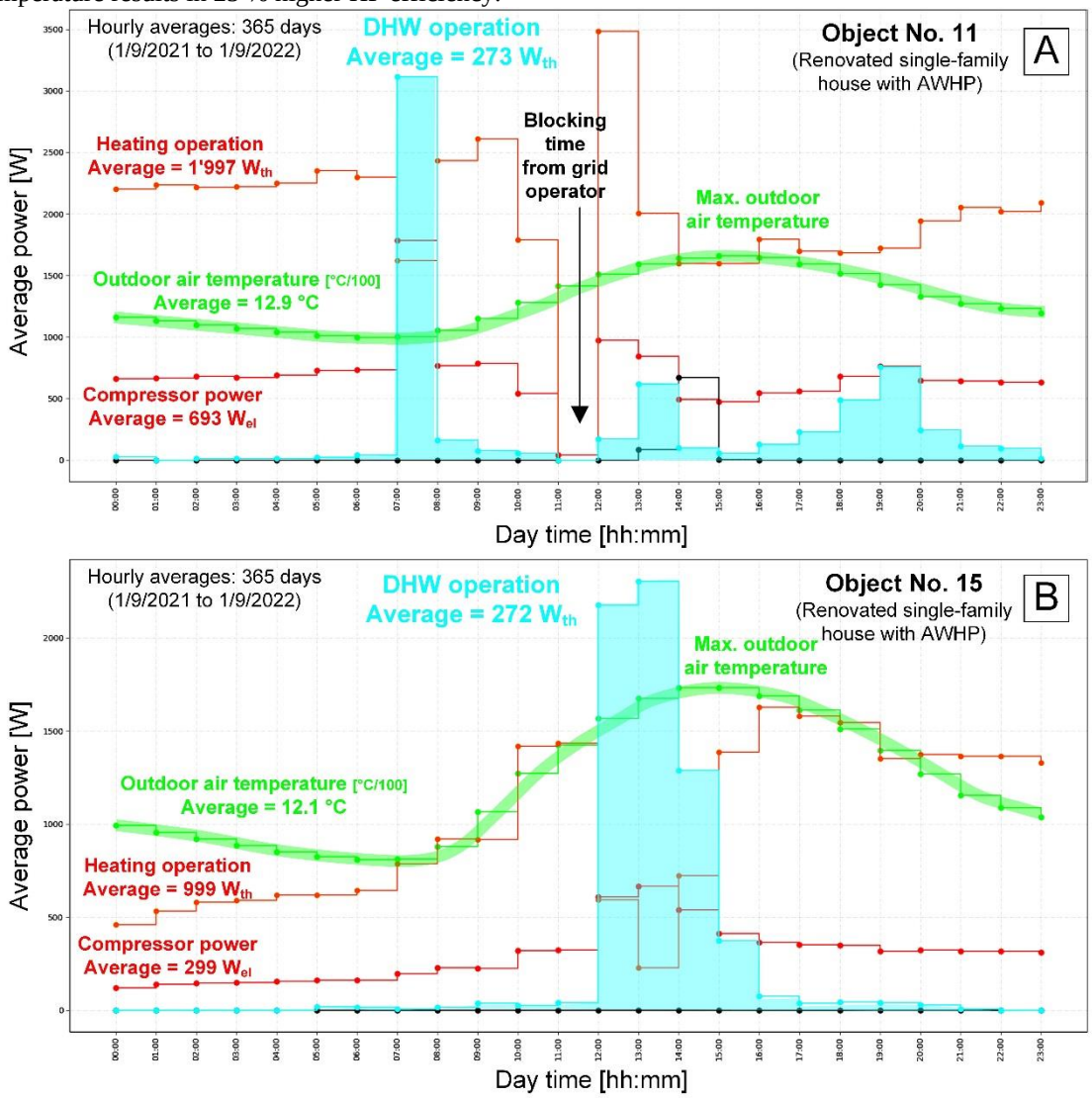


Fig. 3. (A) DHW operation at Object No. 11 occurs predominantly between 7:00 and 8:00 when the outdoor air temperature is low. The highest outdoor air temperatures are measured between 15:00 and 16:00. Between 11:00 and 12:00, blocking times of the electrical grid operator are active. (B) DHW operation at Object No. 15 is shifted to high outdoor air temperatures between 12:00 to 16:00. The operating window could even be moved to 14:00 to 17:00 to profit from the highest outdoor air temperature of 17.2 °C.

3.3. Comparison of fixed speed (on/off) and variable speed (inverter-driven) HPs

Inverter-driven HPs can modulate the compressor speed and thus dynamically adapt the HP performance to the required heating or DHW demand within certain limits. In contrast, the compressor speed is constant in conventional on/off HPs. In the following, some results of inverter-driven and on/off HPs are compared, and topics such as performance, sizing, running time (e.g., the compressor starts, cycling), and standby losses are discussed [8], [9].

Figure 4 shows the seasonal performance factor of 8 variable-speed and 4 fixed-speed AWHPs in heating mode (SPF_{SH}) as a function of the temperature lift between source and supply temperature (outdoor air temperature range between 0 and 10 °C accounts for >70 % of the annual heat demand). Each point represents a daily average. The Carnot efficiency of 30 % and 50 % is also plotted for orientation. Likewise, power function trendlines are added for each compressor group.

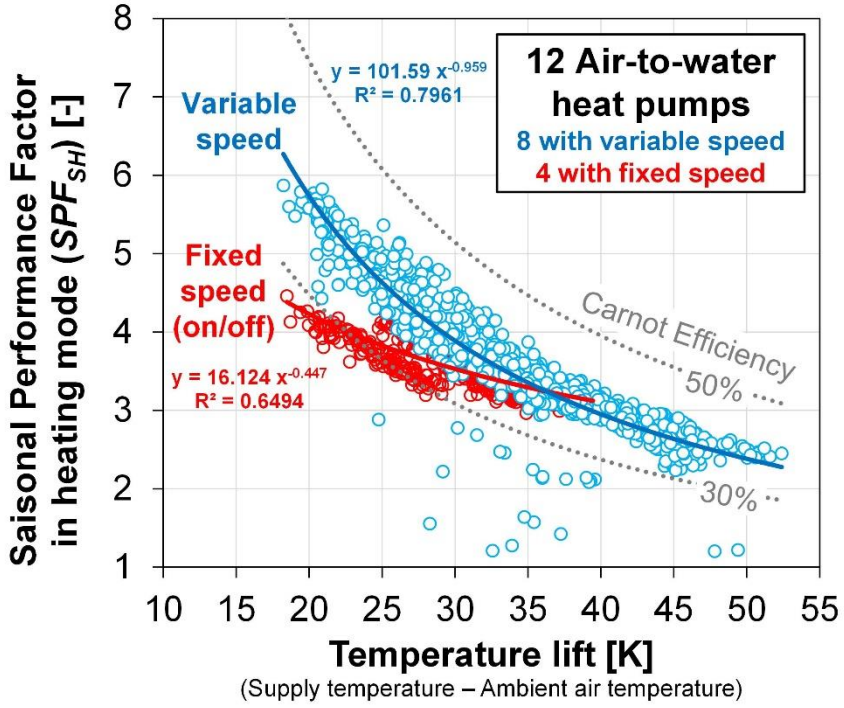


Fig. 4. Comparison of the seasonal performance factor of variable speed and fixed speed (on/off) AWHPs in heating mode as a function of the temperature lift between supply temperature and ambient air temperature as the heat source (ranging from 0 to 10 °C). Each point is a daily average (Data source: [8], [9]).

The evaluation shows that the Carnot efficiency of the variable-speed AWHPs was about 40 % over the entire temperature range. At a temperature lift of 25 K, the examined AWHPs with inverter (SPF_{SH} 4.67, variable speed) were on average 22 % more efficient than those with fixed speed (SPF_{SH} 3.85) [8]. Both compressor types achieved similar Carnot efficiencies for larger temperature lifts of about 40 K. However, the smaller the temperature lift, the lower the efficiency of the on/off HPs. At small temperature lifts, the Carnot efficiency also decreased below 30 %. A major reason is that fixed-speed HPs switch on and off much more frequently than variable-speed AWHPs. In addition, the temperature differences inside the heat exchangers of the HP are smaller with a variable speed compressor in part-load operation. Furthermore, the type of compressor used can also influence efficiency. For example, variable-speed rotary piston compressors usually work more efficiently at small temperature lifts than scroll compressors with fixed speeds [11]. In conclusion, variable speed AWHPs are especially suited for new residential buildings with low supply temperatures, e.g., 30 °C to 35 °C for floor heating.

However, the measured data for the heating season HS 2021/22 also revealed that the potential of inverter-driven HPs is not always fully exploited. Figure 5 shows that not all variable speed HPs have a significantly longer running time per start (red dots on the secondary axis). On average, the evaluated AWHPs with inverters had about 4 times more running time per start than on/off units (2 hours per start vs. 0.5 hours per start). For BWHPs, the average running time per start of inverter HPs was even 9 times higher than for on/off units (6.5 hours per start vs. 0.7 hours per start).

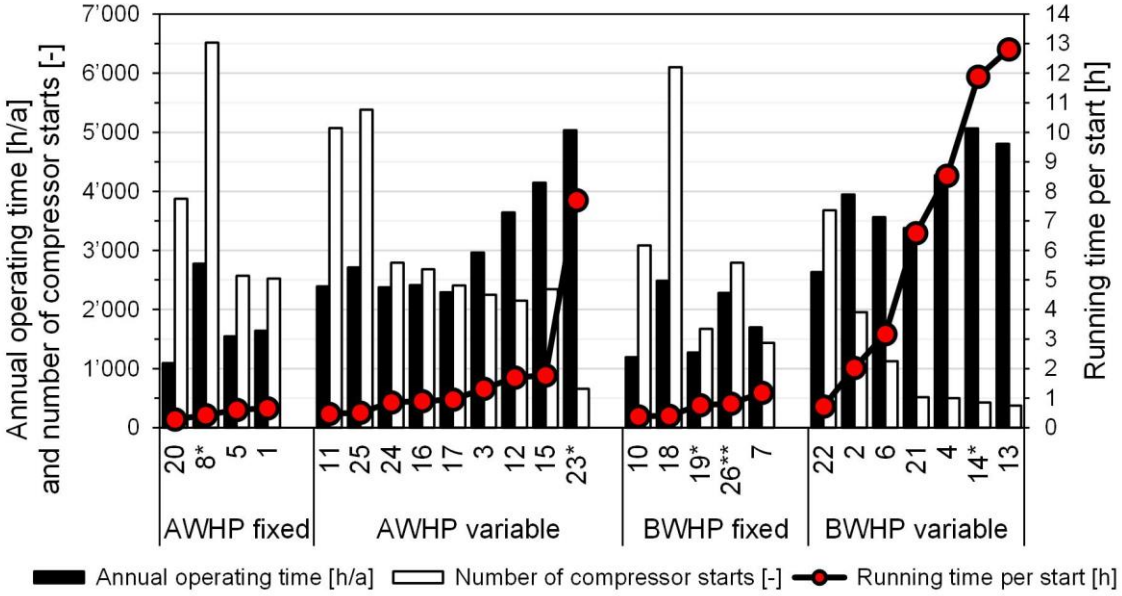


Fig. 5. Annual operating time, number of compressor starts, and running time per start of different fixed speed and variable speed AWHPs and BWHPs in HS 2021/2022, *Objects with separate DHWHP. **2 HPs with 4 parallel compressors (Data source: [9]).

The annual operating times differed considerably in some cases. For example, on average, speed-controlled inverter AWHPs had 1.7 times the operating times of on/off units. The difference was even greater for BWHPs. Here, the inverter machines had, on average, even 2.2 times longer operating hours.

For both AWHPs and BWHPs studied, one inverter system (Objects No. 23 and 14) ran for over 5,000 operating hours in the HS 2021/22. The average running time of the corresponding AWHP was 7.7 hours per start, and that of the BWHP was 11.9 hours per start. Even with optimal design, inverter-driven BWHPs achieved a higher average running time as the power control range depends essentially on the heat source temperature, which varied considerably more for AWHPs than for BWHPs.

In conclusion, the following general recommendations can be made for inverter-driven HPs:

- **Design:** Inverter-driven HPs should be well-matched to the heat demand of the building. Oversizing leads to a limitation of the control range due to the minimum HP capacity. Then, continuous operation of AWHPs is only possible at relatively low outdoor temperatures to deliver the minimum capacity to the building. If the heating demand is lower, an inverter-driven HP must also switch to cycle operation. Therefore, the advantages over an on/off HP are no longer given in these time ranges.
- **Start-up:** Good and solid commissioning is especially important for inverter-driven HPs. Software parameters such as the heating curve, heating limit, legionella activation, etc., must be determined and correctly set.
- **HP manufacturer:** There is potential to increase the efficiency of inverter-driven HPs. Some inverter-driven HPs have high standby losses in combination with long downtimes. In DHW operating mode, attention should be paid to low compressor speeds, as these lead to lower temperature differences in the hot water heat exchanger and thus increase the COP. In many cases, DHW generation is performed at a constant high speed because the main focus is likely to be on a short charging time and less on efficiency.

In addition to significant differences in operating behavior and efficiency, there were also revealing differences in standby losses between fixed-speed and variable-speed HPs. In general, standby losses are the energy that occurs during a HP standstill, i.e., when the compressor, including the auxiliary heater, is not in operation. The main causes of standby losses are the control system, an oil sump heater, and, in the case of inverter-driven HPs, the inverter. In the field monitoring study, these standby losses vary considerably depending on the object.

Figure 6 shows the average standby powers and the resulting annual standby losses grouped by 8 on/off and 16 speed-controlled HPs examined in the field monitoring study. The highest standby losses were found in some inverter-driven HPs. However, others with low standby losses indicate that high standby losses in

inverter-driven HPs were not system related. The average standby power for the measured on/off HPs was 12 W, while the mean value of the inverter-driven HPs was 27 W and, thus, 2.3 times higher. On average, the five HPs with the highest standby losses (all with speed-controlled compressors) consumed 49 W.

Depending on the object, the electrical standby losses ranged between 0.5 % and 10 % of the total annual electrical demand. Across all HPs, the standby losses accounted for 2 % of the total annual electrical energy demand. For some inverter-driven HPs, there is still a relatively high potential for optimization, as a comparison with the "best" systems shows.

Qualitatively, the annual standby losses (secondary axis of Figure 6) showed a similar picture as the average standby power. However, the standby energy depends on the respective running or standby time, which is influenced by many factors, including the HP design (e.g., dimensioning of the heating capacity), the hydraulic integration, parametrization, and the actual user behavior (e.g., selected room temperature or DHW demand). For example, this effect can be seen in the comparison of Objects No. 2 and No. 24, whose average standby power was almost identical. However, the annual standby losses of No. 24 were about 29 % higher than those of No. 2. Thus, lower standby power does not necessarily mean lower standby losses [8], [9].

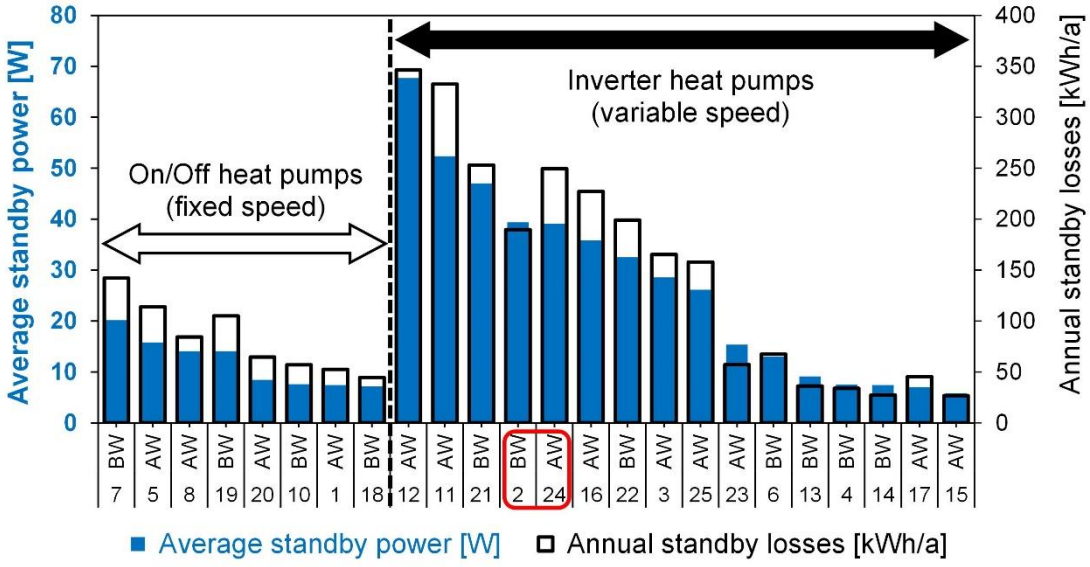


Fig. 6. Average standby power and annual standby losses of 8 fixed-speed on/off HPs and 16 speed-controlled inverter-driven HPs examined in the field study, sorted by decreasing standby power (Data source: [8], [9]).

In summary, comparing variable speed HPs with conventional on/off HPs shows a clear difference in efficiency and control strategies. Furthermore, standstill losses were much higher with an inverter because the HP control and frequency converter were always running. On the other hand, fixed-speed systems started up more frequently than variable-speed systems. The average running time of variable-speed compressors was more than twice that of fixed-speed systems. This indicates that many variable-speed compressors run at a more optimal operating point than units without capacity control, even though they tend to be oversized and often not optimally parameterized.

3.4. Seasonal performance factor for AWHPs and BWHPs by 2050

Table 1 summarizes the average *SPFs* of AWHPs and BWHPs in heating (*SH*), *DHW*, and combined (*SH+DHW*) mode based on 2018 field measurement data and provides an outlook for future development until 2050 for an average scenario with 60 % Carnot efficiency [12]. For the forecast, the considered efficiency strongly depends on the supply temperature of the building category (30 to 35 °C assumed for a new building, 40 to 45 °C for renovation, and 50 to 55 °C for old buildings). AWHPs currently achieve a measured SPF_{SH+DHW} of 3.5 in new single-family houses, while BWHPs achieve an SPF_{SH+DHW} of 4.9. Assuming the average-case scenario, SPF_{SH+DHW} values of 6.3 and 7.9 appear reachable by 2050, corresponding to a significant efficiency increase compared to today [12]. However, a prerequisite is that the economic and political framework conditions are set in such a way that further development of HP technology by the manufacturers takes place.

The difference in efficiency between AWHPs and BWHPs is most evident in the low supply temperature range, where the higher heat source temperatures have relatively more influence. In contrast, the difference in efficiency is smaller for old buildings because much running time of the AWHPs is at high outdoor temperatures. Nevertheless, field measurements show that BWHPs with higher supply temperatures perform better than those in the low-temperature range. Furthermore, BWHPs benefit from a stable geothermal heat source and have an average source temperature (7.9 °C) that is about 4 K higher than AWHPs (3.8 °C) [9].

Table 1. Seasonal performance factor (SPF) of AWHPs and BWHPs in heating (SH), hot water (DHW), and combined mode (SH+DHW) in 2018 and for an average future scenario in 2050 with 60 % Carnot efficiency (Data source: [12]).

Heat pump type	2018			2050 (Carnot efficiency 60 %)		
	SPF_{SH}	SPF_{DHW}	SPF_{SH+DHW}	SPF_{SH}	SPF_{DHW}	SPF_{SH+DHW}
New building: 35 to 30 °C (supply temperature at design point)						
AWHP	3.7	2.8	**3.5**	**6.5**	**4.9**	**6.3**
BWHP	5.7	3.2	**4.9**	**8.4**	**4.7**	**7.9**
Renovation: 45 to 40 °C						
AWHP	3.3	2.8	3.1	**5.2**	**4.9**	**5.1**
BWHP	5.0	3.2	4.6	**6.6**	**4.7**	**6.0**
Old building: 55 to 50 °C						
AWHP	2.9	2.8	2.8	**4.6**	**4.9**	**4.5**
BWHP	4.4	3.2	4.3	**4.9**	**4.7**	**4.8**

4. Conclusions

AWHPs with variable speed compressors are well suited as a heating system for the conditions in Switzerland, especially for new residential buildings with low supply temperatures (e.g., floor heating). Due to the low heat demand in new buildings, AWHPs are usually the most economical and frequently chosen HP type. On the other hand, BWHPs are preferred in renovations due to the higher supply temperatures and heating capacities. However, correct dimensioning, integration, and parameterization are key to the efficient and long-lasting operation of all heat pump types.

Regarding efficiency, the analyzed AWHPs with variable speed compressors perform better on average than fixed speed models at a temperature lift below 40 K. At around 25 K temperature lift, the advantage of inverter-driven AWHPs is approximately 22 % in the SPF. However, in standby mode, inverter-driven HPs revealed considerable standby losses, which, combined with the low compressor running time, can significantly decrease system efficiency. The annual standby losses can vary between 25 kWh/a and 350 kWh/a depending on the system (factor of 14!).

Although good HP efficiencies are already achieved in the field, these can be increased by simple tricks in the controller settings. The greatest potential for optimization was identified on the HP control side. Recommendations are:

- Optimization of the supply temperature (i.e., settings of the heating curve and heating limit, 1 °C lower supply temperature corresponds roughly to 2.5 % efficiency gain)
- Optimizations in the control of the heat sink pump and the compressor speed
- Timing of DHW operation for AWHPs in the early afternoon (e.g., 13:00 to 15:00), as outdoor temperatures are higher than in the early morning hours (activation of summer function if available).

Assuming an average scenario with 60 % Carnot efficiency, SPF values (heating and DHW) of 6.3 for AWHPs and 7.9 for BWHPs seem achievable by 2050 if the economic and political framework conditions are set in a direction favorable for highly efficient HPs. What is needed in the medium term are better control systems for HPs that simplify installation and HPs that optimize themselves according to the heat demands of the building and the customer needs.

Acknowledgments

The results published in this study were funded and obtained in close cooperation with EnergieSchweiz. The content and conclusions of this report are the sole responsibility of the authors.

Nomenclature

AWHP	Air-to-water heat pump	
BWHP	Brine-to-water heat pump (geothermal heat pump system with vertical boreholes)	
COP	Coefficient of performance	[-]
DHW	Domestic hot water	
DHWHP	Domestic hot water heat pump	
E_{Co}	Electrical energy of the heat pump compressor	[kWh]
$E_{CP,Sink}$	Electrical energy of the circulating pump at the heat sink	[kWh]
E_{DHW}	Electrical energy of the heat pump in DHW operation	[kWh]
$E_{ext,HE}$	Electrical energy of the external heating elements	[kWh]
EnergieSchweiz	Federal authority on behalf of the Swiss Federal Office of Energy (SFOE)	
ERA	Energy reference area of the building	[m^2]
E_{tot}	Electrical energy input of the entire heat pump system	[kWh]
FAWA	Field analysis of heat pump installations	
GWHP	Groundwater/water heat pump	
$HGT_{20,12}$	Heating degree days for 20 °C, 12 °C (heating limit) (new building)	[°C]
$HGT_{20,16}$	Heating degree days for 20 °C, 16 °C (heating limit) (renovation)	[°C]
HP	Heat pump	
HS	Heating season	
HUR	Heat utilization ratio according to the definition of SFOE	[-]
IES	Institute for Energy Systems (IES) at OST, Campus Buchs	
OST	Eastern Switzerland University of Applied Sciences	
Q_{DHW}	Thermal energy requirement for DHW	[kWh]
Q_{HD}	Specific heating demand	[kWh/m^2]
Q_{SH}	Thermal energy requirement for space heating (SH)	[kWh]
SH	Space heating	
SPF	Seasonal performance factor according to EnergieSchweiz	[-]
SUR_{DHW}	System utilization ratio according to SFOE	[-]
$T_{source,SH}$	Average source inlet temperature in SH mode of the HP	[°C]
$T_{source,\ DHW}$	Average source inlet temperature in DHW mode of the HP	[°C]
$T_{supply,SH}$	Average supply outlet temperature in SH mode of the HP	[°C]
$T_{supply,\ DHW}$	Average supply outlet temperature in DHW mode of the HP	[°C]
THR	Total specific heat requirement (SH and DHW)	[kWh/m^2]
WPZ	Heat pump test center (in Buchs SG, CH) (in German: Wärmepumpen Test Zentrum)	

References

[1] FWS, “Statistik 2021, Fachvereinigung Wärmepumpen Schweiz,” 2021. https://www.fws.ch/wp-content/uploads/2022/05/FWS-Statistiken-2021-V2.pdf.

[2] C. Arpagaus, M. Berthold, and M. Eschmann, “Report «Messung der Effizienz der Trinkwassererwärmung bei Wärmepumpenanlagen im Feld», Feldmessungen Wärmepumpen-Anlagen 2015-2018, on behalf of EnergieSchweiz,” pp. 1–40, 2018.

[3] R. Kuster, M. Prinzing, M. Berthold, C. Arpagaus, M. Eschmann, and S. S. Bertsch, “Field Performance of Domestic Heat Pumps for Heating and Hot Water in Switzerland,” *13th IEA Heat Pump Conf. May 11-14, 2020, Jeju, Korea*, p. Paper 059, 2020.

[4] M. Erb, P. Hubacher, and M. Ehrbar, “Feldanalyse von Wärmepumpenanlagen FAWA 1996-2003, im Auftrag vom BFE,” 2004, [Online]. Available: https://www.fws.ch/wp-content/uploads/2018/06/FAWA_Auszug_deutsch.pdf.

[5] R. R. Kuster, M. Prinzing, B. Matthias, M. Eschmann, and S. S. Bertsch, “Field Performance Of Domestic Heat Pumps For Heating And Hot Water In Switzerland Part I: Technology, Methods And State Of The Art Of The Field Studies,” *19th Int. Refrig. Air Cond. Conf. Purdue*, p. Paper 2083, 2021, [Online]. Available: https://docs.lib.purdue.edu/iracc/2083.

[6] OST, “OST Website - Wärmepumpen Feldmessungen,” 2022. https://www.ost.ch/de/forschung-und-dienstleistungen/technik/systemtechnik/ies/wpz/waermepumpen-feldmessung.

[7] R. Kuster, M. Prinzing, M. Berthold, M. Eschmann, and S. S. Bertsch, “Field Performance of Domestic Heat Pumps for Heating and Hot Water in Switzerland Part II: Results, Analysis and Optimization,” *19th Int. Refrig. Air Cond. Conf. Purdue*, p. Paper 2084, 2021, [Online]. Available: https://docs.lib.purdue.edu/iracc/2084.

[8] R. Kuster, M. Prinzing, M. Berthold, M. Eschmann, and S. S. Bertsch, “Field Performance of Domestic Heat Pumps for Heating and Hot Water in Switzerland - Insights and Analysis,” *19th Int. Refrig. Air Cond. Conf. Purdue*, p. Paper 2373, 2022, [Online]. Available: https://docs.lib.purdue.edu/iracc/2373.

[9] M. Berthold, M. Uhlmann, S. Bertsch, and M. Eschmann, “Report Feldmessungen von Wärmepumpen-Anlagen Heizsaison 2021/22, Jahresbericht, 2. November 2022, on behalf of EnergieSchweiz,” 2022.

[10] BFE, “Definition von Nutzungsgraden von Wärmepumpen-Anlagen,” 2018.

[11] ASHRAE, “Chapter 38: Compressors,” in *Handbook - HVAC Systems and Equipment*, 2012, pp. 1–38.

[12] M. Prinzing, M. Berthold, and S. Bertsch, “Ausblick auf mögliche Entwicklungen von Wärmepumpen-Anlagen bis 2050, Bericht vom 30. November 2019, im Auftrag vom BFE,” pp. 1–32, 2019, [Online]. Available: https://pubdb.bfe.admin.ch/de/publication/download/9999.

14th IEA Heat Pump Conference
15-18 May 2023, Chicago, Illinois

Multiparametric Analysis of Novel Multilevel Temperature Heat Pumps (LEAP) for Multi-Sink Heating

E.B. Badran[1], M. Yebiyo, C.H. Stignor, M. Axell, O. Gustafssan, M. Willis

RISE, Division of Built Environment, Department of Energy & Resources, Stockholm 114 28, Sweden

Abstract

Industrial sectors are currently seeking ways to decarbonize their processes which rely primarily on fossil fuel boilers. Heat pumps offer high-quality heating that could substitute boilers due to their high coefficient of performance (COP) for moderate temperature lifts. It is proven that the heat pump efficiency deteriorates with increased temperature lifts. This paper examines multilevel heat pumps (LEAP) as an efficient way to produce high and/or variable-level sink temperatures. The LEAP concept operates between 0°C and 160°C with three heating levels at 60°C, 110°C, and 160°C. With a two and three-stage independent layered heat pump system, the sink heat exchanger is divided into two heat exchangers at each stage. One is used to supply the external load requirements, and the other is to cover the source or internal load on the higher consecutive stage cycle. The external load heat exchangers can be connected in series or parallel to control the desired load output temperature. A multi-parameter selection analysis was conducted using EES software to evaluate several natural and synthetic refrigerants with low values of the Global Warming Potential (GWP) index. For different scenarios, selected low GWP refrigerants were investigated based on their thermophysical properties. The multiparametric analysis shows that for each stage a COP of 3.5 was achieved and a total COP of 2.5 can be obtained for the LEAP concept. This is equivalent to an increase of about 40 % more than a single heat pump can provide. The best synthetic refrigerants were R-1234ze (Z), R-1224yd (Z), R-1233zd (E), and R1366mzz (Z). On the other hand, the best natural refrigerants were R-600 (n-Butane), R-600a (Isobutane), R-601 (n-Pentane), and R-601a (Isopentane).

© HPC2023.
Selection and/or peer-review under the responsibility of the organizers of the 14th IEA Heat Pump Conference 2023.

Keywords: Hydrocarbon; Synthetic refrigerants;Natural refrigerants, low GWP; Hydrofluooroolefin (HFO); multi-stage; cascade

1. Introduction

Decarbonization of commercial and industrial processes is a requirement for a sustainable future. There is a great interest in increasing the use of waste heat, making efficient use of thermal energy and replacing fossil fuel boilers with other cleaner technologies. Heat pump systems are considered a greener alternative to fossil fuel boilers because electricity with a high share of renewable sources can power the system. Moreover, in the absence of waste heat sink sources, the heat must be extracted from near ambient temperatures. This would lead to higher temperature difference between both heat source and heat sink reservoirs, therefore; penalizes the system's energy performance and decreasing its environmental benefits.

Multilevel heat pump applications are scarce [1]. The most common solution for increasing energy performance in high-temperature lift applications is using multilevel vapor compression configurations. The LEAP concept, with the multi-layered configuration, offers flexibility in the operation and adaptation to the application. The potential of two-stage heat pump cycles compared to single-stage has been evaluated in terms of energy performance and heating capacity [2]. A two-stage cascade system has been investigated with appropriate configurations for 60 K and 80 K temperature lifts compared to other technologies, such as ejector or parallel compression. In each stage, efforts are mainly devoted to its optimization in terms of intermediate

[1] Corresponding author. *Email address:* bassam.badran@ri.se

temperature and refrigerants [3]. The use of natural refrigerants Butane (R-600) and Isobutane (R-600a), respectively, in a cascade system appeared to be the most viable working fluids in terms of COP for the low-temperature circuit, while R-601a (n-Pentane) and R-1336mzz (Z) were the most promising for the high-temperature stage [4]. Uusitalo et al. studied combinations of refrigerants and concluded that the temperature level in the cascade heat exchanger has a significant effect on the COP [5]. Wang et al. explored the applicability of an auto-cascade heat pump for heating in cold climates. The research found that R-134a / R-600 with a mass ratio of 0.8/0.2 could get a COP of 2.15 [6]. Yu et al. presented a novel auto-cascade heat pump for electric vehicles. Theoretical analysis indicated that the proposed system with CO_2/R-290 improved the COP by 12.3 % compared to a single-stage compression system using CO_2 [7]. Chen et al. proposed a novel vapor injection auto-cascade heat pump for high–temperature water heating, which introduced the liquid branch after the partial condensation into the injection port through a cascade internal heat exchanger based on the conventional auto-cascade cycle [8]. A most recent study investigated a three-stage cascade for very low-temperature refrigeration [9]. They studied different operating, energetic, and exergetic parameters and obtained the most suitable refrigerant combination. They found that this system has an optimum condensation temperature for each intermediate temperature.

R-134a and R-245fa refrigerants will be used as a base reference to select an appropriate refrigerant for each stage since they will be replaced in the upcoming years to prevent the usage of hydrofluorocarbons with high GWP. Dawo et al. investigated and showed that three low GWP refrigerants could replace R-245fa at a constant heat source temperature of 120°C with small variations in efficiency and heating output [10].

Several literature studies show that most multi-layered heat pumps only consider a two-stage system. They do not use the intermediate levels to satisfy other heating consumptions. This paper presents a multiparametric analysis of multilevel temperature heat pumps (LEAP) to obtain multilevel sink temperatures for variable heating applications.

2. LEAP configuration with multilevel sink temperatures.

The multi-layered heat pump concept is used to overcome the problems of decreasing compressor efficiencies and power consumption due to high-temperature lifts and give the user the freedom to choose the required sink temperature for different applications. To reach high-temperature outputs from a low-temperature heat source, moderate steps of temperature lifts can be utilized. This gradual increase is enough to cover greater temperature lifts. If no waste heat source is available, then the heat sink can be the same as ambient or even below ambient temperature. Therefore, additional stages should be considered for operating between ambient and industrial high temperatures. Usually, cascades are designed in two stages with the same working fluid, and this solution is enough to cover greater temperature lifts, for example, commercial refrigeration or air source heat pumps.

However, high-temperature industrial applications can reach 150°C, so additional stages should be carefully considered when operating between ambient and industrial high temperatures. When selecting the refrigerant, it is necessary to consider the thermodynamic and thermophysical properties, the environmental issues, and safety characteristics. Fig. 1 shows the temperature-entropy diagram of an ideal three-stage multi-layered heat pump, in which the different temperature levels in this system are visible.

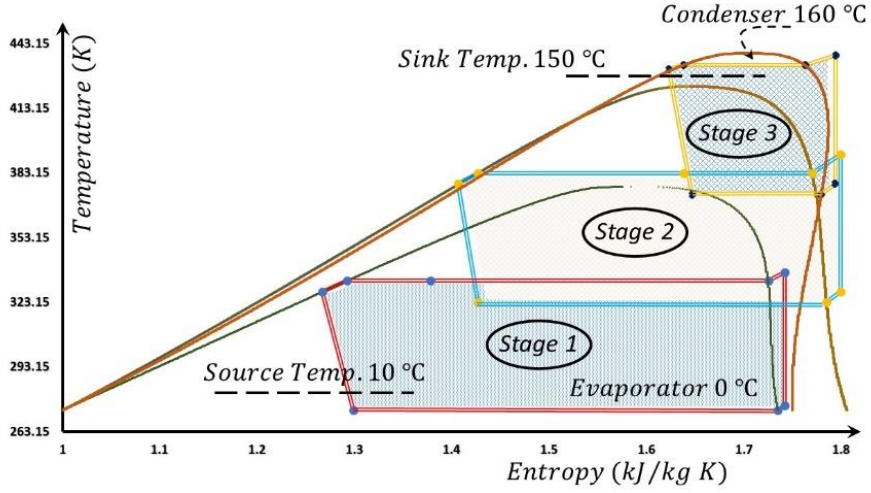


Fig. 1: T-s Diagram for LEAP Concept.

Fig. 2 illustrate the conceptual structure of the LEAP idea where the condenser in the internal cycles is divided into two or several heat exchangers with equal loads. The first heat exchanger will cover the load of the evaporator in the successive cycle, whereas the remaining heat exchangers will supply the external users with the required loads at specific temperature. The external load heat exchangers can be connected in series or parallel to control the desired output temperature. Therefore, this system possesses excellent flexibility in covering different heating consumptions in buildings or industrial applications such as HVAC or domestic hot water systems.

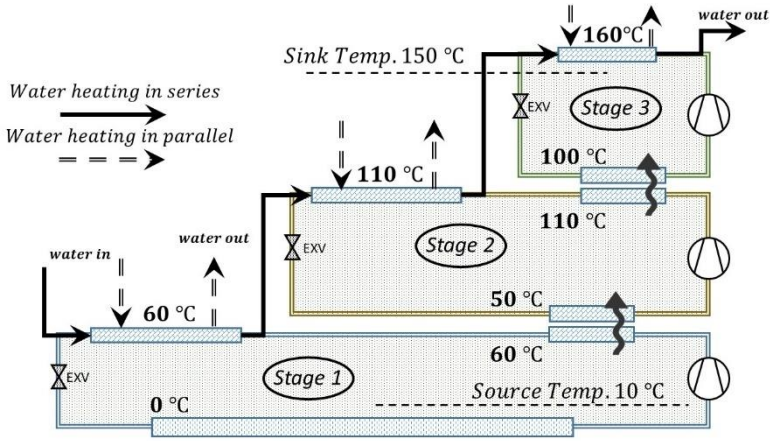


Fig. 2: Components of the LEAP with multiple heating levels.

The main assumptions for each LEAP concept start with an initial source load of 200 kW as the base load for the whole system, an isentropic efficiency of 70% for each compressor within the system, isenthalpic expansion within the expansion valve, constant and equal temperature lifts for each stage, no internal heat exchanger, and pressure drops and heat transfer to the ambient are neglected.

2.1. Low-GWP refrigerants for LEAP concept.

This section provides the various criteria considered to identify the refrigerant with the best thermophysical and thermodynamic properties, which maximizes the system's performance and minimizes the environmental impact. A variety of refrigerant types have been considered in order to choose the best refrigerant for the LEAP concept.

Fig. 3 shows the families of synthetic refrigerants obtained from natural ones and how the chemical processes would be done to obtain the required synthetic refrigerant.

Fig. 4 represents the triangle of elements, Hydrogen on the top, Carbon on the bottom left, and Fluorine on the bottom right. From the triangle, we can locate flammable, toxic, and long atmospheric lifetime (fully halogenated) areas. We can also find areas where refrigerants have high GWP values and high ozone depletion potential (ODP) rates.

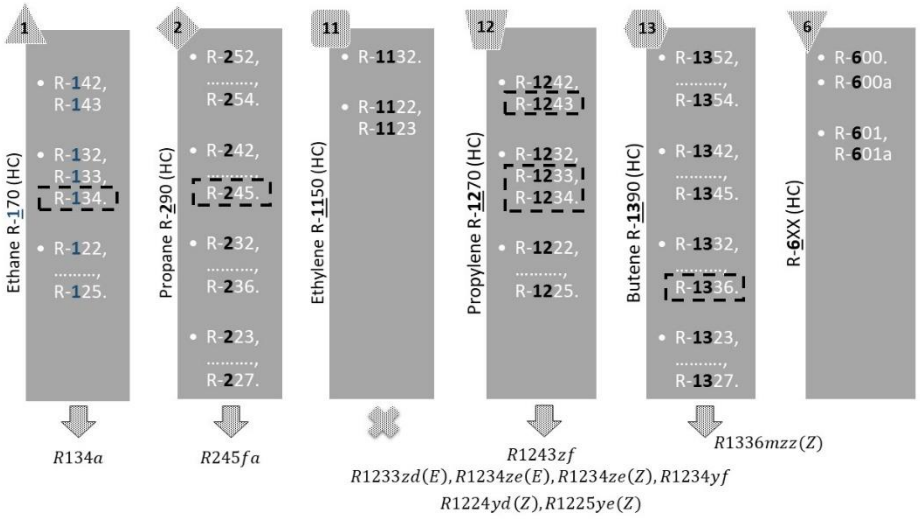


Fig. 3: Synthetic refrigerants families.

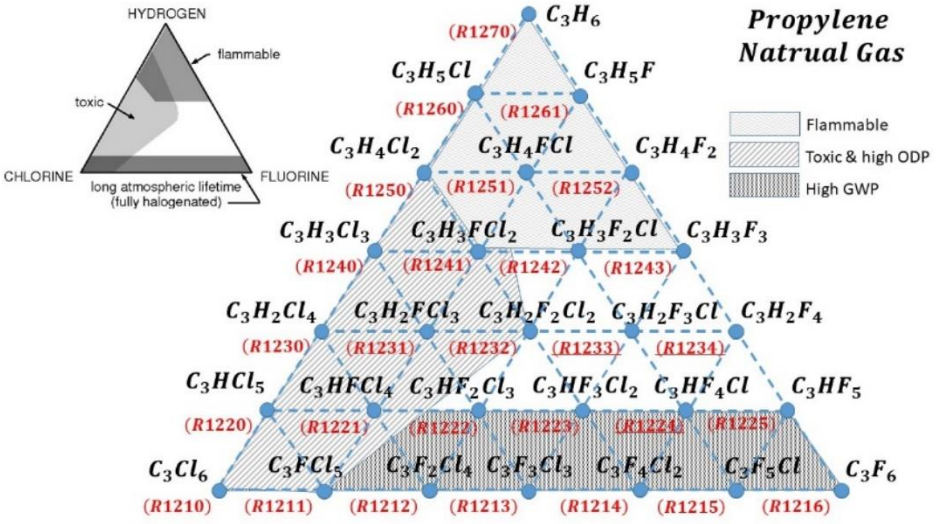


Fig. 4: Synthetic from natural refrigerants (series 12)

All refrigerants will be investigated for a single-stage heat pump with different temperature lifts to eliminate and choose the right media for different stages in the LEAP concept. Table 1 illustrates the refrigerants under investigation in this paper. It shows the trend of increasing the critical temperature of the refrigerants and states the molar mass of the refrigerants' molecules. It is clear from the table that some refrigerants are limited in substituting R-134a and R-245fa, and some are superior thermodynamically. All refrigerants in the table have a GWP around unity and almost zero ODP rates; therefore, their direct impact on climate change can be considered ultra-low.

Table 1: Investigated synthetic & natural refrigerants.

Refrigerants		MW	T_{BP}		T_{cr}		P_{cr}
		$kg/kmol$	(℃)	(K)	(℃)	(K)	kPa
R-1270 (Propylene)	HC	42.08	-47.72	225.43	92.42	365.57	4665
R-1234yf	HFO	114	-29.49	243.66	94.7	367.85	3382
R-290 (Propane)	HC	44.1	-42.1	231.05	96.68	369.83	4247
R-134a	HFC	102	-26.09	247.06	101	374.15	4059

R-1243zf	HCFO	96.05	-25.43	247.72	103.8	376.95	3518
R-1225ye (Z)	HFO	132	-19.54	253.61	106.9	380.05	3528
R-1234ze (E)	HFO	114	-19.28	253.87	109.4	382.55	3632
R-600a (Isobutene)	HC	58.12	-11.68	261.47	134.7	407.85	3640
R-1234ze (Z)	HFO	114	9.72	282.87	150.1	423.25	3531
R-600 (n-Butane)	HC	58.12	-0.52	272.62	152	425.15	3796
R-245fa	HFC	134	15.18	288.33	154	427.15	3651
R-1224yd (Z)	HCFO	148.5	14.61	287.76	155.5	428.65	3337
R-1233zd (E)	HCFO	130.5	18.32	291.47	165.6	438.75	3573
R-1336mzz (Z)	HFO	164.1	33.47	306.62	171.3	444.45	2900
R-601a (Isopentane)	HC	72.15	27.85	301	187.2	460.35	3370
R-601 (n-Pentane)	HC	72.15	35.87	309.02	196.5	469.65	3364

2.2. Refrigerants' selection for each stage.

Simulating a single-stage heat pump with different temperature lifts of 30, 40, 50, 60, 70, and 80K for the same conditions mentioned above, we notice that the heating loads for all "drop-in" refrigerants vary between -8% and 6% for R-134a as base refrigerant and between -14% and 2% for R-245fa as base refrigerant. Similarly, the COP ranges between -17% and 14% for R-134a and between -5% and 24% for R-245fa. Fig. 5 illustrates the COP trend for all refrigerants with a constant temperature lift of 60 K. The evaporator temperature starts with the boiling point temperature of the selected refrigerant with a gradual increase of 2K. The COP values decline as we go higher in the evaporator temperature as we go closer to the critical temperature. It also shows the available refrigerants that can substitute R-134a and R-245fa with respect to COP values.

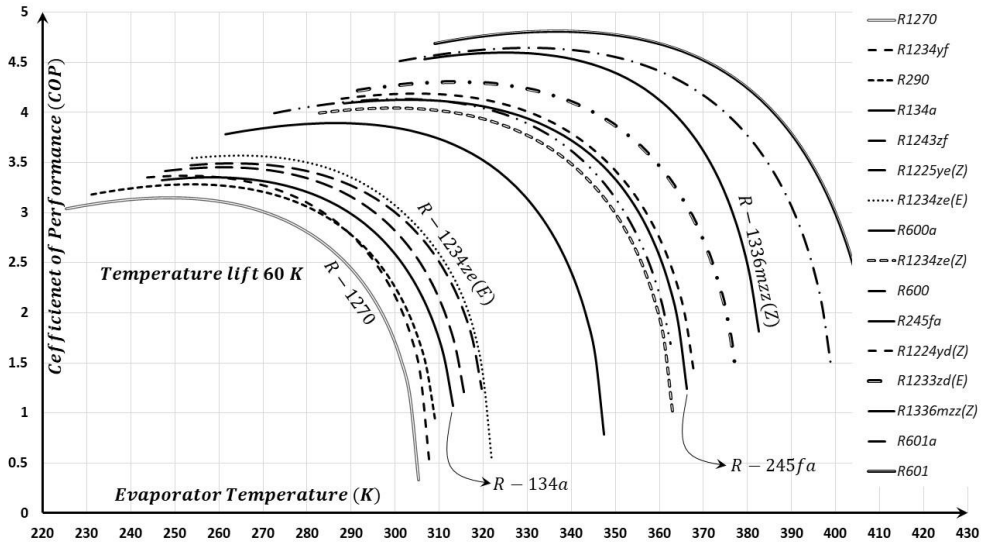


Fig. 5: COP trend for all refrigerants.

Table 2 indicates the variation of COP and heating load (HL) for all investigated refrigerants in a single-stage heat pump with a temperature lift of 60 K as a sample parameter. These values are given in equations (1) and (2) for R-134a and R-245fa as the base refrigerants. We notice from the table that the base refrigerants can be replaced with several refrigerants with an increased COP values and some variation in the heating load on the sink side. The trend is more stable in R-245fa with increasing temperature lifts where the COP values increased while the heating load capacity decreased for all refrigerants. This trend is not clear for R-134a.

Table 2: Data for single-stage heat pump for 60 K temperature lift.

Refrigerants	R-134a		Refrigerants	R-245fa	
	COP%	HL%		COP%	HL%
R-1234ze (Z)	-9.2	1.9	R-1234ze (Z)	-2.7	0.5
R-601 (n-Pentane)	-9.0	-0.8	R-601 (n-Pentane)	-2.5	0.6
R-1233zd (E)	-8.4	1.8	R-1233zd (E)	-2.0	0.3
R-601a (Isopentane)	-7.4	1.7	R-601a (Isopentane)	-1.0	0.3
R-600 (n-Butene)	-6.1	1.4	R-600 (n-Butene)	0.2	-0.1
R-1224yd (Z)	-6.1	1.4	R-1224yd (Z)	0.2	-0.1
R-1336mzz (Z)	-4.9	1.2	R-1336mzz (Z)	1.4	-0.3
R-600a (Isobutene)	-2.8	0.7	R-600a (Isobutene)	3.3	-0.8
R-1234ze (E)	1.0	-0.1	R-1234ze (E)	6.8	-1.6
R-1243zf	1.3	-0.2	R-1243zf	7.1	-1.7
R-290 (Propane)	2.3	-0.6	R-290 (Propane)	8.1	-2.2
R-1270 (Propylene)	2.4	2.1	R-1270 (Propylene)	8.2	-2.3
R-1225ye (Z)	2.6	-0.6	R-1225ye (Z)	8.4	-2.1
R-1234yf	7.7	-1.7	R-1234yf	13.2	-3.2

$$COP\% = \frac{COP_{ref} - COP_{base}}{COP_{base}} \quad (1)$$

$$HL\% = \frac{LH_{ref} - LH_{base}}{LH_{base}} \quad (2)$$

The first stage in the LEAP concept work between 0°C and 60°C and 10°C for the heat source, the second stage operate between 50°C and 110°C, and between 100°C and 160°C for the third stage. This means that the maximum temperature for the heat sink is 150°C. If we take the critical temperature of the refrigerant as a base for comparison with positive COP values and a temperature lift of 60K, several candidates for the first stage, as per Table 2, can be selected. If we, however, open the selection for all COP values, the option to select a suitable refrigerant can widen, and the choice will vary for each LEAP stage.

Table 3 shows the selected refrigerants for each stage with boiling temperature below 0°C and critical temperature above 60°C for the first stage, below 50°C and above 110°C for the second stage, and below 100°C and above 160°C for the third stage.

Table 3: LEAP refrigerants for each stage.

First Stage (0°C and 60°C)	Second Stage (50°C and 110°C)	Third Stage (100°C and 160°C)
Synthetic		
	R-1336mzz (Z)	
	R-1233zd (E)	
R-1224yd(Z)		
R-1234ze(Z)		
R-1234ze (E)		
R-1225ye (Z)		
R-1234yf		
R-1243zf		
Hydrocarbons		
R-290 (Propane)		
R-1270 (Propylene)		
R-600 (n-Butene)		
R-600a (Isobutene)		
	R-601 (n-Pentane)	
	R-601a (Isopentane)	

3. Results & Discussions

3.1. LEAP results with 2-layered heat pump.

Running the simulation software EES for variable combinations of refrigerants between the first and the second stage starting from the boiling point of the refrigerant, we notice that no matter what the selection

would be for the first stage, the second stage will output increasing COP values, as seen in Table 4, and fluctuating heating load values.

Table 4: The 2-layered heat pump results.

First Stage (0°C and 60°C)		Second Stage (50°C and 110°C)	
Refrigerant	COP	Refrigerant	COP
R-1234yf	3.065	R-600a (Isobutane)	3.159
R-1270 (Propylene)	3.202	R-600 (n-Butane)	3.449
R-1225ye (Z)	3.202	R-1224yd (Z)	3.501
R-290 (Propane)	3.208	R-1336mzz (Z)	3.532
R-1243zf	3.242	R-1234ze (Z)	3.603
R-1234ze (E)	3.252	R-601a (Isopentane)	3.617
R-600a (Isobutane)	3.355	R-1233zd (E)	3.675
R-600 (n-Butane)	3.448	R-601 (n-Pentane)	3.722

The structured array of increasing COP values in the second stage is composed of the following refrigerants: R-600a, R-600, R-1224yd (Z), R-1336mzz (Z), R-1234ze (Z), R-601a, R-1233zd (E), and R-601. The best combination for the 2-layered heat pump is R-600 with a COP of 3.448 for the first stage and R-601 with a COP of 3.722 for the second stage. If the choice is to use only synthetic refrigerants, then that R-1234ze (E) with a COP of 3.252 for the first stage and R-1233zd (E) with a COP of 3.675 for the second stage. In the 2-layer heat pump, we obtain two levels of temperatures, 50°C and 100°C, or we can increase the sink source temperature from 10°C to 100°C in one step

If a single-stage heat pump is supposed to deliver the same sink temperature of 100°C from a 10°C source temperature, then the temperature lift is 110 K. By looking at the refrigerants' thermophysical properties, we can see that only R-600 and R-600a will comply, and the COP values will be 1.6 and 1.4 respectively compared to a total COP value of 2.56 for the LEAP two stages. Using a 2-layered heat pump will therefore lead to energy savings of almost 40%.

3.2. LEAP results with 3-layered heat pumps.

In the third stage layer, the compressor enthalpy discharge values will land in the vapor-liquid mixture zone instead of the superheated zone due to the positive slope of the vapor line in the P-h chart. To overcome these discrepancies, the superheat and subcooling temperatures will be increased to overcome the false values.

Using the same analogy from the 2-layered heat pump, Table 5 summarizes the refrigerants that can be selected for each stage. For the first and the second stage, the array of refrigerants is the same. Considering the third stage, fewer options are available. The best option is R-600 for the first and the third stages, with COP values of 4.143 and 5.877 respectively, and R-601 for the second stage with a COP value of 4.527. If a single-stage heat pump is supposed to deliver the same sink temperature of 150°C from a 10°C source temperature, then the temperature lift will be 160K. In this case, only R-601 and R-601a will comply, and the COP values will be 1.336 and 1.264 respectively with high-power compressors. The total COP value for the LEAP three stages is 2.539. The increase in using a 3-layered heat pump is an energy saving of almost 48%.

Table 5: The 3-layered heat pump results.

First Stage (0°C - 60°C)		Second Stage (50°C - 110°C)		Third Stage (100°C - 160°C)	
Refrigerant	COP	Refrigerant	COP	Refrigerant	COP
R-1234yf	3.801	R-600a (Isobutane)	4.11	R-1233zd (E)	5.704
R-1270 (Propylene)	3.907	R-600 (N-butane)	4.315	R-1336mzz (Z)	5.841
R-1225ye (Z)	3.926	R-1224yd (Z)	4.348	R-601a (Isopentane)	5.85
R-290 (Propane)	3.918	R-1336mzz (Z)	4.368	R-600 (n-Pentane)	5.877
R-1243zf	3.959	R-1234ze (Z)	4.441		
R-1234ze (E)	3.973	R-601a (Isopentane)	4.435		
R-600a (Isobutane)	4.06	R-1233zd (E)	4.475		
R-600 (N-butane)	4.143	R-601 (N-pentane)	4.527		

4. Conclusions

This paper analyzes the performance of a three-stage heat pump with multilevel heating based on different working fluids for taking advantage of the flexibility of heat pumps in comparison with other heating technologies. The most suitable low GWP refrigerants for condensing temperatures of 60°C, 110°C and 160 °C (at the evaporation temperature of 0°C, 50°C, and 100 °C respectively) have been studied in terms of

operational and thermodynamic potential. The highest heating production is set at 150 °C, and the nominal heating capacity is 200 kW. The heat transfer to the external flow in the intermediate and low condensing temperature depends on the cycle selection.

Refrigerants have been classified according to the critical temperatures, pressures, and working pressure-temperature relationship. R-1224yd (Z), R-1234ze (Z), R-1234ze (E), R-1225ye (Z), R-1234yf, R-1243zf, R-290, R1270, R600, R00a with positive COP values have been proposed at the first stage to replace R134a; R-1336mzz (Z), R-1233zd (E), R-1224yd (Z), R-1234ze(Z), R-600, R-600a, R-601, and R-601a at the second stage; R-601, R-601a, R-1336mzz (Z) and R-1233zd (E) at the third stage. From that list, carbon dioxide, water, and ammonia have not been considered for this study because of the significant difference in critical temperatures and safety requirements to HFCs traditionally used (R-134a and R-245fa).

Refrigerants with a higher coefficient of performance capacity have been selected for each cycle. R-1234ze (E) and R-1233zd (E) as synthetic refrigerants, and R-600 and R-601 as natural refrigerants for a 2-layered heat pump with a total COP of 40% more than using the single-stage heat pump. R-1234ze (E), R-1233zd, R1336mzz (Z) as synthetic refrigerants, and R-600, R-601, and R-600 as natural refrigerants for 3-layered heat pump with a total COP of 48% more than using the single-stage heat pump. These values of COP are promising since it makes the heat pump a valuable alternative to natural gas boilers in most European countries.

References

[1] Arpagaus, C., Bless, F., Schiffmann, J., Bertsch, S.S.S. Multi-temperature heat pumps: A literature review. Int. J. Refrig. **69**, 437–465. https://doi.org/10.1016/j.ijrefrig.2016.05.014.

[2] Kosmadakis, G., Arpagaus, C., Neofytou, P., Bertsch, S. Techno-economic analysis of high-temperature heat pumps with low-global warming potential refrigerants for upgrading waste heat up to 150 °C. Energy Convers. Manag. 226, 113488. https://doi.org/https://doi.org/10.1016/j.enconman.2020.113488.

[3] Mateu-Royo, C., Arpagaus, C., Mota-Babiloni, A., Navarro-Esbrí, J., Bertsch, S.S. Advanced high temperature heat pump configurations using low GWP refrigerants for industrial waste heat recovery: A comprehensive study. Energy Convers. Manag. 229, 113752. https://doi.org/https://doi.org/10.1016/j.enconman.2021.113752.

[4] Mota-Babiloni, A., Mateu-Royo, C., Navarro-Esbrí, J., Molés, F., Amat-Albuixech, M., Barragán-Cervera, Á. Optimization of high-temperature heat pump cascades with internal heat exchangers using refrigerants with low global warming potential. Energy 165, 1248–1258. https://doi.org/10.1016/j.energy.2018.09.188.

[5] Uusitalo, A., Turunen-Saaresti, T., Honkatukia, J., Tiainen, J., Jaatinen-Värri, A. Numerical analysis of working fluids for large scale centrifugal compressor driven cascade heat pumps upgrading waste heat. Appl. Energy 269, 115056. https://doi.org/10.1016/j.apenergy.2020.115056.

[6] Wang, W., Zhou, Q., Tian, G., Hu, B., Li, Y., Cao, F. The intermediate temperature optimization for cascade refrigeration system and air source heat pump via extreme seeking control. Int. J. Refrig. 117, 150–162. https://doi.org/10.1016/j.ijrefrig.2020.05.007.

[7] Yu, B., Yang, J., Wang, D., Shi, J., Chen, J. Modelling and theoretical analysis of a CO2-propane auto cascade heat pump for electrical vehicle heating, International Journal of Refrigeration, 95, 146-155, https://doi.org/10.1016/j.ijrefrig.2018.07.030.

[8] Chen, J., Chen, Q., Qin, X., Wang, D., Energy, exergy, economic and environmental analyses and optimization of a novel vapor injection auto cascade heat pump for high-temperature water heating, Energy Conversion and Management, 267, https://doi.org/10.1016/j.enconman.2022.115909.

[9] Sun, Z., Cui, Q., Wang, Q., Ning, J., Guo, J., Dai, B., Liu, Y., Xu, Y. Experimental study on CO2/R32 blends in a water-to-water heat pump system, Applied Thermal Engineering, 162, https://doi.org/10.1016/j.applthermaleng.2019.114303.

[10] Dawo, F., Fleischmann, J., Kaufmann, F., Schifflechner, C., Eyerer, S., Wieland, C., Spliethoff, H. R1224yd(Z), R1233zd(E) and R1336mzz(Z) as replacements for R245fa: Experimental performance, interaction with lubricants and environmental impact, Applied Thermal Engineering, 162, 2019, https://doi.org/10.1016/j.applthermaleng.2019.114303

14th IEA Heat Pump Conference
15-18 May 2023, Chicago, Illinois

Integration of High-Temperature Heat Pumps in Swiss Industrial Processes (HTHP-CH)

Cordin Arpagaus[a,*], Frédéric Bless[a], Stefan Bertsch[a], Pierre Krummenacher[b], Daniel A. Flórez-Orrego[c], Eduardo A. Pina[c], François Maréchal[c], Nicole Calame Darbellay[d], Fabrice Rognon[d], Stéphane Vesin[e], Pascal Achermann[f], Christian Jansen[g]

[a]Eastern Switzerland University of Applied Sciences, Institute for Energy Systems, CH-9471 Buchs,
[b]HEIG-VD Haute Ecole d'Ingénierie et de Gestion du Canton de Vaud, Institute of Thermal Engineering, CH-1401 Yverdon-les-Bains,
[c]EPFL Valais, Industrial Process and Energy Systems Engineering, CH-1951 Sion,
[d]CSD Ingénieurs SA, CH-1701 Fribourg,
[e]ESTAVAYER LAIT SA (ELSA), CH-1470 Estavayer-le-Lac,
[f]Cremo SA, CH-1752 Villars-sur-Glâne,
[g]Gustav Spiess AG, CH-9442 Berneck

Abstract

High-temperature heat pumps (HTHP) with supply temperatures above 100 °C are becoming increasingly important for the electrification and decarbonization of industry. However, their adoption is slow because there is still a lack of knowledge about their capabilities, design, control, and optimal integration, resulting in few practical implementation examples. This study investigates the technical and economic feasibility of HTHP integration based on case studies from the Swiss industry. ELSA (Estavayer Lait SA), Cremo SA, and Gustav Spiess AG support the research and provide access to industrial process data. ELSA, Switzerland's largest industrial dairy on a single site, is interested in a HTHP supplying steam for cleaning-in-place processes. Cremo SA manufactures dairy products and sees opportunities to integrate a HTHP in a milk permeate drying plant that consumes a large amount of 3 bar steam. Gustav Spiess AG produces meat products and sees potential for integrating a HTHP into sausage cooking processes for steam generation at about 115 °C. In addition, other Swiss industrial companies in the food, biotech, and chemical sectors also show interest in HTHPs for applications such as distillation, sterilization, drying, and steam generation. This study presents suitable HTHP integration concepts based on case studies with quantified efficiency gains, energy savings, CO_2 reduction, and cost-efficiency results. It also includes an up-to-date review of HTHP suppliers derived from participation in the IEA HPT Annex 58 that shares results and knowledge with international experts on HTHPs.

© HPC2023.
Selection and/or peer-review under the responsibility of the organizers of the 14th IEA Heat Pump Conference 2023.

Keywords: industrial processes; high-temperature heat pumps; techno-economic analysis; payback period; case studies; CO_2 emissions

1. Introduction

1.1. Application potential of industrial HTHPs in Switzerland

Switzerland has been pioneering in developing and commercializing heat pumps (HP). The first European HPs were realized in Switzerland (e.g., in 1877 at the salt works at Bex) [1]. In 2021, HP sales increased to an all-time high of 33'704 units (20% growth compared to 2020) [2]. Especially in the small-capacity range for single- and multi-family houses, HPs are an established technology for space heating and domestic hot water, with a market share of over 90% in new buildings. Above 100 kW heating capacity, 169 HPs were sold (around 0.5% of all units) since, in larger heating capacity ranges, oil and gas boilers still dominate process heat generation [3]–[5]. Therefore, replacing fossil heating systems with electrically-driven industrial HPs is

* Corresponding author. *E-mail address:* cordin.arpagaus@ost.ch

a possible scenario to reduce CO_2 emissions from industry. High-temperature heat pumps (HTHP) with supply temperatures above 100 °C are increasingly important to replace fossil fuels in industries [6]–[8]. The most relevant application areas for HTHPs are the food/beverage, chemicals, and pulp/paper industries for processes like drying, evaporation, sterilization, or similar thermal processes with available waste heat from about 30 °C to 70 °C and process heat demand from 80 °C to 150 °C [9]. Based on annual energy consumption of around 43 TWh in Switzerland [10], a 30% share of process heat and steam below 150 °C [11], and a moderate conversion rate of 40% to HPs and HTHPs [12], the addressable energy savings potential from the use of HTHPs in the Swiss industry can be roughly estimated at 2'893 GW/a which is approximately 6.7% of the total process heat demand [13] (Table 1).

Table 1. Potential energy savings through industrial HTHPs in Switzerland (top-down estimate) [13].

	Energy consumption	**Data source / Estimations**
Swiss industry	42'972 GWh	154,7 PJ as of 2018 [10]
Process heat demand	24'107 GWh	56,1% (>80 °C) [10]
Process heat and steam demand below 150 °C	7'232 GWh	30% (estimate based on Heat Roadmap Europe [11])
Energy savings potential through the use of HTHPs (= addressable process heat share)	2'893 GWh (6.7% of the process heat demand)	40% (moderate estimate of conversion rate to HPs and HTHPs based on technical analysis within SCCER EIP [12])

Compared to natural gas, which has an emission factor of 0.201 kg CO_2 per kWh_{th} of useful heat [14], the consumer electricity mix available in Switzerland is 0.128 kg CO_2/kWh_{el} [15]. On this basis and with an average COP of 3.0 to 4.0 for an industrial HTHP at about 40 K to 60 K temperature lift from heat source inlet to sink outlet (assuming 45% Carnot efficiency [6], [7], [16]), the generated CO_2 emissions per useful heat are about 0.032 to 0.043 kg CO_2/kWh, which is 5 to 7 times lower than for a gas boiler (assuming 90% boiler efficiency). Assuming that integrated HTHPs would run with 5'000 operating hours per year on average, this results in a total heating capacity of 579 MW and, with specific investment costs (incl. installation, without integration, valid for 500 kW_{th} HP size) of approx. 450 to 700 EUR per kW heating capacity [17], a potential market of 260 to 405 million EUR for Switzerland. Assuming an average heating capacity per HTHP unit of 1 MW_{th} is equivalent to installing around 579 HTHP units.

Thus, integrating industrial HTHPs will contribute to energy savings, CO_2 reduction, and a substantial new market. Furthermore, expanding renewable energy and increasing energy efficiency in industrial processes align with the federal government's Energy Strategy 2050 [18]. Consequently, HTHP technology supports the efforts of Switzerland's net carbon emissions to net zero by 2050 [19].

1.2. Existing challenges for the wider spread of HTHPs

However, HTHPs are just beginning to enter the market of industrial heat production. There is still a lack of knowledge about available HTHP technologies and products (>100 °C supply temperature), methods for optimal integration, proper sizing, control, dynamic behavior, and techno-economic feasibility, resulting in few realized references with operational experience. As highlighted in a white paper [20], demonstration projects with increased knowledge sharing at the international level are needed to drive further HTHP technology dissemination and achieve greater visibility, particularly in process electrification. In this context, the authors of this study participate as Swiss representatives in the IEA HPT Annex 58 on HTHPs to exchange results and knowledge with international experts. In recent studies, the techno-economic feasibility of integrating HTHPs for steam generation in distillation applications was investigated [21], [22], and an up-to-date overview of the latest HTHP developments and products for supply temperatures above 100 °C was presented at the China Heat Pump Conference 2022 [16]. The analysis of the integration of HTHPs into ammonia and pulp production was also presented at CPOTE 2022 [23] and ECOS 2022 [24].

1.3. Objectives of this study

This study investigates the technical and economic feasibility of HTHP integration based on case studies in Swiss industrial companies with heat source temperatures from 40 to 80 °C to provide process heat (e.g., steam) at 115 to 150 °C and about 0.5 to 3.5 MW heating capacity. First, a review of current HTHP products and the corresponding working domains (e.g., heating capacity, temperatures) is given. Next, a simple economic model is used at an early planning stage to assess whether a HTHP integration could be economically viable. Then, the investment and operating costs of HTHPs are analyzed for the case studies using a cost model with different

input parameters. Finally, the payback period, the avoided CO_2 emissions, and the energy savings are calculated, and the main influencing factors are discussed in a sensitivity analysis.

2. Market review of industrial HTHPs and operating ranges

The range of industrial HTHP products on the market has grown steadily in recent years (especially since 2018 [6]). Table 2 presents an overview of 33 HTHP products with heat supply temperatures above 100 °C based on information collected in the IEA HPT Annex 58 project [25]. The list includes closed-cycle and open-cycle HPs for mechanical vapor recompression (MVR). It is structured by maximum supply temperature, HTHP supplier, country, compressor type, the working fluid (refrigerant), maximum heating capacity, and technology readiness level (TRL) [16]. The specific investment costs are also given in EUR/kW_{th}. It should be noted that the HTHP suppliers provided the information without third-party validation. Therefore, the data is indicative and may vary in the final installations depending on the application-specific parameters.

Table 2. Overview of HTHP technologies and suppliers structured by maximum supply temperature above 100 °C [16] (Data based on IEA HPT Annex 58 [25]) (Note: The HTHP suppliers provided all information without third-party validation. Therefore, the information is indicative and may vary in final installations depending on application-specific parameters).

HTHP supplier (High-Temperature Heat Pump)	Country	Product	Compressor type	Working fluid (Refrigerant)	Max. heating capacity (MW)	Max. supply temp. (°C)	TRL (Technology Readiness Level)	Spec. invest. cost (EUR/kW_{th})
Spilling	DE	Steam Compressor	Piston (MVR)	R718 (water)	15	280	9	100 to 400
Enerin	NO	HoegTemp	Piston	R704 (helium)	10	250	6	600 to 800
Qpinch	BE	Heat Transformer	Chemical heat transformer	R718, H_3PO_4 and derivatives	2	230	9	1000 to 2000
Piller	DE	VapoFan	Turbo (MVR)	R718	70	212	8 to 9	850
Olvondo	NO	HighLift	Piston (double acting)	R704	5	200	9	1200
Turboden	IT	LHP	Turbo	Application specific	30	200	7 to 9	300 to 700
ToCircle	NO	TC-C920	Rotary vane	R717 (ammonia), R718	5	188	6 to 7	250 to 430
Kobelco MSRC160	JP	MSRC160	Twin -screw (MVR)	R718	0.8	175	9	n.a.
Kobelco SGH165	JP	SGH165	Twin-screw (MVR)	R245fa/R134a (mixture), R718	0.62	175	9	n.a.
Heaten	NO	HeatBooster	Reciprocating, custom design	HFOs (hydrofluorolefins)	6	165	7 to 9	250 to 350
SPH	DE	Thermbooster	Piston	HFOs (hydrofluorolefins)	5	165	6 to 8	150 to 1000
SRM	SE	Compressor for water vapor	Screw (MVR)	R718	2	165	5	n.a.
Siemens Energy	DE	Industrial Heat Pump	Turbo (geared or single-shaft)	R1233zd(E), R1234ze(E)	70	160	9 (to 90 °C)	250 to 800
Enertime	FR	HTHPs	1- or 2-stage centrifugal	R1336mzz(Z), R1224yd(Z), R1233zd(E)	10	160	4 to 8	300 to 400
Weel & Sandvig	DK	WS Turbo Steam	Turbo (MVR)	R718	5	160	4 to 9	150 to 250
Rank	ES	Rank® HP	Screw	R245fa, R1336mzz(Z), R1233zd(E)	2	160	7	200 to 400
MAN	DE	ETES CO_2 Heat Pump	Centrifugal turbo with expander	R744 (CO_2)	50	150	7 to 8	300 to 500
Epcon	NO	MVR-HP	Centrifugal fan / Blower	R718	30	150	9	200 to 400
Ohmia Industry	NO	SPHP	Piston, Centrifugal fan (MVR)	R717, R718	10	150	7 to 8	n.a.
ecop	AT	Rotation Heat Pump K7	Rotational heat pump	ecop fluid 1 (He, Kr, Ar)	0.7	150	6 to 7	700
Mayekawa FC Comp	BE	FC-compressor	Screw	R601 (n-pentane)	1	145	5	720
GEA Refrigeration	NL	CO_2 Heat Pump	Semi-hermetic piston	R744	1.2	130	8	200 to 300
Mitsubishi Heavy Ind.	JP	ETW-S	Two-stage centrifugal	R134a	0.6	130	9	n.a.
Hybrid Energy	NO	HyPAC-S	Piston/screw	R717/R718 mixture	5	120	9	200 to 600
Johnson Controls	DK	Cascade Heat Pump System	Reciprocating	R717, R600 (n-butane) (cascade)	5	120	7 to 8	n.a.
Fenagy	DK	H1800-AW/WW	Reciprocating	R744	1.8	120	5 to 6	250 to 425
Mayekawa HS Comp	BE	HS-compressor	Piston	R600 (n-butane)	0.75	120	7	450
Kobelco SGH120	JP	SGH120	2-stage twin-screw	R245fa	0.37	120	9	n.a.
Mayekawa EcoCircuit	JP	Eco Circuit 100	Reciprocating	R1234ze(Z)	0.1	120	9	n.a.
Fuji Electric	JP	Steam Generation Heat Pump	Reciprocating	R245fa	0.03	120	9	n.a.
Emerson	US	Cascade Solution	Scroll and EVI scroll	R245fa, R410a, R718	0.03	120	6	n.a.
Skala Fabrikk	NO	SkaleUP	Piston (semihermetic)	R290 (propane), R600 (cascade)	0.3	115	7	500 to 700
Mayekawa EcoSirocco	JP	Eco Sirocco	Reciprocating	R744 (CO2)	0.1	100	8 to 9	n.a.

Figure 1 shows the industrial HTHP products sorted by their maximum heat supply temperature and heating capacity. The heating capacities range from laboratory demonstrators of about 10 kW to larger 70 MW units. Illustrated in color are the compressor technologies, including screw, piston, turbo, and others like the rotary vane compressor from ToCircle, the heat transformer from QPinch, or the Rotational HP from Ecop using a noble gas in a Joule cycle. These last examples show various technologies emerging alongside more classical Carnot cycles.

In most cases, turbo compressors are used for large heating capacities. For HTHP applications and high temperature lifts, compressors must be able to handle high pressure ratios. Therefore, the compressor manufacturers offer optimized designs for special applications.

For HTHP application, the steam compressors must preferably offer high flow rates at low suction pressure, high pressure ratios to reduce the number of compression stages, temperature resistance (e.g., need for liquid injection), and long-term corrosion resistance. In particular, a development perspective is small steam compressors for integrating HTHPs in industrial processes with an open cycle or combined in a two-stage cycle with MVR [26].

For example, Spilling's piston steam compressors operate at suction pressures above 1.4 bar(a) (110 °C) and achieve temperature lifts of up to 100 K with a 3-stage compression design in one unit. Piller's VapoFans are used in multi-stage MVR applications with suction pressures down to about 100 mbar(a) (45 °C). Enerin and Olvondo provide HTHPs with helium (R704) as working fluid and double-acting piston compressors in a Stirling cycle, which allow flexible operation conditions, high lifts, and supply temperatures above 200 °C.

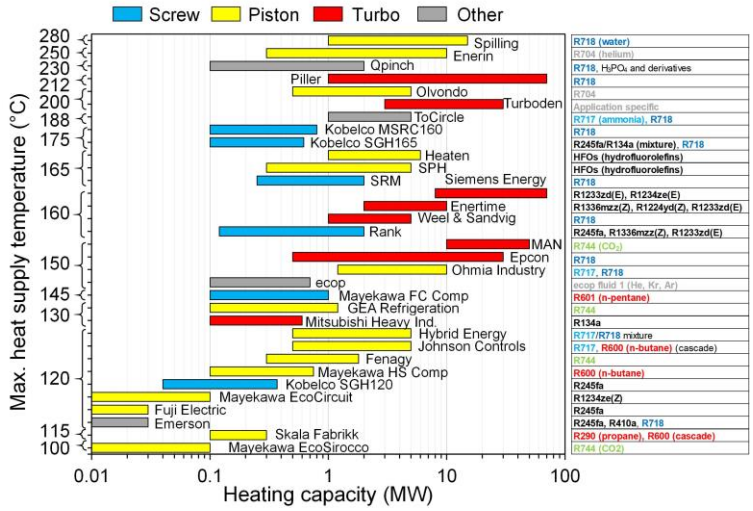


Fig. 1. Industrial HTHPs products sorted by maximum heat supply temperature (>100 °C) and heating capacity. The implemented compressor technology is color-coded (blue: screw, yellow: piston, red: turbo, grey: others). The table indicates the refrigerant [16].

Some HTHP suppliers provide closed-cycle HTHPs with up to 165 °C supply temperature using HFO refrigerants, e.g., the HeatBooster from Heaten or the ThermBooster from SPH. Other suppliers realize steam-generating HP using natural refrigerants, e.g., Ohmia Industry with ammonia (R717) in a bottom cycle and water (R718) in an open top cycle with MVR, Mayekawa with n-butane (R600), or Johnson Controls (Sabroe) with an R717/R600 cascade system using piston compressors.

Hybrid Energy uses ammonia/water (R717/R718) as the working medium in an absorption/compression cycle. As a result, temperatures up to 120 °C are achieved with high efficiency, and potentially high temperature glides on the heat source and sink. Recently, Fenagy commercialized CO_2 HPs for hot water heating from 30 to 120 °C with heating capacities up to about 1,800 kW.

Other manufacturers of HTHP products not listed in Table 2 and Figure 1 are Ago Calora (absorption-compression cycle, R717/R718, up to 150 °C), Ochsner (HFO refrigerants, up to 130 °C), Oilon (R1233zd(E), up to 120 °C), PureThermal (Pure PLUS, up to 120 °C), ThermoDraft (R1233zd(E), up to 120 °C), or Combitherm (HFO refrigerants, up to 120 °C). Finally, several large-scale HTHPs with > 10 MW heating capacity for industrial applications are supplied, for example, by Friotherm, MAN Energy Solutions, Turboden, Mitsubishi MHPS, or Siemens Energy.

Figure 2 shows the operating maps of some industrial HTHPs as a function of the heat source and sink temperature. In particular, there is a higher share around 50 °C heat source and 120 °C sink temperature. The operating limits are determined by the permissible condensation pressure, evaporation pressure, compression ratios, differential pressure across pistons, compressor speed, discharge gas temperatures, lubrication (e.g., oil temperature issues), and lowest allowable suction pressure.

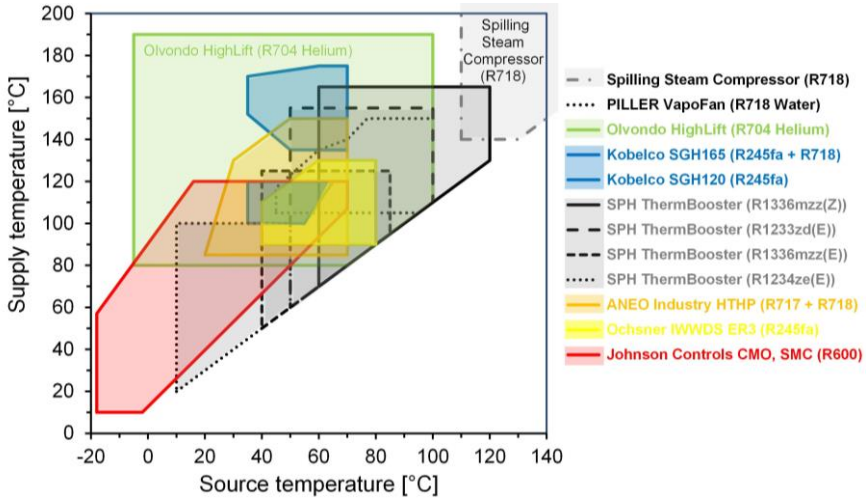


Fig. 2. Operating maps of some industrial HTHPs as a function of heat source and supply temperature.

Overall, Table 1 and Figures 2 and 3 demonstrate the availability of HTHP products and steam compressors and can be used as decision-support data for selecting appropriate HTHP suppliers. A preliminary technical feasibility check for HTHP integration consists of verifying the availability of a HTHP compatible with the temperature levels of the heat source and sink and heating capacity for a given project. In addition, industrial site constraints may further limit the HTHP integration options, such as the choice of refrigerant used (e.g., natural or synthetic), cycle concept (e.g., open, closed, or combinations), and space limitations.

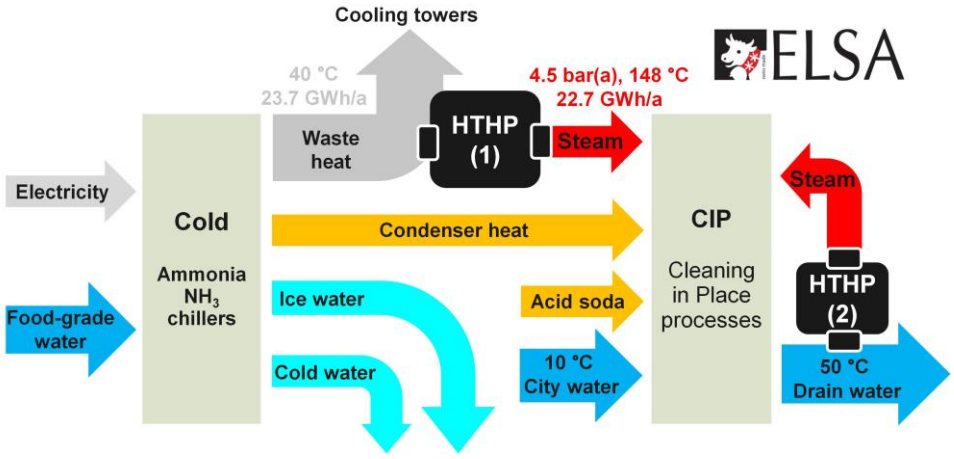


Fig. 3. Potential integration points for a steam-generating HTHP at ELSA using waste heat from the ammonia chillers at 40 °C as a heat source (1) or heat from drain water at 50 °C (2).

Finally, a Pinch analysis can determine the optimal HTHP integration in an industrial context, which also identifies heat recovery options to increase efficiency and reduce energy consumption. Depending on the application, tailor-made HTHP designs are required (i.e., concepts for large temperature glides in the heat sink versus steam generation with no temperature glide).

3. Case studies and economic model

The following section describes case studies of potential HTHP integrations from the industrial companies ELSA, Cremo SA, and Gustav Spiess AG that support the Swiss project Annex 58 HTHP-CH by giving access to industrial process data. Furthermore, various other Swiss industrial companies (e.g., food, biotech, chemical) and HP suppliers are in contact with the project team showing interest in HTHP integration.

3.1. Case Study at ELSA (Estavayer Lait SA)

ELSA (Estavayer Lait SA) is Switzerland's largest dairy on a single site, processing around 260,000 t/a of milk into a wide range of fresh dairy products, such as UP/UHT milk, yogurt, quark, and cream. The main heat treatments are pasteurization and sterilization in the temperature range of 65 to 155 °C. In addition to the production processes, CIP processes (Cleaning in Place) require large amounts of water and are an important steam consumer (e.g., 4.5 bar(a), 148 °C) (Figure 3). Today, process steam is generated by a wood chip steam boiler and several natural gas boilers (71.6 GWh/a or 275 kWh/t milk processed).

The process requirement for CIP is keeping the circulating basic and acidic solutions at 75 °C and 60 °C respectively, while the"sterilization" step of processing equipment, taking place after cleaning and, if needed, before the next operation, requires circulating hot water at 90 °C. These requirements could, in principle, be fulfilled with a hot utility below 100 °C; however, retrofitting the CIP stations (comprising 65 heat exchangers in total) for a hot water utility at 95 to 100 °C instead of steam at 4.5 bar(a) would be both expensive and difficult to implement because of the lack of space.

Therefore, to save energy and water, ELSA is interested in integrating steam-generating HTHPs that use waste heat from the NH_3 chillers (about 23.7 GWh/a at 40 °C, currently discharged through cooling towers) or drain water (about 490,000 m^3/a at 50 °C) as a heat source to replace some of the steam required for the CIP processes (about 22.7 GWh/a steam in 7,200 h of operation corresponding to 3.15 MW). Although the heat sources and sinks have yet to be confirmed, Figure 3 shows potential HTHP integration points for the CIP plants. Measurements are ongoing to determine the mass and heat balance of CIP operations and to check whether a significant share of the consumed 4.5 bar(a) steam could, in practice, be supplied at a significantly lower temperature and affordable costs.

The electricity price for 2023 is around 0.18 CHF/kWh [27] in Estavayer for a large industrial company (Category C7), and the gas price (Type X) is about 0.13 CHF/kWh, including CO_2 tax of 0.02 CHF/kWh [28]. These conditions result in a favorable electricity-to-gas price ratio of around 1.4. Compared with natural gas, which has a CO_2 emission factor of 0.201 kg CO_2 per kWh_{th} [14], an average Swiss consumer electricity mix of 0.128 kg CO_2/kWh_{el} is considered [29]. The cost multiplication factor for planning and integration is assumed to be 3.0 because the installation environment is quite complex, and space is tight.

3.2. Case Study at Cremo SA

Cremo SA in Villars-sur-Glâne processes around 240,000 t/a of milk into various dairy products, including cheese (Gruyère, Vacherin fribourgeois, Raclette), butter, skim milk, milk proteins, and milk permeate powder. Today, the heat is supplied by two 5 MW gas-fired steam boilers (12 t/h steam, baseline consumption). In addition, a district heating network (105 °C/80 °C supply/return) from the nearby waste incineration plant provides heat to an internal hot water loop at 105 °C/60 °C that is connected to spray dryers (for preheating air), a TIXOTHERM™ drying process [30], evaporators, pasteurizers, CIP stations, building HVAC, and tap hot water. In case of a future reduction of the district heating temperature to 80 °C / 60 °C, the possibility of a large-scale HTHP is considered (around 5 to 10 MW_{th}) to adapt to the changing heat transfer rate (Figure 4).

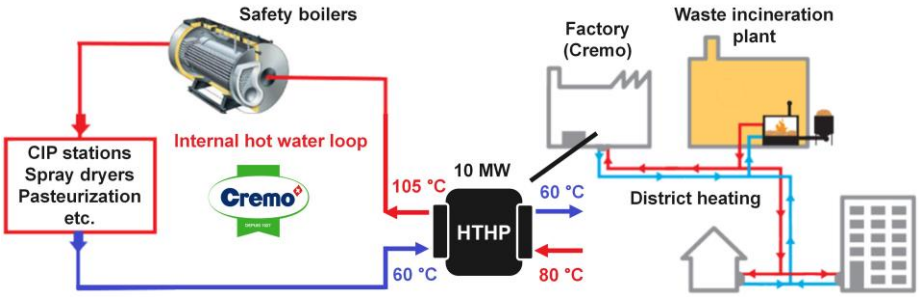


Fig. 4. Potential HTHP integration point at Cremo using district heat as a source and upgrading the heat to the internal hot water loop.

Another potential integration point for a HTHP has been identified in the TIXOTHERM™ drying plant (Figure 5), which produces milk permeate powder (containing milk sugars) and currently consumes about 10% to 15% of the total steam demand for heating a Rosinaire™ paddle dryer [30]. Presently, there is only limited heat recovery on the humid exhaust air. Therefore, this case study is *a priori* suitable for a HTHP integration to supply low-pressure steam at around 1.4 bar(a) (110 °C) to the paddle dryer using humid exhaust air as a heat source (65 °C) and substitute steam generation from the steam boilers.

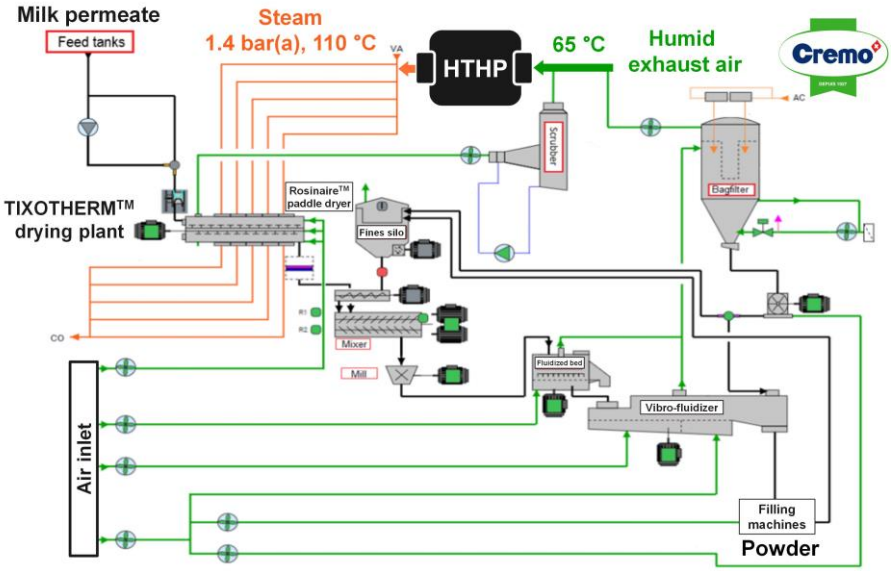


Fig. 5. Potential HTHP integration point at Cremo in the TIXOTHERMTM drying process with a RosinaireTM paddle dryer, where humid exhaust air could be used as a heat source to generate steam.

Figure 6 (left) shows the calculated Composite Curves (CCs) as the initial situation before the integration of a HTHP, indicating a Heat Recovery (HR) potential through direct heat transfer of about 600 kW between air flows and a Pinch temperature at around 70 °C. Furthermore, Figure 6 (middle) shows the corresponding Grand Composite Curve (GCC) with an integrated HTHP, providing a 940 kW condensation capacity at 120 °C and 570 kW evaporation capacity at 38 °C, from which a COP of 2.3 can be derived (see COP-fit formula in Figure 8). Finally, Figure 6 (right) shows the CCs after integrating the HTHP. The example demonstrates a potential reduction of the Hot Utility (HU) by 100% (from 940 to 0 kW) and the unused waste heat by 47% (from 1,204 to 634 kW), and an increase of the HR potential by 249% (from 605 to 2,113 kW).

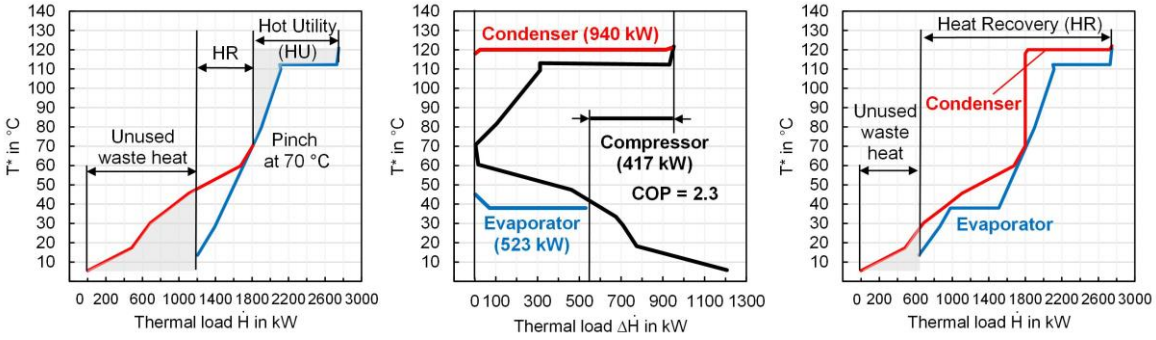


Fig. 6. Composite curves (CC, left) and grand composite curve (GCC, right) of the TIXOTHERM™ process with paddle dryer at Cremo showing the potential HTHP integration providing low-pressure steam at 110 °C and using humid exhaust air as a heat source (Pinch at 70 °C, evaporation temperature at 38 °C, condensation temperature at 120 °C, COP of 2.3).

A challenge is the low evaporation temperature (and thus the large temperature lift of 80 K) and the probably insufficient evaporation capacity if the waste heat is to be recovered exclusively from the drying process. Therefore, additional waste heat sources must be identified at about 35 to 40 °C. The estimated annual operating time of the potential HTHP is about 6,400 hours, which is within the range of various techno-economic studies presented in a literature review [21], [22]. The electricity price for a customer of the size of Cremo is 0.2 CHF/kWh$_{el}$, and the gas price is 0.11 CHF/kWh$_{th}$, corresponding to an electricity-to-gas price ratio of about 1.8. The CO_2 emission factor of electricity at Cremo is around the average Swiss consumer electricity mix of 0.128 kg CO_2/kWh$_{el}$ [29], as the mix contains renewables, just not purely renewables. Furthermore, a discount rate of 2% is used to estimate the discounted payback period of the HTHP investment. The cost multiplication factor for calculating planning and integration costs is assumed to be 2.0.

3.3. Case Study at Gustav Spiess AG

Gustav Spiess AG in Berneck (SG) produces meat products such as sausage, ham, and bacon. Today, a gas boiler provides steam (6 to 8 bar(a)) to heat the pasteurization and cooking/smoking cabinets (Figure 7). The steam pressure is reduced to 1.5 bar(a) (115 °C) to achieve cabinet temperatures of 85 to 90 °C and a sausage core temperature of about 72 °C. Here, integrating a 550 kW$_{th}$ steam-generating HTHP is under consideration, using the waste heat from the NH_3 chillers as a possible heat source at 40 to 50 °C. Typical operation is 12 hours per day, 250 days per year, resulting in an annual operating time of about 3,000 hours. The expected payback period for new energy-related infrastructure investments is about 8 to 10 years. The electricity price for medium-sized customers in the given area is 0.25 CHF/kWh, and the gas price is 0.17 CHF/kWh resulting in an electricity-to-gas price ratio of 1.5, which appears favorable for electricity-powered heating and cooling technologies. The purchased electricity mix is nuclear energy with a low CO_2 emission factor of about 0.012 kg CO_2/kWh$_{el}$. The cost multiplication factor accounting for planning and integration is assumed to be 2.0.

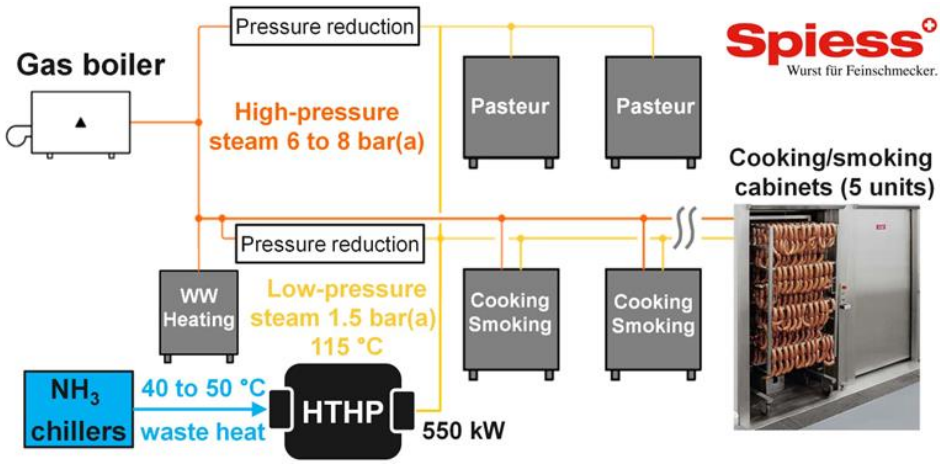


Fig. 7. Possible integration point of a steam-generating HTHP at Gustav Spiess AG for sausage cooking/smoking processes.

3.4. Economic evaluation and COP estimation

The economic evaluation of the case studies is based on a calculation tool developed in MS Excel, illustrated in Figure 8 [21], [22]. It assumes that the investment of the gas boilers is depreciated and that the gas boilers remain for production safety, redundancy, start-up operation, and peak load coverage. Input parameters to the evaluation tool are electricity price (c_{el}), gas price (c_{fuel}), operating hours (t), heating capacity ($\dot{Q}_h$), temperature lift between the heat source and sink (ΔT_{lift}), specific investment costs ($c_{inv,HP}$), maintenance cost factor ($f_{maintain}$), interest rate (i), the emissions factors of electricity and fuel (f_{CO2}), and CO_2 tax refund (subsidies). The output results are the COP, CO_2 emissions reduction ($\dot{m}_{CO2,reduction}$), annual cost savings ($C_{savings}$), and the payback periods (PP). The calculation tool helps to quickly evaluate the economic feasibility as a "go/no-go" decision.

1. First, the efficiency of the HTHP is estimated using the temperature lift (ΔT_{lift}) and a COP fit-curve ($COP = 52.94 \cdot {\Delta T_{lift}}^{-0.716}$) derived from quotes from various heat pump suppliers [21], [22].
2. Next, the investment costs ($C_{inv,HP}$) of the industrial HTHPs are evaluated based on the specific investment costs ($c_{inv,HP} = 3'157 \cdot {\dot{Q}_h}^{-0.322}$) according to price information from heat pump suppliers, the heating capacity ($\dot{Q}_h$), and a cost multiplication factor ($f_{inv,HP}$) accounting for planning and integration (typically between 1.5 to 4.0 depending on the complexity of integration, e.g., including heat storage, site's electrical installation, piping, hydraulics, etc.) [21], [22].
3. Then, the annual cost savings are calculated considering the following:
    - electricity cost (C_{el}) to operate the HTHP,
    - maintenance costs ($C_{maintain}$) of the HTHP using a multiplication factor ($f_{maintain}$) on capital cost (typically between 1.5% to 6%, in the case studies, 4% is used) [21], [22],
    - saved fuel costs (C_{fuel}) (assuming 90% boiler efficiency η_{fuel}), and
    - possible refunds of CO_2 reduction (C_{CO2}) (e.g., carbon taxes or subsidies).
4. After that, the payback period of the HTHP investment is evaluated as a trade-off between the investment costs versus the expected annual cost savings resulting from the heat pump investment.

5. Finally, the discount rates (i) are considered to calculate the discounted payback periods (DPP) [31], depending on the investor's risk tolerance (e.g., sector, company size, energy intensity, funding source, new technology, etc.) [32]. Typical discount rates for HP investments range from 5% to 15%, according to reviewed literature [21], [22]. The DPP (discounted payback period) is the period after which the cumulative discounted cash inflows cover the initial investment [31]. The DPP can therefore be interpreted as a period beyond which a project generates economic profit. In contrast, the static PP gives a period beyond which a project generates accounting profit.

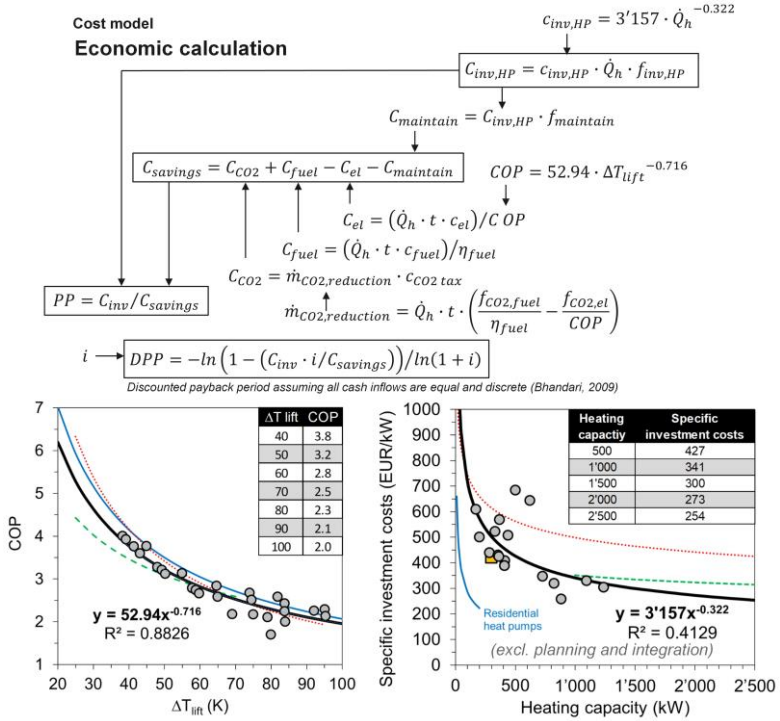


Fig. 8. Economic calculation, COP, and specific investment costs to derive the payback period for HTHP integration [21], [22].

4. Results and discussion

Table 3 summarizes the results of the three case studies. The calculations lead to payback periods of 2.0, 3.7, and 3.3 years, which means that HTHP integration would be cost-effective under current assumptions. Overall, the case study examples show significant annual energy savings of 55%, 60%, and 66%, and CO_2 emission reductions of 71%, 75%, and 98%, respectively. The COP varies between 2.0 and 2.7 according to the COP-fit function shown in Figure 8.

Table 3. Results of the case studies, with COP, energy savings, investment costs, reduction of CO_2 emissions, and payback periods.

Heat pump conditions	**Symbol**	**Unit**	**ELSA CIP process**	**Cremo Milk drying**	**Gustav Spiess Sausage cooking**	**Reference 2023 (Ref)**
Heat sink (outlet) temperature	$T_{h,out}$	°C	148	120	115	120
Heat source (inlet) temperature	$T_{c,in}$	°C	50	38	50	50
Temperature lift	ΔT_{lift}	K	98	82	65	70
Heating capacity	$\dot{Q}_h$	kW	3,150	940	550	1,000
Fuel (gas, oil) price	c_{fuel}	EUR/kWh	0.13	0.11	0.17	0.15
Electricity price	c_{el}	EUR/kWh	0.18	0.20	0.25	0.35
Electricity-to-fuel price ratio	$p_{el/fuel}$	-	1.38	1.82	1.47	2.33
CO_2 tax (or subsidies)	$c_{CO2\,tax}$	EUR/tCO_2	0	0	0	92.5
Electricity CO_2 emissions factor	$f_{CO2\,el}$	kgCO_2/kWh	0.128	0.128	0.012	0.128
Fuel CO_2 emissions factor	$f_{CO2\,fuel}$	kgCO_2/kWh	0.201	0.201	0.201	0.201
Annual operating time	t	h/a	7,200	6,400	3,000	6,400
The efficiency of fuel boiler	η_{fuel}	-	0.90	0.90	0.90	0.90

Maintenance factor (on capital costs)	$f_{maintain}$	-	0.04	0.04	0.04	0.04
Cost factor for planning & integration	$f_{inv,hp}$	-	3.0	2.0	2.0	3.0
COP ($COP = 52.94 \cdot \Delta T_{lift}{}^{-0.716}$)	COP	-	2.0	2.3	2.7	2.5
Specific investment costs ($c_{inv,HP} = 3'157 \cdot \dot{Q}_h{}^{-0.322}$)	$c_{inv,hp}$	EUR/kW	236	348	414	341
Annual CO_2 emissions reduction	$\dot{m}_{CO2,reduction}$	tCO_2/a	3,604	1,002	361	1,105
Annual CO_2 emissions reduction	-	-	71%	75%	98%	77%
Annual energy savings	$E_{savings}$	MWh/a	13,782	4,019	1,214	4,579
Annual energy savings	-	-	55%	60%	66%	64%
Investment costs	$C_{inv,hp}$	kEUR	2,230	655	455	1,024
Annual fuel cost savings	C_{fuel}	kEUR/a	3,276	735	312	1,067
Annual electricity costs	C_{el}	kEUR/a	2,055	533	155	886
Annual heat pump maintenance costs	$C_{maintain}$	kEUR/a	89	26	18	41
Annual CO_2 tax compensation	C_{CO2}	kEUR/a	0	0	0	102
Annual cost savings	$C_{savings}$	kEUR/a	1132	176	139	242
Discount rate	i	-	0.10	0.02	0.05	0.10
Payback period	PP	years	2.0	3.7	3.3	4.2
Discounted payback period	DPP	years	2.3	3.9	3.7	5.8

The case study ELSA has the highest temperature lift of 98 K and consequently the lowest COP as well as a cost multiplication factor for planning and integration of 3.0, but benefits from favorable electricity-to-gas price ratio and low specific investment costs due to the large HTHP (economies of scale).

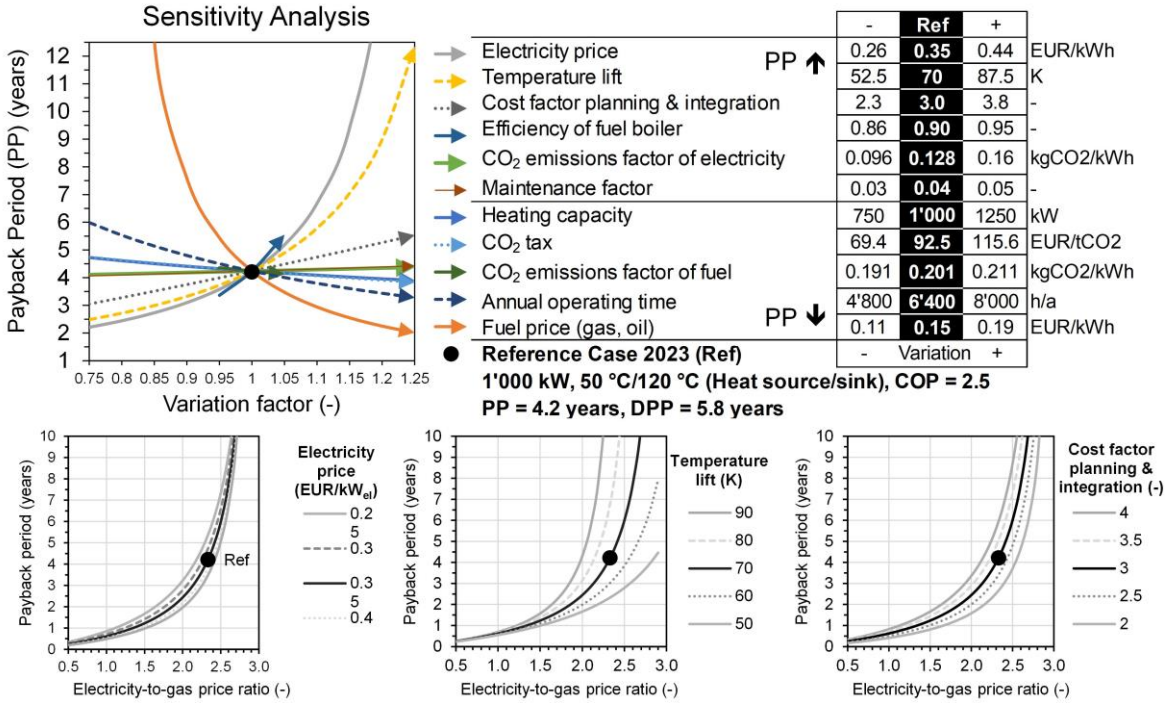
In the Cremo case study, the electricity-to-gas price ratio is higher, and the integration factor is 2.0, but the discount rate is low, leading to a DPP of 3.9 years. The pinch analysis is a powerful tool to determine the optimal placement of a HTHP, its size, and adequate evaporation and condensation temperatures.

The case study of Gustav Spiess AG shows a high CO_2 emission reduction of 98% because the company benefits from low CO_2 emissions by purchasing nuclear power. Using waste heat from the NH_3 chillers as a heat source shows great multiplication potential in other case studies in the Swiss food industry, where refrigeration machines for cooling foods are state of the art.

In addition to the three case studies, Table 3 also shows the results of the payback period for a possible Reference Case 2023 (Ref) with a heat source of 50 °C, a heat sink of 120 °C (COP of 2.5), and 1 MW heating capacity, and specific investment costs of 341 EUR/kW_{th}. This scenario uses a discount rate of 10%, an average Swiss consumer electricity mix with a CO_2 emission factor of 0.128 $kgCO_2/kWh_{el}$ [29], and a possible carbon tax refund of EUR 92.5/tCO_2 due to the reduction of CO_2 emissions. Electricity and gas prices are based on market data for 2023 [33] (0.15 EUR/kWh PEGAS NCG Year Future and 0.35 EUR/kWh Phelix Year Future, price ratio 2.33, as of December 11, 2022).

Figure 9 shows a sensitivity analysis of the payback period for the Reference Case 2023 (abbreviated as Ref). All input factors of the model were individually varied from -25% to +25% (factor 0.75 to 1.25), while the other parameters were kept constant. The sensitivity analysis reveals that the payback period is strongly sensitive to a change in electricity and fuel prices as well as the temperature lift of the heat pump.

Favorable conditions for HTHPs are higher values of fuel prices, operating time, fuel CO_2 emission factor, CO_2 tax, heating capacity, and lower electricity prices. In addition, an increasing CO_2 tax, along with subsidies and possible CO_2 compensation through the European emission trading system increase the financial incentives for HTHPs.



	-	Ref	+	
Electricity price (PP ↑)	0.26	**0.35**	0.44	EUR/kWh
Temperature lift	52.5	**70**	87.5	K
Cost factor planning & integration	2.3	**3.0**	3.8	-
Efficiency of fuel boiler	0.86	**0.90**	0.95	-
CO_2 emissions factor of electricity	0.096	**0.128**	0.16	kgCO2/kWh
Maintenance factor	0.03	**0.04**	0.05	-
Heating capacity	750	**1'000**	1250	kW
CO_2 tax	69.4	**92.5**	115.6	EUR/tCO2
CO_2 emissions factor of fuel	0.191	**0.201**	0.211	kgCO2/kWh
Annual operating time (PP ↓)	4'800	**6'400**	8'000	h/a
Fuel price (gas, oil)	0.11	**0.15**	0.19	EUR/kWh
	-	Variation	+	

Fig. 9. Sensitivity analysis of the payback period for a Reference Case 2023 (Ref) at 50 °C/120 °C heat source/sink, 1'000 kW heating capacity, and an electricity-to-gas price ratio of 2.33. The graphs below show the impact of electricity price, temperature lift, and cost factor for planning & integration on the payback period as a function of the electricity-to-gas price ratio.

On the other hand, low gas and high electricity prices lead to unfavorable conditions and are significant barriers to the investment of industrial HTHPs. As seen in the lower diagrams of Figure 9, the payback period is strongly determined by the electricity-to-gas price ratio. Above a price ratio of 2.7, the payback period is more than 10 years. In addition, the payback period is strongly influenced by the temperature lift, which determines the COP and, thus, the operating cost of the HTHP and the avoided fuel consumption.

For given energy prices and temperature lift, the cost multiplication factor for planning & implementation leads to significant uncertainty in quantifying the payback period. The cost multiplication factor depends on the complexity of the HTHP integration and can only be properly determined after a thorough analysis of the project and indicative price quotations for the entire heating system implementation.

5. Conclusions

A simple cost model was developed to pre-assess the economic feasibility of integrating HTHPs into actual industrial processes based on investment costs and annual cost savings. The analyzed HTHP integrations at ELSA, Cremo, and Gustav Spiess show significant annual energy savings of 55%, 60%, and 66%, and CO_2 emission reductions of 71%, 75%, and 98%, respectively. The calculations lead to payback periods of 2.0, 3.7, and 3.3 years, which means that the integration of HTHP would be cost-effective under the current assumptions. However, it should be noted that the financial evaluation strongly depends on the individual case. A sensitivity analysis has shown that higher fuel prices mainly shorten the payback period. An electricity-to-gas price ratio below 2.7 leads to payback periods below 10 years. Temperature lifts below 70 K appear to be profitable. Economic challenges arise with high temperature lifts, low gas prices, and high discount rates. Overall, the availability of closed-cycle HTHP products and steam compressors shows that the case studies are technically feasible with the integration concepts presented. A wide range of HTHP products is available up to 120 to 160 °C supply temperature. Individual HTHP products achieve temperature lifts of up to 125 K. HTHPs are also available in the large heating capacity range >10 MW. More detailed discussions with HTHP manufacturers are required in the next step to clarify the end-user-specific integration conditions. In addition,

the cost model can be applied to other Swiss case studies for initial cost estimation. Future work could include integrating an advanced heat pump model that considers the effects of refrigerant, compressor efficiency, and cycle design.

Acknowledgments

The project team gratefully acknowledges the Swiss Federal Office of Energy (SFOE) for the financial support of the R&D project Annex 58 HTHP-CH (Contract number SI/502336-01) and the SWEET (SWiss Energy research for the Energy Transition) project DeCarbCH (DeCarbonisation of Cooling and Heating in Switzerland) (www.sweet-decarb.ch).

Nomenclature

$\dot{Q}_h$	Heating capacity	kW	$C_{inv,HP}$	Investment costs of HP	EUR
ΔT_{lift}	Temperature lift	K	$\dot{m}_{CO2,reduction}$	Annual CO_2 emissions reduction	tCO_2/a
$c_{inv,HP}$	Specific investment costs of HP	EUR/kW	$E_{savings}$	Annual energy savings	kWh/a
$f_{inv,HP}$	Cost factor for planning & HP integration	-	C_{fuel}	Annual fuel cost savings	EUR/a
t	Annual operating time	h/a	C_{el}	Annual electricity costs	EUR/a
$f_{maintain}$	Maintenance factor (on capital costs)	-	$C_{maintain}$	Annual HP maintenance costs	EUR/a
η_{fuel}	Efficiency of gas boiler	-	C_{CO2}	Annual CO_2 tax compensation	EUR/a
i	Discount rate	-	$C_{savings}$	Annual cost savings	EUR/a
c_{fuel}	Fuel price (gas, oil)	EUR/kWh	PP	Payback period	a
c_{el}	Electricity price	EUR/kWh	DPP	Discounted payback period	a
$c_{CO2\ tax}$	CO_2 tax	EUR/tCO_2			
$f_{CO2,el}$	CO_2 emissions factor electricity	$kgCO_2/kWh$			
$f_{CO2,fuel}$	CO_2 emissions factor fuel	$kgCO_2/kWh$			

References

[1] M. Zogg, “History of Heat pumps: Swiss Contributions and International Milestones,” 2008. https://www.zogg-engineering.ch/publi/HistoryHP.pdf.

[2] FWS, “Statistik 2021, Fachvereinigung Wärmepumpen Schweiz,” 2021. https://www.fws.ch/wp-content/uploads/2022/05/FWS-Statistiken-2021-V2.pdf.

[3] S. Renz, “Heat Pump Market Development in Switzerland, Market Report,” *Heat Pump. Technol. Mag.*, vol. 38, no. 1, pp. 19–22, 2020, [Online]. Available: https://heatpumpingtechnologies.org/publications/heat-pump-market-development-in-switzerland/.

[4] B. Vonlanthen, “Erfolgsgeschichte der Wärmepumpen in der Schweiz,” in *News aus der Wärmepumpen-Forschung, 25. Tagung des BFE-Forschungsprogramms “Wärmepumpen und Kälte”, 26. Juni 2019, BFH Burgdorf*, 2019, pp. 7–16.

[5] C. Arpagaus, F. Bless, S. S. Bertsch, and J. Schiffmann, “Wärmepumpen für die Industrie: Eine aktuelle Übersicht,” in *25. Tagung des BFE-Forschungsprogramms “Wärmepumpen und Kälte”, 26. Juni 2019, BFH Burgdorf, Schweiz*, 2019, pp. 1–15.

[6] C. Arpagaus, F. Bless, M. Uhlmann, J. Schiffmann, and S. S. Bertsch, “High temperature heat pumps: Market overview, state of the art, research status, refrigerants, and application potentials,” *Energy*, vol. 152, pp. 985–1010, Jun. 2018, doi: 10.1016/j.energy.2018.03.166.

[7] C. Arpagaus, *Hochtemperatur-Wärmepumpen: Marktübersicht, Stand der Technik und Anwendungspotenziale, 138 Seiten, ISBN 978-3-8007-4550-0 (Print), ISBN 978-3-8007-4551-7 (E-Book)*. Offenbach, Berlin: VDE Verlag GmbH, 2018.

[8] N. Calame, F. Rognon, and O. Sari, “High Temperature Heat Pumps for Industrial Processes - State of the Art and Research Needs,” in *23. Tagung des Forschungsprogramms Wärmepumpen und Kälte des Bundesamts für Energie BFE, 14. Juni 2017, Burgdorf*, 2017, pp. 1–17.

[9] C. Arpagaus, J. Payá, A. H. Hassan, and S. S. Bertsch, “Potential Impact of Industrial HTHPs on the European Market,” in *3rd HTHP Symposium, 29-30 March, 2022, Copenhagen, Denmark*, 2022, p. Poster, [Online]. Available: http://hthp-symposium.org/hthp-symposium-2022/.

[10] Bundesamt für Energie (BFE), “Analyse des schweizerischen Energieverbrauchs 2000 - 2018 nach Verwendungszwecken,” 2019. [Online]. Available: https://www.bfe.admin.ch/bfe/en/home/supply/statistics-and-geodata/energy-statistics/analysis-of-energy-consumption-by-specific-use.html.

[11] T. Fleiter *et al.*, “Profile of heating and cooling demand in 2015, Deliverable D3.1 Report, Heat Roadmap Europe,” *HeatRoadmapEU*, no. 695989, p. 70, 2017, [Online]. Available: https://heatroadmap.eu/wp-content/uploads/2018/11//HRE4_D3.1.pdf.

[12] M. J. S. Zuberi *et al.*, “Decarbonizing Swiss industrial sectors by process integration, electrification, and traditional energy efficiency measures,” in *Eceee Industrial Summer Study Proceedings, Industrial Efficiency 2020 Decarbonise industry! 14–17 September 2020 Online event*, 2020, pp. 307–318, [Online]. Available: https://www.eceee.org/library/conference_proceedings/eceee_Industrial_Summer_Study/2020/4-technology-products-and-systems/decarbonizing-swiss-industrial-sectors-by-process-integration-electrification-and-traditional-energy-efficiency-measures.

[13] C. Arpagaus *et al.*, “HTHP-CH – Integration of High-Temperature Heat Pumps in Swiss Industrial Processes,” in *28. Tagung des BFE-Forschungsprogramms «Wärmepumpen und Kältetechnik» 22. Juni 2022, BFH Burgdorf*, 2022, pp. 1–9, [Online]. Available: https://www.sweet-decarb.ch/fileadmin/downloads/Presentations_File/HTHP-CH_Tagungsband.pdf.

[14] BAFU, “CO2 -Emissionsfaktoren des Treibhausgasinventars der Schweiz, Faktenblatt, Januar 2022, Bundesamt für Umwelt BAFU,” 2022. https://www.bafu.admin.ch/dam/bafu/en/dokumente/klima/fachinfo-daten/CO2_Emissionsfaktoren_THG_Inventar.pdf.download.pdf/Faktenblatt_CO2-Emissionsfaktoren_01-2022_DE.pdf.

[15] Bundesamt für Umwelt (BAFU), “8. How climate-friendly is the Swiss energy supply? Last modification 02.10.2018,” 2018. www.bafu.admin.ch/bafu/de/home/themen/klima/klimawandel--fragen-und-antworten.html.

[16] C. Arpagaus, L. Brendel, S. Paranjape, F. Bless, M. Uhlmann, and S. Bertsch, “High-Temperature Heat Pumps for Industrial Applications - New Developments and Products for Supply Temperatures above 100 °C,” 2022, [Online]. Available: https://www.youtube.com/watch?v=HvCEWrG4uR0.

[17] S. Wolf, R. Flatau, P. Radgen, and M. Blesl, “Systematische Anwendung von Großwärmepumpen in der Schweizer Industrie, Endbericht, 10. Mai 2017.” pp. 1–47, 2017, [Online]. Available: https://www.bfe.admin.ch/bfe/de/home/news-und-medien/publikationen.exturl.html/aHR0cHM6Ly9wdWJkYi5iZmUuYWRtaW4uY2gvZGUvcHVibGljYX/Rpb24vZG93bmxvYWQvODY3Ng==.html.

[18] Bundesaft für Energie (BFE), “Energiestrategie 2050,” 2021. https://www.bfe.admin.ch/bfe/de/home/politik/energiestrategie-2050.html.

[19] Bundesamt für Umwelt (BAFU), “Klimastrategie 2050,” 2021. https://www.bafu.admin.ch/bafu/de/home/themen/klima/fachinformationen/emissionsverminderung/verminderungsziele/ziel-2050/klimastrategie-2050.html.

[20] R. De Boer *et al.*, “Strengthening Industrial Heat Pump Innovation, Decarbonizing Industrial Heat, White Paper,” 2020.

[21] C. Arpagaus and F. Bless, “Techno-economic analysis of steam generating heat pumps for integration into distillation processes,” 2022, doi: http://dx.doi.org/10.18462/iir.gl2022.0029.

[22] C. Arpagaus, F. Bless, and S. S. Bertsch, “Techno-Economic Analysis of Steam-Generating Heat Pumps in Distillation Processes,” 2022, [Online]. Available: http://hthp-symposium.org/hthp-symposium-2022/.

[23] D. Flórez-Orrego, M. E. G. Domingos Ribeiro, and F. Maréchal, “A systematic framework for the multi-time integration of industrial complexes and urban systems,” in *7th International Conference on Contemporary Problems of Thermal Engineering, CPOTE 2022, 20-23 September 2022, Warsaw, Poland*, 2022, pp. 1–23.

[24] D. Flórez-Orrego, E. A. Pina, M. Ribeiro Domingos, S. Sharma, and F. Maréchal, “High temperature heat pumps applications for industrial separation and drying processes,” in *Proceedings of ECOS 2022 - The 35th International Conference on Efficiency, Cost, Optimization, Simulation and Environmental Impact of Energy Systems, July 4-7, 2022, Copenhagen, Denmark*, 2022, pp. 1001–1009.

[25] IEA HPT, “IEA HPT Annex 58 about HTHPs (Website), Task 1: Technologies - State of the art and ongoing developments for systems and components,” 2022. https://heatpumpingtechnologies.org/annex58/task1/.

[26] F. Bless, C. Arpagaus, S. S. Bertsch, and J. Schiffmann, “Theoretical analysis of steam generation methods - Energy, CO 2 emission, and cost analysis,” *Energy*, vol. 129, pp. 114–121, Jun. 2017, doi: 10.1016/j.energy.2017.04.088.

[27] ElCom, “Strompreise Schweiz, 17,97 Rp./kWh 2023, Groupe E SA, Estavayer,” 2023. https://www.strompreis.elcom.admin.ch/municipality/2054?category=C7.

[28] WBF, “Preisüberwachung: Gaspreise in der Schweiz, Typ X,” 2022. http://gaspreise.preisueberwacher.ch.

[29] FOEN, “Climate change: Questions and answers, 8. How climate-friendly is the Swiss energy supply? Federal Office for the Environment,” 2022. https://www.bafu.admin.ch/bafu/en/home/topics/climate/questions-answers.html.

[30] J. Písecký, “Spray drying in the cheese industry,” *Int. Dairy J.*, vol. 15, no. 6–9, pp. 531–536, Jun. 2005, doi: 10.1016/j.idairyj.2004.11.010.

[31] S. B. Bhandari, “Discounted Payback Period - Some Extensions,” in *Proceedings of ASBBS Annual Conference, Las Vegas, February 2009*, 2009, vol. 16, no. 1, pp. 1–10.

[32] European Commission, “EU Reference Scenario 2020 Energy, Transport and GHG Emissions - Trends to 2050,” 2021. https://op.europa.eu/s/shWr.

[33] Enerprice Partners AG, “Market prices 2023, as of December 11, 2022, Electricity - Phelix Year Future, Gas - PEGAS NCG Year Future,” 2022. https://www.enerprice.ch/charts.

14th IEA Heat Pump Conference
15-18 May 2023, Chicago, Illinois

Analysis of the performance of a heat pump with subcooling control as a function of the refrigerant charge

Belén Llopis-Mengual[a], Emilio Navarro-Peris[a]*

[a]Instituto Universitario de Investigación de Ingeniería Energética (IUIIE), Universitat Politècnica de València (UPV), Camino de Vera s/n, 46022, Valencia, Spain

Abstract

When using hydrocarbons like propane (R290) as a refrigerant in heat pumps, it is critical to detect if the system is undercharged to find potential leaks, as they are flammable. This is specially challenging in reversible air-to-water heat pumps where a liquid receiver to compensate for the charge fluctuations is commonly installed. This liquid receiver introduces some tolerance of the system to charge fluctuations which are desirable from the system performance point of view but also makes especially difficult the pre-diagnosis of a possible leak. This study has experimentally characterized the performance with different refrigerant charge levels of a reversible air-to-water propane heat pump with a liquid receiver at the compressor inlet and a variable-speed compressor. It has different control strategies: superheat control for cooling and subcooling for heating mode. The work shows the evolution of the most important system variables like discharge, condensation, and evaporation temperature, as well as subcooling and superheat, and which could be the impact on the system performance. Finally, the use of compressor speed as a tool to diagnose potential system undercharge faults have been pointed out as a promising strategy.
© HPC2023.
Selection and/or peer-review under the responsibility of the organizers of the 14th IEA Heat Pump Conference 2023.

Keywords: refrigerant charge; subcooling control; air-to-water heat pump; undercharge fault; R290

1. Introduction

Nowadays, attempts are being made to reduce the energy consumption in heating, cooling, and domestic hot water, since it accounts for the 80% of the energy that citizens consume [1]. Heat pumps that use outdoor air to heat water for heating and domestic hot water can undoubtedly contribute to this. In addition, if they are reversible, they can also provide cold water for air-conditioning. According to [2], heat pump sales grew by 34% in Europe in 2022, and within a short period of time, heat pump installations are expected to increase.

Concerning the refrigerants used in these systems, the European Union currently restricts a large number of hydrofluorocarbons (HFCs), which are the ones that have been used the most. The main alternatives, harmless to the ozone layer and without influence upon the greenhouse effect, are natural refrigerants such as carbon dioxide, ammonia, and hydrocarbons. However, the latter has a safety problem, given the refrigerant's flammability. Thus, it is critical to detect if refrigerant charge leakage occurs. Sensors that detect this are currently expensive or require much maintenance and must be replaced regularly. Besides, understanding how the system will behave if this fault occurs is also essential for early detection and proper maintenance.

Many experimental tests have been conducted to evaluate the system performance with refrigerant charge variation. For example, [3] analyzes the performance with the charge level of several split and rooftop air-source heat pumps with refrigerants R410A and R407C and with different compressors and expansion devices. Another is [4], which also imposes different refrigerant charge levels, among other faults, to a split residential heat pump in cooling mode with a Thermal Expansion Valve, measuring the effect on variables with these faults. In this work [5], they use experimental tests with different refrigerant charge levels to generate a virtual

* Corresponding author. Tel.: +34963879123
E-mail address: emilio.navarro@iie.upv.es

refrigerant charge sensor. They use several types of systems, both air-to-air and water-to-water, with variable speed compressors and some of them reversible for cooling and heating, with accumulators at the condenser outlet to compensate for different charge requirements between modes. In the latter case, they conclude that their virtual sensor does not work well with higher refrigerant levels in the accumulator because charge variations did not significantly change the vapor compression cycle variables. A similar conclusion is reached in this study [6], in which they simulate undercharge faults in a refrigeration system with a liquid line receiver but obtain significant differences in the prediction of system variables under low charge conditions due to the presence of the accumulator.

Nevertheless, there are few studies on reversible air-to-water heat pumps on their performance depending on the refrigerant charge. In this type of system, the analysis is essential because when changing between cooling or heating modes, the refrigerant charge requirements and the difference in internal volume between heat exchangers generate particular behaviors. In this study [7], they experimentally analyze the refrigerant mass distribution of each component of the cycle in an invertible air-to-water heat pump with R32, showing significant differences in the refrigerant charge distribution depending on the conditions.

To address this issue, some studies like [8] have shown that it is beneficial for such reversible systems to use an accumulator in the compressor suction to compensate for charge variations depending on the mode of operation. With this, the subcooling is regulated by the expansion valve instead of the superheat. Besides, some works as [9] study different subcooling control strategies with this system to optimize the performance of a heat pump.

In the present work, it is experimentally investigated the influence of the charge in a reversible air-to-water propane heat pump with different operating modes: cooling mode with superheat control and heating mode with subcooling control. The system has an accumulator at the compressor suction and uses a variable-speed compressor. The study analyzes the variables that would allow the detection of refrigerant leaks in this system in heating mode, given its particularity of subcooling control with an accumulator in the compressor suction which acts as a charge reservoir.

2. Methodology

2.1. Experimental setup

In this study, it is conducted an experimental campaign with a reversible air-to-water heat pump with 7 kW of nominal capacity that uses R290 (propane) as a refrigerant. Figure 1 shows the schematic of the system, whose main components are: a rotary variable speed compressor, a brazed plate heat exchanger (BPHX), a finned-tube heat exchanger, an electronic expansion valve (EEV), and a liquid accumulator at the compressor suction. In addition, the system has a reversible valve or 4-way valve for switching between modes.

The main differences between modes are the following. In cooling mode, the BPHX is the evaporator used to cool water, and the EEV maintains a constant superheat (SH) at the compressor suction (the superheat is taken as the difference between the compressor inlet temperature and the evaporation temperature). However, in heating mode, the BPHX is used as a condenser to heat water, and the EEV maintains a constant subcooling (SC) at the condenser outlet (the subcooling is taken as the difference between the condensing temperature and the condenser outlet temperature). The manufacturer designs this heat pump with the target of optimizing the heating mode. This mode is the one in which the system is going to work more hours during the year.

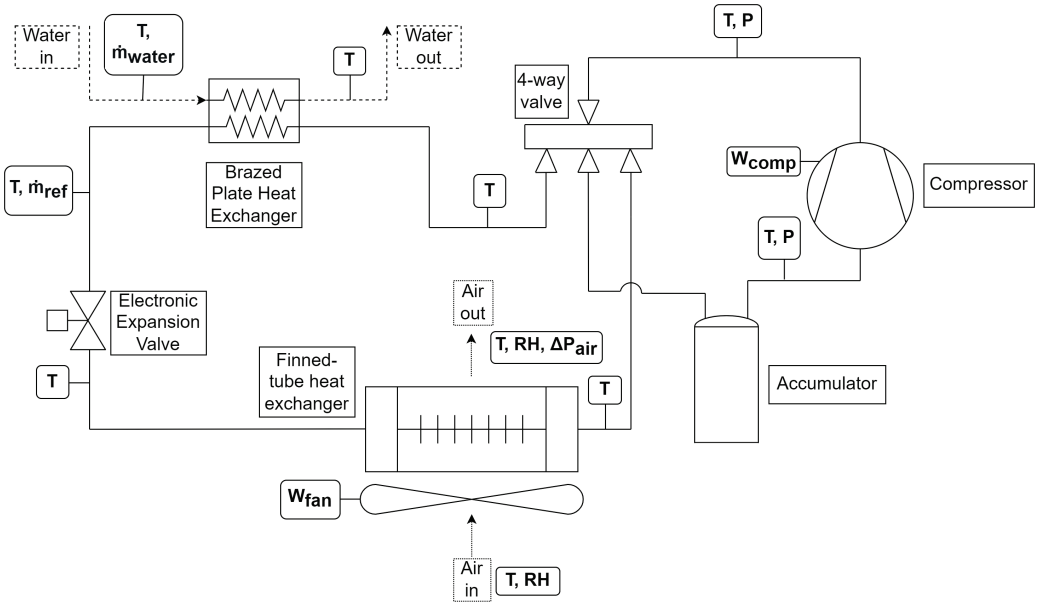


Fig. 1. Experimental setup of the reversible air-to-water heat pump

The unit is tested in a psychrometric chamber capable of recreating the needed working conditions of the heat pump. Figure 1 shows the location of the sensors in the system. These are compressor suction and discharge pressure, refrigerant temperature before and after each component, and water and air temperature. In addition, the refrigerant mass flow rate in heating mode was measured with a Coriolis flowmeter installed at the outlet of the BPHX (condenser in heating). To obtain the refrigerant flow rate in cooling mode, it was measured the water flow rate with a Coriolis flowmeter. From this, it is obtained the refrigerant flow rate with the corresponding balance in the BPHX. In addition, an averaging pitot tube flowmeter is used to obtain the fan's airflow. The refrigerant charge used in each test is measured with a Gram LHK-150 scale, with a resolution of 10g. Table 1 lists the instruments used and their range and total error from the uncertainty analysis.

Table 1. Measurement instruments and their range and uncertainties.

Measurement	**Instrument**	**Range**	**Total error**
Refrigerant temperature	Thermocouple type T	-270-400 ºC	±0.8 (ºC)
Water and air temperature	Thermoresistance PT-100	-220-850 ºC	±0.07 (ºC)
Suction and discharge pressure	Pressure transducer Rosemount 3051	0-15 bar (suction) 10-45 bar (discharge)	±0.06 (bar)
Refrigerant mass flow rate	Coriolis flowmeter Micro Motion CMFS015M	0-5600 kg/h	±0.13 (kg/h)
Water mass flow rate	Coriolis flowmeter Mass 2100	0-245 kg/h	±4.48 (kg/h)
Air relative humidity	Vaisala Humicap 180	0-100%	±2.77 (%)
Pressure drop in the air heat exchanger	Differential pressure transducer DPT-4001	0-25 Pa	±0.2 (Pa)

2.2. Test campaign

Table 2 shows the conditions at which the unit is tested. These correspond to both modes of operation, different air and water inlet conditions, and compressor speeds. Each of these conditions is tested for a range of refrigerant charges, which are defined as:

$$m_{ref}(\%) = \frac{m_{ref-test} - m_{ref-nominal}}{m_{ref-nominal}} \cdot 100 \quad (1)$$

Where $m_{ref-test}$ is the refrigerant charge at a given test and $m_{ref-nominal}$ the unit's nominal (standard) charge, indicated by the manufacturer. Thus, a refrigerant charge percentage of 85% means that the unit is charged with a 15% less refrigerant charge than the nominal that should have.

Table 2. Experimental testing conditions.

Mode	Test Condition	Inlet air dry bulb temperature (ºC)	Inlet water temperature (ºC)	Outlet water temperature (ºC)	Compressor velocity (rps)	Refrigerant charge (%)
Cooling	A23W18-80rps	23	23	18	80	85, 90, 95, 100, 105, 110
	A35W7-30rps	35	12	7	30	
	A35W18-60rps	35	23	18	60	
Heating	A10W45-80rps	10	38	45	80	
	A12W24-40rps	12	20	24	40	
	A2W35-35rps	2	32	35	35	
	A7W70-80rps	7	64	70	80	

2.3. Heat pump model

In this study, a model of the air-source heat pump using the dedicated software IMST-ART has been built, see [10] for a detailed description. This software allows modeling and simulating vapor compression cycles with their real components in detail. Particularly, it is able to perform a detailed simulation of the heat exchangers based on the most relevant heat transfer, void fraction, and pressure drop correlations of the literature considering variables like refrigerant charge or oil in the system.

In order to build the model, detailed geometrical information about heat exchangers and the variable speed compressor must be supplied. In addition, the catalogue data's cooling capacity and compressor power input are introduced for different compressor speeds. When a compressor speed is set as an input, the model calculates interpolating between the various compressor speeds entered. Then, this is converted into volumetric and compressor efficiencies to calculate the whole cycle.

3. Results and discussion

3.1. Cooling mode

In cooling mode, the heat pump has 2 control strategies:

a) Control a target SH to be maintained.
b) Control a subcooling of 3 K. This second condition is activated when the water inlet temperature is 7ºC or lower in order to avoid having evaporating temperatures lower than 0ºC.

To analyze the results obtained after the experimental campaign, the inputs measured in each case have been introduced in the model with the nominal charge. Thus, the refrigerant charge needed by the system in those conditions has been calculated. Table 3 shows the inputs used and the necessary refrigerant charge calculated for each of them. Thus, A23W18-80rps and A35W18-60rps need a higher charge (0.34 and 0.35 kg, respectively) and A35W7-30rps a lower one (0.28 kg). In addition, the target SH of the system in the cases with higher charge is 5-6 K, while the one with the lower charge is around 0 K. This can be achieved by having a liquid accumulator at the outlet of the evaporator that allows having saturation conditions at its outlet.

Table 3. Refrigerant charge needed for each test condition in cooling mode.

Test condition	Air inlet temperature (ºC)	Airflow (m3/h)	Water inlet temperature (ºC)	Water outlet temperature (ºC)	Compressor Speed (rps)	SC (K)	SH (K)	Total refrigerant charge (kg)
A23W18-80rps	23	732	23	18	80	18	5	0.34
A35W7-30rps	35	1257	12	7	30	3.5	0	0.28
A35W18-60rps	35	1226	23	18	60	14	6	0.35

Figure 2 shows the refrigerant charge accumulation in the A23W18-80rps condition, which needs 0.34 kg. Since in this condition, the target SH to be controlled is 5K, the accumulator at the outlet of the evaporator will be almost empty, and the refrigerant in the liquid state will be concentrated at the outlet of the condenser, which in cooling mode is the finned-tube. The SC measured with these conditions is 18K, a significant value since the refrigerant is located there. If the system is undercharged or refrigerant leakage occurs, the charge will be reduced from the condenser outlet, and therefore the main effect of observing is the SC, which decreases (Figure 4a). For the same reason, the condensation temperature (Figure 4b) will also be reduced. Figure 4c shows that the SH can be controlled even if the refrigerant charge increases or decreases to around 5K. Concerning the discharge temperature (Figure 4d), no significant changes are observed either since its variation with the charge will depend mainly on the state of the accumulator at the compressor's suction.

The A35W7-30rps condition requires less refrigerant charge than the previous one, and considering the low water temperature which introduces subcooling control instead of a superheat control, more charge will accumulate in the liquid state in the system (Figure 3). Thus, if refrigerant leakage occurs, it will reduce the amount of refrigerant in the accumulator, but SC (Figure 4a) or condensation temperature (Figure 4b) will be maintained at the same values. However, following Figure 4c, if the refrigerant charge is reduced to 90% of the nominal, it is observed that the measured SH, which controls the EEV, is 2K, and with 85% charge, 5K. It means that the refrigerant charge has been reduced from the accumulator. The system can no longer have saturation conditions at the outlet and maintain 0K of SH, changing the SH target. Furthermore, in Figure 4d, it is seen how the discharge temperature increases as the refrigerant charge is reduced since, by decreasing the level of liquid refrigerant in the accumulator, it enters with a higher vapor quality to the compressor, leading to a higher discharge temperature.

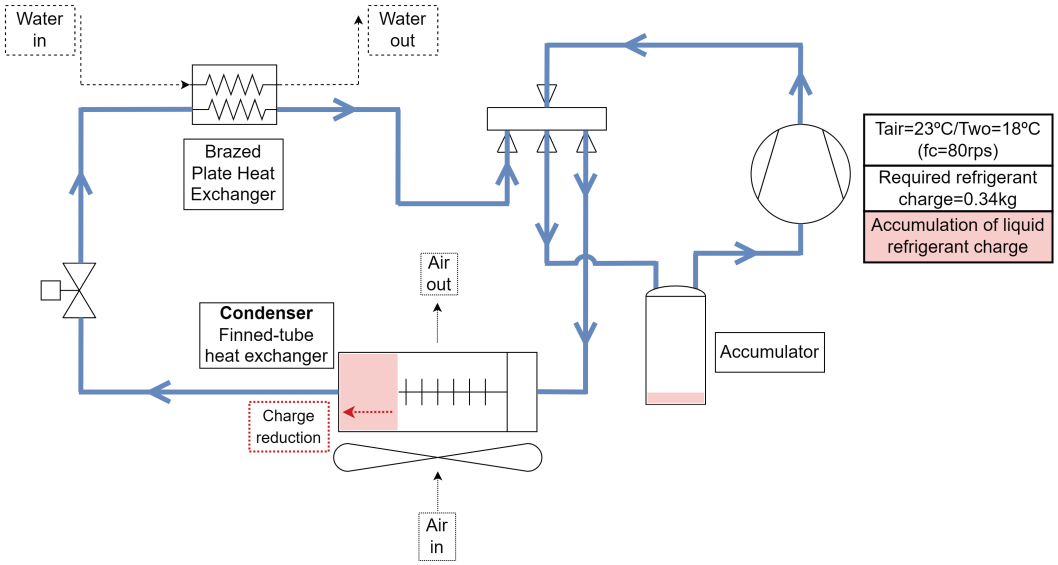


Fig. 2. Description of the accumulation of liquid refrigerant charge with the cooling mode condition of Tair=23ºC/Two=18ºC (fc=80rps).

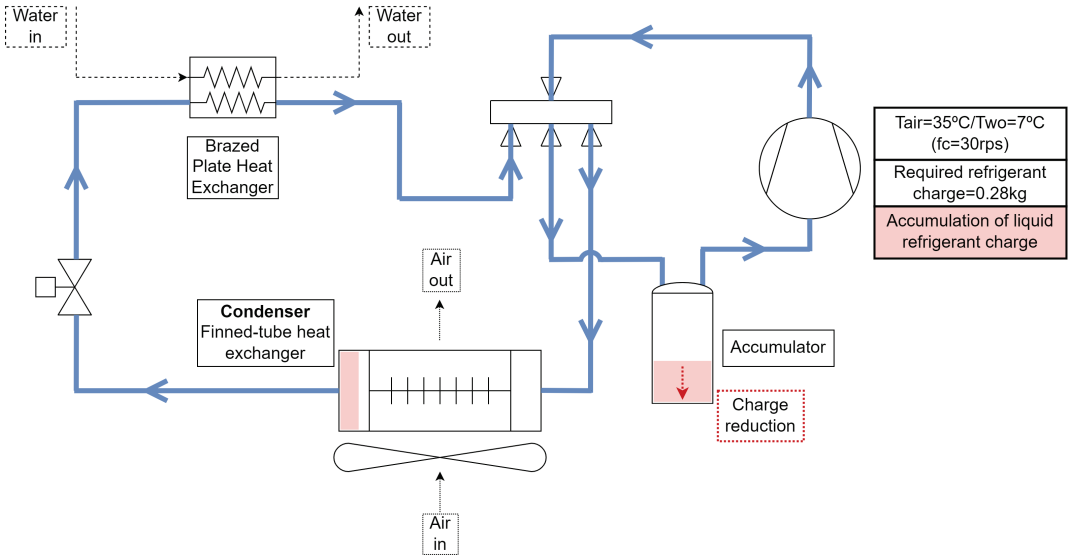


Fig. 3. Description of the accumulation of liquid refrigerant charge with the cooling mode condition of Tair=35ºC/Two=7ºC (fc=30rps).

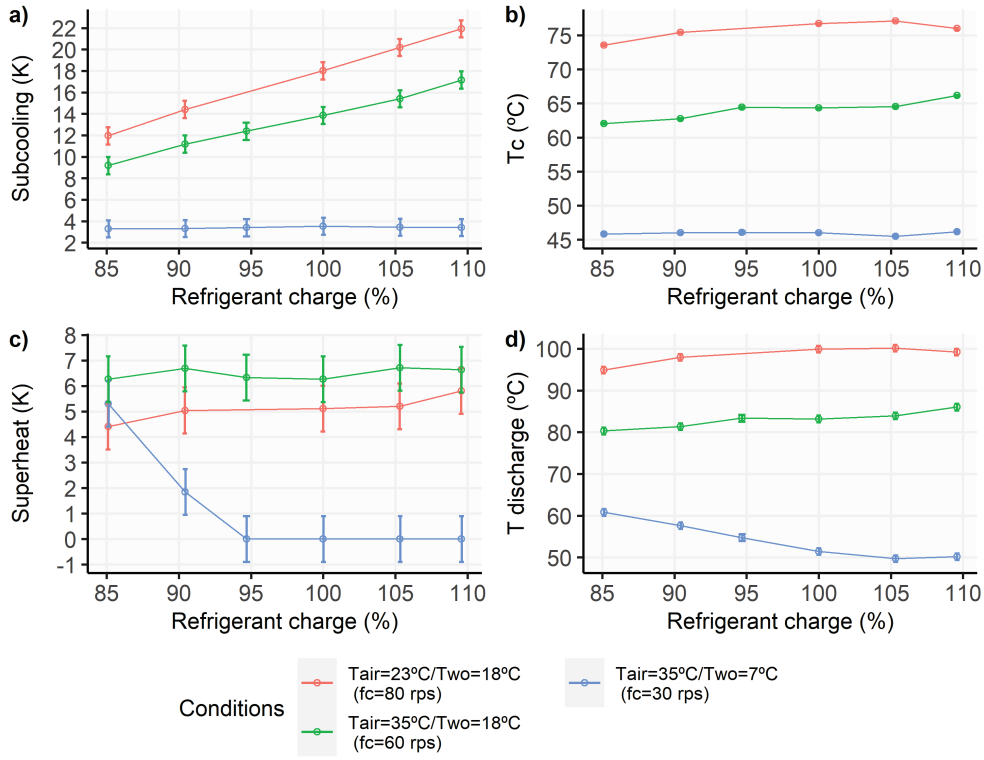


Fig. 4. Experimental measurements in cooling mode of a) subcooling, b) condensation temperature, c) superheat, and d) compressor discharge temperature.

3.2. Heating mode

In this mode, the EEV controls the SC at the condenser output instead of the SH. In this case, the SC target will be determined by a value that maximizes the COP in each condition, like the SH in cooling mode. Concerning the SH, the refrigerant in the liquid state will accumulate in the receiver at the evaporator outlet, ensuring saturation conditions and, therefore, SH of 0K. Table 4 shows the inputs to the model from the

measurements of each condition with 100% refrigerant charge. Thus, this table shows that the SH of each condition is 0K, being the evaporator outlet saturated and the target SC to be controlled by the EEV between 6 and 8 K, depending on the case. In addition, it is calculated with the model the refrigerant charge needed for each condition. Two conditions need more charge, A2W35-35rps, and A12W24-40rps, with required refrigerant charges of 0.53 and 0.47 kg, respectively. The A7W70-80rps and A10W45-80rps conditions need less refrigerant charge, both of them 0.35 kg.

Table 4. Refrigerant charge needed for each test condition in heating mode.

Test condition	Water inlet temperature (ºC)	Water outlet temperature (ºC)	Evaporator inlet temperature (ºC) and Relative Humidity (%)	Airflow (m3/h)	Compressor Speed (rps)	SC (K)	SH (K)	Refrigerant charge (kg)
A2W35-35rps	32	35	2 (60.94%)	1229	35	6.7	0	0.526
A7W70-80rps	64	70	7 (53.51%)	1246	80	7.4	0	0.353
A10W45-80rps	38	45	10 (32.00%)	943	80	8	0	0.346
A12W24-40rps	20	24	12 (36.77%)	796	40	6.4	0	0.465

To analyze how the system performance develops with the refrigerant charge, it is studied the evolution with the charge of some variables from the condition that needs more charge, which is A2W35-35rps with 0.53 kg, and one that needs less, which is A7W70-80rps. Thus, in the case of A2W35-35rps and following Figure 5, as this condition requires more refrigerant charge to operate, it accumulates less liquid refrigerant charge in the receiver at the evaporator outlet. When a situation of undercharge or refrigerant leakage occurs, it will be reduced from the accumulator, as the liquid refrigerant at the outlet of the condenser (in this mode, the BPHX) will be fixed, and the EEV controls that the same amount is maintained to have the same SC value (Figure 7a). However, as this condition needs a lot of refrigerant charge to operate, it is already observed in Figure 7c that for a charge reduction of 5%, saturation conditions cannot be maintained at the outlet of the evaporator (i.e., the accumulator is with a low liquid level) and the SH increases to 2K. At 85% refrigerant charge, a SH of 12K is reached. Furthermore, for this test point, it is seen in Figure 7b how the evaporation pressure and, thus, the evaporating temperature decrease accordingly. Figure 7d shows the evolution of the discharge temperature with the refrigerant charge. It is observed that as the charge decreases, the discharge temperature increases by reducing the level of the accumulator, and the refrigerant enters the compressor with a lower vapor quality.

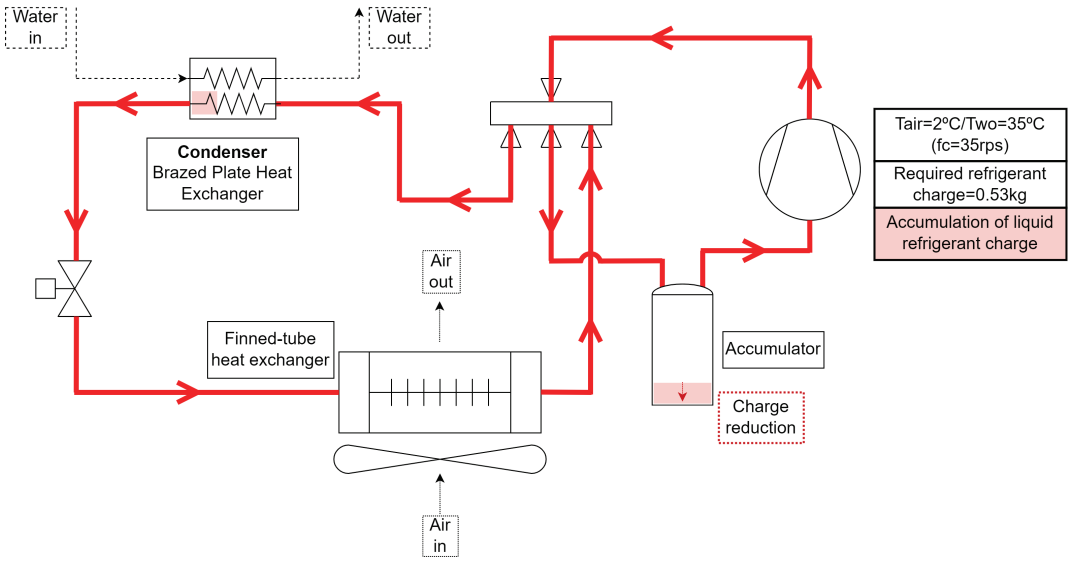


Fig. 5. Description of the accumulation of liquid refrigerant charge with the heating mode condition of Tair=2ºC/Two=35ºC (fc=35rps).

However, in the case of test condition A7W70-80rps, less refrigerant charge is needed than in the previously described condition. Therefore, it will accumulate more liquid refrigerant than in the previous case. This

refrigerant is collected in the accumulator at the evaporator outlet since, as in the previous case, the amount of refrigerant accumulated at the condenser outlet depends on the value controlled by the EEV, which will remain constant regardless of variations in the refrigerant charge (Figure 7a). Likewise, the refrigerant charge required to operate is lower, and the level of liquid refrigerant in the accumulator is higher, reducing the charge to 85% makes the level still enough to maintain saturation conditions at the outlet of the evaporator. Figure 7c shows how the SH is kept at 0K. Similarly, Figures 7b and 7d show how the evaporation and discharge temperature also do not vary when reducing the refrigerant charge, showing that the accumulator has a high refrigerant charge level.

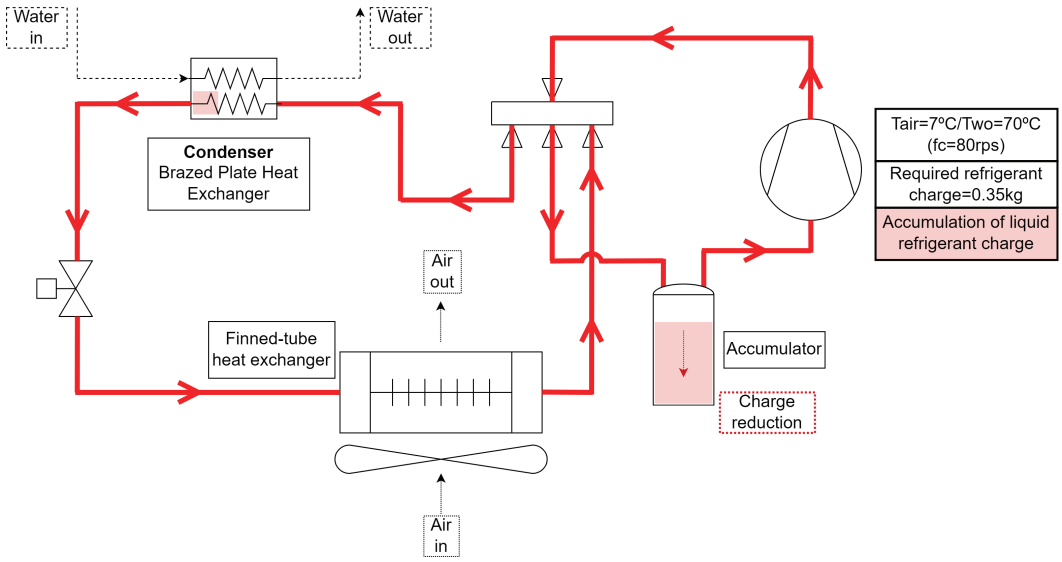


Fig. 6. Description of the accumulation of liquid refrigerant charge with the heating mode condition of Tair=7ºC/Two=70ºC (fc=80rps).

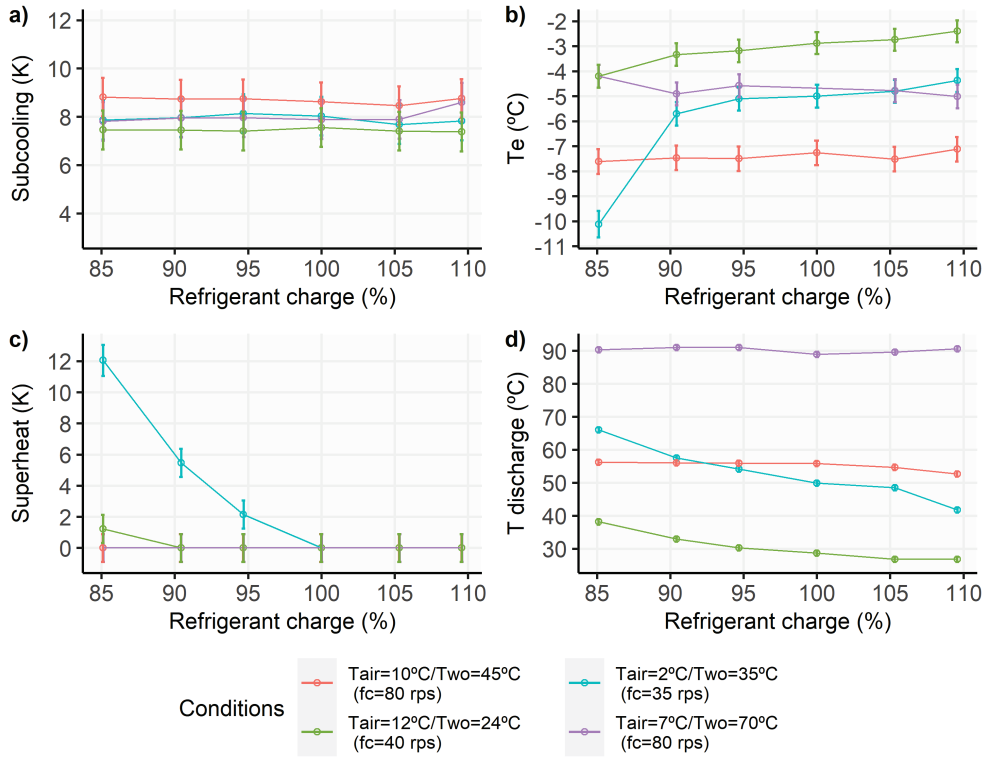


Fig. 7. Experimental measurements in heating mode of a) subcooling, b) evaporation temperature, c) superheat, and d) compressor discharge temperature.

With the experimental tests varying the refrigerant charge and the model it is possible to simulate the required charge in each condition, and it has been done a study varying some parameters. As it has been seen previously, the heat pump's performance will vary with the refrigerant charge depending on the condition. An analysis in heating mode has been done. Using the model, two usual application conditions in this mode have been selected (Twi=30ºC/Two=35ºC and Twi=65ºC/Two=70ºC) changing the compressor speed and the air inlet conditions (evaporator inlet). The SC has been maintained constant with a value of 7 K and a SH=0K, since it is assumed that, there will be enough liquid refrigerant in the accumulator to have saturation conditions at the evaporator outlet.

The refrigerant charge required by the system for each case has been obtained. The results are shown in Figure 8. It is observed that for low compressor speeds and low air temperature, the system needs more charge to operate. This is mainly because of the variation in the compressor speed which changes the suction conditions. By decreasing the compressor speed, evaporating pressure and the density increase, requiring more refrigerant charge. The required charge will be slightly higher for the case of Twi=30ºC/Two=35ºC than for Twi=65ºC/Two=70ºC. The zone denominated as "A" will have the performance previously described for A2W35-35rps (Figure 5). Since it needs more refrigerant charge to operate, the accumulator will have a lower liquid level. A 5% decrease in refrigerant charge will already cause changes in SH and discharge temperature, being much more pronounced with a 15% less charge. In the zone referred to as "B", the system needs a lower refrigerant charge to operate than in "A". It would be a refrigerant charge requirement similar to the tested conditions A12W24-40rps (0.47 kg). In this case, changes in discharge temperature and SH would be seen, but from a higher refrigerant reduction (15% in the case of the performed tests).

The rest of the contour plot that is not zone "A" or "B" in both Twi/Two conditions will follow the performance described for the A7W70-70rps condition (Figure 6). In them, despite reducing the refrigerant charge by 15%, the charge requirements for that operating point can be satisfied because the accumulator still has a high liquid level. Considering this, if a refrigerant leak happens, no change in the operating variables could be observed for conditions outside of zones A and B.

Therefore, an undercharge fault diagnostic method to be explored in heating mode for this air-to-water heat pump with subcooling control can be to change the compressor speed to low values and, to a lower degree, reduce the water outlet temperature, bringing the system to zone A or B. With this, it can be seen if there are deviations from the typical values in the system variables that the heat pump would have in a given operating condition with a 100% refrigerant charge, such as the SH, the discharge temperature, or the evaporation temperature.

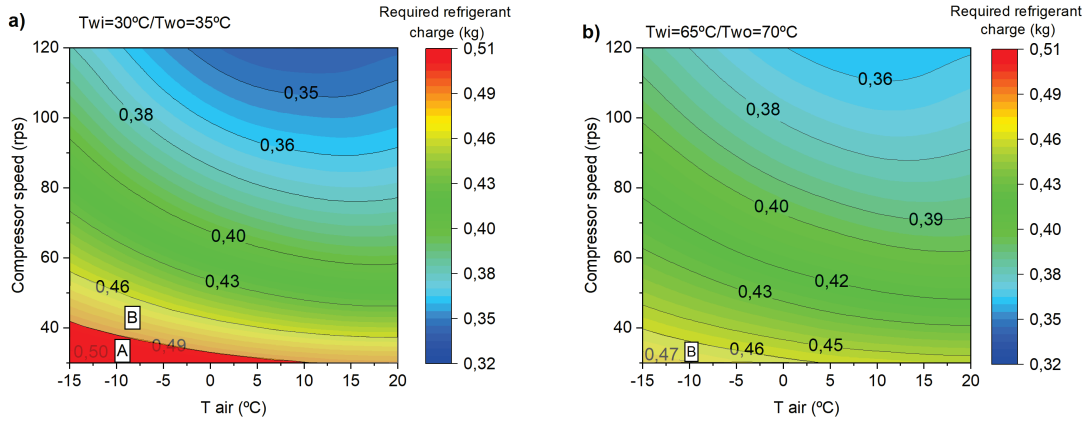


Fig. 8. Required system refrigerant charge with different compressor velocities and air inlet dry bulb temperature in heating mode. a) Twi=30ºC/Two=35ºC, b) Twi=65ºC/Two=70ºC.

4. Conclusions

This study presents an experimental campaign in which the dependence on the charge of a heat pump with a liquid receiver is analyzed, and it can be seen as a first step in order to determine future fault detection strategies in these systems. In cooling mode, the SH is controlled with an EEV, and in heating, the SC is controlled, having an accumulator that ensures SH=0K at the evaporator outlet. The study presents how the system variables change with the refrigerant charge and illustrates how the liquid refrigerant charge varies in the system in different conditions. Finally, the refrigerant charge required depending on the outdoor air conditions and compressor speed in heating mode is presented.

Some conclusions drawn are:

- In cooling mode, this system works by controlling the SH and therefore accumulating the refrigerant in a liquid state, mainly at the outlet of the condenser. Therefore, a refrigerant charge variation controlling SH>0K will cause the SC at the condenser outlet to increase or decrease as the charge increases or decreases respectively. The condensation temperature will also increase or decrease to a lower extent.
- In the case that the system controls the subcooling in cooling mode, a refrigerant charge higher than nominal will not cause changes. However, reducing it will cause changes in the discharge temperature and SH, as the liquid level in the accumulator will drop. The behaviour in these conditions is similar to the heating mode.
- In heating mode, the system controls the SC at the condenser outlet with the EEV, and the accumulator at the suction has a high refrigerant level, with SH=0. In conditions requiring a higher amount of charge, the accumulator will have a lower liquid level. Thus, reducing the refrigerant charge will increase the real SH and discharge temperature. Besides, to a lower degree, the evaporation temperature will drop.
- At these conditions, increasing the charge level will cause the discharge temperature to decrease and the evaporating temperature to increase slightly.
- At points that require a low refrigerant charge in heating mode, the accumulator level will be high, so by reducing the refrigerant charge by up to 15% in the tests, no changes in system variables are observed.
- In heating mode, at low compressor speeds, the heat pump needs more refrigerant charge to operate, being the more critical conditions from the charge point of view. The reduction of compressor speed in conditions that require a low refrigerant charge to diagnose an undercharge condition allows the observation of the deviation from the expected values in the discharge temperature and SH, so it results in an alternative to be explored in fault diagnosis of this kind of systems.

Nomenclature

BPHX	Brazed Plate Heat Exchanger	$m_{ref-nominal}$	Nominal refrigerant charge
EEV	Electronic Expansion Valve	A	Air inlet dry-bulb temperature
SH	Superheat	W	Water outlet temperature
SC	Subcooling	T_{wi}	Water inlet temperature
T	Temperature	T_{wo}	Water outlet temperature
P	Pressure	fc	Compressor speed
RH	Relative Humidity	Tc	Condensation temperature
$m_{ref-test}$	Refrigerant charge at a given test	Te	Evaporation temperature

Acknowledgements

The present work has been supported by the Spanish “Ministerio de Ciencia e Innovación”, through the project ref: PID2020-115665RB-I00 “Decarbonización de edificios e industrias con sistemas híbridos de bomba de calor”, and by the Spanish “Ministerio de Universidades” through the "Formación de Profesorado Universitario" program ref. FPU 19/04012.

References

[1] European Parlament. *Directive 2010/31/EU of the European Parliament and of the Council of 19 May 2010 on the Energy Performance of Buildings*.; 2021. http://data.europa.eu/eli/dir/2010/31/oj

[2] European Heat Pump Association (EHPA). *The European Heat Pump Market and Statistics Report 2022*.; 2022. https://www.ehpa.org/market-data/market-report-2022/

[3] Du Z, Domanski PA, Payne WV. Effect of common faults on the performance of different types of vapor compression systems. *Appl Therm Eng*. 2016;98:61-72. doi:10.1016/j.applthermaleng.2015.11.108

[4] Hu Y, Yuill DP, Ebrahimifakhar A, Rooholghodos A. An experimental study of the behavior of a high efficiency residential heat pump in cooling mode with common installation faults imposed. *Appl Therm Eng*. 2021;184 (July 2020):116116. doi:10.1016/j.applthermaleng.2020.116116

[5] Kim W, Braun JE. Extension of a virtual refrigerant charge sensor. *Int J Refrig*. 2015;55:224-235. doi:10.1016/j.ijrefrig.2014.09.015

[6] Behfar A, Yuill D. Numerical simulation of fault characteristics for refrigeration systems with liquid line receivers. *Int J Refrig*. 2020;119:11-23. doi:10.1016/j.ijrefrig.2020.05.003

[7] Guzzardi C, Azzolin M, Lazzarato S, Del Col D. Refrigerant mass distribution in an invertible air-to-water heat pump: effect of the airflow velocity. *Int J Refrig*. 2022;138(October 2021):180-196. doi:10.1016/j.ijrefrig.2022.03.006

[8] De Carvalho BYK, Hrnjak P. Evaluation Of Subcooling Control In Residential Heat Pumps Through Experimental And Model Analysis. In: *International Refrigeration and Air Conditioning Conference*. ; 2022.

[9] Hervas-Blasco E, Pitarch M, Navarro-Peris E, Corberán JM. Study of different subcooling control strategies in order to enhance the performance of a heat pump. *Int J Refrig*. 2018;88:324-336. doi:10.1016/j.ijrefrig.2018.02.003

[10] Corberán JM, Gonzálvez-Maciá J, Montes P, Blasco R. “ART”, a computer code to assist the design of refrigeration and air conditioning equipment. In: *International Refrigeration and Air Conditioning Conference*. ; 2002. http://www.imst-art.com/

14th IEA Heat Pump Conference
15-18 May 2023, Chicago, Illinois

Evaluation of the potential of heat pumps in the reduction of energy consumption in energy communities: a case study in a Mediterranean district.

Ximo Masip[a,b], Rossana Boccia[c], Emilio Navarro-Peris[b*]

[a] Instituto Universitario de Ingeniería Energética, València, España
Universitat Politècnica de València, Spain
[b] ImpactE, c/ Joan Verdeguer n16, València, 46024, Spain
[c] Section of Thermal Energy, Department of Civil and Mechanical Engineering, Technical University of Denmark, Nils Koppels Alle 403, 2800 Kgs. Lyngby, Denmark
e-mail: xmasip@iie.upv.es

Abstract

Energy communities play a key role to move towards a low-carbon and decentralized energy system with higher penetration of renewable energies, offering new opportunities for citizens to actively participate in the energy transition. However, the term energy community is widely addressed in literature as photovoltaic systems shared by several users to cover their electricity needs. The present work describes the georeferenced modelling and assessment of potential domestic hot water energy communities based on heat pumps thermal energy communities in 150 residential buildings in a representative Mediterranean city. With the objective of contributing to the development of this concept in the literature and provide insights on the potential at a district level for its energy transition. The aggregated economic and emission savings of domestic hot water in the district can reach up to 85% and 73% respectively for heat pumps. The analysis shows that the implementation of domestic hot water energy communities could represent a significant reduction in the CO2 emissions of the residential sector using the air as a heat source with a reduced cost compared with individual air source heat pump systems.

© HPC2023.
Selection and/or peer-review under the responsibility of the organizers of the 14th IEA Heat Pump Conference 2023.

Keywords: Energy communities; energy transition; domestic hot water; positive energy districts; heat pumps

1. Introduction

Tackling climate change is one of the biggest challenges of the humanity. Nowadays, cities are one of the biggest problems, being responsible for 72 % of Global Warming Emissions (GWE) despite occupying only 3 % of the land [1]. Still, cities are the solution at the point where they face a huge transition towards energy efficiency and renewable energy inclusion. European Union (EU) settles the objective of decarbonizing the economy for 2050, with a reduction of 90 % GWE regarding residential sector among others [2].

Residential sector in Europe is responsible for 40 % of total energy consumption and 36 % of GWE. The majority of its energy use is due to HVAC purposes, with a 65 %, followed by 13.9 % due to Domestic Hot Water (DHW) [3]. The HVAC consumption will require energy efficiency actions directed to reduce the energy demand of buildings mainly through energy refurbishment. However, DHW demand cannot be reduced without affecting comfort. Considering that it represents on average 18.9% of the final energy consumption in the residential sector [10], energy efficiency measures will be necessary to reduce the energy consumption of the equipment to satisfy this demand.

* Corresponding author. Tel.: +0-000-000-0000 ; fax: +0-000-000-0000 .
E-mail address: author@institute.xxx .

Many possibilities exist for improving the energy efficiency of current DHW production systems. Not only do there exist different technologies (solar thermal, biomass or heat pump (HP)), but also different options regarding the system production level (individual, building or full district). In the decision-making process on the energy planning of future cities, these decisions could change cities as we know them, as well as citizens and how they relate to the energy topic.

Among these alternatives, HP appears as a very promising solution for urban environments where a high population density living in multifamily houses are quite common. This kind of dwellings have the characteristics of limited amount of space and limited amount of solar surface irradiated, which postulates the HPs as one very reliable alternative overall if the climate conditions are soft like in the Mediterranean European area.

Energy Communities (ECs) are an initiative recently emerged that seeks the active participation of citizens in the energy transition. According to EU, this initiative definition corresponds with collective actions participated by citizens, public and private entities around a renewable energy project [4]. Energy Communities constitute a radical change towards distributed energy systems, promoting people empowerment and contributing to the formation of awareness among citizens regards a sustainable energy use.

In this way, this research work aims to give some hints on the best decision for this transformation and determine up to which level the HP could place an important role in that transformation. The paper focuses on DHW production, analyzing one full-district current state and different alternatives regarding system production level considering only the HP technology. The technologies studied and compared are gas boiler, immersion electric heater, individual Air Source Heat Pump (ASHP) and collective operated ASHP. The paper studies a representative Mediterranean city of the Europe warmer climate.

2. Method

For the study, the city of València with its neighborhood of *Illa Perduda* has been selected to perform the analysis. València city can be a city representative of Warmer EU climate and the conclusions here exposed can be of applicability to other Mediterranean cities. The district consists of an area with 164 total number of buildings, of which 150 are residential ones, mainly built during 60s-70s. The average building contains 17 dwellings, with a maximum of 210 dwellings in one building and a minimum of 6.



Figure 1. Analysis area selected for the study. District of Illa Perduda in València, Spain.

Concerning that the study considers different system level production, the DHW demand has been obtained for an individual dwelling and at a building level, considering each residential building of the district. Figure

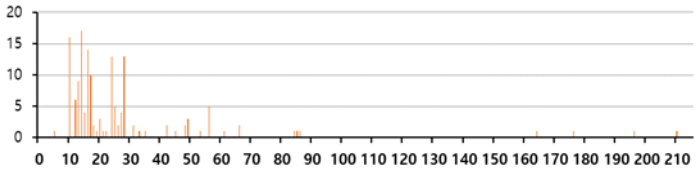


Figure 2. Histogram of the number of dwellings per building of the district.

2 illustrates the number of dwellings per building for the full district. An average value of 2.3 inhabitants per dwelling has been assumed, matching EU average [5].

To model the energy demand, DHWcalc software has been used [6]. DHW 1-minute draw-off profiles have been obtained, including cleaning, shower, bath and cooking consumptions based on published indications in [7]. As an example, Figure 3 includes 2 draw-off profiles for a random day, for 1 dwelling and 20 dwellings.

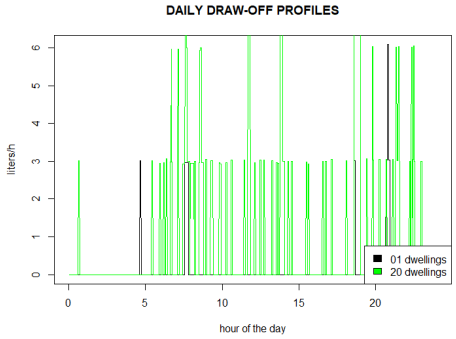


Figure 1. Exemplification of 2 random profiles for a random day of the year.

Concerning the dynamic energy simulations, TRNSYS software has been used [8]. The 4 different DHW production technologies studied and compared have been modelled and simulated in TRNSYS. All the models have been created and validated against commercially available systems. The net water temperature of València has been used, considering an average value for each month. The user demand has been considered at 45 ºC, whereas the set-point temperature for collective cases has been set at 60 ºC considering legionella normative. The models that include storage tank, consider a 0.8 $W/m^2 K$ value for the heat losses.

- **Immersion Electric Heater (IEH)**: it consists of an 80 L storage tank with an aspect ratio of 2 and a nominal capacity of 1.5 kW. The temperature sensor has been placed in the 1st node. 55 ºC set-point temperature has been considered to minimize energy consumption but also guaranteeing user comfort, matching energy-label of the commercial product.
- **Gas Boiler (GB)**: it consists of an instant-heating system of 28 kW and 92 % efficiency. As an instantaneous system, the annual energy consumption is not affected by the set-point temperature considering a fixed demand.
- **Individual ASHP**: an individual ASHP commercially available has been modelled at HP unit level using IMSTart software. A HP performance map has been created and included in a new TRNSYS type. The map was crated varying the external conditions for the operation of the HP, concerning more than 3,500 operating conditions.
  The HP works with propane as natural refrigerant and has 1 kW heating capacity and 180 l storage capacity. It consists of a plate heat exchanger condenser, a finned tube evaporator, an expansion valve, and a scroll compressor. The condenser is directly connected to the DHW stratified-storage tank, and it operates with a variable water inlet temperature (Tci) and a water outlet temperature (Tco) fixed at 64ºC. The HP is designed to heat up water from 10 to 64ºC. The HP unit as been optimized, according to its operation on the system, by the subcooling. In such a way that the high temperature lift on the water side match in an optimum way with the temperature profile in the heat pump.
- **Collective ASHP**: the individual HP unit of the ASHP model has been optimized using IMSTart to work under collective conditions, specifically adjusting the subcooling of the model. The HP unit model developed has been included in a new TRNSYS type. This type is connected to a stratified storage tank. In order to take into account the re-circulation losses, a 10 % annual energy consumption reduction has been considered. The HP size and tank volume have been properly analyzed for each building in the district through a parametric study varying the range of each of them and following comfort criteria explained in the following. For each of the buildings of the district, a performance map of the full system was created concerning different HP and tank sizes and taking into account the comfort restrictions of each simulation. Based on this map, the optimal sizing of HP and tank has been found for the minimum consumption point of the map. Thus. the

proper sized cases have been selected among those that comply with the comfort restrictions and achieve the minimum annual energy consumption.

Constraints settled have to do with comfort restrictions and HP starts. To guarantee user comfort, two restrictions have been defined: (i) the annual percentage of discomfort has to be lower than 0.5 % ; (ii) the maximum available time out of comfort for each hour of the day has been settled to 5 seconds. To guarantee system reliability, a maximum number of starts of 9 per hour has been set. In the collective installation case, the simulations that do not comply with the restrictions would not be considered. Whereas, in the individual DHW production level these restrictions will be considered as outputs, since the sizing is defined by the manufacturer.

In order to analyze each case and compare them, the following system performance indicators have been used:

- SPFuser: as the quotient between the useful heat received by the user and the total system energy consumption (including compressor, fan, and circulation pumps).
- COP: as the quotient between HP heat delivered and energy used by the compressor.
- Annual energy consumption: considering the consumption of the system, including compressor, fan, and circulation pumps.
- Annual emissions: considering an emission factor of 0.201 tCO_2/MWh for gas [9] and 0.112 tCO_2/MWh (ref) for electricity.
- Annual energy cost: considering an energy price of 0.067 €/kWh for gas and 0.2 €/kWh for electricity.

3. Results

In this section, the main results are presented and discussed. First of all, an analysis of the current situation regarding the DHW production of the neighborhood under study is performed. Secondly, the results of the different alternatives to the current DHW production systems are described in terms of performance, energy consumption, emissions and energy costs. Finally, the alternatives technologies are compared, and the outcomes discussed.

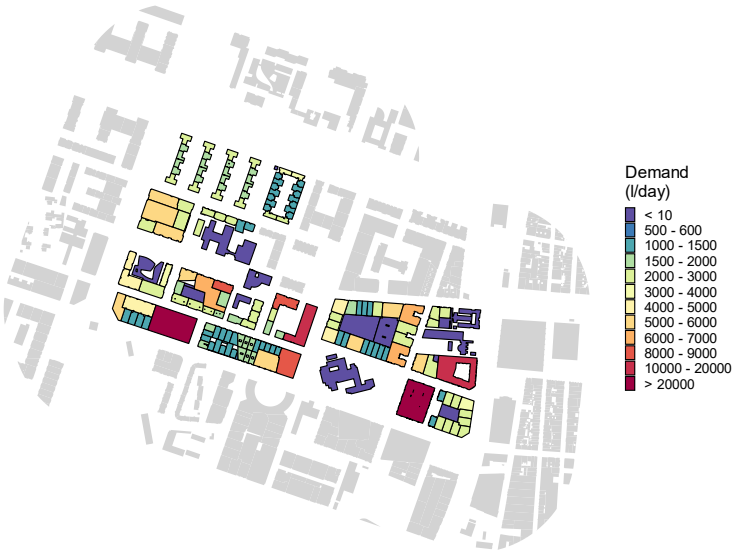


Figure 2. Demand, in l/day, for each building of the district.

Figure 4 depicts the DHW demand of each of the buildings of the neighborhood in liters per day. The demand is directly related with the number of dwellings in each building.

Current scenario

The current state in the neighborhood, regarding the production of DHW, is governed by low energy efficient and high polluting systems, considering the year of construction and the social vulnerability situation

of it. According to recent literature, DHW is produced by 28.6 % of the dwellings using IEH, by 70.4 % using GBs [10].

Table 1 summarizes the current situation regarding the use of GB and IEH. The table shows the annual emissions and energy cost related to the DHW production in the district. On average, one dwelling is responsible for 532 kgCO2/y and has an energy cost of 464 €/y.

Table 1. Emission and energy cost of current DHW production situation

	Emissions ktCO2/y	Energy cost M€/y
Current situation	2.23	1.95

Individual ASHP renovation scenario

Concerning the results of individual ASHP, Table 2 includes the main results for 1 dwelling. In order to obtain global results, it was assumed that each dwelling in the district did the renovation. The results show an average COP of 4, with a reduced annual discomfort, with 200 hours per year year (2.3 % in front of the 0.5% of the collective scenario).. The total energy consumption accounted for 414 kWh/y, with an energy cost of 82.64 € and GWE of 46.28 kgCO2/y.

Table 2. Results from individual ASHP

	SPFuser	COP	Annual discomfort	Working hours	Energy use	Emissions	Energy cost
	-	-	%	h/y	kWh/y	kgCO2/y	€/y
Individual ASHP	3.27	4.05	2.28	1600.63	413.19	46.28	82.64

Collective ASHP renovation scenario

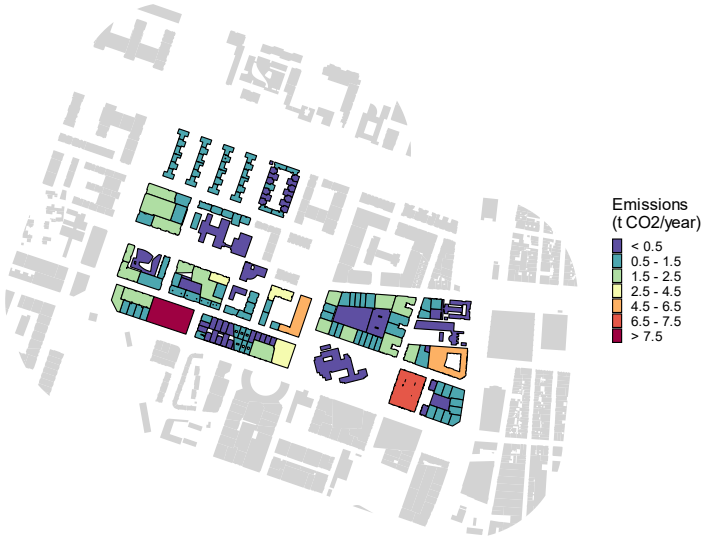


Figure 3. Annual emissions building to building.

Figure 5 and Figure 6 show the emissions and economic costs resulting from the use of the collective ASHP in each building of the district. Assuming every building in the district does the renovation, the total savings are shown in Table 3. The results show a total equivalent annual emissons of 150 tCO2 and 270 k€. The average dwelling was responsible for 36 kgCO2/y and had an energy cost of 65 €/y.

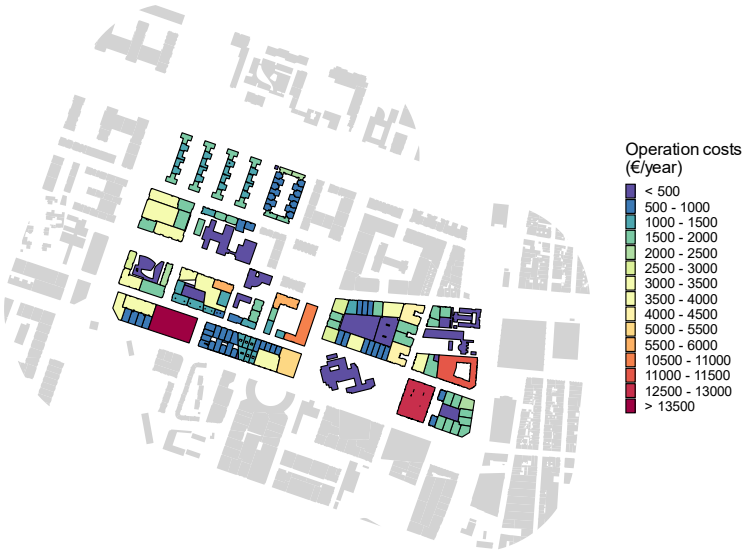


Figure 4. Annual energy cost building to building.

Comparison

Table 3 includes the results for the current scenario and each alternative regarding emissions and energy cost. The results show:

- Emission savings for both the alternatives over 90 % with respect to the current scenario, and energy costs savings above 80 %.
- Absolute annual savings over 2 ktCO2 and 1.6 M€ regarding the current scenario.
- The ASHP collective alternative shows 20 % higher savings than the individual ASHP. In details, the collective ASHP saves 42 tCO2 and 75 k€ more compared to the individual ASHP.
- The individual ASHP shows annual savings of 400 € per dwelling, whereas the collective one shows savings of 2310 € for the average building block.
- The installation of collective ASHPs in the district only requires 150 HP units and tanks, against the 4194 units needed with the installation of individual ASHPs.
- On average, the collective alternative needs 3 % less HP capacity and 85 % less storage volume than the individual one.
- Although this research works does not analyze in detail sustainability and investment efficiency matters, some opinions can be extracted:
    - Regarding sustainability matter, much less equipment is needed, and the HP size and tank volume are more reduced in the case of collective installations. This positions the collective alternative ahead of the individual.
    - Regarding investment efficiency matter, in 10 years the individual option achieves 4,000 € in savings whereas the collective reaches 23,100 € for the average building block. {Bibliography}Considering also that the collective installation needs of HP size and storage are more reduced, this option could be much more cost-effective than the individual installation case.

Table 3. Results comparison of each alternative, regarding GWE and energy cost.

	Emissions ktCO2/y	Energy cost M€/y
Current situation	2.23	1.95
ASHP individual	0.19	0.35
ASHP collective	0.15	0.27

4. Conclusions

This work has shown the high potential of ASHP to reduce the emissions associated to the DHW demand in buildings without the necessity of implementing complicated infrastructures like geothermal wells or having a centralized district heating network. It has been proved that for template climates like the one present in the Mediterranean coast a ASHP installed in each house without the necessity of neighborhood coordination could be the most easy solution to reach remarkable emission reduction objectives.

Nevertheless, the initial investment of this type of installation is far from being suitable and environmental responsibility of the users or some kind of public fundings must be promoted to install that kind of systems. On the other side, the collective installations and the development of thermal energy communities present the advantages of having a slightly higher potential of CO2 emissions reduction, having a significantly lower initial price of the HP components, and having a significantly less space requirements in the building which in some cases could be a critical argument for them. However, this kind of system requires the agreement between all the members of the community and some points regarding the legal implications of it are still under development.

Acknowledgements

This work was supported by Grupo ImpactE Planificación Urbana and by the project "DECARBONIZACI´ON DE EDIFICIOS E INDUSTRIAS CON SISTEMAS H´IBRIDOS DE BOMBA DE CALOR", funded by "Ministerio de Ciencia e Innovación", MCIN, Spain, with code number: PID2020-115665RB-I00

References

[1] European Commission, "100 Climate-Neutral Cities by 2030 - by and for the Citizens Interim Report of the Mission Board for Climate-Neutral and Smart Cities," 2020. doi: 10.2777/62649.

[2] E. Comssion, "2050 long-term strategy," 2018. https://ec.europa.eu/clima/policies/strategies/2050_en (accessed Nov. 12, 2018).

[3] European Comission, "Energy Consumption Buildings," 2019. https://ec.europa.eu/energy/en/topics/energy-efficiency/buildings (accessed Jul. 20, 2019).

[4] Official Journal of the European Union, "Directive (EU) 2018/2001 of the European Parliament and of the Council of 11 December 2018 on the Promotion of the Use of Energy from Renewable Sources (Recast)." 2018.

[5] EUROSTAT, "Living conditions in Europe - housing - Statistics Explained." ttps://ec.europa.eu/eurostat/statistics-explained/index.php?title=Living_conditions_in_Europe_-_housing&oldid=569706 (accessed Sep. 21, 2022).

[6] U. Jordan and K. Vajen, "DHWcalc: Program to generate Domestic Hot Water profiles with statistical means for user defined conditions," *Proceedings of the Solar World Congress 2005: Bringing Water to the World, Including Proceedings of 34th ASES Annual Conference and Proceedings of 30th National Passive Solar Conference*, vol. 3, pp. 1525–1530, 2005, [Online]. Available: http://www.scopus.com/inward/record.url?eid=2-s2.0-84870527781&partnerID=tZOtx3y1

[7] Asociación Técnica Española de Climatización y Refrigeración (ATECYR), *Guia Tecnica de agua caliente sanitaria central*. Instituto para la Diversificación y Ahorro de la Energía, Minsiterio de Industria Gobierno de España, 2010. [Online]. Available: www.idae.ec

[8] "Transient System Simulation Tool (TRNSYS)," 2019. http://www.trnsys.com/ (accessed Jul. 02, 2018).
[9] CNMC, "Documento de consulta pública sobre la propuesta de metodología de cálculo de la tasa de retribución financiera de la actividad de producción de energía eléctrica a partir de fuentes de energía renovables, cogeneración y residuos para el siguiente periodo," 2018.
[10] IDAE, "PROYECTO SECH-SPAHOUSEC," 2011.

14th IEA Heat Pump Conference
15-18 May 2023, Chicago, Illinois

Assessing the peak demand implications of air-source heat pumps in Canada and identifying potential mitigation strategies

Justin Tamasauskas[a*], Sarah Mollier[a], Martin Kegel[a]

[a]CanmetENERGY in Varennes, Natural Resources Canada, Varennes, J3X 1P7 Canada

Abstract

Heat pumps are a critical element of a decarbonized built environment, but their widespread adoption can increase house level electrical demand. This paper uses a simulation-based approach to examine the peak demand implications of replacing natural gas furnaces with air-source heat pumps in four Canadian cities. Results show that the peak demand impacts of heat pumps are closely tied to climate. In colder regions (Ottawa, Winnipeg), peaks occur when outdoor temperatures are lowest and auxiliary heating is needed to supplement or replace heat pump operations. Peak demand increases vs. gas heating may approach up to 8 kW in Ottawa and 9 kW in Winnipeg. In milder regions (Halifax, Vancouver), peak events are linked to heat pump use coincident with higher non-HVAC electrical loads. Peak demand increases may reach up to 3 kW in Halifax and Vancouver. Simulations show these increases may be mitigated by using energy stored in the building thermal mass to reduce heat pump operation during peak hours. Results can be used to understand the implications of greater heat pump adoption in Canada and identify approaches to address potential challenges.

© HPC2023.
Selection and/or peer-review under the responsibility of the organizers of the 14th IEA Heat Pump Conference 2023.

Keywords: air-source heat pumps; heat pump peak electrical demand; cold climate heat pumps; peak electrical demand mitigation

1. Introduction

The *Canadian Net Zero Accountability Act* outlines Canada's commitment to achieving carbon neutrality by 2050 [1]. Heat pumps have strong potential to drive the decarbonization of Canadian buildings via their ability to efficiently electrify space heating and cooling. However, transitioning from fossil fuel to heat pump systems can increase demand on electrical grids, affecting their ability to provide reliable decarbonized energy. Demand increases can be particularly significant for air-source heat pumps (the most common form of heat pump integration in Canada [2]), which often require supplemental electrical heating to maintain space temperatures during colder winter days typical in Canada. Understanding the peak demand implications of heat pumps, and any potential mitigation strategies, is essential in supporting an increased adoption of these systems in Canada.

Quantifying the peak demand of heat pumps via building simulation can be a challenge. Peak demand analysis requires the use of smaller time steps, where the impact of controls, heat pump transients (e.g., defrost and start-up), and the interaction with any auxiliary systems can be represented. Yet, many typical building simulation programs average performance across an hourly time step and are unable to adequately capture shorter term heat pump transients. Several simulation-based studies have examined the peak demand impacts of heat pump adoption in Europe [3,4], and two locations in Canada [5]. However, further work is needed to better understand how the peak electrical demand implications of heat pumps vary across additional Canadian regions, and what measures can be taken to mitigate added demand.

* Corresponding author. Tel.: +1-438-364-1663;
E-mail address: justin.tamasauskas@nrcan-rncan.gc.ca.

This paper uses a simulation-based approach to (I) examine the electrical demand implications of transitioning from natural gas furnaces to air-source heat pumps, and (II) explore how increased demand may be mitigated during peak periods via improved controls. First, detailed models of new construction housing are developed in four Canadian cities (Halifax, Ottawa, Winnipeg, Vancouver), and combined with a series of non-HVAC load profiles to quantify baseline thermal and electrical performance. An enhanced data-driven heat pump model is then used to examine the peak demand implications of air-source heat pump integration, and how this added electrical demand may be minimized via the application of a preheat/setback strategy. Results provide an overview of the potential challenges faced in the widespread deployment of air-source heat pumps, and how they may be addressed using improved controls and other approaches.

2. Base Case Housing Models

Climate and the type of heating system being replaced have an important impact on the magnitude of peak electrical demand increase associated with heat pump systems. This study examines four Canadian regions, each representing a unique set of boundary conditions. Key parameters are summarized in Table 1 [6,7]. The percentage of homes currently heated using fossil fuels is derived from available data at the provincial level [7], in the absence of reliable information for each specific city examined. While this percentage varies greatly between areas, these systems represent at least 50% of single detached homes in all selected regions.

Table 1. Summary of climate characteristics by region [6,7]

Characteristic	Halifax NS	Ottawa ON	Winnipeg MB	Vancouver BC
Climate Type	Cold-Humid	Cold-Humid	Very Cold	Marine
Heating Degree Days (18°C)	4000	4440	5670	2825
Heating Design Temperature (°C)	-16	-25	-33	-7
% Homes Heated Using Fossil Fuels*	63%	75%	53%	59%

*By respective province

All analysis is performed for a typical Canadian single family detached home. Housing geometry is based on the Canadian Centre for Housing Technology (CCHT) test homes located in Ottawa, Canada [8], and consists of two above ground floors and a finished basement with a total heated floor area of 284 m^2. The building envelope is modified to represent new construction in each selected region, based on the requirements specified in the National Building Code of Canada [6]. All base cases use natural gas furnaces for space heating, to examine the impact of transitioning from gas to heat pump systems. Key housing characteristics are summarized in Table 2.

Table 2. Summary of housing characteristics

Characteristic	Description/Value (All Cities)
Central Air Distribution	Yes
Primary Heat Fuel & System	Natural Gas Forced Air Furnace
Heating Efficiency	92%
Space Cooling System	Central AC COP = 3.5*
DHW Fuel	Natural Gas
Heat Recovery Ventilator (HRV)	Yes

* At AHRI Rating Conditions (95°F Outdoor Dry Bulb Temperature, 80°F Indoor Dry Bulb/67°F Wet Bulb)

Non-HVAC Load Profiles: Non-HVAC (i.e., lighting, appliances and plug loads) electrical load profiles have an important impact on house-level electrical demand. Analyzing the peak demand of heat pumps in homes with different electrical load profiles can provide an idea of how the added electrical demand associated with heat pumps may vary under different internal gains and space use types. This work uses a detailed load profile generator model (LPGM) developed using the bottom-up stochastic approach outlined by Wills [9], with additional refinements to better represent the homes and cases used in this study. Further details can be found in Mollier *et al.* [5].

Seven distinct active occupancy profiles are examined to better represent the range of peak demand increases possible when replacing a natural gas furnace with an electrically driven heat pump. For each occupancy profile type, occupancy levels between 2 and 5 people are considered, generating a total of 28 non-HVAC load profiles for each city. Table 3 summarizes the different occupancy profiles examined.

Table 3. Summary of occupancy profiles used in analysis

No.	Type	Description
1	Teleworking	Occupants are home most of the day, except during lunchtime.
2	Normal	67% of occupants are away during the day [10]
3	Pyramidal	Active occupancy slowly increases in the morning and decreases in the evening.
4	Morning and evening	100% of occupants are away during the day.
5	All day	Occupants are home all day.
6	Armstrong	Active occupancy profile such that resulting load profiles match Armstrong *et al.* [11]
7	Armstrong inverse	Morning and evening peaks from Armstrong *et al.* [11] are swapped.

A daily average of each selected load profile is provided in Fig. 1 for a three-person household in Vancouver. While each daily profile is unique, they tend towards the averages shown below.

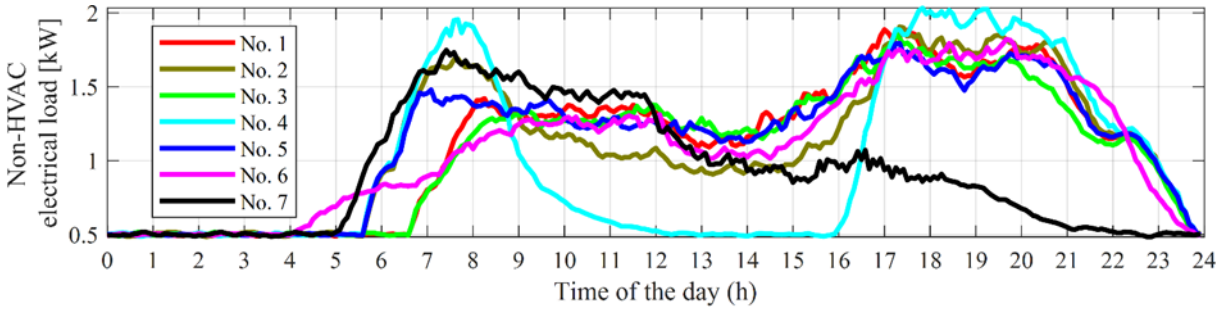


Fig. 1. Average daily occupancy profiles for a three-person household in Vancouver.

3. Heat Pump System Integrations

The added electrical demand associated with heat pump systems in Canada is closely linked to the operating range and cold climate performance of the selected system. Two heat pump performance curves are examined in this paper to better understand the influence of these characteristics.

Variable Capacity Heat Pump (VCHP): This unit is a typical market-available variable capacity heat pump. These systems have achieved a growing market share in Canada, driven by their ability to better modulate to space heating or cooling loads vs. more traditional single or two-stage units. However, these systems are not necessarily well adapted to cold climates, and may experience significant capacity degradations at the colder outdoor temperatures common in Canadian winters.

Cold Climate Variable Capacity Heat Pump (CCHP): As an alternative to the *VCHP*, a second heat pump system is modelled. This heat pump has an extended operating range, and is able to maintain a more substantial portion of its heating capacity at the colder outdoor temperatures common in Canada. As an illustration, the performance of the *VCHP* and *CCHP* are summarized below in Fig. 2.

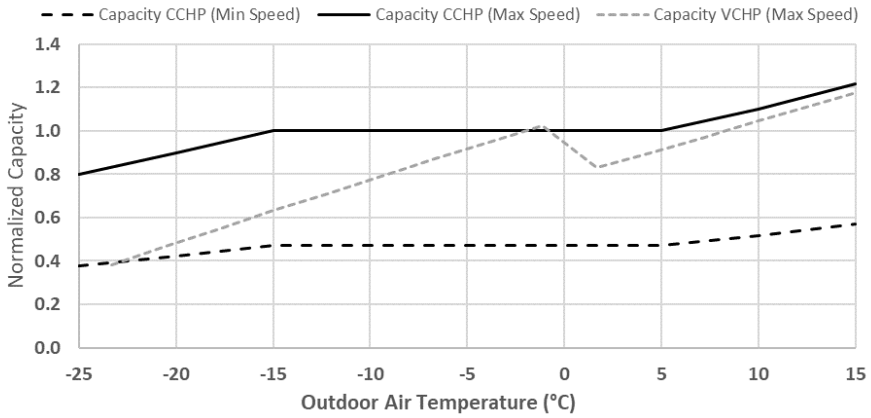


Fig. 2. Comparison of VCHP system performance [12,13].

Table 4 summarizes additional heat pump characteristics for both systems examined.

Table 4. Summary of heat pump performance characteristics [12,13]

	HP Type	
	VCHP	CCHP
Heating COP*	3.7 (2 ton) 4.1 (3 ton)	3.8 (All)
Cooling COP*	3.8 (2 ton) 4.1 (3 ton)	3.3 (All)
Min. Outdoor Operating Temperature, Heating Mode (°C)	-23	-25
% Capacity at Cut-Off Temperature (Max Speed)	38%	80%
Average Min: Max Capacity Ratio	0.3	0.3

*At AHRI Rating Conditions (47°F Outdoor Dry Bulb/43°F Wet bulb, 70°F Indoor Temperature)

Heat pump integration and sizing approaches can also have an important influence on performance. All heat pump systems are examined in a centrally ducted configuration, supplying space heating and cooling to all three levels of the home. Each heat pump integration is sized to cover a majority of the space heating load in each region, as per Option C of NRCan's *Air-Source Heat Pump Sizing and Selection Guide* [14]. CCHP sizing in Vancouver is limited by the lack of available units under 2 tons for the model line used in the analysis [13].

Electric resistance elements in the ductwork are used to supplement heat pump operations as needed to maintain comfort. Details on heat pump and auxiliary sizing are provided in Table 5. All auxiliaries are sized to either meet the difference between heat pump capacity and building load at design conditions (in regions where the design temperature is above the heat pump minimum operating temperature), or the full design load (in regions where the design temperature is below the heat pump minimum operating temperature). Auxiliaries activate in 2.5 kW stages to provide a more realistic representation of their impact on electrical demand.

Table 5. Summary of heat pump and auxiliary sizing

	Heat Pump Size (ton)		Aux. Size (kW)
City	VCHP	CCHP	All
Halifax	3	2	5
Ottawa	3	2	10
Winnipeg	3	2	12.5
Vancouver	2	2	2.5

4. Heat Pump Modelling

Accurately representing the performance characteristics of each heat pump system is critical to properly estimate peak electrical demand. All system models are developed in TRNSYS v. 18 [15] using the appropriate Canadian Weather for Energy Calculation (CWEC) weather file. TRNSYS offers a vast library of components for modelling of space conditioning systems, as well as the ability to easily add custom component models (as was done in this paper with the heat pump component described below). Unlike many building simulation programs which typically use an hourly time step, TRNSYS also allows the user to select a fixed time step for simulation. In this study, all simulations use a 2.5-minute timestep to better represent the control logic of the heat pump and auxiliary heating systems.

Heat Pump Performance Modelling

A custom component is used in TRNSYS to model each heat pump system. This enhanced model (TRNSYS Type 3255) is developed based on extensive test experience at the CanmetENERGY in Varennes facility and integrates a series of new capabilities including performance variations with compressor speed, and short-term transients including start-up, defrost, and cycling. Further details are provided in Breton *et al.* [16].

Type 3255 follows a data-driven approach to heat pump performance, using a performance map to represent variations in heat pump capacity and power with outdoor temperature and compressor speed. Performance data in this study has been derived via available manufacturer literature. Data sources are summarized in Table 6.

Table 6. Summary of data sources for heat pump modelling

Heat Pump System	Rated Performance	Part Load Performance
VCHP	Manufacturer [12]	Manufacturer [12]
CCHP	Manufacturer [13]	Manufacturer [13]

Heat Pump Control

A PID controller is used to vary the speed of the compressor to maintain the first floor of the home at 21°C in heating and 23°C in cooling. The controller also contains a minimum operating frequency, below which the heat pump remains off. This feature enables the model to capture on/off cycling at warmer conditions when building loads fall below the minimum capacity of the heat pump. Additional controls prevent the heat pump from operating beyond its manufacturer specific range of outdoor temperatures.

Capturing the interaction of the heat pump with any electric auxiliary heating is critical to accurately estimate electrical demand. Auxiliary systems have three modes, depending on heat pump operations:

I. Heat pump is defrosting: The auxiliary duct heater turns on at a constant, fixed, limited capacity to minimize occupant discomfort during defrost. This capacity is calculated based on the estimated indoor cooling effect in defrost, to ensure a minimum supply air temperature of 12°C to the home, as per building code minimum requirements [6]. Defrost length is fixed at 5 minutes (future work will add varying defrost lengths). As will be discussed later, the sizing of the auxiliary system for defrost has important electrical demand implications. Future work will examine the use of different sizing methods (e.g., different minimum temperatures) to more fully quantify and illustrate these impacts.

II. Heat pump is operating: The first stage of auxiliary heating operates with a lower setpoint (20°C vs. 21°C for the heat pump) to ensure space temperatures are maintained within an acceptable range while prioritizing heat pump operations. Subsequent auxiliary stages follow a setpoint 0.5°C below the previous stage (e.g., second auxiliary stage activates at 19.5°C). The heat pump and auxiliaries may operate in parallel.

III. Heat pump is unable to operate: When ambient temperatures are too cold for the heat pump to operate, the first auxiliary stage activates when space temperatures fall below the desired setpoint of 21°C. Subsequent auxiliary stages follow a setpoint 0.5°C below the previous stage.

5. Results

This section compares the peak demand implications of the *Base Case*, *VCHP*, and *CCHP* for each city, under each of the 28 load profiles outlined in Section 2. Focus is placed on heating mode, given the importance that space heating electrification has for Canadian electricity grids, with the analysis period defined as Oct. 1st to May 1st.

Transitioning from Natural Gas to Air-Source Heat Pumps in Colder Climates ($T_{Design} < T_{HP,min}$)

This section examines results for two cities (Ottawa, Winnipeg) where outdoor temperatures fall below the minimum operating temperature for the selected heat pump systems. Fig. 3 shows the occurrence of peak electrical demand for each non-HVAC profile over the heating season in Ottawa. Each bar represents the number of simulation runs that experience their maximum house-level electrical demand during the defined time period (i.e., the number of simulation runs where a peak occurs during the time period, out of the 28 times each system is simulated using a different electrical load profile). *Base Case* peaks are far more dispersed vs. the two heat pump systems, as peak demand in these cases is driven by occupant behavior. Conversely, peaks for the *VCHP* and *CCHP* occur when outdoor temperatures fall below the minimum operating temperature of the heat pump and auxiliary heating must be used to maintain space temperatures.

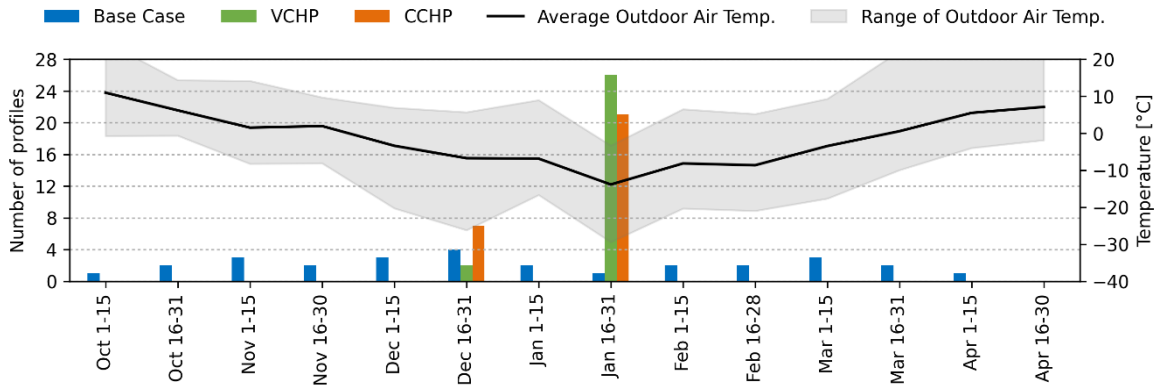


Fig. 3. Occurrence of peak demand by system type over the heating season in Ottawa

Fig. 4 shows the occurrence of peak demand by system in Winnipeg. Results follow a similar trend to Ottawa: *Base Case* peaks are dispersed due to their occupancy driven nature, while heat pump peaks occur during periods when ambient temperatures fall below the operating range of the heat pump. The distribution of peaks is identical for both the *VCHP* and *CCHP* units, as both systems experience an extended period when the heat pump is not able to operate and heating must be met using electric auxiliary elements. In both cities, it is important to note that peaks may occur with a high degree of coincidence across multiple homes, given that all heat pumps in a region will experience similar outdoor temperatures.

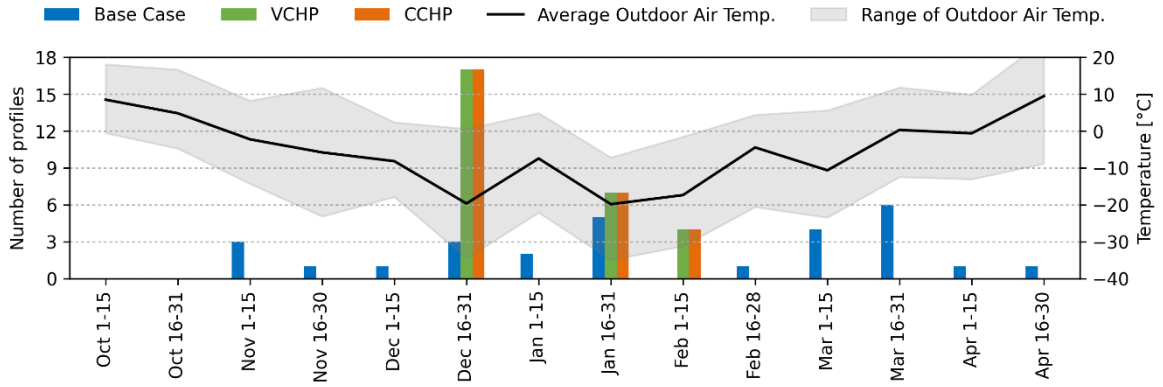


Fig. 4. Occurrence of peak demand by system type in Winnipeg.

Fig. 5 compares the magnitude of peak electrical demand increase associated with each heat pump vs. the *Base Case* in Ottawa and Winnipeg. Given that both the *VCHP* and *CCHP* must rely fully on auxiliary heating during the coldest winter days, both systems demonstrate similar peak demand increases. In Ottawa, peak electrical demand may increase between 2.9 kW and 7.7 kW with the *VCHP*, and between 2.5 kW and 7.6 kW with the *CCHP*. In Winnipeg, *VCHP*s may increase electrical demand between 5 kW to 8.8 kW, while *CCHP* systems may increase electrical demand from 3 kW to 9 kW. It should be noted that the lower minimum increase (3 kW) associated with the *CCHP* system in Winnipeg primarily results from the random nature of the load profiles, rather than a difference between *VCHP* and *CCHP* systems. In all cases (both Ottawa and Winnipeg), peak load increases are driven by a combination of auxiliary electric heating plus some degree of non-HVAC electrical loads. In the Winnipeg *CCHP* case, during one simulation run the non-HVAC loads that coincided with maximum auxiliary energy demand were lower, leading to this smaller minimum increase.

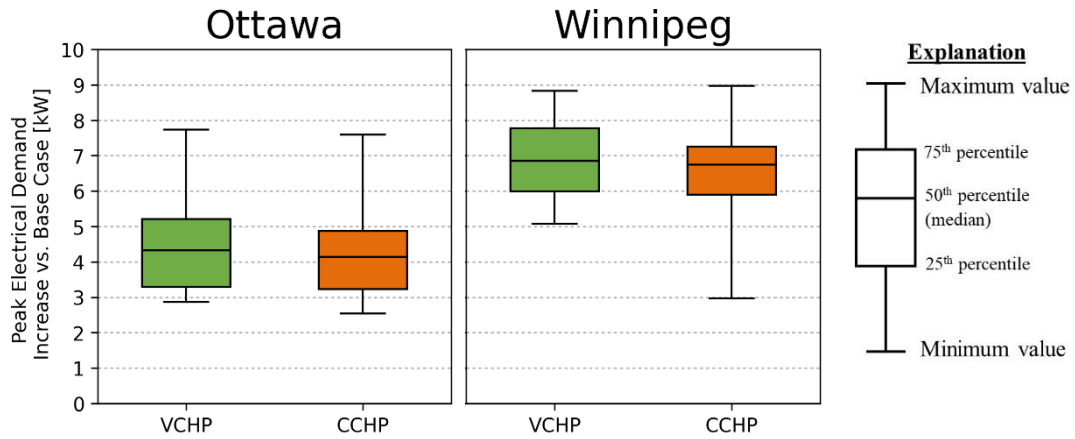


Fig. 5. Peak electrical demand increase for each heat pump system in Ottawa and Winnipeg.

The duration of any peak event can also be of value to electrical utilities. Fig. 6 compares the load duration curves (all load profiles) for both the *VCHP* and *CCHP* units in Winnipeg. Unlike the previous graphs, a comparison of the two insets shows a clear difference between the *VCHP* and *CCHP* systems. The *VCHP* system experiences a plateau at higher load for approximately 180h over the year, primarily associated with an extended duration of auxiliary heating. *CCHP* units reduce the duration of this plateau by over 30 hours, minimizing the added load placed on the grid by the heat pump system. Similar results are seen in Ottawa, although the magnitude of the reduction (8 h *CCHP* vs. 18h *VCHP*) is smaller due to the milder climate.

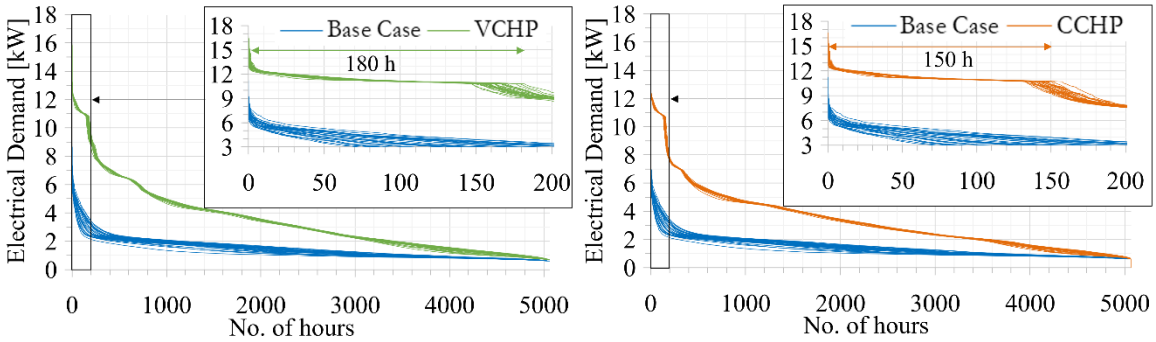


Fig. 6. Load duration curves for VCHP and CCHP systems in Winnipeg over heating season.

Transitioning from Natural Gas to Heat Pumps in Milder Canadian Climates (T_{Design}>$T_{HP,min}$)

The drivers of peak demand differ significantly in climates where the outdoor temperature always remains within the operating range of the heat pumps selected. Fig. 7 shows the distribution of peak electrical demand for all three systems in Halifax. Heat pump peaks are more dispersed, as peak demand is now driven by a combination of heat pump operations and occupancy-based non-HVAC electricity use (rather than aux. heating). Some correlation to colder temperature remains, as the heat pump must operate at higher compressor speeds (and power) to meet building loads during these periods, while defrosting is also needed. Results can have important implications for utilities, as it suggests that peak demand associated with heat pumps in milder climates may occur with a lower degree of coincidence, mitigating grid level peak demand increases.

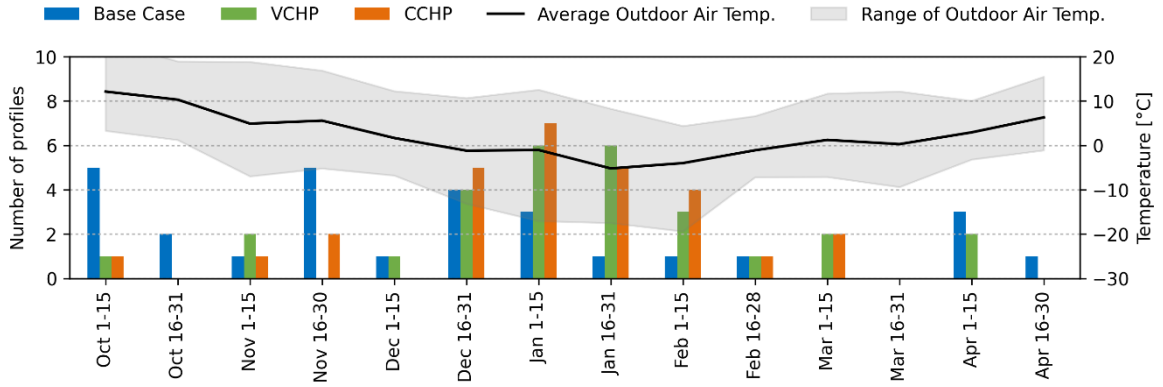


Fig. 7. Occurrence of peak demand for all three systems in Halifax during heating season.

Fig. 8 compares the occurrence of peak demand across all three systems in Vancouver. Results follow a similar trend to Halifax, with a dispersion of peak demand across the heating season. The milder climate in Vancouver allows both heat pump systems to operate consistently without the need for any auxiliary heating (except when the heat pump defrosts), with peak demand events instead driven mainly by heat pump use coincident with non-HVAC end uses.

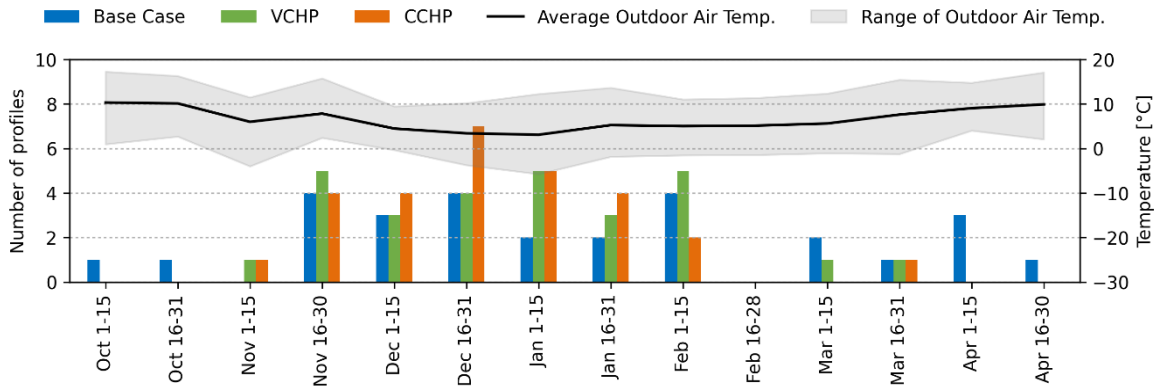


Fig. 8. Occurrence of peak demand for all three systems in Vancouver during heating season.

Fig. 9 compares the range of peak demand increase vs. the *Base Case* for each heat pump system in Halifax and Vancouver. Peak demand increases are smaller vs. the previous cities examined, as the heat pump operates consistently throughout the year. In both cities the *VCHP* and *CCHP* systems exhibit a similar range of peak demand increase, primarily because (i) they are sized according to the same objectives, and (ii) the outdoor temperature is not cold enough to reach the minimum operating temperature of either unit. In Halifax, peak demand increases range from 0.1 kW to 3 kW with the *VCHP*, and between 0.1 kW to 2.9 kW with the *CCHP*. Larger peak demand increases are associated with heat pump defrost (which activates a portion of aux. heating, as noted in Section 4) coinciding with higher non-HVAC electrical demand. Smaller peak demand increases are associated with the heat pump operating at lower speeds in combination with higher occupant driven loads. Peak demand increases are similar in Vancouver, ranging from 0 kW to 1.7 kW with the *VCHP*, and 0 kW to 3.1 kW with the *CCHP* case. Cases with peak demand increases near 0 kW relate to peak events driven solely by non-HVAC electrical loads, with the heat pump remaining in standby mode.

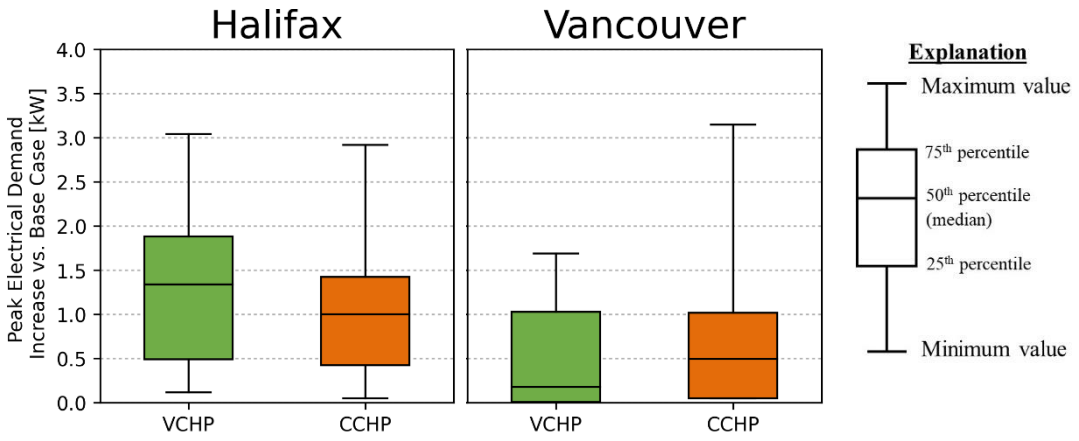


Fig. 9. Range of peak demand increase with each heat pump system in Halifax and Vancouver over the heating season.

While heat pump peaks are more dispersed in Halifax and Vancouver, it is interesting to note when these peaks may occur during the day. Fig. 10 compares the occurrence of peaks over a 24h period for the *Base Case*, *VCHP* and *CCHP* systems in Halifax. Typical peak periods for the grid in the morning (7 AM to 9 AM) and evening (5 PM to 7 PM) are also shown [17]. Given the closer link to occupancy driven loads, it is not surprising to see that peaks are more likely to occur during the core periods of the day when occupants are active. This information is important to grid operators and planners, as it suggests that heat pump peaks may occur during periods of the day when demand is already higher, necessitating some form of demand reduction strategy to ensure grid capacity and stability.

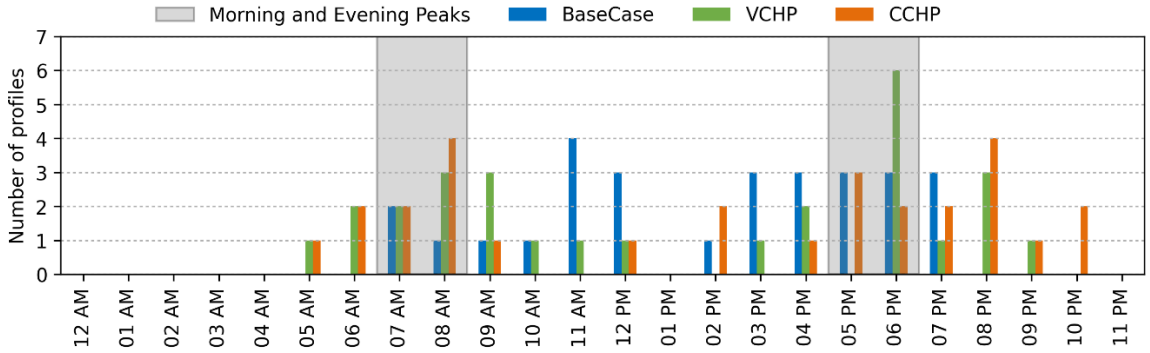


Fig. 10. Occurrence of peak event over day in Halifax during heating season.

Mitigating Peak Demand Associated with Heat Pump Systems

Peak demand increases associated with heat pump systems can also be mitigated in a number of ways, including improved controls or the integration of energy storage. As a simple example, a preheat and setback strategy is examined to reduce heat pump peak demand during defined morning (7 AM – 9 AM) and evening (5 PM – 7 PM) periods. Heat pump indoor temperature setpoints used in the analysis are presented in Fig. 11, and aim to heat up the interior space prior to peak periods, and then utilize the thermal capacitance available in the building mass to coast until the end of the two-hour peak. During all preheat periods, auxiliary setpoints lag behind the heat pump setpoint to prioritize heat pump operations. The setpoint strategy is presented as an initial analysis and will be further examined and optimized in future work.

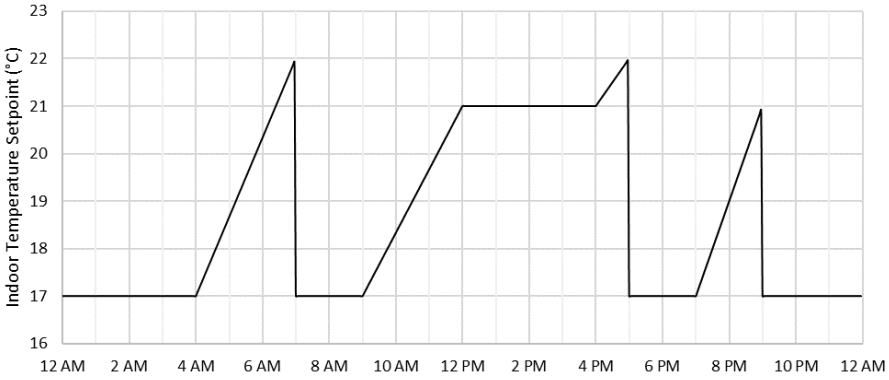


Fig. 11. Setpoint strategy used in initial peak demand mitigation strategy for Halifax.

Fig. 12 compares the peak demand increase during the defined peak periods only (7AM-9AM, 5 PM-7PM) in Halifax with and without the mitigation strategy. It is immediately clear that the applied strategy greatly reduces the electrical demand of the building during peak hours by avoiding the use of the heat pump and any auxiliary systems. However, it is important to note that this demand reduction occurs only during the peak periods: Higher system electrical demand occurs just before and after these periods to preheat and recover space temperatures. In fact, *overall* peak electrical demand increases vs. the base case are actually higher when the mitigation strategy is applied, reaching up to 6 kW (vs. only 3 kW when no preheating/setback strategy is used). Applied on a larger scale, the associated electrical demand before and after the two-hour peak window could pose a significant challenge for utilities. As such, some form of dispersed strategy, where not all systems follow the preheat and setback schedule, may be required to achieve sufficient results at the grid level.

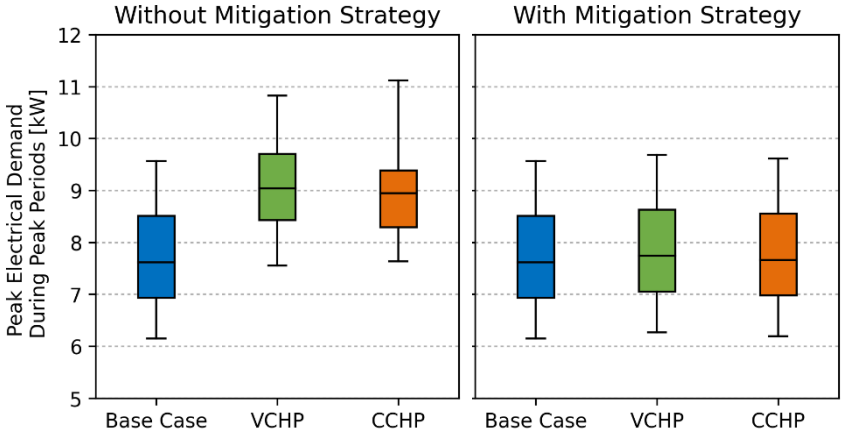


Fig. 12. Comparison of peak demand distribution during peak hours in Halifax with and without mitigation strategy.

Application of this strategy relies on the willingness of the homeowner to accept lower space temperatures over a short duration, and the ability of the building mass to maintain space temperatures within the desired range over the two-hour period. The current analysis shows that this strategy is viable for newer construction buildings but may be more challenging in older housing vintages with poorer envelope construction and higher rates of infiltration. Alternative strategies, including integrating thermal or electrical storage with the heat pump system (e.g., in a Climate & Comfort Box configuration [18]), holds strong promise to extend the peak management and energy flexibility potential of heat pump systems.

Discussion

Results highlight that the peak demand implications of heat pump systems are highly dependent on local climate. In areas where outdoor air temperatures fall below the minimum operating temperature of the heat pump, the occurrence of peak events is tied closely to colder periods when the heat pump requires partial or full auxiliary heating to maintain space temperatures. Given the link to outdoor temperatures, it is also possible that these peaks may occur with a greater degree of coincidence in the same region, imposing a larger aggregated load on the electrical grid. In regions where outdoor temperatures remain within the operating range of the heat pump, peak demand events tend to be more dispersed and may occur with a lower degree of coincidence. However, given that peak demand behavior in these cases is linked to heat pump operations coinciding with non-HVAC electrical use, peaks are likely to occur during periods of higher grid demand.

A brief analysis of the results would appear to show little difference between the *VCHP* and *CCHP* technologies in terms of peak demand. However, *CCHP* systems hold strong promise in reducing auxiliary heating, which has been shown in this study to be a leading driver of peak electrical demand in colder regions. The extended operating range of these systems also minimizes the period of time the home must be heated solely via the auxiliary system, reducing the probability that auxiliary heating will coincide with a larger non-HVAC electrical draw. As climate change brings more extremes in outdoor temperature, *CCHP* systems may also provide a degree of added resilience for both homeowners and grids, particularly in regions like Halifax where the need for heating down to -25°C is not currently required.

Heat pump sizing can also have an important impact on peak demand. In this study, all systems were sized with a focus on heating, as per Option C of NRCan's *Air-Source Heat Pump Sizing and Selection Guide* [14]. Heat pumps sized to meet a smaller portion of the heating load will likely require further supplemental electric heating, increasing the duration and magnitude of peak demand vs. the results presented in this paper. The application of similar sizing objectives for the *VCHP* and *CCHP* cases also explains why peak demand increases are similar for both systems. Should both cases use the same size of heat pump (e.g., both 2 ton) instead of targeting the same percentage of annual heating load, results would likely reflect a strong preference for the *CCHP* system due to a reduced reliance on auxiliary heating.

6. Conclusion

This study has examined the peak demand implications of transitioning from natural gas furnaces to air-source heat pumps in four Canadian regions. Results show a strong link between climate and heat pump peak demand. In colder climates (i.e., Ottawa and Winnipeg, where ambient temperatures fall below the minimum operating temperature of the heat pump), peak demand is closely associated with periods of low outdoor temperatures when the heat pump must be supplemented partially or fully via electric auxiliary heating. Peak demand increases may reach up to 7.7 kW in Ottawa, and 9 kW in Winnipeg vs. a natural gas heated home. Given the link to outdoor temperature, peaks may also occur with a higher degree of coincidence, creating a larger aggregated load on the grid. In milder regions (i.e., Halifax and Vancouver, where outdoor temperatures remain within the operating range of the heat pump) peak demand is more closely linked to heat pump operations coincident with higher non-HVAC electrical loads. These peaks were more dispersed throughout the heating season but often occurred during peak hours when occupant activity was higher. Peak demand increases may reach up to 3.1 kW in both Halifax and Vancouver. An initial analysis of demand mitigation via preheating and temperature setback showed a strong ability to reduce electrical demand in Halifax during two-hour peak events in the morning and evening. However, this strategy also increased electrical demand before and after defined peak periods vs. the non-mitigation case, and as such requires careful application. Further work is needed to examine the viability of this strategy in other regions, and in older vintages of construction where the thermal capacitance of the building is reduced.

Future work will examine the peak demand implications of heat pumps in additional regions, and in a greater variety of residential building archetypes. Planned analysis also includes an in-depth examination of heat pump plus storage systems (e.g., Climate & Comfort Box solutions) to better mitigate peak demand without affecting thermal comfort in the building. Larger scale assessments of mitigation strategies at the grid level should also be performed to ensure that these strategies appropriately address the needs of utilities and avoid any unintended consequences (e.g., large peaks directly after a demand reduction period has ended).

References

[1] Government of Canada (GoC). *Canadian Net Zero Emissions Accountability Act*. Ottawa, CA: GoC; 2020.
[2] Canada Energy Regulator. Market Snapshot: Steady growth for heat pump technology. Ottawa, CA: Govt. of Canada; 2019. Available at: https://www.cer-rec.gc.ca/nrg/ntgrtd/mrkt/snpsht/2018/02-03htpmps-eng.html
[3] Protopapadaki, C., and Saelens, D., 2017. Heat pump and PV impact on residential low-voltage distribution girds as a function of building and district properties. *Applied Energy* **192**: 268–81.
[4] Fischer, D., Wolf, T., Wapler, J., Hollinger, R., Madani, H., 2017. Model-based flexibility assessment of a residential heat pump pool. *Energy* **118**: 853–64.
[5] Mollier, S., Deslauriers, C.A., Tamasauskas, J., Breton, S., Kegel, M. , 2022. "Peak Electrical Demand Impacts of Air-Source Heat Pumps in Canadian Residential Buildings". 2022 ASHRAE Annual Conference. Toronto, CA, paper TO-22-C042.
[6] National Research Council of Canada. *National Building Code of Canada 2015*. Ottawa: NRC; 2015.
[7] Natural Resources Canada. *Comprehensive Energy Use Database*. Ottawa, ON: NRCan; 2022. Available at: https://oee.nrcan.gc.ca/corporate/statistics/neud/dpa/menus/trends/comprehensive_tables/list.cfm
[8] Swinton, M.C., Entchev, E., Szadkowski, F., Marchand, R. *Benchmarking twin houses and assessment of the energy performance of two gas combo heating systems*. Ottawa,CA: Canadian Centre for Housing; 2003.
[9] Wills, A. D. *On the modelling and analysis of converting existing Canadian residential communities to net-zero energy*. Ottawa, Ontario, Canada: Carleton University; 2018.
[10]Mitra, D., Steinmetz, N., Chu, Y., Cetin, K., 2020. Typical occupancy profiles and behaviors in residential buildings in the United States. *Energy and Buildings* **210**, p. 109713.
[11] Armstrong, M. M., Swinton, M. C., Ribberink, H., Beausoleil-Morrison, I., Millette, J., 2009. Synthetically Derived Profiles for Representing Occupant-Driven Electric Loads in Canadian Housing. *Journal of Building Performance Simulation* **2**(1): 15–30.
[12] Daikin. *DZ20VC Specification Sheet*. Houston, USA: Daikin Manufacturing Company; 2019.
[13] Mitsubishi. *MUZ-FE Series Engineering Manual*. Atlanta, USA: Mitsubishi Electric Trane HVAC; 2019.
[14] Natural Resources Canada. *Air-Source Heat Pumps Sizing and Selection Guide*. Ottawa: NRCan; 2021.
[15] Klein, S.A. et al. *TRNSYS 18: A Transient System Simulation Program*. Madison, WI, USA: University of Wisconsin - Madison Solar Energy Laboratory; 2017.
[16] Breton, S., Tamasauskas, J., Kegel, M., 2019. "An Evaluation of Cold Climate Variable Capacity Air-Source Heat Pumps in Canadian Residential Buildings Using an Enhanced Component Model". Building Simulation 2019. Rome, IT, paper #211116.
[17] Hydro Quebec. *Rate Flex D*. Montreal, PQ, CA: Hydro Quebec; 2022. Available at: https://www.hydroquebec.com/residential/customer-space/rates/rate-flex-d.html
[18] International Energy Agency Heat Pump Technologies Programme. Climate & Comfort Box. Gothenburg, SWE: IEA Heat Pump Centre; 2022.

14th IEA Heat Pump Conference
15-18 May 2023, Chicago, Illinois

Experimental Investigation Into The Effect of Charge Optimization And Standard Test Conditions On The Seasonal Performance In An R410A Heat Pump With Dedicated Subcooler

Sugun Tej Inampudi[a], Stefan Elbel[a,b*]

[a]University of Illinois at Urbana-Champaign, Department of Mechanical Science and Engineering, Air Conditioning and Refrigeration Center, 1206 West Green Street, Urbana, IL 61801, USA
[b]Creative Thermal Solutions, Inc., 2209 North Willow Road, Urbana, IL, 61802, USA

Abstract

There is an increased focus on the amount of refrigerant charge used in the HVAC&R systems due to the new restrictions and ongoing phase down of high GWP refrigerants as part of the F-gas regulation. In the current study, seasonal performance for a variable speed compressor in an R410A water ethylene glycol (WEG) heat pump system having a nominal heating capacity of 9 kW is estimated according to EU 14825. This study experimentally studied the effect of charge and the fixed/variable outlet condition on the seasonal performance of the water heat pump equipped with a variable speed compressor. The results of a charge optimization done at part load conditions show an unexpected peak in COP_{dec} and results indicates that optimum charge has a higher impact on the efficiency at part load conditions than the nominal conditions. Based on the experimental results, the difference in the order of 5% in $SCOP$ is found when comparing optimum charge and non-optimum charge in a variable speed compressor. $SCOP$ can change by almost 22% depending on whether fixed/variable condenser temperature outlet operation is used.

© HPC2023.
Selection and/or peer-review under the responsibility of the organizers of the 14th IEA Heat Pump Conference 2023.

Keywords:charge optimization; heat pump; seasonal performance; dedicated subcooler; EU 14825; SCOP

1. Introduction

Due to the new restrictions and ongoing phase down of high GWP refrigerants as part of the F-gas regulation, there is an increased focus on the amount of refrigerant used in the HVAC&R systems. This increases the focus on potential benefits of having the optimum charge in a HVAC&R system. There are experimental studies which show the impact of charge level on cooling/heating capacity and energy efficiency. A refrigerant charge reduction of 25% led to an average energy efficiency reduction of about 15% and capacity degradation of about 20%. When the refrigerant was charged to 75% of design, the SEER value decreased by 16% [1]. An experimental investigation was conducted to study the effect of low charge level of R-22 on the performance of a 3-ton residential air conditioning system. The experimental results show that if a system is undercharged to 90% there is only a 3.5% reduction in cooling capacity however, the system performance suffers serious degradation if the level of charge drops below 80% [2].

Though there are many studies which predict that not operating at the optimum refrigerant charge can impact the cooling capacity and the efficiency of the system. The charge optimization is done at the nominal operating conditions and this charge might not be the optimum for part load operations. Beginning 2023, there are new DOE requirements for the HVAC systems to have higher SEER in USA. This increases the focus on seasonal performance than a single point efficiency. One of the ways to increase the seasonal performance is to use compressor capacity modulation.

* Corresponding author. Tel.: +1-217-721-9621.
E-mail address: elbel@illinois.edu.

An experimental study by the same authors analysed the effect of charge on the COP of a single speed and variable speed compressor in a dedicated subcooler chiller system. A peak was observed in COP at charge before the receiver starts filling up and this peak was more pronounced at the part load conditions. When the variable speed compressor was tested at a lower charge, the IPLV.SI was higher by 5% than when tested with the higher charge. They concluded that the peak in COP occurs due to the relative sizing of the condenser and subcooler and the optimum charge corresponds to the scenario when some portion of the two-phase heat transfer is happening in the subcooler [3]. Additionally, cases with different high side configuration were discussed and the peak COP was only observed for the case with a dedicated subcooler [4].

In the current study, the seasonal performance of an R410A heat pump for water heating application with a variable speed compressor is estimated according to EU 14825 standard [5]. The seasonal performance is estimated for the case with constant and variable $T_{weg,co,out}$. The initial tests are done using the nominal charge of 1.5 kg which was estimated for the same R410A system for cooling application [3,4]. The charge optimization for the heat pump is conducted at part load conditions to see if a peak in COP like the cooling application is observed [3,4]. This study also tries to explain a peak in COP observed in this dedicated subcooler with receiver system when the receiver is empty during the charge optimization test. The variable speed compressor is then tested at the optimum charge with constant and variable $T_{weg,co,out}$ to determine the effect of charge optimization on seasonal performance estimation.

2. Experimental Facility Description

Figure 1 shows the schematic of the R410A Water Ethylene Glycol (WEG) heat pump. A mixture of 20 % water and ethylene glycol is used as the secondary fluid. Two closed WEG loops are connected to the evaporator and condenser. Variable speed pumps and electric heaters are used to control the WEG flow rate and the outlet temperature of the condenser and the inlet temperature of the evaporator. An additional heat exchanger with chilled water flowing through is included in the condenser WEG loop to reject the heat from the condenser WEG loop. All the heat exchangers used in the facility are brazed plate heat exchangers (BPHX) and their dimensions are provided in Table 1. A 0.9 L receiver is connected between the condenser and the subcooler. Superheat is maintained at constant value by an electronic expansion valve (EXV) equipped with a superheat controller while the subcooling is a function of the charge.

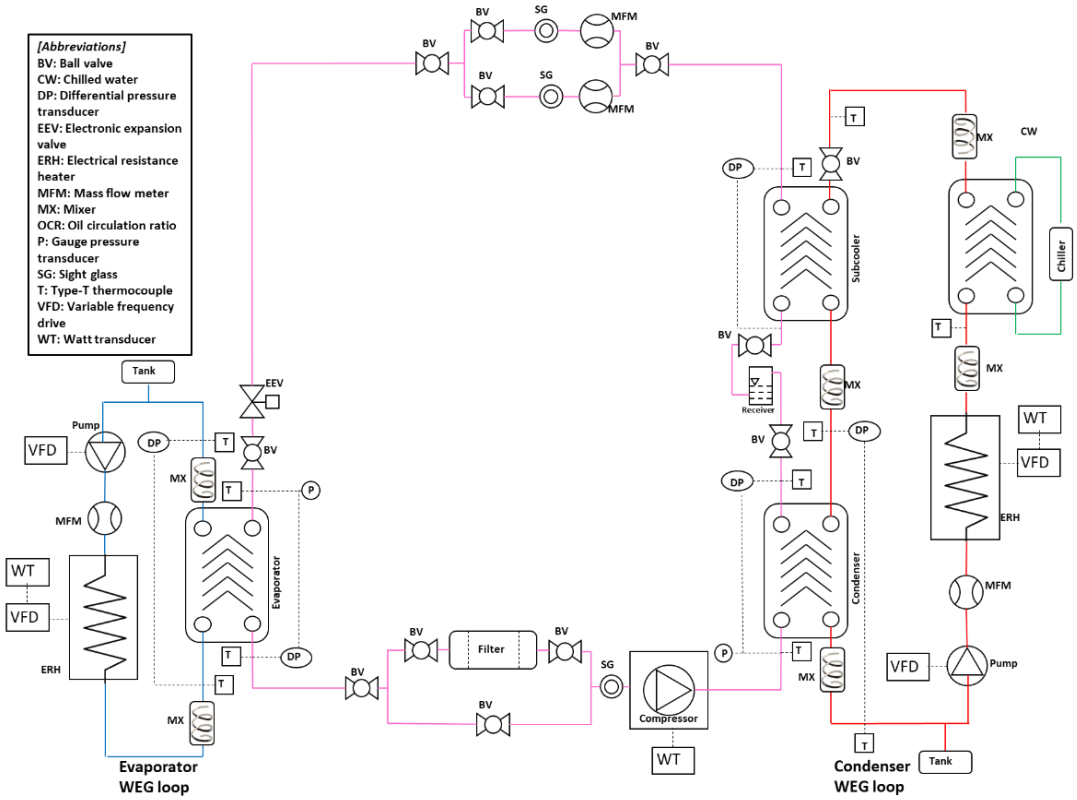


Fig. 1. Schematic of the R410A experimental facility

This experimental facility was also used by the same authors to compare the seasonal performance of different compressor modulation strategies for cooling application and the results show that variable speed compressor has the best seasonal performance [6,7,8]. A variable speed compressor than can operate between 15 and 100 Hz is used for this study.

Type-T thermocouples, absolute and differential pressure transducers, and Coriolis-type mass flow meters are used to obtain the refrigerant side measurements while type-T thermocouples, differential pressure transducers, and Coriolis-type mass flow meters are used to obtain WEG measurements. The data is collected at steady-state conditions at 5s intervals for 15 consecutive minutes, and the data is averaged over the collection period. REFPROP 10.0 was used to calculate the WEG and R410A properties [9]. The uncertainty of the sensors used in the experimental facility is presented in Table 2. This estimation does not include the uncertainty in thermophysical properties. However, the uncertainty in enthalpy difference can be approximated as the uncertainty in specific heat which is around ±0.5% [9]. An uncertainty propagation analysis carried out revealed an experimental uncertainty of ±0.3% for $\dot{Q}_{co+sc,ref}$ and ±5.7% for $\dot{Q}_{co+sc,WEG}$.

Table 1 Dimensions of the BPHX

Heat exchanger	Length (mm)	Width (mm)	Number of plates
Evaporator	311	111	28
Condenser	311	111	14
Subcooler	207	77	14

Table 2 Summary of the measured and calculated uncertainties

Instrument	Thermocouple (°C)	Pressure transducer (kPa)	Mass flow meter (g/s)	Wattmeter (kW)	$\dot{Q}_{co+sc,avg}$ (kW)	$COP_{dec,avg}$ (-)	$COP_{dec,weg}$ (-)
Uncertainty	±0.2	±0.2%	±0.2%	±0.5%	±3.0%	±3.1%	±5.8%

The capacity is calculated on the refrigerant side and the WEG side. For the WEG side, mass flow rate, temperature, and specific heat are used to calculate capacity as shown in Equation (1). For the refrigerant side, temperature and pressure are used to calculate the enthalpy which is then used with the mass flow rate to calculate the capacity as shown in Equation (2). The capacity reported is the average of the refrigerant side and WEG side capacity given by Equation (3). The difference between the two capacities is indicated by the error given by Equation (4). This error is always less than 6% for the part load rating tests. Power consumed by the compressor is measured using a Wattmeter. The ratio of the average capacity and power consumed by the compressor is used to calculate the $COP_{dec,avg}$ as shown in Equation (5). The heating capacity is always the combined heat rejected from the condenser and dedicated subcooler.

$$\dot{Q}_{co+sc,weg} = \dot{m}_{WEG} c_p \Delta T \tag{1}$$

$$\dot{Q}_{co+sc,ref} = \dot{m}_{ref} \Delta h \tag{2}$$

$$\dot{Q}_{co+sc,avg} = \frac{(\dot{Q}_{co+sc,WEG} + \dot{Q}_{co+sc,ref})}{2} \tag{3}$$

$$\varepsilon_{\dot{Q}co+sc} = \frac{(\dot{Q}_{co+sc,avg} - \dot{Q}_{co+sc,WEG}) \cdot 100}{\dot{Q}_{co+sc,avg}} \tag{4}$$

$$COP_{dec,avg} = \dot{Q}_{co+sc,avg} \Big/ \dot{W}_{cp} \tag{5}$$

$\dot{Q}_{co+sc,avg}$ as defined in Equation (3) and $COP_{dec,avg}$ are used for the estimation of the seasonal performance of the compressor (Sections 4.1, 4.3 and 4.4), but $\dot{Q}_{co+sc,weg}$ defined in Equation (1) and $COP_{dec,weg}$ are used during the charge optimization sections (Section 4.2). When the system is undercharged, the refrigerant is a two phase substance at the subcooler outlet which affects the Coriolis mass flow meter measurement. Though this problem does not exist at higher refrigerant charges, $\dot{Q}_{co+sc,weg}$ and $COP_{dec,weg}$ are still used to be consistent across all the refrigerant charges tested.

3. EU 14825 Standard

EU 14825 standard is used for the determination of the seasonal performance of a water heat pump [5]. Though there is an USA standard AHRI 551/591 available for chiller application, there is no such standard for water heat pump [10]. This standard defines the seasonal performance using $SCOP$, seasonal coefficient of performance. $SCOP$ is a representative for the whole designated heating season calculated as the reference annual heating demand divided by the annual electricity consumption for heating. Only the compressor power consumption (W_{cp}) is included in the estimation of $SCOP$. The current study estimates the seasonal performance using part load conditions for water/brine-to-water units for low temperature application for average heating season. These test conditions are given in Table 3. $SCOP$ is calculated using COP_{PL}, outside temperature, number of annual hours in which these temperatures are recorded. EU 14825 standard defines these characteristic reference temperatures and annual hours. The methodology to determine the $SCOP$ according the European standard EN 14825 was explained for a domestic brine-to-water heat pump for low-temperature application in another study [11].

Table 3 Part load conditions for water/brine-to-water units for low temperature application for average heating season

Test point	Part load ratio (%)	Outdoor (Evaporator) BPHX temperature [°C]	Indoor (Condenser) BPHX fixed outlet [°C]	Indoor (Condenser) BPHX fixed outlet [°C]
E&F	100	10/7	30/35	30/35
A	88	10/*	*/35	*/34
B	54	10/*	*/35	*/30
C	35	10/*	*/35	*/27
D	15	10/*	*/35	*/24

In this study, the bivalent temperature was selected equal to the design temperature causing the E and F conditions to become the same. As seen in Table 3, condenser and evaporator inlet and outlet conditions are mentioned for the full load condition (E&F) while for the remaining part load conditions, only the condenser outlet and evaporator inlet temperatures are given. The standard requires that the condenser and evaporator WEG flow rate used for the full load condition be used for the remaining part load conditions as well. The standard requires the evaporator outlet WEG temperature to be 7°C for the 100% load condition but the WEG flow required to achieve a 3°C temperature difference across the evaporator is beyond the maximum flow rate possible with the available pumps in the experimental facility. Hence, a 5°C temperature difference is used for the evaporator as well. A 5°C is used for the condenser in the EU 14825 standard as well as for the evaporator in cooling application in both the USA and EU standard [5,10].

If the compressor cannot be unloaded to the required part load ratio, then the compressor is run at the minimum step of unloading at the same condenser outlet and evaporator inlet condition shown in Table 3 and COP_{dec} is calculated. Then this COP_{dec} is degraded to COP_{PL} using the CR, $C_d = 0.9$ as shown in Equations (6) and (7). CR is the ratio of the required heating demand to the supplied heating capacity by the system. The degradation coefficient C_d can be determined by performing a specific cycling loss test defined in EU 14825 or a value of 0.9 can be assumed according to the standard [5].

$$CR = \frac{\dot{Q}_{load}}{\dot{Q}_{capacity}} \tag{6}$$

$$COP_{PL} = COP_{dec} \frac{CR}{C_d \cdot CR + (1 - C_d)} \tag{7}$$

4. Results And Discussion

4.1. Seasonal performance of a variable speed compressor with 1.5 kg of charge

4.1.1. Constant condenser WEG inlet conditions

Seasonal performance results of a variable speed compressor charged with 1.5 kg of refrigerant are shown in Figure 2. The selected compressor can operate between 15 and 100 Hz. The load is a linear function of the part load conditions. The maximum heating capacity is equal to the load at the E&F condition obtained with the variable speed compressor operating at 72.5 Hz. This operating frequency is equal to the one used for the

cooling performance tests conducted [8]. As the test condition changes from E&F to D, the condenser WEG inlet temperature remains constant at 35°C and the required load changes from 100% to 15%. The variable speed compressor can match the required heating load at E&F, A and B condition by changing the compressor operating frequency. Since this compressor can operate below 28.3 Hz, it should have been able to match the required heating load at C condition. Additionally, at the D condition, the compressor should have been able to operate at 15 Hz (lowest possible frequency) and provide a closer heating capacity. However, if the compressor operates at a frequency below 28.3 Hz, the required pressure ratio is outside the compressor operating envelop and thus it is limited to this 28.3 Hz. This high pressure ratio is caused by the constant condenser outlet test condition on WEG side. The compressor undergoes cycling losses at C and D condition and the magnitude of these losses are higher at the D condition. This can be by the difference between $COP_{dec,avg}$ and COP_{PL} and the cycling losses in Figure 2. $SCOP_{avg}$ calculated for this compressor is 4.33.

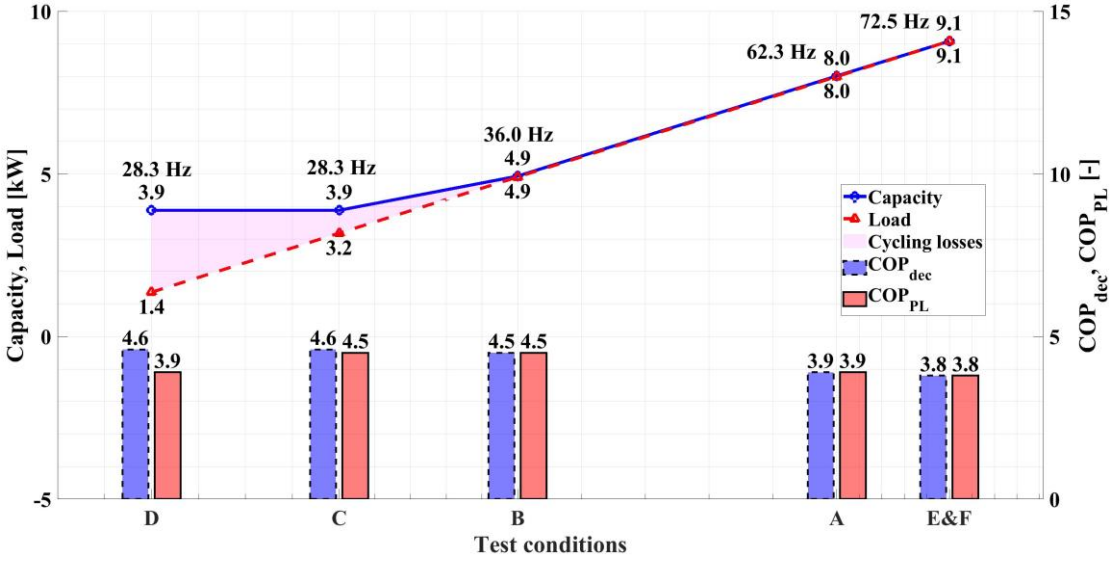


Fig. 2. Seasonal performance of variable speed compressor with constant $T_{weg,co,out}$

4.1.2. Variable condenser WEG outlet temperature

Seasonal performance results of the same variable speed compressor when tested according to the variable condenser WEG outlet temperature requirements are shown in Figure 3.

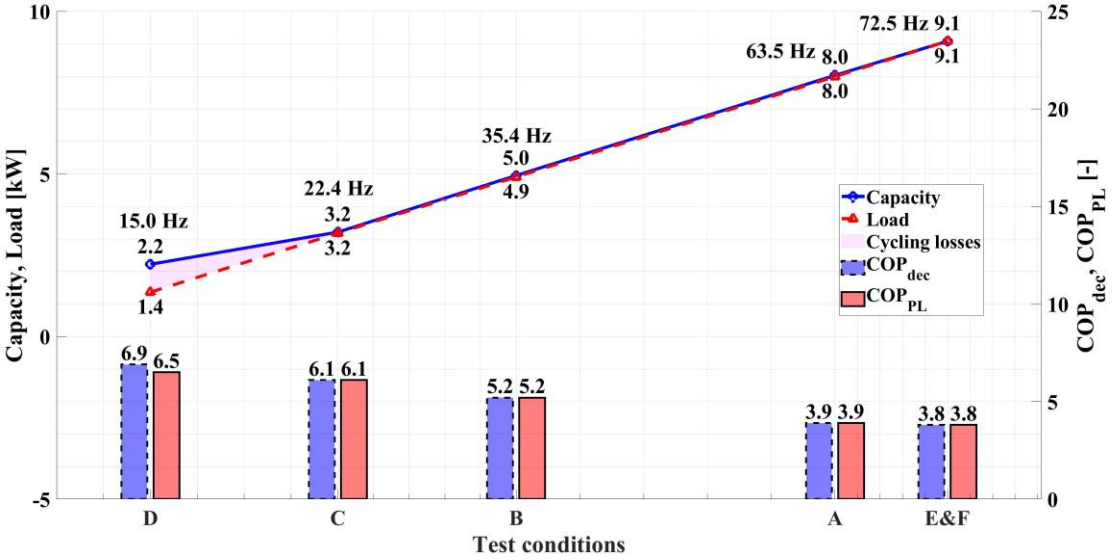


Fig. 3. Seasonal performance of variable speed compressor with variable $T_{weg,co,out}$

The operating frequency and the performance of the compressor are the same at E&F condition due to the similarities between both the standard requirements. However, at the part load test conditions, the required part load ratio remains the same as the case with constant WEG outlet temperature but the condenser outlet temperature changes. This temperature drops from 35°C at E&F condition to 24°C at D condition. This drop in the condenser temperature causes the pressure ratio to be within the compressor operating envelop. Thus, the compressor can match the required cooling load at C condition and operate at its lowest possible frequency of 15 Hz at D condition. This lowers the cycling losses experienced by the compressor and both $COP_{dec,avg}$ and $COP_{PL,avg}$ are higher when using this test matrix. The $SCOP_{avg}$ calculated for this compressor is 5.26.

4.2. Charge optimization of variable speed compressor at B condition

Charge optimization results of the variable speed compressor at B condition are shown in Figures 4, 5 and Table 4. Figure 4 shows the variation of $COP_{dec,weg}$, $\dot{Q}_{co+sc,weg}$ with charge while Figure 5 shows the variation of compressor work, superheat and subcooling with charge.

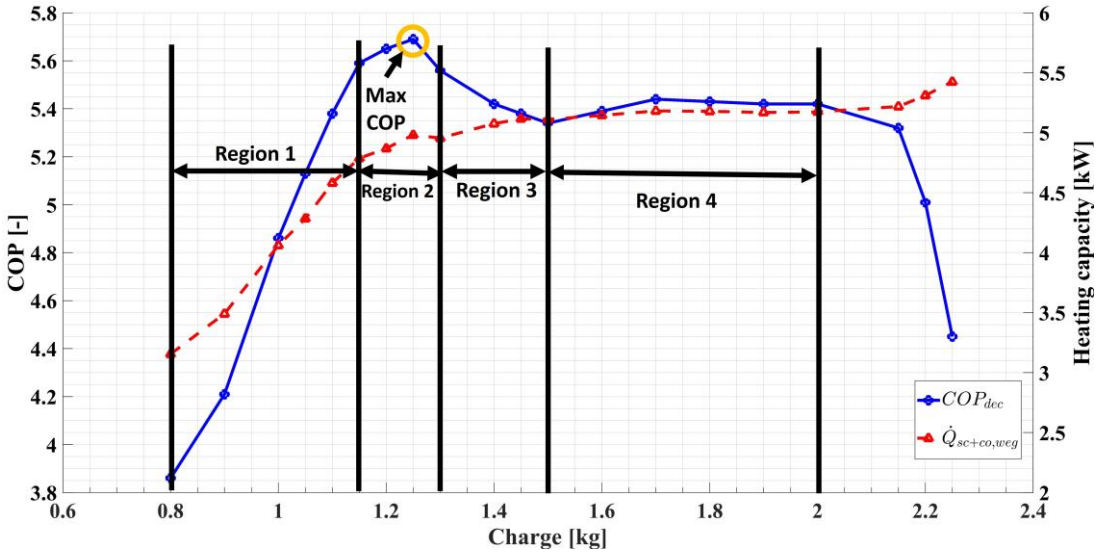


Fig. 4. Variation of $COP_{dec,weg}$ and $\dot{Q}_{co+sc,weg}$ of variable speed compressor with charge at B condition

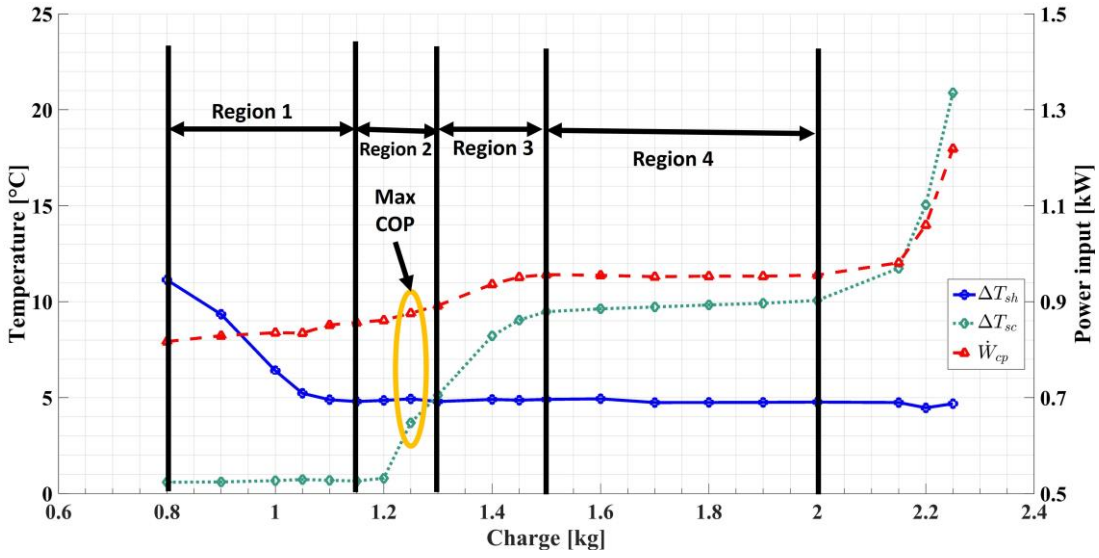


Fig. 5. Variation of W_{cp}, ΔT_{sh} and ΔT_{sc} of variable speed compressor with charge at B condition

Table 4 presents the charge, $COP_{dec,weg}$, percentage change in the heating capacity, power consumption between two consecutive refrigerant charges. It also shows the difference between the subcooler outlet enthalpy of two consecutive charges. The evaporator superheat and UA are also available in Table 4. Though Figure 4 looks like a typical charge optimization curve for a system with TXV/EXV with a receiver, there is an unexpected peak in $COP_{dec,weg}$ that occurs when the receiver is empty. To explain the reason why there is a peak in $COP_{dec,weg}$ and why it occurs at that charge, the entire charge optimization curves are divided into four regions.

Region 1 (0.80 to 1.15 kg): In this region, the refrigerant charge added goes to the evaporator due to the EXV being completely open. Thus, as the charge increases in the evaporator, the superheat at the evaporator outlet reduces. This in turn increases the evaporator UA. A lower superheat, higher evaporator UA increases the heat transfer in the evaporator and thus also increases the condenser heat rejection. Additionally, the subcooler outlet enthalpy increases in this region. Thus, there is no positive impact of the subcooler in this region. At the end of this region, the evaporator superheat reaches a constant value and the EXV can maintain the required superheat.

Region 2 (1.20 to 1.25 kg): The maximum $COP_{dec,weg}$ occurs in this region. The increase in the heating capacity at this point compared to the previous charge is due to the decrease in subcooler outlet enthalpy. This is the first point where the subcooler outlet enthalpy reduces compared to the previous charge. The compressor power also increases; however, the percentage increase of the heating capacity is higher than the percentage increase of power consumption. Thus, this results in a peak in $COP_{dec,weg}$. This is the last point in region 2 and 3 where the relation in Equation (8) is valid.

$$\frac{\Delta\dot{Q}_{co}}{\dot{Q}_{co}} > \frac{\Delta\dot{W}_{cp}}{\dot{W}_{cp}} \tag{8}$$

Table 4 Variation of different parameters with charge for a variable speed compressor at B condition

Charge [kg]	$COP_{dec,weg}$ [-]	$\Delta\dot{Q}_{co}/\dot{Q}_{co}$ [%]	$\Delta W_{cp}/W_{cp}$ [%]	$\Delta\dot{Q}_{co}/\dot{Q}_{co} - \Delta W_{cp}/W_{cp}$ [%]	ΔT_{sh} [°C]	UA_{ev} [kW/°C]	Δh_{scro} [kJ/kg]
0.80	3.86	-	-	-	11.1	0.34	
0.90	4.21	+10.65	+1.49	+9.16	9.3	0.44	+1.13
1.00	4.86	+16.35	+0.75	+15.59	6.4	0.72	+1.56
1.05	5.13	+5.48	-0.09	+5.57	5.2	0.83	+0.15
1.10	5.38	+6.94	+2.02	+4.92	4.9	0.72	+1.06
1.15	5.59	+4.48	+0.60	+3.88	4.8	0.70	+0.41
1.20	5.65	+1.73	+0.57	+1.17	4.9	0.70	-0.05
1.25	5.69	+2.29	+1.71	+0.58	4.9	0.71	-4.27
1.30	5.56	-0.52	+1.79	-2.31	4.8	0.71	-1.65
1.40	5.42	+2.43	+5.01	-2.58	4.9	0.72	-2.17
1.45	5.38	+0.79	+1.58	-0.79	4.9	0.73	-0.37
1.50	5.34	-0.10	+0.54	-0.64	4.9	0.72	-0.41
1.60	5.39	+0.66	-0.15	+0.81	4.9	0.72	-0.24
1.70	5.44	+0.72	-0.30	+1.02	4.7	0.74	-0.14
1.80	5.43	-0.07	0.12	-0.19	4.7	0.74	-0.32
1.90	5.42	-0.17	-0.02	-0.15	4.8	0.74	-0.07
2.00	5.42	+0.09	0.25	-0.16	4.8	0.74	0.03
2.15	5.32	+0.86	2.69	-1.83	4.7	0.74	-1.14
2.20	5.01	+1.77	8.01	-6.24	4.5	0.75	-0.79
2.25	4.45	+2.16	15.02	-12.86	4.7	0.74	-0.66

Quality at the subcooler inlet, ratio of heat transfer happening in the subcooler to the total heat transfer happening in the condenser and subcooler and the single phase (subcooled liquid) heat transfer happening in the subcooler are plotted against the charge in Figure 6. In the region 1, the quality at the subcooler inlet

increases because as the charge is added to the system, refrigerant mass flow rate increases while the heat transfer happening in the condenser does not change significantly. This causes an increase in the quality at the subcooler inlet (condenser outlet). The $COP_{dec,weg}$ maximum occurs when the quality at the subcooler inlet is 34%. This means at the charge corresponding to the $COP_{dec,weg}$ peak, some portion of the two phase heat transfer happens in the subcooler. This can also be seen that 30% of the total heat transfer is happening in the subcooler at the maximum $COP_{dec,weg}$ charge and as the charge increases, more heat transfer occurs in the condenser. Additionally, the single phase heat transfer happening in the subcooler increases as the charge increases beyond the maximum $COP_{dec,weg}$ charge but the ratio of heat transfer happening in subcooler decreases. This indicates that as additional charge is added though the single phase heat transfer increases in the subcooler, the total heat transfer happening in the subcooler decreases.

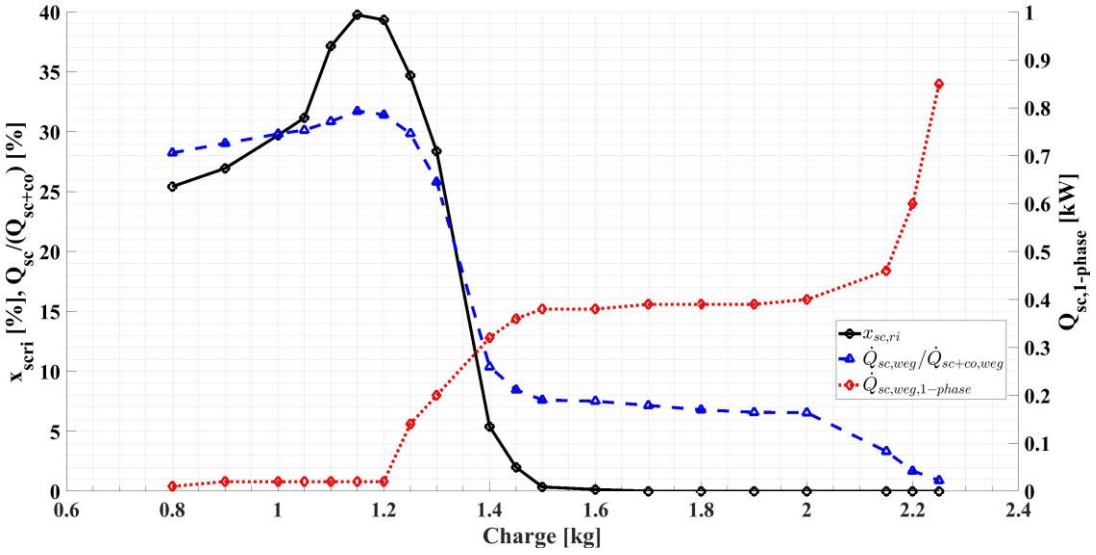


Fig. 6. Variation of refrigerant quality at subcooler inlet, subcooler heat transfer with charge

The maximum $COP_{dec,weg}$ approximately corresponds to a configuration shown in Figure 7 which indicates that the single phase subcooled refrigerant exists only at the outlet of the subcooler.

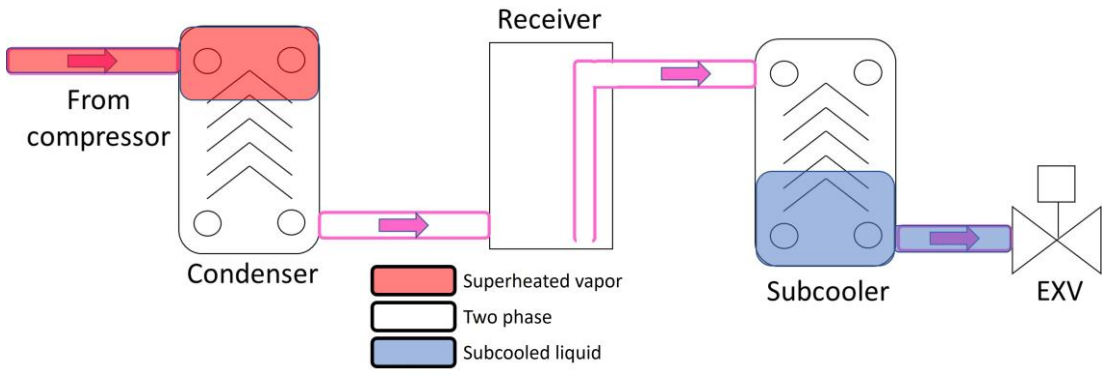


Fig. 7. Approximate distribution of the refrigerant at the maximum COP_{dec} charge

Region 3 (1.30 to 1.50 kg): In this region, the relative increase in compressor power consumption is higher than the relative increase in heating capacity and the relation shown in Equation (9) is valid. Though the amount of subcooling increases 5°C to 9.4°C as shown in Figure 5, the enthalpy at the subcooler outlet only drops by 2.9 kJ/kg in the entire region 3. This drop is lower than the drop of 4.3 kJ/kg observed from the 1.20 kg to the peak $COP_{dec,weg}$ charge of 1.25 kg. As the charge increases in this region, the condensation pressure goes up and the subcooling at the subcooler outlet increase, the heating capacity is determined by the enthalpy at the subcooler outlet not the subcooling. Additionally, there is a limit on the heating capacity due to the minimum

possible subcooler outlet enthalpy determined the inlet temperature of WEG while there is no such limit on the compressor outlet enthalpy and compressor power consumption.

$$\frac{\Delta \dot{Q}_{co}}{\dot{Q}_{co}} < \frac{\Delta W_{cp}}{W_{cp}} \tag{9}$$

At the maximum $COP_{dec,weg}$ charge and in region 3, the subcooler inlet is two phase refrigerant. As the charge increases in region 3, the fraction of two phase heat transfer happening the subcooler reduces. This reduction is seen by the drop in the subcooler inlet refrigerant quality in Figure 6. This increases the amount of two phase heat transfer happening in the condenser. Therefore, to get a higher heat transfer rate in the same condenser area, the temperature difference across the refrigerant and WEG in the condenser must increase. This leads to a higher condensation pressure and subcooling at the subcooler outlet. The increase in power consumption due to this higher condensation pressure is more than the increase in heating capacity as shown in Equation (9), causing a drop in the $COP_{dec,weg}$ in region 3.

Region 4 (1.60 to 2.00 kg) and beyond (2.15 to 2.25 kg): Region 4 starts when the receiver starts filling up with the liquid refrigerant. The additional refrigerant charge gets accumulated in the receiver and thus there is no change in the system performance. When the charge is increased beyond the region 4 and the receiver holding capacity, the additional charge gets accumulated in the condenser which increases the condensation pressure, power consumption and reduces the $COP_{dec,weg}$.

4.3. Seasonal performance of a variable speed compressor with 1.25 kg of charge

The results of the charge optimization study reveal that a peak in $COP_{dec,avg}$ is seen when the system operates at 1.25 kg. To understand the impact of the charge optimization on the seasonal performance ($SCOP_{avg}$), the variable speed compressor is now tested using constant and variable condenser WEG inlet with 1.25 kg of refrigerant charge.

4.3.1. Constant condenser WEG inlet conditions

Seasonal performance results of a variable speed compressor charged with 1.25 kg of refrigerant are shown in Figure 8. The operating frequencies of the compressor are the same as in Section 4.1.1. However, the heating capacities with the reduced refrigerant charge is lower at the full load conditions by 2.2% than the one available when operating with 1.5 kg of charge. This difference in heating capacity drops at the part load conditions. The $COP_{dec,avg}$ is higher for the 1.25 kg compared to 1.5 kg charge. The $COP_{dec,avg}$ is 2% higher at the full load condition while it 4.3% higher at C&D and 6.6% at B condition. This shows that the charge optimization has a higher impact at the part load conditions than the full load conditions.

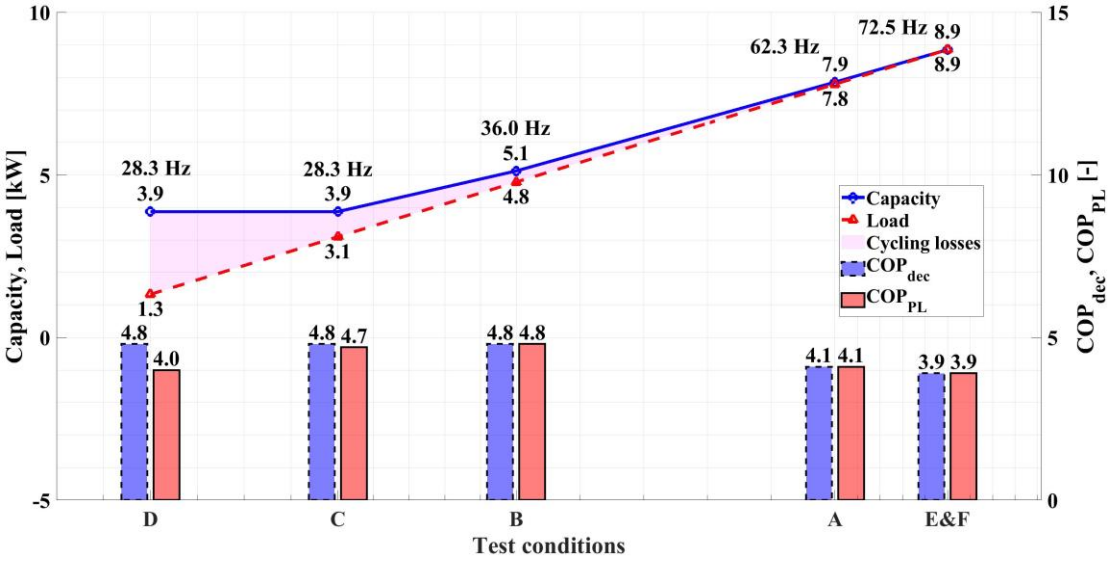


Fig. 8. Seasonal performance of variable speed compressor with constant $T_{weg,co,out}$

Though it can be seen from Figure 8 that the compressor undergoes cycling losses at B condition, no cycling losses were included and $COP_{PL,avg}$ is equal to $COP_{dec,avg}$. The compressor can match the required heating capacity at B condition by operating at a frequency lower than 36.0 Hz, it is still operated at 36.0 Hz to match the frequency used when operating with 1.5 kg. This frequency allows an estimation of the effect of only charge on $COP_{dec,avg}$ for both the cases. And to ensure the case with 1.25 kg is not penalized for this operation, cycling losses are not included. The compressor does undergo cycling losses at C and D conditions for this lower refrigerant charge as well. However, the $COP_{PL,avg}$ are still higher for the lower refrigerant case. The $SCOP_{avg}$ for this compressor at 1.25 kg refrigerant charge is 4.56.

4.3.2. Variable condenser outlet temperature

Seasonal performance is estimated for the variable speed compressor charged with 1.25 kg of refrigerant according to the variable $T_{weg,co,out}$ test matrix. The results of the seasonal performance test are shown in Figure 9. The heating capacity at the full load condition (E&F) is still lower by 2% than when operating with 1.5 kg of refrigerant charge. The operating frequency of the compressor is maintained the same as the test case with higher refrigerant charge to only include the effect of refrigerant charge on the seasonal performance. The $COP_{dec,avg}$ and $COP_{PL,avg}$ are higher with 1.25 kg for all the test conditions and the difference is higher at part load conditions. The compressor only undergoes cycling losses at D condition when the required operating frequency to match the heating load is below minimum possible compressor frequency of 15 Hz. The compressor can match the heating load at C condition because of the reduced $T_{weg,co,out}$ and pressure ratio. The $SCOP_{avg}$ for this compressor at these conditions is 5.47.

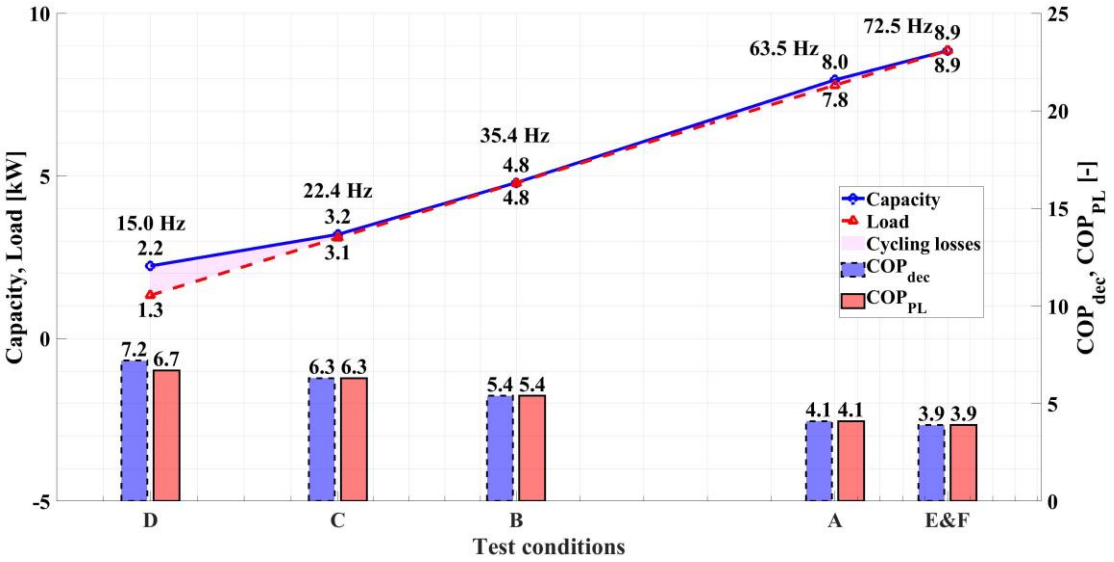


Fig. 9. Seasonal performance of variable speed compressor with variable $T_{weg,co,out}$

4.4. Comparison of $SCOP_{avg}$ for all the investigated cases

The $SCOP_{avg}$ values calculated using the $COP_{PL,avg}$ for all the different tested cases are shown in Table 5. The case 4 with 1.25 kg of refrigerant charge and variable $T_{weg,co,out}$ is 26.3% higher than the case 1 with 1.5 kg of refrigerant charge and fixed $T_{weg,co,out}$. The $SCOP_{avg}$ of the compressor when tested according to the variable $T_{weg,co,out}$ is 21.5% higher than when tested according to constant $T_{weg,co,out}$ with 1.50 kg of charge and it is 21.0% with 1.25 kg of charge. This higher $SCOP_{avg}$ is due to the lower $T_{weg,co,out}$ which causes a drop in the compressor operating pressure and power consumption. Additionally, the compressor can match the heating capacity during the variable $T_{weg,co,out}$ test cases at the C condition and operate at the minimum possible frequency at the D condition. This eliminates the cycling losses at the C condition and reduces the cycling losses at D condition. These lead to a higher $COP_{PL,avg}$ for the case with variable $T_{weg,co,out}$. The $SCOP_{avg}$ for case 2 with fixed $T_{weg,co,out}$ and lower charge is 5.3% than the equivalent case 1 with higher refrigerant charge. Similar improvement of 4.8% is observed when comparing cases 3 and 4 with the variable $T_{weg,co,out}$. These difference cases show that there is an effect of test standard as well as the refrigerant charge on the seasonal performance estimates and the impact of test standard is significantly higher.

Table 5 $SCOP$ estimates for all the cases investigated

Case #	Charge [kg]	Fixed/Variable Condenser WEG outlet	$SCOP_{avg}$ [-]	Difference in $SCOP_{avg}$ [%]	$\dot{Q}_{co+sc,avg}$ at full load condition [kW]	Difference in full load $\dot{Q}_{co+sc,avg}$ [%]
1	1.50	Fixed	4.33	-	9.08	-
2	1.25	Fixed	4.56	+5.3%	8.85	-2.5%
3	1.50	Variable	5.26	+21.5%	9.08	-
4	1.25	Variable	5.47	+26.3%	8.85	-2.5%

5. Conclusions

This study experimentally studied the effect of charge and the fixed/variable outlet condition on the seasonal performance of an R410A water heat pump with a variable speed compressor. The $SCOP_{avg}$ for the variable speed compressor with variable outlet condition was 21.5% higher than the fixed outlet condition. The variable speed compressor cannot match the required heating load at one of the part load conditions with fixed outlet condition due to the required pressure ratio being outside the compressor operating envelop. This problem does not occur for the variable outlet condition, and this leads to a lower cycling losses and higher $SCOP_{avg}$.

Charge optimization for the variable speed compressor was done at part load conditions and a peak in $COP_{dec,weg}$ was observed at a charge before the receiver starts filling up. This maximum $COP_{dec,weg}$ occurs due to the relative amounts of heat transfer happening in the condenser and subcooler and the optimum charge corresponds to the scenario when some portion of the two phase heat transfer is happening in the subcooler. The peak in $COP_{dec,weg}$ is due to the interaction between the increase in power consumption due to reduced two phase heat transfer area in the subcooler and the increased heating capacity due to higher subcooling in the subcooler. The relative difference between these two factors causes a peak in $COP_{dec,weg}$. When the variable speed compressor was operated at this optimum charge, the $SCOP_{avg}$ improved by 5.3% for the fixed outlet condition and 4.8% for the variable outlet condition. Thus, the COP_{dec} can improve if the system is operated in region 2.

However, the heating capacity at the full load drops by around 2% when operating at lower refrigerant charge. Any refrigerant leak in the system can also move the operating charge to region 1 which drops the COP_{dec} significantly. So, it is recommended to operate the system in region 3 to get a higher COP_{dec} but not a huge drop in heating capacity. Additionally, operating a dedicated subcooler system with a receiver installed in between the condenser and subcooler at the peak COP_{dec} does not make use of the installed receiver and the maximum possible subcooling from the dedicated subcooler.

Nomenclature

BPHX	brazed plate heat exchanger [-]	Subscripts	
C_d	degradation coefficient [-]	1-phase	single phase refrigerant
COP	coefficient of performance [-]	2-phase	two phase refrigerant
CR	capacity ratio [-]	avg	average
c_p	specific heat [kJ/kg]	co	condenser
EXV	electronic expansion valve [-]	cp	compressor
GWP	global warming potential [-]	dec	declared
h	enthalpy [kJ/kg]	ev	evaporator
$IPLV.SI$	integrated part load value [-]	in	inlet
LMTD	log mean temperature difference [K]	load	required heating load
m	mass flow rate [g/s]	out	outlet
p	pressure [kPa]	PL	part load
Q	heat transfer rate [kW]	ref	refrigerant
$SCOP$	seasonal coefficient of performance [-]	ri	refrigerant inlet
T	temperature [°C]	ro	refrigerant outlet
UA	overall heat transfer coefficient [kW/K]	sc	subcooler/subcooling
W	power [W]	sc+co	subcooler and condenser
WEG	water ethylene glycol [-]	sh	superheat
x	refrigerant quality [-]	weg	water ethylene glycol

Greek symbols	
Δ	difference [%]
ε	error [%]

Acknowledgements

The authors would like to thank the member companies of the Air Conditioning and Refrigeration Center at the University of Illinois at Urbana-Champaign for their funding to support this project, Emerson / Copeland for compressor samples, Danfoss for brazed plate heat exchangers, and Creative Thermal Solutions for the technical support.

References

[1] Kim, W., & Braun, J. E., 2012. Evaluation of the impacts of refrigerant charge on air conditioner and heat pump performance. International journal of refrigeration, 35(7), 1805-1814.
[2] Goswami, D. Y., Ek, G., Leung, M., Jotshi, C. K., Sherif, S. A., & Colacino, F., 2001. Effect of refrigerant charge on the performance of air conditioning systems. International journal of energy research, 25(8), 741-750.
[3] Inampudi S.T., Elbel S., 2022, "Study of charge optimization and compressor modulation strategies effect on the seasonal performance in a R410A chiller," 19th International Refrigeration and Air Conditioning Conference at Purdue, West Lafayette, IN, USA, July 11 -14, Paper 1199
[4] Inampudi S., Elbel S., 2022, "Experimental investigation into the effect of charge optimization and compressor modulation strategies on the seasonal performance in a R410A chiller," 16th International Conference on Heat Transfer, Fluid Mechanics and Thermodynamics - HEFAT 2022, Amsterdam, The Netherlands, August 08-10, Paper 131
[5] European Committee for Standardization, 2013. Standard EN 14825: 2013, Air conditioners, liquid chilling packages and heat pumps with electrically driven compressors for space heating and cooling. Testing and rating at part load conditions and calculation of seasonal performance.
[6] Inampudi S.T., Botticella F., Elbel S., 2021, "Experimental comparison of seasonal performance in R410A chiller using single speed and two stage compressor," 18th International Refrigeration and Air Conditioning Conference at Purdue, West Lafayette, IN, USA, May 23-28, Paper 1484
[7] Inampudi S., Botticella F., Elbel S., 2021, "Part load performance of single and two stage compressors – a comparative experimental study in a R410A chiller unit," 12th International Conference on Compressors and their Systems, London, UK, September 6-8, Paper 184
[8] Inampudi S.T., Botticella F., Elbel S., 2022, "Comparative experimental analysis of different compressor capacity modulation strategies in R410A chiller with focus on seasonal performance," 19th International Refrigeration and Air Conditioning Conference at Purdue, West Lafayette, IN, USA, July 11 -14, Paper 1198
[9] Lemmon, E. W., Bell, I. H., Huber, M. L., & McLinden, M. O., 2018. NIST Standard Reference Database 23: Reference Fluid Thermodynamic and Transport Properties-REFPROP, Version 10.0, National Institute of Standards and Technology. Standard Reference Data Program, Gaithersburg
[10] A. H. R. I., 2020. AHRI Standard 551/591 (SI): 2020 Standard for performance rating of water-chilling and heat pump water-heating packages using the vapor compression cycle. Air-Conditioning, Heating, Refrigeration Institute, Arlington, VA, USA.
[11] Sieres, J., Ortega, I., Cerdeira, F., Álvarez, E., & Santos, J. M., 2022. Seasonal Efficiency of a Brine-to-Water Heat Pump with Different Control Options according to Ecodesign Standards. Clean Technologies, 4(2), 542-554.

14th IEA Heat Pump Conference
15-18 May 2023, Chicago, Illinois

Assessing the potential of air-source heat pumps in the Canadian residential sector

Justin Tamasauskas[*,a], Laurence Rousseau[a], Alex Lachance[a], Martin Kegel[a]

[a]CanmetENERGY in Varennes, Natural Resources Canada, Varennes, J3X 1P7 Canada

Abstract

Air-source (air-air) heat pumps can play a critical role in driving an efficient electrification of space heating in Canadian buildings. However, the deployment of these systems is often challenging in Canada, complicated by large variations in climate, utility rates and structures, and existing heating energy sources. This paper uses a simulation-based approach, driven by an enhanced data-driven model, to develop a more comprehensive overview of the technical and economic potential of heat pumps as replacements for current common heating systems (natural gas furnace, oil furnace, electric baseboards) in Canadian residential buildings. Results highlight the economic value in transitioning from electric baseboards or oil furnaces to heat pump systems in each of the four regions examined (Halifax, Toronto, Winnipeg, Vancouver), and note the growing potential of heat pumps as replacements for natural gas furnaces, with planned carbon pricing resulting in lifecycle cost savings vs. gas furnaces by 2030 in all regions. Findings can be used to better understand the current and future context for heat pumps to support R&D, policy, and market development.

© HPC2023.
Selection and/or peer-review under the responsibility of the organizers of the 14th IEA Heat Pump Conference 2023.

Keywords: Air-source heat pumps;electrification;residential sector;techno-economic analysis

1. Introduction

The *Canadian Net Zero Emissions Accountability Act* outlines Canada's commitment to achieving carbon neutrality by 2050 [1]. The built environment must play a key role in this transition: Canadian buildings account for 17% of national greenhouse gas (GHG) emissions, with nearly 80% of this total directed towards space heating, cooling, and hot water preparation [2]. Heat pumps are critical in driving decarbonization of the built environment via their ability to efficiently electrify space conditioning. However, supporting greater adoption requires an appropriate understanding of system selection and economics.

The Canadian context represents a particularly challenging set of circumstances for heat pump integration. Wide variations in both climates (mild maritime, to extreme cold) and utility rates and structures (vast differences in prices of natural gas vs. electricity) mean that the impact of heat pumps (e.g., on energy savings, utility costs, greenhouse gas (GHG) emissions) can differ greatly in a given region. Quantifying these impacts is a critical step in driving the policy and R&D required to facilitate a greater uptake of heat pumps in Canada.

Air-source (air-air) heat pumps are a popular choice of heat pump integration in Canadian homes, driven by their relative lower cost and ease of installation. Previous efforts have examined the role and impacts of these systems in Canada [3,4], but often focus on assessing heat pumps in a single building archetype or as a replacement for a single type of existing heating technology (e.g., natural gas furnaces). Recent studies [5] have attempted to present a more complete outlook but employ simplified heat pump models to facilitate analysis, limiting the ability to compare different heat pump technologies or assess the impact of system sizing.

* Corresponding author. Tel.: +1-438-364-1663;
E-mail address: justin.tamasauskas@nrcan-rncan.gc.ca.

This paper uses a simulation-based approach, supported by extensive testing and measured data, to examine the energy, GHG, and economic impacts of electrifying building thermal loads via the implementation of air-source heat pumps. A detailed, data-driven heat pump model is used to represent two common air-source heat pump integrations: A conventional variable capacity unit, and a cold climate (variable capacity) unit aimed at maintaining heating performance in the cold Canadian climate. Each heat pump integration is used to examine the impact of replacing three common heating systems (natural gas furnace, electric baseboards, oil furnace) in three types of typical single family Canadian housing. Results are used to examine the short- and medium-term role of air-source heat pumps in driving an effective, economic decarbonization of Canadian homes.

2. Definition of Base Cases for Heat Pump Integration

Climate, utility rates, and electricity generation methods (and associated GHG emissions) can vary greatly across Canada. Four Canadian regions are selected for this analysis, each representing a unique context for system integration. Table 1 summarizes key parameters for each region [2,6].

Table 1: Summary of Climate and Electricity Generation Methods for Selected Canadian Regions [2,6]

Characteristic	Halifax	Toronto	Winnipeg	Vancouver
Climate Type	Cold-Humid	Cold-Humid	Very Cold	Marine
Heating Degree Days (18°C)	4000	3520	5670	2825
Cooling Degree Days (18°C)	100	280	170	40
Heating Design Temperature (°C)	-16	-18	-33	-7
Cooling Design Temperature (°C)	26	31	30	28
Main Electricity Generation Method(s)	Coal, Fuel Oil	Nuclear, Nat. Gas, Hydro	Hydro	Hydro
GHG Emission Factor, Electricity (g CO_2/kWh)	760	30	1.3	20

Three separate building archetypes are developed to better understand the impact of building size, construction, and heat pump integration method on energy and economic performance. These archetypes have been developed to represent specific segments of the residential building stock, with geometry and floor area derived from available literature and databases [7,8,9]. Each archetype also uses a different base case heating system to examine the impact of heat pumps replacing different common heating technologies. The most common residential heating energy system is highly region-dependent: Natural gas heating is prevalent from Western through Central Canada (Vancouver, Winnipeg, Toronto), while electrical or oil-based heating is more common in the Atlantic provinces (Halifax) [2]. To develop a more comprehensive understanding of the transition to heat pumps, all three of these heating base cases (Natural gas, oil, electricity) are examined in each region, even in situations where particular systems have smaller uptake. This can provide policy makers with information to better tailor potential incentive programs and identify situations where transitioning to a heat pump offers immediate energy and economic benefits. A summary of relevant parameters for each building archetype is presented in Table 2. Where possible, archetype performance has been validated using data from test homes (for L2S [3]) or compared with available literature [2].

Table 2: Summary of Archetype Parameters [7,8,9]

	Archetype		
Characteristic	Small Bungalow (SB)	Medium Two-Storey (M2S)	Large Two-Storey (L2S)
Heated Floor Area	110 m^2	190 m^2	280 m^2
Number of Floors	1	2	2
Basement	No, slab on grade	Yes	Yes
Construction Vintage	1960s	New Build	New Build
Primary Heating Fuel & System	Heating Oil Forced Air Furnace	Electric Baseboard Heaters	Natural Gas Forced Air Furnace
Heating Efficiency	71%	100%	95%
Cooling System	Central AC COP = 3.5*	Split AC Unit COP = 3.3*	Central AC COP = 3.5*
DHW Fuel	Heating Oil	Electric	Natural Gas
Heat Recovery Ventilator	No	Yes	Yes

For each archetype, building envelope performance is modified to represent region specific construction for the four selected cities in Table 1. For the M2S and L2S archetypes, envelope performance was selected based on the National Building Code of Canada (NBC) minimum requirements for the selected climate zones [6]. For the SB archetype, envelope performance was derived from the *Canadian Single-Detached & Double/Row Housing Database* (CSDDRD) [8] for the appropriate regions and 1960s vintage, with this archetype and construction period selected to represent the smaller, older homes where oil systems are typically still seen. A summary of envelope parameters for the SB archetype is provided in Table 3.

Table 3: Summary of Envelope Construction for SB Archetype

Characteristic	City			
	Halifax	Toronto	Winnipeg	Vancouver
Wall RSI (m^2°C/W)	1.8	1.7	1.9	1.9
Roof RSI (m^2°C/W)	3.3	3.9	4.6	3.1
Window U Value (W/m^2°C)	2.9	2.9	2.9	5.5
Infiltration (ach_{50})	7.4	6.7	3.4	9.8

3. Heat Pump System Integrations

The developed housing archetypes serve as a basis to examine three different heating system transitions:

I. Natural Gas Furnaces to Air-Source Heat Pumps
II. Oil Furnaces to Air-Source Heat Pumps
III. Electric Baseboards to Air-Source Heat Pumps

Each transition is selected due to the unique economic boundary conditions imposed, and its relevance and potential impacts in supporting a decarbonization of Canadian residential buildings. In cases that involve a transition from fossil fuels, it is assumed that homeowners will proceed with a complete electrification of space and water heating, including the introduction of an electric (non-heat pump) hot water tank.

Heat Pump Integration and Sizing Methods

The base case mechanical systems for each archetype play a critical role in defining the form of heat pump integration. In cases where central ducted is available (replacing oil or natural gas furnaces), a ducted heat pump configuration is proposed, with the indoor coil of the heat pump integrated into a central air handling unit. For homes without central ducting (replacing electric baseboards), a ductless configuration is used, with the indoor unit of the heat pump integrated into the stairwell linking the first and second floors of the home. In this integration, the basement of the home is heating only using electric baseboards, as per the base case.

Heat pump sizing also has an important impact on system performance and economics. Given the cold Canadian climate, all heat pump systems are sized with a focus on space heating using Option C of NRCan's *Air-Source Heat Pumps Sizing and Selection Guide* [10].

Heat Pump Technologies

Two market available air-source heat pump technologies are assessed to examine their economic and energy savings potential in each of the defined transition cases:

Conventional Variable Capacity Air-Source Heat Pump (**VCHP**): Variable capacity units are an increasingly popular option in the Canadian residential heat pump market. Unlike single stage heat pumps, variable speed systems are able to efficiently modulate their capacity to better match heating or cooling demand. However, these systems are not necessarily well adapted to cold climates, with many market-available options suffering significant performance degradations at the colder ambient temperatures common in Canadian winters. This integration focuses on these more conventional variable capacity systems in each region and transition case.

The performance of variable capacity systems is closely linked both to their rated performance and their ability to modulate their capacity to meet lower heating or cooling loads. Key parameters used in the analysis are provided below in Table 4, and are the same for all sizes of heat pumps used in the simulations.

Table 4: Variable Capacity Heat Pump Parameters [11,12]

	HP Configuration	
	Ductless	Ducted
Heating COP*	3.3 (All)	3.7 (All)
Cooling COP*	4.1 (All)	3.9 (All)
Min. Outdoor Operating Temperature, Heating Mode (°C)	-17	-23
% Capacity at Cut-Off Temperature (Max Speed)	51%	38%
Average Min: Max Capacity Ratio	0.32	0.30

*At AHRI Rating Conditions

Cold Climate Variable Capacity Heat Pumps (**CCHP**): Cold climate heat pumps combine variable speed compressor technologies with other cycle upgrades (e.g., larger outdoor heat exchangers, vapour injection cycles) to maintain a higher portion of heating capacity at low outdoor temperatures. Although multiple definitions of cold climate heat pumps exist in the literature [13,14], they are classified in this paper as systems operating to an outdoor temperature of -25°C and maintaining at least 65% of their rated heating capacity.

Figure 1 compares the normalized capacity of the ducted CCHP and VCHP systems used in this study. The CCHP unit maintains a much larger portion of its heating capacity at low ambient temperatures, while also operating to a lower minimum outdoor temperature. These characteristics have important implications for system efficiency and peak electrical demand.

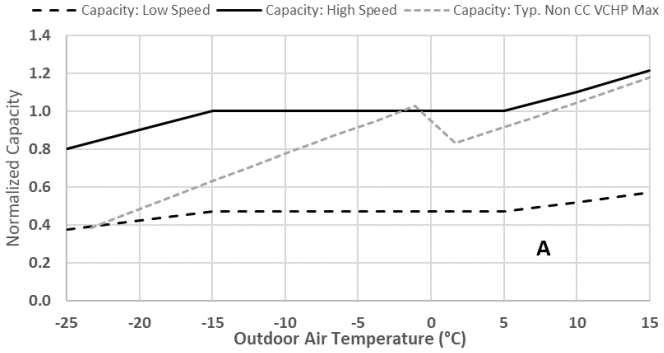


Figure 1: Comparison of CCHP and VCHP Normalized Heating Capacity [12,15]

Table 5 summarizes key parameters for the CCHP systems examined in this study. Variations in rated COP are due to the differences in manufacturer listed performance among units of the same model line.

Table 5: Cold Climate Heat Pump Parameters [15,16]

	HP Configuration	
	Ductless	Ducted
Heating COP*	4.4 (0.75 Ton) 4.2 (1 Ton) 4.1 (1.5 Ton)	3.6 (1.5 Ton) 3.8 (2 Ton)
Cooling COP*	4.5 (0.75 Ton) 3.8 (1 Ton) 4.2 (1.5 Ton)	3.3 (All)
Min. Outdoor Operating Temperature, Heating Mode (°C)	-25	-25
% Capacity at Cut-Off Temperature (Max Speed)	66%	80%
Average Min: Max Capacity Ratio	0.33	0.30

*At AHRI Rating Conditions

4. Modelling Methodology

Appropriately modelling the performance of each heat pump system is critical to properly assess its energy and economic benefits. All system models were developed in TRNSYS v.18 using the appropriate Canadian Weather for Energy Calculations (CWEC) weather file (2020 version). Simulations were run using a time step of 2.5 minutes in order to properly represent the control logic of the heat pump and its interaction with any auxiliary heating systems.

Heat Pump Performance Modelling

Examining the potential of variable and cold climate heat pump systems requires a simulation model capable of capturing their unique performance characteristics. In this study, all heat pump systems are simulated using a new enhanced heat pump model (TRNSYS Type 3255). This model has been developed based on extensive test experience at the CanmetENERGY in Varennes facility and integrates a series of new capabilities including performance variations with compressor speed, and key short term transients including startup, defrost, and cycling. Further details on this model are provided in Breton *et al.* [17].

Type 3255 employs a data-driven approach, using performance maps supplied as inputs to the model to represent variations in heat pump capacity and power as a function of temperature and compressor speed. Where possible, this study uses performance maps derived from detailed testing to drive simulations. In cases where this data is not available, performance data has been derived from manufacturer data sheets and information available in the open literature. For the ductless VCHP system, performance curves are derived from a database of variable capacity heat pump performance [18]. Data sources are summarized in Table 6.

Table 6: Summary of data sources for heat pump modelling

	Ductless Systems		Ducted Systems	
Heat Pump System	Rated Performance	Part Load Performance	Rated Performance	Part Load Performance
VCHP	Literature [18]	Literature [18]	Manufacturer [12]	Manufacturer [12]
CCHP	Test [19]	Test [19]	Manufacturer [15]	Manufacturer [15]

Heat Pump Control

A PID controller is used to vary the heat pump compressor speed to maintain 21°C in heating mode, and 23°C in cooling. The simulated controller also contains a threshold minimum operating frequency, below which the heat pump turns off. This feature enables the model to capture on/off cycling when building loads fall below the minimum capacity of the heat pump. Additional controls ensure that the heat pump only operates within its intended range of outdoor temperatures.

While heat pump systems are sized to cover the majority of annual heating demands, they are not selected to meet the full heating demands of the home at design conditions. As such, electric auxiliary systems are included to supplement heat pump operations as needed. When ambient temperatures are above the minimum operating temperature for the heat pump, auxiliary heaters use a slightly lower setpoint (20°C vs. 21°C for the heat pump) to prioritize heat pump operations while ensuring thermal comfort in the space. When ambient temperatures fall below the minimum heat pump operating temperature, auxiliary heaters maintain 21°C.

5. Economic Analysis

System economics play an important role in defining the pace of heat pump adoption in Canada. In this study, each system integration is evaluated over a 20-year lifespan, with a focus on capital, maintenance and operating costs (replacement costs are neglected). Lifecyle calculations use an inflation rate of 1.8% and a discount rate of 3.3%, based on current Canadian financial markets. Given current economic volatility, these values represent a conservative approach over the defined 20-year analysis period.

System capital costs are based on a component level analysis, and include all required equipment, controls, and ducting (for centrally ducted systems). Included components are summarized in Table 7. Given the focus on decarbonization in this paper, all transitions from fossil fuel heating systems also include replacing the base case hot water tank with an electric resistance equivalent storage tank. Heat pump costs do not include modifications to the electrical service of the home, which can significantly increase overall system costs.

Table 7: Components included in calculation of system capital costs

Category	Components
Equipment	Heat Pump (Both Indoor & Outdoor Sections)
	Auxiliary Electric Baseboards (Ductless Cases)
	Auxiliary Electric Duct Heaters (Ducted Cases)
	Hot Water Storage Tank
Controls	Thermostat
Distribution	Ductwork (Ducted Cases)

System costs are derived via RS Means [20] and available online suppliers [21], and include both material and labour. All costs were adjusted for the appropriate region using factors from RS Means. For clarity, system costs are summarized by integration case in the *Results* section of this paper.

Utility rates and structures also play a critical role in defining the operating costs of the systems. This study uses current rates and structures in each region [22-28]. Rates include both fixed and energy charges, tiered/time of use structures, rate riders, and provincial or federal carbon pricing for 2022. Energy escalation rates were estimated using information from the National Energy Board of Canada [29]. Given the volatility in current (2022) energy markets, escalation rates can be considered a conservative estimate over the system lifespan. A summary of utility rates used in the analysis is provided in Table 8.

Table 8: Summary of utility rates and structures used

Utility	**Charge**	**Halifax**	**Toronto**	**Winnipeg**	**Vancouver**
Electricity	Fixed Charge	$10.83/month	$40.10/month	$6.64/month	$8.86/month
	Energy Charge	$0.1841/kWh	$0.1132/kWh (Off-peak) $0.1508/kWh (Mid-peak) $0.2152/kWh (On-peak)	$0.1015/kWh	$0.111/kWh (First 1,350 kWh/2 Month) $0.166/kWh (> 1,350 kWh/2 Month)
	Escalation Rate	0.10%	0.60%	0.30%	0.30%
Nat. Gas	Fixed Charge	$21.87/month	$22.12/month	$14/month	$12.82/month
	Energy Charge	$0.7658/$m^3$	$0.563/m3 (First 30 m^3/Month) $0.556/m3 (Next 55 m^3/Month) $0.551/m3 (Next 85 m^3/Month) $0.547/m3 (Above 170 m^3/Month)	$0.4571/$m^3$	$0.5713/$m^3$
	Escalation Rate	1.00%	0.70%	1.00%	0.20%
Fuel Oil	Energy Charge	$1.80/L	$2.14/L	$1.89/L	$1.89/L
	Escalation Rate	3%	3%	3%	3%

6. Results and Discussion

The developed methodology provides a basis to explore the energy and economic implications of air-source heat pump adoption across Canada. Results are presented by heating system transition below.

Transitioning from Natural Gas Furnaces to Air-Source Heat Pumps in Large Two-Storey Homes

Table 9 summarizes the energy performance of both heat pump systems as gas furnace replacements in large two-storey homes in Halifax and Toronto. Each system demonstrates a clear reduction in annual energy use, with savings for space heating and cooling ranging from 53% to 60%. Despite the colder climate and higher number of heating degree days in Halifax, annual savings are greater vs. Toronto because of a reduced need for auxiliary heating (Halifax has a smaller number of operating hours below -20°C). It is also interesting to note that the predominance of coal-fired electricity in Atlantic Canada yields an *increase* in GHG emissions with each heat pump case, although this is expected to change as the grid undergoes further decarbonisation.

Table 9: Summary of heat pump energy performance replacing natural gas furnaces in Halifax and Toronto

	Halifax			Toronto	
End Use	Base Case	VCHP	CCHP	Base Case	VCHP	CCHP
Total Heating (kWh)	11,910	5,310	4,570	13,300	5,950	5,290
Furnace	11,910	--	--	13,300	--	--
Heat Pump	--	4,780	4,300	--	5,090	4,900
Aux: Elec Duct Heater	--	530	270	--	860	400
Cooling (kWh)	260	250	250	620	550	570
Fans (kWh)	760	1,110	1,010	860	1,230	1,120
DHW (kWh)	7,080	5,650	5,650	6,650	5,310	5,310
Lighting/Equip. (kWh)	6,930	6,930	6,930	7,020	7,020	7,020
Total Energy Use (kWh)	26,940	19,250	18,410	28,450	20,060	19,310
Total Savings (kWh)	--	7,700	8,540	--	8,400	9,130
% Savings for Htg&Clg*	--	54%	60%	--	53%	58%
Seasonal Heating COP	0.97	2.20	2.57	0.97	2.19	2.47
GHG Emissions (tn CO_2 eq)	9.5	14.6	14	3.8	0.6	0.6
GHG Emissions (%)	--	+54%	+47%	--	-84%	-85%

*Seasonal Heating COP for whole home, inc. HP & aux.

Table 10 summarizes the energy performance of each heat pump system in Winnipeg and Vancouver. The impact of the different climates is immediately clear: The colder climate in Winnipeg reduces energy savings due to a greater reliance on auxiliary energy use, while the milder Vancouver climate yields higher operating efficiencies and greater energy use reductions (aux. heating is only used in Vancouver when the heat pump is in defrost). It is important to note that the savings associated with the CCHP in Vancouver are related to the operating efficiency of this unit across the most common winter temperatures (-5°C to +5°C), rather than a strong need for cold climate performance – This result may change if other VCHP or CCHP units are examined in the analysis, and is not a definitive reflection of VCHP vs. CCHP systems in this area. Future work is needed to investigate the sensitivity of results to the heat pump performance curve used, especially in milder regions where the cold climate capacity of the CCHP may be used less. The value of cold climate performance is evident however in Winnipeg, where the CCHP reduces auxiliary energy use by nearly 1,000 kWh. GHG emissions are nearly eliminated in both cities due to the relatively clean electricity grids.

Table 10: Summary of heat pump energy performance replacing natural gas furnaces in Winnipeg and Vancouver

	Winnipeg			Vancouver		
End Use	Base Case	VCHP	CCHP	Base Case	VCHP	CCHP
Total Heating (kWh)	20,420	10,940	10,370	8,460	3,580	2,410
Furnace	20,420	--	--	8,460	--	--
Heat Pump	--	6,960	7,370	--	3,490	2,320
Aux: Elec Duct Heater	--	3,970	3,000	--	80	90
Cooling (kWh)	410	360	350	140	140	130
Fans (kWh)	850	1,610	1,500	670	910	870
DHW (kWh)	8,160	6,500	6,500	6,390	2,790	2,790
Lighting/Equip. (kWh)	6,890	6,890	6,890	6,990	6,990	6,990
Total Energy Use (kWh)	36,730	26,300	25,610	22,650	14,410	13,190
Total Savings (kWh)	--	10,420	11,100	--	8,240	9,460
% Savings for Htg&Clg	--	46%	49%	--	57%	71%
Seasonal Heating COP*	0.97	1.86	1.97	0.97	2.26	3.38
GHG Emissions (tn CO_2 eq)	5.2	0.03	0.03	2.9	0.3	0.3
GHG Emissions (%)	--	-99%	-99%	--	-90%	-91%

*Seasonal Heating COP for whole home, inc. HP & aux.

Table 11 summarizes the economic performance of each system in all four regions. Except in Halifax, all heat pump integrations result in higher lifecycle costs, primarily due to the increased cost of the heat pump systems vs. base case (natural gas furnace + air conditioner) that they are replacing. Interestingly, some form of utility cost savings is achieved using the CCHP in two of the four regions examined (Halifax, Vancouver), suggesting that an economic incentive to cover a portion of the heat pump system costs could shift the economic balance in favor of these systems (This result assumes a complete shift to electricity for all end uses and a removal of the gas connection). In this context, choosing the appropriate systems to incentivize (i.e., those that achieve the greatest utility cost savings) is of critical importance given the current marginal utility cost savings vs. the base case system.

Table 11: Summary of lifecycle costs for VCHP and CCHP systems as gas furnace system replacements

City	System	Capital Cost ($)	Lifecycle Utility Cost ($)	Lifecycle Maintenance Cost ($)	Total Lifecycle Cost ($)
Halifax	Base	$19,500	$64,200	$3,000	$86,700
	VCHP	$21,200	$54,100	$1,500	$76,800
	CCHP	$25,100	$51,800	$1,500	**$78,400**
Toronto	Base	$21,500	$46,400	$3,700	**$71,600**
	VCHP	$23,500	$50,400	$1,900	$75,800
	CCHP	$27,100	$48,800	$1,900	$77,800
Winnipeg	Base	$21,800	$36,500	$3,400	**$61,700**
	VCHP	$26,600	$41,600	$1,800	$70,000
	CCHP	$28,800	$40,600	$1,800	$71,200
Vancouver	Base	$20,200	$28,400	$3,100	**$51,700**
	VCHP	$21,400	$30,300	$1,600	$53,300
	CCHP	$25,500	$27,300	$1,600	$54,400

A major factor impacting natural gas rates in Canada is the implementation of carbon pricing. Carbon prices evolve according a schedule defined by the federal government, ranging from a current surcharge of \$0.0979/m^3 of natural gas, to a value of \$0.1860/m^3 in 2025 and a final price of \$0.3389/m^3 by 2030 [30]. Table 12 summarizes the impact of 2025 and 2030 carbon pricing on the above results. Increases in carbon pricing allow CCHP systems to achieve operating cost parity with natural gas furnaces by 2025 in nearly all locations except Winnipeg, where CCHP operating costs are slightly higher vs. the base case. Using the 2030 carbon pricing, operating cost savings are enough in all regions to outweigh the higher capital costs associated with the heat pump integrations, although economic incentives may be needed to achieve the shorter-term payback periods (<10 years) often desired by homeowners.

Table 12: Lifecyle cost variation with carbon pricing

		2025 Carbon Pricing		2030 Carbon Pricing	
City	System	Lifecycle Utility (\$)	Total Lifecycle (\$)	Lifecycle Maintenance (\$)	Total Lifecycle (\$)
Halifax	Base	\$66,700	\$89,200	\$71,000	\$93,500
	VCHP	\$54,100	**\$76,800**	\$54,100	**\$76,800**
	CCHP	\$51,800	\$78,400	\$51,800	\$78,400
Toronto	Base	\$49,000	**\$74,200**	\$53,300	\$78,500
	VCHP	\$50,400	\$75,800	\$50,400	**\$75,800**
	CCHP	\$48,800	\$77,800	\$48,800	\$77,800
Winnipeg	Base	\$40,400	**\$65,600**	\$46,700	\$71,900
	VCHP	\$41,600	\$70,000	\$41,600	**\$70,000**
	CCHP	\$40,600	\$71,200	\$40,600	\$71,200
Vancouver	Base	\$29,600	**\$52,900**	\$33,400	\$56,700
	VCHP	\$30,300	\$53,300	\$30,300	**\$53,300**
	CCHP	\$27,300	\$54,400	\$27,300	\$54,400

Transitioning from Oil Furnaces to Air-Source Heat Pumps in Small Bungalows

Table 13 summarizes the energy performance of both heat pump technologies as replacements for oil furnaces in 1960s vintage small bungalows located in Halifax and Toronto. Results also reflect a transition from oil-fired hot water tanks to electrically heated tanks in each heat pump case. Compared to the natural gas cases, energy use reductions are even larger due to the lower efficiency of the oil-fired heating equipment in the base cases. In Halifax, GHG emissions still increase with each heat pump integration due to the carbon intensive nature of electricity generation. As noted previously, emissions associated with electricity are expected to fall in future years as electricity grids undergo further decarbonization.

Table 13: Summary of heat pump energy performance replacing oil furnaces in Halifax and Toronto

	Halifax			Toronto		
End Use	Base Case	VCHP	CCHP	Base Case	VCHP	CCHP
Total Heating (kWh)	17,750	6,480	4,950	14,740	5,690	4,470
Furnace	17,750	--	--	14,740	--	--
Heat Pump	--	5,920	4,650	--	5,150	4,200
Aux: Elec Duct Heater	--	560	300	--	540	270
Cooling (kWh)	340	140	130	950	510	430
Fans (kWh)	470	1,240	1,140	530	1,260	1,120
DHW (kWh)	8,200	4,450	4,450	7,770	4,200	4,200
Lighting/Equip. (kWh)	4,920	4,920	4,920	5,020	5,020	5,020
Total Energy Use (kWh)	31,680	17,230	15,590	29,010	16,680	15,240
Total Savings (kWh)	--	14,450	16,100	--	12,320	13,770
% Savings for Htg&Clg	--	63%	72%	--	60%	69%
Seasonal Heating COP*	0.58	2.09	2.75	0.59	2.02	2.58
GHG Emissions (tn CO_2 eq)	11.40	13.10	11.90	6.30	0.50	0.50
GHG Emissions (%)	--	+15%	+4%	--	-92%	-93%

*Seasonal Heating COP for whole home, inc. HP & aux.

Energy performance results for heat pump system integrations in Winnipeg and Vancouver are provided in Table 14. Each heat pump system offers strong heating and cooling energy use reductions, ranging from 55% to 80% depending on the region and heat pump technology. Heat pump seasonal performance is lower in Winnipeg, due to the colder climate and extended period of time when outdoor temperatures are below the minimum operating limit for the heat pump. Users may also note the higher annual heating energy use for the base case in Vancouver vs. Winnipeg, which relates to higher infiltration and poor envelope performance associated with 1960s construction in this region. As with the natural gas cases, the improved performance of the CCHP vs. the VCHP in Vancouver relates to its higher operating COP over the most common winter temperatures. This result is not suggesting cold climate performance is needed in Vancouver and should not be considered a definitive statement on VCHP vs. CCHP technology in this region. Instead, it highlights the importance of selecting systems that optimize operating efficiency over the most common winter temperatures.

Table 14: Summary of heat pump energy performance replacing oil furnaces in Winnipeg and Vancouver

	Winnipeg			Vancouver		
End Use	Base Case	VCHP	CCHP	Base Case	VCHP	CCHP
Total Heating (kWh)	19,110	8,670	8,100	20,090	6,040	3,990
Furnace	19,110	--	--	20,090	--	--
Heat Pump	--	6,100	5,950	--	5,900	3,840
Aux: Elec Duct Heater	--	2,570	2,150	--	140	150
Cooling (kWh)	680	320	300	350	150	130
Fans (kWh)	590	1,500	1,190	530	1,980	1,170
DHW (kWh)	9,210	5,050	5,050	7,520	4,060	4,060
Lighting/Equip. (kWh)	4,870	4,870	4,870	4,910	4,910	4,910
Total Energy Use (kWh)	34,460	20,410	19,510	33,400	17,140	14,260
Total Savings (kWh)	--	14,050	900	--	16,260	19,140
% Savings for Htg&Clg	--	55%	58%	--	70%	80%
Seasonal Heating COP*	0.59	1.76	1.88	0.60	2.39	3.63
GHG Emissions (tn CO_2 eq)	7.70	0.03	0.03	7.60	0.34	0.29
GHG Emissions (%)	--	-99%	-99%	--	-95%	-96%

*Seasonal Heating COP for whole home, inc. HP & aux.

Table 15 summarizes the lifecycle economics of each heat pump system replacing the oil-fired base cases. The high cost of heating oil means that all heat pump integrations offer strong utility cost savings vs. the base case, demonstrating the value to homeowners in transitioning from heating oil to heat pump systems. In most regions, the CCHP is the preferred option despite its higher initial cost, primarily because of the larger magnitude of energy use reductions it achieves vs. the VCHP. In Vancouver, the CCHP is preferred only because of its improved performance vs. the VCHP over the most common winter temperatures. This result may change when examining a different VCHP unit, and is not a definitive statement on the suitability of the CCHP vs. the VCHP in Vancouver. One challenge for homeowners is the higher cost of heat pump systems, which can be significant vs. furnace systems. Although not examined in this study, the Government of Canada has recently launched an incentive program to support homeowners in the transition from oil-fired to heat pump systems by covering a portion of capital and installation costs [31]. This program further increases the value proposition for heat pumps and will drive uptake in coming years.

Table 15: Summary of lifecycle costs for VCHP and CCHP systems as oil furnace system replacements

City	System	Capital Cost ($)	Lifecycle Utility Cost ($)	Lifecycle Maintenance Cost ($)	Total Lifecycle Cost ($)
Halifax	Base	$19,800	$101,700	$3,800	$125,300
	VCHP	$21,200	$48,600	$1,500	$71,300
	CCHP	$24,600	$44,200	$1,500	**$70,300**
Toronto	Base	$21,900	$109,500	$4,700	$136,100
	VCHP	$22,900	$43,000	$1,900	**$67,800**
	CCHP	$26,600	$39,900	$1,900	$68,400
Winnipeg	Base	$21,400	$107,700	$4,300	$133,400
	VCHP	$26,600	$32,800	$1,800	**$61,200**
	CCHP	$28,700	$31,300	$1,800	$61,800
Vancouver	Base	$20,500	$105,200	$3,900	$129,600
	VCHP	$21,400	$37,100	$1,600	$60,100
	CCHP	$25,500	$29,900	$1,600	**$57,000**

Transitioning from Electric Baseboards to Air-Source Heat Pumps in Medium Two-Storey Homes

The final system transition examined is the replacement of electric baseboards with heat pump systems. As mentioned earlier, this integration varies from the two previous cases in that ductless heat pumps are used, which serve only the first two floors of the home. Table 16 summarizes the energy performance for this system transition in medium two-storey housing in Halifax and Toronto. It is clear that heating and cooling energy use reductions appear to be less than for the previous cases, primarily because the heat pump is no longer serving the whole home. When comparing only the energy used to heat the two above ground floors, energy use reductions are significantly higher, approaching 54% in each heat pump integration. VCHP and CCHP performance is also very close in both cities: Both systems maintain a similar portion of capacity at colder ambient temperatures and are sized using the same objectives.

Table 16: Summary of heat pump energy performance replacing electric baseboards in Halifax and Toronto

	Halifax			Toronto		
End Use	Base Case	VCHP	CCHP	Base Case	VCHP	CCHP
Total Heating (kWh)	6,760	3,860	3,840	7,720	4,470	4,430
Heat Pump	--	2,044	2,072	--	2,383	2,426
Aux: Elec BB (1st, 2nd)	5,470	460	400	6,230	530	440
Aux: Elec BB Basement	1,280	1,360	1,360	1,490	1,560	1,560
Cooling (kWh)	490	290	340	970	530	670
Fans (kWh)	480	620	530	490	670	560
DHW (kWh)	5,640	5,640	5,640	5,300	5,300	5,300
Lighting/Equip. (kWh)	5,250	5,250	5,250	5,280	5,280	5,280
Total Energy Use (kWh)	18,620	15,660	15,600	19,760	16,250	16,240
Total Savings (kWh)	--	2,960	3,020	--	3,510	3,520
% Savings for Htg&Clg	--	43%	42%	--	42%	41%
Seasonal Heating COP*	1.00	1.77	1.74	1.00	1.75	1.73
GHG Emissions (tn CO_2 eq)	14.10	11.90	11.90	0.60	0.49	0.50
GHG Emissions (%)	--	-16%	-16%	--	-18%	-18%

*Seasonal Heating COP for whole home, inc. HP & aux. COP higher when considering only zones served by HP

Table 17 summarizes the energy performance of each heat pump integration in Winnipeg and Vancouver. The value of the CCHP is immediately clear in Winnipeg, with the extended operating range of this unit providing a strong reduction in baseboard energy use on the first and second floors of the home. Results in Vancouver follow a similar trend to Halifax and Toronto, with both the VCHP and CCHP offering similar performance over the heating season. Given the relatively clean electricity grids in Winnipeg and Vancouver, some readers may question the importance of transitioning from baseboards to heat pumps in the overall context of decarbonization. While the magnitude of GHG emission reductions is quite small in these two regions, transitioning to more efficient heat pump systems also frees up additional generating capacity to meet increased demand driven by population growth and a greater electrification of other sectors (e.g., transport).

Table 17: Summary of heat pump energy performance replacing electric baseboards in Winnipeg and Vancouver

	Winnipeg			Vancouver		
End Use	Base Case	VCHP	CCHP	Base Case	VCHP	CCHP
Total Heating (kWh)	12,490	9,480	8,750	6,100	3,510	3,300
Heat Pump	--	2,940	3,840	--	1,620	1,330
Aux: Elec BB (1st, 2nd)	9,430	3,400	1,760	4,580	320	370
Aux: Elec BB Basement	3,060	3,130	3,150	1,520	1,580	1,590
Cooling (kWh)	680	460	380	420	280	220
Fans (kWh)	480	630	640	480	540	510
DHW (kWh)	6,490	6,490	6,490	5,090	5,090	5,090
Lighting/Equip. (kWh)	5,220	5,220	5,220	5,280	5,280	5,280
Total Energy Use (kWh)	25,360	22,280	21,480	17,370	14,700	14,400
Total Savings (kWh)	--	3,080	800	--	2,670	2,970
% Savings for Htg&Clg	--	25%	31%	--	42%	46%
Seasonal Heating COP*	1.00	1.33	1.44	1.00	1.71	1.81
GHG Emissions (tn CO_2 eq)	0.033	0.029	0.028	0.35	0.29	0.29
GHG Emissions (%)	--	-12%	-15%	--	-15%	-17%

*Seasonal Heating COP for whole home, inc. HP & aux. COP higher when considering only zones served by HP

Table 18 summarizes the economic performance of the heat pump systems replacing electric baseboard heating. Smaller capital costs for most CCHPs vs. VCHPs relates to the unit sizes: Given their improved capacity, smaller CCHPs were integrated while meeting the same sizing objective. Heat pump systems offer utility cost reductions in all cities, as would be expected given they are replacing a less efficient base case system using the same energy source. All heat pump systems achieve lifecycle cost savings over the 20-year analysis period, with the VCHP and CCHP systems offering relatively similar total costs. These overall savings tend to be limited somewhat by the higher cost of the heat pump systems vs. inexpensive electric resistance heating. As with the previous transitions examined, it is likely that incentives covering first costs may be needed to drive greater uptake and ensure payback periods fall within the expected range for homeowners.

Table 18: Summary of lifecycle costs for VCHP and CCHP systems as electric baseboard system replacements

City	System	Capital Cost ($)	Lifecycle Utility Cost ($)	Lifecycle Maintenance Cost ($)	Total Lifecycle Cost ($)
Halifax	Base	$6,700	$52,300	$1,500	$60,500
	VCHP	$8,500	$44,300	$1,500	$54,300
	CCHP	$8,300	$44,200	$1,500	**$54,000**
Toronto	Base	$7,700	$50,000	$1,900	$59,600
	VCHP	$9,200	$42,500	$1,900	$53,600
	CCHP	$9,000	$42,400	$1,900	**$53,300**
Winnipeg	Base	$8,100	$40,200	$1,800	$50,100
	VCHP	$10,400	$35,500	$1,800	$47,700
	CCHP	$10,500	$34,300	$1,800	**$46,600**
Vancouver	Base	$6,600	$37,700	$1,600	$45,900
	VCHP	$7,800	$31,100	$1,600	$40,500
	CCHP	$7,900	$30,300	$1,600	**$39,800**

7. Conclusions and Future Work

This study has examined the techno-economic impacts of heat pump adoption in single family Canadian housing. Using an enhanced, data-driven heat pump model, both variable capacity and cold climate variable capacity systems were simulated over a full year as replacements for (i) natural gas furnaces, (ii) oil furnaces, and (iii) electric baseboards. While simulations show the strong energy savings benefits of heat pumps, the economics of these systems are highly dependent on the regional climate, local utility rates and heating energy source being displaced. Integrating heat pumps as replacements for natural gas furnaces represents the most challenging current context, with heat pumps currently offering utility cost savings in only two of the four regions assessed (Vancouver, Halifax), with lifecycle costs higher in all regions. Heat pumps as replacements for oil and electric baseboard systems present a stronger value proposition in the current economic climate, offering both utility and lifecycle cost savings in all cases. An additional analysis using planned carbon pricing shows that by 2030 heat pumps will offer both utility and lifecycle cost savings vs. all three systems examined in this paper (natural gas furnaces, oil furnaces, electric baseboards), representing a significant improvement in system economics vs. the current context. Even when lifecycle cost savings are achieved, the adoption of heat pumps may be challenged by the higher first cost of these systems vs. those they are replacing. Results from this study can be used as a starting point to support the future policy and incentive programs needed to drive decarbonization of Canadian residential buildings.

Heat pump adoption is likely to rise significantly in the coming years as efforts to decarbonize space heating gain momentum. Although not examined in this study, understanding the electrical demand implications associated with this increased uptake is critical to ensure that local electricity grids have the capacity and infrastructure to support a greater electrification of building systems. CanmetENERGY in Varennes has previously used its simulation capabilities to examine the peak demand implications of air-source heat pumps in residential buildings, and will continue this work to complement the energy and economic impacts presented in this article. These peak demand implications also necessitate a new generation of heat pump systems that combine efficient heating and cooling with energy storage to increase flexibility and demand response capabilities. Ongoing research at CanmetENERGY in Varennes has identified novel combinations of heat pumps and thermal storage for the Canadian context, with planned work furthering this research through additional development and a small-scale proof of concept. This work is intended to further compliment the information presented in this paper and support the efficient electrification of Canadian residential buildings.

References

[1] Government of Canada (GoC). *Canadian Net Zero Emissions Accountability Act*. Ottawa, CA: GoC; 2020.
[2] Natural Resources Canada. *Comprehensive Energy Use Database*. Ottawa, ON: NRCan; 2022. Available at: https://oee.nrcan.gc.ca/corporate/statistics/neud/dpa/menus/trends/comprehensive_tables/list.cfm
[3] Kegel, M., Tamasauskas, J., Sunye, R., 2014. "Heat Pumps in the Canadian Building Sector". 11th IEA Heat Pump Conference. Montreal, CA, paper #217.
[4] Tamasauskas, J., Breton, S., Kegel, M., 2021. "A Techno-Economic Assessment of Air-Source Heat Pumping Technologies in the Canadian Residential Sector". 13th IEA Heat Pump Conference. Jeju, KR, paper #252.
[5] Natural Resources Canada. *Cold-climate air source heat pumps: Assessing cost-effectiveness, energy savings and greenhouse gas emissions reductions in Canadian homes*. Ottawa, ON: NRCan; 2022.
[6] National Research Council of Canada. *National Building Code of Canada 2015*. Ottawa: NRC; 2015.
[7] Natural Resources Canada, 2015. *Survey of Household Energy Use 2015*. Available at: https://oee.nrcan.gc.ca/corporate/statistics/neud/dpa/menus/sheu/2015/tables.cfm [Accessed Jan 2020]
[8] Swan, L.G., Ugursal V. I., Beausoleil-Morrison, I. 2009. A database of house descriptions representative of the Canadian housing stock for coupling to building energy performance simulation. *Journal of Building Performance Simulation* 2009; **2**(2):75-84
[9] Swinton, M.C., Entchev, E., Szadkowski, F., Marchand, R. *Benchmarking twin houses and assessment of the energy performance of two gas combo heating systems*. Ottawa: Canadian Centre for Housing Technology; 2003.
[10] Natural Resources Canada. *Air-Source Heat Pumps Sizing and Selection Guide*. Ottawa: NRCan; 2021.
[11] Carrier. *Carrier 38 MHRB Product Data*. Indianapolis, IN, USA: Carrier Corporation; 2018.
[12] Daikin. *DZ20VC Specification Sheet*. Houston, USA: Daikin Manufacturing Company; 2019.
[13] Northeast Energy Efficiency Partnerships (NEEP). *CCASHP Specification and Product List*. Lexington, MA, USA: NEEP; 2022. Available at: https://neep.org/ASHP-Specification
[14] Northwest Energy Efficiency Alliance (NEEA). Cold Climate DHP Specification and Recommendations. Portland, OR, USA: NEEA; 2019. https://neea.org/our-work/cold-climate-dhp-specification
[15] Mitsubishi. *PUZ-HA Series Engineering Manual*. Atlanta,USA: Mitsubishi Electric Trane HVAC; 2019.
[16] Mitsubishi. *MUZ-FE Series Engineering Manual*. Atlanta, USA: Mitsubishi Electric Trane HVAC; 2019.
[17] Breton, S., Tamasauskas, J., Kegel, M., 2019. "An Evaluation of Cold Climate Variable Capacity Air-Source Heat Pumps in Canadian Residential Buildings Using an Enhanced Component Model". Building Simulation 2019. Rome, IT, paper #211116.
[18] Lachance, A., Tamasauskas, J., Breton, S., 2022. "Development of Cold-Climate Variable Heat Pump Performance Adjustment Curves for Building Simulation". 2022 ASHRAE Annual Conference. Toronto, ON, paper #31049.
[19] Kegel, M., Sager, J., Thomas, R., Giguère, D., Sunyé, R., 2017. "Performance Testing of Cold Climate Air Source Heat Pumps". IEA Heat Pump Conference 2017. Rotterdam, NE, paper #340.
[20] RS Means. *RS Means Mechanical Cost Data 2022*. Norwell, USA: Reed Construction Data; 2022.
[21] Bryan's Fuels. *Heat Pumps in Ontario*. Orangeville, ON, CA: Bryan's Fuels; 2022.
[22] Nova Scotia Power. *Domestic Service Tariff*. Halifax, NS,CS: Nova Scotia Power; 2021. Available at : https://www.nspower.ca/about-us/producing/rates-tariffs/domestic-service-tariff
[23] Eastward Energy. *Rates for Home*. Dartmouth, NS, CA: Eastward Energy; 2022. Available at: https://eastwardenergy.com/for-home/rates/
[24] Toronto Hydro. *Residential rates and charges*. Toronto, CA: Toronto Hydro; 2021. Available at: https://www.torontohydro.com/for-home/rates
[25] Enbridge Gas. *Natural Gas Rates*. Toronto, ON: Enbridge Gas; 2022. Available at: https://www.enbridgegas.com/residential/my-account/rates
[26] Manitoba Hydro. *Residential rates*. Winnipeg, MB, CA: Manitoba Hydro; 2021. Avaialble at: https://www.hydro.mb.ca/accounts_and_services/rates/residential_rates/
[27] BC Hydro. *Residential Conservation Rate*. Vancouver, BC, CA: BC Hydro; 2021. https://app.bchydro.com/accounts-billing/rates-energy-use/electricity-rates/residential-rates.html
[28] FortisBC. *Residential Natural Gas Rates*. Vancouver, BC, CA: FortisBC; 202. www.fortisbc.com/accounts-billing/billing-rates/natural-gas-rates/residential-rates
[29]National Energy Board of Canada. *Energy Markets*. Ottawa, CA: National Energy Board of Canada; 2016.
[30] Governemnt of Canada. *Update to the Pan-Canadian Approach to Carbon Pollution Pricing 2023-2030*. Ottawa, CA: Government of Canada; 2022.
[31] Governemnt of Canada. *Making Home Heating More Affordable for Canadians While Fighting Climate Change*. Ottawa, CA: Government of Canada; 2022. Available at: https://www.canada.ca/en/natural-resources-canada/news/2022/11/making-home-heating-more-affordable-for-canadians-while-fighting-climate-change.html

14th IEA Heat Pump Conference
15-18 May 2023, Chicago, Illinois

Development of a gas absorption heat pump for residential applications

Tommaso Toppi[a*], Lorenzo Pistocchini[a], Marco Guerra[a], Luigi Tischer[b], Pietro Brevi[b]

[a]Politecnico di Milano, via G. La Masa 34 , 20156 Milano, Italy
[b]Ariston Group, Via della Vignolina 2, 20864 Agrate Brianza (MB), Italy

Abstract

Thermally Driven Heat Pumps represent an option to reduce the energy consumption for space heating and domestic hot water in hard-to-decarbonize buildings without impacting the electrical grid and utilizing the current and future gaseous energy vectors with high efficiency. Ariston Group and Politecnico di Milano developed a gas absorption heat pump for the residential market, exploiting design and manufacturing solutions to enable large-scale production and introducing technical features to assure high performance over the entire working range.
In particular, the use of a variable restrictor setup coupled with a patented solution, called "booster", can reduce the temperature of the generator at high load and high lift conditions, enabling the heat pump to provide the nominal capacity from -22 °C to +40 °C of outdoor air temperature, with supply temperature up to 70 °C. Moreover, coupled with a specifically designed combustion system, the heat pump can modulate at 1:6 ratio of its nominal capacity. This feature makes it possible to maintain high efficiency also at part load conditions, avoiding the on-off operation and making redundant the installation of inertial buffer.
Additionally, an innovative strategy to perform the defrosting of the air-sourced heat exchanger without the need of acting on the thermodynamic cycle has been developed. This allows defrosting operations extremely fast, while offering an almost negligible effect on the heat pump performance and substantially no interruption to the heating service and contributing to the elimination of the need to install an inertial buffer.
The thermodynamic core of the appliance was built targeting large scale production. It allows for high specific capacity (kg/kW) and a small footprint (m2/kW) with the ability to serve nominal capacities ranging from 8 to 15 kW based on the configurations. Laboratory test to assess the performances based on the European Standard EN 12309 returned a seasonal gas utilization efficiency on the net calorific of 1.50, a seasonal primary energy ratio of 1.27, and extremely low electrical consumption for the auxiliaries.

© HPC2023.
Selection and/or peer-review under the responsibility of the organizers of the 14th IEA Heat Pump Conference 2023.

Keywords: gas absorption heat pump; residential application; seasonal efficiency; defrosting.

1. Introduction

Many authors have already highlighted the importance of the climatization of the building stock toward the reduction of the primary energy consumption and CO_2 emissions. The built environment, particularly in western world, is characterized by several aspects:

- limited presence of high efficiency buildings, i.e. buildings with heat demand lower than 25 kWh/(m^2 year)
- large presence of existing buildings with energy consumption above 150 kWh/(m^2 year)
- low replacement rate, with less than 1% of building stock replaced annually by new buildings [1]
- presence in existing buildings of high temperature emitters, in particular radiators in Europe and heat exchangers for air ducted systems in North America.

* Corresponding author. Tel.: +39 02 2399 3964
E-mail address: tommaso.toppi@polimi.it

To achieve a substantial reduction in primary energy consumption and in CO_2 emissions, a solution that could deliver substantial savings in the retrofit of existing buildings is needed. Indeed, the distinction between the new buildings and the existing buildings is pivotal to ensure that the reduction of emissions is achieved in the shortest possible time. While new buildings enjoy access to state-of-the-art construction technology, and large degrees of freedom in terms of architectural decisions (surface-to-volume ratio, orientation, size and position of windows, etc.), the retrofit of existing buildings has to face a high number of constraints including a limited budget and often the presence of the landlord during the retrofit (existing buildings cannot be easily vacated). Nevertheless, the large number of existing buildings with large yearly energy needs for space heating and the extremely high heat demand of these building make this challenge the most relevant and crucially important to address the overall challenge of reducing emissions.

To facilitate the adoption in the existing buildings the optimal solution needs to minimize the installation hurdles, i.e. not requiring changes to the existing emission systems in the building (radiators and diameter of piping). This requirement implies working with high output temperatures (up to 70 °C) and the limited flow rates typically used in systems designed for boilers that often do not exceed 1000 l/hour. Moreover, limited requirements for auxiliary equipment (inertial buffer, etc.) and the possibility to leverage the skills and competence already available in the installer base by avoiding forcing them toward new certification are crucial. At the same time, the proposed technology would need to meet the following requirements:

- Lower operating costs than state of the art (usually a direct combustion system).
- Low noise level to minimize the possible impact on outdoor quietness, in compliance with local legislation, even in presence of limited distance from the neighborhood's property.
- Ability to deliver heat with constant power output particularly in high thermal lift conditions, typical of the most demanding climates of the North European and North American regions.
- Ability to serve both the space heating and the domestic hot water function to maximize the benefits to the overall heat demand of the building.
- Environmental benefits in terms of reduced global warming emissions (CO_2, F-Gas), reduced ozone depletion emissions (F-Gas) and reduced human health hazardous emissions (PMs, NOx, OGCV).

In addition, a solution that could be rapidly adopted will need to be compatible with the energy system in place and the one prospected in the future. Therefore, the reduced electrical load (not to rely on an already overloaded grid) and the ability to work with green gases (bio-methane, bio-LPG, hydrogen blends) is required.

Gas driven heat pumps meet these requirements, since they can be designed to work at high temperature, matching the needs of high temperature heating systems, and relay on an already existing and high-capacity gas network. Compared with existing fuel driven heating systems, as boilers, gas heat pump provide a substantial reduction of the gas consumption with a minor increase of the electricity needs. In [2] two prototypes with a nominal capacity of 23.5 kW have been tested and a seasonal gas utilization efficiency of 1.36 (based on gross calorific value) has been achieved, considering the climate region IV of the American and Canadian Standard. A value of about 1.25 has been found in [3] from numerical simulations on the use of gas heat pumps in various residential buildings in the average European climate. Looking at the comparison from a life cycle assessment prospective [4], in renovated buildings and with the 2020 European energy mix, the weighted environmental impact of a gas absorption heat pump results about 25% lower than the one of a condensing boiler and about 50% lower than the one of electrical driven heat pumps.

In this work, the development of a gas driven absorption heat pump (GAHP) is presented, with a focus on the innovative solutions adopted to meet the goal of efficient and safe operation over the entire working range. Three technical solutions are presented, i.e., the so-called "booster" function, the use of a double restrictor in the solution branch and the use of an innovative approach to defrosting.

Gas fired absorption heat pumps experience an increase of the temperature of the generator when the thermal lift (difference between source and supply water temperatures) and the capacity increases. Thus, traditionally, the thermodynamic cycle is designed to have the maximum temperature at the generator at the lowest outdoor air temperature, higher supply temperature and design capacity. Consequently, when the working conditions become more favorable, i.e., at lower lift and lower capacity, the temperature of the generator decreases. This has two main consequences. The first is that at very low load conditions the temperature of the generator may become sub-optimal or even decrease below the cut-off limit [5]. The second is that at mild conditions the heat pump results strongly oversized, leading to a poor efficiency and unfavorable weight to power ratio. To overcome these issues the innovative solutions have been implemented. The booster is a patented [6] solution, which allows to reduce the generator temperature at high capacity and high thermal lift. This permits a design of the cycle with a more favorable weight to power ratio, keeping the capability to provide the nominal capacity at design conditions, while maximizing the efficiency at intermediate lift and capacity, i.e., in those conditions when most of the yearly energy is delivered.

The use of a double restrictor allows a better tuning of the generator temperature across the working range, with further benefits on the efficiency.

The third innovative solution introduced in the heat pump concerns the defrosting operation, required to remove the ice layer which builds up on the air-sourced evaporator of all heat pumps. While in vapor compression heat pumps this is usually done by inverting the thermodynamic cycle and operating the evaporator as a condenser, allowing the hot refrigerant to melt the ice, in absorption heat pump the most common solution relies on a bypass of hot refrigerant from the generator to the evaporator, skipping the condenser. The cycle inversion of Vapor Compression HPs has a significant impact on the thermodynamic cycle and on the continuity of the power delivered to the user. The bypass of refrigerant usually implemented in GAHPs is less impacting but affects for a certain period the operation of the cycle and require a fine design of the internal volumes. For the developed heat pump an alternative approach has been selected, taking advantage of the use of an indirect evaporator: a heat exchanger is used to heat up the secondary fluid which circulates in the air-sourced heat exchanger using the supply water. In this work this system is described and details about its operation are provided.

2. Concept description

The Ariston Group initiative on Thermally Driven Heat Pumps focused on a common thermodynamic design that could serve a range of products to accommodate the need of the different local market in which the Group is commercially active. The design of the technological solution was therefore targeted to support different capacity ranges and aeraulic design and installation configurations.

First of all, the thermodynamic design was conceived in order to incorporate products with different capacity range. Indeed, the destination markets include different heat loads due to the different size and different insulation characteristics of the buildings. Therefore, to cover the largest possible portion of the European residential market, the sealed circuit was designed to be able to accommodate an output power in the range from 8 kW to 15 kW measured at air temperature of -22 °C and supply water of 70 °C.

Similarly, the different local market features and the different requirements in terms of expectation for quietness (with the associated legislation) resulted in product design solutions to be customized for such markets. Indeed, in several countries the noise limits are differentiated between day and night, with expectations for extremely low noise performance at night and in proximity to the fence or window of the neighborhood. Therefore, two different aeraulic designs, depicted in Figure 1, have been developed to accommodate the most differentiated acoustic emission targets and the requirements of markets where the form factor and total volume were highly valued. This mass customization approach was implemented in a platform design of the thermodynamics and in two set of aeraulic configurations (horizontal and vertical air flow) with substantially differentiated fans and air heat exchangers.



Fig. 1 – The two aeraulic configuration developed to meet the requirements of the different European markets.

Finally, the specific requirements of the local European market were translated in several options for possible installation configurations. Indeed, the compactness, local regulation on exhaust flue gas, resilience to extreme weather conditions generated different evaporator designs. In details, Ariston developed a technology platform where several features could be incorporated to maximize the customization to the

different markets. Among others, this approach included several unique features for a thermally driven heat pump as described in the following.

- Air sourced design with indirect evaporator: the evaporation of the refrigerant happens in a heat exchanger with a water-glycol mixture. This fluid is then used to exchange with outdoor air by means of an air coil. This design allows lower ammonia content, and an almost transparent defrosting cycle actuation.
- Combustion system designed and tested to comply with both current gases and expected new green gases (Bio LPG, Bio-methane, H2 blend). This feature allows the end-user to perceive the investment in the TDHP technology as something already designed for the future gases that will be injected in the grid.
- Design solutions for industrialization of pumping system, heat exchangers and solution desorber to allow high quality and high-volume manufacturing.

Similarly, the control architecture was developed to include:

- a sophisticated on-board controller able to control the appliance safety and efficient heat generation function,
- a plant controller to control most possible installation schematics used in the destination markets,
- remote access, and connectivity functions to allow functionality and performance monitoring,
- access to the entire ecosystem of accessories that the Ariston Group offers.

In this section, the technological features which have been incorporated in the heat pump to meet the mentioned level of flexibility, efficiency and quietness will be presented.

2.1. Booster

Heat pumps usually experience a performance reduction at high thermal lift, i.e. when the outdoor air temperature is low and when the supply water temperature is high. Therefore, heat pumps result undersized when the heating demand of the building is higher and require a backup system (electrical resistance or gas boiler) which increases the system complexity and cost and reduces the overall efficiency. Alternatively, if the heat pump is sized to handle the full load at design condition, it results largely oversized when the load is lower, i.e. for most of the heating season, again with negative impact on the costs and on the efficiency.

To overcome this issue, the booster concept [6] is aimed at allowing a gas input above the nominal value, while keeping the generator temperature below the maximum value, usually set at 180-200 °C for corrosion control reasons. The booster concept relies on two splits on the solution and the refrigerant circuit aimed at modifying the magnitude of the internal heat recoveries, with the purpose of lowering the temperature and increasing the ammonia mass fraction of the rich solution entering the generator. This has the effect of reducing the temperature in the generator and increasing the maximum amount of gas input.

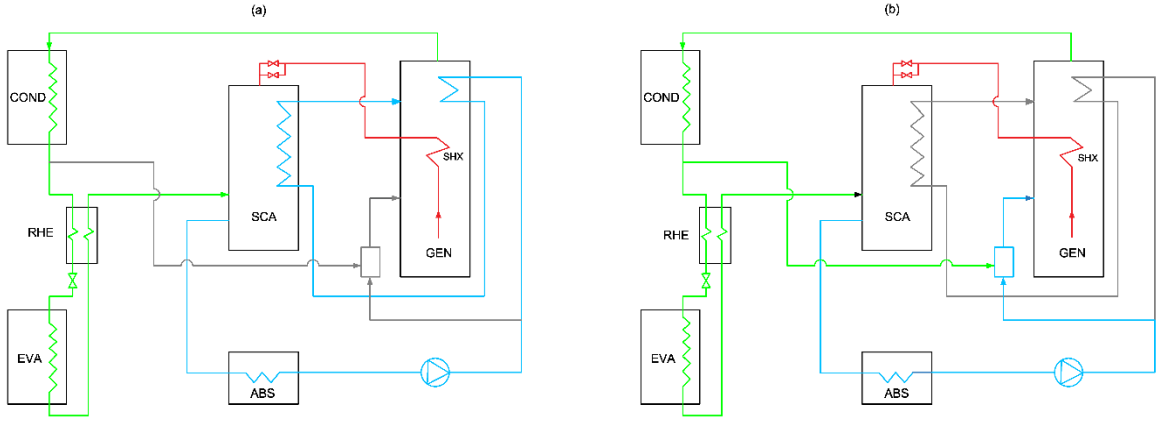


Fig. 2 – scheme of the heat pump cycle during normal operation (a) and with activated booster function (b).

With reference to Figure 2, where the cycle layout is presented both under normal operation (a) and in booster mode (b), the solution which normally flows through the Solution Cooled Absorber (SCA) is deviated and directly sent to the generator, disabling the heat recovery given by the GAX (Generator Absorber heat eXchange) effect. Moreover, making use of a venturi tube, part of the refrigerant leaving the condenser is injected in the rich solution, increasing its ammonia mass fraction. This increases the mass fraction in the generator and its capability to generate vapor, transferring the extra gas input into latent energy. The possibility

to increase the gas input up to 50% more than the design value permits to reach the maximum heating capacity even when the thermal lift is high. Thus, the thermodynamic cycle can be sized to operate with the maximum efficiency in the most frequent conditions, i.e., intermediate thermal lift and load, while keeping the possibility to meet the maximum capacity without the need of auxiliary systems.

A further effect of the activation of the booster is the reduction of the high pressure of the cycle. In fact, when the rich solution is directly routed towards the generator, the rectifier is not cooled anymore. This results in a lower mass fraction of the refrigerant leaving the generator, which causes a reduction of the condensation temperature. This is often beneficial since the booster is usually activated at high supply temperatures, which are also associated to high pressures. Thus, the booster can be used not only to deliver the required capacity without exceeding the maximum temperature at the generator, but also to increase the supply water temperature while keeping the maximum pressure within the design limits.

2.2. Two-stage restrictor

To further extend the capability of the heat pump to operate efficiently in all the loads and thermal lifts, a double stage restrictor has been used on the poor solution branch. The control of the flow rate on the solution branch consent to deal with two well-known correlated issues related to part load operation of gas driven heat pumps, i.e., the reduction of the temperature in the generator and a sub-optimal ammonia mass fraction in the circuit. In fact, gas driven heat pumps deal with part load by reducing the gas input. This automatically translate in a reduction of the generator temperature and a consequent increase of the ammonia mass fraction of the solution contained in the generator volume. These changes have various effects: they reduce the concentration spread between the rich and poor solutions (which impacts on the GAX effect in the SCA) and reduce the amount of ammonia available for the other components. The first issue has a direct impact on the efficiency of the heat pump and can even lead to cut-off conditions when the generator temperature decreases too much, forcing the control system to run the machine in an inefficient on-off operation. The second issue has an impact on the low pressure, which tends to decrease when the amount of ammonia available in the circuit is not sufficient, with a negative impact on the efficiency of the heat pump, which operates in an unnecessary artificially high thermal lift.

The use of a variable solution flow rate to maintain the generator temperature in its optimal value and to maximize the heat pump efficiencies in all the thermal lift and load condition has been proved numerically [5]. In this work, the concept has been deployed in the developed heat pump, opting for a two-stage restrictor instead of a continuously adjustable one to keep the cost and control complexity low. However, through a proper selection of the characteristic of the two restriction stages and in combination with the booster, it has been possible to maintain a high efficiency in the entire range of operating conditions.

2.3. Defrosting

The choice of an indirect evaporation allowed the design of an innovative approach to defrosting operation.

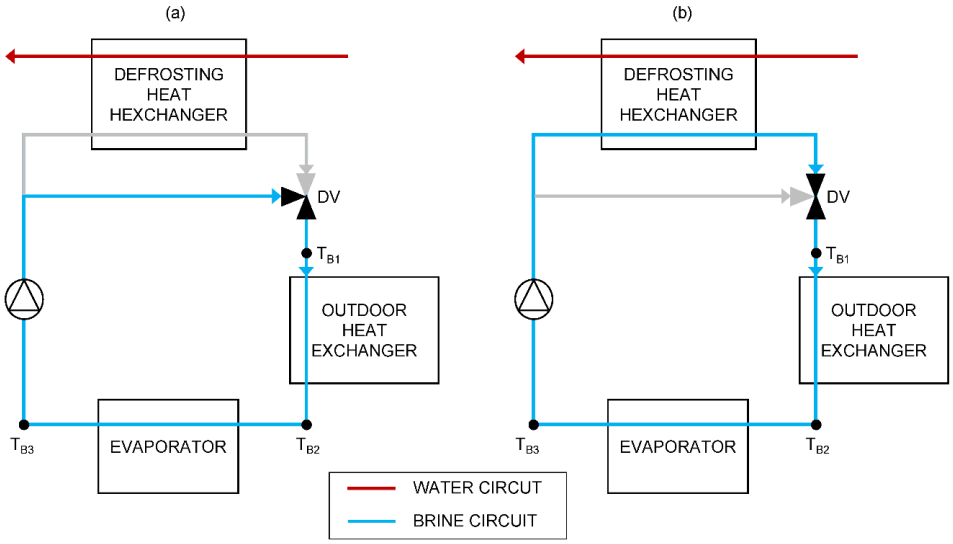


Fig. 3. Schematic representation of the defrosting system during normal operation (a) and defrosting operation (b).

With this system, which schematic operation is reported in Figure 3, the defrosting process is done by heating up the brine in the secondary circuit by means of a heat exchanger, called defrosting heat exchanger, paced in series with the supply water outlet. During normal operation (Figure 3a) the three-way valve DV allows the brine to circulate between the evaporator and the outdoor air heat exchanger, skipping the defrosting heat exchanger through the brine bypass. During defrosting operation (Figure 3b) the valve switches, closing the brine bypass and circulating the brine through the defrosting heat exchanger. Here the brine is heated up by the supply water, reaching a temperature warm enough to defrost the air-sourced heat exchanger.

3. Performances

In this section the measured performances of an initial prototype of a heat pump are presented. A first defrosting operation is reported to prove the effectiveness of the developed solution. Then, the effects of the booster and of the double restrictor on the thermodynamic cycle are showed with reference to some specific tests. Finally, the seasonal performance according to the European Standard EN 12309 and the representation of the operating range of a prototype of a heat pump incorporating the described solutions are reported.

3.1. Defrosting

The relevant temperatures useful to analyze a defrosting operation are reported in Figure 4. In particular, the black line indicates when the defrosting valve DV is opened (at time 18:42) and closed (at about 18:45). In the first part of the chart, the temperatures of the brine entering (T_{B1}) and leaving (T_{B2}) the outdoor air sourced heat exchanger are about -10 °C and -13 °C, significantly lower than the air temperature (0 °C) due to the presence of frost, while the supply water temperature is stable at 55 °C. When the desfroting operation starts, the brine passes through the defrosting heat exchanger and meets the warm water leaving the heat pump. As a result, the temperature of the brine entering the outdoor air heat exchanger (T_{B1}) increases up to a level sufficient to melt the ice. The increase of the temperature of the brine leaving the outdoor air heat exchanger (T_{B2}) is slower due to the intense heat transfer taking place during the melting process. When the process is concluded by the return of the defrosting valve to its initial position, the supply water temperature reaches immediately the original value of 55 °C. The brine temperatures decreases more slowly due to the capacity of the circuit and of the outdoor heat exchanger, meaning that part of the sensible energy used to heat up the system at the beginning of the defrosting process is recovered. After the transient, the brine temperature stabilize few degrees below the air temperature, at the typical value associated to a frost-free heat exchanger.

The entire process lasts about 3 minutes and does not have any impact on the thermodynamic cycle. This makes the operation very efficient and allows to restore the supply temperature to its set value immediately. The basic principle herein described is subject to further improvements and it is associated to control features covered by industrial intellectual property of Ariston Group that include additional function for the management of the indirect evaporation and the defrosting.

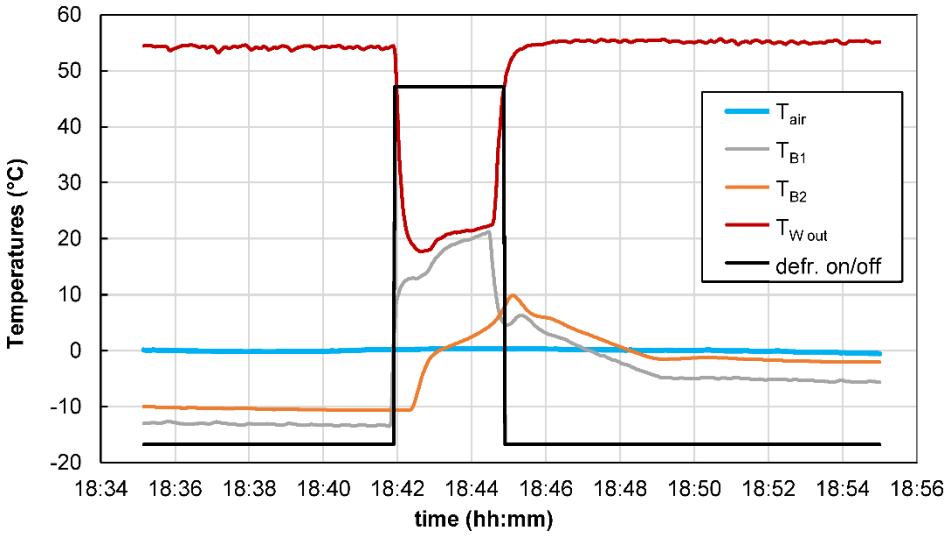


Fig. 4. Trend of the relevant variables of the brine circuit during a defrosting operation

3.2. Effects of the booster

As mentioned in the previous section, the booster can be used for two different purposes, i.e., limiting the generator temperature at high capacity and high thermal lift or limiting the high pressure at high supply temperature. In the chart in Figure 5 the effect of the booster on the cycle when it is used to limit the high pressure can be observed. The test was run at 20 °C of air temperature, while the water inlet/outlet temperature was 50/70 °C. Under this condition the high pressure was the limiting factor to the delivered capacity, which was about 3.6 kW (green line). To increase the heating power without a further increase of the high pressure, the booster was activated at 15:28. As a result, the generator temperature (red line) dropped from 143 °C to 133 °C and the high pressure (blue line) from 25 bar to 22 bar, creating some space for an increase of the gas input and of the delivered capacity. From the chart it is also possible to see that even if the activation of the booster introduces significant variations on the operation of the cycle, the transition is very smooth and does not impact the heat pump stability.

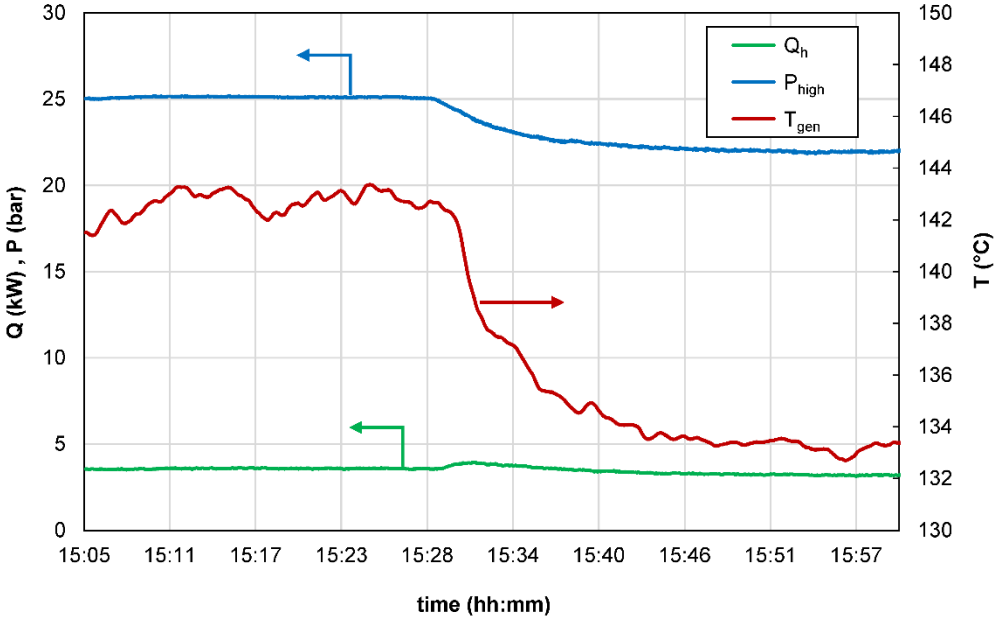


Fig. 5. Effect of the activation of the booster on the generator temperature and

3.3. Effects of the double restrictor

Providing a complete picture about the use of the double restrictor in combination with the booster is complex and would require the disclosure of control strategies that have been specifically developed to maximize the benefits of these solutions and are considered confidential. However, in this section the impact on the thermodynamic cycle of the switch between the two restrictors configurations is described showing the variation of some relevant quantities. In Table 1 the two pressure levels of the cycle, the temperature in the generator, the gas input, the delivered heating capacity and the resulting GUE are reported for the operation with slow and fast restrictor, for two operating conditions. Of the two reported conditions, the first, with air at 0 °C and water temperature of 40/55 °C, has been selected because it shows an efficiency independent on the type of restrictor used. On the other hand, for the second conditions, characterized by a lower thermal lift, a higher efficiency is found with the slow restrictor, which allows for a higher generator temperature.

The two reported conditions allow the use of both the restrictors because they are characterized by an intermediate heating capacity (about 63% of the nominal capacity) and intermediate thermal lift. As the capacity and the lift increase, the fast restrictor becomes the only option available since the slow restrictor would lead to excessively high temperatures in the generator. On the other hand, at lower capacities and lower thermal lift, the slow restrictor is the only available alternative because with the fast restrictor the temperature of the generator would drop and lead to very low efficiency or even to cut-off conditions.

Table 1. Impact of the type of restrictor on the thermodynamic cycle

		T_{air} = 0 °C, T_w = 40/55 °C		T_{air} = 7 °C, T_w = 40/55 °C	
		Slow restrictor	Fast restrictor	Slow restrictor	Fast restrictor
high pressure	bar	15.8	16.4	19.2	19.5
low pressure	bar	2.7	2.5	4.2	4.3
generator temperature	°C	169.3	144.6	172.0	137.9
Q_{gas}	kW	5.24	5.47	4.32	4.43
Q_h	kW	6.33	6.63	6.26	6.27
GUE	-	1.21	1.21	1.45	1.42

3.4. SPER based on the EN 12309

The efficiency of a prototype of such a heat pump has been measured in a certified laboratory at Politecnico di Milano premises following the procedure proposed by the European Standard EN12309 [7]. The Standard gives the possibility to calculate the Seasonal Gas Utilization Efficiency (SGUE) for three different outdoor design temperatures (2 °C, -10 °C, and -22 °C) corresponding to the three reference European climates warmer, average, and colder respectively. Moreover, for each climate, four different climatic curves are available, corresponding to different requirements of the emission system. For the present work, a design supply temperature of 55 °C, corresponding to the high temperature application, has been selected and the results for the average climate conditions are presented.

To calculate the SGUE, the Standard approach considers the GUE, i.e., the ratio between the heating capacity of the heat pump and the gas input, at different load ratios. The Part Load Ratio (PLR), i.e. the ratio between the design and the actual building loads, is calculated as a function of the outdoor design temperature and the actual outdoor air temperature, under the assumption that the building load is proportional to the difference between the indoor and the outdoor temperature and becomes zero at 16 °C.

The SGUE is calculated using the bin method as in Equation 1. The Standard prescribes to measure the GUE under the working conditions reported in Table 2 and to derive the values of GUE for the remaining air temperatures by interpolation. Since the performances of the GAHP are also affected by the return water temperature, the Standard allows a maximum temperature difference between supply and return temperature (ΔT_{max} in Equation 2), function of the outlet water temperature ($T_{w\,out}$).

Besides the GUE, Table 2 reports the Auxiliary Energy Factor (AEF) for each measured condition, i.e., the ratio between the heating capacity and the electrical power required for the auxiliaries of the heat pump, namely electronics, blower, fan, water pump and solution pump. These values are used to calculate the Seasonal Auxiliary Energy Factor when the appliance is running ($SAEF_{ON}$) in a similar way as the one described to calculate the SGUE from the GUE. Adding the electrical consumption in standby mode (E_{SB}) and thermostat off mode (E_{TO}), equal to 6 W and 0 W respectively, the SAEF is obtained. As last step, weighing the GUE and the SAEF with their corresponding primary energy factors (f_{EL} = 2.5 and F_{GAS} = 1), the Seasonal Primary Energy Ratio is calculated as in Eq. 3.

The following seasonal figures have been obtained for the developed heat pump:

- GUE_{NCV}: 1.50
- SAEF: 55.9
- SPER: 1.27

$$SGUE = \frac{\sum_{j=1}^{N} h_j \cdot \dot{Q}_h(T_j)}{\sum_{j=1}^{N} h_j \cdot \frac{\dot{Q}_h(T_j)}{GUE(T_j)}} \quad (1)$$

$$\Delta T_{max} = 7 + \frac{T_{w,out} - 35}{3} \quad (2)$$

$$SPER = \frac{1}{\frac{f_{GAS}}{SGUE} + \frac{f_{EL}}{SAEF}} \quad (3)$$

Table 2. Test conditions and measured GUE and AEF.

part load ratio	T_{air} (°C)	$T_{air\ WB}$ (°C)	$T_{w\ out}$ (°C)	$T_{w\ in}$ (°C)	GUE_{NCV}	AEF
100%	-10	-11	55.0	41.4	1.26	50.0
88%	-7	-8	52.0	39.4	1.33	53.0
54%	2	1	42.0	32.7	1.53	61.1
35%	7	6	36.0	28.7	1.61	59.8
15%	12	11	30.0	24.7	1.38	35.3

It must be mentioned that the test conditions reported in Table 2 have been run without activating the booster. This is due to the design choices, which aimed at delivering the design power at the design condition without the need of activating the booster, with the scope of assuring high efficiency over the space heating conditions. However, the booster can be activated when the outdoor temperature drops below the design conditions or when high water temperatures are required (e.g., during the domestic hot water preparation). Additionally, the booster operation is also influenced by the gas input, which impacts on the generator temperature. In the following section a rough indication about the conditions when the booster is needed is presented.

3.5. Operating range

Gas absorption heat pump is a technology which could be asked to operate over a very wide range of operating conditions. In fact, being the existing building its more natural application, the type of emission system and capacity requirements can differ significantly from case to case. Additionally, existing buildings can present high load and the need for high supply temperature in all type of climate conditions. The innovations described in the previous sections, beside enabling high performances, were introduced also to extend the operating range of the heat pump, to maximize the possible application that can be addressed with the same design. As a result, the described heat pump prototype can provide 70 °C of supply water with air temperature from -22 °C, i.e., the design condition of the reference European colder climate conditions to above 30 °C, typical of the summer season when domestic hot water production is still required. As reported in Figure 6, when the design capacity is required, supply temperatures above 55 °C and air temperatures below -15 °C require the activation of the booster. This region becomes smaller at the minimum capacity, where only the upper part of the supply temperature range requires the activation of the booster. The limitation existing at the combination of high air temperature and high supply temperature is given by the high pressure, which would exceed the design values.

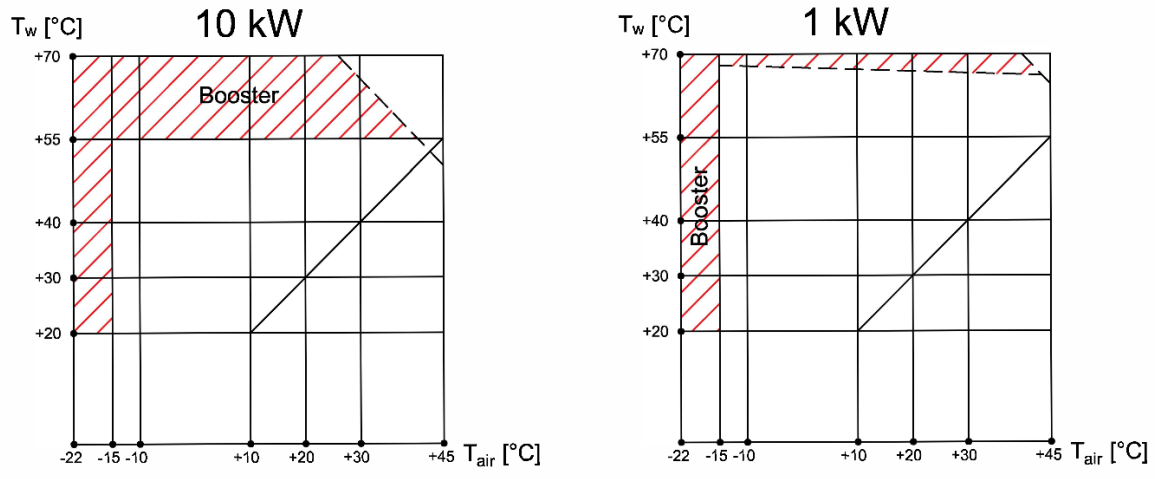


Fig. 6. Graphical representation of the operating range of a 10-kW heat pump at maximum and minimum capacity

1. Conclusions

In this work the development of a prototype of a new product platform of gas absorption heat pumps for residential application has been presented. The main innovations introduced, their motivation and their impact on the heat pump operation have been described.

An innovative defrosting system has been developed, taking advantage of the use of an indirect evaporation configuration, with a brine auxiliary circuit. This system resulted very effective and able to complete the defrosting operation in about three minutes, with minimal impact on the user and no influence on the thermodynamic cycle.

The combined use of the patented concept of the booster and of a double stage restrictor allows the heat pump to operate from -22 °C to more than 30 °C of air temperature, with maximum supply temperature of 70 °C. It also made it possible to design the thermodynamic cycle to reach the maximum efficiency in the most frequent operating conditions in the heating season and to avoid the oversizing of the heat pump, keeping the dimensions and the weight low. Moreover, these solutions enabled efficient operation over the entire operating range, which resulted in a Seasonal Primary Energy Ratio measured according to the European Standard EN 12309 of 1.27 and a Seasonal Auxiliary Energy Factor of 55.9.

From this initial development work, Ariston completed the design of a new platform of TDHP products further enhancing these results.

Acknowledgements

The development of the gas absorption heat pump presented in this work has been done within the i-GAP research project, supported under the Call “Agreements for Research and Innovation of the Lombardy Region” co-financed by the ERDF ROP 2014-2020 of the European Commission. Project ID: 241736. Moreover, the introduction of the double restrictor and the extension of the modulation range has been funded by Regione Lombardia under the LombHe@t Project - Call Hub Ricerca e Innovazione.
These developments are therefore the basis of a scientific and technological work that Ariston Group has considered in preparing its new TDHP platform.

References

[1] W. Eichhammer, T. Fleiter, B. Schlomann, S. Faberi, M. Fioretto, N. Piccioni, S. Lechtenböhmer, A. Schüring, V. Resch, *Study on the Energy Savings Potentials in EU Member States, Candidate Countries and EEA Countries*, Final report, 2009.

[2] M. Garrabrant, R. Stout, C. Keinath, and P. Glanville, *Experimental Evaluation of Low-Cost Gas Heat Pump Prototypes for Building Space Heating*, 16th International Refrigeration and Air Conditioning Conference, Jun. 2016. [Online]. Available at: http://docs.lib.purdue.edu/iracc/1573

[3] R. Scoccia, T. Toppi, M. Aprile, M. Motta, *Absorption and compression heat pump systems for space heating and DHW in European buildings: Energy, environmental and economic analysis*. Journal of Building Engineering 2018;16:94-105.

[4] J. Famiglietti, T. Toppi, D. Bonalumi, M. Motta, *Heat pumps for space heating and domestic hot water production in residential buildings, an environmental comparison in a present and future scenario*, Energy Conversion and Management, 2023; 276: 116527.

[6] Marco Guerra, *Absorption hea t pump for overfeed gener ator oper ating conditions*, Patent application EP2372273B1/ US8950212B2, 2011.

[5] Giorgio Villa, TommasoToppi, Marcello Aprile, Mario Motta, *Performance improvement of gas-driven absorption heat pumps by controlling the flow rate in the solution branch*, International Journal of Refrigeration 2023; 145:290-300.

[7] European standard, *EN12309:2014, Gas-fired sorption appliances for heating and/or cooling with a net heat input not exceeding 70kW*.

14th IEA Heat Pump Conference
15-18 May 2023, Chicago, Illinois

Innovative small capacity gas driven ammonia-water absorption heat pump prototype for space heating and domestic hot water production

Pistocchini Lorenzo [a,*], Villa Giorgio [a], Paulin Cesare [a], Toppi Tommaso [a]

[a]Politecnico di Milano, via G. La Masa 34 , Milan 20156, Italy

Abstract

Gas driven absorption heat pumps are a viable alternative for efficient space heating and domestic hot water production in residential and light commercial buildings with high temperature distribution systems. This work presents a second-generation ammonia-water absorption heat pump prototype, with patent-pending components developed by Politecnico di Milano. The innovative design of desorber and rectifier improves the heat and mass transfer in the generator whilst reducing its height and complexity. All the heat exchangers, except for the generator, are plate heat exchanger and a specifically designed oil driven diaphragm pump is used as solution pump. The overall weight of the prototype, excluding the continuous fin-type outdoor heat exchanger, is kept below 70 kg for a unit with nominal capacity of 10 kW. Variable restrictors for both solution and refrigerant branches are used to improve part load operation and the seasonal efficiency. Laboratory tests confirm high performance over a supply water temperature range between 25 °C and 70 °C and ambient temperatures between -14 °C and 22 °C. The experimental results highlight the importance of installing a variable restrictor on the solution branch to improve performances at partial load, optimizing the generator temperature. The newly designed prototype proved to perform smoothly and to maintain stable operation under the tested steady-state and transient conditions.

© HPC2023.
Selection and/or peer-review under the responsibility of the organizers of the 14th IEA Heat Pump Conference 2023.

Keywords: Absorption Heat Pump; Ammonia; Variable Valves; Gas-fired Generator; Residential Heating

1. Introduction

Absorption heat pumps are a reliable and efficient technology as demonstrated by several applications in the light commercial sector where thousands of gas-driven absorption heat pumps (GHP) are used for many years [1]. This technology is also interesting for the residential market to replace condensing boilers in not or poorly insulated buildings, with high temperature emission systems as radiators, a building typology which represents a large share of the existing European residential buildings [2]. In fact, absorption heat pumps achieve high supply water temperatures with limited performance degradation. For this type of buildings, it has been calculated that absorption heat pumps can provide also higher performances than electric vapor compression heat pumps [2], especially in cold and very cold climates where the COP is reduced by the low outdoor air temperature [3]. Furthermore, the possibility to run absorption heat pumps with green hydrogen or a mix of natural gas and hydrogen, can support the decarbonization of the heating sector, handling the peaks of demand without impacting on the electric grid [1], [4]. Experimental tests confirmed that absorption heat pumps provide higher performances than conventional space heating and water heaters appliances. In [5] two prototypes with a nominal capacity of 23.5 kW have been tested and a Seasonal gas utilization efficiency of 1.36 (based on gross calorific value) has been achieved, considering the climate region IV of the American and Canadian Standard [6]. The seasonal gas utilization efficiency (SGUE) is calculated as the ratio between the useful heat provided by the heat pump during the heating season and the natural gas input. For domestic hot water production (DHW), a 9-month field test has been performed in [7] achieving interesting energy savings, compared to traditional gas tank water heaters. Then, an 18-kW absorption heat pump has been also

* Corresponding author. *E-mail address:* lorenzo.pistocchini@polimi.it

tested obtaining a Season Gas Utilization Efficiencies of 1.43, 1.38, and 1.24 (all based on gross calorific value) for the warm, average, and cold climates respectively [8], as defined by the European Standard [9] test conditions.

Even if gas-driven absorption heat pumps are a viable alternative to condensing boilers, especially for single or two-family houses with space availability for an outdoor installation, the limited number of manufacturers and the relatively high purchase costs of commercially available heat pumps limit a wide diffusion of this technology [3]. Many different absorption cycles are available, the most suitable ones for the residential sector are the single effect cycle (SE) and Generator Absorber eXchanger cycle (GAX) [10]. The GAX is considered one of the most suitable cycles for residential application because it achieves high performances providing the possibility to heat up the rich solution by recovering part of the heat released in the absorber [11]. To perform this heat recovery, an additional component is needed compared to the single effect cycle. However, the GAX effect is affected by high thermal lift and partial load operation, condition often found in residential applications [5]. Moreover, small-capacity heat pumps in real applications experience frequent load variation and different operating conditions, such as changes in inlet/outlet temperatures, mass flow rates, external temperatures etc. [12]. To improve the performances at partial loads, an optimization of the temperature of the generator is essential. This task can be achieved controlling the weak solution mass flow rate with a variable restrictor in the solution branch [13].

In this project, a compact and cost-effective air-source gas-driven ammonia-water absorption heat pump based on the single effect cycle has been developed and tested. The heat pump is the second-generation prototype of a previous concept, where several innovations have been introduced in the generator (under patent pending), optimized plate heat exchangers have been selected and the variable restrictors for both solution and refrigerant branches have been used. The solution pump is an oil driven diaphragm pump specifically designed for this application. After a description of the prototype, in this work the achieved energy performances are presented and analyzed. Seasonal gas utilization efficiency and other relevant working conditions are shown, highlighting the impact of the use of a variable restrictor to assure efficient operation, and giving evidence of the smooth and stable operation of the heat pump under both steady-state and transient conditions.

2. Prototyping and thermodynamic cycle

In this section the thermodynamic cycle and the peculiarities of the prototype are described.

2.1. Thermodynamic cycle

The small-capacity gas driven absorption heat pump analyzed in this study has been designed for residential and small commercial applications. The single effect cycle shown in Figure 1 has been selected to meet the requirements of this application, strongly driven by space-saving, by the purchase cost for what concerns the economic aspects, and by a wide range of operating conditions for what concerns the technical considerations.

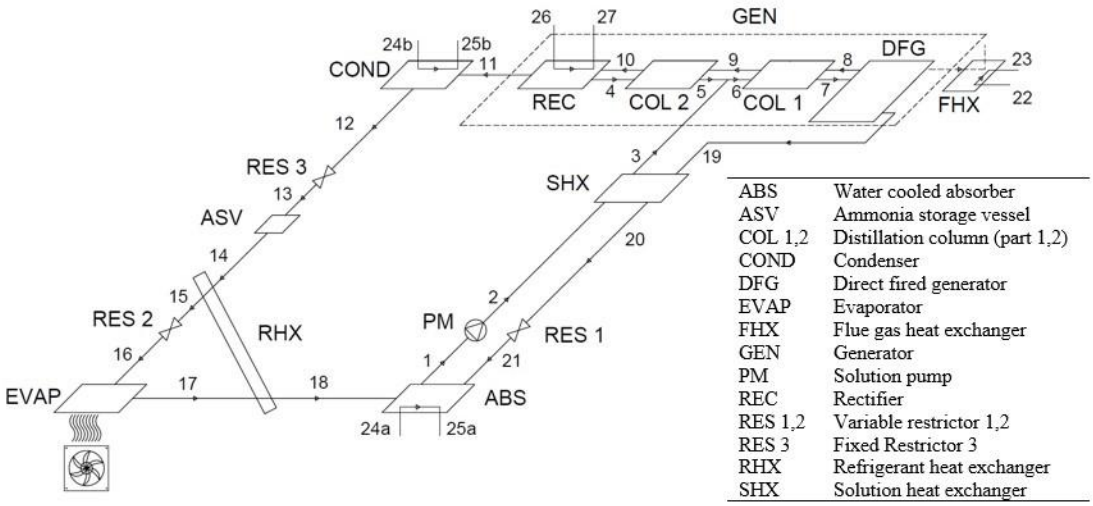


Figure 1: Single effect thermodynamic cycle

The Single effect cycle is composed by the refrigerant and the solution branches. The refrigerant branch is the left side of the cycle in Figure 1 and it is composed by the condenser (COND), the restrictors (RES 2 and RES 3), the refrigerant heat exchanger (RHX), the Ammonia Storage Vessel (ASV) and the evaporator (EVAP). On the other side, the solution branch is composed by the water-cooled absorber (ABS), the solution pump (PM), the restrictor (RES 1), the solution heat exchanger (SHX) and the generator (GEN) that can be divided in the direct fired generator (DFG) directly connected to the distillation column (COL1+COL2) and the water-cooled rectifier (REC). The combustion of natural gas heats up the ammonia-water pool boiling solution in the direct fired generator creating vapor (point 8). The ammonia mass fraction of the vapor is increased, while its temperature is decreased in the first section of the distillation column (COL1) where it flows counter-current with the rich solution (point 6) (high ammonia mass fraction), promoting an intense heat and mass exchange. On the contrary, the rich solution reduces its ammonia mass fraction while increasing its temperature. Since a high ammonia mass fraction (≈99%) of the outlet vapor from the generator (point 11) is needed, a partial condensation takes place in the water-cooled rectifier (REC). Between REC and COL1 there is the second section of the distillation column (COL 2), where the vapor (point 9) meets the liquid produced by the partial condensation (point 4). The outlet vapor (point 11) flows toward the condenser where it is cooled down, providing part of the useful effect, and it is throttled in RES 2 and RES 3. Between the two restrictors there is the ASV that stores/releases the refrigerant when it is required, as described in [1], and the RHX that provides an internal heat recovery between the outlet liquid refrigerant of the ASV (point 14) and the outlet vapor of the evaporator (point 17). The weak solution (point 19) (low ammonia mass fraction) leaves the generator, it is throttled in RES 1 and flows to the absorber (point 21) where it is mixed with the refrigerant (point 18) providing part of the useful heat thanks to the exothermic absorption process. The rich solution (point 1) is pumped up by the solution pump (point 2) and it is heated up (point 3) by the weak solution (point 20) in the SHX providing a remarkable internal heat recovery. Then, the rich solution flows in the generator. Looking at the water circuit, the useful effect of the heat pump is provided by the flue gas heat exchanger (FHX), the condenser, the absorber, and the water-cooled rectifier. The water is pre-heated by the FHX cooling down the flue gas (point 23) and compensating part of their humidity content, then condenser and absorber are connected in parallel (point 24a and point 24b). To conclude, the whole mass flow rate flows in the REC (point 26) providing the cooling for the rectification process.

2.2. Prototype description

The sealed circuit of the 10-kW air-water gas-driven absorption heat pump under analysis is shown in Figure 2. To achieve high performances reducing the manufacturing costs, the design of this prototype is based on a mix of standard components available on the market and customized components.

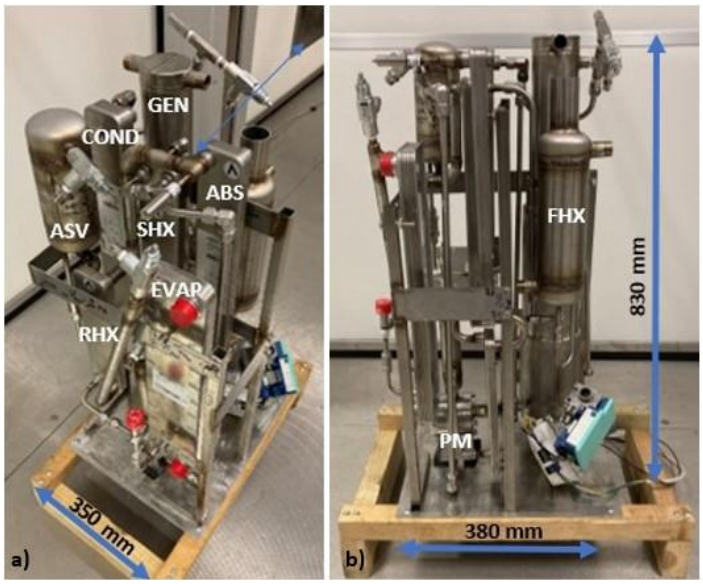


Figure 2: Two side of the GHP sealed circuit, showing its main components and overall dimensions

The customized components are the generator (under patents pending) and the solution pump, i.e. an oil driven diaphragm pump specifically designed for this application, in order to manage the very low flow, the high head pressure, and especially to ensure the complete tightness and maintenance-free reliability in the long term.

The generator has a fire-tube configuration with an innovative geometry that promotes an intense heat exchange between the flue gas and the ammonia water solution maintaining a compact size and reducing the risk of hot spots and local corrosion.

For what concerns the design of the heat exchangers delivering the useful effect of the heat pump, the high difference between the ammonia-water solution mass flow rate and the water mass flow rate represents the most critical issue [1]. In this prototype, standard and custom plate heat exchangers (PHE) developed by Swep have been used. Where possible, an All-Stainless Steel product has been selected, as for the evaporator. When the required All-Stainless Steel PHE is not available, the nickel brazed stainless steel plate PHE has been selected, considering that the corresponding All-Stainless Steel version can be later implemented and produced at a lower cost once you get from GHP prototype to a commercial product.

The solution heat exchanger (SHX) is characterized by a very long thermal length, in order to transfer most of the heat from the weak solution leaving the generator to the rich solution entering the generator. To achieve such a result a multi-pass PHE with a custom configuration has been selected.

The absorber (ABS) consists of two PHE in series, to achieve the required thermal length and manage the different volumetric flow in the refrigerant side, which is mainly a vapor stream at the inlet and a liquid flow at the outlet.

In the evaporator (EVAP) a brine loop (actually filled by a water-glycol mixture) transfers the heat from the outdoor air to the evaporator. This layout may cause a slightly reduction of the performances of the heat pump due to the additional temperature difference caused by use of the intermediate brine loop, however, it offers higher flexibility in installing the sealed circuit indoor and the air heat exchanger outdoor. Furthermore, this option reduces the heat losses towards the environment, partially compensating the performance reduction. Moreover, the use of a brine-water plate heat exchanger as evaporator reduces the internal volume of the sealed circuit, leading to an ammonia content lower than 2 kg, and the risk of refrigerant store-out from the generator into a fin type air-solution heat exchanger, as in case of direct expansion heat pump, during switching on and transients. In addition, thanks to this layout, different defrosting strategies can be implemented. The combination of a compact generator with the use of plate heat exchangers allows for a design of the heat pump able to keep the weight at about 70 kg and to maintain the dimensions close to the ones of a condensing boiler, i.e. 380 x 350 x 830 mm (excluding the outdoor air-brine heat exchanger), as shown in Figure 2. Small capacity heat pumps installed in residential sector works in a wide operating range and under frequent load transient and variable conditions, thus a flexible design under the operating conditions point of view is essential. To achieve this goal, variable restrictors are installed in the solution branch (RES 1) and in the refrigerant branch (RES 2). In contrast, RES 3 is a fixed restrictor that improves the stability of the thermodynamic cycle by introducing a small pressure drop and an intermediate pressure for the ASV and the liquid side of the RHX. The solution branch variable restrictor provides the possibility to optimize the temperature at the base of the generator controlling the flowrate in the solution branch, while RES 2 controls the evaporation temperature to avoid the flooding of the evaporator. The ASV is installed between RES 3 and the RHX to optimize the operation of the RHX [1].

3. Test methodology

The gas-driven absorption heat pump prototype has been tested in an accredited laboratory in the brine-to-water configuration. Temperature measurement is made by high accuracy RTD Pt100 Temperature Sensors (4 wire 1/10 DIN), which coupled to a high precision monitoring system and periodically calibrated allow us to reach an accuracy of +/-0.02 K in the whole operating range.

Flow measurement in the water and brine lines is made by electromagnetic flowmeters, which are periodically calibrated and guarantee 0.1 % of reading accuracy.

Even the particular oil filled volumetric gas flowmeter is periodically calibrated and guarantee 0.5 % of reading accuracy in a wide range of flow rates.

To simulate the impact of the brine loop that transfers heat from the outdoor air to the evaporator, the inlet temperature of the brine is considered 2 K lower than the temperature of the air, with a temperature variation in the evaporator of about 3 K. Consequently, once the ΔT required for the heat transfer between brine and refrigerant is taken into account, the evaporation temperature is about 8-9 K lower than the air temperature, a reasonable value which can be matched when an actual well-designed air-to-brine heat exchanger is used. The

energy performance of a gas-driven heat pump is measured as the ratio between the useful heat provided by the heat pump and the natural gas heat input ($\dot{Q}_{gas}$), which is the measured volumetric flow of methane, corrected on the basis of actual temperature and pressure, times the net calorific value (LHV [MJ/Nm^3]). This ratio is the Gas Utilization Efficiency (GUE) and considers as useful effect the heat provided by the condenser ($\dot{Q}_{cond}$), the absorber ($\dot{Q}_{abs}$), the rectifier ($\dot{Q}_{rec}$) and the flue gas heat exchanger ($\dot{Q}_{fhx}$) as shown in Equation 1. The Seasonal Gas Utilization Efficiency (SGUE) gives an indication about the performance of the heat pump over an entire heating season and it is calculated as suggested by the European Standard EN 12309 [9]. Both GUE and SGUE can be calculated also on the basis of the gross calorific value (HHV [MJ/Nm^3]) simply by substituting LHV with HHV in $\dot{Q}_{gas}$ calculation. The Standard gives the possibility to calculate the SGUE for three different outdoor design temperatures (T_{design}), 2 °C, -10 °C, and -22 °C, that correspond to the three reference climates for Europe, i.e. warm, average, and cold respectively. For each climate, four different climatic curves are available related to low temperature, medium temperature, high temperature and very high temperature applications, to consider different emission systems, i.e., underfloor system, fan coil system, radiators, and high temperature radiators. To define the inlet water temperature, a maximum temperature difference between inlet and outlet temperatures (ΔT_{max}) is calculated by Equation 2 as function of the outlet water temperature ($T_{w\text{-}out}$) [9]. The Standard proposes a calculation method for the SGUE based on the bin method, as for Equation 3, considering the GUE at different load ratios. The partial load ratio (PLR) is calculated as function of the design temperature and the water outlet temperature (T_j) (see Equation 4) assuming that the heating demand of a building decreases linearly with the outdoor air temperature and it is zero when the outdoor air temperature is 16 °C. In this paper, the average climate ($T_{design} = -10\ °C$) and the high temperature climatic curve, with 55 °C as supply water temperature at design condition (for radiators), have been selected to optimize the initial charge of ammonia and water. For the average climate, the Standard prescribes to measure the GUE under the working conditions in Table 1 for the high temperature climatic curve. Moreover, the seasonal efficiency of the heat pump to deal with the very high temperature application (see Table 2) has also been tested.

$$GUE = \frac{\dot{Q}_{cond} + \dot{Q}_{abs} + \dot{Q}_{rec} + \dot{Q}_{fhx}}{\dot{Q}_{gas}} \tag{1}$$

$$\Delta T_{max} = 7 + \frac{T_{w\text{-}out} - 35}{30} * 10 \tag{2}$$

$$SGUE = \frac{\sum_{j=1}^{N} h_j * \dot{Q}_h(T_j)}{\sum_{j=1}^{N} h_j * \frac{\dot{Q}_h(T_j)}{GUE(T_j)}} \tag{3}$$

$$PRL(\%) = \frac{T_j - 16}{T_{design} - 16} * 100 \tag{4}$$

Table 1: Working conditions for the high temperature climatic curve and average climate

	Partial Load Ratio	**Reference air temperature**	**Inlet temperature of brine**	**Inlet temperature of water**	**Outlet temperature of water**
Conditions	**PLR**	T_{air}	T_{brine_in}	T_{w_in}	T_{w_out}
-	**%**	**°C**	**°C**	**°C**	**°C**
1	100	-10	-12	41.3	55
2	88	-7	-9	39.3	52
3	54	2	0	32.7	42
4	35	7	5	28.7	36
5	15	12	10	24.7	30

Table 2: Working conditions for the very high temperature climatic curve and average climate

	Partial Load Ratio	Reference air temperature	Inlet temperature of brine	Inlet temperature of water	Outlet temperature of water
Conditions	**PLR**	T_{air}	T_{brine_in}	T_{w_in}	T_{w_out}
-	**%**	**°C**	**°C**	**°C**	**°C**
1	100	-10	-12	48.0	65
2	88	-7	-9	45.3	61
3	54	2	0	37.3	49
4	35	7	5	32.0	41
5	15	12	10	26.0	32

4. Results

In this section, the experimental results at different working conditions are introduced. Moreover, the additional flexibility provided by variable restrictors is shown.

4.1. Use of valves to control the cycle

The gas-driven absorption heat pump prototype under analysis has variable restrictors for both the solution (RES 1) and the refrigerant (RES 2) branches (see Figure 1). The variable restrictor RES 2 provides the possibility to optimize the evaporation temperature defined as the inlet temperature at the evaporator (point 16), while RES 1 provides the possibility to optimize the temperature at the bottom of the generator.

Figure 3 shows the evaporation temperature variation due to actions on the RES 2 valve. Increasing the aperture of the valve, the evaporator pressure and temperature increase (from point A to point D). This is achieved thanks to an increase of the refrigerant mass flow rate, which reduces the amount of liquid ammonia stored in the receiver and make it available to the thermodynamic cycle. This is normally associated to a lower thermal lift and higher concentration of the rich solution, both beneficial for the efficiency. The higher efficiency is visible from the increase of the difference between inlet and outlet temperatures of the brine circuit. However, when the aperture of RES 2 exceeds its optimal point, the difference between the evaporator temperature and the brine temperature decreases, causing a partial evaporation, which results in the flooding of the evaporator (point E). This phenomenon reduces the heat exchange with the low temperature source and the outlet evaporator temperature decreases. For the selected cycle layout, with the ASV between the condenser and the RHX, a flooded evaporator increases the heat transfer process in the RHX, leading to a higher degree of subcooling in the refrigerant entering the expansion valve. This further increase the flow rate, leading to a deterioration of the performances at the beginning and an interruption of the thermodynamic cycle if this condition persists. To restore a complete evaporation, RES 2 is closed (point F) reducing the refrigerant mass flow rate. As the refrigerant is stored in the ASV and the evaporator temperature decreases, leading to a complete evaporation of the liquid in the evaporator. Thus, the installation of the ASV before the evaporator on the one hand assures the possibility to control the evaporation pressure to optimize the performances, on the other it is required an active control on the restrictor RES 2 to avoid the flooding of the evaporator.

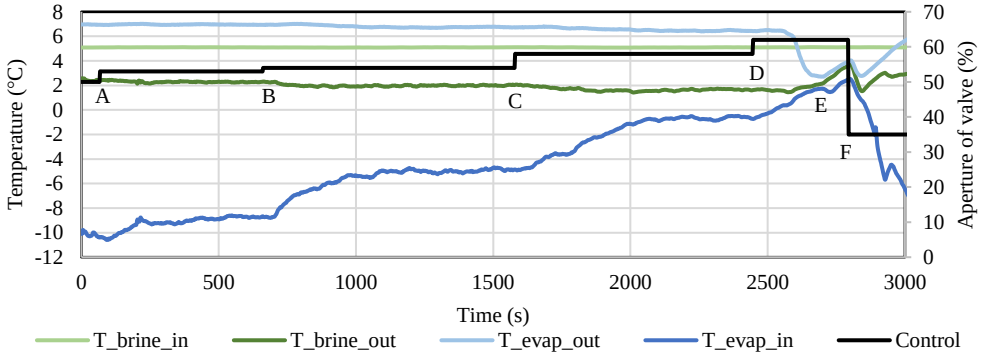


Figure 3: Effect of a variable refrigerant restrictor on the evaporation temperature

Once the control is tuned, the heat pump can operate smoothly and in a stable way under steady-state conditions. This is shown in Figure 4, where inlet and outlet temperatures for both the brine and the refrigerant are reported for a full load (10 kW of heating capacity) condition. The oscillation of all the temperatures is lower than 1 °C with the inlet brine temperature coming from the experimental set-up as the less stable. As for the evaporation temperature, the outlet water temperature variation is lower than 1 °C for the same test (see Figure 5), while the oscillation of the temperature of the weak solution (low ammonia mass fraction) is just slightly higher than 1 °C.

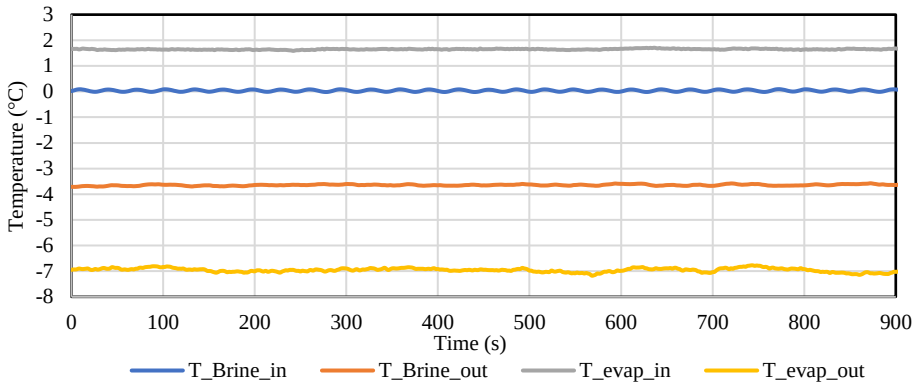


Figure 4: Experimental evaporation and brine temperatures

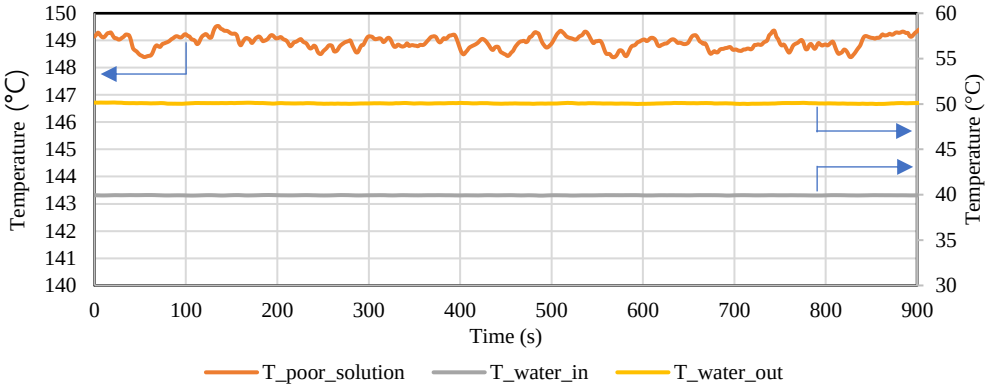


Figure 5: Experimental weak solution and water temperatures

4.2. Seasonal performances

The seasonal performance is calculated in compliance to EN 12309 for the average climate condition, with design temperature of -10 °C, and for the high and very high temperature applications, the former with a nominal supply temperature of 55 °C, the latter with 65 °C, as for the test conditions reported in

Table 1 and Table 2. The actual test conditions for the high temperature application and the measured GUE are reported in Table 3Table 3. The resulting Seasonal Gas Utilization Efficiency is 1.58 on a net calorific value basis or 1.42 on the gross calorific value. Table 4 shows the same information for the very high temperature application. Due to the higher supply temperature, the GUEs are lower than for the high temperature application and so is the SGUE, for which a value of 1.51 based on the net calorific value is achieved.

The climatic room where all the tests have been performed has been kept at 20°C, assuming an indoor installation of the GHP.

It must be mentioned that the amount and the average mass fraction of the water-ammonia solution have been optimized for the high temperature application. One of the constrains that have been applied when designing the heat pump and setting the water-ammonia content and mass fraction is that the maximum temperature at the base of the generator should not exceed 180 °C to avoid corrosion issues and assure reliable and safe operation over the entire lifetime. However, given the water-ammonia solution charge set for the high

temperature application, in Condition #1 of the very high temperature climatic curve, the maximum temperature of the generator is reached in correspondence of a heating capacity of 9 kW. Thus, for this application, with the current settings, the design capacity of the heat pumps is reduced from 10 kW to 9 kW, with the part load conditions recalculated accordingly. However, 10 kW could be reached also for the very high temperature application by properly tuning the solution mass fraction and, if needed, changing the RES 1 to increase the maximum flow rate allowed in the weak solution branch.

Table 3: SGUE calculated for high temperature climatic curve for an average climate (EN 12309)

	Useful heat	**Inlet temp. of water**	**Outlet temp. of water**	**Reference air temp.**	**Inlet temp. of brine**	**Outlet temp. of brine**	**Gas Utilization efficiency**
Condition	Q_h kW	T_{w_in} °C	T_{w_out} °C	T_{air} °C	T_{brine_in} °C	T_{brine_out} °C	GUE -
1	10.0	41.6	55.5	-10	-12.7	-15.4	1.36
2	9.0	39.4	52.6	-7	-9.0	-12.2	1.41
3	5.3	32.6	41.8	2	0.0	-2.6	1.60
4	3.5	29.0	36.3	7	5.0	2.3	1.67
5	1.6	25.0	30.8	12	10.0	8.4	1.59
$SGUE_{NCV}$	-	-	-	-	-	-	1.58
$SGUE_{GCV}$	-	-	-	-	-	-	1.42

Table 4: SGUE calculated for very high temperature climatic curve for an average climate (EN 12309)

	Useful heat	**Inlet temp. of water**	**Outlet temp. of water**	**Reference air temp.**	**Inlet temp. of brine**	**Outlet temp. of brine**	**Gas Utilization efficiency**
Condition	Q_h kW	T_{w_in} °C	T_{w_out} °C	T_{air} °C	T_{brine_in} °C	T_{brine_out} °C	GUE -
1	9.0	48.1	65.3	-10.0	-12.0	-14.8	1.25
2	7.9	44.9	60.6	-7.0	-9.0	-12.1	1.34
3	4.9	37.2	49.0	2.0	0.1	-2.6	1.54
4	3.2	31.9	40.5	7.0	5.1	3.4	1.57
5	1.3	28.0	32.0	12.0	10.1	8.9	1.46
$SGUE_{NCV}$	-	-	-	-	-	-	1.51
$SGUE_{GCV}$	-	-	-	-	-	-	1.35

4.3. Full load conditions and low temperature conditions

The heat pump has been tested in different full load conditions as shown in Table 5. The first experimental test (Test #1) has an inlet water temperature of 30 °C and an outlet temperature of 40 °C. This condition is important to test that the compact generator works properly. In fact, the combination of relatively low supply water temperature, which is translated in a reduced high pressure (P_{high}), and the high natural gas heat input, provides an intense boiling process. It may cause the drag of the liquid ammonia-water solution by the vapor stream from the upper part of the generator to the condenser, reducing the performances. In this case, the described phenomenon is not present and a remarkable performance of 1.541 is achieved, with an inlet brine temperature of 0 °C. Then, additional tests are performed increasing the return water temperature, while maintaining the same temperature difference between inlet and outlet water (10 °C). In Test #2, where both inlet and outlet water temperatures were increased by 10 °C compared to Test #1, a decrease of the GUE is measured. Further temperature increase was performed for Test #3 and Test #4 in Table 5, reaching a supply temperature of 65 °C. As expected, the efficiency of the heat pump decreases as the supply temperature is increases, even if the achieved GUE (1.361 with 60 °C as supply water temperature and 1.323 with 65 °C) underline the capability of the heat pump to operate efficiently also at high lift conditions, e.g. when producing domestic hot water (DHW) or when coupled with heating systems that need supply water temperatures higher than the ones considered by the Standard [9]. As additional condition, similar to the ones for domestic hot water production, a higher supply water temperature of 70 °C was set in Test #5, using 15 °C as temperature

difference between supply and return water. Even in this unfavorable condition for heat pumps, the prototype provides an interesting GUE of 1.295, which is about 30% higher than a condensing boiler operating under the same conditions. Since DHW production is usually needed also during mid-seasons and summer, two tests at higher air temperatures (12 °C and 22 °C respectively) are performed. 40/50 °C and 50/60 °C have been used as return and supply water temperatures, simulating two different phases of the charging of the DHW tank. It can be noticed that at higher air temperatures, the low pressure (P_{low}) is higher (4-7 bar), but the thermodynamic cycle works flawlessly, assuring a gas utilization efficiency between 1.45 and 1.60 as shown by Test #6, #7, #8 and #9 in Table 5.

Table 5: Cycle variables and GUE for different full power tests

	Useful heat	**Inlet temp. of water**	**Outlet temp. of water**	**Reference air temp.**	**Inlet temp. of brine**	**Outlet temp. of brine**	**Inlet temp. of solution at evap.**	**Pressure at cond. inlet**	**Pressure at evap. outlet**	**Gas Utilization efficiency**
Test	Q_h	T_{w_in}	T_{w_out}	T_{air}	T_{brine_in}	T_{brine_out}	T_{evap}	P_{high}	P_{low}	GUE
#	kW	°C	°C	°C	°C	°C	°C	bar	bar	-
1	10.2	30.0	40.2	2.0	-0.1	-3.9	-7.3	13.6	2.9	1.54
2	10.0	39.9	50.0	2.0	0.0	-3.6	-7.0	17.6	3.1	1.48
3	10.1	49.9	60.2	2.0	0.1	-3.2	-7.0	22.2	3.0	1.36
4	10.2	55.1	65.4	2.0	0.1	-3.1	-4.9	24.9	3.2	1.32
5	10.0	55.0	70.1	2.0	0.1	-2.7	-4.9	25.2	3.2	1.30
6	10.0	39.9	50.1	12.0	10.1	5.9	2.9	17.8	4.6	1.57
7	10.2	50.1	60.5	12.0	10.1	5.7	3.2	22.8	4.6	1.47
8	10.0	39.9	50.0	22.0	20.0	15.4	12.1	17.9	6.4	1.60
9	10.0	49.9	60.0	22.0	20.1	15.6	13.9	22.9	6.8	1.49

Moreover, the heat pump has been tested at low air temperature, to verify the operation and the efficiency at cold climatic conditions. Test #10 (see Table 6) shows that the heat pump still achieves a GUE of 1.483 with an inlet brine temperature of -16 °C and a supply water temperature of 35 °C, a condition which corresponds to a system with underfloor heating operating at about -14 °C of outdoor air temperature, usually very severe for most of the heat pumps. The minimum temperature considered by the European Standard for a cold climate is -22 °C [9]. This temperature cannot be reached by the calorimeter where the heat pump has been tested in brine-water configuration, due to freezing protection of the glycol circuit. However, to simulate a possible working condition at -22 °C of air temperature, the evaporation temperature was reduced to -30 °C acting on the variable valve on the refrigerant branch (see Test #12 in Table 6). This process replicates very well the operation of a heat pump at -22 °C, except for the temperature of the refrigerant leaving the evaporator. However, this temperature difference has very limited impact in terms of power due to the shape of the enthalpy-temperature curve of the refrigerant in the last phase of the evaporation process. The achieved GUE of 1.429 is remarkable and indicates that the heat pump can work with high efficiency also in the design conditions of the cold climate. Test#12 is performed at higher water and air temperatures where a GUE of 1.309 is obtained with a supply water temperature of 55 °C and an inlet brine temperature of -16 °C.

Table 6: Cycle variables and GUE for low temperature -20°C air 35W tests

	Useful heat	**Inlet temp. of water**	**Outlet temp. of water**	**Reference air temp.**	**Inlet temp. of brine**	**Outlet temp. of brine**	**Inlet temp. of solution at evap.**	**Pressure at cond. inlet**	**Pressure at evap. outlet**	**Gas Utilization efficiency**
Test	Q_h	T_{w_in}	T_{w_out}	T_{air}	T_{brine_in}	T_{brine_out}	T_{evap}	P_{high}	P_{low}	GUE
#	kW	°C	°C	°C	°C	°C	°C	bar	bar	-
10	9.8	26.1	34.9	-14.0	-15.9	-20.3	-25.3	11.8	1.4	1.48
11	9.9	26.1	34.9	-22.0	-15.9	-19.7	-30.0	11.6	1.1	1.43
12	9.9	41.4	55.1	-14.0	-16.0	-19.2	-22.3	17.8	1.6	1.31

5. Conclusions

This work presented the development of a 10 kW single effect ammonia-water gas driven absorption heat pump and its laboratory performances under various relevant operating conditions. The peculiarities of this prototype are the innovative layout of the generator (under patents pending), the use of variable restrictors for both the solution and refrigerant branches, and the use of commercial plate heat exchangers.

The role of the variable restrictors to optimize the low pressure and the efficiency of the cycle was presented, besides a proof of the stable operation of the heat pump. The efficiency of the heat pump was tested in laboratory conditions on a brine-to-water prototype, taking care of simulating the presence of an outdoor air heat exchanger by means of proper settings of the inlet brine temperatures. A remarkable Seasonal Gas Utilization Efficiency equal to 1.58 was achieved in accordance with the European Standard EN 12309 for the high temperature application, with nominal supply temperature of 55 °C, and the average climate condition. Furthermore, a SGUE of 1.51 was reached for the very high temperature application, with 65 °C of nominal supply temperature. Then, the GHP has been tested also in other relevant conditions which demonstrated its capability to provide hot water up to 70 °C and to operate at an equivalent air temperature of -22 °C.

Compactness, high efficiency in all the operation and the flexibility to operate over the wide range of tested conditions demonstrate that the developed heat pump could represent an interesting and reliable solution for space heating and domestic hot water production in residential application.

References

[1] L. Pistocchini, A. Storoni, T. Toppi, M. Aprile, and M. Motta, “Development of a compact ammonia-water Gas Absorption Heat Pump,” in *Proceedings International Sorption Heat Pump Conference 2021 - Part II Call 2021*, 2021, pp. 187–191. [Online]. Available: https://depositonce.tu-berlin.de/bitstream/11303/13495/3/Meyer_etal_Proceedings_2021.pdf

[2] R. Scoccia, T. Toppi, M. Aprile, and M. Motta, “Absorption and compression heat pump systems for space heating and DHW in European buildings: Energy, environmental and economic analysis,” *Journal of Building Engineering*, vol. 16, pp. 94–105, Mar. 2018, doi: 10.1016/j.jobe.2017.12.006.

[3] M. Garrabrant, R. Stout, M. Blaylock, and C. Keinath, “Residential and Commercial Capacity Absorption Heat Pumps for Space and Domestic Water Heating Applications,” *IEA Heat Pump Conference*, pp. 1–12, 2017, [Online]. Available: http://hpc2017.org/wp-content/uploads/2017/05/O.4.3.3-Residential-and-Commercial-Capacity-Absorption-Heat-Pumps.pdf

[4] G. Villa, R. Scoccia, T. Toppi, and M. Aprile, “Energy, environmental and economic analysis of electric vapour compression and gas driven absorption heat pumps for single-family houses,” *E3S Web of Conferences*, vol. 312, p. 06001, 2021, doi: 10.1051/e3sconf/202131206001.

[5] M. Garrabrant, R. Stout, C. Keinath, and P. Glanville, “Experimental Evaluation of Low-Cost Gas Heat Pump Prototypes for Building Space Heating,” in *16th International Refrigeration and Air Conditioning Conference*, Jun. 2016. [Online]. Available: http://docs.lib.purdue.edu/iracc/1573

[6] American National Standard/Canadian Gas Association Standard, “ANSI Z21.40.4-1996 Performance Testing and Rating of Gas-fired Air Conditioning and Heat Pump Appliances.” 1996.

[7] P. Glanville, “Field Evaluation of Pre-Commercial Residential Gas Heat Pump Water Heaters,” in *ACEEE Hot Water Forum*, Feb. 2016.

[8] T. Toppi, M. Aprile, M. Guerra, and M. Motta, “Experimental characterization of a newly developed air-source water- ammonia gas absorption heat pump for residential applications,” in *International Sorption Heat Pump Conference*, Mar. 2014, pp. 1–10.

[9] European standard, “EN12309 Gas-fired sorption appliances for heating and/or cooling with a net heat input not exceeding 70kW,” 2014.

[10] B. Dehghan B., T. Toppi, M. Aprile, and M. Motta, “Seasonal performance assessment of three alternative gas-driven absorption heat pump cycles,” *Journal of Building Engineering*, vol. 31, p. 101434, Sep. 2020, doi: 10.1016/j.jobe.2020.101434.

[11] B. A. Phillips, “Development of a high-efficiency, gas-fired, absorption heat pump for residental and small-commercial applications,” United States, 1990. [Online]. Available: https://www.osti.gov/biblio/6004697

[12] A. A. Roeder, A. Goyal, and S. Garimella, “Transient simulation of ammonia–water mixture desorption for absorption heat pumps,” *International Journal of Refrigeration*, vol. 100, pp. 354–367, Apr. 2019, doi: 10.1016/j.ijrefrig.2019.01.032.

[13] G. Villa, T. Toppi, M. Aprile, and M. Motta, “Performance improvement of gas-driven absorption heat pumps by controlling the flow rate in the solution branch,” *International Journal of Refrigeration*, Sep. 2022, doi: 10.1016/j.ijrefrig.2022.09.015.

14th IEA Heat Pump Conference
15-18 May 2023, Chicago, Illinois

A modified effectiveness-based approach in performance prediction of simultaneous heat and mass transfer in heat pump operating conditions

Ruozhou Du[a], Jiabao An[a], Long Huang[a*]

[a]Xi'an Jiaotong-Liverpool University, 111 Ren'ai Road, Suzhou, P. R. China, 215123

Abstract

This paper provides a systematic review of mathematical models for simultaneous heat and mass transfer process modeling. Models were categorized into lumped models, zone models, and numerical methods with information on their computation costs and accuracies. Observing the reviewed models, it was revealed that iterative calculations and complicated analytical corrections on fin efficiency are necessary under fully wet conditions. To provide the explicit calculation for the dehumidification process for micro-channel heat exchangers, regression techniques, like Multiple Polynomial Regression, are applied to modify the effectiveness-NTU method. The improved regression models show advances in accuracy and usability within the common geometries and conditions for heat pump applications.

© HPC2023.
Selection and/or peer-review under the responsibility of the organizers of the 14th IEA Heat Pump Conference 2023.

Keywords: Microchannel Heat Exchanger; Dehumidification; Heat Pump; Modeling

1. Introduction

In recent years, the mathematical models for the pure heat transfer process in heat exchangers are well developed. Classic models like Logarithm Mean Temperature Difference (LMTD) method and the effectiveness-NTU method provide a reasonable level of accuracy under fully dry conditions. However, once dehumidification occurs in the cooling process, the prediction of simultaneous heat and mass transfer becomes complicated while both sensible and latent capacity needs to be calculated. For instance, the traditional LMTD method is unable to calculate the latent heat during the condensation of humid air. To properly model this dehumidification process, various modified models were proposed, which are worth a systematic review to foster further studies. Hence, this article comprehensively summarizes current mathematical models for the dehumidification process within heat exchangers in section 2. The review reveals that iterative calculation and complicated analytical correction on fin efficiencies are contained in most of those models to approach reasonable accuracy, which shows little practical usability for engineers. To tackle this problem, regression-based modified explicit models, for Microchannel Heat Exchangers (MCHXs), are proposed in section 3. Finally, the proposed regression models are assessed and compared with traditional methods in section 4.

2. Review of mathematical models

For the modeling of simultaneous heat and mass transfer processes, [1] and [2] summarized several methods for the dehumidifying process of fin-and-tube heat exchangers, providing comprehensive reviews on this topic. Further, [3] gives a general framework for the categorization of those models. The existing models for simultaneous heat and mass transfer prediction of heat exchangers could be generally classified into three types: the lumped model, distributed parameter model (multi-node/numerical model), and the zone model. The

* Corresponding Author. *E-mail address:* long.huang@xjtlu.edu.cn

lumped models compute the cooling performance based on the lumped parameters, with the advantage of fast calculation. However, the details of the mass transfer process, such as the wetting area along the fin, are not considered. To account for detailed heat and mass transfer processes and approach higher prediction accuracy, numerical models can be used. Those methods tend to compute the cooling capacity of heat exchangers cell by cell. Each cell is treated with lumped parameters. Nevertheless, those methods are usually computationally expensive and hence lack practicality for fast performance predictions. The zone model slots in between lumped models and numerical approaches in terms of accuracy and computational cost. Those approaches divide the heat exchangers into different portions. Each portion is considered a lumped model with distinctive working circumstances. With various partitioning procedures, the calculation accuracy would be improved compared with the overall lumped models, yet the time for computation is reasonable in terms of the numerical methods. Based on these categories, the mainstream methods would be further introduced in the following section.

2.1. Lumped models

Based on the formulation of different models, the lumped models could be further summarized into temperature difference-based, effectiveness-based, and enthalpy difference-based models.

2.1.1. Temperature difference-based models

All the temperature difference-based methods originate from the classic LMTD method. However, modifications have to be introduced since the above equation cannot predict the latent heat. According to [2], the simplest way to modify is by introducing an empirical factor. The empirical factor is expressed as

$$\xi = \frac{i_{a,i} - i_{a,o}}{C_{pa} \cdot \left(T_{a,i} - T_{a,o}\right)} \tag{1.}$$

The empirical factor transfers the temperature difference into the enthalpy difference to cover the evaluation of latent heat. Although this is a quick method, the empirical factor may vary along the dehumidification process and a large deviation may be caused by that. Concerning that, McQuiston [4] introduced the condensation factor into the overall heat transfer coefficient with a similar idea. The condensation factor is defined as

$$C_f = \frac{w_a - w_{sat,w}}{T_a - T_w} \tag{2.}$$

The essence of this modification is unifying the sensible heat term and latent heat term in the energy equation and expressing sensible and latent heat by temperature difference.

Several publications modify the temperature difference as well. To reduce the complexity brought by the condensation, the researchers transfer the dehumidification into the equivalent dry cooling process based on the constant enthalpy difference [5], which is named as Equivalent Dry-bulb Temperature (EDT) method. In detail, the dehumidification process 1-2 in the following figure is converted into the 1e-2e process, which owns the constant humidity ratio. The transfer process is shown in Figure 1.

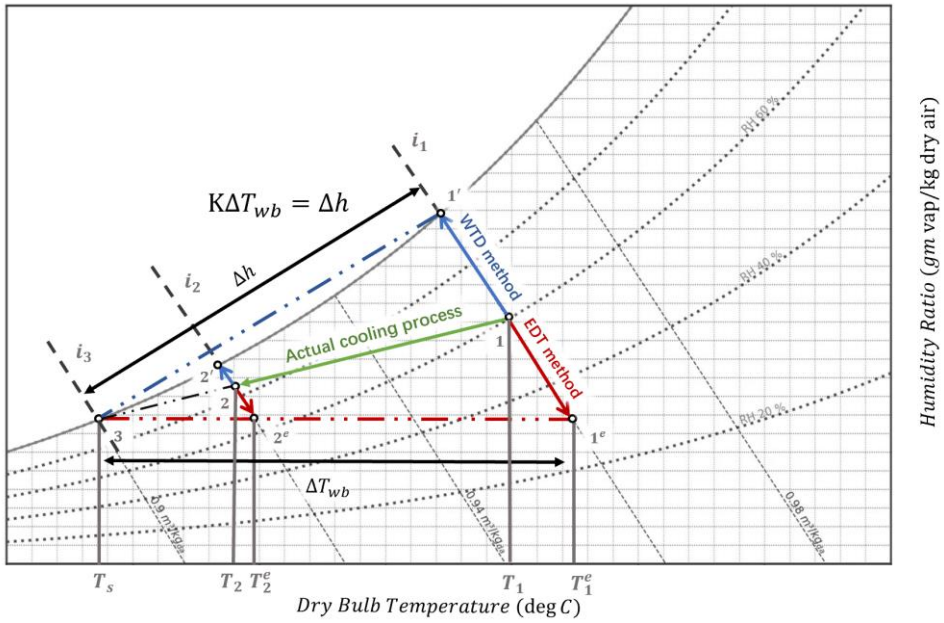


Figure 1 psychrometric charts for illustrating the assumptions of WTD method and the equivalent process of EDT method

Mathematically, the transformation of the heat transfer equation is

$$Q_t = \frac{h_{\text{wet}}A}{C_{\text{pa}}}\left(\frac{i_1 + i_2}{2} - i_{\text{w}}\right) = \frac{h_{\text{wet}}A}{C_{\text{pa}}}\left(\frac{i_1^e + i_2^e}{2} - i_{\text{w}}\right) \approx h_{\text{wet}}A\left(\frac{T_1^e + T_2^e}{2} - T_{\text{w}}\right) \quad (3.)$$

The other similar approach, namely Wet-bulb Temperature Difference (WTD) method [6]. This method was originally proposed for the indirect evaporative heat exchangers, aiming to transfer the enthalpy potential on the side of secondary air into the wet-bulb temperature difference. Considering point 1 in Figure 1 as the inlet of secondary air and point 2 as the outlet, those blue lines schematically exhibit this transformation. This method is based on two assumptions. The first is the linear variation assumption between saturated enthalpy difference and wet-bulb difference (shown as Eq.(4)).

$$K = \frac{\Delta i}{\Delta T_{wb}} \quad (4.)$$

The other one is assuming the lines 1' 2' and 1'3 in Figure 1 share the same value of K to simplify the derivation. Based on those two assumptions, the total heat transfer rate, for a parallel-flow configuration, is modified as

$$Q_t = U_{WTD}A\frac{\left(T_{pr}^{\text{i}} - T_{sc,wb}^{\text{i}}\right) - \left(T_{pr}^{\text{o}} - T_{sc,wb}^{\text{o}}\right)}{\ln\frac{T_{pr}^{\text{i}} - T_{sc,wb}^{\text{i}}}{T_{pr}^{\text{o}} - T_{sc,wb}^{o}}} \quad (5.)$$

Even though this approach is launched from air-to-air evaporators, the air-to-coolant heat exchangers could also use the same idea to rewrite the air-side transfer equation and re-derive Eq. (5) correspondingly.

2.1.2. Effectiveness-based models

As a classic predicting method, Braun[7] stated the effectiveness-NTU method for predicting fully dry conditions,

$$Q_d = \varepsilon_d \dot{m}_a C_{pa}\left(T_{a,i} - T_{w,i}\right) \quad (6.)$$

While under fully wet conditions, the total heat transfer rate is calculated by the enthalpy potential,

$$Q_t = \varepsilon_{wet}\dot{m}_a\left(i_{a,i} - i_{s,w,i}\right) \quad (7.)$$

The effectiveness in Eq. (6) and Eq. (7) is varied in different cases since it is a function of NTU, configurations of heat exchangers, etc. Hence, several basic derivations for effectiveness in different flow

arrangements under fully dry conditions are given by [8] and properly summarized in [9]. Additionally, to facilitate the use of effectiveness, some scholars also put efforts into simplifying the forms of effectiveness through a linear approximation between effectiveness and heat capacity rate ratio [10].

2.1.3. Enthalpy difference-based models

The classic LMED method for the dehumidifying condition was mentioned in several publications [11]–[13]. For instance, the cooling performance for Fin-and-Tube Heat Exchangers (FTHE), using LMED, is calculated as [2]

$$Q_t = U_{LMED} A_{total} \Delta i_{lm} \tag{8.}$$

$$\frac{1}{U_{LMED}} = \frac{b'_r A_t}{h_c A_{w,in}} + \frac{b'_p A_t \ln\left(\frac{D_{out}}{D_{in}}\right)}{2\pi k_w L_w} + \frac{A_t}{h_a \left(\frac{A_{w,in}}{b'_{w,p}} + \frac{\eta_{f,wet} A_f}{b'_{w,f}}\right)} \tag{9.}$$

The $b'_r, b'_p, b'_{w,p}, b'_{w,f}$represent the linear coefficients between saturated enthalpy differences and temperature differences, normally iterative calculations are needed to obtain accurate values. Detailed calculation procedures are given in [11]. According to Xia et al [14], the above LMED expression assumes the Lewis number as unity, which may cause deviations. Therefore, they fundamentally re-formulated the LMTD method to adapt the non-unity cases.

2.2. Zone models

As mentioned before, the zone models are mainly built on the concept of effectiveness and the major discrepancy is in the wet-dry boundary identification. For instance, [15] re-derived the correlations of effectiveness and NTU for counter-flow DX evaporators. The new correlations are integrated into the dry or wet area under partially wet conditions. Therefore, with the additional constraint from the dew point temperature of inlet air when computing the position of the boundary, the equation set can be closed and the areas of wet and dry could be obtained using those re-derived correlations.

Except for the above methods, another proposed explicit zone model is called Equivalent-Capacitance Approach (ECA) [16]. They found an alternative form for the LTMD method and it could avoid iterative calculation without introducing any further assumptions. Utilizing explicit expressions, they considered the two critical conditions, the just-dry-condition and the just-wet condition for coiling coils [17]. With the energy balances and the assumption of the surface temperature at the boundary is equivalent to the dew point temperature of inlet air, the critical coolant temperatures could be obtained. Comparing the two critical inlet refrigerant temperatures at just-dry-condition and just-wet-condition with actual inlet coolant temperature, the coil could be explicitly decided whether it is the fully wet, partially wet, or fully dry mode. Meanwhile, to partition the dry region into partially wet conditions, they formed an empirical correlation to maintain the explicit calculation.

Except for segmenting the heat exchangers from the airside, due to the phase change of the coolant, some publications proposed methods to separate the sub-cooling, saturation, and superheated regions on the refrigerant side. [18] developed the explicit methods of identifying those three portions through the calculation of volume fraction corresponding to the condensers, evaporators, and air coolers. In addition, [19] further divided the saturation region into region 1 and region 2, which was decided from the experiments. With the other two regions, the paper suggests a separate calculation for each portion through the effectiveness-NTU method and energy conservation equations and iteratively repeats the calculation process until the entire system meets the energy balance.

2.3. Numerical models

The numerical methods indicate the procedure that divides the heat exchangers into a large number of small cells and calculates them independently with basic governing equations. The numerical methods own high flexibility and accuracy on simulations, with the drawback of high computational expense. However, some numerical models would introduce some lumped parameters, such as the fin efficiency, to reduce the calculation time while maintaining reasonable accuracy, which is summarized as the semi-numerical models.

2.3.1. Semi-numerical models

The semi-numerical models introduced in this section indicate the methods that separate the entire heat exchangers into various segments and each segment could be considered as a small independent heat exchanger and is evaluated by lumped parameters. One representative semi-numerical model would be the Finite-Circular Fin Method (FCFM). FCFM originated from [20], they tend to evaluate the dehumidifying process of fin-and-tube heat exchangers segment-by-segment and each segment is equivalently considered as a fraction of a coil with a circular fin. The cooling performance is calculated by lumped LMED method, mentioned in section 2.1.2.

Consequently, they extend this method into the fully dry condition [21]. Distinguishing from the fully wet mode, the actual temperature difference is used. Noticing that the fin efficiency used in FCFM for the equivalent circular fin is derived in [22], for both fully dry and fully wet circumstances. In 2008, they added the evaluation to the partially wet condition using FCFM [23], a complicated analytical circular fin efficiency for partially wet conditions formulated by them. Later, as a comparison, FCFM was combined with the aforementioned EDT method to perform the calculation [24]. It was found that the FCFM based on the EDT method shows higher heat and mass transfer characteristics.

[25] also proposed the element-based approach according to the effectiveness-NTU method. It divides the cross-flow heat exchangers into many tiny elements. Each element is calculated independently. This discretizing method would provide higher simulation flexibility compared with the FCFM method.

2.3.2. Numerical models

To eliminate the use of fin efficiency in semi-numerical models, the grids on the fins are generated and each grid is calculated by basic governing equations. Based on this concept, a straightforward numerical method, named as Semi-explicit Method for Wall Temperature Linked Equations (SEWTLE), is proposed [26]. To provide a general numerical approach for any heat exchangers with complex geometry, this method focuses on describing the heat transfer during fluid cells (air cells or refrigerant cells) and wall cells (fin cells or tube wall cells). The governing equations are

$$\dot{m}_{flu} C_{p,flu} dT_{flu} = \sum_{j=1}^{\mathrm{n}} U_{local} \left(T_{\mathrm{w,cell}} - T_f\right) dA_{cell} \qquad (10.)$$

n represents the number of wall cells surrounding the fluid cells. The heat conduction along the wall cells by the two-dimension Laplace equation

$$\nabla\left(k_{local} t_{local} \nabla T_{\mathrm{w,cell}}\right) + \sum_{i=1}^{2} U_{local} \left(T_{\mathrm{w,cell}} - T_f\right) dA_{cell} = 0 \qquad (11.)$$

Eq. (10) could solve the fluid temperatures based on adjacent wall cell temperatures and Eq. (11) could obtain the wall cell temperatures based on neighboring temperatures of wall cells and fluid cells. Therefore, an iterative calculation would be performed once initial guess values are given to wall cells.

However, the mass transfer prediction for the dehumidifying condition was missed in SEWTLE. Therefore, [27] extend the application range of the original SEWTLE method into the fully wet condition and re-named it Fin2D-W. Further, the superheated region on the coolant side was also concerned in later research [28]. However, due to the heavy computation issue of this method, they applied the Fin theory on the fin cells to ease the computation process and therefore developed a new model called Fin2B-MB [29]. According to the authors, the introduction of fin theories would make the model overpredict the latent heat transfer rate by about 2%, and underpredict the sensible heat transfer rate by 4%.

Another constraint of the SEWTLE is its inconvenience in evaluating the irregular geometry boundary, such as the edge of holes on the fin. To improve the model feasibility on this issue, [30] mentioned a 2D model, which introduced several coefficients for irregular grids and changed the discretizing form of the 2D Laplace equation, making it could express irregular grids at boundaries.

3. Regression model development

Except for those models derived from classic methods, statistical tools also could be used for the predictions of the thermal behavior of heat exchangers. According to [31], serval types of techniques are widely applied for the statistical modeling of cooling systems, including the Artificial Neuron Network (ANN), Genetic Programming (GA), Multiple Linear Regression (MPR), etc. [32] specifically pointed out the basic regression

analysis that can be used, such as the linear/nonlinear regression, the multiple polynomial regression, and the stepwise regression, etc. Further, they gave a representative example of utilizing the MPR analysis on the cooling system. In this case, to maintain acceptable model accuracy, they chose the 8th degree during the regression, which causes 494 terms in the model. It is believed that the usability of this model is reduced by the enormous amount of terms. As a comparison, several studies developed regression models with fewer terms, yet fewer input variables [33]–[35]. In regard, another type of strategy to perform the regression is integrating heat transfer equations. For instance, combining several basic governing equations in non-dimensional forms, [36] proposed simpler performance correlations for indirect evaporative heat exchangers, expressed by Eq. (12).

$$\mathrm{T_{c,o}} = \psi \cdot \Pi_1^a \cdot \Pi_2^b \cdot \Pi_3^c \tag{12}$$

ψ, a, b, c are empirical coefficients and Π_1, Π_2, Π_3 are the derived dimensionless parameters.

This type of methodology can be also utilized in the present study. In Section 2, it becomes evident that the majority of dehumidification models require iterative calculations, which increases the computational load for real-time simulation of thermodynamic cycle systems. Additionally, the fin efficiency, which is formulated based on rectangular fin geometry, cannot perfectly suit MCHX due to the assumption of the adiabatic boundary at the middle height of the fin. As result, it causes a deviation in the prediction of heat capacity under both fully wet and dry conditions. To address the raised computational load in fully wet conditions and the accuracy limitations brought about by analytical fin efficiency, a regression-based modification has been made to the explicit effectiveness model under fully wet/dry conditions for two-phase refrigerant in this section. The regression is based on the dataset generated by the numerical model Fin2D-W mentioned in section 2.3.2. The explicit effectiveness-based models for the fully wet and dry conditions are stated in section 3.1 and section 3.2 respectively. In section 3.3, the selected regression variables and corresponding ranges are described to elaborate on the application range of the proposed model.

3.1. Explicit model for fully dry condition

For the pure heat transfer process of MCHX, the classic effectiveness-NTU model is used. With two-phase refrigerant, the effectiveness is described as

$$\varepsilon = 1 - \exp(-NTU_t) \tag{12.}$$

where

$$C_r = \frac{C_{min}}{C_{max}}$$

$$NTU_t = \frac{U_t A_t}{\dot{m}_a C_{pa}}$$

$$U_t = \frac{1}{\left(\frac{1}{h_c} + \frac{t_f}{k_w}\right)\left(\frac{A_t}{A_{f,t}}\right) + \frac{1}{\eta_{sf,d} h_a}}$$

The overall surface efficiency is calculated as

$$\eta_{sf,d} = 1 - \frac{A_{f,t}}{A_t}\left(1 - \eta_{f,d}\right) \tag{13.}$$

Therefore the Q_t is calculated by

$$Q_t = \varepsilon_d \dot{m}_a C_{pa}\left(T_{r,i} - T_{a,i}\right) \tag{14.}$$

To improve the prediction accuracy, efficiency is the regression objective so that the temperature profile along the fin can be better described within the selected variable ranges.

3.2. Explicit model for fully wet condition

To perform an explicit calculation procedure for fully wet conditions, the expression for total heat transfer rate is re-derived as Eq. (15).

$$Q_t = \varepsilon_m \dot{m}_a (i_{a,i} - i_{s,r}) \quad (15.)$$

where

$$\varepsilon_m = \frac{1}{\frac{1}{\varepsilon} + \frac{c_s \dot{m}_a}{\alpha_i A_i}}$$

$$\varepsilon = \left(1 - \exp\left(-\frac{\alpha_o \eta_{sf,wet} A_o}{\dot{m}_a C_{pa}}\right)\right)$$

$$\eta_{sf,wet} = 1 - \frac{A_{f,t}}{A_t}(1 - \eta_{f,wet})$$

$$c_s = \frac{(i_{sat,f} - i_{sat,r,i})}{(T_w - T_r)}$$

And the sensible heat transfer is obtained by Eq. (16).

$$Q_s = \left(1 - \exp\left(-\frac{\alpha_o \eta_{s,wet} A_o}{\dot{m}_a C_{pa}}\right)\right) \dot{m}_a C_{pa} (T_{a,i} - T_f) \quad (16.)$$

Naturally, to formulate the explicit calculation process, c_s has to be regressed based on the input parameters. To provide sufficiently accurate c_s, the MPR technique is selected. In addition, to describe the enthalpy profile and temperature profile more accurately, η_f used in Eq. (15) for the calculation of Q_t and η_f used in Eq. (16) for the calculation of Q_s are independently regressed. the regression results are exhibited in section 3.4. Overall, the explicit calculation procedure is **(i)** calculate the Q_t by Eq. (16), with regressed c_s and $\eta_{f,w}$ for total heat transfer rate, **(ii)** calculate the tube wall temperature by Eq. (17), **(iii)** lastly calculate the Q_s by Eq. (16), with the regressed fin efficiency $\eta_{f,w}$ for the calculation of Q_s.

$$T_w = \frac{Q_t}{h_c A_i} + T_{ref} \quad (17.)$$

3.3. Selection of variables and ranges

To cover most of the influential input variables, nine inputs are selected to design the experiments for dry conditions and ten variables for wet conditions. Selected variables include the mass flow rate of coolant $\dot{m}_r$, the air velocity v_a, the inlet air temperature $T_{a,i}$, the inlet refrigerant temperature $T_{r,i}$, the Relative humidity of inlet air RH, the fin depth L_f and the fin height H_f, the Air-side Heat Transfer Coefficient (AHTC), expressed by h_a, Refrigerant-side Heat Transfer Coefficient (RHTC), expressed by h_c and the half spacing of the MCHX is denoted as hs. All the selected variables are illustrated in Figure 2(a). The input variable RH is ignored under fully dry conditions.

Due to the substantial time cost of the Fin2D-W model, A 5-level 1/8 fractional factorial circumscribed Central Composite Design (CCD) is utilized to minimize the simulation time and optimize the regression results. The travel distance α between the axial point and central point is set at the value of 3.3636. 147 experiments are generated for dry condition simulation and 149 cases are generated for fully wet conditions. The relations between coded levels and actual levels, as well as selected input variables and corresponding ranges, are listed in Table 1. The value of the AHTC for each case is determined by the simple heat transfer correlation form provided by Wang and Chang [38], which is shown as

$$j = 0.425 Re_{Lp}^{-0.496} \quad (18.)$$

Since the prediction results of Eq. (18) are more moderate compared with the final equation in [38] and the correlation for plain fins provided by [39], meaning a wider range of fin geometry could be represented by the prediction. In terms of the RHTC, it is determined based on [40] for two-phase refrigeration flow boiling and based on [41] for condensing refrigerant flow. Moreover, to extend the range of AHTC and RHTC that contains in this regression, coefficients between 0.5-1.5 are multiplied before they are used in the calculation, which is

explained by Eq. (19) and (20). In other words, all the values of AHTC and RHTC randomly fluctuated by about ±50%. Those coefficients of AHTC and RHTC for cases are shown in Table 1.

$$h_c{}' = C_{RHTC} \times h_c \quad (19.)$$

$$h_a{}' = C_{AHTC} \times h_a \quad (20.)$$

Table 1. input variables and relations between coded level and actual level for CCD

General input variables						
Input variables	Unit	Five Coded levels				
		$-\alpha$	-1	0	1	α
$\dot{m}_r$	kg/s	3e-4	6.041e-4	1.05e-3	1.496e-3	1.8e-3
v_a	m/s	0.5	0.9054	1.5	2.0946	2.5
RH	$-$	0.4	0.5216	0.7	0.8784	1
L_f	m	0.015	0.017	0.02	0.023	0.025
H_f	m	0.008	0.0088	0.01	0.0112	0.0120
C_{RHTC}	$-$	0.5	0.7027	1	1.2973	1.5
C_{AHTC}	$-$	0.5	0.7027	1	1.2973	1.5
hs	m	1.1250e-4	1.8669e-4	2.9550e-4	4.0431e-4	4.7850e-4
Specified input temperatures for the fully wet condition with two-phase refrigerant						
$T_{r,i}$	K	277.15	278.37	280.15	281.93	283.15
$T_{a,i}$	K	293.15	295.18	298.15	301.12	303.15
Specified input temperatures for the fully dry condition with two-phase refrigerant						
$T_{r,i}$	K	323.15	327.20	333.15	339.10	343.15
$T_{a,i}$	K	303.15	305.18	308.15	311.12	313.15

Meanwhile, the test dataset, for the validation of regression models, is generated randomly within the ranges listed in Table 1. 24 cases for the test dataset are picked, as roughly 20% of the training dataset for both dry and fully wet conditions.

4. Result and discussion

In this section, the regression results are listed, and the performance concerning the calculation time and prediction accuracy are elaborated.

4.1. Regression results

(a) Fully wet conditions

The wet fin efficiency η_{Qt} used in the calculation of Q_t is obtained by Eq. (47)

$$\eta_{Qt} = \eta_{wet}^{\mu_1} \quad (21.)$$

where

$$\eta_{wet} = \frac{\tanh(mH_f)}{mH_f}$$

$$m = \sqrt{\frac{2.1493\alpha_o}{k_w t_f}}$$

$$\mu_1 = 1.7290\xi_1 + 0.2301\xi_1^2$$

$$\xi_1 = \left(\frac{\alpha_o}{\alpha_i}\right)^{0.0365}\left(\frac{H_f}{L_f}\right)^{-0.1418}\left(\frac{hs}{L_f}\right)^{0.1594}\left(\frac{T_{a,i}}{T_r}\right)^{-0.3249}\left(\frac{\rho_a V_a H_f hs}{\dot{m}_r}\right)^{-0.0331}(RH)^{0.0983}$$

It should be noted that the regression basis η_{wet}, which pertains to fully wet conditions, maintains a similar form to the analytical solution under dry conditions due to its superior predictive performance when compared to other forms. In terms of the wet fin efficiency used in the calculation of Q_s,

$$\eta_{Qs} = \eta_{wet}^{\mu_2} \tag{22.}$$

where

$$\mu_2 = -0.8904\xi_2 + 2.2120\xi_2^2$$

$$\xi_2 = \left(\frac{H_f}{L_f}\right)^{-0.0921}\left(\frac{hs}{L_f}\right)^{0.0742}\left(\frac{T_{a,i}}{T_r}\right)^{2.2396}\left(\frac{\rho_a V_a H_f hs}{\dot{m}_r}\right)^{-0.0138}(RH)^{0.2792}$$

The regression results of c_s that are regressed in the form of MPR are exhibited in the Appendix.

(b) Fully dry conditions

The analytical dry efficiency expression is still maintained as Eq. (23).

$$\eta_d = \frac{\tanh\left(\frac{mH_f}{2}\right)}{\frac{mH_f}{2}} \tag{23.}$$

$$m = \sqrt{\frac{2\alpha_o}{k_w t_f}}$$

Yet the modified fin efficiency for the single-phase refrigerant is shown as

$$\eta_{m,d} = \eta_d^{\mu_3} \tag{24.}$$

Meanwhile, the modifications that apply to the two-phase flow are exhibited as follows.

$$\mu_3 = 1.9307\xi_2 + 2.2470\xi_2^2 \tag{25.}$$

where

$$\xi_3 = \left(\frac{\alpha_o}{\alpha_i}\right)^{0.0670}\left(\frac{H_f}{L_f}\right)^{-0.3489}\left(\frac{hs}{L_f}\right)^{0.1753}\left(\frac{T_{a,i}}{T_r}\right)^{1.4307}\left(\frac{\rho_a V_a H_f hs}{\dot{m}_r}\right)^{-0.1094}$$

4.2. Model assessment

The prediction performance is assessed based on two indexes, the Mean Absolute Error (MAE) and Maximum Error (ME) of training/test datasets, which are shown in Eq. (25) and (26). The performances are exhibited in Tables 2 and 3 for fully dry and fully wet conditions accordingly. Note that the single potential effectiveness-NTU model is used, which is stated in [33].

$$\text{MAE} = MEAN\left(\frac{\left|Q_{num,i} - Q_i\right|}{Q_{num,i}}\right) \tag{26.}$$

$$\text{ME} = MAX\left(\frac{\left|Q_{num,i} - Q_i\right|}{Q_{num,i}}\right) \tag{27.}$$

Based on the test results presented in Table 2, it is evident that the developed regression model exhibits advance in prediction accuracy for two-phase flow conditions. The MAE and ME are improved by 0.1% and 0.3%, respectively. The developed model also shows superior prediction accuracy for dehumidification processes in two-phase refrigerant conditions. For the three types of heat transfer rates, the developed model

shows the advances at both MAE and ME, where the prediction of the sensible heat transfer rate is improved the most. For the sensible heat transfer rate, the MAE is reduced by about 1.2%, while the ME is improved by about 3%.

Furthermore, the developed model exhibits a faster computational process compared to iterative effectiveness-NTU, as shown in Table 4. In a nutshell, the present model is roughly 3 times quicker on average in two-phase refrigerant conditions for calculating one case, compared to effectiveness-NTU. The data presented in Table 4 is gained from the first hundred cases in the training datasets.

Table 2 performances of models in the test dataset under fully dry condition

Models	Two-phase (24 cases)	
	MAE (%)	ME (%)
Present model	0.74	1.99
Effectiveness-NTU	0.88	2.35

Table 3 performances of models in test dataset under fully wet condition

Models		Two-phase (24 cases)	
		MAE (%)	ME (%)
Present model	Q_t	0.54	1.44
	Q_s	0.47	1.13
	Q_l	0.72	2.27
Effectiveness-NTU	Q_t	0.95	3.36
	Q_s	1.69	4.34
	Q_l	0.99	4.88

Table 4 calculation time comparison of models

		Fully wet with two-phase (s)
Present model	Max time	2.4e-3
	Average time	1.3e-3
Effectiveness-NTU	Max time	1.1e-2
	Average time	4.6e-3
Numerical Fin2D-W	Max time	2.22e+3
	Average time	4.09e+2

5. Conclusions

This paper systematically reviews the mathematical models for the prediction of the dehumidification process. Three types of models are classified, and each has its characteristics of computational cost and accuracy. Based on the review models, it is found that most models in wet conditions require iteration computations and complicated correction on fin efficiency based on various geometries. To improve the usability of dehumidification prediction models, fully wet and fully dry explicit models for two-phase refrigerants are proposed based on the analytical effectiveness-NTU method. The regressions are carried out in a wide range of air and refrigerant side conditions, as well as commonly used geometric parameter ranges. Three main advantages of the proposed models are the explicit calculation for dehumidification calculation with improved accuracy as compared with traditional lumped models.

The research carried out here should benefit the academic and engineering communities with the need to conduct fast heat and mass transfer analysis for MCHX in heat pump applications. The regression methods presented here can be employed in the future as part of heat exchanger optimization studies for a wider range of conditions and geometries.

Nomenclature

A	area [m^2]	k	thermal conductivity
b'_p	slope of the air saturation curve between the outside and inside tube wall temperature	ζ_2	regression coefficient for fin efficiency modification
b'_r	slope of the air saturation curve between the mean water temperature and the inside wall temperature	$\dot{m}$	mass flow rate of air [Kg/s]
$b'_{w,f}$	slope of the saturated moist air enthalpy curve at the mean water film temperature of fin surface	L_w	tube length
$b'_{w,p}$	slope of the saturated moist air enthalpy curve at the mean water film temperature of pipe outer-wall surface	L_f	fin depth, exhibit in Figure 2.
C_f	condensation factor [Kg/K]	L_p	louver pitch
C_{pa}	air specific heat capacity [KJ/kg/K]	n	the number of wall cells surrounding the fluid cells
C_s	rate of change of the specific enthalpy with temperature along the saturated air line [kJ kg-1 K-1]	NTU	Heat transfer unit
C_r	Heat Capacity Ratio	Q	heat transfer rate [KJ/Kg]
D	tube diameter	Re_{Lp}	Reynolds number based on louver pitch, defined by $G * L_p/\nu$
H_f	fin height, exhibit in Figure 2.	RH	relative humidity of the inlet air, exhibit in Figure 2
hs	half spacing of the fin, exhibit in Figure 2	T	temperature [K]
h	heat transfer coefficient [W m−2 K−1]	t	fin thickness [m]
i	enthalpy [KJ]	U	overall heat transfer coefficient [W m−2 K−1]
j	the Colburn factor	ν	viscosity [Pa s]
K	slope defined by Eq. (4)	v_a	Velocity of the air [m s-1]
β	parameter defined by Eq. (22)	w	humidity ratio [Kg]
γ	regression coefficient for dry condition modification, defined by Eq. (19)	η	Surface or fin efficiency
ε	effectiveness	ξ	empirical factor [-]

Subscript	Description	**Subscript**	Description
$AHTC$	air-side heat transfer coefficient	$RHTC$	refrigerant-side heat transfer coefficient
a	air	c	coolant
cell	at this cell	**s**	sensible
d	dry	sat	saturated
f	fin	sc	secondary air for indirective evaporators

flu	at a Fluid cell	t	total
i	inlet	WTD	for wet-bulb temperature difference method
in	inside	w	wall
$local$	at local position	wb	wet-bulb
o	outlet	$\mathbf{wet}$	under wet condition
out	outside	$\mathbf{1}$	inlet
pr	primary air for indirective evaporators	$\mathbf{2}$	outlet
sf	surface		

Superscript	Description
e	element
$\mathbf{i}$	inlet
$\mathbf{o}$	outlet

Acknowledgements

This work was supported by the Natural Science Foundation of the Higher Education Institutions of Jiangsu Province, China (Grant No. 21KJB470011), State Key Laboratory of Air-conditioning Equipment and System Energy Conservation Open Project (Project No. ACSKL2021KT01) and the Xi'an Jiaotong-Liverpool University Research Development Fund (RDF 20-01-16).

References

[1] W. Pirompugd, C. C. Wang, and S. Wongwises, "A review on reduction method for heat and mass transfer characteristics of fin-and-tube heat exchangers under dehumidifying conditions," *International Journal of Heat and Mass Transfer*, vol. 52, no. 9–10, pp. 2370–2378, Apr. 2009, doi: 10.1016/j.ijheatmasstransfer.2008.10.019.

[2] G. Zhang, B. Wang, X. Li, W. Shi, and Y. Cao, "Review of experimentation and modelling of heat and mass transfer performance of fin-and-tube heat exchangers with dehumidification," *Applied Thermal Engineering*, vol. 146. Elsevier Ltd, pp. 701–717, Jan. 05, 2019. doi: 10.1016/j.applthermaleng.2018.10.032.

[3] G. liang Ding, "Recent developments in simulation techniques for vapour-compression refrigeration systems," *International Journal of Refrigeration*, vol. 30, no. 7. pp. 1119–1133, Nov. 2007. doi: 10.1016/j.ijrefrig.2007.02.001.

[4] F. C. Mcquiston, "Fin efficiency with combined heat and mass transfer," 1975.

[5] J. Wang and E. Hihara, "Prediction of air coil performance under partially wet and totally wet cooling conditions using equivalent dry-bulb temperature method," 2003. [Online]. Available: www.elsevier.com/locate/ijrefrig

[6] X. Cui, K. J. Chua, M. R. Islam, and W. M. Yang, "Fundamental formulation of a modified LMTD method to study indirect evaporative heat exchangers," *Energy Conversion and Management*, vol. 88, pp. 372–381, 2014, doi: 10.1016/j.enconman.2014.08.056.

[7] J. E. Braun, S. A. Klein, and J. W. Mitchell, "Effectiveness models for cooling tower and cooling coils," 1989.

[8] D. Taler, *Numerical Modelling and Experimental Testing of Heat Exchangers*, vol. Volume 161. Polish Academy of Sciences, 2019. [Online]. Available: http://www.springer.com/series/13304

[9] G. Zhou, Y. Ye, W. Zuo, X. Zhou, and X. Wu, "Fast and efficient prediction of finned-tube heat exchanger performance using wet-dry transformation method with nominal data," *Applied Thermal Engineering*, vol. 145, pp. 133–146, Dec. 2018, doi: 10.1016/j.applthermaleng.2018.09.020.

[10] R. Laskowski, "The concept of a new approximate relation for exchanger heat transfer effectiveness for a cross-flow heat exchanger with unmixed fluids. *Journal of Power Technologies* 91 (2) (2011) 93-101 The concept of a new approximate relation for exchanger heat transfer effectiveness for a cross-flow heat exchanger with unmixed fluids." [Online]. Available:

https://www.researchgate.net/publication/266289611
[11] C.-C. Wang, Y.-C. Hsieh, and Y.-T. Lin, "Performance of Plate Finned Tube Heat Exchangers Under Dehumidifying Conditions," 1997. [Online]. Available: http://heattransfer.asmedigitalcollection.asme.org/
[12] X. Ma, G. Ding, Y. Zhang, and K. Wang, "Airside characteristics of heat, mass transfer and pressure drop for heat exchangers of tube-in hydrophilic coating wavy fin under dehumidifying conditions," *International Journal of Heat and Mass Transfer*, vol. 52, no. 19–20, pp. 4358–4370, Sep. 2009, doi: 10.1016/j.ijheatmasstransfer.2009.03.066.
[13] Q. Liu, J. Liu, L. Zhang, and X. Xu, "Effect of environmental pressure on heat and mass transfer characteristics for fin-and-tube heat exchangers under non-unit Lewis factor," *Applied Thermal Engineering*, vol. 116, pp. 784–791, 2017, doi: 10.1016/j.applthermaleng.2017.01.093.
[14] L. Xia, M. Y. Chan, S. M. Deng, and X. G. Xu, "A modified logarithmic mean enthalpy difference (LMED) method for evaluating the total heat transfer rate of a wet cooling coil under both unit and non-unit Lewis Factors," *International Journal of Thermal Sciences*, vol. 48, no. 11, pp. 2159–2164, Nov. 2009, doi: 10.1016/j.ijthermalsci.2009.04.002.
[15] M. K. Mansour and M. A. Hassab, "Novel lumped modelling for determining thermal performance of DX evaporator under partially-wet and fully-wet conditions," *Applied Thermal Engineering*, vol. 98, pp. 1025–1035, Apr. 2016, doi: 10.1016/j.applthermaleng.2015.12.094.
[16] C. K. Lee and H. Nam, "An equivalent-capacitance approach for determining the performance of a refrigerant coil," in *Progress in Sustainable Energy Technologies Vol II: Creating Sustainable Development*, Springer International Publishing, 2014, pp. 421–429. doi: 10.1007/978-3-319-07977-6_28.
[17] C. K. Lee, "A simplified explicit model for determining the performance of a chilled water cooling coil," *International Journal of Refrigeration*, vol. 43, pp. 167–175, 2014, doi: 10.1016/j.ijrefrig.2014.04.003.
[18] C. K. Lee and H. N. Lam, "Simplified explicit calculation algorithms for determining the performance of refrigerant coils in vapour-compression systems," *International Journal of Refrigeration*, vol. 38, no. 1, pp. 178–188, Feb. 2014, doi: 10.1016/j.ijrefrig.2013.08.023.
[19] Y. T. Ge and R. Cropper, "Performance evaluations of air-cooled condensers using pure and mixture refrigerants by four-section lumped modelling methods," *Applied Thermal Engineering*, vol. 25, no. 10, pp. 1549–1564, Jul. 2005, doi: 10.1016/j.applthermaleng.2004.10.001.
[20] W. Pirompugd, S. Wongwises, and C. C. Wang, "A tube-by-tube reduction method for simultaneous heat and mass transfer characteristics for plain fin-and-tube heat exchangers in dehumidifying conditions," *Heat and Mass Transfer*, vol. 41, no. 8, pp. 756–765, Jun. 2005, doi: 10.1007/s00231-004-0581-x.
[21] W. Pirompugd, C. C. Wang, and S. Wongwises, "A fully wet and fully dry tiny circular fin method for heat and mass transfer characteristics for plain fin-and-tube heat exchangers under dehumidifying conditions," *J Heat Transfer*, vol. 129, no. 9, pp. 1256–1267, Sep. 2007, doi: 10.1115/1.2739589.
[22] K. T. Hong and R. L. Webb, "Calculation of fin efficiency for wet and dry fins," *HVAC and R Research*, vol. 2, no. 1, pp. 27–41, 1996, doi: 10.1080/10789669.1996.10391331.
[23] W. Pirompugd, C. C. Wang, and S. Wongwises, "Finite circular fin method for wavy fin-and-tube heat exchangers under fully and partially wet surface conditions," *International Journal of Heat and Mass Transfer*, vol. 51, no. 15–16, pp. 4002–4017, Jul. 2008, doi: 10.1016/j.ijheatmasstransfer.2007.11.049.
[24] W. Pirompugd, C. C. Wang, and S. Wongwises, "The New Mathematical Models for Plain Fin-and-Tube Heat Exchangers with Dehumidification," *Journal of Heat Transfer*, vol. 137, no. 3, Mar. 2015, doi: 10.1115/1.4029037.
[25] H. A. Navarro and L. C. Cabezas-Gómez, "Effectiveness-NTU computation with a mathematical model for cross-flow heat exchangers," vol. 24, no. 04, pp. 509–521, [Online]. Available: www.abeq.org.br/bjche
[26] J. M. Corberán, P. F. de Córdoba, J. Gonzálvez, and F. Alias, "Semiexplicit method for wall temperature linked equations (SEWTLE): A general finite-volume technique for the calculation of complex heat exchangers," *Numerical Heat Transfer, Part B: Fundamentals*, vol. 40, no. 1, pp. 37–59, Jul. 2001, doi: 10.1080/104077901300233596.
[27] A. H. Hassan, S. Martinez-Ballester, and J. Gonzalvez-Macia, "A comparative study between a two-dimensional numerical minichannel evaporator model and a classical effectiveness–NTU approach under different dehumidifying conditions," *Science and Technology for the Built Environment*, vol. 21, no. 5, pp. 681–692, 2015, doi: 10.1080/23744731.2015.1028866.
[28] A. Hussein Hassan, S. Martínez-Ballester, and J. Gonzálvez-Maciá, "Two-dimensional numerical modelling for the air-side of minichannel evaporators accounting for partial dehumidification

scenarios and tube-to-tube heat conduction," *International Journal of Refrigeration*, vol. 67, pp. 90–101, Jul. 2016, doi: 10.1016/j.ijrefrig.2016.04.003.

[29] A. H. Hassan, S. Martínez-Ballester, and J. Gonzálvez-Maciá, "A new moving boundary model for evaluating the performance of wet fins: Application to minichannel evaporators," *Applied Thermal Engineering*, vol. 127, pp. 566–579, Dec. 2017, doi: 10.1016/j.applthermaleng.2017.08.055.

[30] S. Y. Liang, T. N. Wong, and G. K. Nathan, "Comparison of one-dimensional and two-dimensional models for wet-surface efficiency of a plate-and-tube heat exchanger." [Online]. Available: www.elsevier.com/locate/apthermeng

[31] A. Sohani, H. Sayyaadi, H. Hasani Balyani, and S. Hoseinpoori, "A novel approach using predictive models for performance analysis of desiccant enhanced evaporative cooling systems," *Applied Thermal Engineering*, vol. 107, pp. 227–252, Aug. 2016, doi: 10.1016/j.applthermaleng.2016.06.121.

[32] Y. G. Akhlaghi, X. Ma, X. Zhao, S. Shittu, and J. Li, "A statistical model for dew point air cooler based on the multiple polynomial regression approach," *Energy*, vol. 181, pp. 868–881, Aug. 2019, doi: 10.1016/j.energy.2019.05.213.

[33] F. Comino, S. Milani, S. de Antonellis, C. M. Joppolo, and M. Ruiz de Adana, "Simplified performance correlation of an indirect evaporative cooling system: Development and validation," *International Journal of Refrigeration*, vol. 88, pp. 307–317, Apr. 2018, doi: 10.1016/j.ijrefrig.2018.02.002.

[34] A. Pakari and S. Ghani, "Regression models for performance prediction of counter flow dew point evaporative cooling systems," *Energy Convers Management*, vol. 185, pp. 562–573, Apr. 2019, doi: 10.1016/j.enconman.2019.02.025.

[35] D. Pandelidis and S. Anisimov, "Application of a statistical design for analyzing basic performance characteristics of the cross-flow Maisotsenko cycle heat exchanger," *International Journal of Heat and Mass Transfer*, vol. 95, pp. 45–61, Apr. 2016, doi: 10.1016/j.ijheatmasstransfer.2015.11.060.

[36] X. Cui, M. R. Islam, B. Mohan, and K. J. Chua, "Developing a performance correlation for counter-flow regenerative indirect evaporative heat exchangers with experimental validation," *Applied Thermal Engineering*, vol. 108, pp. 774–784, Sep. 2016, doi: 10.1016/j.applthermaleng.2016.07.189.

[37] W. Pirompugd and S. Wongwises, "Partially wet fin efficiency for the longitudinal fins of rectangular, triangular, concave parabolic, and convex parabolic profiles," *Journal of the Franklin Institute*, vol. 350, no. 6, pp. 1424–1442, Aug. 2013, doi: 10.1016/j.jfranklin.2013.02.019.

[38] Y.-J. Chang and C.-C. Wang, "A generalized heat transfer correlation for louver fin geometry," 1997.

[39] P. Teertstra, M. M. Yovanovich, J. H. Culham, and T. Lemczyk, "Analytical forced convection modeling of plate fin heat sinks," *Annual IEEE Semiconductor Thermal Measurement and Management Symposium*, pp. 34–41, 1999, doi: 10.1109/stherm.1999.762426.

[40] M. M. Shah, "New general correlation for heat transfer during saturated boiling in mini and macro channels," *International Journal of Refrigeration*, vol. 137, pp. 103–116, May 2022, doi: 10.1016/j.ijrefrig.2022.02.019.

[41] M. M. Shah, "A correlation for heat transfer during condensation in horizontal mini/micro channels," *International Journal of Refrigeration*, vol. 64, pp. 187–202, Apr. 2016, doi: 10.1016/j.ijrefrig.2015.12.008.

Appendix

C_s for Two-phase refrigerant under fully wet condition

Regression items	Coefficients
hs	773.3503278912
α_i	0.0000948948
L_f	38.3773722823
RH	−2.0216861869
$T_{r,i}$	−1.0152934629
$T_{a,i}$	−0.0558427117
v_a	−0.4891876154
$\dot{m}_r$	−5723.4507277779
$\alpha_i \times hs$	0.0024117767
α_i^2	0.0000000003
$\alpha_o \times hs$	0.6156383647
$\alpha_o \times \alpha_i$	−0.0000000170
$\alpha_i \times H_f$	−0.0001363495
$\alpha_o \times H_f$	0.0181053785
$L_f \times H_f$	3471.1090492644
$\alpha_i \times RH$	−0.0000059242
$\alpha_o \times RH$	0.0003096243
$RH \times L_f$	−2.0289842690
$\alpha_o \times T_{r,i}$	−0.0000155251
$RH \times T_{r,i}$	0.0033981273
$T_{r,i}^2$	0.0018169769
$T_{a,i} \times hs$	−2.7568565683
$\alpha_i \times T_{a,i}$	−0.0000003349
$\alpha_o \times T_{a,i}$	0.0000134885
$T_{a,i} \times H_f$	0.0131479250
$T_{a,i} \times L_f$	−0.1332461658
$RH \times T_{a,i}$	0.0040033968
$T_{a,i} \times T_{r,i}$	0.0002142941
$hs \times v_a$	−48.2247161957
$\alpha_i \times v_a$	−0.0000016500
$\alpha_o \times v_a$	0.0000684268
$L_f \times v_a$	−0.5824816663
$RH \times v_a$	0.0244457612
$T_{a,i} \times v_a$	0.0018222308
v_a^2	−0.0041959005
$\alpha_i \times \dot{m}_r$	0.0243469441
$T_{r,i} \times \dot{m}_r$	19.4632217323

14th IEA Heat Pump Conference
15-18 May 2023, Chicago, Illinois

Achievement report of NEDO R&D Project on Innovative Thermal Management Materials and Technologies

Yoichi Fujita*, Tetsushiro Iwatsubo*

* Energy Conservation Technology Department, New Energy and Industrial Technology Development Organization (NEDO), 212-8554 Japan

Abstract

The importance of industrial heat pumps toward decarbonization has begun to be widely recognized worldwide. Japan has developed, and applied industrial heat pumps ahead in the world. This paper overviews the current technology and market status of industrial heat pumps in Japan. It reveals that heat-pumping technology has matured to some degree. However, it shows the importance of accelerating the adoption. This study also clarifies the issues for its widespread adoption by questionnaire survey and barrier analysis and discusses measures for the future.

© HPC2023.
Selection and/or peer-review under the responsibility of the organizers of the 14th IEA Heat Pump Conference 2023.

Keywords: R&D Project; Thermal Management; Unutilized Thermal Energy; Industrial Heatpumps; High-temperature Heatpumps

1. Introduction

On October 2020, Japan declared that it would aim to realizing “carbon neutrality by 2050,” and in April 2021, Japan has also set a new target to reduce greenhouse gas emissions by 46% in FY 2030 from FY 2013 levels. Towards 2050, the new plan seeks to achieve energy transitions and decarbonization, considering the global momentum in this direction and in enforcement of the Paris Agreement, and to pursue all tenable options toward this end.

During Japan's energy distribution process, about 30% to 40% of primary energy, mainly fossil resources such as oil, coal, and natural gas, are lost when they are converted into electricity and fuel [1], and at the final consumption, and it is used only a small portion, so total 60% to 70% of primary energy is considered not to be used effectively but discarded as heat. Authors refer to such artificially discharged heat as “unutilized thermal energy,” and it is the key for realizing thorough energy efficiency to effectively reduce, reuse, and recycle this huge amount of unutilized thermal energy discharged into this environment, and it can be said to be a frontier.

Authors introduce an overview of a national R&D project “Research and Development Project for Innovative Thermal Management Materials and Technologies” which aims to realize thorough energy efficiency promoted by New Energy and Industrial Technology Development Organization (NEDO). Above all, they focus on R&Ds of new high-temperature heat pumps that make use of heat efficient in industrial fields by reusing unused thermal energy for process heating instead of boilers.

2. National R&D Project Overview

The goal of this project is to develop three Rs technology to effectively reduce (via insulation, thermal insulation, or heat storage), recover and reuse (via heat-pump technology), or recycle (via thermoelectric conversion or waste heat power generation) untapped thermal energy. The project also aims to develop basic crosscutting heat management technologies for effective reduction, recovery and reuse, or conversion of the

* Corresponding author. Tel.: +81-44-520-5281; fax: +81-44-520-5187.
E-mail address: thermal-energy@nedo.go.jp.

huge amount of unused heat released into the environment to achieve further energy conservation in the industrial, transportation, and consumer sectors.

Figure 1 shows Organizational chart of "Research and Development Project for Innovative Thermal Management Materials and Technologies". The project had been excuted under industry-academia collaboration of the Thermal Management Materials and Technology Research Association (TherMAT).

In this way, this R&D project is intended for a wide range, but here authors introduce an R&D on high-temperature heat pumps, which are the core of this R&D project and can show high energy efficiency effect.

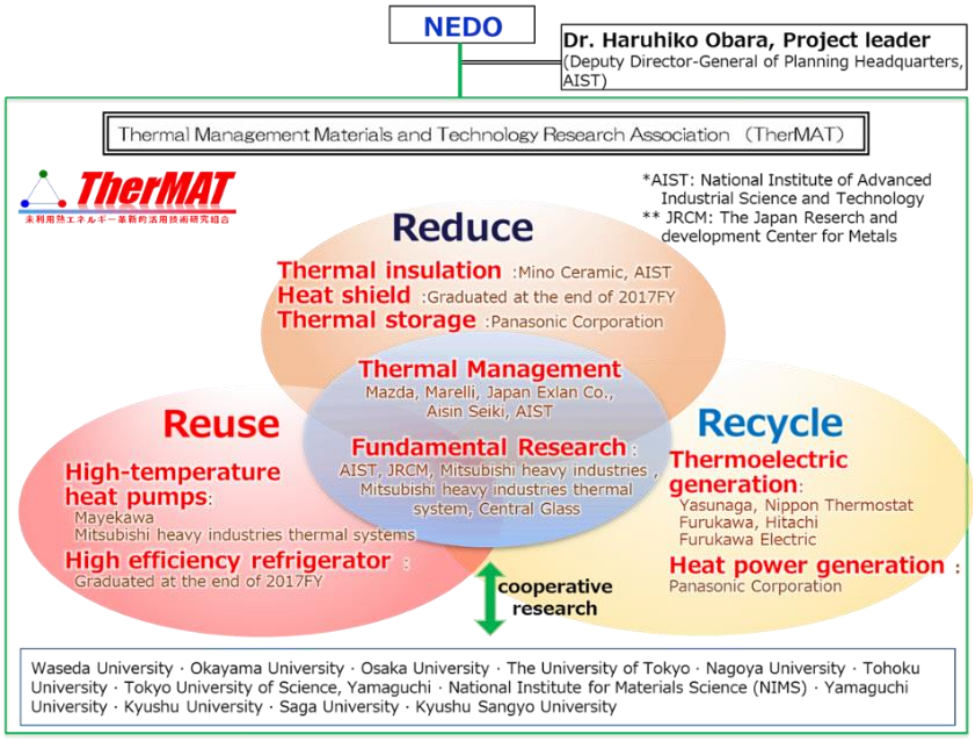


Fig. 1. Organizational chart of "Research and Development Project for Innovative Thermal Management Materials and Technologies"

Figure 2-1 shows the estimated amounts of nationwide unutilized thermal energy, by sector and temperature based on the survey result from 1,273 factories of 15 industries. The nationwide estimation of the amount of unutilized thermal energy (exhausted as gas) was based on results of questionnaires, approximation calculated by the correlation between energy inputs to factories and unutilized thermal energy as exhaust gas by industry, and FY2015 energy consumption statistics of manufacturing industries. [2]

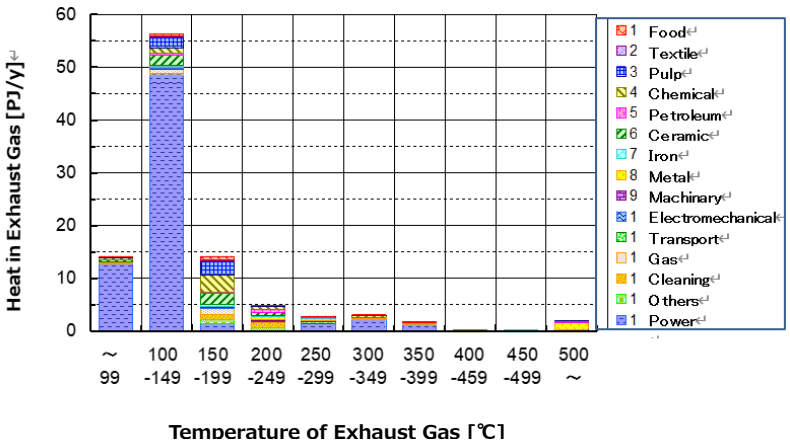


Figure 2-1: Estimation of amount of heat in exhaust gas from industry by temperature range

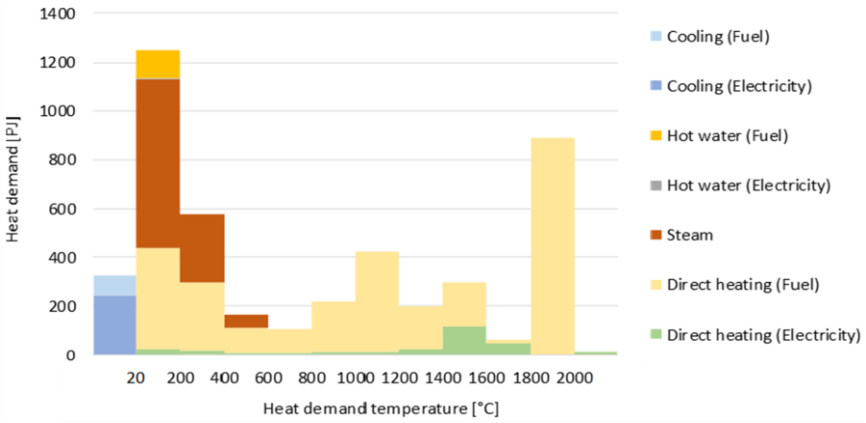


Figure 2-2: Heat demand in the Japanese industry by heat use form

On the other hand, Figure 2-2 shows the estimated amounts of heat demand, by heat form and temperature based on the survey result from 1,155 factories of 15 industries. [3] This heat demand area below 200°C becomes 1250 PJ (= 347 TWh) and accounts for 28% of the total industrial heat demand. Another feature is that temperature distribution of exhaust heat and heat demand are overlapping each other.

As shown in Figure 2-2, main heat source is steam below 200°C and usually boilers using fossil resources are used as heat sources as steam for industrial heating applications, and unutilized thermal energy is discharged from each heating process. By reusing this waste heat as a heat source, it is expected to regenerate it to a higher temperature and replace the heat sources from conventional boilers with high-temperature heat pumps.

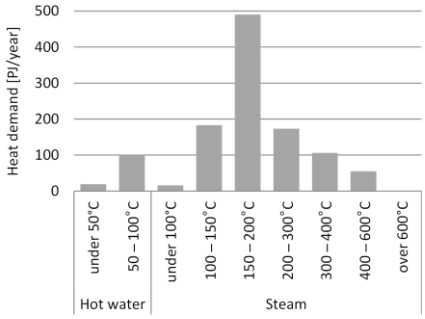


Figure 2-3: Heat demand of hot water and steam

Figure 2-3 shows the graph picking up the heat demand of hot water and steam from Figure 2-2. The applicable potential of heat pump expands as its supply temperature rises. Although it is largest demand at 150°C to 200°C range, unfortunately there is no heat pump which can supply above 150°C.

In this project, it aims to develop high-temperature heat pumps which can supply high-temperature heat about from 160°C to 200°C with high efficiency (e.g. COP: 3.5 or higher), recovering from waste heat of 80°C or 100°C which is discarded from industrial manufacturing processes, and as the result of penetrating them as alternatives to steam boilers, can contribute to use primary energy efficiently and reduce CO_2 emissions.

Figure 3 shows comparison of primary energy basis efficiency between boiler and high-temperature heat pump. Typical conventional heat systems supply steam by boiler with 90% of efficiency. On the contrary COP (Coefficient of Performance) of high-temperature heat pump reaches 3.5, and generation efficiency of thermal power plant is 45%. Therefore, total efficiency of high-temperature heat pump system reaches 158%, which is 1.75 times more efficient than conventional boiler system. It is expected that high-temperature heat pump will prevail by economical advantage.

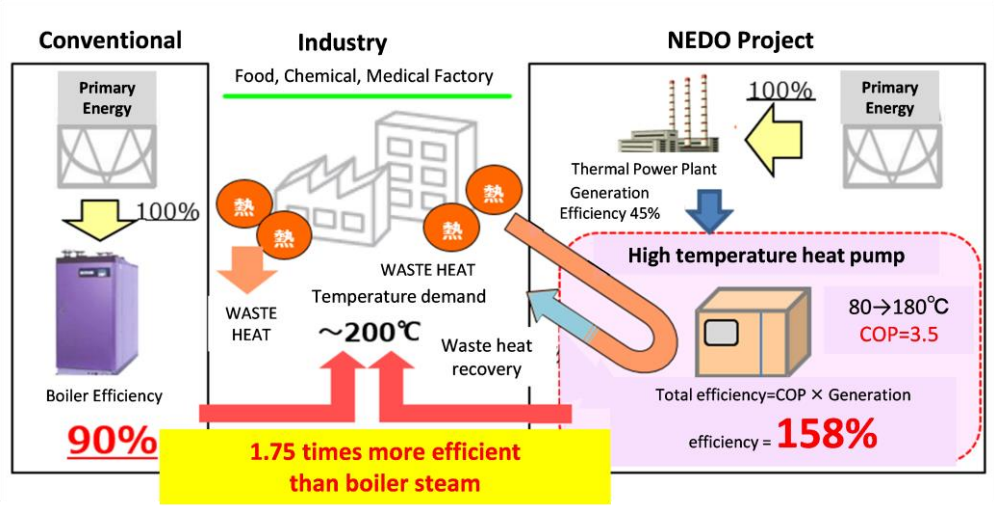


Figure 3: Comparison of efficiency between boiler and high-temperature heat pump

3. Development of industrial high-efficiency and high-temperature heat pump capable of supplying maximum 200°C

3-1. Development target

In this project, Mayekawa Mfg. Co., Ltd. who is the member of TherMAT, is developing heat pump systems with having the target that can meet the supply temperature range up to 200°C and achieve COP: 3.5 or higher by heating from 80°C to 180°C. [4]

There are 2 type of high-temperature heat pump in accordance with heating methods. Type-1 is steam supply circulating type with small temperature glide by Vaper compression cycle as shown in Figure 4-1. There is constant temperature during heating process which water is changed phase to steam. It is difficult to generate above 150°C of steam with presently available refrigerant. Type-2 is thermal oil or air supply transient type with large temperature glide by trans critical cycle as shown in Figure 4-2. There is no constant temperature during heating process. It is possible to generate above 150°C with presently available refrigerant. Therefore, Type-2 was adopted to achieve 180°C for this development.

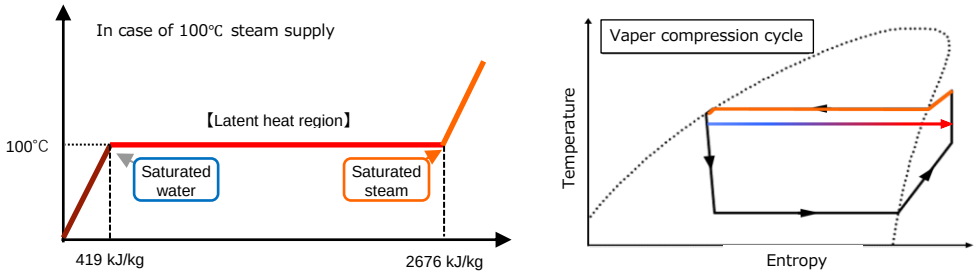


Figure 4-1: Type-1 Steam supply circulating type

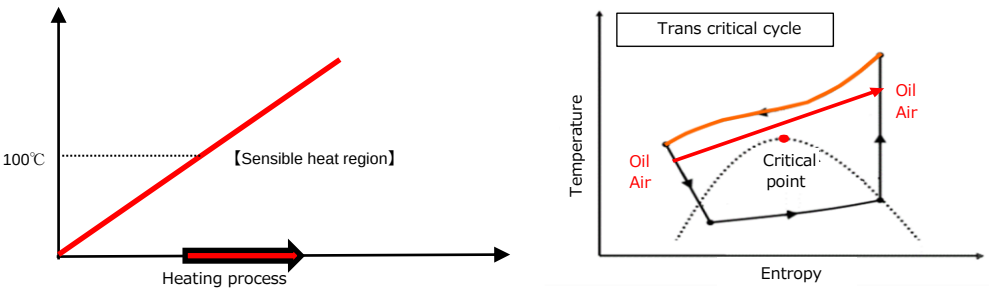


Figure 4-2: Type-2 Thermal oil or air supply transient type

Figure 5 shows the flow diagram of the system. The system consists of heat exchangers, compressors, expansion valve and connecting pipes. The heat exchangers are an evaporator, a gas cooler, and a liquid-gas heat exchanger. Approximately 80°C of waste heat is extracted by the evaporator as the heat source to evaporate the refrigerant which is then compressed and heated to about 200°C in the compressor. The heating medium flowing through the gas cooler is thermal oil with flash point temperature of more than 250°C which is classified as nonhazardous material by the fire service act.

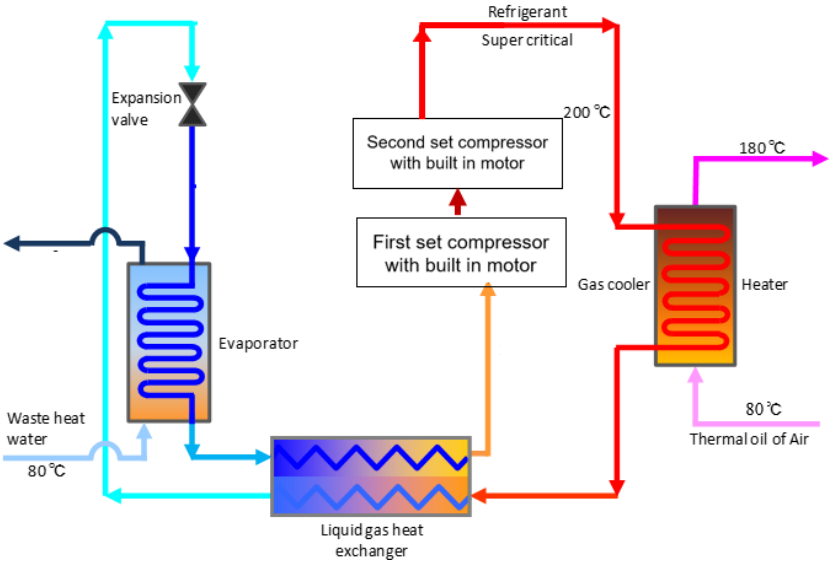


Figure 5: Schematic diagram of the high-temperature heat pump system

3-2. Development of compressor technology

To achieve the development target, it was necessary to develop an epoch-making compressor that had never existed before and to achieve the maximum operating temperatures of 200°C or higher. Due to the high operating temperatures, the conventional lubricating oil was difficult to use. Therefore, an oil-free centrifugal compressor with magnetic bearings is adopted. To improve efficiency, an optimally designed compressor rotor and a high-speed built-in motor are being used.

Magnetic bearings and built-in motors are one of the most important components in the development of this compressor. The magnetic bearings control the attractive force of the electromagnet and supports the rotating body in a non-contact manner. The built-in motor is located between the magnetic bearings at both ends. In consideration of the maximum operating temperature of 200°C, a three-phase induction motor with high heat resistance was adopted.

3-3. Development of the second prototype

NEDO had reported about 300kW of the first prototype which used R600 (n-butane) as refrigerant in the 13th IEA Heat Pump Conference 2020. [5] R600 which is a hydrocarbon-based refrigerant was adopted with a small GWP and high COP. However, R600 is a highly flammable and the test unit had to be enclosed in a casing to provide 24-hour ventilation and explosion-proof specifications. In recent years, it has become clear that new nonflammable low GWP refrigerants such as HFO (Hydro-fluoro-olefin) are available in the market and the rotation speed of the compressor is expected to be lower than that of R600 refrigerants. Therefore, HFO refrigerant is adopted for the second prototype. Table 1 and Figure 6 shows the main changes between the first prototype and the second prototype.

The second prototype comprises of two sets of compressors each with two stages, which makes it four stages compression compared with three stages compression of the first prototype according to fluid analysis result for different refrigerant. The two impellers being back-to-back structure was adopted with the second prototype to reduce thrust load of axial disk in comparison with the two impellers being same direction structure of the first set compressor of the first prototype.

The gas cooler with a capacity of 300 kW consists of two heat exchangers connected in parallel. The heating medium used is thermal oil and exchanges heat with the refrigerant in super critical state in trans critical cycle.

Table 1 The main changes of the first prototype compressor and second prototype compressor

	First prototype compressor	Second prototype compressor
Refrigerant	R600	R 1336mzz(Z)
Number of compression stage	Three stages	Four stages
Rotated speed[rpm]	45,000 (First set) 70,000 (High pressure side)	16,000 (First set) 15,000 (High pressure side)

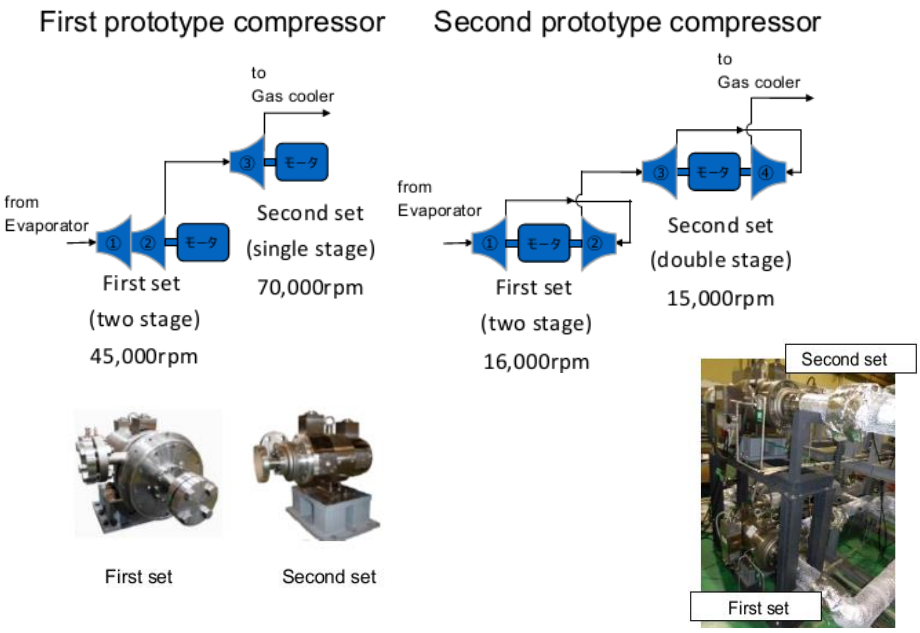


Figure 6: Comparison of the first prototype compressor and the second prototype compressor

Table 2 shows specifications of second prototype heat pump and Figure 7 shows the appearance. Currently, performance and reliability tests are conducted with the second prototype. According to comparison of theoretical values and actual measurements, there is prospect of achieving COP=3.5

Based on the test results, the elemental technologies such as compressors and heat exchangers are optimized, and then it is planned to be put on the market from around 2025.

Table 2 Specifications of test apparatus

Gas cooler	Type	Brazed plate
	Capacity	300 kW
Compressor	Type	Centrifugal
	Oil	Oil free
Refrigerant		R 1336mzz(Z)
Design pressure		5.2 MPaA
Rotation frequency	Low pressure compressor	16,000 rpm
	High pressure compressor	15,000 rpm
Thermal oil inlet temperature		80°C
Thermal oil outlet temperature		180°C



(a) Casing



(b) Inside

Figure 7: Test apparatus of high- temperature heat pump

3-4. Next steps

Toward introduction of the heat pumps after the end of R&D, it would be one of most important initiatives to see the effect or value when they apply to actual heat utilization equipment in factories. Especially it will be even more difficult to conduct verification to grasp the energy efficiency effect in the actual environment using the existing systems. Therefore, authors will proceed with activities of model cases studies, assumed actual heat utilization facilities, and based on the results of this studies, calculation and quantitatively evaluation of the effect or value including energy efficiency, cost merit and heat pump system configuration post introduction. As the result of the activities, "visualization" of introduction effect will be progressed and it will be possible to share the installation image of heat pumps in industrial heating processes with customers, which will be able to lead to acceleration of the commercialization.

On this project, NEDO plans to construct equipment utilizing systems with high- temperature heat pumps including attached facilities, proceed with model case verifications that examine optimal applied processes and clarify economic effects, and studies on "visualization" of introduction effect. Through these activities, the newly developed industrial high-efficiency and high-temperature heat pumps will be properly arranged and used for process heating instead of boilers, thereby promoting energy efficiency in factories and contributing to solving energy and environmental problems in the future.

4. Conclusion

"Energy efficiency" is the primary expectation for the realization of "3E + S" (simultaneously achieving Energy Security, Economic Efficiency and Environment, with coming Safety always at first) in Japan and global carbon neutrality by 2050, but most of primary energy is still discharged as unutilized thermal energy without being effectively used, even though various measures have been taken so far. Among energy forms such as fuel, electricity, and hydrogen that are expected to be used in the future, the last remaining form is heat, and decarbonization of all sectors that use this heat can be the key to construct the sustainable recycling society.

Now all the relevant people are required to promote to implement technologies for effectively reducing or recovering a large amount of unutilized thermal energy discharged into the environment including high-temperature heat pumps, to the society with economic rationality, realize significant energy efficiency of the entire society and a "circular economy", and there can be no doubt that this R&D project had been a driving force for it.

References

[1] Agency for Natural Resources and Energy, *FY2017 Energy Supply and Demand Report*, (2019) (in Japanese).
[2] NEDO, TherMAT, *Industrial Waste Heat Survey Report*, (2019) (in Japanese)
[3] Mitsubishi Research Institute, *FY2017 Heat supply and demand report*, (2018) (in Japanese)
[4] Kimura, *International Symposium on New Refrigerants and Environmental Technology 2021*.
[5] Kondo, *NEDO R&D project "Research and Development Project for Innovative Thermal Management"* ; HPC2020.

14th IEA Heat Pump Conference
15-18 May 2023, Chicago, Illinois

Development of dynamic model of variable refrigerant flow cooling system based on moving boundray method

Jeong Kuk Hong, Hongryul Joo, Min Soo Kim*

Department of Mechanical Engineering, Seoul National University, Seoul 08826, Republic of Korea

Abstract

The use of variable refrigerant flow (VRF) cooling and heating systems is gradually expanding, but the development of system dynamic models for optimal operation and fault diagnosis is still in the research stage. Therefore, in this study, we tried to develop a dynamic model of the entire VRF system by modeling the heat exchanger using the moving boundary method. A dynamic model development method for heat exchangers, a receiver, and an accumulator with dynamic variables was presented. In addition, modelling method of shut-down and start-up process in indoor units was also presented. Based on these models, the entire VRF system model was completed by combining static models for components such as compressors. Combining the thermal zone model with the VRF system model, the indoor unit on/off operation of the VRF system was simulated for 2,400 s. The simulation results showed that the developed model simulated the actual VRF system similarly, although there were some errors. However, if the accuracy of the model is increased using actual experimental results in the future, it is expected that the developed model can be used to perform optimal control of the actual VRF system.

© HPC2023.
Selection and/or peer-review under the responsibility of the organizers of the 14th IEA Heat Pump Conference 2023.

Keywords: Moving boundary method; Variable refrigerant flow; Transient model; Dynamic behavior; Digital twin

1. Introduction

The variable refrigerant flow (VRF) heating and cooling system has higher energy efficiency than duct systems, and it is easy to respond to individual indoor loads, so its market size is continuously increasing [1]. However, the optimal operation method according to changes in indoor load and operating conditions is still in the R&D stage.

Many researchers have struggled to find the optimal operation method of the VRF system. Yun *et al.* [2] developed a load responsive controller for the VRF system which control the evaporating temperature, showing that the new controller could reduce the annual cooling energy consumption by 14%. Moon *et al.* [3] developed two artificial neural network (ANN) model and two control algorithms for finding unoccupied period. Li *et al.* [4] proposed the ANN-based dynamic model for a direct expansion air conditioning system. They showed that the ANN-based model can control appropriately the compressor speed and supply fan speed without other logic.

There are many preceding studies, but in most cases, VRF system models depend on Big Data or utilize VRF system models of commercial programs. However, this method does not guarantee model accuracy for situations where data are not accumulated. Therefore, developing a simulation model that reflects the physical phenomena in the VRF system and using it for optimal control can be a versatile solution.

For this reason, in this study, dynamic model of the entire VRF system by modeling the heat exchanger using the moving boundary method is developed. Also, combining the thermal zone model with the VRF system model, the indoor unit on/off operation of the VRF system is simulated.

* Corresponding author. Tel.: +82-2-880-8362; fax: +82-2-880-4301.
E-mail address: minskim@snu.ac.kr .

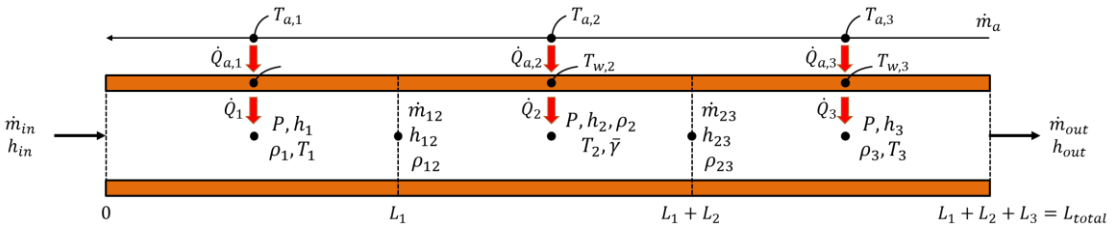


Fig. 1. Illustration of three-zone moving boundary model

2. Model development

2.1. Heat exchanger

2.1.1. Refrigerant mass conservation equations

When modeled by the moving boundary method, the heat exchanger is divided into three regions: subcool, two-phase, and superheat region. In this study, each region was numbered as regions 1, 2, and 3 in order of distance from the heat exchanger inlet. The result of applying the refrigerant mass conservation equation for each region is shown in Eqns. (1)-(3).

$$(\rho_1 - \rho_{12})\dot{L}_1 + \left(\frac{\partial \rho_1}{\partial P}\Big|_{h_1} + \frac{1}{2}\frac{\partial \rho_1}{\partial h_1}\Big|_P \frac{dh_{12}}{dP}\right) L_1 \dot{P} + \frac{1}{2}\frac{\partial \rho_1}{\partial h_1}\Big|_P L_1 \dot{h}_{in} = \frac{\dot{m}_{in} - \dot{m}_{12}}{A} \tag{1}$$

$$(\rho_{12} - \rho_{23})\dot{L}_1 + \left[\bar{\gamma}\rho_g + (1-\bar{\gamma})\rho_f - \rho_{23}\right]\dot{L}_2 + \left[\bar{\gamma}\frac{d\rho_g}{dP} + (1-\bar{\gamma})\frac{d\rho_f}{dP}\right] L_2 \dot{P}$$

$$+ (\rho_g - \rho_f) L_2 \dot{\bar{\gamma}} = \frac{\dot{m}_{12} - \dot{m}_{23}}{A} \tag{2}$$

$$(\rho_{23} - \rho_3)\dot{L}_1 + (\rho_{23} - \rho_3)\dot{L}_2 + \left(\frac{\partial \rho_3}{\partial P}\Big|_{h_3} + \frac{1}{2}\frac{\partial \rho_3}{\partial h_3}\Big|_P \frac{dh_{23}}{dP}\right) L_3 \dot{P} + \frac{1}{2}\frac{\partial \rho_3}{\partial h_3}\Big|_P L_3 \dot{h}_{out} = \frac{\dot{m}_{23} - \dot{m}_{out}}{A} \tag{3}$$

When a certain section disappears within the heat exchanger, the equation derived from that section is no longer applicable. In that case, when section 1 disappears, the equation $\dot{m}_{12} = \dot{m}_{in}$ can be applied instead, and when section 3 disappears, the equation $\dot{m}_{23} = \dot{m}_{in}$ can be applied instead.

2.1.2. Refrigerant energy conservation equations

$$(\rho_1 h_1 - \rho_{12} h_{12})\dot{L}_1 + \left[\left(\frac{\partial \rho_1}{\partial P}\Big|_{h_1} + \frac{1}{2}\frac{\partial \rho_1}{\partial h_1}\Big|_P \frac{dh_{12}}{dP}\right) h_1 + \frac{1}{2}\frac{dh_{12}}{dP}\rho_1 - 1\right] L_1 \dot{P}$$

$$+ \frac{1}{2}\left(h_1 \frac{\partial \rho_1}{\partial h_1}\Big|_P + \rho_1\right) L_1 \dot{h}_{in} = \frac{\dot{m}_{in} h_{in} - \dot{m}_{12} h_{12} + \dot{Q}_1}{A} \tag{4}$$

$$(\rho_{12} h_{12} - \rho_{23} h_{23})\dot{L}_1 + \left[\bar{\gamma}\rho_g h_g + (1-\bar{\gamma})\rho_f h_f - \rho_{23} h_{23}\right]\dot{L}_2$$

$$+ \left[\bar{\gamma}\frac{d\rho_g h_g}{dP} + (1-\bar{\gamma})\frac{d\rho_f h_f}{dP} - 1\right] L_2 \dot{P} + (\rho_g h_g - \rho_f h_f) L_2 \dot{\bar{\gamma}} = \frac{\dot{m}_{12} h_{12} - \dot{m}_{23} h_{23} + \dot{Q}_2}{A} \tag{5}$$

$$(\rho_{23} h_{23} - \rho_3 h_3)\dot{L}_1 + (\rho_{23} h_{23} - \rho_3 h_3)\dot{L}_2 + \left[\left(\frac{\partial \rho_3}{\partial P}\Big|_{h_3} + \frac{1}{2}\frac{\partial \rho_3}{\partial h_3}\Big|_P \frac{dh_{23}}{dP}\right) h_3 + \frac{1}{2}\frac{dh_{23}}{dP}\rho_3 - 1\right] L_3 \dot{P}$$

$$+ \frac{1}{2}\left(h_3 \frac{\partial \rho_3}{\partial h_3}\Big|_P + \rho_3\right) L_3 \dot{h}_{out} = \frac{\dot{m}_{23} h_{23} - \dot{m}_{out} h_{out} + \dot{Q}_3}{A} \tag{6}$$

The result of applying the refrigerant energy conservation equation for each region is shown in Eqns. (4)-(6). When section j disappears, the equation $\dot{L}_j = 0$ can be applied instead of the equation derived from each section.

2.1.3. Tube wall energy conservation equations

$$L_1\dot{T}_{w1} - (T_{w12} - T_{w1})\dot{L}_1 = \frac{\dot{Q}_{a,1} - Q_1}{A_w \rho_w c_w} \tag{7}$$

$$L_2\dot{T}_{w2} + (T_{w12} - T_{w23})\dot{L}_1 - (T_{w23} - T_{w2})\dot{L}_2 = \frac{\dot{Q}_{a,2} - Q_2}{A_w \rho_w c_w} \tag{8}$$

$$L_3\dot{T}_{w3} + (T_{w23} - T_{w3})\dot{L}_1 + (T_{w23} - T_{w3})\dot{L}_2 = \frac{\dot{Q}_{a,3} - Q_3}{A_w \rho_w c_w} \tag{9}$$

The result of applying the tube wall energy conservation equation for each region is shown in Eqns. (7)-(9). The symbol T_{w12} means the tube wall temperature at the boundary between section 1 and section 2, and the T_{w23} means that at the boundary between section 2 and section 3. Some researchers have completed the equation by considering both T_{w12} and T_{w23} to be T_{w2} [5-7]. Also, some researchers have assigned different values to T_{w12} and T_{w23} according to the sign of the time derivative of the length at the boundary point [8-10]. For example, they used T_{w1} for T_{w12} when $\dot{L}_1 < 0$, and they used T_{w2} for T_{w12} when $\dot{L}_1 \geq 0$. However, in this study, Eq. (10) and Eq. (11) were used for expressing T_{w12} and T_{w23} as introduced in [11, 12] because this method is more numerically stable and has no conditional statements.

$$T_{w12} = (L_1 T_2 + L_2 T_1)/(L_1 + L_2) \tag{10}$$

$$T_{w23} = (L_2 T_3 + L_3 T_2)/(L_2 + L_3) \tag{11}$$

2.1.4. Equation for mean void fraction

$$\dot{\bar{\gamma}} = \left(\frac{\partial \bar{\gamma}}{\partial P}\bigg|_{x_{i,2}, x_{o,2}} + \frac{\partial \bar{\gamma}}{\partial x_{i,2}}\bigg|_{P, x_{o,2}} \frac{\partial x_{i,2}}{\partial P}\bigg|_{h_{i,2}} + \frac{\partial \bar{\gamma}}{\partial x_{o,2}}\bigg|_{P, x_{i,2}} \frac{\partial x_{o,2}}{\partial P}\bigg|_{h_{o,2}} \right) \dot{P}$$
$$+ \frac{\partial \bar{\gamma}}{\partial x_{i,2}}\bigg|_{P, x_{o,2}} \frac{\partial x_{i,2}}{\partial h_{i,2}}\bigg|_{P} \dot{h}_{i,2} + \frac{\partial \bar{\gamma}}{\partial x_{o,2}}\bigg|_{P, x_{i,2}} \frac{\partial x_{o,2}}{\partial h_{o,2}}\bigg|_{P} \dot{h}_{o,2} \tag{12}$$

In order to accurately simulate the dynamic behavior of the heat exchanger, the mean void fraction of the two-phase section should be set as a dynamic variable. In this case, one differential equation including quality distribution information within the two-phase section is further required. In this study, Eq. (12) was applied assuming that the refrigerant quality in the two-phase section increases (or decreases) linearly, which was derived in [13, 14]. The subscript $i,2$ means inlet of the two-phase section and the subscript $o,2$ means outlet of the two-phase section

By arranging Eqns. (1)-(12), the dynamic behavior of the heat exchanger is expressed as equations for the vector $[\dot{L}_1, \dot{L}_2, \dot{P}, \dot{h}_{out}, \dot{T}_{w1}, \dot{T}_{w2}, \dot{T}_{w3}, \dot{\bar{\gamma}}]$, and the change in state of the heat exchanger over time can be obtained by integrating this vector.

2.1.5. The situation where the inlet and outlet of the heat exchanger are closed

In a VRF system, some indoor units among several indoor units may stop operating. In this case, generally the fan of the indoor unit still works, but the valves at the inlet and outlet of its heat exchanger are closed and the refrigerant does not flow until the indoor temperature reaches a certain value. In this situation, since the moving boundary method assumes a situation where the refrigerant flows, the governing equations derived in Section 2.1.1 and Section 2.1.2 cannot be applied.

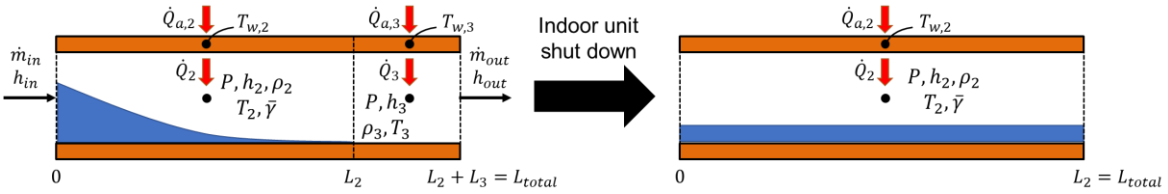


Fig. 2. Change in refrigerant flow inside the heat exchanger when the indoor unit is stopped

$$\left[\bar{\gamma}\frac{d\rho_g}{dP} + (1-\bar{\gamma})\frac{d\rho_f}{dP}\right]\dot{P} + \left(\rho_g - \rho_f\right)\dot{\bar{\gamma}} = 0 \tag{13}$$

$$\left[\bar{\gamma}\left(\rho_g\frac{du_g}{dP} + \frac{d\rho_g}{dP}u_g\right) + (1-\bar{\gamma})\left(\rho_f\frac{du_f}{dP} + \frac{d\rho_f}{dP}u_f\right)\right]\dot{P} + \left(\rho_g u_g - \rho_f u_f\right)\dot{\bar{\gamma}} = \frac{\dot{Q}_2}{AL_2} \tag{14}$$

Therefore, Eq. (13) and Eq. (14) were derived for the situation. Since there is no mass flow of the refrigerant, the mass in the heat exchanger does not change and thus $\dot{\rho}_2 = 0$. Then, since $\rho_2 = \bar{\gamma}\rho_g + (1-\bar{\gamma})\rho_f$, Eq. (13) can be derived. By similar way, from $(m_2 u_2)' = (AL_2\rho_2 u_2)' = \dot{Q}_2$ and $\rho_2 u_2 = \bar{\gamma}\rho_g u_g + (1-\bar{\gamma})\rho_f u_f$, Eq. (14) can be derived.

Since the Eq. (8) still can be used when indoor unit stopped, therefore the dynamic behavior of the heat exchanger is expressed as equations for the vector $[\dot{P}, \dot{T}_{w2}, \dot{\bar{\gamma}}]$.

2.2. Accumulator and receiver

$$\dot{m}_{acc} = \dot{m}_{acc,in} - \dot{m}_{acc,out} \tag{15}$$

$$\frac{d(m_{acc}u_{acc})}{dt} = \dot{m}_{acc}u_{acc} + m_{acc}\dot{u}_{acc} = \dot{m}_{acc,in}h_{acc,in} - \dot{m}_{acc,out}h_{acc,out} \tag{16}$$

$$\dot{u}_{acc} = \frac{\partial u_{acc}}{\partial P}\bigg|_{\rho_{acc}}\dot{P} + \frac{\partial u_{acc}}{\partial \rho_{acc}}\bigg|_{P}\frac{1}{V_{acc}}\dot{m}_{acc} \tag{17}$$

$$m_{acc}\frac{\partial u_{acc}}{\partial P}\bigg|_{\rho_{acc}}\dot{P} + \left(u_{acc} + \frac{\partial u_{acc}}{\partial \rho_{acc}}\rho_{acc}\right)\dot{m}_{acc} = \dot{m}_{acc,in}h_{acc,in} - \dot{m}_{acc,out}h_{acc,out} \tag{18}$$

Since the accumulator and receiver can store the refrigerant mass inside the components, the change in the mass of the refrigerant inside the components is expressed as a dynamic behavior. Taking an accumulator as an example, the change in refrigerant mass in the accumulator is expressed as the difference between the mass flow rate at the inlet and the mass flow rate at the outlet, as shown in Eq. (15). Also, energy balance equation was derived as Eq. (16). By thermodynamics, u_{acc} could be expressed with other two thermodynamic properties such as P and ρ_{acc} and Eq. (17) was derived as a result. Combining Eq. (16) and Eq. (17), finally Eq. (18) was obtained. It is noteworthy that the outlet enthalpy ($h_{acc,out}$) become h_g or h_{acc}, respectively, depending on whether the refrigerant inside the accumulator is in a two-phase state or a single-phase state. As a conclusion, the dynamic behavior of the accumulator and receiver is expressed as equations for the vector $[\dot{P}, \dot{m}_{acc}]$ *or* $[\dot{P}, \dot{m}_{rec}]$.

2.3. Compressor, electronic expansion valve (EEV), and pipe

Since the time constants of a compressor and an EEV are very small compared to that of heat exchangers, a static model is used for the compressor and expansion valve, not a dynamic model. In addition, in the case of a pipe connecting the indoor unit and the outdoor unit, the mass of the refrigerant can be stored therein, but the amount is very small compared to the heat exchanger, the accumulator, and the receiver. Therefore, the static pipe model is also used for pipes.

As a static model for the compressor, refrigerant flow in compressor can be calculated as the product of the compressor frequency, inlet refrigerant density, and stroke volume. The compressor outlet enthalpy can be calculated with an isentropic efficiency. As a static model for the EEV, refrigerant flow in EEV can be

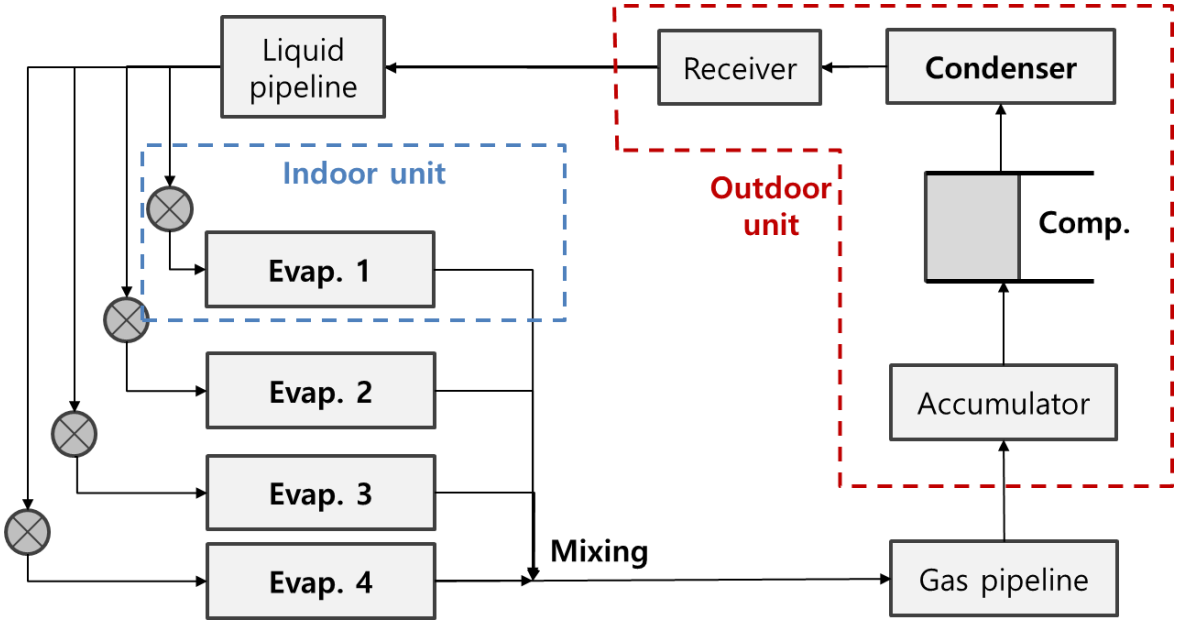


Fig. 3. Schematic diagram of the simulated VRF system

determined by the orifice flow equation, and the outlet enthalpy was the same as the inlet enthalpy. For calculating pressure drop in pipes, Darcy-Weisbach equation was used.

2.4. System configuration

In this study, a dynamic model of a VRF system including one outdoor unit, four indoor units, a compressor, four EEVs, an accumulator, and a receiver was developed as shown in Fig. 3. The simulation was performed only in cooling mode and cooling capacity of the VRF system was set to 30 kW. PI control was applied to the compressor speed so that the accumulator pressure, which is the inlet pressure of the compressor, reached a specific value from the initial condition of 0 Hz. In addition, the openings of the EEVs were also PI controlled so that the superheat at the outlet of each indoor unit be 10 K. In the case of the indoor unit, on/off control was applied, and the refrigerant flow was stopped when the air inlet temperature reached 17.5℃, and the valve was opened to allow the refrigerant to flow when the temperature reached 18.5℃. Other simulation conditions, parameters, and component geometry not mentioned are shown in Table 1.

Table 1. VRF system simulation conditions

Item	Value
Refrigerant	R-410A, Charge = 11.4 [kg]
Indoor/Outdoor T	27, 25, 23, 21 / 35 [℃] at initial
Compressor	$V = 150$ [cc], $\eta_{isen} = 0.75, \eta_v = 1$, Hz = 15 ~ 60 (PID controlled for matching accumulator pressure)
EEV	$\dot{m}_{EEV} = C_V\sqrt{\rho_{in}(P_{in} - P_{out})}$ DSH1 = DSH2 = DSH3 = DSH4 = 10 K (PI controlled)
Condenser	154 × 7.2 × 176 [cm^3] Finned-tube heat exchanger Heat transfer coefficient: single-phase from Gnielinski (1976), two-phase from Chen (1987) Air mass flowrate: 220 [m^3/min]
Evaporator	175 × 4 × 24 [cm^3] Finned-tube heat exchanger Heat transfer coefficient: single-phase from Gnielinski (1976), two-phase from Chen (1966) Air mass flowrate: 19 [m^3/min]
Receiver	*V*=13 [L]
Accumulator	*V*=5.7 [L]

2.5. Thermal zone model

Thermal zone models were constructed to simulate the situation where the indoor temperature decreases due to the cooling operation of the VRF system and the indoor unit repeats on/off. The thermal zone modeling method referred to the study of Lapusan *et al.* [15] Lapusan *et al.* constructed thermal resistance circuit for the multi-room building considering conduction from ceiling, interior and external wall, windows, and floor; ventilation through the windows; radiation from the sun.

By modifying their thermal resistance model, the thermal resistance model to be applied to this simulation was developed as shown in Fig. 4. Cooling effect from the VRF system and heat generation from human beings were added to the previous model.

The size, arrangement, and other simulation conditions of each thermal zone are shown in Fig. 5. The ground temperature was set to 10℃ and the amount of solar radiation and heat generation were set to 160 W and 500 W (5 people in each room), respectively. Additionally, mass flow rate of the ventilation was set to 50 m^3/h. In term of geometry, each room has an area of 25 m^2 and a height of 3 m and all four rooms are placed side by side.

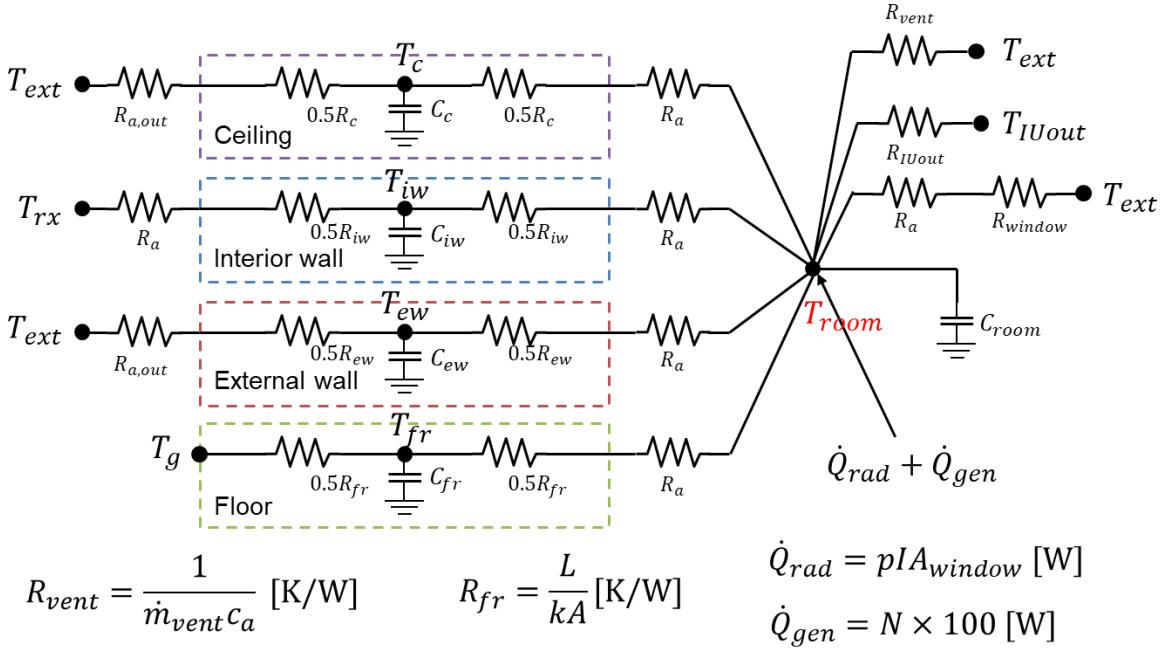


Fig. 4. Thermal resistance circuit for one room in the multi-room building

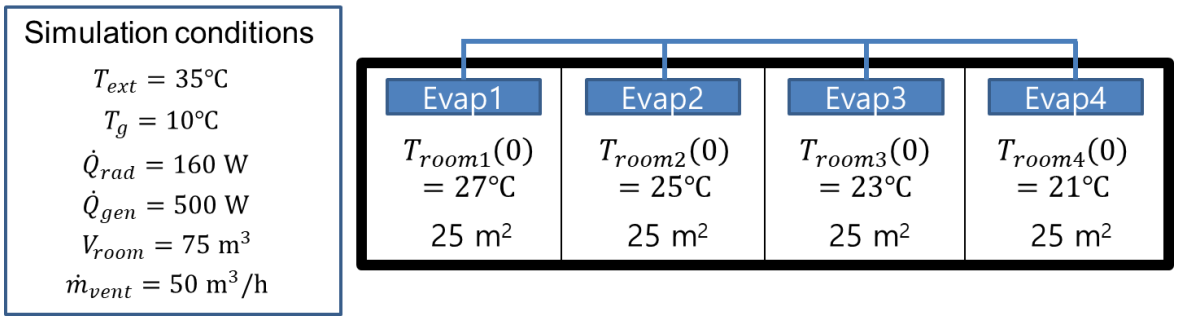


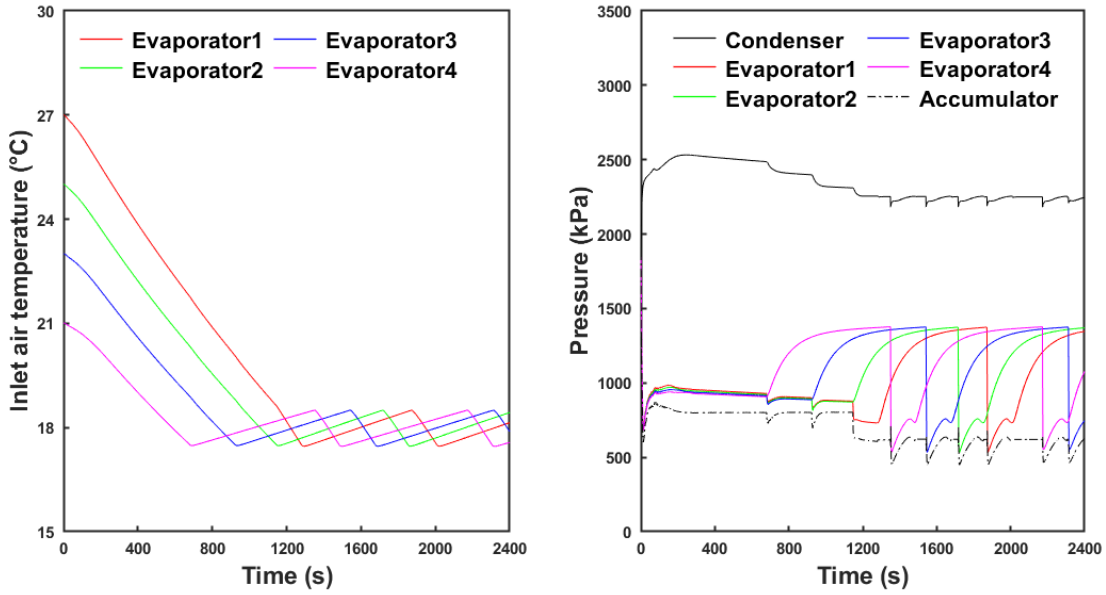
Fig. 5. 4-office zone arrangement for VRF cooling system simulation and simulation conditions

3. Simulation results

Fig. 6 shows the dynamic behaviors of the simulated system from 0 s to 2,400 s. At 690 s, inlet air temperature of the fourth evaporator reached the set lower limit, and the valves of that indoor unit were closed.

Then, the pressure of the refrigerant in the indoor unit rapidly increased as heat was supplied from the indoor air. When the temperature of the refrigerant became the same as the room temperature, the heat transfer decreased and it approached a steady state with no pressure change. Sequentially, the other indoor units also experienced the same process. At 1,350 s, inlet air temperature of the fourth evaporator reached the set upper limit and valves were opened. Then, the refrigerant in the indoor unit quickly moved to the accumulator which had lower pressure, and the indoor unit pressure drastically decreased. Although the slope of decreasing pressure was very large, the simulation was robust and worked without showing numerical instability even when this process was repeated.

However, as the simulation time elapsed, the compressor inlet pressure (accumulator pressure) converged to about 620 kPa. This is the evaporation pressure corresponding to the evaporation temperature of -7.6℃, and it shows a difference from the operating data of the actual VRF system. This difference is expected to be resolved through a model validation process that and reduces the error with the experimental results of the actual VRF system changing the main parameters of the VRF system modeling.



(a) (b)

Fig. 6. Dynamic behaviors of the simulated system (a) Inlet air temperature in each zone (b) Pressure of the components

4. Conclusions

In this study, the heat exchanger was modeled using the moving boundary method, and the dynamic model development and simulation of the entire VRF system was performed by combining it with the main component models of the VRF system. In particular, a modeling method in the stationary state of the indoor unit, which frequently occurs in VRF systems, was included. In addition, the indoor unit on/off operation of the VRF system was simulated by combining the thermal zone model. Based on the system pressure change data derived through simulation, it was confirmed that the developed model simulated the actual VRF system similarly, although there were some errors. However, if the accuracy of the model is increased using actual experimental results in the future, it is expected that the developed model can be used to perform optimal control of the actual VRF system.

Nomenclature

A	=	Cross-sectional area [m^2]
C	=	Heat capacity [J/K]
c	=	Specific heat capacity [J/(kg·K)]
$\bar{\gamma}$	=	Mean void fraction [-]
h	=	Specific enthalpy [J/kg]
η_{isen}	=	Isentropic efficiency [-]
η_v	=	Volumetric efficiency [-]
I	=	Solar radiation = 80 [W/m^2]
k	=	Thermal conductivity [W/(m·K)]
L	=	Length [m]
m	=	Mass [kg]
$\dot{m}$	=	Mass flow rate [kg/s]
N	=	The number of occupants [-]
P	=	Pressure [Pa]
p	=	Fraction of solar radiation transmitted to the floor = 0.6 [-]
$\dot{Q}$	=	Heat transfer rate [W]
R	=	Thermal resistance [K/W]
ρ	=	Density [kg/m^3]
T	=	Temperature [K]
T_{ext}	=	Outdoor temperature [K]
T_g	=	Ground temperature [K]
t	=	Time [s]
u	=	Specific internal energy [J/kg]
V	=	Volume [m^3]
$x_{i,2}$	=	Quality at two-phase section inlet [-]
$x_{o,2}$	=	Quality at two-phase section outlet [-]

Subscript

1	=	Section 1
12	=	Boundary between section 1 and section 2
2	=	Section 2
23	=	Boundary between section 2 and section 3
3	=	Section 3
a	=	Air
acc	=	Accumulator
c	=	Ceiling
ew	=	External wall
f	=	Liquid
fr	=	Floor
g	=	Gas
gen	=	Generation
in	=	Inlet
iw	=	Interial wall
out	=	Outlet
rad	=	Radiation
rec	=	Receiver
$room$	=	Room
rx	=	Adjacent room
$vent$	=	Ventilation

w	=	Tube wall
$window$	=	Window

References

[1] Wan, H., Cao, T., Hwang, Y., Oh, S., 2020. *A review of recent advancements of variable refrigerant flow air-conditioning systems*. Appl. Therm. Eng. 169, 114893.

[2] Yun, G.Y., Lee, J.H., Kim, H.J., 2016. *Development and application of the load responsive control of the evaporating temperature in a VRF system for cooling energy savings*. Energy Build. 116, 638–645.

[3] Moon, J.W., Jung, S.K., 2016. *Development of a thermal control algorithm using artificial neural network models for improved thermal comfort and energy efficiency in accommodation buildings*. Appl. Therm. Eng. 103, 1135–1144.

[4] Li, N., Xia, L., Shiming, D., Xu, X., Chan, M.-Y., 2012. *Dynamic modeling and control of a direct expansion air conditioning system using artificial neural network*. Appl. Energy 91, 290–300.

[5] Willatzen, M., Pettit, N.B.O.L., Ploug-Sørensen, L., 1998. *A general dynamic simulation model for evaporators and condensers in refrigeration. Part I: moving-boundary formulation of two-phase flows with heat exchange: Modèle général dynamique pour évaporateurs et condenseurs frigorifiques. Partic I: Formulation des conditions aux limites variables de flux biphasiques avec échange de chaleur*. Int. J. Refrig. 21, 398–403.

[6] Shah, R., Alleyne, A.G., Bullard, C.W., Rasmussen, B.P., Hrnjak, P.S., 2003. *Dynamic modeling and control of single and multi-evaporator subcritical vapor compression systems.*

[7] Eldredge, B.D., Rasmussen, B.P., Alleyne, A.G., 2008. *Moving-Boundary Heat Exchanger Models With Variable Outlet Phase*. J. Dyn. Syst. Meas. Control 130. https://doi.org/10.1115/1.2977466

[8] Jensen, J.M., Tummescheit, H., 2002. *Moving boundary models for dynamic simulations of two-phase flows*, in: Proc. of the 2nd Int. Modelica Conference.

[9] McKinley, T.L., Alleyne, A.G., 2008. *An advanced nonlinear switched heat exchanger model for vapor compression cycles using the moving-boundary method*. Int. J. Refrig. 31, 1253–1264.

[10] Zapata, J.I., Pye, J., Lovegrove, K., 2013. *A transient model for the heat exchange in a solar thermal once through cavity receiver*. Sol. Energy 93, 280–293.

[11] Zhang, W.J., Zhang, C.L., 2006. *A generalized moving-boundary model for transient simulation of dry-expansion evaporators under larger disturbances*. Int. J. Refrig. 29, 1119–1127.

[12] Bonilla, J., Dormido, S., Cellier, F.E., 2015. *Switching moving boundary models for two-phase flow evaporators and condensers*. Commun. Nonlinear Sci. Numer. Simul. 20, 743–768.

[13] Qiao, H., Aute, V., Radermacher, R., 2014. *An improved moving boundary heat exchanger model with pressure drop*. Int. Refrig. Air Cond. Conf.

[14] Qiao, H., Laughman, C.R., Aute, V., Radermacher, R., 2016. *An advanced switching moving boundary heat exchanger model with pressure drop*. Int. J. Refrig. 65, 154–171.

[15] Lapusan, C., Balan, R., Ciprian, R.A.D., Plesa, A., 2015. *Development of a multi-Room building thermal model for use in the design process of energy management systems*. ACTA Tech. NAPOCENSIS-Series Appl. Math. Mech. Eng. 58.

14th IEA Heat Pump Conference
15-18 May 2023, Chicago, Illinois

Development and application of a new calculation method for double spiral ground heat exchangers

Kunning Yang[a*], Takao Katsura[b], Katsunori Nagano[b*]

[a]Graduate school of Engineering, Hokkaido University, Sapporo, 060-8628, Japan
[b]Faculty of Engineering, Hokkaido University, Sapporo, 060-8628, Japan

Abstract

This study provides a new calculation method for double spiral ground heat exchangers (GHEs) and involves the combination of the analytical infinite line source (ILS), and infinite cylindrical source (ICS) models with the capacity resistance model (CaRM). Method adopts the concept of fin efficiency, enabling it to calculate underground temperature change easily and accurately, followed by integration into a simulation tool for ground source heat pump (GSHP) systems. Verification was done by comparing the simulation results with actual operating data, measured from a zero-energy building (ZEB) in Sapporo, Japan. Under conditions of instantaneous large heat injection, significant differences were observed between the simulation the actual measurements during initial 50 h. the number of temperature nodes in the network was increased to effectively reduce the error between simulations and measurements.

© HPC2023.
Selection and/or peer-review under the responsibility of the organizers of the 14th IEA Heat Pump Conference 2023.

Keywords: ground source heat pump system, double spiral ground heat exchangers, capacity resistence model, energy pile,simulation;

1. Introduction

More than 140 countries have pledged to achieve net-zero emissions at the COP 26 meeting held in UK, 2021 [1], this has reaffirmed that climate change is the greatest threat to all of us. Building energy consumption accounts for 40% of the total global energy consumption, to substantially reduce greenhouse gas emissions, energy supplies for space cooling/heating must be shifted from fossil fuels to renewable energy sources [2].

Ground source heat pump (GSHP) systems are gaining popularity in residential and commercial buildings due to their high energy efficiency, environmental friendliness, and ease of integration with other energy systems. However, the biggest obstacle to promoting GSHP systems is the large amount of land required and the high cost of drilling for ground heat exchangers (GHEs).

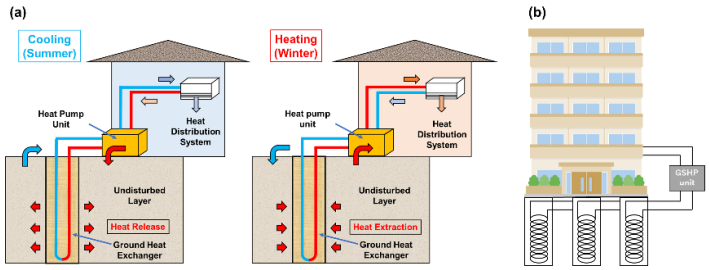


Fig. 1. (a) Operation of GSHP system with borehole U-tube GHE; (b) Buildings with GSHP system using thermal piles

Thermal piles have been adopted in recent years to tackle these problems. Thermal pile is a type of energy structure that incorporates the GHEs of GSHP systems through the foundation elements of the building.

* Kunning Yang. Tel.: +81-011-706-6287; fax: +81-011-706-6287.
E-mail address: kunning.yang.h4@elms.hokudai.ac.jp .

Thermal piles can not only support the structure of the building but also serve as GHEs [3]. In this paper, a new simulation tool is developed by combining this calculation method (for temperature change inside the thermal pile) with a ground temperature simulation program for GSHP systems (for temperature change outside the thermal pile) for temperature simulations of thermal piles with double spiral pipe GHEs.

2. Development of the new calculation method for double spiral pipes

In the previous study, several methods were used to calculate the heat transfer inside the spiral tube. Cui et al. [4] proposed a ring-coil heat source model but did not provide exact solutions for the spiral coil source. Zhang et al. [5] made improvements by considering the arrangement and pitch of spiral pipe and simplified the calculation. This new model, however, cannot be applied if the grouting material differs from that of the surrounding soil. Park et al. [6] created an efficient spiral coil source model along with its analytical solution, but its long-term operational efficiency is yet to be verified.

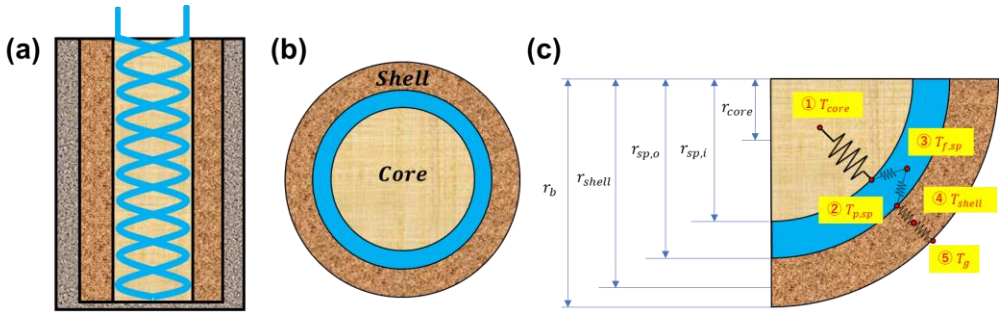


Fig. 2. (a) Sectional view of thermal pile, (b) Top view of thermal pile, and (c) Partial detail of thermal pile

The larger diameters of the thermal pile than the common value of the borehole make it essential to consider the heat capacity of the grouting material when studying the thermal performance of double spiral pipe GHE. Previous works [7] presented a numerical model, CaRM-He, to solve this problem and analyzed the thermal behavior of a short-length spiral pipe GHE.

This study also employed the capacity and resistance model (CaRM) to account for the thermal capacitance of grouting material, temperature nodes were arranged in the radial direction to reduce the amount of calculation while obtaining acceptable calculation accuracy. The volume of the thermal pile is divided into three parts (Fig. 2):

- "core" part: grouting material
- double spiral tube
- "shell" part: thermal pile material between spiral tube and borehole boundary

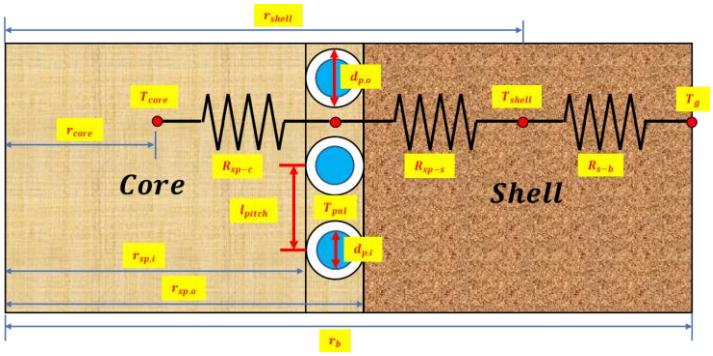


Fig. 3. Sectional drawing of the thermal pile

The heat transfer processes inside thermal pile consist of three parts [7] [8]:

- heat conduction in the "core" part
- heat convection between flowing circulating fluid and pipe surface
- heat conduction in the "shell" part

As the outer diameter of the pipe $d_{p,o}$ is much smaller than the borehole diameter, the double spiral pipe was considered as a line that injects/absorbs heat into/from the ground in summers/winters [8]. Assuming this, the thermal resistances between "core" part and double spiral pipe, double spiral pipe and "shell" part, and "shell" part and surrounding soil can be respectively expressed in form of equations (Fig. 3):

$$R_{sp-c} = \frac{1}{2\pi \cdot l_b \cdot \lambda_{core}} \cdot ln\left(\frac{r_{sp,i}}{r_{core}}\right) \quad (1)$$

$$R_{sp-s} = \frac{1}{2\pi \cdot l_b \cdot \lambda_{shell}} \cdot ln\left(\frac{r_{shell}}{r_{sp,o}}\right) \quad (2)$$

$$R_{s-b} = \frac{1}{2\pi \cdot l_b \cdot \lambda_{shell}} \cdot ln\left(\frac{r_b}{r_{shell}}\right) \quad (3)$$

However, the temperature of the layer between "core" and "shell", which contains double spiral pipe and grout, is difficult to calculate. We have found a calculation method adopting fin efficiency to solve this problem.

Previous studies proposed a calculation method, Kollmar-Liese method, for the thermal emission of flat floor heating panels with a cylindrical heat source [10]. In a hot-water floor heating system, as shown in Fig. 4 (a), it is assumed that a virtual fin with a width (d) equal to the outer diameter ($d_{p,o}$) of the pipe is attached to the pipe. Fig. 4 (b) depicts a combination of a virtual fin and a pipe, fin efficiency η of the virtual fin can be calculated:

$$m = \sqrt{\frac{2\alpha}{\lambda \cdot d}}; h = \frac{l_{pitch} - d_{p,o}}{2}; \eta = \frac{tanh(m \cdot h)}{m \cdot h} \quad (4)$$

Assuming that the surface temperature of the pipe is T_H and the ambient temperature is T_L, the mean temperature T_m of the virtual fin can be calculated using the Kollmar-Liese method [10]:

$$T_m = T_L + \eta \cdot (T_H - T_L) \quad (5)$$

The vertical section of the double spiral pipe GHE resembles a "vertical" floor heating panel (Fig. 4 (c)). The convective thermal resistance between circulating fluid and pipe surface can be expressed as:

$$R_{sp-f} = \frac{1}{2\pi \cdot r_{p,i} \cdot l_{sp} \cdot \alpha_f} + \frac{1}{2\pi \cdot \lambda_p \cdot l_{sp}} \cdot ln\left(\frac{r_{sp,o}}{r_{sp,i}}\right) \quad (6)$$

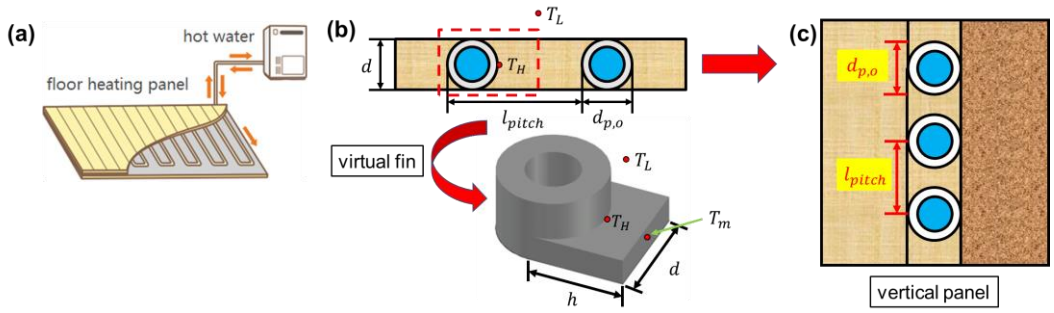


Fig. 4. (a) A typical radiant floor heating system (b) Principle of Kollmar-Liese method (c) Similarity between floor heating panel and double spiral pipe GHE

According to Kollmar-Liese method, heat transfer coefficient between spiral tube and "core" grout, spiral tube and "shell" grout can be calculated [9]:

$$K_{fcore} = \frac{1}{2\pi \cdot r_{core} \cdot l_b \cdot R_{sp-c}} \quad (7)$$

$$K_{fshell} = \frac{1}{2\pi \cdot r_{shell} \cdot l_b \cdot R_{sp-s}} \tag{8}$$

$$Z_{core} = \frac{l_{pitch} - d_{p,o}}{2} \cdot \sqrt{\frac{2 \cdot K_{fcore}}{\lambda_p \cdot d_{p,o}}} \tag{9}$$

$$Z_{shell} = \frac{l_{pitch} - d_{p,o}}{2} \cdot \sqrt{\frac{2 \cdot K_{fshell}}{\lambda_p \cdot d_{p,o}}} \tag{10}$$

$$\eta_{fshell} = \frac{tanh(Z_{shell})}{Z_{shell}} \tag{11}$$

$$\eta_{fcore} = \frac{tanh(Z_{core})}{Z_{core}} \tag{12}$$

Using Kollmar-Liese method, the average temperature of the "vertical" panel T_{pnl} can be expressed as:

$$T_{pnl} = \frac{1}{2}\left[\left(T_{sp} - T_{core}\right) \cdot \eta_{fcore} + T_{core}\right] + \frac{1}{2}\left[\left(T_{sp} - T_{shell}\right) \cdot \eta_{fshell} + T_{shell}\right] \tag{13}$$

Using T_{pnl}, the heat balance equation in each part can be expressed:

- Circulating fluid in double spiral pipe:

$$c_f \cdot \rho_f \cdot \pi \cdot r_{p,i}^2 \cdot l_{sp} \cdot \frac{dT_f}{dt} = c_f \cdot \rho_f \cdot v_f \cdot \left(T_{f,in} - T_{f,out}\right) - \frac{T_{f,sp} - T_{p,sp}}{R_{sp-f}} \tag{14}$$

- The "core" part:

$$c_{core} \cdot \rho_{core} \cdot \pi \cdot r_{sp,i}^2 \cdot l_b \cdot \frac{dT_{core}}{dt} = \frac{T_{pnl} - T_{core}}{R_{sp-c}} \tag{15}$$

- The "shell" part:

$$c_{shell} \cdot \rho_{shell} \cdot \pi \cdot (r_b^2 - r_{sp,o}^2) \cdot l_b \cdot \frac{dT_{shell}}{dt} = \frac{T_{pnl} - T_{shell}}{R_{sp-s}} - \frac{T_{shell} - T_s}{R_{s-b}} \tag{16}$$

Our laboratory has developed a high-speed simulation program for GSHP systems in previous research. It is based on the analytical model of Infinite Line Source (ILS) and Infinite Cylindrical Source (ICS) models [10]. In this research, the new calculation method for double spiral GHEs was integrated into the simulation program in MATLAB R2020b, and the calculation flow is illustrated in Fig. 5.

For one time step $dt = 60s$, the calculation procedures are under:

- Electricity consumption E_{hp} of the heat pump unit and fluid temperature $T_{1,out}$ flowing out of the heat pump unit are calculated using the building load Q_2 (secondary side), heat extraction/injection from/into the ground Q_1 (primary side). $T_{1,out}$ is equal to the inflow temperature of the circulating fluid $T_{p,in}$.
- The heat transfer processes inside the thermal pile and inflow temperature of the circulating fluid $T_{p,out}$ have been calculated using the new calculation method proposed. $T_{p,out}$ is equal to the fluid temperature $T_{1,in}$ flowing into the heat pump unit, which will be used for the next time step.
- The surrounding soil temperature T_s (outside the thermal pile) is calculated in GroundClub, T_s is equal to the thermal pile boundary temperature T_b, which will also be used for the next time step.

The simulation results of the GHSP system for long-term operations can be obtained by performing continuous step-by-step simulations of temperature changes in pipe inlet $T_{p,in}$, outlet $T_{p,out}$, and ground T_s.

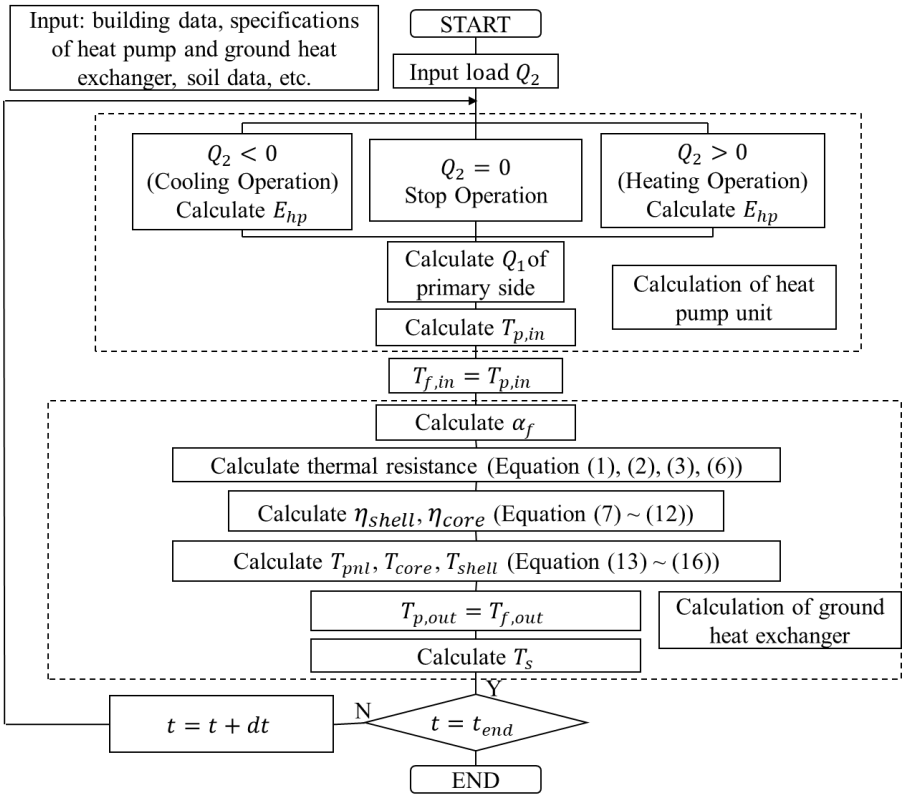


Fig. 5. Calculation flowchart for the GSHP system with double spiral pipe GHEs

3. Results and analyses

The verification work was carried out in a 3-story house in Sapporo, Japan. Table 1 lists the basic information about the house. Energy efficient technologies used in this house include a photovoltaic panel system for electricity supply, heat recovery ventilation system, and GHSP system, FCU (fan coil unit), and radiant air conditioning system. The house has been in operation since 2021/7 and was verified as a nearly-ZEB (zero energy building).

There are 3 GSHP units (rated power 10 kW) and 24 thermal piles installed on each floor of the house to provide space heating and cooling and snowmelt in winter. Figure 14 illustrates the system diagram of each floor. The thermal pile configuration for each floor is as follows: 4 (2 series × 2 parallel) for 1st floor (stores), 6 (2 series × 3 parallel) for 2nd floor (office rooms), 4 (1 + 1 + 2) for 3rd floor (office rooms and meeting rooms) and 10 for snowmelt (Fig. 6 (c)).

Each GSHP unit has temperature sensors and electromagnetic flow meters that collect real time measurements of pipe inlet temperature $T_{p,in}$, outlet temperature $T_{p,out}$, circulating fluid flow v_f, and power consumption of heat pump unit E_{hp}. Data was collected over a period of one year and was used for the purpose of verification.

Table 1. Basic information of the house

Building	**Energy saving technologies**
Location: Sapporo, Japan	Heat recovery ventilation system
Floor area: 650.85 m^2	High thermal insulation
Number of floors: 3	PV system
Operation time: 2021/7 ~ now	Radiant air conditioning system
Structure: Wooden	GSHP system

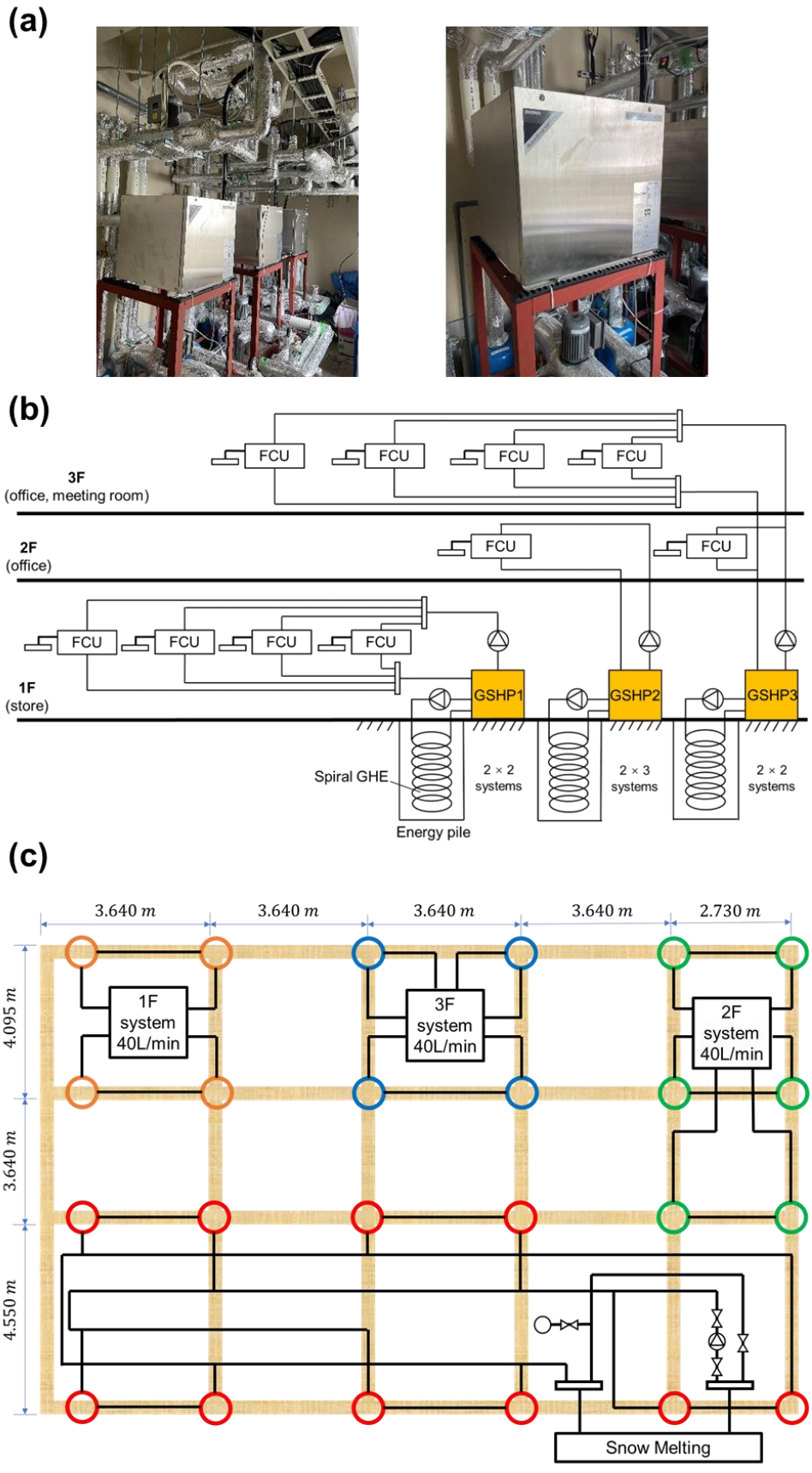


Fig. 6. (a) Heat pump units on the first floor, (b) Schematic diagram of the 3-story house, (c) Layout diagram of thermal piles installed in the house

Table 2. GSHP system specifications

Description	Unit	Value
Thermal pile		
Depth l_b	*m*	20
Outer radius r_b	*m*	0.3
Inner radius $r_{sp,o}$	*m*	0.2
"Core" part (cement & soil)		
Thermal conductivity λ_{core}	*W/m·K*	0.6
Specific heat capacity c_{core}	*kJ/kg·K*	0.9
Density ρ_{core}	*kg/m³*	2100
"Shell" part (concrete)		
Thermal conductivity λ_{shell}	*W/m·K*	2.0
Specific heat capacity c_{shell}	*kJ/kg·K*	0.95
Density ρ_{shell}	*kg/m³*	2500
Double spiral GHE		
Pipe outer diameter $d_{p,o}$	*m*	0.032
Pipe inner diameter $d_{p,\mathrm{i}}$	*m*	0.026
Spiral distance l_{pitch}	*m*	0.25
Thermal conductivity of pipe material λ_p	*W/m·K*	0.38
Length of spiral pipe l_{sp}	*m*	94.63
Soil		
Specific heat capacity λ_s	*kJ/kg·K*	2
Density ρ_s	*kg/m³*	1500
Initial temperature T_s	*℃*	12
Circulating fluid: 40% ethylene glycol solution		

Table 2 gives the specifications of the GSHP system. In October 2021, an in-site thermal response test (TRT) was performed to determine the thermal conductivity of the ground soil. The data were analyzed using the Kelvin Line Theorem, and the effective thermal conductivity of soil was calculated to be λ_s=1.846 (W/m·K). By applying this value to the simulation, the verification work was performed by comparing the measured and simulated data and simulation under two cases discussed below:

3.1. Space cooling in summer

During the space cooling period, the indoor room temperatures were set to 26 °C. As majority of the rooms on the first floor are occupied, GSHP unit 1 ran the longest. As such we chose this unit for data analyses. The heat injection from the house into ground can be calculated using the hourly recorded pipe inlet/outlet temperature and the flowrate data of the circulating fluid during the space cooling period (Fig. 7 (a)):

$$Q_{injection} = \rho_f \cdot c_f \cdot v_f \cdot (T_{p,in} - T_{p,out}) \tag{16}$$

Then heat injection during this period was used as the primary side load Q_1 for subsequent simulations. Except for the preparation time, the verification period was set as 2021/8/1–2021/8/31. Fig. 7 (b) shows the comparative hourly changes of the pipe inlet temperature $T_{p,in}$ for both, measured and simulated data.

The RMSE (Root Mean Squared Error) value between measurement and simulation data from 8/1 to 8/31 was reported to be 0.73, indicating the accuracy of the simulation tool. The simulated and measured average temperatures were reported to be 19.71 °C and 19.77 °C, respectively. Changes in both temperatures display similar trends, with minor differences when the temperatures change rapidly.

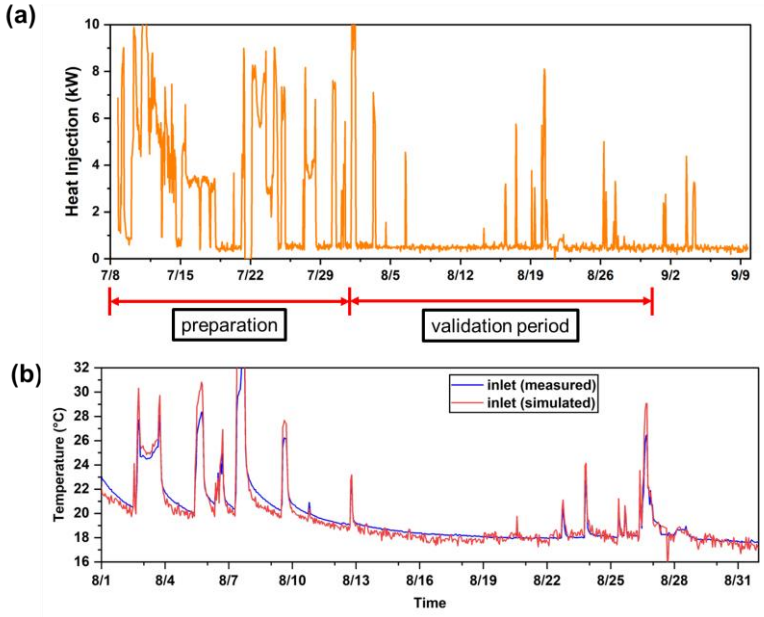


Fig. 7. (a) Heat injection into the ground during space cooling period (b) Pipe inlet temperature during space cooling period

3.2. Space heating in winter

All GSHP units were set to provide 45 °C hot water during the space heating period, while the indoor room temperatures were set to 22 °C. The recorded data was used to calculate the heat extracted from the ground, the results for which are shown in Fig. 8 (a):

$$Q_{extraction} = \rho_f \cdot c_f \cdot v_f \cdot (T_{p,out} - T_{p,in}) \quad (17)$$

Fig. 8 (b) plots the comparison between measured and simulated data for pipe inlet temperature. Excluding maintenance and holiday time, the verification period was selected from 1/7 to 2/7, which is the coldest period in Sapporo, when space heating is most needed. The results show that the temperatures between measurement and simulation are well matched with an RMSE value of 1.06. This value is acceptable and demonstrates the effectiveness of this simulation tool.

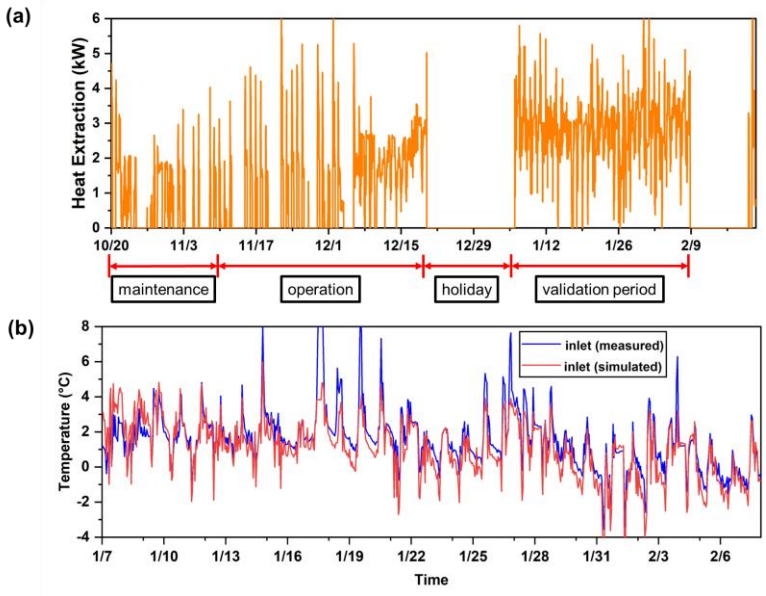


Fig. 8. (a) Heat extraction from the ground during space heating period (b) Pipe inlet temperature during space heating period

This simulation tool has been designed to generate high accuracy performance assessment results to make sound estimates supporting the early-stage decision-making. The summer and winter verifications show that this simulation tool for performance prediction can be applied in the preliminary design phase of future GSHP systems using thermal piles and double spiral pipe GHEs.

4. Discussion

The measurement results of the TRT test were compared with the simulation results during the verification works, as shown in Fig. 9. Although the two sets of data agree well after a period of 100 h, there are significant errors in both pipe inlet and outlet temperatures during initial 50 h. This means that, when applying the CaRM model, there will be a significant difference in the simulated and calculated temperature changes over a short period of time in case of large instantaneous heat injections.

This is mainly because the CaRM or lumped thermal capacity model assumes that the temperature of each solid is spatially independent (uniform) and can be represented by the same temperature. If the volume of the solids corresponding to the temperature nodes is too large, the represented temperatures may deviate from the actual temperatures.

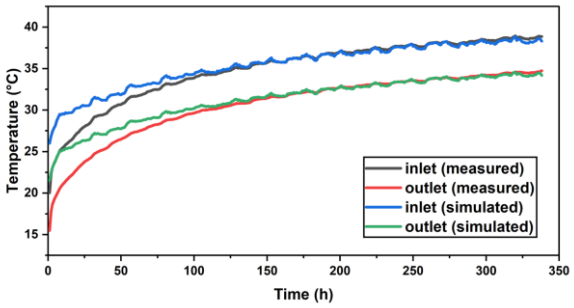


Fig. 9. Comparison of pipe inlet & outlet temperature between simulation and measurement

To solve this problem, the size of solid can be reduced so that the network of interconnected thermal resistances and capacities has a finer mesh. The “core” and “shell” part are divided into n regions (Fig. 10 (a)), corresponding to n temperature nodes. With this, the heat load and circulating fluid flow in the initial 50 h of TRT can be used as an input for the simulation, Fig. 10 (b) shows that the deviation between the simulation results and the actual measured data reduces with increase in temperature nodes during the initial 30 h. This thus proves that the simulation tool can also be used for short-term operation predictions.

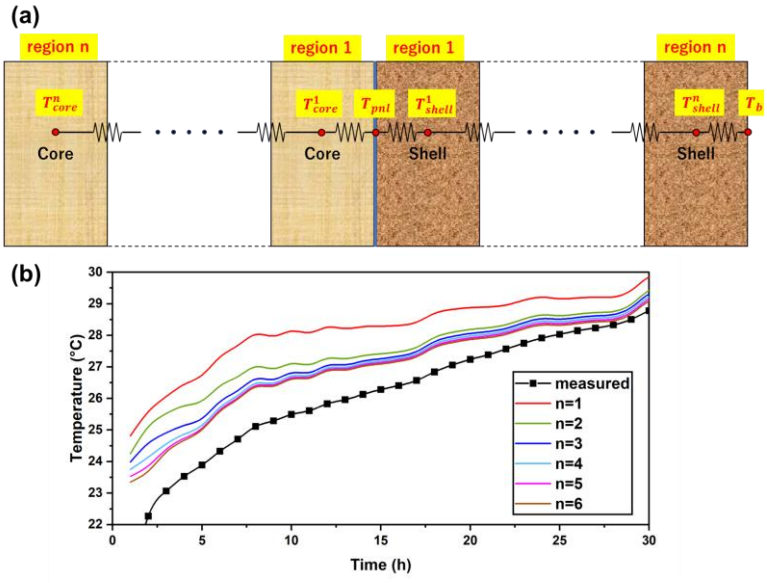


Fig. 10. (a) Concept of dividing “core” and “shell” part into n annual regions (b) Comparison of pipe inlet temperature in initial 30 h

5. Conclusion

The proposed new calculation method based on the CaRM model is an improvement over the previous ones as it adopts the concept of fin efficiency and integrates a simulation program for GSHP system. The main findings of this paper are:

- Different from the traditional U-shaped pipe GHE, the double spiral pipe GHE adopts shorter underground borehole, but has a larger area for heat exchange between the ground and circulating fluid without additional drilling work, which saves the initial costs of the GSHP system and promotes its use in the future.
- By replacing the spiral pipe with a "vertical" heat generating/absorbing panel, the temperature changes in each part of the thermal pile can be easily obtained without a huge amount of calculation.
- Verification work carried out in an energy-efficient house proved that the simulation tool produces reliable and high-precision simulation results for the long-term operation of GSHP systems, both in summers and winters. This would assist in the preliminary designing phase of future GSHP systems.
- For short-term simulations of less than 50 h, the simulated results can still agree well with the measured results by adding more temperature nodes to the thermal network.

Acknowledgements

This work was supported by JST SPRING, Grant Number JPMJSP2119. And this study is based on results obtained from the project "Renewable energy heat utilization technology development for cost reduction", commissioned by the Japan national agency NEDO. The authors also thank M's Industry Co., Ltd and Japan Pile Corporation for their assistance in this research project.

Nomenclature

Symbols		**Subscripts**	
l	length/depth, m	b	borehole of thermal pile
η	fin efficiency	sp	spiral pipe
T	temperature, ℃	s	ground soil
R	heat resistance, K/W	f	circulating fluid
r	radius, m	in	inlet
d	diameter, m	out	pipe outlet
α	heat transfer coefficient, $W/m^2{\cdot}K$	o	outer
λ	thermal conductivity, $W/m{\cdot}K$	i	inner
v	flow rate, m^3/s	$core$	"core" part
Q	thermal load, kW	$shell$	"shell" part
ρ	density, kg/m^3	pnl	"vertical" panel
c	specific heat capacity, $J/kg{\cdot}K$	p	GHE pipe
E	electricity consumption, kW	hp	heat pump

References

[1] UNFCC. *COP26 Explained*.; 2021.
[2] Ma Z, Xia L, Gong X, Kokogiannakis G, Wang S, Zhou X. Recent advances and development in optimal design and control of ground source heat pump systems. *Renewable and Sustainable Energy Reviews*. 2020;131.
[3] Wang D, Lu L, Zhang W, Cui P. Numerical and analytical analysis of groundwater influence on the pile geothermal heat exchanger with cast-in spiral coils. *Appl Energy*. 2015;160.
[4] Cui P, Li X, Man Y, Fang Z. Heat transfer analysis of pile geothermal heat exchangers with spiral coils. *Appl Energy*. 2011;88(11).
[5] Zhang W, Yang H, Lu L, Cui P, Fang Z. The research on ring-coil heat transfer models of pile foundation ground heat exchangers in the case of groundwater seepage. *Energy Build*. 2014;71.

[6] Park Sk, Lee SR, Park H, Yoon S, Chung J. Characteristics of an analytical solution for a spiral coil type ground heat exchanger. *Comput Geotech*. 2013;49:18-24.
[7] Katsura T, Higashitani T, Fang Y, et al. A new simulation model for vertical spiral ground heat exchangers combining cylindrical source model and capacity resistance model. *Energies (Basel)*. 2020;16(3).
[8] Serageldin AA, Radwan A, Katsura T, Sakata Y, Nagasaka S, Nagano K. Parametric analysis, response surface, sensitivity analysis, and optimization of a novel spiral-double ground heat exchanger. *Energy Convers Manag*. 2021;240.
[9] Ishino, H. Research on Calculation Method of Thermal Design Load in Radiant Heating and Cooling Systems. *Sixth International IBPSA Conference (BS' 99)*. 1999; 885-892.
[10]Katsura T, Nagano | Katsunori, Sakata Y, Wakayama H. A design and simulation tool for ground source heat pump system using energy piles with large diameter. Published online 2019.

14th IEA Heat Pump Conference
15-18 May 2023, Chicago, Illinois

Hydronic Optimization for a good Heat Pump Performance

Gaia Balzarini*, Peter Gammeljord[a], Jan Eric Thorsen[b], Torben Funder-Kristensen[c]

* Director Industry Affairs and Strategic Projects, Danfoss, Nordborg, 6430, Denmark.
[a]Application and Control Specialist, Danfoss, Nordborg, 6430, Denmark.
[b]Director, Global Application Expert, Danfoss, Nordborg, 6430, Denmark.
[c] Ph.D. Head of Industry Affairs , Danfoss, 6430 Nordborg, Denmark

* Corresponding author. Tel.: +39 3355698875;
E-mail address: gaia.balzarini@danfoss.com.

Abstract

Many gas-fired boilers are likely going to be replaced with heat pumps in the very close future [1], supported by current energy plans. Air-to-water heat pumps will be increasingly used as sources for hydronic heating systems. Consequently, water-based systems need to have low OPEX for obtaining a solid business case with good ROI. As a common pragmatic solution an A/W heat pump is recommended with low temp. heating systems, typically floor heating, where the temperature curve is lower compared to conventional radiator heating system. However, in most boiler replacement cases radiators are installed in residential and residential like buildings. Acceptable ROI is obtained by having superior SCOP of the HP together with an optimized design of the hydronic system, including distribution and heat emission. This paper describes the role of hydronic controls, which in traditional radiator heating systems is governed by TRVs and Hydronic Balancing, the relation to the HP efficiency, with the goal to achieve best ROI. This is realized without compromising comfort, and is a marginal cost of the additional Building Automation and Control devices to be installed or upgraded together with the HP. Investigations and results are oriented to parameters which leads to reduced operational temperatures and longer lifetime for the HP.

© HPC2023.
Selection and/or peer-review under the responsibility of the organizers of the 14th IEA Heat Pump Conference 2023.

Keywords: heat pump, low temperature readyness, TRVs,residential heating, condensing boiler replacement, electrification of heating, controls, thermostats;

1. Introduction

1.1 Methodology

Best practice and system design was investigated through interviews to technical specialist from the industry in focus markets, mainly designers, project engineers and installers in UK, IT, FR and DE and through a wide search of the recent literature (see Bibliography and References) including e.g., associations white papers, technical articles, and best practice manuals, dedicated to application, and design for residential buildings retrofit. Calculations and theoretical simulations were carried out to investigate limitations on hydronic flows for the building heating installation. Analysis of the building stock was made using available data from BPIE to show potential energy savings when reducing indoor temperatures and thus accepting the performance of the existing radiators, working at lower temperatures with a heat pump.
Unicity of the work is based on the combined knowledge of the authors on heat pumps technology and on building hydronics. These two perspectives are necessary to optimize the system in retrofit applications, as the main system components in heating distribution and emission of existing old buildings were not designed and commissioned to match the characteristics of heat pumps. The paper formalizes a pragmatic methodology based on steps, that helps installers in the system design evaluation and needed corrective actions when heat source technology is changed.

1.2 Acronyms and Nomenclature of relevance.

HP	Heat pump
A/W	Air to Water
SCOP	Seasonal Coefficient of Performance
COP	Coefficient of performance (kWhth/kWhel)
TRV	Thermostatic Radiator Valve
eTRV	Electronic Thermostatic Radiator Valve
W/W	Water to water
RV	Radiator Valve
CAPEX	Capital expenditure
OPEX	Operational Expenditure
ROI	Return on Investment
Tsupply	Supply water temperature from the HP
Treturn	Return water temperature to the HP
Supply	Supply water from the HP
Return	Return water to the HP
Heat sink	Entity to which an amount of energy must be or can be provided

1.3 Boiler replacement with HP in small systems.

The electrification of heating means a tremendous acceleration of the deployment rate of heat pumps. Heat pumps are used with different technologies and capacities, they can be adapted to natural heat sources (i.e., air and water) or recover energy from waste heat sources that would otherwise be lost. Large scale MW sized heat pumps will typically be used in connection with district energy systems and local planning needs to be done to establish the best size and distribution of the heat pumps in connection with heat source locations. In areas where district heating is not foreseen and in buildings where hydronic heat distribution is already installed, a ground source (W/W) heat pump or an air to water (A/W) heat pump will often be preferred as replacement for a gas or oil boiler.

In contrast to a boiler which has a nearly constant efficiency over supply temperature (condensing boiler efficiency mainly depends on return temperature), the heat pump has a more complex nature to observe if the optimal efficiency should be achieved. The energy output from the heat pump consists of the energy from the heat source and of the electricity provided to create the temperature lift between the heat source and heat sink. The electricity consumption increases with the temperature lift i.e., the supply temperature of the hydronic systems should be minimized to have an optimal COP. In new buildings – or building undergoing deep renovation - this can be done by using low temperature floor heating. However, in buildings where deep renovation is not done, the existing heat emitters are often kept, and the risk is that the newly installed heat pumps run with a far lower COP than nominal. This is often because basic optimization parameters on the buildings hydronic system are not sufficiently observed. With other words, the building hydronic system should be optimized for the heat pump operation to ensure consumers the full potential of the “boiler to heat pump” replacement.

Target objective of this paper is to describe what to observe when a small size boiler (typically wall hanging) is replaced in a single-family house or dwelling where radiators are used as heat emitters.

2. Low temperature readiness of buildings

Following EN14825 “low temperature readiness” of a building means its ability to provide the users good comfort when the energy source delivers supply temperatures at 35°C or lower.
The far majority of buildings including their heating systems were designed and built throughout the last century. Past retrofit measures may have changed the primary fuels used to service the building (e.g., coal replaced by oil, then by gas), but many heat distribution components and heat emitters still remain a part of the current heating systems.

2.1. Readiness evaluation

Typical other elements to evaluate the low temperature readiness of the building are:

1) Reduce the basic energy demand: evaluate and optimize the level of envelope insulation. Walls, windows, roofs can be insulated, but also minor means such as improving the backwall of the radiator by installing an insulating/infrared reflecting panel.
2) Optimise the ability to operate at reduced supply temperatures. The size of specific radiators: Often radiators are over dimensioned for the temperatures during boiler operation. This may turn into an advantage for the heat pump operation at lower temperatures, especially when adapting the right controls and using them in the right way. Replacement of critical radiators. A simple way to increase the heat output is change from e.g., 1 panel to multi panel radiators with convectors, of the same installation dimensions. This implies no change on the piping system.
3) Validate and upgrade the installed controls: building automation and control systems play a big role in energy efficiency and the ability to achieve heating needs at lowest possible supply temperatures. Controls should be checked or upgraded to ensure the low temperature demands. E.g., in relation to flow capacity and hydraulic balancing.
4) Behavior of occupants: Are they utilizing the available radiator surfaces in the optimal way by having all radiators emitting heat in a balanced way. Are they able to program the heating according to different time schedule? Low temperature heating needs a more stable temperature setting.

2.2. Resilient buildings

The water flow supply and return temperatures to the heating emitters are impacted by the type of heat source installed. A heating system using traditional boilers operates normally with supply temperatures of 70-80 degrees with temperature drops of 15-20 degrees trough the heat emitters. The high supply temperature is obtained without compromising the efficiency as traditional boilers are much less sensitive on this parameter. When installing a heat pump the supply temperature can be directly set, but this temperature setting has a high impact on the efficiency of the system and thereby also the OPEX. Heat pumps should as a rule of thumb always be operated with the lowest possible supply temperatures.

A good performing heating system, independent of the heating source, relies on efficient controls, appropriate temperature settings, and a well-balanced hydraulic system.
A balanced hydraulic heating system provides a uniform temperature drop across all radiators. This temperature drop, at nominal or design conditions, is expected to be 15-20 °C when applying a condensing boiler or even higher with a connection to district heating. With a heat pump, this drop due to the low supply temperature is likely in the range of 5-10°C. It means the heat emitter has a more uniform temperature distribution to compensate for the lower supply temperature.
A properly balanced building distribution enables to reduce supply temperature [2], as the balancing will avoid overflow by specific bad performing radiators or wrong operated TRVs. Specific radiators that are too small to emit the needed heat output at the desired supply temperature should be replaced. This will likely be limited cost wise, compared to the CAPEX for the heat pump. A study across the EU has shown that hydraulic balancing is unfortunately not common, and only 10% of buildings heating systems are correctly balanced. [3]

3. Radiator design and flow

3.1. Hydronic radiators physics

The heat rate, or emission, from a radiator is defined in EN442-2 and depends on the over temperature ΔT and the radiator constant K_m. Expressed by:

$\Phi = K_m * \Delta T^n$;

Where:
Φ is heat output in W
K_m is the radiator constant.
ΔT is the difference between the mean radiator temperature and the room temperature.
n is an exponent, also defined in the radiator model

Considering that the radiator is not replaced when a heat pump is installed and assuming K_m and n is held constant, the only way to maintain the heat output Φ is to maintain the ΔT of the radiator.
ΔT can be simplified to the difference between the average temperature of the radiator (T_{av}) and the room temperature (T_{amb}).

The simplest method is called the arithmetic over-temperature, where:

$\Delta T = T_{mean} - T_{amb} = (T_{inlet}+T_{outlet})/2 - T_{amb}$.

A more representative method, which takes the nonlinearity of the temperature over the radiator into account, is the logarithmic over-temperature, and will be used in this article, where:

$\Delta T = T_{mean} - T_{amb} = (T_{inlet}-T_{outlet}) / \ln((T_{inlet}-T_{amb})/(T_{outlet}-T_{amb}))$

Maintaining the ΔT requires that when reducing the T_{inlet} ,should be lowest possible for a good HP COP, T_{outlet} should increase, and this requires a higher flow through the radiator [4].

Above simple formulas are used to describe the radiator behavior in a simple way. A more detailed numerical description on the radiator physics can be read in [5] .

3.2. COP vs supply temperature

The COP of the heat pump will increase as the temperature lift is decreasing, see Fig 1 [6], the example of a air to water HP. It means the COP can be maximised by realising a heating system that requires a low supply temperature. This should also be considered when retrofitting a radiator system i.e., the supply temperature should be set as low as possible.

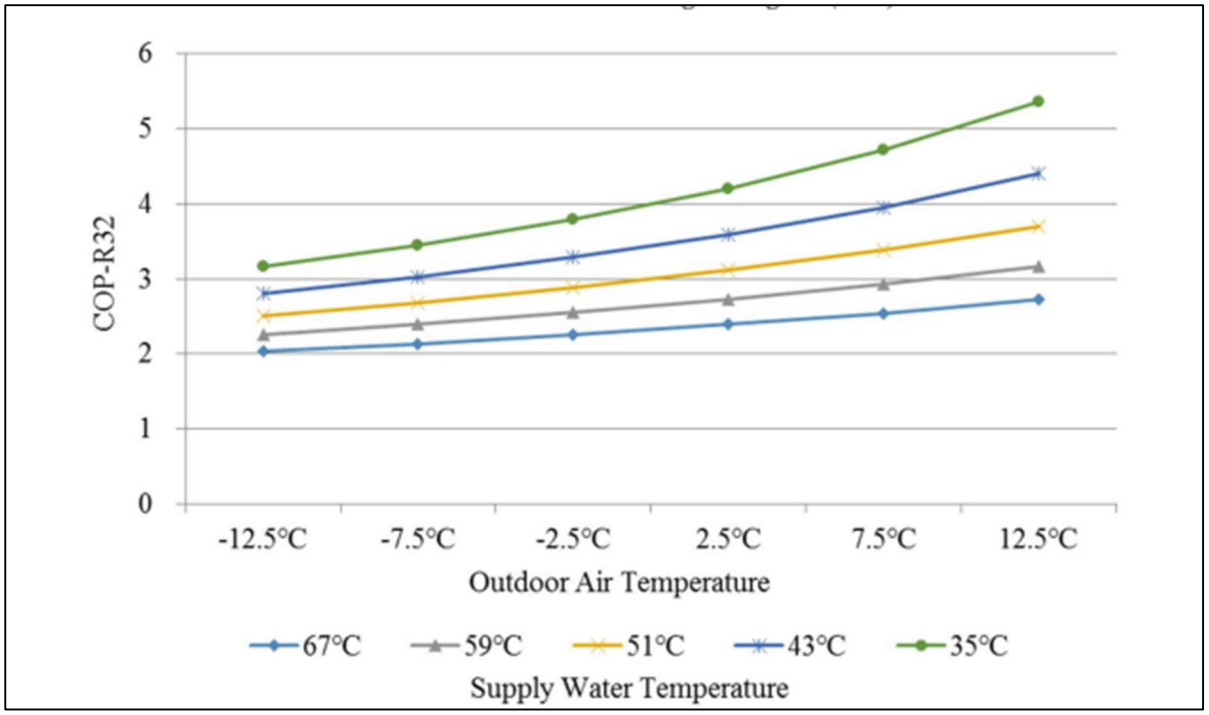


Fig. 1. The COP of air source heat pump operated with R32 under varied outdoor air and supply water temperatures.

3.3. Capacity evaluation and new settings

As mentioned, a challenge when retrofitting is to ensure sufficient capacity or heat emission from the existing radiators when operated at reduced supply temperatures. As described above, the heat emission from the radiators is based on the difference between the mean radiator surface temperature and the room air temperature. E.g., a constant heat emission can be achieved by various sets of inlet and outlet temperatures of the radiator. It basically means by reducing the inlet temperature, the outlet temperature should be increased, and this implies increasing the flow through the radiator. To illustrate this, an example is shown in figure 2. where the flow is uncontrolled, e.g., by a manual radiator valve, RV, and where the flow is controlled, e.g., by a thermostatic radiator valve, TRV.

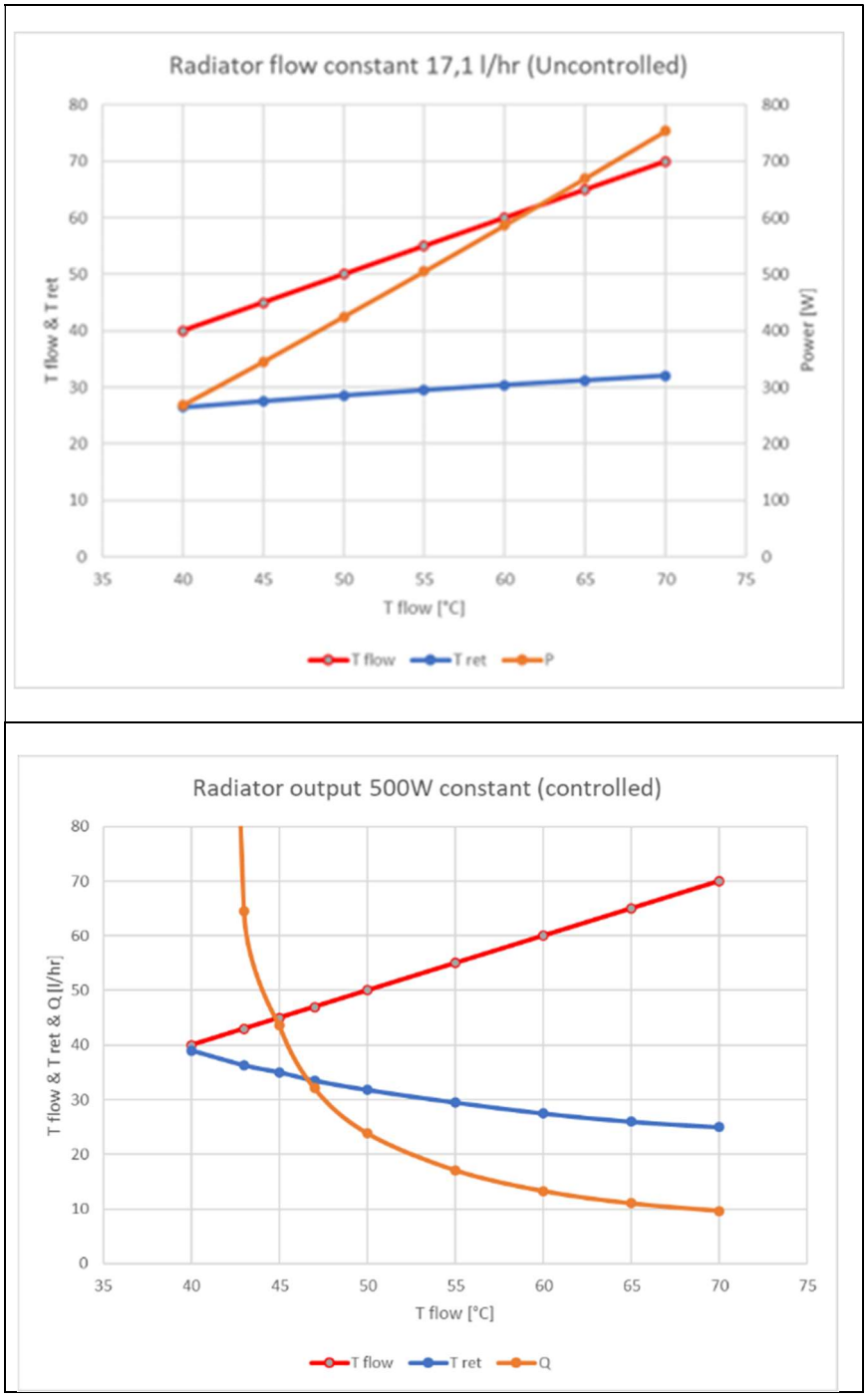


Fig. 2. Radiator basics (example): T flow is supply temperature, T ret is return temperature, P is the heat emission and Q the flow.

In the upper figure the uncontrolled situation or no flow control is shown (RV), represented by a constant flow through the radiator. The heat output is a direct result of the supply temperature, thus only one specific supply temperature is matching the heat load of the room. In this case the example of 500W is used at a supply temperature of 55°C and here the flow of 17,1 l/hr fits. On the lower figure the situation is shown where a flow control is applied (TRV or eTRV). The heat output of the radiator is constant independent on the supply temperature. The supply temperature cannot be below 40°C when emitting 500W is to be kept, and even before reaching 40°C, the maximum flow of the radiator or system is reached. It can also be seen that the radiator return temperature increases when the supply temperature is decreased, this to maintain the mean temperature difference of the radiator surface to the surrounding air, and thus maintaining the same heat emission.

When replacing a traditional high temperature heat source with a Heat pump, with the intention of optimising CAPEX and OPEX, the difference of the radiator inlet and outlet temperature, should be in the range 5-10°C. (Fig.3) The radiator's control concept will therefor need to adapt to the reduced operating temperature. This basically means that the pre-setting and balancing of the radiator and distribution system should have the ability to operate at increased flow levels.

As stated above, it is possible to maintain the heat output of a radiator by increasing the flow rate through it and at the same time reduce the supply temperature (till a maximum acceptable flow level that depends on the radiator, the piping, the flow noise level, the circulation pump head pressure, and control valve capacity). Increasing flow rates create significantly higher head pressure losses and associated higher pump circulator power input. A balance between heat pump COP optimisation, circulation pump consumption and radiator maximum heat emission compared the needs can be simulated. (Fig. 3). The shown COP includes the electricity consumption of the HP and the circulation pump. The HP COP used in the present calculation is based on [7] .

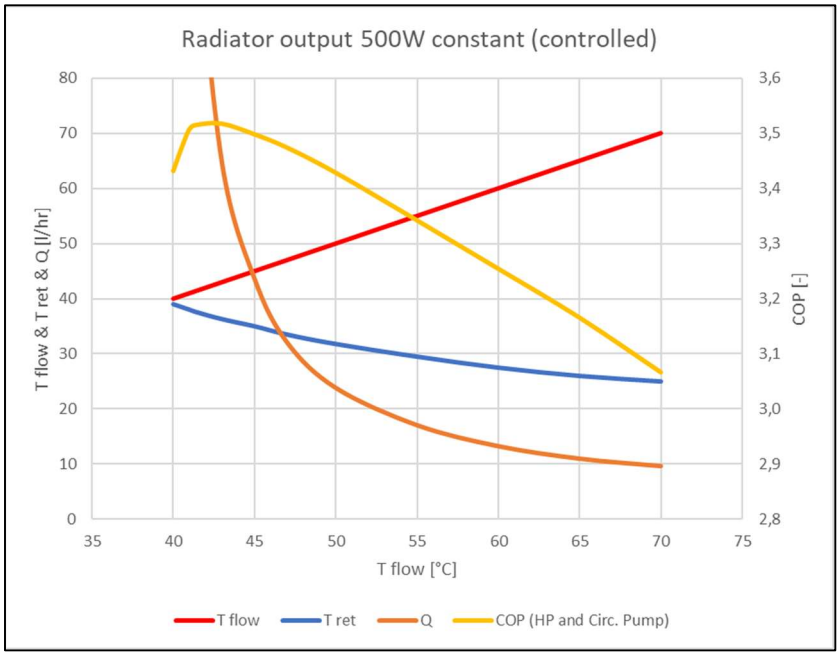


Fig. 3. COP vs other main radiator parameters.

As seen from figure 3, then there is a maximum COP. This point represents the situation where the increased flow, due to the reduced supply temperature, results in reduced electric consumption for the HP but at the same time results in a similar increased electric consumption of the circulation pump. If it is possible to operate at maximum COP depends on the factors mentioned above.

A simple mathematical model has been developed to describe radiator heat emission and flows through radiators when a boiler is being replaced with a heat pump. Through this model it is possible to be guided on different options and parameters when analysing the feasibility of the retrofit. (Fig.4)

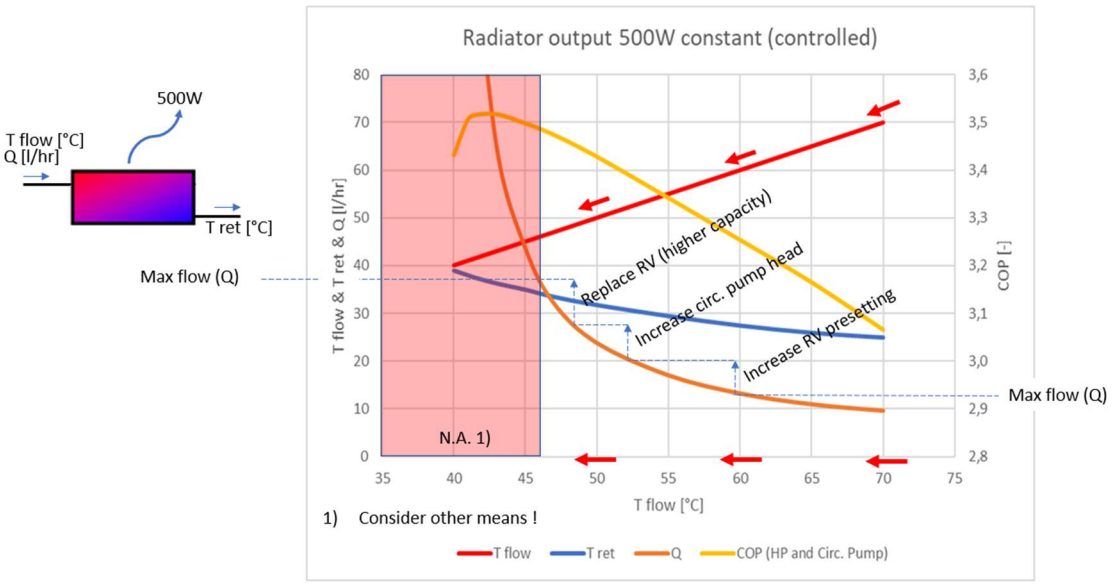


Fig. 4. Relevant steps and changes in parameters at Heat Pump retrofit.

When a heat pump is introduced in the system [8] the temperature drop over the radiator is to be decreased (if possible in the mentioned interval of 5-10°C) and flows are subsequently to be increased. This implies TRVs should be able to provide higher flows through change in the presetting if applicable. Presetting is the predetermined maximum flow at a given differential pressure the valve will pass through the radiator valve. The feasibility of a higher presetting should be evaluated when rebalancing the hydronic system for HP operation. The circulation pump head pressure must likely be increased assuming a reserve as is available. If the radiator valve (RV) is limiting the flow, they can be replaced to RVs with a higher capacity. In the example of figure 4, going even to a lower supply temperature (below 47°C) would require other and more costly means, like replacing radiators and/or pipes.
The tradeoff is found in balancing the investment costs in relation to the operational saving due to a higher COP. In this example the supply temperature to the radiator is reduced from 70°C to 46°C, and at the same time the COP is increased from 3,05 to 3,46. The flow through the radiator is increased from 10 l/hr to 38 l/hr, basically a factor 4. For this example, the maximum COP cannot be fully reached, due to flow limitations, see red area Fig. 4 marked N.A. The remaining potential for improving the COP is anyhow limited. The steps mentioned here are options, and an example of priority.

3.4. End users' behaviour and indoor temperatures

BPIE fresh Hotmaps Building Stock Analysis issued in 2022 [9] was used to check energy demand for space heating for the 3 representative abundant building types in 3 European countries (IT, DE, UK), at the hypothesis that heating is turned on when indoor temperature drops below 19-21°C depending on user behaviour. The calculation on equivalent kWh/m2/y thermal need (fig.5) based on national heating degree days shows the space heating demand at different heat 'turn on', or heating degree base temperature, starting conditions. Besides saving energy in general, the heat emitting area relative to the heating demand can be increased tremendously for the sake of efficient heat pump operation in the light of the previous section 3.3. Consequently, it is heavily recommended, when a heat pump is introduced in a traditional radiator heating system, to explain end users they should set indoor temperature at a reasonably low but still comfortable temperature (ideally max 19-20°C), to fully benefit from the retrofitted HPt and avoid changing the radiators. The market investigation reveals that in many cases designers and installers, over the last 50 years over dimensioned radiators and further the building was improved thermally during the years resulting in a basis for a potential well working HP.

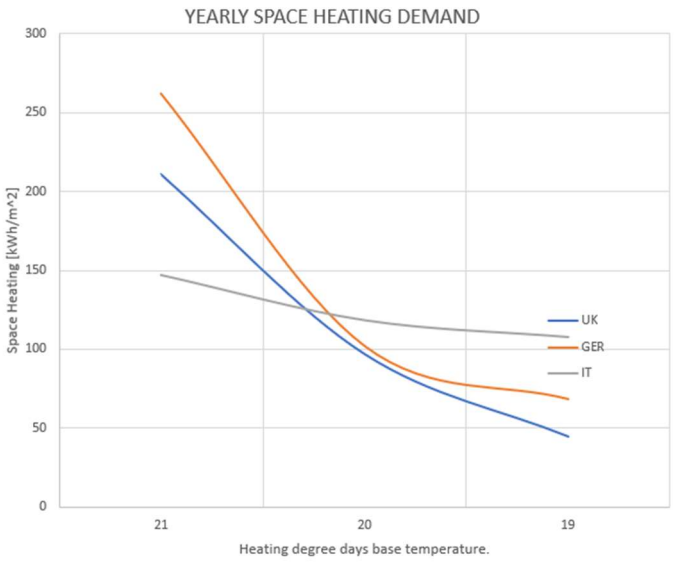


Fig. 5. Yearly space heating demand in UK, GER, IT most abundant buildings.

4. Best practice approach when retrofitting

Previous chapters have described the needed methodology of a efficient retrofit solution.
In practice, there are typical measures to evaluate, that can turn the system into low temperature ready.
Below is a short description of the different options that should be considered prior to retrofit, improving CAPEX, OPEX and ROI:

- Decreasing basic heating loads/losses: when possible and feasible the thermal demands of the building should be decreased by adding insulation to the envelope (walls and roof), changing the windows, or adding winter gardens. The size and cost of the heat pump is related to the improved heating load and thus ROI should be calculated when deciding which means to go for, especially what to do first when doing staged renovation.

- Adding heat emitters. This should be done in the critical rooms only. In fact, the larger the total surface area of the heat emitters, the lower the required supply water temperature for a given rate of heat transfer/thermal load. Normally some of the radiators are over dimensioned for the given room, at the same time their size is set to provide the needed heat power in the coldest day of the winter, while for the remaining time they are more than adequately sized. This means in many cases there is only a need to adding surface in few selected rooms if at all.

- Changing type and/or size of emitters. This includes panel radiators, fan coils, fan assisted panel radiators, fin tube solutions or radiant heating. By changing the emitters, we refer to the intention of adding radiant surface and have a system that can deliver at lower supply temperature. Mostly it is possible to limit this to the critical rooms and the radiator area can be increased by replacing to multi panel radiator on the same wall surface with the same build in dimensions.

- Auxiliary heat source: evaluate how much space-heating energy is needed during the coldest days, when the heat pump due to the limited upper water temperature cannot provide sufficiently high supply water temperature. During that period, an auxiliary heat source is typically used in combination with the HP. If the amount of energy used under such conditions is relatively small in comparison to the total seasonal heating energy required, it would be reasonable to use the heat pump for the majority of the heating load and rely on the auxiliary heat source on top of the HP for the peak load conditions. This represents a typical hybrid system where the auxiliary heat source can be biomass, solar, or more easily direct electric which can be installed into the tank as an resistance based heat coil or alternatively be electric radiators (or hybrid radiators with a small electric resistance that turns on very limited hours a year) or electric underfloor heating. Traditional condensing boilers still represent a solution for an auxiliary source, but this is a transitional and non-logical opportunity when intention is to move towards a fossil free energy system.

- Evaluate the heat demand/supply profile, also including a thermal storage tank. This is out of scope for the present paper and will be investigated in further studies, i.e.: buffer tank and other components for hydraulic separation are needed to properly use controls and avoid over cycling of the HP.

5. Conclusions

The potential market for retrofitting heat pumps in existing building heating systems is substantially larger compared to new buildings. Thereby this is the first opportunity for decarbonising heating through electrification, also in small applications such as phasing out single-family fossil fuel boilers. Retrofitting of heating systems with heat pumps has its own specific characteristics, of which the high distribution/emission temperature used in existing hydronic heating systems is the most prominent.

Old hydronic systems are often designed for higher heating capacities than the actual design heat demands (especially with climate change!). In that case, the distribution temperatures may be reduced below the original design values. The distribution temperatures (supply temperature) may be reduced further by reducing the specific heat demand (W/m2/y). In all cases it should be ensured that the heat pump in combination with the new controls (not only on the primary circuit but even more on distribution and emission components) really saves energy, by a proper design for the new type of heat source.

Approaching retrofit design through the elements described in this paper potentially using the systematic stepwise approach can make clean heating through heat pumps the financially most attractive choice, create trust, and meet the technology acceleration that climate desperately needs.

Acknowledgements

EP 2 646 755 B1, Method For Operating A Heating System
EP 3 506 043 B1, Method For Controlling A Heating Or Cooling System
EP 3 276 266 B1, Method For Controlling A Heating Or Cooling System And Heating Or Cooling System

References

[1] *EHPA; European Heat Pump Market and Statistics Report, 2022.*

[2] *Simulation study on supply temperature optimization in domestic heat pump systems K. Huchtemann*, D. Müller RWTH Aachen University, Institute for Energy Efficient Buildings and Indoor Climate, E.ON Energy Research Center, Mathieustr. 10, 52074 Aachen, Ger.*

[3] *Ahern, C.; Norton, B. Energy savings across EU domestic building stock by optimizing hydraulic distribution in domestic space heating systems. Energy Build. 2015, 91, 199–209..*

[4] *https://www.rehva.eu/rehva-journal/chapter/can-we-still-trust-in-en-442-new-operating-definitions-for-radiators-part-1-measurements-and-simulations-1.*

[5] *Research on heating performance of heating radiator at low temperature Zongjiang Liu a,b , Wei Xu a,b , Zhong Li b,* , Linhua Zhang a , Ji Li b , Aisong Li b , Airong Feng b a School of Thermal Engineering, Shandong Jianzhu University, Jinan, China b Inst.*

[6] Z. L. X. K. D. L. Jinzhe Nie, *Analysis and Comparison Study on Different HFC Refrigerants for Space Heating Air Source Heat Pump in Rural Residential Buildings of North China,* 2017.

[7] *Jensen, J. K., Ommen, T., Reinholdt, L., Markussen, W. B., & Elmegaard, B. (2018). Heat pump COP, part 2: Generalized COP estimation of heat pump processes. In Proceedings of the13th IIR-Gustav Lorentzen Conference on Natural Refrigerants (Vol. 2, pp. 113.*

[8] *For this paper we used the folowing parameters: Refrigerant R134a, Pinch temp cond 5K, evap 5K, Isotropic efficiency compressor0.65, T evap in 8°C, T evap out = 3°C, Heat loss 0.3 (fraction of electric consumption).*

[9] *data · master · Hotmaps / Building stock analysis · GitLab.*

Bibliography

1. Domestic Retrofit Assessment of the Heat Pump System Considering the Impact of Heat Supply Temperature and Operating Mode of Control—A Case Study Muhammad Abid *, Neil Hewitt, Ming-Jun Huang, Christopher Wilson and Donal Cotter
2. Analysis of retrofit air source heat pump performance: Results from detailed simulations and comparison to field trial data. Energy and Buildings.Volume 43, Issue 1, January 2011, Pages 239-245
3. Techno-economic Feasibility of Replacing Oil Boilers with Air-To-Water-Heat-Pumps Coupled with Thermal Energy Storage Paraskevi Vatougiou1 , David P. Jenkins1 , Peter McCallum1 1 Urban Energy Research Group, School of Energy, Geoscience, Infrastructure and Society, Heriot-Watt University, Edinburgh, EH14 4AS, UK
4. VDI 4650. Calculation of heat pumps e simplified method for the calculation of the seasonal performance factor of heat pumps e electric heat pumps for space heating and domestic hot water; 2009 [guideline, Association of German Engineers].
5. Kozarcanin, S.; Hanna, R.; Staffell, I.; Gross, R.; Andresen, G. Impact of climate change on the cost-optimal mix of decentralised heat pump and gas boiler technologies in Europe. Energy Policy 2020, 140, 111386.
6. Valancius, R.; Singh, R.M.; Jurelionis, A.; Vaiciunas, J. A review of heat pump systems and applications in cold climates: Evidence from Lithuania. Energies 2019, 12, 4331.
7. Chen, X.; Liu, C.; Yang, J.; Chen, J. Experimental study on R-22, R-427A, R-161 and R-290 in air-source heat pump for space heating at low ambient temperatures. Int. J. Refrig. 2018, 96, 147–154.
8. Williams, C.J.; Binder, J.O.; Kelm, T. Demand side management through heat pumps, thermal storage and battery storage to increase local self-consumption and grid compatibility of Psystems.In Proceedings of the 2012 3rd IEEE PES Innovative Smart Grid Technologies Europe (ISGT Europe), Berlin, Germany, 14–17 October 2012; pp. 1–6.
9. Heat Pumps. Available online: https://www.iea.org/reports/heat-pumps.
10. Global Energy Transformation: The Remap Transition Pathway. Available online: https://www.irena.org/media/Files/IRENA/Agency/Publication/2019/Apr/IRENA_GET Emap_pathway_2019.
11. 22. Xiao, B.; He, L.; Zhang, S.; Kong, T.; Hu, B.; Wang, R. Comparison and analysis on air-to-air and air-to-water heat pump heating systems. Renew. Energy 2020, 146, 1888–1896.
12. Verhelst, C.; Degrauwe, D.; Logist, F.; Van Impe, J.; Helsen, L. Multi-objective optimal control of an air-to-water heat pump for residential heating. Build. Simul. 2012, 5, 281–291.
13. Daikin. Domestic hot water heat pump technology. https://www.daikin.co.uk/en_g/b/product-group/domestic-hot-water-heat-pump.html.
14. Mitsubishi electric. Document Library: https://library.mitsubishielectric.co.uk/pdf/directory/heating/technical_documents/current/databook; 2020.
15. Renaldi, R.; Kiprakis, A.; Friedrich, D. An optimisation framework for thermal energy storage integration in a residential heat pump heating system. Appl. Energy 2017, 186, 520–529.
16. Kowalski, P.; Szała ´nski, P. Seasonal coefficient of performance of air-to-air heat pump and energy performance of a building in Poland. E3S Web Conf. 2019, 116, 00039.
17. Asaee, S.R.; Ugursal, V.I.; Beausoleil-Morrison, I. Techno-economic feasibility evaluation of air to water heat pump retrofit in the Canadian housing stock. Appl. Therm. Eng. 2017, 111, 936–949.
18. Zhang, Q.; Zhang, L.; Nie, J.; Li, Y. Techno-economic analysis of air source heat pump applied for space heating in northern China.Appl. Energy 2017, 207, 533–542.
19. Pu, J.; Shen, C.; Zhang, C.; Liu, X. A semi-experimental method for evaluating frosting performance of air source heat pumps.Renew. Energy 2021, 173, 913–925.
20. Çakır, U.; Çomaklı, K.; Çomaklı, Ö.; Karslı, S. An experimental exergetic comparison of four different heat pump systems working at same conditions: As air to air, air to water, water to water and water to air. Energy 2013, 58, 210–219.
21. Mitchell, M.S.; Spitler, J.D. Open-loop direct surface water cooling and surface water heat pump systems—A review. Heat. Vent. Air-Cond. Refrig. Res. 2013, 19, 125–140.
22. Renaldi R, Kiprakis A, Friedrich D. An optimisation framework for thermal energy storage integration in a residential heat pump heating system. Appl Energy Jan.2017;186:520–9.
23. Staffell, I.; Brett, D.; Brandon, N.; Hawkes, A. A review of domestic heat pumps. Energy Environ. Sci. 2012, 5, 9291–9306.
24. Kim, D.H.; Park, H.S.; Kim, M.S. Optimal temperature between high and low stage cycles for R134a/R410A cascade heat pump based water heater system. Exp. Therm. Fluid Sci. 2013, 47, 172–179.
25. Le, K.X.; Huang, M.J.; Shah, N.N.; Wilson, C.; Mac Artain, P.; Byrne, R.; Hewitt, N.J. Techno-economic assessment of cascade air-to-water heat pump retrofitted into residential buildings using experimentally validated simulations. Appl. Energy 2019, 250,633–652.

26. Xu, L.; Li, E.; Xu, Y.; Mao, N.; Shen, X.; Wang, X. An experimental energy performance investigation and economic analysis on a cascade heat pump for high-temperature water in cold region. Renew. Energy 2020, 152, 674–683.
27. Boman, D.B. Adsorption Heat Pumps: Fundamentals and Applications; Springer Nature: Cham, Switzerland, 2021.
28. Wu, W.; Skye, H.M.; Domanski, P.A. Selecting HVAC systems to achieve comfortable and cost-effective residential net-zero energy buildings. Appl. Energy 2018, 212, 577–591.
29. American Society of Heating, R.; Air-Conditioning Engineers, I. 2017 ASHRAE® Handbook—Fundamentals (SI Edition); American Society of Heating, Refrigerating and Air-Conditioning Engineers, Inc. (ASHRAE): Atlanta, GA, USA, 2018
30. Matthes P, Hoh A, Müller D. Energieeinsparpotential durch adaptive Vorlauftemperatur-Regelung. HLH Lüftung/Klima e Heizung/Sanitär e Gebäudetechnik 2007;11:29e35 [engl.: Energy saving potential through adaptive supply temperature control].
31. Seifert J, Kozak W, Richter W. Modelling of hydraulic circuit for different heat pump systems in low energy building. Proc. of Eleventh International IBPSA Conference. Building Simul 2009;1:354e60.
32. Beghi A, Cecchinato L. Modelling and adaptive control of small capacity chillers for hvac applications. Appl Thermal Eng 2011;31:1125e34.
33. Zogg M. Wärmepumpen. Last visit 2012/04/23, http://www.zogg-engineering. ch/Publi/WP_ETH_Zogg.pdf; 2009.
34. Russ C, Miara M, Platt M, Günther D, Kramer T, Dittmer H, et al. Feldmessung Wärmepumpen im Gebäudebestand e Kurzfassung zum Abschlussbericht. Technical Report. Fraunhofer Institut für Solare Energiesysteme; 2010 [engl.: Field test measurements of heat pumps in existing buildings].
35. Wärmepumpen-Testzentrum, http://www.ntb.ch/ies/kompetenzbereiche/ waermepumpen-testzentrum-wpz.html. Heat pump test centre of Interstaatliche Hochschule für Technik Buchs, Swiss; 2012.

14th IEA Heat Pump Conference
15-18 May 2023, Chicago, Illinois

Steady state measurements and dynamic behaviour of an absorption heat transformer operating in an industrial environment

J. L. Corrales Ciganda[a], Asier Martinez-Urrutia[a*]

[a]TECNALIA, Basque Research and Tecnology Alliance, Area Anardi 5, Azpeitia , Spain

Abstract

An Absorption Heat Transformer or Type II Absorption Heat Pump is a thermally driven heat pump able to upgrade approximately half of its driving heat up to a higher temperature level with an almost neglectable consumption of electric power. In the frame of a European project a 200 kW industrial pilot heat pump has been designed and installed in the power plant of a petrochemical facility. This work presents operation data of this AHT prototype operating at industrial scale. The presented results include steady state as well as dynamic performance measurements. The pilot AHT had continuously delivered heat flow rates between 220 and 270 kW with a thermal COP of around 0.5. The comparison of the monitoring results with those of a laboratory prototype present a deviation in the performance of around 20 % in terms of usable heat flow rates, but some explanation for this deviation are presented based on the operating conditions. The use of a dedicated adiabatic absorption chamber on the other side, partially compensate this deviation in performance, confirming the advantages of using an absorber with this configuration.

© HPC2023.
Selection and/or peer-review under the responsibility of the organizers of the 14th IEA Heat Pump Conference 2023.

Keywords: Type your keywords here, separated by semicolons ;

1. Introduction

An absorption heat transformer (AHT), also called type II or booster absorption heat pump is a device able to split a heat flow at an intermediate temperature level in two heat flows, one at a higher temperature level (upgraded heat flow) and another one at a lower temperature level (rejection heat flow).

These kind of thermal heat pumps are especially suitable for the recovery and upgrade of waste heat from industrial processes. For the European industry, which accounts for the fourth part of the energy consumption in Europe, approximately 70 % of its energy demand is used for thermal purposes, and a third part of this is directly rejected, being the largest part of this waste heat rejected at low-temperatures below 100 ºC. The Absorption Heat Transformers (AHT) is a ready-to-market technology that can upgrade these large quantities of available low-temperature waste-heat into a usable temperature level with a very reduced electrical consumption.

Applications reported in the literature concentrate in the pulp and paper (during and lamination processes), chemical and petrochemical (distillation and purification processes) and food and beverage sectors (drying, sterilization, fermentation and mold and bacteria processes) [1–4]. The literature reports present installations with capacities between 100 kW and 5 MW, and agree that AHTs presents attractive payback periods, between 2 and 5 years, depending mainly on their capacity. Furthermore, over the past years some market installations by the manufacturers Thermax and Johnson Controls – Hitachi, offering AHTs between 0.5 and 10 MW, have been documented in their respective websites. Despite these recent advancements, there remains a lack of

* Corresponding author. Tel.: +34667101117
E-mail address:joseluis.corrales@tecnalia.com.

knowledge about the integration and performance of such systems in the industry. Furthermore, there is a noticeable lack of open experimental data available regarding the performance of these systems.

Within the Indus3Es Project (Horizon 2020 Project No. 680738) a single stage AHT has been developed, focusing on its design and on its integration into existing plants and its adaptability into various industrial processes. The developed system is being under demonstration in a real environment at the Izmit facilities of Tüpras, the main petrochemical industry in Turkey, enabling to analyze integration aspects, as well as operational and business-related issues. This work presents the monitored experimental performance data of the pilot scale 200 kW AHT and its comparison with previously presented operational results under laboratory conditions.

2. Description of the Heat Upgrade System based on an AHT

A heat upgrade system including a 200 kW nominal capacity AHT has been installed at the power plant of the petrochemical facilities of Tüpras in Izmit (Turkey) in the final phase of the Indus3Es project. The waste-heat that drives the absorption cycle in the AHT system is the condensation heat obtained from an oily steam drum tank, that was released to the ambient before the installation of the Indus3Es system.

The heat upgrade system combines direct recovery of part of the condensation heat of the oily steam in a plate heat exchanger (HX E-7 in Figure 1) with recovery and upgrade of the remaining part of the condensation heat of the oily steam by means of the AHT.

The demineralized water feeding the boilers of the steam cycle of the power plant enters the heat upgrade system with a temperature that is relatively constant throughout the year at 65 °C. The demineralized water is first preheated to a temperature of around 95 ºC at HX E-7, and then further heated up at the heat exchanger HX E-5 by the hot glycol-water stream in the absorber circuit at the temperature level T2.

The heat released by the condensation of part of the oily steam at the heat exchanger HX E-6 heats up the water-glycol stream in the generator/evaporator circuit up to 95 ºC, that enters the generator and evaporator of the AHT driving the cycle. The AHT splits this driving heat flow into a heat flow at the heat rejection circuit at temperature level T0 connected to the condenser, and an upgraded heat flow at the temperature level T2 that is transferred by the absorber circuit between the AHT and the heat exchanger HX E-6. The water-glycol in this absorber circuit is heated up to 140 ºC by the AHT and heats up the demin-water circuit up to 135 ºC before it is sent to the boilers. The temperature of the cooling water entering the condenser at the heat rejection circuit is obtained from the cooling water network of the plant and have a nominal temperature of 25 ºC.

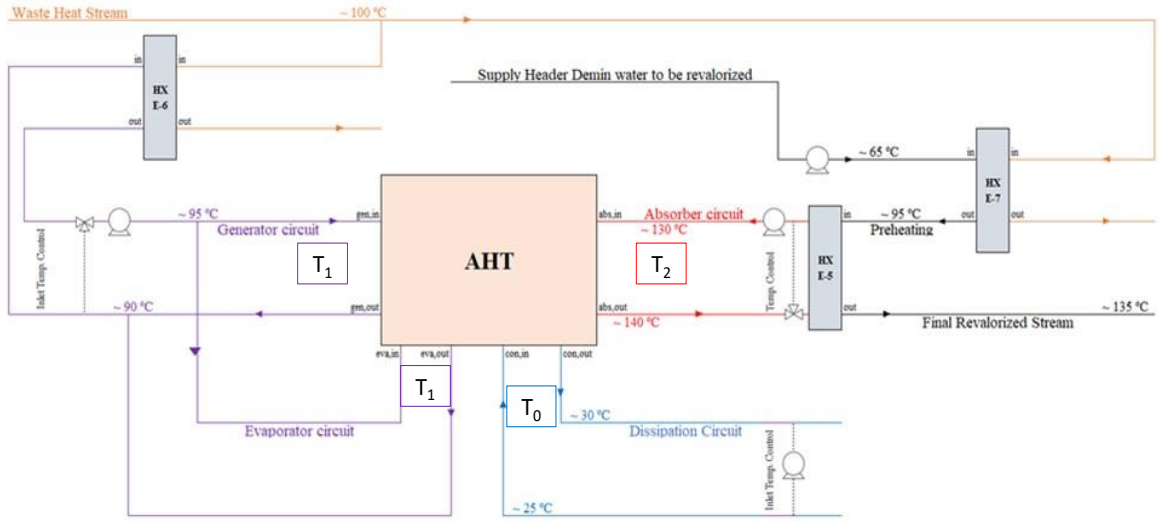


Fig. 1. Scheme of the AHT heat upgrade installation

3. Steady State Measurements of the 250 kW Industrial AHT

3.1. Operational Results

From November 2019 to Mai 2020 (end of the Indus3Es Project), the heat upgrade system has been in operation and monitoring data of the system under different sets of conditions have been analyzed, with the objective of the characterization of the AHT.

The heat upgrade system has been controlled with a dedicated control system developed within the project based on the characteristic equation method with the goal of maintaining the temperature of the demineralized water sent to the boilers at a constant value, that has been changed along the monitoring phase.

A set of valves controlled by the system act on the three circuits connected to the AHT at the temperature levels T_0, T_1 and T_2 according to an internal logic that reduced the use of cooling water from the cooling water network by recirculation at the heat upgrade circuit. The temperature at the circuit T_1 is kept as high as possible to make the best possible use of the waste heat. The pumps at the three circuits T_0, T_1 and T_2 are equipped with frequency variable drivers to control the flow rate.

Table 1 presents the nominal, minimal and maximum temperature and flow rate values registered during the first operation phase. The temperature at the condenser inlet was lower than the nominal one because the tests of this first phase took place in wintertime. Lower generator/evaporator temperature than those used for planning were a consequence of the lower-than-expected flow rate of oily steam. Therefore, lower than planned absorber outlet temperatures were measured in this first phase.

Table 1. Operating conditions of the heat upgrade system for the monitored steady state points

Prototype	design	nominal	minimum	maximum
Flow rate at circuit T_2 (Absorber circuit) in m3/h	24	27	1	5
Flow rate at circuit T_1 (G-E) in m3/h	74	74,7	1,1	5
Flow rate at circuit T_0 (C) in m3/h	36	36	14,8	24,4
Solution Mass Flow Rate in kg/h	3000	2600		
Temperature at Condenser inlet, $T_{0,in}$ in ºC	25	18	15.5	28.4
Temperature at Generator/Evaporator inlet $T_{1,in}$ in ºC	95	90	86.1	95.2
Temperature at Absorber Inlet, $T_{2,in}$ in ºC	130	115	113.1	126.2
Temperature at Absorber Outlet, $T_{2,out}$ in ºC	140	125	121.2	133.9
Gross Temperature Lift, GTL in K	45	35		
Upgraded heat flow rate, $Q_{A,}$ in kW	200	230	218.8	248.5
$COP = Q_A / (Q_G + Q_E)$	0.48	0.50	0.42	0.51

The table also includes the range of values registered for the upgraded heat flow rate, Q_A, and the thermal coefficient of performance COP, that is the ratio between the upgraded heat and the driving heat transferred at the evaporator Q_E and generator Q_G.

Although the COP value remains practically constant at around 0.5, the heat flow rate varies between 218 and 248 kW. As shown in Table 1, the design value of the upgraded heat flow rate, 200 kW, is smaller than the measured values, but the operating conditions in the monitored period are different than the design ones.

The main difference found in the operating conditions is on the T_0 circuit: although the system was designed for cooling water temperature of 25 ºC, the temperature from the cooling water network of the plant was mainly in the range between 16 and 22 ºC. Additionally, the system was designed for temperatures at the absorber circuit T_2 higher than those at which it has operated for most of the time. The reason for this is that the recirculation valve adjusting the absorber temperature in circuit T_2 was not configurated for the operation range required by the new cooling water conditions, and thus the set point value could only be achieved when the cooling water temperature aproached its design value. The necessary adjustments of the control parameters of the absorption recirculation valve could not be made because the visit planned for parameter adjustment in March 2020 was cancelled due the irruption of the COVID-19 pandemic.

A set of 28 steady state points however have been obtained from the first operation phase. Each steady state correspond to a monitored operation period of the system of at least 60 minutes with no relevant change in temperature or flow rate at the three external circuits T_0, T_1 and T_2.

The upgraded heat flow rate and coefficient of performance are presented in the Figure 2 against the cooling water inlet temperatures $T_{c,in} = T_{0,in}$. As the Figure 2 shows, most of the monitored point correspond to points with driving temperature $T_{1,in}$ in the range between 87 and 89 ºC and condenser inlet temperatures $T_{0,in}$ between 16 and 22 ºC. As it was presented in [6] for the results of the first laboratory prototype, for constant values for $T_{1,in}$ and $T_{2,in}$ a decrease of the absorber capacity or heat flow rate Q_2 is expected with increasing $T_{0,in}$. Although a tendency trend can be observed for this results, no conclussions can be obtained since neither T_{1in} nor $T_{2,in}$ are constant for these measurements.

On the lower section of the figures the COP values are presented. The values remain constant at a value around 0.50 with the exception of one point with $T_{1,in}$=95 ºC, $T_{0,in}$=16 ºC and $T_{2,out}$=134 ºC (COP=0.42).

For another point with $T_{1,in}$=95 ºC, $T_{0,in}$=18 ºC and $T_{2,out}$=132 ºC however, the monitored COP value was 0.51. For most of the cases, the COP measured for the system is larger than the expected one for the design conditions at around 0.48.

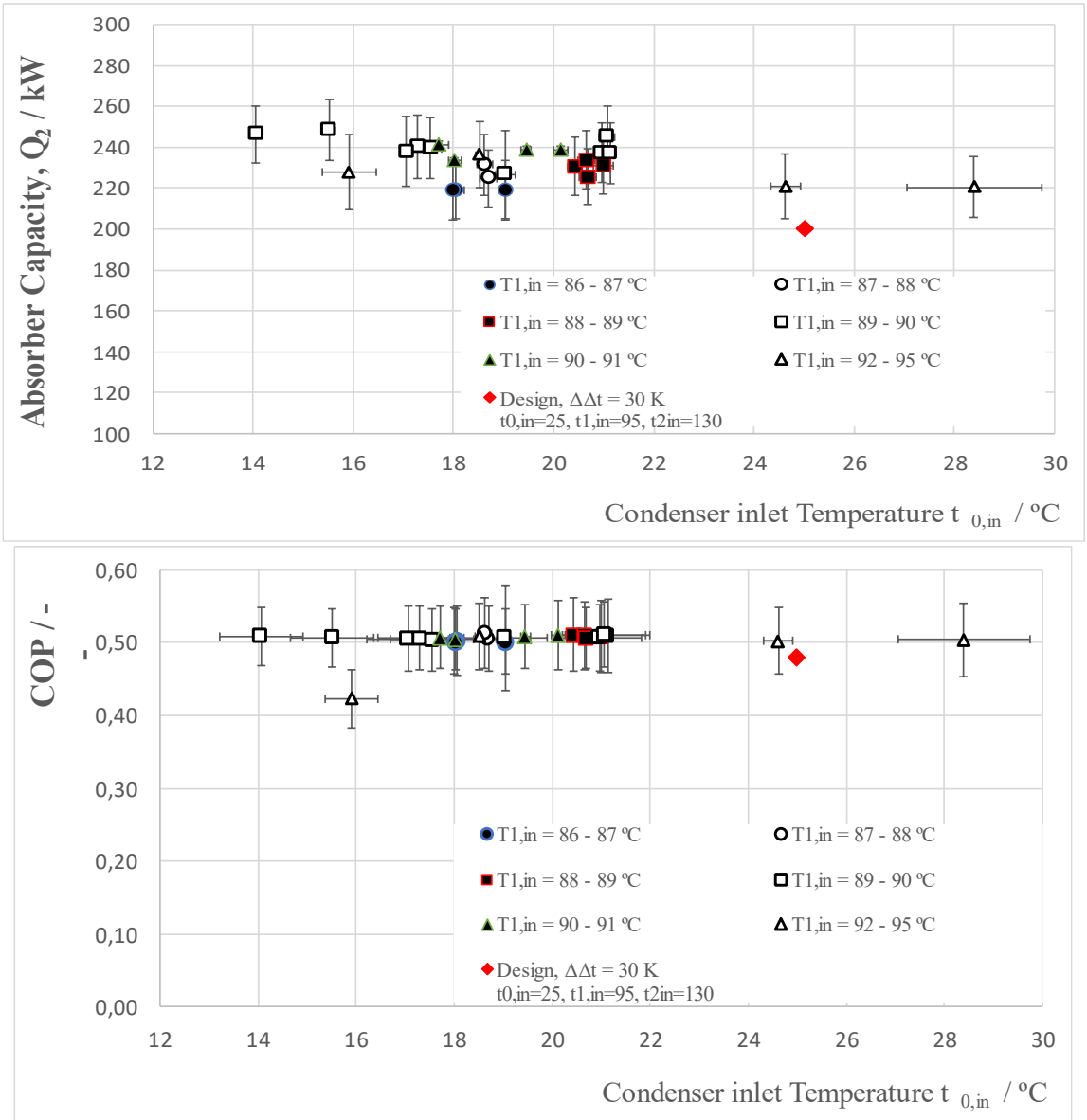


Fig. 2. AHT heat upgrade capacity and COP vs the condenser inlet temperature

In order to have a better overview of the operation map of the AHT during the monitored period, the Absorber capacity Qa and thermal COP values are plotted against the temperature of glycol leaving the absorber $T_{2,out}$ in Figure 3.

The results of Figure 3 reveal that the AHT has been operating in the monitored period for most of the time with temperatures t_{2out} between 122 and 123 ºC. The diagram also shows, that the AHT is able to operate with delivery temperatures of 132 and 134 ºC and heat upgrade capacities between 220 and 240 kW. Due to the difficulties in the control of the valves in the absorber circuit previously mentioned, no measurement values are yet obtained for delivery temperatures t_{2ou} at the design temperature 140 ºC. The COP values presented in the lower part of Figure 3 show that the only point measured with a lower COP correspond to the highest delivery temperature T_{2out}. Although this could be intuitively be interpretated as a correlation of T_{2out} and COP this makes no sense and would contradict the experimental results presented in [6] and [8], that show that COP higher than 0.45 can be obtained with and t_{2out} as high as 138 ºC. More likely, the measurement with the lowest COP correspond to a measurement with NC-gases present in the system [9].

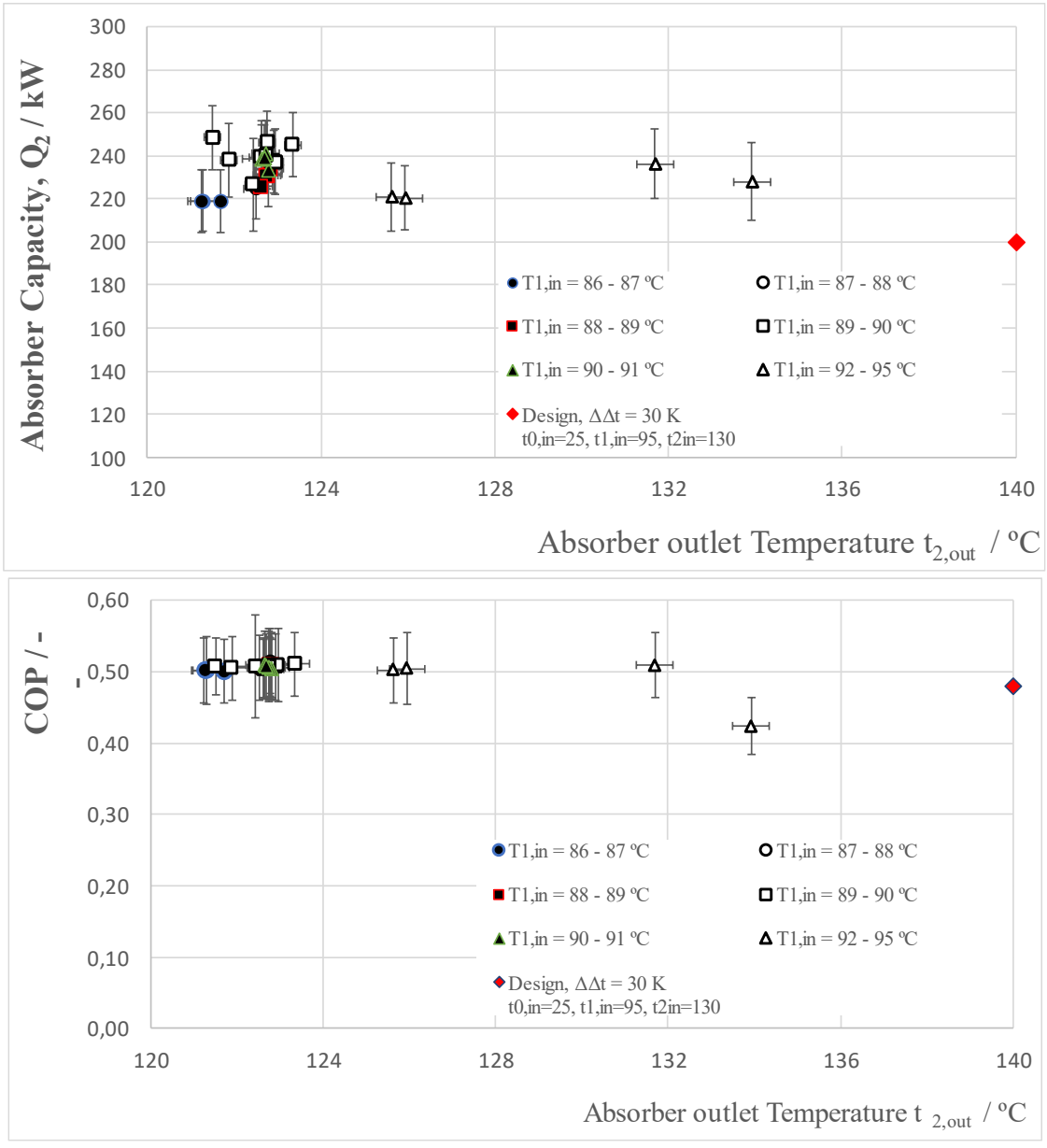


Fig. 3. AHT heat upgrade capacity and COP vs the absorber outlet temperature

3.2. Comparison with laboratory prototype

The results presented in Figures 2 and 3 have been compared with the results previously measured at the laboratory under controlled conditions and presented in [6] and [8]. The measurement results of the first prototype developed within the Indus3Es project have been previously presented in the 12th HPC Conference [6] showing the dependances of absorber capacity and COP with the external circuit temperatures. The measurement results of the second prototype (pr II) developed in the project has been presented in [7] analyzing its differences with those of prototype I. The measurement results of this prototype pr II have been filtered and analyzed in detail in [8], being used also to validate and update the characteristic equation model of an absorption heat transformer.

Table 2. Comparison of prototype characteristics

Prototype	A_A (m^2)	A_G/A_A (-)	A_E/A_A (-)	A_C/A_A (-)	V_A (m^3/h)	$V_G = V_E$ (m^3/h)	V_C (m^3/h)	m_{sol} (kg/h)
Laboratory Prototype pr I [6]	7.6	1	1	1	5	5	5	700
Laboratory Prototype pr II [7]	8.2	1,1	0,8	0,8	5	5	5	700
Pilot Scale Prototype (This work)	43.3	1,1	0,8	0,7	24	37	36	3000

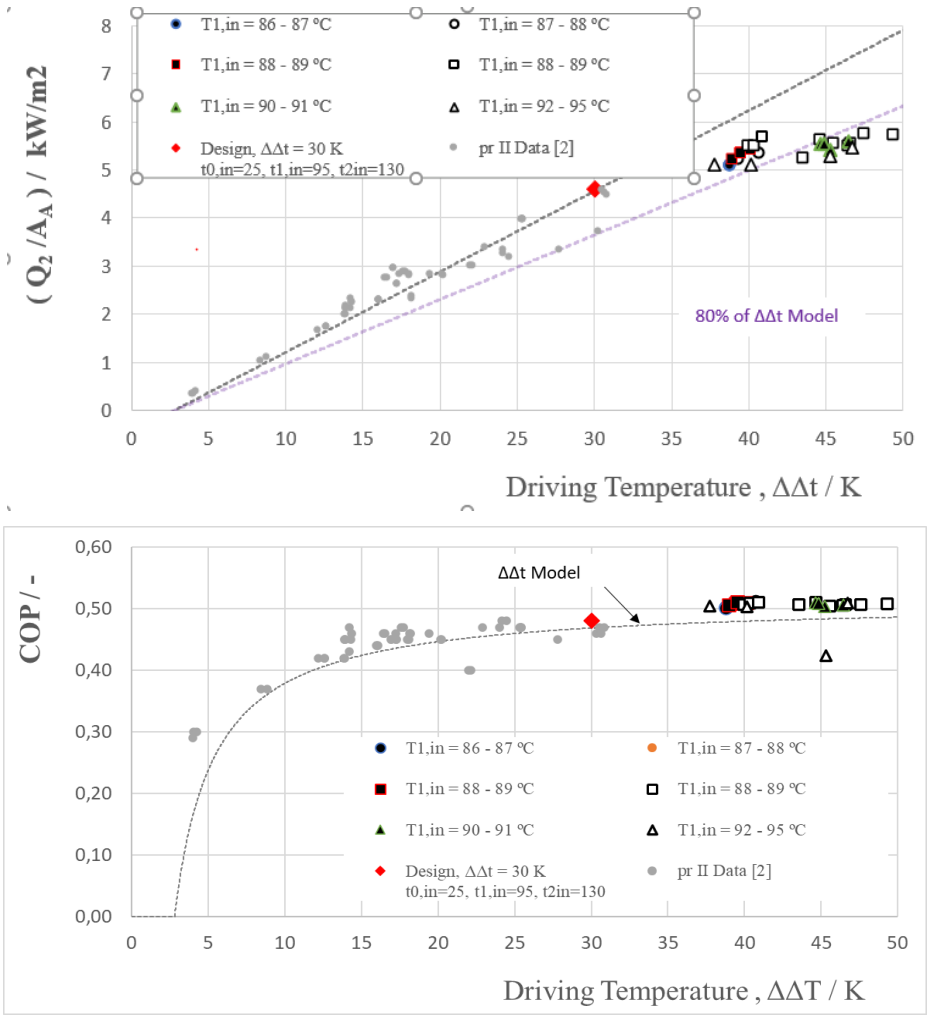


Fig. 4. AHT Absorber capacity and COP compared to that of the laboratory prototype pr II

The characteristic equation model has been previously used for the upscaling process from the lab scale prototype to the 200 kW industrial prototype. The model can also be used to analyze deviations between the expected performance of the AHT and the monitored results

As it is presented in Table 2, the laboratory prototype has been upscaled by enlarging the total heat exchanger area of the absorber (A_A) by a factor of around 5. The relations between the heat exchanger area of the absorber and those of evaporator, absorber and condenser of the pilot scale prototype is the same as that of the laboratory prototype, and the solution flow rate and external heat carrier flow rates have been set in order to have equal heat transfer rates at each exchanger.

With these assumptions, it has been expected that the specific heat upgrade capacity of the AHT expressed in kW/m^2 absorber can be predicted by the characteristic equation line presented in [8].

In the Figure 4, specific absorber capacity and COP of the systems are plotted against the driving temperature difference ΔΔt, that can be defined as presented in equation (1). ΔΔt is the double temperature difference and expresses the driving potential of the AHT for heat upgrade. (R is a constant around 1.15).

$$\Delta\Delta t = \left(t_{gen} - t_{abs}\right) - R \cdot \left(t_{con} - t_{eva}\right) = R \cdot \left(t_1 - t_0\right) - \left(t_2 - t_1\right) \qquad (1)$$

As presented in Figure 4, the driving temperature differences during the monitored operation of the AHT are much larger than expected (between 36 and 48 K instead of 30 K). Therefore, the absorber capacities measured for the AHT are larger than the design value. The Figure 4 reveals however, that the heat flow measured are between 12 and 20 % smaller than those calculated by the characteristic equation model.

The difference between measured and expected capacity could be the consequence of two causes. On the one hand, the dissipation temperature in the condenser was lower than expected in most of the cases. There is scientific evidence that the lower the pressure of the lower pressure vessel, the influence of the NC gases could be increased, which would result in the decrease of the performance [9]. On the other hand, the solution flow rate in these tests was 13 % lower than the one defined from the design phase. During the design phase, the flow rate was set to have the same specific flow rate along the tube´s length. Because of cavitation risk, the solution flow rate was set to about 2600 kg·h^{-1}, representing a decrease of the 13 %.

The lower diagram on Figure 4 on the other side, explains why the monitored COP values are practically constant. The characteristic equation method predicts that as the absorber capacity increases, the impact of the heat losses and other inefficiencies present in the absorption cycle is reduced, and thus for large ΔΔt values the COP remain practically constant. The monitored COP values exceeding expectations may be due to measurement inaccuracies (uncertainties in the COP of 0.05 have been determined from the uncertainties in the determination of Q_A, Q_G and Q_C in the range between 13.9 and 36.0 kW as shown in Figures 2 and 3).

3.3. Improved performance using an adiabatic absorption chamber

One technical innovation included with the AHT Pilot Scale Prototype is the two-chamber absorption design with a separated adiabatic absorption chamber with atomizing spray nozzles distribution system. This design has been adapted to increase the contact area of the solution and vapor in the absorber and optimize the adiabatic absorption process increasing the residence time of the solution. This can be done by atomizing the solution into-small droplets, as it happens in the dedicated adiabatic absorption chamber installed before the solution distribution system based on a conventional dropping tray as in the lab scale prototype.

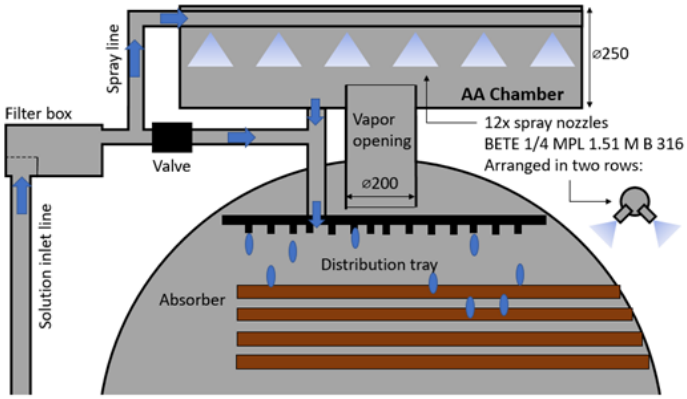


Fig. 5. Schematic view of the adiabatic absorption chamber

This dedicated adiabatic absorption chamber (AA chamber in Fig.5) can be bypassed and cut-off from the system by means of a controlled valve. This valve has been added in order isolate the adiabatic absorption chamber when desired and analyze its contribution separately.

During the second monitoring phase of the system the AHT was set to work under adiabatic mode. In this second monitoring phase both the installed adiabatic-absorption-vessel and the traditional absorber with distribution tray were in operation, while in the previously presented results.

The performance of the AHT in the second monitoring phase using the adiabatic absorption chamber (AAC) was significantly improved compared to that of the first measurements. It is estimated that the revalorization capacity of the AHT using the AAC is about 12 % higher comparing to the non-adiabatic mode, as it is shown in Fig.6 The black triangles symbols correspond to results using the AAC, and the empty circles to results without using it. The main advantage of the use of the AAV is the increase of the temperature entering to the absorber´s tube bundle. With higher temperature at the first row of the tubes, higher temperature energy could be transferred to the external circuit. During the tests performed, it was estimated that the 13 % of the absorption rate occurs in the AAC, increasing in about 20 K the entering solution temperature.

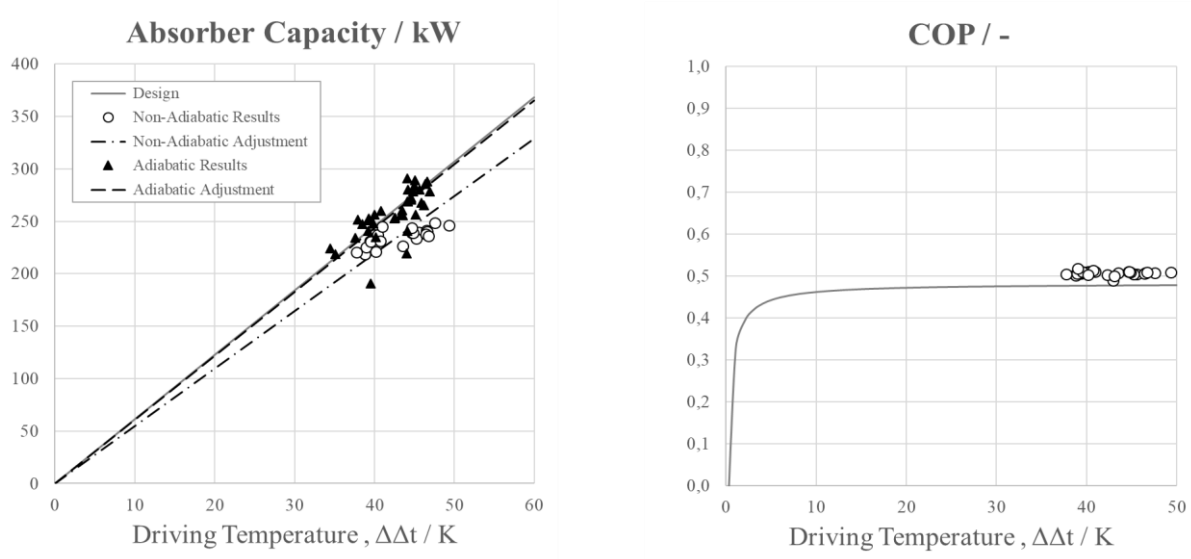


Fig. 6. Pilot Scale AHT absorber capacity and COP under Non-adiabatic(○) and Adiabatic(▲) modes.

4. Dynamic behavior of the absorption heat transformer

Although the parameters of the controller of the heat upgrade system could not be adjusted within the lifetime of the project due to the irruption of the COVID pandemic the control system demonstrated that the heat system could operate autonomously adjusting the outlet temperature at the absorber of the AHT, at the given set point. Figure 7 presents continuous monitored data of the AHT operating between the 19 and 24 of February 2020.

The control system adjusts valves in the circuits in order to maintain T_{2out} at either 120, 125 and 130 ºC. Therefore, the flow rate at the absorber circuit T_2 experiments relatively strong variations. The flow rates at Generator, Evaporator and Demin Water circuits are kept constant but the efforts made in the heat rejection circuit to change the value of T_{0in} are sterile, although the flow rate at the condenser suffer strong variations. The main oscillations in the driving heat Temperature T_1 are due to oscillations in the flow non-monitored flow rate of oily steam entering the condensing heat exchanger HX-6.

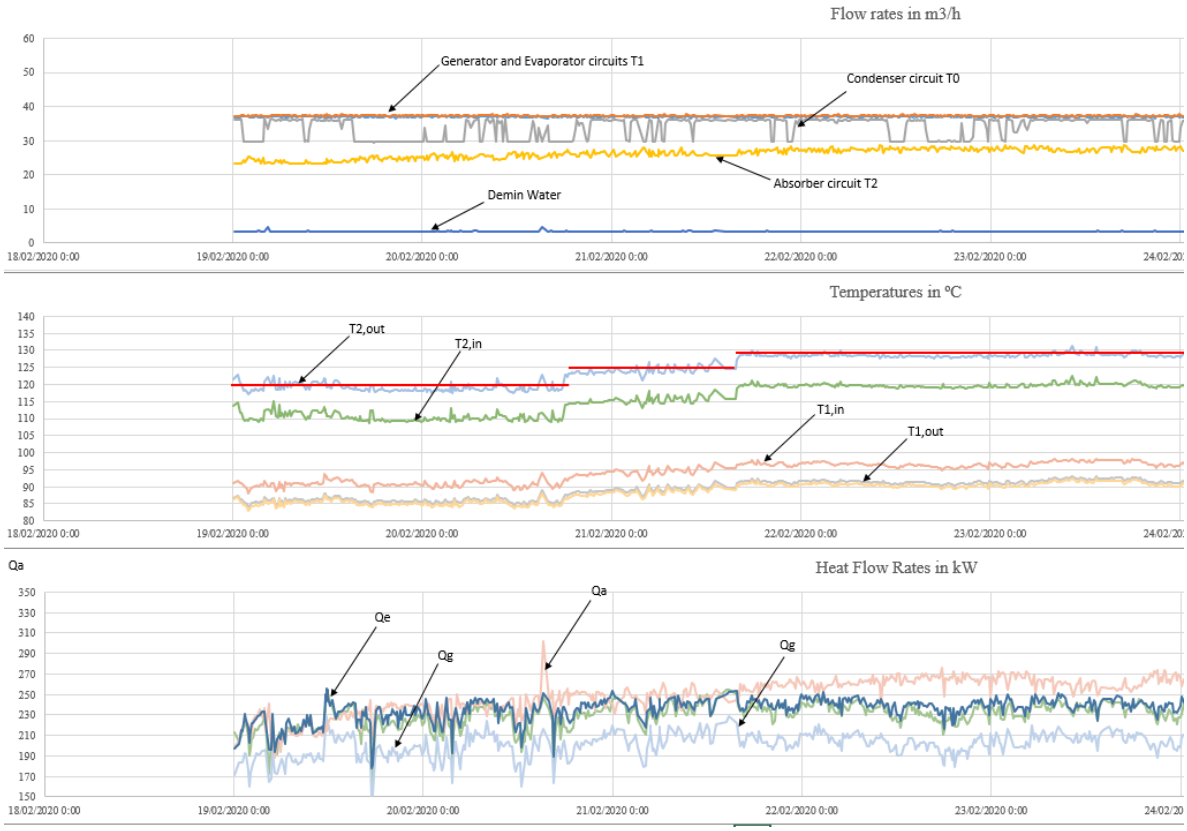


Fig. 7. Dynamic behavior of the AHT in the period between 19 and 24.02.2020

These oscillations are the main difficulty to overcome to find steady state conditions for the analysis of the system and its comparison with the laboratory measurements. Only when this oscillation stops could steady state periods longer than 60 minutes be analyzed as have been presented in the previous figures.

However, although a good comparison between steady state conditions is only possible for some points the results presented in Figure 7 show that the upgraded heat flow rate supplied by the AHT have been continuously above the design value of 200 kW, achieving at moments 270 kW.

5. Final considerations and conclusions

This paper has presented and analyzed the monitored performance of an absorption heat transformer with a design capacity of 200 kW for upgrading heat with up to 140 ºC with a driving heat temperature of 95 ºC. The monitored results presented a very stable thermal coefficient of performance (useful to driving heat ratio) of around 0.50, but with an uncertainty of around 0.05. The measured upgraded heat flow rates are between 218 and 270 kW for heat upgrade temperatures between 115 and 138 ºC, with driving heat temperatures between 88 and 95 ºC. The higher-than-expected measured flow rates are due to more convenient conditions than predicted for the operation. The performance is however somehow lower than expected, although some hypothesis can be formulated for this deviation. The use of the innovative adiabatic absorption chamber, on the other side, increases the performance by around 10%.

The pilot plant prototype also included an innovative motor-less non-condensable (NC) gases purge system solution that due to time limitation within the project and irruption of the COVID Pandemic could not be tested within the project. Additionally, the system a control strategy which prevents the cycle from moving into risky operational conditions. The advanced control system ensures safe operation of the heat transformer minimizing the risk of crystallization while it optimizes the performance characteristics. The control strategies used for the chillers implies the modification of current optimization models. The Characteristic Equation Method has been used for the definition of the control system [5]. The advantages of these technological innovations have not been discussed within this work.

The economical performance of a ready-to-market system with this capacity has been discussed in [10] based on the performance results presented in this work. It concluded that the total cost of the system implementation would be about 420.000 €, i.e. about 1.500 €/kW revalorized by the AHT, and that the investment would be completely recovered within 6 years. If the total considered installation would include a 600 kW prototype, the payback period would be reduced to 3 years, and to 2 years in case 1.2 MW AHT is considered.

Acknowledgements

This work has been developed under the project "Indus3Es: Industrial Energy and Environmental Efficiency" funded by the Horizon 2020 framework of the European Union, Project No. 680738. http://www.indus3es.eu/

References

[1] Parham, K., Khamooshi, M., Tematio, D. B. K., Yari, M., & Atikol, U. (2014). Absorption heat transformers–a comprehensive review. *Renewable and Sustainable Energy Reviews*, 34, 430-452.

[2] Donnellan, P., Cronin, K., & Byrne, E. (2015). Recycling waste heat energy using vapour absorption heat transformers: A review. *Renewable and Sustainable Energy Reviews*, 42, 1290-1304.

[3] Rivera, W., Best, R., Cardoso, M. J., & Romero, R. J. (2015). A review of absorption heat transformers. *Applied Thermal Engineering*, 91, 654-670.

[4] Cudok, F., Giannetti, N., Ciganda, J. L. C., Aoyama, J., Babu, P., Coronas, A., ... & Ziegler, F. (2021). Absorption heat transformer-state-of-the-art of industrial applications. *Renewable and Sustainable Energy Revie*ws, 141, 110757.

[5] Cudok, F., & Ziegler, F. (2015). Absorption heat converter and the characteristic equation method. *In 24th International Congress of Refrigeration ICR-2015*. Yokohama (Japan); Paper 764 E2-Fr-2.

[6] Cudok, F., Ciganda, J. C., Kononenko, N., & Drescher, E. (2017). Experimental results of an absorption heat transformer. *In 12th IEA Heat Pump Conference*. Rotterdam (Netherlands); Abstract O.4.4.2. p. 101 – 102.

[7] Corrales Ciganda J. L., Cudok F. (2019) Thermodynamic analysis of an absorption heat transformer based on experimental measurements. In Proceedings of the 25th IIR International Congress of Refrigeration: Montréal , Canada, August 24-30, 2019. pap. n. 1370 DOI : http://dx.doi.org/10.18462/iir.icr.2019.1370

[8] Corrales Ciganda J. L., Cudok F. (2021) Performance evaluation of an absorption heat transformer for industrial heat waste recovery using the characteristic equation, *Applied Thermal Engineering*,193,

[9] Metzner, D., Corrales Ciganda, J. (2019) Einfluss von nicht-kondensierbaren Gasen auf den thermodynamischen Prozess in Absorptionswaermetransformator. Paper S.04, Tagungsband der DKV-Jahrestagung.

[10] Martinez-Urrutia, A., Ramirez, M., Corrales, J, Cudok, F., Evron, Y, Pérez-Ortiz, A, Ataç, D. (2021) Experimental results and thermoeconomic analysis of an absorption heat transformer operating in a petrol refinery *In Proceedings of the International Sorption Heat Pump Conference 2021 - Part II Call 2021*. Berlin (Germany); DOI: 10.14279/depositonce-12278

14th IEA Heat Pump Conference
15-18 May 2023, Chicago, Illinois

A heat pump system for simultaneous comfort floor cooling and domestic hot water

Tingting Zhu[a,b*], Jierong Liang[b], Jan Eric Thorsen[c], Oddgeir Gudmundsson[c], Wilko Rohlfs[a], Brian Elmegaard[b]

[a]University of Twente, Drienerlolaan 5, Enschede 7522 NB , The Netherlands
[b]Technical University of Denmark, Anker Engelunds Vej 101, Lyngby 2800, Denmark
[c]Danfoss A/S, Nordborgvej 81, Nordborg 6430, Denmark

Abstract

The benefit of ultra-low temperature district heating systems (ULTDH) is their low supply temperature, which increases the heat generation efficiency and significantly reduces the heat loss of the DH network. The present study proposed a dual-effect heat pump system, which in combination of the ULTDH network, fulfills both, comfort floor cooling/heating and domestic hot water (DHW) demands. Depending on the operation the ULTDH system is used as a heat source, DHW preparation, or as a heat sink in cooling operation mode. The application potential of the proposed heat pump unit used for comfort floor cooling has been validated. The cooling experimental tests were performed under designed conditions with fixed heat source temperature (22 °C) and different heat sink temperatures, simulating either DHW preparation or delivering the surplus heat to the ULTDH network. The coefficient of performance (COP) of the dual-effect heat pump system varied from 2.22 to 2.81 in cooling mode, and from 3.0 to 3.4 in heating mode. The cooling capacity ranged from 2.9 kW to 3.4 kW and heating capacity ranged from 3.8 kW to 4.4 kW.

© HPC2023.
Selection and/or peer-review under the responsibility of the organizers of the 14th IEA Heat Pump Conference 2023.

Keywords: Dual-effect; Comfort cooling; Ultra-low district heating; Cooling capacity; Domestic hot water.

1. Introduction

The amount of energy used for heating and domestic hot water (DHW) is high and will keep increasing [1]. Combined cooling and heating systems can achieve efficient utilization of resources and energy through heat recovery, which is providing sustainable solutions to global warming and the energy crisis [2]. A novel compression/ejection transcritical CO_2 heat pump system for simultaneous cooling and heating can realize the utilization of geothermal energy and solar energy [3]. Heat pumps for simultaneous heating and cooling appear as interesting solutions for electric energy saving and residential buildings with a specific mode for DHW production. An air-source heat pump has been investigated by Byrne and Ghoubali [4], which shows a good potential in producing of hot water and chilled air simultaneously.

The idea of the present study is to indicate the performance and application potential of small heat pump used in household comfort floor cooling and domestic hot water supply. Thus, a comfort cooling heat pump prototype has been set up at Technical University of Denmark (DTU) to conduct the investigation experimentally. Thermal behavior of a small heat pump unit with R134a as working refrigerant has been analyzed based on experimental results. The experimental tests were performed under design conditions: different inlet temperature for the heat source, and a fixed inlet temperature for heat sink, which corresponds to the district heating temperature supply and comfort floor cooling temperature. The variations of the heat pump operation for different temperature combinations of district heat water are outlined. The operation parameters are: 3 kW cooling capacity (50 W/m^2 for 40 m^2 room area), with a water temperature inflow of 17 °C and return of 22 °C.

* Corresponding author. Tel.: +31 53 489 8823; fax: +31 53 4893471.
E-mail address: t.zhu@utwente.nl

The application potential of the proposed heat pump unit used for comfort floor cooling has been validated experimentally. Thermal behavior and exergy performance of this small heat pump unit have been analyzed. The variations in heat pump operation under different temperature combinations of DHW are outlined. The structure of this paper is summarized as follows. In Section 2, the experimental setup and the configuration of a comfort cooling heat pump system are introduced. Then, the energy and exergy analysis method to assess the performance of the proposed system has been conducted in Section 3. In Section 4, the results are discussed considering the application scenarios. Finally, the conclusions are summarized in Section 5.

2. Experimental setup and configuration description

2.1. Testing system

The heat pump experimental set up installed in DTU is designed for the application of floor comfort cooling and DHW in the DH system (Fig.1 and Fig.2). The test rig includes four sub-systems: a secondary water cycle to illustrate the DHW system and comfort floor cooling system, a refrigerant cycle with R134a as working medium, a shunt-system and a cooling system to regulate designed test temperatures. The main information of each component is listed in Table 1. The selection of each component is calculated based on heating/cooling capacity using Danfoss calculation software.

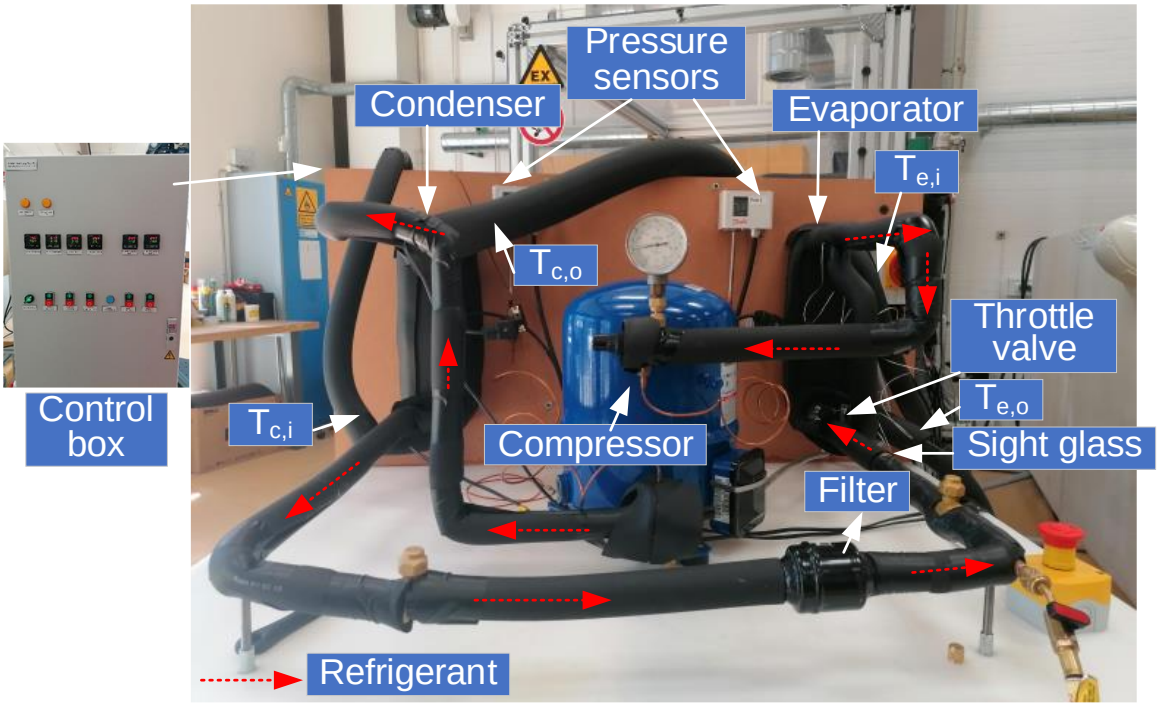


Fig. 1. Picture of Comfort Cooling test rig.

Table 1. Components information

Item	Type	Item	Type
Condenser	Danfoss D22-26	Sight Glass	Danfoss SGP 10s
Evaporator	Danfoss D22-16	TXV	Danfoss TUAE
Compressor	MTZ018-4, R134a	Orifice for TXV	Danfoss TU-6
Pressostat H	Danfoss KP7EW	Temp. sensor	Danfoss AKS-11
Pressostat L	Danfoss KP1E	Pressure sensor L	Danfoss AKS-33
Filter Dryer	Danfoss DML 053/053s	Pressure sensor H	Danfoss AKS-33

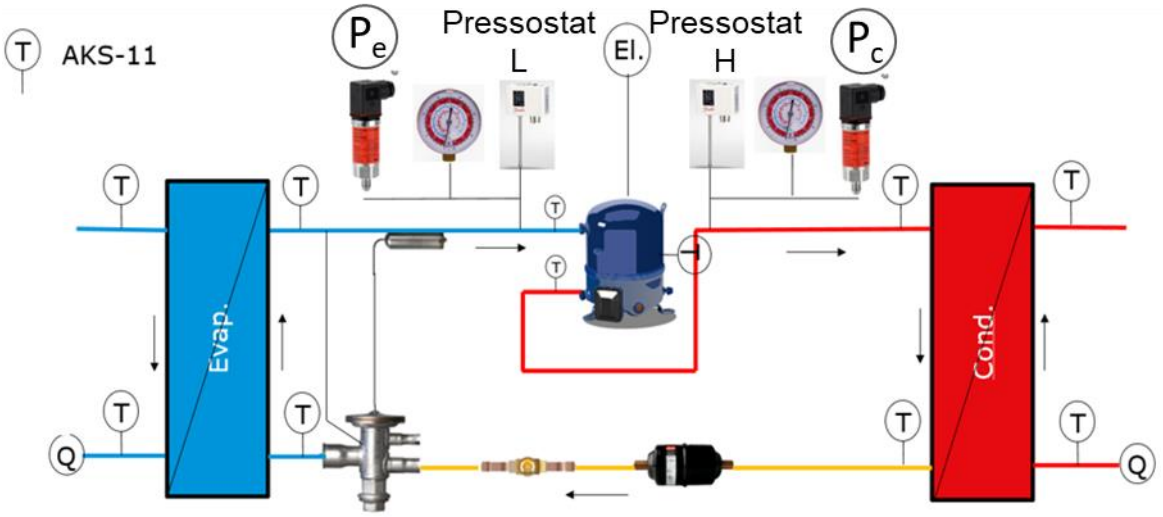


Fig. 2. Test rig diagram of comfort cooling system.

2.2. Operation conditions

A baseline heat pump system loop (1-2-3-4) used for comfort floor cooling and domestic hot water supply is sketched in Fig. 3, which consists of a compressor, a condenser, an expansion valve, and an evaporator. The dynamic process of refrigerant includes: the saturated refrigerant vapor is compressed, increasing both temperature and pressure. Subsequently, the working liquid is cooled by the water-refrigerant heat exchanger of the condenser. Afterwards, before entering the evaporator, the refrigerant turns into two-phase fluid by passing through the expansion valve. Finally, the refrigerant flows back to the compressor and the cycle is finished.

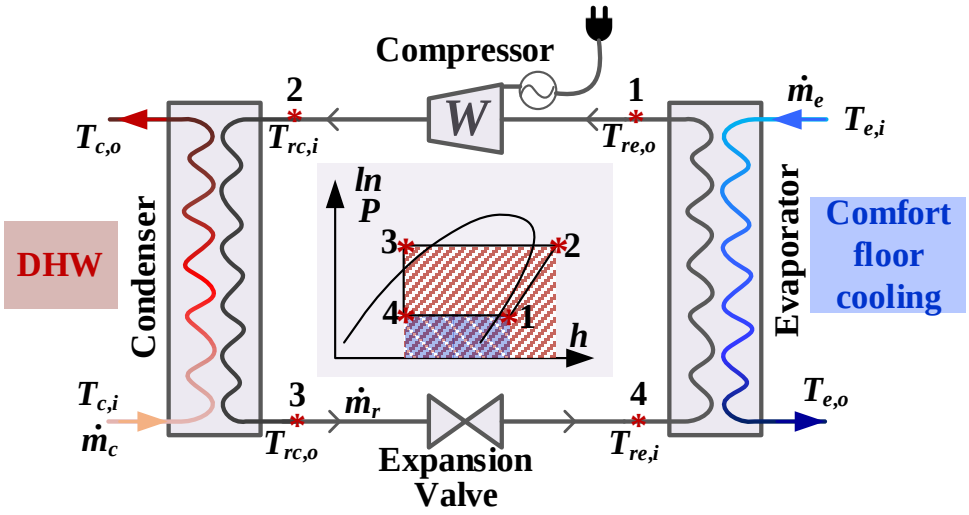


Fig. 3. Thermal-dynamic process of simultaneous comfort floor cooling and domestic hot water.

The tested parameters are listed in Table 2.

The operation conditions are chosen as below,

1) Temperature control (by electric heater and adjusting valve in the shunting system)

2) Flow control (control system to adjust valve in each of the condenser and evaporator cycle)

Parameters setting listed as,

1) Inlet water temperature of the condenser: 30 ℃, 35 ℃, 40 ℃, 45 ℃, 48.5 ℃;

2) Inlet water temperature of the evaporator: 22 ℃~27 ℃.

Experiments have been conducted on different combinations of cooling and heating temperature. Table 2 summaries the test cases.

Table 2 Tested cases

Case No.	F_c [m³/h]	F_e [m³/h]	$T_{c,i}$ [℃]	$T_{e,i}$ [℃]	Case No.	F_c [m³/h]	F_e [m³/h]	$T_{c,i}$ [℃]	$T_{e,i}$ [℃]
1	180.0	499.6	30.4	22.7	14	340.1	500.7	40.0	22.7
2	131.1	501.0	30.4	22.2	15	339.8	499.6	40.0	21.9
3	129.4	498.5	30.3	22.1	16	341.2	500.2	43.6	22.2
4	115.2	501.7	30.0	22.1	17	229.2	539.5	40.1	22.6
5	248.4	501.6	38.5	23.6	18	345.7	500.3	48.5	27.0
6	129.2	499.4	29.9	22.1	19	341.0	500.0	44.7	23.1
7	115.3	519.3	30.1	22.0	20	139.4	499.5	34.2	22.0
8	339.0	570.4	35.9	22.1	21	129.6	499.9	34.2	22.1
9	229.6	540.2	39.9	22.0	22	338.6	499.5	48.1	26.9
10	230.9	539.9	40.3	22.7	23	231.2	500.0	45.2	27.1
11	229.3	650.3	38.5	23.6	24	231.3	500.5	44.0	22.6
12	231.2	500.0	39.4	21.9	25	231.5	230.2	42.9	35.4
13	140.1	500.6	34.1	22.0					

3. Energy and exergy analysis method

3.1. Coefficient of performance (COP) of the heat pump

Due to the compressor heat loss, pipe heat loss, the temperature difference of heat transfer in evaporator and the condenser, pressure drop, and several other irreversible factors, the actual COP of the heat pump cannot reach the value of an ideal cycle. Therefore, the formula of the studied heat pump COP is,

$$\mathrm{COP}_{\mathrm{heating}} = \frac{\dot{Q}_c}{\dot{W}} \tag{1}$$

$$COP_{\mathrm{cooling}} = \frac{\dot{Q}_e}{\dot{W}} \tag{2}$$

$$\dot{Q}_c = \mathrm{c_p}\dot{m}_\mathrm{c}\,(T_{c,i} - T_{c,o}) \tag{3}$$

$$\dot{Q}_e = \mathrm{c_p}\dot{m}_\mathrm{e}\,(T_{e,i} - T_{e,o}), \tag{4}$$

where $\dot{Q}_c$ [kW] is the released heat of condenser/heat capacity; $\dot{Q}_e$ [kW] is the cooling capacity of the evaporator; W [kW] is the power of compressor; $\mathrm{c_p}$ [kJ/kg] is the specific heat capacity at constant of water; $\dot{m}_\mathrm{e}$ [kg/s] is the water mass flow rate in the evaporator; $\dot{m}_\mathrm{c}$ [kg/s] is the water mass flow rate in the condenser; $T_{c,i}$ [K]] is the inlet water temperature of the condenser; $T_{c,o}$ [K] is the outlet water temperature of the condenser; $T_{e,i}$ [K] is the inlet water temperature of the evaporator; $T_{e,o}$ [K] is the outlet water temperature of the evaporator; Figure 1 below is an example which authors may find useful.

The cooling and heating dual-effect coefficient of performance ($\mathrm{COP_{dual}}$) has been used to characterize the efficiency of the system. The measure can be defined as the sum of the absolute values of heating and cooling capacity divided by the input power,

$$\mathrm{COP_{dual}} = \frac{|\dot{Q}_{\mathrm{cooling}}|+|\dot{Q}_{\mathrm{heating}}|}{\dot{W}} \tag{5}$$

The second-law efficiency of the heat pump at the dual-effect heating and cooling working condition, $\eta_{\mathrm{II,dual}}$ can be defined as [5],

$$\eta_{\mathrm{II,dual}} = \frac{\mathrm{COP_{dual}}}{\mathrm{COP_{dual,ideal}}} \tag{6}$$

$$\mathrm{COP_{dual,ideal}} = \frac{\hat{T}_{\mathrm{c,w}}+\hat{T}_{\mathrm{e,w}}}{\hat{T}_{\mathrm{c,w}}-\hat{T}_{\mathrm{e,w}}}\ , \tag{7}$$

where $\hat{T}_{c,w}$ and $\hat{T}_{e,w}$ are average temperatures of heat supply (hot water flow through the condenser and chilled water flow through the evaporator, which are given by Eq. (8) and Eq. (9).

$$\hat{T}_{cw} = \frac{h_{\mathrm{c,o}}-h_{\mathrm{c,i}}}{s_{\mathrm{c,o}}-s_{\mathrm{c,i}}} \tag{8}$$

$$\hat{T}_{ew} = \frac{h_{\mathrm{e,i}} - h_{\mathrm{e,o}}}{s_{\mathrm{e,i}} - s_{\mathrm{e,o}}} \tag{9}$$

3.2. Exergy analysis

Compared to conventional energy analysis, the exergy analysis can accurately pinpoint the location of inefficiencies and quantitatively characterize the thermodynamic imperfection of heat transfer process and the possibility for thermodynamic development for heat pump system [6]. Thus, based on the typical thermodynamic cycle of the studied dual-effect HP (Fig. 3 pressure–enthalpy diagram) an exergy evaluation has been carried out corresponding to the exergy flow of each component. The measured quantities of the refrigerant cycle in the present study are temperatures on condenser side and pressures on both sides. The enthalpy value of the refrigerant at each state point (point Nr. 1, 2, 3 and 4, see Fig.3) can be calculated by REFPROP 10.0 software [7] with the pressure and temperature data recorded in the testing process.

The exergy balance equations of the heat pump components were described in agreement with the work of Rijs and Mróz [8] by

$$\dot{E}_{\mathrm{in}} - \dot{E}_{\mathrm{out}} = \Delta\dot{E}_{\mathrm{component}} \ , \tag{10}$$

where, $\dot{E}_{\mathrm{in}}$ [kW] is flux of exergy entering the studied thermodynamically open system; $\dot{E}_{\mathrm{out}}$ [kW] is flux of exergy leaving the studied thermodynamically open system; $\Delta\dot{E}_{\mathrm{component}}$ [kW] is the exergy loss and destruction occurring in the component.

The exergy balance equations of each component can be calculated as,

$$\Delta\dot{E}_{\mathrm{comp}} = \dot{m}_{\mathrm{r}}(h_1 - h_2 - T_0(s_1 - s_2)) + \dot{W} \tag{11}$$

$$\Delta\dot{E}_{\mathrm{cond}} = \dot{m}_{\mathrm{r}}(h_2 - h_3 - T_0(s_2 - s_3)) + \dot{m}_c \mathrm{c_p}(T_{\mathrm{c,i}} - T_{\mathrm{c,o}} - T_0 ln\frac{T_{\mathrm{c,i}}}{T_{\mathrm{c,o}}}) \tag{12}$$

$$\Delta\dot{E}_{\mathrm{TXV}} = \dot{m}_{\mathrm{r}}(h_3 - h_4 - T_0(s_3 - s_4)) \tag{13}$$

$$\Delta\dot{E}_{evap} = \dot{m}_{\mathrm{r}}\big(h_4 - h_1 - T_0(s_4 - s_1)\big) + \dot{m}_{\mathrm{e}}\mathrm{c_p}(T_{\mathrm{e,i}} - T_{\mathrm{e,o}} - T_0 ln\frac{T_{\mathrm{e,i}}}{T_{\mathrm{e,o}}}) \tag{14}$$

where, T_0 [K] is dead state temperature, (K); $\dot{m}_r$ [kg/s] is refrigerant mass flow rate of the heat pump cycle, (kg/s);

The exergy efficiency of the heat pump system writes,

$$\eta_{\mathrm{ex}} = \frac{\dot{E}_{\mathrm{use}}}{\dot{W} + \Delta\dot{E}_{\mathrm{HS}}} \ , \tag{15}$$

where

$$\dot{E}_{\mathrm{use}} = \dot{m}_{\mathrm{c}} c_{\mathrm{w}}(T_{\mathrm{c,o}} - T_{\mathrm{c,i}} - T_0 \ln\frac{T_{\mathrm{c,o}}}{T_{\mathrm{c,i}}}) \tag{16}$$

$$\Delta\dot{E}_{HS} = \dot{m}_{\mathrm{e}} c_{\mathrm{w}}(T_{\mathrm{e,i}} - T_{\mathrm{e,o}} - T_0 \ln\frac{T_{\mathrm{e,i}}}{T_{\mathrm{e,o}}}) \ , \tag{17}$$

where η_{ex} exergy efficiency of the heat pump system; $\dot{E}_{\mathrm{use}}$ [kW] is useable exergy, which is the physical exergy of the heated water via condenser; $\Delta\dot{E}_{\mathrm{HS}}$ [kW]is exergy change flux of external heat source.

3. Results and discussion

3.1. Uncertainty

The temperature, pressure, mass flow, and power consumption were measured using the instruments specified in Section 2.1. The method proposed by Moffat [9] was used to calculate the maximum relative uncertainties of the experimental data (Equation 18). The relative uncertainty of COP arising with respect to the considered parameters are given by the following correlation [10],

$$\delta R = \left[\sum_{i=1}^{n}\left(\frac{\partial R}{\partial x_i}\delta x_i\right)^2\right]^{1/2} \tag{18}$$

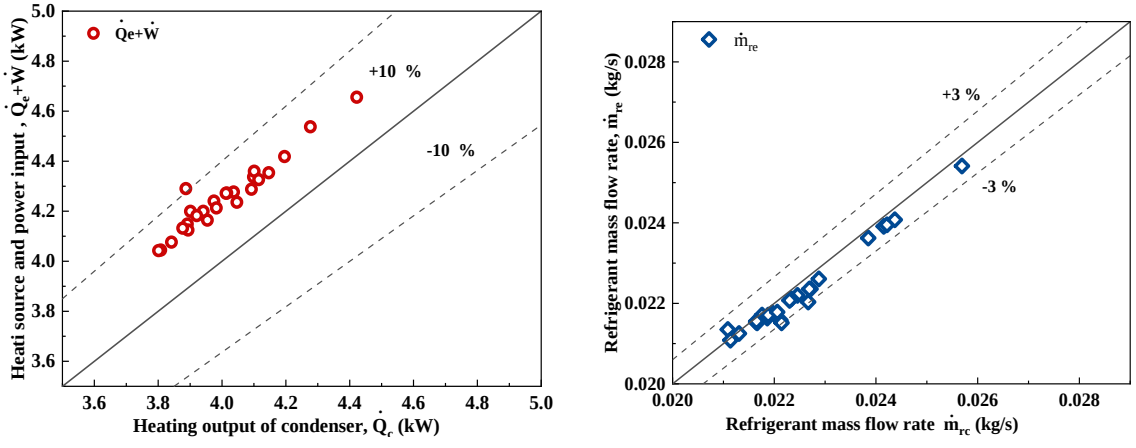
$$\delta \mathrm{COP}_{\mathrm{heating}} = \left[\left(\frac{\Delta\dot{m}_{\mathrm{c}}}{\dot{m}_{\mathrm{c}}}\right)^2 + 2\left(\frac{\Delta T_{\mathrm{c}}}{T_{c,i} - T_{c,o}}\right)^2\right]^{1/2} \tag{19}$$

$$\delta \mathrm{COP}_{\mathrm{cooling}} = \left[\left(\frac{\Delta \dot{m}_{\mathrm{e}}}{\dot{m}_{\mathrm{e}}} \right)^2 + 2 \left(\frac{\Delta T_e}{T_{e,i} - T_{e,o}} \right)^2 \right]^{1/2} \quad (20)$$

Energy balances have been calculated based on the measured data, all of them were within the acceptable range. Thus, the measurements are reliable. Both water flow rate of condenser and evaporator were measured by ISOMAG-ML210 electromagnetic flowmeter with an accuracy of ±0.2 % and a range of 0 kg/s to 0.288 kg/s in the present study. The temperatures were measured by Type T thermocouples with an accuracy of ±0.5 ℃. The range of condenser side temperatures is from 29 ℃ to 62 ℃, thus, its maximum uncertainty was 1.6%; and for the evaporator side is from 15 ℃ to 36 ℃. Thus, its maximum uncertainty was 2.4 %. The maximum uncertainty in $\mathrm{COP}_{\mathrm{heating}}$ and $\mathrm{COP}_{\mathrm{cooling}}$ were 2.3 % and 3.4%, respectively.

Table 3 Tested results

No.	$T_{c,i}$	$T_{c,o}$	$T_{rc,i}$	$T_{rc,o}$	$T_{e,i}$	$T_{e,o}$	$T_{r,eo}$	P_c	P_e	W	Q_c	Q_e	$\mathrm{COP}_{\mathrm{heating}}$	$\mathrm{COP}_{\mathrm{cooling}}$	$\mathrm{COP}_{\mathrm{dual}}$	SH	Sub	Tesat	Tcsat	η_{ex}	$\eta_{II,dual}$
unit	℃	℃	℃	℃	℃	℃	℃	bar	bar	kW	kW	kW	-	-	-	K	K	℃	℃	%	%
1	30.4	48.9	70.6	44.5	22.7	17.3	18.0	13.1	4.4	1.13	3.89	3.16	3.43	2.79	6.23	6.0	5.3	12.0	49.8	14.8	20.1
2	30.4	56.9	77.0	46.3	22.2	16.8	17.6	15.1	4.4	1.13	4.04	3.15	3.57	2.78	6.35	5.7	9.0	11.9	55.4	19.4	25
3	30.3	57.0	77.4	44.6	22.1	16.7	17.8	15.1	4.4	1.13	4.02	3.14	3.55	2.78	6.32	6.2	10.9	11.6	55.6	19.3	25
4	30.0	60.0	80.3	44.9	22.1	16.8	17.9	16.0	4.4	1.16	4.01	3.11	3.45	2.67	6.12	6.2	12.9	11.8	57.9	20	25.3
5	38.5	52.7	74.2	48.4	23.6	18.1	18.9	14.3	4.5	1.15	4.10	3.19	3.57	2.78	6.35	6.1	5.0	12.8	53.4	21.2	25.6
6	29.9	56.3	75.9	46.8	22.1	16.7	17.8	14.9	4.4	1.13	3.97	3.11	3.51	2.75	6.26	6.0	8.2	11.9	55.0	18.6	24.2
7	30.1	59.6	77.5	49.3	22.0	17.0	15.1	15.9	4.5	1.16	3.95	3.00	3.4	2.58	5.98	2.8	8.4	12.3	57.7	19.6	24.6
8	35.9	46.7	67.3	40.8	22.1	17.0	14.9	12.8	4.4	1.13	4.28	3.41	3.78	3.01	6.79	3.0	7.9	11.9	48.7	18.1	24.3
9	39.9	55.2	73.1	46.3	22.0	17.0	13.8	15.3	4.5	1.18	4.09	3.11	3.47	2.63	6.1	1.2	9.8	12.6	56.1	22.8	27.9
10	40.3	55.4	74.4	48.8	22.7	17.7	14.9	15.3	4.6	1.15	4.05	3.09	3.53	2.69	6.22	1.9	7.2	13.0	56.0	23.2	27.9
11	38.5	54.2	73.0	49.8	23.6	19.3	16.6	14.8	4.7	1.16	4.20	3.26	3.6	2.8	6.4	2.5	5.0	14.1	54.8	22	25.9
12	39.4	53.6	70.3	50.5	21.9	16.9	13.3	14.6	4.5	1.15	3.81	2.90	3.32	2.52	5.84	1.1	3.7	12.2	54.2	20.9	25.9
13	34.1	57.4	73.3	51.9	22.0	17.1	13.8	15.5	4.5	1.2	3.80	2.85	3.18	2.38	5.56	1.1	4.7	12.7	56.6	19.3	23.7
14	40.3	50.2	67.9	48.7	22.7	17.5	13.8	13.8	4.5	1.15	3.90	3.05	3.4	2.66	6.06	1.4	3.2	12.4	51.9	20.1	24.9
15	40.0	50.0	72.1	47.6	21.9	16.6	16.4	13.7	4.4	1.13	3.94	3.07	3.48	2.71	6.19	4.8	3.8	11.6	51.4	20.4	26.1
16	43.6	53.4	75.7	50.5	22.2	17.1	16.7	14.8	4.4	1.16	3.89	2.98	3.34	2.56	5.91	4.6	4.3	12.1	54.8	22.8	27.7
17	40.1	55.0	76.2	50.4	22.6	17.8	17.2	15.0	4.5	1.16	3.98	3.05	3.42	2.62	6.04	4.5	4.9	12.6	55.3	22.3	26.9
18	48.5	58.7	80.7	57.0	27.0	21.6	21.4	16.9	5.0	1.24	4.10	3.12	3.29	2.5	5.8	5.6	3.2	15.9	60.3	26.1	27.2
19	44.7	54.6	77.0	52.3	23.1	18.0	17.7	15.3	4.6	1.2	3.92	2.99	3.28	2.5	5.77	4.7	3.7	13.0	56.0	23.3	27.3
20	34.2	58.3	78.3	50.4	22.0	16.9	16.6	15.6	4.4	1.16	3.89	2.96	3.35	2.54	5.89	4.5	6.5	12.1	56.9	20.7	25.6
21	34.2	60.0	79.8	51.3	22.1	17.1	16.7	16.2	4.5	1.2	3.88	2.94	3.24	2.45	5.7	4.5	7.0	12.2	58.3	20.9	25.4
22	48.1	58.5	80.2	56.7	26.9	21.5	21.3	16.8	5.0	1.2	4.11	3.13	3.44	2.62	6.06	5.3	3.4	16.0	60.1	26.9	28.2
23	45.2	60.6	81.2	56.9	27.1	21.7	21.6	17.2	5.1	1.21	4.15	3.14	3.42	2.59	6.01	5.4	4.0	16.2	60.9	26.3	27.4
24	44.0	58.3	79.5	54.1	22.6	17.7	17.4	16.2	4.6	1.2	3.84	2.88	3.21	2.41	5.62	4.5	4.4	13.0	58.5	24.2	28.1
25	42.9	59.3	80.4	55.6	35.4	22.6	24.6	16.7	5.3	1.23	4.42	3.43	3.6	2.79	6.39	7.0	4.0	17.6	59.6	24.9	22.5



(a) (b)

Fig. 4. Uncertainty: a) Energy balance, b) Refrigerant flow rate calculation deviation.

3.2. Thermal performance

Under the proposed operation conditions of simultaneous cooling and heating the temperature of the hot water stream is increased by the heat release from the condenser while cooling down the temperature of cold water stream returned from the floor cooling system. The required temperature of the chilled/hot water differs depending on the demand, and thus sets the operation parameters of the heat pump and determines their efficiency.

Figure 5 summarizes the operation conditions of condenser and evaporator inlet and outlet temperature for the 25 test cases investigated in this study. The colour coding is according to the COP_{dual} reached under these operation conditions (See the colour bar at the bottom of Figure 5) . While Fig. 5a provides a complete overview of the tests, subfigures b-d display specific groups which will be discussed in the following paragraphs in a more detailed manner.

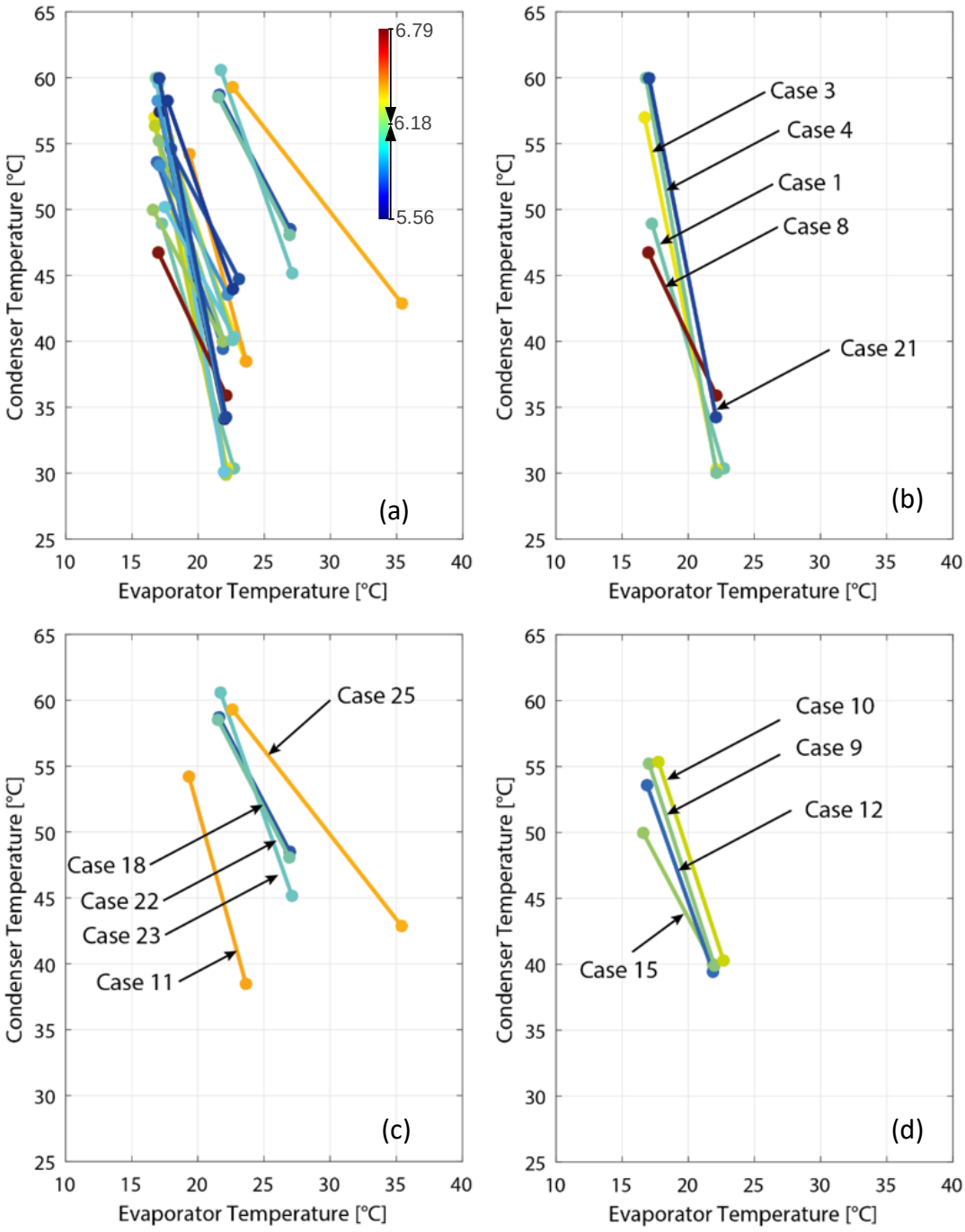


Fig. 5 Operation conditions of condenser and evaporator inlet and outlet temperature for the 25 test cases.

All cases displayed in Figure 5b have a low evaporator inlet temperature of 22 °C and an outlet temperature of 17 °C in common. They differ in the water temperature lift on the condenser side. Case 8 exhibits the highest COP_{dual} with a value of 6.79, which results from the low temperature lift from 35.9 °C to 46.7 °C in the condenser. The lowest COP_{dual} is measured for case 21, caused by the high temperature lift from 34.2 °C to 60.0°C. Increasing the temperature from 30 °C to 60 °C (case 4) results in a higher COP_{dual}. Both cases have a similar pressure level in the compressor. The difference in COP_{dual} is mainly attributed to the lower subcooling temperature reached in case 4 (12.9 K) compared to the subcooling temperature of 7.0 K in case 21. The same effect of the higher subcooling temperature is observed in a comparison of case 1 and case 3. Although the condenser outlet temperature is significantly higher for case 3 (57.0 °C) compared to case 1 (48.9 °C), the COP_{dual} is 0.1 points higher for case 3. Note the subcooling for case 3 is 10.9 K while this is only 5.3 K for case 1.

Figure 5c illustrates a second subset of cases. Note that case 18 and 22 have almost the identical inlet and outlet temperatures. Also all other measured quantities such as pressure and temperature levels are very similar. Nevertheless, the measured value of the COP_{dual} varies between 5.8 and 6.1, which is in the range of the measurement accuracy (5% difference), mainly caused by the given accuracy of the measured power consumption. Cases 11 and 25 both exhibit a high COP_{dual}. In case 25, the evaporator inlet temperature is high (35.4 °C) but also the evaporator outlet temperature is high (22.6 °C). The superheating in the evaporator is 7.0K at a saturation temperature of 17.6 °C. For case 11, the evaporator inlet temperature is 23.6 °C and the outlet temperature is only 19.3 °C. Due to the low temperatures, also the superheating in the evaporator is with 2.5K low. The high efficiency is caused by the low temperature at the condenser outlet of 54.2 °C. It reveals that a high temperature difference between condenser inlet and outlet temperature is beneficial for the COP due to the increased effect of subcooling and the higher subcooling temperature that can be achieved.

All cases shown in Figure 5d have same evaporator drop of around 5 °C. The highest $COP_{dual}$is measured for case 10, caused by the high evaporator inlet temperature of 22.7 °C. Compared with case 15, case 10 has a higher temperature lift from 40.3 °C to 55.4 °C, measured a lower superheating of 1.9 K and a higher subcooling of 7.2 K, which results in a higher COP_{dual} of 6.22. Case 12 exhibits the lowest COP_{dual} with a value of 5.84, which results from the lowest subcooling (3.7 K) among these compared four cases and the high temperature lift from 39.4 °C to 53.6 °C in the condenser. Case 15 has a lower temperature lift from 40.0 °C to 50.0 °C and a lower condenser outlet temperature (50.0 °C) than case 12, causing a high COP_{dual} of 6.19.

Figure 6 summarizes the exergy and second-law efficiency under operation conditions of condenser and evaporator inlet and outlet temperature for the 25 test cases investigated in the present study. The colour coding is according to the exergy efficiency (η_{ex}) /second-law efficiency ($\eta_{II,dual}$) reached under these operation conditions. Exergy efficiency is obtained by dividing the useful exergy gained from condenser by input exergy (Eq. (15)).

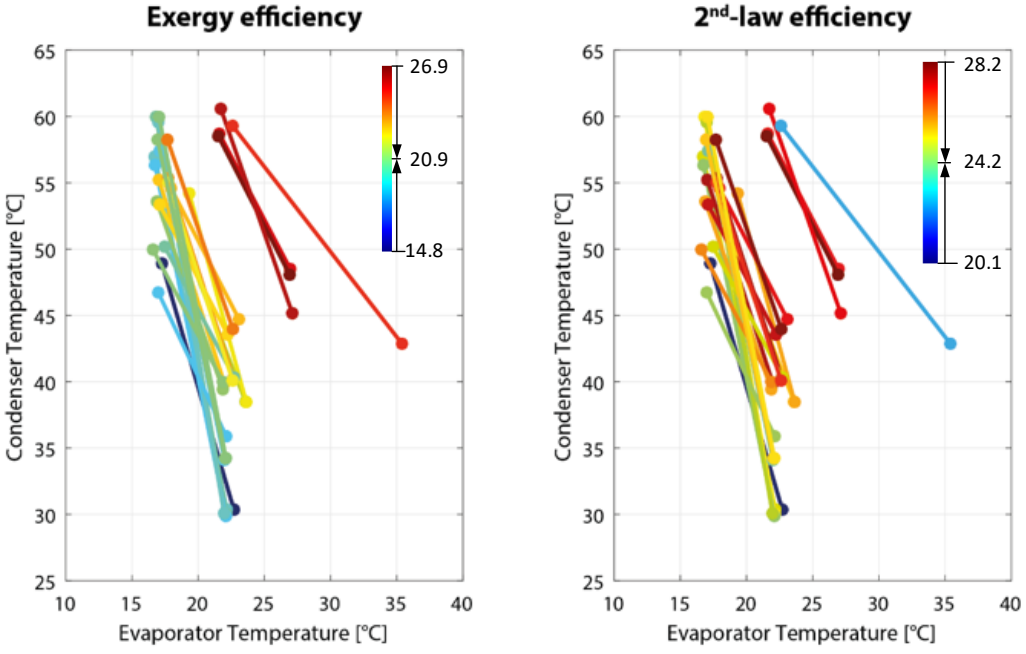


Fig. 6. Effect of condenser and evaporator inlet and outlet temperature on exergy efficiency and second-law efficiency.

Figure 6a shows an exergy efficiency distribution of the studied cases. Figure 6a shows that when the evaporator water inlet temperature ranged from 21.9 °C to 35.4 °C, the exergy efficiency varied from 14.8 to 26.9 %. The exergy efficiency increases with the increase of heat source temperature, which directly reflects the quality of the input energy. The decrease in the exergy efficiency is mainly attributed to the increase in compressor power with superheating degrees. Although Case 25 has a higher heat source temperature in the evaporator side, the temperature difference between inlet and outlet is also high. As the temperature difference increases, the irreversibility of the heat transfer process of evaporator increases, which results in a higher exergy loss corresponding a lower exergy efficiency than cases 18, 22 and 23.

The second-law efficiency of the simultaneous cooling and heating heat pump has been drawn in Fig. 6b based on the experimental results. Second-law efficiency achieved its maximum value at 28.2 % corresponding to a low temperature lift of condenser side and high temperature of DHW. Although the second law efficiency also shows the irreversibility of the system, different from exergy efficiency discussed above, $\eta_{II,dual}$ used in the present paper takes the useful output of $COP_{cooling}$ into consideration, which is numerically higher than exergy efficiency. Case 25 shows that the lower second-law efficiency ($\eta_{II,dual}$) is caused by a higher heat source temperature, with a very high ideal COP_{dual} such that $\eta_{II,dual}$ is significantly reduced to the corresponding 22.5 %.

3.3. Exergy efficiency

The performance of operation conditions with different heat sink temperatures have been studied experimentally. Mass flow rate of the comfort floor cooling water is fixed during testing these working conditions (m_e= 0.138 kg/s). Figure 9 shows five different working conditions with different DHW supply temperatures. The exergy and second law efficiency are highly influenced by the temperature of condenser side. Thus, an increment of the DHW temperature produces an increase of the energy quality and therefore, an increase of the efficiency. However, with the increase of DHW temperature, condensation temperature rises gradually, which make the system COP drop correspondingly.

Figure 9 also shows the exergy destruction ratio of each component in the studied simultaneous heat pump system. It can be found that the higher the temperature difference between inlet and outlet temperature of DHW, the lower the compressor exergy destruction ratio. The higher the temperature lift in the condenser side, the higher exergy destruction ratio of the condenser. The condenser side will be the potential component to improve the performance by decreasing the temperature lift when the evaporator side is fixed.

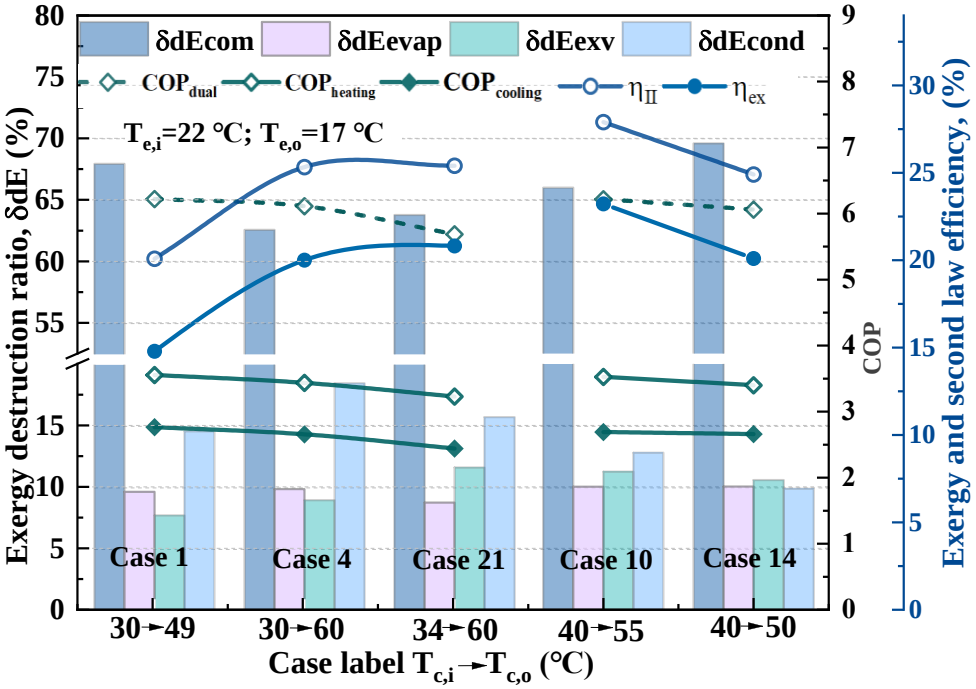


Fig.9. Effect of temperature difference on DHW side on heat pump system simultaneous performance.

4. Conclusions

A prototype of a water-source heat pump for simultaneous heating and comfort floor cooling was built and tested. Based on the experimental results discussed above, the main conclusions of the present study on steady state behavior of the proposed BHP can be drawn as follows,

- It can be found that the $COP_{heating}$ value varies from 3.0 to 3.4 in the studied conditions, and the $COP_{cooling}$ value ranged from 2.22 to 2.81. Test results showed that the cooling capacity ranged from 2.9 kW to 3.4 kW, heating capacity ranged from 3.8 kW to 4.4 kW.
- The lower domestic water temperature and higher temperature lift in the condenser can achieve a higher $COP_{heating}$ under the studied conditions with fixed cooling settings. A high temperature difference between condenser inlet and outlet temperature is beneficial for the COP_{dual} due to the increased effect of subcooling and the higher subcooling temperature that can be achieved.
- For each cooling load, there exists a corresponding heating capacity area, which can be used to regulate the system to operate at high efficiency. The highest dual-effect COP of the studied is 6.79. The second-law efficiency of the simultaneous DHW heating and floor cooling can reach 28.2 % within the studied range.
- The next step is to do the study with ratio of simultaneous DHW heating and cooling needs into consideration. System performance under non-synchronized DHW and cooling demands.

Acknowledgements

The authors gratefully acknowledge the financial support provided by Danfoss on the Comfort Cooling Project. The research also has received funding from the European Union's Horizon 2020 research and innovation program under the Marie Sklodowska-Curie grant agreement no. 713683 (COFUNDfellowsDTU, H. C. Ørsted Postdoc project HPMixPerform: Performance optimization of heat pumps using zeotropic mixtures as working fluid). The authors would also like to express our heartfelt gratitude to Jan Horne Hansen and Benny Edelsten for their help with the test rig.

Nomenclature

Symbols			
COP	Coefficient of Performance	P	Pressure (bar)
c_p	Specific heat capacity (J/(kg· K)	$\dot{Q}$	Energy capacity (kW)
DH	District heating	s	Entropy (kJ/kg·K)
$\dot{E}$	Exergy flow (W)	t	Temperature (℃)
$\dot{F}$	Volume flow rate of water (l/ h)	T	Temperature (K)
h	Specific enthalpy (kJ/kg)	$\dot{W}$	Compressor power (kW)
$\dot{m}$	Mass flow rate (kg/s)	y	Exergy destruction ratio
Subscripts			
comp	Compressor	L	Low
c	Condenser	o	Outlet
d	Exergy destruction	P	Production
e	Evaporator	r	Refrigerant
ex	Exergy	sub	Subcooling
ExV	Expansion valve	sup	Superheat
f	Forward	sat	Saturation state
F	Fuel	w	Water
H	High	0	Dead state
HS	Heat source	1,2,3,4	State point
i	Inlet	II	Second law
l	loss		
Greek Symbol			
Δ	Variation (-)	δ	Variation ratio (-)
η	Efficiency (%)		

References

[1] D.U. Shin, S.R. Ryu, K.W. Kim, Simultaneous heating and cooling system with thermal storage tanks considering energy efficiency and operation method of the system, Energy Build. 205 (2019). https://doi.org/10.1016/j.enbuild.2019.109518.

[2] F. Li, B. Sun, C. Zhang, L. Zhang, Operation optimization for combined cooling, heating, and power system with condensation heat recovery, Appl. Energy. 230 (2018) 305–316. https://doi.org/10.1016/j.apenergy.2018.08.101.

[3] X. Qin, Y. Zhang, D. Wang, J. Chen, System development and simulation investigation on a novel compression/ejection transcritical CO2 heat pump system for simultaneous cooling and heating, Energy Convers. Manag. 259 (2022) 115579. https://doi.org/10.1016/J.ENCONMAN.2022.115579.

[4] P. Byrne, R. Ghoubali, Exergy analysis of heat pumps for simultaneous heating and cooling, Appl. Therm. Eng. 149 (2019) 414–424. https://doi.org/10.1016/j.applthermaleng.2018.12.069.

[5] D.S. Ayou, R. Hargiyanto, A. Coronas, Ammonia-based compression heat pumps for simultaneous heating and cooling applications in milk pasteurization processes: Performance evaluation, Appl. Therm. Eng. 217 (2022) 119168. https://doi.org/10.1016/J.APPLTHERMALENG.2022.119168.

[6] D. Wu, B. Hu, R.Z. Wang, Performance simulation and exergy analysis of a hybrid source heat pump system with low GWP refrigerants, Renew. Energy. 116 (2018) 775–785. https://doi.org/10.1016/j.renene.2017.10.024.

[7] E.W. Lemmon, I.H. Bell, M.L. Huber, M.O. McLinden, NIST Standard Reference Database 23: Reference Fluid Thermodynamic and Transport Properties-REFPROP, Version 10.0, National Institute of Standards and Technology, (2018). https://doi.org/https://doi.org/10.18434/T4/1502528.

[8] A. Rijs, T. Mróz, Exergy Evaluation of a Heat Supply System with Vapor Compression Heat Pumps, Energies. 12 (2019) 1028. https://doi.org/10.3390/en12061028.

[9] R.J. Moffat, Describing the uncertainties in experimental results, Exp. Therm. Fluid Sci. 1 (1988) 3–17. https://doi.org/10.1016/0894-1777(88)90043-X.

[10] T. Zhu, T. Ommen, W. Meesenburg, J.E. Thorsen, B. Elmegaard, Steady state behavior of a booster heat pump for hot water supply in ultra-low temperature district heating network, Energy. 237 (2021) 121528. https://doi.org/10.1016/J.ENERGY.2021.121528.

14th IEA Heat Pump Conference
15-18 May 2023, Chicago, Illinois

Performance evaluation of multi-functional cascade heat pump system for a residential building

Beom-Jun Kim[a], Hye-Jin Cho[a], Soo-Jin Lee[a], Taek-Don Kwon[a], Jae-Weon Jeong[a,*]

[a]Department of Architectural Engineering, College of Engineering, Hanyang University, Seoul, Republic of Korea

Abstract

With increasing fossil fuel usage in building air-conditioning systems, air-source heat-pump systems are in the spotlight as an alternative HVAC system to reduce carbon emissions. The aim of this study is to evaluate a multi-functional cascade heat pump system for a residential building. A design method suited in residential buildings was applied to evaluate system performance of the proposed system. A reference system as separate two heat pumps was selected in charge of cooling, heating and hot water supply. The target building was set to residential of 100m2, 5 occupants are in the building. The thermal load of the target building was derived with commercial transient simulation tool, thermodynamic equations, and model equations built-in EnergyPlus were used. As a result, the proposed system saves 13% energy in cooling mode and 10% in heating mode compared with the reference system. The energy saving effect was occurred at the compression ratio of each high- and low-cycle decreasing due to the effect of recovering unused waste heat in summer and increasing the temperature of the refrigerant in winter.

© HPC2023.
Selection and/or peer-review under the responsibility of the organizers of the 14th IEA Heat Pump Conference 2023.

Keywords: Cascade heat pump; Air-source; Multi-functional system; Building energy-saving; Residential building

1. Introduction

With increasing fossil fuel usage in building air-conditioning systems, air-source heat-pump systems are in the spotlight as an alternative HVAC system to reduce carbon emissions [1]. Heat pump technology can treat indoor air condition and heat domestic hot water through heat absorption in an evaporator and heat dissipation in a condenser [2]. The absorbed heat by the evaporator for indoor cooling should be discharged to outdoor air. In contrast, and the heat should be absorbed from heat sources by the evaporator for indoor or water heating. If the temperature of the heat source is in an extremely low state or the load side requires a high temperature, the temperature difference between the evaporator-condenser increases, which can put a heavy load on the compressor. This may cause problems in that energy consumption increases and system efficiency decreases.

This problem can be solved by reducing the compressor load in each cycle by using a cascade type multi-stage heat pump system. If the heat absorption and heat emission properties of each cycle of the cascade heat pump system are used well, it has the potential to be used as a multi-functional system for zone cooling, heating, and domestic hot water in the building. The previous studies on cascade heat pumps have conducted experimental system performance analysis or optimization according to the refrigerant charging amount and expansion valve opening rate [3,4]. However, the capacity calculation and energy simulation of the system reflects building design constraints, such as thermal load, have not conducted for the case of applying of cascade heat pump system to a building. Therefore, in this study, a design procedure for the application of multi-functional cascade heat pump system was presented, and energy simulation was conducted for a residential building that requires both heating and cooling and domestic hot water. An existing air-source heat pump system responsible for cooling, heating, and domestic hot water was set as a simulation comparison.

* Corresponding author. Tel.: +82-2-2220-2370; fax: +82-2-2220-1945.
E-mail address: jjwarc@hanyang.ac.kr.

2. System overview

2.1. Cascade heat pump system

A cascade heat pump system consists of two heat pump cycles exchanging heat in an intermediate heat exchanger. The low-cycle of the system is in charge of the zone air-cooling, and the high-cycle heats domestic hot water for zone radiant floor heating and hot water supply. It was assumed that the refrigerant of the low-cycle heat pump was R410A, which is widely used in general air conditioners, and that of the high-cycle heat pump was R134a to supply high temperature heat [5] The proposed cascade heat pump in Figure 1 is to supply zone cooling in the low-stage cycle in summer, and supplies hot water in the high-stage cycle in winter.

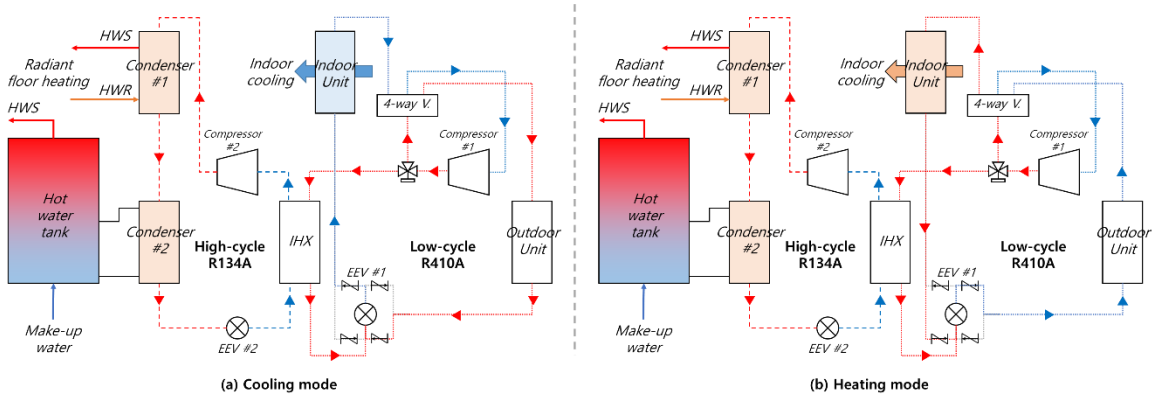


Fig. 1. Schematic of cascade heat pump system.

2.2. Reference heat pump system

In order to compare the performance of the proposed system, single heat pump systems were applied for each function required in a residential building [6]. The system to be compared is an air-source heat pump system as same as the proposed cascade heat pump system. A structure of the reference system is illustrated on Figure 2. The R410A refrigerant was used for the zone cooling cycle, and the R134a refrigerant was used for water heating cycles.

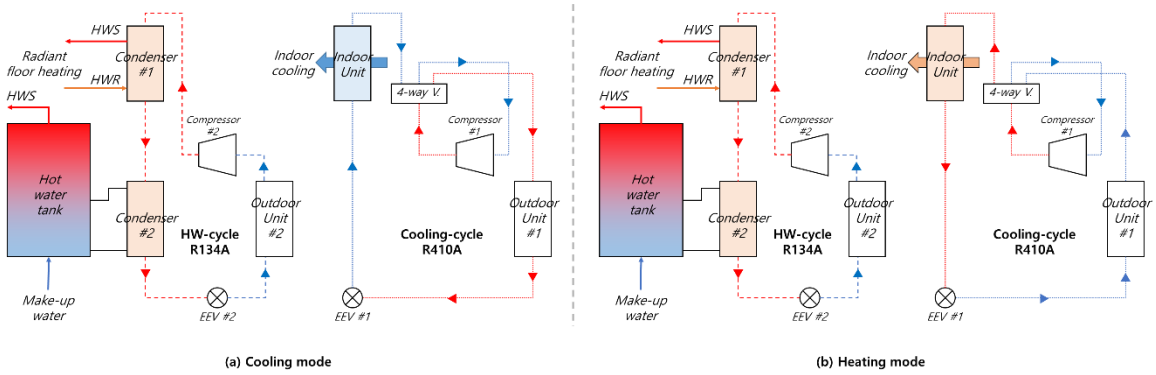


Fig. 2. Schematic of reference heat pump system.

3. Simulation overview

3.1. Sizing process logic

The sizing process algorithm for system capacity calculation was shown in Figure 3. First, design constraints for applying the system to residential buildings are set [7]. After the building information is determined according to the design constraints, the transient thermal-load simulation tool was used to calculate the thermal load of the model building [8]. The capacity of the low-cycle heat pump was determined

preferentially based on the cooling peak load. Finally, the capacity of the high-cycle heat pump that can satisfy the peak load of heating and domestic hot water load was determined.

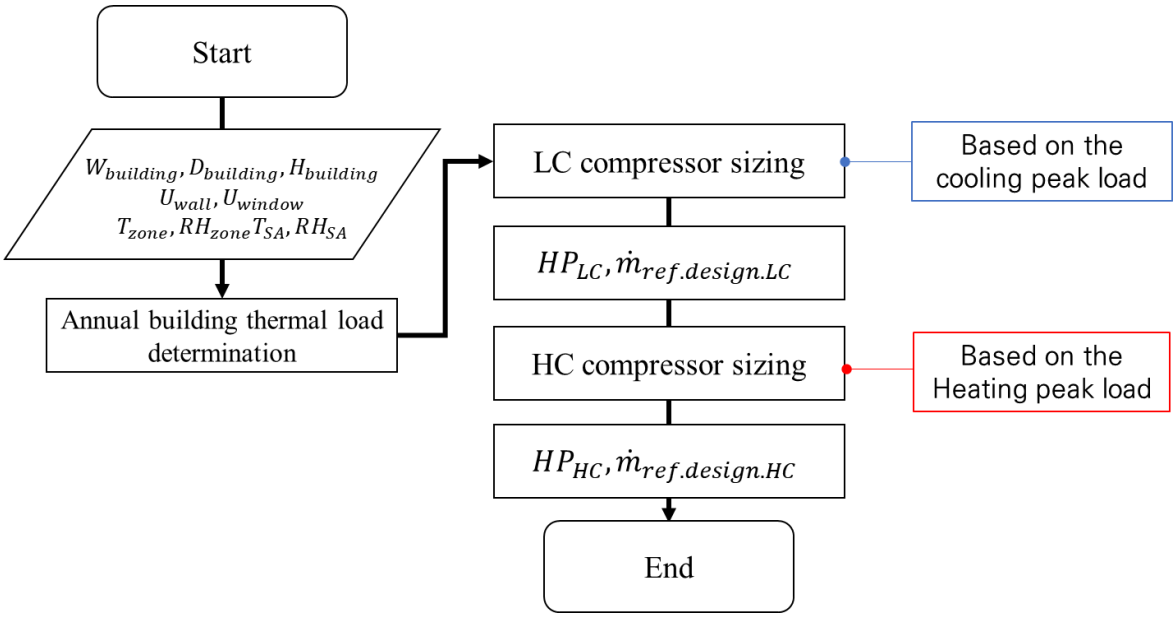


Fig. 3. Flow chart of system sizing for cascade heat pump system.

The parameters of each heat pump can be calculated by thermodynamic equations as follows (Eq.1-5) :

$$\dot{m}_{ref.LC} = \frac{\dot{Q}_{load.zone}}{\Delta h_{evap.LC}} \quad (1)$$

$$\dot{m}_{ref.HC} = \frac{\dot{Q}_{load.hw}}{\Delta h_{cond.HC}} \quad (2)$$

$$\dot{W}_{comp} = \dot{m}_{ref} \Delta h_{comp} \quad (3)$$

$$\dot{Q}_{cond} = \dot{m}_{ref} \Delta h_{cond} \quad (4)$$

$$\dot{Q}_{evap} = \dot{m}_{ref} \Delta h_{evap} \quad (5)$$

3.2. System design constraint

The design constraints necessary to apply the cascade heat pump system to residential buildings were set as follows. First, the air conditioning supply conditions must be 15°C and 80% relative humidity. Second, the target water temperature for floor heating and domestic hot water supply is set to 60°C. Third, the calculated cooling, heating and hot water supply performance of the heat pump must satisfy both the building heat load derived through the heat load simulation tool. R410a refrigerant was used for the LC of the heat pump, and R134a refrigerant was used for high-temperature heat supply for HC. Compressor and heat exchanger efficiencies, which is defined as the ratio of the actual work performed to the work input, were assumed to be 0.75 and 0.8, respectively, and superheat and subcooling degrees were assumed to be ±5°C [9]. Lastly, it is assumed to operate at full load without partial load.

3.3. Building thermal load determination

The building information are shown in Table 1. A 3 m-high-building of 100 m^2 was simulated through the TRNSYS program, and a total of 5 occupants were set based on the ASHRAE standard [10]. After calculating the building heat load, the indoor temperature and humidity conditions and the heat pump simulation were calculated through the EES program.

Table 1. Input data for building thermal load simulation.

Regime types	Parameters	Values
Floor area [m^2]		100
Number of floors [-]		3
Occupants [person]		15
Infiltration [1/h]		0.6
Zone condition	Temperature [℃]	26
	Relative humidity [%]	50
Supply air condition	Temperature [℃]	15
	Relative humidity [%]	80
Heat gain	People [W/person]	130 (sensible, latent)
	Equipment [W/m^2]	0.4
	Lights [W/m^2]	7
U-value	Outdoor wall [W/m^2K]	0.17
	Floor [W/m^2K]	0.17
	Roof [W/m^2K]	0.15
	Window [W/m^2K]	1.12

4. Simulation result

The results of this study were divided into 5 parameters and analyzed. There are capacity of the system derived from the results of the required thermal load simulation, the refrigerant and enthalpy difference by p-h plot, the system COP, waste heat recovery analysis, and primary energy consumption.

4.1. System design capacity

The thermodynamic simulation result of the heat load of the building was shown in Table 2 during peak load in summer and peak load in winter. The cooling cycle HP size was determined based on the summer peak load, and the heating and domestic hot water cycle size was determined based on the heating peak load and domestic hot water load in winter. The capacity of the heating and hot water cycles was designed after the capacity of the cooling cycle was pre-determined.

Table 2. Peak load data of the model building.

Peak data	T_{oa} [℃]	RH_{oa} [-]	T_{zone} [℃]	RH_{zone} [-]	$\dot{Q}_{sen}$ $[kW]$	$\dot{Q}_{lat}$ $[kW]$	$\dot{V}_{hw}$ $[L]$
Cooling	31.3	0.535	39.22	0.3664	2.716	0.8611	20
Heating and water heating	-13.65	0.835	12.24	0.3054	-2.522	-0.6548	26

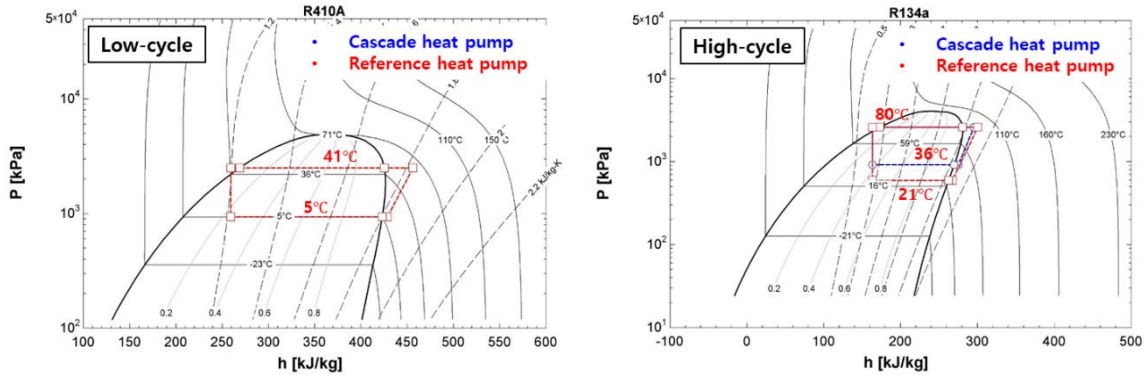
The designed capacity of cooling cycles, which refers the compressor power, were the same at 1.1 HP on both systems. However, the size of the cycles responsible for heating and domestic hot water was three times higher than the proposed system at 1.8 horsepower in the existing heat pump system.

Table 3. Design capacity of each system.

System	For cooling [HP]	For water heating [HP]
Cascade system	1.1	0.6
Reference system	1.1	1.8

4.2. p-h graph on peak day

First, to examine the behavior of the two systems, p-h diagrams were drawn for the two systems during peak load in summer, as shown in Figure 4. The low cycle, (i.e. the cooling cycle), showed the same cycle behavior in summer because the cooling operation of the two systems was the same. Since only domestic hot water was needed in summer, one can see that the thermal load is low, and the temperature difference between the evaporator-condenser of the blue-dash line is smaller. The refrigerant was same in both systems in cooling mode (i.e., 0.03018 kg/s of $\dot{m}_{ref}$). In contrasts, the cascade cycle in the hot water cycle needs more refrigerant (i.e., 0.00364 kg/s for cascade heat pump, 0.00350 kg/s for reference heat pump). As for the enthalpy difference, the heat absorption enthalpy difference of evaporator is large and the enthalpy difference in the compressor is small.

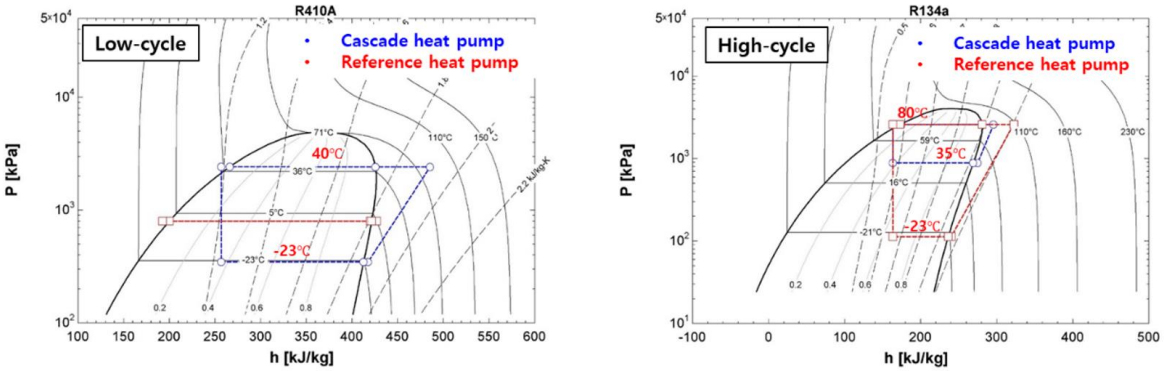


(a) Low-cycle (b) High-cycle

Fig. 4. Flow chart of system sizing for cascade heat pump system in cooling mode

Figure 5 shows the system in the winter condition. Under the condition, only the cycle of the cascade heat pump was visible in that cycle. This is because the reference system does not perform cooling operation in winter. The cascade system should be run a low cycle even in winter for multi-stage temperature rise. In winter, both systems were operated at a high cycle because residential buildings require floor heating and domestic hot water. It can be seen that the temperature difference between the evaporator-condenser of the reference system was very large. However, when matching the thermal load of the target condenser at high cycle, the amount of refrigerant in the reference system is operated with a small amount, and the heat absorption enthalpy difference in the evaporator is also small. This is because it is difficult to absorb a lot of heat from the outdoor air because the outdoor temperature is very low in winter, and it can cause the enthalpy difference of the compressor is up to 4 times larger.

Therefore, Cascade heat pump system has a high heat absorption of evaporator in high-cycle (heating), which reduces the required input power of the compressor and reduces the overall energy consumption. As a result, the amount of work that goes into the compressor is greater with the reference system.



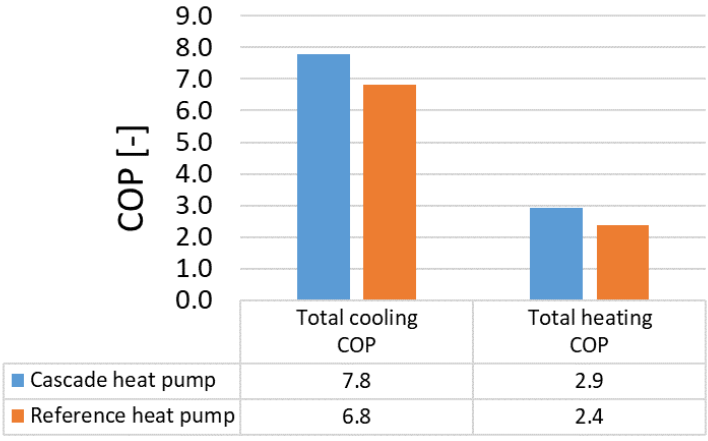
(a) Low-cycle (b) High-cycle

Fig. 5. Flow chart of system sizing for cascade heat pump system in heating mode

4.3. Coefficient of performance

Figure 6 reveals the total COP for each cycle of the heat pump, which was analyzed in 24 hours on the day when the cooling and heating peak load occurred. First, in the cooling mode, Hot water cycle showed higher COP in cascade heat pump system. The compressor load was low by receiving the waste heat of the low-stage cycle and supplying hot water with a higher heat source than the reference system. When operating in the cooling and hot water mode, the COP of the cascade heat pump was relatively high except for the cooling cycle. Conversely, in case of heating mode in winter, the cooling cycle of reference heat pump does not operate in winter, so the COP was zero. Each cycle COP of cascade heat pump is derived relatively high. When operating in heating and hot water mode, the COP of proposed system compared to reference system was relatively higher.

As a result of deriving seasonal COP, the result of high COP of cascade heat pump was derived in each season. This is thought to be the result of relatively low compressor energy consumption of the Cascade heat pump.



	Total cooling COP	Total heating COP
Cascade heat pump	7.8	2.9
Reference heat pump	6.8	2.4

Fig. 6. Seasonal COP of the heat pump system.

4.4. Waste heat recovery in summer

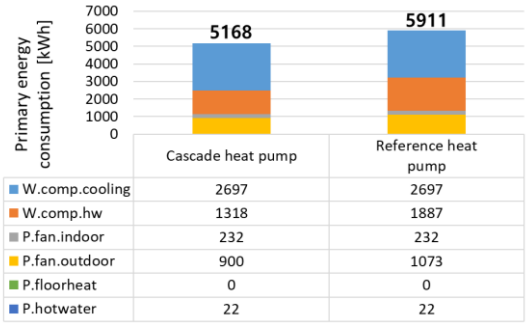
The amount of heat dissipation from the condenser of the cooling cycle in summer was 9621.4 kWh. In summer, the Cascade heat pump recovers heat from the low-stage cycle and uses it as a heat source for the high-stage cycle. About 18% of the waste heat was recovered.

4.5. Primary energy consumption

As a result of energy consumption analysis, along Figure 7, it was confirmed that the energy consumption of the proposed cascade heat pump system was lower than that of the reference system in both seasons. The

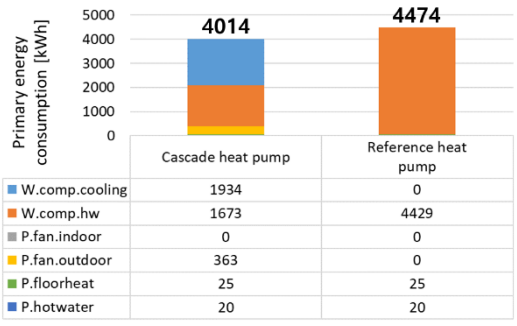
Cascade heat pump compared to the reference heat pump in energy consumption was confirmed to save energy by 13% when operating in cooling mode and 10% when operating in heating mode. In the cooling mode operation, there was no significant difference between the two systems in the cooling cycle, but a difference in energy consumption was confirmed in the hot water cycle.

In heating mode operation, the cascade heat pump system operated all cycles, but the total energy consumption was derived less than reference system, which was only operated with HW-Cycle and had any energy consumption of cooling compressor and outdoor fan. In the case of the fan, it was confirmed that the energy consumption of the reference system was slightly higher in the outdoor fan.



	Cascade heat pump	Reference heat pump
W.comp.cooling	2697	2697
W.comp.hw	1318	1887
P.fan.indoor	232	232
P.fan.outdoor	900	1073
P.floorheat	0	0
P.hotwater	22	22

(a) cooling mode



	Cascade heat pump	Reference heat pump
W.comp.cooling	1934	0
W.comp.hw	1673	4429
P.fan.indoor	0	0
P.fan.outdoor	363	0
P.floorheat	25	25
P.hotwater	20	20

(b) heating mode

Fig. 7. Primary energy consumption of heat pump systems.

5. Conclusion

In this study, when the cascade heat pump system is applied to a building, the High-cycle capacity was determined after the low-cycle capacity is determined according to the cooling load. As a result of the energy simulation, it was confirmed that the energy consumption of the Cascade heat pump is superior to the reference heat pump system (i.e., cooling, heating, and hot water supply, respectively). The cooling season COP improved by 14% and the heating season COP by 22%. In addition, energy consumption during the cooling season was 13%, and energy consumption during the heating season was 10%, resulting in a total annual energy savings of 12%. This indicates that the Cascade heat pump system has a high heat absorption of evap. in the high-cycle (heating), and as a result, the input power required for the compressor is reduced, resulting in a decrease in total energy consumption and an increase in COP. In conclusion, it is considered that each heat pump compressor has a smaller energy load than the compressor of a single stage heat pump system due to waste heat recovery in summer and multi-stage temperature increase in winter. It is necessary to conduct experimental study through future work to validate the energy saving performance of the cascade heat pump system.

Acknowledgements

This work was supported by the National Research Foundation of Korea(NRF) grant funded by the Korea government(MSIT) (No. 2022R1A2B5B02001975 and No. 2022R1A4A1026503), and Korea Environment Industry & Technology Institute (KEITI) through Prospective green technology innovation project, funded by Korea Ministry of Environment (MOE) (RE202103243).

References

[1] A.S. Gaur, D.Z. Fitiwi, J. Curtis, Heat pumps and our low-carbon future: A comprehensive review, Energy Res. Social Sci. 71 (2021).
[2] W. Yunna, X. Ruhang, Green building development in China-based on heat pump demonstration projects, Renew. Energy 53 (2013) 211–219 https://doi.org/10.1016/j.renene.2012.11.021.
[3] H.W. Jung, H. Kang, W.J. Yoon, Y. Kim, Performance comparison between a single-stage and a cascade multi-functional heat pump for both air heating and hot water supply, Int. J. Refrig. 36(5) (2013) 1431–1441, https://doi.org/10.1016/j.ijrefrig.2013.03.003

[4] D.H. Kim, M.S. Kim, The effect of water temperature lift on the performance of cascade heat pump system, Appl. Therm. Eng. 67(1–2) (2014) 273–282, https://doi.org/10.1016/j.applthermaleng.2014.03.036
[5] D.H. Kim, H.S. Park, M.S. Kim, Optimal temperature between high and low stage cycles for R134a/R410A cascade heat pump based water heater system, Exp. Therm. Fluid Sci. 47 (2013) 172–179, https://doi.org/10.1016/j.expthermflusci.2013.01.013
[6] LG Electronics. B2B Catalog. Available online: http://kr.lgeaircon.com/gcac.cussupport.catalogue.RetrieveCatalogueList.dev (accessed on 10 August 2022).
[7] ASHRAE, ANSI/ASHRAE Standard 55-2016, Thermal Environmental Conditions for Human Occupancy, American Society of Heating, Refrigerating and Air-conditioning Engineers, Inc., Atlanta, 2020.
[8] S.A. Klein, W.A. Beckman, J.W. Mitchell, J.A. Duffie, N.A. Duffie, T.L. Freeman, J.C. Mitchell, J.E. Braun, B.L. Evans, J.P. Kummer, R.E. Urban, A. Fiksel, J.W. Thornton, N.J. Blair, P.M. Williams, ,D.E. Bradley, T.P. McDowell, M. Kummert, D.A. Arias, M.J. DuffyTRNSYS 18: A Transient System Simulation Program, Solar Energy Laboratory, University of Wisconsin, Madison, USA, 2017. http://sel.me. wisc.edu/trnsys.
[9] P.G. Jolly, C.P. Tso, P.K. Chia, Y.W. Wong, Intelligent control to reduce superheat hunting and optimize evaporator performance in container refrigeration, ASHRAE Trans. (2011) 243–255, 10.1080/10789669.2000.10391261
[10] ASHRAE, ANSI/ASHRAE Standard 90.1-2016, Energy Standard for Buildings Except Low-Rise residentail buildings, American Society of Heating, Refrigerating and Air-conditioning Engineers, Inc., Atlanta, 2019.

14th IEA Heat Pump Conference
15-18 May 2023, Chicago, Illinois

Preliminary test result of an oil compatibility of a low-GWP refrigerant as an alternative to R410A in a compressor test loop

Junhyun Cho[a,*], Gilbong Lee[a], Bongsu Choi[a], Bong Seong Oh[a], Ho-Sang Ra[a], Sun Ik Na[a], Eunseok Wang[a], Gyunchul Hur[a], Jongjae Cho[a], Beomjoon Lee[a], Young-Jin Baik[a*]

[a]Korea Institute of Energy Research, 152 Gajeong-ro, Yusung-gu, Daejeon 34129, South Korea

Abstract

A new alternative refrigerant has to be tested under real operating conditions to investigate its compatibility with lubricant oil, additives, seals, copper or any metal components and varnish in a compressor driving motor. In this study, oil compatibility characteristics of a low-GWP refrigerant as an alternative to R410A in a compressor test loop is preliminarily studied. To determine short and long-term lubricant oil compatibility of a low-GWP refrigerant in a compressor, a simple heat pump cycle test loop is designed and preliminarily tested under accelerated test protocol. R466A is selected as an alternative to R410A. A 6 hp of compressor for R410A, a 20 kW of condenser are selected. To reduce heat source capacity and to control inlet condition of a compressor, a shell type evaporator with a 15 kW electric heater is designed. An oil characteristic such as a viscosity and a decomposed ion using an ion chromatography are measured after each operation time schedule.

© HPC2023.
Selection and/or peer-review under the responsibility of the organizers of the 14th IEA Heat Pump Conference 2023.

Keywords: Type your keywords here, separated by semicolons ;

1. Introduction

In accordance with global carbon-neutral policies and refrigerant regulations to limit global temperature rise, alternative refrigerants with low global warming potential (GWP) and heat pump technology using them are being developed. System air conditioners used for heating and cooling homes and commercial buildings, that is, variable refrigerant flow (VRF) heat pumps, currently use HFC (hydrofluorocarbons) R410A refrigerant with a global warming potential of 2088. The US CARB (California Air Resource Board), which leads environmental regulations, plans to use refrigerants with a GWP of less than 750 for new residential and commercial products from 2025 and for VRF systems from 2026 [1]. In addition, the European F-gas regulation stipulates that HFC refrigerant usage in 2030 be reduced by 79% compared to 2015, and from 2025, sales of single-split air conditioners with a refrigerant volume of 3 kg or less that uses a GWP of 750 or more refrigerant would be forbidden [2].

R410A is a mixed refrigerant composed of 50% R32 (CH_2F_2) and 50% R125 (C_2HF_5). A mixed refrigerant R466A which is composed of 49% R32, 11.5% R125, and 39.5% R13I1 (CF_3I) was developed as a replacement of R410A by Honeywell who is one of the representative refrigerant manufacturers [3]. The GWP of R466A is 733, and some manufacturers are developing systems for R466A as the safest A1 class refrigerant.

When a new refrigerant is developed, it is essential to evaluate its compatibility with lubricants, especially in compressors. Oil for lubrication is used in the compressor, and this oil serves not only to lubricate but also to cool frictional heat and motor heat. In addition, it serves as a sealing and anti-rust function in mechanical seals and piston rings. To this end, oil flows into the compressor together with the refrigerant, so the heat pump system can be stably operated only when an appropriate combination of new refrigerant and oil is configured.

* Corresponding author. Tel.: +82-42-860-3581; fax: +82-42-367-5067.
E-mail address: jhcho@kier.re.kr.

As a representative method for evaluating refrigerant oil adequacy, the sample accelerated test technique of ASHRAE (American Society of Heating, Refrigerating and Air conditioning Engineers) standard 97-2007 is used [4]. It is a method of evaluating physical properties after sealing in a test tube mixed with oil in a 1:1 weight ratio and aging at a temperature of 175 ° C for 14 days.

Oil and additives are screened through these sample tests, and reliability tests are conducted through actual system operation. R466A has similar physical properties and thermodynamic performance to R410A, and it has been announced in previous studies that the POE (Polyolester) oil used in R410A can be used [5], but the refrigerant-oil compatibility in actual heat pump system operation situation Experimental data are scarce. Therefore, in this study, for the alternative refrigerant R466A, not a sample test, but a core device such as a compressor constituting a heat pump system in an actual operating state, various parts such as valves, and refrigerant-oil compatibility and system reliability were evaluated. Therefore, key factors of the compatibility evaluation method were determined, cycle operating conditions were determined for the accelerated real operation test, and a compressor test loop was designed for the long-term reliability test.

2. Key factors for evaluating refrigerant-oil compatibility

In order to evaluate the suitability of refrigerant and oil, three evaluation factors were determined by referring to the existing literature [4] for the physical property index to be analyzed after deterioration due to long-term real operation of the system.

First, it is possible to evaluate the adequacy with the refrigerant by measuring the acidic product produced by the oxidation of oil as an index of TAN (Total Acid Number). Potentiometric titration using KOH (ASTM D 664) is used.

Second, the degree of decomposition of the refrigerant or oil can be grasped by analyzing the decomposition ions generated by the reaction between the refrigerant and oil as a decomposed ion indicator. When fluoride is detected, the refrigerant is decomposed, and when organic acids such as propanoate and hexanoate are detected, it can be evaluated that oil is decomposed. For this, ion chromatography is used.

Third, the compatibility can be evaluated by measuring the viscosity that decreases with the deterioration of the oil as a viscosity index. Viscosity is measured using a Brookfield viscometer (ASTM D 4402).

3. Previous researches on R466A-oil compatibility

Honeywell's sample accelerated test for R466A refrigerant under the condition of POE oil (ISO 32 3MAF) for R410A and additive combination According to the results of previous research, fluoride was detected at 50 ppm, 25 times higher than 2 ppm for R410A, in the R466A test, and iodide It has been reported that 22 ppm, which is hundreds of times greater than <0.1 ppm of R410A, is detected [6].

Accordingly, after a sample accelerated test in the same POE oil using additives whose components were not disclosed at Honeywell, it was shown that fluoride was 2 ppm and iodide was <1.5 ppm, and compatibility could be satisfied [6].

In addition, it was reported that R23(CF_3H) was decomposed and detected in the combination of zinc-aluminum alloy and R466A-POE base oil [7], and it was also shown that compatibility can be satisfied through the addition of additives. It is evaluated that the iodine component of CF_3I of R466A reacts with oil and zinc-based metal materials.

Some information on the additive material can be obtained from Honeywell's patent, which is a combination of alkylated naphthalene (NA-LUBE), farnesene ($C_{15}H_{24}$), a diene compound, and BHT (Butylated Hydroxi Toluen), a phenolic compound [8].

4. Test scenario for R466A oil compatibility evaluation in actual operation

In order to evaluate the oil suitability of R466A according to the actual long-term operation of the compressor, a heat pump test cycle was constructed and an operating scenario was determined.

In order to accelerate the deterioration by the refrigerant-oil reaction, test scenario of start-continuous operation (8 hours)-stop was determined under the AHRI (Air Conditioning, Heating and Refrigeration Institute) Standard 210/240 MOC (Maximum Operating Condition) condition or more harsh condition. In this operating condition, refrigerant-oil samples would be taken every 100 hours repeatedly and test loop would be operated for a cumulative 300 hours.

Table 1. AHRI Standard 210/240 MOC conditions for R466A

Condensing Temperature (℃)	Outdoor Temperature (℃)	Evaporative Temperature (℃)	Indoor Temperature (℃)
55.1	46.1	7	26.7
Superheat (℃)	Subcooling (℃)	Compressor Rotational Speed	
5.5	5.5	Full	

Table 2. Temperature and Pressure conditions of R410A and R466A cycles

State	Temperature (℃)	Pressure (bar)	Temperature (℃)	Pressure (bar)
1	7.0	9.9	7.0	10.6
2	92.3	34.8	100.1	36.4
3	55.1	34.5	55.1	36.0
4	9.7	10.8	9.8	11.5

As shown in Table 1, the outdoor temperature standard under the MOC condition is 46.1℃, and the corresponding condensing temperature on the refrigerant side is 55.1℃, which is 9℃ higher by referring to Honeywell's AHRI 210/240-A condition performance test reference [8], and the evaporative temperature was selected as 7℃. Superheating and subcooling were selected as 5.5℃.

Cycle design was carried out to derive compressor operating conditions under MOC operating conditions. The cycle was designed using an in-house code that can predict the heat pump design performance using the thermodynamic governing equation, and the calculation was performed using the mixture properties of REFPROP using the composition ratio of R466A.

In addition, calculations were performed for R410A under the same conditions. As shown in Fig. 1, the cycle operating conditions and performance of R466A and R410A under MOC conditions were predicted. The pressure loss was assumed to be 1% in the condenser and 8% in the evaporator.

As shown in Table 2, under the R466A MOC condition, the condensing temperature/pressure was 55.1℃ /36.0 bar, the evaporative temperature/pressure was 7℃/10.6 bar, and the compressor discharge temperature was calculated as 100.1℃. Under R410A MOC conditions, the condensing temperature/pressure was 55.1℃ /34.5 bar, the evaporative temperature/pressure was 7℃/9.9 bar, and the compressor discharge temperature was 92.3℃. Since the conditions are almost similar, commercial parts based on R410A were used when designing and manufacturing the actual test loop.

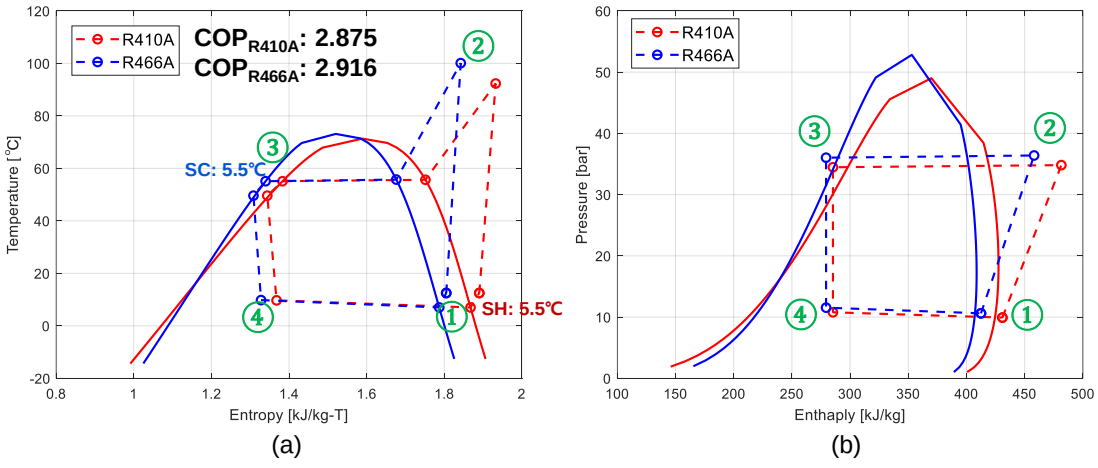


Fig. 1. T-s (a) and P-h (b) charts of R410A and R466A cycles

In this study, the main purpose is to evaluate the refrigerant-oil compatibility and reliability according to long-term cycle operation rather than cycle performance characteristics analysis, a simplified test loop for long-term operation was designed and manufactured

5. Design and construction of test loop

For the evaluation of compressor refrigerant-oil compatibility and reliability in accelerated operation, the test loop was designed as shown in Fig. 2. The core cycle devices such as the compressor, heat exchanger, and electronic expansion valve were selected with commercially available parts for R410A, and a rotary compressor with a capacity of 6 HP and an inverter control system was used. In order to simulate the MOC condition in the long term, we tried to simplify the heat source facilities corresponding to the secondary side of the condenser and evaporator. Therefore, after the compressor, working fluid is discharged (state 2), a bypass loop is placed before entering the condenser, so that the refrigerant that has passed through the condenser is expanded in the EEV (Electric Expansion Valve) 1, and the bypassed refrigerant passes through EEV2 and 3. After expansion, it was configured to be mixed in an evaporator. EEVs were selected with Danfoss' R410A standard commercial product, and the bypass loop is composed of two loops to control the flow rate and expansion ratio fluctuations that may occur when R466A refrigerant is used in the valve. EEV2 and EEV3 are controlled by manual and/or remote signal by PLC controller.

The refrigerant that has passed through EEV1, EEV2, and EEV3 is introduced into a shell containing a 15 kW electric heater and mixed. This shell-type heater operates as an evaporator in order to control the evaporative temperature and superheat of the compressor easily because of uncertain characteristics of R466A. R466A is a mixed refrigerant of three types. In response to the temperature change that can occur during heat exchange, an electric heater that can directly control the temperature is used to allow only gaseous R466A to flow in from the compressor inlet, enabling stable testing.

A visualization window and an oil extraction valve were configured in the loop returning from the oil separator to the compressor after compressor discharge, so that oil sampling was possible, and a mass flowmeter (OVAL, ±0.1%) was installed on the compressor discharge side and the condenser rear side. A pressure gauge (Autrol) of ±0.075% was used at the inlet and outlet of the compressor, and a pressure gauge (Keller) of ±0.5% was used for other parts, and a Class A RTD was used for the temperature, and the temperature for controlling EEV1 was measured using a thermocouple. Temperature and pressure data were obtained through a data logger (Yokogawa GM10), and EEV control was configured with a PLC.

As shown in Figure 3, the test loop was completed, and the stability of the system was verified through the pressure resistance test and air tightness test. Afterwards, R410A refrigerant is sealed, and core device performance, data acquisition, cycle control, and safety issues are checked through a test run, and then the test is conducted with R466A refrigerant.

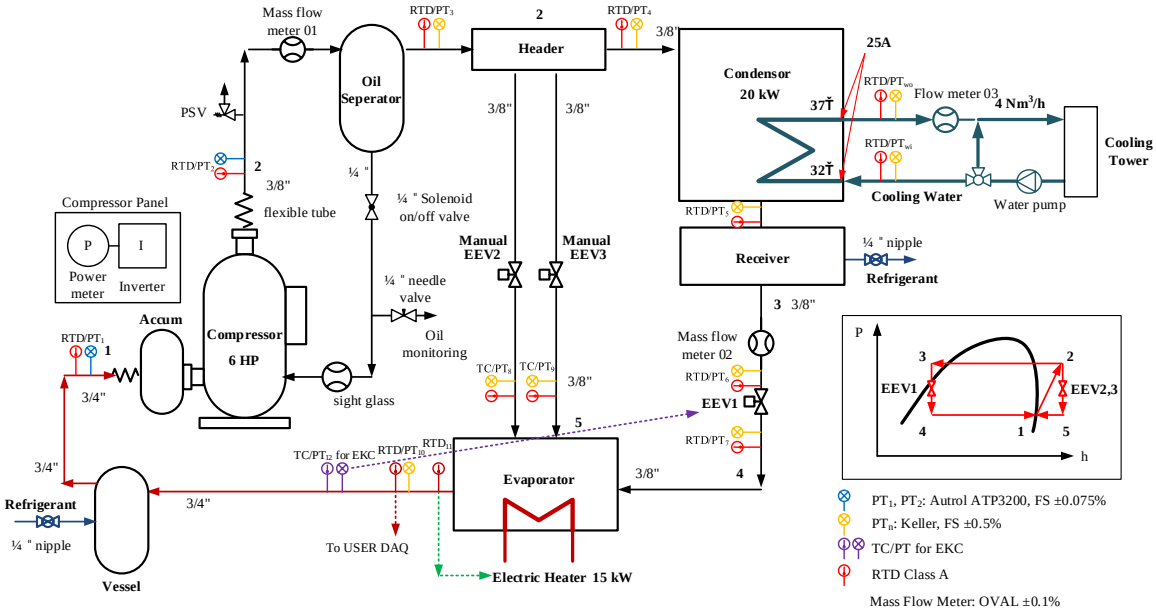


Fig. 2. Schematic of the test loop for refrigerant-oil compatibility test under long-term operation

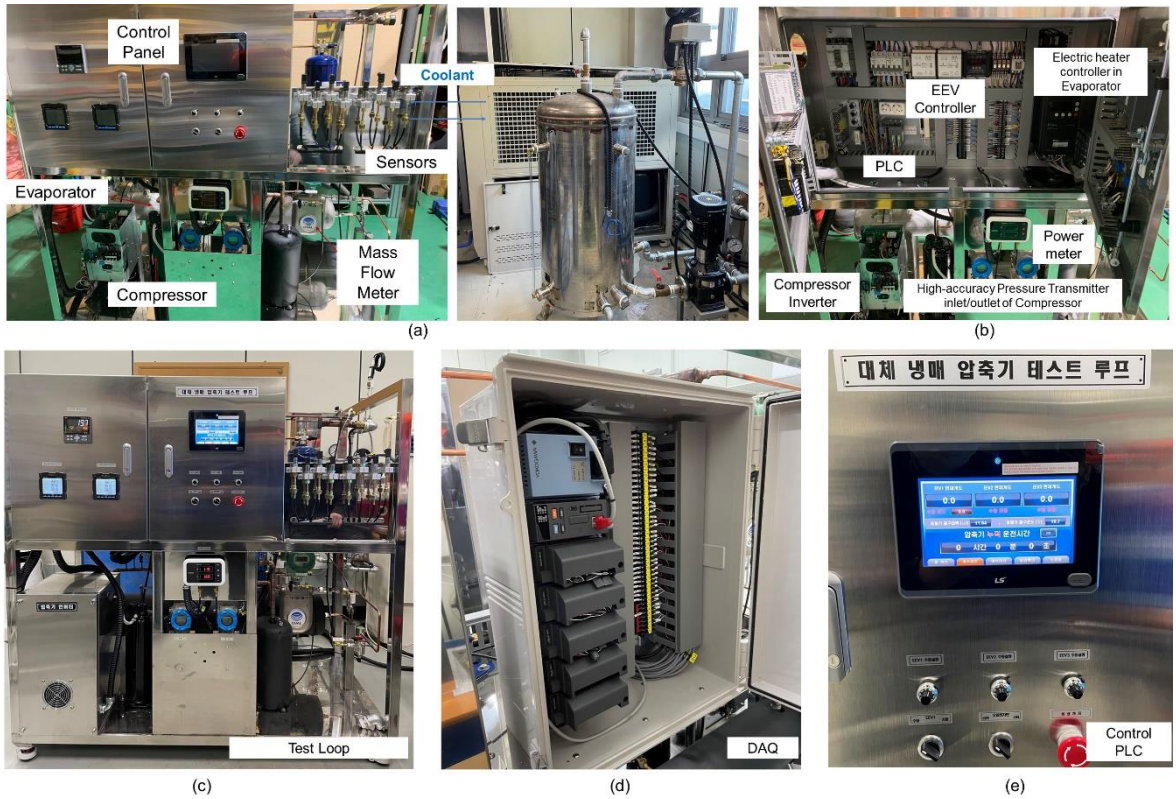


Fig. 3. Components of the test loop with a chiller unit (a), an inverter and controllers (b), the final test loop (c), a data acquisition unit (d) and a control PLC monitor (e)

6. Conclusions and Future works

For the R466A refrigerant of GWP 733, which replaces the R410A refrigerant of GWP 2088 currently used in commercial VRF systems, a test loop that can evaluate the compatibility and reliability of compressor refrigerant-oil that may occur during long-term actual operation was designed and manufactured.

First, TAN, decomposed ion, and viscosity were determined as indicators to be evaluated through the investigation of the refrigerant-oil compatibility evaluation method. Through previous research analysis, it was confirmed that the use of POE-type oil, the same as R410A, but the use of appropriate additives to suppress corrosion due to the influence of CF_3I included in R466A was necessary, and information on target additive candidates was investigated in the refrigerant manufacturer's patents.

AHRI 210/240 MOC conditions that can simulate accelerated deterioration conditions were selected and the corresponding R466A cycle design was performed, and the cycle operating conditions of 10.6 bar in the low-pressure part, 36.4 bar in the high-pressure part, and 100.1 ℃ discharge temperature of the compressor were selected. Based on this, in order to simplify the long-term acceleration test, a test loop including a bypass loop after compressor discharge and a shell-type evaporator using an electric heater was designed and manufactured.

Currently, the test loop verification is in progress based on the R410A refrigerant, and after that, the R466A refrigerant drop-in test would be performed to analyze the change in the characteristics of the refrigerant and oil after long-term room operation, and the deterioration of the compressor and accessories.

Acknowledgements

This work was supported by Korea Institute of Energy Technology Evaluation and Planning (KETEP) grant funded by the Korea government (MOTIE) (20212020800070, Development of next-generation alternative refrigerant and efficient heat pump system)

References

[1] CARB, Prohibitions on Use of Certain Hydrofluorocarbons in Stationary Refrigeration, Chillers, Aerosols-Propellants, and Foam End-Uses Regulation, 2022, 01. https://ww2.arb.ca.gov/ rulemaking/2020/hfc2020
[2] Global trend on refrigerant regulation and alternatives, Trane Korea, 2017
[3] https://sustainability.honeywell.com/us/en/products/ refrigerants/hfo-blends/solstice-n41-r-466a
[4] Ngoc Dung (Rosine) Rohatgi, Robert W. Clark and David R. Hurst, 2012, "Material Compatibility & Lubricants Research for Low GWP Refrigerants - Phase I: Thermal and Chemical Stability of Low GWP Refrigerants with Lubricants", AHRTI Report No. 09004-01
[5] Atilla G. Devecioglu and Vedat Oruc, 2020, "Energetic performance analysis of R466A as an alternative to R410A in VRF systems", Engineering Science and Technology, an International Journal, Vol. 23, pp. 1425~1433
[6] Kaimi Gao, Henna Tangri, Greg Smith, Ankit Sethi and Samuel Yana Motta, 2021, "Reduced GWP Refrigerant for Residential and Commercial Air Conditioning Systems", International Refrigeration and Air Conditioning Conference. Paper 2191
[7] Stephen Anthony Kujak and Elyse Sorenson, 2021, "Chemical Stability and Equipment Reliability Impacts of R-13I1 (CF3I) in R-466A", International Refrigeration and Air Conditioning Conference. Paper 2091
[8] Honeywell Intenational Incorp. Patent 10-2020-7009907, South Korea

14th IEA Heat Pump Conference
15-18 May 2023, Chicago, Illinois

Heat pump application approach to abate plume generation from a cooling tower

Gilbong Lee*, Junhyun Cho, Bong Su Choi, Bong Seong Oh, Ki-Chang Chang

Korea Instititue of Energy Research, 152 Gajeong-ro, Yuseong-gu, Daejeon, 34129, Republic of Korea

Abstract

In Korea, white plume generated by cooling tower is a one of major social conflicts due to its visual pollution. Various methods have been developed to abate plume generation, such as outdoor air condensing, dry/wet hybrid cooling, membrane method, etc. However when cooling towers operate in cold climate without plume generation, both humidity ration and relative humidity have to be reduced with effective methods. Dehumidification and regeneration using heat pump cycle can be a good technical solution for this since it condense water vapor and then reheat the air with condensation heat and compressor power input. The required energy of a heat pump method is 3 to 4 times less than a direct heating method. For further energy reduction, an outdoor air mixing is introduced before heat pump stage and the power input can be reduced up to 10% compared to a direct heating.

© HPC2023.
Selection and/or peer-review under the responsibility of the organizers of the 14th IEA Heat Pump Conference 2023.

Keywords: Cooling Tower; Heat Pump; Plume; Plume Prevention

1. Introduction

Stacks or cooling towers tend to exhaust plume when the outdoor temperature is low and relative humidity is high. The plume is literally water vapor and not environmentally harmful. However it may cause social conflicts due to visual pollution and misperception as fire or smoke [1, 2]. In addition, when the white smoke does not rise and spreads on the road, it may cause icing problems and sometimes cause traffic problems. For this reason, cooling tower plume abatement is one of the biggest technical issues in the related industry.

2. Plume abatement by applying a heat pump cycle

One of the most widely used methods to reduce plume generation from cooling towers is outdoor air mixing method in which exhaust wet air is firstly dry-cooled by lower temperature outdoor air while discharging thermal energy to the outdoor air and reducing water vapor intake. Then the two air streams are mixed together and the humidity ratio and relative humidity of the discharged air of cooling tower are decreased [3]. By adopting this method, it is possible to reduce the absolute discharge of water vapor and reduce water consumption through condensate recovery. This method can be applied with small design changes in existing cooling towers while minimizing additional input energy, but it is difficult to ensure plume abatement in low temperature outdoor condition such as winter morning with high relative humidity or high relative humidity condition such as foggy or snowy weather.

Condensing and removing water vapor using a heat pump can also be another method for reducing plume generation. By applying a more active cooling/heating device, heat pump, it becomes possible to efficiently prevent plume even in sub-zero climate conditions [3]. The heat pump recovers sensible and latent heat from the humid discharged air of cooling tower in the evaporator and the recovered heats is then transferred to the

* Corresponding author. Tel.: +82-42-860-3293;.
E-mail address: giblee@kier.re.kr

discharge stream passing through the condenser. Therefore the relative humidity can be lowered much more than the outdoor air mixing method (Fig.1). Since air in cooling tower is at high relative state, heat transfer in the evaporator is increased due to condensation, and energy consumption can be reduced by the factor of COP of the heat pump compared to the electric heaters.

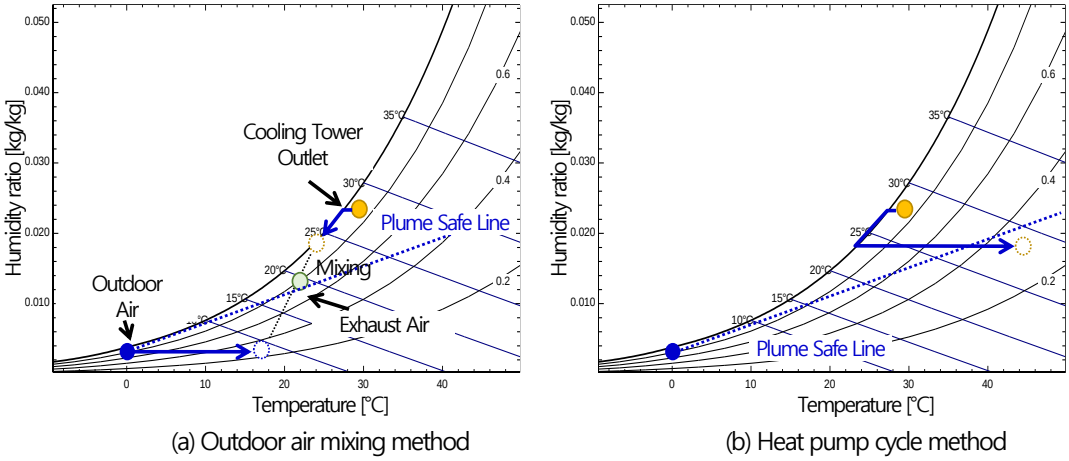


Fig. 1. Plume abatement approaches – outdoor air mixing and heat pump

Fig. 2 shows a reference case of heat pump cycle analysis under typical cooling tower flow conditions. The cycle characteristics in the cooling tower flow condition are the high latent heat ratio in the evaporator (latent heat transfer is more than 95% of the total heat transfer) and the high condenser pressure approaching the compressor operating limit. The high latent heat ratio is due to the high relative humidity, and as the evaporator and the condenser operate at the same air volume rate, the condensation pressure has to increase more compared to the general heat pump system. Under the suggested operating conditions in the figure, the air at the exit of the condenser is heated up to 51.5°C, and plume prevention can be expected to about 0°C outdoor air temperature. The estimated COP obtained by the heat pump is 4.0.

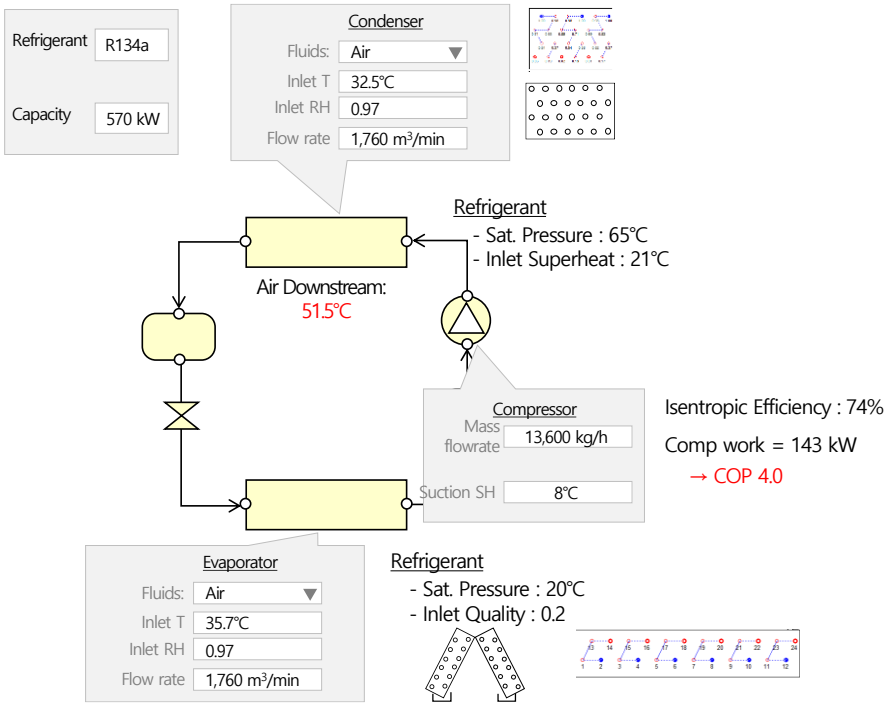


Fig. 2. Heat pump cycle analysis under typical cooling tower flow conditions

3. Plume Prediction based on Psychrometric Chart

From a thermodynamic point of view, plume is generated when condensation occurs in the mixing process between exhaust air of cooling tower discharge and low-temperature outdoor air. The occurrence of condensation means that the humidity ratio of the two mixed stream is higher than the value of saturated condition at the mixed temperature. So the saturated humidity ratio to the mixed temperature and the current humidity ratio were selected as the criterion for plume generation. In order to prevent plume generation in certain outdoor conditions and cooling tower outlet conditions, either the outlet air temperature must be raised or the humidity ratio value must be reduced. The figure below shows the process of estimating the minimum value of outlet air temperature increase on a psychrometirc chart, and the determination process is briefly presented too.

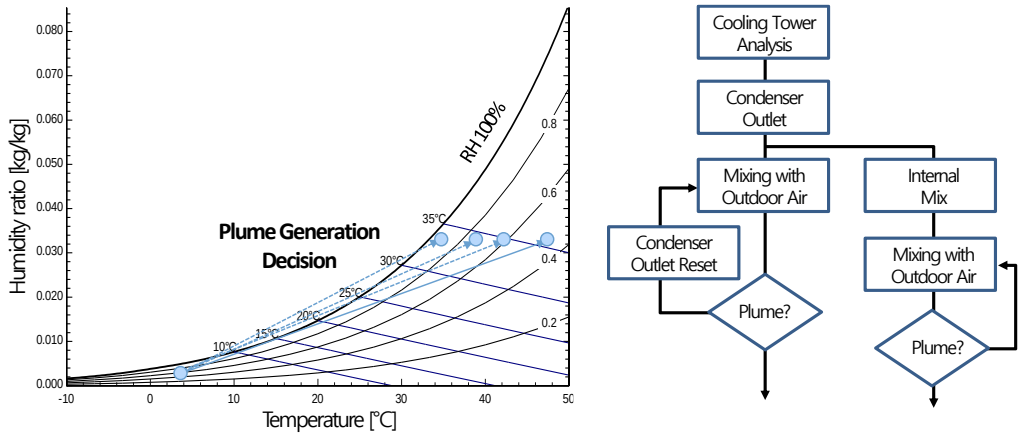


Fig. 3. Process of finding operation conditions for the prevention of plume generation

The plume generation prediction method based on the psychrometic chart can be used for following cases

- (Analysis of outdoor temperature effect) The result of analyzing the temperature required for plume prevention according to the different outdoor temperature with fixed cooling tower outlet condition of 33℃ and RH99% is shown in the below figure and table. When the outdoor temperature is lower than a certain point, the temperature required for plume prevention tends to increase rapidly. For example, for the outdoor temperature of 20ºC, only 1.4 ºC temperature increase is required. However the required values are increased to 9.9ºC at 10ºC outdoor and 37.4ºC at 0ºC outdoor. Reheating temperature prediction tool with outdoor temperature changes makes it possible to derive operational limits for plume prevention in currently constructed facilities.

T_old(℃)	Outdoor T(℃) (RH 75%)	T_new(℃)	h_old(kJ/kg)	h_new(kJ/kg)	Delta T(℃) (Heating)
33	20	34.4	115.6	117.1	1.4
33	19	34.8	115.6	117.5	1.8
33	18	35.2	115.6	118	2.2
33	17	35.8	115.6	118.6	2.8
33	16	36.4	115.6	119.2	3.4
33	15	37.2	115.6	120.1	4.2
33	14	38	115.6	120.9	5
33	13	39	115.6	122	6
33	12	40.2	115.6	123.3	7.2
33	11	41.5	115.6	124.7	8.5
33	10	42.9	115.6	126.2	9.9
33	9	44.6	115.6	128	11.6
33	8	46.4	115.6	129.9	13.4
33	7	48.4	115.6	132	15.4
33	6	50.7	115.6	134.5	17.7
33	5	53.2	115.6	137.1	20.2
33	4	56	115.6	140.1	23
33	3	59.1	115.6	143.4	26.1
33	2	62.5	115.6	147.1	29.5
33	1	66.3	115.6	151.1	33.3
33	0	70.4	115.6	155.5	37.4

T_old/h_old : air temperature/enthalpy exiting base cooling tower
T_new/h_new : air temperature/enthalpy after condenser to prevent plume generation

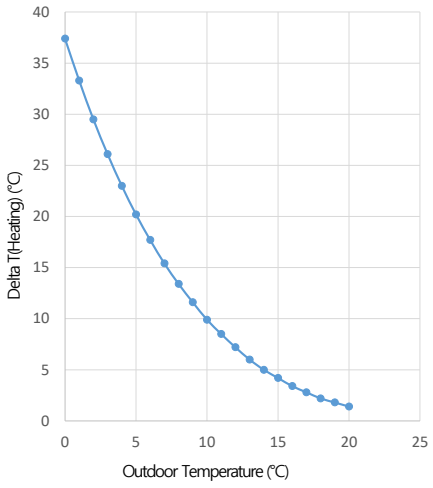


Fig. 4. Analysis of outdoor air temperature effect on plume prevention

- (Analysis of outlet temperature effect) In order to analyze the cooling tower operating conditions for plume prevention in low-temperature outdoor condition, an outdoor plume reduction temperature analysis was performed at −5℃/RH75%. Considering the fact that the heating temperature rapidly increases as the outdoor temperature decreases in the previous case, the cooling tower outlet temperature was arbitrarily lowered in this case, and the plume prevention temperature increase characteristics were analyzed for 20-29ºC outlet temperature. The results are presented in the figure and table below, and compared to the case of 15.1ºC heating requirement a 20ºC outlet temperature, 42.2ºC heating is required at 29ºC outlet (2.86 times more heat required). Therefore, in order to effectively prevent plume, it is necessary to design a control logic that lowers the outlet air temperature and a system in which the output of the heat pump for plume removal is inter-connected with each other.

T_old(℃)	Outdoor T(℃) (RH 75%)	T_new(℃)	h_old(kJ/kg)	h_new(kJ/kg)
20	-5	35.1	57.01	72.59
21	-5	38.2	60.45	78.23
22	-5	41.5	64.04	84.23
23	-5	45	67.78	90.61
24	-5	48.6	71.68	97.26
25	-5	52.6	75.75	104.5
26	-5	56.9	79.99	112.3
27	-5	61.3	84.43	120.4
28	-5	65.8	89.06	128.8
29	-5	71.2	93.91	138.4

T_old/h_old : air temperature/enthalpy exiting base cooling tower
T_new/h_new : air temperature/enthalpy after condenser to prevent plume generation

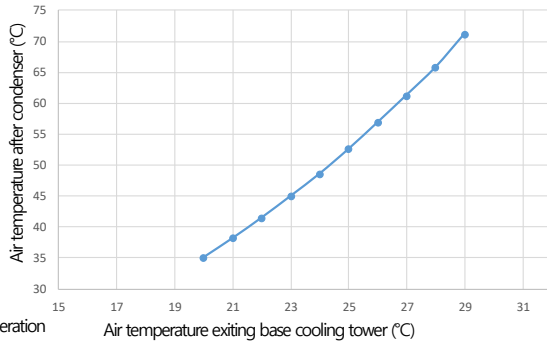


Fig. 5. Analysis of outlet temperature effect on plume prevention

- (New operation proposal and operation characteristic analysis) As the outdoor temperature decreases, the heating temperature required for plume prevention increases rapidly due to the nonlinearity of the humidity curve. In order to reduce the energy required for plume prevention, a new operating mode was suggested. The new operating concept was designed considering the cooling tower operating boundaries for a power plant. Even if the outdoor temperature is lowered, the turbine back pressure must be maintained constantly. Therefore the temperature change of the cooling tower circulation water should be maintained. In order to maintain the same temperature change, the cooling tower air volume flow rate must be reduced. If the outside air is taken as the amount of the difference between design air flow rate and operation air flow rate and then mixed with cooling tower outlet air, the mixed air becomes supersaturated. Assuming that the supersaturated liquid droplets generated inside the cooling tower can be removed relatively easily by methods such as drift eliminator and fog collector, wet air entering the pump can be assumed to be saturated with low temperature. This mixing and droplet elimination process is represented as “Internal Mix” in fig. 3. Then plume reduction temperature after mixing the excess of the design air volume as above was calculated. The result is as follows. From the table, it can be seen that less energy is required for mixed heating compared to direct heat pump application.

Outdoor RH 75%

T_out	Air flow	Heat Pump Output	Output with Mixing	Evap. In Temp.(°C)	Mixed Air Temp.(°C)
-5	488.1	655.9	39.36	34.31	6.954
-4	494.9	604.8	39.38	34.36	7.83
-3	502.1	557.5	39.41	34.42	8.704
-2	509.5	515.1	36.41	34.47	9.577
-1	517.3	474.6	36.44	34.52	10.45
0	525.5	438.2	36.48	34.57	11.32
1	533.7	398.3	36.51	34.62	12.18
2	543.2	362.1	33.5	34.67	13.06
3	552.3	327.6	33.54	34.72	13.92
4	561.8	296.3	30.52	34.77	14.77
5	571.9	267.5	30.55	34.82	15.62
6	582.5	241.2	27.53	34.86	16.47
7	593.6	216.3	27.56	34.91	17.32
8	605.4	192.9	27.6	34.95	18.17
9	618	172.3	27.64	34.99	19.01
10	631.3	152.1	24.6	35.04	19.85

Outdoor Temperature 0°C

RH_out	Air flow	Heat Pump Output	Output with Mixing	Evap. In Temp.(°C)	Mixed Air Temp.(°C)
0.75	525.5	438.2	36.48	34.57	11.32
0.76	525.9	446.9	39.52	34.57	11.33
0.77	526.4	455.7	39.52	34.57	11.34
0.78	526.8	465.5	42.56	34.57	11.35
0.79	527.3	476.4	45.6	34.57	11.36
0.8	527.7	487.3	45.6	34.56	11.36
0.81	528.2	498.3	48.64	34.56	11.37
0.82	528.6	510.3	51.68	34.56	11.38
0.83	529.1	523.4	54.72	34.56	11.39
0.84	529.5	537.6	57.76	34.56	11.4
0.85	530	552.8	60.8	34.56	11.41
0.86	530.4	569.2	66.88	34.56	11.42
0.87	530.9	587.7	69.92	34.56	11.43
0.88	531.3	606.2	76	34.56	11.44
0.89	531.8	630.1	82.09	34.56	11.45
0.9	532.2	654	91.21	34.56	11.46

Fig. 6. Heat pump output reduction effect with suggested operation proposal

4. Conclusion

The characteristics of the heat pump cycle in the cooling tower flow are as follows.

- Since air flow rate is fixed as the cooling tower operating value, the operation conditions of evaporator and condenser are restricted.
- When reheating air flow in condenser with the recovered heat from evaporator, a high condensing temperature is particularly required due to the low heat capacity of air.
- About 50°C discharge air, COP around 4 are expected under typical cooling tower rated conditions

The input energy characteristics for plume reduction are as follows.

- As the outdoor temperature decreases, the input energy needed increases rapidly. (Unsuitable operating conditions even for the heat pump cycle with sub-zero outdoor conditions)
- A design approach that lowers the discharge air temperature of the cooling tower while maintaining the circulating water temperature range is preferred.
- Operation that utilizes the flow rate margin between the design air volume and the operating air volume to take outside air is suggested to reduce the heat pump input energy further.

Heat pump cycle can control the evaporation temperature and condensation temperature. The low temperature heat recovered by heat pump can be upgraded and used for other high temperature purposes. Through this, it is possible to expand heat pump application not only to prevent plume generation, but also to recover and reused waste energy in exhaust gas in energy intense industries such as power generation, petrochemical, and paper manufacturing. The suggested approach will be able to expand its application to cooling towers for building air conditioning, cooling towers for subway heat treatment along with plume prevention for large cooling towers of power generation, petrochemical plants, etc.

Acknowledgements

This work was supported by the Technology Innovation Program (20018456, Development of a 160°C steam generation heat pump with thermal capacity of 350kW using oil-free centrifugal compressor) funded By the Ministry of Trade, Industry & Energy(MOTIE, Korea).

References

[1] Tyagi SK, Pandey AK, Pant PC, Tyagi VV, Formation, potential and abatement of plume from wet cooling towers: A review, *Renewable Sustainable Energy Rev*. 2012;**16**:3409-3429.
[2] Li S, Moradi A, Vickers B, Flynn MR, Cooling tower plume abatement using a coaxial plume structure, Int. J. Heat Mass Transf, 2018;**120**:178-193.

[3] Lee B, et al., Experimental evaluations on the outdoor air-based methods for water saving and plume abatement. International Journal of Low-Carbon Technologies, 2020;doi:10.1093/ijlct/ctz078.

14th IEA Heat Pump Conference
15-18 May 2023, Chicago, Illinois

Performance and safety analysis of charge reduced brine to water heat pumps using R290

Timo Methler[a,*], Hannes Fugmann[a], Clemens Dankwerth[a], Christian Sonner, Katharina Morawietz[a], Lena Schnabel[a]

[a]Fraunhofer Institute for Solar Energy Systems ISE, Heidenhofstraße 2, 79110 Freiburg, Germany
* timo.methler@ise.fraunhofer.de

Abstract

The European implementation of the Montreal Protocol, the F-gas Regulation, restricts the use of refrigerants with high GWP. Thus, low-GWP refrigerants, in particular R290 (propane), are becoming the standard in the growing heat pump market. Within this contribution the results of the research project "Low Charge 150 g" are shown. The focus is on the reduction of charge needed in heat pumps, favorably below 150 g propane. As part of this project different components were combined in brine to water refrigerant circuits and experimentally evaluated. Conclusions and correlations will be described based on ErP standards and a multitude of measured values. All evaluation focus on the behavior based on charge variation and are used to create four distinct operation modes of a heat pump. Additionally, a test bench for refrigerant distribution testing was built to analyze R290 concentration development in controlled indoor scenarios. All measurements are done with compact plate-to-plate refrigerant circuits. The heating capacity reaches up to 12.85kW using 124 g R290. The current best solution achieves a specific heating capacity <10 g/kW with a SCOP (ErP) >4.5.

© HPC2023.
Selection and/or peer-review under the responsibility of the organizers of the 14th IEA Heat Pump Conference 2023.

Keywords: propane; R290; heat pumps; refrigerant; charge reduction; safety

1. Introduction

Heat pumps have become the technology of choice for society and policy makers in the European region and increasing in popularity worldwide. Commonly used refrigerants have been regulated recently and they will be regulated/ banned in the near future. Different regions worldwide follow individual timelines. These timelines were agreed upon by participants of an assembly in Montreal in 1987, commonly referred to as "the Montreal protocol" [1]. The European implementations have led the EU-market to an increasing focus on R290 as refrigerant. R290 (propane) has a low GWP of 0.02 [2]and very good thermodynamic properties but is highly flammable and therefore needs special attention regarding safety. The reduction of charge in the system is an elegant solution to decrease the hazard represented by the system. The following contribution will show the basic concept of charge reduction, visualize the impact, and show taken measures.

2. Infrastructure

All measurements presented below were taken at Fraunhofer ISE. To ensure standardized testing, conditioning modules, were used to simulate source and sink and are referred to as secondary modules/circuits. These conditioning modules are standardized equipment in the laboratory and have the following adjustable/ controllable parameters: fluid temperature, pressure drop and mass flow. The conditioning module for the sink side is filled with water and the module on the source side with a mixture of ethylene/glycol and water with a freezing temperature of -20 °C. For evaluation, the heating and cooling capacities on the secondary sides were calculated by the measurement of the mass flow employing a coriolis sensor, combined with in- and outlet

* Corresponding author. *E-mail address:* timo.methler@ise.fraunhofer.de

temperature measurement, using submerged PT100 sensors and their applicable specific heat capacities. The electrical power consumed by the driver and compressor was measured between the driver and the power grid. Therefore, all frequency converter losses are included in the results. To estimate the power necessary for external pumps on the secondary side, differential pressures across the heat exchangers on the secondary side were monitored by pressure differential sensors. Controllers were used to control the inlet temperatures to the heat pump. The temperature difference between in- and outlet of the two plate heat exchangers on the secondary sides, were controlled by adjusting the mass flows of secondary fluids. The source side was set to 3 K and the sink side to 5 K temperature difference.

3. Test procedure

All prototypes measured by Fraunhofer ISE were built as the flow chart in Fig. 1. The refrigerant circuits (RC) were built in the workshops at Fraunhofer ISE and named following a versioning system RC-version. All manufacturing guidelines are coordinated with partners in the project´s advisory board and with component manufacturer, as well as the component manufacturers.

The components used, were all selected to be able to provide 8 kW heating capacity in their upper rating range. Generally, all pipes were insulated by 1cm foam insulation. The heat exchangers were set up to operate in counter flow arrangement.

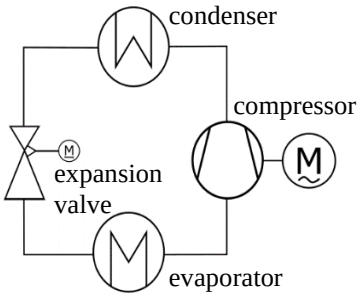


Fig. 1. Simplified Refrigerant Circuit Flowchart

All measurements are taken as charge variations since the main focus lies on the low charge behavior of refrigerant circuits. For this purpose, a special charging station was developed and constructed for automated charging and safe discharging of up to three refrigerant circuits mounted at the same time processed individually. To control the direction of the R290 mass flow the charging station can be heated or cooled. In-depth explanation of the charging station can be found in the article of [3].

For the measurements the charging unit charged an initial amount of refrigerant to the circuit (for instance 80 g). With the initial amount several operation points were measured, which includes several different parameters set by the secondary modules, frequency converter and EEV. Those operation points were measured for 30 minutes in stable conditions, respectively. After running through this measurement matrix of different operation points the charging unit automatically charged 10 g extra refrigerant and the operation points of the measurement matrix were measured again. The procedure continues until high pressure protection is tripped, this commonly occurred between 200 g to 250 g of refrigerant R290 in the circuit. Within the refrigerant circuit the following parameter are recorded: Temperature and pressure in suction and discharge line, temperature in liquid and injection line, pressure difference across the heat exchangers and amount of refrigerant charge. The collected data is compiled in a combined database and enhanced by additional documentation including all pipe lengths, all pipe diameter, insulation type, insulation diameter, pictures, component list, oil type, oil amount, sensor connection length and diameter for differential pressure sensors. The additional base information is used in some following corrections mentioned below. During operation the suction side super heat of the refrigerant circuit is controlled with an electronic expansion valve (EEV), the reference temperature sensor in the suction line, was implements as submerged PT100 sensor. All set values are added to the measurement database and are used in the evaluations below.

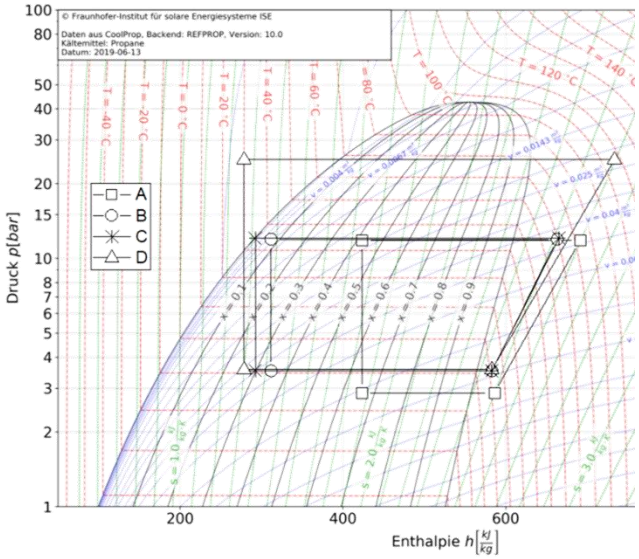


Fig. 2. Log (p) -h diagram visualizing heat pump operation of **RC8-21** at B0/W35/SSH10/F40 for the special attention points A-D, as marked in Fig. 3.

4. Operation with different charge

Fig. 3 shows five stacked graphs ((a)-(e)) with a common x-axis, which displays a full charge variation measurement for refrigerant circuit RC8-21 at operation point B0/W35/SSH10/F40 (brine inlet temperature: 0 °C; water flow temperature: 35 °C; suction super heat: 10 K; frequency: 40 %). When considering the full range of a charge variation measurement as described in Chapter 3, there are four major operation points, where different thermal and fluid dynamic effects have significant impact on the circuit. These four operation points are marked with **A-D** in Fig. 3. Point **A** is under charged with refrigerant. The necessary super heat is not achieved. In point **B** the desired super heat is achieved, but the system did not reach the maximum efficiency and heating capacity. Point **D** is over charged with refrigerant. Efficiency drops significantly. Most common operation is point **C**, which is widely regarded as baseline heat pump cycle. The presence of sub cool is considered essential for the baseline cycle.

Fig. 2 shows point **C**'s cycle in a log(p)-h diagram marked with stars. Operation **C** is expected to have 0-2 K sub cool, which is difficult to measure reliably in the tight physical arrangement. Therefore, the team is using alternative measured values to determine marginal sub cool. The behavior of the EEV (shown in Fig. 3 (b)), is used as main indicator for marginal sub cool. The EEV's task is the expansion of the refrigerant, this can be considered as forced pressure drop. Pressure drop is strongly dependent on fluid velocity, which in term is strongly dependent on density. For this reason, the EEV behavior shift from being strongly charge depended to largely independent, is considered the turning point of marginal sub cool. For this reason, the EEV opening is used to define the "minimal sub cool" points. This is also considered the minimal optimal charge in [3]. The additional charge, with point **C** as reference, does not significantly impact the EEV and therefore no significant density/ velocity changes in front of the EEV are occurring. This shows the existence of sub cool, it does not quantify sub cool reliably but considering fluid dynamics sub cool has to be present. Fig. 3 (d) shows condensation temperature and liquid line temperature; subtracting them from each other results in the sub cool of the system. With increasing charge increasing sub cool is present in the system. Additional charge will accumulate inside the condenser, if no collector is present, the additional inventory reduces the available area for condensation and desuperheating. The loss of available area is balanced with a forced increase in temperature difference and therefore condensation temperature. This is particularly prominent at operation **D**, where overfill has occurred. Fig. 3 (d) shows the significant increase in condensation temperature and therefore pressure. Fig. 3 (b) on the other hand shows the reaction of the EEV to create additional pressure drop the cross-sectional area of the EEV has to be reduced. The significance of the change in operation is also visualized in Fig. 2 where operation **D** is indicated as

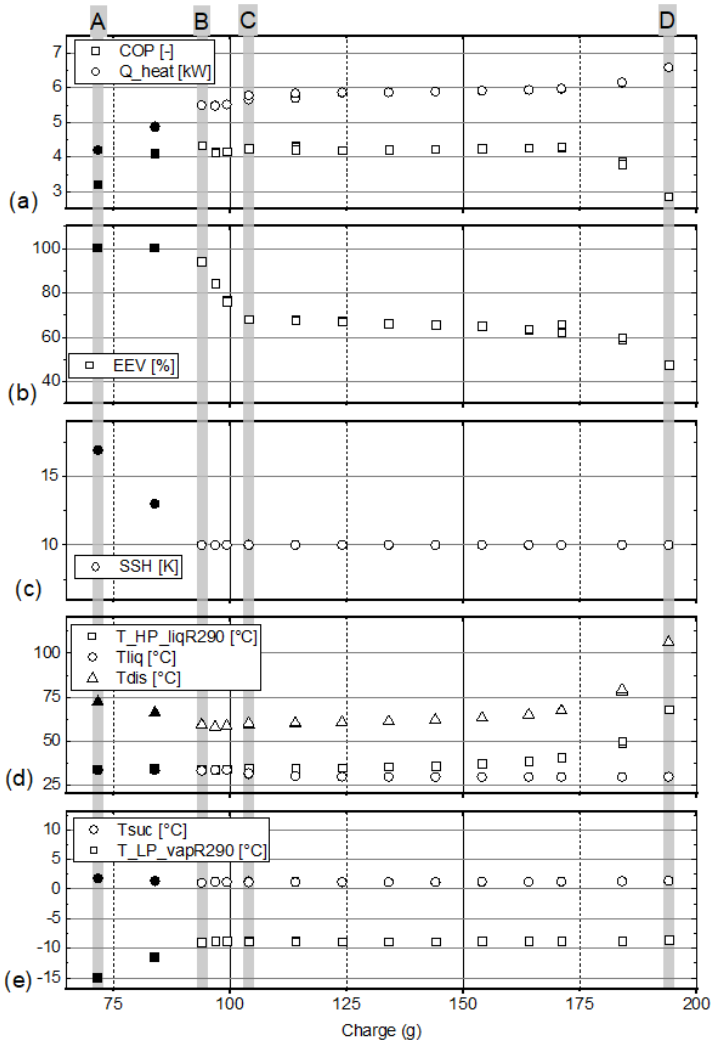


Fig. 3. ((a)-(e)). Charge variation of **RC8-21** at operation point B0/W35/SSH10/F40, 5 stacked graphs showing, (a) COP and heating capacity, (b) EEV opening in %, (c) suction side super heat, (d) high pressure propane condensation temperature as well as condenser outlet and discharge temperature, (e) suction gas temperature and low-pressure propane evaporation temperature. Marked for special interest are charges A-D representing **A** extreme undercharge, **B** undercharge, **C** minimal optimal charge and **D** overcharge operation

triangles. Additional side effects are the increased pressure ratio to be covered by the compressor. This leads to an additional increase in discharge temperature and drop down of COP shown in Fig. 3 (d) and (a) respectively.

When reducing charge, with **C** as reference point, the reduction will have different impacts. First effect will be the reduction of sub cool below 0 K sub cool. This will force the condenser to have two-phase outlet, marked in Fig. 3 as operation **A/B**. This will change the requirements for the expansion valve drastically and any expansion valve made for liquid entry state will reach its physical limit quickly, which is the major difference between operation **A** and **B**. As discussed earlier due to the higher velocities with two-phase flow and a considered constant mass flow. Mass flow can be considered constant, for points **B-D,** due to constant rotational speed of the compressor in combination with the constant pressure and temperature at the compressor inlet shown in Fig. 3 (d) and Fig. 2. Operation **A** does have altered mass flow compared to the operation **B-D**, due to the reduced inlet pressure and increased super heat which leads to lower densities at compressor inlet. This works to reduce the velocity increase at the EEV, which is still dominated by the decrease in density due to two-phase operation. The suction temperature displayed in Fig. 3 (e) shows the constancy of suction side temperature over the full charge range, due to the consistent secondary side source temperature. At operation **A**, where the decreased density and with it required additional EEV opening, exceeded the operation limits of the EEV. As a result, the low pressure is reduced lower than necessary for 10 K SSH, this leads to uncontrolled increase super heat in the circuit and is the dominant reason for the decreased pressure at the compressor inlet. Both operation states are visualized in Fig. 2 **B** as circles with the EEV at maximum operation envelop and **A** as squares with the EEV operated outside of its operation envelop. During their investigations the team Palm et. al. in 2006 found the same correlations for COP and temperature developments over charge, these are shown and discussed in [4]. Additional visualization can be provided by employing IR pictures of the cross section of condensers. The concept of using IR pictures for distribution evaluation was used and described nicely in [5]. In this case the same concept can be used to show the inventory level in condensers rising with charge during the previously described charge variation. For this visualization, a charge variation of refrigerant circuit **RC8-17** at B0/W24/SSH10/F10 has been selected to show charge inventory in the condenser. Operations **B**, **C** and **D** are marked and selected similar as RC8-21 discussed before (see Fig. 4 ((a) - (c))). For circuit **RC8-17** the IR pictures of the condenser cross section for operations **B**, **C, D** and an additional point are shown in Fig. 5. Refrigerant flow is downstream from top right to bottom right of the heat exchangers. The first picture of Fig. 5 (**B**) represents an underfilled system with a total charge of 114 g R290. Except the hot gas region in the upper region of the heat exchanger the IR picture indicates a homogenous temperature profile starting 26 on the y-axis to the bottom part of the heat exchanger. The homogenous temperature profile reflects the process of condensing the refrigerant. Pure liquid phase is not reached. At the outlet of the heat exchanger the refrigerant is still in two phases.

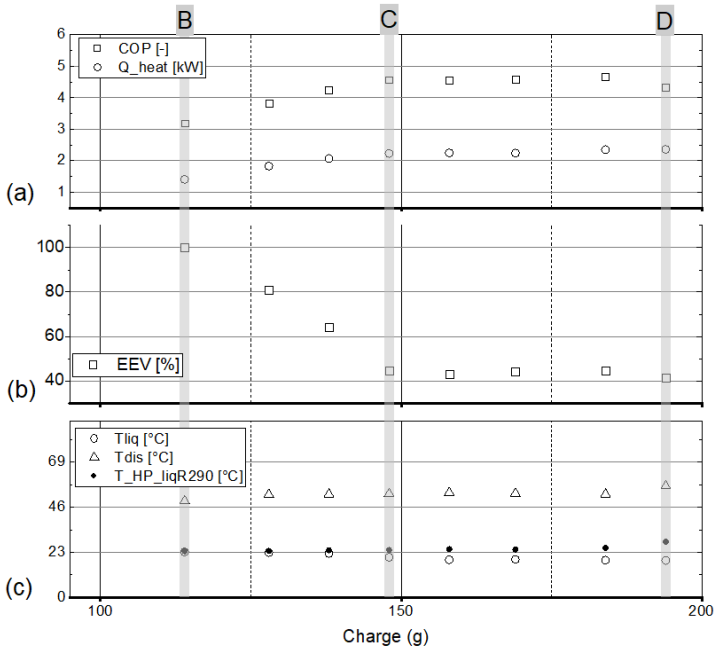


Fig. 4. ((a) - (c)). Charge variation of **RC8-17** at operation point B0/W24/SSH10/F10 stacked graphs showing, (a) COP and heating capacity, (b) EEV opening in %, (c) temperatures in discharge and liquid line as well as condensing temperature. Marked for special interest are charges **B-D** representing **B** undercharge, **C** minimal optimal charge and **D** overcharge operation

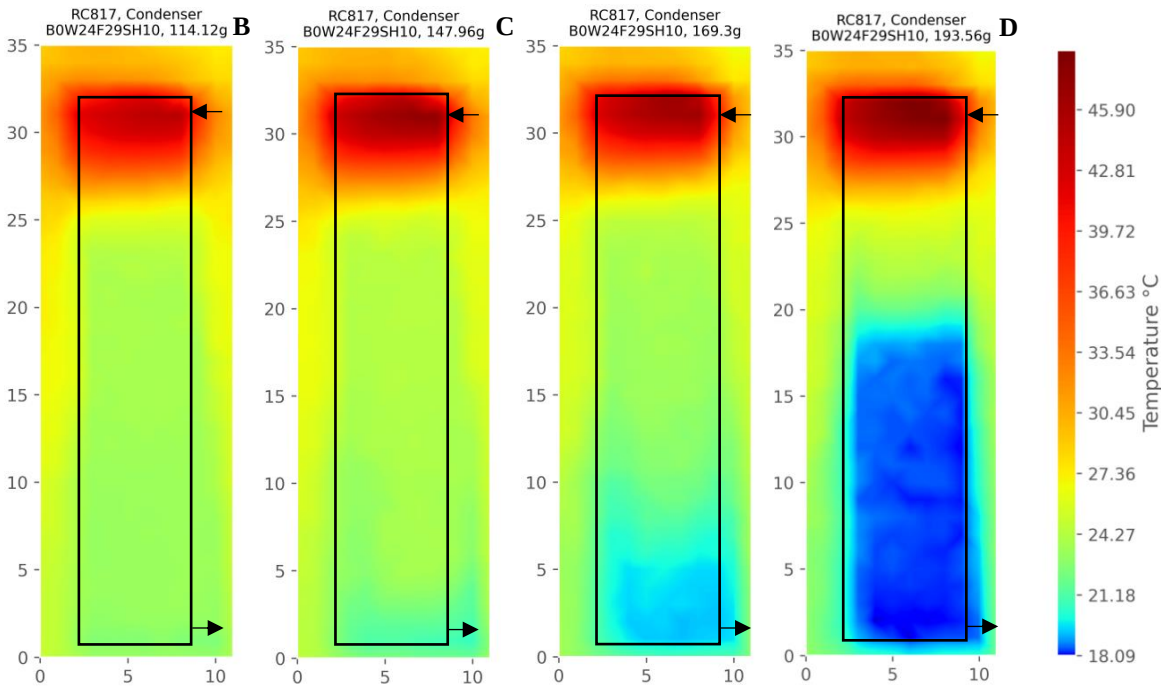


Fig. 5. IR pictures of condenser RC8-17 for operation points **B**, **C**, **D** and one additional operation point at 169 g, heat exchanger outline is marked for all images. Inlet R290 is located top right of the heat exchanger image, whereas the outlet is located in the bottom right. Water is running in counter flow the opposite direction.

The second picture in Fig. 5 (**C**), shows RC8-17 at the minimal optimal charge operation with 147 g R290. The upper region of the heat exchanger shows almost no change in temperature, compared to the image of operation **B**. Whereas the bottom region demonstrates a slight change in temperature level. This indicates a completed condensation and starting of sub cooling of the refrigerant at the bottom of the heat exchanger. This is reflected in Fig. 4 (c) where the condensation temperature (T_HP_liqR290) and measured outlet (T_liq) are shown. The temperature differential represents the measured sub cool. Fig. 5 shows an additional image for 169.3 g of charge to visualize the development of the sub cool region, visible at the bottom of the heat exchanger. The final picture of Fig. 5 (**D**) refers to an overfilled system with a total charge of 193 g R290. As explained earlier for overfilled systems, the discharge temperature rises. The increase in discharge temperature can be seen at the top region of the heat exchanger in a displayed dark red color. Furthermore, with additional charge, the condenser works as a collector. All unnecessary charge stays in the condenser in front of the EEV. The sub cooling increases and the area used for condensing the refrigerant is getting smaller. This can be seen in the blue bottom part of the heat exchanger. The earlier discussed behavior of charge varied refrigerant circuits is applicable to all circuits measured during the project, which were not changed by adding additional components. Therefore, qualitatively visualized process in Fig. 2 applies.

5. Design rules for charge reduced heat pumps

To design low charge heat pumps the following design rules should be in mind to keep the amount of refrigerant low and use the charged refrigerant as efficient as possible.

5.1. Heat exchanger manifolds

Heat exchangers have connection ports/ manifolds/ headers to distribute or collect the refrigerant to/ from the plates and channels. Those ports are often designed to be very simple and easy to manufacture. They are not optimized regarding refrigerant efficiency and often they are holding some amount of refrigerant/ oil which is not used in the circuit. For example the manifold and outlet port of a plate heat exchanger condenser are commonly punched with the same tool as the secondary side ports. This leads to manifold diameters 2-3 times

larger than necessary, and therefore to charge inventories 4-9 the needed mass and volume. Manifolds could be designed much smaller to safe unused refrigerant, for this reason port design is an important part of charge reduced design.

5.2. Oil reduction/ absorption

The oil, commonly used in refrigerant circuits, absorbs 5-18 weight% (depending on the oil) of the refrigerant. The knowledge of adsorption can be measured and is widely known, a good example of behavior can be found in Ginies work of 2016. One example of the work is shown in Fig. 6 [6]. These absorption values occur during heat pump operation. The amount of refrigerant which is absorbed by the oil depends on several factors. The type of oil and refrigerant is important, as well as the physical conditions of the oil (temperature and pressure). The main amount of oil in a refrigerant circuit is present in the oil sump in the compressor. Therefore, it makes a difference if the oil sump is on the suction side or discharge side of the compressor.
The team did not elaborate on the benefits or negatives of either solution and found no clear indication for which system is charge optimal. The general rule in regards of oil remain, avoiding oil traps, reducing oil sump, considering the oil type, will all reduce or impact the required total amount of refrigerant.

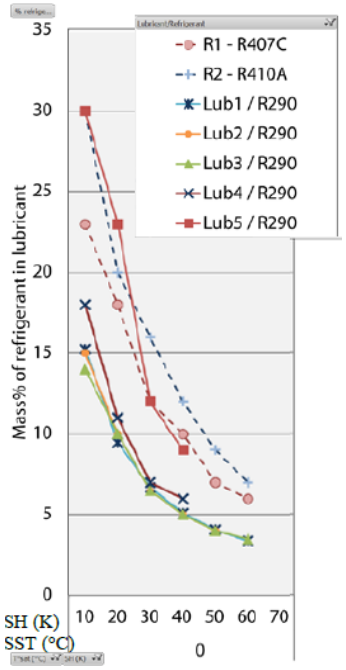


Fig. 6. Oil adsorption overview R290 with different lubricants, partial representation of work published in 2016 by Ginies et. al. [2]. SH= super heat; SST = suction side temperature

5.3. Liquid line

The liquid line should be designed as short and thin as possible. Due to the high density of the refrigerant in the liquid line (see top left Fig. 2) it has a high effect on the total charge of the system.

5.4. Operation strategy

For reverse operation via 4-way-valve the condenser and the evaporator are switched in the refrigerant circuit. This is used for deicing or active cooling mode. In those operation modes much more refrigerant is needed due to higher volumes in the evaporator (evaporator fills up with liquid refrigerant). For highly charged reduced refrigerant circuits other deicing modes are recommended and passive cooling could be an alternative.

5.5. Super heat optimization

Different suction super heat values require different amounts of refrigerant for their minimal optimal charge operation, marked as C in Figure 7. The higher the super heat the lower the required refrigerant charge. Though the suction super heat has a high impact on the efficiency of the unit. The lower the super heat the higher the efficiency.
In some scenarios to achieve a certain maximum refrigerant charge it can be useful to use the suction super heat to regulate the required refrigerant charge. All prototypes during the project had a charge delta between 5 K SSH and 15 K SSH of 20 g to 70 g, main reason for the widespread is the charge absorbed in the oil, due significant impact on oil sump/ suction gas temperature, as well as different inner volumes in evaporators, where the varied super heat has a significant impact on the average density in the evaporator.

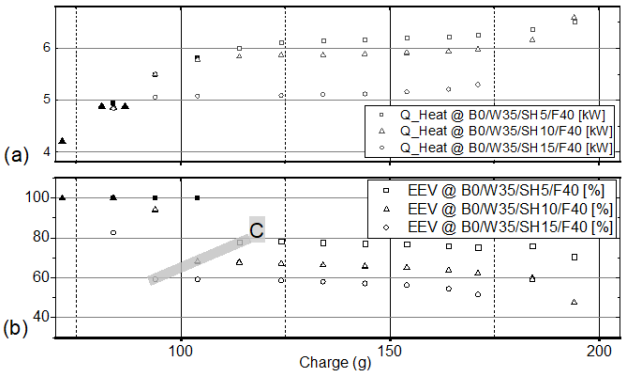


Fig. 7. (a,b) charge variation for **RC8-21** showing SSH 5, 10 and 15 K operations, shared x axis for all graphs, (a) showing heating capacity and (b) shows EEV opening, marked minimal optimal charge region as discussed earlier

5.6. Heat exchanger

A major amount of refrigerant charge in refrigerant circuit stays in the two heat exchangers. The larger the inner volume of the heat exchanger the more charge is needed. In the design process should be kept in mind, that the selection of the heat exchangers has a large impact on the final charge. Specifically additional plates due to safety margins should be considered carefully when designing a charge reduced system. Other options for charge reduction are asymmetric heat exchangers, which enable low secondary side pressure drops but low inner volumes on the primary refrigerant side. A recent publication of Will et. al. showed increased necessary charge if any maldistribution is present. The investigation was done purely theoretically and simulation based, never the less all five most common models for two phase charge estimation were in agreement. [7]

5.7. Heat exchanger

Normally filter dryer are used in the liquid line in refrigerant circuits. The filter dryer is holding liquid refrigerant with a high density. For very compact systems the share of the total refrigerant charge can be quite high. To avoid some refrigerant from the filter dryer in the liquid line, the filter dryer can be shifted to the suction line of the refrigerant circuit where the refrigerant is in gas phase and has a lower density. Due to high gas velocities the filter dryer needs to be larger than in suction line. Nevertheless, some refrigerant can be saved, the team saved 50 % charge during pre-evaluations. Though, the filter dryer in suction line has additional pressure losses which harm the efficiency of the complete unit, the actual impact will vary on a case-to-case bases.

Another option is to renounce the filter dryer completely. The amount of saved refrigerant is the highest. The manufacturing process and needs to be a very careful to have no particles in the refrigerant circuit. And the evacuating needs to be very accurate to remove almost every humidity from the unit.

6. Safety analysis outlook

To evaluate the safety of propane heat pumps during and after a leakage, knowledge of the propane concentration in its surroundings is essential. Of interest are the behavior of concentration development over time in the casing of the refrigerant circuit (heat pump) as well as in the installation room around it. To be able to measure distribution of propane, inside and outside of the casing, a test installation room (see Fig. *8*) has been installed at Fraunhofer ISE. The dedicated room enables the team to test the distribution development over time in a controlled environment. The leaked mass of propane is not limited; however, the leakage mass flow rate is limited. This flow rate represents small leakages to rupture leaks varying between 0.001 g/s to 2 g/s, respectively; and the leakage position can be varied within the casing, focusing on critical positions such as brazing joints, any specific component necessary to evaluate.

The test installation room is built with sandwich panels with a volume of approximately 21 m³ (3,5 m x 2,5 m x 2,4 m), representing a typical size of a cellar. The installed test room includes, a gas warning system, a ventilation system and measurement equipment. The ventilation system can be used for cleaning the installation room during or after a leakage test. Measurement results with desired resolution are recoded with more than 30 gas sensors, temperature sensors and differential pressure sensors, which are installed in the test installation room. The gas sensors (Dynament propane gas sensors with ATEX certificate) detect propane concentration by infrared

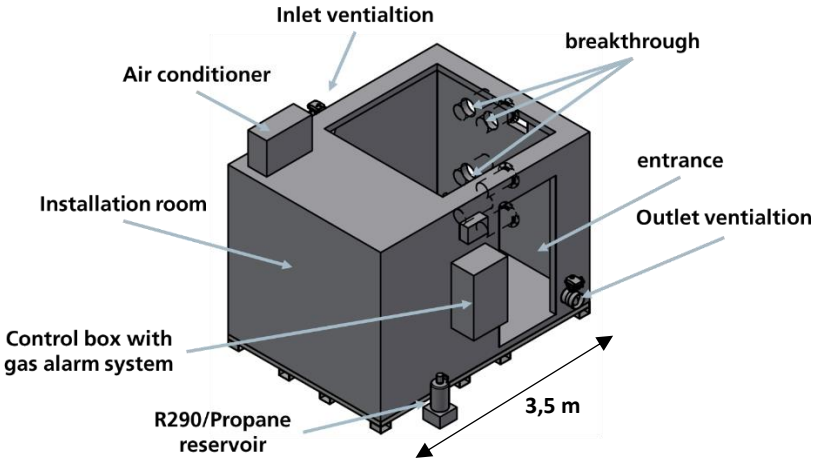


Fig. 8. Installation room for leakage testing of heat pumps

measurement principle and have a response time of ~1.2 s. The gas sensors are installed within the casing and within the test installation room around the casing. As part of the project "Low Charge 150" three types of casings have been defined for testing: (1) without casing / very permeable casing, (2) with a casing that is individually designed, based on the refrigerant mass in the circuit, (3) with a casing, that has a fixed volume according to the "white goods" volume with 60 cm x 60 cm footprint. Casing (2) and (3) are built to have custom side panels to be able to accommodate new designs and component-based additions to housings. The dedicated measurement campaign for "Low Charge 150" will start beginning of 2023. The desired outcome will be, whether a casing can be designed to include a passive safety concept intrinsically. A further goal is the definition of an upper limit of propane with a fixed casing volume and this passive safety concept. The main benefit of such a concept would be to eliminate additional active safety devices in the casing or in the installation room.

7. Conclusions and outlook

The described behavior in Section 4 has been present in more than 20 refrigerant circuits measured during the project "Low Charge 150" and all circuits with no additional components. The thermodynamic relations between the individual components and the thermodynamic behavior with charge reduction has been very consistent and conclusive. Overall charge reduction has a long chain of dependencies attached. The authors summarize the full chain as follows.

Reduced charge (below the minimal optimal charge point) leads to gas parts in the liquid line **(saves charge)**. This reduces the available enthalpy delta in the condenser **(reduce heating/ COP)**. The gas phase in the liquid line leads to additional non desired expansion. This in term leads to higher super heats. Additional super heat reduces absorption in the compressor oil **(saves charge).** Lower evaporation temperatures/pressure created by the additional expansion increases the necessary compression ratio **(increases electric use/ reduces COP)**. The rise in suction side super heat and the additional pressure ratio increases the hot gas temperature. Rising hot gas temperature leads to the less efficient gas-based heat transfer in the condenser **(reduce COP)**. A similar conclusive argument chain forms for overfilling which is explained in section 4, but does not represent special interest for charge reduction.

To summarize the described effects and relations the Fraunhofer ISE derives seven rules for designing charge reduced heat pumps

1. Oil reduction
2. Minimal liquid line
3. Heat exchanger manifolds/ ports
4. Operation strategy
5. Super heat strategy
6. Heat exchanger inner volume/ distribution
7. Minimal / suction side filter dryer

These rules are described in detail above in section 5. Most if not all of the rules can be respected when selecting components. The fundamental relations also give strong areas of attention for future developments. Testing and implementing new oils with lower absorption of refrigerant are a strong contributor to charge reduction, as well as the general reduction of oil. On the thermal dynamics side the quality of fluid-distribution in heat exchangers has an impact on the efficiency as well as on charge efficiency.

Acknowledgements

The study presented in this paper received funding from the German Federal Ministry of Economic Affairs and Climate Action (BMWK) under the grant agreement number FKZ 03EN4001A (LC150).

The cooperation between Fraunhofer ISE and UPV and the ideas for this work were inspired, supported and supervised by Prof. José Miguel Corberán Salvador. He served as Professor in the Department of Applied Thermodynamics and Director of the Institute for Energy Engineering at the Polytechnic University of Valencia (UPV), Spain and died on July 7, 2022 at the age of 65. We will continue the work with his attitude towards professionalism in refrigeration, cooperation and humanity.

References

[1] United Nations Foundation. 1987. Montreal Protocol on Substances that Deplete the Ozone Layer.
[2] IPCC. 2021. *Climate Change 2021: The Physical Science Basis. Contribution of Working Group I to the Sixth Assessment Report of the Intergovernmental Panel on Climate Change* In Press. Cambridge University Press, Cambridge, United Kingdom and New York, NY, USA.
[3] Methler Timo, Dankwerth, C., Schnabel, L., Fugmann, H., Joos, L., and Morawietz, K. 2022. Experimental Analysis of Various Refrigerant Circuit Component Combinations for Low Charge Propane Heat Pumps. *15th IIR-Gustav Lorentzen conference on Natural Refrigerants*.
[4] Palm, B., Fernando, P., Andersson, K., Lundqvist, P., and Samoteeva, O. 2006. Designing a Heat Pump for minimum Charge of Refrigerant.
[5] Navarro-Peris, E., Alvarez-Piñeiro, L., Albaladejo, P., Schnabel, L., and Corberan, J. M. 2021. Refrigerant maldistribution in brazed plate heat exchanger evaporators. Part A: Testing campaign and experimental results. *International Journal of Refrigeration* 131, 119–128.
[6] Pierre Ginies, Guillaume Rebiere, Julie Mandon, Jean Guillaume Cheurlin. 2016. LGWP & HC Refrigerants Solubility Tests Performed in Running Scroll Compressor. *International Compressor Engineering Conference* 23.
[7] Will, T., Köhler, J., Henning, H.-M., Oltersdorf, T., and Schnabel, L. 2020. Kältemittelfüllmengenberechnung in Plattenwärmeübertragern. In *Jahrestreffen der ProcessNet-Fachgruppe Wärme- und Stoffübertragung*, Dechema, Ed., Erfurt.

14th IEA Heat Pump Conference
15-18 May 2023, Chicago, Illinois

Transcritical CO_2 heat pump for tap water heating: experimental validation of an auto adaptive algorithm for high pressure optimization

Chiara Corazzol*, Giovanni Rossanese, Sergio Maria Capanelli, Luca Mattiello

CAREL Industries S.p.A., Brugine 35020, Italy

Abstract

Recent developments pushed by F-gas regulations and European guidelines for the renovation of domestic heating systems have led the HVAC market to use new alternatives to propane (R-290) and fluorinated refrigerants. CO_2 (R-744) heat pumps are a consolidated solution for domestic hot water (DHW) applications, with the advantages resulting from using an environmentally friendly, not toxic and not flammable refrigerant. Another benefit of CO_2, when used in DHW applications, is that high-temperature hot water (up to 70°C) can be obtained without the use of a supplementary heating system. In this case, heat rejection pressure has a strong influence on the efficiency of the unit, and there's an optimal value that makes the system reach the maximum coefficient of performance (COP). In this work, the performance of a real transcritical air/water CO_2 heat pump for tap water heating has been investigated and compared at different heat rejection pressure values.
Considering that the optimal pressure value is strictly affected by the variability of the operating conditions (such as water inlet temperature, water outlet temperature or evaporating pressure), an auto adaptive algorithm has been adopted and the consequent results are reported. The algorithm is based on the CO_2 thermodynamic properties calculated via Artificial Neural Network by the controller; one of its main advantages is that it does not require the system modeling and it is not dependent on the use of a specific unit or component.

Keywords: Carbon dioxide, Heat pump, Domestic hot water, Pressure optimization algorithm, Auto-adaptive.

1. Introduction

The crisis due to the conflict in Ukraine and geopolitical instability in general is causing significant repercussions on the European energy market: the uncontrolled increase in gas and electricity prices due to the cut in supplies has led to an increase in costs in various sectors, especially in industrial processes and home heating, markets that have historically relied on gas and other fossil fuels.

Hence the European Union's decision to establish a very aggressive plan for the transition of energy-intensive processes and the technological evolution of systems towards alternatives to gas for residential and industrial applications, focusing the actions above all on the heat pump market: REPowerEU [1] has identified heat pump technology as one of the key technologies for reducing Europe's dependence on fossil fuels in the short and medium term.

In conjunction with these initiatives, which on their own will drive significant market growth, a new proposal has been drafted for the revision of the F-Gas Regulation 517/2014. When the F-Gas Regulation 517/2014 [2] came into force in 2014, it caused a major upheaval in the market, impacting the prices of refrigerants and bringing about the decommissioning of commonly-used refrigerants in the HVAC/R market, to a great extent than if they had actually been banned by law. The proposed revision [3], published on 5 April 2022, aims to introduce further restrictions on the use of HFC and HFO fluids as early as 2024, setting a GWP threshold of 150 for refrigerants used in air conditioning and refrigeration applications. These new limitations, combined with other proposals to ban the use of compounds containing PFAS, chemicals found in many

* Corresponding author. Tel.:+39 049 9731864.
E-mail address: chiara.corazzol@carel.com.

refrigerants currently on the market or the result of their degradation, clearly define the European Union's intention to favour the use of natural refrigerants only in HVAC/R equipment in the near future. The majority of manufacturers have already addressed the use of hydrocarbons, such as propane R-290, as refrigerants in all segments of units intended for the residential air conditioning and heating market. This type of refrigerant has a series of important benefits in terms of operating range, efficiency and design of the units compared to established fluids such as R-410A, as seen in Capanelli [4], yet its high flammability means it is not easily usable in all applications and unit configurations required by the market. CO_2 (R-744) is a natural refrigerant, with GWP=0, and has countless benefits, especially with a view to being used for domestic hot water heating, even if today the main applications are all in the refrigeration market.

It is therefore extremely important to understand and assess the potential of this fluid also in residential applications, so as to define the best combinations of unit design, component selection and process efficiency, and thus make CO_2 a potentially usable option for home air conditioning.

A transcritical unit efficiency can be maximized by correctly managing the working condition. A key-factor on this side is the high pressure of the system which must be tuned in order to get the highest Coefficient of Performance (COP). Liao et al. [5] correlation is extensively used in this field; however in heat pump systems, COP depends also on the secondary fluid capacity, which is a factor not considered in Liao's correlation. An option to improve the high pressure regulation is to use model-based optimization approaches or "ad hoc" correlations, derived from experimental data, such as Zhang et al. [6]. On the other hand, these solutions are often tailored to specific system structures with poor generalization properties. Cervato et al. [7] proposed the use of an Extremum Seeking Control (ESC) that is a real-time optimization approach that does not use a priori model, relying instead on measurements obtained by monitoring the system. Anyway, the COP real-time calculation may result in a burdensome task due to certain limitations and technological constraints typical of industrial scenarios.

To overcome this complications, the present work characterizes the system efficiency by means of a suitable index, defined as simple as possible to be calculated, but accurate enough to guarantee the unit performance. Besides, we use a simple hill climbing algorithm [8], that is an iterative optimization technique.

2. Test Rig Description

Fig. 1 depicts a simplified scheme of the test rig. The unit has two rotary compressors (C_1 and C_2) Toshiba DY45NIFB-10FU with a $45 \cdot 10^{-6}$ m^3 individual displacement. Lubrication is ensured by the oil circuit, which includes an oil separator (SP) and a solenoid valve (SV). A double-wall plate heat exchanger (H) Swep B16DWHx37/3P carries out the heat rejection while a finned-coil evaporator (E) gives the heat load. A receiver (R) is provided to build up a three-pressure levels cycle. The heat rejection and receiver pressures are regulated by V_H and V_R valves respectively, while the evaporating pressure is controlled by the evaporator fan and the superheat at the evaporator outlet is regulated by V_E valve. The secondary fluid for the heat rejection is brine with 16% volumetric concentration of ethylene glycol; the brine circuit includes a variable-speed brine pump (BP) and a volumetric flow meter, measuring the brine flow rate ($\dot{V}_B$).

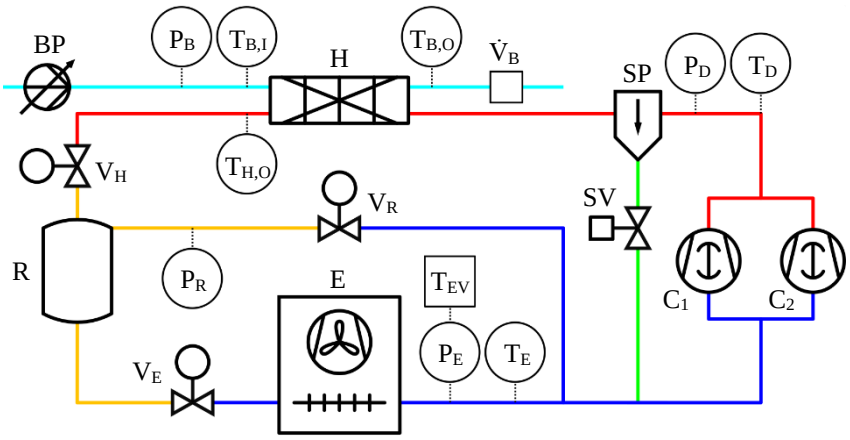


Fig. 1. Transcritical CO_2 heat pump schematic. **B**: brine, **BP**: variable-speed brine pump, **C**: rotary compressor, **D**: discharge, **E**: finned-coil evaporator, **EV**: evaporation, **H**: heat rejection heat exchanger, **I**: inlet, **O**: outlet, **P**: pressure, **R**: receiver, **SP**: oil separator, **SV**: solenoid valve, **T**: temperature, **V**: modulating valve, **$\dot{V}$**: volumetric flow rate.

Temperatures on heat rejection side (T_D and $T_{H,O}$) are measured with ⅒DIN PT100 probes with a 4-wires connection, while on brine side T-type thermocouples are installed ($T_{B,I}$ and $T_{B,O}$). Power consumption of each compressor and its speed-drive is measured by energy meters with ±0.5% of reading accuracy. Brine volumetric flow rate and pressures ranges and accuracies are reported in Table 1.

Table 1. Measuring ranges and accuracies of brine volumetric flow rate and pressures. **RDG**: of reading, **FS**: full scale.

	$\dot{V}_B$ [l h^{-1}]	P_D [barg]	P_B [barg]
Range	40 … 800	0 … 150	-0.5 … 7
Accuracy	± 0.25% RDG	± 1% FS	± 2% FS

All the other variables not described above are gauged by standard industrial sensors.

3. Experimental Tests

The heat pump performance depends on the two fluids capabilities of rejecting and receiving the useful heat load. The unit Coefficient Of Performance (COP) is influenced by the thermodynamic conditions of both CO_2 and brine sides in terms of pressure, temperature and flow rate. For these reasons, a universal correlation able to identify the optimal working point of a particular unit is hard to find, as stated in Fornasieri et al. [9].

The developed algorithm aims to match the two fluid streams through online thermodynamic calculation and simplified modeling of the heat rejection phenomena, without the complication of pure system perturbation as suggested by Cervato et al. [7]. To do so, the measurements on both the heat rejection side (P_D, T_D and $T_{H,O}$) and brine side ($T_{B,I}$ and $T_{B,O}$) are used as inputs of an Artificial Neural Network (ANN) architecture. The ANN has been trained off-line using static data set of CO_2 properties and then implemented inside the unit controller in order to perform the thermodynamic calculations needed.

Assuming that the most stringent constraint is on the brine side, in terms of delivery temperature level, the focus of the present work is dedicated to CO_2 side in terms of heat rejection pressure regulation. During the tests, the discharge pressure P_D has been considered as the independent key-variable to focus on; in fact, the pressure drops recorded across the heat rejection side are comparable with P_D pressure transducer accuracy. The target of the proposed algorithm is then to search for the optimal P_D that maximizes the unit COP, adapting to the imposed brine side conditions.

In the present work, the COP is defined as the ratio between the heat load rejected to the brine side (Q_B) and the electrical power absorbed by the compressors (PWR_C):

$$COP = \frac{Q_B}{PWR_C} = \frac{\dot{V}_B \rho_B c_{P,B} (T_{B,O} - T_{B,I})}{PWR_{C_1} + PWR_{C_2}} \quad [-] \qquad \text{Eq.(1)}$$

Where $\dot{V}_B$ is the brine volumetric flow rate, ρ_B is the brine density and $c_{P,B}$ is the brine specific heat capacity at constant pressure (both calculated using Refprop [10]). Power consumption of the evaporator fan is excluded from the COP calculation, as well as the negligible contributes of variable-speed brine pump and electronics (valves and controls).

The algorithm capability to find the optimal P_D has been tested through different sets of conditions of $T_{B,I}$, $T_{B,O}$ and T_{EV} parameters, while maintaining a 10K constant superheat at the evaporator outlet and a fixed compressors mechanical speed equal to 100rps. Table 2 reports the investigated conditions during the experimental tests.

Table 2. Investigated experimental conditions.

Condition	$T_{B,I}$ [°C]	$T_{B,O}$ [°C]	T_{EV} [°C]
a	15	55 / 65 / 70	-5
b	10	55 / 65 / 70	-5
c	15	55 / 65 / *	-8

* $T_{B,O}$ =70°C not investigated due to system technycal limitations.

$T_{B,I}$ is guaranteed by an auxiliary external chiller, while the brine pump controls $T_{B,O}$. Finally, T_{EV} is controlled at the desired set point by the evaporator fan.

To prove the algorithm quality, the optimal pressure $P_{D,OPT}$ of each investigated condition has been experimentally determined within the transcritical regime $75<P_D<105$barg. To do so, a step-by-step approach has been adopted: for each condition reported in Table 2, P_D has been progressively varied in order to find out the value realizing the maximum COP. Afterwards, the same conditions have been maintained letting the algorithm free to control P_D and converging to a calculated value.

Two indexes are defined for the comparison of the experimental optimal pressure $P_{D,OPT}$ and the algorithm-calculated pressure $P_{D,ALG}$:

$$dev_P = P_{D,OPT} - P_{D,ALG} \ [bar] \quad ; \quad dev_{COP} = \frac{COP_{OPT} - COP_{ALG}}{COP_{OPT}} \cdot 100 \ [\%] \qquad \text{Eq.(2)}$$

These two deviations are considered as representative of the algorithm quality, as they account for both optimal pressure determination accuracy and resulting relative unit performance.

4. Results

Fig. 2(a) reports, by way of example, the experimental curves of Q_B and PWR_C against P_D, while Fig. 2(b) reports T_D and $T_{H,O}$ experimental curves against the same variable. The points resulted by letting the algorithm free to operate in the same conditions are also depicted. The charts are plotted for condition "a" of Table 2 with $T_{B,O}$=55°C.

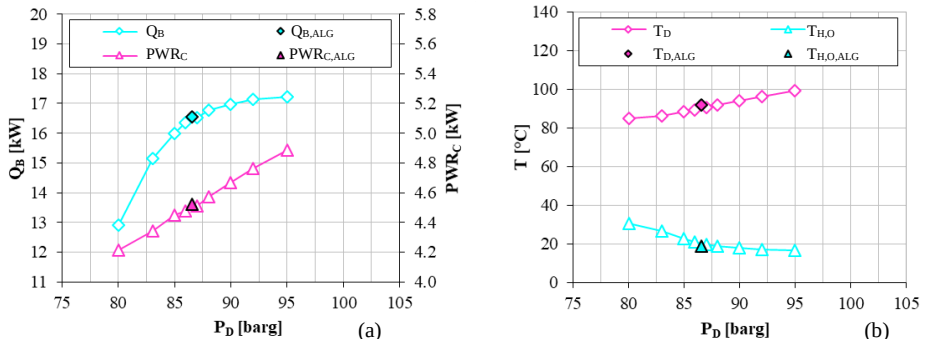


Fig. 2. Condition "a", with $T_{B,O}$=55°C, curves of Q_B, PWR_C (a) and T_D, $T_{H,O}$ (b) with their respective ALG points.

By looking at Fig. 2(a), as expected, both Q_B and PWR_C increase as P_D increases. However, while the first presents a progressively decreasing slope, the second one has a near-linear trend. This justifies the concave shape of the resulting COP curve. It can be also seen that the algorithm is capable of identifying a point where the Q_B curve slope equals the PWR_C curve slope, which is directly related to the optimal point for the heat rejection phenomena. This is also confirmed by Fig. 2(b), as the algorithm point of convergence is close to the change in slope of $T_{H,O}$ curve, i.e. the minimum P_D capable of ensuring a small temperature approach ($T_{H,O}$ - $T_{B,I}$) and an optimized heat rejection. A further increase in P_D, in fact, would have led to a considerable PWR_C increase with a limited increase in Q_B and negligible temperature approach variation.

As additional way of example, the same condition "a" of Table 2 with $T_{B,O}$=55°C is reported in Fig. 3, showing the behavior of the algorithm during a convergence test. It can be seen in Fig. 3(a) an initial pressure set point $P_{D,SET}$ forced to 95barg, then at 00:10 the algorithm is let free to operate. It starts from a value of 88barg, which is the average of condition "a" P_D range, identifying the optimal $P_{D,SET}$. After 10 minutes the algorithm starts to swing around the calculated value of $P_{D,SET}$ close to 86barg and regulates the respective measured pressure $P_{D,MEA}$. The logic correctly reduces $P_{D,SET}$ as the COP increment is visible: from 3.5 to 3.7 as mean values. Correspondingly, Fig. 3(b) shows $T_{B,I}$, $T_{B,O}$ and $\dot{V}_B$ for the same time-frame. It can be seen that $\dot{V}_B$ is correctly regulated by the BP in order to maintain $T_{B,O}$=55°C, so a flow rate reduction is necessary as $P_{D,MEA}$ decreases.

It must be underlined that the BP modulation is completely independent from the algorithm calculation routines. Furthermore, the $P_{D,MEA}$ spike noticeable in Fig. 3(a) at 00:20 (due to an oil refill procedure), does

not destabilize the convergence itself, indicating that the embedded logic is able to bypass harsh disturbances and instabilities.

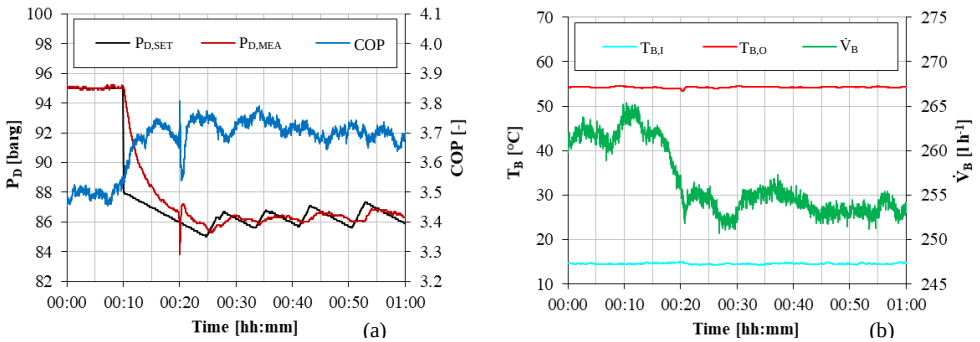


Fig. 3. Condition "a", with $T_{B,O}$=55°C, curves of $P_{D,SET}$, $P_{D,MEA}$ and COP (a) and $T_{B,I}$, $T_{B,O}$ and $\dot{V}_B$ (b).

Fig. 4(a) shows the tests carried out for condition "a", Fig. 4(b) for the condition "b" and Fig. 4(c) for condition "c". Each figure reports the COP trend (Eq.(1)) as a function of P_D for different $T_{B,O}$ ($T_{B,O}$=55°C light blue curve, $T_{B,O}$=65°C green curve and $T_{B,O}$=70°C red curve).

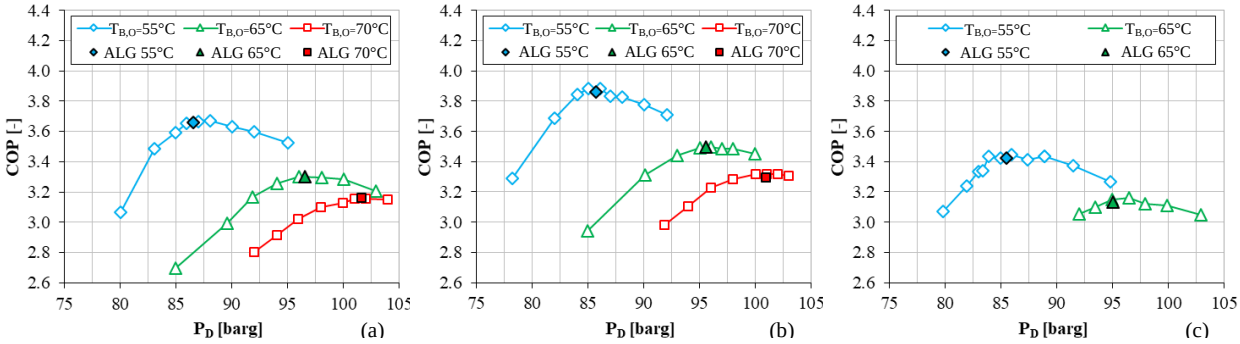


Fig. 4. Experimental COP curves and ALG points for the investigated experimental conditions "a", "b" and "c".

P_D varies within a predefined interval with a higher points density close to the optimal value $P_{D,OPT}$.

As expected, the obtained COP curves are concave functions so that they have a maximum in correspondence of the optimal pressure $P_{D,OPT}$ (i.e. the pressure that allows the best matching of the two fluid streams). For each condition reported in Fig. 4, $P_{D,OPT}$ increases as $T_{B,O}$ increases, causing a consequentially reduction of the COP_{OPT}. As a final step, the auto adaptive algorithm has been tested for the same working conditions: the results are reported in Fig. 4 (solid colour fill markers). It has to be pointed out that the COP_{ALG} reported in the plots are the averages of all the pressure values collected over an observation period of 15 minutes, after the convergence of the algorithm itself.

Results show that the proposed algorithm is capable of converging to a value of COP sufficiently close to the maximum one in all investigated conditions. In fact, dev_{COP} (Eq.(2)) is always less than 1%. Consequently, the resulting discharge pressure $P_{D,ALG}$ is close to the optimal value $P_{D,OPT}$ as $-0.6<dev_P<1.5$bar.

By comparing conditions "a" and "b" it can be noticed that a decreasing in $T_{B,I}$ leads to an increasing of COP_{OPT} for the same $T_{B,O}$ value. This is coherent assuming that the heat rejected is proportional to the brine temperature difference as reported in Eq.(1). Despite the COP_{OPT} values increment, $P_{D,OPT}$ values seems not heavily affected by the different $T_{B,I}$.

By comparing conditions "a" and "c" it can be noticed that a decreasing in T_{EV} causes a decreasing of COP_{OPT} for the same $T_{B,O}$ value. This is coherent assuming that the PWR_C is proportional to compression ratio and this negatively affects the COP value as reported in Eq.(1). Also this comparison shows that $P_{D,OPT}$ values are not heavily affected by the different T_{EV}, even with lower COP_{OPT} values.

Table 3 reports the comparison between the optimal discharge pressures experimentally determined $P_{D,OPT}$ and the ones obtained by the algorithm $P_{D,ALG}$ along with their relatives COP_{OPT} and COP_{ALG}. All the values are referred to the heat load Q_B ranging between 12.9 and 17.8kW.

Table 3. Experimental OPT and ALG pressures P_D and COP with their relative dev_P and dev_{COP} (see Eq.(2)).

Condition	$T_{B,O}$ [°C]	$P_{D,OPT}$ [barg]	$P_{D,ALG}$ [barg]	dev_P [bar]	COP_{OPT} [-]	COP_{ALG} [-]	dev_{COP} [%]
a	55	88.03	86.55	1.48	3.67	3.66	0.27
	65	96.00	96.55	-0.55	3.30	3.30	0.00
	70	102.00	101.61	0.39	3.16	3.16	0.00
b	55	86.06	85.72	0.34	3.88	3.86	0.52
	65	96.00	95.54	0.47	3.50	3.50	0.00
	70	101.02	100.94	0.08	3.32	3.30	0.60
c	55	85.93	85.50	0.43	3.45	3.42	0.87
	65	96.44	95.02	1.42	3.16	3.13	0.95

The values of dev_P are influenced by the arbitrary choice of the pressure values P_D selected to build up the experimental curves in Fig. 4. On the other hand, the values of dev_{COP} are related to the COP resolution chosen (number of significant digits), which justifies the null values appearing in Table 3.

Results indicate that the condition that mostly influences the optimal pressure $P_{D,OPT}$ is the $T_{B,O}$. The variations of $T_{B,I}$ and T_{EV}, have a significant effect in the values of the COP but not a great influence on the optimal pressure determination. The experimental results stated the ability of the proposed auto adaptive algorithm to locate the optimal pressure $P_{D,OPT}$ in all the investigated conditions with a satisfactory approximation.

5. Conclusions

An auto adaptive algorithm for optimal transcritical heat rejection pressure determination has been developed and experimentally investigated on a CO_2 air/water heat pump unit for a Domestic Hot Water (DHW) application. The Artificial Neural Network (ANN) architecture used by the algorithm allows local thermodynamic calculations in order to match the refrigerant and secondary fluid streams so to reach the highest unit Coefficient Of Performance (COP). Experimental tests have been carried out for two levels of evaporating temperature (-5°C and -8°C) and two levels of water inlet temperature (10°C and 15°C) with three values of water outlet temperature (55°C, 65°C and 70°C), maintaining the heat rejection pressure inside the transcritical regime between 75barg and 105barg.

The algorithm showed uniform convergence behavior and robustness against noises and disturbances. Response timings are related to PIDs calibration, which will be considered in future developments.

As expected, the optimal pressure depends on the coupling of CO_2 and water streams capacities. The proposed algorithm is capable of identifying a pressure that matches these two streams, converging on a value close to the optimal one. In fact, the maximum experimental pressure deviation is 1.48bar, resulting in an experimental COP deviation always less than 1% with respect to the maximum. Results show that water outlet temperature is the major factor influencing the optimal pressure, bringing the algorithm to regulate between 85barg and 102barg.

Due to easiness of implementation, a great advantage of such algorithm is the possibility of its inclusion inside an industrial controller with standard computational performances. Furthermore, the absence of a pure system perturbation approach brings significant simplification on its application. Its versatility makes it also suitable for “in situ” direct regulation application as well as laboratory tests on prototype units with the aim of characterization/optimization.

Future works are focused on testing the ability of the algorithm to adapt on different system features such as (but not limited to): fixed-speed water pump with modulating compressors, extended temperature range on water and evaporation sides, heat recovery integrated design, secondary circuit layout coupling.

Nomenclature

Symbols

BP	variable-speed brine pump	[-]	PWR	electrical power	[kW]
C	rotary compressor	[-]	Q	heat load	[kW]
COP	coefficient of performance, Eq.(1)	[-]	R	receiver	[-]
dev	deviation, Eq.(2)	[bar] ; [%]	SP	oil separator	[-]
E	finned-coil evaporator	[-]	SV	solenoid valve	[-]
H	heat rejection heat exchanger	[-]	T	temperature	[°C]
P	pressure	[barg]	V	modulating valve	[-]
PID	Proportional, Integral, Derivative	[-]	$\dot{V}$	volumetric flow rate	[l h^{-1}]

Subscripts

ALG	algorithm-calculated	I	inlet
B	brine	MEA	measured value
C	compressors	O	outlet
D	compressors discharge	OPT	optimal
EV	evaporation	SET	set point value
H	heat rejection		

References

[1] *https://ec.europa.eu/commission/presscorner/detail/en/IP_22_3131* ; Press release.

[2] *https://eur-lex.europa.eu/legal-content/EN/TXT/?uri=CELEX%3A52022PC0150*.

[3] *https://climate.ec.europa.eu/eu-action/fluorinated-greenhouse-gases/eu-legislation-control-f-gases_en*.

[4] Capanelli S.M.; "*Benefits and reliability of air-to-water heat pumps in residential applications, using R-290 refrigerant and an alternative design solution to guarantee high safety with standard components*"; 13th IEA Heat Pump Conference, Jeju, Korea, 2021.

[5] Liao S.M., Zhao T.S., Jakobsen A.; "*A correlation of optimal heat rejection pressures in transcritical carbon dioxide cycles*"; Applied Thermal Engineering 20, pp831-841, 2000.

[6] Zhang X.P., Fan X.W., Wang F.K., Shen H.G.; "*Theoretical and experimental studies on optimum heat rejection pressure for a CO2 heat pump system*"; Applied Thermal Engineering 30, pp2537-2544, 2010.

[7] Cervato A., Corazzol C., Mattiello L., Rampazzo M.; "*Maximizing CO_2 Heat Pump Systems Performance via Extremum Seeking Control*"; 23rd IEEE International Conference on Emerging Technologies and Factory Automation (ETFA), 2018.

[8] Simon D.; "*Evolutionary optimization algorithms*"; John Wiley & Sons, 2013.

[9] Fornasieri E., Girotto S., Minetto S.; "*CO_2 heat pump for domestic hot water*"; 8th IIR Gustav Lorentzen Conference on Natural Working Fluids, Copenhagen, Denmark, 2008.

[10] NIST, "*Refprop Standard Database DLL version 10.0*", Boulder (CO): US Secretary of Commerce, 2018.

14th IEA Heat Pump Conference
15-18 May 2023, Chicago, Illinois

A Study on Isothermal Compression System Applying Electrochemical Compressor

Soyeon Kim[a], Minkyu Jung[a], Donik Ku[a], Soojin Bae[a], Gijeong Seo[b], Dong Kyu Kim[c], Minsung Kim[a,b*]

[a]Department of Intelligent Energy and Industry, Chung-Ang University, 84 Heukseok-ro Dongjak-gu, Seoul 06974, Republic of Korea
[b]School of Energy Systems Engineering, Chung-Ang University, 84 Heukseok-ro Dongjak-gu, Seoul 06974, Republic of Korea
[c]School of Mechanical Engineering, Chung-Ang University, 84 Heukseok-ro Dongjak-gu, Seoul 06974, Republic of Korea

Abstract

Electrochemical compressor (ECC) can produce pressurized refrigerant through electrochemical reaction, and ion selective electrolytes. It can be an ideal replacement for mechanical compressor (MC) that have low compression efficiency and noise problem caused by driving parts. Considering the piston rotating at high speed about 25~30 RPS, it is very difficult to cool the incoming fluid and the gas pressure and temperature increase due to adiabatic compression. However, ECC is prone to lowering temperature of the discharge side as it does not have a driving part, and the surface area of membrane is wide. Therefore, since sufficient inter-cooling can be performed by attaching heat exchangers on multi-stage compression, an isothermal compression process can be achieved. It means, since it is not compressed by volume reduction, compression close to isothermal compression is possible. In this study, a performance of the isothermal compression refrigerator system using ECC is compared with the mechanical compression system. When cooling the ECC with outside air, adiabatic compression is implemented at the compression front-end and isothermal compression at the rear-end.

© HPC2023.
Selection and/or peer-review under the responsibility of the organizers of the 14th IEA Heat Pump Conference 2023.

Keywords: isothermal compression; Electrochemical compressor; mechanical compressor; refrigeration cycle; multi-stage compression;

1. Introduction

The efficiency of refrigeration systems has improved a lot over the past decades due to the rapid increased in cooling loads caused by abnormal climate. The Carnot refrigeration system achieve the highest possible cycle efficiency, which consists of two isentropic processes and two isothermal processes. However, this cycle is not feasible due to various unavoidable irreversibility such as friction, pressure drop, throttling expansion, etc.[1] In particular, the mechanical compressor consumes a lot of energy and the increase in the irreversibility by superheated vapor compression makes it difficult to achieve the refrigeration system closer to the Carnot system.[2] Because the compressor consumes a lot of work in the refrigeration cycle, it is a well-known fact that if isothermal compression is achieved, the efficiency of entire system can be greatly improved. [3] To implement the isothermal compression with the mechanical compressor (MC), it is natural to proceed with multi-stage compression and intercooling. The concept of intercooling is that isothermal compression can theoretically be performed if a cooling step is applied in between each compression stages, and the number of stages becomes infinite. However, in many studies, there is a lack of analysis on how much compression work can be reduce by multi-stage compression and intercooling in practical case. Therefore, in this paper, an analysis of that with MC is included.

The another most potential method to make isothermal compression in the refrigeration cycle is the using electrochemistry.[4] That is called Electrochemical Compressor (ECC), and it can attain an isothermal

* Corresponding author. Tel.: +82-2-820-5973 ; fax: +2-82-3280-5867.
E-mail address: minsungk@cau.ac.kr.

compression efficiency greater than 90%. In ECC, the low GWP refrigerant can be used because the gas that can permeate through the ion exchange membrane in an ion state can be used as cycle refrigerants. It also has no moving parts, so the compression process can be performed without lubrication oil, noise, or vibration. Therefore, in this study, a mechanical multi-stage compressor using intercooling and an ammonia refrigeration system with ECC are analyzed, and a practical cycle modeling considering heat exchanger is conducted.

2. Isothermal compression of multi-stage intercooling compression

2.1. Comparison of configuration and work with number of stages

In this chapter, an ideal case that can make isothermal compression using mechanical compressors (MCs) is analyzed. The intercooling is carried out between each stage of the MC, and this cooling is performed at the outside air or condenser temperature, so that adiabatic compression can be realized in the front-end of compression and isothermal compression in the rear-end compression. The intercooling proceed as the condenser temperature, and ideally, the effectiveness of the heat exchanger is set to 1. The cycle condition is shown in the Table 1. In an ammonia refrigeration cycle in which the evaporator temperature is 5 ℃, the condenser temperature is 50 ℃, and in the case of a 6-stages MC with an isentropic efficiency of 0.75 at each stage to approach practical cycle [5], and assuming that the degree of superheat (DSH) is 5 ℃, the cycle as shown in the diagram below the compressor of cycle is composed.

Table 1. Ammonia refrigeration cycle conditions and result

Parameters	Value
Condenser temperature [℃]	50
Evaporator temperature [℃]	5
Isentropic efficiency of MC (η_{isen})	0.75
Suction superheat [℃]	5
Number of stages	6
W_{comp} of single-stage MC [kJ/kg]	280.9426
W_{comp} of multi-stage MC [kJ/kg]	263.1342
Work reduction [%]	6.34
COP increase [%]	6.78

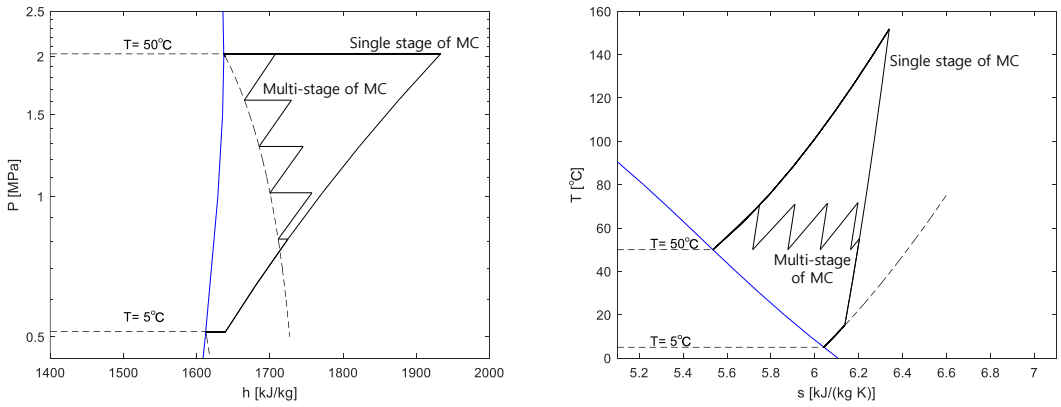


Fig. 1. Diagram of 6-stage MC and 1-stage MC with different configuration (left : *P-h* diagram, right : *T-s* diagram).

The single-stage MC consumes the work about 280.94 kJ/kg, multi-stage MC's work input is 263.13 kJ/kg, so the work reduction from single to multi stages is 6.34%. COP of multi-stage MC can improve approximately 6.78% higher than single MC in standard vapor compression. If the number of stages becomes infinite, isothermal compression can be achieved theoretically.

Consider the case where the number of stages is 100, like the T-s diagram in Fig. 2. If adiabatic compression occurs at the front-end and multi-stage intercooling compression is performed at the rear-end, isothermal

compression can be theoretically implemented at the rear-end. As the number of stages increases, the amount of work required by the compressor will decrease. As shown in Fig. 2, isothermal compression is realized at the latter stage of compression, and the effect of approaching the Carnot efficiency can be obtained. The convergence value of work under the current conditions is about 256.6 kJ/kg in Fig. 3.

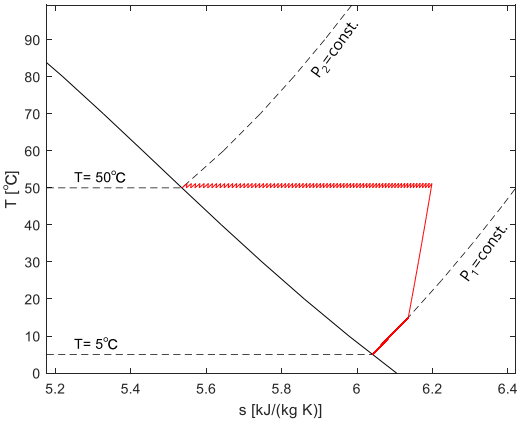


Fig. 2. Configuration of isothermal compression with 100-stage MC.

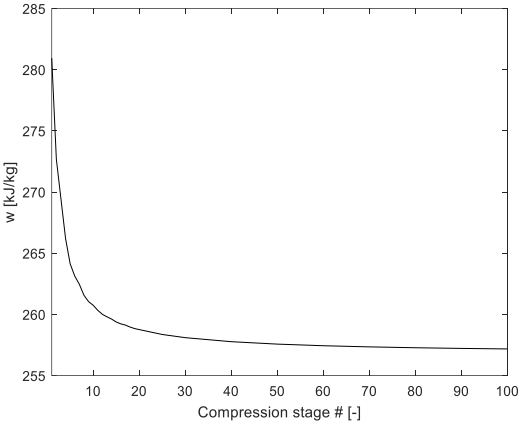


Fig. 3. Work variations according to the stage number of MC.

2.2. Practical cycle of intercooling multi-stage MC

Practical cycle is considered including heat exchanger modeling with compression model. The cycle analysis conditions used for this are shown in Table 2. The simulation model was developed using MATLAB, and the thermal properties were loaded from the REFPROP data base. [6]

Table 2. Practical cycle analysis conditions

	Variables	Value
Main cycle	Refrigerant	Ammonia
	Refrigerant mass flow rate [kg/s]	0.02
Heat exchanger	Condensing water mass flow rate [kg/s]	0.3
	Evaporating water mass flow rate [kg/s]	0.3
	Condensing water inlet temperature [℃]	30
	Evaporating water inlet temperature [℃]	25
	Condensing water inlet pressure [kPa]	101.325
	Evaporating water inlet pressure [kPa]	101.325
	Degree of superheating [℃]	5
	Degree of subcooling [℃]	5
	Heat exchanger length [m]	10
	Finite volume [-]	50
Compressor	Stages of multi-stage MC	6
	Intercooling air temperature [℃]	35
	Isentropic efficiency of MC	0.75

A copper double pipe heat exchanger was used to analyze the heat phenomenon of the two fluids with counter flow, and for the more physically approaching the practical refrigeration cycle the finite volume method (FVM) was used which is one of the most popular numerical methods used to solve heat transfer problems. [7-8] The secant method was used as a numerical analysis method of cycle. The Secant method is similar to Newton's method. Newton's method finds a solution using the gradient at a given point, while the Secant method finds a solution at the gradient of two given points. Unlike Newton's method, which requires knowing the exact function form, the secant method makes it possible to derive a solution without knowing

the exact function of the given graph. The method of finding the approximate value of the solution by the secant method is as follows.

$$x_n = x_{n-1} - y_{n-1}\frac{x_{n-1}-x_{n-2}}{y_{n-1}-y_{n-2}} \quad , \quad n = 2, 3, \cdots \tag{1}$$

x_0 and x_1 are assumed to be random values from the beginning. The desired solution can be found by repeating the above formula until the approximate value falls within the error range of the actual value. In this simulation, assuming P_{cond} and P_{evap} by changing the values of T_{cond} and T_{evap}, the calculation is repeated until the results of each heat exchanger analysis and the enthalpy of cycle point 3 (condenser outlet) and point 4 (evaporator inlet) converge within 1% of the error range.

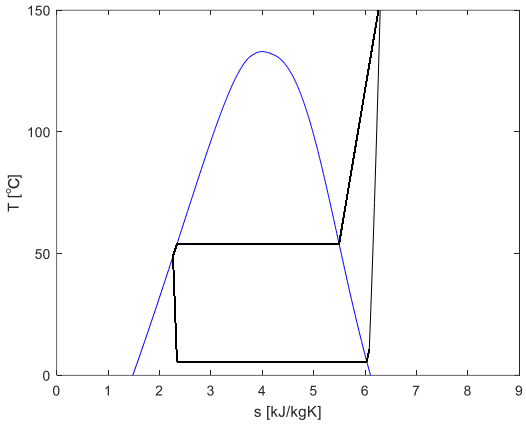


Fig. 4. T-s diagram of cycle with single-stage mechanical compressor.

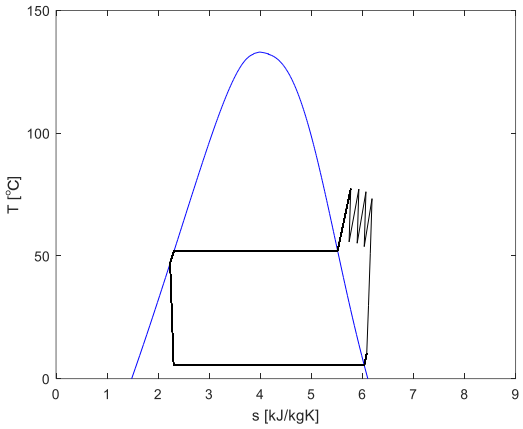


Fig. 5. T-s diagram of cycle with multi-stage mechanical compressor and intercooler.

First, looking at the results of the single MC stage, in this cycle, ammonia has a large vapor compression irreversibility, so it appears as a T-s plot as in Fig. 4. At this time, the condenser temperature and evaporator temperature were 53.99 ℃ and 5.6 ℃, respectively, and the work consumed by the compressor was 309.4576 kJ/kg when the isentropic efficiency was 0.75.

Next is the result when using multi-stage MC including intercooling instead of single MC in the same cycle in the Fig. 5. The effectiveness of the intercooling air heat exchanger between the compression processes was set as an ideal value by obtaining the effectiveness value when the isentropic efficiency is 1 so that the refrigerant at the condenser inlet does not become 2-phase state. When the isentropic efficiency in all stages was given as 0.75, the work input was 230.2457 kJ/kg, which significantly reduced the irreversibility compared to the single-stage MC. As the number of stages approaches infinity, isothermal compression approaches and Carnot efficiency approaches.

In the thermodynamic cycle, the second-law efficiency indicates the degree to which the actual process is close to the reversible process. In this case, the cooling COP can be expressed as the actual performance and the reversible process can be expressed as the Carnot efficiency as shown in the following equation. The second-law efficiency of the multi-stage MC analyzed in this study is 76.77%, and if intercooling and multi-stage compression can be implemented in real, it can be approached close to the Carnot cycle.

$$\frac{COP_R}{carnot\ efficiency} = \frac{Q_{evap}/W_{comp}}{T_{evap}/(T_{cond}-T_{evap})} \tag{2}$$

However, it is actually hard to realize multi-stage compression and intercooling using mechanical compressors.[9] This is why compression using interstage cooling has not been studied much. As shown in Fig. 6, there are studies on two-stage compression with refrigerant injection. [10-11]

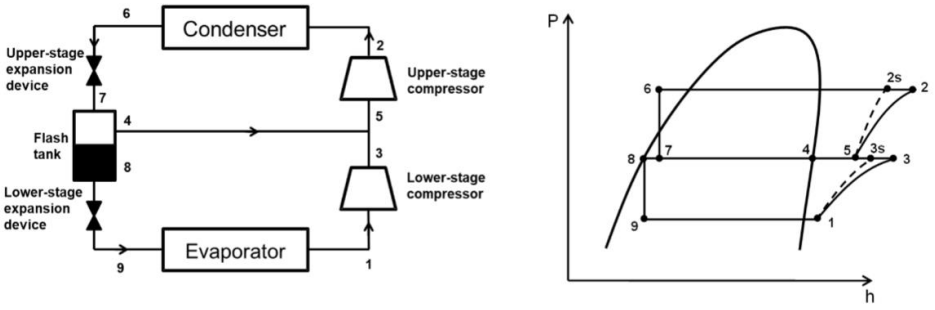


Fig. 6. *Schematic of Two-stage compression cycle (left) with associated P-h diagram (right).[6]*

In contrast, Electrochemical Compressor (ECC) is a technology that compresses gas through an electrochemical reaction and is based on the isothermal compression principle. In the next chapter, the principle of ECC and the practical isothermal compression refrigeration cycle with ammonia ECC are analyzed.

3. Isothermal compression of Electrochemical compressor (ECC)

3.1. Electrochemical Ammonia Compressor

Electrochemical ammonia compressor is an electrochemical compressor that uses the movement of NH_3 from the suction side to the discharge side using H_2 as a carrier gas when the ion exchanger membrane is charged with DC voltage. As shown in Fig. 7, ammonia and hydrogen transfer the membrane at a ratio of 2:1, and the half reaction at each electrode is as follows. [12]

$$2NH_3 + H_2 \rightarrow 2NH_4^+ + 2e^- \quad (anode) \tag{3}$$

$$2NH_4^+ + 2e^- \rightarrow 2NH_3 + H_2 \quad (cathode) \tag{4}$$

Due to the potential difference, H_2 is oxidized to H^+ ions at the anode, and NH_4^+ ions are generated and passed through the polymer electrolyte membrane. At the cathode, NH_3 gas and H_2 gas evolve again. Through pressure sealing on the discharge side, gas compression effect is provided as the number of molecules increases without changing the volume.

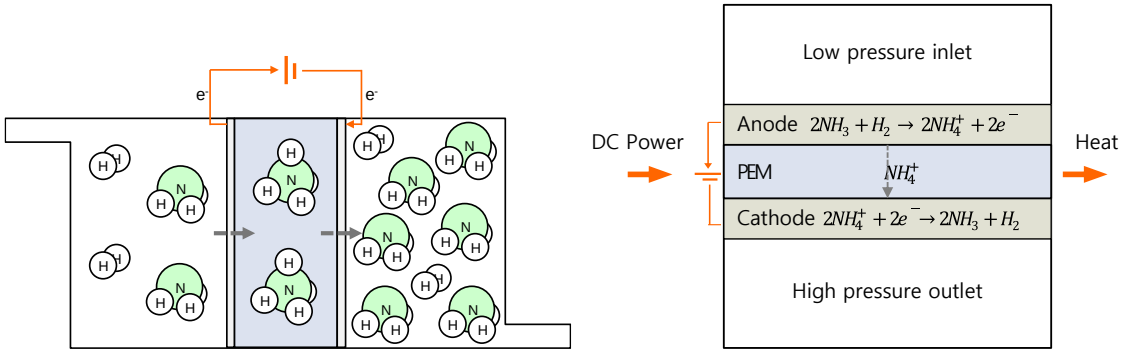


Fig. 7. *Schematic of electrochemical ammonia compressor (left) principle of ammonia ECC (right).*

Unlike traditional MC that is limited by ideal gas law (PV=nRT), the ECC is governed by the Nernst equation and ohmic loss, activation loss, etc. E_0 is standard hydrogen electrode potential, and it is zero because the half reactions on both sides of the membrane are opposite. Where $P_{cathode}/P_{anode}$ is the ratio of pressures across the membrane, and the voltage required for compression is a function of this ratio. [13]

$$V_{comp} = E_{Nernst} + \eta_{ohm} + \eta_{act} \tag{5}$$

$$E_{Nernst} = E_0 + \frac{RT_{ECC}}{nF} ln\ (\frac{P_{cathode}}{P_{anode}}) \quad (6)$$

$$dU = \delta Q + PdV \quad (7)$$

This relationship describes isothermal compression. From a thermodynamic point of view, the internal energy U is a function of Q and W as shown in the equation (7). In the adiabatic process, if the pressure rises without volume change, δQ = 0 and dV = 0, so the change in internal energy is zero. Since internal energy is a function of temperature, isothermal compression can proceed as the temperature change also becomes zero. In addition, since there is no physical driving part, it is a great advantage that there are no problems with noise or lubricating oil.

In comparison with mechanical compressors explained in the previous chapter, the most ideal compression of MC for isothermal compression is adiabatic compression. As can be seen in Fig. 8, multi-stage adiabatic compression is needed intercooling, and it results in high capital and operating cost. The ECC performs isothermal compression like in Fig. 8.

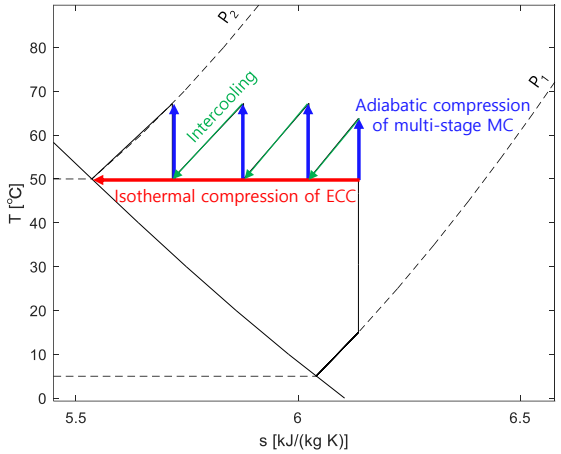


Fig. 8. Compressor temperature profiles during compression with multi-stage MC and ECC. [14]

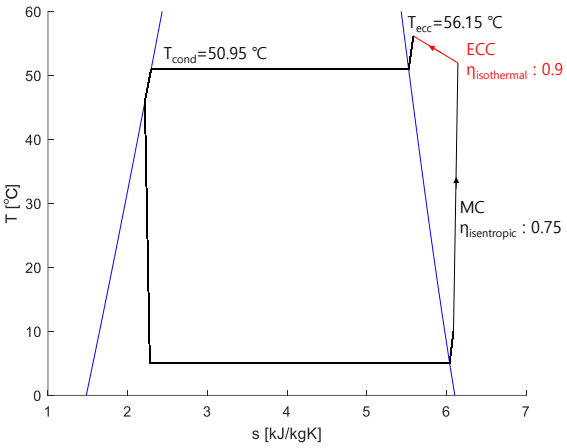


Fig. 9. T-s diagram in practical cycle of semi-isothermal compression using ECC.

3.2. Practical case of isothermal compression cycle modeling with ECC

Practical cycle with ECC was analyzed including single-stage MC compressor in the low-pressure compression part. The cycle analysis conditions used for this also are shown in Table 2. For isothermal compression using ECC, MC with an isentropic efficiency of 0.75 was used at the front-end to adjust the condenser refrigerant inlet temperature to the cycle like Fig. 9, and the isothermal efficiency of ECC is set 0.9. Since the compression of ECC is not volume compression but compression due to the increase in the number of molecules at constant volume, so it cannot be represented as a state point in the T-s plot, but it is plotted in a sense of entropy per mass for better understanding.

From eq. (6), the required work to compress from the MC outlet pressure to the condenser pressure is calculated by dividing the isothermal efficiency ($\eta_{isothermal}$). The work equivalent to the remaining work increases the enthalpy of the refrigerant as a loss of ECC like an eq. (8). So, the refrigerant which temperature determined at the ECC outlet with isothermal compression efficiency flows into the condenser. The ECC consumes the work as 155.84 kJ/kg, and total compression work is required as 243.583 kJ/kg, which is confirmed that the work could be reduced compared to single-MC cycle. Compared to Fig. 4, the cycle using ECC takes advantage at work in the superheat vapor compression over the condenser temperature part and performs close to isothermal compression instead of MC cycle which is barely to implement real intercooling and multi-stage systems.

$$w_{thermal,loss} = RT_{ECC} ln \left(\frac{P_{ECC,out}}{P_{ECC,in}}\right) * \frac{(1-\eta_{isothermal})}{\eta_{isothermal}} = h_{ECC,out} - h_{ECC,in} \quad (8)$$

In other words, due to irreversibility caused by cell resistance, overvoltage is required than Nernst voltage, and it generates heat corresponding to remainder of the isothermal compression efficiency. To maintain

constant performance, this heat must be removed. Normally, the isothermal compression efficiency of ECC is known to be about 93% [4], but if you make a stack to achieve a high-pressure ratio, you must have a thermal management solution [14].

Fortunately, ECC makes it easy to implement intercooling between unit cells in the stack unlike the MC. Since the gas distribution channels are in contact between the cells, the surface area for heat removal is sufficient. Tao et al. proposed an intercooler design to implement isothermal compression in ECC stack. The intercooling has an open channel design using air or a heat exchanger design using water, so the system is not complicated. Therefore, it can be said that it is the closest process to practical isothermal compression.

The second-law efficiency of the Fig. 9 cycle is 73.87%, which is the closest to the Carnot cycle. However, even in this cycle, the effect of isothermal compression is reduced because MC is used for the front-end compression to satisfy the condenser temperature. Therefore, it is necessary to study refrigerant cycles or membranes with low condenser temperatures for use in refrigeration cycles. ECC has a cation exchange membrane and an anion exchange membrane. Research is being conducted on a low GWP refrigerant that can pass through the membrane in a positive ion state by obtaining H^+ while using hydrogen gas as a carrier gas. The most anticipated refrigerant is the HFO series. The biggest barrier to using ECC as a compressor in the refrigeration cycle is the operating temperature of the ECC. In the case of Nafion membrane, which is the most used, since it is mainly used at 5-60℃, the condenser temperature is around that temperature or rather, it requires heating to apply to the cycle and cooled again after compression. Therefore, it is necessary to increase the potential of the refrigeration system through the development of ECC with high efficiency in the low temperature region.

4. Conclusion

In this paper, the concepts of multi-stage mechanical compressor (MC) with intercooling and electrochemical compressor (ECC) are proposed for practical implementation of the isothermal compression. The most ideal and theoretical compression using MC is adiabatic + intercooling compression. With given isentropic efficiency, the work consumed in the refrigeration cycle of single-stage MC and multi-stage MC with intercooling was compared, and the numerical analysis of the cycle reflecting practical elements was performed. As a result, as the number of stages increases, it becomes closer to isothermal compression and the work can be reduced. However, considering the high-speed rotating piston, it is almost impossible to cool the inflowing fluid, and multi-stage compression using MC is not feasible due to the problem that the pressure and temperature of the gas rise simultaneously due to adiabatic compression.

On the other hand, since ECC is not compression by volume reduction, compression close to isothermal compression is possible. In addition, there is no driving parts, and the surface area of the membrane is wide, so it is easy to lower the temperature of the discharge side. Therefore, since sufficient intercooling can be performed by attaching a heat exchanger during multi-stage compression, the possibility of implementing an isothermal compression process is high.

However, when applied to the refrigeration cycle, since the condenser temperature must be matched, the temperature of isothermal compression must still be raised using MC at the compression front-end, and it is difficult to approach Carnot efficiency due to the few stages of isothermal compression. In addition, in the case of ECC, the range of refrigeration cycles that can be applied is not expected to be wide because the operating temperature is high at 5-60 ℃. Nonetheless, ECC has potential for low GWP refrigerants and as membrane technology improves, it can potentially improve the efficiency for the vapor compression systems.

Acknowledgements

This research was jointly supported by National Research Foundation of Korea (NRF No. 2019R1A2C108869414) and by Korea Institute of Energy Technology Evaluation and Planning (KETEP) (20202020900290, 20214000000280, 20212050100010) funded by Ministry of Trade, Industry and Energy. This research was also supported by the Korea Environmental Industry & Technology Institute (KEITI No. 2020003060005) Authors sincerely appreciate their supports.

References

[1] Kim T, Lee CY, Hwang Y, Radermacher R. A review on nearly isothermal compression technology. *J Int Refrig* 2022;144:145-62.
[2] Asdrubali F, Desideri U. Handbook of Energy Efficiency in Buildings: A Life Cycle Approach. Oxford, UK : Elsevier; 2019, p. 441–595
[3] Schorer, L., Schmitz, S. 2017. "Onsite hydrogen generation and hydrogen recycling for refuelling FCEVs using an electrochemical hydrogen compressor," EVS30 Symposium. Stuttgart, Germany.
[4] Tao Y, Hwang Y, Radermacher R, Wang C. Experimental study on electrochemical compression of ammonia and carbon dioxide for vapor compression refrigeration system. *J Int Refrig* 2019;104:180-8.
[5] Ibrahim TK, Rahman M, Alla ANA. Study on the effective parameter of gas turbine model with intercooled compression process. *SRE* 2010;5(23):3760-70.
[6] Lemmon, E. W., Bell, I. H., Huber, M. L., McLinden, M. O., 2018. NIST standard reference database 23: reference fluid thermodynamic and transport properties-REFPROP, Version 10.0, National Institute of Standards and Technology. Standard Reference Data Program, Gaithersburg.
[7] Kim S, Cho Y, Kim MS, Kim M. Characteristics and optimization of supercritical CO2 recompression power cycle and the influence of pinch point temperature difference of recuperators. *Energy* 2018;147: 1216-26.
[8] Na SI, Kim M, Kim MS. Performance simulation of CO2 transcritical cooling system with mechanical subcooling cycle for automobile air conditioning. *J Mech Sci Technol* 2022;36:4797–807.
[9] Coney MW, Stephenson P, Malmgren A, Linnemann C, Morgan RE, Richards RA, Huxley R, Abdallah H. Development Of A Reciprocating Compressor Using Water Injection To Achieve Quasi-Isothermal Compression. *International Compressor Engineering Conference*. 2002; Paper 1508.
[10] Lee D, Seong KJ, Lee J, Performance investigation of vapor and liquid injection on a refrigeration system operating at high compression ratio. *Int J Refrig* 2015;53:115–25.
[11] Huang JM, Chiang CP, Chen JF, Chow YLo, Wang CC, Numerical investigation of the intercooler of a two-stage refrigerant compressor. *Appl Therm Eng* 2007;27:2536–48.
[12] Tao Y, Gibbons W, Hwang Y, Radermacher R, Wang C. Electrochemical ammonia compression. *Chem Commun* 2017;53(41):5637-40.
[13] Nordio M, Rizzi F, Manzolini G, Mulder M, Raymakers L, Annaland MVS, Gallucci F. Experimental and modelling study of an electrochemical hydrogen compressor. *Chem Eng J* 2019;369:432-42.
[14] Lipp, L., 2012. "Electrochemical Hydrogen Compressor," DOE Hydrogen Program.

14th IEA Heat Pump Conference
15-18 May 2023, Chicago, Illinois

Ideal performance analysis of membrane-based vacuum dehumidification systems

Donik Ku[a], Soyeon Kim[a], Minkyu Jung[a], Soojin Bae[a], Young Soo Chang[b], Minsung Kim[a,c,*]

[a]Department of Intelligent Energy and Industry, Chung-Ang University, Seoul 06975, Republic of Korea
[b]School of Mechanical Engineering, Kookmin University, Seoul 02707, Republic of Korea
[c]School of Energy Systems Engineering, Chung-Ang University, Seoul 06975, Republic of Korea

Abstract

Non-vapor compression air-conditioning systems were proposed to overcome the limitation of the traditional air-conditioning systems. It was reported that the membrane heat pump(MHP) has a high energy saving potential. The sensible heat and latent heat removal process can be separated by the system. A membrane-based vacuum dehumidification system(MVD) is the latent heat removal systems, consisting of a membrane mass exchanger and a vacuum compressor. The water vapor discharge type membrane-based vacuum dehumidification system(W-MVD) and condenser combined membrane-based vacuum dehumidification system(C-MVD) show high performance among the several structure of MVDs. One system can show a higher performance than another system according to temperature and humidity conditions, but there is lack of discussion about the ideal COP values for actual system design, analysis, and optimization. In this study, the ideal dehumidification COP of the two systems were defined by reversible cycle analysis. It was achieved by removing all irreversibility of system consisting of membrane mass exchangers, vacuum compressor and heat exchanger, and the ideal COP formulas were derived. Exergy analysis and compressor consumption modeling methods were used to verify the formulas, and the COP values calculated by them show a high consistency. when comparing the ideal COP of the MVDs based on the results, the W-MVD shows higher performance than the C-MVD in unsaturation outdoor air condition.

Keywords: Membrane-based vacuum dehumidification system, Membrane mass exchanger, Vacuum compressor, Irreversibility, Ideal dehumidification COP;

1. Introduction

As the demand for building air conditioning increases worldwide and regulations on fluorine-based refrigerants are strengthened, the problem of using the existing vapor compression air conditioning system continues to be raised. At the same time, with the development of sensible load management technologies such as passive house technology and high-efficiency sensible heat control air conditioning system technology, the importance of the humidity control system is increasing to maintain thermal comfort for residents. Accordingly, a membrane heat pump (MHP) that can overcome the shortcomings of the existing dehumidification system has been proposed as one of the promising technologies [1].

The membrane heat pump uses the principle that water vapor can be separated from indoor humid air by utilizing a dense membrane with selective permeance to water vapor. Fig. 1 shows the change in the state of the theoretical air conditioned by each dehumidification system on the psychrometric chart. Unlike a condensation dehumidification system that simultaneously removes sensible heat and latent heat, the membrane heat pump can separate the sensible heat removal and latent heat removal process. Since it is not necessary to overcool the air and then reheat it, it is possible to take a thermal gain by the cooling path in the psychrometric chart. Since dehumidification using a desiccant is an isenthalpic process, thermal gains by the cooling path cannot be expected, but the disadvantages of desiccant that consume a large amount of heat during the regeneration process can be compensated. However, the coefficient of performance(COP) should be considered along with the state change of humid air to evaluate how efficient the system operates under certain cooling load conditions.

* Corresponding author. *E-mail address:* minskim@snu.ac.kr

Chun et al. constructed a system that combines the membrane-based vacuum dehumidification system(MVD) and the air carrying energy radiant air conditioning system to calculate the COP [2]. Since the dehumidification performance of the MVD varies depending on the vapor separated from humid air discharge structure, various structures have been studied to improve performance. Scovazzo & Scovazzo proposed a system that reduced the compression ratio of the vacuum compressor by bypassing a portion of the dehumidified air [3]. Dais Analytic proposed a system in which two membrane material exchangers were installed at the inlet and outlet of the vacuum compressor to reduce the compression ratio and vapor flow rate at the same time [4], and Bui et al. proposed a system in which a condenser was installed at the outlet of the compressor [5]. Lim et al. compared the dehumidification COP of each system and analyzed the effect of outside air conditions [6].

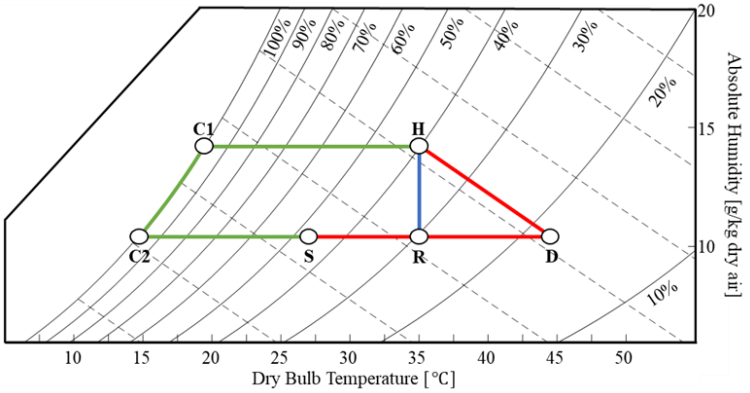


Fig. 1 Cooling path of each system on psychrometric chart; (a) condensation (H-C1-C2-S) (b) desiccant (H-D-S) (c) MHP (H-R-S)

Certain substances can be selectively permeated and separated from the mixture by the membrane, and permeation occurs due to chemical potential differences between two sides of the membrane. In the gas-gas separation membrane, it is divided into a porous membrane and a dense membrane according to the presence or absence of a physical pore through which gas molecules can pass, as shown in Fig. 2, the difference in partial pressure of each gas acts as a chemical potential difference. The permeation performance of the membrane is expressed in terms of permeance, which means the transmittance of a specific material per unit potential difference, and selectivity, which means the transmittance ratio of the two materials. The permeance and selectivity of the dense membranes used in the MVD mainly affect the dehumidification capacity and COP of the system, but they are in trade-off relation as shown in Fig. 3, so it is important to select the appropriate membrane according to the situation. Accordingly, experimental studies are being conducted to accurately measure the permeation characteristic values of the membrane under the operation conditions of the system to be actually used. Lee et al. measured the water vapor permeance and selectivity of the water vapor selective dense membrane that can be used in the MVD according to the pressure difference before and after the membrane and the transmission direction of water vapor and air [7].

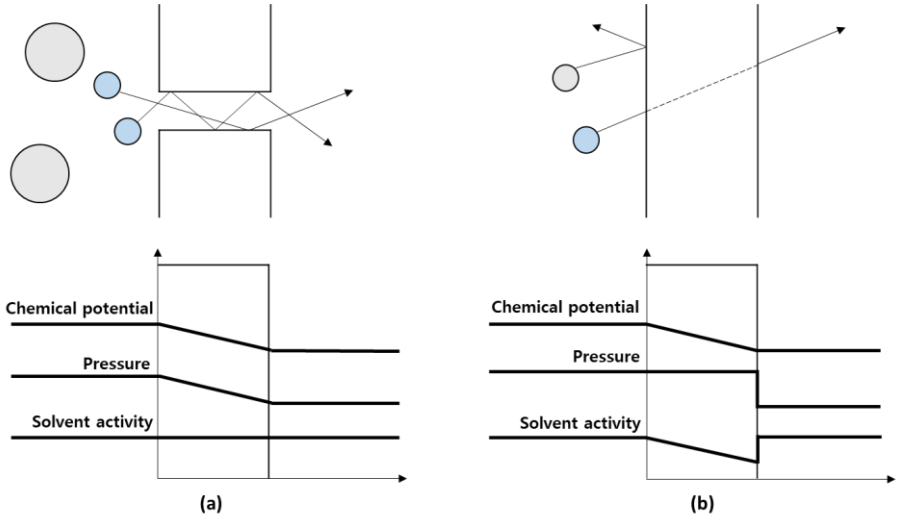


Fig. 2 Gas separation by partial pressure difference between two sides of membrane; (a) porous membrane (b) dense membrane

In previous studies on the performance of the MVD, the analysis was conducted assuming a membrane that completely blocks dry air and transmits only water vapor, that is, a membrane with infinite selectivity. However, since even a selectivity of the membrane is infinite, there is irreversibility by finite pressure difference as driving force of permeation process. So, this study aims to calculate the ideal dehumidification COP of MVDs by removing all irreversibility for systems design and optimization.

In other previous studies on the ideal performance of air-conditioning system, ideal COP of liquid-desiccant dehumidification and condensing dehumidification system were proposed by Zhang et al. as shown follows [8]. The ideal COP of isothermal dehumidification by perfect gas separation without considering the water vapor discharge process was proposed by Bui et al. as shown Eq.(4) [5]. And Labban et al. proposed ideal COP of generalized air-conditioning system discharging water vapor to ambient using exergy analysis as shown Eq.(5) [9]. This exergy model was used as an evaluation criterion of the ideal COP of MVDs.

$$COP_{des.Zhang} = \frac{1}{T_R}\frac{T_{iso.O}T_{iso.I}}{T_{iso.O}-T_{iso.I}} \quad (1)$$

$$COP_{con.Zhang} = \frac{T_{DP.I}}{T_R-T_{DP.I}} \quad (2)$$

$$W_{sep} = -nRT(X_a lnX_a + X_w lnX_w) \quad (3)$$

$$COP_{MVD.Bui} = \frac{m_w h_{fg}}{\Delta W_{sep}} \quad (4)$$

$$COP_{DH.Labban} = \frac{\dot{m}_w(h_{wet}-h_{dry})}{\dot{m}_w\xi_w+\dot{m}_{dry}\xi_{dry}-\dot{m}_{wet}\xi_{wet}} \quad (5)$$

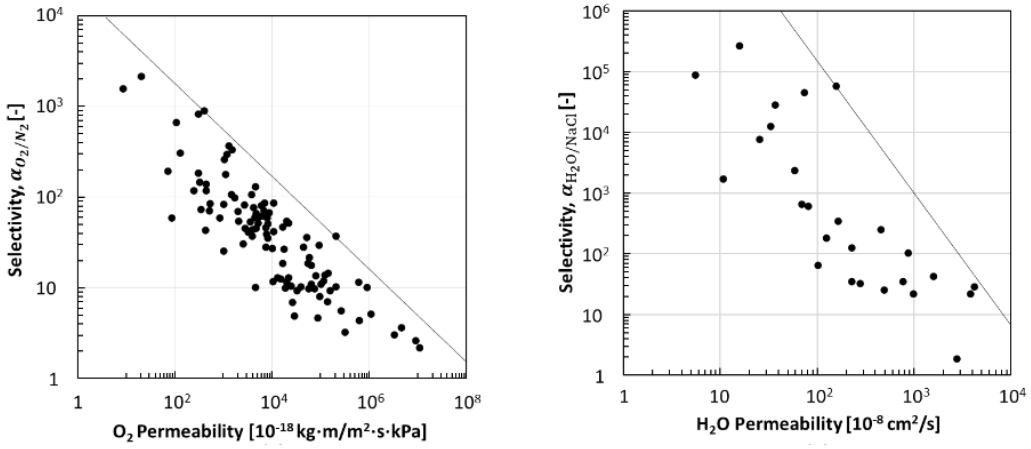


Fig. 3 Membrane permeance and selectivity trade-off; (a, left) O_2/N_2 [10] (b, right) H_2O/Nacl [11]

2. Simulation methodology

2.1. Idealized reversible MVDs

Fig. 4 shows the structure of water vapor discharge type MVD(W-MVD) and condenser-combined type MVD(C-MVD), which are analysis target systems of this study. W-MVD has two membrane mass exchangers installed at the inlet and outlet of the vacuum compressor, and C-MVD has a membrane mass exchanger installed at the inlet and heat exchanger at the outlet of the vacuum compressor. Assumptions to define the ideal dehumidification COP of the two systems were shown below.

- ✓ Both permeance and selectivity, the permeation characteristics of the membrane, are infinite.
- ✓ The effect of concentration polarization near the membrane surface is negligible.
- ✓ The water vapor adiabatically compressed to outdoor dry-bulb temperature and isothermally compressed to outdoor vapor partial pressure within non-condensation conditions.
- ✓ There is no irreversibility by temperature difference in the condenser of the C-MVD.
- ✓ The mass flow rate of indoor and outdoor air passing through the membrane mass exchangers is sufficiently large compared to the amount of water vapor permeation.

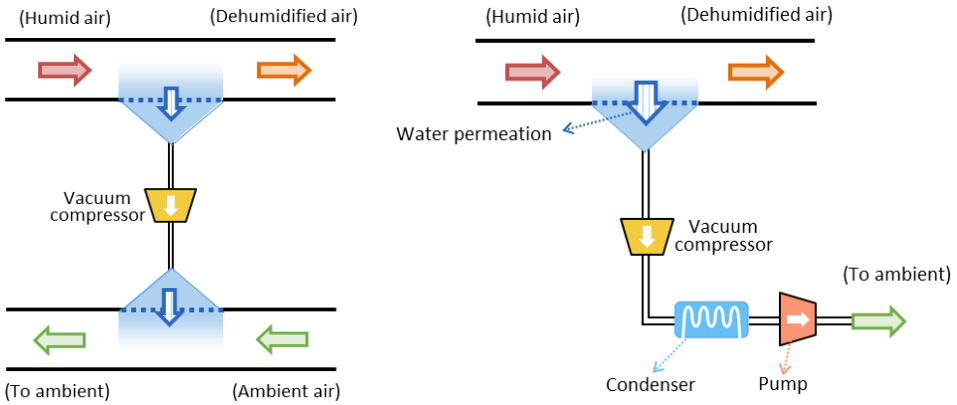


Fig. 4 Structure of the (a, left) W-MVD and (b, right) C-MVD

2.2. Mass transfer and compression model

The dense membrane separates water vapor from humid air according to vapor permeance and selectivity defined by Eqs. (6) and (7), respectively. Permeance is a property of a membrane determined by the water vapor transmission amount through the membrane under the partial pressure difference between the feed and the permeate side. The higher the water vapor permeance, the greater the amount of water vapor permeated through the membrane per unit area, per unit pressure difference, and per unit time. Selectivity is another property of a membrane determined by the transmission ratio between water vapor and dry air. The higher the selectivity, the more water vapor can transfer. Most previous studies have defined a membrane with infinite selectivity that can only permeate pure water vapor from humid air as an ideal membrane.

$$\beta = \frac{\dot{m}}{A \cdot \Delta P} \tag{6}$$

$$\alpha = \frac{\beta_w}{\beta_a} \tag{7}$$

Eq. (6) can be rewritten in the explicit form for mass flow rate of water vapor $\dot{m} = \beta A \cdot \Delta P$ where the formulation is similar to the heat transfer process. When the cross-sectional area is finite, infinite permeance is assumed for a reversible isothermal mass transfer process, such as assuming an infinite overall heat transfer coefficient for a reversible isothermal heat transfer process. Therefore, in this study, a membrane with infinite vapor permeance and selectivity was defined as an ideal membrane for dehumidification, and mass transfer through such a membrane is reversible.

Since the pressure difference between the feed side and the permeate side is zero in the ideal membrane, the inlet pressure of the vacuum compressor is the same as the water vapor partial pressure of the indoor air in both MVDs. The vacuum compressor outlet pressure is the same as the water vapor partial pressure of outdoor air in the case of W-MVD, and the water vapor saturation pressure at the outside temperature in the case of C-MVD. At this time, the suction and discharge pressure of the vacuum compressor must not exceed the saturation pressure at each temperature so that water vapor does not condense. If the indoor water vapor partial pressure is higher than the outdoor water vapor partial pressure, indoor water vapor can be discharged to the outside with only the membrane mass exchanger. This is a passive ventilation process, and MVD is unnecessary. Therefore, this case is out of analysis range. Only the case where the outdoor vapor partial pressure was higher than that of the indoor was considered. Fig. 5 is a T-s diagram showing the compression process of MVDs under the condition that the indoor and outdoor relative humidity is 100%. Since the water vapor partial pressure of outdoor air is the saturation pressure, the two MVDs are expressed in the same diagram. Due to the feasibility of isothermal compression, the water vapor would be adiabatically compressed from point 1 to 2'. Then the temperature difference between the vacuum compressor outlet and the outdoor air cause heat exchange. Since this irreversibility should be removed for ideal dehumidification of MVD, it is assumed that adiabatic compression from point 1 to point 2 and isothermal compression from point 2 to point 3 are performed. Assuming that water vapor is an ideal gas, the dehumidification COP are as follows.

$$COP_{DH} = \frac{\dot{m}_w h_{fg}}{\dot{W}_{isen} + \dot{W}_{isoth}} = h_{fg} \left[\frac{kRT_1}{k-1} \left(r_{p1}^{\frac{k-1}{k}} - 1 \right) + RT_2 \ln r_{p2} \right]^{-1} \tag{8}$$

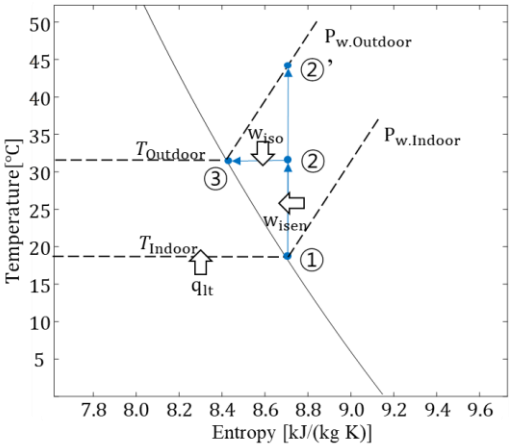


Fig. 5 Compression process on T-s diagram of W-MVD and C-MVD under indoor and outdoor saturation conditions

2.3. Theoretical dehumidification performance

Fig. 6 is a T-s diagram showing the approximate compression process of MVDs under conditions where indoor and outdoor relative humidity is less than 100%. Water vapor separated from indoor humid air is compressed to outdoor water vapor partial pressure in W-MVD and saturation pressure in C-MVD. That is, the outlet pressure of the vacuum compressor depends on both the condenser temperature and humidity in the W-MVD, but on only the condenser temperature in the C-MVD. Therefore, in order to remove irreversibility by heat transfer under unsaturated conditions, water vapor must be isothermally compressed at the dew point temperature of the outdoor air in W-MVD and at the dry-bulb temperature of the outdoor air in C-MVD. The permeation driving force of the membrane mass exchanger is the partial pressure difference of each gas, so the point I and O of W-MVD and point I of C-MVD can be approximated by saturated vapor points on the same pressure line, i.e., points 1 and 3 of W-MVD and 1 of C-MVD. Accordingly, the two MVDs approximately is a rectangular-shape open cycle on T-s diagram, such as a Carnot refrigeration cycle. That is, the ideal dehumidification COP of W-MVD can be expressed as a Carnot refrigeration COP, where the high temperature is the outdoor air dew-point temperature and the low temperature is the indoor air dew-point temperature, as shown in Eq. (9). Similarly, the ideal dehumidification COP of C-MVD can be expressed as a Carnot refrigeration COP, where the high temperature is the dry-bulb temperature of outdoor air and the low temperature is the indoor air dew-point temperature, as shown in Eq. (10).

$$COP_{W-MVD.ideal} = \frac{f(P_{w,I})}{f(P_{w,O})-f(P_{w,I})} = \frac{T_{DP.I}}{T_{DP.O}-T_{DP.I}} \tag{9}$$

$$COP_{C-MVD.ideal} = \frac{T_{DP.I}}{T_O-T_{DP.I}} \tag{10}$$

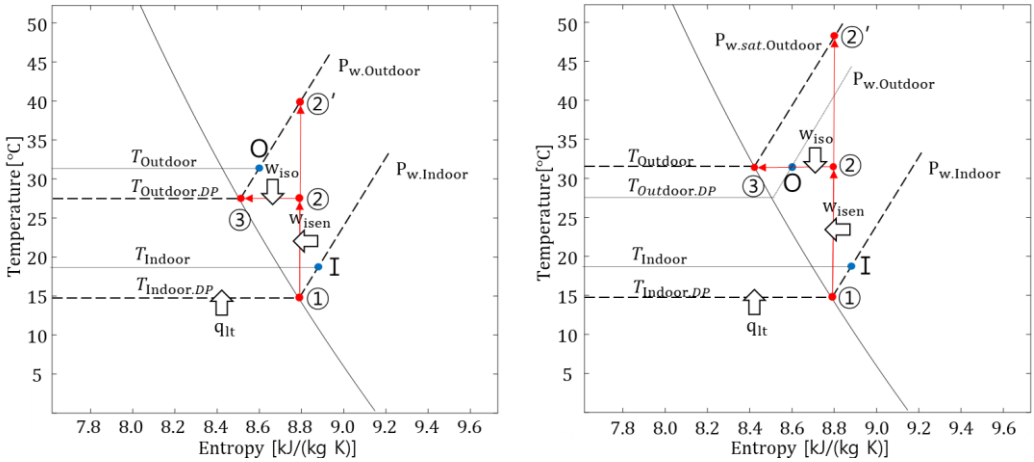


Fig. 6 Approximate compression process of (a, left) W-MVD and (b, right) C-MVD under indoor and outdoor unsaturated conditions

The dehumidification COP of both MVDs was calculated by Eq. (8). In the calculation process, the explicit method using MATLAB was applied based on MVD component modeling, and the thermodynamic properties are based on REFPROP 9.0. The results were mutually verified by comparing the ideal dehumidification COP calculated by Eq. (8) and Eqs. (9), (10). And the values and the theoretical maximum isothermal dehumidification COP calculated by Eq. (5) were compared. The detailed conditions applied to the performance analysis are shown in Table 1. The constraints conditions to analyze the effects of indoor and outdoor air conditions were represented as values in brackets. Both the isentropic efficiency and isothermal efficiency of the vacuum compressor were assumed to be 1.0, and the pump consumption of the C-MVD was ignored. Changes in indoor and outdoor air due to dehumidification and water vapor discharge were ignored, and the atmospheric pressure was assumed to be 101.325 kPa. Since the water permeance and selectivity of the membrane are assumed to be infinite, the compressor inlet and outlet conditions are the same as indoor and outdoor vapor conditions each. The temperature and humidity conditions were based on the ASHRAE 55 standard and KS C 9306 standard.

Table 1. Analysis conditions for ideal COP of MVD calculation

Location	Parameters	Values
Indoor air (Compressor inlet)	Dry-bulb temperature (T_I) [℃]	10~34 (24)
	Relative humidity (RH_I) [%]	50 ~ 100 (62.66)
	Absolute humidity (AH_I) [kgv/kga]	0.0093 ~ 0.0189 (0.0117)
	Dewpoint temperature ($T_{DP,I}$) [℃]	12.98 ~ 24 (16.44)
	Vapor partial pressure ($P_{w,I}$) [kPa]	1.493 ~ 2.985 (1.871)
Outdoor air (Compressor outlet)	Dry-bulb temperature (T_o) [℃]	16 ~ 40 (24)
	Relative humidity (RH_o) [%]	50 ~ 100 (84.22)
	Absolute humidity (AH_o) [kgv/kga]	0.0093 ~ 0.0489 (0.0158)
	Dewpoint temperature ($T_{DP,o}$) [℃]	12.98 ~ 40 (21.18)
	Vapor partial pressure ($P_{w,o}$) [kPa]	1.493 ~ 7.383 (2.513)
Vacuum compressor	Isentropic efficiency ($\eta_{isen,vc}$) [-]	1.0
	Isothermal efficiency ($\eta_{iso,vc}$) [-]	1.0

3. Results and discussion

Fig. 7 shows the ideal dehumidification COP ratio of the two MVDs according to outdoor air relative humidity calculated by Eqs. (9) and (10). By the absence of irreversibility, the ideal dehumidification COP of C-MVD is consistent with the dehumidification COP of W-MVD with 100% outdoor relative humidity. However, under unsaturated conditions of outdoor air, the ideal dehumidification COP of W-MVD is always higher than that of C-MVD, because the dry-bulb temperature is always higher than the dew-point temperature. Under the dehumidification conditions of KS C 9306 standard (T_I=24°C, RH_I=62.66%, T_O=24°C, RH_I=84.22%), C-MVD shows about 63.21% of W-VMD. Since the result of Eq. (9) is consistent with the result of Equation (8) under the saturation condition of outside air, the performance of W-MVD and C-MVD was analyzed with Eq. (8) in the subsequent result analysis.

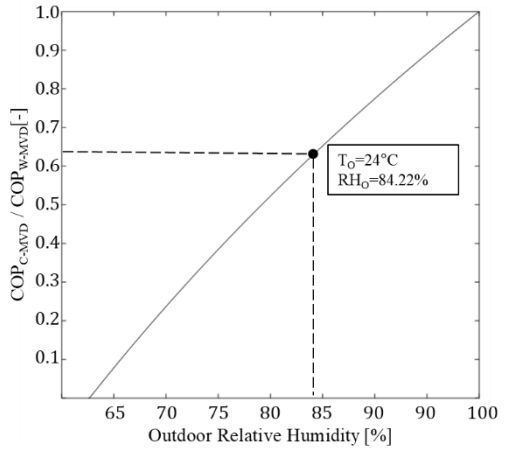


Fig. 7 Ratio of ideal dehumidification performance of W-MVD and C-MVD according to outdoor air relative humidity (T_I=24°C, RH_I=62.66%, T_O=24°C)

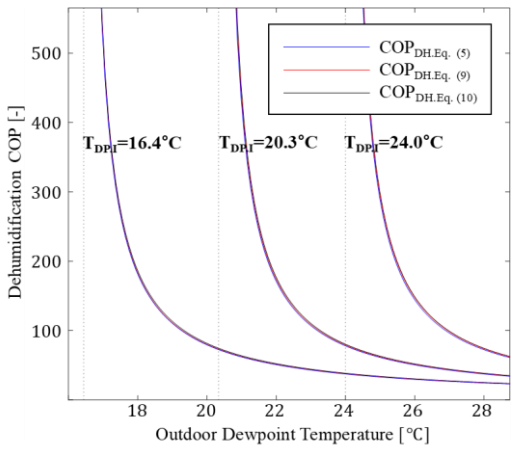


Fig. 8 Theoretical dehumidification COP of MVD according to the outdoor air dew-point temperature by Eqs. (5), (9) and (10) (T_I=24°C, RHo=100%)

Fig. 8 shows the theoretical dehumidification COP according to the outdoor air dew-point temperature for each indoor dew-point $_{temperature}$ calculated by Eqs. (5), (8), and (9). The indoor temperature is 24.0°C and the relative humidity is 62.66% to 100%, and the outdoor temperature varies from 16°C to 30°C and the relative humidity is 100%. The values obtained by the three methods are almost identical, and the ideal dehumidification COP of W-MVD and C-MVD under outdoor air saturation conditions is equivalent to the theoretical maximum COP of any isothermal system that discharges water vapor into the outdoor air.

3.1. Influence of temperature and humidity

In order to consider the effects of climate conditions on dehumidification COP of MVDs, dehumidification COP variation according to outdoor temperature and relative humidity were analyzed. Fig. 9 shows variation by climate conditions. It is assumed that the temperature of the indoor air is 24°C, and the relative humidity is constant at (a) 100% or (b) 50%. The outdoor temperature changed from 23°C to 40°C, and the relative humidity changed from 50% to 100%. As the temperature or relative humidity of outdoor air increased, the dehumidification COP decreased under all conditions. This is because the water vapor separated from the indoor air and passed through the membrane must be compressed to a higher pressure as the partial pressure of outdoor water vapor increases, resulting in an increase in vacuum compressor power consumption. This can also be explained by the fact that under the $T_{DP,I}$ condition set in Eq. (9), the larger the $T_{DP,O}$, the smaller the dehumidification COP, and is consistent with the intuition that the dehumidification system has higher COP in dryer climates.

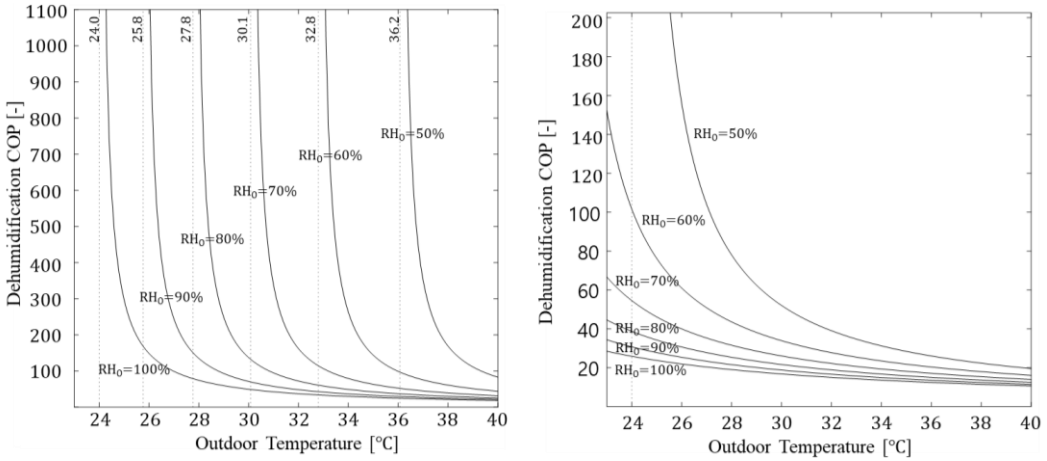


Fig. 9 Ideal dehumidification COP of MVD variation as outdoor air conditions of T_I=24°C; (a, left) RH_I=100%, (b, right) RH_I=50%

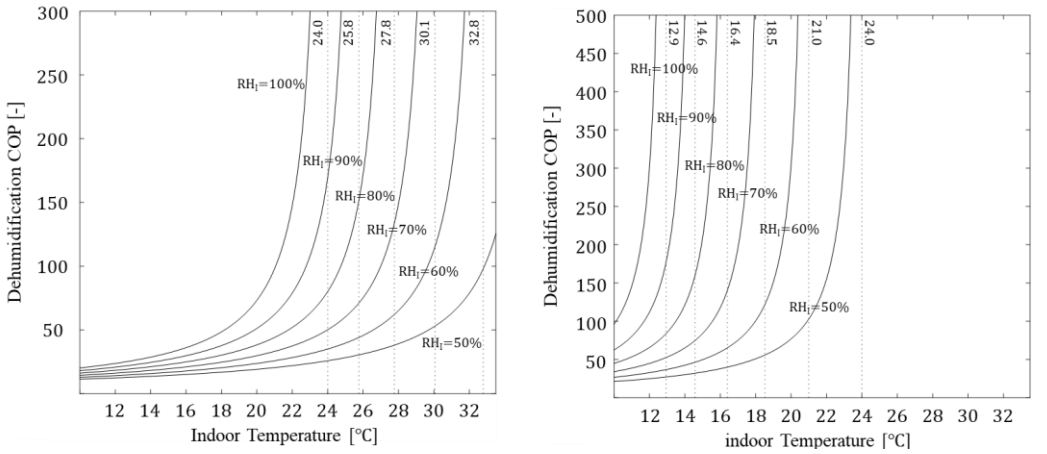


Fig. 10 Ideal dehumidification COP according to indoor air conditions of T_O=24°C; (a, left) RH_O=100%, (b, right) RH_O=50%

Since indoor conditions change when an air-conditioning system is operated, the effects of changes in indoor conditions on dehumidification COP under specific climate conditions was analyzed. Fig. 10 shows the ideal dehumidification COP variation according to the indoor air temperature and relative humidity. It is

assumed that the outdoor air temperature is 24°C and the relative humidity is constant at (a) 100% or (b) 50%. The indoor temperature changed from 10°C to 34°C, and the relative humidity changed from 100% to 50%. As the indoor temperature or relative humidity increased, the ideal dehumidification COP increased. This is because the compression ratio of vacuum compressor decreases as the partial pressure of indoor water vapor increases. This can also be explained by the fact that under the $T_{DP.O}$ condition set in Eq. (9), the larger the $T_{DP.I}$, the larger the dehumidification COP, and is consistent with the intuition that the dehumidification system has lower COP in the humid state at the beginning of dehumidification.

3.2. Irreversibility analysis

The assumptions of the MVD are not valid in a real system due to the inevitable irreversibility, so the actual dehumidification COP of MVD cannot reach the ideal values. Considering the finite permeance of the membrane, the finite pressure difference on both sides of the membrane mass exchanger is required as the driving force of mass transfer, which acts as irreversible. The inlet pressure of the vacuum compressor should be lower than the indoor vapor partial pressure, and the outlet pressure of the vacuum compressor in W-MVD should be higher than the outdoor vapor partial pressure, so the compression ratio increases and the energy consumption of the vacuum compressor increases. Fig. 11 and Fig. 12 (a) show the dehumidification COP according to the outdoor air temperature for each finite pressure difference between both sides of the membrane with finite water vapor permeance and infinite selectivity of W-MVD and C-MVD, respectively. It was assumed that the indoor temperature was 24°C, the relative humidity was 62.66%, and the outdoor relative humidity was 84.22%. The lower the water vapor permeance of the membrane, the greater the required water vapor partial pressure difference, the higher the irreversibility of the system, so the dehumidification COP is lower than the ideal value. If the pressure difference is not required due to infinite water vapor permeance, the dehumidification COP is consistent with the ideal dehumidification COP.

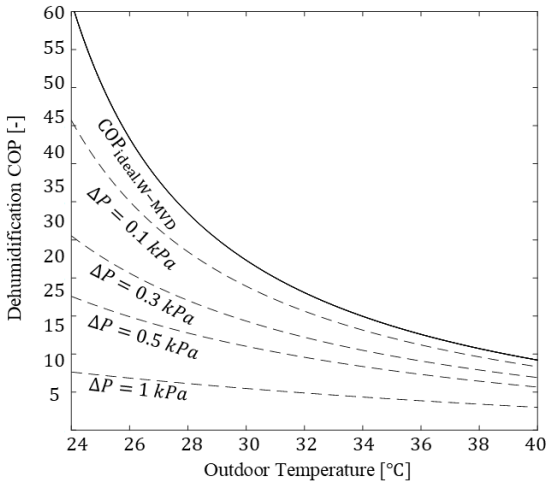


Fig. 11 Dehumidification COP reduction in W-MVD due to finite pressure difference (T_I=24°C, RH_I=62.66% and RH_O=84.22%)

Fig. 10 (b) shows the dehumidification COP of C-MVD with infinite membrane permeance and selectivity for each temperature difference in the condenser. Like the pressure difference between both sides of the membrane, the dehumidification COP approaches an ideal value as the temperature difference decreases, because water vapor must be compressed more at a temperature higher than the outdoor temperature dew to the finite temperature difference. In all results, the finite pressure difference and temperature difference were assumed to be uniform.

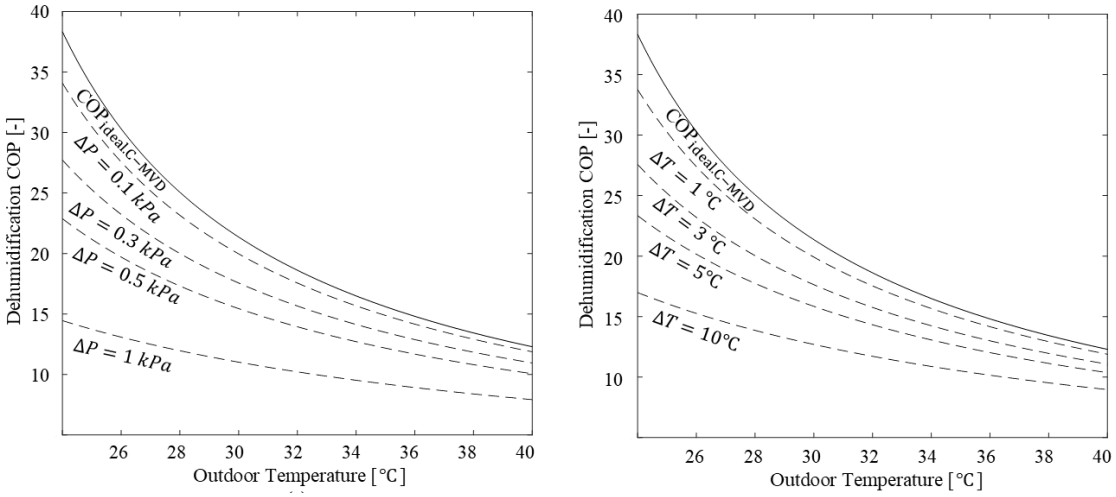


Fig. 12 Dehumidification COP reduction in C-MVD due to (a, left) finite pressure difference and (b, right) finite temperature difference (T_I=24℃, RH_I=62.66% and RH_O=84.22%)

In the compression processes of the ideal MVD, the water vapor separated from the indoor humid air was isothermally compressed at the outdoor temperature. However, in practice, it is difficult to implement isothermal compression as discussed in section 2.2, and a single adiabatic compression causes MVD to consume more energy as it is compressed to a temperature higher than the outdoor air temperature. Fig. 13 compares the ideal dehumidification COP and the dehumidification COP in this case. Systems that have a single adiabatic compression show lower performance under all temperature and humidity conditions than systems that have an ideal compression process.

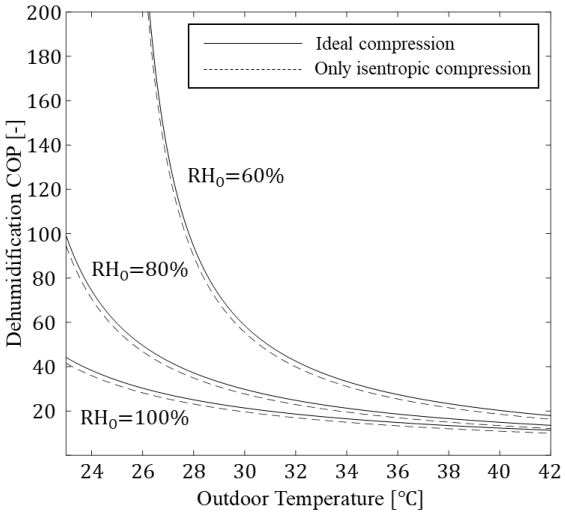


Fig. 13 COP reduction of MVD by single adiabatic compression

4. Conclusion

The ideal dehumidification COP of MVDs was analyzed in this study. Assuming that there is no irreversibility of the membrane mass exchanger, vacuum compressor, and heat exchanger, the ideal dehumidification COP of W-MVD and C-MVD was defined by Carnot cycle analysis. This was compared with the thermodynamical maximum dehumidification COP values calculated by exergy analysis and components modeling. Based on the newly defined ideal dehumidification COP, the influence of operation conditions and irreversibility of actual systems were analyzed. The results of this study were as followed.

- ✓ The dehumidification COP values calculated by the three methods matched. These results show dehumidification COP of MVDs can be predicted by only the temperature and humidity conditions of the indoor and outdoor air where MVDs are operated.

- ✓ The ideal W-MVD has a thermodynamical maximum dehumidification COP, which is 58.2% higher than the ideal dehumidification COP of C-MVD under reference condition.

- ✓ The dehumidification COP of the systems is better in cold, dry climates. The values near the asymptote are very high because the water vapor partial pressure of indoor air is higher than that of outdoor air or the difference is too low. The MVD is not useful in these conditions. however, it is possible to identify temperature and humidity conditions in which the dehumidification can be performed with low energy consumption or only simple passive ventilation without operation of the systems.

- ✓ Under the desirable temperature and humidity requirements, the ideal dehumidification COP of W-MVD is approximately 50-100 and considering the irreversibility inevitable in real systems such as finite pressure difference in mass transfer process or finite temperature difference in heat transfer process, the actual COP is lowered according to the degree of the irreversibility. The presented equations for the ideal dehumidification COP of MVDs can be used as a basis for research on performance of MVDs and for system design and optimization.

Nomenclature

A	Area [m^2]	α	Selectivity [-]
AH	Absolute humidity [kgv/kga]	β	Permeance [kg/m2·s·kPa]
h_{fg}	Specific enthalpy of vaporization [kJ/kg]	ξ	Specific exergy [kJ/kg]
k	Specific heat ratio [-]		
n	Number of moles [mol]	***Subscript***	
m	Mass [kg]	a	Air
$\dot{m}$	Mass flow rate [kg/s]	amb	Ambient air
P	Pressure [kPa]	con	Condensing dehumidification
P_w	Water vapor partial pressure [kPa]	des	Liquid desiccant dehumidification
R	Gas constant [8.314472 J/mol·K]	DH	Dehumidification
RH	Relative humidity [%]	dry	humidified dry air
r_p	Compression ratio [-]	iso	Isothermal compression
T	Temperature [K]	$isen$	Isentropic compression
T_{DP}	Dewpoint temperature [K]	I	Indoor air
T_{iso}	Iso-relative humidity line Temperature [K]	O	Outdoor air
T_R	Temperature of reference point of exergy [K]	sep	Complete gas separation
W	Work [kJ]	w	Water vapor
$\dot{W}$	Power [kW]	wet	Not dehumidified wet air
X	Mole fraction [-]	1,2,3	State point number

Acknowledgements

This research was jointly supported by National Research Foundation of Korea (NRF No. 2019R1A2C108869414) and by Korea Institute of Energy Technology Evaluation and Planning (KETEP) (20202020900290, 20214000000280, 20212050100010) funded by Ministry of Trade, Industry and Energy. This research was also supported by the Korea Environmental Industry & Technology Institute (KEITI No. 2020003060005) Authors sincerely appreciate their supports.

References

[1] USDOE Office of Energy Efficiency and Renewable Energy. (2017). Energy savings potential and RD&D opportunities for non-vapor-compression HVAC technologies, December 2017.
[2] Chun, L., Gong, G., Peng, P., Wan, Y., Chua, K. J., Fang, X., & Li, W. (2021). Research on thermodynamic performance of a novel building cooling system integrating dew point evaporative cooling, air-carrying energy radiant air conditioning and vacuum membrane-based dehumidification (DAV-cooling system). Energy Conversion and Management, 245, 114551.
[3] Scovazzo, P., & Scovazzo, A. J. (2013). Isothermal dehumidification or gas drying using vacuum sweep dehumidification. Applied thermal engineering, 50(1), 225-233

[4] Dais Analytic Corporation. (2017). Membrane based air conditioning, 2017 Building Technologies Office Peer Review.
[5] Bui, D. T., Ja, M. K., Gordon, J. M., Ng, K. C., & Chua, K. J. (2017). A thermodynamic perspective to study energy performance of vacuum-based membrane dehumidification. Energy, 132, 106-115.
[6] Lim, H., Choi, S., Cho, Y., Kim, S., & Kim, M. (2020b). Comparative thermodynamic analysis of membrane-based vacuum air dehumidification systems. Applied Thermal Engineering, 179, 115676.
[7] Lee, J., Kim, H. S., Ku, D., Lim, J., Jung, M., Kim, S., ... & Seo, Y. S. (2021). Experimental Study on the Water Selective Dense Membrane under an Absolute Pressure Difference with Simplified Test Method. Applied Sciences, 11(4), 1710.
[8] Zhang, L., Liu, X. H., & Jiang, Y. (2012). Ideal efficiency analysis and comparison of condensing and liquid desiccant dehumidification. Energy and buildings, 49, 575-583.
[9] Labban, O., Chen, T., Ghoniem, A. F., & Norford, L. K. (2017). Next-generation HVAC: Prospects for and limitations of desiccant and membrane-based dehumidification and cooling. Applied Energy, 200, 330-346.
[10] Robeson, L. M. (1991). Correlation of separation factor versus permeability for polymeric membranes. Journal of membrane science, 62(2), 165-185.
[11] Geise, G. M., Park, H. B., Sagle, A. C., Freeman, B. D., & McGrath, J. E. (2011). Water permeability and water/salt selectivity tradeoff in polymers for desalination. Journal of Membrane Science, 369(1-2), 130-138.

14th IEA Heat Pump Conference
15-18 May 2023, Chicago, Illinois

Strategies to overcome the dilemma in renovating and integrating HPs and RE into the building stock

Fabian Ochs[a*], Alice Tosatto[a], Mara Magni[a], Elisa Venturi[a], William Monteleone[a], Georgios Dermentzis[a]

[a]University of Innsbruck, Technikerstr. 13, 6020 Innsbruck, Austria

Abstract

Considering the overall limited availability of renewable electricity and (district) heat together with the competing demand by industry and transport, deep thermal renovation (TR) of buildings and a rapid phase out of fossil-based heating systems is crucial to achieve the overall climate targets. Independent of the actual choice of the path to the required phase-out of fossils, it will lead to significantly increasing shares of renewables (RE) in the electricity system. This increasing share of RE will lead to a significant reduction of the CO_2 conversion factor for electricity. This will also relevantly influence the CO_2 conversion factor of DH, when, as anticipated to a large extent central large-scale HPs are involved. The dilemma is that in such a scenario, with proceeding time, the deep TR of buildings and the further integration of onsite PV (coupled to HPs) will not any more influence the CO_2 emissions of the building in a relevant way. This would lead to a decreasing motivation to implement high ambition targets on building level. However, high ambition levels will be required to reach the overall goal of the phase-out of fossil energy. This requires an energy policy approach instead of market incentives, i.e. CO_2 tax will not sufficiently trigger the required transition process but instead CO_2 budgets have to be defined.

© HPC2023.
Selection and/or peer-review under the responsibility of the organizers of the 14th IEA Heat Pump Conference 2023.

Keywords: Heat Pumps; Renewables;Thermal Renovation; Phase-out; Energy Scenario; Building Stock; Transition; CO_2; Dilemma

1. Introduction

1.1. Buildings and Energy Transition

On European level (EPBD), ambitious goals have been set implementing nearly zero energy buildings (nZEB) and the target to integrate onsite (or nearby) renewables [1]. Massive integration of renewables (RE) shall lead to Net Zero Energy Buildings (NZEB) or even Positive Energy Buildings (PEB). Extending the system boundary to blocks and districts allows to unlock efficiency potentials of the electric and thermal energy of neighborhoods leading to the goal of Positive Energy Districts (PED) (IEA EBC Annex 83, IEA HPT Annex 61), see e.g. [2].

Contrariwise, with the recently growing need to rapidly phase-out fossil energy-based heating systems, a trend can be seen that HPs and direct electric (DE) heating are implemented in existing buildings (i.e. without thermal renovation) as an apparently cheaper and faster solution (IEA HPT Annex 50).

However, due to the overall limited availability of renewable electricity and (district) heat together with the competing demand by industry and transport, deep thermal renovation (TR) of buildings and a rapid phase out of fossil-based heating systems is crucial to achieve the overall climate targets. The change from gas- or oil-based heating systems to heat pumps (HP) is (often) only technically feasible in combination with deep TR and generally only recommended in combination with it. However, there are both technical and non-technical barriers and challenges [3].

* Corresponding author. Tel.: +43 512 507 63603.
E-mail address: fabian.ochs@uibk.ac.at.

A rapid phase out of fossil-based heating systems requires a significant boost in the exchange rates. The heat demand of buildings will increasingly be covered by HPs and district heating (DH) and in a minor part by DE systems. Biomass, partly in combination with solar thermal can only be applied up to its limited availability and taking into account the need of biomass in the industry and traffic sector [4]. A decarbonized DH system will consist of biomass CHP, heating plants, large-scale HPs and to some extent geothermal and solar thermal. Therefore, a significant increase of DH's extents and a massive increase of HPs should be taken into consideration [5].

Constraints are next to the limit of available biomass for the building sector (with the competition of other energy consuming sectors and growing food), the limit of economically expanding DH networks and the large-scale production and installation of HP and RE. In addition, a number of barriers/gaps have to be addressed in such a transition process, which are acc. to [3]

- Technical gap: Replacing (decentralized) oil, gas and E-boilers in multi-apartment buildings requires solutions for which currently dedicated HP (system) solutions are not available on the market.
- Owner-user gap: The building owner is often not the beneficiary of the investment, but the tenant is.
- Social gap: Mixed housing (tenant, owner structure) might be an unbreachable obstacle, if e.g. some parties did replace gas boilers recently, while others alternatively replaced windows.
- Financial gap: Renovation might be economically feasible considering life-cycle costs, but high investments are required immediately, which may surpass liquidity constraints.

Without energy efficiency measures in buildings, the electric energy demand increases when switching from fossil energies to HP-based heating systems. This would lead to an increase of the so-called winter gap [6] in a future energy system based on volatile renewable resources (wind, PV).

In the perspective of the energy transition the infrastructural and technological lock-in in the building sector is a limiting aspect considering the long lifetime of buildings and building components [7]. Since building components have a typical lifetime of several decades, insufficient measures taken now will have a long-term effect [8]. This so-called 'carbon lock-in' highlights the need of rather deep TR measures than fast incomplete measures. As an example, a newly installed gas boiler with a lifetime of 20 years becomes a 'stranded asset' and will prevent phase-out of gas but replacing it before end of life is critical in terms of economic considerations. In this perspective, the role of buildings with the possibility of deep TR and switching from fossil-based to HP-based heating systems is of primary importance in achieving the goals of the energy transition and has to be seen as one of the important columns of the energy policy strategy.

1.2. Aim of and structure of this work

In such a scenario of the energy transition, with proceeding time, the deep TR of buildings and the further integration of onsite PV (coupled to a HP) will not significantly influence the CO_2 emissions of the building, which would lead to a decreasing motivation to reach high ambition goals on building level. However, high ambition levels will be required to reach the overall goal of the phase-out of fossil energy in the electricity system and in district heating networks.

Using a simple building stock model, different scenarios of deep TR and integrating HPs and RE will be discussed in terms of environmental impact (i.e. CO_2 emissions) highlighting possible strategies to overcome this energy transition dilemma.

In section 2, Methods, the model and the assumptions are described and different scenarios are developed. In section 3, Results, the scenario results are shown in terms of secondary energy and CO_2 emissions and are discussed from the perspective of the building stock and from the perspective of an individual building. From the results strategies are developed and summarized and concluded in section 4.

2. Method

2.1. Building Stock and Energy System Model

The model represents a generic district and analyses the primary energy demand (P-E) and CO_2 emissions considering transport and conversion for a given useful energy demand (U-E) and consists of (from right to left in the Sankey in Fig. 1):

- the demand, i.e. the useful energy (UE): space heating (SH), domestic hot water (DHW) as well as appliances and auxiliaries,

- the heating systems: fuels (oil, gas, biomass), direct electric (DE) heating, heat pump (HP) and district heating (DH) and
- the energy system consisting of combined heat and power (CHP) and district heating plants (DHP).

The supply side (left), the required secondary energy (S-E), is provided by fossil energy sources (oil, gas), biomass (bio) and to some extent renewable electricity (RE E: hydro, wind, PV) and renewable and waste heat (RE H: industrial waste heat, waste incineration, geothermal, solar thermal).

Using conversion factors (see section below), from the S-E the primary energy (P-E) and CO_2 emissions are calculated.

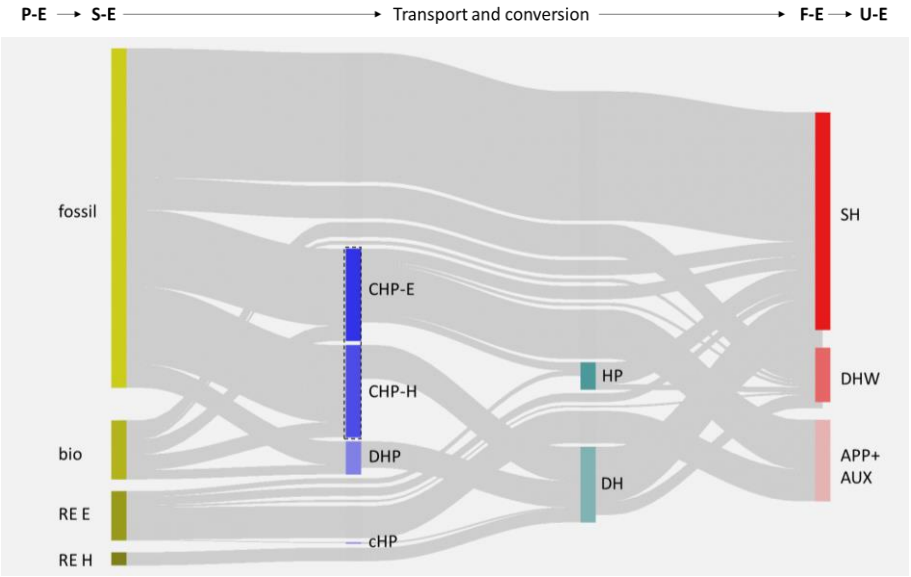


Fig. 1. Sankey Diagram[1] of the Baseline system with high share of fossil (oil, gas) for direct use in buildings (boiler) and for combined heat and power plants (CHP) as well as district heating plants (DHP) and existing (inefficient) building stock with high space heating demand (SH), central heat pumps (cHP) in district heating (DH) play a minor role as do decentral heat pumps (HP) in buildings for space heating (SH) and domestic hot water (DHW).

2.2. Decarbonization Scenarios

The year 2025 is considered as baseline (see section below for details) and the scenario is developed until 2050. For the Building Stock (BS) and for the Energy System (Electricity E and District Heating DH) each three ambition levels (AL) are considered.

- Const (= BAU)
- IMPROVE
- AMBITION

For the Building Stock, BAU means no (relevant) reduction of the HD, IMPROVE means a reduction from 80 kWh/(m² a) to 55 kWh/(m² a) and AMBITION means a reduction to 30 kWh/(m² a) until 2050.

For the Energy System, BAU means slow phase-out of fossil fuels (oil, gas) and no relevant increase of RE in the electricity system and district heating systems, IMPROVE means a relevant reduction of fossil energies and AMBITION a high ambition level, thus that fossils are reduced (directly switching from fuels to electricity (E) and district heating (DH) and indirectly in E and DH) to a remaining very low share. This leads to a massive extension of RE (Biomass CHP as well as wind and PV) in the electricity mix and involves Biomass CHP and HPs in DH.

Furthermore, two different paths are defined, one with focus on individual (i.e. building-wise) HPs and one which is DH dominated and thus includes a higher share of central HPs. This leads to 18 variants in total as shown in Fig. 2.

[1] Ranran Wang (2022). Sankey Diagram (https://www.mathworks.com/matlabcentral/fileexchange/75813-sankey-diagram), MATLAB Central File Exchange. Retrieved November 2022; modified

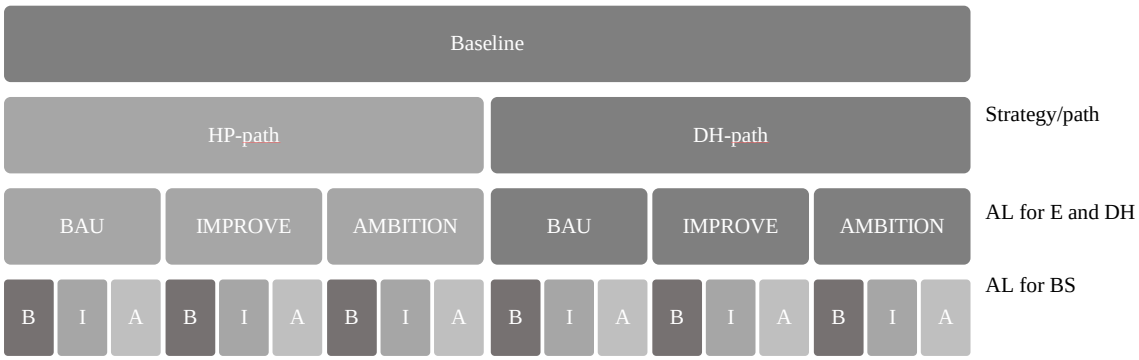


Fig. 2. Overview of Scenarios (transition paths) starting from the baseline with two different paths (individual HP or DH) and with different Ambition Levels (AL) for Electricity (E) and District Heating (DH) as well as for the Building Stock; B: BAU, I: IMPROVE, A: AMBITION

2.3. Building Stock Model - Baseline

The simple building stock (BS) model consists of 100 buildings (i.e. 100 %) with an average treated area of A_T = 150 m². The BS with constant number of buildings with the following properties (Table 1) is heated with a mix of fuel, direct electric heating (DE), decentral heat pumps (HP) and district heating (DH) as in Table 2. In all scenarios fuels for heating are reduced to minor shares of 2.5 % in terms of energy demand. Direct electric heating (DE) is assumed to increase from 10 % in 2025 linearly to 15 % in 2050. In all scenarios a switch from fossil fuels to biomass is assumed but considering that the absolute amount of biomass is limited for the building sector. Gas boiler (condensing) are assumed to have an overall thermal efficiency of 85 %, while oil and biomass boilers are calculated with 80 % efficiency. The share of DH increases in the DH-path from 25 % to 60 % and in the HP-path to 35 %.

Table 1. Building stock characteristics.

	BAU	IMPROVE	AMBITION
Space Heating Demand SH / kWh/(m² a)	80	55	30
Domestic Hot Water Demand DHW / kWh/(m² a)		15 + 5	
Appliances and auxiliaries / kWh_{el}/(m² a)		20 + 5	

Table 2. Baseline building stock (BS) heating system, share in %.

	Baseline	Remark
Fuel (building/flat-wise boiler)	55	Phase-out
- oil	30	Fast phase-out
- gas	60	
- bio	10	Limited absolute amount
DE	10	Limited to slight increase
HP (decentral, i.e. building/flat wise)	10	Strong increase
DH	25	Strong increase in DH-path

2.4. Energy System - Baseline

For sake of simplicity the energy system is modelled by means of annual balancing starting from the baseline until 2050 in steps of 5 years and consists of fuels (oil, gas and biomass), an electric grid and DH. Both systems, electricity and DH are coupled on several levels: directly via CHP, and indirectly via central HPs in the DH system and decentral HPs in buildings and are influenced by the choice of the ambition level in the building stock (BS) through the reduction of SH demand in the DH and via DE and HP in the electricity demand, see also Fig. 1 (above).

Depending on the choice of the ambition level in the BS and the path (DH or HP) the energy demand in the DH can either decrease or increase. The electricity demand can either remain constant (in the DH path and in case of high ambition level), or in all other cases will increase.

The overall goal is to compare different paths for the phase-out of fossils. As shown in Fig. 1 (above) this can be achieved on building level by different combinations of (deep) TR, switching from fossil-based heating to biomass-based heating, DH or HP and by decarbonizing the electricity and DH. Both in the electricity mix and the DH system biomass is present. Due to the limited potential of biomass for energetic use, biomass is limited as direct fuel or as fuel in CHP or District Heating Plants (DHP) in all scenarios to a maximum increase of 100 % with respect to the baseline.

2.4.1. Electricity

The electricity system consists of fossil (gas) and biomass CHP, Hydro (with a constant absolute contribution), Wind and PV. Coal and nuclear energy are excluded in this scenario (baseline 2025).

In a scenario with increasing electricity, to some extend biomass CHP can be increased, the rest hast to be covered by extending wind and PV. On-shore and off-shore wind are not distinguished. Furthermore, onsite (building integrated) and ground-mounted PV are not distinguished. Imports and exports of electricity are disregarded (i.e. either not existing or balanced). The absolute contribution of hydro is assumed to be constant (limited extension potential).

Table 3. Electricity mix of baseline, share in %.

	share	Remark/Constraint
Fossil CHP	50	phase-out
Biomass CHP	10	absolute limit
Hydro	25	absolute limit
Wind	5	
PV	10	

2.4.2. District Heating

District heating (DH) refers to (sufficiently) large DH systems with CHP (block heating is accounted to single building heating systems, here). The contribution to DH of the baseline is summarized in Table 4. DHP are assumed to have an efficiency of 80 %. The thermal efficiency of CHP plants is 40 % and the thermal energy is limited by the electric output (electricity-driven CHP). DH losses are assumed to be 10 % with respect to the useful energy. Waste heat, geothermal and solar thermal absolute contribution is assumed to be constant.

Table 4. District heating (DH) system of baseline, share in %.

	share	Remark/Constraint
Waste Heat and waste incineration	15	absolute limit
Geothermal and solar thermal	2.5	constant absolute contribution
central Heat Pump (Heat)	2.5	
Bio CHP	10	limited by electricity generation, absolute limit
Bio DHP	10	absolute limit
Fossil CHP	35	limited by electricity generation,
Fossil DHP	25	Phase-out (in IMPROVE and AMBITION)

2.4.3. Heat Pumps

Heat pumps play the predominant role in both paths (HP and DH). The central and decentral HPs are modelled with a simple Carnot based approach with a Carnot performance factor η_c:

$$COP_{HP} = \eta_c \cdot COP_c \quad (1)$$

$$COP_c = \frac{T_{max}}{T_{max} - T_{min}} \quad (2)$$

$$COP_{Sys} = (1 - \mathrm{a}) \cdot COP_{HP} + a \cdot COP_{DE} \quad (3)$$

For the decentral (building- or flat-wise) HPs, the following assumptions were made: a Carnot performance factor of 0.36, a flow temperature of 65 °C at an average ambient temperature of 10 °C and share a of direct electric (DE) heating of 15 % with COP_{DE}= 1 (bivalent system) the system COP = 2.

For the central HPs (DH level), the flow temperature is assumed to be 95 °C, the average source temperature is 15 °C and the Carnot performance factor is $\eta_c = 0.44$. This results in an average HP and system COP of 2.

It is noteworthy that a COP of 2 is relatively low with respect to other studies. However, if a fast and broad implementation of HPs in the building stock is assumed, a high-quality low-temperature heating system cannot be hypothesized. Hence, the assumption of higher COP would be very optimistic. In case of the scenario with high ambition level in the BS, a lower heating load and a lower required flow temperature could be expected, which would lead to a slightly better COP. The influence on the resulting electricity demand would be still relatively low as also the demand is anyway significantly lower. As an example, with a COP of 2.5 instead of 2, the required additional renewable electricity would be 25 % less for HPs in DH and 50 % less for building-wise HPs with high ambition level and a COP of 3 as shown in Tab. 3.

Table 3. Influence of COP of the HP on the electric energy demand w_{el} of the building stock (BS).

Scenario (SH + DHW demand in kWh/(m² a))	BAU (80 +20)	IMPROVE (55+20)	AMBITION (30 + 20)	BAU (80 +20)	IMPROVE (55+20)	AMBITION (30 + 20)
		Central			Decentral	
Rel. Loss of DH		10 %			-	
COP (conservative)		2			2	
W_{el} / kWh/(m² a)	55	41.25	27.5	50	37.5	25
COP (improved)		2.5			2.5	
W_{el} / kWh/(m² a)	44	33	22	40	30	20
ΔW_{el} / kWh/(m² a)	11	8.25	5.5	10	7.5	5
COP (depending on AL of BS)				2	2.5	3
W_{el} / kWh/(m² a)				50	30	16.7
ΔW_{el} / kWh/(m² a)				0	7.5	8.33

2.5. Combined Heat and Power

For gas and biomass fired combined heat and power plants (CHP) a CHP coefficient (power to heat ratio) of $\sigma = 1.0$ ($\eta_{el} = 0.4$, $\eta_{th} = 0.4$) is assumed. It is defined as the ratio between electricity generation (W_{el}) and thermal generation (Q_{th}):

$$\sigma = \frac{W_{el}}{Q_{th}} \quad (4)$$

The CO_2 emissions allocated to the electric energy and the thermal energy are evaluated using the Carnot Method. The Carnot-Efficiency η_C is calculated based on the maximum i.e. the flow temperature of the DH system (assumed to be 160°C) and the minimum temperature, i.e. the ambient temperature (10 °C):

$$\eta_C = 1 - \frac{T_{min}}{T_{max}} \quad (5)$$

The so-called fuel fraction of electrical and thermal energy can be calculated based on the thermal and electric efficiency and the Carnot efficiency.

Fuel fraction of electrical energy $A_{F,el}$:

$$A_{F,el} = \frac{(1 \cdot \eta_{el})}{\eta_{el} + \eta_C \cdot \eta_{th}} \quad (6)$$

Fuel fraction thermal energy $A_{F,th}$

$$A_{F,th} = \frac{(\eta_C \cdot \eta_{th})}{\eta_{el} + \eta_C \cdot \eta_{th}} \quad (7)$$

The CO_2 conversion factor is determined based on the fuel fraction and the thermal and electric efficiency.

$$f_{CO2,el} = A_{F,el} \cdot f_{CO2,gas} / \eta_{el} \quad (8)$$

$$f_{CO2,th} = A_{F,th} \cdot f_{CO2,gas} / \eta_{th} \quad (9)$$

CHP is assumed to be purely electricity driven.

2.6. CO_2 emissions

The total CO_2 emissions are determined based on the secondary energy (S-E) and the CO_2 conversion factors (eqs. (10) to (11)) and parameters in Table 4 with hy: hydro, wi: wind, PV: photovoltaic, bCHP-

E/bCHP-H: biomass CHP electricity and heat, fCHP-E/ fCHP-H: fossil CHP electricity and heat, waste/RE: waste heat, waste incineration, geo and solar thermal, W_{el}: electric energy, Q_{DH}: thermal energy and E: fuels

$$f_{CO_2,el} = f_{hy} \cdot CO_{2,hy} + f_{wi} \cdot CO_{2,wi} + f_{PV} \cdot CO_{2,PV} + f_{bCHP} \cdot CO_{2,bCHP-E} + f_{fCHP} \cdot CO_{2,fCHP-E} \quad (10)$$

$$f_{CO_2,DH} = f_{waste/RE} \cdot CO_{2,waste/RE} + f_{bCHP} \cdot CO_{bCHP-H} + f_{fCHP} \cdot CO_{fCHP-H} + f_{HP} \cdot CO_{2,el} \quad (11)$$

$$CO_2 = W_{el} \cdot f_{CO_2,el} + Q_{DH} \cdot f_{CO_2,DH} + E_{Bio} \cdot f_{CO_2,Bio} + E_{Gas} \cdot f_{CO_2,Gas} + E_{Oil} \cdot f_{CO_2,Oil} \quad (12)$$

Table 4. CO_2 emissions of fuels, electricity generation and DH sources based on [9].

	f_{CO2} / [g/kWh]	Remark		f_{CO2} / [g/kWh]	Remark
Fuel			Heat		
- Oil	310		- Waste-Heat	9	Incl. waste incineration
- Gas	247		- Geoth., ST	9	
- Biomass	17		- central HP	var.	El. mix
Electricity			- Fossil CHP	129	
- Fossil CHP	371	σ = 1	- Bio CHP	11	
- Bio CHP	32		- Fossil DHP	247	
- Hydro	1		- Bio DHP	17	
- Wind	5				
- PV	10				

3. Results and Discussion

3.1. Phase-out of Fossil

The phase-out of fossil fuels and the transition to renewable electricity and renewable DH is shown in Fig. 3. In spite of the high ambition level in the building sector (i.e. deep thermal renovation) and a high share of DH the electricity demand is increasing. A major part of the DH is covered by large-scale central HPs which contribute with a relevant share to the increase of the electricity demand. The additional electricity demand is covered by a large extent by PV and wind.

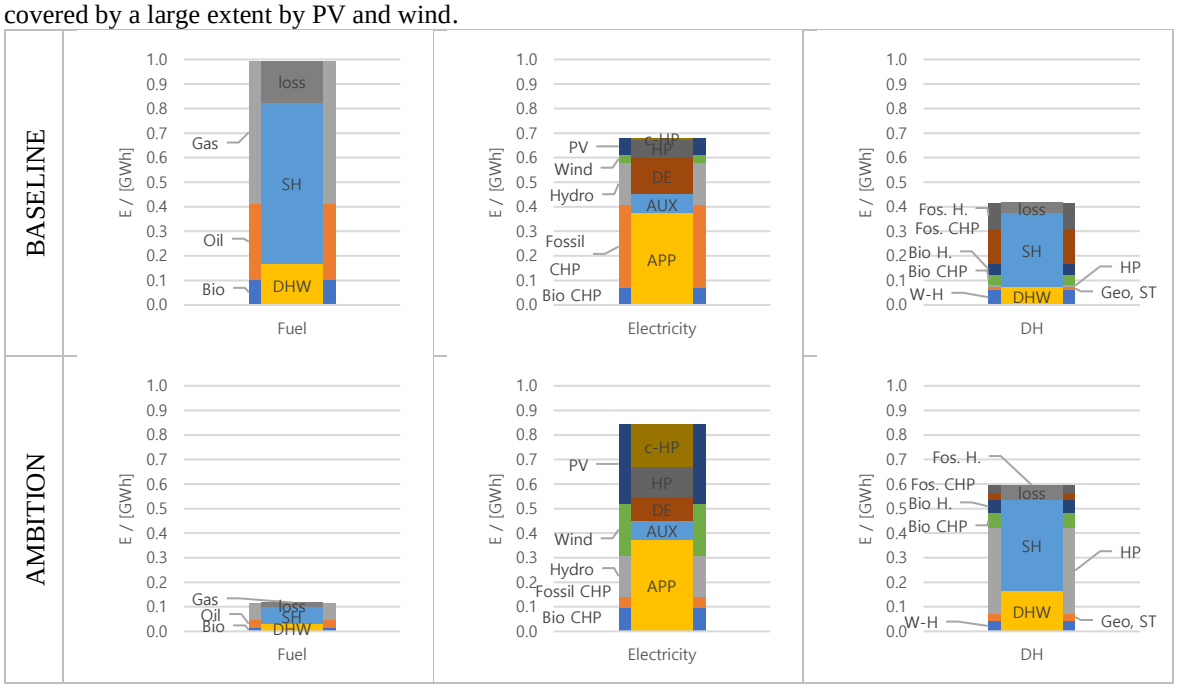
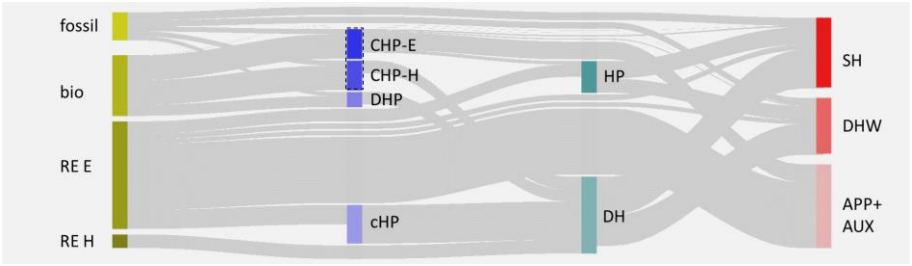


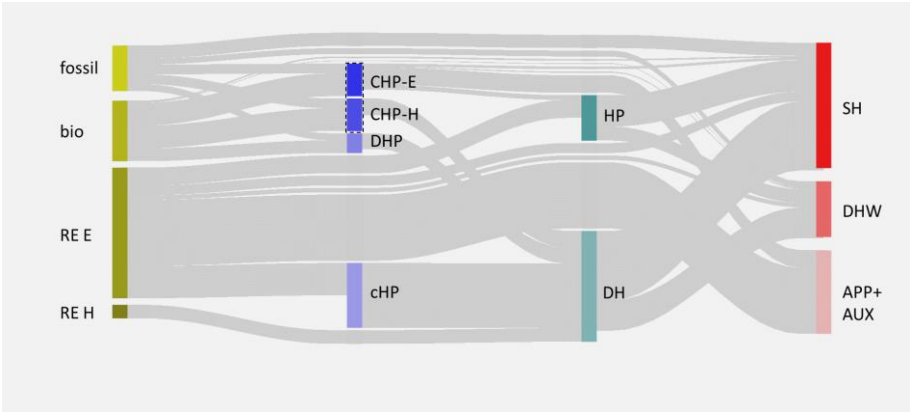
Fig. 3. Transition from fuel-based heating to HP and DH as well es decarbonization of electricity and DH from baseline to AMBITION level scenario.

3.2. Ambition Levels and influence of deep thermal renovation

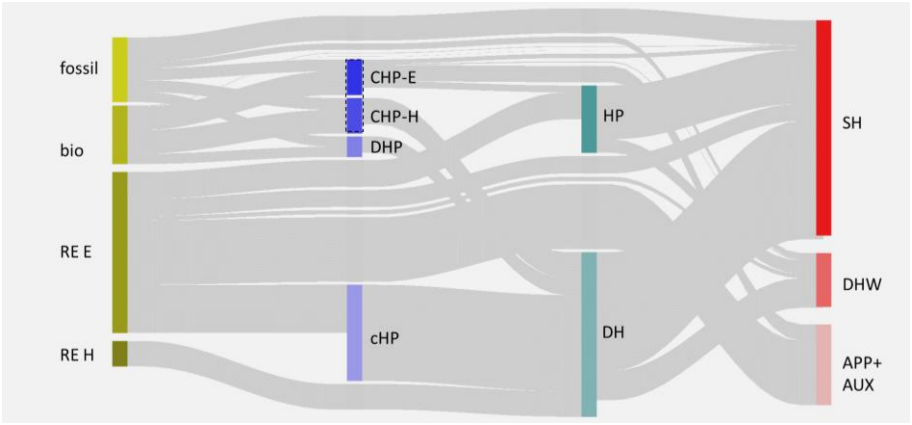
Fig. 3a, b and c show exemplarily the Sankey diagram for the highest ambition level in terms of electricity and DH and three different ambition levels for the building stock (a: AMBITION, b: IMPROVE, c: BAU). The higher ambition level in the building stock leads to the lowest CO_2 emissions, and significantly reduced required amount of electricity for HPs (central and decentral) and this in consequence to a significantly reduced need to extent renewable electricity.



a



b



c

Fig. 4 Sankey diagram[1] of energy system case ”AMBITION” with (a) deep thermal renovation (AMBITION), 41.9 ton CO_2 (b) thermal renovation (IMPROVE), 61.6 ton CO_2 and (c) no thermal renovation (BAU), 107.8 ton CO_2.

3.3. Decarbonization Strategies and Ambition Levels

The resulting development of the CO_2 emissions (Fig. 4a), the electricity (Fig. 4b) and the DH (Fig. 4c) demand as well as of the required extension of PV and wind (d) in the different decarbonization paths (see section 2.2) are summarized in the following diagrams. From Fig. 5 it can be derived that the HP-path leads to the overall lowest CO_2 emissions. However, the implementation of HPs in existing buildings is technically very challenging. It can be seen for all variants that without deep TR, switching from fossil to HP-based heating

will significantly increase the energy consumption of the building stock. The mere phase-out of oil and gas is not sufficient to reduce the CO_2 emissions.

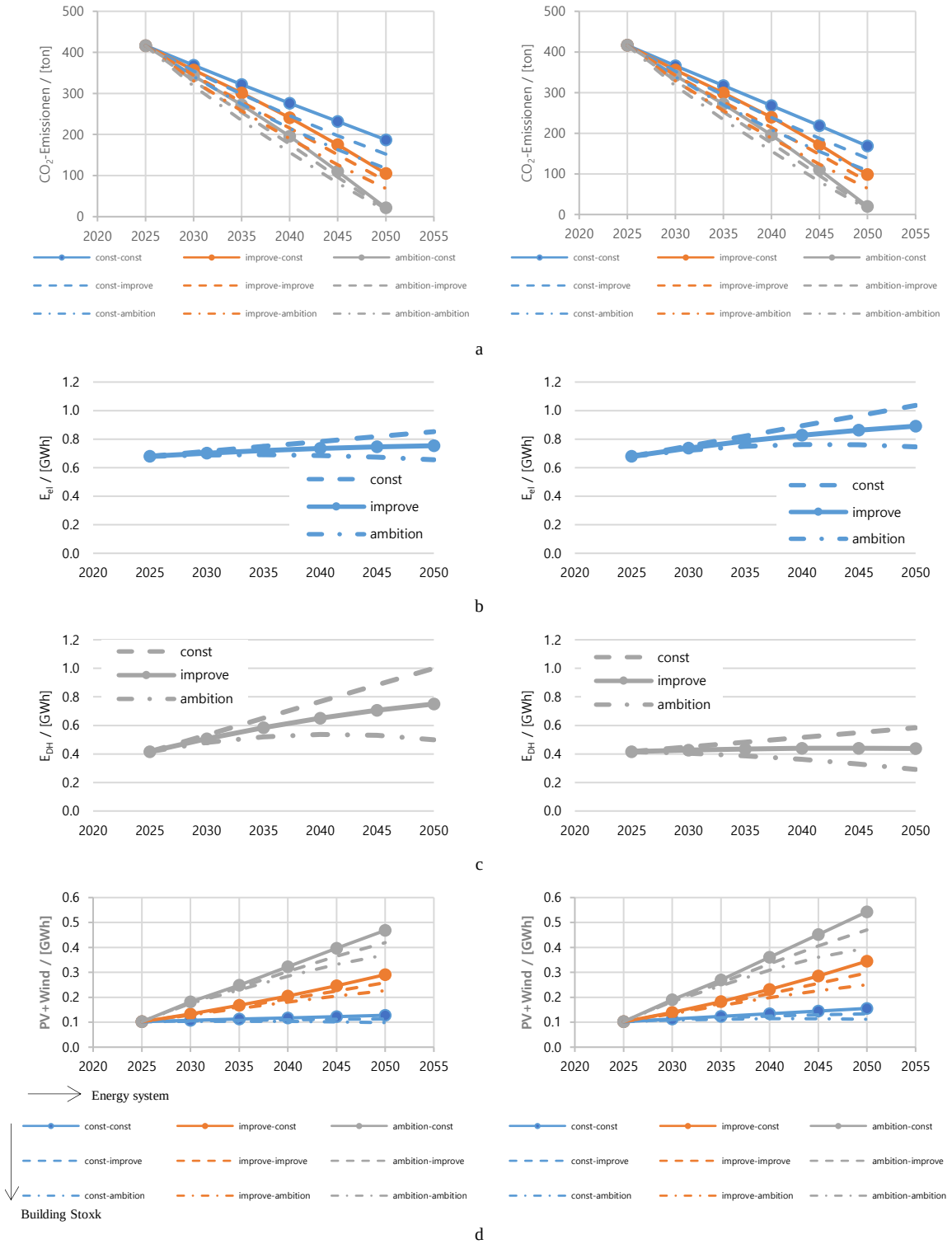


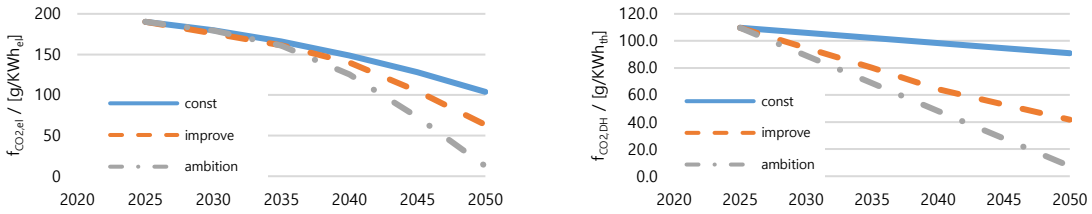
Fig. 5. Development of the annual CO_2 emissions (a), total electricity demand (b), DH demand (c) and extension of PV and wind electricity (d) according to the different paths (left: DH and right HP) and according to the different ambition levels of the building stock (legend: energy system AL – building stock AL).

The IMPROVE energy scenarios do not reach sufficient reduction of CO_2 emissions without ambitious renovation. Instead, in the AMBITIOUS energy scenario a diminishing influence of the ambition level in the BS can be seen, i.e. deep thermal renovation does not seem to change the picture. However, this goes on cost

of a significantly extension of the electricity generation. Without high ambition level in the building sector, the AMBITION scenario in the energy sector can only be achieved by massive extension of PV and/or wind. This would lead to an increasing mismatch between winter and summer (winter gap, see section below). The DH-path requires a massive extension of DH grids with a large number of central HPs. As in all AMBITION scenarios (and to a lower extent also in the IMPROVE) the CO_2 conversion factor will relevantly decrease, CO_2 tax on electricity and DH will lose its relevance with proceeding time, as also shown in the next section.

3.4. Single Building Perspective

Based on the results of the scenario, the CO_2 emission on building level can be evaluated using conversion factors for electricity and in case DH. The resulting conversion factors are summarized in Fig 6.



Electricity: DH-path and HP-path DH: DH-path and HP-path

Fig. 6. Development of CO_2 conversion factor for electricity (left) and DH (right)

In all scenarios the conversion factor for electricity reduces. It reaches nearly zero in 2050 in case of high ambition level (12.4 g/kWh$_{el}$). The conversion factor of DH is connected to that of electricity (due to the central HPs) and also reduced to almost zero in 2050 in case of high ambition level (7.4 g/kWh$_{th}$).

For the building, if no regulations are supposed except phase-out of fossil for a given point of time, any measure or combination of measures could be chosen: DE, HP or if applicable DH

Additional measures are optional

- Thermal renovation (standard, deep)
- Onsite renewables (PV)

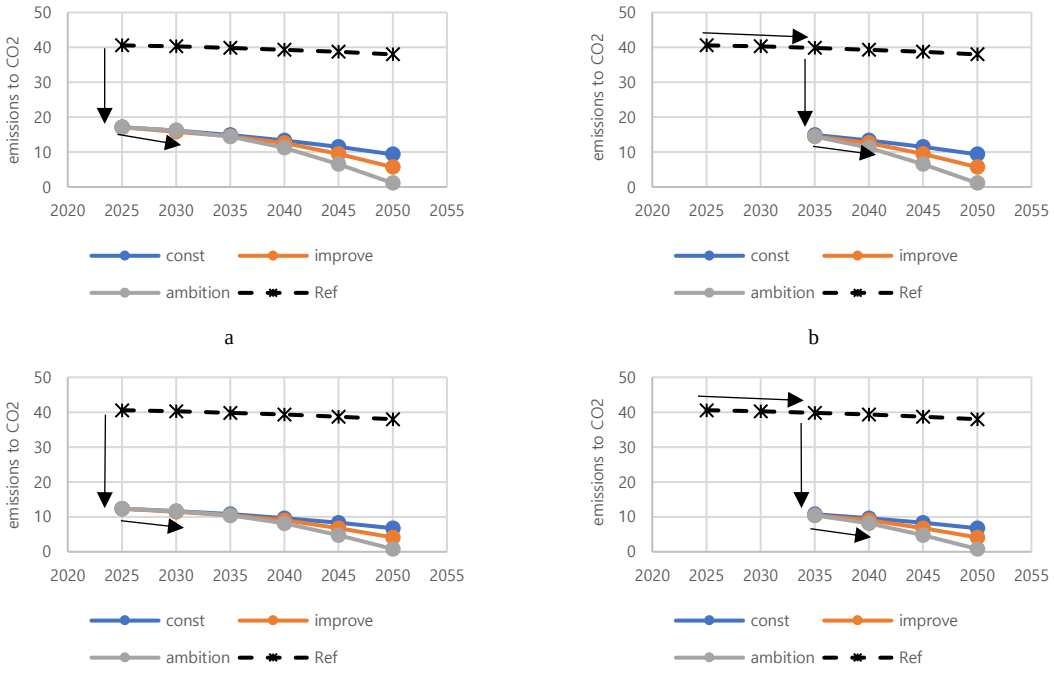


Fig. 7. Development of CO_2 emissions for a single building switching to HP (a in 2025 and b 2035) and optionally in combination with a deep thermal renovation (c in 2025 and d in 2035).

Assuming the building is equipped with a gas-boiler, and has the average characteristics as described in Table 1, the CO_2 emissions can be calculated for different combinations of measures and different points of time (i.e. switching from fossil-based heating to either DE or HP or DH in 2025, 2030, 2035, 2040). Here exemplarily, the results for a switch in 2025 and 2035 are shown. Independent of the point of time of the implementation of the measure, in 2050, the emissions are very low with respect to the baseline. The additional thermal renovation does not significantly influence the CO_2 emissions and even to a lower extent if the measure is implemented later. Hence, a CO_2 tax would, if switching from fossil-based heating to electricity-based, be of minor influence and would not trigger the additional thermal renovation.

3.5. Winter gap and seasonal storage

Additional electricity demand "generated" by means of insufficient efficiency measures (i.e. DE instead of HP, insufficiently or not renovated buildings) has to be provided by RE, i.e. by wind turbines or PV. While the main electricity demand occurs in winter (in particular in case of inefficient buildings), the contribution of PV (and also of hydro) will be available mainly in summer. Wind energy has a less seasonally pronounced characteristic but is volatile, too. If - as can be expected - the share of PV will be dominating because of higher public acceptance, there will be a strong seasonal mismatch between demand and supply. This seasonal gap (also called winter gap) requires (seasonal) storage capacities. To some extent pumped hydro storage may be available, but the main contribution will have to be covered by renewable hydrogen (and/or methane). The cycle efficiency of electrolysis-hydrogen-(mechanization)-storage and re-electrification (with fuel cell or gas turbine) is with optimistic assumptions in the range of 30 %. Consequently, for each kWh of electricity that has to be stored, 3.33 kWh have to be generated in summer at correspondingly very high costs.

3.6. Strategies

From the results of the scenarios, the following strategies for the building stock and energy policy can be derived:

- Develop a clear and transparent energy policy that includes the building stock as a major column;
- Evaluate measures in the building stock from the macro-economic instead of from the micro-economic perspective;
- Identify lock-in effects and avoid/prevent all measures that lead to lock-ins;
- Focus on energy efficiency in the building stock first, then renewables;
- Restrict direct electric heating (neither for SH nor for DHW);
- Set absolute limit for final energy for electricity (or heat in case of DH) for buildings;
- Direct fundings/subsidies in-line with the overall climate and energy policy goals. Cancel all contra-productive fundings/subsidies;
- Balance investments in the building sector with reduced need to invest in the energy system (PV, wind, energy storage);
- Develop a clear long-term strategy for the extension of DH and define dedicated districts;
- Set a CO_2 budget (per person) instead of a CO_2 long term target.

4. Conclusions

This increasing share of RE in future electricity and DH system will lead to a significant reduction of the CO_2 conversion factor for electricity with also a relevant influence on the CO_2 conversion factor of DH when HPs are involved. The dilemma is that in such a scenario, a high ambition level with respect to deep TR, or the further integration of onsite RE coupled to a HP will not significantly influence the CO_2 emissions of a building. Instead, a high ambition level on building level and massive onsite PV will be required to reach the goal of the phase-out of fossil energy. This requires an energy policy approach instead of market initiatives, and for example e.g. CO_2 budgets or other limits and conditions will have to be defined. This dilemma can only be solved if the building sector is seen as part of the energy policy.

Insufficient ambition goals on building level lead to the so-called lock-in, which prevents or delays reaching the climate goals on energy system level. A purely micro-economic focused approach will inevitably lead to fail. The building stock has to be considered as a part of the energy system and planning and implementation of any measure has to be evaluated in the context of the transition to a sustainable (and affordable) energy system. A CO_2 budget (per person) until e.g. 2050 (better 2040) instead of target of CO_2 emissions in 2050 (or

2040) is required. Transparent and reliable goals have to be set for the building sector with limits for the final energy consumption instead of non-directed incentives.

As outlook, an economic analysis should be performed as a next step and also the need of (seasonal) energy storage should be considered in future works.

Acknowledgements

This work is possible through fundings of the following Austrian research projects: INTEGRATE (ACRP-14), PhaseOut (FFG, Stadt der Zukunft); IEA HPT Annex 61 (FFG Energieforschung).

Nomenclature

AL	Ambition Level	H	Heat
BAU	Business as usual	HP	Heat Pump
BS	Building Stock	HVAC	Heating, ventilation and air conditioning
CHP	Combined heat and power	MFH	Multi-family house
CHP-E	Combined heat and power electricity	MVHR	Mechanical ventilation with heat recovery
CHP-H	Combined heat and power heat	nZEB	Nearly zero energy building
cHP	Central heat pump	NZEB	Net zero energy building
COP	Coefficient of performance	PEB	Positive energy building
DE	Direct electricity	PED	Positive energy district
D-E	Delivered energy	RE	Renewable energy
DH	District heating	SFH	Single-family house
DHP	District heating plant	SH	Space heating
DHW	Domestic hot water	SPF	Seasonal performance factor
E	Electricity	S-E	Secondary energy
ETS	Emissions trading system	TR	Thermal renovation
GHG	Greenhouse gas	U-E	Useful energy

References

[1] R. Simson, K.E. Thomsen, K.B. Wittchen, J. Kurnitski, NZEB Requirements vs European Benchmarks in Residential Buildings, Rehva J. (2021) 40–44.

[2] U. Eicker, Editorial: Positive Energy Districts: Transforming Urban Areas Into High Efficiency Districts With Local Renewable Generation and Storage, Front. Sustain. Cities. 4 (2022) 1–2. https://doi.org/10.3389/frsc.2022.838899.

[3] K.W. Steininger, J. Mayer, G. Bachner, S. Duelli, E. Frei, W. Grossmann, R. Maier, S. Nabernegg, K. Williges, W. Streicher, F. Ochs, M. Magni, A. Tosatto, E. Venturi, A. Passer, H. Kreiner, M. Scherz, B. Truger, J. Vogel, I. Offenthaler, The Economic Effects of Achieving the 2030 EU Climate Targets in the Context of the Corona Crisis - An Austrian Perspective, (2021). https://doi.org/10.13140/RG.2.2.20973.51685.

[4] M. Ploss, A. Peter, F. Ochs, F. Sigg, Low-Cost nZEB, Paris-kompatible Mehrfamilienhäuser, AB 231 – Internationale Vernetzung von Wissenschaft und Bauwirtschaft zur Entw, 2021.

[5] F. Ochs, M. Magni, G. Dermentzis, Integration of Heat Pumps in Buildings and District Heating Systems—Evaluation on a Building and Energy System Level, Energies. 15 (2022) 3889. https://doi.org/10.3390/en15113889.

[6] W. Feist, Passive House - the next decade, 18th Int. Passiv. House Conf. (2014) 635–658.

[7] K.C. Seto, S.J. Davis, R.B. Mitchell, E.C. Stokes, G. Unruh, D. Ürge-Vorsatz, Carbon Lock-In: Types, Causes, and Policy Implications, Annu. Rev. Environ. Resour. 41 (2016) 425–452. https://doi.org/10.1146/annurev-environ-110615-085934.

[8] N.H. Sandberg, J.S. Næss, H. Brattebø, I. Andresen, A. Gustavsen, Large potentials for energy saving and greenhouse gas emission reductions from large-scale deployment of zero emission building technologies in a national building stock, Energy Policy. 152 (2021) 112114. https://doi.org/10.1016/j.enpol.2020.112114.

[9] F. Ochs, G. Dermentzis, Evaluation of Efficiency and Renewable Energy Measures Considering the Future Energy Mix, 7th Int. Build. Phys. Conf. Proceedings, IBPC, Int. Assoc. Build. Phys. (IABP), Syracuse, New York, 2018. (2018) 1271–1276. https://doi.org/10.14305/ibpc.2018.pe-1.03.

14th IEA Heat Pump Conference
15-18 May 2023, Chicago, Illinois

Simulation-assisted development of a mini-split air-to-water façade-integrated heat pump for minimal invasive renovations

William Monteleone[a*], Fabian Ochs[a]

[a]Unit for Energy Efficient Building, University of Innsbruck, Technikerstraße 13, 6020 Innsbruck, Austria

Abstract

One of the challenges in renovated multi-apartment buildings is the upgrade or substitution of existing systems delivering space heating (SH), domestic hot water preparation (DHW) and cooling (SC). Construction and installation works are complex and their related costs are high. The European heat pump market currently lacks compact and cost-effective solutions for minimally invasive, so-called serial renovations, which at the same time exhibit high efficiency, an aesthetically pleasing design and low sound emissions. Façade-integrated decentralised small-scale heat pumps (HP) are regarded as a promising solution to increase the general acceptance for flat-wise heating solutions. Because of the compact design, they require a deeper investigation of the fluid-dynamics within the outdoor unit (evaporator) to guarantee an adequate efficiency of the final product. Based on these considerations, a mini-split air-to-water façade-integrated HP for DHW was developed. The design of the outdoor unit was optimised by means of computational fluid-dynamics simulations (CFD) and the overall efficiency evaluated through refrigerant cycle and system simulations. To conclude, the prototype was tested dynamically in a double-room climate chamber with controlled indoor and outdoor temperature conditions.

© HPC2023.
Selection and/or peer-review under the responsibility of the organizers of the 14th IEA Heat Pump Conference 2023.

Keywords: Heat pumps; serial renovation;, alternative refrigerants; façade integration

1. Introduction and state-of-the-art

The European Building Performance Directive (EPBD) 2018/844 [1] stated the commitment of the European Union (EU) to the development of a sustainable, energetically secure and decarbonized energy system, along with a full decarbonization of the building stock by 2050, 35% of which older than 50 years old [2]. The new EPBD indicates also that EU member countries should submit national building renovation strategies within the National Energy and Climate Plans (NECPs) including roadmaps to phase out fossil-based systems supplying heating and cooling by 2040 at the latest. In order to achieve the full decarbonization of the building sector, an improved average yearly renovation rate of 3% is needed (compared to the actual 1%) along with a cost-effective transformation of existing buildings into nearly-zero energy buildings (nZEBs) [3]. Independently from how a carbon neutral energy system will be realized in the future, it is no doubt that HPs will play a crucial role in a sustainable and efficient transformation in the heating, cooling and DHW preparation of buildings [4]. During the renovation of multi-apartment buildings, a complete upgrade or substitution of the existing centralized systems delivering the SH, SC and DHW demands is frequently not possible for techno-economic reasons, among others high investment costs and high degree of invasiveness. The European market offers currently different HP based solutions depending on their construction type [5]:

a) Internal monoblock with integrated hot water storage;
b) Internal monoblock with integrated wall-hanging hot water storage;
c) Split units;
d) DHW HP with integrated or separated hot water storage.

* Corresponding author. Tel.: +43 512 507 63661
E-mail address: william.monteleone@uibk.ac.at .

Split units (air-to-air or air-to-water) are already a standardized product on the market and are offered in all power ranges. A couple of major drawbacks of such system are however the optically unattractive outdoor unit and the high developed sound power level during operation, ranging from 59 to 70 dB(A) for outdoor units and from 43 to 65 dB(A) for the internal module [5,6]. Accordingly, the European market does not yet offer compact, modular and silent split HP solutions with an aesthetically pleasing design of the outdoor unit. Innovative decentral façade-integrated small-scale HP solutions would guarantee a substantial space saving and a high degree of prefabrication, minimizing thus the total investment costs. Additionally, reduced sound emissions should improve their overall acceptance. Within the FFG (Austrian Research Promotion Agency) funded research projects FitNeS and PhaseOut a mini-split air-to-water façade-integrated HP for DHW with a design heating power of 1.5 kW was developed by means of coupled simulation and experimental work to cover an important gap on the wide renovation market and enhance serial renovation in multiple-family buildings. The design and the optimization of the outdoor unit was performed through CFD, refrigerant cycle and system simulations. To supply a proof-of-concept and to verify the efficiency of the developed design, a prototype was tested dynamically with water tapping profiles according to EN 16147 [7] in a double-room climate chamber with controlled indoor and outdoor temperature conditions.

2. Highlight of current research gaps and novelty of developed concept

DHW and SH in renovated buildings are mainly fossil based in continental Europe, with small differences among member countries [8], with more than half of the installed systems relying on either natural gas or oil [9]. New centralized installations are frequently not possible or possible for social, technical or economic reasons, among them high degree of invasiveness, higher investment costs, higher distribution losses and impossibility to provide step-wise renovation. District heating (DH) systems represent a real alternative only if they are already available on site, often not the case especially in densely populated areas. Additionally, the European market does not provide efficient and cost-effective sustainable alternatives to decentral gas-fired or electric boilers that require only minimal construction work. In this paper, a propane-based façade-integrated mini-split HP for the apartment-wise renovation of multiple-family buildings will be presented to tackle the absence of minimally invasive, compact and silent HP solutions on the broad market segment of the refurbishment of buildings. Since the integration takes mainly place within the insulation layer, a deep analysis of the fluid dynamics and the heat transfer is necessary. Firstly, the main boundary conditions of the CFD simulation work will be highlighted and the final design selected based on flow homogeneity, overall pressure drop, sound emissions and electric power consumption of the fans. Secondly, the theoretical performance of the refrigerant cycle will be evaluated under the assumption of uniform flow conditions. Then, the overall performance of the entire system, including the HP, the hot water storage and the fresh water station for the delivery of the DHW demand, will be investigated by means of dynamic system simulation. Lastly, the results of the testing of a prototype of mini-split HP under dynamic conditions will be presented.

3. Methodology

The analysis presented in this work follows a development and optimization approach from the component level up to the system level, as discussed also in [10] where the development of an air-to-air HP for SH is highlighted. The next sections will present the implemented research methodology, starting from the CFD-based design development of the outdoor unit with a brief mention of the criteria used to compare the evaluated designs. Then, the following section will highlight the basic assumptions of a steady-state refrigerant cycle simulation tool developed internally in the MATLAB environment [11] to produce reasonable performance maps of the to-be-developed mini-split HP under the simplifying assumption of uniform airflow. The generated performance maps will be then used as an input in the dynamic system model developed within the Simulink simulation environment [12] to perform a pre-sizing of the optimal size of the DHW storage. Consequently, the primary energy consumption of the entire system supplying the DHW demand will be assessed considering a hot water tapping profile based on the “M” profile according to [7] for a typical household of 2-3 persons. In the last section, the test setup at the University of Innsbruck used to measure the dynamic performance of the prototype will be discussed.

3.1. CFD-based design development and optimization

Several design geometries were simulated in the software ANSYS [13] with the help of the CFX solver in a first phase and pre-selected based on the following criteria:

- Flow homogeneity on the evaporator surface;
- Air-side pressure drop;

The pre-screening included geometrical designs with both axial and radial fans. Crossflow fans were not taken instead into further consideration due to space constraints in façade-integrated installations. Table 1 illustrates the simulated variants based on the geometry of the evaporator, the fan type and the position of the fans related to the evaporator.

Table 1: Overview of simulation cases to assess the optimal geometry of the outdoor unit by means of CFD simulations.

Variant number	Geometry	Type of Fan	Position of the Fans
1	Square	4 axial	Downstream
2.1	Rectangular	4 axial	Downstream
2.2	Rectangular	4 axial	Upstream
3	Rectangular	1 radial	Downstream
4	Rectangular	1 radial	Downstream

For the simulated variants, the boundary conditions highlighted in Table 2 were assumed throughout the CFD simulations:

Table 2: Boundary conditions in CFD simulations. For the simulations involving axial fans, the rotational speed was also varied between 900 rpm and 1700 rpm.

Type of Fan	Boundary Conditions	Value
Radial fans	Inlet	Total pressure = 0 Pa
	Outlet	Mass flow rate = 0.115 kg/s
Axial fans	Inlet	Static pressure = 0 Pa
	Outlet	Average static pressure = 0 Pa

The k-ε turbulence model was adopted for all simulation models, as it is generally suggested for flows over rotating geometries and baffles, as well as being a robust model with a sufficient accuracy [14]. Additionally, the walls of the fluid domain are assumed to be smooth and the velocity on the model boundaries is equal to zero (no-slip wall condition). To model the fluid interface between stationary and rotating domains, the option "Frozen rotor" was selected.

3.2. Refrigerant cycle simulation model and performance maps generation

In parallel to the selection of the optimal outdoor unit design based on the presented criteria, a refrigerant cycle analysis was executed with the purpose of:

a) Generating physics-based reasonable performance maps to be used in the dynamic system simulation in absence of measurement results;
b) Evaluate the maximum theoretical performance of the refrigerant cycle at varying boundary conditions.

The refrigerant cycle is based on propane (R290), an alternative and more sustainable refrigerant with a global warming potential (GWP) equal to 3 and ozone depletion potential (ODP) equal to zero [15]. However it has the drawback of belonging to the A3 class, thus highly flammable and with a maximum allowed refrigerant charge in Europe equal to 150 g for residential installations [16]. A pre-analysis of the performance of the refrigerant cycle, given the knowledge about the single components, is in this sense crucial. The model itself is built in a modular way, so that each component of the refrigerant cycle has its own equations, which will be highlighted in the following section along with the basic assumptions of the model.

3.2.1. Compressor model

The modelled compressor exhibits the characteristics highlighted in Table 3:

Table 3: Technical features of the compressor modelled within the refrigerant cycle simulation

Feature	Value
Compressor type	Rotary
Displacement	12.74 cm^3
Speed control	Single speed – 2900 rpm
Number of phases	1 – 230 V – 50 Hz

For the calculation of the isentropic efficiency associated to a certain pressure ratio, a fourth-order, ten-coefficients equation, depending on evaporation and condensation temperatures, was modelled based on manufacturer data:

$$\eta_{is} = f^4(\vartheta_{evap}, \vartheta_{cond}) \quad (1)$$

The refrigerant mass flow supplied by the compressor is calculated from a physical model, as discussed also in [17], described by equation (2) :

$$\dot{m}_{ref} = \eta_{vol} \frac{n_{rpm}}{60} D_c \rho_{ref,suction} \quad (2)$$

The volumetric efficiency is in turn also deducted from a theoretical model similar to the one described in [18] and [19] depending from the pressure ratio τ and accounting for any deviation from the ideal gas behavior, as depicted in (3) :

$$\eta_{vol} = 0.97 - \left[\left(\frac{Z_s}{Z_d}\right) \tau^{\frac{1}{k}} - 1\right] C_l - e_v \quad (3)$$

It is noteworthy to mention that the clearance volume of a compressor is usually not included in the technical data supplied by the manufacturer, but reasonably lies between 5 and 15 % of the total displacement [20]. Its value needs thus to be calibrated. The same procedure should be executed for the correction factor e_v, since different applications typically exhibit different deviations from the ideal gas behaviour. For the calculation of the electrical power consumption attributed to the compressor, a constant total efficiency of 95% was assumed for sake of simplicity, equal to the product of electrical and mechanical efficiencies.

3.2.2. Condenser and Evaporator models

For the sake of pre-analysis and to maintain the simplicity of the model, no detailed calculation of the heat transfer was implemented at the condenser and at the evaporator sides. It was however decided to take into account the heat exchange through the definition of a pinch point temperature difference between the refrigerant cycle and the primary side (air) as well as between the refrigerant cycle and the secondary side (water). No detailed model was introduced within the steady-state model to account for the performance drop under icing conditions. The power laws shown in the equations (4) and (5) were thus implemented, depending on heating and cooling power respectively:

$$\Delta T_{pp,cond} = \Delta T_{pp,cond,0} \left(\frac{\dot{Q}_{cond}}{\dot{Q}_{cond,0}}\right)^{n_{cond}} \quad (4)$$

$$\Delta T_{pp,evap} = \Delta T_{pp,evap,0} \left(\frac{\dot{Q}_{evap}}{\dot{Q}_{evap,0}}\right)^{n_{evap}} \quad (5)$$

The parameters $\Delta T_{pp,cond,0}$, $\dot{Q}_{cond,0}$, n_{cond} as well as $\Delta T_{pp,evap,0}$, $\dot{Q}_{evap,0}$, n_{evap} are subjected to calibration procedure.

3.2.3. Expansion valve model

An isenthalpic valve model was adopted for sake of simplicity. For this reason, the condition described in (6) was applied to the model:

$$h_{in,exv} = h_{out,exv} \quad (6)$$

3.2.4. Pressure drop and heat losses model

Pressure drop can be taken into account for each component of the refrigerant cycle as a fixed value or through correlations depending on the refrigerant mass flow. The calculation is separated for each phase. Heat losses are solely assigned to the compressor shell and follow the law mentioned in eq. (7):

$$\dot{Q}_{loss} = UA_{compr} \left(\vartheta_{compr} - \vartheta_{amb}\right) \quad (7)$$

3.2.5. Basic assumptions about the refrigerant cycle

The following basic assumptions were made for the simulation of the refrigerant cycle:

Table 4: Inputs assumed for the refrigerant cycle simulation regarding superheating, subcooling, air and water volume flows.

Property	Value
Superheating	6 K
Subcooling	6 K
Air volume flow	350 m^3/ h
Water volume flow	4 liter/min

The value of subcooling usually depends, among other factors, on the actual refrigerant charge in operation within the refrigerant cycle. However, since there is actually no implemented model for the calculation of the optimal refrigerant charge, this effect was neglected throughout the refrigerant cycle simulations and a constant value was used as an input instead. Performance maps were thus generated for -15, -7, 2, 7, 10, 20 °C outdoor air temperature, as well as 35, 45, 55 °C supply water temperature.

3.2.6. Calculation assumptions and convergence criteria

The numerical model uses the heating and cooling power as iterated variables to obtain a full characterization of the refrigerant cycle in terms of pressure, enthalpy, entropy and temperature. The convergence of the model is based on the minimization of an error function, defined in equations (8), (9) and (10).

$$err_{conv} = \left|\dot{Q}_{cond} + \dot{Q}_{loss} - \dot{Q}_{evap} - \dot{Q}_{compr}\right| + err_{\dot{Q}_{evap}} + err_{\dot{Q}_{cond}} \quad (8)$$

$$err_{\dot{Q}_{evap}} = \frac{\left|\dot{m}_{ref}\,(h_{evap,out} - h_{evap,in}) - \dot{m}_{src}\,c_{p,src}\,(\vartheta_{src,in} - \vartheta_{src,out})\right|}{\dot{Q}_{evap}} \quad (9)$$

$$err_{\dot{Q}_{cond}} = \frac{\left|\dot{m}_{ref}\,(h_{cond,in} - h_{cond,out}) - \dot{m}_{sink}\,c_{p,sink}\,(\vartheta_{sink,out} - \vartheta_{sink,in})\right|}{\dot{Q}_{cond}} \quad (10)$$

In the first part of the convergence function, the overall energy balance of the heat pump is checked, while the remaining terms proof the validity of the local energy balances for the evaporator and for the condenser.

3.3. Dynamic system modelling of hot water consumption and performance evaluation

The efficiency of the entire system supplying the DHW demand was evaluated within the simulation environment of *MATLAB* and *Simulink*, where the heat pump was modelled using the built-in model already present in the CARNOT Toolbox. The performance data is supplied by the developed refrigerant cycle simulation tool. The dynamic performance of the system was evaluated at the outdoor air temperatures of 10, 15 and 20 °C to be later compared with laboratory measurements. Four different storage tank sizes were simulated, corresponding to 90, 100, 110 and 120 liters. For sake of simplicity, the height of the storage tank was assumed to be constant and equal to 1.1 m, while the diameter of the tank increases with increasing storage volume. The overall heat transfer coefficient of the tank, including insulation, was selected such that for each storage volume it would correspond to the energy efficiency class ErP B [21]. The temperature of the technical room is constant and equal to 20 °C. Figure 1 shows a conceptual drawing of the hydraulic system supplying the DHW demand, as it was modelled within the simulation environment. Along with the HP and the DHW storage, a freshwater station was included in the simulation as well as in the reality to avoid legal and technical constraints due to legionella. The pipe lengths correspond to the lengths in the experimental setup. The simulation time corresponds to 24 hours, of which 14 and a half hours are reserved for tapping.

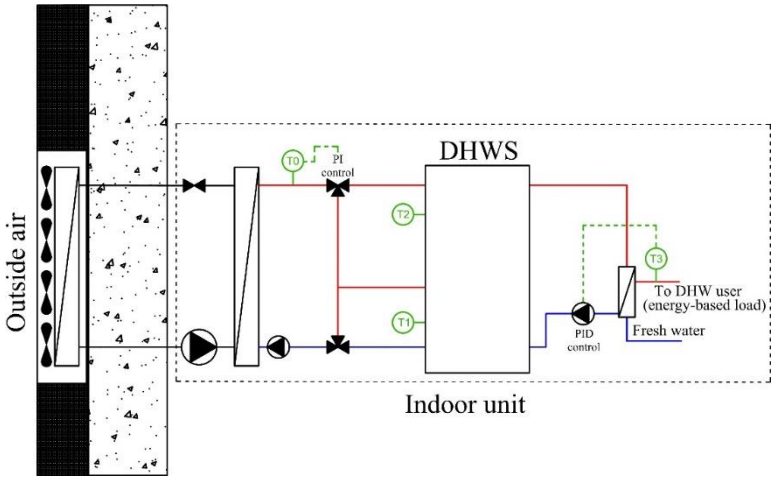


Figure 1: Schematic representation of the system supplying the DHW demand as modelled within the Simulink environment for the assessment of the optimal storage size and performance.

The entire storage tank is heated to a constant temperature equal to 55 °C. During the start-up phase of the heat pump, the temperature of the water supplied to the storage would be much lower than the actual temperature in the tank. If no additional measures were undertaken, this would result in a disturbance of the stratification of the storage and have a detrimental effect on the system performance. Thus, when the supplied water temperature is lower than 52 °C, controlled by means of the temperature sensor T0 (with an inertia of 5 seconds), the upper and lower mixing valves are closed such that water is recirculated in a loop and its temperature increases. As soon as the setpoint temperature is reached, the storage tank is loaded from above by means of fixed-value control so that a certain reserve volume can be guaranteed for short-term taps. After the reserve volume has been charged, the storage tank is also charged via the intermediate layer, whereby the fixed value control is not used here. Then the lowest part of the hot water storage tank is charged. The control of the temperature in the storage tank is performed based on a hysteresis controller coupled to the temperature sensors T1 and T2. When T2 indicates a temperature equal to the setpoint (55 °C), the heat pump is shut down. On the other hand, when T1 measures a temperature equal to 5 K lower than the setpoint (thus 50 °C), the heat pump is turned on again. On the secondary side, the rotational speed of a PID-controlled inverter-based pump is modulated in order to meet the user water temperature request, in this case 45 °C (temperature sensor T3). When the desired hot water temperature is reached, the energy control starts counting and tapping continues until the required energy has been supplied.

A tapping profile based on profile "M" according to the standard EN 16147 [7] was taken into consideration for the simulations, in which two major taps (10 liter/min) take place at 07:15 and 21:30 (i.e. shower in the morning and in the evening). Each simulation starts with a completely charged storage. Minimum and maximum operational time intervals of, respectively 5 and 80 minutes are assumed. For air temperatures lower than 7 °C, a 10 minutes stop interval is considered every 80 minutes to take into account for deicing cycles. However, the additional electric power consumption for deicing, for which calculation a dedicated model would be needed, is not taken into account.

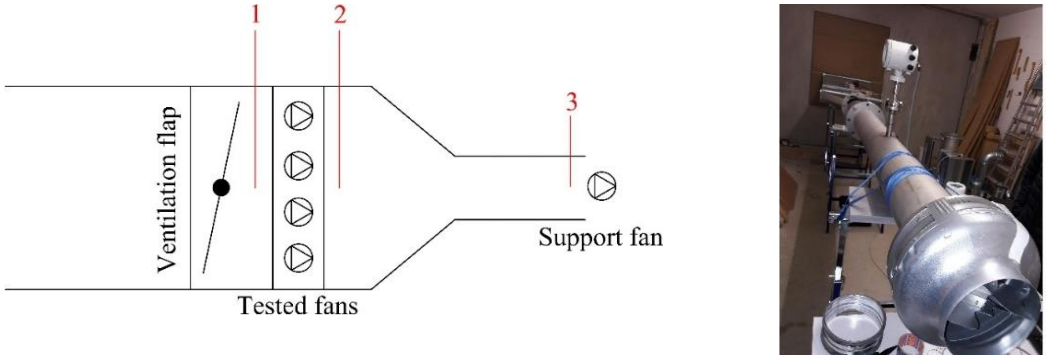
The performance of the system is evaluated through the definition of a coefficient of performance (COP) for the entire system as follows:

$$COP_{sys} = \frac{Q_{DHW}}{Q_{el}} \qquad (11)$$

3.4. Laboratory testing and proof-of-concept

The laboratory infrastructure was used first to compare the electric power consumption and the sound power level of different fan configurations for the outdoor unit and then to test the dynamic performance of a developed prototype of mini-split façade-integrated HP for DHW preparation. To test the electric power consumption as well as the sound power level of the fan configurations, the test rig described in Figure 2 has been set up. The pressure conditions upstream of the fans (1) is imposed by means of a PI controlled ventilation flap. In the same way the pressure difference with the environment downstream of the fans (2) was equaled to zero to replicate outflow in the environment by means of a support fan. The rotational speed of the fans is

either controlled by a PWM module for the axial fans and via a 0-10 V control signal for the radial fans. Air volume flow is measured by means of a hot-wire anemometer (3). For acoustical measurements, the channel downstream of the fans must be opened and the sound power level of the fans assessed according to [22] and [23]. On the other hand, to assess the dynamic performance of the split HP, a double room climate chamber was used. The cold room was reserved to the installation of the outdoor unit of the HP, while the ambient room was dedicated to the indoor element. The temperature in each room is controlled by means of brine-to-air and water-to-air heat exchangers. With the current system configuration, it was possible to reach a minimum outdoor air temperature of 10 °C. A conceptual scheme of the test-rig for the assessment of the dynamic performance of the mini-split HP is depicted in Figure 3. Water withdrawal is controlled by means of a magnetic 2-way valve, the withdrawn volume flow being measured by a magnetic flow meter (MFM). Since the cold water temperature cannot be directly controlled, a flush valve is opened intermittently to keep the cold water temperature as constant as possible. A flush valve is also provided on the hot water side to energetically empty the hot water storage and cool it down approximately to cold-water temperature (i.e. for the measurement of the losses attributed to the DHW storage). The temperature in the storage is measured by means of three Pt100 temperature sensors, positioned respectively at 9 cm, 40 and 70 cm from the top cover of the hot water storage. The water supply and return temperatures are also measured and logged. Thus, the prototype of split-type heat pump was tested at outdoor air temperatures of 10, 15, 20 °C under intermittent tapping (M profile, see also [7]). A temperature of 45 °C was considered as minimum comfort condition for the water supplied to the DHW user. In order to allow for longer measurement stints, a hot water storage size of 120 liters was chosen. The total measurement time corresponds to the simulation time where the water withdrawal is different from zero.



(a) (b)

Figure 2: Test rig set up for the determination of fan power consumption and sound power level. (a) Conceptual scheme and (b) photo of the actual test rig.

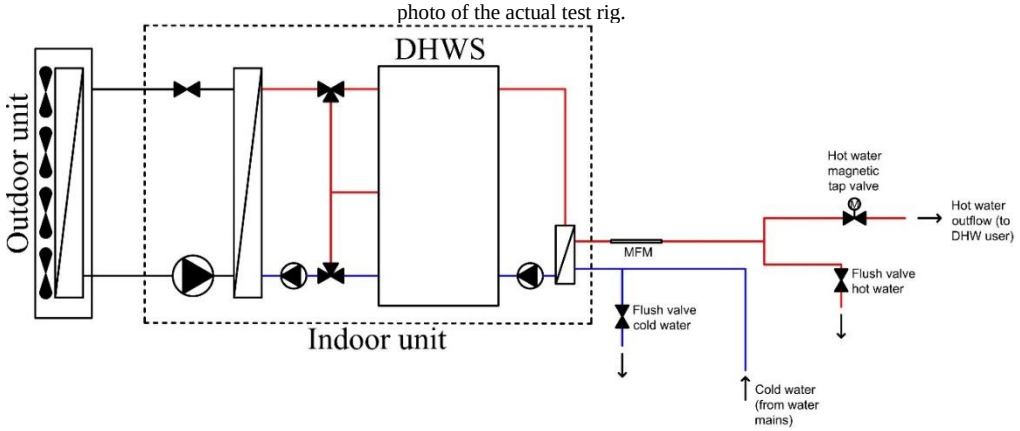


Figure 3: Test rig setup for the measurement of the dynamic performance of the system supplying the DHW demand.

4. Results and Discussion

4.1. CFD-based design development and optimization

The CFD- based pre-analysis yielded the design shown in Figure 4, involving four parallel axial fans (shown in green) and an evaporator tilted of 30° (depicted in red) compared to the inflow direction. The advantage of

axial fans over radial fans was determined with the help of the measurements of the electric power consumption as well as of the sound power level, which will be presented in a later section.

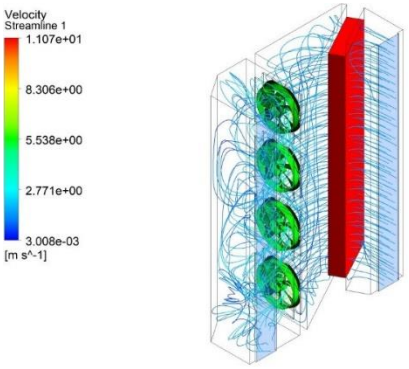


Figure 4: Final design of the outdoor unit featuring four axial fans, flow pattern simulated within the CFD software.

4.2. Refrigerant cycle simulation model and performance maps generation

The refrigerant cycle model presented in section 3.2 produced the performance maps depicted in Figure 5(a) to (d) for a split-type heat pump, with air temperature varying from -15 to 20 °C and supply water temperature of 35, 45 and 55 °C:

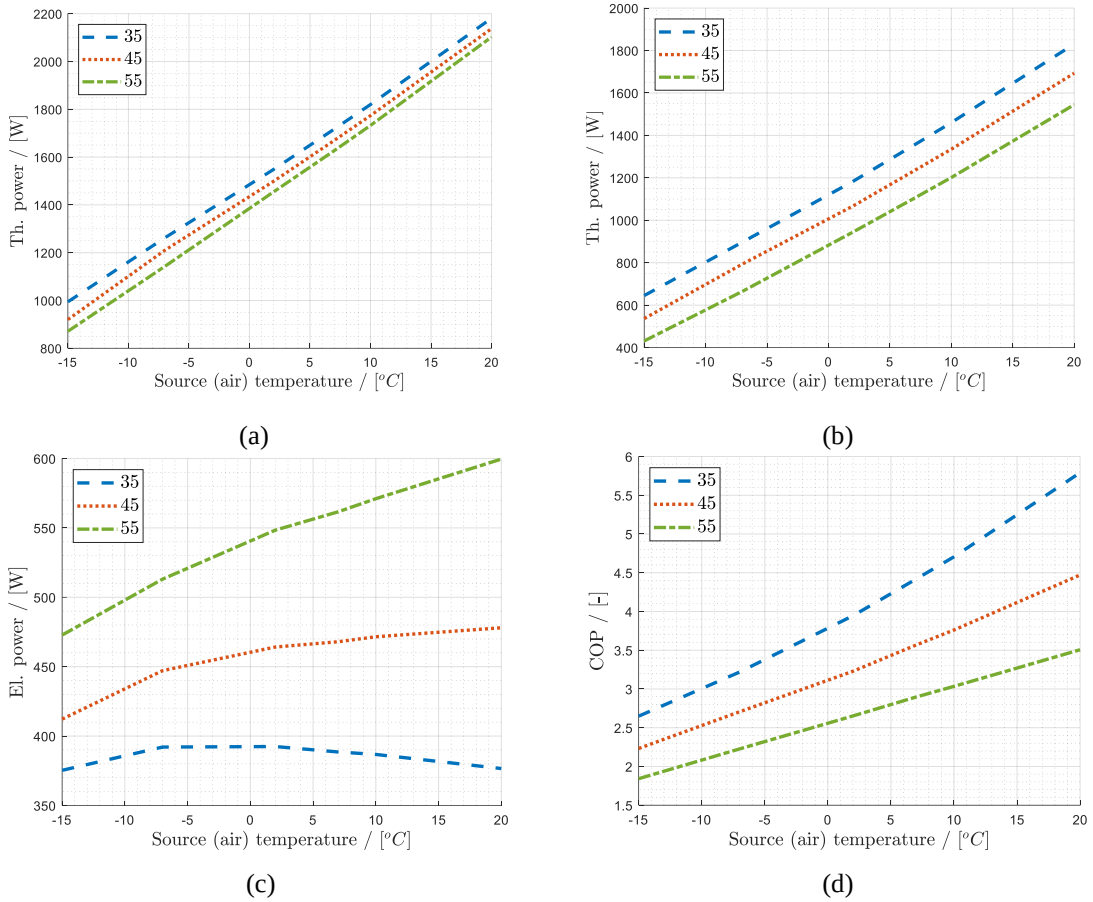


Figure 5: Simulated performance data of a split-type air-to-water heat pump to be used as input for the dynamic system simulation. (a) Heating power, (b) Cooling power, (c) Electric power consumption, (d) Coefficient of Performance with source temperatures ranging from -15 to 20 °C and supply water temperatures of 35, 45 and 55 °C.

As it is possible to discern from Figure 5(a), the design heating power of 1.5 kW at the design conditions of 7 °C air temperature, 55 °C supply water temperature is theoretically guaranteed. The generated performance

data were thus us as an input for the heat pump model in Simulink/CARNOT to investigate the dynamic performance of the entire system.

4.3. Dynamic system modelling of hot water consumption and performance evaluation

The system was simulated within the Simulink environment for multiple storage sizes at the outdoor air temperatures of 10, 15 and 20 °C. Table 5 reports the results in a concise and more compact way for the different temperatures and a storage size of 90 liters, while Table 6 summarizes the results for a storage size of 120 liters. The results show thus, that considering equal outdoor air temperature conditions, a compact 90 liters storage would be sufficient to fulfill the domestic hot water demand of a small family. The adoption of a larger storage size brings an additional 4 to 7 % performance improvement, due to the reduced switch-on frequency in the larger storage size and therefore to the comparatively lower power consumption.

Table 5: Summary of simulation results for a storage size of 90 liters and varying outdoor air temperature.

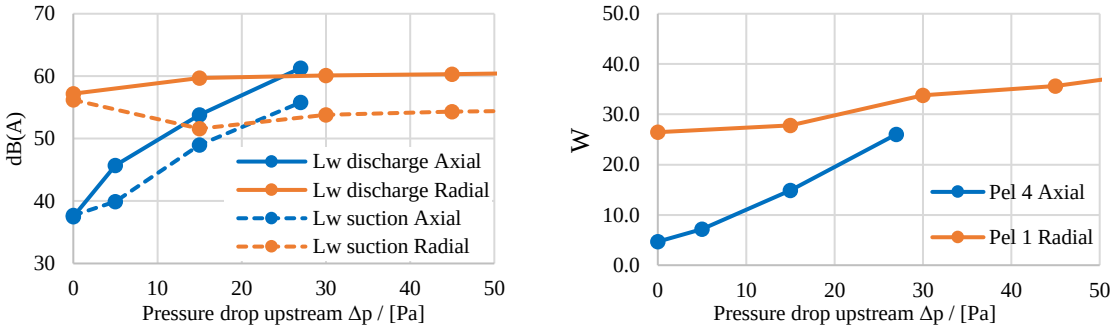
Temperature [°C]	Q_{DHW} [kWh]	Q_{el} [kWh]	COP_{sys}[-]
10	6.05	2.02	2.99
15	6.05	1.88	3.22
20	6.05	1.76	3.43

Table 6: Summary of simulation results for a storage size of 120 liters and varying outdoor air temperature.

Temperature [°C]	Q_{DHW} [kWh]	Q_{el} [kWh]	COP_{sys}[-]
10	6.05	1.88	3.22
15	6.05	1.81	3.35
20	6.05	1.68	3.61

4.4. Laboratory testing and proof-of-concept

Figure 6(a) and (b) highlight the measured sound power level and the electric power consumption for four axial fans and a single radial fan. The tests show that axial fans might be more favorable than radial one, both in terms of sound emissions and in terms of electric power consumption, if the pressure drop attributed to the inflow geometry and the evaporator can be constrained to values lower than 25 Pa. The measured total pressure drop combination of inflow geometry and evaporator in the prototype at the design airflow rate was of 9.8 Pa, confirming the choice of 4 axial fans in spite of radial fans. Figure 7 shows finally the measurement results of the prototype under dynamic conditions. Generally, it is possible to conclude that the minimum comfort requirement is always guaranteed and the minimum temperature is always supplied to the DHW user. The difference between measured and simulated performance, as highlighted by Table 6 and Table 7, is to be attributed to a higher measured storage heat loss coefficient in the experimental specimen, about 2 to 3 times higher than the simulated one due to improper insulation installation and excessive convection within the indoor unit housing the DHW storage.



(a) (b)

Figure 6: (a) Measured sound power levels (A-corrected) on discharge and suction sides for 4 axial fans and 1 radial fan at 350 m^3/h air volume flow and (b) measured electric power consumption for 4 axial fans and 1 radial fan at varying pressure drop conditions.

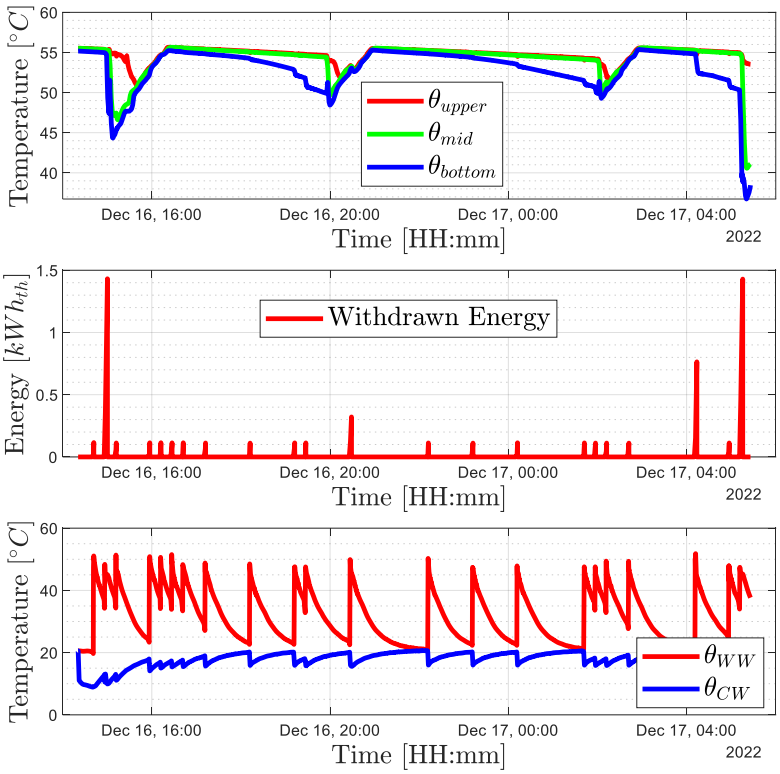


Figure 7: Measurement results of a split-type heat pump under dynamic test conditions (M standard tapping profile) and 10 °C outdoor air temperature. From the top: measured storage temperatures, withdrawn tapped energy, tapped warm and cold water temperatures. The measured storage temperatures refer to the sensors positions indicated in section 3.4.

Table 7: Summary of measurement results for a prototype of a split-type heat pump tested in a double room climate chamber under intermittent tapping and varying outdoor air temperature.

Temperature [°C]	Q_{DHW} **[kWh]**	Q_{el} **[kWh]**	COP_{sys}**[-]**
10	6.05	2.16	2.80
15	6.05	2.07	2.92
20	6.04	1.96	3.09

5. Conclusions and outlook

Decentral heat pump solutions could play a major role in the upcoming years on the renovation market. In order to save space and for sake of cost-effectiveness, one alternative and more sustainable solution to decentral gas or electric boilers is a façade-integrated split air-to-water heat pump. This work has focused on the presentation of a general procedure on how to develop efficient small-scale heat pumps in narrow environments and has given proof of the potential of such solutions. A prototype of a propane-based mini-split air-to-water heat pump was thus conceived by means of CFD, refrigerant cycle and system simulations and tested later dynamically under varying tapping conditions. The fluid-dynamics based pre-analysis has highlighted in axial fans a more favorable alternative in compact installations, due also to their lower sound emissions and lower power consumption. Additionally, system simulations have also remarked that a 90 liters storage would be sufficient to satisfy the DHW demand of a small household (2-3 people) and that slight improvements are seen for larger storage sizes. The analysis must be however extended to lower outdoor air temperatures, for which a correct modelling of ice formation and de-icing is necessary. Laboratory measurements have also shown a performance gap between the simulation performance data and the measured ones. This discrepancy was traced back to a higher measured storage heat loss coefficient in the tested HP due to improper insulation installation and excessive convection within the indoor unit. Such drawbacks will require a complete redesign of the indoor unit. Furthermore, the possibility of supplying the SH demand depending on the delivery system will be assessed for a demonstration building. In this case the condenser of the HP would be connected directly with the radiator loop or floor heating.

Nomenclature

C_l	Clearance volume of the compressor
COP_{sys}	System coefficient of performance
D_c	Displacement of the compressor
e_v	Correction coefficient for non-ideal gas behavior
h	Enthalpy
k	Isentropic expansion factor
$\dot{m}_{ref}$	Refrigerant mass flow
n_{rpm}	Rotational speed of the compressor
$\dot{Q}$	Thermal power
Q_{DHW}	Delivered energy to the DHW user
Q_{el}	Electrical energy supplied to the system for the operation of the heat pump and the auxiliaries
UA_{compr}	Compressor shell overall heat transfer coefficient
z_d	Compressibility factor of the refrigerant at discharge port
z_s	Compressibility factor of the refrigerant at suction port
ΔT	Temperature difference
η_{is}	Isentropic efficiency
η_{vol}	Volumetric efficiency
ϑ_{amb}	Technical room temperature
ϑ_{compr}	Compressor shell temperature
$\rho_{ref,suction}$	Refrigerant suction gas density
τ	Compression ratio

Acronyms

CFD	Computational Fluid Dynamics
compr	Compressor
cond	Condenser
DH	District Heating
DHW	Domestic Hot Water
EPBD	European Building Performance Directive
evap	Evaporator
exv	Expansion Valve
GWP	Global Warming Potential
HP	Heat Pump
NECP	National Energy and Climate Plan
nZEB	Nearly Zero Energy Buildings
ODP	Ozone Depletion Potential
Pp	Pinch Point
ref	Refrigerant
SC	Space Cooling
SH	Space Heating

Acknowledgements

This work is part of the research projects *FitNeS* (Nr. 867327) and *PhaseOut* (Nr. 999895470) funded by FFG (Austrian Research Promotion Agency) within the *Stadt der Zukunft* research program. Special thanks to the project partners Drexel und Weiss, Drexel Reduziert, Element Design, Kulmer Holzbau, Winter, Rothbacher and IIG.

References

[1] European Commission, Directive (EU) 2018/844 of the European Parliament and of the Council of 30 May 2018 amending Directive 2010/31/EU on the energy performance of buildings and Directive 2012/27/EU on energy efficiency, Off. J. Eur. Union. 156 (2018) 1–17. https://eur-lex.europa.eu/legal-content/EN/TXT/PDF/?uri=CELEX:32018L0844&from=EN.

[2] European Commission, Factsheet - Energy Performance of Buildings, (2021) 3. https://ec.europa.eu/commission/presscorner/detail/pt/fs_21_3673.

[3] EU, COMMISSION RECOMMENDATION (EU) 2019/786 of 8 May 2019 on building renovation, Off. J. Eur. Union. 18 (2019) 75. https://op.europa.eu/pt/publication-detail/-/publication/4a4ce303-77a6-11e9-9f05-01aa75ed71a1/language-en.

[4] H.-M. Henning, A. Palzer, Energiesystem Deutschland 2050, Fraunhofer-Institut Für Solare Energiesysteme ISE. (2013) 46.

[5] F. Ochs, D. Siegele, D. Jähnig, C. Rohringer, T. Calabrese, R. Pfluger, C. Fink, Sanierung von Mehrfamilienhäusern mit kleinen Wohnungen – Kostengünstige technische Lösungsansätze für Lüftung, Heizung und Warmwasser, 2020.

[6] M. Vukits, A.M. Fulterer, F. Ochs, D. Jähnig, A. Wegener, D. Siegele, E. Sibille, R. Pfluger, A. Sief, Bericht zum Stand des Wissens Lüftung, Wärmepumpen und Kompaktgeräte - Projekt SaLüH, (2018).

[7] DIN EN 16147, Heat pumps with electrically driven compressors - Testing, performance rating and requirements for marking of domestic hot water units, 2017. https://doi.org/https://dx.doi.org/10.31030/2513808.

[8] P. Biermayr, C. Dißauer, M. Eberl, M. Enigl, H. Fechner, B. Fürnsinn, M. Jaksch-Fliegenschnee, K. Leonhartsberger, S. Moidl, E. Prem, C. Schmidl, C. Strasser, W. Weiss, M. Wittmann, P. Wonisch, E. Wopienka, Innovative Energietechnologien in Österreich - Marktentwicklung 2021, Nachhalt. Wirtschaften. 21b (2022) 18–275. https://nachhaltigwirtschaften.at/de/iea/publikationen/markterhebungen.php.

[9] IEA, Austria 2020: Energy Policy Overview, Int. Energy Agency. (2020). https://www.iea.org/reports/austria-2020.

[10] F. Ochs, W. Monteleone, G. Dermentzis, D. Siegele, C. Speer, Compact Decentral Façade-Integrated Air-to-Air Heat Pumps for Serial Renovation of Multi-Apartment Buildings, Energies. 15 (2022). https://doi.org/10.3390/en15134679.

[11] Mathworks, MATLAB, (2022). https://de.mathworks.com/products/matlab.html.

[12] E. Leonardi, D. Siegele, carnotUIBK Toolbox for MATLAB Simulink, (2018). https://www.uibk.ac.at/bauphysik/forschung/carnotuibk/index.html.en.

[13] Ansys, Ansys 19.2, (2022). https://www.ansys.com/.

[14] C. Abeykoon, Compact heat exchangers – Design and optimization with CFD, Int. J. Heat Mass Transf. 146 (2020) 118766. https://doi.org/10.1016/j.ijheatmasstransfer.2019.118766.

[15] Z. Yang, B. Feng, H. Ma, L. Zhang, C. Duan, B. Liu, Y. Zhang, S. Chen, Z. Yang, Analysis of lower GWP and flammable alternative refrigerants, Int. J. Refrig. 126 (2021) 12–22. https://doi.org/10.1016/j.ijrefrig.2021.01.022.

[16] D. Colbourne, K.O. Suen, T.-X. Li, I. Vince, A. Vonsild, General framework for revising class A3 refrigerant charge limits – a discussion, Int. J. Refrig. 117 (2020) 209–217. https://doi.org/10.1016/j.ijrefrig.2020.04.024.

[17] Institution of Mechanical Engineers, 8th International Conference on Compressors and their Systems, Woodhead Publishing, 2013.

[18] B. Guo, W.C. Lyons, A. Ghalambor, Petroleum Production Engineering, A Computer-Assisted Approach, 2007. https://doi.org/10.1016/B978-0-7506-8270-1.X5000-2.

[19] K. Arnold, M. Stewart, Surface Production Operations: Design of Gas-Handling Systems and Facilities, 1999. https://doi.org/10.1016/b978-0-88415-822-6.x5000-4.

[20] A. Kayode Coker, Ludwig's Applied Process Design for Chemical and Petrochemical Plants, 2013. https://doi.org/10.1016/c2009-0-27268-0.

[21] European Parliament, Directive 2009/125/EC of the European Parliament and of the Council of 21 October 2009 establishing a framework for the setting of ecodesign requirements for energy-related products (recast) (OJ L 285 31.10.2009, p. 10), Off. J. Eur. Union. (2009) 1–40. http://data.europa.eu/eli/dir/2009/125/2012-12-04.

[22] ISO 9614-1:1993 - Determination of sound power levels of noise sources using sound intensity - Part 1: Measurement at discrete points, 1993.

[23] ISO 9614-2:1996 — Determination of sound power levels of noise sources using sound intensity — Part 2: Measurement by scanning, 1996.

14th IEA Heat Pump Conference
15-18 May 2023, Chicago, Illinois

Experimental Assessment of Air-Source and Hybrid Ground-Source Heat Pump Systems

Brian Msizi CINDI[(a)], Tatsuaki IKUNO[(a)], Keishi KARIYA[(b)], Akio MIYARA[(b)*]

[((a)] Graduate School of Science and Engineering, Saga University
1 Honjo-machi, Saga, 840-8502, Japan, 21734001@edu.cc.saga-u.ac.jp
[(b)]Department of Mechanical Engineering, Saga University
1 Honjo-machi, Saga, 840-8502, Japan, miyara@me.saga-u.ac.jp

Abstract

Ground-source heat pump air conditioning systems are more efficient than air-source air conditioning systems in terms of energy consumption. Optimal hybrid utilization of air and ground heat sources has been shown to reduce the heat load on the ground. This study aims to ascertain the performance of hybrid heat pump systems in comparison to the standard air-conditioning system. A field test was conducted for the hybrid air conditioning and air-source systems. For the experiment, two commercial air conditioners were utilized. One of them was set up as a standard air-source air conditioner. Another one was connected with the ground to construct a ground-coupled hybrid air conditioner. The experimental setup was constructed in two small houses, one for each heat pump system. Generally, a hybrid heat pump system performs better over time compared to an air-source system. So, a comparison test between an air-source heat pump and a hybrid heat pump for cooling conditions was conducted to validate this point. The hybrid heat pump system showed an overall higher coefficient of performance (COP) compared to the air source air conditioning system.

© HPC2023.
Selection and/or peer review under the responsibility of the organizers of the 14th IEA Heat Pump Conference 2023.

Keywords: ground-source heat pump; hybrid heat pump systems; cooling capacity; COP, air-source ratio, air-source heat pump

1. Introduction

Energy consumption is growing swiftly with the people's standard of living. The growing demand for renewable energy sources has been driven by the need to reduce greenhouse emissions caused by fossil fuels. Renewable energy technologies research has primarily been focused on solar and wind power because of their ubiquitous and universal applicability **[1]**. Geothermal energy is also part of renewable energy research and is vitally important for building air-space conditioning. Buildings consume tremendous amounts of energy in a form of heating and cooling. It is estimated that on average a building's energy consumption accounts for 19% of the total social energy consumption **[2]**.

Conventional heating methods based on fossil fuels emit a massive amount of pollutants, consume a large amount of energy, and waste high-grade energy. So, heat pump technology has been gaining attention because of its energy-efficient, environmentally friendly, and cost-effective applications **[3]**. Among these heat pump technologies include ground source heat pump (GSHP) which typically yields higher heating and cooling coefficients of performance (COP) compared to the water-source heat pump (WSHP) and air-source heat pump systems (ASHP). A heat pump (HP) is a device capable to transfer thermal energy from the outside using the

* Corresponding author. Tel.: +81 70 9003 6741
E-mail address: 2734001@edu.cc.saga-u.ac.jp.

refrigeration cycle. Heat pumps inject the heat to the ground (GSHP) or release the heat to the ambient air (ASHP) when cooling a building. The decision on the type of HVAC to use depends on the size, reliability, costs, energy efficiency, and maintenance requirements **[4] [5]** The heat pump systems that were investigated in this study were the air-source heat pump (ASHP) and hybrid ground-source heat pump (HBHP). In the case of the HBHP, the heat is transferred from the room and deposited underground during cooling, or heat is transferred from the ground to the indoor space during heating. The air-source heat is the same only that the heat is transferred from the outside air to the indoor space for heating or removed from the indoor space to the outdoor air during cooling.

There have been many studies conducted that compare the performance of ASHP to that of GSHP. Urchueguía *et al.*(2008) demonstrated that a ground-coupled heat pump (GCHP) saved about 20% more energy compared to the air-source heat pump **[6]**. Morrone *et al.* (2014) also showed the economic benefits of using GCHP, particularly in cold climates **[7]**. Conversely, soil thermal imbalance caused by uneven loads of heating-dominant buildings adversely affects heating capacity and the long-term performance of a GSHP system **[8]**. This directly affects the initial borehole investment, which hinders the application of GSHP in cold regions.

This work investigates if HBHP is a more energy-efficient and cost-effective option for cooling (or heating) compare to the ASHP. It has been established by many studies that HBHP operates at a relatively higher COP than ASHP resulting in saving on electricity costs and energy consumption. Moreover, this research aims to investigate the role of each component in the overall system COP.

1.1. Study location

The ASHP and HBHP performance testing system was conducted using three prefabricated buildings located at Saga University, Saga prefecture in Japan (see Figure 1).

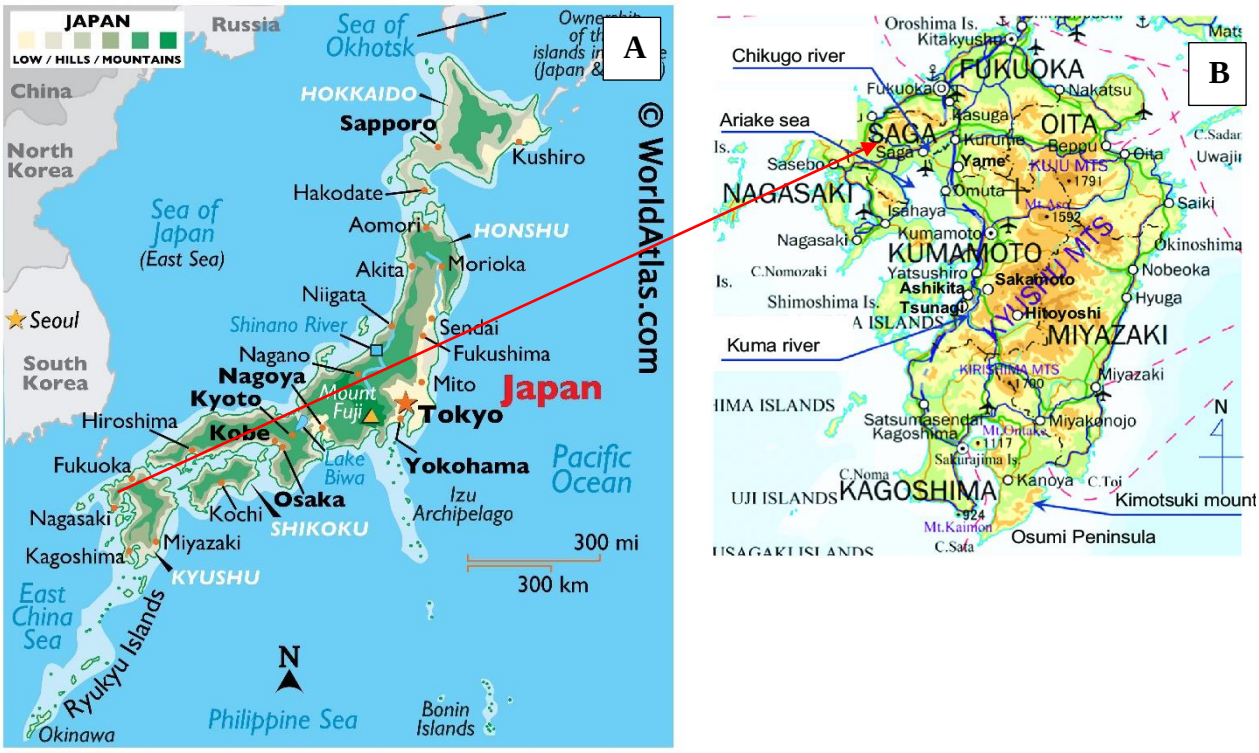


Figure 1: The map of Japan is on the left (a), The red arrow shows the location of Saga Prefecture(b).

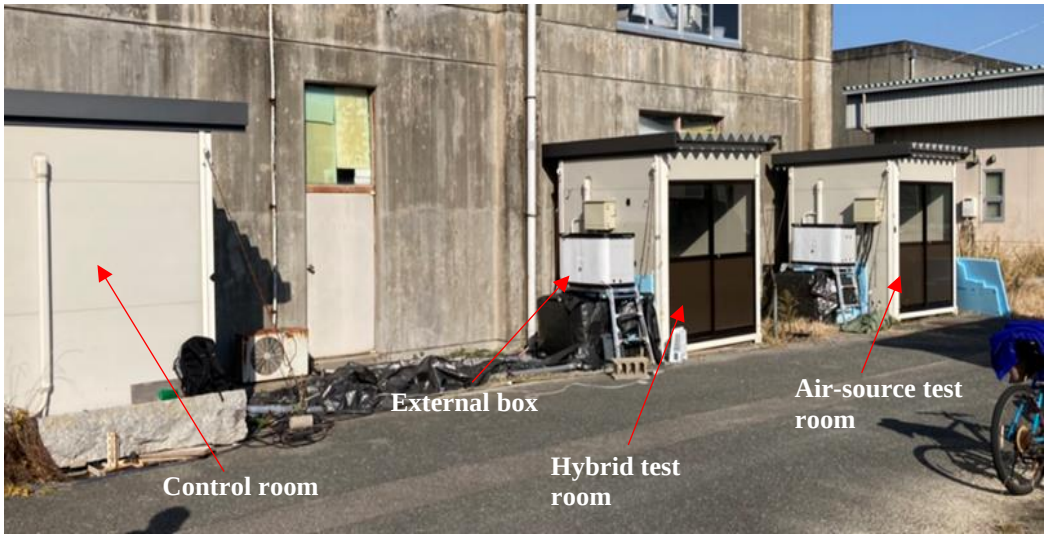


Figure 2: The experimental site for this research.

The control room is on the left, the hybrid test room is in the middle, and the test room for the air-heat source system is on the right. The control room is equipped with a data logger for recording instrument values, a pump for water piping, and a monitor for data observation. The hybrid test room and the Air-source heat pump system test room are each equipped with an indoor unit. In the hybrid heat pump system, the PHE, expansion valve, flow meter, and solenoid valve are installed as a single unit in a box on the side of the prefabricated structure above the outdoor unit (hereinafter referred to as "external box"). Similarly, the expansion valve and flow meter are installed in a box in the air-source heat pump system. The experimental site studied is directed north-south and it receives direct sun radiation from east to west. To avoid heat loss an insulated cover was used (see Figure *3* below).



Figure 3: Insulated experimental room.

2. Experimental Device

This section describes the air-source and hybrid heat pump systems in detail. Figures 4 and 5 show the external box for the air-source system and hybrid heat pump system respectively in cooling operation mode.

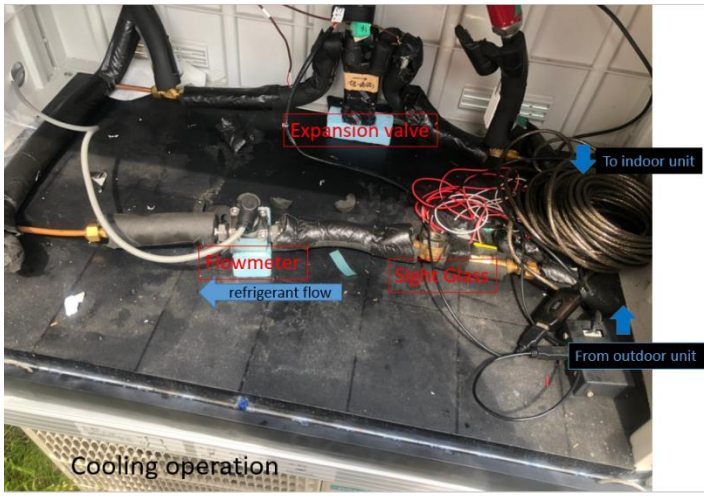


Figure 4: Inside the air-conditioning box for the ASHP system.

The refrigerant used in the refrigeration cycle is R32 (difluoromethane). The refrigerant (R32) becomes a high-pressure gas refrigerant in the compressor and enters the condenser (outdoor unit). In the condenser, the refrigerant condenses from a high-pressure gas refrigerant to a high-pressure liquid refrigerant in order to dissipate heat into the outside air. The refrigerant then enters an expansion valve, where it is expanded to a low-pressure liquid and enters an evaporator (indoor unit). In the evaporator, the refrigerant removes heat from the room, evaporates, and returns to the compressor as a low-pressure gas. In other words, the cycle of compression, condensation, expansion, evaporation, and compression is repeated. The specifications of the components used are described in the table below;

Table 1: Description of the Components of the heat pump.

Component	**Type**	**Operating Principle**	**Working Fluid**	**Flow direction**
Fan	Propeller	Turbo-type	Gas(R32 refrigerant)	Axial
Expansion Valve	Electronic Expansion Value (EEV)	The EEV controls the precise amount of refrigerant that flows into the evaporator.	Gas(R32 refrigerant)	-
Heat Exchanger	Double U-Tube (30 meters long)	Water moves from the pump to the double U-Tube and to PHE (see *Figure 8*).	Water	-

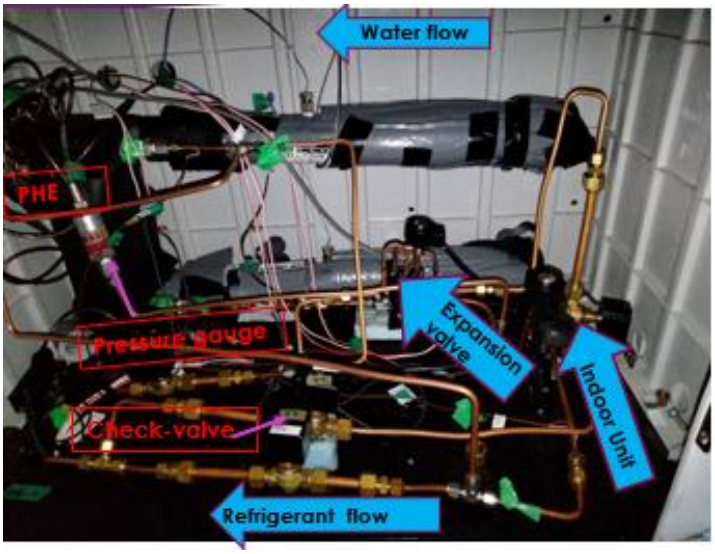


Figure 5: Inside the air-conditioning box for the hybrid heat pump system.

The hybrid heat pump system has a plate heat exchanger (PHE) which is installed in series with the air heat exchanger. The PHE is a heat exchanger between the ground heat source and the refrigerant. The pipes connecting the ground heat exchanger (GHE) and the PHE are filled with water. As in air-source systems, the high-pressure gas refrigerant exiting the compressor enters the condenser (outdoor unit). In a hybrid heat pump system, the refrigerant enters the PHE in a two-phase state, i.e., gas and liquid coexist, after the heat is dissipated to the outside air in the condenser, where it is condensed by dissipating heat to water (underground). In other words, the hybrid heat pump system utilizes both air and water. The high-pressure liquid refrigerant enters the expansion valve, where it is expanded to become a low-pressure liquid, which enters the evaporator, and then the gaseous refrigerant enters the compressor and the cycle repeats again. The measuring instruments for the flow of refrigerant and water are summarized in Table *2* below.

Table 2: Measuring instruments

Instruments	**Type of measurement**	**Accuracy**
T-type Thermocouple	Refrigerant temperature	$\pm 1℃$
K-Type Thermocouple	Water temperature in the GHE	$\pm 2.2℃$
Pressure Gauge	Refrigerant pressure	$\pm 0.25\%$
Resistance Thermometer	Water temperature	$\pm 0.1℃$
Volumetric flowmeter	Refrigerant flowrate	$\pm 1\%$
Solenoid Valve	Allow fluid flow in one direction	$\pm 2.5\%$

Table *2* above shows the measuring instruments used to take data in this study. The accuracy of each device was taken from the manufacturer's websites. The T-type thermocouple and pressure gauge were used to measure temperature and pressure respectively as the refrigerant enters different components in the refrigeration cycle as seen in Figure *6* and Figure *7*. The resistance thermometer was used to measure the temperature of water (see Figure *9*). The volumetric flowmeter measures the refrigerant's flow rate. The solenoid valve is an electromechanically controlled valve that is used to regulate the flow direction of the refrigerant.

2.1. About the experimental apparatus of the Air-source heat pump system

Figure *6* shows the experimental setup for the Air-source heat pump system. The figure shows the cooling operation. T and P in the figure indicate a thermometer (thermocouple) and a pressure gauge, respectively.

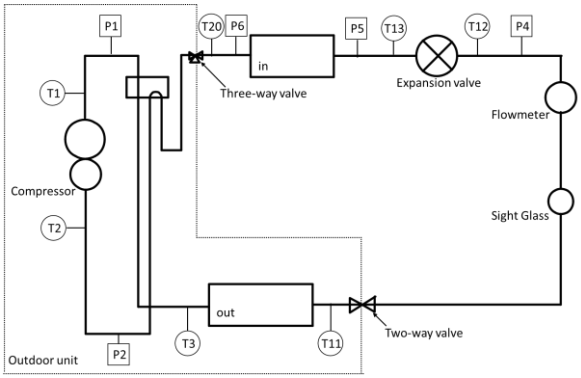


Figure 6: Air-source heat pump system Experimental Schematic.

In Air-source heat pump systems and Hybrid heat pump systems, pressure gauges and T-type thermocouples are installed at the compressor inlet/outlet, heat exchanger inlet/outlet, and expansion valve inlet/outlet. The T-type thermocouple is soldered to the surface of the copper tube. To calculate the mass flow rate of the refrigerant, a volumetric flowmeter is installed at the inlet of the expansion valve. The mass flow rate is obtained by the product of the volume flow rate and the density. Therefore, it is impossible to measure in a two-phase state where the density is not fixed. Therefore, a volumetric flowmeter was installed at the outlet of the condenser (an inlet of the expansion valve) where the liquid condenses to a pure liquid.

2.2. About the experimental apparatus of the Hybrid heat pump system

The solid line shows the refrigerant piping and the broken line shows the water piping. The control software for remotely operating the compressor speed, expansion valve opening, outdoor unit fan speed, and indoor unit fan speed is also the same as for the Air-source heat pump system. Five solenoid valves are installed in the hybrid heat pump system.

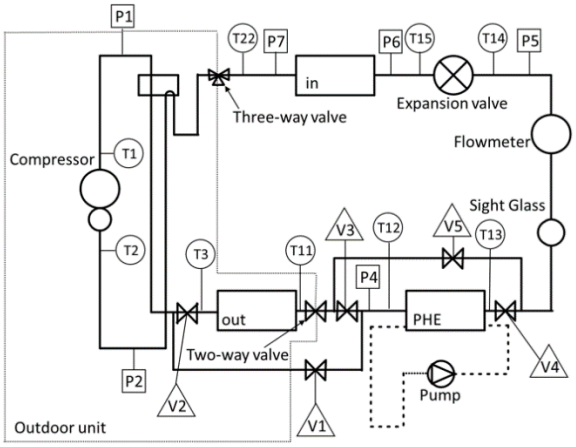


Figure 7: Hybrid heat pump system experimental schematic.

2.3. About Water Piping

The water goes from the pump in the control room to the double U-tube for heat exchange with the ground. After leaving the ground heat exchanger (GHE), the water, which is almost equal to the ground temperature, enters the PHE and exchanges heat with the refrigerant.

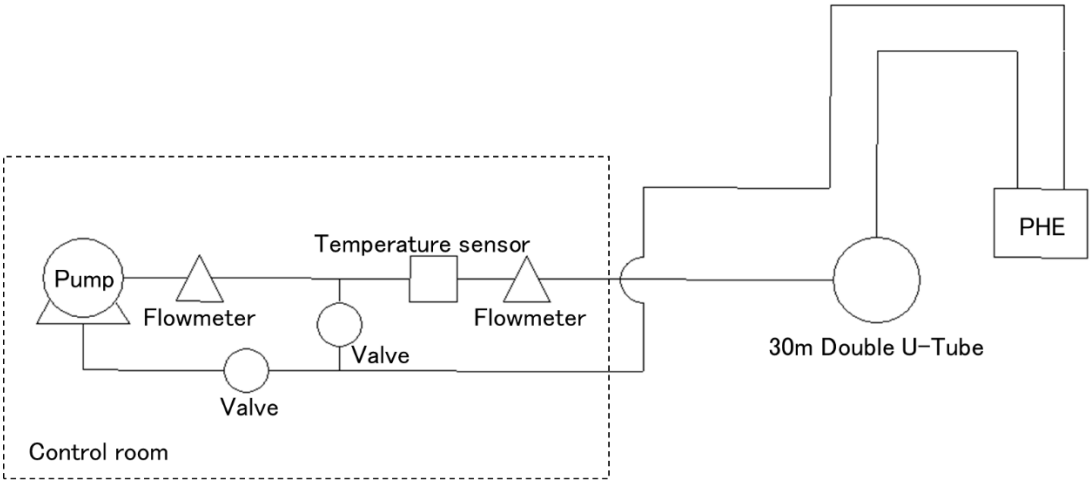


Figure 8: Overall view of water piping.

The two valves in the diagram above regulate the flow rate of water. As the water moves its temperature changes in the circuit. The changes in temperature were measured by the resistance thermometer (Figure *9*). The resistance thermometer measures the temperature by utilizing the fact that the electrical resistance of material changes with temperature. Unlike thermocouples, reference contacts are not required, making temperature measurement relatively easy and accurate (see Table *2*). However, the temperature range is lower than that of thermocouples.



Figure 9: Resistance thermometer.

The water temperature at the inlet/outlet of the GHE is measured by a K-type thermocouple. The water from the GHE goes to the PHE installed in the external box above the outdoor unit.

3. Methodology

3.1. System modeling procedure

The data collected was represented graphically in T-s and P-h diagrams. The system performance was evaluated by the P-h and T-s diagrams. These diagrams monitor the vapor compression refrigeration cycle as it changes states in different components (from the compressor, condenser, metering device, evaporator, and to the compressor again).

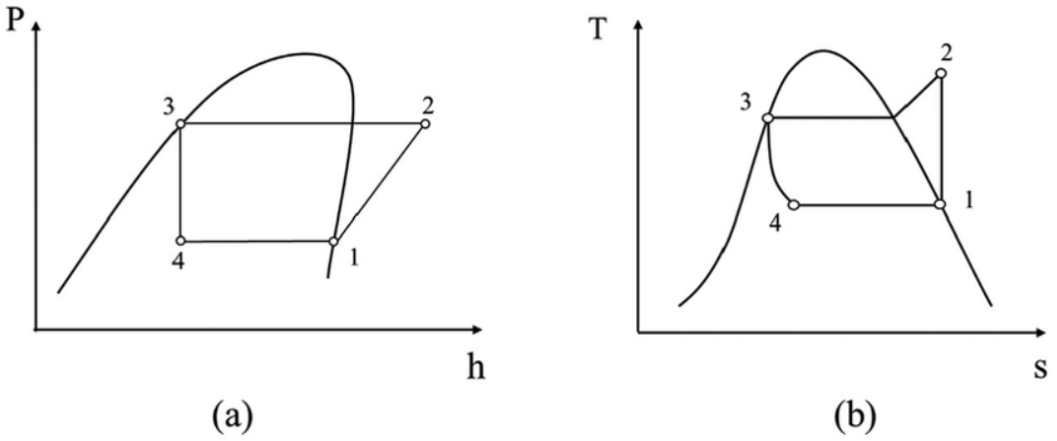


Figure 10: The P-h (a) and T-s diagram (b) **[9].**

The P-h (a) and T-s (b) diagrams above show the vapor compression refrigerant cycle. The numbers in the diagram indicate the different components which the refrigerant will have to pass through. The movement of the refrigerant through these components will result in a phase change. The refrigerant will move from the compressor (1) after it had be compressed resulting in an increase in its pressure, then it will move to a condenser (2) where the temperature will drop. Position (3) is a metering device (expansion valve) that drops the pressure of the refrigerant as it goes to an evaporator (4) and then it goes to the compressor where the cycle repeats again. The evaporator is where the refrigerant absorbs heat from the room.

3.2. Data Reduction

Firstly, hourly dynamic cooling loads for the ASHP and HBHP were calculated using a Visual Basic for Applications (VBA) program in a CSV file. The experimental data were used to calculate COP and evaluate the system performance. The COP is defined as follows:

$$COP_{cooling} = \frac{Q_L}{W_{in}} \quad (1)$$

Where Q_L is the available heat at the evaporator and W_{in} is the amount of energy required for compression. Since $W_{in} = Q_h - Q_L$, COP could also be expressed as follows:

$$COP_{cooling} = \frac{Q_L}{(Q_h - Q_L)} \quad (2)$$

REFPROP ver. 10 was used to calculate enthalpy and entropy which were automatically plotted in the CSV file. The REFPROP ver. 10 was also used to calculate other important parameters such as the mass flow rate, water mass flow rate, cooling capacity, the amount of GHE, PHE heat exchange rate, pump work, and the COP for both heat pump systems. Out of all the parameters mentioned, the mass flow rate, cooling capacity, and COP were the most important for this research.

The mass flow rate $\dot{m}_{ref}$ [kg/s] is obtained by the product of the refrigerant volume flow rate F_{ref} [L/min] and the density ρ_{ref}[kg/m^3]. The density of the refrigerant is calculated from the temperature and pressure using REFPROP. The temperature and pressure are referenced to the measured values at the inlet of the expansion valve, which is the location where the flowmeter is installed. The mass flow rate formula is as below:

$$\dot{m}_{ref} = F_{ref} \times \rho_{ref} \times \frac{1}{60} \times \frac{1}{1000} \quad (3)$$

The cooling capacity $Q_{cooling}$ [kW] indicates the amount of heat the system can remove from the refrigerated space over time. It is obtained by the product of the mass flow rate $\dot{m}_{ref}$ [kg/s] of the refrigerant and the specific enthalpy difference Δh_{eva} [kJ/kg] of the indoor unit (evaporator for cooling operation).

$$Q_{cooling} = \dot{m}_{ref} \times \Delta h_{eva} \quad (4)$$

Enthalpy is defined as the total heat energy of a system and is equal to the sum of internal energy (ΔU) and the product of pressure (P) and volume (ΔV). Mathematically, it can be expressed as,

$$H = \Delta U + P\Delta V \quad (5)$$

The specific enthalpy of the system is defined as the enthalpy per unit mass. It can be expressed as,

$h = \frac{H}{m}$,

Where h is the specific enthalpy, H is the enthalpy of the system and m is the mass. Thus, the specific enthalpy (h) can be defined as the sum of the specific internal energy (u) and the product of pressure (p) and specific volume (v),

$$h = u + pv \quad (6)$$

So, the specific enthalpy difference Δh_{eva} is the enthalpy difference between the inlet and outlet of the evaporator. The evaporator is where the refrigerant absorbs heat from the room in an isobaric heat addition process (see Figure *10*). Using thermodynamic principles, the specific enthalpy can be represented as,

$$\Delta h_{eva} = c_p \Delta T \quad (7)$$

Where c_p is the specific heat capacity at constant pressure, and ΔT is the temperature difference between the inlet and outlet of the evaporator.

Coefficient of performance commonly known as COP is a measurement of the energy efficiency of a system's heating or cooling performance. The COP was used to evaluate the performance of an air-conditioner. It is obtained by the quotient of the air-conditioner's power input W_{HP} [kW] to the amount of cooled heat $Q_{cooling}$[kW]. The COP_{AIR} [-]for the air-heat source system is shown in the formula below:

$$COP_{AIR} = \frac{Q_{cooling}}{W_{HP}} \quad (8)$$

The hybrid heat pump system can be obtained by considering, the pump power W_{pump}[kW]. COP_{HB}[-] of the hybrid heat pump system is shown in the Equation below:

$$COP_{HP} = \frac{Q_{cooling}}{W_{HP}+W_{pump}} \quad (9)$$

3.3. Data Acquisition

The cooling data was collected from the beginning of August to the first week of October. It was taken in four stages. The data were collected in four stages for both ASHP and HBHP. The data collection steps are summarized below:

- Controlling the compressor speed, expansion valve opening, and outdoor fan in an uninsulated room.
- Automatic air-conditioning ("free mode") operation in an uninsulated room.
- Controlling the compressor speed, expansion valve opening, and outdoor fan in an insulated room.
- Automatic air-conditioning ("free mode") operation in an insulated room.

In the first stage; data was collected by controlling the compressor speed, outdoor fan speed, expansion valve, indoor temperature, and PHE. This data was collected to optimize the whole system's performance by getting desirable values for the COP, cooling capacity, superheat, and air-source percentage ratio (for the hybrid heat pump system). The second stage was collecting data by letting the air-conditioning operate freely as in any building. The changes in a compressor, outdoor fan speed, and expansion value over time were recorded in a

CSV file. Over time, the COP, cooling capacity, and indoor temperature variations were also noted.
The third stage involved covering the two experimental rooms with an insulated cover to reduce heat from escaping easily. This was done to mimic how buildings are normally constructed. Buildings in regions with extreme weather like in Japan are built with indoor insulation, so heat doesn't escape easily unless an air-conditioner is used. This stage was performed exactly like in stage one where we controlled for different system components and observed their influence on the COP, cooling, superheat, or air-source percentage ratio (for the HBHP system). The final stage was the "free mode" where we allow the air-conditioner to run without any interference and changes for compressor speed, outdoor fan speed, and expansion valve were recorded in a CSV file. The air-source percentage ratio was also recorded for the HBHP system. The formula for the air-source percentage ratio is defined below:

$$\text{ASR} = \frac{\Delta h_{Air}}{(\Delta h_{Air} + \Delta h_{PHE})} \quad (9)$$

The reason for calculating the ASR for the HB system was to correlate the percentage of air with COP and cooling capacity. This correlation will help us optimize for the correct amount of air-source heat required in the HBHP system to improve the COP and cooling capacity.

4. Results and Discussion

The results focus mainly on comparing the performance (COP), ground heat exchange percentage, cooling capacity, inlet condenser temperature, and percentage of improvement comparison of the two systems.

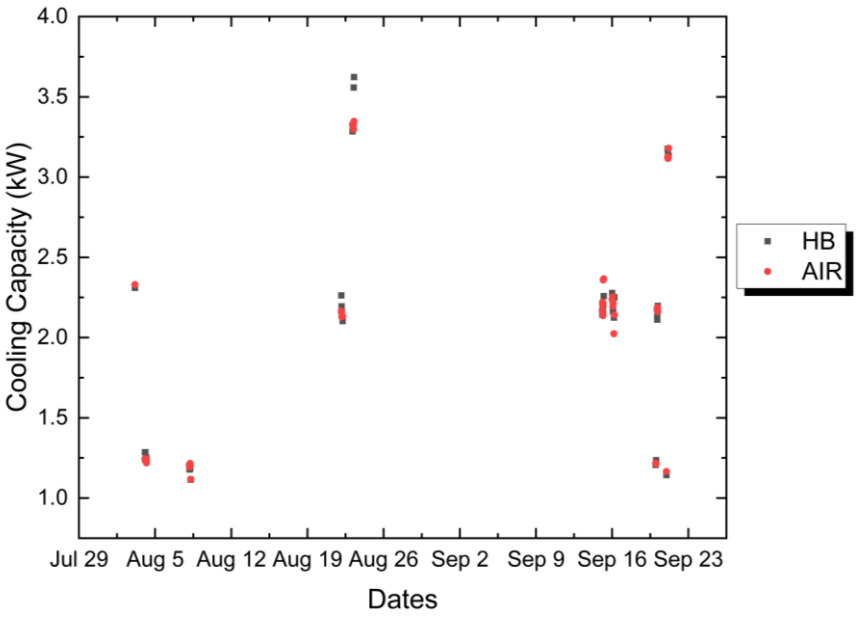


Figure 11: Cooling capacity for different days.

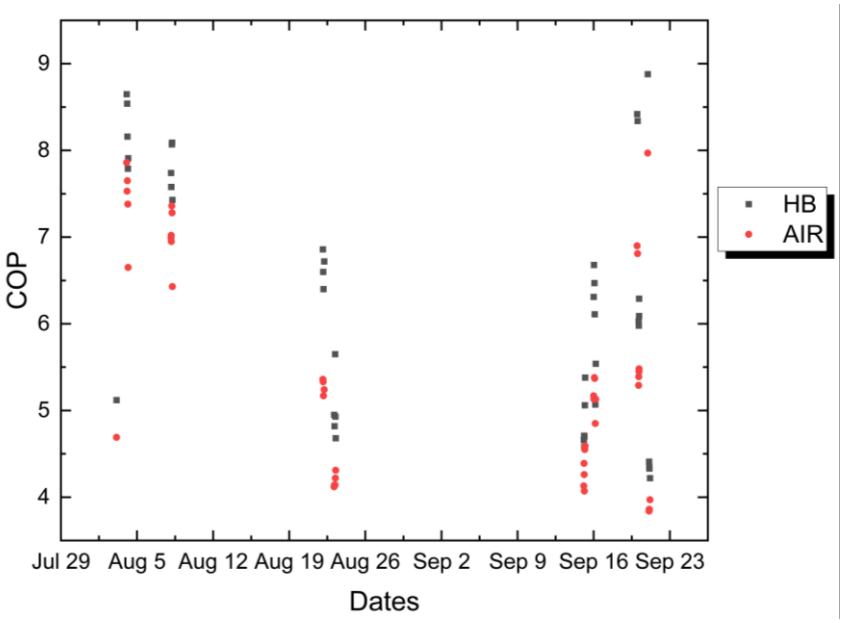


Figure 12: Coefficient of performance for different days.

The two figures above (Figure *11* and Figure 12) compare the hybrid and air source systems. HB stands for the hybrid heat pump system and AIR is for the air-source heat pump system. Figure *11* shows the cooling capacity comparison between HBHP and ASHP for different numbers of days. The HB shows similar cooling capacities for specific days because we controlled each system's specific cooling capacity range. Figure 12 depicts the COP comparison between the two systems. HBHP shows a greater performance overall as compared to the ASHP system.

Table 3: Hybrid and Air source performance comparison data.

Cooling capacity	**HB**		**AIR**		**Percentage Improvement (%)**
	COP	Outdoor Inlet Temperature (℃)	COP	Outdoor Inlet Temperature (℃)	
1kW	8.07	30.77	7.36	30.76	9.65
	8.09	31.16	7.28	31.33	11.13
	7.43	31.3	6.99	31.48	6.29
	7.58	32.5	6.95	31.92	9.06
	7.58	32.94	7.02	32.3	7.98
2.2kW	6.72	30.42	5.24	30.57	28.24
	6.6	32.07	5.33	31.64	23.83
	6.86	32.18	5.36	31.47	27.99
	6.4	33.56	5.17	32.56	23.79
	5.12	34.47	4.69	33.98	9.17
3.3kW	4.68	29.36	4.31	29.5	8.58
	4.93	29.87	4.22	29.91	16.82
	5.65	30.51	4.14	30.85	36.47
	4.82	30.8	4.14	30.99	16.43
	4.95	31.59	4.12	31.17	20.15

Table *3* above shows comparison data for the hybrid and air-source systems. Cooling capacity was controlled to a specific range to monitor the COP and outdoor inlet temperature for both systems. The significant metric of comparison is displayed in the last column where a hybrid percentage improvement is shown relative to the air. Higher cooling capacities display a high percentage improvement. A system that is able to remove heat efficiently will have a higher performance improvement. The reason that the hybrid heat pump system shows a higher performance improvement is that it cools the refrigerant coming from a compressor using two main components. The first component is the outdoor unit (condenser) and the second component is the plate heat exchange (PHE) which reduces the refrigerant temperature using the water cycle (See Figure *7* to see the refrigerant and water circuit).

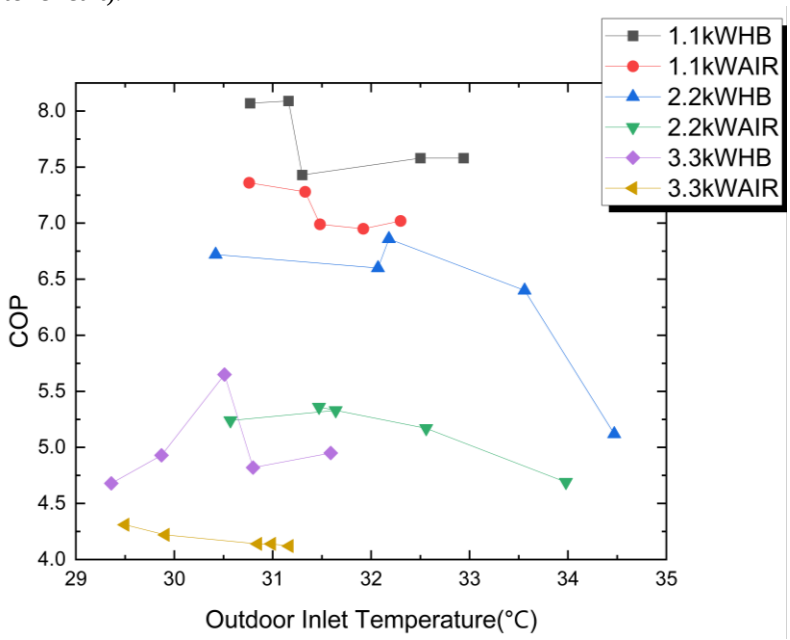


Figure 13: COP comparison against outdoor unit inlet temperature for different cooling capacities.

Figure *13* above depicts the relationship between COP and the outdoor unit inlet temperature for both systems. The COP for both systems dips slightly as the outdoor inlet temperature increases. Increasing the temperature of the gas requires an increase in work output to condense the refrigerant. So, for the same work output, the temperature of the stream leaving the condenser increases for a fixed input temperature to the condenser, and the heat rejection capacity of the condenser decreases. Thus, the COP for both systems decreased slightly. The hybrid heat pump system shows a higher COP compare to the air-source system in each cooling capacity range.

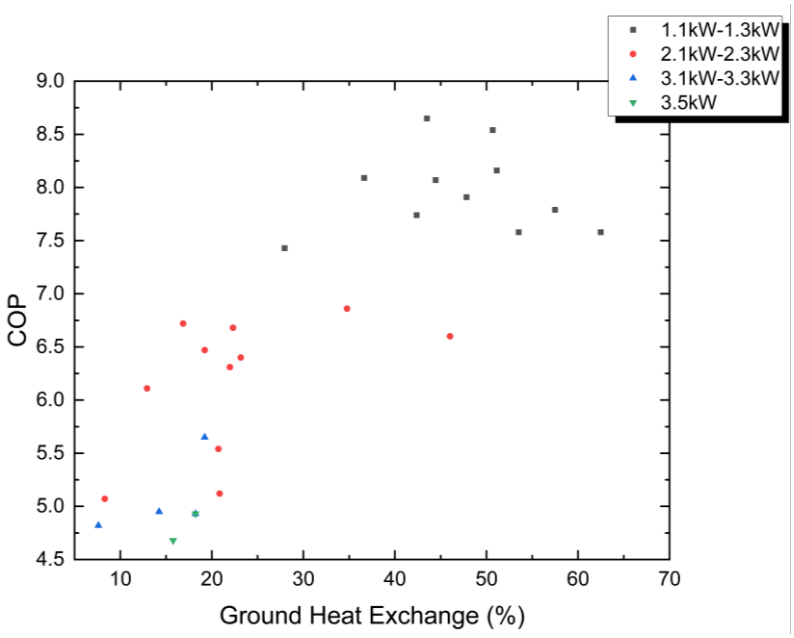


Figure 14: COP comparison against ground heat exchange percentage for different cooling capacities.

The hybrid heat pump system has an additional water circuit that exchanges heat with the refrigerant using the PHE. PHE is the main component in our circuit responsible for the improvement of a hybrid heat pump system compared to an air-source system. The ground source heat percentage was also measured to understand the role of the PHE in improving performance. Figure *14* above shows the relationship between the ground heat exchange percentage and the COP for each specific cooling capacity range. Figure *14* can also be correlated to the air-source ratio which demonstrated the percentage of air in the hybrid heat pump system required for optimum performance. Then, the graph shows that increasing the percentage of ground source heat improves the COP. Varying values of ground heat exchange percentage parameters were obtained by changing the compressor speed, outdoor fan speed, and PHE control valve.

Table 4: The summary table for the COP of the two systems.

Cooling Capacity	**Average COP**		**COP_{improv} % (HB vs AIR)**
	HB	**AIR**	
1.1kW	**8.08**	**7.20**	**10.91**
2.1kW	**5.78**	**4.97**	**13.41**
3.1kW	**4.70**	**4.05**	**13.43**

Table *4* shows the COP comparison between HB and AIR source systems. These are average COP values for each cooling capacity range. The HB performed better in every measurement taken for the COP. The highest disparity between the two systems is at higher cooling capacities. This means that hybrid heat pump systems perform better in regions or buildings that require a lot of energy consumption as a requirement to meet air-conditioning needs. The COP percentage comparison was calculated as follows:

$$COP_{improv} = \left(\frac{COP_{ave_HP} - COP_{ave_AIR}}{COP_{ave_HP}}\right) \times 100$$

Where,

COP_{improv} is the COP percentage improvement of HB against AIR source system, COP_{ave_HP} and, COP_{ave_AIR} is the average coefficient of performance for a specified cooling capacity range for the hybrid and air-source system respectively.

5. Conclusion

In this research, a performance comparison between the hybrid and air-source heat pump systems was experimentally investigated. The findings obtained in this research are as follows:

- As a result of the experiment, the hybrid heat pump system's coefficient of performance (COP) is higher than the air-source system. The average COP for the 3.1kW cooling capacity showed the highest COP improvement between the two systems. The Average COP obtained for the HB and AIR was 4.70 and 4.05 respectively. Thus, this resulted in the HBHP performing 13.43% better than the ASHP.
- An increase in outdoor inlet temperature decreased the COP in both systems. This results from the condenser's inability to reject more heat without affecting the performance of the system. This can be attributed to the higher energy demand by the system to meet the higher cooling requirement.
- The cooling capacity ranges obtained by controlling the compressor speed, expansion valve opening, and outdoor fan speed showed COP values for the two systems that are comparable to other authors. Further research will be focused on system performance comparison for the heating operations. Thereafter, an in-depth component (compressor, condenser, expansion valve, evaporator, and PHE) impact on the overall performance will be fully assessed.

Acknowledgment

This study has been a collaborative effort between Miyara and Kariya Thermal Engineering Lab at Saga University and Fujitsu General company. The authors would also like to thank Saga University, Graduate School of Science and Engineering for providing academic support and facilities to make this research possible.

References

[1] H. V. Nguyen, Y. L. E. Law, M. Alavy , P. R. Walsh, W. H. Leong and S. B. Dworkin, "An analysis of the factors affecting hybrid ground-source heat pump installation potential in North America," *Applied Energy*, pp. 28-38, 2014.

[2] T. You, W. Wu, W. Shi, B. Wang and X. Li, "An overview of the problems and solutions of soil thermal imbalance of ground-coupled heat pumps in cold regions," *Applied Energy*, vol. 177, pp. 515-536, 2016.

[3] T. You, X. Li, W. Wu, W. Shi, B. Wang and K. Soga, "Coupled heating of ground-coupled heat pump system with heat compensation unit: Performance improvement and borehole reduction.," *Energy Conversion and Management*, vol. 148, pp. 57-67, 2017.

[4] K. F. Beckers , G. A. Aguirre and J. W. Tester, "Hybrid ground-source heat pump systems for cooling-dominated applications: Experimental and numerical case-study of cooling for cellular tower shelters.," *Energy and Buliding*, vol. 177, pp. 341-350, 2018.

[5] S. P. Kavanaugh, "A design method for hybrid ground-source heat pumps.," *ASHRAE Transactions*, vol. 104, p. 691, 1998.

[6] J. Urchueguía, M. Zacarés, J. Corberán, A. Montero, J. Martos and H. Witte, "Comparison between the energy performance of a ground coupled water to water heat pump system and an air to water heat pump system for heating and cooling in typical conditions of the European Mediterranean coast.," *Energy Coversion and Management*, vol. 49, no. 10, pp. 2917-2923, 2008.

[7] B. Morrone, G. Coppola and V. Raucci, "Energy and economic savings using geothermal heat pumps in different climates.," *Energy conversion and management*, vol. 88, pp. 189-198, 2014.

[8] T. You, B. Wang, W. Wu, W. Shi and X. Li, "Performance analysis of hybrid ground-coupled heat pump system with multi-functions.," *Energy Conversion and management*, vol. 92, pp. 47-59, 2015.

[9] C. O. Suong and A. Asanakham, "Evaluation of a single stage heat pump performance by figure of merit (FOM)," *Energy Reports*, vol. 6, pp. 2735-2742, 2020.

14th IEA Heat Pump Conference
15-18 May 2023, Chicago, Illinois

Development of a Novel Sorption-Type Heat Pump Water Heater for North American Homes

Paul Glanville[a*], Navin Kumar[a], Abbas Ahsan[a], Alex Fridlyand[a], Magnus Ekblad[b], Ingemar Hallin[b], Corey Blackman[d], Noe Contreras[c]

[a]GTI Energy, 1700 S Mt Prospect Rd, Des Plaines, IL 60018 USA
[b]HeatAmp Sweden AB, Sankt Eriksgatan 65, 113 32, Stockholm, Sweden
[c]Northwest Energy Efficiency Alliance (NEEA), 700 NE Multnomah Street, Suite 1300, Portland, OR 97232 USA
[d]SaltX Technology AB, Västertorpsvägen 135, 129 44, Stockholm,. Sweden

Abstract

Critical to decarbonizing gas-fired water heating, typically up to 26 GJ of natural gas consumed per home per year, is advancing heat pump water heaters (HPWHs). This paper provides an overview of the development and experimental demonstration of this novel sorption-type HPWH, using a nested buffer tank/heat exchanger approach driven by an integrated compact steam boiler. Led by a European technology developer with technology support from multiple U.S.-based partners, this fuel-fired HPWH concept is intended for North American homes, with a hybrid design of both up to 2 kW peak output from the sorption modules and up to 12 kW peak auxiliary output from the steam boiler. With an efficiency target of ≥1.25 UEF and a target first hour rating of 284 L of hot water, this paper focuses on several aspects of this product development and testing, including a) the development and testing of a compact steam boiler loop to drive the desorption process, designed for 14 ng NOx/J output and compatible with up to a 30% hydrogen/natural gas blended fuel, b) immersed sorption modules within the buffer storage tank for water heating with a COP_{gas} > 1.40 using limited moving parts, and c) heat exchange and preliminary system controls, per empirically-calibrated simulation, to meet UEF targets and high usage hot water patterns typical for 4-5 occupant homes. Following this review of testing results, the authors provide an outlook for fuel-fired HPWHs in a rapidly decarbonizing North American market.

© HPC2023.
Selection and/or peer-review under the responsibility of the organizers of the 14th IEA Heat Pump Conference 2023.

Keywords: heat pump water heater; sorption-type heat pump; vapor adsorption cycle; ultra-low NO_x

1. Introduction

Of the more than four million fuel-fired storage-type residential water heaters sold in the U.S. each year, which outnumber sales of tankless water heaters by about six-to-one, only about 5% of these products have efficiencies greater than the minimum allowable efficiency of a uniform energy factor (UEF) of 0.62 to 0.64 (depending on storage tank volume[1]). This is despite concerted efforts on the behalf of manufacturers, technology developers, and researchers to introduce higher-efficiency equipment, which includes condensing-level efficiency storage water heaters, hybrid tank/tankless type solutions, and integrated heat pump water heaters (HPWHs). It is the last category that holds the greatest promise to decarbonize the approximately 26 GJ of natural gas consumed per home per year, through increases in efficiency as a critical emerging solution

* Corresponding author. Tel.: +1 847 768 0782; fax: +1 847 768 0501.
E-mail address: pglanville@gti.energy.

[1] The Uniform Energy Factor (UEF) is a common efficiency metric in the U.S. and Canada, which is a daily efficiency metric (site energy basis) based on serving a specific simulated hot water usage pattern. This is defined in the U.S. Code of Federal Regulations, Appendix E to Subpart B of Part 430 – *Uniform Test Method for Measuring the Energy Consumption of Water Heaters*

to address a market that is challenged by cost-effective energy efficiency with 0.88 UEF storage-type solutions and 0.97 tankless-type solutions available today [1].

While residential electrically-driven HPWHs are mature and available in the U.S. for 10+ years [2], providing multiple options UEF > 2.50 (0.95 on primary energy basis for U.S. average), there are emerging air-source sorption-type HPWHs under development as well that are suitable for direct-fired applications with natural gas, propane, biomethane, and/or hydrogen-based fuels. Sorption-based HPWHs are available for commercial-sized water heating applications but are only now emerging for residential applications. Commercial-sized fuel-fired HPWHs are often able to serve much larger commercial hot water loads than integrated electrically-driven HPWHs (common to have > 3X rated capacity [3]) and have undergone multiple demonstrations in recent years over multiple building types, including hospitality, multifamily buildings, senior care facilities, schools, and restaurants/cafeteria applications [3]. For these commercial-sized products or prototype HPWHs, employing direct-fired vapor absorption cycles (single-effect and GAX-type), units with maximum outputs from 23 kW to 41 kW were operated in conjunction with existing site boilers and/or commercial water heaters as a retrofit for periods of 12 months or more in California, British Columbia, Illinois, Ontario, and Oregon. Results showed a reduction in site fossil gas consumption by 18% to 53% [4-7], with one study using hybrid air/water-source approach to provide supplemental A/C in addition to hot water for two full-service restaurant sites, yielding an additional 14% reduction in electricity demand for A/C in addition to hot water fuel savings, for a net 48% reduction in overall greenhouse gas (GHG) emissions [4].

These residential sorption-type HPWH developments are important, as the regulatory environment in the U.S. is shifting rapidly to accelerate further gains in end-use energy efficiencies. This includes proposed changes to the EnergyStar® specification to have a minimum allowable UEF ≥ 0.86 (original proposal was UEF ≥ 1.0) for gas-fired storage-type water heaters [8] and regional specifications like the Northwest Energy Efficiency Alliance (NEEA) advanced specification creating three performance tiers of minimum allowable UEF from 1.0 to 1.3 [9]. These shifts in performance metrics have been informed by multiple developments of sorption-type HPWHs, such as one approach based on a single-effect vapor absorption cycle (NH_3/H_2O), which was successfully developed and demonstrated in multiple U.S. field trials to reduce fuel consumption by 50% or greater with a projected UEF of 1.20 (1.08 on a primary energy basis) [1]. Another emerging approach described in this paper is based on a vapor adsorption cycle with enhanced chemisorption, with an NH_3/salt working pair. In this paper, lessons learned from parallel and prior sorption-type HPWH developments are provided and then the authors focus on the latter and review the development of a novel adsorption-type HPWH, using a nested buffer tank/heat exchanger approach driven by an integrated compact steam boiler, a collaboration between technology developers, with a hybrid design approach with 2 kW output sorption module and 12 kW auxiliary steam boiler. Performance goals are ≥1.25 UEF, target first hour rating of 284 L of hot water or greater, and a combustion system with less than 14 ng NOx/J output and compatible with 30% hydrogen/natural gas blended fuel, and capacity for typical 4-5 occupant North American homes.

2. Technology Review - Description of Residential Sorption-type HPWHs

For thermally-driven heat pumps (TDHPs) overall, inclusive of not just sorption-type machines but also mechanically-driven vapor compression cycles (e.g. engine-driven) and thermal compression machines (stirling-type, thermoacoustic, etc.), it is sorption-type machines that have the greatest potential be scaled down to sizes appropriate for residential applications (< 25 kW output, often < 5 kW for hot water). This is for many reasons, but for practical concerns, this is primarily due to challenges in cost-effectively scaling down engines for work-activated TDHPs and economies of scale necessary for thermal compression-type machines with commonly high operating pressures (> 50 bar) [3]. Sorption-type TDHPs are commonly used in heating-focused applications, in air-to-water/brine configurations most commonly, as supplements or replacements for water heaters, boilers, and/or furnaces. For these systems, the two primary types of sorption heat pumps are explained as follows:

- **Vapor Absorption** heat pump cycles utilize thermal energy to drive a heat-pump cycle where a refrigerant is cyclically absorbed and desorbed from a secondary fluid (absorbent). While the refrigerant is still compressed by an electro-mechanical pump (solution pump), it is a liquid in solution rather than a vapor – in the case of the predominant vapor compression cycles. Absorption-type heat pumps are an attractive alternative, as lifting the pressure of a liquid versus a vapor requires significantly less energy (1%-2% for standard conditions). Thus, while the job of refrigerant compression is performed by a relatively small, low-power solution pump, the primary input to the process is thermal energy required to drive the refrigerant vapor from its absorbed state in the desorber (or "generator"), taking a low-temperature refrigerant/sorbent mixture and providing a high-temperature, vapor refrigerant. The most common

working fluid pairs are for absorption machines specializing in heating versus cooling, NH_3 (refrigerant) and water (absorbent) for the former and water (refrigerant) and lithium bromide (absorbent) for the latter. For heating applications, regeneration temperatures commonly range from ~115°C (single effect), ~150°C (GAX), to > 175°C (double effect). With significant developments by multiple manufacturers, developments of TDHPs using the vapor absorption cycle were summarized in 2019 by GTI Energy [3].

- **Vapor adsorption** heat pump cycles also referred to as solid sorption cycles, are the adhesion of a gas or vapor (the adsorbate) to form a thin film on a solid surface (adsorbent). Typically, adsorbents are mounted to a heat exchanger that heats and cools the solid. There are many different types of adsorbents, including silicon dioxide, carbon-based compounds, salt matrices, and synthetic compounds such as zeolites. Adsorption is a batch process, a discontinuous process that can continue until a balance between the adsorbent and the adsorbate is achieved. Regeneration temperatures trend lower than vapor absorption overall, depending on cycle and working fluid/sorbent pair, from as low as ~60°C to ~150°C, concerning common open and closed cycle architectures [3]. The adsorption cycle can be applied for multiple end uses, including space conditioning (both heating and cooling) and refrigeration.

As noted, NH_3 is a common refrigerant for sorption-type TDHPs designed for heating applications, used in nearly all of the prototypes and products summarized in the prior section. The table below provides a summary of the broad advantages and disadvantages of TDHPs using NH_3 as a refrigerant, for vapor absorption versus vapor adsorption type cycles. As noted previously and in other efforts [3], the performance advantages of vapor absorption cycles, particularly in heating applications, are well-documented, as are the operational and reliability challenges [10]. TDHPs using the vapor adsorption cycle do have a reduced capacity and efficiency but have significant potential for improved reliability.

Table 1. Qualitative Comparison of NH_3-based Absorption and Adsorption type TDHPs

	NH_3 Absorption TDHPs	NH_3 Adsorption TDHPs
Unique Advantages	Continuous Process, has higher efficiency, ability to modulate capacity	Fewer moving parts for improved reliability, NH_3/salt pair has added capacity from chemisorption effect*
Unique Disadvantages	Pumps with dynamic seals are common failure points; corrosion and non-condensable gases must be managed	As batch process, cyclic & seasonal efficiency/capacity is poorer than absorption in general, commonly by 10%-15%
Common Advantages or Disadvantages relative to other TDHPs	Advantages: Can operate well in cold climate applications, NH_3 has GWP = ODP = 0.0, no issues with freezing climate installations	
	Disadvantages: Hazards associated with NH_3 as B2L refrigerant, compatibility challenges with common materials (e.g. copper/copper alloys)	

*This is primarily an improvement over other common adsorption working fluid/sorbent pairs

Before describing the design of the current HPWH, it is useful to review the features and outcomes of the vapor absorption-type HPWH. In this prior effort, a technology developer, GTI Energy, and multiple manufacturers were successful in developing and demonstrating a retrofit-ready GHPWH unit with a target total installed cost of $1,800 and with Ultra Low NOx certification (< 10 ng NOx/J output). The system used an integrated design, with a 3 kW nominal output NH_3/H_2O single effect absorption cycle atop a 227 L to 302 L tank, driven by a custom 2 kW premix gas burner with a nominal 1100 W heater for supplemental high capacity heating. The ~0.5 kg NH_3 was well below the 3 kg limit allowing for indoor installations and, following initial proof-of-concept developments [11-14], successive demonstrations were performed with ~30 units built, roughly half of which were installed in field environments. In the most recent, five-site demonstration in the Los Angeles area between 2019-2020, the per-site energy and GHG emissions reductions were 50% or greater over a 12-month monitoring period as compared to a measured baseline. Operating COP_{Gas} was consistently 1.25-1.60, electric power demand was 0.2% - 2.0% of total output, and end users surveyed indicated satisfaction with the hot water capacity delivered at average temperatures of 52°C [1]. Laboratory testing of the current pre-production generation of GHPWHs demonstrated a path to achieving 1.20 UEF certification. Subsequent analysis and modeling of the potential interactive effects between the GHPWH and the home's HVAC equipment revealed a minimal impact on false loading, substantially less than the impact of eliminating the natural draft baseline water heater product or an electric-type HPWH, and suggestive that a ducted evaporator is neither necessary nor cost-effective [1]. With a photo of a demo unit and the overall field performance compared to baselines in Figure 1, these efforts have aided in demonstrating the technical and market feasibility of sorption-type HPWHs.

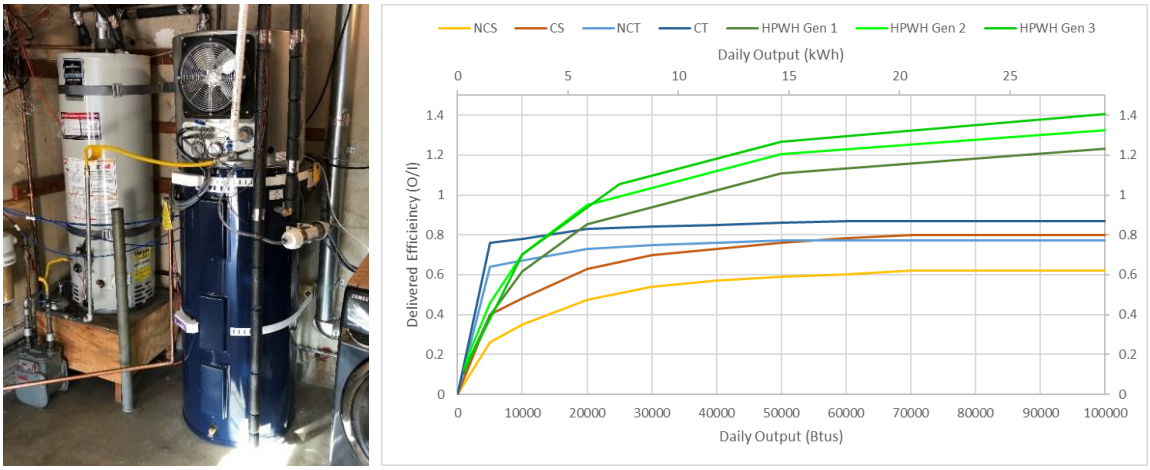


Fig. 1. Photo of Vapor Absorption-type Sorption HPWH in Prior Study and Performance Compared to Non-condensing Storage (NCS)/Condensing Storage (CS) and Non-condensing Tankless (NCT)/Condensing Tankless (CT) Baselines [1]

In developing this sorption-type HPWH, this team determined the performance criteria necessary to meet the original 1.30 Energy Factor (E.F.) and subsequent 1.20 UEF targets, which were as follows [1, 15]:

- *Average Heat Pump Cycle COP$_{Gas}$:* The time-averaged COP$_{Gas}$ of the heat pump cycle needed to exceed 1.65, defined as the ratio of heat recovered from the heat pump cycle (absorber, condenser, flue gas heat recovery) to fuel inputs.
- *Average System COP (COP$_{System}$):* The time-averaged system COP needed to exceed 1.50, defined as the total heat delivered to the storage tank as a ratio of total energy inputs (electricity and fuel inputs). This is often approximately equal to the "recovery efficiency" term as defined in the standard test procedure.
- *Average combustion efficiency ≥ 95% ($T_{flue\ gas} \leq$ 90 °F):* This is a time-average of the net combustion efficiency of the process, on a flue-loss calculation basis.
- *Average $T_{delivered}$ of hot water ≥ $T_{tank,\ initial}$:* To avoid detrimental corrections in the calculation procedure, it is advantageous for time-averaged delivered outlet water temperatures to be at or above the starting average temperature of the storage tank.
- *Standby Heat Losses:* Using the UA term defined in the procedure as a benchmark, a factor of 2.5 Btu/hr-°F or less is prescribed.
- *Power Consumption:* Active and standby power consumption targets were less than 120 W and 10 W respectively.
- *Controls Trigger Early Recovery:* More an artifact of the hot water draw pattern used to yield the UEF metric determination, the product was required to initiate a recovery within the first draw cluster.

While these metrics will not universally apply to all sorption-type HPWHs, nor do they represent the unique set of criteria to meet a 1.20 UEF goal or greater, however, this approach of breaking down these key criteria of HPWH functionality will serve useful in the optimization of the presently described HPWH and others as well.

2.1. Description of the Adsorption-type HPWH Concept

Shown in the diagram and rendering, in both Figures 2 and 4 subsequently, the novel sorption-type HPWH described in this paper embeds a nominal 1 kW output vapor adsorption cycle within a buffer storage tank. The sorption module reactor is driven by a compact steam generator, dubbed a "burner/boiler", which regenerates the sorbate and delivers heat to the buffer storage (via heat recovery). The burner/boiler can also generate hot water directly ("boost" heating). The reactor design uses the NH_3/salt working pair and, as previously developed for space heating applications [16, 17], is modified for this application. The reactor includes calcium chloride, a widely known salt in use in various industrial applications and the adsorption bed uses a shell-and-tube type design as described previously, with the cycling and varying of heat delivery of the batch process evened out by the buffer tank [18]. As shown in the simplified schematic in Figure 2, the heat-driven adsorption HPWH consists of a reactor, a receiver, an evaporator, and a burner-boiler integrated into a 189 L buffer tank. The heat to the buffer tank is delivered either through a sorption cycle or via auxiliary combustion (“boost” heating), which indirectly delivers heat to the potable water. The sorption cycle and

direct-firing can operate both in parallel and in series. In direct-firing mode, the steam generated in the burner-boiler and the remaining heat in the flue gas is recovered to heat the buffer tank directly. The direct-firing mode is utilized during high load periods when the buffer tank temperature drops below set-point during a draw.

In the sorption mode, the heat to the buffer tank is delivered in three different phases: (1) Desorption, (2) Cool-down, and (3) Adsorption. In the desorption phase, the steam generated in the burner-boiler enters the reactor. It condenses in the reactor, releasing heat to the reactor, with the liquid water returning to the boiler. The reactor's temperature increases to a level where ammonia is desorbed from the salt matrix. The desorbed ammonia vapor condenses on the reactor walls and heats the buffer tank with the heat of condensation before returning to the receiver and evaporator through gravity. The communication tube in the buffer tank helps with steam volume expansion. The desorption phase was sized to deliver heat to the buffer tank at 1.5 kW for 20 mins.

In the cool-down phase, the burner-boiler is inactive; the pump circulates water from the buffer tank through the reactor to cool down the salt matrix to the equilibrium pressure. The cool-down phase was designed to last 5 minutes and deliver 0.15 kWh of heat to the buffer tank through sensible heat recovered from the reactor.

In the adsorption phase, similarly, the burner-boiler is inactive. Low-grade heat from the ambient is utilized to heat the ammonia to the gas phase in the evaporator. Ammonia vapor flows through the receiver to the reactor and is absorbed into the salt matrix. The pump circulates water from the buffer tank through the reactor to heat the tank with the heat of adsorption. The adsorption phase was sized to deliver heat to the buffer tank at 0.49 kWh for 95 minutes.

This sorption-type HPWH is sized for residential water heating applications but may be suitably large for space heating, or "combi"-type applications as well. The burner/boiler has a design output of 2-12 kW, sized to regenerate the 3.0 L sorption module and provide excess heating in "boost" operating modes. The system contains approximately 1.2 kg of NH_3, which is sufficiently below the previously noted 3 kg limitation for indoor installations. For this "alpha" prototype, the storage tank is based on a 50-gallon (227 L) platform, however, subsequent versions are expected to be slightly larger to meet the design targets of 2 kW peak output from the sorption module and up to 12 kW peak auxiliary output from the steam boiler. In all cases, the efficiency target is ≥1.25 UEF, with an interim target of the middle tier of 1.15 UEF [9], and in all cases a target first hour rating of 284 L of hot water. To be competitive in all U.S. markets, the product is also targeted to have at least 14 ng NOx/J output emissions and be compatible with up to a 30% hydrogen/natural gas blended fuel.

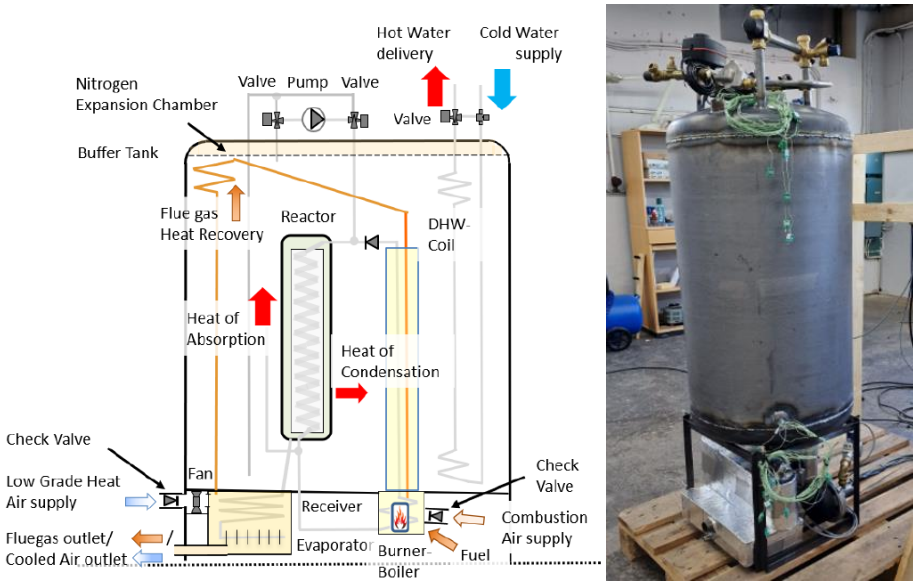


Fig. 2. Simplified Diagram of Concept Novel Sorption-Type HPWH and Prototype Under Construction

3. Progress in Novel Adsorption-Type HPWH Development

3.1. HPWH Design and Integration

A first "alpha" prototype with the design described was manufactured for preliminary testing in the second half of 2022. This design is based on several separate subsystem efforts in parallel, with the main focus on design, manufacturing, and showcasing a prototype that has a bill of materials that can meet the set cost targets within the target product category. The system is currently operational with a measured efficiency that is 15%-20% higher than direct-firing with a condensing-level efficiency. To improve on this performance, the authors note that system heat losses need to be better managed, for both direct-firing and heat pumping modes. With subsequent analysis, several pathways to remedy these performance gaps have been identified, including scaling up certain subsystems to optimize capacity versus these thermal losses. At the time of writing, the team continues to address these performance optimization challenges, with completion expected in 2023. Several aspects of this development are described in the subsequent section.

Guiding this design process is the challenging market of residential water heating, where an aggressive cost target is necessary for consumer acceptability [19]. The goal for this system, as a drop-in replacement in North America, would be competing with lower cost, lower performance existing water heaters but also assuring efficiencies well above levels of performance consistent with condensing-level efficiency. In addition to being considered as a replacement or alternative for existing lower efficiency water heaters, the product may also be considered as an alternative to both high-efficiency boilers and electrically-driven heat pump water heaters. With these factors in mind, the system configuration is intended to meet near-term efficiency and decarbonization goals, while retaining end user comfort in standard and extreme loading scenarios, while meeting a mass production manufactured cost of <$1,000 with an even lower cost as a long-term goal. While sizing described previously is for a proof-of-concept version of this sorption-based HPWH approach, designs and product families may evolve with greater/lesser levels of buffer storage, sorption module capacity, and burner/boiler capacity. Ultimately, it is the authors' sense that the available market for a future product within the category is mainly driven by the cost of the appliance, which drives this optimization process overall, per the simplified representation in Figure 3.

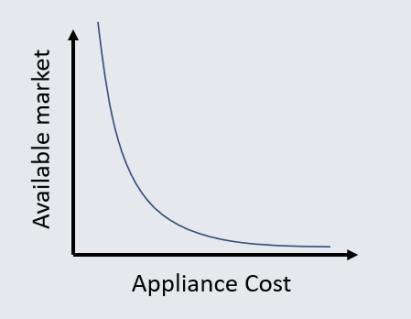


Fig. 3: Representation of Cost Driver

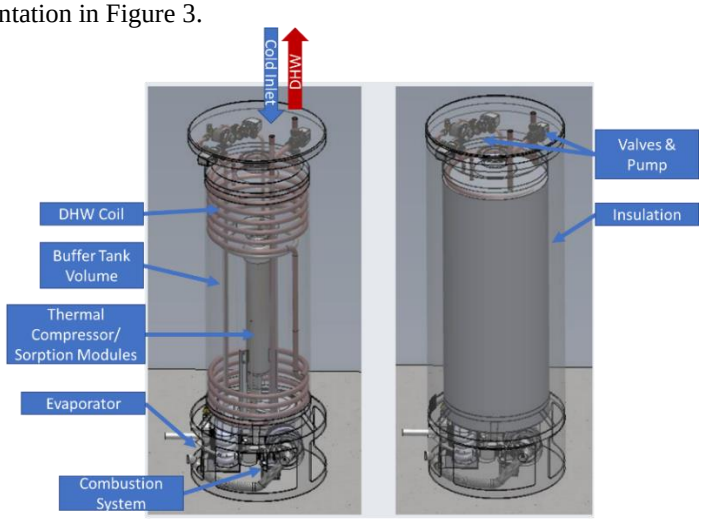


Fig. 4. Rendering and Identification of Key Components of Concept Novel Sorption-Type HPWH

3.2. Burner/Boiler Design and Demonstration

Based on preliminary design exercises, the burner/boiler will need to meet the following basic criteria for performance: greater than 93% overall effectiveness, greater than 83% overall fuel-to-steam efficiency, NO_x emissions of less than 14 ng/J output, CO emissions of 100 ppm air-free or below, and suitable modulation over full range over 2-12 kW. During start-up, the burner/boiler should rapidly reach steady-state steam

circulation and the boiler segment should avoid dry-firing in all operational scenarios.

3.2.1. Combustion Design Lessons Learned from Prior Sorption-type HPWH Efforts

Similar to conventional boilers, direct-fired sorption machines commonly employ either "water-tube" or "fire-tube" designs for the desorber, the vessel where the heat source (combustion, typically) drives the boiler of the refrigerant from the sorbent, typically at a peak temperature/pressure for the cycle. In previous work by a subset of the authors in a separate and parallel effort, the aforementioned prototype development of small-scale absorption heat pumps [1] and commercially-available solutions employ "fire-tube" and "water-tube" designs respectively (see figure below). While the heat transfer coefficient of boiling ammonia/water solution differs from what is expected within low-pressure steam generation, by 10-25X, some lessons can be learned, specifically from the "water-tube" desorber design effort, which includes the following as applicable to a custom approach for premixed, modulating combustion within a compact desorber:

- Radial/cylindrical burners were superior in performance and emissions to up-fired approaches in the cylindrical combustion chamber, using a CFD-assisted design approach the ideal dimensions of the combustion chamber and burner were realized, which were a chamber radius approximately equal to the diameter of the burner.
- On downstream quenching, CO emissions, and stability issues, the height of the chamber (distance from the top of the burner, with a blank surface, from transition/exit from the chamber) was found to have a non-linear response. Increasing heights above a certain limit, the simulation suggested a favorable recirculation zone was weakened, leading to poorer heat transfer and flame liftoff. This allowed for an empirically-tuned gradual increase in the chamber height.
- On the burner surface, the impact of vertical distribution was mitigated by internal structures, preventing the "Christmas tree" effect – wherein fuel/air face velocities are greatest at the burner top and lowest at the bottom. The use of conical or parabolic inserts, in addition to revised perforated plate hole patterns, were all shown to improve this impact, further reducing quenching.
- For outdoor installations, several combinations of gas valves, blowers/mixers, and ignition controls were demonstrated to effectively modulate and ignite at down to -20°F, though not all components performed equally.

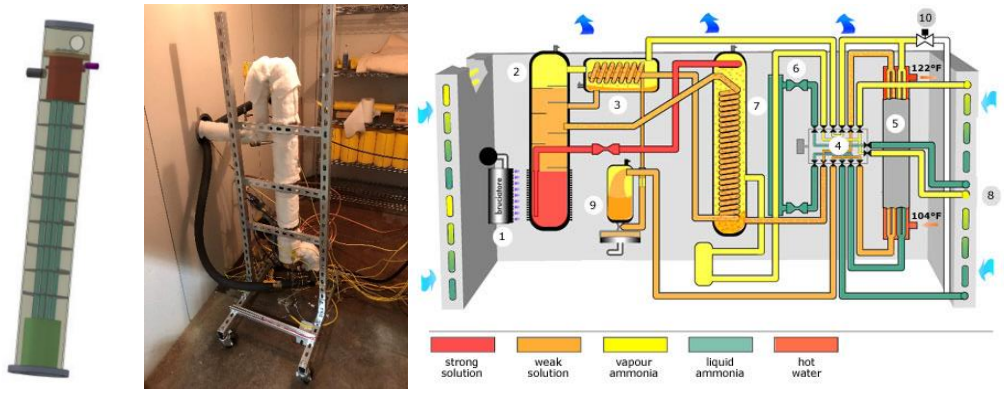


Fig. 5. "Fire-tube" Desorber Design/Testing (Left, Center) and "Water-tube" Desorber Design (Right, Desorber is #2) Examples (Image Source: [15], GTI Energy, Robur)

3.2.2. Burner/Boiler Testing Results

An experimental test stand was designed and built at GTI Energy to perform testing on the burner/boiler component of the novel sorption-type HPWH, as shown in the figure below. A custom-made, cylindrical, radiant-style burner was used in conjunction with off-the-shelf gas train components. The premix burner configuration was assembled using a fuel-air mixer with a nominal output of 27 kW and a turndown ratio of 5:1. During preliminary testing, combustion stability was difficult to maintain, with lean blowoff being the common mode of failure. This may have been caused by insufficient sealing of the burner base and entrainment of secondary combustion air into the burner/boiler, or insufficient drainage of condensate in the flue gas stream leading to abrupt changes in back pressure. Further investigation will be conducted to determine and resolve the flame stability issue.

Despite challenges with maintaining combustion stability, some valuable experimental data was gained from the preliminary testing during stable operation taking place over separate 15 minute and 20 minute

periods. Due to the oversizing of the fuel-air mixer component, the firing rate was set to an average of 14.0 kW with excess air of 170% (air-fuel equivalence ratio of 1.7). Emissions testing results are summarized in Table 2, which indicates NO_x emissions well below the target but outstanding issues with the CO emissions, slightly above the target. For future testing, a new gas train will be assembled with a more appropriate modulation range that will better match the 2-12 kW operating range of the sorption module. The emissions values will be reassessed at excess air ranging between 140-150%, which is more common for boiler applications.

Table 2. Emission Testing Results.

Exhaust Species	Average Measured Emissions	Emissions Target
NO_x Emissions	1.8 ng/J; 1.5 ppm at 3% O_2 Corrected	14 ng/J; 20 ppm at 3% O_2 Corrected
CO Emissions	137.4 ppm, air-free	100 ppm, air-free



Fig. 6. Photo of Un-insulated Burner/Boiler Test Station

3.3. System Simulation and Projected Performance

The adsorption HPWH model was simulated as a stratified water buffer tank as an indirect Domestic Hot Water (DHW) system coupled with an adsorption heat pump and an internal Heat Exchanger (HX), as illustrated in the Figure 7 schematic. The sensible storage energy balance model were developed in Octave based on stratified sensible thermal storage divided into five volume segment nodes. Each equal volume segment is assumed to be thoroughly mixed. The heat loss capacity rate from the buffer tank to the ambient was specified for the bottom, top and zone as highlighted in Table 3, as heat loss capacity rate UA. The model constants and buffer tank properties highlighted in Table 3 were based on an off-the-shelf 50-gal indirect storage tank. The buffer tank was discharged (i.e., heating DHW) via the internal heat exchanger. All temperatures in the buffer tank were computed by solving a set of differential equation energy balance for each node given by:

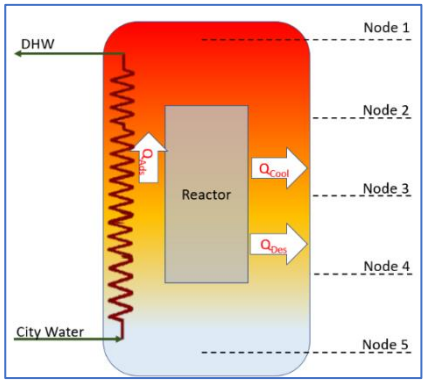


Fig. 7. The schematic for stratified water storage tank model with direct heating and internal heat exchanger.

$$\frac{V_w \rho_w C_{p,w}}{n_{tank}} \frac{\delta T_{i,j}}{\delta t} = k_{water} \frac{A_q}{H_w} n_{tank} \left[\left(T_{i+1,j} - T_{i,j} \right) + \left(T_{i-1,j} - T_{i,2} \right) \right] - \frac{UA_{hx}}{n_{hx}} \left(T_{i,j} - T_{i,j,hx} \right) - \sum \frac{UA_{loss}}{n_{loss}} \left(T_{i,j} - T_{amb} \right) + P_{heat} \quad (1)$$

The internal HX heat transfer area is divided into five segment nodes. Each node was thermally coupled to the corresponding volume segments of the tank. The heat transfer coefficient between the heat exchanger and tank was calculated using H. Druck's correlation for immersed coil heat exchanger [20]. The energy balance for the heat exchanger at each node is given by:

$$\frac{V_{hx}\rho_{hx}C_{p,hx}}{n_{hx}}\frac{\delta T_{i,j}}{\delta t} = \dot{m}_{hx}\, C_{p,hx}\left(T_{i-1,j} - T_{i,j}\right) + \frac{UA_{hx}}{n_{hx}}\left(T_{i,j,tank} - T_{i,j}\right) - \frac{UA_{hx,loss}}{n_{hx}}\left(T_{i,j} - T_{amb}\right) \quad (2)$$

The heating of the buffer tank was either performed by sorption phases at fixed-volume nodes, as shown in Figure 7. The internal heating of the buffer tank was modeled like an electric resistance heater controlled by the average tank temperature (i.e., aquastat). The heat loss capacity rate from the buffer tank to the ambient was specified for the bottom, top, and each volume node, as summarized in Table 3.

Table 3. Constant model parameter.

Model Parameters	
Volume of tank [m^3]	0.19 (50 Gal)
Height of storage tank [m]	1.17
UA_a – Zone heat loss [W/K]	0.7
UA_u – Bottom heat loss [W/K]	0.3
UA_o – Top heat loss [W/K]	0.3
$V_{hx,internal}$ [m^3]	0.01
A_{hx} [m^2]	1.32
Time step – [sec]	10
Number of nodes	5
Max tank temp [°C]	72
Q_{des} – Desorption [kW, Minutes]	1500, 20
Q_{cool} – Cool down [kW, Minutes]	1800, 5
Q_{Ads} – Desorption [kW, Minutes]	315, 95

As illustrated in Figure 8, the model was validated with experimental data for an indirect DHW storage tank previously collected in the field by GTI Energy. The model's accuracy was within ± 15% of the experimental data's tank average temperature. The model's spatial average temperature was computed by averaging the temperatures of the five nodes. Similarly, the water storage temperature was measured in the field at five equally distributed intervals and averaged.

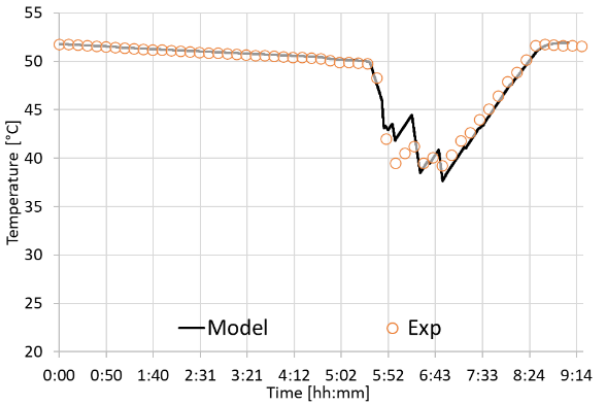


Fig. 8. Model validation with experimental data for average tank temperature.

Energy efficiency standards and labeling metrics (EES&L) for water heaters vary widely among countries [21]. In the USA, the Uniform Energy Factor (UEF) test procedure developed by the U.S. Department of Energy (DOE) is used for the energy efficiency of water heaters [22]. A higher UEF metric means a water

heater is more energy-efficiency and will cost less to operate compared with other water heaters in the same category.

The UEF test is 24 hours long to simulate the use of a water heater over one day. For the medium draw profile in this work, the UEF consists of numerous water draws organized into three draw groups (series of water draws) at two predefined flow rates (1 and 1.7 GPM). The UEF characterizes the system's energy efficiency based on this characteristic hot water use pattern. The UEF has energy-based corrections for the tank's initial and final conditions and energy-based corrections for the outlet temperature differing from the nominal value.

The COP for the adsorption heat pump during the 24-hour model, the UEF test, was assumed at a constant value of 1.25 based on the UEF test condition requirement of 19.7 ± 0.6˚C [20]. The adsorption heat pump operated for a total of 9 hours and 30 minutes, as shown in Figure 9. The heat pump's runtime was divided into two segments, with 3 hours of non-operational period between them. Based on the estimated COP of the adsorption heat pump and the heat loss from the buffer tank, the system achieved a UEF of 1.1 in the model. As illustrated in Figure 9, the tank is vertically stratified, with hotter (lower density) water above cooler (higher density) water, as expected by the model for the stratified tank. Analysis of the tank temperature shows the effect of draws and charging location (i.e., adsorption heating phase) on the stratification.

As illustrated in Figure 10, the buffer tank temperature was set to and maintained at 70˚C (158˚F), compared to 48.9˚C (120˚F) in residential storage water heaters. The buffer was held at a higher temperature than the standard due to the indirect design of the DHW. A higher buffer temperature is required to maintain the DHW supply temperature of more than 43.3˚C (110˚F), accounting for the flow rate and heat transfer limitation on the heat exchanger, as shown in Figure 10 during the UEF testing.

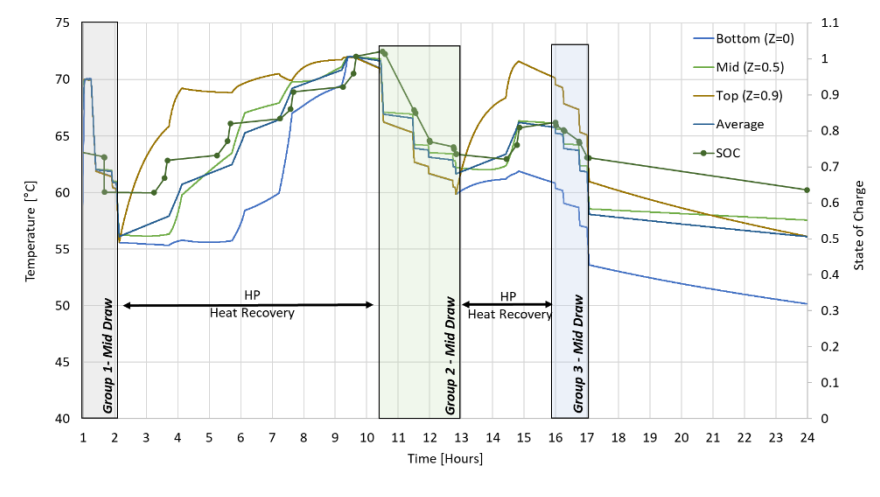


Fig. 9. Uniform Energy Factor (UEF) simulation of adsorption HPWH for 24 hours at medium draw level.

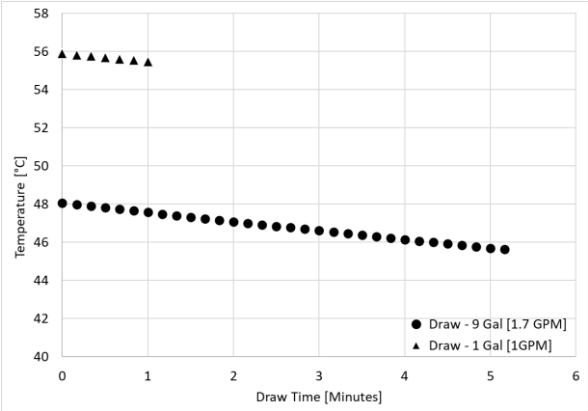


Fig. 10. The effect on DHW supply temperature for the indirect system during the UEF simulation.

4. Conclusions and Next Steps

In this paper, the authors described a novel sorption-type heat pump water heater, sized for residential applications in North America with a hybrid design, of both up to 2 kW peak output from the sorption modules and up to 12 kW peak auxiliary output from the steam boiler, with an efficiency target of ≥1.25 UEF and a target first hour rating of 284 L of hot water. The context of this development is described, in terms of the residential high-efficiency water heating market and the design and performance of sorption-type HPWHs in general. Progress on several aspects of the design and development are described, including a) the development and testing of a compact steam boiler loop to drive the desorption process, designed for 14 ng NOx/J output and compatible with up to a 30% hydrogen/natural gas blended fuel, b) immersed sorption modules within the buffer storage tank for water heating with a COP_{gas} > 1.40 using limited moving parts, and c) heat exchange and preliminary system controls, per empirically-calibrated simulation, to meet UEF targets and high usage hot water patterns typical for 4-5 occupant homes. While these remain performance targets as development and testing are ongoing, a path to reaching these goals is briefly described as are efforts to calibrate a performance model of the novel sorption-type HPWH. In the coming months, the authors anticipate refining system components through successive experimental development, assessing performance in succeeding generations of HPWH prototypes, and if successful in meeting targets, proceeding to initial field trials in the U.S.

List of Acronyms/Nomenclature

CO	Carbon Monoxide
COP	Coefficient of Performance
CFD	Computational Fluid Dynamics
DHW	Domestic Hot Water
GAX	Generator Absorber Exchange
GHG	Greenhouse Gas
GHPWH	Gas-fired Heat Pump Water Heater
GTI	Gas Technology Institute
HPWH	Heat Pump Water Heater
HVAC	Heating, Ventilation, and Air-conditioning
NEEA	Northwest Energy Efficiency Alliance
NOx	Oxides of Nitrogen
TDHP	Thermally-Driven Heat Pump
UEF	Uniform Energy Factor
heat	Heat input
hx	Heat Exchanger
n	Nodes
UA	Heat Transfer coefficient (W/K)
V	Volume (m^3)
Cp	Heat Capacity (kJ/kg K)
T	Temperature (°C)
k	Thermal Conductivity (W/m K)
A	Area (m^2)
P	Heating Power (W)
ρ	Density (kg/m^3)

Acknowledgments

The authors acknowledge the support of Utilization Technology Development (UTD) and the Northwest Energy Efficiency Alliance (NEEA), with contributions from GTI Energy, HeatAmp, SaltX, and NEEA.

References

[1] Glanville, P., Fridlyand, A., Mensinger, M., Sweeney, M., Keinath, C. "Integrated Gas-fired Heat Pump

Water Heaters for Homes: Results of Field Demonstrations and System Modeling", ASHRAE Transactions; Atlanta Vol 126, (2020): 325-332.
[2] Glanville, P., Kosar, D., & Suchorabski, D. "Parametric Laboratory Evaluation of Residential Heat Pump Water Heaters". ASHRAE Transactions, 118(1), 853+, 2012.
[3] GTI & Brio, Gas Heat Pump Technology and Market Roadmap (2019), Industry White Paper, https://www.gti.energy/wp-content/uploads/2020/09/Gas-Heat-Pump-Roadmap-Industry-White-Paper_Nov2019.pdf
[4] Glanville, P., Mahderekal, I., Mensinger, M., Bingham, L., Keinath, C. "Demonstrating an Integrated Thermal Heat Pump System for Hot Water and Air-Conditioning at Full-Service Restaurants", ASHRAE Transactions; Vol. 127 (2021): 363-370.
[5] Toronto Atmospheric Fund (TAF). 2018. "Gas Absorption Heat Pumps: Technology Assessment and Field Test Findings", Prepared for Enbridge Gas and Union Gas.
[6] Pratt, J. et al., 2020. Robur Heat Pump Field Trial, Report #E20-309 prepared for the Northwest Energy Efficiency Alliance.
[7] Glanville, P., Mensinger, M., Blaylock, M., Li, T. and Hardesty, R. "Hybrid Heating and Hot Water in Multifamily Buildings: Demonstration and Analysis of Integrated Boilers and Thermally-Driven Heat Pumps", Proceedings of the ASHRAE Winter Conference, Las Vegas, NV (2022).
[8] U.S. EnergyStar®, Product Specification for Residential Water Heaters, Final Draft Version 5.0 (2022).
[9] Northwest Energy Efficiency Alliance, "Advanced Water Heating Specification for Gas-Fueled Residential Storage Water Heaters - Version 1.0" (2019), Link: https://neea.org/img/documents/Natural-Gas-Advanced-Water-Heating-Specification.pdf
[10]Glanville, P., Fridlyand, A., Keinath, C., and Garrabrant, G., Demonstration and Simulation of Gas Heat Pump-Driven Residential Combination Space and Water Heating System Performance, Proc. of the 2019 ASHRAE Winter Conference, Atlanta, GA.
[11]Garrabrant, M., Stout, R., Glanville, P., Keinath, C., and Garimella, S., Development of Ammonia-Water Absorption Heat Pump Water Heater for Residential and Commercial Applications, Proceedings of the 7th Int'l Conference on Energy Sustainability, Minneapolis, MN, 2013.
[12]Garrabrant, M., Stout, R., Glanville, P., and Fitzgerald, J., Residential Gas Absorption Heat Pump Water Heater Prototype Performance Results, Proceedings of the Int'l Sorption Heat Pump Conference, Washington, DC, (2014).
[13]Glanville, P., Vadnal, H., and Garrabrant, M., Field testing of a prototype residential gas-fired heat pump water heater, Proceedings of the 2016 ASHRAE Winter Conference, Orlando, FL.
[14]Glanville, P. and Vadnal, H., Field Evaluation of Residential Gas-Fired Heat Pump Water Heaters, public Final Report prepared for the Northwest Energy Efficiency Alliance under contract #42385 (2016).
[15]Garrabrant, M., Stout, R., Glanville, P., Fitzgerald, J., and Keinath, Chris. Development and Validation of a Gas-Fired Residential Heat Pump Water Heater - Final Report. United States: N. p., 2013. Web. doi:10.2172/1060285.
[16]Blackman, C., Bales, C., Thorin, E. Experimental Evaluation and Concept Demonstration of a Novel Modular Gas-driven Sorption Heat Pump. Proceedings of the 12th IEA Heat Pump Conference, Rotterdam, NL (2017). Link: https://www.diva-portal.org/smash/get/diva2:1167419/FULLTEXT01.pdf
[17]Blackman, C. Evaluation of Modular Thermally Driven Heat Pump Systems, Doctoral Dissertation prepared for Mälardalen University, Sweden (2020). Link: https://www.hig.se/download/18.27f829b517401fb8b9fe048/1598339666303/Corey%20fulltext.pdf
[18] Gluesenkamp, K.R.; Frazzica, A.; Velte, A.; Metcalf, S.; Yang, Z.; Rouhani, M.; Blackman, C.; Qu, M.; Laurenz, E.; Rivero-Pacho, A.; Hinmers, S.; Critoph, R.; Bahrami, M.; Füldner, G.; Hallin, I. Experimentally Measured Thermal Masses of Adsorption Heat Exchangers. Energies 2020, 13, 1150. https://doi.org/10.3390/en13051150
[19] Northwest Energy Efficiency Alliance, (2018) "Water Heater Market Characterization Report" Link: https://neea.org/resources/water-heater-market-characterization-report
[20] H. Drück, E. Hahne: Thermal Testing of Stores of Solar Domestic Hot Water Systems Proceedings of Eurosun '96, Freiburg, September 1996
[21] C. T. Johnson Alissa, Lutz James, Mcneil Michael A., "An international Survey of Electric Storage Tank Water Heater Efficiency and Standards (LBNL-6725E)," Berkeley, 2013. [Online]. Available: https://eta-publications.lbl.gov/sites/default/files/lbnl-6725e.pdf.
[22] US Department of Energy, "10 e-CFR 430, Energy Conservation Program for Consumer Products; Subpart B, Test Procedures; Appendix E, Uniform Test Method for Measuring the Energy Consumption of Water Heaters," 2019.

14th IEA Heat Pump Conference
15-18 May 2023, Chicago, Illinois

Economic and Environmental considerations for the deployment of VHTHPs in European markets

Kim Högnabba*[a], Ron Zevenhoven[a], Tor-Martin Tveit[b], Stefano Vittor[b]

[a]Åbo Akademi University, Henriksgatan 2, FI-20500 Åbo, Finland
[b]Olvondo Technology AS, Langgata 21 A, NO-3080 Holmestrand, Norway

Abstract

This paper provides an overview of the most important economic and environmental considerations when deploying very high temperature heat pumps (VHTHPs) in the European region. One of the state-of-the-art heat pumps, a process based on the reversed Stirling cycle, can achieve temperatures of up to 200 °C, and temperature lifts over 150 °C. The coefficient of performance (COP) suffers during such large temperature lifts, and thus the relationship between the price of electricity and alternative fuels becomes a crucial factor when determining the feasibility of replacing existing boilers in industrial settings. The environmental impact is quantified using life cycle assessment and mainly depends on the electricity source used to run the heat pump as well as the construction and decommissioning of the heat pump itself.
It was found that factors such as low electricity prices and/or carbon pricing mechanisms are crucial in order to operate low COP heat pumps profitably. Additionally, it was determined that VHTHPs can significantly reduce the environmental impact of steam generation compared to equivalently sized fossil fuel boilers, provided that renewable sources of electricity are used.

© HPC2023.
Selection and/or peer-review under the responsibility of the organizers of the 14th IEA Heat Pump Conference 2023.

Keywords: VHTHP; Life Cycle Assessment; Europe; Electricity mix

1. Introduction

Very high temperature heat pumps (VHTHPs) capable of delivering temperatures of up to 200 °C (392 °F) are beginning to emerge on the market and offer an alternative process for generating high temperature process heat for industries which have traditionally relied on the combustion of fossil fuels [1]. While there is no generally accepted definition of what constitutes a VHTHP, Arpagaus et al. presents a definition for in Figure 1 which involves operating conditions where sink temperatures exceed 100 °C and/or source temperatures exceed 60 °C. Traditional heat pumps operate with sink temperatures below 80 °C and source temperatures below 40 °C, and high temperature heat pumps occupy the space between traditional heat pumps and VHTHPs [2].

The coefficient of performance (COP) decreases due to the high temperature lifts, and as such the economic feasibility of the technology becomes highly dependent on the price ratio between electricity and fossil fuels, typically natural gas. The environmental benefit of replacing fossil fuels boilers with VHTHPs is also largely dependent on the source of the electricity used to power the heat pump. Countries where electricity grid mixes consist mostly of nuclear power and/or renewable energy sources such as wind, solar, and hydropower produce a significantly smaller environmental footprint when operating VHTHPs compared to grids consisting mostly of fossil fuels. This footprint can be quantified using life cycle assessment (LCA).

In this study, a way to estimate the environmental and economic outcomes associated with installing VHTHPs in different European regions is determined using electricity data from ENTSO-E [3], environmental impact data from ecoinvent v3.8 [4], and real-world data from VHTHPs in industrial settings. Two separate

* Corresponding author. Tel.: +358-458816058
E-mail address: kim.hognabba@abo.fi

breweries in Spain utilizing high temperature steam are investigated, and the economic and environmental impacts of replacing existing natural gas boilers with VHTHPs are estimated.

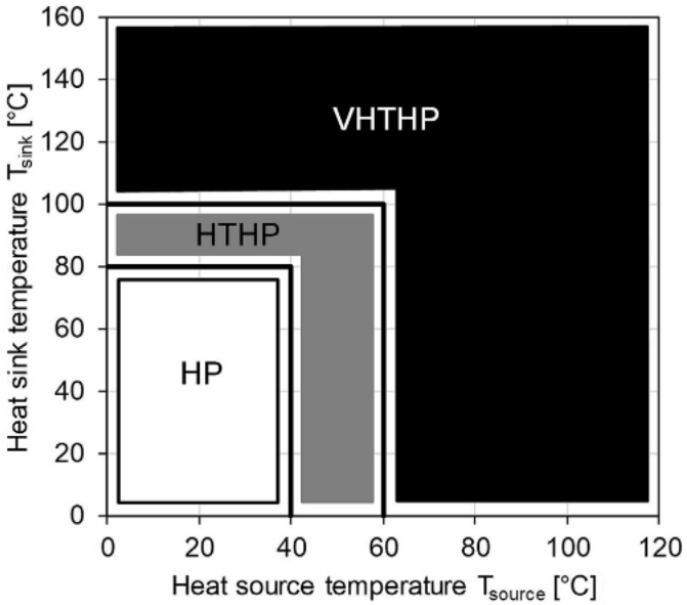


Fig. 1. Temperature operating ranges for heat pumps (HP), high temperature heat pumps (HTHP), and very high temperature heat pumps (VHTHP) [2].

2. Economic considerations

The efficiency of a heat pumps is limited by the theoretical Carnot efficiency, which decreases as the temperature difference between the heat source and the heat sink increases. The VHTHP analyzed in this study, a heat pump based on the reverse Stirling cycle which uses helium as the working medium, can deliver temperature lifts over 150 °C. During these temperature lifts, the COP tends to drop under 2.0 in practice [1, 5]. This means that the price ratio between electricity and fossil fuels, commonly natural gas, becomes a deciding factor when comparing different heating technologies.

Compared to natural gas boilers, industrial VHTHPs are still an emerging technology and therefore tend to have higher upfront costs, as well as potentially higher maintenance costs. Table 1 presents the initial investment and maintenance costs for a natural gas boiler and the VHTHP included in this study. The investment cost of the VHTHP is calculated according to a 1 200 €/kW figure from a product datasheet [6], while the maintenance cost is an internal estimate from the heat pump manufacturer. The values for the reference natural gas boiler are obtained from case study 2 in the EU Commission report *Ecodesign preparatory Study on Steam Boilers* [7], as it is of roughly appropriate size. The values for the natural gas boiler have been adjusted for inflation to 2022 prices.

Table 1. Investment and maintenance cost comparison of a VHTHP and a natural gas boiler

	VHTHP	NG Boiler
Thermal capacity (kW)	750	1 700
Investment cost (k€)	900	76
Maintenance cost (k€/yr)	10	5.5

All European Union member countries as well as Iceland, Liechtenstein, and Norway are participants in the European Union Emissions Trading System (EU ETS), which is a cap-and-trade scheme in which companies purchase emission allowances for the CO_2 they emit. Depending on the industry, companies get a certain number of allocations by default, and must thereafter either purchase enough allowances to cover their carbon dioxide emissions or reduce their overall emissions [8]. Companies always have an incentive to reduce their emissions, as the allowances can be bought and sold on an open market. Therefore, any reduction in CO_2 emissions can be directly tied to a monetary gain. At the time of writing, allocations were trading at 80 €/ton CO_2 [9].

3. Environmental considerations using LCA

A significant portion of the environmental footprint associated with a VHTHP is tied to the electricity generation used to run the heat pump. The European electricity market consists of a diverse set of energy sources that varies between bidding zones. In order to accurately determine the environmental impact of installing and operating a VHTHP, one needs to know the electricity mix in the region in question along with the environmental footprint associated with each energy source.

3.1. Life Cycle Assessment

LCA allows one to estimate the environmental impact of building, operating, and decommissioning a product at a specific location. The overall impact gets categorized into fifteen or so midpoint categories depending on the methodology used, and includes categories such as land use, carcinogenic substances, and ecotoxicity. These factors can be summarized into wider damage categories covering the impact on human health, ecosystem quality, climate change, and resource usage.

The life cycle impact of the VHTHP in this article has been studied and quantified before and will serve as a basis for further analysis [10].

3.2. Methodology and Impact categories

Depending on what methodology is used, one can group the environmental impact into three or four damage categories. The IMPACT 2002+ V2.15 [11] method was chosen in this analysis, as it separates climate change into its own category alongside human health impact, ecosystem quality, and resource usage. These four damage categories can be normalized in order to compare them against each other, and they can also be combined into a single total environmental impact estimate. This impact is measured in points, which are equal to person years (pers×yr) and represent the average impact associated with a single European citizen per year in a given category.

At the midpoint level, life cycle impacts are typically expressed as kg substance $s\text{-}_{eq}$, which is an equivalent amount of a reference substance s appropriate for the impact category in question. Examples of these reference substances are chloroethylene emissions into the air for the human toxicity category, sulfur dioxide emissions into the air and water sources for terrestrial acidification/nutrification and aquatic acidification, and carbon dioxide emissions for global warming. Other units are used where a reference mass equivalent substance is not appropriate, such as Becquerel carbon-14 into $air\text{-}_{eq}$ for the category ionizing radiation.

These emissions are then normalized into the damage category units Disability-Adjusted Life Years (DALY) for human health, Potentially Disappeared Fraction of species over a certain amount of m^2 during a certain amount of years (PDF×m^2×yr), and Mega Joules (MJ) for resource usage. The normalization factors used to further estimate the total environmental impact measured in points are 0.0071 DALY/point for human health, 13 700 PDF×m^2×yr/point for ecosystem quality, 9 950 kg CO_2e into air/point for climate change, and 152 000 MJ/point for resource usage [11].

3.3. Environmental impact of different electricity sources

Table 2 contains a summary of the environmental impact associated with the most common electricity generation sources in Europe and the most relevant midpoint categories expressed in damage category units. The inventories for each electricity source were taken from the database ecoinvent v3.8, and the method IMPACT 2002+ V2.15 was used to assess the life cycle impact. The impact of some electricity sources such as solar power differs considerably between regions. The total amount of solar irradiance received is lower in regions further from the equator and the weather conditions may be harsher, resulting in reduced equipment lifespans. As a result, the environmental impact associated with each individual kWh electricity produced over the panel's lifetime is increased in regions that receive less solar irradiance. The impact of other energy sources such as nuclear power is more consistent across European regions.

The figures in Table 2 are modeled after the "Electricity, *source*, at power plant/UCTE" modules in ecoinvent v3.8, which represent the average impact across power generation stations across Europe. In reality, these figures vary between power plants, with more modern units being more efficient and producing a smaller environmental footprint for a given amount of electricity.

Table 2. Environmental impact assessment per kWh delivered electricity from different electricity sources

Category	Unit	Hard coal	Lignite	Natural gas	Nuclear	Hydro	Solar*	Wind	Pulp**	Wood chips
Human health impact										
Carcinogens	DALY	2.81×10^{-9}	1.2×10^{-9}	1.62×10^{-8}	6.52×10^{-10}	2.56×10^{-10}	5.17×10^{-9}	1.38×10^{-9}	1.4×10^{-8}	9.3×10^{-9}
Non-carcinogens	DALY	1.5×10^{-8}	4.53×10^{-9}	9.43×10^{-10}	4.32×10^{-9}	2.35×10^{-10}	9.38×10^{-9}	1.44×10^{-9}	1.52×10^{-8}	9.53×10^{-8}
Respiratory inorganics	DALY	5.11×10^{-7}	8.48×10^{-7}	8.17×10^{-8}	1.81×10^{-8}	4.32×10^{-9}	4.98×10^{-8}	1.05×10^{-8}	2.54×10^{-7}	2.24×10^{-7}
Ecosystem quality										
Aquatic ecotoxicity	PDF × m^2 × yr	2.23×10^{-3}	7.67×10^{-5}	2.73×10^{-4}	1.85×10^{-3}	1.03×10^{-5}	6.03×10^{-4}	6.41×10^{-5}	2.47×10^{-3}	1.32×10^{-2}
Terrestial ecotoxicity	PDF × m^2 × yr	8.69×10^{-2}	6.46×10^{-3}	1.03×10^{-2}	2.41×10^{-2}	6.19×10^{-4}	2.25×10^{-2}	4.74×10^{-3}	0.12	0.77
Terrestial acid/nutri	PDF × m^2 × yr	1.65×10^{-2}	1.54×10^{-2}	4.19×10^{-3}	2.19×10^{-4}	8.45×10^{-5}	1.38×10^{-3}	1.79×10^{-4}	5.41×10^{-3}	1.25×10^{-2}
Land occupation	PDF × m^2 × yr	8.35×10^{-3}	1.46×10^{-4}	2.51×10^{-5}	2.15×10^{-4}	4.09×10^{-5}	9.73×10^{-4}	7.6×10^{-4}	0.21	0.26
Climate change										
Global warming	kg CO_2e	1.03	1.22	0.619	7.54×10^{-3}	3.64×10^{-3}	8.5×10^{-2}	1.08×10^{-2}	0.13	4.05×10^{-2}
Resources										
Non-renewable energy	MJ primary	12.4	13.8	11.2	12.7	4.32×10^{-2}	1.38	0.17	2.0	0.53
Mineral extraction	MJ primary	1.82×10^{-3}	1.11×10^{-3}	8.32×10^{-4}	2.98×10^{-3}	1.14×10^{-3}	2.18×10^{-2}	1.45×10^{-2}	5.77×10^{-3}	1.86×10^{-3}

* Modelled after solar power generated in German climate conditions
** Modelled after electricity generated from bleached softwood pulp production using the kraft process

3.4. European grid mixes

The European electricity market consists of a diverse mix of energy sources that varies greatly between bidding zones. Table 3 contains the average electricity consumption mixes for the year 2022 in some of the largest economies in Europe which were estimated using data from the ENTSO-E transparency platform [6]. The average consumption mix was estimated as the sum of the electricity generated within a region and the consumption mix of any imported electricity. The mix of any exported electricity was excluded in order to only account for the domestic demand. As ENTSO-E provides hourly updates regarding electricity production across the EU, it is possible to create up-to-date predictions regarding the consumption mixes. By combining the consumption mixes in Table 3 with the environmental impact associated with each electricity source in Table 2, one can estimate the environmental impact of operating a VHTHP with a specific COP in any given country. This estimate is performed in chapter 5.

The ENTSO-E transparency platform does not provide additional details regarding the composition of electricity generated from biomass which makes it difficult to estimate the environmental impact. This electricity might be generated by combusting black liquor from pulp production, biogas from silage, biodegradable waste, woodchips, or other sources.

Table 3. Average electricity consumption mixes for the year 2022

Country	Hard coal	Lignite	Natual gas	Nuclear	Biomass	Hydro	Solar	Wind	Other	Unaccounted Imports
Austria	3.4%	9.5%	16.8%	7.3%	2.8%	39.3%	3.8%	14.7%	2.4%	0 %
Belgium	1.7%	0.7%	22.4%	42.4%	2.2%	0.3%	6.9%	12.5%	8.4%	2.5%
Czech Republic	7.6%	36.3%	7.1%	31.9%	3.3%	2.5%	4.0%	4.1%	3.2%	0 %
Denmark	11.0%	0.9%	5.7%	2.8%	8.5%	12.5%	5.8%	45.7%	7.1%	0 %
Finland	4.7%	0 %	2.3%	31.8%	7.2%	27.3%	0 %	16.4%	5.9%	4.4%
France	1.0%	0.4%	10.4%	60.6%	1.0%	9.6%	4.5%	8.9%	0.9%	2.7%
Germany	12.4%	19.9%	11.2%	7.4%	7.6%	4.0%	10.6%	24.4%	2.5%	0 %
Italy	6.9%	0.8%	45.5%	7.2%	2.3%	12.9%	8.3%	8.5%	7.6%	0 %
Netherlands	20.9%	1.2%	36.7%	5.8%	0.9%	1.9%	1.0%	17.6%	11.6%	2.4%
Norway	0.3%	0.2%	1.0%	1.6%	0.2%	83.5%	0.3%	12.3%	0.6%	0 %
Poland	44.1%	25.5%	5.9%	0.3%	1.3%	1.4%	6.0%	13.4%	2.1%	0 %
Slovakia	8.6%	14.5%	6.8%	45.5%	2.8%	9.5%	3.1%	3.1%	6.1%	0 %
Spain	3.0%	0 %	29.3%	22.1%	1.5%	8.4%	11.6%	22.4%	1.7%	0 %
Sweden	0.1%	0 %	0.1%	29.3%	0.1%	44.7%	0.5%	20.0%	5.2%	0 %
United Kingdom*	2.0%	0 %	38.9%	22.0%	7.1%	2.2%	4.6%	22.1%	1.1%	0 %

* Data from the year 2020

4. Assessment of two breweries

Two different industrial cases were assessed in this study, and the most important case data presented in Table 4. The first case involved a brewery in Spain utilizing high temperature steam at 170 °C (7 barg). 680 kW of heat was available in the form of ammonia condensation at 26 °C during the winter and 32 °C during the summer, and there were expected to be 6 350 operational hours annually. The COP was estimated to be 1.8, which is 58% of the theoretical maximum Carnot COP of 3.1. The second case involved a different Spanish brewery with steam at 162 °C (5.5 barg) as a heat sink. 425 kW of waste process heat was available at 85 °C. The smaller temperature lift results in a higher COP which was estimated to be 2.3, 41% of the Carnot COP of 5.6.

Table 4. Data for the two cases investigated

	Case 1	Case 2
Hot sink temperature	170 °C (7 barg)	162 °C (5.5 barg)
Cold source temperature	26 °C (winter) 32 °C (summer)	85 °C
Cold source availability	680 kW	425 kW
Operational hours	6 350 h	5 200 h

The COP was estimated based on an internal model provided by the heat pump producer. The performance of the heat pump in several different operating conditions can be viewed in the products datasheet [6]. Electricity was to be available in the form of guarantee of origin solar power priced at 70 €/MWh, the price of natural gas was 27 €/MWh, and the ETS carbon price was 90 €/ton CO_2 at the time. The boiler efficiency was estimated to be 90%.

For the first case, two 750 kW heat pumps utilizing the entire cold heat source and delivering 1 370 kW heat while consuming 760 kW electricity was proposed. The second brewery case had enough waste heat to operate one heat pump delivering 690 kW of high temperature steam while consuming 300 kW electricity.

The reduction in on-site CO_2 emissions from combustion were estimated as follows:

$$m_{CO_2} = \frac{q_{NG} Q}{\eta_{boiler} LHV_{NG}}. \quad (1)$$

Here m_{CO_2} is the CO_2 mass, q_{NG} is the specific natural gas CO_2 emission factor of 2.75 kg_{CO2}/kg_{NG}, Q is the heat produced, η_{boiler} is the efficiency of the boiler, and LHV_{NG} is the lower heating value of natural gas which is 13.06 kWh/kg_{NG}. Both the economic assessment and the environmental impact assessment assumed a 15-year lifespan.

4.1. Economic assessment

Table 5 presents the estimated annual cost of operating one or multiple VHTHPs in both cases under the conditions described in the previous chapter. It also includes an estimate of the cost of operating the reference natural gas boiler as well as the annual running cost savings if VHTHPs are used in place. The estimated running cost savings were calculated as the cost of natural gas for the boiler, the cost of maintenance, as well as the cost of the ETS allowances needed to cover the CO_2 emissions minus the cost of electricity needed to operate the heat pump as well as maintenance costs.

Table 5. Annual running cost estimates for the two cases

	Case 1	Case 2
	2 VHTHPs	1 VHTHP
VHTHP costs		
Maintenance (k€/yr)	20	10
Electricity (k€/yr)	338	109
Natural gas boiler costs		
Maintenance (k€/yr)	5.5	5.5
Natural gas (k€/yr)	261	108
ETS allowances (k€/yr)	183	76
Running cost savings (k€/yr)	**91.5**	**70.5**

One factor that limits the running cost savings are the relatively few operational hours in both cases, namely 6 350 and 5 200 hours respectively. When estimating the simple payback period as the cost of investment divided by the annual running cost savings, a VHTHP is assumed to have a retail price of 900 000 €, and the natural gas boiler is assumed to cost 76 000 € in accordance with Table 1. With these figures the simple payback periods for both cases are calculated to be 20 years and 13 years respectively.

A sensitivity analysis on the simple payback period provides more insight into how uncertainty in the price of electricity and natural gas affects the economic viability of an installation. One approach is to conduct Monte Carlo simulations which rely on a large number of random samplings of variable values in order to estimate the probability of different outcomes. These simulations were performed with electricity, natural gas, and ETS prices as independent variables. In practice, these variables are not truly independent, as for example grid electricity prices will be affected by changes in natural gas prices if the grid in question partially operates on fossil fuels.

Figure 2 depicts the results of two Monte Carlo simulations, one for each investigated case. 1 000 000 price conditions were simulated with the relative outcome probability on the y-axis. The price of electricity and natural gas was varied with a standard deviation of 10%, while the price of the ETS allowances had a standard deviation of 15%. Outcomes with payback periods longer than 50 years and outcomes with negative payback periods (i.e., unprofitable outcomes) are not included in the figure. These amounted to 13% of the outcomes in the first case and less than 1% of the outcomes in the second case.

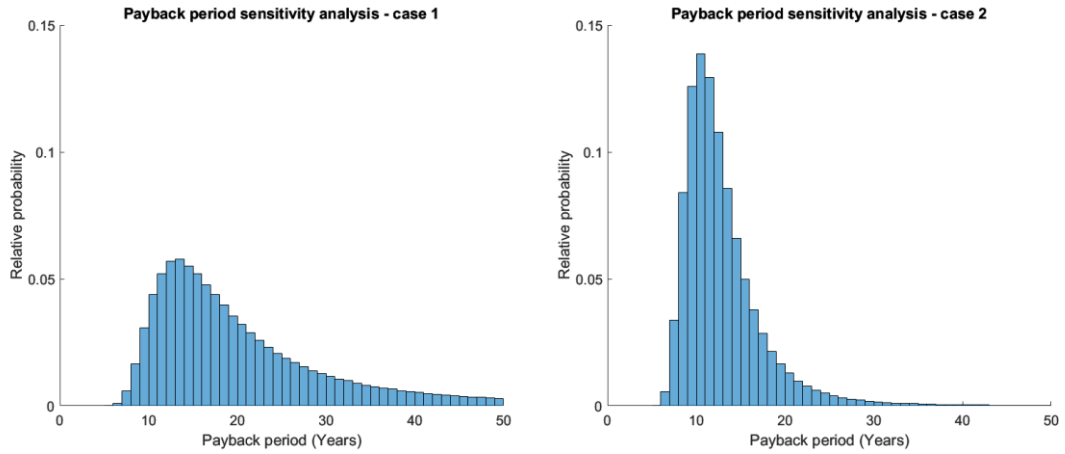


Fig. 2. Sensitivity analysis on the simple payback periods for two different cases using Monte Carlo simulations.

Analysis shows that the first case is more sensitive to price changes compared to the second case. This is likely due to the lower COP and, as a result, higher electricity consumption. Overall, 54% of the outcomes in the first case and 93% in the second case end up with a payback period below 20 years, with median values of 19 and 12 years, respectively.

4.2. Environmental impact

Table 6 contains the estimated environmental impact for the proposed solution of two VHTHPs and an equivalently sized natural gas boiler for the first case, and Table 7 contains the results for the second case. The damage categories are presented in bold text while their most impactful constituent midpoint categories are in roman. An estimated total environmental impact is also included.

In both cases, VHTHPs operating under the previously described conditions and utilizing renewable solar energy in Spain show a significantly smaller total environmental footprint, with large reductions in the damage categories climate change and resource usage. The impact on human health shows a slight improvement, while the impact on ecosystems is slightly increased. Case two shows more significant improvements due to the higher COP.

Table 6. Estimate of the environmental impact of two VHTHPs and a natural gas boiler in the first case

	VHTHP	Natural gas	Reduction
Total environmental impact (kPt)	**1.26**	**7.66**	**84 %**
Climate change (ton CO_2e)	**3 630**	**32 200**	**89 %**
CO_2 emissions on site (ton/a)	0	2 030	
Human health impact (DALY)	**2.84**	**3.67**	**23 %**
Carcinogens (DALY)	0.22	0.85	74 %
Non-carcinogens (DALY)	0.42	0.06	-600 %
Respiratory inorganics (DALY)	2.17	2.74	21 %
Ecosystem (PDF × m^2 × yr)	**1.14×10^6**	**7.44×10^5**	**-53 %**
Land occupation (PDF × m^2 × yr)	4.24×10^4	1.24×10^4	-242 %
Aquatic Ecotoxicity (PDF × m^2 × yr)	2.66×10^4	1.54×10^4	-73 %
Terrestrial Ecotoxicity (PDF × m^2 × yr)	1.01×10^6	5.92×10^5	-71 %
Terrestial acid/nutri (PDF × m^2 × yr)	6.00×10^4	1.24×10^5	52 %
Resources (MJ primary)	**6.16×10^7**	**5.83×10^8**	**89 %**
Non-renewable energy (MJ primary)	6.05×10^7	5.83×10^8	90 %
Mineral extraction (MJ primary)	1.07×10^6	5.23×10^4	-1 946 %

Table 7. Estimate of the environmental impact of one VHTHP and a natural gas boiler in the second case

	VHTHP	Natural gas	Reduction
Total environmental impact (kPt)	**0.41**	**3.16**	**87 %**
Climate change (ton CO_2e)	**1 170**	**13 300**	**91 %**
CO_2 emissions on site (ton/a)	0	840	
Human health impact (DALY)	**0.92**	**1.52**	**39 %**
Carcinogens (DALY)	0.07	0.35	80 %
Non-carcinogens (DALY)	0.14	0.03	-367 %
Respiratory inorganics (DALY)	0.70	1.13	38 %
Ecosystem (PDF × m^2 × yr)	**3.74×10^5**	**3.07×10^5**	**-18 %**
Land occupation (PDF × m^2 × yr)	1.38×10^4	5.10×10^3	-171 %
Aquatic Ecotoxicity (PDF × m^2 × yr)	8.69×10^3	6.33×10^3	-27 %
Terrestrial Ecotoxicity (PDF × m^2 × yr)	3.32×10^5	2.44×10^5	-36 %
Terrestial acid/nutri (PDF × m^2 × yr)	1.95×10^4	5.13×10^4	62 %
Resources (MJ primary)	**2.02×10^7**	**2.40×10^8**	**92 %**
Non-renewable energy (MJ primary)	1.98×10^7	2.40×10^8	92 %
Mineral extraction (MJ primary)	3.68×10^5	2.16×10^4	-1 603 %

The 89% and 91% reductions in CO_2e emissions are almost entirely due to the smaller carbon intensity of solar energy compared to natural gas. Spanish solar electricity is modeled as the "Electricity, production mix photovoltaic, at plant/ES" module in ecoinvent 3.8 which has a carbon intensity of roughly 50 g CO_2e per kWh electricity while natural gas is modeled as the "Heat, natural gas, at boiler modulating >100kW" module in ecoinvent 3.8 which has a carbon intensity of roughly 247 g CO_2e per kWh heat.

A network analysis of the LCA results was conducted in order to identify the sources of the emissions. The lessened impact on human health mostly comes down to a reduction of inorganic emissions causing respiratory illnesses as well as reduced carcinogenic emissions. Particulate matter smaller than 2.5 µm in diameter ($PM_{2.5}$) is the reference substance for the midpoint category respiratory inorganics, and in the case of the natural gas boiler, roughly two-thirds of the $PM_{2.5}$ emissions originated from the production and transport of natural gas while most of the remaining one-third occurred during the combustion process. In the VHTHP case, these emissions stemmed from a mix of copper and aluminum refining, glass production, and freight shipping.

The increased impact on ecosystems consists almost entirely of increased terrestrial ecotoxicity. The process of copper extraction and refining accounted for over half the impact on terrestrial ecotoxicity in both heat pump cases.

The use of non-renewable energy resources sees a substantial reduction as no fossil fuel combustion occurs. At the same time, considerably more energy is needed for the extraction of minerals such as copper, nickel, and aluminum. The extraction of copper accounted for roughly half the energy used for mineral extraction in the VHTHP cases.

5. VHTHPs in different electricity grid mixes

In this section the environmental impact of deploying a VHTHP in the different European countries grid mixes listed in Table 3 is investigated. The operating conditions of the VHTHP is modeled to be similar to that of case 2. Electricity generated from biomass is assumed to consist of natural wood chip combustion as no further insight is provided by ENTSO-E, and the category *Other* is modeled as a mix of waste combustion and biomass, as well as peat in the case of Finland. The *Unaccounted imports* in the case of Finland consists of Russian electricity. These imports have since halted and have been replace with imports from the Swedish grid since the 15th of May 2022. Russian electricity production is also not available in ENTSO-E. As a result, the category *Unaccounted imports* in the case of Finland is modeled after the Swedish electricity mix. The unaccounted imports in the case of Belgium, France, and the Netherlands consist of imports from the United Kingdom, whose production data is not included in the ENTSO-E database for the year 2022. These imports were therefore modeled after the United Kingdom 2020 mix in Table 3.

The total environmental impact of a VHTHP in the second case using grid electricity in the listed countries as well as the total environmental impact of an equivalently sized natural gas boiler is presented in Figure 3, where the red horizontal line indicates the total environmental impact of the natural gas boiler. The four damage categories human health impact, ecosystem impact, climate change, and resource usage have been recalculated into points using the normalization factors in chapter 3.2.

Countries under the red line would see a net environmental benefit by operating a VHTHP instead of a natural gas boiler, while countries over the line would not. The results show that the environmental impact associated with operating a VHTHP across all damage categories is highly dependent on the source of electricity used. In electricity grids reliant on fossil fuels such as Poland or the Czech Republic, the total environmental impact can be greater for a VHTHP compared to an equivalently sized natural gas boiler. This is clearly shown in the damage categories climate change and human health impact, where electricity from the Polish grid results in a significantly larger impact compared to a natural gas boiler. Countries whose grids mostly consist of renewable energy sources, such as Norway or Sweden, would see a significant environmental benefit to installing and operating VHTHPs in place of a natural gas boilers under the conditions described in case 2.

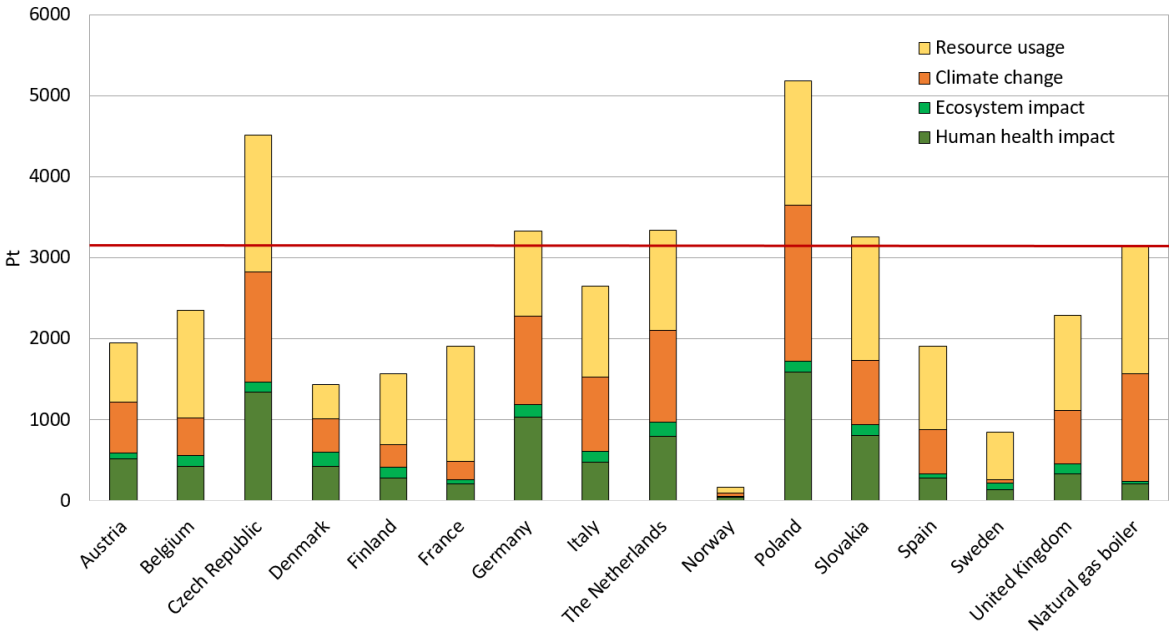


Fig. 3. Estimate of the total environmental impact of one VHTHP with a COP of 2.3 utilizing grid electricity in different European countries and a similarly sized natural gas boiler. The red line indicates the total environmental impact of the natural gas boiler.

6. Conclusion

This article summarized the most important economic and environmental factors that should be considered when assessing the feasibility of introducing VHTHPs in the European region. A way to quantify the environmental impact using LCA and up-to-date data regarding electricity consumption mixes in distinct regions was presented.

Two cases involving breweries in Spain with a demand for steam at 170 °C and 162 °C respectively were considered, and the economic and environmental impacts of replacing natural gas boilers with one or multiple VHTHPs were investigated. Analysis showed that the running cost savings and payback periods are highly dependent on the price ratio between electricity and natural gas as well as the price of CO_2 emission permits. The first case was estimated to have a simple payback period of 19 years and was shown to be more sensitive to utility price changes compared to the second case which was estimated to have a payback period of 12 years.

It was determined that the first case could operate two VHTHPs with an estimated COP of 1.8 which resulted in an 84% reduction in the total environmental impact over a natural gas boiler if solar power was used as an electricity source. The second case could facilitate a single VHTHP with an estimated COP of 2.3 which would reduce the total environmental impact by 87%. The environmental impact of operating VHTHPs in a number of different European settings using grid electricity was also studied, and it was determined that the environmental benefit of replacing natural gas boiler with VHTHPs is highly dependent on the source of electricity used. VHTHPs operating in electricity grids consisting mostly of renewable energy sources showed a substantial reduction in the total environmental impact compared to natural gas boilers, while VHTHPs operating in grids consisting mostly of fossil fuels showed an increase.

Acknowledgements

This project was funded by the Research Council of Norway, regional funding for Vestfold and Telemark, project 332898 “De-carbonization of European industry”. Iberdrola S.A, Madrid, Spain is acknowledged for providing data for case study development and useful discussions. Umara Khan of Åbo Akademi University is acknowledged for providing background information for the LCA calculations.

References

[1] IEA HPT. 2021. Annex 58: High-Temperature Heat Pumps. IEA Heat Pump Technologies. Available at: https://heatpumpingtechnologies.org/annex58/task1/. [Accessed 9.2.2023].

[2] Arpagaus, C., Bless, F., Uhlmann, M., Schiffmann, J., & Bertsch, S.S. 2018. High temperature heat pumps: Market overview, state of the art, research status, refrigerants, and application potentials. Energy, 152. Available at: https://doi.org/10.1016/j.energy.2018.03.166.
[3] European Network of Transmission System Operators transparency platform. Available at: https://transparency.entsoe.eu/.
[4] Wernet, G., Bauer, C., Steubing, B., Reinhard, J., Moreno-Ruiz, E., and Weidema, B., 2016. The ecoinvent database version 3 (part I): overview and methodology. The International Journal of Life Cycle Assessment, 21, pp.1218–1230. Available at: https://doi.org/10.1007/s11367-016-1087-8.
[5] Tveit, T-M., Johansson, M. N., & Zevenhoven, R. 2020. Environmentally friendly steam generation using VHTHPs at a pharmaceutical research facility. 13th IEA Heat Pump Conference, Jeju, South Korea, Paper No. 4.
[6] Olvondo Technology AS. Reversed Stirling Cycle. Annex 58: High-Temperature Heat Pumps. IEA Heat Pump Technologies. Available at: https://heatpumpingtechnologies.org/annex58/wp-content/uploads/sites/70/2022/07/olvondo-highlift.pdf. [Accessed on 12.2.2023].
[7] Gentili, P. et al. 2014. Ecodesign Preparatory Study on Steam Boilers. European Commission. pp.94-95. Available at: https://publications.europa.eu/resource/cellar/8f57cc3b-daeb-4a30-b5dc-e28e506561d8.0001.01/DOC_1.
[8] European Commission. EU Emissions Trading System (EU ETS). Available at: https://climate.ec.europa.eu/eu-action/eu-emissions-trading-system-eu-ets_en.
[9] Ember. 2022. EU Carbon Price Tracker. Available at: https://ember-climate.org/data/data-tools/carbon-price-viewer/. [Accessed 1.11.2022].
[10] Khan, U., Zevenhoven, R., & Tveit, T-M. 2020. Evaluation of the Environmental Sustainability of a Stirling Cycle-Based Heat Pump Using LCA. Energies, 13, 4469. Available at: https://doi.org/10.3390/en13174469.
[11] Humbert, S. et al. 2012. IMPACT 2002+: User Guide. Available at: https://quantis.com/pdf/IMPACT2002_UserGuide_for_vQ2.21.pdf. [Accessed 27.10.2022].

14th IEA Heat Pump Conference
15-18 May 2023, Chicago, Illinois

Detecting Leaks of Flammable Refrigerants below the 5% Lower Flammability Limit with a Low-Cost Sensor Platform

Moonis R. Ally[a*], Stephen Killough[a]

Energy Science and Technology Directorate, Oak Ridge National Laboratory, P.O. Box 20008, Oak Ridge, 37831-6070, USA

Abstract

A new low-cost sensor platform was developed for detecting flammable refrigerant leaks below the 5% lower flammability limit with an intrinsic self-check feature, detection times of under 1 s, no field calibration requirement, and rapid communication with a monitoring station or the fire department using Internet of Things technology. The sensor platform is plug and play and is specifically suitable for environmentally friendly low–global warming potential natural refrigerants, such as propane, that can achieve higher energy efficiency and operate at lower costs compared with hydrofluorocarbons. Because of its flammability, propane is mainly used in secondary and cascade refrigeration systems in supermarkets and chillers. Further adoption and market penetration depends on improved equipment safety because of tight safety standards from regulators and building codes. This sensor platform will provide OEMs and end users with increased safety features and optionality. Adoption of this platform for propane, which has a global warming potential of 3, will help reduce global warming relative to the use of hydrofluorocarbons.

© HPC2023.
Selection and/or peer-review under the responsibility of the organizers of the 14th IEA Heat Pump Conference 2023.

Keywords: Sensors, flammable refrigerants, heat pumps, refrigeration, leak detection

1. Introduction

Phase-out of hydrofluorocarbons (HFCs) and the safe transition to low-GWP hydrocarbon/natural refrigerants are critical global issues[1]. Regulatory, business, and climate impacts are the main drivers of these changes. The 2019 American Innovation and Manufacturing Act and HFC phasedown regulations are requiring original equipment manufacturers (OEMs) and end users to use alternative refrigerants to reduce greenhouse gas emissions. The natural refrigerants market is expected to grow from $1.5 billion in 2020 to $2.45 billion by 2025 at a 12% CAGR [2] . The global market for low-GWP, environmentally friendly refrigerants is estimated at $25.2 billion in 2022 and is forecast to surpass $73.7 billion by 2032, growing at a CAGR of 11.3% from 2022 to 2032 [3]. HFC phasedown and use of low-GWP refrigerants presents an opportunity for a 0.5°C reduction in global warming [4], and to lower energy costs for consumers. HVAC, water heating, and refrigeration systems are the largest energy end uses in buildings, using nearly 50% of all energy in US commercial and residential buildings. DOE is supporting US HFC phasedown efforts that target an 85% reduction by 2035[5], [6] through R&D and testing of low- to zero-GWP technologies.

Propane, with a low GWP of 3, is a strong contender to replace R-134a, which has a much higher GWP of 1,430, in refrigeration equipment. Propane is a natural refrigerant but is also flammable (A3 classification)[7]. Therefore, improving safety features within the equipment is crucial so that propane can be used throughout the heating, refrigeration, and air-conditioning industry in all sectors (residential, commercial, and industrial) of the economy. This paper describes a low-cost plug-and-play sensor platform that is engineered for detecting propane leaks at below the 5% lower flammability limit (LFL) within seconds. The developed sensor platform serves the US Department of Energy's (DOE's) maximum daily energy consumption, energy-related greenhouse gas reduction (83% by 2050 from 2005 levels) [8], and climate change (<2°C rise by 2100) targets.

* Corresponding author. *E-mail address:* allymr@ornl.gov

To reduce GWP, OEMs are replacing R-134a with propane; however, better product safety is needed to meet regulatory and building safety requirements. This requires developing propane sensor platforms that enables rapid detection and response at low concentrations.

The sensor platform consists of (1) an electrochemical sensor and (2) associated electronics and specialized software for a self-check feature, propane detection, and communications to a monitoring station or a fire department. The small size is ideal for use in refrigeration and heat pumping equipment. To improve safety, the goal of the sensor platform is to detect leaks in equipment before they can spread to the building or facility level. A microcomputer chip that retails for $0.50 is programmed to self-check the sensor and transmit a signal that indicates the sensor is working with fidelity while simultaneously monitoring any leaks. When a leak is detected, the microcomputer is programmed to transmit a signal to a monitoring station via a LoRa transceiver. LoRa is a wireless modulation technique derived from chirp spread spectrum technology and is used extensively in Internet of Things (IoT). It encodes information on radio waves using chirp pulses. LoRa-modulated transmission is robust against disturbances [9]. In this study, we display the transmitted signal using a terminal emulator (Putty). The sensor output could also be relayed via a satellite signal or telephone lines to a fire station, depending on customer preferences. Packaging these features in a low-cost plug-and-play platform is important for adoption of low–global warming potential (GWP) flammable natural refrigerants.

To optimize the safe use of propane, early detection of leaks is important to reduce flammability risk of propane. In this paper, we discuss four important metrics to reduce risks: (1) the fidelity of the sensor and its ability to self-check, (2) the level of detection, (3) how quickly a leak is detected at a particular concentration level, and (4) data transmission via LoRa.

2. Sensor platform architecture, metrics, and measurements

The sensor platform consists of two main parts. The first is an electrochemical sensor chosen for its rapid reaction with a flammable gas (propane, isobutane, or hydrogen). A small Ni-Cr heating coil heats a sliver of SnO_2 on an Al_2O_3 ceramic substrate to release O_2, which is subsequently adsorbed on the ceramic surface. In the absence of flammable gases, the donor electrons on SnO_2 are attracted toward the adsorbed O_2, preventing current flow. In the presence of flammable gases, the adsorbed O_2 is consumed, releasing electrons and allowing current to flow through the sensor. The self-check feature of the sensor ensures that the heating element maintains its integrity for the process to work.

The second part of the sensor is the electronics and associated software that perform the sensor self-check and transmission of signal using chirp spread spectrum technology. The qualification, “sensor platform” refers to the specific use of LoRa, a wireless modulation that is widely used in IoT. It encodes information on radio waves using chirp pulses. LoRa radios use the unlicensed 902-928 MHz band and thus do not require any licensing fees. The monitoring organization would need a receiving unit to watch for alarms, or commercial reception service can be purchased to send messages to the customer through the internet. The radio link range can be several miles thus, a single receiving station can cover several square miles. For shorter range requirements, the transmitter power can be reduced to enable more frequency re-use. A microchip is programmed to communicate with the sensor and the LoRa transmitter. It allows self-checks of the sensor every 5 s, although this can be varied arbitrarily via software modification. We selected an interval of 5 s so that the self-check feature can be witnessed frequently for demonstration in a laboratory setting. A voltage output from the sensor indicates that the sensor is working properly. If this output goes to zero, then the sensor has failed. This inexpensive, robust technology [10] is inexpensive and provides more capability and flexibility relative to other sensors available on the market. It is also plug and play, and the sensor can readily be removed and replaced, if needed.

When flammable gases contact the sensor, via a rubber tube from the calibrated gas cylinder to the sensor head, a current is generated, and a corresponding voltage is displayed on a terminal emulator (Putty, which is freeware). The voltage depends on the concentration of the flammable gas. We tested calibrated gases traceable to the National Institute for Standards Technology (NIST) standards at flammability limits of 47.61% LFL (1% propane + air), 28.57% of LFL (0.6% propane + air), and 4.76% of LFL (0.1% propane + air) with response times of less than 1 s. Representative data with response times are shown in **Error! Reference source not found.** where the response times are for propane + air concentrations of 47.61% LFL, 28.57% LFL, and 4.76% LFL, with the concentrations traceable to NIST standards provided by the manufacturer. Modules #1, #2 and #3 refer to three sensors from the same manufacturer. The response times of each of the three discrete sensors (same model and manufacturer) is less than 1 s at the 95% confidence interval (C.I.). For the lowest concentration of propane (4.76% LFL, or 0.1% propane in air), the average response time is 0.386 s ± 0.03 s.

Standard statistical methods are used for calculating C.I. These data demonstrate that the level of detection is below 5% LFL and the presence of propane is detected within 0.5 s.

Table 1. Sensor response times at three levels of propane + air concentrations

	Sensor response times after exposure to 47.61% LFL (1% propane + air)		
	Module #1	Module #2	Module #3
Average time, s	0.37	0.43	0.36
Std. dev., s	±0.12	±0.13	±0.07
95% C.I., α = 0.05	±0.06	±0.05	±0.03
	Sensor response times after exposure to 28.57% LFL (0.6% propane + air)		
	Module #1	Module #2	Module #3
Average time, s	0.34	0.34	0.33
Std. dev., s	±0.03	±0.04	±0.06
95% C.I., α = 0.05	±0.02	±0.02	±0.03
	Sensor response times after exposure to 4.76% LFL (0.1% propane + air)		
	Module #1	Module #2	Module #3
Average time, s	0.41	0.41	0.34
Std. dev., s	±0.07	±0.07	±0.04
95% C.I., α = 0.05	±0.03	±0.03	±0.02

A proprietary software takes readings every 5 s to check the sensor and to check the voltage reading from the sensor above a certain threshold level when no propane is present. This threshold is approximately 0.4 V. As soon as propane is detected, the voltage spikes, which is relayed via a LoRa transmitter to a receiver connected to a laptop and displayed using Putty. Putty is a Secure Shell (SSH) and telnet client and is open source. It is used as a communication vehicle between the host system (e.g., a laptop) and the system command-line interface. The combination of the sensor, transceiver, microprocessor, and software comprising the sensor platform is shown in Fig. 1.

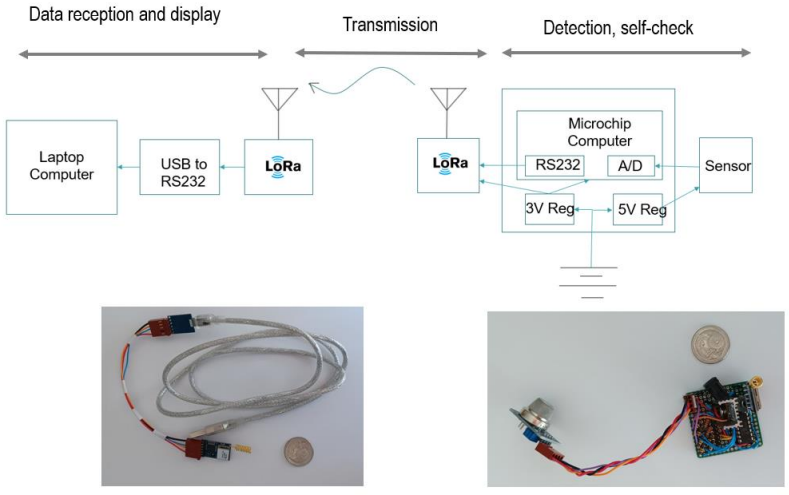


Fig. 1. IoT-based sensor platform with diagnostics and messaging. The size of the module is estimated by comparison to the size of a quarter ($0.25) coin.

The response of the sensor platform to propane at the three distinct concentration levels is shown in Fig. 2. The rapid detections of propane at the three distinct concentration levels are similar, as confirmed by the values in Table 1 and Fig. 2, and the sensor returns to its baseline level of 0.3 V in about 90 s. This pattern of repeated

propane detection and returning to the baseline case is evident in Fig. 2, demonstrating the sensor's repeatability and fidelity.

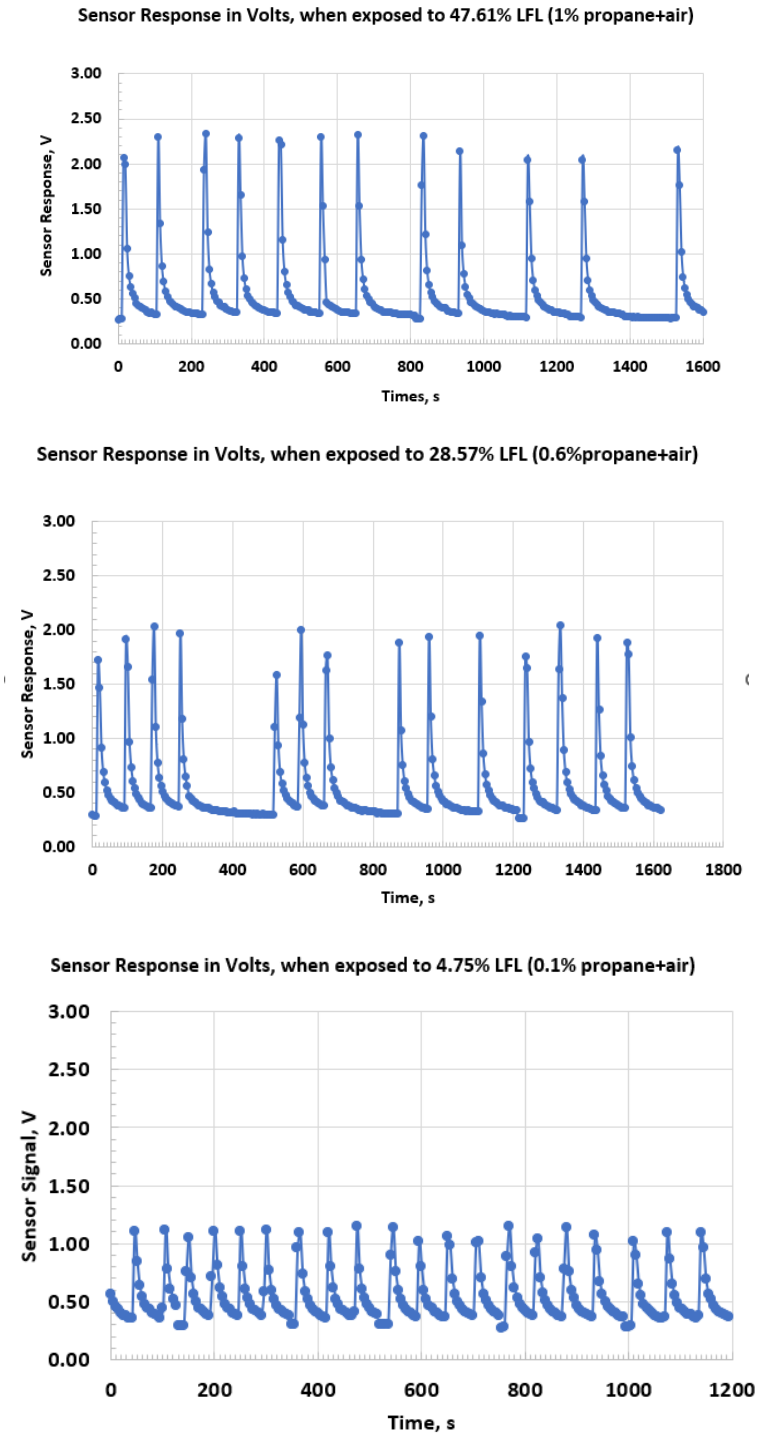


Fig. 2. Repeated responses of the sensor platform when exposed to different propane concentrations: (top) 47.6% LFL (1% propane + air); (middle) 28.57% LFL (0.6% propane + air), and (bottom) 4.75% LFL (0.1% propane + air).

3. Discussion

Many sensors have been evaluated [11][11][11][11] recently to address leak detection of refrigerants, including low-GWP hydrocarbon refrigerants to mitigate global warming and to limit the rise in global

temperature to within 2°C, and preferably to 1.5°C compared with preindustrial levels as per the Paris Agreement adopted by 196 parties on December 12, 2015 and made effective on November 4, 2016[11]. Refrigerant detectors utilize a variety of sensing principles, including micro-machined membrane, nondispersive infrared, thermal conductivity, metal oxide semiconductor, speed of sound, and electrochemical sensors. We selected the electrochemical sensor because of its rapid response, reliability, ease of operation, and low cost. Tighter regulations and safety standards in the United States and the European Union are anticipated for A3 refrigerants. Propane is approved under the US Environmental Protection Agency's Significant New Alternatives Policy Program. The sensor platform has the following capabilities: a self-check feature and diagnosis; rapid detection; ability to detect small leakages at less than 5% LFL in less than 1 s; no field calibration requirement; and communication via IoT technology to a monitoring site, which can be adapted in various ways to meet customer demand. In the current version of the platform as described in this paper, the platform transmits a self-check signal and leak detection signal via radio signal to another radio receiver whose output is read on a laptop for remote monitoring. This platform will assist OEMs looking for long-term solutions with equipment life >15 years and in accordance with regulations and safety standards in the United States and the European Union. The properties and performance metrics of the low-cost sensor platform make it attractive for adoption in industry.

Acknowledgements

We are grateful to Antonio Bouza, Technology Manager, HVAC & Water Heating R&D, for his support and encouragement on this manuscript.

Conflicts of Interest: This manuscript has been authored by UT-Battelle, LLC, under contract DE-AC05-00OR22725 with the US Department of Energy (DOE). The US government retains and the publisher, by accepting the article for publication, acknowledges that the US government retains a nonexclusive, paid-up, irrevocable, worldwide license to publish or reproduce the published form of this manuscript, or allow others to do so, for US government purposes. The DOE will provide public access to these results of federally sponsored research in accordance with the DOE Public Access Plan (http://energy.gov/downloads/doe-public-access-plan).

References

[1] J. H. Koh and Z. Zakaria, "Hydrocarbons as refrigerants? A review," ASEAN Journal on Science and Technology for Development 34(1), 35–50, 2017.
[2] Global Natural Refrigerants Market 2020 by Manufacturers, Regions, Type and Application, forecast to 2025, Report ID: 2441784, December 12, 2020, https://www.marketstudyreport.com/reports/global-natural-refrigerants-market-2020-by-manufacturers-regions-type-and-application-forecast-to-2025?gclid=Cj0KCQjwj7CZBhDHARIsAPPWv3dpVKhEF1X_sGd2GVq-Y2hg2JlSTOEoRun0pXRLnndjnPl5Kh7cb4AaAgDdEALw_wcB
[3] Low GWP Refrigerants Market, FACT3054AMR, April, 2022, Suite 9884, 27 Upper Pembroke Street, Dublin 2, Ireland, https://www.factmr.com/report/3054/low-gwp-refrigerants-market
[4] The Long-Term Strategy of the United States. Pathways to Net-Zero Greenhouse Gas Emissions by 2050, US Department of State and the United States Executive Office of the President, 2021.
[5] Biden Administration Combats Super-Pollutants and Bolsters Domestic Manufacturing with New Programs and Historic Commitments, The White House, 2021. https://www.whitehouse.gov/briefing-room/statements-releases/2021/09/23/fact-sheet-biden-administration-combats-super-pollutants-and-bolsters-domestic-manufacturing-with-new-programs-and-historic-commitments/
[6] Final Phasedown rule-Phasedown of Hydrofluorocarbons: Establishing the Allowance allocation and Trading Program under the AIM Act, US Environmental Protection Agency, July 12, 2022. https://www.epa.gov/climate-hfcs-reduction/final-rule-phasedown-hydrofluorocarbons-establishing-allowance-allocation#:~:text=The%20AIM%20Act%2C%20which%20was,of%20global%20warming%20by%202100.
[7] Designation and Safety Classification of Refrigerants, ANSI/ASHRAE Standard 34-2019, ISSN 1041-2336 (2019).
[8] Buildings Technology Office Multi-Year Program Plan, Fiscal Years 2016-2020, US Department of Energy.
[9] F. Adelantado, X. Vilajosana, P. Tuset-Peiro, B. Martinez, J. Melia-Segui, and T. Watteyne, "Understanding the limits of LoRaWAN," IEEE Communications Magazine 55(9): 34–40, 2017.[10]

Quick detection of flammable refrigerant leaks, diagnostics, and remedial action, Invention Disclosure ID 202205101, UT-Battelle, LLC, Oak Ridge National Laboratory, April 4, 2022.
[10] Quick detection of flammable refrigerant leaks, diagnostics, and remedial action, Invention Disclosure ID 202205101, UT-Battelle, LLC, Oak Ridge National Laboratory, April 4, 2022.[11] J. Zheng and S. Elbel. Refrigerant Detector Characteristics for Use in HVACR Equipment-Phase I, AHRTI, 2020.
[11]. Zheng, J, ElbelS. Refrigerant Detector Characteristics for Use in HVACR Equipment-Phase I. Final Report prepared for, Air-Conditioning, Heating and Refrigeration Technology Institute, Inc., 82311 Wilson Boulevard, Suite 400, Arlington, VA 22201, March 2020
[12] L. Jensen, COP26 Climate Change Conference in Glasgow, European Parliamentary Research Service, 2021. Retrieved from https://policycommons.net/artifacts/1850237/cop26-climate-change-conference-in-glasgow/2596922/ on August 16, 2022. CID: 20.500.12592/txxvrq.

14th IEA Heat Pump Conference
15-18 May 2023, Chicago, Illinois

Analysis of Large-Scale Ammonia Heat Pumps in Transient Operating Conditions

Kenneth Rugholm Kramer [a], Jonas Lundsted Poulsen [a,*], Wiebke Meesenburg [b], Mathias Kjær Christensen [c], Peter Reinholdt [c], Brian Elmegaard [b], Benjamin Zühlsdorf [a]

[a]*Danish Technological Institute, Energy and Climate, Aarhus, Denmark*
[b]*Technical University of Denmark, Department of Civil and Mechanical Engineering, Kgs. Lyngby, Denmark*
[c]*Johnson Controls Denmark ApS, Holme, Denmark*

Abstract

Large-scale ammonia heat pumps are a key technology for enabling sustainable heat supply. Exploiting their potential in integrated systems requires the highest efficiencies and reliability even at varying operating conditions. The varying operating conditions can result from variations in the heat source and sink, such as variations in production processes and sudden changes of weather conditions. The dynamic operating conditions may result in unwanted dynamic effects, risking sub-optimal performance and component damage. This study focuses on the development and validation of dynamic models for the components in an ammonia heat pump system. The various components were assembled in a dynamic model implemented in Dymola and validated against test data from operation of a MW-scale ammonia heat pump. The system responses to sudden changes in the source and sink conditions, compressor speed, and liquid levels in the system were studied. The results from the validation showed that this dynamic model has great potential to be used for developing holistic control strategies and design guidelines in order to further improve the resilience and performance under fluctuating boundary conditions for large-scale heat pumps.

© HPC2023.
Selection and/or peer-review under the responsibility of the organizers of the 14th IEA Heat Pump Conference 2023.

Keywords: Large-scale heat pump; Dynamic model; Experimental validation; Control; Dymola

1. Introduction

Large-scale heat pumps are key components for the decarbonization of district heating and industrial heat supply. In line with the efforts to reduce greenhouse gas emissions from the heating sector, the number of installed large-scale and domestic heat pumps is increasing rapidly worldwide [1]. Large-scale heat pumps integrated with ambient heat sources or industrial processes may be required to operate under variable boundary conditions such as rapid changes in the sink or source temperature or flow. These may e.g. occur due to rapid changes in the outdoor air conditions for air-source heat pumps or due to variations related to the type of industrial process the heat pump is supplying heating (and cooling) to. If the systems is not designed to be able to handle such variations, the rapid change in boundary conditions may lead to unwanted dynamic effects, risking sub-optimal performance and component damages [2].

Designing large-scale heat pumps and the respective control systems to operate optimally under expectable and unforeseen variations in the boundary conditions requires studying the dynamic response of the system to such variations. This may be done using validated dynamic models of the system that are based on fundamental physics and thereby applicable to a broad range of operation conditions. Using models to test the dynamic response of the system to different variations in the boundary conditions is expected to reduce costs and time for testing and to reduce the risk of harming the experimental set-up if too extreme variations are tested. Such

*Corresponding author. Tel: +45 72201378
E-mail address: jlp@teknologisk.dk

models form the basis for tasks such as analysis of system behaviour, system design, model based control design, controller tuning and fault detection and diagnosis [3]. Li et al. provide an extensive overview of the common practices of dynamic modelling of HVAC systems [4-5]. These include component based modelling and the use of the object-oriented programming language Modelica [6] for the implementation, which has been shown to be a suitable approach [7].

This approach has previously been applied to large-scale ammonia heat pumps to assess the ability of large scale heat pumps to supply frequency regulation service to the electricity grid [8]. The same dynamic model was used to assess which components in a two-stage heat pump system have the largest influence on the time constant for changing the load in large-scale heat pumps [9]. Recent studies on large-scale heat pumps used dynamic models to optimize the controller set-points [10] and assess the influence of heat exchanger fouling [11].

The present study aimed to develop and validate a dynamic model for a MW-scale single-stage ammonia heat pump system using a screw compressor and flooded evaporator. The models were developed based on the underlying physics, fitted against design data of the individual components, and validated against measurement data. The available measurement data was obtained from experiments, in which different controller set-points were changed to excite the system. The model was used to analyze the dynamic response of the system to the changes in set-points such as compressors speed, receiver level, sink/source temperature and flow variations. The intended future use of the model is to use it for optimization of both the design and the control of similar large-scale systems to ensure optimal performance during rapidly changing boundary conditions.

2. Methods

2.1. Case description

Fig. 1 shows the overall heat pump cycle layout and control dependencies for the main components as well as the independent input parameters used in the model.

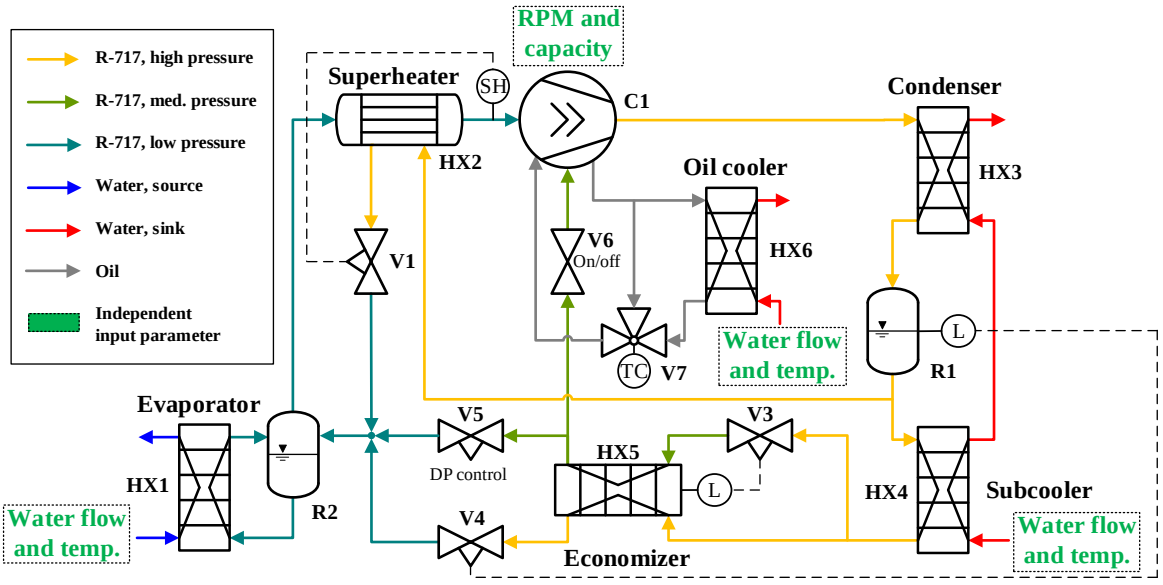


Fig. 1. Layout of heat pump system, including independent input parameters (written in green).

The heat pump consists of the following main components; screw compressor (C1), plate oil-cooler (HX6), plate condenser (HX3), liquid separators (R1 and R2), plate-and-shell sub-cooler (HX4), plate-and-shell economizer (HX5), plate evaporator (HX1), shell-and-tube superheater (HX2), and expansion valve (V4). The controllers modelled included:

- Receiver (R1) level controlled by main expansion valve (V4).
- Economizer (HX5) liquid level controlled by economizer valve (V3).
- Suction gas superheating (HX2) controlled by valve on the liquid side (V1).
- On/off control valve (V6) and differential pressure valve (V5) for economizer gas flow.
- Inlet temperature of oil to the compressor (C1) controlled by 3-way valve (V7).

To validate the dynamic model and compare it with the operating data from the heat pump, it was necessary to have identical boundary conditions between the model and measured data. For this, various independent parameters were used, which were variable inputs to the heat pump. In Fig. 1 these inputs are highlighted in green and consist of input temperatures and flows on the water side of the sub-cooler, oil-cooler, evaporator, as well as the compressor speed and capacity.

The dynamic model of the heat pump was developed in Dymola [12] with the component library TIL suite [13], based on the object-oriented language Modelica [14]. The basis of the dynamic system model was individual component models, which were first developed, tested, and validated against design data before the component models were assembled in the system model. Both the components and the system were modelled based on a finite volume method [15], consisting of mass, energy and momentum balances supplemented with semi-empirical correlations for describing the component characteristics. The process of preparing the validated dynamic model can be seen in Fig. 2. In step 1 (component modelling) the various component models were first developed by inserting relevant parameters for the available data, e.g. material type and geometry specifications for the heat exchangers. After this, other parameters such as e.g. the heat transfer coefficients and pressure loss coefficients were fitted against data available from standard calculations from e.g. manufacturer component design software, data sheets or experiments. In step 2 (system modelling) the component models were assembled in a system model and the control parameters were defined. Finally, in step 3 (validation) the model was validated by comparing the model results with measurement data from experiments with the heat pump system. The modelling process (step 1 to 3) was iterated where needed. Hence, independent datasets have been used for fitting (component design data) and validation (measurement data from experiments) to develop the final system model.

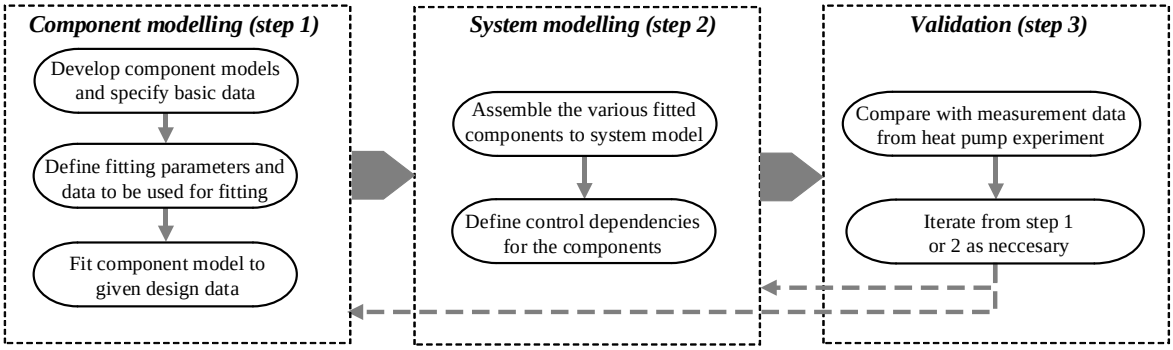


Fig. 2. Illustration for the process in relation to the development of the dynamic model.

Coefficients for the different component models from the TIL component library were fitted in relation to, for example, heat transfer, pressure loss, and friction to match the associated design points in the given component. Examples of the component modelling for the heat exchangers and the compressor are given in the following two sections.

2.2. Heat Exchangers

The heat pump consisted of six heat exchangers of different types and sizes. The three plate heat exchangers are standard components in the TIL suite component library, while the two plate-and-shell heat exchangers and the one shell-and-tube heat exchanger were modelled to be compatible with TIL suite. For all the heat exchangers, the geometry was known, and the models were based on this information. All the heat exchangers were fitted in relation to a series of different design conditions and compared with the heat transfer rate (HTR), outlet temperatures and pressure drops using TLK's Modelfitter tool [16]**.** In addition, pressure loss correlations based on [16,17,18] were used. The fitting procedure used for the evaporator is used as an example of the fitting process.

The model of the evaporator which is a large plate heat exchanger was discretized into 10 cells on the water and ammonia side, respectively. On the water side, a constant heat transfer coefficient was fitted, while on the ammonia side, a heat transfer model was used [20] which was subsequently fitted with a correction factor and a reference heat transfer coefficient. To compare and fit the model against the component design data, a virtual test bench of the component model in Dymola was converted according to the Functional Mock-up Interface standard [21], see Fig. 3, and fitted in TLK's Modelfitter tool. Here, different various independent parameters (input parameters) for the component were inserted and the dependent parameters for the model and design data were compared. For the heat exchanger, five independent parameters were used: enthalpy, mass flow, and pressure of ammonia, and the flow and temperature of water, see Fig. 3.

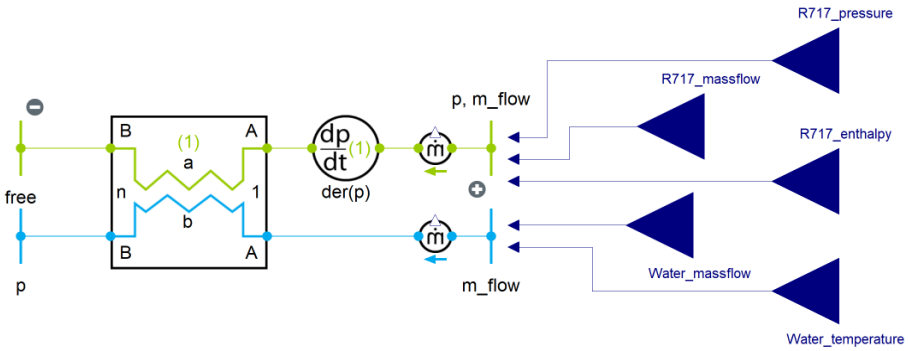


Fig. 3. Content of Functional Mock-up Unit for virtual test bench for model of evaporator plate heat exchanger.

Fig. 4 shows three different dependent parameters for nine different steady-state design points from the manufacturer component design software: heat transfer rate, water temperature out and pressure drop on the ammonia side. The difference between model and design points for the evaporator before and after the fit is shown, and it can be seen the R^2 score was satisfactorily high after fitting.

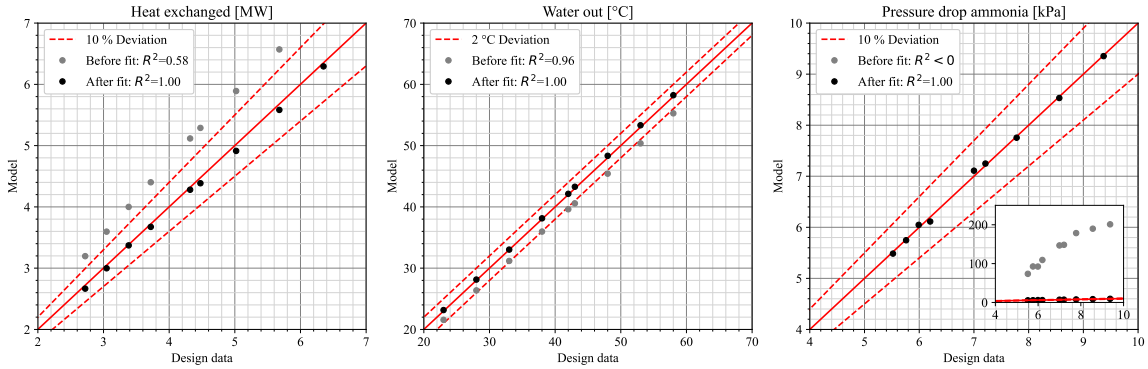


Fig. 4. Differences between mode and design data before and after fitting of evaporator.

2.3. Screw Compressor

The model for the screw compressor was based on the compressor base classes from the TIL suite library [13], but some extra functionalities were added to the model in order for it to include the principles of the modelled heat pump. This included among other things an automatically regulating volume ratio within a predefined interval, a capacity slide valve control, and oil cooling. The model was divided in three volumes (inlet, outlet, and economizer volume) and for each volume dynamic mass and energy conservation equations were implemented. Fig. 5 shows how the different control volumes were connected to each other.

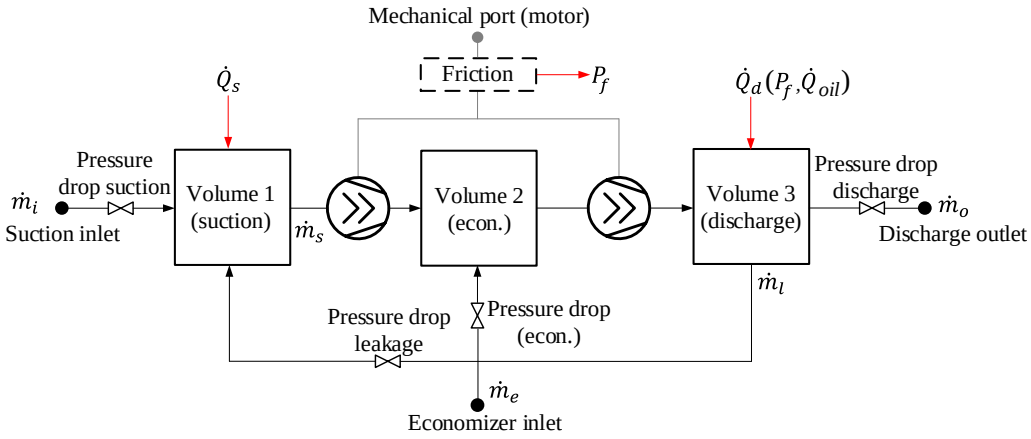


Fig. 5. Modelling of screw compressor with injection from economizer port (adapted from [22]).

The energy balance for the suction and discharge volume were influenced by $\dot{Q}_s$ and $\dot{Q}_d$, respectively. For the discharge volume, $\dot{Q}_d$ was calculated based on the friction power, P_f, which was a function of the compressor RPM, two empirical friction coefficients, and the torque. Furthermore, oil cooling ($\dot{Q}_{oil}$) was modeled and applied in the discharge volume only and thus also a part of $\dot{Q}_d$. The modeling of the oil cooling was based on a dynamic balance equation and formulated independently of the refrigerant volume. In this way, only heat was exchanged between the oil and the refrigerant. In addition, the liquid oil was assumed incompressible (simplified energy balances).

Several steady-state design data points from the compressor were used to fit the screw compressor, e.g. by varying the friction coefficients and cross-sectional areas for the valve areas determining the flow rates with the use of the Saint-Venant and Wantzel equation [23].

The automatic regulating volume ratio and the oil flow were determined using a polynomial fit based on steady-state design data of the screw compressor and were then used in the model to determine the volume ratio and the oil flow. The design data were generated for all combinations of evaporating temperatures in the range of 20 °C to 45 °C and condensing temperatures in the range 65 °C to 95 °C with a 5 °C resolution at 3600 RPM. Fig. 6 shows a comparison of the design data and the respective fits for oil flow and volume ratio. The oil flow polynomial fit was made as a function of the pressure difference, while the volume ratio polynomial fit was made as a function of the pressure ratio, compressor speed and suction pressure.

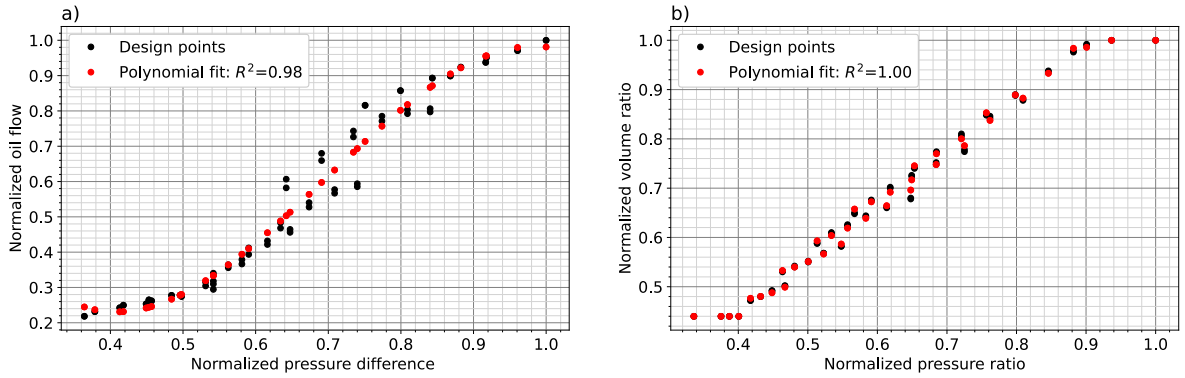


Fig. 6. Comparison of model and design data for a) normalized oil flow as function of normalized pressure difference and b) normalized volume ratio as function of normalized pressure ratio for the screw compressor.

As with the various heat exchangers, the screw compressor was fitted in relation to the design data based on a virtual test bench. The screw compressor model was fitted in relation to refrigerant flow, discharge temperature, and compressor power. The result before and after the fit can be seen in Fig. 7.

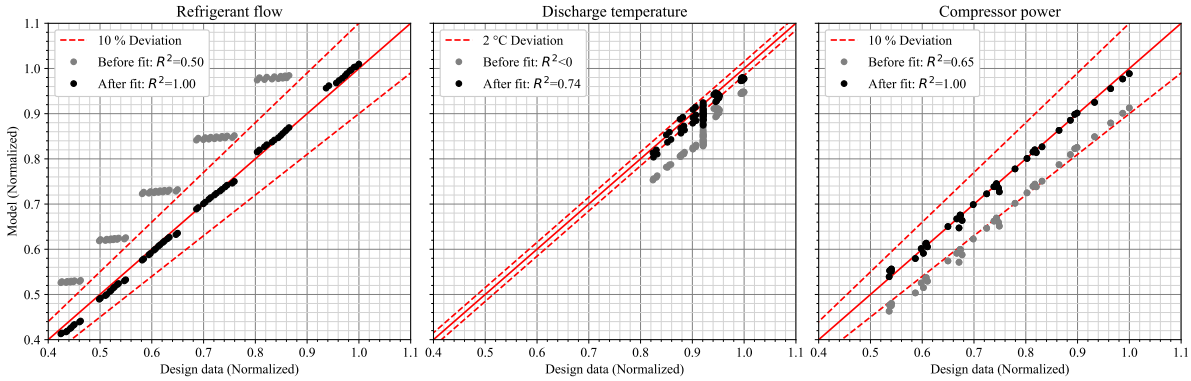


Fig. 7. Refrigerant flow, discharge temperature, and compressor power for the model as a function of the design data.

2.4. System modelling and validation

The heat pump system model was aggregated from the various modelled components and PI-controllers. The P and I gains for the different controllers were tuned by comparison with relevant test data from experiments with the heat pump system including controllers. The experiments were conducted in a controlled test environment with several pressure, temperature, flow rate, and level sensors installed. The media on the source and sink side was water, and the heat was exchanged between the source and sink side in a mixing loop.

To validate the behavior of the system model, the independent input parameters for the model (see Fig. 1) were varied based on three different experimental test cases. The cases defined were:

- Case 0: Test period with relatively stable operating conditions.
- Case 1: First dynamic operating case – variation of receiver level set-point.
- Case 2: Second dynamic operating case – with several simultaneous changes being made in the system at the same time, including gradual change of compressor speed as well as changing inlet water temperatures and flows.

The independent input parameters and results from the three validation cases, including further descriptions of the cases are described in the next section. The three cases were chosen because they illustrated a nuanced view of different operating conditions. Case 0 illustrates the steady state error for the various dependent parameters. Case 1 illustrated what happened when one parameter was changed. And finally, case 2 illustrated what happened to the heat pump when multiple changes were made at the same time. The sampling time for the data was 1 second and all three cases were tested without economizer.

3. Results

For the three cases the model was simulated 10,000 seconds before time = 0 s with the independent input parameters from time = 0 s as inputs. This made the results from the model stable before the input parameters from the data processing stated to change at time = 0 s. In a similar manner the tests of the heat pump were kept in steady state for a period before the start of the logging period.

3.1. Case 0: Stable operating conditions

Case 0 was the baseline case which aimed at verifying that energy- and mass balances for model and test data matched in a steady-state case. The case lasted for around 1300 seconds, and the defined independent input parameters can be seen in Fig. 8. From the figure it can be seen that the operating data for the water inlet temperatures to the evaporator (HX1), sub-cooler (HX4), and oil cooler (HX6), respectively, were relatively stable. The inlet temperature to the oil-cooler and sub-cooler were identical. In addition to this, the water flow and compressor were also relatively stable.

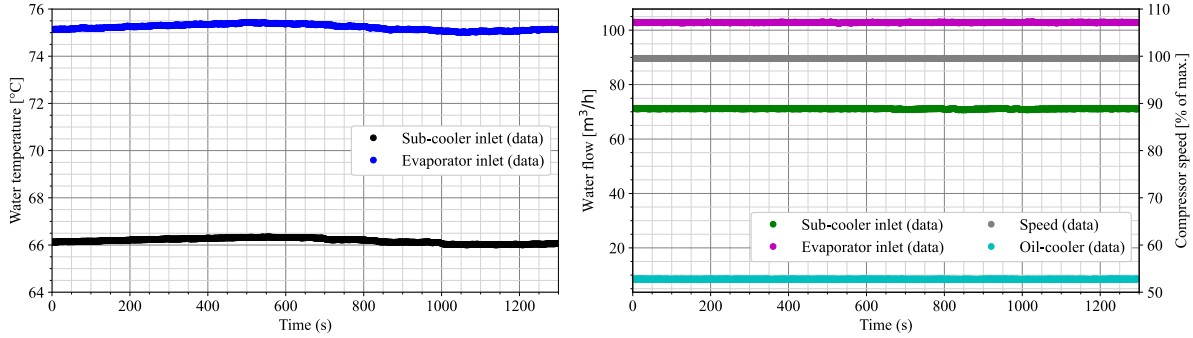


Fig. 8. Independent parameters for case 0 – stable operation.

Fig. 9 shows a log(p)-h diagram and a T-$\dot{Q}$ diagram for case 0 at time = 0 s. The log(p)-h diagram shows the cycle process for both the model and measured data, respectively. The T-$\dot{Q}$ diagram shows the normalized

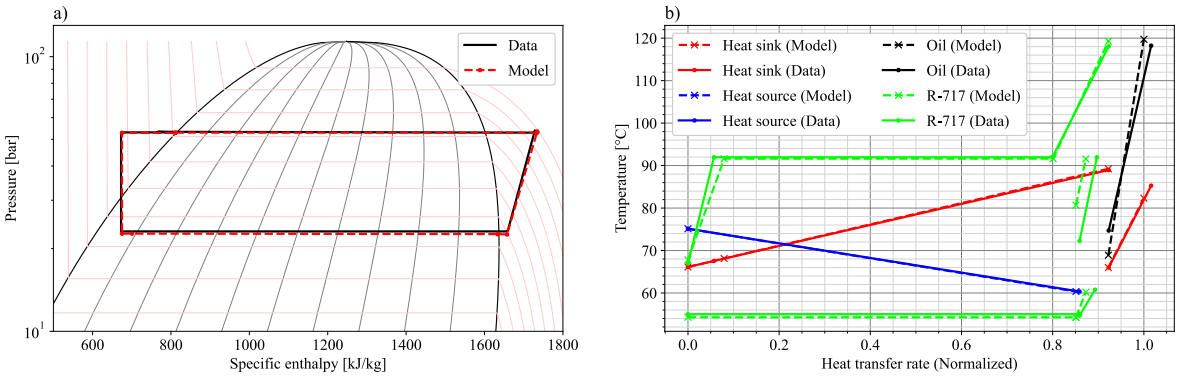


Fig. 9. Case 0 – a) Log(p)-h and b) T-$\dot{Q}$ diagram with comparison of model and test data at time = 0 s.

heat transfer rate (Norm. HTR) for the different heat exchangers on the water, ammonia, and oil side, in relation to the temperature levels. The heat transfer rate for the data was determined from an energy balance using flow and temperature sensors. The heat transfer rate for the oil cooler (HX6) was in parallel with the heat transfer rate from the sub-cooler and the condenser on the water side.

The temperatures and heat transfer rates were generally in good agreement between model and measured data for case 0. The difference between model and test data for selected values can be seen in Table 1.

Table 1. Difference between model and test data at time = 0 s for selected values.

	Data	Simulation	Deviation
Evaporation temperature [°C]	55.00	54.28	0.72 K
Condensing temperature [°C]	91.96	91.62	0.34 K
Discharge temperature [°C]	118.09	119.27	-1.18 K
Sub-cooler outlet temperature [°C]	66.98	67.80	-0.82 K
Superheating before compressor [K]	5.77	6.18	0.41 K
Outlet temperature - water sink [°C]	88.95	89.24	0.29 K
Norm. HTR – water sink [%]	92.28	92.22	0.06 %
Norm. HTR – water source [%]	89.30	87.27	2.03 %
Norm. HTR – oil-cooler [%]	9.32	7.78	1.54 %

The dynamic response of some of the key parameters for case 0 can be seen Fig. 10. Here the discharge pressures (a), evaporation temperature (b), and the oil inlet temperature (c) are shown as a function of time. In this case there were no major differences between measured data and model. It can be seen that for all three parameters the model generally follows the data with an offset of approximately 0.5 bar for the discharge pressure, 0.7 K for the evaporating temperature and 0.1 K for the oil inlet temperature to the compressor (first 700 s).

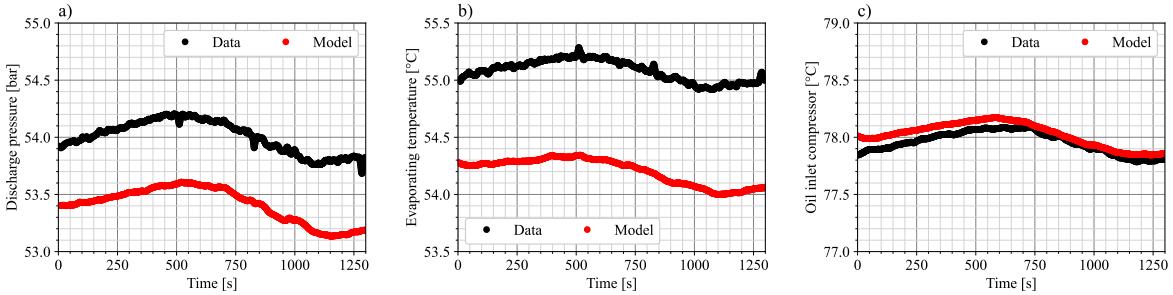


Fig. 10. Dynamic response for a) discharge pressure, b) evaporating temperature, and c) oil temperature in case 0.

3.2. Case 1: Set-point change for the receiver level

Case 1 was a controlled dynamic test, where the system and hereby the independent parameters were kept in steady state until 412 seconds after the defined start of case 1, as seen in Fig. 11. At that time a single set point change of the high-pressure control valve was made, and the level in the receiver was lowered. The change of

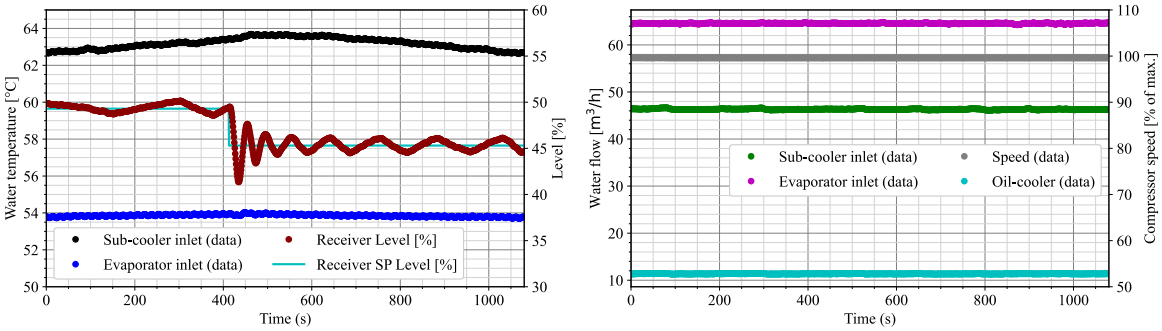


Fig. 11. Independent input parameters for case 1 – change in receiver level.

level was estimated to correspond to a 7.3 % change of the fraction for the liquid volume in the receiver from 54.5 % down to 47.2 % based on a level measurement in the cylindrical formed receiver with horizontal orientation. After the set-point change in the receiver the other input parameters for e.g. the compressor speed and secondary flows on the sink and source side continued to be almost the same.

Fig. 12 shows the influence and the dynamic response for the heat pump system with the change in receiver for both the test data and simulation results. In Fig. 12 (a) the filling level is shown, and it can be seen that for both the test data and the dynamic model the value for the filling level was within the neutral zone (± 1 % of set-point with deactivated PI controller) for the controller before the set-point change. Immediately after the set-point change the level oscillates similarly outside the neutral zone for both the test data and the model before being within the neutral zone again around 150 seconds after the change. Inside the neutral zone the PI-controller in the model was creating a higher oscillating frequency compared to the test data.

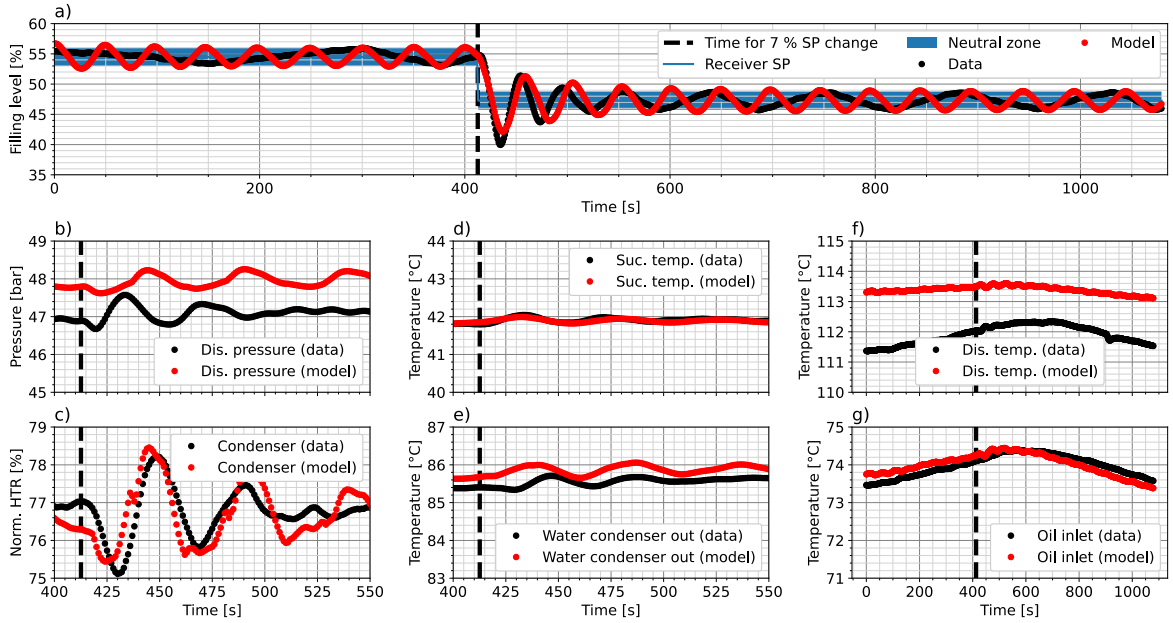


Fig. 12. Comparison of dynamic response in case 1 between data and model for a) the filling level for R1, b) discharge pressure, c) normalized heat transfer rate for the condenser, d) suction temperature, e) temperature for water out of condenser, f) discharge temperature, and g) oil inlet temperature.

Fig. 12 further shows the discharge pressure (b), normalized heat transfer rate for the condenser (c), suction temperature (d), temperature for water outlet of condenser (e), discharge temperature (f), and oil inlet temperature (g) for the dynamic response in case 1. The control of the receiver liquid level has a considerable impact on the dynamic response in the system. The rapid decrease of the set point of the liquid level in R1 immediately caused a small pressure increase on the suction side and subsequently on the discharge side of the compressor. It can be seen that the dynamic response for the outlet pressure was a little slower for the model than for the test data, while the dynamic response for the water outlet temperature from the condenser was a bit faster for the model compared to the test data.

One of the challenges about the system model was to replicate the various controls in the heat pump. For example, the thermostatic valve (V7) in the oil circuit was relatively slow regulating in relation to the set point, which in this case was defined as 73.5 °C, see Fig. 12(g). In the model, this thermostatic valve was modeled with a PI regulator, which then had to reflect the measured data. Another control parameter was the high-pressure control of the liquid level in the receiver. The liquid level was controlled by a PI regulator which was active outside a neutral zone. In order to find the PI gains (proportional gain, k, and the time constant of the integrator block, T_i) that reflected the measured data, a parameter sweep was made to find the best combination. Fig. 13 shows some of the investigated PI gains. The parameters shown for the red curve were used for further work with the model. For this combination of PI gains, it was possible to control the level within the neutral zone before the set-point change, and it had the same characteristics for the overshoot immediately following the set-point change. In addition, a corresponding settlement time of around 150 seconds occurred before the level again was inside the neutral zone.

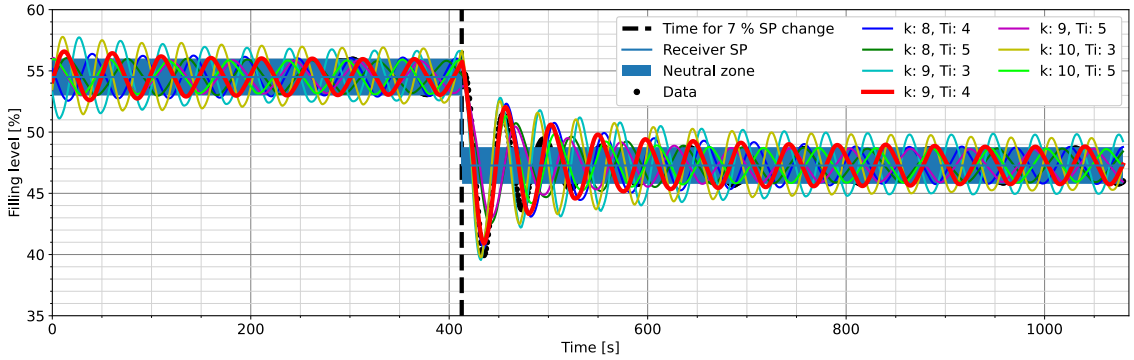


Fig. 13. Different PI gains for the controller for liquid level in receiver R1.

3.3. Case 2: Multiple simultaneous changes

Fig. 14 shows multiple dynamic variations of the independent input parameters for case 2. The graph on the left side shows the inlet temperatures to the evaporator and the sub-cooler which were similar to the inlet temperature for the oil-cooler. The graph on the right shows the water flows for the sub-cooler, evaporator, oil-cooler and the compressor speed, respectively. In this case the inlet water temperatures varied by 2 K to 3 K during the 2500 seconds of the case, and the water flows were increased as the compressor speed was gradually increased from 3060 RPM to 3580 RPM.

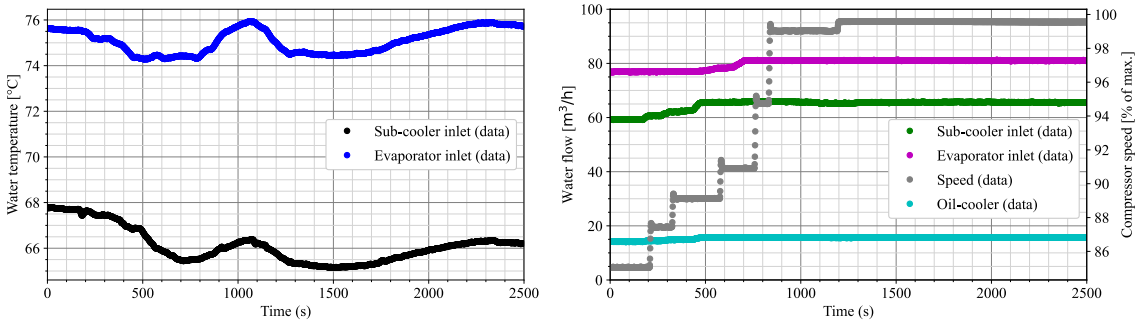


Fig. 14. Independent parameters for case 2 – multiple simultaneous changes.

Although there were several different parameters that were changed at the same time, case 2 still gave a good indication of the ability for the model to predict the dynamic response of the heat pump. Fig. 15 shows the influence and dynamic response of the heat pump system with changes in RPM and inlet water temperatures for both the test data and simulation results.

Fig. 15(a) shows the discharge pressure as a function of time. In addition, the six times with an RPM increase as well as the water inlet temperature to the sub-cooler are highlighted. The model was able to predict a discharge pressure which captures the dynamic fluctuation from the water inlet temperature and changes in RPM. Fig. 15 also shows the dynamic response of normalized heat transfer rate for oil-cooler (b) and condenser (c) as well as the suction temperature (d), water outlet temperature (e) of the condenser, discharge temperature (f), and oil inlet temperature to the compressor (g). In general, there was a good correlation between dynamic patterns in the test data and the model. The model discharge pressure (a) was on average 0.56 bar higher at RPM below 3580, while the average difference at full speed was 0.25 bar. With each RPM change, the pressure level for the test data and the simulation changes. The new pressure levels of the measurements were achieved approximately twice as fast as in the model, but with the same pressure increase. The difference in the normalized heat transfer rate for oil cooling (b) and condensing (e) were on average 1.2 % and 0.7 % lower for the model compared to the measured data. The suction temperature (d) was on average 0.04 °C lower for the model. Here, however, there were a few sudden drops in measured data that the model did not capture. The modelled discharge temperature (d) was on average 2 °C above the measured data, however with a similar dynamic response. The modelled water outlet temperature of the condenser (f) and oil inlet temperature to the compressor were on average 0.2 °C and 0.3 °C above the measured data. For the temperature out of the condenser the dynamic response was similar between the data and simulated values, while for the oil inlet temperature dynamic response also was similar, however with smaller deviation occurring around 1500 seconds.

The dynamic response for the normalized heat transfer rate for the oil cooler was also similar between data and simulated values, however at full load there was an offset of approximately 1.1 %.

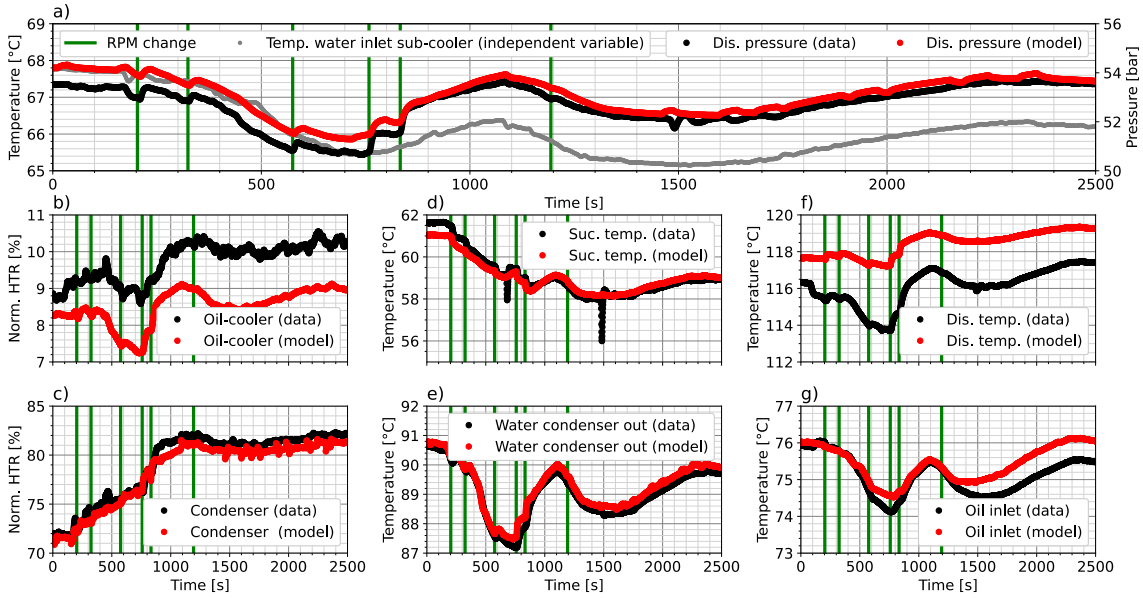


Fig. 15. Comparison of dynamic response in case 2 between data and model for a) the discharge pressure, b) heat transfer rate for oil-cooler, c) heat transfer rate for the condenser, d) suction temperature, e) temperature for the water outlet of the condenser, f) discharge temperature, and g) and oil inlet temperature.

4. Discussion

The validation of the results from the simulation model compared to the test data showed that the model was able to satisfactorily predict the dynamics seen during operation of the heat pump system. This would not be likely to be captured with only quasi-stationary models as also discussed in [24]. The offset difference between the experimental data and the model in relation to the steady state error can for example be attributed to small differences in the fitted parameters (design data in relation to experimental data), not modeled physical aspects, and/or measurement uncertainties. The difference for the dynamic aspects can for example be attributed to the PI controllers.

The validation showed the importance of suitable parameters used in the controllers. Especially the control of the expansion valve (V7) was sensitive for the system operation. In order to tune and validate the controllers further, more tests are suggested where set-point changes are introduced one at a time. These suggested tests including a test program with ramping the compressor speed up and down, on/off operation with the economizer, changing the capacity glider position, changing the sink and source side flow and temperature, while maintaining all other independent input parameters constant. Since there are several different PI-controllers with different PI-gains and neutral zones which simultaneously influencing each other, future structured tests will further show if additional changes to the PI-controllers in the model are necessary.

In some cases, the dynamic response for the simulation model showed shorter settling times with lower amplitude compared to the measured data. This might be due to neglecting pipe connections between the components and the corresponding heat- and pressure losses. If these connections were taken into account a minor contribution to the dynamic response for the model is expected, however it is also expected that the model will be numerically stiffer and has an accordingly higher computation time [8].

For case 1, in which a change of the liquid level in the receiver was imposed, another source of error could be due to a difference in the interpretation of the value of the experimental data for the height measurement in the horizontal receiver. The measured value in the test data was a relative height measurement, while the used filling level in Dymola was the fraction between the volume of liquid and the total volume. The conversion from the relative height measurement to the filling level was based on approximated values. In future work the exact position of the sensor will be investigated in order to precisely compare the receiver fluid level in the measurements and the simulation.

In some cases, the controllers in the physical heat pump use a varying proportional band depending on the difference between the desired set-point value and the actual value. If the error signal is large and outside the proportional band the controller ramps up quicker, while the controller is slower for low error signals. Further

studies are needed to investigate if this effect needs to be included in the model in order to further minimize errors between the dynamic model and the measured data.

In the present study, the heat pump was modeled without details of the components for the secondary streams, which determines the sink and source inlet water temperatures and flows. These were defined by the test setup, and then used as inputs to the model. This approach is suitable for validation of the heat pump system model. In future studies, it may be favorable to also include the modelling of pumps and valves on the secondary sides when investigating holistic control procedures to accommodate fast changes of external parameters.

Several design points have been used to fit the individual components in the system. For most of the parameters, it was possible to fit the design data very well to the individual components. There was, however, a little difference for the discharge temperature of the screw compressor. In order to make this temperature more accurate, further work can be done to incorporate the oil cooling in the model in more detail.

By making a detailed dynamic model and validating the system in different operating conditions, it was possible to get a thoroughly validated model, which then can be used for more in-depth analyses for many different operating conditions. By having a validated model, these analyses can be done much faster compared to full scale testing of the heat pump system in the laboratory. Hence, the presented validated model in this study allows for relatively quick investigation of different control approaches and development of design guidelines in order to be used as a general development tool for large-scale ammonia heat pumps.

5. Conclusion

A dynamic model of a large-scale one-stage ammonia heat pump with a screw compressor and different types of heat exchangers was implemented in Dymola. The model was validated with three different cases: a case with stable operating conditions, a case with a single set-point change for the receiver level, and a case with multiple simultaneous changes. The validation showed a satisfying agreement between the measured data and the model, both in relation to the offset errors and the dynamic response.

The dynamic model was developed by systematically modelling each individual component in the heat pump system, and fitting it mainly against the component design data, before finally combining the components into an overall system model. The different controllers were set up to match the dynamic response for the measured data in order to be able to validate the system model. The various dynamic responses in the model compared to the measured data were highly dependent on the used gains for the PI controllers, but through parameter sweeps of the PI gains it was possible to find values that led to satisfying agreement between the measured data and the model.

Case 0 showed that the model overall in a steady state scenario performed similar to the performance for the measured data. In case 1 the liquid level in the receiver was changed which subsequently led to a change in pressure for the heat pump system which the model captures. For case 1 it was further shown that the dynamic response overall was in good agreement for all the individual components, however also that for a few components small time differences in the dynamic response were observed, which can be refined in future work. Finally, case 2 showed that model and measured data agree well for changes in the temperatures on the sink and source side as well as for fast changes of the compressor speed.

The results from the validation showed that this dynamic system model has great potential to be used for developing holistic control strategies and design guidelines in order to further improve the resilience and performance under fluctuating boundary conditions for large-scale heat pumps.

Acknowledgements

This work was funded by EUDP (Energy Technology Development and Demonstration Programme) under the project ”Development of Fast Regulating Heat Pumps using Dynamic Models” (64020-1077).

References

[1] IEA, “Heat Pumps,” Paris, 2022. [Online]. Available: https://www.iea.org/reports/heat-pumps

[2] J. J. Aguilera, W. Meesenburg, T. Ommen, W. B. Markussen, J. L. Poulsen, B. Zühlsdorf, and B. Elmegaard, “A review of common faults in large-scale heat pumps,” *Renew. Sustain. Energy Rev.*, vol. 168, p. 112826, 2022, doi: 10.1016/j.rser.2022.112826.

[3] B. P. Rasmussen and B. Shenoy, “Dynamic modeling for vapor compression systems-Part II: Simulation tutorial,” *HVAC R Res.*, vol. 18, no. 5, pp. 956–973, 2012, doi:

10.1080/10789669.2011.582917.
[4] P. Li, H. Qiao, Y. Li, J. E. Seem, J. Winkler, and X. Li, "Recent advances in dynamic modeling of HVAC equipment. Part 1: Equipment modeling," *HVAC R Res.*, vol. 20, no. 1, pp. 136–149, 2014, doi: 10.1080/10789669.2013.836877.
[5] P. Li, Y. Li, J. E. Seem, H. Qiao, X. Li, and J. Winkler, "Recent advances in dynamic modeling of HVAC equipment. Part 2: Modelica-based modeling," *HVAC R Res.*, vol. 20, no. 1, pp. 150–161, 2014, doi: 10.1080/10789669.2013.836876.
[6] Modelica Association, "Modelica Libraries — Modelica Association," 2019.
[7] M. Gräber, K. Kosowski, C. Richter, and W. Tegethoff, "Modelling of heat pumps with an object-oriented model library for thermodynamic systems," *Math. Comput. Model. Dyn. Syst.*, vol. 16, no. 3, pp. 195–209, 2010, doi: 10.1080/13873954.2010.506799.
[8] W. Meesenburg, W. B. Markussen, T. Ommen, and B. Elmegaard, "Optimizing control of two-stage ammonia heat pump for fast regulation of power uptake," *Appl. Energy*, vol. 271, no. December 2019, p. 115126, 2020, doi: 10.1016/j.apenergy.2020.115126.
[9] W. Meesenburg, T. Ommen, W. B. Markussen, and B. Elmegaard, "Influence of component sizing on the dynamic behaviour of fast-regulating two-stage ammonia heat pumps," *ECOS 2020 - Proc. 33rd Int. Conf. Effic. Cost, Optim. Simul. Environ. Impact Energy Syst.*, pp. 923–934, 2020.
[10] J. L. Poulsen, J. Joaquín, A. Schulte, S. Försterling, W. Meesenburg, J. Koehler, B. Elmegaard, and B. Zühlsdorf, "Model-based analysis of a heat pump cascade system using seawater and ammonia as working fluids," *35th Int. Conf. Effic. Cost, Optim. Simul. Environ. Impact Energy Syst.*, 2022.
[11] W. Meesenburg, J. Joaquín, R. Kofler, and W. B. Markussen, "Prediction of fouling in sewage water heat pump for predictive maintenance," 2022.
[12] Dassault Systemes, "Dymola 2022 - Dynamic Modeling Laboratory." Dassault Systèmes.
[13] "TIL 3.9 - Model library for thermal components and systems." TLK Thermo GmbH, 2022.
[14] Modelica-Association, "Modelica and the Modelica Standard Library." 2021. [Online]. Available: http://www.modelica.org
[15] M. W and V. H, *An Introduction to Computational Fluid Dynamics - The Finite Volume Method*. Pearson Education (Us), 2007.
[16] TLK-Thermo, "ModelFitter." 2022. [Online]. Available: http://www.tlk-thermo.de
[17] X. Tao and C. A. Infante Ferreira, "Heat transfer and frictional pressure drop during condensation in plate heat exchangers: Assessment of correlations and a new method," *Int. J. Heat Mass Transf.*, vol. 135, pp. 996–1012, 2019, doi: 10.1016/j.ijheatmasstransfer.2019.01.132.
[18] H. Martin, "A theoretical approach to predict the performance of chevron-type plate heat exchangers," *Chem. Eng. Process. Process Intensif.*, vol. 35, no. 4, pp. 301–310, 1996, doi: 10.1016/0255-2701(95)04129-X.
[19] R. L. Amalfi, F. Vakili-Farahani, and J. R. Thome, "Flow boiling and frictional pressure gradients in plate heat exchangers. Part 2: Comparison of literature methods to database and new prediction methods," *Int. J. Refrig.*, vol. 61, pp. 185–203, 2016, doi: 10.1016/j.ijrefrig.2015.07.009.
[20] G. A. Longo, S. Mancin, G. Righetti, and C. Zilio, "A new model for refrigerant boiling inside Brazed Plate Heat Exchangers (BPHEs)," *Int. J. Heat Mass Transf.*, vol. 91, pp. 144–149, 2015, doi: 10.1016/j.ijheatmasstransfer.2015.07.078.
[21] Modelica-Association, "Functional Mock-up Interface," 2022. https://fmi-standard.org/ (accessed Mar. 21, 2022).
[22] TLK-Thermo, "Model development of physical based screw compressor with injection." Braunschweig, 2021.
[23] P. Kurzweil, B. Frenzel, and F. Gebhard, *Physik Formelsammlung*. 2008.
[24] H. Biglarian, M. Abbaspour, and M. H. Saidi, "Evaluation of a transient borehole heat exchanger model in dynamic simulation of a ground source heat pump system," *Energy*, vol. 147, pp. 81–93, Mar. 2018, doi: 10.1016/J.ENERGY.2018.01.031.

14th IEA Heat Pump Conference
15-18 May 2023, Chicago, Illinois

Design and operational optimisation of an integrated thermal energy storage ground-source heat pump with time-varying electricity prices

Paul Sapin[a,*], Andreas V. Olympios[a], Matthias Mersch[a,b], Christos N. Markides[a]

[a] Clean Energy Processes (CEP) Laboratory and Sargent Centre for Process Systems Engineering, Department of Chemical Engineering, Imperial College London, London SW7 2AZ, UK.
[b] Centre for Environmental Policy, Imperial College London, London SW7 2AZ, UK.

Abstract

A detailed methodology is proposed to design and optimise the operation of a ground-source heat pump (GSHP) coupled to a phase-change material (PCM) thermal battery. The objective is to minimise the cost of supplying space heating and hot water to a medium-demand house in the UK during a typical winter day with fluctuating electricity prices. A bespoke 8-kW GSHP is designed and used to optimise the charging schedule of the thermal battery to minimise daily operational costs while meeting the heat demand. If no limit is imposed on the size of the thermal battery, in the best scenario, a 41-kWh thermal battery is required to achieve costs as low as 1.85 £/day. However, large PCM batteries mean high upfront costs and little space restrictions. Therefore, a constraint is imposed on the thermal store capacity to identify the optimal trade-off that can be achieved between PCM battery size and daily power consumption costs. Operational costs strongly depend on the battery size, increasing from 1.85 £/day for a 41-kWh thermal battery to 3.50 £/day for a 6.3-kWh store.

© HPC2023.
Selection and/or peer-review under the responsibility of the organizers of the 14th IEA Heat Pump Conference 2023.

Keywords: ground-source heat pump; optimal control; phase-change material; thermal energy storage.

1. Introduction

Delivering near- and long-term international environmental objectives likely requires significant changes in the way heat is supplied to residential buildings [1]. The ambition to phase out the installation of new natural gas boilers in many countries implies remarkable infrastructural and regulatory changes in the upcoming years [2, 3]. Electricity-driven vapour-compression heat pumps are a proven technology [4] associated with a considerably better thermodynamic performance than gas boilers [5]. Although they are widely recognised as a sustainable alternative to conventional heating systems, the share of heat pumps in the market remains low in most countries [6]. This is mainly due to the high investment cost required [7], the high price of electricity when compared to that of natural gas [8] and the low uptake of control mechanisms that can be used to heat homes in a smart and flexible way [9].

Vapour-compression heat pumps involve many possible design options and heat sources [10]. Common types are air-source heat pumps (ASHPs) and ground-source heat pumps (GSHPs). The former uses ambient air as low-temperature heat source, while the latter draws heat from the ground. GSHPs require heat collector tubes to be buried underground. Therefore, they are associated with higher installation costs than ASPHs [4]. However, since the temperature of the ground experiences smaller fluctuations throughout a year compared to the ambient air, GSHPs can often be operated more efficiently on average than ASHPs. Especially in winter, when the demand for domestic hot water (DHW) and space heating (SH) is the highest, GSHPs typically show superior performance.

* Corresponding author. Tel.: +44 (0)7412913167.
E-mail address: p.sapin@imperial.ac.uk.

The cost competitiveness of vapour-compression heat pumps can be potentially improved by using thermal energy stores (TES) in conjunction with smart control strategies [11-16]. TES can be used to decouple demand and supply. Smart controllers can shift some of the electricity consumption from high- to low-electricity-price periods, leading to notable economic savings for homeowners while at the same time benefiting the wider energy system by providing demand-side flexibility [11].

As countries progress in decarbonising their electricity sector, the capacity of intermittent renewable generation sources is increasing significantly in many systems, while firm generation capacity from, e.g., coal- and gas-fired power plants is decreasing. Therefore, it is widely recognised that the value of demand flexibility is ever increasing. The UK aims to install 600,000 heat pumps per year from 2028 and up to 1.7 million heat pumps per year from 2035 [12], for a total of 7 to 11 million heat pumps in 2035 [13]. These heat pumps, if used with conventional controllers, will significantly add to peak electricity demands. However, if coupled with TES and smart controllers, they can potentially provide significant demand flexibility.

Sensible-heat storage in the form of hot-water cylinders is currently the most widely used TES method in residential applications, as it is cheap and safe. However, latent-heat storage systems based on phase-change materials (PCMs) have experienced significant development and have recently entered the market for residential applications [14]. The main advantages of PCM-TES compared to hot-water cylinders are the potential for higher energy densities and the fact that they can work within smaller temperature ranges. This results in potentially lower required hot-water delivery temperatures and thus higher heat pump system efficiencies.

Most of the recent literature on smart operation of domestic heat pumps has focused on ASHPs. Several studies have examined the potential of shifting the operation of heat pumps from high- to low-electricity-price periods. Some of these studies concluded that a very large TES volume can prove beneficial for homeowners. For example, in the work of Arteconi et al. [15] a 500-L hot-water cylinder was shown to minimise the electricity consumption of an ASHP during high-electricity-price afternoon hours in Northern Ireland. Le et al. [16], also focusing on Northern Ireland, showed that hot-water cylinders with volumes in the range of 600 to 1100 L are optimal, depending on the investigated scenario. Furthermore, Kelly et al. [17] concluded that a 1000-L hot-water cylinder or a 500-L PCM thermal store would be required to shift ASHP operation to off-peak periods for a typical UK household. However, since TESs are typically installed within the internal space of houses, such storage volumes are not viable for many households that have limited space.

In addition to the aforementioned studies, Renaldi et al. [18] predicted that smart ASHP operation in a London house can lead to slightly reduced operational cost (by 6%) compared to a gas boiler. Fischer et al. [19] concluded that the use of model predictive control can reduce operating costs for a multi-family home in Germany by more than 10% compared to simple rule-based control methods. In their most recent work, Olympios et al. [20] identified that the operational optimisation of an ASHP for a single-family dwelling in the UK and Germany can lead to operational cost savings higher than 20% compared to simple heat pump control mechanisms based on temperature sensors. In that work, price and demand forecasts were assumed to be known with perfect accuracy.

Less effort has been devoted to optimising the operation of integrated thermal energy storage ground-source heat pump (GSHP-TES) systems. Salpakari et al. [21] studied cost-optimal and rule-based control strategies for buildings with a PV system, a GSHP, a hot-water cylinder, electrical storage and shiftable loads. They showed that, for a low-energy house in Finland, cost-optimal control can lead to 13–25% savings in the yearly electricity bill compared to an inflexible reference control strategy. Yang et al. [22] proposed operation strategies of a hybrid GSHP system with double-cooling towers for a hotel building, but results are not applicable to domestic buildings. Kajgaard et al. [23] estimated that economical savings achieved by time-shifting the operation of a GSHP heat pump in a typical Danish house can by up to 12%. However, none of the studies focusing on GSHPs considered PCM-TES.

In this work, the operation of an GSHP-TES is optimised for a typical UK household. The novelty lies not only in the development of comprehensive thermodynamic models and their use to perform an operational optimisation of a GSHP system integrated with a PCM-TES for domestic applications, but also in the identification of the optimal trade-off that can be achieved between PCM battery size and daily power costs. The developed heat pump and TES models, as well as the description of the optimisation framework, are presented in Section 2. The results and conclusions are provided in Sections 3 and 4, respectively.

2. Design and operational optimisation of an integrated thermal store ground-source heat pump

An optimisation framework has been developed in-house based on comprehensive first-law thermodynamic and component-costing models with a view to perform simultaneous design and operational optimisation of domestic ground-source heat pumps with integrated thermal energy storage (GSHP-TES). In this paper, we

present a preliminary study aimed at optimising the charging schedule of a phase-change material (PCM) thermal store coupled with a ground-source heat pump to supply both space heating and domestic hot water demands during a typical winter day for a medium-demand house in the UK, as detailed in Figure 1.

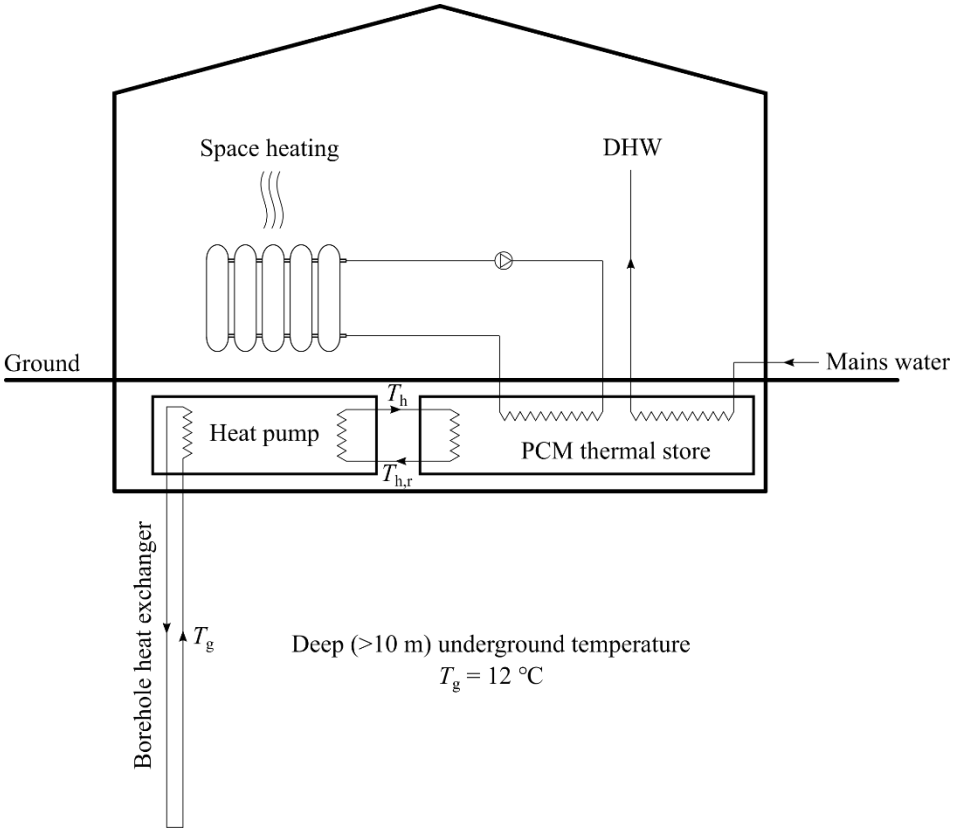


Fig. 1 - Schematic of a domestic ground-source heat pump with integrated latent-heat thermal energy storage.

Heat demand profiles and time-varying electricity prices used for this case study are presented in Section 2.1. The heat pump is first designed for a set heating capacity and prescribed pinch-point constraints for both condenser and evaporator units, as detailed in Section 2.2, while a simplified model is used to predict the PCM thermal battery performance, as detailed in Section 2.3. The charging schedule of the PCM thermal battery is then optimised for various thermal store sizes (ranging from 7 to 60 kWh), as detailed in Section 2.4.

2.1. Case study definition

This study is performed using the hourly heat demand profile of a typical UK household in a typical year. The typical household was identified by applying a kmedoids clustering algorithm to the Cambridge Housing Model dataset [24], which contains a representation of the UK building stock. Since the model only provides annual demand values for SH and DHW, the method developed by Watson et al. [25] was used to determine the hourly SH demand based on the ambient temperature, while the daily DHW demand profile was taken from Herrando et al. [26]. To eliminate any potential bias from choosing a specific year, the weather data was taken from a typical meteorological year, provided by the PVGIS tool [27]

Time-varying electricity tariffs offer end-users an opportunity to shift their electricity usage to low-price periods, which can be achieved with adequate-size thermal batteries coupled to heat pump units. In the current study, we selected the Octopus Agile tariff, which exhibits a high-price period between 4 and 7 pm [28].

Both hourly-defined electricity price and aggregated heat demand profiles for a typical winter day for a medium-demand house in the UK, presented in Figure 2, are used for this study.

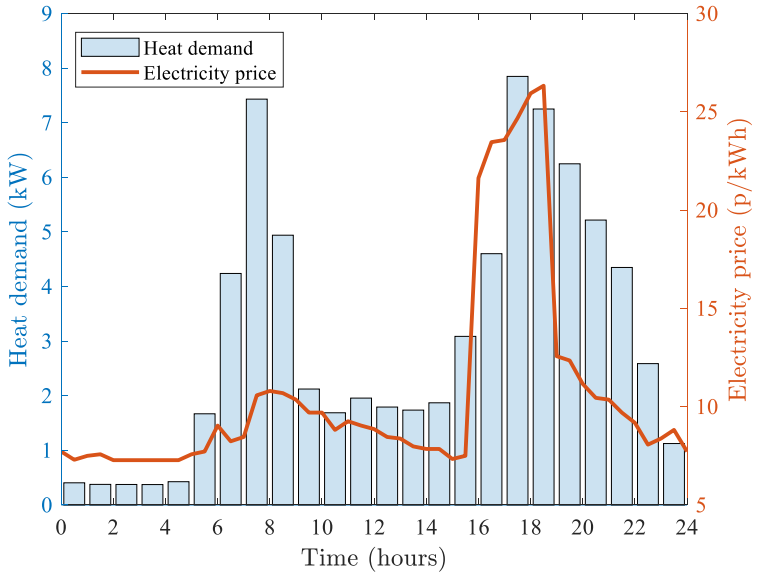


Fig. 2 - Hourly-defined electricity price and heat demand profiles for a typical winter day for a medium-demand house in the UK.

2.2. Ground-source heat pump (GSHP) design

The GSHP used to supply both space heating and DHW demands is a standard electricity-driven vapour-compression heat pump (VCHP) made of 4 main components, namely: a compressor, a condenser, an expansion valve, and an evaporator, as shown in Figure 3, operated with R32 as a working fluid, which exhibits a relatively low 100-year global warming potential of 675, as found in the IPCC 4th Assessment Report.

The GSHP is designed to extract heat from a ground-source water stream entering the evaporator unit at a constant T_g = 12 °C and rejecting heat at T_h = 60 °C, with imposed 5-K pinch-point temperature difference in both the condenser and evaporator units. The return temperature from the PCM thermal store is determined from a heat balance as a function of both the PCM melting temperature, T_m = 48 °C, and the water-to-store heat transfer effectiveness (ε = 0.8), as detailed in Section 2.3. In addition, the compressor is assumed to have a 60-% isentropic efficiency and the expansion valve is set to maintain a constant 6-K superheat at the compressor suction. The working fluid equilibrium and transport properties are obtained using the open-source thermophysical property library Coolprop [29].

The thermodynamic performance of the VCHP unit is assessed with a comprehensive first-law thermodynamic model based on a set of widely accepted assumptions:

- No pressure losses in pipes
- No heat losses
- Zero subcooling at the condenser outlet (which can be achieved with a liquid receiver)
- Dynamic effects are neglected (i.e., cycle assumed to operate under steady conditions)
- Counter-current heat exchangers

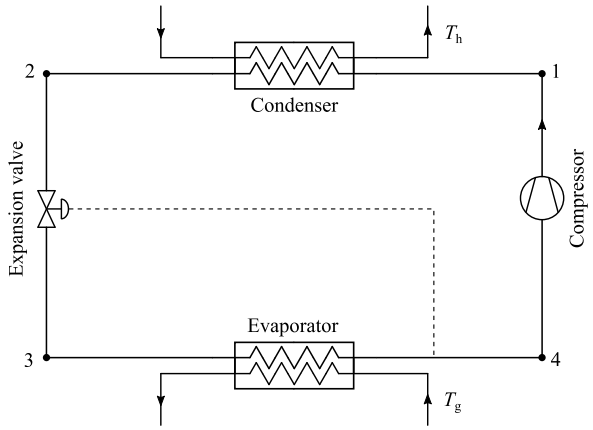


Fig. 3 - Schematic of the domestic vapour-compression heat pump (VCHP) design.

The VCHP cycle and the corresponding performance can then be determined by the condensing pressure, P_{cond}, and evaporating pressure, P_{evap}. With the zero-subcooling assumption at the condenser outlet, the thermodynamic state of the working fluid state in point '2' – as defined in Figure 3 – is fully defined and both equilibrium and transport properties are calculated using Coolprop. The saturated liquid leaving the condenser then undergoes an isenthalpic throttling through the expansion valve, which allows us to calculate the vapour quality and properties of the two-phase mixture resulting from the Joule-Thompson expansion, thus fully defining state '3'. State '4' is also fully defined from the evaporating pressure, P_{evap}, and the prescribed 6-K superheat at the evaporator outlet. The compressor discharge (state '1') is obtained from the assumed 60-% compressor isentropic efficiency, which accounts for various loss mechanisms, including: pressure losses through the intake and exhaust valves, mass leakage through the piston ring and heat transfer.

Finally, both evaporating and condensing pressures are optimised to minimise the power consumption, $\dot{W}_{\mathrm{c}}$, to provide a given heating capacity, $\dot{Q}_{\mathrm{h}}$, while respecting pinch-point constraints in the condenser and evaporator units. This non-linear problem is solved using the sequential least squares programming (SLSQP) implemented in the Python open-source SciPy library [30]. The coefficient of performance (COP), denoted φ, is then defined as the ratio of the heating power to the power input: $\varphi = \dot{Q}_{\mathrm{h}}/\dot{W}_{\mathrm{c}}$.

The design of evaporator and condenser units is then determined using spatially resolved models. Brazed-plate heat exchangers (BPHXs) are used for both units as they offer compact and efficient designs for both water-cooled condensers and water-source evaporators. Heat exchanger units are discretised in equal enthalpy-step nodes and the conjugate heat transfer through the heat exchanger plates are solved for each element to determine the overall required area. Single-phase convective heat transfer is predicted using Bogaert & Böles correlation [31], which is also used to predict the convective-boiling contribution to the heat transfer in the two-phase region of the evaporator unit, while the pool-boiling contribution is estimated with Cooper's correlation [32]. The fluid-to-wall heat transfer in the two-phase region of the condenser unit is predicted using the model proposed by Thonon & Bontemps [33]. No further detail is provided on these models nor is the choice of these correlations further discussed here, as this study focuses on the operational optimisation of GSHP-TESs and on the trade-off between the thermal battery size (or capacity) and the daily operational costs. However, interested readers may refer to recent publications where these models are presented in more detail [5, 34]. The following research questions will be addressed in future studies: (i) whether high-spec high-cost heat pumps perform better than low-spec low-cost ones from an economic point of view; or (ii) whether a large heat pump coupled with a small thermal battery outperform a small heat pump with large thermal stores.

For stated assumptions and component performance indicators, an 8-kW heat pump has been designed, and the corresponding geometry and performance characteristics are detailed in Table 1. The stated performance matches that of real-world ground-source heat pump systems, the price and performance of which are detailed in the online technology library proposed by Olympios et al. [35].

Table 1. Detailed characteristics of an 8-kW heat pump (with R32) designed to extract heat from a water stream at T_{g} = 12 °C and rejecting heat at T_{h} = 60 °C, with imposed 5-K pinch-point temperature difference in both the condenser and evaporator units.

Heat pump performance	
Power consumption	2.64 kW
Coefficient of performance	3.0
Pressure ratio ($P_{\mathrm{cond}}/P_{\mathrm{evap}}$)	4.8
Working fluid mass flowrate	27.10^{-3} kg/s
Condenser design	
Total heat transfer area	0.15 m^2
Number of plates	3
Channel width	50 mm
Channel length	970 mm
Evaporator design	
Total heat transfer area	0.08 m2
Number of plates	2
Channel width	79 mm
Channel length	508 mm

2.3. PCM thermal battery design and performance

The latent-heat thermal battery proposed for domestic applications is based on an existing phase-change material, namely the PCM-A48 from PCM Products Ltd., which has a melting temperature T_{m} = 48 °C, which is deemed adequate for the mid-size dwelling selected for this investigation and for modern radiators. Further details on the selected PCM are provided in Table 2. Underfloor heating installations with proper insulation would require lower melting temperatures, which would obviously benefit the thermodynamic performance of the heat pump by reducing the source-to-sink temperature lift and using the building thermal mass as an additional thermal storage medium, which is though beyond the scope of this study.

Heat transfer to and from the latent-heat thermal battery is represented using a simple fixed-effectiveness method (ε = 0.8), from which the return temperature to the heat pump unit, $T_{\mathrm{h,r}}$, is calculated:

$$T_{h,r} = T_h - \varepsilon(T_h - T_m). \quad (1)$$

Table 2. Thermo-physical properties of the organic phase change material PCM-A48 from PCM Products Ltd.

Material	Melting temperature	Density	Latent heat	Specific heat capacity	Thermal conductivity
PCM-A48	48 °C	810 kg/m^3	230 kJ/kg	2.85 kJ/kg/K	0.18 W/m/K

2.4. PCM thermal battery charging schedule optimisation

The charging schedule is defined as a set of on/off times spanned throughout the day to decide when and for how long the heat pump is turned on to charge the thermal battery. Instead of allowing an unlimited number of charges a day, which would be highly computationally expensive, we decided to impose and increase the number of charges a day incrementally until no further improvement is noticed. The optimisation exercise then boils down to decide, for a given number of charges a day, when and for how long should each charge occur to minimise the daily operational expenditure (OPEX). A couple of constraints have been imposed to ensure feasibility and control the size of the thermal battery: (i) the heat demand must always be met; and (ii) the storage capacity of the thermal battery cannot exceed a prescribed value. The latter constraint is first lifted to measure the maximum savings that can be achieved through smart control of the thermal battery charging schedule (results in Section 3.1), while a range of constrained battery sizes are imposed to identify the optimal trade-off between the thermal battery capacity and the daily operational costs (see Section 3.2).

This optimisation problem was formulated in the Python open-source SciPy library [30] and solved using a differential evolution algorithm, which consists of iteratively improving a population of candidate solutions.

3. Results

3.1. Optimised charging schedules without constraint on the thermal battery size

The charging schedule of an unlimited-size thermal battery is first optimised using the 8-kW heat pump designed in Section 2.2. The results are presented in Figure 4, where the optimum charging profiles are shown for 1-to-4 charges per day along the heat demand and electricity prices throughout the typical winter day selected for this investigation, while the associated daily operational costs (i.e., electricity consumption costs) are detailed in Table 3 along with the required battery size for each scenario.

It appears clearly that, for each scenario, low-price periods are favoured to charge the thermal battery, while the peak-price period is avoided. Increasing the number of charges does lead to significant additional savings, with the daily OPEX reducing from 2.01 £/day for a single charge to 1.85 £/day for 3 or more charges per day. It is worth noting that, although the 3-charge-a-day charging schedule differs from that of the 4-charge-a-day scenario, as shown in Figure 4, similar daily costs are achieved. The battery required to achieve the former schedule (46 kWh) is however larger than that needed to deliver the heat demand following the 4-charge-a-day schedule (41 kWh). Increasing the number of charges per day is thus needed to identify a better trade-off between battery size and daily costs, which is explored further in the next section.

Finally, for the unlimited-size battery optimisation exercise, no improvement is noticed when further increasing the number of charges per day.

Table 3. Daily operational cost (OPEX) and required battery capacities associated with optimised charging schedules with an 8-kW heat pump without constraint on the thermal battery size.

Number of charges a day	1	2	3	4	5
Required battery size (kWh)	53	47	46	41	41
Daily OPEX (£/day)	2.01	1.86	1.85	1.85	1.85

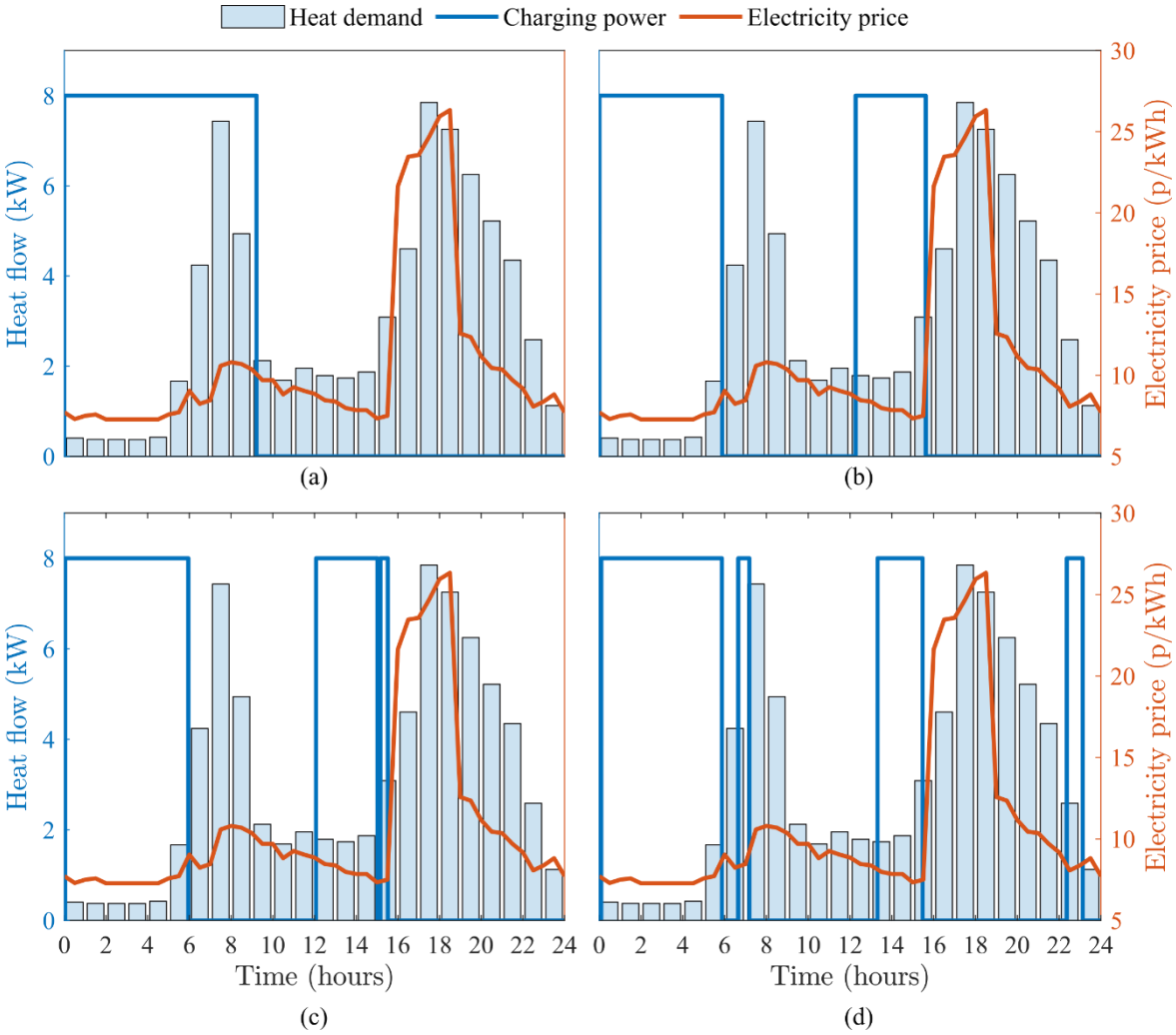


Fig. 4 - Optimised charging schedules with an 8-kW heat pump (design detailed in Table 1) without constraint on the thermal battery size for: (a) 1 charge a day; (b) 2 charges a day; (c) 3 charges a day; and (d) 4 charges a day. Corresponding daily operational and required battery sizes are detailed in Table 3.

3.2. Multi-objective optimisation: trade-off between thermal battery size and daily OPEX

Increasing the thermal storage capacity comes at a cost. First, from an economic standpoint, upfront costs for a large-scale thermal battery are very significant, as the specific cost of PCM batteries typically ranges from 200 to 400 £/kWh. Second, space restrictions are to be considered and several end-users simply will not have enough space to fit large-capacity thermal batteries. Therefore, a multi-objective optimisation has been conducted, whereby a constraint is imposed on the thermal store capacity to measure how the potential savings are impacted and identify the optimal trade-off that can be achieved between PCM battery size and daily costs.

The results of this investigation are presented in Figure 5, where the daily operational costs are plotted against required thermal store capacity for a range of optimised charging schedules. These results have been obtained by varying the number of charges per day and the constraint imposed on the battery size to explore the design/operational space. This allows us to identify the optimal trade-off, which is given by the Pareto

frontier plotted in Figure 5. This curve provides the end-user or installer with a direct relationship between how much savings can be expected by fitting a larger thermal battery.

As expected, higher daily power costs are to be paid with smaller thermal stores. The fact that the evening peak demand coincides with the peak electricity prices, as shown in Figures 2 and 4, explains why operational costs so strongly depend on the battery size, with daily OPEX increasing from 1.85 £/day for a 41-kWh thermal battery to 3.5 £/day for a 6.3-kWh thermal store. Indeed, it becomes impossible to avoid charging the battery during the peak-demand/peak-price period with smaller thermal batteries.

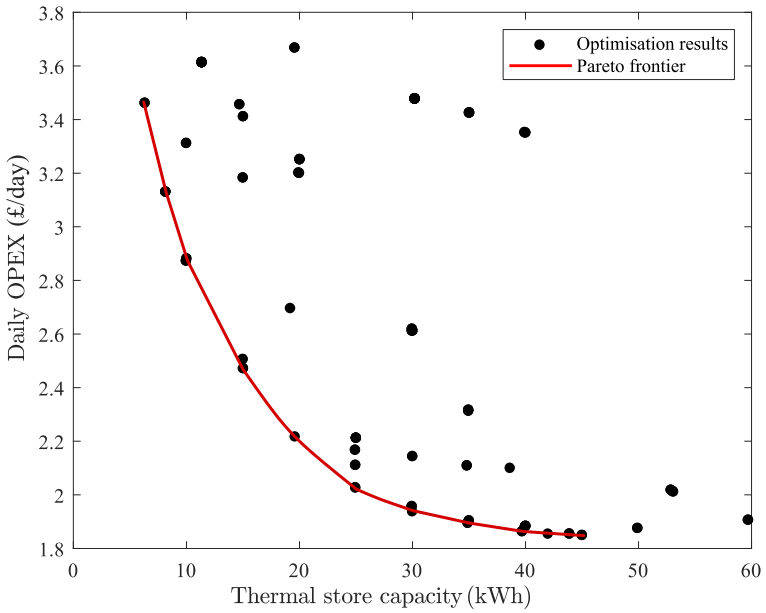


Fig. 5 - Daily operational costs (OPEX) plotted against required thermal store capacity and associated Pareto frontier. Each point corresponds to an optimised charging schedule with specific number of charges per day and constraint on the battery size.

4. Conclusions

Quantifying the savings in the yearly electricity bill that can be achieved through smart control strategies of heat pumps integrated with thermal energy storage is key to promote the uptake of clean heating technologies and help heat decarbonisation. In this paper, a detailed methodology is proposed to design and optimise the operation of a ground-source heat pump (GSHP) coupled to a phase-change material (PCM) thermal battery. The objective is to minimise costs of supplying both space heating and hot water to a medium-demand house in the UK during a typical winter day with fluctuating electricity prices.

Time-varying electricity tariffs offer end-users an opportunity to shift their electricity usage to low-price periods, which can be achieved with adequate-size thermal batteries coupled to the heat pump unit. After designing a dedicated 8-kW GSHP fitted with brazed-plate heat exchangers, charging schedules of the thermal battery have been optimised to minimise daily operational costs (OPEX) while meeting the heat demand.

First, no limit was imposed on the size of the thermal battery. By increasing the number of charges allowed per day from 1 to 5, it was found that increasing the number of charges does lead to cost savings, with the daily OPEX reducing from 2.01 £/day for a single charge to 1.85 £/day for 3 or more charges per day. In the best scenario, a 41-kWh thermal battery is required to achieve costs as low as 1.85 £/day.

However, large-scale thermal stores are costly. First, from an economic standpoint, as higher upfront costs are to be paid for larger thermal batteries. Second, space restrictions are to be considered and several end-users do not have enough space to fit large-capacity thermal batteries. Therefore, a multi-objective optimisation has been conducted, whereby a constraint is imposed on the thermal store capacity to measure how the potential savings are impacted and identify the optimal trade-off that can be achieved between PCM battery size and daily power costs. As expected, higher daily power costs are to be paid with smaller thermal stores. Operational costs strongly depend on the battery size, with daily OPEX increasing from 1.85 £/day for a 41-kWh thermal battery to 3.50 £/day for a 6.3-kWh thermal store. This is largely due to the concomitance of the evening peak heat demand and peak electricity prices as it becomes impossible to avoid charging the battery during the peak-demand/peak-price period with smaller thermal batteries.

Three main research pathways are being explored to extend the findings of this investigation.

- Simultaneous design and operational optimisation are being performed, whereby the size and performance of the heat pump system will be optimised along with yearly charging schedules to minimise the levelised cost of heat using ground-source energy systems.
- The assumption made in the current study to impose a constant return temperature from the underground borehole heat exchanger, although acceptable for a daily performance estimation, is no longer valid for yearly operation. A collaboration with a geotechnics research team is currently ongoing to address this limitation and determine year-round temperature variations associated with heat dissipation and accumulation in the ground.
- The omniscient point of view taken in the current study provides us with an upper bound for potential savings through smart control of the thermal battery charging schedule. At best, a real-life smart meter can be fed with inaccurate electricity prices, weather, and heat demand forecasts, which will lead to sub-optimal charging schedules as compared to those presented in this paper. We are currently investigating how close a smart-meter control strategy can approach this upper bound and what & how many data are needed. In other words, how smart does a smart meter need to be?

Acknowledgements

This work was also supported by the UK Engineering and Physical Sciences Research Council (EPSRC) [grant numbers EP/R045518/1, EP/P004709/1, and EP/V042149/1]. For the purpose of Open Access, the authors have applied a CC BY public copyright licence to any Author Accepted Manuscript version arising from this submission. Data supporting this publication can be obtained on request from cep-lab@imperial.ac.uk.

References

[1] Thomaßen G, Kavvadias K, Jiménez Navarro JP. The decarbonisation of the EU heating sector through electrification: A parametric analysis. *Energy Policy* 2021;**148**:111929. **doi**:10.1016/j.enpol.2020.111929

[2] Secretary of State for Business, Energy & Industrial Strategy. Heat and buildings strategy. 2021.

[3] Kerr N, Winskel M. A Review of Heat Decarbonisation Policies in Europe. *ClimateXChange Publications* 2021. **doi**:10.7488/era/794

[4] Staffell I, Brett D, Brandon N, Hawkes A. A review of domestic heat pumps. *Energy and Environmental Science* 2012; **5**: 9291-9306. **doi**:10.1039/C2EE22653G

[5] Olympios AV, Aunedi M, Mersch M, Krishnaswamy A, Stollery C, Pantaleo AM, Sapin P, Strbac G, Markides CN. Delivering net-zero carbon heat: Technoeconomic and whole-system comparisons of domestic electricity- and hydrogen-driven technologies in the UK. Energy Conversion and Management 2022; 262: 115649. **doi**:10.1016/j.enconman.2022.115649

[6] European Heat Pump Association. European heat pump market data. 2021.

[7] Meles TH, Ryan L. Adoption of renewable home heating systems: An agent-based model of heat pumps in Ireland. *Renewable and Sustainable Energy Reviews* 2022;**169**:112853. **doi**: 10.1016/j.rser.2022.112853

[8] European Commission. Electricity and gas prices for household consumers - bi-annual data. 2022.

[9] Stopps H, Huchuk B, Touchie MF, O'Brien W. Is anyone home? A critical review of occupant-centric smart HVAC controls implementations in residential buildings. *Building and Environment* 2021;**187**:107369. **doi**:10.1016/j.buildenv.2020.107369

[10] von Cube HL, Steimle F. *Heat pump technology*. 1st ed. Norwich: Butterworth-Heinemann; 1981.

[11] Hoseinpoori P, Olympios AV, Markides CN, Woods J, Shah N. A whole-system approach for quantifying the value of smart electrification for decarbonising heating in buildings. *Energy Conversion and Management* 2022;**268**:115952. **doi**:10.1016/j.enconman.2022.115952

[12] Department for Business, Energy & Industrial Strategy. Heat and buildings strategy. 2021.

[13] Department for Business, Energy & Industrial Strategy. Net-zero strategy: Build back greener. 2021.

[14] Midsummer. Sunamp heat batteries. 2022. [Online].
Available: https://midsummerwholesale.co.uk/buy/sunamp-heat-batteries

[15] Arteconi A, Hewitt NJ, Polonara F. Domestic demand-side management (DSM): Role of heat pumps and thermal energy storage (TES) systems. *Applied Thermal Engineering* 2013;**51**(1-2):155-165. **doi**:10.1016/j.applthermaleng.2012.09.023

[16] Le KX, Huang MJ, Wilson C, Shah NN, Hewitt NJ. Tariff-based load shifting for domestic cascade heat pump with enhanced system energy efficiency and reduced wind power curtailment. *Applied Energy* 2020;**257**:113976. **doi**:10.1016/j.apenergy.2019.113976

[17] Kelly NJ, Tuohy PG, Hawkes AD. Performance assessment of tariff-based air source heat pump load shifting in a UK detached dwelling featuring phase change-enhanced buffering. *Applied Thermal Engineering* 2014;**71(**2):809-820. **doi**:10.1016/j.applthermaleng.2013.12.019

[18] Renaldi R, Kiprakis A, Friedrich D. An optimisation framework for thermal energy storage integration in a residential heat pump heating system. *Applied Energy* 2017;**186**:520-529. **doi**:10.1016/j.apenergy.2016.02.067

[19] Fischer D, Bernhardt J, Madani H, Wittwer C. Comparison of control approaches for variable speed air source heat pumps considering time variable electricity prices and PV. *Applied Energy* 2017;**204**:93-105. **doi**:10.1016/j.apenergy.2017.06.110

[20] Olympios AV, Sapin P, Freeman J, Olkis C, Markides CN. Operational optimisation of an air-source heat pump system with thermal energy storage for domestic applications. *Energy Conversion and Management* 2022;**273**:116426. **doi**:10.1016/j.enconman.2022.116426

[21] Salpakari J, Lund P. Optimal and rule-based control strategies for energy flexibility in buildings with PV. *Applied Energy* 2016;**161**:425-436. **doi**:10.1016/j.apenergy.2015.10.036

[22] Yang J, Xu L, Hu P, Zhu N, Chen X. Study on intermittent operation strategies of a hybrid ground-source heat pump system with double-cooling towers for hotel buildings. *Energy and Buildings* 2014;**76**:506-512. **doi**:10.1016/j.enbuild.2014.02.061

[23] Kajgaard MU, Mogensen J, Wittendorff A, Veress AT, Biegel B. 2013. "Model Predictive Control of Domestic Heat Pump," American Control Conference (ACC). Washington, USA.

[24] Department for Business, Energy & Industrial Strategy. Cambridge housing model. 2015.

[25] Watson SD, Lomas KJ, Buswell RA. Decarbonising domestic heating: What is the peak GB demand? *Energy Policy* 2019;**126**:533-544. **doi**:10.1016/j.enpol.2018.11.001

[26] Herrando M, Markides CN, Hellgardt K. A UK-based assessment of hybrid PV and solar-thermal systems for domestic heating and power: System performance. *Applied Energy* 2014;**122**:288-309. **doi**:10.1016/j.apenergy.2014.01.061

[27] European Commission - Joint Research Centre. Photovoltaic geographical information system (PVGIS). 2022. [Online]. Available: https://re.jrc.ec.europa.eu/pvg_tools/en/

[28] Octopus Energy. Introducing Octopus Agile: The 100% green electricity tariff with plunge pricing. 2020. [Online]. Available: https://octopus.energy/agile/#what-does-it-cost

[29] Bell IH, Wronski J, Quoilin S, Lemort V. Pure and pseudo-pure fluid thermophysical property evaluation and the open-source thermophysical property library CoolProp. *Industrial & engineering chemistry research* 2014;**53(**6):2498-508.

[30] Virtanen P, Gommers R, Oliphant TE, Haberland M, Reddy T, Cournapeau D, Burovski E, Peterson P, Weckesser W, Bright J, Van Der Walt SJ, Brett M, Wilson J, Millman KJ, Mayorov N, Nelson A, Jones E, Kern R, Larson E, Carey CJ, Polat I, Feng Y, Moore EW, VanderPlas J, Laxalde D, Perktold J, Cimrman R, Henriksen I, Quintero EA, Harris CR, Archibald AM, Ribeiro AH, Pedregosa F, van Mulbregt P. SciPy 1.0: fundamental algorithms for scientific computing in Python. *Nature methods* 2020;**17**(3):261-72. **doi**:10.1038/s41592-019-0686-2

[31] Bogaert R, Böles A. Global performance of a prototype brazed plate heat exchanger in a large Reynolds number range. *Experimental Heat Transfer* 1995;**8**(4):293-311. **doi**:10.1080/08916159508946508

[32] Cooper MG. Heat flow rates in saturated nucleate pool boiling-a wide-ranging examination using reduced properties. *Advances in heat transfer* 1984;**16**:157-239. **doi**:10.1016/S0065-2717(08)70205-3

[33] Thonon B, Bontemps A. Condensation of pure and mixture of hydrocarbons in a compact heat exchanger: experiments and modelling. *Heat transfer engineering* 2002;**23(**6):3-17. **doi**:10.1080/01457630290098718

[34] Olympios AV, Hoseinpoori P, Mersch M, Pantaleo AM, Simpson MC, Sapin P, Mac Dowell N, Markides CN. 2020. "Optimal design of low-temperature heat-pumping technologies and implications to the whole-energy system," 33rd International Conference on Efficiency, Costs, Optimization, Simulation and Environmental Impact of Energy Systems (ECOS 2020). Osaka, Japan.

[35] Olympios, AV, Mersch M, Sapin P, Pantaleo AM, Markides CN. "Library of price and performance data of domestic and commercial technologies for low-carbon energy systems." (2021). [Data set]. Zenodo. **doi**:10.5281/zenodo.4692649.

14th IEA Heat Pump Conference
15-18 May 2023, Chicago, Illinois

Performance test of a gas-fired absorption heat pump with total recovery of exhaust heat applied for distributed space heating

Ding Lu[a], Zijian Liu[a,b] and Maoqiong Gong[a,b,*]

[a]Technical Institute of Physics and Chemistry, Chinese Academy of Sciences, Beijing 100190, China
[b]University of Chinese Academy of Sciences, Beijing 100049, China

Abstract

Under the background of carbon neutrality, efficient and low-carbon space heating in distributed areas away from the centralized network is a meaningful topic. In this paper, a gas-fired absorption heat pump was built and tested during winter in Langfang, a city near Beijing. The unit was driven by direct combustion of natural gas, and recovered low-grade heat from the ambient air. In order to increase the energy utilization ratio, solution preheating and intermediate evaporation was introduced. In order to enhance the internal heat recovery under low ambient temperatures, intermediate absorption was adopted. The measured performance showed that the outlet temperature of exhaust gas was lower than 35°C, indicating that both the sensible and latent heat were fully recovered. The average daily primary energy efficiency was over 1.58 and heating capacity was 30 kW, at the ambient temperature of -1.2°C, when supplying 45°C hot water for space heating. It was proven that the designed unit has great application potential in cold winter areas away from the centralized heating network.

© HPC2023.
Selection and/or peer-review under the responsibility of the organizers of the 14th IEA Heat Pump Conference 2023.

Keywords: absorption heat pump; performance analysis; natural gas; distributed heating; exhaust heat recoverytemperature

1. Introduction

Under the background of carbon neutrality, the reduction in fossil fuel usage and greenhouse gas emission are urgent and inevitable issues. Over 30% of the worldwide carbon emission is contributed by energy consumption in buildings [1]. Energy consumption for building space heating and cooling accounts for 58% and 41% in the urban and rural areas of China [2]. On the other hand, with the improvement of living standards and the advancement of urbanization in developing countries represented by China, the building area and energy consumption will be further increased [3]. Improving the space heating systems is of vital importance for energy conservation and carbon emission re-duction, and to some extent, is an important step towards achieving carbon neutrality.

In general, space heating can be realized by centralized networks in urban areas. Whereas, the huge initial capital cost for the network construction and the thermal losses along the pipe lines make centralized networks unaffordable in rural areas with low population density [4,5]. In terms of heating methods in areas away from the centralized networks, the wall-mounted gas furnace (GF) [6] and the compression heat pump (CHP) [7] are usually applied. The GF is low-efficient with primary energy efficiency (PEE) lower than 1. Even though the coefficient of performance (COP) of the electrically driven CHP can reach 3 [8], the PEE is still low since thermal power generation with 30-35% efficiency is the major way to generate electricity worldwide [9]. Even worse, these methods of separate heating greatly increase the initial investment of the consumers, and have more carbon emissions during production and operation.

As a result, the decentralized or house-central heating system for areas away from the centralized network has attracted wide attention. The absorption heat pump (AHP) can utilize different kinds of heat sources and provide heating with wide temperature range. For a single-stage system, its heating temperature ranges from

* Corresponding author. Tel.: +86-010-82543739; fax: +86-010-82543739.
E-mail address: gongmq@mail.ipc.ac.cn.

40°C to nearly 80°C, fitting for the heating demands of most occasions. It should be noted that the absorption system needs two kinds of heat sources: one is high-grade driving heat utilized in the generator, and the other is low-grade heat harvested in the evaporator. For a single-stage absorption system using LiBr-H2O or NH3-H2O as the working fluids, the generation temperature is in the range of 75-170°C [10], which can be easily achieved by natural gas combustion.

Compared with other systems including the GF and CHP, the AHP for district heating has the superiority of high PEE that can reach up to 1.3, due to the ability of utilizing additional low-grade heat through the evaporator. Zhang et al. [11] studied a hot water driven ground-source AHP for the district heating. They showed that the energy utilization efficiency was improved and the power consumption was reduced significantly, compared with those from the electrically-driven heat pump. Moreover, Wu et al. [12] studied a water-source AHP for the low temperature heating. The measured COP was 1.2 when the temperatures of the evaporator inlet, generator inlet and hot water outlet were set to -10°C, 130°C and 45°C, respectively. Moreover, the system could operate at the evaporator inlet temperatures of -18°C. Garrabrant et al. [13] studied a gas-fired NH_3-H_2O AHP, and the COP was 1.63 when producing 45 °C hot water under the ambient temperature of 20°C. Keinath et al. [14] investigated a gas-fired NH_3-H_2O AHP. The system achieved a COP of 1.74 when the ambient and water inlet temperatures were 20°C and 32°C, respectively.

The above-mentioned studies were all based on the single-effect system, which means the driving heat only triggered one generation process. Actually, the AHP systems were studied extensively aiming to find out the most suitable system con-figuration for the residential applications and district heating. Wu et al. [15] reviewed various heating methods based on the AHP technology, and discussed their application and development in different fields. Phillip et al. [16] investigated six different configurations, including double-effect, absorber augmented, double-effect regenerated, and generator-absorber heat exchange (GAX), and found that the optimal one is the GAX configuration. Kang et al. [17,18] studied the hybrid GAX system, where a compressor was added between the generator and the condenser to increase the heating temperature of the con-denser. Results showed that the absorber could provide 47°C hot water for district heating, and the condenser could provide hot water up to 100°C for other purposes. However, the GAX system was not suitable for cold regions, because as the ambient temperature decreases, the temperature overlaps between the generator and the absorber decreased or even disappeared. Garimella et al. [19] simulated a GAX system, and found that for the ambient temperature of 5.6°C, the COP reached up to 1.4, while when the ambient temperature de-creases to -30°C, the COP reduces sharply to 1.05. In order to improve the performance in cold regions, a double-stage [20] and a compression-assisted [21] AHP were developed.

In this paper, a gas-fired absorption heat pump was built and tested during winter in Langfang, a city near Beijing. The unit was driven by natural gas direct combustion, and recover low-grade heat from the ambient air. In order to increase the energy utilization ratio, solution preheating and intermediate evaporation was introduced. In order to enhance the internal heat recovery un-der low ambient temperatures, intermediate absorption was adopted.

2. System description

2.1. System Configuration

The schematic diagram of the gas-fired AHP system is shown in Figure 1. The system consists of four branches including the gas, water, solution and refrigerant branch, which are illustrated by the orange, blue, purple and green lines, respectively. Moreover, state points in the four branches are presented as G, W, S and R, separately. For example, W1 presents the return water state point, while G4 presents the flue gas outlet state point.

For the gas branch, the mixture of the natural gas and oxidizing air G1 enters the combustor, and the combustion heat is delivered to the generator. The high temperature flue gas G2 enters the solution preheater, heats the strong solution S1 flowing to the generator, and the temperature is reduced to a medium value. Then the medium temperature flue gas G3 enters the intermediate evaporator and the temperature is further reduced, and finally it is discharged to the ambient.

For the water branch, the return water W1 passes through the condenser, rectifier and absorber subsequently and absorbs the heat generated by each component. The water temperature increases gradually and the supply water W4 is supplied to hot consumers.

For the solution branch, the strong solution S1 is preheated by the flue gas, and after mixing with the reflux solution S0 from the rectifier, enters the generator and flows downward. The strong solution is first heated by

the generated weak solution S2, and generates part of the ammonia vapor. Then the solution is further heated by the gas combustion, and generates large amounts of ammonia vapor. In the meantime, mass transfer occurs between the solution and the vapor, along the packing. The generated weak solution S2 returns back to the generator to undergo the internal heat recovery process, hence its temperature decreases. After the expansion process, the weak solution S4 flows through the intermediate absorber and the absorber, and absorbs the ammonia vapor from the intermediate evaporator and the evaporator respectively. Finally, it turns to the strong solution S7, flowing to the solution tank. After pressurizing by the solution pump, the strong solution S8 enters the intermediate absorber to recover the absorption heat, and then it is further heated by the high temperature flue gas in the solution preheater.

For the refrigerant branch, the ammonia vapor R0 from the generator enters the rectifier. It is partially condensed to the reflux S0, while the remaining enters the condenser and is condensed to the liquid ammonia R2. After the subcooling and expansion process-es, the ammonia refrigerant enters the intermediate evaporator, recovers the waste heat of low temperature flue gas and is partially evaporated. The vapor-liquid mixture R5 enters the separator, where the vapor and liquid are separated. The vapor part R6 enters the intermediate absorber and is absorbed by the weak solution, while the liquid part R7 goes throttling and then enters the evaporator, where it absorbs heat from the ambient and is evaporated completely. After evaporation, the ammonia vapor R9 is superheated in the sub-cooler, and then enters the absorber and is absorbed by the solution.

Except for the above four branches, there exits another branch for defrosting, which is presented with the dotted purple lines in Figure 1. During the defrosting process, the de-frosting valve is opened and part of the intermediate solution S5 enters the evaporator directly, where it absorbs the ammonia refrigerant R8 and releases absorption heat for de-frosting. During this process, the system still operates, however the heating capacity is reduced. The larger the opening of the defrosting valve, the faster the defrosting speed, while the lower the heating capacity.

The main differences between the proposed system and the conventional system are shown in Fig. 2. The *P-T* diagrams were drawn under the basic working condition of -20℃ evaporation temperature and 180℃ generation temperature. The main innovation lies in the introduction of the intermediate evaporation and absorption processes. The ammonia condensate from the condenser was firstly throttled to intermediate pressure, and recovered waste heat from the flue gas. In this process, both the sensible and latent heat could be totally recovered by adjusting the intermediate pressure. Furthermore, the ammonia vapor, partially evaporated from the intermediate evaporator, entered the intermediate absorber, and the intermediate absorption heat was used to carry on internal heat recovery.

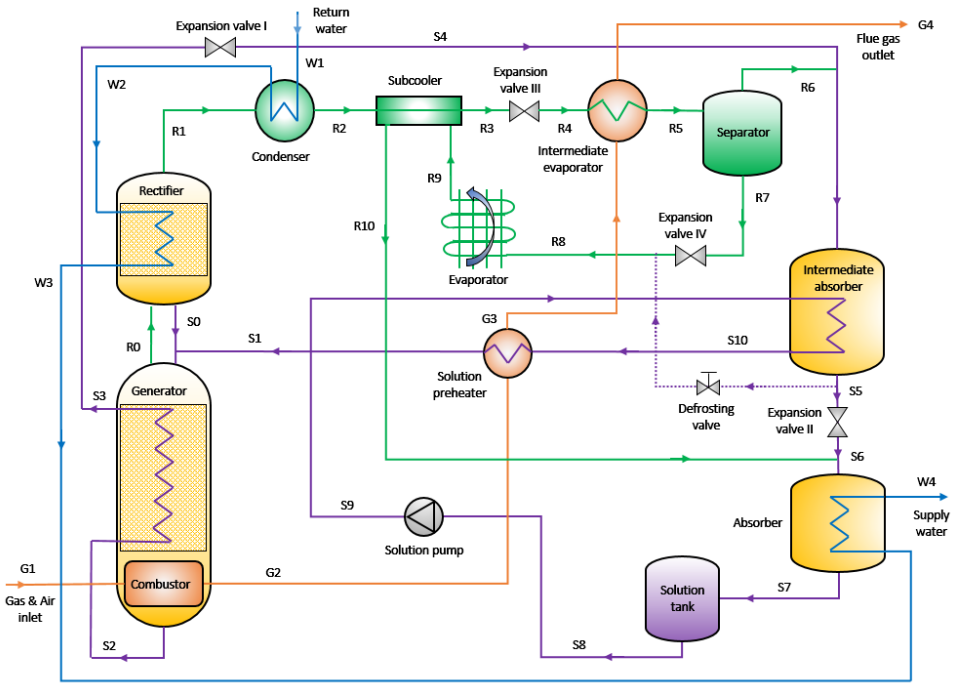
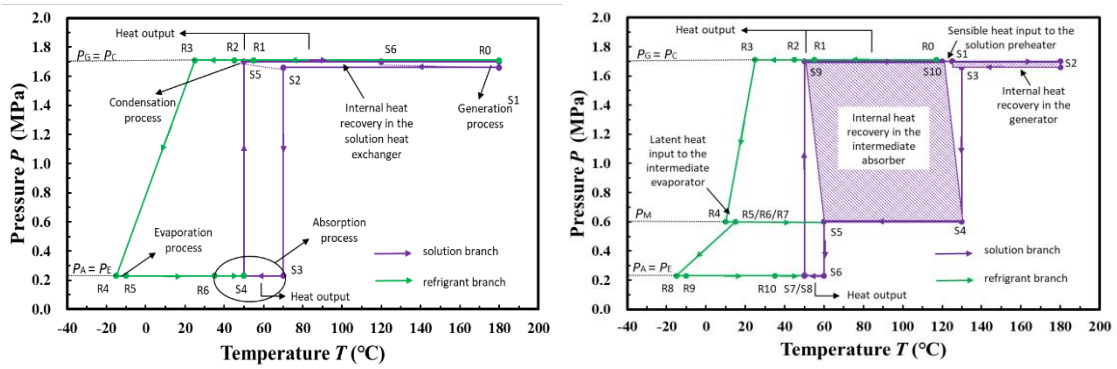


Fig. 1. Schematic diagram of the proposed gas-fired AHP system.



(a) (b)

Fig. 2. Comparison of *P-T* diagrams of the proposed system and the conventional one: (a) conventional system; (b) proposed system.

2.2. AHP unit

The 3D diagram and the photo of the gas-fired AHP unit with 30 kW heating capacity are shown in Figure 3. The unit had a compact design, with the dimension of 1360*1360*2260mm(L*W*H). The built AHP unit was expected to provide space heating for 3-4 families in the north of China in winter. Ammonia-water compare was used as the working fluid, considering that the system operated at low ambient temperatures. Natural gas was burned inside the unit as the driving heat source, and the evaporator could also harvest low-grade heat from the ambient air.



Fig. 3. 3D diagram and the picture of the gas-fired AHP unit.

Table 1. Details of the heat-exchange components of the gas-fired AHP unit.

Components	Types	Rated heat exchange Capacity (kW)
generator	falling film	20
rectifier	shell-and-tube	5
absorber	shell-and-tube	16
condenser	tube-in-tube	14
evaporator	plate-fin	11
intermediate absorber	tube-in-tube	18
intermediate evaporator	plate-fin	3
sub-cooler	tube-in-tube	1
solution preheater	plate-fin	1

Details of the heat-exchange components of the gas-fired AHP unit are shown in Table 1. The absorber was the shell-and-tube heat exchanger, while the condenser, sub-cooler and intermediate absorber adopted the tube-in-tube type. For the evaporator, intermediate evaporator and solution preheater, plate-fin heat exchangers were used. For the gas-fired generator, its structure is shown in Figure 4. Natural gas and air entered the combustion chamber at the bottom, where the natural gas was burned. The combustion heat was delivered to the ammonia-water solution through the solution jacket, which could also prevent the chamber wall from overheating. High-temperature flue gas from the combustion chamber raised through the gas pipeline, delivering heat to the solution flowing downward along the outer wall of the pipes. In order to enhance the heat and mass transfer insider the generator, the embossed threaded pipes and θ-ring packings were adopted.

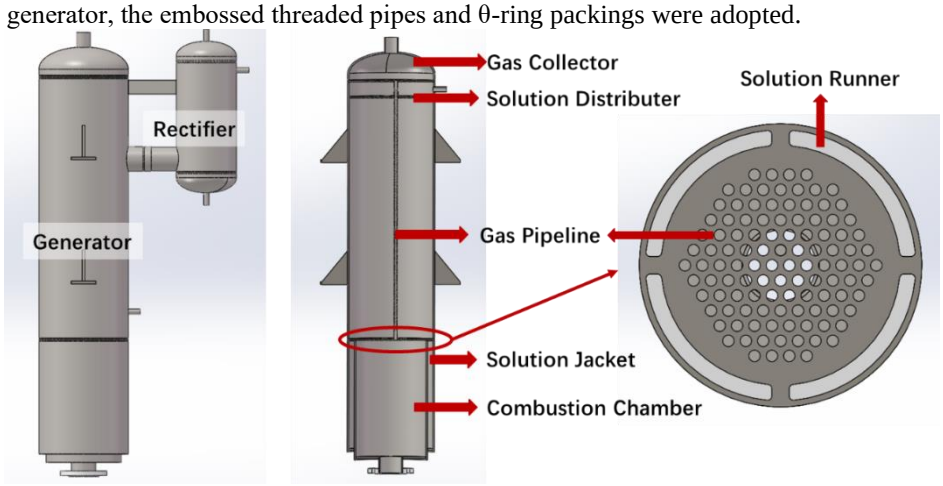


Fig. 4. Structure of the gas-fired generator.

3. Methods

Based on the AHP unit, system performance under typical heating conditions was investigated through the environmental tests in Langfang, a city near Beijing. The unit was designed in accordance with the worst operating conditions according to the preliminary simulation results, and all heat exchangers were designed in accordance with the maximum heat transfer capacity during the year-round operation. Therefore, the prototype could adapt to the change of working conditions with part-load operation in some conditions.

The AHP unit has more than 30 temperature measuring positions, 5 pressure measuring positions and 3 flowrate measuring positions, and the system operating conditions can be measured and recorded comprehensively. Details of the measuring components are shown in Table 2.

Table 2. Details of the measuring components of the gas-fired AHP unit.

Components	Type	Range	Accuracy
thermometers	PT100	-50~300°C	±0.25 °C
pressure meters	capacitance transmitter	0~2.5 MPa	±6.25 kPa
gas flowmeter	vortex	0~3 m^3/h	±0.045 m^3/h
water flowmeter	electromagnetic	0~6 m^3/h	±0.03 m^3/h
solution flowmeter	ultrasonic	0~2 m^3/h	±0.02 m^3/h
liquid level meter	floating ball	0~600 mm	±5mm

In the AHP unit, all the components that exchange heat with the surroundings adopted external medium countercurrent heat exchanger. The flowrate, inlet and outlet temperatures of the medium were measured to calculate the heat transfer capacity of each component, as are shown below [11]:

$$\text{driving heat} \quad Q_{\mathrm{D}} = V_{NG} \cdot q_{\mathrm{NG}} \tag{1}$$

$$\text{condensation heat} \quad Q_{\mathrm{C}} = m_{\mathrm{W}} \cdot c_{\mathrm{W}} \cdot \Delta T_{\mathrm{C}} = \rho_{\mathrm{W}} \cdot V_{\mathrm{W}} \cdot c_{\mathrm{W}} \cdot \left(T_{\mathrm{C,out}} - T_{\mathrm{C,in}}\right) \tag{2}$$

$$\text{rectification heat} \quad Q_{\mathrm{R}} = m_{\mathrm{W}} \cdot c_{\mathrm{W}} \cdot \Delta T_{\mathrm{R}} = \rho_{\mathrm{W}} \cdot V_{\mathrm{W}} \cdot c_{\mathrm{W}} \cdot \left(T_{\mathrm{R,out}} - T_{\mathrm{R,in}}\right) \tag{3}$$

$$\text{absorption heat} \quad Q_{\mathrm{A}} = m_{\mathrm{W}} \cdot c_{\mathrm{W}} \cdot \Delta T_{\mathrm{A}} = \rho_{\mathrm{W}} \cdot V_{\mathrm{W}} \cdot c_{\mathrm{W}} \cdot \left(T_{\mathrm{A,out}} - T_{\mathrm{A,in}}\right) \tag{4}$$

where V_{NG} and q_{NG} are the volume flow rate and calorific value of standard volume of the natural gas; m_W, V_W, and c_W are the mass flowrate, volume flow rate, density and specific heat of the water; ΔT , T_{in} and T_{out} are the temperature difference, inlet temperature and outlet temperature of each component. The total heating capacity of the AHP unit is the sum of the heat from the condenser, rectifier and absorber:

$$\text{total heating capacity} \quad Q_H = Q_C + Q_R + Q_A \tag{5}$$

The heating performance of the AHP unit is presented by the primary energy efficiency PEE, which is the ratio of the heating capacity to the driving heat (i.e., the calorific value of the consumed natural gas):

$$\text{primary energy efficiency} \quad \text{PEE} = \frac{Q_H}{Q_D + W/\eta} \tag{6}$$

where W is the total power consumption of the AHP unit, and η is the power generation efficiency in China, which is about 35% [9].

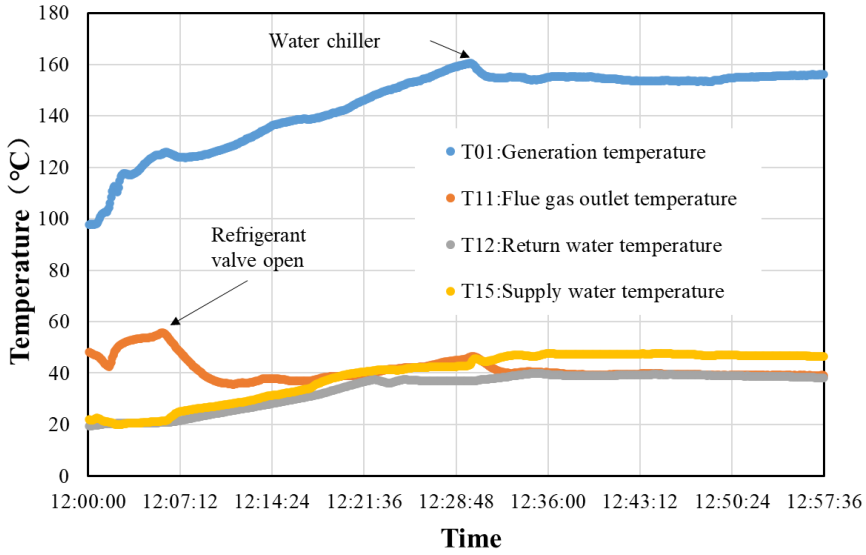
4. Results and Discussion

4.1. Start-up performance

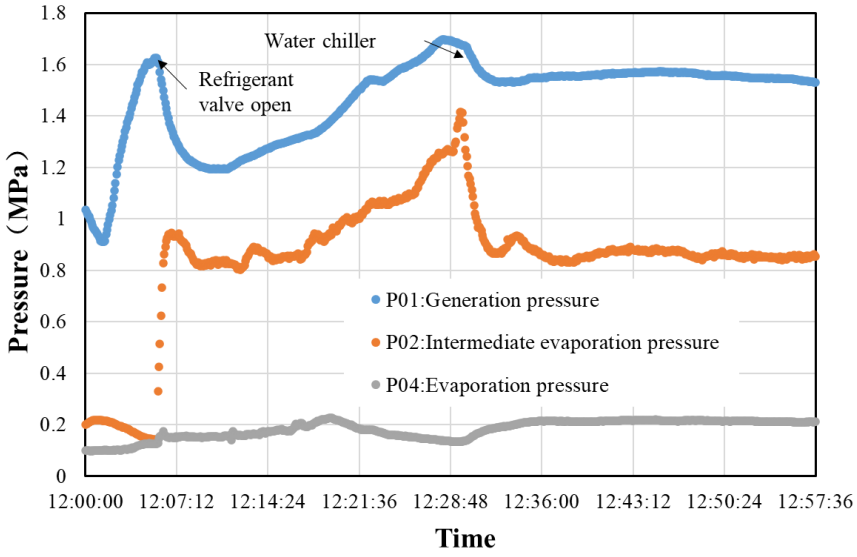
The startup sequence of the AHP unit followed this order: firstly, the gas combustor started, then the refrigerant valve opened, and finally the water chiller started. The refrigerant valve was closed at first, in order to quickly reach the required generation temperature and pressure. Fig. 5 shows the startup performance of the gas-fired AHP unit. It should be noted that a test run was conducted the day before, and the solution temperature in the generator reduced to about 100°C after overnight cooling.

It is found that a rapid growth in the generation temperature and pressure happened after starting the gas combustor, and the generation pressure reached up to 1.6 MPa within 7 minutes. Meanwhile the refrigerant valve opened, and the generation pressure reduced to 1.2 MPa, while the intermediate pressure raised immediately to 0.8 MPa. It should also be noted that the outlet temperature of flue gas reduced to 37°C after the intermediate evaporation process got involved.

When the solution temperature and pressure reached 90% of the target values, the water chiller started. The generated ammonia vapor was condensed in the rectifier, and then flowed into the solution. This process caused reduction in the solution temperature and pressure at first, and then tended to be stationary. 50 minutes after starting up, the supply water temperature reached the stable value of 43°C, and the AHP unit Began normal operation.



(a)



(b)

Fig. 5. Start-up performance of the gas-fired AHP unit: (a) Key temperature parameters variation; (b) Key pressure parameters variation.

4.2. Performance under basic working condition

The performance of the gas-fired AHP unit was analyzed in detail under the basic working condition: the evaporation temperature was -1.2°C, the return water temperature was 37.0°C, and the supply water temperature was 45.2°C. Detailed data of key parameters are shown in Table 3. The return water of 37.0°C passed in sequence through the condenser, rectifier and absorber, and its temperature increased to 40.2, 41.3 and 45.1°C, respectively, with flow rate keeping at 3.26 m3/h. It is shown that by introducing the intermediate process, the outlet temperature of flue gas was reduced to 38.6°C, which was lower than its dew point, indicating that the gas-fired AHP unit had ability to fully recover both the sensible and latent heat. It is also shown in Table 3 that the system high pressure, intermediate pressure and low pressure were 1.6 MPa, 0.8-0.9 MPa and 0.2-0.3 MPa, respectively. Moreover, the intermediate absorption pressure was 60 kPa lower than the intermediate evaporation pressure, and the absorption pressure was 70 kPa lower than the evaporation pressure, due to the flow resistance and the obstruction of check valves.

Table 3. Data of key parameters under the basic working condition.

Parameters	Value
ambient temperature	-1.2°C
evaporation temperature	-7.5°C
generation temperature	156.2°C
return water temperature	37.0°C
condenser outlet water temperature	40.2°C
rectifier outlet water temperature	41.3°C
supply water temperature	45.1°C
generator outlet gas temperature	117.0°C
Outlet temperature of flue gas	38.6°C
generation pressure	1.62 MPa
intermediate evaporation pressure	0.93 MPa
intermediate absorption pressure	0.87 MPa
evaporation pressure	0.29 MPa
absorption pressure	0.22 MPa
natural gas volume flowrate	1.82 Nm^3/h

water volume flowrate	3.26 m^3/h
power consumption	0.52 kW

Based on the measured data, the heat duty or power consumption of the main component, as well as the performance of the AHP unit are shown in Table 4. When the ambient temperature was -1.2°C, the AHP unit could provide 30.8 kW heating capacity to heat the water from 37 to 45°C, and the PEE was 1.58.

Table 4. Performance of the gas-fired AHP unit.

Parameters	Value
ambient temperature	-1.2°C
supply/return water temperature	45/37°C
condensation heat	12.2 kW
rectification heat	4.2 kW
absorption heat	14.5 kW
heating capacity	30.8 kW
calorific of natural gas	18.0 kW
power consumption	0.52 kW
primary energy efficiency PEE	1.58

4.3. Influence of the ambient temperature

Figure 5 shows the influence of the ambient temperature on the system performance. It is indicated that as the ambient temperature reduced from 7.2°C to -7.8°C, the primary energy efficiency reduced from 1.82 to 1.38. At the lower ambient temperature, the ammonia evaporation was impeded, and the opening of the electronic expansion valve decreased. As a result, the recovered low-grade ambient heat and the PEE of the AHP unit reduced.

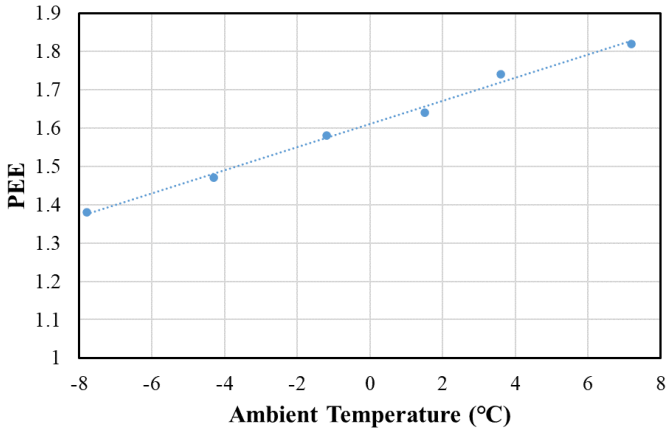


Fig. 5. Influence of the ambient temperature on the system performance.

5. Conclusions

In this paper, a gas-fired absorption heat pump was built and tested during winter in Langfang, a city near Beijing. The unit was driven by natural gas direct combustion, and recovered low-grade heat from the ambient air. In order to increase the energy utilization ratio, solution preheating and intermediate evaporation was introduced. In order to enhance the internal heat recovery under low ambient temperatures, intermediate absorption was adopted.

1. The measured performance showed that the exhaust gas outlet temperature was lower than 35°C, indicating that both the sensible and latent heat were fully recovered.

2. The average daily primary energy efficiency was over 1.58 and heating capacity was 30 kW, at the ambient temperature of -1.2°C, when supplying 45°C hot water for space heating.

It was proven that the designed unit has great application potential in cold winter areas away from the centralized heating network.

Acknowledgements

The authors would like to thank the support of the National Natural Sciences Foundation of China (No. 52206033).

References

[1] Kingma B, Lichtenbelt WV. Energy consumption in buildings and female thermal demand. Nat Clim Chang. 2015;5(12): 1054-1056.
[2] Zheng X, Wei C, Qin P, Guo J, Yu Y, Song F, et al. Characteristics of residential energy consumption in China: Findings from a household survey. Energy Policy. 2014;75:126-35.
[3] Center TUBESR. Annual Report on China Building Energy Efficiency: China Architecture and Building Press; 2020.
[4] Buffa S, Cozzini M, D'Antoni M, Baratieri M, Fedrizzi R. 5th generation district heating and cooling systems: A review of ex-isting cases in Europe. Renew Sust Energ Rev. 2019;104:504-22.
[5] Lake A, Rezaie B, Beyerlein S. Review of district heating and cooling systems for a sustainable future. Renew Sust Energ Rev. 2017;67:417-25.
[6] Zhang QL, Hao YY, Sun DH, Nie Q, Jin LW. Research on the Clean Energy Heating Systems in Rural Beijing. Joint Conference of the World Engineers Summit / Applied Energy Symposium and Forum - Low Carbon Cities and Urban Energy (WES-CUE). Singapore, SINGAPORE: Elsevier Science Bv; 2017. p. 137-43.
[7] Wu D, Hu B, Wang RZ. Vapor compression heat pumps with pure Low-GWP refrigerants. Renew Sust Energ Rev. 2021;138: 110571.
[8] Fumo N, Chamra LM. Analysis of combined cooling, heating, and power systems based on source primary energy con-sumption. Applied Energy. 2010;87:2023-30.
[9] Zoungrana A, Çakmakci M. From non‐renewable energy to renewable by harvesting salinity gradient power by reverse elec-trodialysis: A review. International Journal of Energy Research. 2020;45:3495-522.
[10] Florides GA, Kalogirou SA, Tassou SA, Wrobel LC. Design and construction of a LiBr-water absorption machine. Energy Conv Manag. 2003;44:2483-508.
[11] Qunli Z, Mingkai C, Qiuyue Z, et al. Research on a new district heating method combined with hot water driven ground source AHP. Energy Procedia 2015; 75: 1242-1248.
[12] Wu W, Ran S, Shi W, et al. NH3-H2O water source AHP (WSAHP) for low temperature heating: Experimental investigation on the off-design performance. Energy 2016; 115: 697-710.
[13] Garrabrant M, Stout R, Glanville P, Fitzgerald J, Keinath C. Development and validation of a gas-fired residential heat pump water heater-final report (No.DOE/EE0003985-1). Stone Mountain Technologies, Inc; 2013.
[14] Keinath C M, Garimella S, Garrabrant M A. Modeling of an ammonia–water AHP water heater for residential applications. International Journal of Refrigeration 2017; 83: 39-50.
[15] Wu W, Wang B, Shi W, et al. Absorption heating technologies: a review and perspective. Applied Energy 2014; 130: 51-71.
[16] Phillips B A. Development of a high-efficiency, gas-fired, AHP for residential and small-commercial applications. NASA STI/Recon Technical Report N, 1990, 91.
[17] Kang Y T, Kashiwagi T. An environmentally friendly GAX cycle for panel heating: PGAX cycle. International Journal of Refrigeration 2000; 23(5): 378-87.
[18] Kang Y T, Hong H, Park K S. Performance analysis of advanced hybrid GAX cycles: HGAX. International Journal of Refrig-eration 2004; 27(4): 442-8.
[19] Garimella S, Christensen R N, Lacy D. Performance evaluation of a generator-absorber heat-exchange heat pump. Applied Thermal Engineering 1996; 16(7): 591-604.
[20] Wu W, Zhang XL, Li XT, Shi WX, Wang BL. Comparisons of different working pairs and cycles on the performance of ab-sorption heat pump for heating and domestic hot water in cold regions. Applied Thermal Engineering 2012; 48:349–58.
[21] Wu W, Shi W, Wang B, et al. A new heating system based on coupled air source absorption heat pump for cold regions: Energy saving analysis. Energy Conversion and Management 2013; 76: 811-817.
[22] Lu D, Bai Y, Zhao Y, Dong X, Gong M, Luo E, et al. Experimental investigations of an absorption heat pump prototype with intermediate process for residential district heating. Energy Conversion and Management. 2020;204:112323.

14th IEA Heat Pump Conference
15-18 May 2023, Chicago, Illinois

Single Fault Impact Analysis of a Residential Heat Pump in the Cooling Mode According to the Temperature Conditions

Minkyu Jung[1], Sanghun Jeong[1], Soyeon Kim[1], Donik Ku[1], Minsung Kim[1,2*]

[1]Department of Intelligent Energy and Industry, Chung-Ang University, 84 Heukseok-ro Dongjak-gu, Seoul 06974, Republic of Korea
[2]Department of Energy Systems Engineering, Chung-Ang University, 84 Heukseok-ro Dongjak-gu, Seoul 06974, Republic of Korea

Abstract

Various faults in components of the refrigeration cycle impact on system efficiency degradation differently. In addition, since sensitive features of each fault are different, the severity of the failures varies according to the operating conditions. Therefore, impacts of residential heat pump faults according to different indoor/outdoor air conditions were analyzed. The test was implemented with R410A residential unitary split heat pump with thermostatic expansion valve (TXV). Six types of common faults were imposed individually: compressor leakage, condenser fouling, evaporator fouling, liquid line restriction, refrigerant undercharge, refrigerant overcharge. Performance parameter model using 2nd order multivariate polynomial was built based on no-fault data. The rate of performance degradation according to the change in operating conditions and the change of fault level was calculated, and the effects of each fault were analyzed. For instance, in case of the temperature difference between indoor and outdoor is small, the refrigerant flow rate increases to handle the cooling load, resulting in a steep decrease in performance at condenser fouling. On the other hand, in this case, the required evaporator capacity was reduced, so the effect of evaporator fouling was small.

Keywords: Heat Pump, Fault detection and diagnosis, Thermal expansion valve, Refrigeration cycle, Performance analysis;

1. Introduction

Demand for the air conditioning rapidly grows recently, and it results in increased energy consumption and the CO2 emissions. In the residential and the commercial building, the heating, ventilating and air conditioning (HVAC) system is the significant source of the energy consumption [1]. According to the OECD/IEA 2018, annual sales of the air conditioners increased about four times from that of 1990. [2] The fault occurrence is one of the main reasons of the energy loss in the HVAC system. And also, such inadequate handling of these problems such as degraded functioning of the components or faulty installation could affect the performance of the system substantially [3]. Fault detection and diagnosis (FDD) of the refrigeration systems is one of key methods to maintain and improve the performance [4].

Recent fault studies for the refrigeration system were focused on improving the accuracy of FDD. Rossi et al. [5] applied the Bayesian classification for the fault detection of rooftop air conditioner operation. Kim et al. [6] proposed the rule-based classifier for the residential heat pump cooling mode, with methodology for boundary direction selection. After 2010s, many studies suggested the application of artificial neural network (ANN) in HVAC systems [7-9].

However, studies about the fault impact on the HVAC system performance have been presented less. Kim et al. [10] selected the seven common faults of heat pump in cooling mode, and conducted the experiments with those faults imposed. Performance change by the single fault level was analyzed by comparing the performance parameters of the no-fault and the fault condition. Later, Kim et al. [11] compared the severity of each fault by comparing the fault levels that degrades 5% of energy efficiency ratio (EER). From the result, since the faults such as evaporator fouling fault (EF) or refrigerant overcharge fault (OC) impacts on the system performance less than other faults, so the fault has to be treated differently in real maintenance situations. Moreover, since the indoor and outdoor temperature conditions are the main parameters in heat pump system, the performance also varies with the operating conditions.

* Corresponding author. *E-mail address:* minsungk@cau.ac.kr

In this study, 40 cases of no-fault steady state experiments and 4 cases of fault tests(combination of indoor temperature conditions of 21.1 and 26.7 °C and outdoor temperature conditions of 27.8 and 37.8 °C) by Kim et al. [10] were analyzed, and the change in system performance of six single faults were observed. Six types of common faults were imposed individually: compressor leakage, condenser fouling, evaporator fouling, liquid line restriction, refrigerant undercharge, refrigerant overcharge. Each performance change at each fault implementation was analyzed using the comparison with the estimated fault-free steady-state reference value.

2. Experimental setup

2.1. System description and fault implementation

The system under the test is R410A 8.8 kW (2.5 ton) residential heat pump system with seasonal energy efficiency ratio (SEER) of 13 [12]. Fig. 1 shows the schematic diagram and the measuring parameters of the system. Constant-speed compressor and a thermostatic expansion valve (TXV) was coupled with indoor and outdoor section heat exchanger units. Detailed information of the test setup and the uncertainties of the measurement can be found in Kim et al. [10].

Six types of common faults in heat pump system and the determination of the artificial fault levels are illustrated on Table 1 [10]. Compressor leakage fault, or the valve leakage fault, was simulated by implementing a hot gas bypass line from the compressor discharge line to the suction line. Condenser fault, which implies improper outdoor air flowrate, was simulated by blocking the finned-heat exchange area. Evaporator fault was imposed by reducing the speed of the nozzle chamber fan at the end of the evaporator duct. Liquid line restriction, which is commonly occur by the pipe clogging, was mocked by controlling the pressure drop between the condenser exit and the evaporator inlet with the metering valve. Refrigerant overcharge and the undercharge were set by controlling the charge level of the system.

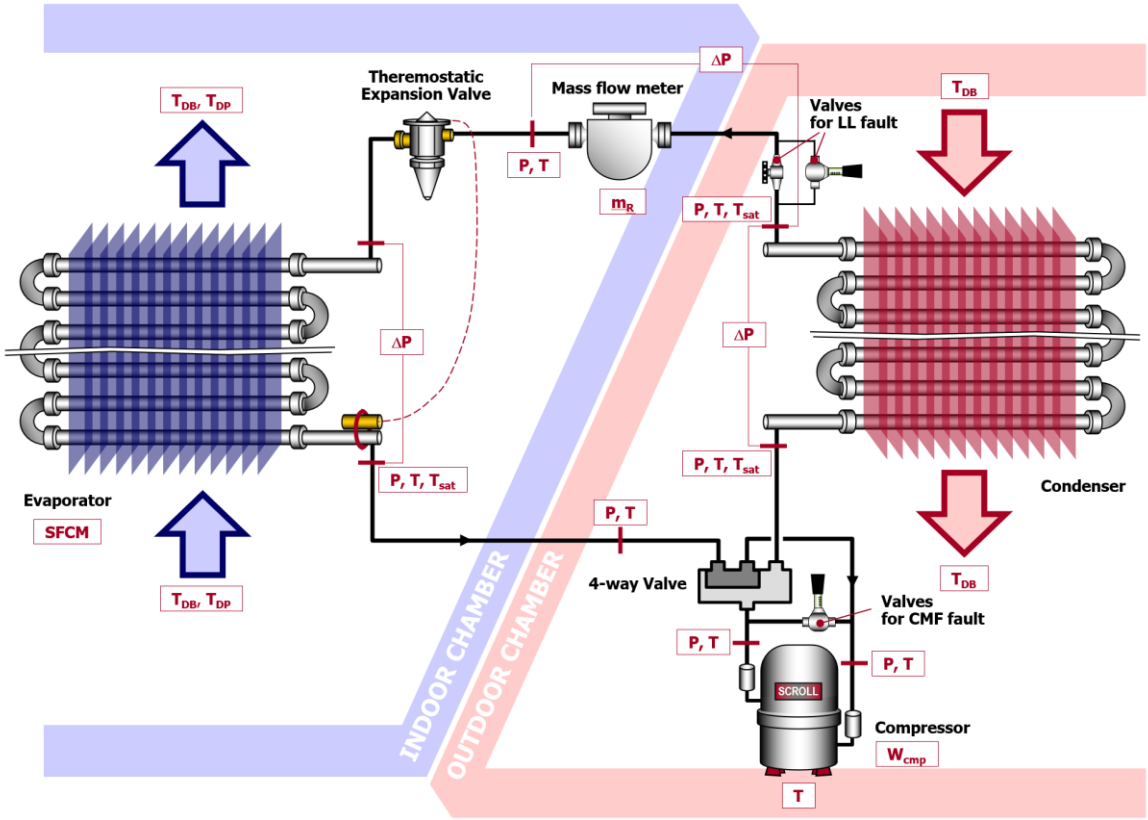


Fig. 1. Schematic diagram of cooling mode heat pump system [10].

Table 1. Description of artificial faults

Abbr.	Fault	Determination of level of artificial faults
CMF	Compressor leakage (4-way valve leakage)	% of refrigerant flow rate
CF	Improper outdoor air flow rate	% of coil area blocked
EF	Improper indoor air flow rate	% of correct air flow rate
LL	Liquid line restriction	% of normal pressure drop through TXV
OC	Refrigerant overcharge	% overcharge from the correct charge
UC	Refrigerant undercharge	% undercharge from the correct charge

2.2. Test conditions

Many studies have been analyzed the impacts of the faults in residential heat pump system, however, indoor and the outdoor temperature was seldom changed since the number of the case becomes large [10, 11, 14, 15, 16]. In order to verify the fault impact in different temperature conditions, experimental data from the Kim's study [10] was adopted. Heat pump system with six kind of single fault was tested under various conditions: indoor temperatures of 21.1, 26.7℃ and outdoor temperatures of 27.8 and 37.8℃. And each faults was tested with various fault levels: CMF (3, 6%), CF (10, 20, 35%), EF (10, 20, 30%), LL (100, 200, 300%), OC (10, 20, 30%), UC (10, 20, 30%).

3. Experimental results

3.1. Performance parameter normalization

Evaporator capacity ($\dot{Q}_{EA}$), condenser capacity ($\dot{Q}_{CA}$) and the coefficient of performance (COP) were selected as performance parameters. Since it is hard to measure the capacities when the refrigerant flows at two-phase state in faulty situations, capacities of the heat exchangers were calculated at air-side. Evaporator air-side capacity was calculated as follows:

$$\dot{Q}_{EA} = \dot{Q}_{EA,sens} + \dot{Q}_{EA,lat} \tag{1}$$

where the $\dot{Q}_{EA,sens}$ and the $\dot{Q}_{EA,lat}$ are the indoor air sensible capacity and the indoor air latent capacity, respectively. Since the measurement of the air flowrate at condenser is hard, condenser air-side capacity was calculated as Eq. (2). And the calculation of the cooling COP was shown in Eq. (3)

$$\dot{Q}_{CA} = \dot{Q}_{EA} + \dot{W}_{comp} \tag{2}$$

$$COP = \frac{\dot{Q}_{EA}}{\dot{W}_{comp}+\dot{W}_{ID,fan}+\dot{W}_{c,trans}} \tag{3}$$

Fault-free steady-state (FFSS) reference model was presented in order to estimate the reference data in no-fault situation for the performance comparison. The model was developed as a form of 2nd order multivariate polynomial equation shown in Eq. (4), with the key system parameters – indoor temperature (T_{ID}), outdoor temperature (T_{OD}) and the indoor dew point temperature (T_{IDP}) [11]. Reference values of three performance parameters at no-fault situation were approximated with regression model, and the coefficients were listed on Table 2.

$$\phi_i = a_0 + a_1 T_{ID} + a_2 T_{OD} + a_3 T_{IDP} + a_4 {T_{ID}}^2 + a_5 T_{ID} T_{OD} + a_6 T_{ID} T_{IDP} + a_7 {T_{ID}}^2 + a_8 T_{OD} T_{IDP} + a_9 {T_{IDP}}^2 \tag{4}$$

Performance variation of the system under single faults were indicated with the $r(\phi)$ of the current value and the reference value with FFSS model. The actual difference of the values, $R(\phi)$ was used when the performance variation through residual ratio is vague.

$$r(\phi) = \frac{\phi_{\text{cur}} - \phi_{\text{ref}}(T_{ID}, T_{OD}, T_{IDP})}{\phi_{\text{ref}}(T_{ID}, T_{OD}, T_{IDP})} \tag{5}$$

$$R(\phi) = \phi_{\text{cur}} - \phi_{\text{ref}}(T_{ID}, T_{OD}, T_{IDP}) \tag{6}$$

Table 2. Coefficients of 2nd-order multivariate polynomial reference model for no-fault performance estimation

ϕ_i	a0	a1	a2	a3	a4	a5	a6	a7	a8	a9
COP	2.58e+1	-5.39e-1	-3.66e-2	-4.52e-3	-4.07e-3	-2.95e-4	-3.79e-4	1.08e-4	-1.97e-4	6.12e-4
$\dot{Q}_E$	2.04e+2	1.69e+2	9.80e+0	-4.73e+1	-4.28e-1	-5.24e-2	-4.17e+1	-1.87e-1	-3.58e-1	1.35e+0
$\dot{Q}_C$	-1.61e+4	6.32e+2	1.91e+0	-5.26e+1	-3.51e+0	-1.16e-1	-2.18e-1	2.99e-2	-3.47e-1	1.23e+0

3.2. Performance degradation with single fault imposed

3.2.1. CMF fault (Compressor/valve leakage)

In Fig. 2 performance parameters with temperature conditions change of CMF fault were shown. Since the COP degradation was not significant in CMF fault, the performance change was shown in $R(\phi)$. According to the Fig. 2 (a), (c), (e), performance decreases as the outdoor temperature increases. Evaporation pressure increases as the indoor temperature increases, which results in the decrease of compression ratio from 3 to 2.2, so the volumetric efficiency increases 8% [13-15]. The specific volume of the refrigerant at compressor suction side decreases 20% as the indoor temperature increases. This leads to the increase of mass flowrate at the compressor, according to the Eq. (7) [16].

$$\dot{m}_{r,comp} = \eta_v \frac{NV_S}{v_{comp,suc}} \tag{7}$$

Since the tendency of the volumetric efficiency change is larger than the specific volume change, the mass flow rate changes inversely proportional to the outdoor temperature. Therefore, the degradation of the performance was greater at the outdoor temperature change.

3.2.2. CF fault (Improper outdoor air flow rate)

According to the Fig. 3, performance degradation was little at such low fault level of 10%, and the low temperature difference at fault level of 20%. In case of largest temperature difference (T_{ID} = 21.1 ℃, T_{OD} = 37.8 ℃) at 20% fault level, the performance drop was large because of the large pressure difference between the condenser and the evaporator. Since the heat exchanger is designed with sufficiently high safety factor, so the performance drop is still tolerable in 20% fault level. But when the fault level reaches 35%, the evaporator and the condenser capacity decrease sharply, which leads in severe performance decrease even at small indoor-outdoor temperature difference.

3.2.3. EF fault (Improper indoor air flow rate)

The decrease of the evaporator air flowrate leads to the decrease of evaporating temperature. According to the Fig. 4, three performance parameter change was less than 8% regardless of the fault level. The evaporator capacity decreases as the fault level gets higher and the condenser capacity decreases similarly. Mass flow rate of the refrigerant decreases with the decreasing evaporating temperature, however the performance of the system increases when the mass flow rate compensated by the increased indoor temperature. Moreover, at high fault level, the refrigerant mass flow rate is too small, so the sufficient system performance could be obtained with little air flow.

3.2.4. LL fault (Liquid line restriction)

LL fault was determined with the pressure difference between the TXV inlet part and discharge part. The flow rate of the refrigerant passing through the evaporator decreases with the fault level increases, so the refrigerant at the rear part of the evaporator superheated, and the opening rate of the TXV increased. At the fault level of 300%, when the temperature difference is smallest, the degradation of the performance was the highest. Condensing pressure was not changed as the operating condition changes, but the evaporating pressure changes drastically. This leads the specific volume of the refrigerant at the compressor suction side increases with the indoor temperature, and the mass flowrate at the compressor gets low. So, the refrigerant flows in two-phase and the performance degradation becomes greater. LL fault shows the largest drop of performance than the other faults.

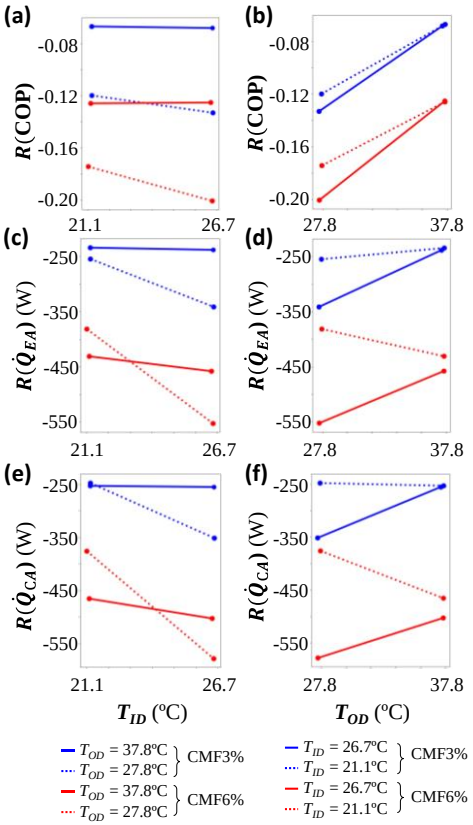


Fig. 2. Performance parameters with temperature conditions of CMF fault

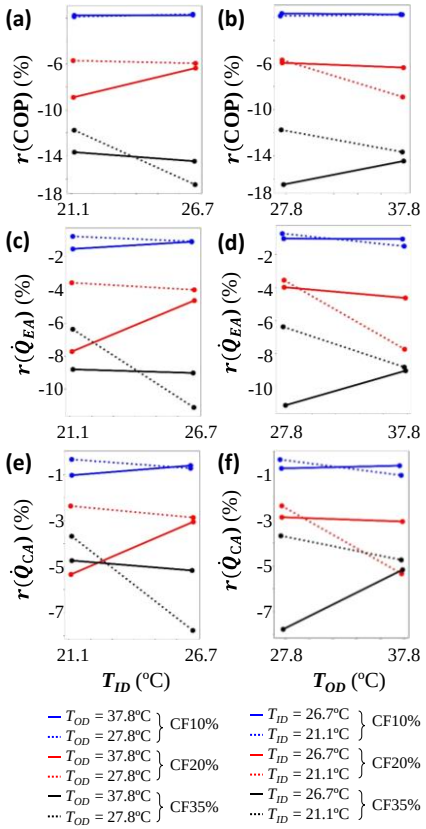


Fig. 3. Performance parameters with temperature conditions of CF fault

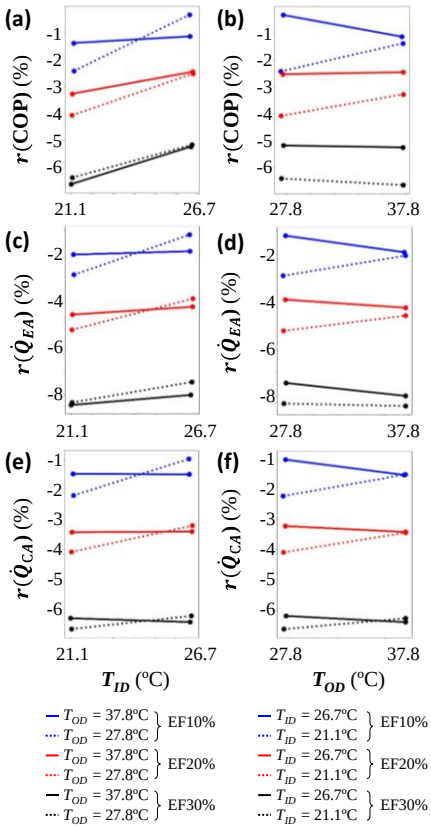


Fig. 4. Performance parameters with temperature conditions of EF fault

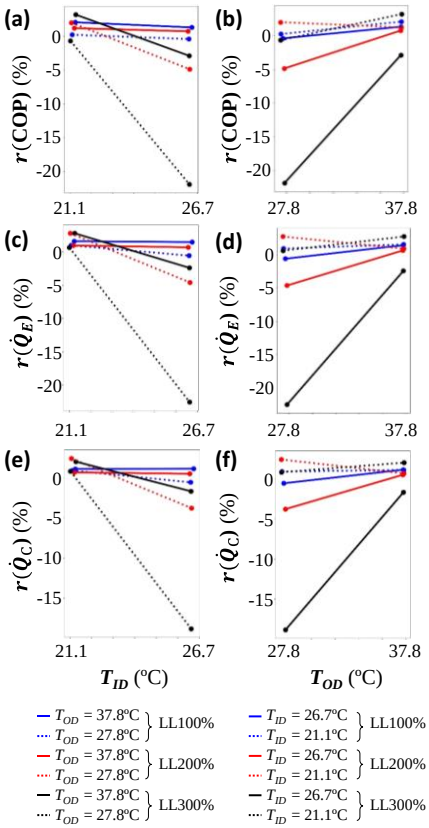


Fig. 5. Performance parameters with temperature conditions of LL fault

3.2.5. OC fault (Refrigerant overcharge)

From the Fig. 6, the system performance degrades a little, at relatively high fault level of 30%. Since the performance of the residential heat pump system is steady even if the amount of refrigerant charge is larger than the normal, performance degradation is not large when the OC fault occurs. In case of 10% fault level, at the refrigerant flowrate gets low when the indoor-outdoor temperature difference is high, the system performance was improved due to the increase of evaporation capacity. However, the OC fault could cause the inflow of liquid refrigerant in compressor, so the fault diagnosis to provide this problem is needed.

3.2.6. UC fault (Refrigerant undercharge)

System performance with the UC fault degrades drastically when the fault level exceeds 20%. As the indoor temperature increases, the mass flowrate increases due to the change of specific volume at the compressor suction side. Therefore, in high indoor temperature condition, required refrigerant is large, so the degree of superheat increased to open TXV. So, the refrigerant flows in two-phase at liquid line and the performance drop exceedingly.

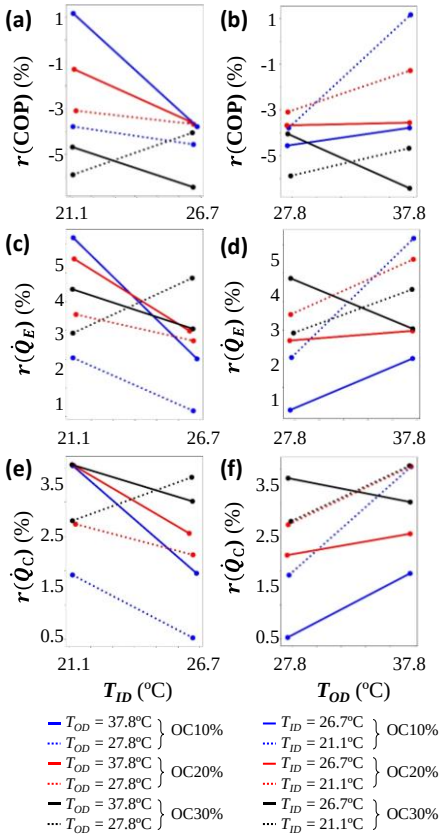


Fig. 6. Performance parameters with temperature conditions of OC fault

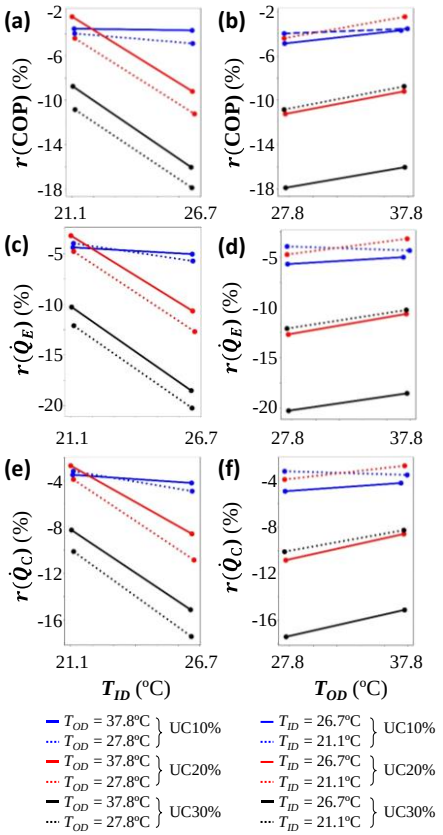


Fig. 7. Performance parameters with temperature conditions of UC fault

3.3. Comparative evaluation of fault effects in operating temperature conditions

Fig. 8 and 9 shows the COP degradation ratio at four different operating temperature conditions in mild fault level and severe fault level, respectively. As shown in Table 1, each fault level was determined in different point of view, so the first and the last fault level was selected.

According to the Fig. 8 COP degrades greatly at CMF, OC and the UC faults. The performance of the system changes intensely by the operating temperature at EF, LL and OC faults. In highest load condition (T_{ID} = 21.1 ℃, T_{OD} = 37.8 ℃), the system performance was improved at LL and OC fault. In LL fault, without lowest load condition (T_{ID} = 26.7 ℃, T_{OD} = 27.8 ℃), system performance was improved rather than the reference value.

In high fault levels, performance drop was severe of maximum 23% at LL fault. In LL fault, the effect of the fault was highlighted at lowest load condition (T_{ID} = 26.7 °C, T_{OD} = 27.8 °C). On the other hand, at highest load condition (T_{ID} = 21.1 °C, T_{OD} = 37.8 °C), system performance was improved. Accordingly, faults that affects the refrigerant mass flow rate such as LL or UC was influenced greatly by the operation temperature.

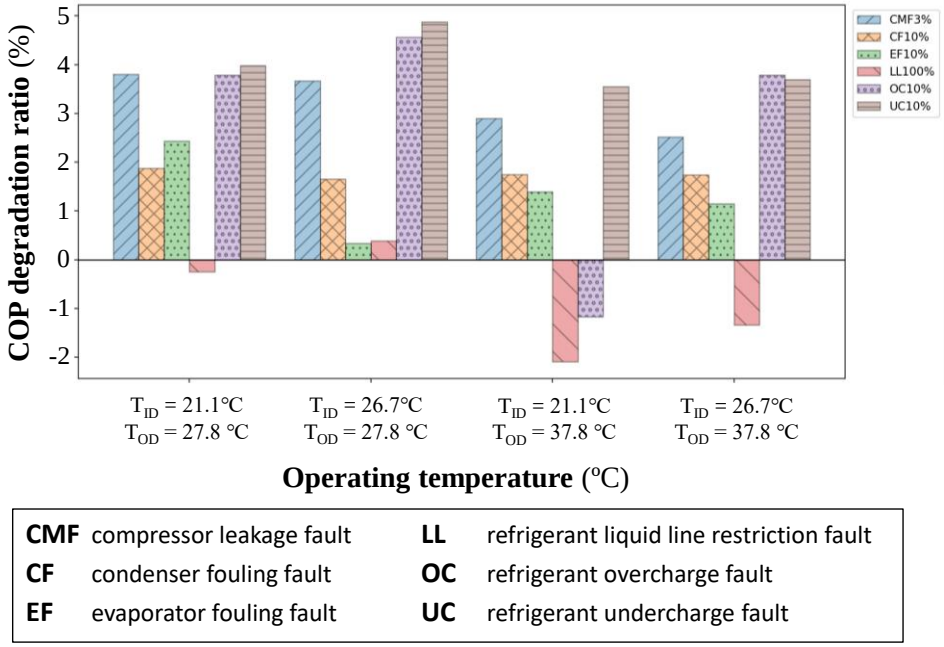


Fig. 8. COP degradation for each mild fault at four different operating temperature conditions.

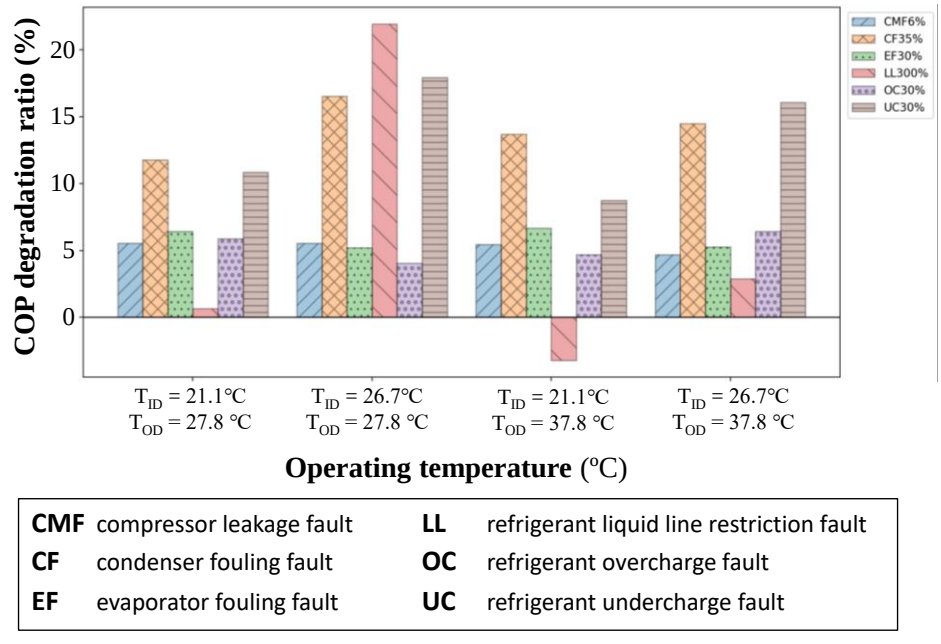


Fig. 9. COP degradation for each high fault at four different operating temperature conditions.

4. Conclusion

In this study, impact of single faults on performance of the residential heat pump system was analyzed at different operating temperature conditions. With the no-fault test data and the 2nd order multivariate

polynomial FFSS model, the reference value for the fault test was approximated. By comparing the difference between the reference value and the test data with six single faults imposed, performance difference was observed.

In CMF fault, three selected performance parameters do not fluctuate greatly, but the refrigerant flow backwards at the compressor so that the COP drops less. For CF fault, as the indoor temperature increased, the mass flowrate of the refrigerant increased, so the performance degrades less but the influence of the outdoor temperature is insignificant since the area of outdoor heat exchanger unit is decreased by the fault. At EF fault, as the evaporator air flow rate decreases, the evaporation pressure gets lower and the specific volume of the compressor suction side changes. In LL fault, as the fault level increases, the density of the fluid decreases as the evaporation temperature drops. Therefore, the refrigerant flowrate decreases greatly, and exceeds the capacity of TXV can rise. In OC fault, as charge level of the refrigerant increases the compressor work also increases which leads in COP drop. When the UC fault level gets higher, discharge line of the evaporator is superheated in order to compensate the fault by opening the TXV, which causes the two-phase flow in liquid line and the system performance reduces poorly.

Nomenclature

CF	condenser fouling	$\dot{Q}_{CA}$	condensing air-side capacity (kW)
CMF	compressor leakage	R	residual
CNN	convolutional neural network	r	residual ratio (%)
COP	coefficient of performance	ref	reference value
cur	current value	SEER	seasonal energy efficiency ratio (BTU/(W h))
DNN	deep neural network	T_{ID}	indoor temperature (℃)
DRNN	deep recurrent neural network	T_{OD}	outdoor temperature (℃)
DSH	evaporator superheat (℃)	T_{IDP}	indoor dew point temperature (℃)
EEV	electric expansion valve	TXV	thermostatic expansion valve
EF	evaporator fouling	UC	refrigerant undercharge
FDD	fault detection and diagnosis	VRF	variable refrigerant flow
FXO	fixed orifice expansion device	$\dot{W}_{c,trans}$	transformer work (kW)
HVAC	heating, ventilating, and air-conditioning	$\dot{W}_{comp}$	compressor work (kW)
LL	liquid line restriction fault	$\dot{W}_{ID,fan}$	indoor fan work (kW)
$\dot{m}_{r,comp}$	compressor mass flow rate (kg/s)		
OC	refrigerant overcharge	*Greek symbols*	
$\dot{Q}_{EA}$	evaporating capacity (kW)	ϕ	characteristic performance parameter
$\dot{Q}_{EA,lat}$	evaporating latent capacity (kW)	η_v	volumetric efficiency of compressor (%)
$\dot{Q}_{EA,sens}$	evaporating sensible capacity (kW)	$v_{comp,suc}$	compressor suction specific volume (kg/m^3)

Acknowledgements

This research was jointly supported by National Research Foundation of Korea (NRF No. 2019R1A2C108869414) and by Korea Institute of Energy Technology Evaluation and Planning (KETEP) (20202020900290, 20214000000280, 20212050100010) funded by Ministry of Trade, Industry and Energy. This research was also supported by the Korea Environmental Industry & Technology Institute (KEITI No. 2020003060005) Authors sincerely appreciate their supports.

References

[1] Afroz Z, Shafiullah GM, Urmee T, Higgins G. Modeling techniques used in building HVAC control systems: A review. *Renewable Sustainable Energy Rev.* 2018;**83**:64-84.
[2] IEA, 2018. “The Future of Cooling”. IEA, Paris, France.
[3] Mirnaghi MS, Haghighat F. Fault detection and diagnosis of large-scale HVAC systems in buildings using data-driven methods: A comprehensive review. *Energy Build.* 2020; **229**:110492.
[4] Kim W, Braun JE. Development, implementation, and evaluation of a fault detection and diagnostics system based on integrated virtual sensors and fault impact models. *Energy Build.* 2020;**228**:110368.

[5] Rossi TM, Braun JE. A statistical, rule-based fault detection and diagnostic method for vapor compression air conditioners. *HVAC&R Res.* 1997;**3**:19-37.
[6] Kim M, Yoon SH, Payne WV, Domanski PA. 2008. "Cooling mode fault detection and diagnosis method for a residential heat pump" NIST Special Publication. 1087
[7] Eom YH, Yoo JW, Hong SB, Kim MS. Refrigerant charge fault detection method of air source heat pump system using convolutional neural network for energy saving. *Energy* 2019;**187**:115877.
[8] Taheri S, Ahmadi A, Mohammadi-Ivatloo B, Asadi S. Fault detection diagnostic for HVAC systems via deep learning algorithms. *Energy Build.* 2021;**250**:111275.
[9] Wan H, Cao T, Hwang Y, Oh S. A review of recent advancements of variable refrigerant flow air-conditioning systems. *Appl. Therm. Eng.* 2020;**169**:114893.
[10] Kim M, Payne WV, Domanski PA, Hermes CJL. 2006. "Performance of a Residential Heat Pump Operating in the Cooling Mode with Single Faults Imposed" NISTIR 7350.
[11] Kim M, Payne WV, Domanski PA, Yoon SH, Hermes CJL. Performance of a Residential Heat Pump Operating in the Cooling Mode with Single Faults Imposed. *Appl. Therm. Eng.* 2009;**29**:770-8.
[12] ARI Standard, 2006. "Standard for Unitary Air Conditioning and AirSource Heat Pump Equipment". Air Conditioning and Refrigeration Institute, Fairfax, VA, p.210-240
[13] Cuevas C, Lebrun J, Lemort V, Winandy E. Characterization of a Scroll Compressor under Extended Operating Conditions. *Appl. Therm. Eng.* 2010;**30**:605-15.
[14] Picavet A, Ginies P., 2014. "Experimental Pressure-Volume diagrams of scroll compressors," International Compressor Engineering Conference. West Lafayette, USA, paper#2305.
[15] Mahfouz HAG, Hassan MNBW, Musa MN., 2004. "Analytical and Experimental Study on a Scroll Compressor," International Compressor Engineering Conference. West Lafayette, USA, paper#1648.
[16] Winandy E, Saavedra C, Lebrun J. Experimental analysis and simplified modelling of a hermetic scroll refrigeration compressor. *Appl. Therm. Eng.* 2002;**22**:107-20.

14th IEA Heat Pump Conference
15-18 May 2023, Chicago, Illinois

Long term performance analysis of a Dual-Source Heat Pump system by means of the Matlab/Simulink tool ALMABuild

Christian Natale*, Claudia Naldi, Matteo Dongellini, Gian Luca Morini

Department of Industrial Engineering, Alma Mater Studiorum – University of Bologna,
Viale del Risorgimento 2, Bologna 40136, Italy

Abstract

In this paper, the performance of a Dual-Source Heat Pump (DSHP), able to exploit energy from both air and ground, has been investigated through the Simulink toolbox ALMABuild. Two different control strategies for the external source selection have been implemented: with the first one, the ambient temperature is compared to a reference value (namely, switching temperature logic); with the second one, the heat pump is forced to operate in air-source mode and ground-source mode during the diurnal and the nocturnal hours, respectively (namely, scheduled times logic). The DSHP has been coupled to a building with unbalanced loads and to a Borehole Heat Exchanger (BHE) field, for which different total lengths of the borefield have been considered. The obtained results show that with undersized BHEs a DSHP achieves better annual performance with respect to Air-Source Heat Pumps (ASHPs) and Ground-Coupled Heat Pumps (GCHPs) coupled to the same borefield. In addition, a DSHP can reduce the ground temperature drift originated by undersized borefield and/or by unbalanced building loads. The paper shows how DSHPs can be selected for the replacement of traditional GCHPs in presence of undersized BHEs.

© HPC2023.
Selection and/or peer-review under the responsibility of the organizers of the 14th IEA Heat Pump Conference 2023.

Keywords: Dual-Source Heat Pump; Borehole Heat Exchangers; Annual Performance Factor; Matlab-Simulink; Control strategies.

1. Introduction

In the last decades the global energy demand, and consequently worldwide greenhouse gas emissions, has significantly increased in parallel with a better population wealth. In order to contrast climate change and simultaneously boosting its own energy security, the European Community is strongly promoting low carbon technologies [1-2]. In Italy, buildings account for about 30% of the total energy consumption [3] and, for this reason, the real estate industry must be involved in a systemic refurbishment. With this aim, the Italian government has granted state allowances to improve the building envelope thermal properties and the heating, ventilating and air conditioning (HVAC) systems [4].

Heat pumps are good candidates for this purpose since they strongly reduce the primary energy demand for space heating and cooling of buildings [5-6] if compared to traditional fossil fuel boilers. In fact, heat pumps are able to exploit significant shares of renewable energy from aerothermal, geothermal and hydrothermal energy sources [2]. In recent years, Air-Source Heat Pumps (ASHPs) have been the most sold units in Europe [1] thanks to the extremely wide source availability and low investment costs. However, the air-to-water heat pumps performance is deeply influenced by the external air temperature and, in particular, their efficiency decreases when the ambient temperature drops in winter and rises in summer, in correspondence of the largest building thermal load. Another drawback is related to the defrost cycles, which occur for heating operating mode when the ambient temperature is low and the relative humidity is high. The frost layer accumulated on the heat pump external heat exchanger can be removed with different techniques, such as the adoption of an

* Corresponding author. Tel.: +39-051-209-0467; fax: +39-051-209-0544.
E-mail address: christian.natale3@unibo.it.

electric resistance to melt the ice, the spray of hot water on the evaporator surface or the use of hot refrigerant by-passed from the compressor discharge port. Among defrost methodologies, the most widespread technique, used by commercial reversible heat pumps, is reverse cycle defrosting (RCD). For this reason, RCD has been considered in this paper as defrosting method [7].

On the contrary, Ground-Coupled Heat Pumps (GCHPs) performance is weakly influenced by the external air temperature. Indeed, starting from a depth of about ten meters the ground temperature is almost stable over the year and equal to the mean annual temperature of the locality. This circumstance, combined to a well-sized Borehole Heat Exchanger (BHE) field, guarantees that the GCHP annual efficiency is substantially higher than that of an ASHP [8]. The main drawback of GCHP systems is the high investment cost linked to the installation of BHEs, which requires an accurate analysis to avoid oversized borefields [9-10].

In order to reduce the BHE field length, guaranteeing high values of the heat pump seasonal performance factors, a Dual-Source Heat Pump (DSHP) able to exploit renewable energy from both air and ground can be adopted. In literature several studies have been carried out on multi-source heat pumps; however, they mostly considered multi-generator systems. Many authors [11-12] integrated solar collectors whilst others [13-14] combined photovoltaic/thermal solar panels to heat pump systems. In this work, only one heat generator has been considered, consisting in a multi-source heat pump prototype. This unit can exploit alternatively geothermal energy, by means of a BHEs field, and aerothermal energy, through a conventional finned tube heat exchanger. In this way, the heat pump can work in air-source mode when the ambient temperature is warmer, as during the milder part of the day, and operate in ground-source mode in the most severe part, avoiding the frost deposition and the consequent defrost cycle. Grossi et al. [15] conducted a preliminary analysis on the adoption of a DSHP similar to the one studied in this paper (i.e., a single unit able to exploit, alternately, air or ground as heat sources). In that work, the Authors utilized a commercial software for buildings dynamic simulation (Trnsys) and a single basic control strategy for the heat pump external source selection.

The aim of the present work is to evaluate the energy performance of a DSHP, comparing the overall efficiency achievable with this kind of unit with those of traditional systems, such as a ASHP and a GCHP. Seasonal and annual performance of these systems has been investigated coupling a BHE field having different sizes to the multi-source generator. By using ALMABuild [16-17], an open-source Matlab-Simulink toolbox, seven-year simulations have been performed to take into account the long-term effects of the ground exploitation on the soil temperature drift. Moreover, when the DSHP is considered as heat generator, two control strategies have been implemented to choose the heat pump external source. The former logic selects the operating heat source by comparing a reference temperature, namely the switching temperature, to the external air temperature. The latter logic considers daily scheduled times in which the external source of the DSHP is pre-defined independent of the climatic conditions. The simulation of two different control strategies for the multi-source generator permits to highlight the benefits of a smart regulation on seasonal and annual performance and, thus, to evaluate the competitiveness of this technology.

2. Building characteristics and climatic data

In order to compare the performance of the different heat pump configurations, a single-storey house [15] has been coupled to the heat pump system. The residential building, located in Bologna (Emilia-Romagna region, Northern Italy, 44°29'N, 11°21'E), has four thermal zones and a non-heated attic. The total net floor area is 111.6 m^2, the net conditioning volume is 301.5 m^3 and the surface to volume ratio is equal to 1.32 m^{-1}. The building main geometrical characteristics are summed up in Table 1, where the external wall surface area, the net floor area and the net volume are indicated for every thermal zone. Moreover, in each thermal zone the infiltration rate has been set to 0.5 vol h^{-1}. In Table 2 the building envelope thermophysical properties are reported.

Table 1. Main geometrical characteristics of each thermal zone

	Zone 1	Zone 2	Zone 3	Zone 4	Non heated-Attic
External wall surface area [m^2]	29.9	32.9	39.0	36.0	107.2
Net floor area [m^2]	18.6	24.8	37.2	31.0	113.9
Net volume [m^3]	50.2	67.0	100.5	83.8	269.1

The insulation level is medium if compared to the current Emilia-Romagna region transmittance limits [18]. The clear components are low-emissivity (equal to 0.1) double glasses (4/12/4) filled with Argon, with a glass transmittance of 1.5 W m^{-2} K^{-1}. The frame transmittance is 2 W m^{-2} K^{-1} and covers 20% of the total window surface. The standards UNI EN ISO 6949 [19] and UNI EN ISO 13370 [20] have been followed to calculate the external opaque components and the slab on grade transmittance values, respectively. Moreover, occupancy and equipment heat gains have not been considered.

The peak heating load is equal to 6.15 kW, whilst the maximum cooling load is 1.66 kW. The heating to cooling load ratio is equal to 3.7, thus, the building loads are strongly unbalanced, with higher values during the winter season. The thermal building loads have been evaluated by means of the ALMABuild tool by setting the indoor set-point temperature equal to 20 °C during winter and to 26 °C during summer. The heating season starts on October 15th and ends on April 30th (198 days), while the cooling season goes from June 15th to August 31st (77 days). The hourly climatic data included in the Meteonorm database [21] have been used in the dynamic simulations (minimum and maximum outdoor air temperature equal to -7 in winter and 35 °C in summer, respectively).

Table 2. Main characteristics of the opaque and clear components

	External wall	Floor	Roof	Window
Thickness [m]	0.34	0.335	0.32	0.02
Insulation thickness [m]	0.06	0.06	0.08	-
Transmittance [W m^{-2} K^{-1}]	0.38	0.28	0.401	1.77
Transmittance limits [W m^{-2} K^{-1}]	0.28	0.29	0.24	1.4

3. HVAC system characteristics

3.1. Sizing of the heat pump

The HVAC system, coupled to the building described above, is based on a single reversible inverter-driven heat pump. No back-up system is present because the heat generator has been sized to cover the maximum heating and cooling loads. To satisfy the building energy demand, three different heat pump systems have been considered: (i) an Air-Source Heat Pump, ASHP (air-to-water); (ii) a Ground-Coupled Heat Pump, GCHP (brine-to-water); (iii) a Dual-Source Heat Pump, DSHP (air/brine-to-water). As mentioned before, the DSHP is able to exploit, alternately, renewable energy from ambient air and soil, depending on the selected control strategy (no parallel exploitation of external sources is possible due to the unit refrigerant circuitation). The GCHP and ASHP manufacturer data on thermal power (cooling *Pc* and heating capacity *Ph*), COP and EER are reported in Figures 1 and 2 for different values of the external source temperature and different inverter frequencies. The curves refer to a load water temperature at the heat pump outlet equal to 10 °C in summer and 40 °C in winter. The DSHP has been modelled by considering the characteristic curves of both the ASHP and the GCHP.

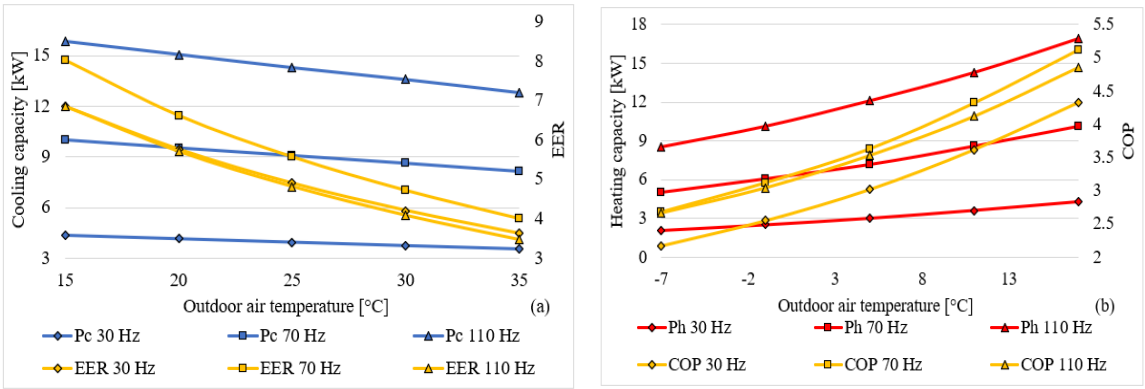


Fig. 1. (a) Cooling capacity and EER and (b) heating capacity and COP as functions of the outdoor air temperature (air-source mode), for three values of the inverter frequency (30 Hz, 70 Hz, 110 Hz).

The selected GCHP and ASHP can satisfy 1.45 and 1.38 times, respectively, the building heating peak load in the most unfavourable conditions (borehole fluid temperature of -5 °C in ground-source mode and external air temperature of -7 °C in air-source mode). Since the building winter energy demand is the most relevant, during summer the heat pump is deeply oversized and this will implicate a large number of on-off cycles.

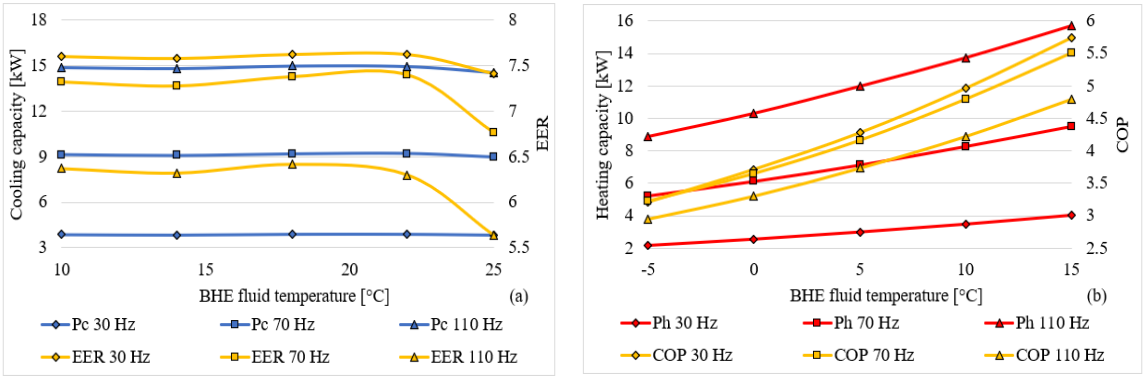


Fig. 2. (a) Cooling capacity and EER and (b) heating capacity and COP as functions of the borehole fluid temperature at the heat pump inlet (ground-source mode), for three values of the inverter frequency (30 Hz, 70 Hz, 110 Hz).

3.2. Heat pump control system

A PI controller is necessary to regulate the heat pump inverter frequency based on the temperature of the water supplied to the emitters. According to the hysteresis cycle adopted, the heat pump is switched off when the water temperature exceeds/goes under 42.5/7.5 °C and switched on when the water temperature decreases below/increases over 37.5/12.5 °C in winter and summer, respectively. When the minimum inverter frequency (30 Hz) is reached, no further thermal capacity modulation is possible, so the heat pump has to perform on-off cycles to satisfy the building thermal energy demand. In addition, the heat pump in air-source mode has to perform defrost cycles when the outdoor air temperature is low and the relative humidity is high.

In order to evaluate the energy losses linked to on-off and defrost cycles, corrective coefficients of the heat pump performance data have been applied. Concerning the on-off cycles, two coefficients have been used [15]. The first one, α, is related to the reduction of the thermal power supplied by the heat pump during the transient start-up of duration τ_α. The second one, β, is related to the reduction of the electric power requested by the heat pump during the transient start-up of duration τ_β. The correct thermal and electric power values have been obtained by multiplying the nominal ones to the corresponding corrective coefficients for the whole transient start-up duration. The values of the penalty coefficients (α, β) and the transient start-up times (τ_α, τ_β) are reported in Table 3.

Table 3. Penalty coefficients and transient start-up time

α	β	τ_α [s]	τ_β [s]
0.69	0.96	216	78

The heat pump cycle inversion due to defrosting occurs when, at the same time and for at least 10 minutes, the outdoor air temperature is lower than 6 °C and the relative humidity is higher than 50%. To model the defrost cycles, three phases have been considered [7]: i) an initial phase τ_1 in which the heat pump is switched-off and the inversing valve is turned on; (ii) an intermediate phase τ_2 during which the cycle is inverted and the heat pump operates in cooling mode, with power P_c and efficiency EER_c; (iii) a final phase τ_3 in which the heat pump is switched-off and the inversing valve is reverted again, to return in heating mode. One hour must pass between two consecutive defrost cycles. Table 4 shows the adopted values of P_c, EER_c, τ_1, τ_2 and τ_3.

Table 4. Main characteristics of the defrost cycle

P_c [kW]	EER_c	τ_1 [s]	τ_2 [s]	τ_3 [s]
-11.4	6	30	360	30

In order to select the most favorable external source (air/ground) when a DSHP is considered, two different control strategies have been analyzed: the switching temperature logic and the scheduled times logic. In the

former, when the external air temperature exceeds a reference value, called switching temperature, the heat pump operates in air-mode, otherwise it operates in ground-mode. In the latter, two daily scheduled time slots, nocturnal and diurnal, have been considered, taking as time limits the monthly average hours of sunrise and sunset in Bologna [22], reported in Table 5. In the diurnal hours the heat pump exploits the aerothermal energy, whereas in the nocturnal hours it uses the geothermal energy.

Four different case studies have been considered: heat pump system based on a GCHP (case A), heat pump system based on an ASHP (case B), heat pump system based on a DSHP with switching temperature logic (case C), heat pump system based on a DSHP with scheduled times logic (case D).

Table 5. Sunrise and sunset monthly average hours in Bologna

	Jan	Feb	Mar	Apr	May	Jun	Jul	Aug	Sep	Oct	Nov	Dec
Sunrise [a.m. h]	7:26	6:52	6:10	5:23	4:43	4:23	4:32	5:07	5:52	6:38	7:17	7:37
Sunset [p.m. h]	4:34	5:08	5:50	6:37	7:17	7:37	7:28	6:53	6:08	5:22	4:43	4:23

3.3. Terminal units and BHE field

In each case study, fan-coils are considered as emitters, that are connected to the heat pump through a hydronic loop where a single-speed circulation pump is present. The HVAC system is activated 24/24 h both during the heating and the cooling season. In order to reduce the heat pump on-off cycles and the thermal zones discomfort during defrost cycles, an inertial tank of 500 l has been placed in the heat pump delivery pipe.

The three-speed fan-coils selected, operating with a constant water flow rate, have been sized to cover the thermal zones load considering an inlet water temperature of 40 and 10 °C in the heating and cooling season, respectively. The fan controller modulates the speed (off, low, medium, or high) based on the room temperature, in order to maintain the set point value of 20 °C in winter and 26 °C in summer. When the fan is switched off, the water flow rate by-passes the terminal unit thanks to a three-way valve. Table 6 reports the fan-coils technical data of air and water flow rate, heating and cooling capacity, in correspondence of the indoor air temperature T_{amb}, inlet/outlet water temperature T_{in}/T_{out}, fan speed *fs* and relative humidity *RH*.

Table 6. Fan-coils technical data. Seasonal reference conditions: T_{amb} =20 °C, T_{in}/T_{out} =40/35 °C, high *fs* in heating mode; T_{amb} =26 °C, T_{in}/T_{out} =10/15 °C, medium *fs* and *RH* 60% in cooling mode

	Zone 1	Zone 2	Zone 3	Zone 4
Air flow rate [$m^3\ h^{-1}$]	442 [1] – 341 [2]	442 [1] – 341 [2]	319 [1] – 233 [2]	319 [1] – 233 [2]
Water flow rate [$l\ h^{-1}$]	253	253	158	317
Heating capacity [W]	1890	1890	1170	1410
Cooling capacity [W]	1540	1540	900	1330

[1] Heating mode

[2] Cooling mode

When the heat pump works in ground-mode (cases A, C, D), another hydronic loop with a single-speed circulation pump connects the heat pump to a BHE field. In Figure 3 a simplified HVAC layout with the multi-source heat pump is shown.

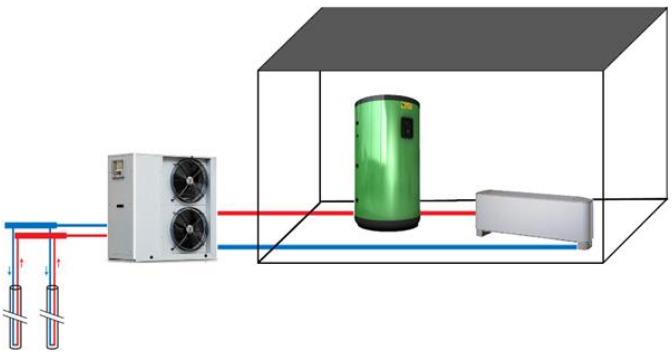


Fig. 3. Simplified HVAC layout with the multi-source heat pump.

The BHE field coupled to the heat pump contains vertical single U-tube boreholes, made of high-density polyethylene pipes in which a mixture of water and 60% Freezium [23] flows. Freezium is a commercial antifreeze borehole fluid, based on organic salts (potassium formate), able to maintain low viscosity and high thermal conductivity in low temperature applications. The gap between U-tubes and ground is filled by a commercial sealant mortar (Termoplast Plus [24]). The main BHE characteristics (borehole diameter D_b, internal pipe diameter $D_{p,i}$, external pipe diameter $D_{p,e}$, grout conductivity k_{gt}, pipe conductivity k_p, shank spacing s, BHE fluid thermal conductivity k_f, kinematic viscosity v_f and freezing temperature T_{ice}) are reported in Table 7.

Table 7. BHE and borehole fluid characteristics

D_b [m]	$D_{p,i}$ [m]	$D_{p,e}$ [m]	k_{gt} [W m^{-1} K^{-1}]	k_p [W m^{-1} K^{-1}]	s [m]	k_f[1] [W m^{-1} K^{-1}]	v_f[1] [m^2 s^{-1}]	T_{ice} [°C]
0.13	0.0262	0.032	1.6	0.355	0.085	0.5	2.2E-6	-25

[1]Property at 0 °C.

The undisturbed ground temperature has been set equal to 13.2 °C, whilst the ground thermal conductivity and diffusivity have been set as 1.97 W m^{-1} K^{-1} and 8.8E-7 m^2 s^{-1}, respectively. The borehole thermal power per unit length, exchanged between BHEs and ground, ranges between 30 and 50 W m^{-1} [25-26]. The borefield in case A (GCHP) is made of 2 BHEs, each 60 m long. For case C (DSHP with switching temperature logic), 4 different borefield configurations have been considered: 2 boreholes each 60 m long (case C1); 1 borehole 90 m long (case C2); 1 borehole 70 m long (case C3); 1 borehole 60 m long (case C4). In cases C2-C4 the total BHEs length is undersized with respect to the building energy demand. Finally, in case D (DSHP with scheduled times logic) only 1 borehole 60 m long has been considered. Table 8 sums up the different case studies.

Table 8. Sum up of the case studies

	A	B	C1	C2	C3	C4	D
Ground	2×60 m	×	2×60 m	1×90 m	1×70 m	1×60 m	1×60 m
Air	×	✓	✓	✓	✓	✓	✓

The ground thermal response has been modeled by means of the *g-functions* method, in which dimensionless thermal response functions simulate the ground temperature trend produced by a uniform and constant dimensionless thermal load [27]. By means of *g-functions*, the BHE fluid outlet temperature has been evaluated at every simulation time step [9], whilst the BHE linear thermal resistance has been calculated with an analytical expression [28].

4. Results

The entire system has been modelled in ALMABuild, a homemade tool developed in the Matlab-Simulink environment for the dynamic simulation of coupled building-HVAC plants [16-17]. ALMABuild contains libraries with blocks to model the different building and HVAC components. The considered system, shown in Figure 4, has been modelled by using blocks from both ALMABuild and Carnot, another Simulink library focused on the HVAC system [29].

Yearly and long-term (7 years) simulations have been carried out to investigate the performance of the considered heat pump systems on the basis of the seasonal and annual efficiency indicators reported in Equation (1). In order to limit the computational time of performed simulations with no lack of reliability, a period of 7 years has been considered idoneous to investigate the (eventual) soil temperature drift, since the variation of the ground temperature stabilizes in a few years for all configurations presented in this paper.

$$SCOP_{net} = \frac{\sum_{j=0}^{\tau_h} E_{h,j}}{\sum_{j=0}^{\tau_h} E_{el,j}} \qquad SEER = \frac{\sum_{j=0}^{\tau_c} E_{c,j}}{\sum_{j=0}^{\tau_c} E_{el,j}} \qquad APF_{net} = \frac{\sum_{j=0}^{\tau_h+\tau_c} E_{h,j} + E_{c,j}}{\sum_{j=0}^{\tau_h+\tau_c} E_{el,j}} \tag{1}$$

The net Seasonal Coefficient of Performance ($SCOP_{net}$) is the winter performance indicator, namely the ratio between the total thermal energy provided by the heat pump during winter $\left(\sum_{j=0}^{\tau_h} E_{h,j}\right)$ and the

corresponding electric energy used by the heat pump compressor $\left(\sum_{j=0}^{\tau_h} E_{el,j}\right)$. The Seasonal Energy Efficiency Ratio (SEER) is the summer performance indicator, that is the ratio between the total cooling energy provided by the heat pump during summer $\left(\sum_{j=0}^{\tau_c} E_{c,j}\right)$ and the corresponding electric energy used by the heat pump compressor $\left(\sum_{j=0}^{\tau_c} E_{el,j}\right)$. The net Annual Performance Factor (APF_{net}) is the annual performance indicator, i.e., the ratio between the total energy supplied by the heat pump during the year $\left(\sum_{j=0}^{\tau_h+\tau_c} E_{h,j} + E_{c,j}\right)$ and the corresponding total electric energy used $\left(\sum_{j=0}^{\tau_h+\tau_c} E_{el,j}\right)$.

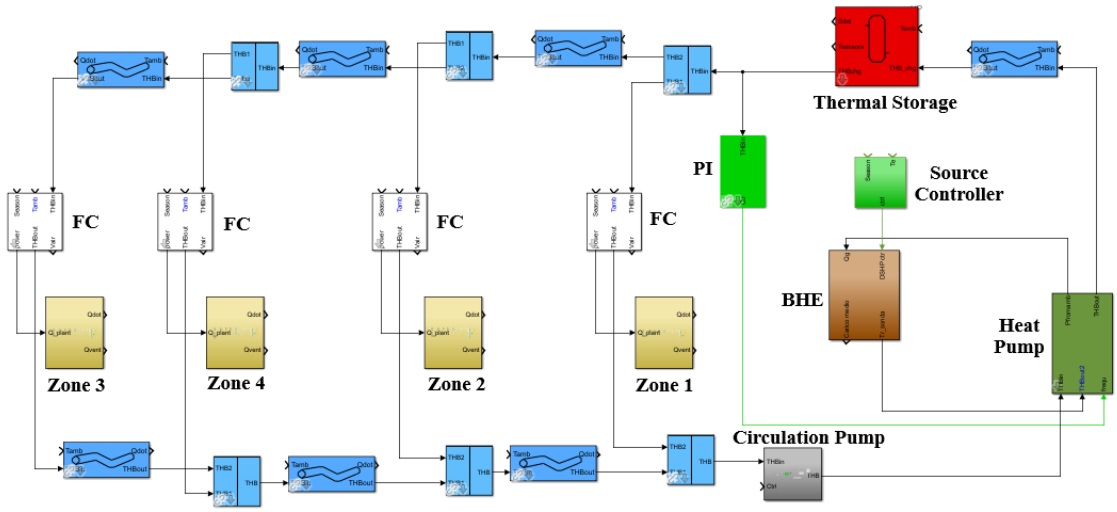


Fig. 4. Building-HVAC system layout (Borehole Heat Exchanger BHE, Proportional Integral controller PI, Fan-coil FC).

4.1. Case A, GCHP

In case A, the GCHP is coupled to the single-storey house and to the BHE field with 2 boreholes, each 60 meters long. The long-term heat pump performance and ground temperature trend have been evaluated. In Table 9 the seasonal and annual performance factors obtained from the first to the 7th year are reported together with the percent variation on the APF_{net} value (Δ_{APF}) with respect to the first year, taken as reference.

Table 9. Seasonal and annual performance factors, GCHP

Year	1	2	3	4	5	6	7
SEER	6.24	6.23	6.23	6.23	6.23	6.23	6.23
$SCOP_{net}$	3.95	3.89	3.86	3.84	3.83	3.82	3.81
APF_{net}	4.07	4.01	3.98	3.96	3.94	3.93	3.93
Δ_{APF} [%]	0	-1.45	-2.17	-2.64	-2.98	-3.24	-3.43

As evident from Table 9, the best efficiency is reached in the cooling season due to an oversized borefield, which allows to keep the maximum BHE fluid temperature at the heat pump inlet below 20 °C. On the contrary, in the heating season the BHE field is well-sized and the seasonal performance ($SCOP_{net}$) remains quite high over the years, with a maximum value of 3.95 in correspondence of the first year. The APF_{net} index follows the $SCOP_{net}$ trend over the 7-years period because the building loads are strongly unbalanced with predominance of the heating demand. Furthermore, it can be observed that the minimum APF_{net} value, obtained at the last year, is only 3.43% lower than that of the first year. This result is explained by the mean winter temperature values at the BHE-ground interface, which drop only slightly over the years, going from 5.7 °C (first year) to 4.35 °C (seventh year). On the contrary, in presence of both unbalanced building loads and undersized borefield, the ground thermal drift can be significant [27].

4.2. Case B, ASHP

In case B, the ASHP is coupled to the same residential building. Since Meteonorm hourly climatic data refer to a typical reference year, one annual simulation is sufficient to investigate the generator efficiency in the long-term period. In Table 10 the seasonal and annual performance indicators are reported.

Table 10. Seasonal and annual performance factors, ASHP

SEER	$SCOP_{net}$	APF_{net}
4.06	2.80	2.87

From Table 10 it can be observed that the minimum seasonal efficiency refers to the winter season: the $SCOP_{net}$ value is equal to 2.80, about 31% lower than the SEER value (4.06). This result is due to the high number of heat pump start-ups: 2873 over the year, where 2547 start-ups occur during the winter period and only 326 during the summer one. The large number of winter start-ups mainly depends on the defrost cycles, which are about 9 per day. This aspect becomes even more critical in the coldest and damp months, from December to February, when the daily average number of defrost cycles overcomes 15. In the summer season the heat pump is often switched off (79% of the conditioning period), given that the cooling demand is much lower than the heating one, so that the generator is deeply oversized during this season. Indeed, the maximum compressor frequency does not overcome 39 Hz during the cooling season (the heat pump frequency range goes from 30 to 110 Hz). The APF_{net} value (2.87) is close to the winter coefficient (2.80), due to the unbalanced building loads.

4.3. Cases C1-C4, DSHP with switching temperature logic

In cases C1-C4, the heat pump is a DSHP able to exploit, alternatively, renewable energy from both air and ground. In the heating season, the adopted source control strategy is the switching temperature logic: the controller compares the ambient temperature with a reference value (switching temperature). In particular, when the external air temperature exceeds the switching temperature, the heat pump operates in air-mode, otherwise in ground-mode. In this way the aerothermal energy can be used when the outdoor air temperature is warmer (with consequent higher COP values) and the defrost cycles can be avoided if a switching temperature higher than 6 °C is selected. On the other hand, in the cooling season the heat pump works in ground-mode only in order to partially recharge the ground due to the unbalanced building loads and to exploit a sink with lower temperature values than the external air, with consequent better EER values.

In case studies C1-C4, 4 different BHE sizes have been coupled to the multi-source heat pump. Figure 5 shows the first year APF_{net} trend as a function of the switching temperature, for the different BHE field lengths. It is worth noting that a switching temperature equal to 26 °C (points on the far right in Figure 5) corresponds to ground-source mode only, namely to a conventional GCHP. From Figure 5 it can be observed that the APF_{net} increases, for a fixed switching temperature, ranging from case C4 (BHE length 60 m) to cases C3 (BHE length 70 m), C2 (BHE length 90 m) and C1 (BHE length 120 m). Indeed, the higher the total BHE length, the higher (the lower) the BHE fluid temperature at the heat pump inlet and, consequently, the better the heat pump winter (summer) performance.

Another important obtained outcome is that an optimal switching temperature can be selected, for a fixed BHE length, that maximizes the APF_{net} value. In particular, this optimal value grows as the borefield length rises: in cases C3 and C4 (shorter borefields) the optimal switching temperature is 6 °C, whereas in cases C2 and C1 (longer borefields) it becomes 8 and 14 °C, respectively. This trend is coherent since the ground utilization increases with the switching temperature, and longer BHEs guarantee higher (lower) borehole fluid temperature values, assuring better heating (cooling) performance. By comparing the results of cases C3 and C4 to each other, it is clear that the adoption of an optimized switching temperature allows to achieve, with a shorter borefield, the same APF_{net} value of a conventional GCHP coupled to a longer (and more expensive) field: the APF_{net} value for case C4 (BHE 60 m long) in correspondence of a switching temperature T_{sw} = 6 °C is 8% larger than that in correspondence of T_{sw} =26 °C (ground-source mode only) and even slightly larger than that achieved in case C3 (BHE 70 m long) with T_{sw} =26 °C (ground-source mode only). Moreover, adopting a switching temperature of 14 °C even in the well-sized case C1 allows to obtain an APF_{net} slightly greater than that of the traditional GCHP (T_{sw} = 26 °C). Indeed, with T_{sw} = 14 °C, the air source is employed when the external air temperature is higher than the ground temperature and this promotes better heat pump performance (compare the heat pump performance data in Figures 1 and 2). Small switching temperature

values can be discarded as they make the heat pump operate for a prolongated time with the aerothermal source even when the ambient temperature is cold and dump.

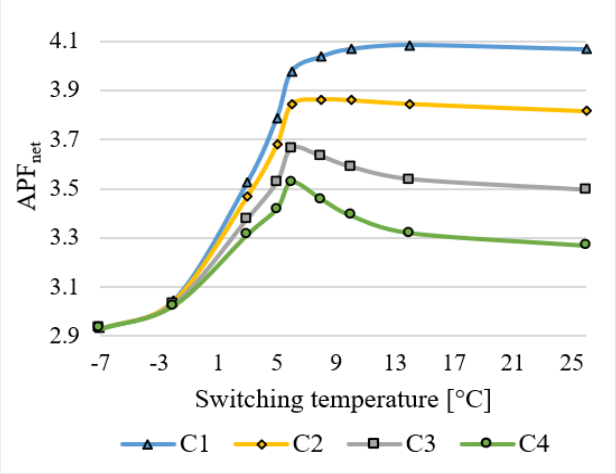


Fig. 5. First year APF_{net} as function of the switching temperature and of the BHE field size (C1, C2, C3, and C4).

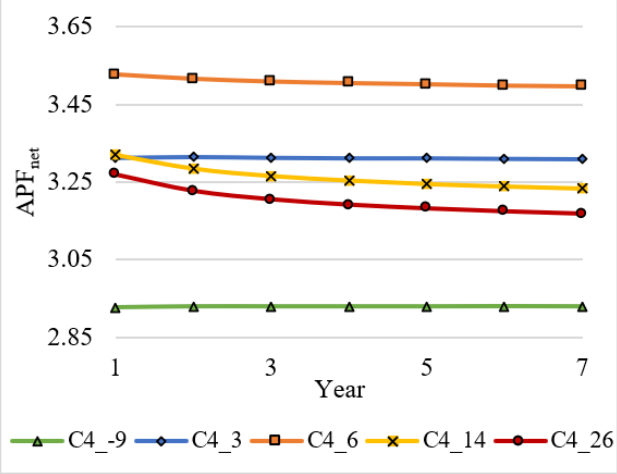


Fig. 6. APF_{net} trend of case C4 over 7 years, for different switching temperature values (-9, 3, 6, 14 and 26 °C).

In order to evaluate the long-term heat pump performance, 7-years simulations have been carried out by coupling the DSHP to the most undersized borefield, namely case C4 (1×60 m). Five switching temperature values (-9, 3, 6, 14, 26 °C) have been selected and the corresponding annual efficiency is reported in Figure 6. It is worth remembering that a switching temperature of 26 °C (red curve in Figure 6) corresponds to simulate a conventional GCHP. It can be observed from Figure 6 that the DSHP APF_{net} with a very low switching temperature (T_{sw} = -9 °C, green curve) has a steady trend since no ground energy is exploited in winter and, therefore, no ground temperature degradation occurs. Additionally, the thermal energy transferred to the ground in the cooling season is insufficient to markedly increase its temperature over the years, thus no influence on the SEER values has been noticed.

On the other hand, the DSHP APF_{net} with a very high switching temperature (T_{sw} = 26 °C, red curve) is always higher than that obtained with T_{sw} = -9 °C, but the ground temperature degradation negatively influences the annual efficiency, which has a drop of 3.1% after 7 years.

As already mentioned before, the optimal switching temperature for case C4 is 6 °C (orange curve in Figure 6): adopting this control logic, the thermal energy extracted in winter from ground decreases by 40% compared to the GCHP case (red curve). As a consequence, the mean winter temperature of the BHE fluid at the DSHP inlet is from 6.6 °C (1st year) to 7.3 °C (7th year) higher than that reached in the same year by the GCHP and the APF_{net} increases from 8 to 10.4% over the considered period.

Therefore, in accordance with the literature results [15, 30-31], the adoption of a DSHP proves to be competitive: (i) to equilibrate the ground loads when the building loads are strongly unbalanced and/or when the borefield is undersized, avoiding the progressive ground temperature drift; (ii) to reduce the HVAC plant investment cost opting for a total BHE field length reduced with respect to the design one.

4.4. Case D, DSHP with scheduled times logic

In case D, the heat generator is composed of a dual-source heat pump coupled to an undersized (60-meters long) borehole. In the heating season the source control strategy is the scheduled times logic: two daily scheduled time slots, nocturnal and diurnal, are defined taking as time limits the monthly average hours of sunrise and sunset in Bologna. In the diurnal hours the heat pump exploits aerothermal energy and in the nocturnal ones geothermal energy. With this control logic the number of defrost cycles depends on the temperature and moisture content of the external air in the diurnal hours. On the other hand, in the cooling season the source controller selects only the ground for the same reasons explained for the switching temperature logic (section 4.3). Table 11 shows the results in terms of seasonal and annual performance coefficients over 7 years. As evident from Table 11, the best seasonal efficiency is reached in summer due to a well-sized borefield, with a mean summer BHE fluid temperature at the heat pump inlet which remains below 17.3 °C over the years. On the contrary, in the heating season the BHE field length is halved with respect to the proper design size and the $SCOP_{net}$ values are 48% lower than the SEER ones. Also in this case the APF_{net} index follows the $SCOP_{net}$ trend over the 7-years period because of the higher building loads for heating. Both

the $SCOP_{net}$ and the APF_{net} factors are quite stable over the years, undergoing a weak decrease, due to the mean winter temperature at the BHE-ground interface which drops from 4.7 °C (first year) to 4 °C (seventh year).

Table 11. Seasonal and annual performance factors, DSHP with scheduled times logic

	1	2	3	4	5	6	7
SEER	6.23	6.23	6.23	6.23	6.24	6.24	6.24
$SCOP_{net}$	3.26	3.25	3.25	3.24	3.24	3.23	3.23
APF_{net}	3.38	3.37	3.37	3.36	3.36	3.36	3.35

4.5. Comparison

The main results in terms of APF_{net} for the investigated cases A-D are summed up in Figure 7.

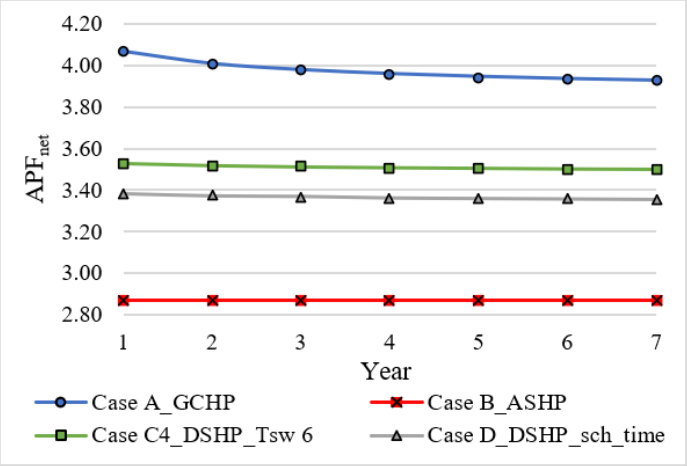


Fig. 7. APF_{net} over 7 years of cases A (blue curve), B (red curve), C4 (green curve) and D (grey curve).

According to the plot of Figure 7, the best annual efficiency is reached adopting a traditional GCHP (blue curve in Figure 7) coupled to a well-sized borefield (case A). In this case, the APF_{net} index drops slightly, especially in the first three years, reaching a value of 3.94 after 7 years. The worst performance is obtained by the ASHP (case B, red curve in Figure 7) due to a colder source in winter and to a large number of defrost cycles. The performance of the DSHP coupled to a strongly undersized borefield (1×60 m) is intermediate between that of cases A and B, with the APF_{net} of the C4 configuration with T_{sw}=6 °C (green curve in Figure 7) 4% better than that of the D one (scheduled times logic, grey curve in Figure 7). This result is due to a better exploitation of the renewable sources in case C4: in the scheduled times logic (case D) the number of defrost cycles cannot be controlled because it depends on the temperature and moisture content of the outdoor air in the diurnal hours (when the heat pump operates in air-mode), whereas the switching temperature logic with an optimized T_{sw} (case C4) avoids the inefficient defrost cycles making the heat pump operate in ground-source mode when the external air temperature is below 6 °C. In both cases C4 and D the APF_{net} is quite stable over the seven years thanks to more balanced ground loads with respect to case A. To summarize, the DSHP guarantees an annual efficiency from 17 to 23% larger than that obtained by a conventional ASHP, independently from the logic chosen to select the operating external source. Furthermore, accepting an APF_{net} value only 11% lower with respect to case A, a borefield strongly reduced up to 50% can be coupled to the DSHP, obtaining, in this way, a consistent reduction of the investment cost.

5. Conclusion

In this paper, the homemade Simulink-MATLAB tool ALMABuild has been employed to investigate the performance of different heat pump systems, coupled to the same single-storey house, located in Bologna (North Italy) and characterized by unbalanced seasonal loads. Three heat pump configurations have been considered: a Ground-Coupled Heat Pump (GCHP), an Air-Source Heat Pump (ASHP) and a Dual-Source Heat Pump (DSHP), modelled through the technical data of both the ASHP and the GCHP. In dual-source

mode two different control strategies have been tested: the switching temperature logic and the scheduled times one. In the former, when the external air temperature exceeds a reference value, called switching temperature, the heat pump operates in air-mode, otherwise in ground-mode. In the latter, two daily scheduled time slots, nocturnal and diurnal, have been considered taking as time limits the monthly average hours of sunrise and sunset in Bologna; in the diurnal hours the heat pump exploits aerothermal energy, in the nocturnal hours the heat pump extracts heat from the ground.

Yearly and long-term (7 years) simulations have been carried out to investigate the different heat pump systems performance. The numerical results demonstrate that, when the borefield is well-sized, the DSHP performance is higher than that of the ASHP and lower than that of the GCHP. Moreover, with the switching temperature logic an optimal value can be adopted to maximize the APF_{net}; the optimal switching temperature value rises as the BHE field length increases. Additionally, in presence of undersized BHEs, annual performance factors higher than that of a GCHP can be obtained by a DSHP with an optimized switching temperature, with a consistent reduction of the borefield investment cost. Furthermore, with the scheduled times logic, lower APF_{net} values are obtained compared to those of the switching temperature logic due to a worst sources selection. More balanced ground loads are guaranteed by the multi-source heat pump, resulting in more stable APF_{net} values than those of the GCHP over the years. The adoption of a DSHP is promising since it allows to reduce the ground temperature drift originated by an undersized borefield and/or unbalanced building loads. As a consequence, DSHPs can be selected for the replacement of conventional GCHPs in presence of BHEs that are undersized (to reduce the investment cost or due to subsequent changes in the building thermal loads).

Acknowledgements

The research leading to these results has received funding from the Italian Ministry of University and Research (MUR) within the framework of the PRIN2017 project «The energy FLEXibility of enhanced HEAT pumps for the next generation of sustainable buildings (FLEXHEAT)», grant 2017KAAECT.

References

[1] E.U. Directive 2018/2002/EU on Energy Efficiency, amending Directives 2012/27/EU, 2009/12/EC and 2010/30/EU and repealing Directives 2004/8/EC and 2006/32/EC, 21 December 2018.
[2] E.U. Directive 2018/844/EU of the European Parliament and of the Council amending Directive 2010/31/EU on the energy performance of buildings and Directive 2012/27/EU on energy efficiency, 30 May 2018.
[3] MISE, Annual Energy Report, 22 July 2021.
[4] MISE, Requirement to obtain tax deduction for building energy upgrading, 6 August 2020.
[5] Madonna F, Bazzocchi F. Annual performances of reversible air-to-water heat pumps in small residential buildings. *Energy and Buildings* 2013;**65**:299–309.
[6] Dongellini M, Naldi C, Morini GL. Seasonal performance evaluation of electric air-to-water heat pump systems. *Applied Thermal Engineering* 2015;**90**:1072–81.
[7] Vocale P, Morini GL, Spiga M. Influence of outdoor air conditions on the air source heat pumps performance. *Energy Procedia* 2014;**45**:653–62.
[8] Urchueguía JF, Zacarés M, Corberán JM, Montero Á, Martos J, Witte H. Comparison between the energy performance of a ground coupled water to water heat pump system and an air to water heat pump system for heating and cooling in typical conditions of the European Mediterranean coast. *Energy Conversion and Management* 2008;**49**:2917–23.
[9] Naldi C, Zanchini E. Effects of the total borehole length and of the heat pump inverter on the performance of a ground-coupled heat pump system. *Applied Thermal Engineering* 2018;**128**:306–19.
[10] Rivoire M, Casasso A, Piga B, Sethi R. Assessment of Energetic, Economic and Environmental Performance of Ground-Coupled Heat Pumps. *Energies* 2018;**11**:1941. doi:10.3390/en11081941
[11] Kaygusuz K, Ayhan T. Experimental and theoretical investigation of combined solar heat pump system for residential heating. *Energy Conversion & Management* 1999;**40**:1377–96.
[12] Lazzarin RM. Dual source heat pump system: Operation and performance. *Energy and Buildings* 2012;**52**:77–85.
[13] Fu HD, Pei G, Ji J, Long H, Zhang T, Chow TT. Experimental study of a photovoltaic solar-assisted heat-pump/heat-pipe system. *Applied Thermal Engineering* 2012;**40**:343–50.

[14] Ammar AA, Sopian K, Alghoul MA, Elhub B, Elbreki AM. Performance study on photovoltaic/thermal solar-assisted heat pump system. *J Therm Anal Calorim* 2019;**136**:79–87. https://doi.org/10.1007/s10973-018-7741-6
[15] Grossi I, Dongellini M, Piazzi A, Morini GL. Dynamic modelling and energy performance analysis of an innovative dual-source heat pump system. *Applied Thermal Engineering* 2018;**142**:745–59.
[16] Campana JP. ALMABEST: A new whole building energy simulation Simulink-based tool for NZEB design (PhD dissertation, Supervisor: Gian Luca Morini). Alma Mater Studiorum - University of Bologna 2019. doi: 10.6092/unibo/amsdottorato/8993
[17] Campana JP, Morini GL. BESTEST and EN ISO 52016 Benchmarking of ALMABuild, a New Open-Source Simulink Tool for Dynamic Energy Modelling of Buildings. *Energies* 2019;**12**:2938. doi:10.3390/en12152938
[18] Dgr Emilia-Romagna. Modifications acceptance to "Deed of regional technical coordination to define energy performance and minimum requirements of buildings, n.967/2015". July 2022.
[19] UNI EN ISO 6946:2008 Building Components and Building Element - Thermal Resistance and Thermal Transmittance - Calculation Method.
[20] UNI EN ISO 13370:2018 Thermal performance of buildings - Heat transfer via the ground - Calculation methods.
[21] METEONORM. Global Meteorological Database for Solar Energy and Applied Climatology. Available: http://www.meteonorm.com
[22] UNI 10349-1:2016 Heating and cooling of buildings - Climatic data – Part 1: Monthly means for evaluation of energy need for space heating and cooling and methods for splitting global solar irradiance into the direct and diffuse parts and for calculate the solar irradiance on tilted planes.
[23] Gernot Krakat. *VDI Heat Atlas.* 2sd ed. Mülheim (Ruhr): Springer D4.2 p 451; 2010.
[24] Termoplast PLUS, pre-mixed for the filling of geothermal weels, technical datasheet. Available: https://www.gtssnc.com/schedetecniche/premiscelato_Termoplast_PLUS.pdf
[25] Lee CK, Lam HN. Computer simulation of borehole ground heat exchangers for geothermal heat pump systems. *Renewable Energy* 2008;**33**:1286–96.
[26] Florides G, Kalogirou S. Ground heat exchangers – A review of systems, models and application. *Renewable Energy* 2007;**32**:2461–78.
[27] Zanchini E, Lazzari S. Temperature distribution in a field of long Borehole Heat Exchangers (BHEs) subjected to a monthly averaged heat flux. *Energy* 2013;**59**:570–80.
[28] Lamarche L, Kajl S, Beauchamp B. A review of methods to evaluate borehole thermal resistances in geothermal heat-pump systems. *Geothermics* 2010;**39**:187–200.
[29] CARNOT Toolbox Ver. 7.0, 07/2019 for Matlab/Simulink R2018b, © Solar-Institut Juelich.
[30] Corberán JM, Cazorla-Marín A, Marchante-Avellaneda J, Montagud C. Dual source heat pump, a high efficiency and cost-effective alternative for heating, cooling and DHW production. *International Journal of Low-Carbon Technologies* 2018;**13**:161–76.
[31] Marinelli S, Lolli F, Butturi MA, Rimini B, Gamberini R. Environmental performance analysis of a dual-source heat pump system. *Energy & Buildings* 2020;223 110180.

14th IEA Heat Pump Conference
15-18 May 2023, Chicago, Illinois

Large scale demand response of heat pumps to support the national power system

Tommy Walfridson[a*], Markus Lindahl[b], Niclas Ericsson[c], Tobias Bergentz[d]
Morgan Willis[a], Ola Gustafsson[b], Caroline Haglund Stignor[b]

[a]Energy and Resources, RISE Research Institutes of Sweden, Stockholm , Sweden
[b]Energy and Resources, RISE Research Institutes of Sweden, Borås, Sweden
[c]Industrial Systems, RISE Research Institutes of Sweden, Västerås, Sweden
[d]Transmission and Distribution, SWECO Sverige, Göteborg, Sweden

Abstract

In a power system with an increased share of electricity from intermittent renewable sources heat pumps can act as a large, aggregated flexibility resource. This can help to balance variations in electricity production and to reduce problems with bottlenecks in the power system. In this study a concept based on using the heat pump manufacturers cloud solutions to communicate demand response between an aggregator and individual heat pumps is investigated. The manufacturers cloud solutions were first released about ten years ago, meaning numerous heat pumps installed are ready to be used for flexibility with the missing piece being communication. Possibilities and constrains related to the concept have been investigated in an interview study with nine technical experts from the major heat pump manufacturers in Sweden. A workshop with those experts and additional stakeholder complemented it. Several barriers to solve were identified. Heat pumps are difficult to securely control rapidly and thus communicating flexibility control on beforehand has clear benefits. The transmission system operator normally has high accuracy demands, something villa heat pumps today cannot meet as most of them lack electricity meters. Here compromising on accuracy is likely necessary. Alternatives to standardize the communication between the aggregator via the cloud services to the individual heat pumps has been investigated. From a heat pump perspective EEBUS and OpenADR are promising.

© HPC2023.
Selection and/or peer-review under the responsibility of the organizers of the 14th IEA Heat Pump Conference 2023.

Keywords: aggregator; demand response; flexibility; heat pump; load control; power system; smart grid

1. Introduction

In a power system with an increased share of electricity from intermittent renewable sources such as wind and solar, the need for demand response is foreseen to increase, to help balance the variations in electricity production. Examples of problems that demand response from residential heat pumps can help to solve are, e.g., peak shaving, reduce problems with bottlenecks in the power system and avoid curtailment of renewable energy sources. This is done by load shifting, where the heat pumps electricity consumption is moved from peak hours to off-peak hours. A standardized way to control heat pumps for demand response would make it easier for aggregators and network owners to use the potential of heat pumps to provide flexibility to the power system.

* Corresponding author. Tel.: +46 10 516 5447
E-mail address: tommy.walfridson@ri.se

1.1. Scope

The scope of this study is to investigate the technical possibilities and constrains for a concept where residential heat pumps are aggregated and controlled via the manufacturers cloud solution in order to support the power system.

- The focus is on technical aspects, other considerations such as legal, and economical are only briefly described.
- The focus is mainly on conditions and available flexibility products for the Swedish power system.
- The solution evaluated is valid for residential heat pumps with hydronic heating systems, meaning ground source, air-to-water and exhaust air heat pumps, that are connected to a manufacturers cloud service.
- Air-to-air heat pumps are excluded because they are (in Sweden at least) relying on direct electric heating as backup. Turning them off at cold weather will likely cause the electric heaters to turn on contradicting the purpose.
- Comfort issues are not thoroughly investigated as demand response will be voluntary and if comfort is too poor, compared to economic benefit, people will terminate their enrollment. In a demand response system comfort can never be the top priority.
- The focus is on space heating as today's power system congestion hours are mainly in the wintertime when heating is the major need, and domestic hot water (DHW) has constraints making it difficult to use for flexibility.

1.2. Background

In Sweden, as in the rest of Europe, more and more electricity from weather-dependent intermittent sources is being installed resulting in larger variations in electricity production, see Figure 1 below. In Sweden, there is a political goal that 100% of the electricity should be fossil-free by 2040 [1] [2]. At the same time there is an ongoing electrification of the whole society and several of the roadmaps from "Fossilfritt Sverige", an initiative to reduce the impact on global warming from different industrial sectors in Sweden, point out an increased electrification as the way forward to reduce the climate impact of the industry [3]. In addition, the Swedish government has published an electrification strategy [4] in order to meet the increasing needs for electricity from renewable sources. The strategy is summarized in twelve points and one of them focus on an increased flexible use of electricity, especially mentioning the need to realize a higher degree of flexible electrical heating. This indicates that an increased load on the power system is to be expected, especially from intermittent sources.

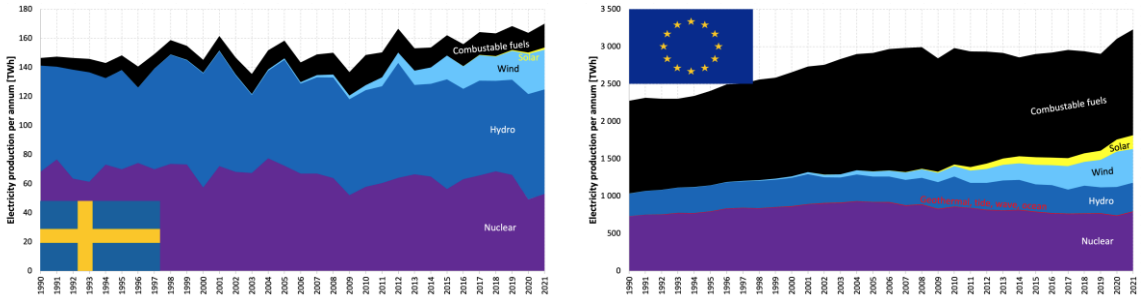


Figure 1. Sources for electricity production in Sweden (left) and EU 28 (right). UK is included, for better readability, in 2020 despite Brexit. Data from Eurostat [5] and the Swedish Energy Agency [6], some data for UK extrapolated in 2020.

Internationally the expected trend with an increasing share of electricity from renewable sources is similar, see Figure 2 below.

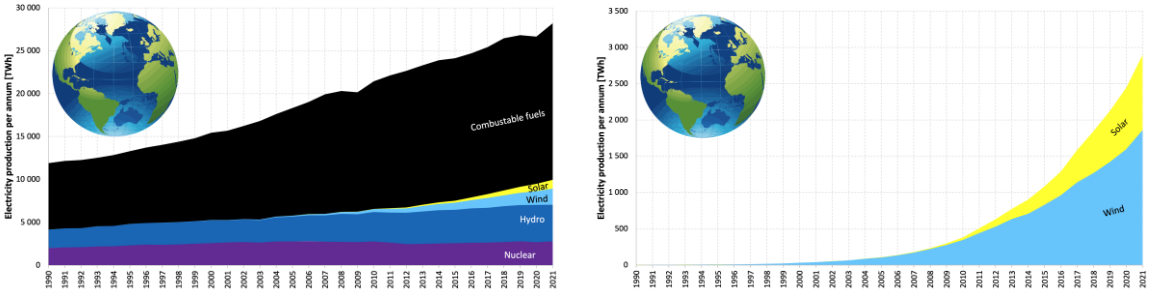


Figure 2. Sources for electricity production of the World (left) and zoom in on wind and solar to see the growth rate (right) [7].

In EUs Renewable Energy Directive towards 2030 [11] there is a binding target for the EU for 2030 that at least 32% of the final energy consumption should come from renewable sources, and there are ongoing discussions to increase the target to 40% as part of the European green deal [10]. Child et.al. has made a scientific forecast that shows how EU will be able to have an almost completely renewable electricity production by 2050. According to the forecast by 2030 60% of the EU's electricity production needs to come from weather-dependent electricity on an annual basis [8].

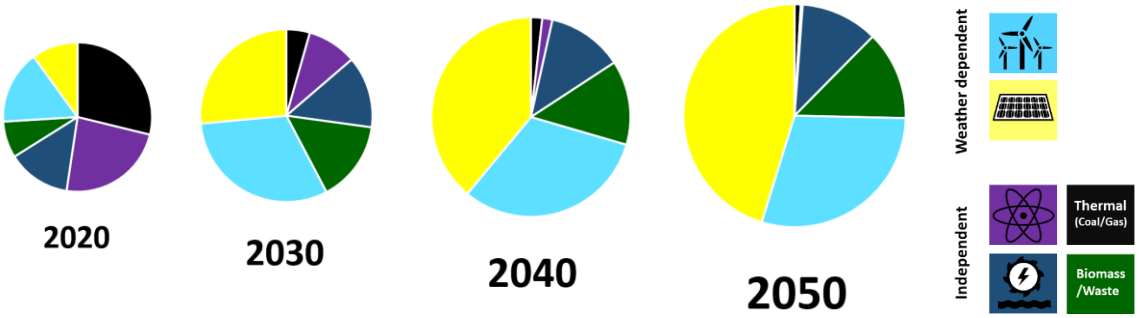


Figure 3. Forecast by Child et. al. [8] to reach a renewable electricity production up to 2050. The diameter of the diagram is proportional to the forecasted electricity produced each year. Note that 2020 also is a forecast here, in reality wind + solar was only 20% in 2020, see Figure 1 above.

1.3. Thermal inertia in buildings

The thermal inertia of a building makes it possible to start or stop the heat production without significant impact on the indoor temperature. The possible duration of the on or off cycle depends highly on the building's thermal inertia, where heavier building types are more flexible to variable heat production. Weiβ et. al. [9] and Le Dréau and Heiselberg [17] have used simulations to investigate the potential with thermal inertia when shifting electrical heating loads in time. Weiβ et. al. showed that for residential buildings in Austria, build according to Austrian standards after 1980, at least 50% of domestic heating peak loads could be shifted to off-peak hours during the day, using a comfort band between 19-22°C. The study by Le Dréau and Heiselberg showed that it is possible to shift the heat production in time for a period of 2-5 h in poorly insulated single-family houses in Denmark and still maintain the set comfort conditions. For homes built according to passive house standard it was possible to switch off the heating system for more than 24 h and still fulfil the comfort criteria.

1.4. Potential for demand response from heat pumps

The vast majority of Sweden's installed heat pumps are currently installed in single family buildings, these heat loads are considered to have the greatest potential for demand response in Sweden. As described in chapter 1.3 the thermal inertia of a building allows the heating to be paused for a few hours without any larger impact on the indoor temperature or comfort, which can be used to provide demand response. But this is a returning load, the loads are only shifted in time and one drawback using heat pumps for demand response is that there is a risk for a new load peak when the heating is started again. Note that, depending on the heating- and ventilation system, a building could have short response to the ambient, especially during cold spells.

Around half of the electricity used by single family houses is used for space heating and production of domestic hot water (DHW), and today there are around 1.5 million heat pumps in operation in Sweden of

which 900,000 in hydronic systems, see Figure 4 below. Around 50,000 new hydronic heat pumps are installed every year [13], where many replace older heat pumps.

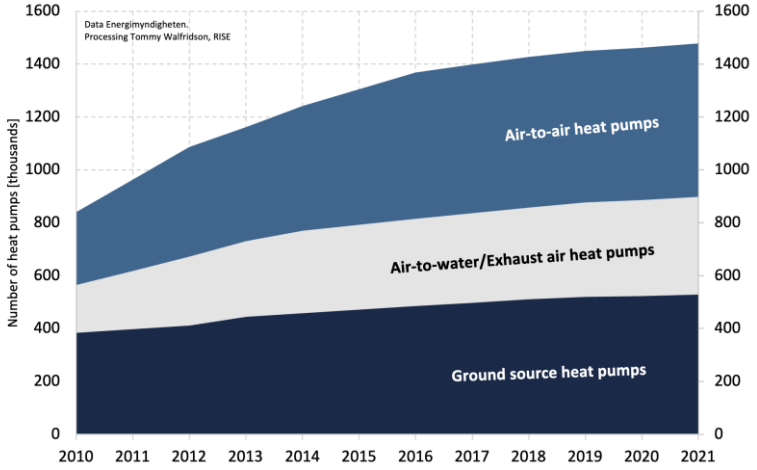


Figure 4. Development of heat pump stock in Sweden. The data source is Energimyndigheten [12] with processing from the author.

Earlier studies have estimated the potential for demand response connected to controlling space heating and production of DHW in Sweden to between 1-6 GW [22]. This can be compared with Sweden's total power need at high load situations which today is about 28 GW and is predicted to increase in the future [3]. Already today we estimate the theoretical potential flexibility from heat pumps to several hundred MW in Sweden, with an additional flexibility of approximately 125 MW per year from hydronic heat pumps only, as older heat pumps are replaced with new ones.

1.5. Flexibility markets

Using heat pumps for demand response is still in the start-up phase, but there are some potential markets for demand response identified, the most likely are either to deliver ancillary services to the Transmission System Operator (TSO) or flexibility to a local flexibility market. An alternative is to have bilateral agreements with a specific partner to provide flexibility. In this study the aggregator is assumed to be a separate actor, but heat pump manufacturers can in the future possibly take the aggregator role as well. In Sweden all local flexibility markets and all ancillary services from the Swedish TSO, Svenska Kraftnät, the smallest bid size is 0.1 MW or higher [26] [27]. Since each individual heat pump can only deliver a smaller amount of flexibility to the power system, this means that domestic heat pumps must be aggregated and controlled together to accomplish the minimum bid size of 0.1 MW. The aggregator uses its pool of heat pumps to deliver services to the power system.

In the EU Directive 2019/944 [36] there are requirements that flexibility must be an option if it is considered an economically viable alternative to regular options, and there are several local flexibility markets under development in Europe, with partly different purposes. In Sweden, the Netherlands and Germany the markets are primarily used for handle bottlenecks in the grid. In France and UK, the flexibility markets are also used for grid planning. The process to develop a regulatory framework has started in several countries in accordance with the EU directive, but none of the countries identified have finished deploying a full regulatory package on the topic [37]. In Sweden there are a few different local marketplaces for flexibility under development and several of them have run as pilots during the latest years, these include Sthlm Flex [19], Coordinet [20] and Effekthandel Väst [21].

One of the main responsibilities of the TSO is to maintain the balance between production and consumption of electricity. To keep the balance the Swedish TSO, Svensk kraftnät, has a well-established market for ancillary services, see Table 1 for details. The different ancillary services have different requirements and complement each other to cover the required balancing needs [27].

Table 1. Overview of requirement of ancillary services in Sweden [27].

	Lowest bid	Volume	Frequency	Activation 1	Activation 2	Endurance	Trade
FFR	0.1 MW	100 MW	49.5 49.6 49.7	0.7 s 1.0 s 1.3 s		30 or 5 s Ready for reactivation within 15 min	Year
FCR-N	0.1 MW	240 MW	49.9–50.1	63% within 60 s	100% within 3 min	1 h	Two (one) day ahead
FCR-D	0.1 MW	<580 MW	49.9–49.5 50.1–50.5	50% within 5 s	100% within 30 s	20 min	Two (one) day ahead
aFRR	5 MW	140 MW	Control signal	100% within 2 min		1 h	A week ahead
mFRR	10 (5) MW	-	Control room	100% within 15 min		1 h	Every hour

Both a decrease and an increase of power consumption can be of interest for the flexibility buyers. In addition, the time it takes to activate a demand response resource is of high importance. A report from the Swedish Energy Markets Inspectorate (Ei) [30] defines the rules for aggregation to implement the EU legislation. The aggregation accuracy is not yet a part of the Ei mission, meaning the accuracy of aggregation is still undefined [29]. Today the accuracy of delivered flexibility is set to the range of 0.5-5% (for FCR-N, FCR-D, aFRR and mFRR) [23] depending on type of nameplate power and position in the power system, but this is as of now not applicable to aggregation [29]. The sampling interval today is 1-10 s [27], meaning each flexibility resource needs to report power consumption or production this often. If an aggregator will have this high sampling rate is still not decided [29].

2. Method

In this study a concept based on using the heat pump manufacturers cloud and application programming interface (API) solutions to communicate demand response between an aggregator and individual heat pumps are investigated. Possibilities and constrains related to the concept have been discussed in an interview study including nine technical experts from the four major heat pump manufacturers in Sweden. Mainly technical issues are evaluated from different aspects and presented in the results. As a complement input from a digital workshop was used. The workshop included the above-mentioned experts complemented with experts from two grid owners, a grid owners association and the Swedish heat pump and refrigeration association. The purpose with the interviews and the workshop was to understand and discuss their opinions and knowledge in using heat pumps to provide flexibility to the power system and how to communicate flexibility information via their cloud solutions.

To cover other areas related to demand response from heat pumps the authors of the study have had input and discussions with researchers and project leaders within different research areas from the Swedish research institute RISE, e.g., cyber security, electric power systems and smart industrial automation as well as literature within the field.

3. Concept for external heat pump control

To enable a rapid deployment of heat pumps as a flexibility resource this study investigates the possibilities to communicate the load control to the individual heat pumps via the manufacturers already existing cloud and application programming interface (API) solutions. Using the manufacturers cloud and API solutions requires no hardware changes to get an initial flexibility solution up and running. The investment cost to start using the heat pump as a flexibility resource and in the next step reach economical breakeven is lower compared to solutions where new hardware needs to be installed. Other studies, e.g., [25], have shown that a barrier to use flexibility from heat pumps is to find a beneficial business model for all attending parties.

The manufacturers cloud/API solutions have been in use for approximately ten years, meaning many heat pumps installed are ready to be used for flexibility once the communication is in place. In Sweden all the major

hydronic heat pump manufacturers have the functionality for the owners to control and monitor their heat pumps via an app, by connecting the heat pump to the manufacturer's clouds solution. This means that many heat pump models can be controlled externally. For example, the heating curve can be altered by the owner via the app, but also automatic planning of the heat and DHW production based on the hourly price of electricity is possible for some heat pump models [31]. Control wise there are still pieces missing to be able to deliver flexibility to the power system via these cloud services, but as the hardware is in place since several years the potential is high. Figure 5 show a schematic overview of the proposed communication flow to deliver flexibility from heat pumps to the power system.

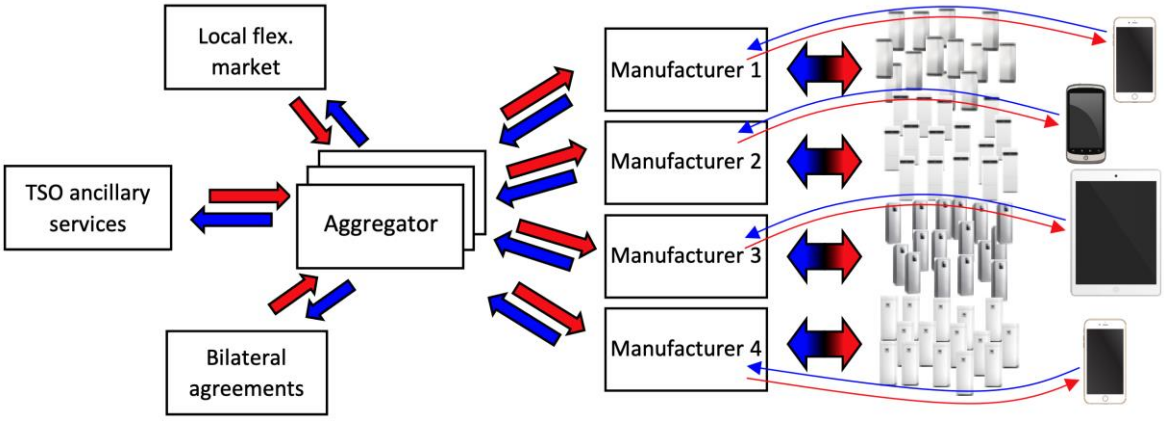


Figure 5. Overview of the communication flow for demand response from heat pumps using the manufacturers cloud solution.

Using the concept proposed in this study the aggregator communicates with the individual heat pumps via the manufacturers cloud services. Depending on how the communication is done and how active the heat pump manufacturer wants to be in the control it gives the manufacturer a possibility to either just forward the control signals to the individual heat pumps or to "translate" the signals for each heat pump type or model. In the latter case each individual heat pump can then react to demand response with less risk for decreased comfort to the end user, as the manufacturers have the deepest knowledge about their products and how to control them, meaning they have the best possibilities to make the heat pump react in the way asked for. Furthermore, this approach adds an additional layer to mitigate cybersecurity risks as the manufacturer can ensure that control signals are withing a reasonable range.

4. Results, evaluation of the concept

In chapter 4 the concept has been evaluated and discussed from different aspects.

4.1. Communication between aggregator and heat pump

With the necessary communication there are signals and feedback sent directly or indirectly between the heat pump and the aggregator. This means that the aggregator could take informed decisions on which heat pumps, or other flexibility resources, that are available, for how long they are available and what the response will be when reduced or increased power consumption is needed.

In most demand response scenarios, there is a need to verify that the agreed change in power consumption has actually happened and there are several options on how this could be done. The problem is that all these options come with different uncertainties, meaning it is not clear what the real outcome of a demand response will be. Domestic heat pumps seldom have dedicated power meters, giving a high degree of uncertainty just there. Examples of functions that can increase the difficulty to calculate the baseline are smart price adaption functionality, meaning the heat pump adapts to the price of electricity or functions to lower the buildings power peaks. Calculating the baseline is thus not trivial. Should it be done before or after the price adaption is set? Huang [28] evaluates seven different methods for baseline calculations with a focus on demand response products currently in use in Sweden.

4.1.1. Placement of logic

There are several options when it comes to where in the information chain different types of logic can be situated. The three main options are:

- The logic is integrated in the heat pump, and the heat pump sends information regarding its availability via the cloud to the aggregator.
- The logic regarding heat pump availability is integrated in the manufacturers cloud.
- The logic is integrated in the aggregator solutions and information is relayed to and from the heat pump via the cloud to the aggregator.

Depending on where the logic is situated the information sent between the heat pump, the cloud and the aggregator will be different. However, the information needed could be the same in all cases. It is assumed that the control logic of the normal heat pump operation for space heating and production of domestic hot water is handled locally in the heat pump or in the heat pump cloud service.

There are several different alternative protocols for standardizing the communication between an aggregator and a heat pump to achieve in-home flexibility. A recent study listed several renown protocols, such as OpenADR, EEBUS, EFI, and OCPP [32]. OpenADR was found possible to use alone or in combination with OCPP [33], and EEBUS [34]. From a heat pump perspective EEBUS and OpenADR are promising and are both open access and license free, in opposite to the international standard for communication in the power system, IEC 61850, meaning the hurdle to start using them is much lower.

EEBUS is a European initiative, while OpenADR has its origin in USA, is sprung from the 2002 electricity crisis in California. While the geographical heritage could have relevance to the choice in different regions, cooperation between the two initiatives is seen. None of the initiatives seems to fulfil all needs from an aggregator to individual heat pumps, but hopefully this will emerge from the cooperation. One complete solution, possible to use worldwide would benefit the heat pump industry.

It is worth noting that IEC 61850 is extended with WAN communication and security [35] and should not be ruled out, since if one or more TSOs point out IEC 61850 as their choice the heat pump industry must adapt and offer solutions based on it.

4.2. Technical possibilities and constrains of heat pumps used for flexibility in the power system

The results in chapter 4.2 is based on interviews with the four major Swedish heat pump manufacturers.

4.2.1. The speed of increased or decreased power consumption

The manufacturers have common ground in how fast their heat pumps can be controlled to decrease or increase power consumption. The auxiliary electric heater can be controlled within a second, both for decreased and increased power consumption, but most likely they will need new software to be used as a flexibility resource. In normal operation the use of the auxiliary heater is minimized, to keep performance up. Clear economic incentives are needed if the auxiliary heater should be used as flexibility resource, this in order to compensate for the much lower performance factor and thus higher power consumption.

On/off compressors can also be turned off within a second, but most of them need the brine pump to start before the compressor is allowed to start. This will delay the start with up to a minute. If anti-freeze brine is used the start delay can likely be removed, but this will need reprogramming of the control systems to be operational. Other technical aspect, for example preheating of compressor sump, could delay startup as well.

The last ten years variable speed drive (VSD) heat pumps have taken a larger and larger share of the market, today more than 50% of the ground source heat pumps (GSHP) sales in Sweden are VSD [13]. These heat pumps are significantly slower to control compared to on/off heat pumps. From turned off to the wanted correct speed it will take several minutes, often the same is true when turning off the compressor. Control wise improvements can likely be done to speed up the process of starting and stopping, but some technical aspects will still limit what is possible.

4.2.2. Measurement on decrease or increase of power consumption

To measure the power consumption of today's heat pumps is difficult, as they normally lack electricity meters and installing it afterwards is expensive and need skilled personnel. VSD heat pumps may have the possibility to measure the power consumption within the inverter controlling the speed of the compressor, while on/off compressors have no technical possibility built in to measure power consumption. The

manufacturers estimate that the uncertainty of the power consumption of VSD heat pumps is ±2-10%, but this is partly estimated and needs further investigations before conclusions can be drawn.

For on/off heat pumps the manufacturers state the uncertainty from under ±10% to ±20%, meaning much lower accuracy than Svenska kraftnäts requires today. This is due to the lack of electricity measurement, the power consumption is calculated from the operating temperatures of the compressor and known compressor equations. Note that the legislative accuracy demand for aggregation is not yet defined, see chapter 1.5.

The uncertainty of the auxiliary electric heater is stated to ±0.5-5% if the voltage is known (as it usually is with VSD heat pumps), else the accuracy is lower as voltage will vary in the power system. For high accuracy on electricity measurement of the entire heat pump the power consumption of fans and circulation pumps needs to be monitored as well. It is not clear if these are part of the measurements/calculations the manufacturers do. The question on accuracy increase with aggregation was not asked in the interviews with the manufacturers, but according to one manufacturer the accuracy would increase significantly with larger number of heat pumps. Further studies on the accuracy increase are needed, especially to understand how to validate the accuracy anticipated.

The necessary measurement interval was not discussed with the manufacturers, but likely a sampling time of 1-10 s as stated today for Svenska kraftnäts ancillary services [27] could be too frequent for today used control system or using the buildings electrical meter. A possible solution is extrapolation or other ways of producing a high frequency of sampling data. As the data management of an aggregator is still pending it is unclear if the sampling interval will be this short or not [29].

4.2.3. Communication to the TSO (Svenska kraftnät) or an aggregator and what product will be possible to fulfill

There are no clear thoughts among the heat pump manufacturers on how to communicate to the TSO (Svenska kraftnät) or to an aggregator. API and ModBus were mentioned. One of the manufacturers states that they have no interest in taking the aggregator roll itself, which could be a possibility, as they don't want that responsibility. Svenska kraftnät has a number of ancillary services to control disturbances in the power system, see Table 1. The possibilities to fulfil the requirements for these services was discussed with the manufacturers.

One manufacturer claims that FFR, the ancillary service with the shortest activation time (0.7-1.3 s), is possible with limited load change, the others have no answer or answers that "it is difficult". All manufacturers but one (where we lack an answer) claims that FCR-N is feasible and for FCR-D, which requires an activation time of 50% within 5 s, all claims that it is possible to fulfil the requirements from a technical point of view. For aFRR and mFRR there are few answers from the manufacturers since this was not discussed in detail in the interviews, but due to the longer activation time compared to FCR-N and FCR-D, it will likely be possible for heat pumps to fulfil the requirements also for these two services.

The answers should not be interpreted that solutions are ready, which might well be the case, but rather that they are technically feasible to solve.

4.2.4. Comfort disturbance at decreased heat production

It was stated by one of the manufacturers that when the heat is turned off the thermal comfort risk to decrease as the temperature in the heating system decrease fast and thus not compensates for cold surfaces (i.e. windows) in the property. Depending on the building envelope this will have different impact on the comfort. How the thermal comfort was before the heat was turned off and how sensitive for variations in temperature the persons living there are also important aspects. Earlier studies based on simulations, see chapter 1.3, indicates that it should be possible to shift heating loads in time and keep a good comfort.

One manufacturer stressed that heat production turned off for one hour could be problematic and that domestic hot water (DHW) is the limiting factor. With a small DHW tank or a high usage, the DHW temperature risk to drop fast, and if the heat pump is blocked new DHW will not be produced.

It was highlighted that underfloor heating (in concrete slab, authors note) should be able to be turned off without any or small comfort impact, even in the winter, as the thermal inertia is very high compared to other types of heating systems.

Concern regarding dimensioning of the heat pump system was raised, meaning at very cold weather the heat pump could not regain the heat in the building without using the electric backup heater after decreased heat production due to lack of heating capacity. According to the manufacturers this problem is low as newer heat pumps generally have spare capacity even at cold spells.

4.2.5. Comfort disturbance at increased heat production

The question on comfort disturbances at increased heat production was asked generally, we didn't get any feedback there. Temporarily and unnecessarily high heat production could be of interest in the future, for example to buffer heat in a property during the night to skip heating at later morning congestion hours in the power system. This needs further discussions to understand what problems could occur. On days with excess electricity production, for example due to windy conditions, buildings with heat pumps could act as heat sinks, meaning wind turbines could keep producing and not being curtailed. To some extent DHW could also be used to store energy, but due to legislative limits on temperature the potential is normally low at least without temperature regulation added to the outlet. From a technical point of view the auxiliary electric heater could be used more freely, meaning it could be used without the compressor running. In this way the heat pump could use more electricity during periods when the power system is in need. Higher electricity consumption, which will be the consequence, will only work at very low electricity prices or other compensations for this aid from the heat pump to the power system. The heat pump manufacturers control systems don't have this functionality to run the auxiliary electric heater today, it needs reprogramming to work.

4.3. Risks related to cybersecurity

To enable flexibility the heat pumps being part of a large-scale flexibility systems need to be remotely controllable, which as of now means controllable over the internet. This opens for cybersecurity risks, as for all internet connected devices. The heat pump industry historically has mainly been a mechanical business, with only the necessary electronics for the fundamental control functionality. Thus, there is most probably a need to raise the awareness and extend the organizations and solutions to cover cyber security sufficiently.

A few potential ways to recruit (hack) connected heat pumps are:

- Cloud service – could have insufficient isolation between users, be misconfigured, have insufficient physical protection
- Communication – could be unencrypted, contain safety holes, or have become outdated due to the lifetime of the product
- Device – could expose services by mistake, contain weak or hardcoded passwords, have unsecure software update
- Employees – needs to be protected against leakage of sensitive information, either by mistake or by extortion

It has been shown that high-wattage IoT devices can cause significant impact to the power system [15], [24]. If large amounts of e.g., heat pumps are hacked or otherwise manipulated to operate in a non-favorable way, for the power system, this could lead to disturbances in the power system even causing safety mechanism to trigger. Saleh et.al. [15] has shown the impact on the Polish power system when simulating IoT attacks via air conditioners and heaters. As heat pumps may require similar or higher power, there is a need to work on rising the awareness of cybersecurity in the heat pump industry and evaluate the system architecture including the communication between individual heat pumps and the server solution. One of the more challenging effects of cyber security is related to the longevity of the systems. While end- customers traditionally expect a heat pump to last for 15-20 years, new vulnerabilities may require software and hardware updates. This is an additional cost due to the Internet connectivity that must be motivated and provide an additional value. Furthermore, as high-wattage IoT devices start offering flexibility services to the electricity grid, they become a critical part of the electricity infrastructure. This also includes all involved companies in the supply chain. Hence heat pump manufacturers will face a new set of challenges.

5. Discussion

The focus in the study is on technical aspects of the heat pumps with less focus on thermal comfort in the heated buildings, business models or to get the concept attractive for the heat pump owners. Some stakeholders were not included in the interviews (e.g., TSO and heat pump owners) and the study is theoretical and not based on tests or field measurements.

The benefits with the flexibility concept evaluated in the study is that all hardware needed to control the heat pump for demand response is already in place and several older heat pumps models have had the hardware for several years. This mean the investment costs to use heat pumps as a flexibility resource will be lower compared to the alternatives. It could make the potential for demand response from today's heat pumps more rapidly accessible for aggregators. Additional hardware to control the heat pump or meters to measure the

electricity consumption will require larger revenues for short enough payback time and will slow the process significantly.

But even if the hardware is in place, there are still several barriers to overcome before the system efficiently can be up and running. Standardization is important, to have the communication standardized will make it easier for the parties involved. The aggregators will know better what is possible to achieve and how to control their heat pump pool and the manufacturers will know what to implement in their control systems. In the longer run an international standard would be optimal, avoid developing different solutions in different countries.

To use many small units aggregated as a flexibility resource is new compared to what historically has been used, when balance services mainly were delivered by large electrical producers and large industrial units. Thus, the requirements need to be adopted to these new flexibility resources to give high enough functionality. One typical example is the low accuracy of electricity metering in heat pumps, meaning the measurement of delivered flexibility risk to be low. Today no villa heat pump identified has a dedicated electric meter factory installed. The first alternative method is to estimate the power consumption through the heat pumps inverter or with help from the operating temperatures, this is in the study shown to have low accuracy. The second alternative is to use the electricity meter of the building, but as it is metering the entire building it could have even lower accuracy than the estimations in the heat pump. High accuracy demand will thus be difficult to fulfill and if it later becomes mandatory it will likely erase older heat pumps as a flexibility resource, as it is costly and time consuming to add meters. Possibly aggregating large number of heat pumps could statistically increase accuracy, but that has not been investigated in the project nor how to validate that accuracy.

Heat pumps are distributed over the grid and can also be used to balance the power system locally. New local flexibility markets might be able to adapt their accuracy requirements more easily as they are under development and their needs are different. One example is the activation time, where the local markets have no frequency control need and the activation could thus be slower or even planned in advance. This means heat pumps could both deliver flexibility and at the same time decrease the risk of too low comfort.

Delivering flexibility to the power system is a new area for the heat pump industry and these new functions are outside their core business today. It is still open how the heat pump manufacturers are going to handle this new opportunity and how an aggregator can communicate through the heat pump ecosystem. Will any manufacturer see the benefit in taking the roll as aggregator themselves? It could mean more accurate control of the heat pumps as the manufacturer has superior knowledge on their different control strategies and heat pump types compared to any other player. Likely at least some manufacturers will distance themselves from controlling their heat pumps in non-comfort optimized way, which any demand response or flexibility solution will do, and simply let another company take the risk. Saving money and at the same time giving the heat pump owners lower comfort level is a delicate path to walk and could risk that company's reputation.

The actual monetary incentive is still unclear with flexible heat pumps aiding the power system. Smart price adaption, meaning producing more heat at low-cost hours is not considered a real direct aid to the power system, but is still a clear and easily understandable way to save money. In Sweden this today normally means producing heat during the night and stopping or running the heat pumps at lower speed at least during the peak hours in the morning and early evening.

Giving the power system, on national level, help to manage congestions or loss of power production is already controlled with the products from Svenska kraftnät (the Swedish TSO), but economic model to distribute the income gained is still not fully mature. On local or regional level, the market is even more immature, there are a few research projects ongoing in Sweden.

6. Conclusion

The study has through expert interviews and literature review investigated the technical possibilities and constrains for a concept where residential heat pumps are aggregated and controlled via the manufacturers cloud solution to support the power system with flexibility. Depending on how the communication is done and how active the heat pump manufacturer wants to be, it gives the manufacturer a possibility to either forward the control signals to the individual heat pumps or to "translate" the control signals for the individual heat pump models. The manufacturers have the deepest knowledge about their products and how to control them, meaning they have the best possibilities to make the heat pumps react in the way asked for with lower risk for decreased comfort.

Technical experts from the four major heat pump manufacturers in Sweden have been interviewed in order to understand and discuss their opinions and knowledge in using heat pumps to provide flexibility to the power system and how to communicate flexibility information via their cloud solutions. The manufacturers are all on somewhat different levels or have different opinions in parts of the discussions, while there is consensus in

other parts. As a complement a lively digital workshop with the above-mentioned experts, experts from two grid owners, a grid owners association and the Swedish heat pump and refrigeration association was performed to get consensus on the needed solution and the obstacles still not overcome.

The experts from the heat pump manufacturers have common ground in how fast their heat pumps can be controlled to decrease or increase power consumption. The auxiliary electric heater can be controlled within a second, both for decreased and increased power consumption, but most likely they will need updated software to be used as a flexibility resource. On/off compressors can also be turned off within a second, but most of them need the brine pump to start before the compressor is allowed to start. This will delay the start with up to a minute. Variable speed heat pumps are significantly slower to control. From turned off to the wanted correct speed it will take several minutes, often the same is true when turning off the compressor. From a technical point of view the manufacturers claims that the requirements for the ancillary services FCR-N and FCR-D, where FCR-D has an activation time of 50% within 5 s, is possible for heat pumps to fulfill. While the requirements for FFR, with an activation time of 0.7-1.3 s, seems difficult.

Today's heat pumps lack electricity meters, giving low accuracy to measurements of demand response delivered. VSD heat pumps normally have the possibility to measure the power consumption within the inverter controlling the speed of the compressor, while on/off compressors have no technical possibility built in to measure power consumption. The manufacturers estimate that the uncertainty of the power consumption of VSD heat pumps is ±2-10%. For on/off heat pumps the manufacturers state the uncertainty around ±10-20%. The uncertainty of the auxiliary electric heater is stated to ±0.5-5% if the voltage is known (as it usually is with VSD heat pumps), else the accuracy is lower.

Alternatives to standardize the communication between the aggregator via the heat pump manufacturers cloud services to individual heat pumps has been investigated. From a heat pump perspective EEBUS and OpenADR are promising. They are possible to use alone or in combination and are both open access and license free. To enable flexibility the heat pumps, need to be remotely controllable, which as of now means controllable over the internet. This opens for cybersecurity risks, as for all internet connected devices. It is worth noting that cybersecurity cannot be addressed lightly in the heat pump industry as hacked heat pumps could, at least in the future, cause severe problems to the power system. This means heat pumps risk being used in cyber warfare. After the renewed Russian attack on Ukraine in February 2022 thousands of wind turbines in Germany were attacked and left offline [16], hence the threat is real and should not be underestimated.

Acknowledgements

This work was supported by the Swedish Energy Agency, project "Storskalig laststyrning av värmepumpar i elnätet" [grant number 50258-1] and Vinnova, project "Standard för laststyrning av värmepumpar".

References

[1] Regeringskansliet, *Mål för energipolitiken*, https://www.regeringen.se/regeringens-politik/energi/mal-och-visioner-for-energi/, 2022-10-25 (In Swedish)
[2] Tidöavtalet, https://www.xn--tidavtalet-gcb.se/, 2022-10-25 (In Swedish)
[3] Energiföretagen & Fossilfritt Sverige, *Färdplan för fossilfri konkurrenskraft -Elbranschen*, 2020 (In Swedish)
[4] Regeringskansliet, *Nationell strategi för elektrifiering*, 2021 (In Swedish)
[5] Eurostat Data Browser https://ec.europa.eu/eurostat/databrowser/product/page/NRG_IND_PEH__custom_2430601, 2022-07-06
[6] Energimyndigheten https://www.energimyndigheten.se/nyhetsarkiv/2022/fortsatt-hog-elproduktion-och-elexport-under-2021/ 2022-07-06 (In Swedish)
[7] Our world in data, https://ourworldindata.org/grapher/electricity-production-by-source, 2022-11-03
[8] Child et al., *Flexible electricity generation, grid exchange and storage for the transition to a 100% renewable energy system in Europe*, Renewable Energy, p. 80-101, 2019
[9] Weiβ, T., Fulterer, A., Knotzer, A., *Energy flexibility of domestic thermal loads -a building typology approach of the residential building stock in Austria*, Advances in Building Energy Research, 13:1, 122-137, DOI: 10.1080/17512549.2017.1420606, 2019
[10] European Parliament, *Fact sheets on the European Union, Renewable energy*, https://www.europarl.europa.eu/factsheets/en/sheet/70/fornybar-energi, 2022-11-02

[11] EU, *Directive (EU) 2018/2001 of the European parliament and of the council of 11 December 2018 on the promotion of the use of energy from renewable sources (recast)*, Official Journal of the European Union, L 328/82, 2018
[12] Energimyndigheten, https://www.energimyndigheten.se/statistik/den-officiella-statistiken/statistikprodukter/energistatistik-for-smahus-flerbostadshus-och-lokaler/?currentTab=0#mainheading, 2022-01-23 (In Swedish)
[13] SKVP, https://skvp.se/statistik/varmepumpsforsaljning 2022-11-18 (In Swedish)
[14] Regeringskansliet, Mål för energipolitiken, https://www.regeringen.se/regeringens-politik/energi/mal-och-visioner-for-energi/, 2022-10-25 (In Swedish)
[15] Soltan, S., Mittal, P., Poor, V., BlackIoT - IoT Botnet of High Wattage Devices Can Disrupt the Power Grid, 27th USENIX Security Symposium, Baltimore, MD, USA, 2018
[16] The Wall Street Journal, https://www.wsj.com/articles/european-wind-energy-sector-hit-in-wave-of-hacks-11650879000 , 2022-11-08
[17] Le Dréau J., Heiselberg P., Energy flexibility of residential buildings using short term heat storage in the thermal mass, Energy 111 p. 991-1002, 2016
[18] E. Abdollahi, P. Chaves-Ávila, T. Gerres, P. Mastropietro, P. Rodilla, and Y. Vardanyan, *Review of the Regulatory Environment for CHP, Identification of Relevant Markets*, Bio-FlexGen, 2022
[19] Svenska kraftnät, *sthlmflex*, https://www.svk.se/sthlmflex, 2022-11-13 (In Swedish)
[20] Svenska kraftnät, *Coordinet*, https://www.svk.se/utveckling-av-kraftsystemet/forskning-och-utveckling/pagaende-fou-projekt/coordinet/, 2022-11-13 (In Swedish)
[21] Göteborg Energi, *Effekthandel Väst*, https://www.goteborgenergi.se/foretag/vara-nat/elnat/effekthandel-vast, 2022-11-13 (In Swedish)
[22] Borgström, S., Norrsén, T., & Lindahl, M., *Laststyrning av värmepumpar i småhus samt Småhusens bidrag till minskade topplaster*, Besmå, 2019 (In Swedish)
[23] Svenska kraftnät, https://www.svk.se/aktorsportalen/balansansvarig/balansansvarsavtalet/, 2022-11-14 (In Swedish)
[24] Shekari, T., Cardenas, A., Beyah, R., MaDIoT 2.0: Modern High-Wattage IoT Botnet Attacks and Defenses, 31st USENIX Security Symposium, Boston, MA, USA, 2022
[25] Lindahl et. al., *Nätflexibla värmepumpar*, 2018
[26] Zagerholm, D., Ackeby, S., & Wiig, C. (2021). *Digitalisering för efterfrågeflexibilitet*, Rapport 2021:737. Energiforsk, 2021 (In Swedish)
[27] Svenska Kraftnät, *Om olika reserver*, Retrieved from SVK.se: https://www.svk.se/aktorsportalen/bidra-med-reserver/om-olika-reserver/, 2022-11-22 (In Swedish)
[28] Huang, Y., Hawkins, Y, Ackeby, S., Baselinemetoder för flexibilitetsprodukter, Energiforsk, 2022
[29] Personal discussion with Roger Abrahamsson, product leader and research engineer, Tekniska Verken Linköping Nät AB, 2022-11-21 and 2022-11-29
[30] Ei 2021:03, Oberoende aggregatorer: Förslag till nya regler för att genomföra elmarknadsdirektivet, I enlighet med NordREGs förslag, Energimarknadsinspektionen, 2021 (In Swedish)
[31] NIBE Smart Price Adaption, https://www.nibe.eu/sv-se/support/vanliga-fragor/faq-items/vad-ar-smart-price-adaption-spa, 2022-11-28 (In Swedish)
[32] Energy Innovation NL, TKI Urban Energy (2020) In-Home Energy Flexibility Protocols
[33] Hoekstra A, Bienert R, Wargers A, Singh H, Voskuilen P (2016) Using OpenADR with OCPP
[34] Zuber J, Bienert R, Böhm R, Prümm R-I, Schwackenberg A (2021) Combining OpenADR and EEBUS for Energy Control
[35] S. M. S. Hussain, T. S. Ustun and A. Kalam, "A Review of IEC 62351 Security Mechanisms for IEC 61850 Message Exchanges," in IEEE Transactions on Industrial Informatics, vol. 16, no. 9, pp. 5643-5654, Sept. 2020, doi: 10.1109/TII.2019.2956734.
[36] EU, DIRECTIVE (EU) 2019/944 OF THE EUROPEAN PARLIAMENT AND OF THE COUNCIL of 5 June 2019 on common rules for the internal market for electricity and amending Directive 2012/27/EU, Official Journal of the European Union, L 158/125, 2019
[37] Jarry, G., Servant, L., An overview of local European flexibility markets, Executive summary, 2021

14th IEA Heat Pump Conference
15-18 May 2023, Chicago, Illinois

Laboratory characterization of a cascade heat pump system with intermediate water loop

Diego Menegon [a] *, Matteo Campidelli [b], Roberto Fedrizzi [a]

[a] Eurac research, viale Druso 1, Bolzano (BZ) 39100, Italy
[b] Innova s.r.l., via 1° Maggio, Storo (TN) 38089, Italy

Abstract

To reach the goal of decarbonization, the thermal loads of buildings are being electrified with the use of heat pumps in replacement of traditional fossil fuel boilers. In the European project HAPPENING, a cascade heat pump system has been designed for the renovation of a building originally heated by a gas boiler. Air-to-water heat pumps provide heat to a water-loop which is the source for a water-to-water heat pump used to produce domestic hot water and for different water-to-air heat pumps, located in the apartments, that cover the heating and cooling loads. The system is controlled with a model predictive control which aim is the optimization of renewable energy consumption. The performance characterization of the heat pumps and the system is crucial for the definition of such advanced control. In the "Heat Pumps Lab" of Eurac research, the system has been characterized in two phases. In this paper we present the first step which includes the investigation of the operational limits, the definition of a performance map and the calculation of the system performance. The second step is the dynamic whole system test where the system is installed in three climatic chambers: one for the external unit, one for the water-loop and one for the internal units.

© HPC2023.
Selection and/or peer-review under the responsibility of the organizers of the 14th IEA Heat Pump Conference 2023.

Keywords: cascade heat pump, laboratory characterization, whole system test, water loop ;

1. Introduction

The decarbonization of the thermal load of building is a key factor to achieve the energy and climate targets since the heating and cooling demands cover near the 50% of the heat demand [1]. The heat pumps cover an important role in the transition of the electrification of the thermal load of the buildings and in the decarbonization process [1–3].

The proper design of the heat pump is important for the performance and therefore for the operational costs, confirmed by the evaluation of the monitored data [4]. For example, Li et al. [5] evaluated the impact of the storage volume identifying in 30-40 l/kW the optimal solution. Also, heat pumps are used in a hybrid system with gas boilers [6], thermal or electrical storages, and are coupled with solar energy (solar thermal or photovoltaic) [7,8]. In all these mentioned cases the proper control of the system is crucial for performance. Advanced control strategies can improve the COP in a range of 5 to 20% [9–13].

Introducing the heat pump system in a new building is simpler than in the renovation of a building since the design of the new building is integrated: the thermal loads are minimized, the space of the technical room is dedicated to the system, the distribution circuit is at low temperature and can be supply both heating and cooling loads, and so on. In this case one single stage heat pump can work with a good coefficient of performance. Instead, in the renovation of a building there are several barriers to overcome. A single stage heat pump could not satisfy all the requirements of the renovation.

In literature different cascade heat pump systems are presented where the refrigerant of the first stage exchanges heat directly with the refrigerant of the second stage through an intermediate heat exchanger. The

* Corresponding author. Tel.: +39 0471 055 639; fax: +39 0471 055 699.
E-mail address: diego.menegon@eurac.edu.

main advantage of a cascade heat pump is the possibility to reach high temperatures, with the downside that at low or medium temperatures a single stage heat pump can reach higher COP than a cascade heat pump [14–17]. The system design and control are important for the performance; for example, Le et al [17] show that despite a nominal COP 2.5 at 7/80 the system can perform with a SCOP of 1.4 using a storage, 2.1 with direct heating, and 1.9 with price-based control. In renovation of the building, cascade heat pump systems are able to cover the heating loads thanks to the high temperature.

The cascade heat pump system with intermediate water-loop has been developed in the H2020 project HAPPENING. The system is presented in the Section 2. The proposed system presents different advantages for building renovation:

- i) the distribution temperature is neutral minimizing the thermal losses of heat distribution; in addition, the efficiency is higher than the high-temperature cascade systems.
- ii) the distribution system is not replaced (reducing the renovation investment) with adding the possibility of covering the cooling loads independently for each room. Otherwise, a medium temperature terminal would require the replacement of distribution piping (due to a different nominal flowrate) or the change of distribution layout (with a three-pipes or four-pipes distribution).
- iii) in summer the domestic hot water demand can be balanced with the space cooling demand.
- iv) the source heat pump can be decoupled to the heat pumps that cover the loads.
- v) the storage can be manged to guaranty flexibility.

The advanced controllers can improve the system performance acting in these last two points. On the other hand, such systems require a higher investment cost. Therefore, the performance and those features should be guaranteed to justify the cost of such systems.

In the HAPPENING project, the system is installed in case studies and this paper presents the laboratory characterization of the same system in a smaller scale. This activity is used to validate the model used to develop the model predictive control [18]. The methodology for the laboratory characterization is presented in Section 3 while the results of the test on the heat pumps are presented in Section 4.

2. Description of HAPPENING cascade heat pump system

The cascade heat pump system developed with the HAPPENING project has been designed for the renovation of buildings originally heated by a gas boiler. The distribution system of the building is maintained while the generation system and the heat emission terminals are replaced by heat pumps. The system includes air-to-water, water-to-water and the water-to-air prototypes developed by Innova within the project. The heat pumps have different refrigerants: the air-to-water and the water-to-water have R32, while the water-to-air R290. The selection of refrigerants followed the phase down foreseen by EU F-Gas Regulation. In the Heat Pumps Lab of Eurac Research, the HAPPENING system has been reproduced in a smaller scale than the system designed for the demo case. The system considers the same units of the demo case except for the air-to-water that is a commercial unit with R410a already available in the laboratory. The results described in this paper refer to the commercial air-to-water unit and to the prototypes of water-to-water and water-to-air heat pumps.

Figure 1 shows the layout of the system installed in the laboratory. An air-to-water heat pump delivers heat at low-temperature to the water-loop through thermal energy storage. The temperature of the water-loop is controlled by a three-way valve connected to a collector that is the source for booster heat pumps. A water-to-water heat pump is used to produce domestic hot water charging a thermal energy storage while two water-to-air heat pumps control the air temperature covering the heating and cooling loads. The two water-to-air heat pumps are of a different size: the larger one is called WL400 while the other is called WL200.

In Figure 1 there are also identified the hydraulic modules (called energy hubs EH) that the laboratory uses to reproduce the control of the system. The figure reports only the used functionalities of those modules showing with a blue dotted line the control logic. Specifically, the EH7 controls the water-loop temperature, the EH8, EH9 and EH10 control the flow rate of the heat pumps. The EH2 on the secondary circuit simulates the DHW tapping, while in the primary circuit can be configured with different controls: P2 always running or running when there is a tapping, and V2 fully open or controlling the supply temperature.

Differently from the system proposed in Figure 1, the demo case has 15 dwelling and therefore the system presents three air-to-water heat pumps connected in parallel, higher capacities of the buffer and thermal energy storage, and the water-to-air heat pumps are installed in each room of the dwellings.

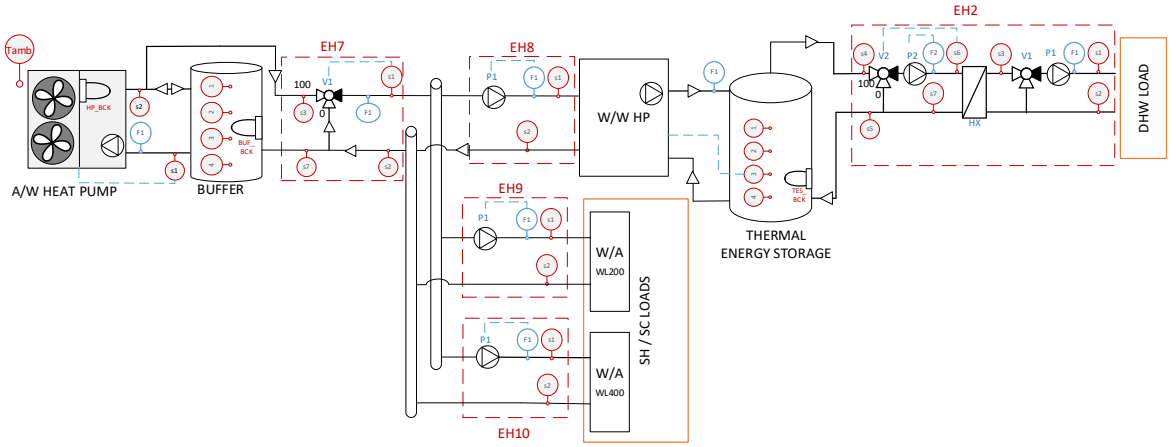


Fig. 1. Layout of the cascade heat pump system

The whole system is tested according to two control strategies: one traditional and a model predictive control. The traditional control is obtained using the heat pumps set point: the air-to-water heat pump controls the return temperature (according to the blue-dotted-line of Figure 1); the water-to-water heat pump controls the storage temperature while the water-to-air heat pumps control the ambient temperature. From the validation of the system model, the model predictive control is developed to optimize renewable energy consumption [18]; than the model predictive control will be implemented in laboratory to control the system. Finally, the system with the model predictive control will be tested.

3. Method

The characterization of the cascade heat pump system was done in two phases:

- Test at component level
- Test at system level

The test at component levels was performed on each unit. The first aim of this activity is the definition of a performance map as a function of the compressor frequency, source temperature and flow rate, and load temperature. Another aim is the comparison of the measurements performed by the laboratory with the internal measurements of the unit in order to validate the algorithms developed by Innova for controlling the performance of the units. Finally, the operational limits of the units are investigated since the demo case can present some boundary conditions out of the nominal and design conditions.

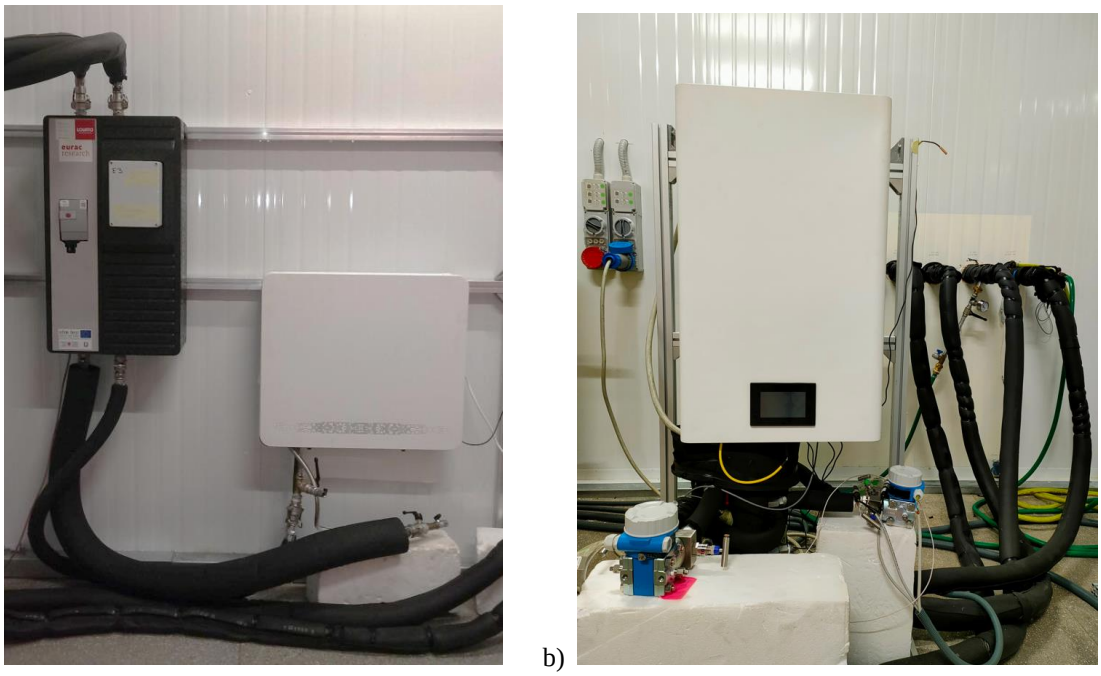
3.1. Test at component level

The heat pumps have been configured according to the instruction of the manufacturer and the compressor frequency has been controlled with different levels.

Table 1 reports the different combinations of test boundaries for the test of the single heat pumps. The boundary conditions considered in the table investigate all the possible operating conditions in order to understand the limits of the units. The choice of the flow rate is explained in the following section for each heat pump.

Table 1. Test boundary conditions at component level.

	Loop Temperature	Load	Flow	Part Load Ratio
W/A – space cooling	10 °C, 17 °C, 25 °C, 30 °C, 40 °C	23 °C, 26 °C	200 l/h, 300 l/h	100%, 75%, 50%, 25%
W/A – space heating	10 °C, 17 °C, 25 °C, 30 °C, 40 °C	19 °C, 22 °C	200 l/h, 300 l/h	100%, 75%, 50%, 25%
W/W – domestic hot water	10 °C, 25 °C, 30 °C	45 °C, 58 °C	1.58 m^3/h	100%, 75%, 50%
	Air temperature	Load	Flow	Part Load Ratio
A/W – space heating	-15 °C, -7 °C, -2 °C, 0 °C, 2 °C, 7 °C, 12 °C	30 °C, 45 °C	1.4 m^3/h, 1.96 m^3/h	100%, 60%, 35%, 20%
A/W – space cooling	20 °C, 25°C, 30 °C, 35 °C, 40 °C	7 °C, 13 °C, 22°C	1.96 m^3/h	Nominal



a) b)

Fig. 2. Installation in laboratory. a) Water-to-air heat pump WL200. b) water-to-water heat pump.

3.1.1. Water-to-air heat pumps

The water-to-air units have a different nominal flow rate corresponding to 480 l/h for the unit WL400 while 240 l/h for the unit WL200. The flow rates indicated in Table 1 are different to the nominal since the demo case is not able to satisfy the nominal flow rate of the unit WL400.

In addition to the points of Table 1, at source temperature of 25 °C and air temperature of 19 °C, the laboratory tested both units at 480 l/h and investigated the minimum flow rate accepted by the unit before presenting faults, warnings, or alarms.

The laboratory has measured the source water inlet and outlet temperatures, the water flow, the internal differential pressure of the source loop, air temperature and humidity, electric consumption and has record the internal registered read by ModBus connection.

In the laboratory installation we recreated a barrier to avoid air recirculation (bypass).

3.1.2. Air-to-water heat pump

The air-to-water heat pump was tested with the nominal flow rate defined according to the EN 14511-3:2018 [19] considering a fixed flow control and nominal condition 7/35 (1.95 m3/h). In addition, some the air temperatures of -15 °C and -7 °C were tested at the minimum speed of the circulator (1.4 m3/h) with the same hydraulic circuit. To measure the different capacities the frequency of the compressor has been limited acting on the internal registers of the unit.

The laboratory has measured the air temperature and humidity, load water inlet and outlet temperatures, the water flow, the internal differential pressure of the load loop, electric consumption.

3.1.3. Water-to-water heat pump

The test of the water-to-water heat pump has been performed with the nominal flow rate defined according to the EN 14511-3:2018 [19]. The load temperature indicated in Table 1 is the supply water temperature where the value at 58 °C has been defined to reach the maximum before presenting faults, warnings, or alarms.

The laboratory has measured the source and load water inlet and outlet temperatures, the water flows, the internal differential pressures, air temperature, electric consumption and has record the internal registered read by ModBus connection.

3.2. Theoretical performance of a cascade system

The equivalent COP of the system composed by two heat pumps connected in cascade, in the hypothetical absence of thermal losses between the exchange from one to the other, can be calculated according to the equation (1). The first heat pump has the subscript "1" while the second heat pump has the subscript "2"; Q is the useful heat, W the electric consumption and COP the coefficient of performance.

$$COP_{syst} = \frac{Q_2}{(W_1 + W_2)} \tag{1}$$

Elaborating the equation (1), the system COP can be described as a function of the COP of the two heat pumps by expressing with energy balances Q and W as a function of COP and source heat.

$$COP_{syst} = \frac{COP_1 \cdot COP_2}{(COP_1 + COP_2 - 1)} \tag{2}$$

The equation (2) is used to evaluate the theoretical performance of the cascade system starting from the COP of the single heat pumps.

3.3. Test at system level

The performance of the cascade heat pump system will be performed with the whole system test procedure PLPE developed by Eurac [20]. The external unit of the air-to-water heat pump is installed in a climatic chamber that reproduces a six-day sequence representative of the year while the hydraulic circuits are installed in another climatic chamber conditioned at internal ambient temperature reproducing the technical room. The water-to-air heat pumps are installed in a calorimeter that reproduces the space heating and cooling loads.

Figure 3 shows the installation prepared in laboratory: in the left part there is the external unit of the air-to-water heat pump; in the middle there are all the components that are installed in the technical room as the internal unit of the air-to-water heat pump, the buffer and the thermal energy storage, hydraulic modules; in the right part there are the two water-to-air heat pumps WL200 and WL400 with the relative pumping hydraulic modules.

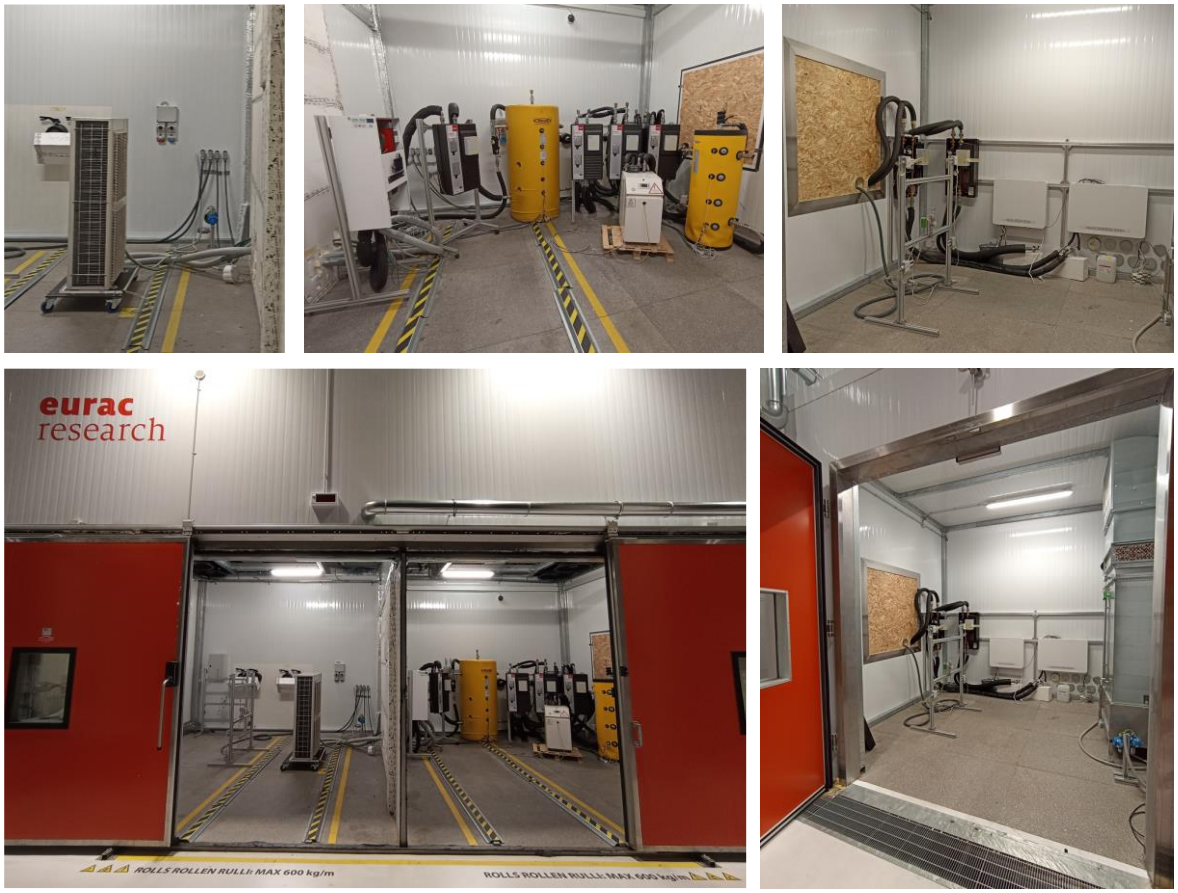


Fig. 3. System reproduced in the Heat Pumps Lab

4. Results

4.1. Test at component level

4.1.1. Water-to-air heat pumps

In order to evaluate the operational limits in terms of source flow rate, in the first stage the two units were installed switching the supply and return piping and in a second moment the installation was corrected. With the wrong installation, the minimum flow rate was varying between 230 l/h and 260 l/h depending to the boundary conditions, while with the correct installation, the minimum flow rate was below 160 l/h.

The request for the demo case is that the unit can work between 200 l/h and 300 l/h even if the nominal flow rate of the unit WL400 is 480 l/h. To verify the effect of the flow rate, a specific test was performed with the water temperature of 25 °C and the air temperature 19 °C controlling the unit according three different capacity levels. Figure 4 shows that the effect of the flow rate is negligible if compared to the effect of variating the compressor speed, but the unit performs better with the nominal flow rate: indeed, the nominal flow rate is higher, and this means a lower temperature difference of the water circuit and therefore a better heat exchange in the evaporator of the heat pump.

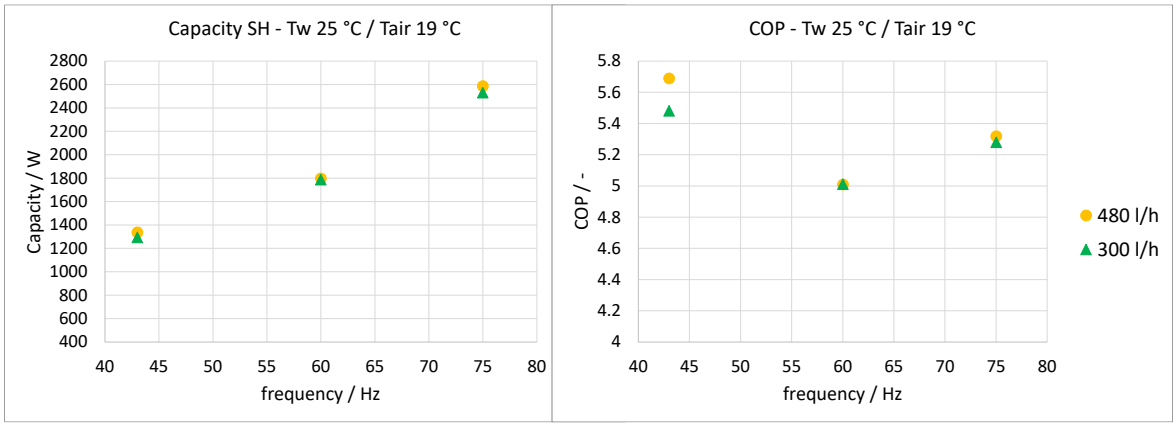


Fig. 4. Effect of source flow rate in the water-to-air heat pump WL400.

The Figure 5 presents all the test points of the unit WL400 while the Figure 6 presents all the test points of the unit WL200. The figures are divided in four diagrams: in the top-left figure it is presented the heating capacity while in the top-right the COP; in the bottom-left figure it is presented the cooling capacity while in the bottom-right the EER. The performance factors are indicated as a function of the source temperature for different series of flow rates and air temperatures. In the capacity graphs it is indicated the frequency of the compressor of one of the four data series.

The operational limits of the units were investigated also in terms of source temperature. The source temperature of 40 °C in space heating as the source temperature of 10 °C in space cooling are not relevant application temperature for a water-to-air heat pump but this test allowed to investigate a wider possibility of the temperature control of the water loop. The COP and EER obtained in those conditions are really high thanks to the very favourable boundary conditions.

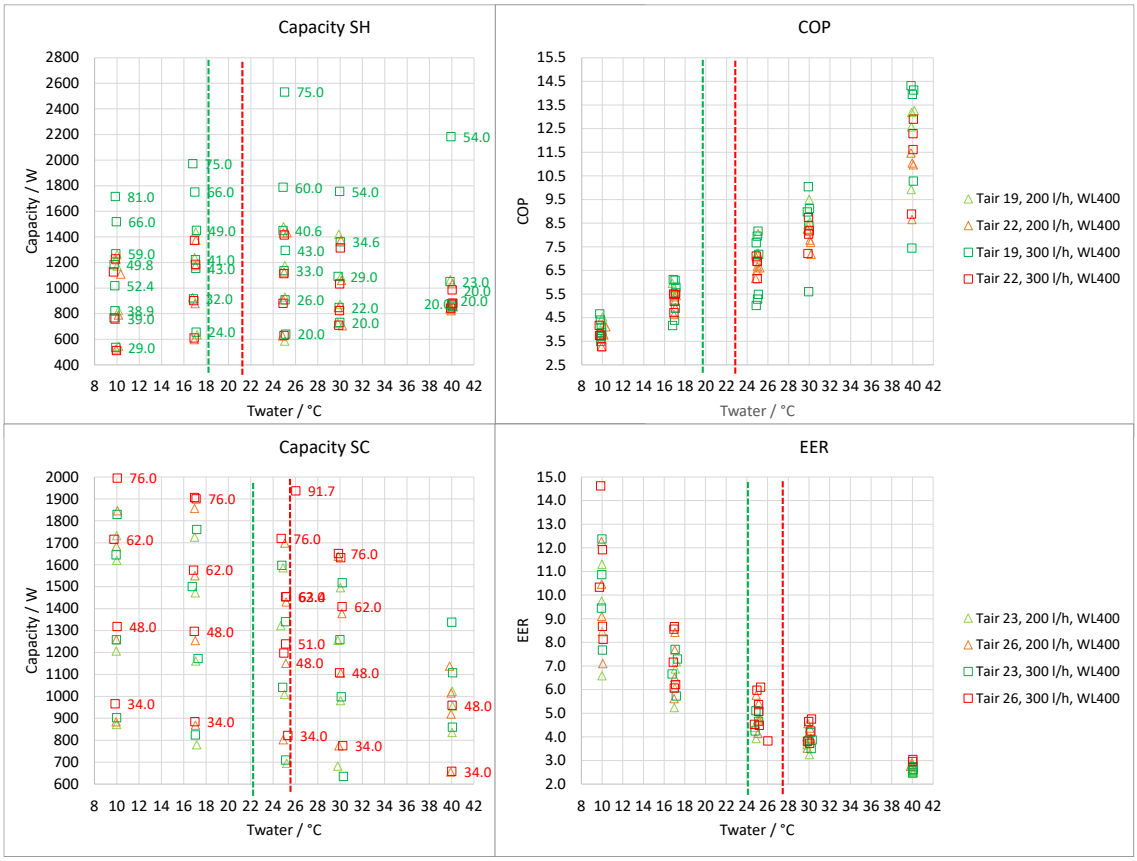


Fig. 5. Performance of water-to-air heat pump WL400.

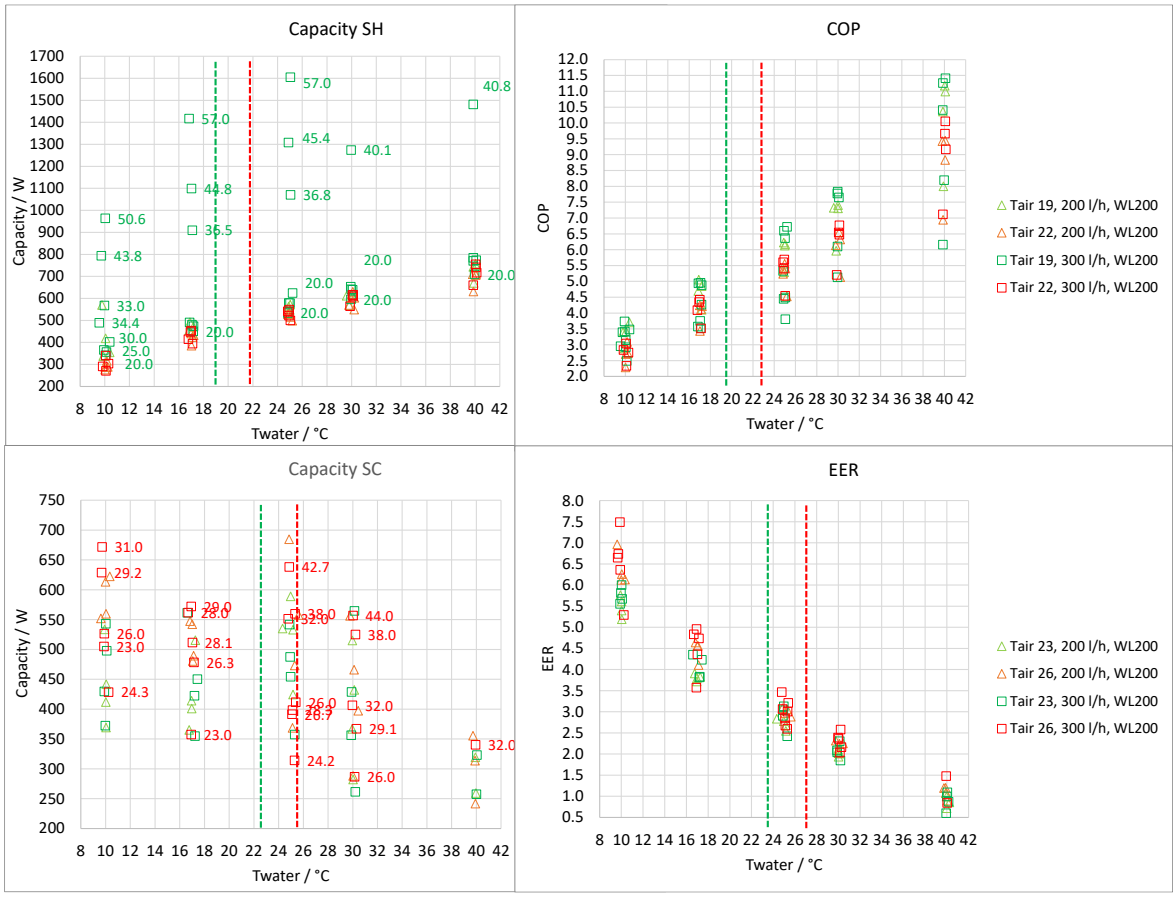


Fig. 6. Performance of water-to-air heat pump WL200.

4.1.2. Air-to-water heat pump

The performance of the air-to-water heat pump presented in Figure 7 shows the heating capacity and the COP according to different compressor frequencies. The limits of the compressor frequency are indicated in one series of the graph. The cooling capacity has been defined only at nominal capacity.

The figure shows the compressor's working range: below 2 °C the compressor does not reach the minimum frequency (since the capacity would be too low) and at 12 °C the compressor is at the top limited due to the high source temperature.

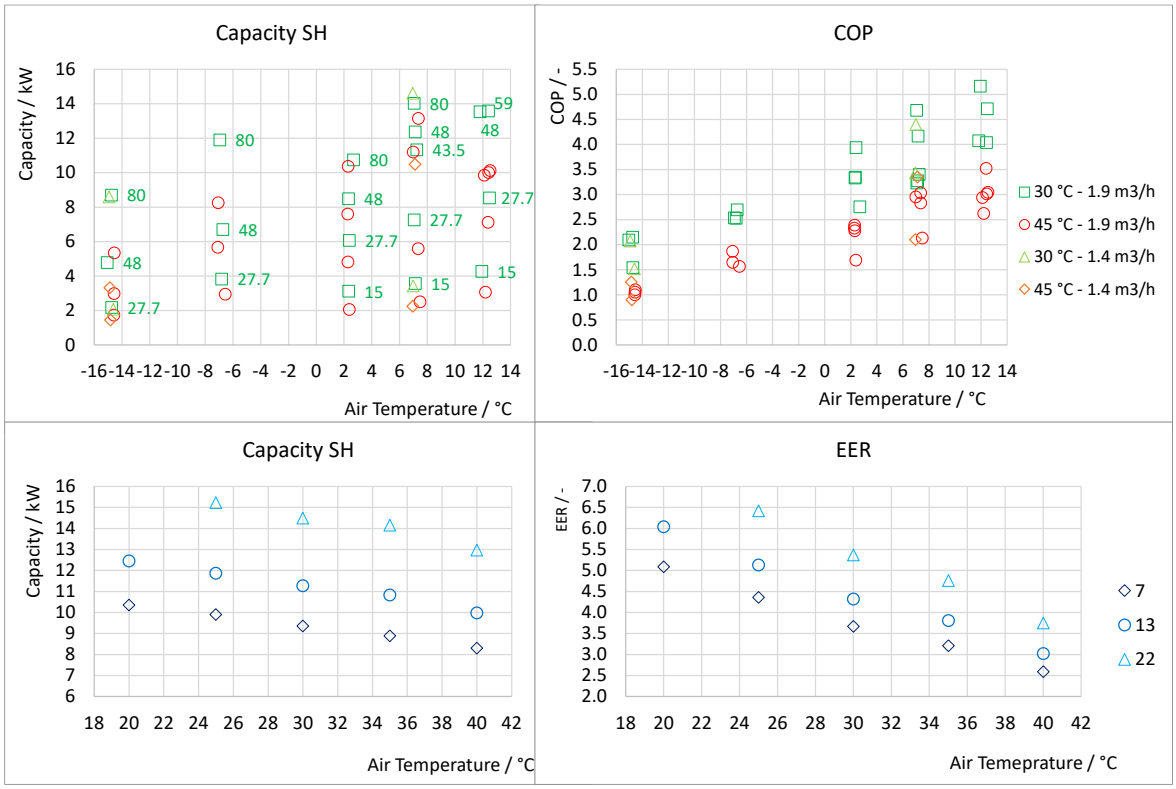


Fig. 7. Performance of air-to-water heat pump.

4.1.3. Water-to-water heat pump

The water-to-water heat pump was tested at two load temperatures at supply temperature 45 °C and 58 °C, that was the maximum temperature identified during the test. This limit is higher than the declared maximum temperature.

Usually, the commercial heat pumps for domestic hot water do not provide a modulation in the preparation of the hot water even if the unit has an inverter (that is used during space heating). In the logic of controlling the system with the model predictive control, the water-to-water het pump was tested with PLR of 50 %, 75% and 100%.

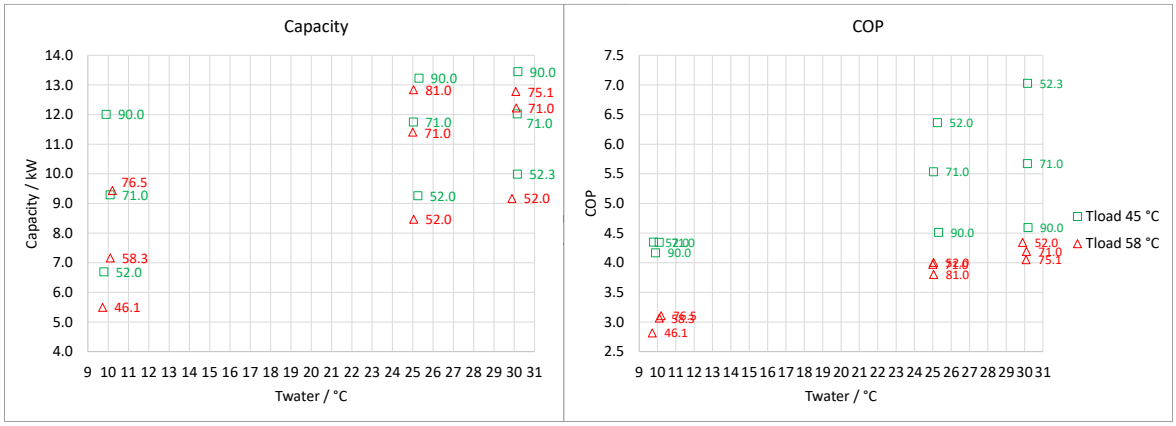


Fig. 8. Performance of water-to-water heat pump.

4.1.4. Cascade performance

Table 2 presents the COP calculation of the cascade heat pump system (COPsys) calculated from the COP of the air-to-water heat pump (COPa2w) as source and water-to-air (COPw2a) for the space heating load and water-to-water (COPw2w) for the domestic hot water according to the equation (2). The COPa2w is defined

with the air temperature (Tair) and water temperature (Twater loop) corresponding as source/load boundary conditions. The COPw2a is defined from the water temperature to the ambient air of 22 °C. At the same time, the COPw2w is defined considering the temperature of the water loop as source and supply hot temperature 45 °C. The last column presents the COP of the air-to-water heat pump used as single-stage (COPa2w sg) to reach the 45 °C considered as supply temperature for the space heating and the domestic hot water; in this case the COP is not dependent from the water loop temperature. The supply temperature of 45 °C for the space heating is to represent a fan coil as heat emission device to have a similar installation of the water-to-air heat pump.

In the calculation of Table 2 we considered two temperatures of the water loop.

In space heating, the cascade heat pump system performs better than the air-to-water heat pump in single stage for air temperatures up to 7 °C; the only exception is at 12 °C. One consideration is that the second stage works with a lower condensing temperature since the second heat pump works with 22 °C of the air while the air-to-water single stage was supposed to work with fan-coils.

The differences between the cascade heat pump system and the single stage heat pump decreases for the domestic hot water. The motivation is that the boundary conditions are the same since both systems have to heat domestic hot water.

The COP presented in Table 2 are defined at full load and the performance of the cascade system can improve at part load conditions. This motivates the necessity of further investigate on the model predictive controller and the necessity of test in laboratory.

Table 2. Calculation of cascade COP and comparison with a single stage air-to-water heat pump.

Space Heating					
Tair	Twater loop	COPa2w	COPw2a (Tload 22 °C)	**COPsys**	COP a2w sg (Tload 45 °C)
-7	25	3.79	6.87	**2.70**	2.13
-7	35	3.43	8.11	**2.64**	2.13
2	25	4.91	7.07	**3.16**	2.76
2	35	4.45	8.24	**3.14**	2.76
7	25	5.70	6.35	**3.28**	3.21
7	35	5.16	7.15	**3.26**	3.21
12	25	6.62	6.15	**3.46**	3.73
12	35	6.00	7.10	**3.52**	3.73
Domestic hot water					
Tair	Twater loop	COPa2w	COPw2w (Tload 45 °C)	**COPsys**	COP a2w sg (Tload 45 °C)
-7	25	3.79	4.51	**2.34**	2.13
-7	35	3.43	7.03	**2.55**	2.13
2	25	4.91	4.51	**2.63**	2.76
2	35	4.45	7.03	**2.99**	2.76
7	25	5.70	4.51	**2.79**	3.21
7	35	5.16	7.03	**3.24**	3.21
12	25	6.62	4.51	**2.95**	3.73
12	35	6.00	7.03	**3.51**	3.73

5. Conclusions

The performance characterization of a cascade heat pumps system has been performed in the “Heat Pumps Lab” of Eurac research.

The system has been characterized in two phases; the first phase presented in this paper, we investigated the operational limits and have defined a performance map of each heat pump. With this data, we calculated the performance of the cascade heat pump system with intermediate loop and compared the system with a

single stage air-to-water heat pump. The results of the detailed performance map obtained in the first phases provided the possibility to the manufacturer to further optimize the units' controllers. The part load performance has been improved to optimize the SCOP; in the water-to-air unit, the manufacturer improved the management of the ventilation and the supply temperature.

The second step of the laboratory characterization will be the dynamic whole system test where the cascade heat pump system is installed in three climatic chambers. In this test we will evaluate a traditional control strategy and the model predictive control developed with the HAPPENING project.

The performance of the cascade system is comparable to the single stage heat pump. Despite the higher cost needed for the installation and similar performance, the cascade system presents several advantages that are optimized with the implementation of the predictive controller: the domestic hot water can be balanced with the space heating during the summer season; the generation part can be decoupled to the loads; the management of the storages (thermal and electrical) guarantees flexibility and renewable energy utilization.

Acknowledgements

This project has received funding from the European Union's Horizon 2020 research and innovation programme under grant agreement No 957007, project HAPPENING – "HeAt PumPs in existing multi-family buildings for achieving union's ENergy and envIromeNtal Goals". The sole responsibility for this content lies with the authors. It does not necessarily reflect the opinion of the European Union. Neither the EASME nor the European Commission is responsible for any use that may be made of the information contained herein

References

[1] M.H. Abbasi, B. Abdullah, M.W. Ahmad, A. Rostami, J. Cullen, Heat transition in the European building sector: Overview of the heat decarbonisation practices through heat pump technology, Sustainable Energy Technologies and Assessments. 48 (2021) 101630. https://doi.org/10.1016/j.seta.2021.101630.

[2] R. Decuypere, B. Robaeyst, L. Hudders, B. Baccarne, D. Van de Sompel, Transitioning to energy efficient housing: Drivers and barriers of intermediaries in heat pump technology, Energy Policy. 161 (2022) 112709. https://doi.org/10.1016/j.enpol.2021.112709.

[3] K.J. Chua, S.K. Chou, W.M. Yang, Advances in heat pump systems: A review, Applied Energy. 87 (2010) 3611–3624. https://doi.org/10.1016/j.apenergy.2010.06.014.

[4] M. Miara, D. Günther, R. Langner, S. Helming, J. Wapler, 10 years of heat pumps monitoring in Germany. Outcomes of several monitoring campaigns. From low-energy houses to un-retrofitted single-family dwellings., in: Rotterdam, 2017.

[5] H. Li, Q. Yang, Z. Xu, S. Shao, Z. Wang, X. Sun, Y. Wang, C. Xu, W. Zhao, Impact of water volume on the energy saving potential of air source heat pump systems, International Journal of Refrigeration. 130 (2021) 128–139. https://doi.org/10.1016/j.ijrefrig.2021.06.025.

[6] M. Beccali, M. Bonomolo, F. Martorana, P. Catrini, A. Buscemi, Electrical hybrid heat pumps assisted by natural gas boilers: a review, Applied Energy. 322 (2022) 119466. https://doi.org/10.1016/j.apenergy.2022.119466.

[7] G. Dermentzis, F. Ochs, N. Franzoi, Four years monitoring of heat pump, solar thermal and PV system in two net-zero energy multi-family buildings, Journal of Building Engineering. 43 (2021) 103199. https://doi.org/10.1016/j.jobe.2021.103199.

[8] T. Schreurs, H. Madani, A. Zottl, N. Sommerfeldt, G. Zucker, Techno-economic analysis of combined heat pump and solar PV system for multi-family houses: An Austrian case study, Energy Strategy Reviews. 36 (2021) 100666. https://doi.org/10.1016/j.esr.2021.100666.

[9] Y. Sun, X. Chen, S. Wu, W. Wei, W. Wang, S. Deng, Performance analysis of air source heat pump space heating system with an adaptive control for supply water temperature, Applied Thermal Engineering. 211 (2022) 118401. https://doi.org/10.1016/j.applthermaleng.2022.118401.

[10] Y. Yao, D.K. Shekhar, State of the art review on model predictive control (MPC) in Heating Ventilation and Air-conditioning (HVAC) field, Building and Environment. 200 (2021) 107952. https://doi.org/10.1016/j.buildenv.2021.107952.

[11] Y. Lu, S. Wang, Y. Sun, C. Yan, Optimal scheduling of buildings with energy generation and thermal energy storage under dynamic electricity pricing using mixed-integer nonlinear programming, Applied Energy. 147 (2015) 49–58. https://doi.org/10.1016/j.apenergy.2015.02.060.

[12] I. Sharma, J. Dong, A.A. Malikopoulos, M. Street, J. Ostrowski, T. Kuruganti, R. Jackson, A modeling framework for optimal energy management of a residential building, Energy and Buildings. 130 (2016) 55–63. https://doi.org/10.1016/j.enbuild.2016.08.009.
[13] J. Allison, A. Cowie, S. Galloway, J. Hand, N.J. Kelly, B. Stephen, Simulation, implementation and monitoring of heat pump load shifting using a predictive controller, Energy Conversion and Management. 150 (2017) 890–903. https://doi.org/10.1016/j.enconman.2017.04.093.
[14] H.W. Jung, H. Kang, W.J. Yoon, Y. Kim, Performance comparison between a single-stage and a cascade multi-functional heat pump for both air heating and hot water supply, International Journal of Refrigeration. 36 (2013) 1431–1441. https://doi.org/10.1016/j.ijrefrig.2013.03.003.
[15] S. Boahen, J.M. Choi, K.O. Amoabeng, R. Opoku, G.Y. Obeng, Efficient control of cascade heat pumps using variable speed compressors, Scientific African. 18 (2022) e01399. https://doi.org/10.1016/j.sciaf.2022.e01399.
[16] B. Dai, X. Liu, S. Liu, D. Wang, C. Meng, Q. Wang, Y. Song, T. Zou, Life cycle performance evaluation of cascade-heating high temperature heat pump system for waste heat utilization: Energy consumption, emissions and financial analyses, Energy. 261 (2022) 125314. https://doi.org/10.1016/j.energy.2022.125314.
[17] K.X. Le, M.J. Huang, N.N. Shah, C. Wilson, P.M. Artain, R. Byrne, N.J. Hewitt, Techno-economic assessment of cascade air-to-water heat pump retrofitted into residential buildings using experimentally validated simulations, Applied Energy. 250 (2019) 633–652. https://doi.org/10.1016/j.apenergy.2019.05.041.
[18] T. Diller, H. Nagpal, A. Soppelsa, G. Henze, A Dynamic Programming Based Method for Optimal Control of a Cascaded Heat Pump System with Thermal Energy Storage, in: SDEWES, Paphos, Cyprus, 2022.
[19] EN 14511-3:2018, Air conditioners, liquid chilling packages and heat pumps with electrically driven compressors for space heating and cooling. Part 3: Test methods, European Committee for Standardization, Brussels, Belgium, 2018.
[20] D. Menegon, A. Soppelsa, R. Fedrizzi, Development of a new dynamic test procedure for the laboratory characterization of a whole heating and cooling system, Applied Energy. 205 (2017) 976–990. https://doi.org/10.1016/j.apenergy.2017.08.120.

14th IEA Heat Pump Conference
15-18 May 2023, Chicago, Illinois

Feasibility Analysis for the Use of Retrofitted Air-Conditioners Using Thermal Energy Storage (TES) for High Ambient Temperature (HAT) Countries

Al-Hussain Othman[a], Vikrant Aute[a*], Daniel Bacellar[a]

[a]Center for Ennvironmental Energy Engineering, Department of Mechanical Engineering, University of Maryland, 3151 Glenn L. Martin Hall Building, College Park, MD 20742, United States

Abstract

In high ambient temperature (HAT) countries, summer temperatures exceed 35°C, degrading the performance of air-conditioning systems and straining power grids. In this paper, a feasibility analysis was conducted to investigate potential savings during the peak using latent Thermal Energy Storage (TES) at near room phase-change temperatures, replacing condensers, thus, minimizing temperature lifts. Weather data, building loads, and baseline air-conditioning systems data were gathered for Dubai. A transient vapor-compression model in Modelica was used to compare the COP, total power input and cooling capacity of the air-conditioner at peak hours when ambient temperatures range between 35 – 45 ºC versus the TES-Phase-Change Material (PCM) melting temperatures from 22 – 28ºC. The results indicate that the TES-PCM can enhance the system COP at the peak by a factor 1.4 and 2 for during for outdoor temperatures of 35 – 40ºC, and 40 – 45ºC, respectively. Lower melting temperature PCMs were able to reduce the required power input by 30-50%, with more savings occurring at higher temperature days. On the other hand, higher temperature PCMs enhancements were minimal especially at outdoor ambient temperatures ranging between 35 – 40ºC. Improvements to the cooling capacity range from 8 – 18 % for the outdoor temperature range of 35 – 45 ºC. An economic analysis was conducted to find the potential saving in utility costs for 30%, 60%, and 90% of the space cooling demands of Dubai, and find the trade-off points between utility savings and cost of PCM-TES implementation. If the peak loads are to be shifted by 6 hours daily, the percentage utility savings for the city is 18%. Using estimated costs of the PCM-TES, ranging from $200-500/kWh, the daily load shifting hours were estimated to range from 4 hours at the lowest cost systems to 2.5 hours at the highest costs.

© HPC2023.
Selection and/or peer-review under the responsibility of the organizers of the 14th IEA Heat Pump Conference 2023.

Keywords: Room-temperature PCMs; High Ambient Temperature Countries; Feasibilty analysis; City Cost Requirements

1. Introduction

Globally, space cooling already consumes 20% of the total electricity to buildings [1]. In high ambient temperature (HAT) countries, challenges in providing sustainable cooling arise in residential and commercial buildings. Gulf Cooperation Council (GCC) countries are characterized as HAT given their extreme conditions during the summer as temperatures exceed 45ºC during the day [2-3].With such hot conditions, more power input is required by compressors to meet cooling demands, and reject heat to such extreme ambient heat sinks. This degrades the COP of air-conditioning equipment that can range from 10 to 30% depending on the refrigerant and cooling system installed [4-5]. Increases in power requirements, maximizes the strain on power grids, specifically during the peak, with air-conditioning being a major contributor to the power demand. For example, around 50% of the annual electricity demand in Dubai is consumed on air-conditioning [6]. With the continuous population growth and urban development, these demands will only grow, increasing carbon dioxide emissions as more powerplants will be required just to meet peak demands.

* Corresponding author. Tel.: 301-405-8726;
E-mail address: vikrant@umd.edu.

Thermal energy storage (TES) systems fitted with phase-change materials (PCMs) provide an opportunity to maximize the COP at peak conditions and shift the electrical demand on the grid during the day. There are several applications on retrofitted air-conditioning systems and buildings with PCM-TES systems. Chaivat & Kiatsiriroat [7] placed a thermal storage heat exchanger in return air duct precooling it prior to ventilation air mixing in Thailand. Using paraffin waxes that melt at around 20ºC, the PCM was discharged at peak hours when the return temperatures are above 25ºC, and recharged with cool air directly at the evaporator exit. Annual electrical cost savings of 9.1% were reported. Real et al. [8] connected PCM tanks to an experimental air-conditioning system through the means of secondary water loops for cooling. On the condenser side, the heat is rejected to the low-than-ambient PCM melting conditions (T_{melt}= 27ºC) during the peak, increasing the COP by 36%. Implementations of solar photovoltaics to power the compressor in the vapor-compression were also added along the thermal energy storage tanks [7, 8].

In many studies conducted the TES-PCM systems were incorporated into a heat pump through the means of a hydronic secondary loop [9–11], whether on the indoor or outdoor heat exchanger. With the exception of Maaraoui et al. [14], where the authors proposed an air-refrigerant-PCM heat exchanger for heat pumps for heating residential buildings. The configuration of the retrofitted heat pump is to have the PCM tank charge at off-peak hours with low heat load, and only the PCM storage discharge the heat at peak conditions. The limiting factor of this design was the lower thermal conductivity of PCMs, resulting in a large HX. On the other hand, the PCM storage tank did last up to 2 hours during the discharge period, which can contribute to improving the annual seasonal performance.

In this paper, the authors propose the inclusion of the TES-PCM storage in the vapor-compression cycle, with the storage tank is both heated (discharged) and cooled (charged) directly with a refrigerant-PCM heat exchanger. For a 17.5-kW (5-tons) R-410A air-conditioning unit, the ability of several PCMs with near-room melting temperatures ranging between 22-31ºC were assessed as replacements for the condenser during the peak for Dubai, UAE. The TES-PCM storage will operate as the condenser for 4-hours during the peak. Using a commercial building prototype, building load data were obtained and a transient model on Modelica was used to predict real-time electrical loads. Using the retrofitted vapor compression cycle, the potential electric savings during the peak hours were assessed, along with their corresponding increases in COP and cooling capacities. Furthermore, the load shifting effect of re-charging the TES-PCM tanks were assessed, and city-level economic analysis was conducted.

2. Methodology

2.1. System Description

In this system, there are two configurations that are shown in Fig. 1. The first configuration (Fig. 1(a)) operation is twofold. The first is the conventional vapor compression cycle, that is running at off-peak conditions, with the TES system (represented as the thermal battery) is fully charged or charging. In this case, the air-conditioning system can provide cooling when lower building loads are there, not requiring excessive electrical demands, thus, not straining the electrical grid. The second operation of configuration 1 occurs when the PCM is partially or fully melted, the conventional cycle can be used to recharge the battery. This can typically occur when the internal load at low, or no indoor cooling is required. In the second configuration shown in Fig. 1(b), the refrigerant flow to the condenser is eliminated and the high-pressure refrigerant is directed to the thermal battery. This occurs during the peak-hours when the outdoor ambient conditions are extreme 35ºC or higher, or when the system COP drops. Given that the thermal battery consists of PCM with melting temperatures that are lower in temperatures than ambient conditions, there is potential to reduce the required power input from the compressor increasing the COP during these hours.

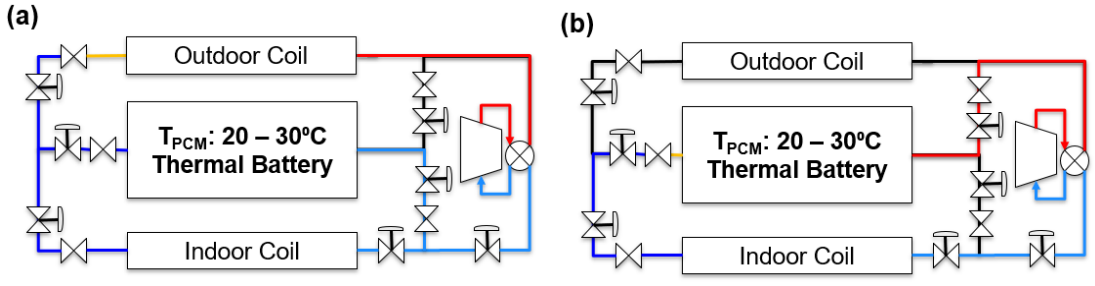


Fig. 1. Proposed cooling system (a) Configuration 1: conventional air-conditioning system for off-peak hours for fully charged or charging battery, (b) Configuration 2: thermal battery discharging cycle for on-peak hours

2.2. System Modeling

The TES-AC integrated cycle consisted of a variable-speed compressor, header microchannel heat exchangers for the evaporator and condenser, and an electronic expansion valve (EXV). The thermal battery model was adapted from the Modelica Standard Library [15], CEEE Modelica Library (CML) [16], Dhumane et al. [17], and Cao & Faghri [18]. The thermal battery model, was a conjugate heat transfer model, between the refrigerant and the PCM material through a material wall (CML [16]). The refrigerant heat transfer and pressure drops are already determine using the control volume available in CML [16]. The PCM transient model [17] considers the solid, two-phase and liquid region to obtain an equivalent specific heat (c), from the enthalpy of fusion (H_{sl}), solid (C_s) and liquid (C_l) specific heats. The equivalent specific heat in the mushy zone considers the average solid and liquid specific heats along with the enthalpy of fusion as per Cao & Faghri [18]. The melting range is assumed to be $(2 \times \Delta T)$, and T_m is the midpoint melting point in the melting range. An additional term s is a correction to the temperature difference to account for any additional changes during the melting and solidification process. Finally, the thermal energy release is predicted depending on the rate of change in enthalpy (dh/dt), and required PCM mass (Equation (1)).

$$
\begin{aligned}
T^* &= T_{pcm} - T_m \\
h &= c(T^* + s) \\
c &= \begin{cases} C_s & \text{if} \quad T^* < -\Delta T \\ \dfrac{C_s + C_l}{2} + \dfrac{H_{sl}}{2\Delta T} & \text{if} \quad -\Delta T < T^* < \Delta T \\ C_l & \text{if} \quad T^* > \Delta T \end{cases} \\
s &= \begin{cases} \Delta T & \text{if} \quad T^* < \Delta T \\ \dfrac{C_s}{C_l}\Delta T + \dfrac{H_{sl}}{C_l} & \text{if} \quad T^* > \Delta T \end{cases} \\
Q &= \frac{dh}{dt} M_{PCM}
\end{aligned}
\tag{1}
$$

To meet the required thermal battery loads of 17.5-kW for 4 hours, the total required loads were summed for the entire time period, over the material density and enthalpy of fusion for the PCM (Equation (2)). For salt-hydrate PCMs, the material densities, range between 1.2 to 2 g/cm^3, with enthalpies of fusion ranging between 100-250 kJ/kg for room temperature PCMs [19]. The reason for selecting salt hydrates as opposed to paraffin waxes, is their higher energy density [19]. To ensure that the heat transfer loads are met at with PCM-TES in place, the overall UA's is in the range of 3000-5000 W/K. In this paper, the following assumptions were made:

1. The PCM-TES UA was 3000 W/K given that this is most likely the least expensive design.
2. The PCM heat transfer coefficient was assumed to be around 10 W/m^{2}K.
3. The enthalpy of fusion was 200 kJ/kg
4. The initial PCM temperatures was 15ºC, with the refrigerant pressure was around 2-MPa
5. The initial conditions in the indoor coil: pressure was 1-MPa, and temperature was 9.5ºC
6. The initial conditions in the outdoor coil: pressure was 2.8-MPa, and temperature was 45ºC

$$
V_{PCM} = \frac{\int_0^{4h} \dot{Q} dt}{\rho_{PCM} \cdot H_{sl}} \tag{2}
$$

The variable speed compressor model, consists of multiple 10-coefficient maps each corresponding to a frequency level. The model switched between the maps based on the required cooling capacity from the building load. Similarly, the EXV model consists of a variable opening orifice, that is adjusted by the manufacturers pulse-capacity curves and degrees of superheat. The dimensions and properties of the microchannel evaporator and condenser were inputted in the CML [16] MCHX models.

Each configuration in Fig. 1 was modeled in a separate cycle, and the cycles were operating based on the required air mass flow rates for the evaporator (indoor coil) and condenser side (outdoor coil) (Fig. 2). When

the required cycles are off, the indoor and outdoor mass flow rates are set to near-zero amounts, according to a time schedule set by the building loads. During the day, the indoor mass flow rates are included based on the corresponding building load, and the outdoor mass flow rate is determined by the manufacturers fan curves at the operating conditions. The remaining outdoor and indoor boundary conditions (temperatures and humidity ratios), were obtained from the weather data sets [20] and prototype commercial building models [21], respectively. When the thermal battery is discharging during peak hours, the only boundary conditions to the cycle are the indoor air temperature, humidity and mass flow rate (Fig. 3(a)), and during the charging stage the outdoor weather data, along with the operating air mass flow rate are the only boundary conditions(Fig. 3(b)). The prototype building model, in EnergyPlus [22], consists of a small office building with 4 office rooms and one corridor, with building loads around 15-18 kW. Using this building prototype EnergyPlus files [21-22] for Dubai along with the locations corresponding weather data, the required boundary conditions were obtained on the indoor coil of the Modelica model.

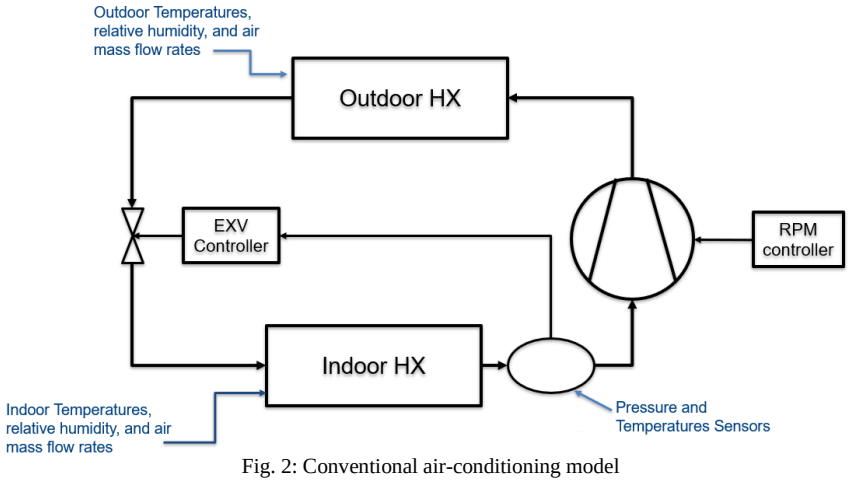


Fig. 2: Conventional air-conditioning model

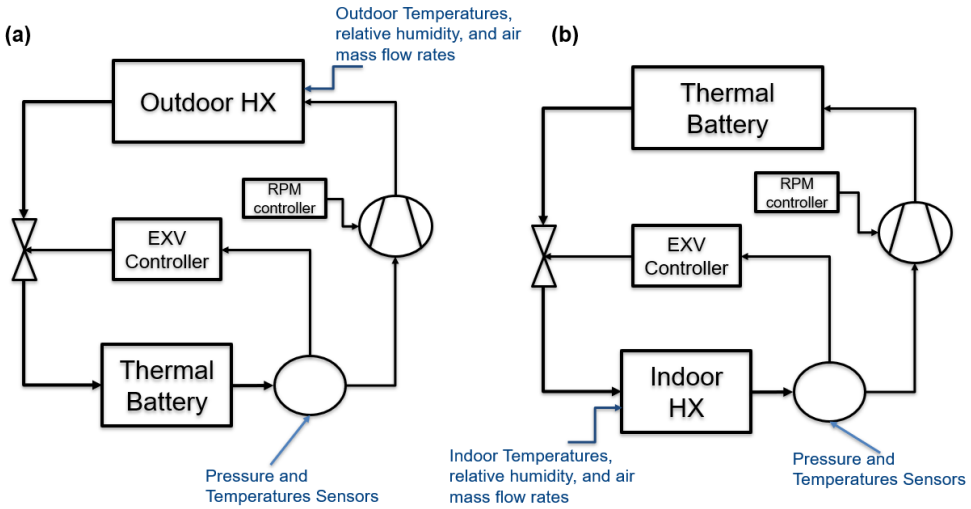


Fig. 3: Thermal battery cycle in (a) discharging mode during the peak, and (b) recharging mode during off-peak conditions

2.3. Selection of Days and PCM Melting Temperatures

For the summer months, between May and September, the weather data [20] obtained was analysed to see the peak temperatures per day. From Fig. 4, the peak temperatures can be divided into two ranges: 35-40ºC and 40-45ºC. While there are other impacts on the building cooling demands, including indoor thermal demands, and outdoor humidity and incoming sun radiation, in this paper, the focus will be more towards the outdoor temperature, as the sole objective of the PCM-TES is to lower the temperature/and pressure lift in the air-conditioning cycle, thus reducing the compressor power during the peak. Three days were selected for each peak range.

In this study, three mid-point melting temperatures were selected (a) 22ºC, (b) 25ºC, and (c) 28ºC. The outputs from each day was averaged for its corresponding peak temperature. According to the Government of

Dubai, the peak hours occur between 12:00 PM and 6:00 PM during the summer [23]. As the first step, the conventional air-conditioning model (Fig. 2) to assess the COPs during the 6-hour peak period. Based on the lowest COPs for these 6-hours, a 4-hour period was selected, and the thermal battery discharging model operation times were set (Fig. 3). Having the TES operate for 4-hour rather than the complete 6-hour period is due to the excessive mass of the TES system. As mention is section 2.2, enthalpies of fusion ranging between 100-250 kJ/kg, the mass of the PCM can range from 1,000-1,200 kg at 4-hours to at 1800-2,000-kg at 6-hours. That increase in mass can pose installation challenges along with the current lack of economic benefits over the entire 6-hours shown in Section 3.3.

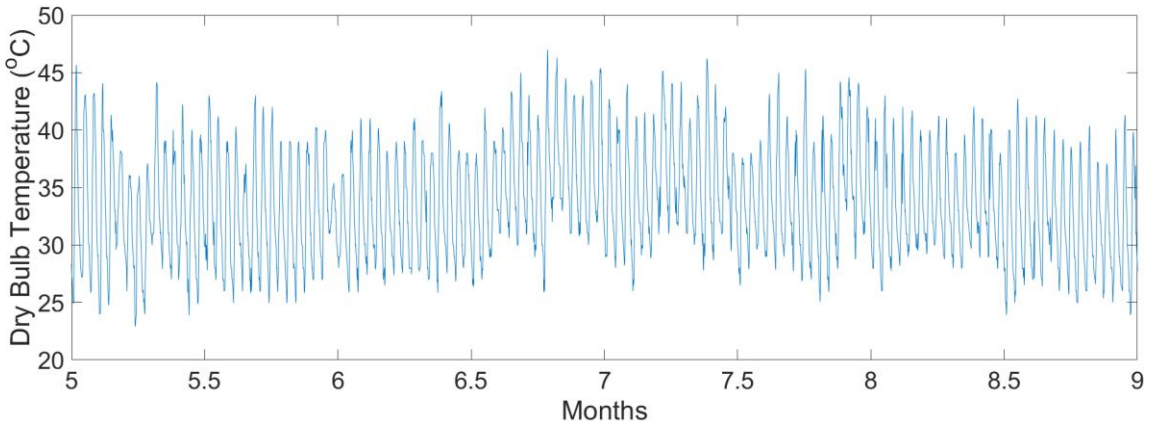


Fig. 4: Temperature Profile for Dubai, UAE

3. Results and Discussion

3.1. Effect of the PCM temperatures on the conventional system

For a day with the peak temperatures ranging between 35-40ºC (Fig. 5a)., it can be seen that near room PCM temperatures have provided a significant increase in COP at the peak, from 15% at T_{PCM} = 28ºC to 51% at T_{PCM} = 22ºC. However, the improvements in COP for higher ambient temperature days (40-45ºC) are significantly higher, shown in Fig. 5(b), with factors ranging from 1.6 to 2 of original system when the PCM melting temperatures are 28ºC and 22ºC, respectively. This increase in COP can provide an excellent opportunity to reduce the strain on the grid and provide a higher cooling capacity, especially during the peak hours at high ambient temperatures.

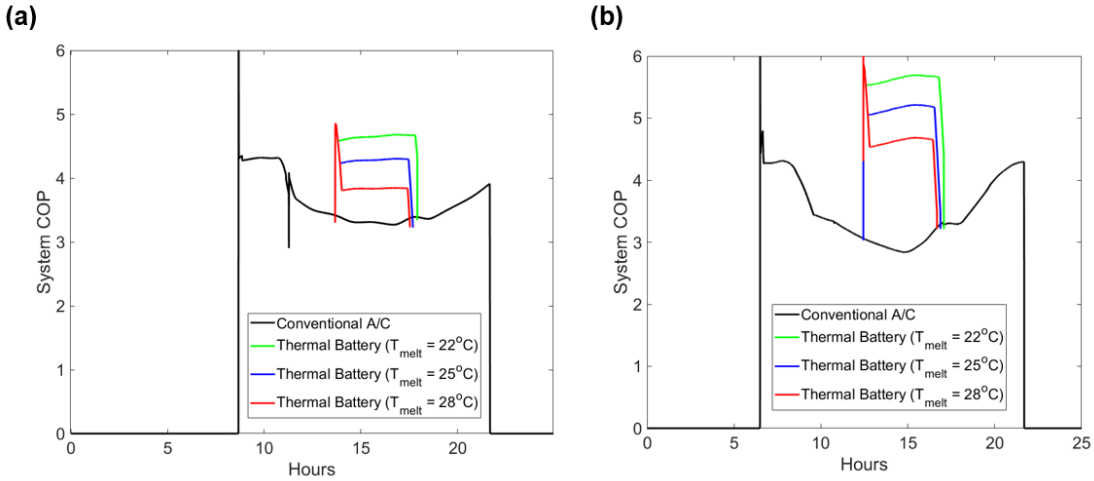


Fig. 5: Improvement in system COP for during the peak hours resulting from the thermal battery for PCM melting temperatures ranging from 22 – 28ºC during the peak, when daily maximum outdoor temperatures are between (a) 35 – 40ºC and (b) 40 – 45ºC

Fig. 6 compares the reduction in the total power demand required by the air-conditioner for the two ambient temperature ranges. This power demand is the total compressor power input from the grid with the outdoor and indoor fans. In Fig. 6(a), the power demand increases from 9 to 11 a.m., given the increase of the building load, therefore increasing the compressor power. Given that at higher outdoor temperatures, the compressor requires higher power input to accommodate the required temperature and pressure lifts just to meet the

required cooling demands. As of such, the reduction in the total power during the peak hours (Fig. 6(b)) are significantly higher when the temperatures are 40-45ºC compared to the lower ambient temperature cases. Furthermore, the reduction in the total is lower with the melting temperatures are higher. Another benefit of the retrofitted PCM-TES, is the elimination of the outdoor fan, therefore, eliminating the fan power consumed during the peak. Table 2**Error! Reference source not found.** shows the percentage savings for each PCM melting temperature. For the higher ambient temperatures, one can see that the potential for power consumption during the peak is between 30 – 45 % of the conventional A/C system. This can be beneficial to high ambient temperature countries, given that such reductions can potentially eliminate plans of building more powerplants, just to meet the electrical loads during the peak hours.

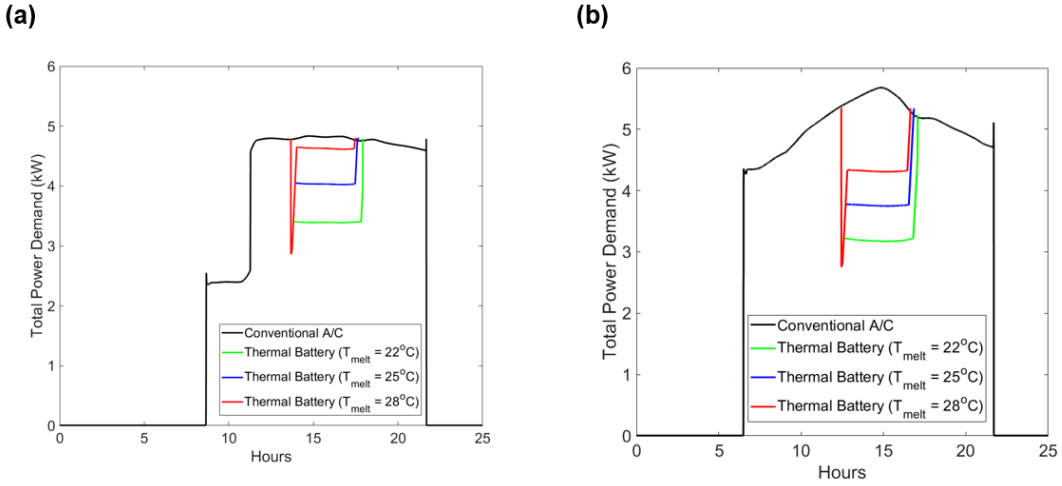


Fig. 6: Reduction in the power demand from the compressor and fans during the peak when the maximum daily outdoor temperatures are between (a) 35 – 40ºC, and (b) 40 – 45ºC

Another reason for the COP improvements during the peak hours for the retrofitted cycle was the increase in the cooling capacity of the system (Table 1). The cooling capacity of the system ranges from 17-18.5 kW. This occurs as the pressure lift decreases, and the PCM thermal battery dissipating almost the same amount of heat as the condenser at a lower pressure, the refrigerant is entering the evaporator at a lower vapor mass fraction (0.15-0.19) than the conventional system (0.22). This has resulted in increases in the cooling capacity ranging from 8% to 18%. The highest increases in the cooling capacity occurs during the with the PCM melting temperature being 22ºC, given that at these conditions the lowest pressure and temperature lifts are obtained. Furthermore, the percentage increase in outdoor temperature ranges of 40 – 45ºC, given that the pressure and temperature lift drops are the higher in these cases as compared to the 35 – 40ºC peak outdoor ambient temperatures. Therefore, the inclusion of thermal battery can provide another advantage as there is a lower need to oversize the air-conditioning system, especially at the summer peak conditions which can in turn have potential savings on the electrical grid.

Table 1. Maximum percentage changes in COP, power consumption and cooling capacities for the different PCM melting temperatures at different ambient conditions during the peak hours

PCM melting temperature	22ºC	25ºC	28ºC
% increase in COP T_{amb} = 35 – 40ºC	42.5	31.2	17.4
% increase in COP T_{amb} = 40 – 45ºC	99.6	82.5	63.5
% power savings for T_{amb} = 35 – 40ºC	30.2	17.1	4.9
% power savings for T_{amb} = 40 – 45ºC	51.2	33.1	24.4
% increase in cooling capacity T_{amb} = 35 – 40ºC	10.1	9.8	8.7
% increase in cooling capacity T_{amb} = 40 – 45ºC	18.1	14.8	12.5

3.2. Energy Required for Load Shifting

In this section, an assessment of the electrical load required to recharge or (solidify) the thermal battery during nighttime was conducted. This is important to quantify the estimated saving during the peak to the energy required to recharge the battery. Table 2 shows the required power consumption by the air-conditioning

system in kWh. The reduction in power input with higher PCM melting temperatures is due to the lower temperature difference between them and the outdoor ambient temperatures which are typically between 25ºC and 30ºC, along with the minor reduction in charging time between the different temperature PCMs (<400 seconds). The selection of PCM appropriate melting temperature relies mostly on the available savings that can be achieved during the peak, without have excessive recharge costs. While the cooling capacity for the three PCMs are close (17-17.5 kW), the choice of the PCM temperature effects mostly how much can be alleviated from the grid during the peak, without excessive energy when recharging. Looking at the saving of the PCM melting at 22ºC, the savings along with the recharge power, it is acceptable to recharge that PCM with this power.

Table 2. Power required in kWh for the thermal battery during night-time for different PCM melting temperatures

PCM Melting Temperature (ºC)	Total Power Input required (kW)	Time required for full recharge (hours)	COP for Cycle Recharge
22	3.81	4.7	4.15
25	3.67	4.5	4.45
28	3.45	4.4	4.65

3.3. Economic Analysis

An economic analysis was conducted to assess to the potential savings for Dubai during the peak hours. This analysis can help predicting the expected savings from increases in meeting the city building more powerplants, just to meet the required cooling demands. According to the Dubai Electricity and Water Authority (DEWA), the peak electrical demand in 2021 was 9,204 MW occurring in August, when the outdoor ambient temperatures exceed 40ºC. So far, the city of Dubai can generate 13,417 MW, with 89% of the power is generated through steam and gas turbines, and 11% is generated by solar photovoltaics [23].

Currently, air-conditioning is responsible for 50% of all the electricity consumed [6]. The thermal battery will consist of the PCM material and heat exchangers. However, even with the low cost PCM ($3-30/kWh [19]), current commercially available thermal battery technologies put their cost between $200-500/kWh [24], given heat exchanger material cost and assembly requirements. In this analysis, the objective was to identify the number of hours for the thermal battery to operate during the peak that can be used to reduce the demand cost for 30%, 60%, and 90% of the city, against the amount the estimated city cost of the thermal battery to meet that required demands.

Table 3: Current Dubai power station capacities [25]

Power Stations	Power Station Type	Current Energy Production Year 2021 (MW) [25]
Aweer Power Station "H" Phases I to III	Natural Gas and Diesel Turbines	1996
Hassyan Power Plant Phases I and II	Natural Gas Turbines (Converted from Coal)	1200
Jebel Ali Station "D"	Natural gas and oil combined cycle	1027
Jebel Ali Station "E"		616
Jebel Ali Station "G"		818
Jebel Ali Station "K"		948
Jebel Ali Station "L" Phases I to II		2401
Jebel Ali Station "M" with Extension		2885
Mohammed bin Rashid Al Maktoum "All Phases until 2022"	Currently Solar PV	1526

Dubai has several powerplants (Table 3), with investments up to 6.6 Billion USD [26]–[29]. During the peak, it is assumed that all the powerplants are operating at full capacity, bringing the estimated cost during the peak at $0.49/kWh. According to DEWA [23], Dubai has a single utility rate per kWh, depending on the amount of electricity consumed per month. Fig. 7, and **Error! Reference source not found.**, shows the estimated cost savings for 30%, 60%, and 90% of the city using the electrical space cooling demands of 2021.

For a PCM with a melting temperature of 22ºC, Table 1 provides us with potential energy savings of a retrofitted air-conditioner with TES at two maximum outdoor temperature ranges. Using the meteorological data in TMY3, it was observed that on average during the summer the outdoor temperature exceeds 40ºC for one hour during the day. For limited operation, the energy savings were calculated for this one-hour using the corresponding percentage reduction of 51%. For longer operating periods the total savings were calculated by a weighted average corresponding to the number of hours per year in the different temperature ranges. From this, we obtain the overall utility reduction estimate of 18% for the entire 6 hours, shown in Fig. 7 and Fig. *8*. This brings the total savings electricity costs to $0.59 and $1.78 billion for 30% to 90% of Dubai's space cooling demand reduction, respectively. That percentage saving is due to the single utility rate per kWh used, rather than having variable rate depending on the peak hours or non-peak hours. In all scenarios, 30% to 90%, the are annual cost savings that increase with more peak hour loads alleviated by the TES, that corresponds to electrical savings at the peak.

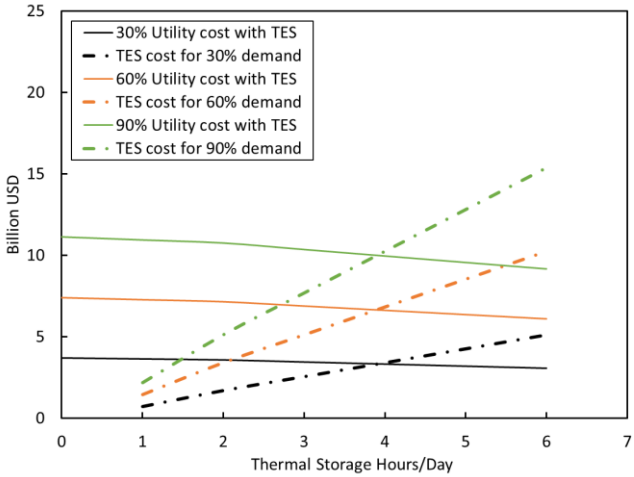


Fig. 7: Predict savings in the utility cost when using TES at against cost of $200/kWh of thermal energy storage per operating hours daily for 30%-90% of the AC requirements

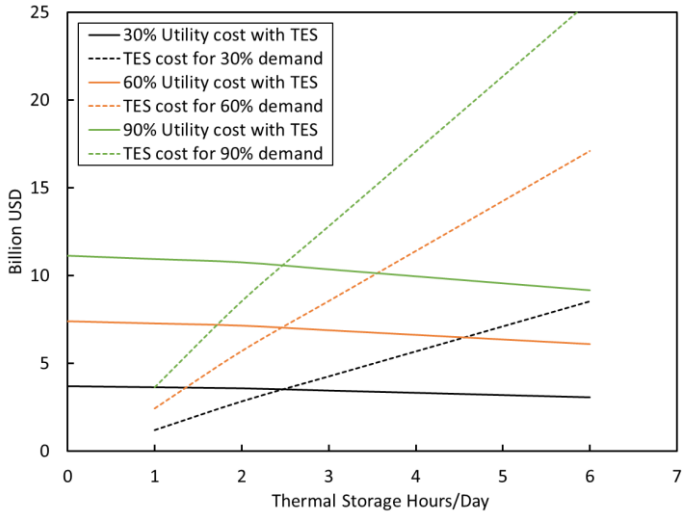


Fig. 8: Predict savings in the utility cost when using TES at against cost of $500/kWh of thermal energy storage per operating hours daily for 30%-90% of the AC requirements

The key challenge is to identify the point which is the trade-off between the cost of the PCM-TES and the number of hours the can be altered. Thus, the cost of TES/kWh is an important factor, and that lower cost TES systems are required, to increase the number of hours that can be used to load shift. For the lower bound of $200/kWh, it is logical to provide TES for 4 hours during the peak, which is the assumed number of TES hours in this study. More hours, will result in higher investment costs than the potential savings. At the higher cost of TES rates, the number of peak load hours shift will reduce to 2.4 hours and if an investment is done at this cost, the operation of TES should only be there at the highest temperature hours of the year. If a cost of $15/kWh of TES is achieved [30] the city of Dubai can provide TES for the entire 6-hour peak for 90% of its citizens at a $1.1 billion, giving a payback period of 2 years only, and not 10 years (TES cost $200/kWh).

3.4. Challenges with the retrofitted TES-PCM air-conditioning system

While the cost of PCM materials are quite low, there still remains challenges in designing and assembling a TES, especially for large applications. This is due to PCMs being constrained by their material properties. PCMs have low thermal conductivities, and a finite energy storage (~100 – 250 kJ/kg for salt hydrates) [19]. To get more thermal energy stored, more PCM is needed, however, the compactness of the TES system must not be affected, not to degrade the heat transfer. Increasing the PCM volumes and heat transfer surface areas, will result in increasing the internal volumes on the refrigerant side, therefore increasing refrigerant charge in the cycle, which is problematic for higher-GWP refrigerants and flammable alternatives. All these challenges can drive the cost of TES systems to increase. Nonetheless, with more research in the design, assembly, and demand for enhanced PCM-TES systems, the cost will start to decrease.

Retrofitting the air-conditioning system with the TES storage has several challenges. Firstly, if the available system has a single-speed compressor, designed for higher temperature lifts, reducing that temperature lift with the TES can potentially degrade the isentropic efficiency of that compressor, degrading the potential savings that can be achieved during the peak. Thus, a variable speed compressor may be used to operate at lower compressor RPMs to meet the building loads at lower temperature lifts, without degrading the isentropic efficiency. Secondly, explicit controls are required to ensure that the cycle can achieve a set point superheat and subcooling when operating with the TES, as lower the pressure and temperature lifts presents hurdles on both the condenser and evaporator obtaining subcooling and superheating. Finally, the air-conditioning refrigerant cycle will require a number of on/off valves to switch refrigerant flows between the outdoor condenser and the TES during peak hours, along with adequate controls to ensure that this switch can occur smoothly, without damaging any cycle component.

4. Conclusions

In this paper, a proposed retrofitted air-conditioning system with near to room temperatures PCM-TES feasibility was investigated for a city in a HAT country (Dubai). A transient model in Modelica was built and used to assess the potential power savings during the peak for a 17.5-kW R-410A air-conditioning unit, and the electrical loads required to recharge the PCM-TES. Using the typical meteorological year data, two types

of days were analyzed, days with peak temperatures ranging between 35 – 40ºC, and others with peak temperatures above 40ºC. For each outdoor temperature ranges, the COP, total power input and cooling capacity was assessed. For higher ambient temperature days, a PCM-melting point of 22ºC, can result in COPs almost doubling, reduction in the power consumption during the peak by up to 50%, and increases in cooling capacities by 18% during the peak hours As the PCM melting temperatures increase, the enhancements to the cycle during the peak hours reduces, especially when outdoor temperatures are below 40ºC. From an economic standpoint, given the higher costs of PCM-TES/kWh, the number of hours for feasible application of PCMs can range between 2.5-hours per day ($500/kWh), to 4-hours a day ($200/kWh) for an entire year with capital investments ranging from $4 – 12 billion depending on the range of the city cooling load to be met (30% – 90%). With more research in the design and assembly of PCM-TES, its cost can further drop, reducing the capital investments into the system to a fraction of the current costs.

Acknowledgements

This material is based upon work supported by the U.S. Department of Energy's Office of Energy Efficiency and Renewable Energy (EERE) under the Building Technologies Office Award Number DE-EE0009681. The views expressed herein do not necessarily represent the views of the U.S. Department of Energy or the United States Government. This work was also funded in part by the Modeling and Optimization Consortium at the University of Maryland.

References

[1] IEA, "The Future of Cooling –Opportunities for energy-efficient air conditioning," International Energy Agency (IEA), 2018. Accessed: Jun. 10, 2022. [Online]. Available: https://www.iea.org/reports/the-future-of-cooling

[2] M. Haddad, "Mapping the hottest temperatures around the world." https://www.aljazeera.com/news/2021/7/1/interactive-mapping-hottest-temperatures-around-world (accessed Jun. 10, 2022).

[3] NASA Earth Observatory, "Land Surface Temperature," Mar. 31, 2022. https://earthobservatory.nasa.gov/global-maps/MOD_LSTD_M (accessed Jun. 10, 2022).

[4] M. A. Ansari, T. Hussain, S. A. Khan, S. Mustafa, and V. Goyal, "Experimental investigation on VCRS by using R-134a and R-410a of air and evaporative cooled condenser," *IOP Conf. Ser. Mater. Sci. Eng.*, vol. 691, no. 1, p. 012071, Nov. 2019, doi: 10.1088/1757-899X/691/1/012071.

[5] R. Bruno, F. Nicoletti, G. Cuconati, S. Perrella, and D. Cirone, "Performance Indexes of an Air-Water Heat Pump Versus the Capacity Ratio: Analysis by Means of Experimental Data," *Energies*, vol. 13, no. 13, Art. no. 13, Jan. 2020, doi: 10.3390/en13133391.

[6] "Dubai Demand Side Management (DSM) –2016 Annual Report 'For an Efficient Cooling,'" Dubai Supreme Council of Energy, Dubai. Accessed: Nov. 09, 2022. [Online]. Available: https://dubaisce.gov.ae/en/taqati/

[7] N. Chaiyat and T. Kiatsiriroat, "Energy reduction of building air-conditioner with phase change material in Thailand," *Case Stud. Therm. Eng.*, vol. 4, pp. 175–186, Nov. 2014, doi: 10.1016/j.csite.2014.09.006.

[8] A. Real, V. García, L. Domenech, J. Renau, N. Montés, and F. Sánchez, "Improvement of a heat pump based HVAC system with PCM thermal storage for cold accumulation and heat dissipation," *Energy Build.*, vol. 83, pp. 108–116, Nov. 2014, doi: 10.1016/j.enbuild.2014.04.029.

[9] Y. Xu and M. Li, "Impact of instantaneous solar irradiance on refrigeration characteristics of household PCM storage air conditioning directly driven by distributed photovoltaic energy," *Energy Sci. Eng.*, vol. 10, no. 3, pp. 752–771, 2022, doi: 10.1002/ese3.1050.

[10] M. Fiorentini, P. Cooper, and Z. Ma, "Development and optimization of an innovative HVAC system with integrated PVT and PCM thermal storage for a net-zero energy retrofitted house," *Energy Build.*, vol. 94, pp. 21–32, May 2015, doi: 10.1016/j.enbuild.2015.02.018.

[11] R. Hirmiz, H. M. Teamah, M. F. Lightstone, and J. S. Cotton, "Performance of heat pump integrated phase change material thermal storage for electric load shifting in building demand side management," *Energy Build.*, vol. 190, pp. 103–118, May 2019, doi: 10.1016/j.enbuild.2019.02.026.

[12] Q. Meng, Y. Xi, X. Ren, H. Li, L. Jiang, and L. Yang, "Thermal Energy Storage Air-conditioning Demand Response Control Using Elman Neural Network Prediction Model," *Sustain. Cities Soc.*, vol. 76, p. 103480, Jan. 2022, doi: 10.1016/j.scs.2021.103480.

[13] B. D. Mselle, G. Zsembinszki, D. Vérez, E. Borri, and L. F. Cabeza, "A detailed energy analysis of a

novel evaporator with latent thermal energy storage ability," *Appl. Therm. Eng.*, vol. 201, p. 117844, Jan. 2022, doi: 10.1016/j.applthermaleng.2021.117844.
[14] S. Maaraoui, D. Clodic, and P. Dalicieux, "Heat Pump With a Condenser Including Solid-Liquid Phase Change Material," *Int. Refrig. Air Cond. Conf.*, Jan. 2012, [Online]. Available: https://docs.lib.purdue.edu/iracc/1194
[15] "Modelica Documentation." https://doc.modelica.org/ (accessed Oct. 12, 2022).
[16] H. Qiao, V. Aute, and R. Radermacher, "Transient modeling of a flash tank vapor injection heat pump system – Part I: Model development," *Int. J. Refrig.*, vol. 49, pp. 169–182, 2015, doi: https://doi.org/10.1016/j.ijrefrig.2014.06.019.
[17] R. Dhumane, J. Ling, V. Aute, and R. Radermacher, "Dynamic Modeling of a Personal Cooling Device with PCM Storage," in *Proceedings of 12th IEA Heat Pump Conference*.
[18] Y. Cao and A. Faghri, "A Numerical Analysis of Phase-Change Problems Including Natural Convection," *J. Heat Transf.*, vol. 112, no. 3, pp. 812–816, Aug. 1990, doi: 10.1115/1.2910466.
[19] J. Hirschey, K. R. Gluesenkamp, A. Mallow, and S. Graham, "Review of Inorganic Salt Hydrates with Phase Change Temperature in Range of 5 to 60°C and Material Cost Comparison with Common Waxes," *Int. High Perform. Build. Conf.*, Jul. 2018, [Online]. Available: https://docs.lib.purdue.edu/ihpbc/320
[20] "EnergyPlus." https://energyplus.net/weather (accessed Nov. 03, 2022).
[21] "Prototype Building Models | Building Energy Codes Program." https://www.energycodes.gov/prototype-building-models (accessed Nov. 03, 2022).
[22] "EnergyPlus." https://energyplus.net/ (accessed Nov. 14, 2022).
[23] "Dubai Electricity & Water Authority | Peak Load." https://www.dewa.gov.ae/en/about-us/sustainability/lets-make-this-summer-green/peak-load (accessed Nov. 07, 2022).
[24] "Sunamp UniQ eHW Heat Battery - Solar and Heat Store," Jul. 12, 2021. https://solarandheatstore.com/product/sunamp-uniq-ehw-heat-battery/ (accessed Nov. 10, 2022).
[25] "Annual Statistics 2021," Dubai Electrcicty and Water Authority (DEWA), Dubai, UAE, 2021. Accessed: Nov. 09, 2022. [Online]. Available: https://www.dewa.gov.ae/en/about-us/strategy-excellence/annual-statistics
[26] "DEWA Completes 84.52% Construction On Phase 4 Of H-Station In Al Aweer - MEP Middle East," Jul. 08, 2021. https://www.mepmiddleeast.com/projects/78681-dewa-completes-8452-construction-on-phase-4-of-h-station-in-al-aweer (accessed Nov. 09, 2022).
[27] "Work on UAE's Mohammed bin Rashid Al Maktoum Solar Park is progressing as per schedule." https://www.zawya.com/en/business/energy/work-on-uaes-mohammed-bin-rashid-al-maktoum-solar-park-is-progressing-as-per-schedule-n5q9dr68 (accessed Nov. 09, 2022).
[28] "Jebel Ali M-Station," *Power Technology*. https://www.power-technology.com/projects/jebel-ali-m-station/ (accessed Nov. 09, 2022).
[29] "Al Aweer Gas Turbine Power Station 'H.'" https://www.besix.com/en/projects/alaweergasturbinepowerstationh (accessed Nov. 09, 2022).
[30] "Thermal Energy Storage," *Energy.gov*. https://www.energy.gov/eere/buildings/thermal-energy-storage (accessed Nov. 10, 2022).

14th IEA Heat Pump Conference
15-18 May 2023, Chicago, Illinois

Cold Climate Field Demonstration of Variable Refrigerant Flow (VRF) Heat Pump and Variable-Air-Volume (VAV) System

Patricia F. Rowley[a*], Alex Fridlyand, PhD[a], David J. Schroeder, PhD[b], Shawn Scott[a]

[a]GTI Energy, 1700 S Mount Prospect Road, Des Plaines, IL 60515, USA
[b]Volta, 28365 Davis Parkway, Suite 202, Warrenville, IL 60555

Abstract

Heat pump variable refrigerant flow (VRF) systems are increasingly used in U.S. small commercial buildings to provide cost-effective efficient heating and cooling for multi-zone applications. The complexity and customized design of VRF systems for specific buildings make it difficult to predict energy savings relative to other HVAC systems. Due to limited VRF field data, especially in colder climates, energy savings are often based on energy modeling or laboratory data obtained under controlled conditions. A field demonstration at Naval Station Great Lakes (NSGL) in Illinois offered a unique opportunity to directly compare measured performance data for a VRF system to the baseline variable-air-volume (VAV) system for the same building. The objective of this demonstration was to evaluate the performance of two VRF systems: an electric cold climate heat pump and a natural gas engine-driven heat pump in a side-by-side installation for a small office building compared to the existing VAV system. This paper will focus on the benefits and limitations of the electric CCHP VRF system compared to the baseline VAV system for cold climate applications. The VRF system paired with a dedicated outdoor air system (DOAS) significantly reduced the facility peak electric demand, greenhouse gas emissions, and energy costs compared to a conventional VAV system.

© HPC2023.
Selection and/or peer-review under the responsibility of the organizers of the 14th IEA Heat Pump Conference 2023.

Keywords: Variable Refrigerant Flow (VRF); Variable-Air-Volume (VAV); Air Source Heat Pump; Cold Climate Heat Pump

1. Introduction

GTI Energy conducted a field demonstration of two side-by-side heat pump technologies with variable refrigerant flow (VRF) at a small office building at Naval Station Great Lakes (NSGL). This demonstration compared the installed performance of an electric cold climate heat pump (CCHP) VRF system and a natural gas engine-driven heat pump (GHP) VRF system relative to the baseline performance of an existing variable-air-volume (VAV) system for the same building. The objective was to quantify the energy use, economics, and qualitative benefits of each technology for cold climate DoD applications. Parameters evaluated included natural gas and electric consumption, peak electric demand, primary energy, full-fuel-cycle emissions, lifecycle costs, and simple payback. Additional details on this demonstration are available on the Environmental Security Technology Certification Program (ESTCP) website. [1] This paper will focus on the benefits and limitations of the electric CCHP VRF system compared to the baseline VAV system for cold climate applications.

* Corresponding author. *E-mail address:* prowley@gti.energy

2. Cold Climate VRF Heat Pumps and DOAS

The selected demonstrated site was a multi-zone office building, a common application for VRF technologies. Heat pump VRF technologies are well suited for multi-zone building types including schools, retail, hospitals, and hotels. VRF systems are often paired with dedicated outside air systems (DOAS) that provide ventilation directly to the conditioned space. For this configuration, DOAS capacity and air flow are sized to meet the ventilation requirements for each zone and to deliver supply air at space neutral conditions. VRF fan coils are used in place of the VAV-boxes to meet the remaining internal and skin loads of the building providing heating and cooling to meet the thermostat setpoints for each individual zones.

Electric VRF heat pumps are a mature technology with several U.S. manufacturers offering products, but have yet to achieve the 30%-50% market share they currently have in Asia and Europe. VRF systems are increasingly used for multi-zone commercial buildings, driven by the potential for energy savings, economic benefits, and improved comfort with zoned temperature control. Studies report energy savings up to 30% compared to conventional HVAC systems [2]; however, energy savings are typically based on manufacturer data and modeled building energy use. Due to the custom nature of VRF installations, direct comparisons of energy use and economics can be difficult to quantify. In addition, the performance of all air source heat pumps varies significantly with ambient temperatures, so performance and energy savings for one climate will not be the same as a different climate.

VRFs are typically installed in warm climates that benefit from their high cooling efficiency. In colder climates, VRFs are often installed in heated mechanical rooms or with backup electric resistance heaters increasing installed costs and reducing energy savings. [4, 5]. Recently manufacturers have introduced cold climate versions of electric VRF systems without supplemental heating. Additional field studies are needed to validate modeled energy savings for VRF systems, especially in colder climates.

3. VRF and DOAS Field Demonstration

This demonstration provided detailed field data on the installed cold climate performance for both the baseline VAV system and an electric CCHP VRF system. A full calendar year of baseline data was used to characterize the performance of an existing VAV system across the full range of heating and cooling loads. The VRF systems were then installed at the field site and monitored from October 2017 to May 2019. These datasets provided a direct comparison between the VRF systems and the baseline equipment to quantify their relative energy savings and site-specific life cycle costs (LCC). Qualitative benefits, such as reliability and comfort, were also addressed.

3.1. Field Site

NSGL, located in northern Illinois in ASHRAE Climate Zone 5, was selected for this cold climate demonstration with cold and moderately long winters averaging 131 days/year below freezing and -5°F design temperature. Based on NOAA 30-year normals, this location averages 1078 cooling degree days per year (CDD55) and 4362 heating degree days per year (HDD60) [3]. Shown in Figure 1, the field site was a single-story multi-zone office building with an existing conventional VAV system. The north wing, circled in red, was selected for the demonstration due to symmetric zones and higher heating loads. The north wing was divided into two equivalent sections with similar zones and thermal loads. One section was served by the electric CCHP VRF while the other was served by an equivalent GHP VRF system.

The baseline HVAC system was a ground-mounted VAV system with 500 MBH modulating gas heating (80% Te) and 30-tons electric cooling (9.5 EER). The system included 19 VAV-boxes with electric resistance reheat to provide zone temperature control. Historic utility data for the total building indicated the system capacity was about twice the typical heating and cooling load.

Two 2-pipe heat pump VRF systems were specified as retrofit equipment for this application. A total of twenty cassette-style VRF fan coil units were installed above the ceiling panels throughout the building. The VRF systems were paired with a conventional DOAS to provide ventilation with gas-fired heating (80%Te) and electric DX cooling (11.3 EER) sized to match the baseline ventilation rate (800 cfm). For cold climates, gas heating is needed to meet the required temperature rise for conditioning 100%OA. The DOAS delivered conditioned air at 64°F (17.8°C) directly to each zone via ceiling diffusers. The DOAS was able to use the existing ductwork which significantly reduced installation costs for this site.



Fig. 1. (a) A multi-zone office building selected for the cold climate demonstration site. (b) The demonstration VRF/DOAS replaced a VAV system serving the north wing, circled in red.

To ensure proper sizing, the design engineering firm developed load calculations based on code-required minimums taking into account a range of DOAS setpoints based on a 60°F (15.6°C) supply temperature to address outdoor latent loads during the cooling season and a neutral 70°F (21.1°C) during the heating season. A 10% safety factor was added to both heating and cooling capacities. Due to its reduced capacity at lower ambient temperatures, the electric CCHP outdoor unit was oversized to meet the heating load at the coldest design conditions. A 12-ton CCHP outdoor unit was paired with approximately 8-ton VRF indoor fan coil capacity.

3.2. Measurement and Verification Approach

3.2.1. Baseline HVAC Monitoring

Gas and electric consumption of the existing VAV system was monitored for a full calendar year. Outdoor air, return air, and supply air temperatures were also measured. Room temperatures and relative humidity were monitored in each conditioned zone to quantify any significant changes in comfort.

3.2.2. Demonstration Monitoring

The CCHP VRF was instrumented with gas and electric meters to measure energy use. One compact watt meter monitored total electric consumption at the outdoor condensing unit; a second watt meter measured the total energy use for the indoor fan coils. DOAS air temperatures, gas and electric consumption were also monitored. The efficiency of the VRF system was calculated by the ratio of total energy (heating and cooling) delivered to total energy consumed for a given period. Due to the design of the cassette-style VRF fan coil units, it was challenging to accurately measure the supply and return air to calculate the total energy delivered by the individual fan coil units to the conditioned space. An alternative approach was used to monitor the total heating and cooling delivered by the VRF system by measuring changes in enthalpy at the refrigerant lines, as shown below in Figure 2.

A Coriolis flow meter was installed in the liquid refrigerant piping to measure the mass flow rate of the refrigerant delivered to/from the indoor fan coils. Thermocouples and pressure sensors were installed in the refrigerant lines adjacent to the outdoor unit. Enthalpy of the liquid and vapor refrigerant was calculated based on R410A properties using the National Institute of Standards and Technology Reference Fluid Thermodynamic and Transport Properties Database [6]. Heating or cooling delivered was calculated based on the enthalpy change between the vapor and liquid refrigerant lines. In previous studies, this method of measurement was successfully validated through comparison of measured field data to laboratory data at similar conditions. This approach improved accuracy and reduced M&V costs compared to air side measurements at each fan coil unit.

3.3. Data Analysis

Data was recorded at 5-minute intervals and downloaded remotely via a cellular modem to provide real time access to performance data. Measured performance data was collected for a calendar year for both the baseline and VRF performance and then normalized based on heating and cooling degree days and the total measured space conditioning load.

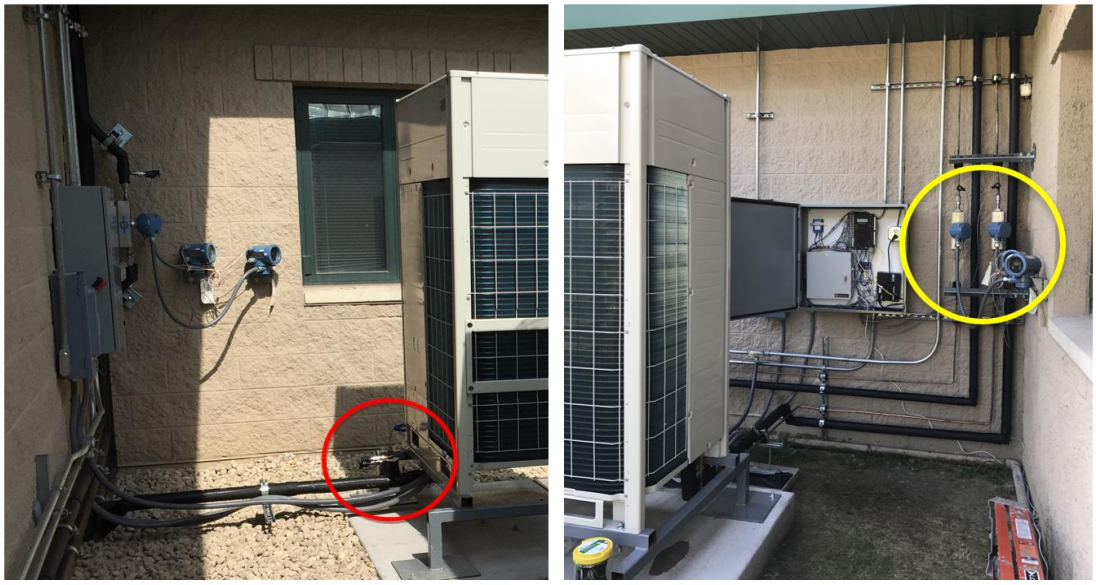


Fig. 2. (a) Pressure and temperature sensors in the refrigerant lines (circled in red) were used to calculate total heating/cooling delivered. (b) Coriolis meters (circled in yellow) measured the mass flow rate of the liquid refrigerant.

3.3.1. Baseline Performance

Measured energy use for the baseline VAV system was highly correlated to heating and cooling degree days. As shown by the graph on the left in Figure 3, cooling energy use was linear with respect to cooling degree days, base temperature 60°F (15.6°C). For heating, natural gas and electric consumption was also linear with respect to with heating degree days, base temperature 55°F (12.8°C).

During heating operation, energy use for the VAV-boxes was higher than expected. Electric resistance heating provided by the VAV-boxes is designed to provide only trim heating and to adjust temperatures between zones. Baseline data shown in Figure 4 shows the VAV-boxes at peak electric heating (orange) while the outdoor unit's modulating gas burner (blue) operated at low fire. Per the manufacturer, a building automation system (BAS) is required to integrate the controls for the gas burner and the VAV-boxes reheat elements. Without a BAS, the outdoor unit and VAV-boxes operate independently resulting in excess electric resistance heating and higher peak electric demand. This may be typical operation for smaller buildings or sites without a central BAS.

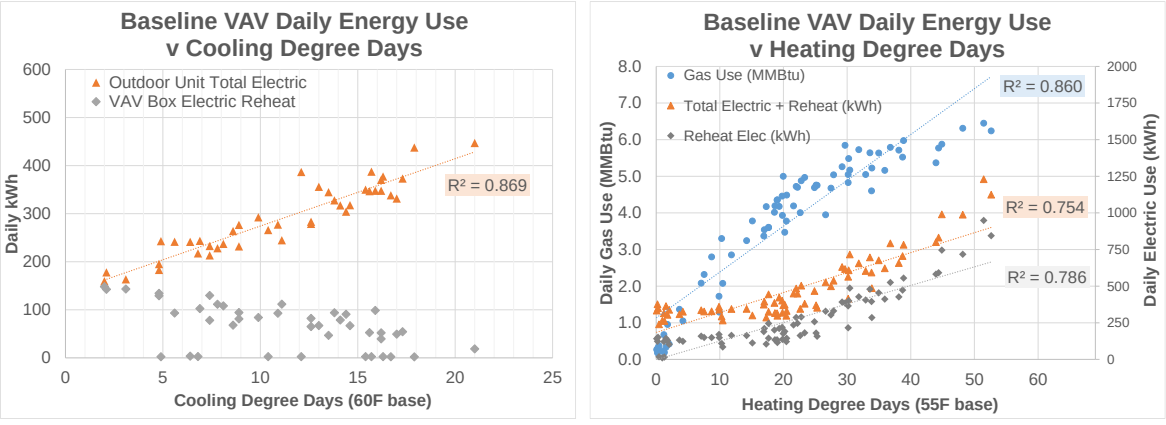


Fig. 3. Graphs show the baseline VAV measured energy use correlated with (a) cooling degree days and (b) heating degree days. VAV electric reheat consumption was higher than expected during heating (shown in gray)

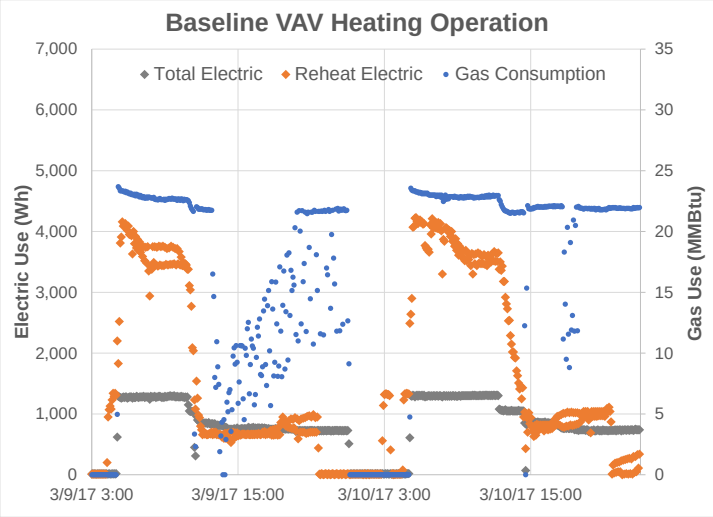


Fig. 4. Electric resistance heating provided by the VAV-boxes (shown in orange) operated at high levels when the modulating gas burner was at low-fire, resulting in higher than expected energy use during heating.

3.3.2. VRF Cooling Performance

In addition to offering higher cooling efficiency, VRF provides zoned cooling eliminating the over-cooling and reheat energy used by VAV systems. Figure 5 shows the measured energy use of the CCHP VRF and DOAS with respect to cooling degree days. Performance was based on a limited dataset due to unrelated component issues and operational outages. Daily average cooling efficiency ranged from 13 to 25 EER, exceeding the specified 12.3 EER rating for 95°F (35°C) due to milder ambient temperatures during this period. Cooling efficiencies decreased with lower part load. Part load for this assessment was calculated as the ratio of measured cooling delivered relative to the rated total capacity. Since the CCHP outdoor unit for this demonstration was oversized to meet peak heating capacity, the system operated at very low part loads (15% to 25%) during cooling. In addition, the DOAS operated with a 64°F set point year-round which reduced the building cooling load.

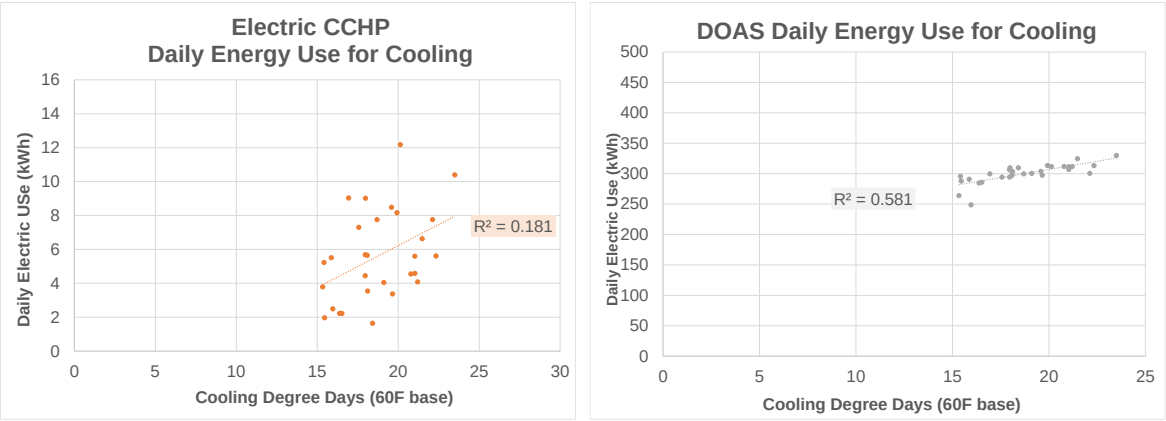


Fig. 5. (a) Left: CCHP VRF measured electricity consumption for cooling with respect to cooling degree days. (b) Right: DOAS measured electricity consumption with respect to cooling degree days

3.3.1. VRF Heating Performance

Figure 6 shows the measured energy use of the CCHP VRF and DOAS during heating correlated with respect to heating degree days. Daily average heating efficiency ranged from 0.5 to 4.0 COP, compared to manufacturer specifications of 4.1 COP at 47°F and 2.3 COP at 17°F.

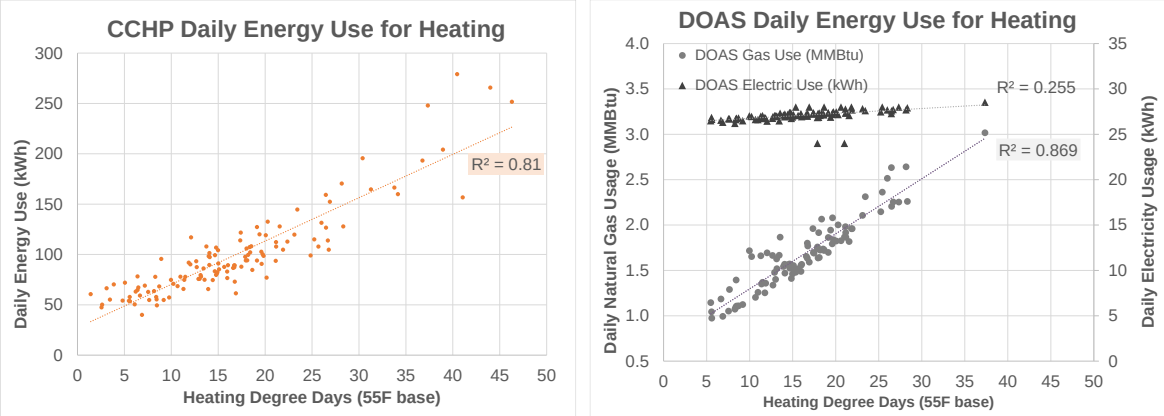


Fig. 6. (a) Left: CCHP VRF measured electricity consumption for heating correlated to heating degree days. (b) Right: DOAS measured electricity consumption correlated to heating degree days.

Ambient temperatures had a larger impact on heating COP than part load operation (Figure 7). For this assessment part load was calculated as the ratio of measured heating delivered relative to the rated total capacity. Heating capacity and efficiency of all air source heat pumps decrease with lower ambient temperatures. For this demonstration, the CCHP did not meet the heating load for seven days at daily average temperatures at or below 16°F, shown circled in the graphs in Figure 7. This indicates the need for supplemental heating for this climate zone. The manufacturer-rated minimum temperature for this CCHP model is -4°F. For this region, the ASHRAE 99% design temperature is -5°F; however, during the demonstration ambient temperatures reached historic lows dropping down to -23°F due to the Polar Vortex in January 2019.

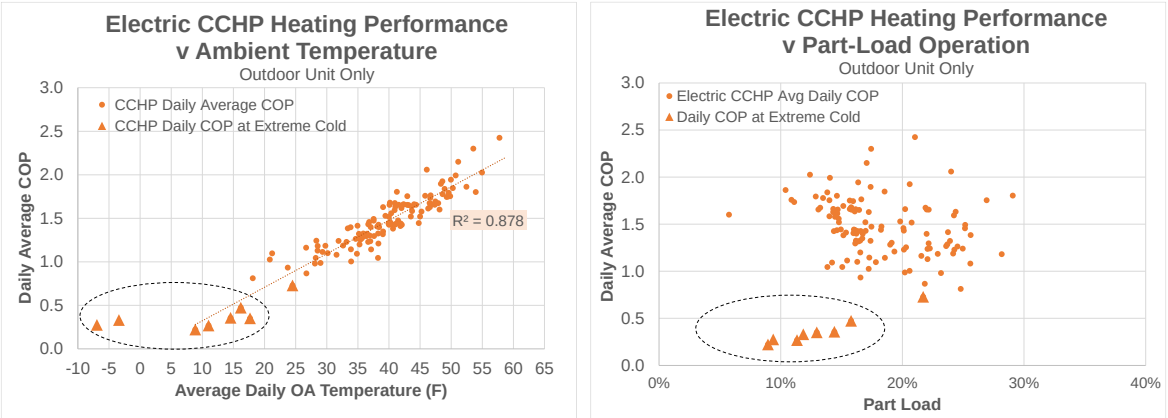


Fig. 7. Graphs show (a) the decreasing measured heating efficiency with respect to ambient temperatures and (b) the minor impact of part load on heating efficiency. During extreme cold temperatures (circled), efficiency dropped below 1.0 COP and the CCHP VRF was unable to meet the building heating load.

3.4. Energy Savings

To estimate annual energy and cost savings, measured energy use data was normalized to published Typical Meteorological Year version 3 (TMY3) cooling and heating degree days based on the National Centers for Environmental Information National Oceanic and Atmospheric Administration Annual Climate 30-year Normals (1981 to 2010) for Waukegan National Airport [3]. Energy use for the CCHP VRF system was normalized with respect to the total building load. Energy savings for the VRF/DOAS were calculated with respect to the baseline VAV system. Primary energy and full-fuel-cycle GHG emissions were calculated based on estimated annual energy use. Primary energy and full-fuel-cycle emissions takes into account all upstream energy used to generate power or to supply fuel to the building meter. Primary energy is a more comprehensive approach to evaluate energy use and may be more relevant to energy security for DoD facilities than the energy metered at the site. A growing number of codes and standards are adopting full-fuel-cycle metrics to quantify the environmental impact of different energy sources and appliances.

A summary of the results is presented in Table 1. The VRF/DOAS system had lower natural gas and electricity use compared to the baseline VAV, reducing primary energy use by 68% and full-fuel-cycle CO2e emissions by 70%. Modeled annual savings for VRF relative to VAV systems range from 20% to 60% for various climates [7]. These results are at the high end of the range due to higher than expected baseline energy use for the VAV system. The VRF/DOAS reduced summer peak electric demand from 43.2 kW to 14.5 kW. The VRF system provides very high efficiency cooling and eliminates the need for electric reheat used in the VAV-boxes. For heating, the baseline VAV peak electric demand (65.4 kW) is higher than expected due to the lack of integrated controls, as previously discussed; however, VRF/DOAS heating operation resulted in a high winter peak electric demand (36.8 kW), exceeding the facility summer peak demand. The peak electric demand in buildings is typically driven by electric cooling, but the use of electric heating creates a secondary winter peak. With the growing use of electric heat pumps, the winter heating peak demand is likely to exceed the summer cooling peak especially in cold climates.

Table 1. Normalized Annual Energy Use

	Baseline VAV with Electric Reheat	Electric CCHP VRF	DOAS	Total VRF/DOAS System	Annual Savings	
Gas Use (therm)	5,474		2,651	2,651	2,823 therms	52%
(kWh)	160,414		77,686	77,686	87,728 kWh	
Electric Use (kWh)	125,713	41,349	9,326	50,675	75,038 kWh	60%
Heating Peak Electric Demand (kW)	65.4	35.5	1.3	36.8	28.6 kW	44%
Cooling Peak Electric Demand (kW)	43.2	8.6	5.9	14.5	28.7kW	66%
Annual Primary Energy (MMBtu)	1,995			853	1,142 MMBtu	57%
(kWh)	584,674			249,877	334,798 kWh	
Full-Fuel-Cycle CO2e Emissions (metric tons)	158.2			66.7	91.5 MT	58%

Assumptions: Natural gas: Primary energy factor: 1.09; Full-fuel-cycle CO2e emissions: 147 lb./MMBtu

Electricity primary energy factor (2016eGrid Non-baseload RFCW): 3.26; Full-fuel-cycle CO2e emissions: 2,133 lb./MWh

3.5. Economic Assessment

Table 2 presents a comparison of annual O&M costs for the baseline VAV system and the CCHP VRF/DOAS. Total energy costs were reduced by 51%. Energy costs per square foot of the facility dropped from the baseline $2.21/sqft ($23.79/sqm) to $1.08/sqft ($11.63/sqm) for the VRF/DOAS. These energy and cost savings may be higher than typical cold climate applications due to higher than expected electric resistance heating for the baseline VAV system. Energy prices were based on incremental composite rates provided by the field site ($0.0559/kWh; $10.3037/kW; $0.49/therm). Utility demand charges and rate structures can vary widely from state to state. Demand charges for the field site were calculated from the highest hourly peak kW during the past 12 months, whether summer or winter. For this demonstration, the highest peak electric demand occurred during the heating season for both the baseline VAV system (65.4 kW) and demonstration VRF/DOAS (36.8 kW).

Table 2. Estimated Annual O&M Costs with Winter Peak Electric Demand

	Baseline VAV with Electric Reheat	VRF/DOAS System	Annual Savings	
Annual Energy Costs ($/yr.)	$9,714	$4,134		
Heating Peak Electric Demand Charge	$8,086	$4,547		
Total Energy Cost	$17,800	$8,680	$9,120	51%
$/Floor Area	$2.21/sqft ($23.79/sqm)	$1.08/sqft ($11.63/sqm)	$1.13/sqft ($12.16/sqm)	
Annual Maintenance Costs	$1,200	$1,200		
Total O&M Costs	$19,000	$9,880	$9,120	48%

Assumptions: $0.0559/kWh; $10.3037/kW; $0.49/therm

Maintenance tasks for CCHP VRF systems differ from more central systems such as VAV. Some sources predict VRF/DOAS have higher maintenance costs than conventional equipment [2], while other publications expect similar or lower maintenance costs [8]. Increasing the number of fan coil units can significantly increase maintenance costs; however, the design for this field site included twenty VRF fan coil units which was similar to the baseline nineteen VAV-boxes. Maintenance for the baseline VAV included annual economizer and terminal unit maintenance, while VRF maintenance included biannual condensate system cleaning and filter changes for the fan coil units [2]. Based on conversations with the manufacturer and facility staff, it was assumed no other repairs or refrigerant replacement are needed over the 15-year equipment lifetime. For the economic assessment, maintenance costs were assumed to be similar for both systems.

Table 3 presents the incremental costs, LCC and simple paybacks for the CCHP VRF compared to the baseline VAV system. VAV installed costs were based on published estimates of $20/sqft ($215/sqm) [13]; a similar range of installed costs were found using R.S. Means. CCHP VRF equipment costs ($2.6K per ton) were based on invoices from the demonstration. VRF installation costs were based on mature market estimate ($6K/ton) plus a $20K engineering design. DOAS installed cost ($1.3K/ton) were based on 2016 R.S. Means. VRF/DOAS installed cost of $22.7/sqft ($454/sqm) and incremental cost of $2.73/sqft ($29.38/sqm) aligns with previous studies [2,7]. Note this includes the additional costs for oversizing the CCHP VRF system for a cold climate which is offset by recent reductions in VRF equipment prices. Based on this assessment, replacing a conventional VAV system with a VRF/DOAS in a cold climate has potential to reduce LCC by about $84,660 (25%) with a simple payback of 3 years. This does not include any equipment or energy use for supplemental heating.

Table 3. Life Cycle Costs

	Baseline VAV with Electric Reheat	VRF/DOAS System	
Equipment Cost	$40,000	$49,600	
Installed Cost (retrofit)	$161,000	$183,000	
$/Floor Area	$20.0/sqft ($215.3/sqm)	$22.7/sq. ft ($454.0/sqm)	
Incremental First Costs		$22,000	$2.73/sq. ft ($29.38/sqm)
LCC Savings		$84,660	25%
Simple Payback		3 years	

Assumptions: 15 years equipment life assuming no component or refrigerant replacement; 3.0% discount rate

4. Conclusion

This field study offered a unique assessment of the cold climate performance of an electric cold climate heat pump VRF/DOAS system for a multi-zone office building. Detailed measured field data allowed a direct comparison of the VRF/DOAS system with the baseline conventional VAV system to quantify their relative energy savings and economic benefits. These results can also be used to validate energy savings and cost savings predicted by energy modeling and simulation tools. Based on this demonstration, VRF/DOAS systems can reduce O&M costs and primary energy use (up to 50%) in cold climates. Several factors contribute to the VRF/DOAS energy savings. VRF with ductless fan coils eliminates duct losses associated with forced air HVAC systems. In addition to higher cooling efficiency, VRF can provide zoned cooling eliminating the need for over-cooling and reheat energy use. During heating operation, VRF trim heating is more efficient than electric resistance heating used in VAV-boxes. Likewise, the use of DOAS has multiple energy-saving benefits including more effective humidity control, less over-ventilation, and lower fan energy [9]. These savings may be higher than some sites due to the higher than expected energy use for the baseline VAV system when operated without a building management system.

This demonstration also identified some limitations for electric CCHP VRF systems. Despite the cold climate design and oversizing to meet the heating load, the electric CCHP required supplemental heating to maintain heating capacity for ASHRAE Climate Zone 5. Although the VRF/DOAS system reduced the summer peak electric demand at the field site, VRF/DOAS operation significantly increased the winter peak electric demand, much higher than the summer peak. For typical buildings, the peak electric demand occurs during the summer cooling operation due to electric air conditioning, but the use of electric heating can create

a secondary winter peak demand. With growing use of electric heat pumps, the winter peak demand is likely to exceed the summer cooling peak especially in cold climates.

Future research will focus on more efficient and cost-effective approaches to use supplemental gas-fired heating to enable electric CCHP VRF systems to operate in cold climates and to minimize the impact and energy costs of increasing winter peak electric demand.

Acknowledgements

We wish to acknowledge the Environmental Security Technology Certification Program (ESTCP) for their financial and technical support. We also appreciate the participation and support from Naval Station Great Lakes staff throughout this demonstration.

References

[1] Rowley, P.F., 2020. Gas Engine-Driven Heat Pump (GHP) Cold Climate Field Demonstration. EW-201515. Environmental Security Technology Certification Program (ESTCP). https://serdp-estcp.org/projects/details/0786546a-b196-4f7a-8524-d62bcf0dba16.
[2] Thorton, B., et. al. 2012. Variable Refrigerant Flow Systems. Prepared by Pacific Northwest National Laboratory for the General Services Administration. December 2012.
[3] National Centers for Environmental Information, National Oceanic and Atmospheric Administration (NOAA). Accessed 05/25/2019. < https://www.ncei.noaa.gov/>.
[4] Schuetter, S. and Hackel, S. 2015. Application of Air Source Variable Refrigerant Flow in Cold Climates. Seventhwave white paper. March 2015.
[5] Swanson, G.A., and Carlson, C.A. 2015. Performance and Energy Savings of Variable Refrigerant Technology in Cold Weather Climates. Minnesota Department of Commerce, Division of Energy Resources Contract No. OES-04042011-37612, February 2015.
[6] Lemmon, E.W., Bell, I.H., Huber, M.L., McLinden, M.O. NIST Standard Reference Database 23: Reference Fluid Thermodynamic and Transport Properties-REFPROP, Version 10.0. National Institute of Standards and Technology, Standard Reference Data Program, Gaithersburg, 2018.
[7] EES Consulting. 2011. Measure Summary Report: Variable Refrigera.nt Flow. Prepared for Bonneville Power Administration by EES Consulting. Accessed June 30, 2019.
[8] Goetzler, W. 2017. Variable Refrigerant Flow Systems, ASHRAE Journal April 2017. pp 24-31
[9] ASHRAE. 2017. ASHRAE Design Guide for Dedicated Outdoor Air Systems (DOAS).

14th IEA Heat Pump Conference
15-18 May 2023, Chicago, Illinois

Impact of the European Building Energy Requirements on the Heat Pump Market

Mara Magni*[1], Fabian Ochs[1], Elisa Venturi[1], Georgios Dermentzis[1], William Monteleone[1]

[a]University of Innsbruck, Technikerstraße 13, Innsbruck 6020, Austria

Abstract

To reach the climate targets set for 2040, it is necessary to increase the efficiency of the building stock and foster the electrification of the buildings' heating system. In this framework, heat pumps will play an important role, in the process of phasing-out fossils. Nevertheless, to enable the efficient operation of a heat pump for heating purposes, low supply temperatures are required. This means that the building should be renovated (i.e. to reduce the heating demand) and the emission system should allow for low supply temperature operation.

In this work, an overview of the development of energy policies in Europe is provided to show the requirements in terms of heating demand. In addition, the effect of the renovation deepness on the heating demand and heating load is shown using a reference multifamily building located in Potsdam (DE). For each renovation scenario, the room-wise heating load is calculated and the effect of the heating load reduction due to renovation in combination with different hypotheses for the sizing of the radiators on the design supply temperature and heat pump performances is described.

© HPC2023.
Selection and/or peer-review under the responsibility of the organizers of the 14th IEA Heat Pump Conference 2023.

Keywords: Type your keywords here, separated by semicolons

1. Introduction

1.1. Energy-efficient buildings - development of requirements

The European Union (EU) aim at limiting the environmental impact of buildings through specific policies ([1] presents a good overview of the history of European standardisation, while in [2] the overview is extended to standardisation in China and the USA). A clear example is the recast of the Energy Performance of Buildings Directive (EPBD) [3]. According to the EPBD recast, all new buildings must be nearly zero energy buildings (nZEB) by the end of 2020. Nevertheless, the definition of nZEB is up to each Member State. However, the common aspect is to achieve very high energy efficiency and to use as much as possible on-site (or nearby) renewable energy to meet the remaining low energy demand of the buildings. In addition, Member States should develop a methodology for cost optimality. The history of the definition of nZEBs in the European context is shown in Fig. 1.

The national nZEB definitions are quite different and hardly comparable [4] and in both Germany and Austria the current level of the requirements fail to achieve the goal of significantly improving energy efficiency in the building sector and thus reducing primary energy consumption and CO_2 emissions. Technical development would allow achieving the Passive House standard already 30 years ago demonstrating that the implementation of energy-efficient buildings does not present any technical hurdles. Calculated over the life cycle, such buildings are also more economical than buildings realised according to the current level of requirements [5]. Fig. 1 shows the development of energy efficiency requirements for buildings in Germany and Austria compared to the Passive House Standard. The heating demand was calculated based on a terraced

* Corresponding author. *E-mail address:* Mara.Magni@uibk.ac.at

house (Passive House Kranichstein). The first German standard dates to 1977, in which the maximum U-value of the individual building components was defined. This was followed by the Heat Conservation Ordinance (WSchV 95) that introduced the calculation of the energy balance and a maximum value for the annual heating demand.

If the tightening of the requirements had continued at the same pace, the maximum heating demand (HD) would have reached the passive house standard already in 2013.

The first Energy Saving Ordinance (EnEV) came into force in 2002 and replaced the annual heating demand as a criterion with the primary energy demand of the building compared to a reference building. In addition, non-renewable primary energy factors were defined.

In Austria, the development towards energy-efficient buildings took place somewhat later: based on the Energy Performance Certificate Act (EAVG) in 2006, the guideline OIB-6:2007 imposed a limit on the HD. The level was then tightened in 2010 and 201. In 2014, the National Plan for the definition of nZEBs in Austria was published (the review took place in 2018). Since the introduction of the guideline OIB-6:2015, the so-called dual path (see Fig. 1 fgee and EEB) has been defined in Austria. With the new version of the OIB guideline, non-renewable primary energy is used as an indicator and excludes household electricity in residential buildings).

The requirements for the thermal quality of the building envelope have remained essentially unchanged since OIB-6:2007 (external wall max. U = 0.35 W/(m² K)).

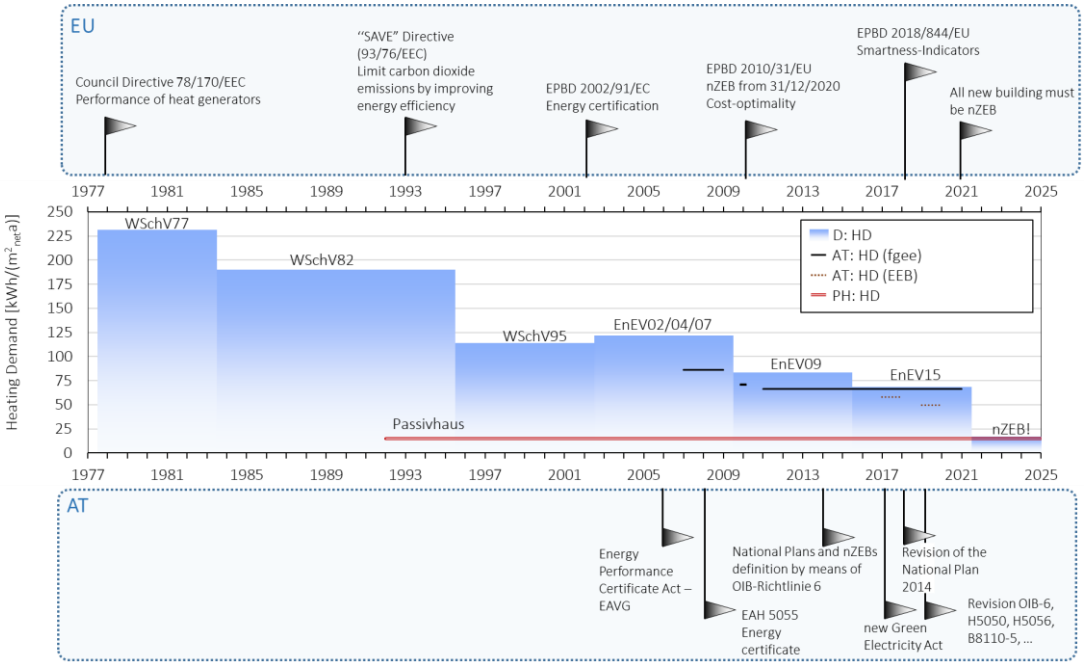


Fig. 1: Heating demand according to the German legal framework compared to the passive house standard [6] and history of nearly zero energy buildings - nZEBs (Directive 2010/31/EC) [7].

In the United Kingdom the Energy Performance of Buildings (England and Wales) Regulations 2012 set the Energy Performance Certificates (EPCs) as a requirement whenever a building is built, sold or rented and, in some circumstances, refurbished. With the Energy Efficiency Regulations 2015, it will be illegal to lease buildings with a EPC rating of F or G [8], [9].

In Spain, the procedure for the calculation of the EPC are defined by Royal Decree 235/2013 [10]. The Royal Decree-Law 14/2022 foresee a wide range of energy saving measures (e.g. limitation of the heating and cooling set points to 19°C and 27°C respectively, encouraging electrifications and penetration of renewables, etc..).

In Italy, the EPBD 2002 was implemented with Decreto Legislativo 192/2005, which introduces the criteria and method for the calculation of the EPC. The DM 26/06/2015 define new rules for the calculation of the EPC and the minimum energy requisite for new and renovated buildings [11].

In Sweden, the Energy Performance Certification Act (Sw. Lag (2006:985) om energideklaration för byggnader) makes the EPC mandatory for certain building categories. A minimum standard (i.e. from A to G) is introduced for buildings classified after 1/1/2014. In 2020, the PBF and the BBR were revised tightening

also the requirements for energy performance for buildings. The Act (2006:985) on energy performance certificates for buildings as well as Boverket's BED was updated in March 2021, regarding inspections [12].

As non-EU-country, Switzerland is not obliged to implement the EPDB, nevertheless Switzerland as member of CEN, agreed to adopt all EU standards [13]. The MuKEn 2014 define the sample regulation used as a reference for the application of the energy regulation in the different cantons.

In Belgium, the first EPB ordinance was defined in 2007. In 2015 a new ordinance (COBRACE) came into force, which transposes the EPBD 2010 [14].

A deep comparison of the nZEB implementation in different European countries is also presented in [4], [15] and [16].

1.2. Plus, zero or near-zero energy building

Various definitions of highly efficient buildings (i.e. good quality of the building envelope) in combination with a high share of renewable energy (usually PV) are in use with the aim of achieving zero, almost zero or plus energy. These definitions sometimes differ significantly with regard to the boundary of the energy balance (space heating, domestic hot water, auxiliary energy, household electricity) and the type of balancing. Plus, usually refers to net-plus, i.e. annual balance. This is possible in very efficient buildings such as the Passive House with a PV system of about 5 kWp; in multi-storey residential buildings, net-zero is usually no longer possible from about 4 storeys upwards if household electricity is also taken into account. It is important to pinpoint that a net-zero building still requires a considerable amount of energy from the grid in winter. According to [17], an NZEB could theoretically be a building with relatively high U-values and consequently a high heating demand having a correspondingly large photovoltaic (PV) system. Such an NZEB would generate a large PV surplus in summer while still having a high grid load during the heating period (so called "winter gap").

The final energy demand and primary energy demand of different building concepts and energy standards are shown in Fig. 2 [18]. In terms of primary energy demand for heating and domestic hot water (DHW), the Solar Active House with a specific limit value (based on the net floor area) of 15 kWh/(m² a) is slightly below that of the Passive House (i.e. 18.5 kWh/(m² a)), this considering that the building is supplied with a heat pump (HP) characterized by an annual performance factor of 2.4 (for heating and DWH purposes and including the losses of the storage and distribution system [19]).

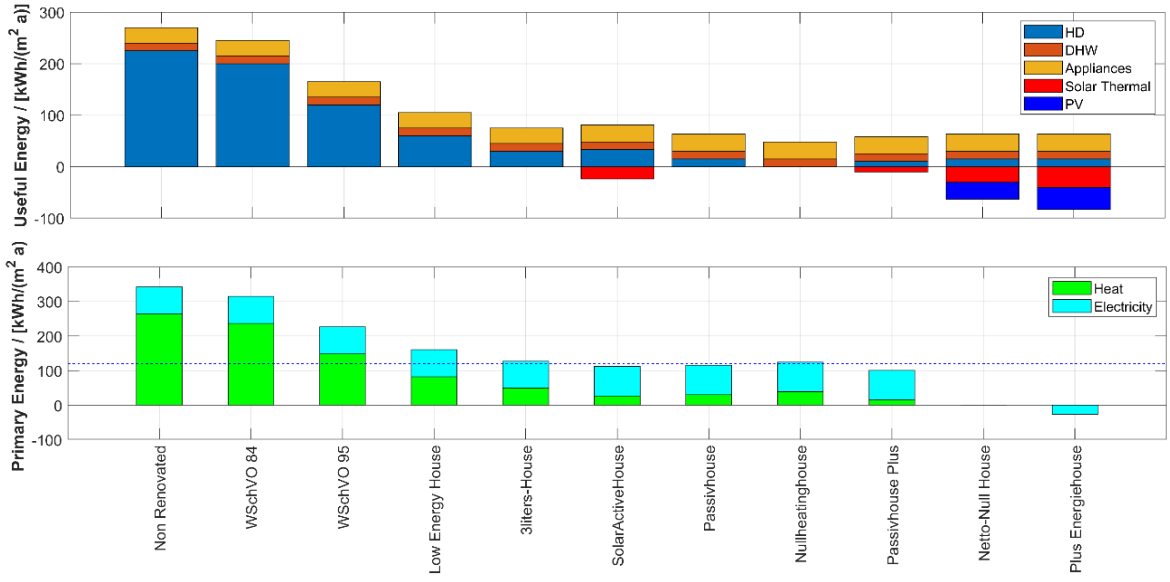


Fig. 2: Final energy demand (top) and primary energy demand (bottom) of different building concepts. The results are normalized with a reference area of 140 m². The following inputs are used for generating the results of the figure: domestic hot water (DHW) 25 l/d/P at 60 °C and 4 persons, no heat losses through distribution and storage; household electricity demand: 3500 kWh/a [18].

Passive House Institute set the limit on the primary energy to 120 kWh/(m²energy reference area a) for heating, domestic hot water, technical and household electricity requirements (incl. ventilation and auxiliary power). In addition, since 2015, the Passive House Standard is assessed with the indicator PER (Primary Energy Renewable)[20].

1.3. Role of Heat Pump

As highlighted in [21], heat pumps are the driving technology for the decarbonization of the heating in the building sector and it is foreseen that the number of heat pumps installed globally will rise from 180 million to 600 million in 2030. This in combination with the renovation of the building stock will enable the transition towards a higher share of renewable energy in the electricity grid (see also [22]). Heat pump is a very flexible and efficient technology that as exhaustively reported in [23] can work with different sources, can be applied at different levels (i.e. district, centrally building or block-wise, decentral flat-wise) and can be used for different services (i.e. heating, domestic hot water, cooling, mechanical ventilation in combination with an exhaust or extract air heat pump).

Nevertheless, some challenges have to be overcome to enhance the application of heat pumps. According to [21] the main challenges are: high upfront, operating cost and emission depending on the electricity mix, space restrictions, heating distribution system, low efficiency of heat pump in combination with high-temperature radiators, permission to install the external unit due to visual and sound reasons, social acceptance.

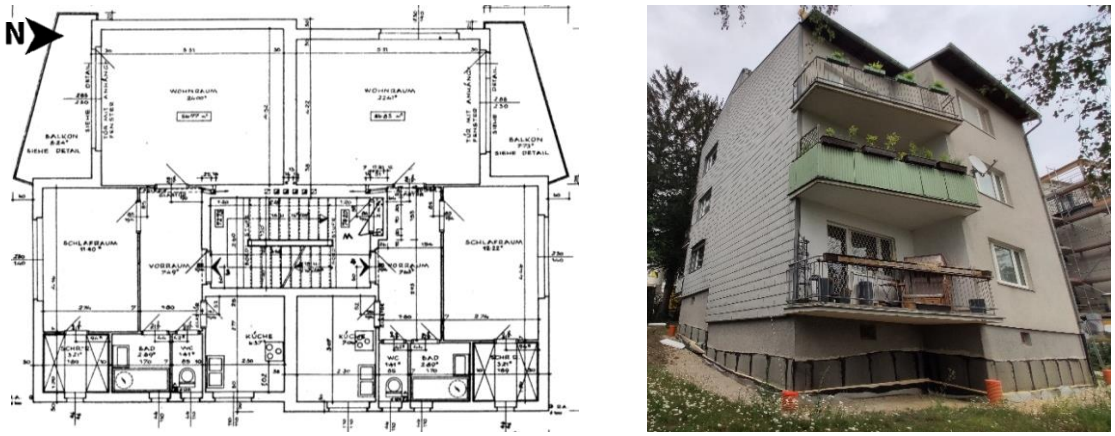
New heat pumps, with adapted refrigerants might help to improve the performances at higher supply temperatures [24]. Nevertheless, the COP will inevitably and drastically decrease as the temperature lift increases (see [25], Figure 58 for a comparison of performances at low and medium temperature level of heat pumps using different refrigerant fluids). In addition it is important to highlight that the performances of the heat pumps under real operating conditions are typically lower compared to the declared performances of the manufacturer [19].

2. Methodology

2.1. Reference Building

The reference building is a typical Austrian multi-family house composed by 3 floors and six flats of 56.8 m^2. The total net floor area of the building is 340.8 m^2 while the total energy reference area is 364.5 m^2. Within this work, the results will be presented using the net floor area as a reference. The walls of the building are made with hollow brick construction, while the roof and floor core construction are based on concrete concave boards.

In Fig. 3 the floor plans and one picture of this building are reported.



(a) (b)

Fig. 3: (a) Floor plan; (b) Picture of the southwest side of the building.

With regards to the weather data, the Test Reference Year (TRY) of Potsdam (generated using Meteonorm v8.1 [26]) is used for the analysis within this work (see Fig. 4).

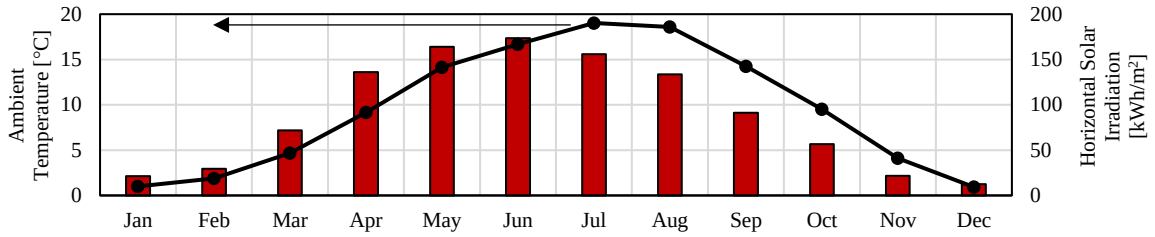


Fig. 4: Monthly average ambient temperature (black line) and monthly horizontal solar irradiation (red columns) for the TRY of Potsdam.

2.2. Renovations

The renovation deepness is very heterogeneous in existing buildings, in fact step wise renovation are often performed. In [27] (see Figures 14-16) an analysis of the average U-values of walls, roof and windows for 45 buildings built between 1979 and 2005 is presented. From this analysis it can be seen that buildings built in the same period can be renovated with very different insulation levels. For this reason in this work, different renovation scenarios are considered for the envelope of the reference building and an overview is provided in Table 1, where the U-values of the building envelope are reported as well as the average U-value (i.e. Ht') considering an envelope area of 779.2 m^2 and the equivalent ventilation rate (which is reduced when a mechanical ventilation system with heat recovery is applied).

Table 1: Overview of the renovation scenarios for the envelope of the reference building.

Renovation scenarios		1	2	3	4	5	6	7	8	9	10	11	12	13
U-Roof	[W/(m^{2}K)]	1.46	**0.37**	**0.16**	0.16	0.16	0.16	0.16	0.16	0.16	0.16	0.16	0.16	0.16
U-Wall N		1.25	**0.49**	0.49	0.49	0.49	0.49	0.49	0.49	0.49	**0.24**	0.24	0.24	**0.15**
U-Wall E		1.25	**0.49**	0.49	**0.12**	0.12	0.12	0.12	0.12	0.12	0.12	0.12	0.12	0.12
U-Wall S		1.25	**0.49**	0.49	0.49	0.49	0.49	0.49	0.49	**0.24**	0.24	0.24	0.24	**0.15**
U-Wall W		1.25	**0.77**	**0.22**	0.22	0.22	0.22	0.22	0.22	0.22	0.22	**0.13**	**0.22**	**0.13**
U-Floor		1.17	1.17	1.17	1.17	1.17	1.17	**0.27**	0.27	0.27	0.27	0.27	0.27	0.27
U-Window S		3.00	**1.92**	1.92	1.92	1.92	1.92	1.92	1.92	**1.55**	1.55	1.55	**0.80**	0.80
U-Windows E		3.00	**1.92**	1.92	1.92	**0.80**	0.80	0.80	0.80	0.80	0.80	0.80	0.80	0.80
U-Windows N		3.00	**1.92**	1.92	1.92	1.92	1.92	1.92	1.92	1.92	**1.55**	1.55	**0.80**	0.80
U-Windows W		3.00	**1.92**	1.92	1.92	1.92	1.92	1.92	1.92	1.92	1.92	1.92	**0.80**	0.80
Thermal Bridges	[W/(m K)]	0.10	0.10	0.10	0.10	0.10	0.10	0.10	0.10	0.10	**0.05**	0.05	0.05	0.05
Ht'	[W/(m$^2_{envelope}$ K)][1]	1.59	0.97	0.76	0.70	0.69	0.69	0.51	0.51	0.47	0.39	0.37	0.32	0.29
Ventilation	[1/h]$_{equiv}$	0.27	0.27	0.27	0.27	0.27	**0.17**	**0.27**	**0.17**	0.17	0.17	0.17	0.17	0.17
Efficiency of the ventilation heat recovery	η [-]	0.00	0.00	0.00	0.00	0.00	0.75	0.00	0.75	0.75	0.75	0.75	0.75	0.75

The yellow marked cells of Table 1 highlight the changes made in one renovation case compared to the previous one to facilitate readability. The first case corresponds to a completely non-insulated building, the second case introduces a few centimetres of insulation material in all the structures and double-pane windows. In all the following cases other improvements to part of the envelope and/or the ventilation system are introduced leading to an always more efficient building. The only exception is between cases 6 and 7 where the envelope is improved but the ventilation system has no heat recovery. The set point temperature is considered to be 20°C[2].

2.3. Heating and Domestic Hot Water demand and Load calculations

For each renovation scenario, the building envelope is designed and the heating demand (HD) and load (HL) for the whole building and flatwise are calculated using the Passive House Planning Package PHPP [28]. In addition, the whole building is evaluated by means of dynamic simulation using the carnotUIBK toolbox [29] developed in Matlab/Simulink to assess the dynamic heating demand (on 10 min basis) of the building throughout the whole year.

[1] $H_t' = \frac{\sum_i A_i \cdot U_i}{\sum_i A_i}$ where i are all the parts of the thermal envelope (i.e. walls, windows, roof, floor) and the thermal bridges.

[2] To assess the real energy demand the prebound effect should be considered for low insulated buildings [35].

PHPP is a quasi-steady-state tool based on Standard ISO 13790:2008 [30] and it has been shown that it can accurately predict the HD of the building [31]. In addition, PHPP can calculate the HL of the building, but in contrast to the standard EN 12831-1 [32], it accounts also for heat gains and considers two different weather scenarios (i.e. cold and sunny day and moderately cold but overcast day).

Therefore, for the sizing process of the radiators, the room-wise heating load is calculated according to the standard EN 12831-1 [32] for each renovation scenario.

As regards the DHW profile, the tapping cycle M described in EN 16147:2017 [33] is used. A reduction factor of 0.625 (resulting in an energy demand of 3.7 kWh/(flat day)) is applied considering an average of 2.5 persons per flat resulting in the profile reported in Table 2. A supply temperature of 55°C is considered for the DHW preparation due to legionella requirements.

Table 2: Hourly useful energy demand for DHW preparation for the whole building.

Hour of day	1-6	7	8	9	10	11	12	13	14	15	16	17	18	19	20	21	22-24
kWh	0	6.04	1.58	0.79	0.39	0.79	1.18	0.00	0.39	0.39	0.39	0.00	1.18	0.39	2.76	5.64	0.00

2.4. Dimensioning of Radiators and supply temperature evaluation

Three different scenarios are considered for the sizing of the radiators: radiators sized in the renovation scenario 1 with a supply temperature of 90°C, radiators sized in the renovation scenario 2 with a supply temperature of 90°C and radiators sized in the renovation scenario 8 with a supply temperature of 45°C. All of these three cases are calculated considering once the room-wise HL according to EN 12831-1 [32] without reheating power and once considering a reheating power of 12 W/m^2.

Since the radiator exponent could range from 1.2 to 1.4 depending on the radiator model and the temperature difference between supply and return over the radiator could range between 10 K and 40 K (except for the low-temperature radiators, where the ΔT could range between 5 K and 10 K) the sizing of the radiators for the different scenarios is performed considering 10 different exponents from 1.2 to 1.4 with a step of 0.02 in combinations with a ΔT ranging from 10 K to 40 K with a step of 10 K for the high-temperature radiators and ranging from 5 K to 10 K with a step of 5 K for the low-temperature radiators.

In the first step the radiators are sized for each room ($n_{el,room_i}$) using equations (1) knowing the room-wise reference HL ($HL_{Ref_{room_i}}$), the nominal power of each radiator element[3] (P_{nom}), the radiator exponent n, the reference temperature difference (fixed to 50 K) between the average radiator temperature and the air temperature (ΔT_{ref})and knowing the supply and return temperature to the radiator by means of equation (2) it is possible to calculate the logarithmic temperature difference ΔT_{log}.

$$n_{el,room_i} = \text{ceil}\left(\frac{HL_{Ref_{room_i}}}{P_{nom}}\right) \cdot \frac{1}{\left(\frac{\Delta T_{log}}{\Delta T_{ref}}\right)^n} \quad (1)$$

$$\Delta T_{log} = \frac{(T_{sup} - T_{air}) - (T_{ret} - T_{air})}{\ln\left(\frac{T_{sup} - T_{air}}{T_{ret} - T_{air}}\right)} \quad (2)$$

Sizing the radiator with different ΔT implies different dimensions (i.e. pipe diameter) of the distribution system as for a given reference power different ΔT are achieved by changing the mass flow. Therefore for every ΔT used during the sizing process, the diameter of the pipe serving one flat is determined using equation (*3*) considering a speed of 0.5 m/s. Considering that this system (distribution and emission) is kept constant during the following renovation steps it is considered that the water velocity can be increased up to 1.5 m/s avoiding noise problems but helping to reduce the ΔT and therefore the supply temperature after the renovation.

$$\dot{m}_{flat} = \frac{HL_{Ref_{flat}}}{cp_{water}\,\Delta T} = v_{water} \cdot \rho_{water} \cdot \pi \left(\frac{d}{2}\right)^2 \quad (3)$$

For each subsequent renovation (with respect to the sizing case) knowing the HL of each room, and the number of elements of the radiator, the ΔT_{log} can be calculated by reversing equation (1). Knowing the minimum and maximum water mass flow and the HL of the renovated flat, the ΔT over the radiator can be determined inverting equation (3) and knowing ΔT_{log} and ΔT the supply and return temperatures can be calculated using equation (2).

[3] This is fixed to 100 W as changing P_{nom} will linearly influence $n_{el,room_i}$ without changing the final conclusions on the minimum required supply temperature. P_{nom} influences the dimension of the radiator that is not fixed within this study.

At this point for each renovation case, a set (i.e. 44 cases for the high radiator temperature and 22 cases for the low-temperature radiator) of possible supply and return temperatures are obtained (considering the different sizing possibilities varying ΔT and n and the mass flow rate). In the results section, for sake of simplicity, the minimum supply temperature (that will be obtained when the radiators are sized with the highest ΔT, the minimum exponent[4] and using the maximum mass flow rate) and the maximum supply temperature (that will be obtained when the radiators are sized with the lowest ΔT, the maximum exponent[4] and using the minimum mass flow rate) are shown and used for the evaluation of the heat pump performances.

2.5. Heat Pump performance evaluation

To estimate the impact of the renovation scenarios and radiator sizing on the performances of a central air to water Heat Pump (HP) a Carnot-based approach is used considering a conservative Carnot performance factor of 0.35 [23]. The building-wise heating demand for each time step (i.e. 10 min) is defined by means of the dynamic building simulation and the ambient temperature is known from the TRY. For each sizing scenario of the radiators (i.e. radiators sized in renovation scenario 1, 2 or 8 considering or not the reheating power due to intermittent operation) a maximum and minimum supply temperature is defined for each renovation scenario and this is used as a constant throughout the year in equations (4) and (5) to calculate the COP and electricity demand of the HP.

$$COP(t) = \eta_{Carnot} \cdot \frac{T_{supply}}{T_{supply} - T_{ambient}(t)} \tag{4}$$

$$P_{el,HP}(t) = \frac{HL_{building,sim}(t)}{COP(t)} \tag{5}$$

Only the cases in which the required supply temperature of the heating system is below 60°C are considered compatible with a HP operation.

As regards the DHW preparation, equations (4) and (5) are used considering T_{supply} equal to 55°C and instead of $HL_{building,sim}(t)$ the DHW demand shown in Table 2 is used.

3. Results

3.1. Heating demand and Heating Load for the different renovation scenarios

Fig. 5 shows the HD calculated using the PHPP flat-wise (i.e. for each of the six flats), PHPP building-wise and by means of dynamic simulation for the whole building. From here it can be noticed that the annual HD predicted by the building-PHPP presents a good match with the annual results of the dynamic simulation with a relative deviation of maximum 8% for the renovation scenario 1.

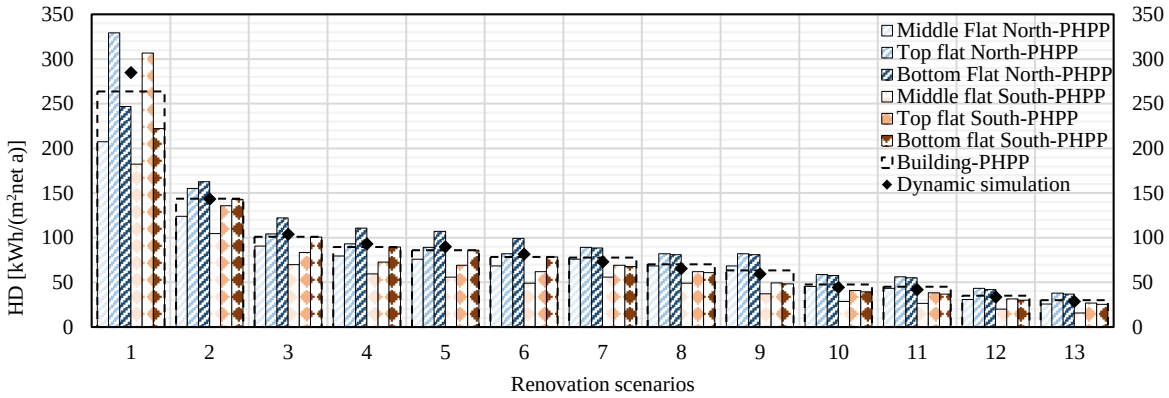


Fig. 5: HD calculated with the PHPP-flat-wise, PHPP-building-wise and by means of dynamic simulation for the whole building for all the renovation scenarios.

In addition, it can be seen that the HD of the flats depends on the orientation (i.e. in this case south-north) due to the solar gains and on the position of the flat within the building. In fact, the middle flats present always

[4] Higher radiator exponent leads to a higher reduction of the radiator emitted power when the average radiator temperature is reduced. Sizing the radiator with higher ΔT for a fixed supply temperature leads to bigger radiators since they have to deliver the required power with a lower ΔT_{log}.

the lowest HD while the top and bottom flats have the highest HD. Insulating the roof in renovation 1 and 2 leads to lower HD of the top flats compared to the bottom flats. When also the floor is insulated (in step 7), top and bottom flats have similar HD. The best renovation scenario (i.e. 13) leads to a building HD of around 30 kWh/(m^2_{net} a). Fig. 6 reports the HL calculated by means of flat-wise PHPP for all the renovation scenarios. Comparing Fig. 5 with Fig. 6 it can be noticed that the HD and HL follow the same trend. In addition, it is important to mention that in the case of installation of a decentral flat-wise HP solution the HL reported in Fig. 6 should be used for the HP sizing process.

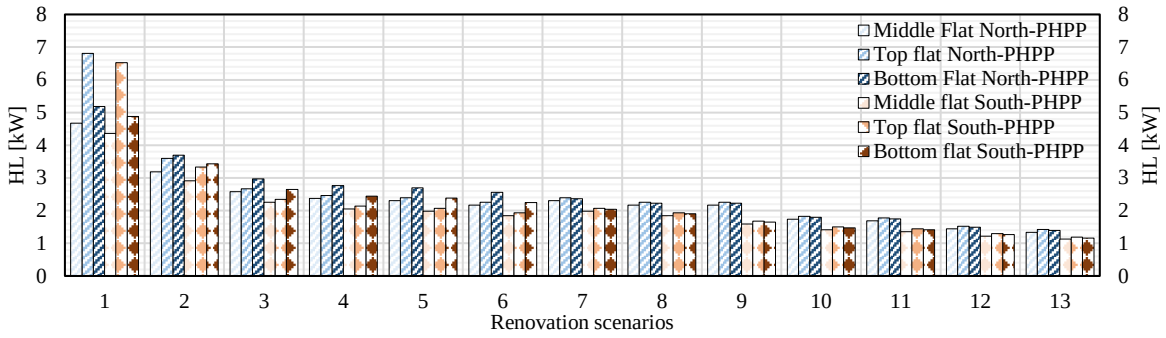
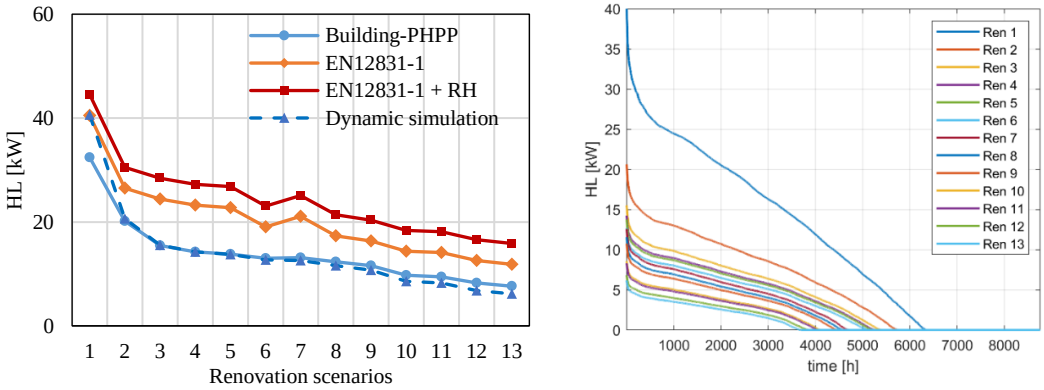


Fig. 6: HL calculated with the PHPP-flat-wise for all the renovation scenarios.

Fig. 7 reports on the left-hand side (a) the HL of all the renovation scenarios calculated with the PHPP-building-wise, the building HL calculated room-wise according to the standard EN 12831-1 considering or not the additional reheating power and the maximum HL derived by means of dynamic simulation. While on the right-hand side (b) of Fig. 7 the load duration curves for each renovation scenario as a result of the whole building dynamic simulation are shown. The HL from the dynamic simulation reported in Fig. 7a corresponds to the maximum of the sorted HL in Fig. 7b (the maximum HL is only required for a few hours a year). From Fig. 7a it can be seen that the HL predicted by the building-PHPP match well with the maximum HL from dynamic simulation except for the renovation scenario 1. It is noteworthy to mention that the HL predicted by the building-PHPP is in average -40% compared to the HL calculated according to EN 12831-1 and -50% when also the reheating power is considered. This is justified by the fact that in the standard stricter conditions are applied for the calculation (i.e. no internal gains, non-heated neighbouring apartments, high ventilation rate, low ambient temperature). These boundary conditions represent the worst-case scenario in terms of HL, which is anyway unlikely to happen at least for long heating periods.

To avoid oversize the HP system, it is recommended to calculate the heating load also through dynamic simulation [34] or using the PHPP (that according to [31] is in good agreement with the results of the dynamic simulation tool). This is important to avoid, a reduction of the HP efficiency due to frequent "on-off" cycles. On the contrary, regarding the dimensioning of the heat emitters, it is recommended [34] to perform a room-wise calculation of the heat load based on the EN 12831. The power needed for the preparation of the DHW has also to be considered during the sizing process of the HP and this depends on the DHW demand, but also the storage capacity and HP operation.



(a) (b)

Fig. 7: (a) HL calculated with the PHPP-building-wise, according to the standard EN 12831-1 considering or not the additional reheating power and by means of dynamic simulation for the whole building for all the renovation scenarios; (b) load duration curve as a result of the whole building dynamic simulation.

3.2. Supply temperature

Fig. 8 shows the possible supply temperature span for each renovation scenario assuming that the radiators could be sized: in the renovation scenario 1 considering the additional reheating power due to intermittent operation of the heating system or not (i.e. Case_1+RH and Case_1), in the renovation scenario 2 (i.e. Case_2+RH and Case_2) and in the renovation scenario 8 with low-temperature radiator (Case_8+RH and Case_8), see also Section 2.4 for additional information. Each case is represented by a temperature span instead of a point as a possible range of radiators was considered (i.e. with different exponent n) sized with different ΔT and run with a range of mass flow that keeps the water speed between 0.5 m/s and 1.5 m/s. The renovation scenarios in which the radiators are installed are exemplarily chosen in this work. In reality, the radiators could be changed/installed in any renovation scenario and could be sized considering different supply temperatures leading to an even wider range of possible supply temperatures required in each renovation.

From Fig. 8 it can be seen that starting from renovation 8 to 13, a wide range of possible supply temperatures could be expected depending on the choice made in the previous renovations of the building. This range goes from low temperatures (i.e. around 35-40°C) up to 80°C (i.e. Case_2).

It is not recommended to apply a monovalent heat pump system if a flow temperature of more than 60°C is required, as its performance would be too low, however, new-generation heat pumps (e.g. propane R290) can reach flow temperatures of 70-75°C. For this reason, the performance of all cases that guarantee a flow temperature below 75°C has been calculated (see Fig. 8, Fig. 9 and Fig. 10). Another noteworthy aspect is that in some countries subsidies for heat pumps are only given if the design flow temperature is below a certain value (e.g. 40°C for Austria). It is important to mention that the temperatures reported in Fig. 8 are design temperatures required in the worst winter conditions and that during the heating season a weather compensation control could be applied reducing the supply temperature based on the ambient temperature allowing higher performances of the HP system and/or longer operation time.

Another aspect highlighted by the supply temperature analysis of Fig. 8 is that renovating only part of the building (e.g. the roof and west-wall from ren. 2 to ren. 3 see Table 1) leads to a reduction in terms of building wise HD and HL (see Fig. 5 and Fig. 6) but might not lower the HL of some rooms, which may then become the bottleneck for the definition of the maximum flow temperature (e.g. see ren. 2 ren. 3 in Fig. 8).

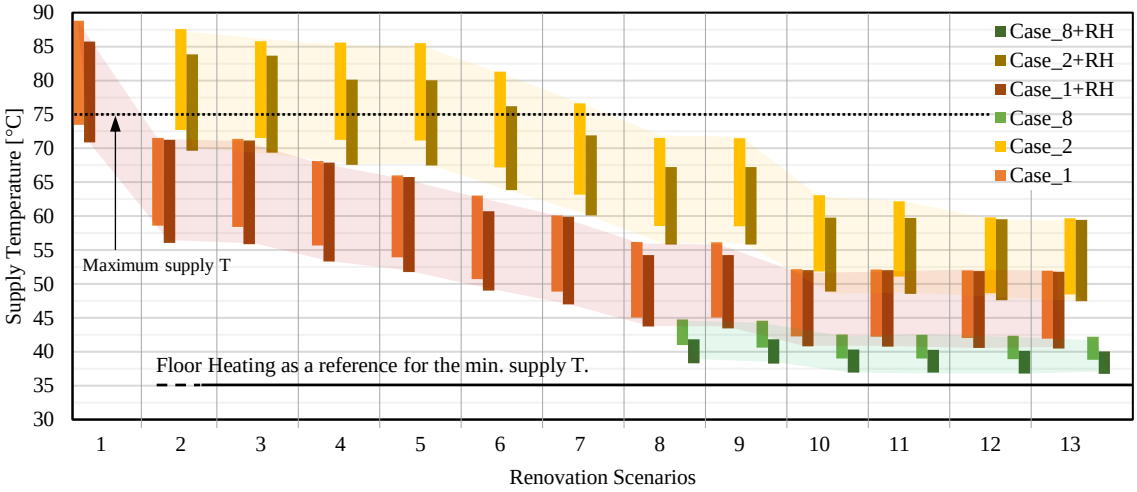


Fig. 8: Design supply temperature ranges required in the different renovation scenarios considering different sizing conditions (i.e. Case 1,2,8 w or w/o reheating (RH)). The different radiator typologies (i.e. different exponent n) sized with different ΔT and considering different mass flows that keep the speed between 0.5 m/s and 1.5m/s define the high of each bar.

3.3. HP performances

Fig. 9 shows the annual electricity demand and Fig. 10 the SPF of the HP for space heating considering the different renovation scenarios (see Fig. 5 and Fig. 7b for annual and sorted heating demands of the different renovations) and the different cases for the design supply temperature (see Fig. 8). The calculation of the electricity demand and SPF of the HP is performed as explained in Section 2.5 considering a Carnot performance factor of 0.35. Only the cases that allow for a supply temperature below 75°C are considered to be compatible with an HP operation and therefore their results are reported in Fig. 9 and Fig. 10. From Fig. 9 it can be noticed that the reduction of the heating demand with increasing quality of the building envelope and

ventilation system leads to a reduction of the electricity demand. Nevertheless, for some specific renovation scenarios (i.e. for the considered cases from 8 to 13) the electricity demand could be further reduced of 38% by reducing the supply temperature and therefore increasing the SPF (see Fig. 10). It is important to mention that the absolute difference in terms of electricity demand between the different cases of one specific renovation scenario is reduced when the heating demand is reduced making the building system more robust against non-optimal operation.

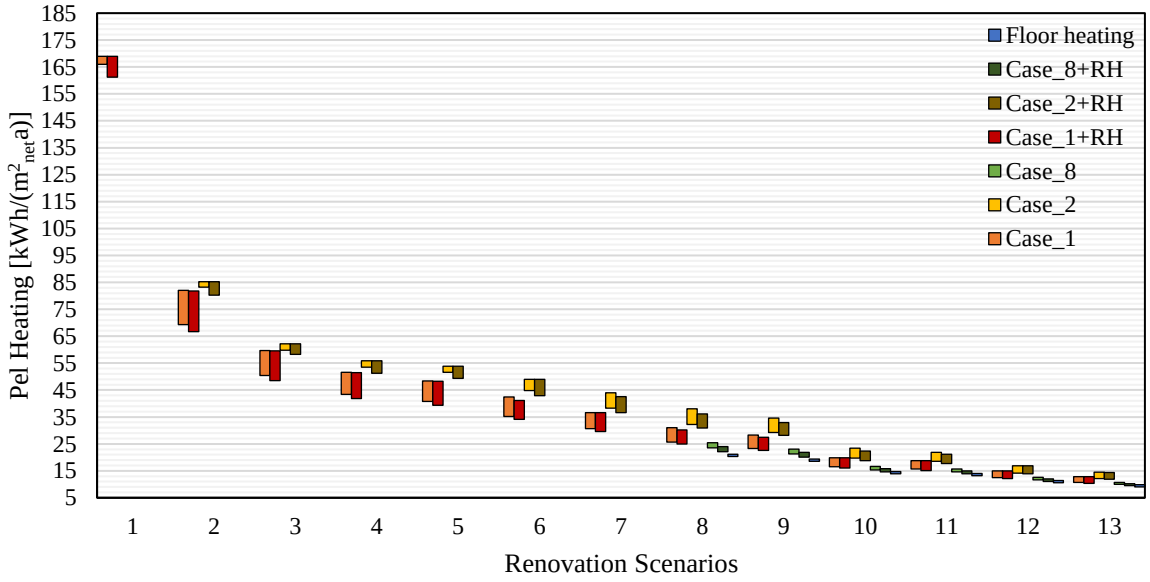


Fig. 9: Annual Electricity demand of the HP for space heating considering the different renovation scenarios and supply temperature.

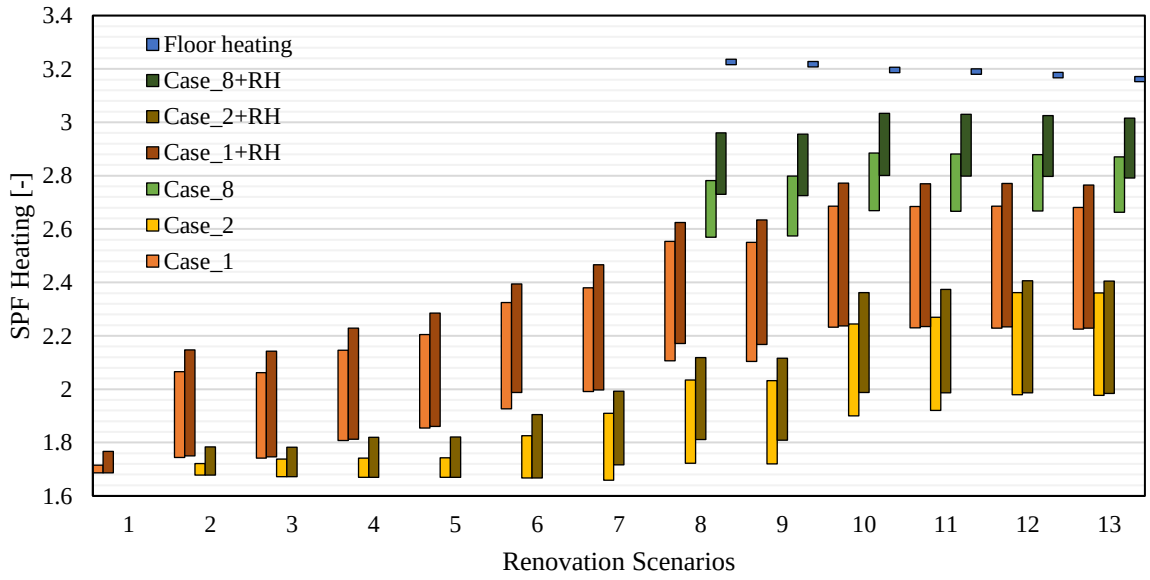


Fig. 10: SPF of the HP for space heating considering the different renovation scenarios and supply temperature.

For all the renovation scenarios the domestic hot water (thermal energy demand of 23.5 kWh/(m^2_{net} a)) is prepared by the air to water HP with a constant supply temperature of 55°C leading to an SPF of 2.5 and an electricity demand of 9.3 kWh/(m^2_{net} a).

4. Conclusions

Within this work, an overview of the development of energy policies in Europe is provided to show the requirements in terms of heating demand. To show the impact of these regulations on the heating load and therefore on the required heat pump size and performance a multi-family house located in Potsdam (DE) is

used as a reference. Thirteen different renovation scenarios are analysed. These lead to progressively reduced heating demand and load, which is calculated on the building and flat level using the Passive House Planning Package (PHPP). The performance of the heat pump and the feasibility of installing this type of system in a renovated building highly depend on the required supply temperature, which is defined by the size and typology of the installed radiators and the design heating load. In this study, the room-wise heating load is calculated according to the EN 12831-1 for each renovation scenario and it is used as a basis for sizing the radiators (different radiator exponents, temperature difference for the sizing process and mass flow are taken into account) considering that high-temperature radiators might be installed in the non-renovated case, or in a slightly renovated case and low-temperature radiators might be installed on a moderately renovated case. Based on the different scenarios for the sizing of the radiators a range of possible supply temperatures for each renovation scenario is defined. Finally, the performances of a central air-to-water heat pump with a Carnot performance factor of 0.35 are evaluated using the calculated supply temperature and the heating demand of the building obtained by means of building-wise dynamic simulations.

The results show that the heating load of the reference building, characterized by a net floor area of 340.8 m^2, can be reduced from 32 kW to 8 kW (the heating demand from 264 to 30 kWh/(m^2a)) by means of thermal renovation of the building envelope and the introduction of mechanical ventilation. The heating load flat-wise, for the worst flat, decreases from 6.8 kW to 1.4 kW. This demonstrates the need of introducing more small-size (i.e. micro) heat pumps on the market as their demand in the future will increase.

The analysis of the supply temperature shows that to enable an efficient heat pump operation it is necessary to have highly over-dimensioned radiators, very deep thermal renovation or to have at least a moderate thermal renovation in combination with a replacement of the existing radiators with low-temperature radiators. Depending on the installed emission system, for a given renovation, the SPF of the heat pump could vary between 1.7 and 3.2 leading to a reduction in electricity demand of up to 46%. As expected, the best efficiency is reached with the floor heating system. Also substituting the existing radiators with low temperature radiators (case 8) might highly contribute to improve the SPF. The worst scenario is represented by the case 2 (high temperature radiators installed during a partial renovation e.g. ren. 2). In this case, the radiators are only slightly oversized compared to case 1 (radiators sized for the non-insulated building – ren. 1), thus they do not allow for significant temperature reduction throughout the various renovation levels.

It is also important to remark that a high-quality thermal renovation not only allows an efficient operation of the heat pump but also makes the building-HVAC system more robust against non-optimal operating conditions.

In a future work, the effect of changing radiators only in the bottleneck rooms should be considered, the performances of the system should be analysed also considering a reduction of the supply temperature throughout the year based on the ambient temperature and different heat pump typologies (e.g., air source or ground source heat pumps) with different performances should be included in the evaluation.

References

[1] M. Economidou, V. Todeschi, P. Bertoldi, D. D'Agostino, P. Zangheri, and L. Castellazzi, "Review of 50 years of EU energy efficiency policies for buildings," *Energy and Buildings*, vol. 225. Elsevier Ltd, p. 110322, Oct. 15, 2020, doi: 10.1016/j.enbuild.2020.110322.

[2] R. Wang, W. Feng, L. Wang, and S. Lu, "A comprehensive evaluation of zero energy buildings in cold regions: Actual performance and key technologies of cases from China, the US, and the European Union," *Energy*, vol. 215, p. 118992, Jan. 2021, doi: 10.1016/j.energy.2020.118992.

[3] European Parliament, "Directive 2010/31/EU," *Off. J. Eur. Union*, vol. L153/13, no. 18.6.2010, pp. 13–35, 2010, doi: 10.3000/17252555.L_2010.153.eng.

[4] C. Wemhoener, F. Ochs, M. Magni, and C. Betzold, "Methodology for comparison of nZEB ambition level in different countries by building and system simulation," in *BS conference*, 2021.

[5] P. Institut, "Are Passive Houses cost-effective?" https://passipedia.org/basics/affordability/investing_in_energy_efficiency/are_passive_houses_cost-effective (accessed Nov. 15, 2022).

[6] Passivhaus Institut, "Nearly Zero Energy Building? Das Passivhaus gibt eine Antwort." https://passipedia.de/grundlagen/energieeffizienz_als_wichtigste_kuenftige_energiequelle/nearly_zero_energy_building_das_passivhaus_gibt_eine_antwort (accessed Nov. 15, 2022).

[7] BPIE, "Nearly Zero Energy Buildings Definitions Across Europe," 2015.

[8] C. Vanessa, "Energy Efficiency (private Rented Property) (England and Wales) Regulations 2015 |

Butler Sherborn," 2020. https://www.butlersherborn.co.uk/property-blog/energy-efficiency-private-rented-property-england-and-wales-regulations-2015 (accessed Mar. 04, 2023).
[9] A. Lionel Delorme and K. Higley, "EPBD Implementation in United Kingdom-England," 2020.
[10] A. D. Martín, "EPBD Implementation in Spain," 2016.
[11] A. Gabriella Azzolini, F. Hugony, and A. Martino, "EPBD Implementation in Italy," 2020.
[12] H.-O. Authors *et al.*, "EPBD Implementation in Sweden," 2021.
[13] G. Zweifel, "Implementation of EN-EPB standards in Switzerland," *REHVA J.*, pp. 13–15, 2019.
[14] C. Danlois, S. Gobiet, Y. Mortehan, and I. Rolin, "EPBD Implementation in Belgium," 2020.
[15] C. Wemhoener, L. Rominger, S. Buesser, M. Magni, F. Ochs, and T. Dippel, "Simulation-based Methodology For Comparison Of nZEB Requirements In Different Countries Including Results Of Model Calibration Tests," in *16th IBPSA International Conference*, 2019, pp. 5060–5067, doi: https://doi.org/10.26868/25222708.2019.210996.
[16] D. D'Agostino and L. Mazzarella, "What is a Nearly zero energy building? Overview, implementation and comparison of definitions," *Journal of Building Engineering*, vol. 21. Elsevier Ltd, pp. 200–212, Jan. 01, 2019, doi: 10.1016/j.jobe.2018.10.019.
[17] F. Ochs, M. Magni, E. Venturi, A. Tosatto, and W. Streicher, "Cost-optimal nZEB HVAC configurations with onsite storage," *E3S Web Conf.*, vol. 246, p. 07001, Mar. 2021, doi: 10.1051/E3SCONF/202124607001.
[18] F. Ochs, D. Bestenlehner, H. Drück, and W. Walter Josef Feist, "Solar-aktiv-Haus und Passivhaus plus als Gebäudekonzept der Zukunft," in *Gleisdorf Solar*, 2012.
[19] R. O'Hegarty, O. Kinnane, D. Lennon, and S. Colclough, "Air-to-water heat pumps: Review and analysis of the performance gap between in-use and product rated performance," *Renew. Sustain. Energy Rev.*, vol. 155, p. 111887, Mar. 2022, doi: 10.1016/J.RSER.2021.111887.
[20] Passivhaus Institut, "Nachhaltigkeitsbewertung mit PER." https://passipedia.de/zertifizierung/passivhaus-klassen/per (accessed Nov. 15, 2022).
[21] IEA, "Installation of about 600 million heat pumps covering 20% of buildings heating needs required by 2030 – Analysis - IEA." https://www.iea.org/reports/installation-of-about-600-million-heat-pumps-covering-20-of-buildings-heating-needs-required-by-2030 (accessed Nov. 14, 2022).
[22] F. Ochs, A. Tosatto, M. Magni, E. Venturi, W. Monteleone, and G. Dermentzis, "Strategies to overcome the dilemma in renovating and integrating HPs and RE into the building stock," *Heat Pump Conf. 2023 Chicago (USA), 15-18 May*, 2023.
[23] F. Ochs, M. Magni, and G. Dermentzis, "Integration of Heat Pumps in Buildings and District Heating Systems - Evaluation on a Building and Energy System Level," *Energies 2022, Vol. 15, Page 3889*, vol. 15, no. 11, p. 3889, May 2022, doi: 10.3390/EN15113889.
[24] M. Lämmle *et al.*, "Performance of air and ground source heat pumps retrofitted to radiator heating systems and measures to reduce space heating temperatures in existing buildings," *Energy*, vol. 242, p. 122952, Mar. 2022, doi: 10.1016/J.ENERGY.2021.122952.
[25] T. Cao and Y. Hwang, "HPT Annex 54: Heat Pump Systems with Low-GWP Refrigerants TASKS 1, 2 AND 3," 2022.
[26] Meteotest AG, "Meteonorm." https://meteonorm.com/en/ (accessed Nov. 14, 2022).
[27] D. Günther *et al.*, "Abschlussbericht: Wärmepumpen in Bestandsgebäuden - Ergebnisse aus dem Forschungsprojekt WPsmart im Bestand," vol. 1, p. 258, 2020.
[28] Passivhaus Institut, "Passive House Planning Package (PHPP)," 2022. https://passiv.de/en/04_phpp/04_phpp.htm (accessed Jan. 13, 2022).
[29] D. Siegele, E. Leonardi, and F. Ochs, "A new MATLAB Simulink Toolbox for Dynamic Building Simulation with B.I.M. and Hardware in the Loop compatibility," *Proc. Build. Simul. 2019 16th Conf. IBPSA*, pp. 2651–2658, 2019, doi: 10.26868/25222708.2019.210641.
[30] ISO 13790:2008, *Energy performance of buildings — Calculation of energy use for space heating and cooling*. 2008.
[31] G. Dermentzis *et al.*, "A comprehensive evaluation of a monthly-based energy auditing tool through dynamic simulations, and monitoring in a renovation case study," *Energy Build.*, vol. 183, pp. 713–726, Jan. 2019, doi: 10.1016/j.enbuild.2018.11.046.
[32] EN 12831-1:2017, "Energy performance of buildings - Method for calculation of the design heat load - Part 1: Space heating load." 2017.
[33] DIN EN 16147, *Heat pumps with electrically driven compressors - Testing, performance rating and requirements for marking of domestic hot water units*. 2017.
[34] M. Grim-Schlink, A. Preisler, and A. Stipsits, "Heizlast optimieren," 2020.

[35] M. Sunikka-Blank and R. Galvin, “Introducing the prebound effect: the gap between performance and actual energy consumption,” *https://doi.org/10.1080/09613218.2012.690952*, vol. 40, no. 3, pp. 260–273, 2012, doi: 10.1080/09613218.2012.690952.

14th IEA Heat Pump Conference
15-18 May 2023, Chicago, Illinois

Ammonia - Steam cascade heat pump for +100˚C steam generation

Kenneth Hoffmann[a*], Michael Bantle[b], Kjetil Evenmo[c]; Vebjørn Nilsen[d]

[a]GEA Heating and Refrigeration Technologies, Unit 9, Conqueror Court, Sittingbourne, Kent, ME10 5BH, United Kingdom
[b]ANEO Industry, Klæbuveien 118, 7031 Trondheim, Norway [c]EPCON Evaporation Technology, Fossegrenda 42, 7038 Trondheim, Norway, [d] Felleskjøpet Agri AS, Nedre Ila 20, 7018 Trondheim, Norway

Abstract

A new innovative high temperature heat pump solution developed by GEA, ANEO and EPCON is presented in this paper: High efficiency and high temperature heat pump for generating steam in the processing industry. By using natural refrigerants ammonia and steam it is possible to ensure the highest possible efficiency without causing any potential harmful damage to the global environment. The heat pump harnesses the heat from the exhaust moist air from the drying process, the air is cooled and dehumidified. It is important to dehumidify the air as a substantial amount of energy is latent energy in the moist exhaust air. Chilled water as low as 20 °C is needed for the energy extraction and a 2-stage ammonia heat pump is used as the first step to generate 85 - 90 °C steam. The dry steam is then compressed to the required steam pressure of 2 bar (around 120 °C) with 4 centrifugal fans in series. This multistage cascade solution gives a high efficiency and minimize the cost by combining two technologies (steam compression and ammonia compression) each operating in the application area where they are the best available technology and hereby achieving a temperature lift of 100K with a heating COP of 3.1.

© HPC2023.
Selection and/or peer-review under the responsibility of the organizers of the 14th IEA Heat Pump Conference 2023.

Keywords: Ammonia, MVR, steam compression, cascade, high temperature heat pump, petfood drier.

1. Introduction

There is an increased focus on decarbonization of industrial processes. The first step in decarbonizations is reducing energy consumption. By closely looking at the whole process and establishing where the quick wins are that, without significant cost, can reduce the primary energy usage. Other improvements are to optimize the heat exchanged within the process and reduce temperature differential across heat exchangers. Many processes are designed for usage of 5 – 10 bar steam (150 °C to 180 °C) for all heating needs even if the temperature needed for the process, is well below 100°C. After energy reduction and optimization, the next step is to establish where waste energy from one process can be used in other parts of the process. This step often leads to installation of heat pumps as the waste energy often are at lower temperatures than required for the process. The many companies who are going through this process often see that most of their heating demand can be met with hot water circuit below 100 °C. This makes the heat recovery easy as it can be provided by standard ammonia heat pumps (preferred refrigerant within the food, beverage and dairy industry). With most of the process heating being decarbonized there is often still some heating demand above 100 °C, which so far have been provided by with either gas fired or electrical boilers. However, this can now be done more efficiently by using natural refrigerant heat pumps (although not ammonia).

Before starting to decarbonize production processes it is important to follow the right strategy. In the pyramid below is shown a sensible approach to decarbonization. The easy and most beneficial gains can be achieved from the bottom of the pyramid, by looking at energy efficiencies in the production. Next step is heat recycling. If the heat demand is large than what can recovered from waste heat the next step is to look for onsite heat generation like solar thermal of geothermal heat. If this is not an option then electrical boilers could

* Corresponding author. *E-mail address:* kenneth.hoffmann@gea.com

be an option and finally the most expensive options of renewable fuels or offsetting emissions, which can achieve the decarbonization but at an added cost making the business less competitive.

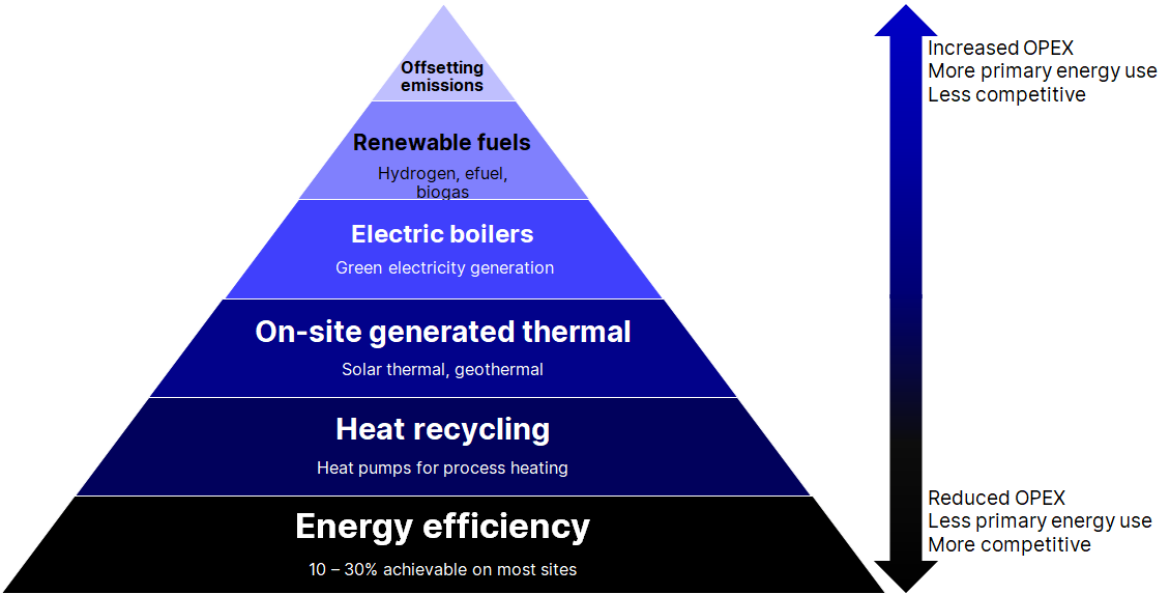


Fig. 1. Decarbonization pyramid.

2. Refrigerants available above 100˚C

Before developing a heat pump solution for delivering temperatures above 100 ˚C, we did an analysis of the available refrigerants for the market. From the table below is a comparison of some of the most common refrigerants considered for heat pump applications above 100 ˚C.

R245 have been around for 20 years and several projects with this refrigerant have been implemented for ultra-high temperature heat pumps (ultra-high = heat pumps delivering more than 100 ˚C). However, R245 have a global warming potential (GWP_{100}) over a 100-year period of 1030. In 2016 the UN countries agreed on phase down of all high GWP refrigerant in the Kigali agreement. Almost all countries have since ratified the agreement and made it local legislation. With a looming ban of high GWP refrigerants it does not make sense to invest in developing solution using these high GWP refrigerants.

R1233zd(E) is one of the new generation F-gasses with low GWP value (<5), This refrigerant has the benefit of being in safety category A1 (non-toxic and non-flammable), which broadens the application area. Unfortunately, the chemical includes Chloride molecules in it structure which is banned in some countries as it leads to ozone depletion (ODP) when released to nature. The ozone depletion is very low for the refrigerant and is registered as having 0 ODP according to UN protocol. The main consideration before applying R1233zd(E) refrigerant is that there now is increased focus on the degradation products of F-gas refrigerants. In Europe long chain Perfluoroalkoxy alkane (PFA) have been banned for several years due to their environmental damage and long life in the nature (also knowns as forever chemicals), but this has led to an increase in use of chemicals which breaks down to shorter chain PFA. These chemicals have proven to be just as damaging to the freshwater environment as the banned PFA, so it is likely that there in the future will be a restriction in the use of chemicals which breaks down to any PFA. One of the breakdown components from refrigerants containing fluoride components are Trifluoroacetic acid (TFA) which is one of the chemicals which is defined as a PFA with short chain fluoride molecules. With these issues in mind there need to a clear efficiency benefit of using these refrigerants with focus on zero leakage system design and a plan for refrigerant recovery at the end of life, to minimize the environmental damage of the refrigerant in the environment.

R601 (Pentane), is one of the hydrocarbons recently identified as suitable for ultra high temperature heat pump applications. With a critical temperature of 196.6 ˚C, it is a suitable refrigerant for delivering hot water or steam above 160 ˚C. This refrigerant has the benefit of being a natural refrigerant with known environmental footprint. When comparing the thermodynamic specifications for the different refrigerants it has been proven

in previous papers that R601 offers a higher efficiency than alternative F-gas refrigerants. The main obstacle for a mass implementation of heat pump solutions with R601 is that it is in safety category A3, which is non-toxic but highly flammable. The high flammability will limit the applications where is can be applied.

R718 (water), have been proven to be a very efficient refrigerant and with a critical temperature of 373.9 ˚C, it is suitable for heat pumps delivering more than 200˚C water or steam. It is non-toxic and non-flammable and no environmental impact of the refrigerant. The main issue is the high boiling point at atmospheric pressure of 100 ˚C with the correlated high-volume flows in vacuum application as well as the high superheat generated during compression. An analysis of the food, dairy and beverage industry have shown that heat sources in general are below 100 ˚C, so steam compressors will have to operate in vacuum and with steam in vapor phase below 100 ˚C, there is a requirement for compressors with a large volume flow.

Table 1. Comparison of refrigerant types suitable for +100˚C

Refrigerant	R1233zd(E)	R245	R601	R718
Molecular structure	CHCl=CH-CF3	CF3CH2CHF2	CH3-3(CH2)-CH3	H2O
Molar weight	130.5	134.0	72.15	18.0
Boiling point at 1.013 bar (°C)	18.3	15.14	36.1	100.0
Critical temperature (°C)	165.6	154.0	196.6	373.9
Critical Pressure (bar)	3.57	3.65	3.37	22.1
Heat of vaporization @ 120 °C (kJ/kg)	123.1	112.4	268	2202.2
GWP100 (CO2=1)	<5	1030	11	0
ODP	0.00034	0	0	0
Lifetime in atmosphere (days)	10 – 40	~2800		-
Occupational Exposure limit (OEL) (ppm v/v)	800	300	2000	1.000.000
Safety group (ASHRAE 34)	A1	A1	A3	A1

3. Heat pump application

Industrial food processes like sterilization, high temperature pasteurization or drying requires more than 100 ˚C heat supply. Outside the food industry there are more processes requiring higher than 100 °C steam like paper, pulp, chemicals etc. for many of these processes it is possible to provide the heat by heat-recycling as the heat added in the front end of the process in most cases can be recovered later in the process. In food processing where pasteurization or sterilization is needed, you will most likely have a refrigeration plant which is used to cool the products after it has been heated and the refrigeration plant reject waste heat to ambient in the process, this heat can via a heat pump be upcycled to the right temperatures for the process. For drying facilities there is not always a refrigeration plant as the drying process removes the moisture content from the product, which gives the product a long shelf life without the need for keeping it refrigerated. For drying processes, you often have large amount of waste heat in the exhaust air, as the air used for drying is collecting the moisture and being heated up across the product. By cooling the air below the dew point sufficient energy can be recovered to recycle the heat and use the exhaust air as the heat source for providing steam for the drying process.

In the diagram below is shown a schematic of a typical pet food pelleting process. The energy flow for pet food pelleting is very similar to a spray drying process. The pellets are formed by mixing the ingredients with process steam and pressing them into their final shape. Hereby the product/pellets are moisturized and heated. In the next process step the pellets are cooled and dried in counterflow with cooling air. The air becomes moist and warm in the process. This exhaust air is used as heat source for a the heat pump and the sensible as well as the latent heat is transferred into the ammonia heat pump. The 2-stage ammonia heat pump system generates low pressure steam at 85 °C. The steam is then compressed via 4-stage centrifugal fans to the required steam pressure for the mixing process of 2 bar.

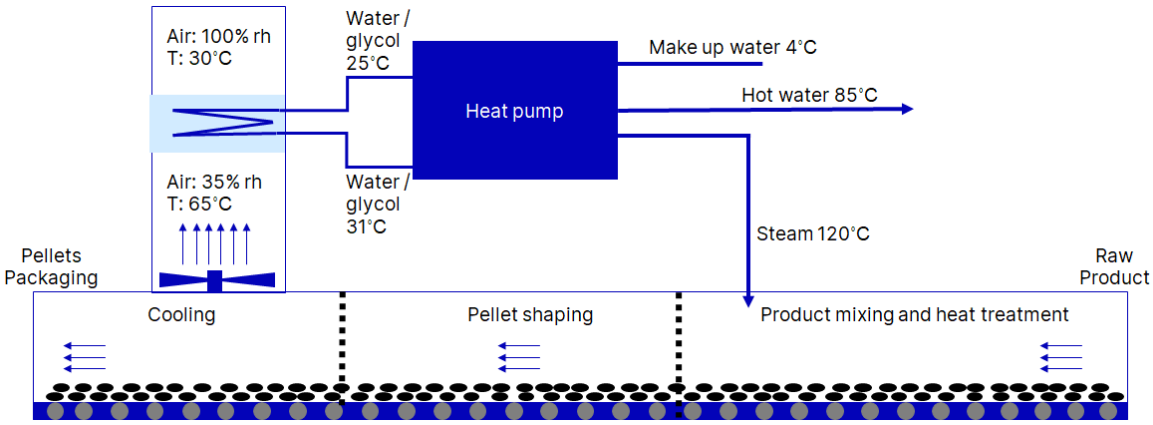


Fig. 2. Schematic of the process to which the heat pump is applied

4. Heat pump design

The pelleting process requires 2000 kg steam per hour at 2 bar (120 ˚C). As the steam is injected into the product, no steam is recovered, and all the steam needs to be generated from the make-up water, which is entering the heat pump at 4 ˚C. The factory also needs hot water at 85 °C for other consumers, which they would like the heat pump to provide in addition to the steam demand. The heat source is via a water circuit in the exhaust air stream. The heat exchanger in the exhaust air is designed for a water temperature supply temperature of 25 ˚C and return temperature to the heat pump of 31 ˚C. With an evaporation temperature of around 22 ˚C for the heat pump and steam delivered at 120 ˚C, it is close to 100K temperature lift, for this to be economically attractive the efficiency of the heat pump needs to be best in class.

To achieve highest possible efficiency of the heat pump system, different heat pump configuration has been considered.

1. Purely steam compression
2. Low stage: Single stage ammonia heat pump. High stage: steam compression
3. Low stage: Two stage ammonia heat pump. High stage: steam compression

4.1. Purely steam compression

There are different compression technologies available for steam compression, however there are large differences in the efficiency of these compression systems. For lower pressures (below 2 bar), the centrifugal turbo compressors have proven to offer the highest efficiency with an isentropic efficiency around 80-85% for the compressors. The centrifugal turbo compressors offer 9 – 10K temperature lift per compression stage for their standard range. There are centrifugal compressors on the market which almost double this temperature lift in a single stage. However, for smaller capacities the cost per kW is not economical for compressors with higher temperature lift and it is more affordable to have 2 compressors with smaller temperature lift. For a project of this size and temperature lift it is necessary with 11 – 12 MVR turbo compressors for the most efficient steam only system. Due to the cost and space requirement this solution was discarded.

4.2. Low stage: Single stage ammonia heat pump. High stage: steam compression

Low stage ammonia piston compressors have an isentropic efficiency of 88% at the chosen design point. Ammonia piston compressors is a price competitive solution with a small footprint and high efficiency. Figure 3 shows the application area for the GEA ammonia piston compressors. The graph shows that at an evaporation temperature of 22 ˚C it is not possible to condense above 80˚C this will give a steam evaporation temperature of 76 ˚C and the compressor will be operating on the limits of its operation area. For delivering steam at 120˚C, we would require 6 or 7 centrifugal compression stages, to lift the steam temperature from 76 ˚C to 120 ˚C. With the operational limitation in mind a 2-stage ammonia heat pump was considered.

4.3. Low stage: Two stage ammonia heat pump. High stage: steam compression

With a two-stage ammonia compression cycle it is possible raise the suction temperature of the high stage ammonia compressor, so it no longer operates at the limits of the application area. This also gives more flexibility of the suction temperature of the steam compressors. The steam evaporation temperature was set at 85 ˚C, with the ammonia heat pump able to increase this to 90 ˚C. This flexibility will give valuable information regarding heat pump design for future projects.

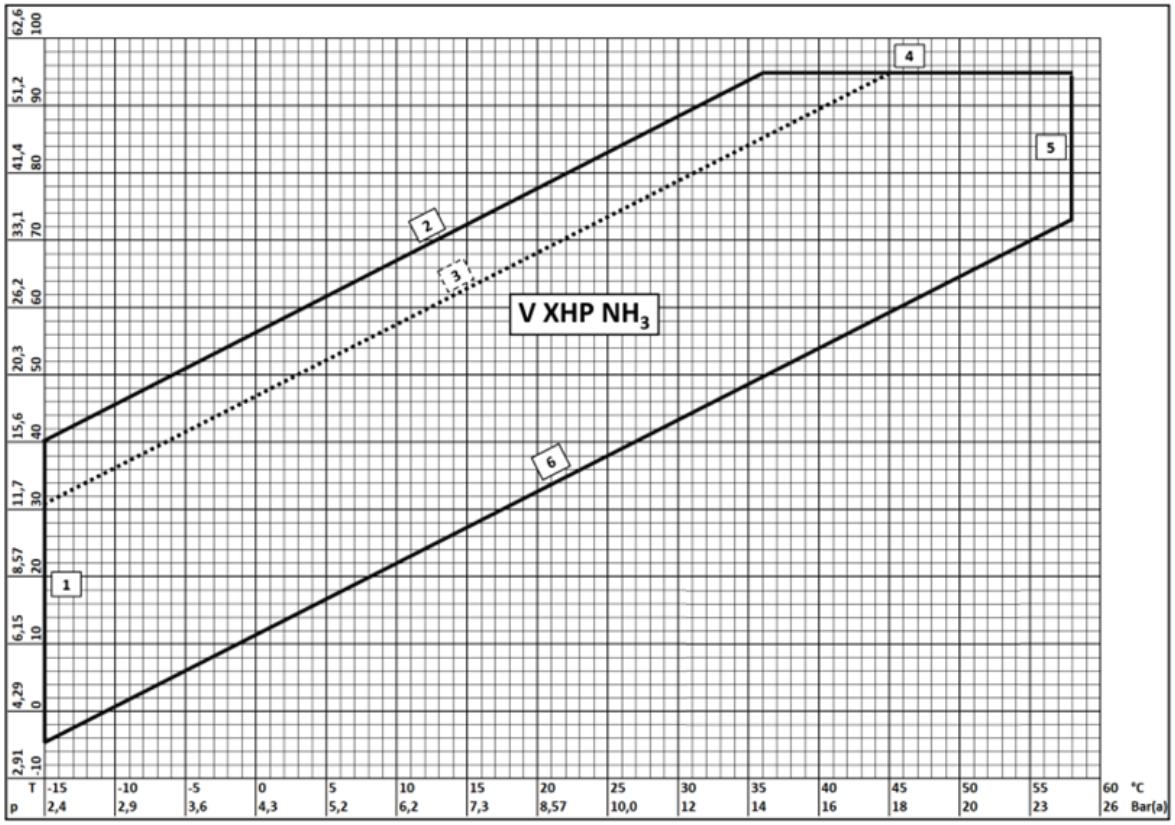


Fig. 3. Application area for the VXHP compressor range, the limitations are: 1: minimum evaporation temperature, 2: maximum discharge temperature at full load when superheat is 0K, 3: discharge temperature with some cylinders disengaged, 4: maximum condensing temperature, 5: maximum evaporating temperature, 6: minimum pressure ratio

4.4. Heat pump system description

The heat pump is designed with a low stage screw compressor operating from +22 ˚C to +45 ˚C. The chilled water circuit is designed for 25 ˚C / 31 ˚C flow and return temperature. If the exhaust air has a higher moisture content or higher outlet temperature, it will be possible to extract sufficient heat with higher chilled water temperatures and approving the efficiency of the heat pump. The absorbed power of the low stage compressor reduces with approximately 2% per degree higher suction temperature. If it is possible to operate at 5K higher suction temperature it reduces the absorbed power with approximately 10% or 15 kW. The screw compressor will need a small amount of oil cooling to ensure sufficient lubrication ability. A high oil temperature will result in a lower viscosity and provide less lubrication, which can lead to increased wear of the compressor. Around 20 kW of oil cooling is provided by the chilled water circuit. Alternative ways of doing the compressor cooling were considered, like thermosyphon oil cooling or liquid injection into the discharge of the compressor. Each solution gives more heat recovery, but are also more difficult to operate, so as this is a trial installation, the system which is easiest to control have been chosen for the oil cooling circuit.

The chilled water circuit is also connected to the oil-cooler on the reciprocating high stage compressor. It is not necessary to have oil cooling of the high stage compressor during normal full load operation, but during part load it might be necessary. Both ammonia compressors are using the same oil.

The evaporator is a plate and frame in stainless steel AISI316L, in combination with the low charge separator it gives a good performance at variable working conditions. After the discharge from the low stage compressor the superheated discharge gas is injected into an open separator vessel below the liquid level in the separator to ensure the gas temperature in the vessel is not superheated. The saturated gas from the low stage screw compressor is compressed in the high stage piston compressor. The high stage compressor is a 6-cylinder high pressure compressor which is able to condense at up to 95 ˚C. It will be operating between the suction pressure of 45 ˚C and the saturated discharge pressure of 89 ˚C. The superheated refrigerant is condensed in a AISI316L stainless steel plate and frame cascade condenser/evaporator. Low pressure (0.58 bar) steam is evaporated in the cascade condenser/evaporator. Due to the large volumetric difference of liquid water and water vapor, 30% of the water entering the heat exchanger at the bottom is exiting the heat exchanger at the top together with the steam bubbles. To separate the water from the steam a separation tank is installed. The dry steam is compressed through 4 stages with centrifugal fans to the desired end pressure of 2 bar steam (120 ˚C). On the inlet side of the centrifugal fans is liquid injection to control the superheat of the discharge steam.

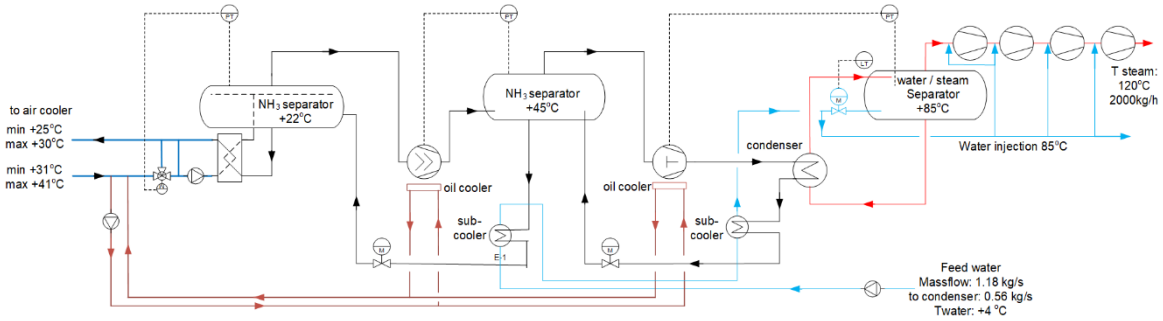


Fig. 4. Flow diagram for the complete heat pump system with both the ammonia compression heat pump and the mechanical vapor compression part.

4.5. Steam generation

With an ammonia design pressure of 60 bar and steam evaporating at 0.56 bar, it is important to select the right heat exchanger for exchanging energy between ammonia and water. Several different types of fully welded heat exchangers were considered. On figure 5 is shown 2 different solutions. The solution to the left has the heat exchanger plate pack within the water/steam separation vessel. This ensures practically 0 kPa pressure drop, which helps with the efficiency, however, there is concerns about potential deformation of the plates within the vessel, as there is no frame support at the end of the plate pack and with a pressure inside the plate pack of 60 bar, it seems like a high risk. To the right is a fully welded heat exchanger with a separation vessel on top of the heat exchanger, this gives a compact design suitable for the required water and ammonia pressures without any risk of leakages. The steam generated from the heat pump is injected into the product, so it is required to have fresh water through the heat exchanger, which for this installation raised concern regarding corrosion of the shell of the heat exchanger as the water would be in direct contact with the carbon steel shell. There was also concern regarding scaling of the heat exchanger, which can be solved by descaling the heat exchanger, but for heavy lime scale it might be necessary with a mechanical cleaning of the heat exchangers which is not possible with the fully welded plate and shell design. It was concluded that these type of heat exchangers are more suitable for closed water circuit systems, which is only fed by recirculated water and a small amount of ionized make-up water.

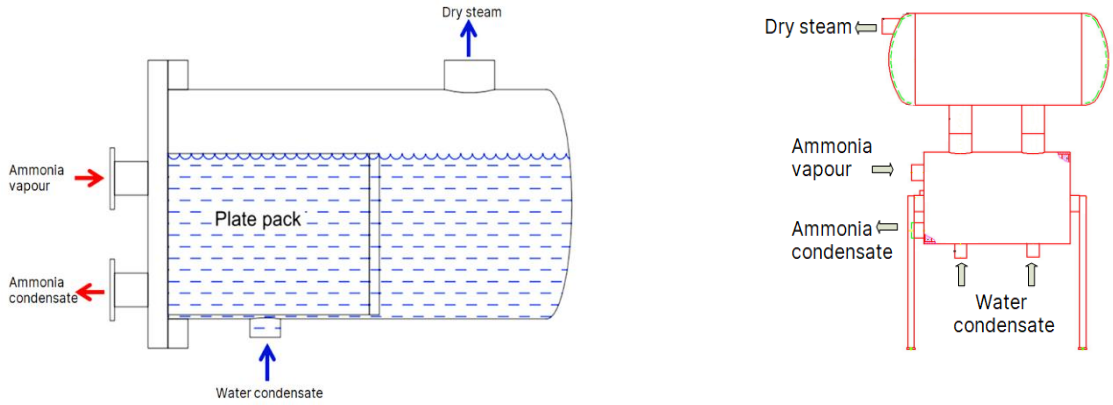


Fig. 5. 2 different heat exchangers for ammonia to water/steam cascade heat pumps

For this project a plate and frame heat exchanger were selected. The plates are welded together on the ammonia side and has gasket between the plates on the water side. This design also add further safety to the system as a potential failed welding of the plates will not leak ammonia into the water system and potential contaminate the products. The pressure drop on the water side is 4 kPa at full load operation, at the low-pressure operation (0.56 bar) this is equal to 1.5K temperature drop.

4.6. Cascade Steam Compression

The steam supplied from the Ammonia heat pump is further compressed to the required steam pressure of the process by a multi-stage Mechanical Vapour Recompression system (MVR-HP). For the MVR system vertical arranged high pressure centrifugal fans (so called MVR compact fans) are used. The MVR fans are characterized by a relative moderate pressure increase which results in a temperature increase of approximately 10K per stage. Since the process requires a steam pressure of 2 bar it is required to install 4 pcs MVR fans in series in order to increase the pressure from 0.56 bar (85 °C) to 2 bar (120 °C).
The compact fans are vertically arranged machines which are equipped with a frequency controlled direct drive and a high-speed motor. Depending on the operational requirements the MVR fans are rotating at up to 13.000 rpm.

Using water-steam in heat pump applications has in general two disadvantages compared to traditional refrigerants. The first is the high volumetric flow at low pressure applications, however this is compensated by the integration of MVR fans in this case. The second is the relatively high superheated steam temperature during compression, which is a consequence of the thermal properties of steam. Due to the 4-stage compression stages, hence moderate pressure ratio each stage, the steam flow is de-superheated by direct water injection. The injected water is hereby evaporated and is cooling the steam back toward the saturation line of the steam. The amount of injected water is controlling by the degree of de-superheating. The production process requires a certain amount of superheat, which is controlled by the water injection in the last stage. The total amount of injected water for the design condition is 150 kg/h and is increasing the amount of supplied steam.

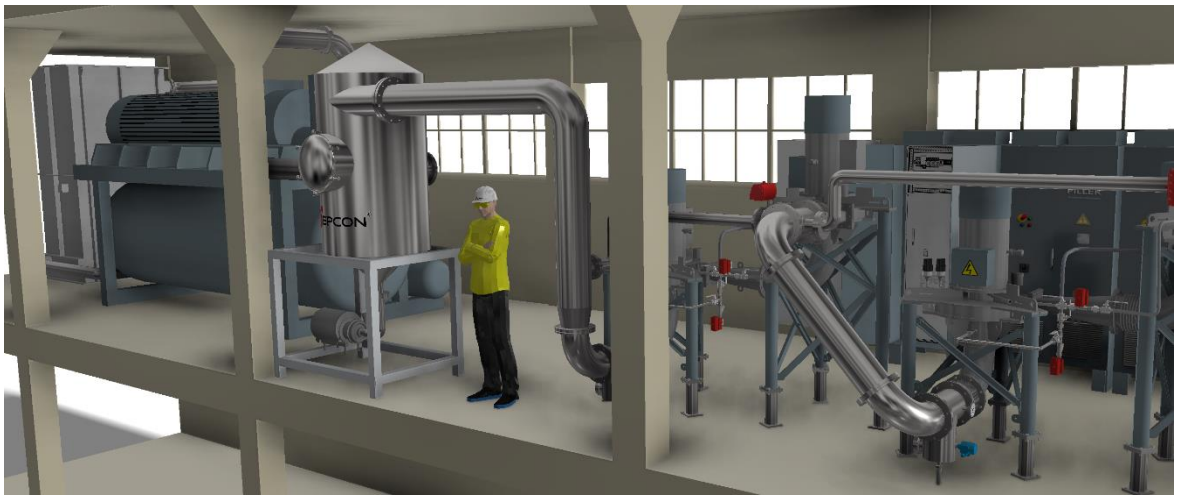


Fig. 6. Preliminary drawing of heat pump installation with ammonia heat pump to the left and steam compression to the right.

For the presented case the efficiency and energy saving potential must be based on the combined energy consumption of the two heat pumps systems and the total amount of delivered energy:
The combined COP considered in this case is the pre-heating of the feed water and the evaporation at low pressure and the required energy to increase the steam pressure to 2 bar.
The total thermal capacity of the system is 1880 kW and consist of approximately 1464 kW for steam generation (equals 2 ton/h of process steam) and 416 kW preheating of feed from 4 °C to 85 °C. The electric power is defined as the shaft power of to the compressors. Auxiliary equipment is not included in the calculation.

Table 2. Heat pump performance

Heat pump performance		
Absorbed power		
Ammonia screw compressor (22 °C to 45 °C)	kW	158.6
Ammonia piston compressor (45 °C to 89 °C)	kW	212.1
4 x MVR steam compressors (85 °C to 120 °C)	kW	189.0
Total shaft power	kW	559.7
Total power (including electrical losses)	kW	601.8
Heat output		
Steam generation	kW	1464
Heating water 4°C -> 85°C	kW	416
Total heat output	kW	1880
Performance		
Shaft COP steam generation only	n/a	2.6
Shaft COP including water heating	n/a	3.4
Heat pump COP (including electrical losses)	n/a	3.1

To produce 2 ton/h of process steam the COP of the Ammonia heat pump is 4.5 and for the water compression is 7.5. This gives a combined COP of 3.1 for the total system for the steam production by the heat pump system from moist air.

The operational time of the system is estimated to be 5000 hours per year for the production site. Hence the system will deliver around 9.40 GWh of thermal energy per year. The alternative energy source is an electric steam boiler with an estimated 90% efficiency. The primary energy consumption for the heat pump solution is hence 3.03 GWh. per year while the boiler would need 10.4 GWh. or fossil; this gives more than 70% energy saving for the production process.

5. Summary and Conclusion

This project has led to a thorough evaluation of different refrigerant and heat pump technologies for providing steam at 120 °C for a commercial petfood manufacturer. Although several refrigerants are available for the temperature range, none of them offer the same longevity, flexibility, and efficiency as the chosen ammonia / steam combination. The chosen technologies are readily available on the market but have for the first time been combined to create a heat pump with a temperature lift from heat source to heat sink of close to 100K. Being able to reduce the energy usage from 10.4 GWh per year for electrical boiler to 3.03 GWh for the heat pump is key to the project being a success. Through the operation of the heat pump further optimization is expected for generating the best-in-class ultra-high temperature heat pump for the future.

6. Acknowledgements

The project gratefully acknowledges the partial funding from Enova SF (Trondheim, Norway) through the project 21/13004.

References

[1] German Enviromental federal office, assesment of HFO refrigerants effect on enviroment 02.19.2021
[2] Industrial heat pumps: Research and Market Update, Dr. Cordin Arpagaus, 10.11.2021, Institue of Energy systems
[3] High temperature heat pumps in Austria: demonstration and application examples, Veronica Wilk, 2019
[4] Analysis of application areas for steam compressors in high temperature heat pump applications, Hans Madsbøll, iir.gl2022.0154

14th IEA Heat Pump Conference
15-18 May 2023, Chicago, Illinois

A novel method for estimation of the annual energy assessment of using an external subcooler in a refrigeration machine

Manuel Diem[a], Lukas Wick[a], Christian Stahel[a], Frank Tillenkamp[a,*]

[a]Zurich Unviersity of Applied Sciences, Institute of Energy Systems and Fluid Engineering,
Technikumstrasse 9, 8400 Winterthur, Switzerland

Abstract

The additional subcooling of the refrigerant is an interesting way to improve the efficiency of the refrigerant system. On behalf of the Swiss Federal Office of Energy, the seasonal saving potential of using an external subcooler in a refrigeration machine considering application limits and plant specific conditions was investigated based on computer simulations.

The result of the investigation is presented as a guideline. With this method, a user can determine the optimum subcooling for his application with the given environmental conditions. By considering the operating limits of the refrigeration machine and the environmental conditions, the method can be used directly for the planning and adjustment of a refrigeration machine.

The results show that a refrigeration machine for air conditioning with a direct evaporator and the refrigerant R290 (propane) can significantly improve efficiency by using an external subcooler. There is an annual energy saving potential of 7% if the external subcooler is used with cold wastewater.

© HPC2023.
Selection and/or peer-review under the responsibility of the organizers of the 14th IEA Heat Pump Conference 2023.

Keywords: Subcooling ; Seasonal saving potential ; Refrigerant cycle ; External subcooler ; Refrigerating machine

1. Introduction

1.1. Related research on the subject

In compression refrigeration systems, subcooling of the liquefied refrigerant is an important issue that can affect the efficiency of the entire cycle. There are many studies in the literature that deal with the subcooling of the refrigerant. This concerns, for example, the type of subcooling that can be realized externally or by means of an internal heat exchanger. Experimental investigations on subcooling with refrigerants R134a and R1234yf have been carried out by *Pottker and Hrnjak* [1], who investigated the operation with internal heat exchanger regarding the efficiency. It was shown that the efficiency of a refrigeration cycle system with R1234yf can be increased up to 18% by using an internal heat exchanger. With R134a, the efficiency could be increased by 9%.

The choice of refrigerant has a significant impact, as various other studies have shown. *Ansari et al.* [2] investigated the effects of subcooling on the operation of the refrigeration machine. They investigated the refrigerants R1243zf and R1233zd(E), which were not considered in our research. The results were compared with the performances of the refrigerant R134a and have shown that R1233zd(E) performs better with subcooling than R134a, while 1243zf is slightly less efficient both energetically and exergetically.

Furthermore, some studies have already been conducted on supercooling by ejector. *Yilmaz and Erdinc* [3] investigated a new ejector subcooling system, where part of the refrigerant is expanded after the condenser.

* Corresponding author. Tel.: +41 (0) 58 934 73 61.
E-mail address: frank.tillenkamp@zhaw.ch

The tests were carried out on seven different refrigerants. With a COP improvement of 20% and an exergy efficiency improvement of 18% the best performance was obtained by R1234yf.

1.2. Purpose of subcooling

Subcooling is necessary to avoid vapor bubbles (flashgas) in front of the expansion valve which is essential for stable and safe operation of the refrigerating machine.

Vapor bubbles before the expansion valve reduce the refrigeration capacity [4] and can lead to cavitation in the expansion valve, which can damage it. If the valve is operated in this condition for a longer period of time, there is a risk of wet operation, as the valve no longer closes completely due to the damage.

With electronic injection control, the amount of refrigerant injected into the evaporator is metered by means of an expansion valve so that the superheat at the evaporator outlet remains constant. The mass flow depends on the pressure difference across the expansion valve, the cross-sectional area, and the inlet density of the refrigerant. The expansion valve changes the cross-sectional area by its degree of opening and thus regulates the flow or the refrigerant charge level in the evaporator. If the refrigerant is not sufficiently subcooled, flashgas may form in the liquid line due to pressure or heat losses, which significantly interferes with the control of the injection rate. The influence of flashgas on the injected mass flow and superheat is shown schematically in Figure 1.

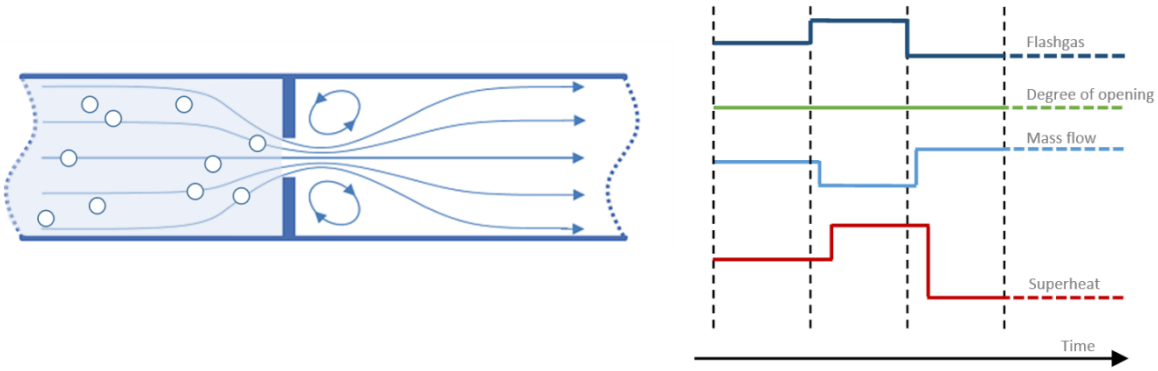


Fig. 1. Influence of flashgas on mass flow and superheat

The gas bubbles have a significantly lower density than the liquid refrigerant. If gas bubbles appear in the liquid refrigerant upstream of the expansion valve, the quantity of refrigerant injected is reduced without the opening position of the expansion valve having changed. This reduction in mass flow leads to an increase in superheat and the controller opens the expansion valve as a countermeasure.

If the proportion of flashgas at the inlet of the expansion valve is reduced, e.g., for a short time completely liquid, the mass flow increases due to the greater density, the superheat decreases, and the controller reduces the opening cross-section of the expansion valve as a counter-reaction. The system may start to oscillate and may no longer be stable [5].

1.3. Aim of the study

The investigations on additional subcooling were carried out for five different subcooling types, five different applications (each with different evaporating temperatures) and eight different refrigerants. All information and results on the investigations are given in the final report on refrigerant subcooling [6] (in German). This paper is limited to the investigation of subcooling with external subcooler for the air conditioning application with a direct evaporator (evaporating temperature of 10 °C) and the refrigerant R290.

The aim of the study is to present the result as a guideline. This allows a user to estimate the potential of additional subcooling in each case for his individual application and the given environmental conditions.

2. Methodology

2.1. Cycle with external subcooler

The investigations for this report were all carried out using computer simulations with MATLAB [7]. To show the influence of subcooling on the refrigeration circuit, a reference process with the same application and the same refrigerant, but without additional subcooling, is calculated in each case. Subsequently, the refrigeration circuit is supplemented by an external subcooler and calculated again. For a seasonal consideration, this procedure is repeated at different operating points. The comparison is shown schematically in Figure 2.

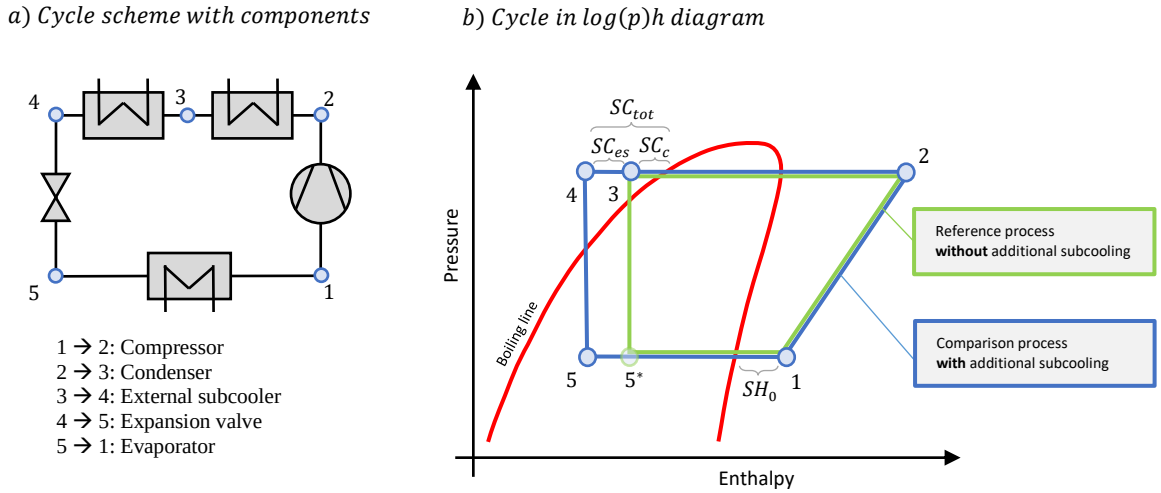


Fig. 2. a) The refrigeration cycle with its components. b) The reference process without additional subcooling (green) and the comparison process with additional subcooling (blue), drawn in log-p-h diagram.

In the case of an external subcooler, the refrigerant is subcooled after the condenser (3) with an additional heat exchanger (4). The total subcooling (SC_{tot}) therefore results from the subcooling by the condenser (SC_c) and the additional subcooling by the external subcooler (SC_{es}). How much the refrigerant can be subcooled depends on the temperature and capacity of the heat sink of the external subcooler. The external subcooling increases the enthalpy difference at the evaporator ($h_1 - h_5$) and thus the refrigeration capacity. The operating point of the compressor and its power consumption remain unchanged. The efficiency of the chiller therefore increases with increasing subcooling. For a correct assessment of the efficiency, however, the required auxiliary energies must also be taken into account. The estimation of the auxiliary energies requires a consideration of the entire system. If the efficiency of another system is reduced due to the subcooling or if additional energy is used to ensure the heat sink (e.g. pump capacities), this must be taken into account. Only if the energy saving at the refrigeration machine is more than the required auxiliary energies, the efficiency of the overall system increases.

2.2. Operating points

The operating point of a refrigeration machine is defined by evaporating and condensing temperature. These are defined as follows:

The **evaporating temperature** T_0 depends on the application and is constant for all operating points. For air conditioning with direct evaporator, the evaporating temperature is 10 °C. The influence of the vapor quality on heat transfer and distribution in the evaporator are not considered.

The **condensing temperature** T_C depends on the ambient temperature and is therefore variable. To consider the operation of the refrigeration machine at different ambient temperatures, the simulations are carried out with five different condensing temperatures at intervals of 5 °C each. These can be seen in Table 1.

Table 1. The five selected operating points in terms of their evaporating temperature T_0 and condensing temperature T_C

Operating point	Evaporating temperature T_0 (°C)	Condensing temperature T_C (°C)
1	+ 10	+ 45
2	+ 10	+ 40
3	+ 10	+ 35
4	+ 10	+ 30
5	+ 10	+ 25

2.3. Parameters of the cycle simulations

Apart from total subcooling, the input parameters for the cycle simulations are identical in both cycles. Table 2 shows the parameters used for the simulations of the reference process and the process with external subcooler. While in the reference process the total subcooling is the same as the subcooling in the condenser, in the external subcooler the total subcooling is varied from 5 K to 25 K (in 5 K steps) at each operating point. How much the refrigerant can be subcooled depends strongly on the available heat sink. This can very differently, depending on the object. Therefore, different degrees of subcooling are investigated in this study.

Table 2. Parameters of the cycle simulations for the circuits investigated

Cycle	Operating points (T_0 / T_C)	1	2	3	4	5
Both (reference and external subcooler)	Subcooling condenser [K]	2	2	2	2	2
	Superheating evaporator [K]	7	7	7	7	7
	Isentropic compressor efficiency [-]	0.7	0.7	0.7	0.7	0.7
Reference	Subcooling total [K]	2	2	2	2	2
External subcooler	Subcooling total [K]	5 - 25	5 - 25	5 - 25	5 - 25	5 - 25

2.4. Computer simulations

The investigations for this report were all carried out using computer simulations with MATLAB [7]. The fluid properties of the refrigerants were calculated using the software REFPROP [8]. The specific enthalpies are calculated for all four or five points of the cycle (see Fig. 2a) and 2b)). The specific enthalpy depends on the pressure and temperature of the fluid and can be calculated for each point. In the 2-phase area, this also allows the vapor quality to be calculated. Accordingly, the most important input parameters are the evaporation temperature T_0 and the condensing temperature T_C, which are listed in Table 1. With the extended cycle parameters of Table 2, the specific enthalpy is calculated for each point in the cycle. The process at the expansion valve (Fig. 2a): 4 → 5) is assumed to be isenthalp, so that $h_5 = h_4$ in each case (compare with Fig. 2b)).

The cooling capacity is calculated according to equation 1:

$$\dot{Q}_0 = \dot{m} \cdot (h_1 - h_5) \quad (1)$$

Since the mass flow $\dot{m}$ is the same everywhere in the refrigeration cycle with external subcooler as well as in the reference refrigeration cycle, the EER is calculated independently of the mass flow $\dot{m}$ according to equation 2:

$$EER = \frac{h_1 - h_5}{h_2 - h_1} \tag{2}$$

The calculation of the EER is performed for both the refrigeration circuit with external subcooling and the reference refrigeration circuit without additional subcooling. The savings potential corresponds to the change in efficiency and is calculated according to equation 3. For all 5 operating points this procedure is repeated.

$$\Delta EER = \frac{EER_{External\ SC}}{EER_{Ref.Process}} \tag{3}$$

3. Limits of subcooling

3.1. Minimum subcooling

The minimum subcooling is essential for stable and safe operation of the plant. Whether this leads to an increase in efficiency is secondary. Subcooling can be reduced by pressure losses and heat inputs between the receiver and the inlet to the expansion valve. The pressure losses are composed of the static height difference between the header and the expansion valve and the pressure losses of the pipelines and fittings. The influence of pressure loss and heat exchange on subcooling (SC) is shown schematically in Figure 3.

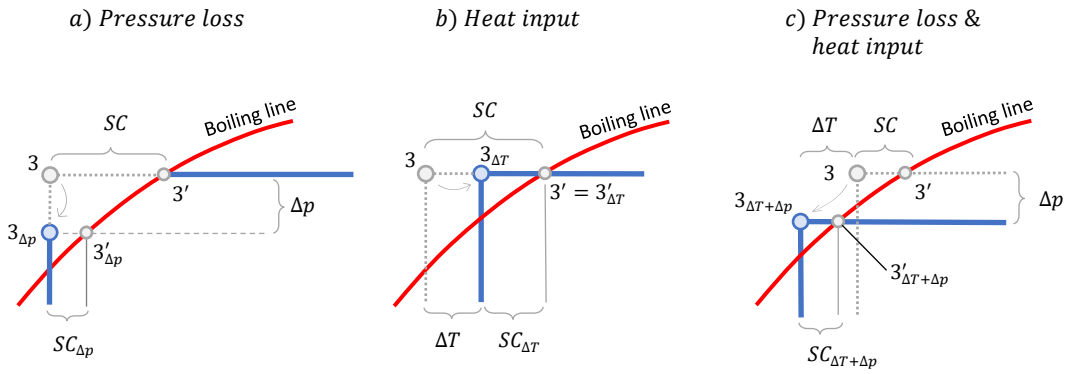


Fig. 3. Reduction of subcooling for a) due to pressure losses, for b) due to heat input, and for c) due to pressure losses and heat input

In Figure 3 the upper left section of the log p-h diagram is shown enlarged. In Figure 3a) the influence of the pressure loss, which is caused by pipelines, fittings, or lines with large height difference, is shown (3 → $3_{\Delta p}$). In case of pressure losses, the refrigerant temperature remains constant ($T_3 = T_{3\Delta p}$). However, the subcooling reduces because the boiling temperature reduces due to the pressure loss ($T_{3'} > T_{3'\Delta p}$). In the plot of Figure 3b), the influence of heat exchange between the pipe and the environment is shown (3 → $3_{\Delta T}$). Heat exchange takes place through the piping and fittings. Depending on fluid and ambient temperature, heat input or heat output results for the refrigerant. During heat exchange, the pressure and thus the boiling temperature remain constant ($T_{3'} = T_{3'\Delta T}$). The subcooling changes as the refrigerant heats up or cools down further due to the heat exchange. In Figure 3c), the combination of pressure losses and heat exchange is shown. These two effects can compensate each other. Due to the pressure loss, the boiling temperature of the refrigerant is reduced. However, if the ambient temperature is lower than the fluid temperature, the refrigerant is additionally cooled via the tube wall.

The minimum subcooling is therefore dependent on pressure losses and heat inputs and is therefore very plant specific.

3.2. Maximum subcooling

The maximum subcooling is primarily about optimizing efficiency and therefore varies depending on the refrigeration machine. In particular, the influence of large subcooling on the piping components and the vapor quality must be considered.

The subcooling beyond the minimum subcooling is only useful if it can increase the efficiency of the system. This may vary depending on the subcooling method, operating control, and refrigerant. How much the refrigerant can be subcooled is limited by the vapor quality at the outlet of the expansion valve. The influence of subcooling on the vapor quality can be seen in Figure 4.

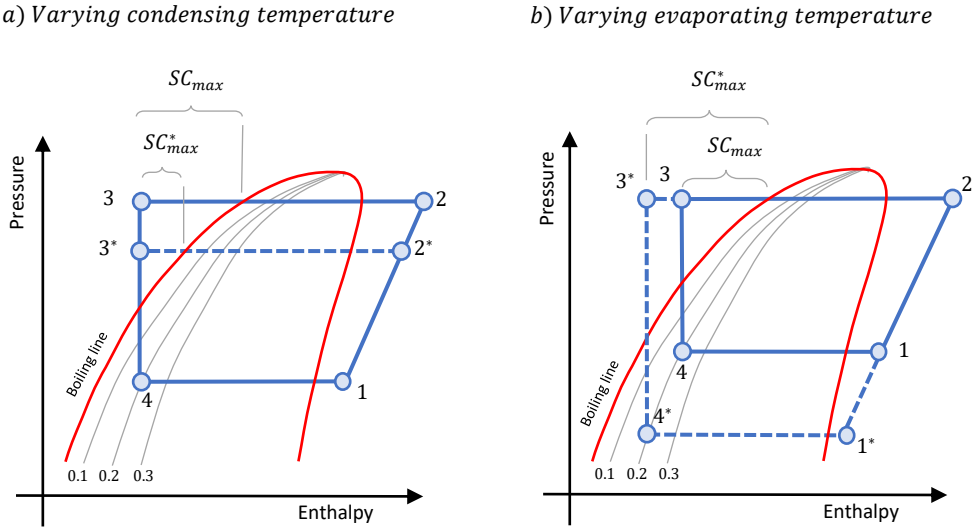


Fig. 4. Influence of subcooling on the vapor quality for a) varying condensing temperature and for b) varying evaporating temperature.

Increasing the subcooling reduces the vapor quality at the outlet of the expansion valve. Thus, the minimum vapor quality there defines a limit to how much the refrigerant can be subcooled. Figure 4a) shows the influence of the condensing temperature (operating point) on the maximum possible subcooling. A reduction of the condensing temperature also reduces the maximum possible subcooling. Figure 4b) shows that a reduction in the evaporating temperature (application) increases the maximum possible subcooling.

4. Results

4.1. Overview

The results of this investigation show the influence of different amounts of subcooling on the efficiency of the system. At the same time, different auxiliary variables are displayed, which are important for the estimation of the minimum necessary and maximum possible subcooling.

The combination of these factors allows a plant specific and seasonal assessment of efficiency improvement. Identical plots have been created for different subcooling types, refrigerants and applications. Therefore, auxiliary variables are also shown, which are not of interest for the assessment in the case of external subcooling. The plots can be seen in the appendix of the final report of the project [6].

Figure 5 shows the influence of additional subcooling on the efficiency as well as important auxiliary variables for a system with an external subcooler and refrigerant R290, for an application with T_0 = 10 °C (air conditioning with a direct evaporator).

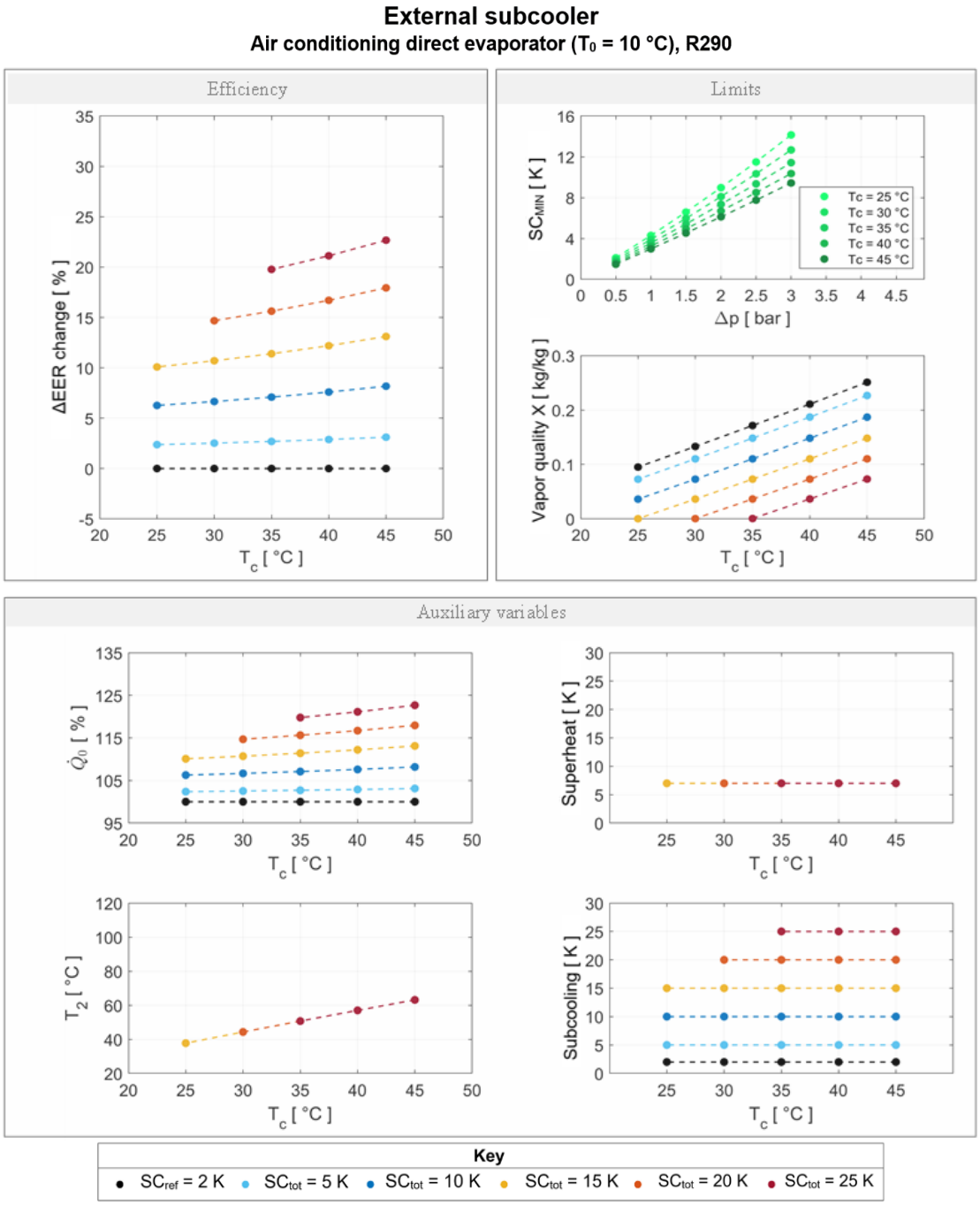


Fig. 5. Influence of additional subcooling regarding efficiency, limits, and auxiliary variables for an example of a refrigeration machine

Figure 5 shows the result as an overview. The top left box shows the potential for EER improvement as a function of condensing temperature for subcooling values of 5 - 25 K. However, in order to determine the efficiency improvement, the limits of subcooling (top right box in Fig. 5) and the auxiliary variables (bottom box in Fig. 5) must also be considered.

The diagrams in Figure 5 allow a comprehensive assessment of the additional subcooling as well as the expected efficiency gain at different operating points. The use of the result, as shown in Figure 5, is described in the following subsection.

4.2. Interpretation and use of the result

To be able to use the result, the heat sink of the external subcooler must be known. As an example, a use of a cold wastewater, which allows cooling of the refrigerant to constant 15 °C, is investigated. The maximum possible subcooling, given by the heat sink, is thus dependent on the operating point and is between 10 - 30 °C. To estimate which subcooling or which efficiency increase can be achieved with this heat sink, the following three limits must be considered and drawn in the upper right diagram in Figure 5 (Limits) and are shown larger for explanation in Figure 6:

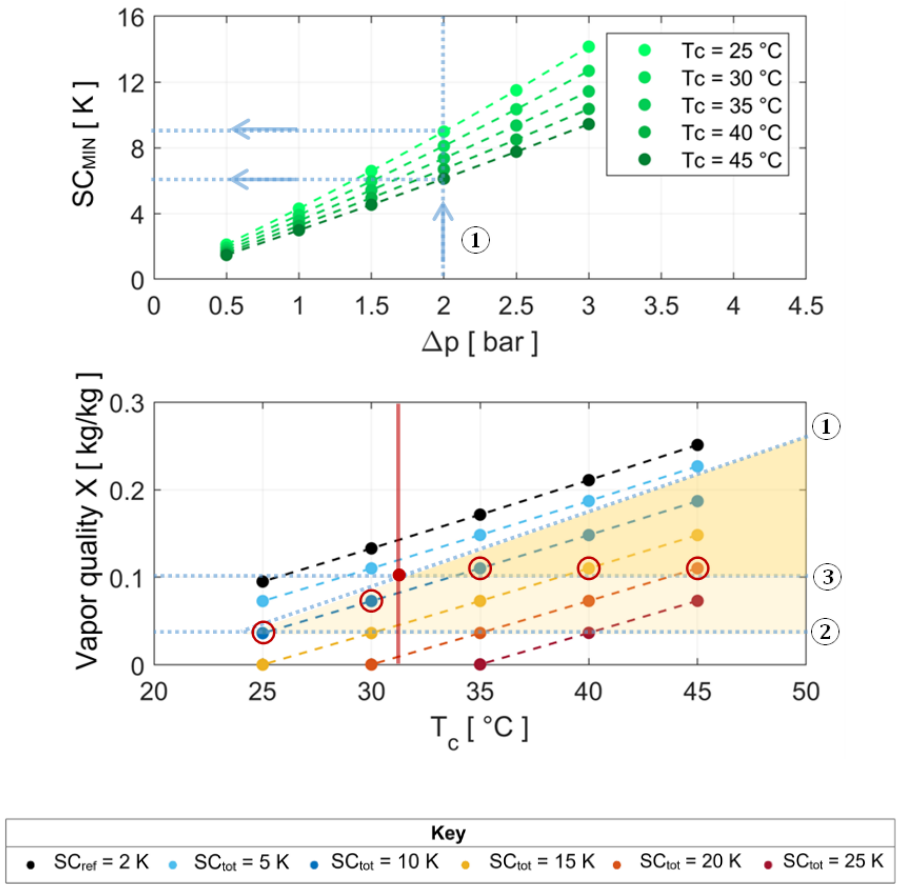


Fig. 6. Description to capture the limits of subcooling

① Minimum subcooling

As described in chapter 4.1, minimal subcooling is necessary for safe and stable operation of the system. Based on the upper diagram, the minimum subcooling can be estimated due to the plant-specific pressure losses. In this example, a plant with large differences in height and therefore 2 bar pressure losses is examined. Due to the pressure losses a minimum subcooling of 6 - 9 K is necessary. This value can also be plotted in the lower diagram and shows the lower limit of subcooling.

② Maximum possible subcooling (Heat sink)

The maximum possible subcooling depends on the heat sink of the external subcooler and its seasonal behavior. In this case, the heat sink is cold wastewater, which allows subcooling to a constant temperature of 15 °C. As can be seen in Figure 4, a steady outlet temperature from the subcooler means different degrees of subcooling, depending on the condensing temperature. This is shown in the Figure 6 by line ②.

③ Maximum subcooling (vapor quality)

The maximum possible subcooling is limited by the heat sink. An additional limitation is the minimum vapor quality at the outlet of the expansion valve. In this case, a minimum vapor quality of 0.1 is examined. This value can be defined by the designer's experience or by the expansion valve's operating limits. This is shown in the Figure 6 by line ③.

Based on the three plant specific limits, a range of possible subcooling results. Between the minimum necessary ① and the maximum possible subcooling ②, which are determined from the pressure losses and the heat sink, there is a range of subcooling which is theoretically possible (yellow area). Considering the minimum vapor quality ③, this area can be further restricted.

At high condensing temperatures (T_C > 31 °C), both the minimum subcooling and the minimum vapor quality can be maintained. All operating points between the two lines are theoretically possible. For efficiency reasons, the optimum subcooling is as close as possible to the minimum vapor quality, provided those other auxiliary variables, such as the end of compression temperature, are not in a critical range.

At low condensing temperatures (T_C < 31 °C), it is not possible to ensure the minimum subcooling without falling below the minimum vapor quality. The designer of the machine should consider operating points in this area in more detail.

Before determining the increase in efficiency of the individual operating points, the influence on other important parameters in the refrigeration cycle can be checked using the additional diagrams. Especially in applications with large pressure differentials, it is possible that the end of compression temperature T_2 comes into a critical range. To verify that the selected subcooling is feasible, the end of compression temperature T_2 must be within the compressor's operating limits. The compressor operating limits are defined by the manufacturer. Figure 7 shows the diagram for estimating the end of compression temperature, which is at the auxiliary variables in Figure 5.

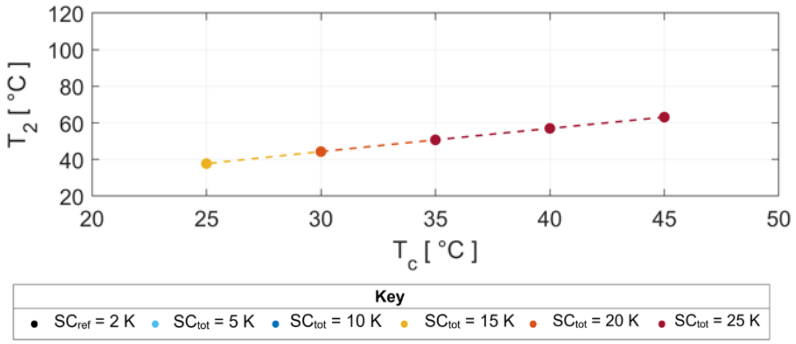


Fig. 7. Plot for estimation of the end of compression temperature (T_2)

The potential efficiency increases from the additional subcooling can be determined in Figure 8.
It shows the savings potential ΔEER of the external subcooler at different operating points. In the case with a wastewater heat sink of 15 °C ΔEER is between 6 – 18 % depending on the condensing temperature T_C. For condensing temperatures of 25 - 35 °C, a total subcooling of 10 K is possible. This was determined using the limits of subcooling (see Fig. 6). The total subcooling for a condensation temperature of 40 °C is 15 K (yellow line), at T_C = 45 °C is SC_{tot} = 20 K (red line).

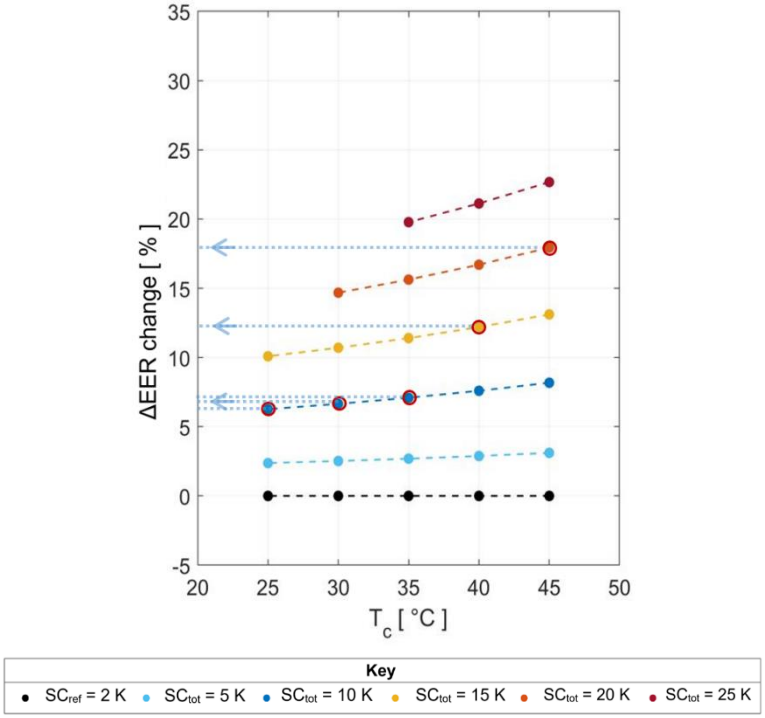


Fig. 8. Change in EER due to subcooling for different operating points

The efficiency improvement values can be used as the basis for an economic efficiency calculation. It should be noted that the operating points vary in frequency depending on the location. The individual operating points must therefore be weighted differently to estimate an annual energy saving, which is described in chapter 5.

5. Application for profitability calculation

The evaluation of the economic efficiency depends on the investment costs, the savings potential of the subcooling type, and the required auxiliary energies. The diagrams created in this report primarily help to estimate the annual savings potential of the subcooling type (ΔEER_a), which is determined according to equation 4.

$$\Delta EER_a = \sum_{i=1}^{5} w_i \cdot \Delta EER_i \tag{4}$$

In the previous chapter, the savings potential (ΔEER) of external subcooling by means of cold wastewater at different condensing temperatures was estimated. Figure 8 shows that the EER increases between 6 - 18 % depending on the condensing temperature.

For a seasonal consideration, the individual operating points must be weighted according to their energetic share of the annual consumption (w_i). The weighting of the individual operating points depends on the location and planned use (load profile). The final report on the investigation of refrigerant subcooling [6] shows in the appendix weighting factors for various locations in Switzerland and load profiles. The methodology for the energetic weighting of several operating points is described in detail in the final report on refrigeration compressors [9] (in German). Table 3 shows the seasonal consideration for the Basel site as an example. The load profile of the application must also be considered.

Table 3. Example of annual savings potential based on seasonal consideration

Operating point	1	2	3	4	5
Condensing temperature [°C]	45	40	35	30	25
Weighting factor [w_i]	0.01	0.05	0.10	0.14	0.70
Savings potential [ΔEER]	18 %	12 %	8 %	7 %	6 %
Annual savings potential [ΔEERa]			**7 %**		

The results in Table 3 show the energy weighting of the individual operating points for the Basel site. The annual savings potential is 7 %. This is due to the hourly frequency of ambient temperatures at the investigated site. It can be seen that the operating points with the highest savings potential are significantly less relevant in terms of energy. It should be noted that this only applies to the refrigeration machine and that any possible changes in the consumption of auxiliary energies have not been considered.

6. Conclusion

The studies on seasonal energy savings potential with additional subcooling have provided a useful basis for proper subcooling. The plots in Figure 5 can be used to determine the limits and energy savings potential of a refrigeration cycle with external subcooling.

It has been shown that there is a significant savings potential for refrigeration machines with direct evaporator and R290 as refrigerant if they can be operated with an external subcooler with constant heat sink.

Based on the seasonal evaluation, an economic efficiency calculation can be performed in addition to the annual savings potential. The study shows that the savings potential is strongly dependent on the operating point due to the limitations. For a seasonal evaluation, it is therefore always necessary to consider several operating points. However, the results are not only important for estimating the energy savings potential, but also for setting the operating limits. Compliance with the limits is important for safe and reliable operation of the refrigeration machine.

The study was carried out only based on computer simulations, which were verified by experts. There is no experimental comparison of the results. Accordingly, it would be interesting if the investigations could be compared with measurements on real refrigeration machines.

Acknowledgements

The authors would like to thank the Swiss Federal Office of Energy for their financial support in this project. In particular Martin Stettler (BFE) and Robert Dumortier (CERT) are expressly thanked. Thanks for the valuable support and constructive cooperation also go to the contributing experts Claudio Müller, Jonas Schönenberger and Matthias Brügger and our project partner Thomas Lang.

Nomenclature and Abbreviations

T_0	Evaporating temperature	COP	Coefficient of Performance
T_C	Condensing temperature	SC	Subcooling
ΔT	Temperature difference	EER	Energy Efficiency Ratio
Δp	Pressure loss	ΔEER	Savings potential
SC_{ref}	Subcooling for a reference process		
T_2	End of compression temperature		
h_i	Specific enthalpy		
$\dot{m}$	Refrigerant mass flow		
$\dot{Q}_0$	Cooling capacity		
ΔEER_i	Savings potential at an operating point to calculate the annual savings potential		

References

[1] G. Pottker and P. Hrnjak, "Experimental investigation of the effect of condenser subcooling in R134a and R1234yf air-conditioning systems with and without internal heat exchanger," Elsevier, Urbana, IL 61801, USA, 04.11.2014.

[2] N. A. Ansari, A. Arora, Samsher and K. Manjunath, "The Effect of Eco-friendly Refrigerants on Performance of Vapor Compression Refrigerant System with Dedicated Mechanical Subcooling," Springer Nature Singapore Pte Ltd., Bawana Road, Delhi 110042, India, 2020.

[3] T. Yilmaz and M. T. Erdinc, "Energetic and exergetic investigation of a novel refrigeration system utilizing ejector integrated subcooling using different refrigerants," Elsevier, 24.11.2018.

[4] A. Brunner, V. Prochaska, M. Kriegers and F. Tillenkamp, Klimakälte heute - Kluge Lösungen für ein angenehmes Raumklima, Faktor Verlag, 02.2019.

[5] Güntner AG & Co. KG, "Fachveröffentlichung - Der Einfluss der Kältemittelunterkühlung auf die Anlageneffizienz," 82256 Fürstenfeldbruck, Germany, 2010.

[6] L. Wick, C. Stahel and F. Tillenkamp, "Kältemittelunterkühlung - Grundlagen und Leitfaden zum Effizienz- und Kältegewinn," Winterthur, Switzerland, 20.07.2022.

[7] MathWorks, "MATLAB - R2021b (9.11.0.1769968)," 17.09.2021.

[8] E. Lemmon, I. Bell, M. Huber and M. McLinden, "REFPROP - NIST Standard Reference Database 23 (DLL version number 10.0)," NIST, 2018.

[9] C. Stahel, L. Wick and F. Tillenkamp, "Kälteverdichter - Schlüssel zu Energieeffizienz und Betriebssicherheit," Winterthur, Switzerland, 24.02.2022.

14th IEA Heat Pump Conference
15-18 May 2023, Chicago, Illinois

Free cooling in air conditioning: Investigation of its potential in Switzerland

Silvan Steiger[a], Christian Stahel[a]
Stefan Rohrer[a], Martin König[a], Frank Tillenkamp[a,*]

[a]Zurich Unviersity of Applied Sciences, Institute of Energy Systems and Fluid Engineering,
Technikumstrasse 9, 8400 Winterthur, Switzerland

Abstract

In air conditioning, free cooling is often used for saving energy. Free cooling is understood here as a bypass water circuit with direct recooling by the environment, not heat removal by nightly ventilation. Contrary to common practice in Switzerland, free cooling is not always economically beneficial. To estimate its potential in air conditioning systems, there are no generally applicable evaluation criteria or guidelines available. The aim of this work is to assess the free cooling potential in Switzerland by applying quasistatic simulations depending on supply temperature, application, location, circuit and type of heat discharge. The results show that supply temperature is the most influential parameter. Below 14 °C all investigated applications (except data centers) show generally less than 10% of free cooling amount in total annual cooling load, therefore not economically benefitting from it. Furthermore, the potential is strongly dependent on climate at the location. Cold regions like the Swiss alps allow longer yearly free cooling operation than warmer regions. If recoolers are used to pre-cool the returning cold water flow, the free cooling potential can almost be doubled.

© HPC2023.
Selection and/or peer-review under the responsibility of the organizers of the 14th IEA Heat Pump Conference 2023.

Keywords: Free cooling; air conditioning; free cooling potential; Switzerland

1. Introduction

Free cooling (FC) is generally used in refrigeration systems for saving energy and reducing refrigeration costs. Recent literature also reflects this trend: Lot of successful effort is put into assessing the worldwide/european/swiss FC potential of data centers [1-3] and reviewing/optimizing existing FC systems in data centers [4-7]. This topic is of utmost importance considering the environmental impact of ever-increasing data traffic around the globe. Furthermore, it strongly improved expertise on how and where FC brings significant energy savings in data centers. Regarding FC potential for general air-conditioning applications, sophisticated work can be found addressing either the FC potential in specific cooling applications [8], [9], assessing it more generally at specific locations [10] or over a wider geographical scope [11]. As FC is a known technology by now, efforts are also put into expanding FC use, for example by applying phase change materials in combination with innovative cooling concepts [12-16]. As to FC potential in Switzerland, specific systems have been reviewed [17], [18]. Matthey and Affolter were able to determine the FC potential of the city of Neuchâtel [19], whereas Artmann, Manz and Heiselberg determined the FC potential by nightly ventilation over Europe [20]. This work aims to gain insight on FC potential in Switzerland with particular attention to influencing factors such as cold water supply temperature (T_{CWS}), application, location, hydraulic integration (circuit) and type of heat discharge.

* Corresponding author. Tel.: +41 58 934 73 61
E-mail address: frank.tillenkamp@zhaw.ch

2. Modelling

The analysis is intended to provide findings on appropriate use-cases for FC in air conditioning. For this purpose, applications in specific sample buildings were considered. With regard to modelling, they were all divided into three subsystems: recooler (refrigeration machine heat discharge), cold generation and cooling distribution/building (see Fig. 1**Error! Reference source not found.**). FC is assigned to the cold generation subsystem.

2.1. Parameter set

To assess influential variables on the FC potential, a suitable parameter set was established. It consists of varying values for the editable subsystems and boundary conditions: hydraulic integration (circuit), type of heat discharge, T_{CWS}, location with associated boundary conditions as well as type of cooling application.

Firstly, to clarify the influence of different hydraulic integrations, a total of five circuits (Fig. 1) were examined in consultation with experts. Each circuit contains the aforementioned subsystems and can be assigned to an operating group. Circuits 1, 2 and 4 are bivalent-alternative systems, where the cooling load is covered either by the refrigeration machine or FC. Circuits 3 and 5 are bivalent-parallel systems, whereby cold water can be precooled by FC and is simultaneously run with the refrigeration machine.

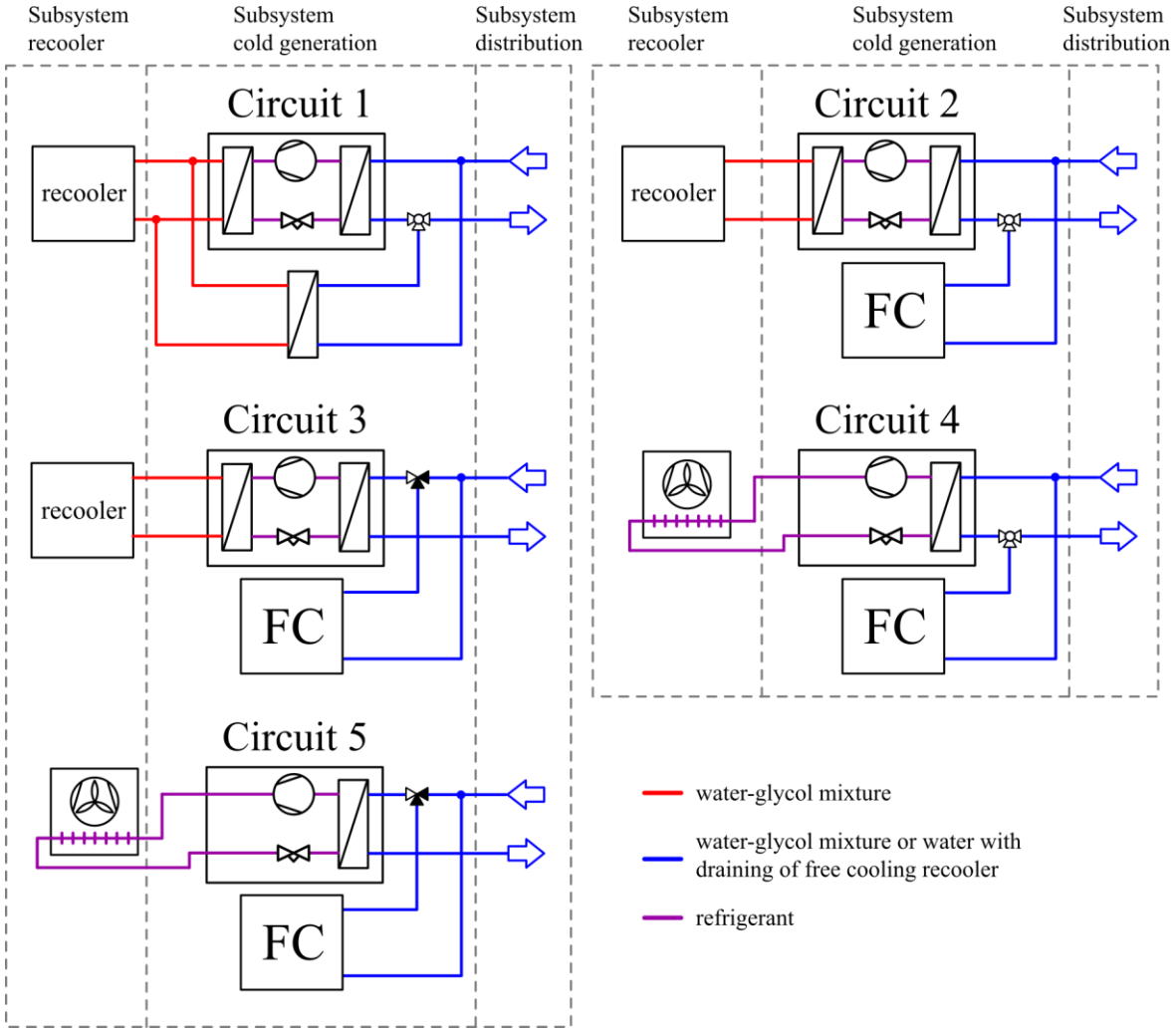


Fig. 1. Simplified scheme of investigated circuits

Secondly, various types of heat discharge systems were investigated. Depending on the type, FC return temperatures and therefore the possible FC operating time is affected. All types were simulated with a maximum capacity, which is never exceeded. This maximum capacity is defined as the design cooling load of the building, which was calculated site and application specific according to the standard of the Swiss Society

of Engineers and Architects (SIA) 2024 [21]. In other words, separate discharge systems for FC (circuit 2 to 5) are able to dissipate the complete design load. The design also takes into account site-specific boundary conditions of the outside air (according to summer design data from SIA 2028 [22]) as well as application-specific sizes (according to SIA 2024 [21]). Every type leads to specific input parameters, which are summarized in Table 1. One value is the temperature difference between wet bulb and heat discharge return line (dT_{WB-RL}), which was assumed to be constant. The second value is the reference temperature (T_{ref}) at which heat can be discharged to.

Table 1: Details of investigated heat discharge systems for FC

Type of heat discharge	**Calculation dT_{WB-RL}**	**Calculation T_{Ref}**
Dry recooler	According to standard SWKI 2003-3 [23]	Location dependent outside air temperature according to standard SIA 2028 [22]
Hybrid recooler	According to standard SWKI 2003-3 [23]	Location dependent wet bulb temperature according to standard SIA 2028 [22]
Geothermal probe	According to standard SIA 384/6 [24]	Location dependent soil temperature according to standard SIA 384/6 [24]
Groundwater collection	Mean of values to strive for according to VDMA 24247-8 [25]	Location dependent wet bulb temperature according to standard SIA 2028 [22]

Some simplifications and delimitations must be considered: Hybrid recoolers were modeled to be sprayed on with water constantly, leading to the maximum possible FC potential. In every simulation run, the used heat discharge system (dry/hybrid) of the refrigeration machine was the same as for FC. Regarding geothermal probes and groundwater collection, soil temperature changes as well as legal regulations were neglected, also resulting in maximum FC potential. Ground temperature could only be estimated and varies strongly with subsurface conditions and drilling depth, only allowing a rough estimation of FC potential. For circuits 2 to 5, separate FC with geothermal probes or groundwater is excluded. Usually, those heat discharge systems are built for recooling the refrigeration machine and are additionally used for FC, which reduces circuits 2 to 5 to circuit 1 in this regard. The effect of water fed heat discharge systems was therefore only calculated with circuit 1.

Thirdly, T_{CWS} was varied to investigate its influence. By choosing the temperature level of the cold water, that for FC is also determined which in turn affects its possible operating time. According to SIA 382/1 [26], temperatures of 6, 10 and 14 °C were used representing typical values for air conditioning applications. 18 °C serves as an interpolation value and with 22 °C a typical temperature for data center cooling was included. T_{CWS} is always assumed to be constant, hence no adjustment to the outside temperature is considered.

Fourth, different locations were evaluated. Due to various environmental conditions, the heating and cooling demand of an application as well as the minimum temperature of heat discharge are affected. To evaluate the site dependency, data of the weather measuring stations Zurich, Basel, Geneva, Lugano and Davos were included (Fig. 2). These can be assigned to one of the three climatic/geographical regions of Switzerland: Central plateau, Swiss alps and Ticino (Table 2). This assignation serves to extrapolate to a more general view over Switzerland. Weather data was obtained from the Federal Office of Meteorology and Climatology (MeteoSwiss) [27]. In the years 2010 to 2016, the year 2013 shows the smallest deviation of annual mean values from the norm across all stations considered (according to MeteoSwiss). Therefore, 2013 was finally used for weather data. Table 3 shows weather parameters (measured in hourly mean values) used for the calculation.

Table 2: Locations and their boundary conditions

Region	**Location**	**Meters above sea level**	**Annual mean air temperature $T_{0,a}$ [°C]**	**Annual mean soil temperature [°C]**
Central plateau	Basel	316	10.3	12.4
	Geneva	410	10.2	12.6
	Zurich	426	9.4	11.3
Swiss alps	Davos	1594	3.6	7.2

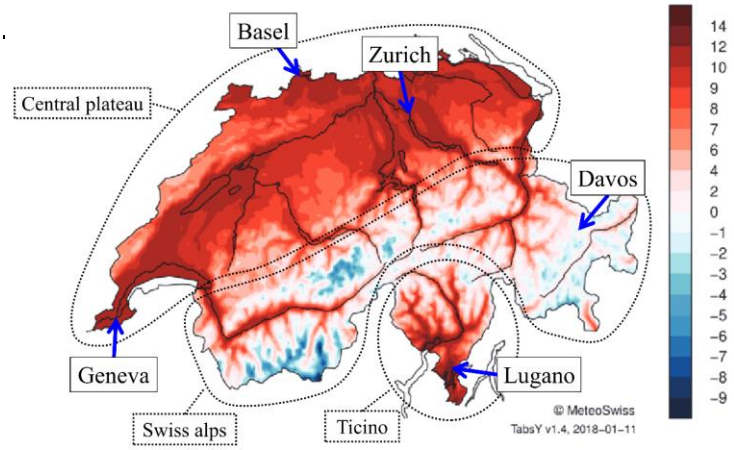


Fig. 2: Annual mean temperature map of Switzerland with marked climatic/geographical regions and locations of used weather data stations [29].

	2.8	14.4

Table 3: Used weather data (hourly values)

Value	Unit
Air temperature 2 m above ground	°C
Wet bulb temperature 2 m above ground	°C
Air pressure at station height	hPa
Relative humidity 2 m above ground	%
Global irradiation	W/m²

Fifth, different proportions of internal heat were evaluated by including different types of applications according to standard SIA 2024 [21]. As Table 4 shows, the selection was based on the widest possible spread of internal heat load share.

Table 4: Investigated types of application

Type of application	**Designation according to SIA 2024** [21]	**Proportion of internal heat load to total heat load [%]**
Hospital/doctors office	Treatment rooms	51
Office building	Open-plan office	57
Department store	Specialty store, department store	83
Data center	Server room	99

2.2. Calculation Model

The applied calculation model is based on thermal energy balances of hourly intervals over a calendar year. This leads to a quasi-static view of the system, which means that storage effects of the building mass and in possible cold or heat storages are not considered. As depicted in Eq. (1), the hourly target thermal load of a building was calculated according to the standard SIA 2024 [21].

$$Q_{dem} = (\Phi_T + \Phi_v + \Phi_i + \Phi_s) \cdot A_{NFA} \quad (1)$$

$$Q_{dem} \leq 0 \quad \Rightarrow \quad Q_{dem,C} = Q_{dem} \quad (2)$$

$$Q_{dem} \geq 0 \quad \Rightarrow \quad Q_{dem,H} = Q_{dem} \quad (3)$$

Here, Q_{dem} is the hourly heating/cooling demand, Φ is the specific heating/cooling load with indexes *T* for transmission, *v* for ventilation, *i* for internal and *s* for solar load. A_{NFA} is the net floor area of the representative building. If the target thermal load is negative, cooling load is present (Eq. (2)) and if it results positive, heat load exists (Eq. (3)). Specific heating/cooling loads were calculated according to the standards SIA 2024 [21] and SIA 2028 [22]. Further information on the calculation can be found in [28].

2.3. Evaluated quantitites

The value of greatest interest is the FC potential, as shown in Eq. (4). It is intended to provide information on the usefulness of FC in relation to the total cooling load. For this purpose, the yearly amount of discharged heat by FC ($\sum Q_{C,FC,a}$) was compared with the yearly total cooling load ($\sum Q_{C,tot,a}$) for each parameter combination.

$$FC\ potential = \frac{\sum Q_{C,FC,a}}{\sum Q_{C,tot,a}} \cdot 100\% \quad (4)$$

In order to provide assistance to the reader, a calculation of the economic efficiency for a 200 kW refrigeration plant was carried out [28]. To keep annual costs of a system with FC at the same level as a conventional one, a FC potential of at least 11% (best case) or 39% (worst case) must be achieved. Otherwise, FC is not considered economically viable. This classification is listed consistently in the results (cf. section 3).

3. Results

A total of 1200 parameter combinations were simulated and evaluated using the procedure described in section 2. The most important findings are outlined below.

3.1. Influence of cold water supply temperature

Out of all parameters T_{CWS} has the most significant influence on FC potential. As an example, the evaluation for Zurich (representing the central plateau region) with dry recooler heat discharge is displayed in Fig. 3. It shows that the FC potential decreases with decreasing T_{CWS}. At $T_{CWS} < 10\ °C$, the FC potential drops below 2 % for all circuits and applications, except the data center. This tendency applies to all locations, heat discharge types, applications and circuits [28]. Applications with a low proportion of internal heat loads (hospital/doctors office, office buildings) show the strongest response to this tendency.

The data center application represents a special case: Due to year-round cooling load, a considerable proportion can be served by FC, even with relatively low T_{CWS}. This confirms the common use of FC in data

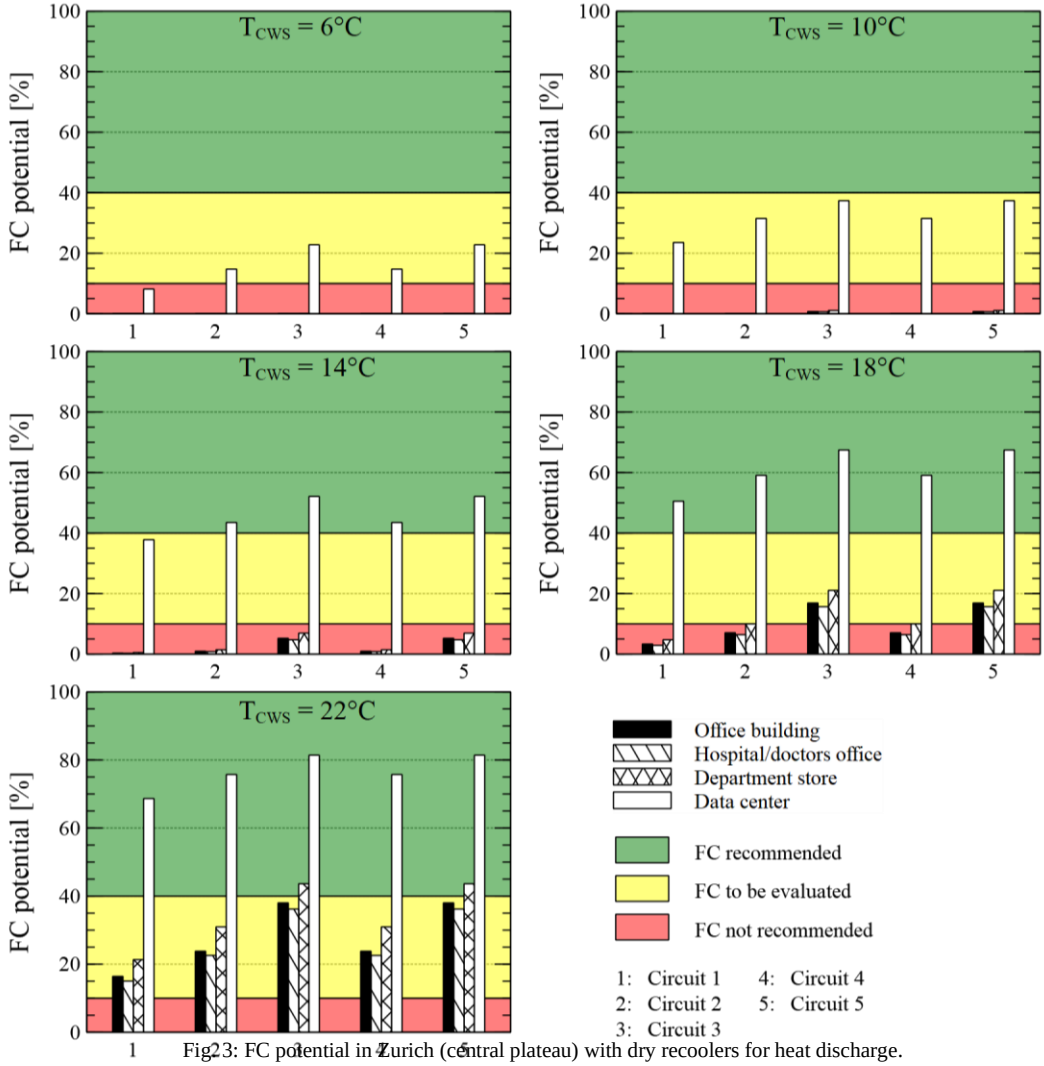


Fig. 3: FC potential in Zurich (central plateau) with dry recoolers for heat discharge.

center chiller systems. However, it stresses the crucial point that cooling with high T_{CWS} leads to great FC potential (up to 81 % in this evaluation) and therefore high energy savings.

3.2. Influence of hydraulic integration (circuit)

The FC potential is further influenced by the choice of hydraulic integration. The evaluation for Zurich with dry recooler heat discharge (cf. Fig. 3) serves as an example again. Across all locations, heat discharge types, applications and T_{CWS}, three main influences of the circuit can be identified:

Temperature difference across heat exchangers

Large temperature differences across heat exchangers have a negative influence on the FC potential since they reduce the necessary spread between T_{CWS} and the return temperature of the FC. Parameter combinations with circuit 1 (largest temperature differences over the heat exchangers) therefore generally have the lowest FC potential.

Operating mode of FC

The operating mode of FC has an influence on the performance, independent of all other parameters. With bivalent-parallel mode the cold water return flow can be precooled as soon as the return temperature of the heat discharge is lower. This allows longer FC operating periods and consequently higher FC potentials. It can be seen that bivalent-parallel systems generally have higher FC potential than bivalent-alternative ones (compare results of circuits 2 & 3 as well as those of circuits 4 & 5).

Type of refrigeration machine condenser

Comparing circuits 2 & 4 as well as circuits 3 & 5, they differ only in the type of refrigeration machine condensation (cf. Fig. 1). No influence on the FC potential can be determined. Circuits which only differ by direct or indirect condensation show the same FC potential for identical parameter combinations.

3.3. Influence of location

The location defines $T_{0,a}$, which influences both T_{Ref} and the application's heat load profile, which in turn significantly influences the FC potential across all parameter combinations. The decisive factor for this influence is the dependence of the heat discharge system return temperature on the outside air temperature.

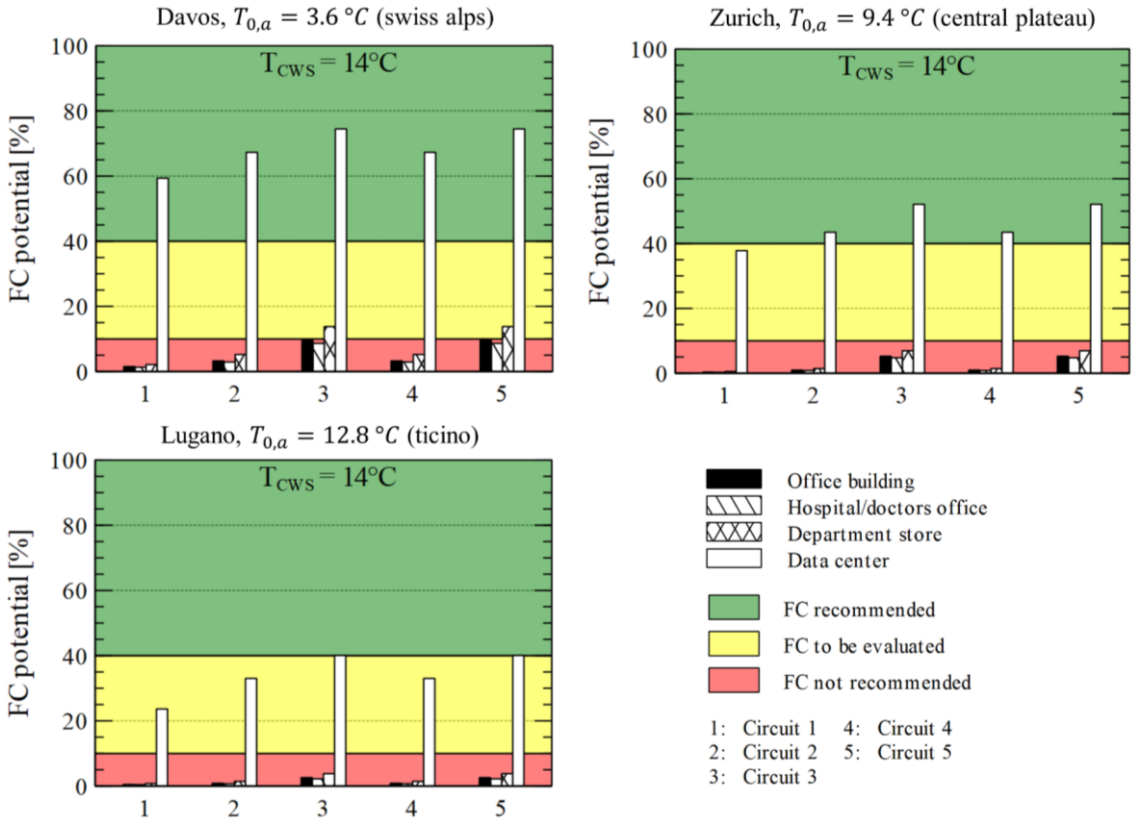


Fig. 4: FC potential for different locations with dry recoolers for heat discharge.

As an example, the FC potential evaluation with dry recooler heat discharge and $T_{CWS} = 14\,°C$ for different regions is shown in Fig. 4. Regardless of the remaining parameters, it can be determined that low ambient temperatures increase the FC potential. Thus, with the same application and circuit, greater potential can be achieved in the Swiss alpine region rather than the Central plateau or Ticino. All investigated locations in the Central plateau show only minor FC potential changes to Zurich.

3.4. Influence of heat discharge system

Dry recooler vs. hybrid recooler

As an example, the evaluation of FC potential at $T_{CWS} = 14\,°C$ and $T_{CWS} = 22\,°C$ for Zurich is shown in Fig. 5. It must be considered that the hybrid recooler was modeled as if it were constantly sprayed on with water. Therefore, the results for hybrid recooling show the maximum possible FC potential. With hybrid recooling, the FC potential can be greatly increased compared to dry recooling. In some cases, it can be even more than doubled.

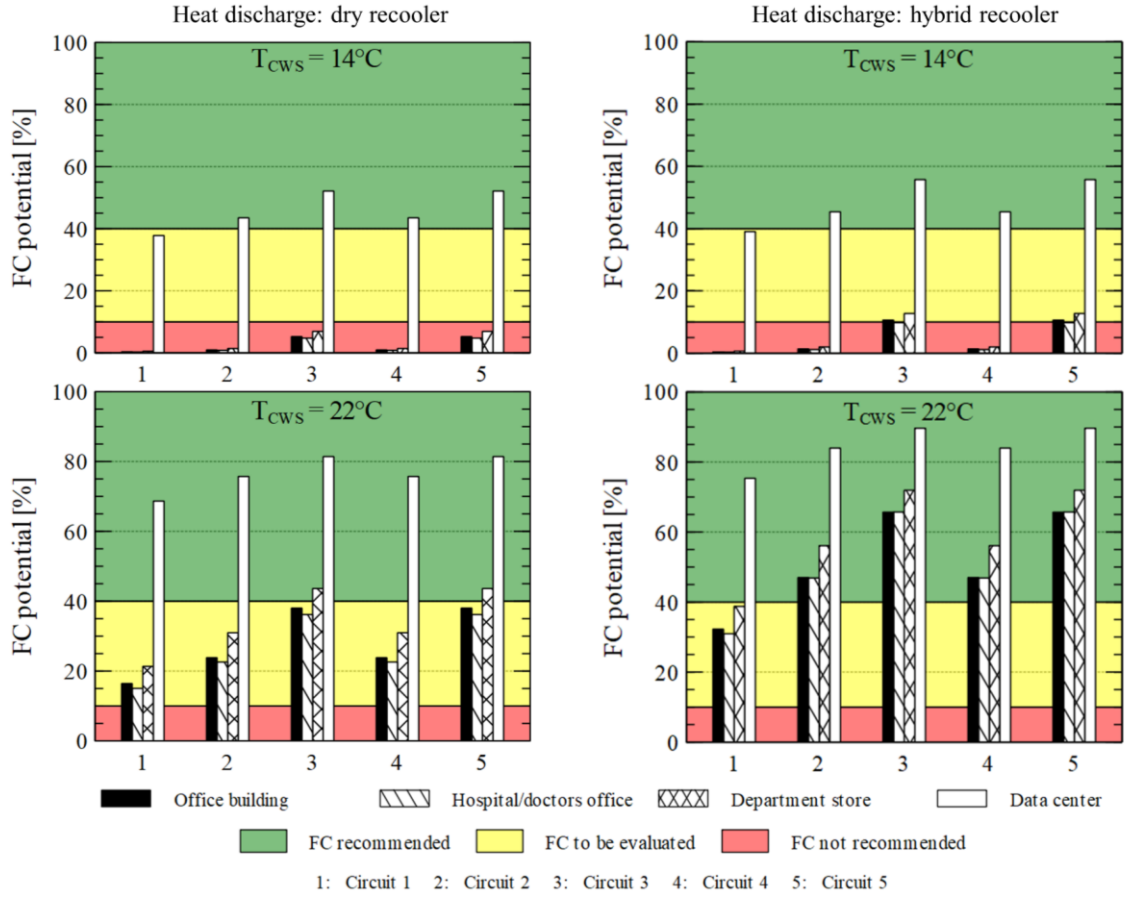


Fig. 5: FC potential for dry and hybrid recooler heat discharge in Zurich.

Geothermal probes and groundwater collection

Due to the simplifications made (cf. section 2.1), only an estimation of the maximum FC potential of geothermal probes and groundwater is possible. Reminder: In order to determine the effects of water-fed heat discharge systems, only circuit 1 was simulated.

The evaluations (Fig. 6) show a large FC potential at high T_{CWS} over all investigated locations. In generally cold regions such as the Swiss alps (Davos), FC by groundwater collection can also be useful with low T_{CWS} due to lower soil temperatures. It should be noted that heat discharge may be limited by legal restrictions. A more exact statement would require a further investigation, in which the dynamic behavior of the geothermal probe as well as groundwater collection is analyzed under consideration of the heat inputs.

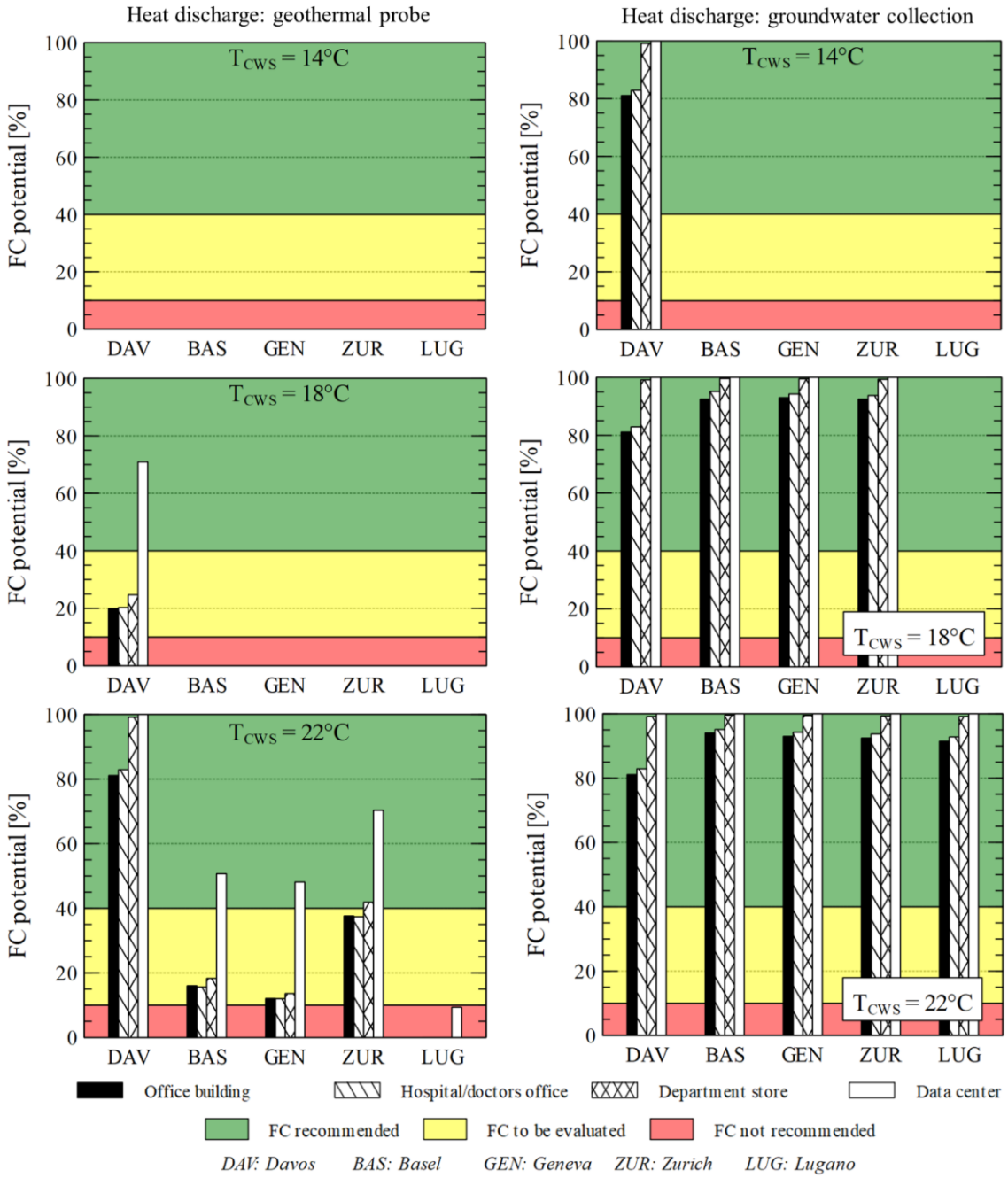


Fig. 6: FC potential with geothermal probes and groundwater collection for circuit 1.

4. Conclusion and Outlook

The main objective of the present study was to investigate the FC potential in Switzerland. This was done by applying quasistatic simulations on typical FC use-cases for different T_{CWS}, applications, locations, circuits, and types of heat discharge. A total of 1200 parameter combinations were calculated where 700 cases (58.3 %) belong into the category "FC not recommended", with FC potential under 11 %. Another 280 cases (23.3 %) belong to the category "FC to be evaluated", with FC potential between 11 % and 39 %. These cases can economically benefit from FC, depending on the exact operating conditions. Last but not least, 220 cases (18.3 %) belong to the category "FC recommended" with FC potential over 39 %. This means that, according to this assessment, only less than half of all parameter combinations considered have a potential for which FC should be evaluated or for which it is recommended. However, it should be noted here: Not all investigated parameter combinations make practical sense (e.g., data centers usually aren't cooled with $T_{CWS} = 6\,°C$). Nevertheless, this study reveals important principles for the use of FC, which are summarized below.

1) Cooling and FC should be carried out at the highest possible T_{CWS}. This increases the FC potential on one hand and the general energy savings on the other.
2) Regarding hydraulic integration (circuit), the difference between direct and indirect condensation of the refrigeration machine is negligible. Bivalent-parallel systems with precooling the cold water return flow generally show higher FC potential than bivalent-alternative systems.
3) In terms of used heat discharge systems, hybrid recoolers or geothermal probes/groundwater collections show large improvements in FC potential in some cases. Especially at high T_{CWS}, water fed heat discharge systems show great advantages.

The analysis of the data center even allows to transfer some conclusions of the results onto industrial refrigeration applications. If it is assumed that an industrial application has a year-round cooling demand, increased FC potential can be expected. If, in addition, high T_{CWS} are present the FC potential can be maximized. From this point of view, FC is a very interesting technology for certain industrial cooling applications. However, the exact relationships would have to be investigated in more detail. In addition, it must not be forgotten for industrial refrigeration applications, that a possible heat utilization is clearly preferable to a heat release to the environment. With the results in this study, it is possible to estimate the FC potential for a specific cooling system. For this purpose, various diagrams and a description of the procedure are provided in the original research report [28]. Furthermore, detailed analyses can also be found there.

With the Swiss Federal Office of Energy as contracting authority, this study was limited to investigations in Switzerland. Further studies for regions with warmer or colder climates than Switzerland can provide information on the validity of this approach as well as further insights on the FC potential in those regions.

Acknowledgements

The Authors would like to thank the Swiss Federal Office of Energy for their financial support in this project. Mr. Martin Stettler is expressly thanked. Thanks for the valuable support and constructive cooperation also go to the contributing experts Arnold Brunner (Brunner Consulting), Robert Dumortier, Michael Kriegers (Meierhans und Partner) and Thomas Lang (zweiweg GmbH). For further technical support we would also like to thank Luk End and Matthias Brügger (Leplan AG).

Nomenclature and Abbreviations

A_{NFA}	Net floor area of representative building	FC	Free cooling
$T_{0,a}$	Annual mean air temperature	MeteoSwiss	Swiss Federal Office of Meteorology and Climatology
T_{CWS}	Temperature of cold water supply line	SIA	Swiss society of engineers and architects
$dT_{WB\text{-}RL}$	Temperature difference between wet bulb and heat discharge return line	SWKI	Swiss association of building services engineers
T_{ref}	Temperature, at which heat can be discharged to (depending on heat discharge system)	VDMA	German mechanical engineering industry association
$\sum Q_{C,FC,a}$	Yearly amount of dircharged heat by free cooling	$\sum Q_{C,tot,a}$	Yearly total cooling load

References

[1] K. P. Lee and H. L. Chen, “Analysis of energy saving potential of air-side free cooling for data centers in worldwide climate zones,” *Energy Build*, vol. 64, pp. 103–112, 2013, doi: 10.1016/j.enbuild.2013.04.013.

[2] T. Malkamäki and S. J. Ovaska, “Solar energy and free cooling potential in European data centers,” in *Procedia Computer Science*, 2012, vol. 10, pp. 1004–1009. doi: 10.1016/j.procs.2012.06.138.

[3] A. Altenburger, “Energieeffizientes Kühlen von IT-Räumen,” 2004. [Online]. Available: www.electricity-research.ch

[4] Y. Yang, B. Wang, and Q. Zhou, “Air Conditioning System Design using Free Cooling Technology

and Running Mode of a Data Center in Jinan," in *Procedia Engineering*, 2017, vol. 205, pp. 3545–3549. doi: 10.1016/j.proeng.2017.09.924.

[5] Y. Udagawa, S. Waragai, M. Yanagi, and W. Fukumitsu, "Study on free cooling systems for data centers in Japan," in *INTELEC, International Telecommunications Energy Conference (Proceedings)*, 2010. doi: 10.1109/INTLEC.2010.5525676.

[6] H. Zhang, S. Shao, H. Xu, H. Zou, and C. Tian, "Free cooling of data centers: A review," *Renewable and Sustainable Energy Reviews*, vol. 35. Elsevier Ltd, pp. 171–182, 2014. doi: 10.1016/j.rser.2014.04.017.

[7] J. Ni and X. Bai, "A review of air conditioning energy performance in data centers," *Renewable and Sustainable Energy Reviews*, vol. 67. Elsevier Ltd, pp. 625–640, Jan. 01, 2017. doi: 10.1016/j.rser.2016.09.050.

[8] U. Berardi, G. Heidarinejad, S. Rayegan, and H. Pasdarshahri, "Enhancing the cooling potential of a solar-assisted desiccant cooling system by ground source free cooling," *Build Simul*, vol. 13, no. 5, pp. 1125–1144, Oct. 2020, doi: 10.1007/s12273-020-0696-0.

[9] B. Li, P. Wild, and A. Rowe, "Free cooling potential of air economizer in residential houses in Canada," *Build Environ*, vol. 167, Jan. 2020, doi: 10.1016/j.buildenv.2019.106460.

[10] H. Bulut and M. A. Aktacir, "Determination of free cooling potential: A case study for İstanbul, Turkey," *Appl Energy*, vol. 88, no. 3, pp. 680–689, 2011, doi: 10.1016/j.apenergy.2010.08.030.

[11] C. Ghiaus and F. Allard, "Potential for free-cooling by ventilation," *Solar Energy*, vol. 80, no. 4, pp. 402–413, Apr. 2006, doi: 10.1016/j.solener.2005.05.019.

[12] A. Maccarini, G. Hultmark, N. C. Bergsøe, and A. Afshari, "Free cooling potential of a PCM-based heat exchanger coupled with a novel HVAC system for simultaneous heating and cooling of buildings," *Sustain Cities Soc*, vol. 42, pp. 384–395, Oct. 2018, doi: 10.1016/j.scs.2018.06.016.

[13] A. Waqas and Z. Ud Din, "Phase change material (PCM) storage for free cooling of buildings - A review," *Renewable and Sustainable Energy Reviews*, vol. 18. pp. 607–625, 2013. doi: 10.1016/j.rser.2012.10.034.

[14] S. A. Nada, W. G. Alshaer, and R. M. Saleh, "Experimental investigation of PCM transient performance in free cooling of the fresh air of air conditioning systems," *Journal of Building Engineering*, vol. 29, May 2020, doi: 10.1016/j.jobe.2019.101153.

[15] K. Panchabikesan, A. A. R. Vincent, Y. Ding, and V. Ramalingam, "Enhancement in free cooling potential through PCM based storage system integrated with direct evaporative cooling (DEC) unit," *Energy*, vol. 144, pp. 443–455, Feb. 2018, doi: 10.1016/j.energy.2017.11.117.

[16] V. A. A. Raj and R. Velraj, "Review on free cooling of buildings using phase change materials," *Renewable and Sustainable Energy Reviews*, vol. 14, no. 9. Elsevier Ltd, 2010. doi: 10.1016/j.rser.2010.07.004.

[17] M. Mosteiro-Romero, E. Riegelbauer, S. Hsieh, and A. Schlueter, "District-scale lake water free cooling in Zurich, Switzerland: System performance simulation and techno-economic feasibility," *Proceedings of ECOS 2020*, 2020, doi: 10.3929/ethz-b-000426953.

[18] M. Eberhard, "Erdwärmesondenfeld Aarau," Aarau, 2005.

[19] B. Matthey and M. Affolter, "Freecooling en milieu urbain," 2009.

[20] N. Artmann, H. Manz, and P. Heiselberg, "Passive cooling of buildings by night-time ventilation," 2008. [Online]. Available: www.empa.ch

[21] Swiss society of engineers and architects SIA, "SIA 2024: Standard-Nutzungsbedingungen für die Energie-und Gebäudetechnik." Zurich, 2006.

[22] Swiss society of engineers and architects SIA, "SIA 2028: Klimadaten für Bauphysik, Energie - und Gebäudetechnik." Zurich, 2008.

[23] Swiss association of building services engineers SWKI, "SWKI 2003-3:2005 Rückkühlung." Schönbühl, 2005.

[24] Swiss society of engineers and architects SIA, "SIA 384/6: Erdwärmesonden." Zurich, 2010.

[25] German mechanical engineering industry association VDMA, "VDMA 24247: Energieeffizienz von Kälteanlagen, Teil 8: Komponenten - Wärmeübertrager," 2011.

[26] Swiss society of engineers and architects, "SIA 382/1: Lüftungs- und Klimaanlagen - Allgemeine Grundlagen und Anforderungen." Zurich, 2014.

[27] Federal Office of Meteorology and Climatology MeteoSwiss, "Measurement values." https://www.meteoswiss.admin.ch/home/measurement-values.html?param=messwerte-lufttemperatur-10min (accessed Nov. 11, 2022).

[28] S. Rohrer, M. König, and F. Tillenkamp, "Free Cooling in der Klimakälte Untersuchung des Potentials in der Schweiz," *IEFE Energy Papers*, vol. 7, no. 1, 2018, doi: 10.21256/zhaw-1369.

[29] Federal Office of Meteorology and Climatology MeteoSwiss, "Klimabulletin Jahr 2017." Zurich, 2018.

14th IEA Heat Pump Conference
15-18 May 2023, Chicago, Illinois

Simulation Towards Demonstration: A Comparison Of Different Control Concepts Of An Industrial-Scale Rotation Heat Pump

Michael Lauermann[1*], Stephan Kling[1], Bernd Windholz[1], Andreas Sporr[1], Andreas Längauer[2], Georg Kaltenbaek[2], Bernhard Adler[2]

[1]AIT Austrian Institute of Technology GmbH, Center for Energy, Giefinggasse 4, 1210 Wien, Austria
[2]ecop Technologies GmbH, Forschungs- und Entwicklungsabteilung, Perfektastraße 73, 1230 Wien, Austria

Abstract

Rotation Heat Pumps (RHP) offer the advantage of a flexible process in terms of temperature with an environmentally friendly, non-flammable working fluid. The application has already proven successful in the operation of a reference plant and prototypes. A RHP uses a Joule cycle in contrast to compression heat pumps using a vapor compression cycle. Due to the rotation of a rotor filled with the working fluid, the temperature of the fluid rises outwards as the working fluid is compressed. Basic elements are the heat exchangers, the compression and expansion pipes, and a fan to circulate the working fluid. Due to the rotation, these components differ in their operating behavior according to available literature data. Regarding control, numerous publications and theoretical principles and commercial controllers are available for compression heat pumps. The current state of the art for an RHP is a fixed/rigid presetting of the parameters to achieve a certain operating state. This results in a simple but non-optimal control, e.g. regarding energy efficiency. In this work, different control concepts based on the fundamentals of a DigitalTwin have been developed and compared to each other (e.g. extremum-seeking control and model predictive control). The proof-of-concept is first performed on the machine controller (PLC) by means of controller-in-the-loop tests. Subsequently, the control concepts are implemented and verified on a real industrial scale RHP.

© HPC2023.
Selection and/or peer-review under the responsibility of the organizers of the 14th IEA Heat Pump Conference 2023.

Keywords: Thermodynamics; Energy; Exergy; Sustainability; Control; Rotation Heat Pump.

1. Introduction

1.1. Rotation Heat Pump

A Rotation Heat Pump (RHP) uses a Joule cycle in contrast to conventional compression heat pumps which use a vapor compression cycle. Basic elements of an RHP are heat exchangers, compression and expansion pipes, and a fan to circulate the working fluid. The Joule process describes the counterclockwise cycle in a closed system, where the working gas never condenses or evaporates, but always remains in the gaseous state. *Figure* 1 shows a schematic comparison of the Joule and the vapor compression cycle.

* Corresponding author. *E-mail address:* michael.lauermann@ait.ac.at

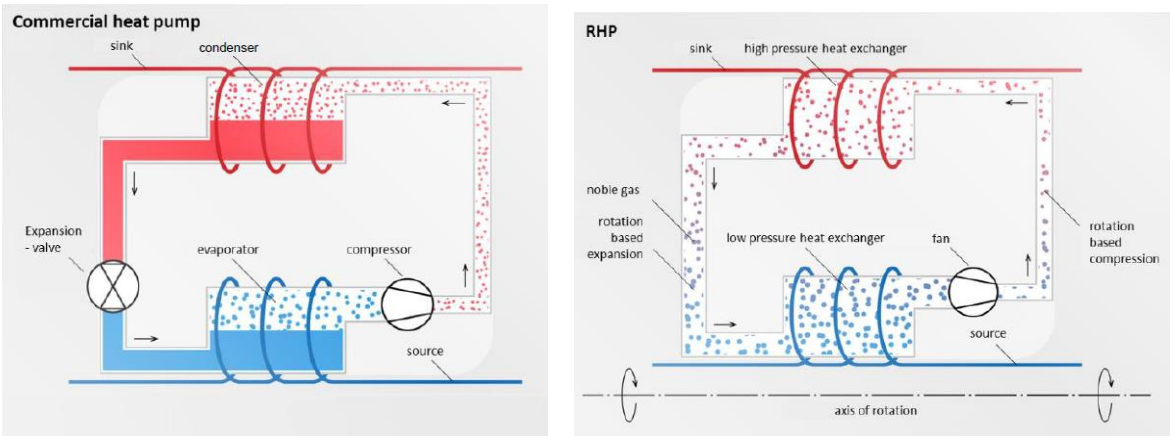


Figure 1: Basic principle of a conventional compression heat pump (left) and an RHP (right).

For implementing the Joule process in an economically viable manner, highly efficient compression of the working gas is necessary. In an RHP this is achieved by centrifugal forces. Due to the rotating rotor filled with a working fluid, the temperature of the fluid rises outwards while the working gas is compressed. This concept is schematically shown in *Figure* 2 (left): Two heat exchangers on low- and high-pressure side as well as compression and expansion pipes and a fan are depicted. These components represent the area flowed through with working gas. Also shown are the connections of source and sink as well as the flow through the heat exchanger. The results of computational fluid dynamics (CFD) calculations for the Joule process are shown in *Figure* 2 (right). Exemplary temperatures are assumed, but the process can be flexibly implemented at different temperature levels.

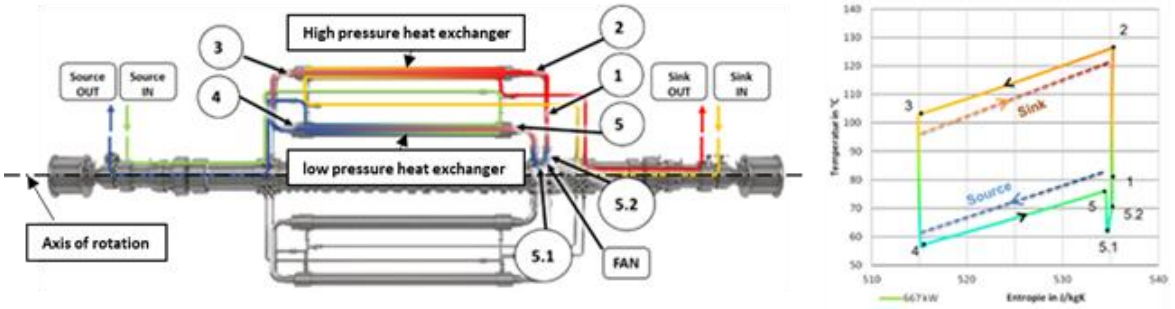


Figure 2: Design and structure of an RHP (left) and associated Joule process (right).

The first reference plant of an RHP, shown in *Figure* 3 (right), is already in operation, measured values from previous test runs have already been published [1]. The design model (left) with opened housing shows the rotor with heat exchangers and pipes.

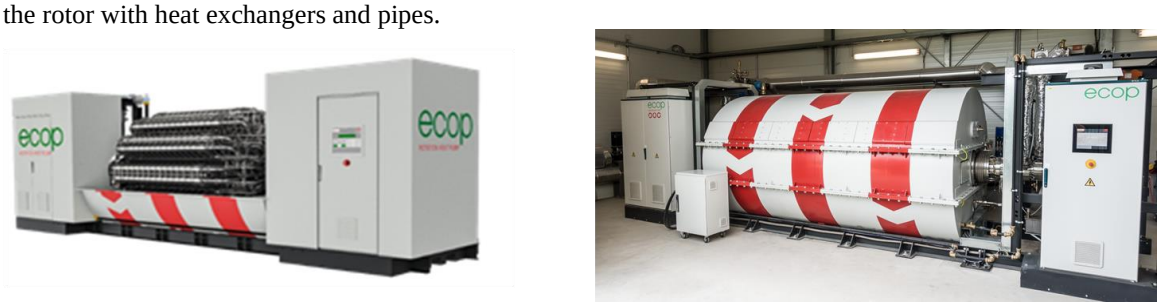


Figure 3: Design model (left) and reference system (right) of an RHP.

1.2. Motivation

For controlling conventional compression heat pumps, numerous publications, theoretical principles and commercial controllers are already available. Here, a well-tuned system can be provided in advance using

"default settings" for e.g. the expansion valve. To determine the main differences between an RHP and a conventional compression heat pump in terms of basic principle, design and operation, basic knowledge must be acquired, and the individual components be analyzed in detail. Control systems and strategies for commercial heat pumps cannot be transferred easily, as additional control parameters are available and further non-comparable complex correlations must be taken into account. Due to the lack of literature, the associated behavior of an RHP regarding the unusual physical relationships of its components needs to be explored, cmp. [2]. The current approach is based on flow simulations of the main components (heat exchangers, fan, pipes) for the entire operating range with variable boundary conditions. Out of these considerations, three major challenges in regard of controlling an RHP were identified:

- **Challenge 1:**

  Due to the rotation the component's operating behavior differs from available literature data. Furthermore, measurements in the system are difficult to establish or even impossible for both, pressure and mass flow sensors, due to high loads on the outer diameter of the rotor, which are problematic for the transducers, and would require complex wiring. Therefore, the modeling approach was chosen and the model is tried to be validated on a global basis (energy balance, efficiency, etc.) for further control development.

- **Challenge 2:**

  The fan like every turbomachine has a characteristic curve with certain operating limits caused by flow phenomena. Both, the fan characteristics and the system curve of the refrigeration cycle furthermore change with the rotor speed of the RHP. Experiments have shown that there are combinations of fan speed and rotor speed, where the fan given the system curve cannot build up enough pressure difference to push the refrigerant mass flow, causing the refrigeration cycle to stop. With the help of CFD for flow phenomena and further modelling, those combinations can be identified and can be considered for controlling and successfully operating the RHP.

- **Challenge 3:**

  The current state of the art in terms of control is a fixed/rigid pre-setting of the fan speed and the rotor speed to achieve a certain operating state. This results in a simple but non-optimal control, especially regarding energy efficiency. A Digital-Twin of the heat pump offers the possibility to carry out the controller development in a time- and resource-efficient way. It requires correlations of the thermodynamic behavior of the components.

2. Digital-Twin

2.1. Method

In a recent work from us [3] the main objective was to gain basic knowledge and to identify physical relationships in an RHP. For this purpose, individual components of the RHP were modeled using CFD. Their behavior across a wide operating range was analyzed using parameter studies. The main components – heat exchangers for source and sink, the fan as well as compression and expansion pipes – were modeled and simulated. At certain boundary conditions (rotation, pressure, flow velocity, etc.), the components showed partly very high deviations from the generally known and validated operating behavior for non-rotational operation. However, by the help of the system simulations, a significant contribution could be obtained for a better understanding of these phenomenological interrelationships of the individual components. Additionally, mathematical relationships from CFD results were also generated and are now available in so-called meta models as functional mockup units (FMU). These FMUs and their position in the schematic refrigeration cycle are shown in *Figure 4*.

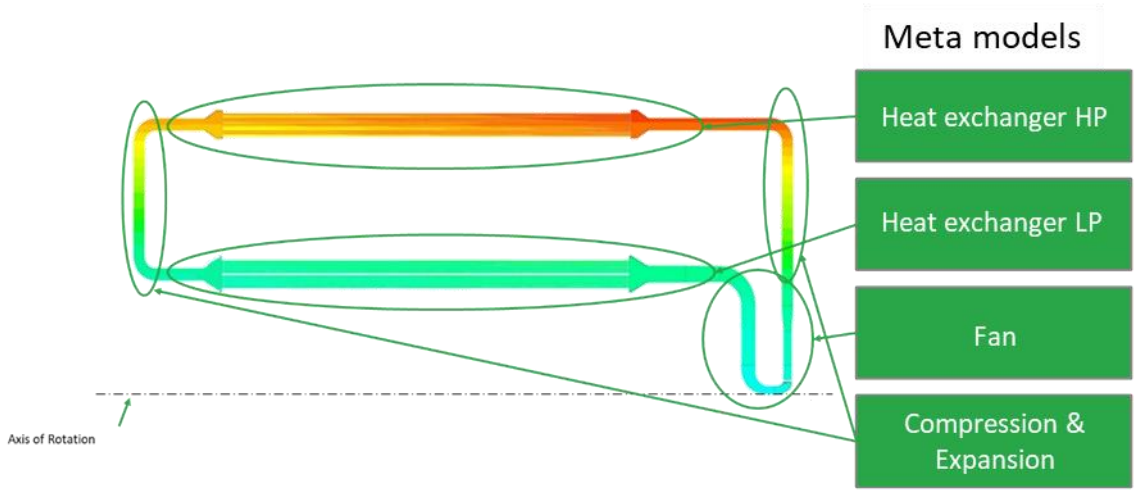


Figure 4: Meta models of the RHP [3].

Within the dynamic simulation environment Dymola/Modelica [4], several FMU models were tested regarding functionality and plausibility in a first step, prepared for the integration (see Figure 5), and finally combined to build the whole RHP system within the framework of the TIL-Library [5], as shown in Figure 6.

Looking at the fan in Figure 5, we adapted the model – compared to [3] - in a way that the flow is given by a mass flow rate directly instead of a total pressure increase. Now, the model is much more robust in terms of initialization and forms a solid basis for further analysis. The two speeds of the rotor and fan as well as pressure, temperature and the total mass flow remain unchanged as input variables into the FMU.

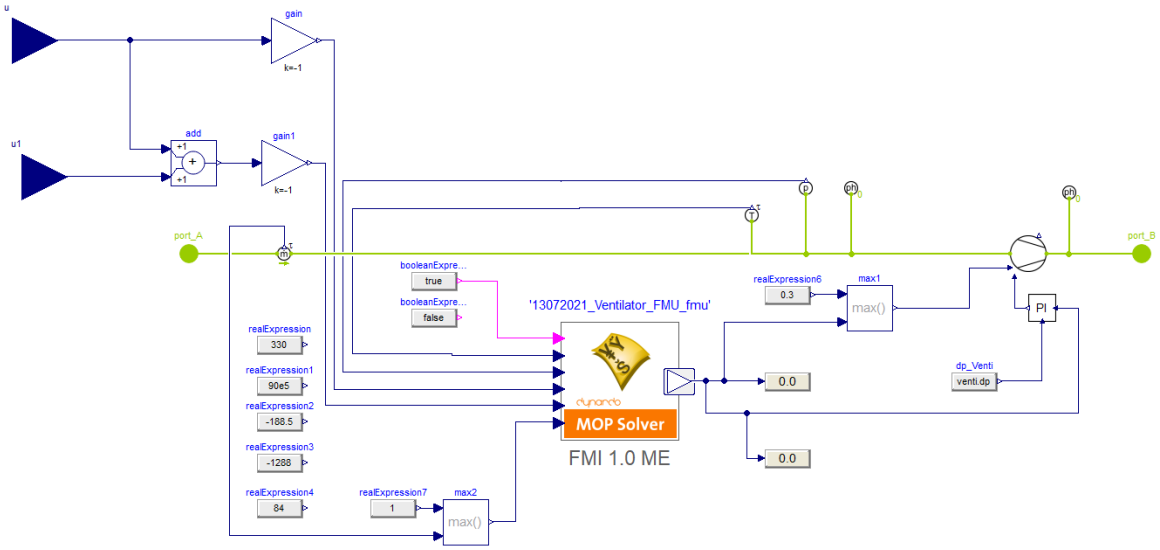


Figure 5: Adapted fan model (FMU from [3]; in the center) operating a general fan block, embedded in Dymola with further components: connectors, ports, concrete values, arithmetic operators etc.

The other two FMUs of the high (sink) and low (source) pressure heat exchangers (*Figure 6*) work on the same principle, but with different input variables. Those FMUs have been upgraded as well compared to [3] as there had been constructive changes on the heat exchangers in the real system.

Figure 6 depicts the complete model with all integrated FMUs. The grey line represents the rotating main axis of the machine. Green is the gaseous refrigerant circuit and blue the water-side heat dissipation and heat absorption of the sink and source. *Figure 6* shows the complete model with all integrated FMUs. The grey line represents the rotating main axis of the machine. Green is the gaseous refrigerant circuit and blue the water-side heat dissipation and heat absorption of the sink and source. Furthermore, temperature, mass flow, volume flow and pressure sensors are integrated to determine the respective system status points.

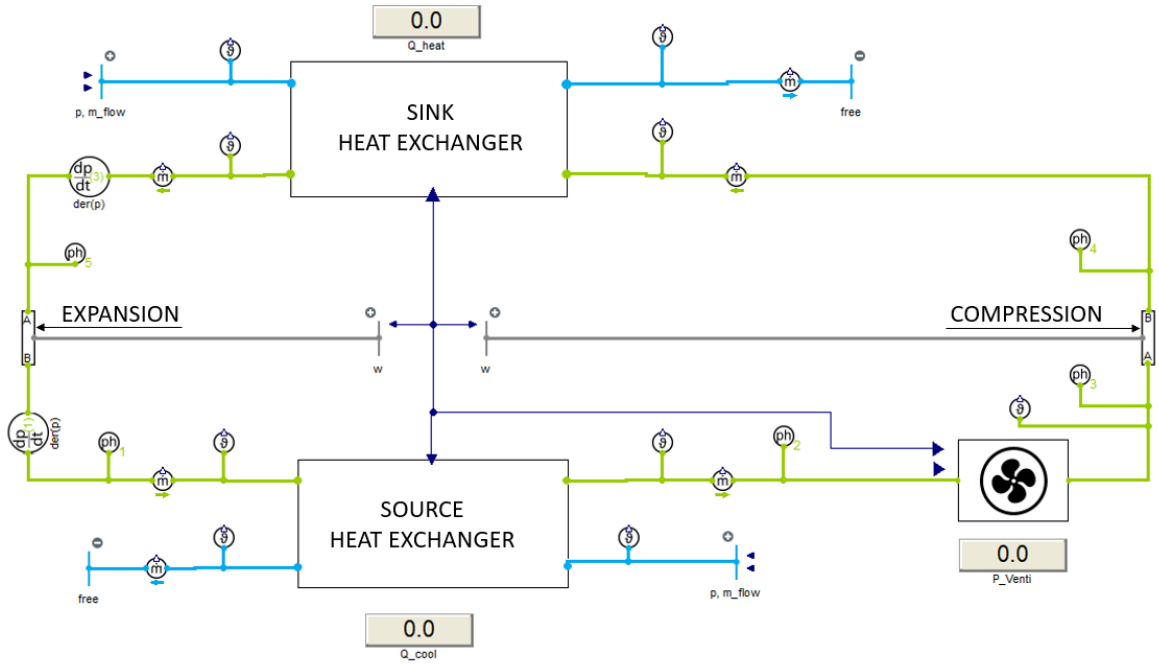


Figure 6: RHP in Dymola/Modelica with integrated meta models as FMUs.

2.2. Results - Validation based on RHP measurement data without controls

In [3] the simulation model was originally validated based on available operating points which were selected from different sets of measurement data of the existing plant. In this work, the operating points were generated with an adapted RHP, see *Figure 7*. The heating capacity based on the supply temperature $T_{sink,out}$ and the temperature lift $T_{lift,meas}$ (temperature difference between source inlet and sink outlet) is shown. Speeds of fan and rotor were fixed. The exact values are shown in Table 1. Compared to [3], 12 operating points are available at a slightly wider range of $T_{lift.meas}$ and higher values of heating capacity $\dot{Q}_{heat.meas}$.

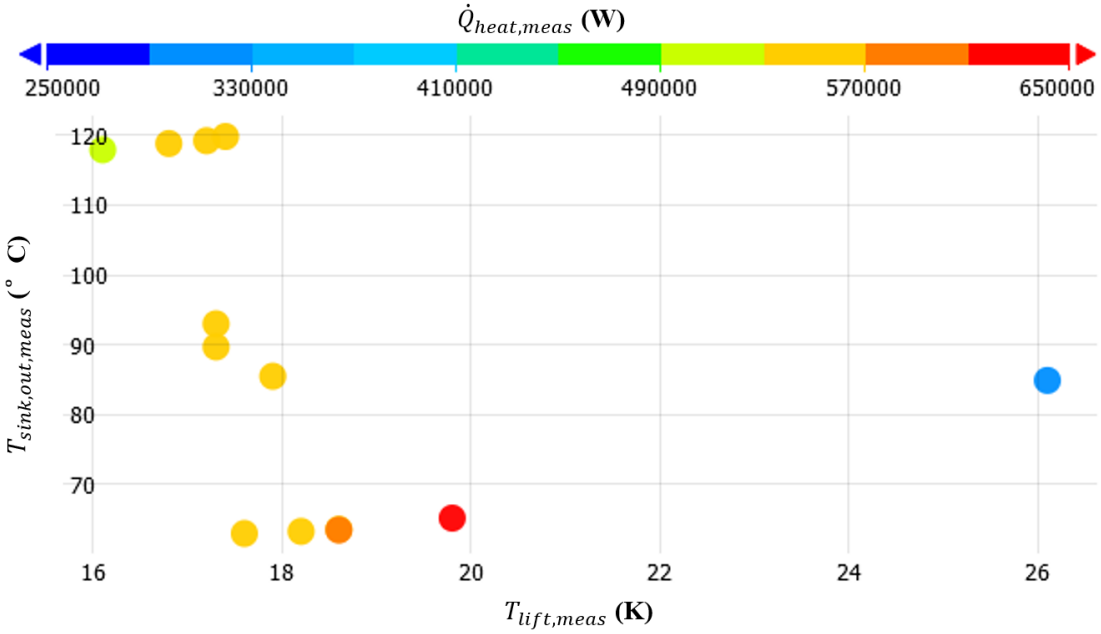


Figure 7: Performance map of the RHP from twelve steady state operating points, cmp. Table 1.

Similar to [3] the following six input variables were implemented into the model:

- Inlet temperatures of source and sink ($T_{source,in}$, $T_{sink,in}$),
- mass flow rates of source and sink ($\dot{m}_{source}$, $\dot{m}_{sink}$), and

- rotational speeds of the rotor and the fan ($n_{rotor},\ n_{fan}$).

Simulation results and experiments are compared on diverse output values such as

- Heating capacity ($\dot{Q}_{heat}$)
- Outlet temperature of the sink ($T_{sink,out}$)
- Coefficient of performance (COP), specifying the relation between the thermal output and electrical input

Table 1 shows the summary of all measured and available simulation results of the above-mentioned twelve operating points. With the simulation model in the current status, the heating capacity $\dot{Q}_{heat}$ is purely overestimated from 3.52% to 9.59%. This makes sense in qualitative perspective as the model is not considering heat losses to the ambient. The supply temperature $T_{sink,out}$ is also overestimated by the model analogous to $\dot{Q}_{heat}$, which corresponds to the relation $\dot{Q}_{heat} = \dot{m}_{sink}\, c_p\left(T_{sink,out} - T_{sink,in}\right)$. The efficiency of the RHP, which is given by the coefficient of performance COP is currently overestimated by the model.

Table 1: Measurement data and available model errors (right) at different operation points (left).

$T_{sink,in}$	$T_{source,in}$	$\dot{m}_{sink}$	$\dot{m}_{source}$	n_{rotor}	n_{fan}	$\dot{Q}_{heat,meas}$	Err. $\dot{Q}_{heat}$	$T_{sink,out,mea}$	Err. $T_{sink,out}$	$T_{lift,mea}$	$COP_{plant,mea}$	Err. COP_{plant}
(°C)	(°C)	(kg/s)	(kg/s)	(rad/s)	(rad/s)	(kW)	(%)	(K)	(K)	(K)	(-)	(%)
45.4	45.4	7.48	7.46	150.2	984.7	619	3.72	65.2	0.71	19.8	3.96	13.39
45.1	45	7.38	7.5	151.4	905.2	570	6.21	63.6	1.11	18.6	4.28	12.6
45.2	45.4	7.27	7.54	150.2	882.9	538	9.59	63	1.61	17.6	4.53	8.81
45.3	45.1	7.52	7.55	147.0	917.4	570	4.54	63.3	0.95	18.2	4.22	13.75
45.1	44.9	7.53	7.48	150.8	917.5	580	5.79	63.5	1.08	18.6	4.28	11.27
102.1	102.4	7.56	7.45	147.0	962.1	554	5.36	119.8	0.54	17.4	3.77	21.39
101.8	102	7.53	7.48	150.2	939.4	553	8.07	119.2	1.35	17.2	3.97	17.39
101.7	102	7.48	7.46	151.4	893.8	538	9.51	118.8	1.51	16.8	4.21	15.37
101.3	102	7.43	7.51	148.3	837.5	508	8.71	117.9	0.98	15.9	4.97	3.84
68	67.6	7.38	7.15	148.9	917.5	539	7.66	85.5	1.26	17.9	4.04	21.33
74.8	58.8	6.76	7.25	148.3	894.4	291	3.98	84.9	0.56	26.1	2.44	36.5
75.7	75.7	7.39	7.12	147.0	894.7	538	4.61	93	0.81	17.3	4.22	20.68
72.5	72.4	7.59	7.62	148.3	905.5	546	7.56	89.7	1.23	17.3	4.28	18.51

Overall, the highest error between simulation and measurement is in the COP of approx. 21%. With the same inlet temperatures and mass flows, the error in the sink outlet temperature $T_{sink,out}$ is max. 1,61 K.

Compared to [3], where the model was under- and overestimating the experiments, now, with the improved components, we see an exclusive overestimation, which is inline with the current modelling approach of no heat losses in place.

The range of the model errors is not a problem per se, it depends on the intended purpose of the model. Using the models for the purpose of controls, errors of this extent should be fine as long as the qualitative tendencies are reproduced. Nevertheless, one aim in [3] of the project team was to reduce the model errors by deeper analyses of the deviations and its reasons, which was successful when comparing Table 1 with [3].

3. Control strategies for the RHP

3.1. Comparison of different principles

With the help of the validated model we develop control strategies in the direction of optimal control. As discussed in [3], Table 2 shows a list of the different control variants including their advantages and disadvantages. In this table we present out initial thoughts and expectations as it is given in the literature. In this work we will tap this and investigate it for the application of RHP.

Table 2: Comparing control concepts.

PI controller	ESC	Model-based look-up table	MPC
+ Proven technology + Reach a wide range of operation + Easy to implement ~ Must be adjusted precisely - Negatively influencing each other (rotor / fan) - Does not necessarily reach an optimal operating point - Undesired operating points can also be reached (e.g. stall)	+ Optimal COPs possible + Adapts to unknown system model ~ Range of operation has to be defined experimentally ~ Thermal inertia of the system can reduce impact based on the controller oscillation principle - slow optimization process - Local minima operation possible	+ Optimal COPs possible + High variety of operation points + Low complexity during operation ~ Moderate development effort ~ Transitions between loads must be smoothed - Models must represent reality very accurate (high modelling effort) - Deviations to reality must be additionally considered (stability)	+ Optimal COPs possible + Any operation point within validity range can be covered + Predictions allow faster response to changes - Models should represent reality very accurate (very high modelling effort) - Very high development effort - Undetected disturbances can destabilize the system

3.2. Definition of the control scenarios

Based on the consideration of the advantages and disadvantages from Table 2, we decided to use the variant of the model-based look-up table. To us, it represents a good trade-off between control quality and feasibility on the RHP control system.

From the possible industrial applications, three main scenarios crystallize. There are, of course, more scenarios but in this work, the following three will be addressed:

- Scenario 1: Heat-driven by controlled $T_{sink,out}$, control variables are rotational speeds of the RHP.
- Scenario 2: Cooling-driven controlled by $T_{source,out}$, control variables are rotational speeds of the RHP.
- Scenario 3: Combination of scenario 1 and 2, controlled by $T_{sink,out}$ and $T_{source,out}$, control variables are rotational speeds of the RHP and secondary mass flows on source and sink side ($\dot{m}_{source}$, $\dot{m}_{sink}$).

The controlled variable, depending on the scenario, is either supply temperature on the cold side or on the hot side or on both sides simultaneously in combination of an optimality condition (either COP or thermal capacity). For each scenario, the control variables and disturbance variables are described in the following *Figure 8*.

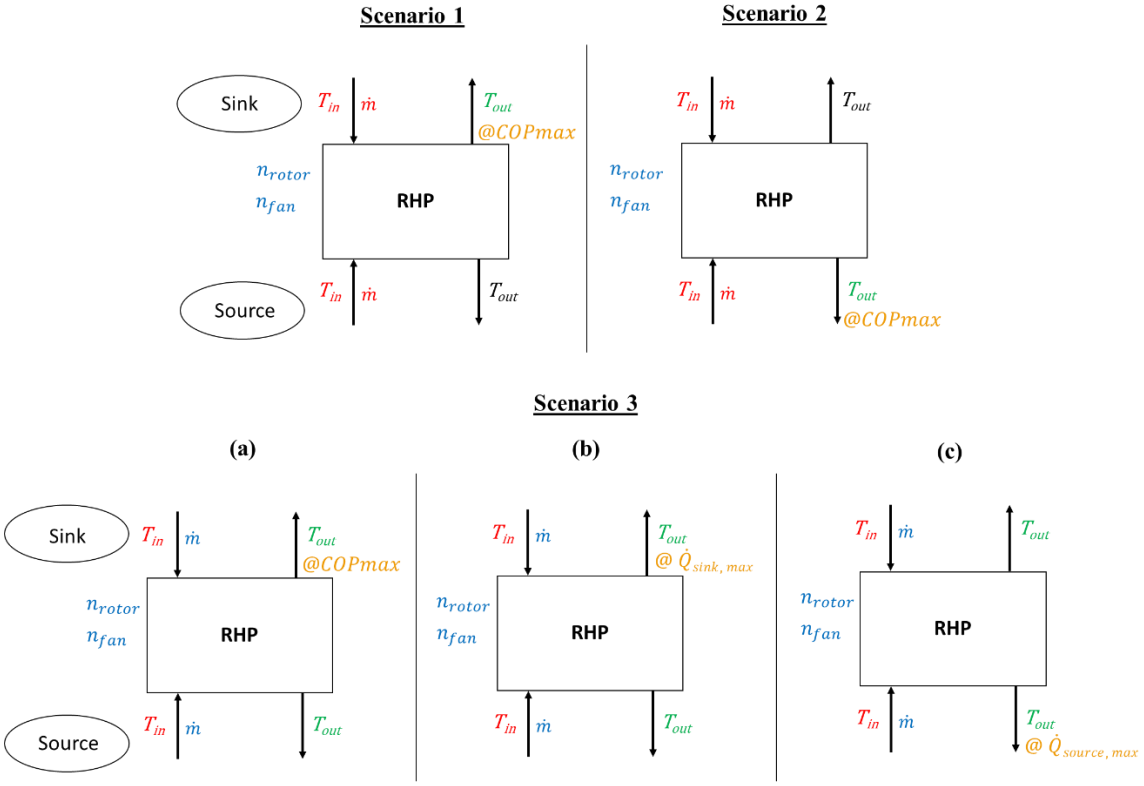


Figure 8: Control scenarios with control variables (green) and optimization targets (orange), boundary conditions / disturbances (red), actuating variables (blue), and resulting variable (black).

3.3. Utilizing the Digital Twin

With the Digital Twin as described in section 2, the characteristic diagram of the entire RHP is created. Taking into account the defined operating limits, see below, a parameter variation is carried out, a so-called parameter sweep. The aim is to capture the optimality variables (green, orange values in *Figure 8*) and their dependence on the boundary conditions (red) and at the same time the influence of the manipulated variables (blue). Finally, this is the data basis for the subsequent analyses. In total, there were about 90,000 variations. However, only about 10,000 of these results were usable by filtering a valid range of heating capacity and pressure increase at the fan, i.e., only points were analyzed that made sense in that manner.

3.4. Results – Operating envelope of the RHP

In general, all boundary conditions result in a lot of superimposed points if showing the results – such as heating capacity or COP - in a 2D-surface plot. Nevertheless, we aim to illustrate the RHP operating limits in order to see unacceptable operating ranges due to stall conditions on the fan, which can be seen *Figure 9*. From our current experience, we assume that based on an actual operating condition, any change in operation, that is pointing to the bottom right can possibly lead to a stall condition on the fan. A change to the top left is limited by the pressure increase of the fan in combination with the fan motor. We also the opposite COP maximum and heating capacity maximum. Here, the temperatures of $T_{sink,out}$ are ranging from 71 to 83°C, *Figure 9*c.

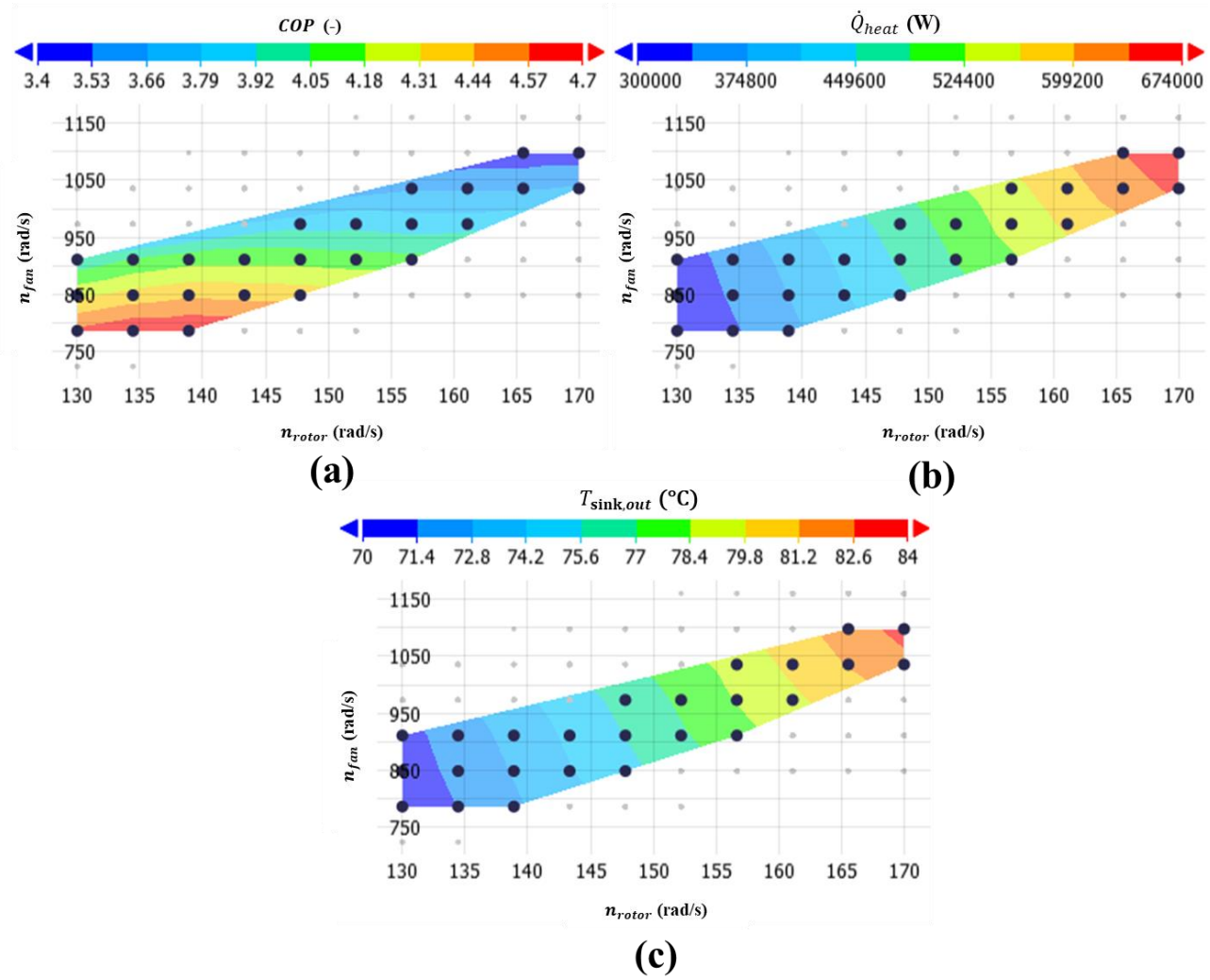


Figure 9: Full operating envelope at given boundary conditions.

In the following we show an exemplary situation for scenario 1 (heat-driven). We set a control target with the temperature range of 80°C ±3K around the desired value. At the same time we also have 4 different combinations of boundary conditions. That means, we do not only "cut out" of the above picture *Figure 9*, but we consider new combinations and thus new ranges than the ones shown above. Additionally, we have a relatively coarse grid, so we consider a control range that seems unusually large at first glance. However, the RHP can regulate to an exact value.

First example:

We consider unchanged rotational speeds of the RHP in combination with a disturbance change, which is a doubled mass flow on the source side. The RHP settled in the optimum point of COP (that is the lowest point in *Figure 10a*, yellow area), which is actually at the "stall limit" considering the total operating range (grey area in the background). When the source mass flow increases, the current speed settings for the maximum COP are suddenly outside the allowable operating range for the desired control target. In the best case, only the outlet temperature on the sink side (which is the controlled variable) cannot not be maintained anymore in the event of a change in the disturbance variable, but in this case a stall at the fan happens, which leads to the immediate shutdown of the machine. This can be seen that the original operating point in *Figure 9a* (the point with the best COP in the yellow area) is now outside of the operating envelope as seen in *Figure 9*c.

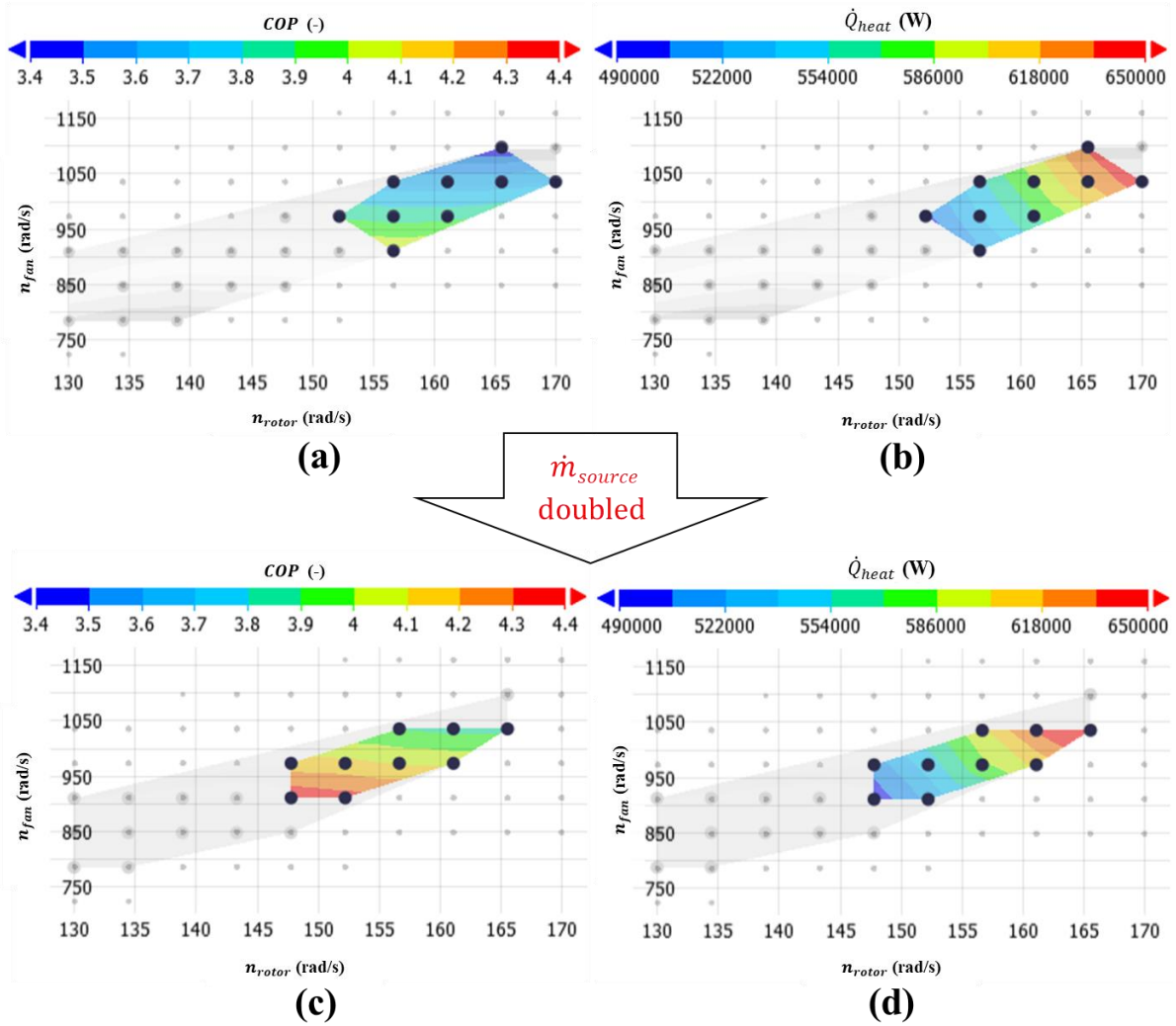


Figure 10: Example 1: Shifting the operating range for deviating boundary conditions.

Second example:

As a second example, for a given set point of the sink outlet temperature $T_{sink,out}$ of 95 °C±3 K, a reduction of the source inlet temperature $T_{source,in}$ of 10 K results, see Figure *11*. The starting point is again the optimum point (COP or heating capacity). In this example, there is a danger of passing through the white area when changing the manipulated variables (rotational speeds) from one operating point to another. To avoid the danger of a stall (area below right), the key message here is to always increase fan speed first and then increase rotor speed when increasing speeds in general. When reducing the rotational speeds, inverse procedure is relevant.

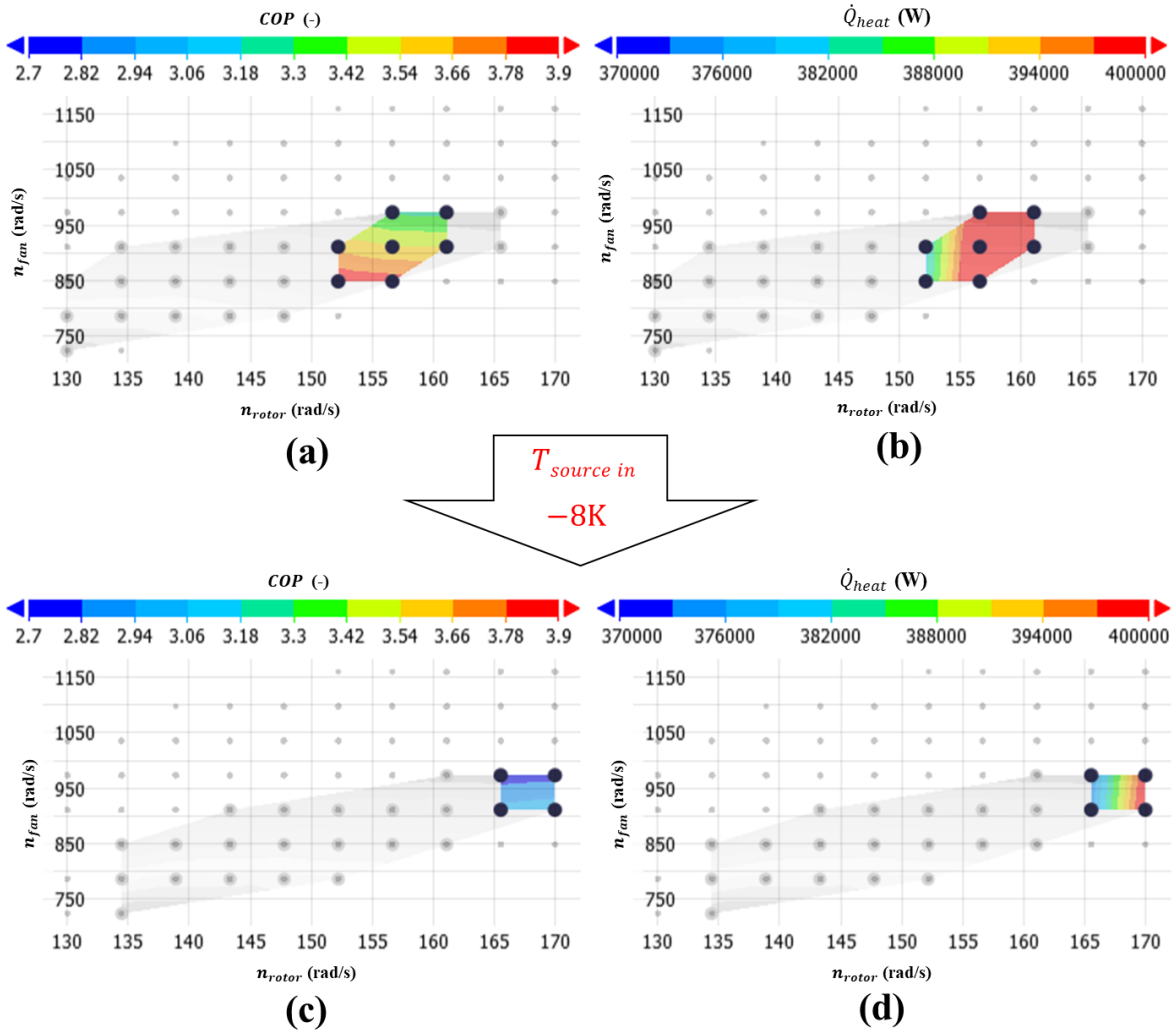


Figure 11: Example 2: Shifting the operating range for deviating boundary conditions.

Our analyses beyond the two examples shown here, show that the optimal operation of the RHP in terms of COP of heating capacity seem to be at the limits of the operating envelope. Here, however, there is, among other things, a danger of stall at the fan, which leads to shutdowns of the RHP. Shutdowns in general are not only bad because of the heat demand, but also for the machine itself. The remedy can be a the definition of a so-called "safety distance consideration", which is therefore already mentioned in the outlook:

- Case A: Fixed speeds (e.g. for maximum COP), and suddenly a disturbance variable (or also several) changes rapidly and unforeseen. How far can they change (stationary!) without the RHP leaving permissible operating ranges?

- Case B: Optimum point is at the edge (because speeds can only be smaller or only larger when the setpoint of the controlled variable is maintained) Safety distance to this limit can be set arbitrarily,

e.g. 5 % away from the edge in the sense of the speeds, or half distance in the direction of the nearest neighbor away from the optimum.

The limits of our considerations are that the results are valid in principle for stationary states, therefore results are generally not valid for start-up or transient changes (e.g. disturbance change or rate).

4. Summary and Outlook

In this paper, essential steps were described to model a digital twin of an RHP and prepare it for controller testing of such a heat pump. In a dynamic simulation environment, existing models, e.g. for pipes, and externally generated models using CFD were connected and simulated.

The RHP model was validated based on real measured operating points moving in realistic ranges. Here, attention was not paid to selecting operating points that could be validated easily, but rather those that could actually occur in real operation and have to be dealt by controls. Overall, the highest error between simulation and measurement is in the COP of approx. 21%. With the same inlet temperatures and mass flows, the error in the sink outlet temperature $T_{sink,out}$ is max. 1,61 K.

A total of approx. 62.500 simulation runs for a heating capacity range up to 750 kW and with different boundary conditions were carried out for the validated model. For example, the fan speed, rotor speed and temperatures were varied to cover a wide range of potentially possible operating points. These runs were performed based on the "parameter sweep" method.

Model errors excluded, valid operating ranges have been identified for specific boundary conditions. Only through the existing work (development and simulation of the Digital Twin) "operating envelopes" of the entire system in the defined operating limits (not only of the individual components) are available.

Permissible control variable combinations for the desired influencing of the controlled variables for given boundary conditions are known. In particular, manipulated variable combinations depending on the scenario for maximum COP, $\dot{Q}_{heat}$, or $\dot{Q}_{cool}$, are known. The "look-up table" for optimal control of different scenarios can now be used for lab tests.

For the implementation in the laboratory, an integration table in the PLC including interpolation between the operating points is necessary and possible. Adaptive modelling is conceivable in order to determine further model errors, in particular at the optimum operating points. A comparison with PID controllers with the controlled variable according to scenario 1 is planned or will be presented at the Heat Pump Conference.

Nomenclature

Acronyms

CFD	computational fluid dynamics
CIL	controller-in-the-loop
COP	coefficient of performance
ESC	extreme seeking control
FMU	functional mockup unit
HP	high-pressure
LP	low-pressure
MPC	model predictive control
PLC	programmable logic controller
RHP	rotation heat pump

Roman symbols

c_p	specific heat, J/(kg K)
$\dot{m}$	mass flow rate, kg/s
n	rotation speed, rad/s
$\dot{Q}$	heat capacity, W
T	temperature, °C

Subscripts and superscripts

fan	fan of the heat pump
in	into the system
lift	temperature lift
meas	measured
rotor	rotor of the heat pump
out	out of the system
sink	sink side of the heat pump
source	source side of the heat pump

References

[1] B. Adler, A. Längauer, Ch. Rakusch, K. Ponweiser, „COP tests of a Rotation Heat Pump“, IIR-ICR-International Congress of Refrigeration 2019, Montreal, DOI: 10.18462/iir.icr.2019.1791

[2] Stephan, P., Kabelac, S., Kind, M., Martin, H., Mewes, D., & Schaber, K. (2010). VDI heat atlas. In VDI-Gesellschaft Verfahrenstechnik und Chemieingenieurwesen.

[3] B. Windholz; As Sporr, S. Kling, M. Lauermann, A.Längauer, B. Adler, „ Simulation towards demonstration: A Digital-Twin for developing control concepts of an industrial-scale Rotation Heat Pump”, ECOS 35th International Conference on Efficiency, Cost, Optimization, Simulation and Environmental Impact of Energy Systems, 2022, Copenhagen.

[4] Dassault Systems, https://www.3ds.com/de/produkte-und-services/catia/produkte/dymola/, accessed 12.3.2022

[5] TLK-Thermo GmbH, https://www.tlk-thermo.com, accessed on 07.03.2022.

Acknowledgments

This work is funded by the Austrians Climate and Energy Fund and is being carried out as part of the Energy Research Program 2020.



14th IEA Heat Pump Conference
15-18 May 2023, Chicago, Illinois

Maximizing operational efficiency of heat pumps with Model Predictive Control: An experimental case study for residential application

Stephan Göbel[a,*], Phillip Stoffel[a], Florian Will[a], Christian Vering[a], Dirk Müller[a]

[a] RWTH Aachen University, Institute for Energy Efficient Buildings and Indoor Climate, Aachen, Germany
[*]Corresponding author

Abstract

In residential heating applications, electrically-driven heat pump systems enable the integration of renewable energy sources (RES) and, thus, systematic sector defossilation. Since the heating demand of buildings and RES availability are time-variant and time-shifted, it is challenging to ensure optimal heat pump system operation. Optimal heat pump system operation requires access to reliable system interfaces and consistent use of higher control strategies such as model predictive control (MPC). However, missing interfaces prevent the spread of MPC in the field and call for conventional controls such as heating curves reducing the overall potential.
This work shows the potential of MPC for heat pump systems by exploiting system interfaces in an experimental case study. We use a heat pump test bench coupled to a dynamic building performance simulation model in the hardware-in-the-loop approach and investigate two control levels: The refrigerant cycle controller ensures stable superheat and resilient operation; the system controller minimizes the heat pump power consumption within the comfort constraints. We analyze two MPC interfaces to control the system: First, the MPC sets the flow temperature, while a PID controls the compressor speed. Second, the MPC directly adjusts the compressor speed. We compare both MPC strategies with a conventional heating curve controller.
The results highlight the need for heat pump interfaces to widespread MPC. Both MPC strategies reduce the heat pump power consumption by up to 20.25 %. Adjusting the flow temperature by MPC results in the lowest energy consumption but many compressor starts and comfort losses. Direct compressor-controlled systems claim the best results concerning comfort constraints and lead to a resilient operation by reducing on-off behavior.

© HPC2023.
Selection and/or peer-review under the responsibility of the organizers of the 14th IEA Heat Pump Conference 2023.

Keywords: system control; hardware-in-the-loop; experiment; simulation; underfloor heating; building performance simulation

1. Introduction

For all sectors, the IPC report shows the need for consistent defossilation to meet climate goals and mitigate climate impact consequences [1]. In particular, the building sector is responsible for up to 30 % of total energy consumption [2]. While, in other sectors, standardized solutions already exist to reduce emissions on a larger scale, there are still major challenges in the building sector due to the high degree of individuality of buildings and occupants [3]. Solving one challenge to reduce the emissions related to heating purposes, heat pump systems can exchange conventional combustion-based heating systems. Electrically-driven heat pump systems are the most efficient solution for defossilation the building sector, as they can provide CO_2-neutral heat when using electricity from renewable energy sources (RES). However, optimal heat pump integration and operation lead to complex system setups and controls since the heating demand and renewable energy sources (RES) availability are time-variant and time-shifted. To capture time-variance and time-shifting, model predictive

* Corresponding author
E-mail address: stephan.goebel@eonerc.rwth-aachen.de

control (MPC) applications are a potential solution in the recent literature. MPC strategies reduce energy consumption by 13 % to 28 %, depending on the heat pump system setup [4]. However, most heat pump systems in the field operate in weather compensation mode using an outdoor temperature-dependent supply temperature (heating curve). As a result, heat pump systems are often not operated optimally, considerably reducing their potential in many cases.

To optimally operate heat pump systems and fully exploit the potential of MPC, there is the need to identify barriers preventing the transfer into practice. In the literature, there are multiple reasons for the slow implementation of MPC approaches in the building sector. First, the development of MPC in building energy systems (BES) needs deep expert knowledge and high hardware and software requirements [5]. Second, individual buildings require individual process models for the controller configuration and, thus, increase the development time [6]. In a recent theoretical study, Stoffel et al. show a data-driven MPC using black-box models (BBMPC) that perform similarly to detailed white-box MPC approaches [7]. In addition, online learning offers continuous improvement of the BBMPC process models reducing the gap compared to more development-intensive MPC approaches. While Stoffel et al. follow a theoretical approach where almost all interfaces can be made available, in practice, interfaces may not be available for safety reasons or the manufacturer's market strategy.

Today, the available interfaces to control heat pumps are very limited, preventing the optimal operation of heat pump systems. In the case of market-available heat pumps, a potential MPC can only control a manipulated variable via the SmartGrid Ready interface that indirectly controls a system variable (e.g., flow temperature). Typically, an internal heat pump controller (usually conventional PID-Controller) still adjusts the control variables of the heat pump (e.g., compressor speed) regardless of whether this is purposeful for the overall system. Hence, the literature shows only studies in which the MPC cannot directly control the compressor speed, which makes the internal controller the limiting factor for optimal system operation [8]. However, to the best of the author's knowledge, such limiting factors are not discussed in the literature.

In the literature, studies show high potential for MPC in BES based on numerical approaches and neglect limiting factors of real-world operation. In addition, many approaches use simplified black-box models or linearized models to predict the heat pump's behavior. However, the heat pump is a closed thermodynamic cycle inherently covering nonlinear dependencies between state and control variables. Considering the complex thermodynamic relationships leads to a complex and computationally intensive model that is often avoided in MPC approaches to solve the underlying optimization problem in a reasonable time. This paper closes the identified research gaps and proves the proposed method in a simulative and experimental case study:

- To reduce expert knowledge for setting up process models, we use data-driven models to minimize the modeling effort.
- To prove consistent thermodynamics and prediction accuracy, we conduct measurement campaigns that substantiate our approaches.
- To avoid manufacturer-related interface limitations, we use a fully controllable heat pump test bench with all relevant interfaces [9].
- To prove the proposed method under realistic, dynamic, and repeatable boundary conditions, we use the hardware-in-the-loop approach by coupling a heat pump test bench to a virtual building.

The paper is structured as follows:

- Section 2 describes the experimental setup and the controller's structure.
- Section 3 shows the results of the simulative and experimental case studies.
- Section 4 discusses the results and underlines the potential of the proposed method.
- Section 5 concludes all findings and gives recommendations for future work.

2. Method: MPC for heat pump systems

The proposed method of this work integrates an MPC system controller into a heat pump test bench., This work uses the experimental hardware-in-the-loop (HiL) approach to assess the potential of MPC compared to conventional controllers under dynamic, realistic, and repeatable boundary conditions. This approach couples real hardware with simulation models that lead to dynamic and realistic environments. This section describes the HiL setup and explains the developed system controller. Furthermore, we introduce the performed case studies and define the used key performance indicators (KPI).

2.1. Experimental Setup

This section presents the HiL approach for the experimental case study. HiL connects virtual buildings with real heat generators. In this work, we focus on the behavior of the heat pump and the potential of the MPC system controller. Figure 1 shows a schematical overview of the implemented HiL framework.

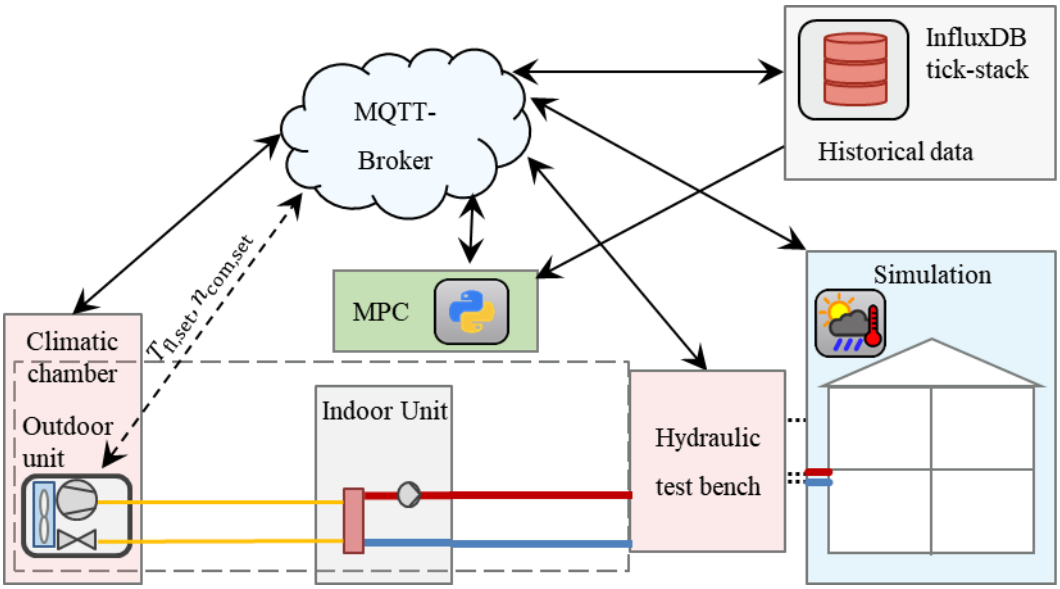


Figure 1: Schematic overview of HiL setup: heat pump test bench (indoor unit and outdoor unit), Climatic chamber, Hydraulic test bench, simulation model, MPC system controller, InfluxDB tick-stack, and MQTT Broker

The system consists of an air-to-water heat pump in split design, test benches (climatic chamber and hydraulic test bench), a building performance simulation model, the cloud-based data infrastructure (MQTT-Broker and InfluxDB tick-stack), and the MPC system controller. The several components are described in the following:

Air-to-water heat pump:

In this work, we use a self-developed air-to-water heat pump with a nominal heating capacity of 7 kW in operating point A7W35 (ambient temperature: 7 °C, supply temperature: 35 °C). We built the heat pump in split design: the outdoor unit (OU) consists of the compressor, evaporator, and expansion valve; the indoor unit (IU) consists of a condenser and a water pump for the hydraulic cycle.

The heat pump uses an inverter-driven scroll compressor operating between 30 Hz and 90 Hz, indicating a possible part load operation of 1/3 of the full load. Using a PLC and measuring terminals, all sensor data are collected, and all set values are written. In previous work, we developed control strategies for a safe and efficient operation regarding superheat control [9]. Thus, the internal heat pump controller controls two subsystems (see Figure 2 and Figure 3).

First, the superheat control (Figure 2) regulates the expansion valve and ensures that gaseous refrigerant enters the compressor's inlet. The detailed controller development is described in Göbel et al. [9].

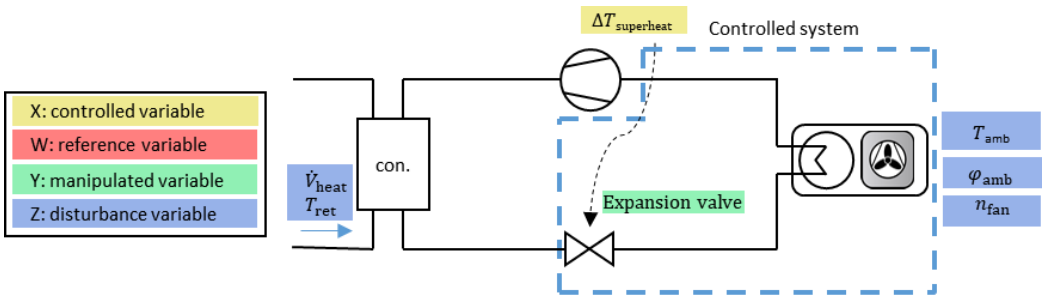


Figure 2: Superheat control of the A/W heat pump

According to Figure 3, the flow temperature T_{fl} can be controlled by manipulating the compressor speed n_{com}. In the market-available heat pumps, an internal PID controller is used to adjust the control variable. However, this controller has no direct interface for MPC applications. In this work, we open this controller interface to manipulate the compressor speed $n_{\mathrm{com,set}}$ directly by the system controller. Within the HiL approach, the air-to-water heat pump is coupled to a virtual building, which is explained in the following.

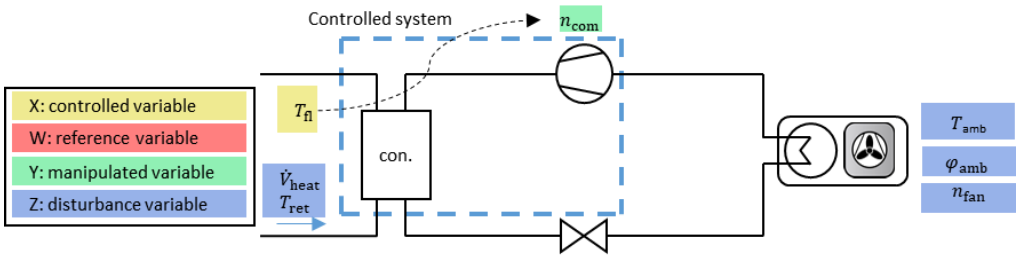


Figure 3: Flow temperature control of the A/W heat pump

Building performance simulation model

We calculate the building performance simulation for the HiL framework using the BESMod Modelica library [10]. In this context, we integrate MQTT communication blocks into the hydraulic subsystem. A single-zone Modelica building performance simulation model calculates the thermal behavior of a building. The air temperature of the single zone represents the room temperature, which is the controlled variable. The model's parameters are obtained from TEASER [11]. The building envelope covers a net floor area of 130 m^2. Following DIN EN 12831, the resulting heat load at -12 °C is 6.596 W. We implement an underfloor heating system model to transfer heat from the hydraulic cycle to the building envelope. The total activated floor's capacity is $52.629\ \mathrm{kJ\ K^{-1}}$ which is equal to a water volume of $12.59\ \mathrm{m^3}$. Due to this high capacity, we avoid an additional buffer tank within the hydraulic system. To connect the described simulation model to the heat pump, we use test benches, which are explained in the following section.

Test benches

The air-to-water heat pump is located in a climatic chamber that emulates dynamic ambient conditions. The climatic chamber captures ambient conditions between -20 °C and 40 °C and humidity up to 100 %. For this purpose, the climatic chamber has an air handling unit with heat exchangers for cooling and dehumidification, an electric heating coil, and an isothermic steam humidifier. The hydraulic test bench controls the return flow temperature and the volume flow of the heating cycle, which the dynamic building performance simulation model calculates. The return temperature is adjusted using a three-way mixing valve, ensuring fast responses and low delay times due to mixing. While the test benches are the physical connection between the simulation model and the heat pump, the cloud-based data infrastructure is the digital connection between all components.

Cloud-based data infrastructure

All components (simulation models, test benches, system controller) communicate with the overall MQTT broker to which they can send data and subscribe to topics. The task of the MQTT broker is to distribute the data. Each component subscribes to the necessary topics. When the broker receives messages for corresponding topics, it is passed on to the corresponding component. The components send their data with a time increment of one second. The communication latency is in the range of milliseconds, allowing the components receive the subscribed messages in the proposed time increment. While the time constants of thermal systems with high capacity (as shown above) are significantly higher than the time increment and the latency, the frequency, and the latency do not affect the system's interaction.

Completing the communication infrastructure, we use the InfluxDB tick-stack to store and visualize all time-varying data, which is communicated via the MQTT broker [12], [13]. Since no historical data is available via the MQTT broker, the system controller requests this data directly from the InfluxDB time series database using HTTP. In this work, we integrate the system controller into the described framework, which we explain in more detail below.

System Controller

The controller needs access to the MQTT brokers and the InfluxDB tick-stack. In this framework, the MPC can run on any server in a cloud system. In this work, the system controller is the device under test, exploiting MPC's potential using different interfaces compared to conventional heating curves. Section 2.2 describes the controller in detail.

2.2. Data-driven model predictive control

The developed MPC maintains thermal comfort by keeping the zone's air temperature within the comfort constraints and simultaneously minimizes the heat pump's power consumption. The cost function of the resulting optimal control problem (OCP) (1) – (7) is given in (1). We penalize the violation ϵ of comfort constraints (4) with $C_1 = 10$. Furthermore, we consider energy consumption by minimizing the control input u. Depending on the experiment, the control input u can either be the actual heat pump modulation (compressor speed) ($C_{2,n_{\mathrm{com}}} = 0.1$) or the flow temperature of the heat pump ($C_{2,t_{\mathrm{flow}}} = 0.1 \cdot 1/300$). The weight $C_{2,t_{\mathrm{flow}}}$ is scaled with 1/300 because the absolute values of the flow temperature are higher than the ones of the heat pump modulation. The third term $C_3 \Delta u_k^2$ ($C_{3,t_{\mathrm{flow}}} = 0.005 \cdot 1/30$) ; $C_{3,n_{\mathrm{com}}} = 0.1$) describes the cost of changing the manipulated variable, which prevents the system from oscillating. The term is squared so that both negative and positive changes are considered. We determine the values of all weights C heuristically. In future work, we also plan to model and minimize the heat pump's electric power.

$$\min_{u,\epsilon} \sum_{k=0}^{N} C_1 \epsilon_k^2 + C_2 u_k + C_3 \Delta u_k^2 \tag{1}$$

$$\text{s.t. } \Delta T_{air,k} = f_{ann}(T_{air,k}, \dots, T_{air,k-m_T}, u_k, \dots, u_{k-m_u}, d_k, \dots, d_{k-m_d}) \tag{2}$$

$$T_{air,k+1} = \Delta T_{air,k} + T_{air,k} \tag{3}$$

$$T_{air,min,k} - \epsilon_k \leq T_{air,k} \leq T_{air,max,k} + \epsilon \tag{4}$$

$$0 \leq \epsilon \tag{5}$$

$$u_{min} \leq u_k \leq u_{max} \tag{6}$$

$$\forall k \in [0, \dots, N-1] \tag{7}$$

Crucial for the successful implementation of MPC is the underlying process model to predict the building's and heat pump's behavior (2) – (3). In this case, we use an artificial neural network (ANN) to predict the zone's temperature with all inherent system dynamics. To predict the temperature change ΔT_{air} during time step k, we consider the last m_T temperatures, the last m_u controls, and the last m_d measured disturbances d (solar radiation and ambient temperature). Thus, we use a nonlinear, autoregressive process model with exogenous inputs (NARX). Using this process model leads to a nonlinear optimization problem, which we solve efficiently using Casadi and Ipopt [14], [15]. Details on the integration of ANNs as process models in an MPC can be found in previous works of the authors [7], [15]–[17]. The OCP's prediction horizon N is 36 with a time step size of 10 min, which results in a prediction of 6 hours.

Safe operation of the MPC requires validity of the underlying process model in the whole operation range. For that reason, we pre-train the ANN with simulation data. The system identification of the simulation model is performed by choosing temperature setpoints according to a square curve for a baseline PID controller for two weeks each in winter, spring, and fall from a test reference year [18]. Here, the data set is split into 80% training, 10% validation, and 10% testing

Besides the training data for setting up a reasonable process model using ANNs, the hyperparameter tuning of ANNs is crucial. Tuneable hyperparameters are the number of layers, the number of neurons in each layer, and the activation function. In this work, a brute-force hyperparameter optimization is performed. For this reason, several ANNs with different architectures are trained and evaluated on the test set. The ANNs with the

highest accuracy are finally used as a process model in the MPC. A batch normalizing layer serves as the input layer since it efficiently scales the features, stabilizes, and speeds up the training process [19]. The output layer uses a linear activation function. We constrain the hyperparameter optimization to use relatively small ANNs with one or two hidden layers and 4 to 32 neurons to compute the optimization problem more efficiently and reduce the risk of overfitting. After hyperparameter tuning, the final ANN has one hidden layer with 16 neurons. The activation function for the hidden layer's neurons is the softsign function. We analyze and benchmark the developed system controller in a case study described below.

2.3. Case Study

In this work, we integrate MPC into a heat pump system controller and investigate the impact of the interface between the system controller and the heat pump system on the overall performance of a building energy system.

For this purpose, we consider two interfaces and a benchmark control:

1. **Benchmark control: Heating curve:**
   The used benchmark control is a weather compensation heating curve which takes the nominal flow temperature $T_{\mathrm{fl,nom}}$, the current room set temperature $T_{\mathrm{room,set}}$, the ambient temperature T_{amb} and the nominal ambient temperature $T_{\mathrm{amb,nom}}$ into account to calculate the set flow temperature $T_{\mathrm{fl,set}}$ for the heat pump. Equation 8 shows the correlation between the variables.

$$T_{fl,set} = \left(T_{fl,nom} - T_{room,set}\right) \cdot \left(\frac{T_{room,set} - T_{amb}}{T_{room,set} - T_{amb,nom}}\right)^{\frac{1}{n}} + T_{room,set} \tag{8}$$

   The parameter *n* describes the heat curve's gradient and is constant at 1.2. The equation results in the nominal flow temperature at the nominal ambient temperature. Because the equation considers the current room set temperature, the set flow temperature is decreased during periods of low room set temperatures. Besides the flow temperature control, a valve manipulates the volume flow into the underfloor heating to further control the room temperature resulting in a dynamic volume flow.
2. **Manipulated variable: Flow temperature**:
   The MPC controls the room temperature by manipulating the flow temperature of the heat pump. The internal controller of the heat pump regulates the supply temperature with the help of the compressor speed. Furthermore, the internal controller considers the heat pump's physical constraints (e.g., min compressor speed = 30 Hz). The volume flow is constant at the nominal flow.
3. **Manipulated variable: Compressor speed**
   The MPC controls the room temperature by manipulating the compressor speed. The heat pump's internal control only interacts with security issues. The MPC knows the heat pump's constraints. Since the manipulated variable has a discontinuous step between 0 and 30 Hz, the heat pump gets turned on above 30 Hz. Below a compressor speed of 30 Hz, the compressor does not operate. The volume flow is constant at the nominal flow.

Figure 4 shows the reference variable for the heating curve and the comfort band for evaluating the room temperature. The approaches with MPC use the band directly as a reference variable. For the heating curve, we shift the reference variable so that the room temperature corresponds approximately to the room setpoint temperature at the beginning of the comfort phase (interval of the higher room setpoint temperature).

We use weather data for the location of Potsdam as a boundary condition of the energy system [18]. We determine reference days with the help of sensitivity analysis and clustering [20]. This work only considers this system's winter reference day, Jan. 11. The day has a mean temperature of 1.32 °C, representing 114 days in the year in Potsdam.

We perform a simulative and experimental case study for this work. The simulative study consists of three cases. The study considers the system with the heating curve controller, the MPC manipulating the flow temperature, and the MPC using the compressor speed as the manipulated variable. We only consider the two MPC controllers for the experimental study without an additional benchmark test since we focus on the interface itself.

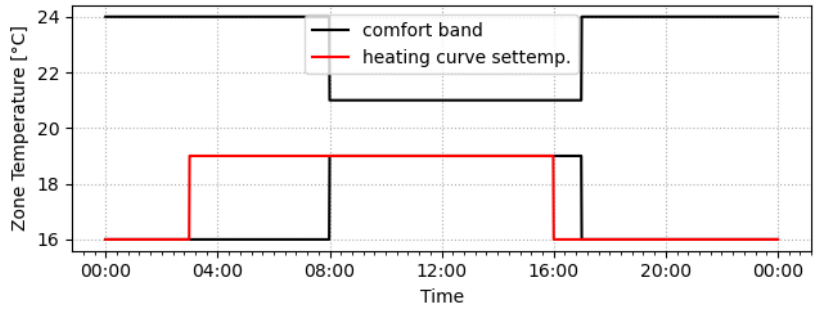


Figure 4: Comfort band for MPC and room setpoint for heating curve for a complete day

2.4. KPI Definition

We evaluate our results with different KPI definitions, which we explain in the following section:

Discomfort:

All building energy systems have a trade-off between discomfort and energy consumption. In our work, we calculate the total discomfort as follows:

$$\int_{t=0}^{t_{end}} |T_{room} - T_{room,set}| \; dt \tag{9}$$

Energy Consumption:

We consider for the energy consumption, the total electrical energy consumption of the heat pump:

$$W_{el,hp} = \int_{t=0}^{t_{end}} P_{el} \; dt \tag{10}$$

Seasonal Coefficient of Performance (SCOP):

To evaluate the heat pump's efficiency, we use the integrated COP of the heat pump over the day considered. To do so, we integrate the provided heat flow into the building $\dot{Q}_{sh}$.

$$SCOP = \frac{\int_{t=0}^{t_{end}} \dot{Q}_{sh} \, dt}{W_{el,hp}} \tag{11}$$

Compressor starts

Due to poor control parameter settings, heat pumps in the field can have many compressor starts, resulting in reduced efficiency. Additionally, compressor manufacturers specify a maximum number of starts to ensure a long service life. For this reason, we evaluate the amount of compressor starts for all use cases.

3. Results

This section presents the dynamic simulation results for the three control approaches (section 3.1) and the experimental comparison between both interfaces (section 3.2).

3.1. Simulation case study: MPC vs. heating curve

Figure 5 shows the benchmark case. The black lines show the upper and lower comfort bounds. Between 8 am and 4 pm, they are between 19 °C and 21 °C, else temperatures between 16 °C and 24 °C are within the bounds. For a reasonable comparison with the MPC approaches, the room temperature of the heating curve is set to 16 °C the night. The control of the volume flow behaves accordingly. We get similar room temperature trends in MPC and heating curve control.

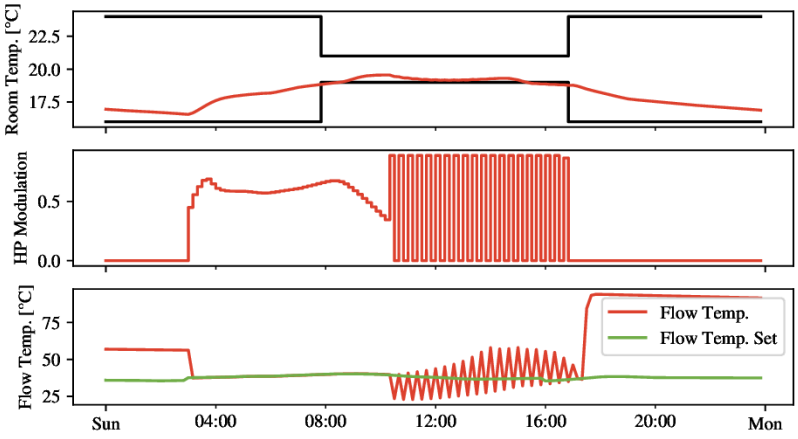


Figure 5: Simulation: Heating the thermal zone on a winter day using a heating curve

It can be seen that the heating curve with the chosen setting can keep the room temperature within the given bounds. The heat pump turns on at around 3:00 am. The heat pump turns on and off frequently as the outdoor temperature rises. The heat pump turns off by lowering the temperature bounds at 4 pm. Since the additional control valve stops the volume flow into the underfloor heating system during low set temperatures, the heat pump can only control the flow temperature during heating hours (3 am – 4 pm; see Figure 4).

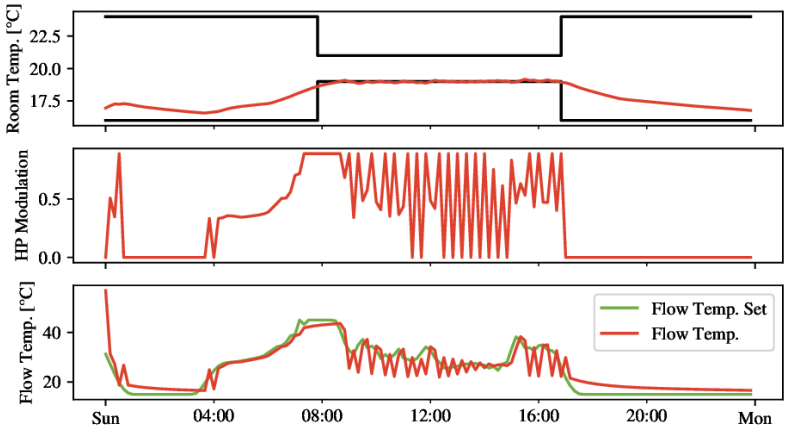


Figure 6: Simulation: Heating the thermal zone on a winter day using an MPC, which controls the flow temperature setpoint.

In Figure 6, the room temperature of the thermal zone is controlled with an MPC that sets the flow temperature setpoint. An internal PID-Controller of the heat pump controls the flow temperature. The MPC can keep the zone temperature within the comfort constraints. To reach the raised bounds at 8 o'clock, the MPC raises the flow temperature setpoint to its upper bound. Between 8 am and 4 pm, a discrepancy between the set and the actual flow temperature is observed. The difference results from frequent on-off cycling of the heat pump caused by the internal PID-Controller. The MPC lowers the flow temperature setpoint by lowering the temperature bounds.

Figure 7 shows the control of the zone temperature with an MPC that directly controls the compressor speed. The MPC is capable of keeping the zone temperature within the comfort constraints. The heat pump gets turned on at around 5 am. Before raising the temperature bounds, the MPC sets the compressor speed to its upper bound to fulfill the temperature bounds. Similar to the MPC with the flow temperature setpoint, the MPC lowers the set value during the day to minimize energy consumption. The discrepancy between the set and the actual heat pump modulation can be explained by the minimum compressor speed of 30 Hz. The compressor gets turned off if the MPC set value is below 30 Hz. Since the relative compressor speed can only

be between 0.33 and 1 and the set value range is between 0 and 1, the compressor can only follow the set fellow from 0.33 to 1.

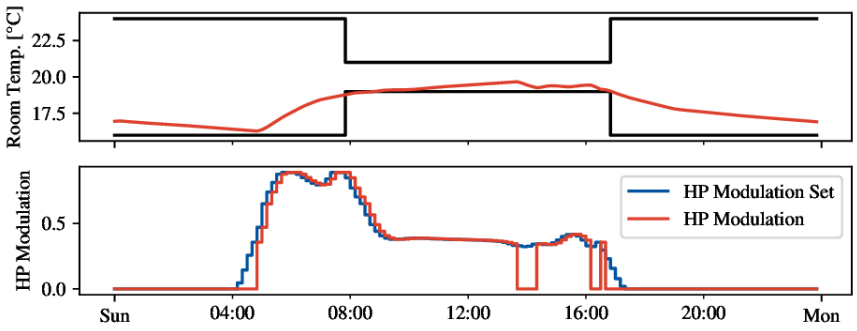


Figure 7: Simulation: Heating the thermal zone on a winter day using an MPC which controls the compressor speed.

Table 1 shows the KPI evaluation of the three simulated control approaches. The consumed electrical energy is 29.38 kWh for the heating curve controller, which is the highest overall value. Both MPC approaches reduce electrical energy consumption. Controlling the flow temperature reduces the energy consumption by 20.25 %, and controlling the compressor speed directly reduces the energy consumption by 5.75 %. The highest discomfort of all control approaches is at 0.32 Kh with the MPC with flow temperature setpoint. The discomfort corresponds to a deviation of the temperature bounds of 0.32 K for one hour, which is negligible for the comfort of occupants.

The heat pump operates the most efficiently with the flow temperature MPC at a SCOP of 2.83. The heating curve controller achieves the lowest SCOP of 2.46. The number of starts for heating curve control and flow temperature MPC is 22 and 24, respectively. Both controllers yield a higher number of starts than compressor speed MPC, which is at 3. Summing up, directly controlling the compressor speed leads to fewer starts. Many compressor starts reduce the service life, but this study cannot measure it. According to the following case study, the heat pump's efficiency needs to be evaluated in real experiments.

Table 1: Simulation: KPI's of the three different control approaches.

Controller	Energy[kWh]	Discomfort[Kh]	SCOP[]	Starts[]
Heating Curve	29.38	0.28	2.46	22
MPC with flow temperature setpoint	23.43	0.32	2.83	24
MPC with compressor speed setpoint	27.69	0.06	2.61	3

3.2. Experimental case study: Integrating MPC into a real heat pump controller

This section demonstrates the successful integration of MPC on a real heat pump system. Figure 8 shows the MPC with flow temperature control. The heat pump first gets turned on at around 4 am, similar to the MPC, which controls the compressor speed. Due to the MPC raising of the flow temperature setpoint, the compressor speed rises until it operates at maximum speed.

With lowering the flow temperature setpoint, we observe several compressor starts between 9 am and 5 pm due to the internal PI controller, which turns off the heat pump if its output is below 0.33. On-off cycling happens if the flow temperature setpoint is too low to be kept with minimum compressor speed. The PI-controller turns off the heat pump, the flow temperature drops below the setpoint, and after the minimum off-time, the heat pump will be turned on again.

Table 2 shows the evaluated KPIs for the experiments with the real heat pump for the two MPC approaches. The electrical energy consumed is 8.15 % lower for the MPC with flow temperature control. The thermal discomfort for this approach is 3.77 Kh and 0.2 Kh for the compressor speed MPC. Table 2 gives an overview of these KPIs. The SCOP is similar to both approaches. Due to the behavior of the internal PI-controller, the flow temperature MPC has 18 starts. With direct control of the compressor speed, the starts are reduced to 2.

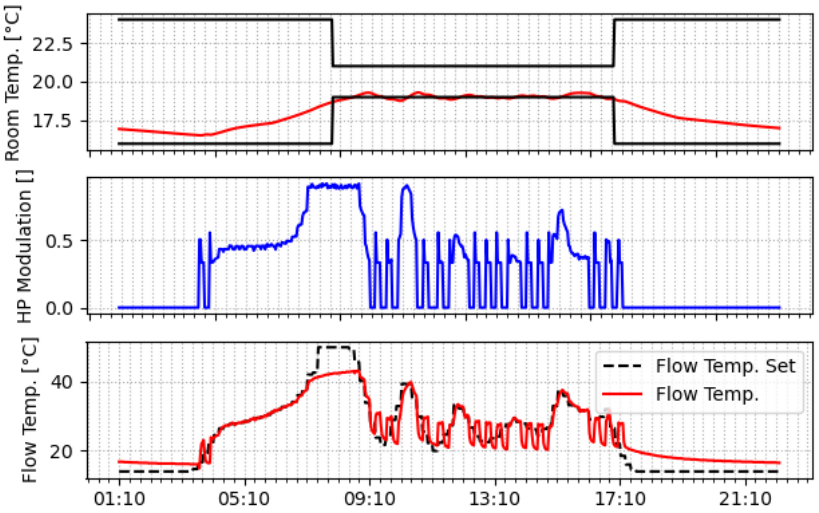


Figure 8: Real experiment: Heating of the thermal zone on a winter day using an MPC, which controls the flow temperature

Figure 9 shows the experimental results of the real heat pump using MPC controlling the compressor speed. The zone temperature and MPC setpoint curves are very similar to the simulated data in Figure 7. The heat pump's compressor can keep the setpoints given by the MPC. Like in the simulations, the heat pump gets turned off at compressor speeds below 30 Hz, corresponding to an MPC setpoint of 0.33.

When the heat pump gets turned on, seen at around 4 am and 11 am, the compressor speed jumps. This starting behavior is given by the prescribed compressor startup program of the compressor's manufacturer. This mode guarantees a safe operation within the highly dynamic starting procedure. After the dynamic starting mode, the heat pump switches to normal mode and accepts set values for compressor speed from the MPC. Staring procedures of heat pumps show real-world limitations, are challenging to model, and underline the importance of dynamic experimental tests. The following section discusses the explained results.

Table 2: Real experiment: KPIs of the three different control approaches.

Controller	Energy[kWh]	Discomfort[Kh]	SCOP[]	Starts[]
MPC with flow temperature setpoint	26.26	3.77	2.69	18
MPC with compressor speed setpoint	28.59	0.2	2.61	2

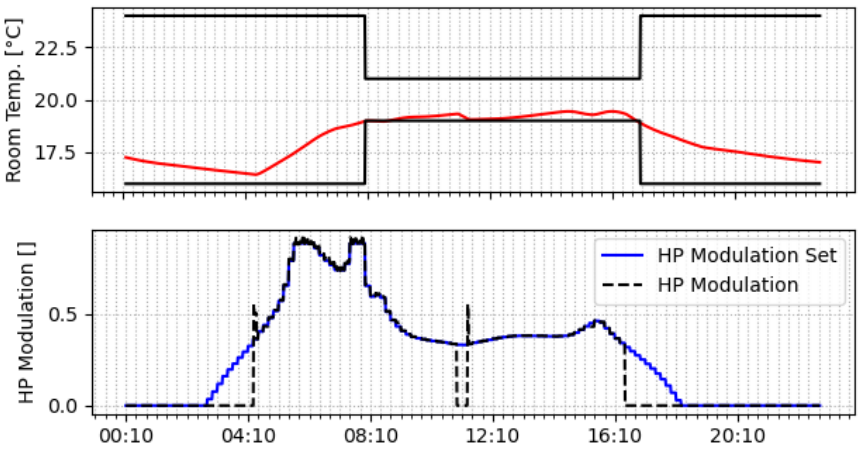


Figure 9: Real experiment: Heating of the thermal zone on a winter day using an MPC, which controls the compressor speed

4. Discussion

In this section, we discuss the results from Section 3 in the context of the identified research gaps. The results show that the simulation and experimental studies provide reasonable results.

The first identified research gap concerns the high implementation effort for MPC. The data-driven MPC method chosen reduces the modeling effort. The results show that the modeling accuracy is sufficient. In the simulative and experimental case studies, the MPC controllers outperform the heating curve controller in energy consumption. The development of the process models requires either field test or simulative data but no physical equations. This work contributes to integrating MPC into practice by overcoming the need for reduced model development effort.

The literature did not investigate the potential of different system controller interfaces on the heat pump system. The results of this work prove the influence of available interfaces on the overall system performance. When comparing the results from Table 2, it is noticeable that the MPC with direct access to the compressor speed leads to lower discomfort (0.2 Kh to 3.8 Kh). If the set flow temperature is manipulated, the heat pump's internal controller calculates the control signal for the compressor. The control signal leads to high inaccuracies that the MPC cannot predict. In addition, the pre-setting of the flow temperature at low modulation increases the number of compressor starts (see Figure 8). As a result, the MPC with flow temperature pre-setting maintains the room setpoint temperature less accurately. If the MPC can control the compressor directly, the number of starts is reduced enormously (from 18 to 2).

One difference between the MPC's setpoint and the heat pump's conversion remains if the modulation setpoint is below 0.33 because the heat pump cannot convert frequencies lower than 30 Hz. Direct compressor control leads to improved comfort and efficient operation with fewer on/off cycles. However, the heat pumps' SCOP does not derivate much between the interfaces. The differences are due to many compressor starts that reduce the average flow temperature. A low flow temperature leads thermodynamically to higher efficiency. Starting processes worsen the efficiency since additional losses occur during the compressor start (high overheating, high friction losses in the compressor). Both effects seem to balance each other out in the investigated experimental case study and should be investigated in more detail in the future.

Finally, purely annual simulative studies usually use simplified models to reduce computational effort. In the simulative case study, the calibrated model accurately describes the steady-state heat pump process. However, the differences between the experiment and simulation, especially in the discomfort, deviate strongly from each other. The differences are not due to MPC computing but due to differences in experimental and simulative heat pump operation. The influence of the compressor starts on the efficiency, and the flow temperature can hardly be represented by a simulation model. Therefore, the experimental data show the real-life behavior and the accurate system technology's influence. The HiL approach, with its dynamic, realistic, and repeatable boundary conditions, contributes to the integration of MPC into the practice.

5. Conclusion

This work contributes to integrating MPC with data-driven process models into practice using simulative and experimental case studies. In this paper, we apply the hardware-in-loop method to prove the functionality of MPC under dynamic, repeatable boundary conditions. We integrate a system controller into an energy system consisting of a self-developed heat pump test bench and a building performance simulation model coupled via a hydraulic test bench and a climate chamber. A conventional heating curve controller represents the benchmark control. The MPC controls the supply temperature or the heat pump's compressor speed exploiting the potential of different controller interfaces. We show that data-driven MPC controllers reduce the modeling effort and still lead to reasonable results outperforming conventional heat pump controller. In all case studies, the MPC reduces the system's energy consumption by up to 20.25 %. Direct access to the compressor frequency reduces the number of startups at from 18 to 2 for one specific day. The reduction of starts leads to a higher control quality and, thus, to low discomfort.

The BES consists only of a heat pump and building in this work. We will extend the system with a DHW tank and PV-System in future work.

Acknowledgments

We gratefully acknowledge the financial support by the German Federal Ministry for Economic Affairs and Climate Action (BMWK), promotional reference 03EN1022B.

References

[1] P.R. Shukla, J. Skea, R. Slade, A. Al Khourdajie, R. van Diemen, D. McCollum, M. Pathak, S. Some, P. Vyas, R. Fradera, M. Belkacemi, A. Hasija, G. Lisboa, S. Luz, J. Malley, 'IPCC, 2022: Climate Change 2022: Mitigation of Climate Change. Contribution of Working Group III to the Sixth Assessment Report of the Intergovernmental Panel on Climate Change'.

[2] IEA, 'Buildings'. 2022. [Online]. Available: https://www.iea.org/reports/buildings

[3] L. Pérez-Lombard, J. Ortiz, and C. Pout, 'A review on buildings energy consumption information', *Energy and Buildings*, vol. 40, no. 3, pp. 394–398, Jan. 2008, doi: 10.1016/j.enbuild.2007.03.007.

[4] J. Drgoňa *et al.*, 'All you need to know about model predictive control for buildings', *Annual Reviews in Control*, Sep. 2020, doi: 10.1016/j.arcontrol.2020.09.001.

[5] G. Serale, M. Fiorentini, A. Capozzoli, D. Bernadini, and A. Bemporad, 'Model Predictive Control (MPC) for Enhancing Building and HVAC System Energy Efficiency: Problem Formulation, Applications and Opportunities', *energies*, Mar. 2018, [Online]. Available: file://eonakku/home/ebc/ses-tsp/Downloads/energies-11-00631-v2.pdf

[6] D. Fischer, J. Bernhardt, H. Madani, and C. Wittwer, 'Comparison of control approaches for variable speed air source heat pumps considering time variable electricity prices and PV', *Applied Energy*, vol. 204, pp. 93–105, Oct. 2017, doi: 10.1016/j.apenergy.2017.06.110.

[7] P. Stoffel, L. Maier, A. Kümpel, T. Schreiber, and D. Müller, 'Evaluation of Advanced Control Strategies for Building Energy Systems', Social Science Research Network, Rochester, NY, SSRN Scholarly Paper 4251878, Oct. 2022. Accessed: Oct. 23, 2022. [Online]. Available: https://papers.ssrn.com/abstract=4251878

[8] T. Pean, R. Costa-Castello, E. Fuentes, and J. Salom, 'Experimental Testing of Variable Speed Heat Pump Control Strategies for Enhancing Energy Flexibility in Buildings', *IEEE Access*, vol. 7, pp. 37071–37087, 2019, doi: 10.1109/ACCESS.2019.2903084.

[9] S. Göbel, T. Fiedler, J. Klingebiel, C. Vering, and D. Müller, 'Development and experimental validation of model-based superheat control strategies for air-to-water heat pumps.' International Institute of Refrigeration (IIR). doi: 10.18462/IIR.GL2022.0143.

[10] F. Wüllhorst, L. Maier, D. Jansen, and D. Hering, 'BESMod - A Modelica Library providing Building Energy System Modules', presented at the American Modelica Conference, Dallas, Texas, 2022.

[11] P. Remmen, M. Lauster, M. Mans, M. Fuchs, T. Osterhage, and D. Müller, 'TEASER: an open tool for urban energy modelling of building stocks', *Journal of Building Performance Simulation*, vol. 11, no. 1, Art. no. 1, Jan. 2018, doi: 10.1080/19401493.2017.1283539.

[12] InfluxData, *InfluxDB key concepts | InfluxData Documentation*. 2023. [Online].

[13] A. Stanford-Clark and A. Nipper, 'Message Queuing Telemetry Transport (MQTT)'. [Online]. Available: http://mqtt.org/

[14] Joel A. E. Andersson, Joris Gillis, Greg Horn, James B. Rawlings, and Moritz Diehl, 'CasADi: a software framework for nonlinear optimization and optimal control', *Math. Prog. Comp.*, no. 11, 2019, doi: https://doi.org/10.1007/s12532-018-0139-4.

[15] A. Wächter and L. T. Biegler, 'On the implementation of an interior-point filter line-search algorithm for large-scale nonlinear programming', *Math. Program.*, vol. 106, no. 1, pp. 25–57, Mar. 2006, doi: 10.1007/s10107-004-0559-y.

[16] J. A. E. Andersson, J. Gillis, G. Horn, J. B. Rawlings, and M. Diehl, 'CasADi: a software framework for nonlinear optimization and optimal control', *Math. Prog. Comp.*, vol. 11, no. 1, pp. 1–36, Mar. 2019, doi: 10.1007/s12532-018-0139-4.

[17] P. Stoffel, C. Loffler, S. Eser, A. Kumpel, and D. Muller, 'Combining Data-driven and Physics-based Process Models for Hybrid Model Predictive Control of Building Energy Systems', in *2022 30th Mediterranean Conference on Control and Automation (MED)*, Vouliagmeni, Greece, Jun. 2022, pp. 121–126. doi: 10.1109/MED54222.2022.9837277.

[18] J. Christoffer, T. Deutschländer, and M. Webs, *Testreferenzjahre von Deutschland für mittlere und extreme Witterungsverhältnisse TRY*. Offenbach: Selbstverlag Deutscher Wetterdienst, 2004.

[19] S. Ioffe and C. Szegedy, 'Batch Normalization: Accelerating Deep Network Training by Reducing Internal Covariate Shift'. arXiv, Mar. 02, 2015. Accessed: Nov. 15, 2022. [Online]. Available: http://arxiv.org/abs/1502.03167

[20] S. Göbel, C. Vering, and D. Müller, 'Experimental Investigation of Rule-Based Control Strategies for Hybrid Heat Pump Systems Using the Smart Grid Ready Interface', in *PROCEEDINGS OF ECOS 2022*, Kopenhagen, 2022.

14th IEA Heat Pump Conference
15-18 May 2023, Chicago, Illinois

Performance Analysis of High-Temperature Heat Pumps with Two-Phase Ejectors

Pengtao Wang, Stephen Kowalski, Cheng-Min Yang, Jian Sun, Zhiming Gao, Kashif Nawaz*

Multifunctional Equipment Integration Group, Building Technology Research and Integration Center, Oak Ridge National Laboratory, Oak Ridge, TN 37831, USA

Abstract

A two-phase ejector recovers the energy in the refrigerant cycles' throttling process, improving the coefficient of performance (COP) of high-temperature heat pumps (HTHPs). This study investigated the effects of the mixing pressure on the performance of two-phase ejectors and ejector-assisted HTHPs. A 1D theoretical model of a two-phase ejector was built to predict the internal fluid dynamics and evaluate ejector performance. A thermodynamic model of an ejector-assisted HTHP was built to evaluate the COP of HTHPs and the volumetric heating capacity of low-global warming potential refrigerants. The results demonstrate that an optimum mixing pressure in a two-phase ejector provides the best performance of a two-phase ejector and ejector-assisted HTHP. The optimum mixing pressure was slightly lower than the evaporation pressure. At this pressure, the two-phase flow in the ejector was subsonic. For ejector-assisted HTHPs using low–global warming potential refrigerants at a sink temperature of 120°C, temperature lift of 40°C, and subcooling of 10°C, a two-phase ejector has an average ejector efficiency of 0.334, and the COP and volumetric heating capacity were improved by 7.2% and 7.3%, respectively.

© HPC2023.
Selection and/or peer-review under the responsibility of the organizers of the 14th IEA Heat Pump Conference 2023.

Keywords: High-temperature heat pump, two-phase ejector, mixing pressure, low–global warming potential refrigerants

1. Introduction

A high-temperature heat pump (HTHP) is one of the emerging solutions for decarbonization and electrification in industry and buildings. Current research focuses on HTHPs operating with electrically driven, single-stage vapor refrigerant compression cycles (VRCCs) [1]. A VRCC uses an expansion valve (EV) to reduce refrigerant pressure from the condenser to the evaporator, which is a throttling process associated with high energy loss. Using a two-phase ejector as an expander device to replace the EV could partially recover this energy loss, resulting in improved performance of the VRCC. A typical configuration of an HTHP operating with an ejector-expansion VRCC (EERC) is shown in Fig. 1(a). The configuration consists of a compressor, a condenser, an internal heat exchanger (IHX), a two-phase ejector, a separator, an evaporator,

* Corresponding author. Tel.: +1-865-241-0972.
E-mail address: nawazk@ornl.gov.

This manuscript has been authored by UT-Battelle, LLC, under contract DE-AC05-00OR22725 with the US Department of Energy (DOE). The US government retains and the publisher, by accepting the article for publication, acknowledges that the US government retains a nonexclusive, paid-up, irrevocable, worldwide license to publish or reproduce the published form of this manuscript, or allow others to do so, for US government purposes. DOE will provide public access to these results of federally sponsored research in accordance with the DOE Public Access Plan (http://energy.gov/downloads/doe-public-access-plan).

and an EV. Figure 1(b) shows that the ejector provides an isentropic expansion process (i.e., process 4→5), resulting in a larger specific enthalpy decrease than that associated with an isenthalpic expansion in an EV (i.e., process 4'→5'). Additionally, the ejector works as a thermo-compressor, providing a higher suction pressure for the compressor (i.e., $p_1 > p_1'$). An EERC could improve the performance of HTHPs by increasing the specific heat absorption capacity in the evaporator and reducing the compression work in the compressor [2].

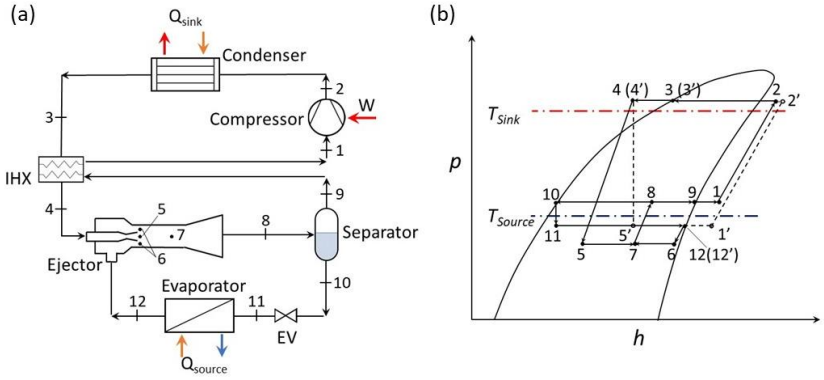


Fig. 1. HTHP assisted with a two-phase ejector: (a) configuration and (b) pressure-enthalpy diagram.

Using a two-phase ejector as an expander in EERCs was proposed in the 1930s. It became an exponentially increased research topic in HVAC and refrigeration (HVAC&R) systems in the 2010s [2, 3]. Two-phase ejectors have been employed in EERCs of transcritical CO_2 [4, 5] and subcritical, low-pressure refrigerants, such as R134a [6], R718 [7], R600a [8], R290 [9], and R410a [10]. For transcritical CO_2 EERCs with a high throttling loss, two-phase ejectors are attractive, increasing the cooling cycle coefficient of performance (COP) by 15%–30% [3]. For low-pressure refrigerant EERCs with a low throttling loss, a two-phase ejector is less effective, increasing the cooling cycle COP by 7%–20% [11]. The research on EERCs in HTHPs is limited. Popovac et al. [12] experimentally quantified the improved performance of an HTHP operating with R600 EERC and suggested that a two-phase ejector could improve the heating cycle COP by approximately 30% at a moderate temperature level (T_{sink} = 80.4°C and T_{source} = 53.2°C). Bai et al. [13] theoretically assessed EERCs operating with low–global warming potential (GWP) refrigerants and demonstrated that an EERC of R1234ze(Z) could improve the heating cycle COP by at least 10.3% at T_{sink} = 105°C and T_{source} = 30°C. Luo and Zou [14] theoretically showed that HTHPs with EERCs of R600 and R1234ze(Z) could reduce expansion losses by 10%–18% and improve the heating cycle COP by 8%–14% at T_{sink} = 120°C and T_{source} = 80°C. Mateu-Royo et al. [15] theoretically demonstrated that an EERC could slightly improve the heating cycle COP and downsize the compressor.

The majority of theoretical research has employed the zero-dimensional model developed by Kornhauser [16]. Kornhauser's model assumed the mixing process was under constant pressure, p_M, and the two-phase fluid was inhomogeneous at equilibrium. The model was built considering the conservation of mass, energy, and momentum with assigned efficiency for different sections within a two-phase ejector. The model required a specified p_M as an input to predict the component-level performance of two-phase ejectors. Pressure p_M is closely related to the ejector's geometry, refrigerants, and operating conditions, which are difficult to determine experimentally [2]. For a mixing process within a constant area under a constant pressure, p_M could be iteratively calculated from the relationship between the mass, flow area, and specific volumes of refrigerant [17-19]. However, the calculated p_M was affected by the condensation shock wave and/or the nonequilibrium two-phase flow at the exit of the mixing chamber. In other literature, p_M was guessed without justification. In transcritical CO_2 EERC for low-temperature refrigeration, $p_{M,opt}$ was assumed to be the evaporation pressure of secondary fluid (SF), p_{Evap}, by Deng et al. [20], or 95% of p_{Evap} by Purjam et al. [21]. In EERC using R134a, R1234yf, and R1234ze(Z) for refrigeration, p_{Evap} was assumed to be the saturated vapor pressure corresponding to a 5 K drop in the evaporation temperature, T_{evap}, by Lawrence and Elbel [22] and Atmaca et al. [23]. Additionally, Kornhauser's primary results showed that the maximum cooling cycle COP of EERC in refrigeration was achieved with an optimum mixing pressure, $p_{M,out}$, which gave the same velocity of the primary fluid (PF) and the SF before mixing. No evidence existed that the calculated or guessed p_M was $p_{M,out}$, which could yield the maximum COP of the investigated EERC for refrigeration applications.

To fully explore the technical merit of using a two-phase ejector in an HTHP, selecting a reasonable value of $p_{M,out}$ is critical. This study analyzes the optimized mixing pressure of two-phase ejectors in HTHPs. An improved 1D thermodynamic model of a two-phase ejector was built with the real properties of refrigerants. The effects of mixing pressure on fluid dynamics within two-phase ejectors were investigated. The optimum mixing pressure was determined for the component-level performance of two-phase ejectors and the system-level performance of HTHPs. The technical merits of HTHPs with EERCs were explored for various low-GWP refrigerants.

2. Theoretical Model of a Two-Phase Ejector

A typical ejector consists of a primary nozzle, a suction chamber, a mixing chamber (including a converging section and a constant area section), and a diffuser, as shown in Fig. 2. The ejector works on the isentropic conversion process of potential work, contained in the PF flow, into kinetic energy. High-pressure PF accelerates into a high-speed jet and creates a low-pressure zone at the nozzle exit plane, which entrains the low-pressure SF vapor into the suction chamber. Depending on the initial state of the PF, the PF flow at the nozzle's exit could be supersonic (e.g., in transcritical CO_2 cycles [24]) or subsonic associated with two-phase change (e.g., flashing evaporation or condensation). PF flow further accelerates and expands, creating a hypothetical throat at the section *y-y*, where the SF flow may be choked at its critical velocity. PF and SF mix in the constant area section of the mixing chamber under a constant mixing pressure, p_M. If the flow of completely mixed PF and SF is supersonic, a condensation shock wave occurs, resulting in a pressure lift. The static pressure of mixed PF and SF further increases in the diffuser by converting its kinetic energy into potential energy.

2.1. Governing Equations

In this study, an improved 1D thermodynamic model of a two-phase ejector was built, considering a constant pressure mixing process [16, 25]. Major assumptions adopted in the theoretical model include the following:

(1) The flow inside the ejector is 1D, steady, and adiabatic.

(2) The frictional and mixing losses are defined in terms of ejector component isentropic efficiencies, including η_N for the primary nozzle, η_S for the secondary flow, η_M for the mixing process, and η_D for the diffuser [26].

(3) Working fluid is in thermodynamic quasi-equilibrium condition (i.e., a homogeneous equilibrium model of two-phase flow [27]).

(4) The mixing PF and SF is initiated at the section *y-y* and completed at the section *m-m* under constant static pressure, p_M.

The governing equations in the thermodynamic model are built with the mass, momentum, and energy conservation across the ejector components. The state points of fluids in the following equations are presented by lowercase Roman numerals "i, ii, iii, …", as shown in Fig. 2

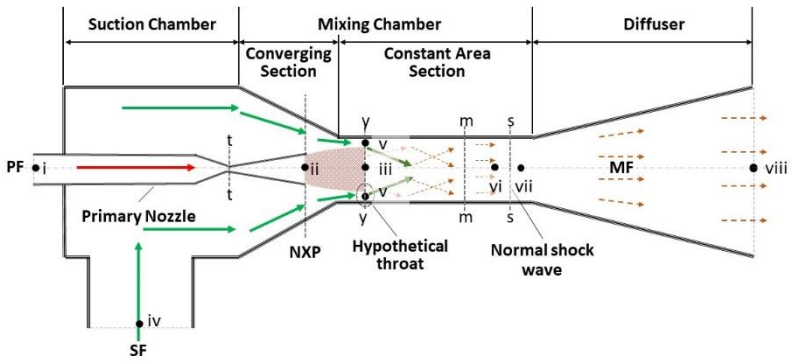


Fig. 2. Typical flow phenomena in a two-phase ejector [28]. (NXP stands for nozzle exit plane. MF represents the mixed PF and SF.)

The energy conservation of PF through an isentropic expansion process within the primary nozzle and the converging section of the mixing chamber is given by Eqs. (1) and (2):

$$h_{\mathrm{iii}} = (1-\eta_{\mathrm{N}})h_{\mathrm{i}} + \eta_{\mathrm{N}}h_{\mathrm{iii,is}} \text{ , and} \tag{1}$$

$$V_{\mathrm{iii}} = \sqrt{2(h_{\mathrm{i}} - h_{\mathrm{iii}})}. \tag{2}$$

The energy conservation of SF within the converging section of the mixing chamber is calculated with Eqs. (3) and (4):

$$h_{\mathrm{v}} = (1-\eta_{\mathrm{S}})h_{\mathrm{iv}} + \eta_{\mathrm{S}}h_{\mathrm{v,is}} \text{ and } h_{\mathrm{v,is}} = h(s_{\mathrm{iv}}, p_{\mathrm{v}}), \text{ and} \tag{3}$$

$$V_{\mathrm{v}} = \sqrt{2(h_{\mathrm{vi}} - h_{\mathrm{v}})}. \tag{4}$$

The maximum value of V_{v} is limited to its local speed of sound, C_{v}. If the flow of SF is chocked, then Eq. (5) gives

$$V_{\mathrm{v,max}} = C_{\mathrm{v}}. \tag{5}$$

The mixing process is under constant static pressure, represented by Eq. (6):

$$p_{\mathrm{iii}} = p_{\mathrm{v}} = p_{\mathrm{vi}} = p_{\mathrm{M}}. \tag{6}$$

The moment conservation in the mixing process is given by Eq. (7):

$$\phi_{\mathrm{M}}(\dot{m}_{\mathrm{PF}}V_{\mathrm{iii}} + \dot{m}_{\mathrm{SF}}V_{\mathrm{v}}) = (\dot{m}_{\mathrm{PF}} + \dot{m}_{\mathrm{SF}})V_{\mathrm{vi}}, \tag{7}$$

where ϕ_{M} is the velocity coefficient accounting for the frictional loss in the mixing process, and $\phi_{\mathrm{M}} = \sqrt{\eta_{\mathrm{M}}}$ [29].

The energy conservation in the mixing process is shown in Eq. (8):

$$(\dot{m}_{\mathrm{PF}} + \dot{m}_{\mathrm{SF}})\left(h_{\mathrm{vi}} + \tfrac{1}{2}V_{\mathrm{vi}}^2\right) = \dot{m}_{\mathrm{PF}}\left(h_{\mathrm{iii}} + \tfrac{1}{2}V_{\mathrm{iii}}^2\right) + \dot{m}_{\mathrm{SF}}\left(h_{\mathrm{v}} + \tfrac{1}{2}V_{\mathrm{v}}^2\right). \tag{8}$$

If the mixed flow is supersonic or sonic (i.e., $M_{\mathrm{vi}} \geq 1$), a condensation shock will occur at the section s-s. The conservation of mass, momentum, and energy across a condensation shock wave are calculated by Eqs. (9), (10), and (11) [25]:

$$\rho_{\mathrm{vii}}V_{\mathrm{vii}} = \rho_{\mathrm{vi}}V_{\mathrm{vi}}, \tag{9}$$

$$p_{\mathrm{vii}} + \rho_{\mathrm{vii}}V_{\mathrm{vii}}^2 = p_{\mathrm{vi}} + \rho_{\mathrm{vi}}V_{\mathrm{vi}}^2, \text{ and} \tag{10}$$

$$h_{\mathrm{vii}} + \tfrac{1}{2}V_{\mathrm{vii}}^2 = h_{\mathrm{vi}} + \tfrac{1}{2}V_{\mathrm{vi}}^2. \tag{11}$$

The thermodynamic state equations for the density and entropy after the condensation shock wave are given in Eqs. (12) and (13):

$$\rho_{\mathrm{vii}} = \mathrm{rho}(p_{\mathrm{vii}}, h_{\mathrm{vii}}), \text{ and} \tag{12}$$

$$s_{\mathrm{vii}} = s(p_{\mathrm{vii}}, h_{\mathrm{vii}}). \tag{13}$$

If the mixed flow is subsonic (i.e., $M_{\mathrm{vi}} < 1$), Eq. (14) applies:

$$V_{\mathrm{vii}} = V_{\mathrm{vi}},\ p_{\mathrm{vii}} = p_{\mathrm{vi}}, \text{ and } s_{\mathrm{vii}} = s_{\mathrm{vi}} = s(p_{\mathrm{vi}}, h_{\mathrm{vi}}) \tag{14}$$

The energy conservation within the diffuser is given by Eqs. (15) and (16):

$$h_{\mathrm{viii}} = h_{\mathrm{vii}} + \frac{1}{2}V_{\mathrm{vii}}^2, \text{ and} \tag{15}$$

$$h_{\mathrm{viii,is}} = h_{\mathrm{vii}} + \eta_{\mathrm{D}}\frac{1}{2}V_{\mathrm{vii}}^2. \tag{16}$$

The static pressure and quality of the two-phase fluid discharged from the ejector are given in Eqs. (17) and (18):

$$p_{\mathrm{viii}} = p(h_{\mathrm{viii,is}}, s_{\mathrm{viii}}) \text{ and } s_{\mathrm{viii}} = s_{\mathrm{vii}}, \text{ and} \tag{17}$$

$$x_{\mathrm{viii}} = x(p_{\mathrm{viii}}, h_{\mathrm{viii}}). \tag{18}$$

Assuming the discharged two-phase fluid could be fully separated in the separator, the fluid loop in an EERC requires Eq. (19):

$$x_{\mathrm{viii}} = \frac{\dot{m}_{\mathrm{PF}}}{\dot{m}_{\mathrm{PF}}+\dot{m}_{\mathrm{SF}}} = \frac{1}{1+\omega}, \tag{19}$$

where ω is the ratio of the mass flow rates of SF, $\dot{m}_{\mathrm{SF}}$, and to that of PF, $\dot{m}_{\mathrm{PF}}$, as shown in Eq. (20):

$$\omega = \frac{\dot{m}_{\mathrm{SF}}}{\dot{m}_{\mathrm{PF}}}. \tag{20}$$

The flow conditions in the ejector are characterized by the Mach number, *M*, and *M* = *V*/*C*. The speed of sound of the two-phase flow, *C*, is given in Eq. (21) [21]:

$$C = \frac{1}{(1-\alpha)\sqrt{\frac{1-\alpha}{C_{\mathrm{l}}^2}+\frac{\alpha\rho_{\mathrm{l}}}{\rho_{\mathrm{v}}C_{\mathrm{v}}^2}}+\alpha\sqrt{\frac{\alpha}{C_{\mathrm{v}}^2}+\frac{(1-\alpha)\rho_{\mathrm{v}}}{\rho_{\mathrm{l}}C_{\mathrm{l}}^2}}}, \tag{21}$$

where α is the void fraction of the two-phase flow, and ρ is the density. The subscripts l and v are for the saturated liquid and vapor phases of refrigerants. In a homogeneous two-phase flow, the void fraction is given by Eq. (22):

$$\alpha = \frac{x\rho_{\mathrm{l}}}{(x\rho_{\mathrm{l}}+(1-x)\rho_{\mathrm{v}})}, \tag{22}$$

where *x* is the vapor quality of the two-phase fluid.

2.2. Calculation Procedure

The two-phase ejector was operated with specified inlet temperature and static pressure of PF and SF, denoted as T_{i}, p_{i}, T_{iv}, and p_{iv}. In investigated ejector-assistant HTHPs, inlet PF was subcooled liquid, and inlet SF was saturated vapor.

$$\begin{aligned} T_{\mathrm{i}} &= T_{\mathrm{sink}} - \Delta T_{\mathrm{sc}} \\ p_{\mathrm{i}} &= p(T_{\mathrm{sink}}, x = 1) \\ T_{\mathrm{iv}} = T_{\mathrm{source}} &= T_{\mathrm{sink}} - \Delta T_{\mathrm{lift}}, \end{aligned} \tag{23}$$

where T_{source} is the sink temperature, ΔT_{SC} is the subcooling temperature of PF from the IHX, and ΔT_{lift} is the lifted temperature of HTHPs. The mixing pressure, p_{M}, is the saturated vapor pressure of SF at an equivalent temperature of SF before mixing, T_{M}, given in Eq. (24):

$$T_{\mathrm{M}} = T_{\mathrm{Evap}} - \Delta T_{\mathrm{M}}, \tag{24}$$

where ΔT_M is the assumed temperature drop of saturated SF before the mixing process.

The calculation procedure for solving the two-phase ejector model is shown in Fig. 3. These governing equations were solved iteratively in the Engineering Equation Solver (EES, F-Chart software). Component efficiencies of two-phase ejectors were assumed with constant values: $\eta_N = 0.8$, $\eta_S = 0.8$, $\eta_M = 0.9$, and $\eta_D = 0.8$ [18]. For a specified p_M, the model could predict the pressure and quality of discharged two-phase fluid from the two-phase ejector, p_{viii} and x_{viii}.

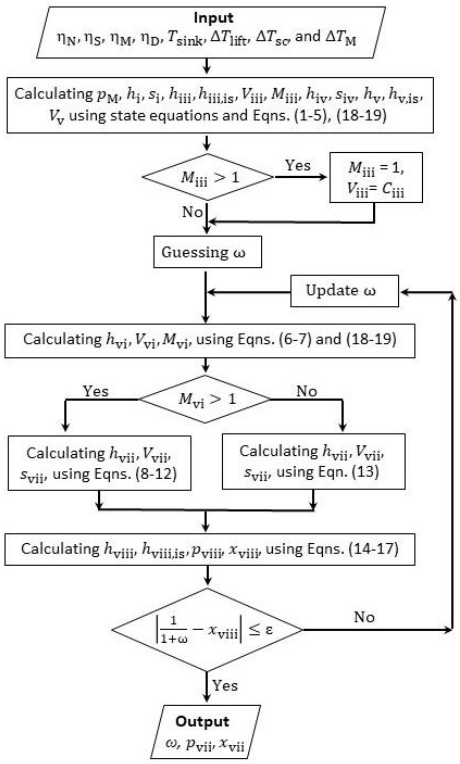


Fig. 3. Flow chart of solving the two-phase ejector model.

3. Thermodynamic Model of an Ejector-Assisted HTHP

A thermodynamic model of an HTHP with EERC was built by applying the mass and energy conservation within each component [15, 30], as summarized in Table 1. The theoretical model was solved using EES with its built-in thermophysical properties of the refrigerants. The system performance of HTHPs was evaluated with selected refrigerants under specified operating parameters of T_{sink}, ΔT_{lift}, and ΔT_{SC}. The system assumed the approach temperature and the pressure drops in the evaporator/condenser were negligible.

Table 1. Mass and energy equations in the thermodynamic model of an ejector-assisted HTHP

Component	Mass equations	Energy equations	Thermal properties equations
Compressor	$\dot{m}_2 = \dot{m}_1 = \dot{m}_{PF}$	$W_{Comp} = \frac{\dot{m}_1(h_{2,is} - h_1)}{\eta_{is}\eta_{em}}$	$h_{2,is} = h(p_2, s_2)$; $h_2 = h_1 + \eta_{is}(h_{2,is} - h_1)$; $p_2 = p_3$; $s_2 = s_1$
Condenser	$\dot{m}_3 = \dot{m}_2$	$Q_{Sink} = \dot{m}_3(h_2 - h_3)$	$h_3 = h(T_3, x = 0)$; $T_3 = T_{sink}$; $p_3 = p(T_3, x = 0)$
IHX	$\dot{m}_4 = \dot{m}_3 = \dot{m}_9 = \dot{m}_1$	$Q_{IHX} = \dot{m}_4(h_3 - h_4)$ $Q_{IHX} = \dot{m}_1(h_1 - h_9)$	$h_4 = h(T_4, p_4)$; $h_9 = h(p_9, x = 1)$; $p_4 = p_3$; $p_9 = p_8$; $T_4 = T_3 - \Delta T_{sc}$

Table 1. Mass and energy equations in the thermodynamic model of an ejector-assisted HTHP (continued)

Component	Mass equations	Energy equations	Thermal properties equations
Two-phase ejector	$\dot{m}_8 = \dot{m}_4 + \dot{m}_{12}$	$\dot{m}_8 h_8 = \dot{m}_4 h_4 + \dot{m}_{12} h_{12}$	$h_{12} = h(p_{12}, x = 1)$; p_8, x_8, and T_8 predicted form the ejector model
Separator	$\dot{m}_9 = \dot{m}_8 x_8$ $\dot{m}_{10} = \dot{m}_8(1 - x_8)$	$\dot{m}_9 h_9 + \dot{m}_{10} h_{10} = \dot{m}_8 h_8$	$h_9 = h(p_9, x = 1)$; $h_{10} = h(p_{10}, x = 0)$; $p_8 = p_9 = p_{10}$
Expansion valve	$\dot{m}_{11} = \dot{m}_{10}$	$\dot{m}_{11} h_{11} = \dot{m}_{10} h_{10}$	$h_{11} = h_{10}$
Evaporator	$\dot{m}_{12} = \dot{m}_{11} = \dot{m}_{\mathrm{SF}}$	$Q_{\mathrm{Source}} = \dot{m}_{12}(h_{12} - h_{11})$	$h_{12} = h(T_{12}, x = 1)$; $T_{12} = T_{\mathrm{source}} = T_{\mathrm{sink}} - \Delta T_{\mathrm{lift}}$

3.1. Compressor

A piston compressor was used in the investigated HTHP for a heating capacity of ≤800 kW. The compressor could provide the maximum discharged temperature of 150°C using hydrofluoroolefins (HFOs) [31]. The volumetric and isentropic efficiencies of piston compressors, represented as η_{vol} and η_{is}, were predicted using Pierre's correlations in Eqs. (25) and (26) [32, 33]:

$$\eta_{\mathrm{vol}} = 1.04\left(1 + 0.15\frac{T_{\mathrm{suc}} - 18}{100}\right) \cdot \exp\left(-0.07\frac{p_{\mathrm{disch}}}{p_{\mathrm{suc}}}\right), \text{ and} \tag{25}$$

$$\left(\frac{\eta_{\mathrm{vol}}}{\eta_{\mathrm{is}}}\right) = \left(1 - 0.1\frac{T_{\mathrm{suc}} - 18}{100}\right) \cdot \exp\left(-2.40\frac{T_{\mathrm{disch}} + 273.15}{T_{\mathrm{suc}} + 273.15} + 2.88\right), \tag{26}$$

where T_{suc} and T_{disch} are refrigerant temperatures in degrees Celsius, and p_{suc}, and p_{disch} are pressures at the compressor's inlet and outlet, denoted by state points 1 and 2 in Fig. 1(b), respectively.

The power consumption of the compress, W_{Comp}, is calculated by Eq. (27):

$$W_{\mathrm{Comp}} = \frac{\dot{m}_{\mathrm{PF}}(h_{2,\mathrm{is}} - h_1)}{\eta_{\mathrm{is}}\eta_{\mathrm{em}}}, \tag{27}$$

where $h_{2,\mathrm{is}}$ is the enthalpy of discharged refrigerant after an isentropic compression process, and η_{em} is the electromechanical efficiencies of compressor; $\eta_{\mathrm{em}} = 0.95$.

3.2. *Internal Heat Exchanger*

An IHX is employed in HTHPs to ensure a dry compression process in the compressor and improve the COP of HTHPs [34]. An IHX exchanges the heat between high-pressure vapor and low-pressure liquid. Refrigerant vapor entering the IHX is saturated at the discharged pressure of the ejector. The enthalpy of superheated vapor leaving the IHX is determined from the energy balance between the liquid and vapor refrigerant in the IHX. In this study, the subcooling temperature of refrigerant leaving the IHX, ΔT_{SC}, was specified as an input in the theoretical model of the two-phase ejector, which should be large enough to ensure the superheating of vapor at the compressor outlet.

3.3. Two-Phase Ejector

The component-level performance of the ejector was evaluated by the entrainment ratio, ω, defined in Eq. (20), and the pressure lift ratio, Π, which is defined in Eq. (28) as the ratio of the ejector's discharged pressure, p_{viii}, to the inlet pressure of SF, p_{iv}:

$$\Pi = \frac{p_{\mathrm{EJT,out}}}{p_{\mathrm{SF,in}}} = \frac{p_{\mathrm{viii}}}{p_{\mathrm{iv}}} = \frac{p_8}{p_{12}}. \tag{28}$$

Elbel and Hrnjak [35] proposed the ejector efficiency, η_{EJT} as an appliable efficiency metric to evaluate the trade-off between ω and Π. η_{EJT} is the ratio of the actual amount of work recovered by the ejector, W_r, and the total work recovery potential for an isentropic process, $W_{r,max}$, given by Eq. (29):

$$\eta_{EJT} = \frac{W_r}{W_{r,max}\frac{h_A - h_B}{h_C - h_D}}, \tag{29}$$

where h_A and h_B are the enthalpy of the PF at the ejector's discharged pressure via isenthalpic and isentropic expansion processes, respectively. The entropy of SF flow before and after an isentropic compression process are h_C and h_D, respectively. For the investigated ejector-assisted HTHP in this study,

$$\begin{aligned} h_A &= h_4, \\ h_B &= h(p = p_8, s = s_4), \\ h_C &= h(p = p_8, s = s_{12}), \\ h_D &= h_{12}. \end{aligned} \tag{30}$$

3.4. Performance of Ejector-Assisted HTHPs

The system-level performance of ejector-assisted HTHPs is evaluated by its heating cycle COP, given in Eq. (31):

$$COP_{EHTHP} = \frac{Q_{Sink}}{W_{Comp}}. \tag{31}$$

The refrigerants for the ejector-assisted HTHPs were evaluated by the volumetric heating capacity (VHC) [36]. A higher value of VHC is desired for a smaller compressor displacement rate to deliver a specified capacity, as shown in Eq. (32):

$$VHC = \eta_{vol}\rho_1(h_2 - h_3). \tag{32}$$

3.5. Low-GWP Refrigerants

Low-GWP refrigerants promising for HTHPs were selected to evaluate the merit of ejector-assisted HTHPs, as listed in Table 2. These refrigerants can be categorized into hydrocarbon (HC), hydrochlorofluorocarbon (HCFO), and HFO. R245fa is R-245fa is a hydrofluorocarbon (HFC) and set as a reference refrigerant because of its wide use in current HTHPs.

Table 2. Low-GWP refrigerants for ejector-assisted HTHPs

Group	Refrigerants	Formula	T_{cr} [°C]	P_{cr} [MPa]	ρ_v* [kg/m³]	*NBP*** [°C]	*MW*** [kg/kmol]	ODP**	GWP	SC***
HC	R601	C_5H_{12}	196.6	3.37	10.1	36.1	72.2	0	5	A3
	R600	C_4H_{10}	152.0	3.80	25.2	−0.5	58.1	0	4	A3
HCFO	R1233zd(E)	$C_3ClF_3H_2$	166.5	3.62	34.8	18.3	130.5	0.00034	1	A1
	R1224yd(Z)	C_3ClF_4H	155.5	3.33	45.6	14.6	148.5	0.00012	<1	A1
HFO	R1336mzz(Z)	$C_4F_6H_2$	171.4	2.90	27.5	33.4	164.1	0	2	A1
	R1234ze(Z)	$C_3F_4H_2$	150.1	3.53	42.2	9.8	114.0	0	<1	A2L
HFC	R245fa	$C_3F_5H_3$	154.0	3.65	44.1	15.1	134.0	0	858	B1

*Saturated vapor at 80.0°C.
**NBP is normal boiling point. MW is molecular weight. ODP is ozone depletion potential.
***ASHRAE safety class (SC): A and B for toxicity from low to high, 1, 2L, 2, and 3 for flammability from low to high.

4. Results and Discussion

The ejector-assisted HTHPs were operated at T_{sink} = 120°C, ΔT_{lift} = 40 K, and ΔT_{SC} = 10 K. The component isentropic efficiencies of a two-phase ejector were η_N = 0.8, η_S = 0.8, η_M = 0.9, and η_D = 0.8. The effects of the

mixing pressure, p_M, on the component-level performance of a two-phase ejector was predicted by the theoretical model with various equivalent temperature drops of SF (i.e., ΔT_M in Eq. (25)). For R1336mzz(Z), p_M in the two-phase ejector almost linearly decreased from 429.2 kPa to 235.0 kPa as ΔT_M increased from 0.1 K to 21.4 K.

4.1. Effects of the Mixing Pressure

4.1.1. Component-level performance of two-phase ejector

With the decrease of p_M, the velocity of PF and SF flows increased, and the velocity of SF flow increased more significantly than that of PF flow, as shown in Fig. 4(a). This difference is because the enthalpy change of SF (saturated vapor) is much larger than that of PF (low-quality two-phase fluid) through an isentropic expansion process across the same pressure drop. The *p-h* diagram of R1336mzz(Z) shows that the isenthalpic and isentropic lines are nearly parallel in the low-quality two-phase region, and the slopes of isenthalpic lines are much smaller than those of isentropic lines in the high-quality two-phase region. With the decrease of p_M, the discharged pressure of ejector, p_{viii}, increased to the maximum value of 456 kPa, giving the maximum pressure lift ratio, Π_{max}. After that maximum, p_{viii} linearly decreased.

From the velocity and the static pressure of PF and SF before the mixing process, four unique points could be identified as: the maximum pressure lift ratio, Π_{max}; no pressure lift effect, $\Pi = 1$; the same velocity of PF and SF, $V_{SF} = V_{PF}$; and a choked SF flow, $M_{SF} = 1$. The effects of p_M on the component performance of two-phase ejectors are shown in Fig. 5. The trends of ω and η_{EJT} related to p_M are similar to that of Π. At the optimum mixing pressure, $p_{M,opt}$ = 424.7 kPa with ΔT_M = 0.6 K, the maximum values of ω_{max} = 0.733, Π_{max} = 1.059, and $\eta_{EJT,max}$ = 0.333 were achieved. At p_M = 358.2 kPa (with ΔT_M = 6.8 K), Π = 1 and η_{EJT} = 0. Further reducing p_M, the ejector could not provide a compression effect because of the overexpansion of PF in the primary nozzle. At p_M = 349.4 kPa (with ΔT_M = 7.7 K), $V_{SF} = V_{PF}$, $\Pi < 1$, and $\eta_{EJT} < 0$. These values indicate that selecting p_M for $V_{SF} = V_{PF}$ is not beneficial for the performance of two-phase ejectors. When p_M was reduced to 235 kPa (with ΔT_M =21.4 K), p_M was sufficiently low to accelerate the SF flow to M_{SF} = 1, and the PF flow was subsonic, with M_{PF} =0.77. At this p_M, the mixed PF and SF flow at the section *m-m* was subsonic; thus, a condensation shock wave did not occur [37]. Further reducing p_M may accelerate the PF flow to supersonic, but the performance of the two-phase ejector would extremely deteriorate.

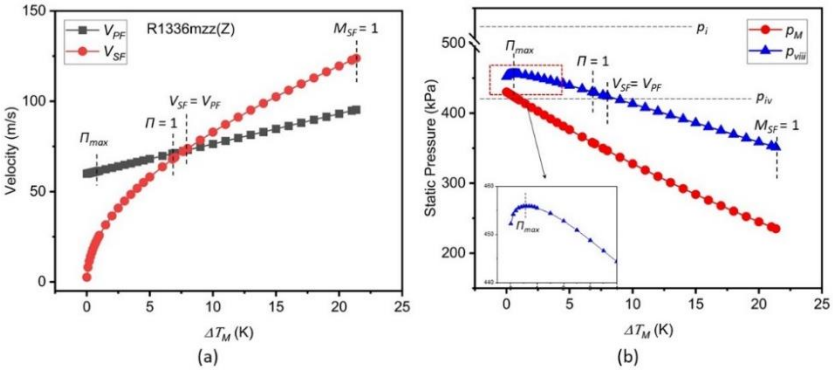


Fig. 4. Effects of the mixing pressure on the gas dynamic properties in a two-phase ejector: (a) velocity and (b) static pressure.

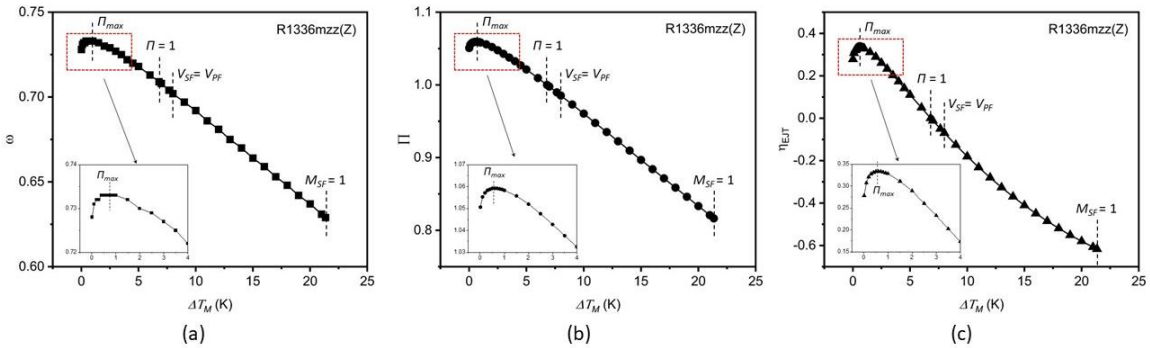


Fig. 5. Effects of the mixing pressure on the two-phase ejector's performance: (a) entrainment ratio, (b) pressure lift ratio, and (c) ejector efficiency.

4.1.2. System-level performance of ejector-assisted HTHPs

The system-level performance of an ejector-assisted HTHP is closely related to the component-level performance of a two-phase ejector. The maximum values of COP and VHC were achieved with $\eta_{EJT,max}$ at $p_{M,opt}$, as shown in Fig. 6. The reference values of COP and VHC, represented as COP_{ref} and VHC_{ref}, are for HTHPs with an EV. COP_{max} = 6.29 and VHC_{max} = 3,272 kJ/m^3 were achieved at $p_{M,opt}$, corresponding to the improvement of ΔCOP_{max} = 7.01% and ΔVHC_{max} = 7.63% for R1336mzz(Z). Replacing an EV with a two-phase ejector becomes unfavorable in HTHPs when the ejector cannot provide the compression effect (i.e., $\Pi \leq 1$).

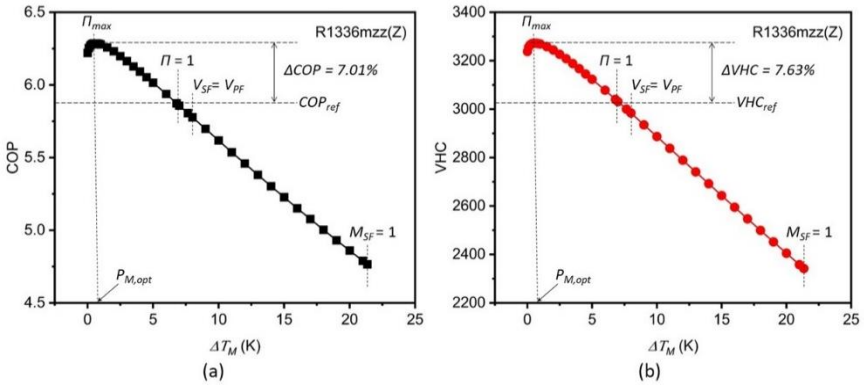


Fig. 6. Effects of the mixing pressure on the performance of an ejector-assisted HTHP: (a) COP and (b) VHC.

4.2. Effects of the Refrigerants

The performance of two-phase ejectors and ejector-assisted HTHPs with selected refrigerants under specified operating conditions (i.e., T_{sink} = 120°C, ΔT_{lift} = 40 K, and ΔT_{SC} = 10 K), as shown in Fig. 7. Similar to R1366mzz(Z), the mixing pressure had an optimum value for the maximum values of η_{EJT}, COP, and VHC, as summarized in Table 3. The averaged value of η_{EJT} was 0.334 ± 0.005, improving the performance of HTHPs by ΔCOP = 7.2% ± 0.9% and ΔVHC = 7.3% ± 0.7%. This work demonstrates that replacing an EV with a two-phase ejector improves the COP of HTHPs and requires more compact compressors than basic HTHPs, which is consistent with previous studies [11]. The contribution of the two-phase ejector in the COP improvement of HTHPs with low-GWP refrigerant is 5.79%–8.47%, which is much lower than moderate-temperature HPs with transcritical CO_2 (ΔCOP = 15%–30% [3]). Compared with R245fa, two-phase ejectors contribute to lower improvements of COP and VHC with the selected low-GWP refrigerants, except for the improved COP with R600. R600 presented the highest COP improvement of 8.47% and the highest VHC values of 6,090 kJ/m^3.

For HTHPs under specified operating conditions, $p_{M,opt}$ was approximately 98.4% ± 0.2% of p_{Evap}, which was slightly larger than 95% of p_{Evap} for a transcortical CO_2 EERC refrigeration system [21]. ΔT_M for $p_{M,opt}$ was 0.7°C ± 0.1°C, which was much smaller than ΔT_M = 5 K for EERC refrigeration using R134a, R1234yf, and R1234ze(E) [22, 23]. A higher value of $p_{M,opt}/p_{Evap}$, associated with a lower ΔT_M, for two-phase ejectors in HTHPs may be because of the high operating temperature of low-pressure refrigerants and the ejector components' isentropic efficiencies adopted in the theoretical model. Additionally, this study demonstrated that p_M for $V_{SF} = V_{PF}$ does not give the maximum COP of ejector-assisted HTHPs. This result disagrees with Kornhauser's primary analysis, which claimed that $p_{M,opt}$ was for $V_{SF} = V_{PF}$ [16]. In a supersonic ejector, the same velocities of PF and SF in the mixing process theoretically results in minimal kinetic energy loss associated with the velocity difference [38]. However, this effect may not be significant in a two-phase ejector because of the subsonic flow combined with a two-phase transition process.

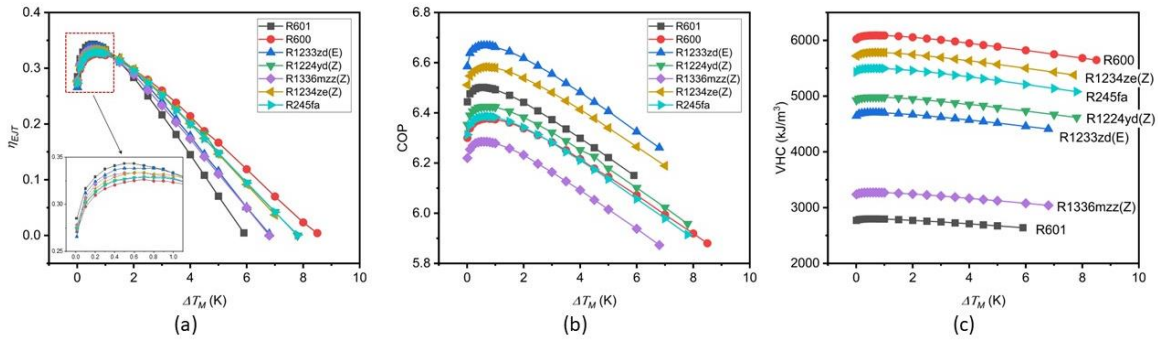


Fig. 7. Ejector-assisted HTHPs with different refrigerants: (a) ejector efficiency, (b) COP, and (c) VHC.

Table 3. Performance of an ejector-assisted HTHP with different refrigerants

Refrigerants	Two-phase ejector			Ejector-assisted HTHP		Maximum improvement	
	ΔT_M (K)	p_M/p_{Evap} (%)	η_{EJT}	COP	VHC (kJ/m^3)	ΔCOP (%)	ΔVHC (%)
R601	0.6	98.5	0.343	6.50	2,798	5.79	6.07
R600	0.7	98.5	0.327	6.38	6,090	8.47	7.85
R1233zd(E)	0.5	98.8	0.339	6.67	4,703	6.5	6.62
R1224yd(Z)	0.8	98.1	0.329	6.43	4,982	7.84	7.91
R1336mzz(Z)	0.6	98.2	0.333	6.29	3,272	7.02	7.63
R1234ze(Z)	0.7	98.3	0.334	6.58	5,784	7.28	7.47
R245fa	0.7	98.2	0.330	6.39	5,499	8.02	8.27

5. Conclusions

The ejector-assisted HTHP used a two-phase ejector to replace an EV, improving energy efficiency and reducing the compressor size. These improvements closely relate to the component-level performance of two-phase ejectors. This study investigated the effects of mixing pressure on the component-level performance of two-phase ejectors and the system-level performance of ejector-assisted HTHPs. A 1D theoretical model was built to predict the fluid dynamic properties of refrigerants within the two-phase ejector and evaluate the ejector's performance. A thermodynamic model of ejector-assisted HTHP was built to evaluate the COP and VHC of HTHPs. Low-GWP refrigerants were selected for the ejector-assisted HTHPs. The effects of the mixing pressure on the component-level performance of two-phase ejectors and the system-level performance of ejector-assisted HTHPs were investigated under specified operating conditions: T_{sink} = 120°C, ΔT_{lift} = 40 K, and ΔT_{SC} = 10 K. The main conclusions are as follows:

(1) An optimum mixing pressure exists in a two-phase ejector, which gives the maximum performance of the two-phase ejector and ejector-assisted HTHP under specified working conditions.
(2) The optimum mixing pressure in a two-phase ejector for HTHPs is slightly lower than the evaporation pressure of SF.
(3) At the optimum mixing pressure, the two-phase flow in a two-phase ejector is subsonic. Choked flow and condensation shock waves do not occur.
(4) A two-phase ejector improves the performance of HTHPs with low-GWP refrigerants. But, the improvement of COP is less than that of transcritical CO_2 HTHPs.

Some limitations of this primary study need to be addressed in future studies. The developed 1D theoretical model of a two-phase ejector adopted constant values for the ejector component isentropic efficiencies. Particularly, the energy loss owing to the difference in the velocity of PF and SF was not considered in the isentropic efficiency of mixing process. These isentropic efficiencies are closely related to the working fluids, the ejector's geometry, and operating conditions. Computational fluid dynamics analysis needs to be employed to determine these isentropic efficiencies. This study provided a comprehensive analysis of the optimum

mixing pressure for ejector-assisted HTHPs operated with specified parameters. The effects of HTHPs operating parameters on the merits of two-phase ejectors needs to be investigated.

Acknowledgments

This work was sponsored by the US Department of Energy's Building Technologies Office under contract No. DE-AC05-00OR22725 with UT-Battelle, LLC. The authors would like to acknowledge the technology manager, Mr. Antonio Bouza, for his support.

NOMENCLATURE

Abbreviations

COP	coefficient of performance
EERC	ejector-assistant vapor compression
EV	expansion valve
GWP	global warming potential
HC	hydrocarbon
HCFO	hydrochlorofluorocarbon
HFC	hydrofluorocarbon
HFO	hydrofluoroolefin
HTHP	high-temperature heat pump
IHX	internal heat exchanger
MW	molecular weight (kg/kmol)
NBP	normal boiling point (°C)
ODP	ozone depletion potential
PF	primary fluid
SC	safety class
SF	secondary fluid
VHC	vapor heating capacity (kJ/m^3)
VRCC	vapor refrigerant compression cycle

Variables

C	speed of sound (m/s)
h	enthalpy of working fluids (kJ/kg)
$\dot{m}$	mass flow rate (kg/s)
M	Mach number
T	temperature (°C)
Q	thermal capacity (kW)
W	power (kJ/kg)
V	velocity (m/s)
x	quality of vapor
ρ	density (kg/m^3)
α	void fraction of two-phase flow
η	component efficiency
Π	pressure lift ratio in ejector
ϕ	velocity coefficient in ejectors
ω	entrainment ratio

Subscripts

1, 2, 3,…	state points within the loop of ejector heat pumps
lv	latent heat of evaporation
D	diffuser
disch	discharged vapor from the compressor

M	mixing chamber
max	maximum
N	primary nozzle of ejector
i, ii, iii, …	state points within an ejector
r	recovery
opt	optimum
S	suction chamber
SC	supercooling
suc	suction vapor into the compressor

References

[1] C. Arpagaus, F. Bless, M. Uhlmann, J. Schiffmann, and S. S. Bertsch, "High temperature heat pumps: Market overview, state of the art, research status, refrigerants, and application potentials," *Energy,* vol. 152, pp. 985-1010, 2018/06/01/ 2018, doi: https://doi.org/10.1016/j.energy.2018.03.166.

[2] S. Elbel, "Historical and present developments of ejector refrigeration systems with emphasis on transcritical carbon dioxide air-conditioning applications," *International Journal of Refrigeration,* vol. 34, no. 7, pp. 1545-1561, 2011/11/01/ 2011, doi: https://doi.org/10.1016/j.ijrefrig.2010.11.011.

[3] S. Elbel and N. Lawrence, "Review of recent developments in advanced ejector technology," *International Journal of Refrigeration,* vol. 62, pp. 1-18, 2016/02/01/ 2016, doi: https://doi.org/10.1016/j.ijrefrig.2015.10.031.

[4] M. Palacz, J. Bodys, M. Haida, J. Smolka, and A. J. Nowak, "Two-phase flow visualisation in the R744 vapour ejector for refrigeration systems," *Applied Thermal Engineering,* vol. 210, p. 118322, 2022.

[5] P. Gullo, M. R. Kærn, M. Haida, J. Smolka, and S. Elbel, "A review on current status of capacity control techniques for two-phase ejectors," *International Journal of Refrigeration,* vol. 119, pp. 64-79, 2020/11/01/ 2020, doi: https://doi.org/10.1016/j.ijrefrig.2020.07.014.

[6] K. Ameur, Z. Aidoun, and M. Ouzzane, "Experimental performances of a two-phase R134a ejector," *Experimental Thermal and Fluid Science,* vol. 97, pp. 12-20, 2018/10/01/ 2018, doi: https://doi.org/10.1016/j.expthermflusci.2018.03.034.

[7] M. N. Šarevski and V. N. Šarevski, "Characteristics of R718 refrigeration/heat pump systems with two-phase ejectors," *International Journal of Refrigeration,* vol. 70, pp. 13-32, 2016/10/01/ 2016, doi: https://doi.org/10.1016/j.ijrefrig.2016.07.007.

[8] Y. Jeon, S. Kim, D. Kim, H. J. Chung, and Y. Kim, "Performance characteristics of an R600a household refrigeration cycle with a modified two-phase ejector for various ejector geometries and operating conditions," *Applied Energy,* vol. 205, pp. 1059-1067, 2017.

[9] Y. Gao, G. He, D. Cai, and M. Fan, "Performance evaluation of a modified R290 dual-evaporator refrigeration cycle using two-phase ejector as expansion device," *Energy,* vol. 212, p. 118614, 2020/12/01/ 2020, doi: https://doi.org/10.1016/j.energy.2020.118614.

[10] Y. Jeon, J. Jung, D. Kim, S. Kim, and Y. Kim, "Effects of ejector geometries on performance of ejector-expansion R410A air conditioner considering cooling seasonal performance factor," *Applied Energy,* vol. 205, pp. 761-768, 2017.

[11] Z. Zhang, X. Feng, D. Tian, J. Yang, and L. Chang, "Progress in ejector-expansion vapor compression refrigeration and heat pump systems," *Energy Conversion and Management,* vol. 207, p. 112529, 2020/03/01/ 2020, doi: https://doi.org/10.1016/j.enconman.2020.112529.

[12] M. Popovac, M. Lauermann, A. Baumhakel, and G. Drexler-Schmid, "Performance analysis of a high-temperature heat pump with ejector based on butane as the refrigerant," in *12th IEA Heat Pump Conference, Vienna, Austria*, 2017.

[13] T. Bai, G. Yan, and J. Yu, "Thermodynamic assessment of a condenser outlet split ejector-based high temperature heat pump cycle using various low GWP refrigerants," *Energy,* vol. 179, pp. 850-862, 2019/07/15/ 2019, doi: https://doi.org/10.1016/j.energy.2019.04.191.

[14] B. Luo and P. Zou, "Performance analysis of different single stage advanced vapor compression cycles and refrigerants for high temperature heat pumps," *International Journal of Refrigeration,* vol. 104, pp. 246-258, 2019.

[15] C. Mateu-Royo, C. Arpagaus, A. Mota-Babiloni, J. Navarro-Esbrí, and S. S. Bertsch, "Advanced high temperature heat pump configurations using low GWP refrigerants for industrial waste heat recovery: A comprehensive study," *Energy Conversion and Management,* vol. 229, p. 113752, 2021/02/01/ 2021, doi: https://doi.org/10.1016/j.enconman.2020.113752.

[16] A. A. Kornhauser, "The use of an ejector as a refrigerant expander," presented at the International Refrigeration and Air Conditioning Conference, West Lafayette, IN, United States 1990, 82. [Online]. Available: https://docs.lib.purdue.edu/iracc/82/.

[17] D. Li and E. A. Groll, "Transcritical CO2 refrigeration cycle with ejector-expansion device," *International Journal of refrigeration,* vol. 28, no. 5, pp. 766-773, 2005.

[18] H. K. Ersoy and N. Bilir Sag, "Preliminary experimental results on the R134a refrigeration system using a two-

phase ejector as an expander," *International Journal of Refrigeration,* vol. 43, pp. 97-110, 2014/07/01/ 2014, doi: https://doi.org/10.1016/j.ijrefrig.2014.04.006.

[19] J. Sarkar, "Optimization of ejector-expansion transcritical CO2 heat pump cycle," *Energy,* vol. 33, no. 9, pp. 1399-1406, 2008/09/01/ 2008, doi: https://doi.org/10.1016/j.energy.2008.04.007.

[20] J.-q. Deng, P.-x. Jiang, T. Lu, and W. Lu, "Particular characteristics of transcritical CO2 refrigeration cycle with an ejector," *Applied Thermal Engineering,* vol. 27, no. 2, pp. 381-388, 2007/02/01/ 2007, doi: https://doi.org/10.1016/j.applthermaleng.2006.07.016.

[21] M. Purjam, K. Thu, and T. Miyazaki, "Thermodynamic modeling of an improved transcritical carbon dioxide cycle with ejector: Aiming low-temperature refrigeration," *Applied Thermal Engineering,* vol. 188, p. 116531, 2021/04/01/ 2021, doi: https://doi.org/10.1016/j.applthermaleng.2020.116531.

[22] N. Lawrence and S. Elbel, "Experimental investigation of a two-phase ejector cycle suitable for use with low-pressure refrigerants R134a and R1234yf," *International Journal of Refrigeration,* vol. 38, pp. 310-322, 2014/02/01/ 2014, doi: https://doi.org/10.1016/j.ijrefrig.2013.08.009.

[23] A. U. Atmaca, A. Erek, and O. Ekren, "Impact of the mixing theories on the performance of ejector expansion refrigeration cycles for environmentally-friendly refrigerants," *International Journal of Refrigeration,* vol. 97, pp. 211-225, 2019/01/01/ 2019, doi: https://doi.org/10.1016/j.ijrefrig.2018.09.013.

[24] Y. Zhu and P. Jiang, "Experimental and numerical investigation of the effect of shock wave characteristics on the ejector performance," *International Journal of Refrigeration,* vol. 40, pp. 31-42, 2014.

[25] Y. Liu, M. Yu, and J. Yu, "An improved 1-D thermodynamic modeling of small two-phase ejector for performance prediction and design," *Applied Thermal Engineering,* vol. 204, p. 118006, 2022/03/05/ 2022, doi: https://doi.org/10.1016/j.applthermaleng.2021.118006.

[26] F. Liu and E. A. Groll, "Study of ejector efficiencies in refrigeration cycles," *Applied Thermal Engineering,* vol. 52, no. 2, pp. 360-370, 2013/04/15/ 2013, doi: https://doi.org/10.1016/j.applthermaleng.2012.12.001.

[27] Ø. Wilhelmsen, A. Aasen, K. Banasiak, H. Herlyng, and A. Hafner, "One-dimensional mathematical modeling of two-phase ejectors: Extension to mixtures and mapping of the local exergy destruction," *Applied Thermal Engineering,* p. 119228, 2022.

[28] S. Elbel and P. Hrnjak, "Ejector refrigeration: an overview of historical and present developments with an emphasis on air-conditioning applications," presented at the International Refrigeration and Air Conditioning Conference, 2008, 884.

[29] B. Huang, J. Chang, C. Wang, and V. Petrenko, "A 1-D analysis of ejector performance," *International journal of refrigeration,* vol. 22, no. 5, pp. 354-364, 1999.

[30] A. Mota-Babiloni, C. Mateu-Royo, J. Navarro-Esbrí, F. Molés, M. Amat-Albuixech, and Á. Barragán-Cervera, "Optimisation of high-temperature heat pump cascades with internal heat exchangers using refrigerants with low global warming potential," *Energy,* vol. 165, pp. 1248-1258, 2018/12/15/ 2018, doi: https://doi.org/10.1016/j.energy.2018.09.188.

[31] M. Nilsson, H. N. Rislå, and K. Kontomaris, "Measured performance of a novel high temperature heat pump with HFO-1336mzz (Z) as the working fluid," in *12th IEA Heat Pump Conference*, 2017, pp. 14-17.

[32] E. Navarro-Peris, J. M. Corberán, L. Falco, and I. O. Martínez-Galván, "New non-dimensional performance parameters for the characterization of refrigeration compressors," *International Journal of Refrigeration,* vol. 36, no. 7, pp. 1951-1964, 2013/11/01/ 2013, doi: https://doi.org/10.1016/j.ijrefrig.2013.07.007.

[33] C. Mateu-Royo, J. Navarro-Esbrí, A. Mota-Babiloni, and Á. Barragán-Cervera, "Theoretical performance evaluation of ejector and economizer with parallel compression configurations in high temperature heat pumps," *International Journal of Refrigeration,* vol. 119, pp. 356-365, 2020.

[34] S. Elbel and P. S. Hrnjak, "EFFECT OF INTERNAL HEAT EXCHANGER ON PERFORMANCE OF TRANSCRITICAL C02 SYSTEMS WITH EJECTOR," 2004.

[35] S. Elbel and P. Hrnjak, "Experimental validation of a prototype ejector designed to reduce throttling losses encountered in transcritical R744 system operation," *International Journal of Refrigeration,* vol. 31, no. 3, pp. 411-422, 2008.

[36] D. Wu, B. Hu, R. Z. Wang, H. Fan, and R. Wang, "The performance comparison of high temperature heat pump among R718 and other refrigerants," *Renewable Energy,* vol. 154, pp. 715-722, 2020/07/01/ 2020, doi: https://doi.org/10.1016/j.renene.2020.03.034.

[37] F. Wang, D. Y. Li, and Y. Zhou, "Analysis for the ejector used as expansion valve in vapor compression refrigeration cycle," *Applied Thermal Engineering,* vol. 96, pp. 576-582, 2016/03/05/ 2016, doi: https://doi.org/10.1016/j.applthermaleng.2015.11.095.

[38] D. Buyadgie, O. Buyadgie, S. Artemenko, A. Chamchine, and O. Drakhnia, "Conceptual design of binary/multicomponent fluid ejector refrigeration systems," *International Journal of Low-Carbon Technologies,* vol. 7, no. 2, pp. 120-127, 2012.

14th IEA Heat Pump Conference
15-18 May 2023, Chicago, Illinois

Comparison of seasonal energy efficiency of different compressor types

Christian Stahel[a], Lukas Wick[a], Frank Tillenkamp[a,*], Silvan Steiger[a], Manuel Diem[a]

[a]Zurich Unviersity of Applied Sciences, Institute of Energy Systems and Fluid Engineering, Technikumstrasse 9, 8400 Winterthur, Switzerland

Abstract

In this work, the energetic behavior of compressor types was investigated and an evaluation method was developed to compare them under variable load profiles and locations. The numerous compressor maps, locations and load profiles lead to a very large number of possible combinations. For the efficient evaluation a freely available compressor tool has been developed which compares the different compressor types. The core of the tool is a database with compressor polynomials of more than 1400 compressors from different manufactures. The same compressor types from different manufacturers we grouped together to represent an average energy performance. Compressor characteristic maps were created which visualize the behavior of each compressor type as well as their application limits and control range. An evaluation method is used to determine the seasonal energy efficiency of the different compressor types depending on the location, load profile and application. The method is based on several operating points, which are weighted according to their energetic share of the annual consumption. Based on the maps, the seasonal efficiency of the compressor types is determined and ranked.

© HPC2023.
Selection and/or peer-review under the responsibility of the organizers of the 14th IEA Heat Pump Conference 2023.

Keywords: Compressor types, compressor characteristic map, seasonal efficiency

1. Introduction

The benefits of refrigeration technologies towards a sustainable energy system are undisputed. The market share of refrigeration machines and heat pump is increasing rapidly. The shortage of skilled workers is therefore becoming a major problem for the industry. On behalf of the Swiss Federal Office of Energy, we developed a freely available tool [4] to support planners in the selection of the optimal compressor type. The focus of this investigation is on air-conditioning and commercial refrigeration applications.

The aim of this work is an energetic comparison of different compressor types based on the data provided by the manufacturers. The performance data of compressors are provided in the form of polynomials and are regulated in the EN 12900 [1] standard. The behavior of the compressors can be summarized in compressor maps. Compressor maps are often created for turbo compressors in the form of shell curves [5][6][7]. However, compressor maps in refrigeration technology are usually not available.

In this study, compressor maps for different compressors were created based on the performance data of the compressor polynomials.

The seasonal comparison of refrigeration machines is regulated in EN 14825 [2]. Here, the seasonal efficiency is determined based on several operating points, which are weighted according to their energetic share. The energy weighting is based on hourly frequencies of ambient temperatures and load profiles. In this study, the SEER evaluation method was adapted to compressors. This allows a seasonal assessment of

* Corresponding author. Tel.: +41 (0) 58 934 73 61.
E-mail address: frank.tillenkamp@zhaw.ch

compressor types based on data provided by the manufacturers. For this purpose, compressor maps are combined with load profiles and weather data.

2. Compressor characteristic maps

The representation of compressor performance data is defined in the EN 12900 [1] standard. Compressor polynomials can be used to determine cooling capacity $\dot{Q}_0$, electrical power consumption P_{el} and refrigerant mass flow $\dot{m}$ as a function of evaporating temperature T_0 and condensing temperature T_c. The compressor polynomials are only valid for a specific frequency, overheating and subcooling. Therefore, several polynomials are required for each compressor to represent the compressor map. Table 1 shows an overview of the collected polynomials.

Table 1. Overview compressor polynomial parameters

Refrigerant	overheating	subcooling	frequency
R1234ze / R454B / R513A / R449A / R744	10 K	0 K	f_{min} - f_{max}
R290	20 K	0 K	f_{min} - f_{max}
R717	5 K	0 K	f_{min} - f_{max}

The coefficients of the compressor polynomials are available in the design tools of the manufacturers. Manufacturers who do not provide their compressor data could not be considered in this study. For turbo compressors are no performance polynomials according to EN 12900 available, therefore only individual operating points are given. These were calculated using the manufacturers' design tools.

Additional quantities such as Coefficient of Performance COP, final compression temperature T_2 and isentropic compressor efficiency η_{is} can be calculated directly from the given compressor polynomials.

2.1. Database (compressor polynomials)

The application of the refrigeration machine has a strong impact on the evaporating temperature of the plant. Therefore, three different applications with different design points are considered in this study. Depending on the application, various refrigerants and design capacities were investigated. Table 2 shows an overview of the selections considered.

Table 2. Overview selections

Application	Design Point (T_0 / T_c)	Design capacity ($\dot{Q}_{0_design}$)	Refrigeration
Air conditioning	5 / 45 °C	20 / 50 / 100 / 300 kW	R1234ze / R290 / R454B / R513A / R717 / R744
Medium temperature	-10 / 45 °C	2 / 10 / 50 / 100 kW	R449A / R513A / R744
Low temperature	-30 / 40 °C	1 / 5 / 25 / 50 kW	R449A / R744

Any combination of application, refrigeration capacity and refrigerant for each compressor type represents a selection. For each selection, compressor data from several manufacturers are collected according to the parameters shown in Table 1. In total, more than 1400 compressors were considered. Figure 1 shows the collected data for semi-hermetic propane reciprocating compressors with a design capacity $\dot{Q}_{0_design}$ of 50 kW ± 30% from various manufacturers.

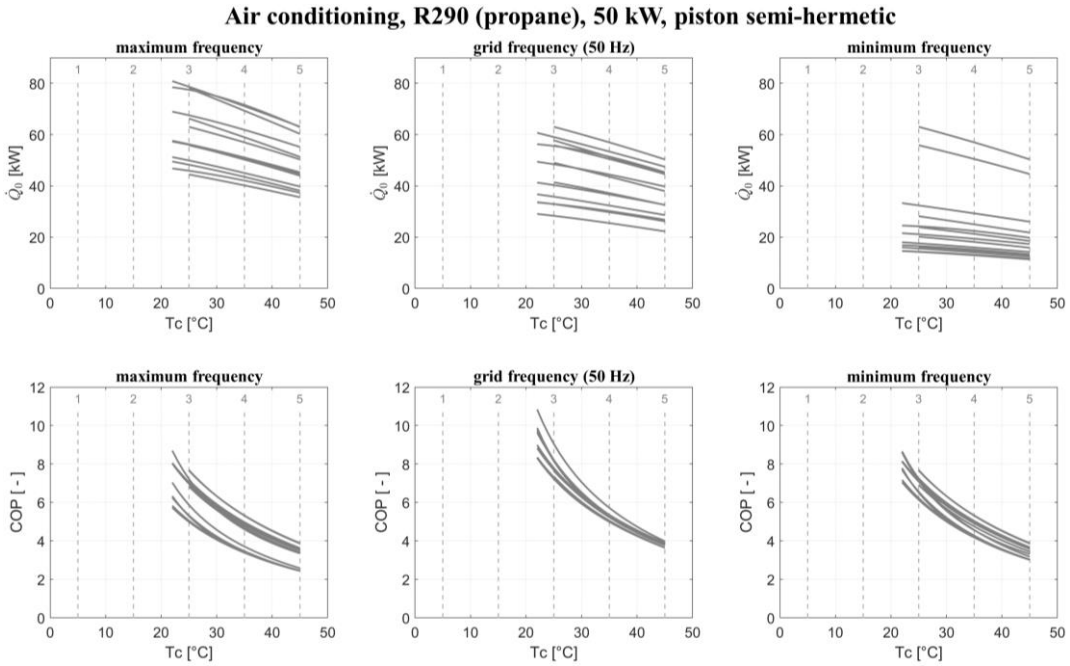


Fig. 1. Compressor data of a selection

In Figure 1 the cooling capacity $\dot{Q}_0$ and the Coefficient of Performance COP of each compressor as a function of the condensing temperature T_c at various frequencies are illustrated. The evaporating temperature T_0 is constant according to the design point. The deviations of $\dot{Q}_0$ at the maximum frequency with T_c = 45 °C are due to the capacity range considered ($\dot{Q}_{0_design}$ ± 30%). It should be noted that the frequency range may differ depending on the manufacturer. Additionally, the operating limit $T_{c,min_}$ of each compressor is taken into account.

2.2. Neutralization

The aim of this study is to compare different types of compressors. To prevent direct comparison between manufacturers, neutralization is applied. In the following, it will be shown how this neutralization is implemented. The compressor data from different manufacturers are combined into one average compressor with each manufacturer equally weighted. This resulting compressor represents the average behavior of the compressor type in the specific selection. Figure 2 shows the compressor characteristic map for the neutralized compressor. This compressor map is based on the twelve individual compressors shown in figure 1.

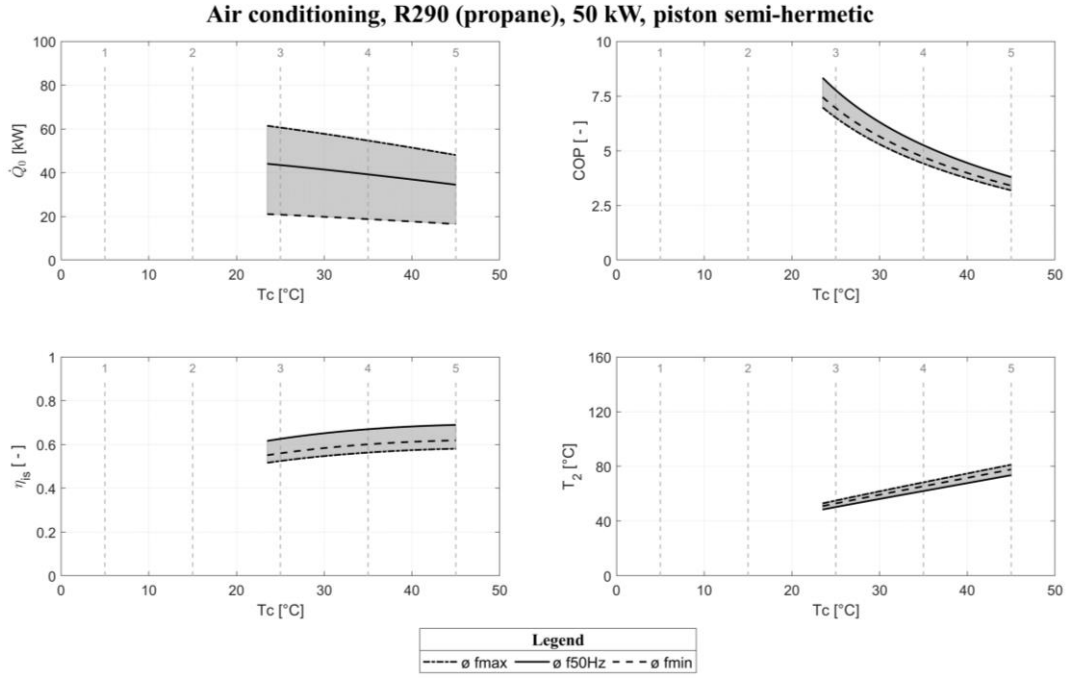


Fig. 2. Compressor characteristic map of a semi-hermetic propane reciprocating compressor

In Figure 2 the compressor characteristic map of a semi-hermetic propane reciprocating compressor with a $\dot{Q}_{0_design}$ of 50 kW for air conditioning applications (T_0 = 5 °C) is shown. The curve of the cooling capacity $\dot{Q}_0$ at different frequencies shows the control range at variable condensing temperatures T_c. The left end of the characteristic diagram corresponds to the average operating limit. The right diagram shows the course of the COP at different frequencies.

The compressor maps are the basis for seasonal efficiency considerations. However, they also allow an assessment of conceptual considerations when planning a plant. For example, the effects of oversized refrigeration systems or compressors can be easily estimated from the compressor map.

2.3. Comparison of different compressor maps

A total of 70 compressor maps were created during the investigation. These maps are located in the appendix of the final project report [3]. To show the differences between the compressor types, sizes or refrigerants used, the compressor maps were also compared. This comparison illustrates the deviations in efficiency, operating limits, and control range. Therefore, this comparison is a very comprehensive resource. Figure 3 is pointing out the deviation of different compressor types with a 2 kW design capacity and the refrigerant R513A. Further comparisons for other selections can be seen in the final report [3].

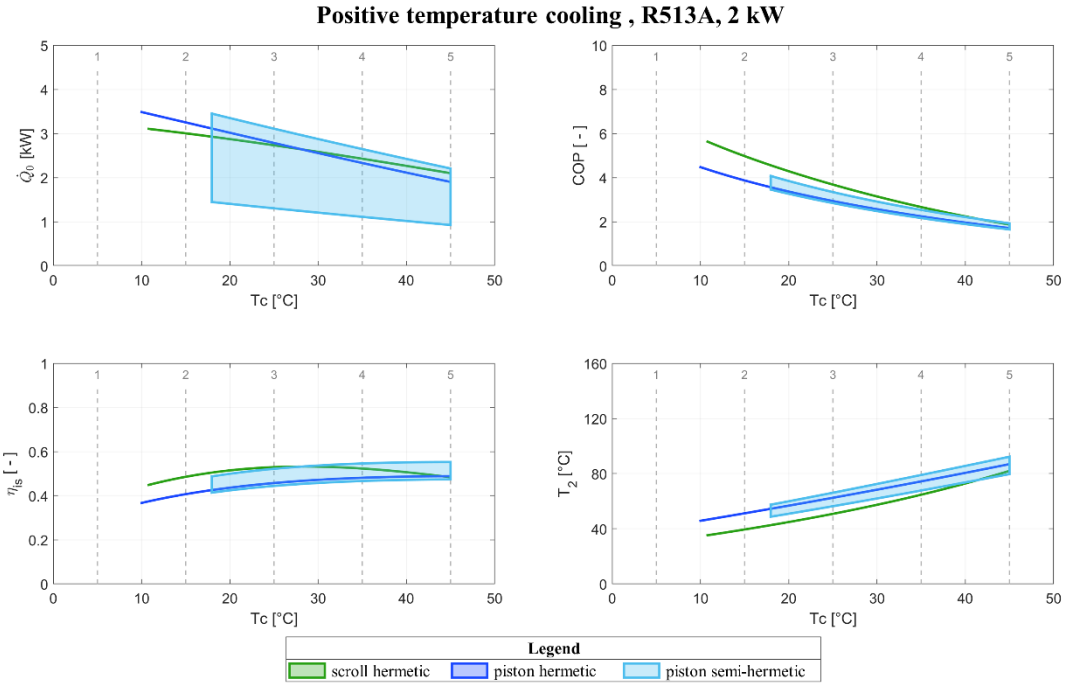


Fig. 3. Comparison compressor characteristic map of different compressor types

The selection in Figure 3 compares compressor types in medium temperature application (T_0 = -10 °C). Due to the small design capacity $\dot{Q}_{0_design}$ selected, no turbo or screw compressors are available. The hermetic piston and scroll compressors don't have capacity control, the compressor map therefore merges into one curve.

At the design point (T_c = 45 °C), the cooling capacity $\dot{Q}_0$ of the reciprocating compressor and the scroll compressor is almost identical. If the condensing temperature T_c is reduced, the cooling capacity $\dot{Q}_0$ of the reciprocating compressor increases significantly more than the one of the scroll compressor. As a result of re-expansion, the volumetric efficiency of the reciprocating compressor increases more in comparison to the scroll compressor if a small pressure differential is applied. Therefore, mass flow of the reciprocating compressor and thus capacity $\dot{Q}_0$ increase over-proportionally at low condensing temperatures T_c.

The internal pressure ratio is particularly characteristic for the behavior of the scroll compressor. This can be seen in the curve of the isentropic compressor efficiency η_{is}. If the pressure ratio of the system and the internal pressure ratio of the compressor match, high efficiencies are achieved. If the compressor is operated at a different pressure ratio, the efficiency is increasingly reduced. When selecting a scroll compressor, it is therefore important to ensure that the internal pressure ratio is at an energetically relevant operating point.

3. Seasonal energy efficiency evaluation method (aCOP)

The seasonal energy efficiency ratio SEER is a seasonal assessment of chillers and is defined in EN 14825. However, due to the different system boundaries as shown in figure 4, the ratio cannot be used to evaluate compressors. For the evaluation of compressor types, the ratio aCOP (annual coefficient of performance) is defined. The methodology of the aCOP is very much based on the existing ratio (SEER) of chillers in part-load operation and is an energetic analysis. The aCOP is calculated according to Eq 1.

$$aCOP = \sum_{i=1}^{5} w_i \cdot c_i \cdot COP_i \qquad (1)$$

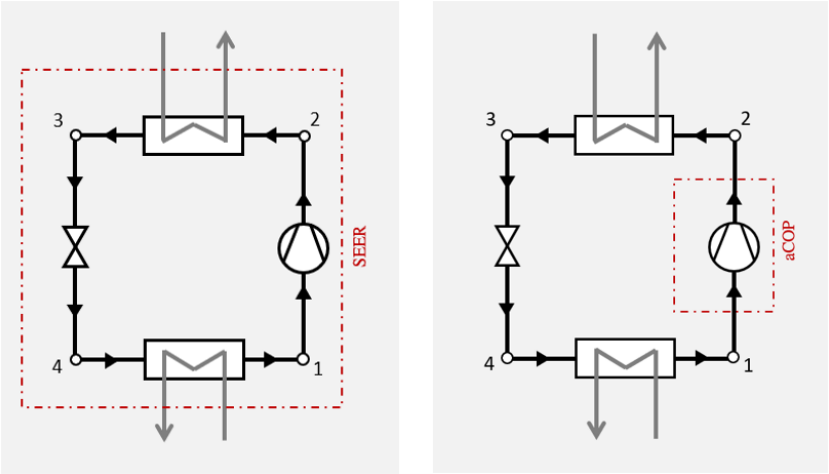


Fig. 4. System boundary SEER and aCOP

To compare different chillers, EN 14825 tests chillers under identical inlet and outlet temperatures in the evaporator and condenser. The temperatures and load profiles are defined to determine a seasonal behavior. The aCOP applies the same methodology to the system boundary compressor. Different compressors are compared under the same evaporating and condensing temperatures.

To calculate the annual coefficient of performance aCOP the compressor maps are combined with load profiles and hourly frequencies of ambient temperatures. This ratio is based on five operating points. The COP of the compressor COP_i is determined from the compressor map. The energetic share of the annual consumption w_i is calculated from the load profile and the hourly frequency of the ambient temperatures. If the cooling capacity of the compressor cannot be adapted to the cooling demand due to the limitations of the capacity control, the COP at the operating point is reduced with a type-dependent cycle factor c_i. In this study, several load profiles and Swiss locations were investigated. The impact of location and load profile are shown in Figure 5.

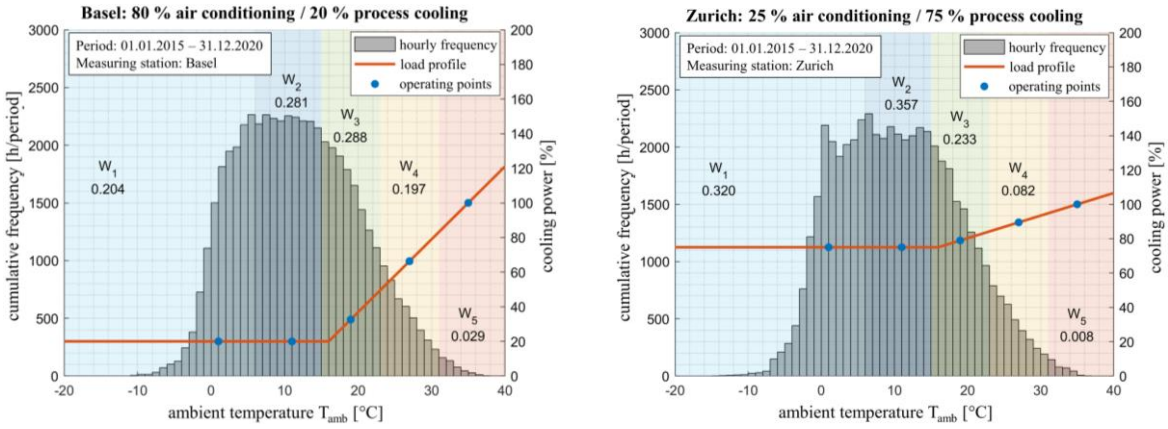


Fig. 5. Influence of location and load profile on weighting

Figure 6 shows the influence of load profile and location on the weighting of the individual operating points. The location has an impact on the frequency of ambient temperatures T_{amb}. This can be seen from the heights of the bars. The load profile shows the cooling capacity $\dot{Q}_0$ in relation to the ambient temperature T_{amb}. The weather data are taken from the data portal IDAweb of the Federal Office of Meteorology and Climatology MeteoSwiss. The hourly average temperature of the years 2015-2020 is used.

3.1. Compressor performance

To determine the coefficient of performance COP of the compressor from the compressor map, the cooling demand $\dot{Q}_{dem}$, evaporating temperature T_0 and condensing temperature T_c has to be defined. The cooling

demand and evaporating temperature are given due to the load profile and application. The condensing temperature depends on the ambient temperature T_{amb} and the operating limit T_{c_min} of the compressor. Thus, the operating point of the compressor may vary depending on the compressor type. Table 3 shows the correlation between the ambient temperature T_{amb} and the condensing temperature T_c regarding the operating limit T_{c_min} of the compressor.

Table 3. Operating Points

Operating point	T_{amb} [°C]	ΔT [°C]	$T_{c_theoretical}$ [°C]	T_{c_min} [°C]	T_c [°C]
1	1	4	5	10	10
2	11	4	15	10	15
3	19	6	25	10	25
4	27	8	35	10	35
5	35	10	45	10	45

The temperature difference ΔT between ambient temperature T_{amb} and theoretical condensing temperature $T_{c_theoretical}$ is not constant for all operating points. This is because the temperature differences dT in the heat exchangers become smaller in part-load operation. The defined temperature differences correspond to an application with dry cooler. If the theoretical condensing temperature $T_{c_theoretical}$ is smaller than the compressor operating limit T_{c_min}, the condensing temperature T_c will be adjusted. The impact of the compressor map on the operating point is shown in Fig. 6.

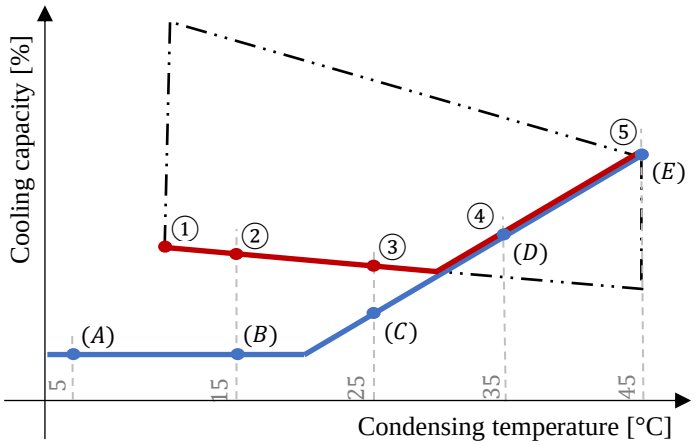


Fig. 6. Influence of compressor map on operating points

Figure 6 shows the differences between theoretical conditions and operating conditions. The theoretical conditions (A-E) resulting from the ambient temperatures T_{amb} and the cooling demand $\dot{Q}_{dem}$ based on the load profile (blue). The operating conditions (① - ⑤) are resulting from the combination of compressor map and theoretical conditions. The operating conditions (red) are therefore depending on the operating limits and control range of the compressor. Thus, the operating points of the compressor types may differ at the same ambient temperatures.

3.2. Operating mode

The cycling factor c_i is determined from the combination of load profile and compressor map. If the cooling demand $\dot{Q}_{dem}$ is within the compressor map, the compressor can modulate and adapt the compressor capacity $\dot{Q}_{comp}$ to the cooling demand. If the cooling demand is less than the cooling capacity at minimum frequency, the compressor goes into on-off operation. This short cycling has a negative influence on the efficiency. The operating mode thus has an influence on the efficiency of the compressor and is considered by a cycling factor c_i. The cycling factor c_i depends on the compressor type and the difference between the

cooling demand $\dot{Q}_{dem}$ of the consumer and the cooling capacity of the compressor $\dot{Q}_{comp}$ and is calculated according to the equations 2 and 3.

$$c_i = \frac{f_{load}}{f_V * f_{load} + (1 - f_V)} \tag{2}$$

$$\mathrm{f}_{load} = \frac{\dot{Q}_{dem}}{\dot{Q}_{comp}} \tag{3}$$

The calculation of the cycling factor c_i is very similar to EN 14825. First, according to equation 3, the load factor f_{load} is calculated from the cooling demand $\dot{Q}_{dem}$ and the capacity of the compressor $\dot{Q}_{comp}$. The load factor f_{load} can take values between 0 and 1 and becomes smaller the more the compressor is short cycling. Subsequently, the cycling factor c_i can be calculated according to equation 2. For this, the load factor f_{load} and the reduction factor f_v of the compressor type are required. The reduction factor can be determined using Table 4.

Table 4. Reduction factor compressor types

Compressor Type	f_v
Rolling piston	0.9
Scroll	0.9
Reciprocating	0.9
Screw	0.85
Turbo	0.8

As shown in Table 4, the reduction factor f_v depends on the compressor type. This is since the influence of the on-off operation on the efficiency varies depending on the compressor type. A turbo compressor has very high speeds and therefore requires energetically demanding switch-on and switch-off routines. For this reason, the differences in compressor types are addressed in the reduction factor f_v. It should be mentioned that the values of the factors were defined in consultation with experts. In further investigations, the values can be validated and optimized.

3.3. Energetic weighting

The concept of energy weighting is already shown in Figure 4. Each operating point covers a range of ambient temperatures T_{amb}. The weighting of the operating point is the ratio of the cooling load in the temperature range to the annual cooling load and is calculated according to equation 3.

$$\mathrm{w}_x = \frac{\sum_{x_{min}}^{x_{max}} (h_i * \dot{Q}_{demand_i})}{\sum_{-20}^{40} (h_i * \dot{Q}_{demand_i})} \tag{4}$$

The weighting factors are depending on the load profile as well as the location. The location defines how many hours a year a certain ambient temperature h_i occurs. The load profile determines the cooling demand $\dot{Q}_{dem}$ at a certain ambient temperature. The cooling load corresponds to the product of cooling demand and frequency at a specific ambient temperature. The sum of all weighting factors is always 1. The temperature ranges of the operating points are shown in table 5.

Table 5. Temperature range weighting factors

Weighting factor	Temperature Range	
	Min.	Max.
w_1	-20 °C	6 °C
W_2	6 °C	15 °C
W_3	15 °C	23 °C
W_4	23 °C	31 °C
W_5	31 °C	40 °C

4. Results

4.1. Compressor characteristic maps

In this study, manufacturer-neutral compressor maps were created for different compressor types, refrigerants, and sizes. The characteristic compressor maps can be used regardless of the presented evaluation method (aCOP) and show their seasonal behavior. Based on the information presented, such as the operating limits, control range or efficiencies, many conceptual impacts can be estimated. In particular, the comparison of compressor maps as shown in Figure 7 clarify the differences between compressor types.

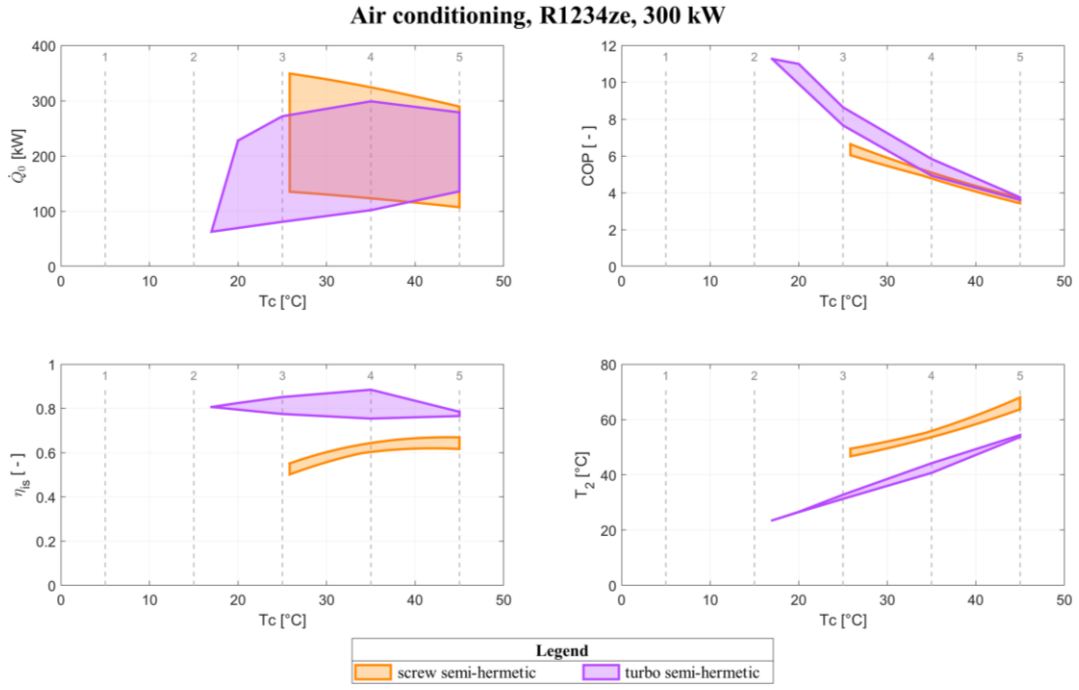


Fig. 7. Comparison of compression principles

Figure 7 shows the deviation between a displacement compressor (screw) and a fluid machine (turbo). In particular, the trend of the cooling capacity $\dot{Q}_0$ as a function of the condensing temperature T_c is most interesting. Cooling demand decreased in many applications as ambient temperatures dropped. Turbo compressors can modulate the cooling capacity $\dot{Q}_0$ to a much greater extent as the condensing temperature T_c drops. It should be noted that the compressor data of the turbo compressors do not consist of polynomials according to EN 12900.

4.2. Seasonal energy efficiency evaluation method (aCOP)

The presented evaluation methodology combines compressor maps with load profiles and weather data from locations and allows an energetic comparison of compressor types. Due to the large number of applications,

refrigerants, cooling capacities, load profiles and locations investigated, a very large number of results have been obtained.

For the efficient evaluation of a specific plant, a compressor tool has been developed which compares compressor types on the basis of a few parameters and supports the selection of the optimum compressor type by providing further additional information. The tool can be downloaded free of charge from the Federal Office for Energy [4]. Figure 8 shows an example of the evaluation of a selection.

Ranking	Compressor-Type	Anual Coefficient of Performance		t_amb	t_c	COP Average	COP Low - Best	Load Profile
1	Reciprocating semi hermetic	**aCOP (Average)**	**6.4**	1 °C	19 °C	8.3	(5.9 - 10.0)	4 kW
				11 °C	19 °C	8.3	(5.9 - 10.0)	4 kW
				19 °C	25 °C	6.4	(4.8 - 7.6)	6.5 kW
		aCOP (Low - Best)	(4.7 - 7.6)	27 °C	35 °C	4.7	(3.9 - 5.1)	13 kW
				35 °C	45 °C	3.1	1.9 - 3.4)	20 kW
2	Scroll hermetic	**aCOP (Average)**	**5**	1 °C	21 °C	7.5	(6.8 - 8.5)	4 kW
				11 °C	21 °C	7.5	(6.8 - 8.5)	4 kW
				19 °C	25 °C	6.6	(6.1 - 7.1)	6.5 kW
		aCOP (Low - Best)	(4.4 - 5.6)	27 °C	35 °C	5	(4.7 - 5.3)	13 kW
				35 °C	45 °C	3.7	(3.4 - 3.9)	20 kW
3	Reciprocating hermetic	**aCOP (Average)**	**4.1**	1 °C	16 °C	7.1	(6.3 - 7.9)	4 kW
				11 °C	16 °C	7.1	(6.3 - 7.9)	4 kW
				19 °C	25 °C	5.6	(5.2 - 5.9)	6.5 kW
		aCOP (Low - Best)	(3.7 - 4.5)	27 °C	35 °C	4.3	(4.1 - 4.4)	13 kW
				35 °C	45 °C	3.2	(3.1 - 3.3)	20 kW

Fig. 8. Example results compressor tool

Figure 8 shows the ranking of R513A compressors with a cooling capacity of 20 kW in an air conditioning application. Only scroll and reciprocating compressors are available in this capacity range. The ranking is made according to the average aCOP. This is calculated according to equation 1. The aCOP average is determined from all compressors in the selection. In addition, the aCOP of the best and worst compressor of the selection (low – best) as well as details of the individual operating points are shown. The results of the tool were randomly checked by the experts who accompanied the project.

5. Conclusion

The created compressor maps are a tool to estimate conceptual considerations. The representation of the seasonal behavior in combination with the control range and the operating limit allow a very comprehensive comparison. This is especially helpful for prospective professionals to better understand the differences in compressor types.

Some of the compressor manufacturers were in the process of converting their product line to the refrigerants studied. Therefore, it is possible that certain compressor data were not yet available at the time of data collection and are therefore not shown. The data basis for the creation of the compressor maps should therefore be updated later. In addition, further distinctions (e.g. three-phase asynchronous motors or permanent magnet motors) could be made to further subdivide the maps in order to better represent differences between series.

The polynomials provided by the manufacturers allow very extensive comparisons regarding the seasonal efficiency of compressors. The evaluation method developed in this thesis adapts the methodology of the SEER to a compressor and allows a seasonal comparison based on different weather data and load profiles. Both the operating limits and the control range of the compressor are taken into account.

The operating limit of a chiller is defined by the most restrictive component. For compressors with a large operating range, it is therefore possible that the operating range is reduced by other components (e.g. expansion valve). This was not considered in this study and can be improved in further investigations.

Especially for large refrigeration capacities, several compressors are often operated in parallel. This increases the operational reliability due to redundancies and increases the control range of the refrigeration machine. In a next step, the evaluation method should be extended so that circuits with several compressors can also be evaluated.

The results show that in particular the desired refrigerant as well as the required refrigerating capacity strongly limit the available compressor types. The tool developed in this work checks which compressor designs are available for a given refrigeration capacity and refrigerant. Subsequently, the available compressor types are compared based on the defined location and load profile according to the method defined in this paper. The result is a ranking of the available compressor types according to aCOP.

The results of the tool were reviewed by the experts. To identify errors in the data acquisition (compressor polynomials) or evaluation method (aCOP), additional checks (e.g. by manufacturers) are useful.

Acknowledgements

The Authors would like to thank the Swiss Federal Office of Energy for their financial support in this project. In particular Mr. Martin Stettler is expressly thanked. Thanks for the valuable support and constructive cooperation also go to the contributing experts Claudio Müller, Jonas Schönenberger, Matthias Brügger, Rolf Löhrer, Robert Dumortier, Michael Kriegers and Thomas Lang.

Nomenclature and Abbreviations

$aCOP$	Annual coefficient of Performance	T_{amb}	Ambient temperature
T_0	Evaporating temperature	ΔT	Temperature difference
T_C	Condensing temperature	SEER	Seasonal Energy Efficiency Ratio

References

[1] EN 12900:2013 Refrigerant compressors - Rating conditions, tolerances and presentation of manufacturer's performance data, European Committee for Standardization CEN, Brussels BE.

[2]] EN 14825:2019 Air conditioners, liquid chilling packages and heat pumps, with electrically driven compressors, for space heating and cooling - Testing and rating at part load conditions and calculation of seasonal performance. European Committee for Standardization CEN, Brussels BE.

[3] C. Stahel, L. Wick, and F. Tillenkamp, “Kälteverdichter – Schlüssel zur Energieeffizienz und Betriebssicherheit” IEFE Energy Paper, Feb. 2022.

[4] Energie Schweiz. Verdichter-Tool BFE www.bfe.admin.ch

[5] H. Desmidt, K. Ekici and K. Young, „Computationally Efficient Axial Compressor Characteristic Map Generation Based on 1-D Meanline Approximation,“ Knoxville, Tennessee, 12.07.2013.

14th IEA Heat Pump Conference
15-18 May 2023, Chicago, Illinois

A proposed methodology to reduce heat pump size with integrated thermal energy storage

Jason Hirschey[a], Kyle R. Gluesenkamp[b*], Bo Shen[b], Zhenning Li[b], Samuel Graham[a]

[a]Georgia Institute of Technology, Atlanta, GA, USA
[b]Building Technologies Office, Oak Ridge National Lab, Oak Ridge, TN, USA

Abstract

Thermal energy storage (TES) offers a unique storage solution wherein heat is stored for later use to thermally condition an application. Heat pumps (HPs) move heat from relatively cold to a relatively hot with an input of work. Integrating TES into a HP system adds a third temperature body, and the HP can be selectively coupled to operate between any two bodies: a constant temperature application, a temporally fluctuating ambient temperature, or a constant temperature TES. Since the HP-TES system enables operation under different conditions depending on the pair of temperature bodies, changes in efficiency and capacity can be expected. Thus, TES can shift HP operation to more favorable conditions to deliver heat to the application. Consequently, TES increases the apparent capacity of the HP which might enable a nominally smaller HP to be used effectively for an application. This paper outlines a method by which TES can reduce the size of a HP without sacrificing heat delivered to the application. The method is demonstrated for a building cooling application which realized a reduction in nominal HP size from 3 tons to 2.4 tons.

© HPC2023.
Selection and/or peer-review under the responsibility of the organizers of the 14th IEA Heat Pump Conference 2023.

Keywords: thermal energy storage; heat pump;

1. Introduction

Thermal energy storage (TES) is posed to be a critical technology for the Energy Transition. TES can benefit many everyday applications and services, but its relevance and performance is dependent on the temperature at which energy is stored. Analogous to electrical energy storage (EES) which might be characterized by its voltage, TES is characterized by its storage temperature. However, unlike EES which can have its voltage transformed to higher or lower values, TES can only transfer heat down a temperature gradient from relatively hot to relatively cold. However, by integrating TES into a heat pump (HP) system, heat may be upgraded to move up a thermal gradient with an input of work. This opens the possibilities for TES to be deployed for a wide variety of applications without needing quite specific storage temperatures (*e.g.*, a cooling application can effectively utilize a TES storage temperature higher than the application temperature). The TES analyzed in this report is assumed isothermal, but real systems might have small TES temperature changes or internal temperature gradients during use.

Notice: This manuscript has been authored by UT-Battelle, LLC under Contract No. DE-AC05-00OR22725 with the U.S. Department of Energy. The United States Government retains and the publisher, by accepting the article for publication, acknowledges that the United States Government retains a non-exclusive, paid-up, irrevocable, world-wide license to publish or reproduce the published form of this manuscript, or allow others to do so, for United States Government purposes. The Department of Energy will provide public access to these results of federally sponsored research in accordance with the DOE Public Access Plan (http://energy.gov/downloads/doe-public-access-plan).

* Corresponding author. Tel.: +1-865-241-2952
E-mail address: gluesenkampk@ornl.gov.

Fig. 1 shows the possible HP-mediated modes that the HP-TES system can take for thermally conditioning an application. A conventional HP might operate only between the application and the ambient, providing heating to the application when the ambient temperature is low and cooling when the ambient temperature is high, simply speaking. For simplification, the ambient in an infinitely large temperature body whose temperature can fluctuate in time, is unaffected by the operation of the HP, and thermally interacts with the application. The efficiency of the HP to thermal condition the application is inversely correlated to the temperature difference between the application and the ambient, typically. Adding TES to a HP system provides a third temperature body with which to operate the HP. At any one time, the HP may only couple to two of the three temperature bodies.

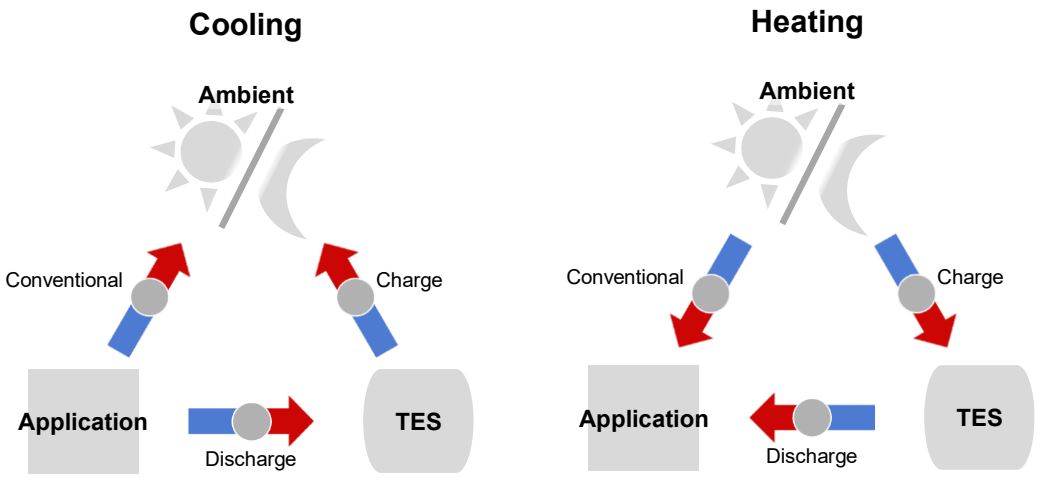


Fig. 1. Heat exchange between three temperature bodies in a HP-TES system.

If the TES is at a different temperature than the ambient, it may provide more advantageous HP operating conditions with which to heat or cool the application. Discharging mode is when the TES is used to provide thermal conditioning to the application and this mode nominally reduces the available energy stored within the TES. Simply speaking, operating in discharging mode is advantageous when the temperature difference between the application and TES is more favorable than the difference between the application and ambient for the thermal conditioning needed. For example, if the application requires cooling and the TES is at a lower temperature than the ambient, it may be more favorable to operate the HP in discharging mode than in conventional mode. If the ambient temperature experiences time-varying fluctuations, there may be an optimal time to operate in discharging mode based on the ambient temperature oscillation. However, the TES has finite energy storage capacity and once it is depleted, it must be returned to its original state before another discharging event can occur. In this system, this charging event is accomplished by thermally coupling the TES to the ambient via the HP, and the HP adds heat to or withdraws heat from the TES, depending on what is needed, to return the TES to its original state. Again, if the ambient temperature presents cyclic fluctuations and the TES temperature is constant, there may be an optimal time to charge the TES when the HP is most effective. Thus, HP-TES systems may shift bulk energy demand for peak heating and cooling loads of an application.

Another value proposition for HP-TES systems is the potential to downsize a HP. Typically, a HP is sized for the most extreme heat load the application might experience, often called the design condition. But most conditions experienced by the application are less extreme than the design condition and thus the HP is oversized for most of its regular use. If instead TES is designed to be utilized during the most extreme conditions by providing more favorable HP operating conditions, a smaller HP, more appropriately sized for a less extreme condition, can be used effectively. In essence, the TES increases the apparent capacity of the HP by providing more favorable HP operating conditions during extreme conditions and thus the requisite heat delivered to the application is met with a nominally smaller HP.

Some published research has examined HP sizing with integrated TES. However, most studies focus on the sizing of the TES storage capacity to meet the thermal loads of a certain event while fewer leverage the TES to reduce HP size. A summary of the reports found in literature follows, first those that include HP sizing then those that exclusively focus on TES capacity sizing. Many also report on the TES storage temperature, but this is often predetermined or chosen from a narrow set of preselected temperatures. It is

observed that the approaches to integrate TES into a HP system differ significantly between studies, and the criterion by which the value of TES or downsized HP vary. Many studies focus on building technologies and systems, but HP-TES can be used in many applications.

Renaldi *et al.* (2017) performed a cost optimization of an integrated HP system to meet indoor heating demands and domestic hot water production in the United Kingdom [1]. The authors explore four HPs that were modeled using regression fits from manufacturer data and six TES capacities each modeled with two storage temperatures, 35°C and 50°C. The TES is modeled as a typical domestic hot water tank which was used for either space heating through radiators and underfloor heating, or for providing domestic hot water. The authors reported HP-TES as compared to gas boilers and concluded that the HP-TES system is not cost effective, even when subsidized. The authors include a baseline HP system without TES in a summary figure, and it is observed that the TES can reduce the operational cost of the HP by approximately 50% with the largest TES size studied. However, the baseline HP and the HP in the HP-TES system are identically sized, therefore it is inferred that the authors found no advantage or mechanism by which the TES reduces the HP size. Furthermore, the authors mention that smaller HPs can lead to increased cost by way of increased energy consumption from auxiliary backup heating systems if the smaller capacity cannot meet all the heating demands even with TES. In the scenario studied, no HP downsizing potential was viable.

Aljehani *et al.* (2018) evaluated a 4-6°C TES system for air conditioning [2]. The TES was coupled to the HP refrigerant loop and the duct air via an ethylene glycol loop. The HP was used to charge the TES, and the temperature difference between the air and TES allowed for direct discharging with a nonzero amount of work to circulate the ethylene glycol. The authors explain that in the conventional system, a 5 kW compressor is needed to meet the thermal loads during the six hour peak, but that it is oversized during off-peak hours. With the integrated TES system, a 2.5 kW compressor was sufficient in meeting peak loads and this size was sufficient for off-peak. Thus, the authors demonstrate a 50% reduction in HP compressor size with the inclusion of TES. Simulations then show that this system can reduce electricity consumption by 30%.

Lyu *et al.* (2022) evaluated the size of an air source HP and of a water tank TES unit for a residential house in Beijing, China [3]. The building model was built in TRNSYS based on measurement data. The water storage tank is modeled between 0.06 – 4.5 m^3, though this is not explicitly related to energy storage capacity. The TES temperature is studied with two setpoint temperatures: 45°C during the hottest 12 hours of the day and 35°C during the coldest 12 hours of the day. The HP size is varied from 80-100% of the HP sized for the design heating load of the building, and all could meet the thermal needs of the building with TES. The authors indicate that HP capacities lower than 80% of the design conditions led to an unacceptable loss of thermal comfort even with large TES. In addition, the authors investigated the startup losses associated with HP cycling. The authors explain that steady HP capacity may not be achieved until several minutes after startup, based on measurement data. Thus, some efficiency loss is observed during the transient startup period. The authors hypothesize that the larger HPs will have shorter operational times and therefore startup losses are more significant and will accumulate with repeated short cycling events. Comparatively the smaller HPs have longer operational times which leads to fewer startup events and therefore less accumulated startup losses. During startup, the TES acts as a buffer tank to compensate for the reduced capacity as described by Meng *et al.* (2021) [4]. Furthermore, the TES can be used to absorb excess heat during steady HP operation, prolonging its operating time and limiting loses due to short cycling. Thus, Lyu *et al.* (2022) conclude that even small TES can reduce HP startup losses compared to lone HP systems. Furthermore, Lyu *et al.* (2022) do not observe significant energy savings with the smaller HP and therefore conclude that the size of the HP has little effect when TES is present. Critically, however, the successful use of a smaller HP is enabled by the presence of the TES. And they note that a smaller HP can reduce the upfront investment. Findings indicate that the large TES sizes can lead to higher energy savings, upwards of 18%.

Marini *et al.* (2019) performed an analysis for the potential of HP-TES to replace existing gas boilers in the UK for space heating and domestic hot water [5]. Data from several residential building were collected operating with the existing gas equipment. A model was then built in TRNSYS to simulate each building with HP-TES equipment, over 400 scenarios in total. A process was used to select an appropriate HP size based on [6] such that the HP-TES thermal service provided to the building matched as closely as possible to the historical data. The HP selection process included information about each house analyzed, the load shifting strategy based on available utility tariffs, and the TES capacity modeled as a hot water tank with a setpoint temperature of 60°C. The authors show that larger TES systems required larger HPs – contrary to the hypothesis proposed that TES adds capacity and thus reduces HP size. However, little discussion was given to the HP selection process as the analysis focused on whether the HP-TES can meet or exceed the thermal conditioning service as compared to the extant gas equipment. It is speculated that the combination of large TES size and relatively high TES temperature requires a large HP to fully recharge. Furthermore,

the approach to mirror historical heat loads with the HP-TES led to a bias towards big systems as there was little opportunity for the load shift flexibility of the HP-TES to be explored. From the data, a minimum TES size could be determined based on the building characteristics, the occupants' idiosyncratic behavior, and the utility tariff. The authors conclude that sizing such HP-TES systems might be specific to certain building and occupant characteristics, and that operational costs to maintain the same level of thermal comfort are likely the largest motivator for HP-TES systems.

Alimohammadisagvand *et al.* (2016) performed a cost optimization of a TES operating with a ground source HP for space heating in Finland [7]. The temperature of TES was evaluated between 55-95°C and the size the TES system varied between 0.3-1.5 m^3, but it is not said how TES physical size correlates to energy storage capacity. The HP and TES selected in this study are based on available products. The authors find that the smallest TES size led to the minimum life cycle cost. Moreover, the authors note that increasing the TES temperature does not lead to increased performance if the TES discharging capacity is sufficient for the application. The optimal TES size was determined by a cost minimization; there is no objective function which would size the TES to the expected heat loads or usage. The authors report the delivered energy from the TES. Unsurprisingly with this metric, the smallest TES unit delivered the lowest amount of energy therefore having the smallest impact of all systems analyzed. Moreover, this study evaluated a ground source HP which are not greatly influenced by the ambient conditions and often have more consistent operation compared to air source HPs. Therefore, without a cost objective related to load shift enabled by the TES, such as a time-of-use or other time varying utility tariff, or a HP that undergoes significant performance changes, it is unsurprising that a small TES tank was found to be cost optimal.

The previous studies evaluate specific building technologies in specific climates to ascertain HP sizing or requisite TES capacity. Many studies focus on operational or life cycle cost to determine an optimal solution. And it is well understood that consumer facing products heavily factor cost into success and deployment. However, the approaches used in determining the equipment size and TES temperature vary considerably between studies and result in some conflicting conclusions. A more methodical approach for determining the potential of TES and its effect on HP size is warranted.

This paper explores the potential of an isothermal TES system to reduce nominal HP size and presents a methodology by which HP and TES size, and TES temperature can be determined for an application. First the method is explained in general terms as it might apply to any application. Then the method is demonstrated using empirical HP data for a building cooling application.

2. Methodology

The method by which TES can reduce HP size is shown here using general terms such that it can be applied to any application. Fig. 2 shows the process flow for determining the downsizing HP for an application in generalized terms. The follow sections provide more detail to how this process is utilized for an application. In Section 2.1, the method is explained as to provide heating to the application, but an identical approach can be used for cooling applications, curtly discussed in Section 2.2.

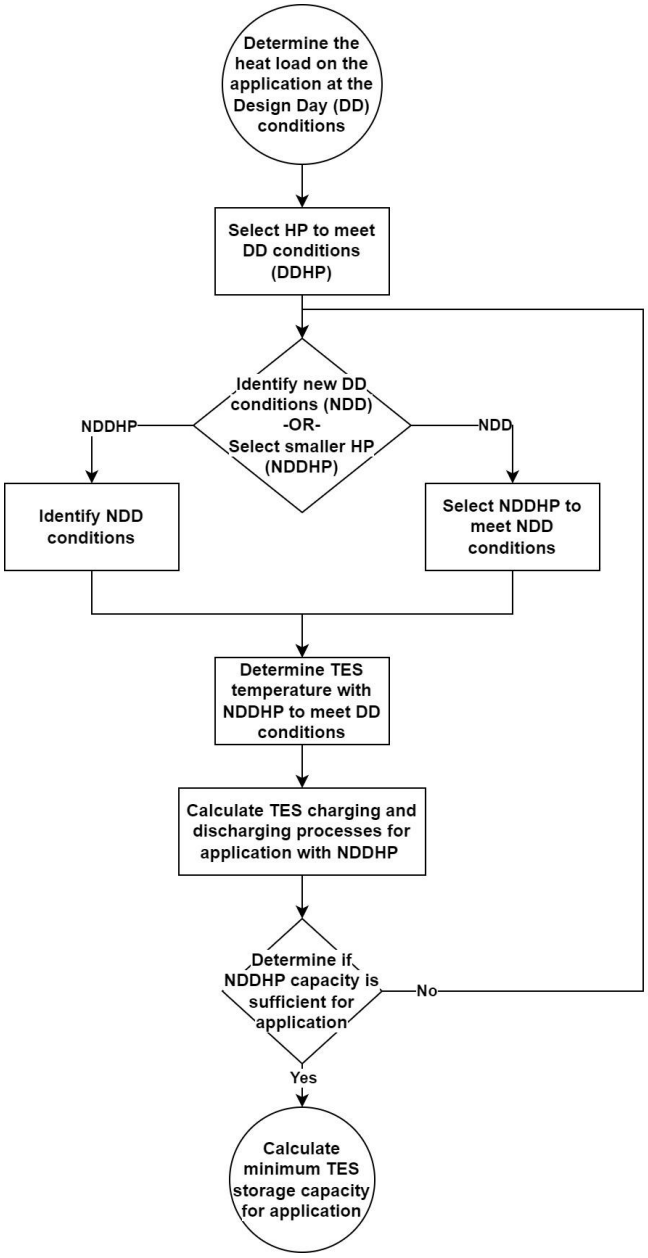


Fig. 2. Generalized HP downsizing with TES approach

2.1. Heating Application

For a heating application it is assumed that a HP provides all heating and no backup heating systems are used. First, the design condition, or design day temperature, $T_{H,DD}$, and associated design heat load on the application, $\dot{H}_{H,DD}$, are determined. For buildings, this could be determined from ACCA Manual J, ASHRAE Standards, or through building energy modeling. Other applications might require unique calculation procedures to determine heating loads against some design conditions. It is uncommon to determine the heating loads for all conditions and commonly, even for real systems. The heating load curve, $\dot{H}_H$, is thus a linear interpolation between the design conditions and the application's balance point temperature, T_{BP}. For applications with special considerations, the heating load might yield a nonlinear curve, but this would be specific to that application and circumstances. But to keep the method general, intermediate heating loads at some ambient temperature, T_O, between T_{BP} and $T_{H,DD}$ the curve is interpolated on the load curve, $\dot{H}_H(T_O)$.

For a heating application, the HP hot side is connected to the application temperature body, T_{app}, which is often at a higher temperature than T_{BP}. The heat might be delivered with some approach temperature above the application temperature, T_{app}^{+} (the approach temperature denoted as a plus sign for brevity). The notation

for HP capacity will be $\dot{Q}(T_{cold\ side}, T_{hot\ side})$. A subscript *H* will indicate HP heating, a *C* will indicate cooling. Additional subscripts will identify the HP design conditions.

The ACCA Manual S includes a methodology for sizing the HP to the design conditions of a building [8]. Other methodologies for sizing the HP might be used, including those that are "tricks of the trade" of contractors, but generally, the HP is sized to meet the design day conditions with some safety factor, f_S. The capacity of the design day HP, *DDHP*, is sized for these conditions: $\dot{Q}_{H,DD}(T_{H,DD}, T_{app}^{+}) = f_s \dot{H}_{H,DD}$

Next, either a smaller HP or a new design day temperature is selected – these are intrinsically linked. If a smaller HP is selected, its maximum capacity, $\dot{Q}_{H,NDD}$, will identify the new design day temperature, $T_{H,NDD}$, to meet the thermal conditioning needs at this temperature. Or if a new design day temperature is identified, the same HP sizing procedures and standards as before may be used to identify a properly sized, presumably smaller, *NDDHP*. The result of both processes yield a *NDDHP* and $T_{H,NDD}$ such that $\dot{Q}_{H,NDD}(T_{H,NDD}, T_{app}^{+}) = f_s \dot{H}_{H,NDD} = f_s \dot{H}_H(T_{H,NDD})$. This process can be done iteratively based on available HP devices and the conditions experienced by the application. Once the *NDDHP* and $T_{H,NDD}$ are determined, the TES temperature, $T_{H,TES}$, is identified as the operating temperature at which the *NDDHP* can supply the heating capacity equal to the design day heat load, $\dot{Q}_{H,NDD}(T_{H,TES}, T_{app}^{+}) = f_s \dot{H}_{H,DD}$. For simplicity, the TES will be used for discharging only when the ambient temperature, T_O, is less than $T_{H,NDD}$, and despite the safety factor included in its sizing. The safety factor will be dropped from further discussion and equations.

The ambient temperature is a function of time, $T_O(t)$, and may take a periodic waveform. Thus, to determine the time spent discharging during a single event, $t_{H,dis}$, information about the amount of time and the magnitude by which the ambient temperature is below $T_{H,NDD}$ is needed for each discharging event. This information will be specific to the application, location of the system, and the previous decisions made to determine $T_{H,NDD}$. An energy balance is then performed such that the time spent discharging at the constant *NDDHP* discharging heating capacity, $\dot{Q}_{H,NDD}(T_{H,TES}, T_{app}^{+})$, is equal to the cumulative heating loads from the ambient during this time, $t_{H,-}$, below $T_{H,NDD}$, Eq. 1 This ignores temperature fluctuations or gradients in the application or the TES as these are considered small compared to the ambient temperature fluctuations. Also note that Eq. 1 is calculated for each discrete discharging event, not cumulatively.

$$t_{H,dis} \cdot \dot{Q}_{H,NDD}(T_{H,TES}, T_{app}^{+}) = \int_0^{t_{H,-}} \dot{H}_H\big(T_O(\tau)\big) d\tau \text{ when } T_O < T_{H,NDD} \tag{1}$$

When the ambient temperature returns above the new design day temperature condition, $T_O \geq T_{H,NDD}$, the *NDDHP* may spend some time heating the application normally, t_{heat}, such that the cumulative heating delivered by the *NDDHP* equals the sum of the heating loads from the ambient conditions. To determine t_{heat}, the amount of time, $t_{H,+}$, and magnitude by which $T_O(t) \geq T_{H,NDD}$ is needed for the period immediately succeeding a discharging event and before the next discharging event. Unlike in Eq. 1, the heating capacity of the *NDDHP* is not constant as it couples between the time-varying ambient and application. Eq. 2 shows the energy balance of the NDDHP to meet the heat loads from the ambient in conventional mode.

$$\int_0^{t_{heat}} \dot{Q}_{H,NDD}(T_O(\tau), T_{app}^{+}) d\tau = \int_0^{t_{H,+}} \dot{H}_H\big(T_O(\tau)\big) d\tau \text{ when } T_O \geq T_{H,NDD} \tag{2}$$

Any time not spent directly heating the application can be used to charge the TES, $t_{H,chg,available} = t_{H,+} - t_{heat}$. As the TES is discharged for heating the application, the TES experiences a cooling load from the *NDDHP* and receives some amount of cooling energy for the duration of discharging, depleting the stored energy by an amount $E_{H,dis}$, Eq. 3. The TES must receive an equal amount of cumulative heating energy to fully charge, $E_{H,chg}$, for the next discharging event, Eq. 4.

$$E_{H,dis} = t_{H,dis} \cdot \dot{Q}_{C,NDD}\big(T_{H,TES}, T_{app}^{+}\big) \text{ when } T_O < T_{H,NDD} \tag{3}$$

$$E_{H,chg} = \int_0^{t_{H,chg,min}} \dot{Q}_{H,NDD}\big(T_O(\tau), T_{H,TES}\big) d\tau \text{ when } T_O \geq T_{H,NDD} \tag{4}$$

Equating Eqs. 3 & 4 informs of the minimum time required to fully charge the TES after a discharging event, $t_{H,chg,min}$, based on the ambient conditions and where $t_{H,dis}$ is determined from Eq. 1. The charging procedure must satisfy the two constraints: 1) $E_{H,chg} = E_{H,dis}$, and 2) $t_{H,chg,min} \leq t_{H,chg,available}$. Failure to satisfy both is ultimately attributed to a lack of available time to complete the charging process before the

next discharging process occurs which is related to the ambient conditions, and the combination of the new design day conditions and the capacity of the *NDDHP*.

For an application that experiences irregular periodic thermal heat loads from the ambient, the minimum energy storage capacity of the TES for heating the application, $E_{H,TES}$, should be equal to the maximum energy discharged, $E_{H,dis,max}$, in any one discharging event as determined by solving Eq. 3 for all events. A factor of safety might be added to the minimum determined TES capacity to provide additional resilience against extreme heating events.

This method might be done iteratively or with several different parameters to determine an array of feasible HP-TES systems for this application. Due to the relationship between the *NDDHP* capacity, TES temperature, and new design day temperature, decisions might percolate throughout the analysis and affect the result in unexpected ways. Furthermore, the availability of HPs might be limited or TES storage temperatures might be offered in discrete selections based on available TES materials or technologies. Therefore, if designing a HP-TES system some concessions might need to be made to the availability of products.

2.2. Cooling Application

The process for a cooling application follows the same approach as described by the heating application in Section 2.1. Dual heating and cooling applications are reserved for future work. To summarize the cooling application, like in the heating application, a design day condition, $T_{C,DD}$, is determined by conventional means based on the application. The design day heat loads are determined, and a linear heat load curve is drawn between the design conditions and the balance point temperature, T_{BP}, to calculate the heat loads as a function of ambient temperature, $\dot{H}_C(T_O)$. Note that for many applications, the balance point temperature might be the same for both heating and cooling. The *DDHP* is selected by conventional means. The *NDDHP* and $T_{C,NDD}$ are determined – these are intrinsically linked and choosing one will affect the other. The maximum TES temperature, $T_{C,TES}$, is identified by the conditions at which the *NDDHP* can provide the maximum heat load experienced by the application, $\dot{Q}_{C,NDD}(T_{app}^{-}, T_{C,TES}) = \dot{H}_{C,DD}$.

Fig. 3 demonstrates the approach graphically for a cooling application: 1) The design day heat load and temperature are determined. 2) A HP is selected to meet this design day load. Here, empirical HP compressor data is used to identify a suitable device, a nominal 3 ton HP. The published compressor map is used to plot its capacity as a function of condensing temperature which is related to outdoor temperature by a designated approach temperature. 3) A smaller HP is selected, a nominal 2.4 ton HP. Its capacity is determined from published compressor map information. Where its capacity intersects with the application's heat load curve is the temperature which describes the new design day conditions, $T_{C,NDD}$. 4) Where the *NDDHP* capacity is equal to the original design day heat load identifies the TES temperature necessary to provide thermal conditioning during the most extreme ambient conditions. Though this application and heat load curve is fictional, the HP compressor data is real and could be used in a similar way to size and design a HP-TES systems.

Like was explained for the heating application, the HP is responsible for cooling the application such that its time spent cooling multiplied by the HP discharging cooling capacity is equal to the heat loads experienced by the application from the ambient, Eq. 5. When the ambient temperature exceeds the $T_{C,NDD}$, discharging mode is activated, Eq. 6, as the *NDDHP* does not have enough capacity at these conditions to provide the necessary heat.

$$t_{C,dis} \cdot \dot{Q}_{C,NDD}\left(T_{app}^{-}, T_{C,TES}\right) = \int_0^{t_{C,+}} \dot{H}_C\left(T_O(\tau)\right)d\tau \text{ when } T_O > T_{C,NDD} \tag{5}$$

$$\int_0^{t_{cool}} \dot{Q}_{C,NDD}(T_{app}^{-}, T_O(\tau))d\tau = \int_0^{t_{C,-}} \dot{H}_C\left(T_O(\tau)\right)d\tau \text{ when } T_O \leq T_{C,NDD} \tag{6}$$

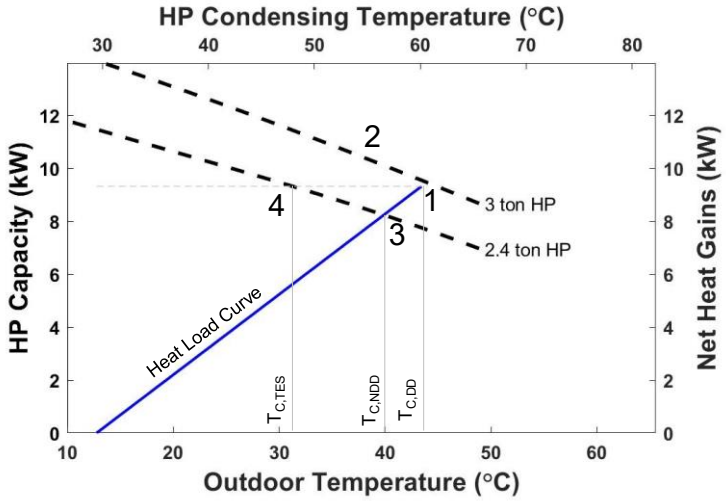


Fig. 3. Generalized HP downsizing with TES based on empirical HP data. 1) The outdoor design day temperature ($T_{C,DD}$) is determined for the application which determines the maximum heat load acting on the application. 2) A *DDHP* is identified to meet this maximum heat load at the $T_{C,DD}$ condition. 3) A smaller *NDDHP* is identified. The intersection of its capacity with the heat load curve indicates the new design day conditions ($T_{C,NDD}$). This can be done in reverse; $T_{C,NDD}$ identified and a *NDDHP* sized for this condition. 4) The temperature at which the *NDDHP* capacity equals the maximum heat load at the DD conditions indicates the TES temperature ($T_{C,TES}$) necessary to provide thermal conditioning at temperatures between T_{NDD} and T_{DD}.

Contrary to the heating application, the TES receives a heating load during discharging. Therefore, the delivered heat to the application is less than the heat stored in the TES; the efficiency of the HP implicitly affects the TES storage capacity which in turn is affected by the TES temperature. The energy depleted from the TES during discharging is shown in Eq. 7. After the discharging event, the TES is charged by coupling the TES to the ambient via the HP, Eq. 8. When charging, the HP still must provide cooling to the application if needed, but any time not spent directly cooling the application can be used for charging the TES, $t_{C,chg,available} = t_{C,-} - t_{cool}$. And likewise, the charging procedure must satisfy the two constraints: 1) $E_{C,chg} = E_{C,dis}$, and 2) $t_{C,chg,min} \leq t_{C,chg,available}$ for every discharge and charge cycle.

$$E_{C,dis} = t_{C,dis} \cdot \dot{Q}_{H,NDD}\left(T_{app}^{-}, T_{C,TES}\right) \text{ when } T_O > T_{H,NDD} \tag{7}$$

$$E_{C,chg} = \int_0^{t_{C,chg,min}} \dot{Q}_{C,NDD}\left(T_{C,TES}, T_O(\tau),\right) d\tau \text{ when } T_O \leq T_{H,NDD} \tag{8}$$

3. Demonstration of HP-TES Sizing

Fig. 3 only demonstrated the HP selection process, and the relationship between the *NDDHP* capacity, the new design conditions, and the TES temperature. However, to size the TES system and determine if the *NDDHP* is capable of supplying all thermal conditioning needs including conventional and charging modes, data on the fluctuating ambient temperature is needed. To demonstrate the approach outlined in Section 2.2 for a cooling application, the process is followed for a building application in Phoenix, Arizona. Typical Meteorological Year version 3 (TMY3) data is used [9]. The TMY3 data presents the median temperature for each hour of the year for building thermal energy simulations. In this analysis, the TMY3 data was interpolated and extrapolated to each minute of the year using Akima spline technique.

Fig. 3 shows the heat load curve for this building and two HP capacity curves calculated from empirical HP compressor data. The nominal 3 ton HP would be selected by conventional means for this building; this is the *DDHP*. Commonly for a building application, the *DDHP* is sized for the 0.4% design condition. The ASHRAE 0.4% design conditions for Phoenix is an ambient dry bulb temperature of 110.2°F (43.4°C). Using the interpolated 2020 TMY3 data, the 0.4% design temperature was identified as 45.2°C. For consistency with the dataset, the calculated 0.4% design condition from the TMY3 data is used. This building is assumed to experience a 9.3 kW net heat load at the 0.4% design condition. The balance point temperature is assumed as 12.8°C where it experiences 0 kW net heat load.

The 2.4 ton HP in Fig. 3 is the next model size smaller in the same family of HPs by the manufacturer; this is the *NDDHP* for this application. The *NDDHP* capacity intersects the heat load curve at 41.8°C, thus any ambient temperatures above this temperature will discharge using the TES; $T_{C,NDD}$ = 41.8°C. This temperature corresponds to the 3% design condition based on the TMY3 data. The TES temperature necessary to provide the necessary capacity at the design conditions is identified as 32°C.

Fig. 4 shows the TMY3 dry bulb temperature data, and 0.4% and 3% design conditions for Phoenix. Using the TMY3 data, all discharging events (when the outdoor temperature is greater than $T_{C,NDD}$) are identified. Then using Eq. 5, the time spent discharging is determined during each event is determined and the energy depleted from the TES found using Eq. 7. These are shown as green pins in Fig. 4 with the energy depleted from the TES for each discharging event on the right vertical axis. The maximum TES storage capacity is found to be 80.3 kWh for the discharging event on July 13 between 9:47am and 5:13pm – nearly 7.5 hours. For reference, if the density and phase change enthalpy of water/ice used, the volume of this TES is about 1 cubic meter or about slightly smaller than a typical domestic refrigerator; if the density and phase change enthalpy of sodium sulfate decahydrate (which has a melting temperature of 32.4°C), the volume of this TES would be approximately 1.5 cubic meters [10]. Note, the published compressor maps only include cooling capacity, thus as a proxy for heating capacity (*i.e.*, heat going into the TES and depleting its stored energy), the cooling capacity plus the electrical power consumed by the compressor was used. It is understood that this might not perfectly represent the heating capacity at the condenser, but from a crude energy balance, this method sufficed.

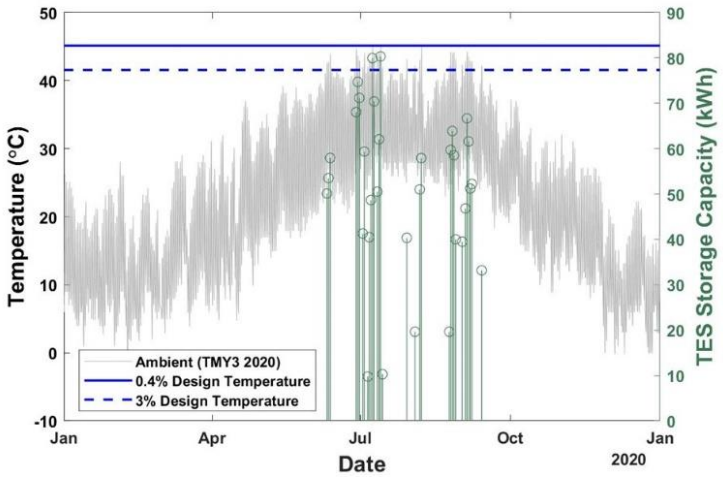


Fig. 4. A building cooling application modeled for Phoenix, AZ with a 2.4 ton HP and 32°C TES. The HP-TES allows for the system to be sized to the 3% design condition. The green pins indicate the 33 TES discharging events where the TES is needed to meet thermal loads greater than the HP capacity and where the HP can fully recharge the TES before the next discharging events.

Between each discharging event, the time required to cool the application in conventional mode was found from Eq. 6, which then informs on the available time to charge the TES. Note, these calculations do not include optimal HP timing to take advantage of diurnal ambient temperature extrema, but future versions and more rigorous simulations can include these considerations. Then by calculating Eq. 7 and comparing to the energy depleted from the previous discharging event, the feasibility of the *NDDHP* to fully recharge the TES was determined. For the conditions outlined, the *NDDHP* with TES can meet all thermal loads to cool the application and recharge the TES between discharging events, thus all discharging event pins in Fig. 4 are green.

As discussed, the performance of the HP is affected by the TES temperature for both charging and discharging. While a colder TES temperature is advantageous for discharging in cooling applications, it may present a larger temperature gradient for the HP to charge depending on the ambient temperature fluctuations. Fig. 5 shows the same building simulation in Phoenix, AZ except where the TES temperature is 25°C, only 7°C lower than in Fig. 4. Here, the necessary TES capacity is reduced to 77.1 kWh because there is a more favorable temperature gradient to cool the application. However, there are three events in which the *NDDHP* fails to fully recharge the TES between discharging events as shown by the red pins in Fig. 5. Thus, this combination of *NDDHP*, $T_{C,NDD}$, and $T_{C,TES}$ is not feasible for this application. This highlights the sensitivity

of designing such HP-TES systems, and the interplay between the TES temperature, HP capacity, and ambient temperature conditions.

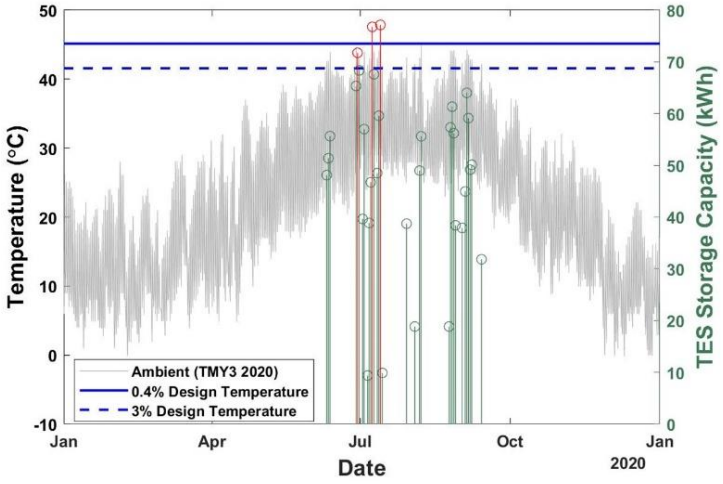


Fig. 5. A building cooling application modeled for Phoenix, AZ with a 2.4 ton HP and 25°C TES, identical conditions compared to Fig. 4 except for a colder TES. With the colder TES, the smaller HP cannot fully recharge the TES after each discharging event. This demonstrates the sensitivity of the HP-TES system; a colder TES provides more favorable cooling during discharging but presents too large a lift for the small HP to recharge.

Lastly, Fig. 6 shows the same building configuration with an even smaller *NDDHP*, nominal 2 ton capacity. From Fig. 6A, the $T_{C,NDD}$ is determined to be 38.1°C (a 6% design condition) and the required $T_{C,TES}$ is equal to 15°C. However, this *NDDHP* proves to be far too small to be effective even with the TES; there are discharging events over 12 hours long which leaves insufficient time to recharge the TES between discharging events with the smaller HP capacity as shown by the numerous red pins in Fig. 6B. This shows there are practical limits to downsizing with a HP-TES system. A HP-TES system with these conditions would need at least 170 kWh of storage to keep the system operational, bridging the gap between discharging events. During the height of the cooling season, the HP would be running continuously to either cool the building (conventional or discharging) or charge the TES, but it is still insufficient in supplying the necessary thermal loads.

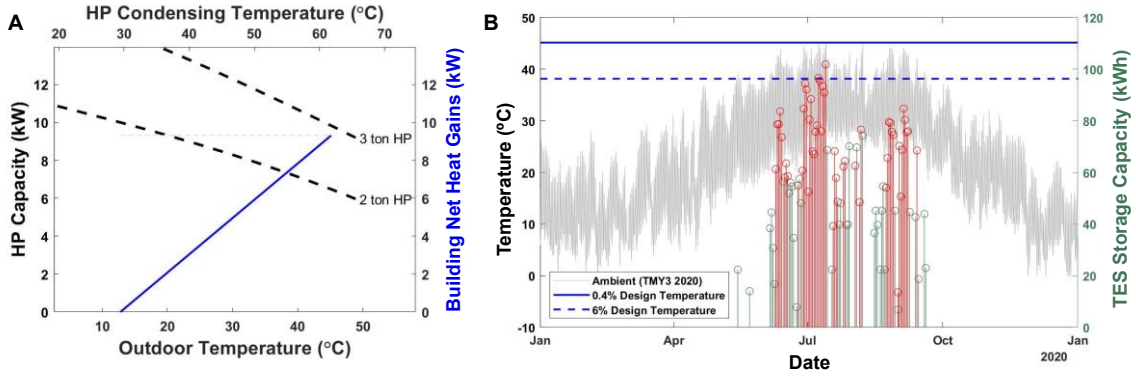


Fig. 6. A building cooling application modeled for Phoenix, AZ with a 2 ton HP and 15°C TES. The HP-TES allows for the system to be sized to the 6% design condition. The TES discharging events are the red and green pins. This HP proves to be too small for the application as the HP cannot fully recharge the TES before the next TES discharging event, evidenced by the red pins.

4. Discussion and Conclusion

This report presents a methodology by which a HP might be downsized when TES is integrated. Data on the specific application, its conventional operating conditions and heat loads, and climate-specific temperature

fluctuations are needed. If this information is known for the HP-TES system to be installed, the TES temperature and its storage capacity can be determined as it relates to the smaller HP size. This report indicates the feasibility of HP compressor downsizing with empirical data but is not comprehensive. The approach can serve as a guideline for other applications or specific uses of HP-TES systems.

This procedure might be performed iteratively to identify an array of possible design conditions, HP equipment, and TES temperatures. HP sizes and TES storage temperatures might be available in discrete options, and thus the design of such systems is subject to these discrete variables. Once a HP-TES system is designed using the methodology outlined here, it might be evaluated in more rigorous simulations to determine the real-world feasibility of such HP-TES systems. Furthermore, more advanced HP-TES control strategies might enable more intelligent use of the TES. For example, simultaneous charging and conventional modes can more effectively utilize excess HP capacity and reduce short cycling, and forecasting heat loads might allow for a TES system to carry partial charges between discharging events while still providing the thermal conditioning necessary. Future work will also evaluate dual heating and cooling applications, and seek to identify HP-TES systems that benefit both modes.

The method was demonstrated on an example building cooling application in Phoenix, AZ with TMY3 weather data. It was shown that the HP could be downsized from a 3 ton system to a 2.4 ton system when TES was added. Furthermore, the TES enabled the HP to be sized based on the 3% design condition (compared to the 0.4% design condition). The HP-TES was shown to be sensitive to the TES temperature as the performance of the HP is affected by this temperature for both charging and discharging; a lower TES temperature is advantageous for cooling during discharging but presents a steeper thermal gradient to charge and thus the smaller HP capacity might be incapable of fully recharging the TES between discharging events.

HP-TES can be valuable for system retrofits. As global temperatures continue to rise due to anthropogenic climate change and thus the prevalence of air conditioning continues to grow, this methodology shows that integrating TES can increase apparent HP capacity. Therefore, adding TES to extant HPs might be a viable solution in applications where the extant HP is now undersized due to the locally changing climate. Thus, rather than replacing the HP, retrofitting with TES can extend its useful life and avoid costly system upgrades.

HP-TES systems are posed to play a critical role in the future of energy. The potential of HP-TES to reduce energy use and shift demand might be specific to the target application and its setting. Nevertheless, this analysis presents the opportunity for HP-TES to be designed more intelligently and reduce unwanted oversized systems. More work to realize these devices in real-world research settings.

Acknowledgements

This material is based upon work supported by the U. S. Department of Energy's Building Technologies Office under Contract No. DE-AC05-00OR22725 with UT-Battelle, LLC. The authors would like to acknowledge Mr. Sven Mumme, Technology Manager, U.S. Department of Energy Building Technologies Office.

References

[1] Renaldi, R., A. Kiprakis, and D. Friedrich, *An optimisation framework for thermal energy storage integration in a residential heat pump heating system.* Applied Energy, 2017. **186**: p. 520-529. DOI: https://doi.org/10.1016/j.apenergy.2016.02.067.

[2] Aljehani, A., et al., *Design and optimization of a hybrid air conditioning system with thermal energy storage using phase change composite.* Energy Conversion and Management, 2018. **169**: p. 404-418. DOI: https://doi.org/10.1016/j.enconman.2018.05.040.

[3] Lyu, W., et al., *Influence of the water tank size and air source heat pump size on the energy saving potential of the energy storage heating system.* Journal of Energy Storage, 2022. **55**: p. 105542. DOI: https://doi.org/10.1016/j.est.2022.105542.

[4] Meng, Q., et al., *Reduction in on-off operations of an air source heat pump with active thermal storage and demand response: An experimental case study.* Journal of Energy Storage, 2021. **36**: p. 102401. DOI: https://doi.org/10.1016/j.est.2021.102401.

[5] Marini, D., R.A. Buswell, and C.J. Hopfe, *Sizing domestic air-source heat pump systems with thermal storage under varying electrical load shifting strategies.* Applied Energy, 2019. **255**: p. 113811. DOI: https://doi.org/10.1016/j.apenergy.2019.113811.

[6] Dwyer, T., *Module 36: Air source heat pumps*, in *CIBSE Journal*. 2012, CIBSE Journal. Available from: https://www.cibsejournal.com/cpd/modules/2012-01/
[7] Alimohammadisagvand, B., et al., *Cost-optimal thermal energy storage system for a residential building with heat pump heating and demand response control.* Applied Energy, 2016. **174**: p. 275-287. DOI: https://doi.org/10.1016/j.apenergy.2016.04.013.
[8] ANSI/ACCA, *Manual S - Residential Equipment Selection*. 2014, Air Conditioning Contractors of America
[9] Wilcox, S. and W. Marion, *Users manual for TMY3 data sets.* 2008
[10] Hirschey, J., et al., *Review of Low-Cost Organic and Inorganic Phase Change Materials with Phase Change Temperature between 0°C and 65°C*, in *International High Performance Buildings Conference*. 2021, Purdue University: West Lafayette, Indiana

14th IEA Heat Pump Conference
15-18 May 2023, Chicago, Illinois

Feasibility study for the application of a high-temperature heat pump in the pulp and paper industry: an Italian case study

Marco Pellegrini[a,b,*], Alessandro Guzzini[a], Cesare Saccani[a]

[a]Department of Industrial Engineering, University of Bologna, Viale del Risorgimento 2, Bologna 40136, Italy
[b]Interdepartmental Centre for Industrial Research in Renewable Resources, Environment, Sea and Energy - CIRI FRAME, Via Sant'Alberto 163, Ravenna 48123, Italy

Abstract

The application of high-temperature heat pump (HTHP) in the pulp and paper industry can promote a more efficient and sustainable use of waste energy. In particular, the paper aims to perform a preliminary feasibility study for the upgrade of heat extracted from the wastewater aiming to increase the circularity of pulp and paper production through a combination of technological innovation. In the analysed case study a 1.3 MW th tailored cascade HTHP is designed to supply heat at 120°C at the thermal dryer while cooling the wastewater from 42°C to 28°C. The proposed solution generates several benefits: i) reduction of sludge mass associated with higher heating value for use as secondary fuel; ii) energy saving (i.e. the heating demand of the thermal dryer is not covered by the steam produced by the existing CHP plant) and consequent recovery of waste heat and CO_2 and pollutants emission reduction; iii) wastewater cooling without cooling tower operation, with a consequent reduction of fan power consumption up to 44 kW; iv) reduction of oxygen demand during the wastewater treatment due to temperature decreasing before aerobic stage, with a further power consumption reduction of the air fan. The preliminary techno-economic analysis shows a negative NPV at year 20 for both HTHP integration strategies analysed, that is completely fed by the power produced by the existing natural gas CHP unit or partially fed by a 0.54 MW el peak PV plant. Despite the contribution to emissions reduction, that is 1,989 ton/year of equivalent CO_2 with PV plant and 1,613 ton/year of equivalent CO_2 without PV, the economic sustainability cannot be guaranteed in the conditions examined. The preliminary sensitive analysis highlights a relevant impact of incentives intensity and duration and of the COP of HTHP.

© HPC2023.
Selection and/or peer-review under the responsibility of the organizers of the 14th IEA Heat Pump Conference 2023.

Keywords: High-temperature heat pump; pulp and paper industry; cascade heat pump; energy efficiency.

1. Introduction

Industrial production processes account for a considerable share of the overall pollution in Europe due to their emissions of greenhouse gases and air pollutants, discharges of wastewater and the generation of waste. The Industrial Emission Directive (IED) aims to achieve a high level of protection of human health and the environment taken as a whole by reducing harmful industrial emissions across the EU [1], in particular through better application of Best Available Techniques (BAT). Increasing energy efficiency and renewable energy in industrial processes is part of the IED and it is also coherent with the Clean energy for all European package (CEP) strategy [2], recently updated after the Covid-19 pandemic through the NextGenerationEU [3] and RePowerEU [4] initiatives. The European industrial sector represents one quarter of the EU28's final energy consumption with 260 Mtoe in 2019 [5], while waste heat sources exist in all industries with a total amount of 300 TWh/year in the EU. Figure 1 shows the distribution of EU28's final energy consumption in the industrial sector for 2019 (based on data extracted from [6]). Chemical and Petrochemical industry ranks first with 20.78% of the whole consumption, while non-metallic minerals (which includes the Ceramic industry in the

* Corresponding author. Tel.: +39-051-2093403.
E-mail address: marco.pellegrini3@unibo.it.

Eurostat classification), Pulp and Paper, and Food industries are, respectively, at the second (13.63%), third (13.05%) and fourth (11.6%) places.

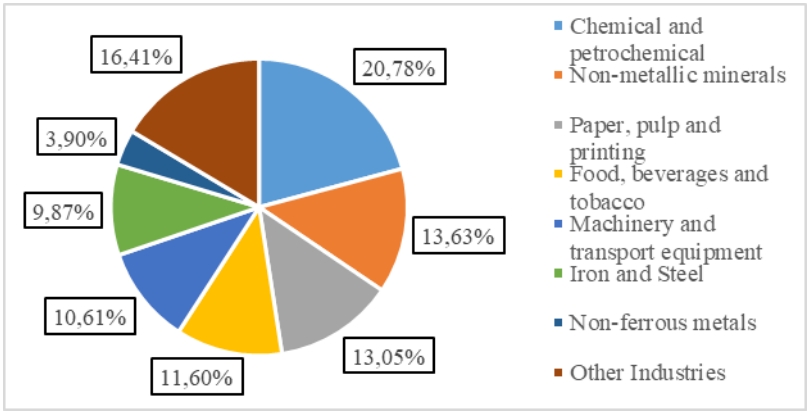


Fig. 1. Distribution of final energy consumption in EU28's industrial sector in 2019 (based on data ex-tracted from [6]).

Industrial process heat accounts for more than two-thirds of total energy consumption in industry, and half of this process heat demand is at low to medium temperatures (i.e. lower than 400°C). Figure 2 shows for each temperature range the final energy consumption share for industrial process heating (based on data extracted from [6]). While more than 85% of heating demand in the iron and steel industry (the industrial sector with the largest final energy consumption) occurs at temperatures over 500°C, Chemical and Petrochemical, Ceramic (included in non-metallic minerals), Food, and Pulp and Paper industries have a relevant heating demand in the range 100-200°C. Furthermore, a good match with the waste heat potential is found in these sectors [7].

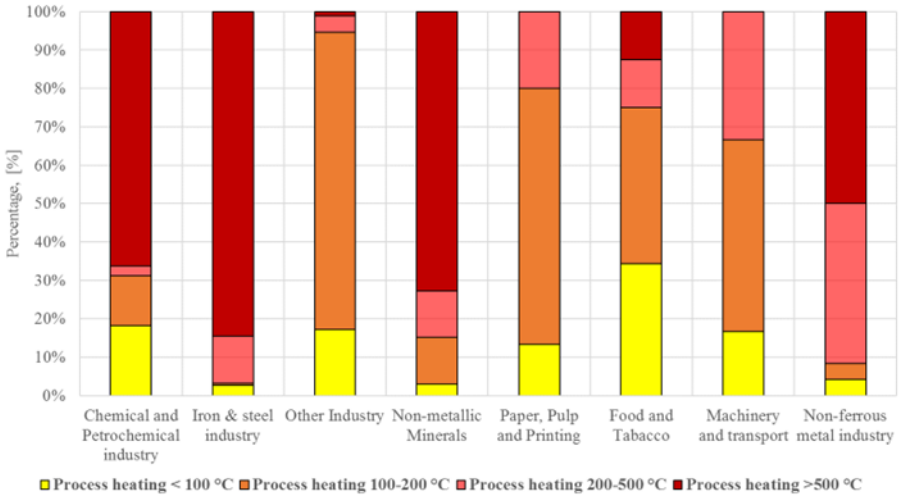


Fig. 2. Industrial final energy consumption for process heating: classification by industrial sectors and by temperature ranges in 2019 (based on data extracted from [6]).

The so-called “heat upgrade technologies” such as traditional heat pumps, mechanical vapour recompression heat pumps, absorption heat pumps and absorption heat transformers allow low-temperature heat (i.e. ambient heat, waste heat or renewable heat) to be upgraded to higher temperatures [8]. Heat upgrade technologies are promising solutions for increasing industrial processes efficiencies and decreasing greenhouse gas (GHG) emissions. In traditional heat pumps the recovered heat vaporizes the working fluid in the evaporator, which is compressed to a higher temperature by electrical power. The working fluid is condensed and expanded in a valve, and then the cycle repeats. In mechanical vapour recompression (MVR) heat pumps the pressure and thus also the temperature of waste gases are increased by a compressor, thereby allowing the heat to be re-used. The most common type of vapour compressed by MVR is steam. MVR heat pumps are widely used in specific industrial applications like in evaporator and distillation installations, in seawater desalination and industrial wastewater treatment plants [9,10]. Absorption heat pumps (AHP) and heat

transformers (AHT) are thermally activated heat upgrading technologies in which the compression of the working fluid is achieved in a solution circuit consisting of a generator, an expansion valve, a solution pump and an absorber. The difference between AHP and AHT is that in an AHT, thermal energy required to vaporize the working fluid in the evaporator is supplied at a higher temperature than that of the heat required for separating the working fluid pair in the generator. In the Sustainable Development Scenario of [11] both electrically and thermally driven heat pumps are considered to be a potentially economically viable solution for heat supply at temperature ranges of up to 400°C. However, accordingly to both IEA HPT Annex 35 [12] and 58 [13] findings the commercially available heat pumps are limited to supply temperatures below 100°C, while the availability of systems capable of higher supply temperatures or high-temperature heat pumps (HTHPs) is limited. In particular, HTHPs integration in existing processes still need to be demonstrated at relevant scale in the medium temperature range (90-150°C) to improve market confidence [14].

In 2020, more than 85 million tons of paper and board and 36 million tons of pulp has been produced in the EU. The leading producing countries are Germany, Sweden, Italy, Finland and France. The turnover for the production of pulp, graphic paper, hygiene paper, packaging paper and special papers is expected to be around EUR 90 billion, with an added value of EUR 20 billion and investments of EUR 4.5 billion, directly providing 178,000 jobs in 891 mills and indirectly 3 million jobs along the forest and paper chain [15]. Pulp and paper mills are highly complex, and involve various process steps to transform the wood into the final product, including wood preparation, pulp production, chemical recovery, bleaching and papermaking. In 2019, the European Pulp and Paper industry consumed 380 TWh of primary energy [15], with drying accounting for up to 70% of the fossil energy use. The sector has reduced its CO_2 emissions by 24% since 1991 thanks to improvements in energy efficiency and the reduction of fossil fuel consumption (from 54.6% in 1991 to 37.6% in 2019) by replacement with biofuels (mostly black liquor) [16]. The Confederation of European Paper Industries (CEPI) has elaborated a roadmap [17] to decarbonize by 80% the European forest fibre and paper industry in 2050 compared to 1990. This will represent a decrease of 37 Mton of CO_2 per year in 2050 compared to 2015 and 32% of the reduction will be achieved through higher energy efficiency and the introduction of emerging and breakthrough technologies, including HTHPs. While there is potential for a high impact of HTHPs in the pulp and paper industry [18,19], several barriers (including regulatory ones to implementation, low fossil-fuel prices, adaptation to the industry processes, high investment cost, lack of knowledge and trust) hinder a wider adoption of HTHPs [20]. The first step for the market uptake of HTHPs in the pulp and paper industry is the preliminary techno-economic evaluation of the HTHP integration in existing facilities. Nevertheless, literature about HTHP application in the pulp and paper industry is limited.

To cover the literature gap about HTHP application in pulp and paper industry, the paper illustrates the design of a 1.3 MW th cascade HTHP to supply heat at 120°C at the thermal dryer of sewage sludge treatment plant of a pulp and paper industry while cooling the wastewater from 42°C to 28°C. The design is optimized to guarantee i) the use of sustainable working fluids and ii) the highest COP. Environmental and economic impact assessments are performed to evaluate CO_2 saving, net present value and payback time of the proposed solution. The sustainability impact of techno-economic parameters on the environmental and economic performances is estimated through a sensitivity analysis.

2. Case study description

The case study is based on a pulp and paper recycling plant located in the North of Italy. The plant, which covers an area of about 290,000 m^2 and employs about 100 workers, currently produces 400.000 tons per year of recycled paperboard. 200,000 Sm^3 of natural gas are daily consumed to supply both electricity and heat to the industrial processes through a gas turbine unit with a nominal power of 21.5 MW el, a recovery boiler with post-combustion for the nominal production of 135 ton/h of steam at 49 bar g and 440°C, and a counter-pressure steam turbine with an electrical power output of approximately 10.44 MW el. The high-pressure steam is sent to the steam turbine which has i) a medium pressure bleed of 105 ton/h of steam at 10 bar g and 275°C for the paper drying machines and ii) a low-pressure discharge of 30 ton/h of steam at 3.5 bar g and 210°C. This steam, after appropriate temperature and pressure adjustments, is destined for the low-pressure processes of the plant. The plant also includes a wastewater and sludge treatment facility. The wastewater treatment plant has the objective of reducing both pollutants and temperature of the water that after being treated is discharged in a superficial water body. The treatment includes both aerobic and anaerobic digestion, which generates 6,000 Sm^3 per day of biogas plus sludge. The sludge is currently dewatered mechanically, reaching a water content of about 50-60%. The relatively high water content of the sludge increases disposal costs and does not allow energy recovery.

3. HTHP integration into pulp and paper industry processes

The first concept was to introduce a new thermal sludge dryer operating in the temperature range 80-120°C to reach a sludge humidity of 5% after treatment. The energy requested for sludge drying process is estimated in 1.3 MW th, that corresponds to a yearly heat demand of 10,920 MWh (i.e. by considering about 8,400 hours of operation per year). The reduction of sludge humidity is beneficial since i) it reduces the mass to be disposed and ii) it increase the lower heating capacity of the sludge, which can be used as secondary fuel. Nevertheless, thermal drying is usually not cost-effective if realized by consuming natural gas. So, sludge thermal drying is not commonly performed in pulp and paper industry facilities [21]. Moreover, due to legislative obligations, the wastewater has to be discharged at a temperature lower to 30°C. In the specific plant the targeted discharge temperature is currently reached by cooling towers, that generate waste heat and high water consumption [22]. Therefore, the second concept was to use the heat content of wastewater as heat source for a HTHP able to dry the sewage sludge, thus generating a combined effect of wastewater cooling and sludge heating.

The identified solution is a cascade HTHP to supply heat at 120°C at the thermal dryer while cooling the wastewater from 42°C to 28°C (see the process flow diagram PFD in Figure 3). A secondary circuit has been foreseen between the HTHP and the wastewater to avoid direct contact and possible fouling of the HTHP evaporator. The configuration generates several benefits for the pulp and paper industry: i) reduction of sludge mass associated with higher heating value for use as secondary fuel; ii) energy saving (i.e. the heating demand of the thermal dryer is not covered by the steam produced by the existing CHP plant) and consequent recovery of heat waste and CO_2 and pollutants emission reduction; iii) wastewater cooling without cooling tower operation, with a consequent reduction of fan power consumption up to 44 kW; iv) reduction of oxygen demand during the wastewater treatment due to temperature decreasing before aerobic stage, with a further power consumption reduction of the air fan.

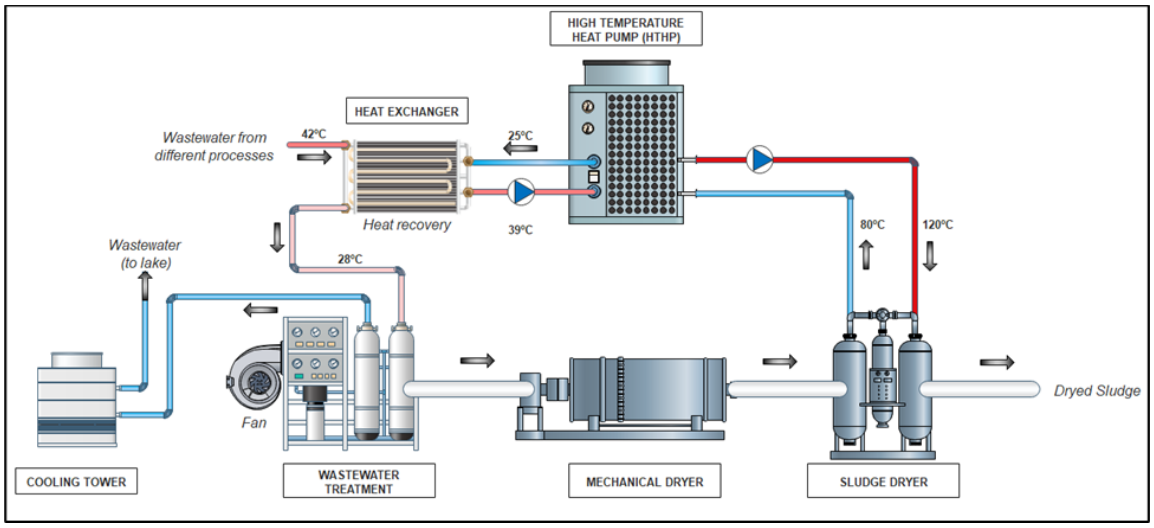


Fig. 3. Process flow diagram of the suggested integration of HTTP in pulp and paper industry.

The cascade HTHP is a 1.3 MW th customized solution offered by a renowned heat pump manufacturer. The size of the HTHP has been identified on the basis of available commercial components and based on heat demand for sludge drying on site. The cascade HTHP (see Figure 4) consists of two separate cycles, called “low temperature” and “high temperature” cycles, interconnected through a cascade heat exchanger. Each of the two cycles will employ two screw compressors in parallel to share the flowrate since the maximum capacity of commercial compressors is not sufficient to cover heat demand. The cascade heat exchanger acts as a condenser for the “low-temperature” cycle and as an evaporator for the “high-temperature” cycle. The pre-selected refrigerants are R1234ze(E) and R1233zd(E), respectively. The heat sink fluid is water, which is pumped from the end-user and recirculates back to it: the water enters the condenser at 80°C and exits as superheated water at 120°C. The economizers play a key role in optimizing heat flows among low and high temperature cycles and contribute to guarantee a relatively high COP despite the large temperature lift requested by the end-user. The expected COP of the whole system is 2.4, but it can be higher (up to 3.5) if the cooling effect on wastewater is considered as positive side effect.

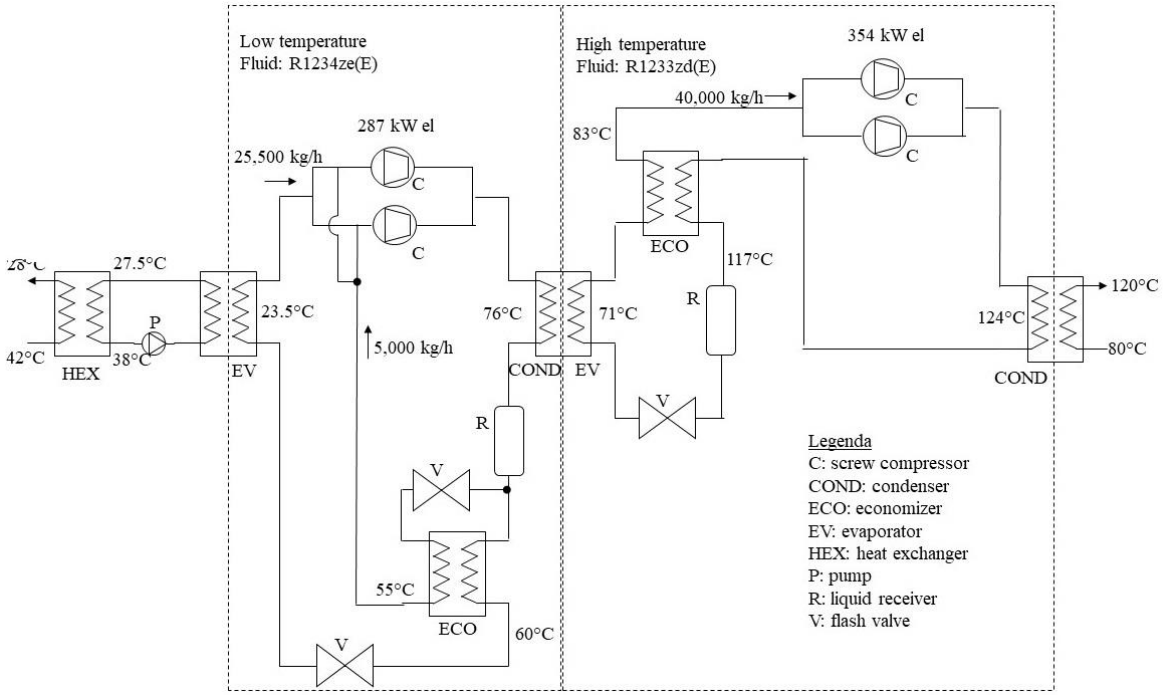


Fig. 4. Process flow diagram of the cascade HTTP. The reported power demand of compressors is the total one.

4. Feasibility study and preliminary techno-economic and environmental assessment

The assessment of HTHP integration into industrial processes requires a detailed techno-economic analysis to justify the investment in a real application. Furthermore, the reduction of the existing environmental impacts should be estimated as well since it can generate benefits from both economic and social community perspectives. The following methodology is proposed for the preliminary assessment. First of all, it is necessary to clearly define the scenarios under assessment. While in the new scenario sewage sludge drying and wastewater cooling are both reached through the integration of HTHP, the existing scenario needs some adaptation to make a proper comparison. In fact, in the current scenario the wastewater is cooled by cooling towers, which are not effective in reaching the expected temperature of 28°C for wastewater discharge in the superficial water body all over the year, especially in summertime. Therefore, in the paper the comparison is made between the cooling effect of the HTHP and the cooling effect that a traditional air-to-water chiller would have to reach the same wastewater output temperature. Figure 5 resumes the two scenarios; the HTHP integration scenario includes also the option of HTHP feeding by renewable electricity (i.e. PV plant), which will be discussed below.

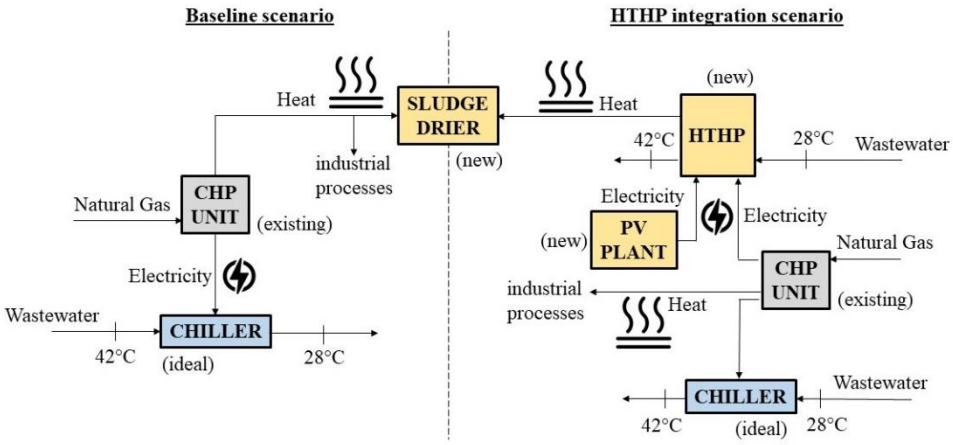


Fig. 5. Scenarios definition.

The comparison among the two scenarios is performed by considering two different parameters: the net present value (NPV), measured in Euros, and the payback time (PT), measured in years. The NPV is computed as in Equation 1, where t (years) is time, n (number of years) is the time period considered for the investment evaluation (which will be assumed equal to both depreciation and technical life time of plants for treatment simplicity purpose), i (%) is the discount rate, F_t (Euro) is the net cash flow at year t. The contribution of tax is not taken into account to simplify the economic assessment.

$$NPV = \sum_{t=0}^{n} \frac{F_t}{(1+i)^t} \quad (1)$$

The net cash flow F_0 at t=0 corresponds to the starting investment: the simplifying hypotheses of full investment payment and plant operation start in the same year (t=0) are also assumed. The net cash flow for period t > 0 was computed taking into account the main costs C_t and revenues R_t components, as highlighted in Equation 2.

$$NPV = -F_0 + \sum_{t=1}^{n} \frac{[R_t \cdot (1+e)^t - C_t \cdot (1+e)^t]}{(1+i)^t} \quad (2)$$

Revenues R_t include i) natural gas consumption saving in sludge drying process due to HTHP integration, ii) power consumption saving in wastewater cooling due to HTHP integration, iii) emission of new energy efficiency certificate, and iv) CO_2 emission certificate saving, both caused by a reduction in natural gas consumption. In this preliminary economic assessment, the benefits related with lower power consumption for the wastewater treatment due to lower air flow rate demand caused by wastewater temperature reduction before entering the anaerobic digestor are not taken into consideration. Energy efficiency certificate can be accounted as revenues only for the first 7 years of HTHP operation, accordingly to the Italian procedure [23]. On the other hand, costs C_t account for i) missed revenues due to electricity not sell to the grid operator while being self-consumed by the HTHP, and ii) operation and maintenance costs of the HTHP integration (not including the sludge dryer, which is the same for both scenarios). Equation 3 and Equation 4 define, respectively, how R_t and C_t have been computed: E_{th} is the yearly heat demand requested for sludge drying (MWh/year), c_{ng} is the cost of natural gas (€/MWh), η_{th} is the thermal efficiency of the existing CHP plant (%), η_{el} is the electric efficiency of existing CHP plant (%), COP is the efficiency of the HTHP (%), E_{fr} is the yearly cooling energy demand for wastewater cooling (MWh/year), c_{el} is the electricity selling price (€/MWh), EER is the efficiency of the traditional air-to-water chiller considered for the comparison with HTHP cooling effect (%), N_{eec} is the yearly number of energy efficiency certificate (#/year), c_{eec} is the market value of one energy efficiency certificate (€/eec), t_{CO2} is the yearly saving of equivalent CO_2 emission (ton of eq CO_2/year), c_{CO2} is the trading emission cost of CO_2 (€/t_{CO2}), $C_{O\&M}$ is the operation and maintenance cost of the HTHP integration. The yearly natural gas saving V_{ng} (Nm^3/year) can be computed as in Equation 5 and is equal to about 781,610 Nm^3.

$$R_t = E_{th} \cdot c_{ng} \cdot \left(\frac{1}{\eta_{th}} - \frac{1}{COP \cdot \eta_{el}}\right) + E_{\text{fr}} \cdot c_{ng} \cdot \left(\frac{1}{EER \cdot \eta_{el}}\right) + N_{eec} \cdot c_{eec} + t_{CO_2} \cdot c_{CO_2} \quad (3)$$

$$C_t = E_{th} \cdot c_{el} \cdot \left(\frac{1}{COP}\right) + C_{\text{O\&M}} \quad (4)$$

$$V_{ng} = \left[E_{th} \cdot \left(\frac{1}{\eta_{th}} - \frac{1}{COP \cdot \eta_{el}}\right) + E_{\text{fr}} \cdot \left(\frac{1}{EER \cdot \eta_{el}}\right)\right] \cdot \frac{1{,}000 \cdot 3{,}600}{LHV} \cdot \frac{273.15}{298.15} \quad (5)$$

Table 1. Assumptions about economic assessment.

Item	Symbol	Value	Comments
HTHP integration cost	F_0	1,115,000 €	HTHP specific cost of 550 €/kW plus integration cost of 400,000 € (including design and permit procedures), as communicated by the HTHP manufacturer.
Heat demand	E_{th}	10,920 MWh/year	For the operation of the 1.3 MW th sludge dryer coupled with HTHP for 8,400 hours per year.
CHP thermal efficiency	η_{th}	56%	Measured in the pulp and paper facility.
CHP electric efficiency	η_{el}	30%	Measured in the pulp and paper facility.

HTHP COP	COP	2.4	Estimated by HTHP manufacturer based on the expected operating conditions.
Natural gas cost	c_{ng}	20 €/MWh	Mean value for March 2021 in Italy.
Cooling energy demand	E_{fr}	6,880 MWh/year	For the operation of the 0.819 MW fr of the HTHP evaporator for 8,400 hours per year.
Electricity selling price	c_{el}	60 €/MWh	Mean value for March 2021 in Italy.
Traditional air-to-water chiller EER	EER	5.5	A high efficiency EER is considered due to the relatively high wastewater outlet temperature.
Number of energy efficiency certificate	N_{eec}	641/year	Equal to the ton of equivalent oil (TOE) saved per year, that is 0.82 TOE per 1,000 Nm^3 of natural gas saved.
Market value of energy efficiency certificate	c_{eec}	267.4 €/eec	Mean value for 2021 in Italy (min 250 €/eec – max 299.99 €/ecc) [24].
Ton of CO_2 emission saved per year	t_{CO2}	1,613 ton/year	Computed by considering an emission factor 1.956 ton CO_2 per 1,000 Sm_3 of natural gas.
Trading emission cost of CO_2 emission	c_{CO2}	56.5 €/ton	Mean value for 2021 (min 34 €/ton – max 79 €/ton) [25].
HTHP O&M costs	$C_{O\&M}$	33,750 €/year	Assumed as 3% of HTHP integration cost.
Natural gas LHV	LHV	35,880 kJ/m^3	As guaranteed by contract to the pulp and paper industry. The reference conditions are 25°C and 1 bar.
Discount rate	i	5%	
Inflation rate	e	2%	
HTHP lifetime	n	20 years	

Figure 6 shows the NPV based on the values included in Table 1. The NPV is computed with and without incentives: the results clearly shows how incentives are crucial to make the investment more profitable. Nevertheless, NPV is negative anyway by considering or not incentives. Therefore, the tuning of incentives duration and intensity is crucial accompanying energy efficiency actions like HTHP integration in industrial processes. The reduction of CO_2 emission during the HTHP lifetime is relevant, being about 32,260 ton. If initial investment F_0 is divided per ton of CO_2 avoided in 20 years, we obtain a value of 34.6 € per ton of CO_2, which is lower than trading emission costs of CO_2. So, incentives are apparently well-designed. Indeed, the high selling price of electricity is the parameter that does not allow to make the investment profitable. So, the main barrier to HTHP integration is the high revenues that electricity selling can generate even by power production through natural gas combustion in CHP units.

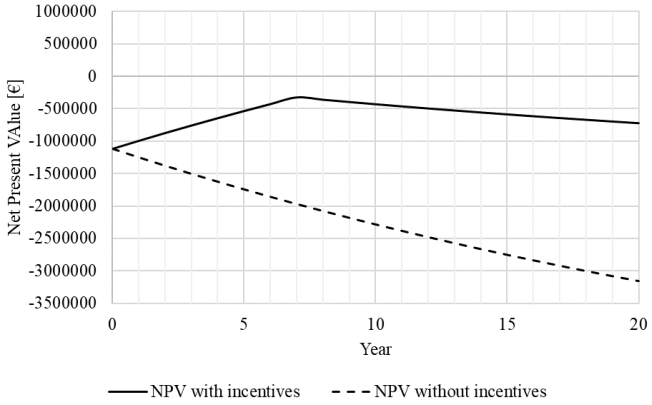


Fig. 6. NPV with and without considering incentives.

But since March 2021 a strong variation in both natural gas cost and electricity selling price has led to enormous stress on the energy market, substantially changes may be expected on the cost framework and related investment NPV and payback time. Table 2 summarizes natural gas cost and electricity selling price variation in 2021. Figure 7 shows how NPV varies by considering the different costs and prices (the NPV is computed with incentives). No relevant results can be reached in terms of investment profitability, since the high selling prices of power produced by natural gas CHP units. Discussion on how disincentivize power

production by fossil fuel combustion is an open question which has implication on both environmental and economic sustainability of electricity market [26].

Table 2. Natural gas cost and electricity selling price variation in 2021.

Item	Symbol	Value at Mar-21	Value at Jun-21	Value at Sep-21	Value at Dec-21
Natural gas cost	c_{ng}	20 €/MWh	30 €/MWh	67 €/MWh	100 €/MWh
Electricity selling price	c_{el}	60 €/MWh	100 €/MWh	160 €/MWh	250 €/MWh

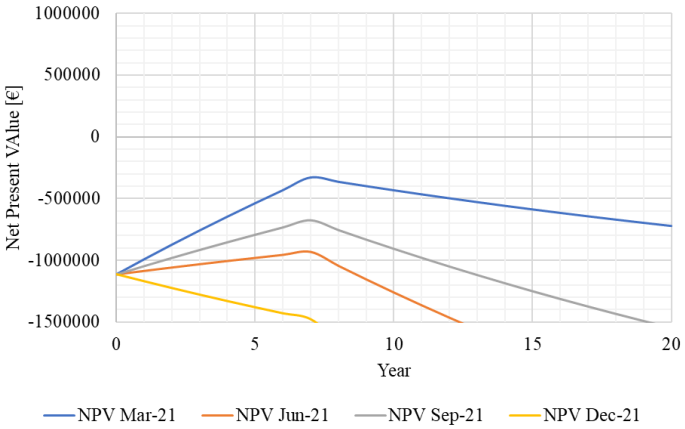


Fig. 7. NPV by considering incentives and with different natural gas cost and electricity selling prices.

The logic consequence of the techno-economic assessment is to prefer HTHP operation fed by renewable energy locally generated. In this case, the requested investment is higher, but the cost related to missing power selling as in Equation 4 can be avoided or, at least, reduced. Renewable energies availability is strongly related with local resources, and so it is highly site specific. When biomass and hydropower are not available in large amount, wind and solar energies are the most common renewable resources available at any site. But both solar and wind sources are characterized by being unpredictable and variable over time (both daily and seasonally) [27]. In the site of the pulp and paper industry under analysis only solar energy can be considered as a sustainable resource, and so photovoltaic (PV) can be taken into account to reduce the carbon footprint of HTHP operation.

Optimization of PV plant and battery storage requires complex modelling taking into account technical, economic and environmental concerns [28]. Since the scope of the paper is only to show how to foster HTHP application in industrial processes, a preliminary assessment of the impact of PV installation is given by considering a size of about 0.54 MW el peak. This configuration simplifies the analysis since no storage is needed and ideally all the electric energy is consumed by the HTHP. Based on the industrial site location, it is expected a mean annual production of 596 MWh. The specific cost of PV plant is assumed equal to 1000 €/kW peak installed [29]. Figure 8 shows the NPV (with and without incentives) in the case of HTHP integration and 0.54 MW el peak PV installation to make HTHP operation less dependent from natural gas consumption. The NPV is computed by considering energy values as in March 2021. The partial switch from natural gas to PV decreases natural gas consumption while increasing CO_2 emission saving, that are, respectively, about 857,679 Nm^3/year and 1,770 ton of CO_2 per year. The increased CO_2 emission reduction also has positive effect in terms of higher number of energy efficiency certificate release, that are 703 per year. But NPV at year 20 is still negative (-490,000 €). Finally, if the initial investment for HTHP plus PV plant is divided per ton of CO_2 avoided in 20 years, we obtain a value of 46.8 € per ton of CO_2, which is in line with the value of trading CO_2 emission certificate considered in Table 1.

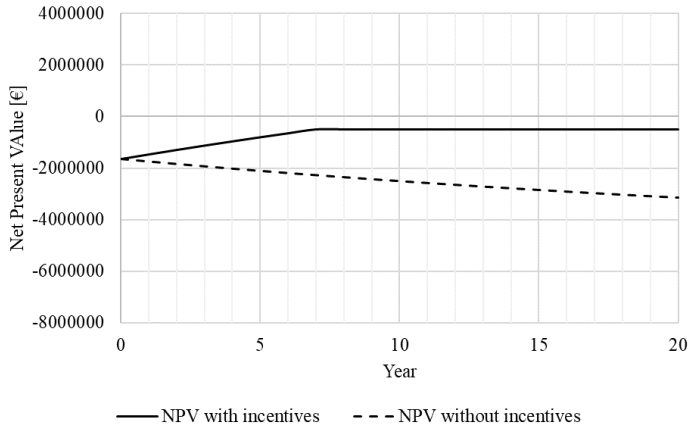


Fig. 8. NPV by considering or not incentives and including a 0.54 MW el peak PV plant for HTHP power feeding. Energy costs are from March 2021.

Due to the innovative design of the HTHP, also the COP of the HTHP needs to be assessed. Figure 9 shows how the NPV is influenced by relatively small COP variation (±8%). The variation has large potential influence on NPV; the increasing of COP generates a NPV increasing at year 20 up to about 0.5 million €, with a payback time up to 7 years. The impact of incentives is high, since without incentives the investment would be negative. A 7 years payback time investment may be perceived as risky since over such a long period variation in the framework conditions (like natural gas and electricity prices, inflation rate, incentives' values) is likely to occur, having potential negative impact on NPV estimation. Therefore, it is essential to pay attention to the COP of the HTHP integration, since an apparently negligible efficiency reduction or increasing can have a huge impact on the economic sustainability of the investment.

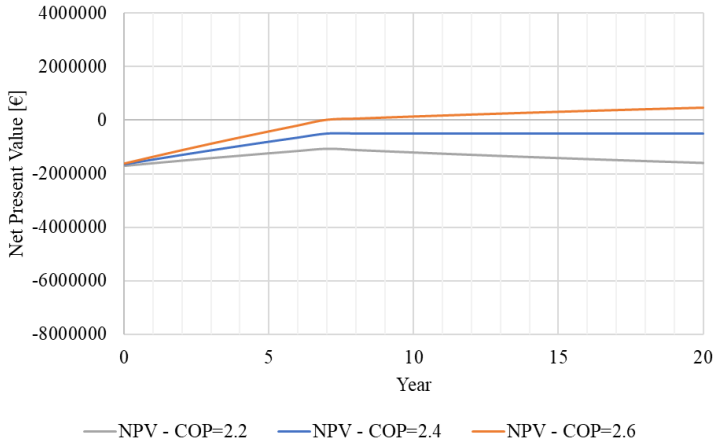


Fig. 9. NPV by considering COP variation ±8%. Energy costs are from March 2021, the integration includes a 0.54 MW el peak PV plant.

5. Conclusions

The paper analyses the application of a HTHP in a pulp and paper industry localized in Northern Italy. In particular, the paper introduces an innovative cascade HTHP to simultaneously generate heat for sludge drying and cool wastewater before wastewater anaerobic digestion treatment section. The temperature lift from the heat source to the heat sink allows to reach a COP limited to 2.4 by applying state-of-the-art technologies. The initial hypothesis is to feed the HTHP with the electricity locally generated by the existing natural gas CHP unit. The HTHP integration in the industrial process produces a more efficient use of the energy. In fact, about 1,613 ton of CO_2 equivalent emission per year can be avoided through the described approach. Nevertheless, the economic sustainability of the HTHP integration is hindered by the high selling price of electricity produced by the existing CHP unit, and that is no longer sold but self-consumed. Despite the rocketing of natural gas

price in 2021 (and still on going in 2022), the connection among natural gas and electricity price makes difficult to predict the existence of a combination of prices able to make the investment profitable.

The solution is to combine the HTHP integration with local renewable power generation. In the paper the realization of a PV plant able to produce the peak power requested by HTHP is considered. The yearly power production is limited to 13% of HTHP power demand, which generates insufficient benefits in terms of NPV increasing. Once again, despite the energy efficiency performance reached by the system (1,770 ton of equivalent CO_2 emission avoided per year), the economic sustainability of the HTHP integration cannot be achieved. Through an optimization of the PV plant, to be coupled with batteries for energy storage, it would be possible to gain positive NPV and sustainable payback time. Such a configuration will be assessed in a following paper. Nevertheless, it is relevant to highlight how incentives intensity and duration play a key role in the promotion of energy efficiency actions. Finally, COP of the HTHP can strongly affect economic performance of the integration process: in fact, by reaching a COP increase of only 8%, it would be possible to have payback time of 7 years with a NPV at year 20 of about 0.5 million €.

References

[1] European Parliament, European Council. Directive 2010/75/EU, 2010.
[2] European Commission, Directorate-General for Energy. Clean energy for all Europeans, Publications Office, 2019.
[3] European Commission, Directorate-General for Budget. NextGenerationEU: Funding plan June-December 2021, Publications Office, 2021.
[4] European Commission, Directorate-General for Communication. REPowerEU, joint European action for more affordable, secure and sustainable energy, 2022.
[5] Eurostat Statistic Explained. https://ec.europa.eu/eurostat/statistics-explained/index.php?title=Energy_statistics_-_an_overview#Final_energy_consumption Available online: (accessed 13/06/2022).
[6] Eurostat. https://ec.europa.eu/eurostat/web/energy/data/database Available online: (accessed 13/06/2022).
[7] Kosmadakis G. Estimating the potential of industrial (high-temperature) heat pumps for exploiting waste heat in EU industries. *Appl Therm Eng* 2019;**156**:287-298.
[8] Oluleye G, Jobson M, Smith R. Process integration of waste heat upgrading technologies. *Process Saf Environ* 2016;**103**:315-333.
[9] Gao X, Gu Q, Ma J, Zeng Y. MVR heat pump distillation coupled with ORC process for separating a benzene-toluene mixture. *Energy* 2018;**143**:658-665.
[10] Zhang C, Wu J, Gao J, Huang X. Experimental study of a novel double-effect evaporation concentration system for high temperature heat pump. *Desalination* 2020;**491**:114495.
[11] International Energy Agency. World Energy Outlook, 2019.
[12] IEA Heat Pump Technologies. https://heatpumpingtechnologies.org/publications/?search=Annex+35 Available online: (accessed 13/06/2022).
[13] IEA Heat Pump Technologies. https://heatpumpingtechnologies.org/annex58/ Available online: (accessed 13/06/2022).
[14] Arpagaus C, Bless F, Uhlmann M, Schiffmann J, Bertsch SS. High temperature heat pumps: Market overview, state of the art, research status, refrigerants, and application potentials. *Energy* 2018;**152**:985-1010.
[15] Confederation of European Paper Industries, Key Statistics 2020 - European Pulp & Paper Industry, 2021.
[16] Sonsale AN, Yashpal Purohit JK, Pohekar SD. Renewable & alternative energy sources for strategic energy management in recycled paper & pulp industry. *Bioresources Technol Rep* 2021;**16**:100857.
[17] Confederation of European Paper Industries. The forest fibre and paper industry in 2050, 2011.
[18] de Boer R, Marina A, Zühlsdorf B, Arpagaus C, Bantle M, Wilk V, Elmegaard B, Corberán J, Benson J. Strengthening Industrial Heat Pump Innovation - Decarbonizing Industrial Heat, 2020.
[19] Mobarakeh MR, Silva MS, Kienberger T. Pulp and Paper Industry: Decarbonisation Technology Assessment to Reach CO_2 Neutral Emissions—An Austrian Case Study. *Energies* 2021;**14**:1161.
[20] Obrist MD, Kannan R, Schmidt TJ, Kober T. Long-term energy efficiency and decarbonization trajectories for the Swiss pulp and paper industry. *Sustain Energy Technol Assess* 2022;**52**:101937.
[21] Faubert P, Barnabé S, Bouchard S, Côté R, Villeneuve C. Pulp and paper mill sludge management practices: What are the challenges to assess the impacts on greenhouse gas emissions? *Resour Conserv Recy* 2016;**108**:107-133.
[22] Hill GB, Pring EJ, Osborn PD. *Cooling Towers - Principles and Practice*. 3rd ed. London: Butterworth-Heinemann; 1990.
[23] GSE. Manuale d'uso - Certificati Bianchi - Applicativo: efficienza energetica, 2022.
[24] GME. https://www.mercatoelettrico.org/It/Statistiche/TEE/StatisticheTEE.aspx Available online: (accessed 29/11/2022).
[25] Trading Economics. https://tradingeconomics.com/commodity/carbon Available online: (accessed

29/11/2022).
[26] Li CT, Peng H, Sun J. Reducing CO_2 emissions on the electric grid through a carbon disincentive policy. *Energ Policy* 2013;**60**:793-802.
[27] Moriarty P, Honnery D. The limits of renewable energy. *AIMS Energy* 2021;**9**:812-829.
[28] Cho D, Valenzuela J. A scenario-based optimization model for determining the capacity of a residential off-grid PV-battery system. *Sol Energy* 2022;**233**:478-488.
[29] IRENA, Renewable power generation costs in 2020, 2021.

14th IEA Heat Pump Conference
15-18 May 2023, Chicago, Illinois

nZEB with GWHP in cold region of Japan

Katsunori Nagano[a], Ye Minzhi[a], Hideki Sato[b]*

[a]Hokkaido University, N13-W8, Sapporo 080-8796, Japan
[b]SANKEN SETSUBI KOGYO CO., LTD., Kinunodai 4-5-1, Tsukuba Mirai 300-2436, Japan

Abstract

The objective of this study is evaluation of the nZEB in a cold region in Japan equipped with an open-loop groundwater source heat pump (*GWHP*) system and radiant ceiling panel (*RCP*) system from both the energy conservation and the thermal environmental points of views. Firstly, the annual energy consumption was calculated based on the recorded measurements. The results indicated that this building could reach the *ZEB*-ready level in Japan. The primary energy consumption can be decreased by approximately 67% compared to that of the reference building by applying this system. Secondly, the indoor thermal comfort was evaluated based on the physical measurements and survey questionnaire. The results showed that the suspended *RCP* system could achieve comfortable indoor thermal conditions during the year. The indoor temperature was maintained within the range of 22–26 °C. Finally, energy conservation and the thermal comfort of the continuous operation methods for heating were compared to those of the intermittent operation method. Benefits of the continuous operation method were proved that a stable indoor thermal environment was maintained, and the *COP* and *SCOP* of the *GWHP* system were increased by 12%.

© HPC2023.
Selection and/or peer-review under the responsibility of the organizers of the 14th IEA Heat Pump Conference 2023.

Keywords: nZEB, groundwater source heat pump (GWHP), radiant ceiling panel (RCP), energy consevation, thermal environment;

1. Introduction

Presently, buildings account for approximately 36% of the total energy consumption and 40% of the energy-related greenhouse gas emissions worldwide [1]. Zero energy building (ZEB) or net zero energy building (nZEB) [2] have been proposed to reduce energy consumption. In Japan, the Society of Heating, Air-Conditioning, and Sanitary Engineers (SHASE) released the definition of ZEB and the evaluation method for ZEBs in 2015. ZEBs are defined as buildings that can reduce the annual net primary energy consumption to zero through renewable energy, highly efficient systems, and controlling the building load through advanced architectural designs (Figure 1). The Ministry of Economy, Trade, and Industry (METI) then issued a national definition of ZEB with four stages to promote its widespread use: ZEB (100% decrease in primary energy consumption), nearly ZEB (75% decrease), ZEB-ready (50% decrease) and ZEB-oriented (40% or 30% decrease) [3] - [5]. On the other hand, radiant heating and cooling (RHC) systems are typically used to achieve ZEB and are accepted worldwide. Specifically, the radiant ceiling panel (RCP) system is a widely used RHC system, that can directly use renewable energy, such as geothermal heat and solar heat, to heat or cool indoor air [6]. In this study, the open-loop groundwater source heat pump (GWHP) is combined with the RCP system.

The objectives of this study are evaluation of the nZEB in a cold region in Japan equipped with an open-loop groundwater source heat pump (GWHP) system and a radiant ceiling panel (RCP) from both the energy conservation and the thermal environmental point of view. Firstly, the annual energy consumption was evaluated. The results showed that this building could reach the ZEB-ready level. The primary energy consumption can be decreased by approximately 67% compared to that of the reference building. Secondly, the indoor thermal environment and comfort were evaluated from both measurement and questionnaire. It was

* Katsunori Nagano. Tel.: +81-11-706-6285; fax: +81-11-706-6285.
E-mail address: nagano@eng.hokudai.ac.jp.

clarified that the suspended RCP system could achieve comfortable indoor thermal conditions during the year, and it contribute energy conservation due to the high performance of the heat pump chiller.

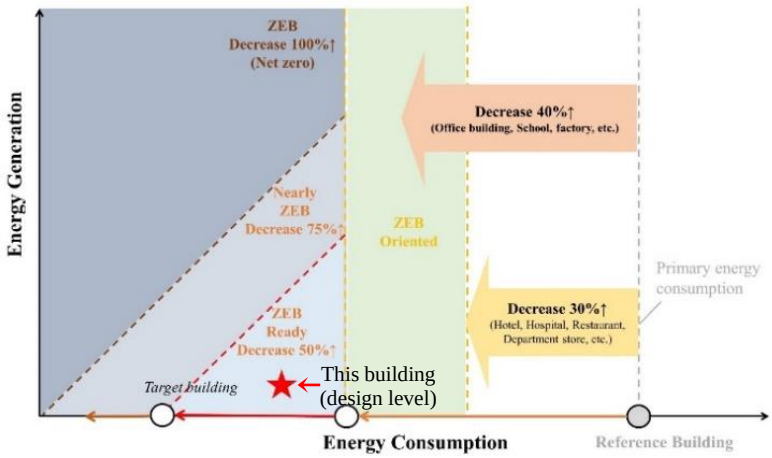


Fig. 1 Definition of the four stages of ZEBs in Japan.

2. ZEB in cold region in Japan

2.1 Building characteristics

The present study was undertaken in a newly constructed two-storey office building, located in Sapporo (latitude: 43°03'00"N, longitude: 141°21'00"E; 32 m above sea level), Hokkaido, Japan. The floor area of this building is 1949.58 m^2. Sapporo falls under the subarctic region, characterized by a mild summer and cold winter. The cold season lasts for 3.5 months from December to March, with an average daily low temperature of -5 °C and an average daily high temperature of 0.8 °C (climate data in 2020).

In this building, the ground floor includes parking, the main entrance, equipment rooms, and meeting and reception spaces. The second floor is primarily the workplace, with two large office rooms. Almost all company employees work there during the day. As shown in Figure 2, eight strings of 112 photovoltaic polycrystalline modules are installed on the south wall. To reduce heat loss, the building envelopes are well-insulated and covered with polystyrene foam plates. Table 1 summarizes the structure and heat transmission coefficients of each element. The windows use pairs of Low-E pair glass with argon gas. The area ratio of the window to the wall is 0.09 for the south and east sides, 0.04 for the west side, and 0.02 for the north side. The heat loss coefficient of this building was estimated to be 0.9 W/(m^2·K), which was calculated based on the heat flow rate and the total floor area. The suggested value is 1.6 W/(m^2·K) in the Hokkaido region in Japan. Thus, it represents that this building has excellent insulation performance.

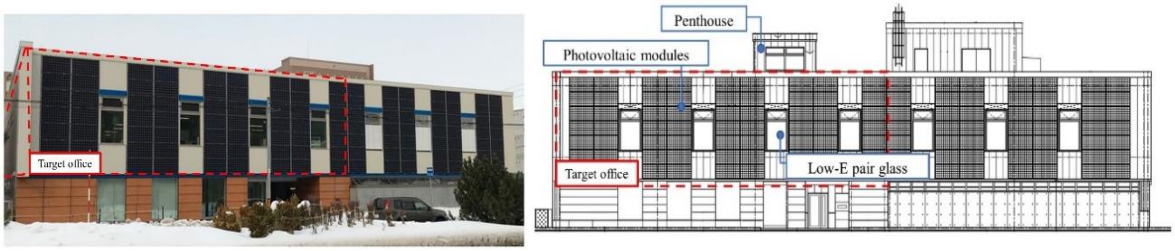


Fig. 2 South view and south elevation of the target nZEB.

2.2 HVAC systems

As illustrated in Figure 3, the radiant ceiling panel (RCP) system heats or cools two office rooms on the second floor. The outdoor-air handling units are used for the central ventilation system, which supplies fresh

processed air to the workspaces through displacement ventilation. The building also uses passive stack ventilation during summer. Figure 4 shows the combined open-loop GWHP system, RCP system, and outdoor-air handling units for the second floor. The groundwater is pumped up from a water well and its temperature is almost constant at 12 °C throughout the year. The temperature of the water supplied to the RCP system is set as 18 °C in the summer and 32 °C in the winter. Free-cooling, which the groundwater directly exchanges heat between RCP and outdoor-air handling though plate type heat exchangers, is adopted during summer (Figure 4 (a)). In winter (Figure 4 (b)), a heat pump (maximum heating output capacity of 45 kW; MCRV-P450E; Mitsubishi Electric) operates and supply hot water to the RCPs, AHU and a water storage tank. The building energy management system (BEMS) controls and monitors all system components and records a total of 167 measuring points every second.

Table 1 Thermal conductivities and heat transmission coefficients of the building envelop.

Elements	Material	Thickness [mm]	Thermal conductivity λ [W/(m·K)]	Heat transmission coefficient U [W/(m^2·K)]
Exterior wall	Galvalume	0.4	45	0.24
	Polystyrene foam	110	0.028	
	Concrete	170	1.6	
Roof	Concrete	80	1.6	0.36
	Polystyrene foam	100	0.028	
	Concrete	170	1.6	
	Air layer	-	-	
	Rock wool sound-absorbing board	12	0.17	
Floor	PVC floor tile	3	0.19	0.40
	Concrete	15	1.6	
	Polystyrene foam	50	0.028	
	Air layer	-	-	
	Concrete	310	1.6	
	Base (Rocks)	150	1	
Window	Low-E glass	26	-	1.40

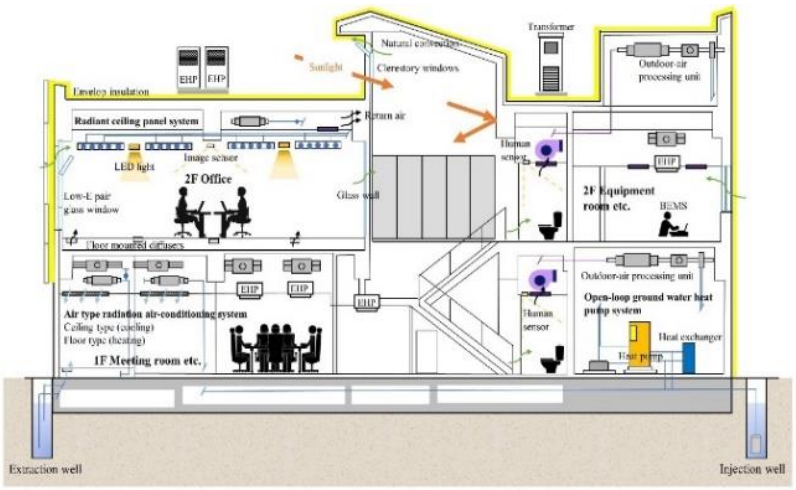
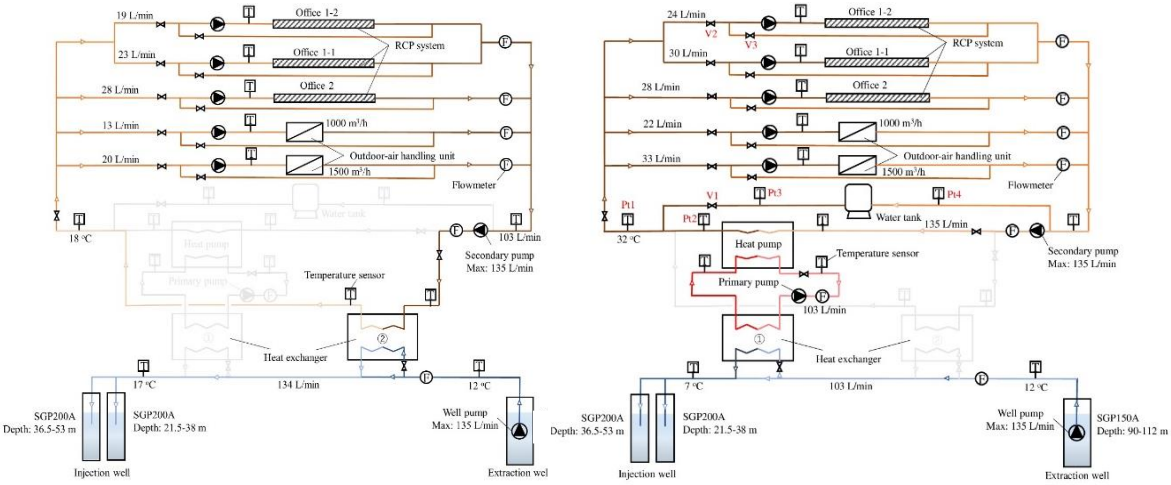


Fig. 3 HVAC systems in the target nZEB.



(a) Summer (b) Winter

Fig. 4 Schematic diagram of an open-loop GWHP system and RCP system for heating and free cooling.

2.3 Indoor space and radiant Ceiling Panels (RCP) for heating and free cooling

The target office has a large open-space office, denoted as Office 1 (457.39 m^2), where all staff sit together without partitions. In this office, the east wall is the internal wall, connected with another office and the stairwell. The west, south, and north walls are well-insulated exterior walls. The south windows (2.2 m × 1.3 m) use roller blinds that cover all window areas to prevent sunlight exposure during mid-day. In contrast, the west and north windows (1.4 m × 0.5 m) are exposed without shading. The thermal time constant of the target building, which represents the building's ability to retain heat, was calculated as 89.7 h based on the thermal mass and heat loss. As shown in Figure 5, radiant ceiling panels are suspended 1.4 m beneath the ceiling and 2.7 m above the floor, covering over 50% of the ceiling area. Each ceiling panel consists of five concave aluminum segments, with a serpentine water pipe fixed on the upper surface. The system is divided into two parts (RCP Group 1 and Group 2), which are independently controlled using different water supply circuits, as shown in Figure 6.

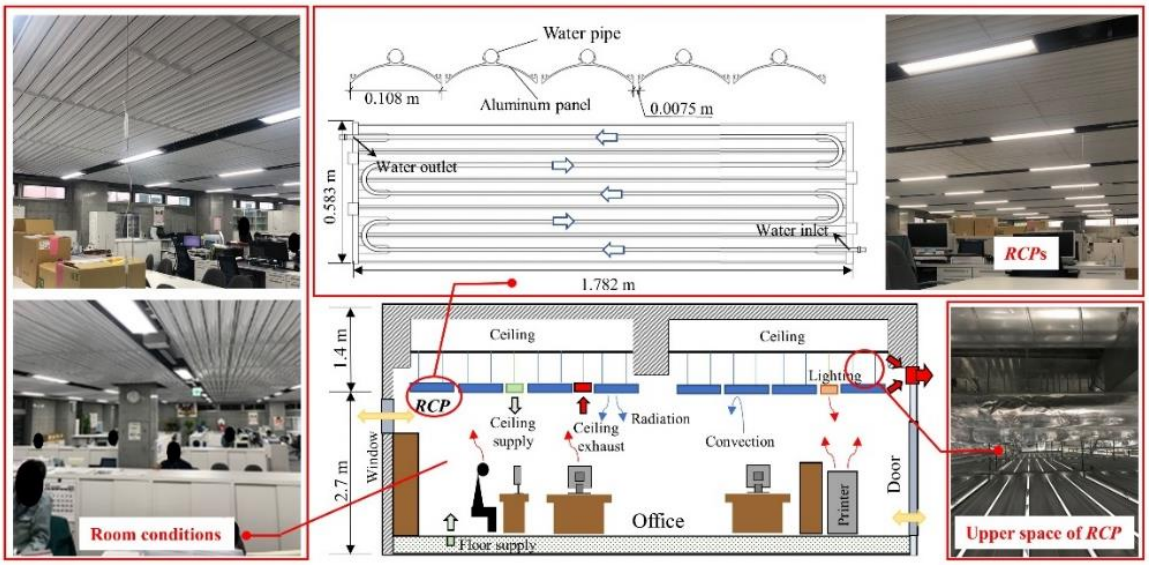


Fig. 5 Room inside views and Radiant ceiling panels (RCP) for heating and free cooling.

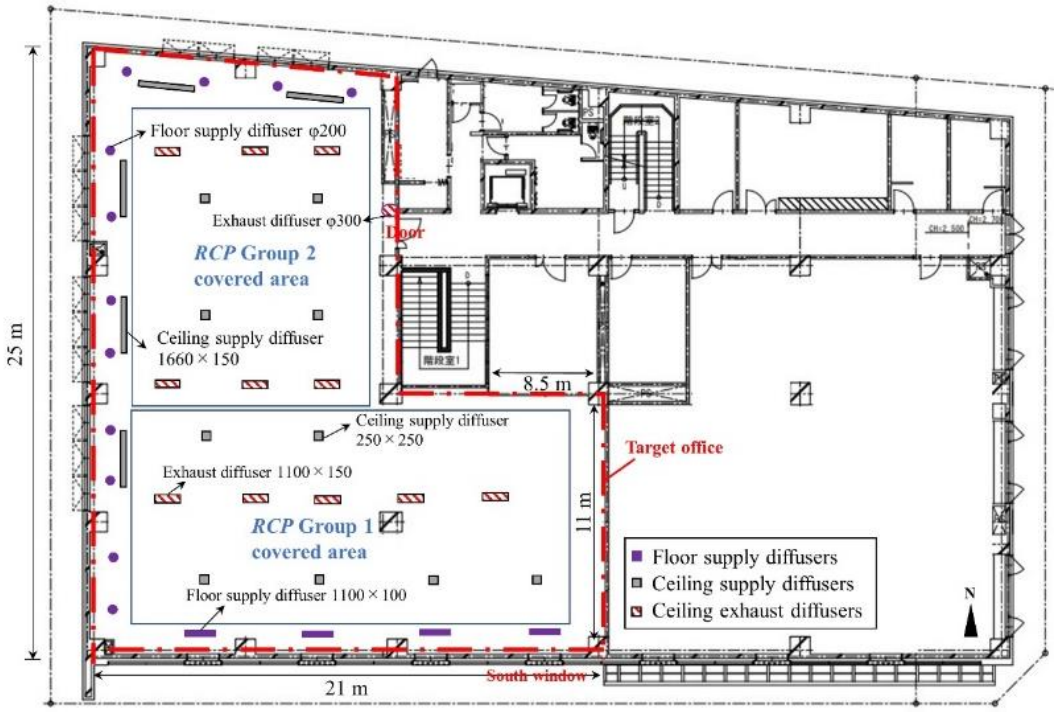


Fig. 6 The Plane of the second floor and two RCP groups.

3. Annual energy consumption

Figure 7 shows changes of the monthly average indoor air temperature and electric energy consumption of each part, including air conditioning, ventilation, lighting, hot water, elevator, and power generated by solar *PV* during 2019. From the breakdown pie chart of the annual energy consumption, it is understood that the energy consumption of the air-conditioning system accounted for 48% of the total annual energy consumed as 61,306 kWh/y, and more than 60% of that from December to March.

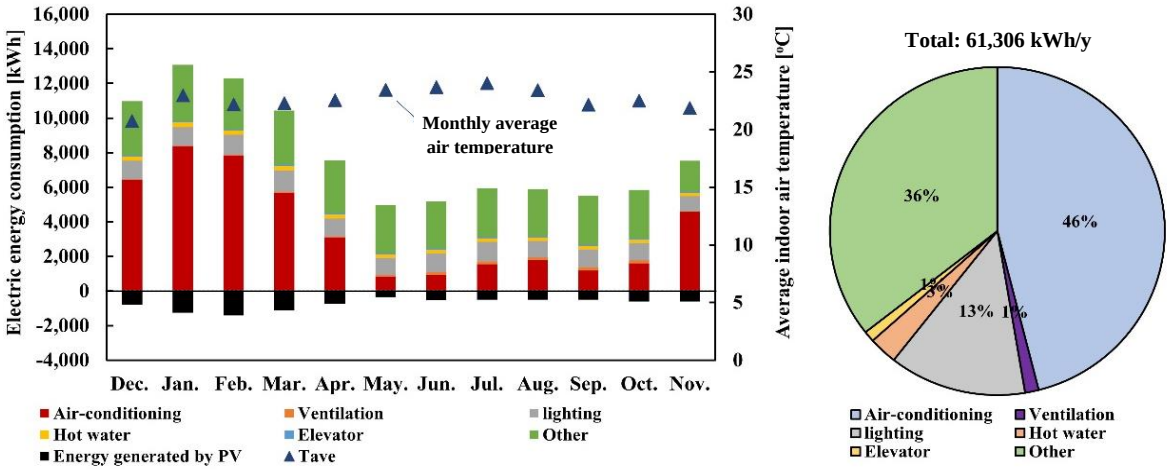


Fig. 7 Monthly electric energy consumptions and breakdown of the annual energy consumption (2019).

Figure 8 is comparisons of primary energy consumptions between for the reference building, design stage and actual measured ones in 2019 and 2020. When primary energy was calculated, conversion coefficients from electric energy to primary energy in energy-saving standards was used as 9,970 kJ/kWh during the day and 9,280 kJ/kWh in the night.

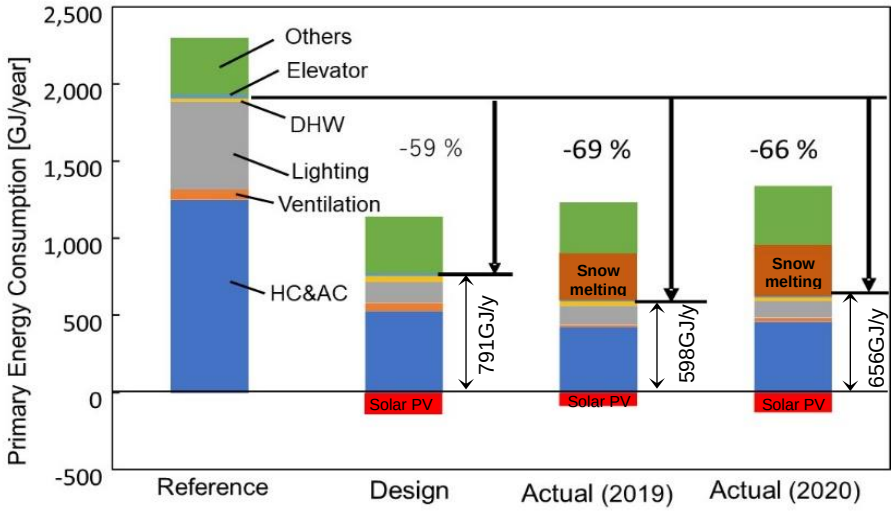


Fig. 8 Reduction of the annual energy consumption compared to those of the reference and design phase.

4. Evaluation of the Groundwater source heat pump system (GWHP)

Table 2 summarizes the operation status and performance of the groundwater heat source heat pump system (GWHP) in the second year of operation. The stand-alone COP of the water-cooled chiller used as a heat pump was 4.11, the SCOP including the primary well water pump and circulation pump was 3.62, the SCOP including the secondary circulation pump and radiant panel circulation pump was 3.28, and the SCOP of the entire heat source system including the external controller was 3.12. The SCOP of the entire heat source system including the external controller was 3.12. The SCOP of the entire heat source system was 26% lower than the COP of the heat pumps alone. This value is in the general category because the energy consumption of the well pump is large in the groundwater heat source utilization system, but the target should be 20% or less when aiming for ZEB.

Table 2 Operation status and performance of the groundwater heat source heat pump system (December 2019 – March 2020).

For heating season from December 2019 to March 2020	
Total heating amount of heat pump chiller (1)	42, 772 kWh
Power consumption of heat pump chiller[kWh] (2)	10419 kWh
Power consumption of pumps [kWh] (3) (well/heat source/room/RCP)	993/555/348/1468 kWh
COP of heat pump chiller [-] (1)/(2)	4.11
SCOP of the heat pump/RCP system [-] (1)/{(2)+(3)}	3.62/3.28/3.12
Supply temp. to the RCP	35 °C
Return temp from RCP	29 °C

The detail operating conditions of GWHP is shown in Figure 9. It can be seen that the temperature at a representative point in the room is stable at around 24°C ± 2°C per year, regardless of whether the room is free cooled in the summer, heated in the middle of the year, or heated in the winter. This room temperature stability is characteristic of an exterior-insulated building with high thermal insulation and huge heat capacity of the concrete construction. However, if the room temperature can be controlled at 22°C for heating in winter and 26°C for cooling in summer, energy savings of approximately 10% over the current level can be expected, based on the temperature difference between the inside and outside.

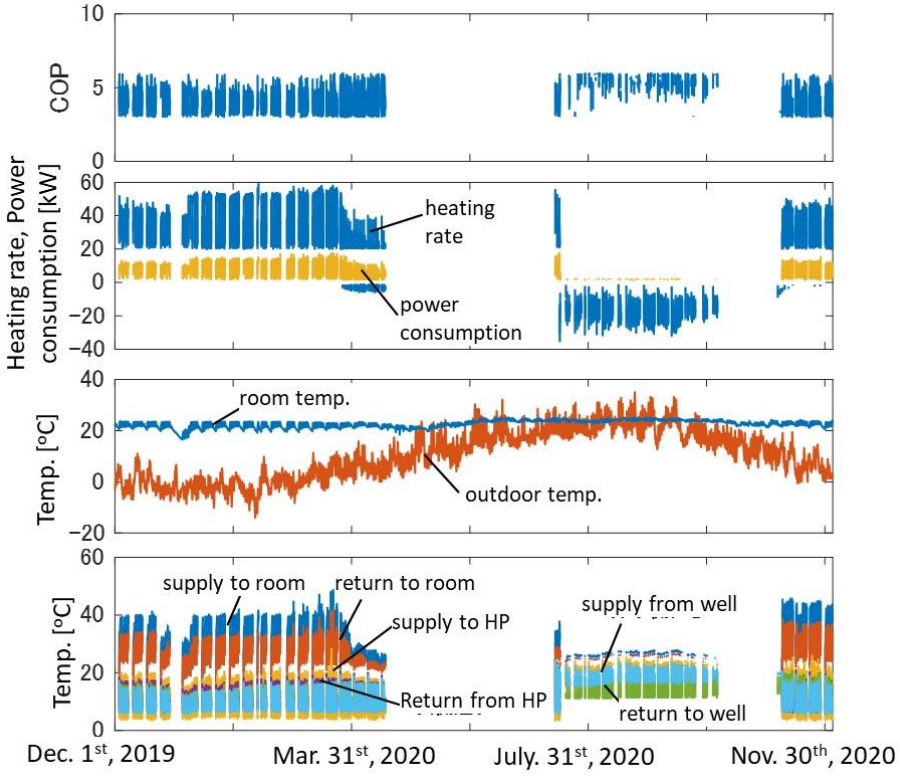


Fig. 9 Operating conditions of Groundwater source heat pump system and room temperature variations (December 1, 2019 - November 30, 2020).

5. Evaluation of vertical room temperature profile

The vertical temperature distribution in the room (6 measuring points; just below the ceiling, 0.1 m below the ceiling, FL +1.8 m, +1.0 m, +0.1 m, and just above the floor) was measured. The daily and period-averaged vertical temperatures at 10 a.m. and noon on weekdays from February 1 to February 12, 2020, including the coldest day, are shown in Figure 10. It is understood that the temperature difference between the upper and lower temperatures at FL+0 m to 1.8 m in the human activity zone is ±0.5 K at noon (the temperature directly above the floor is 23.0 to 23.4°C), except on Monday, but the temperature near the floor is 1.0 K lower than the average temperature at 10 am (the lowest temperature directly above the floor is 22.0 to 23.4°C), more than ±1.0 K. This is the range in which a temperature difference is felt at the foot on the floor. This can be improved by starting the heating earlier every morning or by using continuous heating.

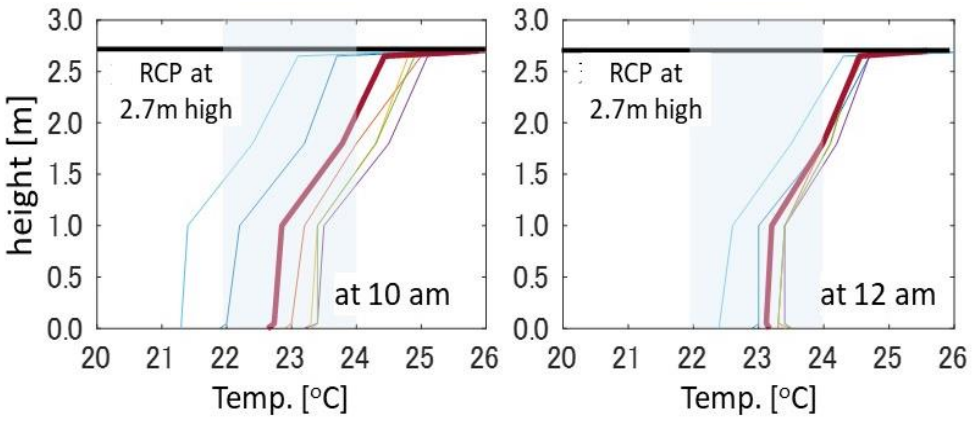


Fig. 10 Variations of average vertical room temperature profile at certain time from February 1 to February 12, 2020.

6. Evaluation of continuous heating operation

6.1 Energy conservation

Continuous heating operation was tested in order to compare the energy consumptions and indoor thermal environment with those of intermittent heating operation in the period with similar weather conditions in winter as shown in Table 3.

Table 3 Weather conditions during each heating conditions.

	Continuous1	Continuous2	Intermittent
Date	16th Dec. 2020	15th Jan. 2021	19th Jan. 2021
Ave. air temp.[°C]	-4.0	-3.3	-3.0
Max. Temp.[°C]	-2.1	-1.8	-0.6
Min. Temp.[°C]	-6.2	-7.1	-6.6
Sunlight hours [hr]	4.4	1.5	6.0
Global solar radiation [MJ/m²]	6.76	5.13	8.00
Snow fall depth [cm]	4	-	4

The results are shown in Fig. 11. In the continuous2 test, the evaporation temperature of the heat pimp was set to 7 °C, and the circulation pump speed was controlled by an inverter, which gives the temperature difference between the supply and return temperatures of the heat pump circuit was 4 K to 5 K. As a result, both COP and SCOP were improved up to 12%. The heating operation time was 22 hours per day. The COP of the heat pump machine was 4.16, and SCOP was 3.70, both 12 % higher than the values in intermittent operation. This result indicates that in an externally well insulated building and huge heat storage capacity, continuous heating can lead the reduction of energy consumption and increasing the thermal comfort by setting the proper circulation pump flow rate and the heat pump evaporation temperature.

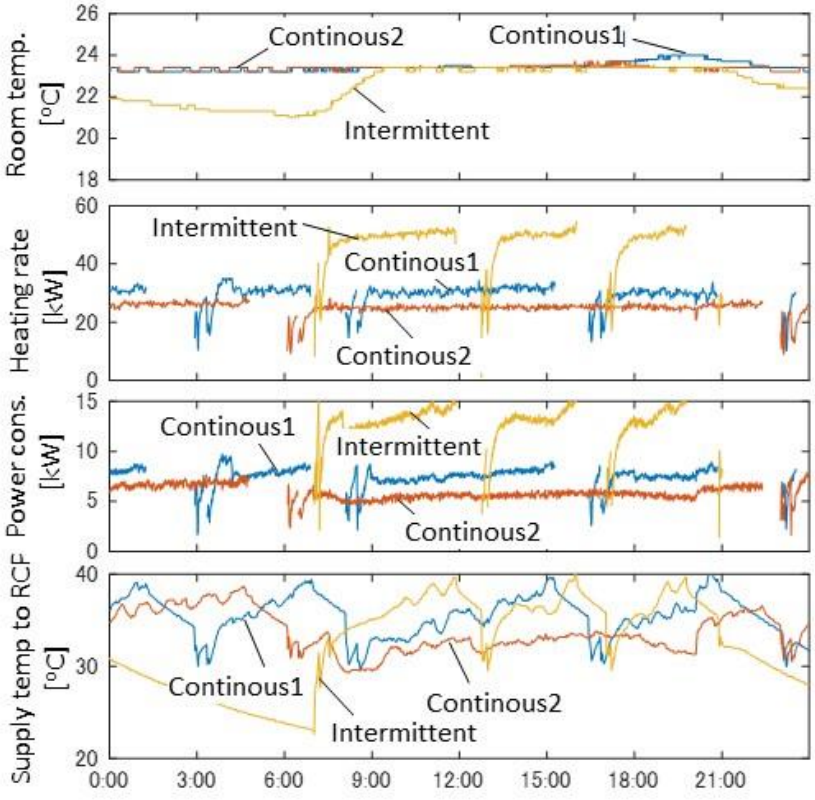


Fig. 11 Variations of room temperatures and power consumptions for three operations.

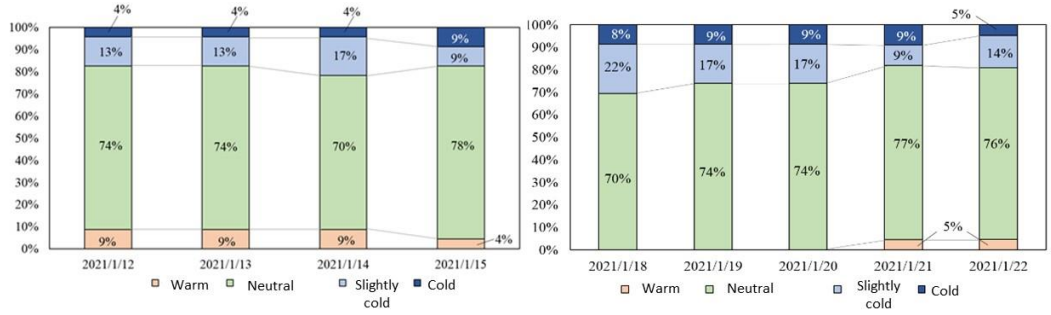
6.2 Thermal environment

The questionnaire was distributed to the workers every morning. Table 4 shows some characteristics of monitored workers. They were asked to fill in the average feeling of warmth and comfort on a 5-point scale, using integer values.

Table 4 Monitored workers in the office.

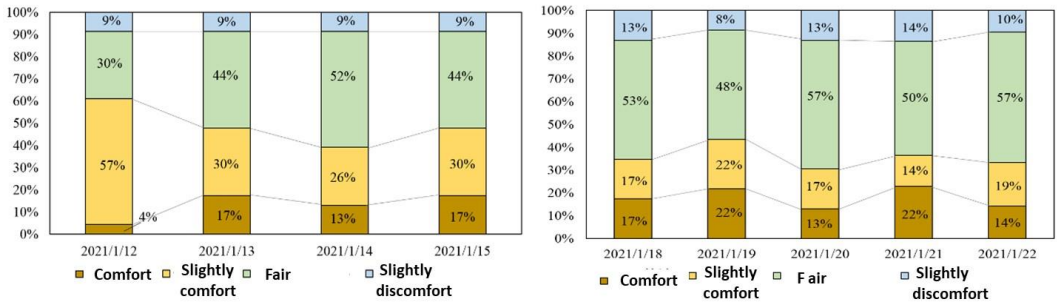
Sex		Male	Female
Total number of persons		19	4
Age/ persons	> 50	10	1
	40-50	5	1
	30-40	0	0
	20-30	5	2
Height / cm	Average	170	156
Weight / kg	Average	68	57

The results of the questionnaire survey are shown in Figure 12 for the daily distributions of thermal sensation, and comfort sensation. The average percentages of respondents who answered "cold" or "slightly cold" during the continuous and intermittent operation periods were 18% and 25%, respectively, which were 7% lower for the continuous operation period. Despite the better thermal sensation in continuous operation, the daily energy consumption of the two types was 129 kWh and 139 kWh, respectively. It is true that the power consumption of auxiliary equipment such as well water pumps and circulation pumps increase almost in proportion to the operation time as the operation time increases, but since the heat pump chiller itself operated in a highly efficient compressor speed band, the power consumption of the heat source including the auxiliary equipment power is also reduced. As a result, the SCOP (including power consumption of primary side pumps) of continuous operation was 12% higher than that of intermittent operation. On the other hand, it can be seen in the lower figures that the percentage of respondents who answered "slightly uncomfortable" was 9 % in continuous operation, while it was 12 % in intermittent operation. The average percentage of respondents who answered "comfortable" or "slightly comfortable" was 48% and 35%, respectively. This means clearly that the continuous operation gives the higher comfort level.



(a) Continuous2 (b) Intermittent

(1) Thermal sensation



(a) Continuous2 (b) Intermittent

(2) Comfort sensation

Fig. 12 Daily distributions of thermal sensation (1) and comfort sensation (2).

7. Conclusions

The building performance of the nZEB in a cold region in Hokkaido equipped with an open-loop groundwater source heat pump (GWHP) system and a radiant ceiling panel (RCP) was evaluated from both the energy conservation and the thermal environmental points of view. The primary energy consumption can be decreased by approximately 67% compared to that of the reference building by applying this system. It was shown this building could reach the ZEB-ready level from the measurement. The results showed that the suspended RCP system could achieve comfortable indoor thermal conditions during the year. The indoor temperature was maintained within the range of 22–26 °C. Finally, both energy consumption and thermal comfort of the continuous heating was compared to those of the intermittent operation. More stable indoor thermal environment was maintained and the COP and SCOP of the GWHP system was increased by 12%.

References

[1] UN, IEA. 2019 Global status report for buildings and construction; 2019. Available at https://www.iea.org/reports/global-status-report-for-buildings-and-construction-2019.

[2] A.J. Marszal, P. Heiselberg, J.S. Bourrelle, E. Musall, K. Voss, I. Sartori, A. Napolitano, Zero Energy Building - A review of definitions and calculation methodologies, Energy Build. 43 (2011) 971–979. https://doi.org/10.1016/j.enbuild.2010.12.022.

[3] Law about energy consumption performance gain of building; Law No.53; Ministry of Land, Infrastructure, Transport and Tourism (MLIT); https://www.mlit.go.jp/jutakukentiku/jutakukentiku_house_tk4_000103.html (in Japanese)

[4] G. Yoon, H. Niwa, G. Onishi, Current Situation and Actions for ZEB in Japan, REHVA J. (2018) 32–37. https://researchmap.jp/yoonlab/published_papers/16155309/attachment_file.pdf

[5] Act on Rationalization of Energy Specifications, etc. Outline of Energy Conservation Law; Ministry of Economy, Trade and Industry Agency for Natural Resources and Energy https://www.enecho.meti.go.jp/category/saving_and_new/saving/summary/ pdf/2017_gaiyo.pdf (in Japanese)

[6] Miriel, J., Serres L., Trombe A., 2002. Radiant ceiling panel heating–cooling systems: experimental and simulated study of the performances, thermal comfort and energy consumptions. Applied Thermal Engineering 22, p. 1861–1873.

14th IEA Heat Pump Conference
15-18 May 2023, Chicago, Illinois

Performance Analysis of Hybrid Ground Source Heat Pump and PVT System for Nordic Climate

Mohammad Liravi [a,*], Carsten Wemhoener [b], Yanjun Dai [c], Laurent Georges [a]

[a] Department of Energy and Process Engineering, Faculty of Engineering, NTNU – Norwegian University of Science and Technology, Kolbjørn Hejes vei 1a, 7034 Trondheim, Norway
[b] IET Institute of Energy Technology, OST Eastern Switzerland University of Applied Sciences, Campus Rapperswil, Oberseestrasse 10, 8640 Rapperswil, Switzerland
[c] School of Mechanical Engineering, Shanghai Jiaotong University, 800 Dongchuan Road, Shanghai, 200240, China

Abstract

During the past few years, Ground Source Heat Pump (GSHP) systems have attracted great attention because of the ability to improve the efficiency compared to air source heat pumps (AHSP), especially in cold climates. This paper aims to evaluate the performance of a GSHP system with series-connected solar PVT collectors for a Multi Family House (MFH) in the heating-dominated region of Oslo, Norway. The system efficiency has been obtained by a detailed simulation of the system model for 50 years using TRNSYS software. The results indicate that using the PVT collectors can significantly influence the Seasonal Performance Factor (SPF) of the system by maintaining the ground temperature compared to the case without PVT. In addition, a parametric study has been carried out to investigate how much the number of the boreholes can be reduced by adding PVT to the system while maintaining the same SPF as a standard GSHP. Hybrid systems combining GSHP and PVT collectors have the potential to contribute to the decarbonization of the MFHs in dense urban areas and to achieve Zero Energy Buildings (ZEB) in Europe.

Keywords: Solar assisted heat pump; Ground source heat pump; PVT; Solar energy; Thermal energy strorage

1. Introduction

The building sector accounts for approximately 40% of the world's energy consumption [1]. Furthermore, space cooling, space heating and Domestic Hot Water (DHW) takes a large proportion of buildings energy consumption, commonly 40-60%, depending on the climate and the type of the building [2]. Also, improving the life standards results in increasing the energy consumption of the buildings during the next years. Therefore, energy saving and further developing the current Heating, Ventilation and Air Conditioning (HVAC) systems play an important role in decreasing the world's total energy consumption.

Heat pump is an energy efficient technology which can be used for heating and cooling purposes. This technology is of interest since it consumes less electricity and primary energy compared to traditional heating systems, such as electric heaters and boilers. There exist different types of heat pumps based on the heat source of this system, such as air-source [3], water-source [4] and ground-source heat pumps [5]. Air-source heat pumps are the most common types in Norway and the main advantage of these heat pumps is the lower electricity consumption in comparison with direct electric heaters. They can be used for both cooling and heating and operate even while the ambient temperature is as low as -20 °C. The performance of these systems strongly depends on the ambient temperature, since by decreasing the source-side temperature of the heat pumps, the electrical energy consumed by the compressor increases considerably, which results in reducing the coefficient of performance (COP) of the whole system [6]. Therefore, using another source of thermal

* Corresponding author. Tel.: +(47) 46585720.
E-mail address: Mohammad.liravi@ntnu.no.

energy which can provide relatively higher and constant temperature during the year is beneficial for enhancing the system performance [7].

Ground Source Heat Pumps (GSHP) can be considered as a good solution, since these systems benefit from the high quantity of thermal energy, which is stored in the ground, and can compensate the low ambient temperature [8, 9]. Solid ground, seawater, soil ground and groundwater can be used as the heat source of GSHP systems. In Norway, the majority of GSHP installations are indirect closed-loop systems utilizing vertical boreholes in crystalline rock [10]. Using this technology, the effect of outdoor air temperature fluctuations on the performance of the system will be reduced, since the ground temperature remains relatively constant throughout the year. One of the main limitations regarding the use of GSHP systems for a region dominated by heat extraction is decreasing ground temperature after a couple of years. Depending on the borehole size and the heating demand, the average temperature of the soil may decrease by 0.5 to 1 °C each year, which results in decreasing the COP of the system after a few years [11]. This reduction in ground temperature can be reduced by increasing the borehole depth and borehole number. It should be noted that increasing the borehole depth is associated with considerable rise in drilling costs and also, increasing the number of boreholes requires large area. The thermal load of Multi Family Houses (MFH) is dominated by heating in Norway. The vast majority of MFHs are located in highly dense locations of urban areas where land for drilling a large borehole field may not be available. Therefore, another solution for maintaining the ground temperature throughout the lifespan of the GSHP should be considered.

One of the methods for overcoming this problem is using the solar heat for regenerating the boreholes by storing the absorbed solar energy during the summer. In this research, the aim is to study the performance of a Solar-Assisted Heat Pump (SAHP) system in heating dominant regions with high latitude, such as Norway. During the conversion of the solar radiation into electricity using a PV module, the surface temperature of the panel increases, which leads to decrement of solar panel efficiency. Therefore, cooling the surface temperature of the panel, which can be conducted using water or air, is necessary to maintain the efficiency. Hence, the concept of PVT collectors has been introduced to enable the potential of reducing the panel temperature to keep the electrical efficiency at a satisfactory level and at the same time, absorb the thermal energy from the received solar radiation by the collector. In other words, these collectors are a hybrid between photovoltaic (PV) and solar thermal panels, which produce electricity and heat, respectively.

Noro et al. [12] studied the energy and economic performance of using PVT panels coupled with an electric compression heat pump to provide space heating in different climates. The results of this study show that up to 65% reduction in primary energy can be achieved by using this hybrid system and also, the discounted payback of the investment can be around 10 years. Lazzarin et al. [13] investigated the effect of using a hybrid system of GSHP-PVT for a refurbished building and optimized the sizing of the system by considering five alternatives, increasing the solar field from 20 m^2 to 60 m^2 and reducing the ground field from 500 m to 300 m. The dynamic simulation of this study reveals that the most efficient alternative for this system is the case with 60 m^2 PVT combined with boreholes of 300 m. Sommerfeldt et al. [6] carried out a parametric study of the technical and economic performance of GSHP-PVT system for a MFH located in Sweden. The results of this study show that using PVT modules can result in reducing the borehole length by 18% and maintaining the SPF of the system compared to the case without PVT.

In this work, PVT collectors are used for the thermal regeneration of the boreholes while they are not operated for heating purposes. TRNSYS, which is a dynamic simulation software, is used for simulating the PVT-GSHP system. The main objective of this paper is to investigate the energy performance of GSHP system combined with glazed and unglazed PVT collectors for a MFH in Oslo. The heating system provides both Space Heating (SH) and Domestic Hot Water (DHW) and is designed in such a way that producing DHW is prioritized over SH when both demands occur at the same time. Moreover, a sensitivity analysis has been carried out to study the effect of using different number of boreholes. The performance of a GSHP with a reduced number of boreholes combined with PVT collectors (to compensate the temperature reduction after some years of operation) is compared to a standard GSHP without PVT.

2. Model description

In this work, the simulation of a GSHP system for providing SH and DHW for a MFH is presented. The simulated building is a four-story MFH with net floor area of 420 m^2 per each floor which has the characteristics of a Norwegian building constructed between 1991 to 2000, i.e., generation 5 in [14]. The heating system designed for this building includes a combined PVT-GSHP system and direct electric heaters for covering the peak load. The simulation is carried out using the dynamic simulation software, TRNSYS 17, with time step of 2 min for the whole period of the study, which is 50 years.

In order to recharge the extracted heat from the ground a series/regenerative system is used, where the PVT loop is connected to a plate heat exchanger on the evaporator side of the heat pump. In this configuration, when the heat pump is on, the PVT boosts the borehole loop temperature and when the heat pump is off, the PVT regenerate the ground. The schematic overview of the system is shown in Figure 1.

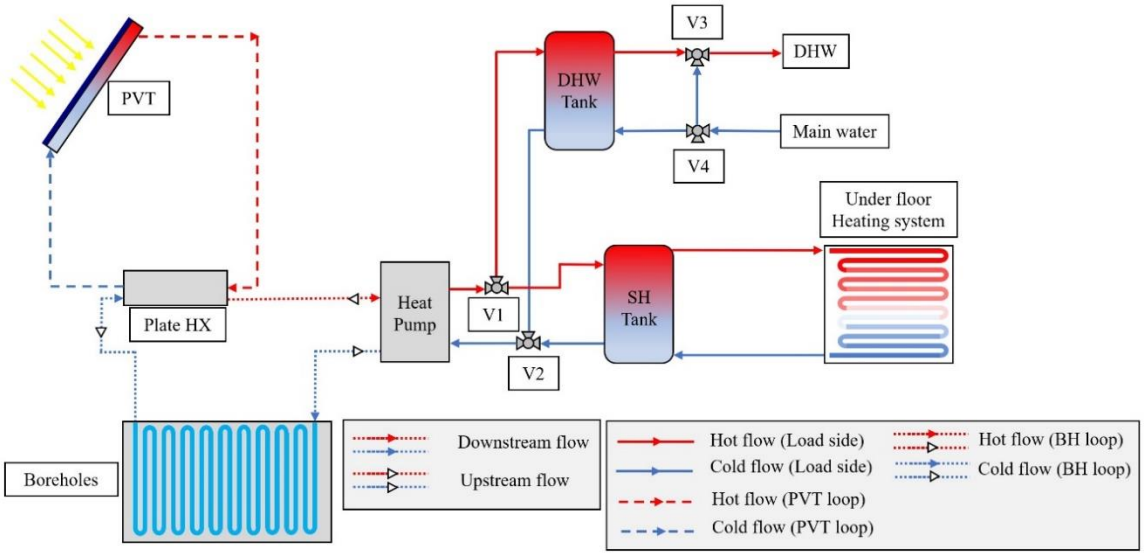


Fig. 1. Base scheme of PVT+GSHP in series/regenerative mode.

The meteorological data has been obtained from Meteonorm Software. The Norwegian standard for calculation of energy needs and energy supply (SN-NSPEK 3031: 2021) [15] has been used to define the internal gains by people, lights and equipment, infiltration rate, ventilation rate and Domestic Hot Water (DHW) demand. Since the building is located in a heating dominant region, there is no need for cooling and only heating is required. Based on Norwegian standards, the set point temperature for heating the residential buildings is 20 °C for the night and 22 °C during the day and 55 °C for DHW. Figure 2 shows the hourly variation of heat generated by internal gains and heating demand for DHW according to [15].

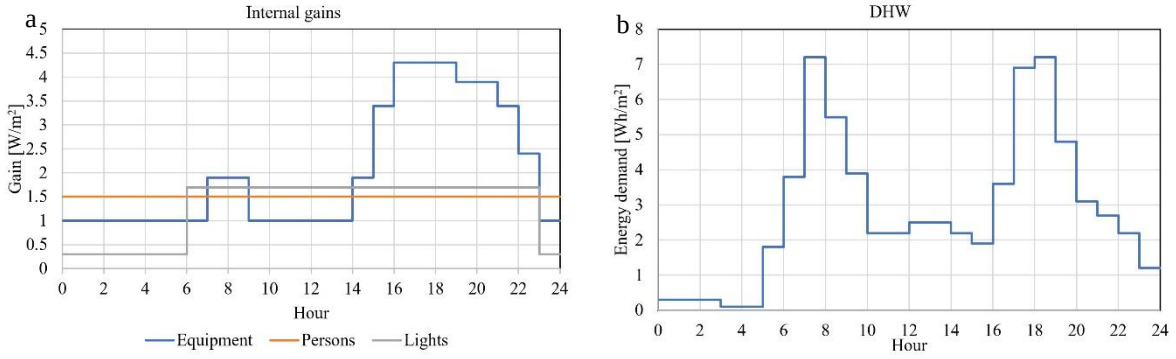


Fig. 2. Hourly variation of a) heat generated by internal gains and b) heat required for DHW.

The yearly simulation gives an annual and specific energy demand for heating of the building by 179 MWh/year and 107 kWh/(year.m^2), respectively. Figure 3 shows the monthly SH and DHW demand during the year. Also, the maximum power required for providing both SH and DHW is 104 kW.

Simulations has shown that a HP covering 70% of the peak power results in a large energy coverage factor., Therefore a water-to-water single-speed heat pump with total heating capacity of 69.44 kW has been chosen. The HP is expected to cover approximately 90% of the energy demand of the building and the remaining comes from direct electric heaters, which can cover the peak load. Three different layouts have been used to provide the required heat for the building, including the standard GSHP system, GSHP-glazed PVT and GSHP-unglazed PVT. The heating system provides both SH and DHW and is designed in such a way that producing DHW is prioritized over SH when both demands occur at the same time. In this study, the baseline model comprises 12 single U-shape and water-filled non-grouted boreholes of 200 m depth with spacing of 20 m. The PVT collectors used for the study have the PV efficiency of 17.02% at reference condition with a temperature coefficient of -0.0041 (1/K). Two different numbers of PVT collectors have been used which correspond to area of approximately 50 m^2 and 100 m^2.

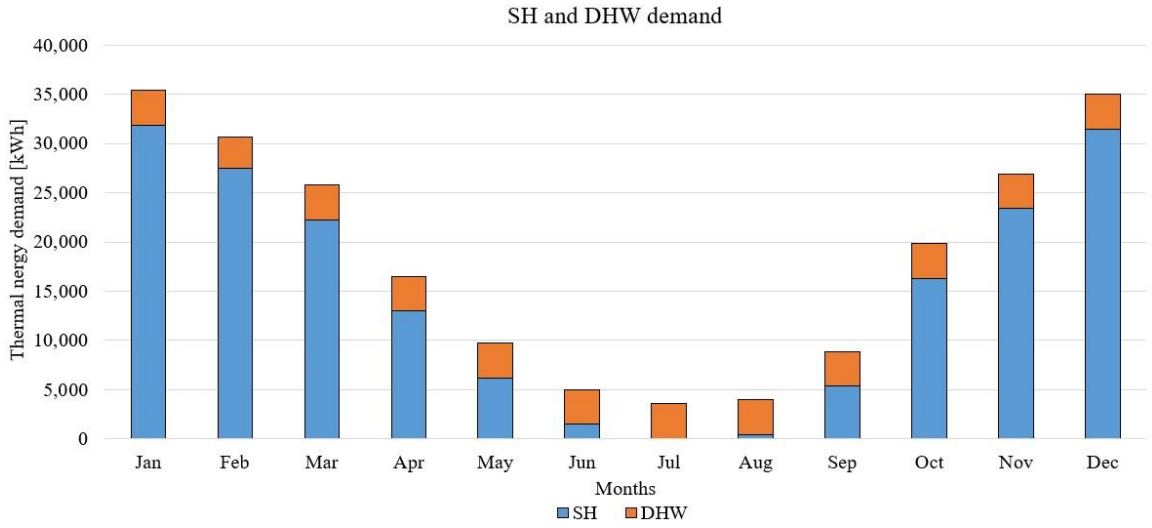


Fig. 3. Monthly SH and DHW demands of the building.

In the standard GSHP layout without PVT, only heat extraction from the boreholes occurs, which results in reducing the borehole temperature after some years of operation. In GSHP-PVT layout, the recharge of the ground temperature occurs when the outlet temperature from the PVT collector is high enough to be able to recharge the borehole. In this study, the PVT circuit turns on when the temperature difference between the outlet of the PVT and inlet of the plate heat exchanger is higher than 6 K. Also, two different modes for GSHP with PVT systems have been used. In downstream mode, the outlet flow from the borehole enters the plate heat exchanger and absorbs thermal energy from the PVT loop, and then enters the evaporator side of the HP. In upstream mode, the flow direction in BH loop has been reversed and the outlet of the BH flows directly to the evaporator side of the HP and then, the outlet from the HP flows into the plate heat exchanger to be recharged by the PVT loop.

The Key Performance Indicators (KPIs) used for assessing the performance of the system are as follows:

$$SPF = \frac{Q_{H,HP}}{E_{Comp}} \tag{1}$$

$$SPF_4 = \frac{Q_{SH}+Q_{DHW}}{E_{Comp}+E_{Aux}+E_{Pumps}} \tag{2}$$

Where SPF is the Seasonal Performance Factor for the HP, $Q_{H,HP}$ and E_{Comp} are heat delivered by the condenser and electricity consumed by the HP, respectively. SPF_4 is the performance factor of the whole system which is equal to the ratio between the heat delivered for SH and DHW over the electricity consumed

by the HP, auxiliary heaters and the pumps in the system. SPF_4 also takes into account the thermal losses of the two hot-water storage tanks.

3. Results and discussion

In this section, the results from the long-term performance analysis of the combined GSHP-PVT system are presented. Figure 4 shows the electricity consumption of each component in the standard GSHP system. Based on this chart, since the HP system cannot cover all the heating demand of the building, a significant amount of electricity is consumed by the auxiliary heaters to cover the peak load in January, February and December. The amount of energy consumed by the peak load system increases after some years of operation, since the heat provided by the HP decreases gradually with the decreasing ground temperature.

Figure 5 shows the average BH temperature (T_m) of the standard GSHP system with 12 BHs. In this system, since there are no other energy resources to recharge the extracted thermal energy from the BHs, a significant reduction in the average BH temperature can be seen. This reduction can result in a considerable reduction in the performance of the HP system. Figure 6 shows the yearly variation of SPF and SPF_4 of the same system with and without PVT collectors in the period of 50 years. Based on this figure, it can be seen that the SPF and SPF_4 decrease as a result of decreasing the outlet BH temperature, but in case of using PVT collectors, since a part of extracted heat from the ground can be recharged, less reduction in SPF and SPF_4 is observed.

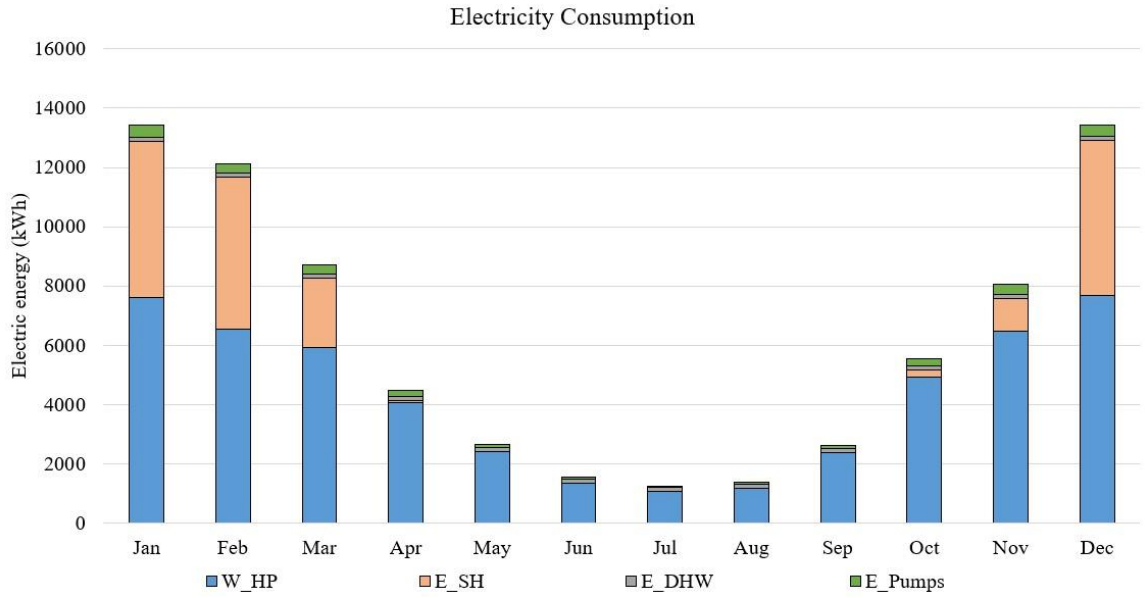


Fig. 4. Monthly electricity consumption of the heat pump and auxiliary heaters in GSHP system with 12 BH.

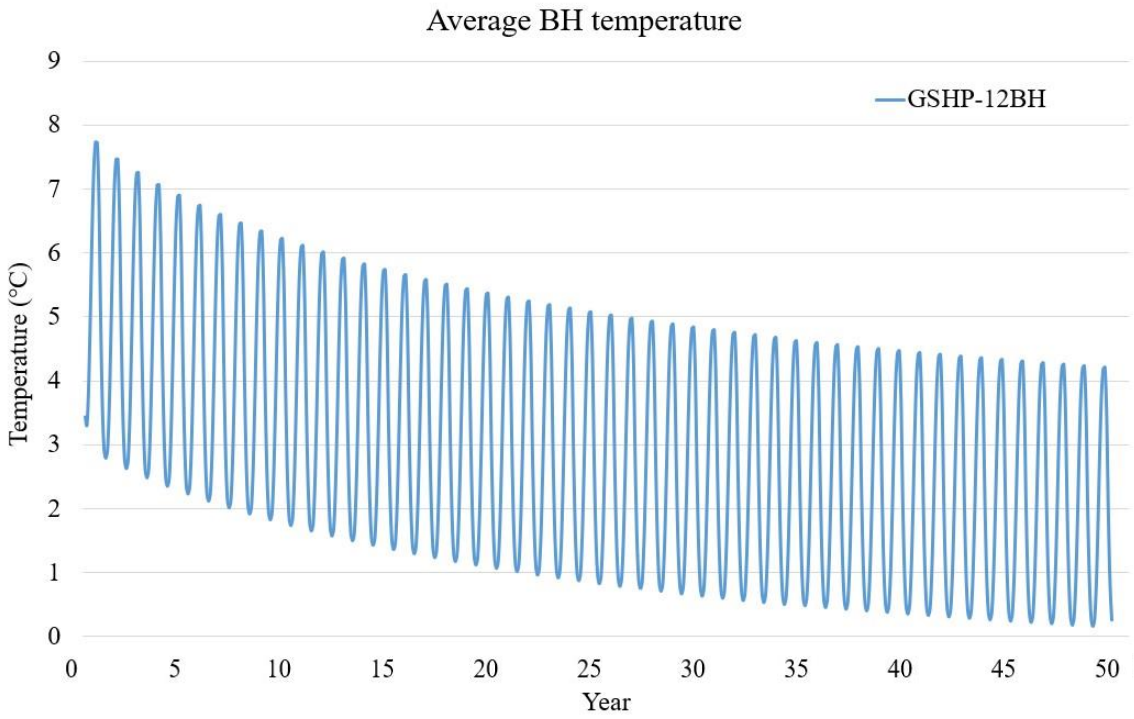


Fig. 5. Variation of average fluid temperature for GSHP simulation with 12 BH in 50 years.

The reason for reducing the SPF_4 of the system after some years of operation can be better seen in Figure 7. According to this figure, the percentage of heat provided using the HP reduces as the result of reducing the BH temperature. This reduction results in increasing the percentage of the heat provided using the peak load system, which subsequently leads to decreasing the SPF_4 of the system.

In Figure 6, the GSHP-PVT system has downstream layout with unglazed PVT collectors. Since the glazed PVT collector has higher thermal efficiency, the same case study has been investigated using the glazed collectors to study the effect of BH temperature reduction and consequently reduction in SPF and SPF_4 using these PVTs. It should be noted that since the glazed PVT collectors typically can produce higher temperatures, the electrical efficiency of these collectors is lower. Therefore, the choice between the glazed and unglazed collectors highly depends on the priority of thermal or electrical energy production.

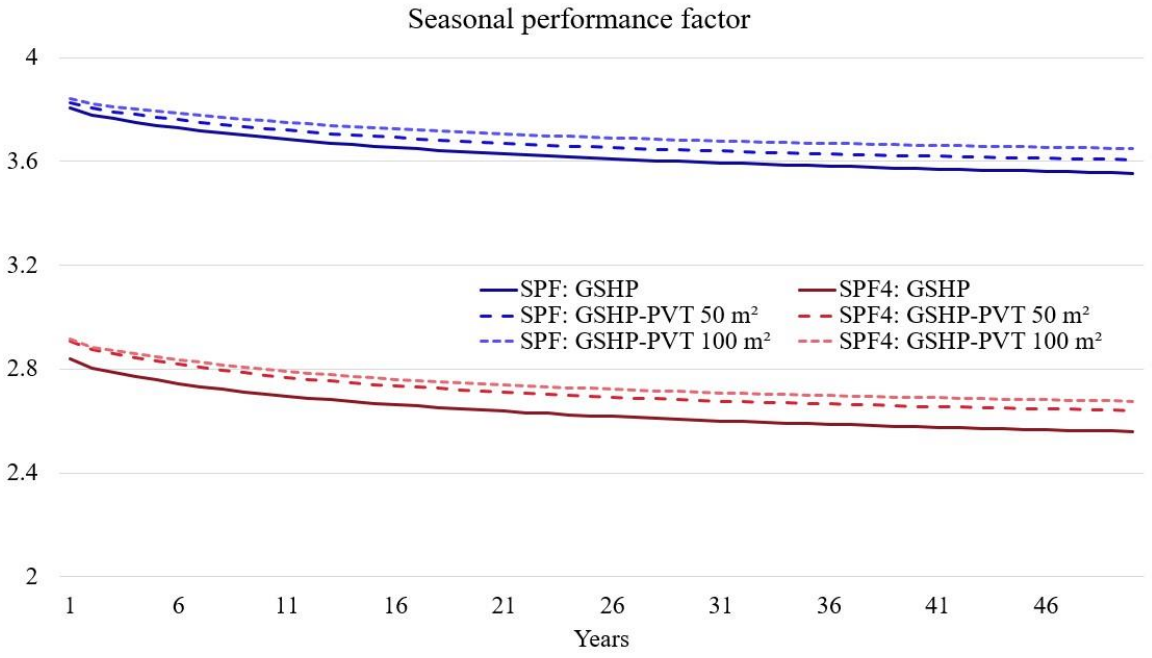


Fig. 6. Yearly variation of SPF and SPF_4 of GSHP and GSHP-PVT systems with 50 m^2 and 100 m^2 collector area.

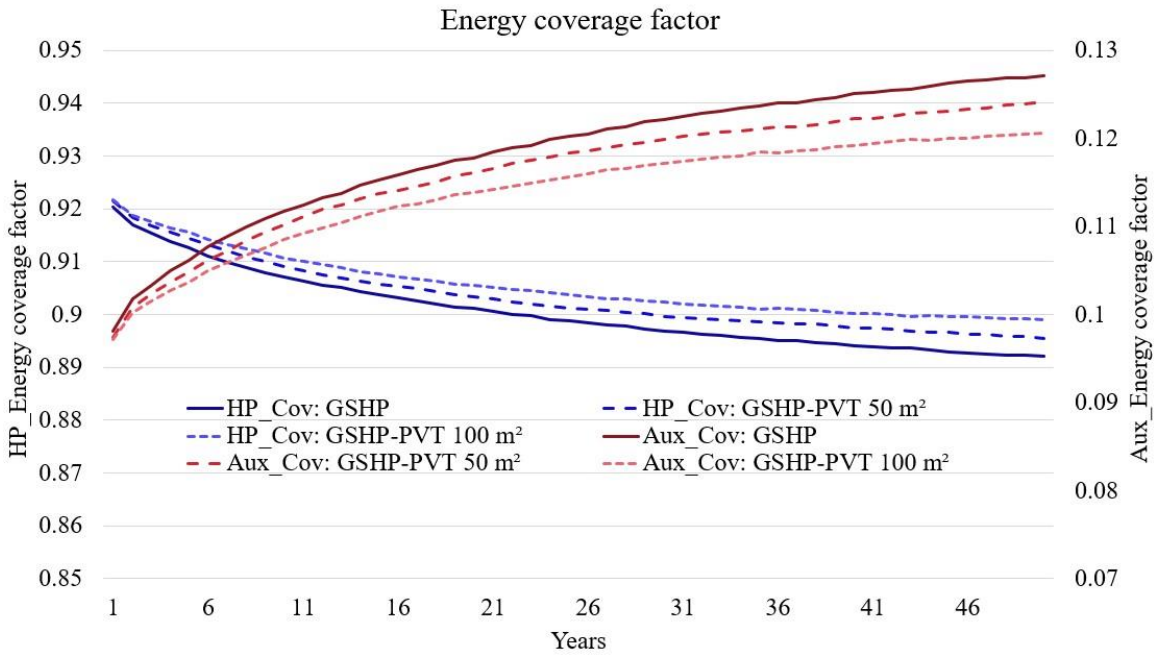


Fig. 7. Yearly variation of HP and auxiliary system energy coverage of GSHP and GSHP-PVT systems with 50 m^2 and 100 m^2 collector area.

In order to investigate the effect of using each system layout on the ground heat extraction, 5 different cases are compared: standard GSHP, GSHP with glazed or unglazed PVT collectors with downstream or upstream layouts. Figure 8 shows the monthly variation of heat extraction/rejection from/to the BH field in different cases with 12 BH and 100 m^2 PVT collectors. According to this chart, the net amount of heat extraction in upstream layout from the BH is insignificantly lower than that of downstream configuration. The reason for this difference can be explained by the difference between the inlet temperature to the BH. In upstream layout, the outlet flow from the evaporator side of the HP flows into the plate heat exchanger and extracts energy from PVT loop and then enters the BH, while in downstream flow, the outlet from the HP directly flows into the BH without being recharged by PVT loop. Also, it can be observed that using glazed PVT collectors, more thermal energy can be injected into the ground compared to the cases with unglazed PVT, which results in having lower net energy extraction from the BH during the year. Therefore, it can be concluded that the upstream layout using glazed PVT collectors has lower BH temperature reduction compared to other cases.

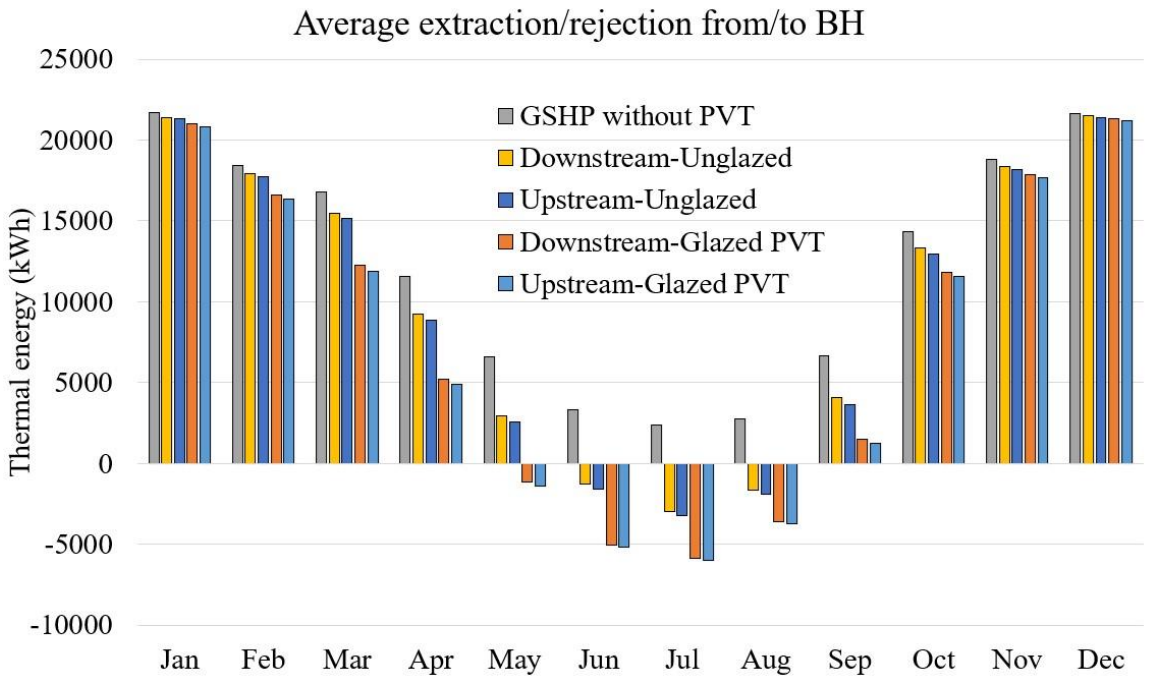


Fig. 8. Monthly variation of heat extraction/rejection from/to BH in different cases with 12 BH and 100 m^2 PVT collectors.

Table 1 shows the SPF and SPF_4 of the standard GSHP, GSHP with glazed and unglazed PVT for both downstream and upstream layouts. In this table the reduction in system performance after 50 years of operation can be observed. According to the table, approximately 6.6% reduction in SPF of GSHP system without PVT collectors can be seen from the first to the last year of operation. As explained earlier, this reduction is due to the reduction in the BH temperature. In case of using PVT collectors, since a part of the extracted heat from the BH can be regenerated, less reduction in SPF and SPF_4 can be seen. For instance, the downstream case with 100 m^2 of glazed PVT shows only 4.1% reduction SPF after 50 years.

Also, it can be concluded that the percentage of the reduction in SPF and SPF_4 in cases of using upstream layout is slightly lower than that of downstream, since in this configuration, the amount of net heat extraction from the BHs is slightly lower than that of downstream. However, the system performance in downstream cases is higher than that of upstream layout. The reason for this statement is the higher inlet temperature of the flow which enters the evaporator side of the HP. As clearly shown in figure 1, in downstream flow, the outlet flow from the BH first enters the plate heat exchanger and absorbs the thermal energy from PVT loop and then, flows into the HP, while in upstream flow, the outlet flow from the BH directly enters the HP.

Also, it can be seen that the system performance in cases with glazed PVT collectors is slightly higher than the cases with unglazed PVT. As explained earlier, glazed PVT collectors have better thermal efficiency because of a layer of air gap between the cover glass and PV cell, which acts as a layer of insulation. Therefore,

it can be expressed that for this system, the downstream layout using the glazed PVT collectors can show better performance, in terms of thermal efficiency, compared to the other investigated cases.

Another interesting fact from this table is that by using PVT collectors, a smaller BH field can be used while achieving the same performance than a standard GSHP (without PVT). For instance, the SPF of the standard GSHP system with 12 BHs in the first and last year of operation is 3.8 and 3.55, respectively, which is close to that of downstream case with 50 m^2 glazed PVT collectors with 10 BHs, which varies from 3.8 to 3.58 after 50 years. By comparing these two cases, it can be concluded that using PVT collectors can compensate the reduction in BH temperature and it can also help the system to have smaller BH fields for a same thermal performance (here a reduction of 16%).

Table 1. SPF and SPF_4 reduction of different cases after 50 years of operation

Case	PVT area [m^2]	Number of BHs	Year	SPF	SPF_4
GSHP	-	12	1	3.8	2.84
			50	3.55	2.56
GSHP	-	10	1	3.75	2.77
			50	3.49	2.49
GSHP-Unglazed PVT Downstream	50	12	1	3.82	2.91
			50	3.6	2.64
GSHP-Unglazed PVT Downstream	50	10	1	3.78	2.84
			50	3.54	2.57
GSHP-Unglazed PVT Downstream	100	12	1	3.84	2.91
			50	3.65	2.68
GSHP-Unglazed PVT Downstream	100	10	1	3.79	2.85
			50	3.59	2.61
GSHP-Unglazed PVT Upstream	50	12	1	3.82	2.9
			50	3.6	2.64
GSHP-Unglazed PVT Upstream	50	10	1	3.77	2.84
			50	3.54	2.57
GSHP-Unglazed PVT Upstream	100	12	1	3.83	2.9
			50	3.64	2.67
GSHP-Unglazed PVT Upstream	100	10	1	3.78	2.84
			50	3.58	2.61
GSHP-Glazed PVT Downstream	50	12	1	3.85	2.92
			50	3.64	2.67
GSHP-Glazed PVT Downstream	50	10	1	3.8	2.86
			50	3.58	2.6
GSHP-Glazed PVT Downstream	100	12	1	3.89	2.95
			50	3.73	2.75
GSHP-Glazed PVT Downstream	100	10	1	3.84	2.88
			50	3.67	2.68
GSHP-Glazed PVT Upstream	50	12	1	3.83	2.91
			50	2.62	2.65
GSHP-Glazed PVT Upstream	50	10	1	3.78	2.84
			50	3.56	2.59
GSHP-Glazed PVT Upstream	100	12	1	3.85	2.92
			50	3.7	2.72
GSHP-Glazed PVT Upstream	100	10	1	3.8	2.86
			50	3.64	2.66

Another parameter which has been studied, is the electricity production using the PVT collectors. Figure 9 depicts the monthly electricity production of 100 m^2 PVT collectors and the annual solar production using glazed and unglazed collectors are 12.6 MWh and 13.5 MWh, respectively. In conclusion, while the glazed PVT collectors improve the thermal performance compared to unglazed PVT, they reduce the electricity production. In future work, this balance between electricity used by the GSHP and the electricity generated by the PVT should be investigated.

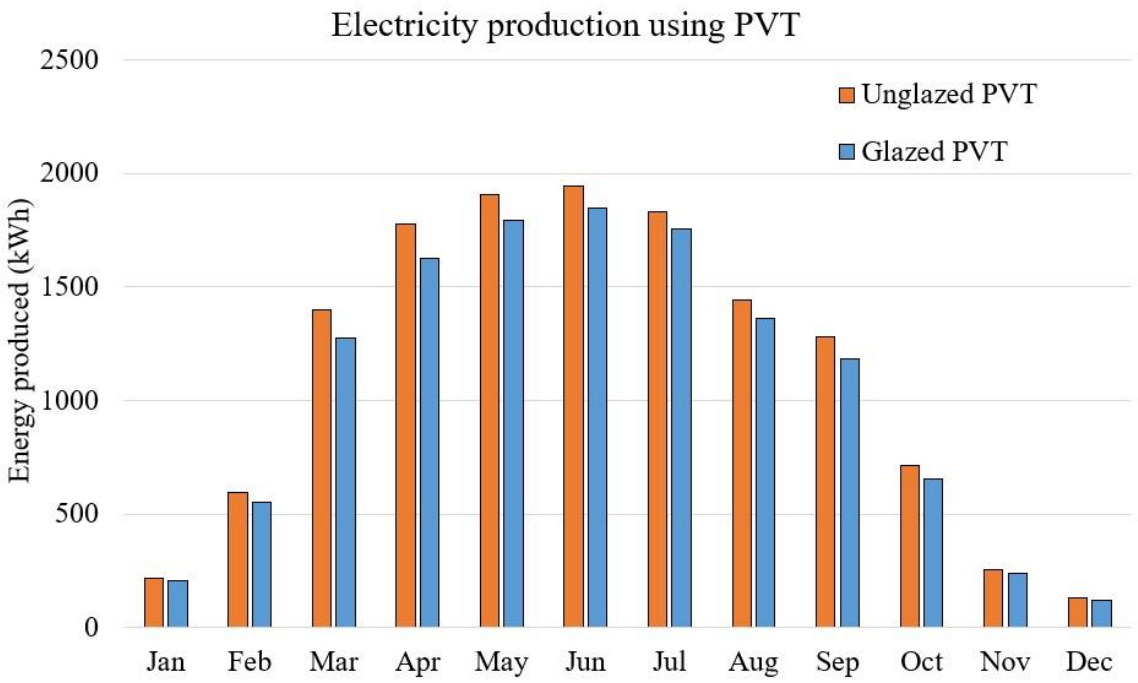


Fig .9. Monthly variation of energy produced by 100 m^2 PVT collectors.

4. Conclusions and future works

In this study, the long-term performance analysis of a combined system of GSHP-PVT with different layouts, downstream and upstream, and glazed and unglazed PVT collectors over the period of 50 years is investigated. The results of this study confirm that using PVT collectors can significantly impact the amount of heat extracted from the BH fields. Also, it can be concluded that the upstream flow results in lower temperature reduction in the BH filed compared to downstream flow. Furthermore, the results show that the downstream flow with glazed PVT collectors can exhibit better thermal performance in comparison with the other investigated cases.

One of the most interesting results obtained by this study is using PVT collectors in GSHP systems to reduce the size of the BH fields. For instance, the SPF of the standard GSHP system with 12 BHs over the period of 50 years is approximately similar to that of the downstream case with 50 m^2 glazed PVT collectors with 10 BHs. As the future works, it is worth studying the techno-economic performance of these systems to evaluate the gains in life cycle costs, including investment costs. In other words, it should be clarified that how much gain, in terms of investment costs, can be achieved by adding PVT collectors to the system and reducing the BH size.

References

1. Cao, X., X. Dai, and J. Liu, *Building energy-consumption status worldwide and the state-of-the-art technologies for zero-energy buildings during the past decade.* Energy and buildings, 2016. **128**: p. 198-213.
2. You, T., et al., *Hybrid photovoltaic/thermal and ground source heat pump: Review and perspective.* Renewable and Sustainable Energy Reviews, 2021. **151**: p. 111569.
3. Huang, S., et al., *Performance comparison of a heating tower heat pump and an air-source heat pump: A comprehensive modeling and simulation study.* Energy conversion and management, 2019. **180**: p. 1039-1054.
4. Cardemil, J., et al., *Thermal analysis of a water source heat pump for space heating using an outdoor pool as a heat source.* Journal of Building Engineering, 2021. **33**: p. 101581.
5. Xu, L., et al., *Hybrid ground source heat pump system for overcoming soil thermal imbalance: A review.* Sustainable Energy Technologies and Assessments, 2021. **44**: p. 101098.
6. Sommerfeldt, N. and H. Madani, *In-depth techno-economic analysis of PV/Thermal plus ground source heat pump systems for multi-family houses in a heating dominated climate.* Solar Energy, 2019. **190**: p. 44-62.
7. Lazzarin, R. and M. Noro, *Lessons learned from long term monitoring of a multisource heat pump system.* Energy and Buildings, 2018. **174**: p. 335-346.
8. Spitler, J.D. and S. Gehlin, *Measured performance of a mixed-use commercial-building ground source heat pump system in Sweden.* Energies, 2019. **12**(10): p. 2020.
9. Busato, F., R. Lazzarin, and M. Noro, *Ground or solar source heat pump systems for space heating: Which is better? Energetic assessment based on a case history.* Energy and Buildings, 2015. **102**: p. 347-356.
10. Stene, J., et al. *Design and operation of ground-source heat pump systems for heating and cooling of non-residential buildings*. in *9th International IEA Heat Pump Conference, Zürich, Switzerland*. 2008.
11. You, T., et al., *An overview of the problems and solutions of soil thermal imbalance of ground-coupled heat pumps in cold regions.* Applied Energy, 2016. **177**: p. 515-536.
12. Noro, M. and R.M. Lazzarin, *Hybrid PhotoVoltaic–Thermal heat pump systems: energy and economic performance evaluations in different climates.* International Journal of Low-Carbon Technologies, 2018. **13**(1): p. 76-83.
13. Lazzarin, R. and M. Noro, *Photovoltaic/Thermal (PV/T)/ground dual source heat pump: Optimum energy and economic sizing based on performance analysis.* Energy and Buildings, 2020. **211**: p. 109800.
14. IEE Project EPISCOPE, launched in April 2013, https://episcope.eu/building-typology/country/no/
15. Norwegian standard for calculation of energy needs and energy supply, accessed 3 March 2021, https://www.standard.no/no/Nettbutikk/produktkatalogen/Produktpresentasjon/?ProductID=1393607

14th IEA Heat Pump Conference
15-18 May 2023, Chicago, Illinois

Quantification of electrical load flexibility offered by an air to water heat pump equipped single-family residential building in Sweden

Sindhu Kanya Nalini Ramakrishna[a], Torbjörn Thiringer[a], Caroline Markusson[b]

[a] Chalmers University of Technology, Hörsalsvägen 11, Gothenburg 412 58, Sweden
[b] RISE Research Institutes of Sweden, Sven Hultins gata 5, Gothenburg 412 58, Sweden

Abstract

Heat pumps are widely used in Swedish single-family houses for space and water heating applications, of which the most common is air-to-water heat pumps. Today, there is an increase in the variability and uncertainty of electricity production due to an increment in the share of electricity generation by intermittent energy sources. Hence, as opposed to the conventional power system operation, there is variability and uncertainty in electricity consumption and production. One possible way of addressing the challenge of balancing the power system is by using heat pumps as a flexibility resource. In this regard, this study quantifies the flexibility potential by developing and integrating a mathematical model of an air-to-water heat pump with the thermal model of a building with a standard way of space heating i.e., radiator heating. The result from this study will provide an estimate of flexibility levels from space heating, in terms of varying levels of reduced electricity consumption as a function of indoor temperature, during different outdoor ambient temperatures. Furthermore, the result of this study helps in employing suitable measures for demand-side-management to support the power system during severe problems.

© HPC2023.
Selection and/or peer-review under the responsibility of the organizers of the 14th IEA Heat Pump Conference 2023.

Keywords: Air-to-water heat pump, Flexibility, Single family residential building, Intermittent energy sources, Power system ;

1. Introduction

The role of electricity is significant for social and economic development. In Sweden, increasing emphasis to reduce greenhouse gas emissions has resulted in a transition of electricity production from conventional fossil fuel-based power plants towards renewable-based power plants[1] i.e., the share of electricity production from wind and solar is increasing. However, the electricity production from these sources is highly intermittent in nature. As a result, in the current power system, there is variability as well as uncertainty in both electricity consumption and production, as opposed to the conventional power system. Hence, one of the major challenges is to ensure the balance between the electricity supply and consumption for hassle-free operation of the power system, especially during power deficit conditions.

Currently, in the scientific literature, a holistic approach is adopted to address the challenge of ensuring the balance between electricity production and consumption in the current as well as future power systems. Most of the technologies like fuel cells and converters aim at making the electricity production side much stronger. However, they have limitations and involve high investment costs [2][3]. On the other hand, several studies focus on reducing electricity consumption during power deficit conditions, often known by the terms demand-side-management and flexibility studies.

Focusing on the total electricity consumption in Sweden, 58 % of it is from the residential and service sector [4]. Moreover, the total electricity consumption in single-family residential buildings is around 4 to 4.5 times higher compared to the multifamily dwellings [5] and mostly electricity is used for space as well as water heating applications, with an air source heat pump as the most common type [6]. The air source heat pumps

are mainly of two types namely, air-to-air and air-to-water heat pumps. Another category of air source heat pump is the exhaust air heat pump (mainly air-to-air but air-to-water also available). This could be used for providing additional heating based on the insulation level and the needs of the building [7]. As water-based heating with radiators is the most common in Sweden, a single-family residential building equipped with an air-to-water heat pump, will be the focus of this article for quantifying the flexibility potential. In this study, flexibility refers to the reduction in the electricity consumption for space heating, to support the electric power system during power deficit conditions.

To use an air to water heat pump as a flexible load, it is important to have information regarding its performance, indicating the quantity of heat delivered, temperature at which heat is rejected, speed and electricity consumption of the compressor, during different outdoor ambient temperatures. Unfortunately, the heat pump manufactures will provide the relevant information only at standard Air Conditioning and Refrigeration (ARI) conditions, where the performance will be optimized. In this regard, in most of literature dealing with demand side management and flexibility studies, the model of air source heat pumps is simplified, where Coefficient of Performance (COP) is only considered as a constant value or as function of outdoor ambient temperature. Furthermore, the variable speed heat pump is assumed to be perfectly modulating between 0 and 100% as the limitations posed by the operating envelope of the compressor in terms of speed and condensor temperatures are not accounted [8][9][10].

Thus, with this background, the purpose of this article is to quantify the potential for flexibility from space heating in a building equipped with an air-to-water heat pump, by obtaining the heat pump's performance, considering the compressor's rating, and operating envelope during different outdoor ambient temperatures to fulfill different heating requirements in the building. The main contribution of this study is that the flexibility quantification serves as valuable information to ensure resilient operation of the electricity grid during power deficit conditions.

2. Methodology

This section describes the method to quantify the heat delivered by a variable speed air-to-water heat pump as a function of condensor and evaporator temperatures together with the speed of the compressor and outdoor ambient temperature, using vapour compression heat pump cycle. This will be followed by the description of the method to obtain the thermal model of a building.

2.1. Vapour compression heat pump cycle

The main components of a heat pump and its operation based on the actual vapour compression cycle, represented on a pressure-enthalpy diagram is shown in figure 1. The four processes involved in this cycle are heat absorption by the refrigerant in the evaporator, compression of the refrigerant by the compressor, heat rejection by the refrigerant in the condensor and the expansion of the refrigerant in the expansion valve.

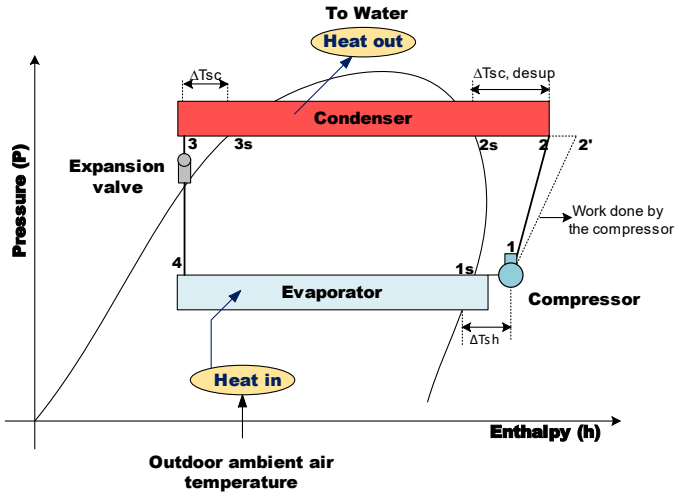


Figure 1: Vapour compression heat pump cycle

The procedure for evaluating the heat delivered and COP is as follows:

- The pressure in the evaporator is determined using the information of the temperature at which evaporation occurs and the quality (100% for saturated vapour (1s)) of the refrigerant.
- The temperature for superheating (ΔT_{sh}) is assumed to be 5K. The enthalpy 'h_1' is determined using the details of the superheated temperature of the refrigerant and the pressure in the evaporator (pressure is assumed to be constant in the evaporator). Also, the entropy and density are determined at the same condition.
- The process of compression is assumed to be isentropic. So, the entropy of the compressed vapour is assumed to be same as that of the vapour at the outlet of the evaporator.
- The pressure in the condensor(pressure is assumed to be constant in the condensor) is determined using the information of the temperature at which condensation occurs and the quality (0 for saturated liquid (3s)) of the refrigerant.
- The temperature of the compressed vapour is determined using the details of pressure in the condensor and entropy of the compressed vapour.
- The mass flow rate of the refrigerant in $\left(\frac{kg}{s}\right)$ is calculated as

$$\dot{m} = \frac{V_{dis}\ \rho_s\ f\ \eta_{\text{vol}}}{10^6}$$

where, 'V_{dis}', ' ρ_s' , 'f' and 'η_{vol}' are the compressor displacement volume $\left(\frac{cc}{rev}\right)$, density at suction $\left(\frac{kg}{m^3}\right)$, compressor speed (Hz) and the volumetric efficiency respectively[11] .

- Using the information of the entropy and temperature of the compressed vapour, the enthalpy 'h_2' $\left(\frac{kJ}{Kg}\right)$is determined. The work done by the compressor to perform the compression is calculated using

$$\dot{W}_{comp} = \frac{\dot{m}(h_2 - h_1)}{\eta_{isent_speed}}$$

where, '$\eta_{\text{isent_speed}}$' is the isentropic efficiency of the compressor for a given speed.

- The temperature for subcooling (ΔT_{sc}) is assumed to be 5K. The enthalpy 'h_3' is determined using the details of the temperature at which the refrigerant is sub cooled completely and the pressure in the condensor .
- The heat delivered at the condensor (kW) and the COP is calculated as

$$COP = \frac{Heat\ delivered}{Work\ done\ by\ the\ compressor} = \frac{\dot{m}\ (h_2 - h_3)}{\dot{W}_{comp}}$$

2.2. The compressor's operating envelope

The compressor is the heart of a heat pump. Manufactures of compressors will provide the operating envelopes indicating the conditions within which the compressors can operate safely, and performance is guaranteed. Before analyzing the vapour compression heat pump cycle, it is important to check if the operating point lies within the operating envelope, otherwise that operating point cannot be used, since the safe operation is not guaranteed outside the envelope.

2.3. Thermal dynamics in the building

With the knowledge of the physical and thermal properties of the building, the thermal mass (C) and the thermal resistance (R) are estimated. A simple way of modelling the thermal dynamics in a building, is in the form of an electric circuit, comprising of a resistance and a capacitance connected in series, powered by a heating system modelled as a current source. The ambient temperature which is an external condition is represented as a voltage source and is shown in figure 2.

The terms 'C_{tot}'and 'R_{tot}'are the total thermal mass and thermal resistance of a building respectively. 'P_{heat}' and 'T_{amb}' are the heat from the heating system and external ambient temperature respectively. The temperature of the room is represented by the voltage 'T_{r}' across the capacitor.

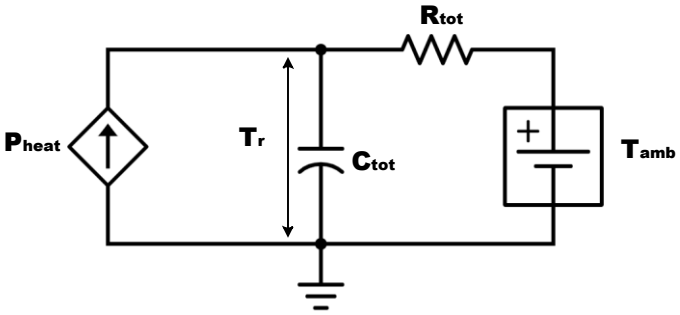


Figure 2: Simple thermal model of a building

3. Case study

This section deals with a brief description of the data considered for the modelling of a variable speed, air-to-water heat pump. This will be followed by a description of the thermal and physical properties of the building, for establishing its thermal model.

3.1. Air to water heat pump

The technical data of a variable speed compressor without enhanced vapour injection, from Copeland Emerson technology is considered for the validation of the model developed. The working fluid considered is the refrigerant 'R410a'. The relevant data together with the operating envelope considered for this study is provided in Table 1 and figure 3 respectively [12]. The operating envelope for this study, adapted for heating application, is considered based on two reasons, the first reason is that the minimum compression ratio should be greater than or equal to 2.3. This assumption is based on the experimental result obtained for Emerson's scroll compressors in [13] and [14]. The second reason is that for heating application, the condenser temperature should be at least 30℃.

Table 1. Technical data of variable speed compressor from Copeland Emerson [12]

Compressor Model	ZPV030	ZPV038
Power (kW)	2.98	3.73
Displacement $\left(\frac{cc}{rev}\right)$	30	38
Speed range (rpm)	900-7200	900-7200
Rated Capacity (kW)@ARI 60Hz	9.7	12.6
Power Input (kW)	2.98	3.80
COP (W/W)	3.25	3.3

3.2. Physical and thermal properties of the building

A single-family residential building in Gothenburg constructed between 1961 and 1975 with an average U-value (rate of heat transfer for climate shell) of $1\frac{W}{m^2\,K}$ and thermal mass of 21.6 $\frac{MJ}{K}$ is considered. The building is assumed have a floor area 125 m^2 and equipped with water radiators for space heating. Sanitary ventilation of $0.35\frac{l}{s\,m^2}$ is also accounted. The maximum supply temperature to the radiators is 55℃. The heating to this building will be provided from an air-to-water heat pump equipped with a variable speed ZPV030 compressor discussed above.

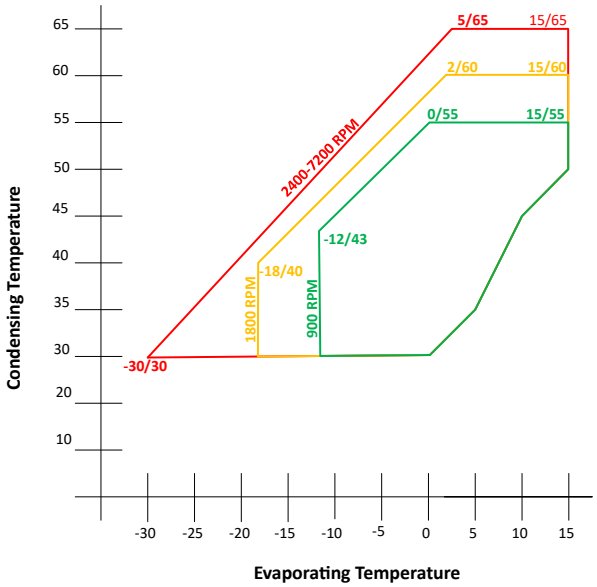


Figure 3: Operating envelope of scroll compressor adapted for the study [12]

4. Results

This section deals with the assumptions made for the analysis and validation of the results obtained from the steady state model of an air-to-water heat pump with ZPV030 and ZPV038 Copeland Emerson scroll compressors. Furthermore, it also deals with the quantification of the flexibility levels from space heating in a single-family residential building dealt with in section 3.2, equipped with an air-to-water heat pump having ZPV030 scroll compressor.

4.1. Validation of simulation result from the air source heat pumps with ZPV030 and ZPV038 scroll compressors @ARI 60 Hz

The following are the assumptions made in the model developed

- The volumetric efficiency 'η_{vol}' of the compressor is 83%
- The isentropic efficiency 'η_{isent}' is 65% at design conditions, considering the aspects of losses [15]
- For air source heat pumps, the temperature difference between evaporator and outdoor ambient temperature is between 5^0C and 8^0C [16]. In this study, a temperature difference of 8^0C is considered.
- The condensor temperature 'T_{cond}' required to heat the water to a desired temperature, is calculated as

$$T_{\text{cond}} = T_{\text{return}} + \frac{T_{\text{supply}} - T_{\text{return}}}{1 - e^{\left(\frac{-(T_{\text{supply}} - T_{\text{return}})}{\Delta T_{log.cond}}\right)}}$$

  where, 'T_{return}', 'T_{supply}' are the return and supply temperatures of the water from and to the heating circuit respectively. '$\Delta T_{log.cond}$' is logarithmic temperature difference of the heat exchanger and is assumed to be 4K.
- The isentropic efficiencies (η_{isent}) during different compression ratios for the Emerson's scroll compressor considered by comparing and analyzing the data available in [13] and [14], is shown in table 2.

Table 2: Variation of isentropic efficiency with respect to compression ratio

Compressor ratio	2.3	3	3.5	4	5	6	7	8	9	11	13.9
Isentropic efficiency	0.59	0.64	0.65	0.645	0.63	0.62	0.6	0.58	0.57	0.524	0.46

- The variation in isentropic efficiency with respect to the speed (f) of the compressor is estimated [17] as

$$\eta_{\text{isent_speed}} = \eta_{\text{isent}}\left(-0.08\left(\frac{f}{f_{60}}\right)^2 + 0.1411\left(\frac{f}{f_{60}}\right) + 0.9337\right)$$

where, 'f_{60}' is the frequency of the compressor at 60 Hz.

The simulation result is compared with the data provided in Table 1 and the observations are tabulated in Table 3. It is observed that the simulation result matches well with the data provided (@ARI 60Hz, i.e.,7℃ evaporator temperature and 55℃ condensor temperature).

Table 3. Comparison of the result obtained from the mathematical model with the technical data provided in [12]

Compressor Model	ZPV030		ZPV038	
	Given	Obtained	Given	Obtained
Speed (RPM)	3600	3600	3600	3600
Rated Capacity (kW) @ ARI 60Hz	9.7	9.85	12.6	12.47
Power Input (kW)	2.98	2.96	3.80	3.74
COP (W/W)	3.25	3.33	3.3	3.33

4.2. The COP as a function of outdoor ambient temperature and condensor temperature for an air to water heat pump with ZPV030 scroll compressor

The condensor temperature as a function of outdoor ambient temperature and COP for an air source heat pump under study is shown in figure 4. It is observed that for a given condensor temperature, as the outdoor ambient temperature increases, COP increases. It is interesting to observe that, at lower outdoor ambient conditions, the heat pump should be complemented with electric heating to deliver desired heat at high temperatures.

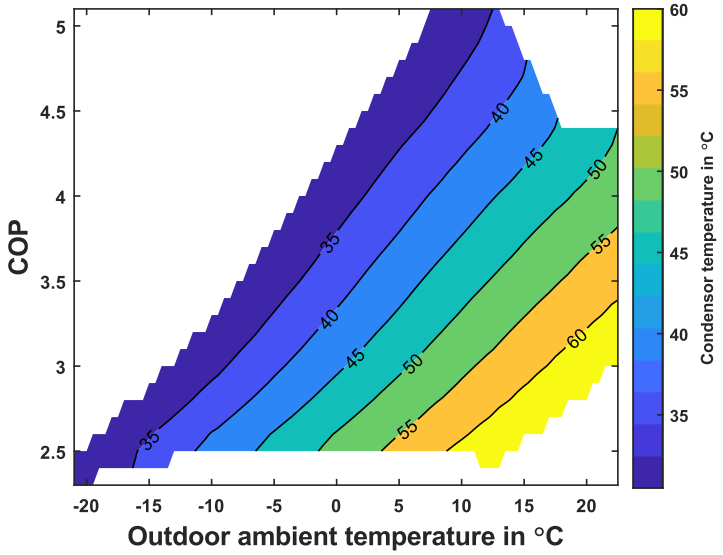
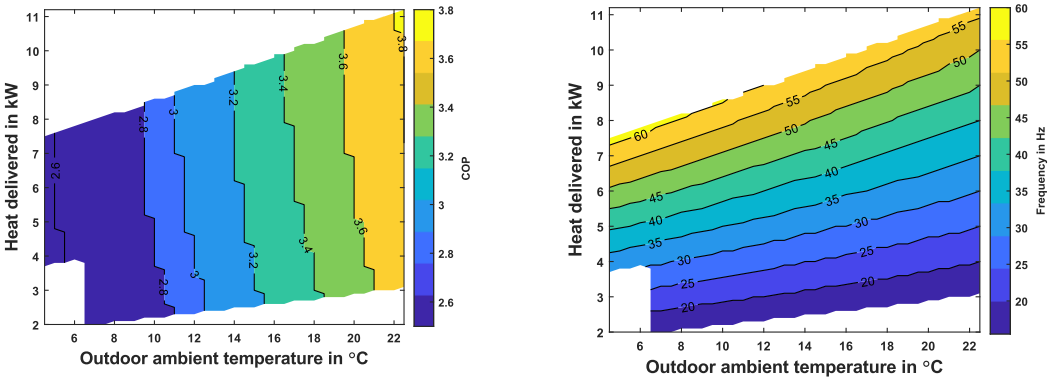


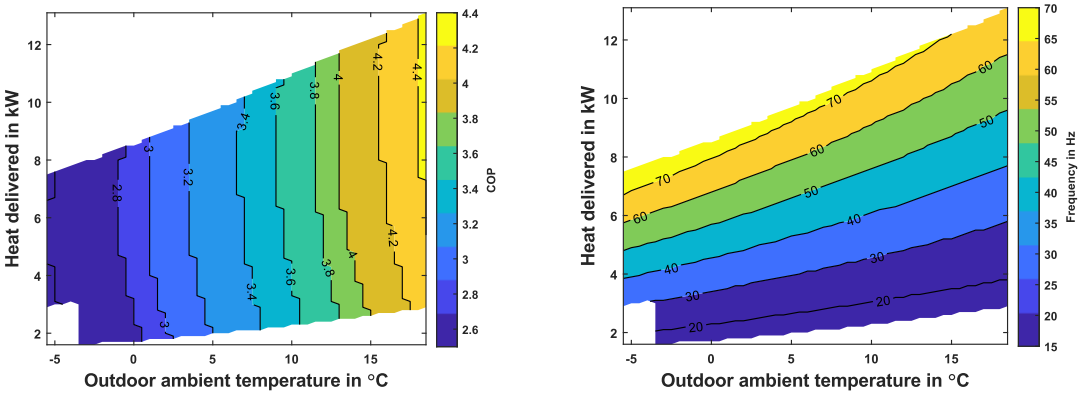
Figure 4: Condensor temperature as a function of outdoor ambient temperature and COP

4.3. The COP and speed as a function of heat delivered and outdoor ambient temperature for supplying water at 55℃, 45℃ and 30℃.

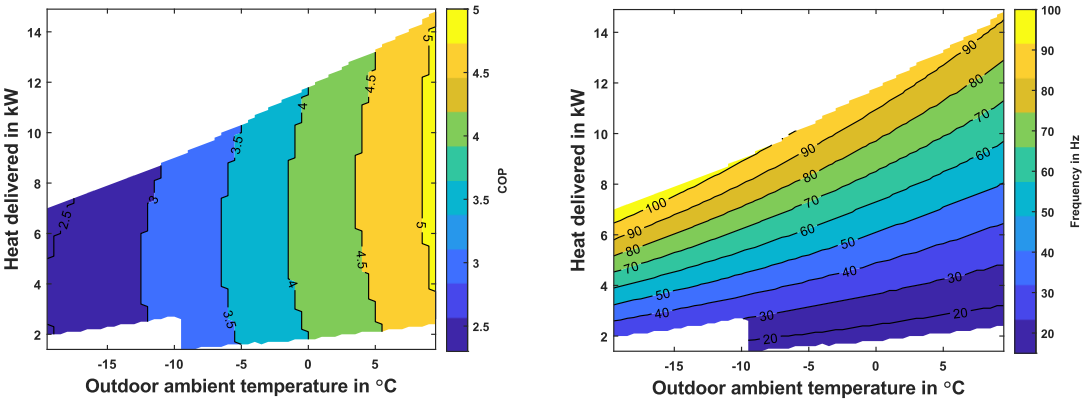
The maximum supply temperature to the panel radiator considered for the analysis is 55℃. However, depending on heating requirements during different outdoor ambient temperatures, the supply temperature of the water to the radiator can vary. In this regard, for the representation purpose, supply water temperatures of 30℃, 45℃ and 55℃ are selected. The COP and the speed as a function of heat delivered and outdoor ambient temperature, for supplying water at temperatures 55℃, 45℃ and 30℃ are shown in figure 5.



(5a) Heat delivering capability of the heat pump to deliver hot water at 55℃



(5b) Heat delivering capability of the heat pump to deliver hot water at 45℃



(5c) Heat delivering capability of the heat pump to deliver hot water at 30℃

Figure 5: Heat delivering capability of the heat pump to deliver hot water at 55℃, 45℃ and 30℃

The COP and amount of heat delivered increases with an increase in ambient temperature, as the temperature of the source increases. Furthermore, for a given ambient temperature, the heat delivered increases with a reduction in the supply temperature of the water.

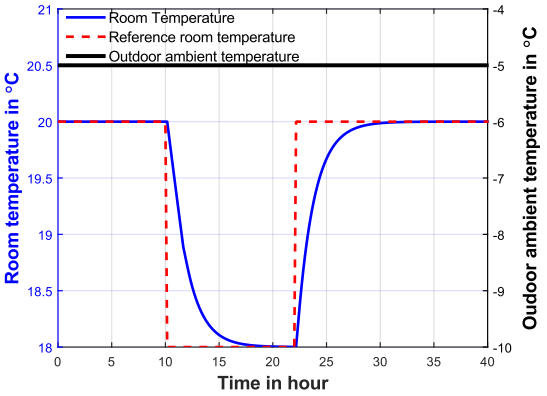
The change in COP at a given condensor temperature and ambient temperature, for delivering different heat loads is due to the variation in isentropic efficiency at different compressor speeds. It is also observed that the speed of the compressor is limited as the power consumption exceeds the rating of the compressor. However, as the supply temperature of the water is reduced, the heat pump can be operated at higher speeds.

4.4. Flexibility offered by the residential building by reducing the indoor temperature from 20℃ to 18℃ during different outdoor ambient temperatures

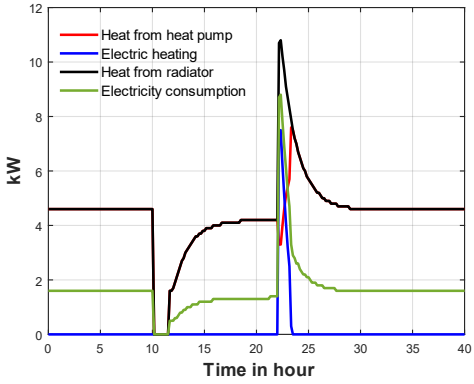
The outdoor ambient temperatures of -5℃, 0℃ and 5℃ are selected.

4.4.1. Flexibility offered by the residential building by reducing the indoor temperature from 20℃ to 18℃ during outdoor ambient temperature of -5℃

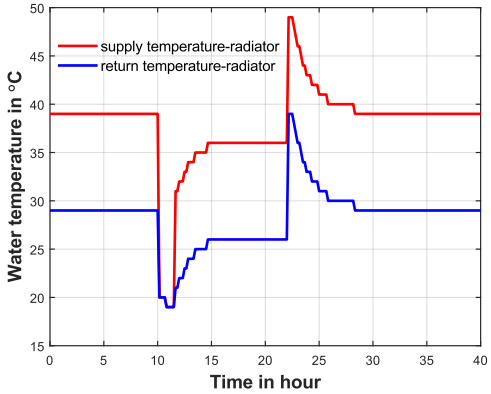
To maintain indoor temperature at 20℃, when the outdoor ambient temperature is -5℃, around 4.6 kW of heat is required. This heat is obtained by setting the supply temperature of the water in the radiators to 39℃ with appropriate mass flow rate to achieve the return water temperature of 29℃. The COP and speed of the heat pump at this condition is 2.89 and 46 Hz respectively. This is shown in figure 6.



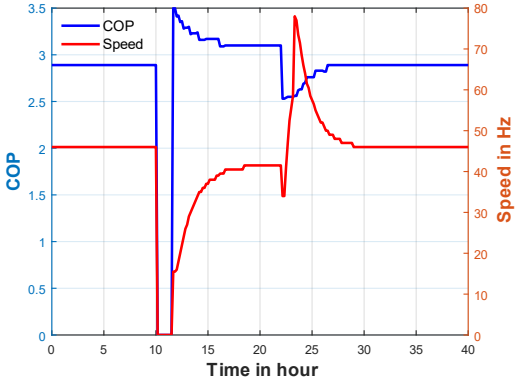
(6a): Variation of indoor temperature



(6b): Heat delivered by the radiators, electric heater in the heat pump, the heat pump and electricity consumed



(6c): Supply and return temperatures of the water in the radiator together with the temperature of water supplied by heat pump



(6d): The variation in the speed and COP of the heat pump while maintaining desired indoor temperature

Figure 6: Thermodynamics in the building during outdoor ambient temperature of -5℃

When the indoor reference temperature is changed to 18℃, there is no heating required for nearly 1.33 hours. After 1.33 hours until reference indoor temperature is reset, the heating requirement gradually increases for maintaining the indoor temperature at the desired level. During this period, it can be observed in figures (6c) and (6d) that, as the supply temperature of water increases, the COP reduces accordingly. When the new steady state has been reached, it is noticed that COP is 3.1 and is higher compared to the COP required for maintaining the indoor temperature at 20℃.

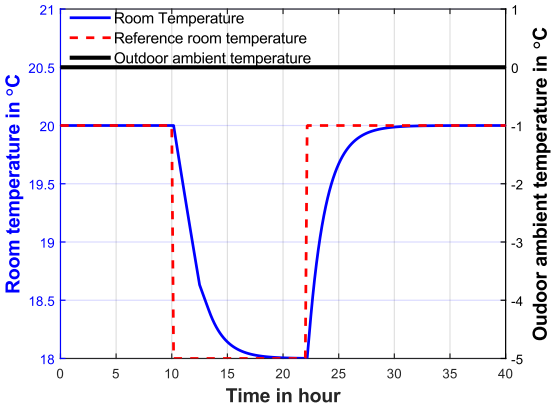
When the indoor reference temperature is reset to 20℃, it can be observed in figures (6b) and (6c) that there is a spike in electricity consumption due to spike in heating requirement. At outdoor ambient temperature of -5℃, the heat pump cannot heat the water to 49℃. In this situation, the heat pump heats the water to 42.5℃ and electric heater is used for heating the water up to 49℃. Correspondingly, it is observed that there is a sudden dip in the COP to 2.53 (to heat water to 42.5℃). As the heat requirement reduces and the supply

temperature of water reduces, COP improves gradually, heating from electric heater also reduces and a new steady state is reached.

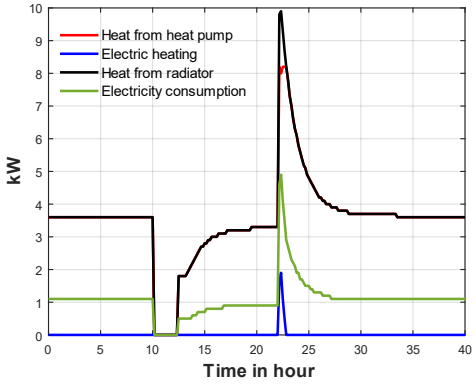
For 1.33 hours, no electrical energy is consumed by space heating, which corresponds to taking 2.13 kWh less electricity from the power grid, and this can be viewed as the flexibility service offered from the building. Furthermore, by continuing to maintain the indoor temperature at 18℃, the strain on the grid during power deficit conditions can be reduced as it is reflected in terms of reduced electricity consumption i.e., higher COP. However, when the temperature is reset to 20℃, initially there is a spike in electricity consumption.

4.4.2. Flexibility offered by the residential building by reducing the indoor temperature from 20℃ to 18℃ during outdoor ambient temperature of 0℃

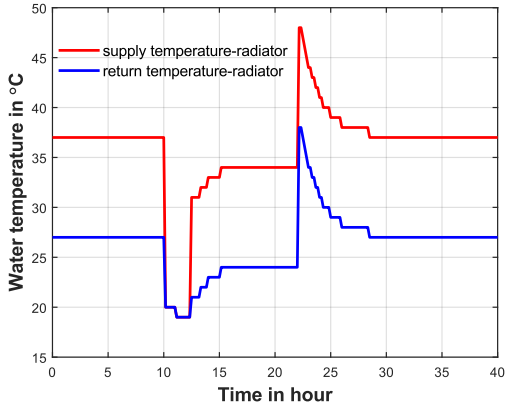
When the outdoor ambient temperature is 0℃, around 3.6 kW of heat is required to maintain indoor temperature at 20℃. This is achieved by setting the supply temperature of the water in the radiators to 37℃ with appropriate mass flow rate to achieve the return water temperature of 27℃. The corresponding COP and speed of the heat pump is 3.41 and 30.5 Hz respectively and is shown in figure 7.



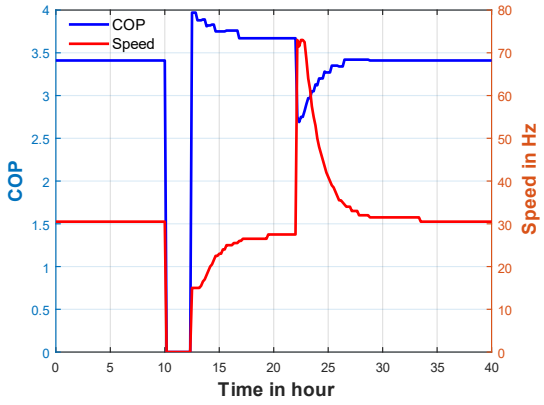
(7a): Variation of indoor temperature



(7b): Heat delivered by the radiators, electric heater in the heat pump, the heat pump and electricity consumed



(7c): Supply and return temperatures of the water in the radiator together with the temperature of water supplied by heat pump



(7d): The variation in the speed and COP of the heat pump while maintaining desired indoor temperature

Figure 7: Thermodynamics in the building during outdoor ambient temperature of 0^0C

When the indoor reference temperature is changed to 18℃, there is no heating required for nearly 2.16 hours. After 2.16 hours until reference indoor temperature is reset, the heating requirement gradually increases for maintaining the indoor temperature at the desired level. During this period, the observations in figures (7b) and (7c) with respect to supply temperature of the water in radiators and COP is similar to as discussed in section 4.4.1.

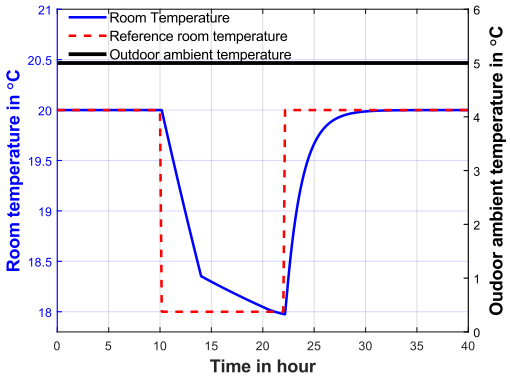
When the indoor reference temperature is reset to 20℃, it can be observed in figures (7b) and (7c) that there is a spike in electricity consumption due to spike in heating requirement. At an outdoor ambient temperature of 0℃, the maximum heat this heat pump can deliver to heat the water at 48℃ is 8.2 kW. In this situation, the

heat electric heater is used for providing extra heat of 1.6 kW. Correspondingly, it is observed that there is a sudden dip in the COP to 2.53 (to deliver heat of 8.2 kW). As the heat requirement reduces and the supply temperature of water reduces, COP improves gradually, heating from electric heater also reduces and a new steady state is reached.

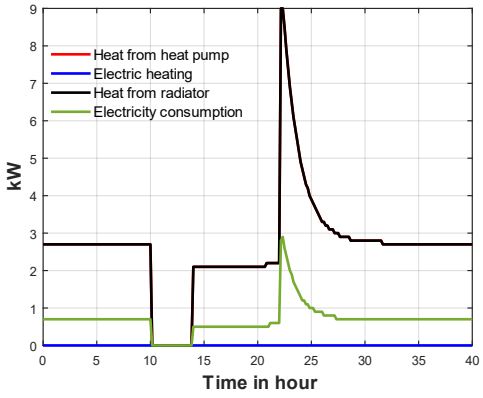
For 2.16 hours, no electrical energy is consumed by space heating, which corresponds to taking 2.38 kWh less electricity from the power grid, and this can be viewed as the flexibility service offered from the building. Furthermore, by continuing to maintain the indoor temperature at 18℃, the strain on the grid during power deficit conditions can be reduced as it is reflected in terms of reduced electricity consumption i.e., higher COP. However, when the temperature is reset to 20℃, initially there is a spike in electricity consumption.

4.4.3. Flexibility offered by the residential building by reducing the indoor temperature from 20℃ to 18℃ during outdoor ambient temperature of 5℃

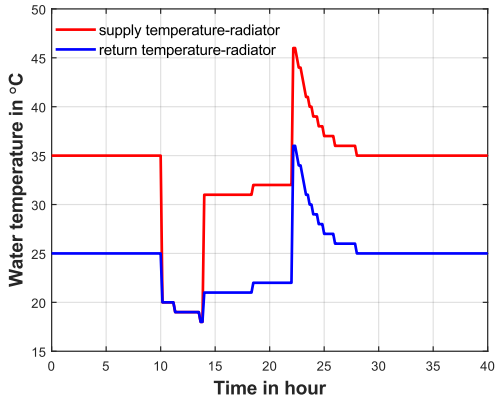
Around 2.7 kW of heat is required to maintain indoor temperature at 20℃, when the outdoor ambient temperature is 5℃. This is realized by setting the supply temperature of the water in the radiators to 35℃ with appropriate mass flow rate to achieve the return water temperature of 25℃. The COP and speed of the heat pump obtained at this condition is 4 and 19.5 Hz respectively. This is shown in figure 8.



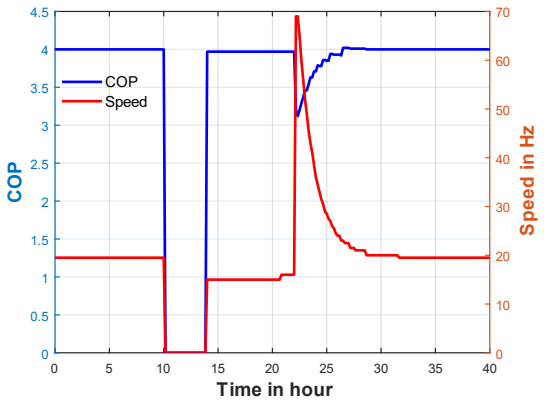
(8a): Variation of indoor temperature



(8b): Heat delivered by the radiators, electric heater in the heat pump, the heat pump and electricity consumed



(8c): Supply and return temperatures of the water in the radiator together with the temperature of water supplied by heat pump



(8d): The variation in the speed and COP of the heat pump while maintaining desired indoor temperature

Figure 8: Thermodynamics in the building during outdoor ambient temperature of 5℃

When the indoor reference temperature is changed to 18℃, there is no heating required for nearly 3.5 hours. After 3.5 hours and some time before the reference indoor temperature is reset, around 2.1 kW of heat is provided as it is the minimum heat which the heat pump can provide at this condition. This heating

is then gradually increased to 2.2 kW. During this period, the observations in figures (8b) and (8c) with respect to supply temperature of the water in radiators is similar to as discussed in section 4.4.1.

When the indoor reference temperature is reset to 20℃, it can be observed in figures (8b) and (8c) that there is a spike in electricity consumption due to spike in heating requirement. Correspondingly, it is observed that there is a sudden dip in the COP to 3.12. As the heat requirement reduces and the supply temperature of water reduces, COP improves gradually, heating from electric heater also reduces and a new steady state is reached.

For 3.5 hours, no electrical energy is consumed by space heating, which corresponds to taking 2.49 kWh less electricity from the power grid, and this can be viewed as the flexibility service offered from the building. Furthermore, by continuing to maintain the indoor temperature at 18℃, the strain on the grid during power deficit conditions can be reduced as it is reflected in terms of reduced electricity consumption i.e., higher COP. However, when the temperature is reset to 20℃, initially, there is a spike in electricity consumption.

5. Discussion

The result obtained in section 4 is consolidated in table 4. It can be observed that the flexibility in terms of power is high when the outdoor ambient temperature is -5℃ compared to 5℃. On the contrary, the flexibility in terms on energy is high during when the outdoor ambient temperature is 5℃ compared to -5℃. Furthermore, by maintaining the reference indoor temperature to a low value, the amount of energy offered as flexible service would be high, considering the contribution from several residential buildings. This can help the electricity grid to be more resilient by avoiding situations which can lead to severe problems during power deficit conditions.

Table 4: Flexibility offered from space heating by reducing the indoor temperature from 20^0C to 18^0C at steady state

Outdoor ambient temperature	Heat in kW to maintain indoor temperature @		COP to maintain the indoor temperature @		Time required for the indoor temperature to reach 18^0C from 20^0C in hours	Reduced power in-take during no space heating in kW	Reduced intake of electrical energy during no space heating in kWh	Electricity consumption by electric heating in kW
	20^0C	18^0C	20^0C	18^0C				
-5^0C	4.6	4.2	2.89	3.10	1.33	1.60	2.13	0
0^0C	3.6	3.3	3.41	3.67	2.16	1.10	2.38	0
5^0C	2.7	2.3	4.00	3.97	3.50	0.71	2.49	0

The future scope of this work involves assessing the flexibility based on different types of single-family residential building i.e., U-value and thermal mass, followed by the different types of heat pumps used. Furthermore, the heat pump technology i.e., with or without enhanced vapour injection, affects the flexibility result, as the heat delivering capability and COP would be high in the latter case. Also, considering the electric heating element used for complementing the heat pump of fixed type, greatly affects the result from flexibility studies focused on shorter time scales.

Acknowledgements

The financial support given by the Swedish Energy agency through grant No. 50343-1 is gratefully acknowledged.

References

[1] Ministry of Environment and Government Offices of Sweden, “Sweden’s long-term strategy for reducing greenhouse gas emissions,” 2020. Accessed: Oct. 10, 2022. [Online]. Available: https://unfccc.int/sites/default/files/resource/LTS1_Sweden.pdf

[2] J. Chen, F. Prystupczuk, and T. O’Donnell, “Use of voltage limits for current limitations in grid-forming converters,” *CSEE Journal of Power and Energy Systems*, vol. 6, no. 2, pp. 259–269, Jun. 2020, doi: 10.17775/CSEEJPES.2019.02660.

[3] D. B. Levin, L. Pitt, and M. Love, "Biohydrogen production: Prospects and limitations to practical application," *International Journal of Hydrogen Energy*, vol. 29, no. 2, pp. 173–185, Feb. 2004, doi: 10.1016/S0360-3199(03)00094-6.

[4] Swedish Energy Agency, "Energy in Sweden – An overview," 2020. Accessed: Oct. 10, 2022. [Online]. Available: https://energimyndigheten.a-w2m.se/Home.mvc?ResourceId=198022

[5] statista, "Final electricity consumption in households in Sweden from 2013 to 2019, by type," *https://www.statista.com/statistics/1027100/final-consumption-of-electricity-in-households-in-sweden-by-type/*, Nov. 2021.

[6] I. Danielski and M. Fröling, "Air source heat pumps and their role in the Swedish energy system," 2012.

[7] EurObser'ER, "HEAT PUMPS BAROMETER," 2021. Accessed: Oct. 24, 2022. [Online]. Available: https://www.statista.com/statistics/864011/heat-pumps-in-operation-sweden/

[8] J. Vivian, E. Prataviera, F. Cunsolo, and M. Pau, "Demand Side Management of a pool of air source heat pumps for space heating and domestic hot water production in a residential district," *Energy Conversion Management*, vol. 225, Dec. 2020, doi: 10.1016/j.enconman.2020.113457.

[9] B. Baeten, F. Rogiers, and L. Helsen, "Reduction of heat pump induced peak electricity use and required generation capacity through thermal energy storage and demand response," *Applied Energy*, vol. 195, pp. 184–195, 2017, doi: 10.1016/j.apenergy.2017.03.055.

[10] L. A. Hurtado, J. D. Rhodes, P. H. Nguyen, I. G. Kamphuis, and M. E. Webber, "Quantifying demand flexibility based on structural thermal storage and comfort management of non-residential buildings: A comparison between hot and cold climate zones," *Applied Energy*, vol. 195, pp. 1047–1054, 2017, doi: 10.1016/j.apenergy.2017.03.004.

[11] N. Park, J. Shin, and B. Y. Chung, "A new dynamic heat pump simulation model with variable speed compressors under frosting conditions," *8th International Conference on Compressors and their Systems, ScienceDirect*, pp. 681–696, 2013.

[12] Emerson Climate Technologies, "Copeland TM Scroll Variable speed compressors for residential air conditioning applications," 2022. Accessed: Oct. 11, 2022. [Online]. Available: https://climate.emerson.com/documents/product-brochure-copeland-scroll-variable-speed-compressors-for-residential-air-conditioning-applications-en-sg-7237218.pdf

[13] T. W. Moesch, A. M. Bahman, and E. A. Groll, "Purdue e-Pubs Performance Testing of a Vapor Injection Scroll Compressor with R407C Performance Testing of a Vapor Injection Scroll Compressor with R407C," 2016. [Online]. Available: https://docs.lib.purdue.edu/icec/2447

[14] E. K. Shungarov and S. A. Garanov, "Comparison of the Characteristics of Low-Temperature Scroll Compressors for Heat Pump Applications," *Chemical and Petroleum Engineering*, vol. 56, no. 5–6, pp. 378–384, Sep. 2020, doi: 10.1007/s10556-020-00784-x.

[15] Scroll compressor and vaccum pump efficiency, "AIR SQUARED ARTICLES," May 02, 2022. Accessed: Oct. 11, 2022. [Online]. Available: https://airsquared.com/scroll-articles/scroll-compressor-and-scroll-vacuum-pump-efficiency-explained/.

[16] C. H. Stignor and T. Walfridson, "Nordsyn study on air-to-air heat pumps in humid Nordic climate". Copenhagen: Nordic Council of Ministers, 2019. doi: 10.6027/TN2019-504.

[17] S. Jain and C. W. Bullard, "Capacity and Efficiency in Variable Speed, Vapor Injection and Multi-Compressor Systems," *Air Conditioning and Refrigeration Center, University of Illinios*, 2004.

14th IEA Heat Pump Conference
15-18 May 2023, Chicago, Illinois

General classification of heat pumps solutions for multi-family buildings

Marek Miara*[a]

[a]Fraunhofer Institute for Solar Energy Systems ISE, Heidenhofstrasse 2, 79110 Freiburg, Germany,

Abstract

The paper documents the results of the IEA HPT Annex 50 "Heat Pumps in Multi-Family Buildings for Space Heating and DHW" and it is based on the final report of the Annex 50. The active Annex group consisted of seven countries (Austria, Denmark, France, Germany, Italy, Netherlands, and Switzerland). The working group has succeeded in creating a general classification of heat pumps solutions for multi-family residential buildings. The solutions have been defined in a standardized way according to eight representative categories. Overall, 13 solutions have been identified, ranging from a fully centralized to a completely decentralized system (each-room solution). The solutions have been grouped into five "families", each grouping specific sub-solutions. In parallel to the theoretical classification of solutions, the Annex collected numerous case studies representing implementation of heat pumps in multi-family buildings. The cases show a wide variety of possibilities for use of heat pumps, depending on the energetical standard of the building, its number of apartments, heat source and further characteristics. For each case study, a corresponding theoretical solution has been defined. All these elements reflect the holistic approach of the Annex, which encompasses the definition, categorisation and the practical implementation of heat pump solutions.

© HPC2023.
Selection and/or peer-review under the responsibility of the organizers of the 14th IEA Heat Pump Conference 2023.

Keywords: multi-familiy buildings; classification of solutions, centalized systems, decentralized system

1. Introduction

The goal was never so clear. We must stop, or at least significantly reduce, the use of fossil fuels. The most important argument to do that is the mitigation of consequences of the climate change. The newest IPCC report [1] does not leave any illusion – the life on our planet as we known it and are used to, will no longer be possible. The consequences of "business as usual" would be dramatic.

In light of the above considerations, the perception of heat pumps by the policy- and lawmakers has changed significantly in favour of heat pumps as a solution for the decarbonisation of heating in the housing sector. New strategies to reach climate neutrality point to heat pumps as the key solution [2, 3].

Most heat pumps installed in Europe are dedicated for single family houses. To reach the climate protection goals, heat pumps must be installed also in multi-family buildings. The analyses provided in the final report of Annex 50 [4] show clearly that one of the major barriers of a broader application of heat pumps in multi-family buildings is a deficit of knowledge. Both on the side of owners of the buildings or apartments, as well as investors.

New domestic buildings are often constructed with a building envelope and heating system designed for low energy consumption and the potential to use new renewable energy technologies, such as heat pumps. For multi-family buildings, the challenge of applying heat pump technologies and renewable energy is more complex. The aspect of ownership varies among member countries of the IEA HPT Implementing agreement. While in some countries multi-family houses are often owned by local cities, communities, or housing corporations, in other countries ownership is private and divided into individual apartments. There are even combinations of ownership by housing corporations and private owners in one building. This implies extra challenges at organizational, financial and implementation level.

* Marek Miara. *E-mail address:* marek.miara@ise.fraunhofer.de

Annex 50 was covering a comprehensive range of topics which relate exclusively to multi-family buildings. A variety of key aspects for usage of heat pumps in multi-family buildings has been considered within this Annex. The outcome allows to better understand the technical and non-technical barriers, comprehensively presents different theoretical solutions of heat pumps implementation in multi-family buildings and visualises numerous case studies with their practical implementation. The connection of theory and the real implementation was an important factor during the whole work within the Annex.

2. National situations

In Europe, the market for heat pumps (HPs) in residential buildings has been steadily growing for several years in most countries [5]. However, this overall trend does not reflect various situations in different types of buildings. Whereas in new individual houses HPs are the most spread solution, their market in multi-family buildings (MFB), both new and existing, remains low.

The first task of Annex 50 was to collect and analyse data from the participating countries with a view to identifying country-relevant characteristics of buildings, their technical aspects and legal regulations relevant for application of heat pumps in MFB.

The shares of individual and collective housing are quite similar among the countries and encompass from 45 to 50% of dwellings in multi-family buildings. In almost all countries, most of multi-family buildings are composed of less than 10 flats; 6 to 8 in average.

In all countries, the multi-family buildings stock is almost equally distributed between owners and tenants, with a slight majority of owners. In all countries participating in the Annex 50, the residential building stock is quite old, with an average share of 52-60% of buildings built before 1970. The main consequence is that space heating constitutes the largest part of energy consumption with a share of about 65%. For old multi-family buildings (<1970), it represents a yearly heating demand of 120-150 kWh/m^2.

Apart from the age of the buildings and an average number of appartements, also the energy carriers for providing the heating needs varied in analysed countries (Figure 1). Natural gas is the main energy source for heating in multi-family buildings in most analysed countries. In France and Switzerland there is a significant share of direct electrical heating. Denmark is the country with the biggest share of district heating (followed by Austria). Switzerland is the exception with more than 50% of oil heating systems.

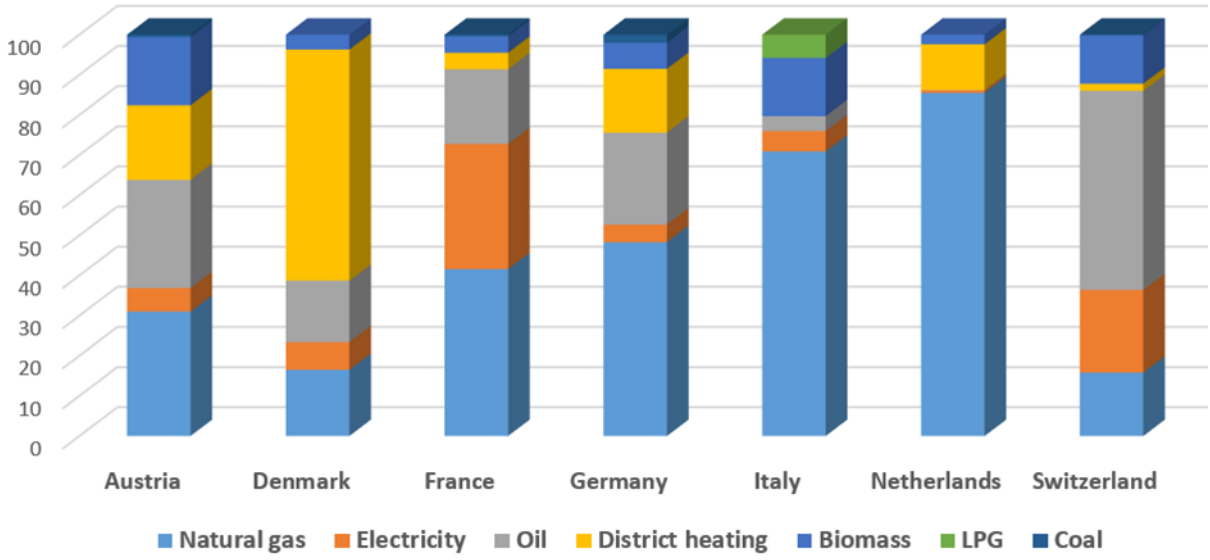


Fig. 1. Energy carriers for providing heating and domestic hot water production in selected European countries

3. Translating complexity

The diversity of multi-family buildings is significantly higher than in the case of single-family buildings. This results in more numerous and complex solutions which can be implemented for covering the heating demand and domestic hot water needs. Consequently, the choice of the most appropriate solution is a much more difficult task.

In the first attempt, the working group tried to create possibly exhaustive categorisation taking into account of various perspectives, such as level of centralisation, heat sources, type of hot water production, energy standard of a building, size, etc. The visual result of this endeavour represents Figure 2 (it is not the intention to show the content of the classification but only its complexity). Although from the scientific and technical point of view the achieved classification was satisfying, its complexity constitutes an obstacle for a readability and comprehension of various possibilities.

To overcome this problem, the Annex 50 group proposed a simplified categorisation of possible heat pumps implementations in multi-family buildings described in following paragraphs. The working group of Annex 50 is aware of the fact that choosing a simplification over completeness results in some of the aspects not being described and presented sufficiently broad and exhaustive. The oversimplification may even be seen as disturbing and artificial, but this approach has a clear goal to "translate complexity". Discussions with the housing industries confirm the need for such simplified classification. To see the potential possibilities in an easy and understandable way can be crucial for taking decisions by building's owners or buildings administrators, who very often do not possess sufficient knowledge and experience to comprehend the complexity.

It is to be mentioned that the way to propose the simplified categorisation was a difficult challenge. The final outcome is a result of longstanding discussions and compromises acknowledging the technical and scientifical shortcomings of this approach.

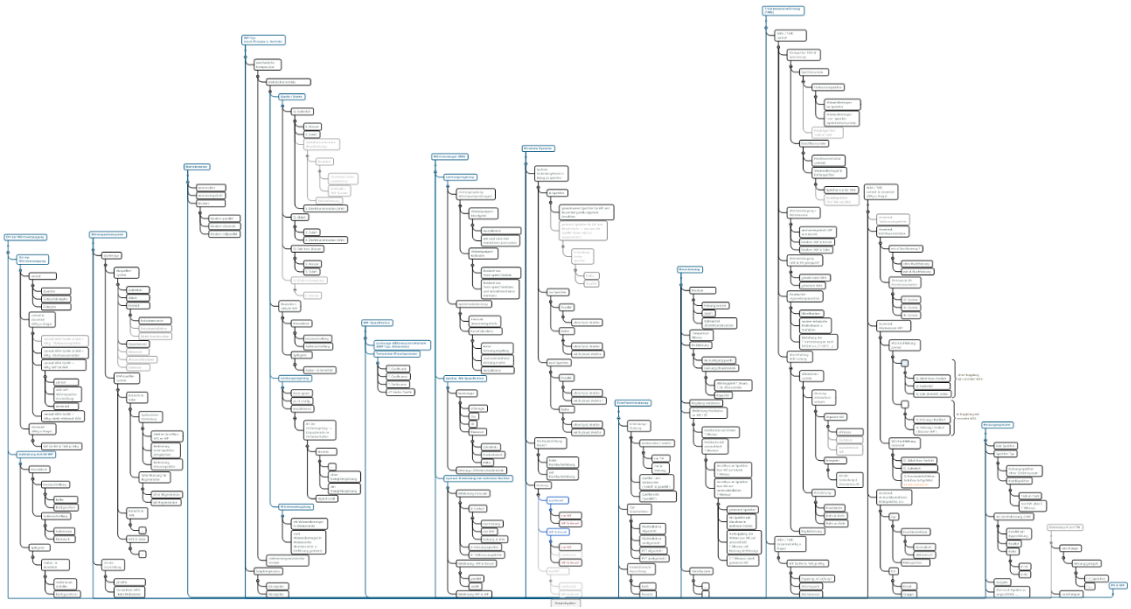


Fig. 2. Visual example of a comprehensive classification of heat pump solutions in multi-family buildings (it is not the intention to show the content of the classification but only its complexity).

4. "Solution matrix"

During the process of gathering knowledge and practice, the work group faced a rich variety of cases and characteristics to consider. Depending on the focus of the system design, for instance, a specific MFB type, the conclusions would vary. Structuring the information in a matrix format provided a response to this issue. The work was carried out with the vision of a description of all solutions in a standardized way. This allowed to explore each scenario, from centralized to completely decentralized HP installation, through the lens of new to non-renovated MFB, building size, heating and/or domestic hot water (DHW) production need, HP only or hybrid system and to reflect on specific issue for each one. It is an attempt to cover all potentially encountered cases. The intention is to help identify the best possible solution for each case and inform on concepts that may be unusual in some countries.

4.1. General classification

A key point to classify heat pump systems, is to define the level at which the integration is realized. This ranges from all centralized to completely decentralized installations with different types of intermediate solutions. This first level of classification consists of five so-called “solutions families”. These generic groups are aligned by their level of system centralization in the following schematic drawings (Figure 3).

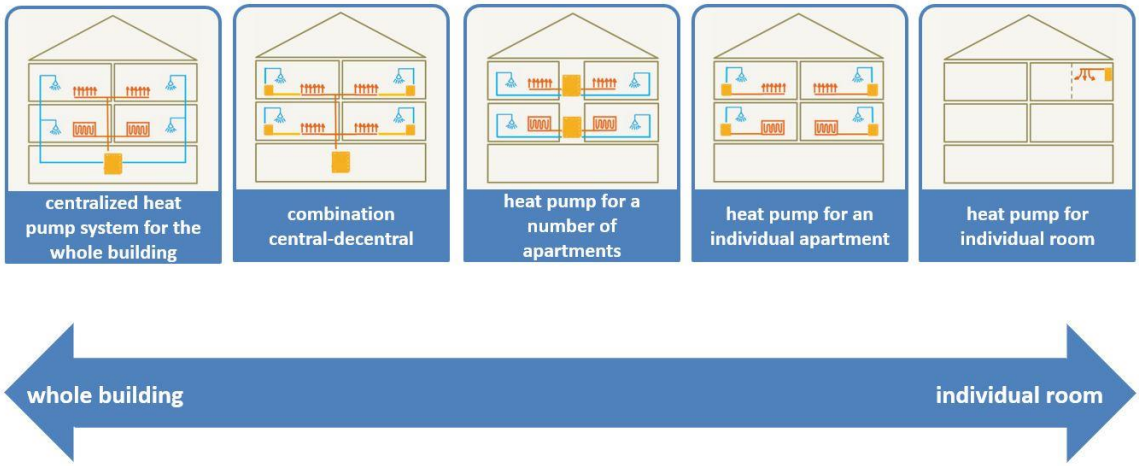


Fig. 3. General classification: solution families

Each “solution family” comprises of several “family members”. The members are variations within one logical group (Figure 4).

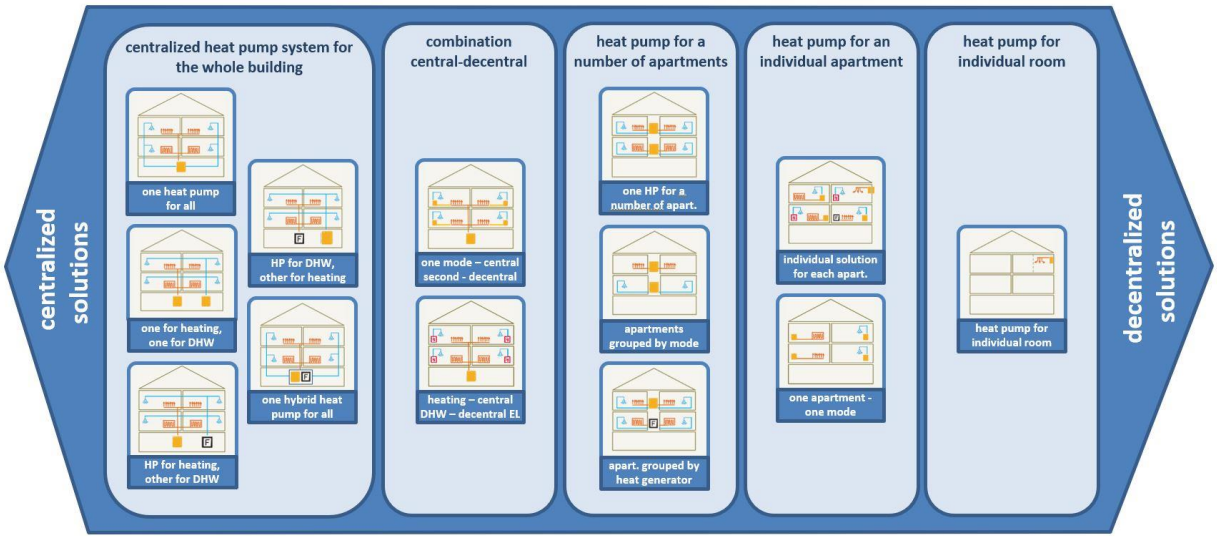


Fig. 4. The overview of the 13 resulting solutions sorted by families according to their degree of system centralization

The following listed solutions have been identified. They are described in order from the most centralized to the most decentralized concept.

- **Solution 1.1 „one heat pump for all“**
  One central heat pump system for the whole building, both for space heating and DHW
- **Solution 1.2 „one for heating, one for DHW“**
  One heat pump system for each mode. One for space heating, separate one for DHW
- **Solution 1.3 „ HP for heating, another device for DHW “**

One heat pump system for the space heating, separate heat generator (fossil, biomass, electric, …) for DHW.

- **Solution 1.4 „HP for DHW, other device for heating “**
  One HP system for DHW, separate heat generator (fossil, biomass, electric, …) for space heating.
- **Solution 1.5 „one hybrid heat pump for all “**
  One hybrid heat pump system for space heating and DHW for the whole building
- **Solution 2.1 „ one mode – central, second - decentral “**
  One central heat pump system for one mode (for example space heating). Decentral heat pumps for the second mode (for example DHW).
- **Solution 2.2 „ heating – central, DHW – decentral EL “**
  One central heat pump system for space heating. Decentral direct electrical heaters for DHW.
- **Solution 3.1 „one HP for a number of apartments “**
  One heat pump system for space heating and DHW for several apartments (usually grouped by levels or staircases).
- **Solution 3.2 „apartments grouped by mode “**
  One heat pump system provides one mode (space heating or DHW) for several apartments (usually grouped by levels or staircases).
- **Solution 3.3 „ apartments grouped by heat generator “**
  The apartments are grouped by heat generators (usually grouped by levels or staircases).
- **Solution 4.1 „ individual solution for each apartment “**
  Each apartment has individual concept of space heating and DHW.
- **Solution 4.2 „ one apartment - one mode “**
  Decentral heat pump for one mode for one apartment.
- **Solution 5.1 „ heat pump for individual room “**
  One heat pump for space heating (or cooling) for one room of the apartment.

4.2. Solutions description

All solutions listed in the above paragraph have been described in detail within 8 categories listed below. The standardized categories allow for a better comparison of solutions.

- **Main characteristic of the concept**
  Maximally concise description of the solution
- **Size of building, number of apartments**
  This category indicates for what size of the building the solution is favourable. For the sake of clarity, three categories of the buildings have been defined. Depending on the number of apartments: “small” buildings consist of 4 to 10 apartments, “average” - 11 to 20 apartments, and “large” – of more than 20 apartments.
- **Energy standard, insulation level**
  In this category three building types have been distinct. New buildings with a high energetical standard; retrofitted with an average energetical standard and old, un-retrofitted buildings with a poor energetical standard. It was decided not to declare strict values expressing the energy demand.
- **Heat Sources**
  The general categorization of the solutions in the “solution matrix” does not consider the heat source of the building. This description category is an attempt to indicate which heat sources are preferable for each solution.
- **Heat distribution and temperatures levels**
  This category describes the type and way of heat distribution for space heating and DHW. Additionally, the temperature levels for each mode are indicated.
- **DHW and storage characteristic**
  This category describes the type and way of provision of the DHW for the building. Also, the necessity of the storage tanks is indicated.
- **Complexity of installation**
  The estimated effort for the installation of the system is described in this section.
- **Specific issues of the concept**
  Any additional information about the solution finds its place under this category.

4.2.1. General remarks to the concept's description

Significant simplification of the presented categorization allows for a quick and understandable overview of heat pump solutions for multi-family buildings. The description of each category is deliberately short and simplified, to be comprehensible for broad audience. This approach consequences with technical superficiality. Presented descriptions do not aim at being fully exhaustive. They rather form a basis for further discussions. Each description is a compromise between different views of the involved Annex partners. In some cases, a specific national perspective results in a different view on the topic. Some descriptions within solutions from the same "family" repeat.

4.2.2. Example of the solution´s description

Comprehensive description of all solutions is available either on the website of the Annex 50 (https://heatpumpingtechnologies.org/annex50/) or in the final report of the project [3]. Below example presents the solution 1.1 called „one heat pump for all"

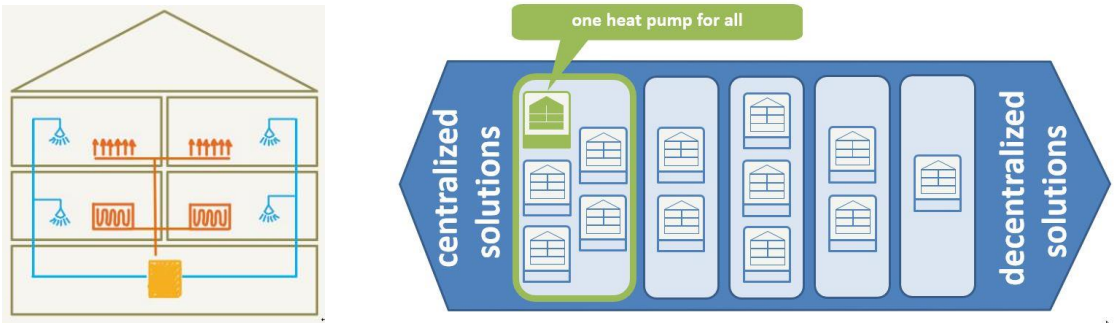


Fig. 5. Schematic hydronic system of the solution and the placement in the "solution matrix"

Description according to the eighth categories:

- **Main characteristic of the concept**
  One central heat pump system for the whole building, both for space heating and DHW.
- **Size of building, number of apartments**
  This solution is a typical solution in SFH (single family house). It may also be common to apply in smaller MFB with a small number of apartments. In case of large buildings, more than 1 heat pump may be necessary to meet the required heating capacity (cascade solution).
- **Energy standard, insulation level**
  Most suitable for buildings with higher energy standards (new buildings). This concept may be used also for buildings with an average energy standard. For poor insulated houses it is not excluded, however more challenging to implement.
- **Heat Sources**
  All heat sources possible. For large buildings with high energy demand the heating capacity can be a restricting factor for the outside air as a heat source. When outside air is used as HP-source, the HPs should preferably be installed on the roof or in dedicated containers near the technical room. For larger systems, the sound emissions may be a problem for air-source heat pumps.
- **Heat distribution and temperatures levels**
  The heat distribution occurs through the whole building, which increases the heat losses. The heat pump must be able to provide two temperature levels for space heating and DHW or the heat production needs to always meet the high temperature requirements for DHW.
- **DHW and storage characteristic**
  In the central solution for DHW the heat losses account for a significant part of the energy consumption. Storage tanks for DHW are needed. Separate consideration about legionella needed (for example ultra-filtration).
- **Complexity of installation**
  In case of retrofitting, the old heating distribution system may be maintained. In some cases, partial or complete exchange of radiators in each apartment may be required. In case of new buildings, long piping through the whole building is necessary.
- **Specific issues of the concept**

The old heat generator can be replaced (during retrofitting) without changing the distribution system.

In addition to the eight categories, the main advantages and disadvantages have been identified. Similarly here, to concisely indicate strong and week sides of the concept was a balancing act between shortness and comprehensiveness. In case of the example solution 1.1. the positive aspects are: optimal for smaller MFB's, one controller, existing distribution maintained and simple replacement of a gas boiler. The negative aspect are the high thermal distribution losses.

5. Holistic approach to present the results of Annex 50

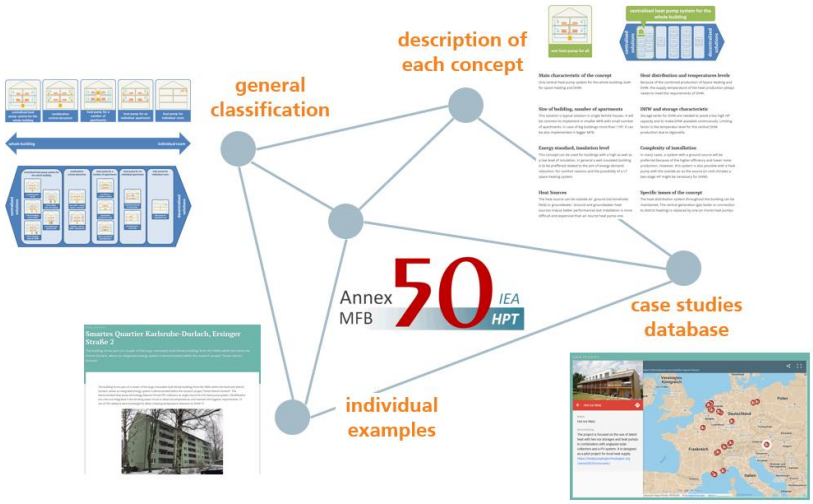


Fig. 6. Main elements of the "solutions matrix", the holistic result of the Annex 50

The approach of the Annex 50 was to find the way to create a holistic (integrated) method of presenting its results. The categorisation of the solutions and the description of each of them is only a part of the "solutions matrix". Other parts are the case study database and the individual examples of case studies of heat pumps in multi-family buildings. Each part of the matrix can be used or presented as a stand-alone component. Figure 6 shows the schematic connection between each component of the matrix.

The elaborated case studies are also linked to the certain examples of solutions from the classification described in the previous section. Through providing concrete examples, the theory has been brought to the practice.

6. Discussion

The results of the Annex 50 have been achieved with the best knowledge and belief of the project partners. Nevertheless, presented outcomes may certainly be flawed with some shortcomings.

The description of the proposed "solution matrix" should rather be seen as a framework prepared for further elaboration, than as an accomplished task. Each description is a compromise between various views of the involved Annex partners. In some cases, a specific national perspective results in a different view on the topic. It is recommended to open the discussion about the characteristic of each concept to the broader audience.

With the simplified approach chosen to classify and to describe the solutions, the planned tool "solution finder", suggesting particular solutions for certain types of buildings etc., cannot be seen and used as a "pre-planning" tool. It is and will be, even with further improvements, solely a hint-assistant on the way to find the right solution and to recognise existing possibilities.

The case studies database should be regarded as a well-established tool with a large expanding potential. The collected cases show explicitly the applicability of heat pumps in multi-family buildings. Despite the significant effort, with the information at the disposal it was not possible to ensure that all case descriptions are of the same level of detail and completeness. The data base should be further developed with more case studies in order to reach its full potential.

7. Conclusions

The importance of implementation of heat pumps in residential buildings, and in multi-family buildings in particular, has grown significantly in the last years and has even further intensified in the days of the crucial and unprecedented debate on independency from fossil energy sources. It`s undeniable that heat pumps technology will play a key role to achieve both the climate neutrality and the fossil fuels independency.

The variety of multi-family buildings and their characteristics make it possible to apply various technical solutions based on heat pumps. Nevertheless, the large heterogenicity of the multi-family buildings leads to individual solutions which are difficult to apply on a large scale. More standardisation of the products and the solutions is therefore needed and crucial.

The proposed categorisation and a simplified schematic visualisation of heat pumps solutions in multi-family buildings provides a user-friendly entry point for the building's owners and/or decision-makers. Rephrasing, it can be the first step towards implementation of heat pumps by disenchanting the complexity of the possible solutions.

The work of Annex 50 will be continued in the newly initiated Annex 62 "Heat pumps for multi-family buildings in cities" (started in January 2023 with the planned duration of 3 years). The tools described in the paper will be consequently improved and developed. Furthermore, new aspects of the application of heat pumps in multi-family buildings will be addressed.

Acknowledgements

This paper and the results behind it would not have been possible without the exceptional support of all partners working within the frame of the Annex 50. I am grateful to all of those with whom I have had the pleasure to work during this project. Namely Odile Cauret (EDF – Research & Development, France), Nicole Calame (CSD INGÉNIEURS SA, Switzerland), Jeannette Wapler (Fraunhofer ISE, Germany), Charles Geelen (Infinitus Energy Solutions, Netherlands), Marco Simonetti (Politecnico di Torino, Italy), Andreas Zottl (AIT Austrian Institute of Technology GmbH, Austria) and Svend Vinther Pedersen (Danish Technological Institute, Denmark).

I would like to express my deep gratitude to all partners for each hour of fruitful discussions, for their patient guidance, enthusiastic encouragement, and useful critiques during the finalization of the final report.

This work was supported by the German Ministry of Economics and Technology (BMWi), under the Grant 03SBE0001B upon decision of the German Bundestag and supervised by the Project Manager Jülich (PTJ).

References

[1] IPCC, 2022: Climate Change 2022: Impacts, Adaptation, and Vulnerability. Contribution of Working Group II to the Sixth Assessment Report of the Intergovernmental Panel on Climate Change [H.-O. Pörtner, D.C. Roberts, M. Tignor, E.S. Poloczanska, K. Mintenbeck, A. Alegría, M. Craig, S. Langsdorf, S. Löschke, V. Möller, A. Okem, B. Rama (eds.)]. Cambridge University Press. In Press.
[2] IEA (2021), Net Zero by 2050, IEA, Paris https://www.iea.org/reports/net-zero-by-2050
[3] Cambridge Econometrics, 2022: Modelling the socioeconomic impacts of zero carbon housing in Europe, Technical Report, Cambridge, UK
[4] Miara, M. 2022. Heat Pumps in Multi-Family Buildings for Space Heating and DHW, Final report of the IEA HPTAnnex50
[5] EHPA 2022: European Heat Pumps Market and Statistics, Report 2022

14th IEA Heat Pump Conference
15-18 May 2023, Chicago, Illinois

Heat pump application in cluster of buildings and positive energy districts

Carsten Wemhoener*

IET Institute of Energy Technology, OST Eastern Switzerland University of Applied Sciences, Campus Rapperswil, Oberseestrasse 10, 8640 Rapperswil, Switzerland

Abstract

A new Annex numbered 61 in the Technology Collaboration Programme (TCP) on Heat Pumping Technologies HPT of the International Energy Agency IEA started in September 2022 and deals with heat pump (HP) application in clusters of buildings as well as positive energy neighborhoods and districts (PED). The focus is on smaller clusters of buildings and new built, but there are also contributions to the district level and retrofit situations, where concepts are developed for larger clusters and to move the cluster or district closer to positive energy or a net zero emission balance, respectively. Based on the state-of-the-art of HP in PED the Annex systematically investigates HP concepts in more detail regarding design and control by simulation. The core activities are techno-economic concept analyses accompanied by monitoring of real case studies both for new built and renovation. The Annex delivers recommendations for HP application in cluster of building and districts to increase market shares of HP also in larger buildings and non-residential applications. The paper gives an outline of the Annex and first interim results of the Annex work.

© HPC2023.
Selection and/or peer-review under the responsibility of the organizers of the 14th IEA Heat Pump Conference 2023.

Keywords: positive energy districts; heat pump; system integration; building clusters; monitoring

1. Introduction

Climate protection is presently the largest challenge for the humankind. The global carbon budget for keeping the 1.5 °C target established in the Paris Agreement of 2015 [1] is reached within a time frame of less than 10 years at current CO_2-equivalent emissions [2]. Thus, efforts in all fields to reduce greenhouse gas emissions are urgently required and many cities have already declared a climate emergency in the recent years.

In many countries worldwide, the built environment plays a key role for carbon emission reduction, since in particular the existing building stock has a poor energetic quality. On the other hand, buildings can thereby also contribute to a fast emission reductions. In the EU, for instance, 36% of the carbon emissions are due to buildings, so reaching ambitious climate targets will be strongly facilitated by transforming the building sector. For new buildings, standards have developed to high performance requirements. Furthermore, buildings shall contribute to cover their own demand, leading to the nearly zero energy concepts (nZEB), which has been established in the EU with the recast of the Energy Performance of Buildings Directive (EPBD) [3] and is the current requirement from January 1, 2021 in the EU member states. In addition, the USA and Canada as well as Japan and China have targets to reach Net Zero Energy Buildings (NZEB) in the time frame of 2020 to 2030. Ambitious targets, though, are harder to achieve in existing buildings. However, the latest version of the EPBD of 2018 also requires the member states to develop retrofit strategies to notably enhance the energy performance of the building stock. For new dwellings, also examples to even transcend the nZEB balance and reach a positive energy balance exist with the ability to export parts of on-site energy production to connected grids. This concept can be extended to clusters of buildings and districts deriving a positive energy district.

* Corresponding author. Tel.: +41 (0)58 257 4325; fax: +41 (0)58 257 44 00.
E-mail address: carsten.wemhoener@ost.ch

However, former work, among others in the HPT Annex 49 on "Design and integration of HP in nZEB" confirmed, that in particular for larger residential and office buildings, reaching a positive energy balance on the individual building level can still be challenging. In this sense, extension to clusters of buildings with different load structures also have potentials to enhance the heat pump (HP) performance and enable to reach ambitious energy targets.

On the other hand, in the Net Zero Roadmap of the International Energy Agency [2], HP are seen as dominating heating systems with a share of 50% globally by 2045.

HP are already establishing as standard heating system in the new built market in many countries, so the integration of heat pumps in the energy system on the large scale is a future task. Application of (larger) HP for the use in cluster of buildings and neighborhoods, though, are not yet as common. Comprehensive recommendations for the best integration of the HP from a purely decentralized use on individual building level to an entirely centralized integration on district level are missing, and performance potentials of HP application in districts depending on load boundary conditions are not obvious. Moreover, further benefits of HP in cluster of buildings regarding storage options and unlocking of energy flexibility as well as economic implications are further investigated to entirely assess potentials and facilitate ambitious energy performance and emission reduction targets.

2. Outline of the Annex

On this background, the new Annex 61 in the Technology Collaboration Programme (TCP) on Heat Pumping Technologies (HPT) of the IEA entitled "Heat Pumps in Positive Energy Districts" studies the application of HP for clusters of buildings and positive energy neighborhoods (PEN) or districts (PED), respectively. A focus is on smaller clusters of buildings and neighborhoods, mainly with residential and office use. While a majority of project contributions concentrates on new built clusters, quite some projects also focus on strategies to increase the energy performance of existing neighborhoods to approach a zero energy/emission balance, which is also in the scope of the Annex. Thereby, renovation strategies include both the improvement of the building envelope and the integration of HP, and optimized concepts of the combination of both approaches to improve the energy performance are to be evaluated.

Besides the unique performance features of HP and the ability to provide the different building services of space (SH)/domestic hot water (DHW) heating and space cooling (SC)/dehumidification (DH) even at the same time, HP are also a key technology to link the on-site electricity production and heating/cooling demands in districts, respectively. Thus, supposed benefits of the HP integration in districts are manifold.

- the high energy performance of HP enables to reach ambitious energy/emission targets
- the simultaneous operation of HP for different building services enables a waste heat recovery for other building services, e.g. by simultaneous space cooling and DHW heating within the district
- the link of electric and thermal energy allows for load balancing within the district of electric and/or thermal loads as well as on-site electricity production for enhanced self-consumption
- the load balancing can also provide energy flexibility for connected grids, so that the district can provide services for other parts of the city

In order to assess the HP potentials the Annex work follows a 4-step methodology divided into Tasks. Based on the state-of-the-art analysis of HP use in already existing clusters of buildings or PED, a concept analysis for HP in PED is carried out. For promising concepts, a detailed techno-economic analysis is accomplished and backed-up by monitoring of HP operation in PED, which are evaluated in parallel to the concept analysis. Details on the individual Tasks is given in the following

2.1. Task 1: State of the art analysis (September 2022 – June 2023)

Starting from already existing HP systems in cluster of buildings, the state of the art is characterized and boundary conditions for the follow-on tasks are gathered. As Key Performance Indicators (KPI) CO_2-eq.-emissions and further technical and economic KPI are considered. As result of Task 1 an assessment of technically realistic options for PED as well as an economic estimation of reachable ambition levels and the economic handicap could be evaluated. Therefore, standardized load profiles are generated and used for archetype district, e.g. entire residential use, mixed residential and office use etc. These archetype districts are to be characterized by the building quality reflected in the loads, the available renewable sources and the on-site energy production options.

2.2. Task 2: Generic concepts development (January 2023 – June 2024)

Task 1 is followed by Task 2 for the analysis of generic system concepts. On the second Annex meeting a first categorization of the generic system concepts has been discussed and the following top level categories have been derived. Starting from decentralized concepts on individual building level as reference, a stepwise path to an entirely central concept with the different steps have been defined, comprising as second category a purely electric connections, as third category a collective heat source, as fourth category a semi-centralized integration and a fifth category the fully central integration. Semi centralized integration is understood in terms of mixed centralized and decentralized HP, e.g. a central SH HP combined with a decentralized second HP, possibly also as "booster" HP for DHW. The categories are to be further detailed into subsystems in order to derive an overview of different possible configurations. For each of the subsystem, a short technical characterization is to be elaborated. As result, an as far as possible complete overview of generic integration options of the HP in districts with pros and cons and favorable applications as well as recommendations are foreseen.

2.3. Task 3: Techno-economic analysis of concepts (January 2024 – December 2025)

Based on the favorable system concepts derived in Task 2 a more detailed techno-economic analysis is carried out, in particular regarding the design and control as well as integration with storage and other generators to optimize the HP operation regarding performance, renewable energy integration, system cost and energy flexibility. The detailed investigations are carried out by simulations where also modelling aspects of larger heat pumps are a research topic. Task 3 also serves to evaluate optimization potentials of real systems in monitoring in Task 4, which in turn yield operation and performance data to validate the models.

2.4. Task 4: Monitoring and system optimization of the real performance of HP in districts (January 2023 – December 2025)

As mentioned above Task 4 is dedicated to the evaluation of the real performance of HP in district applications and to the identification of typical optimization potentials in the real operation for the different heat pump integration options in monitoring. Moreover, a comparison and verification to simulated values is enabled by the real operational data.

Table 1. Overview of possible contributions of participating and interested institutions to the IEA HPT Annex 61

Country	Institutions	Contributions
AT	UIBK, AIT, AEE-INTEC	• Concept analysis in 7 equal multi-family houses (MFH) by simulation/monitoring • Evaluation of HP in clusters of buildings (decentral, semi-central, central) • Investigation of new built district regarding integration option by simulation/monitoring
BE	ULB, KU Leuven, Swecobelgium, vito	• Design and monitoring of clusters of offices/neighbourhoods with sewage water heat source • Development of models and a testing framework for district concepts • Test of different HP technology options in a living lab of a district retrofitted to PED
CA	Concordia	• Model development and case studies of PED by simulation
CH	IET OST	• Simulation and monitoring of PED with centrally integrated heat pumps • Design of larger heat pumps for MFH and clusters of buildings
DE	THN, SIZ energieplus	• Model predictive control of a cluster 8 single family plus energy houses for energy flexibility • (Retrofit) concepts for MFHs/neighborhood by simulation and monitoring
IT	Univ. Firenze	• Monitoring and simulation of neighborhood with seasonal thermal storage, HP and solar collectors/troughs
JP	Univ. Nagoya	• Evaluation of contribution of HP in positive energy district to reach climate protection targets • Case studies of simulation and monitoring of HP in districts
NL	RVO	• Investigation of decentralized and centralized system concepts for HP in new built and retrofit application
NO	SINTEF, NTNU, COWI AS	• Case studies of heat pump application in clusters of buildings by monitoring • Integration of heat sources for clusters of residential buildings and districts
SE	RISE	• HP modelling and development for the use in thermal grids • Control of HP flexibility in thermal grids and large-scale control of HP
US	NIST, ORNL, EPRI	• Simulation, testing and monitoring of high performance ground source integrated HP with different ground-source systems (horizontal/borehole)

2.5. Task 5: Dissemination of interim results (September 2022 – December 2025)

All task are accompanied by dissemination activities like workshops, articles, website information and presentations, which are summarized in an overarching Task 5.

3. Overview of selected contributions and interim results

The IEA HPT Annex 61is still in the starting phase since it officially started in September 2022. However, two meeting have been held, where first definitions and results have been discussed. Thus, in the following, a more detailed description of Annex contributions along the single Annex Tasks linked to first interim results are summarized to give better impression of intended and ongoing Annex work.

3.1. State of the art results in Task 1

First results on the state of the art are given in terms of PED definitions and an evaluation of realized PEDs concepts in Germany and Switzerland.

3.1.1. International and national definitions of PED

Even though the concept of PED is developed since 2015, there is no uniform definition up to now. In Seifried et al. [4] a detailed evaluation of applied definitions is provided by the analysis of five EU programs and nine prominent PED project and common items and differences are analyzed. In Figure 1 left, the PED framework developed by Joint Programming Initiative of Urban Europe (JPI UE) which seeks to create a uniform vision for PED and states PED as "energy-efficient and energy-flexible urban areas or groups of connected buildings which produce net zero GHG emissions and actively manage an annual local or regional surplus production of renewable energy. They require integration of different systems and infrastructures and interaction between buildings, the users and the regional energy, mobility and ICT systems, while securing the energy supply and a good life for all in line with social, economic and environmental sustainability." While this definition has a focus on the operational phase, a Swiss definition of a "*2000 W Areal*" is based on the SIA 2040 efficiency path [5], which takes into account the whole life cycle incorporating also the embodied energy for the construction and demolition phase and the building induced mobility linked to the site as basic energy boundary. However, as can be seen in Figure 2 on the left, also other criteria like management and communication processes, surrounding and use are contained.

A characteristic, though, which is contained in several definitions, is besides the efficiency and the on-site energy generation the requirement for energy flexibility in order to manage the local or regional energy flows also in conjunction with connected local or regional grids.

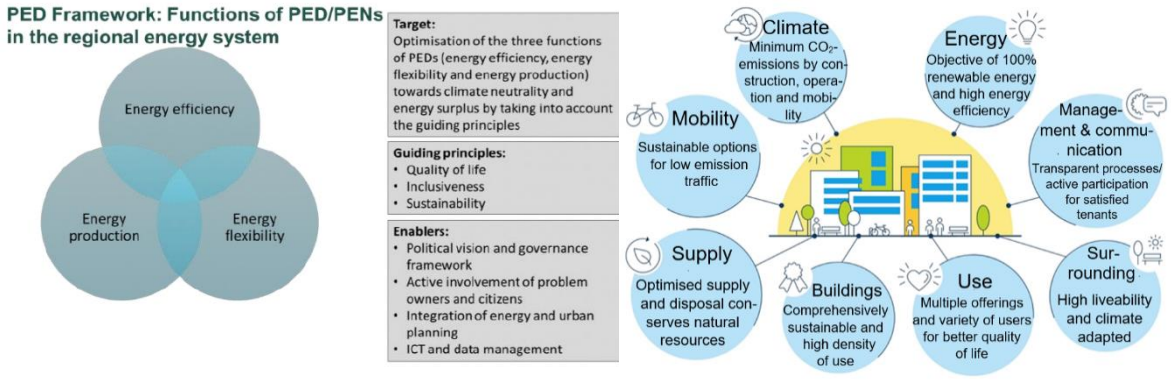


Fig. 1: PED Framework definition according to JPI UE (left) [6] and Swiss definition of 2000 W Areal (www.2000watt.swiss)

Seifried et al. [4] conclude from their evaluation that there are still a lot of differences, among other on the PED boundary, the calculation method of the energy balance and the scope for non-energy matters. An important fact is defining the fundamental purpose and application, which can lead to a universal framework.

3.1.2. Interim results on the evaluation of existing PED in Germany and Switzerland

At the Steinbeis Innovation Center (SIZ) EnergiePlus, a first review of existing PED in Germany with a particular focus on heat pump operation has been compiled and is summarized in the following.

The overall number of PED found adds up to 42 documented projects, of which 2/3 are in realization or already realized, while the remaining 1/3 is still in the planning phase or will not be realized. Thereby, projects are not evenly spread in Germany, but most of the projects are located in just two federal states "Baden-Württemberg" and "Hessen". Based on available data, only 16 of the total of 42 have been evaluated. Regarding the energy system, all PED are equipped with PV-systems, while installed solar thermal systems are below 20%. HP are with 60% the most applied heating system followed by combined heat and power (CHP) with 40%. Further energy generators are small wind turbines as well as district heating.

With respect to the HP, eight of them are centrally integrated, while two are decentral. The CHP is mainly linked to thermal grids within the PED, and only two transcend the PED physical boundary. The size of the PED are quite different in the range of 16 – 480 flats. However, most of the PED have above 50 and below 200 flats, also including the districts in planning.

In Switzerland, PED are currently dominated by the *2000 W districts*, counting 44 projects, which, however, are also differentiated to projects in realization (25%), in planning and in transition (together 75%). Projects in transition are related to transform existing districts to the requirements of a *2000 W district*.

The term 2000 W district is based on a budget approach developed at the Swiss Federal Institute of Technology ETH stating that a continuous global power consumption of 2000 W/P/year (corresponding to 17500 kWh/P/year) for all energy services including transport and industry sector is sustainable. It developed as long-term vision for the Swiss energy consumption. However, due to the newer results on climate change the objectives of the 2000 W vision have been significantly tighten in order to comply with the net zero targets by 2050 [7]. Furthermore, the 2000 W district certification is currently linked to the efficiency label MINERGIE [8] and to the sustainability label SNBS [9], which may also change the name of the certification.

Only 4 projects are listed as so-called "plus energy district", which is a different initiative to document high performance districts with a positive energy balance. For this certification, only operational energy is taken into account for the balance. The 2000 W projects are more evenly spread in 13 of the 26 federal states, but only five federals states have projects in use. Heat pumps are the dominating heat generator besides district heating, with shares in the range of 90%, often combined with PV, which also reaches fractions above 90%. More than half of the projects use heating grids, and about 30% use the ground as heat source. Also almost all projects plan to import certified green electricity. Regarding the use of the districts, the majority has a mixed use with a range of 200 to 1500 workplaces. These districts include also offices, restaurants, hotels etc. 9 districts are only for residential use without any workplace and commercial or retail areas. The number of buildings reaches from one to 53, whereby the total area reaches from 4'500 m^2 to 900'000 m^2. The number of flats reach up to 1500, while the smallest contains just 81. Regarding the supply systems, nearly all districts incorporate heat pumps and PV production partly combined with other heat generators. Imported green electricity is often found, as well, and one district uses a river hydro power plant to generate electricity in the district. The heat production is mostly local, i.e. there is still potential for the extension of heating grids. Some districts use biogas to dampen peak load. One district also produces its own biogas.

3.2. Generic system concepts in Task 2

Based on the outline in chap. 2.2 the different categories are depicted in direction of increasing integration of the heat pump into the district in Figure 2.

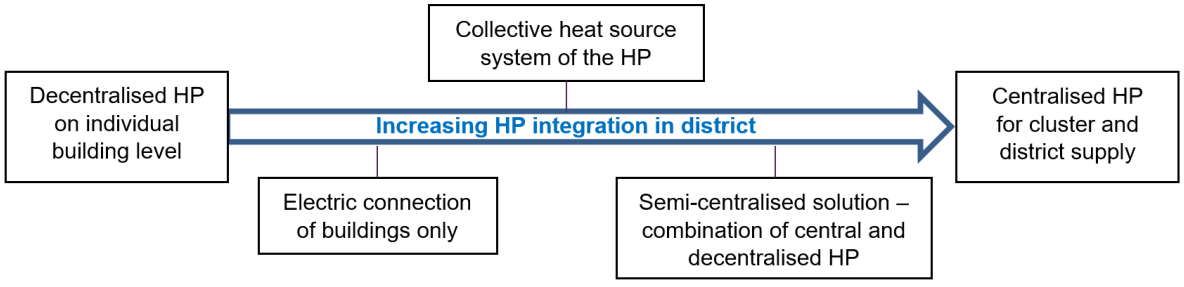


Fig. 2: HP integration categories defined in Task 2 in the direction of increasing HP integration

Currently, the subsystems are gathered and a template is elaborated for the compilation of system characteristics.

3.3. Techno-economic analysis of promising cluster concepts by simulation in Task 3

Task 3 has not yet started, but is dedicated to the in-depth techno-economic analysis for favourable concepts identified in Task 2

3.4. Monitoring of HP application in clusters and districts in Task 4

Monitoring of HP is an important feedback of the real performance, on the one hand for the energy assessment, on the other hand for simulation validation. In turn, simulation in Task 3 are used to identify optimization potentials in order to improve the real operation.

In the following, an outline of four different clusters and districts, respectively are given, which also visualize the different categories of generic concepts for the heat pumps integration in Task 2, see chapter 2.2.

3.4.1. Cluster of eight terraced plus energy single family houses Herzo Base in Herzogenaurach, Germany

The cluster of eight terraced houses is located in Herzogenaurach, Germany in the new district Herzo Base and built in 2017. The buildings were designed as an "all electric buildings", which means that the only source of energy is electricity. A PV-system (88 kW_p) on the roofs delivers an annual surplus of energy. The idea of small neighbourhoods creating an energy community and share energy systems enables higher potential to increase the PV self-consumption. Furthermore, synergies between different electrical loads lead to a more even electrical profile and reduces electrical load peaks. The terraced houses share a central heat pump system of two modulating HP (MHPs) of each 17 kW_{th}, with geothermal heat source as well as a battery system with a capacity of 40 kWh_{el}. The supply of domestic hot water is decentralized in each terraced house by a domestic hot water-HP (Booster), which use the heating buffer storage units as heat source. All eight terraced houses are equipped with floor heating and decentralized ventilation devices. The objectives of the field monitoring is the evaluation of the plus energy balance and PV self-consumption. Another aspect is the field test and evaluation of advanced control strategies in order to increase PV self-consumption and reduce energy costs. Figure 3 shows the building cluster and its position in the district.



Fig. 3: Building cluster Herzo Base, Herzogenaurach, DE

3.4.2. Clusters of multi-family buildings in Konstanz and Wolfsburg, Germany

The planning and implementation of a completely renewable energy supply for a block of residential buildings in an urban structure presents a challenge. This was achieved in the two projects by providing heat using a ground- coupled HP. The multi-family houses in Konstanz and Wolfsburg were completed in 2016 and supply a net floor area of 1140 and 9500 m².



Fig. 4: Cluster of multi-family buildings in Konstanz (left) [source: WOBAK] and Wolfsburg (right), DE

Figure 4 shows the building cluster in Konstanz (two buildings) and Wolfsburg (four buildings). The energy concepts of the residential buildings are based on heat supply via HP.

The generated heat is temporarily stored in buffer tanks and delivered to the low-temperature heating systems. The DHW is heated via fresh water stations or storage tank charging systems. Decentralized exhaust air systems or central ventilation systems ensure a constant air exchange. Natural ventilation via the windows is possible in all properties. Photovoltaic systems are installed to cover the electrical energy needs of the system technology and the connected households. The system technology is optimized for so-called "PV self-consumption", which means direct use of the photovoltaic yields.

Electrical energy from the PV systems that cannot be directly consumed or stored is fed into the public electricity grid. The comparison of the multi-family buildings refers to their efficiency, ecology and economy, with the overall balance and thus the total consumption of electrical energy serving as the basis for evaluation.

The consumption of the buildings is made-up of the electricity consumption of HP and circulation pumps, general electricity (lift, staircase, garage, etc.) and the user electricity of the individual flats (appliances).

Table 2. Key data of the building and supply concept

	Konstanz	Wolfsburg
Building	2 buildings (2016) with 12 apartments in total; 3 floors each; Net Floor Area (NFA) 1140 m² (total)	4 buildings (2016) with 68 apartments in total; 4 floors each; Net floor Area (NFA) 9500 m² (total)
PV-system	59.2 kWp on the roof; roof slope 10° to west and east	27.4 kWp on the roof of house A; Roof slope 45° to south (possible PV size ~160 kWp)
Heat pump	2x brine-to-water-HP (30 + 27 kW)	2x brine-to-water-HP (90 + 50 kW) and 4x air-to-water-HP (each 14 kW)

3.4.3. New built district Campagne, Innsbruck, Austria

A new low-energy residential district is being built in Innsbruck, Austria. The building owners (social housing companies) had to make decisions with respect to the energy quality of the buildings and the heating system with respect to the energy and environmental impact. The district will be composed of 16 buildings grouped in four blocks, see Figure 5. The main part of the buildings is residential and will consist of approximately 1100 new apartments for a total surface of 78027 m^2. Moreover, sport facilities, cafes, schools and kindergartens will be constructed. In the planning phase, a cooperative process was carried out, involving neighboring residents and local associations.



Fig. 5: Building cluster of Campagne, Innsbruck, AT (source: ibkinfo.at; stadtteilzentrum-reichenau.at, Bogenfeld Architekten)

The buildings are built according to Passive House standard (space heating demand lower than 15 kWh/(m^2yr)). The space heating demand is supplied by a groundwater HP and the emission system is floor heating. The domestic hot water is provided by the district heating network, which accounts for a high proportion of heat by renewable sources, industrial waste and bioenergy. The shares of renewable sources and industrial waste heat of the district heating of Innsbruck are higher than other cities in Austria and it is foreseen that these shares are going to increase in the future. Photovoltaic panels are installed on the roof of the buildings to cover the electrical demand of auxiliaries. Moreover, sustainable mobility solutions are planned to enhance the electric mobility. System simulations have already been performed, while also monitoring of the buildings is intended.

3.4.4. Papieri district, Cham, Switzerland

The Papieri district in Cham, CH, is an old estate of the Paper industry, which is rebuild to a comprehensive new neighborhood in six phases over the next years for 1000 inhabitants and 1000 additional workplaces in the final development. Figure 6 left shows a picture of the district, the first development phase is depicted in Figure 6 middle, and the energy concept of the borehole fields connected to the central HP heating and cooling is shown in Figure 6 on the right.

The neighborhood consists of industrial heritage buildings of the paper industry which are preserved and retrofitted for a new use and are amended by new buildings, which create a mix of about 30% of existing and 70% of new buildings. In the first phase depicted in Figure 6 middle, 105 freehold apartments and 160 rental apartments together with 4400 m^2 floor area of commercial and office use will be commissioned by the end of 2022.

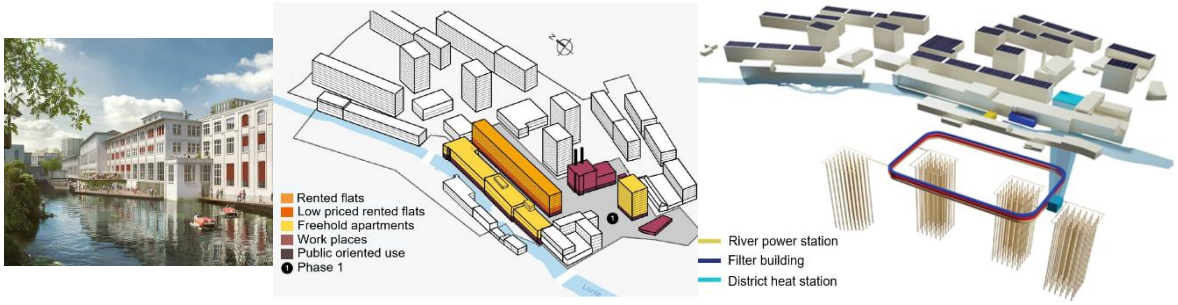


Fig. 6: Papieri neighborhood, Cham, CH, with neighborhood view from the river (left), buildings of the first phase (middle), and the energy concept (right) source: www.papieri-cham.ch, AWIAG, Cham group)

The estate development is designed in a way that all building services of heating, cooling and domestic hot water are entirely supplied by renewable energy. About 40% of the electricity use in the district is generated on-site. The electricity is generated by a 6500 m^2 PV-system of an installed peak capacity of 1.27 MW_p and an estimated annual electricity production of 1.1 GWh, which is installed on the roof of the new buildings. As second electricity generator, a hydro power plant with an installed capacity of 240 kW and a calculated annual production of 1.25 GWh is installed in the river Lorze, which run through the district. The remaining electricity is imported as certified green electricity from the utility in order to reach a zero emission balance.

The space heating and cooling as well as the DHW production is supplied entirely renewable by four central ammonia HP of a total capacity of 4 MW, which use borehole fields of totally 192 ground probes of 320 m depth as heat source. As second heat source, the river water of the Lorze is used either directly as heat source or as regeneration source for the borehole fields. The comfort cooling for the residential and office use is planned to be operated primarily by freecooling from the boreholes. Active cooling by the HP in chiller operation is only provided for peak load cooling, whereby all the recooling (waste) heat from the active chiller operation is to be recovered for other uses like DHW production or for the regeneration of the borehole fields.

Since neither the modelling and simulation nor the monitoring has started, yet, only the above-mentioned energy concept and design data are available of the neighborhood. The HP system will be modelled, simulated and monitored in order to optimize the first operation years and retrieve on-site information for the further development of the neighborhood in the later project phases. The evaluation includes the verification of the system performance of the centralized HP and the zero emission balance.

A special focus of the simulation and the monitoring is a more detailed analysis of the operation and the energy balance of the borehole fields for combined space heating, DHW and cooling operation. Moreover, the options for the interaction of the two heat sources of the borehole fields and the river water is investigated. Performance potentials are seen in the use of the source with most favorable temperature level, the regeneration of the borehole field for space heating and the simultaneous operation of the HP for heating and cooling in combination with high free-cooling shares. Thus, the objective for the system operation is the maximize the system performance of the HP by an optimized management of the borehole field as heat source and (free-) cooling heat sink and the integration of the ground and river water heat source.

3.4.5. Summary of monitoring projects and link to other tasks

The selected monitoring concepts combine both different sizes of the cluster for smaller groups of 2 and 3 buildings to larger neighbourhoods of up to 1000 flats in 16 buildings. Figure 7 depicts the outlined monitoring projects as contributions to the IEA HPT in the categories of the Task 2.

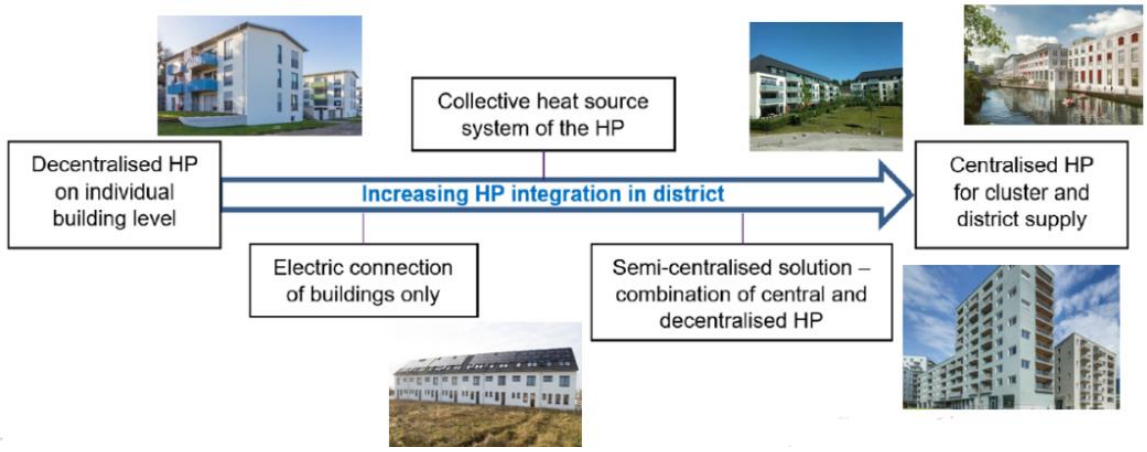


Fig. 7: Presented monitoring project in the categories of Task 2 between central and decentralized integration

Moreover, the uses range from smaller residential to larger multi-family, combined also with commercial and office use in the district. Even though for this selection, the focus is on new built there is also monitoring projects for retrofit concepts, even a variety of concept in 7 nearly identical buildings, which enables a direct concept comparison as well as larger districts build-up of retrofit and new built. By the chosen monitoring projects, it also becomes clear, that the different integration options according to the categories in Task 2 followed by the in-depth analysis in Task 3 can be well covered.

4. Conclusions and outlook

Positive energy districts are an ambitious concept, which is currently promoted in order to enhance a high energy performance and on-site energy production as part of the transition of the urban energy systems. Extending the system boundary from the individual building to clusters of buildings and neighbourhoods offers the combination of different load structures, which can unlock opportunities to increase on-site self-consumption of the produced electricity in the cluster by load balancing and to enhance the performance by waste heat recovery from one building service for another. Heat pumps can play an important role in positive energy district concepts, since they facilitate to reach ambitious energy targets by their high energy performance and can link both electric and thermal loads as well as different thermal uses like heating and cooling. As further aspect, sector coupling within the district and with connected grids can provide energy flexibility within and over the boundaries of the district.

The upcoming Annex 61 in the Technology Collaboration Programme on Heat Pumping Technologies TCP of the IEA investigate heat pump concepts for building cluster and positive energy districts. Starting with decentralized solutions on the individual building level, higher integration of the HP in the districts up to entirely centralized solutions and integration with other energy generators/supply like district heating is evaluated technically and economically. Based on generic concepts a detailed techno-economic analysis shall deliver favorable applications of HP in positive energy districts and recommendations for the integration, design and control of the HP systems.

As insight to the national contributions, the paper presents four case studies with different degree of integration of the heat pump in the cluster or district. Already existing results of the case studies confirm that reaching a positive energy balance is a challenge, which requires high building performance to limit the loads, high performance generators for efficient energy supply and vast energy production with the cluster or district, in particular for larger buildings and non-residential use.

Higher integration of the heat pump can create opportunities of higher on-site energy consumption and waste heat recovery for different building services in the cluster, which may further increase the energy performance and flexibility, but may also increase the cost and losses due to necessary grid connections. Both technical and economic trade-offs with be analyzed in the Annex 61.

Results of the case studies underline that HP reach high performance values in the application in clusters and can facilitate to reach ambitious objectives of zero or plus energy neighbourhoods or districts due to its unique features of even simultaneous provision of different building services with high performance. Furthermore, HP offer energy flexibility for higher PV self-consumption and reduced grid interactions. The upcoming Annex will derive favorable HP concepts for districts by simulation and monitoring in different case studies.

Acknowledgements

The IEA HPT Annex 61 is a collaborative research work and results are based on contributions of all participating persons and institutions. The good collaboration and open exchange is highly appreciated. The support and funding of the Swiss Federal Office of Energy SFOE highly acknowledged.

References

[1] UN, 2016. United Nations,Treaty Series,vol. 3156, CHAPTER XXVII, ENVIRONMENT, 7. d Paris Agreement, Paris, 12 December 2015, United Nations,Treaty Series,vol. 3156, C.N.63.2016.TREATIES-XXVII.7.d of 16 February 2016 (Opening for signature) and C.N.92.2016.TREATIES-XXVII.7.d of 17 March 2016 (Issuance of Certified True Copies.

[2] IEA, 2021. Net Zero by 2050, A Roadmap for the Global Energy Sector, revised version October 2021 (4th revision), International Energy Agency, Paris

[3] European Parliament, 2010. Directive 2010/31/EU of the European Parliament and Council of May 19, 2010 on the energy performance of buildings (recast), Journal of the European Union, p. L 153/13, 18. 6. 2010, Brussels

[4] Albert-Seifried, V. Murauskaite, L., Massa, G., Aelenei, L., Baer, D., Krangsås, S. G., Alpagut, B., Mutule, A., Pokorny, N. Vandevyvere, H. 2021. Definitions of Positive Energy Districts: A Review of the Status Quo and Challenges, in Howlett, R., Jain, L.C., Sustainability in Energy and Buildings 2021, Smart Innovation, Systems and Technologies book Series, Volume 263, Springer

[5] SIA 2040, 2017 *Effizienzpfad Energie*. Swiss engineers and architects society, Zurich, 2017

[6] JPI UE. 2020, *Europe Towards positive energy districts.* A compilation towards sustainable urbanisation and the energy transition, first update, 2020

[7] energie schweiz. 2020. Leitkonzept für die 2000 W Gesellschaft (in german). 2020. Energy Switzerland, Specialist department 2000 Watt, Oct.2020, https://www.local-energy.swiss/arbeitsbereich/2000-watt-gesellschaft-pro/Grundlagen-und-Konventionen/Leitkonzept-2000-Watt-Gesellschaft.html#/

[8] MINERGIE 2022. Produktreglement zu den Gebäudestandards MINERGIE®/MINERGIE-P®/ MINERGIE-A, version 2022.1, MINERGIE Association, Berne, 2022 https://www.minergie.ch/media/211130_produktreglement_minergie_p_a_v2022.1_de.pdf

[9] SNBS 2022. https://www.snbs-hochbau.ch/media/rz_min_204_-_snbs_flyer_148x210_de_02_web.pdf

14th IEA Heat Pump Conference
15-18 May 2023, Chicago, Illinois

European heat pump market data – evolution of the state of the art heat pump over time and its possible knowledge gain

Thore Oltersdorf[1,*], Hannes Fugmann[1], Lena Schnabel[1]

[1]Fraunhofer Institute for Solar Energy Systems ISE
Heidenhofstraße 2, 79110 Freiburg, Germany
thore.oltersdorf@ise.fraunhofer.de
* Person of contact

Abstract

Market data for several thousand heat pumps are available in different databases in Europe. Information therein of different versions over time allow the analysis of the evolution of the state of the art of heat pumps. Contrary to typical investigations of single systems by research groups as kind of "bottom-up approaches" to develop new systems or to argue why a specific refrigerant might be applicable due to reached efficiency etc., we try to gain insights into the state-of-the-art of the European heat pump market with a "top-down approach". The study begins with a comparison of such available databases and their specific differences. The gained product data are aggregated with additional information usually not part of such databases like the age of equipment, dimensions, etc. Thereby a very comprehensive new database arises. Based on this database we show the course over time of important parameters, such as used refrigerants and efficiency, but also sound emissions and refrigerant charge. Where possible the analysis comprises sensitivity analysis of different parameters linked to the used refrigerants and impacts of the applied refrigerant's thermodynamics.

© HPC2023.
Selection and/or peer-review under the responsibility of the organizers of the 14th IEA Heat Pump Conference 2023.

Keywords: market data; heat pumps; air-to-water; brine-to-water; database; CE-marking

1. Introduction

Due to the F-gas regulations and the resulting phase down of high GWP (global warming potential) refrigerants such as R407C and R410A, rising effort is spent in academic and industrial research and development towards the use of refrigerants with low GWP [1]. Especially, natural refrigerants like hydrocarbons and carbon dioxide are of interest. However, how fast can a change on the market towards low-GWP refrigerants happen? Beside the choice of refrigerant type, sound emissions of heat pumps become more and more relevant for installation of heat pumps, especially in dense cities. Is there a trend towards less noisy heat pumps visible in the market data? And lastly, an increase in thermal efficiency is a dominant driver for the industry? Is a stagnation of efficiency in sight? Or what is the efficiencies to compete with when new systems are developed? These questions can partly be answered by looking deeply into available market data for heat pumps in public and non-public databases.

The Eastern Switzerland University of Applied Sciences OST publishes every year performance figures of heat pump measurements in their accredited lab. In the last report [2], they show a significant proportion of outdoor installed heat pump units in the lab testing (increase from 17% in 2014 to 32% in 2020) and an increase in their thermal performance (COP increase from 3.5 in 2014 to 4.2 in 2020; operation condition: A2/W35). They state that outdoor installation of heat pumps might increase in future further on. Another finding from OST was that since 2018 the number of heat pumps with low-GWP refrigerants R32 and R290 increased up to 40% of the tested heat pump models in 2020. The authors state that a further increase is probable. Since 2005 OST has measured 249 air-to-water heat pumps and 217 brine-to-water heat pumps according to the

* Corresponding author. Tel.: +49 761 4588 5239
E-mail address: thore.oltersdorf@ise.fraunhofer.de.

standard EN 14511, such that this database is a good representative of the heat pump market in Europe. However, local boundary conditions in Switzerland, such as a change in the Swiss quality label for heat pumps [3] affect heat pump design and thus performance in the lab tests accordingly.

In the paper [4] from Park et al., the authors present comparative data that might help policy makers to create more effective air conditioning (AC) efficiency market-transformation programs. The paper explores relationships between the room AC efficiency performance metrics of different regions around the world using performance data for split room AC models, including reversible heat pumps which shows the relevance related to the usage of cross-correlated product databases.

Evaluation reports for subsidization programs for the promotion of heat pumps and thus a decarbonization of heat production are another crucial resource to investigate market dynamics and changes in the state-of-the-art of domestic heat pump. Several countries publish such reports in recent years on a regular basis [5–7] which were main resources on a just recently published meta study from IRENA with a global approach on analyzing costs and markets of heat pumps [8].

All research articles and reports listed above show significant trends of performance categorized e.g. for types of heat pumps. Their results can help policy makers and industry to learn from past trends and to estimate future trends. Our work will continue this trend analysis with heat pump data from large European databases and own data collection and adds the time of market introduction into perspective as another relevant figure. It helps to gain knowledge about heat pumps and is a figure which wasn't used before to the best knowledge of the authors.

2. Databases

For the following analysis of the European heat pump market several different databases have been used. These databases are listed in Table 1.

Table 1. List of databases

No.	Database	Country of origin	Number of heat pumps in database	Year	Used as eligibility list for e.g.	Reference	Used in this paper for…
1	**HP Keymark database**	Europe	428 btw hps; 4271 atw hps	11.2022	-	[9]	Efficiencies
2	**SAP Q database**	GB	4010 atw hps; 650 btw hps	11.2022	GB	[10]	Market introduction
3	**GET product database**	Austria	1453 atw hps; 578 btw hps	11.2022	Austria	[11]	Sound power
4	**BAFA database**	Germany	4221 atw hps; 1212 btw hps	11.2022; 12.2020	Germany	[12]	Efficiencies
5	**HARP database**	Ireland	605 atw hps; 163 btw hps	03.2022	Ireland	[13]	Market introduction
6	**Eurovent Certita Certification database**	Europe	12324 atw hps; 394 btw hps	11.2022	France	[14]	-
7	**Propane heat pump database Fraunhofer ISE**	Europe	120 atw hps; 5 btw hps	11.2022	-	this paper	Efficiencies, dimensions, market introduction
8	**Other national databases (IT, DK, CDN, NL)**	Europe, Canada	110 to 25500 (all types)	2020 to 2022	EU members, Canada	[15–18]	-
9	**TOPTEN databases (CH, A)**	Europe	110 to 190 (all types)	2022	-	[19]	-

atw: air-to water; btw: brine-to-water; hps: heat pumps

According to the website the Heat Pump Keymark is *a voluntary certification mark that supports the quality and performance of heat pumps on the European market. It can apply to all heat pumps, combination heat pumps and hot water heaters. The certification is based on independent third-party testing and is compliant with efficiency requirements as set by Ecodesign Lot 1, 2 and 10*[2]. The European heat pump sector is pinning

[2] See website www.ehpa.org/heat-pump-keymark, last accessed 30.11.2022

hopes into the idea to have in the future a standardized eligibility framework within the EEA based on the HP Keymark.[3] The database is of good quality due to the strict work based on test reports.

The GET product database is mainly *for installers to find product lists for boilers and collectors to help them prepare the system design declaration required for grant submissions*.

The BAFA database is a set of heat pump models listed as being eligible in terms of the legal and technical constraints in the framework of the German heat pump subsidization scheme. It comprises EN 14511 efficiencies, heating capacities and certain system and circuit specifications (in versions until 14th December 2020). In recent versions publicly available data were minimized and harmonised towards other product databases being compatible to implementing directives (mainly 206/2012 and 813/2013) of the ecodesign regulation rules which made the list less attractive for statistical purposes as within this study.

The SAP Appendix Q Database provides individual branded product performance information that can be accessed and used as an adjunct to the SAP calculation. A product's performance information is determined by testing against a specification agreed by different stakeholders in England.

The HARP database provides information on the efficiency of heating appliances available in Ireland for use in domestic funding schemes. Product submissions include product test data, product identification documentation and HARP submission forms. The database has been in operation since 2006.[4]

The Eurovent Certita Certification database is the largest and most professional database but more dedicated to commercial appliances and less used for heat pumps in residential houses. Its objectives are in the range of serving R&D departments of participating member companies as well as using the data to participate in bids for public orders.

The propane heat pump database from Fraunhofer ISE, used within this paper, contains market available heat pumps with the refrigerant R290 (propane) in order to show evolution and trends in the market of propane heat pumps. The database is based on the BAFA database but extended with data provided from the manufacturers. The database is non-public and lists more than 100 different types (vapor compression circuits) of propane heat pumps resulting several hundred individual models as variants from those different cycles.

Other national databases are available from different countries that are operating a heat pump funding scheme. Without being complete these are for example Canada, Belgium, Denmark, Spain, Austria, Switzerland, Belgium, Czech Republic as well as Poland.

Topten databases are usually a subset of the large portfolios of heat pumps available in the European Economic Area (EEA). Usually, products are relatively new to serve the aim of solely offering highly efficient, modern and environmentally friendly products to the market.

3. Evaluation

Based on this preliminary work to evaluate the existing databases and to generate a new database an analysis of relevant parameters started.

3.1. Refrigerant charge

The refrigerant charge is strongly dependent on the heating capacity of the heat pump. An increase in capacity usually corresponds to an increase in component size (e.g. heat exchangers) and thus yields higher absolute but not necessarily to higher specific refrigerant charges. The ratio of charge and capacity is shown in Figure 1 and referred to as "specific charge". The figure shows heat pump models from the BAFA database (No. 4 in Table 1). The year is based on the CE-marking dates (market introduction date) of the individual models. The data is separated into heat pumps with heating capacities below (a) and above (b) 12 kW. Comparing graph (a) and (b) regarding the increase in charge it is visible that the baseline is not strongly differing between smaller and larger systems. The inter decile range (between 10-90% of all models) for the smaller systems is in the range of 0,33-0,63 kg/kW and the inter decile range of the larger systems is in-between 0,1-0,52 kg/kW. This means that smaller systems have a faint larger specific charge amount than larger systems. But this strongly depends on the type of the used heat exchangers.

[3] Personal communication to several CEO's of heat pump manufacturer in November 2022.

[4] See website www.seai.ie/home-energy/building-energy-rating-ber/support-for-ber-assessors/software/harp-database/, last accessed 30.11.2022

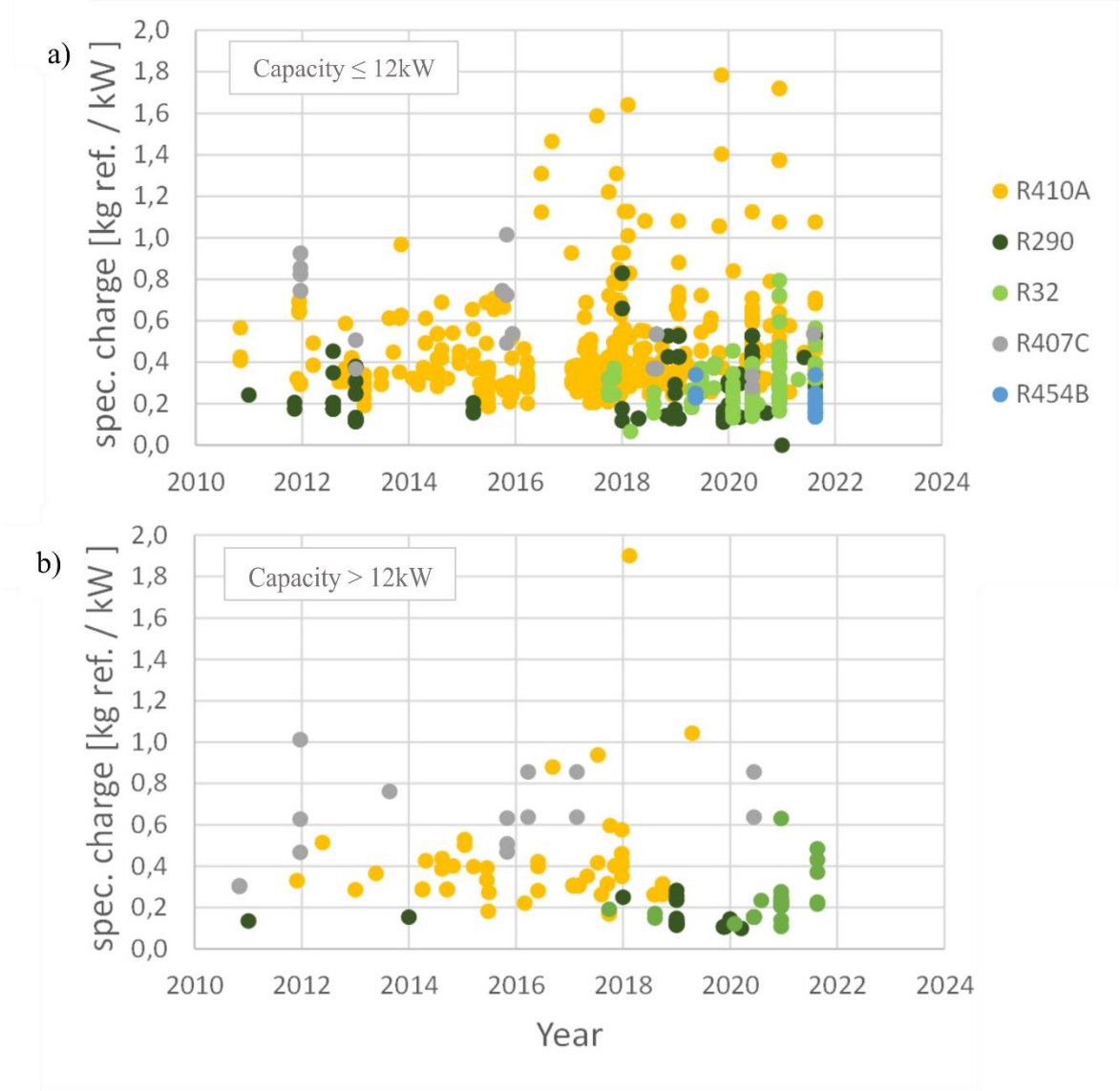


Figure 1. Refrigerant charge in kg per heating capacity in kW for different refrigerant types for air-to-water heat pumps. Operation point is A7/W35. a) for a heating capacity below 12 kW; b) for a heating capacity above 12 kW. Source: Own data and BAFA database (No. 4 in Table 1).

Different reasons for a specific charge higher than ca 0.8 kg/kW can be listed. For the authors, the most probable one is the usage of larger components in order to get a high COP.

A specific charge below 0.1 kg/kW is reached in less than 5% of the data. For these models the authors assume a design of the refrigeration circuits, optimized for low charge operation. Even though there are manufactures on the market with these low refrigerant charge heat pumps, a trend towards low charge cannot be seen from the analysis in Figure 1. At the same time the authors see strong R&D activities of the heat pump manufacturers with the flammable refrigerant R290. A safe operation is thereby linked strongly to the amount of refrigerant used. A reduction of R290 supports the safe operation. As Figure 1 shows the air-to-water heat pump models only, an assertion for brine-to-water heat pumps is not possible. The authors see for these systems market available low charge heat pumps and ongoing R&D activities[5], such that specific charge for brine-to-water heat pumps will further decrease.

[5] See https://www.lc150.eu/more_info/

3.2. Acoustics

Several of the databases includes sound power levels (database No. 1, 3, and 6). We focus on database No. 3 which is the Austrian GET product database. The GET database includes nominal and maximum sound power levels. A lot of models and thus entries in the database show a zero difference which means nominal and maximum sound power level are declared identical. This represents about 40% of all models listed in the database. The considered amount of listed air-to-water heat pumps is 1453 models. This leads to the conclusion that the data is not sufficiently reliable to investigate the sound power trends according to the time of market introduction. This is one of the reasons why for the revision of LOT 1 of the Ecodesign directive it was suggested to define operating conditions stricter than in the past. The taken recommendations are strongly linked to the recommendations and conclusions of the Swedish project on the acoustics of heat pumps to identify more reliable testing conditions [20]. This project was running in parallel to the IEA Annex 51 about the Acoustic Signatures of Heat Pumps [21].

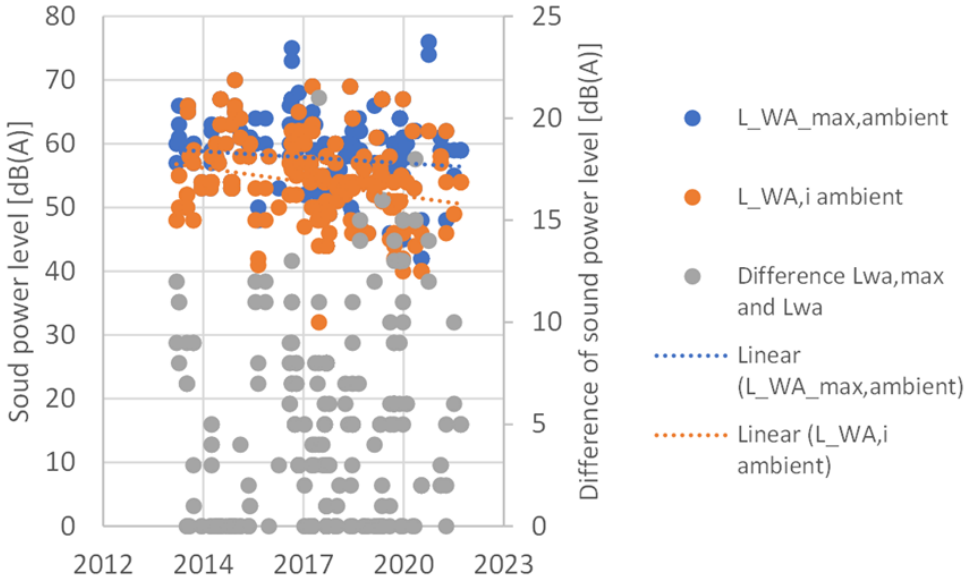


Figure 2: Sound power level of air-to-water heat pumps; L_WA: sound power level. source: get database (No.3 in Table 1).

3.3. Performance

Based on the BAFA database No. 4 from Table 1, an analysis of the eligible heat pumps in Germany is done with focus on performance of heat pumps for different types of refrigerants. Figure 3 shows the coefficient of performance for six different refrigerants for all low-GWP air-to-water heat pumps in the BAFA database. The figure differentiates between four operation points of the heat pump. COPs for the lowest ambient air temperature of -7°C (blue bars) differ from 2.7 to 3.1 as a refrigerant-specific mean value. The variation within a refrigerant category can be more than one COP point (see the error bars) at this operating point; e.g., R32 reaches values up to 4 for a specific heat pump model and down to 2.5 for another model. For ambient conditions of +10°C (yellow bar) the mean COPs are highest, reaching values up to 5.6. Model-specific COPs reach values up to 6 at this operating point.

The number of heat pump models in each refrigerant category (grey boxes) ranges from 4 for R454C to more than 200 for R32. Thus, a comparison of performance should be done with caution for the categories with low number of models. Nevertheless, for the three refrigerants R32, R290 and R454B there are a large number of models and manufactures in the BAFA database, such that Figure 3 can give a good impression on performance.

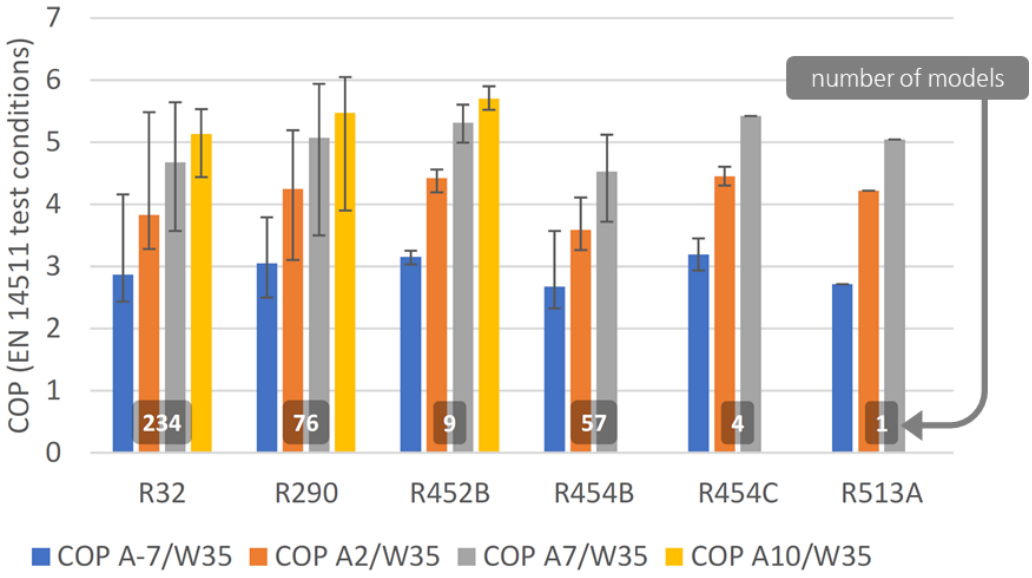


Figure 3. Performance of heat pumps, categorized by type of refrigerant; source: BAFA database (No.4 in Table 1).

Based on the data, we can conclude, that primarily the choice of a specific heat pump model leads to a higher impact on the performance than the secondary choice of a specific low-GWP refrigerant. But in combination best case situations occur. And this situation can be found at the German market. There were high sales numbers until the evaluated subsidization scheme MAP where we concluded that for R290 systems the share of sold units is much larger as for other low-GWP refrigerants, see Annex of [5] for the evaluation and the Annual Report 2021 of IEA Annex 54 [22]. However, R454B shows significant lower COP values than R32 or R290. This is in accordance with the material properties of the refrigerants.

3.4. Proportion of refrigerant type

The date of the CE marking of a heat pump is one criterion to estimate the date of the heat pump release into the market, other resources are for example the SAP Q database No. 2 as well as the HARP database No. 5 in which the assignment of a new model within these funding schemes is monitored. However, it can on the other hand express a revised heat pump which got changes. Therefore, a CE marking date expresses a constant working or improvement process.

Figure 4 shows the type of refrigerant in heat pumps in relation to the date of the last CE marking. The data is based on the BAFA list 2020 and extended by the CE marking date. It can be seen that the proportion of high-GWP refrigerants (GWP > 1500) such as R404A, R407C and R410A is decreasing the last 5 years. However, there is still a proportion of 50% in 2020 and thereafter with high-GWP refrigerants.

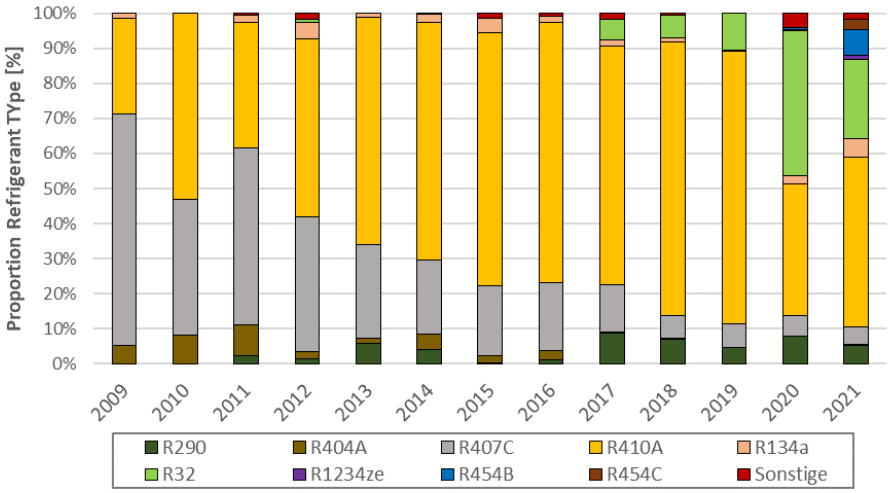


Figure 4. Proportion of refrigerant type for heat pumps based on CE marking date in data sheets; source: extended BAFA Database (No. 4 in Table 1

In Figure 4 it can be seen that within the last five years heat pumps with R290 are constantly marked with the CE marking, but stay below 10% of all heat pump CE markings in the BAFA database. Caution must be taken with the interpretation of Figure 4 for the heat pump market. The figure does not show sales numbers of heat pumps. A link between refrigerant and sales number needs additional data (e.g. [8]) besides the databases in Table 1. Data from before 2009 can be looked up in [2].

3.5. Focus Propane

In order to understand the market of propane heat pumps better, the database No. 4 and 7 from Table 1 (BAFA list and propane heat pump database Fraunhofer ISE) is used to show possible trends. Therefore, Figure 5 shows the efficiency in terms of the seasonal space heating energy efficiency η_S for air-to-water heat pumps with four different refrigerants. The mean efficiency (black line) increased between 2007 and 2021 by more than 10%[6]. However, scattering of data is by a factor of two larger than this mean increase. Remarkingly, there are two strong impacts on the data of this graph.

1. On the right side close to 2020 there are cluster-like structures which is the result of identical CE marking documents which were all updated and provided publicly at the same time from individual manufacturers. This is of course not the market introduction but more a consequence due to the changes/revision anywhere within the legal framework of these conformity declared product.
2. The same effect shows updates and pseudo-market introduction dates for R407C systems within the year 2018 which definitely is not resulting from newly introduced equipment (since no new R407C system should have been developed after about 2012 or earlier) but more to this issue of changes of the legal framework which might leads to regular CE marking updates for individual models. This has also a large impact on Figure 4.

Nevertheless, the dataset for Figure 5 is huge and it is assumed that tendencies and relations between the data are real and can be analyzed.

[6] This is the consequence out of different definitions being used for SCOP (with changes at about 2018/2019) together with an unclear situation if all used resources to digitize and use SCOP values were updated based on the current understanding of this figure. Furthermore, the listed SCOP in product and especially eligible heat pump lists should have change in the time window of end of 2021 beginning of 2022 when BAFA for example at the last one has switched from system-wide calculations of η_S to product-based values and it is not clear if entries of SCOP done by manufacturers themselves is always provided based on the one or the other then valid definition and it is best declared together with the value.

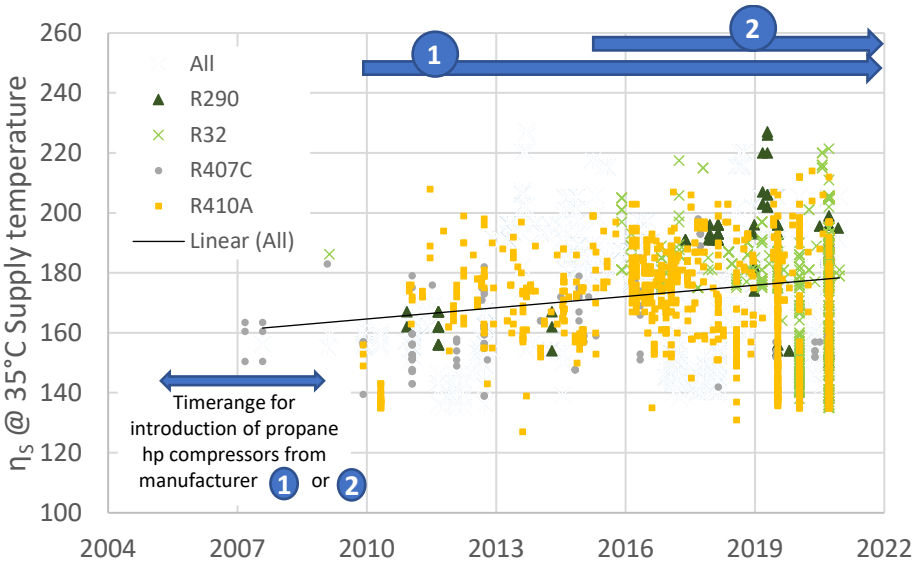


Figure 5. Evolution of η_S at the supply temperature level of 35 °C of BAFA database and additional individual R290 HP specifications for air-to-water heat pumps.

For R290 the evolution shows a clear picture. With the introduction of a new compressor designed for propane and for heat pump application starting from 2010 the first propane refrigerant circuits show similar performance than those of other heat pumps. With the ongoing development improvements of propane-specific compressors on the market in 2016, performances increased strongly, and the propane heat pumps show performance values significantly above average.

4. Summary and Outlook

Several thousand heat pump models are listed in European databases with information such as performance and capacity. An evaluation of these databases individually can help for a view on current market available heat pumps. However, to express trends in performance, usage of refrigerant, acoustics, etc, additional information have to be collected for these datasets. This extension has been done by the authors. Especially the date of market introduction is a meaningful parameter which the authors included. They depicted the date by the CE-marking of the heat pump model as well as listing dates from database No. 2 and 5. Trends based on this representation show reasonable data point progression, with limitations based on revision of the CE-marking. A comparison of the efficiency among each database is difficult due to the different operation points used in the databases.

The main conclusions of the evaluation of these databases are:

- Specific refrigerant charge (in kg refrigerant per kW heating capacity) for air-to-water heat pumps shows a large scattering from 0.1 kg/kW up to 0.8 kg/kW with additional outliers. A clear trend towards reduced amount of refrigerant cannot be seen in the data up to the year 2021. The flammable refrigerant R290 shows lower specific charge than the other refrigerants within the database.
- A trend toward more silent heat pumps can be found in the data. However, a large proportion of the data points shows inconsistencies in terms of nominal and maximum sound power level, which reduces the informative value of the evaluation. Further filtering would be helpful to separate the dataset from non-modified fan blades and serrated trailing-edge fan blades which are nowadays the de-facto standard for quite axial fans.
- The performance of heat pumps (COPs) shows a recognizable dependency on the type of refrigerant. Market available heat pumps listed in the BAFA database show best performance for R290, followed by R32 and R454B (evaluation only for more than 50 different models per refrigerant type). The individual heat pump model has a stronger impact on the performance than the type of refrigerant.

- A large bandwidth of COPs shows large quality or design differences among the models; Simultaneously these differences show potential for performance increase among the majority of heat pumps.
- For R290 new components (e.g. compressor platforms) yielded a significant change in performance in the past. The authors assume still some more performance increase based on improved components in the future for R290 refrigerant circuits before an expected asymptotic final technical maturity level will be reached.

Acknowledgements

The financial support by the German Federal Ministry for Economic Affairs and Climate Action for the Project SafeSENSE [23] under grant no. 03EN2030A is gratefully acknowledged.

References

[1] Europäische Kommission, Verordnung (EU) Nr. 517/2014 über fluorierte Treibhausgase: F-Gase-Verordnung, 2015.
[2] M. Eschmann, Qualitätsüberwachung von Kleinwärmepumpen 2020: Statistische Auswertung der Prüfresultate, Ittingen, Switzerland, 2021.
[3] swiss heat pump quality label, https://www.fws.ch/waermepumpen-guetesiegel/.
[4] W.Y. Park, N. Shah, J.Y. Choi, H.J. Kang, D.H. Kim, A. Phadke, Lost in translation: Overcoming divergent seasonal performance metrics to strengthen air conditioner energy-efficiency policies, Energy for Sustainable Development 55 (2020) 56–68.
[5] Daniel Zech, Evaluation und Perspektiven des Marktanreizprogramms zur Förderung von Maßnahmen zur Nutzung erneuerbarer Energien im Wärmemarkt im Förderzeitraum 2019 bis 2020, Berlin, 2021.
[6] Robert Lowe, FINAL REPORT ON ANALYSIS OF HEAT PUMP DATA ANALYSIS OF HEAT PUMP DATA FROM THE FROM THE RENEWABLE HEAT PREMIUM PAYMENT (RHPP) SCHEME, FINAL REPORT, 2017.
[7] ENOVA, Annual Report 2020, Trondheim, 2021.
[8] IRENA, Renewable solutions in end-uses: Heat pump costs and markets, Abu Dhabi, 2022.
[9] KEYMARK, HP Keymark: product type: Heat Pumps, [November 14, 2022], https://keymark.eu/en/certificates/certificates-data-base.
[10] BRE, Building Energy Performance Assessment: Support Website, SAP Q Database, [November 30, 2022], https://www.ncm-pcdb.org.uk/sap/.
[11] get, GET product database, [November 14, 2022], https://www.produktdatenbank-get.at/#/.
[12] BAFA, Liste der Wärmepumpen mit Prüf-/Effizienznachweis, [November 14, 2022], https://www.bafa.de/SharedDocs/Downloads/DE/Energie/beg_waermepumpen_anlagenliste.html.
[13] HARP, Home Heating Appliance Register of Performance (HARP) database, [November 30, 2022], https://www.seai.ie/home-energy/building-energy-rating-ber/support-for-ber-assessors/software/harp-database/.
[14] Eurovent Certification, Heat pumps Eurovent, [November 14, 2022], https://www.eurovent-certification.com/de/advancedsearch/result?program=Eurovent-HP&product_type=&keyword=#access-results.
[15] ISDE, Investeringssubsidie duurzame energie en energiebesparing, Niederlande, 2022.
[16] Natural Resources Canada, Canada Greener Homes, Canada, 2022.
[17] Energistyrelsen, Varmepumpenlisten, 2022.
[18] GSE, Catalogo Pompe di Calore, 2022.
[19] topten.eu, Energy Efficient Heat Pumps: Database, [November 14, 2022], https://www.topten.eu/private/products/heat_pumps.
[20] O. Gustafsson, H. Hellgren, Metodutveckling – utvärdering av buller från värmepumpar, Borås, Sweden, 2018.
[21] C.e.a. Reichl, Acoustic Signatures of Heat Pumps, IEA Annex 51, [November 30, 2022], https://heatpumpingtechnologies.org/annex51/.
[22] T. Oltersdorf, Country Report Germany: Annual Report 2021, IEA Annex 54, Borås, Sweden, 2022.
[23] C. Sonner, T. Oltersdorf, SafeSENSE, https://www.ise.fraunhofer.de/de/forschungsprojekte/safesense.html.

14th IEA Heat Pump Conference
15-18 May 2023, Chicago, Illinois

Integration of heat sources for heat pump operation in the larger capacity range

Carsten Wemhoener*, Christoph Meier

IET Institute of Energy Technology, OST Eastern Switzerland University of Applied Sciences, Campus Rapperswil, Oberseestrasse 10, 8640 Rapperswil, Switzerland

Abstract

In Switzerland, heat pumps (HP) in buildings with higher capacities still have lower market shares. The paper focuses on overcoming limitations of heat sources for HP capacities higher than 50 kW, e.g. for air-source due to noise problems or for borehole heat exchangers (BHE) due to space or drilling restrictions. By combining heat sources, a monovalent HP operation is enabled and due to synergies between the sources, also cost and efficiency benefits can result. By building and system simulations, it was found that the BHE size can be significantly reduced, if only winter peak loads are covered. This will circumvent both the noise limitations of the air-source and the space/drilling limitations of the BHE, and can even make dual-source operation more cost-effective. Regeneration can also result in smaller BHE design. For solar regeneration, favorable ratios regarding collector costs have been determined; while for air heat exchangers, special attention must be paid to the fan power and control. As conclusion, a dual source application does not only offer a monovalent HP application, but can also reduce cost and increase performance.

© HPC2023.
Selection and/or peer-review under the responsibility of the organizers of the 14th IEA Heat Pump Conference 2023.

Keywords: Dual-source heat pump; peak load coverage; borehole heat exchanger regeneration; heat generator replacement; building renovation;

1. Introduction

Scenarios in many countries assume that heat pumps will be the predominant heating system in the future. In the Net Zero by 2050 report of the IEA of 2021 [1] it is evaluated that heat pumps will cover 50% of the global heat demand by 2045. While heat pumps already have a high market share in newly built, smaller residential buildings in Switzerland, their use in larger residential buildings and non-residential buildings with higher heat loads above 50 kW, especially in existing buildings, is still limited. One of the limitations regarding a higher diffusion of heat pumps for use in the higher capacity range are suitable heat sources, especially for heat generator replacements and renovations of existing buildings, where heat source limitations can be a major obstacle. In densely built areas of city quarters, limitations of air source heat pumps are mainly due to noise emissions, if many heat pumps are used on a small area and in a residential quarter with noise protection requirements. In Switzerland, the sound level is limited to 55 dB(A) at daytime and 45 dB(A) during the night to be approved for the installation permit [2]. On the other hand, also a ground source can be limited due to space restriction of the borehole heat exchanger, drilling limitation regarding depth due to ground layer structure and limitation due to the accessibility of the drilling area for the drilling machinery. Furthermore, the drilling density can also be a limitation, since with many borehole next to each other, the ground temperature is increasingly exhausted. One way to overcome the limitations of individual heat sources can be accessed by combining different heat sources, especially if synergies among heat sources can be exploited.

Thus, in this paper, combinations of heat sources are investigated with the aim of overcoming limitation on the source side and enabling a monovalent use of heat pumps despite limitations of individual sources. In this way, the market shares can be extended for larger capacities and renovation projects.

*Corresponding author. Tel.: +41-(0)58-257 43 25; fax: +41-(0)58-257 44 00.
E-mail address: carsten.wemhoener@ost.ch.

The hypothesis is that synergies between the heat sources can be used for a better system performance and/or economic advantages compared to the use of only one single source, e.g. by using the heat source with the better temperature level or by exploiting design advantages. The project objective is to derive recommendations for the use of multi-source systems for higher capacity range applications.

2. Methodology

A literature review and market research delivered the result that so far hardly any commercial system solutions for multiple heat sources are available on the market from the relevant manufacturers. There are different examples for splitting the total heating capacity to different heat pumps, but only with the same heat source, which does not avoid problems in case of source restriction. This may be due to the several reasons:

- the retrofitting of buildings is emerging step by step
- currently, a peak load coverage by fossil fuels is still accepted in the market, which can relax the limitation on the heat source by downsizing the HP capacity
- multi-source systems are associated with a higher complexity and cost and thereby considered more error-prone and risky for the investor, designer and installer
- there are little reference systems with multi-source application

In research, there are several projects, but mainly covering solar assisted heat pumps, where solar energy is applied as regeneration source for the ground, e.g. [3], or a source storage, e.g. as ice storage, or also applied as heat source and/or in direct operation, e.g. for DHW production in summertime. However, since solar yield in winter cannot be guaranteed, either a source storage is required or the primary heat source has to be designed for the entire design heat load of the building. Natale et al. [4] investigate a dual source configuration of a ground and air-source regarding two control strategies. However, only switching between sources and no parallel operation of the two sources is considered. It was found, that even with smaller borehole design a similar performance can be reached, which enables a retrofitting for undersized borehole heat exchangers. Reum et al. [5] investigate control strategies for the air-source and horizontal ground collector, which also includes a parallel operation below a balance point temperature. The HP modelling is based on a black box model derived by test rig measurement. However, no implications for the design of the sources are given. A systematic evaluation of potentials that can be explored by different heat source integration is missing, though. Therefore, this project started with a characterization of different heat sources and combination options. Based on this characterization of heat sources, four strategies are considered for the integration of dual or multiple heat sources:

(a) peak load coverage by an additional heat source
(b) regeneration of the primary heat source by additional source(s)
(c) year-round base load operation by additional source(s)
(d) Preheating of the primary heat source by additional source(s) to increase the capacity output

Due to the higher practical relevance of the first two strategies, this paper will focus on evaluation of these two strategies. Typical applications for the third variant are e.g. an exhaust air or wastewater heat recovery for the DHW operation. The fourth variant can be interesting in cold climate regions with clear sky winter conditions, where the cold outdoor air can be preheated by solar energy use.

The variants for the above first two strategies were investigated by dynamic building and system simulation. The building and system technology has been modelled in Matlab-Simulink using the Carnot-Blockset [6]. The objective of the simulations is the investigation of the system configuration with respect to integration, design and control. Thereby, the main focus of the investigation is to enable the monovalent use of HP as sole heat generator without a peak load coverage by fossil energy or direct electric back-up heaters, in order to enable efficient and carbon free operation. Direct electric back-up heating for the space heating application is forbidden in Switzerland anyway. Thus, in this paper, the term "monovalent" refers to the heat generator and not to the heat source. It is thus understood as use without auxiliary heating, but possibly with multiple heat sources. The scope is set to the higher capacity range > 50 kW installed capacity of the HP, since for this capacity range the limitations of heat source are increasing, in particular for densely built environments in cities and heat generator replacement in existing buildings.

The investigations are carried out by means of simulations of generic residential buildings in the construction standard "new building" and "existing building" with a heat load of 60 kW (base variant) to 240 kW (upper limit for heat load variation). As a boundary condition for the design of borehole heat exchangers/ borehole fields, the design criterion according to SIA 384/6 [7] was always taken as a requirement for all calculated variants, where it is required that the mean fluid temperature must not fall below -1.5 °C after 50 years of operation, e.g. as -3 °C inlet and 0 °C outlet of the borehole heat exchanger.

Table 1. Building- and system parameters for the simulation studies in new and existing buildings

Parameter	New built	Existing	Variation/remark
Heat demand (SH & DHW)	45 kWh/(m^2yr)	160 kWh/(m^2yr)	No variation
Fraction SH/DHW	33% SH, 66% DHW	80% SH, 20% DHW	No variation
Design heat load	60 kW	60 kW	Varied up to 240 kW
Number of flats	36	12	At 60 kW
Supply temperature heating	35 °C	55 °C	Floor heating/radiators
DHW	55 °C	55 °C	No heating element, HP only
Weather data	Zurich Meteoschweiz	Zurich Meteoschweiz	Zurich Meteoschweiz cold year
Thermal conductivity ground	2.4 W/(mK)	2.4 W/(mK)	Standard Swiss middleland
Thermal conductivity grouting	2.0 W/(mK)	2.0 W/(mK)	0.8 W/(mK)

Legend: SH – space heating, DHW – domestic hot water

Thereby, effects of size scaling (e.g. probe spacing) as well as in the load profile (higher hot water share in new buildings) could be investigated. The different strategies can be compared according to energetic and economic criteria under the same boundary conditions (e.g. limited borehole depth). For this paper the key performance indicators of the seasonal performance factor (SPF) of the HP and the annualized life cycle cost are evaluated.

Table 1 gives an overview of the building and system parameters used for the simulation studies. The loads were used according to the standard use according to SIA 2024 [8] for multi-family houses. The site Zurich Meteoschweiz average year according to SIA 2028 [9] was used as weather data. To test the robustness of the design, variations including a cold year were also performed, both for the same weather data set of the cold year over 50 years and as a periodic variation of four normal years followed by a cold year. The heat pump was evaluated as a performance map based on manufacturer data for an air-to-water and brine-to-water heat pump. The higher loads are calculated by multiplying the load profile of the basic size of 60 kW.

The ground source model corresponds to a common approach of design programmes to have a finite difference model of the ground probe and the near surrounding and a step response function called "g-function" according to Eskilson [10] for the farer surrounding of the ground. The model has been validated by a cross programme comparison with the common design tool in Switzerland EWS [11] and also compared to monitoring data of a system in Feldmeilen, CH [3], which delivered feasible results. However, the validation does not cover the operation mode of a peak load coverage strategy investigated here, which is a future task within a demonstration project of a boiler replacement in two multi-family buildings, see chap. Conclusions. The upcoming demonstration project offers the opportunity to gather monitoring data of the peak load operation of the ground source field and is therefore well suited for further model validation work.

3. Results

The focus of this paper is on the first two integration options of the strategies "peak load coverage" and "regeneration". In the context of this publication, only the sole strategies are considered, although combinations of the strategies are also conceivable, which is particularly obvious for very high capacities in the range of the upper limit for the simulations of 240 kW and more, when the borehole field reaches a size, where regeneration is called for. The combination of the strategies can further improve the respective advantages of the individual strategies presented in the following.

3.1. Strategy (a) – Peak load coverage

For the integration variant (a) peak load coverage with borehole heat exchangers, advantages are offered in combination with capacity limitations of the primary heat source, as they may exist with the heat source outside air due to noise emissions. In the case of a sole ground source by borehole heat exchangers, on the other hand, space limitations may exist for the installation of a sufficient number of probes. Peak capacities, though, are often needed only for a rather short period, since in Switzerland HP are designed monovalently to the design outdoor temperature. Figure 1 shows the relative probe length compared to a 100% borehole heat exchanger heat source for the performed parameter variations with respect to new and existing buildings, different probe arrangements as line and compact rectangular field layout, different capacities of 60 kW and 240 kW, normal and cold weather and different thermal conductivity of the grouting of 2 W/(mK) and 0.8 W/(mK).

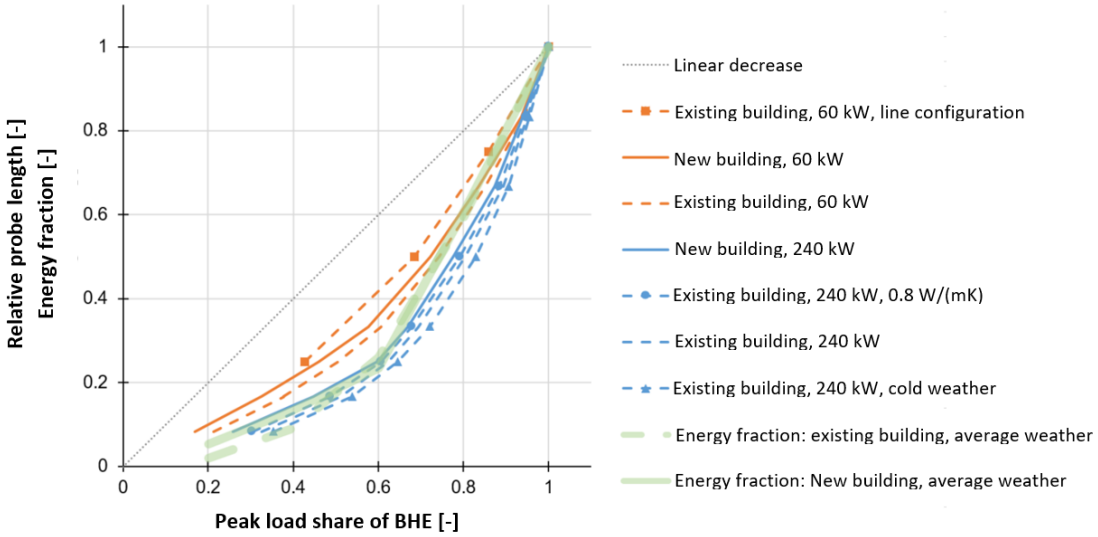


Fig. 1. Parameter variations for the strategy "Peak load coverage" by ground probes

The basic setting is a compact field layout as rectangular. For the 60 kW building also a line configuration has been evaluated, which is closest to the 45° line and thereby has the least saving potentials compared to a 100% borehole heat exchanger. In fact, most results show robust behavior regarding the performed variation, which simplifies the design for different boundary conditions. The biggest difference is found indeed in the probe arrangement between linear and compact field design. The compact field shows a more digressive behavior since natural regeneration is more limited by the field effect, i.e. the shielding of the inner probes in the center from the surrounding undisturbed soil, and therefore, a lower discharging of the field by the operation for peak load coverage has an even higher impact.

As conclusion of the results depicted in Figure 1, with the combination of air as primary source and the ground for peak load operation, significantly less energy is extracted from the ground than with a ground source only, e.g. about 20% of the total energy when designed for 50% of the total heat load. This corresponds to a much shorter probe length of only 20% of the ground source-only case, which can overcome space restrictions that exist in particular in existing buildings. Furthermore, simulations show that a slightly higher capacity in the range of up to 70 W/m can be temporarily extracted, since long "natural" regeneration times exist for the borehole heat exchangers.

The simulation results further confirm that peak load coverage with borehole heat exchangers, in addition to alleviating capacity constraints, can provide performance and economic benefits such as lower overall investment costs and can unlock additional benefits of borehole heat exchangers as a heat sink for summer cooling.

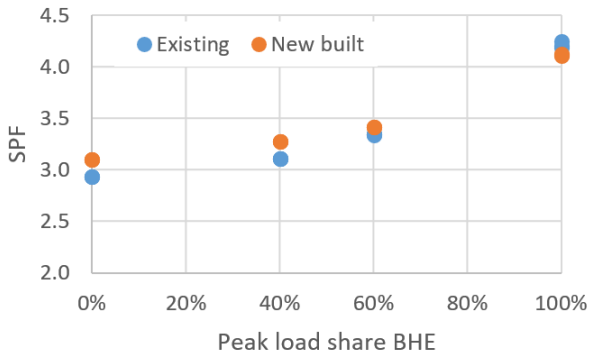


Fig. 2. Performance of the concepts "Peak load coverage" by ground probes

Figure 2 shows the SPF as a function of the peak load share by the borehole heat exchanger for peak load coverage. Compared to an outdoor air source only (0%), the efficiency also increases with increasing peak load share by the ground source. The difference between the new and existing building is relatively small, since the lower space heating supply temperature is compensated by the higher DHW fraction.

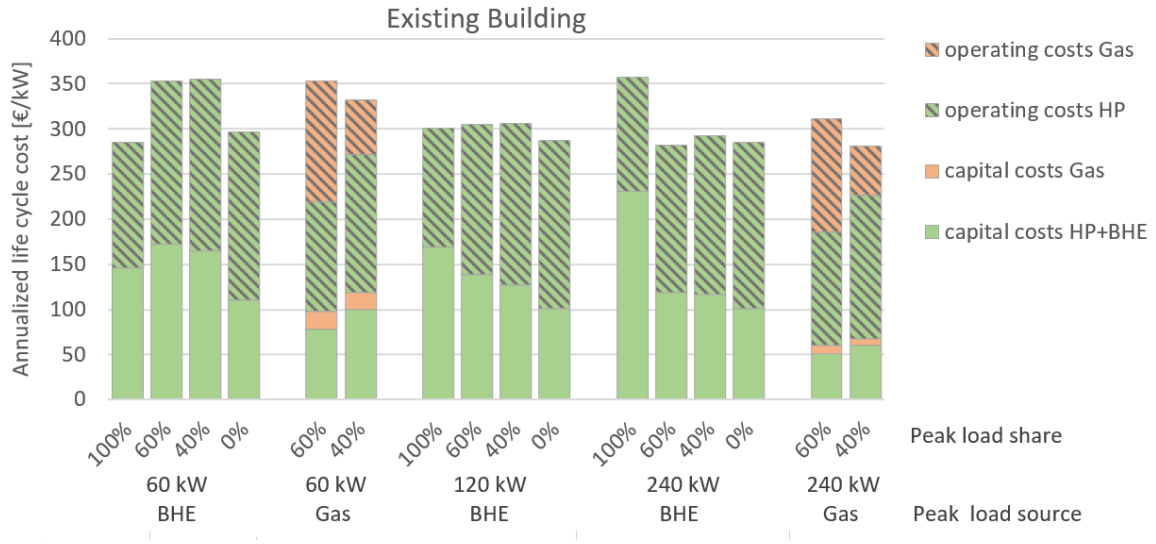


Fig. 3. Economical comparison of the concepts "Peak load coverage" by ground probes

This also explains the slightly better performance of the existing building for the 100% ground-source. Since the existing building is dominated by space heating, the supply temperature decreases, while the DHW stay constant for the entire year. For the air-source heat pump (0%) the performance in new built is better, since the higher DHW share can be provided very efficient due to the high outdoor air temperature during summer, which overcompensates the decreasing temperature in space heating in the existing building. For the ground source (100%), it is vice versa, i.e. the decreasing space heating temperature causes the better performance than the DHW temperatures.

The seasonal performance factor is averaged over the entire operating period of 50 years, since the system variants with higher ground fraction experience a cooling down of the ground and thereby lower source temperatures over the design period of 50 years.

Figure 3 shows an estimation of the cost structure for the case of the existing building depending on the peak load share by the borehole heat exchanger and in comparison to a bivalent solution with a fossil back-up boiler with natural gas as annualized life cycle cost (gas and electricity tariffs as of June 2022, see also Table 2). The used boundary conditions for the economic evaluation depicted in Figure 3 for the strategy "Peak load coverage" and Figure 4 and Figure 5 for the strategy "Regeneration" in section 3.2 are listed in Table 2.

Table 2. Boundary conditions for the economic evaluation in Fig. 3

Parameter	Specific cost/tariff	Variation/remark
Investment cost		
Air-source HP	1700 €/kW	
Ground-source HP	900 €/kW	
Gas boiler system (averaged)	300 €/kW	
Borehole heat exchanger	100 €/m	
Air heat exchanger (60 kW-240 kW)	1500 – 600 €/kW	
PV/T collector	750 €/m2	
Operational cost		
Electricity tariff	0.20 €/kWh	As of June 2022, strongly dependent on market
Gas tariff	0.15 €/kWh	As of June 2022, strongly dependent on market
Feed-in tariff	0.10 €/kWh	Dependent on site
Component lifetime/interest rate		
Ground probes	50 yrs.	
Heating system components	20 yrs.	
Interest rate (real)	1.5%	

The costs of the monovalent solution only with HP can result in lower specific costs than the peak coverage by natural gas, which, however, is strongly dependent on the market prices. For the HP solutions, there are economic advantages of the individual sources ground probes-only or air-source-only for the smaller capacity range of 60 kW. The individual sources, however, may not be possible to realize in case of restrictions. Moreover, the additional costs for a dual source HP solution are moderate at 50 €/kW and allow a monovalent HP operation without back-up heater. For larger capacities, the cost advantages of the individual sources decrease or even show higher costs, in particular for the ground source. This is due to the effect depicted in Figure 1. Due to the significantly smaller design of the ground source in relation to the 100% ground source, larger cost saving occur for higher capacities, which can cover the additional cost of the second heat source. This can reach the cost of the 100% air-source, since the air source has also increasing cost for higher capacities and may not be possible due to restrictions, anyway. Furthermore, in new buildings and compared to air-source only, there may be additional freecooling potential by the dual source HP. If this is taken into account as cost benefit in the economic calculation, the differences to the individual source disappear for the lower capacities, as well (not depicted in Figure 3).

3.2. Strategy (b) - regeneration

For variant (b) with regeneration, it is known that large borehole heat exchanger fields are only insufficiently regenerated by natural heat inflows from the ground, which makes technical regeneration necessary. Furthermore, with regeneration the probes can be arranged with smaller distance to each other without cooling down the ground too much and it may be possible to reduce the total probe length, which opens up options for more probes on less space and thus can overcome space limitations. In the project, the control of the HP using solar absorbers and PV/T collectors as well as outdoor air heat exchangers as synergy to heating/domestic hot water operation was systematically investigated for different building sizes. The parameters that were varied include probe field sizes, drilling depth, probe spacing and probe placement in the field.

While many studies have already been conducted on the regeneration of mostly larger borehole heat exchanger fields, the focus has often been laid on 100% regeneration or even seasonal storage through so-called "active" regeneration, i.e. a higher heat regeneration amount than the heat extraction, so that the ground temperatures can be successively raised [12]. In this project, however, the evaluation is carried out for the investigated regeneration sources with respect to necessary area and possible drilling depth as a trade-off between costs and regeneration demand or degree of regeneration in order to evaluate, how and what extend of space and drilling limitations can be overcome.

The results show that both limitations in the possible field size/probe depth and space as well as economic advantages can be achieved by a shorter overall probe length. For solar regeneration, for example, the focus of the economic analysis is on a cost-effective design as the optimal ratio between the collector area and the probe length. From the results, a representation as a contour plot was developed, from which the cost-optimized degree of regeneration can be found, depending on the regeneration source and the boundary conditions.

Case study:

- Capacity demand: 240 kW
- BHE field area: 3200 m² (13.4 m²/kW)
  → Max. 32 probes @ 10 m spacing
- Probe depth limitations: ca. 300 m
  → not possible without regeneration
  → minimum cost at 60-80% regeneration
  → specific annual cost of 270 €/kW

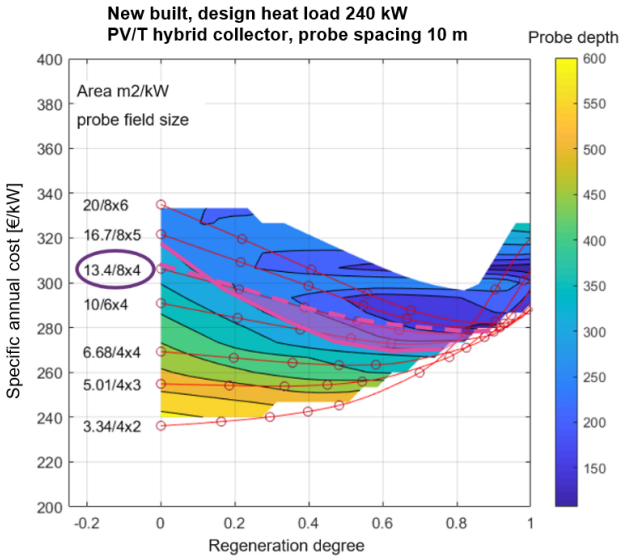


Fig. 4. Evaluation of the concept "Regeneration" with PV/T hybrid collector

Figure 4 shows the results of the parameter variations for the new building with a fixed probe spacing of 10 m and a design heat load of 240 kW and a regeneration by a photovoltaic thermal (PV/T) system.

By means of a reading example, the statements of the graphical representation are clarified. The plot correlates the specific annual costs vs. the degree of regeneration. Parameters of the contour plot are the probe depth (color-coded contours) and the available area per kW of extraction power as parameter curves. If, for example, a heat load of 240 kW is based on a probe field area of 3200 m² (13.4 m²/kW as dashed line), a maximum of 32 probes can be drilled at a probe spacing of 10 m. If additionally a drilling depth restriction of 300 m is considered (line along the middle blue contour), this results in the purple area in the diagram of possible solutions.

Since the area is only reached at a regeneration degree of almost 20%, the design conditions for the ground probes field of -1.5 °C after 50 years can only be achieved with regeneration under these boundary conditions. The regeneration degree with the lowest annual costs is found at regeneration degrees of 60-80%, i.e. clearly below 100%, with annual costs of 270 €/kW (costs for drilling and regeneration, including also the benefits of the electricity generation by the PV/T collector).

Compared to a PV/T system a solar thermal regeneration could offer certain advantages in summer operation, because the DHW operation can be provided directly by the solar thermal system. By the PV/T system, a double benefit with electricity production can be achieved, but for commonly available unglazed PV/T less heat is supplied than with solar thermal collectors systems without PV coupling. Thus, possibly the hot water storage temperature level cannot be reached with PV/T only operation.

However, especially in the case of renovation, the roof area may be limited or may have unfavorable conditions due to orientation or shading. Therefore, regeneration by an air heat exchanger can also be a good option, especially in the case of space limitation in the renovation case. Figure 5 shows the same diagram for the regeneration by an air heat exchanger, i.e. for the same limitations of the borehole heat exchanger as in Figure 4. The economic evaluation for the air heat exchanger is quite similar to the regeneration with the PV/T collector. The field of possible designs also starts at almost 20% of regeneration and the lowest system costs are reached at a regeneration degree of 60-80%. Therefore, also for the regeneration source different combination are available which enables an adaptation to restriction in the concrete situation. While the above limitations of the solar regeneration sources can be avoided, care has to be taken for noise issues and the positioning of the air heat exchanger similar to the use as primary heat source. Further criteria and potentials for a high energy efficiency of the air heat exchanger are the fan power and improved control strategies.

Case study:

- Capacity demand: 240 kW
- BHE field area: 3200 m² (13.4 m²/kW)
  → Max. 32 probes @ 10 m spacing
- Probe depth limitations: ca. 300 m
  → not possible without regeneration
  → minimum cost at 60-80% regeneration
  → specific annual cost of 280 €/kW

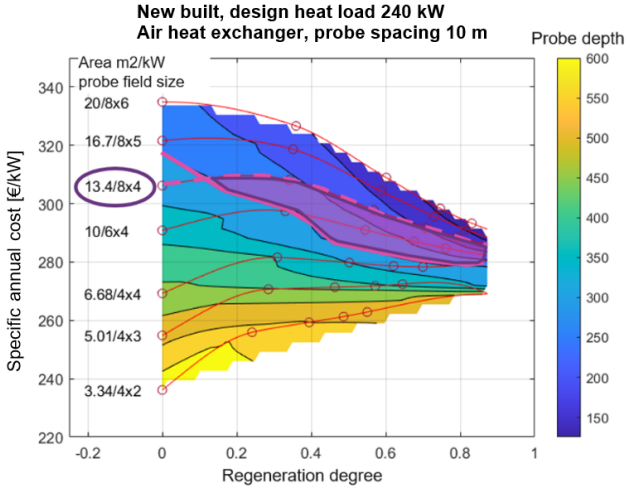


Fig. 5. Evaluation of the concept "regeneration" with air heat exchanger

4. Discussion

The focus of the investigation was the larger diffusion of the use of HP as only heat generator without fossil back-up heating in the higher capacity range above 50 kW. One limitation for the higher capacity range can be limited heat sources, especially in the case of heat generator replacements in existing buildings. In order to enable a monovalent HP application also in the higher capacity range, combinations of heat sources and their integration and design have been investigated.

The hypothesis of the study was, that in particular for the higher capacity range, limitation of individual heat sources can be overcome and even benefits of higher performance and better economic values can be achieved due to the use of synergies between dual or multiple heat sources. In this paper, results of two investigated strategies entitled "peak load coverage" and "source regeneration" are reported.

It could be verified that with synergies between the heat sources, e.g. use of the better temperature conditions of the individual sources, i.e. the ground in winter time and the air in summer time, and adapted use of the ground, also performance advantages (compared to air source) and economic benefits (compared to ground-source) can be exploited.

For the conducted investigations on the strategy "peak load coverage", the combination of the heat sources "outdoor air" and "borehole heat exchangers", which are most frequently used in Switzerland, was considered. However, this does not limit the strategy of peak load coverage to these heat sources. The results can also be transferred to other heat source, where the "outdoor air" stands for a heat source that is limited in capacity, e.g. by noise protection requirements, and the ground stands for a heat source that can be stored, but which can also be subject to restrictions, e.g. by required space, drilling depth or other legal limitations. The combination allows a smaller dimensioning of both heat sources, so that both limitations can be overcome. Other possible combinations include groundwater or surface water with a limited pumping volume, or waste heat with a limited capacity in combination with air or geothermal probes. Depending on which source is considered as primary individual source, the performance may increase as shown in Figure 2 for the case of peak load coverage by ground source where air is considered as primary heat source.

In the strategy of "regeneration", the second source primarily serves to manage the storable primary heat source. In addition, though, the regeneration source can also take over e.g. the summer operation as only source, and thereby use seasonal advantages, in the case of solar thermal regeneration for instance the good summerly solar irradiation availability. In the case of air, heat exchangers the higher summer outdoor temperatures can be used, and thus further promote the regeneration of the primary heat source by a reduced use in summer.

The economic evaluation confirms that dual or multi-source system do not necessary have higher costs, since synergies between the sources may also decrease the cost. For the "peak load coverage" by ground probes, where a high peak capacity, but less energy is delivered by the ground probes, the decrease of the borehole heat exchanger size enables a cost decrease for the ground probes.

On the other hand, by regeneration of the ground, a cost optimized design can refund the investment in the second heat source for the regeneration and decrease the overall system costs. There is also a certain variability of regeneration sources, which can be designed according to respective on-site limitations especially in case of existing buildings. For the example outlined in this paper, the regeneration by PV/T collectors and by air heat exchanger lead to comparable overall system costs.

Moreover, the integration of a second source may also additionally enable further operation modes, such as a freecooling operation in case of additional use of geothermal probes as second source. However, the use of this freecooling option also depends on the installed emission system in the building. In the case of freecooling, larger surfaces for the heat transfer are required, which are classically installed in new buildings. Radiators in existing buildings are normally not suited for a freecooling operation, unless not supported by ventilators for enhanced convective heat transfer.

A drawback of dual or multi-source systems, though, is an increased system complexity. Results of this study should thus be elaborated to derive recommendations for an as far as possible simple and robust integration. However, further steps are required in order to derive more standardized guidelines for a dual or multi-source application.

Two other strategies of a "second source as base load" and a "source preheating" by a second source have not been discussed in this publication.

A "second source as base load" can typically be applied, if the one source has a more or less constant capacity and contributes to the overall coverage with this constant capacity throughout the whole year. As example, a wastewater heat recovery as second source is usually sufficient to constantly cover the DHW load throughout the year. In addition, waste heat from exhaust air can deliver a more or less constant heat source, which can help to overcome limitations of the primary source.

The strategy "source preheating" is particular promising in situations, where the temperature limitations during peak load hours is an obstacle. A situation can be cold days, which, however, have a high solar irradiation potential at clear skies, e.g. in northern or mountainous regions, where winter outdoor temperature can fall down to very low temperatures, even below the operating limit of the heat pumps, but are combined with high solar irradiation, which can be used to preheat the outdoor air source.

5. Conclusions and perspectives

Within the scope of the project, system solutions with the HP as only heat generator and dual source are investigated. However, in addition, the investigated strategies can also be useful for a combination with other heat generators or heat carriers. In combination with district heating, for instance, more buildings can be connected to the grid, if a decentralized coverage of the peak load with borehole heat exchangers is integrated. The load profile for the energy drawn from the grid shifts to a higher base load fraction due to the increase of the hot water share supplied by the district heating. Alternately, the district heat extraction can be better adapted to the application, e.g. existing grids can supply more buildings without increasing the pipe diameter/generator capacity, or more heat is available for high temperature applications, e.g. in existing buildings. These advantages can occur both for higher temperature grids, e.g. from waste incineration, or for low-temperature grids in terms of 5th generation district heating on waste heat level, such as waste heat from a waste water treatment plant.

The promising results both on the performance as on the economic evaluation can raise the question on cost and performance optimized combination of heat sources. Synergies for the individual heat sources in the combination can lead to more attractive multi-source systems than individual sources even in situations without the limitations of the sources. However, also the cost assumptions would need to be assured by practical applications. Furthermore, early adaptions and manufacturers or system developers as prime movers would be needed to enhance market extensions and knowledge to spread dual source systems. This could go hand in hand with an optimization and standardization of the systems for a certain capacity range.

A limitation of the results of the study is that they have been obtained by simulations only, so far. In order to approve their validity in practical application of a real system, monitoring of a system with respective limitations on the source side would be a fruitful verification which can promote the spread of the information on dual source HP applications by a best practice system and deliver further information and verification of systems models as well as on integration, design and control.

5.1. Demonstration project of dual source heat pumps for boiler replacement

In fact, in the course of the project, already a real case with the investigated limitations has been found. The project deals with the heat generator replacement of an old oil boiler, which supplies two existing multi-family buildings built in 1972 with 28 flats each and a heated area of totally 4180 m^2. The buildings have hardly been retrofitted and are mainly in their original state.

The total heating capacity of 200 kW is supplied by a common oil boiler and distribution line between the two buildings. The average annual heat consumption over the last 20 years was evaluated to 600 MWh/a.

The original concept aimed at the boiler replacement by a single-source ground-coupled HP, which significantly improves both the energy performance and the CO_2-emission reduction.

Due to the steep surrounding area, though, the space for the drilling of the boreholes is limited to the parking lot between the two buildings. The concept was detailed with ground probes in a depth of 295 m and an additional air heat exchanger for the regeneration of the ground probes. An air heat exchanger was chosen as regeneration source, since the retrofitting of the roofs of the two building is planned for the next years after the replacement of the heat generator. Therefore, the space on the roof was not available for solar regeneration.

However, during the drilling of the first three boreholes, artesian water has been found at 130 m, so the authorities defined an additional limit of drilling depth of maximum 120 m. With this new limitation, the concept with boreholes only is no longer sufficient to provide the whole source capacity for a heat pump operation and a dual source system of the ground and an extended air heat exchanger is now under consideration.

Since these boundary conditions correspond to the investigated limitations, the buildings are an ideal case study to gather further experience with a dual source combination of the ground heat exchanger and outdoor air heat source. A demonstration project has thus started in January 2023 and the monitoring data of the system can be used to verify simulation results, evaluate the real performance and cost of the dual source system and derive planning and design recommendation by a real monitored buildings.

Acknowledgements

Results outlined in this paper have been investigated in the project "HP-source – integration options for heat sources". The project supervision, support and funding of the Swiss Federal Office of Energy SFOE under the contract SI/502144-01 is highly appreciated and acknowledged.

References

[1] International Energy Agency. *Net Zero by 2050, A Roadmap for the Global Energy Sector*, Special report, revised version October 2021 (4th revision), International Energy Agency, Paris
[2] Cercle bruit. *Lärmrechtliche Beurteilung von Luft / Wasser-Wärmepumpen* (Noise assessment of air/water heat pumps, in German), Implementation guide 6.21, 16 June 2022, Solothurn
[3] Bätschmann, M., Büttgenbach, S., Caflisch, M., Willim, M. *Erkenntnisse über Erdwärmesonden-Regeneration am Beispiel Doppel-Mehrfamilienhaus Ländisch* (Findings on geothermal probe regeneration using the example of a double multi-family house in Ländisch), Final report in German, energieschweiz, 2021
[4] Christian Natale, C., Naldi,C., Dongellini, M., Morini, G.L. 2023. "Long term performance analysis of a Dual-Source Heat Pump system by means of ALMABuild", Proceedings 14th IEA HP Conference, Chicago, USA.
[5] Reum, T., Schmitt, D., Summ, T., Schrag, T. 2023. "Investigation of a Novel Hybrid Heat Pump Concept", Proceedings 14th IEA HP Conference, Chicago, USA.
[6] Solar Institute Juelich. Carnot Blockset, version 7.1, Univ. of Applied Sciences Aachen, 2021.
[7] Swiss engineers and archtects society. *SIA 384/6:2021. Erdwärmesonden* (ground probes), in German, Zurich, 2021
[8] Swiss engineers and archtects society. *SIA 2024:2015. Raumnutzungsdaten für Energie- und Gebäudetechnik* (room use data for the energy and building system technology), in German, Zurich, 2015
[9] Swiss engineers and archtects society. *SIA 2028:2010. Klimadaten für Bauphysik, Energie- und Gebäudetechnik* (climate data for building physics, energy and building system technology), in German, Zurich, 2010
[10] Eskilson, P. *Thermal Analysis of Heat Extraction Boreholes*. Department of Mathematical Physics, Lund Institute of Technology, Lund, Sweden. ISBN 91-7900-298-6
[11] Huber Energietechnik AG. EWS Version 5.5, Zurich
[12] Braun, D., Filleux, Ch., Wehrli, S. 2010. Die Sonne als einzige Energiequelle (The sun as only energy source), in German, Schweizer Energiefachbuch 2010, pp. 32-36

14th IEA Heat Pump Conference
15-18 May 2023, Chicago, Illinois

Assessment of ambient loop-coupled GSHP and WWHP systems in a cold-climate institutional/residential development

Monica Brands[a*], Usama Sohail[b], Alan Fung[c]

[a]Toronto Metropolitan University (formerly Ryerson University), 350 Victoria St., Toronto, ON, M5B 2K3, Canada
[b]Noventa Energy Partners, #440 – 36 Distillery Lane, Toronto, ON, M5A 3C4, Canada
[c]Toronto Metropolitan University (formerly Ryerson University), 350 Victoria St., Toronto, ON, M5B 2K3, Canada

Abstract

Six potential heating and cooling systems were simulated in a large (44-storey) proposed institutional/residential development on a Canadian university campus: a base case including natural gas boilers and a water-cooled chiller; an ambient loop (AL) coupled with conventional equipment (natural gas boilers and cooling tower); an AL-coupled wastewater heat pump (WWHP) system; a hybrid WWHP-conventional AL system; an AL-coupled ground-source heat pump (GSHP) system; and a hybrid GSHP-conventional AL system. The hybrid WWHP-conventional system and the two GSHP systems outperformed the base and conventional AL systems on all fronts, providing energy savings and greenhouse gas (GHG) emissions reductions while also costing less to operate on an annual basis than the base or conventional AL systems under both 2019 and 2030 energy pricing. Of the six systems investigated, the hybrid GSHP-conventional system had the lowest energy use, produced the least GHGs, and cost the least to operate under 2019 and 2030 price schemas. While the results of the simulation mediate towards the adoption of a GSHP-based system for this institutional/residential development, annual cost savings and GHG emissions reductions must be balanced against upfront costs, available energy resources, and logistical concerns such as the construction of a borehole field.

© HPC2023.
Selection and/or peer-review under the responsibility of the organizers of the 14th IEA Heat Pump Conference 2023.

Keywords: Heat recovery ; Wastewater-source heat pumps ; Ground-source heat pumps ; Ambient loop ; Institutional buildings

1. Introduction

Residential and commercial buildings in the US account for approximately 13% of all greenhouse gas emissions [1]. Since most of the buildings that will exist in 2030 have already been constructed, the majority of opportunities to reduce GHG emissions in buildings in the coming decades will come from improving the efficiency of existing building systems and from the electrification of fossil fuel-based space and water heating equipment. Ambient loop (AL) systems, also known as ambient loop heat pump (ALHP) systems, are a relatively clean and efficient substitute for conventional space heating and cooling systems, allowing for flexibility in the choice of coupled auxiliary heating and cooling equipment. Using a planned cold-climate institutional/residential development as a test case, this paper will investigate the performance of ambient loop systems paired with conventional equipment (natural gas boilers and cooling tower), wastewater heat pumps (WWHPs), and ground-source heat pumps (GSHPs). Annual energy usage, greenhouse gas (GHG) emissions, and energy costs will be compared, and recommendations will be made for system selection.

In an ambient loop system, refrigerant is circulated throughout a building at 8-25°C, with water-to-water or, more frequently, water-to-air heat pumps serving to 'upgrade' the energy in the ambient loop at-zone and provide heating or cooling to individual areas of the building [2] [3]. The simultaneous discharge of heat to and extraction of heat from the loop in different zones serves to maintain/moderate loop temperature; for this reason, ambient loop systems are well suited to buildings with simultaneous heating and cooling loads.

* Corresponding author. Tel.: +1-647-915-2017
E-mail address: mbrands@ryerson.ca

Ambient loops are also ideally suited to make use of low-temperature waste heat (e.g., from wastewater, minewater, or industrial discharge), and do not suffer from transmission losses to the same extent as conventional hot/chilled water systems [3].

Soil and urban wastewater, both of which maintain relatively constant year-round temperatures in the 10-25°C range, present promising heat sources/sinks for ALHP systems [4] [5] [6]. In a wastewater heat pump (WWHP) ambient loop system, ambient loop temperature is maintained via heat exchange with urban wastewater. Although institutional-scale WWHP systems have been implemented in a number of buildings worldwide – for example, the Rechts der Isar Medical Centre in Munich, Germany and Okanagan College in Kelowna, Canada – heating and cooling with wastewater remains relatively uncommon in North America, and there exists a substantial underutilized energy resource [7] [8]. A 2009 Canadian study suggested that an area with a population of 100,000 could produce 300,000 GJ of recoverable heat per year, enough to heat 3,000-5,000 single-family homes, while a 2013 Swiss study estimated that cooling Zurich's wastewater by 1°C would correspond to a continuous delivery of 10 MW [6] [9]. An ALHP system which uses the earth as a heat source/sink is referred to as a ground-source heat pump (GSHP) or geo-exchange ambient loop system. GSHP systems share many advantages – including relatively high system coefficients of performance (COPs), and a high energy efficiency and decarbonization potential – with WWHP technology, but are better established in North America [10]. In this paper, WWHP modeling is conducted using Microsoft Excel and coupled thermodynamic plugins, while GSHP modelling is conducted in HyGCHP, a TRNSYS-based software module for analyzing hybrid geothermal systems. Subsequent sections of the report detail the characteristics of the analyzed building development, as well as the building energy model, ALHP system simulation methodology, and comparative results for the six systems under analysis.

2. Development characteristics and energy model

The proposed development will be located in downtown Toronto, Canada, on the campus of Toronto Metropolitan University (formerly Ryerson University). The development will consist of a 15-storey podium (including 14 teaching storeys and one mechanical floor) and an adjacent 44-storey residential tower. The podium is slated to contain: retail areas; a café; a science gallery; a dining hall; conference space; lecture theatres; active learning classrooms; study rooms; and computer, physics, chemistry, and biology labs. The tower will contain student residences. Key parameters of the development are given in Table 1.

Table 1. Characteristics of proposed building development

Development type	Institutional/residential
Floor area	62,297 m^2 (702,850 ft^2)
Volume	339,195 m^3 (11,978,565 ft^3)

Building energy modelling was performed in eQuest by a consulting firm employed by the University, with the podium-tower development being modelled as 204 separate zones. Table 2 gives peak demand and annual loads for heating and cooling, as per the eQuest model. The development is slightly heating-dominated both with respect to energy peaks and with respect to overall load.

Table 2. Development energy usage

	Value
Heating peak	5,765 kW
Cooling peak	5,564 kW
Annual heating load	8,415 MWh
Annual cooling load	7,268 MWh

The development experiences almost year-round heating/cooling loads, with 0 annual no-load hours. Heating loads occur 8,715 hours a year (99.49% of the time) and cooling loads 8,758 hours a year (99.98% of the time), with the development having simultaneous heating and cooling demands for 8,713 hours each year

(99.46% of the time). The presence of simultaneous heating and cooling loads over most of the year renders the development well-suited to an ambient loop system.

The proposed development is to be located in a densely-developed downtown area. This presents an opportunity with respect to WWHP implementation, as the site is adjacent to substantial untapped wastewater resources, but a challenge with respect to GSHP implementation, as a large borehole field would be required to meet the development's heating/cooling loads and available space is limited.

3. Modelled heating and cooling systems

Six systems were modelled supplying the development's heating and cooling needs: a base case with natural gas boilers and a water-cooled chiller (no AL); an ambient loop coupled with conventional equipment (natural gas boilers and cooling tower); an AL-coupled WWHP system; a hybrid WWHP-conventional AL system; an AL-coupled GSHP system; and a hybrid GSHP-conventional AL system.

Modelling for the base case and the two WWHP systems was performed in Microsoft Excel using the XSteam and Psych plugins, while modelling for the two GSHP systems was performed in HyGCHP. Weather data used in air- and sewer-temperature correlations while modelling the conventional and WWHP systems was obtained from Environment Canada (Toronto weather station 6158355).

3.1. Base case (natural gas boilers and water-cooled chiller)

Under the base case, the development's space heating demands are met by natural gas boilers, while its space cooling demands are met by a water-cooled chiller. A constant 75% boiler efficiency was assumed, an industry-standard value as per the work of Kwiatek et al. [11]. Water-cooled chiller performance data was obtained from a reputable manufacturer, and is shown in Table 3. Two 3,285 kW chillers were required to meet the development's cooling needs.

Table 3. Water-cooled chiller operating parameters

% Load	Input power (*kW*)	COP
100	866.3	3.792
90	782.1	3.781
80	703.3	3.737
70	628.8	3.658
60	557.6	3.536
50	486.4	3.378

3.2. Conventional ambient loop

The conventional system model consists of: *(1)* a boiler model, *(2)* a cooling tower model, and *(3)* a heat pump model, integrated with a variable-flowrate ambient loop. Ambient-loop flowrate was set to 4.8×10^{-5}(m^3/s)/kW (2.7 GPM/ton) of net heating/cooling demand and ambient-loop power draw to 0.349 kW/(kg/s) (22 W/GPM), both industry-standard values, the latter drawn from ASHRAE 90.1 [12]. As in the base case, boiler efficiency was kept constant at 75%.

An open-loop cooling tower model was created in Microsoft Excel. XSteam, a MATLAB/Excel plugin, and Psych, a psychrometric plugin, were used to determine the thermodynamic properties of steam/water and moist air, respectively, under Toronto climatic conditions. In-zone water-to-air heat pumps were used to provide heating and cooling to individual building zones. Heat pump COPs for heating and cooling were drawn from TRNSYS. Table 4 shows the coefficients of performance used.

Table 4. Water-to-air heat pump operating parameters

AL Temperature (°C)	Heating COP	Cooling COP
-1.11	3.55	-
10	4.50	6.64
21.11	5.25	5.40
32.22	5.89	4.14
43.33	-	3.02

An open-circuit cooling tower was modelled as per the schematic in Figure 1 below. Temperature (T, in °C) and specific enthalpy (h, in kJ/kg-K) are modelled at each state point, along with the relative humidity (RH, unitless) and humidity ratio (ω, unitless) of the incoming and outgoing air. The specific enthalpy of air is denoted h_a (in kJ/kg-K), while the specific enthalpy of saturated liquid water and saturated water vapour are denoted h_f and h_g, respectively (also in kJ/kg-K). For air entering (State 3) and leaving (State 4) the cooling tower, both dry-bulb (T_{DB}) and wet-bulb (T_{WB}) temperatures are given.

Warm water entering the tower from the ambient loop (State 1) and cooled water returning to the ambient loop (State 2) share a single flowrate, $\dot{m}_w$ (in kg/s), with incoming makeup water ($\dot{m}_5$, in kg/s) compensating for evaporation such that mass balance is preserved. The tower is assumed to run only when there is a net demand for cooling. Further details for how makeup water rate and cooling tower air mass flowrate ($\dot{m}_a$, in kg/s) are determined on an hour-by-hour basis are given below.

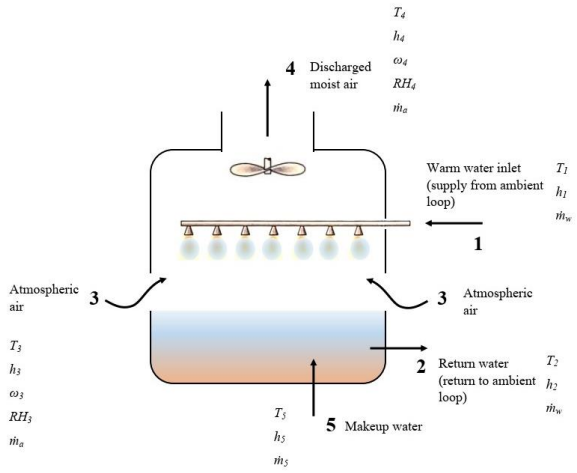


Fig. 1. Schematic of AL-coupled cooling tower (schematic adapted from [13])

Ambient loop flowrate ($\dot{m}_w$) was set to vary with net heating/cooling demand, with makeup water rate and airflow rate determined on an hourly basis as a function of ambient loop flowrate and the properties of supply (State 1) and return (State 2) water in the ambient loop.

For hours in which there is a net demand for cooling, state points were fixed as follows:

- **State 1:** The thermodynamic properties of the supply water from the ambient loop are determined by the amount of heat rejected by the building's water-to-air heat pumps. That is, $T_1 = (\dot{Q}_{cool})/\dot{m}_w C_{p1} + T_2$ where $\dot{Q}_{cool}$ is the heat rejected by all zones (in kW) and $\dot{m}_w$ and C_{p1} are the ambient loop mass flowrate (in kg/s) and specific heat capacity of the water in the ambient loop (in kJ/kg-K).
- **State 2:** Water at State 2 is at the *ambient loop temperature*, which, when there is net demand for cooling, is defined as being 5°C above the outdoor wet-bulb temperature. That is $T_2 = T_{AL} = T_{3WB} + 5°C$. (When there is a net heating demand instead of a net cooling demand, ambient loop temperature is held constant at 11°C.)
- **State 3:** State 3 is outdoor ambient air. Dry-bulb and wet-bulb temperatures from Environment Canada (Toronto weather station 6158355) were used to establish the state.
- **State 4:** State 4 is moist leaving air. The following assumptions were made to determine the properties of leaving air at State 4:

a. Temperature at State 4 was taken as the average of outdoor ambient temperature and supply temperature from the ambient loop. That is, $T_4 = \frac{T_1+T_{3DB}}{2}$.
b. Relative humidity at State 4 was assumed to be 20% higher than outdoor relative humidity, up to a maximum of 100%. That is, $RH_4 = RH_3 + 0.2$.

- **State 5:** Makeup water, which compensates for evaporation, is also treated as being at the same temperature as the ambient loop temperature.

With these relationships in place, the mass flowrate of air through the cooling tower was found through Equation 1:

$$\dot{m}_a = \frac{\dot{m}_1(h_{f1}-h_{f2})}{h_{a4}-h_{a3}+\omega_4 h_{g4}-\omega_3 h_{g3}-(\omega_4-\omega_3)h_{f5}} \quad (1)$$

Note that when the system is in heating mode $h_{f1} = h_{f2}$ and therefore the mass flowrate of air is 0 and the cooling tower is off/bypassed.

Equation 2 below gives the mass flowrate of makeup water in kg/s:

$$\dot{m}_5 = \dot{m}_a(\omega_4 - \omega_3) \quad (2)$$

As with airflow through the cooling tower, the makeup water rate is 0 when cooling is not required. The boiler and cooling tower models were integrated to create a conventional system ambient loop model capable of meeting the complete heating and cooling demands of the proposed development. Once loads were extracted from the eQuest model, heat extracted from and rejected to the ambient loop were defined as follows:

$$\dot{Q}_{cool} = \dot{Q}_{in}\left(1 + \frac{1}{COP_c}\right) \quad (3)$$

Where $\dot{Q}_{cool}$ is heat rejected to the ambient loop (in kW), $\dot{Q}_{in}$ is cooling load (kW), and COP_C is cooling coefficient of performance (unitless).

$$\dot{Q}_{heat} = \dot{Q}_{out}\left(1 - \frac{1}{COP_H}\right) \quad (4)$$

Where $\dot{Q}_{heat}$ is heat extracted from the ambient loop (in kW), $\dot{Q}_{out}$ is heating load (kW), and COP_H is heating coefficient of performance (unitless).

We then define the **net heat rejected** (NHR) as cooling minus heating for a given hour:

$$NHR = \dot{Q}_{cool} - \dot{Q}_{heat} \quad (5)$$

NHR determines how much cooling must be provided by the cooling towers or (if negative) how much heating must be supplied by the boilers. Boiler energy use and cooling tower air mass flowrate and makeup water rate were set to ensure that NHR was always met. Cooling tower power draw was determined as a function of flowrate through the tower, using the minimum efficiency value set by ASHRAE 90.1, 3.23×10^{-3} (m^3/s)/kW (38.2 GPM/hp) [12].

3.3. WWHP-coupled ambient loop (including hybridization)

For the WWHP system, it is proposed that a wetwell – a structure which receives sewage for handling – be constructed to tap into one of the sewers adjacent to the university campus. Wastewater will be screened for debris, passed through a bank of shell-and-tube wastewater-to-water heat exchangers housed in an energy transfer station (ETS), and – once its energy has been extracted – returned to the sewer. The shell side of the heat exchanger will be wastewater, while the tube side will be clean (ambient loop) water. This system configuration will ensure that only clean water circulates on the university side of the heat exchanger. The fluid pressure will also be higher on the tube side of the heat exchanger to ensure that in the event of a rupture clean water enters the wastewater side, and not vice versa, though it should be noted that such an emergency is unlikely.

Although the WWHP system is capable of meeting the development's complete heating and cooling needs, a boiler plant and/or cooling tower(s) for may be retained for redundancy depending on local legislation and the preferences of the building operators. Regulations regarding redundancy may differ depending on the exact configuration of the WWHP system.

3.3.1. Sewer temperature correlation and wastewater energy estimation

Sewer temperature and flow data were received from Toronto Water for several sites in the Greater Toronto Area. In order to estimate available wastewater energy in a manner consistent with the Toronto outdoor air temperatures provided by Environment Canada (and because temperature data was available only for the August-October 2018 period), it was necessary to determine a correlation accounting for the relationship between sewer temperature and: *(1)* outdoor dry-bulb temperature, and *(2)* time of day.

Sewer temperature fluctuates seasonally with outdoor air temperature, with average sewer temperatures being higher in summer and lower in winter. Additionally, sewer temperature varies predictably within a 1-2°C window throughout the day; temperatures are lowest around 7AM-8AM and rise steadily towards a high point in the late morning/early afternoon (11AM-2PM). Temperatures then drop steadily until they reach another low point around 5PM-6PM, before climbing towards their highest point around midnight. While there is considerable day-to-day variation in the exact shape of the sewer temperature curve, this general pattern of two peaks and two valleys holds true throughout the year.

The flows from Sewer MH101, Site 005 were used to generate a correlation between wastewater temperature, seasonal outdoor dry-bulb temperature, and time of day according to the following method:

- A fifth-degree polynomial trendline was generated to represent variation in wastewater temperature as a function of time of day ("Correlation A").
- Mean daily ambient temperature and mean daily wastewater temperature were correlated using a line of best fit ("Correlation B").
- To capture the effect of seasonal variation, the x^0 value of the fifth-degree polynomial (y-intercept) was replaced with the estimated mean daily wastewater temperature as determined from Correlation B.
- An offset of +0.6°C was applied to reduce error.

RMSE between estimated sewer temperature and recorded sewer temperature under this method ("Correlation C") was 0.73. The maximum modelled wastewater temperature was 25.6°C, while minimum modelled wastewater temperature was 19.6°C, values consistent with most urban sewersheds [4] [5] [6]. The coefficients of the line of best fit used are shown in Table 5 below.

Table 5. Coefficients for sewer temperature correlation

x^5	x^4	x^3	x^2	x^1	x^0
9.593×10^{-6}	-0.0005	0.00804	-0.03230	-0.16591	$f(T_{DB})$

Where:

$$x_0 = \overline{T_{sewer}} + 0.6 = f(T_{DB}) = [0.1041 \times T_{DB} + 22.634] + 0.6 \quad (6)$$

The estimated temperature profile was paired with a full year of actual flow data from a different monitoring site (103-119) to generate a complete temperature/flowrate profile.

Maximum available sewer energy (i.e., energy available if the entire sewer flow is utilized) was calculated according to Equation 7 below:

$$\dot{Q}_{sewer} = \dot{m} \times c_p \times \Delta T \quad (7)$$

Where $\dot{m}$ is the mass flowrate of the sewer, c_p is the specific heat capacity of water (wastewater), and ΔT is the inlet-outlet temperature difference across the wastewater side of the heat exchanger, here taken to be 3°C due to municipal safety limits on wastewater temperature.

A 5°C difference between water and wastewater streams was assumed – that is, ambient loop temperature was taken to be 5°C higher than the sewer temperature in the cooling season and 5°C lower than the sewer temperature in the heating season. The lowest available sewer energy at any point during the year was found to be 5,416 kW (occurring in late March), sufficient – once heat pump efficiencies are taken into account – to meet the complete heating and cooling demands of the proposed development.

3.3.2. Hybrid WWHP-conventional ambient loop

As has been mentioned above, it is estimated that the energy content of available wastewater resources near the proposed development – estimated based on the flowrate of a comparably-sized sewer and sewer temperature-outdoor air temperature correlations based on other Toronto sewers – is capable of meeting the heating and cooling demands of the development. However, for the sake of comparison, a hybrid WWHP-conventional ambient loop scenario is also presented.

Under the hybrid scenario, it is assumed that wastewater resources are *not* sufficient to meet the demands of the development, so conventional equipment – namely, natural gas boilers and a water-cooled chiller – is reintroduced to make up the deficit, with wastewater remaining the first source of supply to the ambient loop. It was assumed under this scenario that there would be enough year-round flow to ensure constant supply for a single shell-and-tube heat exchanger; heat exchanger specifications were provided by the manufacturer. At full capacity, this shell-and-tube heat exchanger operates with a wastewater flowrate of 0.057 m^3/s and clean water flowrate of 0.028 m^3/s.

3.4. GSHP-coupled ambient loop (including hybridization)

In the two GSHP-coupled ambient loop scenarios (full geo-exchange and hybrid GSHP-conventional system), the ambient loop is paired with a ground heat exchanger. Modelling for the two GSHP-coupled scenarios was performed in HyGCHP, a module based on TRNSYS (Transient System Simulation Tool) used for analyzing hybrid geothermal energy systems. The parameters used in both simulated scenarios are given in Table 6 below.

Table 6. HyGCHP simulation parameters

Ground temperature (at mid-bore depth)	13.9°C	**Ambient loop fluid**	Propylene glycol
Drilling depth	91.4 m	**Minimum fluid temperature**	-7.78°C
Bore spacing	6.10 m	**Pump power per 100 tons of peak block load**	7,457 W
Header depth	1.80 m	**Fraction of pressure drop attributable to GHX**	0.55
Center-to-center half distance	3.80 cm	**COP heating**	3.42
Borehole radius	5.70 cm	**EER cooling**	15.6 MBH/kW
Ground thermal diffusivity	0.10 m	**Fan operation**	Continuous
Ground thermal conductivity	5.68 W/m^2-K	**Performance curves**	Default
U-tube size	25 mm	**Heating EAT**	21°C
Grout thermal conductivity	4.54 W/m^2-K	**Cooling EAT**	24°C

3.4.1. Hybrid GSHP-conventional ambient loop

The final scenario simulated was a hybrid GSHP-conventional ambient loop. As in the hybrid WWHP-conventional ambient loop scenario, rejection of heat to and extraction of heat from the thermal reservoir (in this case, the ground rather than wastewater) remains the first order of supply, with conventional equipment – in this case, a single cooling tower – making up the remainder of the development's demand. In the hybrid GSHP-conventional scenario, the borehole field is sized to meet heating demand.

4. Energy, cost, and GHG comparison

Natural gas and electricity prices used in estimating energy costs for the six heating/cooling systems are shown in Table 7. 2019 and 2030 prices are derived from Toronto Metropolitan University's *Carbon Reduction Roadmap* (2021) [14]. It should be noted that natural gas costs are extremely volatile; 2022 natural gas costs are substantially higher those of 2019, reflecting current sociopolitical conditions. With respect to electricity pricing, the University is a Class A consumer under the Ontario regulatory structure, meaning that it pays a global adjustment (GA) factor based on the percentage of the province's electrical demand for which it is responsible during the top 5 draw hours every year; costs given in the *Roadmap* are therefore not simple marginal energy costs, but rather reflect estimated global adjustment.

Table 7. Factors used in calculating energy costs [14]

	Natural gas cost (*$CAD/kWh*)	Electricity cost (*$CAD/kWh*)
2019	0.0286	0.1517
2030	0.0595	0.1566

Canada's 2021 *National Inventory Report* for greenhouse gas sources and sinks provided the factors used to calculate greenhouse gas emissions associated with: *(1)* electricity consumption from the Ontario grid, and *(2)* the burning of natural gas; these factors reflect 2019 conditions [15]. For electricity consumption, the average emissions factor ("AEF"), which represents the simplest measure of the grid's GHG intensity, was used. GHG emissions factors are shown in Table 8 below.

Table 8. Factors used in calculating greenhouse gas emissions [15]

	GHG intensity
Natural gas	1,899 gCO_2eq/m^3
Electricity AEF 2019	30 gCO_2eq/kWh

A comparison of annual energy use, GHG emissions, and energy costs for the six modelled systems is given in Table 9 below.

Table 9. Comparison of annual energy use, GHG emissions, and energy costs for the six modelled systems

System	Energy use (*MWh*)	GHG emissions (*tonnes*)	Cost (*$CAD*, 2019)	Cost (*$CAD*, 2030)
Base	13,193	2,118	$630,450	$987,149
Conventional AL	9,566	1,236	$689,332	$897,107
WWHP	5,711	171	$866,423	$894,409
WWHP-conventional	6,007	589	$582,861	$681,656
GSHP	3,261	97	$494,646	$510,623
GSHP-conventional	3,218	96	$488,123	$503,889

The AL-coupled WWHP system provided a meaningful reduction in annual energy use as compared to the base case (57% reduction) and the conventional ambient loop (40% reduction), as well as significant greenhouse gas (GHG) emissions reductions (92% as compared to base case, 86% as compared to conventional ambient loop); however, under 2019 energy pricing, it was more costly to operate than either the base case (37% higher cost) or conventional AL (26% higher cost) systems. By 2030, the AL-coupled WWHP would

provide slight costs savings as compared to the base (9% lower cost) and conventional AL (0.3% lower cost) systems.

By contrast, the hybrid WWHP-conventional was cheaper to operate than the base and conventional AL systems under both 2019 and 2030 energy costs. When compared to the base case, it provided 8% cost savings under 2019 pricing and 31% savings under 2030 pricing; when compared to the conventional AL system, it provided 15% cost savings under 2019 pricing and 24% savings under 2030 pricing. However, GHG emissions were significantly (243%) higher than for the pure WWHP system, and energy use slightly (5%) higher.

Of the six systems studied, the two GSHP systems – and particularly the hybrid GSHP-conventional system – performed best on all metrics (energy use, GHG emissions, 2019 energy costs, and 2030 energy costs). The hybrid GSHP system had an annual energy use of 3,218 MWh, only 56% of the energy used by the WWHP system and less than a quarter of the energy used by the development under the base case. Due to the offsetting of natural gas emissions, GHGs were significantly lower than in the base case for all four renewable-based systems (the hybrid and non-hybrid WWHP and GSHP systems). The hybrid GSHP system produced only 96 tonnes of GHGs annually, about 5% of the GHGs produced by the conventional system and 56% of the GHGs produced by the WWHP system.

The natural gas boilers were the largest energy consumer for the base case and conventional AL systems. For the WWHP AL system, heat pump electrical consumption represented the largest share of energy consumed, slightly edging out electrical consumption by the AL pumps. In the hybrid WWHP AL system, the boilers were again the largest energy consumers, representing the relative inefficiency of natural gas boilers. For the two GSHP systems, electrical draw by the heat pumps represented the majority of energy used.

5. Conclusion

The results of this investigation mediate towards the selection of a GSHP-based system for the proposed campus development, as the two GSHP-based systems had the lowest energy usage and GHG emissions of the systems studied, as well as the lowest costs under both 2019 and 2030 energy prices. However, it should be noted that this analysis had numerous limitations. Upfront costs and capital expenditures were not considered, nor were return-on-investment or the larger economic viability of the systems under study. The implementation of WWHP systems requires the cooperation of municipal authorities, who control access to city wastewater, while GSHP systems require large borehole fields which are often difficult to build in urban areas and whose construction can slow the development process.

In addition to the practical and economic concerns involved in the implementation of WWHP and GSHP systems, the current analysis was limited by the software used. HyGCHP is a software intended for simplified analysis of geo-exchange and hybrid geo-exchange systems; a more detailed analysis would use TRNSYS or equivalent software to analyze both the WWHP and GSHP configurations.

While a more complete analysis remains for future work, it is certain that, as carbon pricing in Canada continues to rise, the economic feasibility of heat pump systems such as those studied in this paper will increase and their implementation will become more widespread. By providing preliminary evidence for the viability of GSHP- and WWHP-based systems in a proposed campus development, the present study suggests two plausible alternatives to conventional heating and cooling; this is particularly significant in light of the underutilization of WWHP systems in Canada. Although it is not possible to draw broad generalizations from the results of this paper, the economic and environmental benefits of GSHPs and WWHPs for the institutional/residential development under study suggest that these types of heating and cooling systems may be worth investigating in other large institutional or residential buildings in Canada, particularly when climatic conditions and wastewater availability resemble the present scenario.

Acknowledgements

The authors would like to thank Noventa Energy Partners and Mitacs Accelerate for their generous support of this research, as well as Toronto Metropolitan University for providing building-related data.

References

[1] United States Environmental Protection Agency. *Inventory of U.S. Greenhouse Gas Emissions and Sinks*. 2022.

[2] London Energy Transformation Initiative. *LETI Climate Emergency Design Guide: How New Buildings Can Meet UK Climate Change Targets*.
[3] Revesz, A., Jones, P., Dunham, C., Davies, G., Marques, C., Matabuena, R., Scott, J., Maidment, G. Developing novel 5th generation district energy networks. *Energy* 2020;**201**.
[4] Xiaodi, H., Li, J., van Loosdrecht, M. C. M., Jiang, H., Liu, R. Energy recovery from wastewater: Heat over organics. *Water Research* 2019;**161**.
[5] Cipolla, S. S., Maglionico, M. Heat recovery from urban wastewater: analysis of the variability of flow rate and temperature in the sewer of Bologna, Italy. *Energy Procedia* 2014;**45**.
[6] Dürrenmatt, D. J., Wanner, O. A mathematical model to predict the effect of heat recovery on the wastewater temperature in sewers. *Water Research* 2014;**48**.
[7] British Columbia Ministry of Community & Rural Development, "Integrated Resource Recovery Case Study: Okanagan College Wastewater Heat Recovery." Available: https://www.waterbucket.ca/gi/sites/wbcgi/documents/media/270.pdf [Accessed 29th April 2022].
[8] Huber, "Wastewater heat utilisation and reuse of process heat at Munich university hospital "Klinikum rechts der Isar"." Available: https://www.huber.de/huber-report/ablage-berichte/energy-from-wastewater/wastewater-heat-utilisation-and-reuse-of-process-heat-at-munich-university-hospital-klinikum-rechts-der-isar.html [Accessed 29th April 2022].
[9] Johnston, C., Lindquist, E., Hart, J., Homenuke, M. Four steps to recovering heat energy from wastewater. *British Columbia Water & Waste Association Watermark, Craig Kelman & Associates* 2009;**18**:2.
[10] Bernier, M. A. Closed-loop ground-coupled heat pump systems. *ASHRAE Journal* 2006;**48**:9.
[11] Kwiatek, C. Techno-economic feasibility of wastewater energy transfer (WET) systems for cold climates (Master's thesis). Toronto, Ontario; 2020.
[12] *ANSI/ASHRAE/IES Standard 90.1-2016: Energy Studies for Buildings Except Low-Rise Residential Buildings (I-P Edition)*. 2016.
[13] Moran, M. J., Shapiro, H. N., Boettner, D. D., Bailey, M. B. *Fundamentals of Engineering Thermodynamics*. 8th ed. Hoboken, NJ: John Wiley & Sons; 2014.
[14] Ryerson University Climate and Energy Working Group. *Carbon reduction roadmap - draft framework*. Toronto, Ontario; 2021.
[15] Ministry of Environment and Climate Change Canada. *National Inventory Report 1990-2019: Greenhouse Gas Sources and Sinks in Canada*. 2021.

14th IEA Heat Pump Conference
15-18 May 2023, Chicago, Illinois

Development of a Simulation Tool for Ground Source Heat Pump Systems Using Horizontal Ground Heat Exchangers

Takao Katsura[a], Motohiro Maeda[a], Yutaka Shoji[a], Katsunori Nagano[a]

[a]Hokkaido University, Kita 13 Nishi 8 Kita-ku, Sapporo, Japan

Abstract

Ground source heat pump (GSHP) systems have been gaining attention in recent years as a one of renewable energy utilization system, but its widespread use in Japan has been delayed due to high installation costs. The introduction of horizontal ground heat exchangers (GHEs) has a possibility to reduce the initial cost, therefore, appropriate system design is required to install the horizontal GHEs. The authors developed a simulation tool for GSHP systems using horizontal GHEs. The developed simulation tool can calculate the ground temperature surrounding the GHE, which is affected by not only the heat extraction/injection via GHEs but also the temperature change at ground surface. In addition, this tool calculates the ground temperature surrounding the GHE by superposing the temperature response, and the temperature response of the spiral coil type GHE is calculated by an applying artificial neural network (ANN). In this paper, outlines of calculation method are firstly introduced. Next, the required length of GHE was estimated as a case study using the developed simulation tool.

© HPC2023.
Selection and/or peer-review under the responsibility of the organizers of the 14th IEA Heat Pump Conference 2023.

Keywords: Ground source heat pump system, Horizontal ground heat exchanger, Simulation tool, Artificaial neural network ;

1. Introduction

In recent years, ground source heat pump (GSHP) systems that utilize underground thermal energy, a renewable energy heat source, have been spreading in many countries as a highly efficient heat source system. However, the total installed capacity in Japan is only 0.2 GW and much smaller than North America, China and European countries [1]. The main reason is the installation costs of ground heat exchangers (GHEs). The vertical type GHE generally used in existing GSHP systems in Japan has a high initial cost of 10,000 ~ 20,000 JPY/meter for installation. On the other hand, horizontal GHEs, which utilize shallow ground several meters deep from the ground surface, requires a large site for installation, but the installation cost is much lower than that of vertical GHE. Therefore, when a large site for GHE burial is available, the adoption of horizontal GHE is expected to expand the introduction of GSHP systems due to the significant reduction in initial costs.

Horizontal GHEs can be classified into (a) Straight pipe type, (b) Spiral coil type, and (c) Comb type, as shown in Photo 1. The spiral coil GHE to be considered in this study is known to have a larger heat exchange rate per heat exchange installation area than the conventional straight pipe type because of the areal heat exchange from the top and bottom of the coil [2]. Therefore, this type of GHE system can reduce the size of the GHE burial site and the initial cost of the GSHP system. On the other hand, appropriate system design is essential for the introduction of this system. Currently, numerical calculation models for the spiral coil GHEs were developed, but it is not suitable as a design tool because of its large computational load. Although Li et al. have derived a theoretical solution to calculate the underground temperature surrounding the spiral coil GHE with a relatively small computational load [3], the computational load becomes large when the average temperature of the pipe surface is calculated.

To address this challenge, the authors have focused on artificial neural networks (ANNs), which have recently attracted attention for their application to regression and classification problems. As an example of the application of ANNs to the calculation of GHE ambient temperature field, Pasquier et al. developed an ANN model to quickly and accurately determine the short-term G-function using a model based on the thermal

resistance and heat capacity [4]. The authors have also developed a regression model that reproduces the numerical results of a moving infinite cylinder problem using ANN, and have shown a fast and accurate method for calculating GHE ambient temperature in groundwater flow fields [5]. Therefore, in this study, we construct a temperature response regression model that reproduces the theoretical analysis results presented by Li et al. [3] based on the high functional representation capability of ANN and its fast computation speed, and develop a fast and accurate simulation model.

Finally, using the developed simulation tool for performance prediction, we will conduct case studies to determine the required scale of GHE.



(a) Straight pipe type (b) Spiral coil type (c) Comb type

Photo 1. Types of horizontal GHEs

2. An artificial neural network model for fast computation of temperature response of spiral coil GHE

2.1. Parameter study with theoretical solution

In order to achieve a fast calculation of the average temperature response of the spiral coil GHE, a regression model is constructed by having ANN learn the results of calculating the average temperature response with the theoretical solution. The parameters that determine the shape of the spiral coil are the loop interval *D*, the ring radius *r*, and the number of rings *N*. The input parameters to the ANN are four variables, including these three variables and the dimensionless time (Fourier number) $F_o = at/r_p^2$. In addition, a dimensionless average temperature $\Theta = \theta_{rs,mean}\lambda r_p/q_r$ was given as output for training.

In the parameter study using the theoretical solution [3], several patterns of coil geometries were prepared and the dimensionless average temperature response of the spiral coil GHE surface over 10 years was calculated at one-hour intervals. As shown in Figure 1, total of 27 patterns were studied, three patterns for each variable. The results of the calculated dimensionless temperature response are shown in Figure 2.

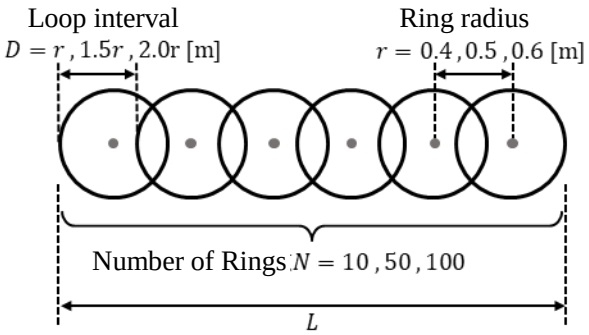


Fig. 1. Parameters that determine the shape of the spiral coil

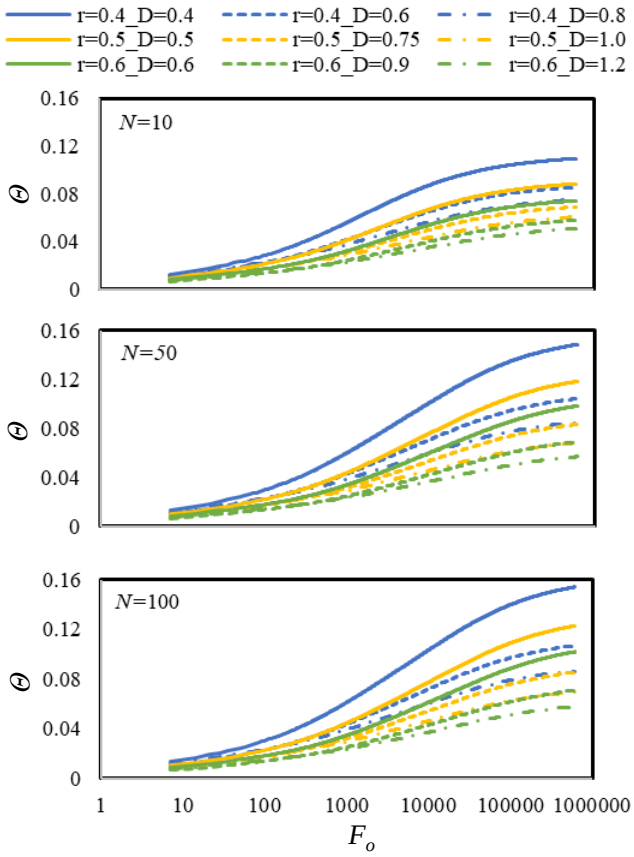


Fig. 1. Dimensionless average temperature calculated by theoretical solution

2.2. Outlines of machine learning

Figure 3 shows a diagram of the ANN. The model is a feed-forward neural network in which all units are coupled, and a ReLU function is set as the activation function in each hidden layer. In machine learning, there are hyperparameters, such as the number of hidden layers and units in ANN, that must be determined in advance during training. In this study, Bayesian optimization was used as the optimization method for hyperparameters. The hyperparameters and their search ranges are shown in Table 1. The maximum evaluation time for Bayesian optimization was 72 hours, and the maximum number of evaluations was 50. To verify the ANN performance, the dataset was randomly divided into a training dataset, a validation dataset, and a test dataset at a certain ratio of 7:1.5:1.5, respectively. The mean squared error (MSE) value was used for the loss function in the ANN learning process.

Figure 4 shows the flowchart of ANN learning. The ANN is trained on the given hyperparameter settings applying the Bayesian optimization algorithm and using the training dataset. The learned ANN is then validated using the validation dataset.

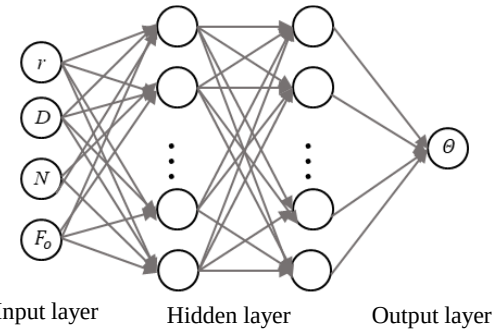


Fig. 1. A diagram of the ANN

Table 1 Hyperparameters and their search ranges

Parameter	Search range
n_{Hidden}	3-8 (Integer)
n_{Unit}	100-500 (Integer)
LR	1.0×10^{-6} – 1.0×10^{-4}
$epoch$	50-120 (Integer)
$Weight_Decay$	1.0×10^{-12} – 1.0×10^{-8}

This is iterated within the maximum evaluation time and number of times, and the MSE for the test data is calculated for the result that finally minimizes the MSE of the verification result. The performance of the ANN is then determined.

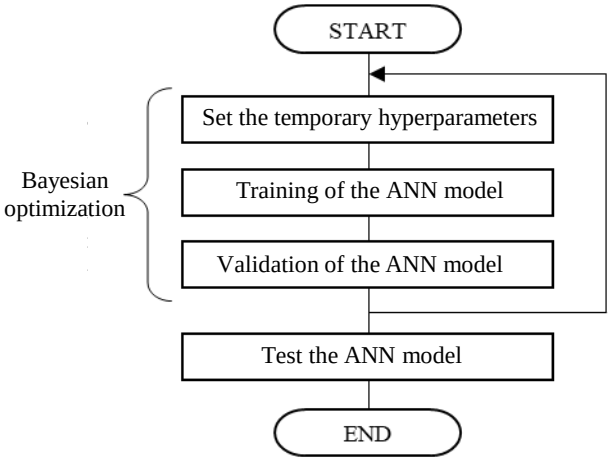


Fig. 4. A Flowchart of ANN learning

2.3. Result of machine learning

The ANN was trained in the search range of hyperparameters in the previous section. The hyperparameters that resulted in the smallest MSE as a result of Bayesian optimization are shown in Table 2. Figure 5 shows the process of determining hyperparameters by Bayesian optimization. Note that n_{Hidden}, n_{Unit}, *LR*, *epoch*, and *Weight_Decay* for each trial are shown in Figure 5 as data labels. From Figure 5, it can be seen that the parameters are updated so that the MSE becomes smaller as the number of training trials progresses.

Table 2 Hyperparameters obtained by Bayesian optimization

Parameter	Optimal value
n_{Hidden}	5
n_{Unit}	499
LR	5.74×10^{-5}
$epoch$	98
$Weight_Decay$	2.52×10^{-12}

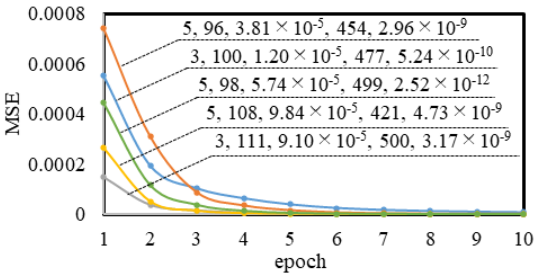


Fig.5 A process of determining hyperparameters by Bayesian optimization

Within the maximum evaluation time and number of iterations, the number of iterations was 50, and the minimum MSE was obtained at the 29th iteration. Bayesian optimization results show that the MSE for the validation data set is 1.46×10^{-9}, which is sufficiently small for a regression model. Figure 6 shows a comparison of the temperature response between the obtained ANN regression model and the theoretical solution under the condition of a ring radius of 0.4 m as an example. The MSE was 2.26×10^{-9} on average. This indicates that the constructed ANN model shows good regression performance and that the generalization performance of the learned ANN is adequate. Furthermore, a comparison of the time required for 10 years of calculations with N=100 rings shows that the ANN model takes about 2 seconds to calculate the temperature response, while the theoretical analysis takes about 20 hours, indicating that the ANN regression model significantly reduces the calculation time. This temperature response was applied to the temperature response calculation of the calculation flow shown in Figure 7, and a simulation tool was created.

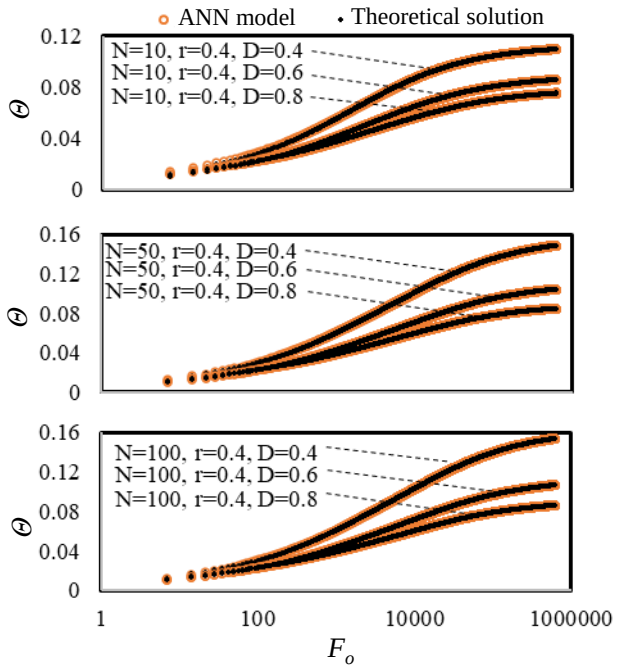


Fig. 6. Temperature response between the obtained ANN regression model and the theoretical solution

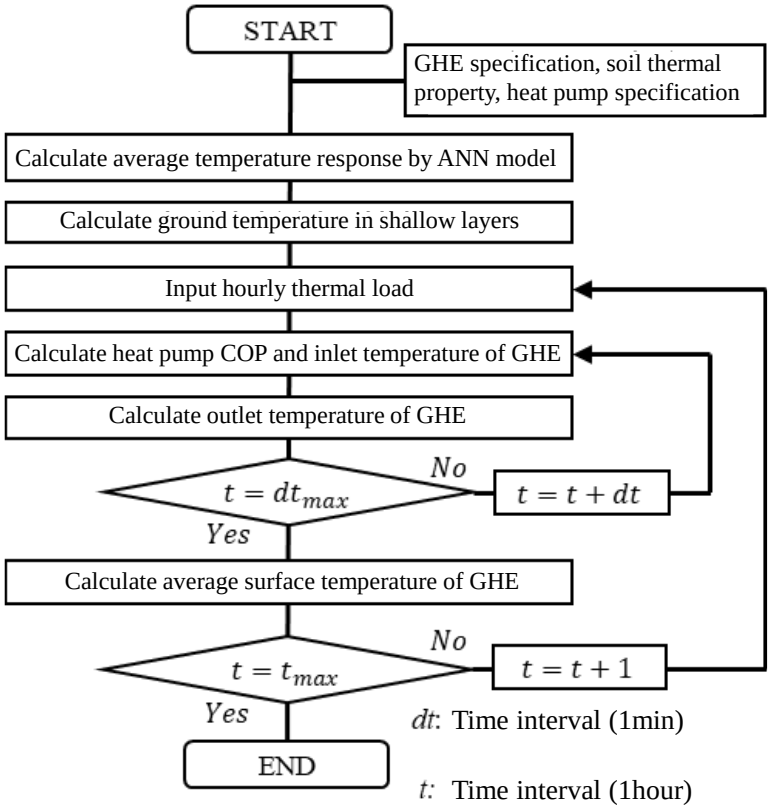


Fig.7 A calculation flowchart of simulation tool for GSHP system with spiral coil GHE

3. Case studies to determine the required scale of GHE

3.1. Calculation conditions

Using the simulation tool for the GSHP system with spiral coil GHEs described above, the GHE size required to cover the annual thermal load for a residential house is investigated. Akita and Tokyo were selected as target cities for semi-cold and moderate climate regions, respectively.

Figure 8 shows the assumed residential house. This model is assumed to have a total floor area of 116m^2 and high insulation performance. The heat loss coefficient per floor area and temperature difference is set as 1.0 W/(m^2・K) in Akita and 1.4 W/(m^2・K) in Tokyo, considering that it should be less than half that of the energy conservation standard in Japan. Air conditioning was set to operate continuously 24 hours a day, with the heating temperature set at 20ºC and the cooling temperature at 26ºC. The hourly heating and cooling load were calculated by using AE-CAD/AE-Simheat [6], which is a commercially available thermal load calculation. Figure 9 shows the hourly cooling and heating loads in annual.

The soil and GHE conditions were set as shown in Table 3. The soil effective thermal conductivity was set at 1.0 W/(m・K) and the circulation flow rate was kept constant at 20 L/min. The minimum GHE size (L in Figure 1) required to keep the fluid temperature of GHE outlet within the range of -5~35ºC throughout the year was defined as the GHE required size in each city.

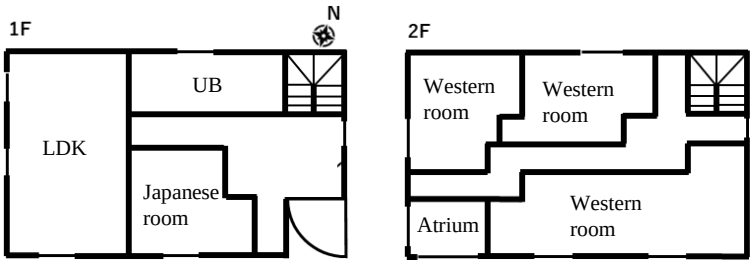


Fig. 8. The subjected residential house

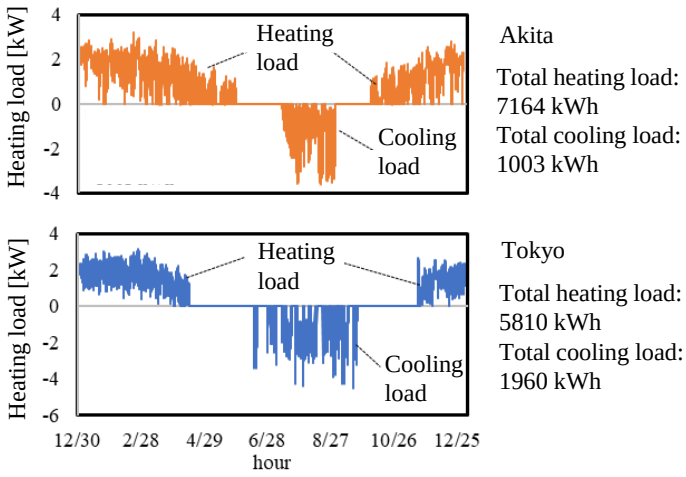


Fig. 9. Hourly heating/cooling load in annual

Table 3 Soil and GHE conditions

Soil conditions	Specific heat	2.0 kJ/(kg・K)
	Density	1500 kg/m^3
	Effective thermal conductivity	1.0 W/(m・K)
GHE conditions	Pipe inside diameter	0.025 m
	Pipe outside diameter	0.032 m
	Loop interval	0.5 m
	Ring radius	0.5 m
	Depth	1 m

3.2. Result and discussions

The minimum GHE sizes were 51 m in Akita and 60 m in Tokyo, respectively. Also, the variation of heat carrier fluid temperature of GHE outlet are shown in Figure 10 when the minimum GHE sizes were given. It was confirmed that the heat carrier fluid temperature reached the lower limit in Akita and the heat carrier fluid temperature reached the upper limit in Tokyo as a result. Based on this result, if spiral coil GHEs with a length L of 10 m are installed at intervals of 2 m, a site area of approx. 80 m^2 (= 2 m intervals × 4 × 10 m) would be required in Akita and about 100 m^2 (= 2 m intervals × 5 × 10 m) in Tokyo. While it is difficult to secure a site area in Tokyo due to the high population density, it is possible to secure a site area in Akita.

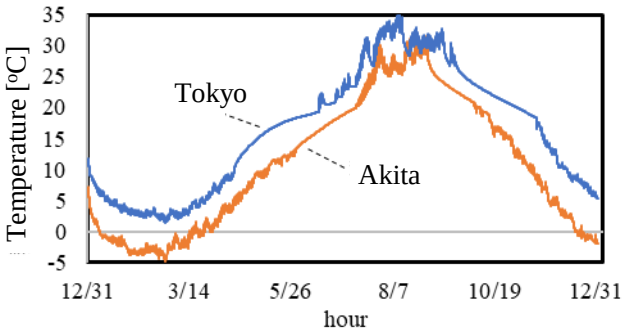


Fig. 8. The subjected residential house

4. Summary

In this study, an ANN regression model of the ambient temperature response of the ground heat exchanger was developed using the theoretical solution in order to develop a simulation tool for horizontal spiral coil type ground heat exchangers. Case studies were conducted in each city to determine the required heat exchanger length, and the following findings were obtained.

1) A regression model of the temperature response function was created by training ANN on the results of the theoretical analysis. As a result, a highly accurate regression model with an MSE of 1.46×10^{-9} was created for the validation data set. Furthermore, the ANN model required only about 2 seconds of computation time over a 10-year period with 100 number of rings, a significant reduction in the computation load.

2) The required GHEX length in each city was examined. In Akita, the required GHEX length was 51 m for the spiral coil method and 46 m for the horizontal unit method. In Tokyo, the GHEX length for the spiral coil method was 60 m and that for the horizontal unit method was 58 m. In both cities, the GHEX length for the horizontal unit method was shorter than that for the spiral coil method.

Acknowledgements

This study is based on results obtained from the project “Research and Development for Total Cost Reduction of Heat Utilization as Renewable Energy,” commissioned by New Energy and Industrial Technology Development Organization (NEDO) in Japan (Grant number P19006).

References

[1] J. Lund and T. Boyd : Direct Utilization of Geothermal Energy 2020 Worldwide Review, World Geothermal Congress 2020
[2] Kavanaugh, S.P., and Rafferty, K. : Ground-Source Heat Pumps, Design of Geothermal Systems for Commercial and Institutional Buildings, ASHRAE (1997)
[3] Li H., K. Nagano, Y. Lai: A new model and solutions for a spiral heat exchanger and its experimental validation, International Journal of Heat and Mass Transfer 55, pp. 4404-4414 (2013)
[4] Pasquier et al. : Application of artificial neural networks to near-instant construction of short-term g-functions, Applied Thermal Engineering 143, pp.910-921 (2018)

[5] Shoji Y., T. Katsura, , K. Nagano : MICS-ANN model: An artificial neural network model for fast computation of G-function in moving infinite cylindrical source model, Geothermics 100 (2022) 102315
[6] Architecture Environment Solutions: AE-CAD/AE-Simheat. Available online: http://www.ae-sol.co.jp/aesol01.html (accessed on 6 July 2018)

NOMENCRATURE

a: Thermal diffusivity [m^2/s], F_o: Fourie number [-], *q*: Heat extraction rate per length [W/m], *r*: Radius [m], *t*: Time [s], θ : Temperature [^oC], Θ : Dimensionless temperature [-], λ : Thermal conductivity [W/m/K]

Subscript

p: Ground heat exchanger pipe, *r*: ring, *rs*, *mean*: average of ring surface

14th IEA Heat Pump Conference
15-18 May 2023, Chicago, Illinois

A novel oscillatory thermal response test for deep U-tube borehole heat exchanger: In situ data

Ahmed A. Serageldin[a,b], Nagano Katsunori[a]

[a]Division of Human Environmental Systems, Faculty of Engineering, Hokkaido University, Sapporo, 060-8628, Japan
[b]Department of Mechanical Engineering, Shoubra Faculty of Engineering, Benha University, Cairo, 11629, Egypt

Abstract

The current study proposed a novel thermal response test methodology to minimize the testing time, and save labor time and testing cost; it utilizes an oscillatory heat flux called OscTRT. The oscillating heating flux has the shape of a sinusoidal wave with a frequency of $1.74x10^{-3}$ Hz, an average value of 14 kW, and an amplitude of ±6 kW. A new TRT machine is customized to control the heating injection pattern frequency and amplitude. Five OTRTs are conducted at sites with various geological and hydrological conditions with an apparent thermal conductivity range of 1.2 ~ 3.1 W/m.K. The sites are located in Sapporo city, Niseko city in Hokkaido prefecture, Miyoshi city in Hiroshima prefecture, Kai city in Yamanashi prefecture, and Tokyo city in Japan. All sites' borehole depths and diameters are 300 m and 250 mm. The fluid temperature and soil undisturbed temperature profiles are measured using optical fiber cables inserted inside the U-tube legs. While, A new analysis method is presented to filter, smooth, and fit the recorded data to find the response temperature amplitude at inlet and outlet to the borehole. The borehole and subsurface thermal response are analyzed to find the amplitude ratio, phase shift angle between inlet and outlet temperature responses, and effective thermal conductivity. The accuracy and validity of the proposed method are examined by comparing the output with the results from the conventional TRTs. Five OscTRTs are carried out for 24 hours, while the normal TRTs are conducted for 60 hours. The results show that the OscTRT shortened the time needed for TRT by 60% with high accuracy. Also, a linear relationship between the amplitude ratio and effective thermal conductivity is derived.

© HPC2023.
Selection and/or peer-review under the responsibility of the organizers of the 14th IEA Heat Pump Conference 2023.

Keywords: Thermal response test;Oscillatory therrmal response test, Ground source heat pumps, Effective thermal conductivity ;

1. Introduction

Ground source heat pump systems (GSHPs) for subsurface heat utilization have recently developed due to their energy saving, high efficiency, and no pollutant emission[1]. The local soil's thermal parameters must be first known when designing GSHPs. The thermal conductivity of the ground (λ) and thermal resistance (R_b)of the ground heat exchanger (GHE) are the two most important design parameters for borehole thermal energy storage (BTES) systems[2]. An in-situ thermal response test (TRT) may determine these two parameters, which gives reliable design data. The common TRT includes boreholes, fluid circulation, temperature control devices, and data acquisition instruments. Temperature sensors are installed at the inlet and outlet of the GHE to measure the average temperature of the circulating fluid. Many portable test devices are small in size and easy to operate[3]. The first step of the test is to determine the undisturbed ground temperature, This is usually made by temperature logging in the borehole or by evaluating the fluid temperature of the circulating fluid before the heating/cooling is switched on. The fluid inlet and outlet temperatures are measured by Pt 100 sensors, while a magnetic flow meter measures the fluid flow rate. The flowing fluid is heated using an electrical heater with 5-10 kW. A data logger records all the data for 48 to 72 hours with a time interval of 30 seconds or 60 seconds[4]. Using the basic theory of heat transfer, the relationship between the average temperature of circulating fluid and the temperature of the borehole wall can be expressed as shown in Eq. (1):

$$q = \frac{\bar{T}(\tau) - T_b(\tau)}{R_b} \quad (1)$$

Where q is the heating injected heat per meter, W/m; $\bar{T}$ is the average fluid temperature, K; T_b is the temperature of the borehole, K; τ is the test time, sec.; R_b is the borehole thermal resistance (m.K)/W; it includes the convection thermal resistance from the fluid to the inner tube surface ($R_{conv.}$), the conduction thermal resistance of the pipe material (R_p), and the conduction thermal resistance through the grouting material[5]. This equation is conditioned to the minimum test time to affirm the steady state of heat transfer inside the borehole and neglect the unsteady heat transfer period. Therefore, the test time $\tau > 10\tau_b$ [6] where τ_b is calculated according to Eq. (2)

$$\tau_b = \frac{r_b^2}{a_g} \quad (2)$$

Where r_b is the borehole radius, m, and a_g is the grouting material thermal diffusivity, m^2/s. Due to the complexity of solving the theoretical basis for the heat transfer analysis outside the borehole, the Boltzmann transformation is used to obtain the mathematical expression of the approximate infinite line source (ILS) model. The average fluid temperature is expressed as indicated in Eq. (3)

$$\bar{T}(\tau) = \frac{q}{4\pi\lambda_s}\ln(\tau) + q\left[R_b + \frac{1}{4\pi\lambda_s}\left(\ln\frac{4a_s\tau}{r_b^2} - \gamma\right)\right] + T_g \quad (3)$$

where T_g is the undisturbed soil temperature, K, a_s is the thermal diffusivity of soil, m^2/s; γ is the Euler's Constant (0.5772 [-]).

Ingerson et al., in 1984, developed the infinite cylindrical source model (ICS) to consider the radial heat transfer through the borehole. While many improved models were developed to describe the heat transfer process more accurately, like the finite line source (FLS) by Zeng et al. in 2002[7], the infinite moving line source model (MILS) [8]and moving finite line source model (MFLS)[9].

Based on the ILS model, the linear regression method takes advantage of the linear relationship between the average inlet and outlet temperature of GHE and the logarithm of test time. Soil thermal conductivity can be obtained according to the fitting curve's slope. The borehole's thermal resistance can be obtained according to the identified thermal conductivity, as calculated from Eq. (4) and Eq.(5).

$$\lambda_s = \frac{q}{4\pi k} \quad (4)$$

$$R_b = \frac{1}{4\pi\lambda_s}\left[\frac{\bar{T} - T_g}{k} - \ln\left(\frac{4a_s\tau}{r_b^2}\right) + \gamma\right] \quad (5)$$

Based on the literature, all the TRT tests considered a constant heat injection through the borehole heat exchangers, and the test lasted for four days of continuous operation. To the author's best knowledge, very few researchers conducted a TRT test with a variable heat injection. Oberdorfer [10] proposed oscillatory injection rates for a short period (OTRT) instead of a constant step; he expected that the new methods could:

- Controle and limit the investigation area by adjusting the oscillatory signal frequency.
- Extract additional information about the borehole and subsurface properties.

The heat injection rate is supposed to be a sinusoidal function with the amplitude P_1 and the angular frequency ω_0. And a constant heat rate P_0, which is larger than the oscillation amplitude, is added to the sinusoidal signal, as shown in Eq. (6)

$$P(t) = P_0 + P_1.\sin(\omega_0 t), \quad |P_0| > |P_1| \quad (6)$$

After carefully scanning the literature, we found that the TRT using oscillatory heating is not comprehensively investigated and is not yet matured. Therefore the current study will focus on advancing this method to predict the subsurface thermophysical properties precisely within a short test time and present the mature version of this new method.

2. Field test set-up

2.1. Borehole construction

The experimental investigation is conducted in five cities to experience various geological and thermal conditions in Hokkaido, Hiroshima, Yamanashi, and Tokyo prefectures in Japan, as shown in Fig (1a). At each site, conventional TRT, which applied a constant heating rate for 60 hours, and OTRT with an oscillatory heating rate for 24 hours are conducted. Each test is followed by a recovery period to affirm the full recovery of the subsurface's thermal condition before the next test. During the drilling, soil samples at various depths are collected and identified accordingly at each site. Fig. (1b) depicts the geological layers associated with depth. The site in Niseko city has volcanic ash at the shallow depth and shall and tuff at the deep layer. Furthermore, the Miyoshi site shows a different profile containing only two layers; conglomerate in the shallow depth, and rhyolite rock occupies the rest of the depth. At last, Kai city is located on almost three layers; gravel, tuff, and sandy clay. The average depth thermal conductivity is 1.4, 1.2, 3.1, 2.1, and 1.6 W/m.K in Sapporo, Niseko, Miyoshi, Kai, and Tokyo cities.

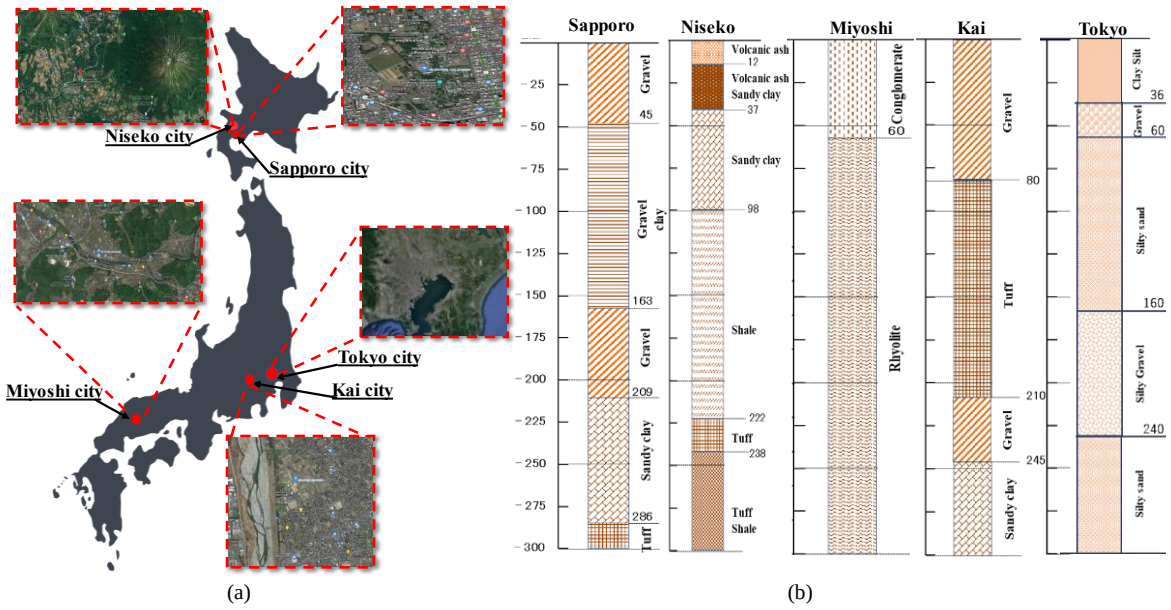


Fig. 1 Field study set-up, (a)Experimental sites locations, (b) Geological column in each site

Five boreholes with a depth of 300 m are drilled in 5 cities in Japan. Fluid based recirculatory method using mud rotary drilling with a rapid rotation speed is used in all sites except the Hiroshima site as shown in Fig(2a). A drilling head with a tricone bit with a diameter of 9" 7/8 inches is used to drill a borehole. While, In Hiroshima, downhole drilling with rotation and vibration is used because the geological column consists of only Rhyolit and Conglomerate rocks. Then A U-tube shown in Fig.(2b) is inserted in the borehole. The U-tube is made by the HakaGerodur company located in Switzerland. The U-tube is made of one unit of extruded Polyethylene PE100-RC (resistance to cracking) and polyamide PA12. Buckling pressure resistance is up to 43 bar, Probe lengths 200 to 410 m in rolls, as shown in Fig. (2b). The cross-section and specifications of the tube is shown in Fig.(2c) and listed in Table (1)



(a) (b) (c)

Fig. (2) Constructing the borehole heat exchanger steps (a) Drilling head, (b) U-tube heat exchanger, and (c) U-tube cross-section

Table (1) U-tube heat exchanger specifications

Parameter	Value	Units
Density	0.95-0.97	(g/cm^3)
Pipe roughness	0.03	(mm)
Thermal expansion	0.18	(mm/m.K)
Thermal conductivity	0.4	(W/m.K)
Specific thermal capacity	1.9	(J/g.K)

A pair of optical fiber sensors are inserted into the U-tube's legs to measure the vertical temperature. Then the OFS is connected to the DTS instrument (made by Ap sensing in German). The temperatures are recorded every 0.5 m every 1 minute, and these results are used to calculate the heat transfer rate's vertical profile and the vertical profile of the effective thermal conductivity. The specification of the DTS

2.2. Oscillatory Thermal Response Test Machine

A new TRT machine is customized and is equipped with a variable speed, three-phase, 200 V centrifugal pump with a power of 1.5 kW and a flow rate of 60 L/m (item No. 9) . Furthermore; the flow rate is controlled by changing the frequency via an inverter (item No. 11). The machine is also equipped with two single-phase electrical heaters connected in series with a total capacity of 20 kW (items No. 6 and 7) . Two three-phase thyristors power regulators control the electric energy supplied to these two heaters (items No. 12, 13). Moreover, a programmable adjusts the heating injection rate using the user interface and software (item No.

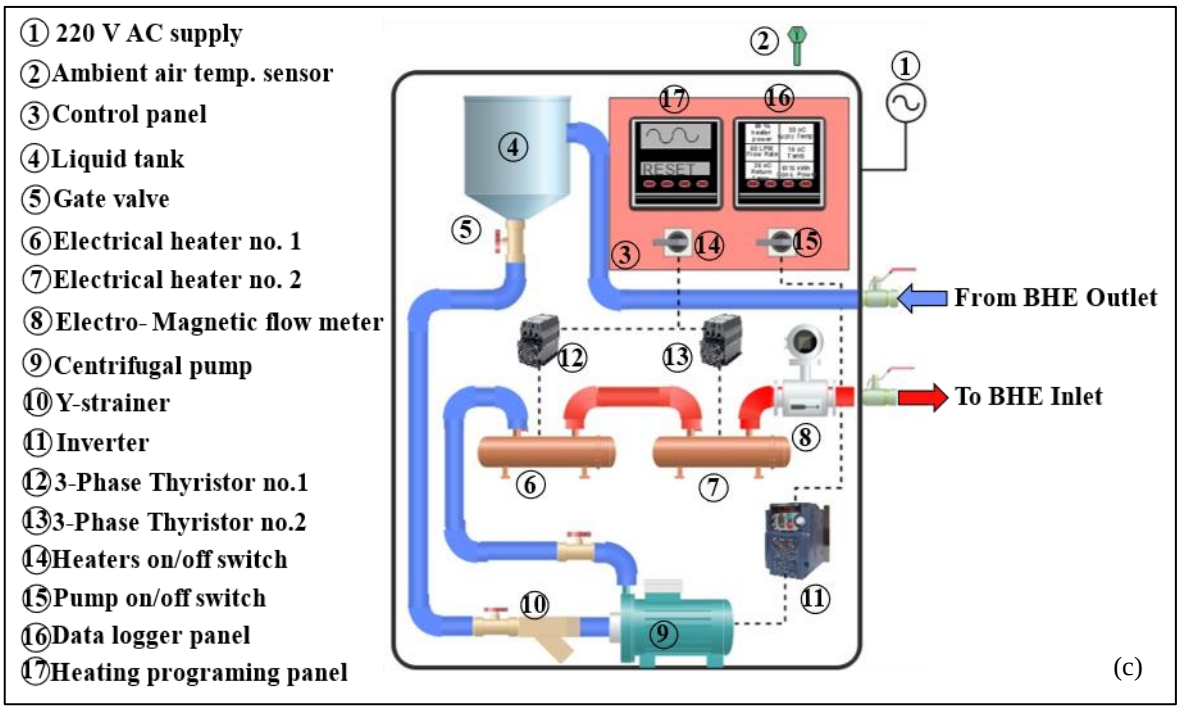


Fig. (3) left side shows The circuit diagram of the new TRT machine

17). An Electromagnetic flow meter is used to measure the fluid flow rate. A liquid tank (60 Litre) is used for liquid backup (item No. 4). These pieces of equipment are fixed inside a mobile carriage with dimensions of 930*1250*1580. Figure 3 illustrates the control panel and a mini data logger (item No. 16). This data logger records the fluid supply and returns temperatures, the ambient air temperature (item No. 2), fluid flow rate, heating power, and accumulated energy consumption. The schematic diagram presented in Fig. (3) explains the circuit diagram of the TRT machine.

2.3. Operation of the TRT test

After finalizing the set-up of the TRT machine, the operation procedure of the conventional TRT is summarized in the following steps:

- The pump is started to circulate the liquid (Ethylene glycol 40% in Sapporo and Niseko, and water in other locations) through the U-tube for 30 minutes to evacuate the air inside the U-tube.
- The flow rate measurement is observed to check the fluctuation until all the air inside the loop is expelled into the atmosphere. Once the flow rate becomes stable, this means the loop is free of any air bubbles and is ready to start heating and collecting the data.
- A constant heat rate of 20 kW(66 W/m) is injected into the BHE for 60 hours during the NTRT. While, The oscillatory heating wave is programmed by the software and transferred to the CHINO controller by means of a USB connection in the following form:
  $Q = q_{avg} + A\,.\sin\left(\frac{2\pi t}{T}\right)$, as shown in Fig. (6b). The q_{avg} is 14 kW, the Amplitude A is ±4 kW. and T is 1 hour.
- Supply and return fluid temperatures, flow rates, power injection, and fluid temperature distribution are instantly measured and recorded every 30 seconds.
- After the NTRT is continually operated for 60 hours and O_{sc}TRT is continuied for 24 hours, the heating and pumping are stopped,

while the soil temperature profile measurements are continued during the recovery period for two weeks

2.4. Analysis method

As explained earlier, the OscTRT is a superposition of constant heating and oscillatory heating with a certain amplitude and frequency. Therefore the new analysis method is proposed to decompose these two cycles and calculate the effective thermal conductivity from the constant heating part while calculating the amplitude ratio and phase shift from the oscillatory part.
The new analysis method includes two main steps; data processing and data analysis. The data processing steps are shown in Fig.(4). The steps are:

1- Inlet and outlet temperature measurements are filtered by using a Savitzky-Golay filter. And it is smoothed using a moving average of the elements using a fixed window length of 0.03 that is determined heuristically. The A Savitzky–Golay filter is a digital filter that can be applied to a set of digital data points to smooth the data.
2- Then the minimum and maximum peaks location and values of the filtered inlet and outlet temperatures data are determined and saved.
3- The average values of the maximum and minimum peaks are calculated.
4- The average values are subtracted from the filtered data to extract the oscillatory part.
5- The slop of the average values is calculated, then used to calculate the effective thermal (λ_{eff}) conductivity using Eq.(4)

The steps of data processing are summarized in Fig.(3)

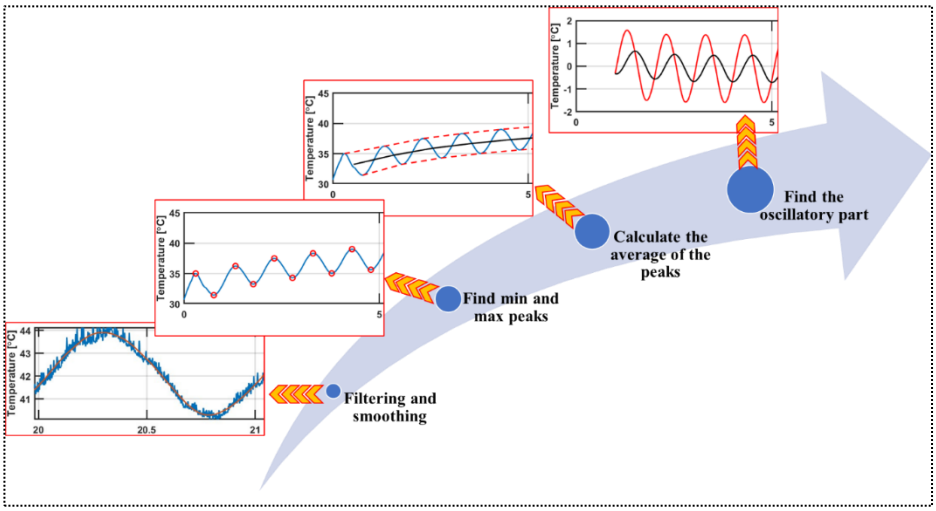


Fig.(4) workflow of data processing step

After the data is processed, the next step is data analysis to calculate the amplitude and phase shift angle of both inlet and outlet temperatures. The following procedure is proposed an depicted in Fig.(5):

1- Fitting the oscillatory part of the inlet and outlet temperature to the oscillatory function indicated in Eq.(7,8)

$$T_{in}(t) = A_{\text{in},0}.\sin(\omega_0 t + \varphi_{in}) \quad (7)$$

$$T_{out}(t) = A_{\text{out},0}.\sin(\omega_0 t + \varphi_{out}) \quad (8)$$

Where $A_{\text{in},0}$, and $A_{\text{out},0}$ are the amplitude of inlet and outlet temperatures (ºC), ω_0 is the frequency (Hz), and φ_{in} , $and\ \varphi_{out}$ are the phase shift (sec).

2- Calculate the amplitude ratio between outlet and inlet temperature $(A_{out,0}/A_{in,0})$

3- Calculate the phase shift lag between the outlet and inlet temperatures $(\varphi_{out} - \varphi_{in})$

4- Find the relationship between the amplitude ratio $(A_{out,0}/A_{in,0})$ and the effective thermal conductivity (λ_{eff}). These steps are summarized in Fig.(8)

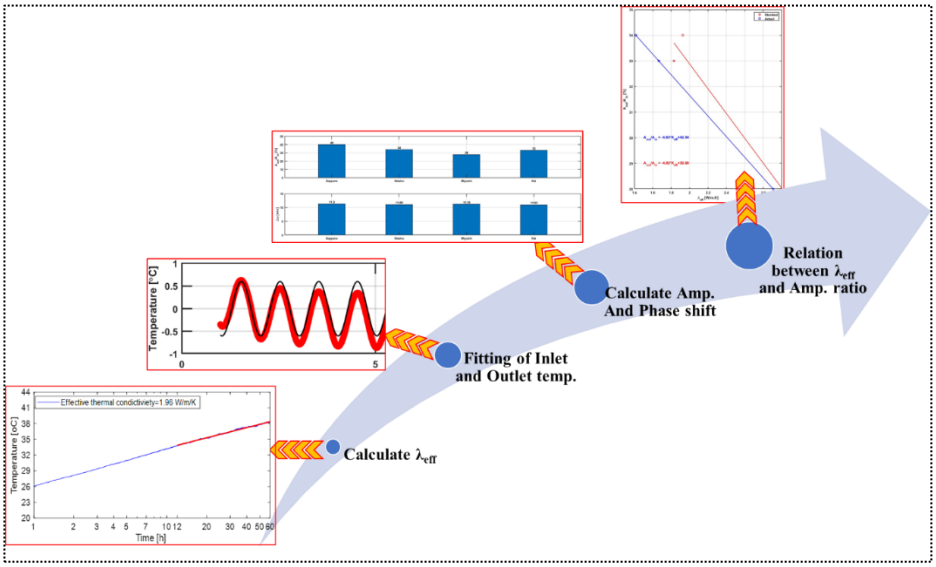


Fig. (5)Data analysis steps

3. Results and discussions

The following subsections indicate the results of the initial soil temperature profiles, the results of both the conventional TRT and OTRT, the fluid temperature profiles, the heat rate distribution profile, the effective thermal conductivity distribution profile, and the relationship between the amplitude ratio and the effective thermal conductivities.

3.1. Undisturbed soil temperature

The OFS measures the undisturbed soil temperature distribution profile before starting the TRT. It shows the natural soil temperature profile without any external disturbance. A comparison between these profiles is depicted in Fig. (6). Moreover, the soil surface temperature is affected by the energy balance on the soil surface at the test time. Generally, each profile also lists the temperature gradient for every 100 m. The Niseko site shows the highest temperature gradient of 10.9 ºC /100 m, where the temperature reaches the value of 42 ºC at the bottom of the borehole. This result shows a significant potential in this site which can be used for a direct heating system or hot spring applications. Meanwhile, the gradient is the lowest at the Tokyo site, with a value of 1.9 ºC/100 m, where the temperature at the bottom of the borehole is 21 ºC. Furthermore, the slop at Sapporo and Kai cities are similar, with values of 3.9 ºC and 3.4 ºC, respectively.

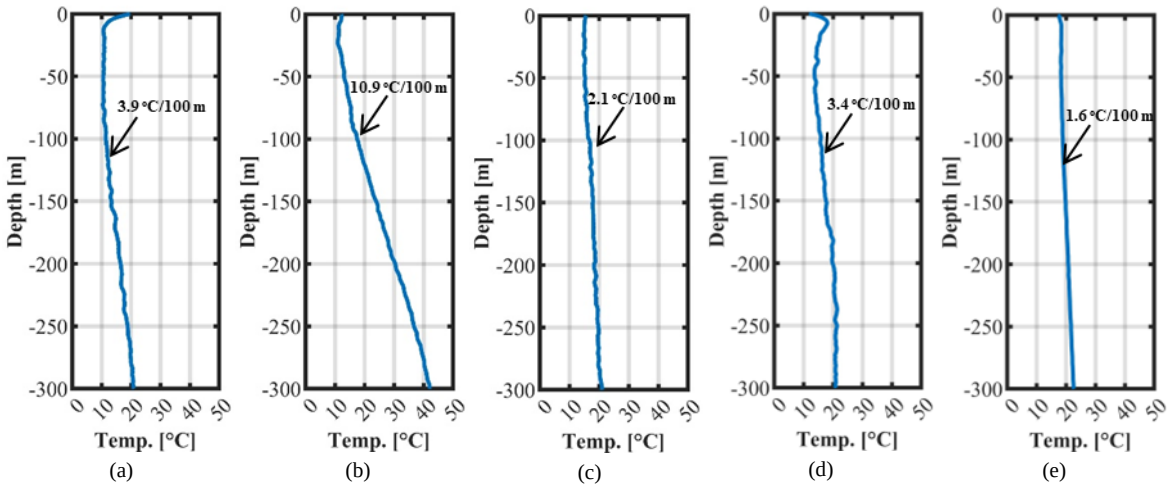


Fig.(6) Undisturbed soil temperature profile at a) Sapporo, b) Niseko, c) Miyoshi, d) Kai, and e) Tokyo cities

3.2. Conventional TRT

The inlet and outlet temperatures are recorded using PT100 sensors every two seconds. The flow rate and injected heat are recorded by the electromagnetic and power meters, respectively. The data are manipulated every 1 minute for 60 hours. The average fluid temperature is calculated, and the relation between the average fluid temperature and the logarithmic value of the time is depicted in Fig. (7). The figures indicate that the temperature increased with time, reaching a maximum value of 48 ºC in Niseko city as shown in Fig. (7b). The heat transferred from the deep surrounding soil affects the fluid temperatures. The linear relationship through the period from 12~ 60 hours is developed. The slope of the linear relationship is used later to calculate the effective thermal conductivity in each city. The slope is varied from one city to another according to the geological and hydrological conditions in each site, the maximum slope in Niseko city reaches a value of 4.34 ºC/hr and a minimum value of 1.79 ºC/hr in Miyoshi city.

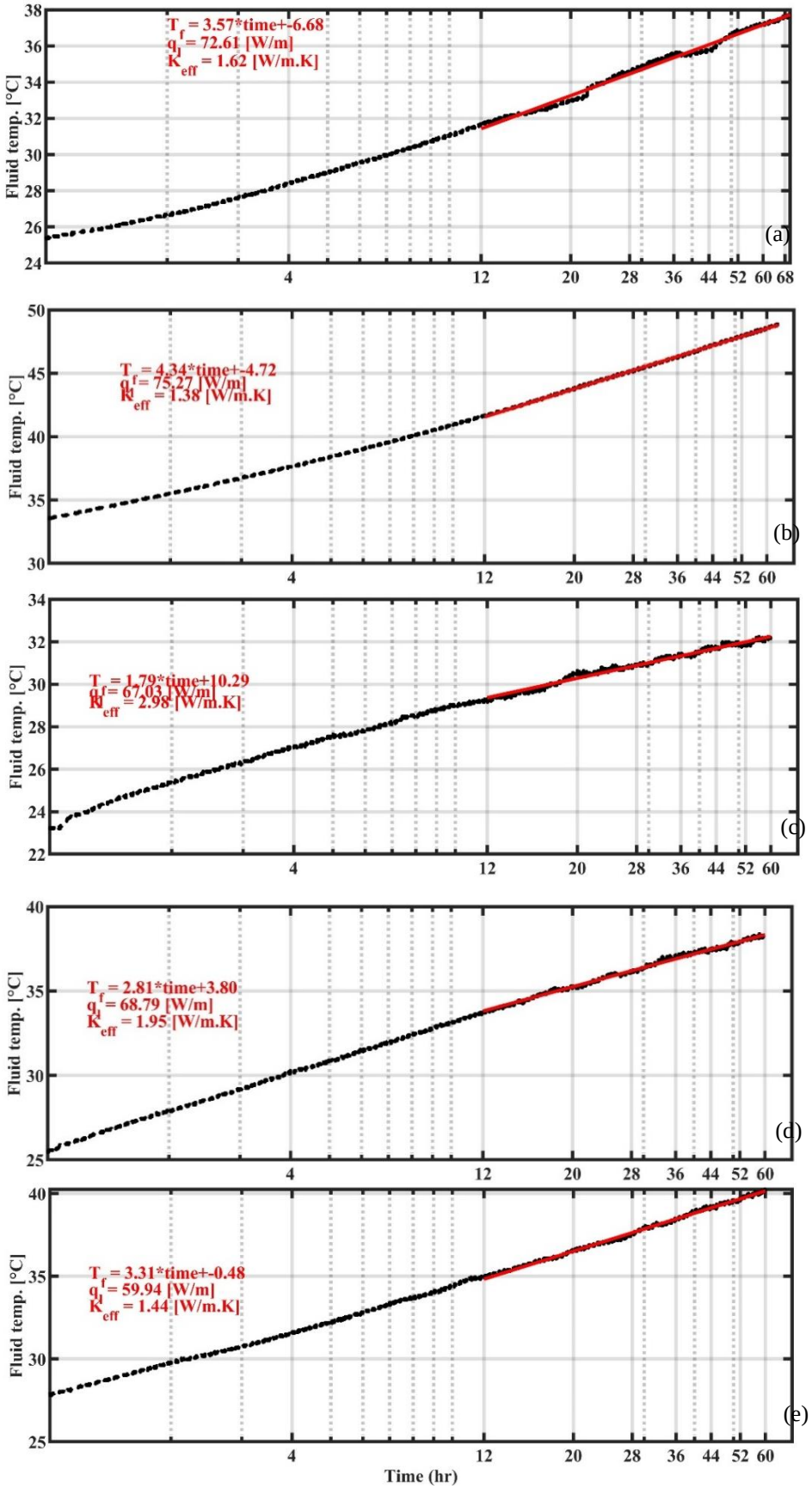


Fig. (7) The linear relationship between log time and Tf, (a) Sapporo, (b) Niseko, (b) Miyoshi, (c) Kai, (e) Tokyo cities

The calculated λ_{eff} are 1.62 W/m.K, 1.38 W/m.K, 2.98 W/m.K, 1.95 W/m.K, and 1.44 W/m.K in Sapporo, Niseko, Miyoshi, Kai, and Tokyo sites, respectively. Compared with the geological column, the error value is maximum in Kai city with a value of 50%, while the minimum value is achieved in Tokyo city. Therefore, these results show a possibility of groundwater flow impact on the measurement results in Kai city and need more investigation to assure this hypothesis.

Table (1) U-tube heat exchanger specifications

λeff	Sapporo	Niseko	Miyoshi	Kai	Tokyo
Geological column	1.4	1.2	3.1	1.3	1.46
NTRT	1.62	1.38	2.98	1.95	1.44
Error %	15.7	15	3.9	50	1.4

Two pairs of optical fiber sensors were inserted in each leg of the U-tube to measure the fluid temperature distribution every 0.5 m and record the measurements every minute, as depicted in Fig. (8). The results are reduced by averaging the temperature every 1 hour and 5 meters. Figure 8 depicts the fluid temperature profile every 10 hours. In Niseko city, the temperature at the bottom of the borehole has recorded the highest value of 47 ºC. Also, the slope of the profile is almost straight through the depth of 180m to 300 m, because of the impact of the heat dissipated from the deep geothermal layer in this site. In comparison, Miyoshi shows the lowest temperature at the bottom edge of the borehole, with a temperature of 32 ºC.

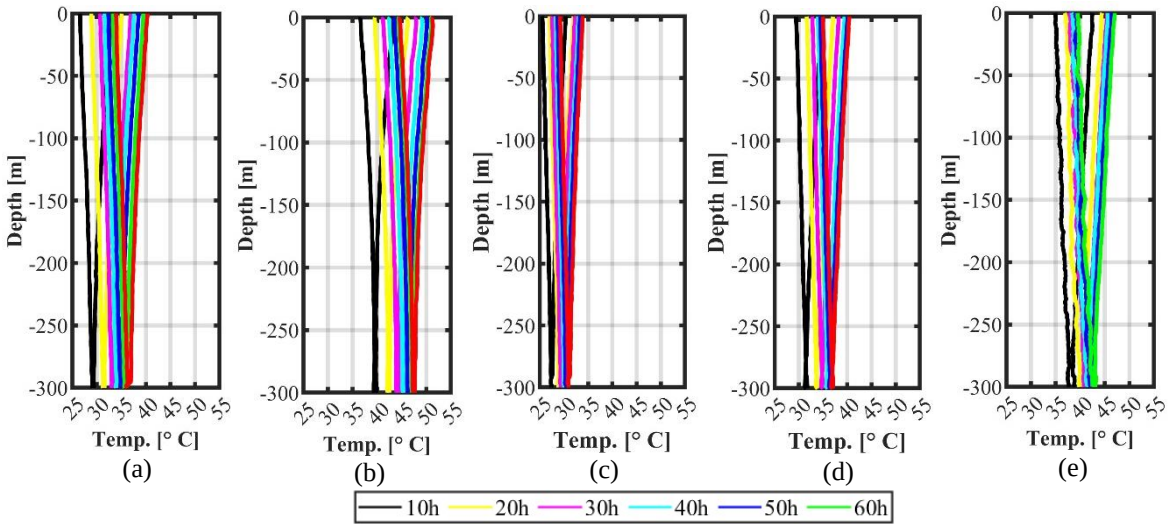
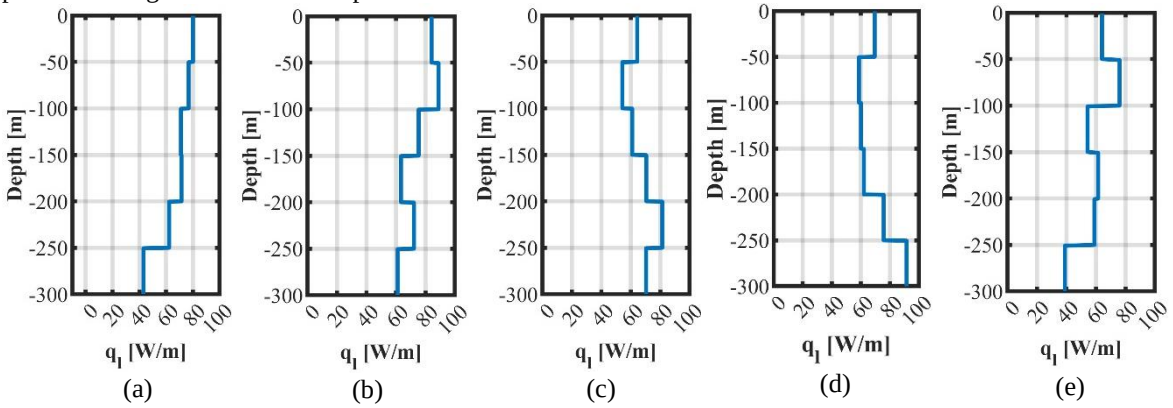


Fig.(8) Fluid temperature profile at a) Sapporo, b) Niseko, c) Miyoshi, d) Kai, and e) Tokyo cities at different time

Using the information of the flow rate and the temperature profile distribution in both DL and UL tubes, the vertical profile of the total heat transfer rate and effective thermal conductivity can be calculated, as shown in Fig. (9). Also, these results are represent the average values of 12 hr~ 60 hr. As a simplification, the depth is divided into 6 layers, but for more insight investigation, these results have to consider the precise calculation of the number of layers. Also, it is clear to define the layer with a potential of groundwater impact and further prediction of groundwater flow speed.



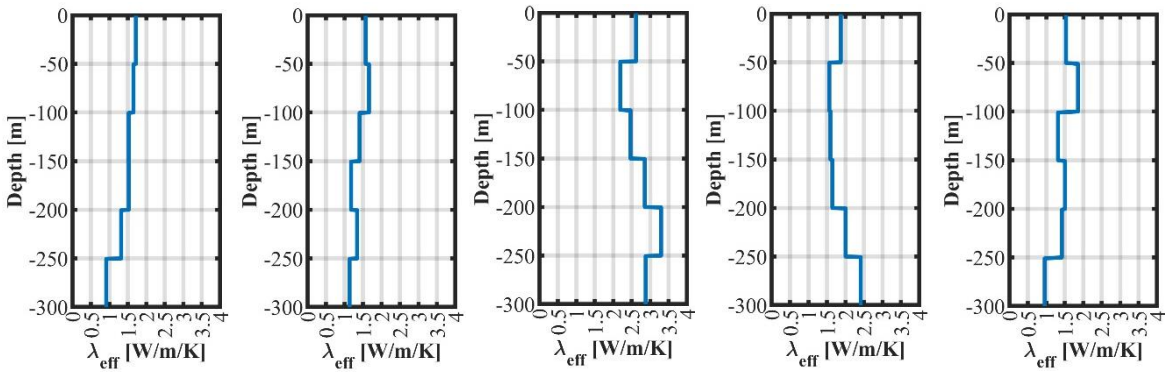


Fig.(7) Heat transfer rate profiles at a) Sapporo, b) Niseko, c) Miyoshi, d) Kai, and e) Tokyo cities, and thermal conductivity profile at f) Sapporo, g) Niseko, h) Miyoshi, i) Kai, and j) Tokyo cities

3.3. Oscillatory TRT

The inlet and outlet temperatures are recorded simultaneously with the flow rate measurement every two seconds. The measurements are filtered and smoothed, as shown in Fig.(A1a) in Appendix A. Then, the maximum and minimum peak location and values are determined, as shown in Fig.(A1b). Moreover, the average values of each inlet and outlet temperature, as well as the heating rate, are calculated as depicted in Fig. (A1c). The oscillating part of the signal is isolated by subtracting the average values from the original smoothed data, as indicated by Fig. (A1d). Finally, the slope of the linear relationship between the average value and logarithmic scale of the time is calculated and used to calculate then the effective thermal conductivity, as shown in Fig. (A1e). Figure A1 depicts the steps of the data processing steps for the test constructed in Kai city, while the same steps are applied for all tests in other sites.

These steps are followed by the data analysis steps, as explained in the previous sections. Figure (B1) in Appendix B depicts these steps for the data recorded in Kai city. The oscillatory part, which is extracted and shown in Fig.(A1d), is fitted with the values calculated from Eq.(7). The *fminsearch* function in Matlab is used to minimize the root mean square errors between the fitted and experimental data by changing the multi variables (Amplitude A, phase shift φ, and cycle time ω_0 in Eq.(7). *fminsearch* uses the Nelder-Mead simplex algorithm; The algorithm first creates a simplex around the initial guess x0 by adding 5% of each component of x0(i) to x0 . Figures B1a, and b, depict the fitting functions for inlet and outlet temperatures.

Figure (8a, and b) depict λ_{eff} calculated from the NTRT and OscTRT in periods of 12~15 hr, 12~30 hr, and 12~60 hr in NTRT, respectively, while the periods are 12~15 hr, 12~20 hr, and 12~24 hr in OscTRT. The NTRT results show instability and differences between the three periods, with a maximum value of 0.54 W/m.K in Miyoshi. While the results of the OscTRT show more stability and robustness with a maximum difference of 0.04 W/m.K in Sapporo city. The NTRT is vulnerable and is affected strongly by the daily variation of the heat energy on the soil surface, while the OscTRT response shows more robustness. As the OscTRT follows the periodic heating pattern with maximum and minimum values of 20 kW and 8 kW with an average value of 14 kW, it absorbs the daily impact on the surface. Also, the same robustness can be noted in the amplitude ratio values in different periods of the OscTRT as shown in Fig. (8c).
These results concluded that the period of 14 hours of an OscTRT is enough to calculate the λ_{eff} with an accuracy of 98 % in three sites (Sapporo, Niseko, and Miyoshi), 87% in one site (Kai city) and 74% in one site (Tokyo city). Hence the OscTRT has a promising potential to save more than 77 % of the time needed for NTRT.

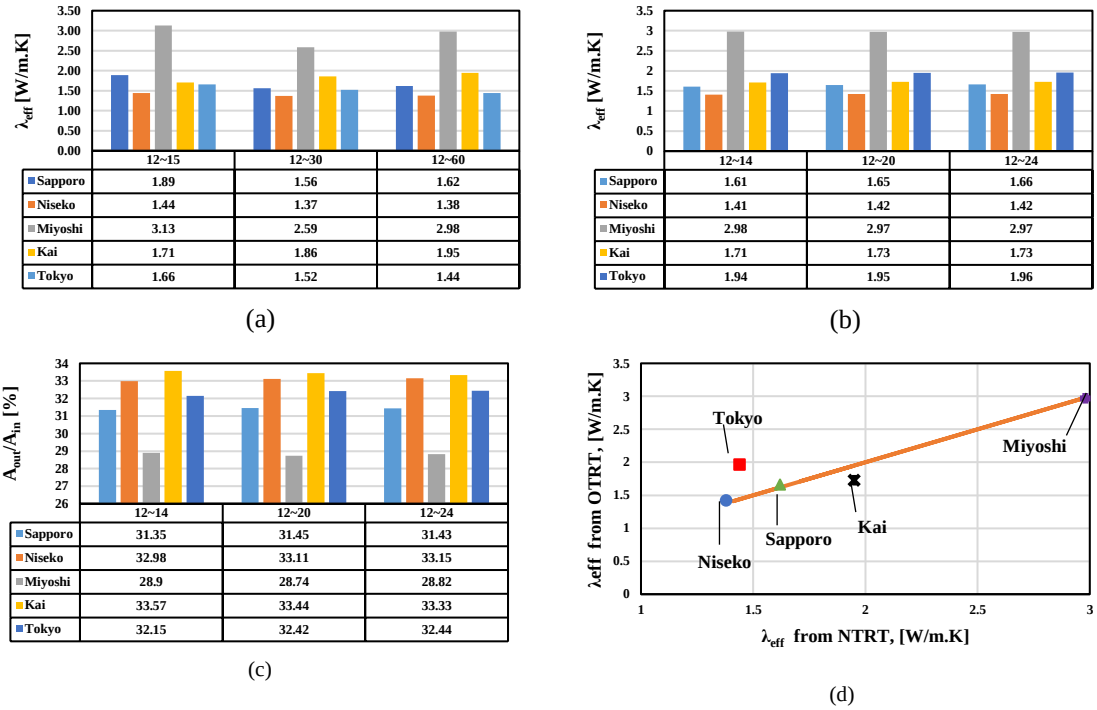


Fig. (8) Summary of the results, a) λeff from NRTR vs OTRT, b) Amp. Ratio vs λeff

3.4. Comparison between the NTRT and OscTRT

The comparison between the effective conductivity, which is calculated from the OscTRT and the NTRT, is indicated in Fig.(8d). The root means square error (RMSE) between the two results is 0.25 W/m.K with a square error maximum value of 0.27 w/m.K in Tokyo city. Be noted that the OscTRT is conducted for 24 hours compared to NTRT with more than 60 hours. The error values are -0.04,-0.04,+0.01,+0.22,and -0.52 W/m.K for Sapporo, Niseko, Kai, Miyoshi, and Tokyo cities. The error value includes the measurements error and operating errors. In addition, the error is maximum in Kai and Tokyo city, where we expected that the groundwater affects the underground's thermal response.

Therefore, it is noteworthy that the relationship between the amplitude ratio of inlet and outlet temperatures and the effective conductivities which are calculated from the NTRT could be a rational alternative to predict the conductivity with the help of numerical simulations and artificial intelligence applications, as shown in Fig. (9). Although The three sites have distinct geological, hydrological, and thermal conditions, a linear relationship can be derived from Fig.(9).

On the other hand, we believe this method needs a comprehensive investigation to explore and clarify the impact of these parameters on the response and amplitude ratio. These goals are the main objectives of future studies using inclusive computational fluid dynamics simulations.

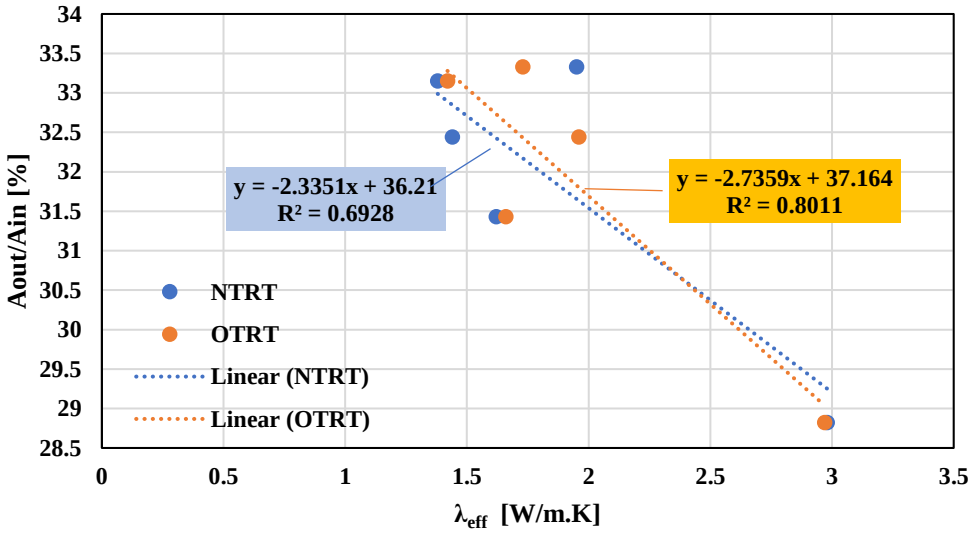


Fig. (9) Relationship between Amp. ratio and calculated λeff.

4. Conclusions

A new thermal response test method is proposed to shorten test time and save test and labor costs, using an oscillating heating signal in the form of a sine wave with a specific amplitude and frequency. In this study there are many conclusions can be derived as follows:

1- A new OTRT is proposed to decrease the TRT time from 60 hours to 14 hours and save test and labor costs by 77 %.
2- The effective conductivity, which the new OTRT calculates, has an RMSE of 0.25 W/m.K compared with the NTRT.
3- The new TRT machine has been built and tested successfully.
4- A new analysis method is developed.
5- A new key parameter (Amp. Ratio between Inlet and Outlet temperatures) is proposed for future investigation
6- A linear relationship is defined between the effective conductivity and amplitude ratio, which shows a good potential to generalize this method in future work.
7- Various geological, hydrological, and thermal conditions are tested.

Although the OscTRt shows promising potential using the experimental measurements in different hydrological, geological, and thermal conditions, this method needs a comprehensive investigation to explore and clarify the impact of these parameters on the response and amplitude ratio. These goals are the main objectives of future studies using inclusive computational fluid dynamics simulations and artificial intelligence.

References

[1] Reuss M. The use of borehole thermal energy storage (BTES) systems. Adv. Therm. Energy Storage Syst. Methods Appl., vol. i, Woodhead Publishing Limited; 2014, p. 117–47. doi:10.1533/9781782420965.1.117.

[2] Spitler JD, Bernier M. Vertical borehole ground heat exchanger design methods. J.D. Spitler and M. Bernier; 2016. doi:10.1016/B978-0-08-100311-4.00002-9.

[3] Sanner B, Hellström G, Spitler J, Gehlin S. Thermal Response Test – Current Status and World-Wide Application. Proc World Geotherm Congr 2005:24–9.

[4] Marcotte D, Pasquier P. On the estimation of thermal resistance in borehole thermal conductivity test. Renew Energy 2008;33:2407–15. doi:10.1016/j.renene.2008.01.021.

[5] Gehlin S. Borehole thermal energy storage. Adv. Ground-Source Heat Pump Syst., Woodhead Publishing Limited; 2016, p. 295–327. doi:10.1016/B978-0-08-100311-4.00011-X.

[6] Zhang X, Han Z, Ji Q, Zhang H, Li X. Thermal response tests for the identification of soil thermal parameters: A review.

Renew Energy 2021;173:1123–35. doi:10.1016/j.renene.2020.12.028.

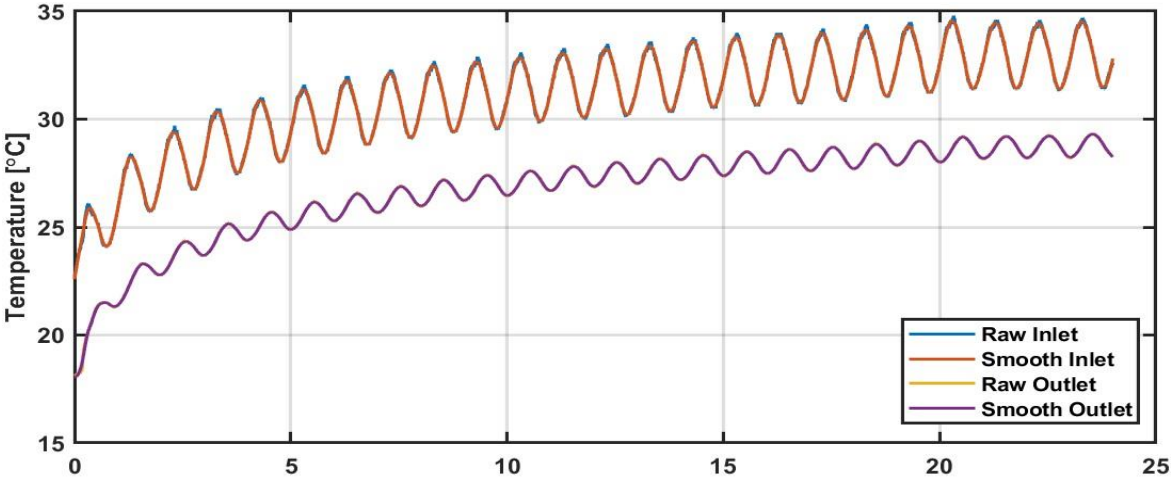
[7] Zeng HY, Diao NR, Fang ZH. A finite line-source model for boreholes in geothermal heat exchangers. Heat Transf - Asian Res 2002;31:558–67. doi:10.1002/htj.10057.

[8] Diao N, Li Q, Fang Z. Heat transfer in ground heat exchangers with groundwater advection. Int J Therm Sci 2004;43:1203–11. doi:10.1016/j.ijthermalsci.2004.04.009.

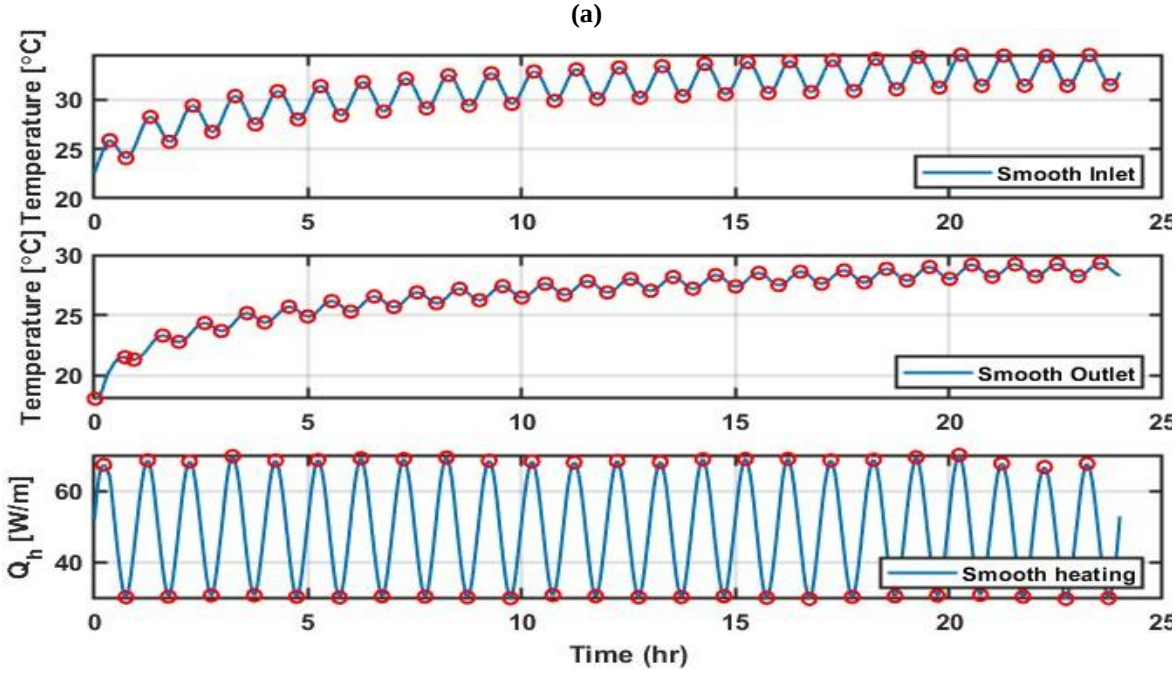
[9] Signorelli S, Bassetti S, Pahud D, Kohl T. Numerical evaluation of thermal response tests. Geothermics 2007;36:141–66. doi:10.1016/j.geothermics.2006.10.006.

[10] Oberdorfer P. Oscillatory Thermal Response Test (OTRT) - an Advanced Method for shallow geothermal applications, developed with comsol, der Georg-August-University at Gottingen, 2014..

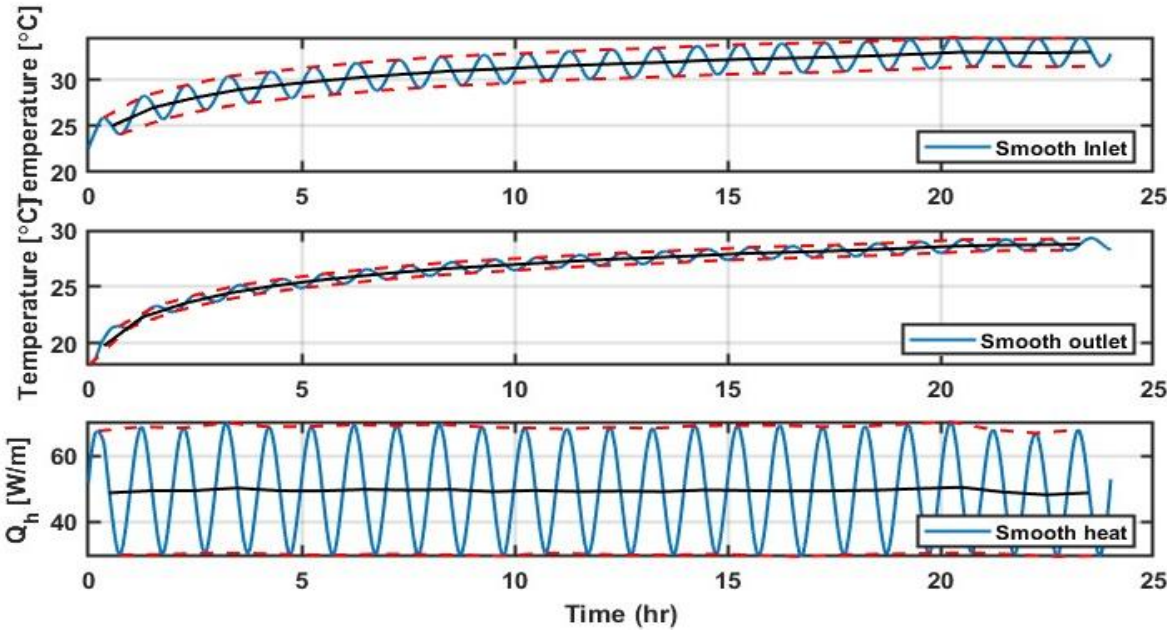
Appendix A



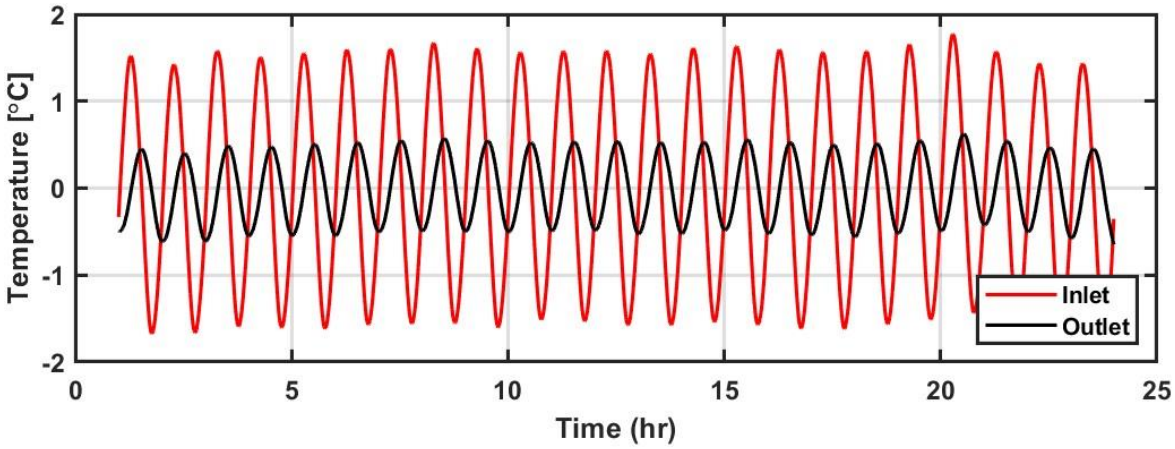
(a)



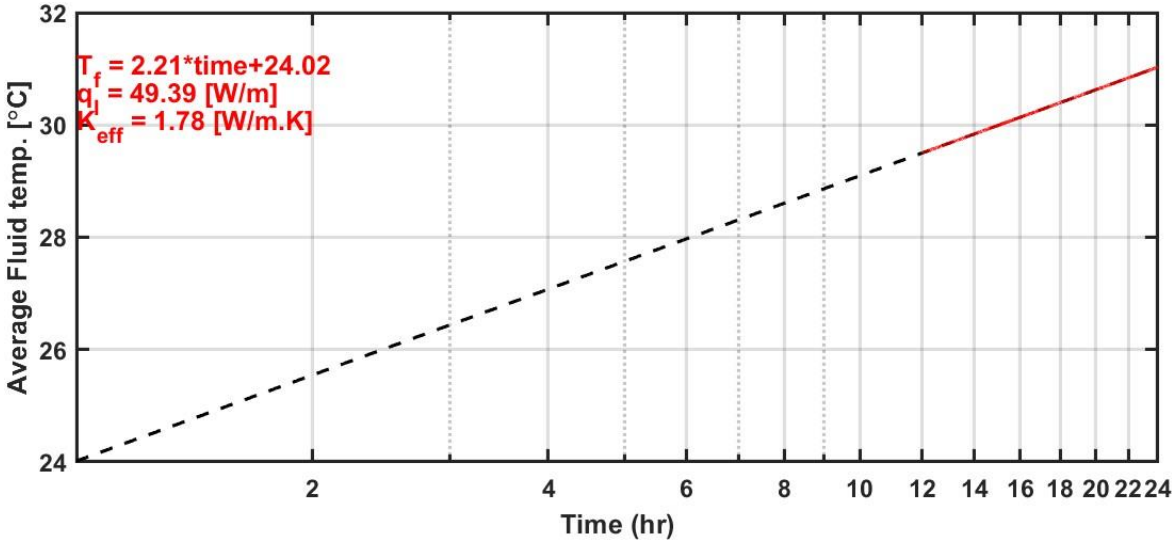
(b)



(c)



(d)



(e)

Fig. (A1) Data processing steps using in OscTRT in Kai city

Appendix B

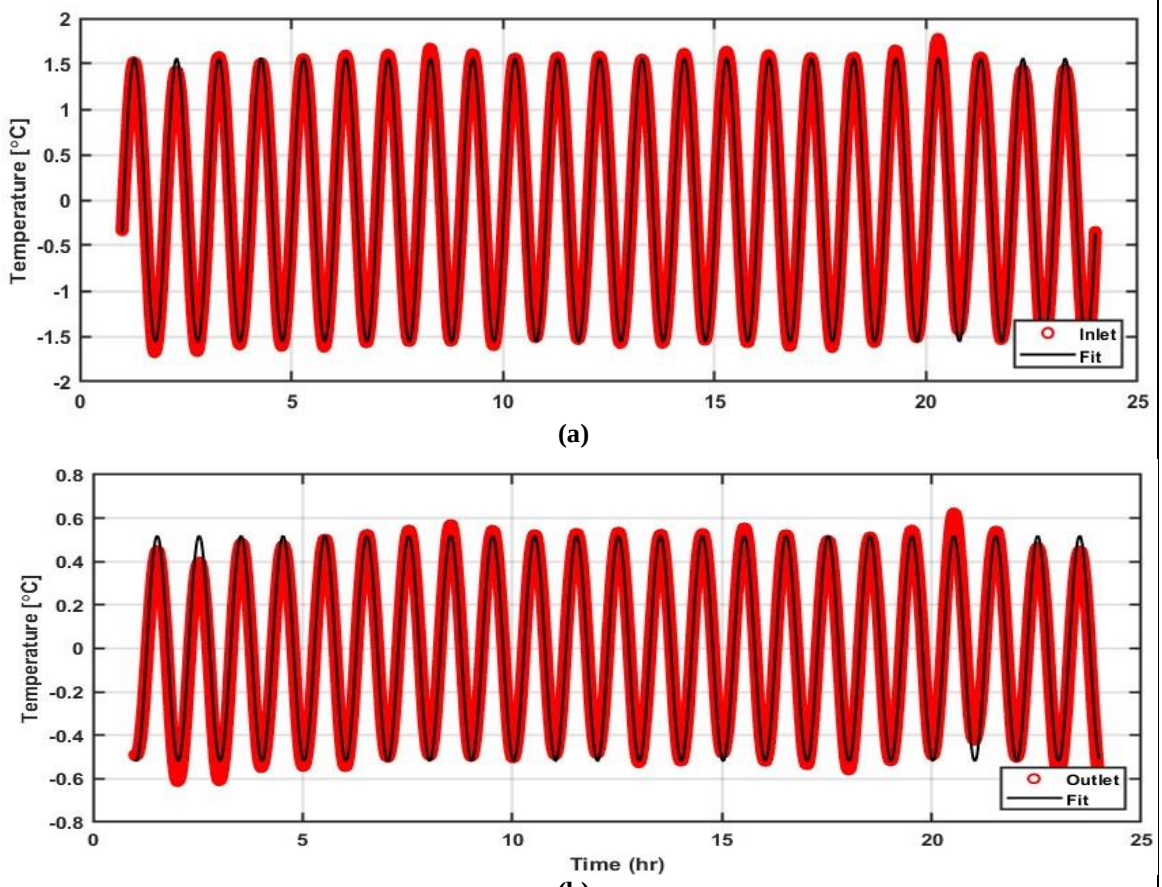


Fig. (15) Fitting of the inlet and outlet smoothed data of Kai city's test

14th IEA Heat Pump Conference
15-18 May 2023, Chicago, Illinois

Experimental study of steam-driven ejector heat pump

Jeremy Spitzenberger [a], Ramy H. Mohammed [a], Pengtao Wang [a, b],
Hongbin Ma [a,*], Ahmad Abu-Heiba [c], Stephen Kowalski [b], Kashif Nawaz [b]

[a] Multiphysics Energy Research Center (MERC), College of Engineering, University of Missouri-Columbia, Columbia, MO 65211, USA.
[b] Multifunctional Equipment Integration Group, Building Technologies, Research and Integration Center (BTRIC), Oak Ridge National Laboratory, (ORNL), Oak Ridge, TN 37830.

Abstract

Ejector-driven systems have been shown to be promising for heating applications. Most of the research works have been devoted to cooling purposes, while little attention has been focused on heating applications. An experimental steam ejector heat pump system (EHP) was designed and constructed to assess its applicability to water heating applications. The effect of the primary nozzle exit position (NXP) on the performance of the steam ejector system was investigated for a primary nozzle throat diameters of 1.5 mm and 2.0 mm. The ejector system was run for high-temperature evaporator (HTE) temperatures of 120, 130, and 140 ˚C and low-temperature evaporator (LTE) temperatures of 10, 15 and 20 ˚C. The target of this investigation was to attain the highest condensing temperature to be able to use the proposed system for water heating purposes. The ejector heat pump coefficient of performance (EHP COP) was used to determine the system efficiency. Larger LTE temperatures were found to result in higher EHP COPs and condensing temperatures. A maximum EHP COP of 2.02 was attained for a HTE and LTE temperatures 120 ˚C and 20 ˚C, respectively, however only resulted in a condensing temperature of 22.88 ˚C. Higher HTE temperatures were found to result in higher condensing temperatures, but at the cost of EHP COP.

© HPC2023.
Selection and/or peer-review under the responsibility of the organizers of the 14th IEA Heat Pump Conference 2023.

Keywords: Type your keywords here, separated by semicolons ;

1. Introduction

In the United States an estimated 18% of residential energy consumption is use ford domestic hot water (DHW) production [1], however a significant portion of the energy required to power these systems is lost in the delivery process, coming in the form of waste heat. Studies have found the more electrically driven a DHW heater is, the higher the primary energy loss will be in the generation and transmission process, and by increasing the share of DHW heaters powered by natural gas, the primary energy efficiency of the system can increase by as much as 65% [2]. These findings indicate an opportunity to pursue the idea of utilizing thermally driven heat pumps for DHW production. Not only are they able to eliminate the primary energy losses in the transmission process of electrical energy, but also, they are able to integrate the waste heat by recycling it back into the system, therefore, they can deliver more useful energy than they consume. A 2015 study conducted by the Lawrence Livermore National Laboratory estimated waste heat accounted for 60% of the total US energy consumption, with 75% of that waste heat being at a temperature of 230 °C or less [3]. If this excess thermal energy can be recycled back into a heat pump system, the electricity demand of a heat pump can be decreased by as much as 80% [4].

Presently, the thermally driven heat pump sector is dominated by sorption technologies [5]. However, research in this sector is ongoing and still at a relatively low maturity level. More research is needed to develop a deeper and more fundamental understanding of the working mechanisms and system performances. One field that has shown promise and great market potential are thermally driven ejector heat pump (EHP) systems. Research on thermally driven ejector systems have been conducted in the past for refrigeration purposes, these are known as ejector refrigeration systems (ERSs). Ejector driven systems are seen as an attractive option as

they require little maintenance due to their lack of moving parts and do not require high ozone potential refrigerant to operate, thus helping to reduce our carbon footprint. Despite this, research on ERS systems has found that these systems yield lower COPs compared to the vapor compression refrigeration systems which continue to dominate the market [6]. Recently there has been a resurgence in ERS research due to a growing environmental concern, yet EHP systems remain relatively untouched. This lack of interest could be attributed to the historical difficulty in understanding the theoretical efficiency of the ejector cycle [7].

A typical ejector system consists of a HTE, LTE, ejector, pump, throttling valve, and a condenser, as seen in Figure 1a. The primary fluid (PF) is superheated in the HTE, which is then accelerated through a converging-diverging nozzle, reaching supersonic speeds at the nozzle exit position (NXP). This creates a low-pressure which leads to a suction effect of the secondary fluid (SF) within the LTE, thus, entraining water vapor into the suction chamber, which leads to a cooling effect. The two steams mix in the mixing chamber and then experience a normal shock at some point along the constant area section. This leads to a sharp increase in pressure and decrease in the velocity of the fluid flow. The fluid mixture then continues to decelerate as it travels along the diffuser and is eventually ejected into the condenser where the fluids then enter a reservoir and are returned to the LTE and HTE through a throttling valve and pump, respectively. The pressure and velocity profiles are shown in Figure 1b.

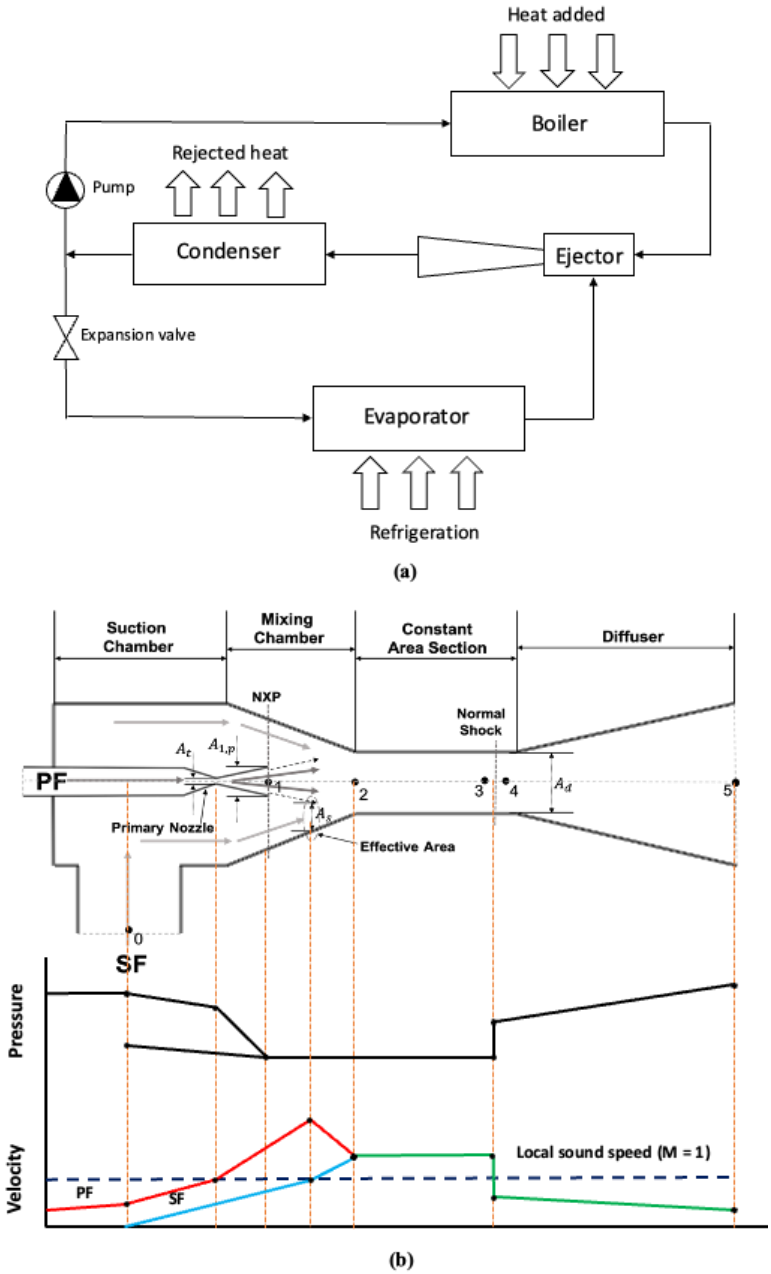


Figure 1: (a) Schematic of typical ejector cycle and (b) pressure and velocity profiles of fluid flow along ejector.

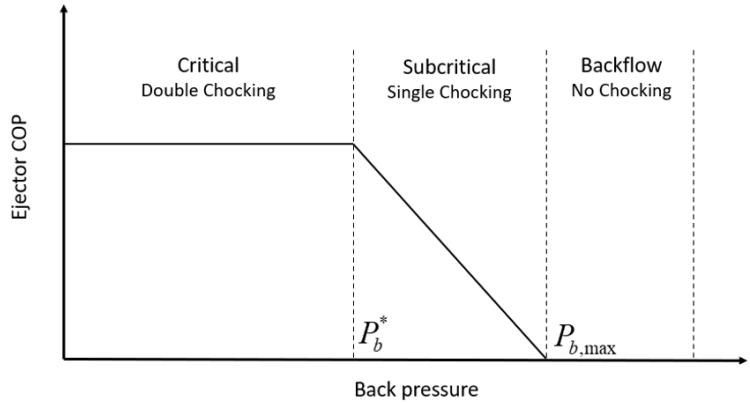


Figure 2: Effect of back pressure on the COP of an ejector

Most ejector experimental studies found in literature focus on operating the ejector system under critical conditions, meaning both the primary and secondary fluids being chocked at their inlets, due to the fact it will result in the highest COPs, as shown in Figure 2. Despite this, the theoretical results from Spitzenberger et al [8], suggest that for an EHP system a high COP_{EJT} does not necessarily correlate to a high COP for the EHP, rather the ejector should be operated within the subcritical zone, in order to maximize the P_b, to achieve the highest condensing temperature possible. The goal of this investigation is focused on the ejector cycle to try and achieve the maximum condensing temperature possible, in order to develop the single-stage gas-fired ejector heat pump water heater first proposed in Spitzenberger et al [8] , which aims to produce a domestic hot water (DHW) supply 14.5 ℃ to a target delivery temperature of 51.7 ℃.

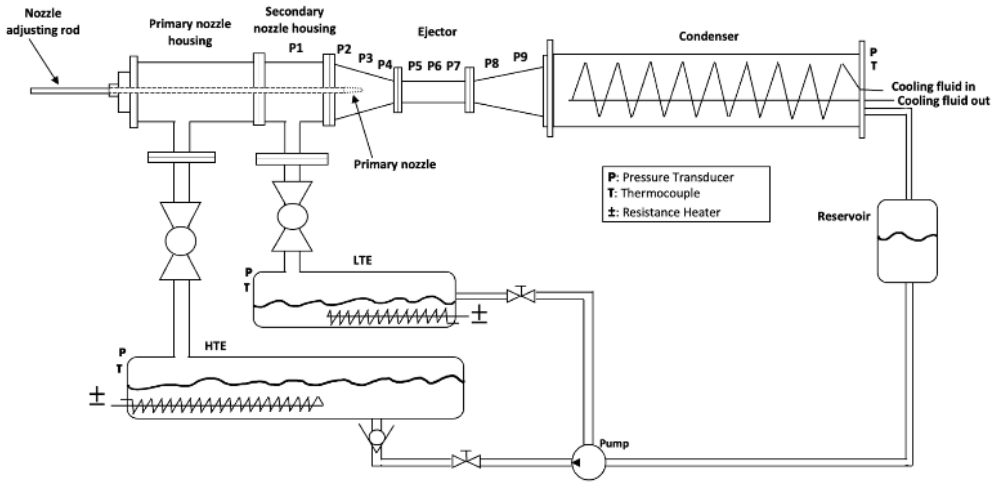
2. Experimental

In this section, the experimental setup in addition to the function of each component is discussed in detail. Error propagation in the COP of the EHP is determined based on the uncertainty of each variable.

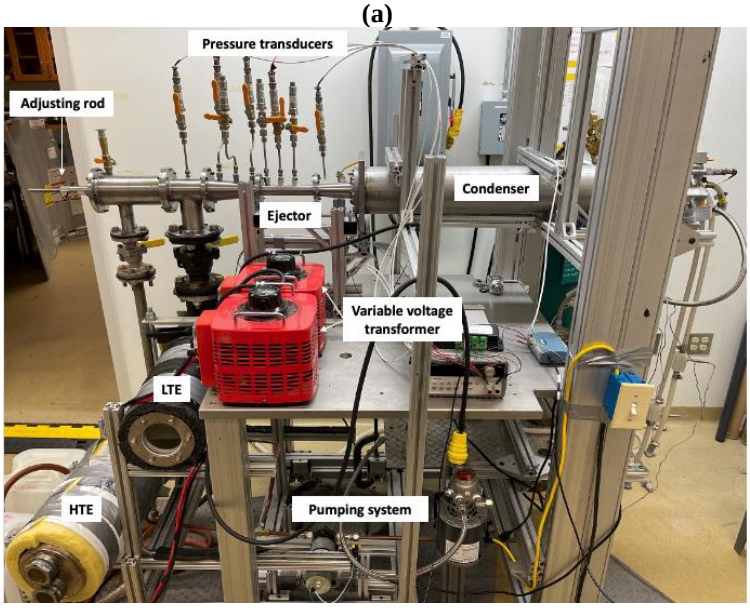
2.1. Experimental setup description

A schematic and image of the experimental setup is shown in Figure 3. The power inputs into the HTE and LTE were supplied by two electrical resistance immersion heaters, connected to a variable voltage transformer capable of supplying 240 V to the system. These allowed the heat added to the HTE and LTE to be set to a specific value to be able to control the pressure and temperature of the working fluid within each vessel. The condenser was a shell-in-tube heat exchanger, consisting of a stainless-steel shell and copper tubing, designed to have a cooling capacity of 7 kW. The cooling fluid was supplied by a constant temperature thermal bath (Maxi Cool Recirculating chiller-RC150-C0021) set to deliver water at a temperature of 14.5 °C to simulate domestic tap water [7].

The input voltages across the electrical heaters within the HTE and LTE were monitored using the Keithley 2701 digital multimeter which had an accuracy of 4% [9]. Type-T thermocouples with an accuracy of ± 0.5 ℃ were used to measure the temperature of the PF in the HTE, SF in the LTE, condenser, and the inlet and outlet temperatures of the cooling water across the condenser. Pressure transducers with an accuracy of 0.08% were installed in the HTE, LTE and condenser to monitor their internal pressures. In addition to this, pressure taps were added along the ejector's axis to measure the static pressure profile along the ejector.



(a)



(b)

Figure 3: (a) Schematic and (b) picture of EHP experimental setup

The heating capacities within the HTE, LTE, along with the cooling capacity in the condenser are calculated using:

$$\dot{Q}_{LTE} = I \times V \quad \text{and} \quad \dot{Q}_{HTE} = I \times V \tag{1}$$

$$\dot{Q}_c = \dot{m}_w c_p (T_{out} - T_{in}) \tag{2}$$

where I is the current, V is the voltage, $\dot{m}_w$ is the cooling water mass flow rate, and T_{out} and T_{in} are the cooling water outlet and inlet temperatures, respectively.

Energy losses within the system were estimated by performing an energy balance across the entire system. Comparing the sum of the thermal load from the HTE and LTE to the condenser cooling capacity. The difference between the two was always found to be less than 4% indicating the system was well insulated. The pumping power was assumed to be negligible compared to the input power into the HTE, therefor the heating-cycle COP of the EHP is determined from [7]:

$$COP_{EHP} = \frac{\dot{Q}_c}{\dot{Q}_{HTE}} \tag{3}$$

Tests were run of HTE temperatures of 120 – 140 °C and LTE temperatures of 10 – 20 °C for primary nozzles with throat diameters of 1.5 and 2 mm. Additional trials were run at LTE temperatures of 25 and 30 °C for the 1.5 mm primary nozzle throat.

2.2. Uncertainty Analysis

To ensure the reliability of the experimental measurements, a few of the trials were repeated three times under the same operating conditions, and the COP values were calculated and compared. The deviation between the similar tests were found to be less than 3%, thus indicating the repeatability and reliability of the experimental setup and measurements. The relative error is estimated by

$$\left(\delta_{COP_{EHP}}\right)^2 = \left(\frac{\partial COP_{HP}}{\partial \dot{Q}_c}\delta_{\dot{Q}_c}\right)^2 + \left(\frac{\partial COP_{HP}}{\partial \dot{Q}_{HTE}}\delta_{\dot{Q}_{HTE}}\right)^2 \tag{4}$$

where

$$\left(\delta_{\dot{Q}_c}\right)^2 = \left(\frac{\partial \dot{Q}_c}{\partial \Delta T_w}\delta_{\Delta T_w}\right)^2 + \left(\frac{\partial \dot{Q}_c}{\partial \dot{m}_w}\delta_{\dot{m}_w}\right)^2 \tag{5}$$

$$\left(\delta_{\dot{Q}_{HTE}}\right)^2 = \left(\frac{\partial \dot{Q}_{HTE}}{\partial I}\delta_I\right)^2 + \left(\frac{\partial \dot{Q}_{HTE}}{\partial V}\delta_V\right)^2 \tag{6}$$

and it is found that it is about 6.5%.

3. Results and Discussion

The pressure profiles inside the ejector are presented at various LTE and HTE temperatures to attempt to understand they affect the flow behaviour withing the ejector and ultimately the performance of the EHP COP. This section ends with a performance diagram that summarizes the COP and back pressure at various operating conditions.

3.1. Effect of HTE temperature

The temperature of the HTE can be changed by adjusting the input voltage to the heater. The pressure profile along the ejector at various HTE temperatures can be observed in Figure 4. It can be observed that when the HTE temperature was increased from 120 °C to 140 °C, the backpressure rose from 2.8 to 3.4 kPa, corresponding to temperatures of 22.88 °C and 26.12 °C, respectively. It should be noted that the first three pressure transducers from the left to right, read the pressures of the entrained flow from the LTE to be nearly the same. Starting at the P4, the variations in the pressure reading were observed, thus indicating the pressure during the mixing process is not constant. The pressure was then observed to increase then decrease at P5, which is in the constant area section. A pressure drop is then observed at P6 and P7, which is a result of an increase in the velocity of the fluid flow. The normal shock appeared to take place somewhere between P7 and P8, which lead to a sharp increase in the static pressure and decrease in the flow velocity. Beyond that, the pressure continued to increase, as the steam travelled along the divergent diffuser section.

The pressure variation depends on the HTE temperature, which controls the mixing pressure and pressure rise across the normal shock. From Figure 4, it can be observed that an increase in HTE temperature from 120 °C to 130 °C, resulted in a 0.29 kPa increase in the backpressure (P9). When the HTE temperature was further increased to 140 °C, the backpressure reached 3.36 kPa, with is 0.53 kPa higher than a HTE temperature of 120 °C. Based on these results it can be concluded that an increase in the HTE can help to attain larger backpressures and in turn larger condensing temperature, thus increasing the temperature life of the heat pump, however, this also results in lower EHP COPs, as shown in Figure 5. The EHP COP was found to decrease from 2.02 to 1.62, when the HTE temperature dropped from 140 °C to 120 °C, which is ~20% decrease in the EHP COP.

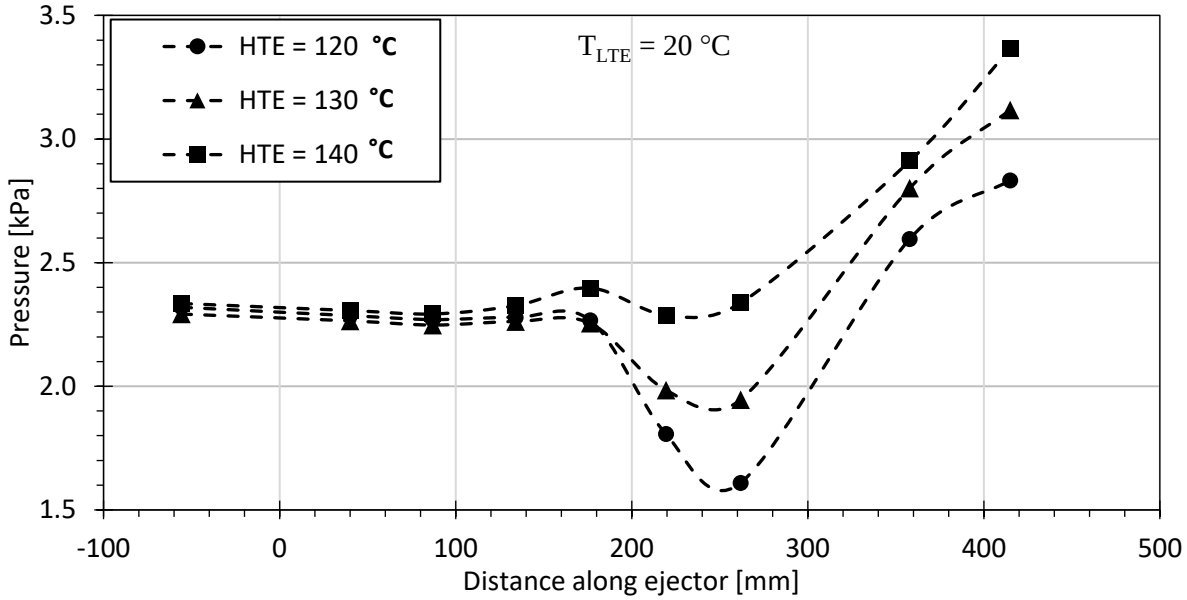


Figure 4: Pressure profile along the ejector at various HTE temperatures for nozzle throat diameter of 1.5 mm.

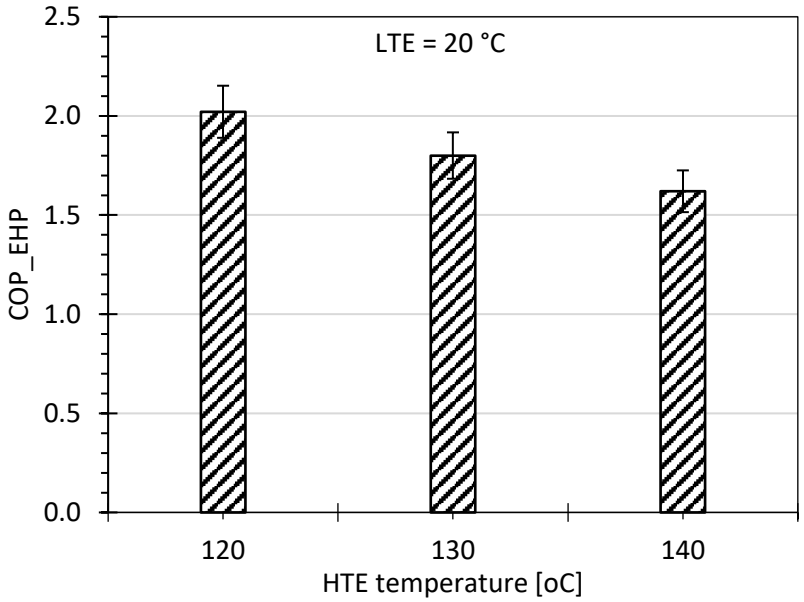


Figure 5: HTE temperature effect on the EHP COP using a nozzle throat diameter of 1.5 mm

3.2. Effect of LTE temperature

The pressure profile along the ejector at various LTE temperatures can be seen in Figure 6. It can be observed that the pressure rises when the LTE temperature increases. For each of the trials the pressures decreased slightly as the steam travelled along the first three pressure transducers, then at the fourth pressure transducer, the pressure was found to significantly depend on the LTE temperature. As shown in Figure 6, a LTE temperature of 20 °C resulted in the largest backpressure. At lower LTE temperatures, a lower amount of water vapor is entrained into the mixing chamber, and the vapor that is entrained has less momentum.

As shown in Figure 7, the temperature of the LTE has a significant effect on the EHP COP, which was found to increase as the LTE temperature increased. A 140% improvement in the EHP COP was observed when the LTE temperature was increased from 10 °C to 20 °C, 1.28 and 1.80, respectively. More importantly, not only did increasing the LTE temperature increase the EHP COP, it also resulted in increased backpressures or temperature life of the heat pump.

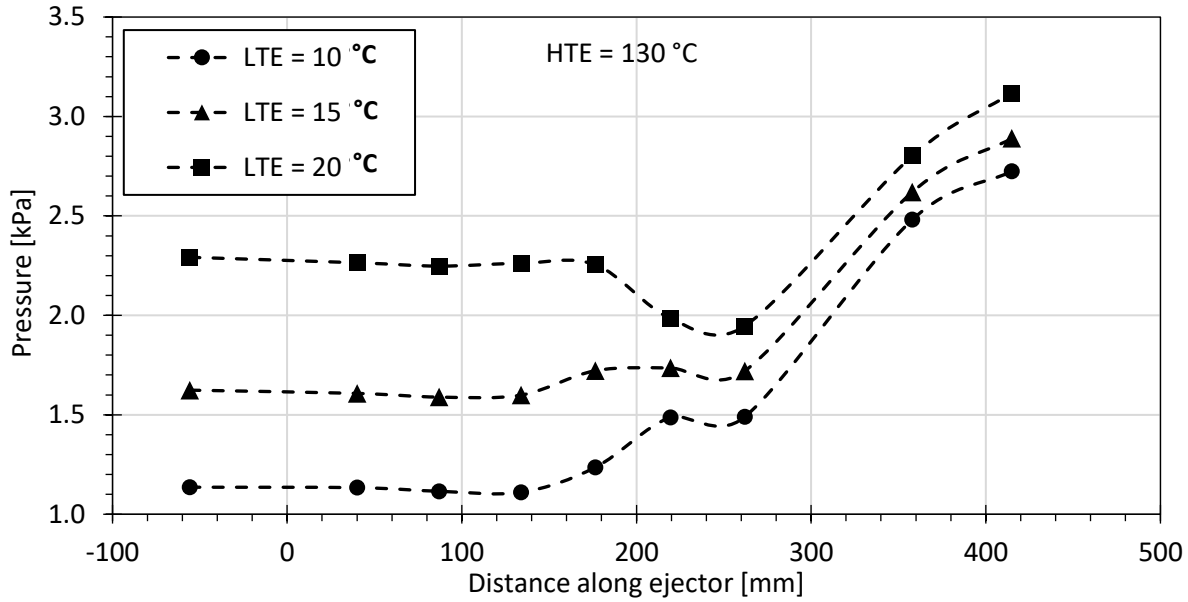


Figure 6: Pressure profile along the ejector at various LTE temperatures for nozzle throat diameter of 1.5 mm.

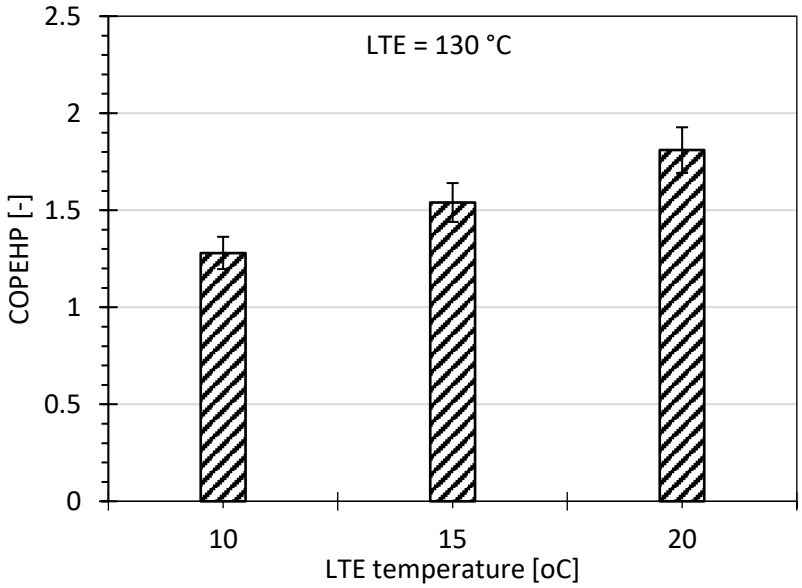


Figure 7: Effect of LTE temperature on the COP of EHP using a nozzle throat diameter of 1.5 mm.

3.3. Effect of nozzle throat diameter

The EHP COP for the two different primary nozzles can be observed in Figure 8. It was found that the nozzle with the smaller throat diameter, 1.5 mm, performed better than that with the 2.0 mm throat diameter. A decrease in the throat diameter, resulted in a decrease in the mass flow rate of the PF travelling through the nozzle. This is also directly related to the heat input to the HTE, which in turn results in a significant increase in the EHP COP. At a nozzle exit position of 0.40, the EHP COP improved from 1.40 to 1.80, a 29% improvement, when the nozzle throat sized was decreased from 2.0 mm to 1.5 mm. A larger backpressure was able to be attained with the 2.0 mm nozzle. This trend shows that a smaller throat size is preferred for larger EHP COPs, while a larger throat diameter is better for larger backpressures. This result emphasizes the importance of optimizing the primary nozzle geometry to find the best compromise between EHP COP and backpressure.

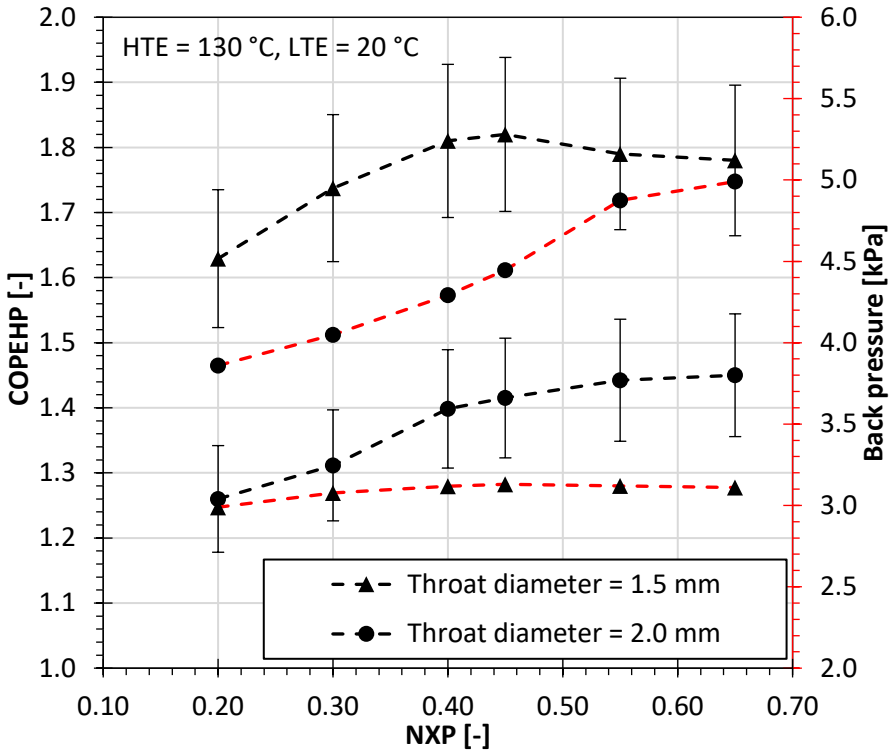


Figure 8: EHP COP and back pressure using two different throat diameters at various NXPs

3.4. Ejector performance

A performance diagram depicting the EHP COP and backpressure at various operating conditions for the 1.5 mm nozzle can be seen in Figure 9. Larger LTE temperatures were found to correspond to larger EHP COPs and backpressures, while larger HTE temperatures resulted in lower EHP COPs and larger backpressures. It is found that to increase the backpressure or temperature lift of an EHP, the EHP COP will need to be sacrificed. The EHP map shown in Figure 9 can be used to select the idea working conditions that provide a compromise between the EHP COP and backpressure, that will best suit the requirements of the EHP system. It should be noted at the values will change with the nozzle size however, the general trend will remain the same.

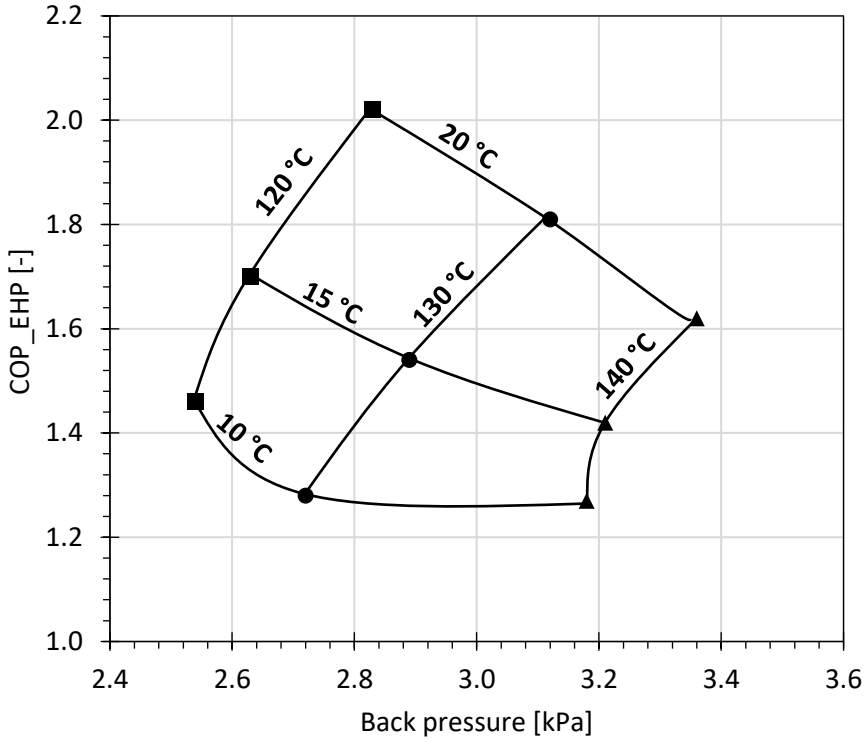


Figure 9: Performance map of EHP using a 1.5 mm nozzle at NXP of 0.40.

4. Conclusion

In this work, on a steam-driven ejector heat pump for water heating purposes was built and tested to determine the effects of the operating conditions and design parameters of the EHP COP and backpressure under sub-critical conditions. Nine pressure transducers were installed along the axis of the ejector to observe the effects the operating conditions had on the static pressure profile of the steam as it travels through the ejector. The experimental results indicate larger LTE temperatures are better for larger EHP COPs and backpressures or a larger temperature lift for the EHP, while larger HTE temperatures also lead to higher backpressures, but the EHP COP is compromised. A larger throat diameter resulted in lower EHP COPs and larger backpressures. Therefore, it is important to carefully design a primary nozzle to get the desired trade-off between the EHP COP and backpressure. An ejector performance map is provided to help select the operating conditions for the desired set point for the EHP system. From this investigation it can be concluded that further work needs to be done to further develop a clear understanding of the behaviour of the fluid flow through an ejector, which can then be used to further improve the EHP system.

Acknowledgements
This material is based upon work supported by the U.S. Department of Energy, Office of Science, Building Technologies Office. This research used resources of the Building Technologies Research and Integration Center (BTRIC) of the Oak Ridge National Laboratory, which is a DOE Office of Science User Facility.

References

[1] Fuentes, E., Arce, L., and Salom, J. “A Review of Domestic Hot Water Consumption Profiles for Application in Systems and Buildings Energy Performance Analysis.” *Renewable and Sustainable Energy Reviews*, Vol. 81, No. February 2017, 2018, pp. 1530–1547. https://doi.org/10.1016/j.rser.2017.05.229.

[2] Abu-Heiba Oak Ridge, TN (United States)] (ORCID:0000000153356180), A. [Oak R. N. Lab. (ORNL). “Literature Review of Potential Thermally Activated Heat Pump Cycles.” 2018.

[3] Forman, C., Muritala, I. K., Pardemann, R., and Meyer, B. “Estimating the Global Waste Heat Potential.” *Renewable and Sustainable Energy Reviews*, Vol. 57, 2016, pp. 1568–1579. https://doi.org/10.1016/j.rser.2015.12.192.

[4] Ayyoub, M. M., Abu-heiba, A., and Vineyard, E. *Multi-Function Gas Fired Heat Pump*. Oak Ridge, TN (United States), 2015.

[5] Dias, J. M. S., and Costa, V. A. F. “Adsorption Heat Pumps for Heating Applications: A Review of

Current State, Literature Gaps and Development Challenges." *Renewable and Sustainable Energy Reviews*, Vol. 98, No. August, 2018, pp. 317–327. https://doi.org/10.1016/j.rser.2018.09.026.

[6] Pounds, D. A., Dong, J. M., Cheng, P., and Ma, H. B. "Experimental Investigation and Theoretical Analysis of an Ejector Refrigeration System." *International Journal of Thermal Sciences*, Vol. 67, 2013, pp. 200–209. https://doi.org/10.1016/j.ijthermalsci.2012.11.001.

[7] Wang, P., Ma, H., Spitzenberger, J., Abu-Heiba, A., and Nawaz, K. "Thermal Performance of an Absorption-Assisted Two-Stage Ejector Air-to-Water Heat Pump." *Energy Conversion and Management*, Vol. 230, 2021. https://doi.org/10.1016/j.enconman.2020.113761.

[8] Spitzenberger, J., Wang, P., Ismael, L., Ma, H., Abuheiba, A., and Nawaz, K. "Theoretical Analysis of a Single-Stage Gas-Fired Ejector Heat Pump Water Heater." *Journal of Thermal Science and Engineering Applications*, Vol. 14, No. 4, 2022, pp. 1–10. https://doi.org/10.1115/1.4051708.

[9] Keithley 2010 Series: 7.5 Digit Multimeter with Scanning | Tektronix n.d. https://www.tek.com/en/products/keithley/digital-multimeter. Accessed Nov. 9, 2022.

14th IEA Heat Pump Conference
15-18 May 2023, Chicago, Illinois

Searching for eco-friendly working fluids for an ejector-driven heat pump for domestic water heating

Ramy H. Mohammed [a], Jeremy Spitzenberger [a], Pengtao Wang [b], Hongbin Ma [a,*], Ahmad Abu-Heiba [c], Stephen Kowalski [b], Kashif Nawaz [b]

[a]Multiphysics Energy Research Center (MERC), College of Engineering, University of Missouri-Columbia, Columbia, MO 65211, USA.
[b]Multifunctional Equipment Integration Group, Building Technologies, Research and Integration Center (BTRIC), Oak Ridge National Laboratory, (ORNL), Oak Ridge, TN 37830.
[c] Rocky Research, Honeywell Aerospace, Boulder City, NV 89005.

Abstract

This study searches for refrigerants with low global warming potential (GWP) and zero ozone depletion potential (ODP) for an ejector heat pump water heater (EHPWH). Several criteria are set, and R1336mzz(Z), R601a, R1233zd(E), R1224yd(Z), R1234ze(Z), and R600a are shortlisted. A theoretical model is built to study the performance of EHPWH and the corresponding ejector design at different operating conditions. For the same ejector design, a refrigerant with a high specific heat ratio produces a high entrainment ratio and heating COP. This is because the expansion wave angle in the ejector is small for refrigerants with a high specific heat ratio, allowing more mass flow rate to be entrained. A higher entrainment ratio does not necessarily correlate to a high COP because the saturation curve of the tested refrigerants is not the same. Results show that the heating COP of R601a is the highest, but it is extremely flammable. R1224yd(Z) and R1234ze(Z) are the most candidates for EHPWH when the trade-off between the COP and safety criteria is considered. The results presented in this work could help building an EHPWH using eco-friendly refrigerants.

© HPC2023.
Selection and/or peer-review under the responsibility of the organizers of the 14th IEA Heat Pump Conference 2023.

Keywords: Ejector; Heat Pump; Water Heating; COP; Working Fluids; GWP.

Introduction

Buildings are responsible for 40% of global energy consumption and 33% of greenhouse gas emissions. Water heating accounts for about 20% of home's energy use. Using energy efficient water heater can reduce the monthly water heating bills. Ensuring new buildings are sustainable and energy-efficient is key to tackling climate change [1]. The Federal Sustainability Plan has been designed and set goals to reduce energy consumption and achieve net-zero emissions buildings by 2045, including a 50% reduction by 2032 [2]. Heat pump is the widely used technology to produce building cooling and heating energy. The proper working fluid selection for heat pump systems is a key parameter to address the Federal Sustainability Plan's ambitious goals by reducing carbon emissions, greenhouse gases, and energy consumption (i.e., achieving a high coefficient of performance (COP)). The suitable working fluids (refrigerants) should be non-toxicity, non-flammable, non-explosive, and eco-friendly with low Global Warming Potential (GWP) and zero Ozone Depletion Potential (ODP) [3], and have desired thermophysical properties, such as high latent heat of vaporization and high thermal conductivity [4].

The working fluids for cooling and heating systems can be classified into Hydrocarbons (HCs), Chlorofluorocarbons (CFCs), Hydrochlorofluorocarbons (HCFCs), Hydrofluorocarbons (HFCs), Hydrofluoroolefins (HFOs), Hydrofluoroethers (HFEs), Fluorocarbons (FCs), and natural refrigerants. CFCs

* Corresponding author. Tel.: +1 573-884-5944.
E-mail address: mah@missouri.edu.

and HCFCs have high ozone depletion potential (ODP) and were phased out under Montreal Protocol. HFCs with high global warming potential (GWP >150) are being phased out. HCs are A3 flammable refrigerants, and only a few HCs, such as Isobutane (R600a), are approved by US Environmental Protection Agency (EPA) [5]. HFOs are developed as alternative refrigerants with low GWPs to replace HFCs and HCFCs [6]. HFEs are non-flammable fluids with low toxicity, chemically inert, and high-temperature stability. Recently, HFOs and HFEs have been investigated as alternative refrigerants for ejector refrigeration systems [4].

The ejector is a thermal-driven compressor that sucks vapor (secondary fluid) from a vessel at low pressure and lifts to a high pressure using a motive fluid (primary fluid) with higher pressure and temperature. The ejector heat pump for cooling and heating applications consists of an ejector, generator, evaporator, condenser, expansion valve, and pump, as shown in Fig. 1. It has many advantages over the electrically driven heat pump, such as simple construction, no moving parts, high reliability, and low cost, making it attractive for residential systems [7]. The ejector heat pump could be driven by different types of heat sources, such as low-grade waste heat (>70 ℃) and renewable energy [8]. Also, it has good potential to boost primary energy efficiency by avoiding the losses in electric generation and transmissions.

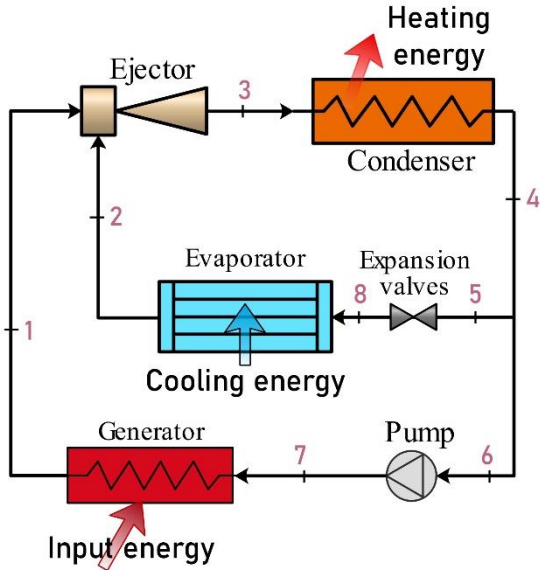


Fig. 1. Schematic drawing of ejector heat pump.

The coefficient of performance (COP) of the ejector heat pump is a function of the entrainment ratio and the ratio between the latent heat of vaporization of secondary fluid and primary fluid. The entrainment ratio is the ratio between the mass flow rate of secondary fluid and primary fluid. It depends on the ejector design, operating conditions, and thermophysical properties of the working fluid. Aphornratana et al. [9] conducted experimental tests for an R11 ejector using two different mixing chambers to study the effect of secondary flow chocking on the ejector performance. The cooling COP of the cycle varied from 0.1 to 0.25. It was found that higher performance is obtained only when the secondary flow is chocked. Ma et al. [10] investigated water and used a spindle to control the water vapor in the primary nozzle according to the heat input. The experimental measurements revealed that a short primary nozzle produces maximum cooling energy, while the longer primary nozzle has a higher COP. Dong et al. [11] reported that the steam ejector cooling cycle could produce a COP of 0.66 when the HTE operates between 55 ºC and 70 ºC. Experimental measurements indicated that the COP decreases when the condenser pressure increases. Shovon et al. [12] tested the performance of a solar refrigeration system's ejector cooling cycle using several working fluids under various operating conditions. The theoretical results highlighted the significant effect of the ejector area ratio on the cycle's COP. Specifically, the COP could be doubled using R718 (water), which increased the ejector area ratio from 6.4 to 12.8, which is defined as the ratio between the constant ejector area and the nozzle throat area. However, the highest COP was calculated using R717 (ammonia), while the maximum cooling effect was produced using water as a working fluid. Geng et al. [13] performed experimental measurements and theoretical analysis to study the performance of the nitrogen ejector cooling cycle. Two primary nozzles with throat diameters of 0.155 mm and 0.185 mm were investigated. Test results showed that the back pressure rises when higher inlet temperatures for the evaporator and generator are used.

Previous studies revealed that the performance ejector cycle depends on the operating conditions and

design parameters. Also, the ejector should be designed for a specific working fluid to achieve higher performance. It is found that little attention has been paid to the ejector cycle for heating applications. Hence, there is a lack of identifying a proper eco-friendly working fluid and corresponding ejector design. Therefore, this study screens different working fluids for ejector heat pump for water heating (EHPWH) that uses a working fluid with low GWP and zero ODP, while the cycle operates under positive pressure with a high heating COP. Criteria for working fluid pairs are established, and candidates for EHPWH are shortlisted. A thermodynamic model for EHPWH is built to evaluate its heating COP using the shortlisted working fluids at various operating parameters. The corresponding geometrical specifications of the ejector are presented.

2. Criteria for selecting the working fluid pairs

The criteria for working fluids screening are established based on having low GWP and zero ODP. Table 1 lists the selected working fluids for GHPWH. In the EHPWH, the evaporator operates at the ambient temperature of 19.4 ℃ as specified for rating air-source heat pump water heaters by the US Department of Energy [33]. It assumed that the evaporator pinch point is 5.0 ℃. Therefore, the evaporation temperature is set at 14.4 ℃. Based on this temperature, the saturation pressure is estimated to identify which working fluid makes the system operates under a vacuum.

The Mach number at the exit of the primary nozzle affects the back pressure. This Mach number is a function of the working fluid's molecular weight and specific heat ratio. R1234ze(Z), R1234ze(E), and R1234yf have the same molecular weight. So, R1234ze(Z) is selected for investigation because its critical temperature is the highest, allowing the generator of heat pump to work at high temperature and subcritical conditions, and hence achieve higher condenser temperature for the same ejector design. R290 and R1270 have relatively low critical temperatures (less than 100 ℃), making them unsuitable for heat pump water heater that could produce hot water at 50 ℃. R717 is usually a suitable refrigerant for chillers, not for heat pumps. Therefore, R601a, R1336mzz(Z), R1233zd(E), R1224yd(Z), R1234ze(Z), and R600a are investigated in this study.

Table 1. Selected refrigerants with low GWP and zero ODP for EHPWH.

	Refrigerants	Chemical Name	P_{sat}* [bar]	T_{cr} [℃]	P_{cr} [bar]	NBP [℃]	γ	MW [kg/kmol]	ODP	GWP (AR4**)	SC+
Under vacuum	R1336mzz(Z)	cis-1,1,1,4,4,4-Hexafluoro-2-butene	0.475	171.3	29	33.5	1.074	164.1	0	2	A1
	R601a	Isopentane	0.620	187.2	33.7	27.9	1.092	72.15	0	4	A3
	R1233zd(E)	Trans-1-chloro-3, 3, 3-Trifluoropropene	0.871	165.6	35.73	18.3	1.105	130.5	0	1	A1
	R1224yd(Z)	cis-1-chloro-2,3,3,3-tetrafluoropropene	0.98	155.5	33.37	14.6	1.104	148.5	0	< 1	A1
Above atmospheric	R1234ze(Z)	cis-1, 3, 3, 3-Tetrafluoropropene	1.21	150.1	35.31	9.7	1.133	114	0	7	A2L
	R600a	Isobutane	2.54	134.7	36.4	-11.7	1.139	58.12	0	< 5	A3
	R1234ze(E)	Trans-1,3,3,3-tetrafluoro-1-propene	3.59	109.4	36.32	-19.3	1.15	114	0	7	A2L
	R1234yf	2,3,3,3-tetrafluoro-1-propene	5.01	94.7	33.82	-29.5	1.177	114	0	< 5	A2L
	R717	Ammonia	7.14	132.3	113.3	-33.3	1.435	17.03	0	0	B2
	R290	Propane	7.20	96.68	42.47	-42.1	1.251	44.1	0	< 5	A3
	R1270	Propylene	8.80	92.42	46.65	-47.7	1.303	42.08	0	2	A3

* Pressure calculated at T = 14.4 ºC.
** AR4 refers to the Intergovernmental Panel on Climate Change (IPCC) Fourth Assessment Report (2007) https://www.ipcc.ch/report/ar4/syr/
+ASHRAE safety class (SC): A and B for toxicity from low to high, 1, 2L, 2, and 3 for flammability from low to high.

3. Theoretical Model

A one-dimensional model is implemented in this study based on the following assumptions [14,15]:

1) The working fluids in the ejector are ideal gas with constant thermodynamic properties.
2) The process of the ejector is a steady state.
3) The flow inside the ejector is one-dimensional.
4) Inlet and outlet kinetic energies are neglected.
5) The irreversibility is respected using experimental coefficients, except that isentropic processes are considered.
6) The ejector walls are adiabatic.
7) Mixing primary (pf) and secondary (sf) streams starts at y–y (refer to Fig. 2).
8) Normal shockwave occurs after mixing primary and secondary streams (at section s-s).

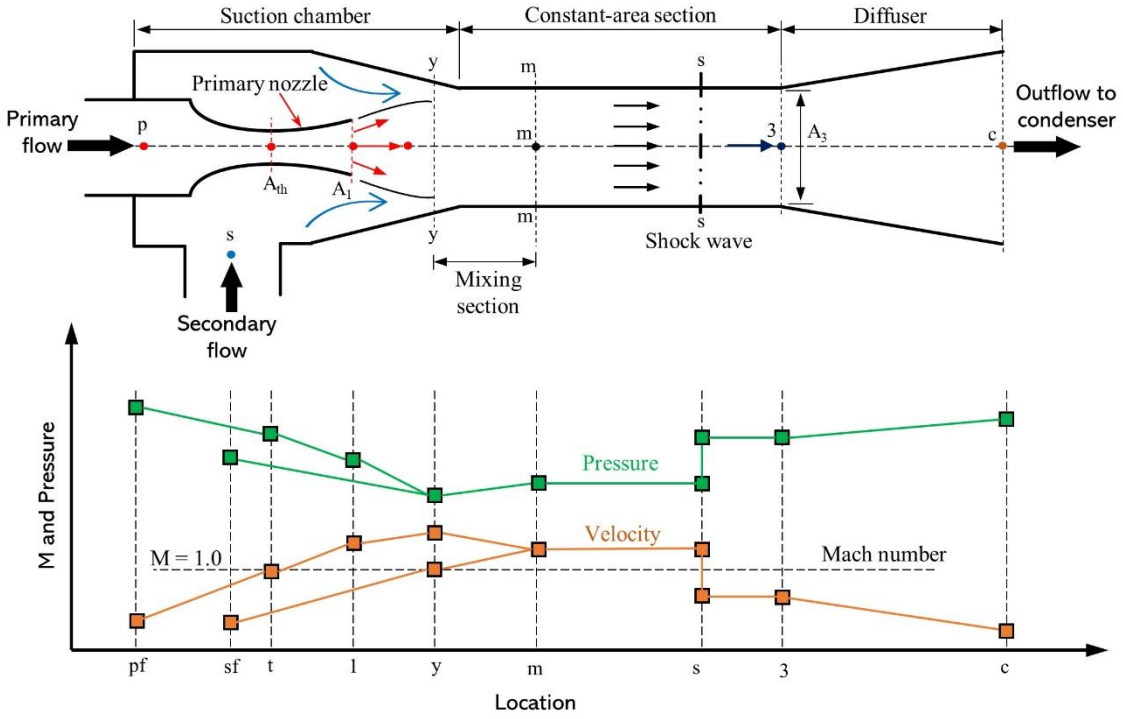


Fig. 2. (a) A detailed schematic of the used ejector and (b) pressure and Mach number variation along the ejector (adapted from [14,16]).

The primary mass flow rate (coming from the generator) can be expressed as a function of temperature, pressure, and throat area.

$$\dot{m}_{pf} = \frac{P_g A_{th}}{\sqrt{T_g}} \sqrt{\frac{\gamma}{R}\left(\frac{2}{\gamma+1}\right)^{\frac{\gamma+1}{\gamma-1}}} \sqrt{\eta_{pn}} \tag{1}$$

where the primary nozzle isentropic efficiency (η_{pn}) is taken as 0.85.

$$\frac{A_1}{A_t} \approx \frac{1}{M_{p1}}\left[\frac{2}{\gamma+1}\left(1+\frac{\gamma-1}{2}M_{p1}^2\right)\right]^{\frac{\gamma+1}{2(\gamma-1)}} \tag{2}$$

$$\frac{P_g}{P_{p1}} \approx \left(1+\frac{\gamma-1}{2}M_{p1}^2\right)^{\frac{\gamma}{\gamma-1}} \tag{3}$$

At y-y location, both streams (p and s) have the same pressure ($P_{py} = P_{sy}$). If it is assumed that the entrained flow is sonic at this location, the pressure ratio can be written as:

$$\frac{P_e}{P_{sy}} \approx \left(\frac{\gamma+1}{2}\right)^{\frac{\gamma}{\gamma-1}} \tag{4}$$

$$\frac{P_{py}}{P_{p1}} \approx \left(\frac{1 + \frac{\gamma - 1}{2} M_{p1}^2}{1 + \frac{\gamma - 1}{2} M_{py}^2} \right)^{\frac{\gamma}{\gamma - 1}} \tag{5}$$

A coefficient ϕ_p is added to the isentropic relation to account for viscous losses at the boundary between both streams. ($\phi_p = 0.95$). The area ratio of the expansion wave can be estimated from the following Equation:

$$\frac{A_{py}}{A_1} = \frac{\phi_p M_{p1}}{M_{py}} \left[\frac{1 + \frac{\gamma - 1}{2} M_{py}^2}{1 + \frac{\gamma - 1}{2} M_{p1}^2} \right]^{\frac{\gamma + 1}{2(\gamma - 1)}} \tag{6}$$

The secondary (coming from the evaporator) mass flow rate is estimated by,

$$\dot{m}_{sf} = \frac{P_e A_{sy}}{\sqrt{T_e}} \sqrt{\frac{\gamma}{R} \left(\frac{2}{\gamma + 1} \right)^{\frac{\gamma + 1}{\gamma - 1}}} \sqrt{\eta_{sn}} \tag{7}$$

Here, the isentropic efficiency of flow expansion (ηsn) is assumed to be 0.85. The total cross-section area at y-y is the same as that of the duct that extends to the aftershock region,

$$A_3 = A_{py} + A_{sy} \quad and \quad AR = \frac{A_3}{A_t} \tag{8}$$

where AR is the ejector area ratio.

Gas dynamic relations are used to specify the temperatures of streams based on upstream Mach number as,

$$\frac{T_g}{T_{py}} = 1 + \frac{\gamma - 1}{2} M_{py}^2 \tag{9}$$

$$\frac{T_e}{T_{sy}} = 1 + \frac{\gamma - 1}{2} M_{sy}^2 \tag{10}$$

A section m-m, both streams are assumed to be totally mixed. Thus, a mixing loss coefficient, ϕ_m, is introduced in the momentum equation between sections m-m and y-y as,

$$\phi_m \left(\dot{m}_p u_{py} + \dot{m}_s u_{sy} \right) = \left(\dot{m}_p + \dot{m}_s \right) u_m \tag{11}$$

Besides, the energy equation is written as,

$$\dot{m}_{pf} \left(h_{py} + \frac{u_{py}^2}{2} \right) + \dot{m}_{sf} \left(h_{sy} + \frac{u_{sy}^2}{2} \right) = \left(\dot{m}_{pf} + \dot{m}_{sf} \right) \left(h_m + \frac{u_m^2}{2} \right) \tag{12}$$

The velocities at different sections can be estimated using Mach number as,

$$\boldsymbol{u_{py} = M_{py} \sqrt{\gamma_{pf} R T_{py}}} \tag{13}$$

$$\boldsymbol{u_{sy} = M_{sy} \sqrt{\gamma_{sf} R_{sf} T_{sy}}} \tag{14}$$

$$\boldsymbol{u_m = M_m \sqrt{\gamma_m R_m T_m}} \tag{15}$$

After the two fluids completely mix, the flow is subjected to a normal shock at section s-s, resulting in an increase in the flow pressure from $P_m = P_{sy} = P_{py}$ to P_3. Then, the state '3' is connecting with state 'c'

(condenser pressure) through a diffusing process.

$$\frac{P_3}{P_m} = 1 + \frac{2\gamma}{\gamma + 1}(M_m^2 - 1) \tag{16}$$

$$M_3^2 = \frac{1 + \frac{\gamma - 1}{2} M_m^2}{\gamma M_m^2 - \frac{\gamma - 1}{2}} \tag{17}$$

$$\frac{P_c}{P_3} = \left(1 + \frac{\gamma - 1}{2} M_3^2\right)^{\frac{\gamma}{\gamma - 1}} \tag{18}$$

After finding the entrainment ratio, the COP of heat pump can be estimated as given:

$$COP = 1 + \frac{\dot{m}_{sf}}{\dot{m}_{pf}} \times \frac{(h_v|_{T_e} - h_l|_{T_c})}{(h_v|_{T_g} - h_l|_{T_c})} = 1 + ER \times \frac{(h_v|_{T_e} - h_f\big|_{T_c})}{(h_v|_{T_g} - h_f\big|_{T_c})} \tag{19}$$

where ER is the ejector entrainment ratio, h_v is the specific enthalpy of saturated vapor, and h_f is the specific enthalpy of saturated liquid.

4. Model validation

The thermodynamic model is built in Engineering Equation Solver (EES) software. The results obtained from the present model are compared with previous experimental data from the literature. Table 2 presents a comparison between the present results and previous ones under the same operating conditions. It is found that the relative error is always less than 4%, indicating that the model is suitable for investigating the performance of ejector cycle.

Table 2. Comparison between present results and previous experimental data for ejector heat pump.

T_g (°C)	Previous results [15]	Present model	Error (%)
120	0.6849	0.6615	3.42
125	0.6074	0.5864	3.45
130	0.5299	0.5158	2.66
135	0.4544	0.4671	2.79
140	0.3822	0.3920	2.56

5. Results and Discussion

This section discusses the effect of the generator pressure and condenser temperature on the ejector area ratio (AR), the entrainment ratio (ER), and COP using the shortlisted working fluids. Discussion is presented about how the thermodynamic properties of the investigated refrigerants affect the ejector behavior and hence the COP of EHPWH.

5.1. Effect of working fluid

For a specific ejector design with an area ratio of 30, the entrainment ratio, mixing Mach number, and corresponding condenser temperature are presented in Fig. 3 for the investigated refrigerants. According to Equation (6), the expansion wave's angle increases when the working fluid's specific heat ratio decreases. This means that the surface area from which the secondary flow is entrained (A_{sy}) decreases when the specific heat ratio of the working fluid decreases. This leads to a decrease in the secondary flow mass flow rate and hence a reduction in the ejector entrainment ratio. So, it is found that the entrainment ratio is the highest using R600a because it has the highest specific heat ratio among the investigated refrigerants (see Table 1). The entrainment ratio of the ejector using R600a is about 3.27 at a heating COP of 3.42. However, R600a produces the lowest value of condenser temperature because the Mach number in the mixing section is found to be the lowest one. On the other hand, R1336mzz(Z) produces the highest condenser temperature of about 50 °C, which is more suitable for heating purposes. However, the entrainment ratio is the lowest and equals 0.4. Thus, for the same ejector, the trend of condenser temperature is always opposite to the trend of the entrainment ratio.

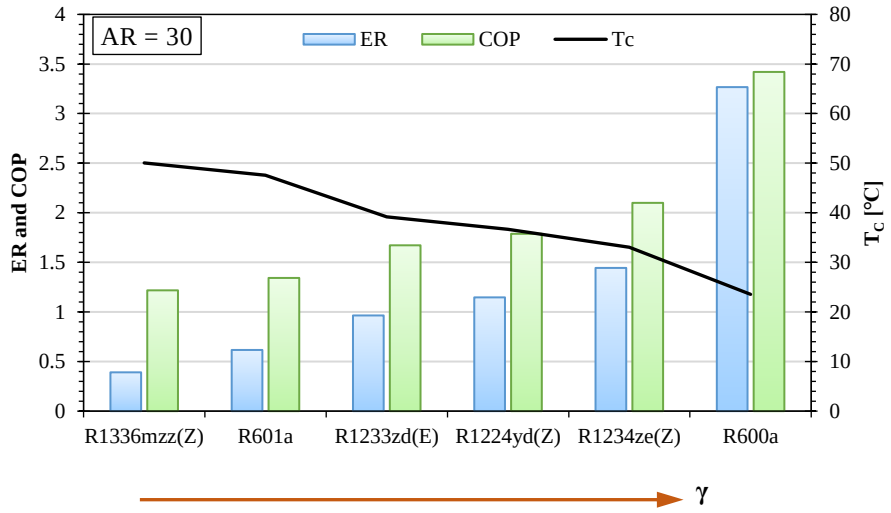


Fig. 3. ER and condenser pressure of ejector heat pump using different refrigerants at constant ejector area ratio at P_g = 25 bar.

Fig. 4 presents the entrainment ratio, Mach number in the mixing chamber, and ejector area ratio using the investigated working fluids to achieve a condenser temperature of 50 °C. All the investigated working fluids achieve almost similar COP of around 1.22 using different ejector area ratios. R601a achieves the highest entrainment ratio of about 0.51 and the highest heating COP of 1.28 using an ejector with an area ratio of 26.5. This behavior is because the generator temperature is the highest for R601a, which is about 168 °C. The ejector area ratio is the largest when the system uses R1336mzz(Z) due to its largest molecular weight of 164.1 kg/kmol. R600a could produce the required condenser temperature of 50 °C using the smallest ejector design of an area ratio of about 6.0 because R600a has the lowest molecular weight (see

Table 1). The entrainment ratio and COP of R1233zd(E), R1224yd(Z), and R1234ze(z) are comparable, but R1224yd(Z) needs a bigger ejector to be able to achieve the desired condenser temperature.

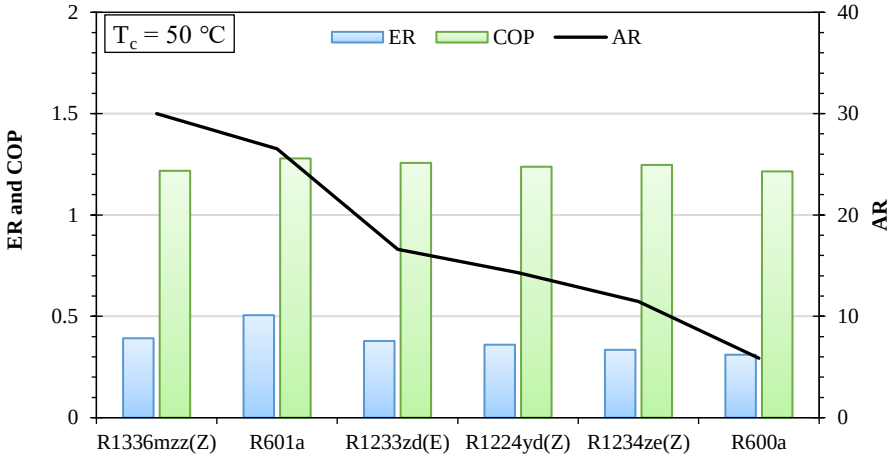


Fig. 4. ER and ejector area ratio of ejector heat pump using different refrigerants at constant condenser pressure at P_g = 25 bar.

5.2. Effect of generator pressure

Fig. 5 presents the variation of ER at various generator pressures for the investigated working fluids. It is found that the ER increases as the generator pressure increases to achieve the same condenser temperature. It can be highlighted that the ER mainly depends on the generator temperature when the generator pressure is fixed. The ER of the ejector using R601a is always the highest and changes from 0.22 to 0.56 when the generator pressure changes from 1000 kPa to 3000 kPa, respectively. The highest ER of R601a is owing to the highest generator temperature. In turn, at any generator pressure, the generator temperature is the lowest when R600a is used, leading to the lowest value of ER.

The area ratio does not follow the same trend, as shown in Fig. 6. To achieve the same condenser pressure, the ejector area ratio should be high for working fluid with large molecular weight. Because R1233mzz(Z) has the highest value of the molecular weight, the ejector area ratio is the highest. For the heating COP, its trends do not follow the trends of ER, as presented in Fig. 7. R601a achieves the highest COP due to its highest ER. Interestingly, the heating COP of EHPWH using R1234ze(Z) rapidly increases and approaches the COP of R601a when the generator pressure increases. This behavior is due to the shape of the saturation curve (P-h diagram) of R1234ze(Z), where the latent heat of vaporization significantly decreases as the pressure increases, and hence the heat added in the generator decreases, leading to a remarkable increase in the heating COP. When the generator pressure changes from 1000 kPa to 3000 kPa, the heating COP produced using R601a and R1234ze(Z) increases by 15% and 26%, respectively. It is worth mentioning that the highest ER does not always correspond to the highest COP of EHPWH. The shape of the P-h diagram of refrigerant affects the amount of heat added in the generator and evaporator and hence the COP accordingly.

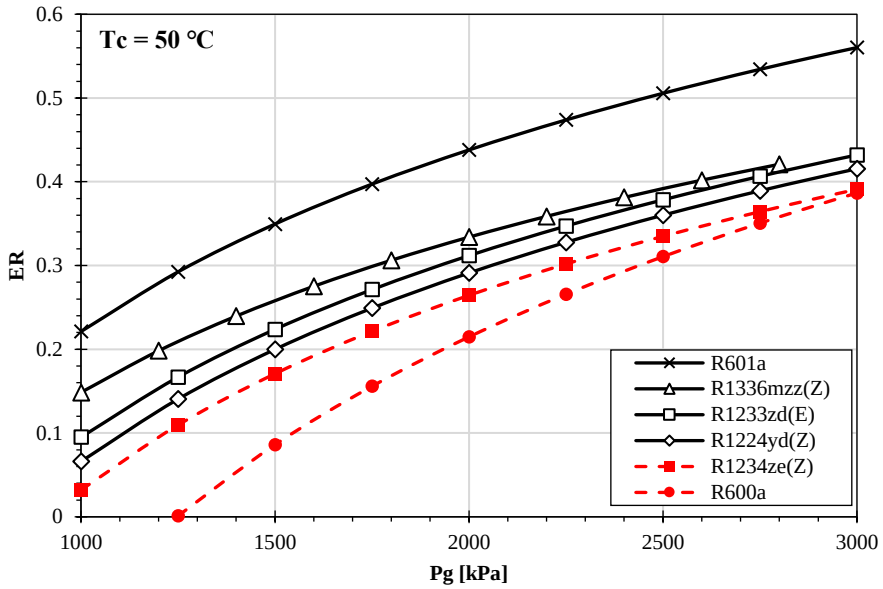


Fig. 5. Effect of generator pressure on the ER at a condenser temperature of 50 °C. (Solid lines indicate operation under vacuum and Dashed lines indicate operation above atmospheric).

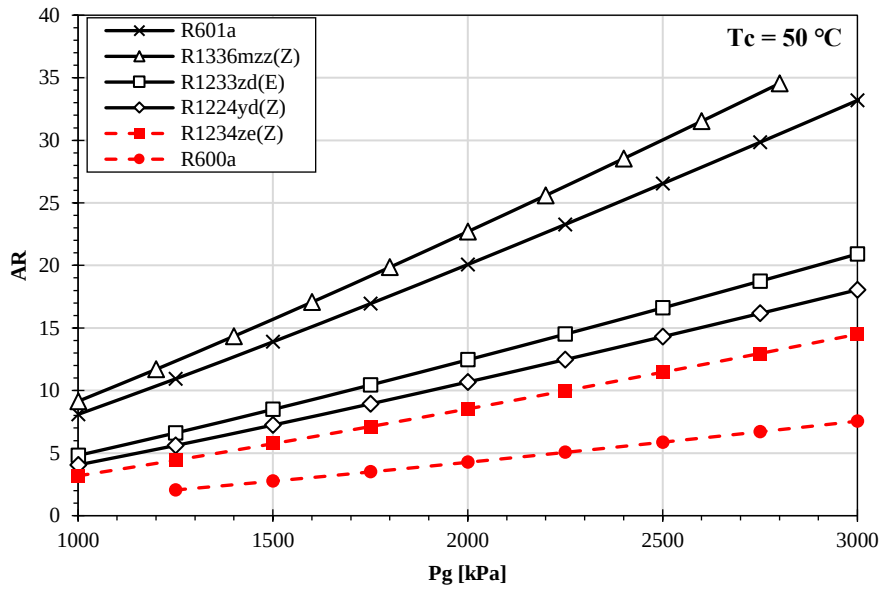


Fig. 6 Effect of generator pressure on the AR at a condenser temperature of 50 °C. (Solid lines indicate operation under vacuum and Dashed lines indicate operation above atmospheric).

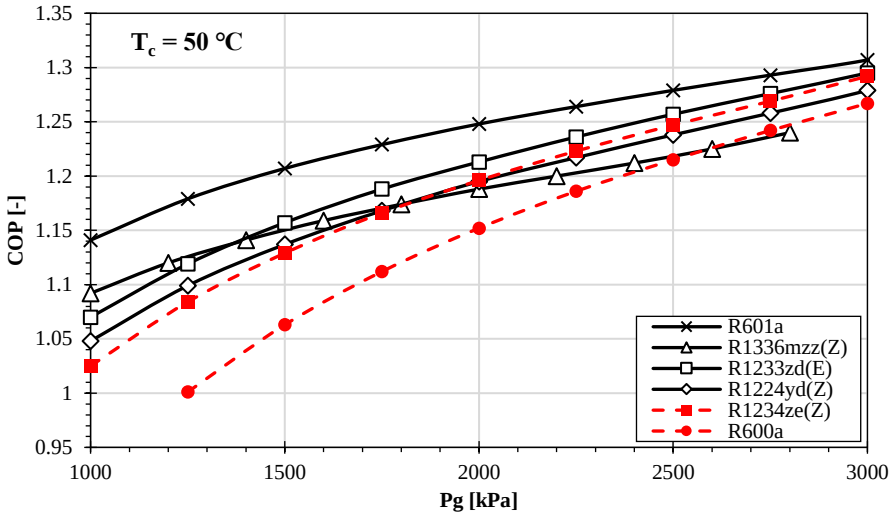


Fig. 7 Effect of generator pressure on the COP at a condenser temperature of 50 °C. (Solid lines indicate operation under vacuum and Dashed lines indicate operation above atmospheric).

5.3. Effect of condenser temperature

The variations of ER for the investigated refrigerants at various condenser temperatures are plotted in Fig. 8. It is found that the ER declines exponentially when the condenser temperature increases for the same ejector design of an area ratio of 30. Regardless of the condenser temperature, the ER is always the highest for R601a, followed by R1336mzz(Z). For R601a, the ER declines from 3.7 to 0.5 (more than 7 times reduction) when the condenser temperature changes 25 °C 50 °C, respectively. This remarkable reduction is observed for all investigated refrigerants. This means that the ejector is very sensitive to condenser pressure, and it should be designed to a specific condenser temperature to be able to achieve higher ER. For Fig. 9, a refrigerant with a larger molecular weight needs a bigger ejector to be able to achieve the desired condenser temperature. Regardless of the variation in ER and AR, the heating COP of EHPWH barely changes when the type of the investigated refrigerant changes, as plotted in Fig. 10. R1234ze(Z) produces the highest COP when the condenser temperature is 25 °C. When the condenser temperature is 25 °C, the heating COP varies between 3.1 and 3.4 when different refrigerants are tested. When the condenser temperature is 40 °C, the heating COP is about 1.22 for the studied refrigerants. Therefore, when the safety class and working around atmospheric pressure or higher, it can be concluded that R1224yd(Z) and R1234ze(Z) are the most suitable candidates for EHPWH to produce hot water at about 50 °C.

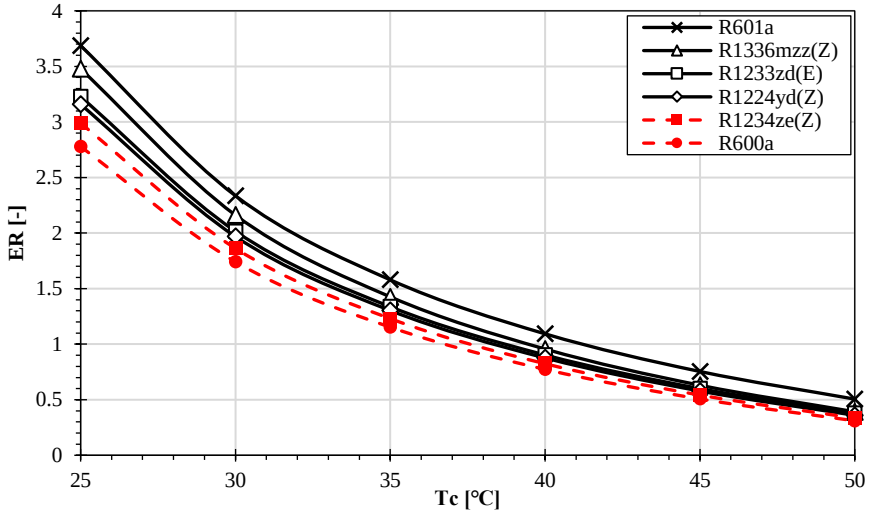


Fig. 8 Effect of condenser temperature on the ER at a generator pressure of 25 bar. (Solid lines indicate operation under vacuum and Dashed lines indicate operation above atmospheric).

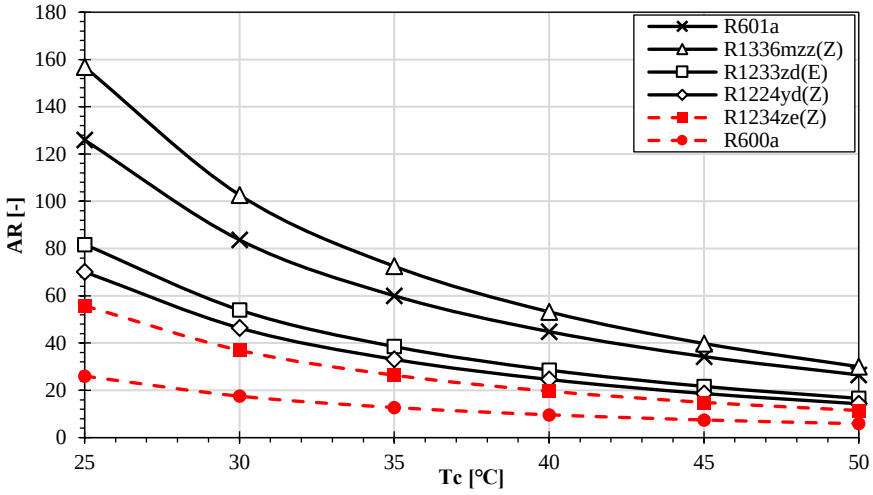


Fig. 9. Effect of condenser temperature on the AR at a generator pressure of 25 bar. (Solid lines indicate operation under vacuum and Dashed lines indicate operation above atmospheric).

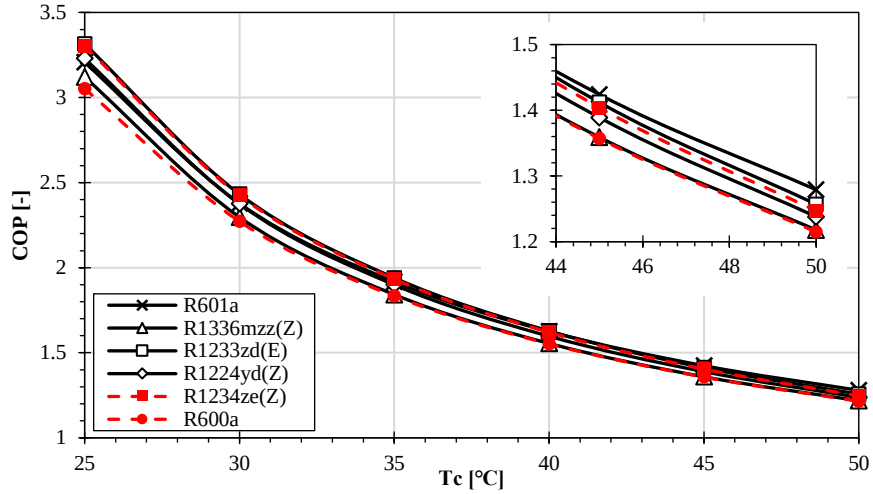


Fig. 10. Effect of condenser temperature on the COP at a generator pressure of 25 bar. (Solid lines indicate operation under vacuum and Dashed lines indicate operation above atmospheric).

6. Conclusion

The present study screens the available working fluids to identify the most suitable environmentally friendly refrigerants for EHPWH. A certain number of refrigerants with low GWP and zero ODP is shortlisted. A mathematical model is built to study the performance of EHPWH using the shortlisted refrigerants at different operating parameters. It is found that refrigerant with large molecular weight always needs a big ejector to achieve desired condenser temperature. It is highlighted that the heating COP is very sensitive to the condenser temperature. Thus, the ejector should be designed for specific operating conditions to be able to achieve high performance. Results indicate that the high ER does not always guarantee the high COP of EHPWH due to the change in the P-h diagram of the tested refrigerants. R601a and R1233zd(E) achieve the highest COP at any condenser temperature, while all the tested refrigerants produce similar heating COP at a condenser temperature of 50 °C. It can be concluded that R1224yd(Z) and R1234ze(Z) are suitable candidates for EHPWH when the trade-off between the COP, toxicity, flammability, and avoiding operating under low vacuum is considered.

Acknowledgments

This material is based upon work supported by the U.S. Department of Energy, Office of Science, Building Technologies Office. This research used resources of the Building Technologies Research and Integration Center (BTRIC) of the Oak Ridge National Laboratory, which is a DOE Office of Science User Facility.

References

[1] Buildings are the foundation of our energy-efficient future | World Economic Forum n.d. https://www.weforum.org/agenda/2021/02/why-the-buildings-of-the-future-are-key-to-an-efficient-energy-ecosystem/ (accessed November 6, 2022).

[2] Federal Sustainability Plan: Catalyzing America's Clean Energy Industries and Jobs | Office of the Federal Chief Sustainability Officer n.d. https://www.sustainability.gov/federalsustainabilityplan/ (accessed October 4, 2022).

[3] Shen B, Nawaz K, Elatar A. Parametric studies of heat pump water heater using low GWP refrigerants. International Journal of Refrigeration 2021;131:407–15. https://doi.org/10.1016/J.IJREFRIG.2021.07.015.

[4] Gil B, Kasperski J. Efficiency analysis of alternative refrigerants for ejector cooling cycles. Energy Convers Manag 2015;94:12–8. https://doi.org/10.1016/j.enconman.2015.01.056.

[5] Chen Q, Yu M, Yan G, Yu J. Thermodynamic analyses of a modified ejector enhanced dual temperature refrigeration cycle for domestic refrigerator/freezer application. Energy 2022;244:122565. https://doi.org/10.1016/J.ENERGY.2021.122565.

[6] Refrigerants With Low Global Warming Potential n.d. https://facilityexecutive.com/2017/02/refrigerants-low-global-warming-potential/ (accessed November 6, 2022).

[7] Tashtoush BM, Al-Nimr MA, Khasawneh MA. A comprehensive review of ejector design, performance, and applications. Appl Energy 2019;240:138–72. https://doi.org/10.1016/J.APENERGY.2019.01.185.

[8] Dong J, Chen X, Wang W, Kang C, Ma H. An experimental investigation of steam ejector refrigeration system powered by extra low temperature heat source. International Communications in Heat and Mass Transfer 2017;81:250–6. https://doi.org/10.1016/J.ICHEATMASSTRANSFER.2016.12.022.

[9] Aphornratana S, Chungpaibulpatana S, Srikhirin P. Experimental investigation of an ejector refrigerator: Effect of mixing chamber geometry on system performance. Int J Energy Res 2001;25:397–411. https://doi.org/10.1002/ER.689.

[10] Ma X, Zhang W, Omer SA, Riffat SB. Performance testing of a novel ejector refrigerator for various controlled conditions. Int J Energy Res 2011;35:1229–35. https://doi.org/10.1002/ER.1766.

[11] Dong J, Hu Q, Xia Y, Song H, Ma H, Cui W, et al. Experimental investigation of a miniature ejector using water as working fluid. J Therm Sci Eng Appl 2020;12. https://doi.org/10.1115/1.4047553.

[12] Shovon MKB, Raman SK, Suryan A, Kim TH, Kim HD. Performance of ejector refrigeration cycle based on solar energy working with various refrigerants. J Therm Anal Calorim 2020;141:301–12. https://doi.org/10.1007/s10973-020-09319-1.

[13] Geng L, Cao H, Meng Q, Li J, Jiang P. Effects of operating conditions and geometries on the performance of nitrogen ejectors for Joule–Thomson cooling. Appl Therm Eng 2022;212:118557. https://doi.org/10.1016/J.APPLTHERMALENG.2022.118557.

[14] Huang BJ, Chang JM, Wang CP, Petrenko VA. A 1-D analysis of ejector performance. International Journal of Refrigeration 1999;22:354–64. https://doi.org/https://doi.org/10.1016/S0140-7007(99)00004-3.

[15] Eames IW, Aphornratana S, Haider H. A theoretical and experimental study of a small-scale steam jet refrigerator. International Journal of Refrigeration 1995;18:378–86. https://doi.org/10.1016/0140-7007(95)98160-M.

[16] Shovon MKB, Raman SK, Suryan A, Kim TH, Kim HD. Performance of ejector refrigeration cycle based on solar energy working with various refrigerants. J Therm Anal Calorim 2020. https://doi.org/10.1007/s10973-020-09319-1.

14th IEA Heat Pump Conference
15-18 May 2023, Chicago, Illinois

Design and energy performance of the heat pump-driven liquid desiccant system with an ultrasonic atomization

Soo-Jin Lee[a], Seong-Yong Cheon[a], Su-Young Jo[a], Jae-Won Joung[a], Jae-Weon Jeong[a,*]

[a]Department of Architectural Engineering, College of Engineering, Hanyang University, Seoul, 04763, Republic of Korea

Abstract

The purpose of this study was to propose and design the heat pump-driven liquid desiccant ventilation system with an ultrasonic atomization. The energy consumption was also compared with the conventional heat pump-driven liquid desiccant system. Because the proposed system could be operated at low solution flow rate than the reference system, the proposed system was suggested for energy benefits. The results indicated that the two systems showed similar heat pump cycle such as temperature of the evaporator and condenser. However, heat pump size could be reduced in the proposed system because of the low solution loads compared with the reference system. Finally, the proposed system could be operated with 30% reduced energy consumption during the summer season than the reference system.

© HPC2023.
Selection and/or peer-review under the responsibility of the organizers of the 14th IEA Heat Pump Conference 2023.

Keywords: Liquid desiccant; heat pump; ultrasonic atomization; energy performance;

1. Introduction

The liquid desiccant (LD) has been suggested as an energy efficiency technology for air dehumidification because of its thermal characteristics [1,2]. The LD technology has based on the mass transfer of the air and solution. The driving force is water vapor pressure difference in the LD system, while the conventional dehumidification method using condensation of the water vapor in the air. LD system has energy saving potential and high efficiency compared with the conventional condensation dehumidification because it does not use unnecessary energy to cool the air below the dew point temperature.

The LD technology was based on the heat and mass transfer between the air and solution by the difference of the water vapor pressure. To make the vapor pressure difference, the solution is cooled and heated before the absorber and regenerator intake. The various heat sources to provide the cooling and heating have been investigated. Badami and Portoraro suggested [3] a trigeneration plant which combined LD system and cooling tower for absorber, natural gas combined heat and power cogeneration system for regenerator. Especially, the heat pump was considered as an energy conservative heat source because it provides cooling and heating concurrently. Shin et al. [4] investigated the energy saving potential of the heat pump-driven LD system compared with conventional LD system which used cooling tower and boiler. The results indicated that the proposed LD system could reduce about 33% primary energy consumption per year. Niu et al. [5] performed the capacity matching between the LD and heat pump hybrid air-conditioning system via novel matching indices to system energy stability. Although many heat pump-driven LD systems have been proposed to reduce the energy consumption, some limitations have been observed; the solution cooling and heating loads are kept constant. Thus, the innovative design that can reduce the heat pump size is required to save the heat pump compressor power.

* Corresponding author. Tel.: +82-2-2220-2370; fax: +82-2-1945.
E-mail address: jjwarc@hanyang.ac.kr.

Meanwhile, LD system applied the solution atomization with ultrasound generator have been studied [6,7]. Yang et al. [6] investigated the mass transfer performance of the ultrasonic atomization LD dehumidification system experimentally. They also investigated the regeneration performance of the ultrasonic atomization LD regeneration system [7]. The results indicated that the proposed system could save about 35 – 60% according to the required regeneration rate. Lee and Jeong [8] evaluated the dehumidification and energy performance of the solution atomization-based LD dehumidifier. The solution atomization-based LD dehumidifier could save 17% solution consumption compared with the conventional LD dehumidifier.

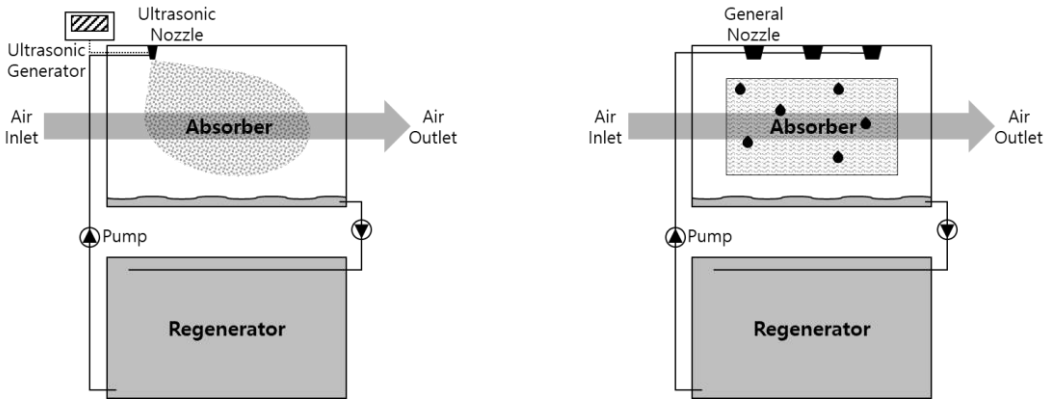
In many researches, the solution atomization-based LD system could reduce the solution cooling and heating load because of the low liquid-to-gas ratio (L/G ratio). However, there are few cases where the solution atomization-based LD system and heat pump are combined and applied as a ventilation or air-conditioning system for buildings. Thus, the heat pump-driven LD system with an ultrasonic atomization was designed and evaluated. The heat pump sizing was performed to apply as a ventilation system via detailed simulation and energy saving potential was also investigated.

2. System Overview

2.1. Liquid desiccant unit

Figure 1 shows the liquid desiccant unit according to the solution atomization methods. Figure 1 (a) is the ultrasonic atomization-based LD unit. The solution was atomized as a fine droplet through the ultrasonic generator and nozzle to increase the heat and mass transfer area between the air and solution by increasing the surface area of the solution droplets. The air and solution contacted directly in the absorber and regenerator, and the dehumidification and regeneration occurred.

Figure 1 (b) is the packbed-based LD units. The solution and air contacted by packing materials such as cellulose type paper. The solution was atomized through the general nozzle onto the packing material. The air was passed through the packing material and dehumidified by contacting with the solution. The packing material was composed of a honeycomb structure to ensure the heat and mass transfer area in limited volume.



(a) Ultrasonic atomized-based (b) Packbed-based

Fig. 1. Schematic of the liquid desiccant unit

2.2. Heat pump-driven liquid desiccant ventilation system

The heat pump-driven liquid desiccant ventilation system consisted of absorber, regenerator, heat pump, indirect evaporative cooler, two fans, and two pump as shown in Figure 2. The outdoor air was introduced to the absorber and dehumidified by the absorber. The air after the absorber passed the primary side of the indirect evaporative cooler and precooled. If the evaporative capacity is remained, the air was additionally cooled by a second evaporator.

Meanwhile, the liquid desiccant solution was circulated from absorber to regenerator. To make the water vapor pressure difference between the air and solution, the solution was cooled and heated before spraying the absorber and regenerator. The heat pump was used for solution cooling and heating concurrently.

The indoor latent load was treated by the heat pump-driven liquid desiccant ventilation system, while the parallel system was required to remove the indoor sensible load. The air-conditioning system based on heat pump cycle was selected as a parallel system.

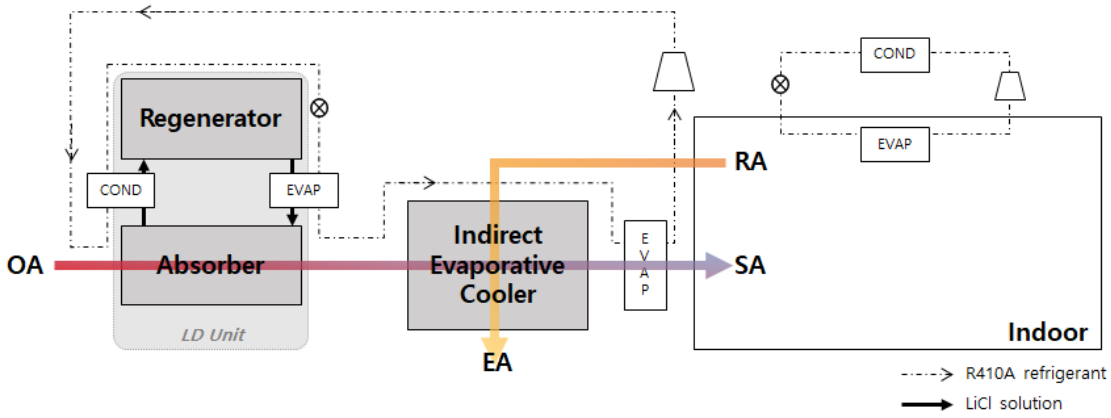


Fig. 2. Schematic of the heat pump-driven liquid desiccant ventilation system

3. Simulation Overview

3.1. Analysis of the liquid desiccant unit

The heat and mass transfer between the air and solution in the counter-flow absorber/regenerator is shown as a one-dimensional problem. Accordingly, the absorber /regenerator model based on the heat and mass conservation relations were expressed using Equations (1) – (5) [9,10]. All the following equations for each differential element are computed numerically using a forward-finite difference algorithm. In the following equations, 101 nodes are segmented along the length of the absorber and regenerator; the unit length (ΔL) is $L/100$. The mass transfer rate was calculated by the number of mass transfer unit (NTU), and the heat transfer rate was also calculated by the NTU and Lewis number (Le). The Lewis number was assumed to be a 0.92 by the heat and mass diffusivity of the air and solution [10].

$$\frac{\omega_a^i-\omega_a^{i+1}}{\Delta L}=\frac{NTU}{L}\times(\omega_{a,in}-\omega_{eq,in}) \quad (1)$$

$$\dot{m}_{a,in}\times(\omega_a^i-\omega_a^{i+1})+\dot{m}_{s,in}\times x_{s,in}\times\left(\frac{1}{x_s^{i+1}}-\frac{1}{x_s^i}\right)=0 \quad (2)$$

$$\dot{m}_s^{i+1}\times x_s^{i+1}=\dot{m}_s^i\times x_s^i \quad (3)$$

$$\frac{h_a^i-h_a^{i+1}}{\Delta L}=\frac{NTU\times Le}{L}\times\left(\left(h_a^{i+1}-h_{eq}^i\right)+\left(\left(\frac{h_{vap,ts}}{Le}-h_{vap,0℃}\right)\times(\omega_{a,in}-\omega_{eq,in})\right)\right) \quad (4)$$

$$\dot{m}_{a,in}\times(h_a^i-h_a^{i+1})+\dot{m}_{s,in}\times x_{s,in}\times(\frac{h_s^{i+1}}{x_s^{i+1}}-\frac{h_s^i}{x_s^i})=0 \quad (5)$$

The number of transfer unit (NTU) was estimated by the open literature [11,12] through the mass transfer coefficient, heat and mass transfer area per system unit volume, system volume, and flow rate of the air (Equation (6)). The mass transfer coefficient (k_m) was assumed to be 0.01 kg/m^{2}s, the heat and mass transfer area per system unit volume can be calculated by Equations (7) and (8).

The heat and mass transfer area per system unit volume is difference with the solution atomization and contact methods between the air and solution. The solution was atomized into the absorber and the air and solution contacted directly without the packing materials in the ultrasonic atomized-based LD unit. Thus, the contact area between the air and solution is related to the surface area of the atomized solution with fine droplets, and calculated by solution flow rate and density, droplet size, cross-sectional area of the absorber and regenerator, and relative velocity between the air and solution (Equation (7)). While the solution wetted the packing materials and the air was passing through the packing materials in the packbed-based LD unit. In the packbed-based LD unit, the area was affected by the dimension of the packing material, and converted by channel sizes of the packing material, efficiency of the wetting area, and solution flow rate (Equation (8)).

$$NTU = \frac{k_m \times S_v \times V}{\dot{m}_a} \quad (6)$$

$$S_{v,UADS} = \frac{6 \times \dot{m}_{s,in}}{\rho_{s,in} \times ds \times S_{cross} \times u_{fa}} \quad (7)$$

$$S_{v,packbed} = a \times \left(1 - 1.203 \left(\frac{u_s^2}{s \times g}\right)^{0.111}\right) \quad (8)$$

3.2. Heat pump sizing process

The heat pump was used for solution cooling and heating, thus the heat pump should be design with capacity to provide the sufficient cooling and heating for the LD unit. Because the solution heating load is bigger than the cooling load in the LD unit, the heat pump was designed with heating priority. The Figure 3 shows the sizing process of the heat pump. The first step is determining the temperature of the evaporator and condenser to satisfy the target solution temperature for absorber and regenerator. The second step is drawing the pressure-enthalpy diagram of the heat pump cycle through the determined temperature of the evaporator and condenser. The subcooled and superheated degrees were neglected at condenser and evaporator, respectively. The compressor outlet enthalpy of the refrigerant was assumed by the isentropic efficiency of the compressor, and it is assumed to be a 0.75 [13]. The third step is estimating the mass flow rate of the refrigerant to satisfy the solution heating load. Finally, the extra solution cooling or extra evaporating load is determined by comparing the real solution cooling load and ideal evaporator capacity. As presented in Figure 3, if the real solution cooling load is greater than the ideal evaporator capacity, the extra solution cooling is needed. The extra solution cooling load was can be obtained by subtracting ideal evaporator capacity from real solution cooling load. Whereas the real solution cooling load is less than the ideal evaporator capacity, the extra evaporating is required to maintain a stable heat pump cycle. The extra evaporating load can be estimated by subtracting real solution cooling load from the ideal evaporator capacity, and it is used for indoor cooling. The R410A was selected as a refrigerant of the heat pump system.

3.3. Energy simulation

The energy was used for the heat pump-driven liquid desiccant system and indoor parallel system. The LD system consumed the energy in the compressor, fan, and pump. The air-conditioning system with heat pump cycle was selected as an indoor parallel system, and the indoor parallel system consumed the energy in the compressor.

The compressor power for LD system could be calculated by the refrigerant mass flow rate, and enthalpy at the in and out point of the compressor (Equation (9)). The remained indoor parallel system load could be estimated using Equation (10) through the extra evaporating load and indoor sensible load. The energy consumption of the parallel system could be calculated using the system COP by Equation (11). The fan is a variable speed, thus, it was estimated by Equations (12). The pump is a constant speed and the energy consumption was estimated by Equations (13) [14].

$$P_{comp} = \dot{m}_{R410A} \times \left(h_{comp,out} - h_{comp,in}\right) \quad (9)$$

$$\dot{Q}_{parallel,remain} = \dot{Q}_{sen} - \dot{Q}_{extra,evap,load} \quad (10)$$

$$\dot{E}_{parallel} = \frac{\dot{Q}_{parallel,remain}}{COP_{indoor,system}} \quad (11)$$

$$P_{fan} = \frac{\dot{V}_a \times \Delta P}{\eta_{fan}} \times (0.0013 + 0.147PLR + 0.9506PLR^2 - 0.0998PLR^3) \quad (12)$$

$$P_{pump} = \frac{\rho \times g \times \dot{V}_s \times H}{1000 \times \eta_{pump}} \quad (13)$$

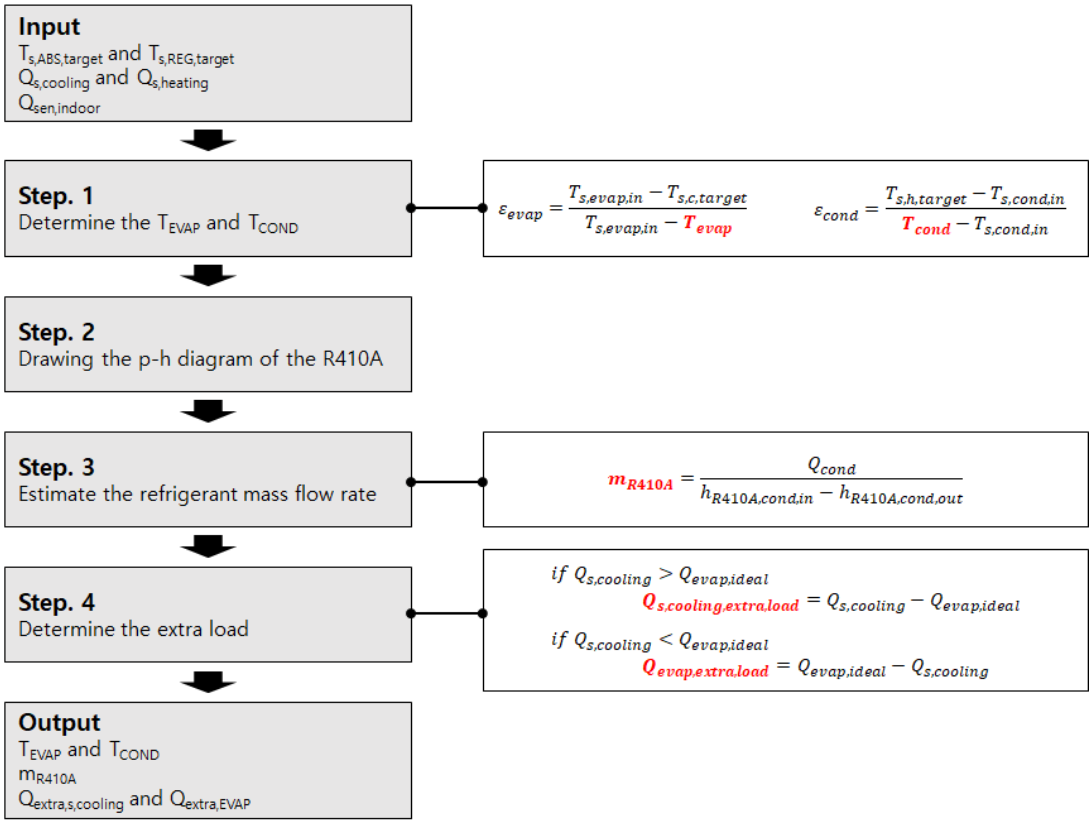


Fig. 3. Flowchart of the heat pump sizing.

4. Results

4.1. Solution cooling and heating load

The solution cooling and heating load was estimated by the solution temperatures at each state of LD unit. Figure 4 shows the maximum solution cooling and heating load comparison of the ultrasonic atomized-based LD unit (i.e., the proposed system) and the packbed-based LD unit (i.e., the reference system).

The proposed system required low solution load than the reference system because the mass flow rate of the solution is different in each system. The proposed system operated 0.4 L/G ratio in the absorber and 0.6 L/G ratio in the regenerator, while the reference system operated 1.0 L/G ratio in the absorber and regenerator under the design condition. Thus, the proposed system needed 0.61 kW and 1.41 kW for solution cooling and heating, whereas the reference system required 1.54 kW and 2.16 kW for cooling and heating, respectively.

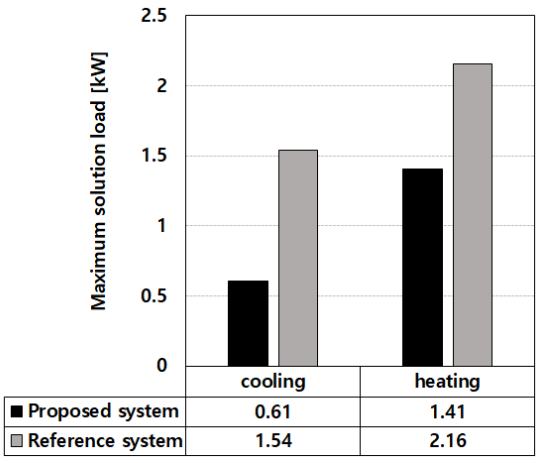


Fig. 4. Maximum solution cooling and heating load in each system.

4.2. Heat pump design

The Figure 5 shows the heat pump cycle for solution cooling and heating. To satisfy the target solution temperature for absorber and regenerator (i.e., absorber target solution temperature = 20℃ and regenerator target solution temperature = 50℃), the evaporator was designed the lower temperature (i.e., about 17℃) than the absorber target and the regenerator was designed the higher temperature (i.e., about 54℃) than the regenerator target. Because the two systems targeted the same temperature for absorber and regenerator, the evaporator and regenerator temperature were almost the same. On the other hand, each system has different in solution cooling and heating load for same target humidity ratio of the supply air because of the L/G ratio. Thus, the mass flow rate of the refrigerant is different. The heating load is greater than cooling load, the extra evaporator load occurred in all summer season. The detailed heat pump sizing results are indicated in Table 1.

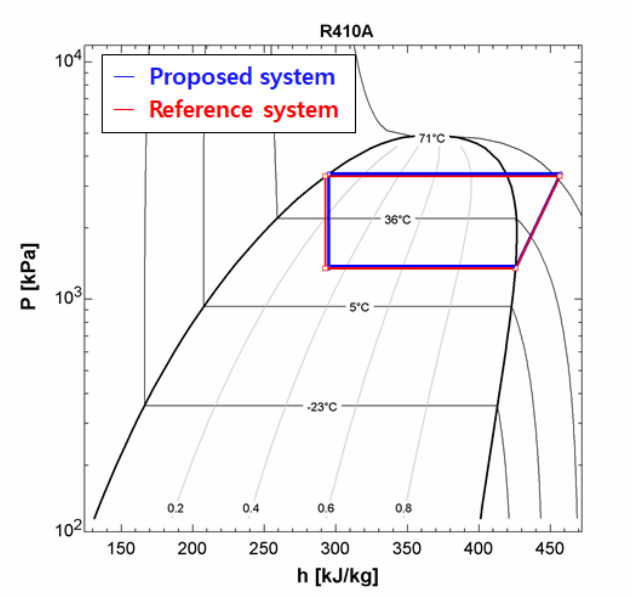


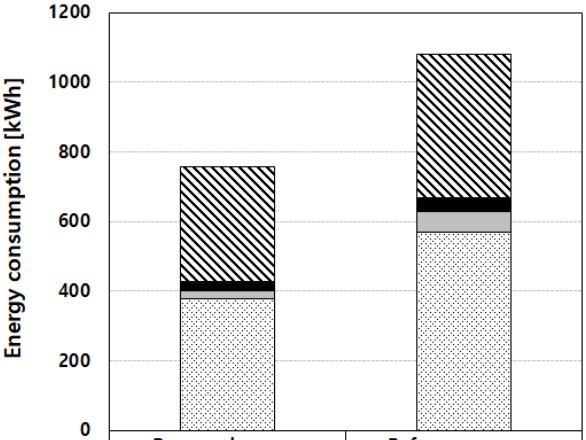
Fig. 5. Pressure-enthalpy diagram of the designed heat pump.

Table 1. Detailed size of the heat pump

	Proposed system	Reference system
Evaporator temperature [℃]	17.8	17.6
Condenser temperature [℃]	54.2	53.2
Refrigerant mass flow rate [kg/s]	0.0087	0.0132
Extra solution cooling load [kW]	0	0
Extra evaporating load [kW]	0.634	0.398

4.3. Energy consumption

The energy consumption of each system during the summer season was shown in Figure 6. The compressor for LD unit power was consumed about 377.1 and 570.3 kWh in the proposed and reference system, respectively. The proposed system used 0.0087 kg/s refrigerant and the reference system used 0.0132 kg/s as indicated in Table 1, thus the compressor power could be reduced in the proposed system because of the low mass flow rate of the refrigerant. Also, because the extra evaporating load in the proposed system is bigger than the reference system, the remained indoor parallel system load is lower in the proposed system. Thus, the proposed system consumed about 330.2 kWh and the reference system consumed 412.3 kWh for indoor parallel system. The fan and pump energy could be reduced in the proposed system even considering PLR (part load ratio) because of the low pressure drop and low solution flow rate in LD unit than the reference system. Finally, the proposed system consumed 757.5 kWh and reference system consumed 1079.7 kWh during the summer season, and the proposed system could save about 30% energy consumption.



	Proposed system	Reference system
Parallel system	330.2	412.3
Pump	26.9	37.8
Fan	23.3	59.3
Ventilation system	377.1	570.3

Fig. 6. Comparison of the total energy consumption during the summer season.

5. Conclusion

This study proposed a heat pump-driven LD ventilation system with a solution atomization technology. The detailed heat pump sizing was conducted to evaluate the energy benefits of the proposed system compared with the conventional LD ventilation system. The total energy consumption during the summer season was predicted.

The results show that the proposed and the reference system had similar heat pump cycle such as temperature of the evaporator and condenser because the target conditions of the LD unit are same. However, the proposed system could reduce the solution cooling and heating load than the reference system. Thus, the mass flow rate of the refrigerant of the heat pump combined with LD unit is difference and the proposed system required less refrigerant. Finally, the total energy consumption during the summer season could be saved about 30% in the heat pump-driven LD ventilation system with ultrasonic atomized compared with the conventional packbed-based LD ventilation system. In the future work, the system will be manufactured and evaluated experimentally.

Acknowledgements

This work was supported by the National Research Foundation of Korea(NRF) grant funded by the Korea government(MSIT) (No. 2022R1A2B5B02001975 and No. 2022R1A4A1026503) and Korea Environment Industry & Technology Institute (KEITI) through Prospective green technology innovation project, funded by Korea Ministry of Environment (MOE) (RE202103243).

References

[1] Kozubal E, Woods J, Judkoff R, Development and analysis of desiccant enhanced evaporative air conditioner prototype, In: National Renewable Energy Laboratory (NREL) Technical Report; 2012.

[2] Dai, Y.J., Zhang, H.F., 2004. Numerical simulation and theoretical analysis of heat and mass transfer in a cross flow liquid desiccant air dehumidifier packed with honeycomb paper. Energy Convers. Manag. 45, p. 1343–1356.

[3] Badami, M., Portoraro, A., 2009. Performance analysis of an innovative small-scale trigeneration plant with liquid desiccant cooling system. Energy Build. 41, p. 1195–1204.

[4] Shin, J.H., Park, J.Y., Jo, M.S., Jeong, J.W., 2018. Impact of heat pump-driven liquid desiccant dehumidification on the energy performance of an evaporative cooling-assisted air conditioning system. Energies. 11.

[5] Niu, X., Xiao, F., Ma, Z., 2012. Investigation on capacity matching in liquid desiccant and heat pump hybrid air-conditioning systems. Int. J. Refrig. 35, p. 160–170.
[6] Yang, Z., Lin, B., Zhang, K., Lian, Z., 2015. Experimental study on mass transfer performances of the ultrasonic atomization liquid desiccant dehumidification system. Energy Build. 93, p. 126–136.
[7] Yang, Z., Zhang, K., Hwang, Y., Lian, Z., 2016. Performance investigation on the ultrasonic atomization liquid desiccant regeneration system. Appl. Energy. 171, p. 12–25.
[8] Lee, S.J., Jeong, J.W., 2022. Dehumidification Performance of a Solution Atomization Based Liquid Desiccant Dehumidifier under Various Operating Conditions. Korean J. Air-Conditioning Refrig. Eng. 34, p. 83–90.
[9] Yao Y, Liu S. *Ultrasound‐atomizing regeneration for liquid desiccants: Ultrasonic Technology for Desiccant Regeneration*. John Wiley & Sons; 2014.
[10] Cengel YA, Ghajar AJ. *Heat and mass transfer: Fundamentals and Applications*. 4th Edition, McGraw-Hill Education: New York, NY; 2014.
[11] Yang, Z., Zhang, K., Yang, M., Lian, Z., 2014. Improvement of the ultrasonic atomization liquid desiccant dehumidification system. Energy Build. 85, p. 145–154.
[12] Al-Farayedhi, A.A., Gandhidasan, P., Al-Mutairi, M.A., 2002. Evaluation of heat and mass transfer coefficients in a gauze-type structured packing air dehumidifier operating with liquid desiccant. Int. J. Refrig. 25, p. 330–339.
[13] Oppermann RH. *Principles ofHeating, Ventilating and Air Conditioning*. ASHRAE: Atlanta, GA, USA; 1936.
[14] EnergyPlus. *Engineering Reference*. US Department of Energy: Washington, DC, USA; 2019, p. 1–1741.

14th IEA Heat Pump Conference
15-18 May 2023, Chicago, Illinois

Monovalent and Hybrid Air-source Heat Pump Concepts for Existing Multifamily Buildings – Energy Performance and CO_2 Savings

Omar Montero[a*], Pauline Brischoux[a], Carolina Fraga[b], Matthias Rüetschi[b], Nicole Calame[c], Fabrice Rognon[c], and Pierre Hollmuller[a*]

[a]Energy Systems Group, University of Geneva, 66 Bd Carl Vogt, 1211 Genève, Switzerland
[b]Services Industriels de Genève, Chemin du Château-Bloch 2, 1219 Le Lignon, Genève, Switzerland
[c]CSD Ingénieurs SA, Avenue des Sports 14, 1400 Yverdon-les-Bains, Switzerland

Abstract

Heat pump suppliers only propose hydronic concepts for buildings up to 15 kW_{th}, and very few suggest diagrams for large air-source heat pumps (> 50 kW_{th}) in existing multifamily building. This paper analyses the energy and environmental performance of hybrid diagrams adapted to existing and large multifamily buildings via a validated numerical simulation model. The concepts correspond to different fuel-switch scenarios with the possibility of using existing boilers as a back-up. For each concept, sensitivity analysis assesses the impact of different levels of heat demand and heat pump capacity. As a result, over the different scenarios, the seasonal performance of the heat pump varies between 2.8 and 3.3, and the overall performance (heat pump and boiler) between 1.5 and 2.9. Considering the hourly CO_{2eq} content of the Swiss electricity mix, emissions of hybrid systems are 1.4 to 2.2 times higher than with a monovalent system. However, they remain 2.3 to 3.5 times lower than a gas boiler, which points out their adequacy as a transitional solution to proceed to a fuel-switch before retrofitting the building envelope.

© HPC2023.
Selection and/or peer-review under the responsibility of the organizers of the 14th IEA Heat Pump Conference 2023.

Keywords: air-souce heat pump; multifamily building; monovalent and hybrid systems; energy performance and CO_2 savings

Nomenclature

ASHP	Air-Source Heat Pump
DHW	Domestic hot water
HP	Heat pump
MFB	Multifamily building
SH	Space heating
SPF_{HP}	SPF_{HP} Seasonal performance of the heat pump
SPF_{global}	Overall seasonal performance of the heat pump and boiler

In Switzerland, buildings account for nearly 50% of the final energy demand (100 TWh/yr) and 24% of the CO_{2eq} emissions (11.2 Mio. t/yr), representing one of the most important sectors for massive decarbonization [1,2]. About 70% of the building stock is still heated with individual fossil fuel boilers, and around 80% of them were constructed before the 21st century [3]. A specific issue concerns multifamily buildings (MFB), which in urban cantons represent 60-70% of the heated area. In parallel to retrofitting of the envelope, large existing MFBs could drastically reduce CO_{2eq} emissions by switching massively from fossil to renewable energy sources, in particular via heat pumps (HP).

* Corresponding author. Tel.: +41 22 379 06 40
E-mail address: omar.monterodominguez@unige.ch

In dense urban areas, air-source heat pumps (ASHP) often turns out to be the only available option for replacing fossil fuel boilers, since other renewable energy sources are often limited: too long distance to a lake or river, no groundwater or prohibition of its use (water protection), no district heating network due to crowded soil, lack of space for borehole fields, wood boilers prohibited in areas of excessive emissions, or limited solar energy due to roof size. In such a context, outside air often is the only renewable energy source for HP [4].

However, while ASHP systems represent the dominant renewable heating system for single-family houses and new buildings, they are rarely installed in large and existing MFBs. This is mainly explained by: i) lack of well-documented case studies proving the feasibility of such systems; ii) noise emissions, which can become a barrier; iii) HP weight and related structural constraints of the roof; iv) HP integration in the existing distribution system, designed originally for boilers; vii) high investment cost; viii) multiple households with diluted decision power and related problems of governance. Nowadays, those constraints make large ASHP (> 50 kW_{th}) an exception rather than a standard solution, especially in non-retrofitted MFB [5–7].

One of the most significant technical challenges for installing ASHP in existing MFBs is the lack of standardized hydronic concepts adapted to existing MFBs (> 50 kW_{th}), which usually concern power ratings up to about 15 kW_{th} [8]. The reason is an obvious lack of market demand, which has yet to lead to the development of such diagrams. On the other hand, most of the literature on the design and operation of ASHP focuses on new or existing single-family houses (< 450 m2 of heated floor area), with capacities below 30 kWth [9–12], for which HPs are mostly standardized, storage capacity within the building usually isn't a technical constraint, and optimal control strategies have already been developed.

1.1. Objective

In order to fill this gap, the objective of this paper concerns the development of monovalent and hybrid ASHP concepts (> 50 kW_{th}), adapted to the specific context of existing MFB, without (or with delayed) renovation of the building envelope. The concepts correspond to different fuel-switch scenarios, with and without the possibility of using the existing modulating or non-modulating boiler. They are analyzed via numerical simulation and calibrated on in-situ measurements. For each concept, sensitivity analysis assesses the impact on energy and environmental performance of different levels of heat demand for space heating (SH) and domestic hot water (DHW), as well as HP capacity (under or oversizing).

The results of this study are part of the AirBiVal project [8] and also contribute to the IEA Annex 50 "Heat Pumps in Multi-Family Buildings for Space Heating and DHW" [13].

2. Hydronic concepts

Figure 1 shows the four hydronic concepts used in this study, which have been developed based on an extant literature review, discussions with experts in the field, and long-term in-situ monitoring of two pilot projects with large ASHP:

- **Monovalent heat pump operation**: corresponds to the case where it is possible (technically and financially) to install a HP to cover 100% of the demand. For this variant, it is essential to consider rooftop static, soundproofing, mechanical vibration, electricity capacity, and extra height construction limits. This concept is based on a monovalent pilot project installed in Geneva, for which a detailed monitoring campaign and related energy analysis were conducted [5].
- **Hybrid parallel operation with modulating boiler**: corresponds to the case where an existing or new modulating boiler is used in parallel operation with the HP. The boiler is positioned after the SH tank to protect the HP from high return temperatures. This is especially important when using existing oil boilers with low modulation. This concept is based on recommendations for HP systems with a thermal output of more than 15 kW_{th}, elaborated on current knowledge from industry and research [14].
- **Hybrid parallel operation with a non-modulating boiler**: corresponds to the case where an existing non-modulating boiler is used in parallel operation with the HP. Ideally, the HP and non-modulating boiler should have their own SH tank, connected in series, to protect the HP from high return temperatures. However, in existing MFB space constraints usually lead to the installation of one tank only, in accordance with the proposed diagram. This concept is based on the hybrid pilot project installed in Geneva, for which an energy analysis and monitoring campaign were conducted [5].
- **Hybrid alternative operation with a non-modulating boiler**: corresponds to the case where an existing non-modulating boiler is used in alternative operation with the HP. It allows temporary

operation in hybrid mode, while waiting for a future retrofit of the building envelope. When the boiler is removed, the existing hydronic connections will not require any major modification. The concept is based on the diagrams developed within the RAVEL program [15].

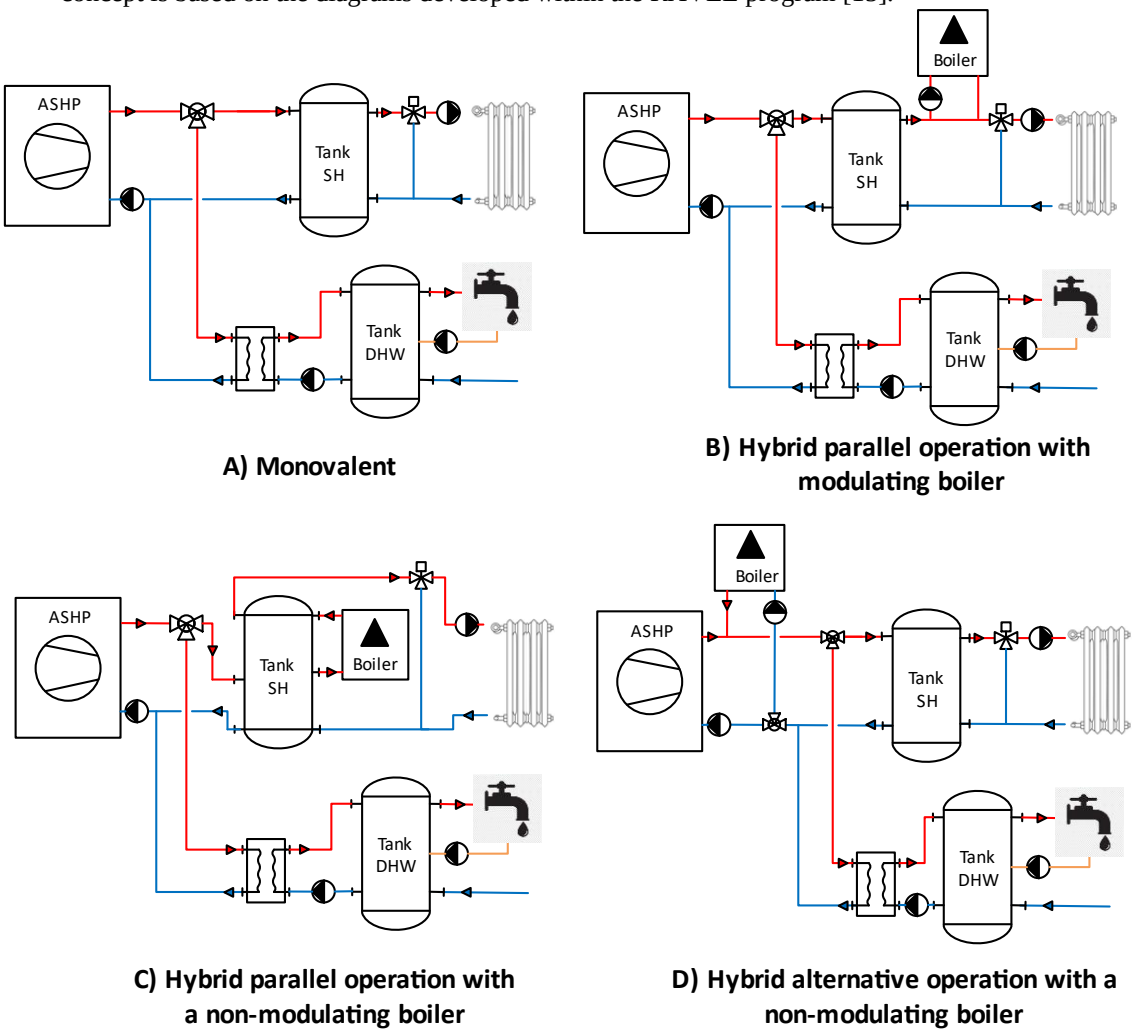


Figure 1. Hydronic concepts

2.1. Diagrams control description

For each of the four concepts, following regulation and design aspects are considered:

- The HP switches between SH and DHW production to maintain the tanks at their respective setpoint temperatures. In the case of a simultaneous demand, priority is given to DHW.
- The HP is the only heat provider for DHW (no boiler backup), so as to force the HP to cover the DHW demand in summer, when outdoor temperatures are most favorable for performance, as well as to simplify the installations diagram.
- The HP reaches 60 °C for DHW to prevent legionella proliferation. An external, rather than internal, heat exchanger is used for DHW to provide enough heat transfer area between the HP loop and the DHW tank.
- For hybrid concepts, the gas boiler only provides heat for SH, in parallel or alternative operation with the HP. The boiler is switched on if the outside temperature is below the bivalence temperature (T_{biv}) and if the HP does not reach the SH setpoint temperatures.
- The operation below the bivalence temperature is as follows (Figure 2, left): a) in the case of a parallel configuration, the HP covers the heat load up to its capacity, and the boiler provides the complement; b) in the case of the alternative configuration, the boiler operates alone. The procedure for identification of the bivalence temperature is given in section 3.3.

Detailed information on functional analysis explaining the switching on/off of the equipment is given in [8].

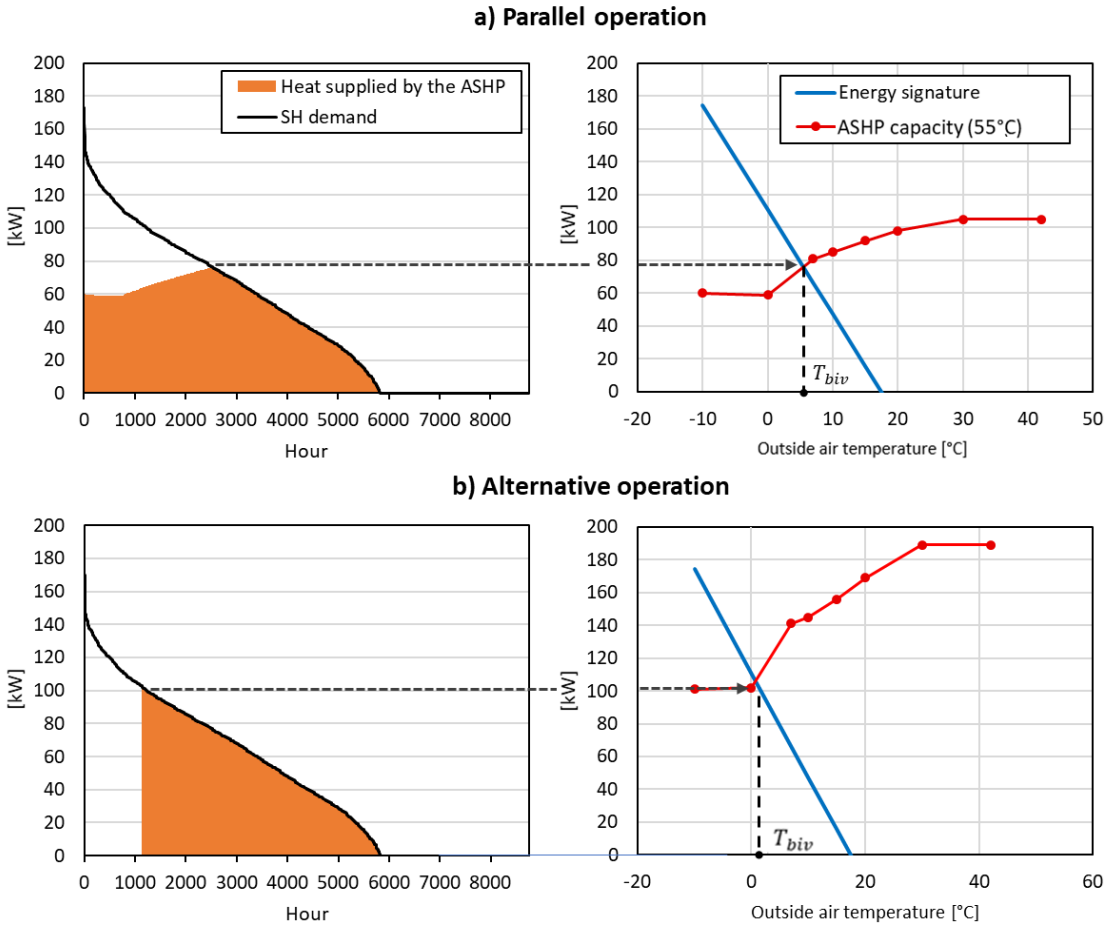


Figure 2. Identification of the ASHP bivalence temperature for a) parallel operation and b) alternative operation.

3. System modeling

In order to evaluate the performance of the proposed concepts and compare them with each other, energy models are set up using TRNSYS [16], with a time step of 1 minute. First, the model is validated based on a monovalent pilot project to ensure that the model can fairly and accurately represent reality. Then, the model is normalized to reference conditions of use, which are also applied to the three-hybrid systems model.

3.1. Validation of the monovalent system model

The model validation is based on the in-situ monitoring of a non-retrofitted MFB (4'047 m^2 of heated floor area), whose original fossil heat supply was replaced by a monovalent ASHP (312 kW$_{th}$ @ 7°/45°C) for DHW and SH production. Monitored daily SH and DHW production, minimum/maximum outdoor temperature, as well as HP and backup boiler production (during HP failure in spring 2019) are presented in Figure 3, over two years of operation.

The model validation is carried out for one year (July 2019 to June 2020). The HP model uses the performance curves provided by the manufacturer. The tanks volume (SH: 1 m³ and DHW: 2 m³) and control parameters correspond to the ones of pilot project. The measured heat demand (SH and DHW), setpoint temperatures, and heating curves are provided to the simulation in hourly values. Detailed information on the controller settings used in the simulation is given in [8].

Figure 4 compares the simulated and monitored HP production as well as related electricity consumption on a daily basis. The simulated HP production faithfully reproduces the monitored values (with an annual error of 1%). On the other hand, the HP electricity consumption (without auxiliaries) is underestimated by around 20%, due to: i) the difficulty of considering all manual changes made to the real system; ii) the discrepancy between the HP performance of the manufacturer (used for the simulation) and of the monitoring (namely

partial load conditions, as well as defrost cycles outside the standard testing conditions). Despite this, the simulation/measurement correlations remain very satisfactory to serve as a basis for modeling the four proposed hydronic concepts.

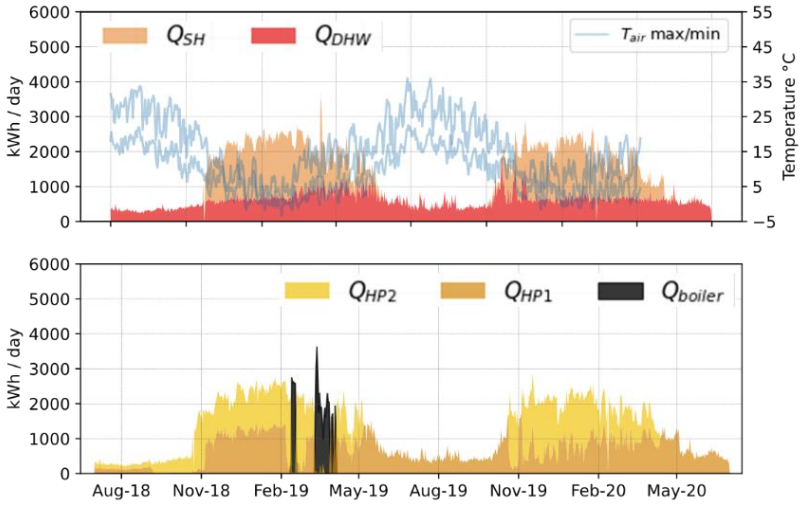


Figure 3. Monitored monovalent ASHP system (July 2018–June 2020): Daily SH and DHW production, as well as minimum/maximum outdoor temperature (top); Daily HP and boiler production, over two years of operation (bottom).

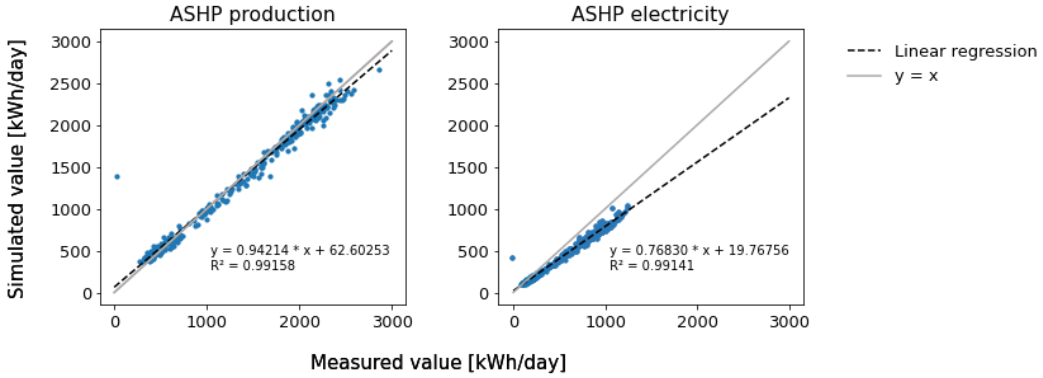


Figure 4. Comparison of simulation results with the pilot project measurements (July 2019 to June 2020, daily values). The electricity consumption of the HP does not include the consumption of the auxiliaries.

3.2. Normalization to reference conditions of use

The model is then normalized to reference conditions of use, which consists in the following modifications:

- Reference climate year for Geneva, according to the SIA 2028 standard [17];
- SH demand derived from the energy signature of the monovalent pilot project (in hourly values), but adjusted to the SIA reference climate to reach an annual demand of 101 kWh_{th}/m^2.year. This value corresponds to the median value of the existing "post-war" building stock (1948-1980) [18];
- DHW demand (35 L/day.person) given by an hourly schedule according to SIA 385/2 standard (SIA 2015) [19], but constant over the year.

The dynamic profile of the reference SH demand is presented in Figure 5, along with two alternatives (high and low demand) which will be used for sensitivity analysis (see section 6).

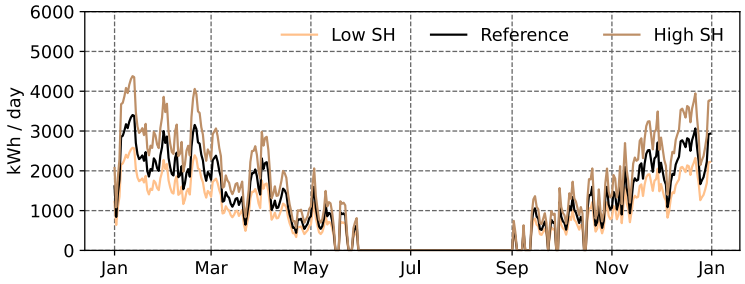


Figure 5. Daily space heating demand used for simulation: reference case as well as high/low alternatives.

3.3. Systems sizing

The three hybrid systems models are derived from the monovalent model, which are adapted according to the hydronic concepts defined above in Figure 1. For each of the four systems, we use the above-defined reference condition of use. The components are sized according to the following procedure, for which the results are shown in Table 1.

Table 1. Design parameters of the four reference systems

	Monovalent	Parallel modulating boiler	Parallel non-modulating boiler	Alternative non-modulating boiler
HP capacity required for SH*	250	78	78	137
HP capacity required for DHW*	84	84	84	84
Mode with the highest capacity requirements	SH	DHW	DHW	SH
HP capacity retained [kW_{th}]*	274	88	88	137
Boiler capacity [kW_{th}]	-	95	95	189
Bivalence temperature [°C]	-	4.5	4.5	0.5
Volume of SH tank [m^3]	2.2	2.9	2.9	2.2
Volume of DHW tank [m^3]	1.9	1.9	1.9	1.9

* HP capacities for 7 °C at the evaporator inlet and 45 °C at the condenser outlet

HP capacity

For DHW, the HP capacity is sized according to the SIA 385/2 [19], assuming a typical demand of 45 L/day.person (as used by engineering companies when the DHW demand is unknown), storage and distribution losses of 30%, as well as 6 daily charging cycles with a duration of 1 hour each. The HP has to ensure the total DHW demand, it must therefore be able to produce at 60°C in the most critical conditions (outside temperature of -7°C for the Swiss plateau).

For SH, the method for sizing the HP capacity is different for monovalent and hybrid systems:

- Monovalent system: The HP supplies 100% of the building demand (DHW and SH). Its SH capacity is defined to be able to provide the maximum daily SH demand within 18 hours (the 6 remaining hours being reserved for 6 DHW cycles of 1 hour each), with a distribution temperature of 55°C and an outdoor temperature of -7°C.
- Hybrid systems: The HP capacity is sized according to a bivalence temperature, which is determined at the intersection between the energy signature of the building and the heating capacity of the HP manufacturer, with the objective of covering 80% of the SH and DHW demand with the HP (see Figure 2). This method results in a HP capacity of 40 – 60% of the maximum hourly heat demand (189 kW_{th}), depending on the configuration (parallel or alternative operation).

Once the above sizing procedure has been applied separately for SH and DHW, the higher of the two HP capacity is selected, and adjusted to existing HP models on the market.

Tank volume

For DHW, the tank volume is sized according to the SIA 385/2, assuming the same conditions used for HP capacity sizing, explained above.

For SH, the tank is sized in relation with the HP capacity, to ensure that the HP runs for at least 20 minutes each time it is switched on. The aim is to prevent short cycling for ensuring the HP lifespan.

Boiler capacity

For the hybrid systems, we assume that an existing gas boiler is reused (installed before the implementation of the HP system), with a total capacity corresponding to the maximum hourly SH demand (189 kW_{th} at -7°C outdoor), subdivided in two capacity levels (95 kW_{th} each).

In the case of the parallel systems, the boiler completes the heat production of the HP below the bivalence point. It is assumed that only the first stage of the boiler is necessary. In the case of the alternative system, the boiler ensures the entire production below the bivalence point, whereby the two stages are therefore necessary.

4. Performance indicators

In order to evaluate and compare the performance of the different hydronic concepts, following energy and environmental performance indicators are used.

4.1. Energy performance

The annual energy performance of the system is evaluated by the seasonal performance factor (SPF_{HP}) according to Equation (1). It is defined as the ratio between annual heat production (Q_{HP}) and annual HP electricity consumption (E_{HP}).

$$SPF_{HP} = \frac{\sum Q_{HP}}{\sum E_{HP}} \quad (1)$$

In the case of the hybrid system, the overall system performance is evaluated by Equation (2), where Q_{boiler} is the annual heat production of the boiler and E_{gas} is the related annual gas consumption. The efficiency of the boilers is assumed to be equal to 90% (relative to the higher heating value).

$$SPF_{global} = \frac{\sum(Q_{HP} + Q_{boiler})}{\sum(E_{HP}+E_{gas})} \quad (2)$$

For all hybrid systems, HP capacity is sized to cover 80% of the annual heat production. In order to check if this objective is respected, the share of the HP production is calculated as follows:

$$HP\ share = \frac{Q_{HP}}{Q_{HP}+Q_{boiler}} \quad (3)$$

4.2. Environmental performance

The emissions related to the HP electricity consumption are calculated using Equation (4), where $E_{HP.h}$ is the hourly electricity consumption of the HP (in kWh_{elec}) and $f_{elec.h}$ is the hourly CO_{2eq} content of Swiss electricity, averaged over the years 2016 to 2019 (in gCO_{2eq}/kWh_{elec}). The latter is taken from Romano et al. [20], which considers domestic generation and imports from neighboring countries. The CO_{2eq} electricity content has an overall average of 99 gCO_{2eq}/kWh_{elec}, but daily peak values in the winter reaching 300 gCO_{2eq}/kWh_{elec}.

$$C_{elec} = \sum_h E_{HP.h} \cdot f_{elec.h} \quad (4)$$

The gas boiler emissions (C_{gas}) are evaluated by a constant emission factor of 203 gCO_{2eq}/kWh_{th} [1].

The total CO_{2eq} emissions of the system (in gCO_{2eq}) are evaluated by Equation (5) and are finally related to the total heat demand (gCO_{2eq}/kWh_{th}) by Equation (6), where Q_{SH} and Q_{DHW} are the annual SH and DHW demand (in kWh_{th}), respectively:

$$C_{global} = C_{elec} + C_{gas} \quad (5)$$

$$C_{th} = \frac{C_{global}}{Q_{SH}+Q_{DHW}} \quad (6)$$

5. Results for reference systems

The energy balances, performances, and CO_{2eq} emissions of the 4 reference systems are shown in Figure 6. Given the boiler backup, in particular during the coldest days, the hybrid systems have a better SPF_{HP} (between 3.13 and 3.20) than the monovalent system (2.85). As planned during sizing (with an objective of 80%), the HP share of the hybrids systems amounts to 79%, except for the parallel non-modulating gas boiler (c), which drops to 71%. In this case, since the boiler cannot modulate its capacity, it overproduces at each start-up, so the storage tank temperature exceeds its set point. As a result, despite a sufficient capacity, the HP is less solicited than it could be. As a result, the latter system consumes 35% more gas than the other two hybrid systems.

The CO_{2eq} emissions of the hybrid systems are 1.7 to 2 times higher than with the monovalent system. Two-thirds of their emissions are related to gas consumption, even though gas covers only 21% to 29% of the total heat demand. Thus, even with a high carbon content of the electricity mix in winter, the use of a HP remains more advantageous in terms of emissions, due to its high efficiency (> 2.8) compared to the boiler efficiency (90 %). For comparison, a system with only a boiler emits nearly 3 times more CO_{2eq} (119 tCO2eq/an) than the hybrid systems, and 5 times more than the monovalent system.

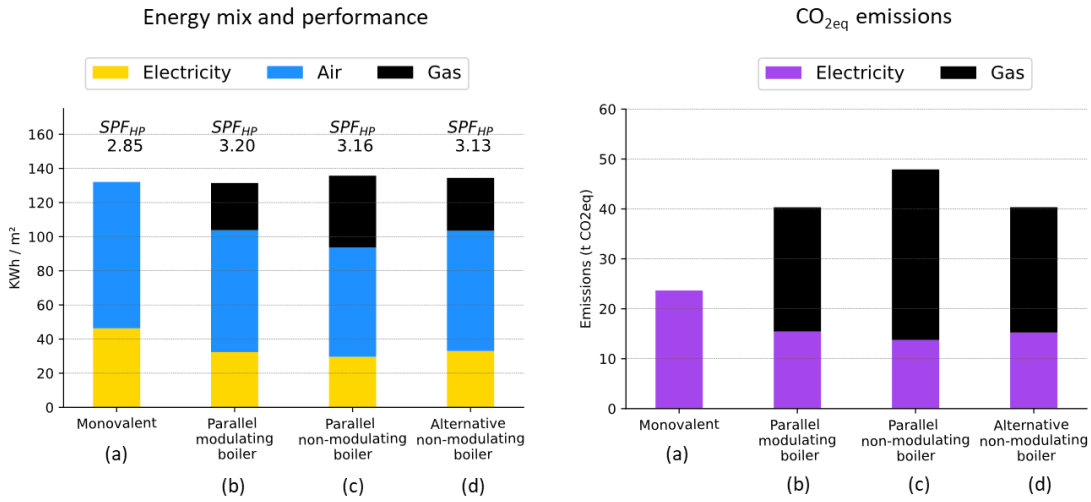


Figure 6. Energy mix and CO_{2eq} emissions of the four reference systems (SPF_{HP} does not include auxiliary consumption).

6. Sensitivity analysis

As a complement to the four reference cases, the impact of different levels of heat demand (SH and DHW) and HP capacity are assessed by following sensitivity analysis (see Table 2):

- Three levels of SH demand, representative of Geneva's post-war MFB stock (1948-1980) [18]: i) 78 kWh_{th}/m^2.year (1st decile of MFB stock); ii) 101 kWh_{th}/m^2.year (median), corresponding to our reference case; and iii) 130 kWh_{th}/m^2.year (9th decile).
- Three levels of DHW consumption: 25, 35 and 50 L/day.person, which correspond approximately to the minimum, median and 9th decile of a benchmark of DHW demand of nearly one million m^2 of heated floor area of MFB in Geneva [21].
- For the hybrid systems, three levels of HP capacity for SH: 30%, 40-60% and 80% of the maximum hourly demand, with their respective bivalence temperature. Note that the intermediate case of 40-60% (reference case) results from the above defined sizing procedure (with the objective to cover 80% of the annual heat demand).

In each case, the HP capacity as well as the SH and DHW tanks are sized according to the method described in section 3.3. This concerns in particular separate HP sizing for SH and DHW, with selection of the higher of

the two values. In this regard, for hybrid systems, the "low capacity" for SH (30%) turns out to be unfit for the DHW constraint, so that these cases actually resume to the respective reference cases (see Table 2).

Table 2. Summary of the cases studied for the sensitivity study

Système	Variant*	#	HP capacity* for SH (@7°C/45°C) [kW_{th}]	HP capacity* for DHW (@7°C/45°C) [kW_{th}]	HP capacity** retained (@7°C/45°C) [kW_{th}]	Boiler capacity [kW_{th}]	T_{biv} [°C]	Volume tank SH [m^3]	Volume tank DHW [m^3]
Monovalent	**Reference**	**A0**	250	(84)	274	-	-	2.2	1.9
	Low DHW	**A1**	250	(84)	274	-	-	2.2	1.9
	High DHW	**A2**	250	(84)	274	-	-	2.2	1.9
	Low SH	**A3**	189	(84)	208	-	-	2.2	1.9
	High SH	**A4**	322	(84)	350	-	-	2.8	1.9
Parallel / modulating boiler	**Reference**	**B0**	(78)	84	88	95	4.5	2.9	1.9
	Low DHW	**B1**	(78)	84	88	95	4.5	2.9	1.9
	High DHW	**B2**	(78)	84	88	95	4.5	2.9	1.9
	Low SH	**B3**	(60)	84	88	72	2	2.9	1.9
	High SH	**B4**	104	(84)	104	122	5	2.2	1.9
	Low capacity	**B5**	(53)	84	88	95	4.5	2.9	1.9
	High capacity	**B6**	201	(84)	208	95	-8	2.2	1.9
Parallel / non-modulating boiler	**Reference**	**C0**	(78)	84	88	95	4.5	2.9	1.9
	Low DHW	**C1**	(78)	84	88	95	4.5	2.9	1.9
	High DHW	**C2**	(78)	84	88	95	4.5	2.9	1.9
	Low SH	**C3**	(60)	84	88	72	2	2.9	1.9
	High SH	**C4**	104	(84)	104	122	5	2.2	1.9
	Low capacity	**C5**	(53)	84	88	95	4.5	2.9	1.9
	High capacity	**C6**	201	(84)	208	95	-8	2.2	1.9
Alternative / non-modulating boiler	**Reference**	**D0**	137	(84)	137	189	0.5	2.2	1.9
	Low DHW	**D1**	137	(84)	137	189	0.5	2.2	1.9
	High DHW	**D2**	137	(84)	137	189	0.5	2.2	1.9
	Low SH	**D3**	104	(84)	104	143	0.5	2.2	1.9
	High SH	**D4**	175	(84)	175	243	0.5	2.8	1.9
	Low capacity	**D5**	(53)	84	88	189	4.5	2.9	1.9
	High capacity	**D6**	201	(84)	208	189	-8	2.2	1.9

DHW: Low DHW = 25 L/hab.day, Reference = 35 L/hab.day, High DHW = 50 L/hab.day;

SH: Low SH = 78 kWh_{th}/m^2.an, Reference = 101 kWh_{th}/m^2.an, High SH = 130 kWh_{th}/m^2.an;

HP capacity (only hybrid sys.): Low capacity: 30%, Reference: 50%, High capacity: 80%

**Values that are not in parenthesis correspond to the highest HP capacity requirements between the two modes.*

*** HP capacity corresponding to an existing HP model, meeting the highest HP capacity required for the system.*

7. Results of sensitivity analysis

The results of the sensitivity analysis are presented in Figure 7. In total, 26 variants are simulated (4 reference cases + 22 variants). For comparison, the CO_{2eq} emissions are also estimated for a "100% gas" system, where a boiler produces all the heat.

In the case of the monovalent system, the SPF_{HP} turns out very stable, at 2.85 ± 0.01. For the hybrid cases, it raises to values between 3.06 and 3.31 (due to boiler backup during the coldest days), except for the HP with *"High capacity"* (B6, C6, D6), for which it drops to around 2.90. For these cases, it turns out that the HP does in fact ensure almost 100% of the heat production, despite a significant reduction of the HP capacity as compared to the monovalent system (208 kW_{th} instead of 274 kW_{th} @7°C/45°C). Such result raises questions regarding the best method for sizing the HP, in particular for monovalent systems, to avoid oversizing and reduce investment costs.

For the hybrid systems (except for the *"High capacity"* cases, for the reason explained above), the SPF_{global}, which considers the gas consumption and related heat production, drops to values between 1.52 and 2.40, with HP shares between 56% and 88%. Furthermore, the higher the overall performance (SPF_{global}) and HP share, the lower the HP performance (SPF_{HP}), due to lesser boiler backup during the colder days.

Emissions of the monovalent systems and hybrid cases with *"High capacity"* are around 49 gCO_{2eq}/kWh_{th}. The hybrid systems reach values between 68 and 127 gCO_{2eq}/kWh_{th} (to be compared with the 247 gCO_{2eq}/kWh_{th} of the "100% gas" system).

At more specific levels:

- For all four system types, the variation of the DHW demand (*"Low DHW"* and *"High DHW"*) has no significant impact, as compared to the respective reference case.
- The same is true for cases with *"High SH"* demand. In parallel systems, the cases with "*Low SH"* demand (B3 and C3) lead to a minor increase of the HP share, with related decrease of SPF_{HP}, increase of SPF_{global} and reduction in CO_{2eq} emissions. Latter is due to an "oversized" HP capacity in SH mode (due to sizing done for the DHW mode, see Table 2), which brings about a colder bivalence temperature (2°C) than for the reference case (4.5°C). As a result, the HP operates over an increased period of time, but in more severe conditions for its performance.
- As explained before, hybrid systems with "*Low capacity"* turn out to be unfit for the DHW constraint, so that these cases actually resume to the respective reference cases. Similarly, for the "*High capacity"* cases where the HP covers almost 100% of the heat production, de facto operating like the monovalent system.

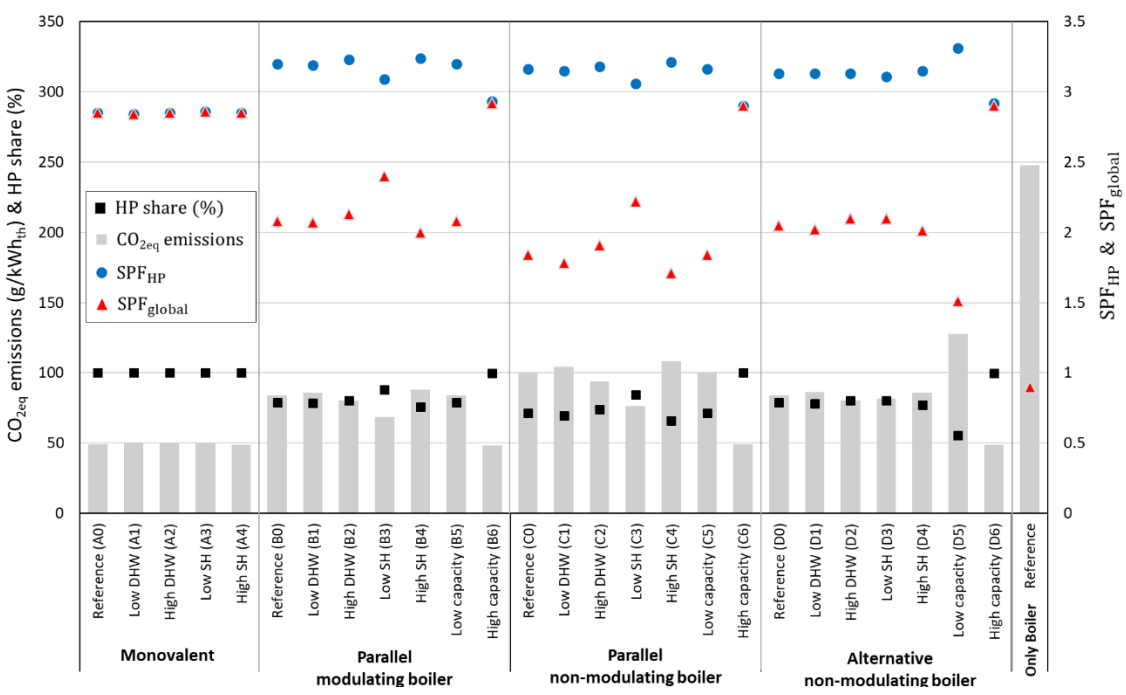


Figure 7. Results of the sensitivity analysis. Left axis: CO_{2eq} emissions per kWh_{th} of demand (bars) and HP share production (square points). Right axis: SPF_{HP} and SPF_{global} (triangles and circles points)

8. Limitations and future work

With the hydronic concepts chosen in this study, the HP provides the entire DHW production, even for hybrid systems. At least for the parallel configurations, linking the boiler to the DHW production system would allow to reduce the HP capacity (see Table 2). While latter would most probably be interesting from an economic point of view, the environmental impact needs to be assessed.

Similarly, the proposed systems consist of a unique HP for SH and DHW, due to space availability and economic constraints. However, the installation of separate HPs for each mode (DHW and SH) could have the advantage of: i) adapting the HP capacity to the respective demands; ii) using refrigerants adapted to the temperature level of each operating mode; iii) simplifying the system hydronic and control.

Further work should also include: i) impact of sizing of storage tanks, in relation with actual constraints in existing MFB buildings; ii) sensitivity analysis regarding SH distribution temperature; iii) diverse climate conditions / locations; iv) sensitivity to / future evolution of the electricity mix and the related CO_2 content.

9. Conclusions

This paper aims to develop hybrid concepts with air-source heat pumps adapted to the specific context of existing multifamily buildings, without renovation of the building envelope. The concepts correspond to different fuel-switch scenarios, with and without the possibility of using pre-existing modulating or non-modulating boilers. They are analyzed via numerical simulations, validated on detailed in-situ monitoring. For each concept, a sensitivity analysis assesses the impact of different levels of heat demand and heat pump capacity (under or oversizing in hybrid mode), in terms of energy and environmental performance.

The sensitivity analysis shows that for optimizing the energy mix and reducing CO_{2eq} emissions, not only the heat pump performance should be considered, but also the overall system performance (heat pump and boiler). Over the different scenarios, the seasonal performance of the heat pump varies between 2.8 and 3.3, while the overall performance (heat pump and boiler) is between 1.5 and 2.9.

Despite reduced HP efficiency and high CO_{2eq} content of the hourly electricity mix in winter, monovalent systems lead to lower emissions than hybrid systems. However, emissions of hybrid systems remain 2.3 to 3.5 times lower than with a fossil boiler, which points out their adequacy as a transitional solution to proceed to a fuel-switch before retrofitting the building envelope (hence avoiding sizing the heat pump to meet the entire demand before the renovation, when only a fraction of the heat pump capacity will be needed in the long term).

Among the hybrid systems, none of the analyzed systems stands out significantly in terms of performance. In addition to performance, the economic aspects also come into play when deciding which system to install. While these were not directly considered, several elements relating to the heat pump sizing were raised. In this regard, monovalent systems require the installation of a heat pump that is 2 to 3 times more powerful than hybrid systems, sized to ensure 80% of the production with the heat pump.

Acknowledgements

This research was co-funded by Services Industriels de Genève (within a pluri-annual partnership related to critical analysis of innovative energy systems in actual condition of use), the Swiss Federal Office of Energy (within the “AirBiVal” project), as well as Innosuisse–Swiss Innovation Agency (within the “Renowave” project).

References

[1] OFEV. Facteurs d’émission de CO2 selon l’inventaire des gaz à effet de serre de la Suisse, 2022. https://www.bafu.admin.ch/bafu/fr/home/themes/climat/etat/donnees/inventaire-gaz-effet-serre.html.

[2] OFEN. Bâtiments 2022. https://www.bfe.admin.ch/bfe/fr/home/effizienz/gebaeude.html (accessed May 19, 2022).

[3] Streicher KN, Padey P, Parra D, Bürer MC, Schneider S, Patel MK. Analysis of space heating demand in the Swiss residential building stock: Element-based bottom-up model of archetype buildings. Energy and Buildings 2019;184:300–22. https://doi.org/10.1016/j.enbuild.2018.12.011.

[4] De Sousa Fraga C. Heat pump systems for multifamily buildings: which resource for what demand? 2017. https://doi.org/10.13097/ARCHIVE-OUVERTE/UNIGE:94939.

[5] Montero O, Brischoux P, Callegari S, Fraga C, Rüetschi M, Vionnet E, et al. Large Air-to-Water Heat Pumps for Fuel-Boiler Substitution in Non-Retrofitted Multi-Family Buildings—Energy Performance, CO2 Savings, and Lessons Learned in Actual Conditions of Use. Energies 2022;15:5033. https://doi.org/10.3390/en15145033.

[6] Calame N. HPT - Heat Pumping Technologies - Heat pump retrofit projects for multi-family buildings – An obstacle run 2021;39:4.

[7] Fabrice R, Alisa Y, Matthias R. Retrofitting fossil-based heating systems with air to water heat pumps in multifamily houses. 12th IEA Heat conferance, Rotterdam: 2017, p. 11.

[8] Calame N, Cuvillier G, Rognon F, Montero Dominguez O, Brischoux P, Callegari SA, et al. AirBiVal: Développement et optimisation de concepts hybrides de pompes à chaleur sur l’air pour des immeubles résidentiels collectifs 2021.

[9] Dongellini M, Naldi C, Morini GL. Influence of sizing strategy and control rules on the energy saving potential of heat pump hybrid systems in a residential building. Energy Conversion and Management 2021;235:114022. https://doi.org/10.1016/j.enconman.2021.114022.
[10] Wüllhorst F, Vering C, Maier L, Müller D. Integration of Back-Up Heaters in Retrofit Heat Pump Systems: Which to Choose, Where to Place, and How to Control? Energies 2022;15:7134. https://doi.org/10.3390/en15197134.
[11] Vering C, Wüllhorst F, Mehrfeld P, Müller D. Towards an integrated design of heat pump systems: Application of process intensification using two-stage optimization. Energy Conversion and Management 2021;250:114888. https://doi.org/10.1016/j.enconman.2021.114888.
[12] Roccatello E, Prada A, Baggio P, Baratieri M. Analysis of the Influence of Control Strategy and Heating Loads on the Performance of Hybrid Heat Pump Systems for Residential Buildings. Energies 2022;15:732. https://doi.org/10.3390/en15030732.
[13] IEA Heat Pump Technologies. Annex 50: Heat Pumps in Multi-Family Buildings for Space Heating and DHW. Annex 50 2018. https://heatpumpingtechnologies.org/annex50/ (accessed May 9, 2022).
[14] Gadola R, Bless C. Wärmepumpen-Heizungszentralen in der Praxis : Vorschläge für eine gesamtheitliche Betrachtung kleiner und mittelgrosser Anlagen. Energie Schweiz; 2017.
[15] Gabathuler HR, Gmür C, Häuselmann E, Mayer H, Schadegg E. Schémas standards. Schémas éprouvés dans la pratique pour pompes à chaleur, couplage chaleur-force et de l'utilisation des rejets thermiques. Ravel; 1995.
[16] Klein S.A. et al. TRNSYS 17: A Transient System Simulation Program 2010.
[17] SIA. Norme 2028:2010 - Données climatiques pour la physique du bâtiment, l'énergie et les installations du bâtiment. Société suisse des ingénieurs et des architectes; 2008.
[18] Khoury J. Rénovation énergétique des bâtiments résidentiels collectifs: état des lieux, retours d'expérience et potentiels du parc genevois. Université de Genève, 2014.
[19] SIA. Norme 385/2:2015 - Installations d'eau chaude sanitaire dans les bâtiments - Besoins en eau chaude, exigences globales et dimensionnement. Société suisse des ingénieurs et des architectes. 2015.
[20] Romano E, Hollmuller P, Patel M. Émissions horaires de gaz à effet de serre liées à la consommation électricité – une approche incrémentale pour une économie ouverte : Le cas de la Suisse 2018.
[21] Quiquerez L. Analyse comparative des consommations de chaleur pour la production de l'eau chaude sanitaire estimées à partir de relevés mensuels: Etude sur un échantillon de bâtiments résidentiels collectifs alimentés par un réseau de chaleur à Genève 2017.

14th IEA Heat Pump Conference
15-18 May 2023, Chicago, Illinois

Thermoacoustic heat pump for very high temperature applications

M.E.H. Tijani*, J.A. Lycklama à Nijeholt

Energy & Materials Transition TNO
P.O. Box 1, 1755 ZG, Petten, The Netherlands

Abstract

Industrial heat pumps are gaining increasing interest as a way to decarbonize the industrial heat system. Waste heat is upgraded to useable temperature levels, leading to lower energy demand, lower energy costs and lower CO_2 emissions. Industry needs heat pumps which can operate at high temperatures (>200°C) and can achieve large temperature lifts. Conventional heat pumps do not have the capability to accomplish these requirements. The thermoacoustic heat pump (TAHP) is an auspicious innovative technology which uses acoustic power to lift heat from a low-temperature source to a high-temperature sink. High temperatures and large temperature lifts can be achieved by making use of Stirling cycle with a gas (helium) as working fluid. This paper presents the design, development, and test of a TAHP driven by a piston compressor which produced steam at 170°C with a high temperature lift. The heat pump has the potential to produce steam at a high temperature of at least 250°C.

© HPC2023.
Selection and/or peer-review under the responsibility of the organizers of the 14th IEA Heat Pump Conference 2023.

Keywords: Heat pump, thermoacoustics, Stirling;

1. Introduction

Industrial heat pumps are rising in popularity as a measure to decarbonize the industrial heat system. Heat pumps are highly efficient systems to upgrade low temperature industrial waste heat to useable temperature levels, resulting in lower energy demand, lower energy costs, and lower CO_2-emissions, especially if renewable electricity is used [1]. Heat pump development is aimed at to achieving higher output temperatures to match the required high process temperatures in industry. Industry needs heat pumps which can operate up to temperatures of 200°C and can achieve large temperature lifts. Conventional heat pumps currently do not have the capability to accomplish these requirements [2]. The temperature that can be delivered by closed-cycle compression heat pumps under development for example is limited to 150°C due to the lack of appropriate refrigerants and compressors for high temperature applications [2].

Different types of heat pump technologies are conceivable for an industrial application [3]. Conventional compression heat pumps are limited in their operating range by the working medium they employ. In contrast, heat pump technology that is based on a gas cycle can be operated at a variety of temperatures, not limited by either condensation or evaporation temperatures/pressures. These include the reverse Brayton cycle heat pump, Stirling heat pump, and TAHP. The TAHP use a Stirling thermodynamic cycle which has the highest COP of all heat pump cycles. The difference between a conventional Stirling and thermoacoustic systems is that thermoacoustic systems have fewer moving parts. The electrically driven TAHP is an auspicious new technology which can operate over a large range of temperatures, up to high temperatures (> 200°C) and can achieve large temperature lifts (e.g. 100 K) using preferably pressurized Helium as working medium. This enables the development of flexible systems that can be applied for large variety of temperature conditions, based on the same design and same working fluid

* Corresponding author. Tel.: +31-665-000-9629
E-mail address: hassan.tijani@tno.nl.

The study presented in this paper is the next step in the development of TAHPs for industrial applications. The first step was a laboratory heat pump setup designed and tested successfully for high temperature applications [4-5]. Secondly, a bench scale TAHP using an acoustic resonator has been developed and tested [6]. The current step in the development is to obtain a more compact and cost-effective heat pump by a TAHP re-design without an acoustic resonator. Another objective is to check the technical feasibility of using a commercial piston compressor as a driver for such a system. The possibility to use a commercially available piston compressors is of crucial importance to pave the path for the upscaling of TAHP to large capacities. Laboratory scale TAHPs use pistons driven by linear motors. However, linear motors are difficult to scale up and are very expensive. Piston compressors are already used in the gas industry and are commercially available at different scales up to MW's which makes upscaling of TAHPs feasible. The last objective is to study the capability of the TAHP to produce steam at temperatures of 200 °C.

The remaining of this paper is organized as follows: section 2 discusses the working principle of the TAHP. Section 3 presents the design and construction of the TAHP. Section 4 discusses the instrumentation. Section 5 presents the experimental results. In section 6 conclusions are drawn.

2. Thermoacoustic heat pump

An illustration of a compact electrically driven TAHP is shown in Figure *1*. TAHP uses acoustic power (W) to pump heat (Q_L) from a low temperature heat exchanger (LHX) and to deliver heat Q_H to a high temperature heat exchanger (HHX). The heat exchangers are linked to an external heat source and heat sink. The heat pump consists of a regenerator (REG) placed between the two heat exchangers which are placed inside a pressure vessel filled with helium gas at high pressure. The regenerator is a porous structure with very small channels where the heat pumping process takes place. An oscillating piston driven by an electrical motor supplies the acoustic power required for the heat pumping process. The acoustic wave generated by the piston forces the helium gas in the regenerator to execute a thermodynamic cycle similar to the Stirling cycle. The acoustic wave performs the compression, displacement, expansion, and the timing necessary for the Stirling cycle. The right phasing between the acoustic pressure and the gas velocity in the regenerator is realized by an acoustic circuit formed by the flow resistance of the regenerator, the acoustic inductance L formed by the annular space around the regenerator and heat exchangers, and an acoustic compliance C (volume of gas). It is worth noting that the functionality of the displacer piston in a conventional Stirling system is replaced by the combination of the inertance (fluidic inertia) and the compliance. This avoids the use of a second piston as mechanical piston displacer [7].

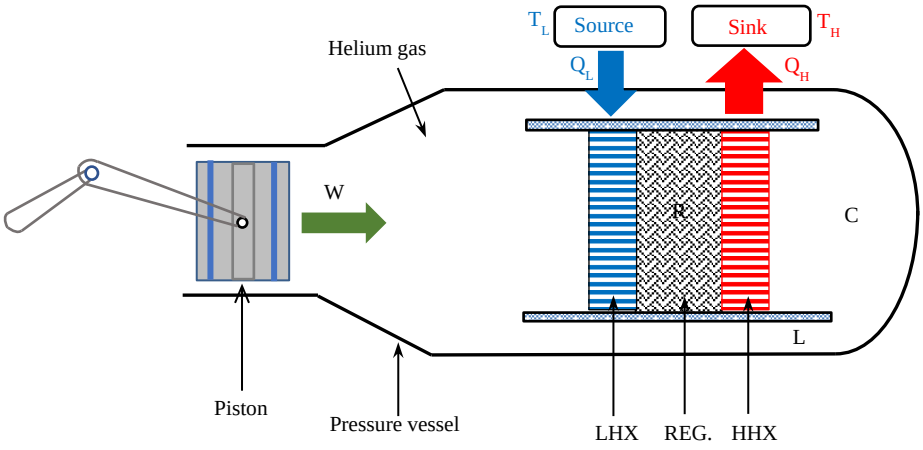


Figure 1 Schematic illustration of the electrically driven thermoacoustic heat pump

The operation of a TAHP will be explained by using an electric analog of the acoustic network, as shown in **Error! Reference source not found.**. The acoustic pressure and velocity are analog to the electrical voltage and current, respectively. The fluidic resistance of the regenerator, the acoustic compliance, and the acoustic inertance are represented by an electric resistance R, electric capacitance C, and electric inductance L, respectively. The function of the network is to create the traveling-wave timing necessary for the Stirling cycle in the regenerator. The ideal phase difference between the acoustic pressure (P) and the acoustic flow (U) in the regenerator is zero (traveling acoustic wave).

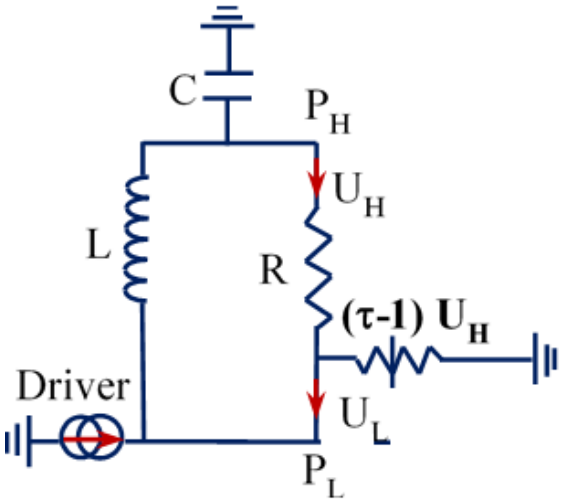


Figure 2 Simplified lumped-element electrical analog of the thermoacoustic heat pump

An analysis of the simplified lumped-element electrical analog of the heat pump can be used to show how the acoustic flows, powers, and timing are determined by the different parameters and components in the circuit. The acoustic flow entering the regenerator at the hot side U_H is damped by the temperature ratio across the regenerator $\tau=T_L/T_H$. An acoustic flow sink $[(1-\tau)\ U_H]$ is used to fulfil the condition of damping. U_H is damped because acoustic power is used to pump heat. The parallel branches of the inertance and regenerator have the same voltage [8]

$$i\omega L U_H = R U_H \tag{1}$$

The flows U_H and U_L are determined by the flow to the compliance

$$U_L + U_H = -i\omega C p_L \tag{2}$$

Combining expressions (1) and (2), U_H is given by

$$U_H = \frac{\omega^2 LC}{R} \frac{P_H}{1+\frac{i\omega L}{R}} \tag{3}$$

Expression (1) shows that the flow in the inertance is 90° out of phase from that in the regenerator. Expression (2) shows that the flows into the regenerator and inertance is controlled by the compliance C. Increasing the compliance volume will results in an increase of the flow through the regenerator. Expression (3) shows that if the impedance of the inertance ωL is much smaller than R, then U_C and p_c will be in phase corresponding to the traveling-wave phasing necessary for the Stirling cycle. Expression (3) shows also that the magnitude of acoustic flow is controlled by R, L, and C. In general R, L, and C are designed to create an impedance in the regenerator which is 15-30 times the traveling wave impedance $\rho_m c/A$ to avoid large losses in the regenerator.

The acoustic power at the hot side of the regenerator in the case $L\omega << R$ (pressure in phase with flow) is given by

$$W_H = \frac{1}{2} p_H U_H \tag{4}$$

Where p_H is the magnitude of the acoustic pressure at the hot side. The acoustic power flowing out the cold end of the regenerator is given by

$$W_C = \frac{T_C}{T_H} W_H \tag{5}$$

An qualitative explanation of the working priciple of the thermoacoustic effect is shown in Figure 3. As mentioned in the foregoing the thermoacoustic thermodynamic cycle is similar to Stirling cycle. **Error! Reference source not found.**a illustrates an acosutic wave treveling through the core of the heat pump. The wave enters at HHX and it is used to pump heat from a heat source to heat sink. As acoustic power is used to

pump heat the wave is damped. **Error! Reference source not found.**b illustrates the thermoacoustic cycle which consists of four steps. Step1: Isothermal expansion (1→2), the gas expands isothermally in LHX and heat is absorbed by the gas. Step 2: Heating, the gas moves through the regenerator from LHX to HHX and it is heated at constant volume. Step 3: Isothermal compression (3→4), the gas is compressed isothermally in HHX and heat is rejected to HHX. Step 4: Cooling, the gas moves back through the regenerator from HHX to LHX and it is cooled at constant volume. **Error! Reference source not found.**c shows the pressure-volume diagram of the cycle which is elleptic due to the overlap between the different steps. The area of the ellipse correpnds to the acoustic power (W) used in the cycle.

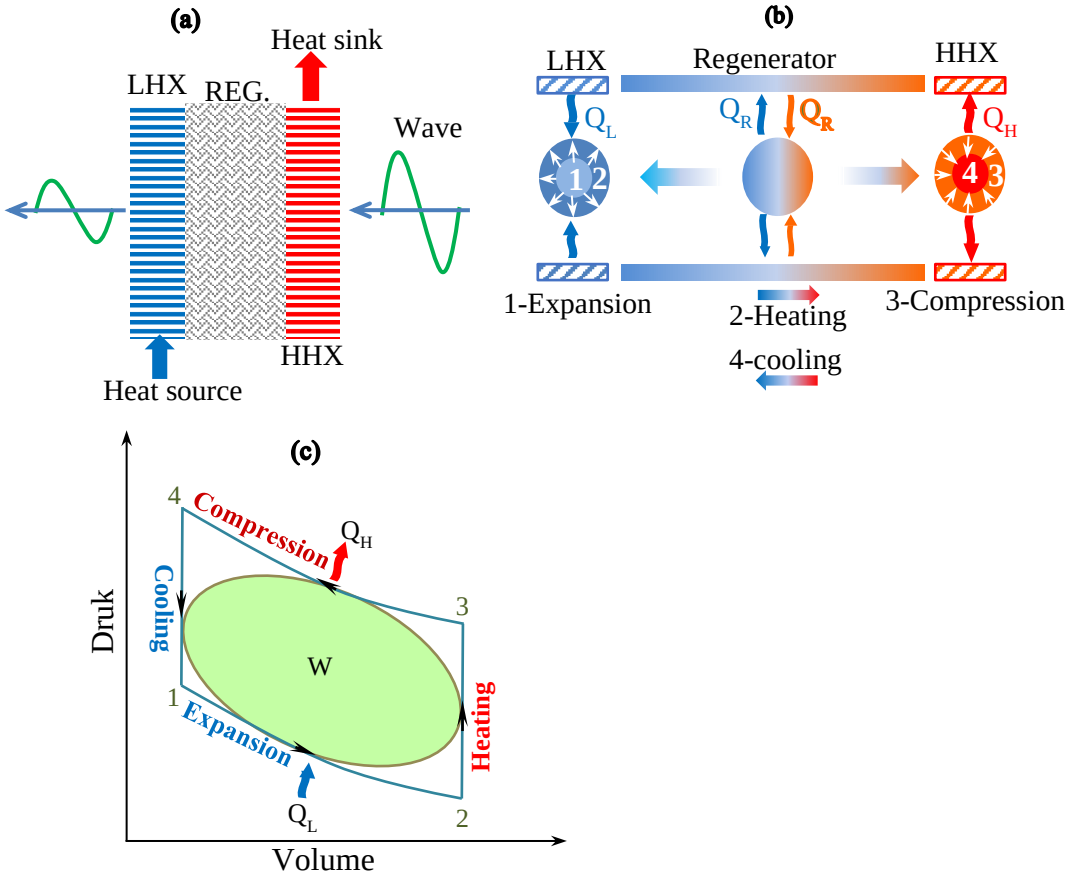


Figure 3 Illustration of the thermoacoustic cycle. (a) Acoustic wave travelling through the core. (b) illustration of the four steps of the cycle. (c) Pressure-volume diagram.

The performance of the heat pump is characterized by the coefficient of performance (COP) which is the ratio of the heat delivered to the heat sink and the acoustic work used by the heat pump.

$$COP = \frac{Q_H}{W} \tag{6}$$

The maximal theoretical limit for the COP of a heat pump is the Carnot coefficient of performance which is determined by the temperatures of the heat sink and the heat source and is given by

$$COPC = \frac{T_H}{T_H - T_L} \tag{7}$$

In practice the COP is always lower than the COPC due to the different losses in the heat pump. It is worth noting that helium is used because of its high power density, thermodynamic performance and safe use. However, it becomes rare and hence expensive. Hydrogen is a better working medium than helium and it will be very abundant in near feature and thus much less expensive. For industrial applications hydrogen could be

the working medium for thermoacoustic systems.

3. Design and construction

As discussed in the foregoing, the aim of the study is to evaluate the feasibility of this compact system, of using a commercial piston compressor as a driver and the capability of the heat pump to produce steam at high temperature (~ 200°C). The starting point for the design is the piston compressor whose operation frequency and stroke will determine the operation conditions for the heat pump. A compressor is selected with a maximal speed of 1200 RPM, a stroke of 230 mm, and the piston diameter is 320 mm. Helium at a mean pressure of 50 bar is used as working fluid. This leads to the operation conditions for TAHP as given in Table 1. The drive ratio is the ratio of the acoustic pressure amplitude at the piston and the mean pressure of the gas.

Table 1 Operation conditions for TAHP

Working gas	Helium
Average pressure (bar)	50
Frequency (Hz)	20
Sink temperatures (°C)	100-200
Thermal power at 180 °C (kW)	6.8
Drive ratio (%)	10.4

The compressor is adapted by the supplier to comply with the expected load on the pin of the crosshead considering the thermoacoustic operation conditions [9]. An illustration of the TAHP as coupled to the compressor is shown in Figure 4. The piston compressor consists of a piston driven by an electric motor via a flywheel and a crankshaft. To limit the load on the pin of the cross-head when starting the compressor, a bypass with a starting valve is used in combination with a back volume. The back volume is a volume of gas at the crank-side of the piston which is used to balance the forces on the piston and hence to limit the load on the pin. When starting the compressor, the forces on the cross-head pin are too high and the valve must be open to limit the load on the pin. The bypass connects the back volume of the piston to the compliance to avoid large loading forces on the pin which might damage the driving system. Once the compressor is started, the valve is automatically closed and the measurements can proceed.

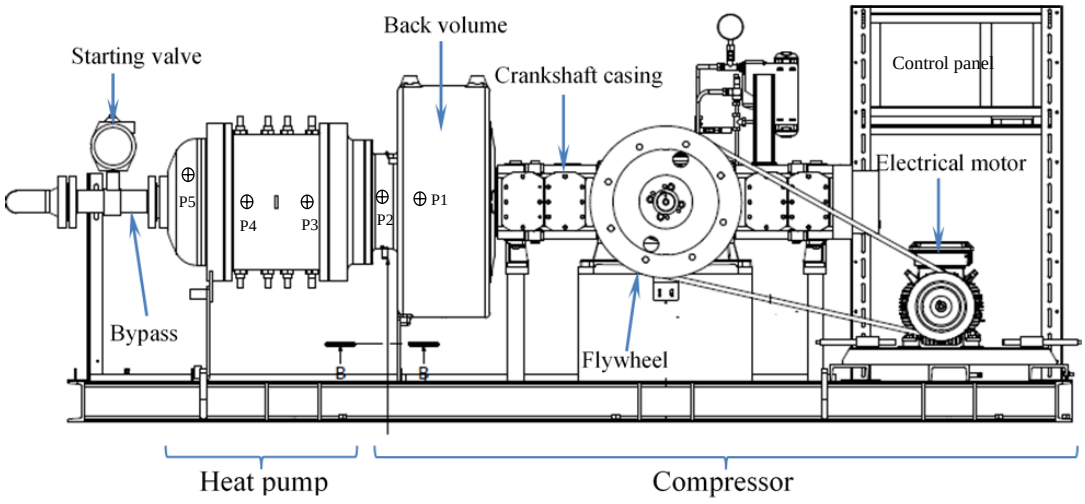


Figure 4 Illustration of the TAHP. The "P's" are pressure sensors

A cross-sectional view of the TAHP is shown in Figure 5. The driver system includes a balance piston connected to the crank which is used to minimize the vibrations due to the oscillating motion of the driving piston.

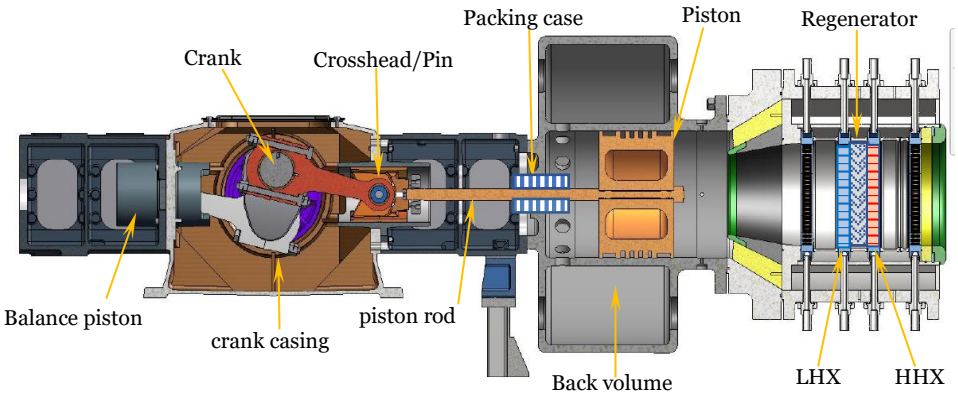


Figure 5 Cross-sectional view of the TAHP

The main parts of the TAHP are the regenerator, heat exchangers, and the acoustic circuit. These parts are discussed shortly in the following. For the sealing, O-rings are used for the nozzles of the heat exchangers and for the connections of the different components of the heat pump. A pressure packing case is placed at the crank side of the piston to limit the helium leakage from the back volume to the housing of the crosshead, which is at atmospheric pressure. The packing is provided with cooling water to remove the heat generated by friction.

Regenerator

The regenerator consists of a stack of stainless steel screen with a diameter of 260 mm and length of 48 mm. The hydraulic radius of the regenerator is 43 µm and the volume porosity is 83 %. A picture of the regenerator is shown in Figure 6. This regenerator is designed for an operation frequency of 80 Hz and an operating pressure of 50 bar and is not optimal for the operational conditions summarized in Table 1. It is used as it is available in our laboratory and can be used directly for the test of the compressor as driver and for the production of steam at high temperature. The use of an optimal regenerator will result in higher thermal power and performance.

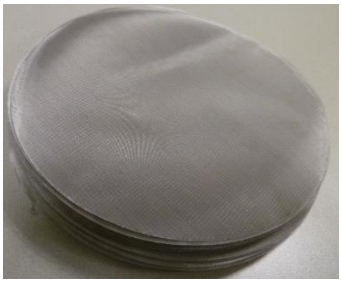


Figure 6 Stack of screen sheets used as regenerator

Heat exchangers

The heat exchangers LHX and HHX are finned, circular tube cross-flow heat exchangers as shown in Figure 7. These heat exchangers are made of copper fins and tubes and stainless steel headers. It consists of a single row of tubes with a diameter of 13.5 mm and the spacing between adjacent tubes (pitch) is 30 mm. The spacing between the fins is 0.88 mm and the fin thickness is 0.25 mm. Helium gas oscillates between the fins and a second fluid (water/steam/thermal oil) flows through the tubes. The maximum design temperature for the heat exchangers is 200°C.

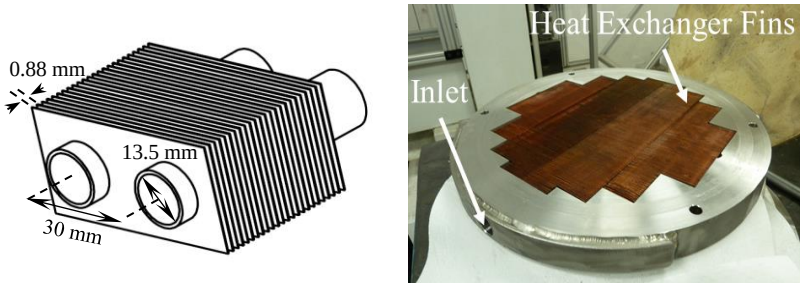


Figure 7 Illustration of the fin-tube structure (left) and picture of the heat exchangers (right)

Acoustic circuit

The feedback inertance, compliance, and regenerator flow resistance are designed to achieve the traveling-wave phasing in the regenerator and minimize viscous losses. The acoustic pressure and acoustic velocity have to be in phase at the regenerator midpoint (Stirling cycle). The feedback inertance L is formed by the annular space between the wall of the pressure vessel and the cylindrical holder of the regenerator and heat exchangers. The length of the annular space is 600 mm and the cross section is about 0.04 m^2. The volume of the compliance is 14 litres.

4. Test bench and instrumentation

A thermal bench using thermal oil has different heating and cooling circuits which can be used to simulate heat source and heat sink for the heat pump. The LHX of the TAHP is coupled to a circuit of the thermal bench that supplies heat between 50-150℃ by thermal oil. The HHX is coupled to a steam vessel where the steam produced by the TAHP can be condensed. The steam vessel contains a condenser which is cooled by the thermal bench. Pictures of the TAHP coupled to the thermal bench are shown in Figure *8*.

Various sensors are placed through the system to measure the operating parameters of the heat pump as indicated in Figure *4* [6]. The oil and water flow into the heat exchangers are measured with flow meters. The temperatures of the oil and water/steam at the inlet and the outlet of the heat exchangers are measured with thermocouples. Several pressure sensors are placed throughout the system to measure the acoustic pressure at different locations in the system. The signals from the thermocouples are read by a PLC-data acquisition system and sent to a computer. The pressure signals (magnitude and phase) are first measured by lock-in amplifiers and then send to a computer. The signals are recorded and displayed using Control Maestro. The acoustic power generated by the piston could not be measured.

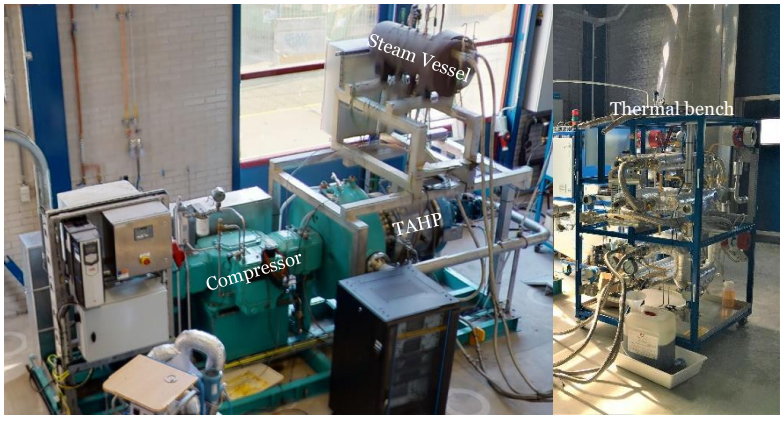


Figure 8 Picture of the TAHP coupled to the steam vessel and to the thermal bench

5. Experimental results

The heat pump is designed to operate at 50 bar helium. However, the electrical motor which drives the compressor reaches its maximum torque at about 32 bars. Therefore, measurements are done with the TAHP at reduced pressure of 30 bars. Steam is produced at different temperatures and the measurement data for the steam production at 150 and 170℃ are summarized in Table 2.

Table 2 Measurements results for the production of steam at 150℃ and 170℃

Dr (%)	T_{LHX}(℃)	T_{HHX}(℃)	T_{reg-H}(℃)	T_{reg-L}(℃)	Q_H(kW)
10.4	94	152	186	45	6.5
10.2	94	170	194	60	4.7

For the steam production at 170℃, the average temperature of the inlet and outlet temperatures of the oil at the LHX is 94℃ and the temperature of the steam in the steam vessel is 170℃. The internal temperatures of the regenerator at the hot side and low temperature side are 194℃ and 60℃, respectively. The external lift is 74 K while the internal lift is 134 K. The heat exchangers are performing poorly as the temperature difference across LHX between helium gas and oil is 33℃ and across HHX between helium and steam is 26℃. The heat pump generates 4.7 kW of thermal power in the form of steam. This is lower than the design value due to the lower used mean pressure of 30 bar. The thermoacoustic computer code DeltaEC [10] predicts that operating at 50 bar, using an optimal regenerator and better heat exchangers with a temperature difference of 10 K, the heat pump would produce 16 kW of thermal power at 170 ℃ with a COP of about 4 and for an external source temperature of 100 ℃.

As mentioned in the foregoing at the moment the acoustic power used by the TAHP can't be measured. An internal energy balance was used to calculate the acoustic power used in the heat pump. This results in an indicative COP of about 3.

6. Conclusions

An electrically driven thermoacoustic heat pump is built and tested and it can be concluded that a piston compressor can be used as acoustic driver for a TAHP. This leads to a compact heat pump without acoustic resonator. Piston compressors are commercially available at different scales up to MW's. This makes upscaling of thermoacoustic heat pumps feasible. The heat pump produces steam at different temperatures up to 170℃, supplying waste heat of 94°C. Higher temperatures can be achieved but not feasible with the current heat exchangers. The heat pump generates 4.7 kW of thermal power with a COP of about 3, excluding the losses in the compressor and internal heat losses. Large temperature differences are measured across the heat exchangers which indicates a poor heat transfer coefficient.

Simulation calculations using the thermoacoustic computer code DeltaEC [10] predicts that operating at 50 bar and using an optimal regenerator and better heat exchangers with a temperature difference of 10 K, the heat pump would produce 16 kW of thermal power at 170℃ with a COP of about 4 for an external source temperature of 100℃.

In the near feature an optimal regenerator and optimized heat exchangers will be implemented to improve the performance of the heat pump and to generate steam at higher temperatures (>200℃). An acoustic power measurement system will be also incorporated enabling the measurement of acoustic power input and performance.

Acknowledgements

This work was funded by TNO and the Dutch Ministry of Economic Affairs and Climate Policy (EZK) under contract TEEI118003.

References

[1] Wolf S, Blesl M. Model-based quantification of the contribution of industrial heat pumps to the European climate change mitigation strategy. ECEEE Ind. Summer Study Proc. 2016:477–87.
[2] Arpagaus, C., Bless, F., Uhlmann, M., Schiffmann, J., & Bertsch, S. S. (2018). High temperature heat pumps: Market overview, state of the art, research status, refrigerants, and application potentials. Energy, 152, 985–1010.
[3] Nellissen P, Wolf S. Heat pumps in non-domestic applications in Europe: potential for an energy revolution. In: 8th EHPA European Heat Pump Forum, Brussels, Belgium; May 28 2015. p. 1-17.
[4] Tijani, M.E.H. Vanapalli, S. Spoelstra, S., Lycklama à Nijeholt, J.A. "Electrically driven thermoacosutic heat pump" 10th IEA Heat Pump Conference 2011, Tokyo, Japan.

[5] Tijani, M.E.H. Spoelstra, S., "High temperature thermoacoustic heat pump" 19th International Congress on Sound and Vibration (ICSV19), Vilinius, Litouwen, , 8-12 juli 2012.
[6] Tijani, M.E.H. Lycklama à Nijeholt, J.A, S. Spoelstra, S.," Development of a thermoacoustic heat pump for distillation column", 12th IEA Heat Pump Conference 2017, Rotterdam, Netherlands.
[7] Vanapalli, S, Tijani, M.E.H. Vanapalli, S. Spoelstra, "Thermoacoustic heat pump for domestic applications" 3rd Joint US-European Fluids Engineering summer meeting, ASME 2010, Montreal, Canada.
[8] Backhaus, S. and Swift, G. W. (2000): A thermoacoustic-Stirling heat engine: Detailed study. J.Acoust.Soc.Am, 107(6), pp. 3148-3166, (2000).
[9] https://www.howden.com/en-gb/contact-us/locations/europe/howden-thomassen-compressors-bv
[10] Ward, W. and Swift, G.W. "Design Environment for Low Amplitude Thermoacoustic Engine", J. Acoust. Soc. Am, 95, 3671 (1994).

14th IEA Heat Pump Conference
15-18 May 2023, Chicago, Illinois

Optimisation of a Novel Dry Air-Ground Source (DAGS) Heat Pump System

Yebiyo, M., Badran B.E., Stignor C. H., Axell, M., Gustafsson O

RISE Research Institutes of Sweden, Drottning Kristinas väg 61, Stockholm

Abstract

Ground temperatures will often fluctuate in response to heat absorption or rejection. It is important to recognize that the ground is not an infinite energy source and that it is appropriate to prevent excessive heat extraction or rejection of the ground. Significant changes in ground temperature are likely to occur if exorbitant heat extraction rates from or rejection to the ground are tolerated for long periods. These variations in the ground temperature can have major adverse effects on the coefficient of performance (COP) of a ground source heat pump (GSHP) system and, thus, the system's overall performance. However, one method of regulating ground temperature imbalance is to reject heat when the ground and ambient temperatures favor this through a dry air cooler (DAC). In order to protect the system, rather than to improve performance, DACs are often fitted to GSHP systems to reject heat in extreme conditions. An empirical transient system simulation model (TRNSYS) was developed in this study and used to analyze the control algorithms to determine the optimal operation and control strategies for the GSHP system's performance. Specifically, the paper explores the impact of using a GSHP device with a DAC. This involves examining (i) the input of energy into the GSHP system, (ii) the annual ground temperature variation and (iii) the COP. The results show that considerable savings can be achieved with optimum operation and control strategies for a GSHP system.

© HPC2023.
Selection and/or peer-review under the responsibility of the organizers of the 14th IEA Heat Pump Conference 2023.

Keywords: Ground Source Heat Pump, ground temperature variation, control optimisiation, TRNSYS

1.0 Introduction.

GSHP systems can provide an efficient and economical alternative to gas, electric, or oil methods for heating and cooling buildings. The GSHP industry has matured from a technology standpoint yet continues to be dynamic with rapid growth rates. Péan et al. (2019) presented a concise review of the past, present, and future research highlighting some of the achievements and advantages of the GSHP system. Sarbu and Sebarchievici (2014) provided a detailed review of the GSHP systems, including their operation, energy, economic and environmental performances and recent advances.

In order to absorb or reject heat from the surrounding soil, GSHP systems have heat exchangers buried in the ground (ground loop). The rate at which heat is absorbed from the ground must not allow the temperature of the ground to fall too low during the winter, and during the summer, the heat absorbed in the winter must somehow be replenished. Otherwise, this will result in soil thermal imbalance (the mismatch between heat extraction and ground rejection) that can degrade the efficiency of the GSHP device.

Researchers are looking at hybrid GSHP systems to help solve the soil thermal imbalance problem. A hybrid GSHP system uses several different geothermal sources, outdoor air and geothermal sources, to balance the annual thermal load.

Three buildings (two cooling-dominated and one heating-dominated) using hybrid GSHP systems for a year were tracked and analysed by Hackel and Pertzborn (2011). In TRNSYS tool, models of hybrid GSHP systems were constructed; a closed-circuit cooling tower (CCCT, also referred to as a fluid cooler) was used as an additional device to meet a portion of the peak heating or cooling load. Their work has demonstrated that cost-effective and environmentally friendly hybrid GSHP systems are available.

Alavy et al. (2013) developed a rigorous mathematical and computational approach for sizing hybrid GSHP systems. They tested their methodology on ten cases, from residential to commercial and industrial buildings, and concluded that the method could result in significant reductions in initial costs of installation, payback period, and operation costs when compared to non-hybrid GSHP systems.

Lee et al. (2014) conducted an experimental study to compare the transient performance characteristics between a GSHP and a hybrid GSHP, accounting for the degradation of the ground thermal condition during long-term operation. They found that the hybrid GSHP lessened the deterioration of the ground thermal condition and increased the system performance during long-term operation. For the hybrid GSHP, supplementary heat rejecters or extractors were incorporated into the GSHP to control some portion of the heat rejection or extraction rate of the ground heat exchanger (GHE) to reduce the cooling or heating load imposed on the GHE.

Lee et al. (2015) proposed a hybrid GSHP system to solve the performance degradation of the GSHP systems under imbalanced load conditions. They designed a hybrid GSHP system composed of three flow loops: a refrigerant flow loop, a ground flow loop, and a supplemental flow loop. In their study, the transient performance characteristics of the hybrid GSHP were measured and analysed in the cooling mode at various flow loop configurations, including the hybrid GSHP systems with serial and parallel configurations. Their research showed that during the hybrid operation, the hybrid GSHP system with serial configuration showed a relatively higher coefficient of performance (COP) than the hybrid GSHP with parallel configuration due to the lower heat accumulation in the ground under the degraded ground thermal condition. In addition, they concluded that under the steady state condition, the COPs in the hybrid GSHP systems with serial and parallel configurations were 15% and 7% higher, respectively, than that in the standard GSHP system.

Beckers, Aguirre and Tester (2018) studied various hybrid and non-hybrid GSHP and air source heat pump (ASHP) configurations using TRNSYS, calibrated with data measured at the cellular tower shelter in Varna, New York, United States (Varna Site). To limit the impact of thermal imbalance, the hybrid GSHP with an air economiser (free cooling) directly blows cold ambient air into the shelter, and the hybrid GSHP with a dry fluid cooler uses cold ambient air to cool down the borehole heat exchanger heat transfer fluid. Their simulations indicated that hybrid GSHP systems allow the owner to save up to 30 per cent of lifetime electricity consumption compared to hybrid ASHP systems for cooling cellular tower shelters for the weather and operating conditions of the Varna Site. They found that a hybrid GSHP system with an air economiser works better if the aim is to minimise energy consumption and CO2 emissions. Omitting an air economiser, the next best alternative is a hybrid GSHP with a dry fluid cooler, followed by a GSHP-only scheme. They also found that increasing the total depth of the borehole heat exchanger would further minimise energy consumption while increasing the total cost of ownership marginally.

Liu et al. (2019) proposed a hybrid GSHP system with an auxiliary cooling tower to relieve soil thermal accumulation and performance degradation over a long-time operation in the cooling-dominated area in Shanghai. To study the proposed system's performance and feasibility, the hybrid GSHP system simulation model was constructed in TRNSYS, and measurement data validated the reliability of the simulation. They concluded that the hybrid GSHP system remained stable in terms of the temperature variation of the soil, and the outlet temperature of the buried pipes were lower compared to standard GSHP systems over a ten-year operation.

Hou and Taherian (2019) designed and assembled a hybrid GSHP system in TRNSYS to examine the overall effectiveness of various pipe lengths. In their design, the hybrid GSHP was presented as a horizontal ground loop in parallel with a liquid dry cooler. They run simulations for a full calendar year to generate important analytical data such as annual energy consumption and heat

rate. After analysing the results of various pipe lengths and diverter setpoint temperatures, the optimal values were recommended by them.

Hou et al. (2020) simulated and tested the effectiveness of a newly-developed temperature-controlled diverter for a hybrid GSHP system which combined a horizontal ground loop and a liquid dry cooler. Their main target was to examine the double-set temperature diverter's overall effectiveness by switching the control strategies. Both short-term and long-term simulations were carried out in TRNSYS to analyse energy variation and soil thermal condition with respect to different diverter heating and cooling set temperatures. The short-term simulation results showed that the system's overall performance was mainly influenced by the diverter's heating set temperatures rather than cooling. Also, the usage ratio of the liquid dry cooler was decreasing while the diverter's heating set temperature was increasing. Combining long-term COP values and soil thermal variation, they recommended that diverter heating set temperatures ranging from 8 °C to 10 °C could provide the system with a favourable COP value and less soil temperature impact in climate zones. They also found that the loss in soil temperature over ten years of operation was shown to be lessened by employing the liquid dry cooler enhanced with the dual setpoint diverter.

In order to protect the system, rather than to boost performance, DACs are often fitted to GSHP systems to reject heat in extreme conditions. Opportunities exist to use a DAC to improve the GSHP 's performance. These control systems are not, however, documented in any literature. This paper presents the development of a new TRNSYS model to investigate the effects of using DAC by selectively rejecting heat through DAC to reduce the degree of ground temperature saturation and thermal imbalance. The overview of the GSHP system and its operation, the setup of the simulation, the GSHP system and the various components used to create an empirical model of GSHP TRNSYS are further presented in this paper.

This paper explicitly explores the impact of using a DAC in combination with a GSHP device. This involves investigating (i) the rejection of heat, (ii) the input of energy to the GSHP system, fan and circulation pumps, (iii) COP and (iv) the variation in ground temperature. Additionally, the TRNSYS model was used to examine a number of control algorithms to identify optimal operation and control strategies for the GSHP system to improve system efficiency.

2.0 Description of the New System and Its Operation.

The proposed system uses the London South Bank University (LSBU) GSHP installation at one of the buildings called (K2) but operates differently from the initial setup. Four HP Reversible EKW130 units (WaterFurnace, Inc) are used by LSBU's K2 building GSHP device. Each has a nominal heating capacity of 120 kW and a cooling capacity of 125 kW. Via a closed device, heat is transported to and from the ground using 159 vertical energy piles that are embedded in the structure's base and drilled into the London clay. The system's source side consists of energy piles and header pipes to which the HPs supply or extract heat through a pumped heat transfer fluide, exchanging energy between the building and the ground. The GSHP system provides the building's heat and cooling output entirely.

The original system used a DAC designed to work when the heat sink temperature was too high or too low. Therefore, the DAC was used to prevent the heat pump from working outside its protected envelope as a safety system. The DAC was tactically used in the proposed system to increase the efficiency and performance of the heat pump and, thus, the system. Figure 1 below illustrates the simulated system. This shows that to accomplish the best COP, the system is managed to provide heat rejection via the DAC rather than the ground loop. This is based on a theory that the Carnot COP of a heat pump is substantially affected with a 1 K decrease of temperature difference , resulting in a 3 % increase in COP. Therefore, when it provides more favorable heat sink temperatures (and thus a higher COP) compared to those produced by the field, the DAC can be used selectively. The proposed system has the potential to save energy but should not require additional components compared to the existing system, although it is controlled differently. The performance improvement of the proposed system is discussed in the following sections.

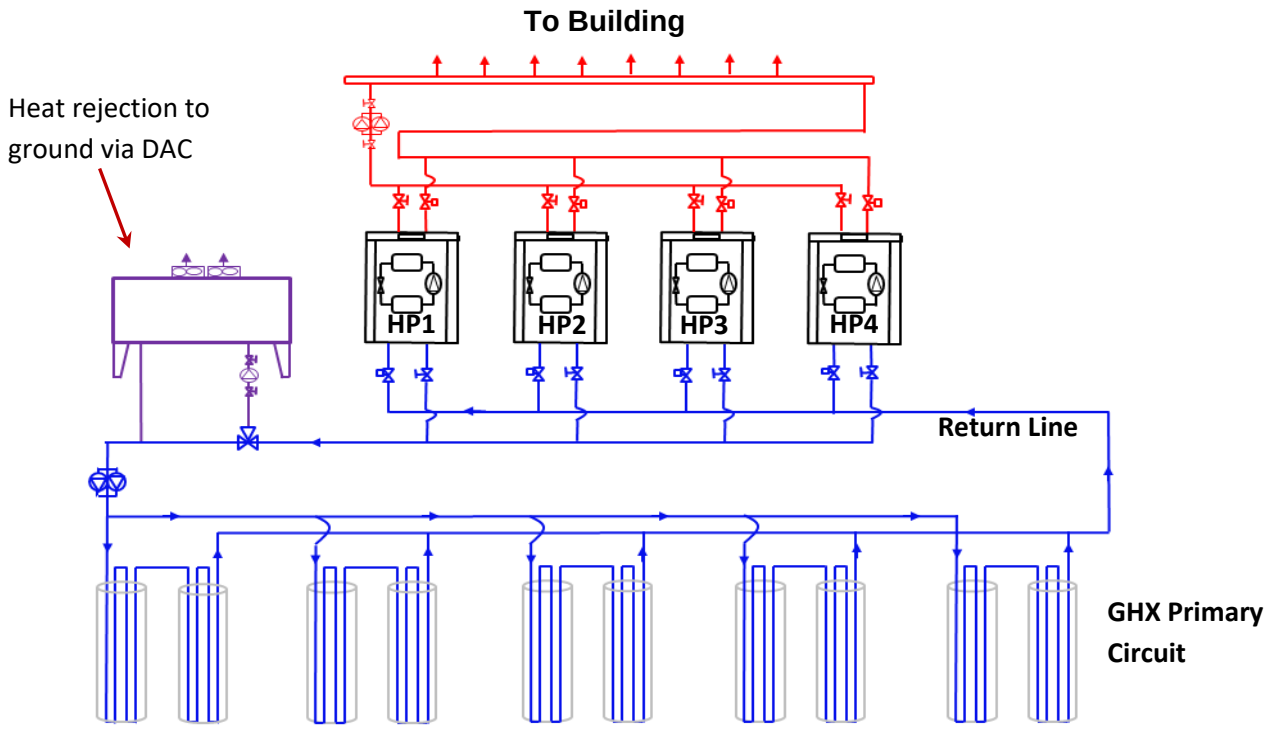


Figure 1: *Schematic of the System Simulated.*

3.0 The Simulation Setup.

In order to simulate the experimental observations, a model was built with the simulation software TRNSYS 17 , (2010). This allows the construction of a GSHP system simulator that closely resembles and simulates the actual HP installation. The main components of the GSHP system that were used to build the simulation model are the ground heat exchanger (Type 557a), the HP model (Type 668), the circulating pumps (Type 682) as flow stream loads, DAC (Type 511), tempering valve (Type 11), and tee piece (Type 511). The following sections describe how the various system components work, which are replicated by interconnecting a set of models.

3.1 Ground Heat Exchanger (Type 557a).

The ground heat exchanger component (Type 557a) was set up with the appropriate geometrical configuration and relevant ground thermal properties, some of which were derived from the thermal response testing carried out in the GSHP design stage. Type 557a models a set of equal vertical U-tube heat exchangers which thermally interact with the ground. This ground heat exchanger model is most used in GSHP applications. Depending on the temperature of the heat carrier fluid and the ground, a heat carrier fluid is pumped through the ground heat exchanger and either rejects heat or absorbs heat from the ground. In the current work, 159 energy piles are used to exploit the ground's heating and cooling capacity.

3.2 Heat Pump Model (Type 688).

The HP model (Type 668) relies upon catalogue data readily available from HP manufacturers for the performance measurement related to the HP that is being simulated. At the heart of the component are two data files: a file containing cooling performance data and a file containing heating performance data. Both data files provide capacity and power draw of the HP (whether in heating or cooling mode) as functions of entering source fluid temperature and entering load fluid temperature; these establish the performance envelope of the HP over a range of ground source side temperatures and a range of load side temperatures.

The Type 668 HP is equipped with two control signals, one for heating and cooling. If the heating and cooling control signals are both ON, the model will ignore the cooling control signal and will operate in heating mode. However, the heating mode takes precedence over the cooling mode. The data used to build this HP model were obtained from the manufacturer WaterFurnace.

The HP's COP in heating is given by equation 1.

$$\mathrm{COP}_{hp} = \frac{\mathrm{Q_{HP}\ [kW]}}{\mathrm{W_{HP}\ [kW]}} \quad (1)$$

The amount of energy absorbed from the source fluid stream in heating is given by equation 2.

$$Q_{absorbed} = Cap_{heating} - P_{heating} \quad (2)$$

The outlet temperatures of the two liquid streams can then be calculated using equations 3 and 4.

$$T_{Source,out} = T_{source,in} - \frac{Q_{absorbed}}{m_{source}Cp_{source}} \quad (3)$$

$$T_{load,out} = T_{load,in} - \frac{Cap_{heating}}{m_{load}Cp_{load}} \quad (4)$$

The HP's COP in cooling mode is given by equation 5.

$$\mathrm{COP}_{R} = \frac{\mathrm{Q_{HP}\ [kW]}}{\mathrm{W_{HP}\ [kW]}} \quad (5)$$

The amount of energy rejected by the source fluid stream in cooling mode is given by equation 6

$$Q_{absorbed} = Cap_{cooling} + P_{cooling} \quad (6)$$

The outlet temperatures of the two liquid streams can then be calculated using equations 7 and 8.

$$T_{Source,out} = T_{source,in} + \frac{Q_{rejected}}{m_{source}Cp_{source}} \quad (7)$$

$$T_{load,out} = T_{load,in} + \frac{Cap_{cooling}}{m_{load}Cp_{load}} \quad (8)$$

3.3 Circulation Pumps (Type 741).

There are two pumps for circulation. The Type 741 pump model may produce any mass flow rate between zero and its rated flow rate; in reality, each pump represents a group of pumps. Similar to the majority of pumps and fans in TRNSYS, Type 741 accepts the mass flow rate as input but only uses it to check the mass balance. Based on its rated flow rate parameter and the current value of its control signal input, Type 741 determines the downstream flow rate. The pressure rise, overall pump efficiency, motor efficiency, and fluid properties are used to compute the pump's power draw.

3.4 DAC (Type 511).

A dry air cooler, represented by Type 511, cools a liquid stream by blowing air across the coils holding the liquid. This model assumes that the device can be modelled as a single-pass, cross-flow heat exchanger.

3.5 Tempering valve (Type 11b).

Thermal systems frequently require the use of pipe or duct "tee-pieces," mixers, and diverters that are controlled externally. This valve enables the system to be managed according to the fluid's temperature, leaving the heat pump.

3.6 Tee piece (Type 511h).

The empirical GSHP system model used to examine various control techniques is schematically depicted in Figure 2. In this application of the Type 511h model, modes 1 and 6 are used to model how a tee-piece would work to thoroughly mix two intake streams of the same fluid at various temperatures and/or relative humidity. Table 1 provides a list of the assumptions used to simulate the TRNSYS system model.

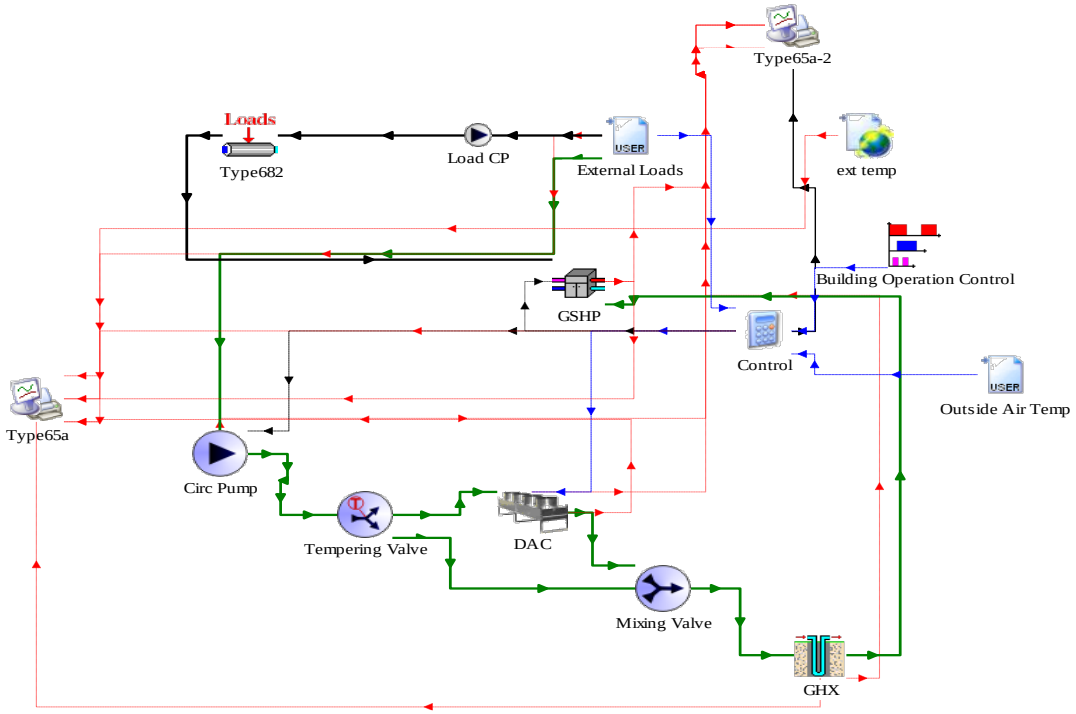


Figure 2: *Schematics of the DAC simulation setup connected to the GSHP system.*

Table 1: *List of model inputs and assumptions*
Occupancy period 13 hours every day except weekends
Historical outside air temperature (OAT)
Flow and return fluid temperatures on both the source and load side of the system
Heating and cooling performance data of the heat pump model
Heat pump and circulation pumps to operate in heating mode if the OAT > 18°C
Heat pump and circulation pumps to operate in heating mode if the OAT < 14°C

4.0 Model Validation.

The empirical TRNSYS model created was validated using experimental data from the real GSHP system installation at LSBU. The many physical elements of the system have been kept as close to reality as feasible, and numerous experiments have been carried out to validate the model. A comparison of the independently calculated COP values with those anticipated by the model shows a reasonable level of agreement. The maximum variance shown in Figure 3 is approximately 7%.

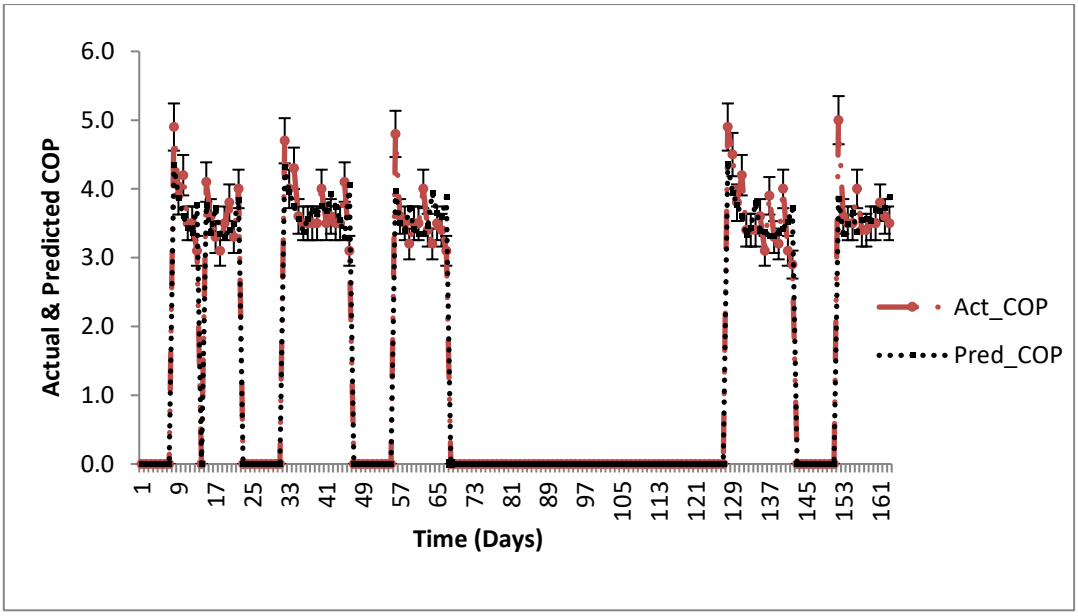


Figure 3: *Comparison of actual and predicted COP.*

5.0 Development of Novel Control Strategies Using DAC.

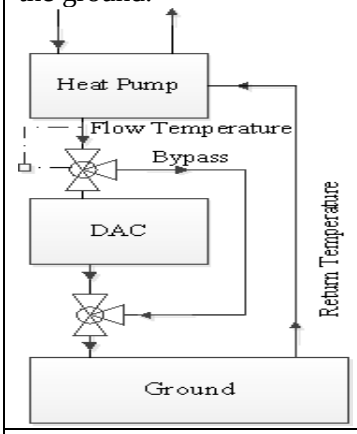
The development of novel control strategies using a DAC is given in this section. When the fluid temperature leaving the HP is higher than a specific threshold, as shown in Table 2, the control methods investigated in this work enable the DAC to activate the various control strategies known as scenarios CS1, CS2, CS3, CS4 and CS5. These conditions have been put to the test and measured against the system's typical operating state in order to explore the impact of operating the DAC at various temperature setpoints. Examining the annual change in ground temperature, the energy input into the GSHP system, and the output coefficient are all necessary for this (COP). The outcomes of the simulated scenarios are thoroughly explained in Sections 5.1 to 5.4.

Controls that have been properly installed and configured are essential for upholding the necessary performance and safety standards while utilizing minimal energy. It is possible to regulate the GSHP system's performance by utilizing a DAC to selectively reject heat to the air. The estimated seasonal or daily ground temperature and the anticipated/available energy demand of the building can be used to manage this. Building energy use and carbon emissions could be reduced if the control system is well-designed, implemented, and uses design temperatures that maximize the system's coefficient of performance (COP).

Table 2: *Different control strategy approaches using DAC*

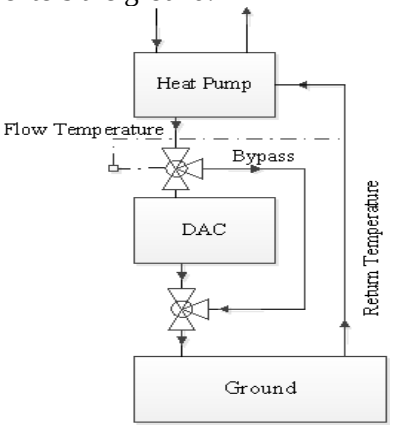
Control Strategy 1 (CS1)

The DAC is controlled based on the fluid flow temperature exiting the HP. When the DAC is on, then the fluid is cooled down using the DAC; otherwise, the fluid bypasses the DAC and enters the ground.



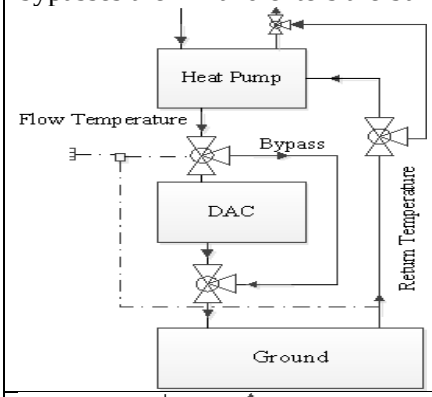
Control Strategy 2 (CS2)

The DAC is controlled based on fluid return temperature leaving the ground. When the DAC is on, then the fluid is cooled down using the DAC; otherwise, the fluid bypasses the DAC and enters the ground.



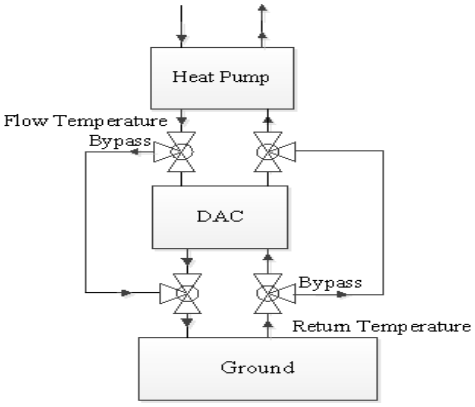
Control Strategy 3 (CS3)

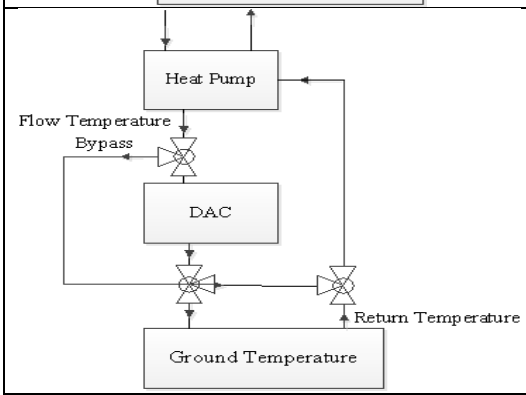
This is a free cooling option; the DAC is controlled based on the difference between fluid return temperature, leaving the ground and outside air temperature. When the DAC is on, then the fluid is cooled down using the DAC; otherwise, the fluid bypasses the DAC and enters the ground. The fluid returning from the ground bypasses the HP and enters the building.



Control Strategy 4 (CS4)

In this control strategy, there is an option of cooling the fluid either on fluid flow temperature exiting the heat pump or on fluid return temperature leaving the ground; otherwise, the fluid bypasses the DAC and enters the ground or the HP.





Control Strategy 5 (CS5)

The DAC is controlled based on the ground temperature and ambient air temperature, when the ground temperature reaches a certain value then the DAC can either be used to reject heat to the ground or the fluid bypasses the ground and enters the heat pump.

In order to reduce ground saturation, which has an impact on the system's performance, the existing system model was modified to reject heat into the ground. The opportunity was therefore seized

to explore the effects of various control strategy approaches employing the DAC on HP performance and ground temperature change after developing and establishing a verified empirical TRNSYS system model. The DAC circuit, circulation pumps, and the HP should all be turned on or off at different times according to the control methodologies used in this study. The three categories of HP power, each circulating pump's power, and DAC fan power add up to the total amount of electrical power used by the system. Figure 4 below displays a flow diagram of the examined control techniques.

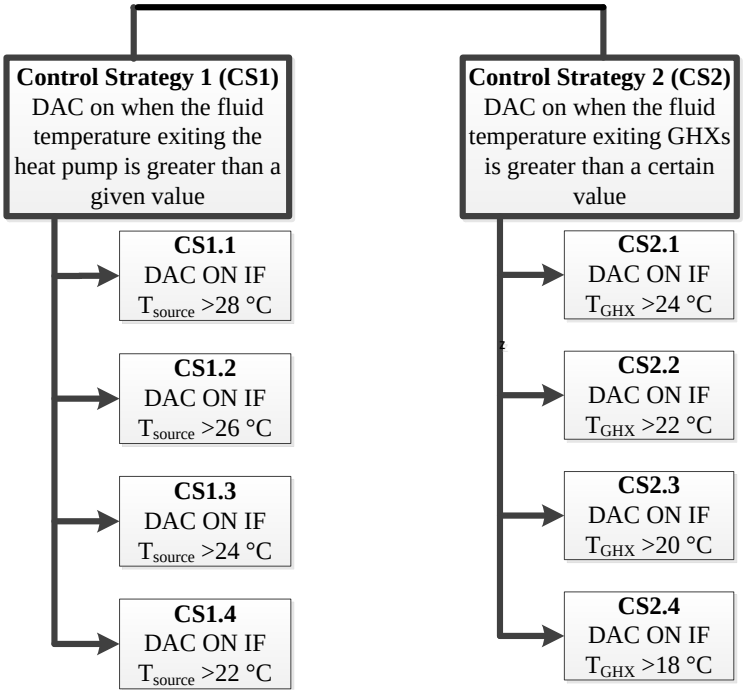


Figure 4: *Flow diagram of the control strategies.*

5.1Effect of DAC on COP.

Figure 5 shows the cooling COP value of the GSHP system at various temperature set points. It should be noted that the COP values for all four of the specified temperature scenarios were quite similar at the start of the season in April to June 2013. Time Period A is the period during which the DAC is not active. In Time Period B, there is a difference in COP between the options, and the DAC is either working fully or partially during the months of June and October 2013. The DAC was used to lower the leaving fluid temperature from the HP by rejecting the heat back to the ground at a lower temperature than the normal operating leaving fluid temperature of the HP, which is the only reason for the difference in COP. The GSHPs COP value decreases continuously with increasing setpoint temperature. For the first year of GSHP system operation, the COP values for cooling are highest for the lowest setpoint temperature.

Setting the temperature setpoint control to 22 ° C results in a cooling COP of 6.2, which is 19.2% higher than the average operating scenario. As a result, the cooling COP value is reduced to 5.2 in comparison to the regular operating scenario. An energy and exergy analysis of a GSHP system in Ontario (Canada) by Kizilkan and Dincer (2015) revealed that the system's efficiency in the heating mode was marginally increased when the fluid temperature entering the HP was greater.

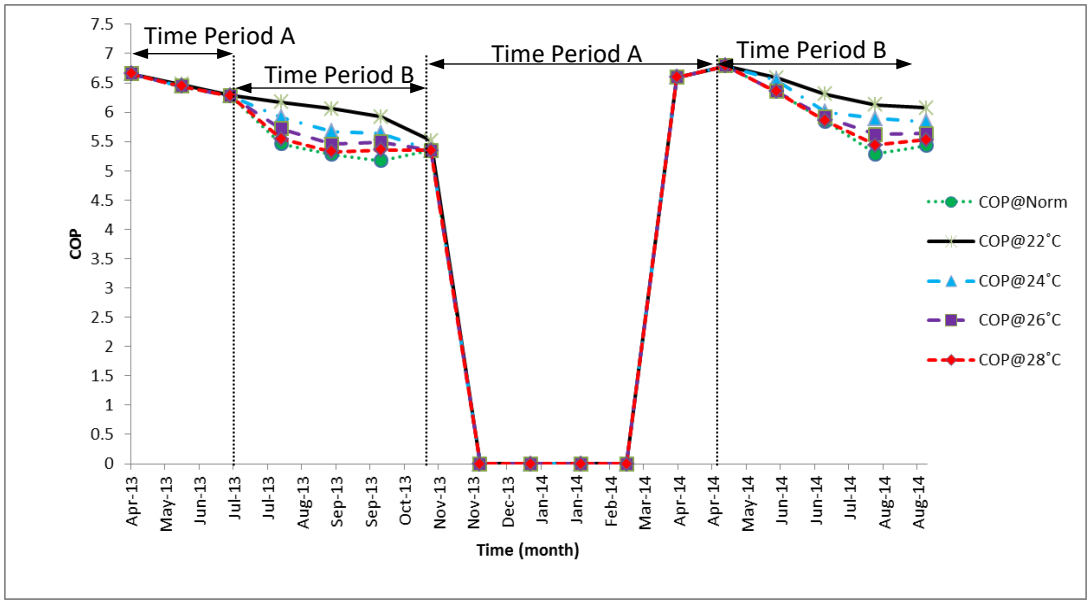


Figure 5: *Average Monthly system COP.*

5.2 Effect of DAC on Ground Temperature

Along with looking into how the DAC's operating cycle affects the device's efficiency, a look into how it affects ground temperature is also conducted. The simulation results for ground temperature over the course of a year are shown in Figure 6. The results demonstrate that when the setpoint temperature varies, the four separate setpoint operation temperatures of the DAC cause variations in the ground temperature.

In Time Period A, when the DAC is not operating at the beginning of the cooling season, the ground temperature is similar, and hence changing the ground temperature setpoints does not affect it at all. Therefore, the ground temperature for all scenarios remains constant. However, in Time Period B, the temperature variation between the scenarios becomes clear that the more the DAC is running, the lower the ground temperature variation is. After one year of cooling mode operation, the maximum ground temperature is 23°C for the normal operation duration, compared to 20°C for the lowest set point temperature, which is 15 per cent lower than the normal operation.

This impacted on COP, and therefore by reducing the ground temperature from 23 to 20 °C, the overall system performance has improved by approximately 9 %, and this can be seen clearly in Figure 5 above. If excessive heat extraction rates from or rejection to the ground are tolerated for prolonged periods, then significant changes in ground temperature are likely to occur; such changes in ground temperature may have a significant detrimental effect on the overall COP system, as well as a significant impact on the atmosphere. By using simpler heat rejection or 'free cooling' techniques, Zoi and Constantinos (2012) suggested three control strategies to mitigate this major change in ground temperature. The first one determines the set point at which a cooling tower starts its operation according to the fluid temperature exiting HP, and ambient air wet-bulb temperature exceeds a given set point. The second one activates the cooling tower when the fluid temperature exiting GHX is higher than a specific value. The third one sets the cooling tower on when the fluid temperature exiting HP is higher than a given value.

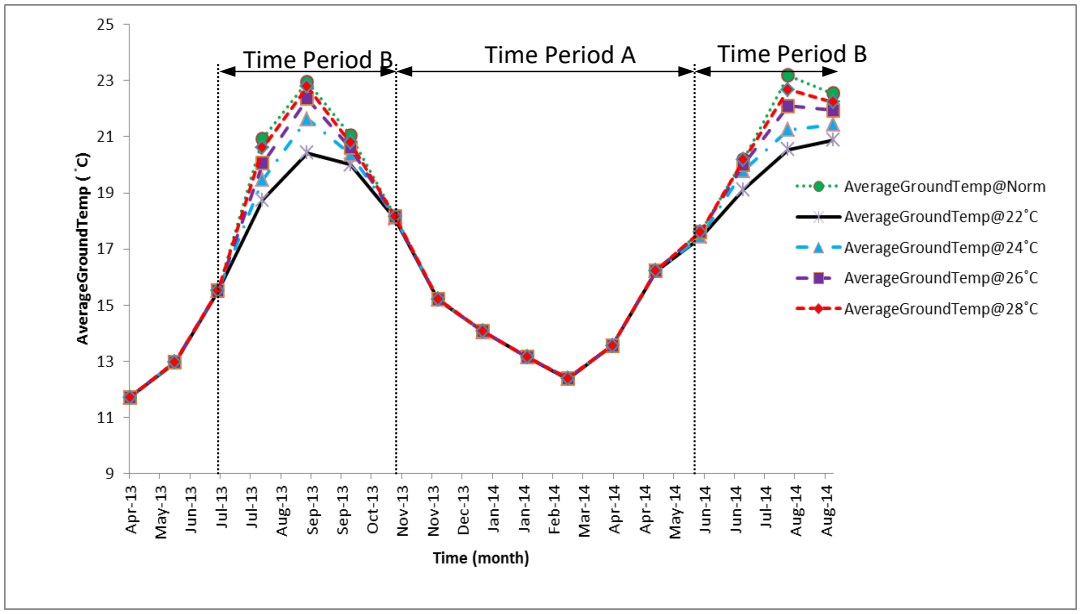


Figure 6: *Monthly ground temperature variations.*

With the decrease of average ground temperature around the ground heat exchanger, the temperature difference between the ground and the circulated heat carrier fluid decreases; this phenomenon has both advantages and disadvantages for the system. While this gradual shift in temperature increases the COP value during the cooling season, it also decreases the system's COP value during the heating season.

5.3 Effect of DAC on Heat Pump Energy Consumption.

The total monthly HP energy consumption for scenarios CS1, CS2, CS3 and CS4 are presented in Figure 7. The operation cycle of the DAC can determine whether the GSHP system consumes more energy compared to a GSHP system without DAC. Figure 7 shows that the maximum energy consumption of the HP was 7923 kWh and 7669 kWh, respectively, between the periods of April 2013 and August 2014, both of which occurred while the system was operating without DAC support. Also, when the DAC was controlled at the highest set point temperature of 28 °C, these dynamics can be shown clearly in Figure 6 during Time Period B. Time Period A demonstrates that the performance of the four set points remains unchanged when the DAC is off. Time Period B shows that this zone also illustrates the advantages of decreasing the ground temperature while the DAC was running at various set points, as shown in Figure 6 of the system's energy input. Reducing the temperature of the ground helps to decrease the temperature differential between the temperature leaving the ground loop heat exchanger and the temperature leaving HP, thus increasing the system's COP.

Comparisons of the four scenarios in Time Period B between the periods of July and September 2013 showed that the system's energy consumption decreased by 8% when the lowest control setpoint of 22 ° C (CS4) was compared to the system's usual operating conditions. Likewise, the system's lowest energy consumption was 267 kWh during the transition period to the heating mode. Zhao et al. (2003) proposed a theoretical and experimental study to investigate the impact of several capacity control techniques on the HP's energy efficiency, i.e. turning the compressor on / off, regulating on / off times of intake and discharge valves, concentration ratios of the refrigerant mixture, and speed of the compressor.

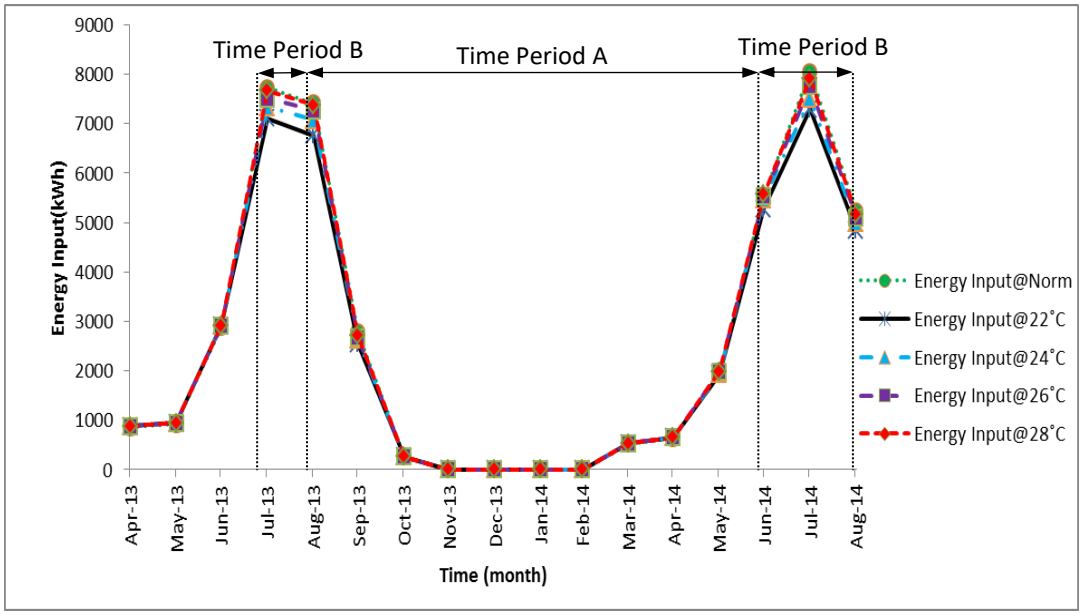


Figure 7: *Monthly HP energy consumption.*

5.4 Proportion of Energy Utilisation

The total proportion of energy consumption of the HP, circulation pump and the fan are shown in Figure 8 below. It indicates that the compressor accounts for 72 per cent of the total system's annual electricity consumption, followed by the circulation pumps, which use 20 per cent of the system's total energy supply. The DAC's 9 per cent energy consumption is comparatively small compared to the energy input of the compressor.

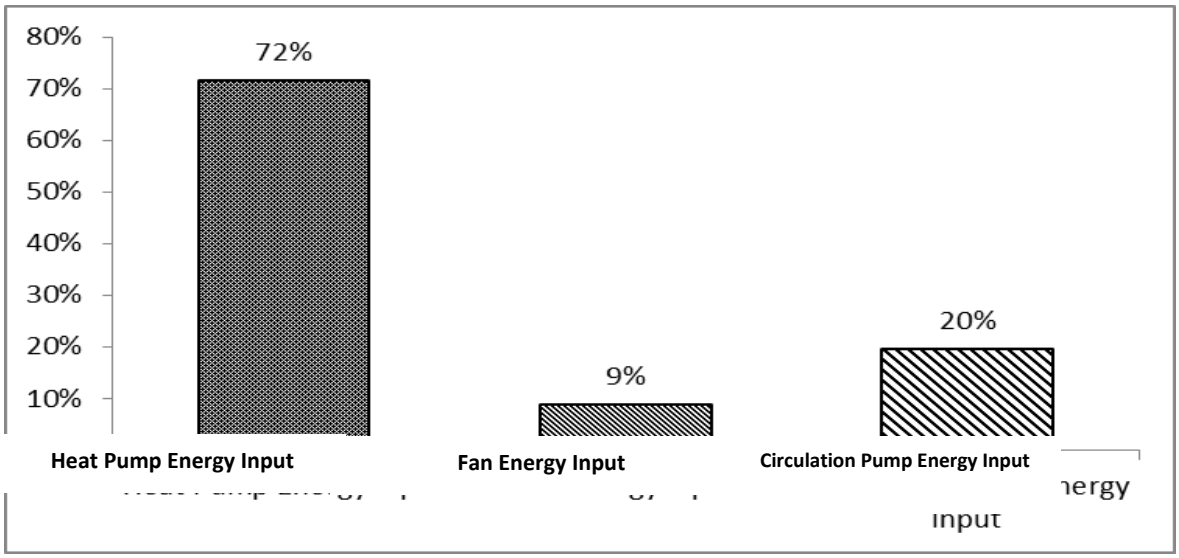


Figure 8: Proportion of energy utilisation of HP, circulation pump and fan CS1.

5.5 Economics of The Control Strategy

The financial and CO2 emission savings for each temperature set point were compared with the regular operation of the system in this section. The additional monthly CO2 emission savings (kgCO2) that can be achieved by enforcing the various temperature control setpoints are shown in figure 8. The graph indicates that a cumulative CO2 emission saving of 420 kgCO2 was achieved in July 2014. This is also the point where the highest COP and highest ground temperature have been reported in connection with Figures 5 and 6. This occurred, notably, at the lowest set temperature point of 22 ° C. In addition, the lowest CO2 emission savings were approximately 20 kgCO2, and this occurred at the

28 ° C maximum temperature set stage. As shown, the lowest temperature set point can produce a saving of approximately 17 per cent relative to the highest temperature set point. The lowest temperature set point will often achieve cost savings of approximately 18 per cent relative to the maximum temperature set point.

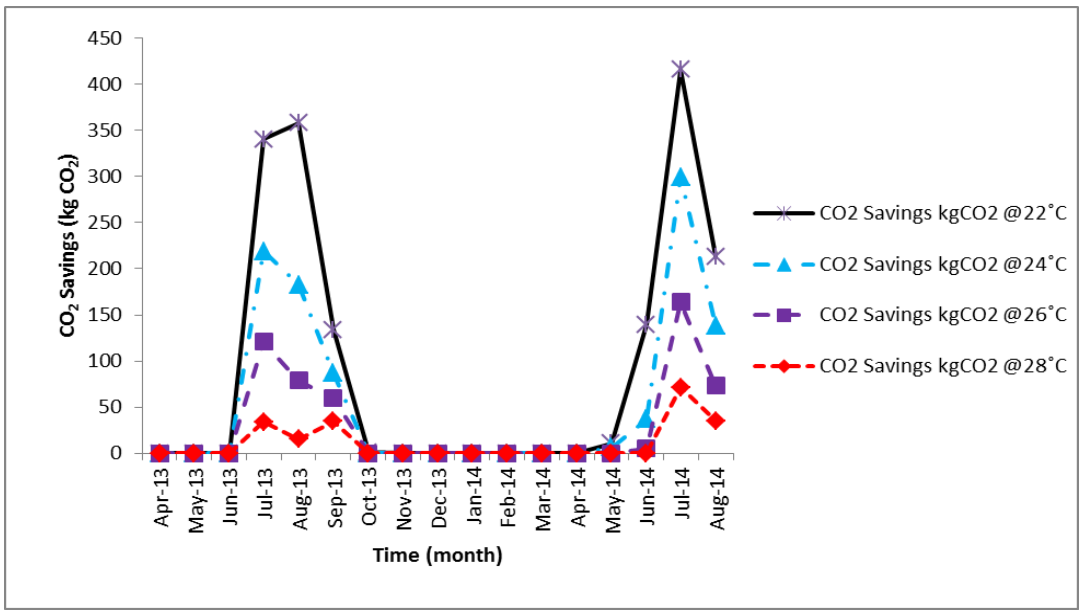


Figure 8: *Monthly CO2 emission savings from the different control strategies.*

Specifically, Figure 9 shows the possible additional cost savings that can be made relative to the standard system operation from the various temperature set points. Figure 9 also shows that using the lowest temperature set point of 22 ° C, a maximum cost saving of £ 110 was achieved in July 2014. In addition, for the same month, the most economical cost savings were around £ 20, and this happened at the maximum fixed temperature point of 28 ° C. Compared to the maximum temperature set point, the lowest temperature set point will achieve cost savings of approximately 18 per cent.

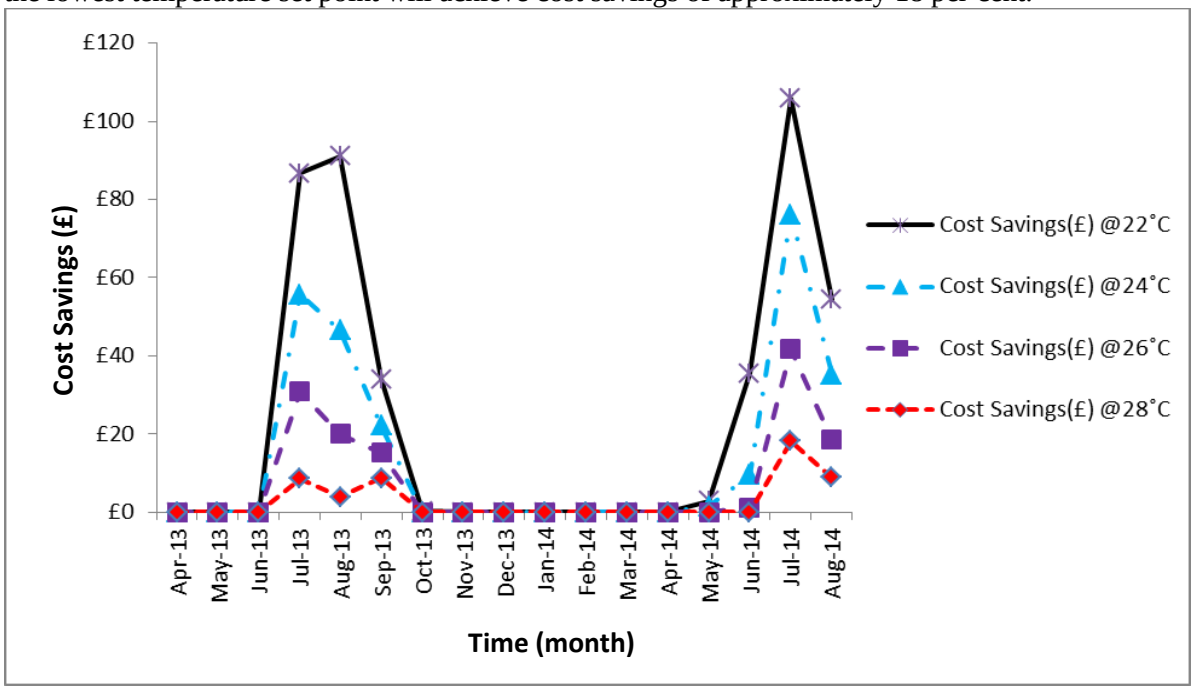


Figure 9 *Monthly cost savings from different control strategies CS1*

6.0 Conclusion

During the net cooling cycle for a university building, this paper identified various control strategies for GSHP device optimisation. The investigation centred on the effect of DAC on ground heat rejection, system COP, variance in ground temperature, minimisation of compressor and circulation pump electrical power consumption, assuming certain building load values, and maximum cooling capacity of HP and DAC.

This paper has shown that a substantial reduction in GSHP running costs, electrical power usage, and an increase in the system's COP could be achieved by using and regulating a DAC using different temperature setpoints. However, it is difficult to argue that this is the most economically profitable example, not only because the heating cycle is not tested, but also because unit selection has not considered the investment and maintenance costs. This is the subject of further work.

This paper has established that the best of those tested to control the activity of DAC in the GSHPs is the lowest temperature setpoint control. A comparison of these four scenarios shows that substantial cost and carbon reductions can be accomplished and that all current control methods achieve improved management of system operations, leading to an additional reduction in energy usage, carbon and cost savings. It is possible to use these remarks as guidelines for potential GSHP designers.

References

Alavy, M., Nguyen, H.V., Leong, W.H., Dworkin, S.B., 2013. A methodology and computerised approach for optimising hybrid ground source heat pump system design. Renewable Energy, 57: 404–412.

Beckers, K.F., Aguirre, G.A., Tester, JW, 2018. Hybrid ground-source heat pump systems for cooling-dominated applications: Experimental and numerical case-study of cooling for cellular tower shelters. Energy and Buildings, 177: 341-350.

Hackel, S., Pertzborn, A., 2011. Effective design and operation of hybrid ground-source heat pumps three case studies. Energy and Buildings, 43(12): 3497–3504.

Hou, G., Taherian, H., 2019. Performance analysis of a hybrid ground source heat pump system integrated with liquid dry cooler. Applied Thermal Engineering, 159: 113830.

Hou, G., Taherian, H., Li, L., Fuse, J., Moradi, J., 2020. System performance analysis of a hybrid ground source heat pump with optimal control strategies based on numerical simulations. Geothermics, 86: 101849.

Kizilkan O, Dincer I. (2015). Borehole thermal energy storage system for heating applications: thermodynamic performance assessment. Energy Convers Manage 2015; 90:53–61.

Lee, J.S., Park, H., Kim, Y., 2014. Transient performance characteristics of a hybrid ground-source heat pump in the cooling mode. Applied Energy, 123: 121–128.

Lee, J.S., Song, KS, Ahn, J.H., Kim, Y., 2015. Comparison on the transient cooling performances of hybrid ground-source heat pumps with various flow loop configurations. Energy, 82: 678-685.

Liu, Z., Li, Y., Xu, W., Yin, H., Gao, J., Jin, G., Lun, L., Jin, G, 2019. Performance and feasibility study of hybrid ground source heat pump system assisted with a cooling tower for one office building based on one Shanghai case. Energy, 173: 28-37.

Sarbu I., Sebarchievici C., 2014. General review of ground-source heat pump systems for heating and cooling of buildings. Energy and Buildings, 70: 441–454.

TRNSYS, (2021). Version 17. Transient system simulation program solar energy engineering laboratory Madison: University of Wisconsin. Available from: http://sel.me.wisc.edu/trnsys/features/features.html. [Accessed: 6th August 2021].

Zoi, S. and Constantinos, R. (2012). Control Strategy for minimising the electric power consumption of Hybrid Ground Source Heat Pump System. Proceeding of ECOS JUNE 26-29, 2012, PERUGIA, ITALY.

14th IEA Heat Pump Conference
15-18 May 2023, Chicago, Illinois

Making progress in the decade of heat pumps – status and trends of the European heat pump markets in 2022

Thomas Nowak[a]

[a]European Heat pump Association aisbl, Rue d'Arlon 63-67, 1040 Brussels, Belgium

Abstract

European heat pump sales grew +38% in 2022. With 3.016 million units sold across Europe, this is a new sales. Assuming a life expectancy of approx. 20 years, the current European heating heat pump stock amounts to 16.97 million units, representing nearly 15% of the EUs building stock of 116 million residential buildings. The main influencing factors for market growth:

- Policy makers focus on heating: 10 years of energy and climate policy is now showing results in national markets.
- Heat pump technology delivers: the needs of new and existing residential and commercial buildings (temperatures up to 75°C) as well as industrial processes (providing between 140°C and 160°C) are met. Solutions are available to fuel the greening of district heating and cooling at temperatures of up to 95°C and capacities of between one and 35 MW.
- Homeowners have focused on upgrading their buildings to improve indoor environmental quality.

The paper explains the underlying market dynamics growth in Europe in 2022 including air-air, air-water, and ground-water heat pumps for heating as well as sanitary hot water heat pumps.

© HPC2023.
Selection and/or peer-review under the responsibility of the organizers of the 14th IEA Heat Pump Conference 2023.

Keywords: heat pumps; market development; sustainable energy system; decarbonisation; Europe; REPowerEU; Renewables; System integration, industrial strategy, heatpump accelerator

1. Background

Over the past decade, the importance of heat pumps has been hailed in the context of climate change. They have been mainly recognized for the highly efficient use of renewable energy and the related much lower emission of CO_2. While the policy framework has been adjusted over time with more ambitious targets for the use of renewable energy, energy efficiency and CO_2 emission reduction, the economic framework has been left untouched until recently [1]. The resulting mismatch between ambition and speed of conversion is observable in the slow transition speed from the use of fossil energy to more renewables as documented by the Eurostat SHARES tool [2]. The average increase of renewables used in heating and cooling has only been 0.6 percentage points for the decade until 2020, far below the target of 1.3 percentage points as set forth in the current European Renewable Energy Directive [3] or the targeted 2.5 percentage points [4] proposed in its future version.

From 2021 onwards, a new momentum was observable.

1. Increasingly recognizable effects of **global warming** made change urgently necessary, including a more ambitious focus on heating and cooling in legislation. Several European countries have started to discuss and/or to introduce measures that are giving an economic advantage to heat pumps over fossil based solutions.

2. Throughout the **COVID pandemic**, end users spent much more time in their homes and buildings, realizing the need for good indoor environmental quality.
3. The **war waged by Russia on Ukraine** has shaken the belief of "gas as a transition fuel" and has destroyed policy makers and end-users trust in Russia as a reliable partner for energy delivery. This recognition has materialized in conceptual papers like the IEA 10 point plan to reduce Europe's dependence on Russian gas [5] and powerful policy packages like "REPowerEU" [6]. Consequently, end-users are now asking for alternatives to their fossil based heating systems.

All three effects trigger additional demand at a level unexpected by industry and installers. The combination of this additional demand and supply shortages of components in a global value chain has led to bottlenecks across the heat pump sector. All three effects will mutually reinforce each other and stabilize the trend away from fossil heating and ensure the necessary exponential growth throughout this decade. Continued policy support both regarding targets and supporting their implementation on all levels is needed to overcome them and to accelerate and stabilise deployment.

2. Status of heat pump market development

The European Heat Pump market has seen positive, uninterrupted growth since 2012. From 2015 onwards double digit growth was observable and 2022 saw a new sales record of +38% (over +34% in 2021). In 2022 more than 3 million heating and hot water heat pumps were installed in the 21 countries covered by EHPA statistics (see figure 1) [7]. This lead to a stock of nearly 20 million units.

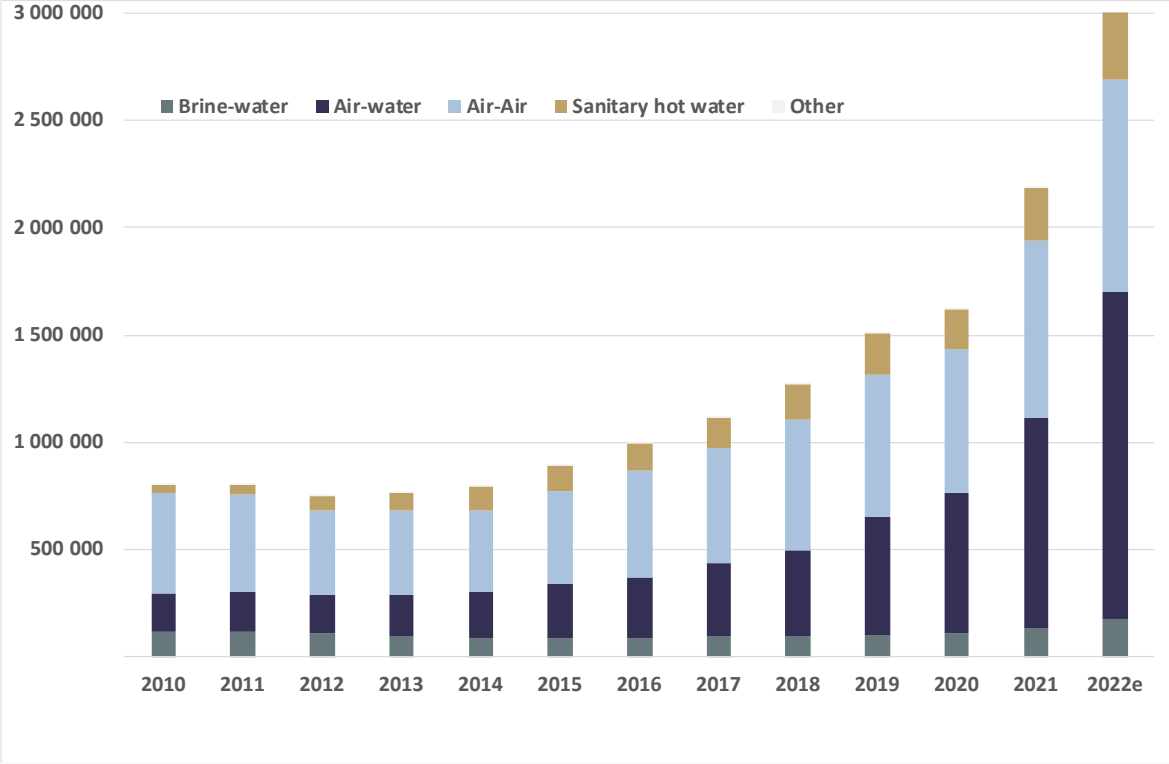


Fig. 1. 2022 heat pump sales in 21 European Countries.

The market was dominated by France (626k), Italy (517k), and Germany (282k). Together with Sweden (215k), Poland (203k), Finland (196k), Spain (185k), Norway (156k), and the Netherlands (125k), these countries form a group of nine markets, in which sales exceeded 100k units and which are jointly responsible for 83% of annual sales.

Figure 2 shows absolute and relative change of annual sales in 2022. Italy leads absolute change in sales with an increase of 134k (+37%) while Poland shows the biggest relative increase with doubling annual sales (+102%, + 99k). It is followed by Czech Republic (+99%), the Netherlands (+80%), Belgium (+66%) and Austria (+59%). Regarding year over year sales increase in absolut numbers the top 5 countries are Italy (+134k), Poland (+99k), Germany (+82k), France (+76k) and Finland (+67k).

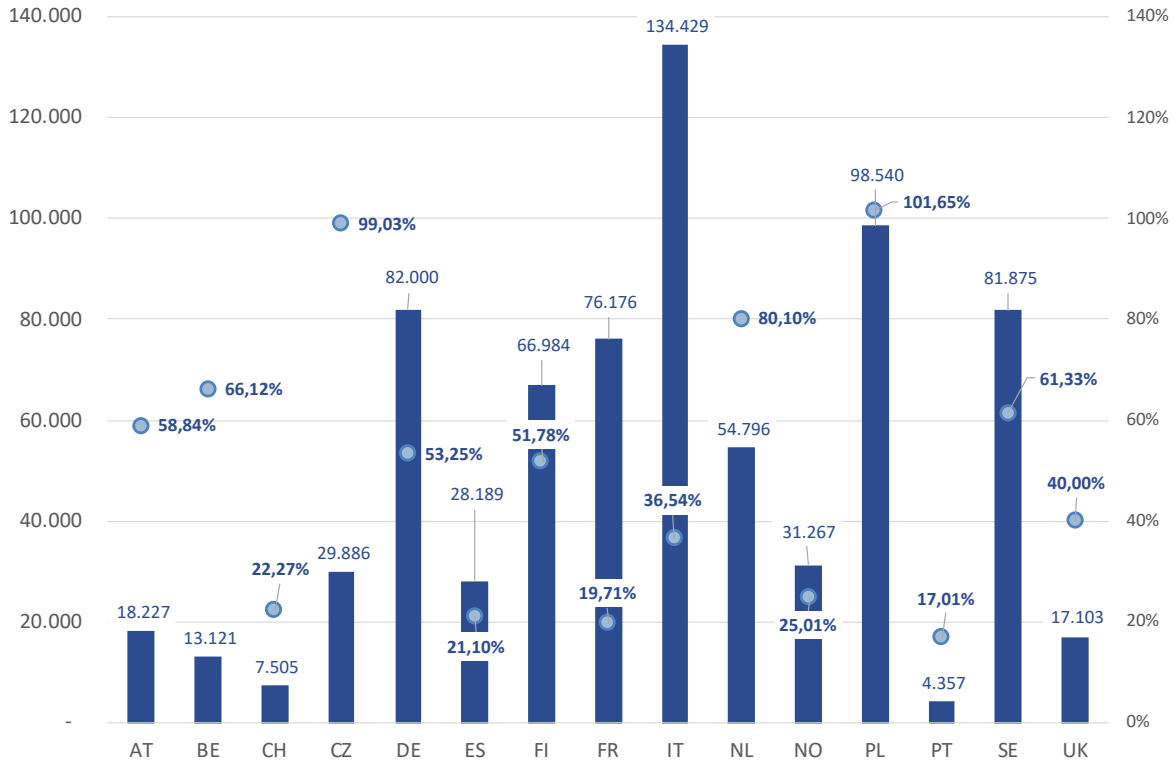


Fig. 2. Absolute and relative changes of 2022 sales compared to 2021 in 15 European Countries.

Growth is expected to continue as national legislation becomes more ambitious, partly as a result of local considerations (e.g., air quality in Poland), partly as a consequence of transposing European legislation. Germany aims at 500k heat pumps to be sold in 2025 supported by a new requirement of a 65% renewables share which is to be met by all heater installations (in new buildings and when replacing an existing heater) from 2024 onwards. Austria has already banned the installation of oil boilers in new buildings in 2020, and followed up with gas boilers in 2023. It aims to ban oil heating by 2035 and gas heating from 2040 onwards [8]. The Netherlands, after having declared the aim to become “gas free” in residential heating, is now mandating hybrid heat pumps as the minimum solution to be installed from 2026 [9]. Denmark has announced a shift of its remaining 400k gas boilers to district heating and individual heat pumps by 2028/2029 [10]. France has banned the installation of new oil boilers in all buildings and the installation of new gas boilers in new buildings from 2023 onwards. Ireland currently discusses the ban of fossil boilers with oil starting this year and gas following in as early as 2025. The European Commission is working on sharpening the regulation on Ecodesign for boilers in a way that would make the installation of fossil-only boilers impossible by 2029 [11]. These measures are fuelling a debate also in countries that have not yet agreed on a specific policy on the matter and their heat pump markets see a positive spill-over from more ambitious neighbours.

This strong increase in sales numbers in 2021 and 2022 is essential to decarbonise heating and to reduce local air pollution. The 2022 heat pump stock to the energy and climate targets is summarized in table 1 [12]. New units with a thermal capacity of 28.18 GW were installed producing approx. 33.95 TWh of useful energy and integrating 19.8 TWh of renewables in heating and cooling.

Table 1. Contribution of the heat pump stock and annual additions to Europe’s energy and climate targets.

	Installed stock end 2022	Addition in 2022
Thermal capacity	175.2 GW	28.2 GW
Useful energy produced	330.7 TWh	48.6 TWh
Renewable energy integrated	208.7 TWh	29.5 TWh
CO_2 emissions saved	53.5 Mt	7.6 Mt

Installing and maintaining these heat pumps is estimated at requiring a total of 162k full time equivalent of employment. Obviously real employment related to the heat pump market is larger, as not all employees work full-time on heat pumps only.

The total stock of heat pumps installed since 2003 amounts to 19.9 million units around 18 million of these being for heating purposes and about 1.9 million providing sanitary hot water. With a thermal capacity of 175.2 GW these heat pumps provided 330.7 TWh of useful energy, 208.7 TWh of which being renewable.

The average emission factor for electricity in Europe has declined from 500 g CO_2/kWh to a value as low as 229 g CO_2/kW in 2020 but has bounced back to 275 g CO_2/kW in 2021. Assuming a continuation of the downward trend, the emission value for 2030 is estimated at 115 g CO_2/kW [13]. The number of heat pumps sold in 2022 have reduced CO_2 emission by 7.6 Mt, arriving at a total annual savings of 53.5 Mt. With the greening of electricity, this number will increase further in the future.

The positive impact of heat pumps on the energy and climate targets is expected to continue, as the technology is not only the #1 heating technology in the new build segment of many national markets but is also making an inroad into the renovation sector. Improved technologies and new business models help their deployment and lead to an increase in demand. This will be further fuelled by the implementation of the "Clean energy for all Europeans", the fit-for-55 and REPowerEU-packages.

3. Legislative background: From EU Green Deal to REPowerEU

Europe's energy and climate policy has traditionally been shaped around:

- the promotion of the use of renewable energy, both in electricity and heating and cooling
- the support of energy efficiency measures in buildings and industry
- the introduction of minimum efficiency requirements for products through the Ecodesign directive and the related regulations on performance and labelling
- the reduction of CO_2 emissions through an emissions trading scheme and an effort sharing mechanism
- a re-design of the electricity grid.

Table 2 shows the increase of ambition on the EU level regarding the block's energy and climate targets. With each revision of the targets on renewable energy, energy efficiency and CO_2 emission reduction arose the need to review the underlying legislation on the EU and the Member State level.

Table 2. Energy and climate targets in the European Union

	Renewable energy	**Renewable energy in buildings**	**Energy efficiency**	**Reduction in CO_2 emissions**
Targets for 2020 [14]	20%		20%	20%
Targets for 2030 [15]	30%	49%	32.5% (9%)	40%
New targets for 2030	45% (EC), 40% (EP) [16]	49% (unchanged)	11.7% [17]	55% [18]
2050				Net zero **[19]**

Currently, the legislation on renewables, energy efficiency, CO_2 emission is undergoing its 3rd review round. New proposals related to heat pumps include:

1. a more ambitious Renewable energy Directive (see [17]) with
   - an increased renewables target for 2030,
   - a faster increase of the share of renewables used in heating (forthcoming Renewable Energy Directive), and
   - the recognition of cooling and waste heat, including in industry and district heating through large heat pumps.
2. the phase out of fossil heating in buildings (Energy Performance of Buildings Directive) [20].
3. a synchronised set of planning measures and assessments (National energy and climate plans, Comprehensive assessment, assessment of the potential from renewable sources, the use of waste heat and cold) (see the forthcoming Energy Efficiency Directive [16]).
4. the inclusion of heating and light commercial uses of fossil energy into the EU Emission Trading System (ETS2) [21].
5. a rebalancing of energy carrier taxation levels making the tax rate applied to electricity the lowest (Energy Taxation Directive [22]).

6. change of the accounting method of energy savings and ruling out the counting of savings from the installation of fossil boilers.

While this review was on its way, the war in Ukraine shattered the belief of gas being a bridge to a more sustainable heat supply and of Russia as a reliable trading partner for fossil gas. Both the International Energy Agency and the European Commission published communications on the need to remove Europe's dependency on Russian gas and both recognised that replacing gas boilers with heat pumps was a suitable approach. Each million of boilers replaced saves around 2 billion cubic meter of fossil gas imports. It hence required about 75 million additional heat pumps to completely remove the amount of gas imported from Russia in 2021 [23].

The European Commission followed up the **REPowerEU** communication **[24]** with a proposal for a sharpened legislation to accelerate the deployment of renewable energy **[25]**. For the first time, heat pump technology was mentioned in the top level communication. This was supported with specific targets on heat pumps, in particular:

1. the installation of 10 million additional hydronic heat pumps until 2026 and a total of 30 million additional units to be installed by 2030.
2. the recognition of renewable energy infrastructure as being of "overriding public interest". This recognition could then be used to justify simplification of administrative procedures.
3. taking additional measures to decarbonise the heat demand in industry, including through high capacity/high temperature heat pumps.
4. the need for additional 210 billion Euro investment identified as necessary to phase out the dependence on Russian gas. In parallel it was suggested to increase the share of renewables in final energy demand to 45% by 2030.

While these suggestions show a recognized need for higher ambition and action, they are not universally supported by neither the European Parliament nor by the Council. The European Heat Pump Industry assessed the proposals as appropriate and feasible but lacking clarity and detail. Achieving the growth numbers as proposed would require an action plan or a heat pump industrial strategy to ensure end-user trust in the technology, trigger and stabilise demand and increase capacity across all stages of the value chain. New technological solutions would have to be developed both for components and products, manufacturing sites would have to be build/redesigned, and experts would need to be trained on all levels. The latter including higher level education on the university level as well as a focus on mathematics, computer science, natural sciences and technology education in schools and a focus on the vocational training of installers, plumbers, or electricians.

4. A pandemic with an impact on home improvement

Regarding the need for a stabilised demand, the more inward focus of end-users on their own homes led to the realisation, that indoor environmental quality could be and should be improved. In consequence, the pandemic influenced demand for comfort and renewable solutions in electricity and thermal energy demand. And there is some evidence pointing to exactly that: When people were forced to stay home during the different lockdowns and home office obligations of the COVID pandemic, they began observing the shortcomings of their properties. With budget that would otherwise have been spent on hobbies, eating out or holidays now at the end user's disposal, they were channelled towards home upgrades. Focus areas were home offices, kitchens and living areas but also ventilation and heating systems. Why representative studies are sparse, (An evaluation of Discover Home Loans concluded that the interest in renovating increased dramatically during the pandemic [26].) anecdotal evidence from personal discussions with installers and other experts in the field support the assumption. An additional plausible explanation of increased demand is the aim to reduce the opearting cost of a building by investing in modern, efficient, and renewables-based power and heat generation solutions.

5. Using energy as a weapon has shattered the belief in gas as a transition fuel

The Russian invasion of Ukraine on 24th of February 2022 had an additional impact on the energy transition in heating. This war "using energy as a weapon" [27] is directly and heavily impacting energy users and may in the end have been the most decisive for the accelerated energy transition, in particular towards the use of renewables in heating [28]. The sudden and unexpected price increase for gas lead to higher cost for heating and – due to determination of the electricity price by merit order – electricity for most of Europe and lead end users to realise that supply security and affordability are at risk when relying on fossil energy. This realisation

has led to a double effect: several international and EU level communications describing the move away from (Russian) gas to the use of more renewables and the REPowerEU legislative package increasing existing energy and climate targets and introducing legislative measures and financing options to achieve them. The IEA 10 point plan to reduce Europe's dependence on Russian Gas lists 10 points to reduce demand of gas, two of which highlight the positive impact of a faster deployment and an increase in sales numbers of heat pump based solutions in residential and industrial applications. The REPowerEU plan aims at a similar target (see above) and identifies additional financing needs. This has a double impact on consumers: on top of their personal experience of the cost impact on energy resulting from the war, the need to shift our energy demand from fossil energy to renewables is re-enforce by the positive policy recognition and support systems that are (announced to be) put in place.

6. Concerted action still needed to fast-track heat pump deployment

Figure 3 shows the mutual support and boost for heat pump demand of three parallel developments. Where the continuous review, sharpening and increase of ambition of the different policy files has created a strong and continuous growth in demand, both the COVID pandemic and the war in Ukraine have added momentum on the end-user side.

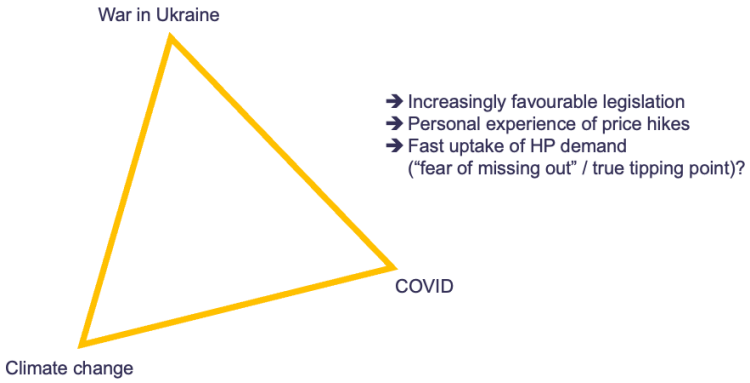


Fig 3: Mutually reenforcing impact on heat pump demand from policy, geopolitics, and pandemic.
Source: own.

The triple effect has steadied out demand not least through engaging hitherto reluctant end-users in considering heat pumps to ensure personal supply and affordability of heat and activating this target groups financing means. Demand must and likely will grow exponentially throughout this decade and while this is generally positive, it comes with a set of challenges that need to be overcome thorough enhancing energy and climate policy by a concerted heat pump industrial policy.

6.1. Are heat pumps becoming the dominant technology for heating in Europe?

Heat pump based heating can efficiently supply all residential and commercial buildings, both in new and renovation, single and multi-family application. Nearly 60% of all buildings are ready to be equipped and solely heated with heat pumps with the rest either having to undergo energetic renovation or be equipped with hybrid heat pumps, using two or more energy sources. As more than 75% of the European building stock are still heated by fossil energy, the necessary speed of change is far bigger than what can be currently observed.

Based on a previous assessment of around 116 million residential buildings in Europe and annual heater sales of around 7 million units, heat pumps now make up for a share of more than 35% in annual sales and about 15% in the stock of heating solutions. To achieve the target of 10 million additional hydronic heat pumps, as set forth by REPowerEU, exponential, double digit growth will be needed. Available data for 2022 shows that this target is within reach, and even the need for continued growth throughout this decade is within reach. Applying the necessary growth rates under REPowerEU also to air-to-air heat pumps, a category that is used for heating in Norway, Sweden, Denmark and Sweden, the Baltics as well as in the Mediterranean countries and that is responsible for about 33% of annual sales, heat pumps could provide 50% of Europe's building stock by 2030.

While the benefits of heat pumps for the energy and climate targets will undoubtedly lead to higher demand, the necessary growth is currently limited by supply shortages regarding components (fans, heat exchangers, pumps, semi-conductors and even tanks) and installation capacity. Related to this the need for a larger, skilled workforce, and the need for a competitive economic offering vs the incumbent fossil heating technology puts a limitation to the possibility of future growth. This needs to be overcome by concerted action.

6.2. A heat pump accelerator is needed to quadruple heat pump markets within this decade!

Europe has a strong position in heat pumps. It has a versatile landscape of research institutions and manufacturing sites and an established process of training and educating a skilled workforce. It should build on this strength to maintain this leadership in this new "industrial age" of renewables [29]. Industry has announced investments close to 5 billion Euro over the next three years [30]. For individual manufacturers, that means about a quadrupling of the 2021 production volume. It is the role of governments to back this growth by further shaping policy ambition and devising an industrial strategy along the whole value chain [31][32]. Making such policy continuity visible to developers and investors will allow them with the confidence needed to go ahead and even intensify their investments.

Hence it needs an all-hands-on-deck approach establishing a "heat pump industrial policy" that supports stakeholders on all stages of the heat pump value chain to implement and even enhance necessary investments to increase capacity. Such a heat pump accelerator will have to address the following points:

1. Maintain **trust** in the future importance of heat pump based solutions for the energy transition in Europe. Heat pumps need to be put forward in political communication on the European and national level. Their importance needs to be mentioned in high level speeches and used as an example of the low hanging fruits to reduce CO_2 emission quickly and significantly from heating and cooling. Heat pumps should be included in the overall energy and climate policy as well as in new, short term measures like EU net zero industry act [source]. Obstacles in component supply, administrative procedures and skilled workforce need to be addressed.
2. **Cost of the energy transition in heating**: The economic framework conditions need to be shaped towards making heat pump based solutions the economically most attractive alternative for private and commercial end-users, including those operating industrial plants and district energy networks. Regarding operation cost, this means improving the relative cost of electricity based heating and cooling solutions vs. their fossil counter parts. Negative external effects of the use of fossil energy need to be internalised, energy taxation needs to give an advantage to electricity and fossil fuel subsidies need to be stopped. Flexibility needs to be given a value, including through offering time-of-use tariffs and at least for the next years, investment cost support needs to be provided through subsidies and advantageous loan offering.
   The decision in favour of a heat pump is not only related to direct, but also to indirect cost. Uncertainty and doubt on the right technical solution, quality of offer and installation can be overcome by providing decision and process support through knowledge centres. This can go as far as providing complete support in form of one-stop-shops [33].
3. **Legal certainty** needs to be established for investors and end-users alike. Legislation should be established with a long term view making investments plannable and profitable. Administrative procedures should be simplified and revised to also allow the provision of new energy services ("heat-as-a-service") even beyond the individual lot. Similarly, the revision of current legislation such as on the use of refrigerants or Ecodesign should take the necessary accelerated deployment of heat pumps into consideration and simplify, not hinder, the path to this goal. Looking at the current review of the refrigerant regulation, the resulting new bans and phasedown trajectory will significantly shape the future of the heat pump industry. The proposed PFAS restriction proposal to the REACH regulation will limit available refrigerants for the industry. Clarity must be created as soon as possible [34][35].
4. In the foreseeable future, there will be a lack of **skilled workers** on several levels of the value chain. From architects, designers, and planners to factory workers to electric and heat pump installers. This needs to be addressed by policy makers through joint initiatives that recognize the importance of skills in the HVAC sector and aim at education and training as much as at re-skilling of existing employees. A focus on heat pump installations may allow a simplification of the extent of skills needed, for example by dropping those needed to install fossil based solutions.
5. Heat pump solutions require further **research and development** to develop residential, commercial, and industrial solutions for enhanced application areas, a reduced footprint, more compact solutions, and units that integrate thermal and energy through sector coupling. Such research can be supported

via different vehicles, Horizon Europe, and Life, but could also be positioned inside one or many Important Projects of Common European Interest (IPCEI).

In order to ensure the necessary growth rate is achieved and maintained, the heat pump accelerator or heat pump industrial policy must include a regular progress review to enable adjustment and modification of EU and national legislation.

7. Conclusion

The European heat pump industry has reached a level of maturity perfectly suited for exponential growth throughout this decade. In 2022 the heat pump share in annual boiler sales have reached about 30%. About 16% of all heating solutions installed in Europe are now heat pump based. Demand is triggered from both policy and individual end-user decisions in residential, commercial, and industrial applications. Growing demand encounters limitations in supply in capacity and skills across the value chain. As demand has increased rather surprisingly for many market players, friction between supply and demand is observable in factory construction, component, and heat pump manufacturing as well as installation. Ongoing investments are expected to overcome this friction over the course of the next 12 months.

The outlook for the heat pump sector is posivie, but more needs to be done in order to remove the use of fossil energy from heating in Europe. Accelerating its growth even further and stabilizing sales needs strong and visible support by governments including through establishing a European heat pump strategy that addresses and supports all parts of the value chain and coordinates the ambition of member states.

If this is established, heat pumps can become the #1 heating and cooling technology in Europe, meaningfully contributing to the continents energy and climate targets and removing its dependance on Russian gas, making renewable heat available and affordable for all. For the next winter and the winters to come.

Acknowledgements

The author thanks numerous experts for their openness in individual discussions that have feed into this text. A particular thank you goes to Sarah Azau for proofreading and critical comments. All remaining errors are entirely my responsibility.

References

1 Nowak, T. Next stop: the mass market! Heat pumps on the verge of large scale deployment in Europe. 13th IEA Heat Pump Conference, 11.-14.5.2020, Jeju, Korea.

2 Eurostat. SHARES (renewables). https://ec.europa.eu/eurostat/web/energy/data/shares. Accessed 4.1.2023.

3 European Parliament and Council: Directive (EU) 2018/2001 of the European Parliament and of the Council of 11 December 2018 on the promotion of the use of energy from renewable sources (recast) (Consolidated text). http://data.europa.eu/eli/dir/2018/2001/2022-06-07.

4 European Commission: Proposal for a Directive amending Directive (EU) 2018/2001 as regards the promotion of energy from renewable sources. https://eur-lex.europa.eu/legal-content/EN/TXT/PDF/?uri=CELEX:52021PC0557&from=EN.

5 International Energy Agency: A 10-Point Plan to Reduce the European Union's Reliance on Russian Natural gas. https://www.iea.org/reports/a-10-point-plan-to-reduce-the-european-unions-reliance-on-russian-natural-gas. Accessed 1.2.2023.

6 European Commission: REPowerEU: affordable, secure and sustainable energy for Europe. https://commission.europa.eu/strategy-and-policy/priorities-2019-2024/european-green-deal/repowereu-affordable-secure-and-sustainable-energy-europe_en. Accessed 1.2.2023.

7 European Heat Pump Association: Heat pump record: 3 million units sold in 2022, contributing to REPowerEU targets. https://www.ehpa.org/press_releases/heat-pump-record-3-million-units-sold-in-2022-contributing-to-repowereu-targets/. Accessed 13.3.2023.

8 Bundesministerium für Klimaschutz, Umwelt, Energie, Mobilität, Innovation und Technology. https://infothek.bmk.gv.at/erneuerbaren-waerme-gesetz-ewg-ab-2023-keine-gasheizungen-in-neubauten/. Accessed 2.2.2023.

9 European Heat Pump Association: Which countries are scrapping fossil fuel heaters? https://www.ehpa.org/2022/12/15/ehpa_news/which-countries-are-ending-fossil-fuel-heaters/. Accessed 2.2.2023.
10 The local: Denmark announces major plan to replace gas heating in homes. 19.4.2022. https://www.thelocal.dk/20220419/denmark-announces-major-plan-to-replace-gas-heating-in-homes/. Accessed 13.3.2023.
11 European Heat Pump Association: Which countries are scrapping fossil fuel heaters? https://www.ehpa.org/2022/12/15/ehpa_news/which-countries-are-ending-fossil-fuel-heaters/. Accessed 13.3.2023.
12 European Heat Pump Association: European Heat Pump Market report and statistics 2022. https://stats.ehpa.org. Publication forthcoming.
13 European Environment Agency. Greenhouse gas emission intensity of electricity generation in Europe. https://www.eea.europa.eu/ims/greenhouse-gas-emission-intensity-of-1. Accessed 3.2.2023.
14 European Commission. 2020 climate & energy package. https://climate.ec.europa.eu/eu-action/climate-strategies-targets/2020-climate-energy-package_en. Accessed 2.2.2023.
15 European Commission. 2030 climate & energy package. https://climate.ec.europa.eu/eu-action/climate-strategies-targets/2030-climate-energy-framework_en. Accessed 2.2.2023.
16 Euractiv. 45% renewable target 'is ambitious but feasible', says EU climate chef. Euractiv. 16.1.2023 https://www.euractiv.com/section/energy/news/45-renewables-target-is-ambitious-but-feasible-says-eu-climate-chief/.
17 European Parliament. Parliament and Council negotiators agree on new rules to boost energy savings. 10.3.2023. https://www.europarl.europa.eu/news/en/press-room/20230309IPR77212/parliament-and-council-negotiators-agree-on-new-rules-to-boost-energy-savings.
18 European Parliament and Council. Regulation (EU) 2021/1119 establishing the framework for achieving climate neutrality (‚European Climate Law'). http://data.europa.eu/eli/reg/2021/1119/oj.
19 European Commission. 2050 long-term strategy. https://climate.ec.europa.eu/eu-action/climate-strategies-targets/2050-long-term-strategy_en. Accessed 2.2.2023.
20 European Parliament. Energy performance of buildings: climate neutrality by 2050. 9.2.2023. https://www.europarl.europa.eu/news/de/press-room/20230206IPR72112/energy-performance-of-buildings-climate-neutrality-by-2050. Accessed 13.3.2023.
21 European Parliament. Climate change: Deal on a more ambitious Emissions Trading System (ETS). 18.12.2022. https://www.europarl.europa.eu/news/en/press-room/20221212IPR64527/climate-change-deal-on-a-more-ambitious-emissions-trading-system-ets. Accessed 1.2.2023.
22 European Parliament. Revision of the energy taxation directive as part oft he European Green Deal. https://www.europarl.europa.eu/legislative-train/theme-a-european-green-deal/file-revision-of-the-energy-taxation-directive. Accessed 10.3.2023.
23 International Energy Agency. How Europe can cut natural gas imports from Russia significantly within a year. 3.3.2022. https://www.iea.org/news/how-europe-can-cut-natural-gas-imports-from-russia-significantly-within-a-year.
24 European Commission. REPowerEU: Joint European Action for more affordable, secure and sustainable energy. 8.3.2022 https://energy.ec.europa.eu/system/files/2022-03/REPowerEU_Communication_with_Annexes_EN.pdf.
25 European Commission. REPowerEU: A plan to rapidly reduce dependence on Russian fossil fuels and fast forward the green transition*. 18.5.2022. https://ec.europa.eu/commission/presscorner/detail/en/ip_22_3131
26 Discover. Comfort, Health and Safety are Top Motivators for Home Improvement Projects During the Pandemic. https://investorrelations.discover.com/newsroom/press-releases/press-release-details/2021/Comfort-Health-and-Safety-are-Top-Motivators-for-Home-Improvement-Projects-During-The-Pandemic/default.aspx.
27 The Economist: Russia is using energy as a weapon. 26.11.2022. https://www.economist.com/interactive/graphic-detail/2022/11/26/high-fuel-prices-could-kill-more-europeans-than-fighting-in-ukraine-has.
28 International Energy Agency. Renewable power's growth is being turbocharged as contries seek to strengthen energy securty. 6.12.2022. https://www.iea.org/news/renewable-power-s-growth-is-being-turbocharged-as-countries-seek-to-strengthen-energy-security.
29 International energy agency. Energy technology perspectives 2023. https://www.iea.org/reports/energy-technology-perspectives-2023.

30 Nowak, T.: Heat pump investment in Europe – an overview. https://www.linkedin.com/posts/thomasnowakeu_conversation-activity-6970985100586950657-VNc1.
31 Lowes, R. et al. The perfect fit: shaping the fit for 55 package to drive a climate-compatible heat pump market. https://www.raponline.org/knowledge-center/the-perfect-fit-shaping-the-fit-for-55-package-to-drive-a-climate-compatible-heat-pump-market/.
32 UK Parliament committee for Business, Energy and Industrial Strategy. Government must 'supercharge' efforts to build up UK's heat pump industry to phase out gas boilers. https://committees.parliament.uk/work/645/decarbonising-heat-in-homes/news/170892/government-must-supercharge-efforts-to-build-up-uks-heat-pump-industry-to-phase-out-gas-boilers/.
33 A great example is the service provided by Electric Ireland Superhomes that covers problem assessment, technology selection, support in finding planers and installers as well as financing, comparison of quotes and a quality check of the final installation. https://electricirelandsuperhomes.ie/.
34 European Commission. Proposal for a regulation of the European Parliament and of the Council on fluorinated greenhouse gases, amending Directive (EU) 2019/1937 and repealing Regulation (EU) No 517/2014.
35 European Chemical Agency. ECHA receives PFASs restriction proposal from five national authorities. Press release. https://echa.europa.eu/-/echa-receives-pfass-restriction-proposal-from-five-national-authorities.

14th IEA Heat Pump Conference
15-18 May 2023, Chicago, Illinois

Numerical evaluation of simultaneous cooling and heating absorption system using H_2O/ionic liquid and R32/ionic liquid as working fluids

Sejun Park[a], Doseong Yun[a], Hyun Uk Cho[b], Nam Soo Lee[b], Yong Tae Kang[c,*]

[a]Graduate school of Mechanical Engineering, Faculty of Engineering, Korea University, 145, Anam-ro, Seongbuk-gu, Seoul, 02841, Republic of Korea
[b]H&A company, LG Electronics
[c]Department of Mechanical Engineering, Korea University, 145, Anam-ro, Seongbuk-gu, Seoul, 02841, Republic of Korea

Abstract

H_2O/LiBr and NH_3/H_2O are commonly used as working fluids of absorption system in that they present high solubility of refrigerant in absorbent. However, the conventional working fluids need to be substituted considering causticity and toxicity. In this study, a simultaneous cooling and heating absorption system, which is combination of type 1 and type 2 absorption systems, has been analyzed using the numerical methods to improve the coefficient of performance (COP) for heating/cooling applications. The ionic liquid absorbents including imidazole, which has non-causticity and non-toxicity, are utilized as working fluids. H_2O and R32 refrigerants are also utilized as working fluids. The thermophysical properties are evaluated by using the non-random two liquid (NRTL) model. The variation of COP is analyzed according to split ratio and generation temperature of each component. It is found that the maximum COP_{tot} of H_2O/LiBr, H_2O/IL, R32/IL are 0.9000, 0.8481 – 0.9066 and 0.4084, respectively. It is also confirmed that when using H_2O/IL, better performance of the absorption system is expected than when using R32/IL, and the crystallization, causticity and toxicity problems are also expected to be solved.

© HPC2023.
Selection and/or peer-review under the responsibility of the organizers of the 14th IEA Heat Pump Conference 2023.

Keywords: Absorption system, COP, H_2O, Ionic liquid, R32, Simultaneous cooling and heating.

;

1. Introduction

The conventional NH_3/H_2O system has problems with refrigerant toxicity, and the H_2O/LiBr system has problems such as crystallization of the absorbent and corrosion with metals. In addition, international regulations are being strengthened step by step to use low global warming potential (GWP) refrigerants after the Montreal Amendment in 1997, the Beijing Amendment in 1999, and the Kigali Amendment in 2016. For this reason, there is a need for research on a new working fluid of absorption type systems.

Ionic liquids have been attracting attention as working fluids due to their unique properties. Kim et al. [1] showed that ionic liquids can maintain a liquid state even at room temperature or below room temperature. Paulechka et al. [2] found that the vapor pressure of ionic liquids is negligible. Domańska et al. [3] confirmed incombustibility and thermal stability, and Trindade et al. [4] confirmed low melting point and high refrigerant solubility, so that it can exist in a liquid state at room temperature. It is expected that these characteristics solve the problems of the previous absorption systems.

* Corresponding author. Tel.: +82-2-3290-5952; fax: +82-2-922-3260.
E-mail address: ytkang@korea.ac.kr.

However, although there is a demand for a simultaneous cooling and heating absorption system in that waste heat can be recovered, there are not many prior studies. In this study, four different working fluids using an ionic liquid as an absorbent were selected based on the previous studies that resulted in a high COP in type 1 absorption system and they were applied to the simultaneous cooling and heating absorption system. Finally, cooling COP, heating COP and total COP were compared according to the variations of split ratio and generation temperature.

2. Research method

2.1. Selecting working fluid

H_2O and R32 were selected as the refrigerant, and the reasons are as follows. In the case of H_2O, the most commercialized working fluid in the previous absorption system is H_2O/LiBr, R32 refrigerant has a smaller specific volume than H_2O, which is advantageous for miniaturization. R32 is HFC and has greater solubility in ionic liquids than HFO.

As the absorbent, imidazolium ($C_3H_4N_2$) ionic liquid was selected. Imidazolium ionic liquid is known as the most stable material among the ionic liquids, and it is easier to obtain necessary physical property data than other ionic liquids because physical properties are measured relatively often. [DMIM][DMP], [EMIM][DMP], and [EMIM][BF_4] were selected as the absorbent for H_2O, and [HMIM][Tf_2N] as the absorbent for R32.

2.2 Simulation model

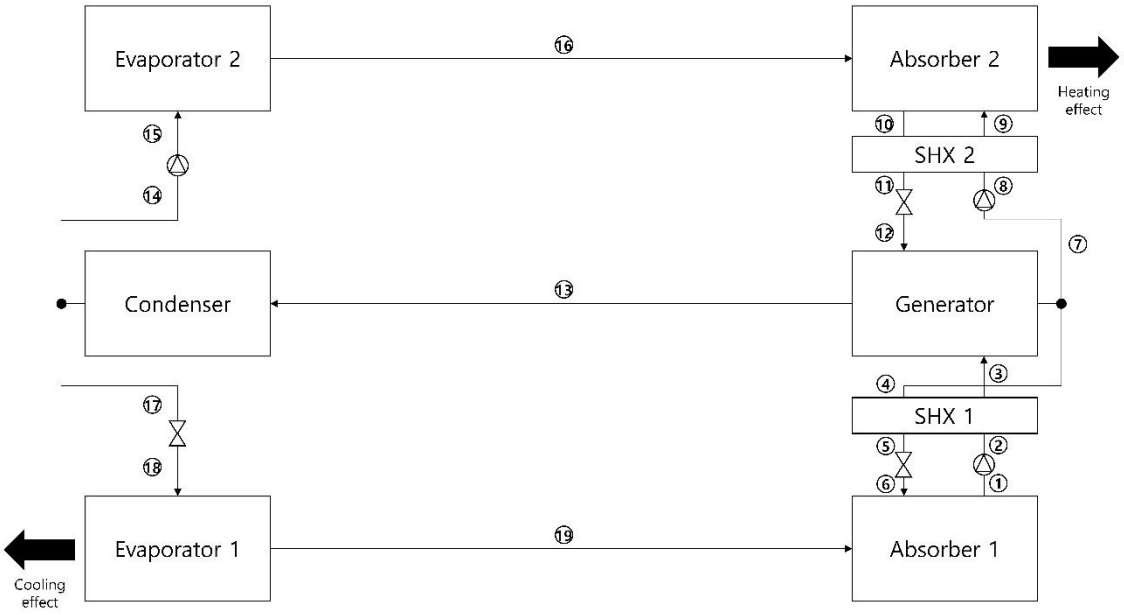


Fig. 1. Schematic diagram of the simultaneous cooling and heating absorption system.

Figure 1 shows the schematic diagram of the simultaneous cooling and heating absorption system. It is a combination of type 1 and type 2 absorption systems. Cooling COP, heating COP and total COP are analyzed under various conditions. To evaluate performance of the system, split ratio and COP were defined as follows;

$$r_g = \frac{\dot{m}_7}{\dot{m}_4+\dot{m}_7} \quad (1)$$

$$r_c = \frac{\dot{m}_{14}}{\dot{m}_{14}+\dot{m}_{17}} \quad (2)$$

$$COP_c = \frac{\dot{Q}_{eva1}}{\dot{Q}_{gen}+W_{pump}} \quad (3)$$

$$COP_h = \frac{\dot{Q}_{abs2}}{\dot{Q}_{gen}+\dot{W}_{pump}} \quad (4)$$

$$COP_{tot} = COP_c + COP_h \quad (5)$$

where r_g is the split ratio of the generator; r_c is the split ratio of the condenser, COP_c is cooling COP, COP_h is heating COP, COP_{tot} is the total COP, $\dot{Q}_{gen}$ is the heat absorbed by the generator, $\dot{Q}_{eva1}$ is the heat absorbed by the low-temperature evaporator, $\dot{Q}_{abs2}$ is the heat emitted by the high-temperature absorber and $\dot{W}_{pump}$ is the pump work. COP_c, COP_h and COP_{tot} are analyzed under various conditions.

In the previous studies, the correlations for the thermal properties of the refrigerant/ionic liquid solution are established using the VLE (vapor-liquid equilibrium) equation and the NRTL (Non-Random Two-Liquid) model. The NRTL model is a chemical model that uses three interaction parameters to obtain an activity coefficient for the phenomenon of deviating from an ideal solution to which the Raoul's law is applied, and uses it to calculate the VLE equation [5–7].

$$Y_i p \Phi_i = X_i \gamma_i p_i^S \ \ (i = 1, 2) \quad (6)$$

$$\Phi_i = \exp\left[\frac{(B_i - V_i^L)(p - p_i^S)}{RT}\right] \quad (7)$$

$$ln\gamma_1 = X_2^2\left[\tau_{21}\left(\frac{G_{21}}{x_1 + x_2 G_{21}}\right)^2 + \frac{\tau_{12} G_{12}}{(x_2 + x_1 G_{12})^2}\right] \quad (8)$$

$$ln\gamma_2 = X_1^2\left[\tau_{12}\left(\frac{G_{12}}{x_2 + x_1 G_{12}}\right)^2 + \frac{\tau_{21} G_{21}}{(x_1 + x_2 G_{21})^2}\right] \quad (9)$$

$$G_{12} = \exp(-\alpha\tau_{12}),\ G_{21} = \exp(-\alpha\tau_{21}) \quad (10)$$

$$\tau_{12} = \tau_{12}^0 + \frac{\tau_{12}^1}{T},\ \tau_{21} = \tau_{21}^0 + \frac{\tau_{21}^1}{T} \quad (11)$$

where Y_i is the vapor molar concentration of ith species; X_i is the liquid molar concentration of ith species; p is the vapor pressure of the solution; p_i^s is the saturated vapor pressure of ith species; Φ_i is the correction factor for ith species; γ_i is the activity coefficient for ith species; B_i is the second virial coefficient of ith species; V_i^L is the saturated molar liquid volume of ith species; R is the ideal gas constant (8.314 kJ/kmol·K), T is the temperature, and α, τ_{12}^0, τ_{12}^1, τ_{21}^0, τ_{21}^1 are adjustable parameters regressed through data from the experimental studies of each solution.

In the simultaneous cooling and heating absorption system, the generator receives waste heat and generates the refrigerant from strong solution. Generated refrigerant moves to the condenser, and the remaining weak solution moves through the splitter to the high temperature solution heat exchanger and the low-temperature solution heat exchanger. In each solution heat exchanger, heat exchange between the strong solution and the dilute solution is performed. After the heat exchange, the weak solutions move to a high-temperature absorber and a low-temperature absorber, respectively. The condenser condenses the generated refrigerant vapor, and the condensed refrigerant moves to the high-temperature evaporator and the low-temperature evaporator through a splitter. Each evaporator evaporates the liquid refrigerant, and a cooling effect corresponding to the cooling load occurs in the low-temperature evaporator. The evaporated refrigerant moves to the absorber and is absorbed by the weak solution to form a strong solution. The strong solution exits the absorber, passes through the solution heat exchanger, and returns to the generator. The simulation conditions for R32/[HMIM][Tf_2N] and H_2O/[DMIM][DMP], [EMIM][DMP], [EMIM][BF_4] are summarized in Table 1 and 2, respectively.

Table 1. Simulation condition of R32/[HMIM][Tf_2N]

Location	1	10	14, 17	16	19
Temperature	30 ºC	77 ºC	30 ºC	50 ºC	5 ºC
Pressure	813.2 kPa	3141 kPa	1928 kPa	3141 kPa	813.2 kPa

State	Solution liquid	Solution liquid	Refrigerant liquid	Refrigerant vapor	Refrigerant vapor

Table 2. Simulation condition of H_2O/[DMIM][DMP], [EMIM][DMP], [EMIM][BF_4]

Location	1	10	14, 17	16	19
Temperature	30 ºC	77 ºC	30 ºC	50 ºC	5 ºC
Pressure	0.6112 kPa	12.35 kPa	4.247 kPa	12.35 kPa	0.6112 kPa
State	Solution liquid	Solution liquid	Refrigerant liquid	Refrigerant vapor	Refrigerant vapor

3. Results

3.1. Effect of split ratio

There are two split ratios in the generator and the condenser, and each value of split ratio has an impact on several performance indicators. The split ratio has an impact on COP_c, COP_h and COP_{tot} for all four refrigerants/ILs. Simulation results according to the changes in r_g and r_c are shown in Figure 2. The COP trends in H_2O/[DMIM][DMP], H_2O/[EMIM][DMP] and H_2O/[EMIM][BF_4] were compared. As r_g increases, the COP_c, COP_h and COP_{tot} increase. As r_c increases, the COP_c and COP_{tot} decrease while COP_h increases. To achieve the reasonable level of cooling and heating effects, it is important to choose r_g and r_c correctly. The COP trends of R32/[HMIM][Tf_2N] were different from those of H_2O/[DMIM][DMP], H_2O/[EMIM][DMP] and H_2O/[EMIM][BF_4]. As r_g increases, the COP_c, COP_h and COP_{tot} increase. However, Ass r_c increases, the COP_c, COP_h and COP_{tot} decrease.

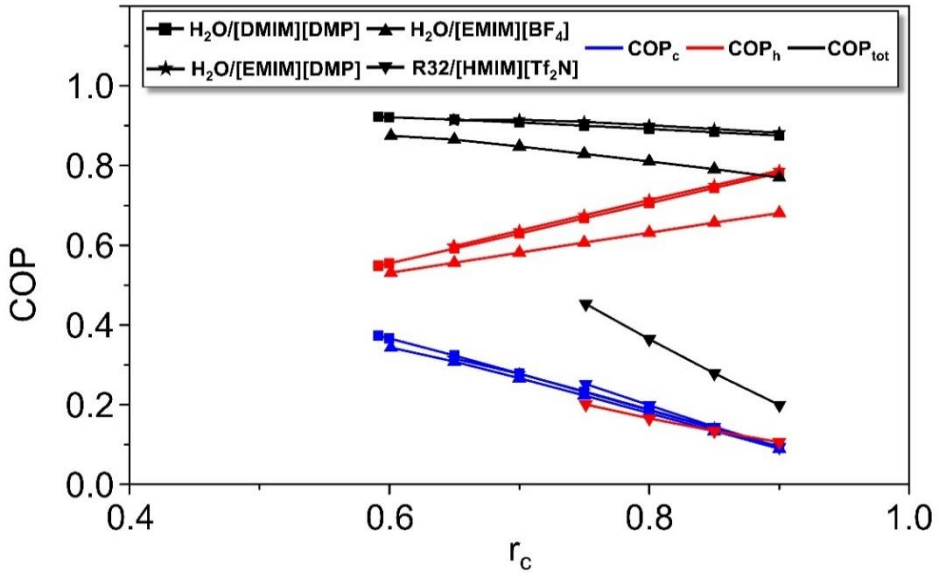


Fig. 2. Simulation result of COP-split ratio for r_g=0.5.

When H_2O/IL applied, cooling effect decreases while heating effect increases as r_c increases. On the other hand, cooling effect increases and heating effect decreases as r_c decreases. When R32/IL applied, the trend of cooling effect is similar to the result of H_2O/IL. However, trend of heating effect is opposite. This is because the factors that influence $\dot{Q}_{abs2}$ are different. In H_2O/IL system, increasing enthalpy of refrigerant vapor which is point 16 in Figure 1 is a dominant factor to influence $\dot{Q}_{abs2}$ as r_c increases. In R32/IL system, increasing enthalpy of solution liquid which is point 10 in Figure 1 is a dominant factor.

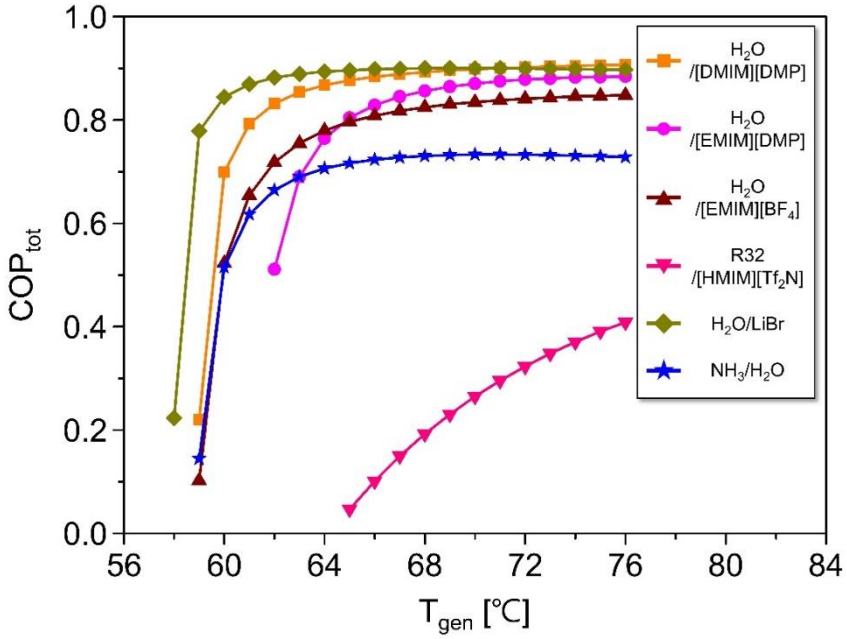


Fig. 3. Simulation result of T_{gen}-COP_{tot} when r_c=0.5.

3.2. Effect of generation temperature

Figure 3 shows the simulation result of T_{gen}-COP_{tot} when r_c=0.5. To show a balanced example of the cooling effect and the heating effect, r_c is set to 0.5. For all four alternative working fluids, COP_{tot} increases as the generation temperature increases. As shown in Figure 3, the maximum COP_{tot} of H_2O/LiBr was 0.90 and NH_3/H_2O was 0.73. Compared with COP_{tot} of H_2O/LiBr, H_2O/[DMIM][DMP] (COP_{tot}=0.91), H_2O/[EMIM][DMP] (COP_{tot}=0.88) and H_2O/[EMIM][BF_4] (COP_{tot}=0.85) results in similar performances. Compared with COP_{tot} of H_2O/LiBr, R32/[HMIM][Tf_2N] (COP_{tot}=0.41) performed 45%.

The trend of increasing or decreasing COP can be explained by the different increasing rates of $\dot{Q}_{gen}$ (heat transfer rate of generator), $\dot{Q}_{eva1}$ (heat transfer rate of low-temperature evaporator) and $\dot{Q}_{abs2}$ (heat flow rate of high- temperature absorber), respectively. As $\dot{Q}_{gen}$ increases, the amount of generated refrigerant increases. Naturally, $\dot{Q}_{eva1}$ and $\dot{Q}_{abs2}$ also increase. Therefore, if the rate of increase in the numerators in Eq (3) and (4) are faster than the rate of increase in the denominators, the COP tends to increase, whereas if the rate of increase in the numerators is slower than the rate of increase in the denominators, the COP tends to decrease. For all four working fluids, the rate of increase in the cooling and heating effects is faster than the rate of increase in the amount of heat input to the generator as the generation temperature increases. Therefore, COP_{tot} increases as the generation temperature increases for all working fluids.

4. Conclusion

In this study, four different working fluids were selected for the simultaneous cooling and heating absorption system, and the COP_c, COP_h and COP_{tot} were compared depending on the variations of the split ratio and generation temperature. From the results, the following conclusions were drawn.

(1) The COP_{tot} of H_2O/IL ranges 0.84–0.90 which is higher value than that of R32/IL.

(2) For all four different working fluids, COP_{tot} increases as generation temperature increases. Maximum COP_{tot} of H_2O/IL is estimated 0.85–0.91. Maximum COP_{tot} of R32/IL is calculated 0.41, showing 55% lower performance than H_2O/IL.

(3) COP_{tot} of refrigerant/IL is similar to that of H_2O/LiBr. Since it can solve the crystallization phenomenon, which is the weakness of H_2O/LiBr, it is confirmed that the ionic liquid will be a strong alternative to the traditional working fluid.

Acknowledgements

Some parts of this study are included in 'Park, S., Choi, H. W., Lee, J. W., Cho, H. U., Lee, N. S., Kang, Y. T. Performance analysis of ionic liquids for simultaneous cooling and heating absorption system' submitted to Energy.

This study is partially supported by the National Research Foundation of Korea(NRF) grant funded by the Korea government (MSIT). (Grant number : NRF-2020R1A5A1018153) and LG Electronics (Grant no. : Q2213281)

References

[1] Kim, J. D., Hayashi, S., Onoda, M., Sato, A., Nishimura, C., Mori, T., & Honma, I., 2008. New organic–inorganic crystalline electrolytes synthesized from 12-phosphotungstic acid and the ionic liquid [BMIM][TFSI]. Electrochimica acta 53(26), 7638-7643.

[2] Paulechka, Y. U., Kabo, G. J., Blokhin, A. V., Vydrov, O. A., Magee, J. W., & Frenkel, M., 2003. Thermodynamic properties of 1-butyl-3-methylimidazolium hexafluorophosphate in the ideal gas state. J Chem Eng Data 48(3), 457-462.

[3] Domańska, U., & Bogel-Łukasik, R., 2005. Physicochemical properties and solubility of alkyl-(2-hydroxyethyl)-dimethylammonium bromide. J Phys Chem B 109(24), 12124-12132.

[4] Trindade, C. A., Visak, Z. P., Bogel-Łukasik, R., Bogel-Łukasik, E., & Ponte, M. N. D., 2010. Liquid− liquid equilibrium of mixtures of imidazolium-based ionic liquids with propanediols or glycerol. Ind Eng Chem Res 49(10), 4850-4857.

[5] Kim, Y. J., Kim, S., Joshi, Y. K., Fedorov, A. G., & Kohl, P. A., 2012. Thermodynamic analysis of an absorption refrigeration system with ionic-liquid/refrigerant mixture as a working fluid. Energy 44(1), 1005-1016.

[6] hang, X., & Hu, D., 2011. Performance simulation of the absorption chiller using water and ionic liquid 1-ethyl-3-methylimidazolium dimethylphosphate as the working pair. Appl Therm Eng 31(16), 3316-3321.

[7] Dong, L., Zheng, D., Nie, N., & Li, Y., 2012. Performance prediction of absorption refrigeration cycle based on the measurements of vapor pressure and heat capacity of H2O+[DMIM] DMP system. Appl Energ 98, 326-332.

14th IEA Heat Pump Conference
15-18 May 2023, Chicago, Illinois

An Experimental Study on the Chemisorption Heat Pump for Low Temperature Heat Source

Hak Soo Kim[a*], Jeong Hyun Kim[a], Dong Ho Kim[a], Young Kim[a], Seok Ho Yoon[a*]

[a]Department of Thermal Energy Solutions, Korea Institute of Machinery and Materials, Daejeon, 34103, Republic of Korea

Abstract

Global interest in carbon neutrality is increasing for a sustainable society in response to the climate crisis. Various studies are being conducted for carbon neutrality, and among them, many studies related to unused energy are being conducted. Many studies focused on the waste heat recovery system regarding the use of unused energy. Recently, interest in a chemisorption heat pump capable of performing a cooling based on low-temperature thermal energy has increased. This research conducted an experimental study to understand the performance characteristics of a chemisorption heat pump consisting of a condenser, an evaporator, and two reactors based on a low-temperature heat source (40℃). Experiments were conducted for cases where the adsorption/desorption operation time was 20, 30, and 50 minutes, and the average cooling capacity, COP, and SCP were presented for each condition when performing six alternating operations. As adsorption/desorption operation time went up, average cooling capacity, SCP were reduced and COP was increased.

© HPC2023.
Selection and/or peer-review under the responsibility of the organizers of the 14th IEA Heat Pump Conference 2023.

Keywords: Chemisorption Heat Pump; Waste heat recovery; Adsorbent; Adsorption; Desorption;

1. Introduction

There is a growing interest in carbon neutrality around the world. The governments of some countries around the world, including South Korea, have announced national plans to achieve carbon neutrality in 2050 [1]. Research institutions around the world are conducting research on the use of renewable energy, process efficiency improvement, and waste energy recovery to achieve carbon neutrality. Among these research topics, in the case of waste energy recovery, many studies have been conducted on waste heat recovery. One study showed the amount of waste heat in each EU country and each industry sector [2]. In most cases, thermal energy of more than 100℃ is emitted in the form of waste heat, and most studies have focused on utilizing waste heat energy in this temperature band. In addition, since the technical difficulty is high to recover low-temperature thermal energy of about 40 to 50℃, relatively little research has been conducted on technologies that utilize low-temperature waste heat energy of about 40 to 50℃.

The chemisorption heat pump is a refrigeration cycle driven by thermal energy. Fig. 1 shows the basic principle and cycle diagram of chemisorption heat pump [3]. Relatively high-temperature (T_h) thermal energy is supplied to the desorption reactor, medium-temperature (T_m) thermal energy is discharged from the condenser and adsorption reactor, and low-temperature (T_l) thermal energy is supplied to the evaporator. A cooling effect occurs in the process of supplying low-temperature thermal energy to the evaporator. In order to drive the chemisorption heat pump, a high-temperature, medium-temperature, and low-temperature heat source is required, and the combination of this temperature is determined by a combination of a working fluid and adsorbent. According to Yang *et al.* [3], When the working fluid of the low-temperature driven chemisorption heat pump is NH_3, NH_4Cl, $PbCl_2$ or NaBr are suitable as an adsorption material. Oliveira and

* Corresponding author. Tel.: +82-42-868-7288; fax: +82-42-868-7338.
E-mail address: haksookim@kimm.re.kr.
* Corresponding author. Tel.: +82-42-868-7064; fax: +82-42-868-7338.
E-mail address: shyoon@kimm.re.kr.

Generoso [4] conducted an experiment using a chemical adsorption heat pump driven by about 70℃ heat energy. Oro *et al.* [5] conducted an analysis study on a chemisorption heat pump using waste heat of about 70 ℃ discharged from the fuel cell. Pacho [6] conducted an analytical and experimental study on a chemisorption heat pump driven by thermal energy of 120℃. In addition to these studies, various studies were conducted on the chemisorption heat pump, such as cycle analysis and Clapeyron curve [7-11].

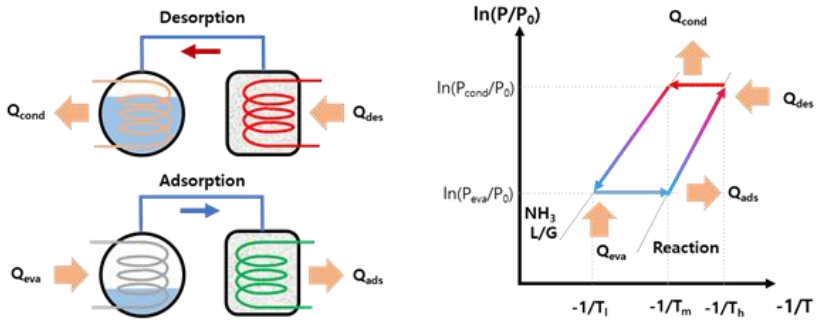


Fig. 1. Schematic and Cycle Diagram of Chemisorption Heat Pump [3].

In this study, a cooling cycle experiment was conducted by using a chemisorption heat pump consisting of an evaporator, a condenser, and two reactors. By performing the alternating operation, cooling performance, COP, and SCP (Specific cooling power) of the system according to the alternating operation time were measured.

2. Experimental Apparatus and Procedures

Fig. 2 shows schematic diagram of chemisorption heat pump. The chemisorption heat pump is operated alternately, and a total of four operation modes are repeated. Each operation mode is implemented using a valve in the system, and the valve's status under each operation mode is in shown in Table 1. In mode A, the working fluid is adsorbed and desorbed from the adsorbent in reactor 1 and reactor 2, respectively. Mode B is a preparation process for mode C, and the chillers connected to each reactor are changed. In mode C, the working fluid is adsorbed and desorbed from the adsorbent in reactor 2 and reactor 1, respectively. Mode D is a preparation process for mode A, and the chillers connected to each reactor are changed. In this study, experiment was conducted by setting T_h, T_m, and T_l to 40, 20, and 15℃, respectively. Chillers 1, 2, 3, and 4 supply cooling water of temperatures of 20°C, 40°C, 20°C, and 15°C to the system, respectively. Mode A, B, C, D were repeated as illustrated in Fig. 3, wherein Δt_1 was set to 20, 30, and 50 minutes, and Δt_2 was set to 5 minutes, and the experiment was conducted. During Mode B and D, Valve 5 was opened at the start of Mode B and D, and closed after 1 minute.

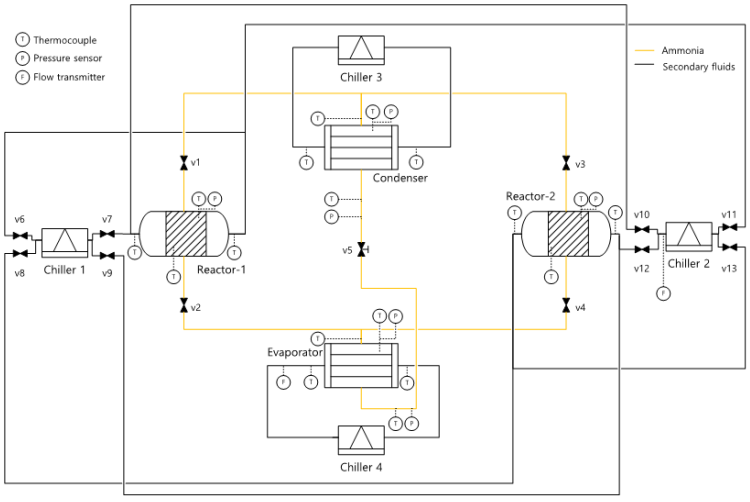


Fig. 2. Schematic Diagram of Chemisorption Heat Pump.

Table 1. Valve Position under each Operation Mode

Valve	1	2	3	4	5	6	7	8	9	10	11	12	13
Mode A	off	on	on	off	off	on	on	off	off	off	off	on	on
Mode B	off	off	off	off	on	off	off	on	on	on	on	off	off
Mode C	on	off	off	on	off	off	off	on	on	on	on	off	off
Mode D	off	off	off	off	on	on	on	off	off	off	off	on	on

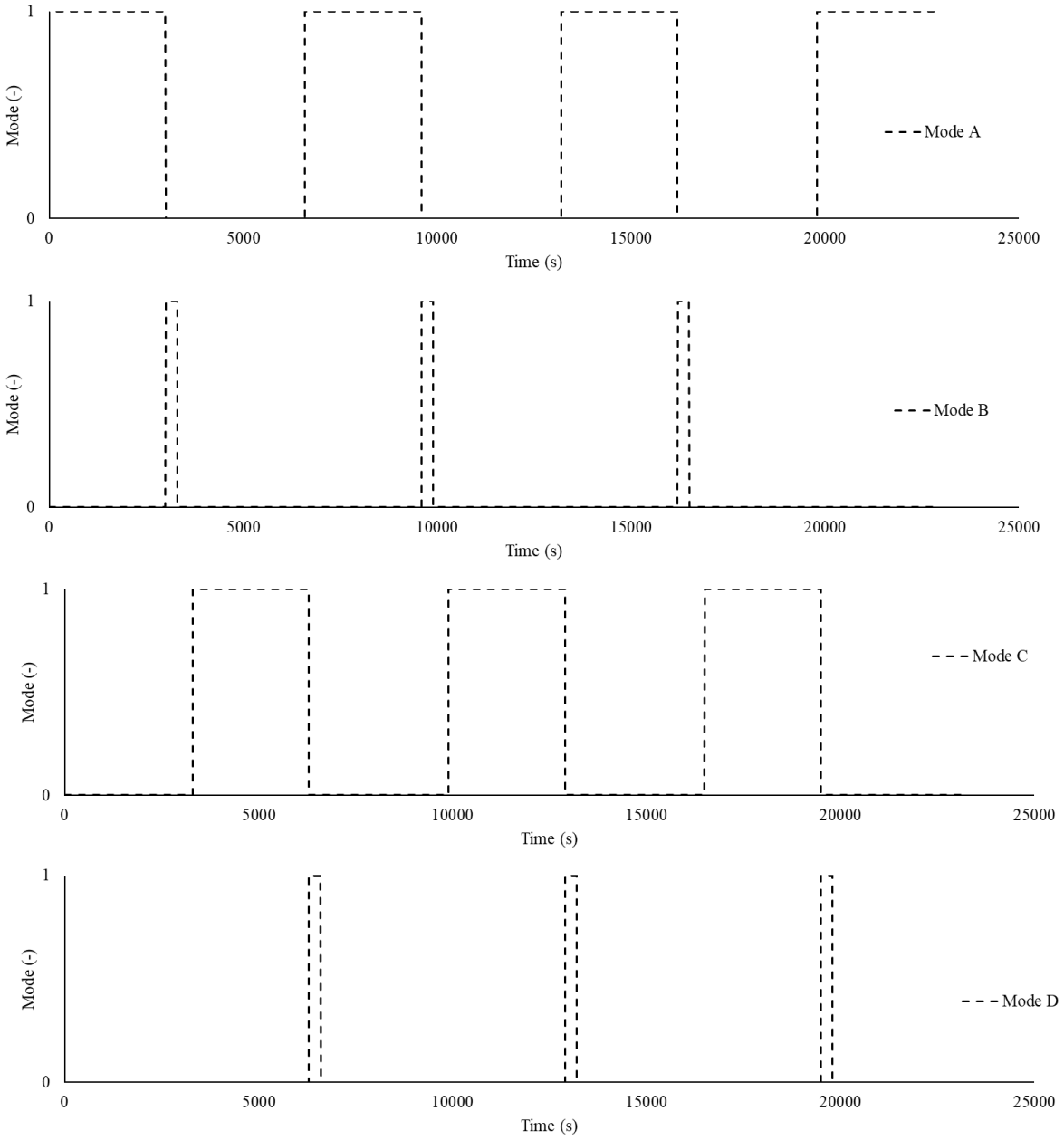


Fig. 3. Each Operation Mode over Time.

Temperature, pressure, and flow rate were measured using thermocouples, pressure transmitters, and flow meters, respectively, and the specifications of each instrument are as shown in the Table 2.

Ammonia was used as working fluid and NaBr was impregnated in Expanded-graphite and used as an adsorbent.

Table 2. Specification of each Instrument

Sensor	Model	Measurement Accuracy
Thermocouple	Omega T-type probe	±0.3℃
Pressure sensor	Sensys PSCH0030BCPG	±1.7 kPa
Flow meter	TCM3100-FA-SGSS-CSMS-	±0.1% of reading

3. Experimental Results and Discussion

Figs. 4 ~ 9 show experimental results when Δt_1 was set to 30 minutes, and Δt_2 was set to 5 minutes. As shown in Fig. 3, Mode A and C were operated 4 and 3 times, respectively. If the alternating operation is repeated continuously, the initial conditions of modes A and C are constant. However, when the alternating operation is first started (0 second of Fig. 3), the initial condition of Mode A is different from the condition when the alternating operation is continuously repeated. Therefore, the data analysis was performed on the conditions under which the alternating operation was continuously performed. The experiment was performed by repeating modes A through D three times. This means that a total of 6 adsorption/desorption operations have been performed. Each adsorption/desorption preparation and adsorption/desorption operation operation are defined as one cycle, and the start and end of each cycle can be expressed like the black dotted line in Fig. 4. In the first, third, and fifth cycles in Fig. 4, the working fluid is adsorbed and desorbed in Reactors 1 and 2, respectively. In the second, fourth, and sixth cycles, the working fluid is desorbed and adsorbed in Reactors 1 and 2, respectively. The working fluid was moved from the desorption reactor to the condenser and condensed. Therefore, the pressure of the desorption reactor is slightly higher than the pressure of the condenser as shown in Fig. 4. Meanwhile, the working fluid evaporated from the evaporator moved to the adsorption reactor and was adsorbed into the adsorbent. Therefore, the pressure of the evaporator is slightly higher than that of the adsorption reactor. It can be seen that the pressure of each component shows a repetitive tendency and is maintained during the alternating operation. Fig. 5 shows cooling capacity of evaporator. Cooling capacity was calculated by using temperature difference and flow rate of secondary flow ($Q = \dot{m}C_p\Delta T$). In Fig. 5, the range 0 ~ 300 seconds is adsorption/desorption preparation operation, and after 300 seconds, it is adsorption/desorption operation. After adsorption/desorption preparation operation starts, the cooling capacity of the evaporator decreases to almost zero, and after adsorption/desorption operation starts, the cooling capacity increases rapidly and then gradually decreases. The cooling capacity was up to about 100 W. It can be found that the cooling capacity shows an almost constant tendency in 6 repeated cycles. Fig. 6 shows heat capacity supplied to desorption reactor. As shown in Figure 6, it can be seen that the heating capacity supplied to the desorption reactor increases rapidly after the start of the adsorption/desorption preparation operation and then gradually decreases. When the adsorption/desorption preparation operation starts, the cooling water of 40℃ is instantaneously supplied to the reactor that had previously been supplied with cooling water of 20℃. Cooling water of 40℃ is instantaneously supplied while the temperature of the structure (Stainless steel) of the desorption reactor is about 20℃, and the cooling water supplies thermal energy to increase the temperature of the desorption reactor structure. Therefore, the heating energy supplied to the reactor increases rapidly after the start of the adsorption/desorption preparation operation. After the temperature of the structure rises, the heat required for the desorption reaction is supplied to the reactor, and as the desorption reaction progresses, the desorption reaction slows down, so the heat supplied to the reactor gradually decreases over time. Olivera and Generoso [4] calculated COP of chemisorption heat pump based on the time averaged cooling capacity of evaporator and time averaged heating capacity supplied to reactor. In this paper, COP is obtained by dividing time averaged cooling capacity of evaporator by time averaged heating capacity supplied to reactor. Figs. 7 – 9 show time averaged cooling capacity of evaporator, time averaged heating capacity supplied to desorption reactor, COP of chemisorption heat pump. Average cooling capacity of evaporator is 73.2 (Cycle 1) ~ 87.3 (Cycle 6) W. Average heating capacity supplied to desorption reactor is 379.9 (Cycle 6) ~ 411.5 (Cycle 1) W. COP of chemisorption heat pump is 0.18 (Cycle 1) ~ 0.23 (Cycle 6) W.

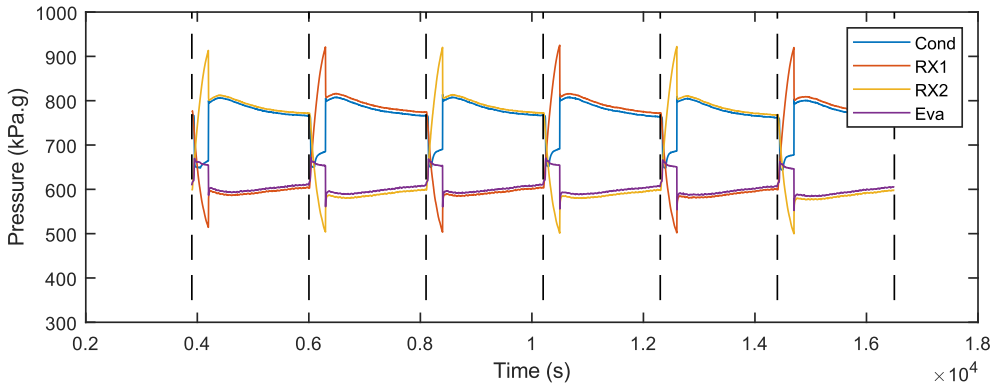


Fig. 4. Pressures of Cond (condenser), RX1 (Reactor 1), RX2 (Reactor 2) and Eva (Evaporator)

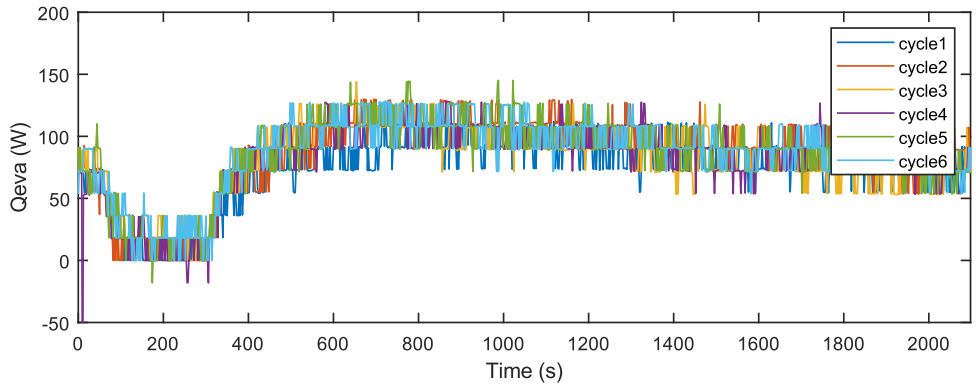


Fig. 5. Cooling Capacity of each Cycle

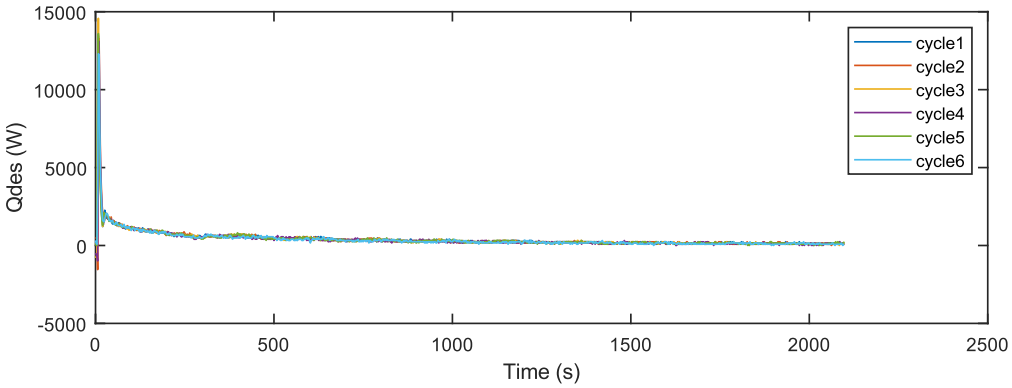


Fig. 6. Heating Capacity Supplied to Desorption Reactor of each Cycle

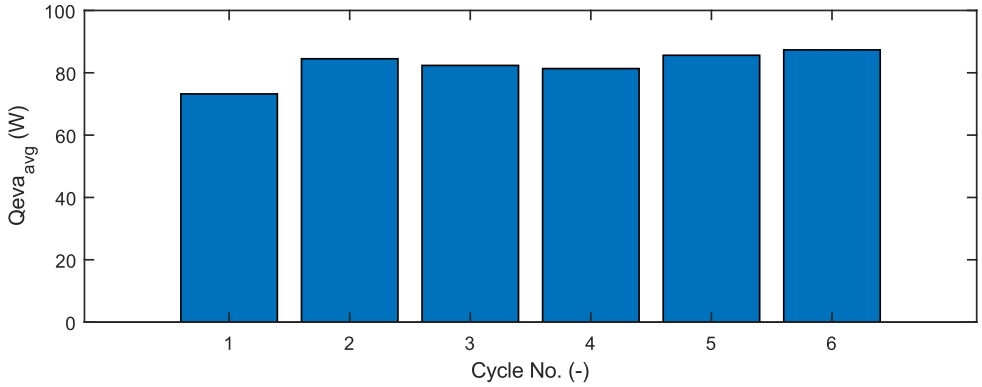


Fig. 7. Time Averaged Cooling Capacity of Evaporator

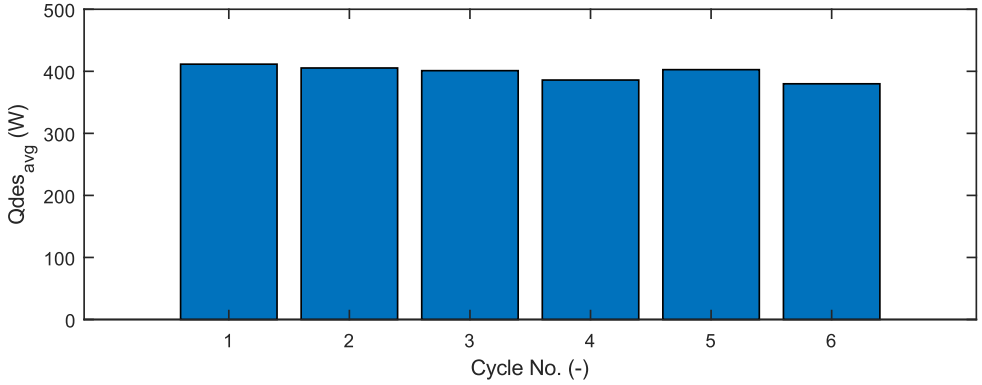


Fig. 8. Time Averaged Heating Capacity Supplied to Desorption Reactor

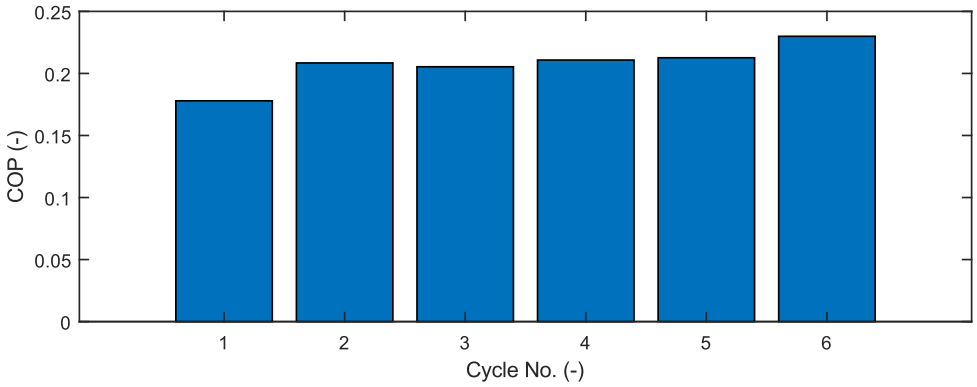


Fig. 9. COP of Chemisorption Heat Pump

As mentioned above, experiments were performed on conditions of 20, 30, and 50 minutes of adsorption/desorption operation time, respectively. Experiments were conducted twice each under the same conditions. Table 3 shows experimental results of each case.

Table 3. Experimental Results of Each Case

Case No.	Δt_1	$Q_{eva,avg}$ (W)	$Q_{des,avg}$ (W)	COP (-)	SCP (W/kg)
1	20	88.3	464.7	0.19	92.8
2	30	82.4	397.7	0.21	86.5
3	50	76.0	307.1	0.25	79.9
4	20	82.9	459.6	0.18	87.0
5	30	78.7	407.5	0.19	82.7
6	50	68.6	313.1	0.22	72.1

As shown in Fig. 5, Q_{eva} decreases as the adsorption/desorption operation time elapses. Thus, as Δt_1 increases, $Q_{eva,avg}$ and SCP decrease. Each time an alternating operation is performed, a large amount of heat energy is supplied to the reactor structure. Therefore, when the system is operated for a specific time span, the COP is increased when the number of alternating operations is reduced. For this reason, as Δt_1 increases as shown in Table 3, COP increases.

4. Conclusion

An experimental study on the refrigeration cycle of chemisorption heat pump system is conducted. Experiment was conducted by using a system consisting of two reactors, a condenser, and an evaporator. Experiment was performed under conditions in which coolant of 40°C, 20°C, 20°C, and 15°C was supplied to the desorption reactor, the adsorption reactor, the condenser, and the evaporator, respectively. Experiments were performed on conditions of 20, 30, and 50 minutes of adsorption/desorption operation time. As adsorption/desorption operation time increases, average cooling capacity, SCP were decreased and COP was increased. Based on this study, it is possible to confirm the performance characteristics of the low-temperature driven chemisorption heat pump system according to the adsorption/desorption operation time.

Acknowledgements

This work was supported by Korea Institute of Energy Technology Evaluation and Planning (KETEP) grant funded by the Korea government (MOTIE) (20212050100010, Chemisorption heat pump system using electrochemical compressor).

References

[1] 2050 Carbon Neutral Strategy of the Republic of Korea: Towards a Sustainable and Green Society; 2020.
[2] Michael P., George K., Andrea C., Umberto La C., Giorgio M., 2018. Industrial Waste Heat: Estimation of the Technically Available Resource in the EU Per Industrial Sector, Temperature Level and Country. Applied Thermal Engineering 138, p. 207-16.
[3] Zhiyao Y., Ming Q., Kyle R. G., 2020. Ammonia-based Chemisorption Heat Pumps for Cold-Climate Heating Applications: A Comprehensive Review. Applied Thermal Engineering 179, 115674.
[4] Rogério Gomes de O., Daniel João G., 2016. Influence of the Operational Conditions on the Performance of a Chemisorption Chiller Driven by Hot Water Between 65°C and 80°C. Applied Energy 162, p. 257-65.
[5] Marcos Vinício O., Rogério Gomes de O.a, Edson B., 2018. An Integrated Solution for Waste Heat Recovery from Fuel Cells Applied to Adsorption Systems. Applied Thermal Engineering 136, p. 747-54.
[6] Angeles Rivero P., 2015. Innovation in Carbon-Ammonia Adsorption Heat Pump Technology: a Case Study. Institute of Rerigeration.
[7] Huashan B., Zhiwei M., Anthony Paul R., 2017. An Optimised Chemisorption Cycle for Power Generation Using Low Grade Heat. Applied Energy 186, p. 251-61.
[8] Huashan B., Yaodong W., Anthony Paul R., 2014. Modelling of a Chemisorption Refrigeration and Power Cogeneration System. Applied Energy 119, P. 351-62.
[9] Z.S. Zhou, L.W. Wang, L. Jiang, P. Gao, R.Z. Wang., 2016. Non-Equilibrium Sorption Performances for Composite Sorbents of Chlorides–Ammonia Working Pairs for Refrigeration. International Journal of Refrigeration 65, p. 60-8.
[10] Ruzhu W., Liwei W., Jingyi W., 2014. Adsorption Refrigeration Technology: Theory and Application. 1st ed. John Wiley & Sons Singapore Pte. Ltd.
[11] Liwei W., Guoliang A., Jiao G., Ruzhu W., 2021. Property and Energy Conversion Technology of Solid Composite Sorbents. 1st ed. Science Press Beijing.

14th IEA Heat Pump Conference
15-18 May 2023, Chicago, Illinois

HpCosy - Heat Pump Comfort System

Christoph Messmer[a,*], Robert Haberl[b], Kanchan Bohara[b], Michel Haller[b], Michele Zehnder[c], Ralph Eismann[a]

[a]FHNW University of Applied Sciences and Arts Northwestern Switzerland, Hofackerstrasse 30, Muttenz CH-4132, Switzerland
[b]OST Eastern Switzerland University of Applied Sciences, Oberseestrasse 10, Rapperswil CH-8640, Switzerland
[c]CTA AG, Hunzigenstrasse 2, Muensingen CH-3110, Switzerland

Abstract

In the project HpCosy the base for a decentralized brine-water heat pump system for flats in multi-family houses is developed and investigated. It encompasses the functions heating, cooling and domestic hot water preparation. Its control shall enable the consideration of availability of on-site produced photovoltaic electricity as a single unit within a swarm of all heat pumps within the building.

The comparison between a centralized and several decentralized heat pump systems clearly shows great advantages of the decentralized solutions (savings up to 31% of electric energy). However, the largest share of the energy saved is due to the elimination of DHW circulation.

The measurement of a HpCosy-unit in realistic and dynamic working conditions showed that an individual adjustment of the control of the individual swarm participants in response to a swarm signal is technically feasible and already leads to a reduction of the grid consumption in the selected and tested week.

The final simulations of the overall system show that - in addition to the savings achieved through the use of decentralized systems - an additional reduction in grid consumption of up to 5% can be achieved by increasing self-consumption by 11% to 17% with a swarm signal, indication whether there is a positive on-site energy production or not.

© HPC2023.
Selection and/or peer-review under the responsibility of the organizers of the 14th IEA Heat Pump Conference 2023.

Keywords: heating; cooling; domestic hot water; multi-family houses; swarm control; photovoltaic self-consumption

1. Introduction

Heat for the provision of domestic hot water (DHW) will become more relevant than heat for heating due to increasingly better building insulation and therefore decreasing space heating demand. Cooling applications will be increasingly realized because of increased comfort demands and not least also due to the advancing climate change. In this context, it makes sense to use the same heat pump to generate both cooling and heating of hot water in the summer, and to operate it as far as possible with self-generated electricity from photovoltaics (PV) or to be able to react to tariff incentives for load shifting (demand side management).

Decentralized heat pump systems for heating and DHW provision in multi-family houses (MFH) with individual units per residential unit offer decisive advantages over central heat pumps. DHW circulation is not required, distribution losses can be avoided, and the lower requirements for DHW storage temperatures in accordance with the Swiss SIA 385/1 [1] standard will increase the efficiency of the provision of DHW. As a result of having several small units, the electrical power drawn can be more finely adjusted to the PV electricity produced.

* Corresponding author. Tel.: +41-61-228-5464 .

E-mail address: christoph.messmer@fhnw.ch .

When combined with geothermal probes as heat sources and heat sinks, the system is expected to have major advantages from both an energetic and an economic point of view.

2. Project goals

The main objective is to develop the basis for a new heat pump system, which has the following characteristics:

- Increased efficiency (30% less electrical energy demand) compared to current solutions with the same hygiene assurance (legionella protection) [2].
- Increased comfort by offering free cooling and/or active heat pump cooling function
- Increased flexibility of the brine circuit, which can be coupled with geothermal probes, energy networks, air heat exchangers or other heat sources.
- Development of a so-called swarm control for skillful consideration of the local PV electricity production.

3. Market potential

In a first step, the market potential for the application was analyzed and the requirements for a decentralized heat pump and storage unit defined, such as the necessary heating and cooling capacities, the power controllability, the necessary communication requirements, and the size of the DHW storage tank.

According to the Federal Statistical Office (FSO), there were a total of around 1.76 million buildings with residential use in Switzerland in 2019 [3]. Of these, around 1.48 million are purely residential buildings, divided into 1.0 million single-family houses (SFH) and 0.48 million MFH, of which around 0.25 million have between 3 and 9 flats. The number of residential buildings with secondary use and 3 to 9 dwellings is about 0.06 million. A first rough estimate for the HpCosy system potential results in about 0.31 million buildings with 6 dwellings on average, which would mean 1.86 million decentralized heat pumps.

A market survey of suitable heat pumps with DHW storage systems showed, that the devices for the application are already available. Of the 27 analyzed models with inverter drives, 13 are with heating powers in the range of 1-10 kW, which is regarded to be sufficient for the individual flats. Heating buffer tanks are not required for part load operation, as the output can be adjusted to a very low demand. The heating power ranges of the 13 selected models are shown in Fig. 1.

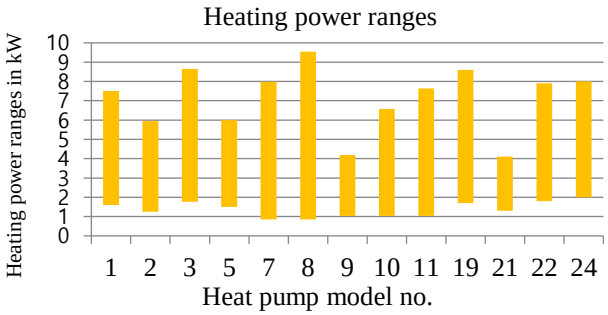


Fig. 1: Heating power ranges of suitable, available heat pumps/storage systems

4. Comparison of centralized and decentralized heat pump systems

A combination of building simulations with the software TRNSYS and spreadsheet calculations for the heating system was used to compare a central with a decentralized heat pump system in an MFH. The modelling was done with the "Type 56" building model in TRNSYS. The modelled building is a three-storey renovated apartment building with six residential units: three residential units on the east side and another three on the west side [4]. Both the internal loads of the flats and the hot water demand are considered via individual user profiles. The location is the city of Zurich. The total heat demand of the flats is shown in Fig. 2 as the sum

of the space heating (SH) demand with ideal heating to a setpoint temperature of 21 °C and the hot water demand.

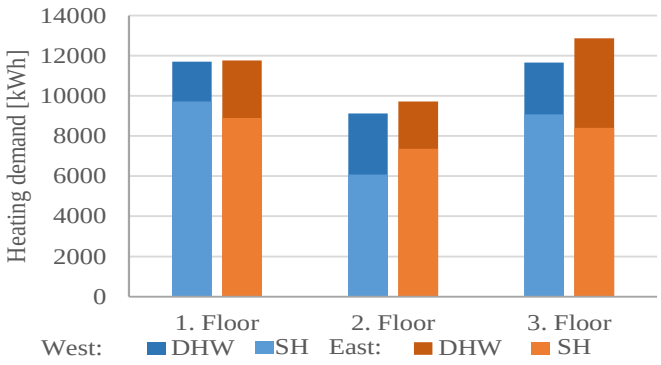


Fig. 2: Heat demand in the MFH

The heat supply of the building is either with a central heating system consisting of an inverter-controlled brine-to-water heat pump, two 600 liter DHW storage tanks and an 850 liter buffer tank for space heating, or six decentralized brine-to-water heat pumps, each with an integrated 220 liter DHW storage tank.

4.1. Centralized heating system

In the central system according to Fig. 3, the room heat is distributed by means of a central heating circuit pump and one line per residential unit. Each apartment is equipped with a room temperature controlled thermostatic valve. An overflow valve is integrated into the heating circuit system to keep the pressure constant and prevent the pump from working against closed valves. The DHW distribution is kept warm by hot water circulation.

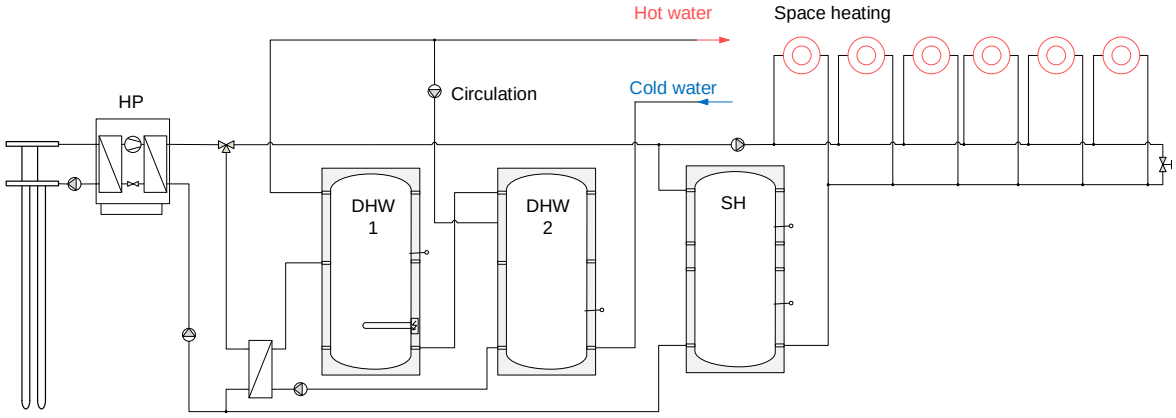


Fig. 3: Hydraulic scheme of the centralized heating system

4.2. Decentralized systems

The decentralized systems shown in Fig. 4 were modeled as compact units with integrated DHW storage tanks (220 l) and direct connection to space heating without an SH buffer tank. The set temperature in the DHW tank is 55°C (SIA 385/1:2020 for systems without DHW recirculation), which can be achieved by the heat pump without the use of an electric heating element; the space heating curve can be set individually in each unit according to the preferences of the occupants and the heat loss rate of the apartment, which is higher for apartments just under the roof or in contact with the basement.

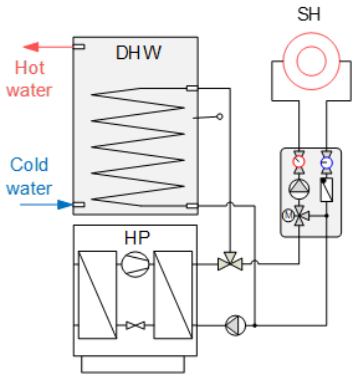


Fig. 4: Hydraulic scheme of a single decentralized unit

The parameterization of the heat pumps for calculating the electricity consumption was carried out according to two models of the company CTA AG:

- Optiheat Inverta 17e for the central system, and
- Optiheat Inverta DHW for the decentralized systems.

The dimensioning of the heat pump for the central heating system was based on the heat demand of the building described above. The aim of the design was a model that can cover the heat demand with 2500 full load hours. The total space heating demand (including losses) in the building is about 58 MWh. Considering the full load hours of 2500 for the heat pump operation, the heat pump capacity is 23.11 kW. The Optiheat Inverta (OHI) 17e model from CTA AG with an output of 25.6 kW at a compressor speed of 70 rps was selected as the basis for the calculations. The COP values of the two HPs were calculated as a function of the condenser outlet temperature and the compressor speed.

The decentralized systems supply the heat directly to the respective heating circuit. For the distribution of DHW, a circulation system with 60/55 °C in the flow and return - and a correspondingly high setpoint temperature in the storage tank - is integrated in the central system; the decentralized systems can operate without the circulation, which is why a temperature of 55 °C in the individual storage tanks is sufficient (SIA 385/1:2020).

Comparing the heat balances of the variants on **Error! Reference source not found.** the difference between the centralized and the decentralized system is relatively small. For space heating, only 1.5 MWh of losses occur in the central system, with a heat demand of 49.6 MWh. For DHW, the losses from storage and distribution amount to 7.4 MWh, with a demand of 17.3 MWh. For the decentralized systems, the only losses are the heat losses from the domestic hot water storage tanks. These amount to a total of 2.9 MWh, which can be credited to the space heating of the respective zone.

However, the comparison of the electricity demand shown in Fig. 6 discloses a big difference between the centralized system and the 6 decentralized systems. It becomes clear that the greatest difference lies in the DHW preparation and distribution.

With a target room temperature of 21°C in each flat, the decentralized systems could save 12% of the electrical energy used for space heating. For hot water production, the total saving, i.e. including coverage of heat losses from circulation, is as much as 53%.



Fig. 5: Heat demand for SH and DHW including losses and inefficiencies, for a centralized heating system compared to 6 decentralized systems.



Fig. 6: Electricity demand to cover SH and DHW and the respective extra-electricity for covering losses and inefficiencies, for a centralized heating system compared to 6 decentralized systems.

5. Swarm signal

The comparison of centralized and decentralized systems in a MFH revealed already a significant advantage of the decentralized systems with a control strategy that is based on the individual demand. The next step was to investigate the potential benefits in terms of self-consumption of the locally generated PV power of an aggregation of the 6 HP systems into a swarm. The individual HP system has its own controller witch also listens to a guide signal, the so called “swarm signal” to rather consume electricity or not. Therefore, a signal is to be calculated and communicated to the individual entities, whose reaction to the signal is programmed to their controllers. There are different concepts of guide/swarm signals feasible:

- A locally generated by regarding the PV production and electric consumption of the building itself
- A remotely generated by the electricity supplier (using tariff models, regarding demand and supply)

For the tests, a locally generated swarm signal was used. The central unit records the target value, namely the difference between local PV power generation and the consumption of all participants for household appliances and the operation of the heat pumps. The aim of the swarm control is to minimize this difference. The difference S is transmitted as a unidirectional signal to the individual HpCosy units. The transmission is linked to the production of the local PV system. Only from a threshold value of 200 W produced PV electricity, the swarm signal processing is enabled. Otherwise, the HP control is purely demand driven.

The signal S is limited to the peak power of the PV plant in kW: $-P_{PV}$ in kWp ... S ... P_{PV} in kWp.

6. Laboratory setup and measurements

A sample of a HP and DHW system from the company CTA AG was measured in the FHNW "hardware-in-the-loop" test stand according to Fig. 7 for the provision of DHW, space heating (SH) and cooling; its functionality was tested and its efficiency evaluated. In the background of the HP, the emulators for the building heating and the geothermal probe are visible, which are operated in a simulation-coupled manner. The DHW tapping takes place in real according to the SN EN 16147:2017 tapping profile L [5].

Fig. 7 shows the schematic of the laboratory measurement with the emulators (highlighted with color). The other five heat pump/storage systems of the other flats are just virtual in the simulation. Temperatures for all supply and return lines, tank layer temperatures, volume flows and electrical powers are recorded.

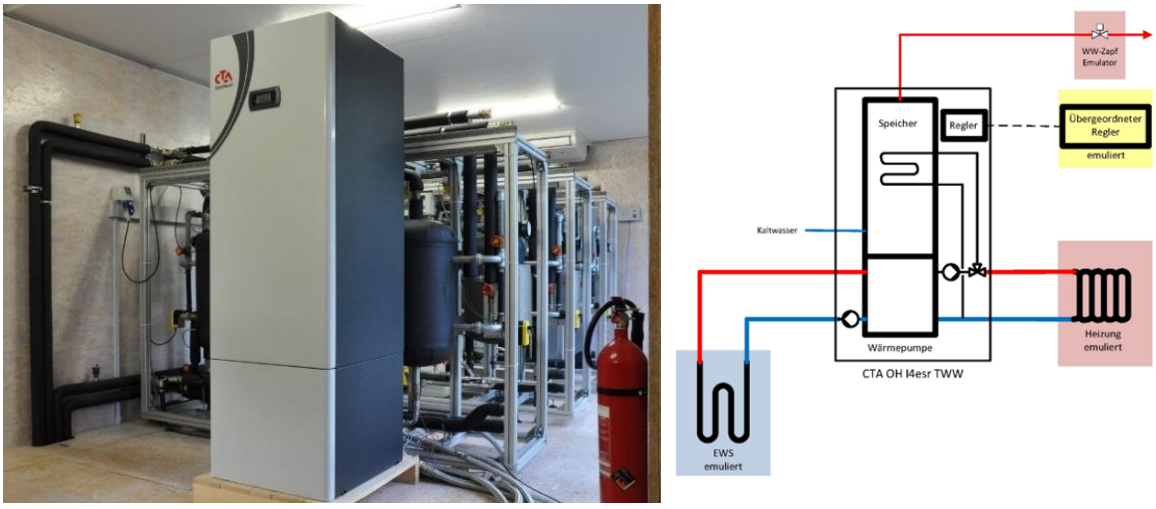


Fig. 7: Laboratory setup of the heat pump system Optiheat Inverta TWW - CTA AG and the according schematic

A total of three different dynamic 7 day test sequences were measured with this setup:

- only DHW preparation and tapping for 4 days and standby mode for 3 days
- heat demand for SH and DHW with a purely demand-driven control without PV power
- heat demand for SH and DHW with the specification of a swarm signal for the measured unit

6.1. DHW Storage Tank CTA Optiheat DHW

Fig. 8 shows the storage tank temperatures measured at 400, 700, 1000 and 1300 mm above the bottom of the tank (Tww1 … Tww4) and the volume flows of the heat pump (HP) charging (Vdot_HP) and hot water tapping (Vdot_DHW) during a 24-hour cycle of the measurement. The storage tank has a total height of 1300 mm. The power-weighted mean flow temperature of the HP during this cycle was 44.5 °C, the power-weighted mean flow temperature of the DHW was 51.4 °C.

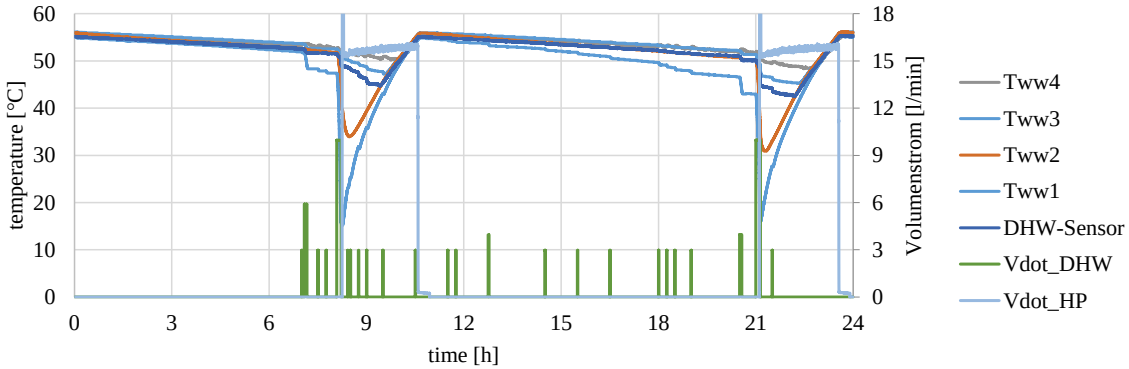


Fig. 8: DHW tank, temperatures and tapping flow rates

For efficient DHW production with the HP, it is particularly important to keep the flow temperature of the HP as low as possible by avoiding mixing in the storage tank. Any mixing of fluids of different temperatures means exergy losses, which must be compensated again via the HP, with the corresponding negative effects on the efficiency of the HP. The temperature curve in Fig. 8 shows the unavoidable mixing processes in the lower part of the storage tank due to the internal heat exchanger. However, the temperatures in the upper part of the storage tank remain unaffected during charging.

The HP had to deliver in total 13.2 kWh to cover the heat demand of 11.9 kWh. The average charging temperature was 44.7 °C, the DHW was delivered with an average temperature of 51.5 °C. The electricity demand of the HP was 4.1 kWh, leading to a power factor (PF) of 3.3 respectively 2.9 considering the thermal losses. The source temperature was held at 5 °C throughout the test.

6.2. Testing of the HP system with demand control (Test 007) and swarm signal control (Test 011)

The developed swarm signal control strategy was transferred to the system installed in the laboratory, but not activated/enabled for the initial tests.

As a reference base, the purely demand controlled system setup was tested (Test 007). The whole building was simulated in advance in detail to generate the time series of the five other heat pump systems of the building. The electric power rates of the five simulated heat pump systems were fed into the real-time simulation running during the laboratory test. The data collected from the “hardware-in-the-loop” measured heat pump system were also used to form a swarm of totally six heat pump systems within the simulation.

Further tests were performed to verify the correct function with the swarm signal control (Tests 008, 009 and 010). During Test 011 the swarm signals for power and control enabling were calculated in the real-time simulation and processed by the heat pump controller.

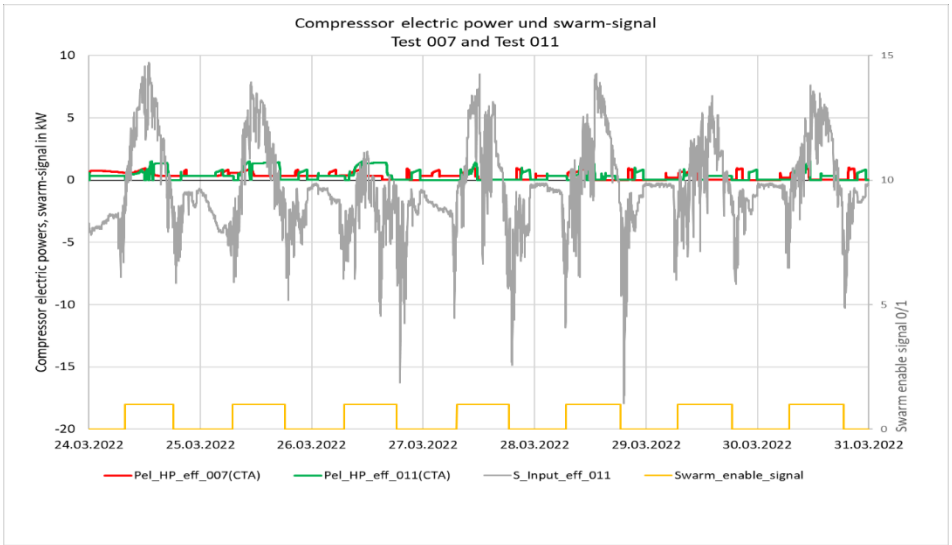


Fig. 9: Compressor electric power and swarm-signal

Comparing the compressor electric powers of test 007 and 011, it can be seen in Fig. 9, that the compressor of the swarm signal controlled system (green curve) runs higher and more during the times with a positive swarm signal.

The HP controller reactions to the swarm signal were:

- Rising or lowering the SH supply temperature setpoint as an offset +/- 5K of the heating curve value
- Rising or lowering the DHW temperature setpoint up to max. 58°C / down to min. 48°C
  and rising or lowering the compressor speed during DHW preparation nom/min/max 44/30/65 Hz

Fig. 10 shows the time series of the two test 007 and 011 for the simulated and measured week of 3/24 - 3/30. This week was selected because it had sufficient PV power, days of SH requirements and days without. Shown are the SH, DHW, electric compressor energies and the generated swarm signals during test 011.

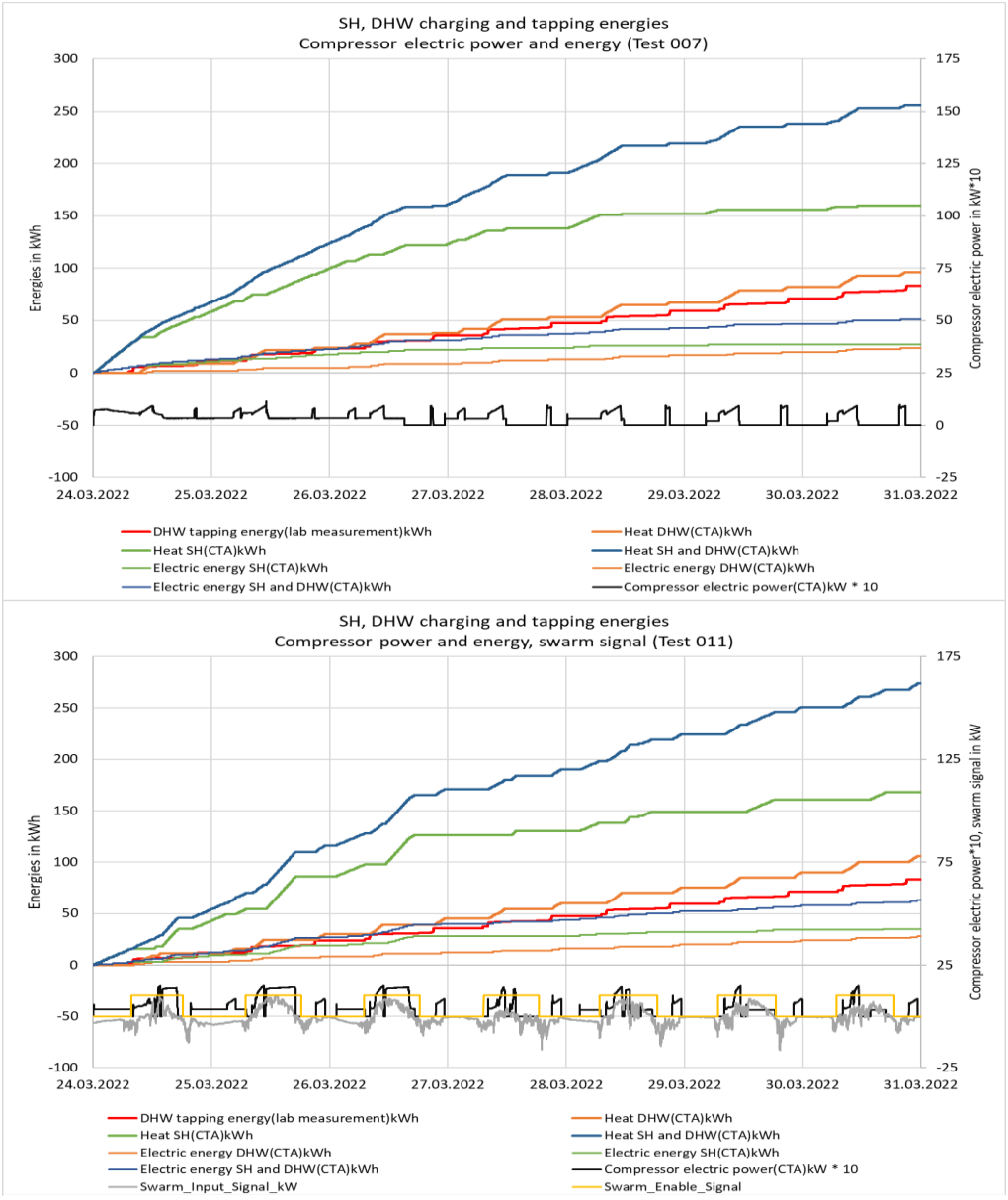


Fig. 10: SH, DHW charging and tapping energies, compressor electric power and energy and swarm input signals

6.3. Comparison of the energy consumption from the grid and PV for the tested week

Table 1. shows the final energies and the average COP values after 7 days of testing. Test 011 showed higher energy values for the SH and DHW and lower values for COP. The swarm signal controlled system had higher temperature setpoints for SH and DHW in average, so the efficiencies were in total 13% less compared to the demand controlled system. On the other hand, the swarm signal controlled system reduced the grid consumption from 36 kWh to 31 kWh (-14%) by enhancing the PV power consumption. With the chosen swarm signal concept, yearly results were evaluated with a series of test-validated simulations in paragraph 7.

Table 1. Comparison of the test 007 and test 011 during week 3/24 – 3/30

Value	Unit	Test 007			Test 011				
		Demand Total	Grid elec-tricity	Self-consumed PV electricity	Swarm Total	Grid elec-tricity	Self-consumed PV electricity	Change Total	Change Grid / PV electricity
Heat for SH	kWh	160			168			+5%	
Heat for DHW	kWh	96			106			+10%	
Heat for SH+DHW	kWh	256			274			+7%	
Electric Energy SH	kWh	27	22	5	35	18	17	+30%	-18% /+240%
Electric Energy DHW	kWh	24	14	10	27	13	14	+17%	-7% / +40%
Electric Energy SH+DHW	kWh	51	36	15	62	31	31	+24%	-14% /+107%
COP avg SH	-	5.93			4.80			-19%	
COP avg DHW	-	4.00			3.79			-5%	
COP avg SH+DHW	-	5.02			4.35			-13%	

The influence of the swarm signal control on the operation can be seen in Fig. 11. The tested week has sufficient PV power, so the during the day, the DHW storage was loaded to higher temperatures. Also, the SH supply temperatures were raised in test 011 and the operations shifted to daytimes with PV power.

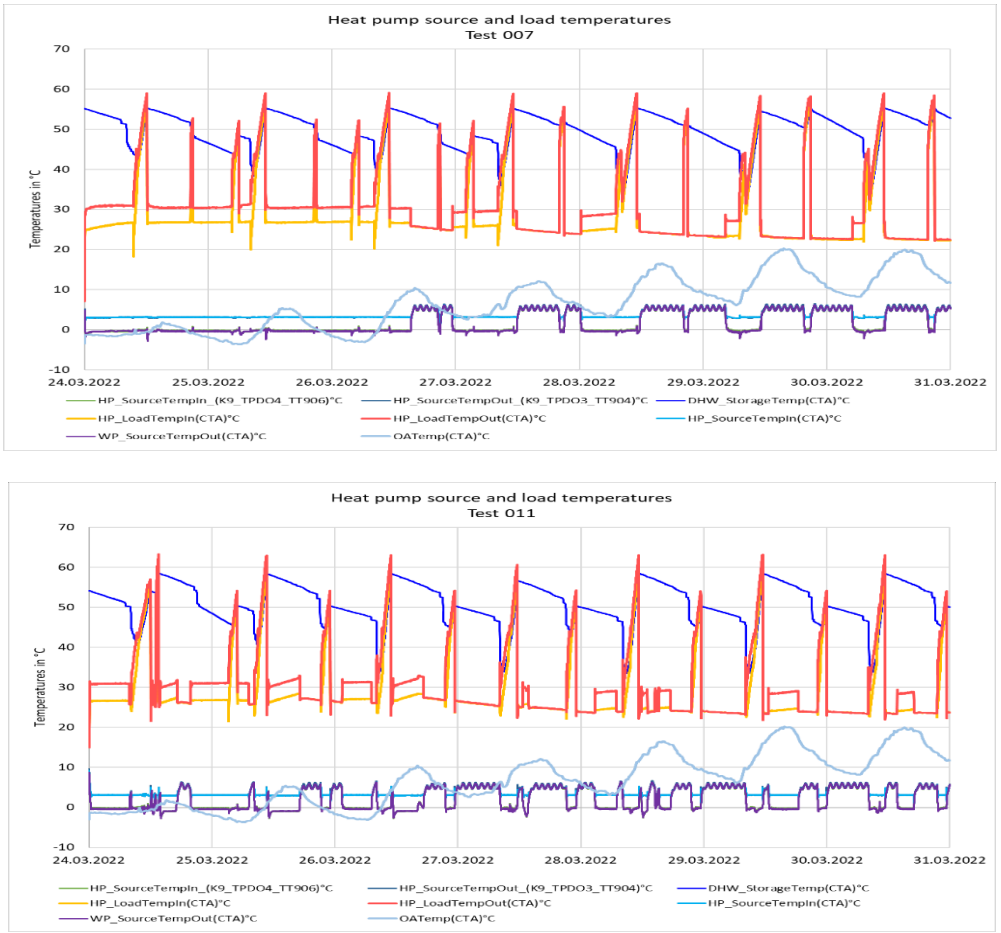


Fig. 11: Heat pump source and load temperatures

7. Annual simulations

Annual simulations of the selected swarm control strategy of the decentralized units with the aim of using PV electricity as efficiently as possible were conducted with a simulation model that has been re-parameterized according to the performed hardware-in-the-loop measurements to obtain viable results.

Figure 12 shows the energy balances with swarm control for different PV areas on a monthly basis. The goal of the simulations is to minimize the term “GridtoHP”, the electric energy from the grid to the HP, and maximize “PVtoHP”, the electric energy from the PV system to the HP. The term “ELfromGrid” is the electric energy from the grid as an input (IN) to the system, “GridtoHH” is the electric energy from the grid used for the household appliances as an output (OUT), in the sense of where it comes from and what it is used for.

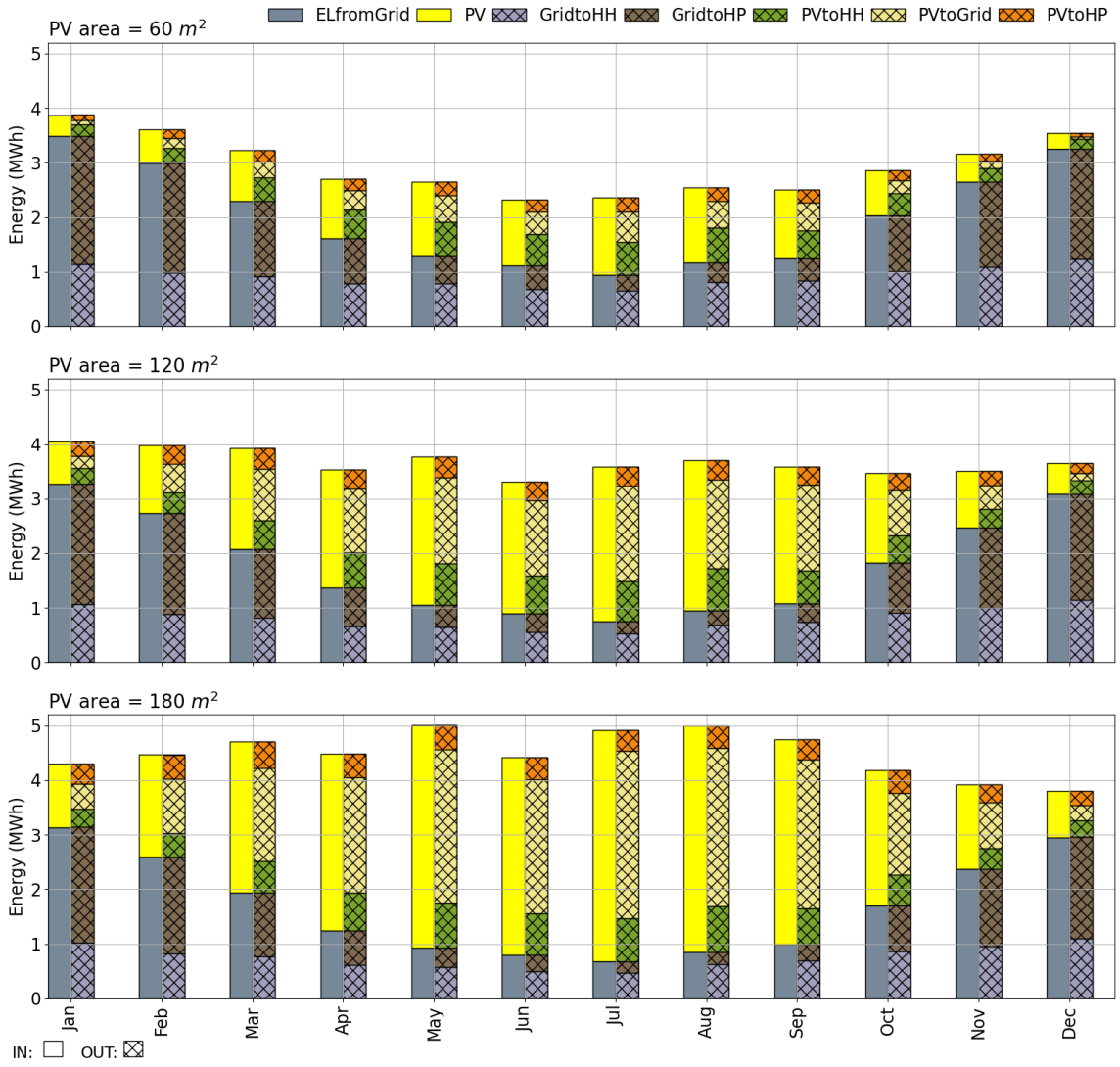


Fig. 12: Energy balance of the complete system with swarm control strategy and different PV areas.

As the swarm signal strength is a function of the PV kWp sizing compared to the totally rated electric consumption of the building, three PV areas 60, 120 and 180 m^2 of specified PV modules were simulated and compared with the base case of purely demand controlled HPs. The grid consumption could be reduced up to 5% and the self-consumption increased by 11 to 17%.

Figure 13 shows the grid purchase and the grid feed-in of the systems with swarm control compared to those with purely demand-based control. The comparison was carried out for different PV system sizes. As expected, the reduction of the grid consumption (blue numbers in the graphic) is smaller than the reduction of the grid feed-in (green numbers). This is due to the reduction in efficiency with forced operation at higher supply temperatures. The ratio of saved grid consumption to lost feed-in is between 2.2 (with 60 m^2 PV area / 11.3 MWh PV yield) and 1.9 (with 180 m^2 PV area / 23.8 MWh PV yield).

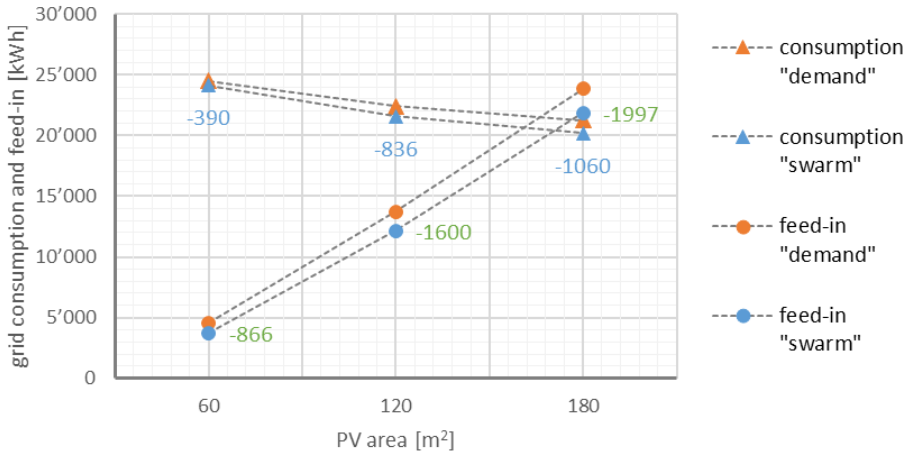


Fig. 13: Grid consumption and feed-in of the demand controlled and the swarm controlled systems for different PV areas.

8. Summary and conclusion

The comparison between a centralized and several decentralized heat pump systems clearly shows great advantages of the decentralized solutions, even in a purely demand controlled operation without taking PV electricity or a swarm control into account.

The savings in the base case with a room set temperature of 21 °C are 28% in electric energy. The variation of room set temperatures revealed that the savings could increase up to 31% when only one of the apartments demands a high room temperature. However, the largest share of the energy saved is due to the elimination of DHW circulation.

The measurements showed that an individual adjustment of the control of the individual swarm participants in response to a swarm signal is technically feasible and already leads to a reduction of the grid consumption in the selected and tested week.

The final simulations of the overall system show that - in addition to the savings achieved through the use of decentralized systems - an additional reduction in grid consumption of up to 5% can be achieved by increasing self-consumption by 11% to 17%.

Acknowledgements

The authors would like to thank the Swiss Federal Office of Energy for supporting the project "HpCosy - Heat Pump Comfort System" under contract number SI/502088-01 and the industry partner CTA AG.

References

[1] Norm SIA 385/1. Anlagen für Trinkwarmwasser in Gebaeuden - Grundlagen und Anforderungen
[2] Vetsch B, Gschwend A, Bertsch A. "Warmwasserbereitstellung mittels Waermepumpen in Mehrfamilienhaeusern"; 2012
[3] Bundesamt für Statistik BFS. «Allgemeine Übersicht «Gebaeude» 2019» Bundesamt für Statistik. 10. Oktober 2020. https://www.bfs.admin.ch/bfs/de/home/statistiken/bau-wohnungswesen/gebaeude.assetdetail.17924951.html
[4] Mojic I, Crameri S, Caflisch M, Carbonell D, and Haller M. "Reference Frame-work for Building and System Simulations: Multifamily Reference Building." SPF Institut für Solartechnik, HSR Hochschule für Technik Rapperswil; 2019
[5] Norm SN EN 16147:2017. Waermepumpen mit elektrisch angetriebenen Verdichtern - Pruefungen, Leistungsbemessung und Anforderungen an die Kennzeichnung von Geräten zum Erwaermen von Brauchwarmwasser
[6] Haller MY, Haberl R, Persdorf P, Reber A. "StorEx – Theoretische und experimentelle Untersuchungen zur Schichtungseffizienz von Waermespeichern." Rapperswil: SPF Institut für Solartechnik; 2015
[7] Haberl R, Tuerk O, Bohren A, Haller MY. "DHWStrat – Methode zur Bestimmung der Schichtungseffizienz von Warmwasserspeichern. " Rapperswil: SPF Institut für Solartechnik; 2021

14th IEA Heat Pump Conference
15-18 May 2023, Chicago, Illinois

Leveraging MultiSource Heat Pump Technology to Produce Electricity and/or Hydrogen Through Enhanced Reverse Electrodialysis Process -

Rahul Nana[a], Rafael Feria[a], Piotr Dlugolecki[b]

[a]Halocline International, LLC; 1209 Orange Street, Wilmington Delaware 19801, USA

[b]Aqua Azure, Hallera 19/5, Gdynia, Poland

Abstract

Reverse electrodialysis (RED) technology provides a way to harness clean and sustainable energy from salinity gradients. First introduced in 1954 [4], this technology has not been widely applied due to limitations requiring direct access to fresh and seawater. The novel approach of introducing a MultiSource heat pump technology into a RED-based system allows users to take full control of the salinity gradient by dissolving and regenerating the salt in a closed-loop system. The heat pump exploits otherwise wasted low-grade heat energy to simultaneously heat and cool salt solutions to produce electricity and/or hydrogen by reverse electrodialysis process. The untapped potential of excess heat as a source of energy is substantial, with Europe and The United States alone boasting an estimated 5791 TWh of accessible waste heat per year [13, 21, 22]. This innovative approach unleashes the full potential of salinity gradient energy, thus offering a solution to the current bottleneck of the seaside water source dependency. Approximately one-third of the global electricity is consumed by residential buildings [8,9]. The unique combination of the reverse electrodialysis process and MultiSource heat pump technology paves the way to significantly reduce energy consumption as well as greenhouse gases (GHG) emissions on a global scale. In this work, we will explore some of the theoretical aspects in more detail.

© HPC2023.
Selection and/or peer-review under the responsibility of the organizers of the 14th IEA Heat Pump Conference 2023.

Keywords: RED; Heat pump; Reverse Electrodialysis; Salinity Gradient Energy; Blue Energy; Clean Energy; Renewable Energy; Circular Economy; Global Warming; MultiSource HeatPump;

Rahul Nana E-mail address: rnana@haloclineinternational.com
Rafael Feria E-mail address: ralphf@haloclineinternational.com

1. Introduction

Air conditioning is a process which allows cooling, heating, and ventilation of an environment. Although the term "air conditioning" is predominantly associated with the cooling process, the process of air conditioning systems also involves humidity control and air cleaning as its key functions. Currently, the use of air conditioners and electric fans for cooling purposes represents 20% to 40% of the global building electricity consumption, which is only projected to increase with elevated global temperatures [2,9]. Presently, air conditioning is used in approximately 90% of homes in the United States, whereas in locations such as India, air conditioning is less prevalent, with an average of around 5% of homes utilizing this technology [3]. Worldwide demand for cooling is rising fast [3]. Currently, more than one-third of the electricity generated in the world is consumed in the residential sector and most of this energy is used for water heating, air conditioning, and space heating [8,9]. Earth's population and global warming are only expected to increase while global energy demand from air conditioners is anticipated to triple by 2050 [3]. In these situations, the demand for air conditioning will surge while imparting a significant impact on the world's overall energy reliance, putting pressure on the electrical grid, and driving up global greenhouse gas (GHG) emissions. On the other hand, at the 2022 United Nations Climate Change Conference of the Parties (COP27), the United States launched the Net-Zero Government Initiative, inviting governments to lead by example and achieve net-zero emissions from national government operations by no later than 2050 [14]. Therefore, renewable energy resources have been one of the most important, widely researched, and discussed global topics for over a decade. With the ever-increasing problem of global warming, there has been a global effort in steering away from carbon-based fuels. There are a wide variety of natural sources for clean energy including solar and wind energy. While it is crucial that we continue to make a switch to these resources, it is important to note that their availability, such as usage during specific times of the day, and reliability are limited. They also require massive amounts of energy storage for them to be a sustainable solution to our energy crisis. Therefore, if we want to address the issue of global warming and achieve a net-zero objective, we must address both restrictions: the availability of energy and GHG-neutral air conditioners. The untapped potential of excess heat as a source of energy is considerable, with Europe alone boasting an estimated 2860 TWh of accessible waste heat per year [13]. This energy source is widely available and abundant, with the added advantage of being constantly accessible, often in the form of unwanted waste. The convergence of a MultiSource heat pump and enhanced Reverse Electrodialysis (RED) promises to become a solution to this problem. The RED Heat Hump (RED-HP) technology relies on waste heat and low-grade heat energy to produce electricity and/or hydrogen, with the added benefit of being entirely carbon-neutral. This technology promises to cool a structure and convert waste and low-grade heat into usable energy. The game-changing RED-HP technology has the ability to significantly reduce energy usage and GHG emissions on a global scale.

2. Salinity Gradient Power

Salinity Gradient Power (SGP) is defined by Gibbs free energy of mixing between two water sources of differing salt concentrations. The concept of SGP was first proposed by R. E. Pattle in 1954 and has since expanded into a variety of methods by which to harness this chemical potential of mixing two water streams with different salinity [4].

During the uncontrolled mixing, $\Delta \boldsymbol{G_{mix}}$ (Gibbs energy of mixing) is released into the environment. This released chemical energy represents the maximum potential energy that can be harvested. The Gibbs free energy [J] released per mole during the mixture of two solutions is given below:

$$\Delta G_{mix} = G_b - (G_c - G_d) \tag{1}$$

Where ΔG_{mix} is the free eneregy of mixing [J/mol], G_b is the Gibbs energy of the mixture, the brakish water [J/mol], G_c is the Gibbs energy of the concentrated salt solution (e.g. brine) [J/mol] and G_d is the Gibbs energy of the diluted salt solution (e.g. fresh water or river water).

$$\Delta G_{mix} = \Delta H - T \cdot \Delta S = -T \cdot (S_b - S_d - S_c) \tag{2}$$

$$S \quad = -R \cdot N_T \sum_i \; x_i ln \; (x_i \cdot \gamma_i \;) \tag{3}$$

Where S is the entropy (J/K), T is the temperature of mixture (K), R is the universal gas constant (8.314 J/(mol·K)), N_T is total number of moles (mol), x_i is the mole fraction of component i, γ_i is the activity coefficient of component i, which accounts for the non-ideal behavior of the solution. The change in enthalpy ΔH (J) is not taken into account in equation 2. The objective of equation 2 is to calculate the theoretically available energy from mixing two dissolved salt solutions with different salinities.

The three primary means of harnessing salinity gradient power from this extraordinary heat pump assisted close loop process are the reversal of the capacitive deionization (RCD) [10], pressure-retarded osmosis (PRO), and reverse electrodialysis (RED). For the basis of this paper, only RED will be discussed in detail as it is believed to have the greatest potential based on its high efficiency [17, 18].

3. Reverse Electrodialysis (RED)

Reverse electrodialysis was first proposed and demonstrated by Richard Pattle between 1954 and 1955, but it was not until a push from the first and second oil crises in 1973 and 1979 that interest in RED was truly heightened [4]. Today several institutions have committed to the RED technology as a way to harness the salinity gradient power (SGP). SGP is a sustainable energy source with a large worldwide potential of 22776 TWh per year, and it is available at deltas where river flows into the sea [20]. Commonly referred to as "Blue Energy", this renewable and carbon-free energy source provides a significant advantage over other renewable sources such as wind and solar power, as it is constantly accessible. The current limitation of this technology is that it can only be applied in specific locations where water with different levels of salinity is available, namely areas where there is access to both low and high salt concentration water.

Reverse electrodialysis utilizes the salinity gradient of two water solutions to produce power in the form of electricity (Figure 1). When salt dissociates in water two ions are formed (anions and cations) containing positive and negative charge. Naturally, concentrations of ions dissociated in the water tend to flow from high concentration to low concentration and can also be further explained by the Donnan exclusion principle [7]. Anions migrate through the anion exchange membrane (AEM) toward anode(s) and cations move through the cation exchange membrane (CEM) towards cathode(s). For example, a positively charged cation can only move through a cation exchange membrane however a negatively charged anion would be blocked by repulsion. It is the opposite for an anion exchange membrane as positive cations are blocked and negatively charged anions can pass thorough. This dynamic allows for the controlled mixing of salts in the RED cell which creates an ionic potential. As ions flow from the concentrated to dilute solution, ions from a separate recirculating rinse solution are pulled from one electrode to the other. This overall movement of ions creates a stack potential that can be harvested through an external load connected to both electrodes and can be calculated using the Nerst equation:

$$\Delta V^0 = N \frac{\alpha RT}{zF} \ln \left(\frac{a_c}{a_d}\right) \tag{4}$$

Where ΔV^0= is the theoretical stack potential [V], N is the number of membranes [-], α is the membrane selectivity [-], R is universal gas constant [8.314J/(mol·K)], T is the absolute temperature [K], z is the electrochemical valence [-], F is the Faraday constant [98485 C/mol], a_c is the activity of the concentrated solution [mol/L]

A RED cell can operate in various modes, the flow of the two solutions can be directed in co-flow, counter-flow, or cross-flow. Furthermore, electrodes can be composed of a single part or multiple segments, with studies showing that multiple segmented electrodes can enhance the efficiency of the cell stack and increase the overall power density [6].

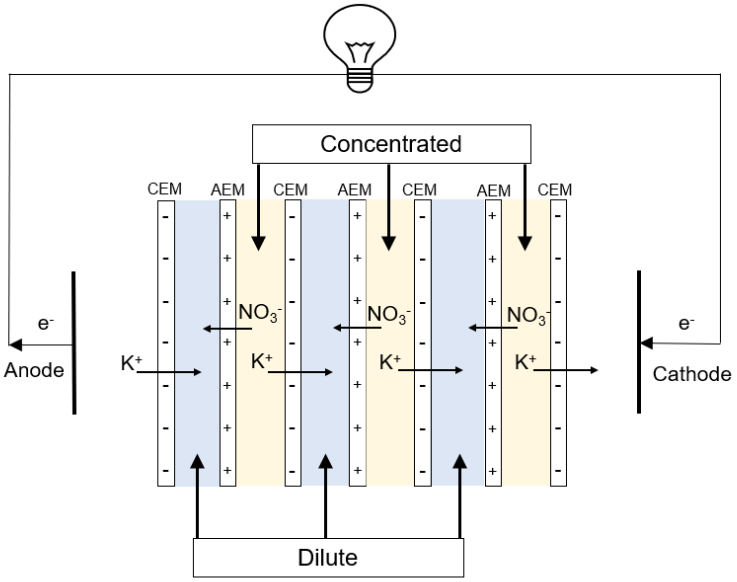


Figure 1. Process of reverse electrodialysis.

At auxiliary electrodes (anode and cathode) red-ox couple solution such as hexacyanoferrate(II) and hexacyanoferrate(III) can be used to minimize losses and produce electricity. In addition, it should be noted that hydrogen gas can also be generated through the process of water splitting reactions:

$$\text{Anode:} \quad 2H_2O \rightarrow O_2\uparrow + 4H^+ + 4e^- \tag{5}$$

$$\text{Cathode:} \quad 4H_2O + 4e^- \rightarrow 2H_2\uparrow + 4OH^- \tag{6}$$

Numerous publications have covered the topic of hydrogen production using reverse electrodialysis [16, 19], and thus our study will not specifically address this area.

The power output of a RED cell stack depends on the stack resistance and electromotive force. The stack resistance R_{stack} [Ω]is a function of the cell resistance R_{cell} [Ω], the number of cell pairs N, A_{mem} is the effective membrane area [m^2] and the resistance of the electrode system $R_{electrode}$.

$$R_{stack} = \frac{N}{A_{mem}} \cdot R_{cell} + R_{electrode} \tag{7}$$

The cell resistance R_{cell} [Ω·m^2] is a function of the resistance of the cation R_{CEM} and anion membrane R_{AEM} [Ω·m^2] and the resistance of the concentrate and dilute cell compartments (R_{con} and R_{dil})

$$R_{cell} = R_{AEM} + R_{CEM} + R_{con} + R_{dil} \tag{8}$$

The resistance of concentrate R_{con} [Ω·m^2] and dilute solution R_{dil} [Ω·m^2] can be calculated as below:

$$R_{con} = \frac{d_c}{\kappa_c} \tag{9}$$

$$R_{dil} = \frac{d_d}{\kappa_d} \tag{10}$$

As shown, R_{con} and R_{dil} are a function of the compartment thickness d_c [m] and solutions conductivity κ [S·m^{-1}].

The maximum power output [W] and power density (W/m^2) can be calculated using the following equation:

$$P_{max} = \frac{(V^0)^2}{4R_{stack}} \quad (11)$$

$$PD_{max} = \frac{P_{max}}{A_{total}} \quad (12)$$

Where A_{total} is the total membrane used and the external load and internal load is assumed to be equal.

4. Heat Pump

Heat pumps offer an energy-efficient alternative to furnaces and air conditioners for all climates. They provide optional year-round cooling or heating utilizing a vapor compression cycle, thermoelectric cooler, and/or chemical absorption process. Heat pumps do not create heat, they redistribute and move heat. Passively, heat moves from hot to cold. With a heat pump, one can actively cool and heat a structure by moving heat from cold to hot. The Coefficient of Performance (COP) of a heat pump can be used to determine a heat pump's efficiency [1]:

$$COP = \frac{Output\ Capacity\ (W)}{Power\ Input\ (W)} \quad (13)$$

Figure 2 provides a visual representation of the heat pump's operation process. As shown, with an input power of 1500 watts, 3000 watts of heat equivalent is harnessed from a cold stream. The heat pump is capable to concentrate the heat and multiply it by a factor of 3 to produce 4500 watts of heating. In the present scenario, the $COP_{Heating}$ is 3, although it should be noted that depending on the season, the $COP_{Heating}$ can reach values as high as 7 [23, 24, 25].

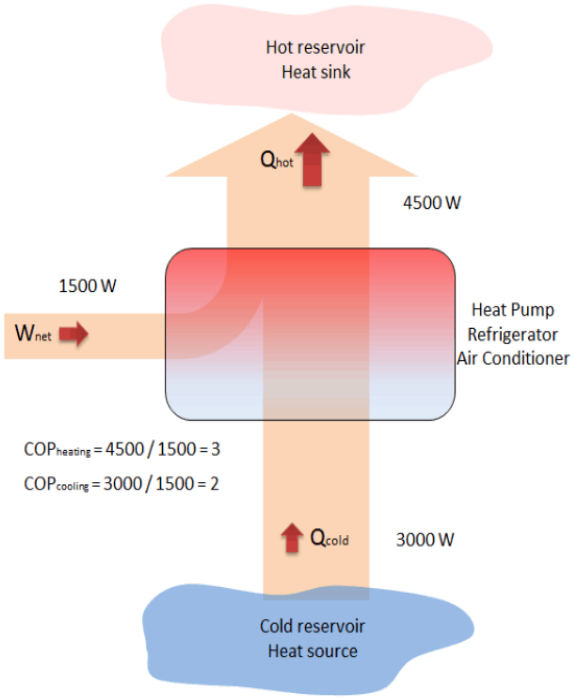


Figure 2. Heat pump COP diagram.

5. Reverse Electrodialysis Heap Pump (RED-HP)

RED is a promising technology for generating renewable energy from the salinity gradient in natural water sources, such as rivers and oceans, without the need for combustion or fuel consumption. The technology has the incredible global potential of 22776 TWh per year of electricity to contribute to a more sustainable and low-carbon energy system, particularly in coastal regions where there is a significant salinity difference between seawater and freshwater [20].

Several attempts have been made to upscale the RED technology to a commercial level [5]. However, no one has yet managed to bring it to a commercially viable level, partly due to the high price of the ion exchange membrane, which is a significant barrier to commercialization. As a general estimate, the cost of an ion exchange membrane can range from around \$20 to \$200 per m^2. To date, the majority of the research and pilot systems have been performed as an open loop system utilizing seawater and fresh water. The dependence on both fresh and seawater not only poses limitations on the applicability of this technology but also restricts the potential locations for implementation. Furthermore, the power output of the system is constrained by the specific types of salts and their concentrations that can be utilized by the technology. Additionally, the use of seawater and freshwater requires large utility costs to pretreat the water. Several steps of microfiltration, ultrafiltration and reverse osmosis filtration is required to remove unwanted sediments, organics and objects out of the natural water streams. This results in the need for large quantities of membranes in order to generate power. Therefore, using closed loop system with a selected salt type and its concentration to deliver the highest available salinity gradient will unlock the potential of reverse electrodialysis globally.

MultiSource heat pump technology utilizes thermal energy and waste heat using proprietary thermal chemical optimization techniques that greatly reduce or eliminate the resulting carbon footprint while providing simultaneous heating and cooling [25]. By introducing MultiSource heat pump technology to a RED-based system, high levels of power efficiency can be achieved in a closed-loop system [25]. Simultaneous heating and cooling provided by the heat pump can be used to create an optimal artificial salinity gradient. Figure 3 shows a schematic representation of the RED-HP closed loop system.

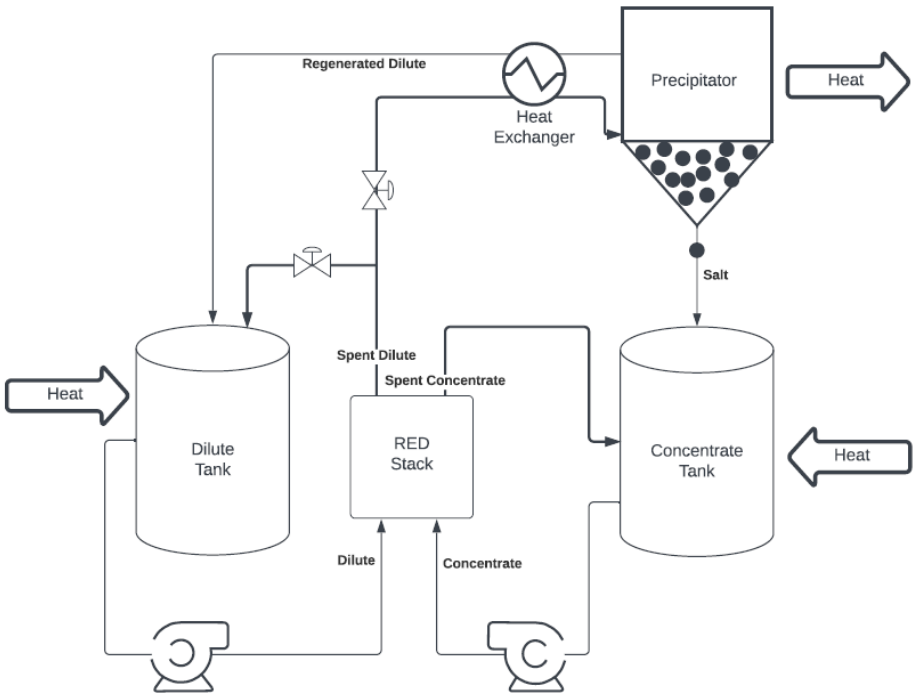


Figure 3. The closed-loop RED-HP system concept.

In this process, a salinity gradient can be regenerated by leveraging the power of a heat pump and using a salt with a steep solubility curve. As shown in the Figure 4 salts such as potassium nitrate and calcium chloride have a steep exponential solubility curve. Consequently, a highly concentrated salt solution can be achieved at temperatures greater than 65ºC and a dilute solution can be achieved by precipitation of salt at lower temperatures ranging from 5-20ºC. To reduce energy consumption, the heat from the spent dilute solution can be exchanged with the refreshed dilute solution, as illustrated in Figure 3. The main contributor to the energy input is heating up dilute solution from, for example, 10ºC to approximately 65ºC. The energy required to heat up 1m^3 of water from 10ºC to 65ºC is 63.9 kWh in the absence of a heat pump. However, the use of an efficient heat pump with a $COP_{Heating}$ of 7 reduces the required electrical energy to heat up 1m^3 of water from 10°C to 65°C to only 9.1 kWh. Furthermore, during the process, the spent dilute solution can be used as a heat source, resulting in a more energy-efficient system. It is important to note that excess heat is one of the largest untapped energy sources and it can be leveraged by utilization of MultiSource heat pump technology [25]. Moreover, it is highly advantageous to have a closed-loop system as the water pre-treatment cost are removed, and various selected salts can be used in a controlled manner.

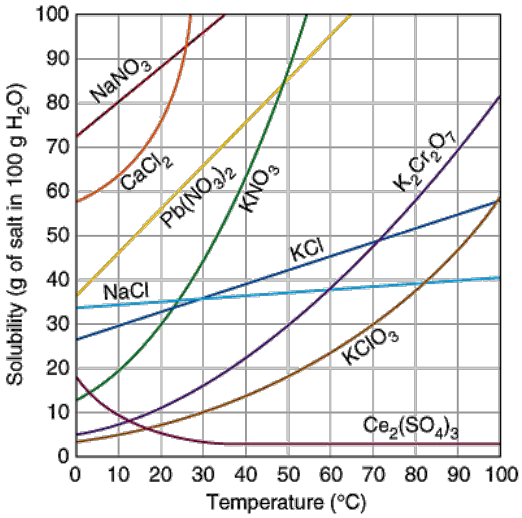


Figure 4. Various salt solubilities at varying temperatures.

The results from the modeled data are presented in Table 1. Salinity gradient, which refers to the difference in salt concentration, is a critical parameter for achieving high power density. To reach a highly concentrated solution of potassium nitrate, the RED process should be operated at an elevated temperature of 65ºC where 12 mol/L KNO_3 solution can be obtained. On the other hand, dilute solution concentration of 2 mol/L is limited by solubility of KNO_3 at low temperature of 10ºC. Both solutions have relatively high molarities above 0.5 mol/L, and therefore, activity coefficients were calculated using the Stokes-Robinson [16]. A higher temperature has a positive impact not only on the potential of the RED stack, which is calculated from the Nernst equation (Equation 4), but also on the membrane resistance, which decreases with increasing temperature [15]. The biggest contributors to RED stack resistance are membranes and dilute compartment resistance, which is related to compartment thickness [11]. Therefore, since we operate at higher salt concentrations and elevated temperatures, we assumed anion and cation exchange membrane resistance of 1 Ω·cm^2. Membranes with resistance of 1 Ω·cm^2 or lower are already commercially available [11]. The thickness of the dilute compartment was set in the RED model to 150µm to limit the dilute compartment resistance. The resistance of the electrodes is assumed to be negligible as a full-size stack will contain at least multiple hundreds of membranes reducing the contribution of the electrode resistance to less than 2%. The average membrane permselectivity is assumed to be 90%. Our RED model, based on equations 4-8, gives a maximal theoretical power density for 400 cell pairs, equivalent to 200m^2 of membrane area. The maximal achievable power density is 5.3W/m^2 of membrane area and the power output of a single stack is 1.06kW. It is important to note that the RED stack dimensions are 0.5m width, 0.5m height and 0.25m length (including 0.05m for auxiliary electrodes). These dimensions translate to a power density of 16.9kW per m^3 of RED stack. However, in practical application of RED,

factors such as spacer shadow effect, current leakage, and concentration polarization phenomenon might limit this power density [15]. Energy spent on pumping dilute and concentrated solution was not taken into account; however, it is estimated to be less than 3-10% of the total power output of the RED system [18].

Dilute and concentrated buffer tanks need to have enough buffer capacity to operate at the most optimal salinity gradient. The theoretical available amount of energy available from the mixing of two salt solutions can be calculated from the Gibbs energy of mixing and thus the theoretical potential of salinity gradient energy can be evaluated. The energy theoretically obtainable from the mixing of 1 m^3 of 12 mol/L concentrated solution with 1 m^3 of 2 mol/L dilute solution at a temperature of 65ºC, calculated from Equation 1-3, equals 9.1kWh (32.8MJ). This allows a 1.06kW system to operate for multiple hours without the need for dilute compartment regeneration and loss of the salinity gradient. However, there is energy needed to heat up the solution after dissolving KNO_3. The enthalpy to dissolve KNO_3 in water equals to -34.9 kJ/mol (-9.69Wh/mol) [16]. This means that potassium nitrate is an endothermic salt and when it dissolves in water, it absorbs heat from its surroundings. If 1m^3 of 12 mol/L concentrated solution is mixed with 1m^3 of 2 mol/L dilute solution, then both solutions end up with a concentration of 7 mol/L. Therefore, to regenerate 1m^3 of dilute solution, 505.5 kg of KNO_3 salt (5000mol) need to be precipitated and dissolved in the concentrated solution tank. The energy required to heat up 1m^3 of concentrated solution is 48.4kW. This means that in order to harvest 9.1kWh of electricity, 48.4kWh of heat needs to be used to heat up 1m^3 of concentrated solution. It is important to note that by using efficient MultiSource heat pump technology with a $COP_{Heating}$ of 7, only 6.89kWh of electrical energy will be spent to compensate for dissolving of 505.5 kg of KNO_3 salt. This energy can be transferred from the dilute solution where the precipitation (dilute solution regeneration) process takes place at a low temperature of 10ºC. On the other hand, it is advantageous if an exothermic salt is selected because the concentrated solution will be heated up by the energy during dissolution.

In addition, it should be noted that energy recovery from salinity gradient energy in reverse electrodialysis is between 20% and 80% [17]. A reverse electrodialysis system was studied for a period of 30 days using natural seawater and river water, and the energy recovery values ranged between 30% and 37% [18]. The obtainable energy recovery from salinity gradient energy depends mainly on the operational current density and the internal stack resistance, which is dominated by the dilute solution resistance and the resistance of membranes.

Table 1: Model input values and the outcome results.

Name	Symbol	Value	Unit
Input parameters			
Concentration of concentrated solution	C_c	12	mol/L
Concentration of diluted solution	C_d	2	mol/L
Activity coefficient of concentrated solution	γ_c	0,4	-
Activity coefficient of diluted solution	γ_d	0,4	-
Specific conductivity of concentrated solution	κ_c	54,1	S/m
Specific conductivity of diluted solution	κ_d	23,2	S/m
Temperature	T	338,15	K
Average membrane permselectivity	α	0,9	
Resistance of anion exchange membrane	R_{AEM}	0,0001	$\Omega \cdot m^2$
Resistance of cation exchange membrane	R_{CEM}	0,0001	$\Omega \cdot m^2$
Thickness of spacer - concentrated solution	d_c	0,00015	m
Thickness of spacer - diluted solution	d_d	0,00015	m
Number of cell pairs	N	400	-
Single membrane active area	A_{mem}	0,25	m^2
Total membrane area	A_{total}	200	m^2
Results			
Open circuit potential	ΔV^0	37,6	V
Resistnace of the RED stack	R_{stack}	0,335	$\Omega \cdot m^2$
Maximum power output	P_{max}	1055	W
Power density	PD_{max}	5,3	W/m^2
Power per volume of stack	PV_{max}	16882	W/m^3

6. Conclusions

The potential of excess heat energy worldwide is substantial and could play a significant role in reducing global energy consumption and greenhouse gas emissions if efficiently harnessed. This energy source is widely available and abundant, with the added advantage of being constantly accessible, often in the form of unwanted waste.

This work identifies and quantifies the potential and operating window of RED as a sustainable energy source for excess heat recovery, utilizing heat pump technology to maintain a constant salinity gradient. The closed-loop 1kW RED-HP system concept was presented, and theoretical power output model was made. The theoretical open circuit potential was 36.7V and the theoretical power density was 5.3 W/m^2 of membrane area and 16.9 kW/m3 of RED stack. To achieve these power density numbers 400 cells pairs of membranes with $0.25m^2$ area per cell are required as well as volume of $1m^3$ of concentrated (12mol/L KNO_3) and $1m^3$ of dilute solution (2mol/L KNO_3). Potassium nitrate salt was selected due to its solubility and temperature relationship, which allows for dilute and concentrated solution regeneration at a lower temperature. However, potassium nitrate is an endothermic salt and when it dissolves in water, it absorbs heat from its surroundings, which works against our heat transfer. The ideal salt for this process should be an exothermic salt that releases energy during dissolving and heating up of a concentrated solution, while absorbing energy during crystallization and cooling down the dilute solution at the same time.

The results of this study have significant implications for reducing global energy consumption and greenhouse gas (GHG) emissions. The RED-HP concept is currently in the process of prototype validation to further investigate its practical applications.

References

1. Canada, Natural Resources. "Government of Canada." *Natural Resources Canada*, Gouvernement Du Canada, 9 Aug. 2022, https://www.nrcan.gc.ca/energy-efficiency/energy-star-canada/about/energy-star-announcements/publications/heating-and-cooling-heat-pump/6817.
2. *Factsheet HVAC Energy Breakdown - | Energy.gov.au*. https://www.energy.gov.au/sites/default/files/hvac-factsheet-energy-breakdown.pdf.
3. Iea. "Air Conditioning Use Emerges as One of the Key Drivers of Global Electricity-Demand Growth - News." *IEA*, https://www.iea.org/news/air-conditioning-use-emerges-as-one-of-the-key-drivers-of-global-electricity-demand-growth.
4. PATTLE, R. E. "Production of Electric Power by Mixing Fresh and Salt Water in the Hydroelectric Pile." *Nature*, vol. 174, no. 4431, 1954, pp. 660–660., https://doi.org/10.1038/174660a0.
5. "REDstack Nears First Green Hydrogen Production at Its Salt-Fresh Water Blue Energy Plant." *REDstack Nears First Green Hydrogen Production at Its Salt-Fresh Water Blue Energy Plant | Dutch Water Sector*, https://www.dutchwatersector.com/news/redstack-nears-first-green-hydrogen-production-at-its-salt-fresh-water-blue-energy-plant.
6. Simões, C., et al. "Electrode Segmentation in Reverse Electrodialysis: Improved Power and Energy Efficiency." *Desalination*, vol. 492, 2020, p. 114604., https://doi.org/10.1016/j.desal.2020.114604.
7. Veerman, J., and D.A. Vermaas. "Reverse Electrodialysis." *Sustainable Energy from Salinity Gradients*, 2016, pp. 77–133., https://doi.org/10.1016/b978-0-08-100312-1.00004-3.
8. Mohamed A. Umbarek, et al. "Energy Consumption in Residential Buildings: Comparison between Three Different Building Styles." *Sustainable Development Research*, vol. 2, 2020
9. Allouhi A. et al. "Energy consumption and efficiency in buildings: current status and future trends." *Journal of Cleaner Production*, vol. 109, 2015, pp. 118-130.
10. Dlugolecki P. et al. "Energy Recovery in Membrane Capacitive Deionization." Environ. Sci. Technol. 2013, 47, 9, pp. 904–4910
11. Dlugolecki P. et al. "Current status of ion exchange membranes for power generation from salinity gradients." Journal of Membrane Science, vol 319, 2008, pp. 214-222
12. Simões, C., et al. "Optimizing multistage reverse electrodialysis for enhanced energy recovery from river water and seawater: Experimental and modeling investigation." Advances in Applied Energy vol. 2, 2021, p100023 (https://doi.org/10.1016/j.adapen.2021.100023)
13. https://www.danfoss.com/en/about-danfoss/news/cf/excess-heat-is-world-s-largest-untapped-source-of-energy/
14. https://www.sustainability.gov/federalsustainabilityplan/emissions.html
15. Dlugolecki P. et al. "Practical Potential of Reverse Electrodialysis As Process for Sustainable Energy Generation" Environ. Sci. Technol. 2009, 43, 17, pp. 6888–6894
16. Krakhella K. et al. "Heat to H2: Using Waste Heat for Hydrogen Production through Reverse Electrodialysis" Energies, 2019, 12, 18, pp. 3428 (https://doi.org/10.3390/en12183428)
17. Post J. et al. "Energy Recovery from Controlled Mixing Salt and Fresh Water with a Reverse Electrodialysis System" Environ. Sci. Technol. 2008, 42, pp. 5785–5790
18. Simões, C., et al. "Scaled-up multistage reverse electrodialysis pilot study with natural waters" Chemical Engineering Journal 2022, 450, pp. 138412
19. Raka Y.D., et al. "Opportunities and challenges for thermally driven hydrogen production using reverse electrodialysis system" International Journal of Hydrogen Energy, 2020, 45, pp. 1212-1225
20. Veerman J., et al. "Reverse electrodialysis: A validated process model for design and optimization", Chemical Engineering Journal, 2011, 166, pp. 256-268
21. Luberti M., et al "An estimate of the ultralow waste heat available in the European Union.", Energy, 238, pp. 121967
22. https://www.energy.gov/quadrennial-technology-review-2015
23. Bin H., et al. "Exergy analysis of R1234ze(Z) as high temperature heat pump working fluid with multi-stage compression." Frontiers in Energy, 2017, 11, pp. 493-502
24. Liu H., et al. "Experimental validation of an advanced heat pump system with high-efficiency centrifugal compressor." Energy, 2020, 213, pp. 118968
25. Feria, R., Heat Source Optimization System, 2018, Patent Nr. US 9,915,436B1

14th IEA Heat Pump Conference
15-18 May 2023, Chicago, Illinois

LCCP Evaluation for Air-to-Air Heat Pumps using Next-Generation Refrigerants - Residential Air Conditioners -

Shigeharu Taira[a] , Eiji Hihara[b]

[a] The Japan Refrigeration and Air Conditioning Industry Association,Tokyo, Japan
[b]University of Tokyo,Tokyo, Japan

Abstract

In Japan, a two-step process is applied to the LCCP evaluation of heat pump-type air conditioners with next-generation refrigerants. This report mainly describes the first step of the process through to the LCCP evaluation methods, together with the concept of the study utilizing field data and hypotheses. In particular, a representative model is selected as an example of general split-type air conditioners, and it is considered in two ways, one of which is only as evaluation for a system drop-in of candidate refrigerants replacement while the other is in terms of system optimization, both using the candidate refrigerants to be examined R290, R32, R454C (and R22, R410A). On the basis of such systems, this report explains a calculation method using the performance simulation that is adopted as a standard tool by the Japan Refrigeration and Air Conditioning Industry Association (hereinafter referred to as "JRAIA").

The report also presents an overview of a project to establish a new concept and hypothesis for LCCP evaluation in which field data related to air conditioners is adopted.

Keywords: LCCP,Air-to-Air,Heat Pump,Next-Generation refrigerant,COP,Residential A/C

1. Introduction

The main issues of recent urgent environmental efforts to address global warming in relation to air conditioners (hereinafter referred to as "AC") are the Kigali Amendment to the Montreal Protocol in globally, the F-Gas Regulation in Europe, and the Act on Rational Use and Proper Management of Fluorocarbons in Japan.

The Kigali Amendment is a regulation aimed at gradually reducing the production and consumption amounts of refrigerants used in CO2 equivalents. This regulation is a global warming countermeasure to be promoted worldwide by focusing on a transition to lower GWP refrigerants. For actual global warming countermeasures, it is important not only to reduce the GWP of the refrigerant, but also to improve the performance of equipment by reducing the amount of greenhouse gas emissions derived from power consumption.

Report of IEA gives an overview of the forecast of demand for residential AC cooling by 2050 by country/region based on the Future of Cooling report published by the International Energy Agency (hereinafter referred to as "IEA") [1]. As can be seen, the chart indicates that the world's demand for residential AC cooling will expand rapidly by 2050. The use of AC in the United States and Japan will increase at a gradual pace. On the other hand, due to growing demand in India, Indonesia, Brazil, China, and EU countries, the world's AC demand is projected to rise considerably – by more than three times – by 2050.

It is anticipated that such an increase in AC demand will not only cause refrigerants to have a direct impact on global warming but also possibly give rise to an increase in the indirect impact on global warming due to the power consumption of AC equipment. Therefore, in addition to the direct impact of refrigerants, the energy efficiency and power consumption of equipment will become the focus of even greater attention in the years to come.

For this reason, we believe the LCCP evaluation to be studied in Task 3 is an important evaluation for selecting the most suitable refrigerants because it takes into account the transition to lower GWP refrigerants

Table 1. Comparison of Refrigerant Properties

	R410A	R32	R454C	R290	R22
Composition	R32/R125 (50/50 wt%)	Pure fluid	R32/R1234yf (21.5/78.5 wt%)	Pure fluid	Pure fluid
GWP	2090	675	148	3	1810
Safety Label	A1	A2L	A2L	A3	A1

and the environmental impact of power consumption. To make the evaluation more realistic, based on the concept of S+3E (Safety, Environment Performance, Energy Efficiency, Economic Feasibility) advocated by JRAIA, it is desirable to conduct a comprehensive evaluation from multiple perspectives, including safety, cost, sustainability, and infrastructure development, in addition to environmental assessment through the LCCP evaluation.

The study conducted by JRAIA in December 2008 [2] is introduced as a previous case study relating to the LCCP evaluation. The LCCP evaluation in this case was based on a simplified simulation, with climate and other conditions set in accordance with Japanese Industrial Standards (hereinafter referred to as "JIS").

There is also a case study concerning IEA-related LCCP evaluation, which was presented by the University of Maryland in the United States (hereinafter referred to as "UMD") [3]. In this paper, mainstream residential ACs in the United States are evaluated; therefore, it is necessary to conduct an evaluation for the split-type heat pump ACs that are in conventional residential use in Japan and Asia.

Accordingly, in Japan, a new LCCP evaluation is carried out in two steps for heat pump-type ACs that use next-generation refrigerants. The first step (this report) examines the LCCP evaluation methods, and the second step to be implemented in the future will mainly describe a new evaluation applying performance simulation and the concept and hypothesis of the study utilizing market data.

In the evaluation in this report, a representative model of typical split-type ACs is selected, and refrigerants R290, R32, R454C, R454C, R22, and R410A are examined. Since the indirect impact of power consumption varies significantly depending on the market and factors such as climate condition and lifestyle, the first step evaluates this under the standard conditions in Japan. The performance evaluation method verified jointly by JRAIA and Waseda University is used. As the second step, evaluation will be conducted on the basis of the possibility of the application of actual market data that varies according to local climate conditions, and Report 2 will explain the established concept and hypothesis about this approach.

2. Concept of LCCP Evaluation

This chapter explains the concept of the LCCP evaluation. Basically, the calculations of LCCP are carried out in accordance with the guidelines published by the International Institute of Refrigeration (hereinafter referred to as "IIR") [4]. The components to be evaluated for LCCP are shown in the report of IIR [4].

This chapter describes how to calculate the amount of refrigerant charge and annual energy consumption.

Table 2. Comparison of Theoretical COP

		Cooling					Heating				
		R410A	R32	R454C	R290	R22	R410A	R32	R454C	R290	R22
Evaporating Pressure	MPa	1.087	1.107	0.591	0.637	0.681	0.799	0.813	0.432	0.474	0.498
Condensing Pressure	MPa	3.067	3.141	1.691	1.713	1.943	2.142	2.190	1.177	1.218	1.355
Temperature glide	K	0.1	0.0	5.6	0.0	0.0	0.1	0.0	6.2	0.0	0.0
Suction Temperature	℃	15.1	15.0	18.5	15.0	15.0	5.1	5.0	8.7	5.0	5.0
Discharge Temperature	℃	71.6	84.3	59.4	58.5	71.7	55.4	67.7	44.5	43.8	56.1
Theoretical COP	-	5.49	5.63	6.02	5.88	5.94	6.72	6.58	7.93	7.61	7.27
Volume Capacity	kJ/m^3	6,404	7,045	3,700	3,737	4,456	5,516	5,749	3,450	3,478	3,826

*Condensing temperature Cooling50/Heating35℃,

Evaporation temperature Cooling10/Heating0℃,

Suction superheat 5K, Sub-cooling 10K

Saturation temperature of zeotropic refrigerants is midpoint temperature of two -phase region under constant pressure.

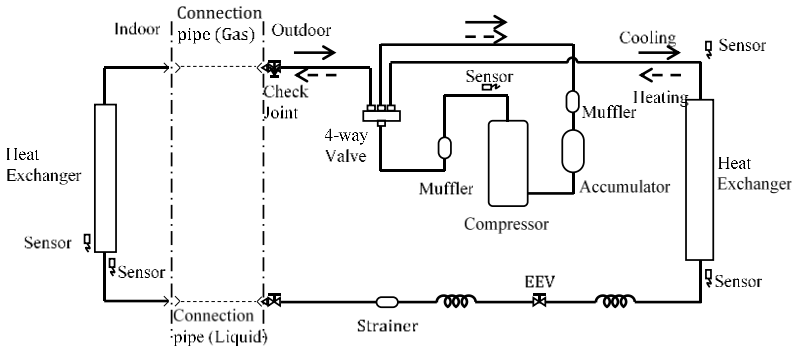


Figure 1. Refrigerant circuits for Split type Air conditioner

2.1. Concept of Candidate Refrigerants

This section explains the concept of candidate refrigerants for examination in the LCCP evaluation in this project.

The candidate refrigerants include R410A, a pseudo- azeotropic refrigerant mixture of an HFC refrigerant, and R32, an HFC single refrigerant, both of which are used in current AC units. In addition, R454C was selected as a zeotropic mixture of HFO and HFC refrigerant with relatively large temperature glide, which is attracting attention as a low-GWP refrigerant. We also selected the natural refrigerant R290, which has a lower operating pressure than R410A and R32, and the HCFC refrigerant R22, which is still adopted in many current ACs in emerging nations and is an important refrigerant for comparison with R290.

Table 1 shows the properties of each refrigerant [5] and Table 2 shows the theoretical COP calculated based on the thermodynamic properties of the refrigerants.

As described above, five refrigerants were selected for the study from the perspective of comprehensively covering the properties of the next-generation refrigerants in relation to system performance: R410A, R32, R454C, R290, and R22.

2.2. Examined AC and Performance Simulation

The AC to be examined is a split-type heat pump AC. Widely distributed ACs are diverse according to the manufacturer and development year; therefore, in this project, we decided to examine a residential AC for which JRAIA defined the standard specifications.

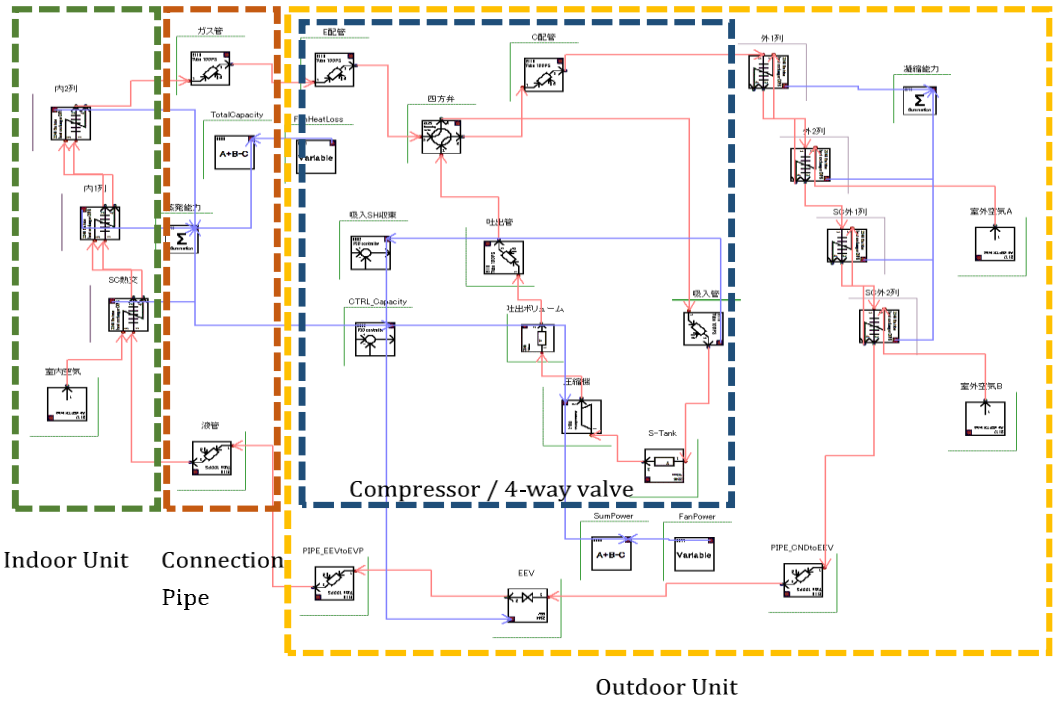


Figure 2. Project Layout for Standard model

Table 3. Calibration results of Standard model

		Cooling		Heating	
		Actual	Calculated	Actual	Calculated
Capacity	%	100	95	100	99
Power consumption	%	100	111	100	102

More specifically, the selected AC is equivalent to a high-end unit, and an analysis model (standard model) with a rated cooling capacity of 4kW was created for the examination. An overview of the AC's refrigerant circuits is shown in Figure 1.

The performance simulation was conducted using the simulation software Energy Flow +M, which was developed by Professor Saito's Laboratory at Waseda University and is used by JRAIA as a standard tool. Figure 2 shows the refrigerant circuit diagram of the standard model constructed with this performance simulation software.

To examine this standard model with greater accuracy, a comparative verification was made between the performance simulation results and the actual equipment test results for the case where the R410A was used for operation. Table 3 shows a comparison with the actual equipment test results. To implement more advanced performance simulation, each element device consisting of the refrigeration cycle was calibrated so that both the capacity and power input in Table 3 have an accuracy of ±10%.

2.3. Performance Simulation Conditions

This section describes the calculation conditions for performance simulation shown in Table 4.

The performance test conditions for ACs have been evaluated by means of JIS C 9612 (2013). Its performance evaluation method is carried out through a relative comparison under the predetermined conditions for the balance point (condensation and evaporation temperatures, suction superheating degree, and subcooling degree), which is the operating status point.

AC performance is evaluated by calculating an Annual Performance Factor (hereinafter referred to as "APF"). To calculate the APF, operation modes are set for each of cooling and heating, and the capacity is set for each of the test conditions and a Coefficient of Performance (hereinafter referred to as "COP") is calculated. AC performance is evaluated based on a relative comparison using the APF.

These evaluations are conducted for each case of using a single refrigerant and using an azeotropic (including pseudo-azeotropic) refrigerant mixture, and for the latter performance is evaluated using a technique called the "cycle midpoint protocol (boiling point/dew point)" as specified in JIS B 8623 (2019), which defines condensation and evaporation temperatures.

In addition, the expansion valve opening degree is adjusted so that the suction superheating degree (= compressor suction gas temperature – saturation temperature in compressor suction gas) is 5°C, and performance is evaluated using the same methods described above. Regarding the subcooling degree, the amount of refrigerant charge is adjusted so that the maximum COP is achieved for each refrigerant.

Table 4. Calculation conditions

TEST		Cooling	Heating
Air Entering of Indoor unit	Dry Bulb[°C]	27.0	20.0
	Wet Bulb[°C]	19.0	15.0
Air Entering of Outdoor unit	Dry Bulb[°C]	35.0	7.0
	Wet Bulb[°C]	24.0	6.0
Cycle Point	Capacity	Same at each operation point	
	SH	5.0 K at Suction Temperature	
	SC	At Optimum Performance	

2.4. *Calculation of LCCP*

Basically, LCCP is calculated in accordance with the guidelines published by the IIR.

The calculation methods for the amount of refrigerant charge, annual energy consumption, and other items are arranged and implemented as follows.

(1) Equipment: JRAIA AC standard model (H/P split type) equivalent to high-end unit with a rated cooling capacity of 4kW

(2) Tool: JRAIA standard tool Energy Flow +M (Prof. Saito's Lab at Waseda University)

(3) Comparison: Optimization is performed for each refrigerant to calculate the amount of refrigerant charge and the annual energy consumption.

(4) Selection of refrigerant types: Five refrigerants (R410A, R32, R454C, R290, and R22) were selected based on the above-mentioned concept.

(5) Calculation conditions: As described above, the power consumption in a refrigeration cycle with the same capacity is calculated under the conditions shown in Table 4.

3. LCCP Evaluation Conditions and Specifications

This chapter describes the evaluation conditions and specifications for LCCP.

3.1. *Definitions of LCCP Equations:*

The definitions of the LCCP equations are stipulated as the LCCP evaluation conditions. LCCP is calculated by obtaining the sum of the direct and indirect emissions according to the method proposed by Dr. Hwang of UMD [3]. The method of calculating the direct emissions is shown in Equation (1). Indirect emissions are calculated using Equation (2). The following is a brief summary of the LCCP calculation.

$$\mathrm{LCCP} = Direct\ Emissions + Indirect\ Emissions$$

$$Direct\ Emissions = C \times (L \times ALR + EOL) \times (\mathrm{GWP} + Adp.\mathrm{GWP}) \quad (1)$$

$$Indirect\ Emissions = L \times AEC \times EM + \sum(m \times MM) + \sum(mr \times RM) + C \times (1 + L \times ALR) \times RFM + C \times (1 - EOL) \times RFD \quad (2)$$

The symbols in the evaluation equations are shown in Table 5.

Table 5. Symbol Description

C	kg	Refrigerant Charge
L	yr	Average Lifetime of Equipment
ALR	% of Ref. Charge	Annual Leakage Rate
EOL	% of Ref. Charge	End of Life Refrigerant Leakage
GWP	$kgCO_2e/kg$	Global Warming Potential
$Adp.\ GWP$	$kgCO_2e/kg$	GWP of Atmospheric Degradation Product of the Refrigerant
AEC	kWh	Annual Energy Consumption
EM	$kgCO_2e/kWh$	CO2e Produced / kWh
m	kg	Mass of Unit
MM	$kgCO_2e/kg$	CO2e Produced / Material
mr	kg	Mass of Recycled Material
RM	$kgCO_2e/kg$	CO2e Produced / Recycled Material
RFM	$kgCO_2e/kg$	Refrigerant Manufacturing Emissions
RFD	$kgCO_2e/kg$	Refrigerant Disposal Emissions

Table 6. Assumption parameters used for LCCP calculation

Symbol	unit
C	kg
L	yr
ALR	% of Ref. Charge
EOL	% of Ref. Charge
GWP	$KgCO_2e/kg$
AEC	kWh
EM	$KgCO_2e/kWh$

3.2. *Influential Factors of LCCP:*

This section describes influential factors when calculating LCCP.

Table 6 summarizes the calculation items used in Equation 1 for the direct emissions and in Equation 2 for the indirect emissions in the LCCP calculation. Table 6 indicates that LCCP involves various influential factors. Therefore, when evaluating LCCP, it is necessary to clarify its influential factors and parameterize them for the study. There is particular concern that the evaluation may significantly differ depending on the country or region.

For example, with regard to energy conversion, since the power generation systems vary by country or region, the data that comes under Equation 1 for the direct emissions and Equation 2 for the indirect emissions are deemed to be influential factor parameters for energy conversion. By replacing these influential factor parameters as appropriate for each country or region, it is possible to estimate valid LCCP.

3.3. *Evaluation Applying Performance Simulation:*

To predict the performance of AC equipment, which will have a major impact on the LCCP evaluation, newly constructed performance simulation with improved prediction accuracy is used in the study.

Figure 4 shows the schematic configuration of the standard model used for performance simulation in this study. The standard model was created based on the specifications of a common commercially available heat pump AC.

In this study, to take into account the design concept for actual ACs, the performance is predicted assuming drop-in (hereinafter referred to as “DI”) and soft optimization (hereinafter referred to as “SO”) in the performance simulation. Specifications optimized with greater awareness of AC product capabilities (e.g., size equivalence and energy efficiency equivalence) are also examined. The DI evaluation in this study refers to performance evaluation where the same AC equipment is used but only the refrigerant is replaced. However, regarding equipment mounted with an inverter compressor and electronic expansion valve, the compressor frequency is changed (change of refrigerant mass flow rate) with the same AC capacity, and the expansion valve opening degree is changed with the same suction superheating degree. In addition, the SO evaluation refers to performance evaluation with minor modifications added on the AC’s hardware, such as changing the diameter of the connection pipe so that almost the same pressure drop occurs in the circuit even when different refrigerants are applied. Table 7 shows the concept of the assumed specification changes.

As shown in Table 7, compared with the base AC (a), in (b) the charged refrigerant (R410A) was changed, the refrigerant amount was adjusted to equalize the subcooling degree, and the compressor frequency was also changed to equalize the capacity before comparison. In (c), for the connection pipes of the liquid side and gas side that connect the indoor and outdoor units, the pipe diameter was optimized so that the pressure drop is equal to that of the current refrigerant. In (d), while maintaining the size of the heat exchanger, the path was changed to achieve the maximum efficiency. In (e), the size of the heat exchanger was changed to equalize the energy efficiency.

The refrigerant used for the base model is R410A.

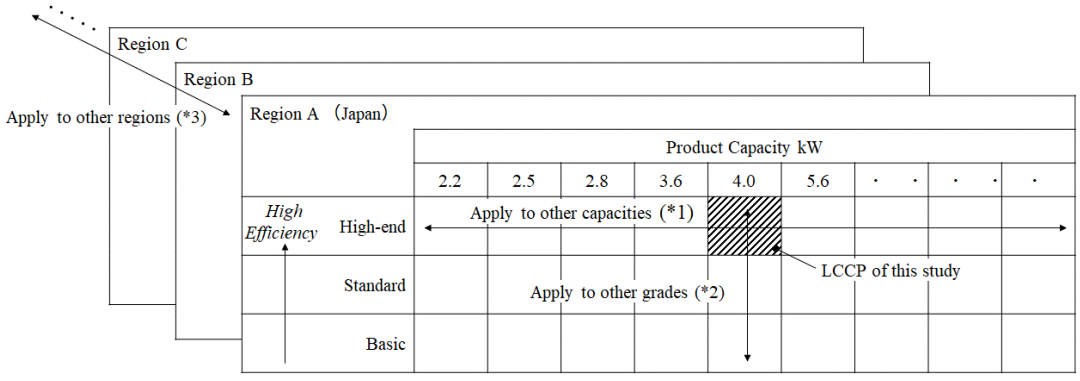
Based on these studies, the values for the refrigerant charge amount, C, and the annual energy consumption, AEC, which are factors affecting the LCCP evaluation, are calculated, and a comparative assessment is made using the obtained values.

Table 7. Specification of refrigeration cycle

		(a)	(b)	(c)	(d)	(e)
		Base model	Drop in	Soft optimization	Optimization (Same size)	Optimization (Same efficiency)
Outdoor unit	Row	2	←	←	←	Optimize
	Column	35	←	←	←	Optimize
	Cooling path	6-3-1	←	←	Optimize	Optimize
Indoor Unit	Row	3	←	←	←	Optimize
	Column	21	←	←	←	Optimize
	Cooling path	1-3	←	←	Optimize	Optimize
Connection pipes	Liquid	Φ6.35	←	Optimize (*1)	Same as (c)	Same as (c)
	Gas	Φ9.52	←	Optimize (*1)	Same as (c)	Same as (c)
Refrigerant charge [kg]		1.1	COP Maximum (*2)	COP Maximum (*2)	COP Maximum (*2)	COP Maximum (*2)
Capacity vs base model [%]		100	←	←	←	←
Expansion valve		As it is	Same as Base model SH	Same as Base model SH	Same as Base model SH	Same as Base model SH

※Note 1： Same as temperature-equivalent pressure drops of base model

※Note 2： Proposal under consideration



How to apply：

※Note 1, ※Note 2： Modify the simulation model (Figure 4)

※Note 3： Modify the assumption parameters (Table 6)

Figure 3. Outline of how to apply the LCCP of this study to various product specifications and global areas

4. Application of LCCP Evaluation and Consideration

With regard to the LCCP evaluation, this chapter formulates a hypothesis for the study with a view to the influential factors and the study of regions both in Japan and abroad, and describes a consideration of these.

4.1. Key points of the Project in the LCCP Evaluation:

Firstly, we will explain the key points of the project in the LCCP evaluation.

The LCCP evaluation is basically examined by utilizing field data in addition to the past study by JRAIA [2] and the paper by UMD [3].

The results of evaluation based on the actual operating conditions will be reported next time in the final report.

4.2. Application of the Project's LCCP Evaluation

The concept of the LCCP evaluation in this project is shown in Figure 3, and the following explains how to apply the evaluation and other matters. The final report of the project will classify and study the regional characteristics of ambient air temperatures and other influential factors in Japanese regions that affect the LCCP evaluation. Therefore, we will study the LCCP evaluation through this task, having in mind that other countries will be able to make broad and general speculation.

(1) Impact of equipment specifications

As explained in Chapter 4, the LCCP values in this project are calculated for the standard model based on a high-end AC unit with a cooling capacity of 4kW that is commercially available in Japan.

However, there is a wide variety of ACs on the Japanese market, and they are even more diversified in other countries. In our view, for such diverse equipment, it is possible to calculate the annual power consumption, namely the indirect emissions in the LCCP evaluation, by modifying the specifications in the refrigeration cycle simulation shown in Figure 2.

(2) Influence of regional characteristics

In addition to the modification of the equipment specifications mentioned in (1), the annual power consumption, namely the indirect emissions in the LCCP evaluation, also requires modifications of the estimation parameters according to environmental characteristics including the temperatures in the region, users' usage conditions, differences in power generation systems, and other factors.

For reference, Figure 6 shows a comparison of the changes of monthly average temperatures around the world in 2020. Climates vary depending on the assumed regional environment, which results in differences in the ambient air temperatures and humidity, operating hours, and required load. These differences strongly affect the annual power consumption during the use of an AC – the indirect emissions of LCCP. For example, in a region where ACs are required to operate throughout the year, annual power consumption is projected to increase throughout the life of the equipment. Regarding the load on the equipment, the higher the ambient air temperature during the cooling mode, the higher the condensing pressure in the refrigeration cycle, increasing the load on the compressor. The heat load entering the building from outdoors also increases, and the room temperature tends to rise; therefore, it is necessary to select an AC with a higher capacity.

Moreover, larger heat exchangers are required as the load increases, leading to the problem of an increase in the amount of refrigerant used. Therefore, it is anticipated that there will be demand for highly efficient refrigerants suitable for large capacity and other influences.

Figure 5 shows the composition of power generation systems in five countries in 2016. Power resources are classified into fossil fuels, such as petroleum, natural gas, and coal, and non-fossil fuels, such as hydraulic power, other renewable energies, and nuclear power, and they are compared in percentage terms. As indicated in Table 6, according to the resource of power generation means, LCCP is affected by EM, which is the amount of CO2 [kgCO2] generated per unit power consumption [kWh]. The EM varies greatly depending on the major power generation systems in each country. For example, in countries where the major systems are renewable energy power generation, such as hydraulic power, and nuclear power generation, the power consumed by

ACs will be unlikely to lead to CO2 emissions, and the indirect emissions will be negligible. On the other hand, in countries where power generation is mainly derived from fossil fuels such as petroleum and natural

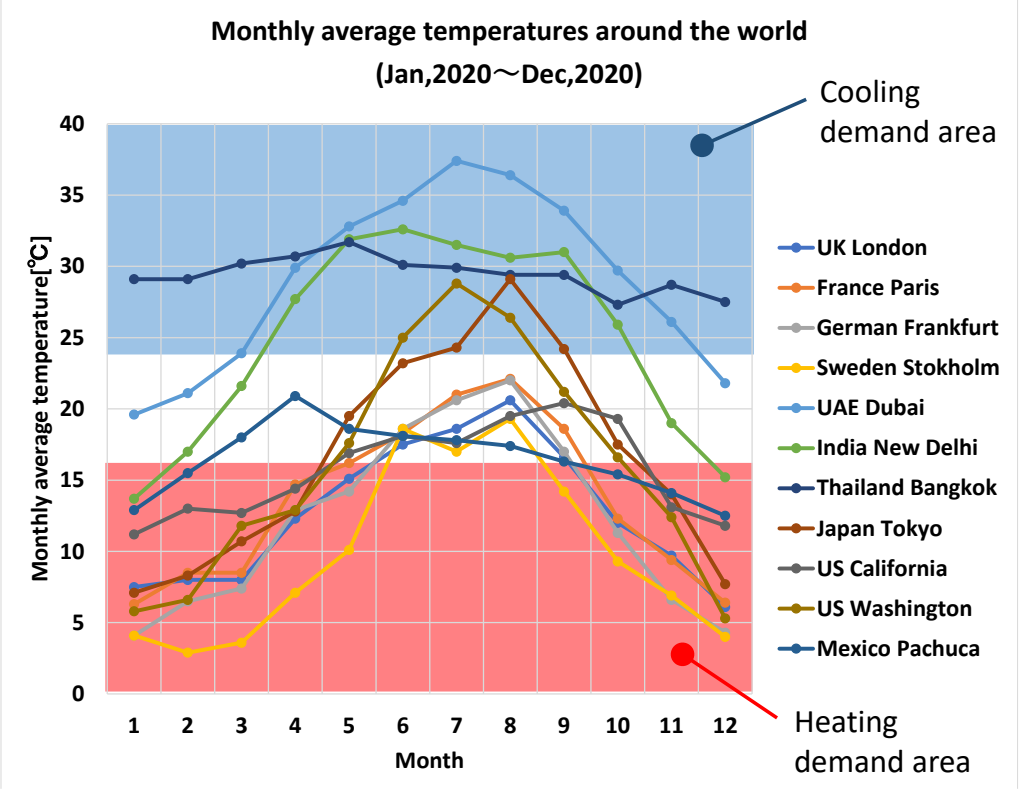


Figure 4. Example of Monthly average temperatures around the world

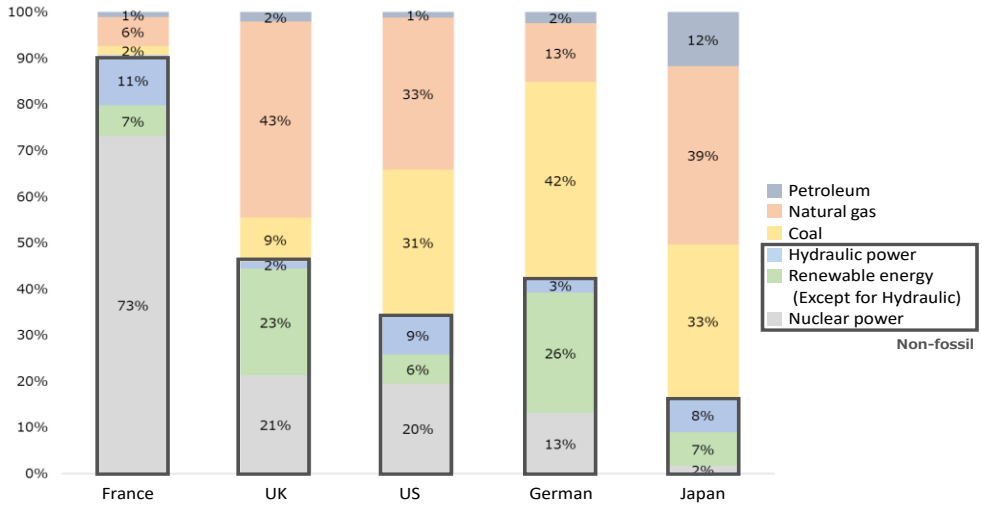


Figure 5. Comparison of non-fossil fuel power resource rates in 2016

gas, CO2 emissions from the use of AC becomes sensitive, and the indirect emissions of LCCP are strongly affected by the equipment efficiency and air-conditioning load.

Concerning the power generation systems, changes in the composition due to changes in power resource demand, shift to renewable energies and other factors may also need to be considered in future predictions.

In our view, by studying the basic values required for the LCCP calculation shown in Table 6, it is possible to apply the LCCP evaluation to the influential factors described above.

(3) Impact of the properties of various refrigerants

This section explains the concept concerning the LCCP evaluation methods for diverse candidate refrigerants.

As mentioned in Chapter 4 and this chapter, in this project, by utilizing new performance simulation with high accuracy and market data, the LCCP evaluation is expected to be closer to actual market conditions than

the previous evaluation was.

The LCCP calculation for various refrigerants in this project is as described in Chapter 4. The method is to examine the factors that affect the LCCP evaluation of various refrigerants through SO or by optimizing the refrigerant circuit for each refrigerant.

For example, the values for the refrigerant charge amount, C, and annual energy consumption, AEC, which are considered major influential factors, can be calculated with high levels of accuracy. In terms of the calculation conditions, it is expected that LCCP for each refrigerant can be compared by reflecting market data and regional characteristics, such as climate and refrigerant recovery rate, which vary in different countries and regions.

5. Conclusion

In Japan, LCCP, LCCP evaluation is studied in a two-step process, and the concept (hypothesis) of the first step described in this report is summarized in the following bullet points:

- The concept (hypothesis) of the LCCP evaluation in this report was established by focusing on the consistency of the criteria of evaluation indicators.
- In the LCCP evaluation, a performance simulation evaluation will be carried out using JRAIA's standard tool (performance simulation program developed by Waseda University) to optimize the system in relation to candidate refrigerants.
- Performance evaluation will be carried out through a relative comparison for each refrigerant under the same capacity.
- A residential heat pump mini-split AC with a capacity of 4.0kW was selected as the standard model of AC equipment to be examined, and calculation will be performed.
- For the standard model, mutual correction will be made between the actual equipment test data and the performance simulation data.
- The calculation conditions of LCCP were clarified so as to share the same data recognition.
  In addition, in the second step, the LCCP evaluation will be studied by utilizing the market data on ACs.
- Influential factors of the LCCP evaluation were clarified and parameterized so that the evaluation can be applied overseas.

Finally, the basic concept on the positioning of the LCCP evaluation in the selection of refrigerants is explained as follows.

We believe that the LCCP evaluation to be studied in Task 3 is one of the important criteria for selecting optimal refrigerants. We also feel that in order to make the evaluation more realistic, it is desirable to conduct a comprehensive evaluation from multiple perspectives, including safety, cost, sustainability, and infrastructure development, in addition to the environmental assessment through the LCCP evaluation.

6. Future Plans

Regarding issues and responses to be addressed in the second step in the future, we plan to verify the concept (hypothesis) of the LCCP evaluation described in this report.

Specifically, the study will be conducted based on the results of the performance simulation to optimize ACs. In addition, the utilization of market data will also be examined.

In the second step, we plan to study the LCCP evaluation not only for Japanese regions with a temperate climate but also, by utilizing market data, for other areas in the world such as India, where ACs are used more often.

Terminology

- **Life Climate Performance (LCCP)**: An index to evaluate the global warming impact of a product throughout its life, from manufacture to disposal. Based on the TEWI, the value is calculated by adding energy consumption (indirect emissions) when manufacturing the gas to be used and the leakage of the gas (direct emissions).
- **Global Warming Potential (GWP)**: Indicates the degrees of the global warming impacts of gases released in the atmosphere. On the basis of carbon dioxide (1.0), the same gas weight and same period (100 years) are assumed to allow relative comparisons of the impact of each gas. When the HFC refrigerant used for ACs is considered with the same gas weight, its GWP is generally hundreds to thousands of times greater than that of carbon dioxide; therefore, its significant impact on global warming is regarded as a problem.

- **Optimization**: In performance simulation, compared with the performance prediction made with conventional DI and SO, optimized performance prediction takes into account the design concept of an actual product; optimization is carried out by adjusting the component parts (piping, heat exchanger, etc.) of the refrigeration circuit so that their specifications conform to the refrigerant characteristics.
- **Performance simulation**: A method to estimate the power consumption of the target equipment under various operating conditions using Energy Flow +M (Prof. Saito's Lab at Waseda University), which is a standard tool of JRAIA. Used to calculate annual power consumption.
- **Coefficient of Performance (COP)**: A factor used as a measure of the energy consumption efficiency of cooling equipment, etc. The value represents cooling/heating capacity per kW of power consumption.
- **Total Equivalent Warming Impact (TEWI)**: A method to evaluate global warming impacts in comprehensive consideration of refrigerant leakage during equipment use, emissions into the atmosphere at the time of disposal, and the amount of carbon dioxide generated from fossil fuel usage due to operating power consumption. TEWI is expressed by the following equation.

TEWI = Direct CO2 emission equivalent + Indirect CO2 emission equivalent
Direct CO2 emission equivalent = $GWP \times L \times N + GWP \times M \times (1-\alpha)$
Indirect CO2 emission equivalent = $N \times E \times \beta$

GWP: Global warming potential per kg on the basis of CO2, 100-year integration period (kg-CO2e/kg)
L: Annual amount of leakage from equipment (kg/year)
N: Service life of equipment (years)
M: Amount of charge to equipment (kg)
α: Recovery rate at equipment disposal
E: Annual energy consumption of equipment (kWh/year)
β: CO2 emissions required for 1 kWh of power generation (kg-CO2e/kWh)

- CO2 emissions: Total of the amount of carbon dioxide generated from fossil fuel usage due to power consumption and the equivalent amount of carbon dioxide using GWP to the degree of the global warming impact of the gas released into the atmosphere.

Acknowledgements (or activity members)

This project is conducted by the following members and observers of JRAIA LCCP Evaluation Study WG. We would like to express our deepest gratitude for their cooperation.

The Chief is PhD. Shigeharu Taira, Daikin Industries, Ltd., and the Sub-Chief is Mr. Seishi Iitaka, Panasonic Corporation.

Members are as follows: Mr. Itaru Nagata, Sharp Corporation; Mr. Tomoyuki Haikawa , Mr.Hayato Nuno and Mr. Katsunori Murata, Daikin Industries, Ltd.; Mr. Hiroichi Yamaguchi and Mr. Kohei Maruko, Toshiba Carrier Corporation; Mr. Ryoichi Takafuji and Mr. Takashi Inoue, Johnson Controls-Hitachi Air Conditioning; Mr. Shunji Itakura, Fujitsu General Limited; Mr. Takanori Nakamura and Mr. Keisuke Mitoma, Mitsubishi Heavy Industries Thermal Systems, Ltd.; Dr. Koji Yamashita and Mr. Yasuhide Hayamaru, Mitsubishi Electric Corporation.

Observers are Professor Kiyoshi Saito and Mr. Yoichi Miyaoka, Chief Researcher, Waseda University; Mr. Takeshi Sakai and Mr. Kazuhiro Hasegawa, JRAIA.

References

[1] The Future of Cooling - Opportunities for energy-efficient air conditioning, 2018, OECD/IEA
[2] Basic Policy of JRAIA on Global Warming Prevention Measures and LCCP-Analogy for HFO1234yf Air Conditioners using a Simulation with R134a Properties, International Symposium on New Refrigerants and Environmental Technology 2008, JRAIA
[3] Y. Hwang, et al, Harmonization of Life Cycle Climate Performance (LCCP) Methodology 2016. International Refrigeration and Air Conditioning Conference. Paper 1724.
[4] IIR LCCP Working Group, Guideline for life cycle climate performance 2015, IIR
[5] TEAP XX VII/4 TEAP Task Force Report, 2016
[6] The data from homepage tool "Climate View" by Japan Meteorological Agency https://www.data.jma.go.jp/cpd/monitor/climatview/frame.php
[7] The data from webpage "Energy circumstances of each country" The Figure made by Japan Agency for Natural Resources and Energy and the original data are from "IEA World Energy Balances" https://www.enecho.meti.go.jp/about/whitepaper/2019html/1-2-3.html

14th IEA Heat Pump Conference
15-18 May 2023, Chicago, Illinois

Development of industrial heat pump simulator

Jongsoo JEONG[a,*], So MUTO[b], Yoichi MIYAOKA[c], and Kiyoshi SAITO[d]

a Research institute for science and engineering, Waseda University, 3-4-1 Okubo, Tokyo, 169-8555, Japan
b Graduate school of fundamental science and engineering, Waseda University, 3-4-1 Okubo, Tokyo, 169-8555, Japan
c Interdisciplinary institute for thermal energy conversion engineering and mathematics, Waseda University, 3-4-1 Okubo, Tokyo, 169-8555, Japan
d Department of Applied Mechanics and Aerospace Engineering, Waseda university, 3-4-1 Okubo, Tokyo, 169-8555, Japan

Abstract

To improve heat conversion efficiency in the industrial field, this research has focused on heat pump technology, which has low CO_2 emissions and high efficiency, and has developed a simulator that can easily study the effects of introducing the technology and can be used for a variety of systems. To achieve this goal, we have selected a model with a good balance between calculation speed and accuracy, and have built a simulator that is easy for users to use and can flexibly respond to changes in refrigerants, systems, and operating conditions. In this paper, we show, compare and analyze the results of an environmental evaluation, as well as verification of its accuracy using actual measurement data from a factory using the simplified simulator calculated by classification of basic system configuration patterns and the integrated simulators based on general-purpose analysis logic for the model.

© HPC2023.
Selection and/or peer-review under the responsibility of the organizers of the 14th IEA Heat Pump Conference 2023.

Keywords: Industrial heat pump; Simplified simulator; Integrated simulator; economic and environmental evaluation

1. Introduction

The New Energy and Industrial Technology Development Organization (NEDO)[1] reported that 70% of waste heat per fuel is generated in boilers, steam pipes, production facilities, and so on, considering the operation of conventional industrial heat systems in factories. Therefore, the introduction of heat pumps as an alternative to conventional combustion methods is attracting attention as a promising method for energy saving. When introducing an industrial heat pump into an existing process, it is necessary to quantitatively evaluate the cost, effectiveness, and desirable configuration of the heat pump system in advance.

However, the hurdles in terms of cost and time are high to determine these factors through actual demonstration construction using heat pumps, and as a result, this has become a factor hindering the spread and expansion of heat pumps. Considering these problems, a simulation-based evaluation method is preferable for quantitatively evaluating the effectiveness of heat pump installation. However, actual processes and systems have complex equipment configurations and are large in scale, and annual performance evaluations must be conducted in response to fluctuating loads and ambient temperatures, etc. This requires complex calculation inputs and a large amount of calculation time. For this reason, the authors have conducted research with the goal of constructing a simulator that is relatively easy to input calculations, has high accuracy, and can significantly shorten calculation time. [2][3]

This paper reports on two simulators that enable the effects of introducing heat pumps with environmental considerations even in complex systems where multiple devices are installed on factory production lines. Specifically, considering the analysis time and convergence for a large annual calculation in hours, the validity of the analysis results is confirmed by comparing them with field data of heat pump systems obtained

* Corresponding author. Tel.: +81-3-5286-3259; fax: +81-3-5286-3259.
E-mail address: jeong@aoni.waseda.jp.

throughout the year. The primary energy consumption and CO_2 emissions of each simulator were evaluated to quantify the efficiency of the heat pump installation system compared to a conventional combustion system.

2. Simulation overview

2.1. Simplified simulator

We suggested the evaluation method of target systems that are classified as 16 basic patterns to evaluate the effects of introducing a heat pump as shown in Table 1, and constructed a simulator that can be handled easily by users with knowledge of heat pumps as a whole to save energy in the entire industrial field. In order to organize a complicated system configuration, patterning methods were proposed based on four indicators (i.e., used equipment, heating method, introduction use) via surveys of heat pump products developed for existing industries.

The conventional “equipment” is set to “boiler” and the introduced equipment is set to the “heat pump” to compare the use of a conventional boiler or burner with a heat pump. We then consider an eco-cute system that supplies hot water as a system that includes a heat pump. Household water heaters are popular although large-scale industrial eco-cutes were developed to generate hot water instead of boilers. This corresponds to an introduction example targeted in the study. In this type of a water heater, there is a difference in the heating method between storing hot water in the tank and temporarily supplying hot water.

Therefore, “heating method” is set to “circulation” and “non-circulation”. Furthermore, the CO_2 hot air generation heat pump can be used for complete replacement of conventional boiler or preheating before conventional boiler. “Introduction use” is set as “replacement” and “preheating”.

Finally, heat pumps that can realize applications including cold / hot water generation, hot water supply, and hot water tank heating with a single unit were developed using waste heat recovery technology. The heat pump can simultaneously extract cold and warm heat from the low temperature side and high temperature side of refrigerant. Therefore, the “thermal utilization” is set as “high-temperature heat utilization” and otherwise “Simultaneous utilization of heat and cold” is set.

In the present study, a total of 16 patterns are proposed by combining the aforementioned "used equipment" (boiler, heat pump), "heating method" (circulation, non-circulation), "introduction use" (preheating, replacement), and "thermal utilization" (high-temperature heat utilization, simultaneous utilization of heat and cold).

The user inputs the target system configuration via a combination of the 16 basic patterns. Similarly, it is possible to perform a comparison with the case where the heat pump is introduced by using the basic pattern and to clarify various effects of introduction.

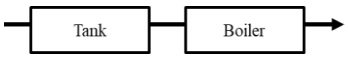
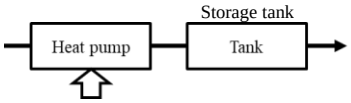
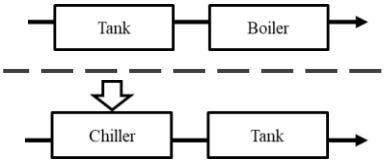
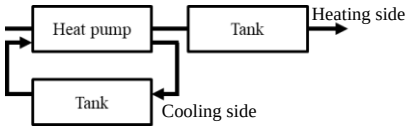
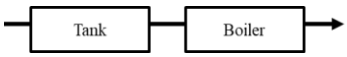
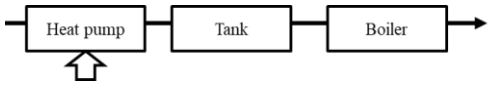
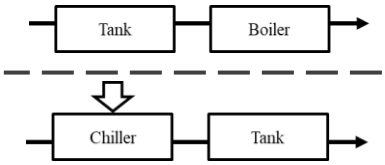
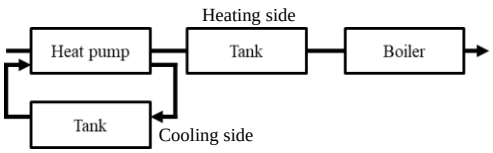
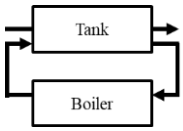
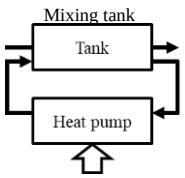
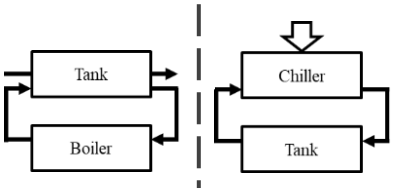
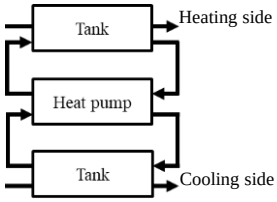
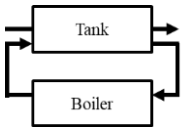
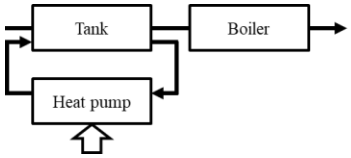
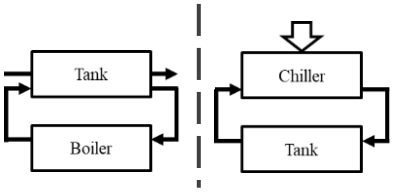
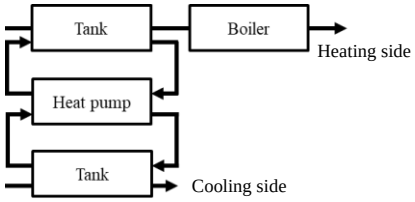
The GUI of the simulator developed using the C++ language is shown in Figure 1. In the simplified simulator, the user first selects one of 16 basic system configuration patterns that correspond to the existing system.

The selected pattern is arranged as the system on the left side shown in Figure 1. The pattern of the heat pump to be newly installed is also selected in the same way, and is placed as the system on the right side shown in Figure 1. Then, input variables for each pattern in csv format (values separated by commas (,)). The input variables are basically the refrigerant type and rated value, as well as the temperature and flow rate at each time point.

Finally, the comparison results are output after running the calculation program. On the screen, the results are displayed in the form of line graphs showing the primary energy consumption during the evaluation period for the input data, and bar graphs and numerical values showing the total primary energy consumption and total CO_2 emissions during the evaluation period, respectively.

In addition, a Moriel diagram of the heat pump is displayed based on the pressure and enthalpy data at the selected time. Since all 16 patterns are used as objective systems for comparison, it is possible to compare the performance of heat pumps with each other, and can respond flexibly to changes in the type of refrigerant and the basic configuration pattern of the system. This simulator is also capable of system economic assessment and LCCP evaluation, however, this paper focuses on the calculation of primary energy consumption and CO_2 emissions. The simulation models are composed of continuity and energy equation in each equipment and the heat transfer performance of the heat exchangers was analyzed as pinch temperature. Details of evaluation assessment are referred to Jeong.[3]

Table 1. Basic pattern of system configuration

Type No.	Conventional type	Heat pump introduction type
Type1 ・Non-circulation ・Replacement ・High-temperature heat utilization		
Type2 ・Non-circulation ・Replacement ・Simultaneous utilization of heat and cold		
Type3 ・Non-circulation ・Preheating ・High-temperature heat utilization		
Type4 ・Non-circulation ・Preheating ・Simultaneous utilization of heat and cold		
Type5 ・Circulation ・Replacement ・High-temperature heat utilization		
Type6 ・Circulation ・Replacement ・Simultaneous utilization of heat and cold		
Type7 ・Circulation ・Preheating ・High-temperature heat utilization		
Type8 ・Circulation ・Preheating ・Simultaneous utilization of heat and cold		

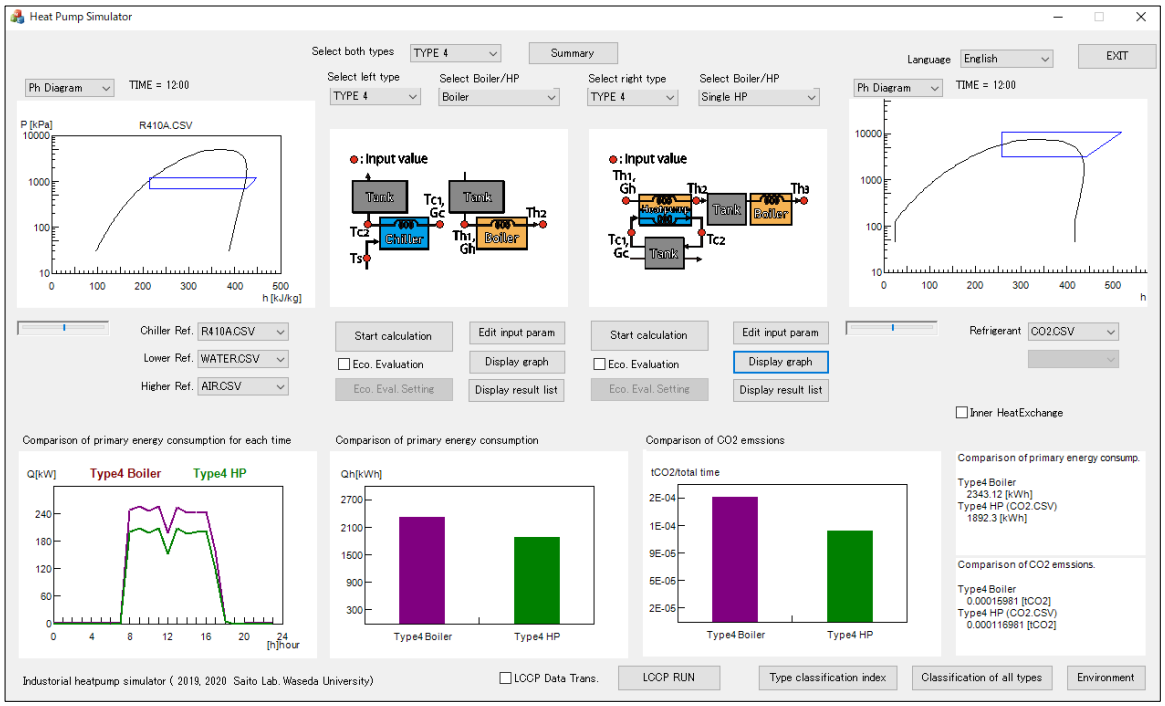
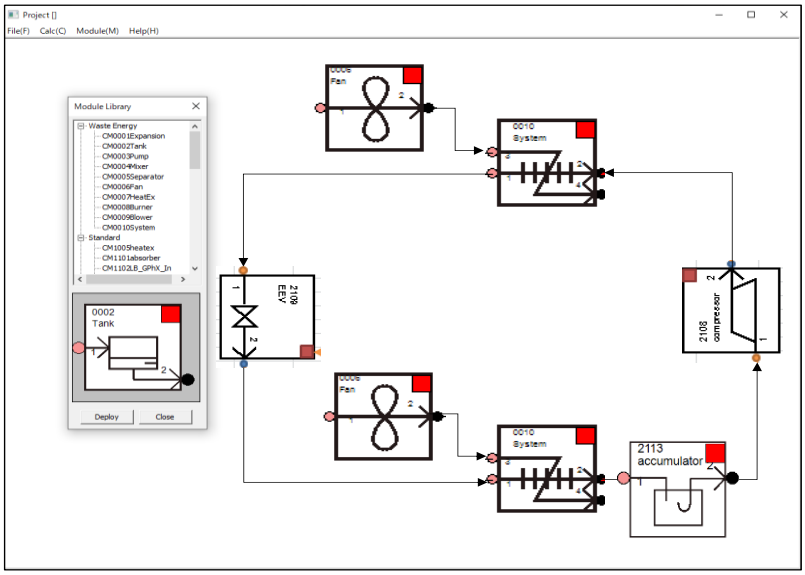


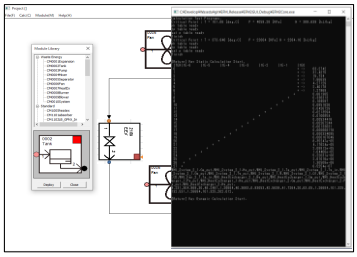
Figure 1. GUI of simplified simulator to compare the effects of installing a heat pump system

2.2. Integrated simulator

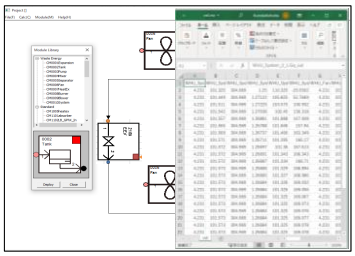
Figure 2 shows GUI of integrated simulator, which features high ability in analyzing the performance of system with various refrigerants, and simulation environment being familiar to engineers and researchers that do not specialize in a simulation on industrial and scientific fields. This simulator extends the capabilities of the simplified simulator to analyze systems with complex configurations and is fully capable of not only designing large-scale heat pump systems, but also predicting and verifying the effectiveness of heat pump installations. As for the tool for examining the performance of air-conditioning systems, a general-purpose energy analysis simulator "Energy Flow+M" has been developed at Waseda University for steady state, dynamic, and control analysis [4-6]. Vapor compression type of air conditioning system expressed by GUI is shown in Figure 2-(a) as an example of simulation. In Figure 2-(b), system simulation is carried on GUI. Figure 2-(c) shows simulation results as output using CSV file. The simulation models are basically the same with those of simplified simulator.



(a) Layout of vapor compression air conditioner



(b) Calculation on GUI



(c) Simulation results on CSV

Figure 2. GUI of integrated Simulator to evaluate the performance of thermal system and effects of installing a heat pump system

Figure 3 shows the analysis process of the integrated simulator. First, the components of the system to be built are selected from the module list and placed on the GUI. Each element or combined pattern is treated as a "module" with its own entrance and exit, and each module is connected to each other with "connections" to construct the system configuration as shown in Figure 2(a). For each of these modules, fixed variables for each device, time-series variables such as temperature conditions, and connection information with each module are stored in xml format, and when the system calculation is executed, the information in the xml file is passed to the calculation main core side. The system is then simulated using the necessary physical properties and convergence algorithms. The final result of the analysis is an environmental assessment of the primary energy consumption and CO_2 emissions of the system and an economic assessment of the life cycle cost. In this paper, it focuses on the calculation of primary energy consumption and CO_2 emissions.

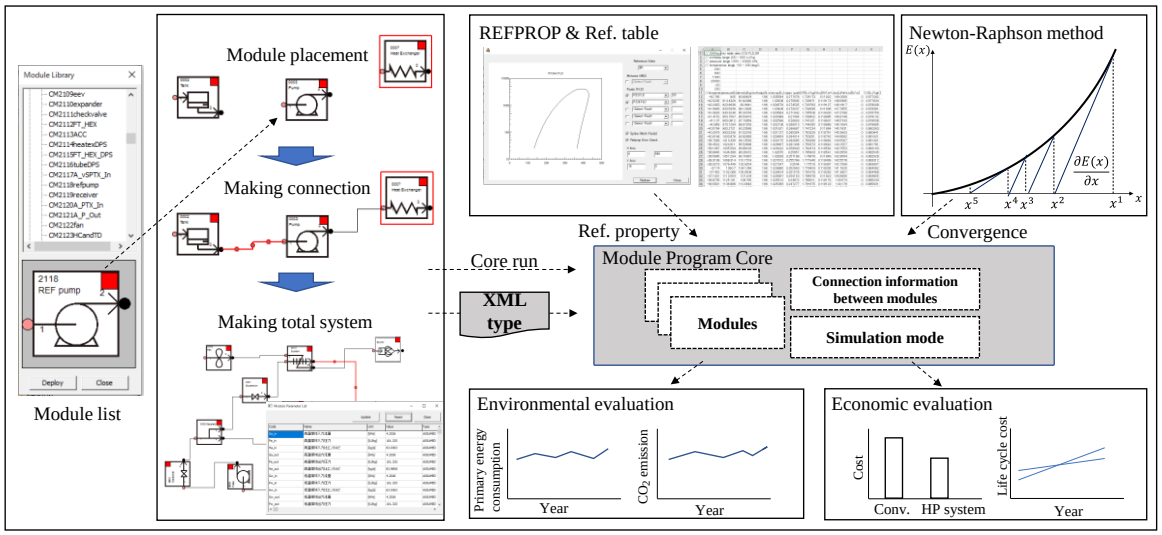


Figure 3. Simulation process of “Integrated simulator” on GUI

3. Simulation example of each simulator

3.1. Objective system

The objective system shown in Figure 4 is a paint drying system in a certain factory. In contrast to conventional combustion-type heating, this system uses a heat pump with CO_2 refrigerant for preheating to generate high-temperature hot air, which is preheated to 90-100°C with the heat pump by the heat pump by taking in outside air at around 15°C, and the heated air is further heated to 170°C by the burner. This system consists of a chiller, a heat exchanger, a burner, and a fan in addition to the heat pump, with multiple heat sources heating and cooling materials in different temperature zones.

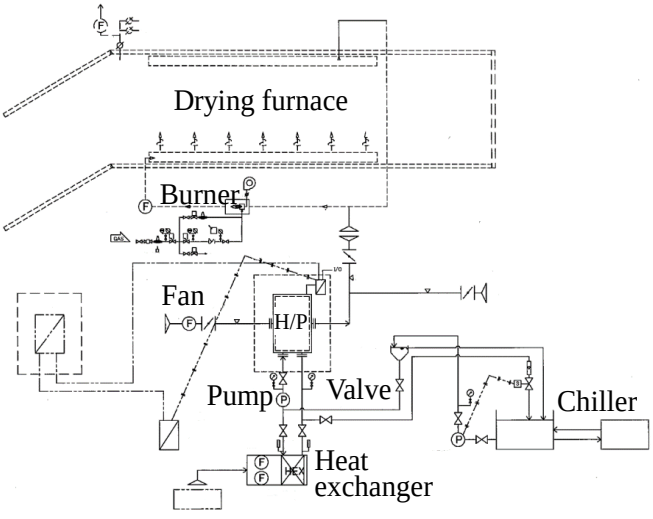


Figure 4. Flow of the target factory

Figure 5 shows annual actual operation data for the objective system with a heat pump as shown in Figure 4, including the temperature and airflow rate of the fan on the hot-air process side, the temperature of the heated hot-air from the heat pump at about 100°C, and the temperature of the hot-air provided by the burner to the drying furnace at about 170°C. Compared to a conventional combustion system, the heat pump is used to raise the temperature from the ambient air to about 100°C. When assessing environmental and economic performance using the simulators, the actual operation data shown in Figure 5 are used as input values for analysis, and energy consumption is calculated to evaluate the effect of the heat pump installation. The heat pump installation system operates for approximately 11 hours from 7:00 to 18:00 on weekdays, with system shutdown on weekends and holidays.

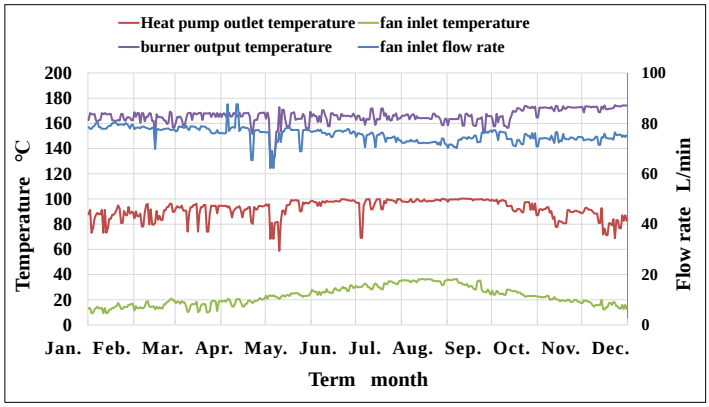
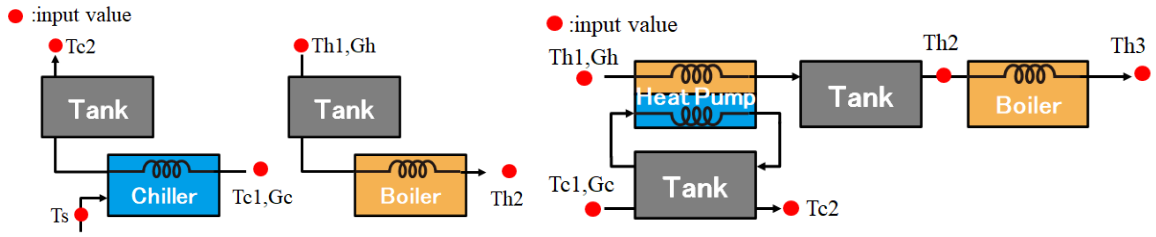


Figure 5. Annual actual operation of heat pump installation system

3.2. Analysis by simplified simulator

For analysis of objective system, the simplified simulator enables evaluating the effects of introducing the industrial heat pump proposed above. The classification for simulation described in Table 1 corresponds to Type 4. This type is without hot water circulation between heat pump and tank and heat pump is for use of preheating in front of boiler or burner to get the target temperature into drying furnace. In addition, to operate efficiently this system, cold and hot water are utilized for drying furnace and electrodeposition process by the heat exchanger in Figure 4. Figure 6 shows the setting of input values for conventional type and heat pump introduction type. Power consumptions are calculated by these input values, for example, final target temperature (Tc1, Th2, Tc2, Th3), environmental air temperature (Th1), air flow rate (Gh), cooling water temperature (Ts), chilled water temperature(Tc1), chilled water flow rate (Gc).



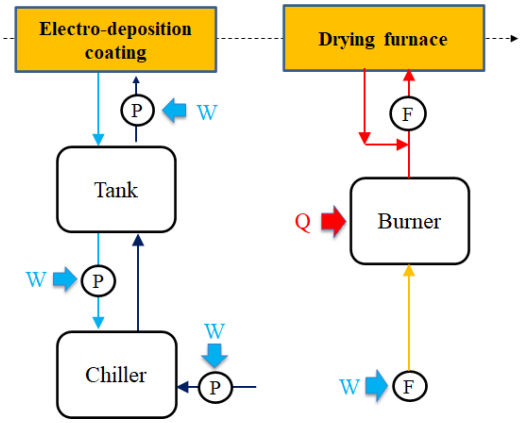
(a) Conventional type (b) Heat pump introduction type

Figure 6. System type classification for simplified simulator

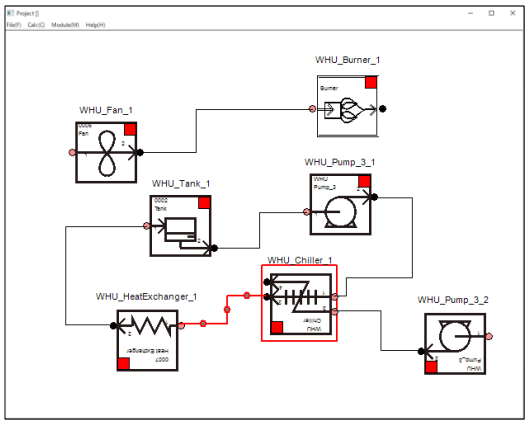
3.3. Analysis by integrated simulator

The integrated simulator is based on the concept of modular analysis as a general-purpose analytical theory for energy systems, particularly thermal-fluid systems. This theory enables the numerical analysis of a wide variety of energy systems using a unified method, and Figure 7(a) shows a flow diagram of a chiller and burner used in conventional industrial process cooling and drying processes. To analyse these systems, the modules of each component of the system are arranged on the graphic user interface (hereinafter referred to as GUI) of the integrated simulator, as shown in Figure 7(b). Figure 7(c) shows a flow diagram of a system that simultaneously utilizes cold and heat by introducing a heat pump, in contrast to the conventional system shown

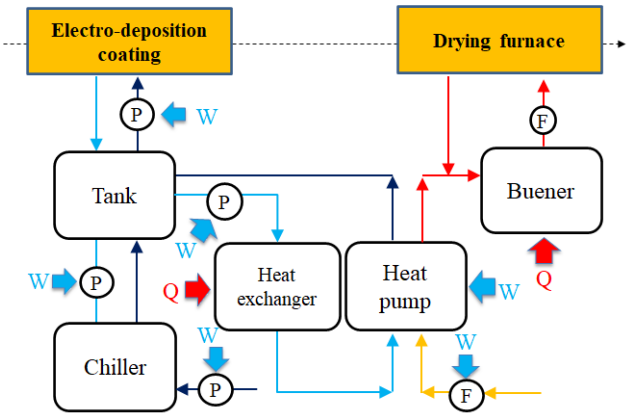
in Figure 7(a). Figure 7(d) shows this system represented as a module of each element in the GUI of the integrated simulator. As shown in Figure 7(b) and Figure 7(d), the integrated simulator was developed in the C++ language, and the GUI was designed to simplify the main screen and make the calculation procedure easy to understand. In addition, the code is structured in a calculation core with independent system analysis, module analysis, convergence calculation, refrigerant properties, and other sections, making it easy to modify and add to the code. The code incorporates a new convergence calculation method to increase speed, and maps refrigerant properties based on the latest REFPROP to improve accuracy and increase speed.



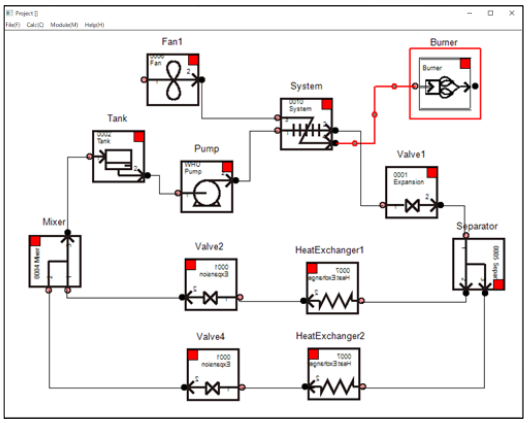
(a) Conventional industrial drying system



(b) Conventional industrial drying system on GUI



(c) Industrial heat pump drying system



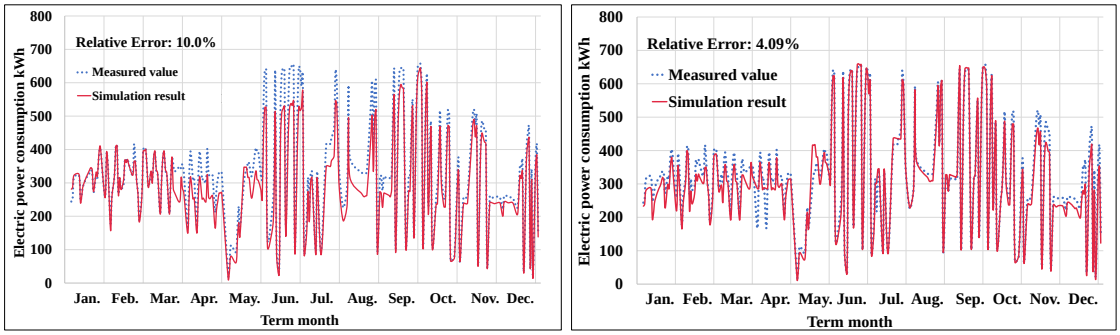
(d) Industrial heat pump drying system on GUI

Figure 7. Flow diagram and expression on integrated simulator of conventional and heat pump introduction industrial drying system

3.4. Simulation results by simplified simulator and integrated simulator

3.4.1. Comparison of simulation results and field data

Figure 8 compares the simulated and measured power consumption of heat pump only by simplified simulator and of heat pump and auxiliary equipment by integrated simulator on a monthly power basis. Integrated simulator considered pump and fan power consumption as auxiliary equipment in addition to heat pump power consumption. The actual measured daily power consumption values used for verification are accumulated as kWh, and data for 365 days are shown. For the simulator analysis, calculations are performed at one-hour intervals throughout the year and compared with the actual measured data. The time required for analysis by the simplified simulator and integrated simulator is about 2 minutes (based on Intel(R) Core(TM) i5) and 7 hours (based on Intel(R) Core(TM) i5) respectively. For the integrated simulator, considering the user's environment, it is assumed that the analysis results can be checked when the user finishes work in the evening and starts work the next morning. The accuracy of the calculation was about 10.0% and 4.1% relative error, confirming the validity of the analysis using the simplified and integrated simulator, respectively.

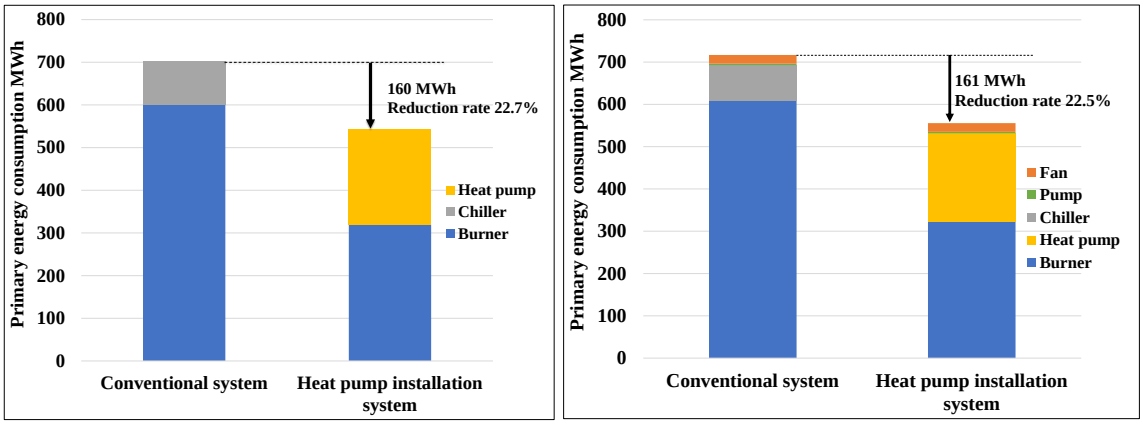


(a) Result by simplified simulator (b) Result by integrated simulator

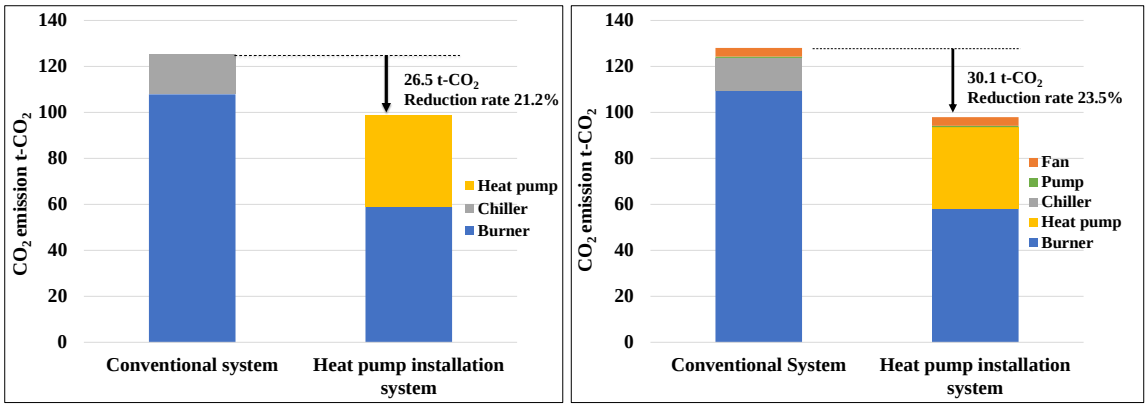
Figure 8. Comparison of simulation and measurement results on electric power consumption of heat pump installation system

3.4.2. Environmental evaluation

The introduction of heat pumps into the industrial heat system field is expected to save energy in industrial processes. This chapter presents a quantitative comparison and evaluation of the degree to which the introduction of heat pumps can save energy and reduce CO_2 emissions for the entire system compared to conventional combustion-type heating equipment such as boilers and burners. The primary energy consumption and converted CO_2 emissions are compared between the conventional system and the heat pump system, including the gas consumption by the gas burner. To calculate the primary energy consumption, the energy conversion efficiency of thermal power generation is 36% and that of burners and boilers is 90%. For the calculation of CO_2 emissions, the emission factor for electricity is set to 0.000462 [t-CO2/kWh] [7] and that for city gas to 0.00017964 [t-CO2/kWh] [7]. Fig. 9(a) and Fig. 9(b) show the monthly primary energy consumption of the conventional system and the system with heat pumps. In the results, it was found that the calculation results of the simplified simulator and the integrated simulator were almost identical, with the only difference being the presence or absence of power consumption by the auxiliary equipment-pump and fan.



(a) Result on primary energy consumption by simplified simulator (b) Result on primary energy consumption by integrated simulator



(c) Result on CO_2 emission by simplified simulator (d) Result on CO_2 emission by integrated simulator

Figure 9. Comparison of conventional and heat pump installation system on primary energy consumption and CO_2 emission

As shown in Fig. 9(a) and Fig. 9(b), although the heat pump system provides the chiller's cooling capacity for the conventional system, the heat pump provides heating up to about 100°C out of the heating capacity of the gas burner up to 170°C. Therefore, the reduction effect cannot be said to be large. Fig. 9(c) and Fig. 9(d) show the monthly CO_2 emissions of the conventional system and the system with heat pumps in the simplified and integrated simulators. It can be seen that CO_2 emissions are reduced by using a heat pump for preheating, which is more efficient than a gas burner, even though the electricity emission factor is about 2.5 times larger than the city gas emission factor.

Based on the above results, it is not important which simulator is better between the simplified simulator and integrated simulator that have been developed so far. The simplified simulator can be effectively used to estimate the effect of installing a heat pump in a short calculation time. The integrated simulator should be used for system design purposes when the energy distribution of the entire system, including auxiliaries, and greater calculation accuracy are required. In this way, we believe that the real strength is found in using different simulators according to the user's application.

4. Conclusions

In this study, we developed a "Simplified simulator" and an "Integrated simulator" that can study the effects of introducing heat pumps from both environmental and economic perspectives in order to help expand the use of heat pumps in the industrial field toward the targeted energy conservation.

As a result of the verification of the accuracy of the analysis, it became possible to calculate with a relative error of approximately 10.0% on simplified simulator and 4.1% on integrated simulator from the annual measured values of the objective system. In addition, a comparison study was conducted between a conventional combustion-type system and a system with a heat pump, and the effects of the introduction were quantitatively compared and evaluated in terms of environmental performance indicators such as energy consumption and CO_2 emissions. This means that the simplified simulator and the integrated simulator can contribute to improving the efficiency of existing systems in the industrial field. Especially, the integrated simulator extends the capabilities of the simplified simulator to analyze systems with complex configurations and is fully capable of not only designing large-scale heat pump systems, but also predicting and verifying the effectiveness of heat pump installations.

Looking ahead, we will continue to develop these simplified and integrated simulators to increase its usefulness and practicality.

Acknowledgements

These results were obtained as a result of the commissioned work (JPNP15007) of the New Energy and Industrial Technology Development Organization (NEDO), and we would like to express our gratitude to all concerned.

References

[1] Industrial Heat Pump Exposition, 2020. New Energy and Industrial Technology Development Organization (NEDO), https://www.nedo.go.jp/content/100925495.pdf. (in Japanese)
[2] J. Jeong, S. Muto, Y. Miyaoka, K. Saito, “Economic and environmental assessment of integrated industrial heat pump simulator”, JSRAE Annual Conference, 2022, Sep. 7-9, Okayama, Japan, A22. (in Japanese)
[3] J. Jeong, Y. Miyaoka, S. Yamaguchi, K. Saito, “Categorization of industrial heat pump for integrated simulation technology”, 13th IEA Heat Pump Conference, 2021,April 26-29, Jeju, Korea, 322.
[4] Ohno K, Saito K, Yamaguchi S, Kishimoto T, Matsumoto K. Intermittent driving simulation of compression type heat pump-1st report: Mathematical model and simulation of single-stage vapor compression type heat pump. *Trans. JSRAE* 2013;**30(2)**:107-122.
[5] Saito K, 2016. “Unified Refrigeration Cycle Evaluation Simulator with Various Refrigerants,” Proceedings of the JRAIA international Symposium 2016, Tokyo, Japan, Japan, pp.369-372.
[6] Saito K, Jeong J. Development of General Purpose Energy System Simulator. *Energy Procedia* 2012;**14**:1595-1600.
[7] Greenhouse Gas Emissions Calculation, Reporting and Publication System, Ministry of the Environment, http://www.env.go.jp/earth/ghg-santeikohyo/index.html, (2021). (in Japanese)

14th IEA Heat Pump Conference
15-18 May 2023, Chicago, Illinois

Design methodology of vapor compression heat pump module in Smart Thermal Energy Design platform

Bong Seong Oh[a], Gilbong Lee[a], Bongsu Choi[a], Hyungki Shin[a], Young-Jin Baik[a], Beomjoon Lee[a], Jongjae Cho[a], Gyunchul Hur[a], Sun Ik Na[a], Ho-Sang Ra[a], Eunseok Wang[a], Min Soo Kim[b], Junhyun Cho[a,*],

[a]Korea Institute of Energy Research, Gajeong-ro 152, Yuseong-gu, Daejeon, 34129, Republic of Korea

Abstract

A design platform, namely Smart Thermal Energy Design Platform (STED platform), for thermal energy-intensive industrial facilities is being developed for any user with an intuitive interface and smart guide during design process. Among design modules in STED platform, the vapor compression heat pump design module gives suitable design results for heat pumps under the given operation conditions. The module can model three heat pump layouts: basic, internal heat exchanger, and injection. To validate the design results from the module, a lab-scale heat pump experimental device, namely heat pump simulator, was made based on the calculation results from the heat pump design module. As a result, the calculated performance from the platform and the measured performance from the simulator had an error of 0.1% in terms of mean COP for 30minutes.

© HPC2023.
Selection and/or peer-review under the responsibility of the organizers of the 14th IEA Heat Pump Conference 2023.

Keywords: Heat pump design algorithm, Internal Heat Exchanger, Injection, Design validation;

1. Introduction

According to the global energy-related CO_2 emissions by sector from IEA data [1], industry sector occupies 23% of total global CO_2 emissions. In 2021, the sector accounted for 38% (169EJ) of total global final energy use, and the fraction of fossil fuel energy in the whole industry sector final energy use was about 68% [2]. To reduce the emissions in the sector, fossil fuel based thermal systems like boilers should be electrified. Reported by Net Zero Roadmap [3], electricity share in light industry should be 76% to accomplish net zero until 2050. Heat pumps could be a great option to electrify the industrial heat because compared to electric heaters heat pumps can generate a few times of generate process heat by inputting a same electric power. Many previous works reported that energy consumption in the industrial sector could be saved about 40 to 60% if process heat under 200℃ that is utilized in most industrial sectors is replaced with heat pumps [4] [5] [6] [7] [8]. Despite these benefits of heat pumps, there is a lack of holistic design algorithms for heat pump systems because they involve various combinations of design parameters, such as cycle layouts, specifications of sub-components, refrigerants, and degrees of superheating and subcooling, and so on [9]. Thus, it is hard for small-, and medium-sized enterprises to design their own heat pump systems because they generally have deficient R&D infrastructure and insufficient capital to pay the license fees of state-of-the-art design platforms to enhance the performance of heat pumps. According to Meng et al. [10], these enterprises approximately accounted for 50% of CO_2 emissions, so that improving the performance of heat pumps used by small-, and medium-sized companies could contribute to reduction of CO_2 emissions in industry sector. To solve the problem, the latest national R&D technologies should be efficiently disseminated to those enterprises.

Smart Thermal Energy Design platform, namely STED platform could be a solution to provide preliminary design results of the thermal energy-intensive facilities such as burners, furnaces, dryers, heat exchangers, and

* Corresponding author. Tel.: +82-42-860-3581;
E-mail address: jhcho@kier.re.kr.

heat pumps to the energy consumers or vendors. Among variety of design modules, heat pump design module could treat three kinds of heat pump layouts which are basic, internal heat exchanger, and injection. In this study, the design algorithms of the layouts were suggested, and the design result of basic layout were validated with experimental test loop for heat pump design module, namely heat pump simulator.

2. Design algorithms for various heat pump layouts

At the first step to design heat pump cycle, inputs are applied into specifications of major components in a heat pump system should be inputted as listed in Table 1.

Table 1. Input list for heat pump design

Category	Input parameters	Symbol
Inputs of hot process (condenser)		
	Mass flow rate	$\dot{m}_h$
	Pressure	P_h
	Inlet temperature	T_{hi}
	Outlet temperature	T_{ho}
Inputs of cold process (evaporator)		
	Mass flow rate	$\dot{m}_c$
	Pressure	P_c
	Inlet temperature	T_{ci}
	Outlet temperature	T_{co}
Inputs of major components		
Basic cycle input *Commonly used in other layouts	Approach temperature (Plate type HX)	ΔT_{pp}
	LMTD (Fin type HX)	ΔT_{lmtd}
	Pressure drop in HX channels	ΔP
	Degree of superheat	ΔT_{sh}
	Degree of subcooling	ΔT_{sc}
	Isentropic efficiency of compressor	η_{comp}
IHX cycle input	Internal HX effectiveness	ε_{IHX}
Injection cycle	Isentropic efficiency of 2nd compressor	$\eta_{comp,2}$

The heat pump design module adopts CoolProp database for utilizing fluid properties [11], but not all fluids are not considered a refrigerant in a heat pump users intend to design owing to the computational resource problem. Instead, the appropriate refrigerants are dynamically selected from the list according to the temperature of process fluid, and the specifications of an evaporator and condenser like approach temperature and LMTD. In the condenser, a refrigerant with high pressure is condensed by the hot-side process fluid such that the critical temperature of the refrigerant is higher than the temperature of the hot-side process fluid considering the pinch point, as shown in Eq.(1). In the evaporator, a refrigerant with low pressure is evaporated by the cold-side process fluid. The refrigerant pressure in the evaporator should be higher than the ambient pressure because of the purity problem in the heat pump system. Thus, the saturation temperature of the ambient pressure considering the pinch point should be lower than that of the cold-side process fluid, as expressed in Eq.(2).

$$T_{crit} > T_{ho} + \triangle T_{pp,cond} \quad (1)$$

$$T_{NBP} < T_{co} + \triangle T_{pp,evap} \quad (2)$$

This is because heat pumps designed by the module should be a subcritical vapor compression heat pump.

2.1. Basic layout

A heat pump system with basic layout is composed of an evaporator, compressor, condenser, and expansion valve. Initially, low pressure and high pressure of the refrigerant in evaporator should be estimated considering atmosphere pressure, critical pressure, and process temperatures. The saturation temperature in evaporator can be calculated from the estimated low pressure by CoolProp database. Adding the superheat inputted by a user to the saturation temperature, the evaporator outlet temperature (i.e. compressor inlet) can be obtained. From the pressure ratio of estimated high to low pressure, and the entered isentropic efficiency of a compressor, the compressor outlet state (i.e. condenser inlet) can be calculated as shown in Eq.(3)(4).

$$T_{comp_in} = T_{sat@P_{evap}} + \Delta T_{sh} \tag{3}$$

$$h_{comp_out} = \left(1 - \frac{1}{\eta_{comp}}\right) h_{comp_in} + \frac{h_{comp_out_ideal}}{\eta_{comp}} \tag{4}$$

The saturation temperature in condenser can be calculated from the assumed high pressure of refrigerant in condenser, and the condenser outlet temperature can be obtained by subtracting degree of subcooling from the saturation temperature in condenser as written in Eq.(5). After condenser inlet and outlet temperature are defined, mass flow rate of the system can be calculated by energy conservation between refrigerant side and process fluid side as shown in Eq.(6)(7). The subscripts 'hot_in,sec' and 'hot_out,sec' mean the inlet and outlet state of hot secondary flow like water and air in condenser. However, the approach temperature point in condenser does not usually exist at the channel inlet or outlet as single-phase heat exchangers do. This is because phase change occurs on refrigerant side in condenser while do not happened in process fluid side. To search the approach temperature in channels, the condenser channel should be divided into finite discrete nodes, and each state can be obtained based on energy conservation equation as shown in Figure. 1. Comparing the calculated approach temperature of condenser to the approach temperature inputted by a user, the error can be defined as Eq.(8). If the error is not met under the entered tolerance, the high pressure in condenser is adjusted until satisfying the convergence tolerance.

$$T_{cond_out} = T_{sat@P_{cond}} - \Delta T_{sc} \tag{5}$$

$$Q_{cond} = \dot{m}_{hot,sec}(h_{hot_out,sec} - h_{hot_in,sec}) \tag{6}$$

$$\dot{m}_{ref} = Q_{cond}/(h_{cond_in} - h_{cond_out}) \tag{7}$$

$$\varepsilon > \left|\Delta T_{pp,cond} - \Delta \hat{T}_{pp,cond}\right| \tag{8}$$

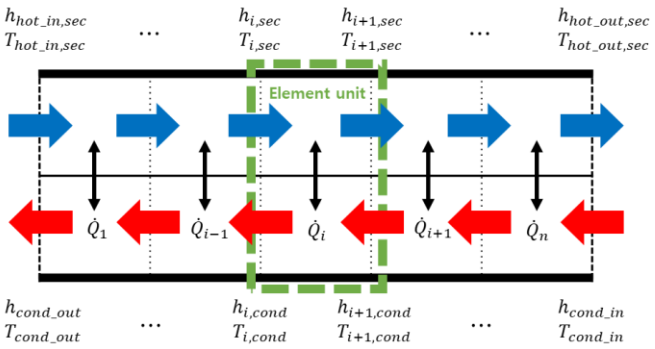


Figure. 1. Internal channel calculation of condenser using finite discrete nodes

After the condenser outlet state is obtained, through expansion valve, evaporator inlet state can be calculated through with isenthalpic process of the condenser outlet state to the low pressure as expressed in Eq,(9).

$$T_{evap_in} = f(P_{evap}, h_{cond,out}) \tag{9}$$

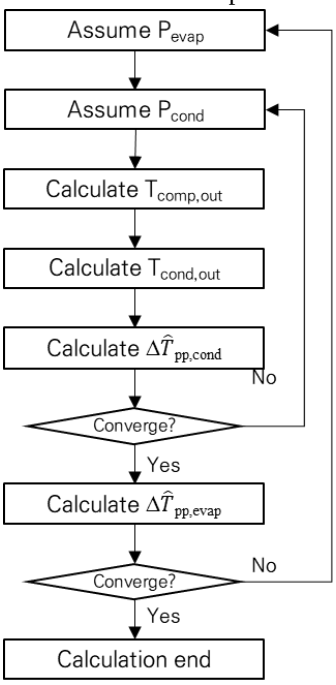
Thus, evaporator inlet and outlet can be determined, and the approach temperature of evaporator is also calculated by the finite discrete nodes method similar to the condenser as shown in Eq.(10)(11)(12). The subscripts 'cold_in,sec' and 'cold_out,sec' mean the inlet and outlet state of cold secondary flow like water and air in evaporator. The error of evaporator's approach temperature is a criterion to judge the convergence of low pressure in evaporator.

$$Q_{evap} = \dot{m}_{ref}\left(h_{evap_out} - h_{evap\,in}\right) \tag{10}$$

$$h_{cold_out,sec} = h_{cold_in,sec} - Q_{evap}/\dot{m}_{cold,sec} \tag{11}$$

$$\varepsilon > \left|\Delta T_{pp,set} - \Delta T_{pp,evap}\right| \tag{12}$$

When both the approach temperature errors of condenser and evaporator are under the user inputted tolerance,



the cycle design is completed. Figure.2 shows the flow chart for designing a basic layout heat pump.

2.2. Internal heat exchanger layout

The design algorithm of IHX heat pump is basically identical with that of the basic layout heat pump but the evaporator outlet and condenser outlet transfer their heat through IHX, so the superheat at the compressor inlet and subcooling at the expansion inlet is more enhanced by the IHX. In the IHX channels, the phases of condenser and evaporator are both single phase. Therefore, the transferred heat can be calculated based on the effectiveness of IHX inputted by a user. Eq.(13) to (18) show the calculation process of IHX cold side and hot side states.

$$T_{\mathrm{IHX}_ci} = T_{sat@P_{evap}} + \Delta T_{sh} \tag{13}$$

$$T_{\mathrm{IHX}_hi} = T_{sat@P_{evap}} - \Delta T_{sc} \tag{14}$$

$$q_{\mathrm{ideal}} = \min\left(h_{\mathrm{IHX}_hi} - h_{\mathrm{IHX}_ho}^{ideal},\ h_{\mathrm{IHX}_co}^{ideal} - h_{\mathrm{IHX}_ci}\right) \tag{15}$$

$$q_{actual} = \varepsilon_{IHX} q_{\mathrm{ideal}} \tag{16}$$

$$h_{IHX_co} = h_{IHX_ci} + q_{actual} \tag{17}$$

Figure.2. Design algorithm of basic layout heat pump

$$h_{IHX_ho} = h_{IHX_hi} - q_{actual} \tag{18}$$

Figure.3 shows the design algorithm of a IHX layout heat pump.

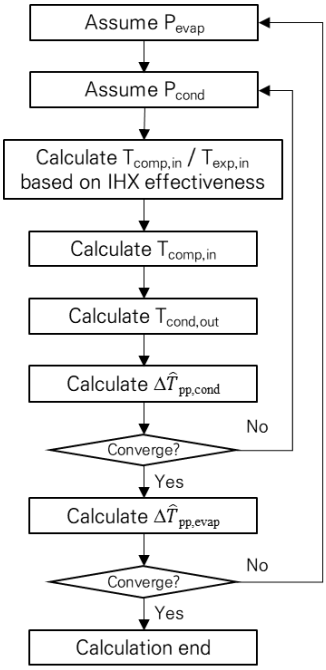


Figure.3. Design algorithm of IHX layout heat pump

2.3. Injection layout

An injection layout heat pump does not directly expand from the high pressure at condenser to the low pressure at evaporator, but there is a flash tank with intermediate pressure between condenser and evaporator. Thus, when the high pressure fluid expands in flash tank, the subcooled refrigerant at the condenser outlet changes saturated state, so that saturation gas partly appears in the tank in Eq.(19). Bypassing the gas to the middle of compression process in a compressor, consumption work of the compressor is substantially decreased due to the intercooling of the compression process in Eq.(20). Remarkably, as intermediate pressure changes, the injection layout heat pump has optimal performance point as illustrated in Figure.4.

$$x_{fsh} = f(P_{inter}, h_{cond_out}) \tag{19}$$

$$h_{comp2_in} = x_{fsh} h_{fsh_v} + (1 - x_{fsh}) h_{comp1_out} \tag{20}$$

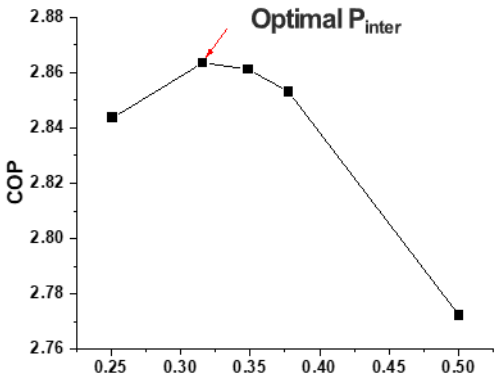


Figure.4. Optimal intermediate pressure for maximal COP

Figure.5 shows the flow chart of injection layout heat pump.

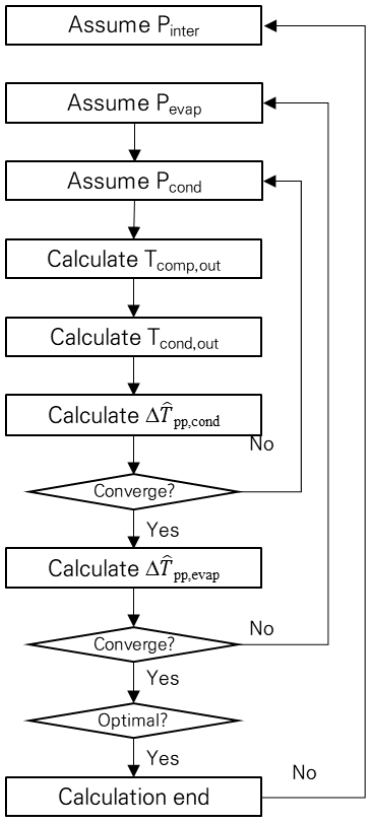


Figure.5. Design algorithm of injection layout heat pump

3. Heat pump simulator

To validate the calculation results from the heat pump design module in STED platform, a simulator was built. The simulator is composed of a compressor, plate type condenser and evaporator, and EEV. The compressor is a twin rotary (two cylinder rolling piston type) with hermetic motor, and PVE oil. Temperatures are measured by RTD with 1/16-inch probe, and pressures of compressor inlet and outlet are measured by high accuracy pressure transmitter with FS ±0.075%. Coriolis flow meter is adopted to obtain the mass flow rate in the system. Figure.5 shows the picture of simulator for heat pump design module in STED platform.



Figure.6. Picture of simulator for heat pump design module in STED platform

The monitoring system of the simulator was implemented by Labview 2020 version. The heat pump design platform was embedded in the Labview, so that the platform results and measurements directly compared on the monitoring system. In Figure.7, the center PFD shows the schematic flow lines of the simulator, and the left side the comparison results of platform calculation and measurements. Especially, the cycle states can be expressed by TS and PH diagrams, and the blue line represents the platform results and red lines shows the measurements from the simulator. They show high agreement between platform and simulator. Moreover, calculating the COPs calculated from the platform and measured from the simulator, the estimated error was only 0.1% with average of 30 minutes. Table 2 shows the differences of major parameters between calculation from the platform and measurements from the simulator. Due to the measurement error of power meter, the compression work showed the largest deviation. Coincidently, the measurement of evaporation heat is also smaller than the calculation so that COP has extremely low error. The difference of subcooling is not reported because the condenser outlet of refrigerant side is in the saturated state so that it is hard to compare the calculation of subcooling to the measurement.

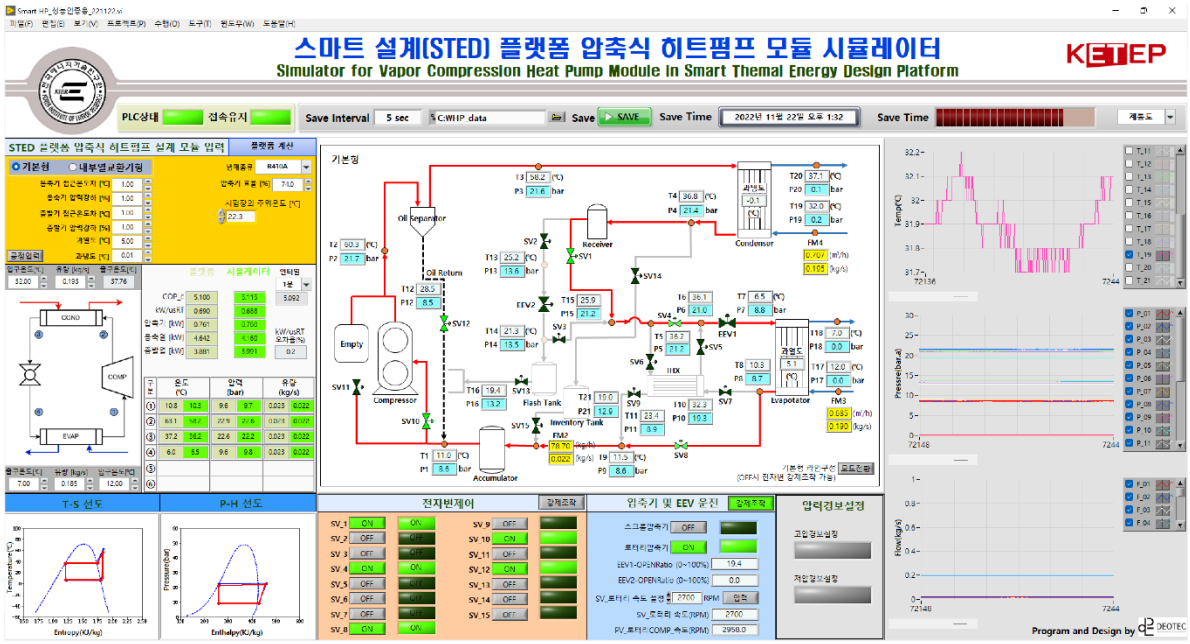


Figure.7. The monitoring system of the simulator

Table 2. Absolute errors between calculation results and measurements

Parameters	Calculation results	Measurements	Differences [%]
COP	5.1	5.093	0.14
Evaporation heat	3.89 kW	4.05 kW	4%
Compression work	0.761 kW	0.795 kW	4.4%
Evaporating pressure	9.6 bar	9.68 bar	0.8%
Condensing pressure	22.9 bar	22.5 bar	1.9%
Superheat	5 ℃	5.17 ℃	3.5%

4. GUI of heat pump design module

After the results of the heat pump design module was demonstrated, the platform was visualized by PyQt5 module in Python library. The first step is selecting heat pump layout a user wants to design. At the next step, the user enter the required inputs as listed in Table 1. Finishing the calculation, the results are summarized with the refrigerant states, and essential diagrams.

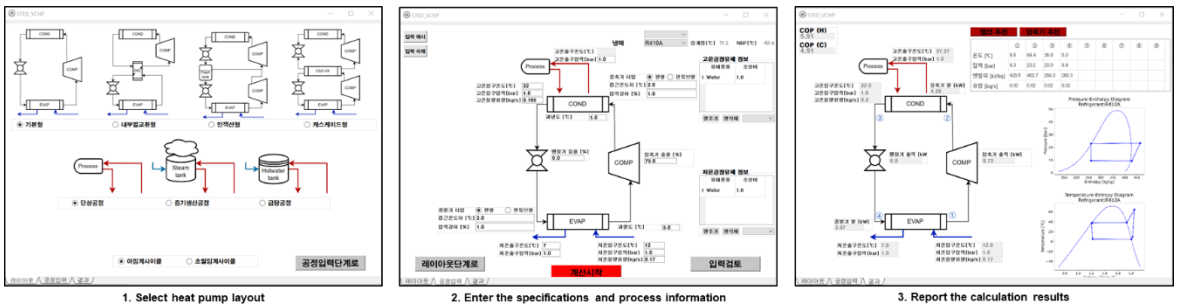


Figure.8. GUI manual

5. Results

To respond to demands for developing user-friendly design platform, Smart Thermal Energy Design platform was developed. Among the thermal energy-intensive facilities the platform treats, the heat pump module algorithms were discussed in this study. Basic, internal heat exchanger, and injection cycles are dealt with, and basic layout heat pump was validated by the simulator with mean error of 0.1%. Thus, the heat pump design module in the platform can provide accurate design results to users.

Acknowledgements

This work was supported by the Korea Institute of Energy Technology Evaluation and Planning (KETEP) and the Ministry of Trade, Industry & Energy (MOTIE) of the Republic of Korea (No. 20202020800200, Development and demonstration of smart design platform technology for thermal energy-instensive industrial facilities).

References

[1] "IEA, Global energy-related CO2 emissions by sector, IEA, Paris." https://www.iea.org/data-and-statistics/charts/global-energy-related-co2-emissions-by-sector, IEA. Licence: CC BY 4.0.

[2] "IEA, Final energy consumption by fuel in the Net Zero Scenario, 2000-2030, IEA, Paris." https://www.iea.org/data-and-statistics/charts/final-energy-consumption-by-fuel-in-the-net-zero-scenario-2000-2030, IEA. Licence: CC BY 4.0.

[3] S. Bouckaert *et al.*, "Net Zero by 2050: A Roadmap for the Global Energy Sector," 2021.

[4] A. K. Jana and A. Mane, "Heat Pump Assisted Reactive Distillation: Wide Boiling Mixture," *AIChE J.*, vol. 57, no. 11, 2011, doi: 10.1002/aic.12518.

[5] M. Yang, X. Feng, and G. Liu, "Heat integration of heat pump assisted distillation into the overall process," *Appl. Energy*, vol. 162, pp. 1–10, 2016, doi: 10.1016/j.apenergy.2015.10.044.

[6] S. Singh and M. S. Dasgupta, "CO2 heat pump for waste heat recovery and utilization in dairy industry with ammonia based refrigeration," *Int. J. Refrig.*, vol. 78, pp. 108–120, 2017, doi: 10.1016/j.ijrefrig.2017.03.009.

[7] Y. Liu, E. A. Groll, K. Yazawa, and O. Kurtulus, "Energy-saving performance and economics of CO2 and NH3 heat pumps with simultaneous cooling and heating applications in food processing: Case studies," *Int. J. Refrig.*, vol. 73, pp. 111–124, 2017, doi: 10.1016/j.ijrefrig.2016.09.014.

[8] B. Zühlsdorf, F. Bühler, R. Mancini, S. Cignitti, and Brian Elmegaard, "High Temperature Heat Pump Integration using Zeotropic Working Fluids for Spray Drying Facilities," *Proc. 12th IEA Heat pump Conf.*, no. July, pp. 1–11, 2017.

[9] J. F. Horn and P. H. Scharf, "Design Considerations for Heat Pump Compressors," *Int. Compress.*

Eng. Conf. Sch., pp. 194–201, 1976.

[10] B. Meng *et al.*, "More than half of China's CO2 emissions are from micro, small and medium-sized enterprises," *Appl. Energy*, vol. 230, no. September, pp. 712–725, 2018, doi: 10.1016/j.apenergy.2018.08.107.

[11] I. H. Bell, J. Wronski, S. Quoilin, and V. Lemort, "Pure and Pseudo-pure Fluid Thermophysical Property Evaluation and the Open-Source Thermophysical Property Library CoolProp," *Ind. Eng. Chem. Res.*, vol. 53, no. 6, pp. 2498–2508, Feb. 2014, doi: 10.1021/ie4033999.

14th IEA Heat Pump Conference
15-18 May 2023, Chicago, Illinois

Development of a Refrigerant Evaluation Tool for Air Conditioners

Yoichi Miyaoka[a,*], Niccolo Giannetti[b], Jongsoo Jeong[a], Kiyoshi Saito[a], Komei Nakajima[c], Koji Yamashita[c], Shigeharu Taira[c]

[a]Waseda University, 3-4-1 Okubo, Shinjuku, Tokyo, 169-8555, Japan
[b]Waseda University, Waseda Institute for Advanced Study, 1-6-1 Nishiwaseda, Shinjuku, Tokyo, 169-8050, Japan
[c]The Japan Refrigeration and Air Conditioning Industry Association, Tokyo, 105-0011, Japan

Abstract

In order to prevent global warming, there is a strong need to reduce greenhouse gas emissions and energy consumption of refrigeration and air conditioning systems. Various new low-GWP refrigerants are being introduced for air-conditioning equipment, such as residential and commercial air-conditioners. The performance of these new working fluids should be effectively evaluated to select their most suitable implementation case and reduce the environmental footprint of this technological field. The actual operation performance of air-conditioning equipment is substantially affected not only by the system design and the properties of the refrigerant, but also by the climate and load conditions of the specific installation. Therefore, a refrigerant evaluation tool may take advantage from the cost effectiveness and flexibility of a reliable simulation platform but requires standardized calculation conditions for achieving unbiased results. Therefore, a system simulator was hence developed for the analysis of next-generation refrigerants, including zeotropic mixtures. This paper discusses about validity verification results of this evaluation tool based on experimental results and assess the performance of residential air conditioners.

Keywords: air-conditioniner; simulator; low-GWP; LCCP; refrigerant;

1. Introduction

In order to curb global warming, it is necessary to reduce greenhouse gas emissions from the refrigeration and air conditioning sector. The operation of such thermal systems leads to both direct and indirect emissions to the environment throughout their life cycle, from manufacturing, through operation, to disposal. In fact, their fundamental functioning is based on the circulation of a refrigerant through various components such as compressors and heat exchangers where heat, mass and momentum transfer take place in order to supply output cooling/heating capacity. The ratio between the magnitude of this output capacity to the corresponding input energy defines the coefficient of performance of the system, which is ruled by the thermophysical and transport properties of the refrigerant. Additionally, the chemical properties define the GWP of the refrigerant, which is commonly used to assess the corresponding direct emissions. Following the Kigali amendment to the Montreal Protocol, research and development of next-generation low-GWP refrigerants and their safety and risk assessment are underway to provide alternative working fluids for refrigerators, air conditioners, and heat pumps. Accordingly, the development of effective refrigerant evaluation techniques is an essential tool for strategizing the decarbonization of this technological field. Contextually, it has been widely recognized that accounting for the sole GWP value cannot comprehensively evaluate the overall environmental footprint of refrigeration and air-conditioning systems. In fact, these systems consume energy during their entire life cycle for equipment manufacturing, operation, and disposal. Energy supply is accompanied by a series of processes that result into corresponding emissions. Under this viewpoint, when selecting optimal refrigerants, LCCP may better represent the performance and environmental footprint of air conditioners and refrigerators. Contextually, the actual operating performance of refrigeration and air conditioning equipment is greatly

* Corresponding author. Tel.: +81-3-5286-3259-4403; fax: +81-35286-3259.
E-mail address: miyaoka@aoni.waseda.jp.

influenced not only by system design and refrigerant characteristics, but also by the climate, load conditions, and characteristics of the energy supply of the installation site [1]. Therefore, to broadly investigate this spectrum of operating conditions, it is important for refrigerant evaluation tools to be cost-effective, flexible, and unbiased.

Common procedures for selecting next-generation refrigerants are either based on the experimental assessment of drop-in tests [2], where refrigerants are replaced without revisiting system design and control, or on the numerical thermodynamic cycle simulations that are determined solely by the refrigerant's thermophysical properties and neglect a thorough evaluation of the interrelationship between the transport properties of the refrigerant and the performance of the equipment [3]. An unbiased refrigerant evaluation approach should assess the potential of each refrigerant under representative operative conditions while also considering the transport performance, component features, and control parameters of the actual equipment. Therefore, a refrigerant evaluation tool may take advantage from the cost effectiveness and flexibility of a reliable simulation platform but requires standardized calculation conditions for achieving unbiased results. To this aim, this study presents the development of a refrigerant evaluation tool based on the integration of a reliable simulation platform with standardized calculation conditions. The validity of the simulator is verified by experimental results, and the performance of residential air conditioners is simulated under some conditions.

2. Overview of the refrigerant evaluation tool

To define representative calculation conditions, it was necessary to bring together different standpoints from academia and industry. Specifically, standardized analysis conditions and equipment models of the most common refrigeration equipment [4] were constructed in cooperation with the Japan Refrigeration and Air Conditioning Industry Association (JRAIA). In November 2015, the JRAIA founded the Refrigerant Evaluation Working Group to develop a standardized environment and corresponding methodology for refrigerant performance evaluation, thereby eliminating complementary discussions on measurement setup, method and accuracy, and enabling prompt evaluation of the actual potential performance of new refrigerants. This will help minimize conflicts between different research efforts and facilitate the effective selection of refrigerants and the development of energy efficient equipment.

As for the tool for examining the performance of air-conditioning systems, a general-purpose energy analysis simulator "Energy Flow+M" has been developed at Waseda University for steady state, dynamic, and control analysis [5-7]. Specifically, the features of the developed evaluation tool and the experimental verification of its computational accuracy are hereby presented and discussed.

3. Features of the simulator

The development of the simulator "Energy Flow+M" is based on the modular analysis theory to consistently represent different thermal systems using different refrigerants on the same simulation platform for energy analysis (Figure 1). Fundamental transport phenomena, together with the laws of energy conservation, mass conservation, and momentum transfer, make up the mathematical relationships that define each module. From this point of view, heat exchangers, compressors, expansion valves, and accumulators are represented as sets of functions that relate the inlet and the outlet states of the circulating refrigerant. As a result, it is possible to construct the Jacobian matrix of the entire system by interconnecting modules according to the system configuration and interfacing with the external environment. Newton-Raphson method drives the simulation towards convergence in stationary conditions and non-stationary conditions with dynamic parameter modulations. For mathematical details of the model formulation employed for the fundamental modules [5-7].

The modular analysis theory as a general-purpose analysis method focused on thermal fluid energy system Modular analysis. Consequently, it was clarified that the modular analysis theory facilitated the numerical analysis of various thermal energy systems, for example, vapor compression system, absorption system, desiccant system, solar thermal application system, etc. by unified methodology. For this theory, the concept of engineering control methods is put into analysis of the energy systems. The user can analyze the thermal system without mathematical procedure. Large scale smart energy system can be also easily analyzed and the user’s burden to make the simulation code can be reduced by using this simulator.

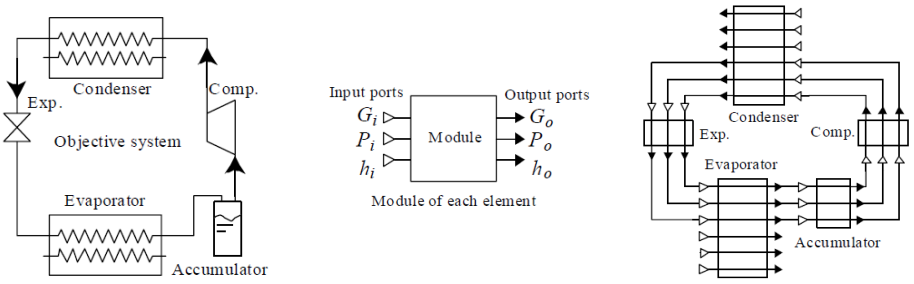


Fig. 1. Conceptual representation of the modular theory adopted for the simulator development

4. Model of the Residential Air Conditioner

Here, we will present the model of a residential air conditioner as a representative example. Single-split residential air conditioner generally feature an independent outdoor unit connected to the indoor heat exchanger with refrigerant pipelines as shown in Figure 2. Additionally, the rotational speed of the compressor and the opening of the expansion valve are adjusted using a PI controller to achieve target room temperature and degree of superheat at the suction of the compressor. The corresponding simulation model is built by assembling compressor, outdoor heat exchanger, expansion valve, accumulator, indoor heat exchanger and extension piping modules according to the reference system characteristics (summarized in Table 1).

Table 1. Reference residential air conditioners characteristics

Refrigerant	Nominal cooling capacity	Extension piping length	Refrigerant charge
R22	2.2 kW	5 m	0.9 kg

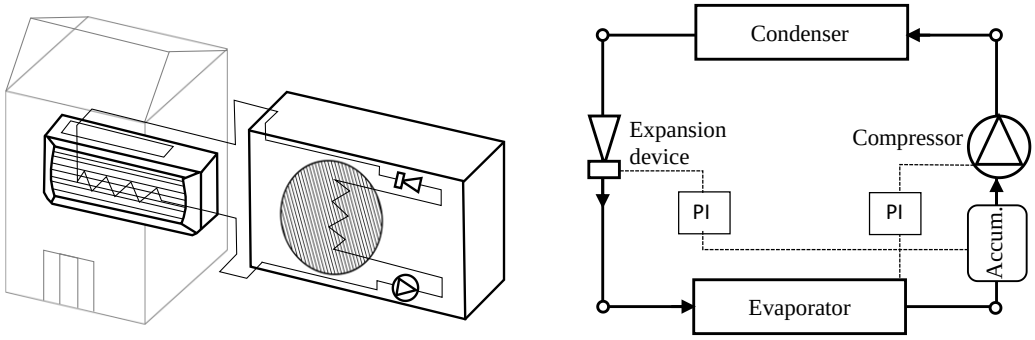
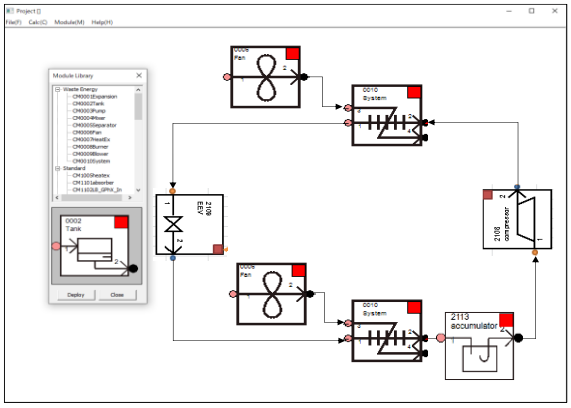


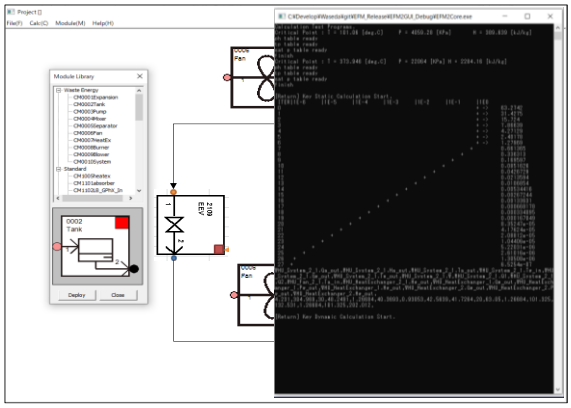
Fig. 2. Illustration of the residential air conditioner system and its flow diagram

5. Characteristics of the GUI

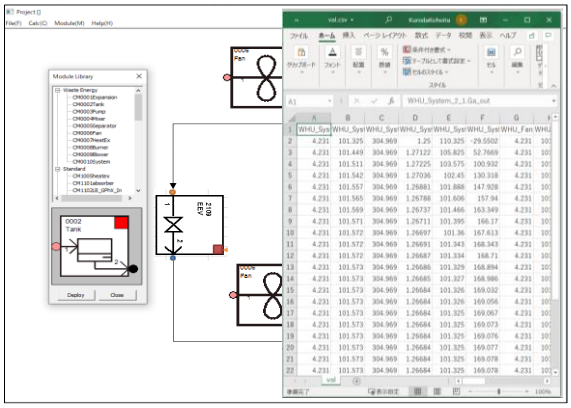
Figure 3 shows the graphic user interface (GUI) of "Energy Flow+M" simulator. The simulation environment makes it user-friendly even to engineers and researchers with minimal background experience in technical and scientific simulations. The combination of modules required to simulate a vapour compression type air conditioning system is shown in Figure 3-(a). Figure 3-(b) shows the appearance of the GUI during system simulations. Figure 3-(c) shows the simulation output in a CSV file format.



(a) Layout of vapor compression air conditioner on GUI



(b) Calculation



(c) Simulation results

Fig. 3. Illustration of the equivalent modular system built in Energy Flow+M

6. Experimental Validation of the Simulation Accuracy

6.1 Experimental test of the air conditioner

6.1.1 Background and purpose of the experiment

When introducing next-generation refrigerants into refrigerating and air conditioning equipment, not only the must the safety and environmental GWP (direct impact) of the refrigerant used in the equipment be considered, but also the impact on global warming owing to energy-derived CO2 emissions (indirect impact). Therefore, the actual operating performance of the refrigerant and air conditioning equipment needs to be evaluated. To fully illustrate the potential of low-GWP refrigerants, an optimized air conditioning unit should be fabricated for each refrigerant and employed to conduct accurate performance tests under actual operating conditions. However, there are a number of next-generation refrigerant candidates; the corresponding financial and time costs required to produce a series of specifically optimized air conditioning units is unrealistic. Therefore, in this study, objective [3] “Simulator development and utilization” was pursued to construct various simulators for heat exchangers and air conditioning systems to shorten the period and cost required for system examination and production. Before using such simulators, the validity and accuracy of the calculated values employed in their construction must be verified. Therefore, the R290 and R454C low-GWP refrigerants were dropped-in to air conditioners designed for use with the R22 refrigerant and their performances were evaluated accordingly.

6.1.2 Overview of the air conditioner used in this experiment

Table 2 shows the specifications of the air conditioner operated during the experimental test. The experimental tests are preliminarily conducted at steady-state for an R22 air conditioner and for drop-in tests of R290 within the same unit.

As the production of the R22 air conditioner had already been discontinued about 10 years ago, it was not possible to obtain a new system. Therefore, tests were conducted on a second-hand wall-mounted room air conditioner with a rated capacity of 2.2 kW. Pressure sensors and thermocouples are installed after thoroughly cleaning the heat exchangers of the outdoor and indoor units. Every time the refrigerant is replaced, the inside

of the refrigerant circuit is cleaned and the refrigeration oil is replaced s with one suitable for each refrigerant, mineral oil for R22 and PAV for R290. In order to measure the refrigerant flow rate, two Coriolis flowmeters were installed for measurements in both cooling and heating modes. In addition, a compressor and expansion valve drive tools were provided by the air conditioner manufacturer to enable free control of the rotational speed of the compressor and free adjustment of the expansion valve opening in 50 steps. Figure 4 shows the mounting positions of the pressure sensors, thermocouples, and refrigerant flow meters. Further details of the equipment and instrumentation of the testing facility are referred to [8]. Fig.4 shows mounting locations of pressure sensors, thermocouples, and flow meters. Figure 5 shows test setup in the dynamic performance evaluation facility.

Table 2. Specification of the room air-conditioner

Item		Contents
Type		Room air-conditioner
Year of manufacture		2001
Original refrigerant		R22
Rated capacity(W)	cooling	2200
	heating	2500

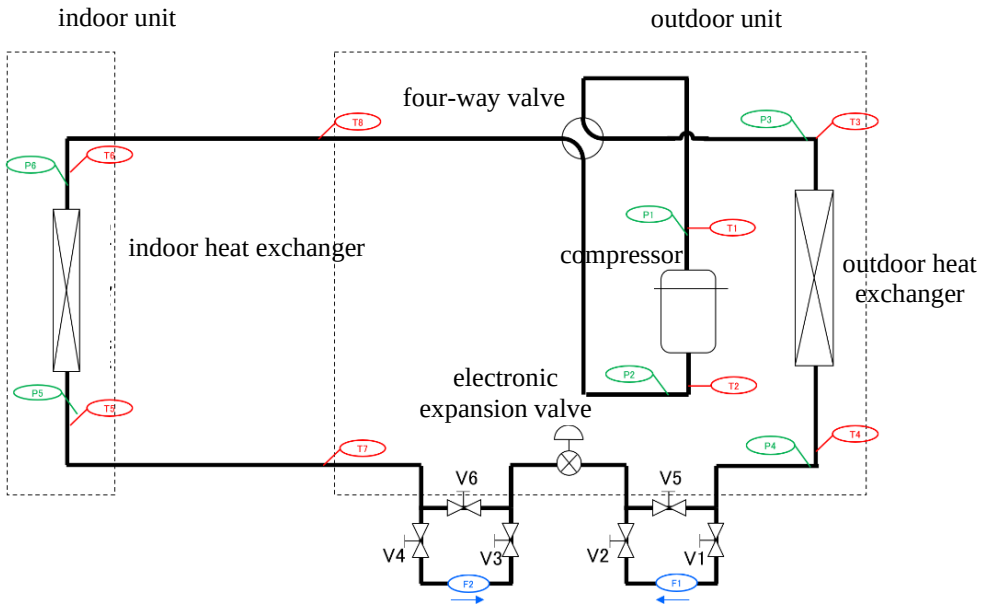


Fig. 4 Mounting locations of pressure sensors, thermocouples, and flow meters



(a) Indoor unit



(b) Outdoor unit

Fig. 5 Test setup in the dynamic performance evaluation facility

6.1.3 Test conditions

Four test conditions comprising four cooling conditions and four heating conditions were evaluated in accordance with the temperature conditions for the outdoor and indoor units provided by JIS C 9612:2013 [3] for room air conditioners. The specific temperature and load conditions are listed in Table 3.

Table 3 Test conditions

	Test condition		Indoor temperature (℃) Dry / Wet	Outdoor temperature (℃) Dry / Wet	Partial load ratio (%)
(a)	Cooling	Standard cooling Full-capacity test	27 / 19	35 / 24	100
(b)		Standard cooling Half-capacity test		35 / 24	50
(c)		Low-temperature cooling Half-capacity test		29 / 19	50
(d)		Low-temperature cooling Minimum-capacity test		29 / 19	25

6.1.4 Test results

The results of the standard cooling full-capacity test conditions represented by (a) at Table 3 are described Table 4 when the refrigerant charge was optimized by fixing the compressor rotation speed to achieve a capacity of 2.2 kW.

Table 4 Comparison of standard cooling full-capacity test results for R22 and R290

Refrigerant type	Refrigerant charge (g)	Compressor speed (Hz)	Mass flow rate (Kg/h)
R22	910	55.0	51.0
R290	400	62.5	28.2

6.2 Experimental results and simulator validation results

6.2.1 Background and purpose of validation

The actual operating performance of refrigeration and air conditioning equipment is the most critical factor in system operation evaluations. As system simulators offer an extremely effective approach for such evaluations, the effects of applying the R290 refrigerants to air conditioners designed for use with the R22 refrigerant, as discussed in previous section, were analyzed using the EF+M system simulator, which is being developed at our university. The differences between the experimental values and simulation results were then evaluated to validate the simulator.

6.2.2 Simulation results for R22 refrigerant and R290 refrigerant drop-in

Table 5 compares the experimental and simulation results for R22 refrigerant at standard cooling full-capacity test conditions represented by (a) at Table 3, Table 6 compares the experimental and simulation results for R290 refrigerant at standard cooling full-capacity test conditions represented by (a) at Table 3.

Table 5 Comparison of system experiment and simulation results (R22)

	Cooling capacity (%)	Power consumption (%)	Mass flow rate (%)	Condensing temperature (℃)	Evaporating temperature (℃)
Experiment	100	100	100	44.6	6.99
Simulation	99.1	100	101	44.7	8.4

	Compressor suction pressure (MPa)	Compressor discharge pressure (MPa)	Compressor suction temperature (℃)	Compressor discharge temperature (℃)	Degree of superheat (℃)	Degree of subcooling (℃)
Experiment	0.621	1.71	19.3	81.8	2.83	2.11
Simulation	0.587	1.72	19.8	82.1	2.14	4.32

Table 6 Comparison of system experiment and simulation results (R290)

	Cooling capacity (%)	Power consumption (%)	Mass flow rate (%)	Condensing temperature (℃)	Evaporating temperature (℃)
Experiment	100	100	100	46.0	6.13
Simulation	101	100	99	46.2	7.43

	Compressor suction pressure (MPa)	Compressor discharge pressure (MPa)	Compressor suction temperature (℃)	Compressor discharge temperature (℃)	Degree of superheat (℃)	Degree of subcooling (℃)
Experiment	0.570	1.57	12.8	64.5	0.10	3.89
Simulation	0.564	1.58	13.2	65.5	0.82	5.00

These numbers are in good agreement overall. However, there is a difference compressor suction pressure and degree of subcooling. The reason for these is that although the former is considered to be affected by the refrigerating machine oil in the actual machine, it is not considered in the simulation. One of the reasons for the latter is thought to be that the fins of the air heat exchanger have slits in the actual machine, but are treated as flat plates in the simulation. In the future, we would like to further investigate and improve the accuracy.

6.2.3 Summary of model validation

A system simulator was applied to reproduce the results of a test in which a room air conditioner designed for use with the standard R22 refrigerant was charged with R22, R290, the latter two of which are low-GWP refrigerants. Comparisons of the experimental values and simulation results confirmed suitable simulation accuracy. In the future, we will also consider dropping in R454C.

7. Conclusions

This study presented the recent progresses in simulation platform adopted for the use in refrigerant performance evaluation analyses. The GUI of the simulator was upgraded with precisely structured and completely independent calculation codes, which enables prompt modification of each component and system module. The new GUI and internal code structure constitute a user-friendly simulation platform that does not require technical experience in coding and numerical simulation development to run accurate air conditioning and refrigeration system simulations with different refrigerants. A standard model for a single-split residential air conditioner was developed and validated with dedicated experimental tests conducted on a 2.2 kW R22 air conditioner. Additionally, numerical simulations with R290 were validated with corresponding drop-in tests of the same air conditioning unit. As a result, it was shown that the simulation results accurately represents the operating performance of actual systems with different refrigerants and may be effectively used for evaluating the performance of new low-GWP fluids.

Acknowledgements

The results of ‘6. Experiments to confirm simulation accuracy’ in this paper were obtained as a result of commissioned work (JPNP18005) by New Energy and Industrial Technology Development Organization (NEDO), and we would like to express our gratitude to everyone involved.

References

[3] Suzuki, T., Ge, Z., Yulianto, M., Miyaoka, Y., Yamaguchi, S., Saito, K. 2021, “Annual performance assessment of heat pump water heaters applying various refrigerants” 13th IEA Heat Pump Conference, Jeju, Korea, paper #297.

[2] Thu, K., Takezato, K., Takata, N., Miyazaki, T., Higashi, Y. Drop-in experiments and exergy assessment of HFC-32/HFO-1234yf/R744 mixture with GWP below 150 for domestic heat pumps, *International Journal of Refrigeration* 2021;121:pp. 289-301.

[3] Domanski, PA., Brown, JS., Heo, J., Wojtusiak, J., McLinden, MO. A thermodynamic analysis of refrigerants: Performance limits of the vapor compression cycle, *International Journal of Refrigeration* 2014;**38**:pp. 71-79.

[4] Giannetti, N., Saito, K., Yamashita, K., Taira, S. 2022. “Development of a Standardized Refrigerant Evaluation Tool for Air Conditioning and Refrigeration Equipment Using a General-Purpose Energy-

Analysis Simulator". 25th International Refrigeration and Air Conditioning Conference, West Lafayette, U.S.A., paper #2488.
[5] Ohno, K., Saito, K., Yamaguchi, S., Kishimoto, T., Matsumoto, K. Intermittent driving simulation of compression type heat pump-1st report: Mathematical model and simulation of single-stage vapor compression type heat pump. *Trans. JSRAE* 2013;30(2):107-122.
[6] Saito, K. 2016. "Unified Refrigeration Cycle Evaluation Simulator with Various Refrigerants," Proceedings of the JRAIA international Symposium 2016, Tokyo, Japan, Japan, pp.369-372.
[7] Saito, K., Jeong, J. Development of General Purpose Energy System Simulator. *Energy Procedia* 2012;14:1595-1600.
[8] Giannetti, N., Matsui, S., Mori, R., Jeong, J., Ariyadi, HM., Miyaoka, Y., Togashi, E., Saito, K. Emulator-type load-based tests for dynamic performance characterization of air conditioners. *Energy and Buildings* 2022;273:112411.

14th IEA Heat Pump Conference
15-18 May 2023, Chicago, Illinois

Development of vapor compression system using natural refrigerant

Jungchul Kim[a,*] , Jin Woo Yoo [a], Kong Hoon Lee [a], Chan Ho Song [a]

[a]Department of Thermal Energy Solutions, Korea Institute of Machinergy & Materials, 156 Gaejeongbuk-Ro, Yuseung-Gu, Daejeon 34103, South Korea

Abstract

Recently, as the life quality has been improved, the demand for the refrigeration system has been increased rapidly. Also, the interest in low GWP chiller is increasing, due to the important environmental problem. Here, we have developed a refrigeration system using R-718 refrigerant, water. Considering the large specific volume and surface tension of the water, we have designed heat exchangers and the compressors. We introduce the performance of the new system with the manufacturing process of the system. Moreover, we show the preparation procedures of the test that are necessary for the system operation.

© HPC2023.
Selection and/or peer-review under the responsibility of the organizers of the 14th IEA Heat Pump Conference 2023.

Keywords: Natural refrigerant; R-718; Turbo compressor; Evaporator; Condenser

1. Introduction

As the quality of life improves, the demand for cooling systems is increasing rapidly. However, since the increase in the manufacture of cooling devices is generally accompanied by an increase in the amount of chemically synthesized refrigerants, a global environmental pollution problem is greatly emerging at the same time. Through the regulation of refrigerants, the use of HFC refrigerants following synthetic refrigerants CFC and HCFC will be greatly reduced. Accordingly, interest in refrigeration and cooling systems using eco-friendly refrigerants with low Global Warming Potential (GWP) is increasing. Korea is the 5th largest producer of refrigeration/air conditioning machinery in the world, showing some technological superiority in the market. In response to the eco-friendly trend of the refrigeration market, research on refrigeration/air conditioning machines that use low GWP and natural refrigerants instead of existing refrigerants is needed. In this study, we would like to introduce the (R-718) cooling system that uses water with zero GWP as a refrigerant. A study on the water refrigerant chiller have not been conducted in Korea, although it has been carried out several times in developed countries such as Germany and Japan.[1-2] In this presentation, water refrigerant chillers developed with domestic technology are introduced. In addition, we would like to disclose the manufacturing method and operating performance.

2. Cycle and components of chiller

This refrigerator is a two-stage compression system, an intercooler is used between the first and second stage compressors, and is manufactured according to the following cycle diagram.

* Corresponding author. Tel.: +82-42-868-7840 ; fax: +82-42-868-7338.
E-mail address: jungchulkim@kimm.re.kr.

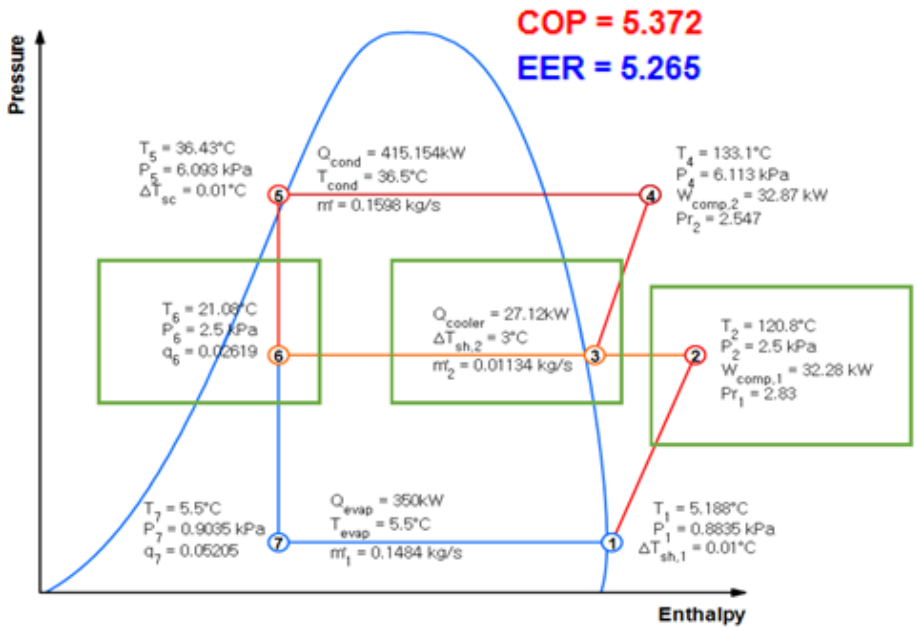


Fig. 1. Cycle of the system

3. Evaporator

Like other turbo chillers, the heat exchanger is designed and manufactured as a shell-and-tube type. Since the pressure difference from outside is not large, the shell is manufactured in an angular shape like an absorption chiller. The evaporator, classified as a falling film evaporator, is driven using a pump and a distributor. Liquid refrigerant is collected at the bottom of the shell, and a pump is installed at the bottom to move the liquid to the top of the evaporator. The liquid, which passes through the distributor, is fallen on the heat transfer tube. The internal pressure is set to 0.9 kpa as a design value, and the internal saturation temperature is set to about 5.4 °C. The inlet temperature of the cold water is 12°C. Since it is higher than the saturation temperature, the droplets, supplied on the heat transfer tube, is immediately evaporated and turned into steam, which is supplied to the first stage compressor. Here, to prevent moisture from entering, an eliminator is installed, as shown in Fig. 2.



Fig. 2. Image of the eliminator installed at the outlet of the evaporator

In order to decide the type and number of tubes, evaporator experiments in lab scale test are performed prior to manufacturing the prototype. A 10 kW evaporator is prepared as shown in the photo, and four (Notched corrugated, Notched floral, Low fin, End cross tubes) different heat transfer tubes are tested. The internal pressure is set to 0.9 kpa, similar to the design pressure. The cold water supply temperature is 12 degrees. As for the evaporator, Notched corrugated tube showed the best performance, but Notched floral tube was the best in terms of low flow stability. So, we decided to use a combination of them. When designing the prototype, at least 130 heat transfer tubes (based on 3 meters) were required in consideration of the cooling capacity. But for stable operation, we installed about additional 50% more, and 204 tubes were installed.

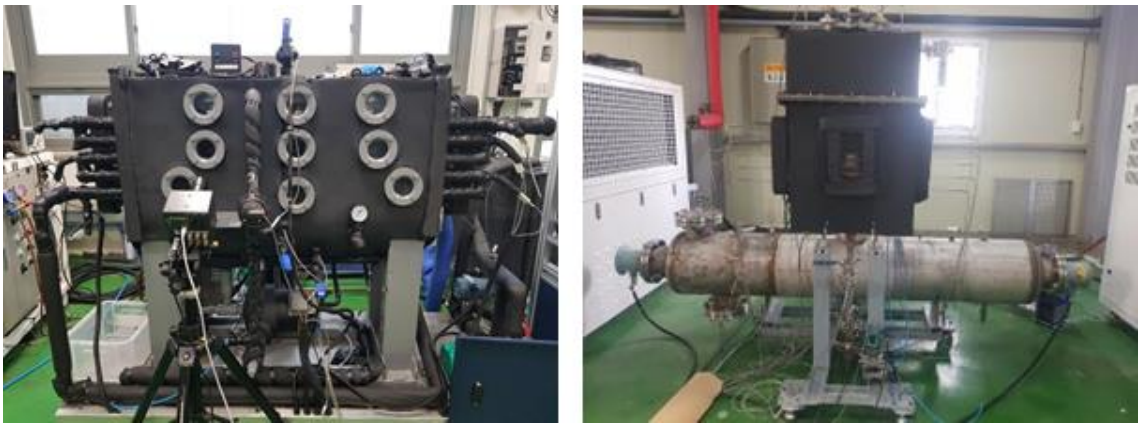


Fig. 3. Images of the 10kW evaporator(left) and condenser(right)

4. Condenser

The internal pressure of the condenser shell is 6.11 kpa, and the saturation temperature is about 36.5 degrees. In the design, the inlet temperature of the cooling water is about 30 degrees, so the refrigerant vapor supplied from the compressor is turned into liquid droplets. The droplets, formed on the upper tubes, fall to the lower ones and are collected at the shell bottom. The liquid moves to the evaporator or intercooler by gravity. Like the evaporator, in order to decide the type and number of heat transfer tubes, lab scale condensation experiments were performed. A 10 kW condenser was prepared as shown in the picture, and 6 different heat tubes (Bare, Corrugated, Floral, Low fin, Notched corrugated, and Notched floral tubes) were employed. The internal pressure is set to 6.1 kpa, similar to the design pressure. The cooling water supply temperature is 30 degrees. Even though the Notched corrugated tubes show the best performance, we decide to use the corrugated, since there was no significant performance difference. Unlike the evaporator which is mainly related to the phase change, the condenser includes the condensing section but also the superheated section, as can be seen in the ph diagram in the figure. Thus, a larger number of heat transfer tubes than for the condensation only are required. Since single-phase heat transfer under vacuum conditions requires a larger heat transfer area, about 4 times more heat transfer tubes were used for cooling the superheated section. Totally, 630 heat transfer tubes are installed. In the overall structure, the condenser should be located at the rear end of the two-stage compressor. But if the connecting parts are arranged in a line, there is a problem that the size becomes excessively large. We also note that the space for the distribution of steam must be added to the front of the condenser, which greatly increases the length of the device. In order to resolve this problem, we erected the condenser, where the refrigerant is supplied vertically to the upper part of the condenser.

5. Intermediate cooler

Since the chiller of this project is a two-stage compression system, an intermediate cooler that cools the vapor that has passed through the first-stage compressor is required. There are two types of intercoolers: an indirect intercooled type and a flash tank type. In this study, the latter is selected to reduce the overall size and

the amount of pressure drop. A nozzle is installed on the top of the intercooler and used to change the refrigerant delivered from the condenser into mist. A small reservoir is installed at the bottom of the intercooler and an additional pump is installed to circulate the refrigerant. The refrigerant vapor passing through the first stage compressor (Lp) meets this mist to exchange heat and mass, and the generated vapor enters the second stage compressor (Hp). At this time, the direction of nozzle injection must be carefully determined so that the droplets do not enter the compressor. (Hp) As shown in the design, the temperature of the refrigerant entering the intercooler is approximately 120 ℃, and the temperature of the refrigerant entering the two-stage compressor approximately 24 ℃, but the exact temperature could not be measured in this experiment.

The liquid refrigerant collected at the bottom of the condenser moves through a pipe. Part of the refrigerant goes into the reservoir of the intercooler, and the rest moves to the evaporator shell. At this time, using the U-trap, (U shaped pipe) the liquid are collected at the lower end of the pipe. Due to the pressure difference, a liquid column is formed in the U-trap, and the column separates the condenser and the other sides, the evaporator and the intercooler. Because of this device, the evaporator and intercooler can maintain a different pressure environment than the condenser. The column height is determined by the pressure difference between both ends and the hydrostatic pressure due to gravity.

6. Compressor

This prototype is a two-stage compression system, and both compressors are of centrifugal type. Since water vapor has a large specific volume and the compressed environment is in a vacuum state, considerably large impellers are required. The diameter of LP is about 970 mm, and the diameter of Hp is about 650 mm. All of the impellers were made of aluminum, and were manufactured with a 5-axis processing machine as shown in Fig. 4. The two compressors are arranged side by side and operated independently. The compression ratio of LP is about 2.8, and the compression ratio of Hp is 2.6. The compressor efficiencies are 76% and 75%, respectively. Bearings are ball bearings and roller bearings. A cooling fan is installed at the rear end, and a cooling line using water connected to the outside is installed to cool the motor. (See Fig. 5)



Fig. 4. Lp(left) and Hp(right) impellers

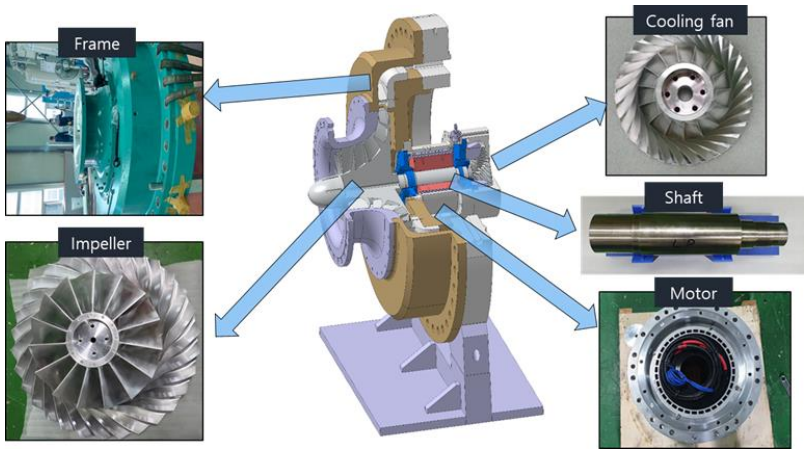


Fig. 5. Structure of the compressor (Lp)



Fig. 6. Image of the prototype

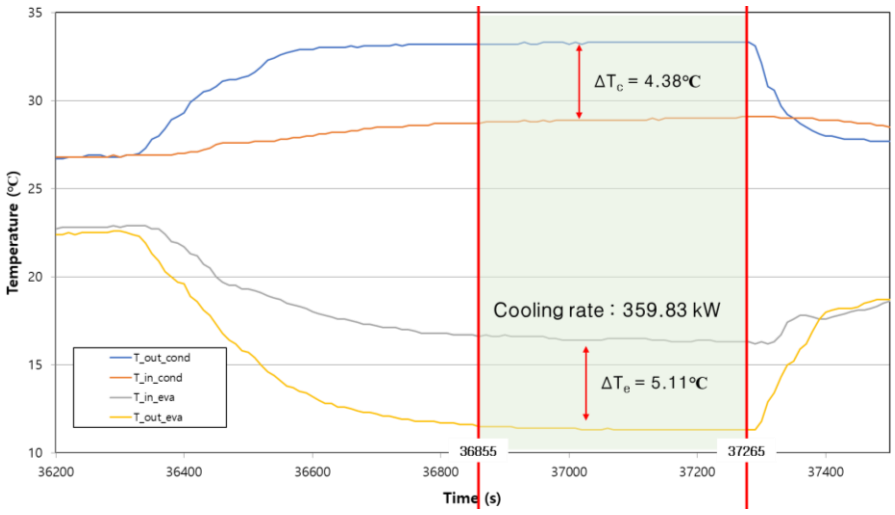


Fig. 7. Temperature change during the operation

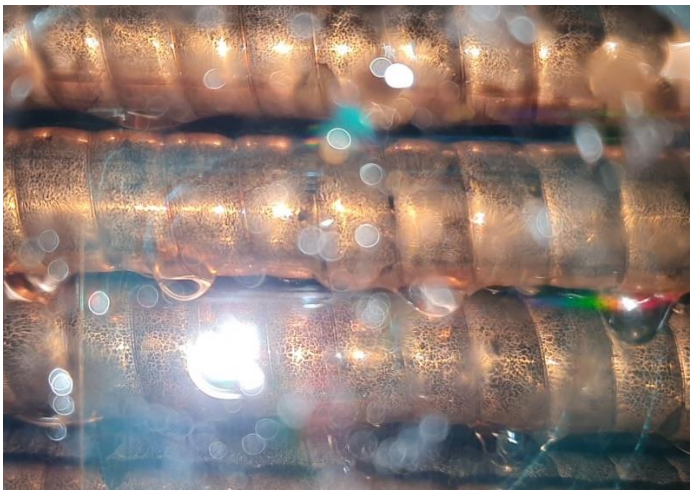


Fig. 8. Image of the condensation

7. Performance of the system

Prior to operating the prototype,(See Fig. 6) we created a vacuum environment and injected water into the evaporator, condenser, and the intercooler. Cold water and cooling water were set to flow at 1,000 lpm and 1,200 lpm. It was operated while increasing the number of revolutions of LP (primary compressor) and HP (secondary compressor) step by step. If the vibration increases or the internal bearing temperature increases while increasing the number of revolutions, we immediately stop the operation. Finally, it was driven up to LP: 10,000 rpm and HP: 16,300 rpm.

As the phase change occurred in the evaporator, the temperature of the cold water was dropped, resulting in a temperature difference of about 5.11 °C at the inlet and outlet.(See Fig. 7) In the condenser, as shown in Fig. 8, condensation actively occurred on the surface of the heat transfer tubes, and the temperature of the cooling water was increased by about 4.38 °C. The total heat capacity was measured as 359.83 kW and 366.60 kW for the evaporator and condenser, respectively. Considering that the total power used by the compressor is 50.48 kW, the calculated heat capacity of the condenser should be about 410.31 kW, but condensation on the inner wall due to conduction occurs together (the amount of condensation on the inner wall was not calculated), resulting in low performance of the condenser.

Upon reaching equilibrium, the average cooling water inlet/outlet temperatures are 16.48 °C and 11.36 °C, and the average cooling water inlet/outlet temperatures are 28.90 °C and 33.27 °C, as shown in Fig. 7. The temperature change is shown in the graph in the figure. The COP considering power consumption and cooling heat was calculated as 6.80, and the overall heat transfer coefficient of the evaporator at this time was calculated as 5,596 $W/m^2°C$. In the case of the condenser, considering the condensing part includes the single phase heat exchange in the superheated and supercooled sections, we derived the overall heat transfer coefficient, 4,596 $W/m^2°C$.

8. Conclusions

In this study, the evaporator, condenser, and compressor were studied in detail to develop the specifications to be applied to the R-718 refrigerator, and the entire system was manufactured by applying them to the prototype. In addition, performance evaluation and analysis were performed by connecting and operating electric devices. For actual product development, several factors, including a huge size, have to be improved, through additional research. We believe that this study has a significant meaning in that it the development direction of the R-718 refrigerant system was investigated through this study.

Acknowledgements

This work was supported by Ministry of Trade, Industry and Energy of Korea (Grant No. 2018-20000187) and Korea Institute of Energy Technology Evaluation and Planning (KETEP) and the Ministry of Trade, Industry & Energy (MOTIE) of the Republic of Korea (Grant Nos. 20212050100010).

References

[1] Marcus Honke, Mathias Safarik and RalfHerzog, 2015, "R718 Turbo Chillers and Vacuum Ice Generation-Two Applications of a New Generation of High Speed, High Capacity R718 Centrifugal Compressors", ICR 2015, August 16-22, Yokohama, Japan, ID:789
[2] Hayato Sakamoto, 2015, "Kawasaki Turbo Chiller Using Water as a Refrigerant", ATOM Sphere Solutions for Asia Natural Refrigerants, 3-5 Feb. 2015 in Tokyo.

14th IEA Heat Pump Conference
15-18 May 2023, Chicago, Illinois

On the Use of CO_2 as a Heat Distribution Fluid for Sustainable Ammonia Heat Pump Solutions

Matt Robinson[a], Aaron Tam[a], Scott Goedeke[a], Dennis Nasuta[b], Paul Kalinowski[b], and Andrea Mammoli[c]

[a]Electric Power Research Institute, 1001 Data Lane, Knoxville, TN, 37932, USA
[b]Optimized Thermal Systems Inc., 7040 Virginia Manor Rd., Beltsville, MD, 20705, USA
[c]Sandia National Laboratories, 1515 Eubank SE, Albuquerque, NM, 87123, USA

Abstract

Supercritical CO_2 is receiving increased interest as a heat transfer fluid, particularly in heat pump applications, due to some favorable physical properties. While supercritical CO_2 is traditionally circulated via compressors, it may be possible to use centrifugal pumps as an alternative. This could lead to substantial energy and cost savings. The design and evaluation of a pumped supercritical test loop is reported in this work. Upon verifying supercritical CO_2 could be circulated with the pump in the given setup, conditions were varied to understand the behavior of the pump and the potential for acting as a heat transfer loop between an outdoor heat pump and the indoor space. These results are presented along with suggestions for improved performance and problems that were encountered in the work.

© HPC2023.
Selection and/or peer-review under the responsibility of the organizers of the 14th IEA Heat Pump Conference 2023.

Keywords: Pumped Supercritical CO_2;HVAC;Low GWP

1. Introduction

There are two interrelated trends in the power and energy industries to meet climate stabilization goals. The first is the electrification of fossil fuel-based end use technologies and the second is the decarbonization of electricity generation. The technology of choice for electrification of heating is generally the heat pump, which can replace fossil fuel-based furnaces and water heaters. The trend of using heat pumps to replace these technologies is likely to increase with next generation heat pumps capable of handling colder ambient conditions.

While heat pumps offer a route to electrify heating technologies, they rely on refrigerants that can have orders of magnitude larger global warming potential (GWP) than CO_2. With this, the Heating, Ventilation, and Air Conditioning (HVAC) industry is experiencing a push to low GWP refrigerants. The American Innovation and Manufacturing (AIM) Act has directed the Environmental Protection Agency (EPA) to *phase down production and consumption of hydrofluorocarbons* (HFCs), due to their high global warming potentials (GWPs) [1]. This planned reduction in production and consumption, while not directed at air conditioners and heat pump systems is consistent with the transition towards more environmentally friendly refrigerants. From a system designer and manufacturer perspective, what options are available? There is a large interest in natural refrigerants such as ammonia (R-717), CO_2 (R-744), and propane (R-290) which are low GWP but *tend* to be more toxic and/or flammable. The synthetic refrigerant alternatives such as R-32 and R-454B have lower GWPs but are still orders of magnitude greater than that of the mentioned natural refrigerants and are more costly. Given the trend towards lower GWPs, facility and plant managers in commercial buildings, and industrial and commercial refrigeration may be faced with decisions of cost and compliance (if it comes to that point) on which systems to utilize to meet their building cooling and heating and/or their refrigeration needs.

Previous research done at the Electric Power Research Institute (EPRI) investigated technologies that can provide solutions/options for low GWP heating and cooling. EPRI performed a laboratory evaluation of a 35

kW (10 RT) ammonia chiller that used CO_2 as the heat transfer fluid to the indoor units [2]. Ammonia was selected as the refrigerant due to its performance and low GWP. The major drawback of this selection is the toxicity of ammonia which requires the ammonia side of the system to be contained outside, requiring a secondary heat transfer loop. Typically, a water-glycol mixture would be used as the working fluid in the secondary loop, however, the work showed the benefits of using liquid CO_2 as the working fluid between the indoor and outdoor units. The main advantage was due to the large latent heat of vaporization of CO_2, taking advantage of phase changes. This resulted in the ability to use smaller diameter pipe and low mass flow rate to transfer heat between indoor air handling units (AHUs) and the ammonia chiller.

This paper presents a novel concept of utilizing a CO_2 secondary loop for space cooling *and* heating with an ammonia based outdoor unit. Specifically, the ability of a CO_2 pump to circulate supercritical CO_2 is investigated, because the critical temperature of CO_2 (304.25 K) is lower than the temperature typically delivered to heating coils (assuming the volume is such that the pressure is beyond the critical pressure; a likely scenario in HVAC applications).

Centrifugal pumps and compressors both move fluid by accelerating it through vanes in a spinning impeller and then increasing the pressure at the outlet by converting part of the kinetic energy imparted. In a pump the fluid is usually a liquid whose density remains approximately constant, while in a compressor the working fluid is a gas whose density is increased. There are substantial differences between impeller designs in centrifugal compressors and pumps. For supercritical CO_2 applications near the critical point, the working fluid is closer to a liquid than to a gas. Nevertheless, the geometry for optimal pumping of supercritical CO_2 is not the same as for an incompressible fluid, and it is a function of the thermophysical properties of the CO_2. A number of studies investigated these issues in connection with applications in oil and gas, and in power generation. Through a CFD analysis, Cubas et al. [3] conclude that typical hydrodynamics similarity laws of pumps used with liquids can be used to evaluate performance when pumping a supercritical fluid. Kim et al. [4] compare experimental and numerical results and conclude that CFD can yield insight into the performance of liquid pumps used for supercritical CO_2, and moreover that liquid pumps can pump supercritical CO_2 effectively. Bergamini et al. [5] provide similar conclusions, namely that centrifugal pumps are efficient means of pumping supercritical CO_2, provided that certain conditions of temperature and pressure are met. While the pump used in this application is much smaller than what would be considered for oil recovery, CO_2 sequestration, or power generation, we too expect the performance in pumping supercritical CO_2 to be similar to the rated performance of the pump for liquid CO_2 applications.

There are numerous benefits of pumping supercritical CO_2 for the current ASHP design, mainly because a CO_2 compressor will not be required. The pumped solution offers lower electrical power consumption, reduces the total cost of the system, and provides a simpler overall design.

This paper presents the testing of a CO_2 pump to circulate supercritical CO_2 in EPRI's Knoxville Thermal Laboratory. The following sections describe the setup that was used to test the idea, the results from the tests that were performed, and a discussion on areas for improvement and further study for this application.

2. Experimental Setup

The experimental setup was designed to mirror the conditions that the supercritical CO_2 would experience in the secondary loop that transfers heat from the condenser to heating coils inside a building. In particular, a test loop was constructed to mimic the heating mode of an ASHP that is connected to the indoor space by a CO_2 loop. The CO_2 is pumped into the condenser of the ASHP where it is heated, routed to the indoor AHUs where it heats the air and then pumped back to the condenser of the ASHP. The test loop is a scaled version of this loop. Heat exchangers (HXs) are paired with valves to simulate behavior of the real heat exchangers, namely heat transfer with pressure drops. The layout of the test loop is explained in detail below.

2.1. Test loop hardware details

The test loop is composed of the CO_2 pump, two compact plate HXs, needle valves to provide controlled pressure drops, a receiver to act as a buffer for the pump, measurement devices (flow meter, digital pressure transducers, analog pressure transducers, and thermocouples), and valves for charging, venting, and vacuuming the system. A schematic of the system is shown in Figure 1 and a part list is presented in **Error! Reference source not found.**. The CO_2 pump is a dual stage centrifugal pump where the impellers are magnetically coupled to the motor. The pump was selected because it is designed to pump liquid CO_2 *and* is rated for

Table 1: Primary components in test loop.

Component	Manufacturer	Part Number	Notes
CO_2 Pump	Hy-Save	820-DS-050-VSD-B	12 MPa Max
Brazed Plate Heat Exchanger	SWEP	B4TMx30	14 MPa Max
Coriolis Flow Meter	Emerson	CMFS025MB67N2BAEKZZ	10.3 MPa Max
Needle Valves	Swagelok	SS-18RS8	> 20 MPa
Digital Pressure Sensor	ProSense	SPT25-10-2000A	0-13.8 MPa F.S.
Cu-Fe Tubing	Mueller Streamline	N/A	13 MPa rating

pressures suitable for handling supercritical CO_2. The tubing connecting the components is copper-iron (Cu-Fe) tube rated for 13 MPa and can be brazed using standard equipment and a high silver content braze rod. The fluid is first circulated through a MicroMotion Coriolis flow meter rated at 10.3 MPa which measures the

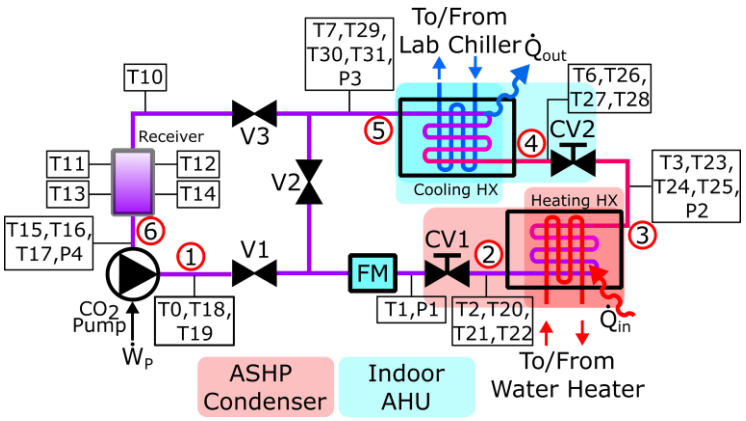


Figure 1: Schematic of test loop for evaluating supercritical CO_2 pumping. T and P indicate location of temperature and pressure measurements, respectively. CV1 and the heating heat exchanger act as the heating portion of the ASHP while CV2 and the cooling heat exchanger act as the indoor air handling unit (AHU).

flow rate and the density of the fluid. The fluid then goes into the part of the loop acting as the condenser of the ASHP. First the fluid passes through a stainless-steel needle valve to simulate pressure drop along the heat exchanger. The CO_2 is then heated in a brazed plate heat exchanger (BPHE) referred to as the heating HX. The heating HX's heat source is 0.15 m^3 (40 gallon) electric water heater coupled with a small circulating pump. The heated CO_2 then passes through the section of the test loop acting as the indoor AHU. The CO_2 passes through another needle valve, providing a controllable pressure drop, and is then cooled by another BPHE, referred to as the cooling HX. The cooling fluid is provided by a water loop in the laboratory, which is cooled by a chiller and heated by electric heaters, following a given setpoint. After the CO_2 is cooled it is collected in a receiver. The receiver has two functions. First it adds additional volume for a fluid reservoir to be available for the pump, ensuring that the pump doesn't run out of fluid to pump. Secondly, the receiver helps ensure that the pressure head requirement for the pump is met. The amount of pressure drop between the receiver and the inlet of the pump is also minimized per the manufacturer recommendation. The CO_2 pump operates on 208 VAC three-phase and a variable speed drive (VSD) is used to control the speed. A bypass was added to the loop in the scenario when not enough fluid is being returned to the pump to cool the motor. This condition has

not been observed with the testing so far. A pressure relief valve was added to protect components and safely reduce the pressure, if exceeded. The system was pressure tested and the pressure relief valve set to 9.75 MPa (1,414 psia). Considerations must be taken with the pressure relief valve if it were ever to exhaust. High pressure CO_2 when rapidly expanded can cause dry ice to form, potentially blocking the exhaust path. Because of this, connecting tubing on the exhaust of a pressure relief valve with CO_2 systems should be avoided. Instead, the CO_2 is allowed to exhaust into the laboratory space where CO_2 sensors are integrated with exhaust fans.

Figure 1 also indicates the measurements being taken and their locations. Temperature is measured using T-type thermocouples and two NI USB-9213 thermocouple modules. 32 temperature measurements are monitored with important measurements (in and out of the heat exchanger, for example) being made with multiple thermocouples. The thermocouples are taped to the pipe and the piping is insulated. The thermocouples were calibrated in a temperature bath prior to installation into the system. Pressure is measured by digital and analog pressure gauges. The four digital sensors output a 0-10 VDC which is read by an NI USB-6001. The flow meter and power meter provide a Modbus over RS-485 interface that the data acquisition computer queries for measured values. Figure 2 shows the completed test setup with major components identified.

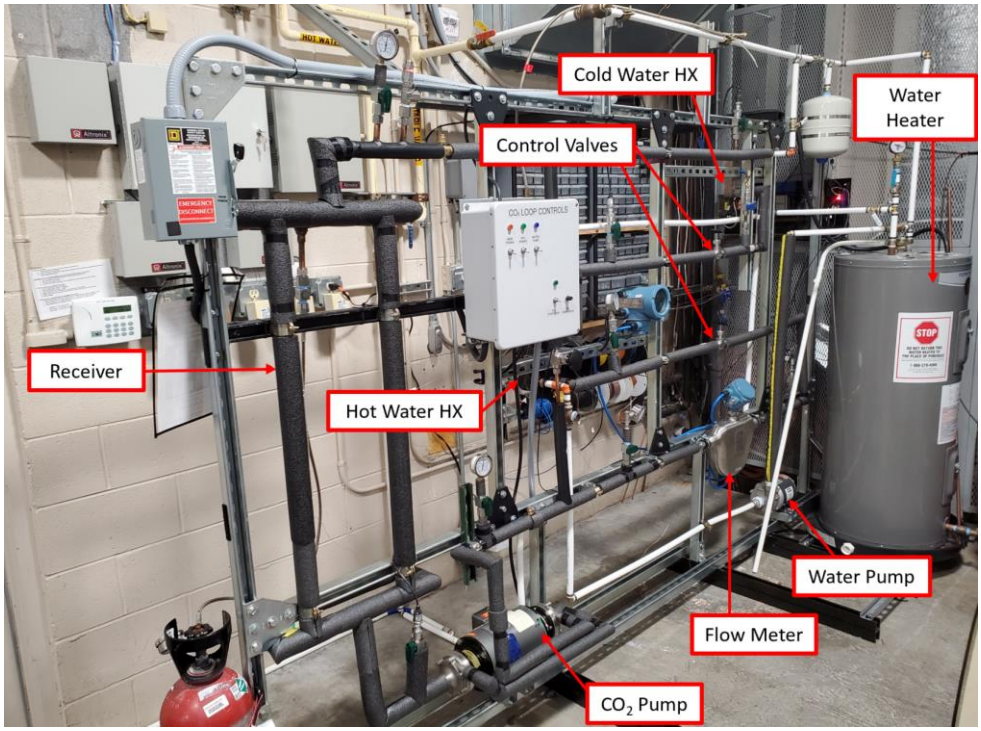


Figure 2: The supercritical CO_2 pump test loop as-built. The insulated lines are the CuFe tubes that contain the CO_2. The water lines, hot and cold, are plumbed in PEX (white pipes in figure).

2.2. Charging of the test loop

The mass of CO_2 to be added to the system (commonly called the charge) was based on the density of supercritical CO_2 at 309 K and 8.5 MPa, and an estimate of the volume of the system. The particular value chosen is a compromise between maximizing the specific heat, c_p, and the stability of c_p at the particular fluid

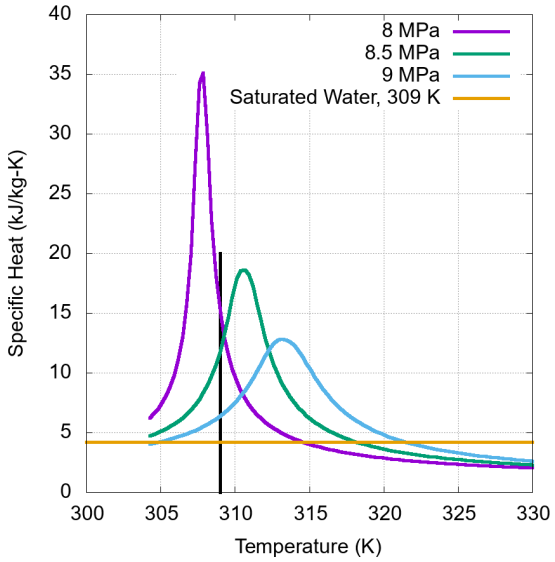


Figure 3: The specific heat of supercritical CO_2 as a function of temperature and pressure. The black vertical line indicates the design temperature for the indoor AHUs.

conditions. Figure 3 illustrates this tradeoff as c_p of supercritical CO_2 is plotted as a function of temperature for different pressures with the black vertical line showing the desired temperature of the fluid going into the indoor AHUs (design condition). As the pressure increases the specific heat decreases but the curves also flatten out, making c_p more stable. It was decided that if we could operate around the 8.5 MPa curve, that would be a reasonable balance between stability and large c_p. For reference, c_p of saturated liquid water at 309 K (4.2 kJ/kg-K) is also shown on Figure 3. The mass required is given by,

$$m = \rho V \tag{1}$$

where ρ is the density at the design condition and V is the volume of the system. The system volume is estimated to be 3.4E-3 m^3 and the density is 568 kg/m^3 at the design condition. The required mass to be fill the system is 1.9 kg. The actual charge of the system was 2.2 kg to provide a slight additional charge for the system in-case of uncertainties in volume estimates. The filling process begins with pulling a vacuum on the system. When the vacuum is sufficient, a CO_2 cylinder with a dip tube is placed on a scale and connected to the fill valve and liquid CO_2 is pulled from the bottom of the cylinder. CO_2 is pressure fed into the system until the correct mass has been reached. If the pressure between the system and the cylinder balances before the required mass is in the loop, heat can be applied to the cylinder to increase the pressure in the cylinder, thereby pushing more liquid CO_2 into the loop.

3. Test Method

The primary goal of testing was to see if it would be possible to pump supercritical CO_2 effectively using a pump designed for liquid CO_2. If pumping was possible, a series of tests would be conducted to examine the performance of the pump over a range of conditions. In particular the following are held constant over the course of a test:

- Temperature entering pump
- Temperature exiting heating HX
- VFD frequency
- Position of CV1 and CV2

The temperatures in the first two bullets were held constant by adjusting valves on the water side of the associated heat exchangers. The frequency of the VFD was set on the drive's front display and the control valves were set before the start of a test. To get the test loop to test conditions (supercritical CO_2 flowing) the cooling water loop and heating water loop were operated until steady state was reached for their control setpoint. The CO_2 pump was started at about 10 Hz with the cooling water valve closed and the heating water valve about a quarter turn open. The temperature and pressure begin to rise in the system until the CO_2 pressure and temperature go beyond the critical point. At this point, the VFD is adjusted to the test's frequency and the cooling water valve is partially opened. The cooling and heating valves are adjusted until the temperature setpoints for the test are met. The test condition is ran for at least 15 minutes while at steady state.

Referring to Figure 1 (numbers in red circles) the rate of heat added to the system, $\dot{Q}_{in}$, can be calculated by

$$\dot{Q}_{in} = \dot{m}(h_3 - h_2) \tag{2}$$

where $\dot{m}$ is the mass flow rate measured by the flow meter, h_3 is the specific enthalpy of the CO_2 leaving the heating HX, and h_2 is the specific enthalpy entering the heating HX. The specific enthalpy is determined using REFPROP [6, 7] and the measured temperature and pressure at the location. The rate of heat leaving the system through the cooling HX, $\dot{Q}_{out}$, is given by

$$\dot{Q}_{out} = \dot{m}(h_5 - h_4) \tag{3}$$

where the h_5 and h_4 refer to the specific enthalpy leaving and entering the cooling HX, respectively. The rate of work on the fluid performed by the pump, $\dot{W}_p$, is determined by

$$\dot{W}_p = \dot{m}(h_1 - h_6) \tag{4}$$

where the specific enthalpy is calculated at the outlet of the pump, location 6, and at the inlet of the pump, location 1. The electrical power consumption of the pump, $\dot{P}_p$, is calculated assuming a balanced three phase load,

$$\dot{P}_p = \sqrt{3} V I pf \tag{5}$$

where V is the applied voltage, 208 VAC, I is the measured current, and pf is the nominal power factor of the pump, 0.67. The work done by the pump and the amount of electrical power are related through the efficiency,

$$\eta = \frac{\dot{W}_p}{\dot{P}_p} \tag{6}$$

which has a nominal value of 72.5%. Heat engine sign convention is used in this study where heat into and work out of the system are considered positive. At steady state, by the First Law of Thermodynamics,

$$\dot{Q}_{in} + \dot{W}_p = \dot{Q}_{in} + \eta \dot{P}_p = \dot{Q}_{out} + \dot{Q}_{lost} \tag{7}$$

where $\dot{Q}_{\text{lost}}$ is the rate at which heat is lost to the environment.

3.1. Uncertainty analysis

Error propagation due to uncertainty in measurements begins with examining Eqns. 2 and 3. In particular, there is a *difference* in enthalpy which is then *multiplied* by the mass flow rate. If uncertainties are independent and random, the uncertainties associated with addition and subtraction is given by [8],

$$\delta \Delta h_{3-2} = \sqrt{\delta h_3{}^2 + \delta h_2{}^2} \tag{8}$$

where $\delta \Delta h_{3-2}$ is the uncertainty that results from taking the difference in enthalpy between points 3 and 2. δh_3 and δh_2 are the uncertainties associated with the enthalpies. These uncertainties are determined by passing through the uncertainties in the thermocouples and the pressure sensors into the enthalpy calculation

performed by REFPROP. In particular, an upper, h_u, and lower, h_l, estimate is made of the enthalpy from the upper and lower bounds of the temperature and pressure. The uncertainty is then determined by

$$\delta h = (h_u - h_l)/2. \tag{9}$$

Given a temperature measurement with associated uncertainty, $T = T_{best} \pm \delta T$, and a pressure measurement, $P = P_{best} \pm \delta P$, h_u, and h_l are determined by examining the pressure-enthalpy diagram which shows that the upper value of the enthalpy is given by,

$$h_u = f(T + \delta T, p - \delta p) \tag{10}$$

and the lower bound of the enthalpy given the uncertainties in temperature and pressure is,

$$h_l = f(T - \delta T, p + \delta p) \tag{11}$$

where f is the function for enthalpy provided by REFPROP. It should be noted that this is the worst-case scenario and may be overly conservative. From calibration, a fractional uncertainty of 0.0028 was determined and is assumed for all thermocouples [9]. The pressure sensors have a stated uncertainty of 0.07 MPa. The Coriolis flow meter has a percent uncertainty of 0.25% (assumed for our supercritical case) and a density uncertainty of 0.2 kg/m^3 for *liquids*.

The next consideration is which temperature is used for enthalpy calculations. Multiple measurements of temperature are done at each location, so an average is used. The uncertainty from each measurement is added in quadrature (Eqn. 8) and scaled by 1/N where N is the number of measurements in the average. For example, the uncertainty of the average of three thermocouples is, δT_{avg},

$$\delta T_{avg} = \frac{1}{N}\sqrt{{\delta T_1}^2 + {\delta T_2}^2 + {\delta T_3}^2} \tag{12}$$

where δT_1, δT_2, and δT_3 are the associated uncertainties with thermocouples 1, 2, and 3, respectively, and N is 3. The relationship between fractional uncertainty, x_{frac}, and uncertainty, δx, is

$$x_{frac} = \frac{\delta x}{|x_{best}|} \tag{13}$$

where x_{best} is the measurement made. Using Eqn. 13, Eqn. 12, with constant fractional uncertainty, can be rewritten as,

$$\delta T_{avg} = \frac{T_{frac}}{N}\sqrt{{T_{best,1}}^2 + {T_{best,2}}^2 + {T_{best,3}}^2}. \tag{14}$$

The final uncertainty consideration is how the error from the mass flow meter and the difference in enthalpy combine. This is straightforward because the fractional uncertainty of products and quotients, is the square root of the sum of the squares of the given fractional uncertainties [8].

4. Results

The first test was to verify that the test loop could circulate supercritical CO_2. Initially the CO_2 is two phase mixture at room temperature. The VFD was operated at a low frequency to circulate the liquid CO_2 while adding heat, to ensure uniformity while avoiding excessive stress on the pump produced by circulating two-

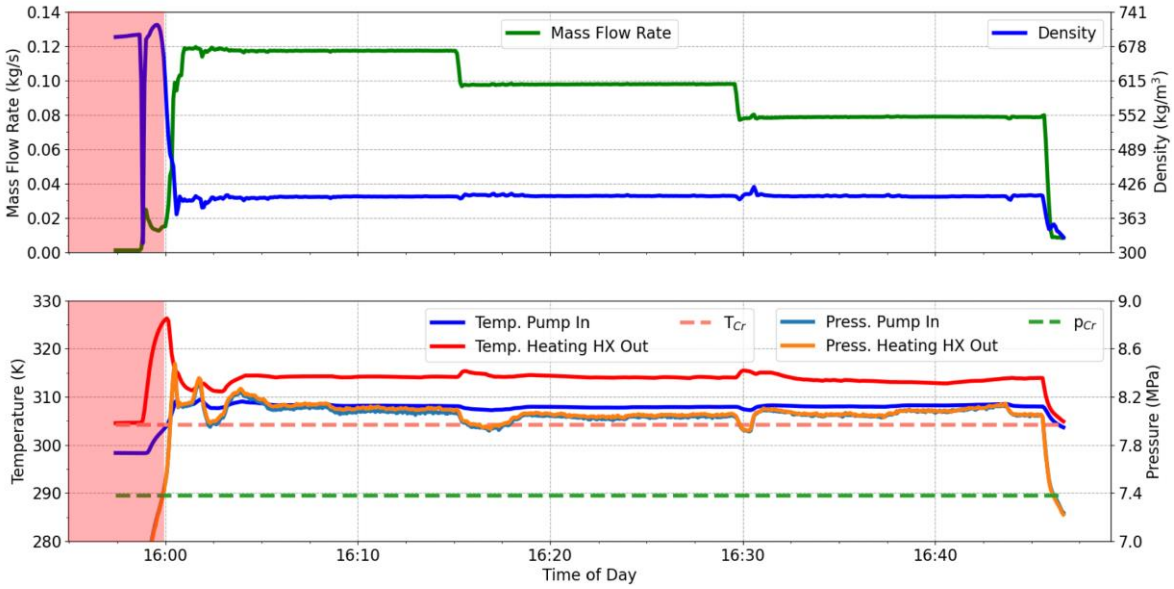


Figure 4: An example of a test performed with a pump inlet temperature of 308.15 K and heating heat exchanger outlet set to 313.71 K. CO_2 goes supercritical after the red transparent rectangles when the temperature and pressure pass their respective critical point values, T_{Cr} and p_{Cr}.

phase fluid. The temperature and pressure increased while the density decreased. When enough heat was added the temperature and pressure surpassed the respective critical points. At this point the density stabilized and the VFD frequency was increased. This showed that the pump could circulate supercritical CO_2 and testing could continue, studying how the pump performed in different conditions.

Figure 4 is an example of a test performed with the pump inlet temperature set to 308.15 K and the heating HX outlet temperature set to 313.71 K. Initially the CO_2 is subcritical as indicated by the shaded red rectangles. As heat is added through the heating HX the temperature and pressure increase until the critical point is passed. At this point the cooling heat exchanger valve is opened to stabilize the temperature and pressure. The VFD is set to the frequency for the specific test. The valves on the heating and cooling water are adjusted such that the test conditions are met; temperature setpoints for pump inlet temperature and heating heat exchanger outlet. The pump inlet and heating HX outlet temperatures are monitored during the test period and adjusted. This was more difficult on the heating water loop due to the smaller capacity of the hot water tank. After about 15 minutes of steady-state operation the VFD is then adjusted to the next speed (60 Hz, 50 Hz, and 40 Hz), the valves adjusted for temperature setpoint, followed by another 15-minute period for steady state conditions. The VFD adjustment is seen in Figure 4 with the decreasing steps in the mass flow rate. As the temperature

setpoints were varied the density changed slightly between tests which yielded insight into how the CO_2 pump performed with a varying fluid density, although the changes were minor. **Error! Reference source not found.** illustrates the performance of the pump as the density changes (slightly) and as the VFD frequency is

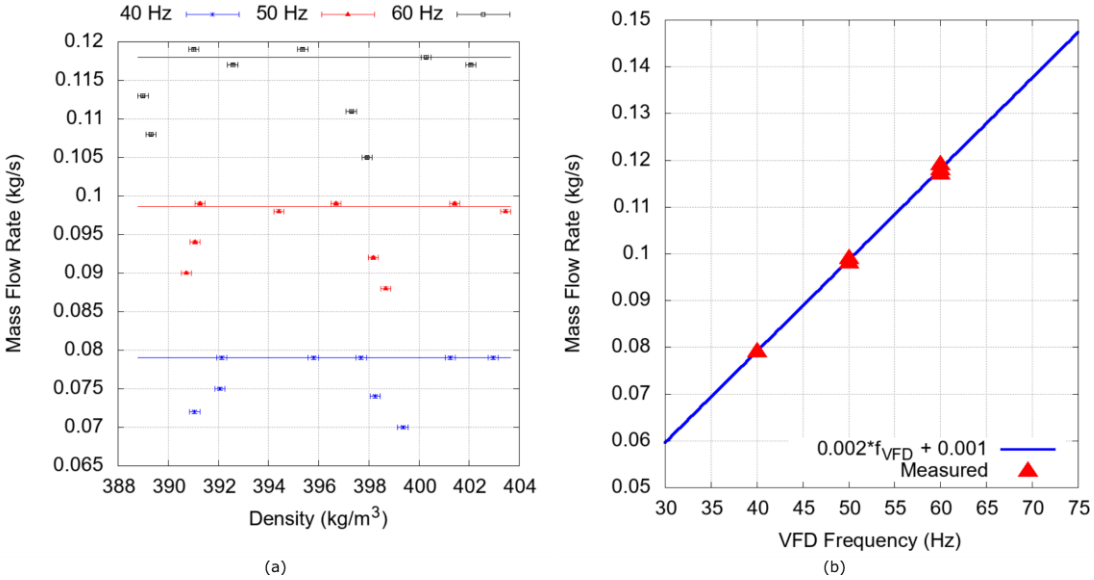


Figure 5: (a) The change in mass flow rate as a function density, VFD frequency, and pressure drop. The blue, red, and black lines represent the average flow rates at 40, 50, and 60 Hz. Large deviations from this average are caused by increased pressure drops due to closing needle valves. (b) The mass flow rate as function of the VFD frequency.

adjusted. For reference, liquid CO_2 at 20 °C has a density around 773 kg/m^3. This performance shows that the mass flow rate is a strong function of the VFD frequency, as expected, and does not vary significantly with the variation in density experienced during these tests. The nominal volume flow rate for this pump when used for liquid CO_2, at 60 Hz, is between 12.1 and 20.8 liters/minute for 19.8 to 13.7 m of head, respectively. The maximum volume flow rate for supercritical CO_2 at the same pump speed was approximately 17.8 liters/minute, confirming expectations that the pumping of supercritical CO_2 would be similar to that of liquid CO_2. **Error! Reference source not found.** also shows the effect of increasing the pressure drop through the

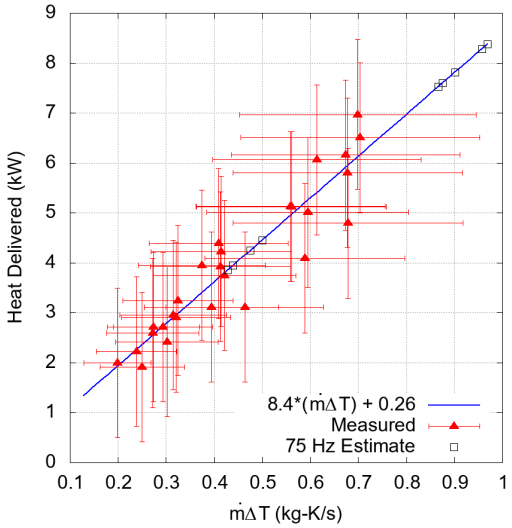


Figure 6: The rate of heat delivered to the cooling heat exchanger as the product of the mass flow rate and change in temperature is varied.

test loop by closing the needle valves a given amount. The blue, red, and black horizontal lines are the average mass flow rates with the needle valves fully open, for 40, 50, and 60 Hz, respectively. Both the heating and

cooling HX valves are closed in equal amounts; first 2 turns and then 3 turns. The decrease in flow rate is seen, again, as expected, by the four points that are away from the averages.

The ultimate purpose of the pump is to deliver heat between the indoor AHU and the ASHP. Figure 6 shows the amount of heat that the pump was delivered as a function of the product of the mass flow rate and temperature difference between the heating HX output and the pump inlet temperature. The rate of heat delivered behaves as expected, increasing as the mass flow rate and/or temperature difference increases.

5. Discussion

The presented results show that circulation of supercritical CO_2 is possible with an appropriately pressure rated/designed CO_2 pump. The mass flow rate varied between 0.07 kg/s at 40 Hz to about 0.12 kg/s at 60 Hz. The electric power provided to the pump for these flow rates is between 150 W and 200 W. The alternative to using the CO_2 pump is a CO_2 compressor. The compressor selected for the current project is estimated to draw

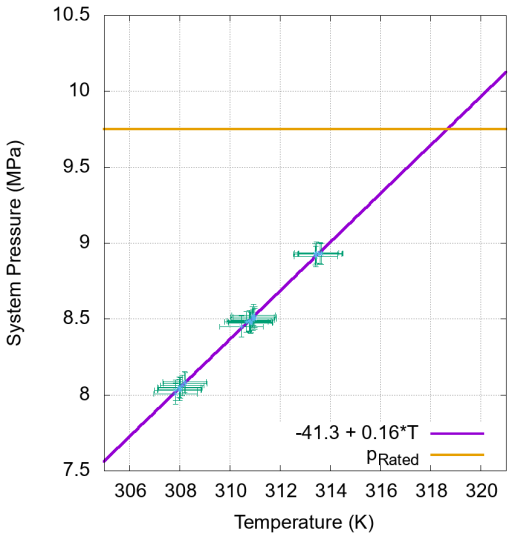


Figure 7: System pressure as function of the pump inlet temperature. The pump inlet temperature should be kept below 319 K to keep the system below the pressure rating.

about 6.5 kW to operate, running at part load. This is a significant difference between using the pump and compressor. The designed heating load is between 35.2 and 70.3 kW which, by inspection of Figure 6, indicates that multiple pumps will be needed if the maximum output is 7 kW, requiring at least 5 pumps. If 5 pumps were being used at 200 W, the total power draw is about 1 kW. This is still significantly less power consumption than the compressor but increases the initial cost of the system. However, from the results presented there are opportunities for increasing the heat output. These include increasing the temperature difference, lowering the mass charge of the system to allow for higher temperature at equivalent pressures, and running the VFD at frequencies greater than 60 Hz.

During the course of the experiments the pressure of the system was a concern. The system was pressure rated to 9.75 MPa and at the time it was not well understood which temperature in the system would dictate the pressure. Understanding the process from subcritical to supercritical and how the cycle executes along with experimental results shows that the system pressure is mainly dependent on the pump inlet temperature. Figure 7 shows the relationship between the system pressure and pump inlet temperature. This indicates that as long as the CO_2 can be sufficiently cooled by the cooling HX, the pressure of the system can be kept at safe operating conditions while increasing the temperature of CO_2 leaving the heating heat exchanger. The result would be a larger temperature difference, leading to an increased heat output. The current setup can be used to test this but is limited by the temperature output of the hot water loop and the HXs. Assuming that the maximum temperature leaving the heating HX is 336 K, and the loop is able to cool this CO_2 to 319 K, just below the maximum pressure condition, the temperature difference is 17 K. If this is done at 60 Hz, the mass flow rate is about 0.12 kg/s. From the fit in Figure 6 the heat output is about 17 kW, more than doubling the heat output that was measured in the experiments, reducing the number of pumps.

Another possible option is to decrease the amount of CO_2 in the system. If the mass present in the system is decreased, the CO_2 could be heated to a higher temperature at the same pressure. This would become an optimization problem in itself because the specific heat also decreases with temperature; what mass charge gives the maximum heat output over the range of temperatures considered? This is not fully understood so an estimate of the benefit cannot be made.

The final opportunity considered for improvement is running the VFD at frequencies greater than 60 Hz. If

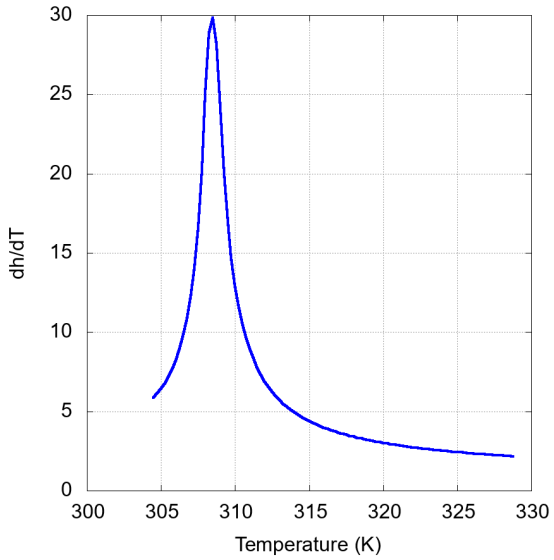


Figure 8: The sensitivity of enthalpy with temperature explains why such large uncertainty is associated with the heat transfer calculations.

the effect of density changes is assumed negligible (reasonable assumption by Figure 5, a) a linear fit between the mass flow rate and the VFD frequency can be made (Figure 5, b),

$$\dot{m} = 0.002 f_{VFD} + 0.001. \tag{15}$$

If the VFD is operated at 75 Hz, the mass flow rate is expected to be 0.151 kg/s, according to Eqn. 15. If this mass flow rate is performed for the same temperature differences, the performance can be estimated by the fit given in Figure 6, and this estimate is given in the figure shown by the black wireframe squares. An increase in maximum output of 1.5 kW is estimated which is about a 13% increase from 60 Hz. If the pump is operated at 75 Hz *and* the temperature difference is increased to the previously stated 17 K, the heat output is estimated at 20.5 kW. The required number of pumps is now 2 for our purposes with this increased performance.

Finally, some of the challenges encountered in this work are acknowledged, in particular, problems that were faced with the CO_2 pump and with the uncertainty in the measurement are discussed.

The CO_2 pump was designed for liquid circulation but modified by the manufacturer to endure the higher working pressure of supercritical CO_2. Unfortunately, the initial design did not consider the aspect of a gas-like fluid being present in the pump and potentially being trapped in any of the internal components. When the system was operated and then vented, gas was trapped in a sleeve in the impeller, which expanded and plastically deformed when the system was vented. The solution was to provide vents on the components that can potentially trap gas.

The final consideration that should be mentioned are the large error bars on the heat calculations (Figure 6). Performing an uncertainty analysis on the measurements it was a surprise that the uncertainty was so large (about 1.5 kW) on the measurements given that calibrated thermocouples were used. Figure 8 gives insight into how slight uncertainty in temperature measurements can lead to large uncertainties in the heat transfer calculations (Eqns. 2 and 3). A number of the experiments were performed between 308 and 313 K where small changes in temperature can lead to large change in enthalpy and thereby increases the uncertainty in the heat transfer calculations. This should have been expected considering the known instability of the specific heat in this temperature and pressure range.

6. Conclusion

This work showed that given an appropriately designed CO_2 pump, supercritical CO_2 can be circulated effectively with a centrifugal pump. The work presented on the ability of the pump and supercritical CO_2 to be used as a secondary loop between a heat source (ASHP) and heat sink (indoor AHU) in a test loop setup. While the amount of heat that was transferred between the source and the sink was somewhat below the requirement for the full scale ASHP, the testing gives indications of how many pumps would be needed if the heat transfer loop was operated as is. More importantly the research showed that there exist opportunities for improvement which included increasing the temperature difference while maintaining system pressure, increasing the VFD frequency, and adjusting the system mass charge. The two former points of improvement could be estimated with the work done and showed that there is a potential to more than double the capacity of the output by appropriate changes in operating conditions. Further work should focus on investigating the concept of optimal charge for pumped supercritical CO_2 systems.

Acknowledgements

The authors would like to acknowledge the California Energy Commission, San Diego Gas and Electric, and Southern California Edison for funding this research under EPC-19-014.

References

[1] Environmental Protection Agency, *Final Rule – Phasedown of Hydrofluorocarbons: Establishing the Allowance Allocation and Trading Program under the American Innovation and Manufacturing (AIM) Act,* 2021.

[2] Electric Power Research Institute, "Environmentally Friendly Advanced Refrigerant Options in Commercial HVAC Applications," Electric Power Research Institute, Palo Alto, 2022.

[3] J. M. Cubas, H. Stel, M. Neto, L. Da Silva, G. Romero and R. Morales, *Numerical Simulation of the Flow of Supercritical CO2 in a Multistage Centrifugal Pump,* Rio de Janeiro, Brazil: SPE Brazil Flow Assurance Technology Congress, 2022.

[4] S. Kim, J. Lee, Y. Ahn, J. Lee, Y. Addad and B. Ko, "CFD Investigation of a Centrifugal Compressor Derived from Pump Technology for Supercritical Carbon Dioxide as a Working Fluid," *The Journal of Supercritical Fluids,* vol. 86, pp. 160-171, 2014.

[5] L. Bergamini, "Centrifugal Pumps For Co2 Applications," in *Twenty-Seventh International Pump User Symposium*, Houston, TX, 2011.

[6] E. W. Lemmon, I. H. Bell, M. L. Huber and M. O. McLinden, *NIST Standard Reference Database 23: Reference Fluid Thermodynamic and Transport Properties-REFPROP, Version 10.0, National Institute of Standards and Technology,* 2018.

[7] R. a. W. W. Span, "A New Equation of State for Carbon Dioxide Covering the Fluid Region from the Triple-Point Temperature to 1100 K at Pressures up to 800 MPa," *J. Phys. Chem. Ref. Data,* vol. 25, no. 6, pp. 1509-1596, 1996.

[8] J. Taylor, Introduction to Error Analysis, the Study of Uncertainties in Physical Measurements, 1997.

[9] A. J. Wheeler and A. R. Ganji, Introduction to Engineering Experimentation, Saddle River: Pearson, 2010.

14th IEA Heat Pump Conference
15-18 May 2023, Chicago, Illinois

Numerical evaluation of high-temperature heat pump and thermal energy storage system for industrial processes

Seon Tae Kim*, Robert Hegner, Göksel Özuylasi, Panagiotis Stathopoulos, Eberhard Nicke

Institute of Low-Carbon Industrial Processes, German Aerospace Center (DLR),
Mandauhöfe, Haus 9, Äußere Oybiner Straße 14/16, 02763, Zittau, Germany

Abstract

A numerical investigation was conducted on a high-temperature heat pump (HTHP) that can supply heat at 200°C and two types of thermal energy storage (TES) systems. The HTHP cycle employs a multistage water vapor compression process to achieve a high-temperature lift. Concrete was used as the sensible heat storage (SHS) system, while strontium bromide/water ($SrBr_2/H_2O$) was used as the working pair for the thermochemical energy storage (TCES) system. The multistage HTHP cycle was first analyzed based on an enthalpy balance with specific temperature conditions, and then the performance of both the SHS and TCES systems connected to the HTHP cycle was estimated.
The HTHP cycle achieved a COP of 4.41 with an evaporation temperature of 90°C and a condensation temperature of 160°C. During storage, 500 kW of heat was supplied at 200 °C for 8 hours. The TCES system required 45% and 68% less mass and volumetric size, respectively, in storage mode. During discharge operation, the TCES system was able to supply heat at a temperature of over 200°C under all conditions, while the SHS system had a maximum cycle out temperature of 180°C. The TCES system also had a heat output rate of ~500 kW and round-trip efficiency (RTE) of 0.82.

© HPC2023.
Selection and/or peer-review under the responsibility of the organizers of the 14th IEA Heat Pump Conference 2023.

Keywords: High-Temperature Heat Pump, Multistage Vapor Compression Cycle, Thermal Energy Storage;

1. Introduction

The global greenhouse gas (GHG) emissions have steadily increased over the past few decades. Among the various emission sectors, the industrial sector is responsible for 34.8% of global GHG emissions after reallocating to the final energy consumption sectors, and the industrial sector is becoming increasingly important [1,2].

In 2019, 120944 PJ of energy were consumed in the industrial sector, and fossil fuels accounted for over 58% (70544 PJ). Thermal energy is the dominant energy carrier in the industrial sector and each industrial sub-sector has a different main temperature level respectively [3].

Waste heat recovery is an excellent solution for improving the efficiency of existing industrial processes [4,5]. However, heat recovery at low temperatures is generally not feasible. Another efficient option for recovering waste heat from industrial processes is to use highly efficient thermal power thermodynamic engines and heat pumps. Heat pumps are widely used in domestic applications and are applied to some niche industrial processes. Electrically driven heat pumps have proven to be suitable for supplying process heat effectively; however, industrial heat pumps can deliver heat at a maximum temperature of 150°C, mainly because of component limitations [6,7]. Despite this shortcoming, there have been several research and development efforts to push the sink temperature of industrial heat pumps to 200-250°C thus extending their availability for a larger proportion of industrial processes [8,9].

* Corresponding author. Tel.: +49-3583-58545-14.
E-mail address: seon.kim@dlr.de.

Thermal energy storage (TES) systems can store heat or cold to be used later at different temperatures, places, or power is mainly used to overcome the mismatch between energy generation and demand [10]. There are three types of TES systems: sensible heat storage, latent heat storage, and thermochemical storage. Sensible heat storage (SHS) is stored by increasing or decreasing the temperature of the storage material. Latent heat storage uses the phase transition of materials, usually a solid-liquid phase change. Upon melting heat is transferred to the material, storing large amounts of heat at a constant temperature. Thermochemical energy storage (TCES) is produced when a chemical reaction with high energy involved in the reaction is used to store energy. TES technology is considered an effective system that can maximize the efficiency of heat pumps [11].

The temperature distribution of the thermal energy demands for individual end-uses can vary substantially. This study focused on a high-temperature heat pump (HTHP) cycle that can supply heat at approximately 200°C. The HTHP consists of a two-stage water vapor (R-718) Rankine cycle with intercooling (IC), and is expected to provide process heat at temperatures ranging from 100°C to 200°C. This temperature range is primarily required in the paper and printing industries and in other non-classified sectors [12]. Additionally, this study numerically evaluated and compared the performance of two different types of thermal energy storage systems, sensible and thermochemical energy storage, when connected to the HTHP.

2. Modeling of HTHP and TES systems

2.1. Multistage water vapor compression cycle

A two-stage water vapor compression cycle with intercooling was introduced as the HTHP cycle, Fig. 1. First, the working fluid, water/steam, is compressed to an intermediate pressure and then cooled close to its condensation temperature. The resulting slightly superheated steam is recompressed to the condensation pressure, which corresponds to the aimed condensing temperature. The International Association for the Properties of Water and Steam, based on the industrial formulation 1997 (IAPWS-IF97), was adopted to calculate the water/steam properties in the HTHP cycle.

The temperature of the heat source, T_{source}, which corresponds to waste heat, was fixed at 120°C. The evaporation and condensation temperatures, T_{evap} and T_{cond}, were set to 90°C and 160°C, respectively, with a temperature difference of ΔT_{lift} = 70 K. The intermediate pressure was determined to have the same pressure ratio between the first and second stages because the two-stage cycle showed the highest coefficient of performance (COP) when both compressors had the same pressure ratio in previous work. Additionally, all the temperature differences between the hot and cold sides after the heat exchangers were assumed to be 10 K ($T_{sup\ \&\ sub}$ = 10 K).

The heat sink flow, which flows through the intercooler and condenser, was designed to supply constant thermal energy to the TES system. It has the same pressure as the condenser, $P_{sink} = P_{cond}$, and the temperature of the sink inlet and outlet, $T_{sink\ in\ \&\ sink\ out}$, were fixed at 25°C and 200°C respectively. The amount of thermal energy obtained from the intercooler and condenser, $\dot{Q}_{sink}$, was determined to be 500 kW.

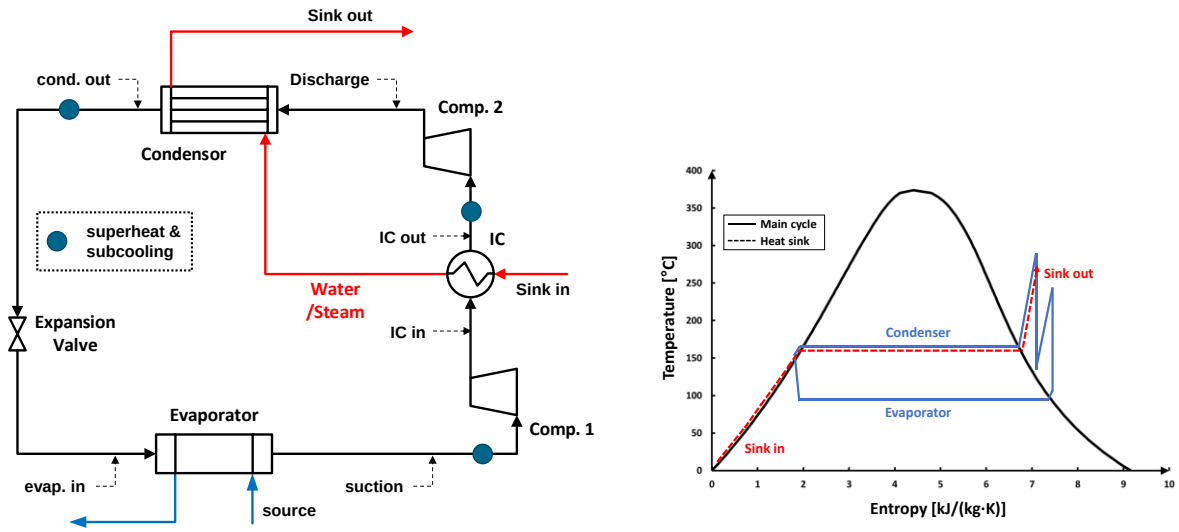


Fig. 1. Image of (left) schematic diagram of the HTHP cycle and (right) T-S diagram.

Table 1. Boundary conditions of HTHP and TES systems

Category	Item	Symbol	Value
HTHP cycle	Evaporation temperature	T_{evap}	90°C
	Condensation temperature	T_{cond}	160°C
	Superheat/Subcooling	$T_{sup\ \&\ sub}$	10 K
TES system	Power in storage mode	$\dot{Q}_{sink}$	500 kW
	Temperature in storage mode	$T_{sink\ out}$	200°C
	Pressure of heat sink	P_{sink}	$P_{sink} = P_{cond}$
	Mass flow rate of TES in discharge mode	m_{dis}	$m_{dis} = m_{stor}$

2.2. Thermal energy storage system

Sensible heat storage involves the use of a material to store thermal energy by increasing or decreasing the temperature of a storage medium. This energy storage method is widely used and is the most common type of TES technology. Many materials can be used for SHS materials such as water, air, oil, rock beds, brick, concrete, and so on. An SHS system using concrete is considered in this study. Concrete can withstand cyclic stress at temperatures of up to 500°C during numerous consecutive charging and discharging periods [13]. Therefore, concrete is suitable for storing sensible heat over long lifetimes.

The SHS system consists of two tanks: a hot tank containing concrete and a cold tank that stores air as a heat transfer fluid (HTF). The operating strategies are shown in Fig. 2. The low-temperature air, T_{amb} = 25°C, is heated by high-temperature steam in the HTHP cycle, T_{sink} = 200°C for 8 hrs, during storage mode, while high-temperature air transfers heat to low-temperature water/steam in the heat sink during the discharge mode. The state of water/steam in the heat sink flow was also calculated using IAPWS-IF97, and the performance of the SHS system was calculated based on the concrete properties at 200°C (Table 2) [14,15].

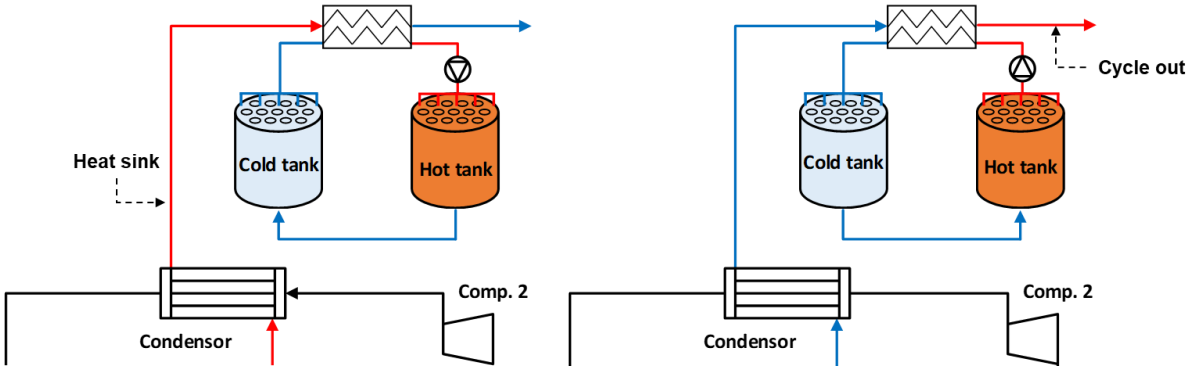


Fig. 2. Image of sensible heat storage system: (left) storage mode and (right) discharge mode.

Table 2. Properties of concrete for SHS systems

Temperature (°C)	Specific heat capacity, *Cp*, (J/(kg K))	Density, ρ, (kg/m^3)	Thermal conductivity, λ, (W/(m K))
100	832	2250	1.80
200	903	2250	1.60
300	1058	2250	1.40

Thermochemical energy storage (TCES) systems use reversible chemical reactions and have the advantages of a high storage density and long storage times without dissipation. Generally, reversible chemical reactions of TCES occur at high temperatures between the solid and gas phases. There are various types of chemical reactions for TCES, such as hydration, carbonation, and oxidation, and each reaction working pair has different working temperature and pressure characteristics. The strontium bromide and water ($SrBr_2/H_2O$) system was selected as the working pair for the TCES system in this study based on its promising performance at temperatures above 150°C [16,17]. The monohydrous $SrBr_2$ and $SrBr_2{\cdot}H_2O$ can store heat via dehydration, and the hydration of anhydrous $SrBr_2$ releases heat, as given in Eq. 1.

$$SrBr_2(s) + H_2O(g) \rightleftarrows SrBr_2 \cdot H_2O(s) \qquad \Delta H = 71.98\ \text{kJ/mol} \tag{1}$$

The operation of the TCES system with a packed bed reactor is shown in Fig. 3. During the heat storage mode, the dehydration of $SrBr_2{\cdot}H_2O$ is caused by a heat sink at 200°C, and the produced water vapor condenses in a water reservoir at 35°C, which is 10 K higher than the ambient temperature. The heat for the hydration, Q_{evap}, is assumed to use waste heat from industrial processes, in the same way as a heat source for the HTHP cycle, therefore, T_{hyd}, is lower than 110°C. Additionally, the molar mass, M, and density, ρ, of anhydrous and monohydrous $SrBr_2$ are shown in Table 3 [18].

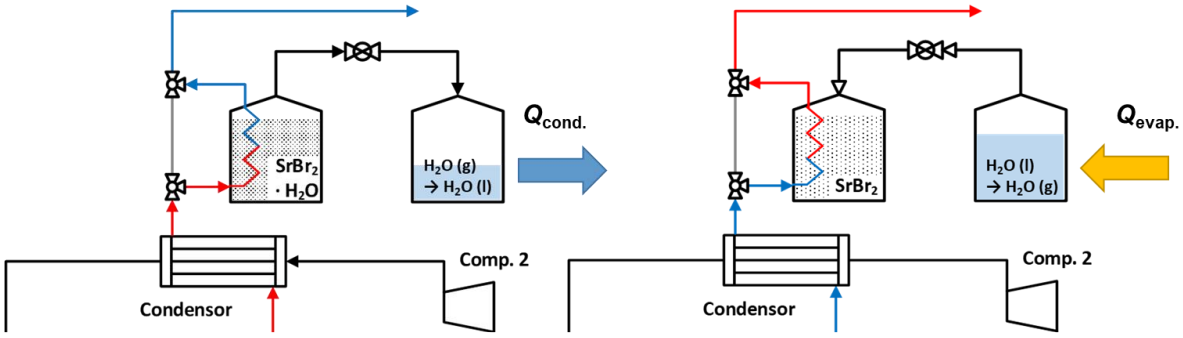


Fig. 3. Image of the thermochemical energy storage system: (left) storage mode and (right) discharge mode.

Table 3. Chemical and physical properties of $SrBr_2/H_2O$ TCES system

Material	Molar mass, M, (g/mol)	Density, ρ, (kg/m^3)	Enthalpy of hydration, ΔH, (kJ/mol)
$SrBr_2$	247.43	4216	71.98
$SrBr_2{\cdot}H_2O$	265.43	3911	

3. Methods and results

3.1. High-temperature heat pump cycle

The HTHP cycle operated at 90°C and 160°C for T_{evap} and T_{cond}, respectively, during storage for 8 hrs. It is assumed that the obtained thermal energy, 500 kW, is fully converted into a TES system, then 14400 MJ will be stored. The thermodynamic heat and energy balance of the multistage high-temperature heat pump cycle were estimated based on the IAPWS-IF97 standards. The intermediate pressure was defined from the suction and discharge pressures, with the assumption that each compression stage had the same pressure ratio. The overall thermodynamic properties, such as the pressure, temperature, and enthalpy, of each point of the HTHP cycle were determined. The important parameters are available from Eq. 2-3. Mass flowrate of the HTHP main cycle, $\dot{m}_{\text{main}}$, was induced as 0.19 kg/s, and the power consumption of two compressors, W_{comp}, was estimated to be 113.36 kW; the isentropic and mechanical efficiency, $\eta_{iso.}$ and $\eta_{mech.}$, are 0.78 and 0.90 respectively. From the obtained thermal energy from the condenser and IC, $\dot{Q}_{\text{sink}} = 500$ kW, and calculated W_{comp}, COP of the HTHP cycle was defined to 4.41, Eq. 4. Additionally, efficiency of the system was compared to that of an ideal cycle by introducing the thermodynamic efficiency, η_{carnot}, in Eq. 5 and 6. The Carnot efficiency, COP_{carnot},

represents the maximum energy efficiency of an ideal process that converts power to heat between two different temperatures, T_L and T_H [19]. The η_{carnot} value was calculated as 0.71.

$$\dot{m}_{main} = \frac{\dot{Q}_{sink}}{((H_{IC\,out} - H_{IC\,in}) - (H_{dis} - H_{cond\,out}))} \quad (2)$$

$$W_{comp} = \left(\frac{(H_{IC\,out} - H_{suc.}) \times \dot{m}_{main}}{\eta_{mech.}}\right) + \left(\frac{(H_{dis} - H_{IC\,out}) \times \dot{m}_{main}}{\eta_{mech.}}\right) \quad (3)$$

$$COP = \dot{Q}_{sink} / W_{comp} \quad (4)$$

$$\eta_{carnot} = \frac{COP}{COP_{Carnot}} \quad (5)$$

$$COP_{carnot} = \frac{T_H}{T_H - T_L} \quad (6)$$

According to the assumption in section 2.1, the mass flow rate of heat sink flow, $\dot{m}_{sink}$, has the same pressure as P_{dis} and it was calculated from the capacity of water/steam, c_p, and enthalpy, ΔH, of vaporization at 160°C, 2081.9 kJ/kg, Eq. 7. Because the c_p is variable by temperature, averaged specific heat capacities for the liquid and gaseous state, $\overline{c_p}_{liquid}$ and $\overline{c_p}_{gas}$, was adopted for the precise estimation. As a result, $\dot{m}_{sink}$ of the HTHP cycle is estimated to be 0.18 kg/s.

$$\dot{m}_{sink} = \frac{\dot{Q}_{sink}}{\left((T_{cond} - T_{sink\,in}) \times \overline{c_p}_{liquid} + (T_{sink\,out} - T_{cond}) \times \overline{c_p}_{gas} + \Delta H_{vap.,T_{cond}}\right)} \quad (7)$$

3.2. Sensible heat storage (SHS)

In storage mode, the HTHP cycle supplies 500 kW of heat for 8 hrs (τ_{stor} = 28800 s). Both TES systems stored thermal energy without any heat loss. The required concrete amounts for the SHS system can be calculated from Eqs. 8-9 based on material properties in Table 2, $m_{concrete} = 96647$ kg and $V_{concrete} = 43.0\ m^3$. As aforementioned in section 2.1, the temperature of the HTF in the TES was defined as 10 K lower than the heat sink out temperature, $T_{stor} = T_{sink\,out} - 10$ K, and the required airflow rate was obtained from Eq. 10, $\dot{m}_{air,stor} = 2.82$ kg/s.

$$m_{concrete} = \left(\dot{Q}_{sink} \times \tau_{stor}\right) / \left(c_{p_{concrete,200°C}} \times (T_{stor} - T_{amb})\right) \quad (8)$$

$$V_{concrete} = m_{concrete} / \rho_{concrete} \quad (9)$$

$$\dot{m}_{air-stor} = \dot{Q}_{sink} / \left(c_{p_{air,190°C}} \times (T_{stor} - T_{amb})\right) \quad (10)$$

On the discharge mode, the SHS system can have various cycle out temperatures, $T_{cycle\,out} < T_{stor} - 10$ K, by controlling heat output rate from the SHS system, $\dot{Q}_{SHS-dis}$. The required $\dot{Q}_{SHS-dis}$ According to the target $T_{cycle\,out}$ can be obtained from the enthalpy balance of heat sink flow and corresponding mass flowrate of air, $\dot{m}_{air-dis}$, on the SHS system are induced from Eq. 11. Additionally, the operation of the SHS system involves an air pump working, unlike the TCES system, for delivering the heat consecutively, Eq. 12. The values of differential the head, $h_{air\,pump}$, acceleration of gravity, g, and efficiency of the pump, $\eta_{air\,pump}$, are 20 m, 9.81 m/s^2, and 0.7 respectively. For what concerns the air mass flow rate, $\dot{m}_{air}$, and densities, ρ_{air}, is changed according to operation modes and conditions.

$$\dot{m}_{sink} \times \left(H_{T_{cycle\,out}} - H_{amb}\right) = \dot{Q}_{SHS-dis} = \dot{m}_{air-dis} \times \left(T_{stor} - T_{cycle\,out}\right) \quad (11)$$

$$W_{air\,pump} = \frac{(\dot{m}_{air} \times h_{air\,pump} \times g \times \rho_{air})}{\eta_{air\,pump}} \quad (12)$$

While the SHS system constantly consumes 3522.77 W for air pump work on storage mode, $\dot{Q}_{SHS-dis}$ and $W_{air\,pump-dis}$ are changed on discharge mode by target cycle out temperature, Fig. 4. Because heat sink flows have the same pressure to discharge pressure, P_{dis}, of HTHP main cycle, it has the same evaporation temperature of 160°C, and mass flow rate, $\dot{m}_{air-dis}$, is increased drastically to satisfy the increase $\dot{Q}_{SHS-dis}$ over the evaporation temperature. It was also found that the power consumption of the air pump increased consistently despite the heat output rate from the SHS system becoming stabilized over 160°C;

$\dot{m}_{\mathrm{air-dis}}$ increased from 22.8 kg/s to 45.9 kg/s on 170°C to 180°C of $T_{\mathrm{cycle\ out}}$ while $\dot{Q}_{\mathrm{SHS-dis}}$ shows stable values 487.45 kW and 497.68 kW.

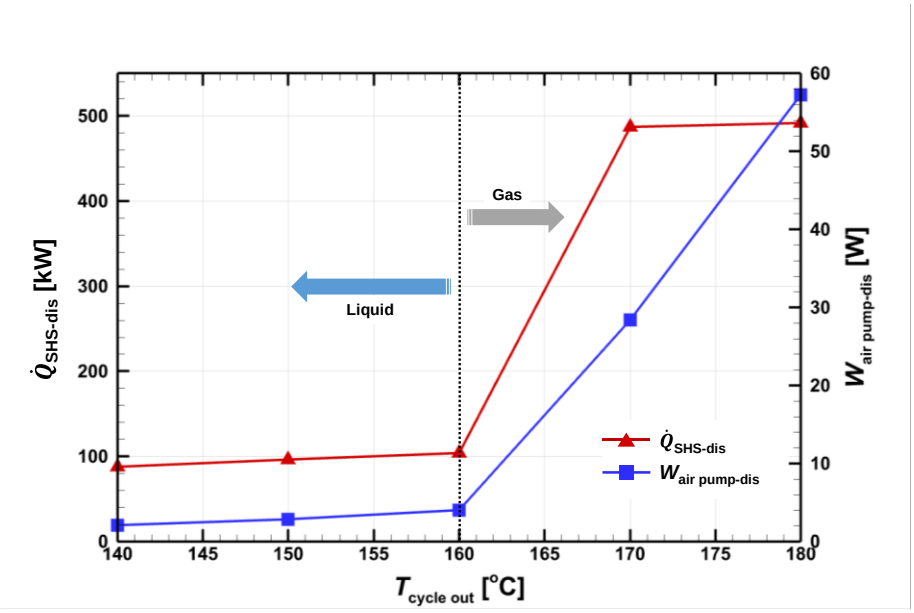


Fig. 4. Change of $\dot{Q}_{\mathrm{SHS-dis}}$ and $W_{\mathrm{air\ pump-dis}}$ by cycle out temperature on discharge mode.

3.3. Thermochemical energy storage (TCES)

The Gibbs free energy change of a reaction, ΔG, is obtained from the reaction enthalpy change, ΔH, and the entropy change, ΔS, as shown in Eq. 13.

$$\Delta G = \Delta H - T\Delta S \tag{13}$$

where ΔG has the following relationship with the reaction equilibrium constant, K_{eq}, for the gas-solid reaction assuming ideal gas properties Eq. 14. The reversible reaction condition is established at around $K_{\mathrm{eq}} = 1$ and the linear form of the Van't Hoff plot is obtained.

$$\ln K_{\mathrm{eq}}(T,P) = \ln\left(\frac{P}{P^0}\right) = \frac{\Delta G}{\mathrm{R}T} = -\frac{\Delta H}{\mathrm{R}T} + \frac{\Delta S}{\mathrm{R}} \tag{14}$$

From the reaction enthalpy, ΔH, molecular mass and density of $SrBr_2{\cdot}H_2O$, $M_{SrBr_2\cdot H_2O}$ and $\rho_{SrBr_2\cdot H_2O}$, in Table 3, the necessary amounts of $SrBr_2{\cdot}H_2O$ for the storage mode can be estimated as a mass, $m_{SrBr_2\cdot H_2O}$, of 53101 kg and volume, $V_{SrBr_2\cdot H_2O}$, of 13.6 m^3 from Eqs. 15-16, in terms of anhydrous $SrBr_2$, 49500 kg and 11.7 m^3.

$$m_{SrBr_2\cdot H_2O} = \left(\left(\frac{\dot{Q}_{\mathrm{sink}}}{\Delta H}\right)/M_{SrBr_2\cdot H_2O}\right) \times \tau_{\mathrm{stor}} \tag{15}$$

$$V_{SrBr_2\cdot H_2O} = m_{SrBr_2\cdot H_2O}/\rho_{SrBr_2\cdot H_2O} \tag{16}$$

Fig. 5 shows the Van't Hoff diagram of $SrBr_2/H_2O$ solid-gas reaction, ΔH = 71.98 kJ/mol and ΔS = 143.93 J/(mol·K) given in the NBS table. This TCES system possible to store heat by the accomplishment of dehydration at a certain temperature, T_{dehyd}, and achieve a higher output temperature than dehydration temperature, $T_{\mathrm{hyd}} > T_{\mathrm{dehyd}}$, particularly, since T_{hyd} is controllable from hydration pressure. Therefore, the discharge mode of the TCES system is also known as the temperature upgrade operation of a chemical heat pump [20].

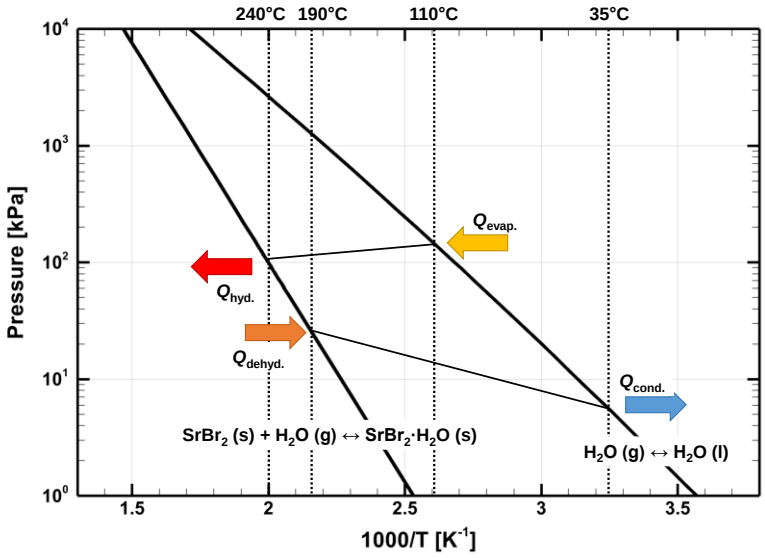


Fig. 5. Van't Hoff plot of $SrBr_2/H_2O$ solid gas-reaction.

In this study, during the heat storage operation, monohydrous $SrBr_2$, $SrBr_2 \cdot H_2O$, was decomposed at 190°C, 10 K lower than T_{sink}, and the produced water vapor was condensed at 35°C, 10 K higher than T_{amb}. Because it was assumed that waste heat from the industrial process was used for evaporation, the temperature for evaporation, T_{evap}, was limited to 110°C. Four different evaporation temperatures were selected, T_{evap} = 80°C, 90°C, 100°C, and 110°C, and hydration temperatures, T_{hyd} = 206°C, 217°C, 227°C, and 238°C, were obtained from the corresponding saturated water vapor pressures of 47.4 kPa, 70.2 kPa, 101.4 kPa, and 143.4 kPa. The heat output rate of the TCES system, $\dot{Q}_{\mathrm{TCES-dis}}$, is obtained from the first half of Eq. 9, and Table 4 shows the cycle out temperature, $T_{\text{cycle out}}$, operable discharge time, τ_{dis}, and $\dot{Q}_{\mathrm{TCES-dis}}$ by evaporation temperature, T_{evap}.

Table 4. Performance of TCES system on discharge mode

Evaporation temperature, T_{evap}, (°C)	Hydration temperature, T_{hyd} (°C)	Operable time, τ_{dis}, (hr)	Heat output rate of TCES, $\dot{Q}_{\mathrm{TCES-dis}}$, (kW)
80	206	8.03	498
90	217	7.96	502
100	227	7.90	506
110	238	7.83	510

3.4. Comparison of both TES systems

The heat output rate and operable discharge time of both the TES systems are compared in Fig. 6. Generally, the TCES system has a higher heat output rate, $\dot{Q}_{\mathrm{dis}}$, and cycle out temperature, $T_{\text{cycle out}}$, than the SHS system. SHS system has a maximum cycle output temperature, $T_{\text{cycle out}}$, of 180°C because the stored temperature, $T_{sotr.}$, is 190°C, however, the $T_{\text{cycle out}}$ of the TCES system obtained from equilibrium pressure on Eq. 12 is higher than 200°C. Additionally, the $T_{\text{cycle out}}$ of the SHS TES system has been decreased rapidly for below 160°C of $T_{\text{cycle out}}$, since the saturation pressure of the heat sink is assumed to have the same condensation temperature as with HTHP main cycle.

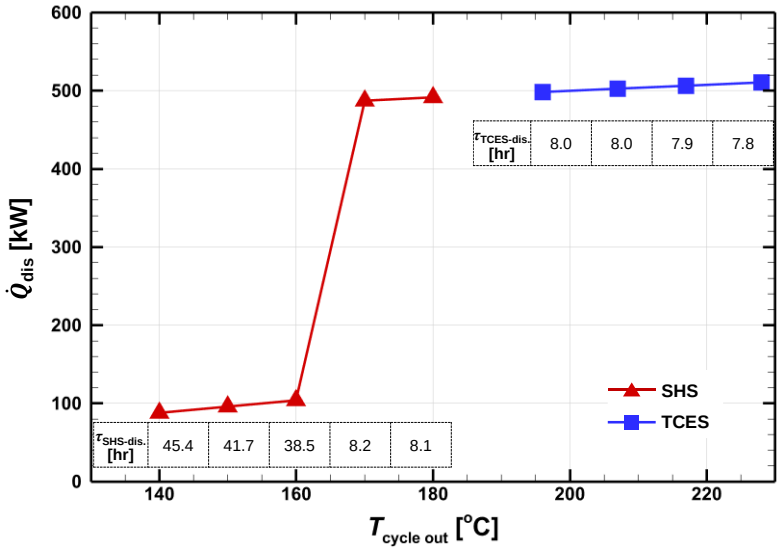


Fig. 6. Comparison of $\dot{Q}_{dis}$ and τ_{dis} in function of the cycle out temperature.

The round-trip efficiency (RTE) of the thermal energy storage system is expressed as the ratio of the energy output to the energy input, as shown in Eq. 17; the power consumption of the air pump, $W_{air\ pump}$, is considered only for the SHS system.

$$\eta_{RTE} = \frac{(\dot{Q}_{dis} - W_{air\ pump-\ dis}) \times \tau_{dis}}{(\dot{Q}_{sink} + W_{comp} + W_{air\ pump-stor}) \times \tau_{stor}} \quad (17)$$

On the RTE, on the other hand, the TCES system has a constant value, 0.82, since the TCES system can be utilizing waste heat from industrial processes for evaporating, Q_{evap}, without additional mechanical power, the RTE of SHS are decreasing from 0.79 to 0.72 with increasing heat output rate. Dramatically increased air mass flow rate on discharge mode, $\dot{m}_{air-dis}$, brings low RTE of SHS system at high cycle out temperature, $T_{cycle\ out}$, and heat output rate, $\dot{Q}_{dis}$. Compared to the concrete SHS system, $SrBr_2/H_2O$ TCES system only requires 45% and 68% less amount of mass and volume for storage; the TCES system also has 4-14% higher round-trip efficiency, Table 5.

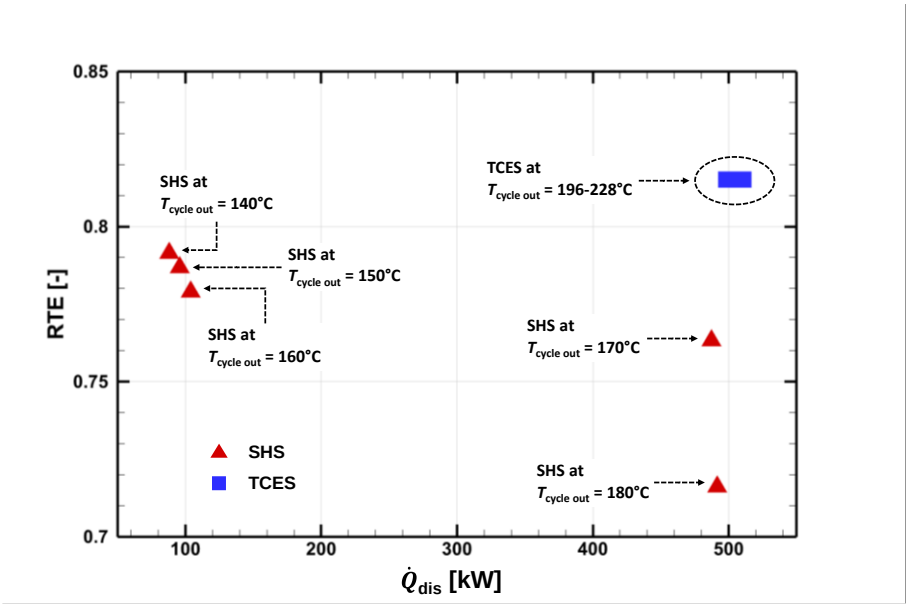


Fig. 7. Comparison of RTE according to heat output rate in the discharge mode.

Table 5. Specifications of TES systems

	SHS	TCES	Note
Material	Concrete	$SrBr_2 \cdot H_2O$ ($SrBr_2$)	TCES/SHS
Weight, *m*, (kg)	96647	53101 (49500)	0.55 (0.51)
Volume, *V*, (m^3)	43.0	13.6 (11.7)	0.32 (0.27)
RTE (-)	0.72-0.79	0.82	1.04-1.14

4. Conclusion

The performances of a multistage high-temperature heat pump (HTHP) and two different thermal energy storage (TES) systems connected to the HTHP cycle were investigated. The HTHP cycle had temperatures of 90°C and 160°C for the evaporator and condenser, respectively, and its performance was analyzed using a thermodynamic enthalpy balance. It was assumed that the HTHP cycle would supply 200°C and 500 kW of thermal energy for 8 hours during storage operation. The heat sink flow transferring thermal energy to the TES system is constrained to have the same pressure as the discharge pressure of the HTHP main cycle, $P_{\text{sink}} = P_{\text{dis}}$, and a constant flow rate, $\dot{m}_{\text{sink}}$.

The thermochemical energy storage system (TCES) has a higher discharge temperature and heat output rate, >200°C and ~500 kW, compared to the sensible heat storage (SHS) system. This is because the $SrBr_2/H_2O$ TCES system release higher temperature than assumed waste heat by considering the equilibrium pressure, whereas the SHS system does not allow for an upgrade in temperature. In particular, the heat output rate of the SHS system was significantly reduced when the cycle out temperature was lower than the condensation temperature, $T_{\text{cycle out}} < T_{\text{cond}}$. In terms of physical requirements, The TCES system has 45% and 68% lower material weight and volume requirements than the SHS system, and its round-trip efficiency is also higher because of the reduced power consumption of the air pump. These results confirmed the advantages of the TCES system for high-temperature thermal energy.

This approach will not only aid in the development of efficient HTHP and TES integration systems but also their effective development. Further study is possible through a detailed analysis of the HTHP cycle with various temperature ranges and different TES system configurations.

References

[1] Lamb WF, Wiedmann T, Pongratz J, Andrew R, Crippa M, Olivier JGJ et al. A review of trends and drivers of greenhouse gas emissions by sector from 1990 to 2018. Environ. Res. Lett. 2021;**16**(7):73005.

[2] Edenhofer O (ed.). Climate change 2014: Mitigation of climate change Working Group III contribution to the fiths assessment report of the intergovernmental panel on climate change.

[3] IEA. Key World Energy Statistics 2021; 2021.

[4] Huang F, Zheng J, Baleynaud JM, Lu J. Heat recovery potentials and technologies in industrial zones. *J Energy Inst* 2017;**90**(6):951-61.

[5] Brueckner S, Miró L, Cabeza LF, Pehnt M, Laevemann E. Methods to estimate the industrial waste heat potential of regions – A categorization and literature review. Renewable Sustainable Energy Rev. 2014;**38**:164–71.

[6] Chamoun M, Rulliere R, Haberschill P, Peureux J-L. Experimental and numerical investigations of a new high temperature heat pump for industrial heat recovery using water as refrigerant. *Ing J Refrig* 2014;**44**:177–88.

[7] German Energy Agency (DENA). Process heat in industry and commerce: Technology solutions for waste heat utilisation and renewable provision; 2016.

[8] van de Bor DM, Infante Ferreira CA. Quick selection of industrial heat pump types including the impact of thermodynamic losses. *Energy* 2013;**53**:312–22.

[9] Arpagaus C, Bless F, Uhlmann M, Schiffmann J, Bertsch SS. High temperature heat pumps: Market overview, state of the art, research status, refrigerants, and application potentials. *Energy* 2018;**152**:985–1010.

[10] Miró L, Gasia J, Cabeza LF. Thermal energy storage (TES) for industrial waste heat (IWH) recovery: A review. *Appl. Energy* 2016;**197**:284-301.

[11] Osterman E, Stritih U. Review on compression heat pump systems with thermal energy storage for heating and cooling of buildings. *J Energy Storage* 2021;**39**:102569.

[12] Fleitern Tobias, Jan Steinbach, Mario Ragwitz, Andreas Müller, Lukas Kranzl, Marcus Hummel et al. Mapping and analyses of the current and future (2020-2030) heating/cooling fuel deployment (fossil/renewables) Work package 1: Final energy consumption for the year 2012 Final report: 54296; 2016.

[13] Laing D, Lehmann D, Fiß M, Bahl C. Test Results of Concrete Thermal Energy Storage for Parabolic Trough Power Plants. *J Sol Energy Eng* 2009;**131**(4): 041007.

[14] Pan J, Zou R, Jin F. Experimental Study on Specific Heat of Concrete at High Temperatures and Its Influence on Thermal Energy Storage. *Energies* 2017;**10**:33.

[15] Anderberg Y, Forsén NE, Hietanen T, Izquierdo JM, A Le Duff, E Richter, RT Whittle, H Bossenmayer, HU Litzner, J Kruppa. Background documents to EN 1992-1-2 Eurocode 2: Design of concrete structures, Part 1-2: General rules - Structural fire design. Brussels, European Committee for Standardization; 2004.

[16] Richter M, Habermann EM, Siebecke E, Linder M. A systematic screening of salt hydrates as materials for a thermochemical heat transformer. *Thermochim. Acta* 2018;**659**:136-50.

[17] Stengler J, Bürger I, Linder M. Thermodynamic and kinetic investigations of the $SrBr_2$ hydration and dehydration reactions for thermochemical energy storage and heat transformation. *Appl. Energy* 2020;**277**:115432.

[18] Perry Dale L, *Handbook of Inorganic Compounds*. 2nd ed. Boca Raton: CRC Press; 2011.

[19] Jan Szargut. Component efficiencies of a vapour-compression heat pump. *Exergy, An International Journal* 2002;**2**(2):99–104

[20] Zamengo M, Yoshida K, Morikawa J. Numerical evaluation of a Carnot battery system comprising a chemical heat storage/pump and a Brayton cycle. *J Energy Storage* 2021;**41**:102955.

14th IEA Heat Pump Conference
15-18 May 2023, Chicago, Illinois

Pool boiling on metal-foam enhanced tube bundle: heat transfer characteristics and flow visualization

Cheng-Min Yang[a], M. Muneeshwaran[a], Pengtao Wang[a], Kashif Nawaz[a,*]
[a]Multifunctional Equipment Integration Group, Building Technologies Research and Integration Center (BTRIC), Oak Ridge National Laboratory, 1 Bethel Valley Rd, Oak Ridge, TN 37831, USA

Abstract

A flooded evaporator configuration is common in large central air conditioning or process cooling systems. It is basically a shell and tube heat exchanger, in which a secondary fluid (brine or water) circulates inside the tube bundle and is cooled by the vaporization of the refrigerant on the outside surface of the tubes. The enhanced pool boiling process enables the compact design of flooded evaporators, which substantially reduces the refrigerant charge. High-porosity metal foam, with a large surface-area-to-volume ratio, could provide an extended heat transfer area and a high-density of nucleation sites. This study experimentally investigated the pool boiling heat transfer and flow characteristics on metal-foam enhanced tube bundles. The enhanced bundle consists of four aluminum tubes with aluminum foam brazed around the outer surface, which are horizontally mounted in a staggered arrangement. The results showed that the metal-foam enhanced tube bundles improved the heat transfer coefficient by 100-160% with a lower wall temperature difference of 1-10°C, compared to the baseline. In addition, the tube pitch played a significant role in determining the pool boiling behavior of the tube bundles.

© HPC2023.
Selection and/or peer-review under the responsibility of the organizers of the 14th IEA Heat Pump Conference 2023.

Keywords: Tube bundle;metal foam;pool boiling;heat transfrer; flow visualization

1. Introduction

Tube bundles have been widely employed in flooded evaporators for air-conditioning and refrigeration, desalination, and absorption chiller industries. In order to reduce the size of heat exchangers and maintain a lower temperature difference between the tube wall and working fluid, improving the pool boiling heat transfer is pivotal. In this regard, several enhanced tube geometries have been developed for industrial applications, such as GEWA, TURBO, and HIGH FLUX tubes. Ayub and Bergles [1] demonstrated 1.5- and 1.75-times heat transfer enhancements for the R-113 pool boiling using GEWA-K and GEWA-T tubes, respectively. Thome [2] demonstrated a 4-10 fold improvement in GEWA-TX tubes compared to the plain tubes.

Recently, utilizing open-cell metal foam to enhance the pool boiling heat transfer has gained significant attention due to its larger area-to-volume ratio and liquid replenishment ability through capillary action. These features of metal foam structures could aid in improving the heat transfer rate and delaying the critical flux. Nosrati et al. [3] studied the flow boiling of R-134a in metal foam filled tubes (metal foam on the tube side). They reported a 220% improvement in the heat transfer coefficient. Similarly, Hu et al. [4] tested the wettability effect of metal foam filled tubes during the flow boiling using R-134a. In their study, they compared the flow boiling behavior of hydrophilic, hydrophobic, and uncoated metal foams. The results showed that the hydrophobic coating offered a 6-30% enhancement in heat transfer compared to the uncoated one, whereas the hydrophilic coating reduced the heat transfer by 2-18%. Manetti et al. [5]

Notice: This manuscript has been authored in part by UT-Battelle, LLC, under contract DE-AC05-00OR22725 with the US Department of Energy (DOE). The US government retains and the publisher, by accepting the article for publication, acknowledges that the US government retains a nonexclusive, paid-up, irrevocable, worldwide license to publish or reproduce the published form of this manuscript, or allow others to do so, for US government purposes. DOE will provide public access to these results of federally sponsored research in accordance with the DOE Public Access Plan (http://energy.gov/downloads/doe-public-access-plan).

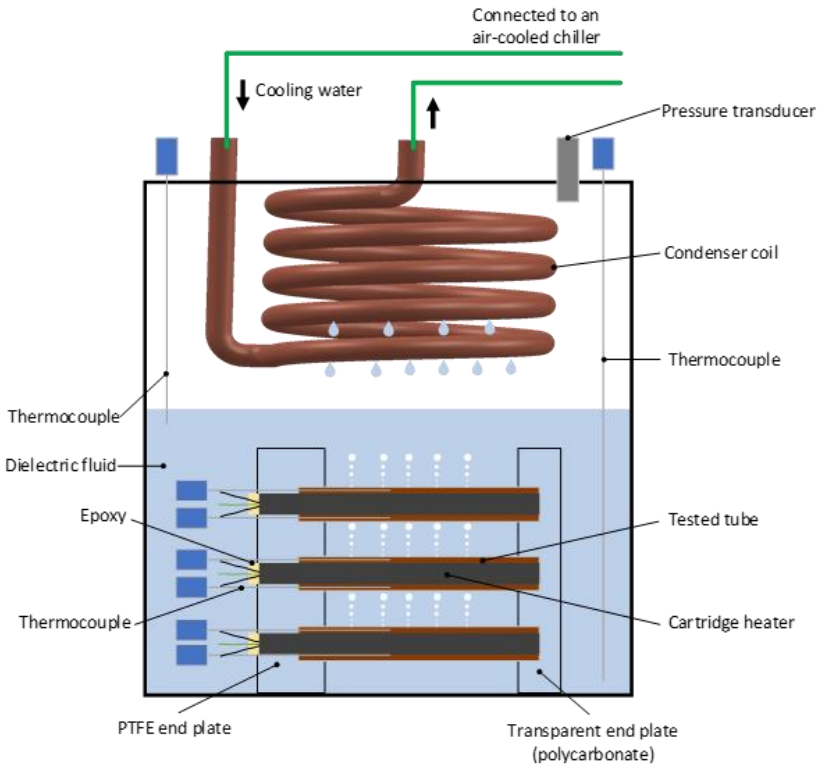
performed the pool boiling experiments on a copper metal foam surface (flat surface) using HFE-7100. They suggested that the metal foam surfaces can overcome the temperature overshoot problem associated with electronic cooling due to their interconnected porous structure that increases the wetted surface area and nucleation site density. Shi et al. [6] analyzed the behavior of a flat copper foam surface under pool boiling conditions for different wettability's. They reported that the superhydrophilic coated foams offered a higher heat transfer rate when the heat flux was above 20 W cm^{-2}, whereas the superhydrophobic coatings outperformed the superhydrophilic ones when the heat flux was below 20 W cm^{-2}. The recent developments in phase change heat transfer in metal foam structures are summarized in [7, 8].

In summary, the pool boiling behavior of metal foam structures is widely studied for the flat surface configuration, and the flow boiling characteristics are analyzed for the metal foam filled tubes (i.e., metal foams are placed inside the tubes). In our previous study, the pool boiling heat transfer over an externally embedded metal-foam tube was experimentally investigated [9]. Yang et al. reported that the effective heat transfer coefficient of the metal-foam enhanced tube was 2.1~4.8 times higher than a bare aluminum tube. However, the studies that pertain to the pool boiling behavior of externally embedded metal- foam *tube bundles* (i.e., shell side) are limited in the open literature. Therefore, the current study aims to develop a metal foam tube bundle to improve the shell side heat transfer rate. The performance of the metal foam tube bundle is compared to the bare tube bundle. In addition, a visualization study is carried out to understand the bubble dynamics on both bare and metal-foam enhanced tube bundles.

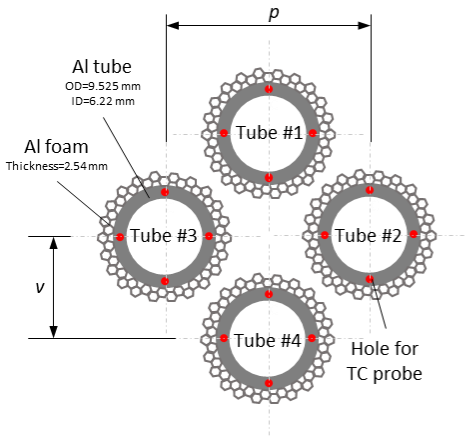
2. Experiments

The schematic of the pool boiling apparatus for tube bundle experiments is shown in Fig. 1 (a). It consists of a pool boiling chamber, a heat transfer test section, a condenser coil, and a cooling system. The pool boiling chamber is made of clear polycarbonate, and its internal dimensions are 222.3 mm × 212.7 mm × 222.3 mm. The chamber is charged with 4 Liters of dielectric liquid at atmospheric pressure, and the heat transfer test section is submerged in the liquid pool. The system pressure is monitored with an Omega absolute pressure transducer with an accuracy of ±0.2% Upper range limit (URL) ranging from 0 to 103.4 kPa. The bulk temperature of the liquid pool is measured with T-type thermocouples at two different locations. A coil condenser located at the upper part of the chamber is designed for condensing the dielectric vapor generated through the pool boiling process. The evaporated vapor rises and condense on the outer surface of the coil. The condensed liquid is dropped and returned to the pool to create a natural circulation. The cooling water for the coil is supplied by a recirculating chiller with a cooling capacity up to 7.5 kW (Thermo Scientific, ThermoFlex 7500).

(a)



(b)



	Case 1	Case 2
Tube pitch *p*	19.05 mm	25.4 mm
Vertical distance between tubes *v*	16.5 mm	22.0 mm

Fig. 1. Schematic diagrams of the (a) experimental apparatus and (b) detailed geometry of the tested tube bundles.

The heat transfer test section of the lab-scale tube bundle experiments has four 3/8" OD aluminum tubes in a staggered arrangement. As demonstrated in Fig. 2(a) and (b), the baseline case consists of bare tubes, whereas the enhanced tube bundle comprises metal-foam tubes. Fig. 1(b) provides the detailed geometry of the tested tube bundles. The tubes have an inner diameter D_i=6.22 mm and an outer diameter D_o=9.525 mm. Two tube pitches of the bundle are investigated in this study. The externally enhanced tubes (metal foam tubes) have a 2.54 mm thick layer of open cell aluminum foam brazed around the outer surface. The aluminum foam used in this study is 40 PPI Duocel foam made of 6101 alloy with heat treated to T6 condition from ERG Aerospace Corporation. The porosity of the metal foam is 81%, estimated through X-ray computed tomography (XCT) 3D scanning. The tested tubes are 76.5 mm long, and they are horizontally mounted to two end plates. One is made of PTFE, while the other is made of transparent polycarbonate for visualizing the boiling process. Two brass pieces are fastened to the end plates as additional weight to ensure the heat transfer test section is submerged. More details of the tube assembly can be found in the work of Yang et al. [9].

(a) (b)

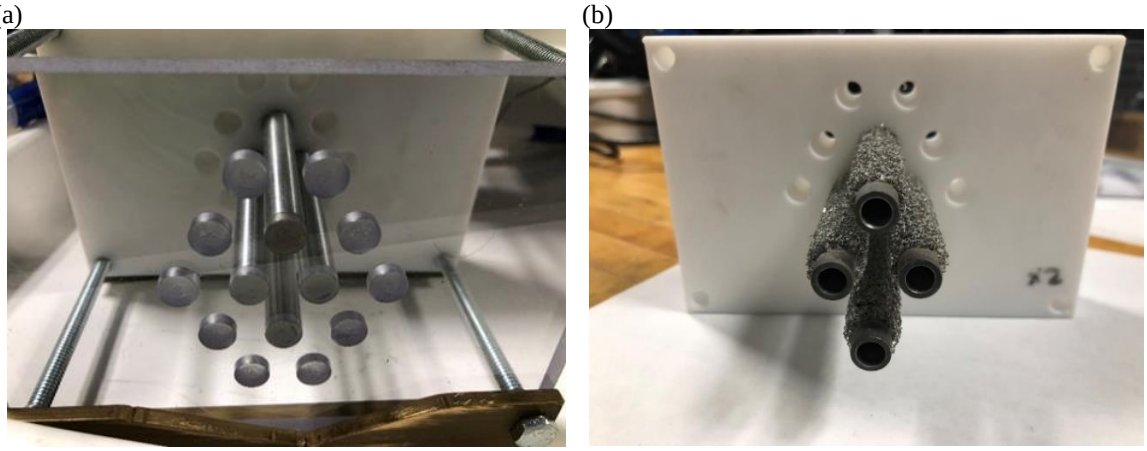


Fig. 2. (a) bare aluminum tube bundle and (b) metal foam enhanced tube bundle.

For each tube, a Watlow cartridge heater with 579W heating capacity is inserted to provide the heat. The outer diameter and the heating length of the heater are, 6.22 mm and 63.5 mm, respectively. To be noted that epoxy is applied to the end of the cartridge heaters to reduce the heat loss in the axial direction. The power to the cartridge heaters is controlled using pulse width modulation, and different outputs can be approximated over a time span of 1 second. The actual heating power is measured using a watt transducer ranging from 0 to 3 kW (Ohio Semitronics, #PC5-020X5Y25). The wall temperatures for each tube are measured at four locations with T-type thermocouple probes. Four holes with the diameter of 1.02 mm are drilled alongside the tube wall at 90 degrees apart. The first 25.4 mm of the thermocouple probes stays inside the tube wall,

and the remaining portion that is directly exposed to the dielectric fluid is insulated with a PVC sleeve. All the thermocouple probes were calibrated against a NIST-certified precision thermometer with an accuracy of ±0.05°C, and all the data are collected and recorded with a Campbell Scientific CR1000 measurement and control datalogger accompanied with an AM25T thermocouple multiplexer.

For the pool boiling experiments of the tube bundles, 3M Novec engineered fluid HFE-7000 is used as the working fluid. HFE-7000 is a type of clear, colorless, thermally stable dielectric fluid with 34°C boiling point under atmospheric pressure. Prior to the experiments, the pool boiling chamber is charged with 4 Liters of the HFE-7000, which provides around 25.4 mm liquid level above the heat transfer test section. At the beginning of the experiments, the cartridge heaters are set to 10% of its maximin heating capacity to heat up the liquid pool to reach saturation temperature. The liquid pool is heated with the same power setting for an additional hour to remove the non-condensable gases dissolved in the fluid. The power of the cartridge heaters is then reduced to 5% to start the heat transfer measurement. Once the steady state is reached, the data is collected and recorded for 10 mins. The experiments are repeated by increasing the heater power with 5% increments.

3. Data Reduction

The effective pool boiling heat transfer coefficient (*HTC*) on the outside of the tube is calculated as the ratio of the heat flux to wall superheat.

$$HTC = \frac{q''}{\Delta T_{\text{sup}}} \tag{1}$$

The heat flux q'' is estimated based on the outer surface area of the bare tube:

$$q'' = \frac{\dot{Q}_{elec} - \dot{Q}_{loss}}{\pi D_o L_h} \tag{2}$$

where D_o and L_h are the outer diameter and the effective heating length of the tested tube. The effective heat transfer rate from the tube wall to the dielectric fluid is determined by the electrical power delivered to the heater, $\dot{Q}_{elec}$ subtracting the conduction heat loss in the axial direction, $\dot{Q}_{loss}$. The conduction heat loss in the axial direction is estimated using a special tube, in which the thermocouple holes alongside the tube have two different depths.

$$\dot{Q}_{loss} = kA_{cs}\frac{T_{wall,R} - T_{wall,L}}{\Delta x} \tag{3}$$

where k and A_{cs} are the thermal conductivity and the cross-sectional area of the tube material, respectively. Δx is the depth difference between the two thermocouple holes in the axial direction. The subscript of the wall temperature shows the location of the thermocouple probe, and *R* and *L* represent the right and left, respectively.

The wall superheat, ΔT_{sup}, is the temperature between the tube wall temperature and the saturation temperature of the dielectric fluid.

$$\Delta T_{\text{sup}} = T_{wall} - T_{sat} \tag{4}$$

The saturation temperature T_{sat} is determined by the average values of the two T-type thermocouple probes located at the top and bottom of the pool boiling chamber. During the experiments, the pool temperature is maintained within 0.3°C. The wall temperature T_{wall} for each tube is the mean temperature of the four thermocouples inserted into the holes alongside the tube wall and corrected using the 1-D heat conduction equation.

$$T_{wall} = T_{m,avg} - \left(\frac{\dot{Q}_{elec} - \dot{Q}_{loss}}{2\pi k L_h}\right)\ln\left(\frac{r_o}{r_m}\right) \tag{5}$$

where r_o is the outer tube radius, and r_m is the mean value of inner and outer tube radius, which is the location of the tip of thermocouple probes.

The overall heat transfer coefficient for the tube bundle is estimated based on the average value of four

single-tube heat transfer coefficients calculated using Eq. (1).

The experimental uncertainties of the effective heat transfer coefficient, the heat flux, and the wall superheat are estimated following the error propagation analysis documented in the work of Moffat [10]. The root-sum-square combination of the effects of the individual measurements gives the overall uncertainty of the target parameter. All the uncertainties are based on a confidence level of 95%.

$$\delta U\left(X_1, X_2, \cdots, X_N\right) = \sqrt{\sum_{i=1}^{N}\left(\frac{\partial U}{\partial X_i}\delta X_i\right)^2} \tag{6}$$

4. Results and Discussion

4.1. Validation of experimental setup

The pool boiling experiments are first performed on a single bare tube to validate the experimental facility. The experimental data are compared against the Cooper [11] and Cornwell and Houston [12] correlations, as shown in Fig. 3. The Cooper correlation and the Cornwell-Houston correlation are given in Eqns. (7) and (8), respectively.

$$HTC_{Cooper} = 90M^{-0.5}\left(q''\right)^{0.67}\left(-\log\left(P_r\right)\right)^{-0.55}\left(P_r\right)^{\left(0.12-0.2\log\left(R_p\right)\right)} \tag{7}$$

where M and P_r are the molecular weight and reduced pressure. R_p is the average surface roughness of the plain tube, and 1 μm was used in the current study.

$$HTC_{Cornwell-Houston} = 9.7P_c^{0.5}\,\mathrm{Re}_b^{0.67}\,\mathrm{Pr}^{0.4}\left(1.8P_r^{0.17} + 4P_r^{1.2} + 10P_r^{10}\right)\left(\frac{k_l}{D_o}\right) \tag{8}$$

Noted that P_c is critical pressure in bar and k_l is the thermal conductivity of dielectric liquid. Re_b is boiling Reynolds number, which is directly related to the heat flux under the saturated pool boiling, as follows.

$$\mathrm{Re}_b = \frac{GD_o}{\mu_l} = \frac{qD_o}{\mu_l h_{fg}} \tag{9}$$

where μ_l is the dynamic viscosity, while h_{fg} is the latent heat of vaporization.

Fig. 3 shows the variation of heat transfer coefficient of HFE-7000 against heat load ranging from 5 to 100 kW/m^2. Similar to the trend predicted by the correlations [11][12], the heat transfer coefficient increases with heat flux. In addition, the Cooper [11] correlation predicts the heat transfer coefficients within a 7% deviation when the heat flux is below 50 kW m^{-2}. At higher heat fluxes (q > 50 kW m^{-2}), the deviation between experimental and predicted data grows. In contrast, the Cornwell-Houston [12] correlation showed better agreement at higher heat fluxes with a maximum deviation of 7% and exhibited a larger deviation at smaller heat fluxes with a maximum deviation of 13%. Overall, the experimental data matches well with the standard correlations, which validates the experimental setup.

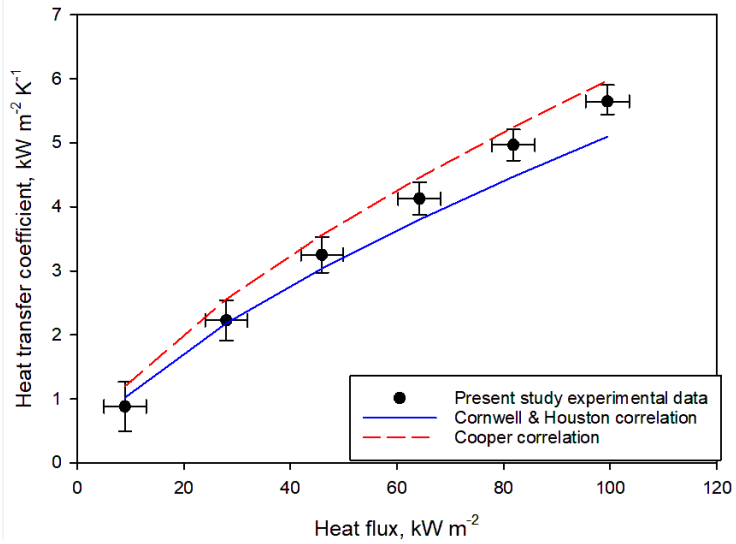


Fig. 3. Validation of experimental facility through comparing single tube pool boiling data against Cooper [11] and Cornwell-Houston [12] correlations.

4.2. Performance assessment of bare and metal foam tube bundles

The performances of a bare single tube and a metal foam tube bundle are characterized in terms of heat transfer coefficient and wall temperature. Note that the results presented in this section pertain to a tube pitch of 19 mm. The experiments are performed for a heat flux range of 5-100 kW m^{-2}, and the corresponding average heat transfer coefficient values are presented in Fig. 4. The HTC of the bare tube bundle is almost 3-5% higher than that of the single bare tube. It indicates that the bundle effect caused by the vapor flow induced convection is minimum for this tube bundle configuration as it only has three rows. However, it can be seen in Fig. 4 that the metal foam tube bundle exhibited a superior performance over the bare tube bundle. The trend of the metal foam tube bundle is consistent with that of the single metal foam tube published in the earlier work [9]. The heat transfer coefficient of the metal foam tube bundle is about 100-160% higher than that of the bare tube bundle for the tested heat flux range. The improvement in the metal foam tube bundle is primarily attributed to the increased surface area. Besides, the metal foam structures possess many active nucleation sites compared to the plain tube, as shown in Fig. 5. The large number of active nucleation sites in metal foam tubes could ameliorate the nucleate boiling heat transfer compared to the bare tube, which in turn increases the heat transfer coefficient.

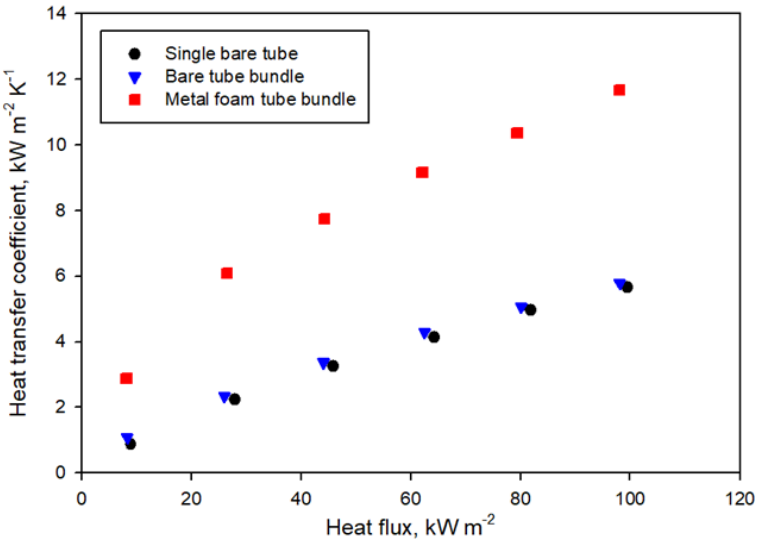
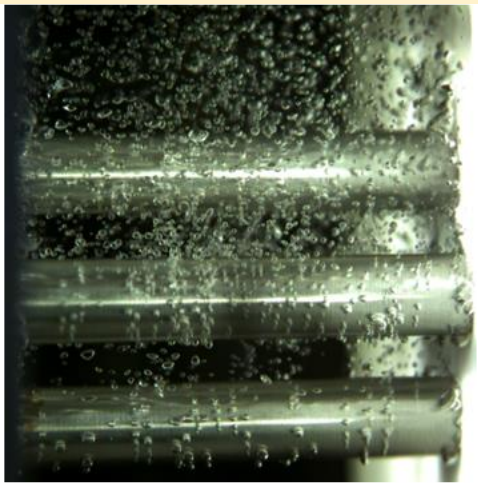
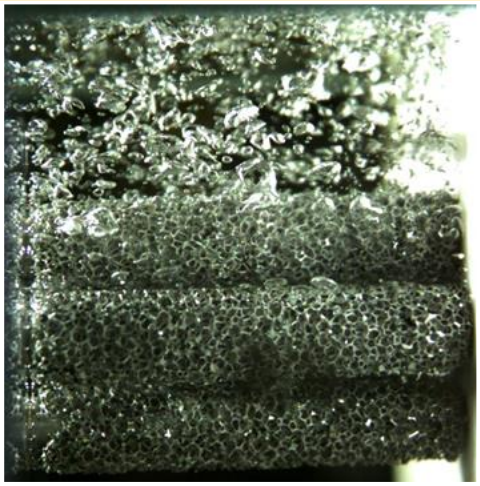
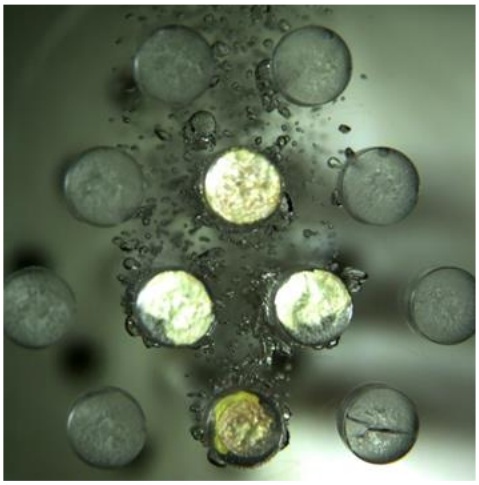
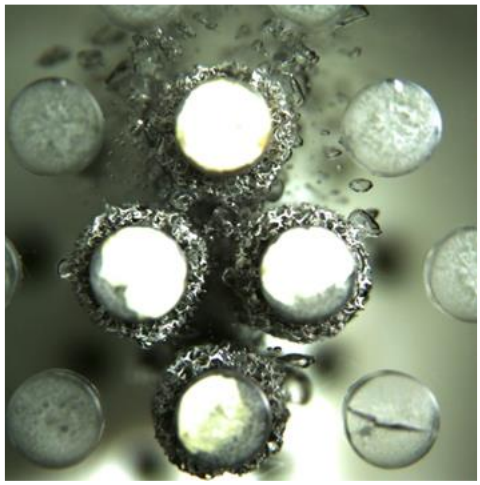


Fig. 4. Performance comparison of bare and metal foam tube bundles.

The photographic comparison of the pool boiling behavior in bare and metal foam tube bundles can be seen in Fig. 5. At lower fluxes ($q < 10$ kW m^{-2}), the wall temperature is close to the saturation temperature of the working fluid (i.e., HFE-7000), as shown in Fig. 6. At this stage, the number of nucleation sites is relatively low, as shown in Fig. 5(a). When the heat flux is increased, the nucleation sites get activated, leading to more bubble formation, as shown in Fig. 5(b). This leads to a bubble coalescence and forms local vapor blankets on the tubes, which hinder the heat transfer from the tubes to the fluid. As a result, the wall temperature keeps increasing with heat load, as shown in Fig. 6. It can be noted that the wall temperature of the bottom tube (i.e., tube 4) is higher than that of other tubes for both bare and metal foam configurations. This is because of the bubble flow pattern. The bubble or vapor column's departure from the bottom tube is mainly impeded by the top (i.e., tube 1) and side (i.e., tubes 2 and 3) tubes. However, the vapor column leaving the bottom tube mainly passes through the gap between tube 2 and tube 3, and finally hits the bottom of tube 1, as shown in Fig. 5 This phenomenon enhances the convection induced heat transfer in tubes 1, 2, and 3. As a result, tubes 1-3 experienced a lower wall temperature compared to that of the bottom tube, as shown in Fig. 6. When comparing Fig. 6(a) and (b), it can be understood that the wall temperature of the metal foam tubes is almost 4-10°C lower than that of the bare tubes. The lower wall temperature of metal foam tubes is attributed to the combination of the following effects: The metal foam on the outside of the tube increases the surface area and thereby the active nucleation site density, which leads to increased latent heat transfer (i.e., pool boiling). Additionally, the open cell metal foam structure could lead to a smaller bubble departure diameter even at the higher heat fluxes, which can potentially delay the local vapor blanket formation. Furthermore, the porous structure of the metal foam can act as a capillary wick to locally feed the liquid to the tube wall due to the capillary action. The combined effect of the above causes could result in a lower wall temperature for the metal foam tubes, as shown in Fig. 6(b).

(a) $q=8$ kWm^{-2}

Bare tubes	***Metal foam tubes***
	
Front view	Front view
	
Side View	Side View

(b) q=98 kWm^{-2}

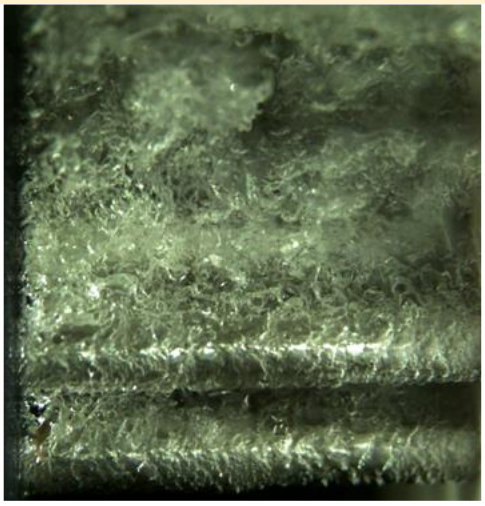
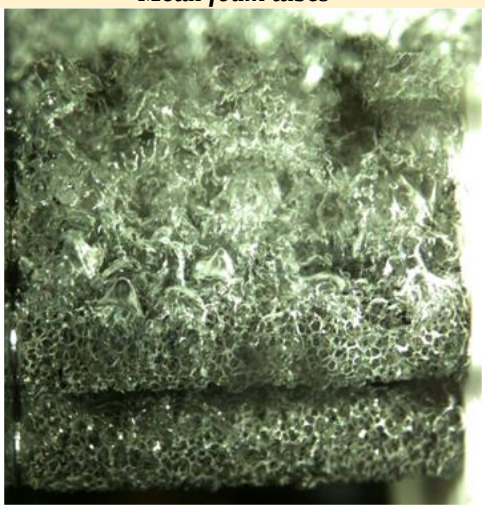
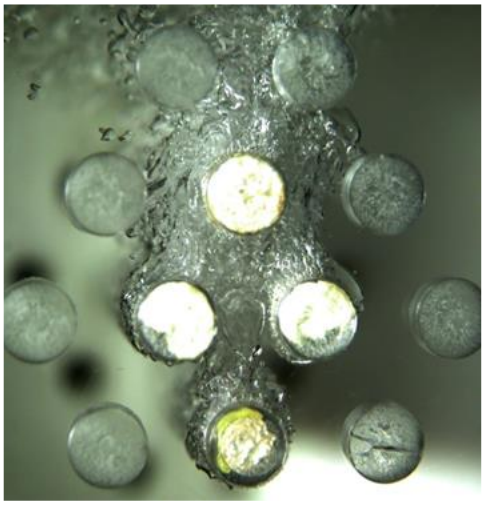
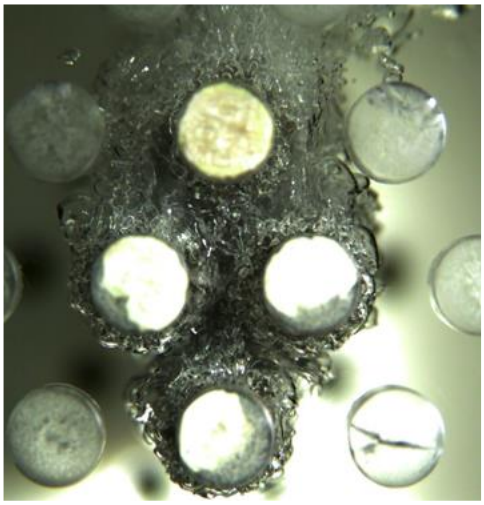
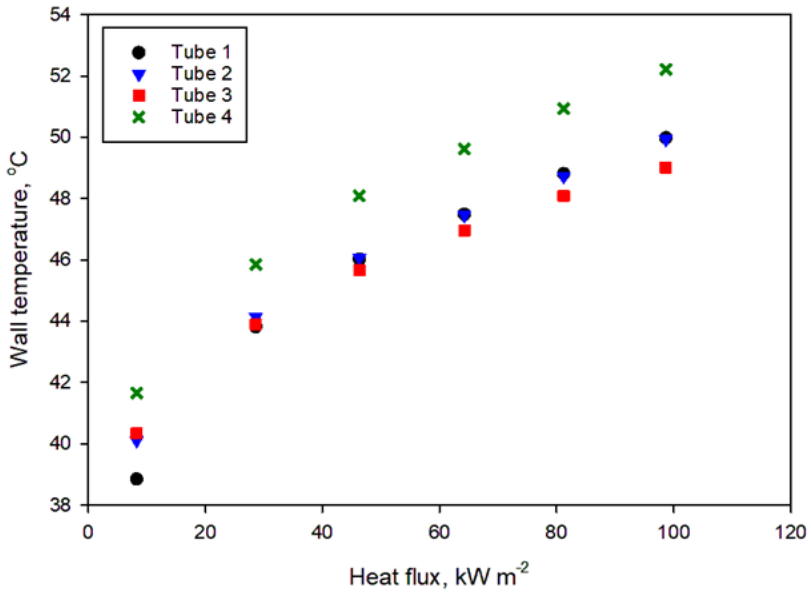
Bare tubes	***Metal foam tubes***
	
Front view	Front view
	
Side view	Side view

Fig. 5. Visualization of pool boiling behavior in bare and metal foam tube bundles.

(a)



(b)

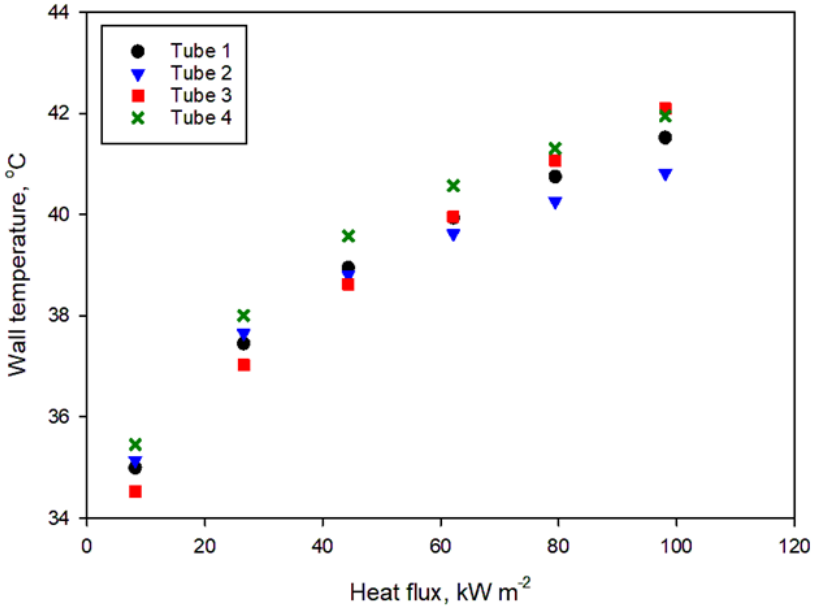


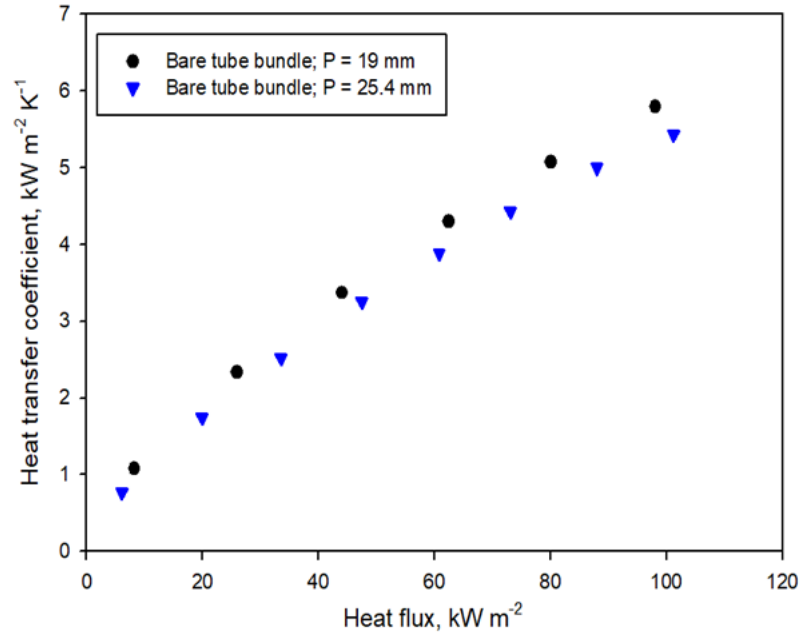
Fig. 6. Wall temperature of different tubes: (a) bare tube bundle and (b) metal-foam enhanced tube bundle.

4.3. Effect of tube pitch on tube bundle performance

To understand the influence of the tube pitch on the heat transfer performance of the tube bundle, two tube pitches, 19 mm and 25.4 mm, are experimentally analyzed for both bare and metal foam tube bundles. The tube pitch effects on heat transfer coefficient are presented in Fig. 7. For both bare and metal foam tube bundles, the heat transfer coefficient value reduces marginally when the tube pitch is increased from 19 mm to 25.4 mm. A maximum of 10% reduction in HTC is observed with an increase in pitch for the bare tube bundle, whereas the same for the metal foam tube bundle is about 14%. In other words, the two-phase flow is more intensive for the tube bundle with lower pitch, and this trend is in agreement with that reported in the

work of Fujita and Hidaka [13] and Swain et al. [14]. Since the increased tube pitch creates a larger gap between the tubes, the vapor column leaving the bottom tubes may not shear along the side tubes. Similarly, the vapor column leaving the side tubes may not shear along the top tubes. As a result, the HTC enhancement caused by the convection effects deteriorates and lead to a lower HTC at a larger tube pitch.

(a)



(b)

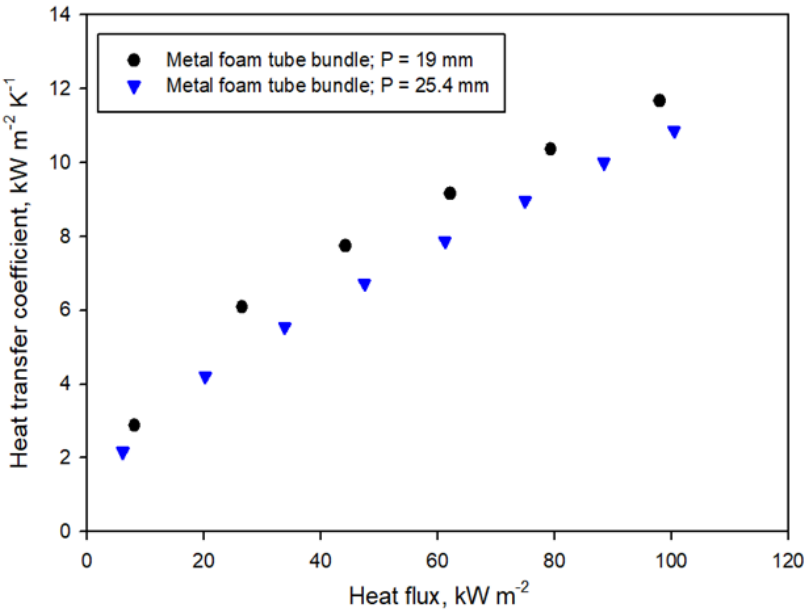


Fig. 7. Effect of tube pitch on heat transfer coefficient (a) bare tube bundle and (b) metal foam tube bundle.

5. Conclusions

In this study, open-cell metal foam tubes are proposed to enhance the shell-side performance of the flooded evaporators. The performance of the bare tube bundle is compared against the proposed metal foam tube bundle under pool boiling conditions. The experiments are carried out for a heat flux range of 5-100 kW m^{-2} and two different tube pitches (19 mm and 25.4 mm). Based on the experimental results, the key outcomes of the study can be outlined as follows:

- The heat transfer coefficient of the bare tube bundle is just 3-5% higher than that of the single tube.
- As compared to the bare tube bundle, the metal foam tube bundle reported a 100-160% enhancement in heat transfer coefficient.
- The wall temperature of the metal foam tubes is about 4-10°C lower than that of the plain tubes due to the combination of increased surface area and nucleation sites, reduced bubble departure diameter, and enhanced liquid suction to the tubes' wall through capillary action.
- The tube pitch played a significant role in determining the pool boiling behavior of the tube bundles. When the tube pitch is increased from 19 mm to 25.4 mm, the heat transfer coefficient values decrease by a maximum of 10% and 14% for the bare and metal foam tube bundles, respectively.

Acknowledgements

The authors are grateful to the colleagues at Oak Ridge National Laboratory who provided useful comments and suggestions to improve the quality of the paper. In addition, the technical support provided by Anthony Gehl, Jeff Taylor, Brian Goins, and Michael Day is greatly appreciated. The authors also acknowledge the support provided by US Department of Energy Building Technologies Office (BTO) and the technology manager, Mr. Antonio Bouza.

References

[1] Z. H. Ayub and A. Bergles, "Pool boiling from GEWA surfaces in water and R-113," *Wärme-und Stoffübertragung*, vol. 21, no. 4, pp. 209-219, 1987.

[2] J. R. THOME, "Nucleate pool boiling of hydrocarbon mixtures on a Gewa-TX tube," *Heat Transfer Engineering*, vol. 10, no. 1, pp. 37-44, 1989.

[3] A. Nosrati, M. Akhavan-Behabadi, B. Sajadi, P. Razi, and R. Mohammadi, "Experimental study on the effects of using metal foam on R-134a flow boiling in annular tubes," *International Journal of Thermal Sciences*, vol. 177, p. 107546, 2022.

[4] H. Hu, Z. Lai, and Y. Zhao, "Heat transfer and pressure drop of refrigerant flow boiling in metal foam filled tubes with different wettability," *International Journal of Heat and Mass Transfer*, vol. 177, p. 121542, 2021.

[5] L. L. Manetti, A. S. O. H. Moita, R. R. de Souza, and E. M. Cardoso, "Effect of copper foam thickness on pool boiling heat transfer of HFE-7100," *International Journal of Heat and Mass Transfer*, vol. 152, p. 119547, 2020.

[6] J. Shi, X. Jia, D. Feng, Z. Chen, and C. Dang, "Wettability effect on pool boiling heat transfer using a multiscale copper foam surface," *International Journal of Heat and Mass Transfer*, vol. 146, p. 118726, 2020.

[7] J. Shi, H. Du, Z. Chen, and S. Lei, "Review of phase change heat transfer enhancement by metal foam," *Applied Thermal Engineering*, p. 119427, 2022.

[8] H. Hu, Y. Zhao, and Y. Li, "Research progress on flow and heat transfer characteristics of fluids in metal foams," *Renewable and Sustainable Energy Reviews*, vol. 171, p. 113010, 2023.

[9] C-M. Yang, W. Asher, M. Sandlin, and K. Nawaz, "Enhanced Pool Boiling Of Low-Pressure Refrigerants On Round Tubes-An Experimental Evaluation," 2022.International Refrigeration and Air Conditioning Conference. Paper 2397. https://docs.lib.purdue.edu./iracc/2397

[10] R. J. Moffat, "Describing the uncertainties in experimental results," *Experimental Thermal and Fluid Science*, vol. 1, no. 1, pp. 3-17, 1988.

[11] M. Cooper, "Saturation Nucleate Pool Boiling: A Simple Correlation, Department of Engineering Science," *Oxford University, England*, vol. 86, pp. 785-793, 1984.

[12] K. Cornwell and S. Houston, "Nucleate pool boiling on horizontal tubes: a convection-based correlation," *International Journal of Heat and Mass Transfer*, vol. 37, pp. 303-309, 1994.

[13] Y. Fujita and S. Hidaka, " Effect of tube bundles on nucleate boiling and critical heat flux, " *Heat Transfer - Japanese Research: Co - sponsored by the Society of Chemical Engineers of Japan and the Heat Transfer Division of ASME*, vol. 27(4), pp. 312-325, 1998.

[14] A. Swain, R.L. Mohanty, and M.K. Das, " Pool boiling of distilled water over tube bundle with variable heat flux ," *Heat and Mass Transfer*, vol. 53, pp. 2487-2495, 2017.

14th IEA Heat Pump Conference
15-18 May 2023, Chicago, Illinois

Performance analysis of hybrid operating modes for dual coolant-source heat pump system applied to electric-driven vehicles

Hoseong Lee[a], Hanbeol Jeon[a], Jaehyeong Seo[a], Dongchan Lee[b], Yongchan Kim[c*]

[a]Thermal Management R&D Departmenet, Korea Automotive Technology Institute, 303 Pungse-ro Pungse-myeon, Cheonan-si 31214, Republic of Korea
[b]Department of Mechanical and Information Engineering, University of Seoul, Seoulsiripdae-ro 163, Dongdaemun-gu, Seoul 02504, Republic of Korea
[c]Department of Mechanical Engineering, Korea University, 145 Anam-ro Sungbuk-ku, Seoul 02841, Republic of Korea

Abstract

An efficient heating system for the cabin of electric-driven vehicles (xEVs) is required to minimize the reduction in the driving range. However, studies regarding heat pumps that use waste heat from fuel cell stack, PE(Power Electronics) and battery in xEVs are limited. In this study, the heating performance of dual coolant-source heat pump using waste heat in xEVs is investigated by varying coolant temperature, and coolant volumetric flow rate to have enough capacity in severe ambient conditions. A developed triple-fluid heat exchanger is introduced to recover waste heat from the fuel cell stack and PE with high level and battery with relatively low level at different temperatures. The heating performance of the coolant-source heat pumps using one coolant and dual coolants shows different characteristics owing to the different temperature levels of the coolants and heat transfer between two coolants. This study suggests optimum heat pump system of xEVs with respect to driving range characteristics under severe ambient conditions.

Keywords: dual coolant-source heat pump; heating performance; triple-fluid heat exchanger; coolant temperature; coolant flow rate;

1. Introduction

In response to regulations pertaining to fossil fuels for addressing environmental concerns [1], automotive companies have developed zero-emission vehicles as an alternative to internal combustion engines (ICEs). Accordingly, numerous studies regarding the development of "green cars," which do not use fossil fuels, have been conducted. The most prominent zero-emission green cars include battery electric vehicles (BEV) and fuel cell electric vehicles (FCEVs) [2–4]. Their power sources are batteries, a hybrid battery system charged by an ICE, and electricity generated by a stack of fuel cells, respectively. All three types of vehicles, so called xEVs, are considered promising, based on the development undertaken by major automotive companies [5,6]. However, laboratory and on-road tests reveal various engineering short-comings of xEVs, including their system efficiency, stack performance, thermal-management technology, and compatibility with other components under high-voltage conditions. These inadequacies must be solved to achieve a performance similar to that of ICE vehicles [7].

Recently developed electric vehicles generally have maximum driving ranges of approximately 400 km for battery-only vehicles and approximately 600 km for FCEVs. However, these driving ranges can be reduced by over 40% when the heating system of a vehicle is operated under cold ambient conditions [8–11]. Conventional positive temperature coefficient (PTC) electric heaters have been widely used in electric vehicles owing to their simple utility. However, it can consume a significant amount of power from the battery because of its low energy transition efficiency (90%–95%) from electricity to heat, resulting in a significantly reduced fuel economy. The efficiencies ranging from 90% to 95% may seem to be enough; however, be-cause a typical heat pump has a heating efficiency of more than 300%, the PTC electric heaters have significantly lower efficiencies than the heat pumps. Therefore, an efficient heating system for the cabin of electric vehicles must be developed to minimize the reduction in the driving range.

In this study, the heating performance of dual coolant-source heat pump using waste heat from the fuel cell stack and PE(high temperature level) and battery(low temperature level) in xEVs was measured and analyzed by varying coolant temperature and coolant volumetric flow rate using developed triple-fluid heat exchanger.

2. Experimental Method

Fig. 1 shows a schematic illustration of the test setup used to measure the performance of a coolant-source heat pump with a triple-fluid heat exchanger for use in xEVs. The heating performance of the coolant-source heat pump was measured in psychrometric chambers. The psychrometric calorimeter in the indoor chamber was designed to precisely maintain the temperature and humidity settings using a cooling coil, heating coil, and humidifier. The temperature and humidity conditions in the outdoor chamber were controlled using an air-handling unit.

The tested coolant-source heat pump comprised an electric compressor, an inner condenser, triple-fluid heat exchangers (evaporator), and an electronic expansion valve (EXV). An electrically driven scroll compressor with a displacement volume of 33.0 cm^3 rev^{-1} at 360 V was adopted along with an inverter driver. The inner condenser, which simulates the cabin of the vehicle, was a parallel-flow type louvered-fin brazed-aluminum heat exchanger measuring 232.0 mm in width, 144.0 mm in height, and 54.0 mm in depth. An EXV with an orifice diameter of 1.6 mm was used to regulate the refrigerant mass flow rate. In addition, an accumulator was installed at the compressor inlet. Table 1 lists the specifications of the coolant-source heat pump with a triple-fluid heat exchanger.

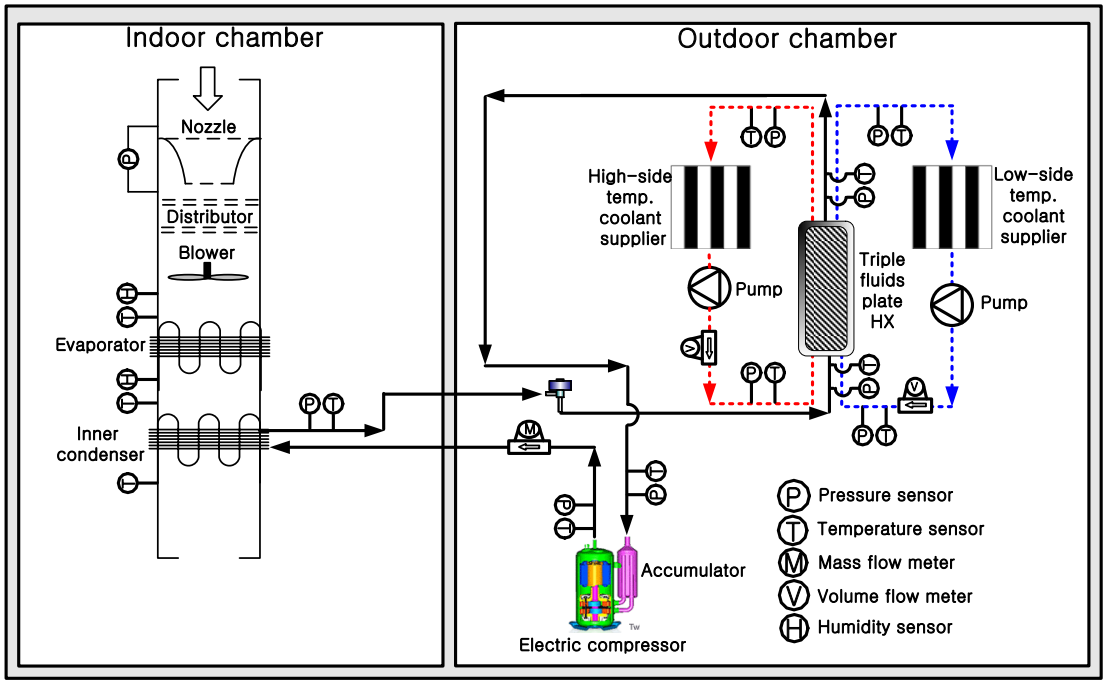


Fig. 1. Schematic of experimental setup for coolant source heat pump system

Table 1. Specifications of coolant source heat pump system

Component	Specifications
Inner condenser (Size, mm)	Parallel-flow type louvered-fin brazed-aluminum heat exchanger 232W × 144H × 54D
Triple-fluid heat exchanger (Size, mm)	Counter-flow plate-type brazed-aluminum heat exchanger 190W × 225H × 80D
Electric compressor (Displacement, cm^3)	Scroll type (33.0)
Expansion devices (Diameter, mm)	Electronic expansion valve (EXV) 1.6

Accumulator (cm^3)	950

A triple-fluid heat exchanger was developed to enable heat exchange between the refrigerant (R-134a) and two types of coolants, where different operating temperatures were considered for the fuel cell stack and PE(Power Electronics, such as driving motors, converters and inverters) (High temp. side) and battery (Low temp. side). The triple-fluid heat exchanger was a counter-flow-type aluminum plate heat exchanger measuring 190.0 mm in width, 225.0 mm in height, and 80.0 mm in depth. Fig. 2 shows the configurations of the triple-fluid heat exchanger. In this heat exchanger, 63 rows (35.0%) were used for high temperature coolant cooling, and 117 rows (65%) were used for low temperature coolant cooling. In the preliminary experiment, excessively high condensing temperature was observed when the channels were equally assigned for high temperature side and low temperature side, because the triple-fluid heat exchanger was used as a heat sink of the heat pump for cooling mode. Accordingly, for high temperature side, the number of channels in the triple-fluid heat exchanger was decreased to 35% owing to higher temperature difference between a coolant and a refrigerant.

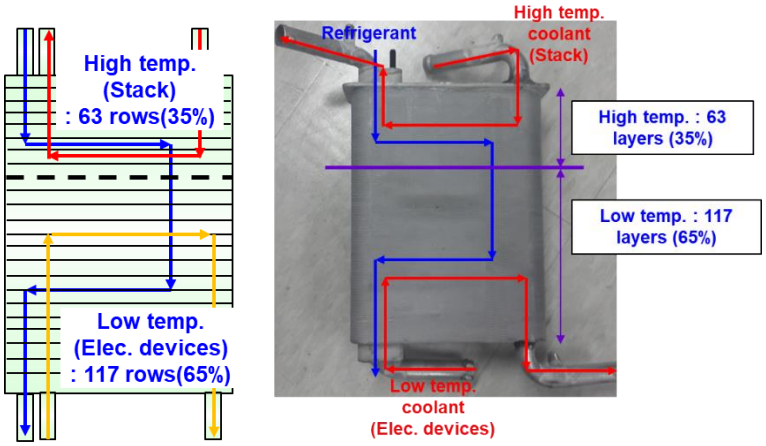


Fig. 2. Triple fluids heat exchanger and channel configurations for coolant source heat pump system

Table 2 lists the test conditions used in the study. The test conditions were set based on the actual coolant temperature profiles of the stack (or PE) and battery under cold ambient conditions under the designed driving pattern, as shown in Fig. 3. The air temperature on the interior side was varied from -20 °C to 0 °C at intervals of 10 °C, and the relative humidity was 50.0%. The air flow rate on the interior side was fixed at 300 $m^3\ h^{-1}$. The stack coolant temperature was maintained within 20 °C–40 °C at intervals of 5.0 °C, whereas the volumetric flow rate at the stack side was varied from 5 to 20 L min^{-1} at intervals of 5 L min^{-1}. The electric device cool-ant temperature was maintained within -20 °C to 0 °C at intervals of 10 °C, whereas the volumetric flow rate at the electric device side was varied from 5 to 20 L min^{-1} at intervals of 5 L min^{-1}. Meanwhile, the compressor speed was varied from 2000 to 4000 rev min^{-1} at intervals of 1000 rev min^{-1}.

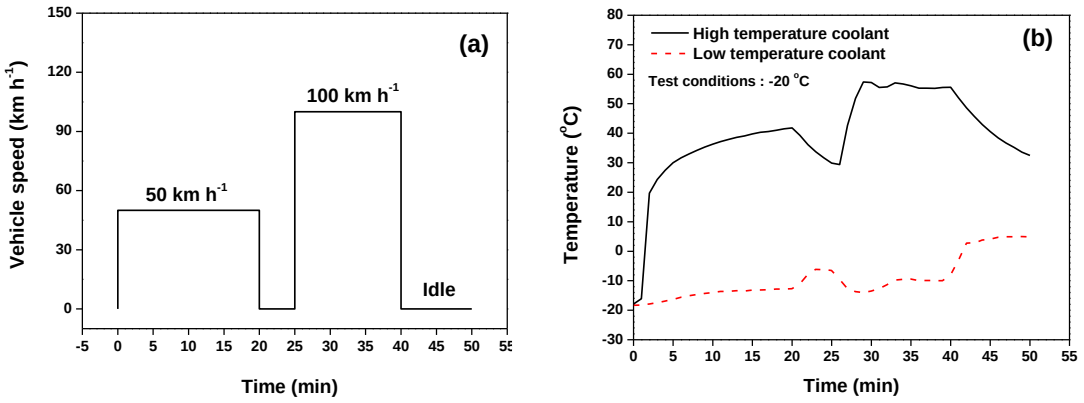


Fig. 3 – (a) Designed driving pattern of xEVs and (b) coolant temperature profiles for high-side and low-side under cold conditions.

Table 2. Test conditions of coolant source heat pump system

Components			Range
Compressor speed (rev min^{-1})			2000, 3000, 3500, 4000
Inner condenser		Air flow rate (m^3 h^{-1})	300
		Air temperature (°C)	-20, -10, 0
Triple-fluid heat exchanger (Coolant)	Stack and PE (High-side temp.)	Volumetric flow rate (L min^{-1})	5, 10, 15, 20
		Coolant temperature (°C)	20, 30, 35, 40
	Battery (Low-side temp.)	Volumetric flow rate (L min^{-1})	5, 10, 15, 20
		Coolant temperature (°C)	-20, -10, -5, 0
Refrigerant			R-134a
Coolant			Ethylene glycol 50%, water 50%
Working fluid			Air

3. Result and Discussion

3.1. Single coolant-sourced heat pump system

Fig. 4 shows the heating capacity and COP of the coolant-source heat pump in the high temperature level's coolant mode with respect to the coolant temperature and volumetric flow rate. Only the high temperature level coolant was used in the high temperature level coolant mode. As the coolant temperature and volumetric flow rate increased at a fixed compressor speed and EXV opening, the heating capacity increased because of the increase in the evaporating pressure. However, the heating COP decreased as the coolant temperature and volumetric flow rate increased owing to the increase in the compressor power consumption. The coolant temperature significantly affected the heat capacity, whereas the heating capacity became constant as the coolant volumetric flow increased beyond 15 L min^{-1}.

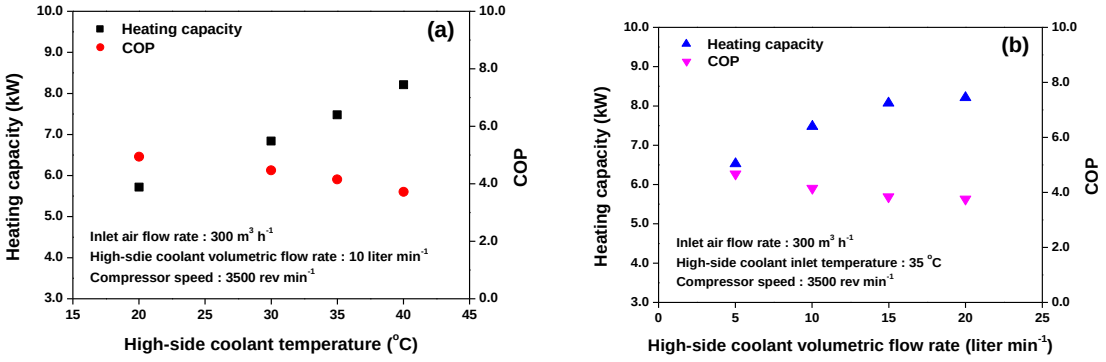


Fig. 4 – Heating capacity and COP in high temperature level coolant mode with respect to (a) temperature and (b) volumetric flow rate of high temperature level coolant.

Fig. 5 shows the heating capacity and COP of the coolant-source heat pump in low temperature level's coolant mode with respect to the coolant temperature and volumetric flow rate of battery cooling. The heating capacity and COP increased with lower-side coolant temperature and volumetric flow rate at a fixed compressor speed and EXV opening. As the coolant temperature increased from -20 °C to 0 °C, the heating capacity increased by 100%, whereas the compressor power consumption increased by 50%, resulting in an increase in the COP. This was attributed to a lower increase in the refrigerant flow rate with respect to the

coolant temperature in the lower temperature coolant mode compared with that in the high temperature coolant mode. Additionally, as shown in Figs. 4 and 5, the low temperature coolant mode exhibited a relatively lower heating capacity than the high temperature level coolant mode. Accordingly, the operation mode in the coolant-source heat pump should be determined based on the heating load under actual driving conditions.

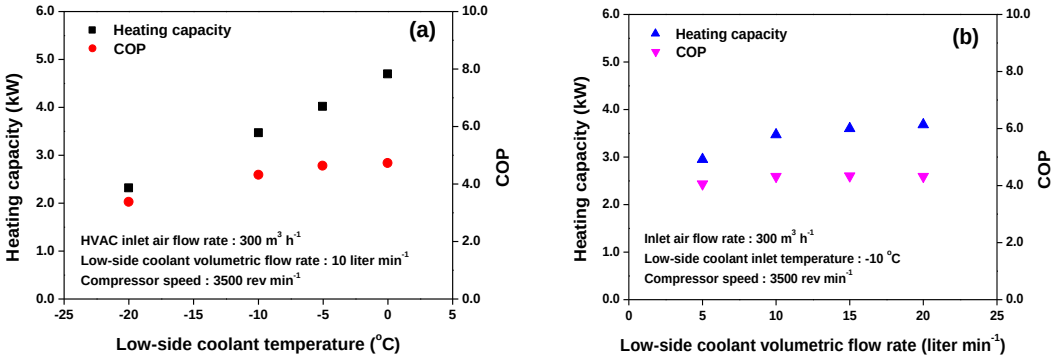


Fig. 5. Heating capacity and COP in low temperature level coolant mode with respect to (a) coolant temperature and (b) volumetric flow rate.

3.2. Dual coolant-sourced heat pump system

The hybrid coolant mode, which uses both coolants as heat sources, was investigated to utilize all possible waste heat in xEVs. When driving under cold ambient conditions, the coolant temperatures in two kinds of coolants remained at -10 °C and -20 °C to 50 °C, respectively. Therefore, the low-side coolant temperature in the hybrid coolant mode was set to -10 °C at various high-side coolant temperatures and EXV opening percentages. As shown in Fig. 6, in the hybrid coolant mode, the EXV opening percentage did not significantly affect the heating capacity and COP of the coolant-source heat pump. However, the heating capacity in the hybrid coolant mode decreased by 50% and 12% compared with that in the high temperature level and low temperature level coolant modes, respectively. This was because the heat was transferred from the higher temperature of the stack (or PE) coolant to the lower temperature of the battery cooling coolant. Owing to a similar reason, as shown in Fig. 6, the heat capacity and COP of the coolant-source heat pump in the hybrid coolant mode were not affected by the high temperature level coolant temperature.

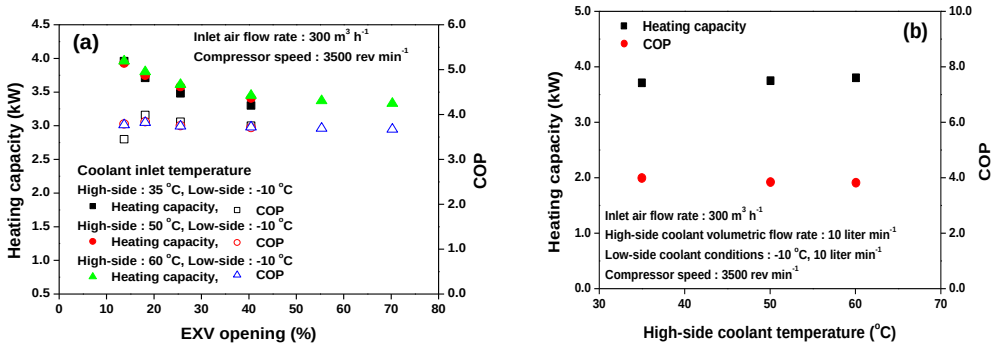


Fig. 6. Heating capacity and COP in hybrid coolant mode with respect to (a) EXV opening and (b) high temperature level coolant temperature.

4. Conclusion

In this study, the heating performance of a coolant-source heat pump using waste heat from the fuel cell stack and PE(high temperature level) and battery(low temperature level) in xEVs was measured and analyzed by varying the inlet air temperature, compressor speed, coolant temperature, and coolant volumetric flow rate. A developed triple-fluid heat exchanger was developed to recover waste heat from battery and fuel cell stack (or PE) which have different temperature levels. The coolant-source heat pump indicated a higher refrigerant flow rate than the air-source heat pump owing to the higher evaporating pressure and higher heat source temperature. Accordingly, the superheats at the compressor inlet and outlet in the coolant-source heat pump were lower than those in the air-source heat pump. The heating performance of the coolant-source heat pump was significantly affected by the compressor speed, and the heating capacity was inversely proportional to the COP.

Additionally, the effects of the coolant temperature on the heating performance of the coolant-source heat pump were investigated in the stack and PE(high temperature level), battery(low temperature level), and hybrid coolant modes. In the high temperature level coolant mode, as the coolant temperature and volumetric flow rate increased, the heating capacity increased owing to the increase in the refrigerant flow rate, whereas the heating COP decreased owing to the increase in the compressor power consumption. However, in the low temperature level coolant mode, both the heating capacity and COP increased with the coolant temperature and volumetric flow rate owing to a lower increase in the refrigerant flow rate. Furthermore, the hybrid coolant mode was inferior to one coolant-source mode in terms of performance; this was because in the hybrid coolant mode, heat was transferred from the stack and PE(high temperature level) to the battery coolant(low temperature level)

Acknowledgements

This work was supported by the Ministry of Trade, Industry & Energy(MOTIE), Korea Evaluation Institute of Industrial Technology(KEIT) through the Automotive Industry Technology Development Program(20018646, Development of optimum control technology for centralized thermal management system using Digital Twin to reduce power consumption and improve driving range for xEV) and through the Hydrogen Electric Tram Verification Program (P0018649, Fuel Cell Element Part and System Technology Development for Fuel Cell Powered Tram).

References

[1] Kim SC, Won JP, Park YS, Lim TW, Kim MS. Performance evaluation of a stack cooling system using CO2 air conditioner in fuel cell vehicles. *Int J Refrig* 2009;32:70–77.
[2] Takahisa S, Katsuya I. Air conditioning system for electric vehicle. *Proceedings of SAE International Congress & Exposition*;1996:960688.
[3] Al-Alawi BM, Bradley TH. Total cost of ownership, payback, and consumer preference modeling of plug-in hybrid electric vehicles. *Applied Energy 2013*;103:488–506.
[4] Brouwer AS, Kuramochi T, Broek M, Faaij A. Fulfilling the electricity demand of electric vehicles in the long term future: An evaluation of centralized and decentralized power supply systems. *Applied Energy 2013*;107:33–51.
[5] Lee HS, Lee MY. Cooling performance characteristics on mobile air-conditioning system for hybrid electric vehicles. *Adv Mech Eng 2013*:1–9.
[6] Lee MY, Lee DY. Review on conventional air conditioning, alternative refrigerants and CO2 heat pumps for vehicles. *Adv Mech Eng 2013*:1–15.
[7] Yamashita T, Ishikawa T, Shimonsono H, Yamada M, Iwasai M. The development of the cooling system for FCV. *Proceedings of JAMA Annual Conference 2004*:88–04.
[8] Doucette RT, McCulloch MD. Modeling the prospects of plug-in hybrid electric vehicles to reduce CO2 emissions. *Appl Energy 2011*;88:2315–2323.
[9] Lee MG, Park YK, Jung KK, Yoo JJ. Estimation of fuel consumption using in-vehicle parameters. *Int J u- and e- Serv, Sci Technol 2011*;4:37–46.
[10] Wang H, Liu Y, Fu H, Li G. Estimation of state of charge of batteries for electric vehicles. *Int J Control Autom 2013*;6:185–194.
[11] Kim DW, Lee MY. Theoretical approach on the heating and cooling system design for an effective operation of Li-ion batteries for electric vehicles. *J Korea Acad-Ind Coop Soc 2014*;15:2545–2552.

14th IEA Heat Pump Conference
15-18 May 2023, Chicago, Illinois

A study on heat and water recovery performance of membrane heat exchanger using different membrane

Van Cong Le[a], Thi Nhan Nguyen[a], Min Sung Lee[b], Jae-il Kwon[c], Dae Hae Kim[d], Sung Joo Hong[e], Min Soo Kim[b], Chan Woo Park [a,b*]

[a] Graduate School of Energy Storage and Conversion Engineering, Jeonbuk National University, Jeonju-si, Jeonrabuk-do 54986, Republic of Korea
[b] School of Mechanical Design Engineering, Jeonbuk National University, Jeonju-si, Jeonrabuk-do 54986, Republic of Korea
[c] G-TECH Co., Ltd, 43-7 Hyeonseok-Ro, 720 Beon-Gil, Gwangjeok-Myun, Yangju-si, Gyeonggi-do, Republic of Korea
[d] Thermalchemical Energy System R&D Group, Korea Institute of Industrial Technology, Cheonan-si, Chungcheongnam-do 31056, Republic of Korea.
[e] Department of Mechanical and Automotive Engineering, Jeonju University, Jeonju-si, Jeonrabuk-do 55069, Republic of Korea

Abstract

Industrial energy consumption is extremely high. Thermal power plants contribute to approximately 40% of total water withdrawal in the US but dissipate a large amount of vapor and heat energy. Transport membrane condensers have been demonstrated to have great potential to recovery waste heat and water as a combination of membrane condensers and heat exchangers. In this study, a laboratory membrane heat exchanger system was developed using plate ceramic membrane and hollow fibers. The heat and water recovery performances were studied to estimate the heat and mass transfer characteristics of membrane heat exchangers. The operating conditions show significant effects on the recovery performances of system. A computational fluid dynamics (CFD) model was developed using experimental data to consider the heat and mass transfer. The simulation model shows great agreements with experimental results. The temperature distribution as well as vapor mass fraction were analyzed to have an insight about the condensation and mass transfer of water vapor.

© HPC2023.
Selection and/or peer-review under the responsibility of the organizers of the 14th IEA Heat Pump Conference 2023.

Keywords: Transport membrane condenser (TMC), heat exchanger, heat recovery, water recovery, computational fluid dynamics (CFD)

1. Introduction

Freshwater sources are steadily decreasing over this decade due to the population growth and living standards [1]. The energy industry consumes an enormous amount of fuel resources. Flue gas in the power plant unit consists of water vapor up to 13% volume fraction and take 50 – 80% heat loss from boiler which accounts for 3-8% total energy of the units [2]. Several efforts have been done to reclaim energy and water from the waste gases. By recovery the heat loss and wastewater, not only the boiler efficiency can be greatly improved but the feed consumption can be significantly reduced [3]. Typically, transport membrane condenser (TMC) is a promising method to recovery the wasted sources and enhance the industrial thermal process efficiency. By the mean of using a proper membrane, the recovery efficiencies of TMC are particularly improved. It has been demonstrated that the TMC can supply 30% of feed water in boiler unit under a proper working condition. In this work, transport membrane condensers with two types of membranes were studied experimentally and numerically.

2. Methodology

The experimental scheme of a hollow fiber transport membrane condenser is shown in figure 1. The dense alumina hollow fibers were assembled in an acrylic round tube. A water boiler was used to generate vapor and control the gas temperature. The air compressor was incorporated with the mass flow control (MFC) to control humid gas circulating though membrane condensers. The cooling water was controlled by a pump and cooling

bath to flow inside the hollow fiber. Thermocouples and humidity sensor were installed to measure the operating conditions. The mass of water transport to water side was measured by a water level sensor.

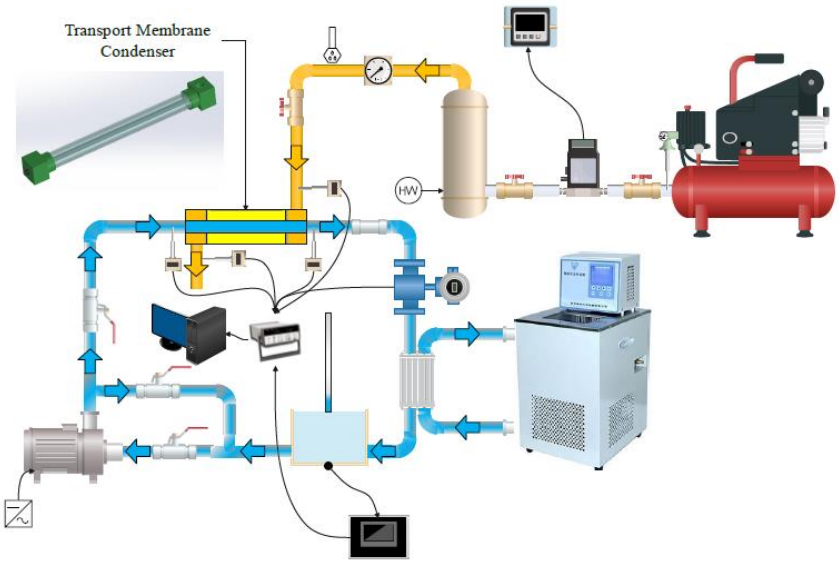


Fig. 1. Experimental scheme of circular type transport membrane condenser

Similarly, a plate membrane was applied in the experiment system for comparison. The humid air and cold water were supplied onto two side of membrane. The velocity and temperature of inlet gas and water were modified to evaluate the recovery behavior. The water and heat recovery can be obtained as following:

$$J = \frac{\Delta m}{\Delta t A} \tag{1}$$

$$Q = \frac{C_p m_l \Delta T + m_T E_w}{A} \tag{2}$$

3. Numerical study

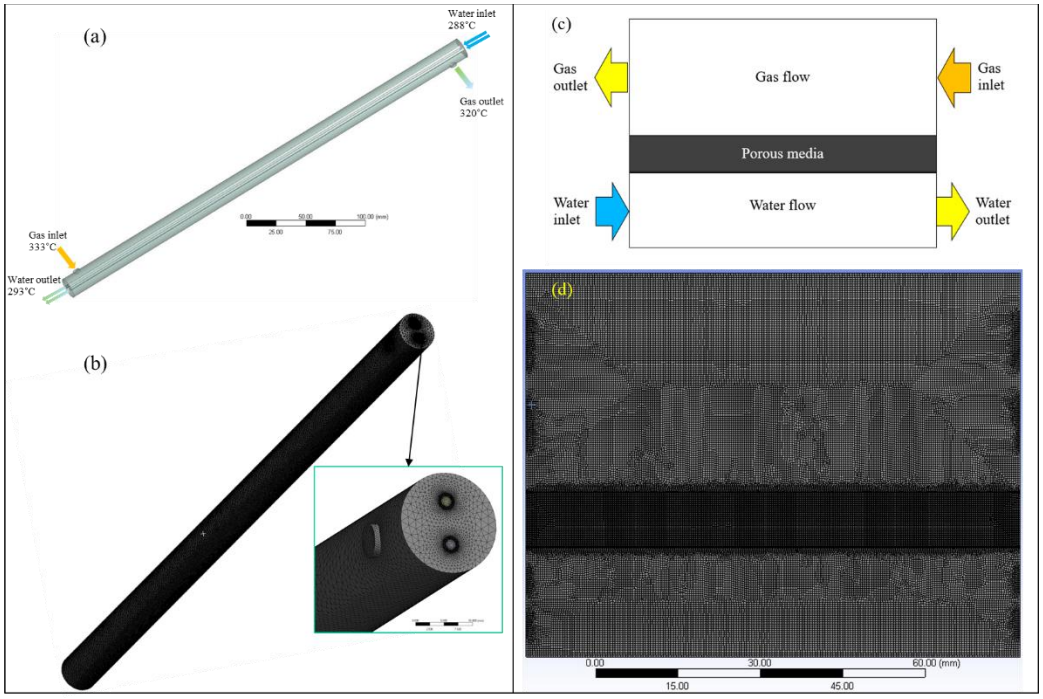


Fig. 2. (a) Schematic and (b) meshing of hollow fiber heat exchanger (c) Schematic and (d) meshing of flat membrane heat exchanger

A CFD code in ANSYS Fluent was used to conduct a simple 2D model of plate membrane condenser, as presented in figure 2c and 2d. The numerical model of a hollow fiber membrane condenser was then developed in 3D configuration . The simulation model consists of three computation zones which are gas, water flow and membrane. The model geometry and parameters were built based on the experiment setup. The simulation conditions are presented in Table 1. The species transport in Volume of Fluid (VOF) multiphase model was utilized with gas mixture as the primary phase and water liquid in the secondary phase. The condensation of water vapor was solved using the evaporation-condensation Lee's model. The condensation rate of vapor was considered as the mass transfer between water liquid and vapor phases. The mass transfer is solved by the following equation:

$$\frac{\partial}{\partial t}(\alpha_v \rho_v) + \nabla \cdot \left(\alpha_v \rho_v \vec{V_v}\right) = \dot{m}_{lv} - \dot{m}_{vl} \tag{3}$$

For the mass transport through the membrane, the permeation of fluid through the ceramic membrane was considered as a laminar flow and solved by the porous media model. A momentum sink comprised of viscosity loss and inertial loss was added as following:

$$S_i = -\left(\sum_{j=1}^{3} D_{ij}\mu v_j + \sum_{j=1}^{3} C_{ij}\frac{1}{2}\rho|v|v_j\right) \tag{4}$$

Table 1. Boundary conditions

Parameter	Value
Water temperature (K)	288
Gas temperature (K)	334
Porosity (%)	35
Water flow rate (LPM)	0.1
Gas flow rate (LPM)	4 to 20
Vapor content (-)	0.13

4. Results and discussions

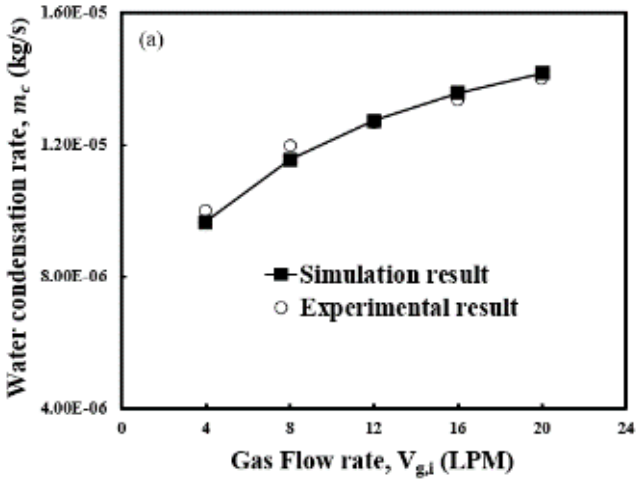


Fig. 3. Comparison of experimental and simulation results at different operating conditions

Fig. 3 shows the comparison between experimental and simulation results with different operating conditions. The simulation results were found to have a great agreement with experimental data. The temperature distribution and vapor mass fraction were studied at different conditions. The temperature and vapor mass fraction of hollow fiber condenser model are presented in Fig. 4 and Fig. 5, respectively. It can be observed that the gas flow temperature decreases along with the flow direction. The decline in gas temperature demonstrated the heat retrieval in the gas stream. On the other hand, the vapor distribution shows a reduction of mass fraction in company with the gas direction. The vapor mass fraction was obtained approximately 0.53 in the gas outlet. Obviously, the moisture content was recaptured into the water side.

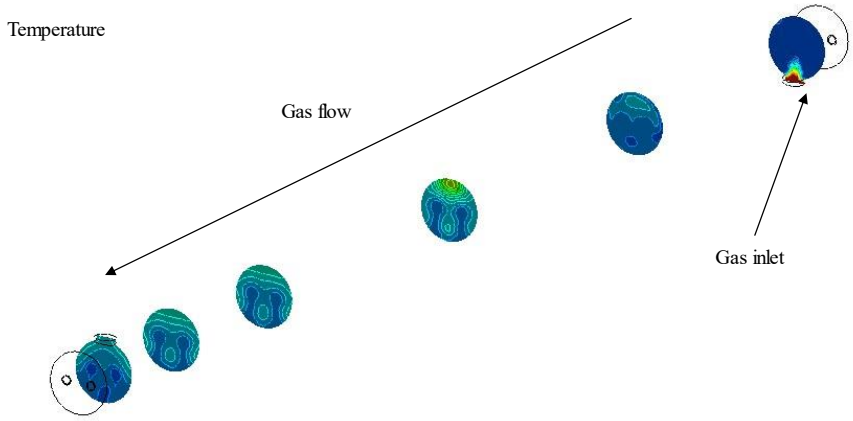


Fig. 4. Temperature of hollow fiber condenser

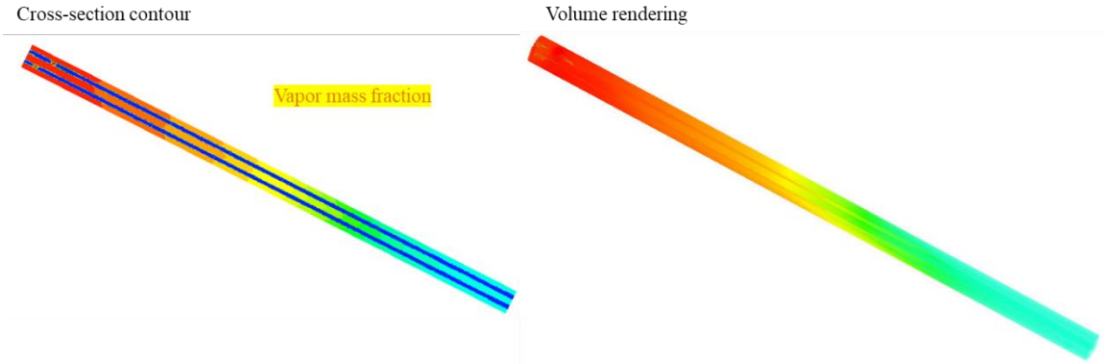


Fig. 5. Vapor mass fraction of hollow fiber condenser

5. Conclusion

In this work, a membrane heat exchanger is proposed for application of heat and wastewater recovery from flue gas using ceramic hollow fiber membranes. A 3D CFD model was developed based on experimental data. A great agreement was found between numerical and experimental results. The simulation results such as temperature contour and mass fraction of vapor in the gas phases have given an insight into the mechanism of the membrane condenser.

Acknowledgements

The authors would like to appreciate the research funds for their support with this project. This research was supported by the Basic Science Research Program through the NRF (National Research Foundation of Korea, grant No. RS-2023-00209123). The authors also appreciate the KETEP (Korea Institute of Energy Technology Evaluation and Planning, grant No. 20192010107020) and the Technology Development Program funded by the MSS (Ministry of SMEs and Startups, grant No. S3276045) for their assistance. And this work was also supported by the Technology Innovation Program (20014699, 20018237. KOITA-RND2-2022-8) funded by the ministry of Trade, Industry & Energy(MOTIE, Republic of Korea).

References

[1] Salman Memon, Young-Deuk Kim, Sadam Soomro, Mujeeb Iqbal Soomro, Woo-Seung Kim. *A new approach for freshwater production and energy recovery from an oil field*, Journal of Water Process Engineering, Volume 34, 2020, 101145, ISSN 2214-7144. https://doi.org/10.1016/j.jwpe.2020.101145

[2] Chen, H., Zhou, Y., Su, X., Cao, S., Liu, Y., Gao, D., An, L., 2018. *Experimental study of water recovery from flue gas using hollow micro–nano porous ceramic composite membranes*. Journal of Industrial and Engineering Chemistry 57, 349–355. https://doi:10.1016/j.jiec.2017.08.042

[3] Wang, Dexin, Ciora, Richard, Lin, Chengxian, and Ma, Zhanhua. *Flue Gas Water Vapor Latent Heat Recovery for Pressurize d Oxy-Combustion*. United States: N. p., 2018. Web. doi:10.2172/1484251.

14th IEA Heat Pump Conference
15-18 May 2023, Chicago, Illinois

Performance evaluation and optimization of lower GWP refrigerants in a residential heat pump

Jethro Medina[a*], Joshua Hughes[a]

[a]The Chemours Company, 201 Discovery Boulevard, Newark, DE 19713, United States

Abstract

R-410A is the prevailing fluid in stationary air conditioning and heat pump applications. Its global warming impact, however, has garnered attention for lower GWP options. Existing alternatives include R-32 and R-454B, which provide notable GWP reductions from R-410A (AR4 GWPs of 2088 vs. 675 and 465 respectively). Although R-454B may prove to be a long-term solution, system optimizations, such as variable speed compressor use and heat exchanger changes, enable the use of even lower GWP fluids.

This paper explores the performance of several low GWP refrigerants (<300 GWP) in stationary air conditioning and heating applications. A commercial, residential R-410A heat pump was modified, per OEM guidance, with a suitable variable speed compressor. The heat pump and corresponding evaporator were placed in a pair of environmental chambers. The evaluated refrigerants consisted of blended HFO-based compositions. Variable speed compressor use allowed each fluid to match R-410A air-side capacities.

Presented data will include the following: air-side capacities, energy efficiencies, compressor speeds, and operating parameters. These performance metrics and operating conditions will be compared to those of R-410A. Performance will consist of both air-conditioning and heating environmental conditions, following the guidelines of AHRI 210/240. These blends further extend the potential options of low GWP alternatives, utilizing optimization technologies such as a variable speed compressor.

© HPC2023.
Selection and/or peer-review under the responsibility of the organizers of the 14th IEA Heat Pump Conference 2023.

Keywords: Residential heat pump; Performance; Refigerat; R-454A; R-454C; Low GWP;R-1234yf; HFO; Variable Speed Compressor

1. Introduction

The phase out of CFC and HCFC refrigerants, due to the Montreal Protocol, has been completed. Consequently, the transition to non-ozone depleting HFC refrigerants resulted in the continued use of high Global Warming Potential (GWP) fluids. With recent regulations, such as the Kigali Agreement to the Montreal Protocol, requiring the phase down of HFC refrigerants, came the advent of hydrofluo-olefin (HFO) refrigerants, such as R-1234yf. With a GWP of <1, R-1234yf and R-1234yf containing refrigerant blends offer significant GWP reductions relative to incumbent HFC refrigerants.

The residential air conditioning and heating space predominantly uses R-410A (GWP 2088) in heat pump systems. Refrigerant blends containing R-1234yf, such as R-454B (GWP 467), are approved for new equipment use and offer significant GWP reductions. In preparation for future regulations calling for further GWP reductions, additional refrigerant blends were studied in a residential heat pump system. Refrigerants R-454C (GWP 146) and R-454A (GWP 288) are binary refrigerant blends consisting of R-32 and R-1234yf. Both fluids are in commercial use in stationary freezer applications. They each have potential in residential heat pump systems with some system optimizations, such as single-speed compressor changes, variable speed compressor use, or heat exchanger adjustments.

2. Fluid Overview, System Architecture, and Thermodynamic Cycle Model Study

2.1. Fluid properties and test system

A comparison of the physical and chemical properties of several lower GWP alternatives to R-410A are shown below in Table 1. Fluids in the comparison include R-410A, R-454B, R-454A, and R-454C.

Table 1. Physical and chemical properties of R-410A and lower GWP alternatives

Fluid	R-410A	R-454B	R-454A	R-454C
Name	R-32/R-125	R-32/R-1234yf	R-32/R-1234yf	R-32/R-1234yf
Composition, wt. %	50.0/50.0	68.9/31.1	35.0/65.0	21.5/78.5
Molecular Weight	72.59	62.61	80.47	90.78
Normal Boiling Point, °C	-51.36	-49.49	-42.16	-37.75
Sat Vap Pres (kPa) @ 20 °C	1443	1323	1012	847
Sat Vap Pres (kPa) @ 60 °C	3834	3541	2793	2368
Critical Temperature, °C	71.3	78.1	81.7	85.7
GWP (AR5)	1924	467	238	146

The alternatives above offer significant GWP reduction relative to R-410A. Each are binary refrigerant blends of R-32 and R-1234yf at differing compositions. Saturated vapor pressures for R-454A and R-454C indicate lower operating pressures in a heat pump system. Normal boiling points of the two fluids indicate capacity differences, which can be mitigated with system optimizations.

Test system architecture consisted of a residential heat pump designed for R-410A, which was an 8.79 kW, 16 SEER ducted, split system heat pump. The single-speed compressor native to the system was replaced with a variable speed compressor with comparable system performance at 60 Hz. The POE 32 centistoke lubricant used for each refrigerant was identical to what was specified for R-410A use. Architectures for both the cooling and heating modes are shown below in Figure 1.

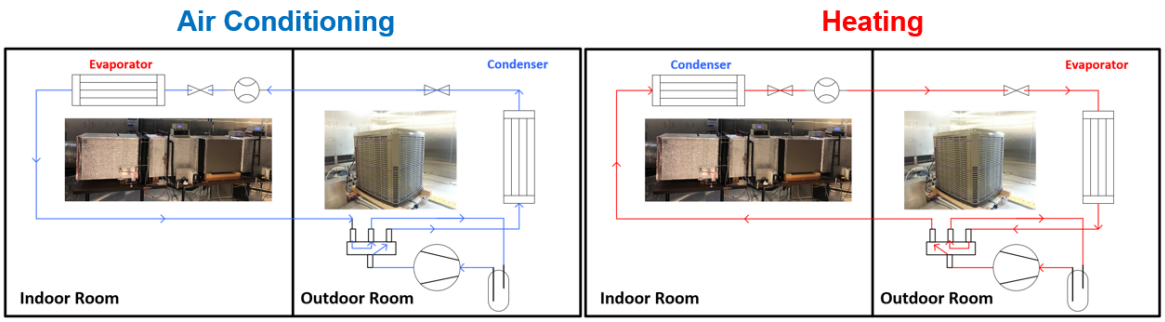


Fig. 1. Heat pump setup and schematic

The test heat pump was comprised of two heat exchangers, a variable speed scroll compressor, a mass flow meter, and a suction line accumulator. The indoor and outdoor room heat exchangers have an electronic expansion valve (EEV) and adjustable thermostatic expansion valve (TXV) respectively. A pair of environmental chambers was used to control the temperature and humidity of the indoor and outdoor units to applicable test conditions. Chamber test conditions are listed below in Table 2, which are compliant with ANSI/AHRI Standard 210/240-2023 and ISO Standard 5151-2017.

Table 2. Chamber test conditions for cooling and heating

Cooling/Heating	Condition	IR DBT °C	IR WBT °C	OR DBT °C	OR WBT °C
Air Conditioning	Cooling B*	26.7	19.4	27.8	18.3
Air Conditioning	Cooling A*	26.7	19.4	35.0	23.9
Air Conditioning	ISO T3**	29.0	19.0	46.0	24.0
Heating	H1*	21.1	15.6	8.3	6.1
Heating	H3*	21.1	15.6	-8.3	-9.4

* ANSI/AHRI 210/240-2023

** ISO Standard 5151-2017

Refrigerant charge optimizations were performed for each fluid at the Cooling A and H1 conditions for cooling and heating respectively. As the system was designed for R-410A, a singular charge optimization was performed for R-410A at the Cooling A condition. Optimized refrigerant charges were different between the modes for both R-454A and R-454C.

2.2. Thermodynamic cycle modelling

Thermodynamic cycle analyses were completed, comparing relative performance of R-454A and R-454C to R-410A at representative air conditioning and heating conditions. Cooling cycle model results are shown below in Table 3. Cycle conditions were as follows: 10 C evaporator, 46.1 C condenser, 11.1 K superheat, 8.3 K subcooling, 70% compressor efficiency, and equivalent compressor displacement. Heating cycle model results are below in Table 4, performed at the following conditions: 0 C evaporator, 55.0 C condenser, 10.0 K superheat, 3.0 K subcooling, and 70% compressor efficiency.

Table 3. Air conditioning thermodynamic cycle analyses

	R-410A	R-454B	R-454A	R-454C
Capacity vs. R-410A	-	-4%	-23%	-33%
COP vs. R-410A	-	2%	3%	5%
Evap Glide [K]	0.1	1.1	4.7	6.1
T, Dis [C]	81	87	77	73
P, Dis [kPa]	2801	2615	2131	1842

Table 4. Heating thermodynamic cycle analyses

	R-410A	**R-454B**	**R-454A**	**R-454C**
Capacity vs. R-410A	-	-1%	-24%	-36%
COP vs. R-410A	-	4%	3%	4%
Evap Glide [K]	0.1	1.0	4.0	4.7
T, Dis [C]	102	111	95	88
P, Dis [kPa]	3435	3207	2615	2261

For both cooling and heating conditions, R-454A and R-454C exhibited notably lower capacities than R-410A but similar COPs. Compressor discharge temperatures and pressures were decreased with both alterative refrigerant blends. Both R-454A and R-45C are zeotropic refrigerant blends, having higher temperature glides than R-410A.

Lower cooling and heating capacities indicate system optimization for use in a residential heat pump. For this work, a variable speed compressor, as described earlier, was installed to compensate for the lower

capacities of R-454A and R-454C. By adjusting refrigerant mass flow rate, cooling and heating capacities can match those of R-410A. Increased compressor speeds will impact total system energy consumption, therefore, impacting efficiencies.

The test system was optimized with a comparable variable speed compressor. The inherent heat exchangers, designed for R-410A use, were unchanged. By optimizing the heat exchangers, the increase in heat transfer area will further account for lower fluid capacities and the increased pressure drop in the heat from lower density refrigerants. Additionally, optimized heat exchangers can better account for fluids with higher temperature glides and greater optimized refrigerant charge sizes relative to R-410A.

3. Results and Discussion

3.1 Air conditioning test results

As specified in the above section, performance evaluations were conducted in a split system residential heat pump designed for R-410A use. A variable speed compressor of similar performance at 60 Hz to the single speed compressor native to the commercial system was installed. The system was installed in a pair of environmental chambers. Testing was conducted following ASHRAE Standard 37, with chamber temperature and humidity set according to ANSI/AHRI Standard 210/240-2023 and ISO Standard 5151-2017, as shown previously in Table 2.

Refrigerant charge size optimizations were performed for both cooling (Cooling A) and heating (H1) modes. For the optimization, R-410A was run at 3600 RPM (60 Hz) to mimic the performance of a single speed compressor. The optimal refrigerant charge yielded the highest COP at the singular compressor speed with appropriate subcooling. The refrigerant charge optimizations for R-454A and R-454C involved adjusting compressor speed to match R-410A capacity at Cooling A and H1, depending on the selected mode. Table 5 displays the results for cooling mode, along with an expected refrigerant charge estimated from liquid densities of each refrigerant.

Table 5. Charge optimization – Air conditioning

Refrigerant	Optimized Charge	Relative to R-410A	*Estimated Charge*	*Relative to R-410A*
	kg	%	*kg*	*%*
R-410A	5.22	0%	*5.22*	*0%*
R-454A	4.99	-4%	*5.02*	*-4%*
R-454C	5.67	9%	*5.12*	*-2%*

Optimized refrigerant charge for R-454A was similar to its estimated charge. The estimated refrigerant charge of R-454C was 2% less than R-410A. However, the optimized refrigerant charge was about 9% greater than that of R-410A. At the lower refrigerant charge, the refrigerant was not fully subcooled entering the expansion valve. The increased refrigerant charge provided the optimal COP and adequate subcooling.

R-454A and R-454C performance was evaluated twice at each condition specified in Table 2. One evaluation was with using a compressor speed of 3600 RPM and matching evaporator superheat of R-410A. The second evaluation had an adjusted compressor speed to match the capacity of R-410A at that temperature condition. Evaporator superheat was also adjusted to better match the evaporator temperature of R-410A for the matched capacity conditions. Figures 2 and 3 depict cooling capacity and COP, relative to R-410A.

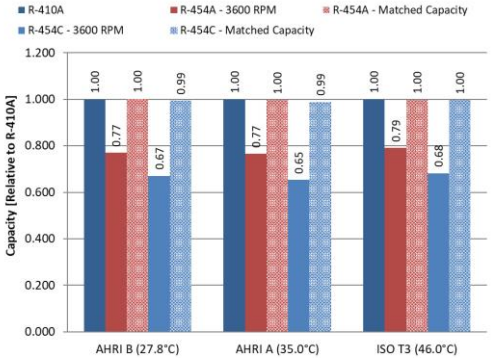


Fig 2. Cooling capacity relative to R-410A

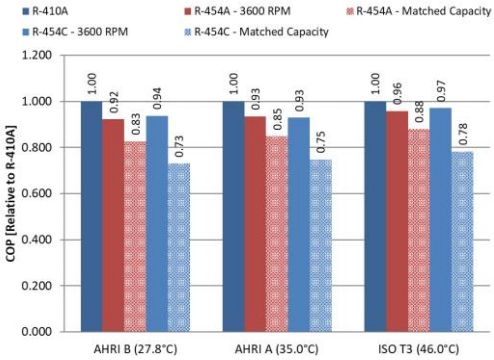


Fig 3. COP relative to R-410A

With compressor speed adjustment, the R-454A and R-454C cooling capacities were within 1% of R-410A capacities at the evaluated conditions. Cooling capacities for both fluids were similar to the thermodynamic cycle model when studied at 3600 RPM compressor speed. Relative COPs at the matched capacity conditions were lower than expected. The lower capacities of R-454A and R-454C required an increase in compressor speed, subsequently increasing energy consumption. The energy penalty is larger than expected considering the comparable COP of both fluids relative to R-410A from the thermodynamic cycle models. Discharge pressures for R-454A and R-454C in the matched capacity tests were higher than cycle models would suggest, indicating a potential penalty from high refrigerant charge. Particularly for R-454C, refrigerant charge was about 9% higher than R-410A with an expected charge being less than R-410A. Additional system optimization or using a system designed for R-454C would likely mitigate this issue. Energy and compressor speed increases are shown below in Figures 4 and 5.

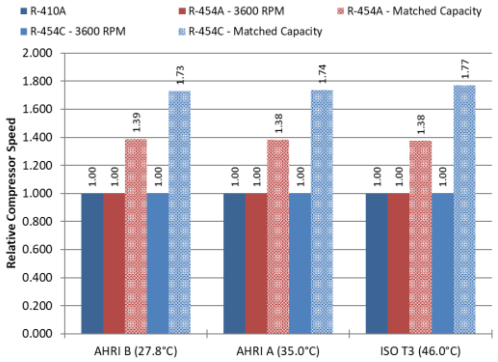


Fig. 4. Relative compressor speed

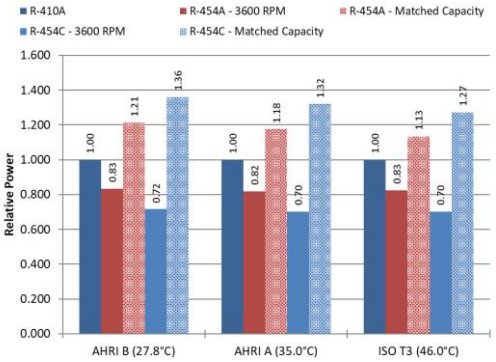


Fig. 5. Relative energy consumption

With lower volumetric capacities, compressor speed increases for R-454A and R-454C are shown above in Figure 4. From Figure 5, relative energy consumption for both fluids at 3600 RPM were about 20% and 30% lower than that of R-410A. Upon increasing speed to match R-410A capacity, increase in energy consumption was greater than the cooling capacity increase, resulting in lower relative COPs shown in Figure 3. This could also be mitigated with further system optimizations or by using a system designed for use with one of the alternative refrigerant blends. Figures 6 and 7 illustrate discharge temperature and refrigerant mass flow rate trends for the testing.

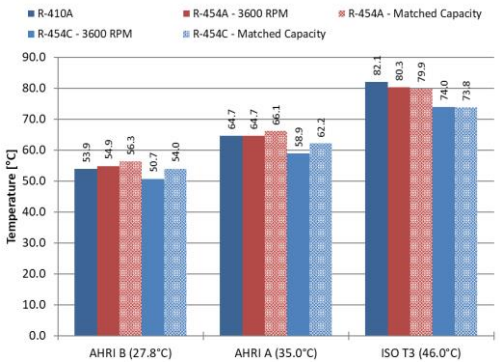


Fig. 6. Compressor Discharge Temperatures

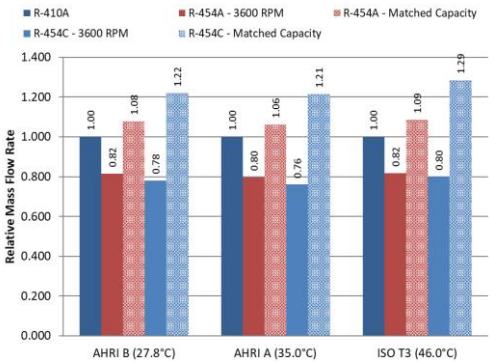


Fig. 7. Relative refrigerant mass flow rate

Compressor discharge temperatures follow the expected trend from cycle model evaluations. R-454C yielded the lowest discharge temperatures, followed by R-454A. The same trend was observed with refrigerant mass flow rate. R-454C relative mass flow rate was greatest due to its lower volumetric capacity among the fluids tested. R-454A and R-454C had flow rates about 8% and 24% higher than R-410A, which accounted for cooling capacity increases of about 23% and 33% respectively. Evaporator superheat and EEV inlet subcooling temperatures are below in Figures 8 and 9.

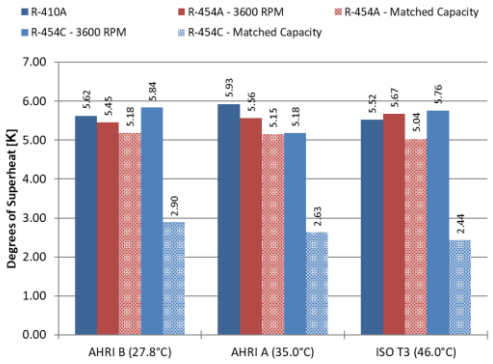


Fig. 8. Evaporator outlet superheats

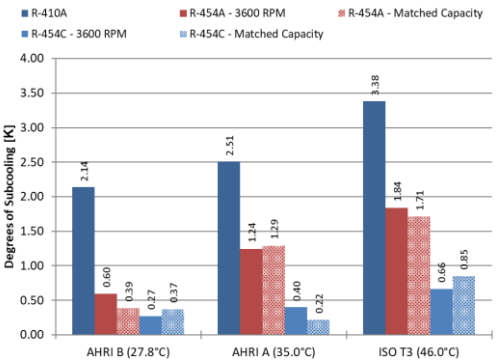


Fig. 9. EEV inlet subcooling

Evaporator superheat was maintained at about 10 F for the 3600 RPM evaluations and adjusted to match the average evaporator temperatures of R-410A at in the matched capacity studies. The higher temperature glide R-454C required more superheat adjustment to match R-410A evaporator temperature. Subcooling values for R-454A and R-454C, though low, were the measured values for the optimal refrigerant charges for both fluids. There is a sight glass on the system before the EEV to visually confirm phase of fluid entering the EEV. For each test, fully subcooled liquid was entering the EEV.

3.2 Heating test results

Performance evaluations in heating mode are in progress. Evaluations for R-454A and R-454C will be complete in 2023.

4. Conclusions

Lower GWP alternatives to R-410A in stationary applications are available in the form of HFO containing refrigerant blends, such as R-454B, and other solutions. The potential for further reducing global warming impact in such systems exists with options such as R-454A and R-454C. Such refrigerants will require optimizations to common designs, such as a variable speed compressor, to achieve comparable cooling

capacities to the incumbent HFC. Evaluations in a R-410A residential heat pump showed the potential of even lower GWP alternatives. Comparable cooling capacity was achieved with R-454A and R-454C. Relative COPs can be improved with further system optimization or choosing a system better suited for use with the alternative refrigerants. The incurred energy penalties can be reduced with these changes. Refrigerant flow increase can compensate for lower capacity fluids, enabling further reductions in GWP.

References

[1] AHRI 2023. *AHRI Standard 210/240-2023: Performance Rating of Unitary Air-Conditioning and Air-Source Heat Pump Equipment*. Arlington, Virginia: Air-conditioning, Heating, and Rerigeration Institute

[2] ASHRAE 2019. *ANSI/ASHRAE Standard 37-2009 (RA 2019): Methods of Testing for Rating Electrcially Driven Unitary Air-Conditioning and Heat-Pump Equipment*. Atlanta, Georgia: American Scociety of Heating Refrigeration and Air Conditioning Engineers, Inc.

[3] Brown, J.S., Domanski, P.A, Lemmon, E.W. *Cycle_D: NIST Vapor Compression Cycle Design Program. Version 6.0*. Gaithersberg, Maryland: National Institute of Standards and Technology, Standard Reference Data Program.

[4] ISO 2017. *ISO 5151 (2017): Non-ducted air conditioners and heat pumps – Testing and rating for performance*. Geneva, Switzerland: International Organiation for Standardization

[5] Lemon, E.W., Huber, M.L., McLinden, M.O. 2018. *NIST Standard Reference database 23: Reference Fliud Thermodynamics nd Transport Properties-REFPROP, Version 10.0*. Gaithersburg, Maryland: National Institute of Standards and Technology, Standard Reference Data Program.

14th IEA Heat Pump Conference
15-18 May 2023, Chicago, Illinois

Study on a hybrid refrigeration cycle by combining an absorption process with a compression process using Low-GWP refrigerant

Tsutomu Wakabayashi[a], Saori Sakurai[a], Ryosuke Takioka[a], Hajime Yabase[b], Naoyuki Inoue[b], Yonezo Ikumi[b] and Kiyoshi Saito[b]

[a]OSAKA GAS CO., LTD., 6-19-9, Torishima, Konohana-ku, Osaka 554-0051, JAPAN
[b]WASEDA UNIVERSITY, 3-4-1, Okubo, Shinjuku-ku, Tokyo 169-8555, JAPAN

Abstract

This research is intended to evaluate a "hybrid refrigeration cycle" which is combining an absorption process driven by utilizing low-temperature waste heat with a compression process in one circulation cycle. A compressor is installed between an evaporator and an absorber in a hybrid refrigeration cycle. In this research, HFO or HCFO refrigerant and an organic solvent were used as a working pair for the absorption process.

The absorption equilibrium solubilities of the working pairs were measured when the experimental temperature and pressure conditions were changed. The parameters of NRTL model were determined by the experimental absorption equilibrium solubilities, and the PTx lines of the working pairs were calculated. Further, the enthalpy-concentration diagrams of the working pairs were calculated by using the material properties of the refrigerants and the absorbents.

It was confirmed that there are the conditions that the estimated cooling COP_c based on the power in the hybrid refrigeration cycle can be more than twice as high as that in the compression refrigeration cycle.

© HPC2023.
Selection and/or peer-review under the responsibility of the organizers of the 14th IEA Heat Pump Conference 2023.

Keywords: hybrid refrigeration cycle; compression; absorption; low-GWP refrigerant; waste heat

1. Introduction

Utilization of waste heat is regarded as one of the effective means to achieve carbon neutrality by 2050. This research is intended to evaluate a "hybrid refrigeration cycle" which is combining an absorption process driven by utilizing low-temperature heat (lower than 100°C) with a compression process in one circulation cycle.

Figure 1 shows the schematic flow diagram of the hybrid refrigeration cycle. A compressor is installed between an evaporator and an absorber. Although the power of a solution pump is necessary, the power of a compressor is reduced more than the increased power for a solution pump. Therefore, it is said that cooling COP_c of the hybrid refrigeration cycle based on power is significantly improved.

Recently, the use of HFCs in air conditioning and refrigeration equipment has been phased out due to their high GWP, and the transition to low GWP refrigerants HFO and HCFO is progressing. As for absorption chillers, working pairs using low GWP refrigerants are being developed, and HFO and ionic liquid working pairs have been proposed [1-2].

In this research, HFO refrigerant (GWP=1 or less) and an organic solvent (glycol ether) were used as a working pair for the absorption process for the purpose of improving the circulation ratio. The absorption equilibrium solubilities of the working pairs were measured when the experimental temperature and pressure conditions were changed. The parameters of Non-Random Two Liquid (NRTL) model were determined by the experimental absorption equilibrium solubilities, and PTx lines of the working pairs were calculated.

Further, enthalpy-concentration diagrams of the working pairs were calculated by using the material properties of refrigerants and absorbents to estimate cooling COP_c of the hybrid refrigeration cycle.

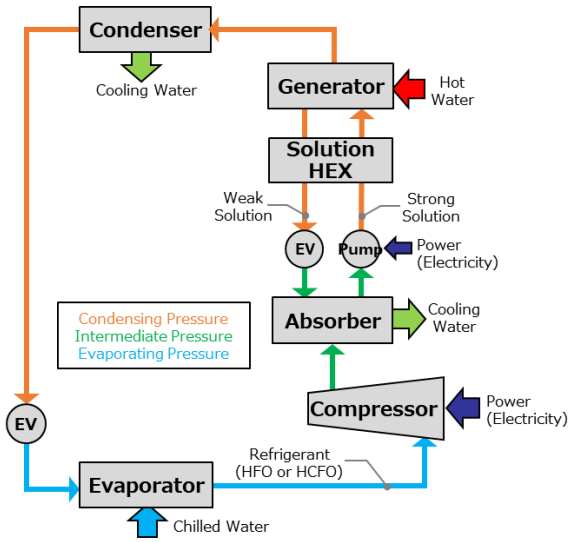


Fig. 1. Schematic flow diagram of a hybrid refrigeration cycle (single expansion).

2. Property of equilibrium state

2.1. Refrigerant and absorbent

R1234yf (GWP < 1) is used as a refrigerant. Tetraethylene Glycol Dimethyl Ether ($C_{10}H_{22}O_5$, Kishida Chemical) is selected as an absorbent. The physical property of the absorbent used in this study is shown in Table 1. The absorbent is one of the organic solvents and is relatively cheap. The ionic liquid of [HMIM][Tf_2N] as the absorbent is also used for validation and comparison.

Table 1. Physical property of the absorbent used this time.

Absorbent	Molecular weight	Boiling Point [℃]	Density [kg/L@20℃]	Specific heat [kJ/(kg・K) @20℃]	Viscosity [Pa・s@ 20℃]
Tetraethylene Glycol Dimethyl Ether	222	275	1.01	2.2	0.0038

2.2. Measurement of absorption equilibrium solubilities

Figure 2 shows the apparatus to measure absorption equilibrium solubilities [1].

The absorbent is set in the equilibrium cell and the refrigerant is set in the reservoir. Both is connected via valve V3.

The refrigerant in the reservoir is added into the equilibrium cell by the procedure that the valve V3 is opened for a certain time and closed. Then the equilibrium pressure P1 and P2 are measured. This procedure is repeated.

The increase of absorption equilibrium solubilities is the quantity of refrigerant moved from the reservoir to the equilibrium cell minus the increase of the quantity of refrigerant in the equilibrium cell.

The quantity of refrigerant moved from the reservoir to the equilibrium cell is estimated using the volume of area in which the refrigerant is present in the reservoir (blue part of Fig. 2, 153mL) and the change of the equilibrium pressure P1 after the addition of the refrigerant to the equilibrium cell.

The increase of the quantity of refrigerant in the equilibrium cell is estimated using the volume of area in which the refrigerant is present (green part of Fig. 2, 148mL minus the volume of the absorbent) in the equilibrium cell and the change of the equilibrium pressure P2 after the addition of the refrigerant to the equilibrium cell. The volume of the absorbent is set to be about 22mL.

The measurement temperature is from 35℃ to 80℃. T1 and T2 are K sheath type thermocouples (1.6mm), and P1 and P2 are the pressure sensors (GP-M025, KEYENCE).

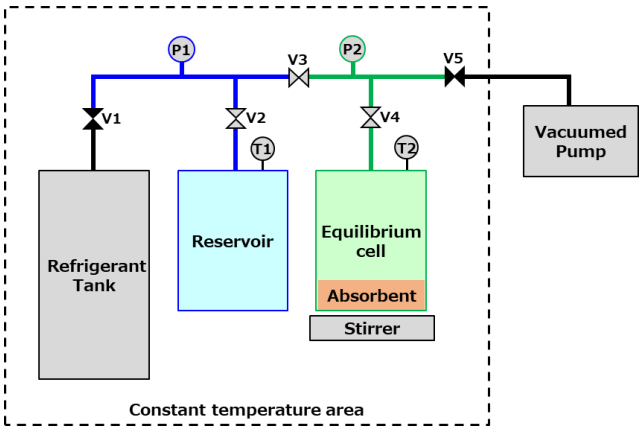


Fig. 2. Outline of apparatus for equilibrium absorption solubilities.

Figure 3 shows the experimental results of the relation between the refrigerant concentration and the pressure at different temperatures. The left of Fig. 3 indicates the result in case of [HMIM][Tf_2N] and the right of Fig. 3 indicates the result in case of Tetraethylene Glycol Dimethyl Ether. The refrigerant concentration is the mass ratio to the sum of the refrigerant and the absorbent. The dotted line in the right of Fig. 3 is fitted to the experimental data by quadratic function.

The refrigerant concentration in case of Tetraethylene Glycol Dimethyl Ether is much higher than that in case of [HMIM][Tf_2N] at the same temperature.

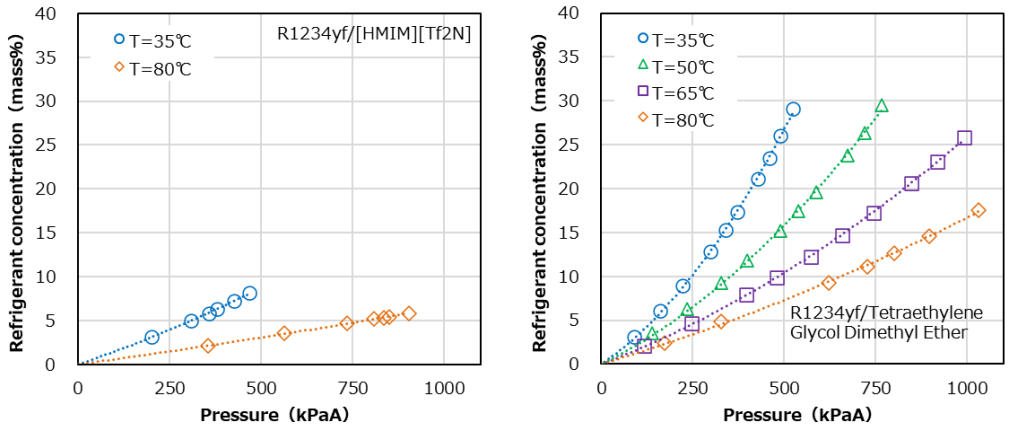


Fig. 3. Experimental results of the relation between the refrigerant concentration and the pressure at different temperatures. The left figure indicates the result in case of [HMIM][Tf2N] and the right figure indicates the result in case of Tetraethylene Glycol Dimethyl Ether.

In order to validate the measured absorption equilibrium solubilities, the data of ref [1] in case of R1234yf/[HMIM][Tf2N] is used.

The temperature conditions for the validation are follows.

- Evaporation temperature T_e is 10℃
- Condensation temperature T_c is 35℃
- Absorption temperature T_a is 35℃
- Generation temperature T_g is 80℃

Table 2 shows the refrigerant concentration of the strong solution x_s and that of the weak solution x_w and the circulation ratio in the condition above including in case of R1234yf/Tetraethylene Glycol Dimethyl Ether. The circulation ratio is defined to be the mass flow ratio of the strong solution to that of the absorbed refrigerant and can be also calculated to be (100% - x_w) / (x_s - x_w). The refrigerant pressure is estimated using Refprop

10.0. In case of R1234yf, the absorption (=evaporation) pressure is 438kPaA, and the generation (=condensation) pressure is 895kPaA. The pressure loss is not considered.

It is confirmed that the refrigerant concentration of the strong and weak solutions and the circulation ratio of ref [1] in case of R1234yf/[HMIM] [Tf_2N] is almost same as this work. Further, the refrigerant concentration difference between the strong and weak solutions in case of R1234yf/Tetraethylene Glycol Dimethyl Ether is increased, and the circulation ratio is significantly improved.

Table 2. Refrigerant concentration of the strong and weak solutions and the circulation ratio at T_e=10℃, T_c=35℃, T_a=35℃, T_g=80℃.

Refrigerant/Absorbent		Refrigerant concentration (mass%)			circulation ratio (-)
		Strong solution x_s	Weak solution x_w	x_s - x_w	
R1234yf/[HMIM][Tf2N]	Ref. [1]	7.3	5.5	1.8	53
	This work	7.5	5.7	1.7	52
R1234yf/Tetraethylene Glycol Dimethyl Ether	This work	22.0	14.7	7.4	12

2.3. PTx lines and enthalpy-concentration diagrams

The Non-Random Two Liquid (NRTL) equation is applied to the experimental results of the relation between the refrigerant concentration and the pressure at different temperatures shown in the right of Fig. 3 for R1234yf/Tetraethylene Glycol Dimethyl Ether. The parameter α of the NRTL equation is set to be constant (α=0.2) in this work [3]. It is confirmed that the deviations of the calculated refrigerant concentration using the NRTL equation from the experimental refrigerant concentration for R1234yf/Tetraethylene Glycol Dimethyl Ether are very small.

The left of Fig.4 shows PTx lines, and the right of Fig.4 shows the enthalpy-concentration diagrams in case of R1234yf/Tetraethylene Glycol Dimethyl Ether. The enthalpy of the solution which absorbed the refrigerant is calculated based on ref [4]. The enthalpy per unit solution mass is plotted against the refrigerant concentration which is the mass ratio of the refrigerant to the sum of the refrigerant and the absorbent. The enthalpy of the saturated liquid of the refrigerant at 0℃ is 200kJ/kg, and the enthalpy of the absorbent at 0℃ is 200kJ/kg.

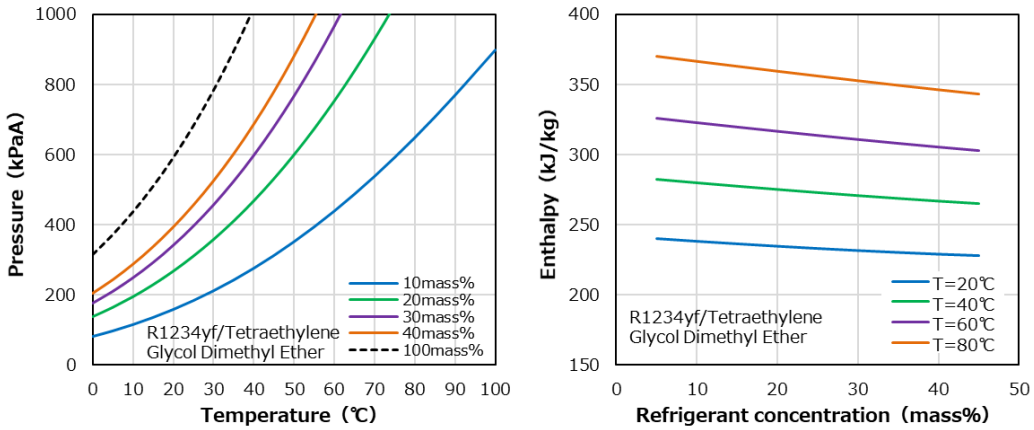


Fig. 4. PTx lines (left) and enthalpy–concentration diagrams (right) in case of R1234yf/Tetraethylene Glycol Dimethyl Ether

3. Process simulation

3.1. Flow and conditions for process simulation

The process simulation in case of R1234yf/Tetraethylene Glycol Dimethyl Ether is conducted for the double expansion flow indicated in Fig. 5.

The refrigerant at the outlet of the evaporator (1) is compressed to the intermediate pressure (2) by the low-stage compressor and is mixed (8) with the saturated vapor refrigerant from the separator (7). The strong solution (10) which absorbs the refrigerant (8) at the absorber is compressed (11) by the solution pump and is heated (12) at the solution heat exchanger and is separated into the refrigerant (9) and the weak solution (13) at the generator. The separated refrigerant (9) is condensed (3) at the condenser and is decompressed (4) by the expansion valve EV2 and is separated into the saturated vapor refrigerant (7) and the saturated liquid refrigerant (5) at the separator. The saturated liquid refrigerant (5) is decompressed (6) by the expansion valve EV1 and is directed to the evaporator. The weak solution (13) is cooled (14) at the solution heat exchanger and is decompressed (15) by the expansion valve EV3 and is directed to the absorber.

The high-stage compressor is provided for operation when the quantality of waste heat is relatively small.

The simulation conditions are follows.

- Compression efficiency is 75%
- Pump efficiency is 50%
- Superheat at the outlet of the evaporator is 5K
- Subcool at the outlet of the condenser is 0K
- Temperature efficiency of the solution heat exchanger is 85% (based on weak solution)
- Pressure and heat loss is none.
- Evaporation temperature T_e is 5°C
- Condensation temperature T_c is 30°C
- Absorption temperature T_a is 30°C

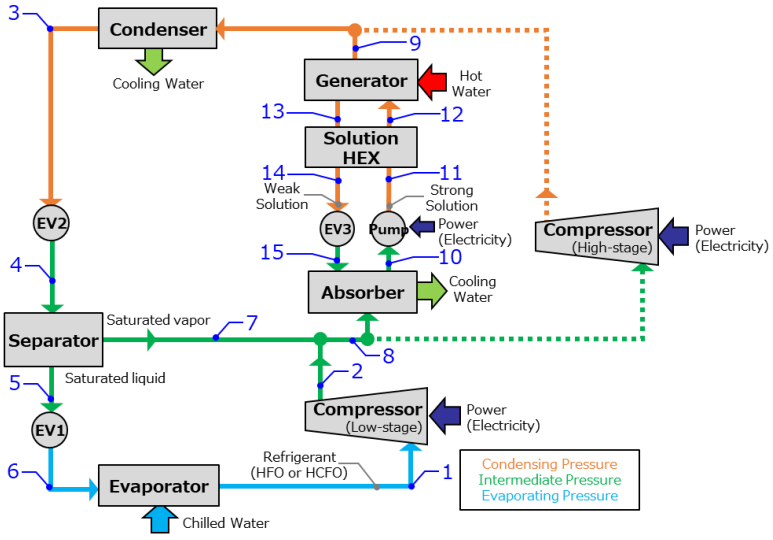


Fig. 5. Flow of the process simulation (double expansion).

3.2. Results of process simulation

Table 3 shows the example of simulation results of the state value at each position and the heat quantity and the power when the high-side compressor is not operated, the intermediate temperature T_m is 12°C, the generation temperature T_g is 80°C and the quantity of evaporation Q_e is 100kW.

The intermediate temperature T_m is defined to be the saturated temperature of the refrigerant at the outlet of the low-stage compressor.

Table 3. Simulation results of the state value at each position (upper) and the heat quantity and the power (lower) at T_e=5°C, T_c=30°C, T_a=30°C, T_g=80°C, T_m=12°C, Q_e=100kW without high-stage compressor.

Position	Pressure (kPaA)	Temperature (°C)	Enthalpy (kJ/kg)	Flow rate (kg/s)	Refrigerant concentration (mass%)
1	373	10.0	371	0.643	100
2	466	17.9	377	0.643	100

3	784	30.0	241	0.765	100
4	466	12.0	241	0.765	100
5	466	12.0	216	0.643	100
6	373	5.0	216	0.643	100
7	466	12.0	371	0.122	100
8	466	17.0	376	0.765	100
9	784	80.0	435	0.765	100
10	466	30.0	251	3.592	31.1
11	784	30.3	251	3.592	31.1
12	784	66.0	323	3.592	31.1
13	784	80.0	365	2.827	12.5
14	784	37.8	274	2.827	12.5
15	466	-	274	2.827	12.5

Part		Quantity of heat or power (kW)
Evaporation	Q_e	100
Condensation	Q_c	149
Absorption	Q_a	162
Generation	Q_g	205
Solution heat exchanger	Q_s	255
Compressor (low-stage)	W_{cl}	3.5
Solution pump	W_{sp}	2.3

Cooling COP_c based on the power in this hybrid cycle is 17.0 (=100kW / (3.5kW+2.3kW)). On the other hand, although the details are omitted, the compression power in the single compression cycle under the same condition is 14.0kW, so cooling COP_c in the single compression cycle is 7.2 (=100kW / 14.0kW). Therefore, cooling COP_c based on the power in the hybrid cycle corresponds to about 238% of that in the single compression cycle. The required quantity of generation heat corresponds to about 2.1 times of that the evaporation heat. The circulation ratio in the absorption process is about 4.7 (=3.592kg/s / 0.765kg/s).

Cooling COP_c based on the power (left) and the quantity of generation heat Q_g (right) are shown in Fig. 6 when the intermediate temperature T_m and the generation temperature T_g are changed in the condition above. Cooling COP_c is expressed as a ratio to that of single compression cycle in the same condition, and the quantity of generation heat Q_g is expressed as a ratio to that of evaporation heat Q_e. The result in the condition of Table 3 (the intermediate temperature T_m is 12℃ and the generation temperature T_g is 80℃) is indicated by "□" in Fig. 6.

It can be seen that COP_c has a local maximum value against the intermediate temperature T_m (indicated by "○"), and the quantity of generation heat Q_g increase as the intermediate temperature T_m decreases. It is considered that although the compression power decreases with the decrease in the intermediate temperature T_m, the power of the solution pump and the quantity of generation heat Q_g increase due to the increase in the circulation ratio.

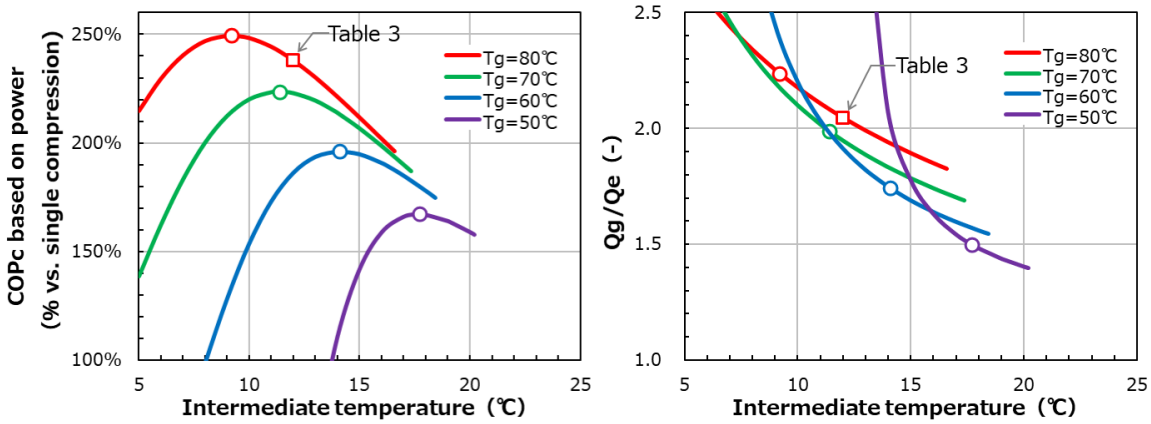


Fig. 6. Cooling COP_c based on the power (left) and the quantity of generation heat Q_g (right) against the immediate temperature T_m at T_e=5℃, T_c=30℃, T_a=30℃, T_g=50-80℃ without high-stage compressor.

Cooling COP_c based on the power against the quantity of generation heat Q_g is shown in Fig. 7 in the condition above. It can be seen that COP_c has a local maximum value against the quantity of generation heat Q_g (indicated by "○").

When the generation temperature T_g decreases, the maximum value of COP_c decreases. However, it can be seen that the required quantity of generation heat Q_g at that time is also reduced.

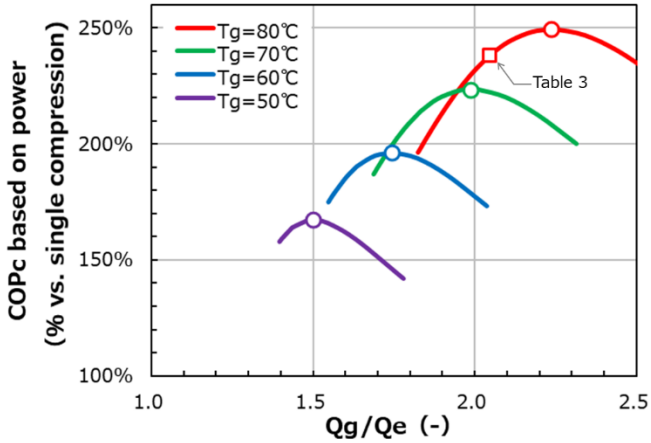


Fig. 7. Cooling COP_c based on the power against the quantity of generation heat Q_g at T_e=5℃, T_c=30℃, T_a=30℃, T_g=50-80℃ without high-stage compressor.

4. Conclusions

After measuring the equilibrium absorption concentration, PTx lines and enthalpy-concentration diagrams were created, and process simulation was performed in the hybrid refrigeration cycle which uses R1234yf as the low-GWP refrigerant and Tetraethylene Glycol Dimethyl Ether (organic solvent) as the absorbent. Below are the conclusions.

- The circulation ratio of the absorption process using Tetraethylene Glycol Dimethyl Ether as the absorbent is significantly lower than that using [HMIM][Tf_2N] (ionic liquid) in case of R1234yf as the refrigerant.
- In the simulation condition of this work, there is a local maximum value of cooling COP_c based on the power of the compressor and the solution pump against the quantity of generation heat. It was confirmed that there are the conditions that the estimated cooling COP_c based on the power in the hybrid refrigeration cycle can be more than twice as high as that in the single compression refrigeration cycle.

References

[1] Liu, et al., 2016, Vapor-Liquid Equilibrium of R1234yf/[HMIM][Tf_2N] and R1234ze(E)/[HMIM][Tf_2N]working pairs for Absorption Refrigeration Cycle, J. Chem. Eng. Data, 61, 3952-3957.
[2] Esaki, 2021, Study on basic characteristics evaluation of a new absorption refrigerator cycle with Hydrofluoroolefin refrigerant and ionic liquid pair, Proceedings of 2021 Annual Meeting of JSRAE, D341.
[3] Shiflett, et al., 2006, Solubility and diffusivity of 1,1,1,2-tetrafluoroethane in room-temperature ionic liquids, Fulid Phase Equilibria, 242, 220-232.
[4] J.M.Smith et al., INTRODUCTION TO CHEMICAL ENGINEERING THERMODYNAMICS (SEVENTH EDITION), McGrawHill.

14th IEA Heat Pump Conference
15-18 May 2023, Chicago, Illinois

The Performance Playbook: A policy strategy for scaling heat pump adoption with happy consumers and utilities

Andy Frank

Nate Kinsey

Sealed, 22 W 38th Street Floor 10, New York, NY 10018
andy.frank@sealed.com
347-609-3508

Abstract

Across the country, states and utilities are implementing programs to accelerate the market adoption of heat pumps to meet energy and climate goals. Through case studies of leading heat pump rebate and incentive programs, including California's Technology and Equipment for Clean Heating initiative, the City of Denver's Climate Action Rebates, and New York State's Clean Heat program, Sealed explores each program's unique market animation strategies and their impact on consumer adoption of heat pumps. These programs attempt to utilize "tried and true" market animation strategies that largely rely on financial incentives for consumers, but they have all caused a market "sugar crash" when program funding is exhausted. Market strategies based solely on large consumer rebates make achieving the adoption of heat pumps difficult, if not impossible, at the speed and scale required to reduce greenhouse gas emissions from commercial and residential buildings.

But while program sugar crashes are a well known phenomenon, little work has been done to quantify the effect and compare the impact across geographies and program designs. This paper takes a first step to track the speed and scale of sugar crash program spending, and offers solutions to the problem.

Specifically, a "Performance Playbook" is proposed that seeks to address this sugar crash problem. Only market-aligned strategies that maximize scarce ratepayer funds can accelerate the consumer adoption of heat pumps and provide utilities with valuable grid services. At its core, the Performance Playbook is built upon the principles that heat pump incentive programs should be:

- Easily accessible for both consumers and market actors,
- Flexible to adapt to evolving market conditions and long-term policy goals, and
- Performance-based to ensure market actors complete high-quality installations.

© HPC2023.
Selection and/or peer-review under the responsibility of the organizers of the 14th IEA Heat Pump Conference 2023.

Keywords:consumer facing rebates, market based incentives, sugar crash, sugar rush.

New York State's Clean Heat Program

Approved by the New York Public Service Commission (NY PSC) in its 2018 Order Adopting Accelerated Energy Efficiency Targets, the New York State Clean Heat program (Clean Heat Program) is the primary rebate program for accelerating the adoption of heat pumps in New York. The program was originally approved in 2018 with a total budget of $250 million and a statewide energy savings goal of 5 million gross MMBtus. On April 1, 2020, the Clean Heat Program began accepting rebate applications with a revised

statewide budget of $454 million and a heat pump energy savings goal of 3.5 million gross MMBtus.[1]

The Clean Heat program is administered on a statewide basis by New York's investor-owned utilities and in coordination with the New York State Energy Research and Development Agency (NYSERDA). Collectively this group is referred to as the "Joint Efficiency Providers" and strives to create a consistent experience and the market conditions to accelerate the adoption of heat pumps in New York.

Table 1 shows the adopted budgets and MMBtu savings goals for each of New York's investor-owned utilities.

Table 1: Clean Heat Program Budget and Savings Goals by Utility[2]

NY Utility	2020	2021	2022	2023	2024	2025	2020-2025 Total
Central Hudson Gas and Electric Corporation ("Central Hudson")							
Base Budget	$3,354,852	$5,559,173	$7,049,949	$8,265,836	$9,186,504	$9,804,997	$43,221,311
Base Energy Savings Target	17,728	30,183	38,850	48,190	56,479	63,863	255,293
Consolidated Edison, Inc. ("Con Edison")							
Base Budget	$18,037,338	$29,128,534	$35,884,450	$42,823,631	$48,526,394	$52,915,488	$227,315,835
Base Energy Savings Target	72,921	119,716	151,334	186,941	219,927	249,162	1,000,001
Niagara Mohawk Power Corporation ("Niagara Mohawk")							
Base Budget	$6,983,416	$11,891,672	$14,789,044	$16,424,789	$17,190,980	$17,118,933	$84,398,834
Base Energy Savings Target	71,239	132,010	172,203	210,694	245,889	280,647	1,112,682
New York State Electric and Gas Company ("NYSEG")							
Base Budget	$6,204,522	$10,605,014	$13,173,160	$14,628,326	$15,300,267	$15,219,288	$75,130,577
Base Energy Savings Target	63,614	117,911	153,328	187,944	219,558	250,383	992,738
Orange and Rockland Utilities, Inc. ("O&R")							
Base Budget	$1,236,326	$1,973,311	$2,397,539	$2,828,131	$3,164,633	$3,403,947	$15,003,887
Base Energy Savings Target	6,440	10,421	13,027	16,109	18,912	21,748	86,657
Rochester Gas and Electric Corporation ("RGE")							
Base Budget	$747,986	$1,278,915	$1,611,466	$1,799,548	$1,900,472	$1,909,389	$9,247,776
Base Energy Savings Target	7,541	14,206	18,304	22,468	26,422	30,282	119,223
Totals							
Base Budget	**$36,564,440**	**$60,436,619**	**$74,905,608**	**$86,770,261**	**$95,269,250**	**$100,372,042**	**$454,318,220**
Base Energy Savings Target	**239,483**	**424,447**	**547,046**	**672,346**	**787,187**	**896,085**	**3,566,594**

Market Animation Strategy and Impact

The initial Order creating the Clean Heat program did not prescribe strategies or tactics the Joint Efficiency Providers should use to animate the market. The Order also did not require a percentage or fixed amount of the program budget to be set aside for certain building types (i.e., small residential, multifamily, or commercial buildings). As such, the Joint Efficiency Providers elected to animate New York's entire building market through a program design that offered a customer-facing rebate structured as 1) a fixed dollar amount per heat pump unit, 2) per heat pump system capacity, or 3) per annual energy savings generated by a heat

[1] In response to the Heat Pump Statewide Framework submitted by the utilities, The Clean Heat program budget and goals were modified in the January 2020 Order Authorizing Utility Energy Efficiency and Building Electrification Portfolios through 2025. See: https://documents.dps.ny.gov/public/Common/ViewDoc.aspx?DocRefId={06B0FDEC-62EC-4A97-A7D7-7082F71B68B83}

[2] Table 1 is a recreation of Appendix C Table C1: 2020-2025 Heat Pump Budgets and Targets (Gross MMBtu) from the January 2020 Order Authorizing Utility Energy Efficiency and Building Electrification Portfolios through 2025. See: https://documents.dps.ny.gov/public/Common/ViewDoc.aspx?DocRefId={06B0FDEC-62EC-4A97-A7D7-7082F71B68B8}

pump project.[3] At the program's launch in April 2020, the Joint Efficiency Providers offered 9 distinct rebate categories.

Over the life of the Clean Heat Program, the Joint Efficiency Providers have increased rebate values, decreased rebate values, and created entirely new rebate categories to influence heat pump installations in their respective service territories. As of November 23, 2022, the Clean Heat Program has 12 different rebate categories that provide financial rebates for air-source heat pumps, ground-source heat pumps, and heat-pump water heaters to customers, contractors, distributors, and, in some categories, all three market actors.

As of November 23, 2022, over 26,000 buildings have participated in the Clean Heat Program. On December 19, 2022, the Department of Public Service staff supporting the NY PSC filed a comprehensive Energy Efficiency and Building Electrification Report. This report summarizes the performance of all of New York's efficiency programs, including the Clean Heat Program, and asks stakeholders for comment on the future direction of these programs.

California's Technology and Equipment for Clean Heating Program

In response to the passage in 2018 of California Senate Bill 1477: Low-emissions buildings and sources of heat energy, the California Public Utilities Commission (CPUC) created the Technology and Equipment for Clean Heating (TECH) initiative to serve as the state's main incentive program for accelerating the market adoption of heat pumps.[4] Originally approved with a total budget of $120 million, the TECH initiative was bid out to a third party non-utility program administrator. The winning bid was led by the Energy Solutions firm and a group of 11 supporting companies that together are responsible for:

1. Offering midstream and upstream incentives to animate the market,
2. Administering regional pilots and quick-start grants designed to overcome identified market barriers to heat pump adoption,
3. Providing low-interest financing for projects in environmental justice communities,
4. Informing future clean space and water heating policies in California through meter-based data driven analysis.[5]

Of the $120 million approved by the CPUC for the TECH initiative, approximately $37.5 million was reserved for single-family heat pump and heat-pump water heater incentives, and approximately $13.3 million was reserved for multi-family heat pump and heat-pump water heater incentives.[6]

Market Animation Strategy and Impact

By statute, the TECH initiative can provide incentives only through midstream or upstream techniques to encourage customer adoption.[7] The TECH team identified contractors as key stakeholders in the heat pump supply chain and elected to issue cash incentives directly to those contractors. The TECH initiative doesn't have requirements for how much or how little of the TECH incentive contractors must pass through to the end customer.

The TECH initiative's focus on the residential building sector allowed the TECH team to design a simpler and more sector-specific set of incentives. Single-family incentives launched on December 7, 2021, utilized a

[3] Specific utilities also provided "kicker" rebates for heat pump installations completed in "High Priority Electrification Zip Codes" identified having natural gas distribution system capacity constraints. See: https://cleanheat.ny.gov/assets/pdf/national-grid-high-priority-electrification-zip-codes.pdf

[4] Decision 20-03-027 approved the TECH program. See: https://docs.cpuc.ca.gov/PublishedDocs/Published/G000/M331/K772/331772660.PDF

[5] The Tech California Team consists of the following firms: Energy Solutions, VEIC, Frontier Energy, Association for Energy Affordability, Building Decarbonization Coalition, Recurve, the Ortiz Group, Ardenna Energy, Electrify My Home, National Comfort Institute, Tre'Laine, and Energy Outlet. For more details on each firm and links to the company websites, see: https://techcleanca.com/about/

[6] Initial funding for the TECH initiative was provided natural gas utility cap and trade proceeds. This funding source restricted the ability of TECH to offer rebates only to customers in natural gas territories.

[7] Senate bill 1477 low-emissions buildings and source of heat energy. (2017-2018) only allows the TECH initiative to provide "upstream and midstream incentives to install low-emission space and water heating equipment in existing and new buildings, with technologies identified pursuant to subdivision." See: https://leginfo.legislature.ca.gov/faces/billNavClient.xhtml?bill_id=201720180SB1477

two-tier and a fixed-dollar amount, per unit, incentive for air-source heat pumps and heat-pump water heaters.[8] Tier 1, or the baseline incentives, were available to all participants. Tier 2, or enhanced incentives, were higher incentives only available in geographies where other energy efficiency heat pump program offerings were available. The TECH initiative was able to "stack," or "braid," their incentives with other heat pump incentives because the program wasn't bound by other regulatory compliance metrics, such as energy efficiency savings goals.

On May 12, 2022, the TECH initiative announced that funding for its heat pump and heat-pump water heater incentives had reached capacity and were no longer processing applications.[9] As of November 23, 2022, the TECH program has incentivized the installation of 9,555 air-source heat pumps and 1,270 heat-pump water heaters. The average incentive provided for these installations was $3,422 for air-source heat pumps and $3,555 for heat-pump water heaters.[10]

Denver's Climate Action Rebates

In November 2020, Denver voted in favor of Ballot Initiative 2A, approving the increase of the city's and county's sales tax rate by 0.25% starting in 2021. Additionally, the initiative created a new city budget fund called the Climate Protection Special Revenue Fund (Climate Action Fund).[11] At the time of passage, the Climate Action Fund was estimated to be valued at approximately $40 million annually and could provide financial and technical support to a range of clean energy investments.

In November 2021, in response to the creation of the Climate Action Fund, and to provide direction on how the funds should be invested, the Office of Climate Action, Sustainability, and Resiliency filed the Climate Protection Fund Five-Year Plan. The plan identified the investments and strategies the office intends to make to achieve the city's goal of reducing greenhouse gas emissions by 65% by 2030.[12] One of these investments and strategies included residential energy rebates designed to accelerate the adoption of clean energy technologies, including "highly efficient, all-electric energy equipment such as space/water heat pumps, electric vehicle charging, [and] solar and energy storage."[13]

On Monday March 14, 2022, Denver's City Council approved Resolution 22-0227, and created a new, three-year $9 million residential energy rebate program, called the Climate Action Rebate program.[14] Unlike other heat pump rebate programs, the Climate Action Rebate program sought to incentivize a range of residential electrification technologies, including electric modes of transportation, rooftop solar, battery-energy storage, and other climate-action related technologies as determined by the program administrator, Aptim Environmental and Infrastructure. The Resolution covered the period from April 1, 2022, to March 1, 2025, and had the goal of reaching between 1,500 and 2,000 households annually.

Market Animation Strategy and Impact

As described by Grace Rink, the Chief Climate Officer for the City and County of Denver, and Executive Director of its Office of Climate Action, Sustainability, and Resiliency, the Climate Action Rebates sought to animate the market for electrification technologies and drive down future installation costs.[15] The program was also intentionally designed to amplify and stack with air-source heat pump and heat-pump water heater rebates available from Xcel Energy (Xcel), the City and County of Denver's investor-owned electricity utility. This was achieved by requiring homeowners to utilize Xcel's trade ally network to complete their installations.

---

[8] See: http://bit.ly/3hXCnty

[9] See: https://tech.freshdesk.com/support/solutions/articles/69000812680)

[10] For the most up to date install data, see: https://techcleanca.com/public-data/maps-and-graphs/

[11] For the full ballot text, see: https://ballotpedia.org/Denver,_Colorado,_Ballot_Measure_2A,_Sales_Tax_to_Fund_Environmental_and_Climate-Related_Programs_and_TABOR_Spending_Limit_Increase

[12] For the full report, see: https://denvergov.org/files/assets/public/climate-action/cpf_fiveyearplan_final.pdf

[13] See, p.34: https://denvergov.org/files/assets/public/climate-action/cpf_fiveyearplan_final.pdf

[14] Resolution 22-0227 accessed November 23, 2022. See: https://denver.legistar.com/LegislationDetail.aspx?ID=5456765&GUID=F009AA24-4619-4036-9BA1-91C85CCBB56E

[15] March 2, 2022, Business, Arts, Workforce, & Aviation Services Committee meeting, agenda item 22-0214. See: https://denver.granicus.com/player/clip/14737?view_id=180&meta_id=1040268&redirect=true&h=9c5f97992620a733cc4c092ffbcc0ba3

On April 22, 2022, the Climate Action Rebates went live, making city residents eligible for the heat pump rebates summarized in Table 2.

Table 2: Summary of Denver's Climate Action Rebates Available on April 22, 2022[16]

Eligible Equipment	Climate Action Rebate Value	Rebate Cost Cap
Ducted air source heat pumps (Cold climate certified)	$9,000	Up to 80% of total project costs
Ducted air source heat pumps (High-Efficiency)	$7,200	
Ground source heat pumps	$1,800/ton up to $9,000	
Ductless air source heat pumps (Cold climate certified)	$5,400	
Ductless air source heat pumps (High-Efficiency)	$4,500	
Heat Pump Water Heater ("Smart")	$3,200	
Heat Pump Water Heater (High-Efficiency)	$1,400	

On June 24, 2022, the city announced that funding for its heat pump and heat-pump water heater rebates had reached capacity and was no longer processing applications. During the 63 days between program launch and program pause, 350 households took advantage of the Climate Action Rebates for heat pumps.[17]

Market Sugar Rush and Sugar Crash

The Clean Heat Program, the TECH initiative, and the Climate Action Rebates all deployed different strategies and tactics to animate the heat pump market. In the case of the Clean Heat Program and the TECH initiative, these efforts were able to animate the market on a statewide basis and, in the process, reached thousands of homes. In the case of the Climate Action Rebates, the program was able to animate the market on a city level and, in the process, reached hundreds of homes. These efforts should be celebrated, as every heat pump installation represents progress toward a more stable climate. However, in the process of animating these markets, each program caused a market effect that Sealed refers to as a market sugar rush, followed by a sugar crash.

Also known as boom-bust cycles, sugar rushes and sugar crashes are a symptom of rebate or incentive programs that have a combination of short-term goals, short-term budgets, and financial incentives that are too generous. Together these program design elements can inject greed as well as fear, uncertainty, and doubt, commonly referred to as "FUD," into the market.

Con Edison's Clean Heat Program is the largest example of a sugar rush and crash. At the program's launch, in April 2020, the rebate offered to customers was simple and generous: Customers who installed a 3-ton heat pump, a standard size for most homes, received a $7,200 rebate. However, due to low initial participation, Con Edison dramatically increased the program's rebate values starting August 1, 2021. For that same 3-ton heat pump, homeowners now received an $18,000 rebate, but only if they decommissioned their existing fossil-fuel heating system.[18] Installations skyrocketed — with monthly installations almost doubling — but this 150% increase in rebate value turned out to be too generous for the market.

Due to an overwhelming market response, Con Edison made a pivotal announcement at the end of 2021: Starting March 1, 2022, rebates would be reduced by approximately 50%, decreasing the value of a 3-ton heat pump to just $9,720. This pivot by Con Edison to manage its short-term program budget infused the

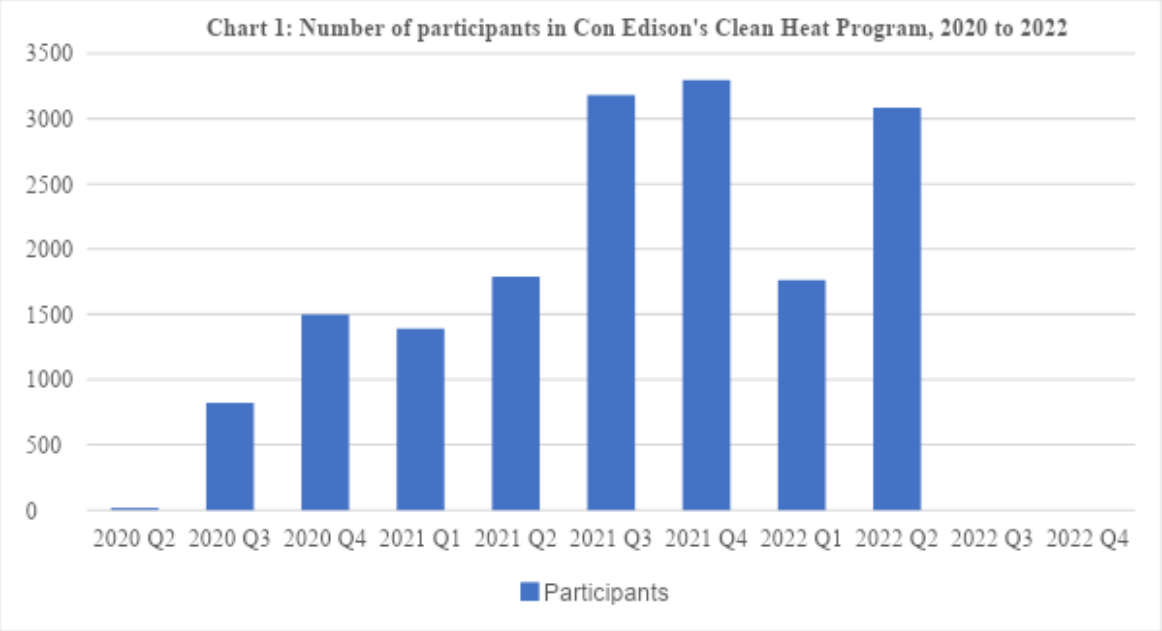
[16] The program also provided rebates for e-bikes, electric vehicle (EV) charging home wiring, rooftop solar, battery energy storage, and electric service upgrades to enable another measure. See: https://www.eebco.org/resources/Documents/POLICY%20ACTION%20COMMITTEE/HVACHP%20ACTION%20GROUP/Flier%20-Denver%20Climate%20Action%20Rebates%20Summary_Overview_4.15.22.pdf

[17] See: https://www.eenews.net/articles/denver-passed-a-sales-tax-for-climate-is-it-working/

[18] Con Edison and other stakeholders initially believed the de-commissioning requirement would slow market demand for the largest tier of heat pump incentives that included decommissioning.

market with additional FUD, resulting in another rush in rebate applications from consumers trying to beat the new deadline, followed by another market crash in March and April.

Because of the huge demand caused by the pivot to lower rebates, on May 9, 2022, Con Edison announced the Clean Heat program would no longer accept rebate applications starting May 14, 2022. This announcement caused another FUD-driven sugar rush, as customers and contractors hurried to meet the May 13, 2022, deadline. Chart 1 documents the sugar rush and sugar crash by quarter.



On July 18, 2022, Con Edison announced they had received rebate applications worth $642 million in 2022, bringing total applications to the program since its launch to $755 million — $528 million more than originally planned. On August 11, 2022, the NY PSC approved Con Edison's petition to transfer unspent energy efficiency funding to cover the cost overrun. The NY PSC also approved Con Edison's request for a new $10 million monthly Continuity Funding Mechanism to restart the Clean Heat Program in their service territory, with the program re-starting on January 17, 2023.

The Performance Playbook

To address these market dynamics and accelerate consumer adoption of heat pumps in alignment with utility price signals, Sealed has developed a three-part market transformation strategy called the Performance Playbook. The Performance Playbook pairs proven market-animation strategies, such as consumer-facing rebates, with flexible market incentives for market actors, along with performance-based incentives to sustainably accelerate market growth while avoiding sugar highs and sugar crashes. Each component is explored below.

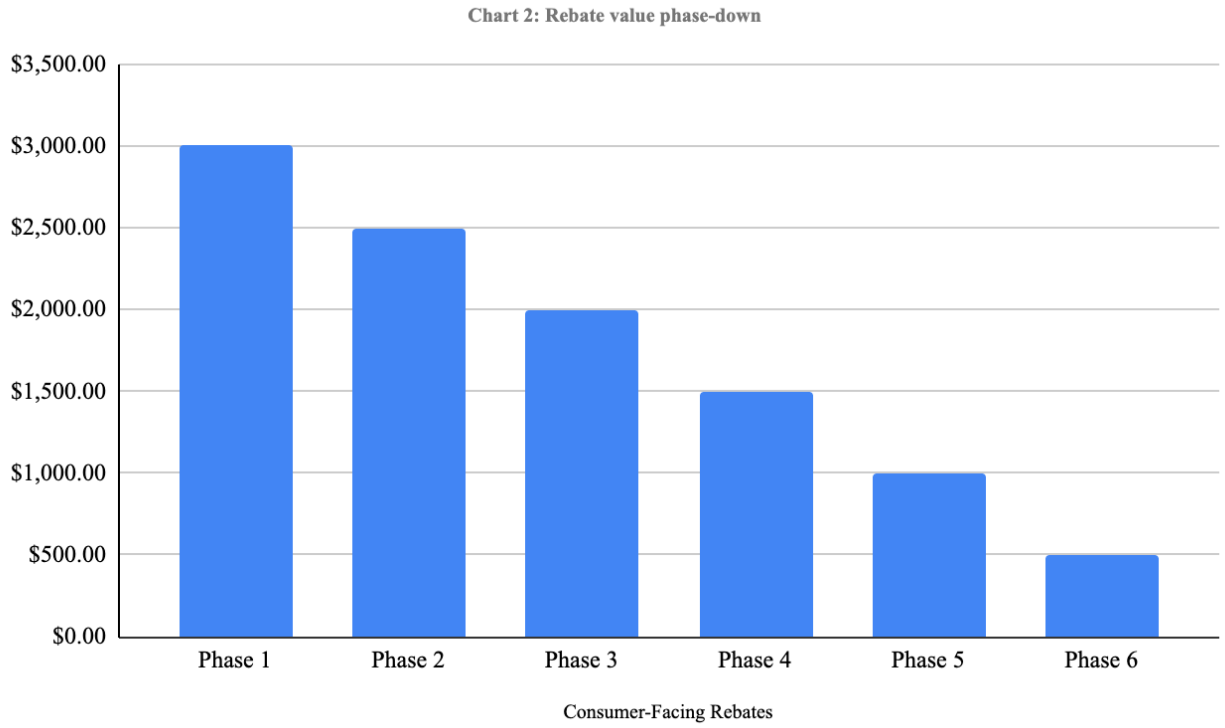
Consumer-Facing Rebates and Rebate Blocks

First, heat pump programs that provide consumer-facing rebates, like New York's Clean Heat Program and Denver's Climate Action Rebate program, should be restructured to predictably decrease in value as market adoption increases. In many leading heat pump markets, consumers have become accustomed to the rush of receiving a rebate for installing a heat pump, but what causes a subsequent crash is the fear of missing the opportunity to receive the rebate. Program designs that set clearer and more sustainable expectations of how much money customers will receive negate this fear.

Incentive blocks, or phase-downs, have been utilized by multiple rooftop-solar programs, including New York's NY-Sun program and the California Solar Initiative, to reduce incentive amounts over time in a transparent way. These programs were by no means perfect, but they helped grow their states' solar markets in a predictable fashion by providing long-term incentive certainty. Ideally, these declining incentive blocks

should be executed over multi-year program budgets to minimize year to year fluctuations in program budgets.

Chart 2 provides an illustrative example of decreasing rebate blocks, starting with a $3,000 heat pump incentive and decreasing the incentive value by $500 over time. Each incentive block should represent a market milestone, such as 10,000 units installed.



Market-Based Incentives

Second, smaller and more stable consumer-facing rebates should be paired with market-based incentives that numerous market actors, or aggregators, can receive. Studies have found that such market-based midstream and upstream incentive programs drive heat pump adoption better than stand-alone consumer-facing rebates.

In addition, the traditional rebate-heavy approach often suffers from being complicated and expensive. One study of more than 600 utilities found that just 60% of the money underpinning such energy efficiency programs was allocated to incentives. The rest? Spent on administrative and marketing costs. While we do not know the administrative allocation of the programs cited in this paper, it is clear that administrative costs are often higher than necessary or sustainable.

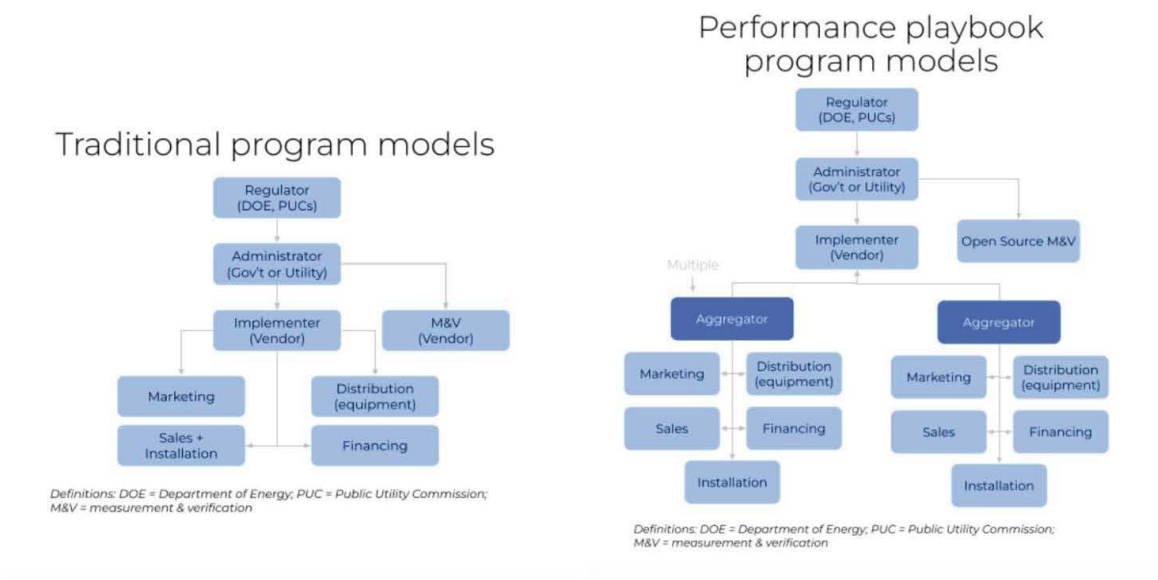
Under the Performance Playbook, aggregators receive incentives that can be used in a variety of ways. Upfront rebates can be used to offset the cost of energy efficiency projects. Incentives can also be used to lower financing costs, minimize sticker price or fund project "extras," like smart thermostats. In other words, market-based incentives provide flexibility, as aggregators compete to discover innovative ways to drive heat pump adoption and performance at the lowest possible cost.

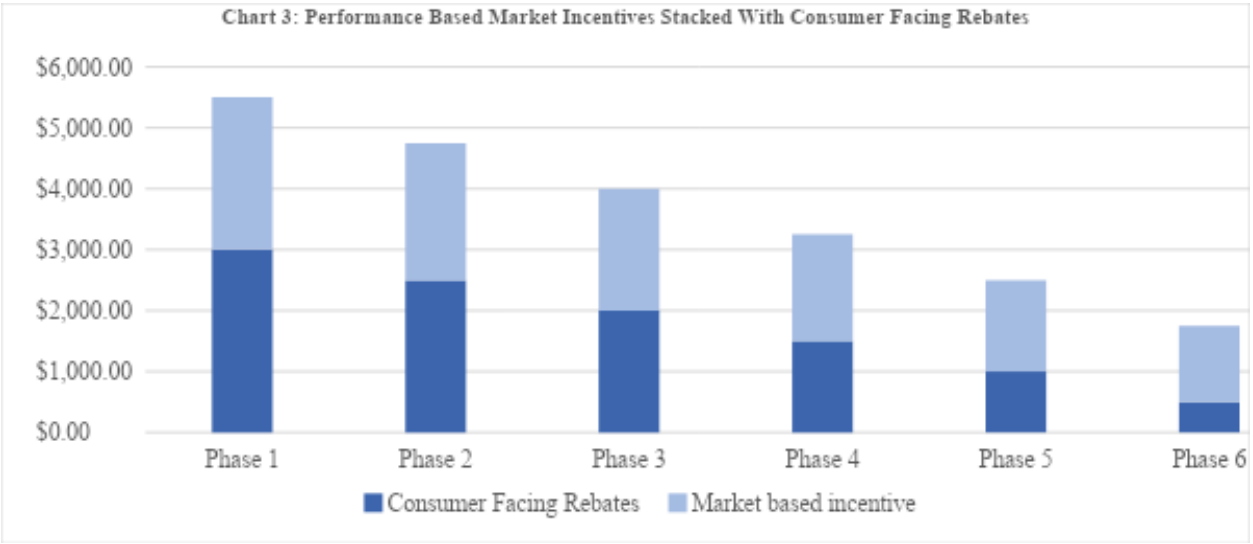
These market-based incentives, like the ones available through California's Market Access Program or the Inflation Reduction Act's HOMES program, motivate market actors to invest in market transformation activities, such as customer marketing, software, and infrastructure, necessary to have a sustainable market. And since these incentives are delivered midstream, they can be lowered if market demand is higher than initially expected.

Graph 1 summarizes the key differences between a traditional approach and one based on the Performance

Playbook. And Chart 3, beneath that, provides an illustrative example of how market incentives could "stack" with consumer-facing rebates and decrease over time.

Graph 1

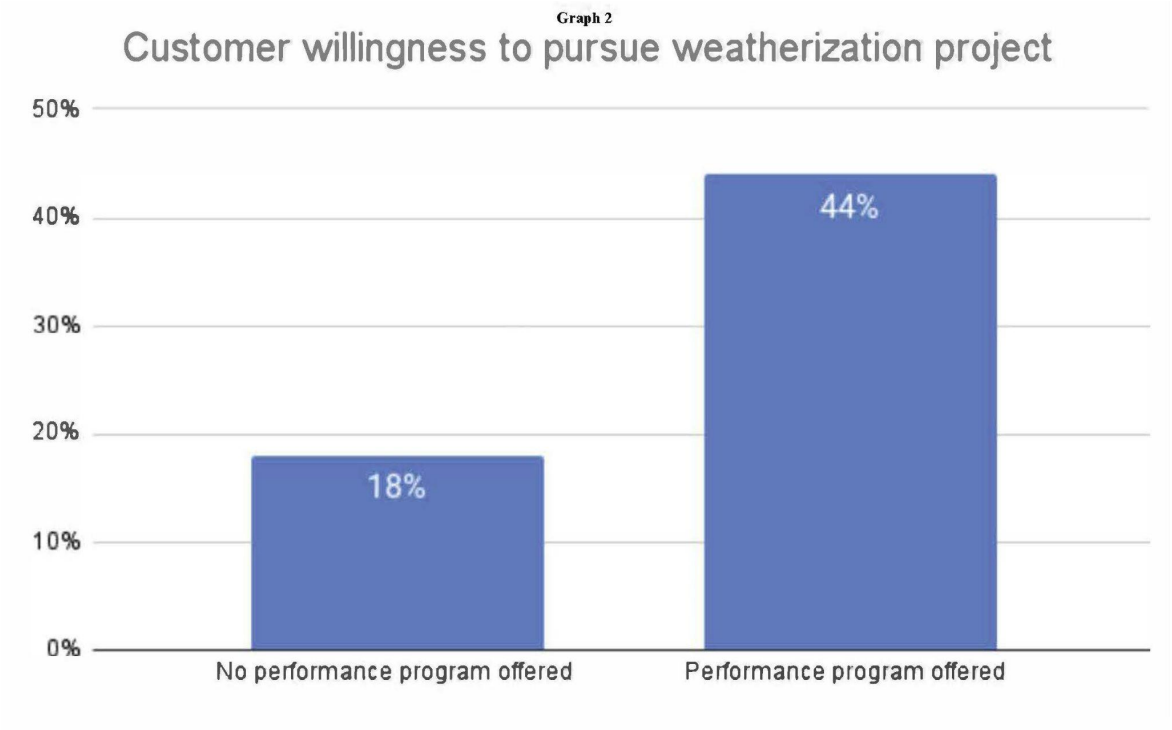




Performance-Based Incentives Ensure Consumer, Ratepayer, and Taxpayer Protection

Third, any incentives paid out to drive the installation of heat pumps should be based on how those energy efficiency projects ultimately perform. This is the measured savings approach that is one pathway defined in the Inflation Reduction Act's HOMES program. The risks of energy efficiency projects are currently shared by consumers, ratepayers, and taxpayers alike, whereas under the Performance Playbook these risks lie with aggregators.

With the Performance Playbook, therefore, incentives are valued based on measured energy savings in order to drive consumer adoption. One survey of New York homeowners discovered that while incentives of 50% of project costs drove significant uptake in heat pump installations, the bigger impact came from performance-based financing. In other words, consumers were more willing to pursue energy efficiency projects if market actors, like aggregators, could take on the project performance risk, as Graph 2 shows.



Conclusion

The rebate and incentives provided for heat pump technologies is exploding, with the August 2022 passage of the Inflation Reduction Act injecting billions of additional dollars into the market. Policymakers across the country will have to grapple with how best to design programs to accelerate heat pump adoption without crashing the market.

Now is the time to learn from previous programs, set realistic incentive amounts and, most importantly, design programs that can last and achieve true market transformation. The Performance Playbook can do this by leveraging taxpayer and ratepayer investments to accelerate the market rather than crash it. By focusing on flexible, performance-based incentives that have long-term budget certainty, precious public resources can be used to unlock multiples of private capital.

But this will only happen if policymakers, utilities, and other stakeholders take a hard look at past program experience, and better understand the relationship between incentive levels, program design, and market demand.

14th IEA Heat Pump Conference
15-18 May 2023, Chicago, Illinois

Exploration of Heat-Driven Ejector High-Temperature Heat Pumps

Pengtao Wang, Stephen Kowalski, Cheng-Min Yang, Jian Sun, Zhiming Gao, Kashif Nawaz*

Multifunctional Equipment Integration Group, Building Technology Research and Integration Center, Oak Ridge National Laboratory, Oak Ridge, TN 37830, USA

Abstract

Heat-driven ejector heat pumps use a supersonic ejector as a thermo-compressor to replace the mechanical compressor. Supersonic ejectors have many advantages in high-temperature heat pump (HTHP) applications, including high operating temperature tolerance, no need for lubrication, low maintenance, and low cost. The coefficient of performance of ejector HTHPs could be improved by selecting binary fluids with unique thermodynamic properties. Although supersonic ejectors have been widely used in refrigeration systems, their application in spaces and water heating is limited. This study explores the theoretical potential of ejector HTHPs with a sink temperature of 100°C–130°C and a lift temperature of 10°C–30°C. Ejector HTHPs were evaluated with single-fluid ejectors (SFEs) and binary-fluid ejectors (BFEs). A comprehensive, geometry-free theoretical model of BFEs was developed to predict the theoretical maximum entrainment ratios. HFE7500 and R718 (water) were selected as working fluids for SFEs and BFEs. SFEs operating with R718 provided a higher coefficient of performance of ejector HTHPs than SFEs operating with HFE7500 and BFEs. This study preliminarily demonstrates the technical potential of ejector HTHP applications in recovering moderate-temperature heat sources.

© HPC2023.
Selection and/or peer-review under the responsibility of the organizers of the 14th IEA Heat Pump Conference 2023.

Keywords: Ejector, High temperature heat pump, binary fluid, COP;

1. Introduction

High-temperature heat pumps (HTHPs) have great potential to improve energy efficiency and reduce CO_2 emissions by replacing gas-fired boilers for industrial process heating. Many HTHPs under development and case demonstrations operate with electricity-driven vapor compression cycles, as reported by International Energy Agency (IEA) Annex 58. A basic configuration of HTHPs working with a vapor compression cycle is shown in Fig. 1(a), in which a mechanical compressor is used to lift the pressure of the refrigerant vapor (Process 1→2). The compressor is the main component in electric-driven HTHPs, accounting for 48.2%–

* Corresponding author. Tel.: +1-865-241-0972; fax: +0-000-000-0000 .
E-mail address: nawazk@ornl.gov.

This manuscript has been authored by UT-Battelle, LLC, under contract DE-AC05-00OR22725 with the US Department of Energy (DOE). The US government retains and the publisher, by accepting the article for publication, acknowledges that the US government retains a nonexclusive, paid-up, irrevocable, worldwide license to publish or reproduce the published form of this manuscript, or allow others to do so, for US government purposes. DOE will provide public access to these results of federally sponsored research in accordance with the DOE Public Access Plan (http://energy.gov/downloads/doe-public-access-plan).

57.3% of the total cost of 100 kW HTHPs using R245fa [1]. Corresponding to a high sink temperature (T_{sink} > 100°C) in HTHPs, the high pressure and temperature of refrigerants challenge state-of-the-art compressor technologies in the following ways:

- Risk of wet compression: Emerging refrigerants with a low global warming potential (GWP), such as R1336mzz(Z), have a saturated vapor curve with a positive slope ($\frac{dT}{ds}$), requiring internal heat exchangers to provide substantial superheating of suction vapor [2].
- Overheating of compressors: Auxiliary cooling technology and components are used in HTHPs to effectively control the temperature of compressors, such as the vapor injection technique with an economizer [3].
- Availability of lubricant oils: High temperature and pressure challenge the thermal stability of lubricant oil and its material compatibility with refrigerants and sealing materials [4].
- Limited drop-in operation with alternative refrigerants: Mechanical compressors have complex designs, infrastructure, and process controls [5], making it difficult to operate with various refrigerants.

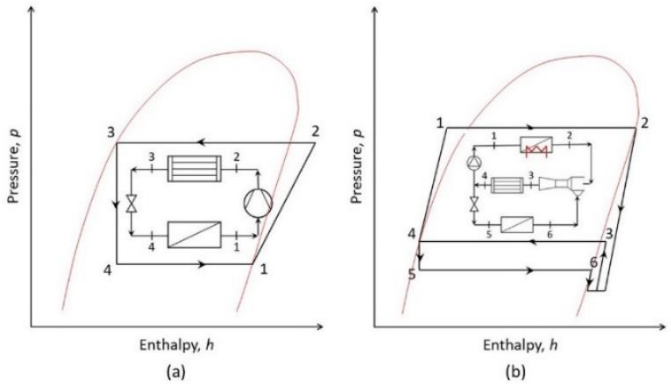


Fig. 1. Schematic of thermodynamic cycles of HTHPs.
(a) Mechanical compressor and (b) ejector thermocompressor.

These challenges associated with electric-driven HTHPs could be alleviated by using heat-driven heat pumps [6]. Heat-driven heat pumps use thermal chemical and physical processes, such as adsorption or absorption HTHPs and transformers; thermal engines, such as Stirling engines and Vuilleumier engines; thermal acoustic coupling effects [7]; and thermo-compressors. The ejector-based HTHP is a typical heat-driven heat pump that uses a supersonic ejector as a thermo-compressor, which replaces the mechanical compressor in a conventional vapor compression cycle, as shown in Fig. 1(b). Primary fluid (PF), at high temperature and pressure (state point 2), accelerates into a supersonic flow and creates a vacuum in the suction chamber of the ejector, which entrains the secondary fluid (SF), at low temperature and pressure (state point 6), into the ejector. PF and SF mix, and the pressure of mixed PF-SF is sequentially lifted to a moderate level (state point 3) through a normal shock wave and a diffusing process. Supersonic ejectors are desirable in HTHPs because of their simple structure, high reliability, low cost, and low maintenance (without moving parts) [8-10]. Furthermore, the ejector could operate with a wide range of refrigerants via drop-in replacement [11], and it is scalable to large systems and multi-stage systems at high temperatures. For example, a steam ejector used in a thermal power plant, driven with a PF at 4.33 MPa and 350°C, could upgrade the low-pressure SF from 1.152 MPa and 400°C to 1.3 MPa and 366°C [12].

Supersonic ejectors in heat-driven refrigeration applications have been extensively studied, and they are attractive for using available waste heat [13] and solar thermal energy [14]. However, few studies have examined ejector-based heat pumps. The technical barriers in ejector-based heat pumps are a low heating cycle coefficient of performance (COP), a small pressure lift ratio, and poor performance under off-design conditions. Theoretically, a low heating cycle COP of ejector heat pumps could be addressed by replacing a single fluid with a binary-fluid pair (i.e., a PF and SF with unique thermal properties) [15]. The heating cycle COP of heat pumps with a binary-fluid ejector (BFE) is approximate to [16, 17]

$$COP_{\mathrm{HP}} = 1 + \omega \frac{\Delta h_{SF}}{\Delta h_{PF}} \approx 1 + \omega \frac{h_{lv,SF}}{\Delta h_{sh,PF} + h_{lv,PF}} \quad (1)$$

where $h_{lv,PF}$ and $h_{lv,SF}$ are the latent heat of evaporation of the PF and the SF, respectively. $\Delta h_{sh,PF}$ is the increased sensible heat of the PF in the high-temperature evaporator (HTE). The entrainment ratio, ω, is defined as the ratio of mass flow rates of the SF and PF, denoted by $\dot{m}_{SF}$ and $\dot{m}_{PF}$.

$$\omega = \frac{\dot{m}_{SF}}{\dot{m}_{PF}} \quad (2)$$

Equation (1) shows that choosing an SF with a larger h_{lv} than PF, and a PF-SF pair yielding a large ω in BFEs, could significantly increase COP_{HP} [18]. Previous theoretical research demonstrated that, for an ejector heat pump water heater with ΔT_{sink} = 65°C, using a binary-fluid pair of HFE7500 and water, $\frac{h_{lv,SF}}{h_{lv,PF}} \approx 25.1$, and neglecting Δh_{PF}, the heating cycle COP could reach 2.0 with a low entrainment ratio of 0.1 [16].

This study explored the technical potential of supersonic ejectors for heat-driven HTHPs operated with T_{sink} = 100°C–130°C and ΔT_{lift} = 10°C–30°C. The single-fluid ejector (SFE) and BFE were theoretically evaluated for the performance of HTHPs. The entrainment ratios of SFEs and BFEs were theoretically predicted with a comprehensive, geometry-free model of an ejector. HFE7500 and R718 (water) are selected as the working fluids for SFE or BFE. The performance of ejectors and ejector HTHPs are investigated for various working conditions.

2. Thermodynamic Model of Heat-driven Ejector HTHPs

A heat-driven ejector HTHP essentially consists of a HTE, a low-temperature evaporator (LTE), an ejector (EJT), a condenser (COND), a separator (SEP), an expansion valve, and a circulation pump, as shown in Fig. 2(a). In Fig. 2, "1, 2, 3, . . ." and "i, ii, iii, . . ." denote the state points in the system-level loop of the HTHP and the component-level process within the EJT, respectively. The working fluid loops are as follows:

1→2, the liquid PF evaporates in the HTE;

i(2)→iii, the high-pressure PF steam accelerates into a supersonic flow and creates a vacuum in the suction chamber of the EJT;

iii→vi←v, PF and SF mix in the constant section of the mixing chamber of the EJT;

vi→vii, the supersonic flow of the mixed PF-SF flows through a normal shock wave;

vii→viii, the subsonic flow of the mixed PF-SF diffuses in the diffuser section of the EJT;

3(viii)→4, the mixed PF-SF vapor condenses in the COND;

4→5 and 5→6, the liquid PF and SF are separated in the SEP;

5→1, the liquid PF is pumped to the HTE;

6→7, the liquid SF throttles in the expansion valve;

7→8, the SF evaporates in the LTE.

iv(8)→v, the SF vapor accelerates into a sonic flow within the EJT.

The EJT in the investigated ejector HTHP could be an SFE or BFE, depending on the selected PF and SF. For the BFE, the separation of PF-SF in the SEP could be a gravity-driven process for an immiscible fluid pair with a large difference in density, or a thermal-driven fractional condensation process for a miscible fluid pair with a large difference in normal boiling point [19]. In this study, a gravity-driven separator was employed for the binary-fluid pair of HFE7500 and R718, as discussed in the following section. If the same working fluid is selected for the PF and SF, the BFE is reduced to the SFE, and the SEP is not needed.

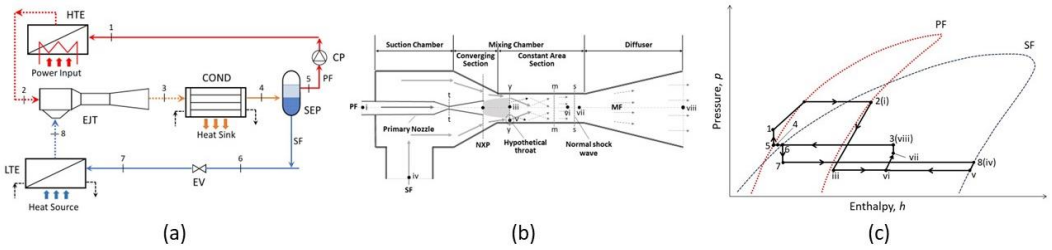


Fig. 2. Schematic of a heat-driven ejector HTHP.
(a) System configuration, (b) gas-dynamic process within an ejector [20], and (c) pressure–enthalpy diagram.

2.1. Thermodynamic Model of an Ejector HTHP

A thermodynamic model of a two-stage BFE HPWH was developed by applying the mass and energy conservation for each component, as summarized in Table 1 [16, 20, 21]. The operating parameters specified for the ejector-drive HTHPs include the sink temperature, T_{sink}, the source temperature, T_{source}, and the driven temperature, T_{HTE}. T_{sink} is the temperature of heat delivered by HTHPs, and $T_{\text{sink}} = T_{\text{COND}}$. T_{source} is the temperature of waste heat available for HTHPs, and $T_{\text{source}} = T_{\text{LTE}}$. The lift temperature of HTHP, ΔT_{lift}, is defined as

$$\Delta T_{lift} = T_{\text{sink}} - T_{\text{source}} = T_{\text{COND}} - T_{\text{LTE}} \tag{3}$$

The system-level performance of an ejector HPWH was evaluated by its heating cycle COP, COP_{HP}, given as

$$COP_{HP} = \frac{Q_{\text{COND}}}{Q_{\text{HTE}}} \approx 1 + \frac{Q_{\text{LTE}}}{Q_{\text{HTE}}} \tag{4}$$

where Q_{COND} is the thermal capacity of the ejector HTHP, which equals the released heat of the mixed PF-SF discharged from the ejector. Q_{HTE} and Q_{LTE} are the heat input in the HTE and the LTE, respectively.

Table 1. The mass and energy equations in the thermodynamic model of the BFE HTHP

Components	Working fluid	Mass equations	Energy equations	Thermal properties equations
HTE	PF	$\dot{m}_1 = \dot{m}_2 = \dot{m}_{PF}$	$Q_{HTE} = \dot{m}_1(h_2 - h_1)$	$h_2 = h(PF, T_2, x = 1)$ $T_2 = T_{HTE}$ $h_1 = h_5$
LTE	SF	$\dot{m}_7 = \dot{m}_8 = \dot{m}_{SF}$	$Q_{LTE} = \dot{m}_8(h_8 - h_7)$	$h_8 = h(SF, T_8, x = 1)$ $T_8 = T_{source}$ $= T_{sin\,k} - \Delta T_{lift}$ $h_7 = h_6$
EJT	PF-SF	$\dot{m}_3 = \dot{m}_2 + \dot{m}_8$	$\dot{m}_3 h_3 = \dot{m}_2 h_2 + \dot{m}_8 h_8$	—
COND	PF-SF	$\dot{m}_4 = \dot{m}_3 = \dot{m}_2 + \dot{m}_8$	$Q_{COND} = \dot{m}_2(h_3 - h_{4,PF}) + \dot{m}_8(h_3 - h_{4,SF})$	$h_{4,PF} = h(PF, T_4, x = 0)$ $h_{4,SF} = h(SF, T_4, x = 0)$ $T_4 = T_{\text{sink}}$
SEP	PF-SF	$\dot{m}_5 = \dot{m}_{PF}$ $\dot{m}_6 = \dot{m}_{SF}$	—	$h_5 = h_{4,PF}$ $h_6 = h_{4,SF}$
EV	SF	$\dot{m}_7 = \dot{m}_6$	—	$h_7 = h_6$
CP	PF	$\dot{m}_1 = \dot{m}_5$	$W = \frac{1}{\eta_{PM}} \frac{\dot{m}_5(p_1 - p_5)}{\rho_5}$ and $\eta_{PM} = 0.5$ $h_1 = h_5 + \frac{W}{\dot{m}_1}$	$\rho_5 = \rho(PF, T_5, x = 0)$ $p_5 = p(PF, T_5, x = 0)$ $p_1 = p(PF, T_1, x = 0)$ $T_5 = T_4$

For the investigated ejector HTHP with a specified thermal capacity, the mass flow rates of the PF and SF were predicted by a theoretical model of the BFE. The comprehensive, geometry-free model predicted the

optimized performance of ejectors under specified operating parameters of HTHPs. The theoretical model was developed based on the gas-dynamic equations and the conservation equations [22, 23]. Detailed information of the theoretical model of the BFE was reported in previous publications [20, 21]. The theoretical model of the BFE was solved with the real properties of working fluids using the Engineering Equation Solver (EES, F-Chart software). The model predicted the theoretical maximum value of ω for an ejector operated under on-design conditions [21]. It is assumed that

- The isentropic efficiencies of ejector components in the theoretical model include 0.92 for the primary nozzle, 0.86 for the secondary nozzle, 0.95 for the mixing chamber, and 0.81 for the diffuser [15];
- The PF and SF entering the ejector are saturated vapor at T_{HTE} and T_{LTE}, respectively; and
- The critical backpressure of the ejector is the saturated vapor pressure of the mixed PF-SF (in a two-phase condition) at T_{COND}.

3. Working Fluids for Heat-driven Ejector HTHPs

The performance of an ejector is closely related to the ejector's backpressure, which equals the saturated vapor pressure of the working fluid in the COND. For an ejector with a fixed geometry, its optimum performance could be achieved under on-design conditions, which require the backpressure to be no larger than the ejector's critical backpressure. For the heat-driven ejector HTHPs in this study, high normal boiling points corresponding to low saturated vapor pressure at T_{sink} were prioritized in selecting the working fluids. Additional considerations in selecting binary-fluid pairs included the following:

- The PF has a much larger molecular weight (*MW*) than the SF for a high entrainment ratio of BFEs;
- The SF has a much larger latent heat of evaporation for a high COP of HTHPs; and
- The PF and SF are immiscible and have significant different density for gravity-driven separation; or the PF and SF have a significant difference in normal boiling point (*NBP*) for thermal separation.

HFE7500 and R718 were selected as the working fluids, as described in Table 2. HFE7000 is a hydrofluoroether (HFE) with a relatively low GWP and zero ozone depletion potential. HFEs are nonflammable fluids with low toxicity, are chemically inert, and have high-temperature stability [24]. HFEs are considered to be third-generation refrigerants to replace chlorofluorocarbons, hydrochlorofluorocarbons, and hydrofluorocarbons [25].

R718 is a natural refrigerant that has been extensively used in ejector-based refrigeration systems. The challenges of using R718 in HTHPs are high compression ratio, large adiabatic coefficient, and low vapor density. Therefore, large-scale multi-stage compressors with intermediate cooling are required in conventional HTHPs. R718 is an ideal working fluid for ejector HTHPs because of the large latent heat of evaporation, high critical temperature, and relatively low vapor pressure at T_{sink}.

Table 2. Working fluids for heat-driven ejector HTHPs

Fluid	Formula	*MW*	*NBP* (°C)	T_{cr} (°C)	P_{cr} (MPa)	h_{lv}* (kJ/kg)	GWP	Group
HFE7500	$C_9H_5F_{15}O$	414	128.4	261.0	1.55	84.0 at 140°C	90	HFE
R718	H_2O	18	99.97	373.9	22.064	2,333.0 at 70°C	0	Natural

4. Performance of Heat-driven Ejector HTHPs

The investigated ejector HTHP was operated with T_{sink} = 100°C–130°C and ΔT_{lift} = 10°C–30°C. The temperature difference for heat transfer in the COND and the LTE was neglected. The inlet of the SF and the discharged PF-SF mixture for the ejector were saturated vapor at T_{LTE} and T_{COND}, respectively. The inlet of the PF is saturated vapor at the operating temperature of T_{HTE}, which is a variable parameter in a range of 190°C–260°C. The maximum pressure of HTE, $P_{\text{HTE,max}}$, is 4.7 MPa for R718 and 1.5 MPa for HFE7500. The theoretical model of the ejector predicted the entrainment ratio, ω, with the inlet and outlet conditions of the working fluids. The performance of the ejector HTHP was evaluated with a unit mass flow rate of PF (1 kg/s), which corresponds to an SF mass flow rate of ω kg/s.

4.1. BFEs and BFE HTHPs

The BFE operated with HFE7500 as the PF and R718 as the SF. Figure 3 shows the component-level performance of BFEs, ω_{BFE}, and the system-level performance of BFE HTHPs, COP_{HP}, under various T_{HTE} and ΔT_{lift}. For a specified ΔT_{lift}, ω_{BFE} increased as T_{HTE} increased until ω_{BFE} reached its maximum value, $\omega_{BFE,max}$; after that, further increasing T_{HTE} significantly reduced ω_{BFE}. The existing optimum temperature of HTE, $T_{HTE,opt}$, for $\omega_{BFE,max}$ was consistent with previous experimental and theoretical results of SFEs in heat-driven refrigeration systems [26] and ejector heat pump water heaters [20, 27]. $T_{HTE,opt}$ is related to the critical points of the PF, T_{cr}, as the thermal physical property of the PF significantly deteriorates near its critical point. For HFE7500 with T_{cr} = 261.0°C, $T_{HTE,opt}$ = 240°C. For a specified T_{sink}, ΔT_{lift} had no obvious effects on $T_{HTE,opt}$ because ΔT_{lift} was only related to the inlet condition of the SF. The trends of COP_{HP} vs. T_{HTE} and ΔT_{lift} were similar to those of ω_{BFE}, indicating that ω_{BFE} dominated the performance of ejector HTHPs. For T_{sink} = 120°C, as ΔT_{lift} increased from 10°C to 30°C, $\omega_{BFE,max}$ decreased from 0.12 to 0.05, and $COP_{HP,max}$ decreased from 2.14 to 1.43.

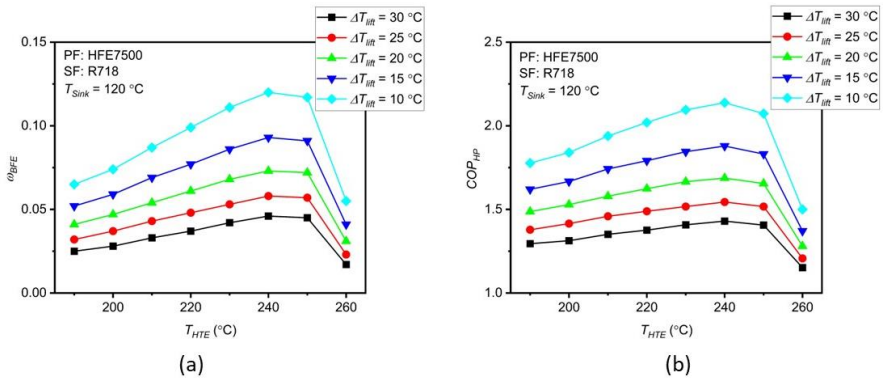


Fig. 3. Typical performance of BFEs and BFE HTHPs. (a) Entrainment ratio and (b) COP.

Figure 4 shows $\omega_{BFE,max}$ and $COP_{HP,max}$ vs. ΔT_{lift} with various T_{sink}. Generally, higher ΔT_{lift} and/or T_{sink} result in lower $\omega_{BFE,max}$ and $COP_{HP,max}$, and the influences of T_{sink} weaken at higher ΔT_{lift}. The largest values of $\omega_{BFE,max}$ and $COP_{HP,max}$ were 0.16 and 2.48, achieved at ΔT_{lift} = 10°C and T_{sink} = 110°C. The smallest values of $\omega_{BFE,max}$ and $COP_{HP,max}$ were 0.04 and 1.39, achieved at ΔT_{lift} = 30°C and T_{sink} = 130°C. Regarding the thermo-compressor, the ejector increased the low pressure of the SF vapor (i.e., $p_{sat,SF}$ at T_{evap}) to moderate pressure (i.e., $p_{sat,SF}$ at T_{sink}). For a specified T_{sink}, a higher ΔT_{lift} provided a lower vapor pressure of the SF entering the BFE. For a specified ΔT_{lift}, a higher T_{sink} required a higher vapor pressure of the SF discharged from the BFE. Therefore, higher ΔT_{lift} and/or T_{sink} consumed more power provided by the kinetic energy of the PF, resulting in lower energy efficiencies of BFEs and HTHPs.

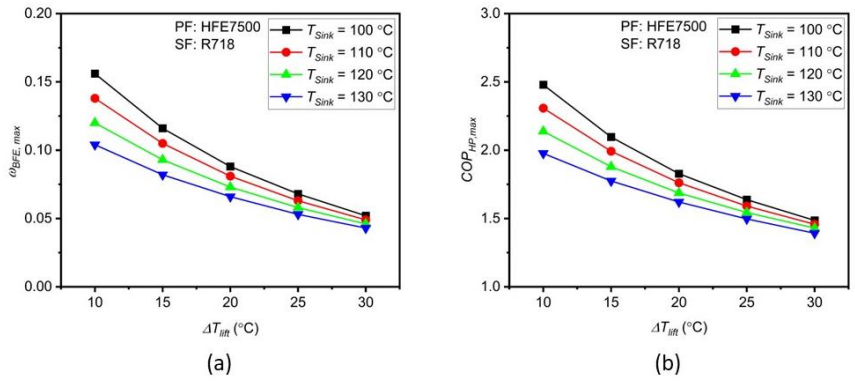


Fig. 4. The maximum performance of BFEs and BFE HTHPs. (a) Maximum entrainment ratio and (b) maximum COP.

4.2. SFEs and SFE HTHPs

The $T_{HTE,opt}$ for the maximum performance of SFEs and SFE HTHPs was 230°C for HFE7500 and 260°C for R718. Figures 5 and 6 show the performance of SFEs and SFE HTHPs operating with HFE7500 and R718, respectively. Similar to BFEs, higher ΔT_{lift} and/or T_{sink} result in lower $\omega_{SFE,max}$ and $COP_{HP,max}$. However, the influences of T_{sink} on $\omega_{SFE,max}$ and $COP_{HP,max}$ were less sensitive than those of BFEs, particularly for HFE7500 at higher ΔT_{lift}, and for R718. SFEs with HFE7500 had higher $\omega_{SFE,max}$ than SFEs with R718 because of the much higher molecular weight of HFE7500 than R718 [28]. However, HFE7500 provided lower $COP_{HP,max}$ than R718. For HFE7500, the largest value of $\omega_{SFE,max}$ was 2.86, and the largest value of $COP_{HP,max}$ was 2.14, achieved at ΔT_{lift} = 10°C and T_{sink} = 130°C. For R718, the largest value of $\omega_{SFE,max}$ was 1.771, and the largest values of $COP_{HP,max}$ was 2.67, also achieved at ΔT_{lift} = 10°C and T_{sink} = 130°C.

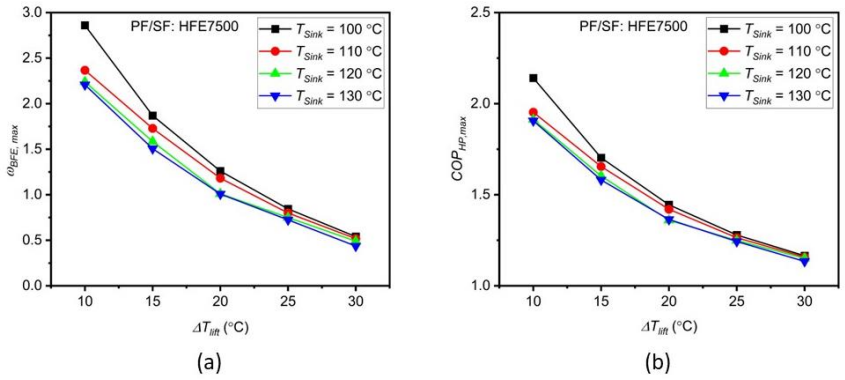


Fig. 5. The maximum performance of SFEs and SFE HTHPs with HFE7500. (a) Maximum entrainment ratio and (b) maximum COP.

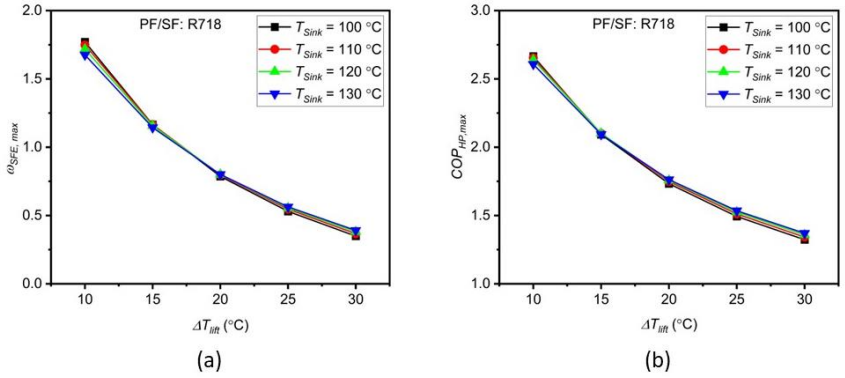


Fig. 6. The maximum performance of SFEs and SFE HTHPs with R718. (a) Maximum entrainment ratio and (b) maximum COP.

4.3. Comparison of BFEs and SFEs

Figure 7 compares the performance of ejectors and ejector HTHPs with single and binary fluids. Generally, ω_{max} of the BFEs was much lower than that of SFEs, but $COP_{HP,max}$ of BFE HTHPs was comparable to that of SFE HTHPs. For SFEs, HFE7500 has larger $\omega_{SFE,max}$ but smaller $COP_{HP,max}$ than R718. The discrepancy in $\omega_{SFE,max}$ and $COP_{HP,max}$ is due to the difference in changed specific enthalpy of the PF in the HTE, Δh_{PF}, and the SF in the LTE, Δh_{SF}. The binary fluids have a much larger $\Delta h_{SF}/\Delta h_{PF}$ but a much smaller $\omega_{SFE,max}$, as described in Table 3. According to Eq. (1), $COP_{HP,max}$ is linearly related to the product of $\omega_{SFE,max}$ and $\Delta h_{SF}/\Delta h_{PF}$. Therefore, BFE HTHPs and SFE HTHPs had comparable values of $COP_{HP,max}$. SFEs with R718 provided the best performance of HTHPs at a low ΔT_{lift}, whereas BFEs with HFE7500/R718 only provided a slightly better performance of HTHPs at ΔT_{lift} > 25°C. This indicates that selecting HFE7500/R718 as a binary-fluid pair for BFE HTHPs cannot fully extract the technical potential of BFE HTHPs. Considering the system

simplification of ejector HTHPs, SFEs with R718 are recommended for heat-driven ejector HTHPs. In addition, operating a SFE HTHP with R718 in an open-loop system may improve $\omega_{SFE,max}$.

For SFE HTHPs with R718 operated at T_{sink} = 120°C and ΔT_{lift} = 10°C–30°C, Carnot efficiencies (i.e., the second law efficiencies) ranged from 6.7% to 10.4%, which are much lower than those of conventional HTHPs—typically 40%–60% from experimental measurements [29].

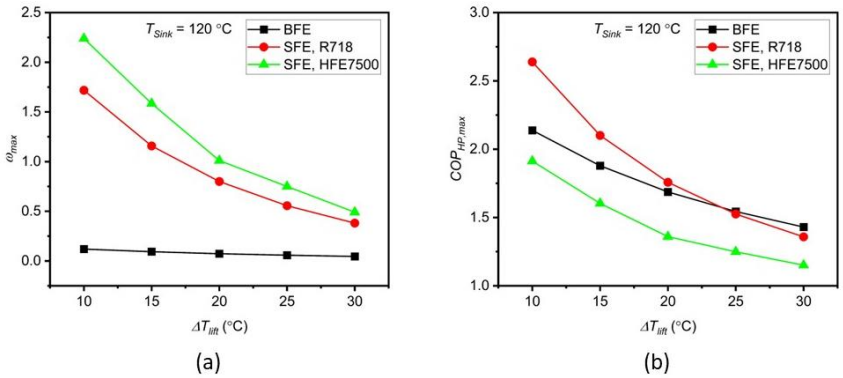


Fig. 7. Comparation of BFE HTHPs and SFE HTHPs. (a) Maximum entrainment ratio and (b) maximum COP.

Table 3. Working fluids for heat-driven ejector HTHPs

Ejectors	PF-SF	T_{HTE} (°C)	T_{sink} (°C)	ΔT_{lift} (°C)	$\Delta h_{SF}/\Delta h_{PF}$	ω	COP_{HP}
BFE	HFE7500-R718	240	120	10	9.50	0.12	2.14
SFE	HFE7500	230	120	10	0.41	2.24	1.91
SFE	R718	260	120	10	0.95	1.72	2.64

5. Conclusions

This study explored the technical potential of heat-driven ejector HTHPs. SFEs and BFEs were theoretically evaluated regarding the performance of ejector HTHPs. The entrainment ratios of ejectors were predicted with a geometry-free model. A thermodynamic model of an ejector HTHP was developed with mass and energy conservation equations. HFE7500 and R718 were selected as the working fluids for SFEs and BFEs. The performance of ejector HTHPs was investigated under the operation of T_{sink} = 100°C–130°C and ΔT_{lift} = 10°C–30°C. The conclusions from this primary study are as follows:

- SFEs had better component-level performance than BFEs in terms of the entrainment ratio, and BFEs had a much smaller entrainment ratio than SFEs.
- HTHPs with BFEs and SFEs had comparable heating cycle performance.
- The binary-fluid pair of HFE7500 and R718 cannot fully extract the technical potential of BFEs. An SFE with R718 could be a candidate for heat-driven ejector HTHPs.
- The Carnot efficiency of heat-driven ejector HTHPs was much lower than the state-of-the-art electric-driven HTHPs

Future research will focus on

- Seeking binary-fluid pairs for BFEs to provide a large entrainment ratio and a large difference in the increased enthalpy in the HTE and LTE; and
- Identifying the deployment of steam ejector HTHPs in open-loop applications.

NOMENCLATURE

BFE	binary-fluid ejector	(-)
COP	coefficient of performance	(-)
COND	condenser	(–)

EJT	ejector	(-)
GWP	global warming potential	(-)
h	enthalpy	(kJ/kg)
HTE	high-temperature evaporator	(-)
HTHP	high-temperature heat pump	(-)
LTE	low-temperature heat pump	(-)
MW	molecular weight	(kg/kmol)
$\dot{m}$	mass flow rate	(kg/s)
NBP	normal boiling point	(°C)
PF	primary fluid	(-)
Q	thermal capacity	(kW)
T	temperature	(°C)
SEP	separator	(–)
SFE	single-fluid ejector	(–)
SF	secondary fluid	(–)
W	power	(kJ/kg)

Symbol

ω	entrainment ratio	(-)
ρ	density	(kg/m^3)
η	component efficiency	(-)
x	quality of vapor	(-)

Subscript

lv	latent heat of evaporation
opt	optimum
max	maximum
i, ii, iii, . . .	state points within an ejector
1, 2, 3, . . .	state points within the loop of ejector heat pumps

Acknowledgements

This work was sponsored by the US Department of Energy's Building Technologies Office under contract no. DE-AC05-00OR22725 with UT-Battelle LLC. The authors would like to acknowledge the technology manager, Mr. Antonio Bouza, for his support.

References

[1] C. Mateu-Royo, C. Arpagaus, A. Mota-Babiloni, J. Navarro-Esbrí, and S. S. Bertsch, "Advanced high temperature heat pump configurations using low GWP refrigerants for industrial waste heat recovery: A comprehensive study," *Energy Conversion and Management*, vol. 229, p. 113752, 2021/02/01/ 2021, doi: https://doi.org/10.1016/j.enconman.2020.113752.

[2] G. Kosmadakis, C. Arpagaus, P. Neofytou, and S. Bertsch, "Techno-economic analysis of high-temperature heat pumps with low-global warming potential refrigerants for upgrading waste heat up to 150 °C," *Energy Conversion and Management*, vol. 226, p. 113488, 2020/12/15/ 2020, doi: https://doi.org/10.1016/j.enconman.2020.113488.

[3] Y. He, F. Cao, L. Jin, X. Wang, and Z. Xing, "Experimental study on the performance of a vapor injection high temperature heat pump," *International journal of refrigeration*, vol. 60, pp. 1-8, 2015.

[4] G. F. Frate, L. Ferrari, and U. Desideri, "Analysis of suitability ranges of high temperature heat pump working fluids," *Applied Thermal Engineering*, vol. 150, pp. 628-640, 2019.

[5] C. Arpagaus and S. Bertsch, "Experimental Comparison of HCFO and HFO R1224yd (Z), R1233zd (E), R1336mzz (Z), and HFC R245fa in a High Temperature Heat Pump up to 150 C Supply

Temperature," presented at the International Refrigeration and Air Conditioning Conference. , 2021, 1875.
[6] J. M. Pinheiro, S. Salústio, J. Rocha, A. A. Valente, and C. M. Silva, "Adsorption heat pumps for heating applications," *Renewable and Sustainable Energy Reviews*, vol. 119, p. 109528, 2020/03/01/ 2020, doi: https://doi.org/10.1016/j.rser.2019.109528.
[7] Q. Chen, M. Yu, G. Yan, and J. Yu, "Thermodynamic analyses of a modified ejector enhanced dual temperature refrigeration cycle for domestic refrigerator/freezer application," *Energy*, p. 122565, 2021/11/06/ 2021, doi: https://doi.org/10.1016/j.energy.2021.122565.
[8] A. Abu-Heiba, "Literature Review of Potential Thermally Activated Heat Pump Cycles," United States, 2018. [Online]. Available: https://www.osti.gov/biblio/1480616. https://www.osti.gov/servlets/purl/1480616
[9] S. Elbel and P. Hrnjak, "Ejector refrigeration: an overview of historical and present developments with an emphasis on air-conditioning applications," presented at the International Refrigeration and Air Conditioning Conference, 2008, 884.
[10] S. Elbel and N. Lawrence, "Review of recent developments in advanced ejector technology," *International Journal of Refrigeration*, vol. 62, pp. 1-18, 2016/02/01/ 2016, doi: https://doi.org/10.1016/j.ijrefrig.2015.10.031.
[11] Y. Fang, S. Croquer, S. Poncet, Z. Aidoun, and Y. Bartosiewicz, "Drop-in replacement in a R134 ejector refrigeration cycle by HFO refrigerants," *International Journal of Refrigeration*, vol. 77, pp. 87-98, 2017/05/01/ 2017, doi: https://doi.org/10.1016/j.ijrefrig.2017.02.028.
[12] J. Zheng, Y. Hou, Z. Tian, H. Jiang, and W. Chen, "Simulation Analysis of Ejector Optimization for High Mass Entrainment under the Influence of Multiple Structural Parameters," *Energies*, vol. 15, no. 19, p. 7058, 2022. [Online]. Available: https://www.mdpi.com/1996-1073/15/19/7058.
[13] F. Riaz, P. S. Lee, and S. K. Chou, "Thermal modelling and optimization of low-grade waste heat driven ejector refrigeration system incorporating a direct ejector model," *Applied Thermal Engineering*, vol. 167, p. 114710, 2020.
[14] K. Braimakis, "Solar ejector cooling systems: A review," *Renewable Energy*, vol. 164, pp. 566-602, 2021/02/01/ 2021, doi: https://doi.org/10.1016/j.renene.2020.09.079.
[15] D. Buyadgie, O. Buyadgie, S. Artemenko, A. Chamchine, and O. Drakhnia, "Conceptual design of binary/multicomponent fluid ejector refrigeration systems," *International Journal of Low-Carbon Technologies*, vol. 7, no. 2, pp. 120-127, 2012.
[16] P. Wang, H. Ma, J. Spitzenberger, A. Abu-Heiba, and K. Nawaz, "Thermal performance of an absorption-assisted two-stage ejector air-to-water heat pump," *Energy Conversion and Management*, vol. 230, p. 113761, 2021.
[17] M. El Hassan, "Numerical Characterization of the Flow Dynamics and COP Estimation of a Binary Fluid Ejector Ground Source Heat Pump Cooling System," *Fluids*, vol. 7, no. 7, p. 250, 2022.
[18] O. Drakhnia, D. I. Buyadgie, T. Miyazaki, O. D. Buyadgie, G. Herrera, and A. Chamchine, "Binary Fluids Application In The Ejector Energy Systems," in *ASTFE Digital Library*, 2017: Begel House Inc.
[19] D. Oleksii, T. Miyazaki, B. Olexiy, B. Dmytro, and A. Sergei, "Fractionating Condenser for Binary Fluid Ejector Refrigerating System," presented at the International Exchange and Innovation Conference on Engineering & Science(IEICES), Kyushu University, Japan, 2017.
[20] J. Spitzenberger, P. Wang, L. Ismael, H. Ma, A. Abuheiba, and K. Nawaz, "Theoretical Analysis of a Single-Stage Gas-Fired Ejector Heat Pump Water Heater," *Journal of Thermal Science and Engineering Applications*, vol. 14, no. 4, p. 041009, 2021.
[21] D. A. Pounds, J. Dong, P. Cheng, and H. Ma, "Experimental investigation and theoretical analysis of an ejector refrigeration system," *International Journal of Thermal Sciences*, vol. 67, pp. 200-209, 2013.
[22] I. W. Eames, S. Aphornratana, and H. Haider, "A theoretical and experimental study of a small-scale steam jet refrigerator," *International Journal of Refrigeration*, vol. 18, no. 6, pp. 378-386, 1995/07/01/ 1995, doi: https://doi.org/10.1016/0140-7007(95)98160-M.
[23] B. Huang, J. Chang, C. Wang, and V. Petrenko, "A 1-D analysis of ejector performance," *International journal of refrigeration*, vol. 22, no. 5, pp. 354-364, 1999.
[24] G. J. Sherwood, "Hydrofluoroethers as low temperature refrigerants," ed: Google Patents, 1998.

[25] J. G. Owens, "Low GWP alternatives to HFCs and PFCs," in Proceedings of the 1999 Taipei International Conference on Atmosphere Protection, 1999.
[26] J. Dong, X. Chen, W. Wang, C. Kang, and H. Ma, "An experimental investigation of steam ejector refrigeration system powered by extra low temperature heat source," *International Communications in Heat and Mass Transfer,* vol. 81, pp. 250-256, 2017/02/01/ 2017, doi: https://doi.org/10.1016/j.icheatmasstransfer.2016.12.022.
[27] J. Spitzenberger *et al.*, "Experimental performance of ejector heat pump operating in the sub-critical mode," *Energy Conversion and Management,* vol. 278, p. 116724, 2023.
[28] D.-W. Sun, "Comparative study of the performance of an ejector refrigeration cycle operating with various refrigerants," *Energy conversion and management,* vol. 40, no. 8, pp. 873-884, 1999.
[29] C. Arpagaus, F. Bless, M. Uhlmann, J. Schiffmann, and S. S. Bertsch, "High temperature heat pumps: Market overview, state of the art, research status, refrigerants, and application potentials," *Energy,* vol. 152, pp. 985-1010, 2018/06/01/ 2018, doi: https://doi.org/10.1016/j.energy.2018.03.166.

14th IEA Heat Pump Conference
15-18 May 2023, Chicago, Illinois

Research Progress of Defrosting Methods for Air Source Heat Pump

NIU Jianhui[a*], LIANG Zheng[a], LI Yongliang[a], Feng Lianyuan[b]
[a]College of Environmental and Energy Engineering, Hebei University of Architecture, Zhangjiakou, 075000, China
[b]Hebei Technology Innovation Center of Phase Change Thermal Management of Data Center, Hebei University of Water Resources and Electric Engineering, Cangzhou, 061016, China

Abstract

With the proposal of the national "double carbon" strategic goal, air source heat pump (ASHP), as a high-efficiency and energy-saving product, will be more and more widely used. Frosting is one of the main factors to reduce the heating capacity of ASHP in winter. The main technical solution for the problem is delaying frosting and high efficient defrosting. The research of domestic and foreign scholars on restraining frosting technologies and defrosting methods for ASHP are summarized. The researches show that changing the inlet air parameters and the structure of evaporators can realize restraining frosting without or only consuming less energy; electric heating defrosting needs consuming additional electrical energy; for small scale refrigeration and heat pump equipment, reverse-cycle defrosting and hot gas by-pass defrosting are most commonly used; a new defrosting method with small energy loss, continuous heating and non-stop defrosting needs to be developed in the future.
© HPC2023.
Selection and/or peer-review under the responsibility of the organizers of the 14th IEA Heat Pump Conference 2023.

Keywords: ASHP; restraining frosting; defrosting;heating performance ;

1. Introduction

In recent years, with the implementation of the “coal-to-electricity” project in China, air source heat pump (ASHP) has been widely used in northern China. However, when the ASHP is running in winter, especially when the outdoor air humidity is high, when the outdoor temperature is lower than 0℃, Frost will grow on the fins of the evaporator. Frosting will not only increase the heat transfer resistance, but also increase the wind resistance, reduce the heat transfer efficiency and the performance of the unit, and even in case of severe frost, the unit will be shut down. Therefore, the frost layer on the fins of the outdoor heat exchanger must be removed periodically. Seeking a suitable defrosting method has been a hot topic of domestic and foreign scholars. This paper summarizes the research on frost suppression and defrosting technology of ASHP by domestic and foreign scholars. The existing problems of frost suppression and defrosting technology are analyzed. The defrosting technology of large and medium-sized ASHP has been prospected.

2. Study on restraining frosting for ASHP

The evaporator frosting is greatly affected by the surrounding environment. Air parameters, surface characteristics, cold surface temperature, and fin structure have significant effect on frosting process and frost layer characteristics [1]. At present, the main methods to inhibit frost growth are to reduce the relative humidity of air around the evaporator, increase air temperature and speed.

* NIU Jianhui. Tel.: +86+313+418+7742; fax: +86+313+418+7742.
E-mail address: zjknjh@163.com.

2.1. Reducing the relative humidity of the air

Xia et al. [2] found that after 50 min of heat exchanger operation, the frost deposition was 1. 34 times higher at 80% RH than at 70%. The former evaporator heat exchange decreased by 23. 1% and the latter by 17. 2%. This indicates that the higher the inlet air humidity, the higher the thickness of frost formation, the greater the frost deposition, and the greater the impact on the evaporator performance. For the ASHP, using the solid or liquid desiccant is mainly used to reduce the air humidity around the evaporator. Wang et al. [3] proposed a novel frost-free heat pump water heater system incorporating an energy storage device and an auxiliary heat exchanger covered by a solid desiccant. Experimental results showed that the relative humidity increased from 75 % to 85 % at a temperature of 0 °C, and the average COP of the system decreased by 6.7 %. A novel frost-free air source heat pump (ASHP) combined with membrane-based liquid desiccant dehumidification and humidification is proposed and investigated by Su et al. [4]. Results demonstrate that the COP_{sen} and the COP_{tot} of the novel system are at least 37.7% and 64.3% higher than that of the $COP_{reverse}$ of conventional reverse-cycle defrosting ASHP system in the variation ranges of the analyzed parameters, respectively.

2.2. Raising the temperature of the air

Increasing the inlet air temperature of evaporator can restrain frost growth effectively. Chen [5] proposed of setting a plate collector at the inlet of the outdoor heat exchanger, using solar preheating inlet air can effectively improve the evaporative temperature, so as to improve the system coefficient of performance (COP). Liu et al. [6] pointed out that in order to ensure energy saving and improve the efficiency of heat pump, the wet air can be heated by heat recovery technology. Kwak et al. [7] set the electric heater at the outdoor heat exchanger air inlet and turned on the electric heater to increase the outdoor heat exchanger inlet air temperature when the outdoor environment reached the frost condition, and the experiment concluded that the heat supply increased by 38.0% and the COP increased by 57.0% compared with the conventional heat pump, and the heat supply could be continuous and stable throughout the defrost period.

2.3. Increasing the speed of inlet air

Increasing air velocity can suppress frosting. Gu et al. [8] studied to compare the evaporation temperature of coils at windward velocity of 3m/s and 1.2m/s and found that the decrease in wind speed led to a rapid decrease in evaporation temperature, which resulted in faster frosting of the coils. Guo et al. [9] studied the influence of wind speed on frost layer growth. The results showed that the frost layer growth rate of outdoor heat exchanger increased with the decrease in air speed. Sheng et al. [10] concluded that increasing the flow rate may delay the formation of the early frost layer. When some frost layers appear, increasing the flow rate will lead to an increase in the density of the frost layer and promote the frost formation process.

2.4. Changing the structure of evaporator

Domestic and foreign scholars mainly studied increasing the evaporator area, changing the structure and spacing of fins, and the number of tube rows along the airflow direction to restrain frosting on the evaporator surface. Huang et al. [11] used three outdoor units with different fins to compare the performance of ASHP, and found that flat fins had the best thermal properties. A defrost-free heat exchanger that has fin surfaces with fine irregularities was proposed by Yajima et al [12]. It could be confirmed that the heat pump, fitted with the defrost free heat exchanger where the fine irregularities were formed only on the fin-ends. The use of the defrost-free heat exchanger has made it possible to achieve a higher COP. Cheng et al. [13] simulated the air-side heat exchanger of air-source heat pump chiller and hot water unit with different fin spacing, tube diameter and tube spacing. The study shows that the fin spacing: 2 mm for light frost zone, 2.5 mm for general frost zone, and 3.5 mm for heavy frost zone is the optimal value; tube diameter 8 mm is better than 10 mm and 12 mm; tube spacing 27.4 mm is better than 25.4 mm.

2.5. Changing evaporator surface characteristics

Some scholars in China and abroad have studied the inhibition of frosting by surface treatment technology (hydrophobic coating or hydrophilic coating). He et al. [14] prepared a superhydrophobic aluminum-based fin

with a contact angle of 158.3°, and the experimental study results showed that the superhydrophobic surface exhibited good frost inhibition and rapid frost melting properties.

Shan [15] conducted a theoretical and simulation study on fins with a superhydrophobic composite coating of epoxy resin + 2 wt% graphene and found that the coated fins could provide frost suppression, shorten defrosting time, and improve heat transfer efficiency.

2.6. Changing the temperature of cold surfaces

The effect of cold surface temperature and air humidity on frosting is more obvious than air temperature, flow rate and heat exchanger structure [16]. Wang et al [17] found that when air temperature is 10.5℃, relative humidity is 80%, wind speed is 3m/s, cold surface temperature is -3.5℃~-19.7℃, the temperature of cold surface has a significant influence on frosting rate, defrosting frequency and frosting height.

3. Study on defrosting technology for ASHP

Common defrosting methods include reverse cycle defrosting (RCD), hot-gas bypass defrosting (HGBD), and electric heating defrosting (EHD). In recent years, researchers have proposed a variety of new ASHP defrosting methods for reverse RCD and HGBD technology, and studied the defrosting effect, system performance and indoor comfort. In addition, in recent years, scholars have proposed energy storage defrosting (ESD), liquid defrosting (LD) and so on.

3.1. Study on Reverse Cycle Defrosting

3.1.1. Conventional reverse cycle defrosting

RCD is an effective defrosting method widely used at present. RCD is mainly used in small household air conditioning, heat pump and refrigeration equipment.

A large number of theoretical and experimental studies on RCD methods have been carried out in China and abroad. Song et al. [18] proposed that the distribution of chillers in the circuit has an effect on the reverse cycle defrost performance, and that the defrost efficiency of vertically installed multi-circuit heat pump units was improved by 7.4% compared to the uneven distribution of refrigerant in each circuit. Reverse cycle defrosting will cause the room temperature to decrease by about 2~5℃, and it will take about 10min for the system to return to normal heating state after defrosting [19].

It can be seen that the conventional RCD inevitably needs to absorb heat from the room. It causes a large fluctuation of indoor temperature and causes discomfort to human body. In addition, when the four-way valve is switched. In addition, when the four-way valve is switched, it has a great pressure impact on the compressor and pipeline.

Hu et al. [20] developed a novel reverse cycle hot gas defrost method for air source heat pumps. The experimental results suggested that the use of the novel reverse-cycle hot gas defrosting method for the experimental ASHP unit was able to help shorten the defrosting time by 3 min or 38%, and minimize the risk of shutting down the ASHP unit due to low suction pressure through increasing the compressor's suction pressure by about 200 kPa, when compared to the use of the traditional standard reverse-cycle hot gas defrosting method.

3.1.2. Reverse cycle defrosting with new heat dissipation terminal

In order to reduce the influence of RCD on indoor thermal comfort and improve the heating performance of the heat pump system, some scholars proposed an ASHP system with radiation heat dissipation terminal [21-24].

Xu et al. [25] effectively coupled the condenser of the heat pump system with the radiation heat pipe. The refrigerant medium is filled inside as the heat dissipation medium. Experimental studies showed that the heating apparatus of heat pump-driven heat pipe has a fast start-up speed. After defrosting, the surface temperature of radiator recovered quickly and distributed evenly. Qu et al. [26] proposed a thermal storage based reverse cycle defrost method, stating that the optimal defrost strategy is to keep the low-level cycle compressor frequency at 90 Hz and the high-level cycle expansion valve opening at 80%. This method can reduce the energy consumption of air source heat pump defrosting. The principle is shown in Fig.1.

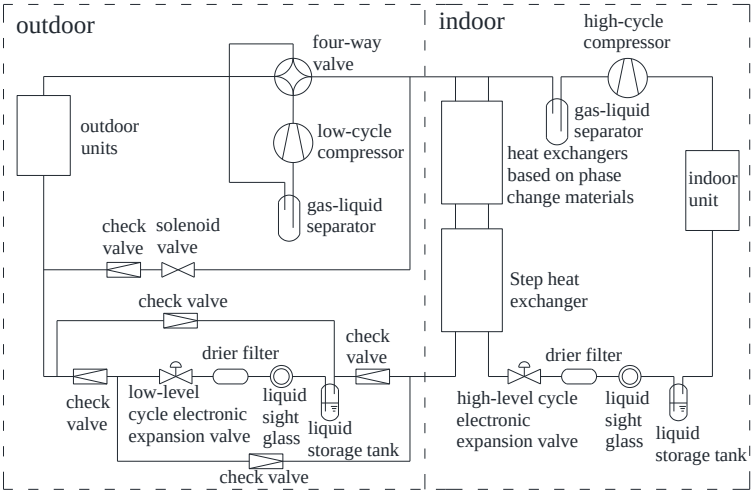


Fig. 1. Reverse circulation defrosting system based on regenerative [26].

3.2. Study on hot-gas bypass defrosting

3.2.1. Conventional hot-gas bypass defrosting

The HGBD is to set a bypass pipeline between the compressor discharge pipe and the evaporator inlet pipe. When defrosting, the solenoid valve on the bypass pipeline is opened, and the compressor discharge vapor was directly discharged into the frosting evaporator.

Lai et al. [27] concluded that the most influential factors of bypass defrost efficiency are the bypass volume, the point of entry into the defrost, and the defrost frequency, and the optimal time entry point for defrost can be determined by the frost inflection point. Xi et al. [28] proposed a new intelligent control strategy based on the maximum heating capacity of the hot gas bypass defrost system and designed a suitable defrost start-stop point. The results showed that the heating capacity of the hot gas bypass defrost was increased by 10.17 % and the overall energy efficiency was improved by 4.06 %. Huang et al. [29] pointed out that the time of HGBD is 2.89 times of RCD. The superheat in suction of compressor is always around 0℃ during defrosting. The discharge temperature and superheat of the compressor continuously reduce, and the safe operation of the compressor is threatened. For heat pumps and water heaters with trans critical CO_2, the power consumption of RCD is lower than that of HGBD, and the average heating COP is higher [30-32].

3.2.2. Hot-gas bypass defrosting with continuous heating

In view of the problem that the system heating is insufficient or even stopping heating during defrosting, some scholars upgraded the defrosting method of hot-gas bypass with double/multiple circuits hot-gas bypass defrosting to achieve continuous heating.

Si et al. [33] proposed a double-loop bypass defrosting technology, in which the indoor unit keeps continuous heating operation under experimental conditions, and as the outdoor temperature decreases, the amount of frosting decreases, the heating operation time is extended, and the proportion of heating time in the whole defrosting/heating cycle keeps increasing. Liu et al. [34] proposed an ASHP system with continuous heating in defrosting. The system has at least two outdoor heat exchangers, one is defrosting, the other one continues to absorb heat from the outdoor air. Part of the heat is used for heating and the other is used for defrosting the outdoor heat exchanger to achieve defrosting while continuing to heat. The system principle is shown in Fig.2 and it is still part of the discharge defrosting of the bypass compressor.

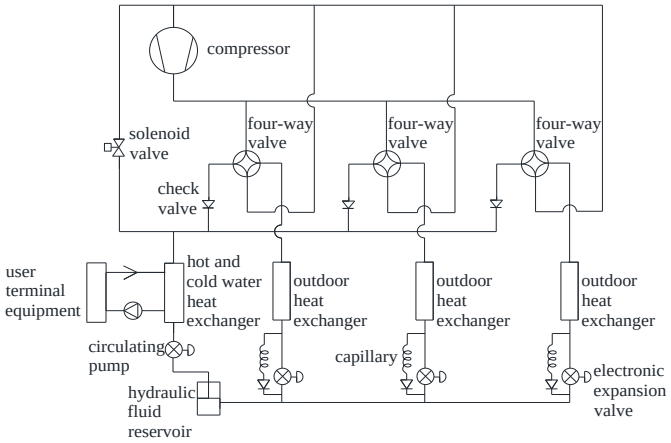


Fig. 2. ASHP with continuous heating and defrosting [34].

Fu et al. [35] proposed a new grouping throttle defrosting method based on the HGBD method. The principle is shown in Fig. 3. The outdoor heat exchanger is divided into two rows, the parallel capillary and solenoid valve are connected in the middle. In defrosting the front and rear heat exchange tubes are used as condenser and evaporator respectively, and the four-way valve is used to defrost them respectively. Under the working condition of outdoor temperature of 2℃ and relative humidity of 80%, the defrosting time of reverse cycle is about 440s, and the defrosting time of this system is about 430s, which is slightly shorter than the defrosting time of reverse cycle method.

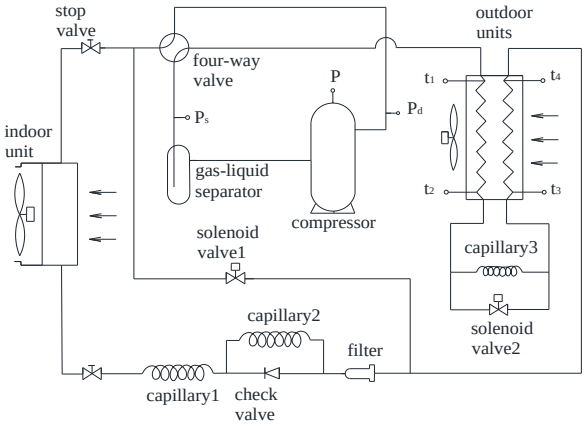


Fig. 3. Principle of group throttle defrosting system [35].

3.3. Study on electric heating defrosting

EHD usually installs an electric heater in the evaporator shell, or installs a heater element on the evaporator fin to defrost. Wang et al. [36] proposed an air-source heat pump system with auxiliary heating from an external heat source, with an additional electric heater between the expansion valve and the condenser. The principle is shown in Fig. 4. The system can extend the operating time of the air-source heat pump for heating under low temperature and high humidity conditions and achieve continuous heating during defrost, but the COP under each condition will be reduced, resulting in increased power consumption.

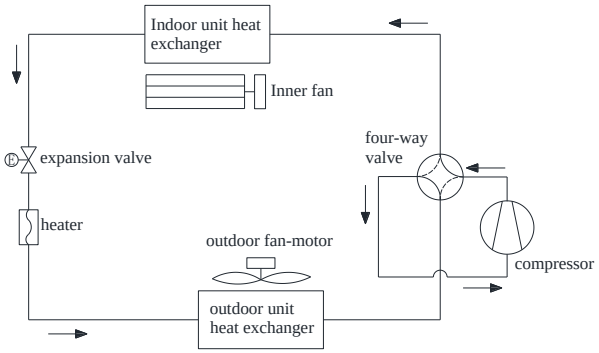


Fig. 4. Heating / defrosting flow chart of new external heat source assisted heating air source heat pump system [36].

The EHD control is convenient, and the electric heating system is relatively independent of the heat pump system. The defrosting ability is not limited by environmental conditions, and the reliability is high [37]. EHD is easy to control, but at the cost of additional power consumption, it is generally only applicable to small window air conditioning [38] and refrigerators [39-40]. The heat requirement of EHD is determined by the thickness of the frost layer and the surface temperature of the evaporator. However, the EHD not only has low defrosting efficiency, but also increases power consumption.

3.4. Study on energy storage defrosting

The ESD method can fundamentally solve the problem of energy shortage of the traditional defrosting method [41], and improve the running stability of the ASHP to a certain extent.

Liu et al. [42] designed a phase change heat storage exchanger through an air source heat pump defrost system with compressor housing heat storage combined with hot gas bypass circulation, and the experimental results showed that the defrosting time and energy consumption were reduced by 10s (9%) and 12.1kJ (21.7%), respectively, compared to reverse cycle defrosting. Zhao et al. [43] used paraffin wax as the heat storage medium and adopted the idea of "waste heat storage and waste heat defrost" to achieve the "frost-free effect", and the system suction and discharge pressure and compression ratio changed smoothly compared with RCD. Chen et al. [44] used the heat storage module with electric heating layer matrix structure to realize VRV system defrosting with heating without shutdown. Zhu et al. [45] proposed a new air source heat pump thermal storage heating system using peak and valley electricity and variable flow operation to achieve economical operation. Through simulation calculation and analysis, the results showed that the operating cost of the system in the heating season can be reduced by more than 50% compared with the annual cost of central heating. Zhao et al. [46] proposed an energy storage air source heat pump system for rapid heating and defrosting, as shown in Fig. 5. Tests were conducted under experimental conditions, and the results showed that the defrosting time of the new system was 68% shorter and the defrosting energy consumption was 51.4% less than that of the conventional system.

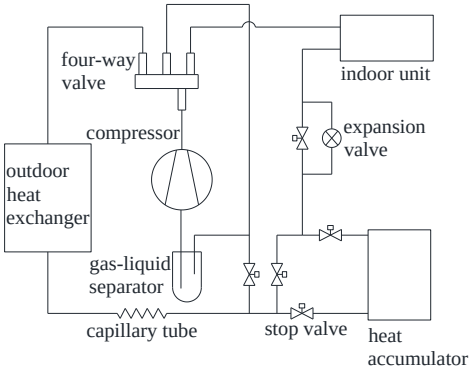


Fig. 5. Principle diagram of storage type air source heat pump system [46].

3.5. Study on liquid defrosting

The LD was first used in the cold storage refrigeration system [47]. This system includes two parallel evaporators. Through valve switching, the sub-cooling liquid after refrigerant defrosting can be evaporated and cooled in another evaporator. Although the system can realize defrosting without stopping cold storage refrigeration, defrosting will also lead to temperature rising for the cold storage.

Niu et al. [48] proposed a heat pump system with multi-outdoor units in parallel defrosting in turn, which principle is shown in Fig. 6, and carried out detailed theoretical and experimental research. The results showed that the system performance achieve best when 4 outdoor units are used for defrosting, and the heating capacity of the system can still reach 60% of that without frost. This method can achieve defrosting with heating at the same time, but for the multiple evaporators, the distribution of refrigerant flow becomes a key factor affecting the operation stability of the system during defrosting.

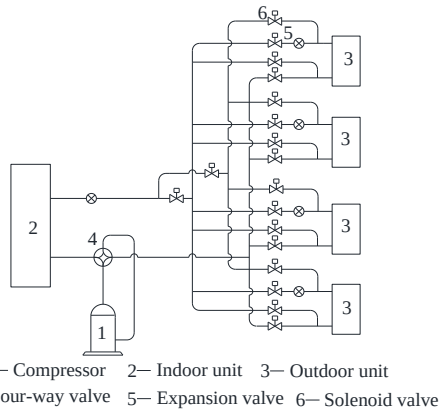


Fig. 6. Principle of sub-cooling defrosting with multi-outdoor units [48].

3.6. Other defrosting methods

Lin et al. [49] put forward hot water defrosting. The defrosting device that can produce hot water is placed on the condenser of the outdoor unit. Through this device, the defrosting is carried out, and the systematic frosting and heating of the air conditioning are carried out at the same time. The defrosting device is an independent additional system with high reliability.

A new defrosting strategy through injecting medium-pressure vapor refrigerant into compressor during defrosting process was proposed by Wei et al. [50]. For the ASHP in the experiment, with the injected electronic expansion valve opening less than 50%, the experimental unit can run safely and defrosting performance improve gradually with the opening increase.

Cai [51] found through simulation studies that the morphology of the frost layer changed significantly after the electric field intensity was applied to the environment, and the individual areas of frost aggregation gradually showed elongated morphological changes, and the frost layer was significantly suppressed.

Tan et al. [52] found through experiments that ultrasonic waves can remove the frost in a certain area of the evaporator surface, and the energy consumption is less than 50% of the energy consumption of the reverse defrost, and the defrosting efficiency is 7~29 times higher than the reverse defrost.

4. Conclusions

In view of the problem of frosting/defrosting in the ASHP system, the research on restraining frosting and defrosting technology is analyzed and reviewed, the conclusions are as follows:

1) Changing air parameters, evaporator structure and surface conditions can play an important role in restraining frosting. However, it can only delay frosting to a certain extent, once the evaporator getting frosting, a certain defrosting method must be used to remove the frost layer.

2) Reverse cycle defrosting and hot-gas bypass defrosting are the most common methods. At present, the research is more focused on the combination of new heat dissipation terminals to improve indoor comfort for reverse cycle defrosting. Based on hot-gas bypass defrosting, multiple evaporators are used to realize non-

stopping heating operation. Due to part of discharge vapor of the compressor is used for defrosting, the system heating capacity decreases and the heating performance deteriorates.

3) Electric heating defrosting is widely used in refrigerators at the cost of extra electric energy. Energy storage defrosting is in the experimental and simulation stage, and has not been applied widely yet. The application of the liquid defrosting method in the defrosting of the evaporator of the cold storage will lead to a temperature increase in the cold chamber. Four outdoor units are used in the ASHP to obtain the optimal defrosting performance.

4) Restraining Frost Formation has attracted much attention due to no energy consumption or low energy consumption. If frost can be restrained or delayed from the source, it will further promote the development of ASHP. At present, the commonly used defrosting methods are mainly used for small-sized ASHP. For large or medium-sized ASHP, due to the excessive thermal inertia of the system, the heat loss of cold and hot fluid mixing cannot be ignored. In the future, it is necessary to develop a defrosting method with small energy loss, continuous heating and uninterrupted defrosting.

Acknowledgements

This project was funded by the Science and Technology Project of Hebei Education Department (ZD2022116), the Open Project Program of the Hebei Technology Innovation Center of Phase Change Thermal Management of Data Center (SKF-2022-08), the project of Hebei Provincial Innovation Ability Training Fund for Postgraduates (CXZZSS2023161).

References

[1] Zhang, Y., Zhang, G.M., Zhang, L.L., Ma, X.X., Xv, P., Tian, M.C., 2018. Research progress on frost formation mechanism of air-source heat pump and its defrosting /anti-frosting technology [J]. Journal of Refrigeration, 39 (05): 10-21+46.

[2] Xia, D., Zhou, X.X., Zhou, Z.Y., 1998. Effect of different parameters on performance of finned-tube evaporators and optimal defrosting period of heat pump [J]. Journal of Shanghai Jiaotong University, 07: 116-118.

[3] Wang, Z.H., Wang, F.H., Wang, X.K., Ma, Z.J., Wu, X.Z., Song, M.J., 2017. Dynamic character investigation and optimization of a novel air-source heat pump system [J]. Applied Thermal Engineering, 111: 122-133.

[4] Su, W., Zhang,X.S., 2017. Performance analysis of a novel frost-free air-source heat pump with integrated membrane-based liquid desiccant dehumidification and humidification [J]. Energy & Buildings, 145: 293-303.

[5] Chen, Y., 2006. Experiment and simulation study on solar-assisted ASHP for space heating [D]. Tianjin: Tianjin University.

[6] Liu, D., Zhao, F.Y., Tang, G.F., 2007. Frosting of heat pump with heat recovery facility [J]. Renewable Energy, 32(7): 1228-1242.

[7] Kwak, K.M., Bai, C.H., 2010. A study on the performance enhancement of heat pump using electric heater under the frosting condition: Heat pump under frosting condition[J]. Applied Thermal Engineering, 30(6/7): 539-543

[8] Gu, B., Sun, T., Tan, L., 2001. Study on the frosting performance of air cooled heat pump units [J]. Journal of HV&AC, 01: 81-82.

[9] Guo, X.M., Wang, D.L., Chen, Y.G., Wang, W.H., 2012. Effects of face velocity of outdoor heat exchanger on frosting characteristics of ASHP system [J]. CIESC Journal, 63 (Suppl. 2): 32-37.

[10] Sheng, W., Liu, P.P., Dang, C.B., Liu, G.X., 2017. Review of restraint frost method on cold surface [J] Renewable and Sustainable Energy Reviews, 79: 806-813.

[11] Huang, D., Ri-Jing, Z., Liu, Y., De-Bo, Yi., 2014. Effect of fin types of outdoor fan-supplied finned-tube heat exchanger on periodic frosting and defrosting performance of a residential air-source heat pump [J]. Applied Thermal Engineering, 69 (1-2): 251-260.

[12] Yajima, T., Ohkubo, H., Seki, M., 2020. Research on defrost free air-source heat pump with surface stripe concavo-convex fins [J]. Energy and Buildings (prepublish). 110568.

[13] Cheng, W.H., Yao, Y., Ma, Z.L., 2006. Effect of air-side heat exchanger structure parameters on frost characteristics of air-source heat pumps [J]. Journal of Shenyang Jianzhu University (Natural Science), 03: 458-461.

[14] He, G.X., Gu, Y.X., Duan, J.H., 2021. Mechanism analysis and performance research on superhydrophobic frost suppression of air source heat pump [J]. Journal of Xi'an University of Architecture & Technology, 53(06): 860-866.

[15] Shan, Y.T., 2021. Research on defrosting and energy-saving characteristics of air source heat pump coating [D]. Zhengzhou: North China University of Water Resources and Electric Power.

[16] Sheng, W., Liu, P., Dang, C.B., Liu, G.X., 2017. Review of restraint frost method on cold surface [J]. Renewable & Sustainable Energy Reviews, 79(nov.): 806-813.
[17] Wang, W., Zhang, F.R., Zhao Y.H., Xiao, J., Guo, Q.C., 2010. Experimental study for frost characteristics of dynamic frosting process under variable cold surface temperature [J]. Journal of Engineering Thermophysics, 31 (4): 663-666.
[18] Song, M.J., Liu, S.C., Deng, S.M., Sun, Z.L., Yan, H.X., 2017. Experimental investigation on reverse cycle defrosting performance improvement for an ASHP unit by evenly adjusting the refrigerant distribution in its outdoor coil[J]. Applied Thermal Engineering, 114: 611-620.
[19] Jang, J.Y., Bae, H.H., Lee, S.J., 2013. Continuous heating of an air-source heat pump during defrosting and improvement of energy efficiency[J]. Applied Energy, 110: 9-16.
[20] Hu, W.J., Jiang, Y.Q., Qu, M,L., Ni, L., Yao, Y., Deng S.M., 2010. An experimental study on the operating performance of a novel reverse-cycle hot gas defrosting method for air source heat pumps [J]. Applied Thermal Engineering, 31(2): 363-369.
[21] Li, M.Z., Zhang, B.H., 2015. Characteristics analysis of radiant heating room air conditioner [J]. Building Energy & Environment, 34 (2): 22-25.
[22] Tang, H.D., Zhang, T., Liu, X.H., 2017. On-site measured performance of radiant slab floor and fan-coil unit heating systems for residences in Yangtze River basin [J]. Heating Ventilating & Air Conditioning, 47(11): 97-103.
[23] Li, T.B., Qin, H., 2016. Research progress in floor radiant heating system [J]. Journal of Building Energy Efficiency, 44(4): 15-18 + 40.
[24] Zhao, J.H., Fang, Z.J., Cui, D., Duan, J., 2019. Experimental study of heat pipe used in floor radiant heating system of ASHP [J]. Energy Conservation, 38(02): 43-45.
[25] Xu, S.X., Ding, R.C., Niu, J.H., Ma, J.Y., 2018. Investigation of air-source heat pump using heat pipes as heat radiator [J]. International Journal of Refrigeration, (90): 91-98.
[26] Qu, M.L., Lu, M.Q., Li, Z., Song, X.J., Chen, J.O., Ziviani, D., Braun, J.E., 2020. Thermal energy storage based (TES-based) reverse cycle defrosting control strategy optimization for a cascade air source heat pump[J]. Energy & Buildings, 219(prepublish).
[27] Lai, X.Q., Zhang, T., 2017. Research on application of hot gas bypass in the frequency conversion heat pump air conditioner[J]. Refrigeration and Air-conditioning, 17(6): 24-27.
[28] Xi, Z.L., Yao, R.M., Li, J.B., Du, C.Q.,Yu, Z.X., Li, B.Z., 2021. Experimental studies on hot gas bypass defrosting control strategies for air source heat pumps[J]. Journal of Building Engineering, 43.
[29] Huang, D., Li, Q.X., Yuan, X.L., 2009. Comparison between hot-gas bypass defrosting and reverse-cycle defrosting methods on an air-to-water heat pump [J]. Applied Energy, 86: 1697-1703.
[30] Ye, Z.L., Wang, Y.K., Yin, X., Song, Y.L., Cao, F., 2021. Comparison between reverse cycle and hot-gas bypass defrosting methods in a transcritical CO_2 heat pump water heater [J].Applied Thermal Engineering, 196: 117356.
[31] Wang, Y.K., Ye, Z.L., Song, Y.L., Yin, X., Cao, F., 2021. Experimental analysis of reverse cycle defrosting and control strategy optimization for transcritical carbon dioxide heat pump water heater [J].Applied Thermal Engineering, 183: 116213.
[32] Wang Y.K., Ye, Z.L., Song, Y.L., Yin, X., Cao, F., 2020. Experimental investigation on the hot-gas bypass defrosting in air source transcritical CO_2 heat pump water heater [J]. Applied Thermal Engineering, 178: 115571.
[33] Si, C.Q., Shao, S.Q., Liu, Y.J., 2019. Experimental investigation on control strategy of defrosting with two bypass loops for air source heat pump[J]. Refrigeration and Air-conditioning, 19(04): 56-60+65-66.
[34] Liu, X., Zhang, H.B., Liu, Z.H., Wang, Y.Q., Li, Z.R., Tao, X.Y., 2017. A unit of ASHP capable for continuous heating and defrosting [J]. Building Energy & Environment, 36(12): 80-82.
[35] Fu, W.C., Guo, X.M., Tao, X.C., 2009. Experiment on a novel defrost cycle for air source heat pumps [J]. Journal of Refrigeration, 30(3): 16-24.
[36] Wang, X.L., Yu, B., Peng, G.Q., Wang, X.C., Wu, J.H., Che, W., Wang, R.F., Yang, W., Yang, X.D., Ma, R.J., 2020. Novel air-source heat pump system with external heat source auxiliary heating[J]. Journal of HV&AC, 50(10):120-124.
[37] Li, Y.H., Zang, R.Q., 2018. Research and development of defrosting methods for air source heat pump [J]. Cryogenics and Superconductivity, 46(09): 82-86. DOI : 10.16711/j.1001-7100.2018.09.016.
[38] Mei, V.C., Domitrovic, R.E., Chen, F.C., Kilpatrick, J.K., Keuper, E., 2002. A frost-less heap pump [J]. ASHRAE Transactions, 108: 452-459.
[39] Amer, M., Wang, C.C. 2017. Review of defrosting methods [J]. Renewable and Sustainable Energy Reviews. 73: 53-74.
[40] Song, M.J., Deng, S.M., Dang, C.B., Mao, N., Wang, Z.H., 2018. Review on improvement for ASHP units during frosting and defrosting [J]. Applied Energy, 211: 1150-1170.
[41] Ma, S.X, Jiang, Y.M., Wen, B., et al. 2015. Experimental study on performance of phase change heat storage evaporative ASHP [J]. Acta Energy Solaris Sinica, 36 (03): 604-609.
[42] Liu, Z.B., Fan, P.Y., Wang, Q.H., 2018. Air source heat pump with water heater based on a bypass-cycle defrosting system using compressor casing thermal storage [J]. Applied Thermal Engineering, 128: 1420-1429.
[43] Zhao, H.Y., Yu, S.P., Qiu, G.D., Shen, C., 2021. Experimental study of heat storage air source heat pump system with “frost-free” effect [J]. Acta Energiae Solaris Sinica, 42(4): 61-67.
[44] Chen, M., Wang, Y.X., Fang, T., Qi, S.Q., Yang, H.D., Liu,Y.C., 2021. Design and experimental study of heat storage module for multi-line non-stop defrosting [J]. Thermal science and technology, 20 (6): 572-577.

[45] Zhu, M., Liu, X., Li, L.W., Qian, Y.Z., Ye, Z.C., Wang, Y.J., 2020. Economic analysis of a novel air-source heat pump heating system with an energy storage tank [J]. Building Energy & Environment, 39(03): 38-42.
[46] Zhao, H.Y., Qiu, G.D., Yu, S.P., 2021. Experimental study on energy storage air source heat pump system for rapid heating and defrosting[J]. Acta Energiae Solaris Sinica, 42(03): 184-190.
[47] Wang, M., Zang, R.Q., Feng, H., 2018. Performance analysis and optimization of liquid refrigerant defrosting system [J]. Fluid Machinery, 46(6): 78-82.
[48] Niu, J.H., Ma, G.Y., Xv, S.X., Fan, X.S., 2019. Experimental study on ASHP with multiple parallel outdoor machines defrosting alternatively [J]. Journal of Beijing University of Technology, 45(8): 787-792.
[49] Lin, C.H., Zhang, J., Liu, J.D., 2017. Study on the new model of the defrosting of the room air conditioner [J]. Electrical Appliances, (5): 67-70.
[50] Wei, W.Z., Ni, L., Dong, Q., Wang, W., Ye, J.Y., Xu, L.F., Yang, Y.H., Yao, Y., 2022. Experimental investigation on improving defrosting performance of air source heat pump through vapor injection [J]. Energy & Buildings, 256,111696.
[51] Cai, C.H., 2021. Defrosting research of air source heat pump based on high voltage field [D]. North China University of Water Resources and Electric Power, 2021.
[52] Tan, H.H., Tao, T.F., Xu, G.H., Wan, X., Zhang, X., 2015. Ultrasonic defrosting theory and technology for finned-tube evaporator [J]. Journal of xi'an Jiaotong university, 49(9): 105-113.

14th IEA Heat Pump Conference
15-18 May 2023, Chicago, Illinois

Impact Analysis of Transitioning to Heat Pump Rooftop Units for the U.S. Commercial Building Stock

Chris CaraDonna†, Andrew Parker, and Ryan Meyer

National Renewable Energy Laboratory, Golden, Colorado, United States

Abstract

Twenty percent (25%) of the energy consumed by the U.S. commercial building sector is from on-site combustion of fossil fuels for space heating. Part of decarbonizing U.S. energy systems to meet climate initiatives will require electrification of space heating equipment, often by transitioning to heat pumps. Rooftop units (RTU) are the most prominent commercial building HVAC system type and should therefore be prioritized for electrification solutions. However, there is limited understanding of the impact on emissions when considering regional electricity generation methods, as well as the impact of ambient temperature on capacity and efficiency, defrost operation, realistic sizing methodologies, and supplementary heating on overall heat pump performance. This study explores the effects of transitioning all installed, existing RTUs to high-performance heat pump RTUs for the U.S. commercial building stock. The analysis is performed using ComStock™, the U.S. Department of Energy's calibrated model of the U.S. commercial building stock. Results show 10% and 9% reductions in stock aggregate energy consumption and greenhouse gas emissions, respectively. This analysis will help inform the transition to heat pump RTUs for the U.S. commercial building stock.

© HPC2023.
Selection and/or peer-review under the responsibility of the organizers of the 14th IEA Heat Pump Conference 2023.

Keywords: heat pump energy modeling; commercial building stock energy modeling; ComStock; heat pump rooftop unit modeling; commercial building electrification; commercial building HVAC modeling

1. Introduction

1.1. Decarbonizing the U.S. commercial building stock

Several simultaneous market transformations must occur to decarbonize the U.S. energy systems. These include renewable power supply and storage options, widespread adoption of energy efficiency and electric demand flexibility, as well as ending the burning of on-site fossil fuels such as natural gas, propane, fuel oil and others. Buildings burn fossil fuels on-site primarily for space heating, water heating, equipment loads and cooking. The combined on-site natural gas combustion of the residential and commercial sectors is estimated to contribute to 9% of all U.S. carbon dioxide (CO_2) emissions annually [1].

Natural gas is the primary space heating and water heating fuel source for half of all commercial buildings in the U.S. by number, representing almost 70% of commercial building floor space, with more than half of the natural gas consumed for space heating [2]. In addition to natural gas, almost 10% of commercial buildings report using fuel oils and propane for primary space heating purposes [2]. This leaves only 25% of all commercial buildings currently relying on electricity as their only source for space heating needs [2].

† christopher.caradonna@nrel.gov

1.2. Heat pump rooftop units as a decarbonization pathway

Many technologies are used to provide space heating in commercial building HVAC systems. Packaged rooftop units (RTUs) are currently used to heat 37% of commercial buildings in the U.S. (representing 50% of the total commercial floor space) [2]. Heat pumps currently provide space heating for only approximately 11% of commercial buildings (representing 15% of the total floor area) [2].

Heat pumps offer a high-performance electric option for commercial building space heating. Their use of electricity for heating enables pathways toward decarbonization with heat pumps delivering space heating 2-4 times more efficiently than electric resistance options. Based on the 2018 Commercial Buildings Energy Consumption Survey (CBECS) data, it is estimated that fewer than 15% of commercial buildings utilize heat pumps for space heating equipment, and when they are in use they are more commonly found in the warmer southern region of the U.S. [2].

Heat pump technologies are available on the market today to replace existing gas-fired or electric resistance RTU systems. Most manufacturers offer heat pump rooftop units (HP-RTU) with compressors capable of providing 105 kW or less of cooling capacity (30 tons). There is remarkable opportunity for growth and widespread adoption of this technology, and expansion of the field will have an extensive impact on electrification efforts.

1.3. ComStock energy modeling

ComStock™ is a physics-based model of the U.S. commercial building stock built from an ensemble of 350,000 OpenStudio® whole-building energy models using the EnergyPlus® simulation engine. As used in this analysis, ComStock represents 66% of the U.S. commercial building stock by floor area. Unlike analyses that use a small number of "typical" building energy models to represent the stock, ComStock includes a diverse range of building and HVAC system configurations, construction vintages, hours of operation, etc. The relative prevalence of these building characteristics is informed by a wide range of data sources, including commonly used datasets such as CBECS [3], proprietary data sources such as CoStar [4], and difficult-to-acquire data sources such as whole-building hourly electricity consumption data from a large sample of buildings. The diversity of building characteristics helps create more robust conclusions because the models reflect the diversity found in reality. ComStock has gone through extensive calibration and validation, particularly on the electricity consumption side, as documented in detail in [5].

For this paper, two of the most important ComStock inputs are the prevalence of HVAC system types and heating fuels. Both model inputs are derived from the CBECS 2012 microdata, in particular the HVAC-related questions [3]. Rather than assuming a uniform distribution of the prevalence of natural gas or electric heating across each census division, data from the residential American Communities Survey (ACS) [6] was used to supplement the CBECS data. The CBECS totals for each census division were maintained, while counties with more residential natural gas heating according to ACS were scaled to have a higher percentage of the commercial natural gas heating, and vice-versa. For a more detailed description of the ComStock model, including the data sources and assumptions referred to above, see the "ComStock Documentation" National Renewable Energy Laboratory (NREL) report expected to be published in March 2023.

2. Methodology

2.1. Analyzing measures with ComStock

ComStock uses a representative set of 350,000 unique OpenStudio energy models to represent the energy usage and behavior of the U.S. commercial building stock [7]. ComStock's bottom-up engineering model approach is especially well-suited for studying the impact of proposed changes to the existing building stock [8], [9]. For this workflow, the baseline set of ComStock OpenStudio models is modified to represent the proposed change to be studied. For example, if increasing the efficiency of cooling equipment in all commercial buildings by 10% was proposed, then the baseline (representing the building stock circa ~2018) set of OpenStudio energy models would be modified to have 10% higher cooling efficiency. The results of this modified run can then be compared back to the original ComStock baseline results to understand the various changes that occurred due to the modification.

In this study, the ComStock baseline is modified to represent replacing all RTUs in the existing building stock, either gas-fired or electric resistance, with high-performance HP-RTUs. This change affects HVAC equipment serving ~45% of the floor area in the ComStock baseline; the floor area representation of all HVAC

system types in ComStock is shown in Fig. 1 [7]. High-performance HP-RTUs are defined to include the following features:

- Single-zone variable air volume (VAV) fan operation
- High-efficiency variable-speed compressor(s) for heating and cooling (>17 IEER)
- High-efficiency variable-speed fans
- Cold climate suitable with low temperature capabilities (minimum compressor operating temperature ≤ -17.8°C) and compressor defrost operation

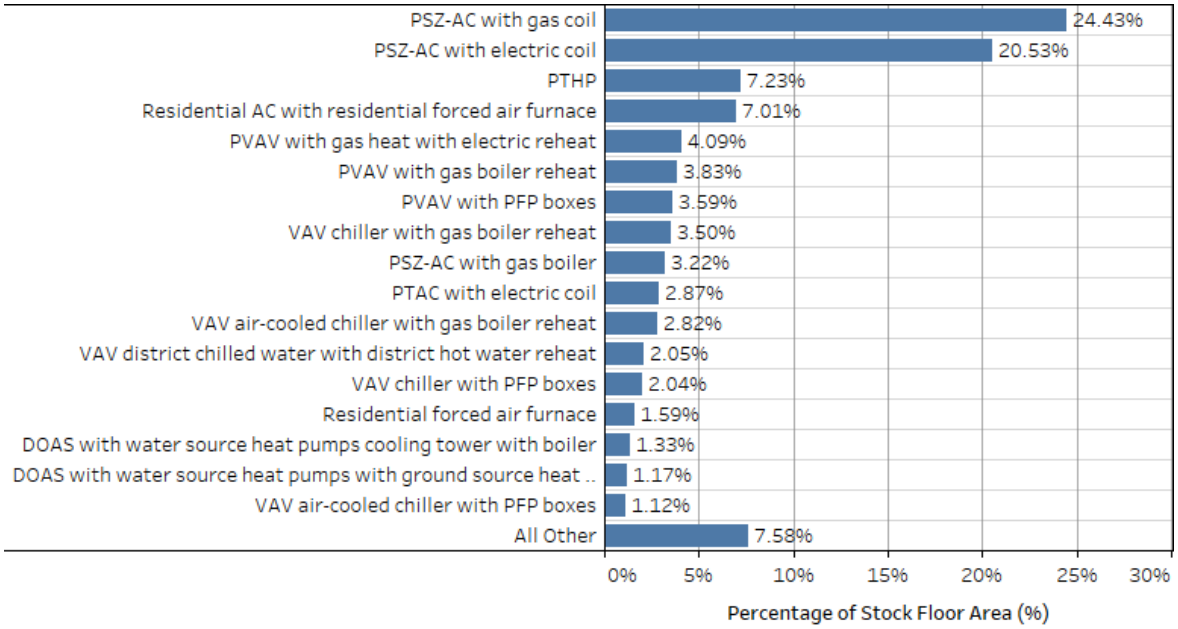


Fig. 1. ComStock HVAC system type prevalence by stock floor area.

Note that PSZ-AC stands for packaged single-zone air conditioner, PTHP stands for packaged terminal heat pump, PVAV stands for packaged variable air volume, DOAS stands for dedicated outdoor air unit, and PFP stands for parallel fan-power.

2.2. Baseline building stock RTU modeling

The state of the existing RTUs in ComStock is based on a combination of when the buildings were built and how the equipment has been updated over time, described in detail in the "ComStock Documentation" NREL report expected to be published in March 2023. Equipment performance is assumed to meet the energy code requirements in force at the time and place of installation. For this reason, most of the existing RTUs are modeled as constant air volume with single speed compressors. This is influential to the results in this analysis since energy savings will be calculated based on the energy performance of the ComStock baseline models versus an updated version of the ComStock baseline that uses the proposed HP-RTUs.

The in force energy code for the ComStock baseline is shown as a percentage of applicable floor area in Fig 2. Applicable floor area for this analysis includes ComStock buildings with "PSZ-AC with gas coil" and "PSZ-AC with electric coil" HVAC system types. Most ComStock baseline RTUs follow energy code requirements from the early 2000s. Other energy efficiency features such as demand control ventilation, energy recovery, and economizer control are only applied to baseline ComStock RTUs if required by the in force energy code for the particular model. The ComStock workflow checks the necessary characteristics of each RTU to determine if the feature is required. Similarly, heating, cooling, and fan efficiencies are set based on the in force code year. For models with the "PSZ-AC with electric coil" HVAC system type, the ComStock baseline will use electric resistance coils with a coefficient of performance (COP) of 1. For models with the "PSZ-AC with gas coil" HVAC system type, the ComStock baseline will use a gas furnace efficiency of generally around 80%.

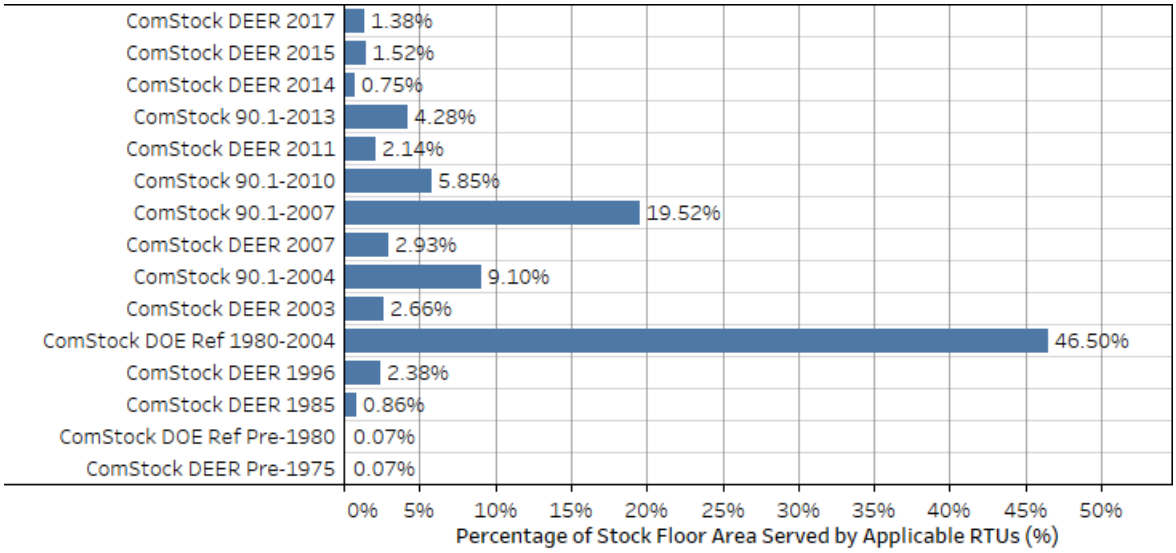


Fig 2: ComStock baseline in force energy code followed as a percentage of applicable floor area. Applicable floor area includes ComStock buildings with "PSZ-AC with gas coil" and "PSZ-AC with electric coil" HVAC system types.

2.3. Heat pump RTU modeling

The HP-RTUs are modeled using the EnergyPlus "AirloopHVAC:UnitarySystem" object [10], [11]. An OpenStudio measure is used in conjunction with the ComStock workflow to modify/remove any applicable RTUs in the ComStock baseline models ("PSZ-AC with gas coil" and "PSZ-AC with electric coil" in Fig. 1) and articulate the appropriate HP-RTU objects and settings. Non-applicable systems are not affected, nor are core operational parameters of systems such as schedules, thermostat setpoints, unoccupied operation behavior, and design outdoor airflow rates. Furthermore, energy-saving features found in applicable baseline RTUs such as airside heat/energy recovery, economizers, or demand control ventilation are preserved as-is for the new HP-RTU systems. This provides even comparability, noting that these features are feasible and available in HP-RTU systems. The modeling details of the HP-RTU system are described further in the following subsections.

2.3.1. Single-zone VAV operation

The modeled HP-RTUs utilize a single-zone VAV operation, which varies the supply airflow and discharge air temperature to efficiently maintain zone thermostat setpoints. During heating operation, as loads increase, first the supply air temperature is gradually raised until it hits a maximum threshold, and then supply airflow is increased until loads are met. During cooling operation, as loads increase, supply air temperature is gradually lowered until it meets a minimum threshold, and the supply airflow is increased until loads are met (Fig. 3) [12]. This is generally expected to provide fan energy savings during periods of reduced loads. The minimum supply airflow ratio modeled is 40%, which is common for single-zone RTUs [13]. The exception to the 40% minimum is when higher outdoor airflow rates are required to maintain ASHRAE Standard-62.1 minimum outdoor airflow rates: in these cases, the minimum flow rate to satisfy design outdoor air ventilation rates are modeled [14].

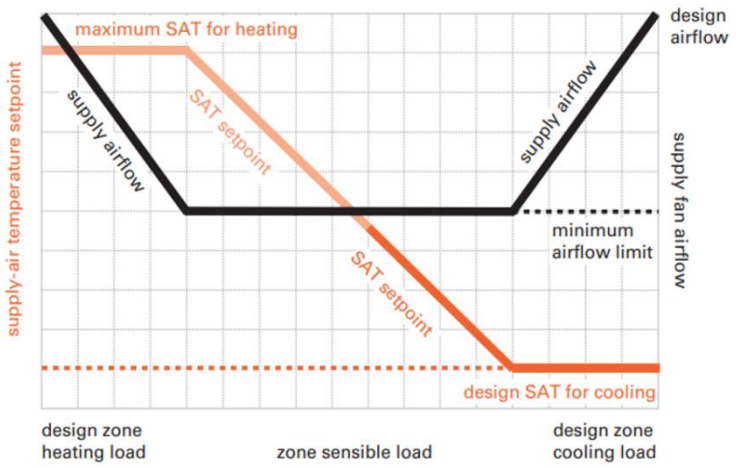


Fig. 3. Visual representation of single-zone VAV operation. Image from *[10]*.

2.3.2. Cooling performance

The variable-speed direct expansion (DX) cooling system in the proposed HP-RTUs is modeled using the EnergyPlus "Coil:Cooling:DXMultiSpeed" object using four speeds of cooling [10], [11]. The highest speed (speed 4) represents the cooling performance at rated conditions with the compressor fully loaded. The efficiency values used for this study are based on a 10-ton variable-speed RTU with a full-load COP of 3.6 at rated conditions with Integrated Energy Efficiency Ratio (IEER) above 17 [15]. Because the EnergyPlus COP input is compressor-only, and therefore removes supply fan energy, the modeling input is adjusted to 4.11 COP using the methodology from the Pacific Northwest National Laboratory's (PNNL's) Daikin Rebel study [15].

The other speed levels (speeds 1 through 3) represent lower compressor speeds, which would occur when the required load to be met is less than the full capacity of the unit. Each speed corresponds to a fraction of the rated capacity, a rated COP, and a rated airflow. Lower compressor speeds generally show higher COP values, which allows for higher efficiencies during these periods of partial loading. For instance, a PNNL lab testing and modeling study showed 20-50% annual cooling energy savings for variable speed RTUs over conventional RTU cooling systems [15]. The capacity fractions and COPs for the different compressor speeds were determined using NREL lab testing data for three variable-speed central ducted AC systems. Because the testing is based on residential central AC units rather than commercial RTUs, the values derived from the testing are normalized to the rated COP of 4.11 to better represent a commercially available HP-RTU for this study (Table 1) [15]. Variable speed HP-RTUs are capable of modulating to the specified fractions, but they may not do so in the same manner as the residential units the performance parameters are based on [13].

Table 1. Multispeed cooling coil performance parameters. Units with high outdoor air fraction may not achieve lower compressor speeds if it violates ventilation requirements.

Compressor Speed Level	Capacity Fraction of Rated	COP Fraction of Rated	Applied HP-RTU COP	Sensible Heat Ratio Fraction
Rated	1.00	1.00	4.11	1.00
4	1.00	1.00	4.11	1.00
3	0.67	1.08	4.44	1.01
2	0.51	1.11	4.56	1.03
1	0.36	1.07	4.40	1.11

Five performance curve modifiers are used for modeling the DX multispeed cooling objects. The performance curves were derived from separate work that used NREL lab testing data of three variable speed central ducted AC systems where values representative of the three systems are used. For multispeed objects, these modifier curves are specific to the compressor speed to which they are applied, so each speed will have its own set of curves. They are described as follows.

1. **Energy input ratio (EIR) as a function of part load ratio** – uses the calculated part load ratio to determine an EIR modifier from compressor cycling, which is multiplied against the full-load EIR for the stage (Fig. 4). Note that EIR is the inverse of COP, so decreasing the EIR increases the realized efficiency. For the multispeed units modeled in this work, this curve is only used for the lowest compressor speed where cycling losses may occur.
2. **Capacity as a function of temperature** – uses outdoor drybulb and indoor wetbulb temperatures to predict a capacity modifying factor that is multiplied against the rated capacity for each stage (Fig. 5). For heat pumps, the available capacity decreases with temperature.
3. **EIR as a function of temperature** – uses outdoor and indoor drybulb temperatures to determine an EIR (1/COP) modifying factor that is multiplied against the rated EIR for each stage for the time step (Fig. 6). Note that other modifier functions can also affect the final COP.
4. **Capacity as a function of flow** – modifies capacity based on the determined flow rate for a time step. This curve is not used since capacity is already accounted for in the speed level.
5. **EIR as a function of flow** – modifies EIR based on the determined flow rate for a time step. This curve is not used since the EIR is already accounted for in the speed level.

The cooling performance maps for EIR as a function of part load ratio, COP as a function of temperature, and capacity as a function of temperature are shown Fig. 4, Fig. 5, and Fig. 6, respectively.

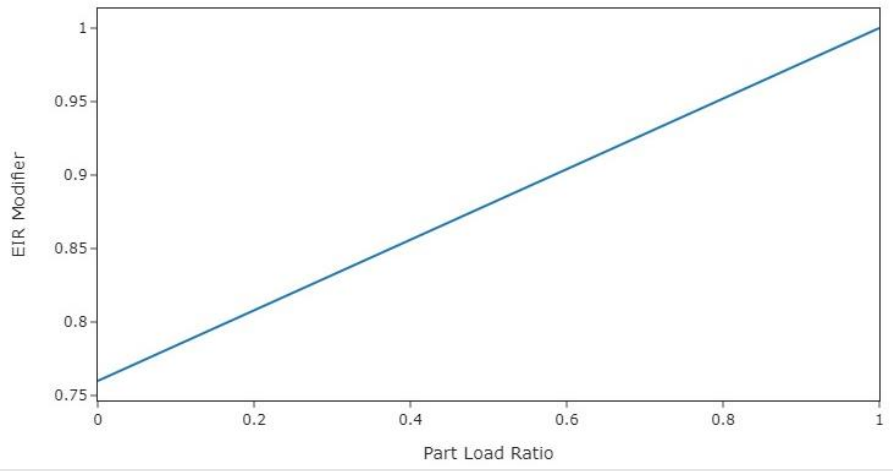


Fig. 4. Heating and cooling energy input ratio modifier as a function of part load ratio for all speed levels. This curve primarily captures losses to due part-load cycling at compressor speed 1. This value is divided by the EIR for the time step, which effectively decreases efficiency at lower part load ratios.

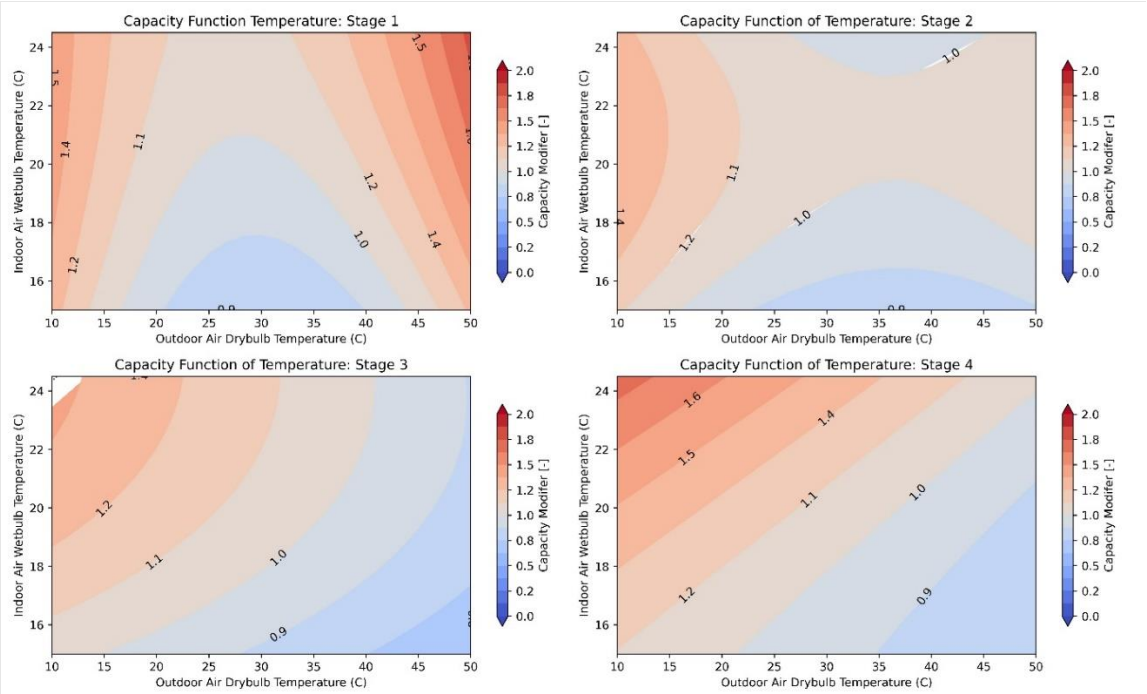


Fig. 5. Capacity as a function of temperature performance map for the four stages of cooling. This value is multiplied by the nominal capacity for each time step to determine the actual available capacity for the time step.

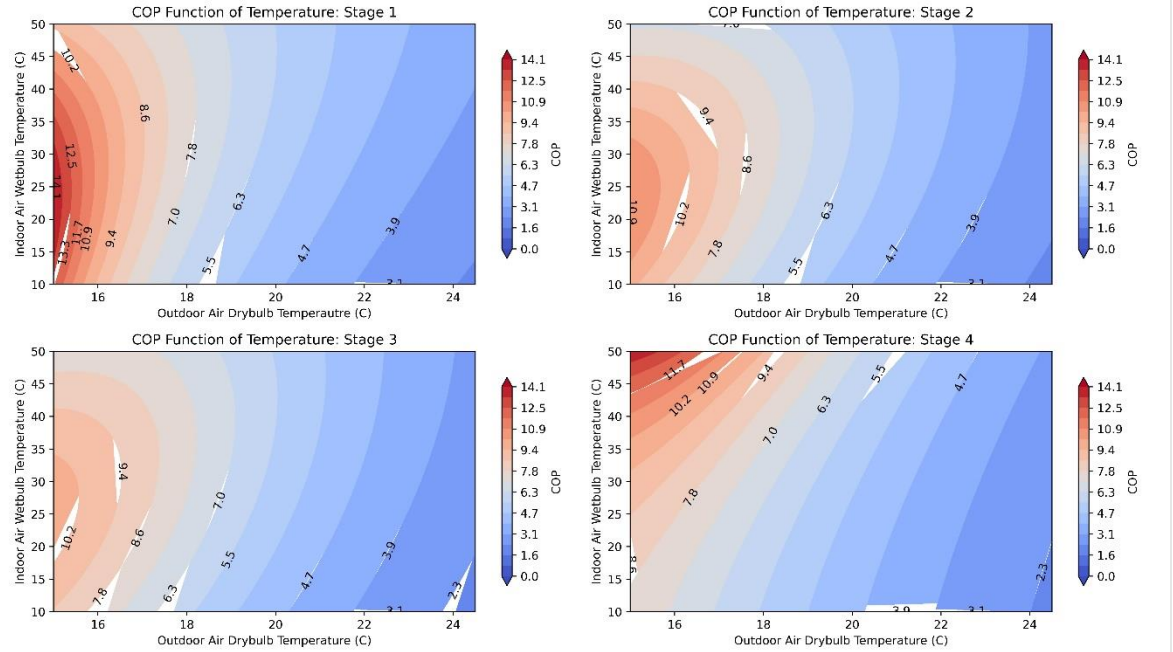


Fig. 6. COP as a function of temperature performance map for the four stages of cooling. Note that these COP values are for the compressor only – adding in supply fan energy would decrease the values presented.

2.3.3. Heat pump heating performance

The variable speed heat pump heating in the proposed HP-RTUs is modeled using the EnergyPlus "Coil:Heating:DXMultiSpeed" object using four speeds of heating [10], [11]. This object performs similarly to the "Coil:Cooling:DXMultiSpeed" object described previously. The rated efficiency values used for this

study are based on a 10-ton variable-speed RTU with a full-load COP of 3.42 at rated conditions (8.3°C outdoor air temperature entering the condenser and 21.1°C drybulb indoor air temperature entering the coil) [15]. Because the EnergyPlus COP input is compressor-only, and therefore removes supply fan energy, the model input is adjusted to 3.8 COP, using the methodology from PNNL's study [15]. The parameters for each stage of heating are shown in Table 2. The capacity and COP fractions for each speed level were determined using manufacturer-provided data for a variable-speed central ducted forced air heat pump system (Table 2). The data is roughly 10 years old but is expected to be a reasonable representation of a variable speed system. The heating COP increases with lower speed levels similarly to what was described for the cooling COPs. Because the testing is based on residential central HP units rather than commercial RTUs, the values derived from the testing are normalized to the rated COP of 3.8 to better represent a commercially available HP-RTU for this study (Table 1) [15]. Variable speed HP-RTUs are capable of modulating to the specified fractions, but they may not do so in the same manner as the residential units the performance parameters are based on which emphasizes the need for additional research in this area [13]. The minimum operating temperature for the heat pumps is modeled at -17.8°C, which is the default setting for some manufacturers. The compressor will lock out below this temperature and only backup heat will be available.

Table 2. Multispeed heating coil performance parameters. COP values are at rated conditions and vary based on temperature.

Compressor Speed Level	Capacity Fraction of Rated	COP Fraction of Rated	Applied HP-RTU COP
Rated	1.00	1.00	3.80
4	1.00	1.00	3.80
3	0.85	1.05	3.98
2	0.48	1.24	4.71
1	0.28	1.45	5.51

Similar to the DX multispeed cooling objects, five performance curve modifier types are used for modeling the DX multispeed heating objects. The descriptions of these are discussed in the cooling performance section of this document, with the only difference being that the heating coils use indoor air drybulb temperature as opposed to indoor air wetbulb temperature used for the cooling coils. The performance curves were derived from manufacturer-provided data for a central ducted variable speed heat pump system. The resulting performance maps for all speed levels are shown in Fig. 4, Fig. 7 and Fig. 8 for EIR as a function of part load ratio, COP, and capacity retention, respectively. As expected with heat pumps, heating COP and capacity generally reduce with outdoor air drybulb temperature.

Heat pump performance maps are especially impactful due to the general reduction of capacity and efficiency at lower outdoor air temperatures where increased heating loads often occur. This study attempts to utilize the best available data, as described previously, as this will notably impact the results. However, it should be emphasized that complete heat pump performance data is still scarcely available at the time of this study, especially for variable speed commercial RTUs and low temperature operation. This adds limitations to the understanding of heat pump performance and operation in this analysis. Further research on heat pump performance could increase confidence in heat pump modeling, and this study may be updated as more data becomes available.

Comparisons of modeled performance data versus alternative data sources were made, where possible, for validation that the performance data used is reasonable. Table 3 and Table 4 compare some key points on the modeled heat pump performance maps for COP and capacity retention as a function of outdoor air temperature, respectively, with other available data sources for validation. The first data source is for the variable speed Daikin Rebel HP-RTU, with specification sheet data specifying capacity and COP at 8.3°C (rated) and -8.3°C [11]. The second source is a Rheem two-stage HP-RTU with heating performance data at various outdoor air temperatures [16]. The last data source is from a study that performed lab testing on a Carrier cold climate variable speed HP-RTU, which provides COP values at various outdoor air temperatures [17].

The modeled HP-RTU outperforms the capacity retention of the reference units by 5 to 9%, with the largest difference occurring with the Rheem unit at -17.8°C (Table 3). For COP retention, the modeled HP-RTU outperforms the reference units by 3% to 14%, with the largest difference occurring with the Rheem unit at -17.8°C (Table 4). Although there are some notable differences between the modeled and reference unit performance, and the modeled HP-RTU outperforms the reference units in all cases, these comparisons still suggest the modeled HP-RTU performance is reasonably appropriate compared to other available data,

especially considering they are different units from different data sources. Note that no alternative data sources were found for comparing part-load performance or the impacts of cycling on variable speed heat pump units, further emphasizing the need for more research in this space to increase modeling confidence.

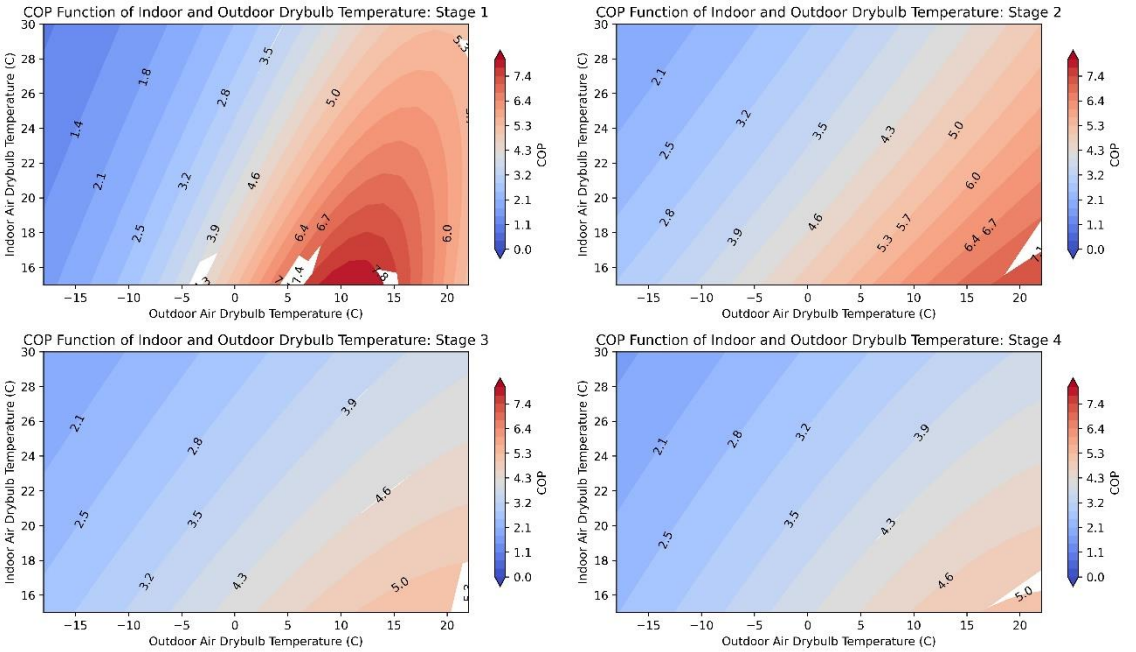


Fig. 7. COP as a function of temperature performance map for the four stages of heating. Note that these COP values are for the compressor only – adding in supply fan energy would decrease the values presented.

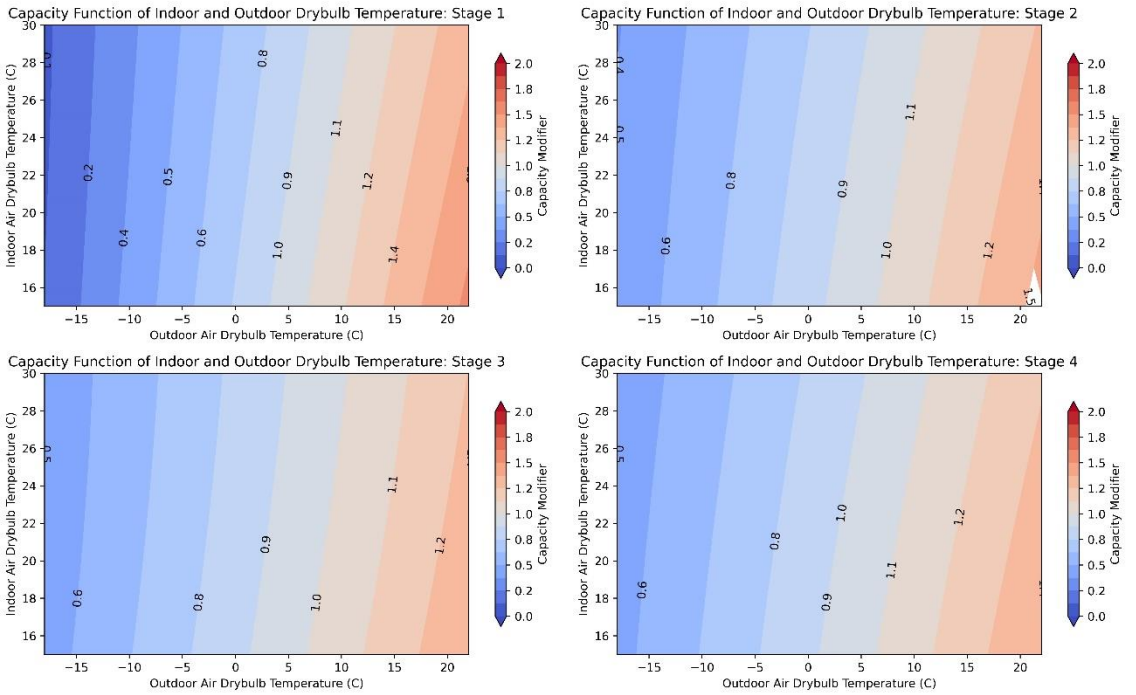


Fig. 8. Capacity as a function of temperature performance map for the four stages of heating. This value is multiplied by the nominal capacity for each time step to determine the actual available capacity for the time step.

Table 3. Capacity retention as a function of outdoor air temperature comparison for Daikin Rebel, Rheem Renaissance, and the modeled HP-RTU performance curves.

Reference Temperature, °C	**8.3°C**	**-8.3°C**	**-17.8°C**
Modeled HP-RTU Capacity Fraction	1	0.64	0.45
Daikin Rebel Capacity (kW)	30.8	18.0	-
Daikin Rebel Capacity Fraction	1	0.59	-
% Diff. Modeled HP-RTU vs. Daikin Capacity Fraction	-	7.80%	-
Rheem Renaissance Capacity (KW)	31.5	19.1	12.9
Rheem Renaissance Capacity Fraction	1	0.61	0.41
% Diff. Modeled HP-RTU vs. Rheem Renaissance Capacity Fraction	-	5.47%	9.33%

Table 4. COP comparison of the modeled HP-RTU, the Daikin Rebel, and a lab-tested Carrier unit. Note that the COPs associated with the modeled HP-RTU and Rheem unit are compressor only while the other include the supply fan. Including the supply fan in the calculation will decrease the COP.

Reference Temperature, °C	**8.3°C**	**-8.3°C**	**-17.8°C**
Modeled HP-RTU COP (compressor only)	3.80 (speed 4)	2.66 (speed 4)	2.11 (speed 4)
Modeled HP-RTU COP Fraction (compressor only)	1	0.70	0.55
Daikin Rebel COP	3.42	2.38	-
Daikin Rebel COP Fraction	1	0.70	-
% Diff Modeled vs. Daikin COP Fraction	-	0%	-
Carrier COP Estimate	3.1	2.1	1.62
Carrier COP Fraction	1	0.68	0.52
% Diff Modeled vs. Carrier COP Fraction	-	2.9%	5.5%
Rheem Renaissance COP (compressor only)	4.2	2.77	1.98
Rheem Renaissance COP Fraction (compressor only)	1	0.66	0.47
% Diff Modeled HP-RTU vs. Rheem Renaissance COP Fraction	-	5.8%	14.3%

2.3.4. Heat pump sizing & backup heating

The sizing of heat pumps is non-trivial since the same system is used for both heating and cooling. Heat pumps in colder climates usually require a source of supplemental heat, which today is often sized to meet the entirety of the heating load. This is because heat pump capacity is reduced as outdoor ambient temperatures decrease, which generally corresponds to the highest heating loads for the building. Furthermore, compressor lockout controls are often implemented in heat pump systems, which disable heat pump operation below a certain temperature [13]. This would require the supplemental heat source to be sized to meet loads below this temperature. Because the supplemental heat source in colder climates is then often sized to meet the design heating load, the system can then be sized based on the required cooling capacity with the assumption that the supplemental heat source will address any heating load beyond the corresponding capacity of the heat pump, avoiding the need to purchase a larger capacity unit. Supplemental heat is less of a concern in warmer climates where the design cooling load exceeds the design heating load, even when accounting for heat pump capacity degradation at lower temperatures, and where the design heating temperature is well above any minimum compressor lockout temperature.

The supplemental heat source is often electric resistance, which has an effective site COP of 1, while the heat pump system will often demonstrate a site COP much higher than this even at temperatures down to -17.8°C. Sizing heat pump systems to address more of the heating load is sometimes suggested since the heat pump heating is more efficient than electric resistance, so long as the sizing of heat pump system still enables effective operation for both heating and cooling [18], [19]. However, this analysis simply sizes the heat pumps based on cooling load, and reserves studying the impact of other sizing approaches for future analyses. The

minimum outdoor air temperature for heat pump operation is modeled as -17.8°C, which aligns with the default minimum temperature for some manufacturers, noting that this default value can change between manufacturers and can be overridden, which would impact performance [13].

2.3.5. Defrost operation

Frost formation can occur on the outdoor unit during heat pump heating operation due to humidity in the outdoor air condensing and freezing on the cold outdoor coil. Frost needs to be periodically removed so the coil can function properly. This is generally done using either an electric resistance coil or by reversing the operating of the heat pump to remove the frost buildup, both of which result in additional energy consumption. This analysis uses reverse cycle as it is common in practice and does not require additional heating coils.

Reverse cycle defrost inhibits the heating capacity of the heat pump system which may require the use of lower-efficiency supplemental heating during these times. Additionally, reversing the cycle of the heat pump causes additional heating load in the RTU since the system is essentially in cooling mode, which EnergyPlus adds to the total effective heating load [10], [11].

Control of the defrost cycle can also vary. Some units use a set time fraction, where the unit operates in defrost mode for a specified time when outdoor air temperatures are below a specified temperature. This analysis uses EnergyPlus' "on-demand" defrost operation, which estimates the amount of time needed for defrost based on a set of empirical calculations dependent on outdoor air wetbulb temperature, coil temperature, and other parameters: these calculations are described in detail in the EnergyPlus Documentation [10], [11].

2.3.6. Greenhouse gas emissions

Greenhouse gas (GHG) emissions savings are estimated in this work using similar methods to those presented in [9]. For direct fuel combustion, the impact of GHG emissions was estimated using emissions factors published by the ANSI/RESNET/ICCC: natural gas = 63.27 kg/GJ (147.3 lb/MMBtu), propane = 76.4 kg/GJ (177.8 lb/MMBtu), and fuel oil = (84.15 kg/GJ) 195.9 lb/MMBtu [20], [21].

Estimating GHG emission impacts due to electricity consumption is more complicated. It requires projecting the resource composition of the electric grid as a result of load increase, which may be substantial when electrifying commercial building HVAC equipment as is done in this study. This is important since the prevalence of cleaner grid resources will directly impact the GHG emissions per kWh of electricity used. Furthermore, the resources producing electricity on the electric grid vary based on location and time of day, which can impact GHG estimates if not accounted for properly [22], [23].

The choice of grid emissions scenario will impact emissions factors and therefore analysis results [24]. This analysis uses NREL's Cambium dataset. The Cambium dataset provides emissions factors that vary based on time of day and U.S. grid region to capture geospatial and temporal variation in converting consumed kWh to GHG emissions [22], [23]. The Cambium dataset includes various grid scenarios to choose from: this analysis uses Cambium long-run marginal emissions rate "low renewable energy cost 15-year" scenario data [22], [23]. The timeseries grid emission factors in this dataset are coupled with ComStock timeseries electricity consumption outputs for each model based on time of day and the location-based Cambium grid region to estimate the GHG emissions impacts of transitioning to HP-RTUs. The published emissions values presented represent a single year of emissions, which are calculated using a weighted average year over the levelization period.

2.3.7. Heat pump annual performance

For this analysis, annual effective heating COP is calculated for the ComStock simulations to understand the performance of the heat pump heating system, as shown in Equation 1.

$$COP_{effective} = \frac{q_{hp} + q_{supp}}{E_{hp} + E_{supp} + E_{defrost}} \quad (1)$$

$q_{hp} = annual\ heating\ output\ energy\ from\ heat\ pump$
$q_{supp} = annual\ heating\ output\ from\ supplemental\ heating\ coil$
$E_{hp} = annual\ heat\ pump\ heating\ electricity\ input$
$E_{supp} = annual\ supplemental\ heating\ electricity\ input$

$E_{defrost} = annual\ reverse\ cycle\ defrost\ electricity\ input$

The effective annual COP calculation in Equation 1 includes performance and capacity degradation with temperature, heat pump sizing limitations, and heat pump defrost cycles and the associated supplemental heating coil operation. This calculation does not include supply fan energy, which is commonly included in product specification sheet values for rated COP values. It is also important to note that natural gas furnaces and boilers are often rated on thermal efficiency and exclude the delivery system (fans or pumps). Including supply fan energy in the COP calculation could lower the values presented in this study by 20-40%.

3. Results and Discussions

3.1. Annual energy and GHG savings

Ten percent (10%) total annual site energy savings (130 TWh) can be achieved for the modeled U.S. commercial buildings, including savings of 8% for electricity, 17% for natural gas, and 50% for other fuels (fuel oil and propane). Savings numbers reflect the 66% of the U.S. commercial building stock currently modeled in ComStock at the time of this analysis. The total site energy savings for just the 45% of buildings with RTUs is 21% (Fig. 9b). The site energy savings for electricity are primarily from fan energy savings from the single-zone VAV operation with high-efficiency fans and cooling savings from high-efficiency variable-speed compressor operation. Notably, these fan and cooling energy savings could also be achieved with high-performance non-heat-pump RTUs. The median fan and cooling energy savings are approximately 35% and 40%, respectively, which align with the results from a lab testing and modeling study performed by PNNL on variable-speed RTUs [15]. There are also substantial electricity savings in the heating end use from converting electric resistance RTUs ("PSZ-AC with electric coil") in the baseline to HP-RTUs which have higher heating COPs. The electricity savings presented in this study would be reduced, possibly causing a net electricity penalty, if replacement of baseline electric resistance RTUs was omitted from the analysis.

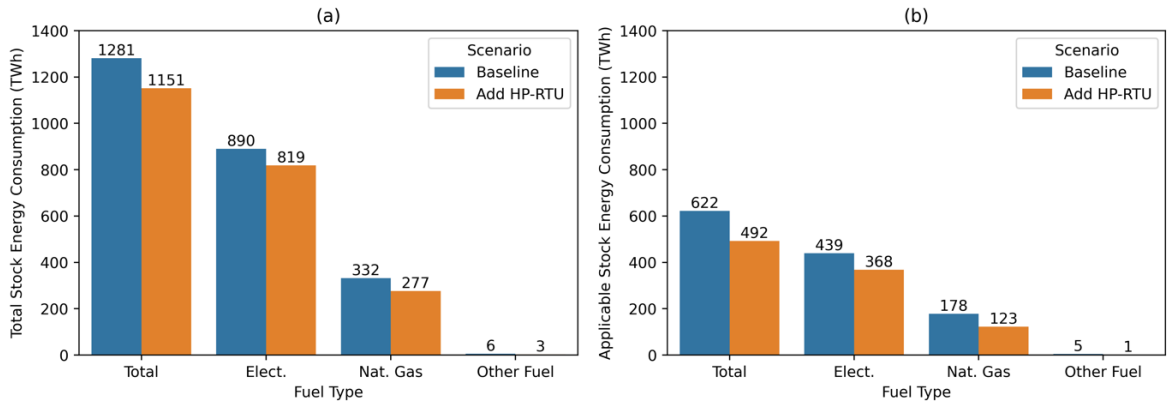


Fig. 9. Aggregate annual site energy consumption by fuel type for (a) the total U.S. commercial building stock modeled by ComStock and (b) the U.S. commercial building stock applicable to the HP-RTU scenario.

The site energy savings from the combustion fuels (natural gas and other) can be attributed to transitioning the baseline gas-fired RTUs to electric heat pump heating. Switching from a gas heated system to an electric heated system will add electricity consumption to the building, although some of the increase in electricity may be offset by fan and cooling savings. HP-RTU replacement alone may not completely electrify applicable buildings if combustion fuels are still used for water heating, appliances, and non-RTU HVAC systems.

Nine percent (9%) total annual GHG emissions savings (32.4 MMT) can be achieved for the modeled U.S. commercial buildings by replacing all existing RTUs with HP-RTUs (Fig 10a). This represents 6.6% GHG emissions reduction for electricity consumed by these buildings, 16.6% GHG emissions reduction for natural gas, 66.7% for fuel oil, and 50% for propane. Similar to the site energy savings projections, these savings numbers reflect the 66% of the U.S. commercial building stock currently modeled in ComStock at the time of this analysis. The reductions in GHG emissions are primarily caused by net reduced energy consumption across all fuel types (Fig. 9). However, emissions for electricity are also impacted by temporal and geospatial variation in grid emissions factors informed by the Cambium dataset. Electricity consumption may be shifted to times

with higher or lower grid emissions factors based on the predicted grid resources for that time. As previously mentioned, this study chose a single Cambium scenario for grid emissions factors. The choice of scenario impacts emissions results [24]. Electrification will become more attractive from a GHG emissions standpoint as the grid continues to generate more electricity from lower GHG sources, effectively lowering grid emissions factors. Geospatial variation in emissions factors between grid regions will impact the GHG reductions from electrification in the particular region [22], [23].

The baseline ComStock model currently underestimates natural gas consumption by around 30% for the modeled buildings, as shown in Figure 193 of the technical report on calibration of ComStock [5]. The source of this error is unknown but may be attributable to some combination of underestimation of heating load, overestimation of primary combustion equipment efficiencies, or misrepresentation of inefficiencies in controlling or maintaining HVAC systems. Because the baseline natural gas consumption is used as a starting point for comparison, the savings potential for HP-RTUs may be higher than the results shown described above.

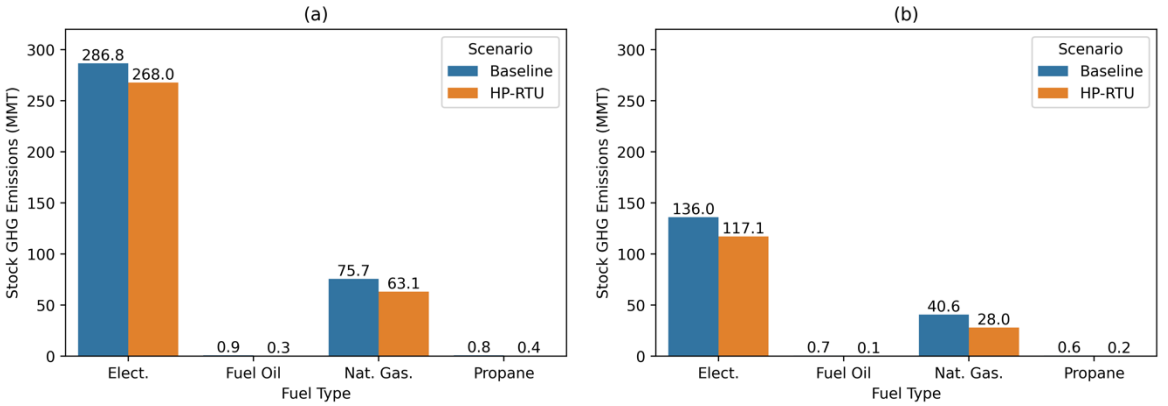


Fig 10. Aggregate GHG emissions by fuel type for (a) the total U.S. commercial building stock and (b) the U.S. commercial building stock applicable to the HP-RTU scenario.

3.2. Heat pump annual performance

Simulation results show variation by state in average annual effective heating COP of the HP-RTUs, with lower values around 2 COP and the highest values above 5 COP (Fig. 11). This annual average heating COP includes performance and capacity degradation, heat pump sizing limitations, and heat pump defrost operation and associated supplemental heating coil operation, but does not include supply fan energy which would lower the COP. Note that some of these higher COPs are attributed to operating the HP-RTUs at lower compressor speeds during part-load conditions (Table 2; Fig. 7), which is possible with the variable speed units modeled in this study. These average COPs would likely be reduced with constant speed HP-RTUs that cycle the full compressor capacity to meet loads.

States with warmer climates generally show higher heating COPs for HP-RTUs than states with colder climates (Fig. 11). This behavior is expected since heat pumps have better performance in warmer conditions. Additionally, in warmer climates the design heating load is generally closer to or below the design cooling load. Since this study sizes heat pumps based on the cooling load, the heat pump heating capacity in warmer climates will naturally meet a larger portion of the design heating load compared to cooler climates, leading to higher annual average heating COP values. However, the heating energy use intensity (annual energy used for heating divided by floor area) in colder states can be more than 10 times higher than in the heating intensity in warmer climates, which stresses the importance of cold climate performance (Fig. 12).

State average percentage of total heating electricity used by the supplementary system ranges from 6% to 56% (Fig. 13). This is due to the reduced capacity of heat pumps under cold ambient conditions, as well as the fact that the heat pumps are generally being sized to a smaller fraction of the design heating load (when sized to design cooling load, as is done in this study). States with higher fraction of supplementary heating generally correspond to lower COPs as expected (Fig. 11 & Fig. 13). Note that supplementary heating can also be induced by reverse-cycle defrost operation which temporarily disables heat pump from heating.

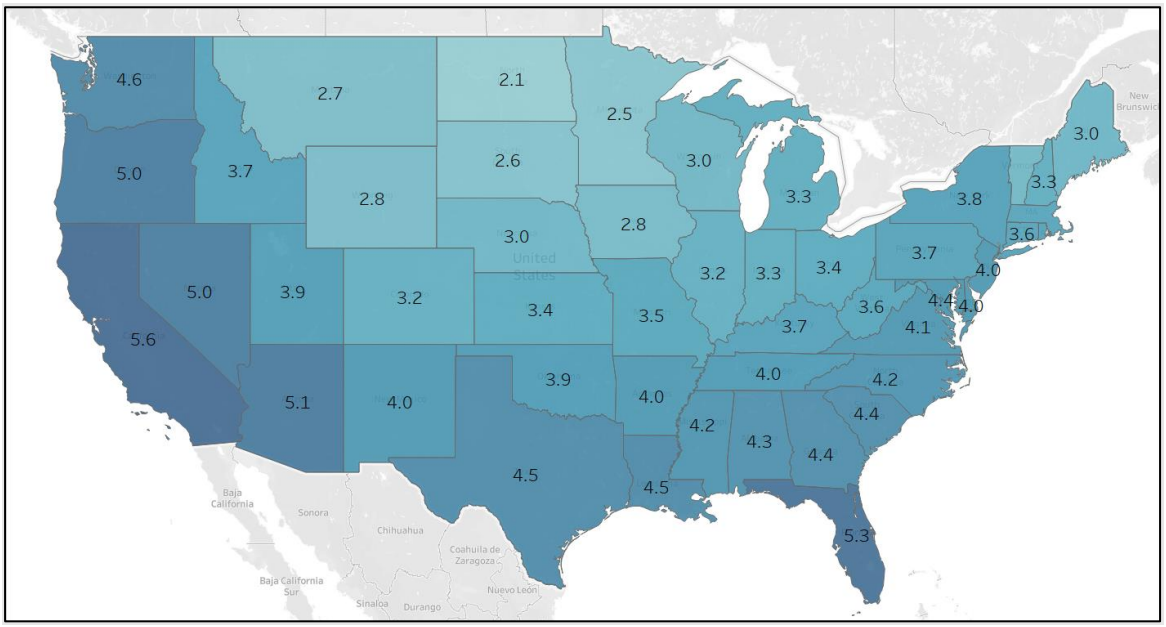


Fig. 11. Stock annual average effective heating COP by state. Effective heating COP is the total heating energy output divided by total heating energy input. Heating energy output includes heating from the heat pump and supplemental heating. Heating energy input includes heat pump compressor and outdoor fans, supplemental heating, and defrost. The heating energy input does not include associated supply fan energy use. Including supply fan energy use would reduce COPs.

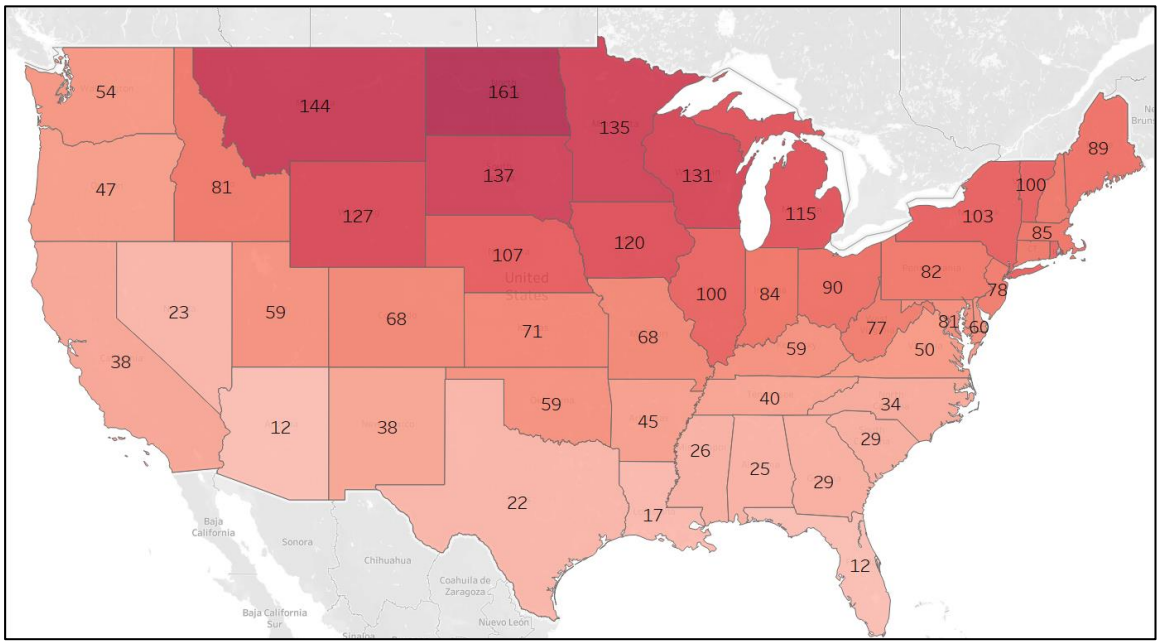


Fig. 12. ComStock baseline stock annual average heating energy use intensity (EUI; kWh/m^2/year) by state.

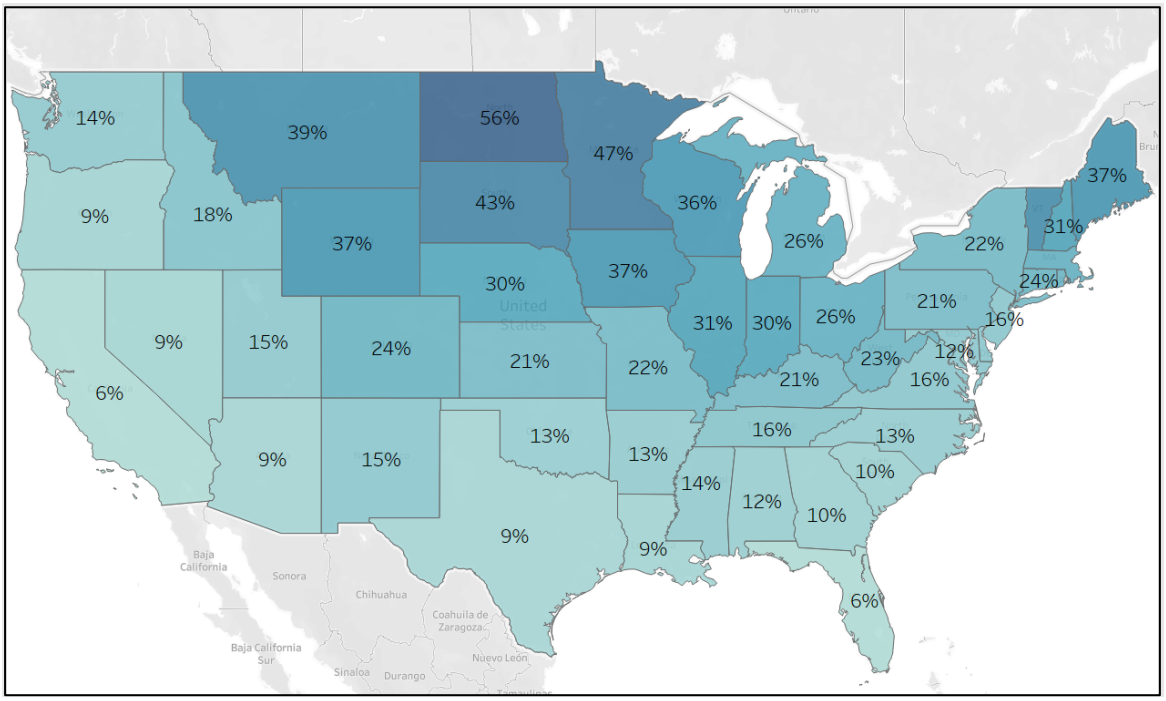


Fig. 13. Stock annual average percent heating electricity input used for supplement heating by state. Note that supplemental heating occurs due to insufficient heating capacity of the heat pump which can be further exacerbated from defrost operation.

Most states have multiple climate zones represented and therefore state average values do not tell the whole story. Fig. 14 shows the distribution of annual heating COPs for two different states. The average for South Carolina is 4.2, but the distribution extends from a COP of 3.1 up to 5.7, while the distribution for Michigan is more closely distributed to its average heating COP of 3.2. One question is why the range of annual heating COPs is so large in a single climate zone. A full analysis and discussion of the reasons for this range is outside the scope of this paper, but generally includes sizing considerations, particularly for buildings with either very unbalanced heating and cooling capacity requirements, heating energy consumption, or both. In some cases, climate can vary substantially within it state which could also cause wider COP distributions.

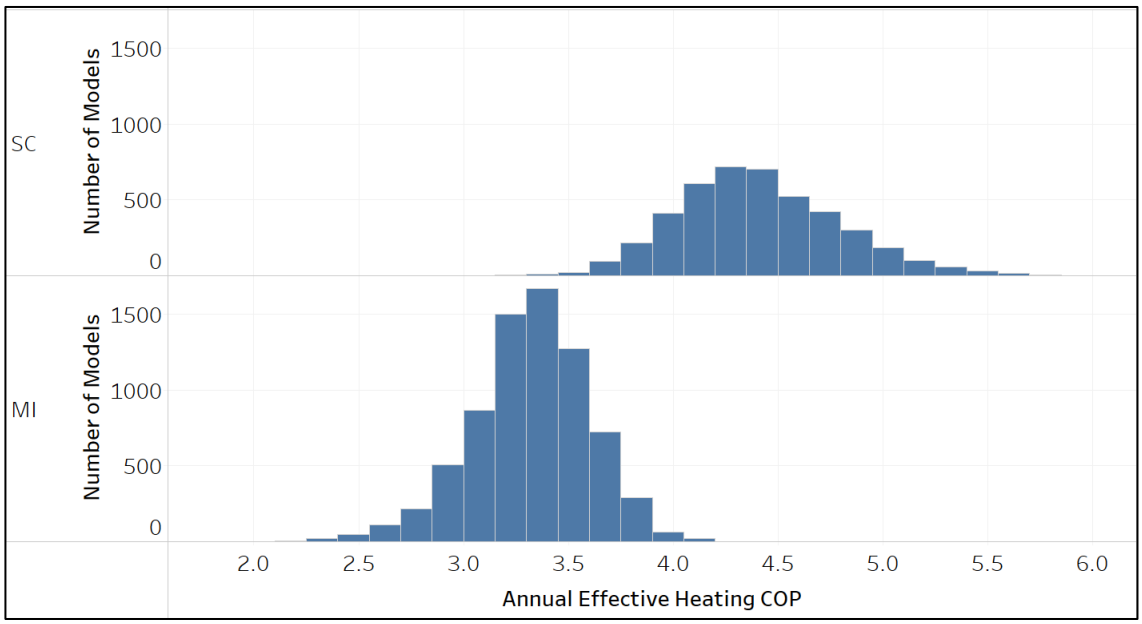


Fig. 14. Distribution of annual effective heating COPs for models in South Carolina (SC) and Michigan (MI)

4. Conclusion

Transitioning the existing RTUs (gas fired and electric resistance) in the U.S. commercial stock to high-performance HP-RTUs is a promising pathway toward electrification and reducing GHG emissions. Comstock energy modeling results show 10% total site energy savings (130 TWh) for the modeled building stock from this transition, noting that ComStock currently models 66% of the building stock at this time. GHG emissions also showed savings totaling around 9% (32.4 MMT CO_2) for the modeled building stock, noting that this analysis uses a single reference scenario from the Cambium dataset for grid emissions factors, the choice of which can impact these estimates. GHG and site energy and savings are achieved by transitioning from gas furnace and electric resistance heating to high-efficiency heat pump heating, and from fan and cooling savings by converting the older, less efficient RTUs currently in the U.S. commercial stock to high-performance variable speed RTUs. Note that the fan and cooling savings could also be achieved with high-performance non-heat-pump RTUs. GHG savings would be expected to increase from electrification pathways as the U.S. electric grid becomes less carbon intensive, therefore reducing the carbon contribution per kWh of electricity.

This analysis also presents average annual heating system COPs by state from the ComStock simulations, which demonstrates the effective COP that can be expected when factoring in impactful heat pump considerations such as supplementary heat, defrost cycles, realistic/economical sizing practices, and efficiency/capacity degradation at lower temperatures. ComStock modeling results suggest annual effective heating COP averages vary considerably by state, with a low of 2.1 and a high of 5.6, and even within a state. As expected, states with warmer climates generally show higher COPs, noting that states in colder climates generally require substantially more energy for heating, which increases the importance of cold climate performance.

Future research could analyze the impact of transitioning existing RTUs to HP-RTUs on electric peak demand, as well as the impact of adding air side energy recovery or utilizing different fuel sources for supplemental heat. Furthermore, although this study attempts to utilize the best available heat pump performance data and makes comparisons to alternative data sources where possible, limitations exist due to the small amount of performance data available for commercial variable speed HP-RTUs. Heat pump energy modeling can be sensitive to performance assumptions such as the variation in COP and available capacity under different operating conditions, which can impact analysis results. Future research could expand this body of knowledge through additional lab testing and field evaluation of HP-RTUs to increase confidence in heat pump modeling, which this work could be updated to include.

Acknowledgements

This work was authored by the National Renewable Energy Laboratory, operated by Alliance for Sustainable Energy, LLC, for the U.S. Department of Energy (DOE) under Contract No. DE-AC36-08GO28308. Funding provided by the U.S. Department of Energy Office of Energy Efficiency and Renewable Energy Building Technologies Office. The views expressed in the article do not necessarily represent the views of the DOE or the U.S. Government. The U.S. Government retains and the publisher, by accepting the article for publication, acknowledges that the U.S. Government retains a nonexclusive, paid-up, irrevocable, worldwide license to publish or reproduce the published form of this work, or allow others to do so, for U.S. Government purposes.

References

[1] "Decarbonizing U.S. Buildings." [Online]. Available: https://www.c2es.org/document/decarbonizing-u-s-buildings/. [Accessed: 15-Nov-2022].

[2] "2018 COMMERCIAL BUILDINGS ENERGY CONSUMPTION SURVEY (CBECS)." [Online]. Available: https://www.eia.gov/consumption/commercial/. [Accessed: 14-Nov-2022].

[3] "Commercial Buildings Energy Consumption Survey (CBECS)," 2012.

[4] "CoStar Property - Commercial Property Research and Information," 2018. [Online]. Available: https://www.costar.com/products/costar-property-professional. [Accessed: 15-Nov-2022].

[5] P. Wilson, Eric J. H., Parker, Andrew, Fontanini, Anthony, Present, Elaina, Reyna, Janet L., Adhikari, Rajendra, Bianchi, Carlo, CaraDonna, Christopher, Dahlhausen, Matthew, Kim, Janghyun, LeBar, Amy, Liu, Lixi, Praprost, Marlena, Zhang, Liang, DeWitt, "End-Use Load Profiles for the U.S. Building Stock," no. November, 2022.

[6] U.S. Census Bureau, "2009-2011 American Community Survey 3-year Public Use Microdata Samples [SAS Data file]," 2012. .
[7] A. Parker *et al.*, "ComStock Documentation," Golden, CO, 2022.
[8] W. Li *et al.*, "Modeling urban building energy use: A review of modeling approaches and procedures," *Energy*, vol. 141, pp. 2445–2457, 2017.
[9] C. CaraDonna and K. Dombrovski, "Air Handling Unit Shutdowns During Scheduled Unoccupied Hours: US Commercial Building Stock Prevalence and Energy Impact," *ASME J. Eng. Sustain. Build. Cities*, vol. 3, no. 3, Aug. 2022.
[10] "EnergyPlus™ Version 22.1.0 Documentation Engineering Reference," 2022.
[11] "EnergyPlus™ Version 22.1.0 Documentation Input Output Reference," 2022.
[12] TRANE, "Understanding Single-Zone VAV Systems," pp. 1–10, 2013.
[13] Daikin, "Installation and Maintenance Manual OM 1141-3 MicroTech ® III Unit Controller for Rebel ® Commercial Packaged Rooftop Systems," no. October, 2014.
[14] "ANSI+ASHRAE+62.1-2019."
[15] W. Wang, "Part-Load Performance Characterization and Energy Savings Potential of the RTU Challenge Unit : Daikin Rebel," no. September, 2013.
[16] "Commercial 7.5-10 Ton Renaissance ™ Line Package Heat Pump RHPDZT Commercial Prestige ® Series RHPDZS Commercial Classic Plus ® Series Compliant Models Air Package Heat Pump RHPD Series."
[17] Frederick Cogswell and D. A. Mahmoud, "High-Performance Air-Source Cold Climate Heat Pump (CCHP)," no. October, 2020.
[18] ASHRAE, *2015 Ashrae Handbook HVAC applications*. 2015.
[19] N. Resources Canada, "AIR-SOURCE HEAT PUMP SIZING AND SELECTION GUIDE." 2020.
[20] "Workflow Inputs — OpenStudio-HPXML documentation." [Online]. Available: https://openstudio-hpxml.readthedocs.io/en/latest/workflow_inputs.html#default-values. [Accessed: 02-Sep-2022].
[21] "ANSI/RESNET/ICCC 301 Standard for the Calculation and Labeling of the Energy Performance of Dwelling and Sleeping Units using an Energy Rating Index," 2019.
[22] P. Gagnon, W. Frazier, W. Cole, and E. Hale, "Cambium Documentation: Version 2021," 2021.
[23] "Cambium | Energy Analysis | NREL." [Online]. Available: https://www.nrel.gov/analysis/cambium.html. [Accessed: 02-Sep-2022].
[24] E. Present, Pieter Gagnon, Eric J.H. Wilson, Noel Merket, Philip R. White, and Scott Horowitz, "Choosing the Best Carbon Factor for the Job: Exploring Available Carbon Emissions Factors and the Impact of Factor Selection," 2022.

14th IEA Heat Pump Conference
15-18 May 2023, Chicago, Illinois

Addressing the barriers to heating electrification in the US

Ed Vineyard[a*], Jim Young[b], Samuel Yana Motta[a], Brian Fricke[a]

[a]Oak Ridge National Laboratory, P.O. Box 2008, MS 6070, Oak Ridge, TN, 37831, USA
[b]Guidehouse, 77 South Bedford Street, Burlington, MA, 01803

Abstract

One of the greatest challenges in US electrification efforts to reduce carbon emissions is to utilize electric heat pumps for space and water heating rather than fossil fuels. Although the number of *heat pumps* for space conditioning is growing, they still represent only 35% of sales and only 12% of installed base. While it has been over forty years since one of the first *heat pump water heaters* was introduced, they only account for 2% of sales and less than 1% of the installed base.

Several barriers exist that impede the widespread adoption of heat pump technology for space and water heating in the US, especially for retrofit applications. This paper will examine the various barriers and identify potential solutions and strategies to address those barriers, including various research activities related to equipment, and potential cost reduction strategies, both for the product and installation. Also included will be a discussion of programs and incentives by utilities and efficiency organizations.

© HPC2023.
Selection and/or peer-review under the responsibility of the organizers of the 14th IEA Heat Pump Conference 2023.

Keywords: Electrification;heat pump;barriers;heat pump water heater;incentives;cost reduction

1. Introduction

The United States (US) has set an ambitious goal to reduce greenhouse gas (GHG) emissions by at least 50% by 2030. Achieving this goal would put the United States on a path to limit global warming to 1.5 degrees Celsius, the target scientists say is required to avoid the worst consequences of the climate crisis.

A recent study by a team of scientists and policy analysts from across the nation indicates there are multiple pathways to achieve this goal. However, commitments to the actions need to be made as soon as possible. The study consolidates findings from six recently published techno-economic models that simulate U.S. energy system operations. According to the authors, the separate models all agree on four major points:

- The majority of the country's greenhouse gas emissions come from power generation and transportation, so to reduce overall emissions by 50%, the electricity grid needs to run on 80% clean energy (up from today's 40%), and the majority of vehicles sold by 2030 need to be electric. Other important sources of GHG emissions reduction include *electrification of buildings* and industries.
- The primary barrier to increased alternative energy use will not be cost, it will be enacting new policies. A coordinated policy response between states and the federal government will be necessary to succeed.

* Corresponding author. Tel.: +1-865-207-5729. *Email address:* vineyardea@ornl.gov

This manuscript has been authored by UT-Battelle, LLC, under contract DE-AC05-00OR22725 with the US Department of Energy (DOE). The US government retains and the publisher, by accepting the article for publication, acknowledges that the US government retains a nonexclusive, paid-up, irrevocable, worldwide license to publish or reproduce the published form of this manuscript, or allow others to do so, for US government purposes. DOE will provide public access to these results of federally sponsored research in accordance with the DOE Public Access Plan (http://energy.gov/downloads/doe-public-access-plan).

- Thanks to advances in wind, solar, and energy storage technologies, powering the electric grid with renewables will not be more expensive; and electric vehicles could save every household up to $1,000 per year in net benefits.
- A clean-energy transition would reduce air pollution, prevent up to 200,000 premature deaths, and avoid up to $800 billion in environmental and health costs through 2050. Many of the health benefits will occur in communities of color and frontline communities that are disproportionately exposed to vehicle, power plant, and industrial pollution. [1]

The US Department of Energy (DOE) is one of the primary US government agencies involved with ensuring America's security and prosperity by addressing its energy, environmental and nuclear challenges through transformative science and technology solutions.

DOE's analysis of greenhouse gas pollution reductions from the clean energy provisions of the Inflation Reduction Act and Bipartisan Infrastructure Law finds that the combined impact of both laws could reduce emissions by approximately 1,000 million metric tons (MMT) in 2030, with a total of nearly 1,150 MMT when considering other provisions of each law. The expected emissions reduction from these measures is equivalent to the approximate combined annual emissions released from every home in the U.S. [2]

"The Inflation Reduction Act (IRA) is a triumph of historic scope and ambition that will enable a whopping 40% reduction in greenhouse gas emissions below 2005 levels. Combined with President Biden's Bipartisan Infrastructure Law and the CHIPS and Science Act, these investments will transform our economy and bring us closer to achieving our nation's climate goal," said U.S. Secretary of Energy Jennifer M. Granholm. "These historic legislative accomplishments are delivering on the President's promise to build a new American clean energy economy that creates millions of good jobs while lowering energy bills for families and combating the climate crisis." [2]

In support of the IRA, the Building Technologies Office in DOE's Office of Energy Efficiency and Renewable Energy develops, demonstrates, and accelerates the adoption of cost-effective technologies, techniques, tools and services that enable high-performing, energy-efficient and demand-flexible residential and commercial buildings in both the new & existing buildings markets, in support of an equitable transition to a decarbonized energy system by 2050, starting with a decarbonized power sector by 2035.

2. Carbon Dioxide Emissions

As shown in Figure 1, the transportation sector has the highest percentage CO_2 emissions (37%), followed closely by the combined emissions (35%) from the buildings sector [3]. Electricity used to power equipment in the residential and commercial sector comprises the largest source of CO_2 emissions (67%), followed by natural gas (26%).

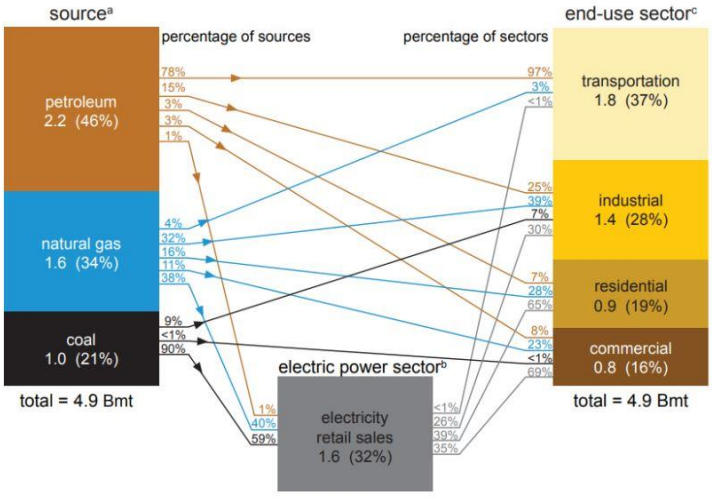


Fig. 1. U.S. CO_2 Emissions from Energy Consumption by Source and Sector.

One of the strategies to address decarbonization in the buildings sector is to increase the use of renewables to replace existing fossil-fueled power plants and address future growth. An additional strategy is to replace natural gas equipment, such as furnaces and water heaters, with heat pumps. As shown in Figure 2, space heating with natural gas is the largest contributor to direct emissions in both residential and commercial buildings [4]. Natural gas water heating is the next largest contributor in residential buildings. Together, space and water heating with natural gas account for over 90% of the *direct* emissions in the residential buildings and approximately 60% in commercial buildings.

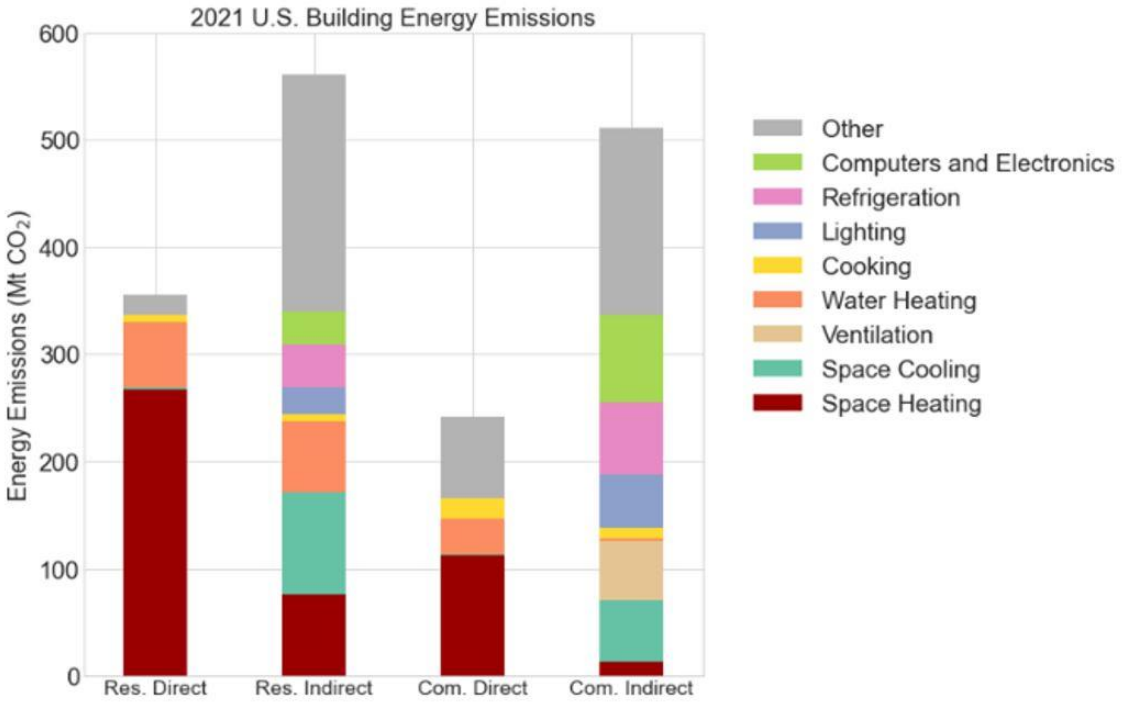


Fig. 2. U.S. CO_2 Emissions from Energy Consumption by End Use.

3. Heat Pump/Heat Pump Water Heater Market

The number of heat pumps in the US for space conditioning is growing (Figure 3) [5]. Since 2000, sales have increased 20%. However, they still represent only 35% of sales and 12% of the installed base. The highest saturation is in the south, accounting for 24% of the installed base (Figure 4) [6].

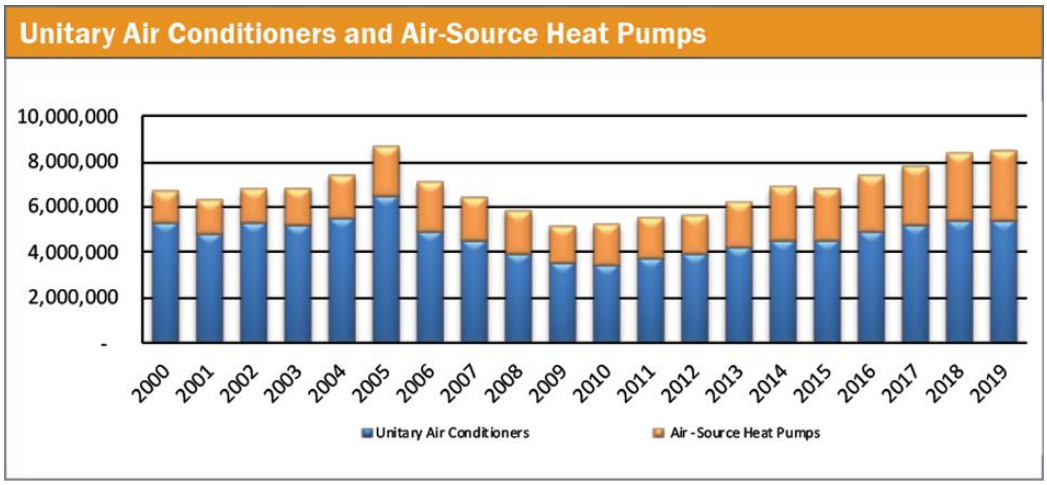


Fig. 3. US Heat Pump Annual Sales.

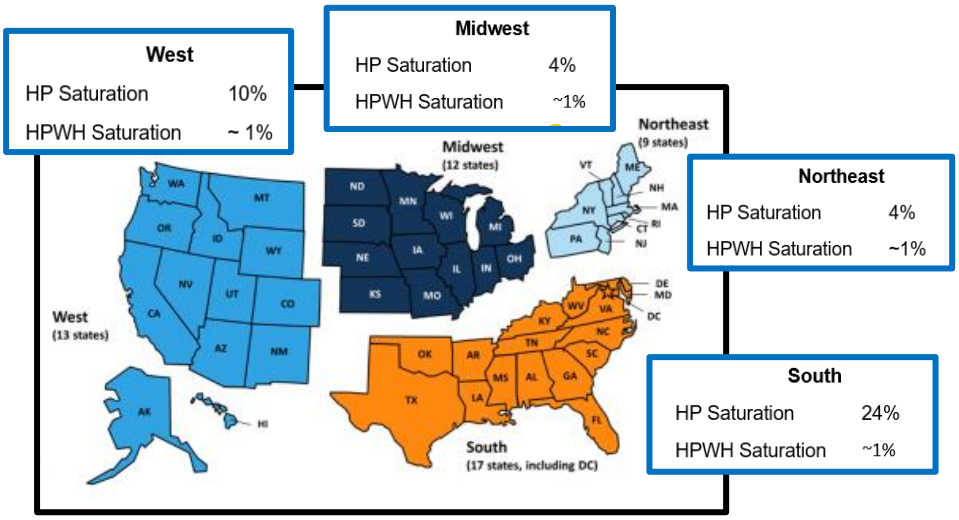


Fig. 4. US Heat Pump Installations by Region.

Heat pump water heaters are the future of water heating, with local jurisdictions promoting all-electric buildings and a new national effort to accelerate market transformation. Numerous reputable water heating manufacturers have released their own models, and by 2017-2018, HPWH shipments totalled about 70,000 on average (Figure 5) with an estimated market penetration of almost 2% [7]. Factors driving the future growth of the heat pump water heater market include their efficiency relative to electric resistance coupled with the ability to use renewable sources of energy to power the unit, which requires three to four times less energy. In addition, supportive regulations and incentives are also expected to play a key role in the growth of this market [8].

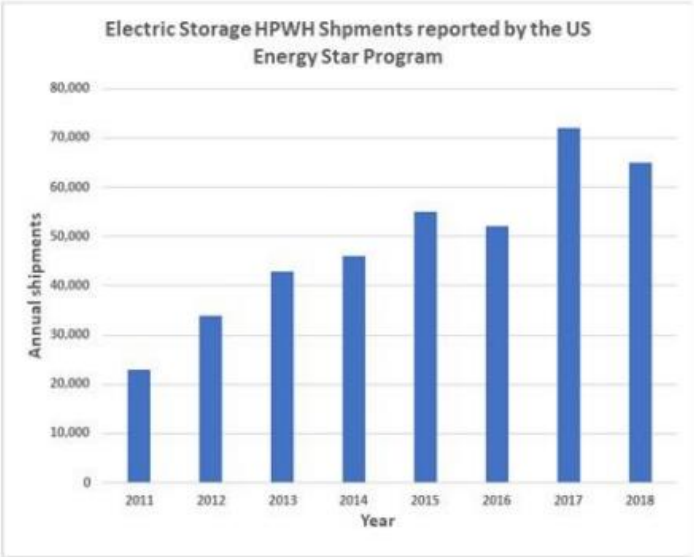


Fig. 5. US Heat Pump Water Heater Annual Sales.

4. Barriers to Heating Electrification

As shown in Figure 6, all states are not equal in the amount of carbon emissions [9]. The main contributors, highlighted in green, are some of the most populous states, such as California, Texas, and Florida. However, population alone doesn't impact carbon emissions. Other factors, such as the fuel used for building equipment (natural gas, electricity, fuel oil), the energy source for power generation (natural gas, nuclear, hydropower, coal), and the climate all influence the amount of carbon released from buildings to the atmosphere.

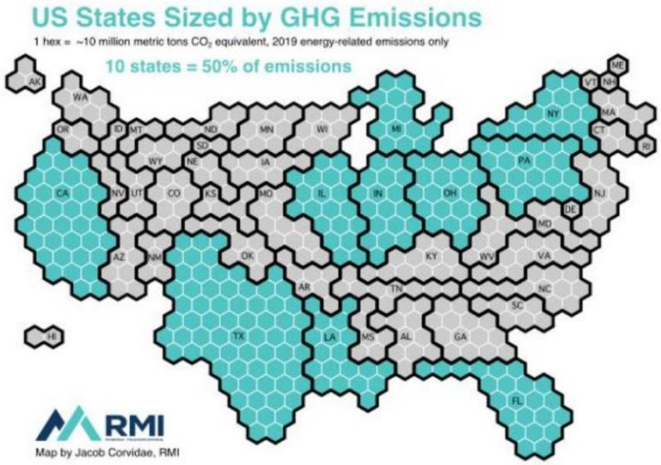


Fig. 6. U.S. States Sized by CO_2 Emissions.

To significantly reduce carbon emissions in the buildings sector, the US must concentrate on addressing some of the main barriers to electrification of building equipment in the ten states, many of which are also problematic in the other states. Following are the major barriers encountered when consumers consider replacing their fossil-fired equipment with an electric heat pump.

4.1 Heat pump barriers

Several barriers exist that inhibit greater numbers of heat pumps being installed in the US. Among these are installed cost, operational cost, space constraints, panel upgrades required when replacing natural gas equipment, installer familiarity, shortage of trained installers, product availability, and consumer acceptance. These barriers can be generally grouped by 1) cost; 2) installation challenges; 3) consumer issues; 4) work force issues, and 5) capacity. Most of these barriers apply to both retrofit and new installations in residential and commercial markets. However, there are some differences which are unique to the building type, especially for multifamily housing, which will be highlighted in section *4.1.6*.

4.1.1 Cost

Installation costs are one of the main barriers to increasing the number of heat pumps, especially in northeastern regions where the present equipment is a natural gas or oil-fired furnace. In the Northeast, natural gas fuels 55% of homes; this is broken down by 75% of New Jersey homes, 61% of New York's, and 51% of Pennsylvania's [10]. In Figure 7, installation costs were estimated in New York for an air-source heat pump compared to a gas furnace with an air-conditioning (3-ton unit) [11]. Estimated costs were based on an average from Long Island, New York City, and the Hudson Valley/Upstate/Western New York region databases and vetted through stakeholder conversations. The average shows the cost difference between an air-source heat pump versus a furnace/electric air-conditioner is $4584, an increase of 55% over the cost for the furnace/electric air-conditioner.

HVAC System Type	Installed Cost
Air-Source Heat Pump	$12,964
Gas Furnace w/ AC	$8,380
Incremental Cost	$4,584
Incremental Cost %	55%

Fig. 7. Installation Cost Estimates for New York.

One of the main drivers for the higher installed cost is that heat pumps in colder climates require larger units to provide sufficient heating at lower temperatures (capacity drops at lower temperatures) and variable-speed compressors and fans to reduce capacity in the summer to prevent frequent cycling that would otherwise result from oversizing the units for winter operation.

Another factor is that in some areas where contractors are unfamiliar with heat pumps, they charge a premium to install a heat pump system versus a natural gas or oil furnace since they will need to spend more time properly designing the system. In addition, they may be concerned about call backs if the customer is unhappy with their new system due to cooler temperatures leaving the register. This would result in less profit for the installer due to the increased cost for labor and vehicle charges (gas and maintenance) to address the issue with the consumer.

In addition to installation costs, operating costs must also be considered to evaluate the overall life-cycle cost for an electric heat pump versus a natural gas/electric air-conditioner. The American Council for an Energy Efficient Economy investigated the life-cycle costs in all regions of the US [12]. The results, shown in Figure 8, indicate that, in general, heat pumps have lower life-cycle costs in states with lower rates for electricity versus natural gas (Southern, Pacific Northwest) and higher life-cycle costs in states with higher rates for electricity versus natural gas (Northeast and Midwest). The higher installed costs in those regions are also a large factor in the differences.

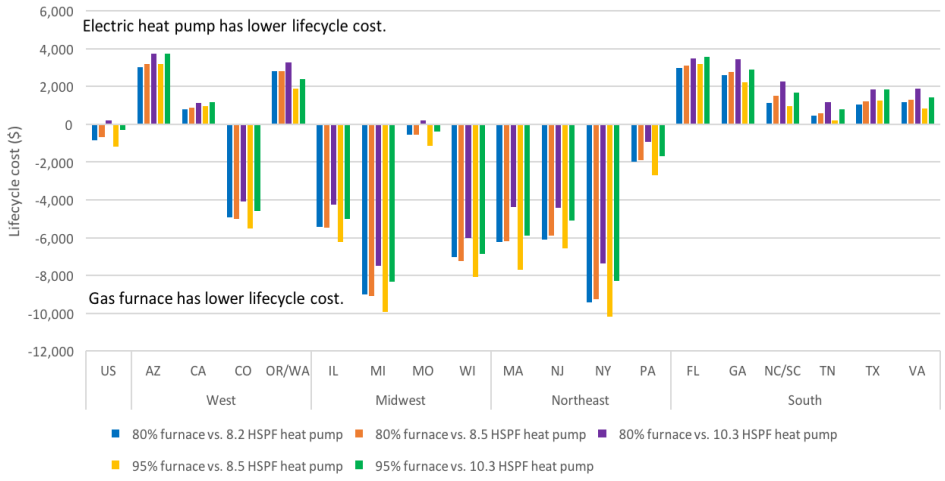


Fig. 8. Life-Cycle Cost Estimates for Various Equipment Types.

4.1.2 Installation challenges

According to new research from residential electricity research group Pecan Street, electric panels in up to 48 million U.S. single-family homes will need to be upgraded to fully transition away from fossil fuels and use electricity for space and water heating, and other applications. Most older homes have a 100-amp breaker panel and heat pumps require a circuit breaker up to 60 amps. With an average cost of $2,000 for an upgraded panel, that represents a nearly $100 billion impediment to residential electrification [13]. This can be problematic when replacing a natural gas furnace to a heat pump in some states, especially California, where natural gas is the most popular residential heating fuel type. Some 64 percent of occupied housing units in the state rely on natural gas for heating in 2020 [14].

4.1.3 Consumer issues

The majority of consumers don't evaluate the total cost of ownership when purchasing a heat pump. They gravitate towards the lowest cost product which is usually minimum standard efficiency. However, it was shown in section *4.1.1* that a higher cost product, such as the cold climate heat pump, can save enough money in energy costs over its lifetime such that the life-cycle costs that are lower than a 97% AFUE furnace in St. Louis.

Consumers are also reactive, meaning they don't plan replacements of heating and cooling equipment ahead of time, but only replace in emergency situations (failure). In addition, they typically replace like for like, e.g., a natural gas furnace is replaced with another natural gas furnace.

4.1.4 Work force issues

Contractors are a key stakeholder in electrification retrofits because they are the main point of contact for home and building owners. In many parts of the US, there are simply not enough contractors trained to properly install heat pumps, particularly in retrofit situations. At the same time, many trained contractors are retiring and not enough people are entering the contractor workforce to replace them. This gap can severely limit the number of electrification retrofits in each area [15].

Contractors may also be hesitant to learn about new equipment because they have limited resources for training and they may worry that there is not enough market demand to justify retraining and changing their business model.

4.1.5 Capacity

Heat pump capacity drops as the outdoor temperature gets colder. The capacity for single-speed heat pumps at low outdoor temperatures can be roughly half of what it is at the rated condition. One remedy for this is to equip heat pumps with electric resistance heaters to maintain the set-point temperature in the house. However, this increases the operating cost since electric resistance heaters only have an efficiency of 1 versus heat pump efficiencies as high as 4. Another remedy is to use variable-speed motors to increase the capacity at low temperatures by increasing the speed (moving more refrigerant through the system) to better match the house load. Unfortunately, variable-speed designs tend to be more expensive than single-speed. Thus, trade-offs must be made when deciding on which heat pump design is most cost-effective.

4.1.6 Multifamily applications

Multi-family housing is a large portion of the U.S. housing stock, with 26% of total housing units located in multifamily buildings [15]. Space constraints are one of the major barriers to heating electrification in multifamily housing since many apartments and condo buildings do not have sufficient space for heat pumps, especially the associated ductwork necessary to distribute conditioned air evenly throughout the space. The locations where electric heat pumps are installed may result in noise complaints, particularly if located in common spaces, balconies or other locations that could disrupt tenants.

Multifamily buildings can also face market barriers with respect to renter occupied units, which comprise the majority (86%) of multifamily units. The large number of renters in multifamily buildings leads to the issue of *split incentives* which refers to building owners being unwilling to invest energy upgrades for tenants who pay for their own utility costs. Because the value of energy efficiency upgrades benefits the tenant, property owners see little to no return which creates a motivational barrier to the installation of heat pumps [15].

4.2 Heat pump water heater barriers

Barriers for heat pump water heaters are similar to those for heat pumps, such as cost, installation challenges, consumer issues, and capacity. For heat pump water heaters, there are a few barriers that are unique or more pronounced, such as space constraints, location of the unit, and availability of units. As in the case with heat pumps, most of these barriers apply to both retrofit and new installations in residential and commercial markets. However, there are some differences, which will be highlighted in section *4.2.6*.

4.2.1 Cost

Installation costs for heat pump water heaters can be approximately $1000 higher when replacing an existing natural gas water heater with a heat pump water heater. This is a 65% increase and for homeowners that base their decisions on first cost, it is difficult hurdle to overcome [16]. Replacing an existing electric resistance water heater with a heat pump water heater may seem to be an easier upsell, especially with paybacks

of around 3 years for a family of four [17]. However, the first cost difference is even higher than that for a gas water heater scenario (approximately $1300) [16].

4.2.2 Installation challenges

Heat pump water heaters face the same electrical panel upgrade challenge as heat pumps when replacing an existing gas unit. Although the breaker required is only 30 amps versus 60 amps for a heat pump, this still can be a difficult hurdle to overcome, especially if there is no wiring in the vicinity of the gas water heater to provide power to the unit. The additional labor and materials for wiring and condensate piping further increase the cost by approximately $500 [16]. This issue can be extremely problematic for states like California where 90% of water heating is supplied by natural gas [18].

4.2.2.1 Space constraints

In residential applications where the water heater is located in a closet, the installation space requirements for heat pump water heaters are much different than for the existing water heater (electric resistance or natural gas) they will replace. The National Building Code requirements for a gas water heater are: 1) it should have a minimal 1-inch clearance between it and any combustible material, such as wall framing or wall finish; 2) it must have a self-closing gasketed door that prevents carbon monoxide or other products of combustion from entering the home; and 3) fresh air needed for combustion must be drawn from *outside* the home using double wall metal pipe [19]. On the other hand, electric water heaters don't require even a minimal clearance space. This is because, unlike their gas-powered counterparts, they don't release exhaust. The main difference when locating a heat pump water heater in a closet is that it has to have adequate ventilation from the *indoor* space. In order to run efficiently, heat pump water heaters need 700 to 800 cubic feet of available space (air in the room) to operate properly, which requires louvered doors when this space is not available [20].

4.2.2.2 Location

Another issue regarding the installation space concerns the ambient temperature at which the heat pump water heater must operate. Since it is a heat pump, the efficiency and capacity get worse as the surrounding air temperature gets colder. Therefore, for a northern climate, locating the heat pump water heater in a garage or attic will severely degrade its performance during the winter.

4.2.3 Consumer issues

Heat pump water heaters are an unfamiliar technology to most consumers. When it comes to replacing their water heater, consumers typically replace in kind because of their familiarity with what has been working for them. One complaint from consumers is that heat pump water heaters are perceived as being noisy. Although they make about as much noise as a refrigerator, consumers are not used to hearing a noise from their electric resistance water heater [18]. Also, for consumers replacing a fossil-fired water heater, they may expect a heat pump water heater to be less noisy than their existing unit.

Because heat pump water heaters transfer heat from ambient air, they do not work well, or sometimes at all, in colder temperatures. For this reason, it may be difficult to utilize a heat pump water heater in certain regions due to a loss in capacity [21]. If hot water recovery is limited to the heat pump alone, it will take a lot longer to reheat the tank after a long draw. Electric resistance heat can hasten the recovery, but at the price of eliminating much of the savings [22].

4.2.4 Capacity

Heat pump water heaters take a relatively long time to heat a volume of water to the pre-set temperature, approximately 3 to 4 hours when running in compressor-only mode for a 40-gallon tank. For comparison, an electric resistance water heater takes 40 to 60 minutes and a natural gas water heater takes 30 to 45 minutes. In order to keep up with the hot water demand, particularly at peak times, most heat pump water heaters are equipped with electric heating elements which would enable them to match the recovery performance of an electric resistance water heater. When properly installed, a heat pump water heater rarely needs to revert to its less efficient backup mode where the heating elements are energized [23]. One strategy for reducing the

amount of time a heat pump water heater avoids turning on the back-up electric resistance heaters is to install a larger tank, 50- to 80-gallon versus a traditional 40 gallon.

4.2.5 Product availability

Another main drawback to heat pump water heaters is the availability of residential products both in big box stores and stocked by plumbers. Plumbers install 43% of all residential water heaters. Homeowners (26%) and retailers (17%) account for another 43% of installations (Figure 9) [24]. Typically, water heaters are an emergency installation following a catastrophic tank failure. Thus, product availability is critical. The majority of plumbers and retailers don't routinely stock heat pump water heaters, thus the only type of water heater available is a standard natural gas or electric resistance version. The reason availability is limited is due to the market demand. Since heat pump water heaters represent 2% of all water heaters sold, there is no incentive for retailers and plumbers to stock them.

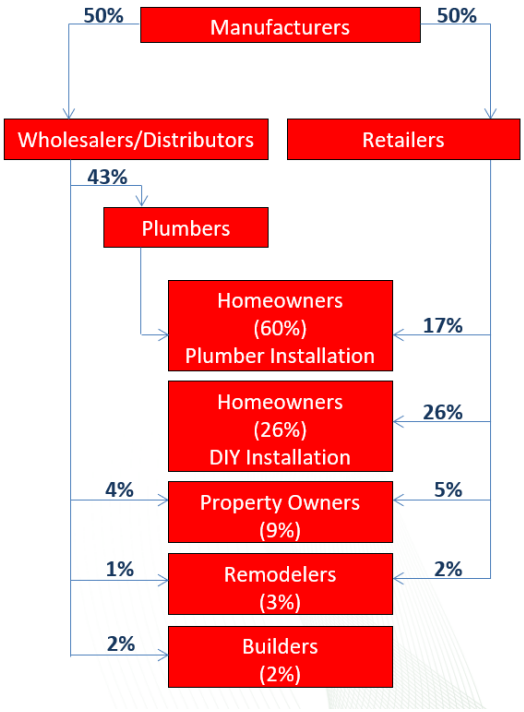


Figure 9. Heat Pump Water Heater Installations.

4.2.6 Multifamily and large commercial applications

For multifamily housing, two options are commonly used: 1) a central domestic hot water system with one or more commercial storage water heaters or one or more boilers coupled with a storage tank to serve the entire building, or 2) alternatively, water heaters are installed in each dwelling unit (similar to single-family). The availability of large heat pump water heater models for central systems is limited compared to residential products. This is especially true for applications that require higher temperatures, such as boiler applications and in large buildings where recirculation losses would require electric resistance boosters. For applications where a single heater services each unit, tankless and low boy water heaters are more popular due to their ability to be located in small spaces, However, this becomes an impediment for replacing with a heat pump water heater since they necessitate more space due to their size and ventilation requirements.

5. Solutions: Heat Pumps/Heat Pump Water Heaters

5.1 Incentives

Financial incentives, whether provided through utility programs or by state agencies, can spur market development. Incentives directly to consumers for heat pumps for space and water heating can aid in mitigating

barriers associated with upfront cost. Incentives to distributors and retailers (rather than through customer rebates) can also be tied to the sale of high-efficiency electric equipment. Incentives can also encourage distributors and plumbers to keep heat pump water heaters in stock for use in emergency replacement situations.

Beginning in 2023 and through the end of 2032, all homeowners will be eligible for a 30% federal tax credit on the total cost of buying and installing their new heat pump, with a maximum credit of $2,000. For heat pumps installed in 2022, there is currently a smaller tax credit of 10% of the cost up to $500 or a specific amount from $50-$300 [25].

The High-Efficiency Electric Home Rebate Act, part of the Inflation Reduction Act, can also help offset the cost of purchasing a heat pump, depending on your income. Homeowners could be eligible for up to $1,750 for a heat-pump water heater and $8,000 for a heat pump if household income is less than 150% of their state's median income. If household income is less than 80% of their state's median household income, then homeowners qualify for the full rebate; meaning if both the heat pump and heat pump water heater are purchased, the homeowner could get $9,750 back. If income is between 80 to 150% of their state's median income, the homeowner would be eligible for 50% of the rebate, and they could receive up to $4,875 back [25].

One potential drawback to incentives is that once they are removed, the market may return to pre-incentive levels. The aftereffects could be that manufacturers would have to absorb the excess inventory as a result of scale-up during periods of higher demand and contractors may have to lay off workers. A better approach would be to create demand for high efficiency space and water heating equipment that is sustainable without the need for incentives.

5.2 Installation challenges

In an older home or a home with a natural gas for heating and water heating, installing a heat pump or heat pump water heater might require a panel upgrade. Several water heater manufacturers are responding to this issue by introducing 120v heat pump water heaters in the market. Presently, at least four manufacturers have brought products to the market that operate on 120v electrical power and others will soon follow. The 120v heat pump water heaters are available in both shared circuit and dedicated circuit models [26]. Field tests are ongoing in California that will provide useful information on the performance of 120v water heaters.

Tall, slim, natural gas water heaters typically found in manufactured homes where space is limited. The market for these units is limited. However, there is a project underway by a national laboratory to develop a 120v heat pump water heater with equivalent first hour rating that can be replace water heaters of this type.

More demonstrations of multi-split heat pump water heaters (i.e., one outdoor unit tied to multiple indoor storage tanks) are needed to prove the technology and facilitate their use to displace electric resistance and fossil-fired water heaters for medium-sized commercial and multi-family buildings. Replacing low-boy water heaters in multi-family buildings is a prime candidate for a demonstration of this type.

5.3 Consumer education

Lack of awareness is one of the key barriers to adoption of this clean energy technology. Programs to raise awareness and educate on a heat pump technology's availability, financial, health, safety, and comfort benefits would help consumers to make informed decisions when it comes time to replace their existing space conditioning or water heating equipment.

The National Resources Defense Council details three successful program designs used by Efficiency Vermont, Association for Energy Affordability in California, and Efficiency Maine [27]. To summarize, the features of currently-successful programs are:

- A midstream/upstream design with incentives that bring costs into parity or better
- Customer education through mass market and targeted outreach
- Strong engagement of supply chain participants
- Trade ally networks that provide a range of benefits to contractor and distributors

- Positive referrals by word of mouth
- Planned and emergency replacements can be installed within one day if panel upgrade isn't required

5.4 Reduce costs

Beyond incentives, several ways to reduce installation/product/operating costs for heat pumps and heat pump water heaters have been proposed. Among these are modular designs that enable homeowners to install the units, reducing installation costs with better tools for right-sizing and smart diagnostic tools to reduce installation time, increasing the efficiency of to reduce operating costs, and reducing the manufacturing cost.

Developing modular designs that enable homeowners to install the units themselves is a novel idea that has merit. Recently, two companies were awarded contracts to develop a window unit heat pump for multifamily housing that operates in cold climates, only requires 120v electrical power, and can be installed by the consumer [28]. One of the main benefits of modular designs is that they are portable and can be taken with the consumer when moving to another location. This is especially beneficial for tenants that live in apartments. It also helps to solve the split incentive issue by shifting the responsibility for the cost of the unit to the tenant rather that the building owner.

Improved tools for sizing heat pumps help to avoid over-sizing which could result in a smaller, lower cost unit being specified. Smart diagnostic tools, comprised of wirelessly connected digital measuring probes, enable real-time fault detection and diagnostics during installation and can reduce costs by reducing the time it takes to verify units are correctly installed.

Increasing the efficiency of the units to reduce operating costs seems to be a reasonable idea. However, this usually comes at a higher unit cost which is then passed down through the value chain, resulting in multiplying the difference in the manufacturer's cost of the unit by three times. The higher unit cost needs to be evaluated to determine if the reduction in operating cost over the life of the product justifies the higher cost.

Reducing manufacturing cost is challenging. However, research is presently being funded by the DOE to reduce costs through lower cost, more compact heat exchangers and compressors. More compact heat exchangers also have the added benefit of reducing the refrigerant charge to enable the possible use of lower GWP refrigerants that are flammable.

5.5 Work force development

Work force training on how to build and maintain equipment for low-carbon buildings is a promising candidate for public-private partnerships. Such training aligns the interests of the public (emissions reduction and safe and comfortable buildings), the building trades (quality installations with high customer satisfaction), and equipment suppliers (having their products installed correctly in homes and businesses).

While consumer awareness is important to drive demand, it is equally necessary to train installers to be able to support and fulfil the demand. There is a focus within the Advanced Water Heating Initiative to develop training and tools to support both contractors and designers. Several hours of training material and videos have been developed and more are planned to support the central systems [29].

Acknowledgements

The authors would like to thank the US Department of Energy Building Technologies Office for support of this work. In addition, they would like to thank Xudong Wang of AHRI, along with Jared Langevin and Aven Satre-Meloy, both of Lawrence Berkeley National Laboratory for information and statistical data in this work.

References

[1] John Bistline, Nikit Abhyankar, Geoffrey Blanford, Leon Clarke, Rachel Fakhry, Haewon McJeon, John Reilly, Christopher Roney, Tom Wilson, Mei Yuan, Alicia Zhao, Actions for reducing US emissions at least 50% by 2030, SCIENCE, 26 May 2022, Vol 376, Issue 6596, pp. 922-924.

[2] DOE Projects Monumental Emission Reductions from Inflation Reduction Act; https://www.energy.gov/articles/doe-projects-monumental-emissions-reduction-inflation-reduction-act

[3] U.S Energy Information Administration (EIA), Monthly Energy Review (April 2022).

[4] Aven Satre-Meloy, 2021. Data drawn from Scout modelling tool v0.7 (https://github.com/trynthink/scout/releases/tag/v0.7) and EIA Annual Energy Outlook 2021.

[5] Air-Conditioning, Heating, and Refrigeration Institute

[6] https://www.eia.gov/consumption/residential/data/2015/2015/hc/php/hc6.7.php

[7] https://heatpumpingtechnologies.org/annex46/wp-content/uploads/sites/53/2020/10/hpt-an46-02-task-1-general-report-hpt-annex-46.pdf

[8] https://www.prnewswire.com/news-releases/global-heat-pump-water-heater-air-source-geothermal-market-to-2026-integration-of-iot-with-heat-pump-water-heaters--positive-outlook-toward-use-of-geothermal-energy-301150085.html

[9] https://www.linkedin.com/posts/jacobcorvidae_infographics-climateaction-activity-6950489060142432256-p-9A/?trk=public_profile_like_view

[10] https://www.northeastgas.org/converting_gas.php

[11] New Efficiency: New York Analysis of Residential Heat pump Potential and Economics, Final Report, Report Number 18-44, New York State Energy Research and Development Authority, January 2019

[12] Nadel, S., Comparative Energy Use of Residential Gas Furnaces and Electric Heat Pumps, Report A160, American Council for an Energy Efficienct Economy, May 2016

[13] https://www.utilitydive.com/news/residential-electric-panels-represent-a-nearly-100b-roadblock-to-full-el/605829/

[14] https://www.statista.com/statistics/1231025/residential-heating-fuel-distribution-in-california/

[15] Bastian, H., and C. Cohn. 2022. *Ready to Upgrade: Barriers and Strategies for Residential Electrification.* Washington, DC: American Council for an Energy-Efficient Economy.

[16] *Cost Stack Estmates for Space Heating and Water Heating*, Guidehouse

[17] https://www.energystar.gov/products/water_heaters/high_efficiency_electric_storage_water_heaters/

[18] https://www.synapse-energy.com/sites/default/files/Decarbonization-Heating-CA-Buildings-17-092-1.pdf

[19] https://homeguides.sfgate.com/specs-gas-water-heater-closet-88425.html

[20] https://www.attainablehome.com/where-to-install-a-heat-pump-hot-water-heater-in-your-home/

[21] https://www.forbes.com/home-improvement/plumbing/heat-pump-water-heaters/

[22] https://www.contractormag.com/management/marketing/article/21255187/14-things-to-know-about-heat-pump-water-heaters

[23] https://www.bobvila.com/articles/heat-pump-water-heaters/

[24] *Energy Star Water Heater Market Profile*, US Department of Enegy, September 2010

[25] https://moneywise.com/taxes/heat-pump-tax-credit-rebate

[26] https://hotwatersolutionsnw.org/partners/news/120-volt-heat-pump-water-heater-product-overview

[27] https://newbuildings.org/wp-content/uploads/2021/05/BuildingDemandforUnitaryHPWH2021_final.pdf

[28] https://www.protocol.com/climate/gradient-nycha-heat-pumps-queens

[29] https://newbuildings.org/scaling-up-market-transformation-for-heat-pump-water-heaters/

14th IEA Heat Pump Conference
15-18 May 2023, Chicago, Illinois

Techno-economic comparative analysis of solar thermal collectors and high-temperature heat pumps with PV for industrial steam generation

Mohammad Ghasemi[a,c], Puneet Saini[a,b,c] Cordin Arpagaus[d], Frédéric Bless[d], Stefan Bertsch[d], Xingxing Zhang[a].

[a] Department of Energy and Construction Engineering, Dalarna University, Falun, S-79188, Sweden.
[b] Department of Civil and Industrial Engineering, Uppsala University, Uppsala, S-75236, Sweden.
[c] Absolicon solar collectors AB, Fiskaregatan 11, Härnösand, S-87133d, Sweden.
[d] Eastern Switzerland University of Applied Sciences, Institute for Energy Systems, Werdenbergstrasse 4, CH-9471 Buchs, Switzerland
*

Abstract

As industrial heat production is responsible for about 20% of total GHG emissions in Europe, shifting to sustainable sources is inevitable in achieving Paris Agreement goals. This paper focuses on two decarbonisation technologies for industrial process heat supply for multiple locations a) Electricity-driven high-temperature heat pumps powered with photovoltaic (HTHP+PV), as an advanced efficient technology in generating steam, and b) parabolic trough collectors (PTC), which produces heat economically with minimal carbon footprint. The aim of this paper is to evaluate the levelized cost of heat (LCOH) of these technologies to fulfil a comparative techno-economic analysis. A maximum PTC collector's solar fraction limit (SFlimit) is defined to indicate when the LCOH for these two technologies is equal. The evaluation is carried out through the annual energy yield using TRNSYS and MATLAB. The result shows that the design of a PTC system with optimal SF can reach cost parity with hybrid system of HTHP and PV for the locations with medium to high direct normal irradiation locations.

Keywords:
High-Temperature Heat Pump; Photovoltaic; Parabolic Trough Collector; Solar Fraction; Techno-Economic Analysis

1. Introduction

"Heat is half" of the global primary energy consumption [1]. The generation of heat from various fuel sources results in nearly 40% of the global CO2 emissions. Decarbonizing the heating supply is the "elephant in the room" and needs significant attention from policymakers to promote the right technological solution to facilitate the rapid replacement of gas, coal, and other fossil fuels.

Heat is consumed in buildings for space heating, domestic hot water, and industries to generate steam or hot water. The major focus regarding technical solutions for clean heating is often on electrification using electrical heaters or heat pumps (HPs). Residential heating demand can be decarbonized using commercial HPs, and their significance is further emphasized in Repower EU, which aims to deploy 60 million HPs by 2030, a projected 4-fold increase from current numbers [2].

It is important to note that industrial process heating demand constitutes 66 % of the EU's overall heating demand [3]. In addition, the concepts of positive energy district (PED) and climate-neutral city are promising nowadays, but they have not yet included industrial heating demand within their boundaries. With the ongoing challenges in gas supply, natural gas prices have increased exponentially in the past few years, thus creating an energy-tense situation in the EU [4]. This implies that a less price-volatile and reliable supply of fuels for industrial process heat should be prioritized. The process heat required in most industries is in the medium temperature range (i.e., 80 to 250 °C). Several technologies in the market can achieve this temperature with low carbon emissions, such as solar thermal (ST) collectors, high-temperature heat pumps (HTHP), and boilers utilizing green fuels such as waste biomass or biogas, or renewable electricity.

Industries typically use fossil fuel boilers to generate steam, which is used as a heat transfer fluid to carry out several processes. Retrofitting any new technology in an existing boiler system requires a detailed understanding of system boundary conditions. Economic feasibility is a crucial decisive criterion for industries to evaluate any technology. From market experience, it is realized that large multinationals can facilitate the capital expenditure (CAPEX) for an efficiency improvement process (such as the implementation of ST, HTHP) only if the payback is less than 5 years.

An indicative pre-feasibility assessment using economic key performance indicators (KPIs) can facilitate industries toward quick decision-making for a go/no-go decision concerning a detailed evaluation of any technology. Therefore, this paper is themed around doing a comparative techno-economic analysis for heat generation using typical boundary conditions encountered in industries. The focus is on two technologies to generate steam, i.e. (a) steam-generating HTHPs and (b) Parabolic trough collector (PTC), which is a type of concentrating ST collector. The sections provide a literature review and the current development status of using these technologies for industrial applications.

1.1. Hybridization of solar thermal with heat pumps

Terrestrial irradiation has daily and seasonal variations. For a typical solar PV system, the grid acts as a large battery that balances the production and demand with minimal waste of electricity. However, the solar heating systems are often retrofitted with individual/stand-alone boilers to continue the operation for non-sunny hours.

As most industries have constant heating demand throughout the day (and year). ST System design with a low SF allows the solar production to always be less than the user's heat demand, thus increasing the system's utilization. Therefore, SHIP systems are typically designed with low solar fraction and backup systems. However, if an ST is designed without thermal storage, the fraction of the overall heat demand met with solar collectors be limited.

To achieve high solar fraction, steam storage is often a limiting component restricting the cost feasibility of the system. Due to its very low density, steam storage is not economical. It is usually stored as sensible heat in solid media or liquid using oil or pressurized hot water. It is observed that for a given constant load profile, the economic feasibility of the solar thermal installation decreases after a threshold solar fraction due to the need for high thermal storage capacity. As the specific heat cost of a pressurized thermal storage is higher than that of a solar thermal collector, thus large tank volumes in the system result in a relatively high cost of heating. This situation puts a financial limit on the maximum solar fraction achievable.

As industries are looking for nearly 100% renewable heating systems, solar thermal has the opportunity to collaborate with other technological alternatives to compensate for the solar irradiation lack or fluctuation during the night and day to reach high renewable heating fractions using a concept involving several technologies, such as thermal storage and a heat pump driven by green electricity. The existing boiler use can be minimised if the system components are sized optimally.

Previous studies have shown that hybridizing the heat pump with solar thermal collector results in the lowest levelized cost of heating (LCOH) compared when these technologies are used individually [5]. Therefore, more research is needed to understand the techno-economic boundaries of solar thermal and HTHP in stand-alone and hybrid modes. This paper takes a step by looking into a comparative analysis of these two technologies. The current study is a base to investigate the combined hybrid systems in future applications.

2. Objectives

The central objective of this paper is a comparative analysis of both HTHP+PV and PTC systems for steam applications using industrial boundary conditions. Previous studies have performed a general feasibility analysis for solar thermal technologies or heat pumps. However, only a few have investigated comparing these technologies on with techno-economic boundaries. The most relevant work to the current paper is by Meyers et al. (2018), where the authors have developed a techno-economic comparison method using maximum turn-key solar investment as an indicator. This method can be used as a criterion to quickly compare and select between solar thermal and heat pumps based on boundary conditions. However, the study did not consider the effect of SF on LCOH. This variation is critical to consider while comparing technologies, especially with high-temperature solar thermal, due to the lack of steam storage technologies. The LCOH of the ST system increases exponentially after a threshold SF due to the diminishing added value of heat storage. Therefore, when comparing other technologies with ST, the SF is a critical criterion to define and is not considered in

previous studies. Meanwhile, the LCOH of hybrid system of HTHP+PV would decrease in most cases while it is also dependant on many other factors such as: GHI, electricity prices and CAPEX. The current paper has overcome the limitations by using comprehensive variables as a comparison basis for both HTHP+PV and ST.

3. Method

This study aims to assess the energy and economic performances of Industrial PTC and HTHP+PV in four European climates. Figure 1 shows the flow chart of the method used for analysis. First, the evaluation is carried out through annual energy simulations performed with dynamic simulation software. After this, a systematic approach is followed to provide the reader with the information needed to understand the results. The analysis is carried out for two load profiles with constant peak demand to capture a broad range of industrial load conditions. However, the results obtained are parametrised to direct normal irradiation (DNI) and global horizontal irradiation (GHI) which can be used to assess the performance for any given location.

In Step 1, simulations for HTHP are conducted using TRNSYS for given load profiles to calculate the COP and thermal output [6]. The outputs are based on a performance map obtained from an HTHP supplier for a broad range of operating conditions. For PV part the annual yield have been simulated based on the results from renewable ninja while in calculating LCOH of hybrid HTHP+PV, the balance of PV yield and power consumption of HP has been considered. It is also assumed that all excess production over consumption been wasted.

In Step 2, dynamic simulations for PTC collectors are done. The product chosen for this study is restricted to a PTC manufactured by a Swedish company named Absolicon solar collector AB[7]. The product is designed for industrial applications and fits this study well. Simulation of the PTC system is done in two sub-steps. The component performance is analysed using TRNSED, and the system performance is simulated using the developed model in OCTAVE. Storage sizing optimization obtains each location's SF vs. LCOH curve. The LCOH calculations for ST and HTHP+PV are done using Excel spreadsheet.

Finally, in Step 3, based on the results obtained, the LCOH of both technologies is compared to provide boundary conditions to identify the strong economic hold of each technology. An indicator SFlimit is introduced to distinguish the economic advantage and to generalize the results.

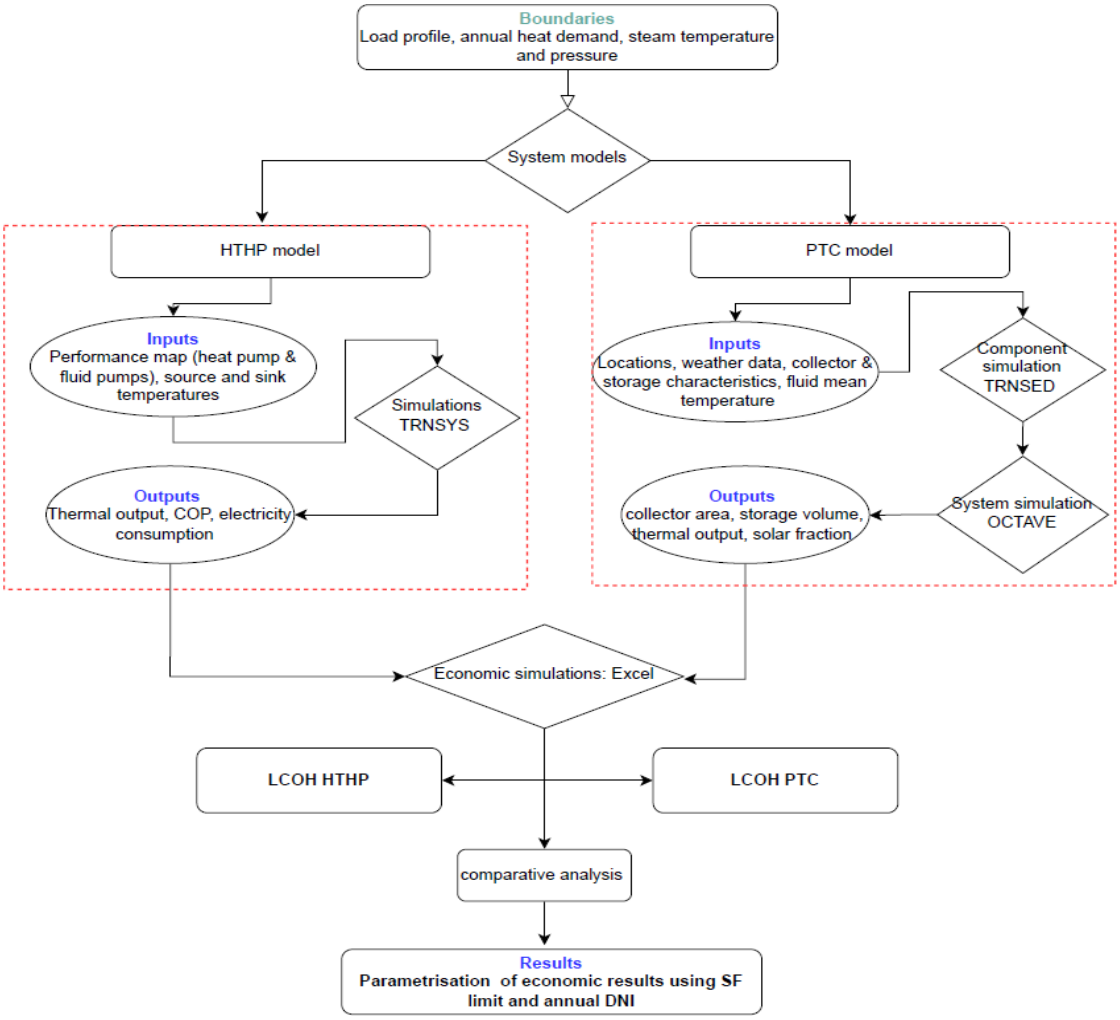


Figure 1 Flow chart for the method used for this study

4. System boundaries and Model

4.1. Load profiles and heating demand

The heat demand in the industries depends on the process characteristics and varies, which is difficult to capture by one study. However, the selection of load profiles to represent a significant share of industries is the focus of this paper. Two different load demand profiles are considered for the analysis. The peak heat demand is fixed at 500 kWth (steam flow of 0.8 tonnes per hour), typical of many process industries. As ST and HTHP are subjected to the same load constraints, the comparative results are not affected by the selection of peak load value. The steam demand is assumed at a constant temperature of 140 °C (saturation pressure 3.7 bara). The steam temperature range is commonly used in many food processing industries and fits well with temperature constraints for both medium-scale PTC and HTHP products. The two chosen load profiles are explained as follows:

- **Continuous demand**: Uniform demand throughout the year with 8760 annual operational hours, which results in annual heat demand of 4380 MWh/year. Such load profiles are prevalent in many large production factories, such as the pharmaceutical sector.
- **Daytime demand**: Uniform demand only during the day (10 hours per day starting 8:00 to 18:00 for whole week), resulting in an annual heat load of 1825 GWh/year. This load profile is typical for a small/medium production facility.

Weekly variation for considered load profiles is shown in Figure 2 . The presented week pattern is repeated for a whole year to obtain the annual heat demand.



Figure 2 Weekly variation of different load profiles considered for the analysis

4.2. HTHP integration

After industrial boundary conditions, the next step is to design an HTHP system and evaluate the techno-economic conditions. HTHP can be integrated at several points, for example, central steam generation for the whole plant or a specific process. This integration type will decide the inlet temperature of the fluid stream at the sink of HTHP to further convert into steam. Steam generated by the HTHP will be fed to the steam line. Therefore, the sink inlet fluid can be tapped feed-water or de-aerator of the existing boiler system. The feed-water pump used for the boiler can be utilized to obtain the required flow in the HTHP. If integrated with the boiler steam header, HTHP must generate steam at slight overpressure to ensure that steam from HTHP is preferred over boiler steam.

The HTHP is designed for peak heating capacity in this study. Therefore, it is considered the sole heat source for the energy system without any backup boiler. On the source side, the available wastewater stream is considered at the inlet, which transfers heat to the HP refrigerant and exits at a lower temperature depending on the temperature glide. On the sink side, the feed water stream enters the inlet and receives heat from HP to convert to steam, which is fed to the process line. A commercial HTHP (Kobelco model SGH 165) capable of generating steam at a maximum temperature of 165 °C is used to meet the steam requirement [8].

4.3. HTHP model

The HTHP used for this study can produce steam up to maximum temperature and pressure of 165 °C and 0.8 MPa-gauge, respectively. The applied refrigerant in this HP is a mixture of R134a and R245fa. The heat pump utilizes a semi-hermetic inverter twin screw compressor. The rated COP of the modelled HTHP is 2.5, specified at source and sink temperatures of 70 °C and 165 °C, respectively. A performance map based on data from the commercial HTHP [8] is used to calculate the electricity consumption. The performance map consists of the COP of the HTHP for various temperature lifts. The temperature lift represents the difference between the fluid temperature at the heat source inlet and the heat sink outlet. The heat pump has a variable speed capacity to operate at the part load conditions. The electrical consumption derived from the annual simulations is then used to calculate the LCOH.

The design temperatures for the HP model are shown in Figure 3. The source for the HP evaporator is considered a wastewater stream with a fixed temperature of 40 °C, available throughout the year. A temperature glide of 6 K is considered on the evaporator. The resulting temperature lift of the HTHP is 100 °C, corresponding to steam temperature of 140 °C. The feed-water temperature entering the HTHP arrives at 110 °C, resulting in a 30 K temperature difference on the heat sink side. The flow rate in the source and sink are varied to obtain the designed temperature glide and thermal capacity, respectively.

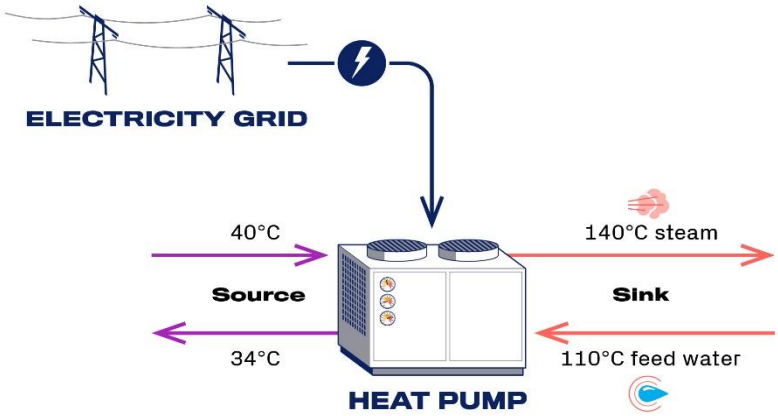


Figure 3 Various fluid stream temperatures of the HTHP system considered for this study

Other than the electricity consumption of the HTHP, there are water pumps on the source and sink side, which also consume electricity and is important in LCOH calculations. The pumps are sized to provide the desired flow rate in the network. Pressure drop calculations are done to estimate the total head in the network using Serghide's method [9]. The pump is designed for the total pressure drop of the network is 1 bar, assuming 20% safety factor while accounting for bends and joints, etc. Based on the flow and pressure drop, a commercial pump is selected from the manufacturer catalogue. The products are used to derive the pump curves (flow vs. head and efficiency vs. head) to simulate the working points of a given scenario and thus used for electricity consumption to calculate LCOH.

4.4. Economic inputs for HTHP

For the heat pump LCOH, it is necessary to include various costs. The analysis is done for three different capital expenditures (CAPEX) of 500, 1'000, and 1'500 Euro/kWth values derived from data based on implemented HTHP case studies [10]. The operational costs for HTHP consider the electricity to run the heat pump compressor and fluid pumps. The O&M costs for HTHP are usually higher than those for boilers and are set to 5% of the CAPEX value with the system degradation rate equal to 0.5%. The LCOH of both HTHP and PTC systems are compared for a time horizon of 15 years. The period is chosen to reflect the suitable timeline various multinational companies consider for energy-related investments. Three different electricity prices are chosen for analysis considering the range of industrial electricity tariffs in the EU.

For sensitivity analysis of LCOH, a total of 6 cases are analysed, accounting for three different cases with HP CAPEX and electricity prices for both load profiles (i.e., CAPEX, electricity price, and load profiles). The values of these variables are shown in

Table *1*.

Table 1 Different scenarios for the variables used in HTHP LCOH calculations

Description	Abbreviation	scenario 1	scenario 2	scenario 3
Load Profile [h/year]	LPR	8’760	8’760	8’760
HP CAPEX [Euro/kW_{th}]	CAP	500	1’000	1’500
Electricity Price [Euro/MWh]	ELP	70	100	150
Description	Abbreviation	scenario 4	scenario 5	scenario 6
Load Profile [h/year]	LPR	3’650	3’650	3’650
HP CAPEX [Euro/kW_{th}]	CAP	500	1’000	1’500
Electricity Price [Euro/MWh]	ELP	70	100	150

4.5. ST simulations-*PTC product description*

The ST product considered for analysis is a PTC collector manufactured by the Swedish company Absolicon solar AB. The product T160 is a concentrating parabolic trough collector that focuses direct solar irradiance onto an absorber tube that runs along the focal line of the concentrator and contains a working fluid that gets heated when solar radiation is concentrated on it. The collector works on single-axis tracking using the astronomical watch, which tracks the solar collectors, so they always face the sun. The product can generate steam and hot water from 60 °C to 160 °C, and is therefore suitable for many industrial sectors (e.g., dairy, brewery, chemical, etc.). The collector can be categorized as a small PTC type and is certified by solar Keymark. The optical efficiency of the collector is 76.6 % based on aperture area. The key technical specifications of the collector are shown in Table 2.

The main components of a collector consist of:

- Reflector, which reflects the incoming radiation onto the receiver.
- The receiver tube absorbs reflected radiation and converts it into heat; this heat is then dissipated by the agent fluid that is pumped through the receiver tube
- The protective glass avoids heat losses and protects the collector from dust, snow etc.

Table 2 Key technical specifications of T160 PTC collector

Item	*Description*
Collector type	Glass-covered PTC with one-axis tracking
Recommended heat transfer fluid	Water. Propylene Glycol (max 40%)
Volume of heat transfer fluid in receiver tube[Litre]	2.2
Operational temperature [°C]	60 to 160
Stagnation temperature [°C]	460
Maximum operating pressure[bar]	16
Receiver	Stainless steel, optically selective coating
Glass	4mm hardened glass, anti-reflective coating
Reflector	Polymer-embedded silver on steel sheet
Weight [kg]	148

4.6. Modelling PTC system

A dynamic simulation of the collector performance was carried out for a statistically normal year based on climate data from Meteonorm using time step of 15 minutes. Simulations are based on the Solar Keymark ISO 9806 collector parameters of the Absolicon T160.

The simulation approach for PTC is based on 2 steps. In the first step, the collector is modelled without interacting with the heating load. This can be considered as if the collector operates under infinite load, and thus all the heat generated by the collector is fully utilized. The simulations are done using TRNSED, which is an add-on to TRNSYS. The collector performance parameters based on the aperture area used in the TRNSED are shown in Table 3.

Table 3 Input Performance characteristics of T160 collector used for model [11]

Parameter	Value
Optical efficiency [%]	76.6
a_1 [W/m^{2}K]	0.368
a_2 [W/m^{2}K^2]	0.00322
K_d [-]	0.120
β, tilt [°]	Single-axis tracking E-W
γ, azimuth [°]*	0

The output of the component analysis results in an hourly profile of collector output with other variables. The output is used in the system model for defined industrial boundaries. System simulations are done using the OCTAVE tool, on an hourly time-step basis for a year. The tool simulates the collector interaction with the load. Several iterations are performed to obtain the collector area and storage volume for a range of solar fractions for specific loss factors. The loss factor represents the maximum quantity of heat allowed to spill from the collector at any time step and is fixed at 20 % of the collector production. The loss factor is chosen based on previous experience. Based on the simulations, a curve representing the collector area and storage volume needed for a range of solar fractions is obtained. The range of SF is restricted from 1 % to 91 %. It is possible to run simulations for SF approaching 100 %. However, this is avoided so to reduce the computational effort.

Moreover, it is uncommon to design a solar thermal system for such high SF due to the excessive tank volume required, which negates the installation's economic gains. The power consumption of the PTC system due to tracking and fluid pumps is also derived from simulation results. The collector area and tank volumes required for various solar fractions are then used to calculate the LCOH of the system, as explained in the next section.

4.7. Economic boundaries & geographical inputs

The data for PTC economic analysis includes the capital and O&M cost. The economic input values are based on data collected from the PTC manufacturer as shown in Table 4.

Table 4 Assumptions regarded in PTC T160 simulations

Item	Symbol	Value	Unit	Remarks
Capital expenditure	CAPEX	350	Euro/m^2	Represents the installed cost
O&M cost	$EX_{O\&M}$	0.1	%	of CAPEX
Solar collector lifetime		25	Years	
LCOH evaluation period		15	Years	
System degradation rate	SD	0.1	%	

5. Key performance indicators

Levelized cost of heating: LCOH is a comparative indicator representing the cost of heating from any system considering capital, operation, and maintenance costs during the system's lifetime [12]. If the LCOH of a new solution is lower than the LCOH of the existing system, it implies that the new system implementation will have positive returns. It is a suitable performance indicator to compare various heat generation technologies. The LCOH is calculated based on Equation 1.

$$\mathrm{LCOH} = \frac{\mathrm{CAPEX} + \mathrm{Price_{el}} \cdot \sum_{n=1}^{N} \left(\frac{W_{Sys}}{(1+\mathrm{DR})^n} \right) + \sum_{n=1}^{N} \left(\frac{EX_{O\&M}}{(1+\mathrm{DR})^n} \right)}{\sum_{n=1}^{N} \left(\frac{Q_{Yield}(1-\mathrm{SD})^n}{(1+\mathrm{DR})^n} \right)} \qquad (1)$$

Where:
$CAPEX$ = Capital cost of technology used (including installation and commissioning) (€]
W_{Sys}= Annual power consumption of technologies (Electricity for fluid pumps, heat pump, and collector tracking system) (kWh)
$EX_{O\&M}$ = operation and maintenance cost per year (€/year]
$Price_{el}$ = Current unit price of grid electricity (€/MWh)
DR=Discount rate (%)

SD=degradation rate (%] of each technology
N= Project lifetime (years)
Q_{Yield} =Heat yield of the system (kWh/year)

SF_{limit}: To compare the cost of heating between HTHP+PV and ST based on location-specific characteristics such as annual DNI, a new comparative indicator SF_{limit} is defined for the analysis. The SF_{limit} refers to the point on the SF-LCOH curve of a PTC when the LCOH of HTHP for the analyzed condition becomes equal to the LCOH of ST. Therefore, if a PTC system is designed for an SF which exceeds the SF_{limit}, then the LCOH of PTC at the designed SF will be higher than HTHP. In other words, below the SF limit value, the LCOH of the ST system will always remain below the HTHP+PV LCOH. Therefore, a higher value of SF_{limit} would represent better cost feasibility and favorable conditions for PTC installation.

6. Results

6.1. HTHP simulation results

Table 5 shows the results for LCOH calculations for HTHP for 6 simulated scenarios representing load profiles, investment cost, and electricity price variation. For any specific load profile, the CAP1-ELP1 represents the LCOH of HTHP assuming CAPEX 1 (500 €/kWth), and Electricity prices 1 (70 €/MW), as shown previously in

Table *1*.

The results show that the LCOH of HTHP varies from 45-130 €/MWh for the simulated scenarios. The minimum LCOH (45 €/MWh) is obtained for the lowest CAPEX and ELP values in LPR1, when the HTHP is utilised throughout the year. For the same CAP and ELP combination, LCOH increases moving from LPR1 to LPR2 due to decreasing operational hours.

Table 5 HTHP LCOH [€/MWh] for simulated scenarios

Case	HP CAPEX EUR/kW	Electricity price EUR/MW	LCOH of HTHP (Euros/MWh)	
			Load profile 1 LPR.1 8'760 h/a	Load profile 2 LPR.2 3'650 h/a
CAP.1-ELP.1	500	70	45	58
CAP.2-ELP.2	1'000	100	66	89
CAP.3-ELP.3	1'500	150	98	130

6.2. PTC simulation results

The results from PTC simulations suggest that LCOH has a higher variation than HTHP. The reason can be attributed to a wide range of solar irradiation variations across simulated European locations. Furthermore, the LCOH also varies with solar fraction for any specific location.

The range of LCOH obtained from PTC varies is huge depending on the solar fraction. The minimum LCOH obtained is obtained for high DNI regions and at a lower solar fraction. A decreasing trend of LCOH with increasing DNI is due to high collector output. Furthermore, for the same DNI, the LCOH increases with an increase in solar fraction due to lower utilization of heat.

It is also important to consider that LCOH depends not only on the absolute annual DNI value but also on the temporal variation. The high temporal variation makes it difficult to achieve large SF due to the large tank volume needed, thus increasing the LCOH.

Then while comparing the LCOH of PTC or any ST product with other technologies, it is important to specify the SF at which the comparison is made.

The simulation results are used to generate SF-LCOH curve for a location, the LCOH will have a minimum constant value up to a certain SF, till all the collector heat is utilized by the system resulting in no excess heat and no storage tank. However, after a threshold solar fraction, the thermal production of the collector exceeds the load demand, bringing the need for thermal storage. The introduction of thermal storage adds additional

cost to the system, increasing the LCOH. After this point on the curve, the LCOH increases exponentially as the thermal storage size required is very high with an increase in SF. Increasing collector areas/tank volumes would diminish the returns for utilized heat, increasing the LCOH. This curve is obtained for all the simulated locations and for two different load profiles. It is then compared with HTHP's LCOH to obtain the corresponding SF limit.

Figure 4[a] illustrates the LCOH comparison for both technologies for the Spain-Seville location. The curves shows the variation of PTC LCOH with SF for two different load profiles. For sake of comparison, the two horizontal lines in the graphs represent the minimum and maximum LCOH of HTHP for all simulated cases. Due to the high DNI in Spain, the minimum LCOH of PTC is always lower than HTHP for all simulated cases. It has been shown that for such a location for LPR 1, even with low CAPEX and OPEX of HTHP (bottom horizontal line), the SFlimit is at 37 %. SFlimit increases up to 65 % if the highest value of CAPEX and OPEX for HTHP are considered (top horizontal line).

The minimum LCOH of HTHP in LPR2 is higher than in LPR1. The reason is a lower number of operational hours while having the same CAPEX of HTHP, which results in high LCOH.

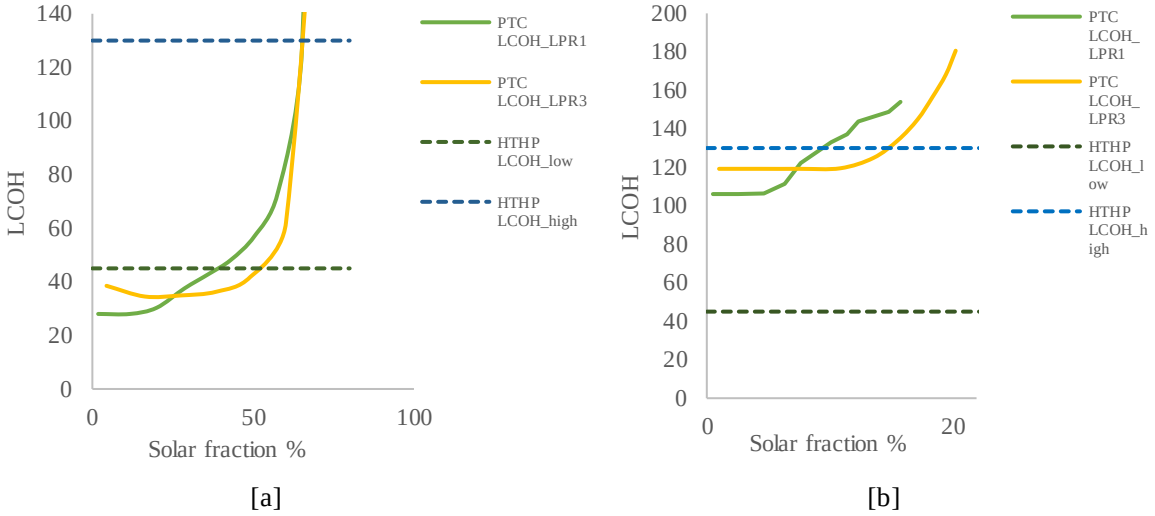


Figure 4 LCOH comparison for HTHP (horizontal lines) and PTC (capex 350 €/m2) for Spain-Seville [a] (DNI: 1848 [kWh/(m2·year]) & Czech- Prague[b] (DNI: 708 [kWh/(m2·year)])

Comparative results are shown for a low DNI location (Czech-Prague) in Figure 4[b]. As can be seen, the PTC LCOH for Prague in LPR.1 are even higher than the worst case of HTHP LCOH (CAP3-ELP3). This implies that for such a case and under the analysed boundaries, HTHP would be more cost-effective option for heat generation than PTC. However, there would be a change by considering LPR.2, where PTC has lower LCOH up to SF of 15 % compared to CAP3-ELP3 scenarios. The SFlimit for this case is at 15.6 %.

6.3. Comparative analysis using SF_{limit}

Based on the analysis in PTC simulation results section, the values of SFlimit for simulated cases is shown in Table 6. The locations where no value of SFlimit is defined (such as in UK-London) indicate that LCOH of ST is always higher than LCOH of HTHP in all simulated cases. These countries often have very low annual DNI, resulting in lower economic feasibility for PTC.

Table 6 Summary of SF limit (%) of ABSOLICON PTC (T-160) and HTHP with and without PV for LPR.1 and LPR.2. Empty values indicate that LCOH of ST is higher than LCOH of HTHP or HTHP+PV

LPR.1

Location	Description	DNI[1]/GHI[2]	ABSOLICON LCOH	CAP1-ELP1	CAP2-ELP2	CAP3-ELP3
			HTHP LCOH without PV	45	63	98
	PV-500 kW_P	1128[2]	LCOH HTHP+PV	43	62	88
Sweden-Borlange	SF without PV	1075[1]	74.1			14
	SFWith PV	1075[1]	74.1			11
	PV-400 kW_P	1399[2]	LCOH HTHP+PV	42	60	85
UK-London	SF without PV	642[1]	122.8			
	SF With PV	642[1]	122.8			
	PV-500 kW_P	1507[2]	LCOH HTHP+PV	42	59	84
France-Paris	SF without PV	790[1]	86.9			
	SF With PV	790[1]	86.9			
	PV-500 kW_P	2124[2]	LCOH HTHP+PV	39	55	79
Spain-Seville	SF without PV	1848[1]	28	39	55	64
	SF With PV	1848[1]	28	30	49	59

LPR.2

Location	Description	DNI[1]/GHI[2]	ABSOLICON LCOH	CAP1-ELP1	CAP2-ELP2	CAP3-ELP3
			HTHP LCOH without PV	58	89	130
	PV-500 kW_P	1027[2]	LCOH HTHP+PV	57	82	111
Sweden-Borlange	SF without PV	1075[1]	74.1		17	29
	SF With PV	1075[1]	74.1			26
	PV-400 kW_P	1356[2]	LCOH HTHP+PV	53	75	102
UK-London	SF without PV	642[1]	122.8			18
	SF With PV	642[1]	122.8			
	PV-500 kW_P	1468[2]	LCOH HTHP+PV	52	74	100
France-Paris	SF without PV	790[1]	86.9			21
	SF With PV	790[1]	86.9			
	PV-500 kW_P	2103[2]	LCOH HTHP+PV	45	64	85
Spain-Seville	SF without PV	1848[1]	28	60	62	70
	SF With PV	1848[1]	28	57	60	63

7. Discussions

The cost aspects of any technology for low-carbon process heat assessment are extremely case-sensitive. The developed method serves as a valuable guide to quickly determine a preferred lower carbon heat solution just by looking at the annual DNI of any location and finding the optimal SF limit for that location. The analysis is comprehensive but restricted by the absolute values of the variables assumed. Several other aspects can change the techno-economic results in the near future. For example, the carbon tax can play a significant role in reducing the cost of heating. ST technologies consume significantly low electricity compared to HTHP technologies. If the CO2 emission cost is accounted for, the results will favour ST technologies and HTHP

with PV. Also, as the electricity grid will have more renewable penetrations, the HTHP will keep getting attractive from a cost and emission perspective.

The land usage for HTHP is much smaller compared to solar thermal collectors. This is a big advantage for HTHP, especially if the industries have limited ground or roof space for solar collector installations. HTHP, on the other hand, needs more developments for low-GWP refrigerants.

A way forward could be to use both technologies in conjunction where ST is designed up to the SFlimit, and HTHP is used to meet the rest of the load. A hybrid system of optimized solar thermal collectors with a small tank volume and HTHP can produce process heat at lower LCOH compared to the technologies used individually. Technology combination is imperative to reach clean and economical industrial heat ambitions. Such a hybrid system could have significant potential to decrease the cost and emission and will be of focus for future studies and publications. For new energy system planning, a bivalent system where only PTC and HTHP are used together, there is a possibility to reach 100% renewable heating fraction if the electricity for HTHP is renewable. Such system can run without any need for boiler backups. In case of retrofitting with existing boiler system, ST can be used as a starting point to cover part heat demand. Then HTHP can be introduced in the system designed for peak heat load demand to phase off the boiler completely.

In addition, to accelerate the decarbonisation aims, the EU has set an ambition to build 100 positive energy districts and smart cities (climate-neutral cities) by the year 2025. However, the focus of current PEDs is mainly on residential and commercial buildings. The PED boundary unfortunately does not include industrial energy system at the moment. Nevertheless, there is a strong need to factuality the industrial decarbonisation and include industrial energy system in the PED development since it belongs to whole city energy infrastructure. If a city wants to achieve the climate-neutral goal, it must consider industrial segment. On the other hand, industry segment fits high synergies if it is considered in PED concept. For instance, the low temperature waste heat can be recovered from industries to meet space heating and DHW demand through 5th generation district heating network. In return, when PED produces extra energy, it can be exported to industries through above-addressed district heating via heat pumps to upgrade heat to the required temperature level. Therefore, to address the technologies for industrial heat is critical to fulfil the PED and climate-neutral city goals, such as HTHP and PTC, which can be the key technologies for a fully decarbonised urban energy system.

8. Conclusions

This paper compares the techno-economic aspects of HTHPs and PTC collectors for various industrial boundary conditions. The focus is on steam generation at 140 °C (3.6 bara), commonly used in many process heating industries. The characteristics of commercial HTHP and PTC products are used as input in the simulation model to obtain energetic results. For LCOH calculation, an excel spreadsheet is used. Finally, results are generalized using SFlimit as an indicator to distinguish the economic advantage of each technology.

The major conclusions of the study are as follows:

- The LCOH of HTHP for the analysed boundary conditions ranges from 45 to 130 €/MWh. There is a clear trend of increasing LCOH with higher electricity prices and specific CAPEX costs. As the HTHP was sized for a peak load capacity of 500 kW, the total CAPEX is the same for both load profiles. However, the LCOH can be lowered by operating the HTHP for more hours. Therefore, the LCOH in scenario LPR1 is always lower than in LPR2 for the same cost of electricity prices.
- The least obtained LCOH comes from the PTC collector for high DNI regions and low solar fractions. If the meteorological conditions are suitable, PTC is a cheaper alternative to generate steam compared to HTHP. The LCOH range obtained from PTC simulations is 28 to 160 €/MWh up to 50% SF. Lower values of LCOH can be observed for high DNI regions and vice versa. High DNI regions are, for example, Spain, Portugal, and Southern Italy. Furthermore, LCOH has an increasing variation with SF. The SF-LCOH curve is not dependent on the absolute DNI but on the distribution of the DNI on a temporal basis, which decides the storage volume needed to increase the SF.
- As the LCOH increases with SF, a specific SF_{limit} exists when producing heat from ST gets more expensive compared to HTHP. This limit is higher for high DNI regions and lower for low DNI regions. The limit increases with higher ELP and CAP for the HP. In low CAPEX and electricity cost situations for an HTHP, a threshold DNI of 764 kWh/m^2 is needed for PTC to produce heat at a cheaper rate. In the high CAPEX scenario, this threshold DNI changes to 1'200 kWh/m^2, and the average SF limit varies from 25% to 55%. In high DNI locations (1'500 to 2'000 kWh/m^2), 15% to 30% for medium DNI (1'001 to 1'499 kWh/m^2), and 0% to 10% for low DNI locations (0 to 999 kWh/m^2).

- The decrease in PTC CAPEX results in lower LCOH for any given solar fraction, eventually leading to high SF_{limit}. When the CAPEX of PTC is lower and load profiles are favorable, a solar fraction limit of 32 % is obtained, even for the lowest DNI location. This situation indicates that cost decrease can result in PTC as the most economic heating source for low DNI locations.
- The industry segment fits high synergies if considered in the PED concept, while both HTHP and PTC can be the key technologies for a fully decarbonized urban energy system.

Author Statement
Puneet Saini: Idea formulation, simulations, method, analysis, writing.
Mohammad Ghasemi: Simulations, writing, reviewing, editing.
Cordin Arpagaus: Project administration, supervision, writing, reviewing.
Fredric Bless: Project administration, supervision, writing, reviewing.
Stefan Bertsch: Reviewing
Xingxing Zhang: Supervision, writing, reviewing

Declaration of competing interest
The authors declare no competing financial interests or personal relationships that could have appeared to influence the work reported in this paper.

Acknowledgement
The authors would like to appreciate Absolicon solar collectors AB for their support to carry this study. The Swiss authors gratefully acknowledge the financial support of the Swiss Federal Office of Energy SFOE as part of the SWEET (SWiss Energy research for the Energy Transition) project DeCarbCH (www.sweet-decarb.ch) and the projects Annex 58 HTHP-CH (Contract number SI/502336-01) and IntSGHP (Contract number SI/502292).

References

[1] "Heating – Analysis," *IEA*. https://www.iea.org/reports/heating (accessed Apr. 11, 2023).
[2] "Article - EHPA." https://www.ehpa.org/about/news/article/repowereu-heat-pump-strategy-required-to-help-sector-deliver/ (accessed Aug. 14, 2022).
[3] "Heating and cooling." https://energy.ec.europa.eu/topics/energy-efficiency/heating-and-cooling_en (accessed Aug. 14, 2022).
[4] L. Cebotari, "EU-Russia energy relations: problems and perspectives," *Proceedings of the International Conference on Business Excellence*, vol. 16, no. 1, pp. 1001–1014, Aug. 2022, doi: 10.2478/PICBE-2022-0093.
[5] Saini, P., Ghasemi, M., Arpagaus, C., Bless, F., Bertsch, S., & Zhang, X. (2023). Techno-economic comparative analysis of solar thermal collectors and high-temperature heat pumps for industrial steam generation. Energy Conversion and Management, 277. Published. https://doi.org/10.1016/j.enconman.2022.116623
[5] S. Meyers, B. Schmitt, and K. Vajen, "The future of low carbon industrial process heat: A comparison between solar thermal and heat pumps," *Solar Energy*, vol. 173, pp. 893–904, Oct. 2018, doi: 10.1016/j.solener.2018.08.011.
[6] "TRNSYS : Transient System Simulation Tool." https://www.trnsys.com/ (accessed Aug. 14, 2022).
[7] "Absolicon - Production Line for T160 concentrating solar collector," *Absolicon*. https://www.absolicon.com/ (accessed Mar. 14, 2023).
[8] "Standard Compressors/ KOBELCO COMPRESSORS CORPORATION | KOBELCO Kobe Steel,. Ltd." https://www.kobelco.co.jp/english/products/standard_compressors/ (accessed Aug. 14, 2022).
[9] M. Asker, O. Emrah Turgut, and M. Turhan Coban, "A review of non iterative friction factor correlations for the calculation of pressure drop in pipes," *Bitlis Eren Univ J Sci & Technol*, vol. 4, no. 1, pp. 1–8, 2014.
[10] "Home - Annex 58." https://heatpumpingtechnologies.org/annex58/ (accessed Aug. 14, 2022).
[11] "Absolicon - Production Line for T160 concentrating solar collector." https://www.absolicon.com/ (accessed Aug. 14, 2022).
[12] K. Branker, M. J. M. Pathak, and J. M. Pearce, "A review of solar photovoltaic levelized cost of electricity," *Renewable and Sustainable Energy Reviews*, vol. 15, no. 9, pp. 4470–4482, Dec. 2011, doi: 10.1016/j.rser.2011.07.104.

14th IEA Heat Pump Conference
15-18 May 2023, Chicago, Illinois

Upscaling and case study design: Influence on the environmental impact assessment of high-temperature heat pumps using LCA

Lukas Zeilerbauer[a,b*], Stefan Puschnigg[a,c], Johannes Lindorfer[a], Felix Hubmann[d], Bernd Windholz[d]

[a]Energieinstitut an der Johannes Kepler Universität Linz, Altenberger Straße 69, 4040 Linz, Austria
[b] Johannes-Kepler-University Linz, Institute for Chemical Technology of Organic Materials, Altenberger Straße 69, 4040 Linz, Austria
[c] Montanuniversität Leoben, Chair of Energy Network Technology, Franz-Josef-Straße 18, 8700 Leoben, Austria
[d] AIT Austrian Institute of Technology GmbH, Giefinggasse 2, 1210 Vienna, Austria

Abstract

Existing high-temperature heat pumps were investigated by means of life cycle assessment with thermal outputs of 0.19, 0.66, 1.2 and 10 MW. Scale up was performed linearly, due to a better fit than other methods presented in the literature. It was shown that the electricity consumed during the usage phase has a greater impact in the majority of damage categories rather than manufacturing or the production/leakage of the working fluid. The European grid mix was compared to the French and Spanish one, showing that a low-carbon power source is vital. Finally, a benchmark with other common steam sources was done in terms of global warming potential, showing the substitution of fossil-based steam sources is the biggest lever when implementing heat pumps for better sustainability.

© HPC2023.
Selection and/or peer-review under the responsibility of the organizers of the 14th IEA Heat Pump Conference 2023.

Keywords: High temperature heat pumps, scale-up, Life Cycle Assessment, LCA, Environmental assessment

1. Introduction

When it comes to assessing sustainability of technologies and their development, life cycle assessment (LCA) is an apt tool to assess environmental impacts on a multidimensional level. Hence, heat pumps (HPs) are no exception and have been the target of several studies. [1] – [4] However, most studies only target residential HPs and/or low temperature systems with larger, high-temperature systems being more of an exception. When it comes to the roll-out of "green" technologies, investors and policy makers face a "hen-or-egg" type of question. Subsequently, potential investors want reliable information concerning economic & environmental implications, this data is hard to generate as hands-on cases are hardly found. While there are already profound approaches for other technologies such as for power-to-gas [5], [6], biorefineries [7], [8], or chemical conversions [9], High-Temperature Heat Pumps (HTHPs) are lacking in this area.

While it is common in LCA-modelling to omit the material needed for the plant as impacts are mostly of a minor nature, this notion will be put to the test in this study, as modelling of a material balance will be investigated. Caduff et al. [10] developed a scale-up framework of domestic HPs based upon exponential power laws. The applicability of this framework will be tested for commercial HPs, with its data being based upon results of IEA Task Annex 58. [11] Data gaps were filled by literature research and discussions with experts on the field. The final results were objected to an LCA with the functional unit to produce 1 GJ of steam.

* Corresponding author. Tel.: +43 732 2468 5646;
E-mail address: Zeilerbauer@energieinstitut-linz.at

2. Materials and methods

2.1 LCA

LCA has been described numerous times in literature, thus for an introductory reading, the authors would like to refer the reader to the following standard works. [12]–[14]. Yet, LCA will be performed following ISO 14044, with its 4 phases being:

- Definition of Goal and Scope
- Life Cycle Inventory (LCI) analysis
- Life Cycle Impact Assessment (LCIA)
- Interpretation and Discussion

2.1.1 Definition of Goal and Scope

The goal of the LCA case study in this paper is the modelling of a HTHP, located in Europe producing steam from low-temperature heat sources, mainly water. The four cases have an output of thermal energy of 0.19, 0.66, 1.2 and 10 MW. The cases are exemplarily conducted for France, Spain and the EU-28, which means the respective electrical grid is considered. The system boundary is cradle-to-gate, as no assumptions about the steam usage are made, with the functional unit of 1 GJ of steam produced. The system entails the production of the machinery and the usage phase, which is assumed to be 15-30 years. The machines are all assumed to operate 8000 hours per year and the End-Of-Life operations were not modelled in this study.

2.1.2 Life Cycle Inventory (LCI) analysis

Life cycle inventory is mostly based upon the Ecoinvent process “Heat Pump Production, brine-water, 10kW”. [15] Other inputs came from manufacturers of the featured HPs. The full inventory is presented in Table 4.

2.1.3. Life Cycle Impact Assessment (LCIA)

The damage impacts will be assessed by the CML-method [13], utilizing the standardized midpoint categories shown in Table 1.

Table 1: Midpoint categories used in this study as introduced by Guinée et al. [13]

Impact categories within the CML method	Unit
Global warming potential (GWP 100 years)	[kg CO_2-Equiv.)
Ozone layer depletion potential (ODP, steady state)	[kg R11-Equiv.]
Acidification potential (AP)	[kg SO_2-Equiv.]
Eutrophication potential (EP)	[kg Phosphate-Equiv.]
Photochemical ozone creation potential (POCP)	[kg Ethene-Equiv.]
Human toxicity potential (HTTP inf.), Terrestic ecotoxity potential (TETP inf.)	[kg DCB-Equiv.]
Freshwater aquatic ecotoxity potential (FAETP inf.), Marine aquatic ecotoxity potential (MAETP inf.)	[kg DCB-Equiv.]
Abiotic depletion (ADP)	[kg Sb-Equiv.]

2.2. Modelling of scaling laws

In the past, researchers found that the cost and material balance of scaling up process equipment does not show linear behavior, as in fact they follow a power law, as presented in Equation 1. With C being the cost/material need of interest, a being the normalization factor, X the capacity/scale of interest and b the scaling factor. If this factor is 1 the relationship is linear, however empirical data did show a value of 0.6 being best suited for many different applications.

Equation 1: The power law found for scale up of process equipment.

$$C = a * X^b \quad (1)$$

As mentioned in the introduction, Caduff et al., [10] applied this approach to HPs and biomass boilers. They tried to correlate HP's mass, working fluid use and coefficient of performance (COP) to the respective masses, by transforming Equation 1 logarithmically, as shown in Equation 2. In this case i is the property of interest, mass, COP, or working fluid, while a & b are scaling factors.

Equation 2: Equation 1 transformed logarithmically to allow for linear regression.

$$\log(i) = \log a_i + b_i \log(X) \quad (2)$$

3. Results and Discussion

3.1.1. Scale-Up of the HP

As in the original manuscript by Caduff et al., [10] the regressions for COP and the mass of working fluids had quite bad correlation, those were omitted for further analysis. For the material balance, the regression slope for the water/water HP was chosen. Two other additional slopes were drawn, based upon the standard-deviation in the 95 % confidence interval. Thus, the following slopes were plotted, as shown in Table 2.

Table 2: Linear regressions found by Caduff et al., [10] and the case studies on our study.

Slope Name	log (a_i)	b_i	X (P / MW)
Low	0.73	0.48	0.19; 0.66; 1.2; 10
Mean	0.75	0.55	0.19; 0.66; 1.2; 10
High	0.78	0.64	0.19; 0.66; 1.2; 10

As shown in the LCI (Table 4), the mass of a 10 kW HP was determined to be 128 kg of materials. Thus, a linear scale up was plotted as reference too. Table 3 shows the heat pumps of Annex 58 and their consecutive masses.

Table 3: HP case studies used to compare real-life scaling data; all data taken from IEA Annex 58.

Machine Name / Manufacturer	Thermal Power/ MW	$Mass/\ kg$
Steam Generation HP / Fuji Electric	0.03	850
CO_2 Air Heater Heat Pump / Eco Sirocco Mayekawa Mf	0.1	1750
ThermBooster / SPH Sustainable Process Heat GmbH	0.3	4000
Steam Grow Heat Pump / SGH120 / KOBELCO Compressors	0.37	4250
SkaleUP / Skala Fabrikk AS	0.45*	4200
130°C Hot Water Supply Heat Pump ETW-S /Mitsubishi Heavy Industries Thermal System	0.627	6500
Hydrocarbon Heat Pump / HS-compressor / Mayekawa Europe NV	0.75	13750
Micro Steam Recovery Compressor MSRC160L / KOBELCO Compressors Corporation	0.8	2700
Hydrocarbon Heat Pump / FC-compressor / Mayekawa Europe NV	1.0	20000
HoegTemp UHT heat pump / Enerin AS	1.0	10000

*0.3 MW Heating & 0.15 MW Cooling

The results of the linear regressions in Table 2 and the data presented in Table 3 are plotted in Figure 1. Apparently, the fitting done in the work by Caduff et al., [10] was futile in the case at hand, as the HTHP mass data follows a linear trend line in the closest manner. Thus, linear trendlines are explored further in the right part of Figure 1. In this comparison, a good fit for masses of HPs up to 0.7 MW was found, which quickly deteriorates as higher masses are also included. This finding is confirmed by the fact that for HPs with a power output > 1 MW their masses are not outlined and are commonly described with phrases such as “depends heavily on the installation and the parameters at the specific site”.

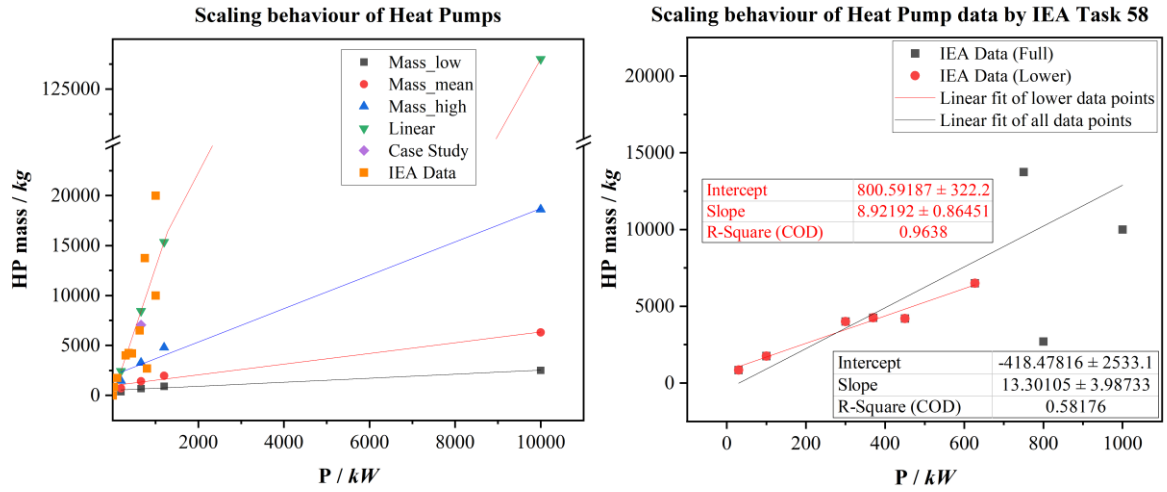


Figure 1: The left part of the figure shows the scaling results by Caduff et al., also taking into account the boundaries of the confidentiality interval, in comparison with the HP data collected in IEA Annex 58 (Task) 1. The right part of the figure shows only the IEA data and two fits, one encompassing the entire data set, the other one only the ones with lower outputs.

3.1.2. Life Cycle Inventory

The LCI was compiled for four HTHPs. The full inventory pertaining to mass for the machinery of the HPs is presented in Table 4. The original Ecoinvent process is shown with the linear scaling results for the selected case studies. On the right part, the four different case studies are presented. All processes were modelled after the Ecoinvent database, except for Copper where a process by Sphera was used [16].

Table 4: The LCI for the materials for all four case studies and basic information provided in the Ecoinvent process.

Input Stream	**Reference 10 kW**	**Unit**	**0.19 MW**	**0.66 MW**	**1.2 MW**	**10 MW**	**Unit**
Copper	22	Kg	418	1452	2640	22000	kg
Electricity, Medium Voltage	140	kWh	2660	9240	16800	140000	kWh
Heat, district or industrial, natural gas	1.33	GJ	25.27	87.78	159.6	1330	GJ
Lubricating oil	1.7	Kg	32.3	112.2	204	1700	kg
Polyvinylchloride, bulk polymerized	1.0	Kg	19	160	120	1000	kg
R134a (1,1,1,2-Tetrafluoroethane)	3.09	Kg	See Table 5				
Reinforcing Steel	75	Kg	1425	4950	9000	75000	kg
Steel, low-alloyed hot rolled	20	Kg	380	1320	2400	20000	kg
Tube insulation	10	Kg	190	660	1200	10000	kg
Outputs/Emissions	Amount	Unit					
Waste Plastic mixture	11	Kg	209	726	1320	11000	kg
R134a (1,1,1,2-Tetrafluoroethane)	0.69	Kg	See Table 5				

Moreover, the LCI consisted of a part containing the working fluid and the power consumed/generated. Those results are found in Table 5 and Table 6. Due to the limited availability of steam-generating heat pumps on the market not all heat pumps in Table 5 are capable of producing steam on their own. This applies to cases 1 –

DryFiciency Wienerberger and 3 - Combitherm. To overcome this issue the COPs of these water-to-water heat pumps were considered and for steam production a flash tank was connected downstream. The internal mechanism of a flash tank only evaporates a relatively small portion of water at the flash valve. The percentage of the mass flow that is converted into steam depends on the pressure difference the fluid experiences at expansion. This added resistance requires more power to pump the sink stream. To take these effects into account circulation pumps were included in the calculation. Their electrical power consumption is estimated based on similar heat pump configurations that use flash tanks. The reference application was based on the design power of the pump. Therefore, the presented estimates for circulation pump power in Table 5 can be seen as an upper bound. The COPs for case studies 1 and 3 include the extra power consumption of the circulation pumps. Documentation of the different HTHP models is given in the citations.

Table 5: LCI data containing energy inputs and outputs as well as additional data.

	Case Study 1 [17]	**Case Study 2** [18]	**Case Study 3** [19]	**Case Study 4** [20]
Model Name / Manufacturer	**Dryficiency / Wienerberger**	**SGH 165 / Kobelco**	**Combitherm**	**Industrial HP / Siemens Energy**
Power Output / MW	0.19	0.66	1.2	10
Useful life / a	15	15	15	30
Runtime / $h*a^{-1}$	8000	8000	8000	8000
Heat source in / °C	91	70	45	115
Heat source out / °C	88	65	40	105
Heat sink in / °C	131	/	112	105
Heat sink out / °C	160	/	120	/
Temperature of steam produced / °C	145*	165	105*	150
Circulation Pump / $MWh*a^{-1}$	160*	0	480*	0
Circulation Pump / MWh (total life)	2400	0	7200	0
Upgrading / $MWh*a^{-1}$	691	2112	4364	19048
Upgrading / MWh (total life)	10364	31680	65455	571429
COP (Steam generating HP)	1.79	2.5	1.98	4.2
Heat Output / $GJ*a^{-1}$	5472	19008	34560	288000
Heat Output / TJ (total life)	82.08	285.12	518.40	4320
Documentation	[17]	[18]	[19]	[20]

** Expert's estimate*

Table 6: LCI data pertaining to working fluid use and leakage.

	Case Study 1	**Case Study 2**	**Case Study 3**	**Case Study 4**
Working fluid	1336mzz (Z)	R134a + R245fa	R1233zd (E)	R1233zd (Z)
IUPAC name	1,1,1,4,4,4-Hexafluorobutene	1,1,1,2-Tetrafluoroethane & 1,1,1,3,3-Pentafluoropropane	*trans*-1-Chloro-3,3,3-trifluoroprop-1-ene	*cis*-1-Chloro-3,3,3-trifluoroprop-1-ene
Initial filling / kg	82	140	285	5000
Total leakage (life) / kg	12.3	21	42.75	1500
Total demand (life) / kg	94.3	161	327.25	6500
GWP / kg CO_2-eq.*kg^{-1} *[Source]*	2 [21]	1050* [22]	6 [22]	6 [22]
GWP (leakage over life) / kg CO_2-eq	24.6	22050	42.75	1500
ODP / kg R11-eq.*kg^{-1} *[Source]*	0 [23]	0* [23]	0.00034** [23]	0.00034** [23]
ODP (leakage over life) / kg R11-eq	0	0	0.014535	0.51

*The manufacturer told the authors that the two WF are in a secret mixture, but for the sake of calculation 100 % R245fa should be assumed.

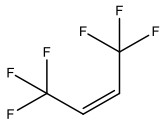
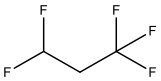
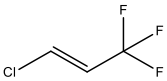
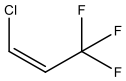
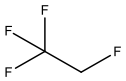
** The value was assumed to be similar for both enantiomers.

The original inventory from Ecoinvent listed significant amount of working fluid (WF) needed for the initial fillings and nearly 20 % of loss during production and decommissioning. [15] After having talks with experts, it was concluded, that those values were too high for state-of-the-art processes. A leakage of 1 % per year and a refilling was hence assumed and modelled.

3.1.3. Transforming the inventory to the model

As presented in Table 4, the production of the HP features also the production of a WF. As R134a is not used in any of the model cases, production data had to be found for the remaining WFs. Literature shows that synthesis routes are manifold, mostly too complicated for LCA studies, as non-standard chemicals and rare-element catalysts are used. [24], [25] As a process was found in the Ecoinvent database for R134a, which outlines a GWP of 17.6 kg CO_2-eq. / kg R134a, it was decided to use it as a proxy [26]. The reason was that literature only lists values for GWP and ODP and we wanted the other midpoint categories to be accounted for, too. Chemical structures of the different WF's Table 7.

Table 7: Overview of the WFs used in the study.

Working fluid	**1336mzz (Z)**	**R245fa**	**R1233zd (E)**	**R1233zd (Z)**	**R134a**
IUPAC	(Z)-1,1,1,4,4,4-hexafluor-2-butene	1,1,1,3,3-pentafluorpropane	*(E)*-1-chloro-3,3,3-trifluoroprop-1-ene	*(Z)*-1-chloro-3,3,3-trifluoroprop-1-ene	1,1,1,2-tetrafluorethane
Structure					

For modelling the mass balance, the Ecoinvent standard processes were used given in the documentation of the process describing the 10 kW HP, if not stated else. Exceptions include the supply for thermal energy, which was modelled with the Sphera process "EU-28: Thermal energy from natural gas" [27], or the plastic waste mixture which was assumed to be treated with the "EU-28: Plastic packaging in waste treatment plant" [28] Sphera process. As for incineration, steam and power are produced, substitution had to be modelled. For the thermal energy, the beforementioned process was taken; while for the grid, the grid used in the scenario was chosen. According to the country selections, the grid mixes featured the Sphera processes for "1KV-60KV grid mix" in the EU-28, France and Spain. [29], [30], [31]. To further clarify matters from chapter 3.1.2, the proxy production of the working fluids was modelled with Ecoinvent process given in the 10kW HP process, but connected to "use phase".

3.2. LCIA results

As a first group of results, the base cases of the four heat pumps are presented. For those the EU:28 electricity mix was used. The absolute values results are listed in Table 8, as well as percentual impacts which were normalized to the 10 MW case, case 4.

Table 8. They are accompanied by percentual values in relation to the 10 MW case.

Table 8:CML LCIA results for the scenarios obtained in the LCA base case.

CML-Midpoint category	**Case 1**	**Case 2**	**Case 3**	**Case 4**
Abiotic Depletion (ADP elements) [kg Sb eq.]	2.26E-05	2.08E-05	2.19E-05	1.34E-05
In %	168.82%	155.71%	163.64%	100.00%
Abiotic Depletion (ADP fossil) [MJ]	2.00E+02	1.43E+02	1.81E+02	1.70E+02
In %	117.87%	84.53%	106.42%	100.00%

Acidification Potential (AP) [kg SO2 eq.]	3.85E-02	2.76E-02	3.48E-02	3.25E-02
In %	118.53%	85.06%	106.92%	100.00%
Eutrophication Potential (EP) [kg Phosphate eq.]	4.38E-03	3.17E-03	3.96E-03	3.69E-03
In %	118.94%	85.99%	107.33%	100.00%
Freshwater Aquatic Ecotoxicity Pot. (FAETP inf.) [kg DCB eq.]	0.15	0.13	0.14	0.09
In %	165.08%	148.21%	157.56%	100.00%
Global Warming Potential (GWP 100 years) [kg CO_2 eq.]	18.39	13.20	16.53	15.57
In %	118.12%	84.77%	106.13%	100.00%
Global Warming Potential (GWP 100 years). excl biogenic carbon [kg CO_2 eq.]	1.84E+01	1.32E+01	1.65E+01	1.56E+01
In %	118.12%	84.77%	106.13%	100.00%
Human Toxicity Potential (HTP inf.) [kg DCB eq.]	9.25E-01	6.93E-01	8.41E-01	7.42E-01
In %	124.64%	93.37%	113.31%	100.00%
Marine Aquatic Ecotoxicity Pot. (MAETP inf.) [kg DCB eq.]	2.45E+03	1.79E+03	2.22E+03	2.03E+03
In %	120.86%	88.11%	109.35%	100.00%
Ozone Layer Depletion Potential (ODP) [kg R11 eq.]	1.12E-06	5.54E-07	6.20E-07	7.93E-07
In %	141.52%	69.90%	78.19%	100.00%
Photochem. Ozone Creation Potential (POCP) [kg Ethene eq.]	2.70E-03	1.95E-03	2.44E-03	2.28E-03
In %	118.38%	85.35%	106.81%	100.00%
Terrestric Ecotoxicity Potential (TETP inf.) [kg DCB eq.]	2.29E-02	1.65E-02	2.07E-02	1.92E-02
In %	118.92%	85.80%	107.73%	100.00%

Generally speaking, the results are relatively uniform throughout the impact categories. The 0.66 MW machine yields the lowest results, owing to the high COP, especially compared to 0.2 and 1.2 MW. While the 10 MW HTHP exhibits a COP of 4.2, one must not forget that this figure comes form of a heat source of > 100°C. Moreover, case study 1 and 3 need the circulating pump, thus higher emissions due to the power used were found. However, lower emissions due to scaling effects were not found. Moreover, the impacts were grouped into the three different stages of the life cycle of the HTHPs. The results are shown in Figure 2.

Upon reviewing the percentual contributions it becomes clear the influences are very similar among the different HTHP systems. Except for ADP elements, FAETP, and ODP, the usage phase of HPs was responsible for the majority of the impacts. The leakage was only noticeable in the case of the 10 MW case, which resulted in a 7 % contribution to ODP, which was again based on very low overall numbers. Especially for GWP, HP production and leakage's impacts were under 1 %, thus confirming the hypothesis that in energy-intensive operations the plant plays only a minor role. Interestingly enough, when comparing case studies 2 & 3, case study 2 featuring a working fluid with a GWP > 20.000, no difference is visible to case study 3 which uses a WF with a GWP of 43, thus indicating that over the lifetime of one HP the GWP of the working fluid should not influence decision making too much.

As mandated by ISO 14044, sensitivity analysis should be used in comparative LCA in order to account for weak spots in the analysis and to further insights into the comparative model. For this, the grid mixes were changed to the Spanish and French one, as well as material balances were changed by + 50 % and reduced by – 50 %. Results for the CML midpoint categories are presented in Figure 3.

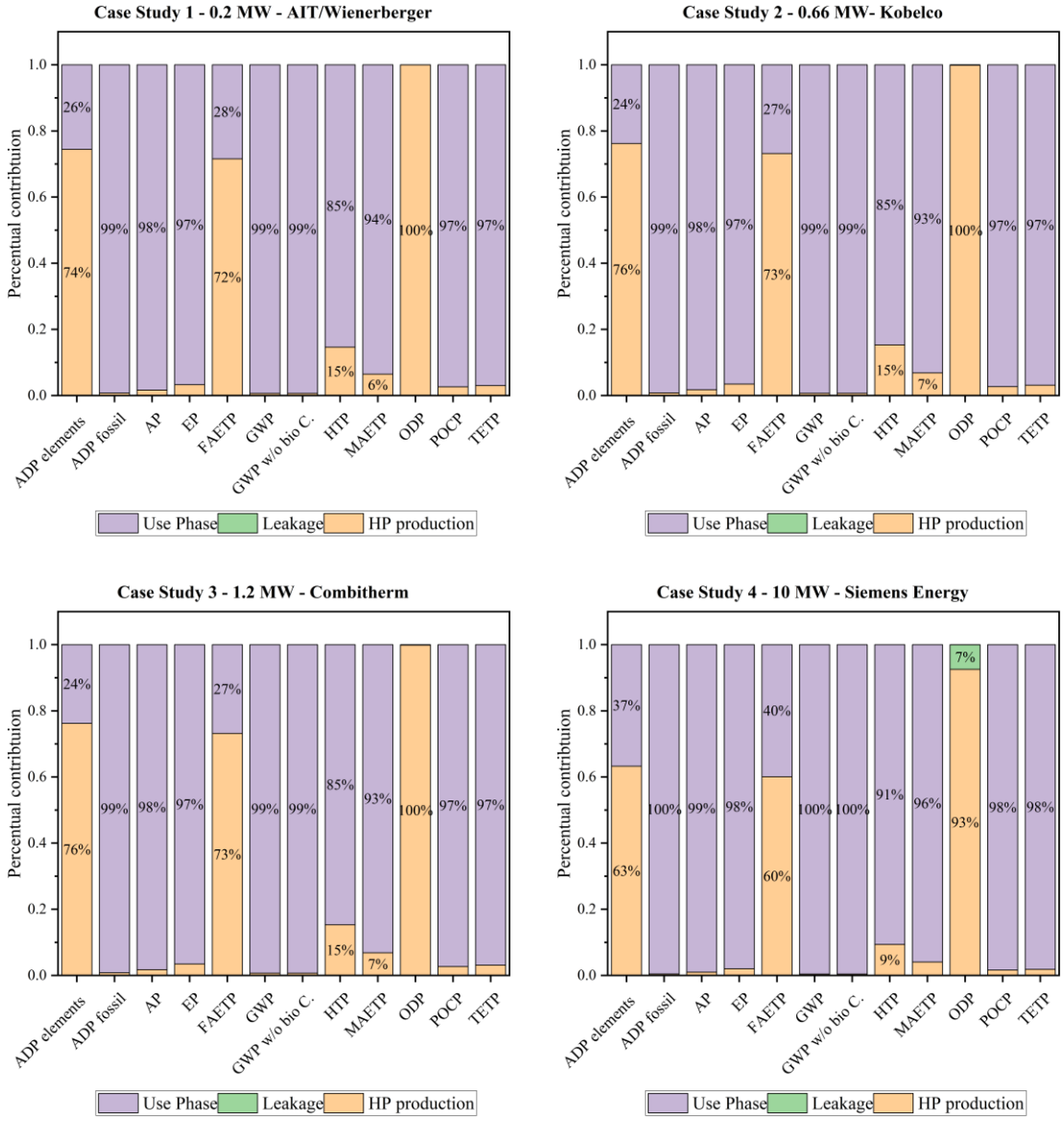


Figure 2: Percentual contributions to the midpoint categories by the three different life style changes.

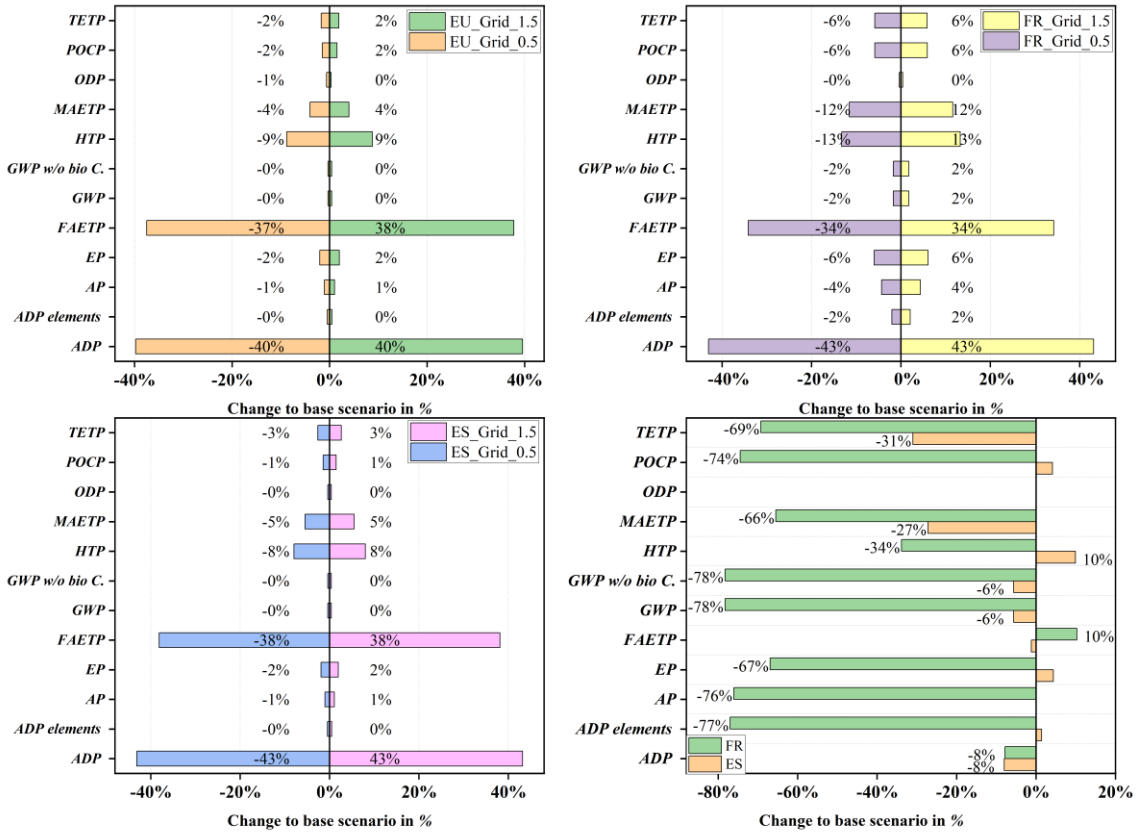


Figure 3: The results of the sensitivity analysis. The top figures and the bottom left ones indicate percentual changes in scenarios varying the three grid mixes and the material balances. The bottom right scenario features no change of material solely the grid mixes changed. Changes smaller than 5 % were not shown for reasons of readability.

The findings of Figure 3 match the ones made in Figure 2. The increased/decreased material demands altered ADP and FAETP by less than 50 %, while leaving the majority of other categories, including GWP, largely unaltered. Due to the linear scaling, the tornado chart is highly symmetrical. This once again highlights, that if GWP is the main focus of a HTHP study, the material balance plays a minor role at most. For toxicity related impacts however, the scaling effects are of interest. Acidification and eutrophication were also only influenced on a minor level. If only the electricity grid mixes were changed from the EU-28 mix to the Spanish or French one, the results turned out very different. The influence is mostly indirectly proportional to the previous analysis, as categories change more drastically. I.e., the French grid provides significant reductions of 77 % in the ADP elements category as well as -78 % for GWP, which was due to its low carbon intensity. AP and EP show similar behaviour, as they are also hardly influenced by the material balance's scaling. The Spanish mix does provide some reductions, yet its influence is notably smaller than the French one. However, in a direct comparison, the Spanish grid provided little improvement over the French one, only in the FAETP category it yielded minuscule better results.

As it was shown, when aiming for an improved carbon balance, the usage phase provides the biggest lever. Aiming for a high efficiency and clean energy can help to significantly reduce the GWP. While this is one part of the equation, the other side in LCA is the energy provision, which will be replaced using a HTHP. Therefore, a last case study was prepared, comparing the 1 GJ produced by the HTHP to common other technologies such as solid biomass, biogas, light fuel oil (LFO) and natural gas. Data was obtained from Sphera's Professional database and is presented in Figure 4. [32], [33], [34], [35]

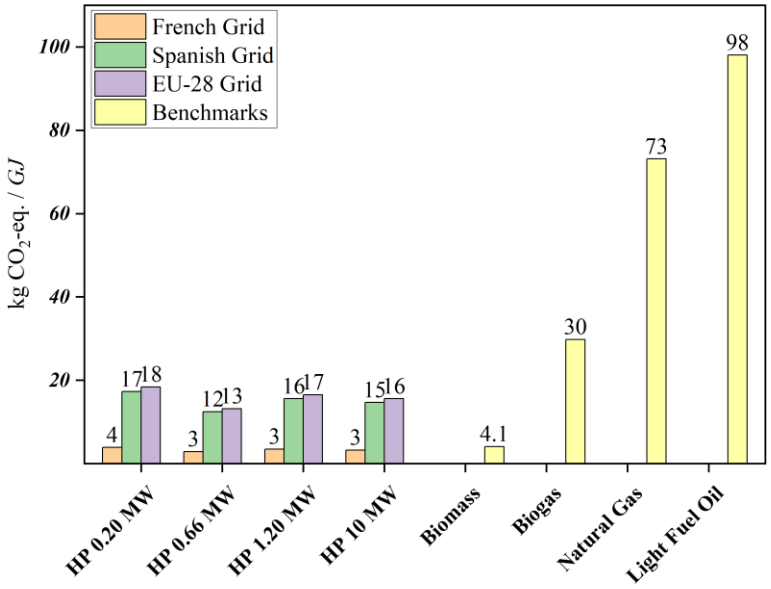


Figure 4: The results for the four HTHP cases in comparison with other established steam sources in terms of GWP.

When assessing the GWPs of the different steam generating technologies it becomes clear that the differences between the different HTHPs, their production and usage parameters are negligible when compared to the figures obtained by different steam generating technologies. This means if one of the HTHPs is implemented, the largest lever to lower the carbon balance is the technology which is replaced. The best case for example, the 0.66 MW design, powered by a French grid, replacing steam from LFO would yield a reduction of emissions by over 97 %. The real case would probably be not as straight-forward, as 1:1 replacement is a very optimistic assumption, and it all comes down to the case at hand and its thermodynamic and process properties. But even replacing smaller fossil steam sources can provide significant emissions savings due to the emission's slope's sizes.

4. Conclusion, final remarks and further outlook

While the power-laws used for scaling up equipment/cost in process engineering have come in handy many times in the past, this was not true in this case of industrial sized HTHPs. It was shown that the power-law was not applicable to the HTHP case, as the scaling behaved mostly in a linear fashion. Especially in the range between 0.1 and 0.7 MW_{th} a good linear correlation was found. However, those results were of methodological interest only as it was shown that manufacturing is not as influential as the usage when it comes to life cycle impacts, especially GWP. This was confirmed in the sensitivity analysis. The usage/choice of working fluid also was shown to be not as influential as assumed, as no considerable difference was observed between cases with a WF with high and low GWPs. Therefore, it is recommended that manufacturers should care about thermodynamic properties foremost, which are mostly met by working fluids with low GWPs in the HTHP area anyways. In the case studies, it was shown that a grid with low carbon intensity can help significantly in decreasing environmental impacts. This effect can be further amplified if carbon-intensive steam sources are replaced. If e.g., a HTHP powered by the French grid replaces steam from LFO GWP savings of over 97 % could be achieved. However, one must not forget that as of now the HTHPs can only supply lower temperature and lower pressure steam, while the fossil sources are not limited in that sense. Moreover, biogenic carbon CO_2 emissions are not further considered in this work as Sphera's modelling approach assumes a full cycle from uptake in biomass, to the release when generating thermal power. [36] This is accurate for the system boundary in this case but may change drastically if different system boundary in terms of biomass is applied.

Acknowledgements

This project has received funding from the European Union's Horizon 2020 research and innovation program under grant agreement No 820771-BAMBOO, as well as by Energieinstitut an der Johannes Kepler Universität Linz.

References

[1] F. J. Rey *et al.*, 'Life Cycle Assessment and External Environmental Cost Analysis of Heat Pumps', *Env. ENG SCI*, vol. 21, no. 5, p. 15, 2004, doi: 10.1089/ees.2004.21.591.

[2] U. Khan, R. Zevenhoven, and T.-M. Tveit, 'Evaluation of the Environmental Sustainability of a Stirling Cycle-Based Heat Pump Using LCA', *Energies*, vol. 13, no. 17, p. 4469, Aug. 2020, doi: 10.3390/en13174469.

[3] A. Nitkiewicz and R. Sekret, 'Comparison of LCA results of low temperature heat plant using electric heat pump, absorption heat pump and gas-fired boiler', *Energy Convers. Manag.*, vol. 87, pp. 647–652, Nov. 2014, doi: 10.1016/j.enconman.2014.07.032.

[4] M. Smith, A. Bevacqua, S. Tembe, and P. Lal, 'Life cycle analysis (LCA) of residential ground source heat pump systems: A comparative analysis of energy efficiency in New Jersey', *Sustain. Energy Technol. Assess.*, vol. 47, p. 101364, Oct. 2021, doi: 10.1016/j.seta.2021.101364.

[5] H. Böhm, S. Goers, and A. Zauner, 'Estimating future costs of power-to-gas – a component-based approach for technological learning', *Int. J. Hydrog. Energy*, vol. 44, no. 59, pp. 30789–30805, Nov. 2019, doi: 10.1016/j.ijhydene.2019.09.230.

[6] H. Böhm, A. Zauner, D. C. Rosenfeld, and R. Tichler, 'Projecting cost development for future large-scale power-to-gas implementations by scaling effects', *Appl. Energy*, vol. 264, p. 114780, Apr. 2020, doi: 10.1016/j.apenergy.2020.114780.

[7] R. Nitzsche, M. Budzinski, and A. Gröngröft, 'Techno-economic assessment of a wood-based biorefinery concept for the production of polymer-grade ethylene, organosolv lignin and fuel', *Bioresour. Technol.*, vol. 200, pp. 928–939, Jan. 2016, doi: 10.1016/j.biortech.2015.11.008.

[8] L. Zeilerbauer, J. Lindorfer, R. Süss, and B. Kamm, 'Techno-economic and life-cycle assessment of a wood chips-based organosolv biorefinery concept for production of lignin monomers and oligomers by base-catalyzed depolymerization', *Biofuels Bioprod. Biorefining*, vol. 16, no. 2, pp. 370–388, Nov. 2021, doi: 10.1002/bbb.2315.

[9] V. Rodin, L. Zeilerbauer, J. Lindorfer, C. Paulik, and D. Finger, 'Life cycle assessment of a novel electrocatalytic process for the production of bulk chemical ethylene oxide from biogenic CO2', *Front. Sustain.*, vol. 3, p. 799389, Sep. 2022, doi: 10.3389/frsus.2022.799389.

[10] M. Caduff, M. A. J. Huijbregts, A. Koehler, H.-J. Althaus, and S. Hellweg, 'Scaling Relationships in Life Cycle Assessment: The Case of Heat Production from Biomass and Heat Pumps', *J. Ind. Ecol.*, vol. 18, no. 3, pp. 393–406, May 2014, doi: 10.1111/jiec.12122.

[11] 'Heat Pumping Technologies - Annex 58', *Annex 58*. https://heatpumpingtechnologies.org/annex58/ (accessed Oct. 05, 2022).

[12] R. Frischknecht, *Lehrbuch der Ökobilanzierung*. Berlin, Heidelberg: Springer Berlin Heidelberg, 2020. doi: 10.1007/978-3-662-54763-2.

[13] J. B. Guinée *et al.*, Eds., *Handbook on Life Cycle Assessment: Operational Guide to the ISO Standards*, vol. 7. Dordrecht: Springer Netherlands, 2002. doi: 10.1007/0-306-48055-7.

[14] W. Klöpffer and B. Grahl, *Life Cycle Assessment (LCA): A guide to best practice*. Weinheim: Wiley-VCH, 2014.

[15] T. Heck, 'Heat pump production, brine-water, 10 kW, GLO, Ordinary transforming activity, Ecoinvent database version 3.8'. Ecoinvent.org, Jul. 28, 2010.

[16] Sphera, 'Process data set: Copper mix (99,999% from electrolysis); from electrolysis; consumption mix, to consumer; 99,999% Cu (en)'. https://sphera.com/2022/xml-data/processes/301d375b-4f27-43f2-bbe0-89f87cae0df1.xml (accessed Feb. 16, 2023).

[17] S. Puskas and V. Wilk, 'DryFiciency - Industrial heat pump for a climate-neutral European industry'. 2019. Accessed: Oct. 10, 2022. [Online]. Available: https://heatpumpingtechnologies.org/annex58/wp-content/uploads/sites/70/2022/07/hthpannex58dryfwbgfinal-1.pdf

[18] T. Kaida, 'SGH 165 / KOBELCO Compressors Corporation'. Accessed: Oct. 10, 2022. [Online]. Available: https://heatpumpingtechnologies.org/annex58/wp-content/uploads/sites/70/2022/07/technologykobelcosgh165.pdf

[19] 'Heat Pumps - Combitherm', Oct. 10, 2022. https://combitherm-h8mjbutwz-dualmeta.vercel.app/produkte-und-loesungen/waermepumpen/ (accessed Oct. 10, 2022).

[20] C. Hüttl, 'Industrial Heat Pump / Siemens Energy'. Accessed: Oct. 10, 2022. [Online]. Available: https://heatpumpingtechnologies.org/annex58/wp-content/uploads/sites/70/2022/07/siemens-energy-hthp-technology.pdf

[21] J. Navarro-Esbrí, A. Fernández-Moreno, and A. Mota-Babiloni, 'Modelling and evaluation of a high-temperature heat pump two-stage cascade with refrigerant mixtures as a fossil fuel boiler alternative for industry decarbonization', *Energy*, vol. 254, p. 124308, Sep. 2022, doi: 10.1016/j.energy.2022.124308.

[22] F. Heberle, C. Schifflechner, and D. Brüggemann, 'Life cycle assessment of Organic Rankine Cycles

for geothermal power generation considering low-GWP working fluids', *Geothermics*, vol. 64, pp. 392–400, Nov. 2016, doi: 10.1016/j.geothermics.2016.06.010.
[23] C. Mateu-Royo, J. Navarro-Esbrí, A. Mota-Babiloni, M. Amat-Albuixech, and F. Molés, 'Thermodynamic analysis of low GWP alternatives to HFC-245fa in high-temperature heat pumps: HCFO-1224yd(Z), HCFO-1233zd(E) and HFO-1336mzz(Z)', *Appl. Therm. Eng.*, vol. 152, pp. 762–777, Apr. 2019, doi: 10.1016/j.applthermaleng.2019.02.047.
[24] C. Zhang, X. Jia, and H. Quan, 'Synthesis of Z-1,1,1,4,4,4-hexafluoro-2-butene from hexachlorobutadiene', *J. Fluor. Chem.*, vol. 191, pp. 77–83, Nov. 2016, doi: 10.1016/j.jfluchem.2016.09.012.
[25] R. M. Bellabarba, 'Catalysts for modern fluorinated refrigerants', *J. Fluor. Chem.*, vol. 244, p. 109741, Apr. 2021, doi: 10.1016/j.jfluchem.2021.109741.
[26] T. Heck, 'Refrigerant R134a production, RER, Ordinary transforming activity, Ecoinvent database version 3.3'. Ecoinvent.org, Jul. 28, 2010.
[27] Sphera, 'Process data set: Thermal energy from natural gas; technology mix regarding firing and flue gas cleaning; production mix, at heat plant; 100% efficiency (en)'. http://gabi-documentation-2022.gabi-software.com/xml-data/processes/cfe8972e-6b51-4a17-b499-d78477fa4294.xml (accessed Oct. 14, 2022).
[28] Sphera, 'Process data set: Plastic packaging in municipal waste incineration plant; waste-to-energy plant with dry flue gas treatment, without collection, transport and pre-treatment; production mix (region specific plants), at plant; 36.0 MJ/kg net calorific value (en)'. http://gabi-documentation-2022.gabi-software.com/xml-data/processes/df791c88-1c61-4bb2-b21f-01c99806066d.xml (accessed Oct. 14, 2022).
[29] Sphera, 'Process data set: Electricity grid mix 1kV-60kV; AC, technology mix; consumption mix, to consumer; 1kV - 60kV (en)'. http://gabi-documentation-2022.gabi-software.com/xml-data/processes/0a1b40db-5645-4db8-a887-eb09300b7b74.xml (accessed Oct. 14, 2022).
[30] Sphera, 'Process data set: Electricity grid mix 1kV-60kV; AC, technology mix; consumption mix, to consumer; 1kV - 60kV (en)'. http://gabi-documentation-2022.gabi-software.com/xml-data/processes/e9d82aa9-0160-4993-8945-6c4a41dc594f.xml (accessed Oct. 14, 2022).
[31] Sphera, 'Process data set: Electricity grid mix 1kV-60kV; AC, technology mix; consumption mix, to consumer; 1kV - 60kV (en)'. http://gabi-documentation-2022.gabi-software.com/xml-data/processes/6f918155-8d6f-4d95-aaaa-eba7f2be25e2.xml (accessed Oct. 14, 2022).
[32] Sphera, 'Process data set: Process steam from biogas 90%; technology mix regarding firing and flue gas cleaning; production mix, at heat plant; MJ, 90% efficiency (en)'. http://gabi-documentation-2022.gabi-software.com/xml-data/processes/363c5d1c-8797-491f-8234-12b925ea5aa9.xml (accessed Oct. 20, 2022).
[33] Sphera, 'Process data set: Process steam from biomass (solid) 90%; technology mix regarding firing and flue gas cleaning; production mix, at heat plant; MJ, 90% efficiency (en)'. http://gabi-documentation-2022.gabi-software.com/xml-data/processes/6f053940-bbe1-44e9-8a74-b8a2e5a6f91e.xml (accessed Oct. 20, 2022).
[34] Sphera, 'Process data set: Process steam from light fuel oil (LFO) 90%; technology mix regarding firing and flue gas cleaning; production mix, at heat plant; MJ, 90% efficiency (en)'. http://gabi-documentation-2022.gabi-software.com/xml-data/processes/49f9634e-5c1c-4f75-9a74-901f48498e7e.xml (accessed Oct. 20, 2022).
[35] Sphera, 'Process data set: Process steam from natural gas 90%; technology mix regarding firing and flue gas cleaning; production mix, at heat plant; MJ, 90% efficiency (en)'. http://gabi-documentation-2022.gabi-software.com/xml-data/processes/d8454c30-29f7-4767-a067-978ea0447ca1.xml (accessed Oct. 20, 2022).
[36] T. Kupfer *et al.*, 'GaBi Databases & Modeling Principles 2020'. Sphera, Feb. 2020. [Online]. Available: https://gabi.sphera.com/fileadmin/GaBi_Databases/Modeling_Principles_-_GaBi_Databases_2020.pdf

14th IEA Heat Pump Conference
15-18 May 2023, Chicago, Illinois

Development and Evaluation of Ammonia Vapor Compression Coupled to a CO_2 Convection Loop

Ron Domitrovic[a], Ethan Tornstrom[b], Troy Davis[c], Jerine Ahmed[d]

[a]EPRI, 942 Corridor Park Blvd, Knoxville, TN 37932, USA
[b] TRC Companies, 424 Church St., Nashville, TN 37215
[c]Mayekawa (MYCOM), 130 Smart Park Drive, Lebanon, TN 37090, USA
[d]Southern California Edison, PO Box 800, Rosmead, CA 91770, USA

Abstract

A novel approach to the application of zero GWP refrigerants for commercial space cooling was demonstrated using ammonia vapor compression chilling coupled to pumped carbon dioxide convection. Following the lead of emerging supermarket refrigeration systems, this approach is both modeled after and meant to substitute halocarbon-based pumped chilled water cooling. Compared to pumped chilled water, the use of CO_2 coupled with ammonia-based chilling could provide a system targeting multiple paths of optimization: reduced cost, increased efficiency, lower GWP potential, improved flexibility. Potential cost reduction may come from reduced piping cost, reduced installation cost, reduced physical building load and reduced pumping cost. These are all derivatives of the higher heat capacity of phase-changing CO_2 as compared to pumped water. Furthermore, low-charge ammonia provides a cheaper alternative to high GWP refrigerants. Efficiency gains potentially come from the use of ammonia as the vapor compression refrigerant—a fluid with inherently favorable thermodynamic properties as an HVAC refrigerant. Additionally, power may be reduced in pumping liquid CO_2 compared to pumping water. GWP reduction potential comes from eliminating the use of halocarbon refrigerants and from higher system efficiency. There is also potential for reduction related to embedded manufacturing cost, though this study did not evaluate those possibilities. In this first prototype system, the concept was proven to be technically feasible. The ability to operate a convection loop at a wide range of temperatures, including below water's freezing point, allows for design and operational flexibility that isn't possible with a water loop. Cooling coils may be operated colder in order to adjust the sensible heat ratio (SHR) and thus have flexibility for greater dehumidification without energy intensive re-heat. This paper summarizes the technical approach to design and shares testing results of the prototype 8-ton system.

© HPC2023.
Selection and/or peer-review under the responsibility of the organizers of the 14th IEA Heat Pump Conference 2023.

Keywords: Heat pump; Hydronic

1. Introduction

In California 14.9% of electricity is used for cooling applications (high temperature applications, not refrigeration). California commercial building cooling energy consumption was estimated to be 10,017 GWh in 2004. The majority of the existing stationary HVAC systems use R22, R410A, R134a, or R407C as the working fluid (refrigerant). R22, a very common HCFC has ozone depleting potential (ODP) as well as GWP. HFCs such as R134a have zero ODP, but still have high GWP.[1]

Environmental concerns have drawn the attention of many regulatory bodies which have undertaken various initiatives to reduce the effect of HCFC's and CFC's. The most famous legislative action in this area is the Montreal Protocol, which mandated the phasedown first of CFCs, and more gradually of HCFCs such as R22. This action was primarily focused on preventing ozone depletion. Later legislation such as the Kyoto Protocol targets global warming, and with that, sets goals for HFC phase-down. The Montreal Protocol was signed by the US, and the Clean Air Act includes actions relating to this protocol. The US did not sign the Kyoto Protocol, but the US EPA is authorized to act through the Significant New Alternatives Policy (SNAP) Program, also under the Clean Air Act, and is doing so to phase down the usage of many high-GWP refrigerants. On a state level, California's Air Resources Board (CARB) has a Refrigerant Management Program (RMP)[2] which institutes requirements for leak checking, reporting, and logging of usage of

refrigerants, first for heavy users (such as supermarkets and refrigerated warehouses), and later for smaller equipment.

Abroad, the European Union's "F-Gas" bans include aggressive requirements to phase down production, and eventually recovery and use of refrigerants with "high GWP" (150-2000, depending on application). Some European nations further have specific taxes targeting refrigerants. In Europe, these legislative actions are significant enough that alternative refrigerant adoption is considerably higher than in the US.[3]

Some promising, low GWP refrigerants may have other considerations, like toxicity or high pressure, making requiring specific protocols for safe operation. The above concerns – safety and environmental considerations – must be considered in parallel to equally important fundamental thermodynamic behavior of the fluid, which determines component sizing, operating pressures, efficiency and capacity, and so on. Combining all of these factors leads to a challenge, as no substance provides the ultimate combination of traits for all applications.

A long-term objective is to provide HVAC&R solutions using natural refrigerants. Natural refrigerants are defined as compounds that are naturally occurring and have thermo-physical properties suitable to be used in a refrigeration cycle with zero ODP and zero or near-zero GWP. Natural refrigerants like ammonia (NH_3) and carbon dioxide (CO_2) which are environmentally benign are possible alternatives but introduce certain other considerations that require tradeoffs. For NH_3, flammability and toxicity are primary concerns whereas CO_2 has challenges in high-ambient cooling operation and system operating pressures. Another potentially attractive option is the use of hydrocarbons, such as propane, which have high efficiency, but are restricted in how they may be applied because of flammability.

This paper describes the construction and evaluation of a first-of-its-kind ammonia to carbon dioxide chiller and convection loop. It is designed as a potential replacement for traditional chiller/hydronic HVAC systems. The system was shown to reliably and safely operate through a range of typical operating condition. The system has some inherent adjustability, allowing flexibility in the sensible heat ratio. Efficiency was reasonable with coefficients of performance ranging from ~2 – 3, considering that components were mostly taken from other, low temperature refrigeration applications, and the system was not fully optimized for HVAC operation. There is likely room for improvement in further designs.

There is potential for reducing material and installation cost because of the smaller (and lighter) piping requirements for pumped carbon dioxide compared to traditional pumped chilled-water. Simple economic analysis shows install cost may be reduced by a factor of 2-3.

Future development in this area should focus on optimizing for HVAC temperatures to push efficiency higher, design systems that incorporate heating or dual-purpose systems and field testing prototype systems.

2. System Design

A system was designed and constructed that uses natural refrigerants with low to zero GWP. The system is comprised of a low-charge Ammonia (NH_3) based direct-exchange (DX) vapor compression air-cooled chiller coupled to a pumped Carbon Dioxide (CO_2) convection loop. Refrigerant charge was less than 1 pound NH_3 per ton. This arrangement is aligned with traditional systems for space cooling using halocarbon based chillers coupled to chilled-water pumped loops. The evaluation is a hybrid between laboratory and field setup, using the EPRI, Knoxville laboratory space as the "field" installation, but taking measures such that indoor conditions could be held reasonably fixed. Figure 1 shows a schematic for the NH_3/CO_2 system.

The chiller is a nominal 8-ton semi-hermetic chiller with ammonia as the working fluid. It was a beta prototype unit at the time of evaluation, designed to exchange heat on the source (cooling) side through an ammonia to carbon dioxide plate heat exchanger.

Carbon dioxide was piped in a separate convection loop, coupled to the chiller, much as a chilled water loop would be coupled in traditional systems. CO_2 remained in a saturated state throughout evaluation, maintained at pressures between ~3.1-3.8 MPa (450 – 550 psig). A central receiver tank acted as the repository for CO_2. Vapor from the top of the receiver entered the chiller heat exchanger, condensed while flowing through it and returned to the receiver through gravity—there was no pumping for the chiller-CO_2 heat exchange.

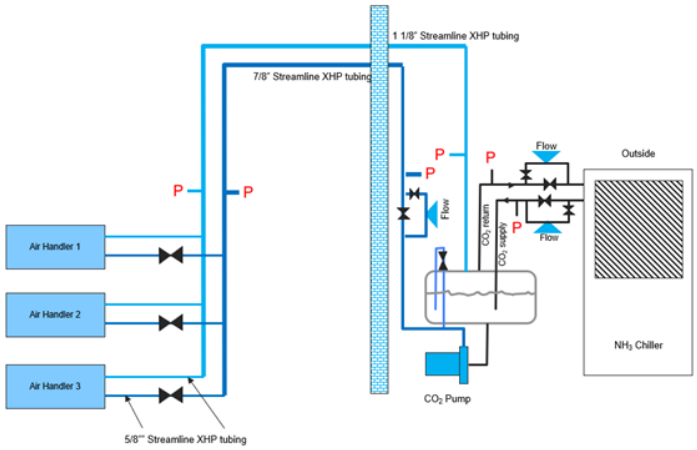


Figure 1. System Schematic

3. Evaluation Approach

The objective was to evaluate overall system operation, with a focus on measuring cooling capacity, power draw characteristics and system efficiency as functions of ambient temperature conditions. Other system characteristics were observed and measured as appropriate. Such other characteristics may include part-load dynamics, standby pressure conditions and cycling behavior.

The system can be viewed with multiple control volumes:

- Control volume around the entire system, measuring overall system input (electrical power) and output (cooling capacity). This approach gives insight on the overall system efficiency for comparison to other comparable approaches (e.g. halocarbon chiller with pumped chilled water).
- Separate control volumes around the NH_3 chiller and the pumped CO_2 loop. This approach isolates each subsystem so that capacity, power draw details and efficiency can be measured for each.

Instrumentation of the setup is designed to accommodate both approaches.

3.1. System Control Volume Approach

Referencing the system control volume in Figure 2, overall system capacity is determined through air-side measurement on the indoor air handlers. Capacity is calculated by:

$$\dot{Q}_{air\ capacity} = \sum_{i=1}^{4} \dot{m}_{air,i}\,[h_{air,out} - h_{air,in}]_i \qquad [1]$$

Where:
$\dot{m}_{air}$ is the mass flow rate of air discharged from each air handler. h is air enthalpy.

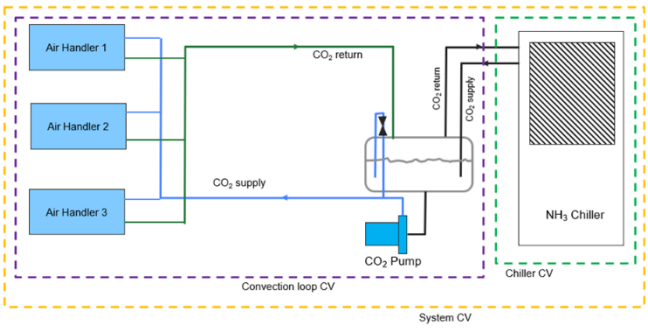


Figure 2. Control Volumes

System power is measured at five points, summing to the total power use of the system:

- Chiller unit power
- CO_2 pump rack and controls power
- 3-6 -> Air handler 1-3 power

$$Total\ Power = \sum_{i=1}^{6} Power_i \qquad [2]$$

Overall system efficiency, termed the Coefficient of Performance (COP) is thus defined as:

$$Overall\ system\ efficiency\ (COP) = \frac{\dot{Q}}{Power} \qquad [3]$$

These three quantities constitute the primary metrics of system performance. All three are functions of operating conditions, namely the outdoor and indoor dry bulb temperature and the indoor relative humidity.

$$\dot{Q}, Power, COP \sim f(T_{out}, T_{in}, RH_{in}) \qquad [4]$$

Air side capacity measurement is an industry accepted method for determining total delivered system capacity. It captures the heat transfer usefully delivered to the space and does not capture otherwise lost heat—losses. In a true building arrangement, there may be additional losses associated with the details of ducting. These are not captured in a laboratory style evaluation. The method of test is generally guided by AHRI 340/360 approaches and methods of measurement, though strict ambient air conditions are not maintained with psychrometric-style testing).

Air temperature is measured with type T thermocouple arrays; relative humidity is measured with capacitive RH sensors and air volume flow is measured via a pitot tube array. Air mass flow is calculated from air density, via measured static air pressure, temperature and relative humidity.

3.2. Subsystem Control Volume Approach

Referencing **Error! Reference source not found.** an additional control volume is shown around the air-cooled chiller. With both the full system CV and the chiller CV, then three overall sets of output metrics (capacity, power draw and efficiency) can be calculated:

- Full system
- Air-cooled chiller
- Convection loop

Because of complexities of measurement, only the full system CV was used for analysis of the experiment. Following is a discussion of some of the associated complexities for sub-component measurement, owing primarily to the nature of 2-phase CO2 flow.

Convection loop metrics are then the difference between the full system and the chiller. For example:

$$\dot{Q}_{conv\ loop} = \dot{Q}_{system} - \dot{Q}_{chiller} \qquad [5]$$

$\dot{Q}_{conv\ loop}$ is expected to be negative, indicating losses in the piping network.

3.2.1. Chiller CV Measurement

Measuring the chiller capacity is somewhat challenging. An air side approach can be used, though accurately measuring air volume flow is difficult on the type of low-static fans that move air through the condensing coil. The act of measuring can substantially change the volume flow rate, so some method of boosting airflow, with a secondary fan, back to its non-disturbed state, is necessary. This approach is sometimes also employed for indoor unit testing, if air flow is significantly affected by the act of measuring.

A more direct method of measuring chiller cooling output is to measure the convection loop heat transfer. In water cooled chillers this is straightforward as the product of mass flow, specific heat of water and temperature differential:

$$\dot{Q}_{chilled\ water} = \dot{m}_{water}[h_{in} - h_{out}] \qquad [6]$$

Which can be simplified to:

$$\dot{Q}_{chilled\ water} = \dot{m}_{water} C_{p,water}[T_{in} - T_{out}] \qquad [7]$$

Since enthalpy is a direct function of temperature for liquid water (a sub-cooled liquid).

For the NH_3 system, using pumped CO_2 as the convection fluid, the method is not as simple. The CO_2 undergoes condensation in the heat exchange process with the chiller and is therefore usually in a 2-phase state—shown by the green line in **Error! Reference source not found.**. Though equation [6] still governs the heat exchange process experienced by the CO_2, there is no effective way to measure the enthalpy of 2-phase CO_2 with only temperature and pressure measurements.

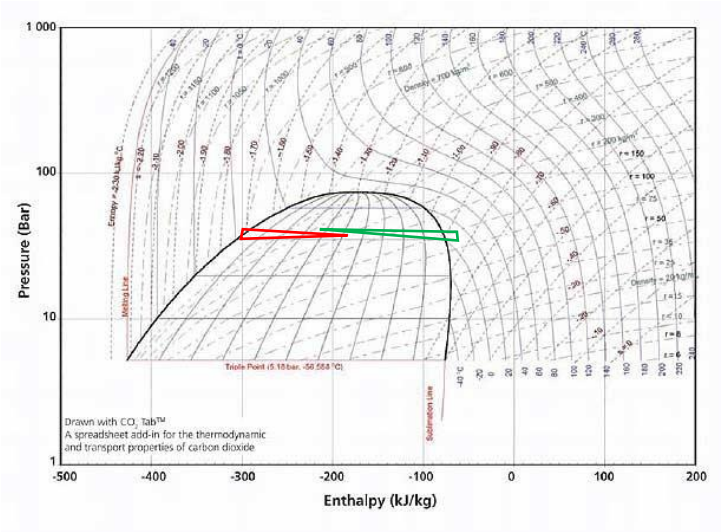


Figure 3. Illustration of Possible CO2 State Points (Green→ Chiller-to-Receiver Loop; Red → Receiver-to-AHU Loop)

For this evaluation, it was not possible to measure the enthalpy change across the chiller CO_2 loop. The h_{in} (the enthalpy of CO_2 returning to the chiller) is saturated or slightly superheated vapor, because of the geometry of its draw from the top of the receiver tank, enabling enthalpy to be calculated from measured temperature and pressure. h_{out} is a different matter, it can be 2-phase, saturated or sub-cooled. An enthalpy calculation is only possible if it is reliably saturated or sub-cooled (though there is no way to confirm saturation, so some small amount of sub-cooling is required).

4. Test Set Up

The test performed in this report was set up as a hybrid laboratory/field installation, where the laboratory space could be conditioned with reasonable control over the indoor ambient conditions. The chiller, CO_2 receiver, and the CO_2 pump were positioned outside and were subject to the outdoor ambient conditions of the summer testing period. The three indoor units were positioned in a horizontal orientation and stacked on top of each other in parallel so that temperature and humidity could be easily controlled. Supplemental heating load to the conditioned space could be adjusted to any wattage, up to ~30 kW. A variety of fans and deflectors were used to de-stratify the air and to ensure uniform entrance temperature to the three air handlers.

Humidity was supplied through manually controlled steam injection. Steam flow was adjusted to reach a rough target, return air, relative humidity of >40%. In steady-state operation of the tested system, return air conditions could be held reasonably stable (+/- 1.1C and 5%RH). Each indoor unit was assembled and setup to accommodate air-side capacity measurements.

5. Testing Results

In addition to some general break-in and operational familiarity testing, five general tests were performed on the system:

- Low Ambient (~21-26°C)
- Moderate Ambient (~28-31°C)
- High Ambient (~32+°C)
- Standby Operation
- Power Failure

5.1. Low Ambient

Low ambient testing was performed with an outdoor ambient range of 21°C to 26°C as the outdoor temperature increased over the course of the test. The system was initially started with all three air handlers on and was then allowed to equilibrate. Air handlers 1 and 2 were successively turned off which is represented in Figure 4 as the test stepped down from three, to two, to one IDUs operating. Figure 4 shows cooling capacity versus time, and shows that with two and three IDUs operating, the chiller runs continuously, whereas with only one IDU operating, the chiller cycles. Figure 5, a graph of the chiller power consumption as a function of time, also shows the cycling where the power drops significantly during the cycling period and drops to zero when an IDU is turned off (transition effect). The data collected below is an average across a pseudo steady state temperature during that portion of the test. This low ambient test produced an operating COP range from 2.45-3.14.

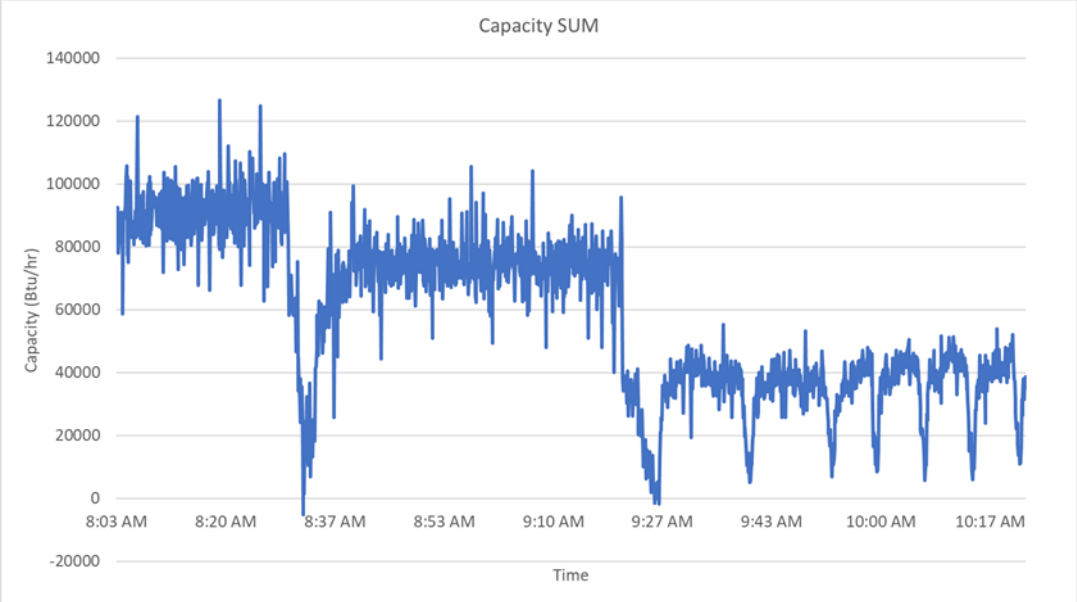


Figure 4. Cooling capacity vs time (low ambient test)

5.2. Moderate Ambient Test

Medium ambient testing was performed with a steady-state outdoor ambient temperature of approximately 30°C. The system was initially started with all three IDUs turned on and was then allowed to equilibrate. The indoor temperature was held constant at approximately 27°C as the system reached equilibrium. After collecting the data in the steady-state, IDUs 1 and 2 were successively turned off similarly to the Low Ambient test. The moderate ambient test produced lower cooling capacity while increasing the ODU power. This moderate ambient test produced an operating COP range from 2.01-2.55 as shown in Table 1.

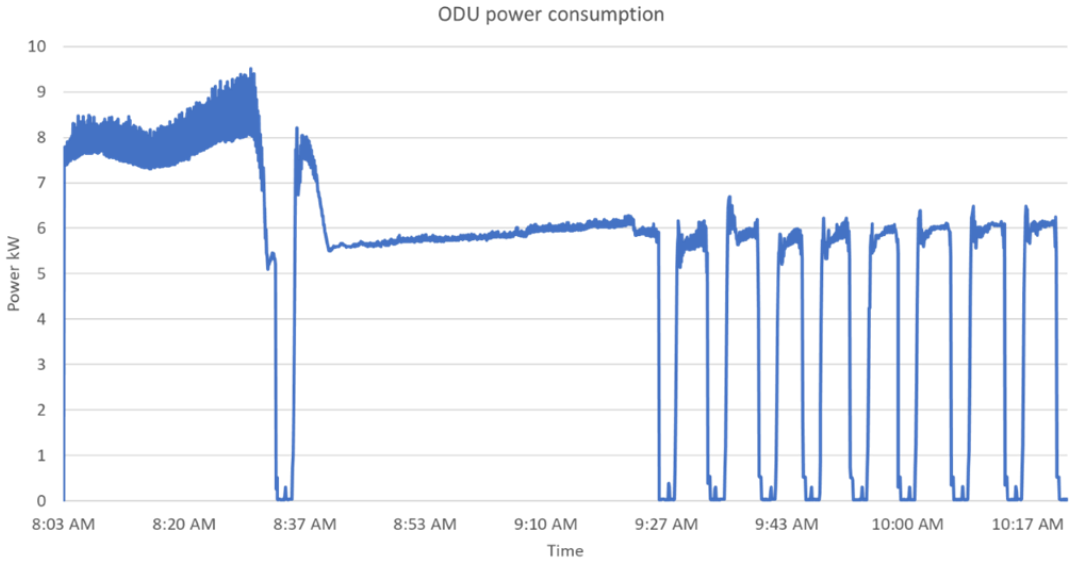


Figure 5. Chiller power vs. time (low ambient test)

Table 1. Steady-state operation for moderate ambient testing

Number of IDU ON		1	2	3
Outdoor Temp	°C	30	30	30
CO_2 Pressure	MPa	3.5	3.4	3.6
Capacity	kW	8.44	19.27	24.44
COP	-	2.01	2.51	2.55
IDU Power	Watts	327	643	949
Pump Power	Watts	184	200	200
ODU Power	Watts	3,692	6,846	8,432
Total Power	Watts	4,202	7,689	9,581

5.3. High Ambient Test

High ambient testing was performed by adding supplemental electric heat to the condenser inlet in addition to the ~29°C ambient outdoor air at the time of testing. This additional heat boosted the condenser inlet air temperature to approximately 33°C. All three IDUs were in operation throughout the entire test. The high ambient temperature with three IDUs running consumed total power around 12.6 kW. Total air-side cooling capacity was 28.84 kW (~8.2 tons), which operated at a COP of 2.14 (Table 2). Figure 6 shows the relationship between the ambient temperature with additional resistive heat and the cooling capacity of the system. The data observed was taken from operating temperatures of ~91°F which are featured in Figure 6. CO_2 tank pressure remained stable between ~3.4-3.6 MPa (500-525 psig).

Table 2. Steady-state operation for high ambient testing

Number of IDU ON		3
Outdoor Temp	°C	33
CO_2 Saturation Temp	°C	4
Capacity	kW	28.85
COP	-	2.14
IDU Power	Watts	943.7
Pump Power	Watts	192
ODU Power	Watts	11,543.7
Total Power	Watts	12,679.4

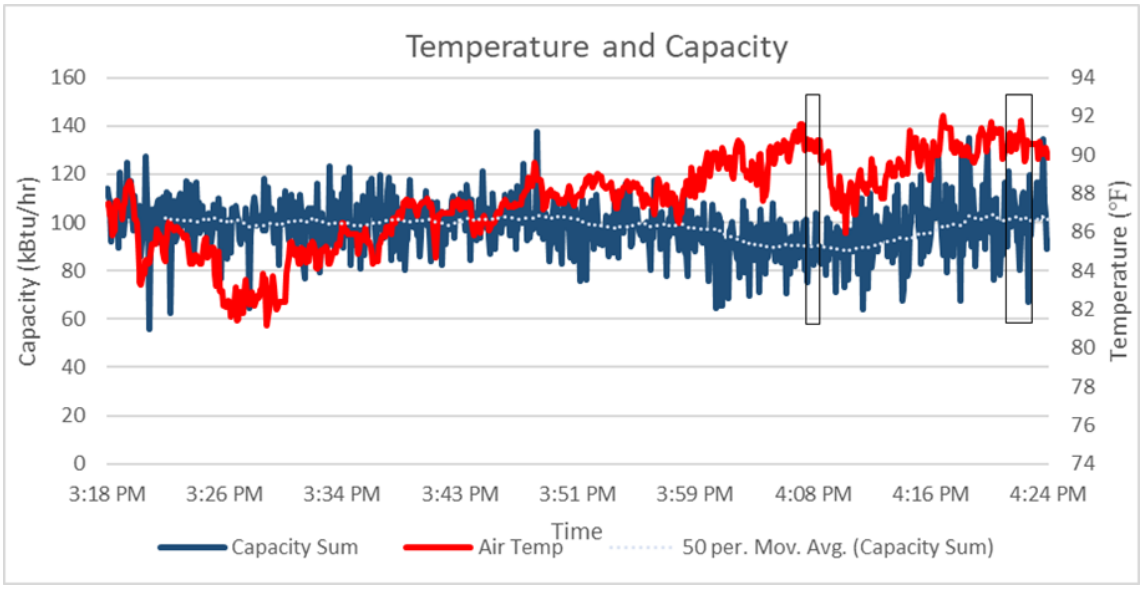


Figure 6. Cooling capacity and outdoor temperature versus time (high ambient test)

5.4. Standby Operation

A standby test was performed to observe how the chiller operates when there is no cooling load imposed on the system. The chiller periodically cycles on to cool the CO2 receiver tank as shown in Figure 7—as CO_2 tank pressure and Chiller power as a function of time. The pressure in the tank oscillates between ~3.27-3.59 MPa (475 – 520 psig) over a period of approximately 20 minutes. The time between intervals decreases slightly as the ambient outdoor temperature increases over the course of the test.

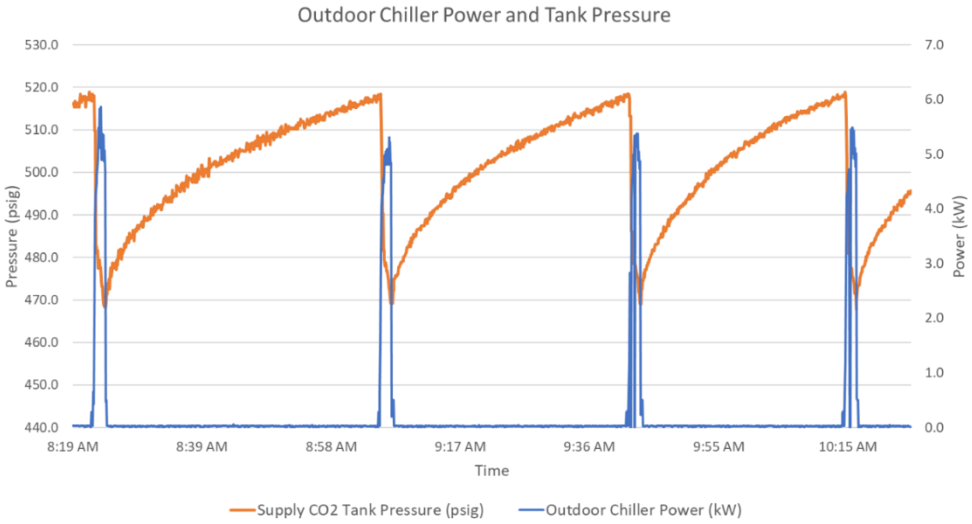


Figure 4. Outdoor chiller and tank pressure versus time (standby operation test)

5.5. Simulated Power Failure

This test was performed to ensure that the system would properly re-energize and reset after a power outage or power failure. The system was initially fully turned on with all three IDUs in operation. All power was then cut from the system by de-energizing the main circuit breakers. After a 10-minute standby, the power was re-applied to the system and observations regarding the test were as follows:

- When power was off, CO_2 tank pressure naturally drifted up ~0.007 MPa/min (1 psi/minute)
- When power was re-applied, the chiller began its restart sequence.
- After 5-minute built-in delay, the compressor and ancillary systems restarted.
- CO_2 tank temperature dropped accordingly, and the system began cycling normally.

The test setup required the CO_2 pump and the three IDUs to be manually restarted after a power failure to restart the cooling process. This was a design choice for this particular experimental setup and is not necessarily indicative of how a system would actually be set up in a field deployment. Automatic restart of pumping and cooling could be easily accommodated with proper control strategies.

6. Economic Analysis of Aspects of Installation

There is potential installation cost savings from using phase-change CO_2 as the convection fluid instead of water. CO_2 is used in some refrigeration systems because it can provide low-temperature (sub-freezing) convection. For HVAC applications where the convection temperature can remain above freezing, CO2 still may offer an advantage of smaller pipe size and, in turn, lower installation cost. The following is an example per-unit calculation of relative material and installation cost for CO_2 convection. This analysis is focused on the CO_2 convection loop, not the ammonia chiller. It is assumed that capital cost per unit of installed capacity of an ammonia or halocarbon chiller is roughly equivalent, leaving any difference in cost to the convection loop only.

The boiling heat capacity of CO_2 at ~3.44 MPa (500 psig), is approximately 416 kJ/kgK (99.3 Btu/lbm°F), while for water, the heat capacity is ~4.19 kJ/kgK (1 Btu/lbm°F). If typical chilled water applications undergo a 5.5°C-temperature change, then phase-changing CO_2 can provide up to 10 times the convection heat transfer per unit mass of pumped fluid. This 10x heat transfer is the key point of exploration for potential installation cost reduction. The full 10x may not be realized in actual systems because full phase transition may not occur as systems may be designed to return a partially boiled mixture of liquid and vapor CO_2 from the evaporator.

Chilled water is typically piped in welded steel or grooved connected steel pipe. CO2 for HVAC applications can be piped in braised high-pressure copper alloy which is a variant of standard ACR type K copper refrigerant tubing. The 8-ton system under test used 7/8" (22mm) O.D. braised copper/iron tubing for the CO_2 supply line and 1-1/8" (28.5mm) for the return. A similarly sized chilled water convection loop would use ~1.5"-4.0" (38-102mm) steel pipe. The CO_2 system with its respective hardware would accommodate ~7.95 lpm (2.1 gpm) of CO_2 flow compared ~72.7lpm (19.2 gpm) of water flow for the similar-sized chilled water convection loop. For an 8-ton system, as described in this report, the CO_2 copper piping would cost 2.67 times less to install than the chilled water steel pipe. Table 30 shows a comparison of installation costs of variously sized ACR copper and welded steel pipe in price per linear foot.

Table 3. Comparison of installation cost of various sizes of ACR copper and welded steel pipe

Tubing/Pipe Size	Raw Material	Raw Labor	Total Installed (with O&P)
Type K Copper (ACR)	Cost ($) per linear foot		
7/8"	$4.97	$2.83	$10.10
1 1/8"	$7.00	$3.2	$12.95
1 3/8"	$9.35	$3.68	$16.35
Schedule 40 Welded Steel	Cost ($) per linear foot		
1 ½"	$5.70	$8.50	$21.06
2"	$11.25	$10.60	$30.76
3"	$16.55	$15.05	$44.14
4"	$17.00	$17.45	$48.87

7. Summary and Conclusions

A first-of-its-kind, natural refrigerant based HVAC system was constructed and evaluated. The system uses ammonia (NH_3) in a low-charge packaged chiller as the primary refrigerant for vapor compression, and carbon dioxide (CO_2) as the convection fluid to distribute cooling to remote indoor air handlers. This combination takes advantage of the high efficiency of NH_3 and the high heat capacity of CO_2 to provide an environmentally friendly option for medium to large HVAC applications. The technology builds on advances made in the supermarket refrigeration sector where refrigerant management is highly important and the shift toward zero GWP refrigerants is already underway.

The general workability of the system approach was demonstrated successfully. Cooling capacity and efficiency were reasonable, with limited effort to optimize the component selection and system controls, likely leaving room for substantial improvement in future designs.

This system was only designed and tested for cooling operation. The concept can be extended to include heating with additional consideration and componentry to accommodate high-pressure CO2 for heat convection.

The smaller size of piping required for CO2 convection (compared to hydronic convection) offers potential for material and installation cost savings, that could help to offset any capital premium for this new type of equipment.

Acknowledgments

The authors would like to thank Southern California Edison (SCE) and Mayekawa (MYCOM) for their participation in this project.

References

[1] California Commercial End-Use Survey (CEUS), CEC Publication # CEC-400-2006-005, March 2006.

[2] Final Regulation Order: Regulation for the Management of High GWP Refrigerants for Stationary Sources (California Code of Regulations, Title 17, Division 3, Chapter 1, Subchapter 10 Climate Change, Article 4)

[3] Natural Refrigerants: State of the Industry, ATMO Report, 2022.

14th IEA Heat Pump Conference
15-18 May 2023, Chicago, Illinois

Optimization of a Residential Air Source Heat Pump using Refrigerants with GWP <150 for Improved Performance and Reduced Emission

Zhenning Li[a], Samuel F. Yana Motta[a], Bo Shen[a], Hanlong Wan[a]

[a]Oak Ridge National Laboratory, Oak Ridge, TN, 37830 USA

Abstract

Using low-GWP refrigerants can reduce the Green House Gas (GHG) emission of heat pump systems. Heat exchangers and compressors are the key components and have a prominent impact on system performance, significant research is devoted to reducing the cost of the heat exchangers while achieving the same or better system performance with refrigerant charge reduction.

To better understand the environmental impacts of optimized systems with low-GWP refrigerants, Life Cycle Climate Performance (LCCP) evaluation method was used to evaluate the direct and indirect emissions of the system over the course of its lifetime from manufacturing to disposal. The DOE/ORNL Heat Pump Design Model (HPDM) is used to evaluate the performance of heat pumps. Multi-objective optimizations using Particle Swarm Optimization (PSO) algorithm are performed on a 3-ton R410A residential air source heat pump on market. Seven R410A alternatives, i.e., R32, R454B, R454C, R455A, R457A, R1234yf and R1234ze(E) are investigated. The last five fluids have GWP lower than 150.

As a result, 5.5%-12.8% seasonal energy efficiency ratio 2 (SEER2) improvement is achieved, and the optimized systems reduce life cycle CO_2 emission by 8.5%-28.6% with GWP lower than 150 refrigerants. The optimal heat exchangers can fit into the original R410A fan-coil units; therefore, the proposed design method establishes a production and installation path to produce cost-effective low-GWP heat pumps easily accepted by end users.

© HPC2023.
Selection and/or peer-review under the responsibility of the organizers of the 14th IEA Heat Pump Conference 2023.

Keywords: Low GWP; Heat exchange;, Heat pump; Optimization; LCCP Introduction

1. Introduction

Modern cooling technologies are significant sources of greenhouse gas emissions (GHGs) with total CO_2 equivalent emissions from the HVAC sector accounting for 7.8% of global GHG emissions ([1]. Considering the commitment to reduce the impact of GHGs on climate in the HVAC&R sector, a transition from fluorinated substances to alternative refrigerants with reduced global warming potential (GWP) values is supported by F-gas Regulation ([2], the Montreal Protocol with the Kigali Amendment [3] of which 146 countries have not ratified, and the Paris Agreement [4] and the US AIM ACT. The requirements as set forth by the F-gas Regulation banned the use of refrigerants with a GWP of 2500 or greater for high refrigerant charge stationary HVAC equipment in 2020. Beginning in 2022, a GWP limit of 150 has been set for multi-circuit cascade

This manuscript has been authored by UT-Battelle, LLC under Contract No. DE-AC05-00OR22725 with the U.S. Department of Energy. The United States Government retains and the publisher, by accepting the article for publication, acknowledges that the United States Government retains a non-exclusive, paid-up, irrevocable, world-wide license to publish or reproduce the published form of this manuscript, or allow others to do so, for United States Government purposes. The Department of Energy will provide public access to these results of federally sponsored research in accordance with the DOE Public Access Plan (http://energy.gov/downloads/doe-public-access-plan).

systems for commercial use with a nominal capacity of 40 kW or more, and for 2025, the GWP limit for single split AC on the European Union (EU) market is set as 750. This ban will not permit the use of R410A (2088 as GWP value) in small charge system applications. In this regard, much research has been conducted to find alternative low-GWP refrigerants.

Reducing the environmental impacts of HVAC&R systems has been an important research topic due to recent severe global climate changes. In residential buildings, space heating and cooling are the main energy consumers, which are relying on vapor compression-based heat pumps. The HVAC&R industry has moved to phase out refrigerants with high global warming potentials (GWP), e.g., R410A, R22, R134a, R404A, etc. The next-generation refrigerants are mostly mixtures of HFO (Hydrofluoroolefins) refrigerants, e.g., R1234yf and R1234ze(E) combined with the HFC (Hydrofluorocarbons) refrigerant, e.g., R32. Since most of these low-GWP mixtures are in the new A2L lower flammability, research [5] has shown that promoting the use of smaller diameter tubes in heat pump systems is an effective way to reduce refrigerant charge and avoid explosion risk. But it may cause performance degradation.

One characteristic of these low-GWP alternative refrigerants is their high glide, i.e., temperature glides from the bubble point to the dew point at one pressure. High-glide refrigerants prefer multi-row, counter-flow heat exchanger configurations for a single-mode operation. If switching mode, the counter-flow heat exchanger (HX) becomes a parallel-flow heat exchanger. The reversed flow causes significant efficiency degradation. Therefore, improvements in components and system configurations are needed to make the high-glide refrigerants work for both cooling and heating modes to achieve good energy efficiency and protect the environment.

This study demonstrates a low-GWP heat pump design method with a particular focus on the use of a new system configuration for dual-mode reversible heat pumps and 5-mm, 7-mm and 9-mm tube optimized heat exchangers and required modification in compressors. The goals of the study include:

- Investigate the effect of a new system configuration to maintain heat exchanger flow configuration under both cooling and heating modes.
- Optimize multi-row 5-mm, 7-mm, and 9-mm tube coils with low-GWP refrigerants and compressors to determine the performance improvements.
- Analyze the annual performance indices of optimal heat pumps and access their life cycle climate performance (LCCP) to assess carbon footprints.

2. Methodology

2.1. System Model

The DOE/ORNL Heat Pump Design Model (HPDM) [6] is used to model the performance of heat pumps. HPDM is a public-domain HVAC equipment and system modeling and design tool, which supports a free web interface and a desktop version for public use. A finite volume (segment-to-segment) tube-fin HX model is used to simulate the performance of the heat exchanger with different circuitries. This model has been validated by the experimental data [7]. The dehumidification model used in the evaporator simulation is an heat & mass transfer effectiveness-based model [8]. More details of HPDM can be found in [9]. In HPDM, REFPROP 10.0 [10] is used to produce performance look-up tables and simulate the refrigerant properties.

2.2. Selection of Refrigerants

In literature [11], near-term refrigerant candidates have GWP<750 and R32 and R454B can be good drop-in options. Long-term options require GWP<150, and those fluids usually do not match the incumbent fluid (R410A) properties. For fluids with GWP lower than 150 such as R454C, R455A and R457A, they require significant changes in heat exchanger structure to address the high temperaturere glide (temperature rise from the refrigerant bubble point to dew point at constant pressure) and redesign of the compressor to compensate the capacity and efficiency degradation. R1234yf and R1234ze(E) have ultra low GWP values and they are of interest in long term. Table 1 shows the characteristics of R410A and its low-GWP alternatives for a typical residential air source heat pump. The temperature glides are evaluated at saturation pressure corresponding to 8 °C dew-point temperature.

Table 1. Characteristics of refrigerants investigated in this research.

Refrigerant	GWP	Safety Class	Composition: Mass Fraction	Glide in Evaporator [K]	Critical Temperature [°C]
R410A	2088	A1	R32/R125: 50%/50%	0.1	72.8
R32	675	A2L	R32: 100%	0	78.1
R454B	466	A2L	R32/R1234yf: 68.9% /31.3%	1.3	78.1
R454C	146	A2L	R32/R1234yf: 21.5% /78.5%	7.7	85.7
R457A	139	A2L	R32/R1234yf/R152a: 18%/70%/12%	6.9	90.1
R455A	145	A2L	R32/R1234yf/CO_2: 21.5%/75.5%/3%	11.71	85.61
R1234yf	4	A2L	R1234yf: 100%	0	94.7
R1234ze(E)	4	A2L	R1234ze(E): 100%	0	153.7

2.3. Heat Pump System Configuration and Heat Exchanger Structural Parameters

In this study, a 3-ton R410A residential single-stage heat pump product on market is modelled. Fig. 1 shows the schematic of the baseline heat pump operating under cooling mode and heating mode. The refrigerant direction inside the heat exchangers is reversed between mode switching.

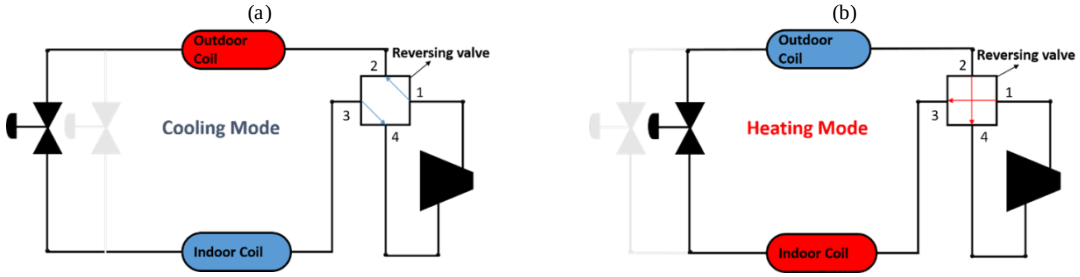


Fig. 1. R410A Baseline Heat Pump System: (a) Cooling Mode Operation; (b) Heating Mode Operation.

To model the baseline system, HPDM has been closely calibrated against experimental data. Table 2 lists the structural parameters of the baseline heat exchangers. The condenser fan moves 2876 CFM of airflow across the outdoor HX and consumes 263 W of power; the indoor blower provides 1205 CFM of supply airflow and consumes 435 W of power. The fan/blower powers and flow rates were the same among all refrigerants.

Table 2. Parameters of Indoor and Outdoor Units of Baseline 3-ton R410A Heat Pump.

Parameters	Indoor HX	Outdoor HX
Coil length [mm]	431.80	2496.82
Coil height [mm]	1248.20	609.60
Coil depth [mm]	35.61	22.00
Number of tubes	120	24
Number of rows	2	1
Number of tubes per row	60	24
Number of circuits	6	3
Circuit pattern (Fig. 2)	cross mixed flow	cross mixed flow
Fin type	Louver fin	Louver fin
Fin density [fins/inch]	16	22
Tube outside diameter [mm]	7.95	9.52
Tube thickness [mm]	0.2794	0.3048
Tube horizontal spacing [mm]	17.81	22.00
Tube vertical spacing [mm]	20.80	25.40

Table 3 lists the empirical correlations used for local heat transfer and pressure drop. For air-to-refrigerant heat exchangers, the thermal resistance is mostly dominated by airside, therefore, it is crucial to model the airside heat transfer coefficient accurately. Different correlations are used according to its suitable application range to improve the prediction of small diameter tube and large diameter tube heat exchangers.

Table 3. Correlations adopted in condenser and evaporator simulations

Operating Mode	Heat Transfer Correlations	Pressure Drop Correlations
Refrigerant - Liquid Phase	Dittus and Boelter (1985) [12]	Blasius (1907) [13]
Refrigerant - Two Phase Boiling (Evaporator)	Thome and Hajal (2003b) [14]	Choi et al. (1999)[15]
Refrigerant - Two Phase Condensation (Condenser)	Cavallini et al. (2006) [16]	Choi et al. (1999) [15]
Refrigerant - Vapor Phase	Dittus and Boelter (1985) [12]	Blasius (1907) [13]
Air	Wang et al. (1999) [17] for 7 & 9-mm tube	Wang et al. (1999) [17] for 7 & 9-mm tube
	Sarpotdar et al. (2016) [18] for 5-mm tube	Sarpotdar et al. (2016) [18] for 5-mm tube

Fig. 2 illustrates 3 typical circuitry patterns by a simple six-tube HX. For the conventional system configuration as used in the baseline system, if the heat exchanger has counter-flow configuration (Fig. 3 (a)) in cooling mode, after the refrigerant flow is reversed in heating mode, the circuitry will become parallel-flow (Fig. 3(c)). And this yields undesirable performance degradation in heating mode.

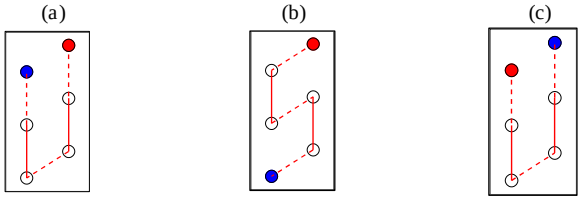


Fig. 2. Heat exchanger circuitry patterns: (a) counterflow, (b) mixed flow, (c) parallel flow

To mitigate the heating performance degradation, the heat exchanger in baseline system is designed as mixed-flow configuration (Fig. 3 (b)) as a compromise solution to balance between cooling and heating modes. The detailed circuitries of the baseline indoor and outdoor heat exchangers are shown in Fig. 3. The indoor HX has 60 tubes per row and 2 tube rows and is divided into 6 mixed flow circuits. The outdoor HX has 24 tubes and 1 tube rows and is divided into 3 circuits. Different colors represent different circuits. The baseline indoor heat exchanger uses 7.95 mm diameter tubes, and the outdoor heat exchanger uses 9.52 mm diameter tubes.

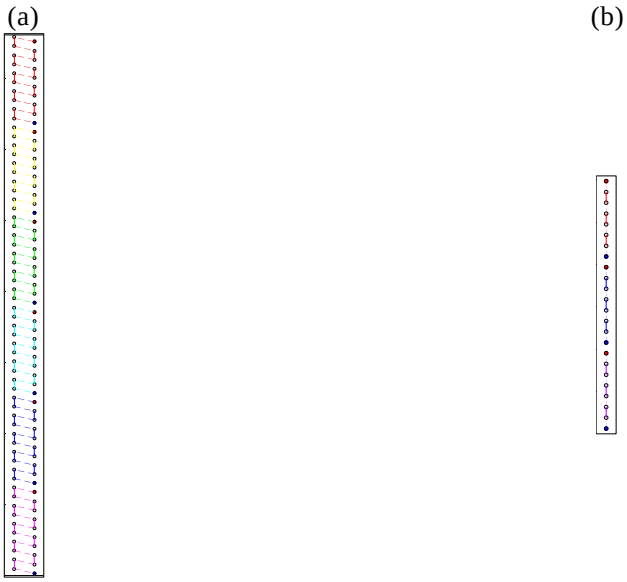


Fig. 3. Baseline tube-fin heat exchanger circuitries: (a) Indoor HX with 7 mm tube; (b) Outdoor HX with 9 mm tube.

As mentioned in the previous section, research has shown that for low-GWP zeotropic mixtures, the counter flow configuration has the most efficient heat transfer performance due to significant saturation temperature glide [5]. With this consideration, one goal of this research is to develop a new system configuration to maintain the same refrigerant flow direction inside the heat exchangers between cooling and heating mode switching. Fig. 4 shows the proposed reversible heat pump system configuration evaluated in the study as the optimized systems. The new configuration has 4 one-way check-valves at the inlet of indoor and outdoor heat exchangers and the heat exchangers have bi-directional distributors. Under both heating and cooling modes, this system configuration can maintain the same heat exchanger circuitry pattern.

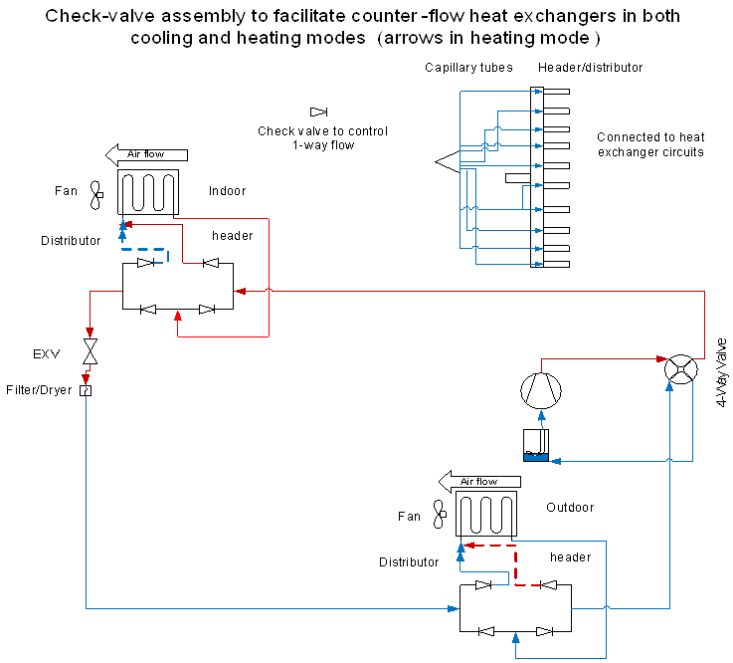


Fig. 4. New System Configuration with Check-valves and Bi-directional distributors Maintaining Counter-flow HXs in Dual Modes

2.4. Optimization Problem Formulation

Shen et al. (2012) [19] developed an optimization framework that integrates HPDM with GenOpt ([20]), a public domain optimization package. In this research, the Particle Swarm Optimization (PSO) algorithm implemented in GenOpt is used to optimize the heat pump system. Regarding PSO setting, the optimization runs use 100 as population size and 200 as number of generations.

Equation (1) shows the optimization problem formulation. The objective is to maximize the Energy Efficient Ratio (EER) of the heat pump under AHRI Standard 210/240 [21] cooling test A condition (95 °F). In Equation (1), the number of circuits for indoor and outdoor heat exchangers are two design variables, which varies between 1 and the number of tubes in each row of the heat exchangers. The number of circuits has a adaptive upper limit to coordinate with the number of tubes in each row.

$$
\begin{aligned}
&\textit{Maximize}: \ EER \\
&\textit{Subject to}: \\
&\quad \textit{Heat exchanger tube diameter} \text{ varies among } 5\ mm, 7\ mm, 9\ mm \\
&\quad 1 \le N_{circuits,evaporator} \le Ntubes\ per\ bank\ of\ evaporator \\
&\quad 1 \le N_{circuits,condenser} \le Ntubes\ per\ bank\ of\ condenser \\
&\quad \Delta T_{superheat,\ evaporator\ outlet} = 10 - \frac{\Delta T_{glide}}{2}\ [R] \\
&\quad 2\ [R] \le \Delta T_{subcooling,\ condenser\ outlet} \le 15\ [R] \\
&\quad Q_{evaporator} = 10.55\ kW \\
&\quad |\ SHR_{evaporator} - SHR_{baseline,evaporator}\ | \ \le 1\% \\
&\quad Height_{evaporator} = Height_{baseline} \\
&\quad Length_{evaporator} = Length_{baseline} \\
&\quad Height_{condenser} = Height_{baseline} \\
&\quad Length_{condenser} = Length_{baseline}
\end{aligned}
\tag{1}
$$

In terms of constraints on operating conditions, the evaporator outlet superheat degree is specified based on the temperature glide of refrigerants as recommended by refrigerant OEM. The condenser outlet subcooling degree is automatically adjusted, but it is constrained between 2 R to 15 R. the cooling capacity of evaporator is a HPDM solving target and set to be the same as the baseline 3-ton R410A heat pump. The compressor displacement volume is altered in HPDM to meet the target evaporator cooling capacity. When modeling the optimized systems using low-GWP refrigerant other than R410A, the compressor isentropic efficiency is fixed as 0.74 and the volumetric efficiency is fixed as 0.98 to be consistent with the baseline R410A system. The goal is to investigate the required displacement volume of the compressor to meet the system capacity for low-GWP refrigerants.

In terms of constraints on heat exchanger dimensions, the last four constraints in Equation (1) guarantee that the optimized indoor and outdoor heat exchangers have the same frontal shapes as the baseline heat exchangers, i.e., the optimal heat exchangers can fit into the original indoor and outdoor fan-coil unit perfectly. This can ease the retrofit effort of upgrading the R410A heat pump to the new low-GWP system by minimizing the change in manufacturing and installation processes and guarantee that the optimized systems have the best compatibility with end-users' house structure. As a result, the new products can be easily accepted by manufacturers and end-users.

The stagg

nm tubes used in the optimized coils are shown in Fig. 5. These tube layout and spacings are off-the-shelf designs from a heat exchanger manufacturer. The heat exchanger circuitry pattern is fixed as counter flow configuration, since counter-flow pattern has the most efficient heat transfer for high-glide zeotropic mixtures [5].

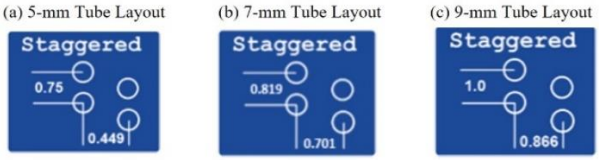


Fig. 5. Horizontal spacing and vertical spacing in inch for (a) 5-mm tube HX; (b) 7-mm tube HX; (c) 9-mm tube HX.

3. Results

3.1. Drop-in Performances



Fig. 6 (a)), R32 induces a capacity increase by 8.3% and R454B shows 1.48% capacity decrease compared with the R410A baseline. If the baseline R410A heat exchangers and compressor are used, R454C, R455A, R457A, R1234yf and R1234ze(E) induce 29.4%, 26.8%, 32.9%, 46.9% and 55.5% capacity degradation, respectively, without changing any component.

In terms of EER, the variation is very small. R32, R454B, R457A and R1234yf induces EER increases by 2.2%, 3.2%, 1% and 3.3%, while R454C, R455A and R1234ze(E) and induces EER decreases by 0.7%, 2.6% and 0.4%, respectively.

For the drop-in test, the compressor isentropic efficiency and volumetric efficiency are predicted by 10-coefficient compressor map provided by the compressor manufacturer. Despite the compressor map is regressed for R410A test data, a scaling method assuming the same isentropic and volumetric efficiencies at the same suction and discharge saturation temperatures for R410A is used to predict the compressor performance when other refrigerants are used. This compressor scaling method is validated against experiment data [11] and demonstrates good prediction accuracy.

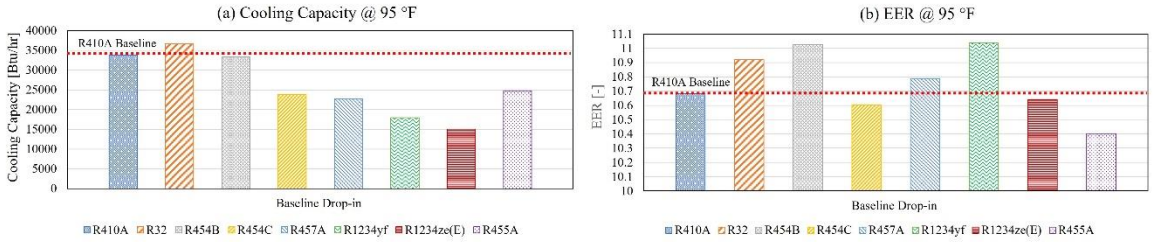


Fig. 6. Baseline System Drop-in Cooling Performance at 95 °F (a) Cooling Capacity; (b) EER



Fig. 7 shows the drop-in performance for heating operation under AHRI 210/240 heating C_1 condition at 47 °F. R32 shows a 6.7% capacity increase and 0.03% COP increase. R454B shows comparable performance to R410A, i.e., a 3.9% capacity decrease and 1.72% COP increases. R454C, R455A, R457A, R1234yf, R1234ze and induces 6.5%, 27.6%, 38.9%, 52.3% and 62.5% capacity degradation, respectively.

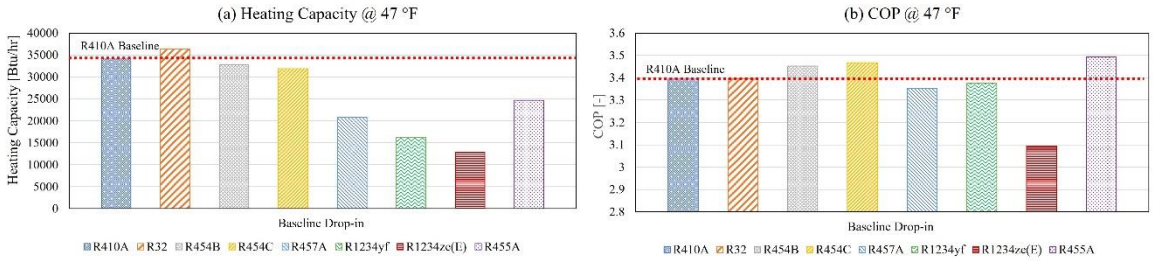


Fig. 7. Baseline System Drop-in Heating Performance at 47 °F (a) Heating Capacity; (b) COP

As a conclusion, these results show that R32 and R454B are good drop-in candidates. However, GWP<150 refrigerants cannot be directly drop-in due to the significant capacity degradation. For low-GWP refrigerants, it is necessary to redesign the system configuration and components to meet the performance metrics. One required change for the compressor is to increase the displacement volume to increase capacity.

3.2. Optimization Results

The previous section shows the drop-in test results, which demonstrates the system efficiency and capacity degrade with drop-in of low-GWP refrigerants. This section shows the results after conducting design optimization of the components and adopting the new system configuration. For all optimization cases, the suction line is sized such that the saturation temperature drop of the suction line for different refrigerants is the same as that of the baseline R410A system. The goal is to investigate the required displacement volume of the compressor to match the R410A system capacity and efficiency requirements.

All cooling-optimized systems using 5-mm [illegible] capacity requirements (i.e., 36000 BTU/hr) to [illegible] of using 5 mm tube HXs attributes to the increase as shown in Table 4. Despite the optimized heat [illegible] he baseline coils, 5-mm tube heat exchangers consi [illegible] ler horizonal and vertical tube spacing as shown i[illegible]

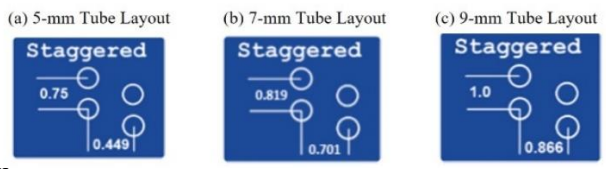


Fig. 5.

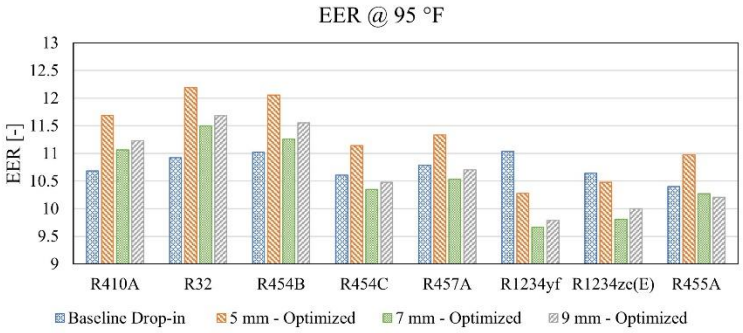
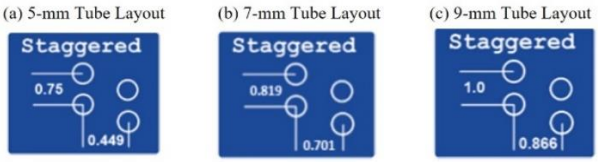


Fig. 8 shows the cooling performance comparison at 95 °F. For R410A, R32, R454B, R455A and R457A, the optimized 5-mm tube heat exchangers yield 9.4%, 11.6%, 9.4%, 5.5% and 5.1% EER improvements, respectively. Except R32 and R454B, using 7-mm tube and 9-mm tube with GWP less than 150 refrigerants yields performance degradation compared with the baseline drop-in test. For refrigerants with GWP less than 150, heat exchanger design optimization does not show efficacy to improve system performance. In this study, increased heat transfer area and reduced mass flux in heat exchangers have the same coil width and coil consist of more tubes in each row and more tube rows al tube spacing as shown in Fig. 5.



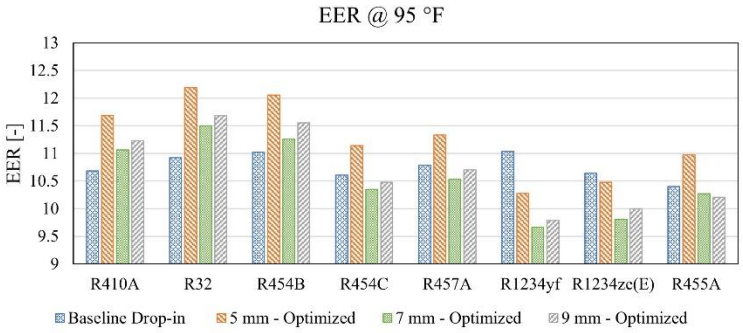


Fig. 8. Cooling Performance Comparison of Baseline and Optimal Systems at 95 °F (a) Cooling Capacity; (b) EER

The cooling optimized designs are evaluated under heating mode at 47 °F. Their performances are depicted in Fig. 9. As shown in Fig. 9(a), the optimal systems using most refrigerants fluids can satisfy the heating capacity of R410A baseline, except R1234ze(E) which induces significant capacity degradation.

In terms of COP (Fig. 9(b)), systems using 5-mm tube optimized heat exchangers show the most performance improvements, i.e., 11.4%, 12.7%, 10.2%, 0.05%, 1.2%, 6.3%, 1.0% and 10.0% for R410A, R32, R454B, R455A, R457A, R1234yf and R1234ze(E), respectively. The performance of optimized 7-mm tube HX is close to the baseline system and the performances of system using 9-mm tube HXs are better than the baseline for R32, R454B, R454C, R457A and R1234ze(E), but worse than the baseline for R455A and R1234yf.

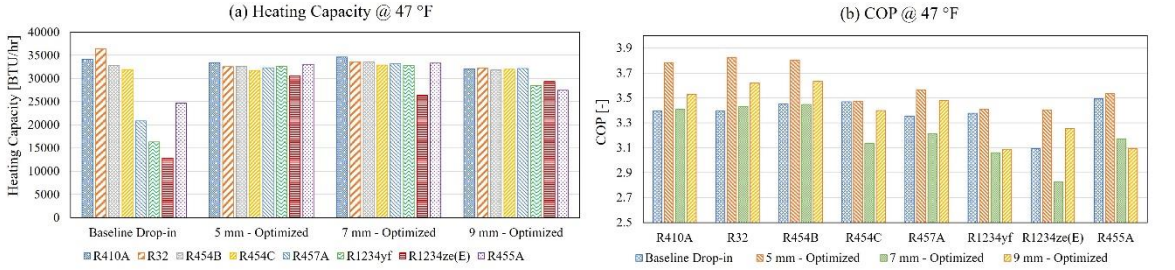


Fig. 9. Heating Performance Comparison of Baseline and Optimal Systems at 47 °F (a) Heating Capacity; (b) COP

Fig.10 (a) shows the refrigerant charge of the optimized systems. Use of 5-mm tube heat exchanger yields charge reduction. The charge reductions range from 28.4% to 43.7%. While 7-mm tube heat exchangers increase the system charge, and 9-mm tube heat exchangers have the comparable charge amount compared with the baseline system.

Fig.10 (b) shows the redesigned compressor displacement volumes for each refrigerant to match the baseline cooling capacity. The required compressor displacement volume is not sensitive to the tube diameters used in the heat exchanger, rather, it is sensitive to the property of fluids. In general, R32 induces displacement volume decreases by 15.8% while R454B, R455A, R457A, R1234yf and R1234ze(E) induce increased displacement volume increases by 4.7%, 40.2%, 50.7%, 62.2%, 152.6% and 224.2%. These results demonstrate the importance of compressor redesign for low-GWP heat pumps. In general, systems using low-GWP refrigerants require larger compressors than systems using R410A.

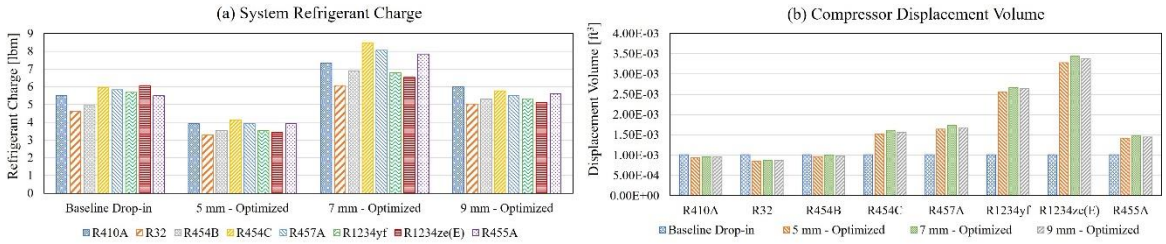


Fig.10. (a) System Refrigerant Charge; (b) Designed Compressor Displacement Volume.

To access the annual performance of optimized systems. The seasonal energy efficiency ratio-2 (SEER2) and heating seasonal performance factor-2 (HSPF2) are calculated according to AHRI 210/240 test standards [21]. Effective January 1st, 2023, SEER2 and HSPF-2 are used to rate system performance following a more stringent testing procedure. The new testing procedure increases the systems' external static pressure by a factor of five to better reflect field conditions of installed equipment in a typical ducted system and results in a lower numerical rating value for the same product. The performance degradation owing to frost accumulation has been considered by applying performance degradation factors, i.e., 0.91 for heating capacity and 0.985 for power consumption at the 35˚F dry bulb/33˚F wet bulb frosting condition.



Fig. 11 (a), the SEER2 of the baseline R410A system is 11.42. R32 and R454B optimized coils can satisfy the baseline SEER2 criteria. Among the five GWP less than 150 refrigerants, the three fluids which overperform baseline is R454C, R457A and R455A using 5-mm tube heat exchangers. The optimized system using R1234yf and R1234ze(E) shows smaller SEER2 after dimension-constrained heat exchanger optimization and compressor sizing.

Fig. 11 (b) shows the HSPF2 of the baseline and optimal systems. The HSPF2 of the baseline R410A system is 7.17. R32 and R454B can satisfy the HSPF requirement regardless of the choice of heat exchanger tubes. When using 5-mm tube heat exchangers with GWP<150 refrigerants, HSPF2 of the optimized systems exceeds HSPF2 of the baseline.

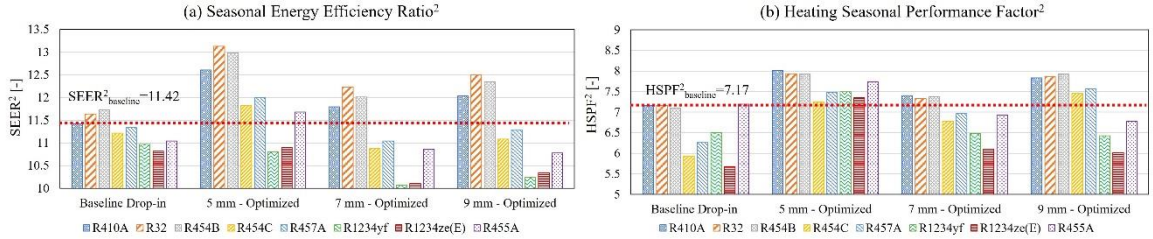


Fig. 11. Heat Pump Systems Performance Comparison (a) Seasonal Energy Efficiency Ratio; (b) Heating Seasonal Performance Factor

To streamline the performance of different heat exchangers with different low-GWP refrigerants, the SEER2 and HSPF2 are shown in Fig. 12. The marker shapes represents different system types, i.e., either the baseline system or optimal systems with different diameter tubes. And the marker colors show different refrigerants. The performance of the baseline R410A system (SEER2-11.4/HSPF2-7.2) is highlighted as the cross in the center . By comparing the baseline performance with optimized systems, the design space is divided into 4 regions. The system designs located in the upper right region has both cooling and he ating performance superior to the baseline and the system designs located in the bottom left region has dual-mode performance inferior to the baseline. The other two regions have designs with only 1 mode better than the baseline. In the upper right region. The best performances are achieved using R32 (SEER2-13.1/HSPF2-7.9), followed by R454B (SEER2-13.0/HSPF2-7.9) and R410A (SEER2-12.6/HSPF2-8.0). For the GWP <150 fluids, three design candidates using R457A (SEER2-12.0/HSPF2-7.5), R454C (SEER2-11.8/HSPF2-7.2) and R455A (SEER2-11.7/HSPF2-7.7) satisfy both heating and cooling performance requirements.

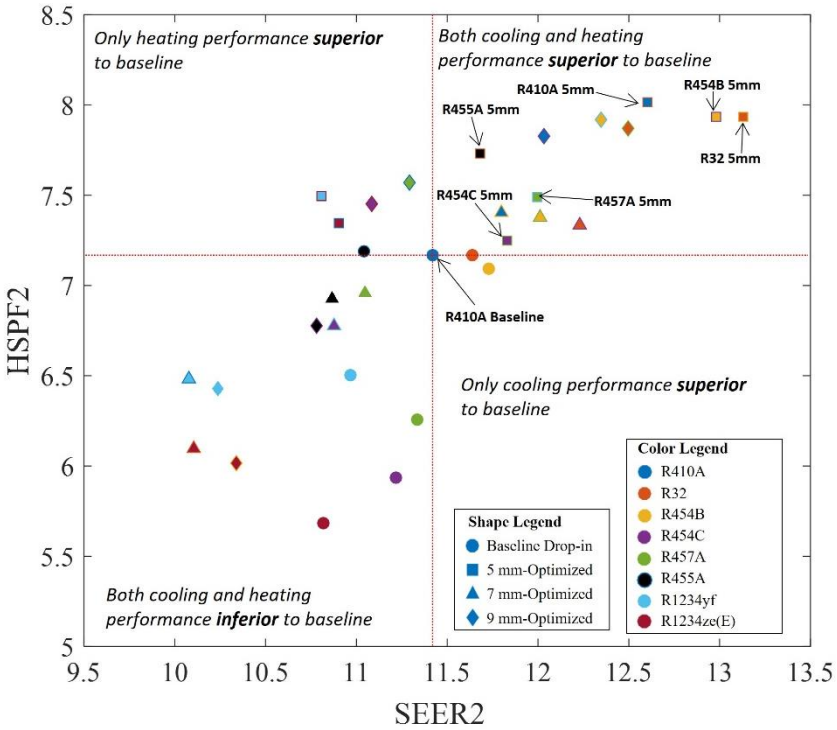


Fig. 12. SEER2 and HSPF2 of Baseline Drop-in Tests and Optimized Systems

Table 4 shows the heat exchanger structures for those optimal systems in Fig. 12. For brevity, the heat exchanger structure is denoted as *Number of Tubes per Row* x *Number of Rows* - *Number of circuits*. For example, the 7-mm tube indoor baseline heat exchanger in Fig. 3 has 60 tubes per row, 2 rows and has 6 circuits, so its structure is 60x2-6, and the 9-mm tube outdoor baseline heat exchanger has 24 tubes per row, 1 row and 3 circuits, so its structure is 24x1-3. Following this convention, the heat exchanger structures of the optimized system are listed in Table 4.

Table 4. Heat Exchanger Structure of Optimized Systems

HX Structure	5 mm - Optimized		7 mm - Optimized		9 mm - Optimized	
	Indoor HX	**Outdoor HX**	**Indoor HX**	**Outdoor HX**	**Indoor HX**	**Outdoor HX**
R410A	64x3-16	32x2-16	60x2-6	30x2-6	48x2-6	24x1-2
R32	64x3-16	32x2-16	60x2-6	30x2-5	48x2-6	24x1-2
R454B	64x3-16	32x2-16	60x2-6	30x2-10	48x2-4	24x1-2
R454C	64x3-32	32x2-16	60x2-12	30x2-6	48x2-6	24x1-3
R457A	64x3-32	32x2-16	60x2-12	30x2-6	48x2-6	24x1-3
R455A	64x3-32	32x2-16	60x2-15	30x2-6	48x2-8	24x1-3
R1234yf	64x3-32	32x2-16	60x2-15	30x2-6	48x2-8	24x1-3
R1234ze(E)	64x3-32	32x2-16	60x2-15	30x2-6	48x2-8	24x1-3

From Table 4, the optimal 5-mm tube indoor HX has two structures depending on the fluids, either 64x3-16 or 64x3-32. The optimal 5-mm tube outdoor HXs regardless of fluids have the same structure, i.e., 32x2-16. Compared with the baseline indoor 7-mm tube HX (60x2-6) and baseline outdoor 9-mm tube HX (24x1-3), the number of circuits are significantly increased for optimal HXs using 5-mm tube. The optimizer increases number of circuits to distribute refrigerant mass flow such that the refrigerant pressure drop in the heat exchangers can be reduced and the effect caused by the decreased tube cross sectional area is mitigated.

3.3. Life cycle climate performance analysis

To understand the environmental impacts of optimized heat pumps using the new system configuration and the optimal HX structures with low-GWP refrigerants, life cycle climate performance (LCCP) evaluation is used to analyze the direct and indirect greenhouse gas (GHG) emissions of the system over the course of its lifetime from manufacturing to disposal. It is calculated as the sum of direct and indirect emissions generated over the lifetime of the system "from cradle to grave". Direct emissions include all effects from the release of refrigerant into the atmosphere during the lifetime of the system. Direct emissions include:

- Annual refrigerant loss from gradual leaks
- Losses at the end-of-life disposal of the unit
- Large losses during operation of the unit
- Atmospheric reaction products from the breakdown of the refrigerant in the atmosphere

The indirect emissions include:

- Emissions from electricity generation
- Emission from the manufacturing of materials
- Emissions from the manufacturing of refrigerants
- Emissions from the disposal of the unit

More details about LCCP evaluation method can be referred to Wan et al. (2021) [22]. The input values used for evaluating the LCCP are shown in Table 5 including the cut-off outdoor temperature and the temperature at which the heat pump starts. A critical part of the LCCP is the assumed leak rate and end of life recovery. 2% leak rate per year with 18 years lifetime and 20% end of life recovery are specified based on ASHRAE 189.1. To compare systems using different low-GWP refrigerants, Chicago is selected for a case study and its TMY-3 weather data is used for annual performance evaluation.

Table 5. Input Values for Baseline and Optimal Systems LCCP Evaluation

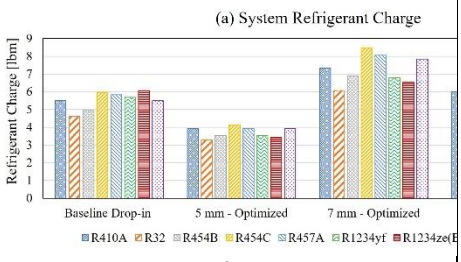
Factor	Value
Refrigerant	R-410A or its alternatives
Refrigerant charge (kg)	As shown in  Fig.10 (a)
Unit weight (kg)	190
Annual refrigerant leakage (%)	2
EOL leakage (%)	80
Lifetime (years)	18
Cut-off temperature (°C)	−17.8
Temperature at which the heat pump starts (°C)	−12.2
Weather data	Chicago TMY-3

Fig.15 shows the comparison of the direct and indirect emissions for systems. Compared to R410A baseline, systems using other refrigerants reduce direct emissions as shown in Fig.15 (a). This attributes to their lower GWP value and the reduced system charge as shown in

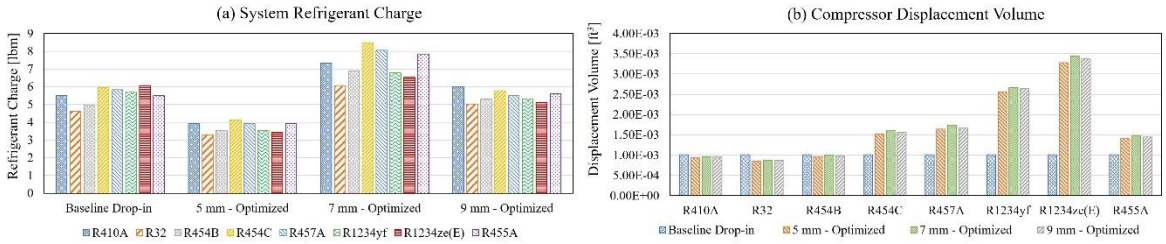


Fig.10 (a).

Fig.15 (b) shows the comparison of the indirect emissions. The optimized systems have 10%-16% lower indirect emissions than the baseline system due to the improved EER (Fig.13 (a)) and improved COP (Fig. 14). The 5-mm optimal designs with R454C and R457A induces significant indirect emission reductions. This indirect emission reduction attributes to improved SEER2 and HSPF2 as shown in

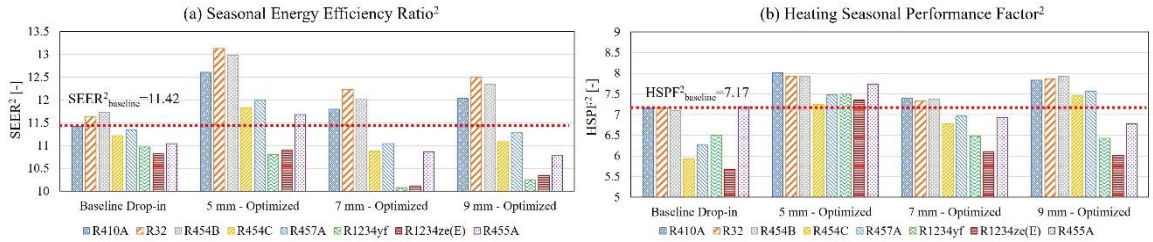


Fig. 11 and Fig. 12. Since Chicago is a city in the heating climate region IV with both significant number of heating and cooling days, the indirect emissions are affected by both cooling and heating performance.

It is worthwhile to mention that the reduction potential is different in another climate zone. For example, in a location with warm or mild climate, the SEER2, i.e., the cooling efficiency plays a more dominant role since the heat pump is mostly operated in cooling mode.

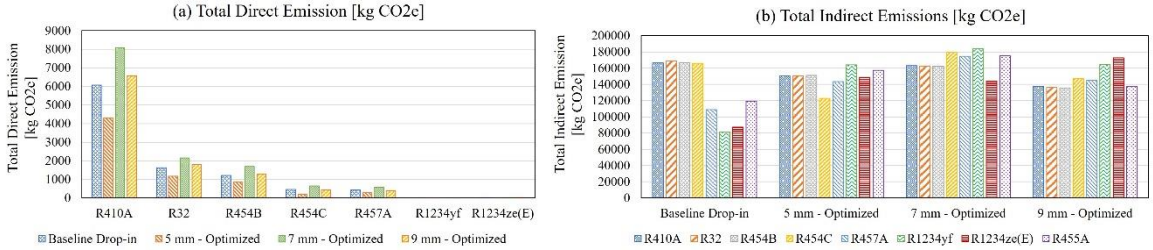


Fig.15. Greenhouse gas emissions of the baseline and low-GWP optimized systems (a) Direct Emission; (b) Indirect Emission.

Fig. 16 shows the comparison of the total emissions. In fact, 96%-98% of the total emission is comprised of indirect emissions. So indirect emission dominates the total emission. Although many designs using 7-mm tube and 9-mm tube heat exchangers show great emission reduction potential, they cannot meet the cooling and heating efficiency requirements as shown in Fig. 12. The three feasible designs satisfying the efficiency requirements are systems using 5-mm tube heat exchangers with R454C, R455A and R457A. The optimal 5-mm tube systems using R454C, R455A and R457A yields 28.6%, 8.5% and 16.5% lifetime emission reduction compared to the baseline R410A system.

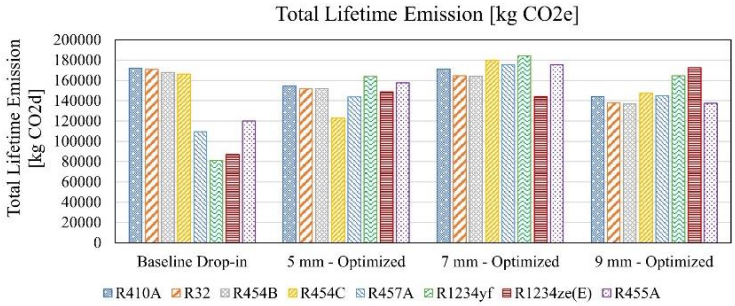


Fig. 16. Total greenhouse gas emissions of the baseline and low-GWP optimized systems.

4. Conclusion

This study presents heat exchanger and system development technologies to support the transition to refrigerants with GWP lower than 150. Higher than baseline R410A system efficiency levels in cooling and heating modes are achieved by a model-based design optimization approach based on simulation using detailed hardware information. The new reversible heat pump systems with low-GWP refrigerants adopt a new system configuration, the optimized indoor and outdoor heat exchangers, an optimized compressor. The potential of 5-mm, 7-mm and 9-mm tube in heat exchangers are investigated. The optimal systems using R454C, R455A and R457A with 5-mm tube heat exchangers outperform the baseline R410A heat pump product. Life cycle climate analysis shows that the optimized systems using GWP lower than 150 fluids reduce the lifetime CO_2 emissions by 8.5%-28.6%, while guaranteeing the same or better capacity and efficiency performance than the baseline.

The optimal heat exchanger designs obtained from this research can fit into the original R410A heat exchanger ducts and chasses, which helps to minimize changes in manufacturing and installation. As a result, the system retrofit impacts on manufacturers and end users are minimized. The proposed design approach establishes a production and installation path to produce cost-effective high-performance low GWP reversible heat pumps.

Acknowledgments

The research used resources at the Building Technologies Research and Integration Center, a DOE Office of Science User Facility operated by the Oak Ridge National Laboratory. The authors would like to acknowledge Antonia Bouza, the DOE Building Technologies Office technology manager for his support.

References

1. Coulomb, D., J. Dupont, and V. Morlet, *The impact of the refrigeration sector on the climate change. 35th Informatory Note on Refrigeration Technologies.* Paris (France), 2017.
2. Schulz, M. and D. Kourkoulas, *Regulation (EU) No 517/2014 of The European Parliament and of the council of 16 April 2014 on fluorinated greenhouse gases and repealing Regulation (EC) No 842/2006.* Off. J. Eur. Union, 2014. **2014**(517): p. L150.
3. Clark, E. and S. Wagner, *The Kigali Amendment to the Montreal Protocol: HFC Phase-Down.* Ozon Action UN Environment (UNEP), 2016: p. 1-7.
4. Agreement, P. *Paris agreement*. in *Report of the Conference of the Parties to the United Nations Framework Convention on Climate Change (21st Session, 2015: Paris). Retrived December*. 2015. HeinOnline.
5. Li, Z., B. Shen, and K.R. Gluesenkamp, *Multi-objective optimization of low-GWP mixture composition and heat exchanger circuitry configuration for improved system performance and reduced refrigerant flammability.* International Journal of Refrigeration, 2021. **126**: p. 133-142.
6. Shen, B. and K. Rice, *DOE/ORNL heat pump design model.* Web link: http://hpdmflex. ornl. gov,

2016.
7. Abdelaziz, O., et al., *Alternative Refrigerant Evaluation for High-Ambient-Temperature Environments: R-22 and R-410A Alternatives for Rooftop Air Conditioners.* Energy and Transportation Science Division. Oak Ridge National Laboratory. ORNL/TM-2016/513, 2016.
8. Braun, J., S. Klein, and J. Mitchell, *Effictiveness models for cooling towers and cooling coils.* ASHRAE Transactions (American Society of Heating, Refrigerating and Air-Conditioning Engineers);(USA), 1989. **95**(CONF-890609--).
9. Shen, B., et al., *Model-based optimizations of packaged rooftop air conditioners using low global warming potential refrigerants.* International Journal of Refrigeration, 2018. **87**: p. 106-117.
10. Lemmon, E.W., M.L. Huber, and M.O. McLinden, *NIST standard reference database 23.* Reference fluid thermodynamic and transport properties (REFPROP), version, 2010. **9**.
11. Shen, B., Z. Li, and K.R. Gluesenkamp, *Experimental study of R452B and R454B as drop-in replacement for R410A in split heat pumps having tube-fin and microchannel heat exchangers.* Applied Thermal Engineering, 2022. **204**: p. 117930.
12. Dittus, F. and L. Boelter, *Heat transfer in automobile radiators of the tubular type.* International Communications in Heat and Mass Transfer, 1985. **12**(1): p. 3-22.
13. Blasius, H., *Grenzschichten in Flüssigkeiten mit kleiner Reibung*. 1907: Druck von BG Teubner.
14. Thome, J.R. and J.E. Hajal, *Two-phase flow pattern map for evaporation in horizontal tubes: latest version.* Heat Transfer Engineering, 2003. **24**(6): p. 3-10.
15. Choi, J.-Y., M.A. Kedzierski, and P. Domanski, *A generalized pressure drop correlation for evaporation and condensation of alternative refrigerants in smooth and micro-fin tubes*. 1999: US Department of Commerce, Technology Administration, National Institute of ….
16. Cavallini, A., et al., *Condensation in horizontal smooth tubes: a new heat transfer model for heat exchanger design.* Heat Transfer Engineering, 2006. **27**(8): p. 31-38.
17. Wang, C.-C., et al., *Heat transfer and friction correlation for compact louvered fin-and-tube heat exchangers.* International journal of heat and mass transfer, 1999. **42**(11): p. 1945-1956.
18. Sarpotdar, S., D. Nasuta, and V. Aute, *CFD Based Comparison of Slit Fin and Louver Fin Performance for Small Diameter (3mm to 5 mm) Heat Exchangers.* 2016.
19. Shen, B., O. Abdelaziz, and K. Rice, *Auto-calibration and control strategy determination for a variable-speed heat pump water heater using optimization.* HVAC&R Research, 2012. **18**(5): p. 904-914.
20. Wetter, M. *GenOpt-A generic optimization program.* in *Seventh International IBPSA Conference, Rio de Janeiro*. 2001.
21. AHRI, A., *Standard 210/240-2008.* Performance Rating of Unitary Air Conditioning and Air-Source Heat Pump Equipment, AHRI, Ed, 2008.
22. Wan, H., et al., *A comprehensive review of life cycle climate performance (LCCP) for air conditioning systems.* International Journal of Refrigeration, 2021. **130**: p. 187-198.